ENCYCLOPEDIA OF BIOCOLLOID AND BIOINTERFACE SCIENCE

ENCYCLOPEDIA OF BIOCOLLOID AND BIOINTERFACE SCIENCE

VOLUME 1

Edited by

HIROYUKI OHSHIMA

WILEY

Copyright © 2016 by John Wiley & Sons, Inc. All rights reserved

Published by John Wiley & Sons, Inc., Hoboken, New Jersey
Published simultaneously in Canada

No part of this publication may be reproduced, stored in a retrieval system, or transmitted in any form or by any means, electronic, mechanical, photocopying, recording, scanning, or otherwise, except as permitted under Section 107 or 108 of the 1976 United States Copyright Act, without either the prior written permission of the Publisher, or authorization through payment of the appropriate per-copy fee to the Copyright Clearance Center, Inc., 222 Rosewood Drive, Danvers, MA 01923, (978) 750-8400, fax (978) 750-4470, or on the web at www.copyright.com. Requests to the Publisher for permission should be addressed to the Permissions Department, John Wiley & Sons, Inc., 111 River Street, Hoboken, NJ 07030, (201) 748-6011, fax (201) 748-6008, or online at http://www.wiley.com/go/permission.

Limit of Liability/Disclaimer of Warranty: While the publisher and author have used their best efforts in preparing this book, they make no representations or warranties with respect to the accuracy or completeness of the contents of this book and specifically disclaim any implied warranties of merchantability or fitness for a particular purpose. No warranty may be created or extended by sales representatives or written sales materials. The advice and strategies contained herein may not be suitable for your situation. You should consult with a professional where appropriate. Neither the publisher nor the author shall be liable for any loss of profit or any other commercial damages, including but not limited to special, incidental, consequential, or other damages.

For general information on our other products and services or for technical support, please contact our Customer Care Department within the United States at (800) 762-2974, outside the United States at (317) 572-3993 or fax (317) 572-4002.

Wiley also publishes its books in a variety of electronic formats. Some content that appears in print may not be available in electronic formats. For more information about Wiley products, visit our website at www.wiley.com.

Library of Congress Cataloging-in-Publication Data

Names: Ohshima, Hiroyuki, 1944– editor.
Title: Encyclopedia of biocolloid and biointerface science / edited by Hiroyuki Ohshima.
Description: Hoboken, New Jersey : John Wiley & Sons, Inc., 2016– | Includes index.
Identifiers: LCCN 2016004182 | ISBN 9781118542767 (set) | ISBN 9781118542682 (cloth : v. 1)
Subjects: LCSH: Biocolloids–Encyclopedias. | Biological interfaces–Encyclopedias. | Surface chemistry–Encyclopedias.
Classification: LCC QD549 .E53 2016 | DDC 547/.134503–dc23 LC record available at http://lccn.loc.gov/2016004182

10 9 8 7 6 5 4 3 2 1

1 2016

CONTENTS

List of Contributors **xxiii**

Preface **xxix**

A

Aerogel

1 Studies On Biocompatible Surface-Active Silica Aerogel and Polyurethane−Siloxane Cross-Linked Structures for Various Surfaces **1**
K. Seeni Meera, R. Murali Sankar, S. N. Jaisankar, and Asit Baran Mandal

1.1 Introduction, 1
1.1.1 Silica Aerogel, 1
1.1.2 Ionic Liquids, 2
1.1.3 Polyurethane–Siloxane Cross-Linked Structures, 2
1.2 Experimental Section, 3
1.2.1 Preparation of Silica Aerogel Using Choline Formate, 3
1.2.2 Preparation of Polyurethane–Siloxane Cross-Linked Films, 3
1.2.3 Characterization, 4
1.3 Results and Discussion, 5
1.3.1 Results of Surface-Active Silica Aerogel, 5
1.3.2 Results of Polyurethane–Siloxane Cross-Linked Structures, 8
1.4 Conclusions, 12
Acknowledgment, 14
References, 14

Anesthetics

2 Interaction of Anesthetics with Globular Proteins **17**
Makoto Nishimoto, Michio Yamanaka, and Hitoshi Matsuki

2.1 Introduction, 17
2.2 Anesthetic Effect on FFL, 18
2.3 Anesthetic Effect on Mgb, Lys, and BSA, 22
2.4 Intrinsic Interaction Mode of an Anesthetic with Proteins, 29

2.5 Conclusions, 32
Acknowledgments, 33
References, 33

3 Lipid Monolayer and Interaction with Anesthetics 36
Yasushi Yamamoto and Keijiro Taga

3.1 Introduction, 36
3.2 Monolayer Formation, 36
3.2.1 Dipalmitoyl Phosphatidyl Choline (DPPC), 37
3.2.2 Dimyristoyl Phosphatidyl Choline (DMPC), 39
3.2.3 Cholesterol, 40
3.2.4 DPPC and Cholesterol Mixture, 41
3.2.5 Usefulness of Dropping Method, 44
3.3 Interaction between Lipid Monolayer and Anesthetics, 44
3.3.1 Quartz Crystal Oscillator (QCO) Method, 45
3.3.2 Apparatuses and Procedure, 46
3.3.3 Time Course of Frequency (QCM) and Resistance (QCI), 48
3.3.4 Concentration Dependence of Frequency (QCM) and Resistance (QCI), 49
3.3.5 True Anesthesia Phenomenon, 56
Acknowledgment, 56
References, 57

Atomic Force Microscopy

4 Atomic Force Microscopy for Measuring Interaction Forces in Biological Materials and Cells 59
Naoyuki Ishida, Yasuyuki Kusaka, Tomonori Fukasawa, and Hiroyuki Shinto

4.1 Introduction, 59
4.2 Measurement of Interaction Forces Using AFM, 60
4.3 Interaction of Model Membranes, 61
4.4 Interaction of Proteins, 62
4.5 Interaction of Cells, 63
4.6 Concluding Remarks, 65
References, 65

B

Bacterial Interaction

5 Bacterial Interactions 68
Masanori Toyofuku, Yosuke Tashiro, Tomohiro Inaba, and Nobuhiko Nomura

5.1 Introduction, 68
5.2 Gram-Positive and Gram-Negative Bacteria, 68
5.3 Cell–Cell Communication in Bacteria, 69
5.3.1 Cell–Cell Communication in Gram-Negative Bacteria, 69
5.3.2 Cell–Cell Communication in Gram-Positive Bacteria, 71
5.3.3 A Common Language for Gram-Negative and Gram-Positive Bacteria: AI-2, 71
5.4 Membrane Vesicles, 72
5.4.1 Components of MVs, 72
5.4.2 Biological Roles of MVs, 73

5.4.3 Surface Characteristics of MVs, 73
5.4.4 Future Perspectives in MV Research, 74
5.5 Biofilm Formation, 74
5.5.1 Surface-Attached Biofilms, 75
5.5.2 Bacterial Aggregates, 76
5.6 Concluding Remarks, 77
References, 77

Biocompatible Polymer

6 2D and 3D Biocompatible Polymers for Biomedical Devices 82
Masaru Tanaka

6.1 Introduction, 82
6.2 Biocompatible Polymeric Biomaterials, 82
6.3 Protein Adsorption on Polymeric Biomaterials, 83
6.4 Water Structure of Polymers, 84
6.5 3D Polymer Surfaces for Tissue Engineering, 85
6.6 Methods of 3D Polymer Fabrication, 86
6.6.1 Top–Down Fabrication, 86
6.6.2 Bottom–Up Fabrication, 86
6.7 Control of Cell Adhesion and Functions, 88
6.8 Conclusions and Perspectives, 90
Acknowledgments, 91
References, 91

Biofilm

7 Biofilm 94
Hisao Morisaki

7.1 Introduction, 94
7.2 Formation Process of Biofilm, 94
7.3 Biofilm Constituents, 95
7.3.1 Substratum Surface, 95
7.3.2 Biofilm Microbes, 96
7.3.3 Extracellular Polymeric Substances (EPSs), 97
7.3.4 Interstitial Water among EPSs, 98
7.4 Biofilm and Surrounding Environment, 99
7.4.1 Influence of Surrounding Environment on Biofilm, 99
7.4.2 Influence of Biofilm on Surrounding Environment, 99
7.5 Present and Prospective Biofilm Research, 100
References, 101

Bioflotation

8 Use of Microorganisms for Complex ORE Beneficiation: Bioflotation as an Example 108
Akira Otsuki

8.1 Introduction, 108
8.2 Characterization of Complex Ores, 108
8.2.1 Mineral Analysis in Dry State, 108
8.2.2 Mineral/Particle Analysis in Water, 109
8.2.3 Mixture of Complementary Analyses, 111

8.2.4 Refractory Gold Ore Beneficiation, 111
8.2.5 Sulfide Flotation Using a Microorganism as a Flotation Reagent, 111
8.3 Summary, 116
References, 116

Biofouling

9 Biofouling **118**
Kazuho Nakamura

9.1 Definition of Biofouling, 118
9.2 Formation of Biofilms, 118
9.3 Biofouling in Industries, 118
9.3.1 Biofouling in Heat Exchangers, 119
9.3.2 Biofouling of Medical Devices, 119
9.3.3 Biofilms in Wastewater Treatment Processes, 120
9.3.4 Biofouling in Membrane Processes, 121
References, 121

Bio-inspired Microemulsion

10 Bioinspired Microemulsions and Their Strategic Pharmacological Perspectives **122**
Soumik Bardhan, Kaushik Kundu, Gulmi Chakraborty, Bidyut K. Paul, Satya P. Moulik, and Swapan K. Saha

10.1 Introduction, 122
10.2 A Brief Outline of Microemulsion Systems, 123
10.2.1 Types of Microemulsion Systems, 124
10.2.2 Role of Surfactant in Formation of Microemulsions, 124
10.2.3 Role of Cosurfactant in Formation of Microemulsions, 124
10.2.4 Role of Oil in Formation of Microemulsions, 125
10.2.5 Solubilization in Microemulsions, 125
10.2.6 Characterization of Microemulsions, 125
10.2.7 Stability of Microemulsions, 125
10.3 Design Strategy for Bioinspired Microemulsion Systems, 126
10.3.1 Selection of Ingredients, 126
10.3.2 Types of Bioinspired Microemulsions, 127
10.3.3 Decisive Factors for Pharmaceutical Applications, 129
10.4 Recent Advances in Bioinspired Microemulsions in Pharmaceutical Science, 129
10.4.1 Microemulsions as in Vitro Drug Delivery Systems, 129
10.4.2 Microemulsions as in Vivo Drug Delivery Systems, 131
10.4.3 Microemulsions in Cancer Therapy, 132
10.4.4 Microemulsions in Biotechnology, 133
10.4.5 Antimicrobial Activity of Microemulsions, 134
10.4.6 Biocompatible Ionic Liquid Microemulsions in Drug Delivery and Biotechnology, 135
10.4.7 Patents in Microemulsion Drug Delivery Systems, 136
10.5 Biocompatibility and Toxicity Issues, 137
10.6 Future Outlook, 138
Acknowledgment, 138
References, 138

Biomaterial

11 Development of Nonfouling Biomaterials **145**

Ruey-Yug Tsay and Toyoko Imae

11.1 Introduction, 145
11.2 Why Nonfouling is Relevant in Biomaterials, 145
11.2.1 Antithrombogenesis and Anti-inflammatory Response, 145
11.2.2 Host Response to Biomaterials, 146
11.2.3 Antibacterial Property, 147
11.3 Protein Adsorption and Material Properties, 148
11.3.1 Adsorption Mechanism of Protein, 148
11.3.2 Protein–Surface Interactions, 148
11.3.3 Surface Hydration, 149
11.3.4 Strategies for Nonfouling Design, 149
11.4 Nonfouling Biomaterials, 150
11.4.1 Surface Immobilization Techniques, 151
11.4.2 Nonionic Hydrophilic Materials, 153
11.4.3 Zwitterionic Materials, 154
11.4.4 Amphiphilic Materials, 156
11.5 Conclusions and Future Perspectives, 157
References, 157

12 Surface Characterization of Silver and Fe_3O_4 Nanoparticles Incorporated into Collagen-based Scaffolds as Biomaterials for Tissue Regeneration: State-of-the-Art and Future Perspectives **161**

Abhishek Mandal, N. Chandrasekaran, Amitava Mukherjee, and Thothapalli P. Sastry

12.1 Introduction, 161
12.2 Structural Information, 163
12.2.1 SDS-PAGE Analysis, 163
12.2.2 Circular Dichroism (CD) Studies, 164
12.2.3 Differential Scanning Calorimetry (DSC), 165
12.2.4 X-Ray Diffraction (XRD), 166
12.3 Chemical Information, 167
12.3.1 Fourier Transform Infrared (FT-IR) Spectroscopy, 167
12.3.2 X-Ray Photoelectron Spectroscopy (XPS), 168
12.4 Morphological Information, 171
12.4.1 Scanning Electron Microscopy (SEM), 171
12.4.2 Atomic Force Microscopy (AFM), 173
12.5 Conclusions and Future Perspectives, 175
Acknowledgment, 175
References, 175

Biomimetics

13 Biomimetic Polymer Aggregates: Self-Assembly Induced by Chemical Reactions **181**

Eri Yoshida

13.1 Introduction, 181
13.2 Self-Assembly Induced by Electron Transfer, 181
13.2.1 Oxidation-Induced Self-Assembly, 182
13.2.2 Reduction-Induced Self-Assembly, 184
13.2.3 Disproportionation-Induced Self-Assembly, 184

13.3 Self-Assembly Induced by Irreversible Photoreactions, 186
13.3.1 Photolysis-Induced Self-Assembly, 188
13.3.2 Photo-Claisen Rearrangement-Induced Self-Assembly, 189
13.3.3 Photoelectron Transfer–Induced Self-Assembly, 190
13.4 Conclusions, 191
References, 191

14 Molecular Interaction in Biomimetics and Biosystems: Chirality and Confinement at Nanodimension 195
Nilashis Nandi and Saheb Dutta

14.1 Introduction, 195
14.2 Methods of Theoretical Calculation, 198
14.3 Chiral Discrimination in Biomimetic Monolayers, 198
14.4 Experimental Studies on Chiral Discrimination in Peptide Synthesis and Aminoacylation Reaction, 199
14.5 Computational Analysis of Chiral Discrimination in Aminoacylation Reaction, 202
14.6 Computational Studies of the Chiral Discrimination in Peptide Bond Formation Reaction, 204
14.7 Concluding Remarks, 206
Acknowledgments, 207
References, 207

Biosensing

15 Softinterface on Biosensing 211
Yukichi Horiguchi and Yukio Nagasaki

15.1 Introduction, 211
15.2 Advantages of Suppressing the Nonspecific Adsorption on a Surface by PEGylation, 212
15.3 Peg Chain Behavior on Surfaces, 212
15.4 Functionalization of PEG End for PEGylation on Surface, 214
15.5 Hybrid Immobilization of PEG with Ligand Molecules, 215
15.6 Conclusion, 217
References, 217

Bioseparation

16 Bioseparation Using Thermoresponsive Polymers 220
Kenichi Nagase and Teruo Okano

16.1 Introduction, 220
16.2 Thermoresponsive Chromatography with Hydrophobic Interactions, 220
16.3 Thermoresponsive Chromatography with Electrostatic Interactions, 222
16.4 Thermoresponsive Chromatography Using Volume Exclusion Effect of PIPAAm, 224
16.5 Thermoresponsive Chromatography for High-Speed Separation, 226
16.6 Thermally Modulated Cell Separation Using PIPAAm, 227
16.7 Conclusions, 228
Acknowledgment, 229
References, 229

Biosurfactant

17 Biosurfactants **231**
Etsuo Kokufuta

17.1 Introduction, 231
17.2 Classification, 231
17.3 Chemical and Physical Properties, 239
17.4 Applications, 242
References, 243

Blood-brain Barrier

18 Structure and Regulation of the Blood–Brain Barrier **244**
Yung-Chih Kuo, Chin-Lung Lee, and Jyh-Ping Hsu

18.1 Introduction, 244
18.2 Cellular System of the BBB, 244
18.2.1 Tight Junctions, 244
18.2.2 Neurovascular Unit, 245
18.2.3 BMECs, 245
18.2.4 Astrocytes, 245
18.2.5 Pericytes, 246
18.3 In Vitro BBB Model, 246
18.3.1 Primary Culture, 247
18.3.2 Coculture, 247
18.4 ABC Transporters in the BBB, 247
18.4.1 Mechanism of ABC Transporters, 247
18.5 Secreted Factors for BBB Regulation: Mechanism and Inhibitor, 247
18.5.1 TGFβ1, 248
18.5.2 VEGF, 248
18.5.3 MMP-9, 248
18.6 Nanoparticles for Delivering Pharmaceuticals Across the BBB, 248
Acknowledgments, 250
Abbreviations, 250
References, 250

Boron Tracedrug

19 Boron Tracedrugs as Theranostic Agents for Neutron Dynamic Therapy **255**
Hitoshi Hori and Hiroshi Terada

19.1 The Real Crisis for Twenty-First-Century Medicinal Chemists in Pharmaceutical Industries and Academia, 255
19.2 Boron Tracedrugs as a Challenge to Traditional Drug Design Methodology, 255
19.3 Boron Tracedrugs for Neutron Dynamic Therapy (NDT), as Physician-Friendly Tools, 257
19.4 Conclusions, 258
Acknowledgment, 259
References, 259

C

Carbohydrate

20 Carbohydrates as Biocolloids in Nanoscience **260**
Zaheer Khan, Shokit Hussain, Ommer Bashir, and Shaeel Ahmed Al-Thabaiti

20.1 Introduction, 260
20.2 Types of Biocolloids, 261
20.3 Properties, 262
20.4 Carbohydrates in Nanoscience, 262
References, 265

Cartilage

21 High-Strength Poly(Vinyl Alcohol) Hydrogels for Artificial Cartilage **269**
Atsushi Suzuki and Teruo Murakami

21.1 Introduction, 269
21.2 Fundamental Properties of Physical PVA Gels, 270
21.2.1 Network Structure: Swelling Ratio and Crystallinity, 270
21.2.2 Conditions for Starting Raw Materials, 271
21.3 Typical Examples of Physical PVA gels: Preparations and Mechanical Properties, 272
21.3.1 Swelling Ratio and Compression Stress, 273
21.3.2 Tearing Energy by a Trouser Tear Test, 274
21.3.3 Dynamic Friction Coefficient and Wear Ratio, 274
21.4 Mechanical Strengthening and Future Visions, 276
Acknowledgment, 277
References, 277

22 Superior Tribological Behaviors of Articular Cartilage and Artificial Hydrogel Cartilage **278**
Teruo Murakami and Atsushi Suzuki

22.1 Introduction, 278
22.2 Various Lubrication Modes in Natural Synovial Joints, 278
22.3 Biphasic Lubrication in Natural Synovial Joints, 280
22.4 Boundary Lubrication in Natural Synovial Joints, 282
22.5 Lubrication Modes in Artificial Joints, 284
22.6 Frictional Behaviors of Artificial Hydrogel Cartilage, 285
22.6.1 Artificial Cartilage, 285
22.6.2 Articular Cartilage, 286
22.7 Biphasic Finite-Element Analyses for Artificial Hydrogel Cartilage, 286
22.8 Boundary Lubrication in Freeze-Thawing PVA Hydrogel, 287
22.9 Superior Tribological Behavior of Artificial Hydrogel Cartilage, 288
22.10 Conclusion, 289
Acknowledgment, 289
References, 289

Cell Mimicking Vesicle

23 Self-Assembled Cell-Mimicking Vesicles Composed of Amphiphilic Molecules: Structure and Applications **292**
Swati De and Ranju Prasad Mandal

23.1 Introduction, 292

23.2 Principles of Vesicle Formation, 292
23.2.1 Parameters, 292
23.3 Classical Vesicles, 295
23.3.1 Classification, 295
23.3.2 Dynamic Processes Occurring in Vesicles, 295
23.3.3 Formation of Vesicles, 296
23.4 Novel Vesicular Systems–Going Beyond Lipids, 300
23.4.1 Niosomes, 301
23.4.2 Ethosomes, 301
23.4.3 Transferosomes, 301
23.4.4 Sphingosomes, 301
23.4.5 Pharmacosomes, 302
23.4.6 e-Liposomes, 302
23.4.7 Polymerosomes, 302
23.4.8 Catansomes, 302
23.5 Vesicle Characterization Techniques, 303
23.5.1 Morphology, 303
23.5.2 Size Distribution, 303
23.5.3 Membrane Thickness, Lamellarity, and Fluidity, 303
23.5.4 Zeta-Potential and Surface Properties, 304
23.5.5 Stability, 304
23.5.6 Entrapment Efficiency, 304
23.5.7 In Vitro Release Study, 304
23.5.8 pH Sensitivity Assessment, 304
23.6 Applications of Vesicles, 304
23.6.1 Drug Delivery, 304
23.6.2 Cosmetic Applications, 305
23.6.3 As Self-Assembled Nanoreactors, 305
23.6.4 As Organized Assemblies for Fluorescence-Based Studies, 306
23.7 Future Perspectives and Directions of Research on Vesicles, 307
Acknowledgments, 307
References, 308

Cell Regulation

24 Integrin-Dependent Cell Regulation and its Clinical Application 313
Takuya Iyoda, Takuya Matsunaga, and Fumio Fukai

24.1 Introduction, 313
24.2 Inactivation of β1-Integrin by FNIII14 Increases Chemosensitivity of Acute Myelogenous Leukemia (AML) Cells, 314
24.3 Forced Adhesion to Fibronectin Through Sustained Activation of β1-Integrin by TNIIIA2 Caused Apoptosis in Hematopoietic Tumor Cells, 317
24.4 TNIIIA2-Induced Activation of β1-Integrin Enhances Intracellular Drug Accumulation in Hematopoietic Tumor Cells, 318
24.5 TNIIIA2-Mediated β1-Integrin Activation Accelerates Erythroid Differentiation of Hematopoetic Tumor Cells, 320
24.6 TNIIIA2-Mediated β1-Integrin Activation Leads Deregulated Hyperproliferation to Nontransformed Fibroblastic Cells, 320
24.7 Concluding Remarks, 321
References, 323

Chitosan

25 Depth Profile of Kr^+-Irradiated Chitosan **325**
Kazunaka Endo

25.1 Introduction, 325
25.2 Computational Method, 325
25.3 Experimental Method, 326
25.4 Results and Discussion, 326
25.4.1 Raman Shift Spectral Analysis, 327
25.4.2 Valence Band X-Ray Photoelectron Spectral Analysis, 328
25.5 Conclusion, 329
References, 330

26 Electronic Structure of Chitosan **331**
Kazunaka Endo

26.1 Introduction, 331
26.2 Experimental Method, 331
26.3 Theoretical Background, 332
26.3.1 NMR Chemical Shielding Tensor, 332
26.3.2 XPS, 332
26.4 Calculations, 332
26.4.1 NMR Chemical Shielding Tensor, 332
26.4.2 XPS, 333
26.5 Results and Discussion, 333
26.5.1 ^{13}C-NMR Chemical Shielding Tensor, 333
26.5.2 XPS, 336
26.6 Conclusion, 337
References, 338

Collagen Matrix

27 Aligned Fibrillar Collagen Matrices **340**
Ralf Zimmermann, Jens Friedrichs, Babette Lanfer, Uwe Freudenberg, and Carsten Werner

27.1 Introduction, 340
27.2 Shear Flow Deposition of Collagen Matrices, 341
27.2.1 Fibers in Shear Flow, 341
27.2.2 Experimental Approach, 341
27.2.3 Possible Mechanism of Fibril Alignment, 347
27.2.4 Comparison with Other Methods, 347
27.3 Collagen Self-Alignment on Mica, 347
27.3.1 Directing Collagen Self-Assembly into Ultrathin Matrices, 347
27.3.2 Adjusting the Collagen Matrix Density by pH Change, 348
27.3.3 Role of Electrolytes in Determining Final Collagen Matrices, 349
27.3.4 Structural Features of Self-Assembled Collagen Fibrils Resembling in Vivo Fibrils, 349
27.3.5 Reshaping Collagen Matrices on Nanoscale, 349
27.3.6 Collagen Matrices Showing Enhanced Stability after Maturation, 350
27.3.7 Insight into Collagen Self-Assembly through Time-Lapse AFM, 350
27.4 Summary, 352
Acknowledgment, 352
References, 352

Colloidal Crystallization

28 Colloidal Crystallization **355**

Tsuneo Okubo

28.1 Introduction, 355
28.2 Preparation and Characterization of Biological and Synthetic Colloidal Particles, 356
28.2.1 Biological Colloidal Particles, 356
28.2.2 Polymer Colloidal Particles, 356
28.2.3 Inorganic Colloidal Particles, 357
28.2.4 Basic Characteristics of Colloidal Particles, 358
28.3 Why Crystal Structures Form, 358
28.4 Morphology and Phase Diagram of Colloidal Single Crystals, 359
28.5 Lattice Structure of Colloidal Crystals, 360
28.6 Alloy Crystals of Colloidal Mixtures, 361
28.7 Colloidal Crystallization Kinetics, 361
28.8 Static and Dynamic Light Scattering and Small-Angle Neutron Scattering, 362
28.9 Structural Relaxation Times of Colloidal Crystals, 363
28.10 Rigidity of Colloidal Crystals, 364
28.11 Viscosity and Viscoelasticity of Colloidal Crystals, 365
28.12 External Field Effects on Colloidal Crystals, 365
28.13 Colloidal Crystallization in Microgravity, 367
28.14 Two-Dimensional Colloidal Crystals, 367
28.15 Biological Colloidal Crystals, 368
28.16 New Colloidal Crystal Systems, 368
28.17 Miscellaneous, 369
28.18 Application of Colloidal Crystals, 369
28.19 Concluding Remarks, 370
References, 370

D

Dielectric Property

29 Dielectric Properties of Biological Macromolecules and Biomolecule–Water Interfaces **380**

Brandon Campbell, Lin Li, and Emil Alexov

29.1 Background, 380
29.2 Macromolecular Dynamics and Its Effect on the Macromolecular Interior and Molecular Surface, 381
29.2.1 Thermal Fluctuations of Atoms, Amino or Nucleic Acids, or Entire Domains, 381
29.2.2 Conformational Changes Induced by Macromolecular Function, 381
29.2.3 Intrinsically Disordered Macromolecules, 382
29.2.4 Conformational Changes Caused by a Change in Environment Due to pH or Salt Concentration, 383
29.3 Water Molecule Dynamics and Its Effect on Protein Interior and Molecular Surface, 383
29.4 Modeling Macromolecular Interior and Macromolecule–Water Interfaces, 384
29.5 Role of Ions, 384

29.6 Dielectric Properties of Biological Macromolecules and Biomolecule–Water Interfaces, 384
29.7 Concluding Remarks, 386
Acknowledgments, 386
References, 386

Drug Delivery

30 NMR of Drug Delivery Coupled with Lipid Membrane Dynamics 391
Emiko Okamura

30.1 Introduction, 391
30.2 Dynamics of Membranes as a Platform of Vital Functions, 391
30.2.1 Diffusion, 392
30.2.2 Protrusion, 394
30.3 Drug Delivery Related to Membrane Dynamics, 394
30.3.1 Diffusion of Drugs in the Membrane, 395
30.3.2 Kinetics of Membrane Binding and Dissociation, 396
30.3.3 Thermodynamic Stability, 399
30.3.4 Dynamic Binding Probability, 399
30.3.5 Effect of Cholesterol, 400
30.4 Concluding Remarks and Future Perspectives, 400
Acknowledgments, 401
References, 401

31 Stimulus-Responsive Intelligent Drug Delivery System Based on Hydroxyapatite-Related Materials 403
Makoto Otsuka

31.1 Introduction, 403
31.2 Slow Drug Release from Self-Setting Apatite Cements, 403
31.3 Effect of Calcium Level on in Vitro Drug Release from Apatite Cement, 404
31.4 Calcium-Level-Responsive Drug Release of Apatite Cements Containing Antiosteoporosis Drug in Healthy and Diseased Rats and Therapeutic Effects, 404
31.5 Drug Delivery System Containing VK2 Based on Self-Setting Apatite/Collagen Composite Cements (AC), 406
31.6 Biodegradation of the AC Block with Interconnecting Pores as a Skeletal Bone Cell Scaffold, 407
31.7 Drug Release from Biodegradable Apatite/Collagen Composite Cements with Interconnective Macropores, 408
31.8 In Vitro Bone Cell Activity–Responsive Drug Release from Biodegradable Apatite/Collagen Bone Cell Scaffold with Interconnective Macropores, 408
31.9 In Vivo Bone Cell Activity–Responsive Deoxyribonucleic Acid (DNA) Release from Injectable Self-Setting Apatite Cement and Application to Gene Therapy, 409
Acknowledgments, 411
References, 411

Drying Structure

32 Drying Structure 412
Tsuneo Okubo

32.1 Introduction, 412

32.2 Convectional Patterns, 413
32.3 Sedimentation Patterns, 416
32.4 Drying Patterns of Colloidal Dispersions and Colloidal Crystals, 417
32.5 Drying Patterns of Polymer Gel Spheres, 419
32.6 Drying Patterns of Synthetic and Biological Polymers, 421
32.7 Drying Patterns of Ionic and Neutral Surfactants, 423
32.8 Drying Patterns of Simple Electrolytes, 424
32.9 Drying Patterns of Other Solutes, 424
32.10 Transferring Information on Solutions and Suspensions Toward the Drying Patterns, 424
32.11 Miscellaneous, 426
32.12 Concluding Remarks, 426
References, 427

E

Electrophoretic Mobility

33 Electrophoretic Mobility of Colloidal Particles 430
Hiroyuki Ohshima

33.1 Introduction, 430
33.2 Smoluchowski's, Hückel's, and Henry's Equations, 430
33.3 General Theory of the Electrophoretic Mobility of Spherical Hard Particles, 431
33.4 Relaxation Effect, 433
33.5 Electrophoretic Mobility of Soft Particles, 435
References, 437

Electrostatic Interaction

34 Electrostatic Interaction Between Colloidal Particles 439
Hiroyuki Ohshima

34.1 Introduction, 439
34.2 Interaction Between Hard Particles, 439
34.2.1 Interaction between Two Parallel Plates: Low-Potential Case, 439
34.2.2 Derjaguin's Approximation for Calculation of Interactions between Two Spheres or Cylinders, 440
34.2.3 Low-Potential Case, 440
34.2.4 Linear Superposition Approximation: Arbitrary Potential Case, 441
34.3 Interaction Between Soft Particles, 443
34.4 Interaction Between Two Soft Particles After Contact, 444
34.4.1 Two-Stage Model, 444
34.4.2 Three-Stage Model, 446
34.5 Electrostatic Interaction Between Two Interpenetrating Soft Particles, 448
34.5.1 Linearized Poisson–Boltzmann Equations for Two Interacting Charged Porous Spheres, 448
References, 449

Emulsion

35 Physicochemical Properties and Clinical Applications Of Surfactant-Free Emulsions Prepared with Electrolytic Reduction Ion Water (ERI) 451
Ken-ichi Shimokawa and Fumiyoshi Ishii

35.1 Introduction, 451

35.2 Preparation and Physicochemical Properties of Surfactant-Free Emulsions Prepared with ERI Containing Magnesium Aluminum Silicate, 453
35.3 Effects of Electrolytic Reduction Ion Water (ERI) Lotion Prepared with Surfactant-Free Emulsions on Burn Wound Healing (Case Report), 456
References, 457

Enzyme Membrane

36 Steady-State Coupling in Enzyme Membrane 459
Kazuo Nomura

36.1 Introduction, 459
36.2 Theoretical Background, 459
36.3 Results and Discussion, 462
36.3.1 Membrane Permeation across the Ionomer Membrane, 462
36.3.2 Immobilization of Enzyme, 463
36.3.3 Hydrolysis of 4-Nitrophenylphosphate across Immobilized Enzyme Membrane, 463
36.3.4 Degree of Coupling between Reaction Rate and Diffusional Flux in the Enzyme Membrane System, 464
36.3.5 Quantity of Immobilized Acid Phosphatase, 466
References, 468

Exosome

37 Evaluation of Zeta-Potential of Individual Exosomes Secreted from Biological Cells Using a Microcapillary Electrophoresis Chip 469
Takanori Akagi and Takanori Ichiki

37.1 Introduction, 469
37.2 Exosome Preparation, 469
37.3 Electrophoresis System for Exosomes, 470
37.4 Relation Between Zeta-Potentials of Exosomes and Their Originating Cells, 470
37.5 Effect of Sialidase on the Zeta-Potential of Exosomes, 472
37.6 Conclusion, 473
References, 473

F

Flocculation Dynamics

38 Flocculation Dynamics on the Basis of Collision-Limited Analysis 474
Yasuhisa Adachi

38.1 Introduction, 474
38.2 Population Balance Equation, 474
38.3 Brownian Coagulation, 475
38.3.1 Collision Process under Brownian Motion, 475
38.3.2 Smoluchowski Solution, 476
38.3.3 Self-Similar Solution, 477
38.3.4 Effect of Fractal Structure of Flocs on Flocculation Rate, 478
38.4 Coagulation in Shear Flow, 479
38.4.1 Collision Frequency in Shear Field, 479

38.4.2 Interaction between Colloid Particles in Laminar Shear Flow, 480
38.4.3 Effect of Formation of Floc Structure on Shear Coagulation Rate, 480
38.5 Initial Stage of Bridging Flocculation in a Turbulent Mixing, 481
38.5.1 Schematic Picture of Flocculation with Polymer Flocculants in a Practical System, 481
38.5.2 Collision Process in Turbulent Flow, 481
38.5.3 Historical Review of Concept of Nonequilibrium Flocculation, 483
38.5.4 Initial-Stage Dynamics of Bridging Flocculation of PSL Particles Induced by Polyelectrolytes under High Ionic Strength, 484
38.6 Conclusion and Future Perspectives, 485
Acknowledgment, 485
References, 485

G

Gel

39 Anisotropic Gel Formation Induced by Dialysis **487**
Toshiaki Dobashi and Takao Yamamoto

39.1 Introduction, 487
39.2 Dialysis-Induced Gelation, 487
39.2.1 Boundary Conditions, 487
39.2.2 Birefringence of Dialysis-Induced Gel, 488
39.2.3 Trigger for Gelation, 489
39.2.4 Dynamics of Gelation, 489
39.3 Theoretical Treatment of Analysis of Dialysis-Induced Gelation, 489
39.3.1 Dynamics of Gelation Induced by a Cross-Linking Agent, 490
39.3.2 Dynamics of Gelation Induced by pH Change, 493
39.3.3 Dynamics of Gelation Accompanied by Transition in Mechanism, 496
39.3.4 Dynamics of Gelation Induced by Dual Mechanisms, 496
39.4 Applications of Dialysis-Induced Anisotropic Gels, 497
References, 497

40 Gels **498**
Etsuo Kokufuta

40.1 Introduction, 498
40.2 Outline of Volume Phase Transition (VPT), 498
40.3 Theories of VPT, 500
40.4 Understanding VPT at the Molecular Level, 503
40.5 Effects of Distribution of Ionic or Hydrophilic Monomer Units Within the Network, 505
40.6 Effects of COIL-TO-HELIX Transition in Polypeptide Gels, 507
40.7 Effects of Surfactant Binding, 507
40.8 Network Inhomogeneity and Swelling–Shrinking Kinetics, 510
40.9 Microgels, 511
40.10 Conclusions, 512
References, 512

41 Gel Crystals **514**
Tsuneo Okubo

41.1 Introduction, 514
41.2 Gel Spheres used for Type I Gel Crystals, 517

41.3 Phase Diagram and Morphology of Type I Gel Crystals, 518
41.4 Lattice Structure of Type I Gel Crystals, 519
41.5 Kinetics of Type I Gel Crystallization, 521
41.6 Role of Electrical Double Layers on Type I Gel Crystallization, 522
41.7 Rigidity of Type I Gel Crystals, 523
41.8 Type II Gel Crystals, 524
41.9 Type III Gel Crystals, 524
41.10 Type III Gel Crystallization of Gel Agglomerates During Dryness, 524
41.11 Conclusions and Future Perspectives, 524
References, 526

Gemini Surfactant

42 Oleic Acid-Based Surfactants as Cost-Effective Gemini Surfactants 529
Kenichi Sakai and Masahiko Abe

42.1 Introduction, 529
42.2 Syntheses and Molecular Structures, 529
42.3 Dilute Aqueous Solution Properties, 530
42.4 Temperature–Concentration Phase Behavior with Water, 533
42.5 Characterizing Insoluble Monolayer Films Formed at the Air–Water Interface, 535
42.6 Adsorption Characteristics at Solid–Aqueous Solution Interfaces, 535
42.7 Concluding Remarks, 537
References, 537

43 Synthesis and Properties of Heterocyclic Cationic Gemini Surfactants 539
Avinash Bhadani, Sukhprit Singh, Hideki Sakai, and Masahiko Abe

43.1 Introduction, 539
43.2 Pyridinium Gemini Surfactants, 539
43.3 Imidazolium Gemini Surfactants, 547
43.4 Pyrrolidinium Gemini Surfactants, 552
43.5 Piperidinium Gemini Surfactants, 552
References, 553

H

Hydrogel

44 Functional Hydrogel Microspheres 554
Daisuke Suzuki, Takuma Kureha, and Koji Horigome

44.1 Introduction, 554
44.2 Microgel Synthesis, 554
44.3 Microgel Characterization, 556
44.4 Functional Microgels, 558
44.4.1 Hybrid Microgels, 558
44.4.2 Janus Microgels, 558
44.4.3 Oscillating Microgels, 560
44.5 Concluding Remarks, 567
References, 567

Hydrophilic-Lipophilic Balance

45 Hydrophilic–Lipophilic Balance (HLB): Classical Indexation and Novel Indexation of Surfactant **570**

Yuji Yamashita and Kazutami Sakamoto

45.1 Introduction, 570
45.2 Calculations of HLB Number, 570
45.3 Practical Side of HLB Theory, 572
45.4 Evaluation of Hydrophilicity and Lipophilicity, 572
45.5 TLC Evaluation of Amino Acid-Derived Surfactants, 573
45.6 Conclusions, 574
References, 574

LIST OF CONTRIBUTORS

Masahiko Abe, Department of Pure and Applied Chemistry, Faculty of Science and Technology, Tokyo University of Science, Chiba, Japan

Yasuhisa Adachi, Faculty of Life and Environmental Science, University of Tsukuba, Ibaraki, Japan

Silvia Ahualli, Department of Applied Physics, School of Sciences, Campus Fuentenueva, University of Granada, Granada, Spain

Takanori Akagi, Department of Bioengineering, Graduate School of Engineering, University of Tokyo, Bunkyo-ku, Tokyo, Japan

Md. Sayem Alam, Council of Scientific and Industrial Research (CSIR)—Central Leather Research Institute (CLRI), Industrial Chemistry Laboratory, Adyar, Chennai, India

Emil Alexov, Computational Biophysics and Bioinformatics, Physics Department, Clemson University, Clemson, South Carolina, United States

Shaeel Ahmed Al-Thabaiti, Department of Chemistry, Faculty of Science, King Abdulaziz University, Jeddah, Saudi Arabia

S. Angayarkanny, CSIR—Central Leather Research Institute (CLRI), Adyar, Chennai, India

Stefano Angioletti-Uberti, Department of Physics, Humboldt University Berlin, Berlin, Germany

Kenji Aramaki, Graduate School of Environment and Information Sciences, Yokohama National University, Hodogaya-ku, Yokohama, Japan

Makoto Aratono, Department of Chemistry, Faculty of Sciences, Kyushu University, Higashi-ku, Fukuoka, Japan

Rajat Banerjee, Department of Biotechnology and Dr. B.C. Guha Centre for Genetic Engineering and Biotechnology, University of Calcutta, Kolkata, India

Victor Banerjee, Department of Chemistry, Laboratory of Protein Chemistry, Bose Institute, Kolkata, West Bengal, India

Soumik Bardhan, Department of Chemistry, University of North Bengal, Darjeeling, India

Ommer Bashir, Department of Chemistry, Jamia Millia Islamia, Jamia Nagar, New Delhi, India

Geetha Baskar, CSIR—Central Leather Research Institute (CLRI), Adyar, Chennai, India

Avinash Bhadani, Department of Pure and Applied Chemistry, Faculty of Science and Technology, Tokyo University of Science, Noda, Chiba, Japan

Marian Brestic, Institute of Soil and Water Conservation, Northwest A&F University, Yangling, China and Department of Plant Physiology, Slovak Agricultural University, Nitra, Slovak Republic

Brandon Campbell, Computational Biophysics and Bioinformatics, Physics Department, Clemson University, Clemson, South Carolina, United States

Félix Carrique, Department of Applied Physics II, School of Sciences, Campus Teatinos, University of Málaga, Málaga, Spain

Gulmi Chakraborty, Department of Chemistry, University of North Bengal, Darjeeling, India

N. Chandrasekaran, Centre for Nano-Biotechnology, School of Bio-Sciences and Technology, VIT University, Vellore 632014, Tamil Nadu, India

Sudeshna M. Chatterjea, Department of Biotechnology and Dr. B.C. Guha Centre for Genetic Engineering and Biotechnology, University of Calcutta, Kolkata, West Bengal, India

Aritra Chowdhury, School of Chemistry, University of Manchester, Manchester, United Kingdom

K.P. Das, Department of Chemistry, Bose Institute, Kolkata, West Bengal, India

Swati De, Department of Chemistry, University of Kalyani, Kalyani, West Bengal, India

Ángel V. Delgado, Department of Applied Physics, School of Sciences, Campus Fuentenueva, University of Granada, Granada, Spain

Kabir-ud-Din, Department of Applied Chemistry, Aligarh Muslim University, Aligarh, India

Toshiaki Dobashi, Graduate School of Science and Technology, Gunma University, Gunma, Japan

Saheb Dutta, Department of Chemistry, University of Kalyani, Kalyani, West Bengal, India

Kazunaka Endo, Division of Colloid and Interface Science, Research Institute for Science and Technology, Tokyo University of Science, Kagurazaka, Shinjuku-ku, Tokyo, Japan

Dotchi Exerowa, Institute of Physical Chemistry, Bulgarian Academy of Sciences, Sofia, Bulgaria

Jens Friedrichs, Leibniz Institute of Polymer Research Dresden, Max Bergmann Center of Biomaterials Dresden, Dresden, Germany

Uwe Freudenberg, Leibniz Institute of Polymer Research Dresden, Max Bergmann Center of Biomaterials Dresden, Hohe Strasse 6, D-01069 Dresden, Germany; Technische Universität Dresden, Center for Regenerative Therapies Dresden, Tatzberg 47, 01307 Dresden, Germany

Keiji Fujimoto, The Center for Chemical Biology, School of Fundamental Science and Technology, Graduate School of Science and Technology, Keio University, Hiyoshi, Kohoku-ku, Yokohama, Japan

Fumio Fukai, Department of Molecular Patho-Physiology, Faculty of Pharmaceutical Sciences, Center for Drug Delivery Research, and Center for Physical Pharmacology, Research Institutes for Science and Technology, Tokyo University of Science, Noda, Chiba, Japan

Tomonori Fukasawa, Department of Chemical Engineering, Hiroshima University, Japan

Yuuka Fukui, The Center for Chemical Biology, School of Fundamental Science and Technology, Graduate School of Science and Technology, Keio University, Hiyoshi, Kohoku-ku, Yokohama, Japan

Makoto Gemmei-Ide, Department of Applied Chemistry, Graduate School of Science and Engineering, University of Toyama, Toyama, Japan

Masaki Goto, Department of Life System, Institute of Technology and Science, The University of Tokushima, Tokushima, Japan

Christof Gutsche, Department of Experimental Physics I, Leipzig University, Leipzig, Germany

Yusuke Hattori, Research Institute of Pharmaceutical Sciences, Musashino University, Shin machi, Nishitokyo, Tokyo, Japan

Hitoshi Hori, Department of Pharmacology, Faculty of Pharmaceutical Sciences, Niigata University of Pharmacy and Applied Life Sciences, Niigata, Japan and NDT Research Institute, Tokushima, Japan

Koji Horigome, Graduate School of Textile Science & Technology, Shinshu University, Ueda, Nagano, Japan

Yukichi Horiguchi, Graduate School of Pure and Applied Sciences, University of Tsukuba, Ten-noudai Tsukuba, Ibaraki, Japan

Jyh-Ping Hsu, Department of Chemical Engineering, National Taiwan University, Taipei, Taiwan, Republic of China

Shokit Hussain, Department of Chemistry, Jamia Millia Islamia, Jamia Nagar, New Delhi, India

Takanori Ichiki, Department of Bioengineering, Graduate School of Engineering, University of Tokyo, Bunkyo-ku, Tokyo, Japan

Makoto Gemmei-Idek, Department of Applied Chemistry, Graduate School of Science and Engineering, University of Toyama, Toyama, Japan

Toyoko Imae, Graduate Institute of Applied Science and Technology, National Taiwan University of Science and Technology, Taipei, Taiwan, Republic of China

Tomohiro Inaba, Graduate School of Life and Environmental Sciences, University of Tsukuba, Tsukuba, Ibaraki, Japan

Naoyuki Ishida, Department of Applied Chemistry and Biotechnology, Okayama University, Okayama, Japan

Munehide Ishiguro, Laboratory of Soil Conservation, Research Group of Regional Environment, Research Faculty of Agriculture, Hokkaido University, Sapporo, Japan

Fumiyoshi Ishii, Department of Pharmaceutical Sciences, Meiji Pharmaceutical University, Noshio, Kiyose, Tokyo, Japan

Makio Iwahashi, Department of Chemistry, School of Science, Kitasato University, Kitasato, Minami-ku, Sagamihara, Kanagawa-ken, Japan

Takuya Iyoda, Department of Molecular Patho-Physiology, Faculty of Pharmaceutical Sciences, and Center for Drug Delivery Research, Center for Physical Pharmacology, Research Institutes for Science and Technology, Tokyo University of Science, Noda, Chiba, Japan

S.N. Jaisankar, Polymer Division, CSIR—Central Leather Research Institute, Adyar, Chennai, Tamil Nadu, India

María Luisa Jiménez, Department of Applied Physics, School of Sciences, Campus Fuentenueva, University of Granada, Granada, Spain

Haruma Kawaguchi, Department of Chemistry, Faculty of Engineering, Kanagawa University, Yokohama, Japan

Zaheer Khan, Chemistry Department, Faculty of Science, King Abdulaziz University, P. O. Box 80203, Jeddah 21413, Saudi Arabia

Jong-Duk Kim, Department of Chemical and Biomolecular Engineering, KAIST, Yuseung-gu, Daejeon, Republic of Korea

Hiromi Kitano, Department of Applied Chemistry, Graduate School of Science and Engineering, University of Toyama, Toyama, Japan

Etsuo Kokufuta, Faculty of Life and Environmental Sciences, University of Tsukuba, Tsukuba, Ibaraki, Japan

Friedrich Kremer, Department of Experimental Physics I, Leipzig University, Leipzig, Germany

Kaushik Kundu, Surface and Colloid Science Laboratory, Geological Studies Unit, Indian Statistical Institute, Kolkata, India

Yung-Chih Kuo, Department of Chemical Engineering, National Chung Cheng University, Chia-Yi, Taiwan, Republic of China

Takuma Kureha, Graduate School of Textile Science & Technology, Shinshu University, Ueda, Nagano, Japan

Yasuyuki Kusaka, Flexible Electronics Research Center, National Institute of Advanced Industrial Science and Technology (AIST), Tsukuba, Ibaraki, Japan

Babette Lanfer, Leibniz Institute of Polymer Research Dresden, Max Bergmann Center of Biomaterials Dresden, Dresden, Germany

Chin-Lung Lee, Department of Chemical Engineering, National Chung Cheng University, Taiwan, Republic of China

Sannamu Lee, Department of Biophysical Chemistry, Faculty of Pharmaceutical Sciences, Nagasaki International University, Sasebo, Nagasaki, Japan

Lin Li, Computational Biophysics and Bioinformatics, Physics Department, Clemson University, Clemson, South Carolina, United States

Hideyuki Maekawa, Department of Chemistry, Faculty of Sciences, Kyushu University, Higashi-ku, Fukuoka, Japan

Kimiko Makino, Faculty of Pharmaceutical Sciences, Tokyo University of Science, Noda, Chiba, Japan

Abhishek Mandal, Centre for Nano-Biotechnology, School of Bio-Sciences and Technology, VIT University, Vellore 632014, Tamil Nadu, India

Asit Baran Mandal, Industrial Chemistry Laboratory, Council of Scientific and Industrial Research (CSIR) — Central Leather Research Institute (CLRI), Adyar, Chennai 600 020, India; Polymer Division and Chemical Laboratory, CSIR—Central Leather Research Institute, Adyar, Chennai, Tamil Nadu, India

Ranju Prasad Mandal, Department of Chemistry, University of Kalyani, Kalyani, West Bengal, India

Kausik Manna, Department of Chemistry, University of North Bengal, Darjeeling, West Bengal, India

Hiroki Matsubara, Department of Chemistry, Faculty of Sciences, Kyushu University, Higashi-ku Hakozaki, Fukuoka, Japan

Hitoshi Matsuki, Department of Life System, Institute of Technology and Science, The University of Tokushima, Tokushima, Japan

Daisuke Matsukuma, Faculty of Science Division I, Department of Applied Chemistry, Tokyo University of Science, Shinjuku-ku, Tokyo, Japan

Hidetoshi Matsumoto, Department of Organic and Polymeric Materials, Tokyo Institute of Technology, Meguro-ku, Tokyo, Japan

Takuya Matsunaga, Division of Endocrinology and Metabolism, Hematology Rheumatology and Respiratory Medicine, Department of Internal Medicine, Kagawa University, Kita-gun, Kagawa, Japan

K. Seeni Meera, Polymer Division, CSIR—Central Leather Research Institute, Adyar, Chennai, Tamil Nadu, India

Kiyoshi Mishima, Yorozu Kohboh, Dome, 2-2804-1 Makuhari Hanamigawa-ku, Chiba-shi, Chiba 262-0032, Japan

Toshio Mitsui, Graduate School of Engineering Science, Osaka University, 1-3 Toyonaka, Osaka, 560-8531, Japan

Hisao Morisaki, Graduate School of Life Sciences, Ritsumeikan University, Kusatsu, Shiga, Japan

Satya P. Moulik, Department of Chemistry, Center for Surface Science and Technology, Jadavpur University, Kolkata, West Bengal, India

Xingmin Mu, Institute of Soil and Water Conservation, Northwest A&F University,Yangling, China

Amitava Mukherjee, Centre for Nano-Biotechnology, School of Bio-Sciences and Technology, VIT University, Vellore 632014, Tamil Nadu, India

Teruo Murakami, Research Center for Advanced Biomechanics, Kyushu University, Nishi-ku, Fukuoka, Japan

R. Murali Sankar, Polymer Division, CSIR—Central Leather Research Institute, Adyar, Chennai, Tamil Nadu, India

Yukio Nagasaki, Graduate School of Pure and Applied Sciences and Master's School of Medical Sciences, University of Tsukuba, Tsukuba, Ibaraki, Japan, and Satellite Laboratory of International Center for Materials Nanoarchitectonics (WPI-MANA), National Institute of Materials Science (NIMS), Tsukuba, Ibaraki, Japan

Kenichi Nagase, Institute of Advanced Biomedical Engineering and Science, Tokyo Women's Medical University (TWIns), Shinjuku, Tokyo, Japan

Hiromichi Nakahara, Department of Biophysical Chemistry, Faculty of Pharmaceutical Sciences, Nagasaki International University, Sasebo, Nagasaki, Japan

Kazuho Nakamura, Faculty of Engineering, Yokohama National University, Hodgaya-ku Yokohama, Japan

Nilashis Nandi, Department of Chemistry, University of Kalyani, Kalyani, West Bengal, India

Andleeb Z. Naqvi, Department of Applied Chemistry, Aligarh Muslim University, Aligarh, India

Makoto Nishimoto, Department of Materials Science, Wakayama National College of Technology, Gobo, Wakayama, Japan

Kazuo Nomura, Department of Chemistry, Faculty of Science, Kyushu University, Higashi-ku, Fukuoka, Japan

Nobuhiko Nomura, Graduate School of Life and Environmental Sciences, University of Tsukuba, Tsukuba, Ibaraki, Japan

Hiroyuki Ohshima, Faculty of Pharmaceutical Sciences, Tokyo University of Science, Noda, Chiba, Japan

Emiko Okamura, Faculty of Pharmaceutical Sciences, Himeji Dokkyo University, Himeji, Japan

Teruo Okano, Institute of Advanced Biomedical Engineering and Science, Tokyo Women's Medical University (TWIns), Shinjuku, Tokyo, Japan

Tsuneo Okubo, Institute for Colloidal Organization, Uji, Kyoto, Japan

Hidenori Otsuka, Faculty of Science Division I, Department of Applied Chemistry, Tokyo University of Science, Shinjuku-ku, Tokyo, Japan

Makoto Otsuka, Research Institute of Pharmaceutical Sciences, Musashino University, Shin machi, Nishitokyo, Tokyo, Japan

Akira Otsuki, Université de Lorraine, GeoRessources UMR 7359 CNRS-CREGU, ENSG, Vandœuvre-lès-Nancy Cedex, France

Amiya Kumar Panda, Department of Chemistry, University of North Bengal, Darjeeling 734 013, West Bengal, India

Koustubh Panda, Department of Biotechnology and Dr. B.C. Guha Centre for Genetic Engineering and Biotechnology, University of Calcutta, Kolkata, West Bengal, India

Chan Woo Park, Department of Chemical and Biomolecular Engineering, KAIST, Yuseung-gu, Daejeon, Republic of Korea

Bidyut K. Paul, Surface and Colloid Science Laboratory, Geological Studies Unit, Indian Statistical Institute, Kolkata, India

Dimo Platikanov, Department of Physical Chemistry, University of Sofia, Sofia, Bulgaria

Rafiuddin, Department of Chemistry, Aligarh Muslim University, Aligarh, Uttar Pradesh, India

Swapan K. Saha, Department of Chemistry, University of North Bengal, Darjeeling, India

Hideki Sakai, Department of Pure and Applied Chemistry, Faculty of Science and Technology, Tokyo University of Science, Noda, Chiba, Japan

Kenichi Sakai, epartment of Pure and Applied Chemistry, Faculty of Science and Technology, Tokyo University of Science, Noda, Chiba, Japan

Kazutami Sakamoto, Department of Pharmaceutical and Life Sciences, Faculty of Pharmacy, Chiba Institute of Science, Choshi, Chiba, Japan

Thothapalli P. Sastry, Centre for Nano-Biotechnology, School of Bio-Sciences and Technology, VIT University,

Vellore 632014, Tamil Nadu, India; Bio-products Laboratory, CSIR-Central Leather Research Institute, Adyar, Chennai 600020, Tamil Nadu, India

Akira Satoh, Faculty of Systems Science and Technology, Akita Prefectural University, Honjo City, Akita Prefecture, Japan

Hongbo Shao, Institute of Soil and Water Conservation, Northwest A&F University,Yangling, China; Key Laboratory of Coastal Biology & Bioresources Utilization, Yantai Institute of Coastal Zone Research (YIC), Chinese Academy of Sciences (CAS), Yantai, China; and Institute for Life Sciences, Qingdao University of Science & Technology (QUST), Qingdao, China

Osamu Shibata, Department of Biophysical Chemistry, Faculty of Pharmaceutical Sciences, Nagasaki International University, Sasebo, Nagasaki, Japan

Ken-ichi Shimokawa, Department of Pharmaceutical Sciences, Meiji Pharmaceutical University, Kiyose, Tokyo, Japan

Hiroyuki Shinto, Department of Chemical Engineering, Faculty of Engineering, Fukuoka University, Jyounan-ku, Fukuoka, Japan

Yukihide Shiraishi, Department of Applied Chemistry, Tokyo University of Science, Yamaguchi, Sanyo Onoda-shi, Yamaguchi, Japan

Rekha Goswami Shrestha, Department of Pure and Applied Chemistry, Faculty of Science and Technology, Tokyo University of Science, Noda, Chiba, Japan

David Singer, Center for Biotechnology and Biomedicine (BBZ), Institute for Bioanalytical Chemistry, Leipzig University, Leipzig, Germany

Sukhprit Singh, Department of Chemistry, UGC Sponsored-Centre for Advance Studies I, Guru Nanak Dev University, Amritsar, India

Konstanze Stangner, Molecular Oncology, Medical School, Leipzig University, Leipzig, Germany

Tim Stangner, Department of Experimental Physics I, Leipzig University, Leipzig, Germany

Atsushi Suzuki, Department of Materials Science & Research Institute of Environment and Information Sciences, Yokohama National University, Hodogaya-ku, Yokohama, Japan

Daisuke Suzuki, Graduate School of Textile Science & Technology, Shinshu University, Ueda, Nagano, Japan

Tharwat Tadros, 89 Nash Grove Lane, Wokingham, Berkshire RG40 4HE, United Kingdom

Keijiro Taga, Department of Life and Materials Engineering, Nagoya Institute of Technology, Gokiso-cho, Showa-ku, Nagoya, Japan

Youichi Takata, Department of Chemical and Biological Engineering, Ube National College of Technology, Ube, Yamaguchi, Japan

Takanori Takiue, Department of Chemistry, Faculty of Sciences, Kyushu University, Higashi-ku Hakozaki, Fukuoka, Japan

Nobutake Tamai, Department of Life System, Institute of Technology and Science, The University of Tokushima, Tokushima, Japan

Masaru Tanaka, Biomaterials Science and Tissue Engineering Group, Department of Biochemical Engineering, and Department of Polymer Science and Engineering, Graduate School of Science and Engineering, Yamagata University, Yonezawa, Japan; Soft Materials Chemistry, Institute for Materials Chemistry and Engineering, Kyushu University, Fukuoka, Japan

Xiaoli Tang, Key Laboratory of Coastal Biology & Bioresources Utilization, Yantai Institute of Coastal Zone Research (YIC), Chinese Academy of Sciences (CAS), Yantai, China and University of Chinese Academy of Sciences, Beijing, China

Akihiko Tanioka, Department of Organic and Polymeric Materials, Tokyo Institute of Technology, Meguro-ku, Tokyo, Japan

Yosuke Tashiro, Graduate School of Engineering, Shizuoka University, Hamamatsu, Shizuoka, Japan

Hiroshi Terada, Department of Pharmacology, Faculty of Pharmaceutical Sciences, Niigata University of Pharmacy and Applied Life Sciences, Niigata, Japan

Roumen Todorov, Institute of Physical Chemistry, Bulgarian Academy of Sciences, Sofia, Bulgaria

Naoki Toshima, Department of Applied Chemistry, Tokyo University of Science Yamaguchi, Sanyo Onoda-shi, Yamaguchi, Japan

Masanori Toyofuku, Graduate School of Life and Environmental Sciences, University of Tsukuba, Tsukuba, Ibaraki, Japan

Ruey-Yug Tsay, Institute of Biomedical Engineering, National Yang-Ming University, Taipei, Taiwan, Republic of China

Carolin Wagner, Department of Experimental Physics I, Leipzig University, Leipzig, Germany

Hongyan Wang, Key Laboratory of Coastal Biology & Bioresources Utilization, Yantai Institute of Coastal Zone

Research (YIC), Chinese Academy of Sciences (CAS), Yantai, China and University of Chinese Academy of Sciences, Beijing, China

Carsten Werner, Leibniz Institute of Polymer Research Dresden, Max Bergmann Center of Biomaterials Dresden, Dresden, Germany, and Technische Universität Dresden, Center for Regenerative Therapies Dresden, Dresden, Germany

Takao Yamamoto, Graduate School of Science and Technology, Gunma University, Gunma, Japan

Yasushi Yamamoto, Department of Life and Materials Engineering, Nagoya Institute of Technology, Gokiso-cho, Showa-ku, Nagoya, Japan

Michio Yamanaka, Department of Chemistry, Faculty of Sciences, Kyushu University, Higashi-ku, Fukuoka, Japan

Yuji Yamashita, Department of Pharmaceutical and Life Sciences, Faculty of Pharmacy, Chiba Institute of Science, Choshi, Chiba, Japan

Tamaki Yasui, Department of Chemistry, Faculty of Sciences, Kyushu University, Higashi-ku, Fukuoka, Japan

Li-Hsien Yeh, Department of Chemical and Materials Engineering, National Yunlin University of Science and Technology, Yunlin, Taiwan

Shoko Yokoyama, School of Pharmaceutical Sciences, Kyushu University of Health and Welfare, Miyazaki, Japan

Eri Yoshida, Department of Environmental and Life Sciences, Toyohashi University of Technology, Tempaku-cho, Toyohashi, Aichi, Japan

Zoya Zaheer, Department of Chemistry, Aligarh Muslim University, Aligarh, Uttar Pradesh, India

Ralf Zimmermann, Leibniz Institute of Polymer Research Dresden, Max Bergmann Center of Biomaterials Dresden, Dresden, Germany

PREFACE

The principal aim of this encyclopedia is to provide a physicochemical tool for interpreting various biological phenomena in terms of a language of colloid and interface science. The present book concentrates on subjects in the field of biocolloid and biointerface science, since there are already excellent encyclopedias on colloid and interface science available in the literature. This field is the youngest—but is becoming a very important—branch in the area in colloid and interface science. Actually, however, colloid and interface science has been closely related to biological science. Colloids, or more specifically, colloidal particles with diameters ranging from 1 to 1000 nm, which are one of the major subjects in colloid and interface science, can be found quite often in biological systems as biocolloids such as biological cells. Surfactant molecules, which are also one of the most important subjects in colloid and interface science, adsorb at interfaces between two immiscible media (e.g., water and oil), forming micelles and vesicles, which are a prototype of living cells. The Derjaguin–Landau–Verwey–Overbeek (DLVO) theory explains well the stability of colloidal suspensions in terms of the electrostatic and van der Waals interactions between the particles. In their book *Theory of Stability of Lyophobic Colloids*, Evert Verwey and Jan Overbeek, two of the founders of DLVO theory, stated that an ordered structure formed by tobacco mosaic viruses can be explained via DLVO theory.

This encyclopedia consists of 71 topics, which are ordered alphabetically. Each topic contains 1–4 review articles, so that there are a total of 89 review articles.

Finally, I would like to gratefully acknowledge the assistance provided by Ms. Anita Lekhwani, Senior Acquisitions Editor at John Wiley and Sons.

HIROYUKI OHSHIMA

ENCYCLOPEDIA OF BIOCOLLOID AND BIOINTERFACE SCIENCE

ENCYCLOPEDIA OF BIOCOLLOID AND BIOINTERFACE SCIENCE

VOLUME 2

Edited by

HIROYUKI OHSHIMA

WILEY

Copyright © 2016 by John Wiley & Sons, Inc. All rights reserved

Published by John Wiley & Sons, Inc., Hoboken, New Jersey
Published simultaneously in Canada

No part of this publication may be reproduced, stored in a retrieval system, or transmitted in any form or by any means, electronic, mechanical, photocopying, recording, scanning, or otherwise, except as permitted under Section 107 or 108 of the 1976 United States Copyright Act, without either the prior written permission of the Publisher, or authorization through payment of the appropriate per-copy fee to the Copyright Clearance Center, Inc., 222 Rosewood Drive, Danvers, MA 01923, (978) 750-8400, fax (978) 750-4470, or on the web at www.copyright.com. Requests to the Publisher for permission should be addressed to the Permissions Department, John Wiley & Sons, Inc., 111 River Street, Hoboken, NJ 07030, (201) 748-6011, fax (201) 748-6008, or online at http://www.wiley.com/go/permission.

Limit of Liability/Disclaimer of Warranty: While the publisher and author have used their best efforts in preparing this book, they make no representations or warranties with respect to the accuracy or completeness of the contents of this book and specifically disclaim any implied warranties of merchantability or fitness for a particular purpose. No warranty may be created or extended by sales representatives or written sales materials. The advice and strategies contained herein may not be suitable for your situation. You should consult with a professional where appropriate. Neither the publisher nor the author shall be liable for any loss of profit or any other commercial damages, including but not limited to special, incidental, consequential, or other damages.

For general information on our other products and services or for technical support, please contact our Customer Care Department within the United States at (800) 762-2974, outside the United States at (317) 572-3993 or fax (317) 572-4002.

Wiley also publishes its books in a variety of electronic formats. Some content that appears in print may not be available in electronic formats. For more information about Wiley products, visit our website at www.wiley.com.

Library of Congress Cataloging-in-Publication Data

Names: Ohshima, Hiroyuki, 1944– editor.
Title: Encyclopedia of biocolloid and biointerface science / edited by Hiroyuki Ohshima.
Description: Hoboken, New Jersey : John Wiley & Sons, Inc., 2016– | Includes index.
Identifiers: LCCN 2016004182 | ISBN 9781118542767 (set) | ISBN 9781118542675 (cloth : v. 2)
Subjects: LCSH: Biocolloids–Encyclopedias. | Biological interfaces–Encyclopedias. | Surface chemistry–Encyclopedias.
Classification: LCC QD549 .E53 2016 | DDC 547/.134503–dc23 LC record available at http://lccn.loc.gov/2016004182

10 9 8 7 6 5 4 3 2 1

1 2016

CONTENTS

List of Contributors **xxi**

Preface **xxvii**

I

Insulin

46 Insulin Fibrillation and Role of Peptides and Small Molecules in its Inhibition Process **575**

Victor Banerjee and K.P. Das

46.1 Introduction, 575
46.1.1 Protein Fibrillation, 575
46.1.2 Diseases Associated with Protein Fibrillation, 575
46.1.3 Fibrillation of Insulin, 576
46.2 Prevention of Insulin Fibrillation, 580
46.2.1 General Strategies to Prevent Insulin Fibrillation, 580
46.2.2 Peptide-Based Inhibitors of Insulin Fibrillation, 580
46.2.3 Small Molecule Inhibitors of Insulin Fibrillation, 585
46.3 Summary and Conclusion, 588
References, 588

Interfacial Water

47 Interfacial Water Between Charge-Neutralized Polymer and Liquid Water **592**

Hiromi Kitano and Makoto Gemmei-Ide

47.1 Introduction, 592
47.2 Polymer Film Systems, 592
47.3 Zwitterionic Polymer Brush System, 595
47.4 Amphoteric Polymer Brush System, 596
47.5 Conclusion, 596
References, 596

L

Langmuir Monolayer Interaction

48 Langmuir Monolayer Interaction of Perfluorooctylated Long-Chain Alcohols With Biomembrane Constituents **597**
Hiromichi Nakahara and Osamu Shibata

48.1 Introduction, 597
48.2 Thermal Properties of *F*8*Hm*OH, 597
48.3 Langmuir Monolayer Behavior of *F*8*Hm*OH, 598
48.4 Binary Monolayers of DPPC and *F*8*Hm*OH, 599
48.4.1 The π–A and ΔV–A Isotherms, 599
48.4.2 Excess Gibbs Free Energy, 599
48.4.3 Two-Dimensional Phase Diagram, 601
48.4.4 Brewster Angle Microscopy (BAM), 602
48.4.5 Fluorescence Microscopy (FM), 603
48.4.6 Atomic Force microscopy (AFM), 604
48.5 Miscibility of *F*8*Hm*OH With Lipids, 605
48.6 Conclusions and Perspectives, 606
References, 606

Latex

49 Affinity Latex **609**
Haruma Kawaguchi

49.1 Introduction, 609
49.1.1 Bioseparation, 609
49.1.2 Affinity Chromatography, 609
49.2 Immunolatex, 610
49.3 Materials Composing Affinity Latex, 610
49.3.1 Latex Particle as a Ligand Carrier, 610
49.3.2 Procedure for Binding Ligands to a Latex Particle Surface, 610
49.3.3 Binding Site of Ligand Molecule, 611
49.4 Comparison Between Affinity Column Chromatography and Affinity Latex, 611
49.5 Features of Affinity Latex, 611
49.5.1 Specific Base Sequence ssDNA-Carrying Affinity Latex, 611
49.5.2 Speedy Recovery of Target-Capturing Affinity Particles, 612
49.6 Novel Affinity Latex, 613
49.6.1 Capture and Cutting Affinity Latex, 613
49.6.2 Affinity Latex for the Detection of Telomerase, 613
49.7 Concluding Remarks and Future Prospects, 613
References, 613

50 Latex Diagnosis **614**
Haruma Kawaguchi

50.1 Introduction, 614
50.2 Materials Composing Immunolatex, 614
50.2.1 Antigen and Antibody, 614
50.2.2 Latex Particle, 614
50.3 Design of Immnolatex, 614
50.3.1 Hemagglutination, 614
50.3.2 Use of Latex Particle as Carrier of Immunocomponents, 615
50.3.3 Improvement of Immunolatex in Terms of Sensitization Mode, 615

50.4 Measurement of Agglutination, 616
50.4.1 Patterns of Agglutination Test, 616
50.4.2 Antigen Excess Zone, 617
50.5 Latex Diagnostics Independent from Agglutination, 617
50.6 Multiplex Assay Using Affinity Latex, 618
50.7 Concluding Remarks and Future Prospects, 618
References, 618

Light Scattering

51 Light Scattering and Electrophoretic Light Scattering of Biopolymers 619
Etsuo Kokufuta

51.1 Introduction, 619
51.2 Static Light Scattering, 619
51.3 Dynamic Light Scattering, 620
51.4 Electrophoretic Light Scattering, 623
51.5 Discussion and Conclusion, 624
References, 627

Line Tension

52 Impact of Line Tension on Colloidal Systems 628
Hiroki Matsubara, Takanori Takiue, and Makoto Aratono

52.1 Introduction, 628
52.2 Domains in Langmuir Monolayers, 628
52.3 Modification of Domain Line Tension, 630
52.4 Vesicles, 631
52.5 Line Tension at Wetting Transitions, 633
52.6 Particles at Liquid Surfaces, 636
52.7 Foam Films, 637
52.8 Summary, 639
References, 639

Lipid

53 Liquid Structures and Properties of Lipids 642
Makio Iwahashi

53.1 Introduction, 642
53.2 Comparison of Alcohols with Their Corresponding Fatty Acids in Their Aggregated Structures and Properties, 642
53.2.1 Density and Molar Volume, 642
53.2.2 Viscosity of Fatty Acids and Alcohols, 643
53.3 Aggregation Number of Alcohol and Stability of Fatty Acid Dimer, 645
53.3.1 Effect of Molecular Structure on Aggregation Number of Alcohol in CCl_4 and in Its Pure Liquid, 645
53.3.2 Stability of Fatty-Acid Dimers in CCl_4 and in the Pure Liquid State (Melt), 646
53.4 Intra- or Intermolecular Movements of Lipids, 647
53.4.1 Segmental Movements (Intramolecular Movements), 647
53.4.2 Intermolecular (Transfer) Movements and Apparent Hydrodynamic Radius for Alkane, Alcohol, Fatty Acid, and Fatty-Acid Ester, 649

53.5 Liquid Structures of Fatty Acids, 650
53.5.1 Fatty Acid Having a Longer Hydrocarbon Chain, 650
53.5.2 Fatty Acid Having a Medium Hydrocarbon Chain, 651
53.6 Effect of Cholesterol and Other Additives on the Cluster Structure and Properties of Oleic Acid, 652
53.7 Aggregated Structures and Properties of Acylglycerols, 655
53.7.1 Triacylglycerols, 655
53.7.2 Diacylglycerols, 655
53.7.3 Monoacylglycerol, 655
53.8 New Application of Fatty-Acid Esters, 656
53.8.1 Application of Fatty-Acid Ester as Insulating Oil in Transformers, 656
53.8.2 An Application of Fatty-Acid Ester for Hepatoma Operation Using a Microcatheter, 656
References, 658

Lipid Bilayer Membrane

54 Birefringence in Lipid Bilayer Membranes 661
Kiyoshi Mishima

54.1 Introduction, 661
54.2 Birefringence in Uniaxial Crystals, 661
54.3 Birefringence in Lipid Bilayers, 663
54.4 Interference with Birefringent Materials, 664
54.5 Birefringence Techniques for Analyzing Lipid Bilayer Membranes, 666
54.5.1 Dual-Polarization Interferometry (DPI), 667
54.5.2 Optical Waveguide Lightmode Spectroscopy (OWLS), 668
54.5.3 Coupled Plasmon–Waveguide Resonance (CPWR), 668
54.5.4 Polarized Transmitted Light Spectroscopy (PTL), 669
References, 672

Lipid Monolayer

55 Surface States of Lipid Monolayers Containing Gangliosides 674
Shoko Yokoyama

55.1 Introduction, 674
55.2 Experimental Materials, 674
55.3 Measurement of Surface Pressure, 674
55.4 Preparation of LB Film, 675
55.5 AFM Observation, 675
55.6 Results and Discussion, 675
55.6.1 Single System of Ganglioside Monolayer, 675
55.6.2 Binary System of Ganglioside–Phospholipid, 675
55.6.3 Ternary System of Ganglioside/DPPC/DOPC, 676
55.6.4 Ternary System of Ganglioside/DPPC/Chol, 679
55.6.5 Quaternary System of Ganglioside/DPPC/DOPC/Chol, 680
55.6.6 Five-Component System of Gangliosides/DPPC/DOPC/Chol, 681
55.7 Conclusion, 683
References, 683

Liponano-capsule

56 Liponanocapsule: A Nanocapsule Built From a Liposomal Template 684
Yuuka Fukui and Keiji Fujimoto

56.1 Introduction, 684
56.2 Multilayer Coating to Produce *Liponanocapsule*, 685
56.3 Release Behavior of Liponanocapsules, 685
56.4 Interaction of Liponano Capsules with Cells, 686
56.5 Assembly of Liponanocapsules to Create Freestanding Bioscaffold, 686
56.6 Coating with Minerals to Prepare Organic–Inorganic Hybrid Liponanocapsule, 687
56.7 Conclusions, 688
References, 688

M

Magnetic Suspension

57 Physical Phenomena of Magnetic Suspensions for Application to Bioengineering 690
Akira Satoh

57.1 Introduction, 690
57.2 Simulation Methods for Colloidal Suspensions, 691
57.2.1 Monte Carlo Method, 691
57.2.2 Brownian Dynamics Method for Axisymmetric Particles, 692
57.3 Surface Modification, 693
57.3.1 Magnetic Spherical Particle System, 693
57.3.2 Rodlike Particle System, 695
57.3.3 Disklike Particle System, 696
57.4 Sedimentation, 699
57.4.1 Introductory Remarks, 699
57.4.2 Particle Model and Simulation Method, 700
57.4.3 Results and Discussion, 700
57.5 Conclusion, 701
References, 702

Membrane Electrode

58 Ion-Sensing Membrane Electrodes in Study of Surfactant–Biopolymer Interaction 704
Sudeshna M. Chatterjea, Koustubh Panda, and Satya P. Moulik

58.1 Introduction, 704
58.2 Development of Surfactant Ion-Selective Electrodes (SISEs), 705
58.2.1 Liquid Membrane Electrodes (LMEs), 705
58.2.2 PVC-Based ISEs, 706
58.3 Study of Surfactant Biopolymer Systems Using SISEs, 710
58.3.1 Interactions between Ionic Surfactants and Biopolymers, 711
58.3.2 Kinetic Studies of Surfactant–Biopolymer Interactions Using SISEs, 714
58.4 Conclusion, 714
Acknowledgment, 715
References, 715

Membrane Potential

59 Membrane Potential as a Function of Dielectric Constant **721**
Akihiko Tanioka and Hidetoshi Matsumoto

59.1 Introduction, 721
59.2 Theoretical Background, 722
59.2.1 Donnan Potential, 722
59.2.2 Membrane Diffusion Potential, 723
59.2.3 Mean Activity Coefficient in Mixed Solvent–Salt Systems, 723
59.2.4 Membrane Potential, 723
59.2.5 Effective Membrane Charge Density, 723
59.2.6 Permeability Coefficient, 725
59.2.7 Mobility of Ions in a Membrane, 725
59.3 Materials and Experimental Procedures, 726
59.3.1 Materials, 726
59.3.2 Potentiometric Titration and Measurement of Equilibrium Water Content, 727
59.3.3 Membrane Potential Measurements, 727
59.3.4 Measurement of Modified Degree of Hydration, 727
59.3.5 Measurement of Permeability Coefficient, 727
59.4 Results and Discussion, 728
59.4.1 Organic Solution System, 728
59.4.2 Low-Water-Content System, 731
References, 734

Micellar Protein Alpha-crystalline

60 Biophysical Studies of a Micellar Protein α-Crystallin by Fluorescence Methods **737**
Aritra Chowdhury, Rajat Banerjee, and K.P. Das

60.1 α-Crystallin, 737
60.2 A Brief Introduction to Fluorescence in Proteins, 737
60.3 Challenges in Determining α-Crystallin Structure and Preliminary Structural Models Based on Micellar Architecture, 738
60.4 Hydrophobicity of α-Crystallin and Its Chaperone Function, 738
60.5 Effect of Temperature on Chaperone Function of α-Crystallin, 740
60.6 Identification of Chaperone Sites of α-Crystallin Using Hydrophobic Fluorophores, 741
60.7 Substrate Conformation Recognized by α-Crystallin: Comparison with Other Chaperones, 741
60.8 Subunit Exchange of α-Crystallin and Its Diverse Role, 743
60.9 Oligomeric Assembly and Unfolding of α-Crystallin, 746
60.10 Summary and Conclusions, 750
References, 751

Muscle Contraction

61 Modeling Muscle Contraction Mechanism in Accordance with Sliding-Filament Theory **753**
Toshio Mitsui and Hiroyuki Ohshima

61.1 Introduction, 753
61.2 Muscle Structures and the Sliding-Filament Theory, 753

61.3 Thermodynamic Relationship that any Models Based on Sliding-Filament Theory Should Fulfill, 754
61.3.1 Work Done by One Crossbridge Using ATP Hydrolysis energy, 755
61.3.2 Relation between p and T in Sliding-Filament Theory, 755
61.3.3 Thermodynamic Relationship, 756
61.3.4 Values of D/r Estimated from Literature Data, 757
61.4 Difficulties of the Power Stroke Model, 757
61.4.1 Difficulty Concerning Magnitude of r, 757
61.4.2 Values of r and D Estimated from Experimental Data, 757
61.5 Requirements for any Models Based on Sliding-Filament Theory, 758
61.6 Construction of a New Model, 758
61.6.1 Formation of Complex MA_3 by a Myosin Head and Three Actin Molecules, 758
61.6.2 Molecular Model for MA_3, 759
61.6.3 Cooperative Interaction among Crossbridges, 759
61.6.4 Chemical Reactions and Energy Liberation Associated with Force Production, 762
61.6.5 Role of Thermal Fluctuations, 763
61.7 Characteristics of the Model That are Helpful for Numerical Calculations, 763
61.7.1 Relation between p and T, 763
61.7.2 Cyclic Force Generation and Parameter y_c, 763
61.8 Comparison of Calculation Results with Experimental Data, 764
61.8.1 Existence Probability of Myosin Molecule in Wells in MA_3, 764
61.8.2 Steady Filament Sliding, 764
61.8.3 Transition Phenomena, 766
61.9 Summary and Discussion, 768
61.9.1 Requirements for Models, 768
61.9.2 Discussion, 769
References, 769

N

Nanocarrier

62 Nanocarriers of Functional Materials From Amino Acid Surfactants 771
Geetha Baskar, S. Angayarkanny, and Asit Baran Mandal

62.1 Introduction, 771
62.2 Self-Assembly and Aggregated Structures, 772
62.2.1 Self-Aggregated Structure Formation in Simple Amphiphiles, 772
62.2.2 Different Chemical Architectures in Surfactants, 773
62.3 Polymeric Amphiphiles, 774
62.3.1 Architectures and Formation of Self-Aggregated Structures in Polymeric Amphiphiles, 774
62.3.2 Self-Organisation in Graft Polymers and Other Polymeric Amphiphiles, 774
62.4 Amino Acid Surfactants, 775
62.4.1 Highlights of Unique Characteristics of Amino Acid Surfactants, 775
62.4.2 Types of Amino Acid Surfactants, 775
62.4.3 Self-Assembled Structure Formation in Amino Acid Surfactants, 776
62.4.4 Polymeric Amphiphiles from Amino Acids, 777
62.5 Polymeric Nanocarriers in Pharmaceutical and Other Applications, 778
62.5.1 Polymeric Nanoparticles, 779
62.5.2 Amino Acid Templates for Synthesis of Nanoparticles, 779

62.6 Summary, 780
Acknowledgments, 780
References, 780

Nanocolloid

63 Syntheses of Metallic Nanocolloids and the Quenching Abilities of Reactive Oxygen Species **784**
Yukihide Shiraishi and Naoki Toshima

63.1 Introduction, 784
63.2 Monometallic Nanocolloids, 785
63.2.1 Preparation of Monometallic Nanocolloids, 785
63.2.2 Characterization of Metallic Nanocolloids, 786
63.2.3 Application to Reactive Oxygen Species (ROS) Scavengers by Monometallic Nanocolloids, 786
63.3 Bimetallic Nanocolloids, 787
63.3.1 Preparation of Bimetallic Nanocolloids, 787
63.3.2 Application to ROS Species Scavengers by Bimetallic Nanocolloids, 788
Acknowledgments, 789
References, 789

Nanocomposite

64 Silver and Gold Nanocomposites: Amino Acid Sidechain Effect on Morphology **790**
Zoya Zaheer and Rafiuddin

64.1 Introduction, 790
64.2 Role of Sidechain, 791
64.3 Mechanism in the Formation of Silver Nanoparticles, 792
References, 796

Nanogel

65 Nanogel, an Internally Networked Poly(Amino Acid) Nanoparticle for pH-Responsive Delivery **799**
Jong-Duk Kim and Chan Woo Park

65.1 Introduction, 799
65.1.1 pH Sensitivity of Nanogels, 799
65.1.2 Modified Poly(amino acid)s, 800
65.2 Preparation of Poly(Amino Acid) Nanogels, 801
65.2.1 Physical Association, 801
65.2.2 Chemical Cross-Linking of Poly(amino acid)s, 801
65.2.3 Morphology of Nanogels prepared from Amphiphilic Polymers, 804
65.3 Structure and Characteristics of Nanogel, 805
65.3.1 Shape and Size, 805
65.3.2 Internal Structure, 806
65.3.3 Swelling of Nanogel, 808
65.4 pH-Responsive Nanogels, 808
65.4.1 pH-Sensitive Property of Nanogels, 808
65.4.2 pH-Responsive Release of Payloads from Nanogels, 809

65.5 Conclusions, 810
References, 810

Nanoparticle

66 Strategies of Metal Nanoparticles for Nanobiology 812
Daisuke Matsukuma and Hidenori Otsuka

66.1 Introduction, 812
66.2 Metal Nanoparticles, 812
66.2.1 Basic Key Aspects of Metal Nanoparticles for Nanobiology, 813
66.2.2 Noble Metal Nanoparticle, 813
66.2.3 Quantum Dots, 813
66.2.4 Magnetic Nanoparticles, 814
66.3 Bioconjugation of Metal Nanoparticles for Nanobiology, 814
66.4 Surface Modification of Metal Nanoparticles by Functional Polymers, 815
66.4.1 Natural Polymer Coating of Nanoparticles, 815
66.4.2 Synthetic Polymer Coating of Nanoparticles, 815
66.4.3 Structural Regulated Copolymer for Coating Agent, 816
66.5 Reducing Polymers Act as Dispersants for Nanoparticles, 817
66.6 Conclusion, 818
References, 818

O

On-chip Electrophoresis

67 On-Chip Electrophoresis for Evaluating Zeta-Potential of Nanoliposomes 821
Takanori Akagi and Takanori Ichiki

67.1 Introduction, 821
67.2 Nanoliposome Preparation, 821
67.3 Zeta-Potential Measurement System, 822
67.4 Calculation of Zeta-Potential of Liposomes, 822
67.5 Capillary Electrophoresis of Liposomes, 823
67.6 Conclusion, 824
References, 824

P

Phase Separation

68 Phase Separation in Phospholipid Bilayers Induced by Cholesterol 825
Nobutake Tamai, Masaki Goto, and Hitoshi Matsuki

68.1 Introduction, 825
68.2 Historical Background, 826
68.3 Solid–Liquid Phase Diagrams of Binary Mixtures, 827
68.4 Phase Transitions of C*n*PC–Cholesterol Binary Bilayers, 829
68.4.1 Prodan Fluorescence Spectra of Pure and Cholesterol-Containing CnPC Bilayers, 829
68.4.2 Characterization of Phase Transitions of CnPC–Cholesterol Binary Bilayers by DSC, 830
68.5 Phase Diagrams of C*n*PC–Cholesterol Binary Bilayers, 833

68.6 Acyl Chain Length Dependence of Characteristic Cholesterol Compositions, 836
68.7 Summary, 838
References, 838

69 Phase Separation Phenomena in Drug Systems 841
Andleeb Z. Naqvi and Kabir-ud-Din

69.1 Introduction, 841
69.2 Drug-DDS Interactions: Effect of Temperature on Solution, 842
69.2.1 Effect of pH/Concentration, 844
69.2.2 Effect of Electrolytes, 845
69.2.3 Effect of Urea/Thiourea, 846
69.2.4 Effect of Alcohols, 847
69.2.5 Effect of Amines, 848
69.2.6 Effect of Amino Acids, 848
69.2.7 Effect of Sugars, 849
69.2.8 Effect of Polymers, 850
69.2.9 Effect of Surfactants, 850
69.2.10 Effect of Fatty Acids (Sodium Salts), 852
69.2.11 Effect of Bile Salts, 852
69.2.12 Effect of Hydrotropes, 853
69.2.13 Effect of Cyclodextrins, 853
69.2.14 Effect of Phospholipids, 854
References, 854

Phosphatidylcholine

70 Bilayer Imaging of Phosphatidylcholines by High-Pressure Fluorometry 860
Masaki Goto, Nobutake Tamai, and Hitoshi Matsuki

70.1 Introduction, 860
70.2 Prodan Fluorescence Spectra, 860
70.2.1 Fluorescence Measurements, 860
70.2.2 Location of Prodan Distributed in PC Bilayer Membranes, 861
70.3 Factors Affecting the Packing State in the PC Bilayer, 862
70.3.1 Effect of Acyl Chain Length, 862
70.3.2 Effect of Vesicle Size, 863
70.3.3 Effect of Acyl Chain Asymmetry, 865
70.4 Packing State in the L_c Phase, 866
70.5 Conclusions, 868
Acknowledgments, 868
References, 868

Plant-responding Mechanism

71 Physiological and Molecular Aspects of Mechanisms Involved in Plant Response to Salt Stress 870
Xiaoli Tang, Xingmin Mu, Hongbo Shao, Hongyan Wang, and Marian Brestic

71.1 Introduction, 870
71.2 Growth and Photosynthesis, 871
71.3 Osmotic Stress Effects and Tolerance, 872
71.4 Ion Toxicity and Ion Homeostasis, 872
71.5 Oxidative Stress and Antioxidant Defense Responses, 875

71.6 Phytohormone in Salt Stress, 876
71.7 Conclusions, 876
Acknowledgments, 878
References, 878

Pulmonary Surfactant

72 Interfacial Phenomena of Pulmonary Surfactant Preparations 885
Hiromichi Nakahara, Sannamu Lee, and Osamu Shibata

72.1 Introduction, 885
72.2 Isotherm Behavior of the Lipids and Peptide, 886
72.3 Interaction Between the Lipids and Peptide, 888
72.4 Hysteresis in $\pi-A$ and $\Delta V-A$ Isotherms, 890
72.5 Morphological Phase Behavior, 891
72.5.1 Fluorescence Microscopy (FM), 891
72.5.2 Atomic Force Microscopy (AFM), 892
72.6 Polarized ATR-FTIR Spectra, 894
72.7 PM-IRRAS Spectra at the Air–Water Interface, 895
72.7.1 The in situ PM-IRRAS Spectra in the Amide Region, 895
72.7.2 Secondary Structure Transformation of Hel 13–5, 897
72.7.3 Lipid Stretching Vibration Modes, 898
72.8 Conclusions, 901
References, 902

73 Using Thin Liquid Film for Study of Pulmonary Surfactants 905
Dotchi Exerowa, Roumen Todorov, and Dimo Platikanov

73.1 Introduction, 905
73.2 Experimental Technique, 905
73.3 Physicochemical Properties Studied by the Thin Liquid Film Method, 907
73.4 Pulmonary Surfactants, 909
73.5 Method for Lung Maturity Assessment, 909
73.6 Foam Films from Pulmonary Surfactant and Its Components, 910
73.7 Thin Liquid Wetting Films from Pulmonary Surfactant Solutions, 912
73.8 Conclusion, 913
References, 913

R

Receptor-ligand Interaction

74 Probing Receptor–Ligand Interactions on a *Single* Molecule Level Using Optical Tweezers 915
Tim Stangner, Carolin Wagner, Christof Gutsche, Konstanze Stangner, David Singer, Stefano Angioletti-Uberti, and Friedrich Kremer

74.1 Introduction, 915
74.2 Methodology, 916
74.2.1 The Setup, 916
74.2.2 Trapping Basics and Force Calculation, 917
74.2.3 Position Detection in Three Dimensions, 917
74.2.4 Other Methods for Characterizing Receptor–Ligand Interactions, 920

74.3 Theoretical Description of Receptor–Ligand Interactions, 921
74.3.1 An Ideal Bond, 921
74.3.2 Force-Induced Bond Rupture: The Dudko—Hummer–Szabo Model, 922
74.4 Case Studies, 923
74.4.1 Measurement Procedure, 923
74.4.2 Ensuring Single Binding Events and Specificity, 924
74.4.3 Reducing the Data Variance in Dynamic Force Spectroscopy Measurements Using Presorted Particles, 924
74.4.4 Dynamic Force Spectroscopy on the Binding of Monoclonal Antibodies and τ-Peptides, 926
74.4.5 Determining the Specificity of a Monoclonal Antibody Using Dynamic Force Spectroscopy, 927
74.5 Conclusion, 929
References, 929

S

Soft Particle

75 AC Electrokinetics of Concentrated Suspensions of Soft and Hairy Nanoparticles: Model and Experiments 933
Silvia Ahualli, Ángel V. Delgado, Félix Carrique, and María Luisa Jiménez

75.1 Introduction, 933
75.2 Basic Equations, 934
75.2.1 General Overview and Notation Used, 934
75.2.2 The Case of Grafted Polymer: Spherical Polyelectrolyte Brushes (SPBs), 937
75.2.3 Expressions for Electrophoretic Mobility and Permittivity of the Suspension, 937
75.3 Some Predictions, 938
75.3.1 Soft Particles, 938
75.3.2 Brushlike Particles, 939
75.4 Experimental Verification, 941
75.4.1 Soft Particles, 941
75.4.2 Polyelectrolyte Brushes, 941
75.5 Conclusion, 943
Acknowledgment, 944
References, 944

76 Electrophoretic Behavior of pH-Regulated Soft Biocolloids 946
Li-Hsien Yeh and Jyh-Ping Hsu

76.1 Introduction, 946
76.2 Theoretical Model, 947
76.2.1 General Electrokinetic Equations, 947
76.2.2 Boundary Conditions, 948
76.2.3 Forces Acting on a Soft Particle, 948
76.2.4 Perturbation Approach, 949
76.3 Electrophoresis of a pH-Regulated Soft Biocolloid, 950
76.3.1 Governing Equations, 951
76.3.2 Boundary Conditions, 952
76.3.3 Solution Procedure, 952

76.3.4 Model Validation by Experimental Data, 953
76.3.5 Electrokinetics of a pH-Regulated Soft Biocolloid, 955
76.4 Summary, 956
76.5 Notations, 957
Greek Letters, 958
Superscripts, 959
Subscripts, 959
Prefix, 959
References, 959

77 Electrophoretic Mobility of Soft Particles 961
Kimiko Makino and Hiroyuki Ohshima

77.1 Introduction, 961
77.2 Electrophoretic Mobility of Hard Particles, 961
77.3 Electrophoretic Mobility of Soft Particles, 962
77.4 Analysis of Electrophoretic Mobility of Soft Particles, 965
77.4.1 RAW117 Lymphosarcoma Cells and Their Variants, 965
77.4.2 Poly(*N*-isopropylacrylamide) Hydrogel–Coated Latex, 966
77.5 Electrophoresis of Nonuniformly Charged Soft Particles, 967
References, 968

78 Potential Distribution Around a Hard Particle and a Soft Particle 970
Hiroyuki Ohshima

78.1 Introduction, 970
78.2 Hard Particles, 970
78.3 Soft Particles, 974
78.4 Discrete-Charge Effect, 975
References, 978

Soil

79 Soil Interfacial Electrical Phenomena 979
Munehide Ishiguro

79.1 Introduction, 979
79.2 Ion Transport in Soils, 979
79.2.1 Influence of Electric Charge on Ion Transport, 979
79.2.2 Influence of Selectivity Coefficient, Distribution Ratio, and Peclet Number on Ion Transport, 982
79.3 Soil Dispersion and Flocculation, 983
79.4 Influence of Dispersion on Soil Permeability, 985
79.5 Surfactant Adsorption, 988
79.6 Ion Exclusion and Salt Sieving, 991
References, 992

Solid-water Interface

80 Pharmaceutical Solid–Water Interface Phenomena Measured by Near-Infrared Spectroscopy 994
Yusuke Hattori and Makoto Otsuka

80.1 Introduction, 994
80.2 Exploration of Interface Phenomena Using Near-Infrared Spectroscopy, 995

80.2.1 Initial Dissolution of Compressed Solids, 996
80.2.2 Hydration and Swelling of Disintegrating Agents: Two-Dimensional Correlation Spectroscopy (2DCOS), 998
80.3 Conclusion, 1001
References, 1002

Stability

81 Colloid Stability of Biocolloidal Dispersions 1004
Tharwat Tadros

81.1 Introduction, 1004
81.2 Kinetic Stability of Biocolloidal Dispersion Systems and General Stabilization Mechanisms, 1004
81.2.1 Electrostatic Stabilization, 1004
81.2.2 Steric Stabilization, 1006
81.3 Nanoemulsions, 1007
81.3.1 Preparation of Nanoemulsions, 1008
81.3.2 Steric Stabilisation and Role of Adsorbed Layer Thickness, 1008
81.3.3 Ostwald Ripening, 1009
81.4 Nanobiodegradable Dispersions, 1010
81.5 Liposomes and Vesicles in Pharmaceuticals, 1011
References, 1013

82 Stability Ratio and Early-Stage Aggregation Kinetics of Colloidal Dispersions 1014
Hiroyuki Ohshima

82.1 Introduction, 1014
82.2 DLVO Theory of Colloid Stability and the Stability Ratio, 1014
82.3 Approximate Analytic Expressions for the Stability Ratio W, 1016
82.4 Rate Equations for Early-Stage Aggregation Kinetics of Colloidal Particles, 1017
82.5 Approximate Solution to the Rate Equation, 1018
References, 1019

Surfactant

83 Catanionic Surfactants: Novel Surrogates of Phospholipids 1020
Kausik Manna and Amiya Kumar Panda

83.1 Introduction, 1020
83.2 Classifications, 1021
83.3 Preparation and Isolation, 1029
83.3.1 Extraction Method, 1029
83.3.2 Precipitation Method, 1029
83.3.3 Ion Exchange Method, 1029
83.3.4 Evaporation Method, 1029
83.3.5 Proton Exchange Method, 1029
83.4 Characterization of Isolated IPA, 1029
83.4.1 ^{1}H-NMR Spectroscopy, 1029
83.4.2 FT-IR Spectroscopy, 1030
83.4.3 X-Ray Diffraction Study, 1030

83.5 Properties, 1031
83.5.1 Properties of Catanionic Surfactants as Functions of Composition and Concentration, 1031
83.5.2 Properties of Isolated IPA, 1035
83.6 Catanionic Micelles, 1036
83.7 Catanionic Vesicles: Catanosomes, 1037
83.7.1 Preparation Methods, 1037
83.7.2 Stability of Catanosomes, 1038
83.8 Applications of IPA/Catanionic Surfactants, 1039
83.8.1 Drug Delivery, 1039
83.8.2 Templates for Nanomaterial Synthesis, 1040
83.9 Challenges and Future Perspectives, 1041
References, 1041

84 Phase Behavior of Natural-Sourced Surfactant Systems 1044
Kenji Aramaki

84.1 Introduction, 1044
84.2 Sugar-Based Surfactants, 1044
84.3 Glycerol-Based Surfactants, 1046
References, 1050

85 Surfactants and Biosurfactants 1051
Youichi Takata

85.1 Introduction, 1051
85.2 General Surfactants, 1051
85.2.1 Hydrophobic Group, 1051
85.2.2 Hydrophilic Group, 1052
85.2.3 Novel Surfactants, 1053
85.3 Biosurfactants, 1054
References, 1055

Surface Active Drug

86 Effect of Additives on Self-Association and Clouding Phenomena of Various Surface-Active Drugs 1056
Md. Sayem Alam and Asit Baran Mandal

86.1 Introduction, 1056
86.2 Surface Properties, Self-Association, and Mixed Micellization of Surface-Active Drugs with and Without Additives, 1059
86.3 Effect of Additives on Clouding Behavior of Amphiphilic Drug Solutions, 1062
86.3.1 Effect of pH, 1062
86.3.2 Effect of Electrolytes, 1062
86.3.3 Effect of Surfactants, 1064
86.3.4 Effect of Additives at Different Fixed pHs, 1064
86.3.5 Effect of Additives at Different Fixed Drug Concentrations, 1064
86.4 Thermodynamics at CP, 1065
86.4.1 Effect of Surfactants, 1066
86.5 Conclusions, 1067
Acknowledgment, 1067
References, 1067

T

Thermodynamic Analysis of Partial Molar Volume

87 Thermodynamic Analysis of Partial Molar Volume in Biocolloidal Systems **1071**

Michio Yamanaka, Hideyuki Maekawa, Tamaki Yasui, and Hitoshi Matsuki

87.1 Introduction, 1071
87.2 Definition of Partial Molar Volume and Elementary Thermodynamic Equations of the Volume Behavior of Solutions, 1072
87.3 Partial Molar Volumes in a Protein–Ligand System, 1073
87.4 Partial Molar Volume in Mixed Membrane Systems, 1079
87.4.1 Binary Mixtures of Water-Insoluble Lipids, 1082
87.4.2 Binary Mixtures of a Water-Insoluble Lipid and a Water-Soluble Substance, 1083
Acknowledgments, 1086
References, 1086

V

Van der Waals Interaction

88 Van Der Waals Interaction Between Colloidal Particles **1087**

Hiroyuki Ohshima

88.1 Introduction, 1087
88.2 Van Der Waals Interaction Between Two Molecules, 1087
88.3 Van Der Waals Interaction Between Two Colloidal Particles, 1088
88.4 Various Geometries, 1088
88.4.1 A Molecule and a Plate, 1088
88.4.2 Two Parallel Plates, 1089
88.4.3 A Molecule and a Sphere, 1089
88.4.4 Two Spheres, 1089
88.4.5 A Molecule and a Rod, 1090
88.4.6 Two Parallel Rods, 1090
88.4.7 A Molecule and a Cylinder, 1090
88.4.8 Two Parallel Cylinders, 1090
88.4.9 Two Crossed Cylinders, 1091
88.4.10 Two Parallel Rings, 1091
88.4.11 Two Parallel Torus-Shaped Particles, 1091
88.4.12 Two Particles Immersed in a Medium, 1092
88.4.13 Two Parallel Plates Covered with Surface Layers, 1093
References, 1093

W

Wormlike Micelle

89 Wormlike Micelles with Nonionic Surfactants **1095**

Rekha Goswami Shrestha, Kenji Aramaki, Hideki Sakai, and Masahiko Abe

89.1 Introduction, 1095
89.2 Wormlike Micelles in Nonionic Surfactants, 1097
89.3 Conclusion, 1102
References, 1102

Index **1105**

LIST OF CONTRIBUTORS

Masahiko Abe, Department of Pure and Applied Chemistry, Faculty of Science and Technology, Tokyo University of Science, Chiba, Japan

Yasuhisa Adachi, Faculty of Life and Environmental Science, University of Tsukuba, Ibaraki, Japan

Silvia Ahualli, Department of Applied Physics, School of Sciences, Campus Fuentenueva, University of Granada, Granada, Spain

Takanori Akagi, Department of Bioengineering, Graduate School of Engineering, University of Tokyo, Bunkyo-ku, Tokyo, Japan

Md. Sayem Alam, Council of Scientific and Industrial Research (CSIR)—Central Leather Research Institute (CLRI), Industrial Chemistry Laboratory, Adyar, Chennai, India

Emil Alexov, Computational Biophysics and Bioinformatics, Physics Department, Clemson University, Clemson, South Carolina, United States

Shaeel Ahmed Al-Thabaiti, Department of Chemistry, Faculty of Science, King Abdulaziz University, Jeddah, Saudi Arabia

S. Angayarkanny, CSIR—Central Leather Research Institute (CLRI), Adyar, Chennai, India

Stefano Angioletti-Uberti, Department of Physics, Humboldt University Berlin, Berlin, Germany

Kenji Aramaki, Graduate School of Environment and Information Sciences, Yokohama National University, Hodogaya-ku, Yokohama, Japan

Makoto Aratono, Department of Chemistry, Faculty of Sciences, Kyushu University, Higashi-ku, Fukuoka, Japan

Rajat Banerjee, Department of Biotechnology and Dr. B.C. Guha Centre for Genetic Engineering and Biotechnology, University of Calcutta, Kolkata, India

Victor Banerjee, Department of Chemistry, Laboratory of Protein Chemistry, Bose Institute, Kolkata, West Bengal, India

Soumik Bardhan, Department of Chemistry, University of North Bengal, Darjeeling, India

Ommer Bashir, Department of Chemistry, Jamia Millia Islamia, Jamia Nagar, New Delhi, India

Geetha Baskar, CSIR—Central Leather Research Institute (CLRI), Adyar, Chennai, India

Avinash Bhadani, Department of Pure and Applied Chemistry, Faculty of Science and Technology, Tokyo University of Science, Noda, Chiba, Japan

Marian Brestic, Institute of Soil and Water Conservation, Northwest A&F University, Yangling, China and Department of Plant Physiology, Slovak Agricultural University, Nitra, Slovak Republic

Brandon Campbell, Computational Biophysics and Bioinformatics, Physics Department, Clemson University, Clemson, South Carolina, United States

Félix Carrique, Department of Applied Physics II, School of Sciences, Campus Teatinos, University of Málaga, Málaga, Spain

Gulmi Chakraborty, Department of Chemistry, University of North Bengal, Darjeeling, India

N. Chandrasekaran, Centre for Nano-Biotechnology, School of Bio-Sciences and Technology, VIT University, Vellore 632014, Tamil Nadu, India

Sudeshna M. Chatterjea, Department of Biotechnology and Dr. B.C. Guha Centre for Genetic Engineering and Biotechnology, University of Calcutta, Kolkata, West Bengal, India

Aritra Chowdhury, School of Chemistry, University of Manchester, Manchester, United Kingdom

K.P. Das, Department of Chemistry, Bose Institute, Kolkata, West Bengal, India

Swati De, Department of Chemistry, University of Kalyani, Kalyani, West Bengal, India

Ángel V. Delgado, Department of Applied Physics, School of Sciences, Campus Fuentenueva, University of Granada, Granada, Spain

Kabir-ud-Din, Department of Applied Chemistry, Aligarh Muslim University, Aligarh, India

Toshiaki Dobashi, Graduate School of Science and Technology, Gunma University, Gunma, Japan

Saheb Dutta, Department of Chemistry, University of Kalyani, Kalyani, West Bengal, India

Kazunaka Endo, Division of Colloid and Interface Science, Research Institute for Science and Technology, Tokyo University of Science, Kagurazaka, Shinjuku-ku, Tokyo, Japan

Dotchi Exerowa, Institute of Physical Chemistry, Bulgarian Academy of Sciences, Sofia, Bulgaria

Jens Friedrichs, Leibniz Institute of Polymer Research Dresden, Max Bergmann Center of Biomaterials Dresden, Dresden, Germany

Uwe Freudenberg, Leibniz Institute of Polymer Research Dresden, Max Bergmann Center of Biomaterials Dresden, Hohe Strasse 6, D-01069 Dresden, Germany; Technische Universität Dresden, Center for Regenerative Therapies Dresden, Tatzberg 47, 01307 Dresden, Germany

Keiji Fujimoto, The Center for Chemical Biology, School of Fundamental Science and Technology, Graduate School of Science and Technology, Keio University, Hiyoshi, Kohoku-ku, Yokohama, Japan

Fumio Fukai, Department of Molecular Patho-Physiology, Faculty of Pharmaceutical Sciences, Center for Drug Delivery Research, and Center for Physical Pharmacology, Research Institutes for Science and Technology, Tokyo University of Science, Noda, Chiba, Japan

Tomonori Fukasawa, Department of Chemical Engineering, Hiroshima University, Japan

Yuuka Fukui, The Center for Chemical Biology, School of Fundamental Science and Technology, Graduate School of Science and Technology, Keio University, Hiyoshi, Kohoku-ku, Yokohama, Japan

Makoto Gemmei-Ide, Department of Applied Chemistry, Graduate School of Science and Engineering, University of Toyama, Toyama, Japan

Masaki Goto, Department of Life System, Institute of Technology and Science, The University of Tokushima, Tokushima, Japan

Christof Gutsche, Department of Experimental Physics I, Leipzig University, Leipzig, Germany

Yusuke Hattori, Research Institute of Pharmaceutical Sciences, Musashino University, Shin machi, Nishitokyo, Tokyo, Japan

Hitoshi Hori, Department of Pharmacology, Faculty of Pharmaceutical Sciences, Niigata University of Pharmacy and Applied Life Sciences, Niigata, Japan and NDT Research Institute, Tokushima, Japan

Koji Horigome, Graduate School of Textile Science & Technology, Shinshu University, Ueda, Nagano, Japan

Yukichi Horiguchi, Graduate School of Pure and Applied Sciences, University of Tsukuba, Ten-noudai Tsukuba, Ibaraki, Japan

Jyh-Ping Hsu, Department of Chemical Engineering, National Taiwan University, Taipei, Taiwan, Republic of China

Shokit Hussain, Department of Chemistry, Jamia Millia Islamia, Jamia Nagar, New Delhi, India

Takanori Ichiki, Department of Bioengineering, Graduate School of Engineering, University of Tokyo, Bunkyo-ku, Tokyo, Japan

Makoto Gemmei-Idek, Department of Applied Chemistry, Graduate School of Science and Engineering, University of Toyama, Toyama, Japan

Toyoko Imae, Graduate Institute of Applied Science and Technology, National Taiwan University of Science and Technology, Taipei, Taiwan, Republic of China

Tomohiro Inaba, Graduate School of Life and Environmental Sciences, University of Tsukuba, Tsukuba, Ibaraki, Japan

Naoyuki Ishida, Department of Applied Chemistry and Biotechnology, Okayama University, Okayama, Japan

Munehide Ishiguro, Laboratory of Soil Conservation, Research Group of Regional Environment, Research Faculty of Agriculture, Hokkaido University, Sapporo, Japan

Fumiyoshi Ishii, Department of Pharmaceutical Sciences, Meiji Pharmaceutical University, Noshio, Kiyose, Tokyo, Japan

Makio Iwahashi, Department of Chemistry, School of Science, Kitasato University, Kitasato, Minami-ku, Sagamihara, Kanagawa-ken, Japan

Takuya Iyoda, Department of Molecular Patho-Physiology, Faculty of Pharmaceutical Sciences, and Center for Drug Delivery Research, Center for Physical Pharmacology, Research Institutes for Science and Technology, Tokyo University of Science, Noda, Chiba, Japan

S.N. Jaisankar, Polymer Division, CSIR—Central Leather Research Institute, Adyar, Chennai, Tamil Nadu, India

María Luisa Jiménez, Department of Applied Physics, School of Sciences, Campus Fuentenueva, University of Granada, Granada, Spain

Haruma Kawaguchi, Department of Chemistry, Faculty of Engineering, Kanagawa University, Yokohama, Japan

Zaheer Khan, Chemistry Department, Faculty of Science, King Abdulaziz University, P. O. Box 80203, Jeddah 21413, Saudi Arabia

Jong-Duk Kim, Department of Chemical and Biomolecular Engineering, KAIST, Yuseung-gu, Daejeon, Republic of Korea

Hiromi Kitano, Department of Applied Chemistry, Graduate School of Science and Engineering, University of Toyama, Toyama, Japan

Etsuo Kokufuta, Faculty of Life and Environmental Sciences, University of Tsukuba, Tsukuba, Ibaraki, Japan

Friedrich Kremer, Department of Experimental Physics I, Leipzig University, Leipzig, Germany

Kaushik Kundu, Surface and Colloid Science Laboratory, Geological Studies Unit, Indian Statistical Institute, Kolkata, India

Yung-Chih Kuo, Department of Chemical Engineering, National Chung Cheng University, Chia-Yi, Taiwan, Republic of China

Takuma Kureha, Graduate School of Textile Science & Technology, Shinshu University, Ueda, Nagano, Japan

Yasuyuki Kusaka, Flexible Electronics Research Center, National Institute of Advanced Industrial Science and Technology (AIST), Tsukuba, Ibaraki, Japan

Babette Lanfer, Leibniz Institute of Polymer Research Dresden, Max Bergmann Center of Biomaterials Dresden, Dresden, Germany

Chin-Lung Lee, Department of Chemical Engineering, National Chung Cheng University, Taiwan, Republic of China

Sannamu Lee, Department of Biophysical Chemistry, Faculty of Pharmaceutical Sciences, Nagasaki International University, Sasebo, Nagasaki, Japan

Lin Li, Computational Biophysics and Bioinformatics, Physics Department, Clemson University, Clemson, South Carolina, United States

Hideyuki Maekawa, Department of Chemistry, Faculty of Sciences, Kyushu University, Higashi-ku, Fukuoka, Japan

Kimiko Makino, Faculty of Pharmaceutical Sciences, Tokyo University of Science, Noda, Chiba, Japan

Abhishek Mandal, Centre for Nano-Biotechnology, School of Bio-Sciences and Technology, VIT University, Vellore 632014, Tamil Nadu, India

Asit Baran Mandal, Industrial Chemistry Laboratory, Council of Scientific and Industrial Research (CSIR) — Central Leather Research Institute (CLRI), Adyar, Chennai 600 020, India; Polymer Division and Chemical Laboratory, CSIR—Central Leather Research Institute, Adyar, Chennai, Tamil Nadu, India

Ranju Prasad Mandal, Department of Chemistry, University of Kalyani, Kalyani, West Bengal, India

Kausik Manna, Department of Chemistry, University of North Bengal, Darjeeling, West Bengal, India

Hiroki Matsubara, Department of Chemistry, Faculty of Sciences, Kyushu University, Higashi-ku Hakozaki, Fukuoka, Japan

Hitoshi Matsuki, Department of Life System, Institute of Technology and Science, The University of Tokushima, Tokushima, Japan

Daisuke Matsukuma, Faculty of Science Division I, Department of Applied Chemistry, Tokyo University of Science, Shinjuku-ku, Tokyo, Japan

Hidetoshi Matsumoto, Department of Organic and Polymeric Materials, Tokyo Institute of Technology, Meguro-ku, Tokyo, Japan

Takuya Matsunaga, Division of Endocrinology and Metabolism, Hematology Rheumatology and Respiratory Medicine, Department of Internal Medicine, Kagawa University, Kita-gun, Kagawa, Japan

K. Seeni Meera, Polymer Division, CSIR—Central Leather Research Institute, Adyar, Chennai, Tamil Nadu, India

Kiyoshi Mishima, Yorozu Kohboh, Dome, 2-2804-1 Makuhari Hanamigawa-ku, Chiba-shi, Chiba 262-0032, Japan

Toshio Mitsui, Graduate School of Engineering Science, Osaka University, 1-3 Toyonaka, Osaka, 560-8531, Japan

Hisao Morisaki, Graduate School of Life Sciences, Ritsumeikan University, Kusatsu, Shiga, Japan

Satya P. Moulik, Department of Chemistry, Center for Surface Science and Technology, Jadavpur University, Kolkata, West Bengal, India

Xingmin Mu, Institute of Soil and Water Conservation, Northwest A&F University,Yangling, China

Amitava Mukherjee, Centre for Nano-Biotechnology, School of Bio-Sciences and Technology, VIT University, Vellore 632014, Tamil Nadu, India

Teruo Murakami, Research Center for Advanced Biomechanics, Kyushu University, Nishi-ku, Fukuoka, Japan

R. Murali Sankar, Polymer Division, CSIR—Central Leather Research Institute, Adyar, Chennai, Tamil Nadu, India

Yukio Nagasaki, Graduate School of Pure and Applied Sciences and Master's School of Medical Sciences, University of Tsukuba, Tsukuba, Ibaraki, Japan, and Satellite Laboratory of International Center for Materials Nanoarchitectonics (WPI-MANA), National Institute of Materials Science (NIMS), Tsukuba, Ibaraki, Japan

Kenichi Nagase, Institute of Advanced Biomedical Engineering and Science, Tokyo Women's Medical University (TWIns), Shinjuku, Tokyo, Japan

Hiromichi Nakahara, Department of Biophysical Chemistry, Faculty of Pharmaceutical Sciences, Nagasaki International University, Sasebo, Nagasaki, Japan

Kazuho Nakamura, Faculty of Engineering, Yokohama National University, Hodgaya-ku Yokohama, Japan

Nilashis Nandi, Department of Chemistry, University of Kalyani, Kalyani, West Bengal, India

Andleeb Z. Naqvi, Department of Applied Chemistry, Aligarh Muslim University, Aligarh, India

Makoto Nishimoto, Department of Materials Science, Wakayama National College of Technology, Gobo, Wakayama, Japan

Kazuo Nomura, Department of Chemistry, Faculty of Science, Kyushu University, Higashi-ku, Fukuoka, Japan

Nobuhiko Nomura, Graduate School of Life and Environmental Sciences, University of Tsukuba, Tsukuba, Ibaraki, Japan

Hiroyuki Ohshima, Faculty of Pharmaceutical Sciences, Tokyo University of Science, Noda, Chiba, Japan

Emiko Okamura, Faculty of Pharmaceutical Sciences, Himeji Dokkyo University, Himeji, Japan

Teruo Okano, Institute of Advanced Biomedical Engineering and Science, Tokyo Women's Medical University (TWIns), Shinjuku, Tokyo, Japan

Tsuneo Okubo, Institute for Colloidal Organization, Uji, Kyoto, Japan

Hidenori Otsuka, Faculty of Science Division I, Department of Applied Chemistry, Tokyo University of Science, Shinjuku-ku, Tokyo, Japan

Makoto Otsuka, Research Institute of Pharmaceutical Sciences, Musashino University, Shin machi, Nishitokyo, Tokyo, Japan

Akira Otsuki, Université de Lorraine, GeoRessources UMR 7359 CNRS-CREGU, ENSG, Vandœuvre-lès-Nancy Cedex, France

Amiya Kumar Panda, Department of Chemistry, University of North Bengal, Darjeeling 734 013, West Bengal, India

Koustubh Panda, Department of Biotechnology and Dr. B.C. Guha Centre for Genetic Engineering and Biotechnology, University of Calcutta, Kolkata, West Bengal, India

Chan Woo Park, Department of Chemical and Biomolecular Engineering, KAIST, Yuseung-gu, Daejeon, Republic of Korea

Bidyut K. Paul, Surface and Colloid Science Laboratory, Geological Studies Unit, Indian Statistical Institute, Kolkata, India

Dimo Platikanov, Department of Physical Chemistry, University of Sofia, Sofia, Bulgaria

Rafiuddin, Department of Chemistry, Aligarh Muslim University, Aligarh, Uttar Pradesh, India

Swapan K. Saha, Department of Chemistry, University of North Bengal, Darjeeling, India

Hideki Sakai, Department of Pure and Applied Chemistry, Faculty of Science and Technology, Tokyo University of Science, Noda, Chiba, Japan

Kenichi Sakai, epartment of Pure and Applied Chemistry, Faculty of Science and Technology, Tokyo University of Science, Noda, Chiba, Japan

Kazutami Sakamoto, Department of Pharmaceutical and Life Sciences, Faculty of Pharmacy, Chiba Institute of Science, Choshi, Chiba, Japan

Thothapalli P. Sastry, Centre for Nano-Biotechnology, School of Bio-Sciences and Technology, VIT University,

Vellore 632014, Tamil Nadu, India; Bio-products Laboratory, CSIR-Central Leather Research Institute, Adyar, Chennai 600020, Tamil Nadu, India

Akira Satoh, Faculty of Systems Science and Technology, Akita Prefectural University, Honjo City, Akita Prefecture, Japan

Hongbo Shao, Institute of Soil and Water Conservation, Northwest A&F University,Yangling, China; Key Laboratory of Coastal Biology & Bioresources Utilization, Yantai Institute of Coastal Zone Research (YIC), Chinese Academy of Sciences (CAS), Yantai, China; and Institute for Life Sciences, Qingdao University of Science & Technology (QUST), Qingdao, China

Osamu Shibata, Department of Biophysical Chemistry, Faculty of Pharmaceutical Sciences, Nagasaki International University, Sasebo, Nagasaki, Japan

Ken-ichi Shimokawa, Department of Pharmaceutical Sciences, Meiji Pharmaceutical University, Kiyose, Tokyo, Japan

Hiroyuki Shinto, Department of Chemical Engineering, Faculty of Engineering, Fukuoka University, Jyounan-ku, Fukuoka, Japan

Yukihide Shiraishi, Department of Applied Chemistry, Tokyo University of Science, Yamaguchi, Sanyo Onoda-shi, Yamaguchi, Japan

Rekha Goswami Shrestha, Department of Pure and Applied Chemistry, Faculty of Science and Technology, Tokyo University of Science, Noda, Chiba, Japan

David Singer, Center for Biotechnology and Biomedicine (BBZ), Institute for Bioanalytical Chemistry, Leipzig University, Leipzig, Germany

Sukhprit Singh, Department of Chemistry, UGC Sponsored-Centre for Advance Studies I, Guru Nanak Dev University, Amritsar, India

Konstanze Stangner, Molecular Oncology, Medical School, Leipzig University, Leipzig, Germany

Tim Stangner, Department of Experimental Physics I, Leipzig University, Leipzig, Germany

Atsushi Suzuki, Department of Materials Science & Research Institute of Environment and Information Sciences, Yokohama National University, Hodogaya-ku, Yokohama, Japan

Daisuke Suzuki, Graduate School of Textile Science & Technology, Shinshu University, Ueda, Nagano, Japan

Tharwat Tadros, 89 Nash Grove Lane, Wokingham, Berkshire RG40 4HE, United Kingdom

Keijiro Taga, Department of Life and Materials Engineering, Nagoya Institute of Technology, Gokiso-cho, Showa-ku, Nagoya, Japan

Youichi Takata, Department of Chemical and Biological Engineering, Ube National College of Technology, Ube, Yamaguchi, Japan

Takanori Takiue, Department of Chemistry, Faculty of Sciences, Kyushu University, Higashi-ku Hakozaki, Fukuoka, Japan

Nobutake Tamai, Department of Life System, Institute of Technology and Science, The University of Tokushima, Tokushima, Japan

Masaru Tanaka, Biomaterials Science and Tissue Engineering Group, Department of Biochemical Engineering, and Department of Polymer Science and Engineering, Graduate School of Science and Engineering, Yamagata University, Yonezawa, Japan; Soft Materials Chemistry, Institute for Materials Chemistry and Engineering, Kyushu University, Fukuoka, Japan

Xiaoli Tang, Key Laboratory of Coastal Biology & Bioresources Utilization, Yantai Institute of Coastal Zone Research (YIC), Chinese Academy of Sciences (CAS), Yantai, China and University of Chinese Academy of Sciences, Beijing, China

Akihiko Tanioka, Department of Organic and Polymeric Materials, Tokyo Institute of Technology, Meguro-ku, Tokyo, Japan

Yosuke Tashiro, Graduate School of Engineering, Shizuoka University, Hamamatsu, Shizuoka, Japan

Hiroshi Terada, Department of Pharmacology, Faculty of Pharmaceutical Sciences, Niigata University of Pharmacy and Applied Life Sciences, Niigata, Japan

Roumen Todorov, Institute of Physical Chemistry, Bulgarian Academy of Sciences, Sofia, Bulgaria

Naoki Toshima, Department of Applied Chemistry, Tokyo University of Science Yamaguchi, Sanyo Onoda-shi, Yamaguchi, Japan

Masanori Toyofuku, Graduate School of Life and Environmental Sciences, University of Tsukuba, Tsukuba, Ibaraki, Japan

Ruey-Yug Tsay, Institute of Biomedical Engineering, National Yang-Ming University, Taipei, Taiwan, Republic of China

Carolin Wagner, Department of Experimental Physics I, Leipzig University, Leipzig, Germany

Hongyan Wang, Key Laboratory of Coastal Biology & Bioresources Utilization, Yantai Institute of Coastal Zone

Research (YIC), Chinese Academy of Sciences (CAS), Yantai, China and University of Chinese Academy of Sciences, Beijing, China

Carsten Werner, Leibniz Institute of Polymer Research Dresden, Max Bergmann Center of Biomaterials Dresden, Dresden, Germany, and Technische Universität Dresden, Center for Regenerative Therapies Dresden, Dresden, Germany

Takao Yamamoto, Graduate School of Science and Technology, Gunma University, Gunma, Japan

Yasushi Yamamoto, Department of Life and Materials Engineering, Nagoya Institute of Technology, Gokiso-cho, Showa-ku, Nagoya, Japan

Michio Yamanaka, Department of Chemistry, Faculty of Sciences, Kyushu University, Higashi-ku, Fukuoka, Japan

Yuji Yamashita, Department of Pharmaceutical and Life Sciences, Faculty of Pharmacy, Chiba Institute of Science, Choshi, Chiba, Japan

Tamaki Yasui, Department of Chemistry, Faculty of Sciences, Kyushu University, Higashi-ku, Fukuoka, Japan

Li-Hsien Yeh, Department of Chemical and Materials Engineering, National Yunlin University of Science and Technology, Yunlin, Taiwan

Shoko Yokoyama, School of Pharmaceutical Sciences, Kyushu University of Health and Welfare, Miyazaki, Japan

Eri Yoshida, Department of Environmental and Life Sciences, Toyohashi University of Technology, Tempaku-cho, Toyohashi, Aichi, Japan

Zoya Zaheer, Department of Chemistry, Aligarh Muslim University, Aligarh, Uttar Pradesh, India

Ralf Zimmermann, Leibniz Institute of Polymer Research Dresden, Max Bergmann Center of Biomaterials Dresden, Dresden, Germany

PREFACE

The principal aim of this encyclopedia is to provide a physicochemical tool for interpreting various biological phenomena in terms of a language of colloid and interface science. The present book concentrates on subjects in the field of biocolloid and biointerface science, since there are already excellent encyclopedias on colloid and interface science available in the literature. This field is the youngest—but is becoming a very important—branch in the area in colloid and interface science. Actually, however, colloid and interface science has been closely related to biological science. Colloids, or more specifically, colloidal particles with diameters ranging from 1 to 1000 nm, which are one of the major subjects in colloid and interface science, can be found quite often in biological systems as biocolloids such as biological cells. Surfactant molecules, which are also one of the most important subjects in colloid and interface science, adsorb at interfaces between two immiscible media (e.g., water and oil), forming micelles and vesicles, which are a prototype of living cells. The Derjaguin–Landau–Verwey–Overbeek (DLVO) theory explains well the stability of colloidal suspensions in terms of the electrostatic and van der Waals interactions between the particles. In their book *Theory of Stability of Lyophobic Colloids*, Evert Verwey and Jan Overbeek, two of the founders of DLVO theory, stated that an ordered structure formed by tobacco mosaic viruses can be explained via DLVO theory.

This encyclopedia consists of 71 topics, which are ordered alphabetically. Each topic contains 1–4 review articles, so that there are a total of 89 review articles.

Finally, I would like to gratefully acknowledge the assistance provided by Ms. Anita Lekhwani, Senior Acquisitions Editor at John Wiley and Sons.

HIROYUKI OHSHIMA

1

STUDIES ON BIOCOMPATIBLE SURFACE-ACTIVE SILICA AEROGEL AND POLYURETHANE–SILOXANE CROSS-LINKED STRUCTURES FOR VARIOUS SURFACES

K. Seeni Meera,[1] R. Murali Sankar,[1] S. N. Jaisankar,[1] and Asit Baran Mandal[1,2,*]

Polymer Division[1] and Chemical Laboratory,[2] CSIR–Central Leather Research Institute, Adyar, Chennai 600020, Tamil Nadu, India

1.1 INTRODUCTION

Nanomaterials are one of the important classes of materials having unique properties. Several methods have been recommended in the literature for the preparation of nanomaterials. The important wet chemical method to prepare nanocrystalline and nanostructured amorphous materials is the sol-gel approach [1]. The term *sol-gel* was introduced by Thomas Graham (Scottish chemist, 1864) during his extensive study on the properties of silicic acid and some other colloids [2]. The sol-gel method is a room-temperature process, which requires very mild synthetic conditions to prepare porous glasslike materials and ceramics. The main advantages of using the sol-gel approach for preparing nanomaterials are low temperature and pressure processing conditions, mild solvents, easily available metallorganic precursors, and easy processing versatility of the prepared colloidal silica [3]. These porous materials have wide applications in optical sensors, biomolecule encapsulation, separation and chromatographic techniques, catalysis, hybrid coatings, controlled release, adsorption, and other processes [4, 5].

*Corresponding Author: Prof. Dr. Asit Baran Mandal
Phone No.: +91-44-24910846/0897; Fax No.: +91-44-24912150
Email: abmandal@hotmail.com, abmandal@clri.res.in

1.1.1 Silica Aerogel

The most important material to be prepared using sol-gel approach is aerogel. *Aerogels* are a new class of interesting materials prepared using metal alkoxide precursors in slightly acidic or basic medium. They have several unique properties, such as large pores, high surface area, low density, and low thermal conductivity [6]. The most widely synthesized and studied aerogel is silica aerogel, which is obtained primarily from silicon alkoxide precursor [tetraethylorthosilicate (TEOS) and tetramethylorthosilicate (TMOS)] by employing the sol-gel approach. This unique class of material finds several applications in catalysis, adsorbents, optical sensors, drug delivery systems, thermal insulations, and chemical separations [7–9]. Apart from its chemical and mechanical behavioral advantages, it has the important activity of biocompatibility. The biocompatibility of silica aerogel finds application as a biochip for molecular recognition of nucleotide acids and antigens [10, 11], entrapment of membrane proteins [12], in situ protein entrapment [13], and virus detection [14]. The sol-gel-processed silica aerogel have several unique properties and various applications. However, they have a disadvantage of matrix shrinkage as well as gel network collapse during the long-term aging process [15]. To overcome this hurdle, some superior drying techniques have been employed, namely, supercritical drying, freeze drying, ambient pressure drying, the use of drying control chemical additives (DCCAs; e.g., formamide, *N*-methylformamide, *N*-*N*'-dimethylformamide, acetamide, glycerol and oxalic acid),

Encyclopedia of Biocolloid and Biointerface Science, Volume 1, First Edition. Edited by Hiroyuki Ohshima.
© 2016 John Wiley & Sons, Inc. Published 2016 by John Wiley & Sons, Inc.

and drying in organic solvents [16, 17]. Most of the drying techniques employed to prepare aerogel require vigorous conditions such as high temperature and pressure and use of organic solvents. During the drying process, the evaporation of solvent results in shrinkage and collapse of the gel network, which can be avoided by using novel solvents with low vapor pressure. The fact that these solvents do not exert any external pressure on the walls of the silica aerogel surface and thereby retain the gel network structure is of current interest.

1.1.2 Ionic Liquids

In the recent past, a new class of solvent called *ionic liquids* (ILs) received much attention in preparing nanomaterials due to their exceptional physical and chemical properties. They have several interesting properties, including low vapor pressure, high polarity, high ionic conductivity, and thermal stability [18]. Because of these favorable conditions and excellent properties, ionic liquids could be used to prepare silica aerogel. The use of ILs as solvent during the sol-gel process could provide control over the structure, pore size, and distribution of the resultant aerogel [19]. Ionic liquids avoid the shrinkage and matrix collapse often observed during long-term aging as well as the drying process [9]. The risky supercritical drying process was eliminated with the use of ionic liquid {1-ethyl-3-methylimidazolium bis[(trifluoromethyl)sulfonyl]amide} during the preparation of silica aerogel in one study [20]. More recently, another team [21] used ionic liquids based on 1-butyl-3-methylimidazolium tetrafluoroborate and 1-butyl-3-methylpyridinium tetrafluoroborate salts for the preparation of silica aerogel, and they achieved control over the pore size of xerogel as well as aerogel. ILs are used for the preparation of silica nanoparticles as well as bulk aerogel [22, 23]. Most of the ILs used for the synthesis of these types of nanomaterials are based mainly on the imidazolium, pyridinium, phosphonium, and other organic salts.

At present, ionic liquids containing components (cations and anions) with widely studied biological and toxicological properties are of interest. One of these is choline, which is an important cation having several metabolic activities in the human body. Choline cation–based ionic liquids containing a number of anions such as formate, acetate, dihydrogen phosphate, aminoacetate, and levulinate have been reported [24]. Choline-based ILs have been reported to have the ability to retain the stability and structure of proteins [25]. Based on the merits of choline based ILs, we have chosen choline formate ionic liquid for the preparation of biocompatible silica aerogel. Our approach is to prepare mesoporous surface-active silica aerogel using a biocompatible ionic liquid and study its effect on the surface properties as well as biocompatibility.

1.1.3 Polyurethane–Siloxane Cross-Linked Structures

Polyurethanes (PUs) are reported to have very promising applications due to their excellent properties and environmental suitability. Various polyurethanes are available to meet the specific requirement of applications such as coatings, elastomers, foams, adhesives, fibers, paints, resins, and development of liquid crystal [26, 27]. PUs offer a wide variety of improved properties such as high thermal stability, mechanical flexibility, barrier properties, hardness, and chemical resistance. More recently, we have reported [28] thermoplastic interpenetrating polymer networks (IPNs) based mainly on polyurethane ionomers and poly(vinyl chloride) with different concentrations of calcinated clay filler, which exhibit as tough films with better miscibility, and thermal stability. These IPNs may find application in the area of damping field for footwear and allied products [28]. Very recently, another group. [29] reported that surface modified and medicated polyurethane sheets could be used as insole material in footwear for athletic shoes, which avoids foot odor and other foot problems. Most of the PU systems can be synthesized by using polyol/diol with diisocyanates. The main concern associated with the use of conventional polyol/diol for the polyurethane preparation is environmental, due to the depletion of petroleum resources and environmental risks. These petrochemical products have increased the threat to the environment and also concomitantly have discharged into the natural environment, creating global environmental pollution problems [30]. More recently, researchers have focused on the use of natural resources for the preparation of polyurethanes, thermosets, interpenetrating networks, elastomers, coatings, and other compounds [31, 32]. Among different oils derived from plants and animals, castor oil (CO) is an important one as it contains hydroxyl groups in 90% of the fatty acid chain [33]. This hydroxyl group is used to react with diisocyanates to obtain PUs. Several studies utilizing the hydroxyl functionality of CO to obtain PUs have been reported [34–37].

In the recent past, the combination of polyurethane and siloxane has represented an important advancement in combining the mechanical properties of polyurethanes and biostability of the siloxane unit [38]. Siloxane linkages are used mainly to alter the surface energy and wettability of the materials surface, and these linkages also provide high thermal stability to the PUs [39]. Polyurethane–siloxane copolymers exhibit superior flexibility, resistance to humidity, acid–base solvents, and thermal stability compared to conventional PUs [40]. Often, siloxane linkages are introduced in to the PU matrix through cross-linking. The cross-linking resulted mainly from Si−O−Si linkage via sol-gel hydrolysis and condensation of the alkoxysilane moiety, which attached to the PU matrix [41]. One group of investigators [42] reported that siloxane cross-linked polyether urethane elastomers have inflammatory

response with controlled biodegradation with relatively short time. Siloxane- coated polymer systems possessing hydrophobicity are reported to have higher protein adsorption over the hydrophilic surface [43]. Another group. [44] reported that cross-linked polyurethane-*block*-poly(trifluoropropylmethyl)siloxane elastomers may find very good application in the field of biomedicine. Novel poly(*N*-vinylpyrrolidone)-grafted poly(dimethylsiloxane) surfaces were prepared by the grafting technique, exhibiting antibiofouling properties with long-term stability [45]. Recently, cross-linked hybrid materials have been obtained by forming stronger covalent bonds between organic and inorganic compounds [46]. The most commonly used organic moiety is polyurethane, and the inorganic part is siloxane linkage, which can be coupled by using different silane coupling agents: 3-aminopropyltrimethoxysilane (APTMS), 3-aminopropyltriethoxysilane (APTES), 3-glycidyloxypropyltriethoxysilane (GPTES), 3-glycidyloxypropyltrimethoxysilane (GPTMS), and 3-isocyanatopropyltriethoxysilane (ICPTES). The main goal of this work is to prepare biorenewable castor oil–based polyurethane–siloxane cross-linked film structures and elaborate studies of physicochemical properties using various structural, thermal, surface, and morphological techniques.

1.2 EXPERIMENTAL SECTION

1.2.1 Preparation of Silica Aerogel Using Choline Formate [47]

Silica aerogel was prepared using tetraethylorthosilicate precursor, formic acid catalyst, and biocompatible ionic liquid (choline formate). Choline formate was synthesized by following the reported procedure [24]. The formic acid–catalyzed sol-gel silica aerogel was prepared using a modified method following the procedure in the literature as follows [5,20] Tetraethylorthosilicate, formic acid, and choline formate were mixed in a ratio of 1:2:1 under magnetic stirring at room temperature in a bottle. The silica sol formed within 3 h after mixing of the precursor, catalyst, and ionic liquid. The mixture gelled overnight and was allowed to age at room temperature for 3 weeks. The bottle was closed with parafilm, and small holes were drilled for the evaporation of solvent formed during the aging process. A white transparent silica aerogel was obtained after 3 weeks of aging. The ionic liquid entrapped in the gel matrix was removed by Soxhlet extraction overnight using ethanol as solvent. The solvent was then freeze-dried to remove the frozen ethanol present in the gel. The gel in wet condition (presence of IL) was labeled as SAGIW, and the dried gel was labeled as SAGID. In addition, we prepared a transparent gel without ionic liquid, which was labeled as SAG (Fig. 1.1a; shrinkage indicated by red arrow). Gel shrinkage during the aging process was high in the case of SAG, whereas the shrinkage reduced for gel in wet conditions (SAGIW; Fig. 1.1b).

1.2.2 Preparation of Polyurethane–Siloxane Cross-Linked Films [48]

Castor oil polyurethane–siloxane cross-linked films were prepared using a convenient two- step process. In the first step, polyurethane prepolymer was synthesized, and the second step involved the attachment of silane moiety followed by hydrolysis and condensation to form cross-linked structures. Polyurethane prepolymer was prepared in a three-necked round-bottomed flask fitted with a condenser, nitrogen (N_2) gas inlet, and addition funnel. Then 2.796 g of castor oil

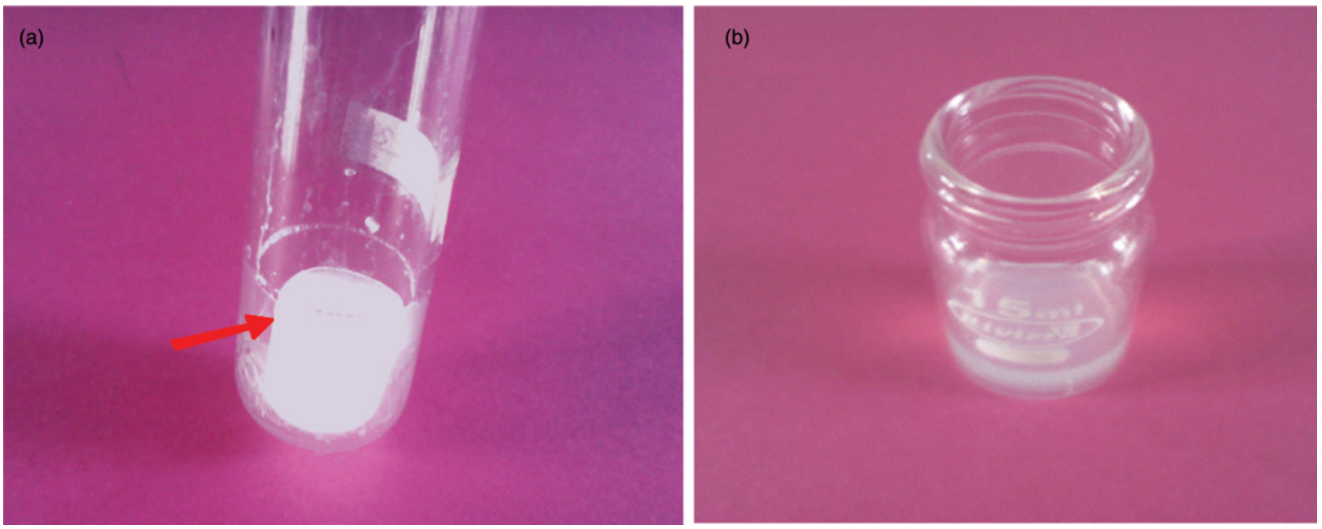


FIGURE 1.1 Image of gel prepared (a) without IL (SAG) and (b) with IL (SAGIW).

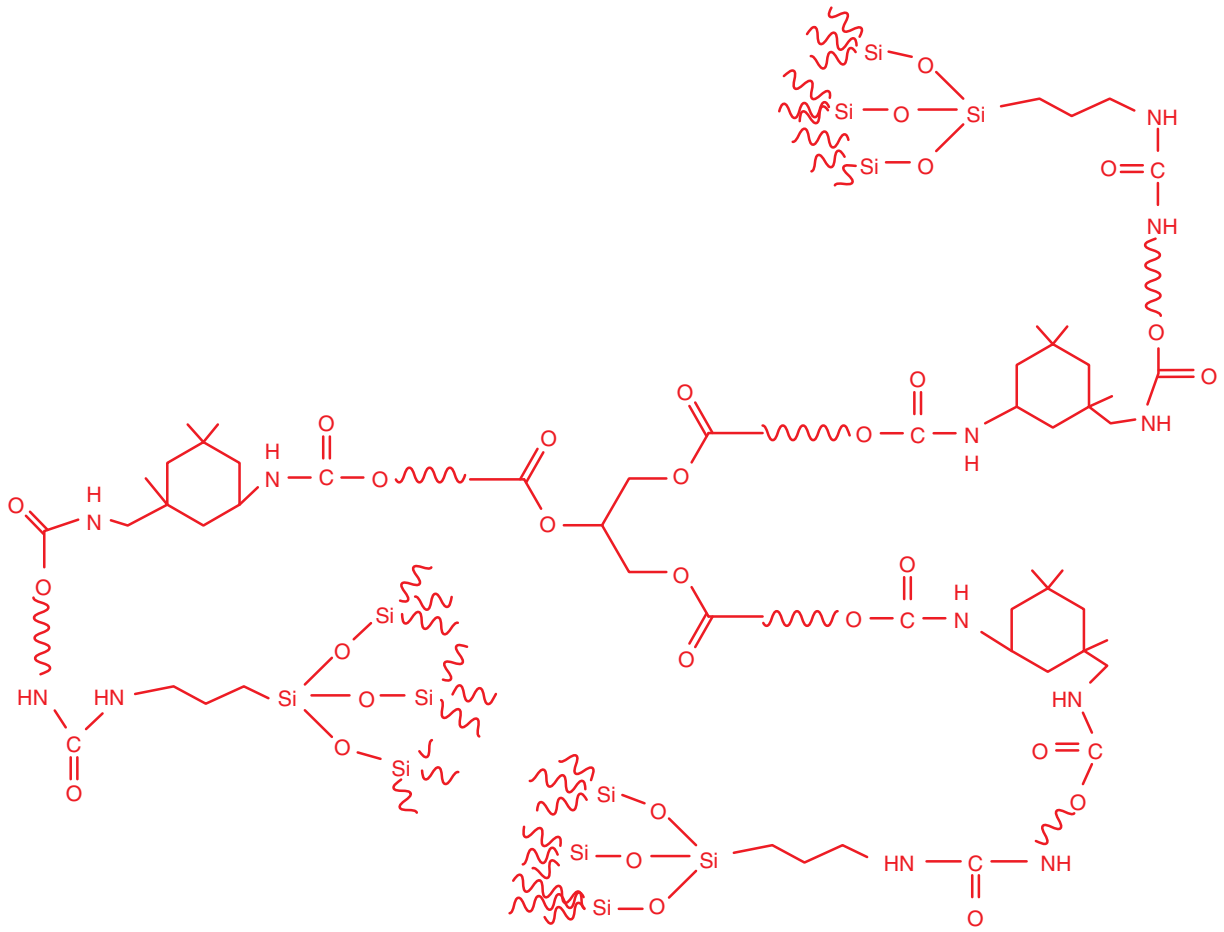


FIGURE 1.2 Scheme showing castor oil polyurethane–siloxane structures [48].

was poured into the reaction vessel and dissolved in 10 mL of chloroform and heated to 70°C with magnetic stirring. The required amount of isophorone diisocyanate (IPDI) was introduced into the reaction vessel dropwise under magnetic stirring, and dibutyltindilaurate (0.001%) catalyst was added also in dropwise fashion. The reaction further continued for 4 h to obtain PU prepolymer solution. To the PU prepolymer solution, a different ratio of 3-aminopropyltrimethoxysilane was added and heated at 70°C for another 4 h and was mold-casted to obtain polyurethane–siloxane cross-linked films. The PU cross-linked structures were obtained as transparent films. The sample codes and compositions are depicted in Table 1.1, and the polyurethane–siloxane cross-linked structures are shown in Fig. 1.2.

1.2.3 Characterization

1.2.3.1 Characterization of Silica Aerogel. Fourier transform infrared (FT-IR) spectra of the gel samples were recorded on a Perkin–Elmer FT-IR spectrometer over a range from 4000 to 400 cm^{-1}. Rheological measurements of the gel samples were performed using a MCR52 rheometer (Anton Paar Inc., USA). Thermogravimetric analyses were done using TG Analyzer-Model Q50 (TA Instruments, USA), under N_2 atmosphere with a heating rate of 20°C/min over a temperature range of 30–800°C. Differential scanning calorimetric analyses were conducted in DSC-Model Q200 (TA Instruments, USA) at a heating rate of 10 °C/min over the range from −70 to 300°C under N_2 flow. The morphology of the aerogel samples was examined using a FEI Quanta 200 (USA) environmental scanning electron microscope. The

TABLE 1.1 Codes and Compositions of Polyurethane–Siloxane Cross-Linked Film Structure

	Compositions (g)			
Codes	CO	IPDI	APTMS	Thickness (mm)
PU-0.0	2.796	2.152	–	0.87 ± 0.05
PU-1.0			1.613	0.93 ± 0.06
PU-1.1			1.747	0.93 ± 0.05
PU-1.2			1.933	1.13 ± 0.12
PU-1.3			2.092	0.92 ± 0.07
PU-1.4			2.253	1.12 ± 0.11
PU-1.5			2.457	1.08 ± 0.05

reduction of live cells during MTT assay was monitored using a synergy HT-1 microreader at 570 nm.

1.2.3.2 Characterization of Polyurethane–Siloxane Cross-Linked Film Structures. Thicknesses of the PU films were measured using Mitutoyo absolute thickness cage (ID-C1012EBS; Mitutoyo Corp., Japan), and the values reported were averages of 10 values taken at different sites on the films. The formation of polyurethane was monitored using attenuated total reflectance Fourier transform infrared (ATR-FTIR) spectroscopy on ABB MB 3000 (Canada), by keeping the film samples on ZnSe surface. The solution state ^{1}H-NMR spectra were used to confirm the formation of polyurethane–siloxane cross-linked structure and spectra taken in a JEOL 500-MHz NMR spectrometer by using deuterated chloroform ($CHCl_3$-d_1) solvent. The solid-state NMR spectra (^{29}Si CP/MAS) for the polyurethane films were carried out using a Bruker Avance 400 spectrometer (Germany), over a range from −150 to 150 ppm. Contact-angle studies were carried out using a contact-angle meter (Holmarc Opto Mechatronics Pvt. Ltd., India). The optical properties of polyurethane films were recorded using a Varian Cary 50 Bio (USA) UV–visible spectrophotometer. Moisture sorption isotherm analysis was performed using moisture sorption analyzer, Q5000 SA (TA Instruments, USA). The adsorption–desorption behavior was noticed over a time interval ranging from 0 to 3000 min. The morphology of the polyurethane films was observed using a Quanta 200 FEG (USA) scanning electron microscope. The surface roughness and topography were analyzed using Atomic Force Microscopy (AFM). Agilent Technologies (USA) 5500 scanning probe microscope instrument in tapping mode.

1.3 RESULTS AND DISCUSSION

1.3.1 Results of Surface-Active Silica Aerogel

1.3.1.1 FT-IR Spectra. The FT-IR spectra of prepared gels are shown in Fig. 1.3. In the FT-IR spectra, the region 3200–3700 cm^{-1} is the characteristic O−H stretching vibration of the Si−OH groups present in the surface of aerogel.

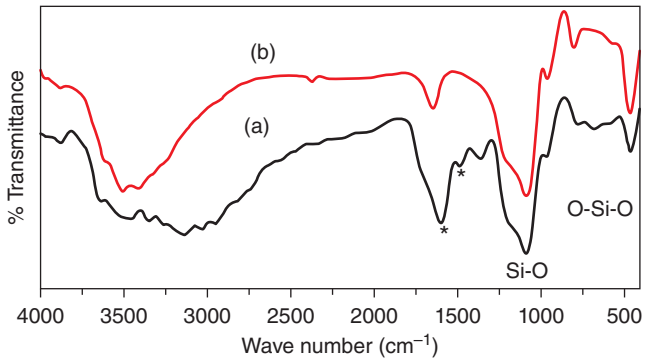


FIGURE 1.3 FT-IR spectra of (a) SAGIW, and (b) SAGID.

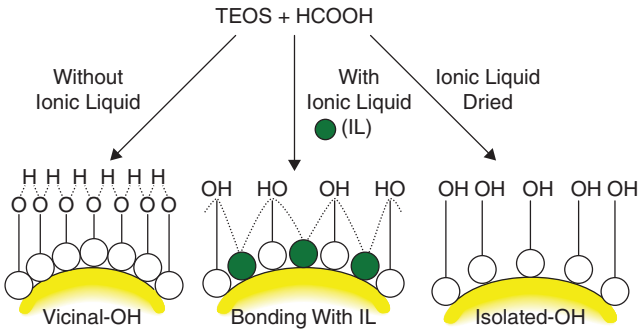


FIGURE 1.4 Schematic representation of –OH groups on silica aerogel surface.

The peak at 1088 cm^{-1} is due to the presence of Si−O stretching vibration ($\nu_{Si\text{-}O}$) and also two peaks observed at around 460 and 790 cm^{-1} are the characteristics of O−Si−O vibration. Importantly, two peaks marked with asterisks in the spectrum (Fig. 1.3a) are the characteristics of ionic liquid (peaks at 1595 cm^{-1} and 1482 cm^{-1} are characteristic C=O of formate ion), which are invisiible in Fig. 1.3b because of the removal of ionic liquid by Soxhlet extraction and freezing. In the case of gel prepared with IL, a negative bandshift at 769 cm^{-1} corresponding to O−Si−O was observed as a result of the physical confinement and interaction between silica gel and IL [49].

The −OH groups present on the surface of silica gel schematically represented in Fig. 1.4. The gel prepared without ionic liquid (SAG) contains vicinal hydroxyl groups (3438 cm^{-1}) on the surface of silica gel, whereas gel prepared with ionic liquid (in wet condition, SAGIW) contains a hydroxyl group bonded with ionic liquid, which shifts the peak position from 3438 to 3475 cm^{-1}. The ionic liquid (i.e., choline formate) shows a −OH peak at 3421 cm^{-1}. Once the ionic liquid is removed from the gel matrix (SAGID), a free hydroxyl group appears on the surface of the gel at 3510 cm^{-1} [50]. These free hydroxyl groups can be further functionalized to get desired functionalities on the surface of the aerogel.

1.3.1.2 Rheological Studies. The rheological measurements of the aerogels showed elastic properties (Fig. 1.5). The storage modulus (G′) of gel with IL increased beyond that of the loss modulus (G″) with respect to the variation of angular frequency from 100 to 0.1 rad/s (data not shown). On the other hand, the complex viscosity (η^*) of gel with IL also shows improved viscosity (Fig. 1.5b). The gelation temperature was increased from 65 to 115°C for SAG and SAGIW, respectively. This shows that the presence of IL plays a major role in improving the viscosity and elastic properties of silica aerogel. Gel prepared with ionic liquid shows viscoelastic properties, which means that the presence of ionic liquid favors more formation of large number of interconnected silica network in colloidal gel [51].

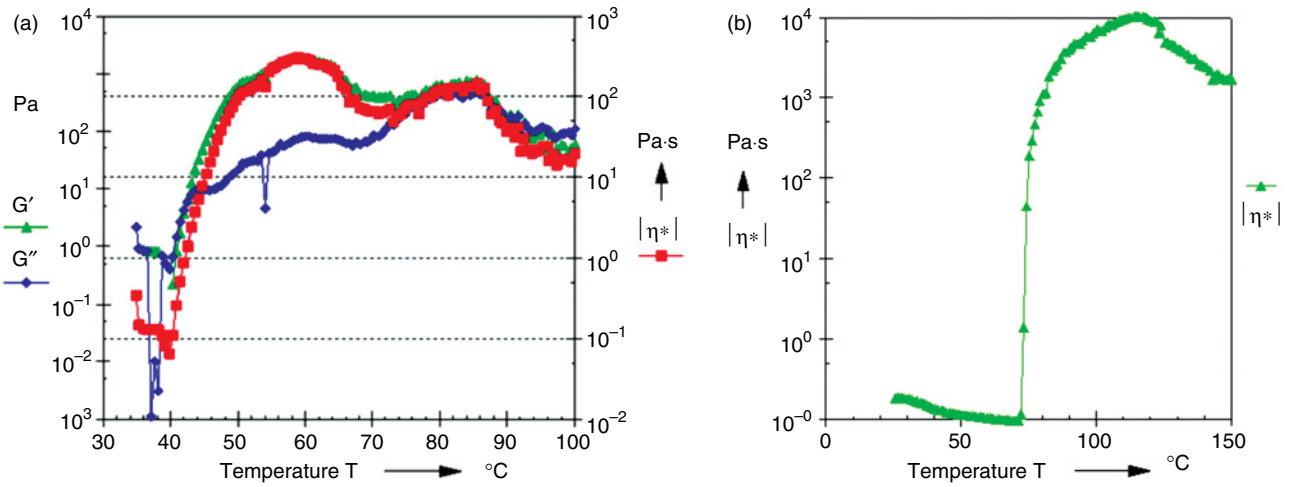


FIGURE 1.5 Rheological behaviors of (a) silica aerogel and (b) silica aerogel with IL.

1.3.1.3 Thermal Properties of Gels. Thermal studies (TGA and DSC) were conducted for the prepared gels and the data presented in Table 1.2. TGA results show that all the gel samples possess weight loss up to 100°C, due to the elimination of water and alcohol formed during the sol-gel process [52]. In the case of SAGIW, a new degradation was observed at 190°C. This corresponds to the degradation of IL presence in the gel matrix, which degrades at 190°C. A similar type of degradation was not obtained for SAGID, which confirms the removal of IL from the pores of the gel by solvent extraction and freeze drying. Furthermore, weight loss behavior at 100°C clearly shows that the presence of IL improves the thermal stability of the gel. In the presence of IL, the percent weight loss at 100°C decreased from 72.1% to 11.8% for SAG and SAGIW, respectively.

Although DSC studies reveal that SAG and SAGID give single endothermic peaks at 147.7 and 141.6°C, respectively, SAGIW yields two endothermic peaks at 140.6°C and 241.3°C. The appearance of new peak in DSC for SAGIW corresponds to the presence of IL in the pores of the gel matrix. The ionic liquid (choline formate) gives two peaks at 148.2°C and 176.5°C. In the case of SAGIW, the second melting peak shifted to 241.3°C, which may be due to the confinement IL in the pores of the gel [53]. This confinement of IL in the pores of the gel plays a crucial role in shifting the melting behavior and controlling the pore volume as well as surface hydroxyl group on the gel surface (Fig. 1.4).

1.3.1.4 Morphology of the Gels. The morphologies of the gels were examined using scanning electron microscopy, and the micrographs are depicted in Fig. 1.6. The gel prepared without ionic liquid shows very dense network structure (Fig. 1.6a). One group of investigators. [21] reported an interconnected network structure of silica particles for aerogels and xerogels made with ionic liquid. SAGIW shows an agglomerated silica particle with network structure due to the presence of ionic liquid (Fig. 1.6b). The increase in size of the silica particle (∼40 nm) was observed for the aerogel prepared with ionic liquid, whereas a smaller size (∼20 nm) was observed for the aerogel prepared without ionic liquid in another study [52]. In the case of SAGID, the structure becomes more porous due to the removal of IL from the gel matrix by solvent extraction (Fig. 1.6c). SEM studies show that the presence of IL yields a network structure of silica particles.

1.3.1.5 Biocompatibility of the Prepared Gels. Biocompatibility of IL and gel samples were tested by following a standard MTT (3-[4,5-dimethyltriazol-2-y1]-2,5-diphenyltetrazolium bromide) assay method [54] using

TABLE 1.2 Thermal Properties of IL and Gels

	TGA		DSC			
Codes	Weight loss at 100°C (%)	Residue (%)	T_{m1} (°C)	ΔH_1 (J/g)	T_{m2} (°C)	ΔH_2 (J/g)
CF	24.2	0.03	148.2	60.4	176.5	37.8
SAG	72.1	22.5	147.7	640.7	–	–
SAGIW	11.8	33.5	140.6	467.4	241.3	372.4
SAGID	25.3	68.9	141.6	630.3	–	–

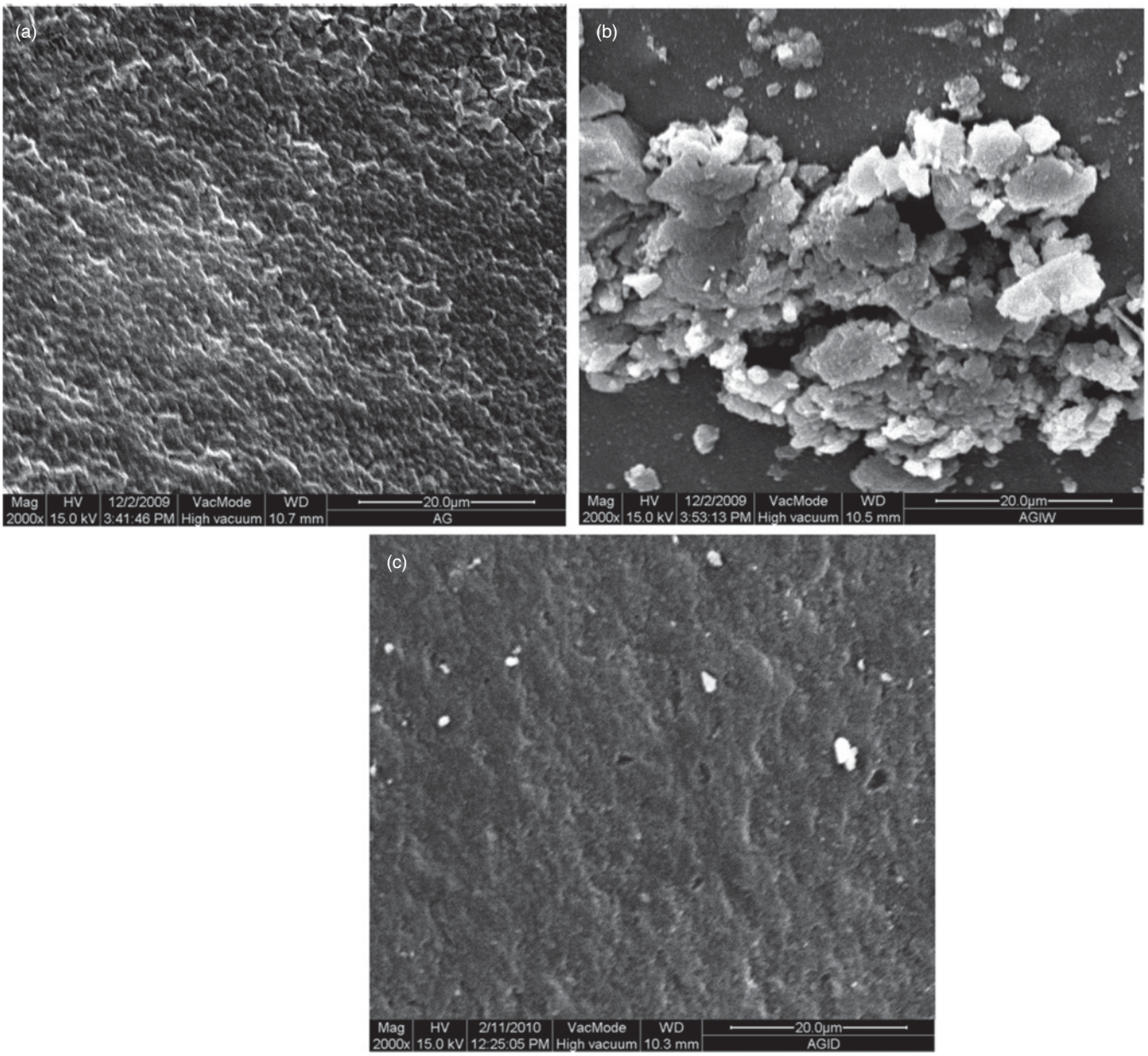


FIGURE 1.6 SEM micrographs of (a) SAG, (b) SAGIW, and (c) SAGID (2000×).

3T3-L1 cells and the obtained results compared with the control. The cell viability of the samples were tested for 24, 48, and 72 h with different concentration of gel samples (viz., 20, 40, 60, 80, and 100 mg), and the results are depicted in Figs. 1.7–1.9. In all the concentrations, the cell viability of IL and gels were high. In the case of SAGIW, the cell viability was around 120% for 20 and 40 mg of samples at 24, 48, and 72 h. The cell viability of gel sample prepared with IL shows very good results at higher concentration (60, 80, and 100 mg) for all the time durations. These results show that the presence and confinement of IL (choline formate) in the pores of gel increases and enhances the cell viability and proliferation of the prepared aerogel [55]. The percent cell viability of IL and gel samples was calculated using the following equation [56]:

$$\text{Cell viability (\%)} = \frac{A_t}{A_c} \times 100 \tag{1.1}$$

where A_t and A_c are absorbance values of treated and control cells, respectively.

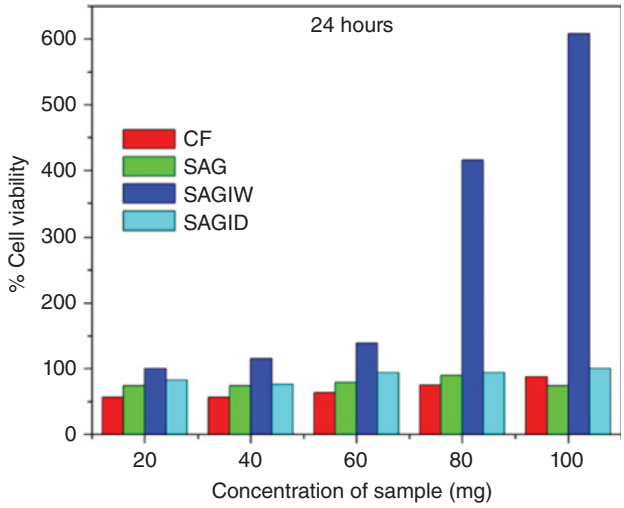


FIGURE 1.7 The MTT assay of IL and gels at 24 h.

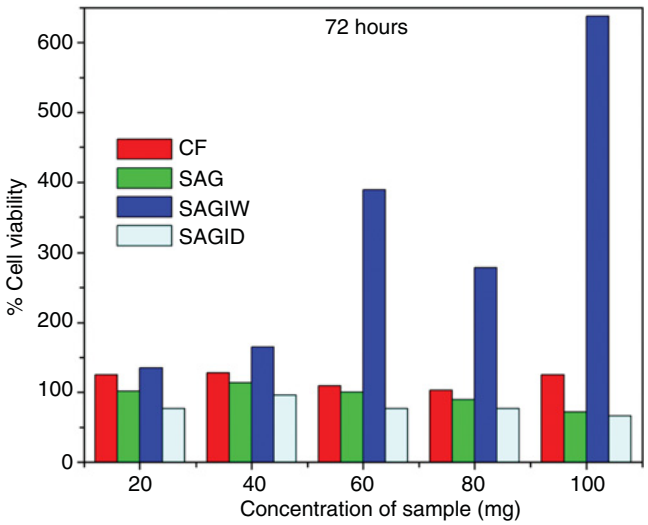


FIGURE 1.9 The MTT assay of IL and gels at 72 h.

1.3.2 Results of Polyurethane–Siloxane Cross-Linked Structures

1.3.2.1 ATR-FT-IR Spectra. The formation of PU and siloxane structure was evidenced from the ATR-FT-IR spectra, shown in Fig. 1.10. Control castor oil polyurethane shows all the characteristic peaks such as C=O, N−H, and −NCO peaks. The free −NCO peak appeared at 2259 cm^{-1}, but completely disappeared in the case of polyurethane–siloxane systems [57]. Control polyurethane (PU-0.0) contains only a urethane peak, whereas siloxane cross-linked samples show a new peak at 1637 cm^{-1} corresponds to a urea peak formed by the attachment of NH_2 group present in silane moiety to the free −NCO of polyurethane prepolymer [58]. Further, two new peaks were observed for the cross-linked systems at 772 and 1094 cm^{-1} corresponding to O−Si−O and Si−O stretching vibrations, respectively. These results confirm the attachment of silane moiety as well as their cross-linkage. In addition to this, the introduction of siloxane shifts the peak position of characteristic N−H, urethane C−O, urea C−O, and Si−O peaks and also the intensity of the respective peaks increased. These results clearly give an idea about the formation of polyurethane, attachment of silane moiety, and cross-linking of siloxane groups in the polyurethane–siloxane cross-linked films.

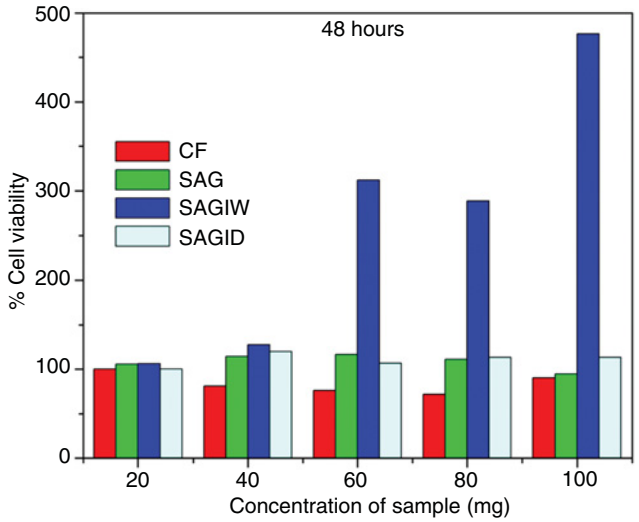


FIGURE 1.8 The MTT assay of IL and gels at 48 h.

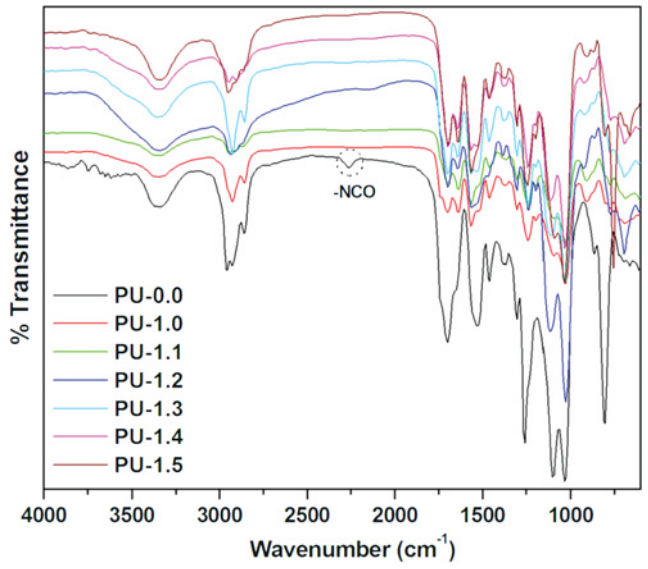


FIGURE 1.10 The ATR-FT-IR spectra for polyurethane–siloxane films.

TABLE 1.3 Chemical Shift Values for ^{1}H-NMR Spectra of Polyurethane–Siloxane Structures

Castor oil [59, 60] δ (ppm)	Castor oil polyurethane prepolymer δ (ppm)	Castor oil polyurethane-siloxane δ (ppm)
4.06–4.28 (m), $-CH_2$ of glycerol moiety	New peaks in addition to castor oil peaks	New peaks in addition to castor oil peaks
5.18–5.24 (m), −CH of glycerol moiety		7.08–7.12, urethane N−H
2.23–2.29 (t), CH_2 attached to ester −C−O	Urethane peak appears at 7.0–7.05	5.89, urea N−H
1.35–1.63, $-CH_2$ chain		3.06, $-CH_2$ next to urea N−H [61]
1.96–2.04, $-CH_2$ attached to C=C on aliphatic side		4.60–4.76, −C−H attached to N−H of urethane
2.13–2.19, $-CH_2$ attached to C=C on −OH side		1.39 and 1.52, CH_2 of APTMS
3.51–3.60 (m), C−H attached to −OH		
0.80–0.87, terminal $-CH_3$		5.0, Si−OH
5.26–5.53 (m), −CH=CH − [62]		

1.3.2.2 ^{1}H-NMR Spectra. The formation and structure of CO polyurethane–siloxane cross-linked film structure was identified and confirmed using solution-state ^{1}H-NMR spectra, and their corresponding chemical shift values are given in Table 1.3. The ^{1}H-NMR spectrum of castor oil polyurethane–siloxane gives all the characteristic peaks of CO. In addition to CO peaks, some new peaks appeared in the ^{1}H-NMR spectrum of polyurethane–siloxane. The appearance of urethane N−H and urea N−H confirms the formation of polyurethane and attachment of silane moiety to PU chain. Furthermore, two new peaks appeared in the range of 1.3–1.6 ppm, which are the characteristic peaks of APTMS. The appearance of a new broad peak at around 5.0 ppm provides evidence for the formation of Si−OH groups. The ^{1}H-NMR spectrum of castor oil PU prepolymer gives only urethane peak (not urea peak), which shows that the urea formation occurs in the second stage of the reaction (after adding APTMS).

1.3.2.3 Solid-State ^{29}Si-NMR Spectra. The formation and cross-linking of siloxane groups in polyurethane– siloxane cross-linked structure occurred through hydrolysis and condensation of Si−OCH_3 groups present in the APTMS moiety. In order to ensure a clearer understanding of the cross-linking, the hydrolysis and condensation of polyurethane–siloxane films were analyzed by using ^{29}Si CP/MAS NMR spectroscopy. Control polyurethane (PU-0.0) doesn't have any silica moiety on its chain, whereas polyurethane–siloxane cross-linked structures contain siloxane linkages. The polyurethane–siloxane structure contains three hydrolyzed (Si−O−Si) and one nonhydrolyzed ($-Si-CH_2-CH_2-CH_2-NH_2$) parts, which are designated as Q (Q^1, Q^2, and Q^3) and T (T^3) terminologies, respectively in ^{29}Si CP/MAS NMR [63, 64]. In case of PU-1.0, ^{29}Si NMR spectra give all the four characteristic peaks (Q^1, Q^2, Q^3, and T^3) ranging from −75 to 100 ppm. This shows that the lower concentration of silane results in a mixed Si environment. Further, increasing the concentration of silane from 1.0 to 1.4 yields three peaks corresponding to Q^2, Q^3, and T^3 ranging from −78 to −98 ppm [65]. The higher concentration of silane (1.5) results in only two peaks (Q^3 and T^3) at −82.4 and −98.7 ppm, which confirms the occurrence of complete cross-linking in polyurethane–siloxane cross-linked systems (PU-1.5). The increase in silane ratio provides a similar kind of Si environment with complete cross-linking in the polyurethane–siloxane system. The major peaks of Q^3 and T^3 play a vital role in forming the complete network structure. ^{29}Si CP/MAS NMR spectra provide a clear picture about the cross-linking state of silica species present in the polyurethane–siloxane system.

1.3.2.4 Contact-Angle Studies. The surface behavior of polyurethane–siloxane films was studied using static contact-angle measurements by placing water (polar) and hexadecane (dispersive) droplets over the film surface. Control PU (PU-0.0) exhibits relatively hydrophilic behavior for water droplets (θ=74.0°; see Fig. 1.11). The introduction of siloxane linkage to the PU chain provides hydrophobicity to the PU surface. In the case of PU-1.5, a higher concentration of

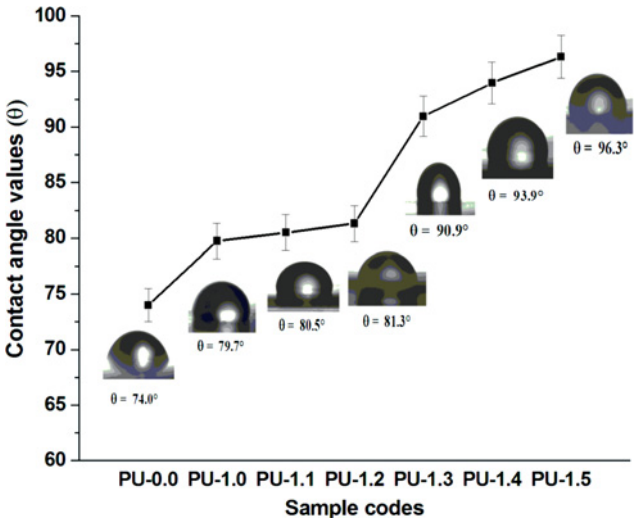


FIGURE 1.11 Contact-angle values for polyurethane–siloxane cross-linked films on a water droplet at 25°C.

silane ratio results in an increment of approximately 23° in the water contact angle (polar component), which proves that siloxane linkage provides hydrophobicity to the film surface. The siloxane linkage present in the PU film surface easily migrates to the surface and imparts antiwettability to the PU surface [66,67]. However, in the case of hexadecane droplets (dispersive component), the contact-angle value decreased from 8.9° to 6.5° for PU-0.0 to PU-1.5, respectively. Overall, this results in decrease of total surface free energy of polyurethane surface from 37.6 (PU-0.0) to 29.7 mJ/m^2 (PU-1.5). The introduction of siloxane helps to ensure a hydrophobic surface with low surface free energy. The low-free-energy surface resulted from the incorporation of siloxane linkages having low surface tension present on the surface of PU films [68]. The chemical modification of cellulose acetate with siloxane cross-linking results in increased contact angle, which provides water repellance to the surface [69].

1.3.2.5 UV–Visible Spectra. The UV–visible absorbance spectra for the prepared polyurethane–siloxane films are given in Fig. 1.12. The incorporation of siloxane cross-linking influenced the absorbance of PU films. All the film samples show very good absorbance in the range of 200–350 nm, whereas in the range of 350–800 nm the absorbance decreased. That means the transmittance of the polyurethane–siloxane films increased in the range of 350–800 nm with increasing concentration of silane ratio from 0.0 to 1.2. Further, increasing the concentration of silane from 1.3 to 1.5 slightly decreased the absorbance of the polyurethane films. Polyurethane films containing a silane ratio of 1.2 show very good transmittance in the range of 350–500 nm. The transparency of the polyurethane–siloxane

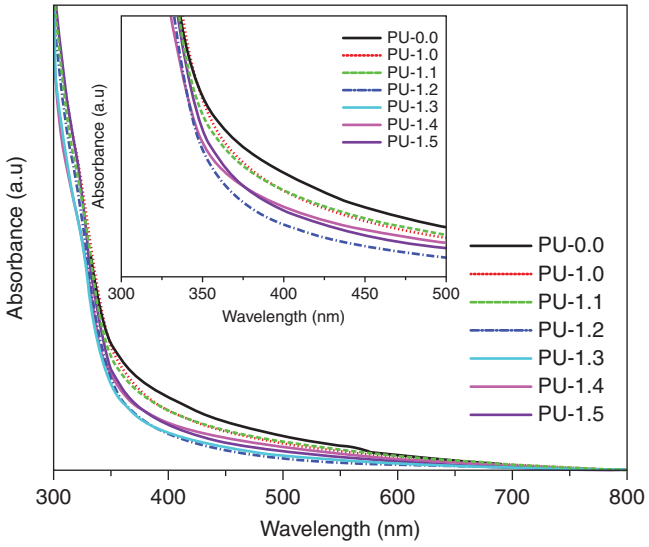


FIGURE 1.12 UV–visible spectra of castor oil polyurethane–siloxane films.

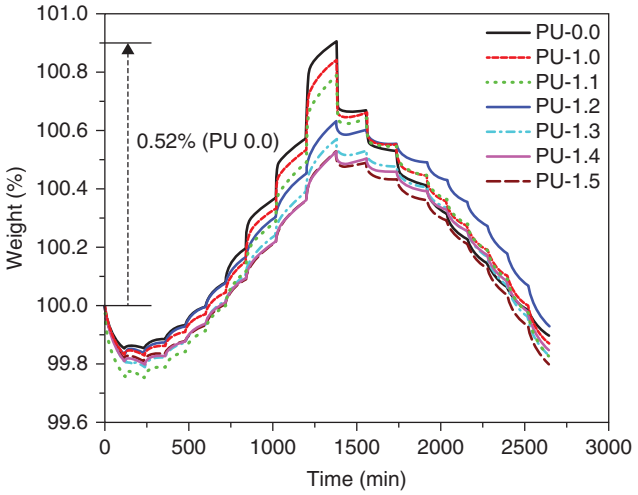


FIGURE 1.13 Time-dependent moisture sorption behavior of polyurethane–siloxane films.

films can be altered by changing the concentration of the silane content. In general, all the polyurethane films show very good transmittance in the visible range, which help us to find applications in the development of leather coatings, transparent coatings, lens, optical fiber, and so on [70,71].

1.3.2.6 Moisture Sorption. The moisture sorption property of polyurethane–siloxane cross-linked film samples were analyzed using a moisture sorption isotherm over a long time duration (2700 min) and are shown in Fig. 1.13. Sorption phenomena occurred up to 1400 min, followed by the occurrence of desorption phenomena until 2700 min. The maximum weight gain during sorption for PU-0.0 sample is 0.91%. In the case of siloxane cross-linked films, the maximum weight gain was found to be 0.83%, 0.78%, 0.62%, 0.57%, 0.53%, and 0.52% for PU-1.0, PU-1.1, PU-1.2, PU -1.3, PU-1.4, and PU-1.5, respectively (Table 1.4). This clearly indicates that the control polyurethane sample shows a slightly hydrophilic characteristic due to the presence of free –OH and –NCO groups, which contributes to its hydrophilicity. The maximum weight gain during sorption decreased

TABLE 1.4 Moisture Sorption Behavior of Polyurethane–Siloxane Films

Codes	Moisture sorption weight (%)
PU-0.0	0.91
PU-1.0	0.83
PU-1.1	0.78
PU-1.2	0.62
PU-1.3	0.57
PU-1.4	0.53
PU-1.5	0.52

with increasing silane content, thus demonstrating that the siloxane cross-linking imparts hydrophobicity to the films [72, 73]. The increased hydrophobicity with respect to silane ratio was already evidenced from contact-angle measurements (Fig. 1.11). The decreased moisture sorption capacity was observed in another study [74] for cellulose–siloxane cross-linked polyester materials.

1.3.2.7 SEM Images. The surface morphology of the polyurethane films was investigated using SEM micrographs and is depicted in Fig. 1.14. In the case of control polyurethane PU 0.0, the surface was almost uniform (Fig. 1.14a). However, siloxane cross-linked film samples exhibit slightly phase-separated structures. In case of PU-1.0, small domains were observed, which originated mainly from within siloxane domains (Fig. 1.14b). Microphase separation with domain structure has been reported for siloxane-modified poly(IPDI-PTMO) copolymers [75]. SEM images of polydimethylsiloxane–polyurethane dispersion (PDMS-PUD) shows a very smooth and uniform surface, whereas block and random PDMS-PUD film samples exhibit better microphase separation with improved tensile properties such as tensile strength and tensile modulus [76].

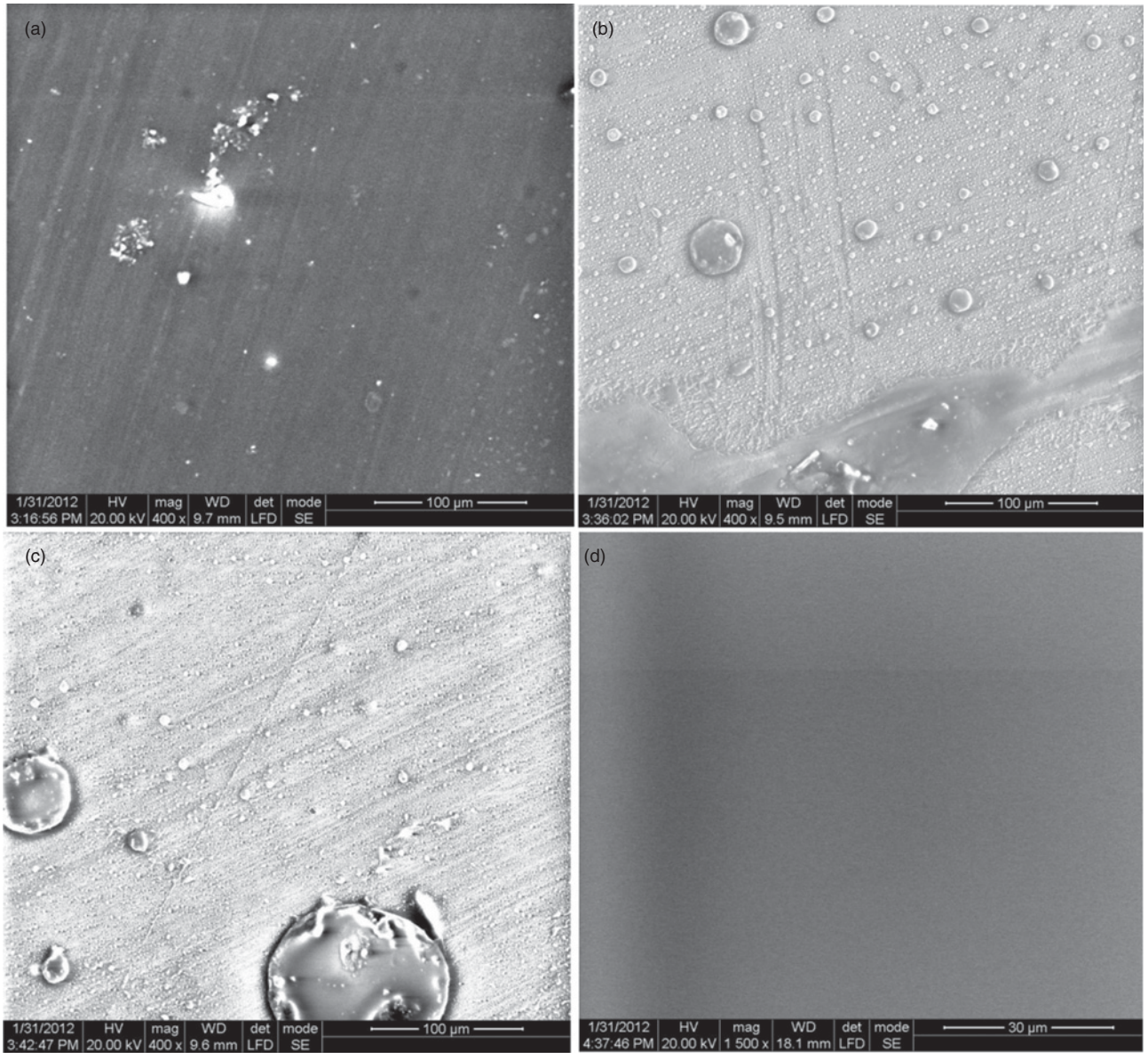


FIGURE 1.14 SEM images of polyurethane–siloxane cross-linked films: (a) PU-0.0 (400×); (b) PU 1.0 (400×); (c) PU 1.1 (400×); (d) PU 1.4 (1500×).

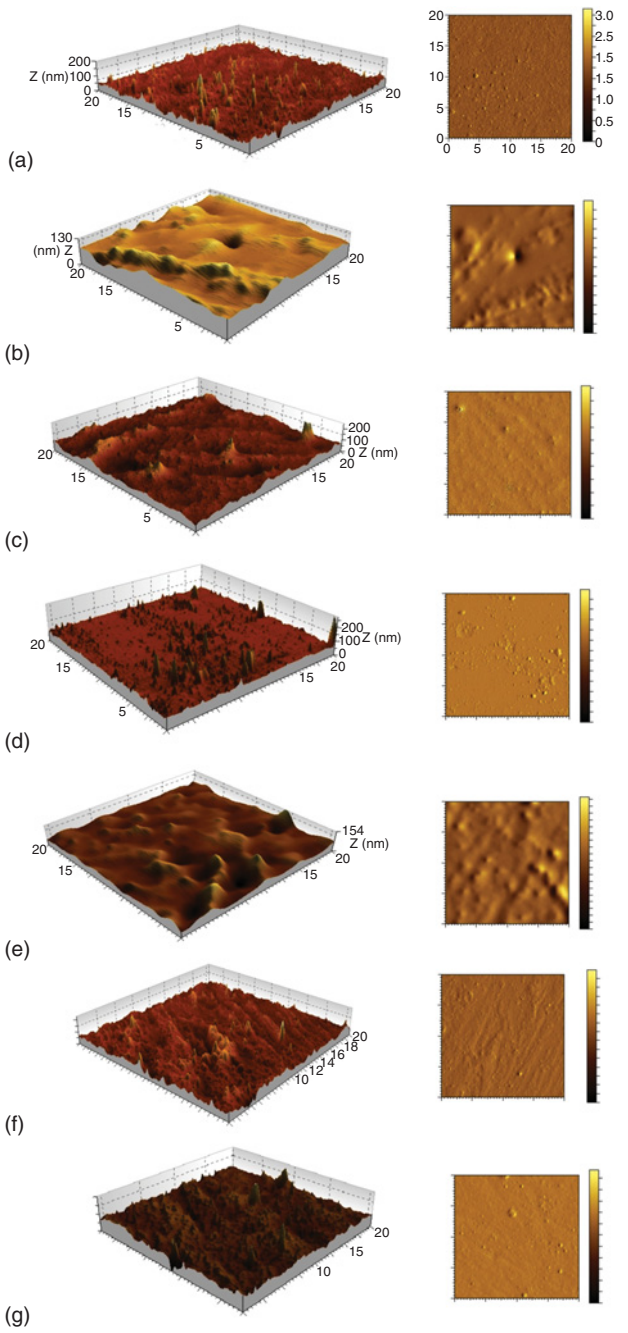


FIGURE 1.15 AFM images of polyurethane films.

1.3.2.8 AFM Studies. The surface roughness as well as topography of the polyurethane films was analyzed using atomic force microscopy, and the images are presented in Fig. 1.15. The incorporation of siloxane cross-linking greatly influences the surface roughness of the film surface. Control polyurethane PU-0.0 shows an irregular surface with a surface roughness value of 13.4 nm (Fig. 1.15a). The incorporation of siloxane cross-linking transforms the surface into a smoothed surface. In the case of higher silane ratios (PU-1.5), the roughness value decreased to 4.7 nm (Table 1.5). This clearly indicates that the introduction of siloxane cross-linking provides smoothness to the film surface. This is due mainly to the presence of siloxane linkages on the surface of polyurethane films, which increases the hydrophobicity of the film surface (Fig. 1.11). The increased contact angle induces the surface to acquire low surface free energy; the roughness profile images are given in Fig. 1.16 The presence of siloxane group gives some relatively dark and light parts, indicating that microphase separation was observed with lower siloxane content (Fig. 1.15c) [48, 77]. Siloxane groups tend to stratify during the formation of film structure and also allow to complete the hydrolysis and condensation of silane moiety, which result in a smoothed surface with low surface free energy [78]. A similar observation has been reported [79] for polyurethane dispersions modified with dihydroxylpropyl terminated siloxane oligomer. The presence of siloxane groups on the polyurethane film surface is schematically represented in Fig. 1.17. This siloxane group covers the surface of polyurethane films, which is responsible for the increased water contact angle with low surface energy. The covering of siloxane group over polyurethane surface reduces the surface roughness and forms a uniform surface [80].

TABLE 1.5 Root-Mean-Square (RMS) Surface Roughness Values of Polyurethane Films [48]

Codes	RMS surface roughness R_q (nm)
PU-0.0	13.4
PU-1.0	13.3
PU-1.1	12.2
PU-1.2	8.2
PU-1.3	7.7
PU-1.4	6.9
PU-1.5	4.7

1.4 CONCLUSIONS

A new class of sol-gel-derived silica aerogel was developed using ionic liquid, with choline formate as pore-forming agent. The presence of ionic liquid in the sol-gel matrix increases the aging time, thereby avoiding collapse of the gel structure. Ionic liquid plays a vital role in controlling the surface behavior of hydroxyl groups. Further, removal of ionic liquid from the gel matrix leaves a free hydroxyl group, which can be further functionalized for some other potential applications. Rheological studies reveal the viscoelastic nature of the prepared gels. Thermal studies clearly show that the presence of ionic liquid greatly influenced the degradation as well as melting behavior of

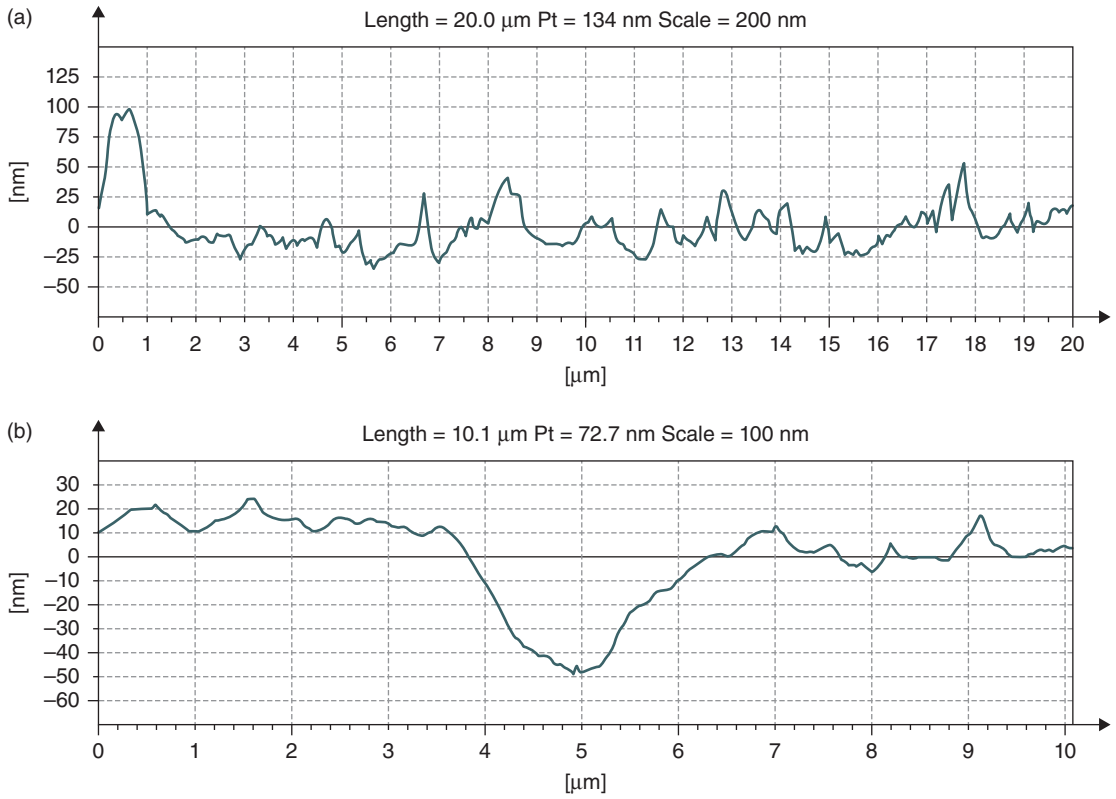


FIGURE 1.16 Surface roughness profile for the PU–siloxane films: (a) PU-0.0; (b) PU-1.5

the gels. The role of ionic liquid on the morphology of silica aerogel was observed using the SEM technique. Furthermore, biocompatibility studies clearly indicate that choline formate ionic liquid enhanced the cell viability as well as proliferation of the aerogels. Higher cell viability was observed irrespective of the concentration of the gel and time duration for the prepared aerogel samples with ionic liquid. These studies clearly indicate that the prepared silica aerogel could be used for the encapsulation of biomolecules such as proteins, enzymes, and other substances for longer time duration, which could help retain their conformational stability.

We adopted a similar sol-gel strategy to prepare polyurethane–siloxane cross-linked film structure. The polyurethane was prepared using a biorenewable castor oil as a polyol, and the siloxane moiety was introduced by coupling the silane agent on to the polyurethane prepolymer. Structural, surface, and morphological properties of the polyurethane–siloxane cross-linked films were extensively studied using ATR-FT-IR, solution ^{1}H NMR, solid-state ^{29}Si CP/MAS NMR, contact-angle, moisture sorption, UV–visible, SEM, and AFM techniques. The ATR-FT-IR spectra confirmed the formation of polyurethane prepolymer, attachment of silane moiety, and siloxane cross-linking. The confirmation of polyurethane formation as well as silane attached to polyurethane prepolymer moiety was analyzed using solution ^{1}H-NMR studies. The cross-linking state of silane moiety on increasing the silane concentration from 1.0 to 1.5 was monitored using solid-state ^{29}Si-NMR spectra. The surface behavior of the film surface was studied using contact-angle measurements, which proves the hydrophobicity of the cross-linked films. Furthermore, adsorption behavior of the films shows that the polyurethane surface has a hydrophobic character. UV–visible studies provide information about the transmittance of the polyurethane films. AFM studies shows that the surface roughness of the films decreased from 13.4 to 4.7 nm for PU-0.0 and PU-1.5, respectively. These hydrophobic polyurethane surfaces may be used for the development of leather coatings, lens, and other materials.

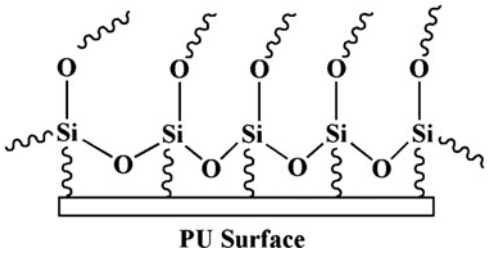


FIGURE 1.17 Schematic representation of siloxane groups on PU surface.

Overall, the study shows that these kinds of sol-gel-derived surface-active silica aerogel and biorenewable castor

oil–based polyurethane–siloxane cross-linked hydrophobic surfaces may find potential applications in the area of development of biomaterials and further widen the scope in the material science.

ACKNOWLEDGMENT

K. Seeni Meera thanks the Council of Scientific and Industrial Research (CSIR), India, for a senior research fellowship (Grant 31/6(362)/2012/EMR-I).

REFERENCES

[1] Schottner, G. (2001). Hybrid sol-gel-derived polymers: Applications of multifunctional materials. *Chem.Mater*. **13**, 3422–3435.

[2] Graham, T. (1864). On the properties of silicic acid and other analogous colloidal substances. *J. Chem. Soc*. **17**, 318–327.

[3] Seeni Meera, K.M., Murali Sankar, R., Murali, A., Jaisankar, S.N., Mandal, A.B. (2012). Sol-gel network silica-modified montmorillonite clay hybrid nanocomposites for hydrophobic surface coatings. *Colloids Surf. B: Biointerfaces* **90**, 204–210.

[4] Monton, M.R.N., Forsberg, E.M., Brennan, J.D. (2012). Tailoring sol-gel derived silica materials for optical biosensing. *Chem. Mater.* **24**, 796–811.

[5] Li, Y.K., Chou, M.J., Wu, T.Y., Jinn, T.R., Chen-Yang, Y.W. (2008). A novel method for preparing a protein-encapsulated bioaerogel: Using a red fluorescent protein as a model. *Acta Biomaterialia* **4**, 725–732.

[6] Duan, Y., Jana, S.C., Lama, B., Espe, M.P. (2013). Reinforcement of silica aerogels using silane-end-capped polyurethanes. *Langmuir* **29**, 6156–6165.

[7] Pouretedal, H.R., Kazemi, M. (2012). Characterization of modified silica aerogel using sodium silicate precursor and its application as adsorbent of Cu^{2+}, Cd^{2+}, and Pb^{2+} ions. *Int. J. Industr. Chem.* **3**, 20–27.

[8] Gurav, J.L., Jung, I-K., Park, H-H., Kang, E.S., Nadargi, D.Y. (2010). Silica aerogel: Synthesis and applications. *J. Nanomater.* 1–11.

[9] Wu, C.-M., Lin, S.-Y., Chen, H.-L. (2012). Structure of a monolithic silica aerogel prepared from a short-chain ionic liquid. *Micropor. Mesopor. Mater.*, **156**, 189–195.

[10] Li, Y.K., Yang, D.-K., Chen, Y.-C., Su, H.-J., Wu, J.-C., Chen-Yang, Y.W. (2010). A novel three-dimensional aerogel biochip for molecular recognition of nucleotide acids. *Acta Biomaterialia* **6**, 1462–1470.

[11] Li, Y.K., Chen, Y-C., Jiang, K-J., Wu, J-c., Chen-Yang, Y.W. (2011). Three dimensional arrayed amino aerogel biochips for molecular recognition of antigens. *Biomaterials* **32**, 7347–7354.

[12] Besanger, T.R., Easwaramoorthy, B., Brennan, J.D. (2004). Entrapment of highly active membrane-bound receptors in macroporous sol-gel derived silica. *Anal. Chem.* **76**, 6470–6475.

[13] Wang, G-H., Zhang, L-M. (2009). A biofriendly silica gel for in-situ protein entrapment: Biopolymer-assisted formation and its kinetic mechanism, *J. Phys. Chem. B* **113**, 2688–2694.

[14] Power, M., Hosticka, B., Black, E., Daitch, C., Norris, P. (2001). Aerogels as biosensors: Viral particle detection by bacteria immobilized on large pore aerogel. *J. Non-Cryst. Solids* **285**, 303–308.

[15] Husing, N., Schubert, U. (1998). Aerogels-airy materials: Chemistry, structure, and properties. *Angew. Chem. Int. Ed.* **37**, 22–45.

[16] Estella, J., Echeverria, J.C., Laguna, M., Garrido, J.J. (2007). Effects of aging and drying conditions on the structural and textural properties of silica gels. *Micropor. Mesopor. Mater.* **102**, 274–282.

[17] Kim, C.E., Yoon, J.S., Hwang, H.J. (2009). Synthesis of nanoporous silica aerogel by ambient pressure drying. *J. Sol-Gel Sci. Technol.* **49**, 47–52.

[18] Li, Z., Jia, Z., Luan, Y., Mu, T. (2008). Ionic liquids for synthesis of inorganic nanomaterials. *Curr. Opin. Solid State Mater. Sci.* **12**, 1–8.

[19] Klingshirn, M.A., Spear, S.K., Holbrey, J.D., Rogers, R.D. (2005). Ionic liquids as solvent and solvent additives for the synthesis of sol-gel materials, *J. Mater. Chem.* **15**, 5174–5180.

[20] Dai, S., Ju, Y.H., Gao, H.J., Lin, J.S., Pennycook, S.J., Barnes, S.E. (2000). Preparation of silica aerogel using ionic liquids as solvents. *Chem. Commun.* **3**, 243–245.

[21] Karout, A., Pierre, A.C. (2007). Silica xerogels and aerogels synthesized with ionic liquids. *J. Non-Cryst. Solids* **353**, 2900–2909.

[22] Pang, J., Luan, Y., Li, F., Cai, X., Li, Z. (2010). Ionic liquid-assisted synthesis of silica particles and their application in drug release. *Mater. Lett.* **64**, 2509–2512.

[23] Moganty, S.S., Srivastava, S., Lu, Y., Schaefer, J.L., Rizvi, S.A., Archer, L.A. (2012). Ionic liquid-tethered nanoparticle suspensions: A novel class of ionogels. *Chem. Mater.* **24**, 1386–1396.

[24] Winther-Jensen, O., Vijayaraghavan, R., Sun, J., Winther-Jensen, B., MacFarlane, D.R. (2009). Self polymerising ionic liquid gel. *Chem. Commun.* 3041–3043.

[25] Weaver, K.D., Vrikkis, R.M., Van Vorst, M.P., Trullinger, J., Vijayaraghavan, R., Foureau, D.M., McKillop, I.H., MacFarlane, D.R., Krueger, J.K., Elliott, G.D. (2012). Structure and function of proteins in hydrated choline dihydrogen phosphate ionic liquid. *Phys. Chem. Chem. Phys.* **14**, 790–801.

[26] Alexandru, M., Cazacu, M., Cristea, M., Nistor, A., Grigoras, C., Simionescu, B.C. (2011). Poly(siloxane-urethane) crosslinked structures obtained by sol-gel technique. *J. Polym. Sci. A: Polym. Chem.* **49**, 1708–1718.

[27] Jaisankar, S.N., Nelson, D.J., Brammer, C.N. (2009). New synthesis and characterization of ionic polyurethane-urea liquid crystals. *Polymer* **50**, 4775–4780.

[28] Jaisankar, S.N., Murali Sankar, R., Seeni Meera, K., Mandal, A.B. (2013). Thermoplastic interpenetrating polymer

networks based on polyvinyl chloride and polyurethane ionomers for damping application. *Soft Mater.* **11**, 55–60.

[29] Gnanasundaram, S., Ranganathan, M., Das, B.N., Mandal, A.B. (2013). Surface modified and medicated polyurethane materials capable of controlling microorganisms causing foot skin infection in athletes. *Colloids Surf. B: Biointerfaces* **102**, 139–145.

[30] Babu, B.R., Meera, K.S., Venkatesan, P., Sunandha, D. (2010). Removal of fatty acids from palm oil effluent by combined electro-Fenton and biological oxidation process. *Water Air Soil Pollut.* **211**, 203–210.

[31] Jaisankar, S.N., Lakshminarayana, Y., Ganga Radhakrishnan, Ramasami, T. (1996). Modified castor oil based polyurethane elastomers for one-shot process. *Polym. Plastics Technol. Eng.* **35**, 781–789.

[32] Knight, S.C., Schaller, C.P., Tolman, W.B., Hillmyer, M.A. (2013). Renewable carvone-based polyols for use in polyurethane thermosets. *RSC (Roy. Soc. Chem.) Advances* **43**, 20399–20404.

[33] Xia, Y., Larock, R.C. (2010). Castor oil-based thermosets with varied crosslink densities prepared by ring-opening metathesis polymerization (ROMP). *Polymer* **51**, 2508–2514.

[34] Hablot, E., Zheng, D., Bouquey, M., Averous, L. (2008). Polyurethanes based on castor oil: Kinetics, chemical, mechanical and thermal properties. *Macromol. Mater. Eng.* **293**, 922–929.

[35] Robertson, M.L., Paxton, J.M., Hillmyer, M.A. (2011). Tough blends of polylactide and castor oil. *ACS (Am. Chem. Soc.) Appl. Mater. Interfaces* **3**, 3402–3410.

[36] Gao, Z., Peng, J., Zhong, T., Sun, J., Wang, X., Yue, C. (2012). Biocompatible elastomer of waterborne polyurethane based on castor oil and polyethylene glycol with cellulose nanocrystals. *Carbohydr. Polym.* **87**, 2068–2075.

[37] Allauddin, S., Narayan, R., Raju, K.V.S.N. (2013). Synthesis and properties of alkoxysilane castor oil and their polyurethane-urea-silica hybrid coating films. *ACS Sustain. Chem. Eng.* **1**, 910–918.

[38] Adhikari, R., Gunatillake, P.A., McCarthy, S.J., Bown, M., Meijs, G.F. (2003). Low-modulus siloxane-polyurethanes. Part II. Effect of chain extender structure on properties and morphology. *J. Appl. Polym. Sci.* **87**, 1092–1100.

[39] Milanesi, F., Cappelletti, G., Annunziata, R., Bianchi, C.L., Meroni, D., Ardizzone, S. (2010). Siloxane-TiO_2 hybrid nanocomposites. The structure of the hydrophobic layer. *J. Phys. Chem. C* **114**, 8287–8293.

[40] Liao, S.K., Jang, S.C., Lin, M.F. (2005). Phase behavior and mechanical properties of siloxane urethane copolymer. *J. Polym. Res.* **12**, 103–112.

[41] Bai, C., Zhang, X., Dai, J., Wang, J. (2008). Synthesis of UV crosslinkable waterborne siloxane-polyurethane dispersion PDMS-PEDA-PU and the properties of the films. *J. Coat. Technol. Res.* **5**, 251–257.

[42] Rhodes, N.P., Bellon, J.M., Bujan, M.J., Soldani, G., Hunt, J.A. (2005). Inflammatory response to a novel series of siloxane-crosslinked polyurethane elastomers having controlled biodegradation. *J. Mater. Sci.: Mater. Med.* **16**, 1207–1211.

[43] Stallard, C.P., McDonnell, K.A., Onayemi, O.D., O'Gara, J.P., Dowling, D.P. (2012). Evaluation of protein adsorption on atmospheric plasma deposited coatings exhibiting superhydrophilic to superhydrophobic properties. *Biointerphases* **7**, 31–42.

[44] Shi, Z. (2013). Preparation and characterization of crosslinked polyurethane-*block*poly(trifluoropropylmethyl)siloxane elastomers with potential biomedical applications. *Polym. Int.* **62**, 1351–1357.

[45] Liu, X., Tong, W., Wu, Z., Jiang, W. (2013). Poly(N-vinylpyrrolidone)-grafted poly(dimethylsiloxane) surfaces with tunable microtopography and anti-biofouling properties. *RSC Advances* **3**, 4716–4722.

[46] Silva, S.S., Ferreira, R.A.S., Fu, L., Carlos, L.D., Mano, J.F., Reis, R.L., Roch, J. (2005). Functional nanostructured chitosan-siloxane hybrids. *J. Mater. Chem.* **15**, 3952–3961.

[47] Meera, K.M.S., Sankar, R.M., Jaisankar, S.N., Mandal, A.B. (2011). Mesoporous and biocompatible surface active silica aerogel synthesis using choline formate ionic liquid. *Colloids Surf. B: Biointerfaces* **86**, 292–297.

[48] Seeni Meera, K.M., Murali Sankar, R., Jaisankar, S.N., Mandal, A.B. (2013). Physicochemical studies on polyurethane-siloxane cross-linked films for hydrophobic surfaces by the sol-gel process. *J. Phys. Chem. B* **117**, 2682–2694.

[49] Shi, F., Deng, Y. (2005). Abnormal FT-IR and FT-Raman spectra of ionic liquids confined in nano-porous silica gel, *Spectrochim. Acta A: Mol. Biomol. Spectrosc.* **62**, 239–244.

[50] Brinker, C.J., Scherer, G.W. (1990). *Sol-Gel Science: The Physics and Chemistry of Sol-Gel Processing.* Academic Press, New York, pp. 617–625.

[51] Tuncaboylu, D.C., Okay, O. (2010). Hierarchically macroporous cryogels of polyisobutylene and silica nanoparticles. *Langmuir* **26**, 7574–7581.

[52] Karout, A., Pierre, A.C. (2009). Porous texture of silica aerogels made with ionic liquids as gelation catalysts. *J. Sol-Gel Sci.Technol.* **49**, 364–372.

[53] Christenson, H.K. (2001). Confinement effects on freezing and melting. *J. Phys. Condensed Matt.* **13**, R95–R133.

[54] Mosmann, T. (1983). Rapid colorimetric assay for cellular growth and survival: Application to proliferation and cytotoxicity assays. *J. Immunol. Methods* **65**, 55–63.

[55] Sankar, R.M., Seeni Meera, K.M., Samanta, D., Jithendra, P., Mandal, A.B., Jaisankar, S.N. (2013). The pH-sensitive polyampholyte nanogels: Inclusion of carbon nanotubes for improved drug loading. *Colloids Surf. B: Biointerfaces* **112**, 120–127.

[56] Sankar, R.M., Meera, K.M.S., Samanta, D., Murali, A., Jithendra, P., Mandal, A.B., Jaisankar, S.N. (2012). The reinforced hydrogel for drug loading: Immobilization of single-walled carbon nanotubes in cross-linked polymers via multiple interactions. *RSC Advances* **2**, 12424–12430.

[57] Murali Sankar, R., Seeni Meera, K., Mandal, A.B., Jaisankar, S.N. (2013). Thermoplastic polyurethane-single-walled

carbon nanotube composites with low electrical resistance surfaces. *High Perform. Polym.* **25**, 135–146.

[58] Mishra, A.K., Chattopadhyay, D.K., Sreedhar, B., Raju, K.V.S.N. (2006). FT-IR and XPS studies of polyurethane-urea-imide coatings. *Progress Organic Coat.* **55**, 231–243.

[59] Xia, Y., Larock, R.C. (2010). Castor oil-based thermosets with varied crosslink densities prepared by ring-opening metathesis polymerization. *Polymer* **51**, 2508–2514.

[60] Martinelli, M., Luca, M.A., Bechi, D.M., Mitidieri, S. (2009). Hybrid films based on hydroxylated castor oil and titanium(IV) isopropoxide. *J. Sol-Gel Sci. Technol.* **52**, 202–209.

[61] Prabhakar, A., Chattopadhyay, D.K., Jagadeesh, B., Raju, K.V.S.N. (2005). Structural investigations of polypropylene glycol (PPG) and isophorone diisocyanate (IPDI)-based polyurethane prepolymer by 1D and 2D NMR spectroscopy, *J. Polym. Sci. A: Polym. Chem.* **43**, 1196–1209.

[62] Karak, N., Rana, S., Cho, J.W. (2009). Synthesis and characterization of castor-oil-modified hyperbranched polyurethanes, *J. Appl. Polym. Sci.* **112**, 736–743.

[63] Yu, Y-Y., Chen, W-C. (2003). Transparent organic-inorganic hybrid thin films prepared from acrylic polymer and aqueous monodispersed colloidal silica. *Mater. Chem. Phys.* **82**, 388–395.

[64] Radi, B., Wellard, R.M., George, G.A. (2010). Controlled poly(ethylene glycol) network structures through silsesquioxane cross-links formed by sol-gel reactions. *Macromolecules* **43**, 9957–9963.

[65] Chiang, C-L., Ma, C-C.M. (2002). Synthesis, characterization and thermal properties of novel epoxy containing silicon and phosphorus nanocomposites by sol-gel method. *Eur. Polym. J.* **38**, 2219–2224.

[66] Pergal, M.V., Dzunuzovic, J.V., Ostojic, S., Pergal, M.M., Adulovic, A., Jovanovic, S. (2012). Poly(urethane-siloxane)s based on hyper branched polyester as cross-linking agent: Synthesis and characterization. *J. Serbian Chem. Soc.* **77**, 1–22.

[67] Kulkarni, S.A., Ogale, S.B., Vijayamohanan, K.P. (2008). Tuning the hydrophobic properties of silica particles by surface silanization using mixed self-assembled monolayers. *J. Colloid Interface Sci.* **318**, 372–379.

[68] Mequanint, K., Sanderson, R., Pasch, H. (2003). Adhesion properties of phosphate- and siloxane-containing polyurethane dispersions to steel: An analysis of the metal-coating interface. *J. Appl. Polym. Sci.* **88**, 900–907.

[69] Stiubianu, G., Nicolescu, A., Nistor, A., Cazacu, M., Varganici, C., Simionescu, B.C. (2012). Chemical modification of cellulose acetate by allylation and crosslinking with siloxane derivatives. *Polym. Int.* **61**, 1115–1126.

[70] Tan, H., Yang, D., Xiao, M., Han, J., Nie, J. (2009). Preparation of silica-polyurethane nanocomposites by UV-induced polymerization from surfaces of silica. *J. Appl. Polym. Sci.* **111**, 1936–1941.

[71] Jaisankar, S.N., Sathya, R., Hariharan, S., Mohan, R., Saravanan, P., Samanta, D., Mandal, A.B. (2013). Cloisite-g-methacrylic acid copolymer nanocomposites by graft from method for leather processing. *Industr. Eng. Chem. Res.* **52**, 1379–1387.

[72] Alexandru, M., Racles, C., Cazacu, M., Nistor, A., Macsim, A.-M. (2011). Polysiloxanes modified with aromatic diamines interconnecting with silica network. *J. Composite Mater.* **45**, 621–630.

[73] Alexandru, M., Hamciuc, E., Nistor, A., Musteata, V., Cazacu, M. (2010). Polysiloxanes cross-linked by bisimide bridges. *IEEEXplore* **2**, 313–316.

[74] Stiubianu, G., Racles, C., Nistor, A., Cazacu, M., Simionescu, B.C. (2011). Cellulose modification by cross-linking with siloxane diacids. *Cellulose Chem. Technol.* **45**, 157–162.

[75] Li, C.Y., Chen, J.H., Chien, P.C., Chiu, W.Y., Chen, R.S., Don, T.M. (2007). Preparation of poly(IPDI-PTMO-siloxanes) and influence of siloxane structure on reactivity and mechanical properties. *Polym.Eng. Sci.* **47**, 625–632.

[76] Chen, R.-S., Chang, C.-J., Chang, Y.-H. (2005). Study on siloxane-modified polyurethanedispersions from various polydimethylsiloxanes. *J. Polym. Sci. A: Polym. Chem.* **43**, 3482–3490.

[77] Jiang, X., Gu, J., Shen, Y., Wang, S., Tian, X. (2011). New fluorinated siloxane-imide block copolymer membranes for application in organophilic pervaporation. *Desalination* **265**, 74–80.

[78] Partha, M., Dean, C.W. (2006). Influence of solvent composition and degree of reaction on the formation of surface microtopography in a thermoset siloxane-urethane system. *Polymer* **47**, 4172–4181.

[79] Zhang, Q., Hu, J., Gong, S. (2011). Preparation and characterization of aqueous polyurethane dispersions with well-defined soft segments. *J. Appl. Polym. Sci.***122**, 3064–3070.

[80] An, Q., Wang, Q., Li, L., Huang, L. (2009). Study of amino functional polysiloxane film on regenerated cellulose substrates by atomic force microscopy and X-ray photoelectron Microscopy. *Textile Res. J.* **79**, 89–93.

2

INTERACTION OF ANESTHETICS WITH GLOBULAR PROTEINS

MAKOTO NISHIMOTO,[1] MICHIO YAMANAKA,[2] AND HITOSHI MATSUKI[3]

[1]*Department of Materials Science, Wakayama National College of Technology, 77 Nada, Noshima, Gobo, Wakayama 644-0023, Japan*
[2]*Department of Chemistry, Faculty of Sciences, Kyushu University, 6-10-1 Hakozaki, Higashi-ku, Fukuoka 812-8581, Japan*
[3]*Department of Life System, Institute of Technology and Science, Tokushima University, 2-1 Minamijosanjima-cho, Tokushima 770-8506, Japan*

2.1 INTRODUCTION

It is well known that organic compounds with a small and simple structure such as ethers and alcohols induce anesthetic action. More than 150 years have passed since the phenomenon of anesthesia was discovered; however, the action mechanisms still have not been clarified thus far. There are some common characteristics in anesthetic action as follows:

1. *No Structural Specificity of Anesthetics*. Most volatile organic liquids exhibit anesthetic potency, although they cannot be clinically used because of the strong toxicity. Laughing gas (nitrous oxide) and inactive-gas xenon also have anesthetic potency. Figure 2.1 shows various molecular structures of anesthetics. Such molecular diversity undoubtedly indicates that functional groups needed for the anesthetic action cannot be determined.
2. *High Effective Anesthetic Concentration*. The EC_{50} (the concentration needed for 50% drug action) values of anesthetics take values of mM (M = mol dm^{-3}) order while those of receptor-binding drugs take values of from nM order to μM order, indicating that they are more than 1000 times larger than the latter.
3. *Pressure Reversal of Anesthesia.* These phenomena were first reported in anesthetic experiments of luminous bacteria [1, 2]; subsequently, they were [3] also confirmed in swimming experiments of tadpoles that pressure antagonisms the anesthetic action.
4. *Cutoff Phenomenon*. The anesthetic effect of organic compounds such as alcohols vanishes suddenly beyond a certain chain length [4, 5].

These characteristics of anesthetic action distinctly describe that the action is quite different from that of most drugs biochemically or physiologically oriented and closely related to fields of not only medical science but also natural science such as colloid and surface chemistry and biophysical chemistry.

Studies of anesthetic mechanisms go back to one rule proposed by Meyer and Overton [6, 7] at the beginning of twentieth century. They described that there exists an excellent correlation between olive oil/water partition coefficients of anesthetics and the anesthetic potency. Because biological membranes provide similar hydrophobic environments with moderate hydrophilicity to olive oil, it was believed that the anesthetic action is produced by a certain amount of an anesthetic incorporated into the membrane; that is, the Meyer−Overton rule suggested that the location of anesthetic action is the membrane. There has been a repeated dispute between two theories in studies of anesthetic mechanisms since the proposal of the Meyer−Overton rule. One theory is that nonspecific binding of the anesthetics into the membranes changes the membrane properties such as fluidity and phase state, and the secondary effect by anesthetics

Encyclopedia of Biocolloid and Biointerface Science, Volume 1, First Edition. Edited by Hiroyuki Ohshima.
© 2016 John Wiley & Sons, Inc. Published 2016 by John Wiley & Sons, Inc.

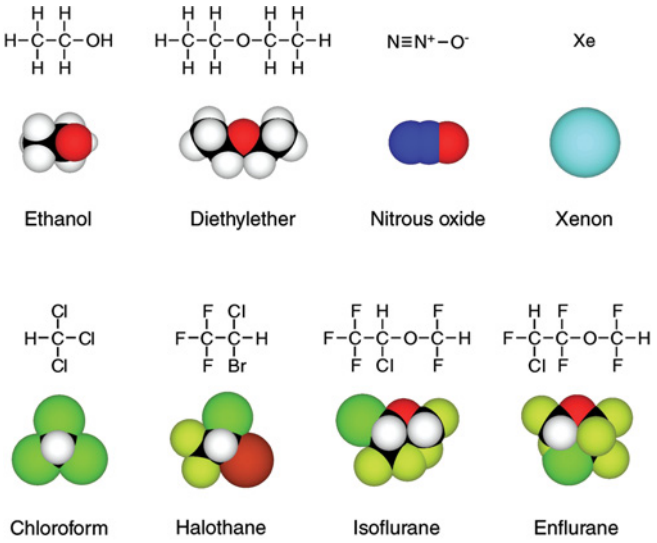


FIGURE 2.1 Molecular structures of inhalation anesthetics.

into the membrane proteins causes anesthesia [8–10]. This is called a *lipid hypothesis* and flourished up to the mid-1980s, but the lipid hypothesis suffers from several criticism [11]: effects of stereoisomers [12, 13] and nonimmobilizers [14,15], low-temperature enhancement of anesthesia [16,17], and cutoff phenomenon [4, 5]. In addition to the backlash of the lipid hypothesis, the rapid development of protein and genetic engineering brought about the prosperity of another theory called a *protein hypothesis*, explaining that anesthesia is caused by the specific binding of anesthetics into several signal receptor proteins in the membrane [18–20]. The protein hypothesis has became popular until now; hence, more recent anesthetic studies concentrate on examinations of specific interactions between anesthetics and various kinds of proteins for the purpose of the identification of anesthetic binding sites in these proteins.

Some water-soluble globular proteins with a relatively simple structure have been used as model proteins for anesthetic studies. However, It has been reported in these model protein systems that the action of anesthetics on proteins varies depending on the kinds of the proteins, namely, the anesthetic sensitivity among the proteins is different from one another. This became a hindrance to the understanding of interaction modes between anesthetics and proteins. Recently, other investigators [21, 22] and we [23–25] have shown that the essential interaction modes of anesthetics to proteins can be revealed by comparing them with the interaction modes of substrates or substrate analogs, what is called specific or competitive binders, to the proteins. In this chapter, comparative studies of interaction modes of anesthetic and specific binders performed on several model globular protein systems are reviewed. At first, a comparative study on a luminescence enzyme firefly luciferase (FFL), which was reported as an anesthetic-specific protein for the first time in 1984 [26], is discussed. Next, studies using several globular proteins, which were also considered to be other anesthetic-specific proteins until now, an oxygen transporter myoglobin (Mgb), a hydrolytic enzyme of polysaccharide lysozyme (Lys), and a carrier enzyme in blood plasma bovine serum albumin (BSA), are demonstrated. Finally, we describe the reason for the diversity of anesthetic sensitivity among proteins by recent our idea of anesthetic–protein interactions.

2.2 ANESTHETIC EFFECT ON FFL

Most enzymes require anesthetic concentrations higher than the clinical level to show significant effects. However, FFL is uniquely sensitive to anesthetic actions; therefore, this enzyme has been used as a lipid-free protein model for the study on the anesthetic interaction with proteins. One investigator [27] first reported that FFL is highly sensitive to anesthetics about 50 years ago. Subclinical concentrations of inhalation anesthetics inhibited partially purified cell-free FFL from Japanese species (*Luciola cruciata*). Later, the authors of a report [28] on the temperature dependence of the anesthetic effects on partially purified American FFL (*Photinus pyralis*) concluded that anesthetics inhibited FFL by reversibly denaturing the structure into the less active unfolded form. On the other hand, another team [26, 29] reported that anesthetics and alcohols inhibited FFL in competition with the substrate luciferin. A controversy of anesthetic mechanism between the above investigators continued in late 1990s. Although the final conclusion has not yet been settled at present, for reasons mentioned in the introduction, now their idea for the anesthetic effect on FFL has been widely recognized as evidence for the specificity of anesthetic action and the paper was regarded as a milestone in the protein hypothesis [30].

The FFL protein is globular, with a molecular weight of 62 kDa, and emits a flash of light when mixed with luciferin and ATP in the presence of oxygen. The initial flash of light is followed by a weak light intensity with a slow decline continuing for hours. The reaction sequence of light emission was clarified [31–33] as follows:

$$E + LH_2 + ATP \Leftrightarrow E \bullet LH_2 \bullet AMP + PP_i \quad (2.1)$$

$$E \bullet LH_2 \bullet AMP + O_2 \Rightarrow E \bullet L_{ox} \bullet AMP + CO_2 + \text{light} \quad (2.2)$$

$$E \bullet L_{ox} \bullet AMP \Rightarrow E + L_{ox} + AMP \quad (2.3)$$

where E is the FFL, LH_2 is the reduced form of luciferin, L_{ox} is oxiluciferin, and PP_i is inorganic pyrophosphate. Initial reaction of FFL is to activate luciferin by ATP to form acyl-AMP between carboxyl moiety of luciferin and phosphate moiety of AMP, releasing PPi [Eq. (2.1)]. More recently, other studies [21,22] have revealed that long-chain fatty acids

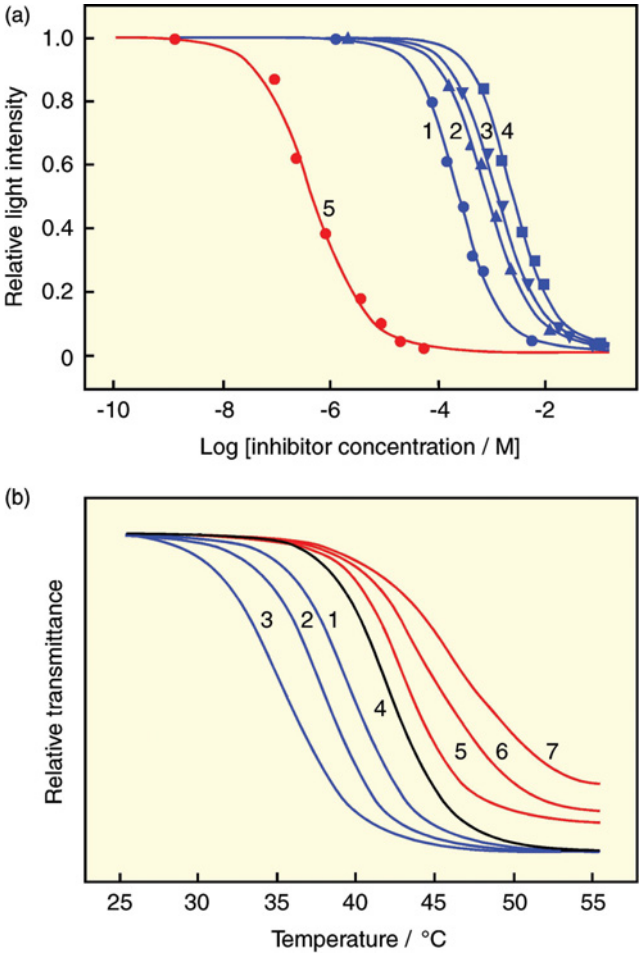


FIGURE 2.2 (a) Dose–response curves of inhalation anesthetics and myristic acid on light intensity of FFL: (1) halothane; (2) isoflurane; (3) enflurane; (4) chloroform; (5) myristic acid. The light intensity is expressed by the fraction of the control light intensity without ligands. (b) Dose-dependent effects of isoflurane and myristic acid on thermal denaturation temperature of FFL: (1) isoflurane concentration 0.96 mM; (2) 1.92; (3) 2.88; (4) control without ligands; (5) myristic acid concentration 5.0 μM; (6) 15.0; (7) 24.9.

such as myristic and palmitic acids inhibit FFL luminescence greater than do alcohols or anesthetics and that they are strong luciferin competitors. The acylation of AMP by carboxylates is often the initial step in activating the carboxylates in many biochemical reactions. Fatty acids are activated by ATP to form acyl-AMP and release PPi during β-oxidation by acyl-coenzyme A (acyl-CoA) synthetases [34] as follows

$$\text{R–COOH} + \text{ATP} \Leftrightarrow \text{R–COO} \bullet \text{AMP} + \text{PP}_\text{i} \quad (2.4)$$

$$\text{R–COO} \bullet \text{AMP} + \text{CoA} \Leftrightarrow \text{R–COO} \bullet \text{CoA} + \text{AMP} \quad (2.5)$$

where R−COOH is a fatty acid. The reaction is identical to the initial interaction of luciferin with ATP in Eq. (2.1). The homology between FFL and acyl-CoA synthetases has been

TABLE 2.1 Effects of Inhalation Anesthetics and Fatty Acids on FFL

Ligand	IC_{50} (μM)	n^a	$\Delta T_{1/2}$ (μM)^b	log P^c
Anesthetics				
Halothane	219	1.13	273	2.30
Isoflurane	694	1.11	634	2.10
Enflurane	871	1.10	852	2.10
Chloroform	2130	1.26	2110	1.97
Fatty acids				
C4	13600	3.02	10340	–2.70
C6	3400	1.04	3280	–1.70
C8	2900	0.81	2460	–0.70
C10	13.2	0.83	7.4	0.30
C12	1.2	0.89	2.3	1.30
C14	0.68	0.89	1.2	2.31
C16	0.67	0.95	1.0	3.31
C18	0.63	0.95	0.87	4.31

[a] Ligand concentrations that change the denaturation temperature of 1.0°C.
[b] Hill number.
[c] Octanol/water partition coefficient.

mentioned [35, 36]. Long-chain fatty acids bind luciferin recognition sites with high affinity by the negative charge of the carboxyl moiety. Therefore, the inhibition modes of anesthetics are different from fatty acids. Here we review several experimental results obtained by comparative studies on FFL−ligand interactions [21, 22, 37−40].

Figure 2.2a shows the dose-response curves of FFL light intensity measured at steady-state conditions when inhalation anesthetics or myristic acid, were added. The values of concentrations needed for 50% inhibition (IC_{50}) are shown for anesthetics and fatty acids in Table 2.1, respectively. The IC_{50} values for anesthetics are in mM ranges, while that of myristic acid is in μM range. Despite almost three orders of magnitude difference in IC_{50} values, the octanol/water partition coefficients are similar: myristic acid 199 [41], halothane 199, enflurane 126, and chloroform 93 [42]. The slopes of the dose-response curves of ligands are related to the Hill coefficients, n, of ligands, and the n values were calculated by the equation at constant temperature and pressure

$$\ln[(I_1/I_2 - 1)] = n \ln[I] + \text{constant} \quad (2.6)$$

where I_1 and I_2 are the intensity without the inhibitor and that with the inhibitor and $[I]$ is the inhibitor concentration, respectively. The calculated n values of inhalation anesthetics exceed one while that of myristic acid is below one. The n value does not necessarily indicate that n molecules of anesthetics bind to the protein. The derivation assumes a highly cooperative reaction between enzyme, E, and ligand, L, where only two species are present, E and EL_n. The intermediate n species, EL_1, EL_2,…, EL_{n-1}, are not counted. When the Hill number exceeds one, at least two

ligand molecules bind to one enzyme molecule cooperatively. The above results mean that inhalation anesthetics interact cooperatively with multiple hydrophobic pockets while the binding sites of myristic acid are limited.

The change in thermal denaturation temperature of a protein by ligand binding gives useful information regarding the ligand effect on structural stability of the protein. If the denaturation is irreversible, the thermal denaturation can be estimated by the ratio between the folded native fraction and the irreversibly denatured fraction. We found that the FFL solution suddenly becomes turbid at the denaturation temperature. The irreversibly denatured fraction was measured by the turbidity. Since the transition temperature varies by the protein concentration and scan rate because of the irreversibility [21], the ligand effects on the transition were compared at a fixed protein concentration and scan rate by using the temperature at which the denaturation was half completed ($T_{1/2}$). Figure 2.2b shows the thermal transmittance tracings of the effects of isoflurane and myristic acid together with a control with no ligand (thick curve). In the case of anesthetics, they are effective at mM range. At μM range, anesthetics show no effect. By contrast, myristic acid increases $T_{1/2}$ dose-dependently at μM range. The anesthetic concentrations that decreased $T_{1/2}$ by 1.0°C and the myristic acid one that increased $T_{1/2}$ by 1.0°C are also shown in Table 2.1. We can understand that the $T_{1/2}$ data are well correlated with the IC_{50} values.

A similar competitive effect of myristic acid with luciferin was observed in the fatty-acid homologs with the carbon number of ≥10 [22] as given in Table 2.1. On the other hand, during the FFL study, we observed that the inhibitory potency of fatty acids on FFL suddenly decreases at the certain carbon chain length. This is the similar cutoff phenomenon of the anesthetic potency observed in the series of homologous alcohols [4, 5, 43]. In the alcohol series, however, the longer alcohols lose their potency unlike the FFL inhibition by fatty acids. Here we compared the effects of butyric acid (C4), hexanoic acid (C6), and octanoic acid (C8) with those of the longer-chain fatty acids on the steady-state luminescence intensity and the thermal denaturation temperature of FFL [37]. We immediately notice from Table 2.1 that there is a sudden discontinuous change from μM to mM at C10–C8. The IC_{50} values change a 220-fold from C10 to C8. In contrast to this, the change in IC_{50} from C12 to C10 is only 11-fold. The dose–response curves of the three fatty acids are shown in Fig. 2.3a. The obtained dose–response curves are not parallel. This is unusual because the dose–response curves of similar compounds such as 1-alkanol series and those of the fatty acids with a longer acyl chain than C10 are parallel [22,24]. Therefore, a large change in shape among the curves shown in Fig. 2.4 means that the Hill numbers change from less than one at C8 to more than one at C6. The result reveals that the binding number suddenly increases when the carbon chain length becomes shorter than C8; that is, the

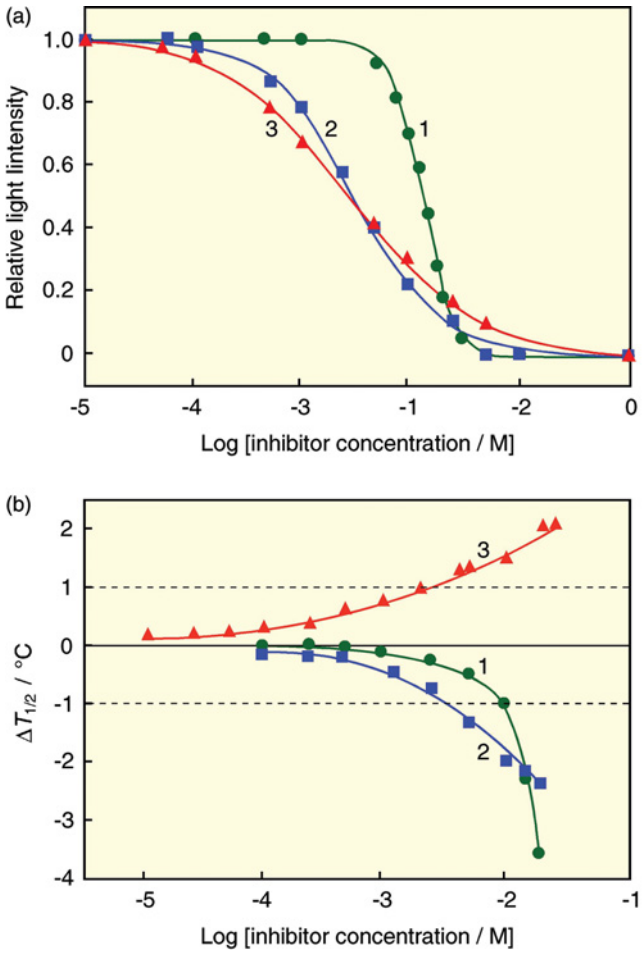


FIGURE 2.3 (a) Dose–response curves of short-chain fatty acids on light intensity of FFL (1) butyric acid (C4), (2) hexanoic acid (C6), and (3) octanoic acid (C8). The light intensity is expressed by the fraction of the control light intensity without ligands. (b) Dose-dependent effects of short-chain fatty acids on thermal denaturation temperature of FFL: (1) C4; (2) C6; (3) C8. Broken lines indicate the lines of denaturation-temperature change of 1.0°C.

binding mode changes from noncooperative limited number of binding sites to highly cooperative multiple binding sites. Further, a more dramatic change was observed with the transition temperature. The dose-dependent effects of C8, C6, and C4 on the thermal denaturation temperature are shown in Fig. 2.3b. The fatty acids with a longer acyl chain than C10 increase the denaturation temperature, whereas those with a chain shorter than C8 decrease the temperature. The latter mode is identical to that of anesthetics and alcohols. The concentration that changed the transition temperature 1.0°C (negative or positive) increases a 332-fold from C10 to C8. The change from C12 to C10 is only 3.2-fold.

The above results show that there are two modes in the action of fatty acids on luciferase. The action mode of fatty acids switches from specific to nonspecific when the carbon

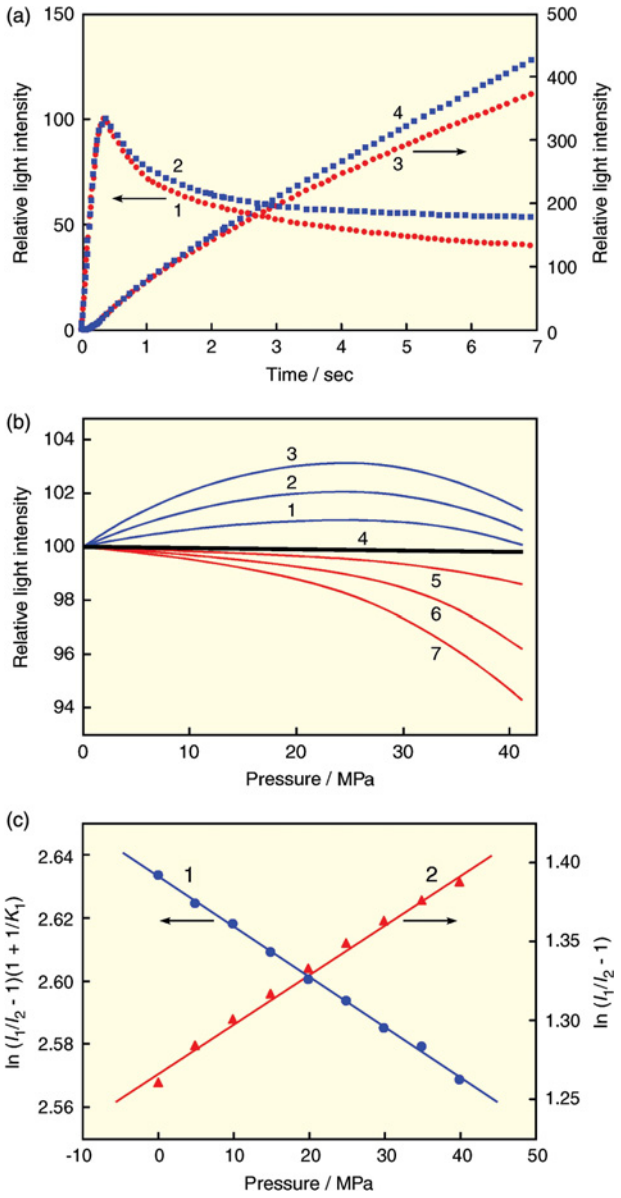


FIGURE 2.4 (a) Stopped-flow tracings of the effect of 1-octanol (0.7 mM) on the light intensity of FFL (initial flash intensity): (1) 0.1 MPa, (2) 12 MPa, and the integral of the tracings (steady-state intensity): (3) 0.1 MPa, (4) 12 MPa. (b) Effect of hydrostatic pressure on the steady-state light intensity of FFL in the presence of halothane and myristic acid at 19.1°C: (1) halothane concentration 0.1 mM; (2) 0.5; (3) 1.0; (4) control without ligands; (5) myristic acid concentration 0.5 μM; (6) 2.5; (7) 5.0. The relative light intensity is taken as the values at ambient pressure as 100. (c) Johnson–Eyring plots for anesthetic and specific-binder inhibition at 25°C: (1) 0.5 mM halothane; (2) 2.5 μM myristic acid.

chain length is reduced below C8. Another author [44, 45] proposed the induced-fit model where the ligands that bind to the substrate binding sites induce the protein structure to a high-energy native state. Another investigator [46] proposed the rate process model where anesthetics and alcohols bind nonspecifically to proteins and reversibly unfold the protein into a less active state by releasing the surface-bound water molecules. Fatty acids with a longer acyl chain than C10 are high-affinity specific binders and follow the induced-fit model. On the other hand, because of the strong hydrophobicity of the luciferin binding site [32], fatty acids with a chain shorter than C8 are apparently excluded from the luciferin binding site and they are low-affinity nonspecific denaturants and follow the rate process model. These results contradict the general consensus that the size of the receptor cavity discriminates specific binders.

The antagonizing effect of high pressure against anesthesia is well known. The pressure reversal of anesthesia has been generally accepted as a standard feature of anesthetic actions. There was a controversy about the anesthetic effect on FFL under high pressure. Another team [47] reported that application of high pressure does not affect the initial flash intensity (i.e., the initial peak heights) of FFL. In contrast, another group [38, 48] reported that high pressure decreases the steady-state light intensity at low temperatures but increases it at high temperatures and that the discrepancy between them is caused by the difference in the choice of parameters to represent the reaction velocity: initial flash intensity versus steady-state light intensity. Figure 4(a) demonstrates the stopped-flow tracings of the light intensity at 25°C in presence of 0.7 mM 1-octanol at ambient pressure and at 12 MPa, respectively, to compare the pressure effects on the initial flash intensity and the steady-state light intensity. The light intensity decays rapidly and the weak light lasts for hours. The initial flash is a transient event and is not in a steady state. We can understand that the flash intensity does not change with the application of hydrostatic pressure in the presence or absence of 1-octanol, but the tailings are different. On the other hand, the steady state is represented by the slope of the linear part of the integral of the light output. It is evident that high pressure increases the steady-state light intensity when the light intensity is integrated with respect to time. The rapid reaction kinetics of the transition state theory [49] shows the initial peak intensity approximately corresponds to the total amount of active enzyme and is unrelated to the reaction rate. Anesthetics inhibit the initial flash intensity by decreasing the amount of the active enzyme by reversibly unfolding the enzyme into the less active state, whereas pressure affects the steady-state light intensity by changing the reaction rates.

Here let us compare the effect of high pressure up to 40 MPa on the light inhibition of an anesthetic (halothane) and a fatty acid (myristic acid) under the steady-state condition, which can be obtained by eliminating the initial peak with addition of pyrophosphate [31, 39, 48]. The temperature scan of the steady-state light intensity of FFL showed that the maximum light intensity is observed at 19.1°C. When pressurized at the temperature that gives maximum light, hydrostatic pressure does not show any effect in the absence of

inhibitory ligands. Figure 2.4b shows the pressure effect on the steady-state light intensity in the presence of ligands at 19.1°C [39]. Here the pressure effect on the light intensity of the ligand-bound FFL is expressed against the light intensity at ambient pressure in the presence of inhibitors as reference states (controls). When halothane is added, pressure increases the light intensity with a maximum effect at about 25 MPa, and then further increase of pressure decreases the light intensity to the control. It is also noticed that pressure increases the light intensity with increasing the halothane concentration. In contrast to the observed effect of halothane, application of hydrostatic pressure in the presence of myristic acid decreases the light intensity monotonously and there is no minimum on the intensity curve. The myristic acid concentration synergizes the pressure effect in direct opposition to the case of halothane. From the pressure effects on the light intensities of the control and the ligand-bound FFL, the volume changes of the host protein (ΔV) were estimated. The Johnson−Eyring rate−process model calculates the volume change by plotting the logarithm of the ratio between the ligand-induced decrement of the light intensity and the control light intensity against the applied pressure [39, 50]

$$\ln[(I_1/I_2 - 1)(1 + 1/K_1)] = -p\Delta V/RT + \text{constant, for anesthetics} \quad (2.7)$$

$$\ln[(I_1/I_2 - 1)] = -p\Delta V/RT + \text{constant, for specific binders} \quad (2.8)$$

where K_1 is the equilibrium constant between the unfolded inactive fraction and the native fraction of the enzyme. Results of the Johnson−Eyring plots of 0.5 mM halothane and 2.5 μM myristic acid at 25°C are demonstrated in Fig. 2.4c. Here the light intensity curves at 25°C in Figs. 2.3 and 2.4 in Ref. 52 were used for data analysis. From the slope values of these curves, the ΔV values of FFL were estimated to be +3.94 cm^3 mol^{-1} for halothane and –7.66 cm^3 mol^{-1} for myristic acid, respectively. These results show that there are distinct differences between these ligands in their response to high pressure, that is, the effect of myristic acid is unambiguously the reverse of that of halothane.

The three-dimensional (3D) molecular structure of FFL (*Photinus pyrali*) in the absence of substrates (luciferin and ATP) was established in 1996 [51]. The enzyme takes an "open" conformation with a large solvent exposed cleft between a large *N*-terminal domain and a smaller *C*-terminal domain (Fig. 2.5a), which was constructed from PDB data (1LCI). The same team [52] also identified anesthetic binding sites on FFL without substrates from X-ray crystallography (Fig. 2.5b) constructed from 1BA3 that two bromoform molecules lie close to one another and bind within pockets in the large *N*-terminal domain: one is bound in a luciferin binding pocket, whereas the other is bound to a pocket accessible from the external surface of the enzyme. Another group [53] determined the FFL (*Luciola cruciata*) structure in the presence of substrates (Fig. 2.5c) constructed from 2D1R. They revealed that the enzyme takes a "closed" conformation, which involves a rigid-body bending of the *C* domain toward the the *N* domain and a ∼90° counterclockwise rotation of the *C* domain relative to the *N* domain, and luciferin and ATP bind closer to the domain interface and the cleft. This is a typical example of the induced-fit model. These facts clearly indicate that the binding of anesthetics to FFL hardly induces any change in structure, while there is a significant structural change in binding of the substrates. Concerning fatty-acid binding to FFL, other investigators [54] reported that FFL has a catalytic activity to synthesize fatty acyl-CoA via fatty acyl−adenylate as an intermediate from fatty acid in the presence of ATP, Mg^{2+}, and CoA. This is because that FFL belongs to adenylate-forming superfamily of enzymes and can produce an intermediate of acyl−adenylate (luciferyl-AMP) similar to fatty acyl−adenylate (fatty acyl-AMP) as seen in Eqs. (2.1) and (2.4) [55−57]. More recently, the structures of long-chain fatty acyl-CoA synthetase (LC-FACS) and its complexes with substrates (Fig. 2.5d,e) constructed from 1ULT and 1V26 have been reported [58]. The structure of LC-FACS in the absence of the substrates (fatty acid and ATP) is markedly similar to that of FFL under the same conditions, and surprisingly, the enzyme changes the conformation from "open" to "closed" by the large structural change between a large *N*-terminal domain and a smaller *C*-terminal domain, due to the substrate binding. The situation is essentially identical to the case of the substrate binding to FFL. Judging from the structural information with the experimental results as mentioned above, we can conclude that fatty acids, which compete with luciferin, stabilize the FFL conformation against thermal perturbation and decrease the FFL volume, indicating that they are a specific binder characterized by high affinity and small binding numbers. On the contrary, anesthetics, which do not compete with the substrate, destabilize the FFL conformation and increase the FFL volume, indicating that they are a nonspecific binder characterized by low affinity and large binding numbers.

2.3 ANESTHETIC EFFECT ON Mgb, Lys, AND BSA

An idea that anesthetics reduce the protein stability, namely, the promotion of protein unfolding, has found general acceptance and holds the anesthetic effect on FFL. However, in more recent reports [59], an opposite effect by anesthetics has been found on BSA, and this attracted a great deal of attention. The authors observed that the thermal denaturation temperature of BSA elevates by adding halothane and pointed out that halothane stabilizes the BSA structure. They explained that this stabilization is caused by the specific

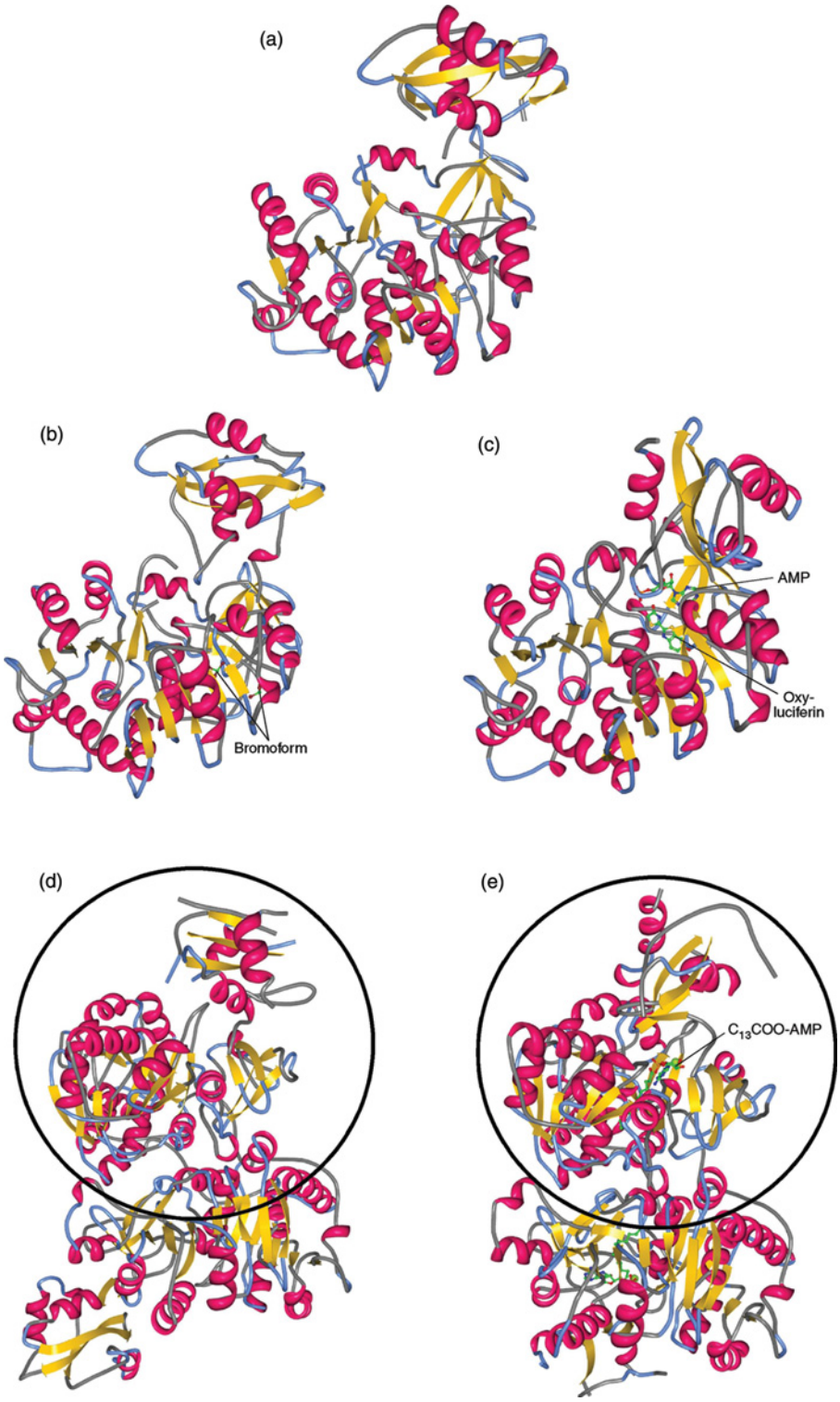


FIGURE 2.5 Structures of FFL and LC-FACS dimer complexed with ligands: (a) FFL without ligands; (b) FFL with bromoform; (c) FFL with AMP and oxyluciferin; (d) LC-FACS dimer without ligands; (e) LC-FACS dimer with C13COO-AMP. LC-FACS monomer is surrounded by a circle, and the ligand in each site is represented by ball-and-stick models. These figures were prepared from PDB data (1LCI, 1BA3, 2D1R, 1ULT, and 1V26) by using MBT Protein Workshop.

binding of halothane to the binding sites of native BSA. Another group [60] investigated the volume behavior of BSA in the absence and presence of medium-chain alcohol octanol and elucidated that the volume change of BSA-octanol binding is large negative, indicating that octanol decreases the BSA volume. These results form a great contrast to the destabilization (unfolding) of FFL by the addition of anesthetics, which was described in the preceding section. Further, investgtigators [61] have also observed that the effects of halothane on other globular proteins such as Mgb and Lys are markedly different from each other. The above findings suggest that an anesthetic acts on a protein in different ways depending on the kinds of the proteins, and this diversity of anesthetic sensitivity among proteins makes it difficult to systematically understand the mode of the interaction between an anesthetic and proteins. To clarify the intrinsic binding mode of anesthetics on globular proteins, we have recently performed a comparative study of ligand interactions on Mgb, Lys, and BSA from three viewpoints [23,25]: (1) comparison of interaction modes of anesthetics to the proteins to those of substrates or substrate analogs, (2) comparison between thermal and volume changes by ligand binding, and (3) comparison of the obtained macroscopic data with the structural data from X-ray crystallography.

The thermal changes of the proteins by anesthetic binding were estimated comparatively by differential scanning calorimetry (DSC). The DSC thermograms of Mgb, Lys, and BSA solutions in the absence and presence of halothane are demonstrated in Fig. 2.6, respectively. The effect of halothane on the thermal denaturation for all proteins appears at concentrations of mM range, however, the extent of the effect varies. The endothermic peak of Mgb shifts to a lower-temperature region with increasing halothane concentration, while Lys shows only a slight peak shift to a lower-temperature region with the concentration. On the contrary, the peak of BSA conversely shifts to a higher-temperature region with increasing halothane concentration. In Fig. 2.7, the denaturation temperatures (T_D) and denaturation enthalpy (ΔH_D) obtained for Mgb, Lys, and BSA at pH 7.0 are plotted against halothane concentration, respectively. For Mgb, the T_D value is depressed and the ΔH_D value decreases with increasing halothane concentration. The depression of T_D and the decrease in ΔH_D means that the binding of halothane to Mgb reduces the thermal stability of the native Mgb; in other words, halothane unfolds the structures as observed in the case of FFL [21]. On the other hand, the variation in the T_D and ΔH_D values of Lys is considerably small although both values decrease only slightly with increasing halothane concentration, which indicates that halothane produces little effect on the unfolding of Lys structures. In contrast to the cases of Mgb and Lys, the T_D and ΔH_D values for BSA increase with increasing halothane concentration, implying that halothane brings about the thermal stabilization of the native BSA by folding the structure. The

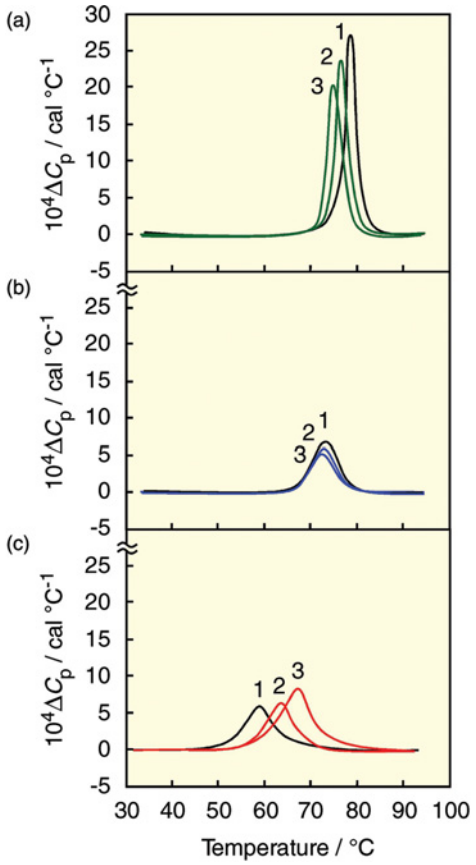


FIGURE 2.6 DSC thermograms of protein solutions at pH 7.0 in the absence and presence of halothane: (a) Mgb, (1) 0 mmol kg^{-1}, (2) 7.9, (3) 16.9; (b) Lys, (1) 0 mmol kg^{-1}, (2) 4.9, (3) 12.1; (c) BSA, (1) 0 mmol kg^{-1}, (2) 5.0, (3) 10.0.

corresponding results for the proteins at other pH levels exhibited a similar behavior for all the proteins [23,62,63].

The abovementioned anesthetic effect on the thermal change of the proteins was compared with that of their specific binders (substrates). The DSC thermograms of Lys solutions in the absence and presence of *N*-acetyl-D-glucosamine (NAG) are shown in Fig. 2.8 together with those of BSA solutions in the absence and presence of palmitic acid. Here NAG and palmitic acid are substrates of Lys and BSA, respectively. The endothermic peak of Lys shifts only slightly with the addition of NAG, while a greater peak shift is caused by the addition of palmitic acid for BSA. The effect of NAG on the T_D and ΔH_D values of Lys and that of palmitic acid on those values of BSA are shown in Fig. 2.9, respectively. The T_D and ΔH_D values of Lys increase very slightly with increasing NAG concentration unlike the case of halothane. In the case of BSA, peculiar behavior is observed for T_D with increasing palmitic acid concentration in the μM range, not mM range: there exists a bimodal increase in T_D, which is originated from the appearance of a new endothermic peak at a higher temperature. The ΔH_D value (total enthalpy of

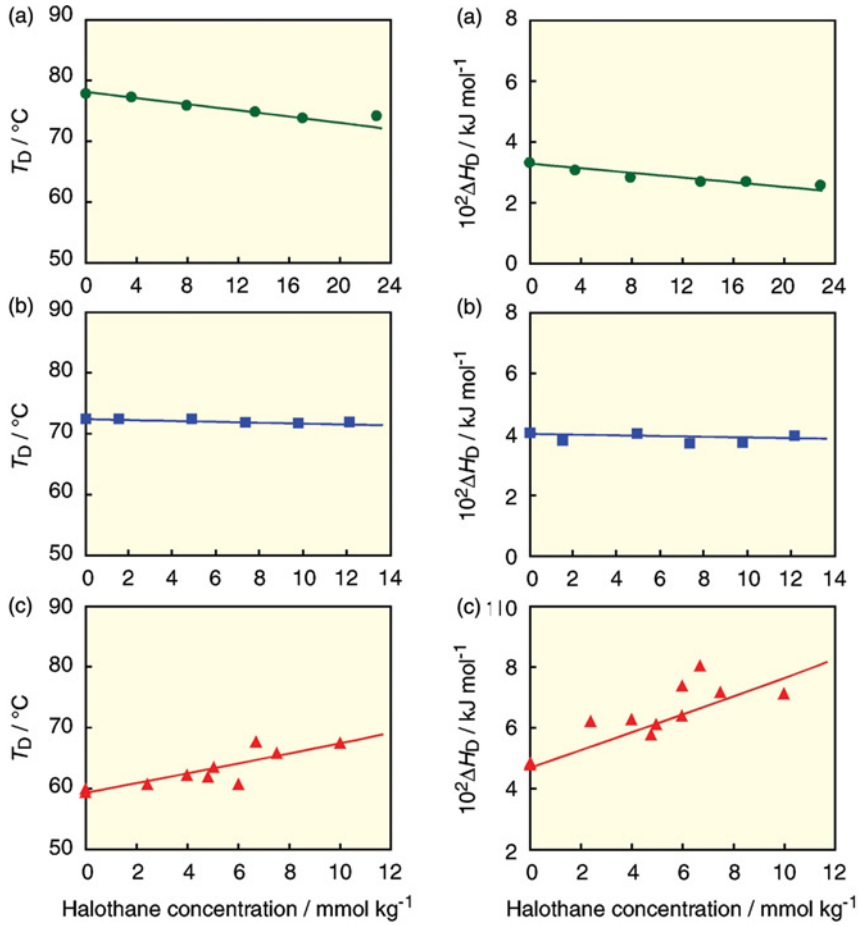


FIGURE 2.7 Thermal denaturation temperatures and enthalpies of proteins at pH 7.0 as a function of halothane concentration: (a) Mgb; (b) Lys; (c) BSA.

the two peaks) greatly increases with palmitic acid concentration. We can say from these results that the mode of the interaction between a specific binder and the protein is also different depending on the kinds of proteins, and also that the specific binder essentially produces the stabilization of the protein structure. The effect of the specific binder is in distinct contrast to that of halothane when considering their much lower effective concentrations.

Ligands affect not only the thermal behavior of a protein but also the volume behavior. Pressure study on FFL definitely suggests that pressure reversal of anesthesia is closely related to the volume change of proteins by binding of ligands. A comparative study of ligand effects on the volume behavior of Mgb, Lys, and BSA by using viscometry was performed [23, 25]. The pH dependence on the reduced viscosity (η_{red}) values of three kinds of protein solutions in the absence of halothane is shown in Fig. 2.10 by open symbols, respectively. The η_{red} values of the Mgb and BSA solutions are almost constant irrespective of pH values, while those of the Lys solution increase in the weak alkaline pH region. The η_{red} values of the three protein solutions in the presence of halothane at various pHs are also presented in Fig. 2.10 by closed symbols. Here the halothane concentration of 5.0 mmol kg^{-1} was adopted in the measurements considering the change in the thermal behavior of the proteins induced by halothane (Fig. 2.7). The changes in the η_{red} values of the protein solutions by the addition of halothane are different from one another: the η_{red} values of the Mgb, Lys, and BSA solutions in the presence of halothane become respectively larger, slightly larger and smaller than those in the absence of halothane at all pHs measured. The variation in the η_{red} value with halothane suggests that the volume of the protein in the solution changes by the addition of halothane, that is, that halothane causes a volume expansion of Mgb and a slight volume expansion of Lys, but a volume shrinkage of BSA.

The effect of the specific binder on the protein volume in the solution was investigated in the same way. The η_{red} values of the Lys solution in the absence and presence of NAG are plotted against pH together with those of BSA in the absence and presence of palmitic acid in Fig. 2.11. Here the NAG concentration of 690 μmol kg^{-1} and the palmitic acid concentration of 150 μmol kg^{-1} were selected by taking

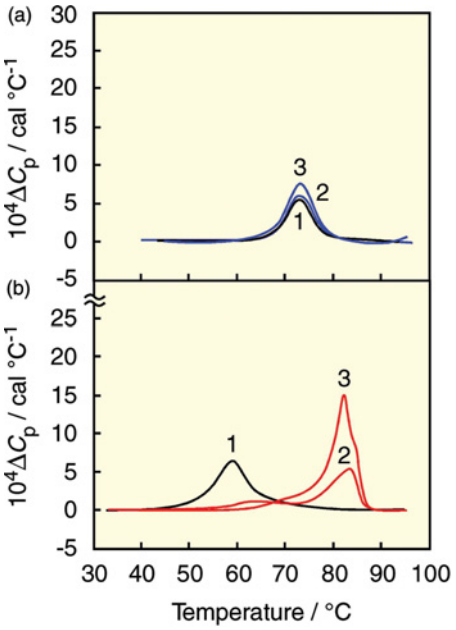


FIGURE 2.8 DSC thermograms of protein solutions at pH 7.0 in the absence and presence of specific binders: (a) Lys, (1) 0 μmol kg^{-1}, (2) 159, (3) 359; (b) BSA, (1) 0 μmol kg^{-1}, (2) 100, (3) 200. Here the binders of Lys and BSA are NAG and palmitic acid, respectively.

account of their effective concentrations (Fig. 2.9). The η_{red} values of the Lys solution in the presence of NAG are almost the same as those in the absence of NAG. The invariance of the η_{red} value suggests that the structural change of Lys by the NAG binding is not large enough to affect the volume. On the other hand, the η_{red} values of the BSA solution in the presence of palmitic acid become larger than those in the absence of palmitic acid, indicating that the BSA volume in the solution expands by the addition of palmitic acid. It is noteworthy that although the thermal behavior of BSA by halothane and palmitic acid (Figs. 2.7 and 2.9) is consistent with the direction of folding of the BSA structure, the volume expansion of BSA by palmitic acid is apparently the direction of unfolding of the structure in contrast to the volume shrinkage caused by halothane.

Mgb, Lys, and BSA are generally regarded as globular proteins. Hence, by assuming that the protein molecule is a hard-sphere particle, we roughly estimated the percentage of the volume change of the protein by the addition of the ligand. The viscosity of a dispersion of hard-sphere particles in homogeneous medium at a low concentration is expressed by Einstein's equation as

$$\eta_{red} = 2.5(v/V)C \tag{2.9}$$

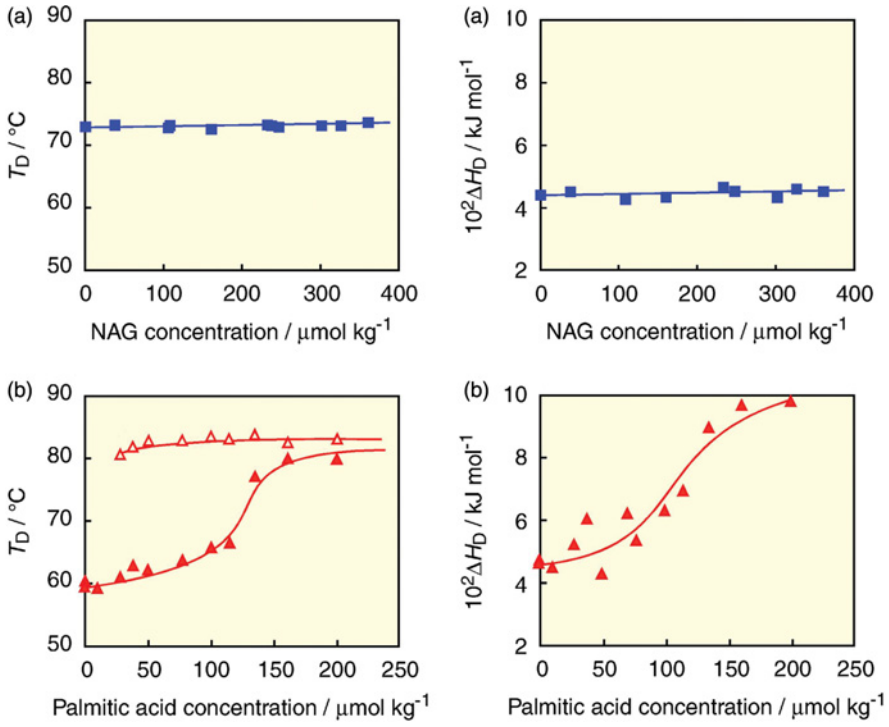


FIGURE 2.9 Thermal denaturation temperatures and enthalpies of proteins at pH 7.0 as a function of specific binder concentrations: (a) Lys; (b) BSA. For BSA, temperatures of low- and high-temperature denaturation are shown and total enthalpies of denaturation are given.

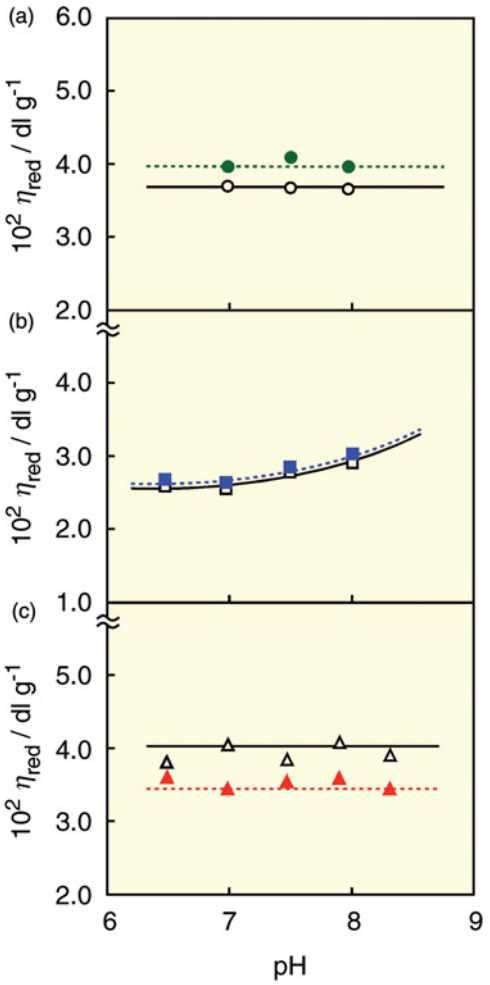


FIGURE 2.10 Reduced viscosity of protein solutions as a function of pH in the absence and presence of halothane: (a) Mgb; (b) Lys; (c) BSA. The open and closed circles correspond to the results for protein solutions in the absence and presence of halothane. The concentrations of halothane is 5 mmol kg^{-1}. The solid and broken were obtained from a least-squares method.

where v and V are the volume of all the hard-sphere particles in the dispersion and the total volume of the system, respectively, and C is the concentration of a protein in units of g dL^{-1}. For nonspherical particles, although the numerical coefficient of v/V is larger than 2.5, it should be constant for any given shape provided the shear rate is sufficiently low. The percentage can be given by the following equation derived by use of Eq. (2.9)

$$[v(\mathrm{P}+\mathrm{L})/v(\mathrm{P})-1]^{*}100 = [\eta_{red}(\mathrm{P}+\mathrm{L})/\eta_{red}(\mathrm{P})-1]^{*}100 \qquad (2.10)$$

where $v(\mathrm{P}+\mathrm{L})$ and $v(\mathrm{P})$ are the volumes occupied by all the protein molecules in the solutions in the presence and absence of the ligand, respectively, and $\eta_{red}(\mathrm{P}+\mathrm{L})$ and $\eta_{red}(\mathrm{P})$ are

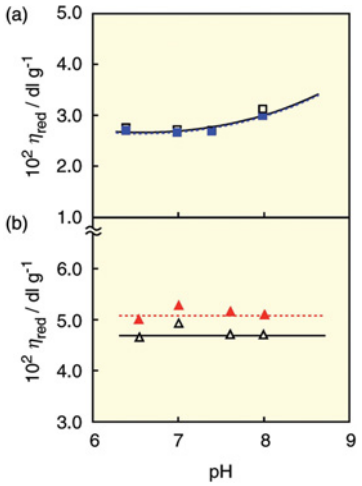


FIGURE 2.11 Reduced viscosity of protein solutions as a function of pH in the absence and presence of specific binders: (a) Lys; (b) BSA. The open and closed circles correspond to the results for protein solutions in the absence and presence of specific binders. The concentrations of NAG and palmitic acid are 690 and 150 μmol kg^{-1}, respectively. The solid and broken lines were obtained from a least-squares method.

the reduced viscosities of the protein solutions in the same situation. The calculated volume change for each protein by the addition of 5 mmol kg^{-1} halothane at pH 7.0 was 7.7% for Mgb, 1.3% for Lys, and –14.7% for BSA. With regard to the specific binders, we obtained the values of –0.72 % for Lys at the NAG concentration of 690 μmol kg^{-1} and pH 7.0, and 10.4 % for BSA at the palmitic acid concentration of 150 μmol kg^{-1} and pH 7.0. It can be said that the volume behavior of proteins is affected in different manners by the specific binder as well as the anesthetic.

For serum albumin, the structural data of several albumin complexed with ligands (anesthetics and substrates) are available from the Protein Data Bank. Let us consider the thermal and volume changes of BSA by the binding of ligands in reference to the structure. The determination of the first high-resolution crystal structure of human serum albumin (HSA) was from X-ray structural analysis in 1992 [64]. The binding sites of anesthetics and fatty acids in HSA have been recently determined by Bhattacharya et al. [65, 66], respectively. Since BSA has a very similar primary structure to HSA and forms almost the same tertiary structure as HSA [67], it is conceivable that the binding sites of halothane and palmitic acid in BSA are virtually the same as those in HSA. HSA has 585 amino acid residues (BSA: 583 residues) and consists of three homologous α-helical domains (I, II, and III). Each domain contains ten helices and is divided into six-helix and four-helix subdomains (A and B). Figure 2.12 demonstrates the structures of HSA, HSA complexed with halothane, palmitic acid, or halothane and myristic acid, respectively, which are constructed by use of PDB

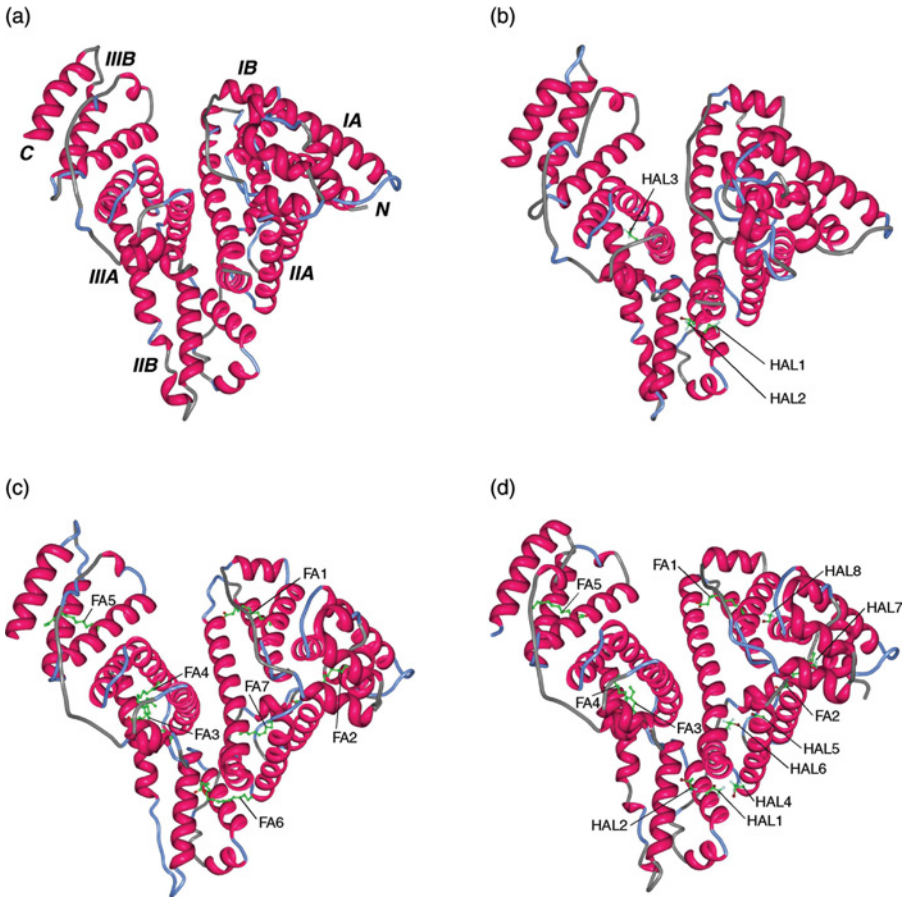


FIGURE 2.12 Structures of HSA complexed with ligands: (a) HSA without ligands; (b) HSA with halothane; (c) HSA with palmitic acid; (d) HSA with halothane and myristic acid. Three domains, I, II, and III, with subdomains A and B in each domain, are shown in figure (a) schematically. The ligand in each site is represented by ball-and-stick models. In part (d), the fatty-acid-binding site FA3 prevents the binding of halothane to the site (HAL3). These figures were prepared from PDB data (1BM0, 1E7B, 1E7H, and 1E7C) by using MBT Protein Workshop.

data (1BM0, 1E7B, 1E7H, and 1E7C). Halothane binds at three discrete sites on HSA in the clinically relevant concentration range (around 15% of the saturated vapor pressure): two sites at the interface between subdomains IIA and IIB (HAL1 and HAL2) and one site in subdomain IIIA (HAL3). The binding of halothane to HSA causes only very minor changes in local structure. On the other hand, palmitic acid binds at seven discrete sites on HSA: one site in subdomain IB (FA1), one at the interface between subdomains IA and IIA (FA2), two in IIIA (FA3 and FA4), one in IIIB (FA5), one at the interface between IIA and IIB (FA6), and one IIA (FA7). Unlike the case of halothane, the binding of palmitic acid to HSA causes the conformational changes among three domains as described below. Furthermore, at high halothane concentrations (around 60% of the saturated vapor pressure) in the presence of myristic acid, there exist seven halothane-binding sites on HSA together with five myristic acid-binding sites. These halothane-binding sites are amphiphilic pockets and clefts preformed on HSA, and all reside at the location of fatty-acid-binding sites.

The above structural data were compared with the thermal results. The effective concentration of halothane on BSA is significantly different from that of palmitic acid. Because we used the overall concentrations to express the ligand concentrations, the binding and free concentrations between BSA and ligand at equilibrium cannot be determined. However, it is useful to compare the molar ratio of ligand to BSA by use of the overall concentration. The molar ratio of effective halothane concentrations of 5 and 10 mmol kg^{-1} correspond to 165 and 330 moles per 1 mol of BSA, while that of effective palmitic acid concentrations of 100 and 200 μmol kg^{-1} correspond to 3.3 and 6.6 mol, respectively. The structurally determined binding numbers of halothane and palmitic acid are not very different from each other. However, in the molar ratio of both ligands, 50−100 times greater ratio of halothane compared with that of palmitic acid is necessary for the

appearance of ligand actions; in other words, the greater numbers of halothane molecules are required for the appearance of the ligand action on BSA whereas palmitic acid suffices for several molecules. Comparing the molar ratio of both ligands at the effective concentrations with the structural data of HSA complexed with ligands, the ratio of halothane is not consistent with the binding numbers on HSA, whereas that of palmitic acid is in good agreement with the numbers. This fact suggests that there is an only slightly observable anesthetic effect on BSA even if the halothane concentration corresponding to the binding numbers determined from X-ray analysis as the overall concentration is added to the BSA solution. Considering the fact that the molar ratio of halothane at the effective concentration is much larger than the concentration of binding number, there are undoubtedly a lot of free halothane molecules in the BSA solution at the concentration. Therefore, we can conclude that halothane is an essentially nonspecific binder to BSA and affects BSA by the nonspecific solvent effect in the higher concentration range. In contrast with the case of halothane, the binding mode of palmitic acid is quite different. The consistency of molar ratio and structural data exhibits that the overall concentration of palmitic acid added can be substantially regarded as the binding concentration, and then there is almost no free plamitic acid in the BSA solution. Further, it should be noted that the molar ratio of BSA to palmitic acid at optimal stabilization is very close to the maximum binding number 7 determined from X-ray analysis. We can thus conclude that palmitic acid is a specific binder to BSA and stabilizes the BSA structure at the transition state in the lower concentration range.

Moreover, it was revealed from the structures of HSA/fatty-acid complexes that binding of fatty acids to HSA produces a distinct conformational change [66,68,69]: fatty-acid binding causes domains I and III to be displaced to the left, opening up the central crevice and increasing the width of the molecule from 80 to 90 Å. The rotation of domain I relative to domain II is stabilized by the fatty-acid binding at FA2 to the interface between subdomain IA and IIA. More recent studies of ^{13}C NMR [70] and molecular dynamic simulation [71] exhibited that fatty acid binding sites FA2, FA4, and FA5 are identified as high-affinity sites, with sites FA1, FA3, FA6, and FA7 as low-affinity sites. Therefore, a few molecules of palmitic acid occupy the binding site of BSA, probably high-affinity sites, including at the interface of subdomains IA and IIA (FA2); the conformational change of BSA from a native state to a transition state occurs; and the structure of BSA becomes thermally stable. An abrupt change in the thermal behavior in the vicinity of the molar ratio of 4 shown in Fig. 2.7 may be in good agreement with the above behavior. Further increase in palmitic-acid concentration increases stabilization, and when seven molecules of palmitic acid occupy all the binding sites, the maximum stabilization effect appears. Concerning the volume behavior of BSA in the presence of palmitic acid, we may say simultaneously that the conformational change due to the binding of palmitic acid produces an increase in volume of BSA, although the thermal stabilization seems to contradict the volume expansion because both trends are apparently mutually inverse to each other in terms of the folding-related stabilization. This behavior is in accord with the fact revealed from the drug-binding study on HSA by X-ray structural analysis [72] that the binding of fatty acids increases the volume of drug site 1 (a preformed binding pocket within the core of subdomain IIA). We speculate that the transformation may be accompanied with a volume increase. This stabilization mechanism of palmitic acid forms a striking contrast to that of halothane.

In contrast to this, almost no change in thermal and volume behavior of Lys is caused by the binding of NAG to Lys (rigorously speaking, very slight thermal stabilization and volume shrinkage). Because it is known that a hexamer of NAG binds at the binding site within Lys [73, 75], the monomers of NAG can also bind at the same sites [73, 74]. However, the DSC measurements revealed that the stabilization of the Lys structure by the binding of NAG is extremely small. Therefore, the binding of NAG does not induce so large a structural change of Lys as to affect its thermal and volume behavior. It was reported from the X-ray structural analysis [73] that oligomers of NAG bind in the cleft of active sites of Lys and cause the induced-fit type interaction. The monomer binds in subsite C with 4 hydrogen bonds and 30 van der Waals contacts and the interaction increases in proportion to oligomerization of NAG. Then, the structural change of Lys by the binding of the monomer of NAG seems to be considerably small as compared with the binding of other oligomers like dimer and trimer. Gekko et al. [76] have shown that the change in partial specific volume and partial adiabatic compressibility of Lys by the binding of the monomer of NAG is smaller than those of the dimer and trimer. One possible reason why the binding of the monomer of NAG to Lys does not produce the detectable structural change accompanied by the stabilization is the imperfect packing in the binding site in addition to the rigid structure of Lys, as mentioned below.

2.4 INTRINSIC INTERACTION MODE OF AN ANESTHETIC WITH PROTEINS

We showed by comparative studies of ligand−protein interaction that the mode of the interaction between an anesthetic and a protein is markedly different from that between a specific binder and a protein. On the other hand, the interaction mode is also remarkably different depending on the kinds of proteins. What is the cause of the difference in ligand sensitivity among globular proteins? We speculate that the difference in anesthetic sensitivity among globular proteins is attributable to two factors: (1) the magnitude of the hydrophilicity on the protein surface, namely, the balance

TABLE 2.2 Properties Related to Hydrophilicity on Protein Surface

Protein	Molecular weight (kDa)	Hydropathy value	H_ϕ[a]	P[b]
Mgb	17.8	−280.1	1038	1.09
Lys	14.3	−210.8	893	1.04
BSA	66.3	−1235.1	990	1.23

[a]The total hydrophobicity divided by the number of residues (cal/residue).
[b]Polarity parameter of Bigelow.

between the hyrophilicity and hydrophobicity on the surface, and (2) the rigidity of the protein structure, that is, whether the protein is hard or soft.

Although it is difficult to quantify the hydrophilicity of the protein surface directly, we can qualitatively infer the hydrophilicity of the protein surface from several parameters determined on the basis of the primary structure of the protein. Table 2.2 lists the values of hydropathy index [77], hydrophobic energy [78] and polarity parameter [79] for Mgb, Lys, and BSA. As the hydrophilicity of a protein becomes large, the hydropathy index and the hydrophobic energy decrease while the polarity parameter increases. From these values, the hydrophilicity of the proteins is Mgb ≈ Lys < BSA but the difference between Mgb and Lys cannot be distinguished. The surface hydrophilicity of a protein is closely related to the solubility of the protein in a buffer solution, or the protein crystallization in the solution. In other words, the more hydrophilic the protein surface is, the larger the concentration at which the crystallization occurs becomes. Therefore, we selected the crystallization concentrations of these proteins as the index of the surface hydrophilicity. Since it is known that the protein crystallization is remarkably dependent on solution conditions such as kinds of solvent and added salts, pH, and so on, we determined the crystallization concentrations under the same buffer condition (0.1 M and pH 7.0). The results of the solubility measurements are given in Fig. 2.13. Although

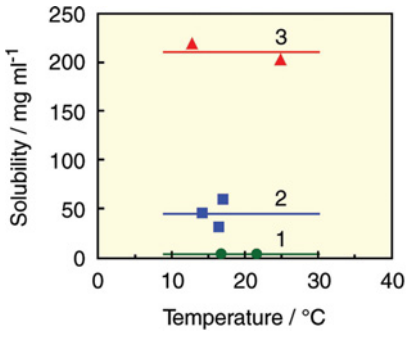


FIGURE 2.13 Solubility of proteins as a function of temperature: (1) Mgb; (2) Lys; (3) BSA. Here all solubilities were determined at the same solution condition: 0.1 M phosphate buffer, pH 7.0.

the solubilities of these proteins are almost constant in the temperature range measured, a pronounced difference in solubility among the proteins is found: the solubility is large for Lys (∼40 mg mL^{-1}) and very large for BSA (ca. 210 mg mL^{-1}) while remarkably small for Mgb (∼4 mg mL^{-1}). Taking into account the above parameters and the solubility for the proteins, we elucidated that the surface hydrophilicity increases in the order of Mgb < Lys < BSA. Regarding FFL, although there are no available data for the hydrophilicity, it seems to have similar hydrophilicity to Mgb, judging from the fact that the solubility of FFL in a Gly-Gly buffer is considerably low.

Inhalation anesthetics are amphiphilic molecules, and the hydrophobicity is relatively large as is seen from the solubility in water [80]. Since almost all the globular proteins are water-soluble, unlike membrane proteins, the proteins used in this study are fundamentally hydrophilic. The difference in the halothane sensitivity of the proteins is closely related to the interaction mode of a hydrophilic protein with an amphiphilic ligand, and the magnitude of the hydrophilicity is one of the determinants of the sensitivity. Proteins maintain the structural integrity by the balance between hydrophilic and hydrophobic interactions on the protein surface surrounded by water. This means that the extensive hydrogen bonding capability of water essentially dominates the behavior of a protein. Anesthetics act in the protein/water interface region and thus interrupt the interaction between proteins and water. They decrease the restrictive force of water (hydrophobic hydration) and loosen the structure for a protein with predominantly hydrophobic residues on the surface. To the contrary, they decrease the attractive force of water (electrostriction) and tighten the structure for a protein with predominantly hydrophilic residues at the surface.

The circumstances around the protein molecule are identical to those for polymer chains in a poor or a good solvent that is often dealt with in general polymer science. Water is repulsive to hydrophobic solutes and act as a poor solvent, but is strongly attractive to hydrophilic solutes and becomes a good solvent. A polymer chain tends to expand in a good solvent while it is inclined to shrink in a poor solvent. Adding a high concentration of an anesthetic can induce a local change of the nature of the solvent in the vicinities around the protein molecules from pure water to a mixed solvent of water and the anesthetic. Such a microscopic mixed-solvent environment produces an effect as a good solvent for a protein with relatively low hydrophobicity, and then they are expected to unfold. As for a protein with large hydrophilicity, on the other hand, such an environment has an effect as a poor solvent, and then the protein is conversely expected to fold. We call this effect a *microscopic solvent effect*. Therefore, the anesthetic effect on proteins may vary according to the difference in the hydrophilic and hydrophobic balance of the protein−water interface. It can be said from the thermal and volume behavior of FFL, Mgb, Lys, and BSA in the presence

of an anesthetic that the former microscopic solvent effect is predominant for FFL and Mgb while the latter solvent effect is predominant for BSA. In the case of Lys, the intermediate situation may be expected to hold and probably another factor mentioned in the next section greatly contributes to the structural stability.

We think that another factor that determines the anesthetic sensitivity of globular proteins is the rigidity of the protein structure. The rigidity of a protein can be estimated from its compressibility in the aqueous solution. Another research group [81−83] have measured the sound velocities and the densities for dozens of aqueous globular protein solutions to determine the adiabatic compressibilities of the proteins in water. They clarified the correlation between the compressibility and several factors affecting the compressibility, such as molecular size, hydrophobicity, and secondary structure, and categorized each of them as a hard or a soft protein. The adiabatic and the isothermal compressibilities of Mgb, Lys, and BSA at 25°C [82] are summarized in Table 2.3 together with other molecular properties of the proteins, such as partial specific volume, fraction of α-helix and β-sheet, and numbers of S-S bond. We immediately notice that the compressibility values of Mgb and BSA are large, while the value of Lys is as low as about half of the values of BSA and Mgb. The compressibility values suggest that Mgb and BSA are fairly soft proteins, while Lys is a rather hard protein, and hence, the rigidity of the structure for the proteins increases in the order of BSA $\approx$ Mgb $<$ Lys. For FFL, the compressibility value has not yet been determined for the enzyme; however, considering the large structural change by the binding of substrates, the rigidity of the structure is expected to be a relatively soft protein.

It is understandable from the secondary structures of the proteins in Table 2.3 that Mgb and BSA contain high percentages of α-helical structures in comparison with Lys. High-pressure studies on volume properties of peptides [84−86] have proved that the compressibility of α-helix or β-sheet itself is negligibly small: they have very hard structures. However, an increase in the α-helix content in a whole protein molecule may cause the insufficient packing between an α-helix and another α-helix or its surrounding hydrophobic region due to its bulky structure, which, in turn, causes the number and the size of cavities to increase. As a result, higher content of α-helix generally tends to soften the protein structure, that is, the α-helix-rich proteins are highly compressible [82]. Therefore, the large variation of Mgb (expansion by unfolding) and BSA (shrinkage by folding) by nonspecific microscopic solvent effect of halothane may result from their soft structures, due to the large α-helical content. It has been reported in the molecular simulation study [87] that the inside of α-helix of Mgb is difficult to compress; however, cavities between α-helices are easily compressed. In contrast to Mgb and BSA, Lys with low α-helix content shows very low sensitivity to halothane. This is also explainable from the same viewpoint: the low halothane sensitivity is probably attributable to the hard structure of the Lys molecule.

As mentioned above, the anesthetic sensitivity of globular proteins is closely correlated with the hydrophilicity of the protein surface and the rigidity of the protein structure. On the basis of the above idea, we can roughly classify the globular proteins into four categories as follows: (1) a protein with large hydrophilicity and soft structure, (2) a protein with small hydrophilicity and soft structure, (3) a protein with large hydrophilicity and hard structure, and (4) a protein with small hydrophilicity and hard structure. From the surface hydrophilicity and the structural rigidity of the present proteins, we can say that FFL and Mgb belong to category 2, Lys belongs to category 3, and BSA belongs to category 1, respectively. Figure 2.14 demonstrates the classification of the proteins schematically. Here FFL is omitted from the figure since the relative position cannot be determined in the figure due to the paucity of property data. These findings imply that the effect of an anesthetic is remarkable for a soft protein, and the degree of hydrophilicity of the protein surface determines the direction of the structural change, that is, folding or unfolding. On the other hand, in the case of a hard protein, the effect of an anesthetic is appreciably small even though the structure of the protein shifted to a folded or an unfolded state depending on the surface hydrophilicity.

The volume information obtained from anesthetic binding on proteins indicates that volumes of FFL and Mgb expand, a volume of Lys slightly expands while a volume of BSA

TABLE 2.3 Properties Related to Rigidity of Protein Structure

Protein	v^{0a} (mL g^{-1})	Fraction (%) of α-Helix	Fraction (%) of β-Sheet	S–S bond[b]	$\beta_S\times10^{12c}$ (cm^2 dyn^{-1})	$\beta_T\times10^{12d}$ (cm^2 dyn^{-1})
Mgb	0.747	77	2	0	8.9	13.1
Lys	0.712	29	16	4	4.6	7.7
BSA	0.735	70	15	17	10.5	14.6

[a]Partial specific volume.
[b]Number of disulfide bonds per molecule (subunit).
[c]The values of adiabatic compressibility.
[d]The values of isothermal compressibility.

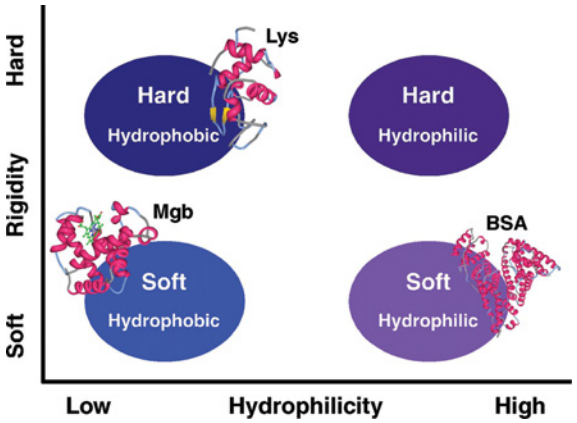


FIGURE 2.14 Schematic representation of the correlation between rigidity of protein structure and hydrophilicity of protein surface. Scales in abscissa and ordinate are depicted relatively in arbitrary units. The protein structures were obtained from the PDB, sperm whale Mgb (1MBN), hen egg Lys (2LYZ), and HSA (1BM0), respectively, and HSA was used instead of BSA.

shrinks by the addition of halothane. The behavior of the volume changes for the proteins well corresponds to that of the structural changes (i.e., unfolding, slight unfolding and folding) expected from the changes in the thermal stability that turbidity and DSC measurements have revealed. Thus, it is interesting to consider the correlation between the volumetric results and the pressure reversal of anesthesia. The standard volume change (ΔV^0) associated with the binding of an anesthetic to a protein can be written as

$$\Delta V^0 = -RT(\partial \ln K/\partial p)_T \tag{2.11}$$

where K is the binding constant between the anesthetic and the protein, and R is a gas constant. Since the ΔV^0 value can be approximately regarded as equal to the ΔV value, the sign of the ΔV value determines whether the number of the anesthetic molecules being bound to the protein will increase or decrease with increasing pressure. The positive ΔV value means the antagonism of the binding by pressure, while the negative value does the synergism of the binding. When considering the pressure antagonism occurs only in the case of the positive ΔV value, it turns out that FFL and Mgb is suitable as a model protein for anesthetic mechanism, and Lys and BSA are not suitable. Especially, BSA may not be involved with the anesthetic mechanism [60]. Therefore, we can conclude that it is reasonable to use proteins belonging to category (2) as model proteins of anesthetic action such as FFL and Mgb.

2.5 CONCLUSIONS

The effect of an anesthetic on globular proteins is different depending on the kinds of the proteins. Hence, it seems that the interaction mode of an anesthetic with proteins is quite complicated at first sight. However, comparing the effect with that of a substrate or a specific binder, the intrinsic interaction mode of the anesthetic with the proteins becomes clear. Taking into account the Meyer–Overton rule, we propose here that the intrinsic interaction mode between an anesthetic and a water-soluble globular protein can be systematically interpreted by considering the following four factors: (1) hydrophobicity of an anesthetic, (2) hydrophilicity of a protein surface, (3) rigidity of a protein structure, and (4) molar ratio of an anesthetic to a protein at the effective concentration. When considering that the effective concentrations of anesthetics is larger than those of specific binders and also that a protein surface and a protein structure are relevant to the interaction mode, the binding to a protein by the nonspecific weak interaction such as a microscopic solvent effect may be an intrinsic interaction mode of an anesthetic, which forms a pronounced contrast to the modes of specific binders of which the binding numbers are exactly determined from physicochemical measurements as the X-ray structural analysis of the protein.

The volume change of a protein by ligand binding provides us with useful information regarding the interaction between ligands and a protein because the ligand binding to a protein is sensitively reflected in the protein volume. The volume change of the protein is closely related to the pressure antagonism of anesthesia and one of key factors to elucidate the anesthetic mechanism. Volume studies of proteins [88–90] showed that the volume change of a protein associated with the unfolding is attributable to the volume changes of hydrated water on the protein surface and that of cavity in the protein. These determinants have almost the same meaning as the hydrophilicity of a protein surface and the rigidity of the protein structure, respectively. We expect that the anesthetic–protein interactions should also be considered in detail from the viewpoint of cavity and hydrated water in the future.

Finally, we focus here on anesthetic–protein interactions, but the location of anesthetic action is biological membranes. The anesthetic effect on lipid membranes cannot be neglected. Although the protein hypothesis only emphasizes the anesthetic–protein interactions and refutes the involvement in lipid membranes for anesthetic mechanism, anesthetics affect almost all proteins and lipid membranes. We recently investigated the ligand effect on phospholipid bilayer membranes by means of a comparative study similar to that described here and showed [91] that the interaction modes of an anesthetic, saturated and unsaturated fatty acids with dipalmitoylphosphatidylcholine (DPPC) bilayer membranes are markedly different from one another. This study proved that the DPPC bilayer membranes have high ability to recognize kinds of ligand molecules as well as proteins and can discriminate among them with specific interaction by the membrane states. Considering the anesthetic

sensitivity of lipid membranes and the fact that the ratio of proteins to lipids in real nerve membranes is about 2:8, we cannot eliminate the lipid membranes for the mechanism. Furthermore, we are now thinking that the anesthetic effect on lipid membranes may also be explained similarly to that on proteins: (1) hydrophobicity of an anesthetic, (2) hydrophilicity of a membrane surface, (3) rigidity of a membrane structure, and (4) molar ratio of an anesthetic to a lipid at the effective concentration. Here, in lipid membranes, the hydrophilicity and rigidity are closely related to the membrane states and lipid molecular structures. The hydrated crystalline or gel state has small hydrophilicity with a hard structure, while the liquid crystalline state has large hydrophilicity with a soft structure. Additionally, lipid ingredients in membranes such as saturated or unsaturated lipids and neutral or acidic lipids also affect the factors mentioned above. Because the anesthetic activities exhibit common characteristics and the anesthetic sensitivity between proteins and lipid membranes can be interpreted similarly, we can say that the action is essentially physical and nonspecific, not chemical and specific.

ACKNOWLEDGMENTS

Financial support by Grant-in-Aid for Challenging Exploratory Research (Grant 24659698) from the Japan Society for the Promotion of Science is gratefully acknowledged.

REFERENCES

[1] Johnson, F.H., Eyring, H., Williams, R.B. (1942). The nature of enzyme inhibitors in bacterial luminescence. Sulfanilamide, urethane, temperature and pressure. *J. Cell. Compar. Physiol.* **20**, 247−268.

[2] Eyring, H., Magee, J.L. (1942). Application of the theory of absolute reaction rates to bacterial luminescence. *J. Cell. Compar. Physiol.* **20**, 169−177.

[3] Johnson, F.H., Flagler, E.A. (1951). Hydrostatic pressure reversal of narcosis in tadpoles. *Science* **112**, 91−92.

[4] Pringle, M.J., Brown, K.B., Miller, K.W. (1981). Can the lipid theories of anesthesia account for the cutoff in anesthetic potency in homologous series of alcohols? *Mol. Pharmacol.* **19**, 49−55.

[5] Chiou, J.-S., Ma, S.-M., Kamaya, H., Ueda, I. (1990). Anethesia cutoff phenomenon: Interfacial hydrogen bonding. *Science* **248**, 583−585.

[6] Meyer, H. (1899). Weiche eigenschaft der anaesthetica bedingt ihre narkotische wirkung? *Arch. Exp. Pathol. Pharmacol.* **42**, 109−118.

[7] Overton, E. (1901). *Studien uber die Narkose zugleich ein Beitrag zur allgemeinen Phamakologie*; Verlag von Gustav Fischer, Jena.

[8] Ueda, I., Kamaya, H. (1984). Molecular mechanisms of anesthesia. *Anesth. Analg.* **63**, 929−945.

[9] Miller, K.W. (1985). The nature of the site of general anesthesia. *Int. Rev. Neurobiol.* **27**, 1−61.

[10] Trudell, J.R. (1991). Role of membrane fluidity in anesthetic action. In Aloia, R.C., Curtain,C.C., Gordon, L.M. (eds.), *Drug and Anesthetic Effects on Membrane Structure and Function.* Wiley-Liss, New York, pp. 1−14.

[11] Cameron, J.W. (2006). The molecular mechanisms of general anaesthesia: Dissecting the $GABA_A$ receptor. *Contin. Educ. Anaesth. Crit. Care Pain* **6**, 49–53.

[12] Franks, N.P., Lieb, W.R. (1991). Stereospecific effects of inhalational general anesthetic optical isomers on nerve ion channels. *Science* **254**, 427−430.

[13] Dickinson, R., Franks, N.P., Lieb, W. (1994). Can the stereoselective effects of the anesthetic isoflurane be accounted for by lipid solubility? *Biophys. J.* **66**, 2019−2023.

[14] Koblin, D.D., Chortkoff, B.S., Laster, M.J., Eger, E.I.II, Halsey, M.J., Ionescu, P. (1994). Polyhalogenated and perfluorinated compounds that disobey the Meyer-Overton hypothesis. *Anesth. Analg.* **79**, 1043−1048.

[15] Koubi, L., Tarek, M., Bandyopadhyay, S., Klein, M.L., Scharf. D. (2002). Effects of the nonimmobilizer hexafluoroethane on the model membrane dimyristoylphosphatidylcholine. *Anesthesiology* **97**, 848−855.

[16] Franks, N.P., Lieb, W.R. (1996). Temperature dependence of the potency of volatile general anesthetics. *Anesthesiology* **84**, 716−720.

[17] Yamamoto, Y., Taga, K., Yoshida, T., Kamaya, H., Ueda I. (2006). Temperature dependence of thermodynamic activity in volatile anesthetics: Correlation between anesthetic potency and activity. *J. Colloid Interface Sci.* **301**, 488−492.

[18] Franks, N.P., Lieb, W.R. (1978). Where do general anesthetics act? *Nature* **274**, 339−342.

[19] Franks, N.P., Lieb, W.R. (1982). Molecular mechanisms of general anaesthesia, *Nature* **300**, 487−493.

[20] Franks, N.P., Lieb, W.R. (1994). Molecular and cellular mechanisms of general anaesthesia. *Nature* **367**, 607−614.

[21] Ueda, I., Suzuki, A. (1998). Irreversible phase transition of firefly luciferase: Contrasting effects of volatile anesthetics and myristic acid. *Biochim. Biophys. Acta* **1380**, 313−319.

[22] Ueda, I., Suzuki, A. (1998). Is there a specific receptor for anesthetics? Contrary effects of alcohols and fatty acids on phase transition and bioluminescence of firefly luciferase. *Biophys. J.* **75**, 1052−1057.

[23] Nishimoto, M., Komatsu, U., Tamai, N., Yamanaka, M., Kaneshina, S., Ogli, K., Matsuki, H. (2009). A comparative study on specific and nonspecific interactions in bovine serum albumin: Thermal and volume effects of halothane and palmitic acid. *Colloid Polym. Sci.* **287**, 979−989.

[24] Nishimoto, M., Morimitsu, T., Tamai, N., Kaneshina, S., Nagamune, H., Matsuki, H. (2010). Inhibition of anti-fluorescent probe monoclonal antibody by long-chain amphiphiles. *Colloids Surf. B: Biointerfaces* **75**, 80−87.

[25] Nishimoto, M., Komatsu, U., Tamai, N., Yamanaka, M., Kaneshina, S., Ogli, K., Matsuki, H. (2011). Intrinsic interaction mode of an inhalation anesthetic with globular proteins: A comparative study on ligand recognition. *Colloid Polym. Sci.* **289**, 1785−1797.

[26] Franks, N.P., Lieb, W.R. (1984). Do general anaesthetics act by competitive binding to specific receptors? *Nature* **310**, 599−601.

[27] Ueda, I. (1965). Effects of diethyl ether and halothane on firefly luciferin bioluminescence. *Anesthesiology* **26**, 603−606.

[28] Ueda, I., Kamaya, H. (1973). Kinetic and thermodynamic aspects of the mechanism of general anesthesia in a model system of firefly luminescence in vitro. *Anesthesiology* **38**, 425−436.

[29] Dickinson, R., Franks, N.P., Lieb, W. (1993). Thermodynamics of *anrsthetic/protein interactions. Temperature studies on firefly luciferase*. *Biophys. J.* **64**, 1264−1271.

[30] Franks, N.P., Lieb, W.R. (2004). Seeing the light. Protein theories of general anesthesia. *Anesthesiology* **101**, 235−237.

[31] McElroy, W.D., Seliger, H.H. (1962). Mechanism of action of firefly luciferase. *Fed. Proc.* **21**, 1006−1012.

[32] DeLuca, M., McElroy, W.D. (1974). Kinetics of the firefly luciferase catalyzed reactions. *Biochemistry* **13**, 921−925.

[33] DeLuca, M., McElroy, W.D. (1978). Purification and properties of firefly luciferase. *Methods Enzymol.* **57**, 3−15.

[34] Berg, J.M., Tymoczko, J.L., Stryer, L. (2011). *Biochemistry*, 7th ed. Freeman, New York, Chap. 22.

[35] Suzuki, H., Kawarabayasi, Y., Kondo, J., Abe, T., Nishikawa, K., Kimura, S., Hashimoto, T., Yamamoto, T. (1990). Structure and regulation of rat long-chain acyl-CoA synthetase. *J. Biol. Chem.* **265**, 8681−8685.

[36] Babbitt, P.C., Kenyon, G.L., Martin, B.M., Charest, H., Slyvestre, M., Scholten, J.D., Chang, K.H., Liang, P.H., Dunaway-Mariano, D. (1992). Ancestry of the 4-chlorobenzoate dehalogenase: Analysis of amino acid sequence identities among families of acyl:adenyl ligases, enoyl-CoA hydratases/isomerases, and acyl-CoA thioesterases. *Biochemistry* **31**, 5594–5604.

[37] Matsuki, H., Suzuki, A., Kamaya, H., Ueda I. (1999). Specific and non-specific binding of long-chain fatty acids to firefly luciferase: Cutoff at octanoate. *Biochim. Biophys. Acta* **1426**, 143−150.

[38] Ueda, I., Minami, H., Matsuki, H., Inoue, T. (1999). Does pressure antagonize anesthesia? High-pressure stopped-flow study of firefly luciferase and anatomy of initial flash. *Biophys. J.* **76**, 478−482.

[39] Ueda, I., Matsuki, H., Kamaya, H., Krishna, P.R. (1999). Does pressure antagonize anesthesia? Opposite effects on specific and nonspecific inhibitors of firefly luciferase. *Biophys. J.* **76**, 483−488.

[40] Takehara, K., Kamaya, H., Ueda, I. (2005). Inhibition of firefly luciferase by alkane analogues. *Biochim. Biophys. Acta* **1721**, 124−129.

[41] Hansch, C., Clayton, J.M. (1973). Lipophilic character and biological activity of drugs. II. The parabolic case. *J. Pharm. Sci.* **62**, 1−21.

[42] Hansch, C., Vittoria, A., Sipiro, C., Jow, P.Y. (1975). Partition coefficients and the structure-activity relationship of the anesthetic gases. *J. Med. Chem.* **18**, 546−548.

[43] Kamaya, H., Matubayasi, N., Ueda, I. (1984). Biphasic effect of long-chain *n*-alkanols on the main-phase transition of phospholipid vesicle membranes. *J. Phys. Chem.* **88**, 797−800.

[44] Koshland Jr., D.E. (1958). Application of a theory of enzyme specificity to protein synthesis. *Proc. Natl. Acad. Sci. USA* **44**, 98−104.

[45] Koshland Jr., D.E. (1963). Correlation of structure and function in enzyme action. *Science* **142**, 1533−1541.

[46] Eyring, H. (1966). Untangling biological reactions. *Science* **154**, 1609−1613.

[47] Moss, G.W.J., Lieb, W.R., Franks, N.P. (1991). Anesthetic inhibition of firefly luciferase, a protein model for general anesthesia, does not exhibit pressure reversal. *Biophys. J.* **60**, 1309−1314.

[48] Ueda, I., Shinoda, F., Kamaya, H. (1994). Temperature-dependent effects of high pressure on the bioluminescence of firefly luciferase. *Biophys. J.* **66**, 2107–2110.

[49] Hiromi, K. (1979). *Kinetics of Fast Enzyme Reactions.* Wiley, New York, pp. 226−232.

[50] Johnson, F.H., Eyring, H., Stover, B.J. (1974). *The Theory of Rate Processes in Biology and Medicine.* Wiley, New York, pp. 385−444.

[51] Conti, E., Franks, N.P., Brick, P. (1996). Crystal structure of firefly luciferase throws light on a superfamily of adenylate-forming enzymes. *Structure* **4**, 287–298.

[52] Franks, N.P., Jenkins, A., Conti, E., Lieb, W.R., Brick, P. (1998). Structural basis for the inhibition of firefly luciferase by a general anesthetic. *Biophys. J.* **75**, 2205–2211.

[53] Nakatsu, T., Ichiyama, S., Hiratake, J., Saldanha, A., Kobashi, N., Sakata, K., Kato, H. (2006). Structural basis for the spectral difference in luciferase bioluminescence. *Nature* **440**, 372–376.

[54] Oba, Y., Ojika, M., Inouye, S. (2003). Firefly luciferase is a bifunctional enzyme: ATP-dependent monooxygenase and a long chain fatty acyl-CoA synthetase. *FEBS Lett.* **540**, 251–254.

[55] Gulick, A. M. (2009). Conformational dynamics in the acyl-CoA synthetases, adenylation domains of nonribosomal peptide synthetases, and firefly luciferase. *ACS Chem. Biol.* **4**, 811−827.

[56] Leitão, J.M.M., Estevas da Silva, J.C.G. (2010). Firefly luciferase inhibition. *J. Photochem. Photobiol. B: Biol.* **101**, 1−8.

[57] Inouye, S. (2010). Firefly luciferase: An adenylate-forming enzyme for multicatalytic functions. *Cell. Mol. Life. Sci.* **67**, 387−404.

[58] Hisanaga, Y., Ago, H., Nakagawa, N., Hamada, K., Ida, K., Yamamoto, M., Hori, T., Arii, Y., Sugahara, M., Kuramitsu, S., Yokoyama, S., Miyano, M. (2004), Structural basis of the substrate-specific two-step catalysis of long chain fatty acyl-CoA synthetase dimer. *J. Biol. Chem.* **279**, 31717−31726.

[59] Tanner, J.W., Eckenhoff, R.G., Liebman, P.A. (1999). Halothane, an inhalational anesthetic agent, increases folding stability of serum albumin. *Biochim. Biophys. Acta* **1430**, 46−56.

[60] Yamanaka, M., Kaneshina, S., Kamaya, H., Ueda, I. (2001). Volumetric study on the protein-anesthetic binding. *Colloid Surf. B: Biointerfaaces* **22**, 23−29.

[61] Tanner, J.W., Liebman, P.A., Eckenhoff, R.G. (1998). Volatile anesthetics alter protein stability. *Toxicol. Lett.* **100-101**, 387−391.

[62] Privalov, P.L., Khechinashvili, N.N. (1974). A thermodynamic approach to the problem of stabilization of globular protein structure: A calorimetric study. *J. Mol. Biol.* **86**, 665−684.

[63] Stigter, D., Alonso, D.O.V., Dill, K.A. (1991). Protein stability: Electrostatics and compact denatured states. *Proc. Natl. Acad. Sci. USA* **88**, 4176−4180.

[64] He, X.M., Carter, D.C. (1992). Atomic structure and chemistry of human serum albumin. *Nature* **358**, 209−215.

[65] Bhattacharya, A.A., Curry, S., Franks, N.P. (2000). Binding of the general anesthetic propofol and halothane to human serum albumin. *J. Biol. Chem.* **275**, 38731−38738.

[66] Bhattacharya, A.A., Grüne, T., Curry, S. (2000). Crystallographic analysis reveals common modes of binding of medium and long-chain fatty acids to human serum albumin. *J. Mol. Biol.* **303**, 721−732.

[67] Peters Jr., T. (1985). Serum albumin, *Adv. Protein Chem.* **37**, 161−245.

[68] Curry, S., Brick, P., Franks, N.P. (1999). Fatty acid binding to human serum albumin: New insight from crystallographic studies. *Biochim. Biophys. Acta* **1441**, 131−140.

[69] Petitpas, I., Grüne, T., Bhattacharya, A.A., Curry, S. (2001). Crystal structures of human serum albumin complexed with monounsaturated and polyunsaturated fatty acids. *J. Mol. Biol.* **314**, 955−960.

[70] Simard, J.R., Zunszain, P.A., Hamilton, J.A., Curry, S. (2006). Location of high and low affinity fatty acid binding sites on human serum albumin revealed by NMR drug-competition analysis. *J. Mol. Biol.* **361**, 336−351.

[71] Fujiwara, S., Amisaki, T. (2008). Identification of high affinity fatty acid binding sites on human serum albumin by MM-PBSA method, *Biophys. J.* **94**, 92−103.

[72] Ghuman, J., Zunszain, P.A., Petitpas, I., Bhattacharya, A.A., Otagiri, M., Curry, S. (2005). Structural basis of the drug-binding specificity of humen serum albumin. *J. Mol. Biol.* **353**, 38−52.

[73] Chipman, D.M., Sharon, N. (1969). Mechanism of lysozyme action. Lysozyme is the first enzyme for which the relation between structure and function has become clear. *Science* **165**, 454−465.

[74] Von Dreele, R.B. (2001). Binding of N-acetylglucosamine to chicken egg lysozyme: A powder diffraction study. *Acta Crystallogr. D: Biol. Crystallogr.* **57**, 1836−1842.

[75] Von Dreele, R.B. (2005). Binding of N-acetylglucosamine oligosaccharides to hen egg-white lysozyme: A powder diffraction study. *Acta Crystallogr. D: Biol. Crystallogr.* **61**, 22−32.

[76] Gekko, K., Yamagami, K. (1998). Compressibility and volume changes of lysozyme due to inhibitor binding. *Chem. Lett.* **27**, 839−840.

[77] Kyte, J., Doolittle, R.F. (1982). A simple method for displaying the hydropathic character of a protein. *J. Mol. Biol.* **157**, 105−132.

[78] Nozaki, Y., Tanford, C. (1971). The solubility of amino acids and two glycine peptides in aqueous ethanol and dioxane solutions: Establishment of a hydrophobicity scale. *J. Biol. Chem.* **246**, 2211−2217.

[79] Bigelow, C.C. (1967). On the average hydrophobicity of proteins and the relation between it and protein structure. *J. Theor. Biol.* **16**, 187−211.

[80] Seto, T., Mashimo, T., Yoshiya, I., Kaneshiro, M., Taniguchi, Y. (1998). Solubility and preparation of volatile anesthetic solution. *J. Anesth.* **12**, 41−42.

[81] Gekko, K., Noguchi, H. (1979). Compressibility of globular proteins in water at 25°C. *J. Phys. Chem.* **83**, 2706−2714.

[82] Gekko, K., Hasegawa, Y. (1986). Compressibility-structure relationship of globular proteins. *Biochemistry* **25**, 6563−6571.

[83] Gekko, K. Hasegawa, Y. (1989). Effect of temperature on the compressibility of native globular proteins. *J. Phys. Chem.* **93**, 426−429.

[84] Takekiyo, T., Shimizu, A., Kato, M., Taniguchi, Y. (2005). Pressure-tuning FT-IR spectroscopic study on the helix–coil transition of Ala-rich oligopeptide in aqueous solution. *Biochim. Biophys. Acta* **1750**, 1−4.

[85] Takekiyo, T., Imai, T., Kato, M., Taniguchi, Y. (2006). Understanding high pressure stability of helical conformation of oligopeptides and helix bundle proten, high pressure FT-IR and RISM theoretical studies. *Biochim. Biophys. Acta* **1764**, 355−363.

[86] Imamura, H., Kato, M. (2009). Effect of pressure on helix-coil transition of an alanine-based peptide: An FTIR study. *Proteins Struct. Funct. Bioinform.* **75**, 911−918.

[87] Yamato, T., Higo, J., Seno, Y., Go, N. (1993). Conformational deformation in deoxymyoglobin by hydrostatic pressure. *Proteins Struct. Funct. Bioinform.* **16**, 327−340.

[88] Kauzmann, W. (1959). Some factors in the interpretation of protein denaturation. *Adv. Protein Chem.* **14**, 1−63.

[89] Ohmae, E., Murakami, C., Tate, S., Gekko, K., Hata, K., Akasaka, K., Kato, C. (2012). Pressure dependence of activity and stability of dihydrofolate reductases of the deep-sea bacterium *Moritella profunda and Escherichia coli*. *Biochim. Biophys. Acta* **1824**, 511−519.

[90] Ohmae, E., Miyashita, Y., Kato, C. (2013). Thermodynamic and functional characteristics of deep-sea enzymes revealed by pressure effects. *Extremophiles* **17**, 701−709.

[91] Nishimoto, M., Hata, T., Goto, M., Tamai, N., Kaneshina, S., Matsuki, H., Ueda, I. (2009). Interaction modes of long-chain fatty acids in dipalmitoylphosphatidylcholine bilayer membrane: Contrast to mode of inhalation anesthetics. *Chem. Phys. Lipids* **158**, 71−80.

3

LIPID MONOLAYER AND INTERACTION WITH ANESTHETICS

YASUSHI YAMAMOTO AND KEIJIRO TAGA

Department of Life and Materials Engineering, Nagoya Institute of Technology, Gokiso-cho, Showa-ku, Nagoya, Japan

3.1 INTRODUCTION

Surfactant (or *surface-active agent*) is a general term referring to compounds in which the hydrophobic moieties compatible with oil (alkyl chain) and the hydrophilic moieties compatible with water coexist in one molecule by a chemical bond (covalent bond). This molecule is also called an *amphiphilic molecule* as it possesses both hydrophobicity and hydrophilicity; therefore, it forms various aggregations such as micelles, vesicles (liposomes), an emulsion, a monolayer, or bilayers, in the water phase and/or on the various interfaces. Extensive investigations on the properties of these aggregations have been performed not only from an industrial perspective such as cleaning, emulsification, and dispersion, but also from a biological perspective on the biomembranes of various composition and functions [1–3].

The monolayer on the water surface, using the above surfactant, points to a monomolecular layer whose molecules arrange two-dimensionally on the water surface, orienting hydrophobic alkyl chains toward the air phase and also hydrophilic moieties toward the water phase. It is possible to form a stable flat film (ultraorganic thin film) comparatively easily on the monomolecular level and also to control the number of monolayer molecules arbitrarily. The monolayer is found in industrially applications such as a nano-level insulator, frictional reduction film, and organic thin-film device applied electronically, by moving the monolayer on the substrate. From the biological perspective, it is also possible to regard it as a half of the biomembrane. Therefore, the monolayer is selected as a biomembrane model; it is applied to investigate cellular functions such as membrane structure, transmission of compounds into and/or out of membrane, interaction with substances, and molecular recognition [1–3].

In this chapter, we focus on the developing monolayer on the water surface (Langmuir monolayer), using a lipid of the biomembrane model substance. We will describe the method of monolayer formation and investigations on monolayer properties, as well as interactions between the monolayer and anesthetics.

3.2 MONOLAYER FORMATION

Benjamin Franklin was the first scientist to observe the monolayer. He was interested in a phenomenon that a *wake* (water) created by a ship or boat sailing became smoothly by throwing way the water that had been polluted with cooking oil. He also observed that when about one-teaspoonful of the oil was dropped on the pond side, the oil spread in a $\sim$1000 m^2 area and the amplitude of the wave in the pond quickly subsided (this is termed the *formation of calm*). These observations were published by the British Royal Association (Royal Society) in 1773 [4]. Thus, the manner in which monolayer molecules float on the water surface, followed by formation of the monolayer, is now called the *dropping method*. This method consists in dropping volatile solution droplets, including monolayer molecules, continuously (one by one) on the water surface, resulting in formation of the monolayer by spreading the molecules throughout the water surface. By using this method, the spontaneous monolayer, in which the monolayer molecules are maintained in their most comfortable state, is formed on the water surface.

Encyclopedia of Biocolloid and Biointerface Science, Volume 1, First Edition. Edited by Hiroyuki Ohshima.
© 2016 John Wiley & Sons, Inc. Published 2016 by John Wiley & Sons, Inc.

A more systematic study of monolayers was performed by Agnes L. W. Pockels, who was interested in spreading of an oil stain in water. She noticed how the oil stain spread on the washing water surface in her kitchen, using handmade equipment with a movable partitioning board, and she observed how the area of a soap monolayer of the stain changed on contact with the water. Pockels' experimental result was published in 1892 through Lord Rayleigh of the Royal Society [5]. Later, the foundation of the present monolayer technology was further developed by Irving Langmuir [6, 7]. Thus, the manner in which monolayer molecules float on the water surface, followed by subsequent formation of the monolayer by squeezing (compressing) it using a partitioning board, is now called the *compression method*. This method consists in dropping small aliquots of the fixed volatile solution on the water surface, resulting in formation of the monolayer by squeezing the partition board horizontally, or by compressing the monolayer molecules. This is the main method for monolayer formation at present. This is also currently applied by forming a high-density monolayer on the water surface by compressing monolayer molecules using an artificial power supply and the partitioning board.

Here, we will describe the formation process and the properties of various lipid monolayers that are formed by the dropping method that enable formation of the flexible monolayer, compared with the corresponding monolayers formed by the compression method. Three processes are applied in the formation of a flexible monolayer by the dropping method: (1) concentration of the dropping solution including monolayer sample (0.5–1.0 mM), (2) dropping volume per time (1.0 μL by microsyringe), and (3) dropping time interval per time (>1 min for the droplet to spread sufficiently on the water surface; droplet spreading is checked as the constant value of surface tension after dropping by the recorder). Process 3 continue until the monolayer was formed, and the monolayer formation was confirmed by the formation of a lens on the water surface. The lens did not spread (move), so the surface tension value didn't change. With the dropping method, many dropping volumes and times are needed for monolayer formation. However, the above process would enable us to form the spontaneous monolayer in which molecules maintain comfortable (equilibrium) states. Therefore, the flexible monolayer, incorporating the interaction between hydrophilic groups in monolayer and water molecules sufficiently, is formed on the water surface. Those monolayers would also be suitable for model membranes.

3.2.1 Dipalmitoyl Phosphatidyl Choline (DPPC)

Dipalmitoyl phosphatidyl choline (DPPC) is a typical phospholipid, composed of two palmitc acids (C16) and a phosphatidyl choline group. DPPC is one of the main components in the biomembrane and possesses many biological

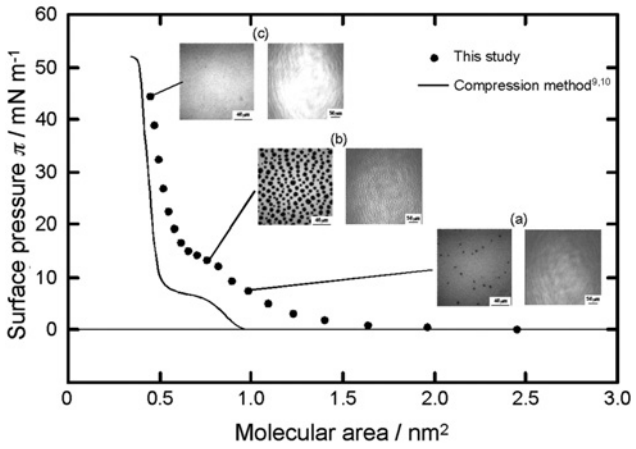


FIGURE 3.1 Surface pressure versus molecular area (π–A) isotherm curve of DPPC monolayer at 26°C. Solid circles (•) indicate dropping method; solid lines, compression method.

characteristics such as formability and flexibility of membrane; therefore, DPPC has been widely used and researched for the elucidation of various biofunctions as biomembrane model substances [8].

Figure 3.1 shows the surface pressure versus molecular area (π–A) isotherm curve of DPPC monolayer at 26°C using the dropping method [indicated by solid circles (•)] together with a typical π–A isotherm curve using the compression method (solid lines) [9, 10]. Chloroform is used as a spreading solvent for DPPC monolayer formation. The horizontal axis (abscissa) represents the molecular area calculated from molecular values in the dropping volume, and the vertical axis (ordinate) represents the surface pressure at which enough time had passed after infusion of the DPPC-chloroform droplet to allow the pressure value to become constant.

Many isotherm studies on the DPPC monolayer using the compression method have shown that the DPPC monolayer forms the following three states; a liquid-expand (LE) state at low surface pressure, a liquid-condensed (LC) state at higher surface pressure, and a LE-LC transition state (plateau range) at a surface pressure of approximately 8 mN/m (indicated by solid lines in Fig. 3.1) [11]. In the LE state, cylinderlike alkyl chains in DPPC molecules [8, 12] lie on the water surface and/or remain in mutually open state. In the LC state, alkyl chains interact with each other and rise to the water surface.

The π–A isotherm curve obtained by the dropping method (solid circles) presented a curve shape [13] different from than that obtained using the compression method (solid line) [9, 10]. The surface pressure increased gradually from about 1.7 nm^2 molecular area and after an unclear, small plateau range (LE-LC transition state, around 12 mN/m), increased up to 42 mN/m.

Two remarkable points are shown in Figure 3.1: (1) *the maximum pressure in the π–A isotherm curve observed*; the

pressure value obtained by the dropping method (42 mN/m) is lower than that due to the compression method (~50 mN/m), and (2) *the limiting molecular area* (A_0). A_0 obtained by the dropping method is 0.65 ± 0.05 nm^2/molecule (~40 mN/m), and this value is approximately 30 % larger than that obtained by the compression method (0.48 nm^2/molecule). These results indicate that the DPPC monolayer obtained by the dropping method is in a *semi-expanded state* and has a *flexible and fluid structure*, similar to the fluidity-rich biomembrane.

In the case of dropping method, a sufficient time interval is maintained between the introduction of different, consecutive droplets on the water surface. This time interval enables DPPC molecules to spread throughout and reach equilibrium state on the water surface. Dropping in succession also results in disentanglement of the unbalanced domain of DPPC molecules, due to redissolution of the domain by the spreading of the solution (DPPC-chloroform). Consequently, DPPC are expected to disperse over the entire water surface and begin to form the monolayer. In a DPPC molecule, the redissolution causes the hydrophobic alkyl chains in the DPPC molecule to open freely in three dimensions, thereby facilitating the intermolecular interactions (hydrophobic interaction) between DPPC molecules. Using the dropping method, the DPPC monolayer passed through the monolayer-forming process in which the priority was given to the intermolecular interaction by alkyl chains in DPPC molecules. This corresponds to an increase in the surface pressure (decrease in the surface tension) at the initial stage in DPPC monolayer formation. Actually, all measurements showed the curve beginning with an initial dispersion of 1.4–1.8 nm^2 molecular area. After the LE-LC transition, two alkyl chains in one DPPC molecule interacted with each other and the alkyl chains in the DPPC molecules rose to the water surface; these results were also observed using the compression method. In this case, the DPPC molecules might have become compatible with water molecules under the special conditions of the dropping method. Therefore, the hydrophilic group of DPPC molecules and water molecules would structure and maintain themselves in the most comfortable (highest-equilibrium) hydrogen-bonding network (hydrophilic interaction) [14]. This is quite different from the scenario obtained using the compression method; the compression collapses the hydrogen-bonding network, and the hydrophilic groups of DPPC molecules and the alkyl chains continue to be compressed, resulting inthe high-density state. This finding is consistent with the assumption that the range of LE-LC transition obtained using the compression method is wider than that using the dropping method. An increase in the dropping volume of solution (increase in DPPC molecule) promotes monolayer growth and hence a higher density finally resulting incompletion of the DPPC monolayer. In the general monolayer formation obtained using the compression method, the interactions between hydrophobic alkyl chains and between hydrophilic groups are very important factors, and such interactions promote the formation of high-density monolayer. In the DPPC monolayer using the dropping method, the hydrophilic interaction between the hydrophilic group of DPPC molecules and water molecules would be maintained and consequently prevent condensation of hydrophobic alkyl chains (hydrophobic interaction) in DPPC molecules. Semi-expanded DPPC monolayer would be formed on the water surface [15], compared to the condensed DPPC monolayer using the compression method. Such a hydrophilic interaction would ultimately control the formation process of DPPC monolayer obtained by the dropping method.

The inset images in Fig. 3.1 show fluorescence microscopy (FM) and Brewster angle microscopy (BAM) images at three surface pressures: (a) 8 mN/m, (b) 12 mN/m, and (c) 42 mN/m). The left images are FM, and the right BAM. On the FM measurement, FM probes (Rh-DMPE) of 0.1 mol% are included in the monolayer. The DPPC monolayer of each surface pressure value is moved on the surface-treated (piranha solution) cover glass with a scooping-up motion [16] and observed by FM. On the BAM measurement, the DPPC monolayer formed at each surface pressure is directly observed in situ by BAM.

In the compression method, the molecular area of 1.2 nm^2 shows zero surface pressure (gaseous monolayer), and both FM and BAM images are homogeneous in dark contrast [17–19]. In the dropping method, on the other hand, that area maintains 8 mN/m surface pressure, and the corresponding images are slightly bright [13]. This indicates that DPPC molecules are already forming a LE-state monolayer with a molecular area of 1.2 nm^2. At the surface pressure of 12 mN/m (b), both FM and BAM images are shown inbright contrast and indicated a LE-LC transition. A remarkable point is the appearance of images. The hole-type LE domain (in dark contrast) appeared in the whole LC phase, thereby indicating a coexistence state. This is completely opposite to the island-type conformation reported with the compression method [17–19], at which small and very bright condensed LC domains disperse in a continuous background of the darker LE phase. Those images (b) would correspond to the π–A isotherm curve that showed unclear LE-LC transition in Fig. 3.1; FM and BAM images also indicate that a flexible and fluid-structured DPPC monolayer is being formed on the water surface. At the surface pressure of 42 mN/m (c), both FM and BAM images became homogeneously bright with the completion of LC-type phase and fluidic DPPC monolayer. The FM needs some additional action for the observation such as mixing of FM probes to DPPC molecules and scooping up the monolayer on the substrate such as a cover glass. However, such actions are not influenced by the formation of DPPC monolayer, and semi-expanded and flexible monolayer is maintained even on the glass, from direct BAM observation [13].

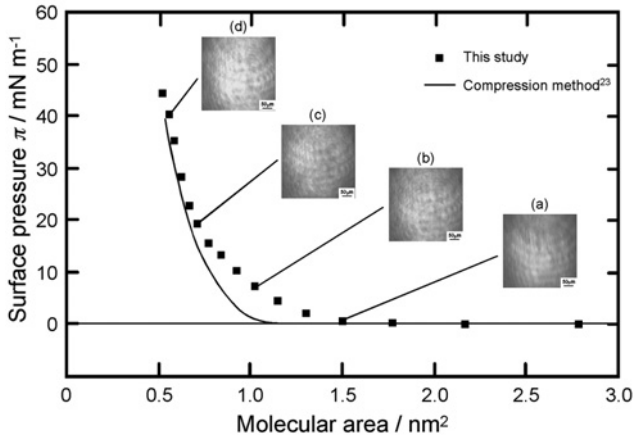


FIGURE 3.2 Surface pressure versus molecular area (π–A) isotherm curve of DMPC monolayer at 26°C. Solid squares (■) indicate dropping method, solid lines, compression method.

It was found that the DPPC monolayer obtained by the dropping method traced a unique monolayer formation process, different from that obtained by the compression method. The comfortable (equilibrium) state between hydrophilic groups of DPPC molecules and water molecules, compared to the interactive state between hydrophobic alkyl chains in DPPC molecules, would lead to the appearance of semi-expanded and flexible DPPC monolayer.

3.2.2 Dimyristoyl Phosphatidyl Choline (DMPC)

Dimyristoyl phosphatidyl choline (DMPC) is also a typical phospholipid as well as DPPC, and composed of two myrisitc acids (C14) and a phosphatidyl choline group. DMPC is one of the components in the biomembrane. DMPC also transforms its state from gel (solid) to a liquid–crystal phase at 24°C (transition temperature); many studies on the phase state of DMPC have been performed relating with biofunctions [8, 20–22].

Figure 3.2 shows the surface pressure versus molecular area (π–A) isotherm curve of DMPC monolayer at 26°C, using the dropping method [solid squares (■)] together with a typical π–A isotherm curve using the compression method (solid lines) [23]. The horizontal axis (abscissa) represents the molecular area calculated from molecular values for the dropping volume, and the vertical axis (ordinate) represents the surface pressure (see also Fig. 3.1).

Many isotherm studies for DMPC monolayer using the compression method have shown that DMPC monolayer forms only one state, a LE state [11]. Therefore, the surface pressure increased gradually from 1.1 nm^2 of molecular area and the pressure increased gradually and monotonously up to 36 mN/m (solid line). In the LE state, two alkyl chains were disordered partially at 26°C. The structure includes a *gauche*-type conformation and a disturbed state; these chains possess expandability, and the cross-sectional area would be larger than that of the hydrophilic group.

The π–A isotherm curve obtained by the dropping method (solid squares) also presented a typical LE state [24]. Therefore, the surface pressure increased gradually from about 1.4 nm^2 molecular area, and increased monotonously up to 43 mN/m. The shape of curve is smooth and similar to that obtained by the compression method (solid line). The limiting molecular A_0 is 0.80 ± 0.05 nm^2/molecule (~40 mN/m), and the value is quite similar to that obtained by the compression method reported previously [0.78 nm^2/molecule (~40 mN/m)].

As well as in the case of DPPC, both sufficient dropping-time interval and the dropwise succession obtained by the dropping method result in dispersal of DMPC molecules over the entire water surface and commencement of the monolayer formation. This corresponds to the increase in surface pressure from the initial stage by the preferential intermolecular interaction of the alkyl chains in DMPC molecules. An increase in the dropping volume of solution (i.e., increase in DMPC molecule) promotes growth of the monolayer and increases the density, as in the case of DPPC. However, partially disordered alkyl chains do not occur in the DPPC-like phase transition, and the molecules also maintain their structure. This is different from the case of DPPC monolayer using the dropping method, where hydrophilic interaction between the hydrophilic group of DPPC molecules and water molecules is dominant. Therefore, the expanding DMPC monolayer forms on the water surface and maintain the expanding state (disordered alkyl chains) of DMPC molecules, and ultimately leading to completion of the DMPC monolayer [15]. This corresponds to the shape of the π–A isotherm curve, which increases gradually and monotonously. The partially disordered alkyl chains that possess larger molecular space than that of hydrophilic group, control the formation process of DMPC monolayer; the differences in the π–A curve between the compression and dropping methods would not appear to be significant. On such the DMPC monolayer, the limiting molecular area A_0 of DMPC monolayer is certainly larger than that of DPPC monolayer; nevertheless, both DMPC and DPPC possess the same hydrophilic group (phosphatidyl choline group). In other words, this indicates that the alkyl chains in DMPC are partially disordered and those in DPPC are cylinderlike at 26°C, as mentioned above.

The π–A isotherm curve of DMPC obtained by the dropping method showed the initial curve starting at higher density (more to the left, about 1.4 nm^2) than that of DPPC (about 1.7 nm^2; see Fig. 3.1). As mentioned above, alkyl chains in DPPC molecules are cylinderlike and the DPPC molecule itself possesses rigidity. In the initial stage of DPPC monolayer formation, the repulsion between DPPC molecules is comparatively large because of its rigidity; therefore, the curve would result in a surface pressure value at lower

molecular density. On the other hand, the DMPC molecule itself possesses expandability because of the partially disordered alkyl chains in DMPC molecule. This expandability may absorb the repulsion energy between DMPC molecules. In other words, the disordered structure of DMPC alkyl chains is somewhat deformable; therefore, the curve may show the surface pressure value at a density higher than that of DPPC.

The inset images in Fig. 3.2 show BAM images at four surface pressures: (a) 1 mN/m, (b) 8 mN/m, (c) 19 mN/m, and (d) 38 mN/m). On the BAM measurement, their treatments are as same as those shown in the Fig. 3.1 insets.

At quite a low surface pressure of 1 mN/m (a), the whole image is shown in slight bright contrast. This indicates that DMPC molecules are beginning to form an expanding monolayer at less than 1 mN/m. As indicated by an increase in surface pressure (8 and 19 mN/m; see Fig. 3.1b, c), the image became brighter but did not result in any morphology change in DPPC molecules (Fig. 3.1b, right); therefore, the DMPC monolayer continued to form homogeneously. At 38 mN/m (Fig. 3.1d), the image became still brighter and consequently the homogeneous DMPC monolayer was formed and completed on the water surface. Such a gradual increase in brightness corresponds to the gradual increase in the surface pressure on the π–A isotherm curve. The brightness of image at 38 mN/m (Fig. 3.1d) was not greater than that of DPPC (Fig. 3.1c, right). On the BAM, thickness and refractive index of monolayer on the water surface is closely related to the brightness [25–27]. DMPC monolayer forms an expandable structure, which also fluctuates on the water surface. Such characteristics of DMPC monolayer would change the refractive index and might also weaken the reflected BAM light compared to the DPPC monolayer.

It was found that the DMPC monolayer obtained by the dropping method traced a monolayer formation process similar to that obtained by the compression method. The comfortable (equilibrium) state of partially disordered alkyl chains in DMPC molecules at 26°C would lead to the appearance of expandable DMPC monolayer, even though hydrophilic DMPC molecules and water molecules maintain equilibrium and interact with each other. Such a partially disordered hydrophobic structure may not be dependent on the pattern of monolayer formation. This is quite different from the DPPC monolayer whose molecules possess cylinderlike alkyl chain structures at 26°C.

3.2.3 Cholesterol

Cholesterol (Chol) is classified under the steroid group, and is composed of a steroid skeleton and hydroxyl group (–OH). Chol is one of the main components in the biomembrane and also the important organic compound in connection with various biological phenomena. Chol is distributed widely in the living body; many studies on biofunctional aspects

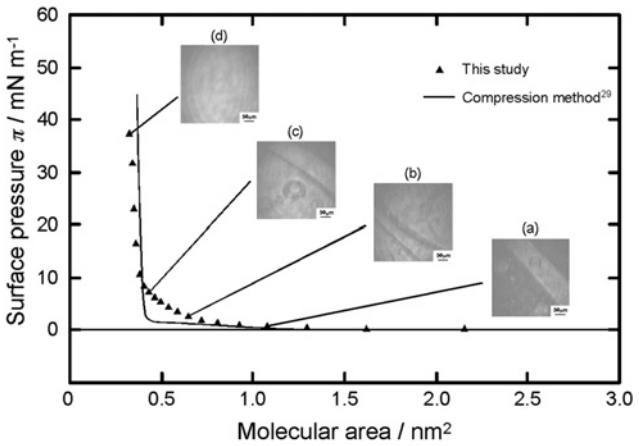


FIGURE 3.3 Surface pressure versus molecular area (π–A) isotherm curve of Chol monolayer at 26°C. Solid triangles (▲) indicate dropping method; solid lines, compression method.

such as its usefulness and toxicity have been performed [8, 14, 28].

Figure 3.3 shows the surface pressure versus molecular area (π–A) isotherm curve of Chol monolayer at 26°C, using the dropping method [solid triangles (▲)] together with a typical π–A isotherm curve using the compression method (solid lines) [29]. The horizontal axis (abscissa) represents the molecular area calculated from molecular values in the dropping volume, and the vertical axis (ordinate) represents surface pressure (see also Fig. 3.1).

Many isotherm studies on the Chol monolayer using the compression method have shown that this monolayer forms only one state, a condensed (solid) state [11]. Therefore, the surface pressure shows extremely gradual increase from 0.6 nm^2 of molecular area (< 2 mN/m) and sudden and steep increase to 40 mN/m at less than 0.45 nm^2. The shape of the π–A isotherm curve is very sharp, similar to a titration curve, and does not change its shape at various temperature (20–40°C). In the condensed state, the Chol molecules orient almost vertically to the water surface and are found in a vertical high-density stacking conformation [30].

The π–A isotherm curve obtained by the dropping method (solid triangles) presented a condensed-type state. Therefore, the surface pressure increased gradually from about 1.0 nm^2 of molecular area and monotonously until about 10 mN/m, and after that increased steeply up to 37 mN/m. The limiting molecular area A_0 is 0.41 ± 0.02 nm^2/molecule (~36 mN/m), and the value is quite similar to that obtained by the compression method reported previously (0.40 nm^2/molecule (~40 mN/m) [23]. On the other hand, the π–A isotherm curve was slightly different from that obtained by the compression method; initially the curve showed only a gradual increase and also a larger molecular area compared to that obtained by the compression method.

As in the case of DPPC, both sufficient dropping-time-interval and the the successive dropping, obtained by the dropping method, supply the dispersion of Chol molecules over the entire water surface, accompanied by the beginning of monolayer formation. This corresponds to the increase in the surface pressure from the initial stage by the preferential intermolecular interaction of steroid skeleton in Chol molecules. An increase in the dropping volume of solution (increase in Chol molecule) strongly promotes the hydrophobic interaction between steroid skeletons in Chol molecules because of its stacking characteristics; thus Chol molecules would form a condensed monolayer on the water surface. This corresponds to the steep increase in the π–A isotherm curve to >10 mN/m. The small hydrophilic group (–OH) may also originate in such formation process of Chol monolayer. This is different from the scenario obtained by the compression method. In the latter method, after the dropwise addition of several aliquots of the condensed aggregates (island-type), dispersion of Chol molecules already appeared partially on the water because of the strong hydrophobic steroid skeleton interaction between these molecules. The compression only gathers those condensed islands on the water surface and forms Chol monolayer of only a solid-type condensed state and, thereby, a steep increase in the π–A isotherm curve. On the other hand, using the dropping method, the Chol monolayer undergoes a liquid-type expanding state, leading to the formation of a condensed state. Although both moieties are the same condensed states at the completion of monolayer, the degrees of uniformity may differ.

Inset images in Fig. 3.3 show BAM images at four surface pressures: (a) 1 mN/m, (b) 3 mN/m, (c) 8 mN/m, and (d) 36 mN/m. On the BAM measurement, the pressures are treated the same as those shown in the Fig. 3.1 insets.

At a relatively low surface pressure (1 mN/m), the image showed the existing line- and circle-type domain states. This indicates that aggregates of Chol molecules already exist on the water surface and begin to form an expanding monolayer at 1 mN/m. As indicated by an increase in surface pressure (3 and 8 mN/m), a number of those domains increased and the domains also enlarged gradually. The brightness of those images also increased. Chol molecules themselves possess high condensation forces and continue to form the monolayer. At 36 mN/m, those domains obtained at ≤8 mN/m disappeared and subsequently the image manifested a homogeneous state. The brightness of the image increased beyond that at 8 mN/m; the homogeneous Chol monolayer was formed and completed on the water surface. Brightness of the image at 36 mN/m (Fig. 3.3d) did not increase beyond that of completed DPPC and DMPC monolayers (Fig. 3.1c right and Fig. 3.2d). Chol molecules are smaller than DPPC and DMPC molecules, and their molecular length is nearly half that of DPPC and DMPC molecules. A size-dependent characteristic such as this would change the refractive index and also might weaken the reflected BAM light compared to the completed DPPC and DMPC monolayer.

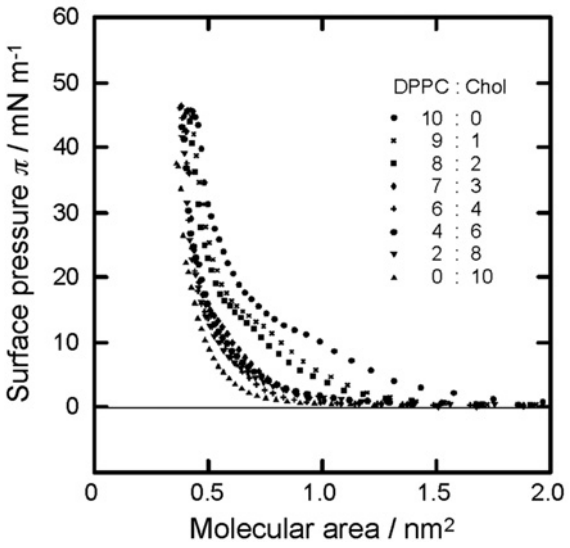


FIGURE 3.4 Surface pressure versus molecular area (π–A) isotherm curve of various DPPC–Chol mixed monolayer at 26°C. Mole fraction of Chol: 0.0, 0.1, 0.2, 0.3, 0.4, 0.6, 0.8, 1.0 from the right π–A isotherm curve.

It was found that the Chol monolayer obtained by the dropping method traced a slightly different monolayer formation process compared to that obtained by the compression method. Sufficient spreading-time interval and the continuous dropping may improve the spreading state at the initial stage of monolayer formation. The strong hydrophobic interaction between steroid skeletons ultimately leads to the formation of a condensed Chol monolayer, similar to that obtained by the compression method.

3.2.4 DPPC and Cholesterol Mixture

Figure 3.4 shows the surface pressure versus molecular area (π–A) isotherm curves of various DPPC-Chol mixed monolayers at 26°C, using the dropping method. Mole fractions of Chol are 0.0, 0.1, 0.2, 0.3, 0.4, 0.6, 0.8, and 1.0. The horizontal axis (abscissa) represents the molecular area calculated from mixed molecular values, and the vertical axis (ordinate) represents surface pressure (see also Fig. 3.1). The curves of 0.0 [pure DPPC (•)] and 1.0 [pure Chol (▲)] are as almost the same as those in Figs. 3.1 and 3.3.

The curves of DPPC-Chol mixed monolayer shift to the left relative to those of the pure DPPC monolayer, as inedicated by an increase in the mole fraction of Chol, and approach the pure Chol monolayer [31]. The unclear small plateau range observed in the pure DPPC monolayer (LE-LC transition) becomes narrower and its surface pressure also decreases, and then completely disappear at >0.3 mole

fraction of Chol. The shape of curves with >0.3 mole fraction of Chol is closely similar to that of pure Chol monolayer. This tendency is also similar to that obtained by the compression method [9, 10, 32, 33]. These observations indicate that Chol molecules strongly influence the DPPC monolayer (condensation effect of Chol) even using the dropping method, and at >0.3 mole fraction of Chol the condensed mixed monolayers form on the water surface. Therefore, the mixed monolayer with <0.3 mole fraction of Chol forms LC-type phase and with >0.3 mole fraction of Chol, the condensed phase.

The mean limiting molecular area of DPPC-Chol mixed monolayer obtained by the dropping method can be compared to that of the ideal mixed monolayer, which is calculated from each A_0 of pure DPPC and Chol monolayer. The excess area A_{ex} can be obtained by using the following equation [9, 10]

$$A_{\text{ex}} = A_{DC} - (X_D A_D + X_C A_C)$$

where A_{DC} is the mean limiting molecular area of the mixed monolayer, A_D and A_C are the limiting molecular area of each pure DPPC and Chol, respectively, and x_D and x_C are the mole fractions of the DPPC and Chol components.

Figure 3.5 shows the dependence of the Chol mole fraction on A_{ex}. The horizontal axis (abscissa) represents the mole fraction of Chol, and the vertical axis (ordinate) represents the excess area A_{ex}. Figure 3.5 also shows typical Chol mole fraction dependences of A_{ex} on previously reported data obtained by the compression method; those data were recalculated by the original calculation method based on those π–A isotherm curves [9, 10, 32, 33]. The present study of the shape of Chol dependence is similar to that of previous data; therefore, the

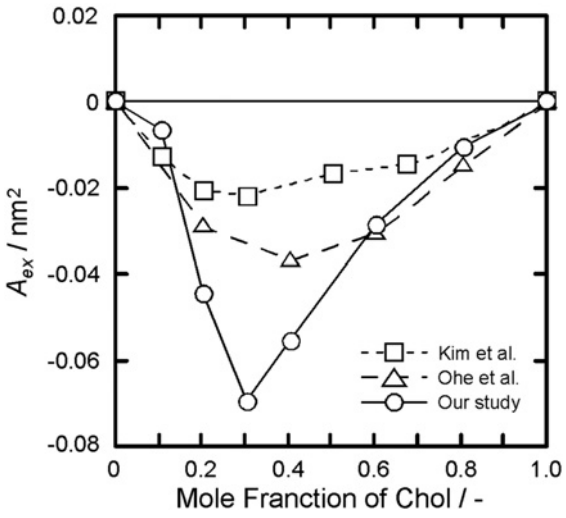


FIGURE 3.5 Chol mole fraction dependence of the excess area A_{ex}. Solid lines indicate dropping method, dashed and dotted lines, compression method.

addition of Chol in the DPPC monolayer showed a negative deviation from the ideal line, and the extreme value is at the ~0.3 mole fraction of Chol. These findings indicate again that Chol molecules cause condensation of the DPPC monolayer at various Chol mole fractions. The present A_{ex} is about twice those of previous data, ranging within $x_C = 0.2$–0.4.

As mentioned in Section 3.2.1, the DPPC monolayer obtained by the dropping method has a fluidic structure, where the hydrophilic interaction between phosphatidyl choline groups in DPPC molecules and water molecules predominates in the hydrophobic alkyl chain interactions between DPPC molecules. Such a state is quite different from that found using the compression method, where intermolecular interaction (hydrophilic and hydrophobic interaction) between DPPC molecules occurs because of the effect of artificial force exerted by the movable partitioning board. The fluidic, loose structure of alkyl chains in the present DPPC monolayer would be a strongly causative factor in the high-condensation effect of Chol; therefore, the easily inserted hydrophobic Chol molecules in DPPC molecules strongly attract weakly interacting alkyl chains in DPPC molecules. Such an attractive force may also collapse the hydrogen-bonding network structured by the hydrophilic interaction between hydrophilic groups of DPPC molecules and water molecules. The present negative large A_{ex} obtained by the addition of Chol indicates that the fluidic pure DPPC monolayer obtained by the dropping method certainly forms on the water surface.

Figure 3.6 shows FM and BAM images on DPPC-Chol mixed monolayer of the 0.2 mole fraction of Chol at various surface pressures (1, 4, 11, and 43 mN/m).Upper images are FM, and lower ones are BAM. The FM (upper) and BAM (lower) images shown in Fig. 3.6 indicate that their treatments are the as same as those shown in in the Fig. 3.1 insets.

At quite a low surface pressure (1 mN/m), the FM image shows a bright state and the irregular spot-type pattern is partially revealed in the image (this pattern could not be detected in the BAM image). The brightness of both FM and BAM images is higher than that of the pure DPPC monolayer at 1 mN/m (not shown). Therefore, Chol molecules assemble DPPC molecules at 1 mN/m, and the mixed monolayer is already formed as the aggregate of DPPC molecules by Chol (condensing state) on the water surface. These findings correspond to the π–A isotherm curve at the 0.2 mole fraction of Chol (Fig. 3.4), which shifts to the left by the condensation effect of Chol. At 4 mN/m, the unique image is obtained in the FM; the image showed the plural dark-spot-type pattern and the size is smaller than that of pure DPPC monolayer at 12 mN/m (insetin Fig. 3.1b, left). Compared to the pure DPPC monolayer, such a spot-type pattern is revealed at 8 mN/m lower surface pressure (4 mN/m); therefore, the LE-LC transition of mixed monolayer of the 0.2 mole fraction of Chol occurred at about 4 mN/m. Such an image was also observed in the BAM, but it was indistinct because of the low

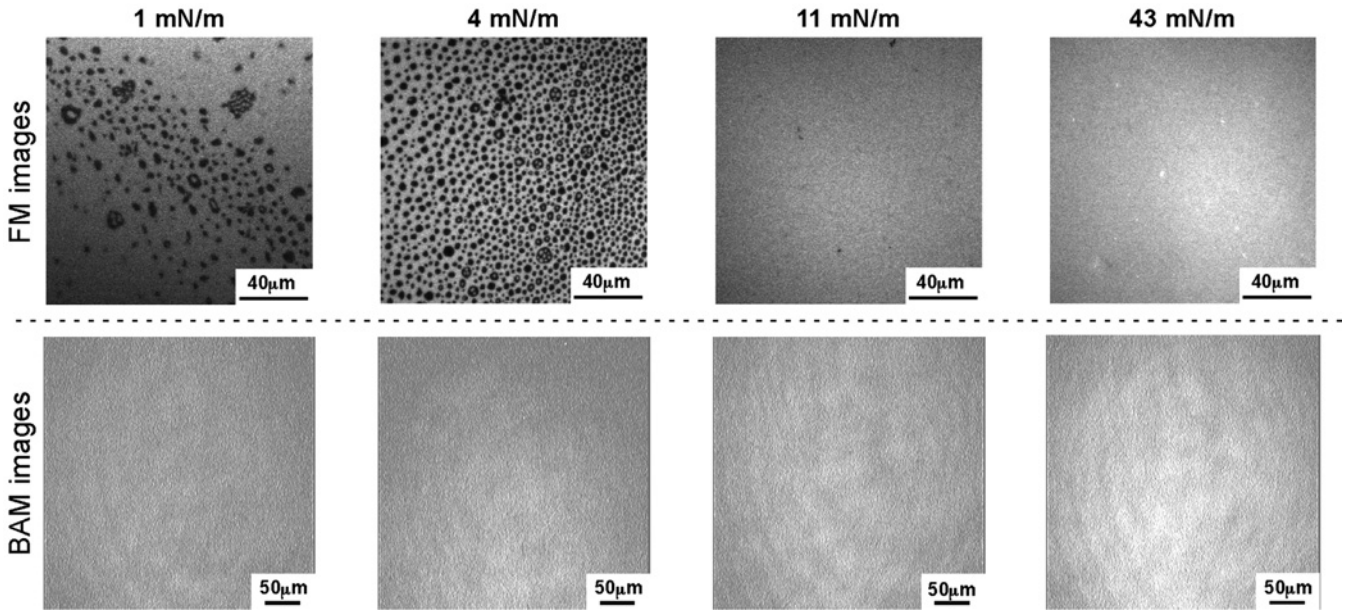


FIGURE 3.6 FM and BAM images on DPPC–Chol mixed monolayer of 0.2 mol fraction of Chol at various surface pressures (1, 4, 11, and 43 mN/m). Upper: FM images; lower: BAM images.

resolution of BAM. The brightness of both FM and BAM at 4 mN/m was greater than that of pure DPPC monolayer at 4 mN/m (not shown), as well as in the case of 1 mN/m. The mixture with Chol and DPPC molecules strengthens the hydrophobic interaction between hydrophobic alkyl chains in DPPC molecules and also relatively weakens the hydrophilic interaction between hydrophilic groups of DPPC molecules and water molecules; therefore, the difficult-to-spread DPPC-Chol mixture would reassemble and form the condensed mixed monolayer on the water surface. This corresponds to a decrease in the size of the dark spot compared to the pure DPPC monolayer. Actually, several island-type aggregates exist in the dark spot, and they are similar to the transition state by the compression method [17–19]. At 11 mN/m, the dark-spot-type pattern of both FM and BAM observed at 4 mN/m disappeared and subsequently those images became homogeneously bright. On the FM image, the brightness is approximately same as that of the bright part observed at 4 mN/m. After the end of the LE-LC transition at the previously observed 4 mN/m caused by Chol molecules, the condensed mixed monolayer is continuously formed on the water surface. This corresponds to the continuous increase in π–A isotherm curve at the 0.2 mole fraction of Chol (Fig. 3.4). At 43 mN/m, a further homogeneous image was observed at both FM and BAM, and the brightness was greater than that observed at 11 mN/m; the formation of homogeneous mixed monolayer was completed. Compared to the pure DPPC completed monolayer, the brightness of BAM was somewhat darker (Fig. 3.1c right). The mixing of Chol would change the mean monolayer thickness of the mixed monolayer compared to the pure DPPC monolayer, The surface roughness would also increase, and consequently a change in the refractive index, and might also weaken the reflected BAM light compared to the pure DPPC monolayer. As shown in the πA isotherm curve, FM and BAM images also revealed that the DPPC-Chol mixed monolayer at the 0.2 mole fraction of Chol forms higher condensed monolayer than the pure DPPC monolayer on the water surface, by the Chol condensation effect.

Figure 3.7 shows BAM images on the DPPC-Chol mixed monolayer of the 0.3 mole fraction of Chol at various surface pressures (1, 4, 11, and 43 mN/m). On the BAM measurement, their treatments are the same as those shown in the insets in Fig. 3.1.

Those images of the mixed monolayer of Chol 0.3 were quite different from those of pure DPPC monolayer (Fig. 3.1 insets) and Chol 0.2 (Fig. 3.4). Therefore, at quite a low surface pressure (1 mN/m), the image showed the existed line- and circle-type domain state. It was indeed the same as that of the following pure Chol monolayer (1 mN/m; Fig. 3.6) at which Chol molecules form a condensed monolayer from quite a low surface pressure. This indicates that the condensed aggregates of DPPC and Chol molecules were already visible on the water surface at 1 mN/m. According to an increase in surface pressure (4 and 11 mN/m), a number of those domains increased and those domains also enlarged gradually. The brightness of the image also increased. As was the case at 1 mN/m, those morphology changes were the same as those of the following pure Chol monolayer (3, 8 mN/m; Fig. 3.6). At 43 mN/m, those domains obtained at 11 mN/m disappeared and subsequently the image exhibited a homogeneous state. The brightness of the image increased

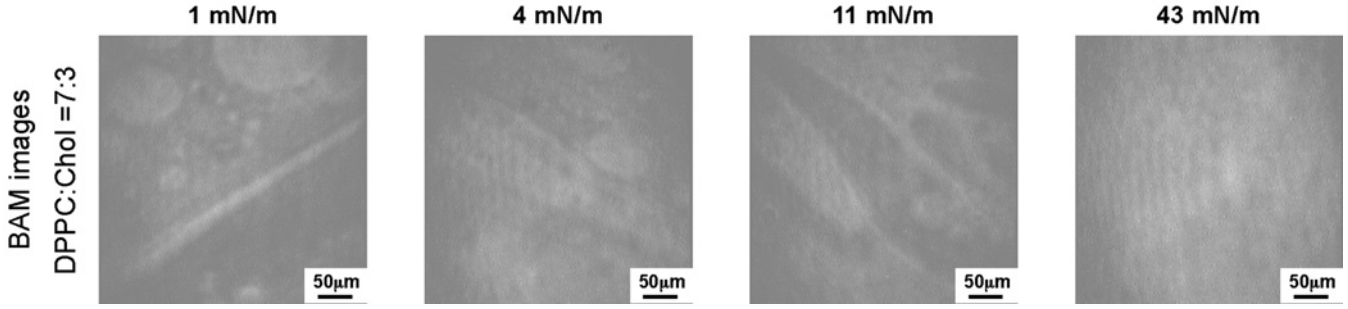


FIGURE 3.7 BAM images on DPPC–Chol mixed monolayer of 0.3 mol fraction of Chol at various surface pressures (1, 4, 11, and 43 mN/m).

beyond that at 11 mN/m and was also similar to that of the 0.2 mole fraction of Chol. As was the case at 1, 4, and 11 mN/m, it was the pure Chol-type morphology change (Fig. 3.3). This indicates that the mixed monolayer at the 0.3 mole fraction of Chol forms Chol-type condensed monolayer and forms on the water surface from the initial stage (low surface pressure) of its monolayer formation. These findings also correspond to the result that the shape of π–A isotherm curve of Chol 0.3 is quite similar to that of pure Chol monolayer (Fig. 3.4), and the condensation rate shows a maximum value at the 0.3 mole fraction Chol (Fig. 3.5). In other words, the pure DPPC monolayer obtained by the dropping method forms flexible monolayer, which is influenced easily on the condensation effect of Chol.

It was found that the DPPC monolayer obtained by the dropping method is strongly affected by the condensation effect of Chol; from the π–A isotherm curve, the excess area A_{ex} was about twice larger than that obtained by the compression method in the range from 0.2 to 0.4 mole fraction of Chol. Both FM and BAM images also supported the condensation effect of Chol; more than the 0.3 mole fraction of the Chol DPPC-Chol mixed monolayer showed Chol-type condensed state. It is known that the condensation effect of Chol also occurs at the DPPC-Chol mixed monolayer formed by the compression method. The present DPPC monolayer obtained by the dropping method certainly forms fluidic state, and hydrophilic groups of DPPC molecules and water molecules retain equilibrium while interacting with each other. Therefore, the monolayer would be strongly affected by the condensation effect of Chol.

3.2.5 Usefulness of Dropping Method

It is interesting that the influence on the monolayer formation by the dropping method differs among DPPC, DMPC, and Chol; DPPC molecules form fluidic and flexible monolayer, DMPC expanding monolayer, and Chol condensed monolayer. In the compression method, DPPC and Chol form condensed monolayer, and DMPC expanding monolayer. Recent research on a phosphatidyl ethanolamine (PE) series also showed such influence; dimyristoyl-PE (DMPE) molecules form fluidic and flexible monolayer, whereas dipalmitoyl-PE (DPPE) molecules form condensed monolayer. With the compression method, both DMPE and DPPE form condensed monolayer. The dropping method may be directly capable of forming reflected the original properties of molecules themselves, such as flexibility or rigidity, dispersion or aggregation, on the water surface. In other words, the monolayer formed by the dropping method would supply the suitable measurement field for the elucidation of membrane function at the present when the membrane flexibility attracts attention in the functional revelation of biomembrane.

3.3 INTERACTION BETWEEN LIPID MONOLAYER AND ANESTHETICS

Biomembranes have fundamental fluid structures as represented by the *fluid mosaic model* proposed by two researhers [34], which buries functional proteins in lipid bilayers composed of various kinds of phospholipids [28]. At the fluidic field of membrane, intermolecular interactions such as hydrogen bonding, hydrophobic interactions, and van der Waals interactions play an important role in various cellular functions, for example, the construction of tertiary structures of protein, the hybridization of DNA, the molecular recognition of membranes, and the transport of nutrition and various medicines [28, 35, 36], as mentioned in Section 3.1.

An anesthesia phenomenon would also belong to the same category as the above interaction, at the point of the interaction between a biomembrane and an anesthetic [37–43]. Anesthetics do not have a common molecular structure; various molecules, such as those of alcohol, diethyl ether, chloroform, and dinitrogen monoxide, and even familiar gas molecules of CO_2, N_2, and Xe, cause the anesthesia phenomenon. At the present, some halogenated compounds, called *halothane*, *enflurane*, *isoflurane*, and *sevoflurane*, are used as anesthetic drugs. The anesthesia phenomenon occurs at the high concentration of millimolar order (mM) in body fluid different from general medicine [nanomolar

order (nM)], and the effect naturally shows reversibility depending on the medication concentration. An anesthetic strength (anesthetic potency) is also known to show temperature dependence; diethyl ether and alcohol weaken the anesthetic potency at a low temperature, whereas chloroform and halogenated compounds strengthen this potency.

Although some anesthetic theories (lipid theory, protein theory, etc.) have been suggested since Meyer and Overton proposed the *lipoid hypothesis* [44, 45], it would probably, be clear that the anesthesia phenomenon is a *physisorption phnomenon*, in which an anesthetic aggregation acts indirectly on a biomembrane interface, according to the above various experimental and clinical findings [38–40, 46, 47]. The details of anesthesia theory and its mechanism are entrusted to another chapter on anesthesia, so we will discuss the action mechanism of anesthetics to the lipid monolayer on the water surface and the correlation with the mechanism and anesthesia phenomenon, describing the principle of measurement technique and the contents of the apparatuses actually used.

3.3.1 Quartz Crystal Oscillator (QCO) Method

Among various interface chemistry techniques, we adopted a quartz crystal oscillator (QCO) method to investigate the interaction between membrane and anesthetic. The QCO method is now a useful and powerful tool for investigating various physicochemical properties, including interfacial phenomena [48, 49].

The QCO apparatus was originally used as a quartz crystal microbalance (QCM) that could detect a mass change in the nanogram-order level [50]. The QCM method has been applied to a gas adsorption measurement in gas phases to monitor the thickness of a vacuum evaporation device [51, 52]. In one study, where the QCM was used for quantitative analysis of cyanide ion in liquid phases, the QCO was shown to have a stable resonance frequency in liquid phases [53]. That pioneering work was preceded by many extensive experimental methods. Another team investigated the adsorbtion of oxygen on the Au surface (electrode of QCO) in perchloric acid solution, and reported that the adsorption process of oxygen proceeded via a three-step reaction sequence from the analysis of mass change [54]. Another group also investigated the cation selectivity on ITO/Au surface (electrode of QCO) modified by a Prussian blue (PB) thin film in propylene carbonate solution, and reported that the selectivity coefficient of Na^+ versus Li^+ on the PB film was about 15 [55]. More recently, another group performed systematic studies of nanogram-order detection on the molecular recognition (chemical adsorption and desorption) using DNA strands and lipid monolayers [56–64]. Those studies were characterized by the use of an oscillator surface modified by the functional film and/or biomembrane and the detection as the mass change on such adsorption processes.

In the QCM method, the resonance frequency of the QCO changes because of the adsorption of substances on the QCO surface. The relation between the resonance frequency and the adsorbed mass is shown according to the following proportional equation [50]

$$\Delta f = -2f_0^2 \Delta m / A(\rho_q \mu_q)^{1/2}$$

where Δf is the measured frequency change (Hz), f_0 is the resonance frequency of the oscillator, Δm is the mass change (g), A is the electrode area (cm^2), ρ_q is the density of quartz (2.648 g/cm^3), and μ_q is the shear modulus (2.947×10^{11} dyn/cm^2). For example, using a 6-MHz AT-cut QCO, the change in 1 Hz of QCO corresponds to 12.2 ng/cm^2; therefore, QCM can detect the volume down to the nanogram level.

These quantitative analyses are based on the above Sauerbrey equation [50]. On the other hand, it has been also reported that the resonance frequency changes in response to a change in not only in mass but also in properties such as density, viscosity, and elasticity of adsorbed substance. This indicates that the Sauerbrey equation is not always applicable to the measurements, especially in liquid phases. Later, another new QCO method, termed the *quartz crystal impedance* (QCI) method, was proposed by several authors [65–68]. The QCI method is now used as a powerful tool for detecting the viscosity/elasticity of adsorbed layers independently of mass of adsorbed layers on the QCO. Yet another team investigated the adsorbed mass and the viscosity change about the action of DNA on the –OH-modified QCO electrode, and reported that the viscosity on the QCO electrode also changed with the adsorption, immobilization, and hybridization of DNA, as well as its mass change [69]. Another group also investigated the temperature dependence of Langmuir–Blodgett (LB) films (1,3-dioctadecyl-*rac*-glycer-2-ol) adsorbed on the QCO, and reported that the phase transition of LB films caused the viscosity change of LB films themselves [70]. Recently another group performed detailed analyses of the molecular properties such as adsorption, precipitation, and denaturation of proteins using piezoelectric QCI system [71–73].

In the QCI method, the mechanical oscillation of QCO is exchanged with the electrical equivalent circuit, including resistance R_1, capacitance C_1, inductance L_1, and capacitance C_0 as shown in Fig. 3.8a, according to the theory of electro-mechano-acoustical analogy [52, 65–68, 74, 75]. In the circuit, R_1, C_1, and L_1 correspond to the viscosity, elasticity, and mass of the oscillating body (quartz plate, electrode, and adsorbed layer), respectively. C_0 is the capacitance between the two electrodes on the QCO. The admittance Y of the circuit is expressed by the following equation

$$Y = 1/(R_1 + 1/j\omega C_1 + j\omega L_1) + j\omega C_0$$

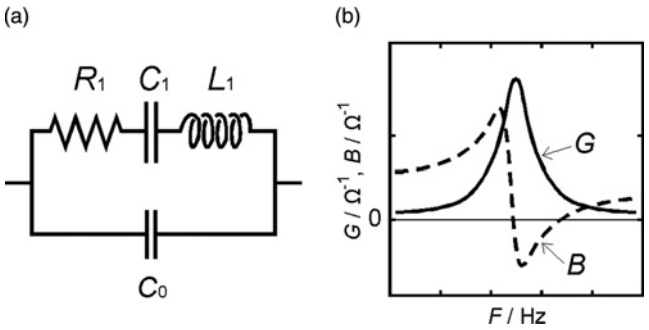


FIGURE 3.8 (a) Electrical equivalent circuit for an AT-cut QCO (R_1 = resistance; C_1 = capacitance; L_1 = inductance; C_0 = capacitance) for QCO; (b) conductance (G) and susceptance (B) spectra of an AT-cut QCO.

This equation is also converted using the conductance G and the susceptance B, which are real and imaginary parts of Y, respectively. R_1, C_1, L_1, and C_0 are calculated using the following equations from analysis of the above G and B obtained by an impedance analyzer at scanned frequency (Fig. 3.8b):

$$R_1 = 1/G_{\max}$$
$$C_1 = 1/L_1 \left(2\pi f_{G_{\max}}\right)^2$$
$$L_1 = 1/2\pi \left(f_{B_{\min}} - f_{B_{\max}}\right)$$
$$C_0 = B_{fG_{\max}}/2\pi f_{G_{\max}}$$

In these equations, G_{max} is a maximum value of G, f_{Gmax} is the frequency at the maximum of G, f_{Bmin} and f_{Bmax} are the frequencies at a minimum value of B and a maximum value of B, respectively, and B_{fGmax} is a value of B at f_{Gmax}. Among those various components, we specifically address the analysis of R_1 (viscosity) in the circuit from the viewpoint of membrane fluidity [36–38, 76, 77].

The details of QCM and QCI are entrusted to many reviews, articles cited above, and another chapter on the QCO method. From these useful characteristics of QCM and QCI, it can be expected that QCM and QCI methods would give the key of the elucidation of anesthesia phenomenon.

3.3.2 Apparatuses and Procedure

In order to investigate the interaction between anesthetics and the biomimetic flexible lipid monolayer on the water surface using the dropping method, as mentioned in Section 3.2, we applied the procedure of attaching QCO horizontally on the lipid monolayer, which employs the flexible properties of lipid monolayer. It was Okahata group who first designed and introduced the QCM method [56], which is now applied to various investigations of intermolecular interactions such as monolayer-protein, Gangliosides-WGA and virus, molecular recognition such as the hydrogen bonding and van del Waals interaction [57–63, 78–84].

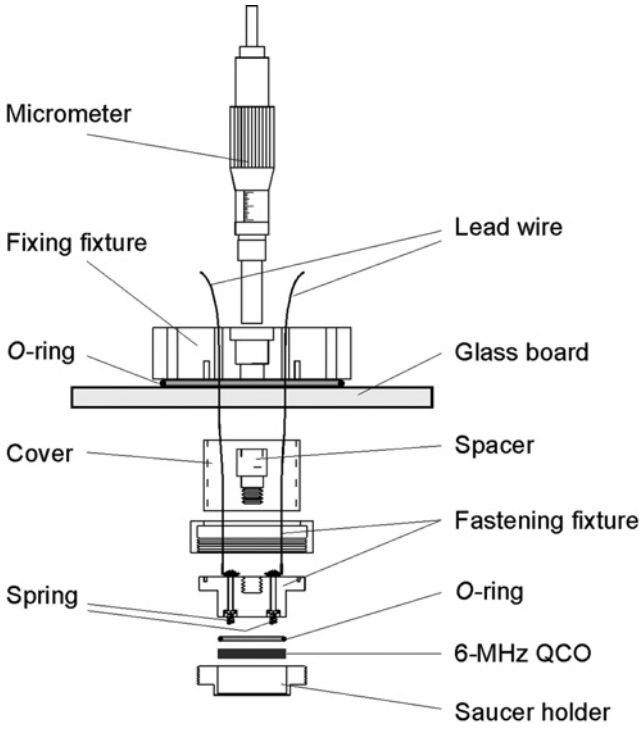


FIGURE 3.9 Central part of the QCO sensor. As the QCO attaches horizontally to the lipid monolayer, the saucer holder is specially processed. By installing a micrometer, it is possible to attach the QCO under the micrometer-order level and gentle condition.

For the detection of a very small physisorption behavior of anesthetic–lipid monolayer interaction, we also developed horizontally adhering type QCO apparatuses uniquely. Figure 3.9 shows a central part of the QCO sensor. An AT-cut QCO with a 6-MHz oscillator (manufactured by Hokuto Denko Corp.) is selected in the measurement. The area of QCO electrode and its thickness are 133 mm^2 and 0.25 mm, respectively. This QCO consists of two separate circuits one side for oscillating the QCO, and an opposite side for attachment to the lipid monolayer. The QCO is fixed with an O-ring in the poly(tetrafluoroethylene) saucer holder by pushing the fastening-type poly(tetrafluoroethylene) fixture. The saucer holder is specially processed so that only one side of QCO can attach horizontally to the lipid monolayer on the water surface. Two springs contacting with the QCO circuits are incorporated into the inside of the fastening-type fixture as two lead wires. A micrometer is also installed through the acrylic resin spacer in a center part of the fastening-type fixture. This micrometer makes it possible to attach the QCO horizontally and carefully on the lipid monolayer, at the micrometer-level and under slow-speed conditions (10 μm/s). The lipid monolayer attaches physically on the electrode surface of QCO by the hydrophobic interaction between the hydrophobic Au electrode surface and hydrophobic group (alkyl chain) of the

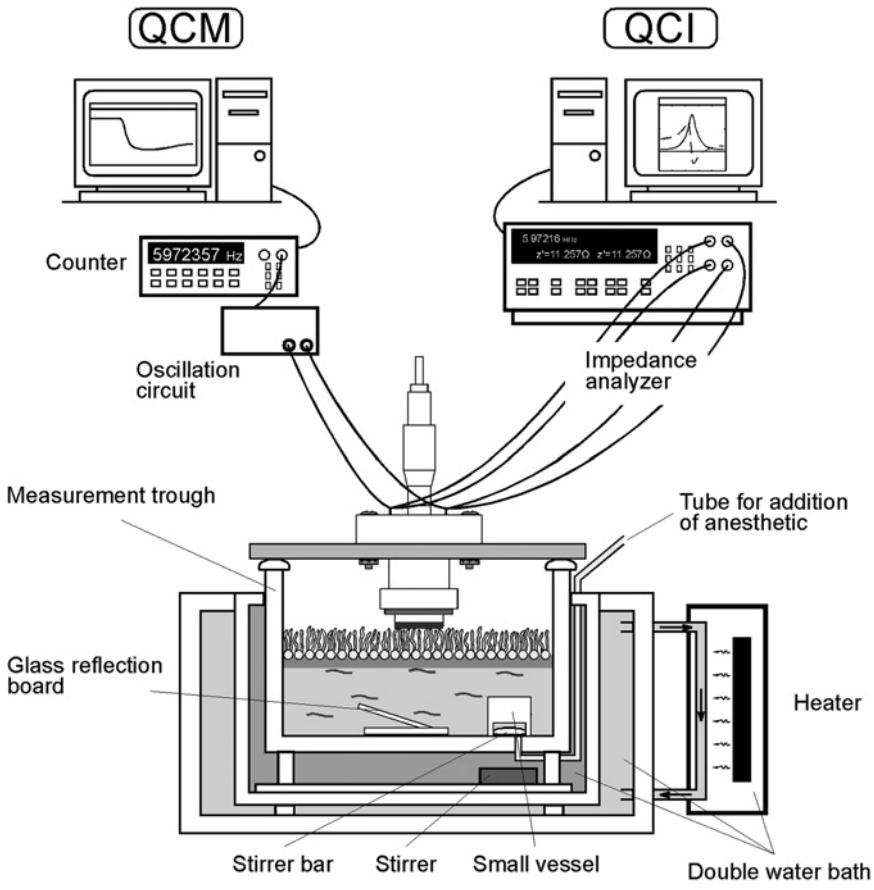


FIGURE 3.10 Schematic diagram of experimental apparatuses for both QCM and QCI measurements.

monolayer [78–84]. The whole QCO sensor is installed with a poly(tetrafluoroethylene) fixing fixture in a center of a glass board, which serves as a cover.

Figure 3.10 is a schematic representation of experimental apparatuses for both QCM and QCI measurements [47, 85, 86]. The measurement trough consists of polypropylene. A glass reflection board is mounted on the bottom of the trough to prevent wave reflection from the bottom [48,49]. A small poly(tetrafluoroethylene) vessel is mounted at the side of trough and a stirring bar is also placed in the vessel. The bar is stirred gently in the trough containing water at the rate of 1 rev/s by magnetic stirrer; the bar rotation is controlled by a slow-speed controller. Since the stirring is very slow, it does not affect the stability of lipid monolayer on the water surface. The vessel is also processed as the dissolved anesthetics by diffuse stirring into the water phase. The anesthetic (liquid) is injected into water phase through the poly(tetrafluoroethylene) tube and anesthetic droplet is stirred by the bar. The temperature of the measurement trough is maintained at 26 ± 0.01°C by use of a double water bath and also by controlling experimental environment at 27 ± 0.5°C. At the QCM, the resonance frequency is counted directly by the frequency counter through the oscillation circuit. At the QCI, the impedance measurement is performed continuously on the QCO, and the resistance is analyzed by the software for the impedance analyzer. QCM and QCI measurements are performed independently, respectively.

Figure 3.11 shows the typical time course of resonance frequency (F, Fig. 3.11a) and resistance (R, Fig. 3.11b) of QCO in contact with dipalmitoyl phosphatidyl choline (DPPC) monolayer on the water surface at 26°C. The horizontal axis (abscissa) represents time (hours), and the vertical axis (ordinate) represents the actual frequency and resistance. The horizontal axis zero corresponds to the time that QCO attached to the DPPC monolayer. When the QCO attached to the monolayer, F decreased by ∼1000 Hz and R increased by ∼200 Ω. Each amount of change was similar to the theoretical and empirical value [55–63, 65–68, 74, 75, 78–84, 87, 88]. After attaching the QCO, it is found that both F and R remain stable for several hours. This initial nonequilibrium state (time dependence) would be due to the equilibration of temperature of QCO and/or hydrophobic interaction between QCO and monolayer by attaching the QCO on the monolayer. Those stabilities were maintained within ± 0.5 Hz at QCM and ± 0.02 Ω at QCI for >8 h; therefore, the QCO

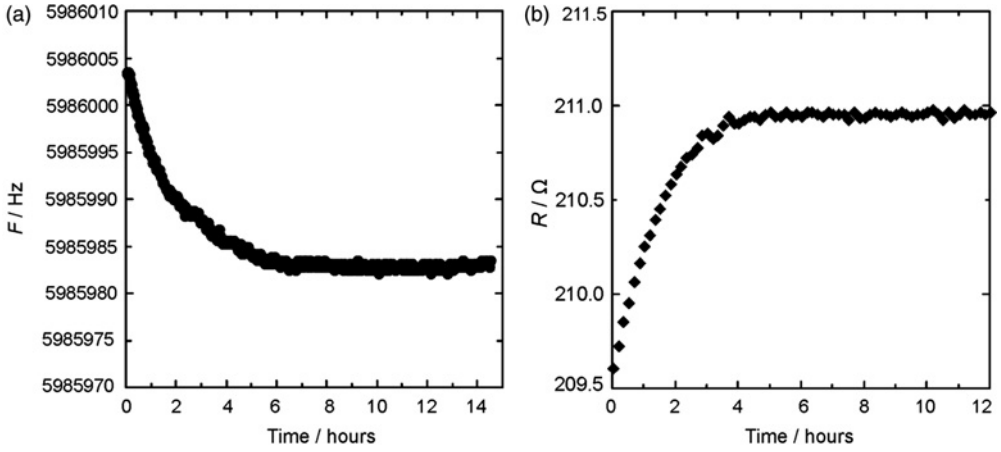


FIGURE 3.11 Typical timecourse of F and R of QCO in contact with DPPC monolayer on the water surface at 26°C. Both F and R are stable after passing for several times. These stabilities are maintained within ± 0.5 Hz at QCM and ± 0.02 Ω at QCI for longer than 8 h.

surface is maintained intact on the monolayer and is sensitive to each change under the monolayer [56–63]. There were some time-dependence patterns besides those shown in Fig. 3.10 until both F and R stabilized. However, when such stabilities were confirmed for ≥3 h, an experiment demonstrating the action of anesthetic on the lipid monolayer was subsequently conducted by the addition of anesthetic into the water phase (Fig. 3.9).

3.3.3 Time Course of Frequency (QCM) and Resistance (QCI)

It is known that the frequency and resistance of QCO are affected by the density and viscosity of the attached liquid phase (water phase in this study) [87, 88]. Since the concentration of anesthetic is on the mM level as mentioned above, the density and viscosity in the solution hardly change compared to those of water even if the anesthetic is dissolved in the water phase. Therefore, the change of frequency and resistance in this study is certainly due to the interaction between the lipid monolayer and anesthetic [56–64].

Here, we will explain how the time course is observed at both QCM and QCI by the addition of anesthetic, giving the interaction between DPPC monolayer and anesthetic enflurane as an example. Figure 3.12 shows the typical timecourse of frequency (QCM) and resistance (QCI) for QCO in contact with a DPPC monolayer after adding enflurane of 7 mM concentration (bulk phase) at 26°C. The lower half of the plot represents frequency and the upper half, resistance. The horizontal axis (abscissa) represents time (hours), and the vertical axis (ordinate) represents each frequency and resistance change [ΔF (Hz) and ΔR (Ω)] based on each stable frequency and resistance (Fig. 3.11) before the addition of enflurane. Enflurane was added in the water phase at the time of line A. After the addition of enflurane, ΔF decreased gradually (increase in adsorption) and ΔR also increased gradually (increase in viscosity) in response to the enflurane, and both ΔF and ΔR approached an equilibrium state. A typical hydrophobic enflurane possesses solubility, and the stirring bar is rotated gently in the water (1 rev/s); therefore, the delayed response (∼1 h) after the addition probably corresponds to the necessary time for the dissolution of enflurane into the water phase and the diffusion of enflurane from bulk solution (water phase) toward the DPPC monolayer/water interface [47, 85, 86, 89]. When both ΔF and ΔR begin to change, ΔF shifts steeply according to the

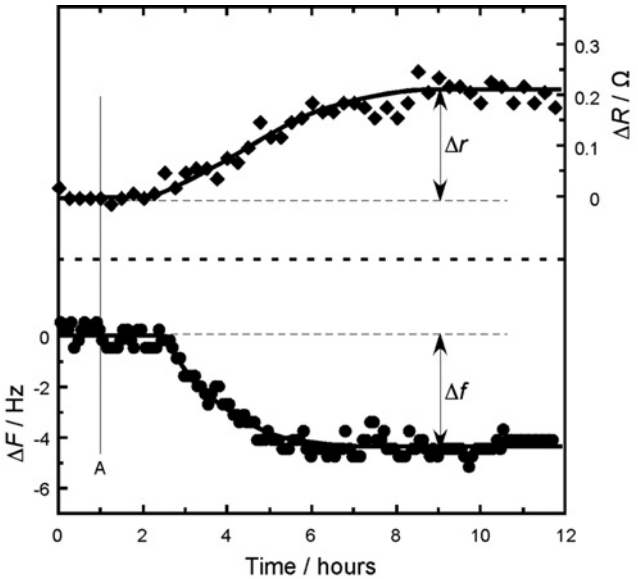


FIGURE 3.12 Typical timecourse of ΔF and ΔR of QCO in contact with DPPC monolayer after adding anesthetic enflurane of 7 mM concentration (bulk phase) at 26°C. Lower: ΔF; upper: ΔR. Enflurane was added in the water phase at the time of line A. Inserts Δf and Δr show each amount of change in frequency and resistance.

general adsorption phenomenon [78–84]; on the other hand, ΔR shifts gently. Because the viscosity change in the DPPC monolayer occurs by the adsorption of enflurane, the difference between ΔF and ΔR would appear in the process of change. The time interval between the beginning and end of the change is approximately several hours on both ΔF and ΔR. In the general observation of adsorption phenomenon by QCO using the monolayer [78–84], the addition reaction (chemical adsorption) to the specific part in the monolayer is often performed and the reaction time ends within several minutes in many cases. On the other hand, the present research consists in observing the physisorption phenomenon of the interaction between the lipid monolayer and anesthetics, as mentioned above. Actually, a specific part in which enflurane combines is not found in the DPPC monolayer, on comparison of the structure of DPPC molecule with enflurane molecule. Probably, it would take a long time for the dissolved enflurane to interact with and physisorb gently on the DPPC monolayer/water interface befoere it reaches an equilibrium state. It follows that this long time lapse (before reaching equilibrium state) would indicate that the reaction is not chemisorption but physisorption.

In the following section, the difference between the values before and after the addition of anesthetic [i.e., the difference between the standard value (zero position) before addition and the equilibrium value after addition] is defined as respective Δf for QCM and Δr for QCI (see Fig. 3.12 inset), and we will discuss the amount of these changes and their dependence on anesthetic concentration.

3.3.4 Concentration Dependence of Frequency (QCM) and Resistance (QCI)

3.3.4.1 DPPC versus Enflurane. Enflurane (CF_2H-O-CF_2-CClFH), a typical inhalation anesthetic, was synthesized in 1963, and this was the first research that was later applied clinically by another group in 1966 [41–43]. Enflurane is a halogenated ether-type anesthetic that is based on the structure and properties of previously administered anesthetics such as diethyl ether and chloroform. Compared to the first-synthesized halogenated anesthetic halothane (CF_3H-CBrClH), enflurane is superior with respect to its lower metabolic rate, smaller blood/gas partition coefficient, and higher analgesic action. Enflurane is a typical semihydrophobic molecule found in oxygen, fluorine, and chlorine atoms, and possesses a solubility of ~10 mM at 26°C [90]. In aqueous solution, water molecules surround the enflurane molecule and thereby form an enflurane-water hydrate in the solution (hydrophobic hydration).

Figure 3.13 shows enflurane concentration–dependent behavior in frequency [QCM (a)] and resistance [QCI (b)] for QCO in contact with a DPPC monolayer at 26°C [47]. The horizontal axis (abscissa) represents the enflurane concentration (bulk phase), and the vertical axis (ordinate) represents each frequency change (Δf) and resistance change (Δr), as defined in the previous section. In addition, the increase in Δf shows the decrease in actual value F. On the QCM (a), Δf gradually increased with an increase in enflurane concentration and asymptotically approached a saturation value of 3.4 Hz at around 6 mM. A further increase in concentration showed discontinuous increase and subsequent continuous increase: a second saturation value of 5.0 Hz. These processes are similar to the scenario of Langmuir's and/or BET's adsorption isotherm. On the QCI (b), there was no change in Δr at <2 mM. At >2 mM, Δr gradually increased with an increase in concentration and asymptotically approached a saturation value of 0.24 Ω at around 6 mM. A further increase in concentration showed discontinuous increase and subsequently a slight increase: a second saturation value of 0.29 Ω, similar to the case of the QCM (a). The amount of Δr change is somewhat small compared to the recent QCI measurement [65–73]. However, as the object that causes change is near

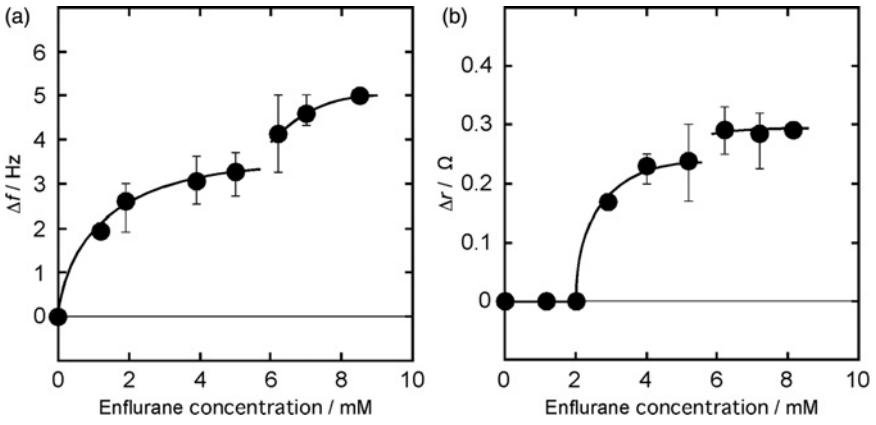


FIGURE 3.13 Enflurane concentration–dependent behavior of Δf (a) and Δr (b) for QCO in contact with DPPC monolayer at 26°C. Changes in Δf and Δr are defined in Fig. 3.12. Increase in Δf shows the decrease in actual value F.

the interface, including the lipid monolayer on the QCO, it is logical to assume that the amount of change will be small and certainly will be changing enough. It is quite interesting that the concentration at which Δf began to change ($\geq$ 1 mM) differed from that at which the Δr began to change ($\geq$ 3 mM), in other words, there is a specific concentration range where Δr does not change. These findings suggest that the action of enflurane to the DPPC monolayer is specific compared to the general adsorption process [78–84].

Another team [91] reported a study using ^{1}H-NMR spectroscopy, demonstrating that anesthetics (halothane, enflurane, methoxyflurane, and chloroform) show different actions on the isothermal phase transition between the lipid core and the hydrophilic interface in a DPPC vesicle. Therefore, the concentration of anesthetics that induced the transition of the lipid core is 2 times that required for the transition of a hydrophilic interface. Yet another group reported using ^{2}H-NMR spectroscopy to show that the interfacial structured water (restricted water) in the emulsion/water interface on the glycerol α-monooleate (GMO)/decane/^2H_2O reversed system (water-in-oil emulsion) changes into free water by enflurane–water hydrates [92]. Other investigators [93, 94] reported studies using ^{1}H- and ^{19}F-NMR spectroscopy and solubilization parameters to show that halothane and enflurane interact with the sodium dodecyl sulfate (SDS) micelle–water interface, at which the molecular axis of the halothane (C–C axis) is perpendicular to the interface (the hydrophobic F_3C– site penetrates the interface, and the hydrophilic –CHClBr site remains in a water phase); on the other hand, the molecular axis of enflurane (C–O–C–C axis) is parallel to the interface [93, 94]. Another team reported, using DSC and X-ray scattering, that enflurane preferentially interacts with DPPC lamellar-phase/water and DPPC liposomes/water interface, and causes the structural change of each lamellar phase and liposome [95]. These reports on anesthetic activity indicate that anesthetic hydrates interact with and release the interfacial structured water formed on the membrane/water interface without penetrating into the membrane lipid core; in other words, anesthetic hydrates physisorb on the interface.

As mentioned in the Section 3.2.1, the present DPPC monolayer obtained by the dropping method is of a semi-expanded state and also has a flexible and fluid structure, therefore elasticity-rich monolayer. Based on such the characteristic of the present DPPC monolayer and the reports cited above, the following model of the enflurane action of the DPPC monolayer would be possible in terms of *interfacial action* [47, 86]. In the first saturation range at ~6 mM, when the enflurane is added and dissolves into the water phase, enflurane hydrates physisorb on the interfacial structured water formed on the DPPC monolayer–water interface. Enflurane hydrates merely physisorb into the structured water and do not cause the interaction that disturbs the structured water at a small amount of enflurane hydrate ($\leq$ 2 mM). Therefore, Δf increases (adsorption mass of enflurane hydrate increases) and Δr does not change [i.e., the viscosity of the interfacial layer (DPPC monolayer/structured water) does not change]. An increase in the enflurane concentration corresponds to an increase in the amount of enflurane hydrates physisorbed on the DPPC monolayer/water interface, thereby further increasing Δf. On the local field such as the monolayer/water interface, an increase in the amount of physisorbed enflurane hydrates would generate the interaction and aggregation between physisorbed enflurane hydrates, and would also influence the structured water formed on the interface, thus leading to *distortion* and *release* of the structured water that is maintained by the week hydrogen bonding between hydrophilic groups of DPPC molecules and water molecules [96]. As a result, the interfacial structured water including enflurane molecules would be reconstructed at the interface. These processes promote the interaction between hydrophilic groups of DPPC molecules and also decrease the distance between those groups. Moreover, the interfacial structure may be strengthened by the existence of enflurane molecule because semi-hydrophobic enflurane interacts more strongly with hydrophilic groups of DPPC molecules than with structured (restricted) water molecules. These synergistic effects would show up as an increase in Δr (increase in viscosity) on the interface. This implies that the fluctuation of the fluid-structured DPPC monolayer is suppressed, leading to an increase in the density of the DPPC monolayer. Hydrophobic alkyl chains in DPPC molecules may also draw mutually (through attractive forces) by the suppression.

The experimental observation that both Δf and Δr eventually attain saturation values indicates that the physisorption of enflurane hydrates on the DPPC monolayer/water interface attained the initial equilibrium states at ~6 mM. From the amount of enflurane hydrates [3.4 Hz = 41.5 ng/cm^2 (Sauerbrey's equation)] by QCM, we roughly estimated the mean molecular area of enflurane hydrate. Here, we neglected the effect of the interfacial viscosity change. According to another report [92] the amount of hydrated water surrounding one enflurane molecule is approximately 30. By using this value, the molecular area of the enflurane hydrate is calculated as 2.9 nm^2 per each hydrate. It is assumed that enflurane hydrate has an *elliptical shape*, in which the molecular axis of the hydrate is the major axis, with the apparent molecular areas along the major and the minor axes measuring ~1.0 and ~0.63 nm^2 per each hydrate, respectively. The calculated value (2.9 nm^2 per each hydrate) is greater than that obtained for the major axis (1.0 nm^2 per hydrate). Considering the findings cited above, demonstrating that it is easy to orient the molecular axis of enflurane molecule in parallel to the micelle/water interface [94], the calculated molecular area indicates the formation of physisorption layer of enflurane hydrates where enflurane molecules are not in a dense state, and where those molecular axes orient parallel to the DPPC monolayer/water interface, in other words, the

formation of a complicated interface combining hydrophilic groups of DPPC molecules, enflurane molecules, and water molecules.

On the higher concentration at >6 mM, enflurane hydrates would physisorb still more on the interface, because the interface is already occupied at the semi-saturation level by the physisorbed enflurane hydrates at ∼6 mM and also loses its function as a barrier to the next physisorbed hydrates. Therefore, there exist the following two possibilities: (1) multi-physisorption of enflurane hydrates and (2) promotion of aggregation between hydrates. In the *multi-physosorption* model, enflurane hydrates physisorb easily and continuously (increase in Δf) because of the existence of the initial semi-saturated enflurane hydrate layer. That continuous physisorption process leads to the formation of an enflurane hydrate multilayer [47, 86, 97, 98]. Multilayering also further suppresses the interface, including the DPPC monolayer. This effect would cause a discontinuous increase and subsequent slight increase in Δr (increase in viscosity) on the interface. In the *promotion of aggregation* model, an increase in the physisorption of enflurane hydrates on the interface (increase in Δf), promotes the interaction between those physisorbed enflurane hydrates. That interaction process leads to the formation of a large enflurane hydrate cluster on the interface [41, 85, 86]. Clustering also strongly suppresses the interface, including the DPPC monolayer. This effect would cause a discontinuous increase and subsequent slight increase in Δr (increase in viscosity) on the interface. The increase in both Δf and Δr on the higher concentration range ($\geq$ 6 mM) may occur as a synergistic and/or simultaneous effect of both multi-physisorption and promotion of aggregation. Such easy physisorption of enflurane hydrates on the interface also causes a rapid second saturation state.

3.3.4.2 DPPC versus Isoflurane. Isoflurane (CF_2H–O–$CClH$–CF_3), a typical inhalation anesthetic, was synthesized by the Terrell group in 1965. Clinical use was permitted in the United States in 1980, and thereafter its use spread quickly [41–43]. Isoflurane is a structural isomer of enflurane. Compared to enflurane, isoflurane is superior with respect to the following points; low metabolic rate, small blood/gas partition coefficient, and almost no toxicity over the liver and kidneys. As well as enflurane, isoflurane is a typical semi-hydrophobic molecule and also possesses a solubility of ∼10 mM at 26°C [90, 99]. In aqueous solution, water molecules surround the isoflurane molecule and thereby form an isoflurane–water hydrate in the solution (hydrophobic hydration), as well as enflurane.

Figure 3.14 shows the isoflurane concentration–dependent behavior of frequency [QCM (a)] and resistance [QCI (b)] for QCO in contact with a DPPC monolayer at 26°C [24]. As in Fig. 3.13, the horizontal axis (abscissa) represents the isoflurane concentration (bulk phase), and the vertical axis (ordinate) represents each frequency change (Δf) and resistance change (Δr). In addition, the increase in Δf is accompanied by a decrease in the actual value of F. On the QCM (a), there was no change in Δf at <2 mM. At >2 mM, Δf gradually increased with an increase in isoflurane concentration and asymptotically approached a saturation value of 1.6 Hz at ∼6 mM. A further increase in concentration showed discontinuous increase and subsequent continuous increase: a second saturation value of 3.1 Hz. These processes are similar to the picture of Langmuir's and/or BET's adsorption isotherm. On the QCI (b), there was no change in Δr at <4 mM. At >4 mM, Δr gradually increased with an increase in concentration and asymptotically approached a saturation value of 0.14 Ω at ∼6 mM. A further increase in concentration showed discontinuous increase and subsequent slight increase or remained almost constant: a second saturation value of 0.18 Ω. As shown in Fig. 3.13, the concentration at which Δf began to change ($\geq$ 2 mM) differed from that at which Δr began to change ($\geq$ 4 mM). In the case of isoflurane, the action to the DPPC monolayer is specific.

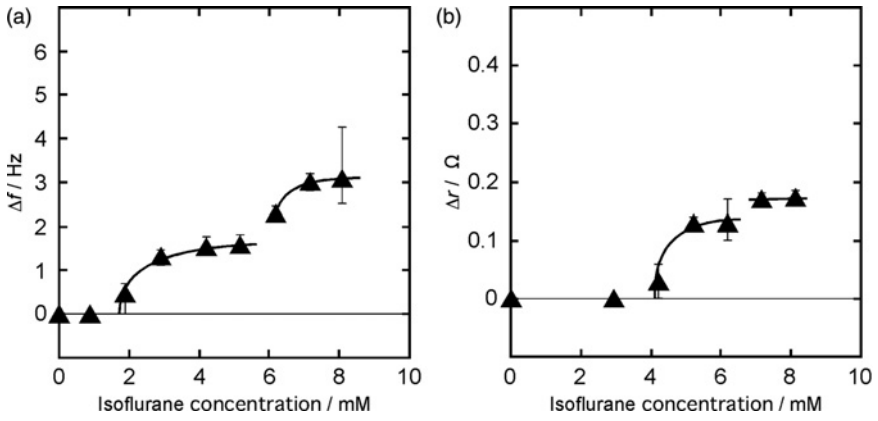


FIGURE 3.14 Isoflurane concentration–dependent behavior of Δf (a) and Δr (b) for QCO in contact with DPPC monolayer at 26°C. Changes in Δf and Δr are defined in Fig. 3.12. Increase in Δf shows the decrease in actual value F.

The general tendency, therefore, of the first and second saturation states with an increase in concentration, is similar to that for enflurane as seen in Fig. 3.13. However, there are two major differences between enflurane and isoflurane. One is the concentration at which both Δf and Δr began to change. With enflurane, Δf began to change at >1 mM; with isoflurane, change began at >2 mM. Therefore, it is more difficult to physisorb isoflurane than enflurane on the DPPC monolayer/water interface. In line with those phenomena, Δr began to change at >2 mM for enflurane and at >4 mM for isoflurane. Another difference is the amount of change for Δf and Δr. For example, first and second saturation values for Δf are 3.4 and 5.0 Hz for enflurane, respectively, while those of isoflurane are 1.6 and 3.1 Hz, respectively. Δr is also obtained at 0.24 and 0.29 Ω for enflurane, respectively, while those of isoflurane are obtained at 0.14 and 0.18 Ω, respectively. On the whole, the amount of change at isoflurane is about 50–60% smaller than that of enflurane. It is interesting that the mode of physisorption differs between enflurane and isoflurane, although these compounds have related isomeric forms.

Figure 3.15 shows the molecular structure of enflurane (left) and isoflurane (right) obtained by density functional theory (DFT) calculation with the B3LYP/6-31G(d) basis set (Gaussian 03 program) [100]. From the calculated optimized structure, enflurane molecule has a zigzag structure, with hydrophobic CF_2H– and –CF_2– separate from hydrophilic –O– and –CClFH, bordering on the molecular axis. Isoflurane also has a zigzag structure as well as enflurane. However, both the hydrophobic ends of CF_2H– and –CF_3 sandwich hydrophilic –O and –CClH–. Therefore, the hydrophobic and hydrophilic components of isoflurane do not differ significantly. The ellipticity of enflurane is less than that of isoflurane. Certainly, such clear structure of both enflurane and isoflurane would not necessarily be maintained in the water phase. However, the difference in arrangement of hydrophobic and hydrophilic components between enflurane and isoflurane (donor site) may appear as differences in hydration structure and also, more subtly, as differences in physisorption potency (easy for enflurane, difficult for isoflurane) in the specific reaction field such as the DPPC monolayer/water interface.

The curve shapes for both Δf and Δr in Fig. 3.14 are similar to those in Fig. 3.13 (enflurane). Therefore, it could possibly be explained by the physisorption model as well as enflurane. In the first saturation range, from 2 mM to approximately 6 mM, isoflurane hydrates physisorb on the interfacial structured water formed on the DPPC monolayer/water interface (increase in Δf). A small amount of isoflurane hydrate does not affect the structured water physically (no change in Δr). The increase in the amount of physisorbed isoflurane hydrate (further increase in Δf) does affect the structured water because of the interaction and aggregation between physisorbed isoflurane hydrates at the interface. As a result, *distortion* and *release* occur in the structured water, and the interfacial structured water, including isoflurane molecules, is reconstructed at the interface. This also implies a suppression of the interface, including the fluid-structured DPPC monolayer, and then subsequently an increase in Δr (increase in viscosity).

When the initial saturation values of both Δf (1.6 Hz) and Δr (0.14 Ω) were attained at around 6 mM, we roughly estimated the mean molecular area of isoflurane hydrate, as well as enflurane. Unfortunately, the amount of hydrated water surrounding one isoflurane molecule is not clear. When we assume 30 with molecules for isoflurane, the molecular area of the isoflurane hydrate is calculated as 6.2 nm^2 per each hydrate. Additionally, when we assume that the isoflurane hydrate is of elliptical shape, where the molecular axis of the hydrate is calculated as the major axis, the apparent

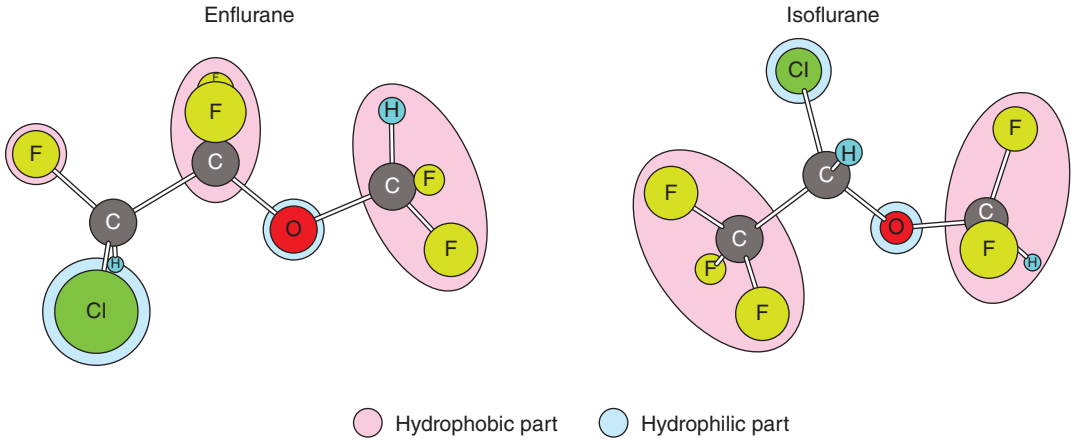


FIGURE 3.15 Molecular structure of enflurane (left) and isoflurane (right) by DFT calculation. Both enflurane and isoflurane have a zigzag structure. Gray indication (F–, –CF_2–, –CHF_2 in enflurane, and CF_3–, –CHF_2 in isoflurane) is the hydrophobic part, and light gray indication (Cl–, –O– in both enflurane and isoflurane) is the hydrophilic part.

molecular areas along the major and the minor axes are ~1.5 and ~1.3 nm^2 per each hydrate, respectively. Although the orientation of isoflurane hydrate on the interface is not clear, the experimental value (6.2 nm^2 per hydrate) is greater than that obtained by calculation (1.5 or 1.3 nm^2 per hydrate), regardless of the orientation of the hydrate. Therefore, physisorption layer of isoflurane hydrates is formed on the interface, where isoflurane molecules are not in a dense state and reach the saturation state by maintaining a certain amount of intermolecular distance, as found in enflurane as well.

At higher concentrations (>6 mM), *multi-physisorption* and/or *promotion of aggregation* of isoflurane hydrates would occur at the composite interface, which consists of hydrophilic groups of DPPC molecules, isoflurane molecules, and water molecules [40, 47, 85, 86, 97, 98], as well as enflurane. Continuous physisorption of isoflurane hydrates leads to multilayering of isoflurane and subsequently further suppression of the interface (multi-physisorption). Increase in physisorbed isoflurane hydrate also leads to aggregation of isoflurane and subsequently further suppression of the interface (promotion of aggregation). These effects cause the increase in Δf (increase in physisorbed isoflurane hydrates) and the increase in Δr (increase in the viscosity of interface). This physisorption mode experienced by the isoflurane hydrates also induces a rapid second saturation state.

3.3.4.3 DMPC versus Isoflurane. Figure 3.16 shows the isoflurane concentration–dependent behavior of frequency [QCM (a)] and resistance [QCI (b)] for QCO in contact with a dimyristoyl phosphatidyl choline (DMPC) monolayer at 26°C [24]. As shown also in Fig. 3.14, the horizontal axis (abscissa) represents the isoflurane concentration (bulk phase), and the vertical axis (ordinate) represents each frequency change (Δf) and resistance change (Δr). In addition, the increase in Δf shows the decrease in actual value F. On the QCM (a), Δf gradually increased with an increase in isoflurane concentration and asymptotically approached a saturation value of 2.2 Hz at around 5 mM. A further increase in concentration showed discontinuous increase and subsequent continuous increase: a second saturation value of 3.8 Hz. These processes are similar to the scenarios of Langmuir's and/or BET's adsorption isotherm, as well as in Figs. 3.13 and 3.14. On the QCI (b), there was no change in Δr at the measured concentration range.

Compared to the result in the action of isoflurane to the DPPC monolayer, two large differences exist. One is the concentration at which Δf began to change. For DPPC monolayer, Δf began to change >2 mM, while it was >1 mM for DMPC. Therefore, it may be easier to physisorb on the DMPC monolayer/water interface than on the DPPC monolayer/water interface. In line with these phenomena, the first and second saturation values (2.2 and 3.8 Hz) are larger than those at the DPPC monolayer/water interface (1.6 and 3.1 Hz). Another difference is the behavior of Δr. For the DPPC monolayer, Δr changed as a result of the action of isoflurane hydrate at the DPPC monolayer/water interface (Fig. 3.14). This tendency is shown in Fig. 3.13 for enflurane. On the other hand, Δr did not change at the DMPC monolayer/water interface. This suggests that the physisorption state of isoflurane differs between DPPC and DMPC monolayers.

As mentioned in the Section 3.2.2, the present DMPC monolayer state obtained by the dropping method is liquid-expanded (LE), in which two alkyl chains are disordered partially and the structure has *gauche*-type shape and disturbed state, indicating an expandability-rich monolayer. Such properties are quite different from those of DPPC monolayer that has an elasticity-rich state. In other words, the DMPC monolayer itself does not expand and/or shrink further, and maintains the expanding state. The interaction between the hydrophilic group of DMPC and water molecule is also weak (not structured), and the properties of water molecules in the

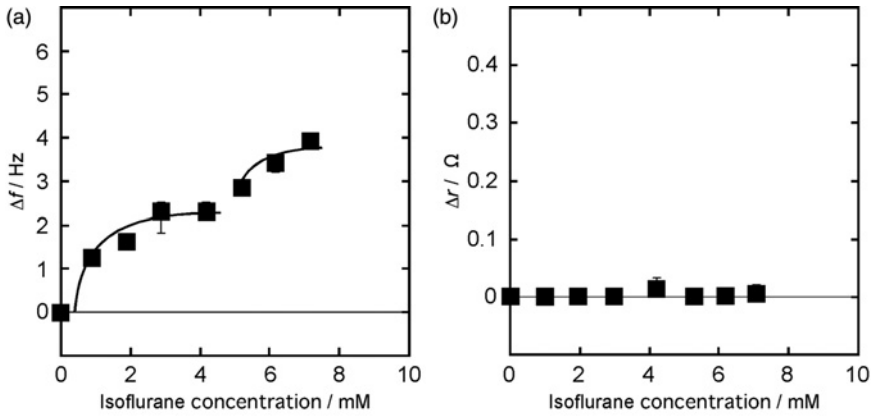


FIGURE 3.16 Isoflurane concentration–dependent behavior of Δf (a) and Δr (b) for QCO in contact with DMPC monolayer at 26°C. Changes in Δf and Δr are defined in Fig. 3.12. Increase in Δf shows the decrease in actual value F.

vicinity at the interface may be similar to those of bulk water phase. This state causes the action of isoflurane hydrate to differ from that of DPPC monolayer, namely, easy physisorption of hydrate on the DMPC monolayer/water interface and no change in the properties of the DMPC monolayer (no change in Δr) with the physisorption of hydrate. Therefore, it can be explained as a simple physisorption model of isoflurane hydrate to the DMPC monolayer. In the first saturation range, to ~5 mM, isoflurane hydrates physisorb on the DMPC monolayer/water interface (increase in Δf). An increase in isoflurane concentration leads to an increase in the amount of physisorbed isoflurane hydrate (further increase in Δf). On the other hand, isoflurane hydrates merely physisorb on the interface and would not give a physical influence to the interface [no change in Δr (viscosity)], even if those form aggregation on the interface.

After the first saturation value of Δf (2.2 Hz) was reached at ~5 mM, we roughly estimated the mean molecular area of isoflurane hydrate. As in Fig. 3.14, we assume the amount of hydrated water surrounding one isoflurane molecule to be 30. The molecular area of the isoflurane hydrate is calculated as 4.5 nm^2 per each hydrate. Considering the size of isoflurane hydrate as mentioned in Section 3.3.4.2, the physisorption layer of isoflurane hydrates is formed on the DMPC monolayer/water interface, where isoflurane molecules are not in a dense state and reach the saturation state by maintaining a certain amount of intermolecular distance, similar to the DPPC monolayer/water interface.

The calculated value (4.5 nm^2 per each hydrate) is smaller than that of the one on the DPPC monolayer/water interface; in other words, the amount of isoflurane hydrate is understandably more. As mentioned above, it would be difficult for the expandability-rich DMPC monolayer to cause the change of the interfacial properties by the physisorption of isoflurane hydrate. If such expandable state spread on the whole water surface, the DMPC monolayer/water interface may be more easily utilized to cause isoflurane hydrate to physisorb (many physisorption sites) compared to the elasticity-rich DPPC monolayer/water interface. As a result, isoflurane hydrates begin to physisorb at lower concentration and the amount of physisorption becomes large, compared to the DPPC monolayer/water interface. This also corresponds to the approach to the first saturation state at lower concentration. The difference in interfacial state (acceptor site) may be related to the difference in physisorption potency.

At higher concentrations (>5 mM), isoflurane hydrates would physisorb still more on the DMPC monolayer/water interface. On the other hand, the composite interface composed of hydrophilic components (hydrophilic groups of DMPC molecules, isoflurane molecules, water molecules), such as the DPPC monolayer/water interface, would not be formed at the first saturation state as discussed above. Therefore, it can also be explained as a simple *multiphysisorption* and/or *promotion of aggregation* model of isoflurane hydrate to the DMPC monolayer. This theory is supported by the observation that Δr does not change by >5 mM. Continuous physisorption of isoflurane hydrates leads to multilayering and/or aggregation of isoflurane themselves, and thereby a further increase in Δf (increase in physisorbed isoflurane hydrates). Compared to the composite DPPC monolayer/water interface (>6 mM), the existence of simple physisorbed isoflurane hydrates would facilitate the physisorption of further hydrates. Such a physisorption caused by the isoflurane hydrates also results in a rapid second saturation state.

3.3.4.4 DPPC-Cholesterol versus Enflurane. Figure 3.17 shows the enflurane concentration–dependent behavior of frequency [QCM (a)] and resistance [QCI (b)] for QCO in contact with a DPPC-cholesterol mixed monolayer at which a mole fraction of cholesterol (Chol) is 0.2 at 26°C. As in Fig. 3.13, the horizontal axis (abscissa) represents the enflurane concentration (bulk phase), and the vertical axis (ordinate) represents each frequency change (Δf) and resistance

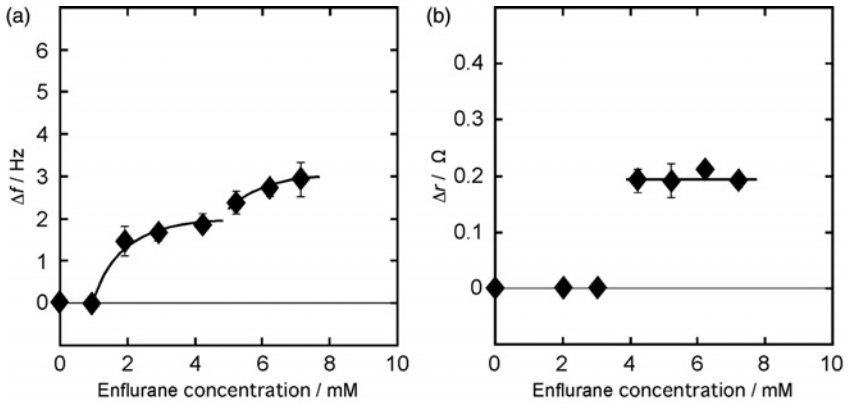


FIGURE 3.17 Enflurane concentration–dependent behavior of Δf (a) and Δr (b) for QCO in contact with a DPPC–cholesterol mixed monolayer at which a mole fraction of cholesterol is 0.2 at 26°C. Changes in Δf and Δr are defined in Fig. 3.12. Increase in Δf shows the decrease in actual value F.

change (Δr). In addition, the increase in Δf shows the decrease in actual value F. We decided to examine the action of enflurane to the mixed monolayer of 0.2 mole fraction of Chol, because the mixed monolayer shows unique monolayer morphology among various mole fractions of Chol, as mentioned in Section 3.2.4. On the QCM (a), there was no change in Δf at <1 mM. At >2 mM, Δf gradually increased with an increase in enflurane concentration and asymptotically approached a saturation value of 2.0 Hz at around 4 mM. A further increase in concentration showed discontinuous increase and subsequent continuous increase: a second saturation value of 3.0 Hz. These processes are similar to the scenario of Langmuir's and/or BET's adsorption isotherm, as well as those in Figs. 3.8, 3.14, and 3.16. On the QCI (b), there was no change in Δr at <3 mM. At ~4 mM, Δr showed sudden and discontinuous increase, and subsequently almost constant value of 0.20 Ω to 7 mM.

Compared to the result in the reaction of enflurane to the pure DPPC monolayer shown in Fig. 3.13, some important differences are found. On the change in Δf, the tendency is similar to the case of pure DPPC monolayer; however, the concentration at which Δf began to change is different. At the pure DPPC monolayer, Δf began to change from 1 mM; on the other hand, it is >2 mM at the DPPC-Chol mixed monolayer. Therefore, it is more difficult to physisorb on the mixed-monolayer/water interface than on the pure DPPC monolayer/water interface. The amount of change is also different. The first and second saturation values for Δf are each 3.4 and 5.0 Hz at the pure DPPC monolayer; on the other hand, those of mixed monolayer are each 2.0 and 3.0 Hz. The amount of change at the mixed monolayer is about 60% smaller than that at the pure DPPC monolayer. On the Δr change, a somewhat specific change was observed: discontinuous increase and subsequent constant value (0.20 Ω) at around 4 mM. This is quite different from that for the pure DPPC monolayer: first and second saturation states with increase in concentration (Fig. 3.13).

As mentioned in Section 3.2.4, the present DPPC-Chol mixed monolayer obtained by the dropping method is more highly condensed than the pure DPPC monolayer (elasticity-rich) on the water surface, as obtained by the Chol condensation effect. On such the mixed monolayer, the limiting molecular area A_0 was 0.48 nm^2 (Fig. 3.4) [31] and larger than that using the compression method (0.43 nm^2) [10]. Therefore, the difference between both values implies that the monolayer elasticity still remains in the mixed monolayer using the dropping method, even if it is subject to the influence of the Chol condensation effect. We have also found from QCM measurement that enflurane (4 mM) does not physisorb on the *n*-hexadecanol ($C_{16}H_{33}OH$: HA) monolayer/water interface [101]. HA forms a highly condensed (solid) monolayer using the dropping method (A_0 = 0.20 nm^2), as does that using the compression method. The HA monolayer/water interface would be stable and also have poor fluidity. These results indicate that enflurane cannot physisorb easily on the condensed monolayer/water interface.

On the basis of these mixed monolayer characteristics and our experimental results, we propose that the following model of the enflurane action to the DPPC-Chol mixed monolayer would be possible. At 1 mM, enflurane hydrates does not physisorb on the mixed-monolayer/water interface because of its more highly condensed state compared to the pure DPPC monolayer. On the first saturation range from 1 mM to approximately 4 mM that was observed at QCM measurement, hydrates physisorb on the interfacial structured water formed on the mixed-monolayer/water interface (increase in Δf). A small amount of enflurane hydrate does not physically influence the structured water (no change in Δr). At the point where interfacial properties (viscosity) do not change in the first saturation range, this process can be explained as a simple physisorption model of enflurane hydrate and is also similar to that of isoflurane physisorption to the DMPC monolayer (Fig. 3.16).

After the first saturation value of Δf (2.0 Hz) was reached at ~4 mM, we roughly estimated the mean molecular area of enflurane hydrate. Assuming the amount of hydrated water surrounding one enflurane molecule to be 30, as shown in Fig. 3.13, we calculated the molecular area of enflurane hydrate as 5.0 nm^2 per each hydrate. Considering the size of enflurane hydrate as mentioned in Section 3.3.4.1, the physisorption layer of enflurane hydrates is formed on the mixed-monolayer/water interface, where enflurane molecules are not in a dense state and reach saturation state by maintaining a certain of intermolecular distance, as is the case for the pure DPPC monolayer.

The calculated value (5.0 nm^2 per each hydrate) is larger than that on the pure DPPC monolayer/water interface; in other words, the amount of enflurane hydrate is understandably less. As mentioned above, the mixed monolayer is more highly condensed than the pure DPPC monolayer. If such a highly condensed state were to spread on the entire water surface, enflurane hydrates could not physisorb easily on the mixed-monolayer/water interface. As a result, the amount of hydrate is smaller than that of pure DPPC monolayer. The difference in interfacial state (acceptor site) may be related to the difference in physisorption potency. This may also be similar to the interpretation that the pattern of isoflurane physisorption differs between DPPC and DMPC monolayers.

At ~4 mM, Δr suddenly caused a discontinuous increase (0.20 Ω). Although the DPPC-Chol mixed monolayer is already condensing to some extent as a result of the Chol condensation effect, the mixed monolayer still has room to condense, as mentioned above. The amount of enflurane hydrate (physisorption-layer level of enflurane), to the extent that the mixed-monolayer/water interface is covered, would probably be required for further condensation. Such covering would cause distortion and release of structured water at the mixed-monolayer/water interface and the

reconstruction of the interface including enflurane molecules. This implies potential suppression of the interface and, therefore, an increase in Δr (increase in viscosity). Furthermore, the Δr did not cause a gradual or two-step change such as in the case of pure DPPC monolayer (Fig. 3.13), and showed discontinuous increase and subsequent constant value (0.20 Ω) to 7 mM. When the interface was reconstructed by covering the physisorption layer of enflurane, Chol condensation effect may function as a synergistic effect. Therefore, the reconstruction process of the interface may further strengthen the interaction between two hydrophobic alkyl chains in DPPC molecules with Chol (promotion of Chol condensation effect) and also cause them condense to a specific limit. This corresponds to Δr maintaining constant value (0.20 Ω) after discontinuous increase, despite an increase in concentration. In other words, above 4 mM, this phenomenon can be also explained as a simple physisorption model of enflurane hydrate to the mixed monolayer as described below.

At the higher concentration (>5 mM) that was observed at QCM measurement, enflurane hydrates would physisorb still more on the DPPC-Chol mixed-monolayer/water interface. Although the mixed monolayer is itself in a condensed state (not easily physisorbed), the interface would somewhat lose its function as a barrier to the next physisorbed hydrates because some enflurane hydrates would already be physisorbed on the interface. Therefore, this phenomenon can be explained as a simple *multi-physisorption* and/or *promotion of aggregation* model of enflurane hydrate on the mixed monolayer, as in the case of DMPC monolayer. This theory is also supported by the fact that Δr does not also change in this concentration range (5–7 mM), as mentioned above. Continuous physisorption of enflurane hydrates leads to multilayering and/or aggregation of enflurane, and thereby further increase in Δf (increase in physisorbed enflurane hydrates). Because there is no change in Δr (no influence on the interface), such a simple physisorption caused by the enflurane hydrates would also occur easily and lead to a rapid second saturation state. The amount of physisorbed hydrate is smaller than that of the pure DPPC monolayer (Fig. 3.13), and probably the change in interfacial properties (condensation) that occurred at ∼4 mM would reduce the physisorption potency of the acceptor site (interface) compared to the pure DPPC monolayer.

3.3.5 True Anesthesia Phenomenon

In the present study, the interaction between various lipid monolayers on the water surface and anesthetics has been investigated using a horizontally adhering type QCM and QCI measurement. It was found that anesthetics physisorb to the elasticity-rich DPPC monolayer and change its monolayer properties (viscosity), but that they physisorb only to the expandability-rich DMPC monolayer, and to the condensed DPPC-Chol monolayer, and that this results in specific changes in monolayer properties. In terms of physisorption (QCM measurement), the process described here showed a two-step change bordering on the concentration of 5–6 mM in all cases investigated, and it was suggested that anesthetic aggregation is probably formed on the monolayer/water interface [40]. It is interesting that anesthetics physisorb to the monolayer on the water surface, which is a comparatively simple system, and also change its monolayer properties depending on the type of monolayer.

More recent studies on the anesthesia phenomenon have regarded anesthetic action as the specific interaction between anesthetic and protein, and have focused on identifying the receptor of anesthetic. Many studies have also been conducted to identify the $GABA_A$ (γ-aminobutyric acidtype A) receptor, which is widely distributed, especially throughout the central nervous system, which is a major target, and many studies have also been performed on the interaction between anesthetics and $GABA_A$ [102, 103]. However, the characteristics of the anesthesia phenomenon, such as the anesthesia revelation at high concentration in body fluid and the reversibility of the phenomenon, cannot be explained only by a specific interaction corresponding to the simple relation between "key" and "keyhole" as in a generic drug. Actually, our measurement results suggest that the lipid parts and/or lipid/body-fluid interface in biomembranes also may be potential targets of anesthetic action.

It is clear from many studies spanning more than one century that only direct action on the lipid membrane (lipid theory) is not the origin of anesthesia revelation [2, 37–47, 85, 86, 90–94, 99–103]. However, it is also appropriate to assume that the results of these studies are not limited to the anesthetic–protein interaction, but that they include the wide-ranging effects of anesthetics on the molecular aggregate in the living body, which contains various lipid molecules and proteins. Although the action mechanism of anesthesia is very complicated and has not yet been elucidated, we believe that, with further investigation, clarification of the molecular action mechanism of anesthetics in response to the molecular aggregate that constitutes the biomembrane will not only deepen our understanding of the anesthesia phenomenon but will also contribute to future guidance in the proposed development of new anesthetics and improvement in the quality of medical treatment involving the use of clinical anesthesia.

ACKNOWLEDGMENT

These work reported in this chapter was supported in part by a Grant-in-Aid from the Ministry of Science, Education, Sports and Culture (Grants 15750118, 21750143, and 24550154), DVA Medical Research and Development Funds, and a Grant-in-Aid from the Sakakibara Memorial Hospital Incorporated Foundation.

REFERENCES

[1] Kawai, T. (2005). *Interfaces and Surfactants –Fundamentals and Applications*. Japan Oil Chemists' Society, Tokyo.

[2] Simabayashi, S., Terada, H., Okabayasi, H. (1990). *Biocolloid 1&2*. Hirokawa Publishing, Tokyo.

[3] Suezaki, Y. (2007). *Physics of lipid membrane*. Kyusyu Univ. Press, Fukuoka.

[4] Franklin, B. (1773). *Stilling the Waters*. Royal Society, London.

[5] Pockels, A. (1892). *Nature* **46**, 418–419.

[6] Blodgett, K.B. (1935). *J. Am. Chem. Soc.* **57**, 1007–1022.

[7] Blodgett, K.B. (1937). *Langmuir Phys. Rev.* **51**, 964–982.

[8] Hatta, I., Murata, M. (2000). *Dynamics of Biomembrane*. Kyoritsu Shuppan Co., Ltd., Tokyo.

[9] Vilallonga, F. (1968). *Biochim. Biophys. Acta* **163**, 290–300.

[10] Ohe, C., Sasaki, T., Noi, M., Goto, Y., Itoh, K. (2007). *Anal. Bioanal. Chem.* **388**, 73–79. (*Note*: The π –*A* isotherm curve described by these authors was almost the same as that at 25°C [9]; therefore, it was similar to that shown in Fig. 3.1.)

[11] Mingotaud, A.F., Mingotaud, C., Patterson, L.K. (1993). *Handbook of Monolayers*, Vols. 1 and 2. Academic Press, San Diego.

[12] Nagle, J.F. (1993). *Biophys. J.* **64**, 1110–1112.

[13] Yoshida, D., Yokoyama, T., Shimoaki, T., Tomita, T., Yoshida, T., Yamamoto, Y., Taga, K., Sumino, A., Dewa, T., Nango, M., Yamamoto, M., Sheravani, Z. (2013). *J. Biophys. Chem.* **4**, 115–121.

[14] Yamamoto, M., Yoshida, D., Yokoyama, T., Mori, H., Sekiguchi, K., Yamamoto, Y., Taga, K. (Manuscript in preparation.)

[15] Nagayama, K. (2000). *Water and Life*. Kyoritsu Shuppan Co., Ltd., Tokyo.

[16] Kato, T., Matsumoto, N., Kawano, M., Suzuki, N., Iriyama, K. (1994). *Thin Solid Films* **242**, 223–228.

[17] Brun, A., Brezesinski, G., Möhwald, H., Blanzat, M., Perez, E., Rico-Lattes, E. (2003). *Colloids Surf. A: Physicochem. Eng. Aspects* **228**, 3–16.

[18] Li, J.B., Miller, R., Vollhardt, D., Möhwald, H. (1998). *Thin Solid Films* **327–329**, 84–86.

[19] Minones, Jr., J., Conde, O. (2004). *Rec. Res. Develop. Surf. Colloids* **1**, 375–399.

[20] Langner, M., Hui, S. (2000). *Biochim. Biophys. Acta Biomembr.* **1463**, 439–447.

[21] Taly, A., Baciou, L., Sebban, P. (2002). *FEBS Lett*. **532**, 91–96.

[22] Kusube, M., Matsuki, H., Kaneshina, S. (2005). *Colloids Surf. B: Biointerfaces* **42**, 79–88.

[23] Nakagaki, M., Tomita, K., Handa, T. (1985). *Biochemistry* **24**, 4619–4624.

[24] Yamamoto, Y., Yokoyama, T., Yoshida, D., Mori, H., Sekiguchi, K., Shimoaki, T., Yoshio, A., Taga, K., Shervani, Z., Yamamoto, M. (2015). *J. Biophys. Chem* **6**, 42–53.

[25] Frey, W., Schief, Jr., W.R., Vogel, V. (1996). *Langmuir* **12**, 1312–1320.

[26] Minones, Jr., J., Dynarowicz-Latka, P., Minones, J., Rodriguez Patino, J.M., Iribarnegaray, E. (2003). *J. Colloid Interface Sci.* **265**, 380–385.

[27] Teixeira, A.C.T., Fernandes, A.C., Garcia, A.R., Ilharco, L.M., Brogueira, P., Goncalves, D.S., Amelia, M.P.S. (2007). *Chem. Phys. Lipids* **149**, 1–13.

[28] Gennis, R.B. (1990). *Biomembrane, Molecular Structure and Function*. Springer, New York.

[29] Hirshfeld, C.L., Seul, M. (1990). *J. Phys. France* **51**, 1537–1552.

[30] Birdi, K.S. (1999). *Self-Assembly Monolayer structures of Lipids and Macromolecules at Interfaces.* Kluwer Academic Publishers, New York.

[31] Yokoyama, T., Yoshida, D., Mori, H., Okabe, M., Shervani, Z., Taga, K., Yamamoto, Y., Sumino, A., Dewa, T., Nango, M. (Manuscript in preparation.)

[32] Kim, K., Kim, C., Byun, Y. (2001). *Langmuir* **17**, 5066–5070.

[33] Kodama, M., Shibata, O., Nakamura, S., Lee, S., Sugihara, G. (2004). *Colloid Surf. B: Biointerfaces* **33**, 211–226.

[34] Singer, S.J., Nicolson, G.L. (1972). *Science* **175**, 720–731.

[35] Gellman, S.H. (1997). *Chem. Rev.* **97**, 1231–1232.

[36] Okamura, Y., Nakamura, M. (1999). *J. Phys. Chem. B* **103**, 3505–3509.

[37] Ueda, I., Yoshida, T. (1999). *Chem. Phys. Lipids* **101**, 65–79.

[38] Ueda, I., Yoshida, T. (2002). *Encyclopedia of Surface and Colloid Science*. Marcel Dekker, New York, p. 2607.

[39] Matsuki, H., Ueda, I. (2001). *Seibutsu Butsuri* **41**, 4–8.

[40] Yoshida, T., Okabayashi, H., Kamaya, H., Ueda, I. (1989). *Biochim. Biophys. Acta* **979**, 287–293.

[41] Arai, T. (2001). *Lectures for Anesthesia and Resuscitation*. Kokuseido Co. Ltd., Tokyo.

[42] Yoshimura, N. (2002). *Standard Anesthesia Science*. Igaku-Shoin Ltd., Tokyo.

[43] Hyodo, M. (2006). *Anesthesiology 11 Rev*. Kinpodo Inc., Kyoto.

[44] Meyer, H. (1899). *Naunyn-Schmiedeberg's Arch. Exp. Athol. Pharmakol*. **42**, 109–118.

[45] Overton, E. (1901). *Studien uber die Narkose zugleich ein Beitrag zur allgemeinen Pharmakologie*. Verlag von Gustav Fischer, Jena.

[46] Cantor, R.S. (1997). *Biochemistry* **36**, 2339–2344.

[47] Yamamoto, Y., Shervani, Z., Shimoaki, T., Yokoyama, T., Ando, T., Somekawa, A., Takayama, M., Tamaoki, K., Yoshida, T., Taga, K., Kamaya, H., Ueda, I. (2010). *Colloid Surf. A: Physicochem. Eng. Aspects* **367**, 47–51.

[48] Lin, Z., Ward, M.D. (1995). *Anal. Chem.* **67**, 685–693.

[49] Furlong, D.N. (1999). *Modern Characterization Methods of Surfactant Systems.* Marcel Dekker, New York [reprinted in *Surf. Sci. Ser*. **83**, 481 (1999)].

[50] Sauerbrey, G. (1959). *Zeitschr. Phys.* **155**, 206–222.

[51] Masuda, H., Baba, N. (1990). *Hyoumen* **28**, 222–232.

[52] Shimazu, K. (1998). *Gendaikagaku* **6**, 14–19.

[53] Nomura, T., Minemura, A. (1980). *Chem. Soc. Jpn.* **10**, 1621–1625.

[54] Bruckenstein, S., Shay, M. (1985). *J. Electroanal. Chem.* **188**, 131–136.

[55] Aoki, K., Miyamoto, T., Ohsawa, Y. (1989). *Bull. Chem. Soc. Jpn.* **62**, 1658–1659.

[56] Ebara, Y., Okahata, Y. (1993), *Langmuir* **9**, 574–576.

[57] Ebara, Y., Okahata, Y. (1994). *J. Am. Chem. Soc.* **116**, 11209–11212.

[58] Sato, T., Serizawa, T., Ohtake, F., Nakamura, M., Terabayashi, T., Kawanishi, Y., Okahata, Y. (1998). *Biochim. Biophys. Acta* **1380**, 82–92.

[59] Fukushima, T., Hayakawa, T., Inoue, Y., Miyazaki, K., Okahata, Y. (2004). *Biomaterials* **25**, 5491–5497.

[60] Matsuno, H., Furusawa, H., Okahata, Y. (2005). *Biochemistry* **44**, 2262–2270.

[61] Hoshino, Y., Kawasaki, T., Okahata, Y. (2006). *Biomacromolecules* **7**, 682–685.

[62] Furusawa, H., Komatsu, M., Okahata, Y. (2009). *Anal. Chem.* **81**, 1841–1847.

[63] Takahashi, S., Iida, M., Furusawa, H., Shimizu, Y., Ueda, T., Okahata, Y. (2009). *J. Am. Chem. Soc.* **131**, 9326–9332.

[64] Nihira, T., Mori, T., Asakura, M., Okahata, Y. (2011). *Lagmuir* **27**, 2107–2111.

[65] Buttry, D.A., Ward, M.D. (1992). *Chem. Rev.* **92**, 1355–1379.

[66] Takada, K., Tatsuma, T., Oyama, N. (1993). *Tyouonpa TECHNO* **6**, 43–46.

[67] Yamaguchi, S., Shimomura, T., Tatsuma, T., Oyama, N. (1993). *Anal. Chem.* **65**, 1925–1927.

[68] Tatsuma, T., Oyama, N. (1995). *Hyoumen* **33**, 689–697.

[69] Tatsuma, T., Oyama, N. (1993). *Tyouonpa TECHNO* **5**, 33–36.

[70] Muramatsu, H., Kimura, K. (1992). *Anal. Chem.* **64**, 2502–2507.

[71] Xie, Q., Zahang, Y., Xiang, C., Tang, J., Li, Y., Zhao, Q., Yao, S. (2001). *Anal. Sci.* **17**, 613–620.

[72] Yuan, Y., Cai, Y., Zie, Q., Yao, S. (2002). *Anal. Sci.* **18**, 767–771.

[73] Xie, Q., Xiang, C., Zhang, Y., Yuan, Y., Liu, M., Nie, L., Yao, S. (2002). *Anal. Chim. Acta* **464**, 65–77.

[74] Muramatsu, H., Tamiya, E., Karue, I. (1988). *Anal. Chem.* **60**, 2142–2146.

[75] Vanysek, P., Delia, L.A. (2006). *Electroanalysis* **18**, 371–377.

[76] Makino, M., Yoshikawa, K., Ishii, T. (1997). *Pharm. Tech. Jpn.* **13**, 31–40.

[77] Makino, M., Kamiya, M. (1996). *Langmuir* **12**, 4211–4217.

[78] Sato, T., Serizawa, T., Okahata, Y. (1994). *Biochem. Biophys. Res. Commun.* **204**, 551–556.

[79] Sato, T., Serizawa, T., Okahata, Y. (1996). *Biochim. Biophys. Acta* **1285**, 14–20.

[80] Ebara, Y., Itakura, K., Okahata, Y. (1996). *Langmuir* **12**, 5165–5170.

[81] Sato, T., Ishii, M., Terabayashi, T., Kawanishi, Y., Okahata, Y. (1997). *Chem. Lett.* **26**, 669–670.

[82] Hashizume, M., Sato, T., Okahata, Y. (1998). *Chem. Lett.* **27**, 399–400.

[83] Okahata, Y., Furusawa, H. (2004). *J. Surf. Sci. Soc. Jpn.* **25**, 131–138.

[84] Kawasaki, T., Asaoka, K., Mihara, K., Okahata, Y. (2006). *J. Colloid Interface Sci.* **294**, 295–303.

[85] Yamamoto, Y., Taga, K., Yoshida, T., Kamaya, H., Ueda, I. (2006). *J. Colloid Interface Sci.* **298**, 529–534.

[86] Yamamoto, Y., Ando, T., Takayama, M., Egami, T., Ohtsu, Y., Sakurai, A., Yoshida, T., Taga, K., Kamaya, H., Ueda, I. (2008). *Colloid Surf. A: Physicochem. Eng. Aspects* **317**, 568–575.

[87] Kanazawa, K.K., Gordon, J.G. II (1985). *Anal. Chim. Acta* **175**, 99–105.

[88] Matin, S., Granstaff, V.E. Frye, G.C. (1991). *Anal. Chem.* **63**, 2272–2281.

[89] Matsuura, N., Elliot, D.J., Frulong, D.N., Grieser, F. (1997). *Colloid Surf. A: Physicochem. Eng. Aspects* **126**, 189–195.

[90] Seto, N., Mashimo, T., Yoshiya, I., Taniguchi, Y. (1991). *Anesth. Resusc.* **27**, 321–324.

[91] Yokono, S., Shieh, D.D., Ueda, I. (1981). *Biochim. Biophys. Acta* **645**, 237–242.

[92] Yoshino, A., Yoshida, T., Takahashi, K. (1989). *Magn. Reson. Chem.* **27**, 344–347.

[93] Yoshida, T., Takahashi, K., Kamaya, H., Ueda, I. (1988). *J. Colloid Interface Sci.* **124**, 177–185.

[94] Yoshida, T., Takahashi, K., Ueda, I. (1989). *Biochim. Biophys. Acta* **985**, 331–333.

[95] Hauet, N., Artzner, F., Boucher, F., Gabrielle-Madelmont, C., Clouteir, I., Keller, G., Lesieur, P., Durand, D., Patermostre, M. (2003). *Biophys. J.* **84**, 3123–3137.

[96] Ohe, C., Ida, Y., Matsumoto, S., Sasaki, T., Goto, Y., Noi, M., Tsurumatru, T., Itoh, K. (2004). *J. Phys. Chem. B* **108**, 18081–18087.

[97] Ruths, J., Essler, F., Decher, G., Riegler, H. (2000). *Langmuir* **16**, 8871–8878.

[98] Tsuboi, K., Seki, K., Ouchi, Y., Fujita, K., Kajikawa, K. (2003). *J. Appl. Phys.* **42**, 607–613.

[99] Bergadano, A., Lauber, R., Zbinden, A., Schatzmann, U., Moens, Y. (2003). *Br. J. Anaesth.* **91**, 276–278.

[100] Frisch, M.J., Trucks, G.W., Schlegel, H.B., Scuseria, G.E., Robb, M.A., Cheeseman, J.R., Scalmani, G., Barone, V., Mennucci, B., Petersson, G.A., Nakatsuji, H., Caricato, M., Li, X., Hratchian, H.P., Izmaylov, A.F., Bloino, J., et al. (2009). *Gaussian 09, Revision **D.01***; Gaussian, Inc., Wallingford, CT.

[101] Yamamoto, Y., Shervani, Z., Shimoaki, T., Yoshida, D., Yokoyama, T., Yoshida, T., Taga, K., Kamaya, H., Ueda, I. (2011). *J. Biophys. Chem.* **2**, 68–74.

[102] Mashimo, T., Ogli, K., Uchida, I. (2005). *Basic and Systemic Mechanisms of Anesthesia.* Elsevier, The Netherlands.

[103] *Proc.8th Int. Conf. Mechanisms of Anesthesia (MAC 2010)* (2010). J.J.R. Macleod Auditorium, Toronto.

4

ATOMIC FORCE MICROSCOPY FOR MEASURING INTERACTION FORCES IN BIOLOGICAL MATERIALS AND CELLS

Naoyuki Ishida,[1] Yasuyuki Kusaka,[2] Tomonori Fukasawa,[3] and Hiroyuki Shinto[4]

[1]*Department of Applied Chemistry and Biotechnology, Okayama University, Japan*
[2]*Flexible Electronics Research Center, National Institute of Advanced Industrial Science and Technology (AIST), Japan*
[3]*Department of Chemical Engineering, Hiroshima University, Japan*
[4]*Department of Chemical Engineering, Fukuoka University, Japan*

4.1 INTRODUCTION

Currently, atomic force microscopy (AFM) occupies a very important position in a wide range of research areas in the sciences and engineering. Since its invention in 1984 by Binning et al. [1], AFM has been used as a powerful tool to explore surface structures down to the molecular scale, or even to the atomic scale depending on the samples and environment. In AFM, a nanostylus (probe tip) attached to the end of a microfabricated cantilever is scanned over a sample. A sensitive four-segment photodiode detects the vertical and lateral positions of the laser beam reflected off the back of the cantilever, which follows the surface undulations of the sample. Owing to this relatively simple optical lever method, AFM can be operated in various environmental conditions, including liquids and gases. This feature is particularly advantageous for biology-related research fields since it enables *in situ* imaging of biomolecules (e.g., proteins, DNA, peptides) and biological cells in aqueous solutions without requiring the complicated pretreatments of samples that are necessary for electron microscopy and fluorescence microscopy. In addition to surface imaging, AFM enables measurement of forces between the probe tip and the sample substrate; the tip and the substrate are scanned vertically (z-direction) and the tip−substrate interaction force is then estimated from the vertical deflection of the probe cantilever. Consequently, AFM enables measurement of the interaction forces of even a few piconewtons between the probe tip and the sample surface at subnanometer resolution in the z-direction. Such highly sensitive force measurements can be conducted in a local area ($<10 \times 10$ nm) along the x and y directions. Once a micrometer-sized particle is attached to the end of the cantilever, often called the colloid probe [2], one can measure the surface forces between the particle and the substrate.

Understanding the interaction forces between two opposing surfaces in liquids has been one of the central topics in colloid science for the past several decades because these forces directly influence the dispersion/aggregation state of colloidal systems, including suspensions and emulsions. The Derjaguin−Landau−Verway−Overbeek (DLVO) theory, developed in the 1940s, provided a way to estimate the dispersion stability of colloidal particles and is still widely used as a standard theory to quantitatively describe the surface forces in aqueous solutions. On the other hand, there was no experimental method to directly measure the interaction forces as a function of separation distance between two opposing interfaces before the 1970s; therefore, one had to rely on indirect methods such as the turbidity measurements of colloidal dispersions, observation of coalescence of two mercury drops, and measurements of soap film thickness [3,4]. In the 1970s, an innovative instrument called a surface force apparatus (SFA) was invented for directly measuring

Encyclopedia of Biocolloid and Biointerface Science, Volume 1, First Edition. Edited by Hiroyuki Ohshima.
© 2016 John Wiley & Sons, Inc. Published 2016 by John Wiley & Sons, Inc.

interaction forces between two macroscopic surfaces in liquid and gaseous media [5]; since then, a number of SFA studies have helped to deepen the understanding of surface forces in various systems. Subsequently, since the early 1990s, AFM has been applied to the direct measurements of interaction forces in a variety of colloidal and biological systems. In force measurements with AFM, a probe tip or a colloid probe can be coated/functionalized with many kinds of molecules, including biological substances. This versatility has made AFM force measurement one of the most important methods in various research fields.

Biological systems comprise a number of the dynamic, physicochemical interactions between their components such as proteins, membranes, phospholipids, endocytic vesicles, and DNAs in biological fluids. Therefore, one of the best approaches to explore and explain the phenomena occurring in biological systems is to evaluate and quantify the dynamic interaction forces acting between these components. In addition, because of the recent rapid growth in the field of nanobiotechnology, engineered materials often come into contact with biointerfaces, including human bodies and environments, as exemplified by research focused on biocompatible materials, cell culture surfaces, and drug delivery systems. Thus, exploration and understanding of various interactions between a variety of materials and biointerfaces from the viewpoint of colloid science would enable the development of a conceptual framework for the predictive and effective design of engineered material surfaces with biological applications. AFM has been viewed as one of the most powerful instruments to achieve these goals.

In this chapter, we provide an overview of the rapid advances in AFM applications for force measurements in bioscience research. We describe developments and the keystone research results of force measurements, focusing mainly on the interactions of membranes, proteins, cells, and various material surfaces, together with descriptions of the methodologies employed for these measurements.

4.2 MEASUREMENT OF INTERACTION FORCES USING AFM

Before reviewing the measurements of interactions for various biointerfaces, we will provide a brief overview on the techniques for direct force measurement using AFM. As shown in Fig. 4.1, the sample is moved vertically (in z-direction) by expanding the piezo scanner to allow the probe to approach the sample surface and make contact with it, and contracting the piezo to retract the probe to the original position. The cantilever deflection (Δz) resulting from the probe−sample interaction is measured by the optical lever method. An attractive force, called the adhesion force, often appears after the probe and sample establish contact with each other. Most commercial AFMs have an operation mode so that these procedures can be conducted automatically. The probe−sample force (F) is calculated by Hooke's law, $F = k_c \Delta z$, where k_c is the spring constant of the cantilever. The surface of the probe tip can be modified with a variety of molecules by either physical adsorption or chemical reaction.

For the colloid probe, spherical particles typically in the diameter range of 1–30 μm are used. A particle is attached to the probe with epoxy glue or hot-melt epoxy resin using a micropositioning device such as a micromanipulator under observation with an optical microscope or a CCD camera.

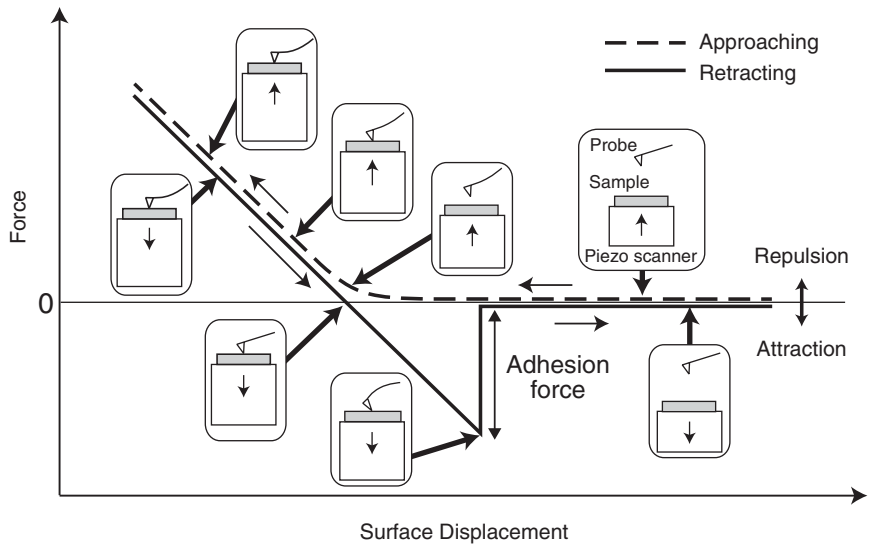


FIGURE 4.1 Schematic illustration of a force measurement between two surfaces using AFM shown along with a plot of force versus displacement.

The surface of the particles can be modified with various molecules before or after attaching to the probe tip.

Since the surface force is usually described as a function of the separation distance between two surfaces, it is of critical importance to determine this separation distance precisely. However, a standard AFM is not equipped to measure the separation distance directly and the following conversion procedure is consequently required to determine the separation distance [6]. Figure 4.2a illustrates a typical raw data trace for the force measurement between two hard, solid surfaces (such as metal oxides) obtained from a standard AFM. The raw output signals by AFM are the deflection of a probe cantilever bent upward/downward by the probe−sample interaction and the surface displacement of a sample stage (or a probe) driven by a piezoelectric transducer. One can easily calculate the probe−sample force from the deflection of the probe cantilever with Hooke's law, as mentioned above. When the probe comes closer to the sample surface (moving from right to left in Fig. 4.2a), the probe cantilever starts to deflect because of the probe−sample interaction. In the case of a sufficiently hard surface of samples, the force−displacement curve exhibits a linear profile after the closest contact between the probe and sample surfaces, where the deflection of the probe becomes equivalent to the displacement of the sample surface. The region of this linear profile can be assumed as that of the zero separation distance between the probe and sample surfaces and is often called the constant-compliance region. One can then transform the surface displacement into the separation distance, and a force−distance curve is obtained as shown in the inset of Fig. 4.2a.

When the surface of the samples is soft, it is more difficult to estimate the separation distance from the AFM force−displacement curve due to surface deformability. This is the case for the force measurements of biomolecules and cells, where they are usually attached to either or both the probe surface and substrate surface. As shown in Fig. 4.2b, the surface deformation changes significantly in the compliance region of the force−displacement curve. When the surface deformation is proportional to the applied force (e.g., a large bubble and a large droplet), a straight constant compliance region still appears with a more gradual slope compared with that of the rigid surfaces. In this linear deformation system, one can estimate the separation distance between two surfaces and their contact point on the assumption that the force from the deformed body or bodies is given by $k_d \Delta z$, where k_d represents a spring constant of the deformed body or bodies [7]. On the other hand, in the event of nonlinear deformation, the compliance region exhibits a curved profile instead of a straight line, and there are no distinct criteria for determining the contact region and the separation distance between the two surfaces. Apart from the separation distance, one can still measure the adhesion force (see Fig. 4.1) that would be influenced by several parameters such as the approaching/retracting velocity, the indentation depth, the applied load, and the contact time. Therefore, the main focus of AFM studies of biological materials and cells is often placed on these adhesion (or pull-off) forces.

4.3 INTERACTION OF MODEL MEMBRANES

Force measurement studies of biomembranes often employ artificial model membranes (i.e., lipid bilayers and giant unilamellar vesicles) as well as actual cell membranes, which are described in Section 4.5. In early-stage studies, SFA,

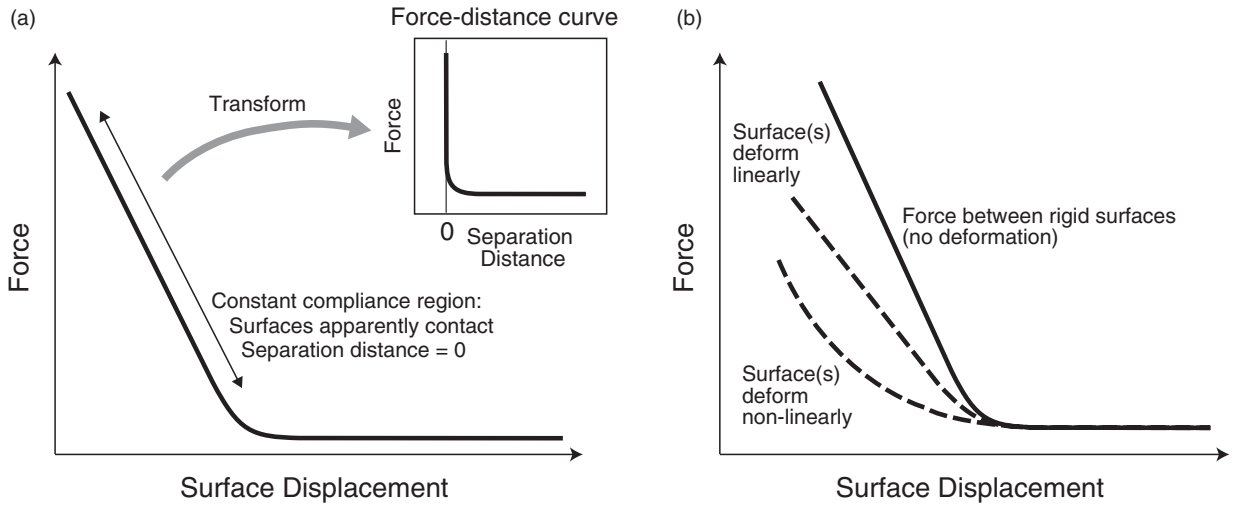


FIGURE 4.2 Schematic illustration of typical force−displacement curves between two surfaces obtained from AFM: (a) rigid surfaces and (b) deformable surfaces. The inset of panel (a) shows a force−distance curve transformed from the force−displacement curve.

which measures the forces between two macroscopic surfaces of area ∼1 cm^2, was used to investigate the interaction between lipid bilayers supported on mica surfaces [8]. These SFA measurements revealed that the short-range hydration/steric interactions between the supported lipid membranes are affected by the type and composition of the phospholipid molecules comprising the membranes. In contrast, application of AFM to the force measurements between lipid membranes was delayed by the difficulty in preparing the lipid bilayers on the AFM probe surface. Therefore, the early-stage AFM studies of lipid bilayers were largely limited to the imaging of lipid membranes supported on substrates [9], the measurement of mechanical strength of the supported lipid membranes [9], and the imaging of aggregation of polypeptides in supported lipid membranes [10].

Pera et al. [11] were the first to develop a method for forming a stable lipid bilayer on the surface of an AFM probe tip, which they used to measure the interaction force between two lipid bilayers supported on the surfaces of the tip and the planar mica in aqueous solution. They found that the salt concentration in the solutions drastically changes the interaction between the supported lipid bilayers, and that the addition of phosphate-binding proteins to the lipid bilayers increases the stability of the lipid bilayers. Following this study, the lipid bilayer was also successfully created on the surface of a colloid probe, which has a larger radius of curvature compared with a probe tip [12, 13]. This colloidal probe microscopy enabled the investigation of interactions between macroscopic bilayers that are more comparable in size to biological membranes.

The interactions of biomolecules with model membranes have also been studied. Carneiro et al. [14] measured the interactions of vesicular stomatitis virus attached to an AFM probe with membranes of different phospholipid compositions. They discovered that the adhesion forces differ drastically depending on the composition of the membrane phospholipids, revealing the high specificity of G protein binding to membranes containing phosphatidylserine. Wang et al. [15] measured the interactions of lysenin, a sphingomyelin-specific binding protein, attached to an AFM tip with the lipid membranes to successfully map the sphingomyelin-rich and -poor domains from the force curves. These types of measurements, however, have been reported by only a few researchers, mainly because of the difficulty in performing such precise measurements and in detecting false interactions such as membrane molecules being pulled out from a lipid membrane by a functionalized tip due to the strong tip−membrane interactions [16].

4.4 INTERACTION OF PROTEINS

One of the main applications of AFM to the force measurements of biomolecules has been single-molecule force spectroscopy (SMFS), where molecules of interest are attached on an AFM tip and allowed to interact with a solid surface with or without other molecules. The SMFS technique was first used by Florin et al. for proteins [17], and by Lee et al. for DNA [18]. The ligand−receptor binding force of individual biotin−avidin pairs was successfully quantified by measuring the adhesion forces between an avidin-immobilized tip and a biotin-functionalized agarose bead [17]. Following this study, much progress has been made to determine the static and dynamic interaction forces of a variety of biomolecule pairs. A number of papers have been published using the SMFS technique to investigate different types of interaction forces, including ligand−receptors [19–21], antigen−antibodies [22, 23], cell surface proteins [24, 25], and protein−DNA [26, 27]. In addition, SMFS has been applied not only to intermolecular force measurements, but also to the intramolecular force measurements of individual molecules such as the folding/unfolding of proteins, where a single molecule is held between the AFM tip and support and stretched thereby [28–30]. A detailed picture of the complex mechanical unfolding pathway of single proteins can be obtained through an energy landscape of the measured interactions [31].

The force curves obtained using SMFS look different from those between solid surfaces mentioned in Section 4.2. The molecules attached onto a cantilever and/or a substrate surface often interact with multiple binding sites when the two surfaces are brought into contact. By retracting the probe from the surface, the multiple bonds gradually rupture to cause "sawtooth" patterns with multiple attractive force maxima in the force curve. During the stretching of the molecule(s) bridging the probe and the substrate before the rupture, the force curve exhibits a specific curved profile, which is similarly observed for the polymer coils extended between two surfaces, as shown in Fig. 4.3. The force profiles obtained from SMFS are sometimes analyzed by fitting the physical models proposed originally for polymer stretching, such as the wormlike chain (WLC) model [32], so that an elastic property of the stretched molecule(s) can be characterized. This analysis is particularly useful to investigate the unfolding of proteins.

SMFS has also been applied to measure protein interactions with solid material surfaces such as glass [33], gold [34], and polystyrene [33,35]. In general, the protein−material interaction forces before their contact are dominated by electrostatic repulsion at large separation distances. Once the protein comes close to a material surface and contacts it, other forces such as hydrogen bonding, hydrophobic interactions, and hydration forces contribute to the adhesion force between the protein and the material. In addition to the simple material surfaces, one can explore the adsorption of protein onto model surfaces coated with various functional groups. Some examples include the self-assembled monolayers (SAMs) of alkanethiols on gold, where the alkanethiols have various

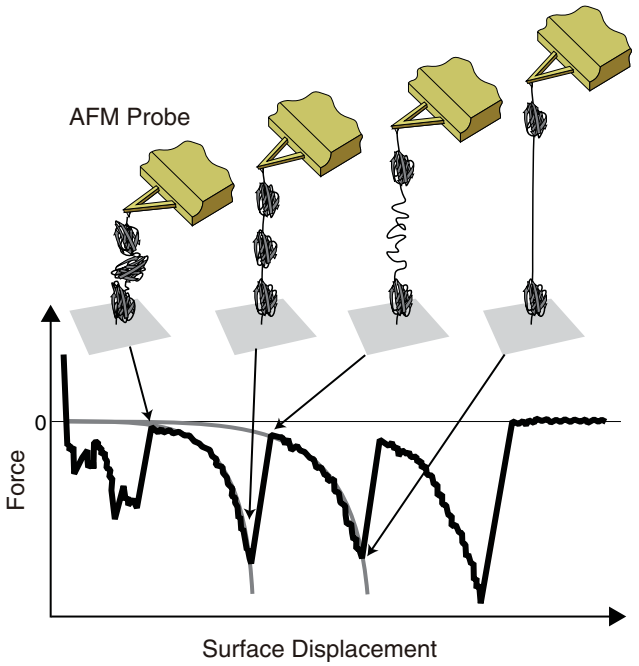


FIGURE 4.3 Schematic illustration of typical force curves for a protein stretching and the hypothesized structure of proteins. Gray lines show the fitted curves using the WLC model.

terminal groups. The investigations of protein interactions with model surfaces that have the terminal groups of $–CH_3$, $–NH_2$, –OH, and –COOH [34,36] revealed that among the four terminal groups, $–CH_3$ has the greatest effect and the strongest affinity for all the investigated proteins. The affinities of the $–NH_2$, –OH, and –COOH surfaces for proteins depend largely on the type of the protein, indicating that this interaction varies in a complicated fashion depending the type of model surface and protein applied.

For engineered surfaces, poly(ethylene oxide) (PEO) [also known as poly(oxyethylene) (POE) or poly(ethylene glycol) (PEG)] is most often used to create biologically inert, protective coatings. The graft polymerization of PEO layers onto material surfaces is used to protect against protein adsorption. The detailed mechanism of the interaction of the PEO layers with proteins, however, had been unclear despite numerous studies; the adsorption tests produced contradictory results showing that the net protein−PEO interactions were both attractive and repulsive. The direct force measurements using AFM with the protein-immobilized probe tip [37] or colloid probe [38] have revealed that the grafting density of the PEO layers has a significant influence: the PEO surfaces of low grafting density make attractive contact with human serum albumin (HSA) [37], whereas those of high grafting density have no affinity for HSA. The attractive forces observed for the PEO surfaces of low grafting density may originate from hydrogen bonds, van der Waals forces, and hydrophobic interactions between the proteins and the sparsely grafted PEO chains that have a sufficiently large degree of conformational freedom to interact with the proteins. Through experiments with bovine serum albumin (BSA) and three different hydrophilic polymer layers, Inoue et al. [39] found that the thickness of the polymer brush layer also has a relatively larger effect on the adhesion force than the chemical structure of the polymer brush layers.

By grafting polymers that can change their properties and structures in response to external stimuli, one can create environment-sensitive functional surfaces. A typical example of temperature-responsive polymers is poly(*N*-isopropylacrylamide) (PNIPAM), which undergoes a volume phase transition by swelling/shrinking in water at a temperature of ∼32°C. Because of this temperature-responsive behavior, PNIPAM has a wide range of practical applications such as in cell culture sheets, the attachment/detachment surfaces for biomolecules, and in medical diagnostic devices. From a fundamental perspective, the intermolecular forces between grafted PNIPAM chains and proteins have been studied by AFM [40, 41], indicating that the PNIPAM−protein interaction is almost repulsive at temperatures below the phase transition point, whereas it tends to be attractive at temperatures above the phase transition point. This temperature-sensitive behavior of the PNIPAM−protein interaction is caused by temperature-dependent hydration/dehydration of PNIPAM chains. Such an AFM method enables the evaluation of whether the surfaces grafted with a variety of stimuli-responsive polymers perform necessary environment-sensitive functions (for examples, see Ref. [42]). These studies demonstrate that the direct AFM measurement of adhesion force of proteins onto the engineered surfaces is a powerful tool for understanding the relationship between the physicochemical property and biocompatibility of the surfaces at the nanometer scale, whereby we can obtain useful information on the effective/efficient design of biomaterial surfaces with high functionalities.

4.5 INTERACTION OF CELLS

The AFM measurement of cells was first developed to investigate the nanomechanical properties of them, where the viscoelastic forces are monitored after an AFM probe makes contacts with and pushes downward the surfaces of cells attached to a substrate. Weisenhorn et al. [49] were the pioneers to quantify the elastic behavior of a living (lung carcinoma) cell from force curves and to obtain a Young's modulus for the cell. Radmacher et al. [44] successfully mapped the local Young's moduli of human platelets with a lateral resolution of ∼100 nm by analyzing the force curves obtained at different positions of the cell. In order to estimate the elastic modulus of the cell from force curves, the constant compliance region of the curves mentioned in Section 4.2 is

used. When an AFM probe is pushed against a cell surface, one obtains the constant compliance region, which is still straight for most cells due to their almost linear deformation against an applied load. The slope of the constant compliance region deviates from that for the force curve between hard surfaces. This deviation represents the degree of surface deformation, from which one can calculate the elastic moduli by fitting the physical models (e.g., the Hertz model) to the experimental data [45]. An example of the unique applications of AFM to such cell nanomechanics is cancer diagnosis [46], by taking advantage of an elastic property of cancerous cells exhibiting a lower Young's modulus value than normal cells.

On the other hand, in order to understand the process of microbial adsorption and adhesion to materials, cell–material interaction forces are measured and often analyzed in the context of DLVO theory assuming that cells act as spherical colloid particles. This approach inevitably includes a lot of approximation, because the DLVO theory is applicable only when surfaces are nondeformable and physicochemically homogeneous without any local structures, which is clearly not the case for biological cells. In addition, it is difficult to determine the separation distance for deformable cell surfaces, as mentioned in Section 4.2. To overcome these difficulties, several extended DLVO models have been proposed, which incorporate additional terms that are mainly steric interactions originating from polymeric structures [47, 48]. In general, the approaching forces measured between cells and AFM probes are strongly repulsive from long separation distances, much longer than the range of the electric double layer repulsion, regardless of the cell species used and their medium conditions (i.e., the ionic strength and pH). This indicates that the contribution of the steric force due to the compression of brush-like biopolymers on the cell surfaces is much larger than the classical DLVO force for such systems.

The adhesion forces between chemically modified AFM tips and cell surfaces are of great interest for evaluating the local properties of cell surfaces. Ahimou et al. [49] reported that the adhesion force between a yeast cell and a COOH-terminated probe varies with pH of the aqueous solution, indicating that the interaction between the cell and material surfaces is influenced by the electrostatic charges on their surfaces (i.e., the surface potentials). Similarly, Dorobantu et al. [50] showed that the force curves can be used to map the bacterial surface hydrophobicity using hydrophilic (OH) and hydrophobic (CH_3) tips. The force measurements between an AFM probe modified with proteins, such as receptors [51] and carbohydrate-binding protein [52], and cells have revealed strong adhesion forces due to specific binding, and their corresponding binding energies were also estimated quantitatively. These methods have been further developed to visualize the chemical heterogeneity of cell surfaces under native conditions by mapping the contour of adhesion forces over cell morphology.

An increasing number of reports have focused on the force measurements between a cell and a microsphere using a colloid probe (Fig. 4.4a), where the interaction forces have been measured at the single-cell, single-particle level. This is because in recent years many researchers have had a growing interest not only in cell surface recognition for drug delivery systems, but also in risk analysis of nanomaterials in the human body, where it is of fundamental importance to understand the adhesion/uptake of nanoparticles (NPs) onto/into cells and their resultant cytotoxicity. Pyo et al. [53] measured the adhesion forces of a silica microsphere toward three different types of cells, and concluded that the difference in adhesion force is reflected by the difference in van der Waals forces and/or hydrogen bonds at the cell–microsphere interface. Shinto et al. [54] measured the interaction forces of a melanoma cell with microspheres of different surface chemistries in a culture medium, and found that the presence/absence of interfacial serum proteins on the microsphere surfaces has a great impact on the measured adhesion forces. It is noted that serum contains extracellular matrix proteins and is usually added to the culture media to help the anchorage-dependent cells adhere to the surfaces of culture dishes. This suggests that some proteins are adsorbed from culture media onto the surfaces of materials and thus influence the cell–material interactions. Using smaller particles, Vasir and Labhasetwar [55] measured the force of NP–cell membrane interactions and related them to cellular uptake of the NPs. They covered an AFM tip with poly(D,L-lactide-*co*-glycolide) NPs with a diameter of approximately 300 nm, and demonstrated that the strength of the adhesive force of NPs with the cell membrane can be correlated with

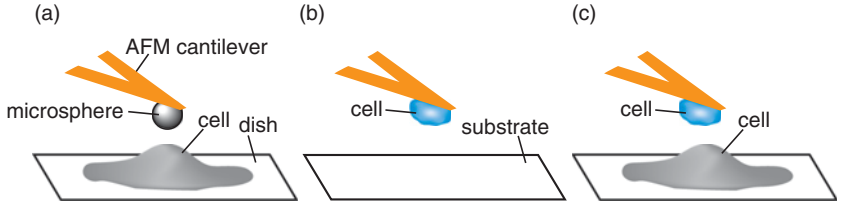


FIGURE 4.4 Illustrations of a colloid probe and a cell probe for the AFM force measurements of (a) microsphere–cell, (b) cell–substrate, and (c) cell–cell interactions.

the uptake amount of NPs by the cells, and hence the extent of the intracellular delivery of the encapsulated materials therein.

There have also been attempts to immobilize cells to the top of AFM tips to investigate cell adhesion. In order to immobilize relatively small cells such as *Escherichia coli*, Ong et al. [56] developed a procedure for coating the tip of an AFM cantilever with a confluent layer of cells, using polyethyleneimine to coat the tip for cell attachment and glutaraldehyde to form cross-linking bonds between the cells and the coated tip. Poly-L-lysine [57], concanavalin A [58], aminosilane [59], and polydopamine [60] are also used as adherent materials to immobilize cells onto tip ends. Alternatively, colloid probes coated with these adherent materials are also used to create a multiple-cell probe [61]. For relatively larger cells, Benoit et al. [62] succeeded in inventing a method to immobilize a single living cell on the top of an AFM cantilever (Fig. 4.4b). A cell in a culture medium was picked up by a tipless cantilever functionalized covalently with lectin under observation with an optical microscope. After this, the single-cell probe was positioned just above a target cell adhered on a dish surface and the cell–cell interaction forces were measured (Fig. 4.4c). The force measurements using such cell probes are often called single-cell force spectroscopy (SCFS).

The measurements of cell–cell interaction forces by SCFS have provided fresh insight into cellular adhesion and aggregation processes at the molecular level. Waar et al. [63] measured the adhesion forces between *Enterococcus faecalis* cells in a medium supplemented with specific antibodies, which act as inhibitors against the aggregation substance (Agg) that is a surface protein on the bacteria. They found that the Agg plays a key role in the strong adhesion forces between the cells. Panorchan et al. [64] investigated the role of vascular endothelial (VE) cadherin, the surface glycoprotein cadherin specific to the endothelium, in the adhesion between living endothelial cells, and revealed that VE-cadherin molecules expressed on the cell surfaces form bonds at a higher tensile strength than bonds formed by classical cadherin. Heterogeneous cell–cell interactions have also been studied using SCFS. Puech et al. [65] used SCFS to measure the binding forces of a melanoma cell line to human umbilical vein endothelial cells and demonstrated the capabilities of this technique. Alsteens et al. [66] quantified the forces between pathogenic *Candida albicans* yeast and hyphae cells, and found that hyphal formation induces strong cell–cell adhesions and that hyphal transition is important for strong biofilm formation.

In addition, the versatility of SCFS enables not only quantification of the single-molecule interactions occurring at the cell surface [58], where the interactions between a cell probe and target molecules immobilized on a substrate were measured, but also measurement of cell–material surface interactions [56,67] for exploring cell adhesion to the material surfaces. These results show that SCFS still has great potential in a variety of biological and medical applications.

4.6 CONCLUDING REMARKS

This chapter has presented an overview of how AFM has been employed for investigating the interaction forces involving biomolecules, cells, and engineered surfaces across various fields of bioscience. The studies introduced herein clearly show that AFM is arguably one of the best tools to help us gain direct understanding of how biomolecules and biosubstances behave down to the nanometer scale level in various environments.

Future applications of AFM will undoubtedly address even more important biological problems, and to achieve this goal, AFM force measurements should be further improved. For example, immediately required technological advances include increasing the sensitivity and the throughput of force measurements, as well as the improvement of protocols for attaching biomolecules and cells to probes and substrates. Further development of theoretical descriptions and treatments is also required to characterize in greater detail how the molecules behave and interact at the interfaces during force measurements. For SMFS, tracking the behavior of single molecules during force measurement by using additional techniques such as fluorescence resonance energy transfer (FRET) and total internal reflection fluorescence microscopy (TIRFM) will show fascinating potential. For SCFS, the combination of AFM with advanced light microscopy or other techniques for evaluating the changes in cell morphology and behavior will likely emerge in the foreseeable future. With these technological and methodological improvements, it is highly expected that the nanometer-scale analysis of interactions between biological substances using AFM will become a central subject to achieve a more comprehensive understanding of the complex behaviors of various biosystems.

REFERENCES

[1] Binning, G., Quate, C.F., Gerberl C. (1986). *Phys. Rev. Lett.* **56**, 930–933.

[2] Ducker, W.A., Senden, T.J., Pashley, R.M. (1991). *Nature* **353**, 239–241.

[3] Craig, V.S.J. (1997). *Colloids Surf. A* **130**, 75–93.

[4] Butt, H.-J., Cappella, B., Kappl, M. (2005). *Surf. Sci. Reports* **59**, 1–152.

[5] Israelachvili, J.N., Adams, G.E. (1978). *J. Chem. Soc. Faraday Trans. I* **74**, 975–1001.

[6] Ducker, W.A., Senden, T.J., Pashley, R.M. (1992). *Langmuir* **8**, 1831–1836.

[7] Chan, D.Y.C., Dagastine, R.R., White, L.R. (2001). *J. Colloid Interface Sci.* **236**, 141–154.

[8] Marra, J. (1985). *J. Colloid Interface Sci.* **107**, 446–458.

[9] Dufrêne, Y.F., Boland, T., Schneider, J.W., Barger, W.R., Lee, G.U. (1999). *Faraday Discuss.* **111**, 79–94.

[10] Mou, J, Czajkowsky, D.M., Shao, Z. (1996). *Biochemistry* **35**, 3222–3226.

[11] Pera, I., Stark, R., Kappl, M., Butt, H.-J., Benfenati, F. (2004). *Biophys. J.* **87**, 2446–2455.

[12] Abdulreda, M.H., Moy, V.T. (2007). *Biophys. J.* **92**, 4369–4378.

[13] Lorenz, B., Keller, R., Sunnick, E., Geil, B., Janshoff, A. (2010). *Biophys. Chem.*, **150**, 54–63.

[14] Carneiro, F.A., Lapido-Loureiro, P.A., Cordo, S.M., Stauffer, F., Weissmüller, G., Bianconi, M.L., Juliano, M.A., Juliano, L., Bisch, P.M., Poian, A.T. (2006). *Eur. Biophys. J.* **35**, 145–154.

[15] Wang, T., Shogomori, H., Hara, M., Yamada, T., Kobayashi, T. (2012). *Biochemistry* **51**, 74–82.

[16] Andre, G., Brasseur, R., Dufrêne, Y.F. (2007). *J. Mol. Recognition* **20**, 538–545.

[17] Florin, E.-L., Moy, V.T., Gaub, H.E. (1994). *Science* **264**, 415–417.

[18] Lee, G.U., Chrisey, L.A., Colton, R.J. (1994). *Science* **266**, 771–773.

[19] Ros, R., Schwesinger, F., Anselmetti, D., Kubon, M., Schäfer, R., Plückthun, A., Tiefenauer, L. (1998). *Proc. Natl. Acad. Sci. USA* **95**, 7402–7405.

[20] Wong, S.S., Joselevich, E., Woolley, A.T., Cheung, C.L., Lieber, C.M. (1998). *Nature* **394**, 52–55.

[21] Zhang, X., Craig, S.E., Kirby, H., Humphries, M.J., Moy, V.T. (2004). *Biophys. J.* **87**, 3470–3478.

[22] Hinterdorfer, P., Baumgartner, W., Gruber, H.J., Schilcher, K., Schindler, H. (1996). *Proc. Natl. Acad. Sci. USA* **93**, 3477–3481.

[23] Sulchek, T., Friddle, R.W., Noy, A. (2006). *Biophys. J.* **90**, 4686–4691.

[24] Baumgartner, W., Hinterdorfer, P., Ness, W., Raab, A., Vestweber, D., Schindler, H., Drenckhahn, D. (2000). *Proc. Natl. Acad. Sci. USA* **97**, 4005–4010.

[25] Dupres, V., Menozzi, F.D., Locht, C., Clare, B.H., Abbott, N.L., Cuenot, S., Bompard, C., Roze, D., Dufrêne, Y.F. (2005). *Nat. Methods* **2**, 515–520.

[26] Bartels, F.W., Baumgarth, B., Anselmetti, D., Ros, R., Becker, A. (2003). *J. Struct. Biol.* **143**, 145–152.

[27] Kühner, F., Costa, L.T., Bisch, P.M., Thalhammer, S., Heckl, W.M., Gaub, H.E. (2004). *Biophys. J.* **87**, 2683–2690.

[28] Mitsui, K., Hara, M., Ikai, A. (1996). *FEBS Lett.* **385**, 29–33.

[29] Rief, M., Gautel, M., Oesterhelt, F., Fernandez, J.M., Gaub, H.E. (1997). *Science* **276**, 1109–1112.

[30] Harris, N.C., Song Y., Kiang, C.-H. (2007). *Phys. Rev. Lett.* **99**, 068101.

[31] Afrin, R., Takahashi, I., Shiga, K., Ikai, A. (2009). *Biophys. J.* **96**, 1105–1114.

[32] Doi, M., Edwards, S.F. (1986). *The Theory of Polymer Dynamics*. Clarendon Press, Oxford, UK.

[33] Sagvolden, G., Giaever, I., Feder, J. (1998). *Langmuir* **14**, 5984–5987.

[34] Rixman, M.A., Dean, D., Macias, C.E., Ortiz, C. (2003). *Langmuir* **19**, 6202–6218.

[35] Chen, X., Davies, M.C., Roberts, C.J., Tendler, S.J.B., Williams, P.M., Davies, J., Dawkes, A.C., Edwards, J.C. (1997). *Langmuir* **13**, 4106–4111.

[36] Kidoaki, S., Masuda, T. (1999). *Langmuir* **15**, 7639–7646.

[37] Rixman, M.A., Dean, D., Ortiz, C. (2003). *Langmuir* **19**, 9357–9372.

[38] Bremmell, K.E., Kingshott, P., Ademovic, Z., Winther-Jensen, B., Griesser, H.J. (2006). *Langmuir* **22**, 313–318.

[39] Inoue, Y., Nakanishi, T., Ishihara, K. (2011). *React. Funct. Polym.* **71**, 350–355.

[40] Kidoaki, S., Ohya, S., Nakayama, Y., Matsuda, T. (2001). *Langmuir* **17**, 2402–2407.

[41] Cole, M.A., Voelcker, N.H., Thissen, H., Horn, R.G., Griesser, H.J. (2010). *Soft Matter* **6**, 2657–2667.

[42] de las Heras Alarcón, C., Twaites, B., Cunliffe, D., Smith, J.R., Alexander, C. (2005). *Int. J. Pharm*. **295**, 77–91.

[43] Weisenhorn, A.L., Khorsandi, M., Kasas, S., Gotzos, V., Butt, H.-J. (1993). *Nanotechnology* **4**, 106–113.

[44] Radmacher, M., Fritz, M., Kacher, C.M., Cleveland, J.P., Hansma, P.K. (1996). *Biophys. J.* **70**, 556–567.

[45] Heinz, W.F., Hoh, J.H. (1999). *Trends Biotechnol.* **17**, 143–150.

[46] Cross, S.E., Jin, Y.-S., Rao, J., Gimzewski, J.K. (2007). *Nat. Nanotechnol*. **2**, 780–783.

[47] Abu-Lail, N.I., Camesano, T.A. (2003). *Environ. Sci. Technol*. **37**, 2173–2183.

[48] Considine, R.F., Drummond, C.J., Dixon, D.R. (2001). *Langmuir* **17**, 6325–6335.

[49] Ahimou, F., Denis, F.A., Touhami, A., Dufrêne, Y.F. (2002). *Langmuir* **18**, 9937–9941.

[50] Dorobantu, L.S., Bhattacharjee, S., Foght, J.M., Gray, M.R. (2008). *Langmuir* **24**, 4944–4951.

[51] Hanley, W., McCarty, O., Jadhav, S., Tseng, Y., Wirtz, D., Konstantopoulos, K. (2003). *J. Biol. Chem*. **278**, 10556–10561.

[52] Francius, G., Lebeer, S., Alsteens, D., Wildling, L., Gruber, H.J., Hols, P., De Kaarsmaecker, S., Vanderleyden, J., Dufrêne, Y.F. (2008). *ACS Nano* **2**, 1921–1929.

[53] Pyo, N., Tanaka, S., McNamee, C.E., Kanda, Y., Fukumori, Y., Ichikawa, H., Higashitani, K. (2006). *Colloids Surf. B* **53**, 278–287.

[54] Shinto, H., Hirata, T., Fukasawa, T., Fujii, S., Maeda, H., Okada, M., Nakamura, Y., Furuzono, T. (2013). *Colloids Surf. B* **108**, 8–15.

[55] Vasir, J.K., Labhasetwar, V. (2008). *Biomaterials* **29**, 4244–4252.

[56] Ong, Y.-L., Razatos, A., Georgiou, G., Sharma, M.M. (1999). *Langmuir* **15**, 2719–2725.

[57] Touhami, A., Jericho, M.H., Boyd, J.M., Beveridge T.J. (2006). *J. Bacteriol*. **188**, 370–377.

[58] Zhang, X., Wojcikiewicz, E., Moy, V.T. (2002). *Biophys. J.* **83**, 2270–2279.

[59] Cail, T.L., Hochella, M.F. (2005). *Geochim. Cosmochim. Acta* **69**, 2959–2969.

[60] Kang, S., Elimelech, M. (2009). *Langmuir* **25**, 9656–9659.

[61] Herman, P., El-Kirat-Chatel, S., Beaussart, A., Geoghegan, J.A., Vanzieleghem, T., Foster, T.J., Hols, P., Mahillon, J., Dufrêne, Y.F. (2013). *Langmuir* **29**, 13018–13022.

[62] Benoit, M., Gabriel, D., Gerisch, G., Gaub, H.E. (2000). *Nat. Cell Biol.* **2**, 313–317.

[63] Waar, K., van der Mei, H.C., Harmsen, H.J.M., de Vries, J., Atema-Smit, J., Degener, J.E., Busscher, H.J. (2005). *Microbiology* 151, 2459–2464.

[64] Panorchan, P., George, J.P., Wirtz, D. (2006). *J. Mol. Biol.* **358**, 665–674.

[65] Puecha, P.-H., Poole, K., Knebel, D., Müller, D.J. (2006). *Ultramicroscopy* **106**, 637–644.

[66] Alsteens, D., Van Dijck, P., Lipke, P.N., Dufrêne, Y.F. (2013). *Langmuir* **29**, 13473–13480.

[67] Thwala, J.M., Li, M., Wong, M.C.Y., Kang, S., Hoek, E.M.V., Mamba, B.B. (2013). *Langmuir* **29**, 13773−13782.

5

BACTERIAL INTERACTIONS

Masanori Toyofuku,[1] Yosuke Tashiro,[2] Tomohiro Inaba,[1] and Nobuhiko Nomura[1]

[1]*Graduate School of Life and Environmental Sciences, University of Tsukuba, Tsukuba, Ibaraki 305-8572, Japan*
[2]*Graduate School of Engineering, Shizuoka University, Hamamatsu, Shizuoka, 432-8561 Japan*

5.1 INTRODUCTION

For a long time, bacteria were regarded as isolated cells that do not actively interact with each other. However, more recent findings have revealed that bacteria do interact with each other in several ways. For example, bacteria can communicate with each other by utilizing signaling molecules that coordinate their group behaviors. More recently, membrane vesicles (MVs) that derived from the cell membrane were shown to be involved in bacterial and bacteria-host interactions. These MVs are released from the bacteria and are packed with proteins, DNA, and even cell–cell signaling molecules. MVs are released into the environment and can be shuttled to the neighboring cells. Furthermore, bacteria can dynamically interact with each other by aggregating and forming multicellular biofilms. In the environment, it is assumed that the primary habitat for many bacteria is biofilms. The cell adhesions are usually mediated by extracellular polymers known collectively as an *extracellular polymeric substance* (EPS). EPS is also the key component in biofilm formation that holds the cells together.

Bacterial genetic experiments have greatly enhanced our knowledge of what is involved in these interactions and how such interactions are regulated. Still, biophysical knowledge is limited. Biophysical knowledge should be important to fill the gap of our understanding of what is exactly happening in the interface of these interactions. For instance, it is not clear how the signaling molecules enter and exit the cells or diffuse in different environments. It is not fully understood how MVs pinch off from the cell surface and furthermore how they fuse to the neighboring cells. In biofilm, many EPSs are identified but how they exactly hold tight of the cells is poorly understood. Answering these questions could enhance our knowledge and may also lead to new treatment of the bacteria.

Among many exciting bacterial interactions that have been reported, in this chapter we introduce the basic knowledge in cell–cell communication, MVs, and biofilm. We hope that this chapter would give a general introduction.

5.2 GRAM-POSITIVE AND GRAM-NEGATIVE BACTERIA

The bacteria average 0.5–10 μm in diameter, and certain shapes such as rods, bacilli, and cocci are common in many taxonomic groups. Bacteria can be divided into two major groups with respect to their cell envelope composition: Gram-positive and Gram-negative bacteria, and these bacteria will frequently be referred to as such in this chapter. *Gram-positive bacteria* have an inner membrane that is covered by a thick cell wall consisting of multiple layers of peptidoglycan. Teichoic acids reinforce the peptidoglycan. Gram-negative bacteria have a thinner peptidoglycan,which is covered by an outer membrane. The outer membrane contains lipopolysaccharides (LPSs) in its outer leaflet and phospholipids in its inner leaflet. Between the inner and outer membranes, including the peptidoglycan layer, is the periplasm. The periplasm contains specific enzymes that are not found in the cytoplasmic space. As we will see further, these two groups of bacteria have distinct systems in terms of bacterial interactions.

Encyclopedia of Biocolloid and Biointerface Science, Volume 1, First Edition. Edited by Hiroyuki Ohshima.
© 2016 John Wiley & Sons, Inc. Published 2016 by John Wiley & Sons, Inc.

Generally, both Gram-positive and Gram-negative bacterial cells are negatively charged. Thus, the bacterial cells are often considered as a negatively charged colloidal particles in physical studies of surface interactions. Since the cell surfaces are usually decorated with fiberlike extracellular cell appendages such as flagella, pili, fimbriae, or EPS, the theory of soft particles in *Derjaguin–Landau–Verwey–Overbeek* (DLVO theory) [1] is applied to bacterial cells.

5.3 CELL–CELL COMMUNICATION IN BACTERIA

In cell–cell communication of bacteria, signaling molecules are produced in the environment and are detected by specific receptors that further modulate gene expressions. The main difference between secondary metabolites and signaling molecules is the presence of a receptor that specifically recognizes the molecule (Fig. 5.1). Many of the signaling molecules enhance their own production and are also called *autoinducers* (AIs). AIs accumulate in the environment as cell density increases. Cell–cell communication involving AIs is also called *quorum sensing* (QS), since gene expression is altered when the cell reaches a certain density [2]. Although several cell–cell signaling molecules are known, two main types of signaling molecules have been thoroughly investigated: (1) *N*-acyl homoserine lactones (AHLs) and small peptides [3] (Fig. 5.2). AHLs are produced in Gram-negative bacteria, while many Gram-positive bacteria use small peptides as their cell–cell signaling molecule. In addition to these molecules, a furanosyl borate diester (AI-2) has been shown to be produced by various Gram-negative and Gram-positive bacteria, suggesting that this molecule may represent a universal language used among bacteria. More recently, *diffusible signal factor* (DSF) was shown to be produced in a variety of Gram-negative bacteria. Cell–cell signaling is likely to be widely conserved among bacteria, and novel signaling molecules are yet to be identified.

5.3.1 Cell–Cell Communication in Gram-Negative Bacteria

5.3.1.1 AHL-Mediated QS. AHL is the typical signaling molecule produced by Gram-negative bacteria. It is not universal, but it is estimated that over 100 species of Proteobacteria use AHLs as signaling molecules [4]. The AHL QS systems generally consist of AHL synthetase, the LuxI family enzyme, and a LuxR family AHL receptor-transcriptional regulator [5]. The chemical structure of the AHL signal consists of a homoserine lactone that is usually coupled to fatty-acid chains. The fatty-acid chain varies in length, saturation, and substitution at the C3 position. The variations in the acyl sidechain confer signal specificity that is recognized by their cognate LuxR receptors. Once AHL binds to its cognate LuxR receptor, the LuxR induces or represses their target genes. Target genes include genes that are associated

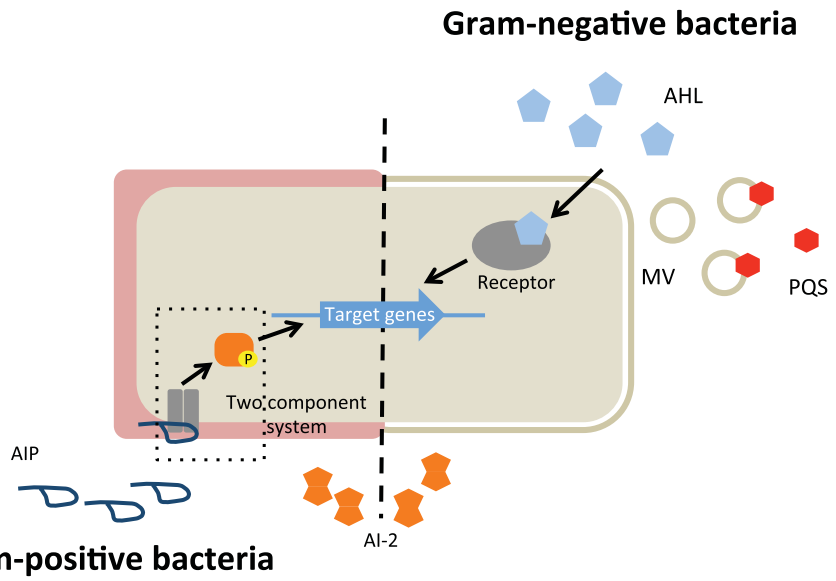


FIGURE 5.1 Cell–cell communication in bacteria. Serected signaling molecules are received by specific receptors. In Gram-negative bacteria, AHL signaling is one of the most widely characterized QS systems. PQS, produced in *P. aeruginosa,* is associated with MVs. Gram-positive bacteria use peptide signals (AIP) as signaling molecules. AIPs are sensed through two component systems. AI-2 is widely used among Gram-negative and Gram-positive bacteria.

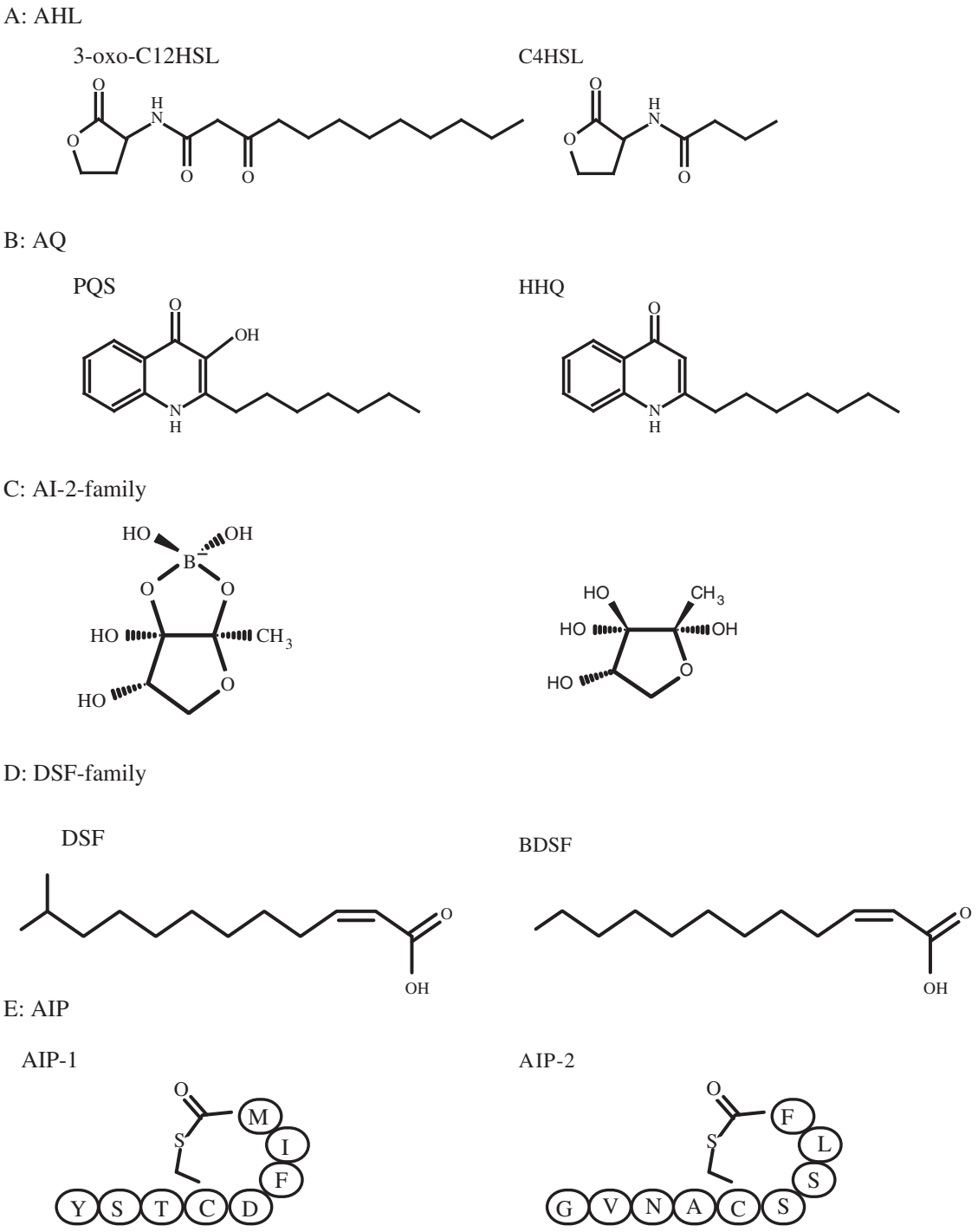


FIGURE 5.2 Chemical structures of selected bacterial cell–cell communication signals.

with biofilm formation, bioluminescence, plasmid transfer, motility, respiration, and virulence factors [6–10].

AHL signaling was first discovered in a marine bacterium *Vibrio fischeri,* which colonize the light organs of a specific squid species. *V. fischeri* produce the light in the light organs of the squid and in response to the bacterial cell density. This light production was found to be mediated by an AHL, 3-oxo-hexanoyl-homoserine lactone (3-oxo-C6HSL), which is produced by the *luxI* gene product [11, 12]. It has been reported that 3-oxo-C6HSL diffuse from the cell by passive diffusion [9]. Like the other AHLs, 3-oxo-C6HSL induces the expression of *luxI* by binding to LuxR. This positive

autoregulation enables the AHL concentration to increase rapidly once it is induced. This allows *V. fischeri* to switch from the low cell density free-living lifestyle from high cell density, host-associated lifestyle.

In some cases such as *Pseudomonas aeruginosa*, QS may regulate up to 300 genes, representing 5% of the genome [13], indicating the huge impact of QS on the cell physiology. *P. aeruginosa* is a ubiquitous environmental bacterium that is also known as an *opportunistic pathogen*. This bacterium is one of the model organisms in QS, which has been studied extensively. In *P. aeruginosa*, two complete QS systems, the *las* system and the *rhl* system, have been identified [5]. Each of these systems is composed of a LuxI and a LuxR family protein. The LuxI family proteins, LasI and RhlI produce *N*-(3-oxododecanoyl)-HSL (3-oxo-C12HSL) or *N*-butyryrl-HSL (C4HSL), respectively. 3-oxo-C12HSL is recognized by LasR and C4HSL is recognized by RhlR, LuxR family proteins. The two QS systems compose a hierarchial regulatory cascade where the *las* sytem positively regulate the *rhl* system. An additional QS system, which uses a chemically distinct type of signals known as the *Pseudomonas* quinolone signal (PQS) is also incorporated in the AHL QS systems. Many virulence factors are positively controlled by QS in *P. aeruginosa*. This has been investigated in various model systems, and the results show that mutants defective in QS are less virulentthan the parent strains [3]. Thus, QS blockers are expected as a strong candidate of therapeutic agents [14]. The QS systems are also affected by environmental conditions through several regulators that enable the bacteria to tune QS in response to the environment [15].

Although homoserine lactone signals typically possess fatty-acid sidechains, a new class of non-fatty-acid-based homoserine lactone signals was discovered in the phototrophic soil bacterium *Rhodopseudomonas palustris* [16]. *R. palustris* produce *p*-coumaroyl homoserine lactone by using *p*-coumaric acid rather than fatty acids. Similar to the fatty-acid sidechain AHLs, *p*-coumaroyl homoserine lactone is recognized by a LuxR family receptor, RpaR. Interstingly, *p*-coumaroyl homoserine lactone is produced from environmental *p*-coumaric acid, which is suggested to be obtained from the plant host. This is unique among all forms of AHL production because the fatty-acid sidechain AHLs are usually produced within the cell. Aryl-homoserine lactone is also produced in *Bradyrhizhobium* sp. BTAi1 and *Silicibacter pomeroyi* DSS-3[16, 17].

5.3.1.2 Quinolone Signal. In *P. aeruginosa,* a 2-heptyl-3-hydroxy-4(1H)-quinolone kwon as PQS has also been identified as a QS molecule [18] (Fig. 5.2). In addition, the precursor of PQS, 2-heptyl-4(1H)-quinolone (HHQ), acts as a signal, although PQS has a much higher affinity with their receptor PqsR [19]. PQS is involved in the regulation of virulence factors, and the molecule also chelates iron, which affects the iron metabolism of the cells [20]. Although the precise mechanism is unclear, PQS was shown to inhibit the anaerobic respiratory activity in *P. aeruginosa* [21]. Structurally related 2-alkyl-4-quinolones (AQs) are known to have antimicrobial activity, and PQS was also shown to repress the growth of Gram-negative and Gram-positive bacteria [22,23]. HHQ production is reported in *Burkholderia* species and in *P. putida*, and chemically related AQs are also produced in a number of *Burkholderia* species [24]. The main AQs produced in *Burkhlderia* species are 3-methyl derivatives of AQs and are implicated to regulate the AHL QS systems [25]. Although mutants deficient in AQ production presented altered colony morphology and increased elastase production in *B. pseduomallei*, the receptor remains to be identified [24].

5.3.2 Cell–Cell Communication in Gram-Positive Bacteria

QS in Gram-positive bacteria also relies on a signaling molecule and a receptor that specifically recognizes the signaling molecule. In many Gram-positive bacteria oligopeptides, called *autoinducing peptides* (AIPs), are used as a signaling molecule (Fig. 5.2) [26]. AIPs are encoded as precursors and become active signal peptides, once they are modulated. The final processed AIPs typically range in size from 5 to 17 amino acid residues and can be linear or cyclized. The signal peptides can also be posttranslationally modified. Because the peptide signals cannot pass the membrane, specialized transporters are required to secrete AIPs. Once secreted, AIPs are detected at the membrane through a two-component system, in which a sensor kinase is located at the membrane, and relay the signal to the intercellular response regulator by phosphorylation.

5.3.3 A Common Language for Gram-Negative and Gram-Positive Bacteria: AI-2

AI-2 is widely produced among Gram-negative and Gram-positive bacteria, indicating its role as a common language [27]. The presence of an interspecies signaling was first suggested by a work in which bioluminescent response of *V. harveyi* was induced by the addition of a supernatant from cultures of other bacteria [28]. The signal that induced this bioluminescent response was AHL-independent and was identified as AI-2 [29, 30]. AI-2 is produced by a spontaneous reaction of a very unstable molecule, 4,5-dihydroxy-2,3-pentanedione (DPD), which is synthesized by LuxS. DPD spontaneously cyclizes into different isomers in solution, and there is a possibility that the AI-2 molecule detected by the bacteria may differ [31, 32] (Fig. 5.2). LuxS homologs have been identified in more than 500 bacterial genomes that have been sequenced [27]. Still, it is not known whether AI-2 is used as a signal in these species, since LuxS has a crucial role in the central metabolic pathway, and AI-2 may be a

metabolic byproduct in some species. To distinguish whether AI-2 is used as a signal or it is a mere byproduct, the presence of a receptor that specifically detects AI-2 is important. So far, three types of receptors–LuxP, LsrB, and Rbs-like receptors–have been identified as being involved in the AI-2 response.

5.4 MEMBRANE VESICLES

Many microorganisms secrete intracellular substances to extracellular milieu to interact with other microbial cells for DNA transfer, small-molecule signaling, and predation. Encapsulation of microorganism-produced substances is an effective way to carry them to other organisms because they are highly concentrated and kept stable against numerous ambient stresses. MVs, which are spherical bilayered structures, ranged from approximately 50 to 250 nm in diameter, and naturally released from microbial cell surfaces of many microorganisms, are used for secretion of many kinds of substances produced in microbial cytoplasm to extracellular milieu (Fig. 5.3a). The observation of MVs in Gram-negative bacteria can be traced back to about the mid-1960s, along with the developments in the electron microscopic analysis [33–35]. MVs are found in every environment, from laboratory cultures, including planktonic and surface-attached biofilm, to natural environments [36, 37]. Conventionally, it has been assumed that MVs are liberated from only Gram-negative bacteria, but more recent studies have indicated that MV production is conserved among organisms spanning both prokaryotes and eukaryotes: Gram-negative and Gram-positive bacteria, archaea, and fungi [38]. MV had been considered as one secretion mechanism that is important for delivering certain toxic proteins, and studies of these vesicles have concentrated on pathogenic bacteria, but more recent studies indicate that nonpathogenic microbes also secrete MVs [39–41]. Because MV production is conserved among many microorganisms, it is likely to be crucial to microbial life.

5.4.1 Components of MVs

The components of MVs were studied mainly in Gram-negative bacteria. In Gram-negative bacteria, MVs consist mainly of phospholipids, LPS, outer-membrane proteins (OMPs), and periplasmic components.

5.4.1.1 Proteins Associated with MVs. The components of vesicular proteins have been developed by biochemical analyses. MVs derived from Gram-negative bacteria contain mainly OMPs and periplasmic proteins, but also contain proteins localized at inner membrane and cytoplasm [42, 43]. In Gram-negative pathogenic bacteria, many extracellular virulence factors are also packaged in MVs. In Gram-positive bacteria, extracellular proteins, membrane proteins, and cytoplasmic proteins are contained in purified vesicles. In many cases, the MV protein profile is quite different from that of cells, suggesting that a specific sorting mechanism may exist for vesicular proteins.

5.4.1.2 Phospholipids Associated with MVs. Phospholipid is also one of major components of MVs. The phospholipid consists of two fatty acids and a phosphate group attached to a glycerol backbone. Both components of the phosphate group and fatty acid in MVs are different from

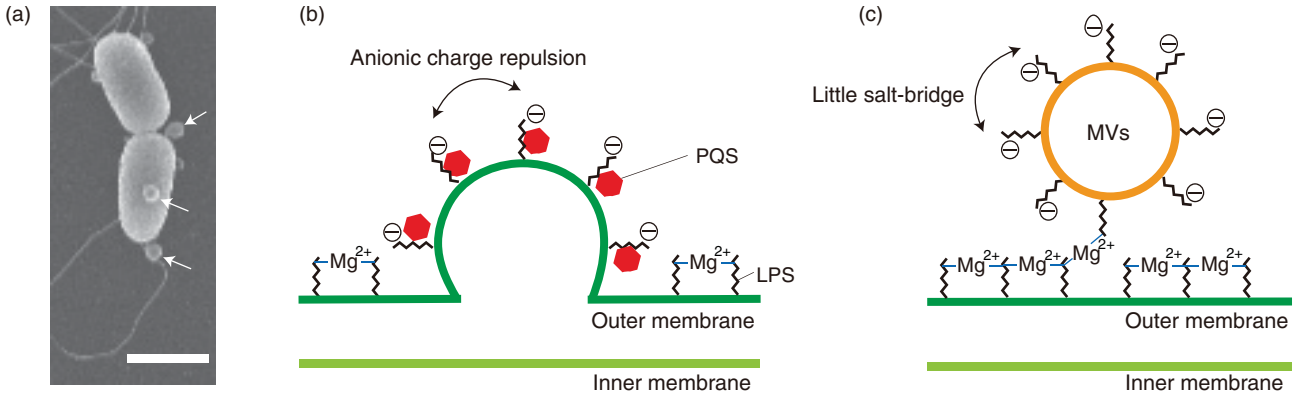


FIGURE 5.3 (a) Membrane vesicle production in *P. aeruginosa*. Bar indicates 1 μm. (b) One of the proposed models for MV formation in Gram-negative bacteria. Divalent cations usually stabilize outer membrane by forming salt bridges between negative charged phosphates of neighboring LPS. PQS strongly interacts with LPS, and anionic repulsion enhances membrane blebbing. (c) A proposed model of interaction of MVs with Gram-negative bacterial cells. Because of loose packing of anionic LPS, there is likely little salt bridge between neighbor LPSs in MVs. It is plausible that LPS of MVs is easily salt-bridged to the surface of cellular outer membrane.

those of the cells in *P. aeruginosa*. The major phosphate groups are phosphatidylethanolamine (PE), phosphatidylglycerol (PG), and phosphatidylcholine (PC), and PE is usually most abundant in Gram-negative bacterial cells. On the other hand, MVs contain a high ratio of PG in *P. aeruginosa* [41,44]. The components of fatty acids are also different from cellular outer membrane and MVs in *P. aeruginosa* and other *Pseudomonas* strains; the percentage of stearic acids is highest in MVs in *P. aeruginosa* [41,44,45]. Abundant saturated and longer-chain fatty acids are known to decrease membrane fluidity [46], and MV membrane is considered to be more rigid than the cellular OM. Analyses using artificial lipid vesicles showed that lipid chain length is critical in achieving stability of vesicles [47]. These results suggest that abundant stearic acids contribute to the stability of MVs. Furthermore, fatty-acid profiles of extracellular MVs are different from cells in Gram-positive bacteria [48], MVs seems to be liberated from specific region on cellular membrane.

5.4.1.3 Other Components in MVs. The lumens of MVs can contain cytoplasmic components, containing DNA and RNA [49–52]. DNA is not only associated with the MV surface but is also localized inside of MVs [52], and DNA is protected from degradation by environmental stresses such as DNase. In *P. aeruginosa*, both chromosomal DNA and plasmids are packaged in MVs.

MVs also possess a cell–cell communication signal, PQS in *P. aeruginosa* [53] (Fig. 5.1). PQS is strongly associated with LPS on bacterial surfaces and stimulates MV liberation. Although hydrophobic substances seem to have difficulty in dissemination between bacterial cells, MVs serve as a mediator of the hydrophobic signal, PQS.

5.4.2 Biological Roles of MVs

It has been hitherto proposed that there exist multiple functions of MV liberation for microbes. MVs consistute a unique secretion system that transfers cellular substances to the environment, and some MVs fuse to other cells. Biological roles of MVs are roughly divided but not limited to the following three functions: delivery system, secretion of unnecessary substances, and maintenance of biofilm structure.

5.4.2.1 Delivery System. A primary biological role of MVs is trafficking vehicles of substances from donor cells to recipient cells that can be both prokaryotes and eukaryotes. Many pathogenic bacteria produce MVs, and several kinds of toxins are associated with MVs. MVs serve as vehicles for delivering these toxins to eukaryotic target cells. Because MVs are coated with LPS and phospholipids, which act as ligands against eukaryotic cells, MVs help to deliver toxic substances from bacterial cells to host cells effectively. In microbial communities, MVs also have a predatory role as they contain peptidoglycan hydrolase and induce cell lysis. It has been shown that MVs derived from various Gram-negative bacteria including *P. aeruginosa* possess antimicrobial activity against both Gram-negative and Gram-positive bacteria [54, 55].

On the other hand, MVs also play a role in bacterial communication. Although hydrophobic PQS rarely freely diffuses out of bacterial cells in *P. aeruginosa*, MVs serve as a shuttle for this compound [53]. Because PQS regulates motility, biofilm formation, and many virulence factor productions in *P. aeruginosa*, MVs help intraspecies communication.

DNA transfer from cell to cell via MVs has also been observed in Gram-negative bacteria and archaea [49, 56]. Packing DNA in MVs prevents DNA degradation from DNase in the environment and facilitates long-distance delivery of DNA from donor to recipients. As only intraspecies DNA transfers via MVs have been observed, it remains unknown whether interspecies DNA transfer actually occurs.

5.4.2.2 Secretion of Unnecessary Substances. MVs can also affect disposal of unnecessary substances accumulated in microbial cells. Accumulation of unnecessary compounds in the periplasm exerts a turgor pressure of the cell envelope in Gram-negative bacteria. For example, peptidoglycan fragments accumulated in the periplasmic spaces increase turgor pressure and MVs are discharged [57]. The production of MVs is also induced by internal damage such as the accumulation of misfolded envelope proteins or internal and external stress, which ultimately leads to cell death [58–63]. In addition, high concentrations of an antibiotic, such as gentamicin, and persistent organic pollutants, such as toluene, increase MV formation, and these compounds are highly concentrated in liberated MVs [64–66]. In this way, MVs can also function in defensive roles to survive by responding to stress and eliminating unnecessary substances from the cells.

5.4.2.3 Maintenance of Biofilm Structure. The third biological role of MVs is maintenance of biofilm structure formed by microbes. Biofilms are composed of cells and EPS that include exopolysaccharides, proteins, DNA, and lipids. The existence of MVs in biofilms has been confirmed in both mixed-environment and laboratory-generated single-species biofilms [37,67–70]. It is known that extracellular DNA is a critical matrix component of biofilm and maintains the stability of biofilm against environmental stresses [71]. MVs possess extracellular DNA on their surfaces, and MV surface-bound DNA in biofilms appears to be an electrostatic bridging component that is central to the interaction among MVs, bacterial cells, and other biofilm matrix components [72].

5.4.3 Surface Characteristics of MVs

The surface characteristics of MVs have been studied using Gram-negative bacteria. Similar to the cell surface, MV surface possess negative zeta potential [73]. On the cell

surface, LPS is negatively charged, and salt bridges consisting of divalent cations such as Mg^{2+} and Ca^{2+} are frequently formed between adjacent LPS molecules (Fig. 5.3b). PQS interacts strongly with LPS, and ionic interactions between PQS and LPS in the outer membrane enhance the anionic repulsion between neighboring LPS molecules [74]. Therefore, PQS enhances MV formation in Gram-negative bacteria [53, 75]. Particularly in *P. aeruginosa*, MVs secreted in the stationary phase possess more negative charges than that in the exponential phase [73], presumably due to the incorporation of PQS that is synthesized in the stationary phase.

Negatively charged MVs facilitates interaction with bacterial cells (Fig. 5.3c). Because MVs have higher surface curvature than the cells, the LPS terminal oligosaccharide sidechain, which is charged, is loosely packaged and the components are separated from each other. For loosely packed LPS, there is slight salt bridging by divalent cations such as Mg^{2+} and Ca^{2+} between adjacent LPSs. Because of cation depletion on MV surface, it is likely that the anionic MV surface would become salt bridged to cations around bacterial cells [54]. Indeed, negatively charged MVs rather than relatively neutral MVs interact easily with bacterial cells [73]. In this way, MV surface charge is a critical factor that affects the interaction with bacterial cells through physiochemical forces. Still, it remains largely unknown, how exterior MVs are incorporated to microbial cells in detail.

5.4.4 Future Perspectives in MV Research

Biochemical and biological studies have developed our understanding of the physiological roles of bacterial MVs, and growing evidence suggests that MVs are essential for microbial survival and pathogenesis. However, previous biological studies have been limited to obtaining comprehensive information for understanding their physicochemical behaviors and the mechanism of their formation. Surfaces of MVs are coated with several substances, including polysaccharides, pili, extracellular proteins, and extracellular DNA, and thus it is difficult to directly apply kinetic and equilibrium models, contrary to vesicles composed of pure phospholipids. Even though that is the case, physicochemical analyses are expected to stimulate the developments of comprehensive understanding in dynamics of bacterial MVs.

5.5 BIOFILM FORMATION

Biofilms are bacterial multicellular consortia covered with an EPS matrix that is often selfproduced. It is thought that the primary habitat for many of the bacteria is biofilms. Biofilms are not necessarily attached to the surface, but floating cell aggregates known as *flocs* or *activated sludge* share common characteristics with biofilms and can also be categorized as certain types of biofilms [76–78] (Fig. 5.4). Practical applications of biofilms include biological wastewater as activated sludge. On the other hand, they have negative effects on human activity and are associated with a wide range of problems in industry and infections. Until recently, most of our knowledge in bacteriology has been based on the studies of planktonic cells, but it is well known that biofilms differ from their planktonic counterpart. For instance, biofilms have increased antibiotic resistance, compared to planktonic

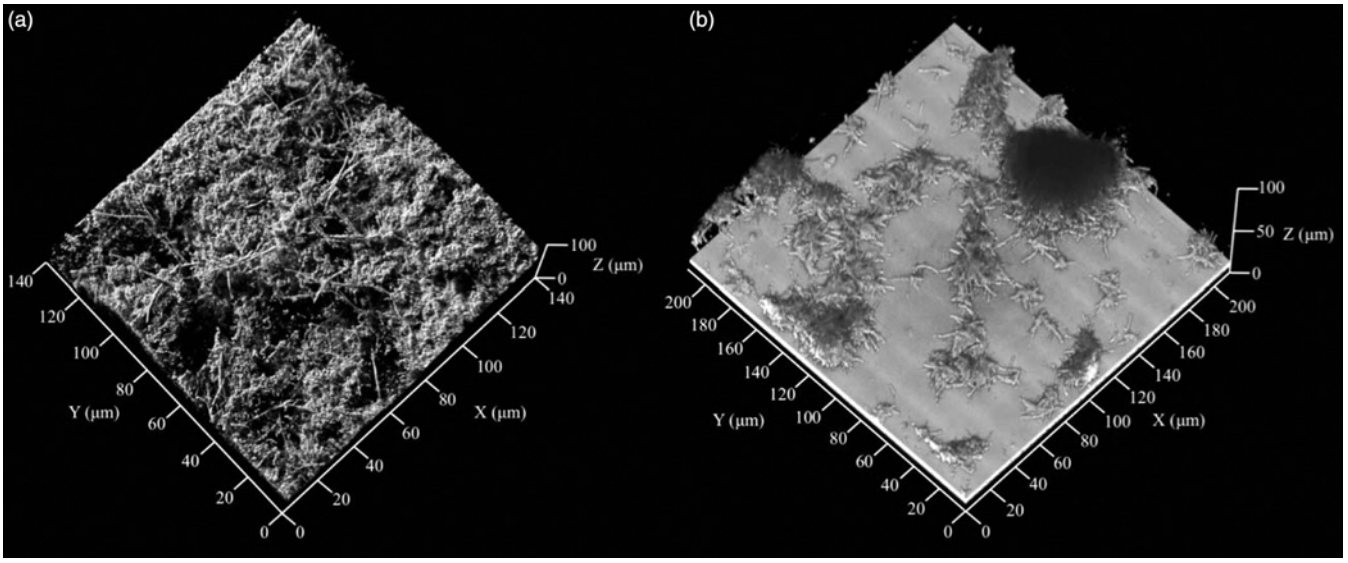


FIGURE 5.4 Microscopic image of surface-attached biofilms and bacterial aggregates visualized by confocal microscopy. (a) Surface-attached biofilms. Oral biofilm was formed on hydroxyapatite disk. The projection shows field of 140 × 140 μm (*x*–*y*) as indicated. (b) Bacterial aggregates of *Rhodococcus* sp. strain SD-74. The projection shows field of 220 × 220 (*x*–*y*). For related informations please see ref. 108.

cells, making it much more difficult to eradicate biofilms [79]. Hence there are wide demands for treating biofilms, and a better understanding of biofilms is necessary to tackle these problems.

5.5.1 Surface-Attached Biofilms

Surface-attached biofilms are relatively well studied compared to cell aggregates. Typically, surface attached biofilms undergo five stages [80]:

1. The cells attach to the surface reversibly (reversible attachment) at the pole of the cells. Fiber-like structures such as flagella, pili, and fimbriae are involved in this process.
2. Cells lie on the surface and attach to it irreversibly (irreversible attachment). EPS such as DNA, proteins, and LPS assist the adhesion between the cell and the surface.
3. Cells replicate and grow into microcolonies. At this stage, the cells are encapsulated in EPS that adhere the cells together.
4. Eventually, microcolonies grow into matured biofilms covered with EPS.
5. The biofilm mode of life terminates when some of the cells switch their lifestyle from biofilm to planktonic cells and disperse from the biofilms.

While physical properties of the surface determine whether the cells are able to attach to the surface, bacteria control the attachment by regulating motility and EPS production or cell appendages involved in surface attachment. With a combination of surface engineering technologies, the surface properties that effect cell attachment have been extensively studied. These studies not only should help us better understand the mechanism of cell–surface attachment but also may lead to design of materials that repel bacteria.

5.5.1.1 Surface Properties Affecting Bacterial Attachment.

Electrostatic and Hydrophobic Interactions. The interactions between the bacteria and the surface are primarily influenced by electrostatic and van der Waals forces [81]. Since most bacteria have a negative charged cell surface, bacteria are attracted to positively charged surfaces and electrostatic repulsion occurs with negatively charged surfaces. Electrostatic repulsion between the cell and the negatively charged surface can be overcome by extracellular appendages of the cells such as flagella, pili, fimbriae, and EPS that decorate the cell surface. In this case, the interaction of bacterial cells and the surface follow the theory of soft particles in DLVO theory proposed by Ohshima et al. [1]. After overcoming the electrostatic interactions, hydrophobic interactions influence the attachment of bacteria to the surface. Many bacteria prefer hydrophobic surfaces, while some bacteria prefer hydrophilic surfaces. It is important to note that bacteria may alter the surface property by secreting EPS or proteins.

Surface Roughness. In addition to the physicochemical properties of the surface, surface roughness has also been shown to affect cell attachment. Recent studies show that two surfaces with chemically identical properties may exhibit different cell attachment patterns, due to differences in surface topographies. In general, rougher surfaces in micrometric scale may support bacterial attachment by offering higher surface area for attachment and also protecting the cells from unfavorable conditions such as shear forces [82]. The effect of nanometer-scale roughness is more complex. Some bacteria attach better to nanoscale rough materials, while others attach better to nanometer-smooth material. A recent study shows that bacteria alter their cell appendage depending on the nanoscale surface topography, presumably to achieve a stronger and more stable attachment [83]. The study suggests that bacteria may sense the surface and topography and utilize different mechanisms to attach. How bacteria sense the surface topography is poorly understood and would be an interesting issue for future works.

5.5.1.2 Biological Regulation in Biofilm Formation.

c-di-GMP: The Central Biofilm Regulatory System. As physicochemical interactions determine the cell attachment to the surface, bacteria can decide whether to attach to or leave the surface by controlling the expression of cell appendages and motility. In a number of bacteria, including the biofilm model organisms, *P. aeruginosa*, a intracellular second messenger, bis-(3′-5′)-cyclic dimeric guanosine monophosphate (c-di-GMP), control EPS and motility in opposite directions [84]. In other words, when the c-di-GMP level is high, EPS production is stimulated and motility is inhibited, thus allowing the cells to irreversibly attach to surfaces and form biofilms. On the other hand, low c-di-GMP levels induce motility and inhibit EPS production. While c-di-GMP levels are elevated during formation of biofilms, they become low when cells disperse from biofilms. c-di-GMP levels are controlled by regulating the enzymes responsible for the production and degradation of c-di-GMP. There are several proteins involved in this process that are usually involved in sensing the changes in environmental conditions. These environmental conditions include nitric oxide, carbon and nitrogen limitation, and oxygen limitation [85]. Taken together, the c-di-GMP signaling network allows the bacteria to sense the environment and decide whether to settle down to form a biofilm. Hence bacteria have a sophisticated regulatory system that controls the bacterial adhesion to the surface.

Effect of Cell–Cell Communication on Biofilms. While c-di-GMP functions as part of the central regulatory system in biofilm formation, cell–cell communication has also been observed to affect biofilm formation in both Gram-negative and Gram-positive species.

In Gram-negative species, typically AHL-based QS has a positive effect on biofilm formation. For instance, in *P. aeruginosa,* a *lasI* mutant defective in 3-oxo-C12HSL productions, build a poorly structured biofilms compared to that of the wild type [6]. The *lasI* mutant biofilm was more sensitive to detergent removal. Because AHLs control diverse genes, the AHLs may affect biofilm formation through multiple pathways, such as the regulation of motility, respiration, and production of biosurfactants [86]. The studies in *P. aeruginosa* also indicate that the effects of AHLs on biofilm formation can be conditional, and may act differently due to the environmental condition [87].

In Gram-positive bacteria, the AIP signals affect biofilm in a species-dependent manner. *Staphylococcus aureus* is a leading cause of nosocomial infections, and many infections are related to biofilm formation. In *S. aureus*, AIP is encoded by *agrD*. The inactivation of the Agr QS system negatively regulated biofilm formation and is involved in biofilm dispersal [88]. In contrast, the Agr system positively control cell adherence biofilm formation in *Lactobacillus plantarum* and *Listeria monocytogenes* [89, 90].

Biofilms comes to an end when the cells inside biofilms disperse from the biofilms. Recent findings of intercellular signals that facilitate biofilm dispersal indicate that the cells can initiate this event in a coordinated fashion. *Diffusible signal factor* (DSF) is responsible for inducing cell dispersal in Gram-negative bacteria. DSF is a fatty-acid molecule. For example, *cis*-11-mehyl-2-dodecenoic acid is known as a DSF involved in dispersal in *Xanthomonas campestris* [91] (Fig. 5.2). Rpf sensors respond to the DSF signal and further control the gene expressions. Addition of DSF to *X. campestris* induces the dispersion of aggregates in the DSF deficient mutant, but not in the sensor-deficient mutant. A DSF-related signal, BDSF, has been characterized in *Burkholderia cenocepacia* [92] (Fig. 5.2). In *B. cenocepacia,* BDSF signaling has been linked with c-di-GMP [93]. The presence of BDSF results in the reduction of intercellular c-di-GMP levels, which, in turn, results in altered biofilm formation. To note, in *B. cenocepacia* H111, elevated c-di-GMP leads to reduction of surface associated biofilm production, which is an exception of the typical c-di-GMP regulation of biofilm. The presence of DSF family signal among phylogenetically distinct bacteria leads to the idea that this signal may serve as an interspecies signal.

5.5.2 Bacterial Aggregates

Biofilms that are not attached to the surface are usually referred to as *cell aggregates* or *flocs*. In addition, the biofilms formed in the liquid-air interface are called *pellicles*. In contrast to the surface-attached biofilms, where the initial step of biofilm formation is the attachment to the substratum, it is assumed that the bacterial aggregation is initiated by clustering of planktonic cells. Several factors that initiate cell clustering have been studied. As we will see, the underlining physical interactions are common in many aspects, between surface-attached biofilms and free-floating cell aggregates. However, some bacteria form surface-attached biofilms, while others form cell aggregates and what determines these lifestyles are not fully understood.

5.5.2.1 EPS Involved in Cell Aggregations. Since bacteria are negatively charged, cells must overcome the negative repulsion between the cells. As in the case of surface-associated biofilms, cell appendages are likely to help overcome the electrostatic repulsion. Degradation of the EPS usually results in the decomposition of the cell aggregates, suggesting that the EPS is also important in holding the cells together.

One of the main components of the EPS matrix is polysaccharides, which have been shown to play important roles in the formation of bacterial aggregation. For instance, in *Azospirillum brasilense*, extracellular polysaccharides and capsular polysaccharide, which is located at the outermost of the cell membrane, is important for cell aggregation [94]. In streptococci, highly organized hyaluronic acid in the capsule serves as extracellular polysaccharides that support cell aggregation [95].

Besides polysaccharides, nucleic acids such as deoxyribonucleotide (DNA) and ribonucleotide (RNA) are often found in the EPS. In many bacteria, extracellular DNA (eDNA) is produced by cell lysis that is induced by autolysis [96–98]. eDNA has been reported as one of the major components in surface-associated biofilms [99]. In line with these observations, it is reported that eDNA is involved in bacterial aggregation [100]. In *Micrococcus halodenitrificans* and *Vibrio costicolus* growing in nutritionally poor media, eDNA is secreted to the environment to maintain the cell aggregates [101]. The eDNA from different sources can stimulate bacterial aggregation, and the eDNA does not necessarily have to be self-produced [102]. Rather than the source of DNA, physicochemical factors such as the concentration and the length of eDNA is important for cell aggregation. Furthermore, thermodynamic analysis indicate that eDNA causes acid–base interaction between *S. epidermidis* cells that leads to cell aggregation [100].

5.5.2.2 Hydrophobic Interactions. A number of extracellular substances that are highly hydrophobic are reported to support cell aggregations. In *Lactobacillus acidophilus*, the S-layer protein is important for auto- or coaggregation with other bacteria [103]. The S layer is located at the outermost of the cell and consists of protein and glycoprotein. In

L. acidophilus, the S-layer protein increases the hydrophobicity of the cell surface, leading to the aggregation [104]. In *L. coryniformis,* it is known that a cell surface protein Cpf mediate coaggregation with other bacteria. Although the main biological function of Cpf is still unknown, Cpf exhibits a high content of hydrophobic amino acid, which is important for coaggregation with other bacteria. These findings suggest that the hydrophobicity of the cell surface is an important factor for bacterial aggregation.

5.5.2.3 Target-Specific Aggregation. Cell aggregations mediated by EPS or hydrophobic cells are unspecific events where, basically, any bacteria that may physically interact can coaggregate. In contrast, specific interactions that select their target cells for aggregation are reported. *Escherichia coli* require a specific protein to autoaggregate and adhere to host intestinal cells. The well-characterized aggregation-related protein referred to as an *autotransporter protein* is a membrane-associated protein that is transported by itself and displayed on cell membrane. The autotransporters antigen 43 and AIDA have a self-recognizing domain, and antigen 43–AIDA interactions mediate autoaggregation by binding specifically to each other [105, 106]. In *Neisseria meningitides,* a pilinlike protein PilX was shown to be essential for cell aggregation [107]. Cell aggregates were formed among the cells that possess PilX, whereas PilX-deficient mutants were not able to form aggregates with the wild-type strain. This result indicates PilX is required for each cells in the aggregates.

In the oral environment, tooth-associated biofilms are well known as dental plaques, which are formed by coaggregation of diverse oral bacteria [108, 109]. The polymicrobial aggregations is not a random event, but is well organized, and the constituent bacteria have specific partners with which to coaggregate. Lectins are one of the factors that are known to be involved in these specific aggregation events [110]. Lectins are carbohydrate-inding proteins, and each lectin has a specific target carbohydrate, thus allowing it to recognize the cell surfaces. Lectins are also involved in adhesion to host cell in many cases of infection as well as bacterial aggregations. In the case of *Streptococcus mutans,* a primary causative bacterium of the dental cavities, extracellular glucan, is required for cell aggregation. *S. mutans*, for instance, have a membrane-associated glucan-binding protein that specifically interacts with glucans present in the EPS [111]. This binding between glucans and cell associated glucan binding proteins causes aggregation.

5.6 CONCLUDING REMARKS

Bacteria interact with each other in many ways, such as through small molecules, MVs, and cell appendages that lead to the formation of biofilms. Much of our present understanding of these events is based on single-species pure culture. However, the real environment is a more complex polymicrobial world, where many bacterial species coexsit and interact with one another. Our understanding of such a polymicrobial world is just beginning. One of the ways to handle such a complex system may be physical approaches, where bacteria are often considered as particles. A successful application of the physical control of polymicrobial system is in wastewater treatment. Many bacteria are involved in this process to purify the water. In this process, physical control of the cell aggregates (also called *activated sludge*) is performed to regulate the aggregation of the cells. Aluminum salts, such as aluminum sulfate and poly(aluminum chloride), are added to the plant to neutralize the negative charge of the cells and therefore stimulate cell aggregation. Importantly, unlike stable colloidal particles, bacteria can alter their surface in response to the environment. Therefore, understanding both the biological and physical aspects of the bacteria would go hand-in-hand with our strides to obtain a deeper understanding of bacterial interactions and to develop further applications.

REFERENCES

[1] Ohshima, H. (1995). Electrophopretic mobility of soft particles. *Electrophoresis* **16**(8), 1360–1363.

[2] Fuqua, W.C., Winans, S.C., Greenberg, E.P. (1994). Quorum sensing in bacteria: The LuxR-LuxI family of cell density-responsive transcriptional regulators. *J. Bacteriol.* **176**(2), 269–275.

[3] Rutherford, S.T., Bassler, B.L (2012). Bacterial quorum sensing: Its role in virulence and possibilities for its control. *Cold Spring Harb. Perspect. Med.* **2**(11), a012427.

[4] Shrout, J.D., Nerenberg, R. (2012). Monitoring bacterial twitter: Does quorum sensing determine the behavior of water and wastewater treatment biofilms? *Environ. Sci. Technol.* **46**(4), 1995–2005.

[5] Schuster, M., Sexton, D.J., Diggle, S.P., Greenberg, E.P. (2013). Acyl-homoserine lactone quorum sensing: from evolution to application. *Annu. Rev. Microbiol.* **67**, 43–63.

[6] Davies, D.G., Parsek, M.R., Pearson, J.P., Iglewski, B.H., Costerton, J.W., Greenberg, E.P. (1998). The involvement of cell-to-cell signals in the development of a bacterial biofilm. *Science* **280**(5361), 295–298.

[7] Eberl, L., Winson, M.K., Sternberg, C., Stewart, G.S., Christiansen, G., Chhabra, S.R., Bycroft, B., Williams, P., Molin, S., Givskov, M. (1996). Involvement of N-acyl-L-hormoserine lactone autoinducers in controlling the multicellular behaviour of *Serratia liquefaciens*. *Mol. Microbiol.* **20**(1), 127–136.

[8] Toyofuku, M., Nomura, N., Fujii, T., Takaya, N., Maseda, M., Sawada, I., Nakajima, T., Uchiyama, H. (2007). Quorum sensing regulates denitrification in *Pseudomonas aeruginosa* PAO1. *J. Bacteriol.* **189**(13), 4969–4972.

[9] Kaplan, H.B., Greenberg, E.P. (1985). Diffusion of autoinducer is involved in regulation of the *Vibrio fischeri* luminescence system. *J. Bacteriol.* **163**(3), 1210–1214.

[10] Piper, K.R., Beck von Bodman, S., Farrand, S.K. (1993). Conjugation factor of *Agrobacterium tumefaciens regulates* Ti plasmid transfer by autoinduction. *Nature* **362**(6419), 448–450.

[11] Engebrecht, J., Nealson, K., Silverman, M. (1983). Bacterial bioluminescence: Isolation and genetic analysis of functions from *Vibrio fischeri*. *Cell.* **32**(3), 773–781.

[12] Eberhard, A., Burlingame, A.L., Eberhard, C., Kenyon, G.L., Nealson, K.H., Oppenheimer, N.J. (1981). Structural identification of autoinducer of *Photobacterium fischeri luciferase*. *Biochemistry* **20**(9), 2444–2449.

[13] Whiteley, M., Lee, K.M., Greenberg, E.P. (1999). Identification of genes controlled by quorum sensing in *Pseudomonas aeruginosa*. *Proc. Natl. Acad. Sci. USA* **96**(24), 13904–13909.

[14] Hentzer, M., Wu, H., Andersen, J.B., Riedel, K., Rasmussen, T.B., Bagge, N., Kumar, N., Schembri, M.A., Song, Z., Kristoffersen, P., Manefield, M., Costerton, J.W., Molin, S., Eberl, L., Steinberg, P., Kjelleberg, S., Høiby, N., Givskov, M. (2003). Attenuation of *Pseudomonas aeruginosa* virulence by quorum sensing inhibitors. *EMBO J.* **22**(15), 3803–3815.

[15] Williams, P., Cámara, M. (2009). Quorum sensing and environmental adaptation in *Pseudomonas aeruginosa*: A tale of regulatory networks and multifunctional signal molecules. *Curr. Opin. Microbiol*. **12**(2), 182–191.

[16] Schaefer, A.L., Greenberg, E.P., Oliver, C.M., Oda, Y., Huang, J.J., Bittan-Banin, G., Peres, C.M., Schmidt, S., Juhaszova, K., Sufrin, J.R., Harwood, C.S. (2008). A new class of homoserine lactone quorum-sensing signals. *Nature* **454**(7204), 595–599.

[17] Ahlgren, N.A., Harwood, C.S., Schaefer, A.L., Giraud. E., Greenberg, E.P. (2011). Aryl-homoserine lactone quorum sensing in stem-nodulating photosynthetic bradyrhizobia. *Proc. Natl. Acad. Sci. USA* **108**(17), 7183–7188.

[18] Pesci, E.C., Milbank, J.B., Pearson, J.P., McKnight, S., Kende, A.S., Greenberg, E.P., Iglewski, B.H. (1999). Quinolone signaling in the cell-to-cell communication system of *Pseudomonas aeruginosa*. *Proc. Natl. Acad. Sci. USA* **96**(20), 11229–11234.

[19] Xiao, G., Déziel, E., He, J., Lépine, F., Lesic, B., Castonguay, M.H., Milot, S., Tampakaki, A.P., Stachel, S.E., Rahme, L.G. (2006). MvfR, a key *Pseudomonas aeruginosa* pathogenicity LTTR-class regulatory protein, has dual ligands. *Mol. Microbiol.* **62**(6), 1689–1699.

[20] Diggle, S.P., Matthijs, S., Wright, V.J., Fletcher, M.P., Chhabra, S.R., Lamont, I.L., Kong, X., Hider, R.C., Cornelis, P., Cámara, M., Williams, P. (2007). The *Pseudomonas aeruginosa* 4-quinolone signal molecules HHQ and PQS play multifunctional roles in quorum sensing and iron entrapment. *Chem. Biol.* **14**(1), 87–96.

[21] Toyofuku, M., Nomura, N., Kuno, E., Tashiro, Y., Nakajima, T., Uchiyama, H. (2008). Influence of the *Pseudomonas quinolone* signal on denitrification in *Pseudomonas aeruginosa*. *J. Bacteriol.* **190**, 7947–7956.

[22] Hoffman, L.R., Déziel, E., D'Argenio, D.A., Lépine, F., Emerson, J., McNamara, S., Gibson, R.L., Ramsey, B.W., and Miller, S.I. (2006). Selection for *Staphylococcus aureus* small-colony variants due to growth in the presence of *Pseudomonas aeruginosa*. *Proc. Natl. Acad. Sci. USA* **103**((252), 19890–19895.

[23] Toyofuku, M., Nakajima-Kambe, T., Uchiyama, H., and Nomura, N. (2010). The effect of a cell-to-cell communication *molecule*, *Pseudomonas* quinolone signal (PQS), produced by *P. aeruginosa* on other bacterial species. *Microbes Environ*. **25**(1), 1–7.

[24] Diggle, S.P., Lumjiaktase, P., Dipilato, F., Winzer, K., Kunakorn, M., Barrett, D.A., Chhabra, S.R., Cámara, M., Williams, P. (2006). Functional genetic analysis reveals a 2-alkyl-4-quinolone signaling system in the human pathogen *Burkholderia pseudomallei* and related bacteria. *Chem. Biol.* **13**(7), 701–710.

[25] Vial, L., Lépine, F., Milot, S., Groleau, M.C., Dekimpe, V., Woods, D.E., Déziel, E. (2008). *Burkholderia pseudomallei, B. thailandensis,* and *B. ambifaria* produce 4-hydroxy-2-alkylquinoline analogues with a methyl group at the 3 position that is required for quorum-sensing regulation. *J. Bacteriol.* **190**(15), 5339–5352.

[26] Dunny, G.M., Leonard, B.A. (1997). Cell-cell communication in gram-positive bacteria. *Annu. Rev. Microbiol.* **51**, 527–564.

[27] Pereira, C.S., Thompson, J.A., Xavier, K.B, (2013). AI-2-mediated signalling in bacteria. *FEMS Microbiol. Rev.* **37**(2), 156–181.

[28] Greenberg, E.P., Hastings, J.W., Ulitzur, S. (1979). Induction of luciferase synthesis in *Beneckea harveyi* by other marine bacteria. *Arch. Microbiol.* **120**(2), 87–91.

[29] Bassler, B.L., Wright, M., Showalter, R.E., Silverman, M.R. (1993). Intercellular signalling in *Vibrio harveyi: S*equence and function of genes regulating expression of luminescence. *Mol. Microbiol.* **9**(4), 773–786.

[30] Bassler, B.L., Wright, M., Silverman, M.R. (1994). Sequence and function of LuxO, a negative regulator of luminescence in *Vibrio harveyi*. *Mol. Microbiol.* **12**(3), 403–412.

[31] Chen, X., Schauder, S., Potier, N., Van Dorsselaer, A., Pelczer, I., Bassler, B.L., Hughson, F.M. (2002). Structural identification of a bacterial quorum-sensing signal containing boron. *Nature* **415**(6871), 545–549.

[32] Miller, S.T., Xavier, K.B., Campagna, S.R., Taga, M.E., Semmelhack, M.F., Bassler, B.L., Hughson, F.M. (2004). *Salmonella typhimurium* recognizes a chemically distinct form of the bacterial quorum-sensing signal AI-2. *Mol. Cell* **15**(5), 677–687.

[33] Bladen, H.A., Waters, J.F. (1963). Electron microscopic study of some strains of *Bacteroides*. *J. Bacteriol.* **86**(6), 1339–1344.

[34] Bayer, M.E., Anderson, T.F. (1965). The surface structure of *Escherichia coli*. *Proc. Natl. Acad. Sci. USA* **54**(6), 1592–1599.

[35] Chatterjee, S.N., Das, J. (1967). Electron microscopic observations on the excretion of cell-wall material by *Vibrio cholerae*. *J. Gen. Microbiol.* **49**(1), 1–11.

[36] Beveridge, T. (1999). Structures of gram-negative cell walls and their derived membrane vesicles. *J. Bacteriol.* **181**(16), 4725–4733.

[37] Beveridge, T.J., Makin, S.A., Kadurugamuwa, J.L., Li, Z. (1997). Interactions between biofilms and the environment. *FEMS Microbiol Rev.* **20**(3–4), 291–303.

[38] Deatherage, B.L., Cookson, B.T. (2012). Membrane vesicle release in bacteria, eukaryotes, and archaea: A conserved yet underappreciated aspect of microbial life. *Infect. Immun.* **80**(6), 1948–1957.

[39] Kuehn, M., Kesty, N. (2005). Bacterial outer membrane vesicles and the host-pathogen interaction. *Genes Devel*.**19**(22), 2645–255.

[40] MacDonald, I.A., Kuehn, M.J. (2012). Offense and defense: Microbial membrane vesicles play both ways. *Res. Microbiol.* **163**(9), 607–618.

[41] Tashiro, Y., Uchiyama, H., Nomura, N. (2012). Multifunctional membrane vesicles in *Pseudomonas aeruginosa*. *Environ. Microbiol.* **14**(6), 1349–1362.

[42] Lee, E., Bang, J., Park, G., Choi, D., Kang, J., Kim, H., Park, K., Lee, J., Kim, Y., Kwon, K., Kim K.P., Gho, Y.S. (2007). Global proteomic profiling of native outer membrane vesicles derived from *Escherichia coli*. *Proteomics* **7**(17), 3143–3153.

[43] Lee, E., Choi, D., Kim, K., Gho, Y. (2008). Proteomics in gram-negative bacterial outer membrane vesicles. *Mass Spectrom. Rev.* **27**, 535–555.

[44] Tashiro, Y., Inagaki, A., Shimizu, M., Ichikawa, S., Takaya, N., Nakajima-Kambe, T., Uchiyama, H., Nomura, N. (2011). Characterization of phospholipids in membrane vesicles derived from *Pseudomonas aeruginosa*. *Biosci Biotechnol Biochem*, 1. **75**(3). 605–607.

[45] Baumgarten, T., Sperling, S., Seifert, J., von Bergen, M., Steiniger, F., Wick, L.Y., Heipieper, H.J. (2012). Membrane vesicle formation as a multiple-stress response mechanism enhances *Pseudomonas putida* DOT-T1E cell surface hydrophobicity and biofilm formation. *Appl. Environ. Microbiol.* **78**(17), 6217–6224.

[46] Mansilla, M.C., Cybulski, L.E., Albanesi, D., de Mendoza, D. (2004). Control of membrane lipid fluidity by molecular thermosensors. *J. Bacteriol.* **186**(20), 6681–6688.

[47] Marshall, S.E., Hong, S., Thet, N.T., Jenkins, A.T.A. (2013). Effect of lipid and fatty acid composition of phospholipid vesicles on long-term stability and their response to *Staphylococcus aureus* and *Pseudomonas aeruginosa* supernatants. *Langmuir* **29**(23), 6989–6995.

[48] Rivera, J., Cordero, R.J.B., Nakouzi, A.S., Frases, S., Nicola, A., Casadevall, A. (2010). *Bacillus anthracis* produces membrane-derived vesicles containing biologically active toxins. *Proc. Natl. Acad. Sci. USA* **107**(44), 19002–19007.

[49] Kolling, G.L., Matthews, K.R. (1999). Export of virulence genes and Shiga toxin by membrane vesicles of *Escherichia coli* O157:H7. *Appl. Environ. Microbiol*. **65**(5), 1843–1848.

[50] Yaron, S., Kolling, G., Simon, L., Matthews, K. (2000). Vesicle-mediated transfer of virulence genes from *Escherichia coli* O157:H7 to other enteric bacteria. *Appl. Environ. Microbiol.* **66**(10), 4414–4420.

[51] Kahn, M., Maul, G., Goodgal, S. (1982). Possible mechanism for donor DNA binding and transport in *Haemophilus*. *Proc. Natl. Acad. Sci. USA* **79**(20), 6370–6374.

[52] Renelli, M., Matias, V., Lo, R.Y., Beveridge, T.J. (2004). DNA-containing membrane vesicles of *Pseudomonas aeruginosa* PAO1 and their genetic transformation potential. *Microbiology* **150**(Pt. 7), 2161–2169.

[53] Mashburn, L.M., Whiteley, M. (2005). Membrane vesicles traffic signals and facilitate group activities in a prokaryote. *Nature* **437**(7057), 422–425.

[54] Kadurugamuwa, J.L., Beveridge, T.J. (1996). Bacteriolytic effect of membrane vesicles from *Pseudomonas aeruginosa* on other bacteria including pathogens: Conceptually new antibiotics. *J. Bacteriol.* **178**(10), 2767–2774.

[55] Li, Z., Clarke, A.J., Beveridge, T.J. (1996). A major autolysin of *Pseudomonas aeruginosa:* Subcellular distribution, potential role in cell growth and division and secretion in surface membrane vesicles. *J. Bacteriol.* **178**(9), 2479–2488.

[56] Soler, N., Marguet, E., Verbavatz, J.-M., Forterre, P. (2008). Virus-like vesicles and extracellular DNA produced by hyperthermophilic archaea of the order Thermococcales. *Res. Microbiol.* **159**(5), 390–399.

[57] Zhou, L., Srisatjaluk, R., Justus, D., Doyle, R. (1998). On the origin of membrane vesicles in gram-negative bacteria. *FEMS Microbiol. Lett.* **163**(2), 223–228.

[58] McBroom, A.J., Kuehn, M.J. (2007). Release of outer membrane vesicles by Gram-negative bacteria is a novel envelope stress response. *Mol. Microbiol.* 7. **63**(2), 545–558.

[59] Tashiro, Y., Sakai, R., Toyofuku, M., Sawada, I., Nakajima-Kambe, T., Uchiyama, H., Nomura, N. (2009). Outer membrane machinery and alginate synthesis regulators control membrane vesicle production in *Pseudomonas aeruginosa*. *J. Bacteriol.* **191**(24), 7509–7519.

[60] Tashiro, Y., Nomura, N., Nakao, R., Senpuku, H., Kariyama, R., Kumon, H., Kosono, S., Watanabe, H., Nakajima, T., Uchiyama, H. (2008). Opr86 is essential for viability and is a potential candidate for a protective antigen against biofilm formation by *Pseudomonas aeruginosa*. *J. Bacteriol.* **190**(11), 3969–3978.

[61] Macdonald, I.A., Kuehn, M.J. (2013). Stress-induced outer membrane vesicle production by *Pseudomonas aerugi nosa*. *J. Bacteriol.* **195**(13), 2971–2981.

[62] Toyofuku, M., Zhou, S., Sawada, I., Takaya, N., Uchiyama, H., Nomura, N. (2013). Membrane vesicle formation is associated with pyocin production under denitrifying conditions in *Pseudomonas aeruginosa* PAO1. *Environ. Microbiol.* **16**(9), 2927–2938.

[63] Maredia, R., Devineni, N., Lentz, P., Dallo, S.F., Yu, J., Guentzel, N., Chambers, J., Arulanandam, B., Haskins, W.E.,

Weitao, T. (2012). Vesiculation from *Pseudomonas aeruginosa* under SOS. *Sci.World J*. 2012, 402919.

[64] Ramos, J., Duque, E., Huertas, M., Haidour, A. (1995). Isolation and expansion of the catabolic potential of a *Pseudomonas putida* strain able to grow in the presence of high concentrations of aromatic hydrocarbons. *J. Bacteriol.* **177**(14), 3911–3916.

[65] Kobayashi, H., Uematsu, K., Hirayama, H., Horikoshi, K. (2000). Novel toluene elimination system in a toluene-tolerant microorganism. *J. Bacteriol.* **182**(22), 6451–6455.

[66] Kadurugamuwa, J.L., Beveridge, T.J. (1995). Virulence factors are released from *Pseudomonas aeruginosa* in association with membrane vesicles during normal growth and exposure to gentamicin: A novel mechanism of enzyme secretion. *J. Bacteriol*. **177**(14), 3998–4008.

[67] Schooling, S., Beveridge, T. (2006). Membrane vesicles: An overlooked component of the matrices of biofilms. *J. Bacteriol.* **188**, 5945–5957.

[68] Kamaguchi, A., Nakayama, K., Ichiyama, S., Nakamura, R., Watanabe, T., Ohta, M., Baba, H., Ohyama, T. (2003). Effect of *Porphyromonas gingivalis* vesicles on coaggregation of *Staphylococcus aureus* to oral microorganisms. *Curr Microbiol.* **47**(6), 485–491.

[69] Inagaki, S., Onishi, S., Kuramitsu, H., Sharma, A. (2006). *Porphyromonas gingivalis* vesicles enhance attachment, and the leucine-rich repeat BspA protein is required for invasion of epithelial cells by *"Tannerella forsythia"*. *Infect. Immun.* **74**(9), 5023–5028.

[70] Toyofuku, M., Roschitzki, B., Riedel, K., Eberl, L. (2012). Identification of proteins associated with the *Pseudomonas aeruginosa* biofilm extracellular matrix. *J. Proteome Res.* **11**(10), 4906–4915.

[71] Whitchurch, C.B., Tolker-Nielsen, T., Ragas, P.C., Mattick, J.S. (2002). Extracellular DNA required for bacterial biofilm formation. *Science*. **295**(5559), 1487.

[72] Schooling, S.R., Hubley, A., Beveridge, T.J. (2009). Interactions of DNA with (2010). Variation of physiochemical properties and cell association activity of membrane vesicles with growth phase in *Pseudomonas aeruginosa. Appl. Environ Microbiol.* **76**(11), 3732–3739.

[73] Tashiro, Y., Ichikawa, S., Shimizu, M., Toyofuku, M., Takaya, N., Nakajima-Kambe, T., Uchiyama, H., Nomura, N. (2010). Variation of physiochemical properties and cell association activity of membrane vesicles with growth phase in *Pseudomonas aeruginosa*. *Appl. Environ. Microbiol*. **76**(11), 3732–3739.

[74] Mashburn-Warren, L., Howe, J., Garidel, P., Richter, W., Steiniger, F., Roessle, M., Brandenburg, K., Whiteley, M. (2008). Interaction of quorum signals with outer membrane lipids: Insights into prokaryotic membrane vesicle formation. *Mol. Microbiol.* **69**(2), 491–502.

[75] Tashiro, Y., Ichikawa, S., Nakajima-Kambe, T., Uchiyama, H., Nomura, N. (2010). *Pseudomonas* quinolone signal affects membrane vesicle production in not only Gram-negative but also Gram-positive bacteria. *Microbiol. Environ.* **25**(2), 120–125.

[76] de Beer, D., Stoodley, P. (2006). Microbial biofilm. In Dworkin, M., et al. (eds.), *The Prokaryotes*, Springer-Verlag, New York.

[77] Flemming, H.C., Wingender, J. (2010). The biofilm matrix. *Nat. Rev. Microbiol.* **8**(9), 623–633.

[78] Zheng, Y.T., Toyofuku, M., Nomura, N., Shigeto, S. (2013). Correlation of carotenoid accumulation with aggregation and biofilm development in *Rhodococcus* sp. SD-74. *Anal. Chem.* **85**(15), 7295–7301.

[79] Stewart, P.S., Costerton, J.W. (2001). Antibiotic resistance of bacteria in biofilms. *Lancet* **358**(9276), 135–138.

[80] Davies, D. (2003). Understanding biofilm resistance to antibacterial agents. *Nat. Rev. Drug Discov.* **2**(2), 114–122.

[81] Renner, L.D., Weibel, D.B. (2011). Physicochemical regulation of biofilm formation. *MRS* (Materials Research Society) *Bull.* **36**(5), 347–355.

[82] Scheuerman, T.R., Camper, A.K., Hamilton, M.A. (1998). Effects of substratum topography on bacterial adhesion. *J. Colloid Interface Sci.* **208**(1), 23–33.

[83] Hsu, L.C., Fang, J., Borca-Tasciuc, D.A., Worobo, R.W., Moraru, C.I. (2013). Effect of micro- and nanoscale topography on the adhesion of bacterial cells to solid surfaces. *Appl. Environ. Microbiol.* **79**(8), 2703–2712.

[84] Hengge, R. (2009). Principles of c-di-GMP signalling in bacteria. *Nat. Rev. Microbiol.* **7**(4), 263–273.

[85] McDougald, D., Rice, S.A., Barraud, N., Steinberg, P.D., Kjelleberg, S. (2012). Should we stay or should we go: Mechanisms and ecological consequences for biofilm dispersal. *Nat. Rev. Microbiol.* **10**(1), 39–50.

[86] Yoon, S.S., Hennigan, R.F., Hilliard, G.M., Ochsner, U.A., Parvatiyar, K., Kamani, M.C., Allen, H.L., DeKievit, T.R., Gardner, P.R., Schwab, U., et al. (2002). *Pseudomonas aeruginosa* anaerobic respiration in biofilms: Relationships to cystic fibrosis pathogenesis. *Devel. Cell* **3**(4), 593–603.

[87] de Kievit, T.R. (2009). Quorum sensing in *Pseudomonas aeruginosa* biofilms. *Environ. Microbiol.* **11**(2), 279–288.

[88] Boles, B.R., Horswill, A.R. (2008). Agr-mediated dispersal of *Staphylococcus aureus* biofilms. *PLoS Pathogens* **4**(4), e1000052.

[89] Fujii, T., Ingham, C., Nakayama, J., Beerthuyzen, M., Kunuki, R., Molenaar, D., Sturme, M., Vaughan, E., Kleerebezem, M., de Vos, W. (2008). Two homologous Agr-like quorum-sensing systems cooperatively control adherence, cell morphology, and cell viability properties in *Lactobacillus plantarum* WCFS1. *J. Bacteriol.* **190**(23), 7655–7665.

[90] Riedel, C.U., Monk, I.R., Casey, P.G., Waidmann, M.S., Gahan, C.G., Hill, C. (2009). AgrD-dependent quorum sensing affects biofilm formation, invasion, virulence and global gene expression profiles in *Listeria monocytogenes*. *Mol. Microbiol.* **71**(5), 1177–1189.

[91] Dow, J.M., Crossman, L., Findlay, K., He, Y.Q., Feng, J.X., Tang, J.L. (2003). Biofilm dispersal in *Xanthomonas campestris* is controlled by cell-cell signaling and is required for full virulence to plants. *Proc. Natl. Acad. Sci. USA* **100**(19), 10995–11000.

[92] Boon, C., Deng, Y., Wang, L.H., He, Y., Xu, J.L., Fan, Y., Pan, S.Q., Zhang, L.H. (2008). A novel DSF-like signal from *Burkholderia cenocepacia* interferes with *Candida albicans* morphological transition. *ISME* (International Society for Microbial Ecology) *J*. **2**(1), 27–36.

[93] Deng, Y., Schmid, N., Wang, C., Wang, J., Pessi, G., Wu, D., Lee, J., Aguilar, C., Ahrens, C.H., Chang, C., Song, H., Eberl, H., Zhang, L.H. (2012). *Cis-2*-dodecenoic acid receptor RpfR links quorum-sensing signal perception with regulation of virulence through cyclic dimeric guanosine monophosphate turnover. *Proc. Natl. Acad. Sci. USA* **109**(38), 15479–15484.

[94] Burdman, S., Jurkevitch, E., Soria-Diaz, M.E., Serrano, A.M., Okon, Y. (2000). Extracellular polysaccharide composition of *Azospirillum brasilense* and its relation with cell aggregation. *FEMS Microbiol. Lett.* **189**(2), 259–264.

[95] Scott, J.E., Thomlinson, A.M., Prehm, P. (2003). Supramolecular organization in streptococcal pericellular capsules is based on hyaluronan tertiary structures. *Exp. Cell Res.* **285**(1), 1–8.

[96] Ahn, S.J., Burne, R.A. (2006). The atlA operon of *Streptococcus mutans:* Role in autolysin maturation and cell surface biogenesis. *J. Bacteriol.*,**188**(19), 6877–6888.

[97] Allesen-Holm, M., Barken, K.B., Yang, L., Klausen, M., Webb, J.S., Kjelleberg, S., Molin, S., Givskov, M., Tolker-Nielsen, T. (2006). A characterization of DNA release in *Pseudomonas aeruginosa* cultures and biofilms. *Mol. Microbiol.* **59**(4), 1114–1128.

[98] Petersen, F.C., Tao, L., Scheie, A.A. (2005). DNA binding-uptake system: A link between cell-to-cell communication and biofilm formation. *J. Bacteriol.* **187**(13), 4392–4400.

[99] Steinberger, R.E., Holden, P.A. (2005). Extracellular DNA in single- and multiple-species unsaturated biofilms. *Appl. Environ. Microbiol.* **71**(9), 5404–5410.

[100] Das, T., Sharma, P.K., Busscher, H.J., van der Mei, H.C., Krom, B.P. (2010). Role of extracellular DNA in initial bacterial adhesion and surface aggregation. *Appl. Environ. Microbiol.* **76**(10), 3405–3408.

[101] Smithies, W.R., Gibbons, N.E., Bayley, S.T. (1955). The chemical composition of the cell and cell wall of some halophilic bacteria. *Can. J. Microbiol.* **1**(8), 605–613.

[102] Liu, H.H., Yang, Y.R., Shen, X.C., Zhang, Z.L., Shen, P., Xie, Z.X. (2008). Role of DNA in bacterial aggregation. *Curr. Microbiol.* **57**(2), 139–144.

[103] Kos, B., Suskovic, J., Vukovic, S., Simpraga, M., Frece, J., Matosic, S. (2003). Adhesion and aggregation ability of probiotic strain *Lactobacillus acidophilus* M92. *J. Appl. Microbiol*. **94**(6), 981–987.

[104] Schachtsiek, M., Hammes, W.P., Hertel, C. (2004). Characterization of *Lactobacillus coryniformis* DSM 20001T surface protein Cpf mediating coaggregation with and aggregation among pathogens. *Appl. Environ. Microbiol.* **70**(12), 7078–7085.

[105] Kjaergaard, K., Schembri, M.A., Hasman, H., Klemm, P. (2000). Antigen 43 from *Escherichia coli* induces inter- and intraspecies cell aggregation and changes in colony morphology of *Pseudomonas fluorescens*. *J. Bacteriol.* **182**(17), 4789–4796.

[106] Sherlock, O., Schembri, M.A., Reisner, A., Klemm, P. (2004). Novel roles for the AIDA adhesin from diarrheagenic *Escherichia coli:* Cell aggregation and biofilm formation. *J. Bacteriol*. **186**(23), 8058–8065.

[107] Helaine, S., Carbonnelle, E., Prouvensier, L., Beretti, J.L., Nassif, X., Pelicic, V. (2005). PilX, a pilus-associated protein essential for bacterial *aggregation, is a key to pilus-facilitated attachment of Neisseria meningitidis* to human cells. *Mol. Microbiol*. **55**(1), 65–77.

[108] Inaba, T., Ichihara, T., Yawata, Y., Toyofuku, M., Uchiyama, H., Nomura, N. (2013). Three-dimensional visualization of mixed species biofilm formation together with its substratum. *Microbiol. Immunol.* **57**(8), 589–593.

[109] Kolenbrander, P.E., Palmer, R.J., Jr., Periasamy, S., Jakubovics, N.S. (2010). Oral multispecies biofilm development and the key role of cell-cell distance. *Nat. Rev. Microbiol.* **8**(7), 471–480.

[110] Kolenbrander, P.E., Andersen, R.N., Blehert, D.S., Egland, P.G., Foster, J.S., Palmer, R.J., Jr. (2002). Communication among oral bacteria. *Microbiol. Mol. Biol. Rev.* **66**(3), 486–505.

[111] Sato, Y., Yamamoto, Y., Kizaki, H. (1997). Cloning and sequence analysis of the gbpC gene encoding a novel glucan-binding protein of *Streptococcus* mutans. *Infect. Immun.* **65**(2), 668–675.

7

BIOFILM

Hisao Morisaki

Graduate School of Life Sciences, Ritsumeikan University, Kusatsu, Shiga, Japan

7.1 INTRODUCTION

Biofilms are aggregations of microorganisms attached to and growing on a surface [1]. Biofilms are not simple accumulations of attached microbial cells; rather, they contain extracellular polymeric substances (EPSs) as well as the microbial cells. The EPSs consist of several kinds of polymers such as polysaccharides, proteins, nucleic acids, and lipids [2]. These polymers are produced by the microbes attached to solid surfaces and play crucial roles in holding the biofilm itself and enclosing the microbial cells. The polymers form a network in which microbial cells and various materials are retained. The movement of materials inside the biofilm is limited by the network structure, which results in a gradient of materials such as nutrients and oxygen. These gradients and their combinations produce complex microscale environments inside biofilm and render the biofilm heterogeneous, containing various niches for microbes, resulting in a variety of microbes inhabiting therein [2].

Microbial cells in biofilm differ from the planktonic cells in three basic respects: (1) microbial cells are in an attached state, (2) their cell density is much greater, and (3) they live in a characteristic structure consisting primarily of microbial cells, EPS produced by the microbes, and the interstitial water occupying the regions among the EPS network. The gene expression of cells in biofilm is different from planktonic ones, and the high cell density in biofilm enable or force the cells in biofilm to interact with each other in various ways, such as cometabolism or competition over nutrient materials, cell communication via DNA fragment, or specific informative molecules such as *N*-acyl homoserine lactone and modified oligopeptide [3–10]. Thus, biofilm is not a simple mass of microbial cells but is functionally similar to a multicellular organism living in the characteristic structure [9, 10].

Biofilm is not isolated from its surrounding environment. It can trap various materials from outside and condense it inside as well as metabolize it into a variety of products that may alter the inside and/or outside environments. Thus, the surrounding environment and biofilm can affect each other. Studies concerning these effects are also important in biofilm research [11, 12].

Many articles examining various aspects of biofilms as described above have been published. A growing body of excellent reviews [2–15] have plotted the highlights of biofilm research carried out over the decades. For details on each topic or research field, the reader is referred to these articles and reviews.

Hereafter, in this chapter, the following aspects of the biofilm are overviewed and discussed: (1) biofilm formation process, (2) biofilm constituents, (3) biofilm and surrounding environment, and (4) review of biofilm research to date and future research prospects.

7.2 FORMATION PROCESS OF BIOFILM

Biofilm is ubiquitous in aquatic environments. We can find biofilms on the surfaces of various kinds of solids immersed in aquatic environments. The biofilm biomass increases along with time typically as a shape of sigmoid curve [16, 17]. Biofilm formation has been considered as the net result of the following physical, chemical, and biological processes

Encyclopedia of Biocolloid and Biointerface Science, Volume 1, First Edition. Edited by Hiroyuki Ohshima.
© 2016 John Wiley & Sons, Inc. Published 2016 by John Wiley & Sons, Inc.

occurring in sequence [16, 18]: (1) adsorption of ions and/or macromolecules present in the bulk liquid resulting in the formation of conditioning film; (2) attachment, including both reversible and irreversible, of bacterial cells to the conditioning film; (3) bacterial growth and production of extracellular polymeric substances (EPSs) strengthening cell attachment and developing network structure formed by EPSs; (4) development of various kinds of microscale environments inside biofilm due to the concentration gradient of various kinds of materials (e.g., oxygen, nutrients), caused by differences in mass transfer and/or microbial utilization or production of the materials; (5) increase in the microbial cell number, including other kinds of bacterial species and microbes resulting from the establishment of various niches inside biofilm; (6) detachment of biofilm biomass, balancing with the biofilm biomass increment at later stages of biofilm formation, due to shearing by fluid shear stress, sloughing of random and sporadic event, which is observed more frequently in thicker biofilm, and abrasion caused by particle collisions to biofilm [19].

7.3 BIOFILM CONSTITUENTS

The formation and development of biofilm and the resultant biofilm properties are affected depending on (1) the substratum surface, (2) microbes, (3) EPS, and (4) interstitial water occupying the region between EPS network, as described below.

7.3.1 Substratum Surface

Biofilms can be formed on surfaces of various kinds of solid, either biotic or abiotic, such as stone, sand, concrete, bottom of a ship, inner face of a pipe, catheter, teeth, soil, food, and plants. These surfaces affect cell attachment, biofilm formation, activity, and community structure of microbes in biofilms. Additionally, biofilm can affect the surface and/or the solid on which it is formed.

7.3.1.1 Cell Attachment. Bacterial cell attachment is an essential step for biofilm formation. Under typical conditions (pH $\sim$ 7), both the bacterial cells and the substratum surfaces are usually negatively charged. Under these conditions, two kinds of opposite interactions exist between the cells and the surfaces: electrostatic repulsive and van der Waals attractive interactions. For cell attachment, the surface properties of bacterial cells relating to these interactions have important influence as well as substratum surface properties such as electric charge, hydrophobicity, and roughness [20–26]. Various studies on the cell attachment mechanism have also been conducted by applying colloidal theory [27] and considering the specific feature of microbial cells as "soft" colloidal particles [28–33].

7.3.1.2 Microbial Activity, Function, and Community Structure. The environment inside biofilm is different from that on the outside, affecting the activity, function, and microbial community structure of biofilm.

Even in the same stream, biofilms formed on sands and rocks are different in enzymatic activity and response to nutrient addition [34]. It has been reported that the bacterial isolates from biofilm formed on reeds (*Phragmites australis*) showed high hydrolysis activities for biopolymer [35] or biodegradable plastic [36].

Bacterial community structure of the biofilms formed on the submerged stem of reeds (*Phragmites australis*) varied with season not related with the lake water [37]. A characteristic community structure of the biofilms formed on reeds has also been observed [35]. Different microbial community structures were observed among biofilms formed on different kinds of materials [25, 38, 39].

7.3.1.3 Surface Deterioration. Biofilm can cause deterioration of the underlying substratum, including metal corrosion, dental caries, and food spoilage.

Metal or metal alloy corrosion by biofilms, referred to as *microbially influenced corrosion* (MIC), has been studied from various aspects, such as phenomenologically [40], thermodynamically [41], and theoretically [42]. Although there have been many studies on MIC mechanisms, the process is relatively poorly understood [43]. In situ monospecies biofilm is rare, so any study regarding the influence of multispecies biofilm as a whole and/or biofilm components on MIC [43] would seem to be useful to prevent and control MIC.

Dental plaque is a biofilm formed on teeth and is defined as the diverse microbial community found on tooth surface embedded in a matrix of polymers of bacterial and salivary origin. Since the 1960s, there has been an enormous expansion of knowledge of the biochemistry and bacteriology of the plaque microflora [44]. Biofilms on teeth also contain multibacterial species as other biofilms formed in natural environments. In the multispecies biofilms on teeth, cell–cell distance is fundamental for intermicrobial communication processes [10]. In further studies including the factors characterizing the oral ecosystem, the oral multispecies biofilms may serve as a paradigm for other biofilm system in general [10].

The surfaces of epithelial cells and medical devices also can be subjects of biofilm formation causing serious infectious problems [7, 45, 46]. Biofilm bacteria can be $\leq$1000 times less susceptible to antimicrobial stress than their freely suspended counterparts. Using compounds that kill or inhibit growth of microbe may lead to frequent development of resistance to antibiotics. Some *antibiofilm* strategies, such as iron metabolism interferences, negating quorum sensing and self-vaccinating biomaterials, which are assumed not to lead to the development of resistance, have been discussed [46].

Biofilms have caused problems in many branches of the food industry. The mechanisms involved in the biofilm formation and behavior, deleterious effects associated with their presence, and some of the current and emergent control strategies have been reviewed and discussed [12, 15, 47, 48].

The various activities of biofilms may be employed to aid the breakdown of a variety of pollutants and other unwanted compounds [49] such as polycyclic aromatic hydrocarbons [50, 51], PET [52], oil residue [53], and herbicide [54].

Biofilms contain multispecies bacteria in common and are formed under the effect of the surrounding environments that may also be influenced by biofilm. These features, containing multispecies microbes and mutual effects between biofilms and the surrounding environments, may provide the foundation for further studies.

7.3.1.4 Plant Surface. Biofilms can be formed on a variety of surfaces as described above. In the case of plants, surface-attached bacteria can be found on seeds, leaves, and roots [55, 56]. The surface of the older parts of roots often becomes encased within a tightly adhering amalgam of soil particles, plant- and microbial-derived mucilage, as well as microbial and plant cells. This so-called *rhizosheath* completely covers the root hairs [57]. These intimate associations between plant roots and microbes are considered as biofilms [58]. Biofilms grow on and around plant tissues, and an increasing number of studies have begun to reveal their importance in plant–microbe interactions [59, 60].

Plant-associated bacteria interact with host tissue surfaces during pathogenesis and symbiosis, and in commensal relationships. Biofilm-type structures that vary from small clusters of cells to extensive biofilms have been revealed through observations of bacteria associated with plants [61], such as at the root tip of *Arabidopsis thaliana* [62], in sweet corn leaf xylem vessels [63], and on bean leaves [64].

Studies concerning the interaction between biofilm-forming microbes and plants have begun at molecular level. Exudates of tomato roots strongly stimulating *Bacillus subtilis* to form biofilm ex planta, with an abundant small molecule in the exudates, L-malic acid, able to stimulate biofilm formation at high concentrations, have been reported [65]. They [65] proposed that small signaling molecules released by the roots of tomato plants are directly or indirectly recognized by the sensor histidine kinase KinD, triggering biofilm formation. Another team [66] showed that *B. subtilis* biofilm formation was triggered by certain plant polysaccharides. These polysaccharides served as a signal for biofilm formation as well as a source of sugars for the synthesis of the matrix exopolysaccharide.

7.3.2 Biofilm Microbes

Microbes living in a biofilm are different from the planktonic cells floating outside biofilm for the following reasons: (1) they are in an attached state; (2) they live in an environment inside biofilm, which is different from that outside biofilm, as will be discussed later (in Section 7.3.4); and (3) the cell density inside biofilm is far greater (>100–1000 times) than that outside biofilm, hence intermicrobe interactions are much more intensive. These differences influence the microbes inside biofilm as described below.

7.3.2.1 Phenotype and Gene Expression. As described by one group of investigators [67], the biofilm bacteria are phenotypically different from the planktonic state [68–70], and generally much more tolerant to antibiotics, biocides, and hydrodynamic shear forces compared with planktonic counterparts [7, 71]. These differences were attributed to significant changes in the patterns of gene expression between the two growth modes [72, 73]. In fact, different gene expression patterns, although the extent is varying, has been revealed between planktonic and biofilm cells in a variety of bacteria [67, 72, 74–76].

7.3.2.2 Multispecies Biofilm. Biofilms formed in nature contain multispecies of microbes. The species constituting a mixed biofilm and the interactions between these microorganisms critically influence the development and shape of the community [13]. Thus, extrapolation from the results using a model microbe, such as *Pseudomonas aeruginosa*, to biofilms in general is not suitable [8].

The bacterial cell density in biofilm is far greater than the outside environment, enabling gene transfer by transformation, transduction, and conjugation between biofilm organisms [77–79]. There are increased opportunities in biofilms for the transfer of mobile genetic elements (e.g., plasmids) that might encode the traits, such as resistance to antibiotics and/or heavy metals and the ability to degrade pollutants [78, 79]. Horizontal gene transfer in bacteria under both natural and engineered environments occurs through transposons and the transformation of naked DNA or plasmids, which leads to transfer of genetic traits [80].

Biofilm microbes frequently appear to differ metabolically from their free-living counterparts due to two possible reasons [81]: (1) physicochemical conditions of microscale environment inside biofilm differ from outside biofilm, and (2) the close proximity between microbes induces various interactions among biofilm members.

In general, interspecies interactions involve communication, typically via quorum sensing (see Section 7.3.2.3), and metabolic cooperation or competition. Interactions among species within a biofilm can be antagonistic, such as competition over nutrients and growth inhibition, or synergistic, such as the promotion of biofilm formation by coaggregation, metabolic cooperation where one species utilizes a metabolite produced by a neighboring species, and increased resistance to antibiotics or host immune responses compared to the monospecies biofilms [13].

Biofilm in nature contain various kinds of microbes such as algae, fungi, and protozoa as well as various species of bacteria. These microbes also interact antagonistically or synergistically. EPS polymers produced by diatoms have been implicated in promoting growth of specific bacterial taxa in estuarine biofilms [82]. Some bacterial strains can grow without organic nutrient when cocultured with diatom; *Cymbella microcephala*, in turn, in the presence of bacteria, enhance the growth and polysaccharide secretion of the diatom [83]. Other investigators [84] reported that in addition to desmids (a group of evolutionarily advanced green algae), diatoms, filamentous green algae, and transient nonmotile phases of flagellates represented the photosynthetic eukaryotes in a wetland biofilm. The corresponding information on protozoa in biofilms, such as their grazing rates, evidence of nutrient remineralization, and their susceptibility to mesoinvertebrate grazing, has been reviewed [85]. There are studies reporting the protozoan capacity to graze biofilm bacteria [86,87]. Contrary to this, in a natural bacterial biofilm, it was shown [88] that bacterial communities are much better buffered against influences of protozoan grazing than reported for their planktonic counterparts.

7.3.2.3 Cell–Cell Communication. Bacterial populations can communicate with one another using signal molecules such as *N*-acyl homoserine lactone in many Gram-negative bacteria such as *Vibrio fisheri* [89], and modified oligopeptide in a number of Gram-positive bacteria as *Staphylococcus aureus* [90]. By the accumulation of the signal molecules in the surrounding environment, a single cell can sense the number of bacteria (i.e., bacterial density), and therefore the population as a whole can make a coordinated response, such as swarming, toxin production, and biofilm formation [91].

The signal produced regulates its own production (autoinduction) leading to a positive-feedback response and greatly increased signal production. At critical densities, the binding of a regulator protein to the signal leads to the switching on of genes controlled [92, 93]. Cell communication involving the production and detection of diffusible signal molecules has become commonly known as *quorum sensing* (QS). Intra- and interspecies QS of bacteria have been reported in many articles. Interspecies QS between bacteria and fungi has also been reported [94].

It has been revealed that bacterial QS molecules are also recognized by eukaryotes that are colonized by QS-active bacteria. In this case, the cross-kingdom interaction can lead to specific adjustment and physiological adaptations in the colonized eukaryote [95].

The QS process can be disrupted by different mechanisms [96]. The degradation [97–101] or interference with [102–104] the signaling molecule is probably another important integral part in the complex QS circuit [95].

In addition to QS molecules, a diversity of other signals trigger biofilm formation. These include secondary metabolites such as antibiotics, pigments, and siderophores [105]. On the other hand, nonbiocidal molecules such as biosurfactants, enzymes, and metabolites produced by bacteria and other microorganisms can cause competitive interactions ranging from inhibition of initial adhesion to matrix degradation, jamming of cell–cell communications, and induction of biofilm dispersion [14].

7.3.3 Extracellular Polymeric Substances (EPSs)

Microbes in biofilm are enclosed in a complex structure composed of extracellular polymeric substances (EPSs). EPSs were initially termed *extracellular polysaccharides*; however, it has become clear that the biofilm matrix also contains proteins, nucleic acids, lipids, and other biopolymers such as humic substances [2]. The participation of multiple types of these molecules in the formation of extracellular matrix makes it impossible to present a single summary of biofilm matrix [105].

These EPS materials mechanically stabilize biofilm, mediate biofilm adhesion to surfaces, and form a cohesive, three-dimensional polymer network (biofilm matrix). In the biofilm matrix extracellular enzymes are immobilized as well as microbial cells, enabling metabolization of dissolved, colloidal, and solid biopolymers [2]. The EPS provides microbial habitats affected correspondingly by EPS characteristics, such as being structural, sorptive, surface-active, active, informative, redox-active, and nutritive as categorized in one report [8]. Each EPS component is discussed below.

Polysaccharides are a major fraction of the EPS matrix [106, 107], mostly long molecules, linear or branched, with a molecular mass of wide range: $0.5–2 \times 10^6$ Da (daltons) [2], wider than the range of $0.5–5 \times 10^6$ Da reported in another study [108]. Most exopolysaccharides are heteropolysaccharides consisting of a mixture of neutral and charged sugar residues. Owing to the presence of uronic acids (and, in some cases, ketal-linked pyruvate or, rarely, sulfate), many known exopolysaccharides are polyanionic [2]; sulfate is reported to be rich in marine biofilm [109]. In multispecies biofilms the presence of a species that produces exopolysaccharides may lead to the integration of other species that do not synthesize matrix polymers [110].

The biofilm matrix can contain considerable amounts of proteins that can far exceed the polysaccharide content on a mass basis [106, 111], functioning as enzymes or structural proteins. Various extracellular enzymes, such as protein-degrading enzymes, polysaccharide or oligosaccharide-degrading enzymes, phosphomonoesterases, and oxidoreductases [112], have been detected in biofilms, many of which are involved in the degradation of biopolymers. The low-molecular-mass resultings can be taken up and utilized as carbon and energy sources. The degradation of

structural EPS may also promote the detachment of bacteria from biofilms [2]. The nonenzymatic proteins in the matrix, such as the cell-surface-associated and extracellular carbohydrate-binding proteins (called *lectins*), and proteinaceous cell appendages (e.g., pili, fimbriae, flagella) can function to form and stabilize biofilm network structure through the interactions with EPS components [2].

Biofilms of various origins have been found to contain extracellular DNA (eDNA) varying in produced amount even between closely related species and in origin, such as generated through lysis of subpopulation of bacteria and active excretion from cells [2]. The eDNA is an integral part of the matrix [113, 114] and of the biofilm mode of life efficient in gene transfer [18]. Extracellular DNA can be used as C, N, and P sources by heterotrophic microorganisms and plays a significant role in bacterial biofilm formation in soil, and sediment environment [115].

Lipids are also found in the biofilm matrix [111]. Lipopolysaccharides are crucial for *Thiobacillus ferrooxidans* adherence to pyrite surfaces [116]. *Serratia marcescens* produces extracellular lipids with surface-active properties (known as *serrawettins* [117]) [2], capable of decreasing water surface tension by which the microbial cells can spread over a surface, although details of the mechanism remain to be clarified [118]. Other surface-active EPSs include surfactin, viscosin, and emulsan, which can disperse hydrophobic substances and render them bioavailable [2]. Biosurfactants can have antibacterial and antifungal properties and are important for bacterial attachment, detachment from oil droplets [119], or enhancement of oil degradation [120].

7.3.4 Interstitial Water among EPSs

Biofilm microbes live in the EPS matrix; thus the water occupying the interstitial region among EPSs is the immediate inhabiting environment for the microbes. The properties of interstitial water and the microbial behaviors inside biofilm will mutually affect each other. Some studies on interstitial water are described in this section.

7.3.4.1 Water Content and Mass Transfer. EPS biopolymers are highly hydrated and form a matrix, which keeps the biofilm cells together and retains water [8]. The water content of biofilm in a natural lake-water environment has been reported at >90% [17]. In general, the water content of biofilms reaches 90–99% of the total wet mass [121]. Although biofilm water content is high, mass transfer in biofilm is not the same as in water outside biofilm, due to the characteristic structure of biofilm matrix. Biofilm matrix is a kind of *bimodel pore structure* containing large macropores (water channels) between different cell–polymer aggregates and micropores inside these aggregates [121]. A significant amount of literature has been published on the relation between internal mass transfer and the physical characteristics of the biofilms [122–126]. The commonly accepted interpretation is that the effective diffusivity depends on the biofilm dry density (the mass of dry biofilm per unit wet volume); a decrease in diffusivity values has been empirically correlated with an increase in biofilm dry density [122]. However, one investigator [121] argued that the concept of tortuosity is more relevant for describing mass transfer inside biofilm matrices than is the more commonly accepted biofilm dry density. Tortuosity has a simple geometric meaning; it describes "the longer connecting path imposed by obstacles within porous solids relative to that for motion in unconstrained free space" [127].

EPSs affect the properties of interstitial water physically and chemically through functions such as selective material uptake with sieving by EPS network structure [2], thereby forming gradients of various materials by diffusion limitation in the matrix, resulting in formation of various niches for microbes.

Examples of experimentally measured gradients in biological activity within biofilms include adenylate charge [128], growth rate [129, 130], culturability [131], and the capacity for protein synthesis [132–134].

7.3.4.2 Ion Concentration in Biofilm. Nutrient ion concentration in biofilm has been reported to be far greater than that in the surrounding water. One team of investigators [135] examined the concentration of ammonium, nitrite, nitrate, and phosphate ions in biofilms formed on reed and stone surface in Lake Biwa (Japan), and found that the concentrations were 100s–1000s times higher compared with the lake water surrounding biofilm. They also found that the concentrations of the ions changed seasonally synchronizing with those of lake water. The higher ion concentrations in other biofilm samples compared with surrounding water were also confirmed in Lake Biwa [17].

Another group [136] measured the concentration of Ca, Sr, and Ti, as well as Fe, Mn, K, and Zn in biofilms and found the enrichment factor of 10^3–10^4 for these elements. An enrichment factor of 10^2–10^4 for Ca, K, Fe, Sr, Mn and Zn was reported in another study [137]. Another team [138] showed that a mineral fraction could reach between 2% and 40% of the EPS dry weight depending on the extraction method used, in which main minerals were Ca, Mg, Na, K, Al, Fe, Mn, P, Si, and S.

7.3.4.3 Condensation Mechanisms. Biofilm polymers contain both electrically positively and negatively charged sites. In other studies measuring the electrophoretic mobility (EPM) of biofilm fragments in buffer solution of various pHs [17, 139], biofilm fragments showed a negative EPM at neutral pH decreasing under acidic conditions, especially around pH 4, indicating the presence of functional group such as carboxylic acid. Those authors also observed positive EPM at

pH 2 indicating the presence of amino group. These observations are consistent with the reports that EPSs contain anionic groups (in uronic acids and proteins) and cationic groups (e.g., in amino sugars) [2, 140], and also indicate the excess existence of the functional groups carrying negative charge over the groups carrying positive charge resulting in a net negative charge of biofilm at neutral pH.

The existence of both negative and positive charges on EPS enables an electrostatic attractive interaction between biofilm and oppositely charged ions existing in surrounding water. The condensation mechanism of biofilm was analyzed by comparison with ion exchange resins [139]. A high ion uptake capacity of biofilm compared to that of ion exchange resins was reported, and the difference in the condensation mechanism between biofilm and ion exchange resin was suggested [139]. It was concluded the ions may be reserved in the interstitial region among EPS polymers as well as the charged sites on the polymers.

7.4 BIOFILM AND SURROUNDING ENVIRONMENT

Biofilm formation is a multistage dynamical process governed by various physicochemical principles and biological protocols [141], as has been described above in this chapter. Biofilms can be seen as catalysts (living ones). As opposed to chemical catalysts, they are able to grow and modify their internal structure in order to adapt to the operating conditions [121].

Data from a great number of authors have revealed how biofilm physical structure, formation, and development change with regulating conditions such as the hydrodynamics and composition of the external liquid, temperature, oxygen concentration, and pH [125, 142–148].

Contrary to the biofilms formed under controlled conditions, biofilms in nature are formed under the ever-fluctuating effects of the external environment. Biofilms are open and highly dynamic communities [149]. Biofilm-associated microbes, because of their ubiquity, diverse metabolic capabilities, and high enzymatic activity [150], have significant effects on external environments. This section focuses on these effects with respect to the formation of biofilms in nature.

7.4.1 Influence of Surrounding Environment on Biofilm

Light intensity has a significant effect on biofilm formation, development, and activity. Light-grown biofilms show significantly higher photosynthetic activity, bacterial density, ectoenzymatic activity (especially β-glucosidase) [151], and abiotic adsorption of organic matter [34] than do dark-grown biofilms. Algal photosynthesis can have a significant impact on bacterial productivity, biomass, biovolume, and enzyme production (α- and β-glucosidase and β-xylosidase) over longer time periods (24 h) at low photon flux densities ($\leq$100 μmol m^{-2} s^{-1}) [152]. A clear dependence of biofilm microbial community structure on light intensity is revealed; under high light conditions in one study, the initial colonizers of the substratum predominantly consisted of green algae, whereas at low light intensities, heterotrophic bacteria were the initial colonizers [153].

Higher-nutrient conditions combined with other factors, including light intensity, influence biofilms to a greater extent than do oligotrophic conditions [154–156].

Some studies report the significant effects of pH, temperature, and water flow on biofilm. One team [157] found significant differences in community structure among the streams varying in pH. An increase in river-water temperature (+4°C above an ambient temperature) induced the enhancement of degradation of recalcitrant [158]. High shear stresses decreased biofilm diversity and thus may slow down biofilm maturation, tending to maintain a younger biofilm [159].

Combination of several factors affects biofilms. It has been reported that bacterial biofilm community composition on the submerged macrophytes *Myriophyllum spicatum* and *Potamogeton perfoliatus* depends mainly on environmental factors (water level, conductivity, temperature, pH) and the plant chemical composition, especially the carbon and total phenolic content [160]. Another study [157] revealed that bacterial communities in streams located within rural catchments were significantly different from those within urban catchments.

Seasonal variation of biofilm microbial community structure in various sites such as lakes, rivers, and estuaries has been reported [37, 150, 161, 162].

7.4.2 Influence of Biofilm on Surrounding Environment

Positive relationships between the extracellular enzymatic activity of biofilm and DOC and biodegradable DOC content in flowing water have been found [34], with the suggestion that biofilm metabolism contributes to DOC dynamics in fluvial systems. The release of a significant amount of dissolved free amino acids into stream has also been reported [163]. Biofilm can condense various ions into EPS matrix through electrostatic interaction between electrically charged sites on polymers constituting the matrix and oppositely charged ions existing outside biofilm [17, 135, 139], as discussed in Section 7.3.4.3. Biofilms can condense various ions into the matrix, and also can release ions to the outside environment [139]. Biofilms are present in various sites and play a key role in the uptake or retention of inorganic and organic nutrients [11]. Biofilms may significantly influence on microbial ecology through the aquatic food web [11, 164].

7.5 PRESENT AND PROSPECTIVE BIOFILM RESEARCH

Biofilm is a consortium of microbes enclosed in the network structure formed by extracellular polymeric substances (EPSs). The biofilm microbes are in an attached state and they interact with each other in various ways physiologically and genetically to result in an assemblage of cells that are functionally similar to multicellular organisms.

Van Leeuwenhoek, using his simple microscopes, first observed microorganisms on tooth surfaces and can be credited with the discovery of microbial biofilms [5]. We now have a more comprehensive understanding of biofilm, specifically, that it is not a simple accumulation of microbial cells but is some sort of population of microbes tightly coordinating each other, inhabiting a characteristic structure composed of EPSs.

Microbial biofilms play a prominent role in the functions of many aquatic ecosystems, such as streams and rivers [4, 165] as well as in several industrial facilities, including sewage plants [166]. Researchers in the fields of clinical, food- and water-related, and environmental microbiology have begun to investigate microbiologic processes from a biofilm perspective [8]. Correspondingly, there is great interest in understanding the mechanisms that modulate the structure and function of microbial biofilms. Research on microbial biofilms is proceeding on many fronts. In this section, some of these will be discussed from a research perspective.

Biofilms have detrimental effects on a variety of solids such as metals, medical devices, industrial facilities, and foods. Biofilm also can contain pathogens causing serious infectious diseases. The demand for preventing or controlling biofilm formation and development has promoted various studies as described below.

The use of ultrasound coupled with pressure and/or heat may be promising to inactivate biofilm bacteria [167]. Carbon nanotube composites may be useful to prevent biofouling associated with biofilm formation [168].

Another study [14] reviewed how nonbiocidal molecules, involving nonbiocidal biosurfactants, enzymes, and metabolites produced by bacteria and other microorganisms, affect microbial interactions in multispecies biofilm, and discussed potential biological roles and perspectives of these compounds as alternative antibiofilm molecules of industrial and biomedical interest.

The use of enzyme-based detergents as biocleaners is expected as a viable option to overcome the biofilm problem in the food industry [12].

Bacillus subtilis was reported [169] to produce a factor (a mixture of D-leucine, D-methionine, D-tyrosine, and D-tryptophan) that prevented biofilm formation and could break down existing biofilms, acting at nanomolar concentrations. D-Amino acids have also been shown to prevent biofilm formation of *Staphylococcus aureus* and *Pseudomonas aeruginosa*, and the acids are produced by many bacteria. Thus it was deduced that D-amino acids might be a widespread signal for biofilm disassembly.

It is reported that the coating of substratum surface with an aqueous fish muscle extract, composed primarily of fish muscle α-tropomyosin, significantly reduced or delayed biofilm formation by all the isolates (urinary tract infectious isolates with various pathogenic and adhesive properties) under every condition examined [170]. A new type of drug delivery system using liposomes and various polymers may be useful in preventing biofilm formation on the surface of devices implanted into the human body [171].

Biocontrol strategies based on mechanisms regarding degradation of or interference with signaling molecule in quorum sensing seem to be sustainable methods because they have a more limited selective pressure for microbial survival than do biocide treatments [172].

There have also been studies on promoting biofilm formation and development, with the objective to apply the biofilm functions in various fields such as water treatment [173, 174], bioremediation [80, 175], and agriculture [176].

Biofilm function may be utilized electrochemically. Bacterial biofilms can generate electric power, and the underlying reasons for the exocellular electron transfer, including cellular respiration and possible cell–cell communication, have been discussed [177]. Another team [178] discussed the role of biofilm on the electric current production in microbial fuel cells (MFCs) and pointed out that the production of electric current is not the major advantage, but wastewater treatment or bioremediation using a cathode or anode may be much more promising than the electric current production of the MFC itself. Other researchers [179] showed that the EPS matrix produced by a *Sphingomonas* strain provides a favorable microenvironment for enzyme (horseradish peroxidase) while retaining its activity when immobilized on a biosensor electrode.

For further progress in biofilm microbiology, a variety of perspectives have been proposed. Another team [149] suggested a concept for biofilm research that is spatially explicit and solidly rooted in ecological theory, which might serve as a universal approach to the study of the numerous facets of biofilms. They stressed that in the wild, biofilms are open and highly dynamic communities and exist as part of a larger microbial network forming a metacommunity. Oral diseases are influenced by microbial communities, not by single pathogens. Thus, another report [10] suggested that substitution of "the community" for "the agent" would make Koch's first postulate applicable to oral polymicrobial diseases.

Biofilm microbes are submerged in the interstitial water occupying the EPS matrix. Thus, studies concerning the properties of the interstitial water seem to lead a new insight into biofilm formation and development. Inside, biofilm is nutrient-rich [180–182] and has been shown to depend on ion

exchange processes [183] and on ion reservation in the EPS network region [139]. It has been deduced that the EPSs, usually electrically charged, attract the charged materials such as nutrient ions from the surrounding water [17]. The nutrient enrichment will cause rapid growth of microbes, resulting in more EPS production, which accumulate nutrients further. This cycle may accelerate the nutrient accumulation and explain the very rapid formation and development of biofilm in natural environments where water quality is not so eutrophic. Other investigators [184] also reported a fast formation process of biofilm in a stream and found that younger biofilms ($\leq$8 days old) showed higher respiratory activity per cell, indicating a fast response of microorganisms to substrate availability. The gradient of nutrient concentration in biofilm may contribute to the spatial stratification and physiological differentiation in biofilms [185].

Regarding the biofilm formation process, another team [186], based on a new approach using 16S rRNA gene sequences for virtual metagenome reconstruction, reported that transporter- and biosynthesis-related modules enrichment extent changed along with biofilm maturation; initially both modules, then biosynthesis-related modules, and finally transporter-related modules were enriched.

Direct observation of biofilm formation process using micro-culture method as reported by Yamada et al. [187] may provide further insights in physiology of biofilms.

It has been reported that more colonies can be formed in a nutrient-poor agar medium than in a nutrient-rich medium for biofilm sample [17, 188]. Improvement of culture media may enhance our understanding about culturability of biofilm microbes.

Not only living cells but also regulated cell death and lysis may be important for biofilm development [189]. Biofilm formation by pathogens in the environment can play a role in the transmission of those pathogens. Another team [190] pointed out that occurrence of viable but nonculturable (VBNC) bacteria, including *Vibrio cholerae* in biofilms, has been reported and most likely such cells were overlooked previously because appropriate methods of detection were not employed. Various approaches to researching VBNC bacteria are now developed [191] and seem to be applicable for further studies.

REFERENCES

[1] Costerton, J.W., Stewart, P.S. (2001). Battling biofilms. *Sci. Am.* **285**, 74–81.

[2] Flemming, H.-C., Wingender, J. (2010). The biofilm matrix. *Nat. Rev. Microbiol.* **8**, 623–633.

[3] Davey, M.E., O'Toole, G.A. (2000). Microbial biofilms: From ecology to molecular genetics. *Microbiol. Mol. Biol. Rev.* **64**, 847–867.

[4] Watnick, P., Kolter, R. (2000). Biofilm, city of microbes. *J. Bacteriol.* **182**, 2675–2679.

[5] Donlan, R.M. (2002). Biofilms: Microbial life on surfaces. *Emerg. Infect. Diseases* **8**, 881–890.

[6] Parsek, M.R., Fuqua, C. (2004). Emerging themes and challenges in studies of surface-associated microbial life. *J. Bacteriol.* **185**, 4427–4440.

[7] Hall-Stoodley, L., Costerton, J.W., Stoodley, P. (2004). Bacterial biofilms: From the natural environment to infectious diseases. *Nat. Rev. Microbiol.* **2**, 95–108.

[8] Flemming, H.-C., Neu, T.R., Wozniak, D.J. (2007). The EPS matrix: The "house of biofilm cells." *J. Bacteriol.* **189**, 7945–7947.

[9] Moons, P., Michiels, C.W., Aertsen, A. (2009). Bacterial interactions in biofilms. *Crit. Rev. Microbiol.* **35**, 157–168.

[10] Kolenbrander, P.E., Palmer, Jr., R.J., Periasamy, S., Jakubovics, N.S. (2010). Oral multispecies biofilm development and the key role of cell–cell distance. *Nat. Rev. Microbiol.* **8**, 471–480.

[11] Romaní, A.M. (2010). Freshwater biofilms. In Dürr, S., Thomason, J.C. (eds.), *Biofouling*. Wiley-Blackwell Publishing, UK, pp. 137–153.

[12] Simões, M., Simões, L.C., Vieira, M.J. (2010). A review of current and emergent biofilm control strategies. *LWT Food Sci. Technol.* **43**, 573–583.

[13] Elias, S., Banin, E. (2012). Multi-species biofilms: Living with friendly neighbors. *FEMS Microbiol. Rev.* **36**, 990–1004.

[14] Rendueles, O., Ghigo, J-M. (2012). Multi-species biofilms: How to avoid unfriendly neighbors. *FEMS Microbiol. Rev.* **36**, 972–989.

[15] Srey, S., Jahid, I.K., Ha, S.-D. (2013). Biofilm formation in food industries: A food safety concern. *Food Control* **31**, 572–585.

[16] Bryers, J.D., Characklis, W.G. (1992). Biofilm accumulation and activity: A process analysis approach. In Melo, L.F., Bott, T.R., Fletcher, M., Capdeville, B. (eds.), *Biofilms–Science and Technology*, Vol. 223, NATO ASI Series E: Applied Sciences. Kluwer Academic Publishers, pp. 221–237.

[17] Hiraki, A., Tsuchiya, Y., Fukuda, Y., Yamamoto, T., Kurniawan, A., Morisaki, H. (2009). Analysis of how a biofilm forms on the surface of the aquatic macrophyte *Phragmites australis*. *Microbes Environ*. **24**, 265–272.

[18] Molin, S., Tolker-Nielsen, T. (2003). Gene transfer occurs with enhanced efficiency in biofilms and induces enhanced stabilisation of the biofilm structure. *Curr. Opin. Biotechnol.* **14**, 255–261.

[19] Brading, M.G., Jass, J., Lappin-Scott, H.M. (1995). Dynamics of bacterial biofilm formation. In Lappin-Scott, H.M., Costerton, J.W. (eds.), *Microbial Biofilms.* Cambridge Univ. Press, Cambridge, UK, pp. 46–63.

[20] Morisaki, H. (2012). Surface characteristics and attachment behaviors of bacterial cells. In Ohshima, H. (ed.), *Electrical Phenomena at Interfaces and Biointerfaces: Fundamentals and Applications in Nano-, Bio-, and Environmental Sciences.* Wiley, Hoboken, NJ, pp. 737–754.

[21] Katsikogianni, M., Missirlis, Y.F. (2004). Concise review of mechanisms of bacterial adhesion to biomaterials and of the techniques used in estimating bacteria-material interactions. *Eur. Cells Mater.* **8**, 37–57.

[22] Hogt, A.H., Dankert, J., Feijen, J., De Wries, J.A. (1982). Cell surface hydrophobicity of *Staphylococcus* species and adhesion onto biomaterials. *Antonie van Leeuwenhoek* **48**, 496–498.

[23] Rad, A.Y., Ayhan, H., Piskin, E. (1998). Adhesion of different bacterial strains to low-temperature plasma-treated sutures. *J. Biomed. Mater. Res.* **41**, 349–358.

[24] Roosjen, A., Busscher, H.J., Norde, W., van der Mei, H.C. (2006). Bacterial factors influencing adhesion of *Pseudomonas aeruginosa* strains to a poly (ethylene oxide) brush. *Microbiology* **152**, 2673–2682.

[25] Yu, J., Kim, D., Lee, T., (2010). Microbial diversity in biofilms on water distribution pipes of different materials. *Water Sci. Technol.* **61**, 164–171.

[26] Characklis, W.G., McFeters, G.A., Marshall, K.C. (1990). Physiological ecology in biofilm systems. In Characklis, W.G., Marshall, K.C. (eds.), *Biofilms.* Wiley, New York, pp. 341–394.

[27] Marshall, K.C. (1976). *Interfaces in Microbial Ecology*. Harvard Univ. Press, Cambridge, MA.

[28] Ohshima, H. (1994). Electrophoretic mobility of soft particles. *J. Colloid Interface Sci.* **163**, 474–483.

[29] Ohshima, H. (1995). Electrophoresis of soft particles. *Adv. Colloid Interface Sci.* **62**, 189–235.

[30] Ohshima, H. (2002). Electrophoretic mobility of a charged spherical colloidal particle covered with an uncharged polymer layer. *Electrophoresis* **23**, 1993–2000.

[31] Kogure, K., Ikemoto, E., Morisaki, H. (1998). Attachment of *Vibrio alginolyticus* to lass surfaces is dependent on swimming speed. *J. Bacteriol.* **180**, 932–937.

[32] Morisaki, H., Nagai, S., Ohshima, H., Ikemoto, E., Kogure, K. (1999). The effect of motility and cell-surface polymers on bacterial attachment. *Microbiology* **145**, 2797–2802.

[33] Morisaki, H., Tabuchi, H. (2009). Bacterial attachment over a wide range of ionic strengths. *Colloids Surf. B: Biointerfaces* **74**, 51–55.

[34] Romaní, A.M., Giorgi, A., Acuña, V., Sabater, S. (2004). The influence of substratum type and nutrient supply on biofilm organic matter utilization in streams. *Limnol. Oceanogr.* **49**(5), 1713–1721.

[35] Rusznyák, A., Vladár, P., Molnár, P., Reskóné, M.N., Kiss, G., Márialigeti, K., Borsodi, A.K. (2008). Cultivable bacterial composition and BIOLOG catabolic diversity of biofilm communities developed on *Phragmites australis. Aquat. Botany* **88**, 211–218.

[36] Yamamoto, M., Murai, H., Takeda, A., Okunishi, S., Morisaki, H. (2005).Bacterial flora of the biofilm formed on the submerged surface of the reed *Phragmites australis. Microbes Environ*. **20**, 14–24.

[37] Tsuchiya, Y., Hiraki, A., Kiriyama, C., Arakawa, T., Kusakabe, R., Morisaki, H. (2011). Seasonal change of bacterial community structure in a biofilm formed on the surface of the aquatic macrophyte (*Phragmites australis*). *Microbes Environ.* **26**, 113–119.

[38] Jones, P.R., Cottrell, M.T., Kirchman, D.L., Dexter, S.C. (2007). Bacterial community structure of biofilms on artificial surfaces in an estuary. *Microbial Ecol.* **53**, 153–162.

[39] Kim, L., Pagaling, E., Zuo, Y.Y., Yan, T. (2014). Impact of substratum surface on microbial community structure and treatment performance in biological aerated filters. *Appl. Environ. Microbiol.* **80**, 177–183.

[40] Liao, J., Fukui, H., Urakami, T., Morisaki, H. (2010). Effect of biofilm on ennoblement and localized corrosion of stainless steel in fresh dam-water. *Corrosion Sci.* **52**, 1393–1403.

[41] Jones, D.A., Amy, P.S. (2002). A thermodynamic interpretation of microbiologically influenced corrosion. *Corrosion* **58**, 638–645.

[42] Hamilton, W.A. (2003). Microbially influenced corrosion as a model system for the study of metal microbe interactions: A unifying electron transfer hypothesis. *Biofouling* **19**, 65–76.

[43] Fint, S., Wolfaardt, G. (2012). Corrosion and fouling. In Lear, G., Lewis, G. (eds.), *Microbial Biofilms.* Caister Academic Press, Norfolk, UK, pp. 111–128.

[44] Marsh, P.D., Martin, M.V. (1992). *Oral Microbiology*, 3rd ed. Chapman & Hall, London.

[45] Donlan, R.M. (2001). Biofilm formation: A clinically relevant microbiological process. *Clin. Infect. Diseases* **33**, 1387–1392.

[46] Bryers, J.D. (2012). Biofilms in disease. In Lear, G., Lewis, G. (eds.), *Microbial Biofilms.* Caister Academic Press, Norfolk, UK, pp. 25–42.

[47] Poulsen, L.V. (1999). Microbial biofilm in food processing. *Lebensm. Wissenschaft. Technol.* **32**, 321–326.

[48] Shi, X., Zhu, X. (2009). Biofilm formation and food safety in food industries. *Trends Food Sci. Technol.* **20**, 407–413.

[49] Brumølle, M., Kjølleer, A., Sørensen, S.J. (2012). An invisible workforce: Biofilms in the soil. In Lear, G., Lewis, G. (eds.), *Microbial Biofilms.* Caister Academic Press, Norfolk, UK, pp. 61–71.

[50] Stach, J.E.M., Burns, R.G. (2002). Enrichment versus biofilm culture: a functional and phylogenetic comparison of polycyclic aromatic hydrocarbon-degrading microbial communities. *Environ. Microbiol.* **4**, 169–182.

[51] Jonsen, A.R., Lukas, W.Y., Harms, H. (2005). Principles of microbial PAH-degradation in soil. *Environ. Pollut.* **133**, 71–87.

[52] Webb, H.K., Crawford, R.J., Sawabe, T., Ivanova, E.P. (2009). Poly(ethylene terephthalate) polymer surfaces as a substrate for bacterial attachment and biofilm formation. *Microbes Environ.* **24**, 39–42.

[53] Dasgupta, D., Ghosh, R., Sengupta, T.K. (2013). Biofilm-mediated enhanced crude oil degradation by newly isolated *Pseudomonas* species. *ISRN* (*International Scholarly Research Notices*) *Biotechnol.* **2013**, 1–13.

[54] Breugelmans, P., Barken, K.B., Tolker-Nielsen, T., Hofkens, J., Dejonghe, W., Springael, D. (2008). Architecture and

spatial organization in a triple-species bacterial biofilm synergistically degrading the phenylurea herbicide linuron. *FEMS Microbiol. Ecol.* **64**, 271–282.

[55] Bais, H.P., Fall, R., Vivanco, J.M. (2004). Biocontrol of *Bacillus subtilis* against infection of Arabidopsis roots by *Pseudomonas syringae* is facilitated by biofilm formation and surfactin production. *Plant Physiol.* **134**, 307–319.

[56] Rudrappa, T., Czymmek, K.J., Pare, P.W., Bais, H.P. (2008). Root-secreted malic acid recruits beneficial soil bacteria. *Plant Physiol.* **148**, 1547–1556.

[57] Angus, A.A., Hirsh, A.M. (2013). Biofilm formation in the rhizosphere: Multispecies interactions and implications for plant. In de Bruijn, F.J. (ed.), *Molecular Microbial Ecology of the Rhizosphere*, Vol. 2. Wiley, Hoboken, NJ, pp. 701-712.

[58] Fujishige, N.A., Kapadia, N.N., Hirsch, A.M. (2006). A feeling for the microorganism: Structure on a small scale. Biofilms on plant roots. *Botan. J. Linnean Soc.* **150**, 79–88.

[59] Lakshmanan, V., Kumar, A.S., Bais, H.P. (2012). The ecological significance of plant-associated biofilms. In Lear, G., Lewis, G. (eds.), *Microbial Biofilms.* Caister Academic Press, Norfolk, UK, pp. 43–60.

[60] Bogino, P.C., Oliva, M.M., Sorroche, F.G., Giordano, W. (2013). The role of bacterial biofilms and surface components in plant-bacterial associations. *Int. J. Mol. Sci.* **14**, 15838–15859.

[61] Ramey, B.E., Koutsoudis, M., von Bodman, S.B., Fuqua, C. (2004). Biofilm formation in plant–microbe associations. *Curr. Opin. Microbiol.* **7**, 602–609.

[62] Timmusk, S., Grantcharova, N., Wagner, E.G.H. (2005). *Paenibacillus polymyxa* invades plant roots and forms biofilms. *Appl. Environ. Microbiol.* **71**, 7292–7300.

[63] Koutsoudis, M.D., Tsaltas, D., Minogue, T.D., von Bodman, S.B. (2006). Quorum-sensing regulation governs bacterial adhesion, biofilm development, and host colonization in *Pantoea stewartii* subspecies *stewartii*. *Proc. Natl. Acad. Sci., USA* **103**, 5983–5988.

[64] Monier, J.M., Lindow, S.E. (2005). Spatial organization of dual-species bacterial aggregates on leaf surfaces. *Appl. Environ. Microbiol.* **71**, 5484–5493.

[65] Chen, Y., Cao, S., Chai, Y., Clardy, J., Kolter, R., Guo, J.-H., Losick, R. (2012). A *Bacillus subtilis* sensor kinase involved in triggering biofilm formation on the roots of tomato plants. *Mol. Microbiol.* **85**, 418–430.

[66] Beauregarda, P.B., Chai, Y., Vlamakisa, H., Losickb, R., Koltera, R. (2013). *Bacillus subtilis* biofilm induction by plant polysaccharides. *Proc. Natl. Acad. Sci.* (published online April 8, E1621–E1630).

[67] Shemesh, M., Tam, A., Steinberg, D. (2007). Differential gene expression profiling of *Streptococcus mutans* cultured under biofilm and planktonic conditions. *Microbiology* **153**, 1307–1317.

[68] Gilmore, M.S. (2003). Growth, development, and gene expression in a persistent *Streptococcus gordonii* biofilm. *Infect. Immun.* **71**, 4759–4766.

[69] Marsh, P.D. (2005). Dental plaque: Biological significance of a biofilm and community life-style. *J. Clin. Periodontol.* **32**, 7–15.

[70] Steinberg, D. (2000). Studying plaque biofilms on various dental surfaces. In An, Y.H., Friedman, R.J. (eds.), *Handbook of Bacterial Adhesion: Principles, Methods, and Applications.* Humana Press, Totowa, NJ, pp. 353–370.

[71] Stewart, P.S., Costerton, J.W. (2001). Antibiotic resistance of bacteria in biofilms. *Lancet* **358**, 135–138.

[72] Whiteley, M., Bangera, M.G., Bumgarner, R.E., Parsek, M.R., Teitzel, G.M., Lory, S., Greenberg, E.P. (2001). Gene expression in *Pseudomonas aeruginosa* biofilms. *Nature* **413**, 860–864.

[73] Wen, Z.T., Burne, R.A. (2002). Functional genomics approach to identifying genes required for biofilm development by *Streptococcus mutans*. *Appl. Environ. Microbiol.* **68**, 1196–1203.

[74] Beenken, K.E., Dunman, P.M., McAleese, F., Macapagal, D., Murphy, E., Projan, S.J., Blevins, J.S., Smeltzer, M.S. (2004). Global gene expression in *Staphylococcus aureus* biofilms. *J. Bacteriol.* **186**, 4665–4684.

[75] Domka, J., Lee, J., Bansal, T., Wood, T.K. (2007). Temporal gene-expression in *Escherichia coli* K-12 biofilms. *Environ. Microbiol*. **9**, 332–346.

[76] He, X., Ahn, J. (2011). Differential gene expression in planktonic and biofilm cells of multiple antibiotic-resistant *Salmonella typhimurium* and *Staphylococcus aureus*. *FEMS Microbiol. Lett*. **325**, 180–188.

[77] Ghigo, J.M. (2001). Natural conjugative plasmids induce bacterial biofilm development. *Nature* **412**, 442–445.

[78] Roberts, A.P., Mullany, P., Wilson, M. (2001). Gene transfer in bacterial biofilms. *Methods Enzymol.* **336**, 60–65.

[79] Fux, C.A. (2005). Survival strategies of infectious biofilms. *Trends Microbiol.* **13**, 34–40.

[80] Singh, R., Paul, D., Jain, R.K. (2006). Biofilms: Implications in bioremediation. *Trends Microbiol.* **14**, 389–397.

[81] Fletcher, M. (1992). Bacterial metabolism in biofilms. In Melo, L.F., Bott, T.R., Fletcher, M., Capdeville, B. (eds.), *Biofilms–Science and Technology*, Vol. 223. NATO ASI Series, Series E: Applied Sciences. Kluwer Academic Publishers, pp. 113–124.

[82] Haynes, K., Hofmann, T.A., Smith, C.J., Ball, A.S., Underwood, G.J.C., Osborn, A.M. (2007). Diatom-derived carbohydrates as factors affecting bacterial community composition in estuarine sediments. *Appl. Environ. Microbiol.* **73**, 6112–6124.

[83] Bruckner, C.G., Bahulikar, R., Rahalkar, M., Schink, B., Kroth, P.G. (2008). Bacteria associated with benthic diatoms from Lake Constance: Phylogeny and influences on diatom growth and secretion of extracellular polymeric substances. *Appl. Environ. Microbiol*. **74**, 7740–7749.

[84] Domozych, D.S., Domozych, C.R. (2008). Desmids and biofilms of freshwater wetlands: Development and microarchitecture. *Microbial Ecol.* **55**, 81–93.

[85] Parry, J.D. (2004). Protozoan grazing of freshwater biofilms. *Adv. Appl. Microbiol.* **54**, 167–187.

[86] Huws, S.A., McBain, A.J., Gilbert, P. (2005). Protozoan grazing and its impact upon population dynamics in biofilm communities. *J. Appl. Microbiol.* **98**, 238–244.

[87] Chabaud, S., Andres, Y., Lakea, A., Le Cloirec, P. (2006). Bacteria removal in septic effluent: Influence of biofilm and protozoa. *Water Res.* **40**, 3109–3114.

[88] Wey, J.K., Jürgens, K., Weitere, M. (2012). Seasonal and successional influences on bacterial community composition exceed that of protozoan grazing in river biofilms. *Appl. Environ. Microbiol.* **78**, 2013–2024.

[89] Nealson, K.H., Platt, T., Hastings, J.W. (1970). Cellular control of the synthesis and activity of the bacterial luminescent system. *J. Bacteriol.* **104**, 313–322.

[90] Novick, R.P., Geisinger, E. (2008). Quorum sensing in staphylococci. *Annu. Rev. Genet.* **42**, 541–564.

[91] Goldstone, R.J., Popat, R., Fletcher, M.P., Crusz, S.A., Diggie, S.P. (2012). Quorum sensing and social interactions in microbial biofilms. In Lear, G., Lewis, G. (eds.), *Microbial Biofilms.* Caister Academic Press, Norfolk, UK, pp. 1–24.

[92] Williams, P., Winzer, K., Chan, W., Cámara, M. (2007). Look who's talking: Communication and quorum sensing in the bacterial world. *Phil. Trans. Roy. Soc. B.* **362**, 1119–1134.

[93] Ng, W.L., Bassler, B.L. (2009). Bacterial quorum-sensing network architectures. *Annu. Rev. Genet.* **43**, 197–222.

[94] Bamford, C.V., d'Mello, A., Nobbs, A.H., Dutton, L.C., Vickerman, M.M., Jenkinson H.F. (2009). *Streptococcus gordonii* modulates *Candida albicans* biofilm formation through intergeneric communication. *Infect. Immun.* **77**, 3696–3704.

[95] Hartmann, A., Schikora, A. (2012). Quorum sensing of bacteria and trans-kingdom interactions of N-acyl homoserine lactones with eukaryotes. *J. Chem. Ecol.* **38**, 704–713.

[96] Kalia, V.C. (2013). Quorum sensing inhibitors: An overview. *Biotechnol. Adv.* **31**, 224–245.

[97] Dong, Y.H., Wang, L.H., Xu, J.L., Zhang, H.B., Zhang, X.F., Zhang, L.H. (2001). Quenching quorum-sensing-dependent bacterial infection by an N-acyl homoserine lactonase. *Nature* **411**, 813–817.

[98] Roche, D.M., Byers, J.T., Smith, D.S., Glansdorp, F.G., Spring, D.R., Welch, M. (2004). Communications blackout? Do N-acylhomoserine-lactone-degrading enzymes have any role in quorum sensing? *Microbiology* **150**, 2023–2028.

[99] Dong, Y.H., Zhang, L.H. (2005). Quorum sensing and quorum-quenching enzymes. *J. Microbiol.* **43**, 101–109.

[100] Czajkowski, R., Jafra, S. (2009). Quenching of acyl-homoserine lactone-dependent quorum sensing by enzymatic disruption of signal molecules. *Acta Biochim. Pol.* **56**, 1–16.

[101] Bhardwaj, A.K., Vinothkumar, K., Rajpara, N. (2013). Bacterial quorum sensing inhibitors: Attractive alternatives for control of infectious pathogens showing multiple drug resistance. *Recent Patents Antiinfect. Drug Discov.* **8**, 68–83.

[102] Persson, T., Givskov, M., Nielsen, J. (2005). Quorum sensing inhibition: Targeting chemical communication in gram-negative bacteria. *Curr. Med. Chem.* **12**, 3103–3115.

[103] Janssens, J.C., De Keersmaecker, S.C., De Vos, D.E., Vanderleyden, J. (2008). Small molecules for interference with cell-cell communication systems in Gram-negative bacteria. *Curr. Med. Chem.* **15**, 2144–2156.

[104] Truchado, P., Gil-Izquierdo, A., Tomás-Barberáan, F., Allende, A. (2009). Inhibition by chestnut honey of N-acyl-L-homoserine lactones and biofilm formation in *Erwinia carotovora*, *Yersinia enterocolitica*, and *Aeromonas hydrophila*. *J. Agric. Food Chem.* **57**, 11186–11193.

[105] López, D., Vlamakis, H., Kolter, R. (2010). Biofilms. *Cold Spring Harbor Perspect. Biol.* **2**, a000398.

[106] Frølund, B., Palmgren, R., Keiding, K., Nielsen, P.-H. (1996). Extraction of extracellular polymers from activated sludge using a cation exchange resin. *Water Res.* **30**, 1749–1758.

[107] Wingender, J., Strathmann, M., Rode A., Leis A., Flemming, H.-C. (2001). Isolation and biochemical characterization of extracellular polymeric substances from *Pseudomonas aeruginosa*. *Methods Enzymol.* **336**, 302–314.

[108] Ras, M., Lefebvre, D., Derlon, N., Paul, E., Girbal-Neuhauser, E. (2011). Extracellular polymeric substances diversity of biofilms grown under contrasted environmental conditions. *Water Res.* **45**, 1529–1538.

[109] Nichols, C.A.M., Guezennec, J., Bowman, J.P. (2005). Bacterial exopolysaccharides from extreme marine environments with special consideration of the southern ocean, sea ice, and deep-sea hydrothermal vents: A review. *Marine Biotechnol.* **7**, 253–271.

[110] Sutherland, I.W. (2001). The biofilm matrix–an immobilized but dynamic microbial environment. *Trends Microbiol.* **9**, 222–227.

[111] Conrad, A., Kontro, M., Keinanen, M.M., Cadoret, A., Faure, P., Mansuy-Huault, L., Block, J.C. (2003). Fatty acid lipid fractions in extracellular polymeric substances of activated sludge flocs. *Lipids* **38**, 1093–1105.

[112] Wingender, J., Jaeger, K.-E. (2002). Extracellular enzymes in biofilms. In Bitton, G. (ed.), *Encyclopedia of Environmental Microbiology*, Vol. 3. Wiley, New York, pp. 1207–1223.

[113] Wingender, J., Neu, T.R, Flemming, H.-C. (1999). What are bacterial extracellular polymeric substances? In Wingender, J., Neu, T.R., Flemming, H.-C. (eds.), *Microbial Extracellular Polymeric Substances*. Springer, Berlin, pp. 1–2.

[114] Persson, T., Givskov, M., Nielsen, J. (2005). Quorum sensing inhibition: Targeting chemical communication in Gram-negative bacteria. *Curr. Med. Chem.* **12**, 3103–3115.

[115] Pietramellara, G., Ascher, J., Borgogni, F., Ceccherini, M.T., Guerri, G., Nannipieri, P. (2009). Extracellular DNA in soil and sediment: Fate and ecological relevance. *Biol. Fertil. Soils* **45**, 219–235.

[116] Sand, W., Gehrke, T. (2006). Extracellular polymeric substances mediate bioleaching/biocorrosion via interfacial processes involving iron(III) ions and acidophilic bacteria. *Res. Microbiol.* **157**, 49–56.

[117] Matsuyama, T., Nakagawa, Y. (1996). Surface-active exolipids: Analysis of absolute chemical structures and biological functions. *J. Microbiol. Methods* **25**, 165–175.

[118] Matsuyama, T., Tanikawa, T., Nakagawa, Y. (2011). Serawettins and other surfactants produced by *Serratia*. In Soberón-Chávez, G. (ed.), *Biosurfactants*, Microbiology Monographs 20. Springer-Verlag, Berlin, pp. 93-120.

[119] Ron, E.Z., Rosenberg, E. (2001). Natural role of biosurfactants. *Environ. Microbiol.* **3**, 229–236.

[120] Iwabuchi, N., Sunairi, M., Urai, M., Itoh, C., Anzai, H., Nakajima, M., Harayama, S. (2002). Extracellular polysaccharides of *Rhodococcus rhodochrous* S-2 stimulate the degradation of aromatic components in crude oil by indigenous marine bacteria. *Appl. Environ. Microbiol*. **68**, 2337–2343.

[121] Melo, L.F. (2005). Biofilm physical structure, internal diffusivity and tortuosity. *Water Sci. Technol.* **52**, 77-84.

[122] Fan, L.-S., Leyva-Ramos, R., Wisecarver, K.D., Zehner, B.J. (1990). Diffusion of phenol through a biofilm grown on activated carbon particles in a draft-tube three-phase fluidized bed bioreactor. *Biotech. Bioeng.* **35**, 279–286.

[123] Bishop, P.L., Zhang, T.C., Fu, Y.-C. (1995). Effects of biofilm structure, microbial distributions and mass transport on biodegradation processes. *Water Sci. Technol.* **31**, 143–152.

[124] Stewart, P. (1998). A review of experimental measurements of effective diffusive permeabilities and effective diffusion coefficients in biofilms. *Biotechnol. Bioeng.* **59**, 261–272.

[125] Beyenal, H., Lewandowski, Z. (2002). Internal and external mass transfer in biofilms grown at various flow velocities. *Biotechnol. Progress* **18**, 55–61.

[126] Stewart, P. (2003). Diffusion in biofilms. *J. Bacteriol.* **185**, 1485–1491.

[127] Zalc, J., Reyes, S.C., Iglesia, E. (2004). The effects of diffusion mechanism and void structure on transport rates and tortuosity factors in complex porous structures. *Chem. Eng. Sci.* **59**, 2947–2960.

[128] Kinniment, S.L., Wimpenny, J.W.T. (1992). Measurements of the distribution of adenylate concentrations and adenylate energy charge across *Pseudomonas aeruginosa* biofilms. *Appl. Environ. Microbiol.* **58**, 1629–1635.

[129] Wentland, E., Stewart, P.S., Huan, C.-T., McFeters, G.A. (1996). Spatial variations in growth rate within *Klebsiella pneumoniae* colonies and biofilm. *Biotechnol. Progress* **12**, 316–321.

[130] Sternberg, C., Christensen, B.B., Johansen, T., Nielsen, A.T., Andersen, J.B., Givskov, M., Molin, S. (1999). Distribution of bacterial growth activity in flow- chamber biofilms. *Appl. Environ. Microbiol.* **65**, 4108–4117.

[131] Wimpenny, J.W.T., Kinniment, S.L. (1995). Biochemical reactions and the establishment of gradients within biofilms. In Lappin-Scott, H.M., Costerton, J.W. (eds.), *Microbial Biofilms.* Cambridge Univ. Press, Cambridge, UK, pp. 99–117.

[132] Huang, C.-T., Xu, K.D., McFeter, G.A., Stewart, P.S. (1998). Spatial patterns of alkaline phosphatase expression within bacterial colonies and biofilms in response to phosphate starvation. *Appl. Environ. Microbiol.* **64**, 1526–1531.

[133] Xu, K.D., Stewart, P.S., Xia, F., Huang, C.-T., McFeters, G.A. (1998). Spatial physiological heterogeneity in *Pseudomonas aeruginosa* biofilm is determined by oxygen availability. *Appl. Environ. Microbiol.* **64**, 4035–4039.

[134] Xu, K.D., McFeters, G.A., Stewart, P.S. (2000). Biofilm resistance to antimicrobial agents. *Microbiology* **146**, 547–549.

[135] Tsuchiya, Y., Ikenaga, M., Kurniawan, A., Hiraki, A., Arakawa, T., Kusakabe, R., Morisaki, H. (2009). Nutrient-rich microhabitats within biofilms are synchronized with the external environment. *Microbes Environ.* **24**, 43–51.

[136] Kröpfl, K., Záray, Gy., Vladár, P., Mages, M., Ács, É. (2003). Study of biofilm formation by total-reflection X-ray fluorescence spectrometry. *Microchem. J.* **75**, 133–137.

[137] Záray, G., Kröpfl, K., Szabó, K., Taba, G., Ács, É., Berlinger, B., Dogan, M., Salih, B., Akbulut, A. (2005). Comparison of freshwater biofilms grown on polycarbonate substrata in Lake Velence (Hungary) and Lake Mogan (Turkey). *Microchem. J.* **79**, 145–148.

[138] Bourven, I., Joussein, E., Guibaud, G. (2011). Characterisation of the mineral fraction in extracellular polymeric substances (EPS) from activated sludges extracted by eight different methods. *Bioresource Technol.* **102**, 7124–7130.

[139] Kurniawan, A., Yamamoto, T., Tsuchiya, Y., Morisaki, H. (2012). Analysis of the ion adsorption–desorption characteristics of biofilm matrices. *Microbes Environ.* **27**, 399–406.

[140] Van Hullebusch, E.D., Zandvoord, M.H., Lens, P.N.L. (2004). Metal immobilization by biofilms: Mechanisms and analytical tools. *Rev. Environ. Sci. Biotechnol.* **2**, 9–33.

[141] Wang, Q., Zhang, T. (2010). Review of mathematical models for biofilms. *Solid State Commun.* **150**,1009–1022.

[142] Vieira, M.J., Melo, L.F., Pinheiro, M.M. (1993). Biofilm formation – hydrodynamic effects on internal diffusion and structure. *Biofouling* **7**, 67–80.

[143] Peyton, B.M. (1996). Effects of shear stress and substrate loading rate on *Pseudomonas aeruginosa* biofilm thickness and density. *Water Res.* **30**, 29–36.

[144] Hermanowicz, S.W. (1999). Two-dimensional simulations of biofilm development: Effects of external environmental conditions. *Water Sci. Technol.* **39**, 107–114.

[145] Melo, L.F., Vieira, M.J. (1999). Physical stability and biological activity of biofilms formed under turbulent flow and low substrate concentration. *Bioprocess Eng.* **20**, 363–368.

[146] Wijeyekoon, S., Mino, T., Satoh, H., Matsuo, T. (2004). Effects of substrate loading rate on biofilm structure. *Water Res.* **38**, 2479–2488.

[147] Bonaventura, G.D, Stepanovi, S., Picciani, C., Pompilio, A., Piccolomini, R. (2007). Effect of environmental factors on biofilm formation by clinical *Stenotrophomonas maltophilia* isolates. *Folia Microbiol.* **52**, 86–90.

[148] Ramli, N.S.K., Guan, C.E., Nathan, S., Vadivelu, J. (2012). The effect of environmental conditions on biofilm formation

of *Burkholderia pseudomallei* clinical isolates. PLoS ONE **7**(9), e44104.

[149] Battin, T.J., Sloan, W.T., Kjelleberg, S., Daims, H., Head, I.M., Curtis, T.P., Eberl, L. (2007). Microbial landscapes: New paths to biofilm research. *Nat. Rev. Microbiol.* **5**, 76–81.

[150] Moss, J.A., Nocker, A., Lepo, J.E., Richard, A., Snyder, R.A. (2006). Stability and change in estuarine biofilm bacterial community diversity. *Appl. Environ. Microbiol.* **72**, 5679–5688.

[151] Romaní, A.M., Sabater, S. (1999). Effect of primary producers on the heterotrophic metabolism of a stream biofilm. *Freshwater Biol*. **41**, 729–736.

[152] Espeland, E.M., Francoeur, S.N., Wetzel, R.G. (2001). Influence of algal photosynthesis on biofilm bacterial production and associated glucosidase and xylosidase activities. *Microbial Ecol.* **42**, 524–530.

[153] Roeselers, G., van Loosdrecht, M.C.M., Muyzer, G. (2007). Heterotrophic pioneers facilitate phototrophic biofilm development. *Microbial Ecol.* **54**, 578–585.

[154] Jones, S.E., Lock, M.A. (1993). Seasonal determinations of extracellular hydrolytic activities in heterotrophic and mixed heterotrophic/autotrophic biofilms from two contrasting rivers. *Hydrobiologia* **257**, 1–16.

[155] Olapade, O.A., Leff, L.G. (2005). Seasonal response of stream biofilm communities to dissolved organic matter and nutrient enrichments. *Appl. Environ. Microbiol.* **71**, 2278–2287.

[156] Proia, L., Romaní, A.M., Sabater, S. (2012). Nutrients and light effects on stream biofilms: A combined assessment with CLSM, structural and functional parameters. *Hydrobiologia* **695**, 281–291.

[157] Lear, G., Niyogi, D., Harding, J., Dong, Y., Lewis, G. (2009). Biofilm bacterial community structure in streams affected by acid mine drainage. *Appl. Environ. Microbiol.* **75**, 3455–3460.

[158] Ylla, I., Romaní, A.M., Sabater, S. (2012). Labile and recalcitrant organic matter utilization by river biofilm under increasing water temperature. *Microbial Ecol*. **64**, 593–604.

[159] Rochex, A., Godon, J.-J., Bernet, N., Escudié, R. (2008). Role of shear stress on composition, diversity and dynamics of biofilm bacterial communities. *Water Res.* **42**, 4915–4922.

[160] Hempel, M., Grossart, H.-P., Gross, E.M. (2009). Community composition of bacterial biofilms on two submerged macrophytes and an artificial substrate in a pre-alpine lake. *Aquat. Microbial Ecol.* **58**, 79–94.

[161] Brümmer, I.H.M., Fehr, W., Wagner-Döbler, I. (2000). Biofilm community structure in polluted rivers: Abundance of dominant phylogenetic groups over a complete annual cycle. *Appl. Environ. Microbiol.* **66**, 3078–3082.

[162] Lyautey, E., Jackson, C.R., Cayrou, J., Rols, J.-L., Garabétian, F. (2005). Bacterial community succession in natural river biofilm assemblages. *Microbial Ecol.* **50**, 589–601.

[163] Ishizawa, S., Yamamoto, Y., Denboh, T., Ueda, H. (2010). Release of dissolved free amino acids from biofilms in stream water. *Fish. Sci.* **76**, 669–676.

[164] Battin, T.J., Kaplan, L.A., Newbold, J.D., Hansen, C.M.E. (2003). Contributions of microbial biofilms to ecosystem processes in stream mesocosms. *Nature* **426**, 439–442.

[165] Findlay, S. (2010). Stream microbial ecology. *J. North Am. Benthol. Soc.* **29**, 170 –181.

[166] Hao, X.D., Wang, Q.L., Zhu, J.Y., van Loosdrecht, M.C.M. (2010). Microbiological endogenous processes in biological wastewater treatment systems. *Crit. Rev. Environ. Sci. Technol.* **40**, 239–265.

[167] Piyasena, P., Mohareb, E., McKellar, R.C. (2003). Inactivation of microbes using ultrasound: A review. *Int. J. Food Microbiol.* **87**, 207–216.

[168] Upadhyayula, V.K.K., Gadhamshetty, V. (2010). Appreciating the role of carbon nanotube composites in preventing biofouling and promoting biofilms on material surfaces in environmental engineering: A review. *Biotechnol. Adv.* **28**, 802–816.

[169] Kolodkin-Gal, I., Romero, D., Cao, S., Clardy, J., Kolter, R., Losick, R. (2010). D-Amino acids trigger biofilm disassembly. *Science* **328**, 627–629.

[170] Vejborg, R.M., Klemm, P. (2008). Blocking of bacterial biofilm formation by a fish protein coating. *Appl. Environ. Microbiol.* **74**, 3551–3558.

[171] Tamilvanan, S., Venkateshan, N., Ludwig, A. (2008). The potential of lipid- and polymer-based drug delivery carriers for eradicating biofilm consortia on device-related nosocomial infections. *J. Control. Release* **128**, 2–22.

[172] Uroz, S., Dessaux, Y., Oger, P. (2009). Quorum sensing and quorum quenching: The yin and yang of bacterial communication. *Chem. Biol. Chem.* **10**, 205–216.

[173] Wyndham, R.C., Kennedy, K.J. (1995). Microbial consortia in industrial wastewater treatment. In Lappin-Scott, H.M., Costerton, J.W. (eds.), *Microbial Biofilms.* Cambridge Univ. Press, Cambridge, UK, pp. 183–195.

[174] Mendez, R., Lema, J.M. (1992). Biofilm reactors technology in wastewater treatment. In Melo, L.F., Bott, T.R., Fletcher, M., Capdeville, B. (eds.), *Biofilms–Science and Technology*, Vol. 223. NATO ASI Series, Series E: Applied Sciences. Kluwer Academic Publishers, pp. 409–419.

[175] Pastorella, G., Gazzola, G., Guardarrama, S., Marsili, E. (2012). Biofilms: Application in bioremediation. In Lear, G., Lewis, G. (eds.), *Microbial Biofilms.* Caister Academic Press, Norfolk, UK, pp. 73–98.

[176] Sen, R. (2003). The root–microbe–soil interface: New tools for sustainable plant production. *New Phytologist* **157**, 391–398.

[177] Logan, B.E. (2009). Exoelectrogenic bacteria that power microbial fuel cells. *Nat. Rev. Microbiol.* **7**, 375–381.

[178] Franks, A.E., Nevin, K.P. (2010). Microbial fuel cells, a current review. *Energies* **3**, 899–919.

[179] Tian, M., Kanavillil, N., Davey, L., Leung, K.Y., Schraft, H., Chen, A. (2007). Direct growth of biofilms on an electrode

surface and its application in electrochemical biosensoring. *J. Electroanal. Chem.* **611**, 133–139.

[180] Blenkinsopp, S.A., Costerton, J.W. (1991). Understanding bacterial biofilms. *Trends Biotechnol.* **9**, 138–143.

[181] Costerton, J.W., Cheng, K.J., Geesey, G.G., Ladd, T.I., Nickel, J.C., Dasgupta, M., Marrie, T. (1987). Bacterial biofilm in nature and disease. *Annu. Rev. Microbiol.* **41**, 435–464.

[182] Hamilton, W.A. (1987). Biofilms: Microbial interactions and metabolic activities. In Fletcher, M., Gray, T.R.G., Jones, J.G. (eds.), *Ecology of Microbial Communities.* Cambridge Univ. Press, Cambridge, UK, pp. 361–385.

[183] Freeman, C., Chapman, P.J., Gilman, K., Lock, M.A., Reynolds, B., Wheater, H.S. (1995). Ion exchange mechanisms and the entrapment of nutrients by river biofilms. *Hydrobiologia.* **297**, 61–65.

[184] Sabater, S., Romaní, A.M. (1996). Metabolic changes associated with biofilm formation in an undisturbed Mediterranean stream. *Hydrobiologia* **335**, 107–113.

[185] Serra, D.O., Richter, A.M., Klauck, G., Mika, F., Hengge, R. (2013). Microanatomy at cellular resolution and spatial order of physiological differentiation in a bacterial biofilm. *mBio* **4**(2), e00103–e00113.

[186] Okuda, S., Tsuchiya, Y., Kiriyama, C., Itoh, M., Morisaki, H. (2012). Virtual metagenome reconstruction from 16S rRNA gene sequences. *Nat. Commun.* **3**, 1203 (doi:10.1038/ncomms2203).

[187] Yamada, H., Takahashi, N., Okuda, S., Tsuchiya, Y., Morisaki, H. (2010). Direct observation and analysis of bacterial growth on an antimicrobial surface. *Appl. Environ. Microbiol.* **76**, 5409–5414.

[188] Furuhata, K., Ishizaki, N., Fukuyama, M. (2010). Characterization of heterotrophic bacteria isolated from the biofilm of a kitchen sink. *Biocontrol Sci.* **15**, 21–25.

[189] Bayles, K.W. (2007). The biological role of death and lysis in biofilm development. *Nat. Rev. Microbiol.* **5**, 721–726.

[190] Huq, A., Whitehouse, C.A., Grim, C.J., Alam, M., Colwell, R.R. (2008). Biofilms in water, its role and impact in human disease transmission. *Curr. Opin. Biotechnol.* **19**, 244–247.

[191] Trevors, J.T. (2011). Viable but non-culturable (VBNC) bacteria: Gene expression in planktonic and biofilm cells. *J. Microbiol. Methods* **86**, 266–273.

9

BIOFOULING

Kazuho Nakamura
Faculty of Engineering, Yokohama National University, Japan

9.1 DEFINITION OF BIOFOULING

Fouling is the process of accumulation of unwanted material at an interface and impedes the function of the surface in a component or system [1–3]. For example, the performance of reverse-osmosis membrane in desalination plants can be decreased by scale formation or bacteria adhesion on the membrane surface [4, 5]. The material that accumulates on surface can consist of either living organisms or nonliving organic/inorganic substances. Biofouling is caused by the accumulation of microorganisms, bacteria, fungi, plants, algae, or animals on solid surface in contact with water. The features of these living organisms in biofouling processes are growth and multiplication, and they can form biofilm, which is complex, multispecies, multidimensional communities on the surface. In the natural environment there are some advantages for living organisms when they are attached to an interface between a solid surface and water because nutrients are brought to them and waste products are carried away.

The impact of biofouling is higher economical costs for preventing and controlling it. Biofouling can occur under circumstances where water is in contact with other materials. In our living environments or certain industrial systems, biofouling usually decreases the performance of systems or devices, necessitating the development and implementation of biofouling prevention an removal methods. In shipping industries biofouling on the ship's hull significantly increases drag for hydrodynamic performance and the cost of fuel, and antifouling paints with toxic molecules are usually applied to prevent the biofouling [2].

In this chapter the impact of biofouling in some industries, mechanisms of the biofouling process, and antibiofouling strategies are introduced.

9.2 FORMATION OF BIOFILMS

The development of biofilm depends on complex behaviors of microorganisms at the interface between solids and water. The mechanism of biofilm formation significantly impacts in various industries as biofouling and its controlling methods. Figure 9.1 shows a typical sequence of events that lead to the formation of biofilms [6, 7]; (1) formation of conditioning film, (2) initial adhesion of microorganisms, (3) production of extracellular polymer substance (EPS) and multiplication, and (4) maturation of biofilm. In the formation of conditioning film, various organic and inorganic matter adsorbs to the solid surface and the formed layer is called *conditioning film*. The adhesion of microorganisms bacteria to the surface occurs via various physicochemical interactions, which can be described by the Derjaguin–Landau–Verwey–Overbeek (DLVO) theory, and bridging with EPS and cell appendages [6]. Biofilm is formed by growth and multiplication of the attached microorganisms and EPS produced by them. The matured biofilm has complex, multispecies, multidimensional communities.

9.3 BIOFOULING IN INDUSTRIES

When biofouling occurs in industrial operation, it interferes with efficiency of the operation. Effective control of biofouling is important to reduce operating costs, while some

Encyclopedia of Biocolloid and Biointerface Science, Volume 1, First Edition. Edited by Hiroyuki Ohshima.
© 2016 John Wiley & Sons, Inc. Published 2016 by John Wiley & Sons, Inc.

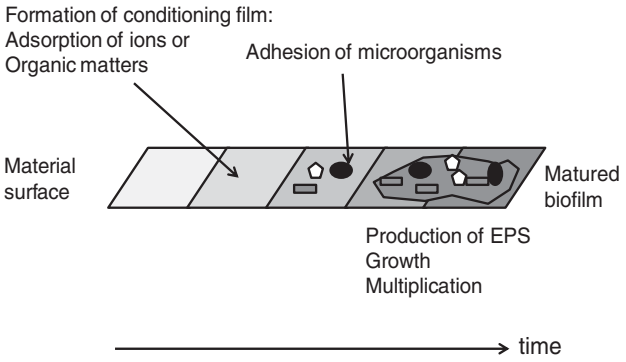


FIGURE 9.1 Adhesion of microbes and formation of biofilm.

biofilms are useful for the operation. In this section typical problems of the biofouling in some industries are introduced.

9.3.1 Biofouling in Heat Exchangers

Heat exchange systems are widely used in various industries, including power plants. Figure 9.2 shows the condenser in a power plant, which is core equipment and has heat exchange surfaces for condensing exhaust steam and for heat removal with the cooling fluid. Seawater is a typical cooling fluid employed in the condenser. The flow of the cooling fluid provided to adsorb the heat from condensing steam tends to create deposits on the heat exchange surface. The deposits are known as *fouling* and consist of biological deposits, sedimentation, precipitation, corrosion, and some inorganic substances [1].

The energy losses and economic cost associated with this fouling are significant. Fouling in heat exchangers is highly problematic for efficient operation and additional costs for design and maintenance. In coastal power plants using seawater as cooling fluid, the biological growth on the heat exchange surface is severe. The biological fouling layer causes higher heat transfer resistance and higher hydrodynamic resistance to flow of the cooling seawater in the heat exchangers. In addition to these difficulties in heat exchange operation, the design of excess heat transfer surface area and the maintenance needed for removing the fouling layer also increase the cost caused by the fouling.

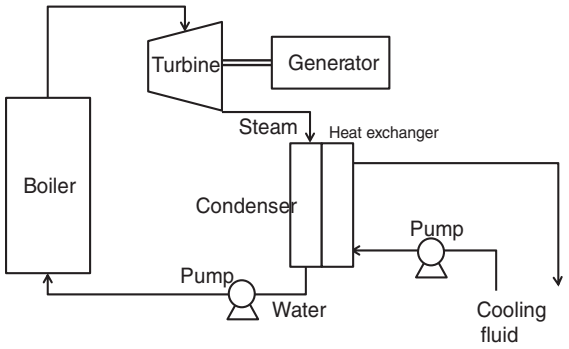


FIGURE 9.2 Heat exchanger in power plant.

Various methods have been used for preventing and removing fouling layer. The methods can be categorized into chemical and physical treatments. *Chemical* treatment consists in *oxidizing biocides*, which are chlorine, ozone, bromine, and peracetic acid; and *nonoxidising biocides*, which include glutaraldehyde and biodispersants. *Physical* treatment includes flushing, abrasive sponge balls, brushing, ultrasonic energy, and ultraviolet light. Chemical treatment with biocides are the most common approach to control biofouling, while these chemicals present toxic and carcinogenetic pollutants in the environment. Chlorine has been a measure biocide because of its effectiveness and relatively low cost. Chlorine can react with many organic substances found in water systems. Free chlorine reacts with water and the hypochlorous acid ionize:

$$Cl_2 + H_2O \rightarrow HOCl + HCl$$

$$HOCl \leftrightarrow H^+ + OCl^-$$

Hypochlorous acid shows effective biocidal activity.

9.3.2 Biofouling of Medical Devices

Biofouling in medical devices has been considered as a critical issue because it causes a wide range of health-related problems, including a risk of infectious diseases. Biofouling involves biofilm, which can develop on various surfaces such as living tissues, tooth surfaces, and medical devices. Bacteria within biofilms are much more resistant to antimicrobials than are those in planktonic condition. According to an estimate by the US National Institutes of Health (NIH), about 80% of all human bacterial infections are caused by biofilms and over 45% of all hospital-acquired infections in the US are caused by the medical device administered [1].

The development of biofilm by microbial involves the formation of conditioning film on the surface, irreversible attachment of bacteria; development of biofilm by attached bacteria, and detachment of single cell or large pieces from the biofilm. The bacteria in the biofilm produce EPSs. The EPS includes polysaccharides, proteins, and nucleic acids and determines physical properties of the biofilm. The features of the microorganism in biofilm in comparison with those in planktonic condition are high population density; presence of EPS matrix; a wide range of physical, metabolic, and chemical heterogeneities; and gene transcription profile. The negatively charged EPS is very effective in protecting bacteria from cationic antibiotics by restricting their permeation. The insensitivity of biofilm bacteria to antibiotics is also attributed to slow antimicrobial penetration, the stress response, substrate limitation, and the presence of persister cells [1].

For prevention and eradication of biofilm formation on medical devices, many studies have focused on developing novel materials, surface coatings, antimicrobial combinations, antifouling, antibiofilm agents, and physical treatments against biofilms [1,2]. In actual medical systems most devices used in medical environments are disposed of after a single use to reduce the risk of infection from contaminated products. The treatment of waste from medical industry, which is highly regulated, including these disposal devices, requires the most care and incurs high costs, and it is also an issue caused by biofouling.

9.3.3 Biofilms in Wastewater Treatment Processes

Biofilms in the natural environment are responsible for the removal of dissolved contaminants in environmental water and influence the quality of the water in which they exist. This characteristic is the basis for the employment of biofilms in wastewater treatment and the improvement of drinking water [3]. The wastewater discharged from various industries in addition to domestic sewage contains undesirable material that provides nutrients for microbial activity. The suitable biofilm systems convert the unwanted components to CO_2 and H_2O in aerobic reactions and to CO_2 and CH_4 in anaerobic conditions. The formation of biofilms and microbial aggregates is applied in biofilm reactors, such as trickle filter, rotating biological filter, aerobic fluidized-bed contactors, and anaerobic fluidized-bed contactors. These reactors are used for oxidation of organic matter, nitrification, denitrification, or anaerobic digestion of wastewater.

The trickling filter is a common aerobic biofilm reactor. Figure 9.3 shows the trickling filter with a reactor consisting of a bed of filter media such as stones, ceramic material, or plastic media, providing a large surface area for microbial growth. The wastewater is distributed over the top surface of the filter medium bed with a bed depth of 1–2 m. The oxygen for the biological activity is available throughout the filter bed. The treated effluent from the bottom of the bed is collected in a settlement tank. The biofilm formed on the surface of the filter media in trickling filters is composed of bacteria, fungi, algae, protozoa, and other life forms, and the microorganisms in the biofilm degrade the organic matter in wastewater. The increase in biofilm thickness leads to limited oxygen diffusion to the deeper layers of the biofilm, which creates an anaerobic environment near the filter media surface. Figure 9.4 shows the structure of the biofilm on the surface of filter media and mass transfer around the biofilm. The efficiency of trickle filters depends on both reaction rate in biofilm and the operating conditions that affect the mass transfer condition among air, water and biofilm.

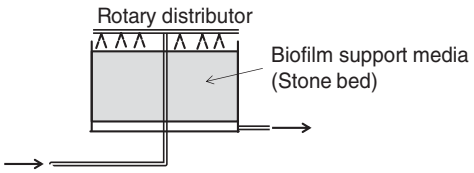


FIGURE 9.3 Trickling filter used for wastewater treatment.

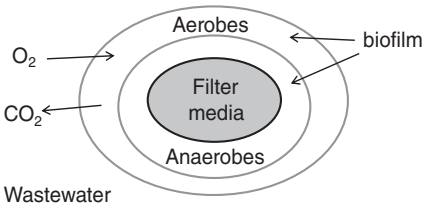


FIGURE 9.4 Biofilm on the surface of filter media.

Figure 9.5 is a schematic representation of a rotating biological filter. This filter has a series of disks mounted on a horizontal shaft. The disks consist of flat or corrugated plastic material. They are made to rotate so that biofilms accumulated on both sides of the disk are alternatively exposed to the wastewater and to the atmosphere. Rotation of the discs ensures effective mass transfer from the wastewater to biofilm, which improves the efficiency of the operation [3].

Figure 9.6 shows the fluidized-bed processes. Aerobic fluidized-bed processes use the media supporting active biofilms, including sand particles, glass, anthracite, polyester foam, or activated-carbon granules. The medium shows a higher surface area, which allows a large amount of biofilm to develop, compared to the media in static systems. The oxygen for the biofilm activity is provided by the injection of air from the bottom of the reactor. In this reactor highly efficient contact between wastewater and biofilm is achieved while the relatively higher energy consumption is required, due to the air injection and pumping. Anaerobic wastewater treatment processes are becoming popular because of their lower energy consumption compared to aerobic treatment processes with aeration. Biogas with a high concentration of methane produced as byproduct may be used as an energy source for the running power of the process. The *upflow anaerobic sludge blanket* (UASB) reactor is an anaerobic fluidized-bed reactor. Wastewater flows upward through the blanket of granular sludge. The granules are dense compact biofilms and are formed by aggregation of bacteria without any support matrix in the flow condition.

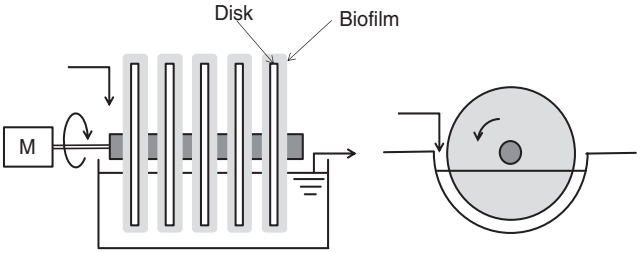


FIGURE 9.5 Rotating biological filter.

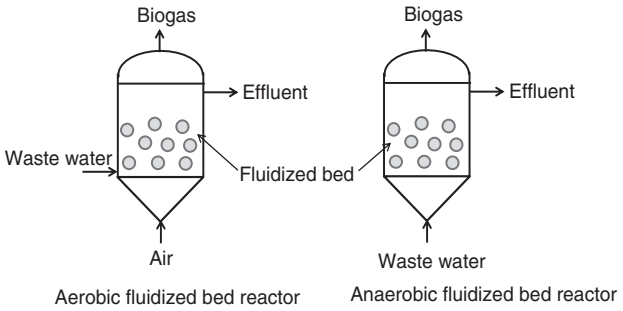


FIGURE 9.6 Fluidized-bed biofilm reactors.

9.3.4 Biofouling in Membrane Processes

The membrane filtration processes producing high-quality water are a key countermeasure against global shortage of water. Membranes are classified by the range of materials separated. *Microfiltration* (MF) membranes are capable of removing particulate matter, including pathogens such as *Cryptosporidium oocystsm*, while reverse-osmosis (RO) membranes retain solutes as water permeates through the membrane. The performance of membrane systems can be characterized as permeate flux, that is, a mass of water across a unit area of membrane per unit time. During membrane operation materials accumulate on and within the membrane structure and reduce the permeate flux by blocking or constricting pores and by forming a layer of additional resistance to flow across the membrane. Figure 9.7 shows the fouling layer formed on the membrane surface by the accumulated materials. This reduction in permeate flux is observed as a consequence of membrane fouling. The fouling is caused by matter presenting in feedwater such as particles, colloids, macromolecules, and ions. Microorganisms may also cause biofouling. They attach onto and within the membrane structure and grow and multiply and finally form biofilm, which compromises membrane performance [1, 2, 5].

Biofouling control strategies fall into two categories: (1) optimization of design and operation of membrane processes, including effective feedwater pretreatment methods, membrane cleaning methods, and operating pressure; and (2) development of antifouling membrane. As the water produced by membrane processes is intended for human consumption, the method of fouling removal is consists in backwashing or chemical cleansing using caustic solution or oxidants such as chlorine. However, the chemical cleansing can attack the membrane structure and reduce the life of the membrane. The design and fabrication of surface chemistries of membrane that are optimized with respect to not only flux and rejection properties but also chlorine resistance and retard adhesion and growth of biofilm, which are desired.

Membrane surface properties such as hydrophobicity, surface charge, and surface roughness will affect the membrane biofouling. The hydrophobic membranes would be easily fouled by bacteria compared with hydrophilic membranes because of the hydrophobic interaction between membrane surface and microorganisms. The membranes with negatively charged surfaces would show lower initial adhesion rate of bacteria on the membrane surface because of the electrostatic repulsive force between membrane surface and the surfaces of bacteria, which are negatively charged around neutral pH. The surface roughness is thought to promote bacterial adhesion. It can be considered that the membranes that have a hydrophilic, neutral or negatively charged, and smooth surface would be more effective in reducing the initial adhesion of microorganisms, which will cause the biofouling [5].

A strategy to control biofouling in the membrane processes is development of antibiofouling surface on the membranes. The membranes with neutral or negatively charged hydrophilic surface will deduce the electrostatic attraction force and hydrophobic interaction between the membrane and microorganisms. The membrane surface immobilized with antibacterial agents will kill the microorganism attached on the surface. The TiO_2 photocatalysis generates various active oxygen species, which decompose organic chemicals and kill bacteria, under light. The silver nanoparticle is also known as an antibacterial agent. Membranes that immobilized these antibacterial agents were reported to manifest antibiofouling activity [1, 2, 5].

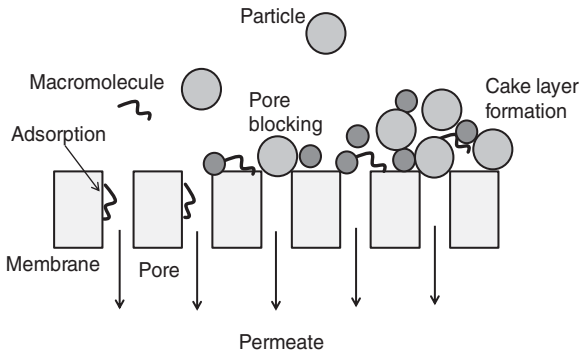


FIGURE 9.7 Accumulation of materials during filtration processes with membrane.

REFERENCES

[1] Chan, J., Wong, S. (eds.) (2009). *Biofouling: Types, Impact and Anti-fouling.* Nova Science Publishers, New York.

[2] Durr, S, Thomason, J.C. (eds.) (2010). *Biofouling.* Wiley-Blackwell, Hoboken, NJ.

[3] Boot, T.R. (2011). *Industrial Biofouling.* Elsevier, Oxford, UK.

[4] Hori, K., Matsumoto, S. (2010). *Biochem. Eng. J.* **48**, 424–434.

[5] Al-Juboori, R.A., Yusaf, T. (2012). *Desalination* **302**, 1–23.

[6] AWWARF, LdE, WRC. (1996). *Water Treatment Membrane Processes.* McGraw-Hill, New York

[7] Melo, L.F., Bott, T.R., Fletcher, M., Capdeville, B. (eds.) (1992). *Biofilms – Science and Technology.* Kluwer Academic Publishers.

11

DEVELOPMENT OF NONFOULING BIOMATERIALS

Ruey-Yug Tsay[1] and Toyoko Imae[2]

[1]*Institute of Biomedical Engineering, National Yang-Ming University Taipei, Taiwan, ROC*
[2]*Graduate Institute of Applied Science and Technology, National Taiwan University of Science and Technology, Taipei, Taiwan, ROC*

11.1 INTRODUCTION

Biofouling, which is the deposition of particles such as proteins, cells, and bacteria at material surfaces, is a major concern in applications including biomedical implants, extracorporeal medical devices, drug delivery carriers, and biosensors. There are significant needs for the development of antifouling materials. The two strategies generally applied for antifouling are either (1) preventing the attachment of the biofoulants or (2) degrading them. Strategy 2 includes incorporating proteases or microbicidals into a coating to impart protein-degrading or bactericidal properties to the surfaces. This approach is less favorable because the degraded proteins and bactericides might cause biocompatibility problems in vivo, and there is a possibility for the emergence of antibiotic-resistant pathogenic strains. Instead of trying to "destroy" the attached particles, the first approach intends to develop "nonfouling" biomaterials that prevent protein adsorption to material surfaces from the beginning.

The development of a nonfouling surface is a major challenge in biomaterials. It is generally believed that nonspecific protein adsorption could activate thrombosis coagulation, elicit inflammatory responses, and cause adverse effects on the healing process for medical implants. A surface that is prone to nonspecific protein adsorption is usually also favorable for the adhesion of bacteria and thus increases the risk of infection. For ex vivo blood-circulating or surface-based diagnostic devices, nonspecific protein adsorption will degrade their performance.

In this chapter, a brief introduction of the major role of nonspecific protein adsorption on the performance of biomaterials will be given and the correlations between biofouling and material properties will be addressed from the perspectives of the adsorption mechanism and driving forces for protein adsorption. Key indices of material properties for protein adsorption will also be discussed. In Section 11.4, recent developments in the design of surfaces of low-fouling/nonfouling biomaterials will be reviewed in detail.

11.2 WHY NONFOULING IS RELEVANT IN BIOMATERIALS

11.2.1 Antithrombogenesis and Anti-inflammatory Response

Coagulation is the instant response of a normal tissue to an injury. It mainly involves a cellular (platelet) and a protein (fibrinogen) component in blood plasma. When the endothelium is damaged, exposure of the circulating blood to the underlying collagen substrate and tissue factor initiates the primary and secondary hemostasis processes. In primary hemostasis, platelets are activated and immediately form a plug at the site of injury. In the meantime, proteins of coagulation factors in the blood plasma respond in a complex cascade (secondary hemostasis) to cross-link fibrinogen to form fibrin strands and strengthen the platelet plug.

The coagulation cascade of secondary hemostasis includes two pathways: the intrinsic (contact activation) pathway and the extrinsic (tissue factor) pathway. Coagulation

Encyclopedia of Biocolloid and Biointerface Science, Volume 1, First Edition. Edited by Hiroyuki Ohshima.
© 2016 John Wiley & Sons, Inc. Published 2016 by John Wiley & Sons, Inc.

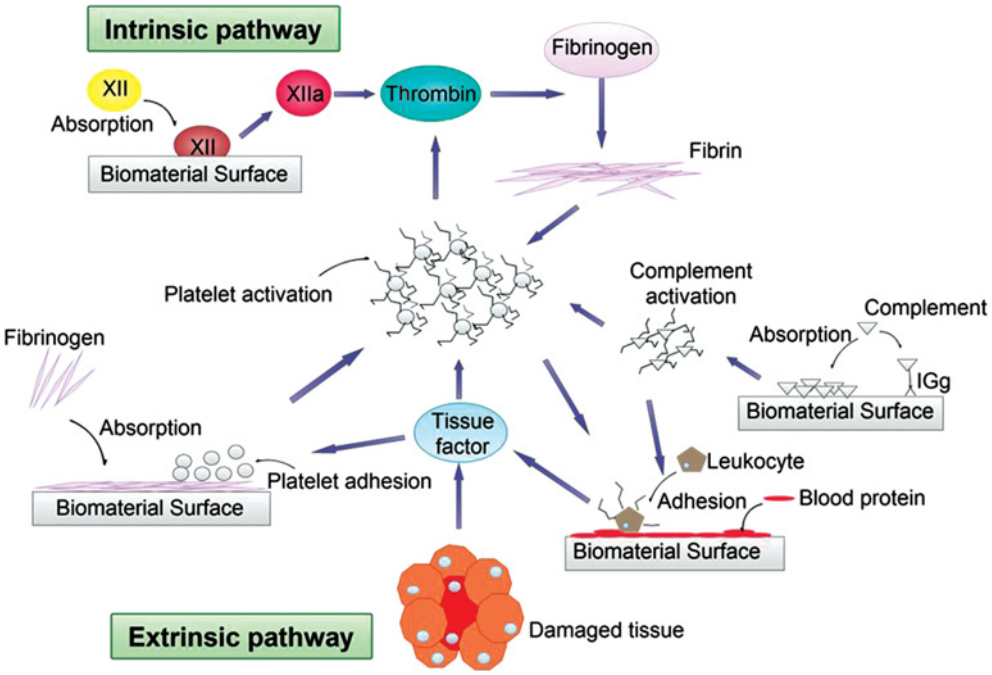


FIGURE 11.1 Relationship between the adsorption of blood proteins and the activation of the coagulation cascade, complement and platelets.

factor XII and tissue factor (TF) are the initiators of the intrinsic and extrinsic pathway, respectively. Both pathways lead to a common pathway for the generation of thrombin and the conversion of fibrinogen to fibrin.

Contact of blood and interstitial fluids with a biomaterial induces different responses. Immediately after the contact, proteins from the blood and interstitial fluids adsorb onto the material surfaces. Therefore, it is the adsorbed layer of protein, rather than the surface itself, that determines the activation of the platelets, coagulation cascade, complement system, and immune cells. Detailed descriptions of biomaterial-associated thrombosis and inflammatory response can be found in recent reviews [1, 2]. In brief, as illustrated in Fig. 11.1, the intrinsic pathway of coagulation can be induced by the contact activation of coagulation factor XII on material surfaces, which induces subsequent thrombin formation and further activates platelets and coagulation factors of the intrinsic and extrinsic systems and, thus, amplifies the coagulation cascade on biomaterial surfaces. Fibrinogen also tends to adsorb on biomaterial surfaces and initiates excess platelet adhesion. The attached platelets can be activated by TF released by damaged cells or activated leukocytes and complements resulting further thrombus formation on material surfaces.

Protein adsorption can also affect the inflammatory response of a biomaterial. For example, the exposure of integrin-binding domains of adsorbed fibrinogens could activate phagocytes and launch an inflammatory response [3]. Additionally, it is known that a high concentration of activated complements can contribute to the onset of inflammatory responses [4]. Because it is well established that complement is activated on contact with a biomaterial and the material surface is always coated with a layer of adsorbed protein, the inflammation due to complement activation is therefore associated with the protein adsorption of the biomaterial.

11.2.2 Host Response to Biomaterials

The normal healing response to a tissue injury is an intricate process and includes three sequential phases: (1) hemostasis and inflammation, (2) proliferation and granulation, and (3) remodeling. The immediate response to injury is the platelet aggregation and fibrin clot formation to reduce bleeding. Cytokines and growth factors are then released to attract white blood cells. Neutrophils are the major white blood cells appearing during the early stage of wound healing. This process is then followed by the migration of monocytes, which later differentiate into macrophages to clean up the wound site. In the proliferation phase, fibroblast and endothelial cells are recruited and grow to convert the fibrin clot into granulation tissue and form new blood vessels. Finally, in the remodeling phase, the granulation tissue is gradually replaced by extracellular matrix (ECM) deposited by fibroblasts. Usually, there is scar tissue formation, although it is possible to restore a completely normal tissue.

The biological response to an implant, termed the *foreign-body reaction*, is different from the response to an injury.

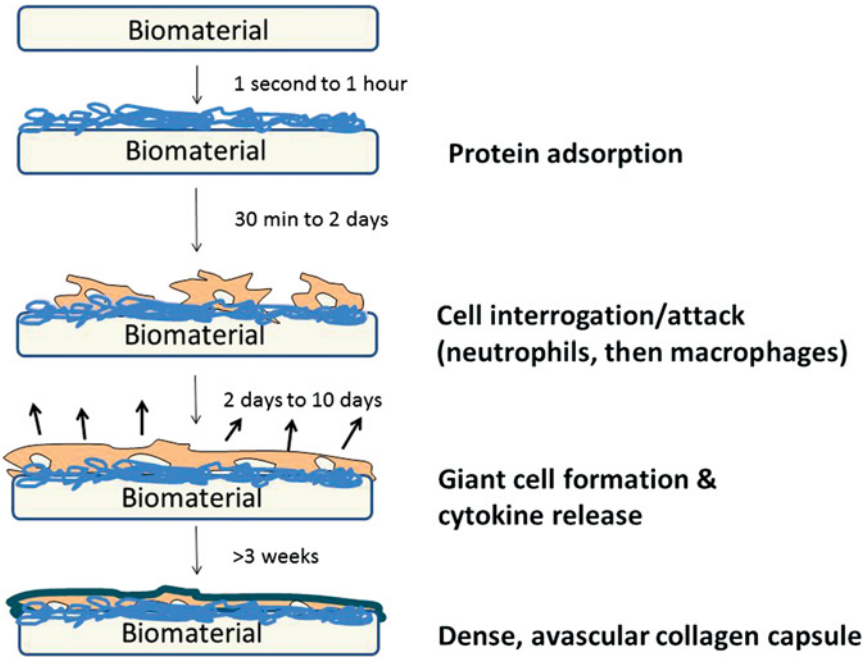


FIGURE 11.2 Sequential stages of a foreign-body reaction proposed by Ratner and Bryant [6].

Detailed reviews on this issue have been provided [1, 5]. Figure 11.2 is a simplified flowchart showing the key steps of the response suggested in one study [6]. The major difference in a foreign-body reaction is that the implantation of a biomaterial elicits immediate nonspecific protein adsorption, and the adsorbed proteins may undergo a different degree of conformational changes due to the effects of the interfacial energy between the material surfaces and the surrounding contacted body fluids. The adsorbed denatured protein can induce the adhesion of various cells, such as leukocytes, monocytes, and platelets, and consequently activate the release of cytokines and the subsequent inflammatory process. For small and degradable implants, the debris can eventually be cleaned up by the white blood cells. However, for implants much larger than the adhered macrophages, because the foreign body cannot be phagocytosed, the adhered macrophages therefore fuse together to form multinucleated foreign-body giant cells at the material surface, which may result in chronic inflammation and last for a lifetime. The final stage of the foreign-body reaction for this type of implant is the formation of an avascular, fibrous tissue to encapsulate the implant.

11.2.3 Antibacterial Property

Microbe-associated infection is one of the major causes for the failure of medical devices. For example, biofilm formations on medical devices such as dental/orthopedic/ cardiovascular prosthesis, catheters, and contact lenses lead to infections [7, 8]. Key strategies for designing implants that prevent microbial infections include the coating of biocidal agents on material surfaces. However, this practice cannot exclude the concern of developing an antibiotic-resistant pathogenic strain and the resulting contamination. Another strategy is to design surfaces that prevent the attachment of bacteria. The attachment of bacteria to a surface is usually followed by subsequent colonization and biofilm formation. Numerous studies indicate that the adhesion of bacteria increases the risk of infection. In vivo, the adhesion of bacteria often is mediated by the adsorbed protein film [9]. A surface that is less subjected to the nonspecific adsorption of proteins usually also has better resistance to bacteria adhesion [10, 11].

In general, the contact of blood or other body fluids to a normal tissue does not elicit nonspecific protein adsorption. However, a material that is identified by the biological system as a foreign body or as an abnormal tissue will trigger the defense system of the body and cause a substantial amount of protein adsorption. The amount, types, orientation, and conformational change of the adsorbed proteins on surfaces will all affect the subsequent biological response of the body to the material. Nonspecific protein adsorption, especially for those accompanied with conformational changes, often activates thrombogenesis and an inflammatory response and renders a surface prone to bacteria adhesion. However, because of the complexity of the determining factors on protein adsorption, the development of a truly nonfouling surface, also called a "stealth surface," remains a major challenge in the field.

11.3 PROTEIN ADSORPTION AND MATERIAL PROPERTIES

A *protein* is a macromolecule that consists of a polypeptide bond and is folded into a specific three-dimensional structure. The distribution of the primary sequence and the manner of protein folding provide the molecular surface with domains of various properties such as charge density and hydrophilicity. Because the properties of a protein surface are not uniform, the protein–surface interaction therefore depends not only on the "average" surface properties but also on the "nanoscale" variation in the surface topography and chemistry [11].

In addition to binding affinity, sometimes the behavior of protein adsorption is also affected by kinetic factors, such as the competitive adsorption of the three major plasma proteins of albumin, immune globulin, and fibrinogen immediately after the contact of the material with blood plasma. Dynamic effects also play a role in protein adsorption, due to the surface denaturation. Because the manner of protein folding might be perturbed by changing the microenvironment around the molecule, one expects to see conformational change induced by protein adsorption. A conformational change will alter protein surface properties, which, in turn, will affect the subsequent protein adsorption.

Under aqueous conditions, the protein adsorption behavior is affected not only by the properties of the protein molecule and material surface but also by the conditions of the water solutions. It is the cohesive and adhesive forces between these three substances that determine the protein–surface, surface–water, and protein–water interactions. Previous studies on protein adsorption tend to focus on the behavior of the surface–protein interaction. However, more recent studies indicate that in addition to the surface–protein interaction, the surface–water interaction (i.e., the hydration properties of the material) also plays a crucial role in determining the nonfouling property of the materials [12–14].

11.3.1 Adsorption Mechanism of Protein

As shown in Fig. 11.3, the dynamic protein adsorption mechanism includes two stages. In the first stage, protein molecules adsorb to the material surface rapidly and reach a pseudo–steady state. At this stage, the adsorbed protein retains its native conformation, and the adsorption is kept in the monolayer and reversible; thus, the protein can still be removed from the material surface. Later, in the second stage, the conformation of the adsorbed protein gradually deteriorates into a denatured form due to the effects of interfacial energy. The denatured protein exposes its hydrophobic core region and therefore tightly binds to the material surfaces. Thus, the adsorption becomes irreversible, and the adsorbed protein can hardly be removed from the surfaces [15–17]. A surface covered with denatured proteins can further induce multilayer protein adsorption. Judging from the abovementioned protein adsorption mechanism, a material can be made favorable for nonfouling by reducing the retention time of the protein molecules on the material surface or by preserving the adsorbed protein in its native form.

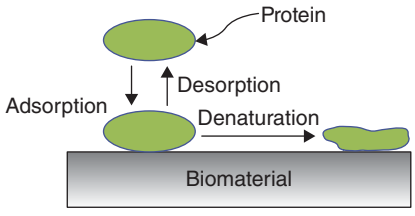


FIGURE 11.3 Two-stage protein adsorption mechanism: first stage, reversible adsorption; second stage, irreversible denaturation.

11.3.2 Protein–Surface Interactions

The major driving forces for protein adsorption include hydrophobic, electrostatic, van der Waals, and hydrogen bond interactions [18]. Adsorption induced by hydrophobic interaction is an entropy-driven process, which consists mainly in the release of "frozen waters" on the hydrophobic surfaces. A nonpolar hydrophobic surface usually exhibits significant protein adsorption because the interfacial energy between the surface and water is large, and its contact with an amphiphilic protein molecule often induces protein denaturation due to the effect of hydrophobic interaction.

Electrostatic interaction is a long-range force. Because most of the serum proteins are negatively charged in vivo, a negatively charged surface should be less favorable for protein adsorption, due to the electrostatic repulsive force. Nevertheless, it is unrealistic to design an antifouling surface based on the function of electrostatic repulsive force because the electrostatic force can be easily attenuated by the presence of abundant ions in the solution, and there are always proteins carrying either a "net" or "localized" positive charge, which is favorable for adsorption.

In contrast to the electrostatic force, the van der Waals interaction is a short-range force, which decays rapidly with the distance between the interacted surfaces. Therefore, introducing a surface-coated film that prevents close contact of the protein and surface can effectively reduce the protein adsorption of a surface. The superior protein resistance of PEG-functionalized surfaces is one of the most successful cases. It is believed that the grafted PEG layer on the material surface provides a repulsive elastic force, sometimes referred to as a *steric hindrance effect*, and substantially reduces the van der Waals interaction between proteins and the substrate materials.

In addition to the steric hindrance effect, many experimental and theoretical studies also suggest that the hydrogen bond interactions between the grafted PEG chains and water

molecules, or the hydration property of PEG, play an important role in its nonfouling property. For protein adsorption in an aqueous solution, both the surface–protein association and the surface–water dissociation processes are involved. Therefore, the affinities of not only the surface–protein but also the surface–water interactions need to be considered. A surface with a higher affinity to water than to protein molecules should exhibit a better nonfouling property. In other words, protein molecules are competing for the material surfaces with water molecules, and the hydration property of the material surfaces is thus crucial in determining the nonfouling property of the materials.

11.3.3 Surface Hydration

It has been demonstrated by many experimental and theoretical studies that various hydrated states of interfacial water exist. The water in a hydrated polymer system was categorized into nonfreezing, freezing bound, and freezing states in one study [19]. Water in the nonfreezing state is tightly associated with the polymer and does not exhibit a crystallization–melting transition. Freezing bound water exhibits a crystallization–melting transition but with considerably more supercooling than that of bulk water, suggesting that it is less closely associated with the polymer. Freezing water is water with a melting temperature and enthalpy close to those of bulk water. The same study [19] indicated that the bound water content (i.e., the nonfreezing and freezing bound water), depends on the chemical and high-order structure of each polymer. For a water content above a threshold, many water-soluble polyelectrolytes, such as hyaluronic acid and xanthan gum, form a gel. Water in such gels mostly exists as freezing bound water, which plays an important role in the junction formation of gelation. Similarly, the structure of water molecules adsorbed in different hydrophilic polymers was studied by differential scanning calorimetry (DSC) and Fourier transform infrared (FT-IR) spectrometry [20]. These researchers also observed that the adsorbed water first bound to the hydrophilic site to form nonfreezable water. Then, above a water content threshold, the adsorbed waters become freezable but at a temperature lower than 0°C. The melting peak of this freezable water merged together with the melting peak of a bulklike water frozen at 0°C at very high water contents.

On the basis of the DSC data for poly(2-methoxyethyl acrylate) (PMEA), a team of researchers classified hydrated waters into three types: nonfreezing water, freezing bound water, and free water [21]. These researchers attributed the excellent blood compatibility of the material to the existence of freezing bound water crystallized at approximately −40°C. Nevertheless, another team observed that poly-MPC hydrogel contained a larger amount of nonfreezable water than did the poly–Me$(EG)_n$MA hydrogel [22]. Because the equilibrium water contents for the two hydrogels were similar, these researchers suggested that instead of freezing bound water, the amount of nonfreezable water may play a crucial role in the nonfouling property of the materials. Other researchers proposed another viewpoint by suggesting that the nonfouling ability of a surface functional group can be evaluated with respect to its intrinsic hydration capacity, which represents the overall hydrating water and is estimated based on the partial molar volume of the functional group at infinite dilution [23]. From experimental measurements and simulation evaluations for a series of hydrophilic materials, including oligo(ethylene glycol), mannitol, sorbitol, and primary amine glycine, the authors suggested a critical threshold value of hydration capacity of approximately 0.15 for the initial screening of nonfouling materials. Additionally, instead of trying to establish a specific correlation between different hydrating states and protein resistance, some authors suggest that it is the existence of a nativelike hydrogen-bounded network of water near the surface that is essential for the antifouling property of a biomaterial [24–26].

11.3.4 Strategies for Nonfouling Design

One way to judge whether a system is prone to protein adsorption is to examine the interfacial energy difference of the system prior to and after protein adsorption. Consider the molecular association-dissociation behavior of a protein adsorption process in water as the simple diagram presented in Fig. 11.4. The free-energy change of the protein adsorption process ΔG_{ads} can thus be expressed as

$$\Delta G_{ads} = \gamma_{SP} + \gamma_{WW} - (\gamma_{SW} + \gamma_{PW}),$$

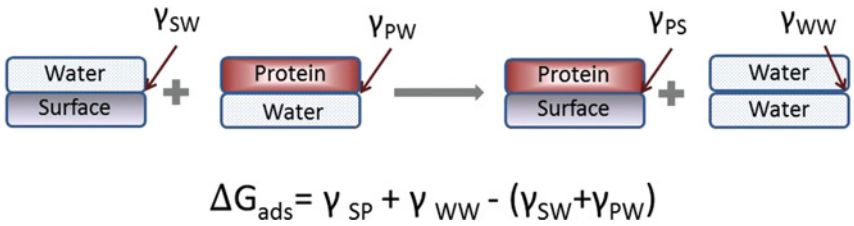


FIGURE 11.4 Illustration of the molecular association–dissociation behavior of a protein adsorption process.

where γ_{SP}, γ_{WW}, γ_{SW}, *and* γ_{PW} represent the surface–protein, water–water, surface–water, and protein–water interfacial energy, respectively, and $\gamma_{WW} = 0$. To minimize protein adsorption, the material surface should be designed to keep ΔG_{ads} as high as possible. There are two possible approaches for this goal: (1) to keep the interfacial energy between the material surface and the adsorbed protein γ_{SP} high and (2) to keep the interfacial energy between the surface and water γ_{SW} low. Proteins are amphiphilic molecules. The adsorption of a protein tends to reduce the surface-protein interfacial energy. Therefore, one expects to keep γ_{SP} high if the intermolecular forces between the surfaces and proteins are minimized. γ_{SW} is generally correlated to the hydrophilicity of the material surfaces. A hydrophilic antifouling biomaterial, such as PEG, usually exhibits a sufficiently low interfacial energy with water.

Previous research on protein–surface interactions has identified two main classes of surface coatings that can resist biofouling [11]. Among them, hydrophobic surfaces such as those of a copolymer with semifluorinated sidechains are known as *fouling release* materials, whereas hydrophilic surfaces of polymers such as PEG, are truly antifouling surfaces, often referred to as 'stealth surfaces." A hydrophobic surface exhibits a high interfacial energy with water and therefore exhibits significant protein adsorption on the surface to minimize the free energy. Nevertheless, because the interaction force between the nonpolar surfaces and proteins is low, the adsorbed proteins can be easily released by external forces such as a shear force due to fluid flow. However, because the prolonged retention of the protein molecules on a hydrophobic surface can induce protein denaturation, the antifouling characteristic of the 'fouling release' type surfaces usually is not stable and cannot last long.

Unlike the hydrophobic surfaces, a hydrophilic surface acquires its antifouling characteristic by reducing the surface–water interfacial energy and keeps the surface "undetected" by proteins in an aqueous environment [27, 28]. Water molecules, which are strong dipoles, exhibit a stronger interaction with a hydrophilic polar group than with a hydrophobic nonpolar group and therefore tend to bind on a polar/charged surface. Previous spectroscopic studies have demonstrated the existence of a nanometer-scale water layer with an increase in ordering on both hydrophobic and hydrophilic surfaces. The viscosity of the ordered water layer near a hydrophilic silica surface was demonstrated to be approximately 2–10^6 times greater than that of bulk water, which, however, is not observed for hydrophobic surfaces such as methylated silica or hydrogenated diamond [29]. The formation of a viscous interface provides evidence for the bonding between water molecules and the hydrophilic surfaces. Numerous studies have identified a strong correlation between surface hydration and nonspecific protein adsorption [12, 14, 23]. It is believed that the bound water layer forms a barrier to prevent protein adsorption on the surface. Nevertheless, the detailed correlation between the hydrated state and the nonfouling feature of the surfaces has yet to be clarified.

11.4 NONFOULING BIOMATERIALS

The nonfouling ability of a surface depends on its physicochemical properties. To obtain an antifouling surface, the use of materials with an intrinsic nonfouling chemical nature and with appropriate physical properties is necessary. There have been many attempts to identify the criteria for protein adsorption-resistant surfaces. In terms of material chemistry, several investigators tested the protein resistance of SAM surfaces terminated with various functional groups and proposed four common parameters that were likely to be important for protein resistance, including the presence of polar functional groups, the absence of any net charge, the presence of hydrogen bound acceptor groups, and the absence of hydrogen bond donor groups [30–32]. The first two criteria are generally accepted. Nevertheless, the criteria concerning the absence of hydrogen bond donor groups for protein adsorption-resistant surfaces remain controversial. Although one series of observations support the statement that the protein-resistant ability of a surface increases with the reduction of the number of hydrogen bond donor groups, this finding appears to contradict other findings [33]. For instance, SAMs of mannitol resist protein adsorption even though they contain a large number of hydrogen donors [34]. Additionally, there are nonfouling zwitterionic materials that form strong interactions with water molecules via charge–dipole interactions instead of hydrogen bonding [35].

In addition to chemical factors, the physical factors of surface packing and surface homogeneity of a material also play important roles in determining the antifouling performance of a surface. Therefore, finding an appropriate coating method to ensure optimized physical properties of a surface is also crucial in the development of an antifouling surface. Numerous studies have indicated that the protein resistance of a modified surface is dependent on the packing density, thickness, and molecular conformation of the surface film. In general, to assure protein resistance, it is necessary to have complete coverage of the surfaces by antifouling materials. For example, by making the grafting density of a PEGylated surface fall in the polymer brush regime, one can obtain a completely covered PEG-grafted surface [36]. Studies have indicated that as long as a surface is fully covered by PEG groups, the chain length does not have a strong effect on the protein resistance [37,38]. This statement was also supported by two studies [39,40] that revealed that SAMs of alkanethiolate with as few as two ethylene oxide terminal groups yielded superior protein resistance. This result occurred because the chain density of a short-chain SAM is much larger than the chain density of a grafted long-chain polymer. Nevertheless,

TABLE 11.1 Common Nonfouling Materials for Protein Adsorption

Category	Types	Materials
I	Nonionic hydrophilic materials	• OEG-/PEG-based materials • PEG-mimetic materials – Propylene suloxide – Polyglycerol dendrons and derivatives • Native/Natural-inspired materials – Peptide-based materials – peptoid-based materials – Polyoxazoline polymers – Saccharides-based materials – dextran, mannitol
II	Zwitterionic materials	• Polybetaines/ Zwitterionic SAMs – phosphobetaine (PB) – sulfobetaine (SB) – carboxybetaine (CB) • Polyampholytes/1:1 mixture of cationic and anionic SAMs
III	Amphiphilic materials	• Polymer with perfluoroalkyl tagged OEG as side chains • Hyperbranched amphiphilic fluoropolymers

an increase in surface chain density does not always increase protein resistance. Other workers reported that the packing density of OEG-SAM on silver is higher than that on gold, while the protein resistance of OEG-SAM on silver is worse [41–43]. The authors suggested that the OEG-SAMs on silver with a *trans* conformation are too dense to incorporate as much water as the OEG-SAMs on gold with a "helical" conformation. Studies on molecular dynamic simulations for protein adsorption on mixed SAMs of OEG-SAM and OH-SAM indicated that there is a correlation between the hydration and the protein resistance properties for surfaces with different OEG packing densities [44–46]. Mixed SAM surfaces with an OEG packing density that is either too high or too low exhibit higher protein adsorption. These results suggest that the appropriate packing density of an antifouling surface film should be dense enough to avoid the penetration of protein molecules and yet loose enough to allow for the incorporation of the hydrated waters.

Surface homogeneity is another important issue. As mentioned previously, a protein is a macromolecule with surface heterogeneity in charge and in hydrophobicity, and therefore, it is prone to bind to a defect site of a surface. A protein-resistant surface is thus expected to be homogeneous and defect-free. Nevertheless, certain data have indicated that some surfaces with mixtures of alternating positively/negatively charged groups or hydrophilic/hydrophobic groups also exhibit superior protein resistant ability [35, 47, 48]. These results do not contradict the abovementioned hypothesis, as it appears that a protein-resistant surface should be homogeneous. As long as the distance between the alternating groups is much smaller than the size of a protein molecule, the detailed structural distribution on the surface cannot be sensed by the protein molecule, and the surface can be considered homogeneous. For example, a polymer with zwitterionic sidechains, such as phosphatidylcholines, consists of both positive and negative charges in each pendent group, is homogeneous on a nanometer scale, and exhibits an excellent antifouling property. According to these arguments, a surface with nanometer-scale homogeneity can be considered as one of the criteria for protein-adsorption-resistant surfaces.

Various protein-resistant materials have been reported in the literature. As summarized in Table 11.1 herein, the nonfouling materials are classified into three categories: nonionic hydrophilic materials, zwitterionic materials, and amphiphilic materials. The listed materials all satisfy the criteria for protein-adsorption-resistant surfaces: the presence of polar functional groups, the absence of any net charge, and the exhibition of nanometer-scale homogeneity. In the following sections, the general methods for surface immobilization of these nonfouling materials will be first introduced. A detailed description of the antifouling mechanism, representative materials, and the design of network architecture of these three types of nonfouling materials will also be presented.

11.4.1 Surface Immobilization Techniques

There are two major methods to tether oligomers/polymers to surfaces: physisorption and covalent attachment [49]. In physisorption, nonfouling materials are typically tethered to a surface via conjugating of the nonfouling polymer chains to an anchoring group. For example, synthetic block copolymers of PEO-PPO-PEO (Fig. 11.5a) have been shown to reduce protein adsorption via the physisorption of the PPO anchoring group to the hydrophobic surfaces [50, 51]. Surface modification via physisorption usually has difficulty in reducing the protein adsorption below a certain limit because

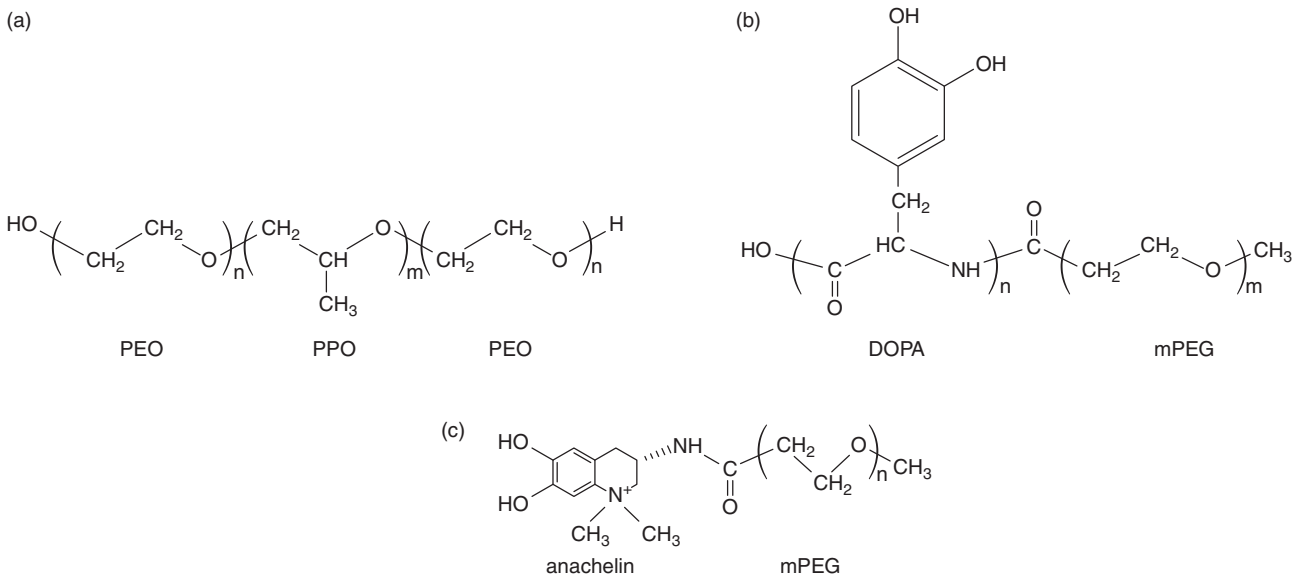


FIGURE 11.5 Structure of (a) PEO-PPO-PEO, (b) mPEG-DOPA, and (c) mPEG-anachelin derivative.

the adsorbed chain density is limited by the steric issue and the binding strength is not robust enough. Several anchoring groups, such as 3, 4-dihydroxyphenylalanine (DOPA) (Fig. 11.5b), a fragment of anachelin (Fig. 11.5c), and poly-L-lysine (PLL), have been developed on the basis of biomimetic strategies. DOPA is an unusual amino acid that is present in large amounts in mussel adhesive proteins. DOPA can form moisture-resistant bonds with various substrates including metals, metal oxides, glass, and plastics [52–54]. Anachelin is a compound used by cyanobacteria for biofilm formation [55], and PLL is a positively charged polypeptide [37]. The conjugation of various nonfouling groups with either one of these two compounds can promote adhesion to metal oxide substrates and provide surfaces with excellent protein-resistant ability.

In general, there are two main routes for the covalent attachment of nonfouling groups to a surface: (1) the *graft-to method*, where end-functionalized nonfouling polymer chains react with appropriate surface sites; and (2) the *graft-from method*, where nonfouling chains grow in situ from pregrafted initiator sites [56]. The graft-to method is simpler for preparation but tends to form a looser network with more defects [57–59]. The graft-from method is a better approach to grow polymer brushes with a high chain density and well-controlled film thickness because of the easy access of the reactive groups to the chain ends of the growing polymer. This method has been widely implemented with controlled free-radical polymerization to build high-density polymer brushes from planar surfaces. For instance, one group of investigators formed SAMs of initiator–mercaptoundecyl bromoisobutyrate on gold and then immersed the SAM-modified surfaces into a solution of oligo(ethylene glycol) methyl methacrylate (OEGMA) monomer for subsequent surface-initiated atom transfer radical polymerization (SI-ATRP). CuBr/bipyridine is added to the solution as a catalyst [60]. Figure 11.6 is a schematic representation of the structure of the OEGylated network prepared via this SI-ATRP method. The resulting surfaces successfully resisted the nonspecific adsorption of proteins when exposed to solutions of fibronectin and 10% fetal bovine serum. This SI-ATRP method is also applicable for the grafting of zwitterionic polymers such as p-SBMA and p-CBMA. Experiments indicated that polymer surfaces of p-OEGMA, p-SBMA, and p-CBMA formed using the SI-ATRP method all exhibited an increased resistance to nonspecific protein adsorption compared with SAMs with similar terminal groups. The authors attribute this improvement to an increase in the surface packing density of nonfouling groups on the surface as well as a steric repulsion from the flexible polymer brush surfaces [14, 61, 62].

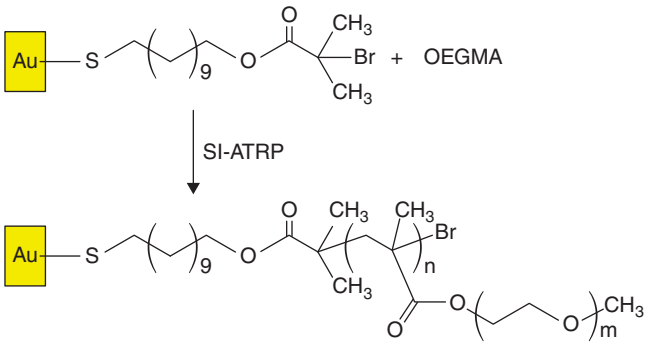


FIGURE 11.6 Schematic diagram of SI-ATRP of OEGMA.

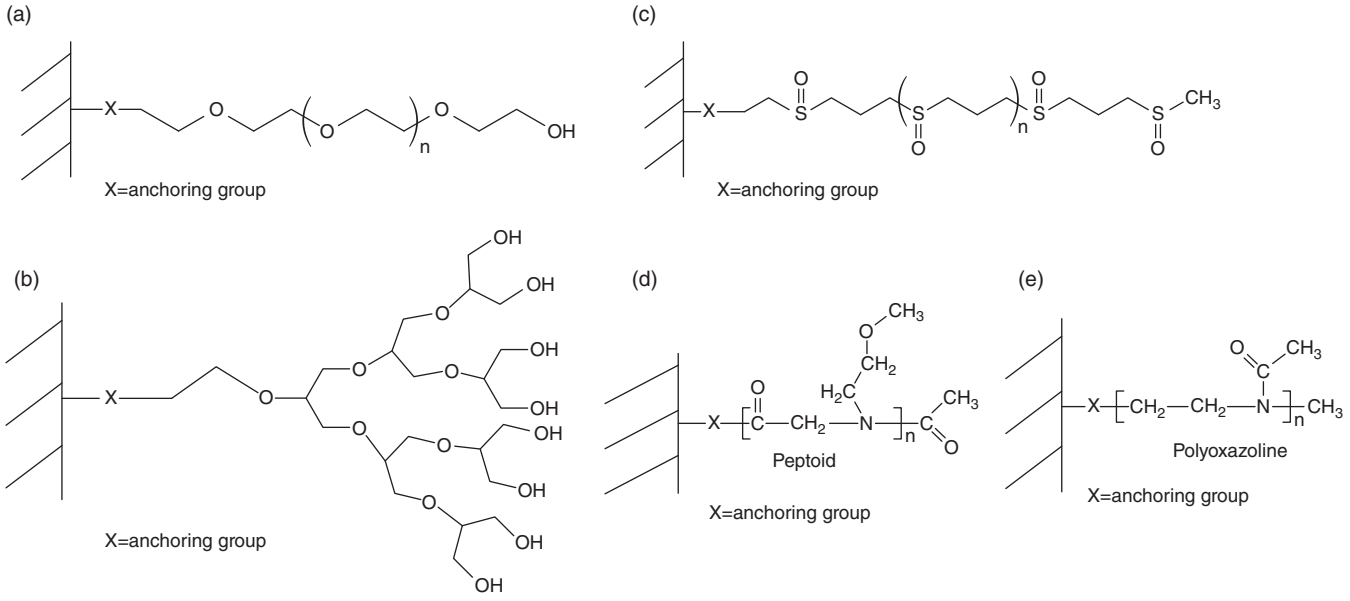


FIGURE 11.7 Structure of (a) polyethylene oxide, (b) dendritic polyglycerol (PG), (c) polypropylene sulfoxide, (d) peptoid-based materials, and (e) polyoxazoline.

11.4.2 Nonionic Hydrophilic Materials

Nonionic hydrophilic nonfouling materials contain polar groups but carry no electrostatic charges in the molecules. The primarily causes for the antifouling characteristic of this type of material is generally attributed to the formation of a hydration layer via hydrogen bonding. Because hydrogen bonding is relatively easy to break, the hydration state and nonfouling property of this type of material is closely correlated to the surface packing density [14]. For surfaces modified with polymer chains via direct attachment, the chain density is relatively low. It is essential to keep the distance between two adjacent chains smaller than the radius of gyration of the polymer chains in solution to ensure complete coverage and antifouling ability of the surfaces [36, 38]. In contrast, for surfaces modified with short-chained molecules, such as self-assembled monolayers (SAM), the chain density is usually high. Studies have indicated that sometimes reducing the packing density of a SAM-coated layer by changing the substrate [42, 63] or the solvent [44] and temperature [64] used in SAM preparation can increase the surface hydration and improve protein adsorption resistance. In addition to surface hydration, some authors have suggested that the steric repulsion [65–67] and chain flexibility [68] of the grafted polymer chains also contribute to the protein resistance of the surfaces.

11.4.2.1 OEG-/PEG-based Materials. Major nonionic hydrophilic nonfouling materials reported in the literatures are listed in the first category of Table 11.1. The oligo(ethylene glycol)/ poly(ethylene glycol) (OEG/PEG)-based materials are among the best and the most commonly used protein-resistant surfaces currently. PEGylated surfaces created using the linear/hyperbranched architectures of PEG grafts or comblike polymers with PEGylated sidechains in general exhibit good resistance to protein adsorption [14,36,69–71]. One study demonstrated that linear PEG (Fig. 11.7a) is more effective in preventing bacterial attachment than a surface with a PEG-like hyperbranched architecture (Fig. 11.7b) [64]. This effect was attributed to the differences in the strength of steric repulsion between the two molecular arrangements. However, whether the same effect works for protein resistance is yet to be confirmed. PEG is a long-chain ether consisting of many hydrogen bond acceptors. Many studies have shown that the methylation of its terminal hydroxyl group can reduce the number of hydrogen bond donors of the molecule and improve its resistance to protein adsorption [30, 32]. Similar effects of decreasing the number of hydrogen bond donors on the increasing of protein resistance ability were also observed for functional groups such as amino acids and saccharides. By replacing the hydrogen atom in the hydroxyl group with a methyl group, the protein resistance ability of these materials also increased.

The long-term stability problem of PEGylated polymers is a major limitation for their applications as antifouling coatings. PEGylated polymers tend to autoxidize and form aldehydes and ethers in a biological environment [72]. Nonfouling hydrophilic material alternatives have been continuously desired. Figure 11.7b–e shows the molecular structures of some promising nonfouling materials. Some of these

materials were designed based on the concept of preserving the main properties of PEG, such as dendritic polyglycerol (PG) and its derivatives and propylene sulfoxide. The others are either natural or bioinspired molecules. Peptide-based materials, peptoid-based materials, polyoxazoline, and saccharide-based materials all belong to this category. All of these materials displayed resistance to protein adsorption comparable to that of PEG SAMs.

11.4.2.2 PEG-Mimetic Materials. Dendritic polyglycerols (PGs) (Fig. 11.7b) and their derivatives are polyethers based on glycerol dendrimers and linear/hyperbranched polyglycidols [73–75]. These materials are highly biocompatible, and bulk PG exhibited higher thermal and oxidative stability than PEG. The protein resistance ability of this type of materials was attributed to their structural features, such as the presence of highly flexible aliphatic polyether or hydrophilic groups. Similar to hydroxyl-terminated OEG/PEGs, the methylation of all-terminal hydroxyl groups of PGs resulted in a significant improvement in protein resistance. Propylene sulfoxide (Fig. 11.7c) is derived from a parent functional group of dimethyl sulfide, which mimics the characteristics of the EG group and is more biocompatible than ethylene glycol [76].

11.4.2.3 NATURAL/Natural-Inspired Materials. Peptide-based materials were designed according to the rules of using amino acids that were hydrophilic, with uncharged sidechains, providing hydrogen bond acceptor groups and forming α-helical structures [77]. These design rules were consistent with the ones proposed by several coworkers [30–32]. The peptide bonding of this type of materials is expected to be more robust than the ether bonding of PEG-based materials. Peptoid-based materials (Fig. 11.7d) represent a promising class of bioinspired polymers that have a protein-like backbone with side chains on the nitrogen atom instead of the α-carbon [78–80]. Peptoids are highly designable because of the ease of introducing chemically diverse sidechains from simple building blocks. Poly(oxazoline) polymers (Fig. 11.7e) are generally obtained via the polymerization of 2-substituted oxazolines via a living cationic ring-opening mechanism (CROP), which yields polymers with narrow molecular weight distributions. Because of the versatility of this class of polymer, poly(oxazoline)s have the superior characteristic of the ease of preparation of polymers with various chemical functionalities and architectures [81]. For instance, one team prepared comb polymers with a polycationic poly(L-lysine) (PLL) backbone and poly(2-methyl-2-oxazoline) (PMOXA) sidechains. This PLL-*g*-PMOXA copolymer is able to spontaneously adsorb onto metal oxides surfaces and provides the adsorbed surfaces with excellent protein resistance [82]. Dextran and mannitol are saccharide-based natural materials. Surfaces grafted with saccharide-based materials mimic the antifouling glycocalyx present at endothelial cell surfaces. Polysaccharide is the major component of the glycocalyx, which prevents nonspecific protein adsorption with cell surfaces in serum. For example, polymers with hydrophilic dextrans or maltose dendrons grafted to a flexible polyvinylamine backbone as sidechains have been shown to effectively reduce protein adsorption [83–85]. Mannitol is a sugar alcohol derived from mannose by reduction. This material exhibits superior protein-resistant ability, although it contains a large number of hydrogen bond donors of hydroxyl groups, which is contradictory to the criteria of nonfouling materials proposed by several coworkers [30–32].

11.4.3 Zwitterionic Materials

Biomimetic zwitterionic materials, such as phosphorylcholine (PC), have attracted extensive attention recently because of their excellent antifouling performance. Similar to hydrophilic nonfouling materials, water hydration on the surfaces of zwitterionic materials is also believed to play a crucial role in their antifouling ability. Various studies have indicated that more bound water was observed around zwitterionic surfaces than other nonionic hydrophilic or hydrophobic surfaces [22, 86]. Another group of coworkers attributed the hydration of a zwitterionic material to the ionic solvation due to the strong charge–dipole interactions between the positive and negative charge units of the zwitterionic groups and water molecules [14, 87]. These authors suggested that the strength and nature of hydrations between ionic solvation for zwitterionic materials are different from those of hydrogen bonding for hydrophilic materials. However, based on Raman and infrared spectroscopy data, another team raised a different viewpoint, suggesting that the existence of an unperturbed native hydrogen bonded network near the surface is a necessary feature for antifouling properties [24–26, 88]. Another report suggested that the protein resistance ability of a surface is related to the accessibility of the protein surface to the surface molecules [35]. This hypothesis is based on the observation by Kane et al. that most of the protein-resistant surfaces contain kosmotropes. *Kosmotropes* are moieties known to be able to stabilize a protein structure by being excluded from protein surfaces [88]. A surface with zwitterionic moieties, such as betaine and taurine, exhibits a strong interaction with water molecules, which may cause the ordering of the water molecules near the surface and thus cause the surface molecules to be preferentially excluded from the protein surface.

Zwitterionic polyelectrolytes contain both cationic and anionic charges on the same macromolecular chain. There are two types of poly-zwitterionic materials: polybetaines and polyampholytes. Polybetaines possess the opposite charged groups on the same monomer units, while polyampholytes possess the anionic and cationic groups on different monomer units. Schematic diagrams similar to that

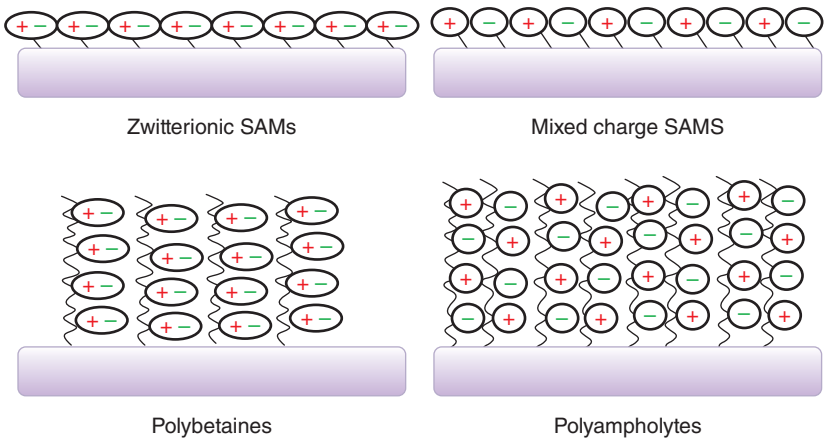


FIGURE 11.8 Schematic diagrams illustrating the ideal charge distributions of (a) zwitterionic SAM, (b) 1:1 mixture of cationic and anionic SAM, (c) polymer grafts of polybetaines, and (d) polymer grafts of polyampholytes.

proposed in one report [14] illustrate the ideal charge distributions of self-assembled monolayers containing zwitterionic terminal groups/a 1:1 mixture of cationic and anionic groups (Fig. 11.8a,b) and surfaces immobilized with polybetaines/polyampholytes (Fig. 11.8c, d). The extremely high dipole moment of zwitterionic groups in polymeric and SAM structures leads to strong inter- and intramolecular dipolar interactions and the association of the polymer chains, which provides the surface with a range of unique properties, such as ultralow protein resistance and stability over a wide range of pH values and ionic strengths [90]. Previous studies indicated that the charge balance, minimized dipole, uniformity of charge distribution, and packing density were key factors in determining the nonspecific protein resistance of the zwitterionic surfaces [14, 46, 91, 92]. A surface covered with a nanometer-scale homogeneous mixture of balanced charge groups can provide the surface with stable ultralow fouling properties. Experiments also indicated that due to the wetting transitions of the polyzwitterionic brushes driven by self-association, optimum chain lengths exist for the nonfouling polyzwitterionic grafts formed by the ATRP method [93,94].

11.4.3.1 Polybetaines. Betaine is a neutral compound with a positively charged functional group and a negatively charged anionic functional group, which may not be adjacent to the cationic site. In nature, various types of betaines can be synthesized by cells to serve as biological osmolytes for the protection of cells, proteins, and enzymes against environmental osmotic stress, high-salinity drought, or extreme temperature. The name of a betaine generally reflects its anionic moiety. Three major types of biomimetic polybetaines–phosphobetaine (PB), sulfobetaine (SB), and carboxybetaine (CB) (Fig. 11.9), all with the same cationic ammonium group–have been reported for their applications in nonspecific protein resistance. Among these polybetaines, a PB such as phosphorylcholine (PC) mimics the zwitterionic structure of the PC headgroups of membrane lipids. SB is an analoge of taurine betaine, which has been extensively studied due to the ease of synthesis [60, 94–98]. Polycarboxybetaine is the first synthetic polybetaine. CB groups are usually more hydrophilic than SB [99]. Because of the unique features of its dual functionality, polycarboxybetaine has the advantage of carrying abundant functional groups for ligand immobilization [100]. Nevertheless, by lowering the pH of the aqueous medium, a CB group can be protonated more easily than a SB group and consequently render the surface cationic [101]. Various immobilization methods, including physisorption via DOPA linkage [54], covalent fixation via SI-ATRP [98], and self-assembly [102], have been applied to demonstrate the non-fouling properties of the zwitterionic materials.

11.4.3.2 Polyampholytes. Polyampholytes, which carry both the positive and negative moieties along the polymer backbone or on the sidechains, have been synthesized by copolymerization of both anionic and cationic monomers.

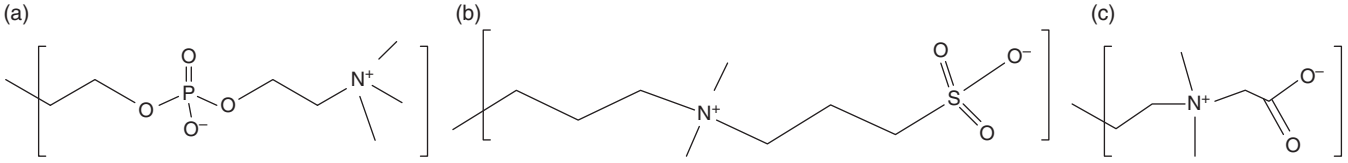


FIGURE 11.9 Chemical structures of (a) phosphobetaine (PB), (b) sulfobetaine (SB), and (c) carboxybetaine (CB).

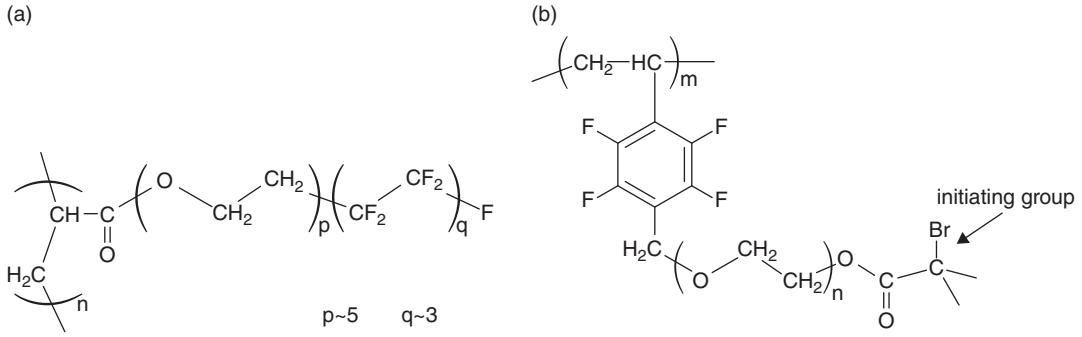


FIGURE 11.10 Molecular structures of amphiphilic polymers: (a) polymer with perfluoroalkyl tagged OEG as sidechains; (b) hyperbranched amphiphilic fluoropolymers.

Although these materials have received less attention in the literature than polybetaine systems, polyampholyte systems are promising for antifouling because the charge neutrality and the uniformity of the charge distribution of the polymers can be obtained by controlling the ratio of the two oppositely charged monomers of the reaction mixture before co-polymerization [103, 104]. It has been demonstrated that the ion pair comonomer polymers with negligible defects can be achieved, and the polymer surfaces displayed excellent resistance to protein adsorption for various polyampholytes such as negatively charged 2-carboxyethyl acrylate (CAA)-based or 3-sulfopropyl methacrylate(SA)-based mixtures with positively charged NH_2, dimethylaminoethyl methacrylate (DM), diethylaminoethyl methacrylate (DE), and [2-(acryloyloxy)ethyl] trimethyl ammonium chloride (TMA) [45,105,106]. Another promising polyampholyte system is polypeptides consisting of alternating positively charged residues such as arginine (Arg) or lysine (Lys) and negatively charged residues such as aspartic acid (Asp) or glutamic acid (Glu). Similar to natural proteins, this type of polyampholyte is biodegradable and the degradation products are nontoxic amino acids. Two reports demonstrated that peptides with alternating Glu/Lys or Asp/Lys have ultralow protein adsorption to various plasma proteins [107, 108]. SAMs with a 1:1 mixture of cationic and anionic charged groups also exhibit similar characteristics. It is believed that the possible rearrangement of charge groups due to the soft backbone of polyampholytes or the mobility of thiols on gold might reduce the defects in the charge distribution of polyampholytes and mixed SAM, respectively, and rendered both surfaces with nanometer-scaled homogeneity [14]. The polyampholytes/mixed SAMs system provides easy routes for the design of a wide range of new nonfouling zwitterionic surfaces.

11.4.4 Amphiphilic Materials

Amphiphilic nonfouling materials are polymers containing both of the hydrophobic fluorinated and hydrophilic PEGylated groups. These materials were designed to combine the *fouling release* characteristic of the low-energy fluorinated groups and the antifouling feature of the hydrophilic PEGylated groups. Amphiphilic nonfouling polymers with different molecular architectures have been reported, including a polymer with perfluoroalkyl tagged OEG as sidechains (Fig. 11.10a) and hyperbranched amphiphilic fluoropolymers synthesized by atom transfer radical polymerization from an amphiphilic monomer with an initiating group (Fig. 11.10b). The polymers with the amphiphilic sidechains tend to form a uniform lamellar structure parallel to the substrate [109]. The wettability of the surfaces of this type of polymer is environmentally responsive due to the rearrangement of the perfluoroalkyl and PEG groups in the lamellar structure. Surfaces coated with hyperbranched amphiphilic fluoropolymers exhibit a completely different surface molecular structure. The surfaces were designed based on the hypothesis that a surface composition with heterogeneity small enough in size will enhance resistance to protein adsorption [11]. Although this hypothesis lacks solid evidence, surfaces grafted with zwitterionic materials, which consist of nanometer-scaled heterogeneity in charge distribution, are consistent with this hypothesis. Hyperbranched amphiphilic fluoropolymers enhance the surface resistance to protein adsorption by introducing nanometer-scale variation in surface hydrophilicity/hydrophobicity. One study indicated that high protein resistance of this type of fluoropolymers can be achieved at an optimal hydrophilic-to-hydrophobic monomer ratio [47]. Another team also reported that surfaces coated with the hyperbranched fluoropolymers synthesized by atom transfer radical polymerization of an inimer shown in Fig. 11.10b exhibit surface heterogeneity small enough to resist protein adsorption [48]. It is believed that the effectiveness of the amphiphilic materials on protein resistance is closely related to the dedicate balance of the hydrophilicity between the polar and nonpolar groups. Further studies on the mechanism for protein resistance of this type of material are necessary.

11.5 CONCLUSIONS AND FUTURE PERSPECTIVES

The development of materials with ultralow protein adsorption has a wide range of industrial and biomedical applications. From the results of numerous studies on the mechanism of protein adsorption, it is generally accepted that the nonfouling properties of a material are closely related to the surface hydration behavior of the materials. General criteria for protein adsorption-resistant surfaces include the presence of polar functional groups, the absence of a net charge, the possession of nanometer-scale homogeneity, and being defect-free. PEG-based materials have long been the most commonly used antifouling materials. To overcome their limitation for long-term usage caused by the oxidation of the materials, various alternative materials have been developed. On the basis of the polarity of the materials, from high to low, these nonfouling materials are classified into three categories: zwitterionic materials, nonionic hydrophilic materials, and amphiphilic materials. Among these materials, the zwitterionic materials, which have the strongest interaction with water and tend to form a dense film on surfaces via interchain association, reveal especially promising outcomes for future development. It has been well documented that the protein resistance of a surface is determined not only by the chemical properties of the materials but also by the physical properties, such as the packing density and chain mobility, of the surfaces. Future studies on correlating the molecular-level details of a surface and the water hydration states for surfaces under various physicochemical conditions should provide useful information on understanding the antifouling mechanism and in developing adequate surface modification techniques for antifouling surfaces.

REFERENCES

[1] Franz, S., Rammelt, S., Scharnweber. D., Simon, J.C. (2011). Immune responses to implants–a review of the implications for the design of immunomodulatory biomaterials. *Biomaterials* **32**, 6692–6709.

[2] Gorbet, M.B., Sefton, M.V. (2004). Biomaterial-associated thrombosis: Roles of coagulation factors, complement, platelets and leukocytes. *Biomaterials* **25**, 5681–5703.

[3] Hu, W.J., Eaton, J.W., Ugarova, T.P., Tang L. (2001). Molecular basis of biomaterial mediated foreign body reactions. *Blood* **98**, 1231–1238.

[4] Sarma, J.V., Ward, P.A. (2011). The complement system. *Cell Tissue Res*, **343**, 227-35.

[5] Anderson, J.M. (2001). Biological responses to materials. *Annu. Rev. Mater. Res.* **31**, 81–110.

[6] Ratner, B.D., Bryant, S.J. (2004). Biomaterials: Where we have been and where we are going. *Annu. Rev. Biomed. Eng.* **6**, 41–75.

[7] Norowski, P.A., Jr., Bumgardner, J.D. (2009). Biomaterial and antibiotic strategies for peri-implantitis: A review. *J. Biomed. Mater. Res. B: Appl. Biomater.* **88B**, 530–543.

[8] Page, K., Wilson, M., Parkin, I.P. (2009). Antimicrobial surfaces and their potential in reducing the role of the inanimate environment in the incidence of hospital-acquired infections. *J. Mater. Chem.* **19**, 3819–3831.

[9] Roosjen, A., van der Mei, H.C., Busscher, H.J., Norde, W. (2004). Microbial adhesion to poly(ethylene oxide) brushes: Influence of polymer chain length and temperature. *Langmuir* **20**, 10949–10955.

[10] Banerjee, I., Pangule, R.C., Kane, R.S. (2011). Antifouling coatings: Recent developments in the design of surfaces that prevent fouling by proteins, bacteria. *Adv. Mater.* **23**, 690–718.

[11] Krishnan, S., Weinmanb, C.J., Ober, C.K. (2008). Advances in polymers for anti-biofouling surfaces. *J. Mater. Chem.* **18**, 3405–3413.

[12] Israelachvili, J., Wennerstrom, H. (1996). Role of hydration and water structure in biological and colloidal interactions, *Nature* **379**, 219–225.

[13] Zheng, J., Li, L., Chen, S., Jiang, S. (2004). Molecular simulation study of water interactions with oligo (ethylene glycol)-terminated alkanethiol self-assembled monolayers. *Langmuir* **20**, 8931–8938

[14] Chen, S.F., Li, L., Zhao, C., Zheng, J. (2010). Surface hydration: Principles and applications toward low-fouling/nonfouling biomaterials. *Polymer* **51**, 5283–5293.

[15] Claesson, M.P., Blomberg, E., Froberg J., Nylander T., Arnebrant T. (1995). Protein interactions at solid surfaces. *Adv. Colloid Interface Sci.* **57**, 161–227.

[16] Hunter, J.R., Kilpatrick, P.K., Carbonell, R.G. (1990). Lysozyme adsorption at the air/water interface. *J. Colloid Interface Sci.* **137**, 462–482.

[17] Haynes C.A., Norde W. (1994). Globular proteins at solid/liquid interfaces. *Colloids Surf. B: Biointerfaces* **2**, 517–566.

[18] Silin, V., Weetail, H.,J., Vanderah, D. (1997). SPR studies of the nonspecific adsorpiton kinetics of human IgG and BSA on gold surface modified by self-assembled monolayers (SAMs), *J. Colloid Interface Sci.* **185**, 94–103.

[19] Hatakeyama, H., Hatakeyama, T., (1998). Interaction between water and hydrophilic polymers. *Thermochim. Acta* **308**, 3–22.

[20] Ping, Z.H., Nguyen, Q.T., Chen, S.M., Zhou, J.Q., Ding, Y.D. (2001). States of water in different hydrophilic polymers–DSC and FTIR studies. *Polymer* **42**: 8461–8467.

[21] Tanaka, M., Mochizuki, A. (2004). Effect of water structure on blood compatibility– thermal analysis of water in poly(meth)acrylate. *J. Biomed. Mater. Res. A* **68A**(4), 684–695.

[22] Morisaku,T., Watanabe, J., Konno, T., Takai, M., Ishihara, K. (2008). Hydration of phosphorylcholine groups attached to highly swollen polymer hydrogels studied by thermal analysis. *Polymer* **49**(21), 4652–4657.

[23] Hower, J.C., Bernards, M.T., Chen, S., Tsao, H.K., Sheng, Y.J., Jiang, S. (2009). Hydration of "nonfouling" functional groups. *J. Phys. Chem. B* **113**, 197—201.

[24] Ishihara, K., Fukumoto, K., Iwasaki, Y., Nakabayashi, N. (1999). Modification of polysulfone with phospholipid polymer for improvement of the blood compatibility. Part 1. Surface characterization. *Biomaterials* **20**, 1545–1551.

[25] Kitano, H., Nagaoka, K., Tada, S., Gemmei-Ide, M., (2007). Structure of water in the vicinity of amphoteric polymers as revealed by Raman spectroscopy. *J. Colloid Interface Sci.* **313**, 461–468

[26] Kitano, H., Nagaoka, K., Tada, S., Gemmei-Ide, M., Tanaka, M. (2008). Structure of water incorporated in amphoteric polymer thin films as revealed by FT-IR spectroscopy. *Macromol. Biosci.* **8**, 77–85.

[27] Vogler, E.A. (1999). Water and the acute biological response to surfaces. *J. Biomater. Sci. Polymer Ed.* **10** (10), 1015–1045.

[28] Vogler, E.A. (2001). How water wets biomaterial surfaces. In Morra, M. (ed.), *Water in Biomaterials Surface Science.* Wiley, New York, pp. 269–290.

[29] Sendner, C., Horinek, D., Bocquet, L., Netz, R.R. (2009). Interfacial water at hydrophobic and hydrophilic surfaces: Slip, viscosity, and diffusion. *Langmuir* **25**, 10768–10781.

[30] Chapman, R.G., Ostuni, E., Takayama, S., Holmlin, R.E., Yan, L., Whitesides, G.M. (2000). Surveying for surfaces that resist the adsorption of proteins. *J. ACS* **122**(34), 8303–8304.

[31] Chapman, R.G., et al. (2001). Polymeric thin films that resist the adsorption of proteins and the adhesion of bacteria. *Langmuir* **17**(4), 1225–1233.

[32] Ostuni, E., Chapman, R.G., Holmlin, R.E., Takayama, S., Whitesides, G.M. (2001). A survey of structure-property relationships of surfaces that resist the adsorption of protein. *Langmuir* **17**(18), 5605–5620.

[33] Yang, Q., Kaul, C., Ulbricht, M. (2010). Anti-nonspecific protein adsorption properties of biomimetic glycocalyx-like glycopolymer layers: Effects of glycopolymer chain density and protein size. *Langmuir* **26**, 5746–5752.

[34] Luk, Y.Y., Kato, M., Mrksich, M. (2000). Self-assembled monolayers of alkanethiolates presenting mannitol groups are inert to protein adsorption and cell attachment. *Langmuir* **16**, 9604–9608.

[35] Kane, R.S., Deschatelets, P., Whitesides, G.M. (2003). Kosmotropes form the basis of protein-resistant surfaces. *Langmuir* **19**, 2388–2391.

[36] Krishnan S., Wang, N., Ober, C.K., Finlay, J.A., Callow, M.E., Callow, J.A., Hexemer, A., Sohn, K.E., Kramer, E.J., Fischer, D.A. (2006). Comparison of the fouling release properties of hydrophobic fluorinated and hydrophilic PEGylated block copolymer surfaces: Attachment strength of the diatom navicula and the green alga ulva. *Biomacromolecules* **7**, 1449–1462.

[37] Kenausis, G.L., Vörös, J., Elbert, D.L., Huang, N.P., Hofer, R., Ruiz-Taylor, L., Textor, M., Hubbell, J.A., Spencer, N.D. (2000). Poly(L-lysine)-g-poly(ethylene glycol) layers on metal oxide surfaces: Attachment mechanism and effects of polymer architecture on resistance to protein adsorption. *J. Phys. Chem. B* **104**, 3298–3309.

[38] Michel, R., Pasche, S., Textor, M., Castner, D.G. (2005). The influence of PEG architecture on protein adsorption and conformation. *Langmuir* **21**, 12327–12332.

[39] Prime, K.L., Whitesides, G.M. (1991). Self-assembled organic monolayers: Model systems for studying adsorption of proteins at surfaces. *Science* **252**, 1164–1167.

[40] Prime, K.L., Whitesides, G.M. (1993) Adsorption of proteins onto surfaces containing end-attached oligo(ethylene oxide): a model system using self-assembled monolayers. *J. Am. Chem. Soc.*, **115**, 10714–21.

[41] Harder, P., Grunze, M., Dahint, R., Whitesides, G.M., Laibinis, P.E. (1998). Molecular conformation in oligo(ethylene glycol)-terminated self-assembled monolayers on gold and silver surfaces determines their ability to resist protein adsorption. *J. Phys. Chem. B* **102**, 426–436.

[42] Herrwerth, S., Eck, W., Reinhardt, S., Grunze, M. (2003). Factors that determine the protein resistance of oligoether self-assembled monolayers –internal hydrophilicity, terminal hydrophilicity, and lateral packing density. *J. ACS* **125**(31), 9359–9366.

[43] Wang, R.L.C., Kreuzer H.J., Grunze, M. (2000). The interaction of oligo(ethylene oxide) with water: A quantum mechanical study. *Phys. Chem. Chem. Phys.* **2**, 3613–3622.

[44] Li, L., Chen, S., Zheng, J., Ratner, B.D., Jiang, S. (2005). Protein adsorption on oligo(ethylene glycol)-terminated alkanethiolate self-assembled monolayers: The molecular basis for nonfouling behavior. *J. Phys. Chem. B* **109**(7), 2934–2941.

[45] Li, G.Z., Xue, H., Gao, C.L., Zhang, F.B., Jiang, S. (2010). Nonfouling polyampholytes from an ion-pair comonomer with biomimetic adhesive groups. *Macromolecules* **43**(1), 14–16.

[46] Zheng, J., He, Y., Chen, S., Li, L., Bernards, M.T., Jiang S. (2006). Molecular simulation studies of the structure of phosphorylcholine self-assembled monolayers. *J. Chem. Phys.* **125**(17), 174714–17417.

[47] Gudipati, C.S., Finlay, J.A., Callow, M.E., Wooley, K.L. (2005). The antifouling and fouling-release performance of hyperbranched fluoropolymer (HBFP)-PEG composite coating evaluated by adsorption of biomacromolecules and the green fouling Alga Ulva. *Langmuir* **21**, 3044–3053.

[48] Powell, K.T., Cheng, C., Wooley, K.L. (2007). Complex amphiphilic hyperbranched fluoropolymers by atom transfer radical self-condensing vinyl copolymerization. *Macromolecules* **40**, 4509–4515.

[49] Llanos, G.R., Sefton, M.V. (1993). Does polyethylene oxide possess a low thrombogenicity? *J. Biomater. Sci. Polym. Ed.* **4**, 381–400.

[50] Sheu, M.S., Hoffman, A.S., Feijen, J. (1992). A glow discharge treatment to immobilize PEO/PPO surfactants for wettable and non-fouling biomaterials. *J. Adhes. Sci. Technol.* **6**(9), 995–1009.

[51] Liou, Y.B., Tsay, R.Y. (2011). Adsorption of PEO–PPO–PEO triblock copolymers on a gold surface. *J. Taiwan Inst. Chem. Eng.* **42**, 533–540.

[52] Dalsin, J.L., Messersmith, P.B. (2005). Bioinspired antifouling polymers. *Mater. Today* **8**, 38–46.

[53] Lee, B.P., Huang, G, K., Nunalee, F.N., Shull, K., Messersmith, P.B. (2004). Synthesis of 3,4-dihydroxyphenylalanine (DOPA) containing monomers and their co-polymerization with PEG-diacrylate to form hydrogels. *J. Biomater. Sci. Polym. Ed.* **15**(4), 449–464.

[54] Li, G., Cheng, G., Xue, H., Chen, S., Zhang, F., Jiang, S. (2008). Ultra low fouling zwitterionic polymers with a biomimetic adhesive group. *Biomaterials* **29**, 4592–4597.

[55] Gademann, K., Kobylinska, J., Wach, J.Y., Woods, T.M. (2009). Surface modifications based on the cyanobacterial siderophore anachelin: From structure to functional biomaterials design. *Biol. Metals* **22**(4), 595–604.

[56] Auroy, P., Auvray, L., Leger, L. (1992). Silica particles stabilized by long grafted polymer chains: From electrostatic to steric repulsion. *J. Colloid Interface Sci.* **150**, 187–194.

[57] Mahmoodian, H., Moradi, O., Shariatzadeh, B. (2014). Grafting chitosan and polyHEMA on carbon nanotubes surfaces: "Grafting to" and "grafting from" methods. *Int J. Biol. Macromol.* **63**, 92–97.

[58] Prucker, O., Ruhe, J. (1998). Polymer layers through self-assembled monolayers of initiators. *Langmuir* **14**, 6893–6898.

[59] Prucker, O., Ruhe, J. (1998). Synthesis of poly(styrene) monolayers attached to high surface area silica gels through self-assembled monolayers of azo Initiators. *Macromolecules* **31**, 592–601.

[60] Ma, H., Hyun, J., Stiller, P., Chilkoti, A. (2004). "Non-fouling" oligo(ethylene glycol)- functionalized polymer brushes synthesized by surface-initiated atom transfer radical polymerization. *Adv. Mater.* **16**, 338–341.

[61] Ladd, J., Zhang, Z., Chen, S., Hower, J.C., Jiang, S. (2008). Zwitterionic polymers exhibiting high resistance to nonspecific protein adsorption from human serum and plasma. *Biomacromolecules* **9**(5), 1357–1361.

[62] Zheng, J., Li, L., Tsao, H.K., Sheng, Y.J., Chen, S., Jiang, S. (2005). Strong repulsive forces between protein and oligo (ethylene glycol) self-assembled monolayers: A molecular simulation study. *Biophys. J.* **89**(1), 158–166.

[63] Pertsin, A.J., Grunze, M. (2000). Computer simulation of water near the surface of oligo(ethylene glycol)-terminated alkanethiol self-assembled monolayers. *Langmuir* **16**(23), 8829–8841.

[64] Lutz, J.F., Akdemir, Ö., Hoth, A. (2006). Point by point comparison of two thermosensitive polymers exhibiting a similar LCST: Is the age of poly(NIPAM) over? *J. ACS* **128**(40), 13046–13047.

[65] Jiang, H., Manolache, S., Wong, A.C., Denes, F.S. (2006). Synthesis of dendrimer-type poly(ethylene glycol) structures from plasma-functionalized silicone rubber surfaces. *J. Appl. Polym. Sci.* **102**, 2324–2337.

[66] Jeon, S.I., Lee, J.H., Andrade, J.D., De Gennes, P.G. (1991). Protein-surface interactions in the presence of polyethylene oxide. I: Simplified theory. *J. Colloid Interface Sci.* **142**(1), 149–158.

[67] Szleifer, I. (1997). Protein adsorption on surfaces with grafted polymers: A theoretical approach. *Biophys. J.* **72**(2), 595–612.

[68] Benhabbour, S.R., Liu, L., Sheardown, H., Adronov, A. (2008). Protein resistance of surfaces prepared by chemisorption of monothiolated poly(ethylene glycol) to gold and dendronization with aliphatic polyester dendrons: Effect of hydrophilic dendrons. *Macromolecules* **41**, 2567–2576.

[69] Malmsten, M., Emoto, K., Van Alstine, J.M. (1998). Effect of chain density on inhibition of protein adsorption by poly(ethylene glycol) based coatings. *J. Colloid Interface Sci.* **202**, 507–517.

[70] Dalsin, J.L., Lin, L., Tosatti, S., Voros, J., Textor, M., Messersmith, P.B. (2005). Protein resistance of titanium oxide surfaces modified by biologically inspired mPEG−DOPA. *Langmuir* **21**, 640.

[71] Zhao, Y.H., Zhu, B.K., Kong, L., Xu, Y.Y. (2007). Improving hydrophilicity and protein resistance of poly(vinylidene fluoride) membranes by blending with amphiphilic hyperbranched-star polymer. *Langmuir* **23**, 5779–5786.

[72] Hucknall, A., Rangarajan, S., Chilkoti, A. (2009). In pursuit of zero: Polymer brushes that resist the adsorption of proteins. *Adv. Mater.* **21**(23), 2441–2446.

[73] Kainthan, R.K., Janzen, J., Levin, E., Devine, D.V., Brooks, D.E. (2006). Biocompatibility testing of branched and linear polyglycidol. *Biomacromolecules* **7**(3), 703–709.

[74] Siegers, C, Biesalski, M., Haag, R. (2004). Self-assembled monolayers of dendritic polyglycerol derivatives on gold that resist the adsorption of proteins. *Chem. A Eur. J.* **10**, 2831–2838.

[75] Wyszogrodzka, M., Haag, R. (2009). Synthesis and characterization of glycerol dendrons, self-assembled monolayers on gold: A detailed study of their protein resistance. *Biomacromolecules* **10**, 1043–1054.

[76] Deng, L., Mrksich, M., Whitesides, G.M. (1996). Self-assembled monolayers of alkanethiolates presenting tri(propyl sulfoxide) groups resist the adsorption of protein. *J. ACS* **118**, 5136–5137.

[77] Chelmowski, R., Koster, S.D., Kerstan, A., Prekelt, A., Grunwald, C., Winkler, T., Metzler-Nolte, N., Terfort, A., Woll, C. (2008). Peptide-based SAMs that resist the adsorption of proteins. *J. ACS* **130**, 14952–14953.

[78] Sun, J., Zuckermann, R.N. (2013). Peptoid polymers: A highly designable bioinspired material. *ACS Nano* **7**(6), 4715–4732.

[79] Statz, A.R., Meagher R.J., Barron A.E., Messersmith P.B. (2005). New peptidomimetic polymers for antifouling surfaces. *J. ACS* **127**, 7972–7973.

[80] Statz, A.R., Barron, A.E., Messersmith, P.B. (2008). Protein, cell and bacterial fouling resistance of polypeptoid-modified surfaces: Effect of side-chain chemistry. *Soft Matter* **4**, 131–139.

[81] Adams, N., Schubert, U.S. (2007). Poly(2-oxazolines) in biological and biomedical application contexts. *Adv. Drug Deliv. Rev.* **59**, 1504–1520.

[82] Konradi, R., Pidhatika, B., Muhlebach, A., Textor, M. (2008). Poly-2-methyl-2-oxazoline: A peptide-like polymer for protein-repellent surfaces. *Langmuir* **24**, 613–616.

[83] Holland, N.B., Qiu, Y., Ruegsegger, M., Marchant, R.E. (1998). Biomimetic engineering of non-adhesive glycocalyx-like surfaces using oligosaccharide surfactant polymers. *Nature* **392**, 799–801.

[84] Vacheethasanee, K., Marchant, R.E. (2000). Surfactant polymers designed to suppress bacterial (Staphylococcus epidermidis) adhesion on biomaterials. *J. Biomed. Mater. Res. A* **50**(3), 302–312.

[85] Zhu, J., Marchant, R.E. (2006). Dendritic saccharide surfactant polymers as antifouling interface materials to reduce platelet adhesion. *Biomacromolecules* **7**, 1036–1041.

[86] Kitano, H., Mori, T., Takeuchi, Y., Tada, S., Gemmei-Ide, M., Yokoyama, Y. Tanaka, M. (2005). Structure of water incorporated in sulfobetaine polymer films as studied by ATR-FTIR. *Macromol Biosci*. **5**(4), 314–321.

[87] Chen, S., Jiang, S. (2008). An new avenue to nonfouling materials. *Adv. Mater.* **20**, 335–338.

[88] Kitano H., Tada, S., Mori, T., Takaha, K., Gemmei-Ide, M., Tanaka, M., Fukuda, M., Yokoyama, Y. (2005). Correlation between the structure of water in the vicinity of carboxybetaine polymers and their blood-compatibility. *Langmuir* **21**, 11932–11940.

[89] Athawale, M.V., Dordick, J.S., Garde, S. (2005). Osmolyte trimethylamine-N-oxide does not affect the strength of hydrophobic interactions: Origin of osmolyte compatibility. *Biophys. J.* **89**, 858–866.

[90] Rubinstein, M., Dobrynin A.V. (1999). Associations leading to formation of reversible networks and gels. *Curr. Opin. Colloid Interface Sci.* **4**, 83–87.

[91] He, Y., Chang, Y., Hower, J.C., Zheng, J., Chen, S., Jiang, S. (2008). Origin of repulsive force and structure/dynamics of interfacial water in OEG- protein interactions: A molecular simulation study. *Phys. Chem. Chem. Phys.* **10**(36), 5539–5544.

[92] Chen, S., Zheng, J., Li, L., Jiang, S. (2005). Strong resistance of phosphorylcholine self-assembled monolayers to protein adsorption: Insights into nonfouling properties of zwitterionic materials. *J. ACS* **127**(41), 14473–14478.

[93] Azzaroni, O., Brown, A.A., Huck, W.T.S. (2006), UCST wetting transitions of polyzwitterionic brushes driven by self-association, *Angew. Chem.* **118**(11), 1802–1806.

[94] Yang, W., Chen, S., Cheng, G., Vaisocherova, H., Xue, H., Li, W., Zhang, J., Jiang, S. (2008). Film thickness dependence of protein adsorption from blood serum and plasma onto poly(sulfobetaine)-grafted surfaces. *Langmuir* **24**(17), 9211–9214.

[95] Chang, Y., Chen, S., Yu, Q., Zhang, Z., Bernards, M., Jiang, S. (2007). Development of biocompatible interpenetrating polymer networks containing a sulfobetaine-based polymer and a segmented polyurethane for protein resistance. *Biomacromolecules* **8**(1), 122–127.

[96] Chang, Y., Liao, S.C., Higuchi, A., Ruaan, R.C., Chu, C.W., Chen, W.Y. (2008). A highly stable nonbiofouling surface with well-packed grafted zwitterionic polysulfobetaine for plasma protein repulsion. *Langmuir* **24**, 5453–5458.

[97] Chang, Y., Chen, W.Y., Yandi, W., Shih, Y.J., Chu, W.L., Liu, Y.L., Chu, C.W., Ruaan, R.C., Higuchi, A. (2009). Dual-thermoresponsive phase behavior of blood compatible zwitterionic copolymers containing nonionic poly(N-isopropyl acrylamide). *Biomacromolecules* **10**, 2092–2100.

[98] Zhang, Z., Zhang, M., Chen, S., Horbett, T.A., Ratner, B.D., Jiang, S. (2008). Blood compatibility of surfaces with super-low protein adsorption. *Biomaterials* **29**, 4285–4291.

[99] Bonte, N., Laschewsky, A. (1996). Zwitterionic polymers with carbobetaine moieties. *Polymer* **37**, 2011–2019.

[100] Zhang, Z., Vaisocherva, H., Cheng, G., Yang, W., Xue, H., Jiang, S. (2008). *Biomacromolecules* **9**, 2686–2692.

[101] Wielema, T.A., Engberts, J.B.F.N. (1988). An ESR spin label study of the dynamics of a zwitterionic polymer, a polyelectrolyte, poly(methacrylic acid) and poly(acrylic acid) in aqueous solution. *Eur. Polym. J.* **24**, 647–650.

[102] Chang, Y., Chen, S., Zhang, Z., Jiang, S. (2006). Highly protein-resistant coatings from well-defined diblock copolymers containing sulfobetaines. *Langmuir* **22**(5), 2222–2226.

[103] McCormick, C.L., Johnson, C.B. (1988). Water-soluble polymers. 28. Ampholytic copolymers of sodium 2-acrylamido-2-methylpropanesulfonatwe with (2- acrylamido-2-methylpropyl) dimethylammoniu chloride: Synthesis and characterization. *Macromolecules* **21**(3), 686–693.

[104] Yang, J.H., Jhon, M.S. (1995). The conformation and dynamics study of amphoteric copolymers, P(sodium 2-methacryloyloxy ethanesulfonate- co-2-methacryloyloxy ethyltrimethyl ammonium iodide), using viscometry, 14N-, and 23Na-NMR. *J. Polym. Sci. A: Polym. Chem.* **33**(15), 2613–2621.

[105] Tah, T., Bernards M.T. (2012). Nonfouling polyampholyte polymer brushes with protein conjugation capacity. *Colloids Surf. B Biointerfaces* **93**, 195–201.

[106] Bernards, M.T., Cheng, G., Zhang, Z., Chen, S., Jiang, S. (2008). Nonfouling polymer brushes via surface-initiated, two-component atom transfer radical polymerization. *Macromolecules* **41**(12), 4216–4219.

[107] Chen, S.F., Cao, Z.Q., Jiang, S. (2009). Ultra-low fouling peptide surfaces derived from natural amino acids. *Biomaterials* **30**(29), 5892–5896.

[108] Yang, Q., Wang, L., Lin, W., Ma, G., Yu, J., Chen, S.F. (2014). Development of nonfouling polypeptides with uniform alternating charges by polycondensation of the covalently bonded dimer of glutamic acid and lysine. *J. Mater. Chem. B* **2**, 577–584.

[109] Krishnan, S., Ramakrishnan, A., Hexemer, A., Finlay, J.A., Sohn, K.E., Perry, R., Ober, C.K., Kramer, E.J., Callow, M.E., Callow, J.A., Fischer, D.A. (2006) Anti-biofouling properties of comblike block copolymers with amphiphilic side chains. *Langmuir* **22**, 5075–5086.

12

SURFACE CHARACTERIZATION OF SILVER AND Fe_3O_4 NANOPARTICLES INCORPORATED INTO COLLAGEN-BASED SCAFFOLDS AS BIOMATERIALS FOR TISSUE REGENERATION: STATE-OF-THE-ART AND FUTURE PERSPECTIVES

Abhishek Mandal,[1] N. Chandrasekaran,[1] Amitava Mukherjee,[1] and Thothapalli P. Sastry[1,2]

[1]*Centre for Nano-Biotechnology, School of Bio-Sciences and Technology, VIT University, Vellore 632014, Tamil Nadu, India*
[2]*Bio-products Laboratory, CSIR-Central Leather Research Institute, Adyar, Chennai 600020, Tamil Nadu, India*

12.1 INTRODUCTION

The molecule-level interactions between materials and biological systems are not clear and completely understood. There is a need to decipher these interactions, as the surface modification of the biomaterial influences the response of proteins and cells, known as *biocompatibility* and *blood compatibility*, respectively. Thus, it is vital to comprehend the biomaterial surface to obtain insight on the nature of biological reaction [1]. It is well known that biomaterials have to satisfy many conditions for its successful use in biomedical applications [2, 3]. However, the nature of the surface of a biomaterial is the most important criterion, as biological reactions occur on the surface and at interfaces [1, 4, 5]. The surface properties such as hydrophilicity, chemical structure, and topography govern the adhesion and proliferation of cells, which play significant roles in biocompatibility as well as in tissue engineering applications [6–10].

The surface is a miniscule part and differs from the bulk of the biomaterial. This is due to the mode of preparation and the thermodynamics involved, which leads to structural reorganization, resulting in the change of the adsorption behavior and other related surface reactions in the biomaterial [11]. Therefore, it is essential to have a set of analytical techniques that can perform comprehensive characterization of both the bulk and surface properties of a biomaterial to evaluate and correlate the changes in the biological performance.

Collagen, the biopolymer, is found abundantly in the extracellular matrix and connective tissue of the mammals [12, 13]. The ease of preparation has enabled it to be widely used as a biomaterial [14]. This fibrous protein provides structural integrity and performs a vital role in the formation of tissues and organs [15]. The advantages of using a naturally derived material such as collagen as biomaterial are its high biocompatibility and intrinsic biological recognition [16–19]. Also, this biopolymer possesses features such as biodegradability and reduced antigenicity, which renders it as an excellent substrate for cell attachment and its growth [20–22], the criteria essential for its application as a biomaterial. Moreover, the structure of collagen and its interaction with host tissue allow it to act as an efficient matrix to produce diverse forms of biomaterials and therefore, it is used extensively in various biomedical fields such as scaffold in tissue engineering applications [23]. The structure and use of collagen scaffolds in various forms are depicted in Fig. 12.1. In addition to the above mentioned desired features, collagen is nontoxic and has a safe profile as a scaffold for biomedical purposes [14]. Thus, collagen-based biomaterials as scaffolds

Encyclopedia of Biocolloid and Biointerface Science, Volume 1, First Edition. Edited by Hiroyuki Ohshima.
© 2016 John Wiley & Sons, Inc. Published 2016 by John Wiley & Sons, Inc.

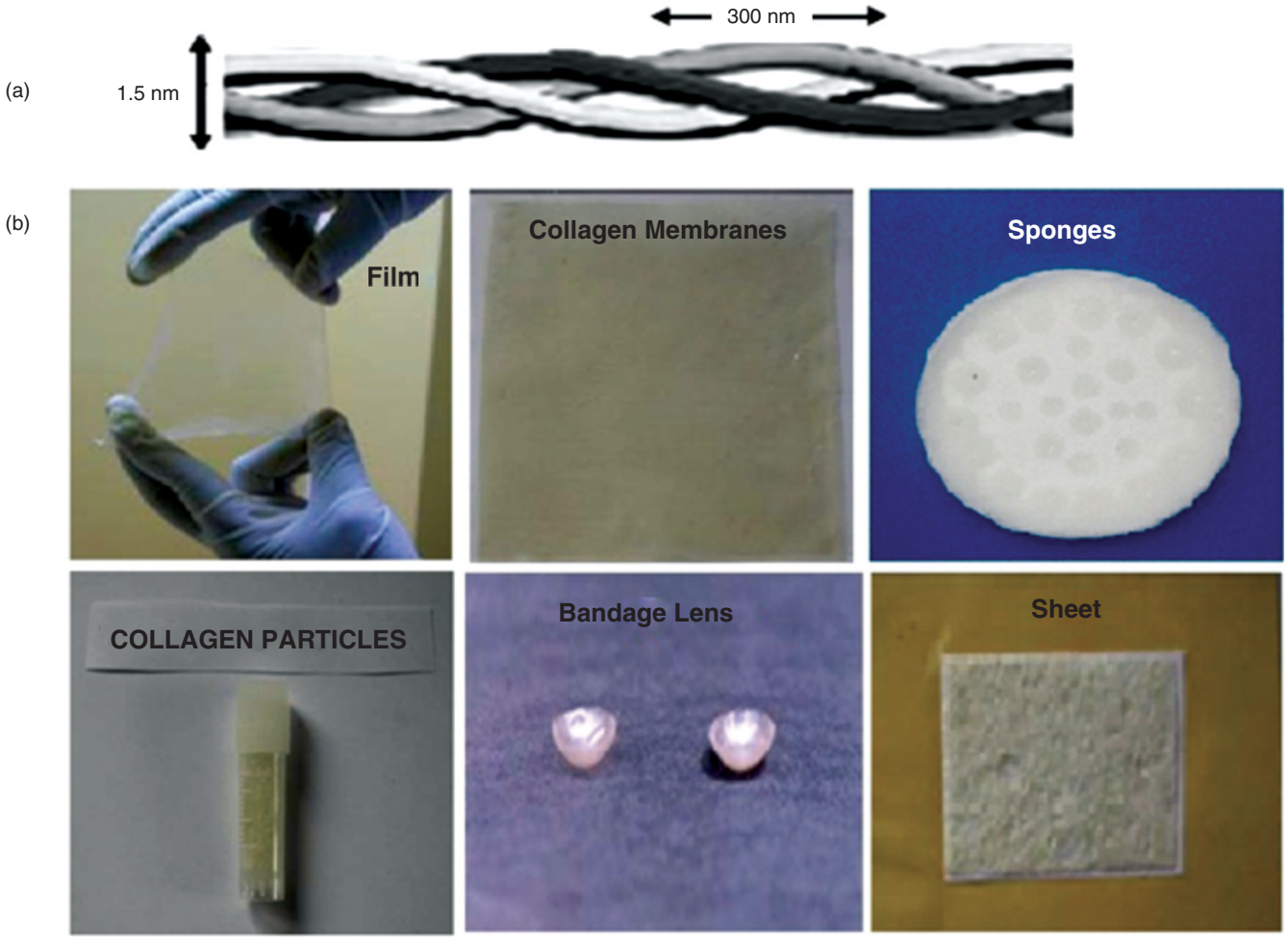


FIGURE 12.1 Schematic representation of collagen (a) triple helical structure and (b) its use as a scaffold in different forms for biomedical applications.

prepared in our CLRI laboratories have found application in tissue engineering and in regenerative medicine.

The use and application of nanoparticles for biomedical applications have gained significant importance. Among them, the role of silver nanoparticles as antimicrobial agent is well established and has been extensively utilized in the preparation of wound-dressing materials [24–26]. Moreover, it has found use as imaging agent [27, 28] and also in sustained-release drug delivery [29, 30]. Iron oxide (Fe_3O_4) nanoparticles have also found use in the biomedical field, where its magnetic properties have been used in the cell seeding into 3D scaffolds [31], cell labeling [32], contrast agent in MRI [33, 34], and as targeted delivery systems in the treatment of cancer-related diseases [35, 36]. Therefore, the incorporation of nanoparticles, particularly silver and Fe_3O_4, and their interactions with various biological molecules such as collagen have been the subject of investigation. This review presents an overview of the state of the art on the major tools applied to the characterization of collagen-based biomaterials as scaffolds for tissue engineering applications and in regenerative medicine. The characterization of nanoparticle-incorporated collagen scaffolds is divided into three main parts in this review: (1) *structural aspects*–focused mostly on determination of molecular mass, purity, and helical content confirmation in addition to other associated bulk thermal properties; (2) *chemical characteristics*–focused primarily on surface elemental analysis; and (3) *morphological characteristics*–observed at different length scales. It is expected that this type of evaluation can offer a reliable basis for comparison of collagen-based biomaterials as scaffolds and also assist in attaining new insights into the nature of reactions with these biomaterials. The techniques employed for the characterization of collagen-based biomaterials as scaffolds along with the format and obtained information are listed in Table 12.1. Although numerous methods can be used for the characterization of collagen scaffolds, the selected techniques mentioned in the table are the most preferred for the collagen-based scaffolds and thus, the

TABLE 12.1 Characterization Techniques for Collagen-Based Biomaterials Used as Scaffolds

Techniques	Collagen Format	Required Concentration	Obtained Information
SDS-PAGE [39]	Soln.	10–30 μg	*Structural* Size (Mol. wt)
CD [10]	Soln. or Film	Soln.: 0.125 μg/L Film: 100% dry wt.	*Structural* 2° and 3° structure
DSC [10]	Film	10 mg dry wt.	*Structural* Denaturation Temperature Heat capacity
XRD [10]	Film, sheets, sponges	<100 mg	*Structural* Crystalline phases
FTIR [11]	Film, sheet, sponges	<100 mg	*Chemical* Chemical Composition Molecular Orientation
XPS [5, 11]	Films, gels, sponges	Films: 20–650 μg/cm^2	*Chemical* Elemental Composition Chemical bonds Surface functional groups Film thicknesses
SEM [5,10]	Films, fibers, sponges	Films: 20–650 μg/cm^2	*Morphological* Topography Phases Defects (cracks, pits)
AFM [6]	Films and fibers	Films: 20–650 μg/cm^2	*Morphological* Topography Phases & defects Mechanical properties/Surface roughness

information acquired from these techniques enable to assess the suitability of the scaffolds for various biomedical applications.

12.2 STRUCTURAL INFORMATION

12.2.1 SDS-PAGE Analysis

Electrophoresis is the study of movement of charged molecules under the influence of an electric field. For low-molecular-weight molecules such as amino acid and carbohydrates, cellulose is used as support medium, while thin gels of agarose and polyacrylamide are widely used for larger molecules such as proteins (e.g., collagen). The mobility of a substance in the gel is governed by both its charge and its size. Thus, the general electrophoretic technique is not suitable and cannot be used to measure molecular weight of the biological molecules. For biological molecules such as collagen, the electrophoretic mobility will depend on size, provided it possesses uniform charge. The molecular weight of collagen is estimated when subjected to electrophoresis in presence of a detergent, sodium dodecyl sulfate (SDS) and a reducing agent β-mercaptoethanol. The SDS treatment disrupts the structure of the protein (2°, 3°, and 4°) such as in collagen to produce a linear polypeptide chain coated with negatively charged SDS molecules. The reducing agent β-mercaptoethanol cleaves the disulfide bonds in proteins and facilitates the denaturation process [10].

Assessment of collagen source is based on purity, and its breakdown into smaller fragments is performed via sodium dodecyl sulfate polyacrylamide gel electrophoresis (SDS-PAGE). Visualization of protein fragments is done by loading of collagen sample in the wells of a thin gel when electric voltage is used to drive the protein fragments. The electrophoretic patterns of type I collagen obtained from Achilles tendon and fish scales are shown in Fig. 12.2.

The molecular weight for a chain of these collagens, using globular proteins as standards, was found to be approximately 100–150 kDa. In general, the molecular weight of collagen could be overestimated when globular proteins are used as molecular weight markers, due to high content of smaller amino acid residues, glycine, proline, and alanine, respectively [37]. Collagen isolated from fish scales and Achilles tendon is composed largely of α chain along with considerable amounts of inter- and intramolecular cross-linked components of α chains and β (dimer), as observed by other

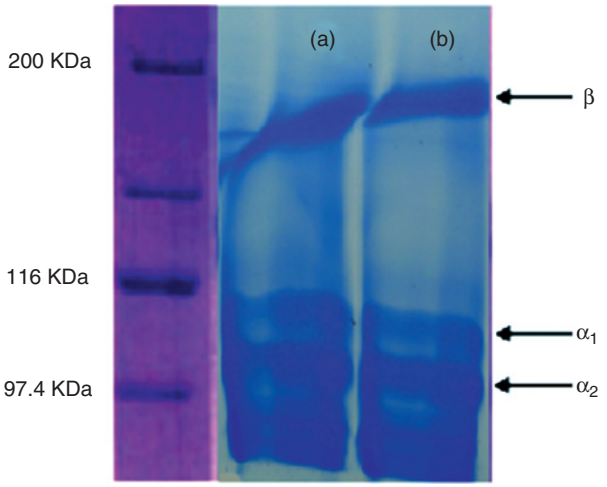


FIGURE 12.2 SDS-PAGE of collagen isolated from (a) Achilles tendon and (b) fish scales, respectively.

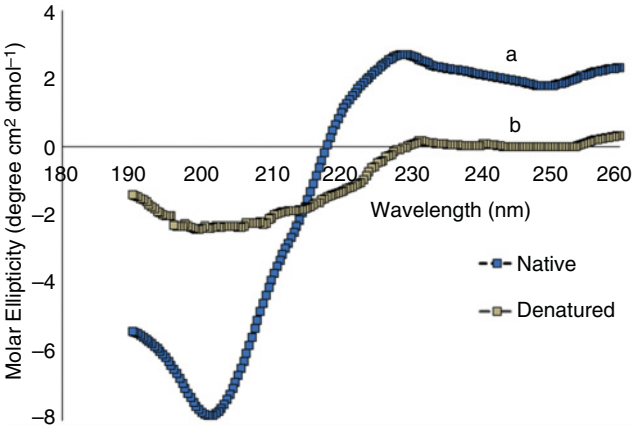


FIGURE 12.3 Circular dichroism spectra of collagen solution in its (a) native and (b) denatured states, respectively.

researchers [38, 39]. Thus, it is evident that lysine-derived cross-link was present in the soluble collagen fraction of tendons [40–42]. The extracted collagen from Achilles tendon comprised of at least two different α chains (αl and α2) with different mobilities, as evidenced in type I collagen from fish scales [43, 44]. Hence, SDS-PAGE can be used to determine purity and to elucidate the type of collagen.

12.2.2 Circular Dichroism (CD) Studies

The differential absorption of polarized light in asymmetric and circular manner forms the basis of circular dichroism and can be used to determine structure and conformation of proteins or the biological molecules [10, 45]. This technique has been extensively utilized to characterize the conformation and helical content of collagen extracted from different source materials. The structural, conformational changes of collagen extracted from different sources such as rat tail tendon, catfish and sepia cartilage, and fish scales in the presence of different surfactants have been studied in detail [46–48] using different techniques. The use of CD, for instance, enables us to determine the specific optical activity resulting from the orientation of amide bonds in highly ordered regions, which is used to elucidate and determine α helices and β sheets of the collagen structure [45, 49]. This is very essential as the triple-helical structure of the collagen imparts required structural properties to the cells and tissues that are utilized when used as scaffolds for tissue engineering applications [42, 50]. For example, CD as a technique has been employed for conformational analysis of collagen and structural effect even when incorporated in the polymer–collagen matrices, fabricated as scaffolds for tissue engineering purposes [9,51]. Also, for a comparative study to understand the behavior of MG63 osteoblast cells grown on the electrospun collagen and gelatin matrix, CD analysis indicated a massive loss of triple-helical structure in an electrospun collagen matrix and the random coils were similar to those found in gelatin [52].

Circular dichroism can be used to inspect helical content of collagen as a function of temperature and assists in understanding the changes in structure and its related chemistry [53]. The helical content of 3D-gelatin-based scaffolds prepared for biomedical applications was confirmed by CD studies [54]. In gelatin, the denatured form of collagen, a significant decrease in positive peak at 221 nm and also reduction in negative peak at 197 nm was recorded, respectively (see Fig. 12.3). This observation suggests that the thermal denaturation causes disruption of the collagen triple-helical structure, and this process is normally irreversible because the self-assembly of collagen chains in an appropriate manner is complex and complicated [55]. In collagen-based biomaterials, helicity of collagen plays an important role in the cellular remodelling responses [56, 57]. The in vitro remodelling rates and cell count of fibroblast improved drastically in gelatin compared to collagen matrix. This observation supports the fact that denatured collagen is responsible for the enhancement of remodelling rate needed for integration of implants [56]. However, it is also documented that mechanical properties of subchondral bone are greatly reduced with the increase in denatured collagen content [58]. Hence, the rate and extent of the helicity of collagen is vital in order to achieve better cell response both in vitro and in vivo as well as to maintain desired mechanical properties required for the efficient function of the tissue-engineered matrix.

The effect of incorporation of silver and iron nanoparticles in collagen has been documented in the literature. CD spectroscopy has also been widely used to characterize the interaction of collagen with that of other small molecules or with nanoparticles such as silver and iron oxide and also to

determine the effect on the stability of the collagen [59–62]. A study Xiufang *et al*. [63] using CD to determine the effect of metallic ions such as Fe^{3+}, Al^{3+}, and Ca^{3+} on the collagen molecules, found a large negative peak near 194 nm and a small positive peak near 222 nm in the CD spectra. The observed loss in ellipticity near 194 nm is attributed to the fact that the incorporation of metallic ions induces a change in secondary structure of collagen. The structural transition from random-helix coil in collagen occurs when the trivalent ions, especially Fe^{3+}, binds with negatively charged free carboxyl groups of collagen and results in cross-linking of the three strands of helices to induce a stretch force, which causes the helix to loosen and become random at the binding sites [63]. The effect of UV irradiation on the physicochemical properties of iron-cross-linked collagen examined via circular dichroic studies reveal changes in the collagen conformation only when subjected to prolonged UV irradiation [64]. This consequence is attributed to the additional stability provided by the crosslinking effect with iron nanoparticles. Recently, the interaction between the collagen-binding domain of Rhusiopathiae surface protein B ($rRspB_{31–348}$) and AgNPs by employing different methods such as CD spectroscopy has been investigated [65]. The CD spectroscopy was used to ascertain the cause for the loss of binding of $rRspB_{31–348}$ with collagen in presence of AgNPs. In order to evaluate this effect, three different ratios, 1:2, 1:6 and 1:10 of AgNPs were added to $rRspB_{31–348}$ and analyzed with far-UV CD spectroscopy. Since, nanoparticles that are not chiral don't affect the protein CD spectra [66], no shift in ellipticity was observed in the CD spectra for two different concentrations of 1:2 and 1:6 and similar secondary structure of $rRspB_{31–348}$ with well-defined antiparallel β-pleated sheets was noted. However, in case of 1:10 ratio, AgNPs did have some effect on $rRspB_{31–348}$, and the increase in ellipticity suggests loss of secondary structure of the protein. This analysis evidently indicates that AgNP-mediated inhibition to collagen binding is not due to a loss in the structural integrity of $rRspB_{31–348}$ but mainly due to the complex formation and its interaction with AgNPs [65].

The biocompatibility and antibacterial properties of photochemically synthesized silver nanoparticles stabilized by collagen were studied [67]. In the study, the UV-CD measurements for the changes in the secondary conformation of collagen in presence of AgNPs were carried out. The UV-CD spectra reveal that the presence of AgNPs in collagen neither alters its position (195 and 220 nm) nor the intensity and thus, the right-handed triple helical conformation of collagen is preserved. However, in another study, UV-CD as a scientific tool when employed to evaluate the secondary structure of proteins in solution showed silver nanoparticles capable of interacting with collagen in aqueous medium in presence of some commonly used cross-linkers [68]. More recently, collagen scaffolds containing AgNPs coated by different concentrations of mixed surfactant of PEG/TX-100 systems have been synthesized and characterized [69]. It would be interesting to study, if there is any difference in helicity as a function of temperature at these different concentrations. Also, no reports on the effect of conjugated silver and Fe_3O_4 NPs on collagen triple helicity as a function of temperature is available and can be conducted in near future. Furthermore, the conformational changes in the collagen cross-linked with AgNPs and also the effect of temperature on the protein conformation using CD technique are not well documented in the literature. However, it is important to note that the precision of the quantitative assessment of helicity is based on the accuracy to determine the solution concentration, molecular mass, and amino acid content. Also, the algorithms employed to convert the signals to obtain structural information are based on globular proteins and thus, the interpretation of CD data is usually difficult for fibrous proteins such as collagen [10].

12.2.3 Differential Scanning Calorimetry (DSC)

Differeential scanning calorimetry measures the temperature dependence of partial heat capacity and thus allows determination of the enthalpy. The heat capacity is calculated by the change in electrical energy needed to increase temperature of the sample compared to that of reference solvent regulated by heating rate. When the mass and temperature are known, heat capacity and melting temperature of the samples can be obtained [70].

DSC is employed to establish the bulk thermal properties of collagen-based biomaterials and also in the case of cross-linked collagen scaffolds [71,72]. Denaturation of collagen, an endothermic reaction, occurs at a very slow rate in equilibrium conditions and corresponds to the breakdown of triple collagen helix, yieling a random structure, gelatin. DSC studies of both collagen (native and anionic) and respective blends with chitosan confirmed the preservation of collagen triple helix because denaturated collagen do not have any thermal transition in the region of 47–51°C, which is the denaturation region [73]. The thermal denaturation of type I collagen vitrified gels using DSC has been conducted [74]. In thermal denaturation, the kinetic energy generated due to the heat interaction disrupts and denatures the secondary and tertiary structure of collagen. This denaturation process can be reversible or irreversible depending on the heating rate [75]. The activation energy of collagen vitrigels for the irreversible process ranges from 100 to 200 kJ/mol, while the reversible enthalpy was found to be 250–300 kJ/mol [74]. The temperature at which the protein like collagen unfolds is known as the *melting temperature* (T_m). The rate of sample heating can impact thermal transitions and so collagen like peptides are heated at rates no greater than 0.2°C/min for accurate determination [76]. The limitation here is that incomplete drying of sample can lead to errors in determination of the melting temperature.

Although DSC has been widely used to determine thermal transitions of collagen-based materials, only limited information on the interaction of nanoparticles, especially silver and Fe_3O_4, with collagen are available in the literature. An investigation of collagen scaffolds incorporated with silver nanoparticles capped by mixed surfactant PEG-TX-100 system was conducted [69]. The DSC results exhibited an increase in denaturation temperature (T_d) of collagen from 40°C to 45°C in presence of PEG+AgNPs system in collagen scaffold. However, it was observed that with the increase in concentration of PEG from 0.3 mM to 0.9 mM, the T_d value decreases. A similar trend was observed for collagen scaffolds having AgNPs+TX-100 systems. For mixed systems, namely, AgNPs coated with PEG+TX-100 into collagen scaffolds, the T_d values of collagen were noted to increase and reach maximum value of 47°C when the surfactant concentration was 0.6 mM. This suggests that mixed surfactants at optimum concentration stabilize the collagen structure [69]. However, no reports on the effect of cross-linking of silver nanoparticles with collagen scaffolds using DSC have been carried out. Similarly, limited information is available on the effect of Fe_3O_4 NPs incorporation on collagen using DSC technique. Collagen-based magnetic nanocomposites for oil removal applications have been performed [77]. The study used DSC to evaluate the changes in the hydrothermal stability of the collagen in presence of Fe_3O_4 NPs. The pristine collagen displayed an irreversible shrinkage known as *shrinkage temperature* or *hydrothermal stability* at 65°C. However, in presence of Fe_3O_4 NPs, the hydrothermal stability of collagen increased to 86.8°C. This observed increase in shrinkage temperature is attributed to the electrostatic interaction between citric acid coated on the Fe_3O_4 NPs and the side chain groups of collagen molecules present in the pentafibril assembly. Thus, DSC can serve as a tool to obtain valuable information on the structural changes along with thermal stability when nanoparticles such as silver and Fe_3O_4 are incorporated in collagen-based systems and thereby enabling to evaluate its applications in biomedical fields.

12.2.4 X-Ray Diffraction (XRD)

X-ray diffraction is a versatile and nondestructive technique used for the determination of the crystallographic identity of the synthesized biomaterial, structural composition, and phase purity and for calculating the mean particle size based on the broadening of the most prominent peak in the XRD profile [78]. Scherrer's equation: $D = K\lambda/\beta \cos\theta$ is used to calculate the average particle diameter D (in Å) [79]. Moreover, the intensity of the diffraction can be used to quantify the proportion of the synthesized nanoparticles (e.g., Ag/Fe_3O_4 NPs) formed in a mixture by comparing experimental peaks and reference peak intensities [80, 81].

In a report [82] on the synthesis and characterization of silver nanoparticles capped by PEG, the film XRD showed

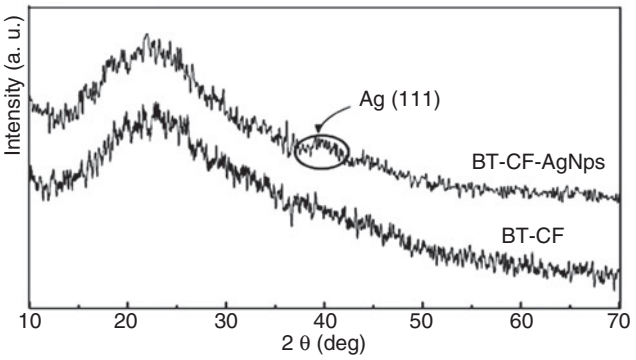


FIGURE 12.4 XRD pattern of BT-CF and BT-CF-AgNPs, respectively [85].

prominent peaks at 2θ values of about 38°, 44.2°, 64.4°, and 77.6°, which represent the (111), (200), (220), and (311) Bragg's reflections of silver having a face-centered cubic (fcc) structure, respectively. These are in accordance with the values reported for silver nanoparticles in the literature [83, 84]. Similarly, XRD showed these characteristic peaks for silver nanoparticles capped by the mixed surfactant (PEG+TX-100) systems. However, when these capped silver nanoparticles were incorporated in collagen scaffolds, an amorphous peak at 23° was noticed [68]. Also, XRD was employed to determine the structural information of the synthesized AgNPs stabilized by bayberry (BT) grafted collagen fiber (CF) [85]. The XRD pattern of BT–CF and BT–CF–AgNPs is shown in Fig. 12.4.

An amorphous peak at 23° attributed to the collagen fiber was observed in both while the XRD spectrum of BT–CF–AgNPs exhibited a weak peak at 39.3°, which is consistent with the Ag(111) plane diffraction peak of the Ag crystal [86]. Also, the broad and weak intensity of the Ag(111) face noticed was attributed to the small crystalline and good dispersion of AgNPs. In another study, XRD patterns of size-controlled silver nanoparticles on polyphenol-grafted collagen fiber ($Ag–EGCG_{0.3}–CF$) also exhibited a broad signal around 23° attributed to the amorphous polymer phase of the collagen fiber [87]. In addition, four diffraction peaks at 2θ = 38.3°, 44.4°, 64.6°, and 77.6° corresponding to the (111), (200), (220), and (311) crystal planes, respectively, which are characteristic of fcc crystalline silver, were observed. Similarly, XRD has been used to study the structural modifications and their effects on Fe_3O_4 NPs [88]. The XRD patterns of both bare and amine-functionalized Fe_3O_4 NPs synthesized their position and relative intensity of all diffraction peaks matched with the reference Fe_3O_4 diffraction data provided in the literature [79, 89]. A series of characteristic peaks at 2θ = 31°, 36°, 43°, 54°, 57°, and 63° corresponding to (200), (311), (400), (422), (511), and (440) Bragg reflections of cubic spinel structure of Fe_3O_4, respectively (see Fig. 12.5). Also, the particle size of bare and

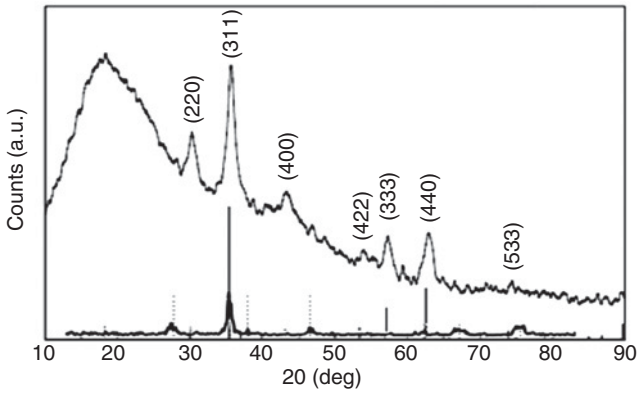


FIGURE 12.5 XRD pattern of bare and amino functionalized Fe_3O_4 nanoparticles [88].

amine- functionalized Fe_3O_4 nanoparticles were calculated by scans using Scherrer's equation. The diameters of bare and amino-functionalized Fe_3O_4 NPs were found to be 19 and 21 nm, respectively. Similarly, another team [90] compared the XRD spectra for Fe_3O_4 and surface- functionalized Fe_3O_4 NPs coated with 3-aminoprpyltriethyloxysilane (APTES) and mercaptopropyl triethyoxysilane (MPTES). The data (all curves) showed diffraction peaks at 2θ values of 18.6°, 30.4°, 35.7°, 37.3°, 43.2°, 53.7°, 57.3°, and 62.8°, indexed to the (111), (220), (311), (222), (400), (422), (511), and (440) planes, respectively. The structure was not changed in the functionalized Fe_3O_4 NPs as the samples patterns follow the standard Fe_3O_4 crystal pattern. However, the diffraction lines were narrowed to some degree, confirming that the XRD diffraction line becomes narrowed as the NPs size becomes larger after surface modification. Thus, XRD is a versatile, nondestructive technique that provides detailed information about the crystallographic structure of the material.

When Fe_3O_4 nanoparticles are introduced in collagen-based nanocomposites, most of the characteristic collagen peaks remain unchanged [77]. However, the XRD patterns of pristine collagen fibers and collagen-Fe_3O_4 nanobiocomposite revealed that the collagen-to-amorphous ratio decreased significantly in the case of nanobiocomposite. The decrease in peak is due to the reduction of intermolecular lateral packing of collagen and is attributed to the interaction of Fe_3O_4 NPs with collagen, which affects the packing order of collagen. It was concluded that the introduction of cross-links between collagen molecules and Fe_3O_4 NPs most probably lead to the decreased order in collagen organization.

The synthesis of collagen scaffolds cross-linked with functionalized (APTES and MPTES) Fe_3O_4 NPs can be attempted, which will have potential biomedical application in tissue engineering. Therefore, XRD can be employed to study and ascertain the crystallinity as well as to determine the particle size of these functionalized Fe_3O_4 NPs in the collagen matrix. Similarly, XRD can also be used to obtain valuable structural information for collagen scaffolds containing the conjugated Ag–Fe_3O_4 NPs as well as to estimate their particle sizes when incorporated in the collagen scaffolds.

12.3 CHEMICAL INFORMATION

12.3.1 Fourier Transform Infrared (FT-IR) Spectroscopy

Infrared (IR) spectroscopy, a vibrational spectroscopic technique capable of providing details of the chemical composition and molecular structures in cells and tissues by measuring the frequency of IR radiation needed to excite vibrations in molecular bonds, is applied to address various biomedical and pharmaceutical issues [91]. The simple IR instrumentation and also faster data collection leading to a superior signal-to-noise ratio (SNR) facilitates assessment of tissue specimens [92]. Biological macromolecules such as proteins and other nucleic acids have specific, fingerprint region (400–4000 cm^{-1}). Since changes in the molecular structure and cellular chemistry govern these spectral fingerprints; IR spectroscopy has to detect abnormal changes in cell and tissues. Also, the fingerprint region can be used to analyze the probe chemical composition and to determine the structural changes occurring in tissues and cells in real time at the molecular level without the help of markers [93, 94]. Therefore, FT-IR as an analytical technique has been employed in medical diagnostics [93].

Fourier transform infrared is a very sensitive probe of the H-bonded states within the triple helix and thus has been utilized to deduce the structure and also to characterize collagen [95]. The FT-IR spectrum of collagen shows characteristic bands sensitive to secondary and tertiary structural changes, which include the N–H stretching (3330 cm^{-1}), amide I, C=O stretching (1650 cm^{-1}); amide II, N–H bending and C–N stretching (1550 cm^{-1}); and amide III, C–N stretch, N–H bending vibrations (1250–1150 cm^{-1}). The 3330 cm^{-1} N–H stretching band shifts to 3300 cm^{-1} in gelatin, the denatured form of collagen. The absorbance ratio of the 1450 cm^{-1} band (C–H deformations) to the 1235 cm^{-1} band (amide III) has been used by many investigators to qualitatively determine the tertiary structure, although the exact ratio associated with the tertiary structure of collagen is not known. However, a band in the amide III region at 1235 cm^{-1} is not present in the spectrum of denatured collagen following a 60°C heat treatment. A team of investigators [96] reported absorbance ratio values ranging from 1.25 to 1.43 depending on the source of the collagen. The absorbance ratio for the collagen used in one study [97] was 1.1, indicating that the collagen was pure. Moreover, the IR absorption ratio A_{1234}/A_{1454} was found to be close to 1.0 in all collagen samples, which indicated that triple-helical structure of collagen

was preserved as compared to gelatin membranes showed a value of 0.59 in the same conditions [73].

Fourier transform infrared was also used to classify the interaction of template type I collagen with AgNPs [69, 98]. The prominent amide I (C=O stretching) band at 1650 cm^{-1}, amide II (N–H stretching) band at 1538 cm^{-1}, and the peaks in the range 1143-1301 cm^{-1} due to amide III (C–N stretching and N–H stretching) observed are due to pure collagen, owing to the rich amines in glycine and proline residues in this protein. However, the shift in bands results when AgNPs were added to collagen. This shift in the peaks is attributed to the association of the collagen molecules with AgNPs as the amines groups present in collagen moiety binds strongly with AgNPs via covalent–electrostatic interaction [69, 98]. In addition, the antisymmetric and symmetric vibrations of CH_2 alkyl chains observed at 2916 and 2849 cm^{-1} indicates that collagen forms a complex with AgNPs [98, 99]. A one-step in situ assembly of size-controlled AgNPs has been synthesized [87] on polyphenol-grafted collagen fiber with enhanced antibacterial properties. FT-IR studies confirmed the graft of epigallocatechin-3-gallate (EGCG) onto collagen fiber (CF) and the presence of phenolic hydroxyls of EGCG involved in the reduction of Ag^+. The FTIR spectrum displayed three characteristic adsorption bands at 1660, 1548, and 1238 cm^{-1} attributed to the amide I, II, and III bands of the collagen molecule, respectively. The adsorption band of EGCG–CF around 3385 cm^{-1} broadened mainly due to the strong hydrogen bond interaction between the phenolic hydroxyls of ECCG and the amino/amide groups of CF. New adsorption peak was observed at 1120 cm^{-1} due to C–O–H stretching vibration of phenolic hydroxyls in EGCG. However, the adsorption bands at 3385 cm^{-1} became narrow and shifted to longer wavelength most probably due to the partial destruction of hydrogen bonds between EGCG and CF, which implies the involvement of the OH groups in the reduction of silver. In addition, the damping of the peak at 1120 cm^{-1} further supported the reduction of silver ions coupled to the oxidation of phenolic hydroxyls of EGCG.

The characteristic absorption peak of Fe_3O_4 is at 582.85 cm^{-1}, which relates to strength of Fe−O bond [100]. Another group [101] reported the synthesis and characterization of biocompatible Fe_3O_4 NPs by the modified controlled chemical coprecipitation method from the solution of ferrous/ferric mixed-salt solution in alkaline medium. Fe_3O_4 NPs coated with sodium oleate were characterized using FT-IR. The peak at 3439.4 cm^{-1} was attributed to the stretching vibrations of –OH assigned to –OH absorbed by Fe_3O_4 NPs. Also, the peak at 583 cm^{-1} attributed to Fe–O bond was observed. For Fe_3O_4 NPs coated with sodium oleate, the peaks at 2924 cm^{-1} and 2854 cm^{-1} were observed, which are attributed to the stretching vibrations of $–CH_2$ and $–CH_3$ in sodium oleate. Also, addition peaks at 1702 and 1590 cm^{-1} due to C=O and C=C in sodium oleate was observed. All these indicated that sodium oleate was absorbed in the surface of Fe_3O_4 nanoparticles. Similarly, FTIR employed to characterize Fe_3O_4 NPs coated with oleic acid and oleyl amine revealed the nature of the bond formed between the surfactant and the surface atoms of Fe_3O_4 NPs [102].

Fourier transform infrared spectra of Fe_3O_4 NPs coated with silanes displayed S–H stretch vibration band at 2590 cm^{-1} due to presence of mercaptosilane in amino functionalized Fe_3O_4 NPs. Also, additional bands are observed in the spectra for silane modified Fe_3O_4 NPs compared to as synthesized uncoated Fe_3O_4 NPs. The main difference is the appearance of bands between 1000 and 1150 cm^{-1}, characteristic of silane layers and originates from Si–O–Si vibrations. i.e., the presence of bands at about 950, 1035 and 1128 cm^{-1} corresponds to the condensation of siloxane (Si-O) molecules onto the surface of the Fe_3O_4 NPs [103, 104]. However, no reports on cross-linking of these functionalized Fe_3O_4 and silver nanoparticles with collagen are available. Surface modification of both Ag and Fe_3O_4 NPs with oraganosilanes is an attractive approach in this context, as it can be biocompatible with collagen and find potential use in tissue engineering applications.

To the very best of our knowledge, only one report on Fe_3O_4 NPs cross-linked with collagen has been documented in the literature [105]. The investigation demonstrates that Fe_3O_4 modified via gum arabic (GA) and cross-linked with collagen can be used for the isolation of *Staphylococcus aureus* bacteria at ultralow concentrations. However, they have not used FT-IR as a tool to study the interaction of GA with Fe_3O_4 or with collagen. FT-IR is beneficial for identification of organic molecular groups and compounds due to the range of functional groups, side chains and cross-links involved. FT-IR studies can be conducted to gain more insight into the effect of these nanoparticles on the triple-helical structure of collagen. Hence, FT-IR can be employed to study coated Fe_3O_4 NPs and their interaction with cross-linked collagen, which find potential biomedical application in tissue engineering. Furthermore, no reports on the synthesis, characterization, and interaction of conjugated Ag–Fe_3O_4 NPs with collagen have been documented, and this aspect is yet to be studied. Hence, FT-IR as a characterization technique can be utilized for this purpose and might serve as an important tool for characterization of collagen-based biomaterials and scaffolds impregnated with Ag–Fe_3O_4 NPs.

12.3.2 X-Ray Photoelectron Spectroscopy (XPS)

X-ray photoelectron spectroscopy, also termed *electron spectroscopy for chemical analysis* (ESCA), is another nondestructive surface characterization method, which provides qualitatively or quantitatively elemental and chemical information from elements present on the solid surface (uppermost 10 nm) of the biomaterials [5,11].

The principle of XPS is based on the emission of electrons from matter in response to irradiation of the surface

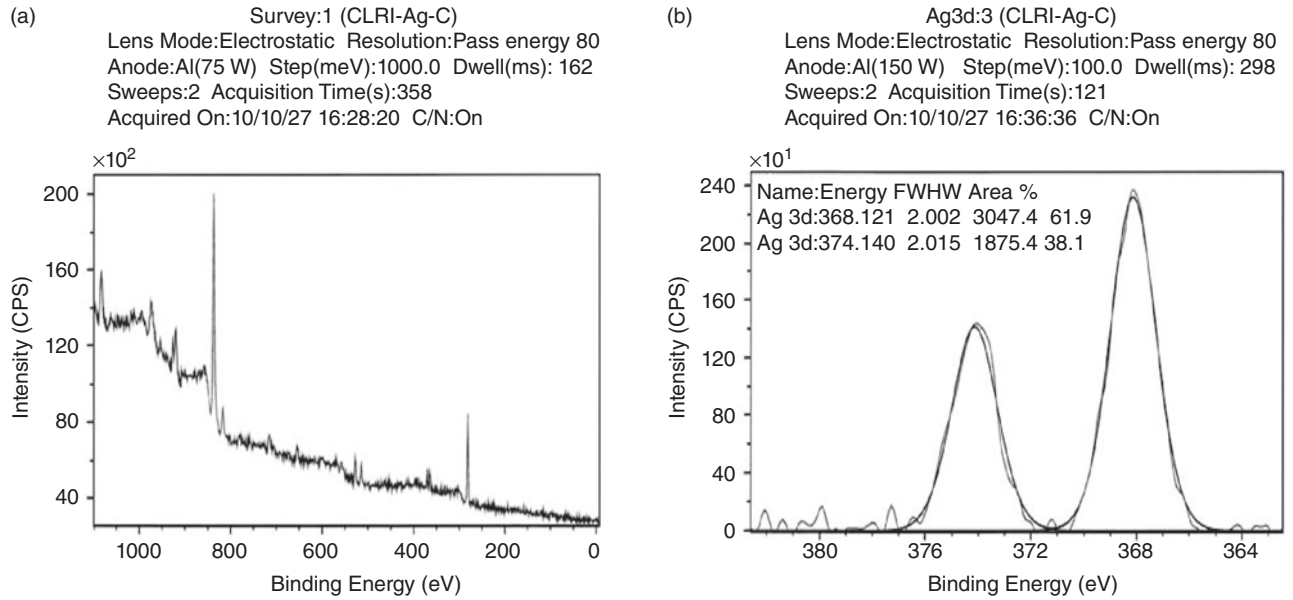


FIGURE 12.6 XPS spectra show (a) wide scan and (b) Ag 3*d* core level of AgNPs incorporated in collagen scaffold, respectively.

by a beam of monochromatic X rays. The kinetic energy (KE) of the ejected photoelectrons is unique for the different elements as well as sensitive to the chemical state of the atoms [106, 107]. The commonly used energies of X rays in experimental practice are 1253.6 eV (MgK_{α}) and 1486.6 eV (AlK_{α}). Since the emitted electrons have little ability to penetrate matter, only those electrons ejected near or from the outermost 100 Å of a polymeric sample can escape from the surface and thereby be quantified [106,108].

Isolation of collagen from animal tissues involves many crude preparation steps, and so it is important to characterize the chemical composition to assess contaminants, material homogeneity such as film formation in tissue culture wells and surface modification with adsorbed or chemically coupled growth or adhesion factors. The effect of fibroblast cell adhesion on the collagen-modified polystyrene plate was investigated [109]. The study used XPS as a characterization method to determine the effect of the structural changes of graft-polymerized polystyrene and the influence of surface amine group concentration on the extent of collagen (Col) immobilization. The peak with binding energy at 288.1 eV confirms the formation of CONH bonding and the covalent interaction between collagen and polystyrene. Also, the surface of the polystyrene grafted film showed the peak at 399.4 eV for C–N, whereas the collagen immobilized film exhibited amide components at the binding energies of 399.8 eV. The increase of CONH from 0% to 13% is probably due to covalent interaction, which results in the immobilization of collagen on the polystyrene film.

Poly(ethylene glycol) hydrogel surfaces modified to covalently attach cell adhesion protein such as collagen was performed to promote cell adhesion [110]. XPS demonstrated the immobilization of collagen on the PEG hydrogel surface. The XPS spectra show the formation of a new nitrogen peak, and it was found that immobilized collagen was dependent on the concentration of bifunctional linker NHS. The cell adhesion studies revealed that collagen immobilization resulted in a significant improvement of cell adhesion. Similarly, XPS has been employed to verify the biosynthesis of collagen by cells and for the confirmation of collagen coating to enhance the biocompatibility of titanium implants used for bone growth [111, 112]. The XPS scan spectra of collagen scaffold containing AgNPs is depicted in Fig. 12.6.

Similarly, spectra of Ag–$EGCG_{0.3}$–CF showed the presence of C 1*s*, N 1*s*, O 1*s*, Ag 3*p*, and Ag 3*d* core levels with no evidence of impurities [87]. The Ag 3*d* core level is fitted to two peaks, at 368.1 and 374.1 eV, assigned to $3d_{5/2}$ and $3d_{3/2}$, respectively. Splitting of the 3*d* doublet of Ag is 6.0 eV, which suggested the formation of silver nanoparticles. The core level O 1*s* at 523 eV can be attributed to presence of hydroxyl groups and surface adsorbed water on EGCG. The peak corresponding to lattice oxygen O^{2-} from Ag_2O was not observed; it can be concluded that the formed silver was predominantly metallic. The C 1*s* signal deconvoluted to three peaks by curve fitting using a mixed Gaussian and Lorentzian lineshape exhibited peaks at 284.5, 286.7, and 287.9 eV corresponding to C–C, C–O and C=O, respectively. Similarly, the N1s signal was deconvoluted as contributions arising from the presence of pyridinic, pyrrolic, and quaternary N parts [87].

X-ray photoelectron spectroscopy is useful for identifying oxidation states of metal/oxide ratio and also information on

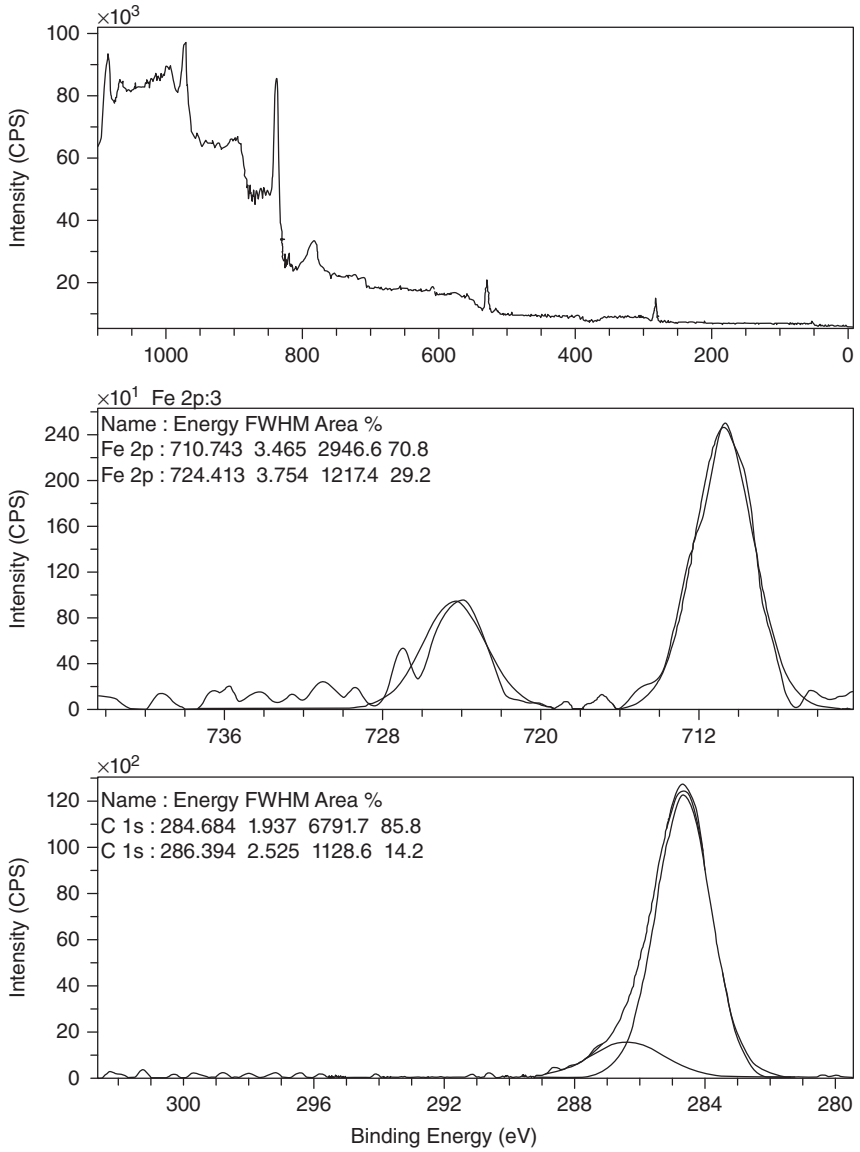


FIGURE 12.7 XPS of PEG capped Fe_3O_4 nanoparticles showing wide scan, Fe 2*p* and C 1*s* regions [114].

oxide thickness can be obtained. Zhang *et al*. [113] reported the synthesis of oleic acid coated monodisperse Fe_3O_4 NPs. The XPS spectrum shows peak at 284.6 eV ascribed to the carbon atoms in the aliphatic chain (C–C), and peaks at 287.4 and 288.3 eV to the carboxylate ($-COO^-$) moiety. The characteristic peak from Fe $2p_{3/2}$ core level electrons at 710.8 eV was noted. The Fe $2p_{1/2}$ peaks at 724.1 eV for 7 nm and 725.0 eV for 19 nm Fe_3O_4 NPs were attributed to the carboxylate–Fe bond. XPS can also provide information on the extent of coating on the nanoparticle or biomaterial surface. The XPS spectra of Fe 2*p* core level for Fe_3O_4 nanoparticles coated by PEG is a proof for the chemical structure of the Fe_3O_4 NPs illustrated in Fig. 12.7. The bonding energies at 710.8 and 724 eV, the characteristic peaks from Fe $2p_{3/2}$ and Fe $2p_{1/2}$ core-level electrons respectively were noticed. Two C 1*s* peaks positioned at 284.6 and 286.4 eV are ascribed to carbon atoms in the aliphatic chain (C–C) of the PEG molecules. XPS determines the elemental composition of the surface, typically to a depth of 3.5 nm at a takeoff angle of 45°, which was used in the experiment. The XPS spectra revealed almost complete coverage of the surface with the PEG stabilizer as the increased carbon and nitrogen signatures, compared to the precursor Fe_3O_4 NPs, was noted, which supported the hypothesis of polymer coverage. However, the detection of low levels of iron suggested that the polymer-layer depth may be lower than 3.5 nm [114].

In a study [115] of the surface organic modification of Fe_3O_4 NPs with KH570, XPS was used to analyze

unmodified and modified Fe_3O_4 with KH570. An Si 2*p* peak appeared at the binding energy of 101.3 eV along with prominent absorption peaks of C 1*s* and O 1*s* at 285.0 eV and 530.61 eV for KH570-modified Fe_3O_4 NPs. Surface composition (*w*) and binding energy (E_b) of Fe_3O_4 unmodified and modified obtained from XPS show that the content of Si was 1.36 wt% in modified Fe_3O_4 NPs, while the content of Fe decreased from 47.84 to 31.37 wt%. The electron binding energy of Fe $2p_{3/2}$ shifted from 711.0 to 711.46, eV due to surface modification. The reason is based on the fact that electronegativity of Si is stronger than that of H, which causes electron density around Fe and shielding effect to decrease, so the binding energy of Fe $2p_{3/2}$ increased. The binding energy shift of 0.46 eV was observed for Fe_3O_4 NPs after modification. This also proved the deduction that Fe–O–Si chemical bond between KH570 and Fe_3O_4 NPs were formed instead of the chemical bond Fe–OH. Similarly, another author [90] reported the silane bridged surface tailoring on Fe_3O_4 NPs using APTES and MPTES. The amino-coated and thiolated Fe_3O_4 showed a lower shift of binding energy of Fe $2p_{3/2}$ compared to bare Fe_3O_4 NPs. The peak of carbon at 284.9 eV is close to the data of the E_b of a long-chain alkyl, and the authors attributed it to the long-chain alkyl of APTES or MPTES. Also, the signal intensities increased as compared to bare Fe_3O_4. The E_b of Si 2*p* was 102.5 eV, close to the standard data for silane (101.9 eV). The E_b of N 1*s* was found to be 399.5 and 164.1 eV for S 2*p*, which is close to the standard data of N-C group (399.8 eV) and S–C group (163.8 eV). Hence, the above results reveal that silane coating of Fe_3O_4 NPs is successful. However, no report on the interaction of these coated Fe_3O_4 NPs with collagen is available in the open literature.

XPS is useful for identifying functional groups. For example, peak shapes of C 1*s* gives information about functional groups in organic materials. The limitation of XPS is the poor lateral resolution (10 μm), and the drawback of XPS, especially for the biological application, is the UHV condition that does not allow the analysis of the sample in liquid state. Hence, valuable information on the elemental composition, chemical state, quantification (imaging, depth profile) for collagen scaffolds cross-linked with aminosilane functionalized silver and Fe_3O_4 NPs can be obtained from XPS. Moreover, XPS can substantiate FT-IR data, indicating the formation of chemical bonds between the nanoparticles, and can serve as a valuable tool in determining the conjugation of Ag–Fe_3O_4 NPs and studying the interaction with collagen.

12.4 MORPHOLOGICAL INFORMATION

12.4.1 Scanning Electron Microscopy (SEM)

Scanning electron microscopy is generally used for studying the surface morphology and their cellular response to biomaterials [116, 117]. This technique uses a primary beam of electrons that interact with samples in vacuum causing emission of different types of electrons and electromagnetic waves. The ejected secondary electrons from the sample surface are gathered to demonstrate a high-resolution micrograph. Fixation is required for SEM sample preparation (if proteins, cells, or tissue are present). Also, drying and coating process are essential as they can modify surface morphology of surfaces that are subjected to changes in a hydrated environment [5]. For example, collagen films, if denatured, can collapse under the force of sputter coating and vacuum of the SEM imaging due to absence of sufficient structural integrity needed for analysis of collagen-based scaffolds.

Cell death and low proliferation rates are a common problem encountered on biomaterial matrices, and therefore, modifying the collagen matrix properties that lead to improved cell proliferation and their survival is necessary to develop novel and superior tissue-engineered constructs. The cell viability of poly anionic collagen (PAC) was assessed on rat cardiac fibroblasts, L6 myoblasts, and NIH 3T3 fibroblasts, respectively. When viewed under SEM, all these cell types were found to be grown uniformly with normal morphologies and the extra negative charges and RGD sites on the PAC support the enhanced cell proliferation [42]. Thus, SEM could be utilized to analyze the in vitro and in vivo biocompatibilities and the efficacy of different cell lines on PAC scaffolds incorporated with nanoparticles such as silver and iron oxide, which could be effective in the treatment of bone defects and regeneration of other soft tissues. The microstructures of collagen matrices with and without EDC/NHS-cross-linking (0, 2 mg/mL-EDC/NHS) were analyzed by SEM [118]. The EDC/NHS-collagen cross-linking led to parallel alignment of collagen with the size of interconnected pores ranging from 33 to 220 μm. MC3T3-E1 cells were found to attach and displayed improved cell proliferation on the surface of cross-linked collagen matrix. The crosslinking due to EDC/NHS facilitates the ability for self-assembly and self-organization of collagen into more ordered structure. The enhanced physicochemical properties of EDC/NHS-cross-linked collagen show promise as bioactive and bioresorbable scaffolds in bone tissue engineering applications. Silane, when cross-linked with collagen using EDC-NHS, has also shown proliferation of osteoblast cells [119]. Thus, silane- coated silver nanoparticles cross-linked with collagen via EDC-NHS has potential for treatment of cartilage defects and other hard-tissue repairs where SEM could be used to analyze the surface morphology and cell proliferations of the scaffolds.

Porous collagen scaffolds for the regeneration of soft tissues, SEM was used to analyze the morphology of the surface [50]. The collagen scaffold has shown better wound reduction and complete epithelialization on day 8 compared to day 16 required for the control. Thus, the scaffold could find use in the treatment of dermal wounds for effective within shorter time period and has potential in skin tissue engineering

applications. A comparison of gelatin and collagen scaffolds to ascertain the applicability of the scaffolds as a skin substitute, in vitro cell adhesion and cell proliferation tests for cultured fibroblast cells were conducted [120]. The morphology of scaffolds investigated by SEM displays a membrane like structure with interconnected pores for collagen scaffolds, while the gelatin scaffolds had some fibers among the continuous wall-like structure. The gelatin scaffolds possessed comparable properties particularly cell proliferation, with that of collagen scaffolds, although the increased degradation rate of gelatin significantly hinders its use in wound healing [120]. Therefore, it is essential to modify the gelatin scaffolds to decrease the degradation rate and be used as a substitute for collagen scaffold to lower the cost of materials for scaffold fabrication. Efficacy of collagen/gelatin sponge (CGS) with a gelatin concentration of 10 wt% as scaffold for sustained release of basic fibroblast growth factor (bFGF) for regeneration of skin tissues was studied using an in vivo animal model [121]. The study evaluated the wound area to determine the neoepithelial cells formation. The observed SEM images of the implanted collagen/gelatin sponges (CGS) impregnated with different concentrations of bFGF $\leq$50 $\mu g/cm^2$ after 1 and 2 weeks show that the CGSs impregnated with normal saline solution (NSS) became infected and degraded, whereas the CGSs impregnated with 7 or 14 $\mu g/cm^2$ bFGF displayed accelerated dermis like tissue formation. Furthermore, increase of bFGF to 50 $\mu g/cm^2$ did not enhance the wound healing process and faster tissue regeneration. This suggests that CGS can release positively charged growth factors bFGF (14 $\mu g/cm^2$) in a controlled manner and could solve the problem of the existing artificial dermis and has potential as a scaffold for the treatment of skin defects [121]. The surface morphology of a trilayer dermal equivalent (TDE) of chitosan-impregnated silver nanoparticles on chitosan–collagen scaffold displays the microstructure having pore size ranging from 80 to 200 μm, which facilitates the fibroblast to infiltrate and can be used to treat different types of skin defects [122]. Also, the SEM image of the cross-sectional morphology of TDE shows that the thickness of the trilayer equivalent as 1 mm, which has collagen–chitosan scaffold in addition to the silver nanoparticles incorporated chitosan films and silicone membrane.

The SEM images of the collagen-based scaffolds, along with the AFM, facilitate the assessment of collagen surfaces, and the information gathered can be used in the fabrication of better tissue-engineered scaffolds. The advantage of SEM technique is that acquisition of the micrographs of the inserted sample can usually be done fairly quickly, allowing for a large number of images to be obtained with varying magnifications. Apart from imaging the surface morphology of biomaterials, it can be combined with EDX for elemental distribution determination and IR or Raman spectroscopy to examine surface modification procedures [5]. Fabrication and characterization of assembled type I collagen–silver nanoparticle multilayered films showed that the intensity of the SERS spectra of assembled films in presence of 5 ng/μL collagen is twofold higher than that of 2 ng/μL collagen [98]. The AgNPs adsorbed on the 5-ng/μL collagen surface was higher as a result of the more positive charges available compared to the 2-ng/μL collagen surface (see Fig. 12.8). Hence, it was concluded that increase in collagen concentration provides a large surface area and porosity, along with a

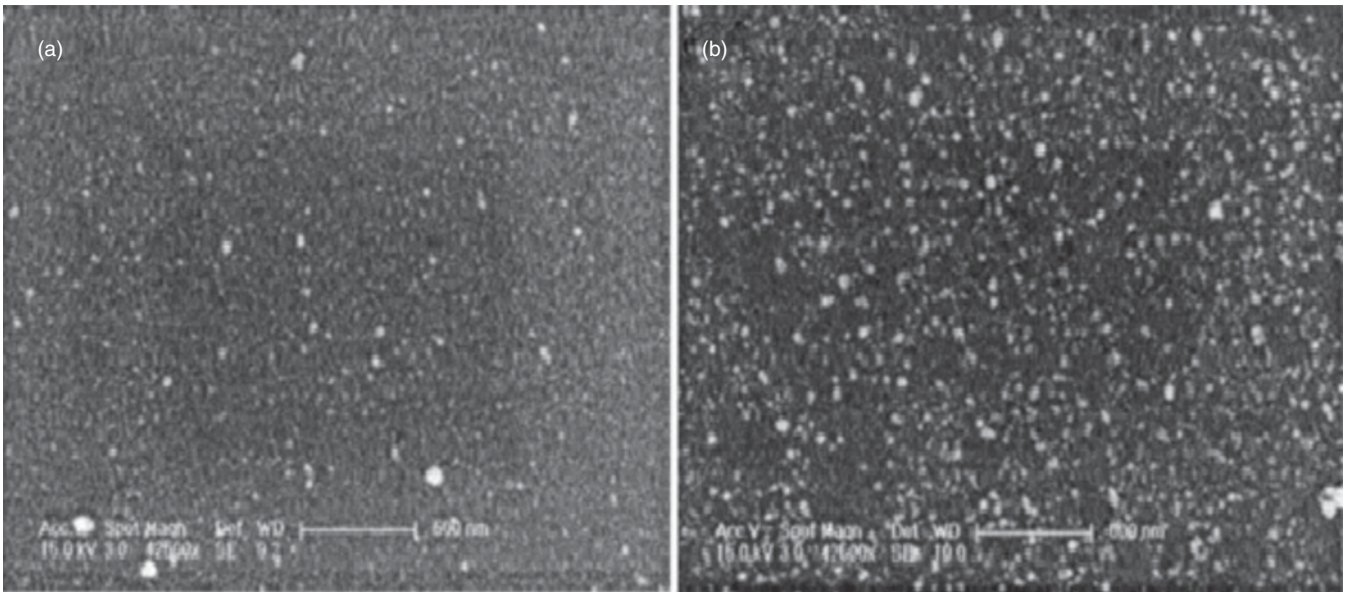


FIGURE 12.8 SEM images of substrate PDDA/AgNPs/collagen with different concentrations of collagen: (a) 2 ng/μL; (b) 5 ng/μL [98].

well-interconnected pore network to accommodate AgNPs. The SEM images showed that AgNPs anchored on a collagen scaffold increased with an increase in the collagen concentration, and the AgNPs tend to grow up simultaneously. Also, the effect of the number of layers of AgNPs was studied using SEM technique. The morphologies of multilayer quartz/PDDA/ AgNPs/(collagen/AgNPs)$_n$ films where n = 0,3,6 exhibit the uniform distribution of AgNPs on the surface. However, the increase of the number of AgNP layers results in the NP aggregations. This effect is due to the uniform distribution of positive charges of the collagen molecules on the surface and also the 3D collagen scaffolds facilitate the space required for the growth of the aggregates [98]. Likewise, the SEM images of a similar kind of study involving the collagen-templated assembly of silver nanoparticles indicate that the maximum formation of monodispersed AgNPs resulted when the Ag colloid:collagen ratio was 1:1(v/v) in comparison to 2:1 and 3:1 ratios, respectively [123]. Furthermore, at the incubation time of 2.5 h, uniform distribution with the least aggregation of AgNPs on the collagen surface was noted. At higher incubation time (>2.5 h), the AgNPs aggregation increased on the collagen surface [123].

The effect of AgNPs on collagen formation and deposition at the point of complete wound healing was carried out using an in vivo model [124]. SEM imaging showed regular and organized arrangement of collagen fibrils in the AgNP-treated group, whereas the untreated group display aggregated and random alignment of collagen fibrils. When observed under higher magnification (60,000×), the average diameters of the surface fibril were found to be 78.6 and 64.8 nm for AgNPs treated and untreated groups, respectively. Moreover, thorough examination at the region close to the fracture site reveals that the collagen fibers have a more regular and compact pattern in the case of AgNP-treated groups, while in the untreated groups the collagen fibers were found to be intermingled with a sparse arrangement. These findings are attributed to the uncontrolled deposition of collagen during the natural wound-healing process and thus, support the fact that collagen fibers directed with a particular orientation or arranged in an ordered manner demonstrates improved mechanical properties for healed skin treated by AgNPs compared to that of the untreated group. Therefore, it can be ascertained that AgNPs modulate collagen deposition in wound healing and demonstrate fetal wound healing rather than forming scars [125].

The nanohydroxyapatite synthesized using Fe_3O_4 NPs extracted from goat blood coated on collagen matrix was visualized with SEM [125]. The image displays the formation of flower shaped nHap with a particle size of 19 nm having a porous crystalline structure on the Fe_3O_4-collagen matrix. FESEM has been used to obtain information on the surface morphology of the collagen-based nanobiocomposite [126]. The image displays the banded structure having a characteristic *D*-periodicity of 64.61 nm indicative of quarter-staggered arrangement of collagen molecules into a pentafibril assembly. The attachment of Fe_3O_4 NPs on the collagen results in reduction of *D*-periodicity to 59.61 nm due to the dense packing of collagen molecules from the displacement of water molecules. Similarly, for the *in vitro* evaluation of the iron oxide nanoparticles coated with gelatin (GIOPs) derived from collagen, FESEM was carried out to investigate the morphological changes occurring on the GIOPs surface after soaking at different time intervals. Formation of needle-shaped type B carbonated apatite from the GIOPs in 12 days mimics the natural bone composition and signifies the bioactivity of the material [126].

One team of investigators [127] applied the Mag-TE technique to a cell-seeding process termed *Mag seeding* and studied the enhancement of cell-seeding efficiency into 3D porous scaffolds for tissue engineering. NIH 3T3 fibroblast cells (FBs) were used as model cells and MCLs (containing 10 nm Fe_3O_4 NPs) were added to FBs at a concentration of 100 pg/cell (lower than the cytotoxicity value) for magnetic labeling. Five collagen scaffolds with different pore sizes were chosen for the study. Histological observation using SEM revealed that cells were distributed in the scaffolds both by static and Mag seedings, with more cells being observed in the case of Mag seeding. The collagen scaffold (Col 1) with small pore size exhibited unique pattern of cell distribution as cells were distributed at the top of the scaffold instead of uniform distribution throughout observed in other cases. The histological observation also revealed that cells formed aggregates after Mag seeding particularly in Col 1 suggesting that the magnetic force in Mag seeding enhanced cell–cell interactions within the scaffold. In addition to cell–cell interactions, the authors speculated that *cell–scaffold* interactions within the scaffold could be enhanced by magnetic force. Moreover, cell-seeding efficiency by Mag seeding showed a good relationship with pore size. Hence, Mag-seeding efficiency may not depend on the composition of the scaffold. However, further study in this direction is needed to determine the cell-seeding efficiency of Mag seeding using scaffolds of various compositions. Since no reports are available on the conjugation of Ag–Fe_3O_4 NPs, their interaction with collagen, and their cell seeding with the Mag TE technique, an attempt can be made in this direction where SEM technique could prove vital for the histological study as well as cell compatibility studies of collagen scaffolds containing the conjugated Ag–Fe_3O_4 NPs.

12.4.2 Atomic Force Microscopy (AFM)

Topography, roughness, and mechanical properties of a biomaterial are essential factors that govern and influence the attachment of cells and their adherence on to the surface of the scaffolds [128–133]. AFM, a powerful tool, is used to determine surface morphology of the collagen-based

scaffolds along with the mapping of the mechanical and adhesive properties of the cells–scaffolds in high resolution [134, 135].

The surface topography of blends of collagen–elastin films for tissue regeneration was investigated via AFM [136]. The AFM images display collagen films having long folded pattern owing to the helical rod like structure of collagen. The morphology remained unaltered when the ratio of collagen/elastin blend was 19:1. However, with the increase in elastin concentration (>5%) results in the formation of buldges with the of diameters 1–2 mm due to rougher surfaces of the mixtures compared to elastin and collagen individually. Moreover, AFM images corroborate the predominant prevalence of collagen in the uppermost layers of the blends and also indicate that collagen when combined with elastin slows down the aggregation process of elastin and also the 3T3 cell adhesion and their proliferations. Also, the effect of UV radiation on the topography of these blends was monitored via AFM. It was observed that the size of the bulges of the blends became smaller and eventually disappeared with the increased level of exposure to UV radiation for longer duration. This observed effect was attributed to the effect of conformational changes caused by the modification of hydrophilic/hydrophobic properties and the loss of water in films due to photooxidation, which enhances the biocompatibility of the materials [136].

In an investigation of fabrication of assembled type I collagen-AgNPs multilayered films, AFM technique has been used to examine the morphology [98]. The images of collagen film immersed for 2 h in Ag colloids and assembled on different concentrations (10, 50, and 100 ng μL^{-1}) of the mica surface confirm the uniform coating of AgNPs for the highest concentration (100 ng μL^{-1}) with no significant aggregations on the collagen surface. This also suggests that the AgNP-coated collagen film has the largest surface for holding probe molecules such as 4-aminothiophenol (4-ATP) and methylene blue (MB) and can be utilized for SERS detection [98]. Similarly, the structural investigations of AgNPs doped on collagen and keratin based materials via AFM indicated a specific surface structure modification at micrometric scale in terms of roughness [137]. The elastic properties of the type I collagen fibrils formed by self-assembly were determined with the help of AFM [138]. The tip of the AFM was used as nanoindentor to determine the elastic properties from the force–displacement curves. The investigations show banding of the shell in the core of collagen fibril. The measurements display higher adhesion in the core of the collagen fibril compared to the shell, although the Young's modulus was found to be the same for both. Thus, AFM as a microdissection tool to probe local elasticity can be useful to gain insights into the collagen assembly and to determine mechanical properties [138].

The influence and effect of cross-linking and composition on the surface and mechanical properties, which affect the cell reactivity of collagen-based films, was determined using AFM [139]. AFM, along with SEM image analysis, reveals that the collagen bundles with diameter 0.82 ± 0.16 μm compared to 0.18 ± 0.28 μm observed for gelatin. The calculated height and roughness of the gelatin–collagen films were found to be 727 nm and 147 ± 30.5 nm, respectively, and these values were intermediate between the pure collagen and gelatin films. Moreover, the obtained average fibre diameter of 238 ± 29 nm for all collagen films and 64.4 ± 2.91 nm for the periodic banding of collagen for all films containing both non-cross-linked and cross-linked collagen indicate that altering the composition or cross-link status had no effect on the collagen fibril size or banding pattern. Cross-linking of collagen with NHS/EDC resulted in a significant increase in the stiffness of the collagen films and also tended to reduce the roughness of the films ($R_q = 0.417 \pm 0.035$ μm, $E = 31 \pm 4.4$ MPa). Gelatin films were generally smoother and more compliant than comparable collagen films ($R_q = 7.9 \pm 1.5$ nm, $E = 15 \pm 3.1$ MPa). As a result, the reactivity of myoblast C2–C12 and C2–C12-α2+ cell lines with all the films were reduced from the initial composition, stiffness, or roughness. Modification of physical properties of the films due to cross-linking results in decrease in the number of accessible cell binding sites and thereby reduces their capacity to support cell activity and curtails the efficiency of the collagen-based films and scaffolds [139]. Thus, it would be worthwhile to investigate the interaction of the surface-modified nanoparticles such as silver and Fe_3O_4 cross-linked with collagen and also their effects on the cellular responses. In this regard, AFM along with advanced optical microscopy can serve as a valuable asset and the obtained quantitative information can be used for the fabrication of better and novel tissue-engineered scaffolds with desired properties having potential applications in tissue engineering fields.

Cellular remodeling of collagen fibrils envisaged by time-lapse AFM exhibit that during alignment of cells, the matrix becomes deformed, due to the reorientation of individual collagen fibrils [140]. The cells caused the deformation of the matrix in an asymmetric manner, thereby leading to anisotropy in matrix rigidity. Thus, high tensile strength and flexibility of collagen fibrils add to the anisotropic rigidity of the matrix, which results in formation of directional cellular traction and cell polarization. This kind of complex entanglement of cellular protrusions with collagen fibrils maximizes the cellular traction, which further enhances the cell alignment process [140]. A more recent study shows that modulation of AgNPs foster the alignment of collagen and improves the mechanical properties required for tissue regeneration [124]. However, AFM was not employed to determine the tensile strength and surface roughness of the regenerated tissues. Also, experiments can be performed to determine the modulating effect of Fe_3O_4 NPs on the alignment of collagen fibrils where AFM can serve as a valuable tool to determine the morphology in addition to the surface roughness and

other mechanical properties that affect the tissue regeneration process.

12.5 CONCLUSIONS AND FUTURE PERSPECTIVES

The characterization of collagen-based biomaterial is necessary for the design of novel tissue- engineered matrices. Collagen, the versatile biomaterial, along with nanoparticles, especially silver and Fe_3O_4, finds application as tissue scaffolds and has been used in various fields of tissue engineering. With the development of new collagen-based biomaterial as scaffolds for tissue engineering applications, the need and search for special and improved analytical techniques for the characterization of these scaffolds has received attention. Several analytical tools have been employed to obtain details and insights on the effect of the collagen structure, its chemistry and the changes in the surface morphology when the silver and iron oxide nanoparticles interact with collagen molecule. Also, the cell morphologies in conjunction with the helicity and topography need to be evaluated as the response of cells to these collagen matrices is based on the characteristics of the biomaterial and thus, involve the changes in the secondary and tertiary structures of collagen in addition to the parameters such as chemical composition and surface roughness. Therefore, the choice of the techniques is crucial for the comprehensive characterization of collagen-based scaffolds and to investigate their influence and interaction with nanoparticles and cells.

The benefits and limitations along with the scope for future work for the methods of characterization that can be suitably applied to collagen biomaterials as scaffolds and to study their association or interaction with nanoparticles such as silver and Fe_3O_4 along with different cells needed for the development of novel biomaterials have been described. Hence, these types of characterizations are vital in the fabrication of collagen-based biomaterial as scaffolds for development of novel tissue-engineered matrices and to assess their cellular responses, which determines their potential in applications related to pharmacy and pharmaceutical sciences.

ACKNOWLEDGMENT

We would like to thank Professor Asit Baran Mandal, Director, CSIR-Central Leather Research Institute (CLRI), India, for the stimulating discussions and valuable suggestions, which are highly appreciated.

REFERENCES

[1] Ratner, B.D. (1993). Characterization of biomaterial surfaces. *Cardiovasc. Pathol.* **2**, 87S–100S.

[2] Hutmacher, D.W. (2000). Scaffolds in tissue engineering bone and cartilage. *Biomaterials* **21**, 2529.

[3] Parenteau-Bareil, R., Gauvin, R., Berthod, F. (2010). Collagen-based biomaterials for tissue engineering applications. *Materials* **3**, 1863–1887.

[4] Healy, K.E., Rezania, A., Stile, R.A. (1999). Designing biomaterials to direct biological responses. *Ann. NY Acad. Sci.* **875**, 24–35.

[5] Merrett, K., Cornelius, R.M., McClung, W.G., Unsworth, L.D., Sheardown, H. (2002). Surface analysis methods for characterizing polymeric biomaterials. *J. Biomater. Sci. Polym. Ed.* **13**, 593–621.

[6] Cunningham, T., Serry, F.M., Ge, L.M., Gotthard, D., Dawson, D.J. (2000). Atomic force profilometry and long scan atomic force microscopy: new techniques for characterisation of surfaces. *Surf. Eng.* **16**, 295.

[7] Klee, D., Hocker, H. (2000). Polymers for biomedical applications, improvement of the interface compatibility. *Adv. Polym. Sci.* **149**, 1.

[8] Knowles, G.C., McKeown, M., Sodek, J., et al. (1991). Mechanism of collagen phagocytosis by human gingival fibroblasts: Importance of collagen structure in cell recognition and internalization. *J. Cell Sci.* **98**, 551–558.

[9] Zeugolis, D.I., Paul, R.G., Attenburrow, G. (2008). Post-self-assembly experimentation on extruded collagen fibres for tissue engineering applications. *Acta Biomater.* **4**, 1646–1656.

[10] Abraham, L.C., Zuena, E., Perez-Ramirez, B., Kaplan, D.L. (2008). Guide to collagen characterization for biomaterial studies. *J.f Biomed. Mater. Res. B: Appl. Biomater.* **87**, 264–285.

[11] Ratner, B.D. (1983). Surface characterization of biomaterials by electron spectroscopy for chemical analysis. *Ann. Biomed. Eng.* **11**, 313–336.

[12] Sekar, S., Manikandan, R., Mandal, A., Sankar, S., Sastry, T.P. (2014). Synthesis and characterization of chemically modified collagen nanobiocomposite containing silver nanorods incorporated with ciprofloxacin. *Int. J. Innov. Res. Sci. Eng.Technol.* **3**, 9618–9625.

[13] Brodsky, B., Ramshaw, J.A.M. (1997). The collagen triple-helix structure. *Matrix Biol.* **15**, 545–554.

[14] Forti, F.L., Goissis, G., Plepis, A.M.G. (2006). Modifications on collagen structures promoted by 1,4-dioxane improve thermal and biological properties of bovine pericardium as a biomaterial. *J. Biomater. Appl.* **20**, 267–285.

[15] Lee, C.H., Singla, A., Lee, Y. (2001). Biomedical applications of collagen. *Int. J. Pharm.* **221**, 1–22.

[16] Peng, Y.Y., Yoshizumi, A., Danon, S.J., Glattauer, V., Prokopenko, O., Mirochnitchenko, O., et al. (2010). A Streptococcus pyogenes derived collagen-like protein as a non-cytotoxic and nonimmunogenic cross-linkable biomaterial. *Biomaterials* **31**, 2755–2761.

[17] Song, E., Kim, S.Y., Chun, T., Byun, H.J., Lee, Y.M. (2006). Collagen scaffolds derived from a marine source and their biocompatibility. *Biomaterials* **25**, 2951–2961.

[18] Nagai, N., Mori, K., Munekata, M. (2008). Biological properties of crosslinked salmon collagen fibrillar gel as a scaffold for human umbilical vein endothelial cells. *J. Biomater. Appl.* **23**, 275–287.

[19] Nam, K., Kimura, T., Funamoto, S., Kishida, A. (2010). Preparation of a collagen/polymer hybrid gel for tissue membranes. Part II: In vitro and in vivo biological properties of the collagen gels. *Acta Biomater.* **6**, 409–417.

[20] Srivastava, S., Gorham, S.D., Courtney, J.M. (1990). The attachment and growth of an established cell line on collagen, chemically modified collagen, and collagen composite surfaces. *Biomaterials* **11**, 162–168.

[21] Shanmugasundaram, N., Ravikumar, T., Babu, M. (2004). Comparative physico-chemical and *in vitro* properties of fibrillated collagen scaffolds from different sources. *J. Biomater. Appl.* **18**, 247–264.

[22] Croce, M.A., Silvestri, C., Guerra, D., Carnevali, E., Boraldi, F., Tiozzo, R., et al. (2004). Adhesion and proliferation of human dermal fibroblasts on collagen matrix. *J. Biomater. Appl.*, **18**, 209–222.

[23] Glowacki, J., Mizuno, S. (2008). Collagen scaffolds for tissue engineering. *Biopolymers* **89**. 338–344.

[24] Furno, F., Morley, K.S., Wong, B., Sharp, B.L., Arnold, P.L., Howdle, S.M., et al. (2004). Silver nanoparticles and polymeric medical devices: A new approach to prevention of infection?. *J. Antimicrobial Chemother.* **54**, 1019–1024.

[25] Riley, D.K., Classen, D.C., Stevens, L.E., Burke, J.P. (1995). A large randomized clinical trial of a silver impregnated urinary catheter: Lack of efficacy and staphylococcal superinfection. *Am. J. Med.* **98**, 349–356.

[26] Arockianathan, P.M., Sekar, S., Kumaran, B., Sastry, T.P. (2012). Characterization and evaluation of biocomposite films containing chitosan and sago starch impregnated with silver nanoparticles. *Int. J. Biol. Macromol.* **50**, 939–946.

[27] Hellebust, A., Richards-Kortum, R. (2012). Advances in molecular imaging: targeted optical contrast agents for cancer diagnostics. *Nanomedicine* **7**, 429–445.

[28] Javier, D.J., Nitin, N., Roblyer, D.M., Richards-Kortum, R. (2008). Metal-based nanorods as molecule specific contrast agents for reflectance imaging in 3D tissues. *J. Nanophoton.* **2**, 23506.

[29] Shanmugasundaram, N., Sundaraseelan, J., Uma, S., Selvaraj, D., Babu, M. (2006). Design and delivery of silver sulfadiazine from alginate microspheres-impregnated collagen scaffold. *J. Biomed. Mater. Res. B: Appl. Biomater.* **77**, 378–388.

[30] Wang, Y., Newell, B.B., Irudayaraj, J. (2012). Folic acid protected silver nanocarriers for targeted drug delivery. *J. Biomed. Nanotechnol.* **8**, 751–759.

[31] Duguet, E., Vasseur, S., Mornet, S., Devoisselle, J.M. (2006). Magnetic nanoparticles and their applications in medicine. *Nanomedicine* **1**, 157–168.

[32] de Montferrand, C., Hu, L., Milosevic, I., Russier, V., Bonnin, D., Motte, L. (2013). Iron oxide nanoparticles with sizes, shapes and compositions resulting in different magnetization signatures as potential labels for multiparametric detection. *Acta Biomater.* **9**, 6150–6157.

[33] Sulek, S., Mammadov, B., Mahcicek, D.I., Sozeri, H., Atalar, E., Tekinav, A.B. et al. (1981). Peptide functionalized superparamagnetic iron oxide nanoparticles as MRI contrast agents. *J. Mater. Chem.* **21**, 15157–15162.

[34] Pouliquen, D., Le Jeune, J.J., Perdrisot, R., Ermias, A., Jallet, P. (1991). Iron oxide nanoparticles for use as an MRI contrast agent: Pharmacokinetics and metabolism. *Magn. Reson. Imag.* **9**, 275–283.

[35] Mandal, A., Sekar, S., Kanagavel, M., Chandrasekaran, N., Mukherjee, A., Sastry, T.P. (2010). Collagen based magnetic nanobiocomposite as MRI contrast agent for cancer therapy. *Biochim. Biophys. Acta Genet. Subjects* **6**, 502–510.

[36] Shubayev, V.I., Pisanic, T.R., Jin, S. (2009). Magnetic nanoparticles for theragnostics. *Adv. Drug Deliv. Rev.* **6**, 467–477.

[37] Kittiphattanabawon, P., Benjakul, S., Visessanguan, W., Nagai, T., Tanaka, M. (2005). Characterisation of acid-soluble collagen from skin and bone of bigeye snapper (*Priacanthus tayenus*). *Food Chem.* **89**, 363.

[38] Sankar, S., Sekar, S., Mohan, R., Sunita, R., Sundaraseelan, J., Sastry, T.P. (2008). Preparation and partial characterization of collagen sheet from fish (Lates calcarifer) scales. *Int. J. Biol. Macromol.* **42**, 6–9.

[39] Noelken, M.E., Wisdom, B.J.J., Hudson, B.G. (1981). Estimation of the size of collagenous polypeptides by sodium dodecyl sulfate-polyacrylamide gel electrophoresis. *Anal. Biochem.* **110**. 131–136.

[40] Kimura, S., Miyauchi, Y., Uchida, N. (1991). Scale and bone type I collagens of carp (Cyprinus carpio). *Compar. Biochem. Physiol.* **99B**, 473–476.

[41] Kimura, S. (1992). Wide distribution of the skin type I collagen $\alpha 3$ chain in bony fish. *Compar. Biochem. Physiol.* **102B**, 255–260.

[42] Sripriya, R., Kumar, R., Balaji, S., Senthil Kumar M., Sehgal, P.K. (2011). Characterizations of polyanionic collagen prepared by linking additional carboxylic groups. *React. Funct. Polym.* **71**, 62–69.

[43] Kimura, S., Ohno, Y. (1987). Fish type I collagen: Tissue-specific existence of two molecular forms, $(\alpha 1)2\alpha 2$ and $\alpha 1\alpha 2\alpha 3$, in Alaska Pollack. *Compar. Biochem. Physiol.* **88B**, 409–413.

[44] Nagai, T., Izumi, M., Ishii, M. (2004). Fish scale collagen. Preparation and partial characterization. *Int. J. Food Sci. Technol.* **39**, 239–244.

[45] Greenfield, N.J. (1996). Methods to estimate the conformation of proteins and polypeptides from circular dichroism data. *Anal. Biochem.* **235**, 1–10.

[46] Rose, C., Mandal, A.B. (1996). Interaction of SDS and urea with cat fish collagen: Hydrodynamic thermodynamic, conformation and geometric studies. *Int. J. Biol. Macromol.* **18**, 41–43.

[47] Mandal, A.B., Ramesh, D.V., Dhar, S.C. (1987). Physicochemical studies of micelle formation on sepia cartilage

collagen solutions (pepsin extracted) in acetate buffer and its interaction with ionic and nonionic micelles: Hydrodynamic and thermodynamic studies. *FEBS Eur. J. Biochem.* **169**, 617–628

[48] Mandal, A.B., Ramesh, D.V., Chandrasekaran, F., Dhar, S.C. (1985). The extent of hydration and thermodynamics activation parameters of intramuscular collagen in fish from viscometric studies. *Leather Sci.* **32**, 127–133.

[49] Rose, C., Kumar, M., Mandal, A.B. (1988). The hydration and thermodynamic studies on warm water and cold water fish collagens. *Biochem. J.* **249**, 127–133.

[50] Kirubanandan, S., Sehgal, P.K. (2010). Regeneration of soft tissue using porous bovine collagen scaffold. *J. Optoelectron. Biomed. Mater.* **2**, 141–149.

[51] Balaji, S., Kumar, R., Sripriya, R., Rao, U., Mandal, A., Kakkar, P., et al. (2012). Characterization of keratin–collagen 3D scaffold for biomedical applications. *Polym. Adv. Technol.* **23**, 500–507.

[52] Tsai, S., Liou, H., Lin, C., Kuo, K., Hung, Y., Weng, R., et al. (2012). MG63 osteoblast-like cells exhibit different behavior when grown on electrospun collagen matrix versus electrospun gelatin matrix. *PLoS ONE* **7**, e31200.

[53] Tiffany, M.L., Krimm, S. (1972). Effect of temperature on the circular dichroism spectra of polypeptides in the extended state. *Biopolymers* **11**, 2309–2316.

[54] Balaji, S., Kumar, R., Sripriya, R., Kakkar, P., Ramesh, D.V., Reddy, P.N.K., Sehgal, P.K. (2012). Preparation and comparative characterization of keratin–chitosan and keratin–gelatin composite scaffolds for tissue engineering applications. *Mater. Sci. Eng. C* **32**, 975–982.

[55] Leikina, E., Mertts, M.V., Kuznetsova, N., Leikin, S. (2002). Type I collagen is thermally unstable at body temperature. *Proc. Natl. Acad. Sci.* **99**, 1314–1318.

[56] Abraham, L.C., Vorrasi, J., Kaplan, D.L. (2004). Impact of collagen structure on matrix trafficking by human fibroblasts. *J. Biomed. Mater. Res. A* **70**, 39–48.

[57] Li, Y., Foss C.A., Summerfield, D.D., Doyle, J.J., Torok, C.M., Dietz, H.C., et al. (2012). Targeting collagen strands by photo-triggered triple-helix hybridization. *Proc. Natl. Acad. Sci.* **109**, 14767–14772.

[58] Day, J.S., Van Der Linden, J.C., Bank, R.A., Ding, M., Hvid, I., Sumner, D.R., et al. (2004). Adaptation of subchondral bone in osteoarthritis. *Biorheology* **41**, 359–368.

[59] Consonni, R., Zetta, L., Longhi, R., Toma, L., Zanaboni, G., Tenni, R. (2000). Conformational analysis and stability of collagen peptides by CD and by 1H- and 13C-NMR spectroscopies. *Biopolymers* **53**, 99–111.

[60] Mitra, T., Sailakshmi, G., Gnanamani, A., Mandal, A.B. (2011). Di-carboxylic acid cross-linking interactions improves thermal stability and mechanical strength of reconstituted type I collagen. Part I. Oxalic acid. *J. Therm. Anal. Calorim.* **105**, 325–330.

[61] Fathima, N.N., Bose, M.C., Rao, J.R., Nair, B.U. (2006). Stabilization of type I collagen against collagenases (type I) and thermal degradation using iron complex. *J. Inorg. Biochem.* **100**, 1774–1780.

[62] Gopal, R., Park, J.S., Seo, C.H., Park, Y. (2012). Applications of circular dichroism for structural analysis of gelatin and antimicrobial peptides. *Int. J. Mol. Sci.* **13**, 3229–3244.

[63] Xiufang, Z., Yandao, G., Jiangang, D., Tianjie, S., Nanming, Z. (1997). Circular dichroism analysis of the effect of metallic ions on structure of collagen molecules. *Tsinghua Sci. Technol.* **2**, 508–511.

[64] Fathima, N.N., Rao, J.R., Nair, B.U. (2011). Effect of UV irradiation on the physico-chemical properties of iron crosslinked collagen. *J. Photochem. Photobiol. B* **105**, 203–206.

[65] Devi, A.S., Ogawa, Y., Shimoji, Y., Balakumar, S., Ponnuraj, K. (2012). Collagen adhesin–nanoparticle interaction impairs adhesin's ligand binding mechanism. *Biochim. Biophys. Acta* **1820**, 819–828.

[66] Li, L., Mu, Q., Zhang, B., Yan, B. (2010). Analytical strategies for detecting nanoparticle–protein interactions. *Analyst* **135**, 1519–1530.

[67] Alarcon, E.I., Udekwu, K., Skog, M., Pacioni, N.L., Stamplecoskie, K.G., Gonzalez-Bejar, M., et al. (2012). The biocompatibility and antibacterial properties of collagen-stabilized, photochemically prepared silver nanoparticles. *Biomaterials* **33**, 4947–4956.

[68] Gaidau, C., Petica, A., Micutz, M., Danciu, M., Vladkova, T. (2013). Progresses in treatment of collagen and keratin-based materials with silver nanoparticles. *Central Eur. J. Chem.* **11**, 901–911.

[69] Mandal, A., Meda, V., Zhang, W.J., Farhan, M.K., Gnanamani, A. (2012). Synthesis, characterization and comparison of antimicrobial activity of PEG/TritonX-100 capped silver nanoparticles on collagen scaffold. *Colloids Surf. B: Biointerfaces* **90**, 191–196.

[70] Jelesarov, I., Bosshard, H.R. (1999). Isothermal titration calorimetry and differential scanning calorimetry as complementary tools to investigate the energetics of biomolecular recognition. *J. Mol. Recogn.* **12**, 3–18.

[71] Flandin, F., Buffevant, C., Herbage, D. (1984). A differential scanning calorimetry analysis of the age-related changes in the thermal stability of rat skin collagen. *Biochim. Biophys. Acta* **791**, 205–211.

[72] Kumar, T.R., Shanmugasundaram, N., Babu, M. (2003). Biocompatible collagen scaffolds from a human amniotic membrane: Physicochemical and in vitro culture characteristics. *J. Biomater. Sci. Polym. Ed.* **14**, 689–706.

[73] Martins, V.C.A., Plepis, A.M.G., Machado, A.A.S. (2002). Thermal and rheological behavior of collagen: Chitosan blends. *J. Therm. Anal. Calorim.* **67**, 491–498.

[74] Xia, Z., Calderon-Colon, X., Trexler, M., Elisseeff, J., Guo, Q. (2012). Thermal denaturation of type I collagen vitrified gels. *Thermochim. Acta* **527**, 172–179.

[75] Wright, N., Humphrey, J.D. (2002). Denaturation of collagen via heating: an irreversible rate process *Annu. Rev. Biomed. Eng.* **4**, 109–128.

[76] Rochdi, A., Foucat, L., Renou, J.P. (1999). Effect of thermal denaturation on water–collagen interactions: NMR

relaxation and differential scanning calorimetry analysis. *Biopolymers* **50**, 690–696.

[77] Thanikaivelan, P., Narayanan, N.T., Pradhan, B.K., Ajayan, P.M. (2012). Collagen based magnetic nanocomposites for oil removal applications. *Sci. Reports* **2**, 1–7.

[78] Sosa, Y.D., Rabelero, M., Trevino, M.E., Saade, H., Lopez, R.G. (2010). High yield synthesis of silver nanoparticles by precipitation in a high-aqueous phase content reverse microemulsion. *J. Nanomater.* **2010**, 1–6.

[79] Eken, A.E., Ozenbas, M. (2009). Characterization of nanostructured magnetic thin films produced by sol-gel processing. *J. Sol-Gel Sci.Technol.* **50**, 321–327.

[80] Inouye, K., Endo, R., Ostsuka, Y., Miyashiro, K., Kaneko, K., Ishikawa, T. (1982). Oxygenation of ferrous ions in reverse micelle and reversed microemulsion. *J. Phys. Chem.* **86**, 1465–1469.

[81] Faraji, M., Yamini, Y., Rezaee, M. (2010). Magnetic nanoparticles: Synthesis, stabilization, functionalization, characterization and applications. *J. Iran. Chem. Soc.* **7**, 1–37.

[82] Luo, C., Zhang, Y., Zeng, X., Zeng, Y., Wang, Y. (2005). The role of poly(ethylene glycol) in the formation of silver nanoparticles. *J. Colloid Interface Sci.* **288**, 444–448.

[83] Raffi, M., Hussain, F., Bhatti, T.M., Akhter, J.I., Hameed, A., Hasan, M.M. (2008). Antibacterial characterization of silver nanoparticles against *E. coli* ATCC-15224. *J. Mater. Sci. Technol.* **24**, 192–198.

[84] Khanna, P.K., Singh, N., Charan, S., Subbarao, V.V.V.S., Gokhale, R., Mulik, U.P. (2005). Synthesis and characterization of Ag/PVA nanocomposite by chemical reduction method. *Mater. Chem. Phys.* **93**, 117–121.

[85] He, L., Gao, S., Wu, H., Liao, X., He, Q., Shi, B. (2012). Antibacterial activity of silver nanoparticles stabilized on tannin grafted collagen fiber. *Mater. Sci. Eng. C* **32**, 1050–1056.

[86] Jacob, J.A., Mahal, H.S., Biswas, N., Mukherjee, T., Kapoor, S. (2008). Role of phenol derivatives in the formation of silver nanoparticles. *Langmuir* **24**, 59–63.

[87] Wu, H., He, L., Gao, M., Gao, S., Liao, X., Shi, B. (2011). One-step in situ assembly of size controlled silver nanoparticles on polyphenol-grafted collagen fiber with enhanced antibacterial properties. *N. J. Chem.* **35**, 2902–2909.

[88] Ma, M., Zhan, Y., Shen, Y., Xia, X., Zhang, S., Liu, Z. (2011). Synthesis of amino-group functionalized superparamagnetic iron oxide nanoparticles and applications as biomedical labeling probes. *J. Nanopart. Res.* **13**, 3249–3257.

[89] Xuan, S.H., Wang, Y.X.J., Yu, J.C., Leung, K.C. (2009). Tuning the grain size and particle size of superparamagnetic Fe_3O_4 microparticles. *Chem. Mater.* **21**, 5079–5087.

[90] Wu, W., He, Q., Chen, H. (2007). *Proc.1st Int. Conf. Bioinformatics and Biomedical Engineering* (Wuhan), Vol. 1, p. 76.

[91] Ratner, B.D., Chilkoti, A., Castner, D.G. (1992). Contemporary methods for characterizing complex biomaterials surfaces. *Clin. Mater.* **11**, 25.

[92] Krafft, C., Sergo, V. (2006). Biomedical applications of Raman and infrared spectroscopy to diagnose tissues. *Spectroscopy* **20**, 195–218.

[93] Dukor R.K. (2002). *Applications of Vibrational Spectroscopy in Live and Natural Sciences.* Wiley, Hoboken, NJ, pp. 3335–3361.

[94] Falamas, A., Cinta-Pinzaru, S., Dehelean, C., Krafft, C.H., Popp, J. (2010). Raman and FT-IR imaging of *in vivo* damaged tissue induced by 7,12-dimethylbenzanthracene (DMBA) in mouse models. *Rom. J. Biophys.* **20**, 1–11.

[95] Leikin, S., Parsegian, V.A., Yang, W.H., Walrafen, G.E. (1997). Raman spectral evidence for hydration forces between collagen triple helices. *Proc. Natl. Acad. Sci. USA* **94**, 11312–11317.

[96] Yannas, I.V., Burke, J.F., Gordon, P.L., Huang, C., Rubenstein, R.H. (1980). Design of an artificial skin. II. Control of chemical composition. *J. Biomed. Mater. Res. A* **14**, 107–131.

[97] Gilbert, D.L., Okano, T., Miyata, T., Kim, S.W. (1988). Macromolecular diffusion through collagen membranes. *Int. J. Pharm.* **47**, 79–88.

[98] Sun, Y., Wang, L., Sun, L., Guo, C., Yang, T., Liu, Z., et al. (2008). Fabrication, characterization and application in surface enhanced Raman spectrum of assembled type-I collagen–silver nanoparticle multilayered films. *J. Chem. Phys.* **128**, 074704.

[99] Liu, Q., Wang, Y., Li, W., Wu, L. (2007). Structural characterization and chemical response of an Ag coordinated supramolecular gel. *Langmuir* **23**, 8217.

[100] Hoa, L.T.M., Dung, T.T., Danh, T.M., Duc, N.H., Chien, D.M. (2009). Preparation and characterization of magnetic nanoparticles coated with polyethylene glycol. *J. Phys. Conf. Series* **187**, 012048.

[101] Sun, Y., Ding, X., Zheng, Z., Cheng, X., Hu, X., Peng, Y. (2007). Surface initiated ATRP in the synthesis of iron oxide/polystyrene core/shell nanoparticles. *Eur. Polym. J.* **43**, 762.

[102] Dallas, P., Bourlinos, A.B., Niarchos, D., Petridis, D. (2007). Synthesis of tunable sized capped magnetic iron oxide nanoparticles highly soluble in organic solvents. *J. Mater. Sci.* **42**, 4996–5002.

[103] Palma, R.D., Peeters, S., Van Bael, M.J., Rul, H.V.D., Bonroy, K., Laureyn, W., et al. (2007). Silane ligand exchange to make hydrophobic superparamagnetic nanoparticles water-dispersible. *Chem. Mater.* **19**, 1821–1831.

[104] Launer, P.J. (1987). *Infrared Analysis of Organosilicon Compounds. Silicone Compounds Register and Review*, Petrarch Systems, Levittown, PA, p. 70.

[105] Chockalingam, A.M., Babu H.K.R.R., Chittor, R., Tiwari, J.P. (2010). Gum arabic modified Fe_3O_4 nanoparticles cross linked with collagen for isolation of bacteria. *J. Nanobiotechnol.* **8**, 30.

[106] Ratner, B.D., Tyler, B.J., Chilkoti, A. (1993). Analysis of biomedical polymer surfaces: Polyurethanes and plasma-deposited thin films. *Clin. Mater.* **13**, 71–74.

[107] Werner, C., Jacobasch, H.J., Reichelt, G. (1995). Surface characterization of hemodialysis membranes based on streaming potential measurements. *J. Biomater. Sci.* **7**, 61–76.

[108] Jablonski, A. (2000). Quantitative surface analysis by X-ray photoelectron spectroscopy. *Polish J. Chem.* **74**, 1533–1566.

[109] Choi, L., Park, H., Chun, H.J., Kim, C., Jang, J.W. (2009). Collagen modified polystyrene plate for enhanced cell cultivation. *Tissue Eng. Regen. Med.* **6**, 432–437.

[110] Kim, D., Park, J., Koh, W. (2009). Control of cell adhesion on poly(ethylene glycol) hydrogel surfaces using photochemical modification and micropatterning techniques. *J. Industr. Eng. Chem.* **15**, 5.

[111] Morra, M., Cassinelli, C., Cascardo, G., Cahalan, P., Cahalan, L., Fini, M., et al. (2003). Surface engineering of titanium by collagen immobilization. Surface characterization and *in vitro* and *in vivo* studies. *Biomaterials* **24**, 4639–4654.

[112] Zambonin, G., Losito, I., Triffitt, J.T., Zambonin, C.G. (2000). Detection of collagen synthesis by human osteoblasts on a tricalcium phosphate hydroxyapatite: An X-ray photoelectron spectroscopy investigation. *J. Biomed. Mater. Res. A* **49**, 120–126.

[113] Zhang, L., He, R., Gu, H. (2006). Oleic acid coating on the monodisperse magnetic nanoparticles. *Appl. Surf. Sci.* **253**, 2611–2617.

[114] Mandal, A., Sekar, S., Chandrasekaran, N., Mukherjee, A., Sastry, T.P. (2013). Poly(ethylene)glycol-capped silver and magnetic nanoparticles: Synthesis, characterization and comparison of bactericidal and cytotoxic effects. *Proc. Inst. Mech. Eng. H: J. Eng. Med.* **227**, 1224–1236.

[115] Cui, S., Shen, X., Lin, B., Jiang, G., Zhang, W. (2008). Surface organic modification of Fe_3O_4 magnetic nanoparticles. *J. Wuhan Univ. Technol. Mater. Sci. Ed.* **23**, 436–439.

[116] Battistioni, C., Casaletto, M.P., Ingo, G.M., Kaciulis, S., Mattogno, G., Pandolfi, L. (2000). Surface characterization of biocompatible hydroxyapatite coatings. *Surf. Interface Anal.* **29**, 773.

[117] Sodhi, R.N.S. (1996). Application of surface analytical and modification techniques to biomaterial research. *J. Electron Spectrosc. Related Phenom.* **81**, 269.

[118] Yang, C. (2012). Enhanced physicochemical properties of collagen by using EDC/NHS cross linking. *Bull. Mater. Sci.* **35**, 913–918.

[119] Raghavan, N.R., Muthukumar, T., Somanathan, S., Sastry, T.P. (2013). Biomimetic mineralization of novel silane crosslinked collagen. *Mater. Sci. Eng. C* **33**, 1983–1988.

[120] Ratanavaraporn, J., Damrongsakkul, S., Sanchavanakit, N., Banaprasert, T., Kanokpanont, S. (2006). Comparison of gelatin and collagen scaffolds for fibroblast cell culture. *J. Metals Mater. Minerals* **16**, 31–36.

[121] Kanda, N., Morimoto, N., Ayvazyan, A.A., Takemoto, S., Kawai, K., Nakamura, Y., et al. (2014). Evaluation of a novel collagen-gelatin scaffold for achieving the sustained release of basic fibroblast growth factor in a diabetic mouse model. *J. Tissue Eng. Regen. Med.* **8**, 29–40.

[122] Huang, A., Xu, S., Wei, G., Ma, L., Gao, C. (2009). A trilayer dermal equivalent containing silver nanoparticles with enhanced antibacterial property. *Chinese J. Polym. Sci.* **27**, 865−871.

[123] Sun, Y., Wei, G., Song, Y., Wang, L., Sun, L., Guo, C., et al. (2008). Type I collagen-templeted assembly of silver nanoparticles and their application in surface-enhanced Raman scattering. *Nanotechnology* **19**, 115604.

[124] Kwan, K.H.L., Liu, X., To, M.K.T., Young, K.W.K., Ho, C., Wong, K.K.Y. (2011). Modulation of collagen alignment by silver nanoparticles results in better mechanical properties in wound healing. *Nanomed. Nanotechnol. Biol. Med.* **7**, 497–504.

[125] Chamundeeswari, M., Kumar, B.S., Kumar, T.M., Muthuraman, L., Purna Sai, K., Sastry, T.P. (2012). Iron nanoparticles from blood coated with collagen as a matrix for the synthesis of nanohydroxyapatite. *Bull. Mater. Sci.* **1**, 3.

[126] Gaihre, B., Khil, M.S., Kang, H.K., Kim, H.Y. (2009). Bioactivity of gelatin coated magnetic iron oxide nanoparticles: In vitro evaluation. *J. Mater. Sci. Mater. Med.* **20**, 573–581.

[127] Shimizu, K., Ito, A., Honda, H. (2006). Enhanced cell-seeding into 3D porous scaffolds by use of magnetite nanoparticles. *J. Biomed. Mater. Res. B: Appl. Biomater.* **77**, 265.

[128] Carlisle, C.R., Coulais, C., Guthold, M. (2010). The mechanical stress–strain properties of single electrospun collagen type I nanofibers. *Acta Biomater.* **6**, 2997–3003.

[129] Park, Y.J., Choi, G.J., Kim, S., Hahn, J., Lee, T.G., Lee, W.J., et al. (2012). Nanoscale characterization of acid and thermally treated collagen fibrils. *Acta Biomater.* **8**, 3381–3391.

[130] Damodaran, G., Collighan, R., Griffin, M., Navsaria, H., Pandit, A. (2009). Tailored laminin-332 α3 sequence is tethered through an enzymatic linker to a collagen scaffold to promote cellular adhesion. *Acta Biomater.* **5**, 2441–2450.

[131] Denning, D., Abu-Rub, M.T., Zeugolis, D.I., Habelitz, S., Pandit, A., Fertala, A., et al. (2012). Electromechanical properties of dried tendon and isoelectrically focused collagen hydrogels. *Acta Biomater.* **8**, 3073–3079.

[132] Niwa, D., Fujie, T., Lang, T., Goda, N., Takeoka, S. (2012). Heterofunctional nanosheet controlling cell adhesion properties by collagen coating. *J. Biomater. Appl.* **27**, 131–141.

[133] Campbell, S.E., Ferguson, V.L., Hurley, D.C. (2012). Nanomechanical mapping of the osteochondral interface with contact resonance force microscopy and nanoindentation. *Acta Biomater.* **8**, 4389–4396.

[134] Baclayon, M., Roos, W.H., Wuite, G.J.L. (2010). Sampling protein form and function with the atomic force microscope. *Mol. Cell. Proteom.* **9**, 1678–1688.

[135] Ye, Z., Zhao, X. (2010). Phase imaging atomic force microscopy in the characterization of biomaterials. *J. Microsc.* **238**, 27–35.

[136] Skopinska-Wisniewska, J., Sionkowska, A., Kaminska, A., Kaznica, A., Jachimiak, R., Drewa, T. (2009). Surface

characterization of collagen/elastin based biomaterials for tissue regeneration. *Appl. Surf. Sci*. **255**, 8286–8292.

[137] Gaidu, C., Petic, A., Ciobanu, C., Martinescu, T. (2009). Investigations on antimicrobial activity of collagen and keratin based materials doped with silver nanoparticles. *Rom. Biotechnol. Lett.* **14**, 4665–4672.

[138] Strasser, S., Zink, A., Janko, M., Heckl, W.M., Thalhammer, S. (2007). Structural investigations on native collagen type I fibrils using AFM. *Biochem. Biophys. Res. Commun.* **354**, 27–32.

[139] Grover, C.N., Gwynne, J.H., Pugh, N., Hamaia, S., Farndale, R.W., Best, S.M., et al. (2012). Crosslinking and composition influence the surface properties, mechanical stiffness and cell reactivity of collagen-based films. *Acta Biomater.* **8**, 3080–3090.

[140] Friedrichs, J., Taubenberger, A., Franz, C.M., Muller, D.J. (2007). Cellular remodelling of individual collagen fibrils visualized by time-lapse AFM. *J. Mol. Biol.* **372**, 594–607.

13

BIOMIMETIC POLYMER AGGREGATES: SELF-ASSEMBLY INDUCED BY CHEMICAL REACTIONS

Eri Yoshida

Department of Environmental and Life Sciences, Toyohashi University of Technology, Aichi, Japan

13.1 INTRODUCTION

Molecular self-assembly is the spontaneous association of molecules into thermodynamically and structurally stable aggregates joined through noncovalent bonds by van der Waals interaction, electrostatic attraction, and hydrogen bonding. Once the self-assembly occurs, the molecules construct three-dimensional structures on micro- and nanometer scales according to the respective rules. The self-assembly into the high-dimensional structures can be seen in many places in vivo, including protein folding [1], stacking of a base in the double helix of DNA [2], formation of biomembranes [3], and transport of lipophilic compounds by fatty-acid micelles [4]. The static self-assembly maintains the structure of the vital tissue, while the dynamic self-assembly provides the tissue with functions through dissociation and association. Such self-assembly is seen in the polymerization–depolymerization of tubulin proteins forming microtubules and in the formation of actin filaments [5]. This reversible self-assembly is controlled by the protein concentrations [6].

Based on the formation of the vital tissue through the self-assembly, proteins can perform individual functions, and the biomembranes can maintain fluidity to sustain life processes. The fluidity of the biomembranes also promotes the transport of substances including ions, electrons, and photons as mitochondria [7], erythrocytes [8], and chloroplasts [9]. Hence, many vital reactions involving electron transfer and photoreactions, such as the oxidation of a fatty acid in the citric acid circle [10] and oxidative phosphorylation [11], occur on the surface of or close to the biomembrane. These reactions often produce changes in the high-dimensional structure formed by the self-assembly [12, 13].

Artificially synthesized amphiphilic block copolymers form micelles and bilayer structures including vesicles in solution, as are the vital surfactants of lipids and fatty acids. The copolymers have often been used for the studies of the self-assembly into micelles [14] and already have many applications in industry such as separation technologies [15] and drug delivery [16]. The micellization of the block copolymers is promoted not only by the copolymer concentration but also by variation in the surroundings, such as temperature [17–21], pressure [22–26], pH [27–31], salt formation [30–35], and noncovalent bond cross-linking [36–38]. During the micellization caused by these environmental stimuli, the block copolymers molecularly dissolved in a solvent are converted in situ into amphiphilic copolymers.

This chapter describes the biomimetic self-assembly induced by electron transfer and irreversible photoreactions as new triggers using block copolymers.

13.2 SELF-ASSEMBLY INDUCED BY ELECTRON TRANSFER

Electron transport systems perform important functions concerning respiration and energy metabolism in eukaryotes [39, 40]. Electron transfer occurs at the mitochondria inner membrane consisting of the electron transport proteins [41] and the lipid bilayer built up by the self-assembly of

Encyclopedia of Biocolloid and Biointerface Science, Volume 1, First Edition. Edited by Hiroyuki Ohshima.
© 2016 John Wiley & Sons, Inc. Published 2016 by John Wiley & Sons, Inc.

phospholipids [3, 11]. The electron transport proteins contain redox catalysts, such as nicotinamide, iron [42, 43], and quinones [44]. The electrons produced by these redox reactions transfer through the lipid bilayer. While the mechanisms of electron transport and the correlation to self-assembly have been clarified, self-assembly triggered by electron transfer has been applied to artificial polymeric surfactants.

The electron transfer-induced self-assembly has been found using some redox catalysts. The electrochemical self-assembly was established using the redox system of ferrocene for polyisoprene-*block*-poly(ferrocenyldimethylsilane) [45]. Other investigators also used the polyferrocenylsilanes composing block copolymers to obtain spherical micelles [46]. Other authors employed the redox of catechol for the self-assembly of 3,4-dihydroxyphenylalanine-containing poly(ethylene glycol) to prepare metal core–polymer shell nanoparticles [47], while other coworkers used the aniline oxidation for an oligoaniline-containing dendron–rod–dendron dumbbell-shaped block oligomer and succeeded in controlling the morphology through oxidation [48].

The redox system of 2,2,6,6-tetramethylpiperidine-1-oxyl (TEMPO) is useful as a trigger of the self-assembly of block copolymers. TEMPO is a stable nitroxyl radical [49] known as a *spin trapping reagent* [50], a *spin label reagent* [51], and a mediator for the controlled/living radical polymerization [52–55]. TEMPO forms a redox system in which the radical is converted into the oxoaminium cation by a one-electron oxidation and is converted into the aminoxy anion by a one-electron reduction (Fig. 13.1) [49,56]. The oxidation of TEMPO into the oxoaminium cation is caused by halogens, such as chlorine [49] and bromine [49, 57] and by metallic ions of copper(II) [58] and iron(III) [59], while the reduction into the aminoxy anion is brought about by phenylhydrazine [60], hydrazobenzene [61], quinones [62], ascorbic acid [63,64], and organometallic compounds [65]. Oxidation into the oxoaminium cation and reduction into the aminoxy anion is simultaneously caused by the disproportionation of TEMPO in ether by the strong acids of hydrochloric acid, nitric acid, tetrafluoroboric acid, fluoroantimonic acid, and perchloric acid [66, 67].

13.2.1 Oxidation-Induced Self-Assembly

Oxidation-induced self-assembly was determined using the oxidative redox system from TEMPO to the oxoaminium cation for a poly(4-vinylbenzyloxy-TEMPO)-*block*-polystyrene (PVTEMPO-*b*-PSt) diblock copolymer

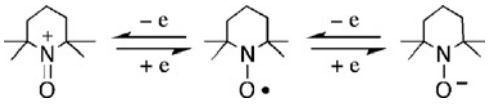


FIGURE 13.1 The redox system of TEMPO.

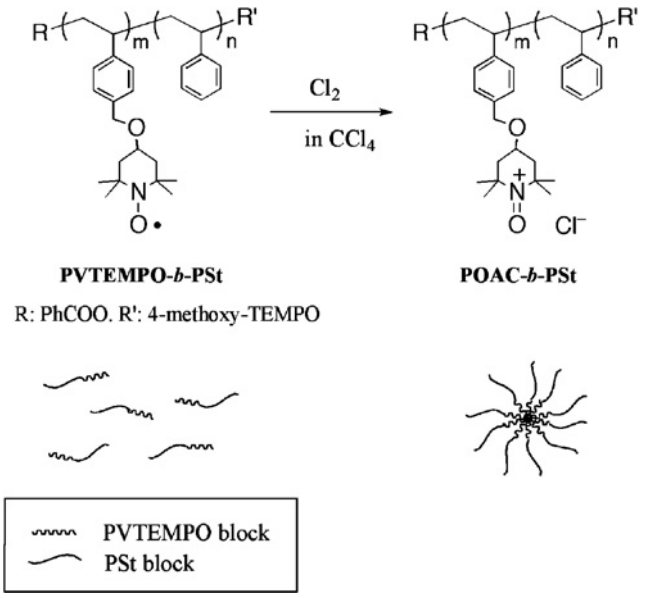


FIGURE 13.2 The oxidation-induced self-assembly of PVTEMPO-*b*-PSt. Mn(PVTEMPO-*b*-PSt) = 31,000-*b*-49,000.

supporting TEMPO on the sidechains (Fig. 13.2) [68]. PVTEMPO-*b*-PSt showed no self-assembly in carbon tetrachloride, a nonselective solvent. The isolated copolymer had a 15.6-nm hydrodynamic diameter. The copolymer self-assembled into micelles with a 49.5-nm diameter by the reaction with chlorine. ESR studies verified that the radical concentration of the TEMPO in the copolymer decreased due to the reaction with chlorine (Fig. 13.3a, b). The broad signal of the TEMPO based on the random orientation due to the restriction of its mobility by supported on the sidechains changed to a characteristic triplet attributed to the isotropy along with a decrease in the signal intensity by the reaction with chorine. The *g* values of the radicals before and after the reaction were 2.0066 and 2.0064, respectively. This negligible difference in *g* values indicates that they are identical radicals originating from the TEMPO. The conversion of the TEMPO was estimated to be 97% based on the integral curves of the radicals. UV analysis confirmed that the TEMPO was oxidized into the oxoaminium chloride (OAC) by chlorine based on the observed absorption at 360 nm originating from the OAC. It was found that PVTEMPO-*b*-PSt was converted into an amphiphilic poly(4-vinylbenzyloxy-OAC)-*b*-PSt (POAC-*b*-PSt) through the reaction with the chlorine to undergo micellization because OAC itself is insoluble in carbon tetrachloride. Figure 13.4 shows plots of the UV absorbance at 360 nm, the relative scattering intensity (I/I_0), and the hydrodynamic diameter (D_H) of the copolymer versus the molar ratio of chlorine to the TEMPO. The induction period of $\leq$0.2 of the chlorine ratio was observed for the plots of the hydrodynamic diameter. The scattering intensity also showed a slight increase up to 0.2, followed by a rapid

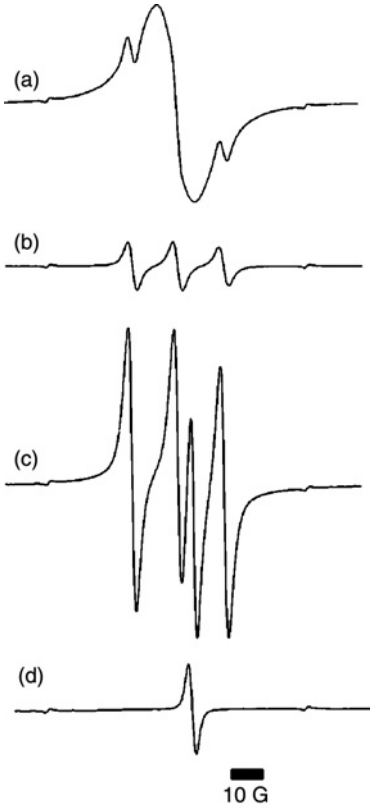


FIGURE 13.3 The ESR spectra of PVTEMPO-*b*-PSt in CCl_4 before (a) and after (b) the reaction with the chlorine, and after the reaction with TMPD (c), and of Wurster's blue chloride separately prepared (d).

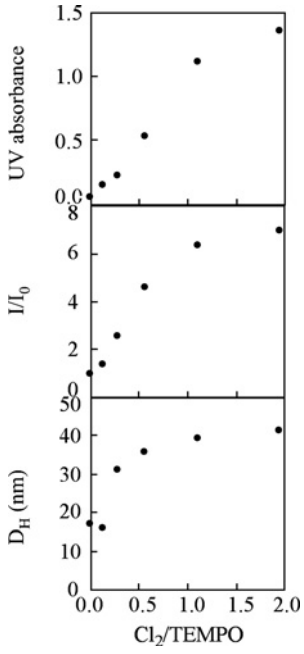


FIGURE 13.4 The variation in UV absorbance at 360 nm, relative scattering intensity (I/I_0), and hydrodynamic diameter (D_H) of PVTEMPO-*b*-PSt versus the molar ratio of chlorine.

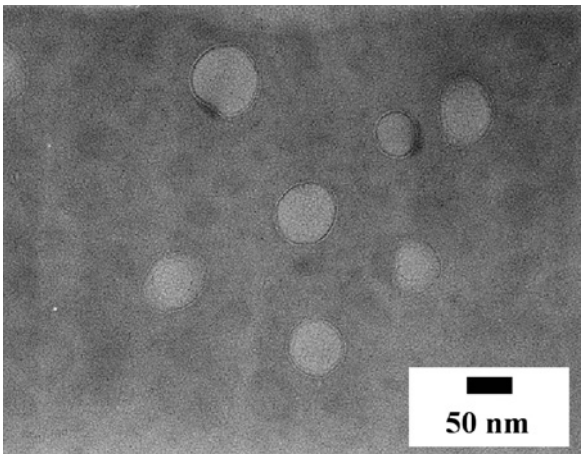


FIGURE 13.5 TEM image of the POAC-*b*-PSt micelles.

increase. It was found that the formation of only 16% of the OAC induced the micellization. TEM observations revealed that POAC-*b*-PSt formed spherical micelles (Fig. 13.5). The size of the micelles was almost equal to that estimated by the dynamic light scattering, suggesting that the micelles have difficulty in swelling in carbon tetrachloride due to the low affinity of OAC for the solvent.

The oxoaminium salts act as a two-electron oxidizing agent for converting alcohols into an aldehyde [69, 70] and ketone [69, 71], while the salts also serve as a one-electron oxidizing agent for water [49], amines [49, 56], sulfides [56, 72], and organometallic compounds [65, 73] to produce their radical cation salts or radical intermediates.

The POAC-*b*-PSt micelles quantitatively oxidized benzyl alcohol into benzaldehyde. Lack of change in the micellar size and the scattering intensity indicated that the copolymer maintained the micellar structure during the oxidation because the OAC was converted into the insoluble hydroxylamine hydrochloride salt, based on the two-electron oxidation for benzyl alcohol. Whereas signals of the pendant groups forming the micellar cores were not observed in the ^{1}H-NMR spectra due to the shielding by the PSt coronas, the signals of benzaldehyde were confirmed. The micelles oxidized benzyl alcohol in the cores and released benzaldehyde from them while maintaining the micellar structure.

The POAC-*b*-PSt micelles also oxidized *N,N,N′,N′*-tetramethyl-1,4-phenylenediamine (TMPD) to produce Wurster's blue chloride (Fig. 13.3c, d). Observation of the characteristic purple color and UV absorption of Wurster's blue indicated that the insoluble Wurster's blue chloride existed in the cores of the micelles. The ESR analysis revealed that the OAC reverted to the TEMPO by the one-electron oxidation of TMPD. The micelles were gradually dissociated into the isolated copolymers, due to the regeneration of the TEMPO.

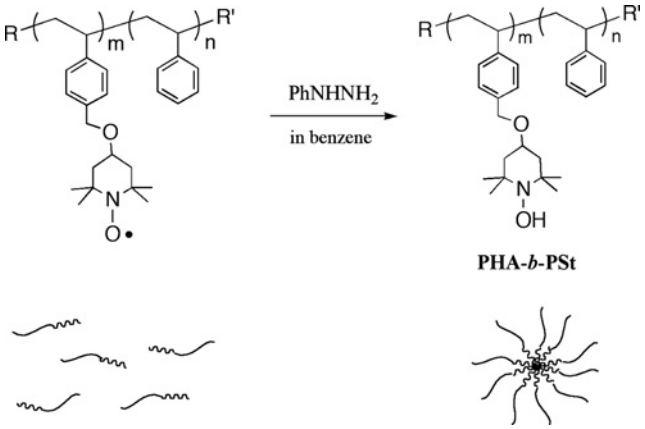


FIGURE 13.6 The reduction-induced self-assembly of PVTEMPO-*b*-PSt.

13.2.2 Reduction-Induced Self-Assembly

Reduction-induced self-assembly was attained using the reductive system from TEMPO to the aminoxy anion [74]. Red-colored PVTEMPO-*b*-PSt was converted into colorless micelles of poly(4-vinylbenzyloxy-hydroxylamine)-*b*-PSt (PHA-*b*-PSt) by the reduction with phenylhydrazine (PH) (Fig. 13.6). Formation of the hydroxylamine by this reduction was also confirmed by ^{1}H NMR. Variation in the scattering intensity distributions of the copolymers by the reduction is shown in Fig. 13.7. The size of the micelles was 55.6 nm, while that of the isolated copolymers was 19.2 nm. The plots of the UV absorption at 500 nm, relative scattering intensity, and hydrodynamic diameter of the copolymer versus the ratio of PH to the TEMPO (PH/TEMPO) are

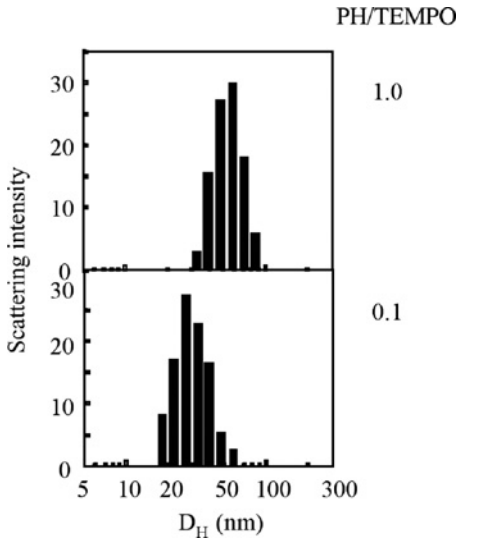


FIGURE 13.7 Scattering intensity distribution of the hydrodynamic diameter of the copolymer at 0.1 (a) and 1.0 (b) of PH/TEMPO.

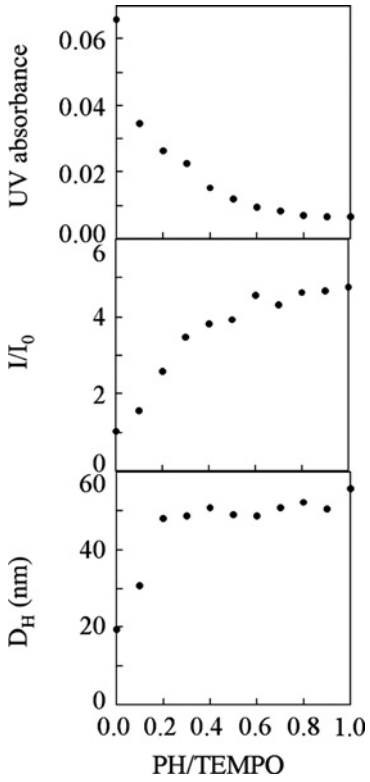


FIGURE 13.8 Plots of the UV absorbance at 500 nm, relative scattering intensity (I/I_0), and hydrodynamic diameter (D_H) versus the PH/TEMPO ratio.

shown in Fig. 13.8. As the PH ratio increased, the hydrodynamic diameter rapidly increased without an induction period and became steady over 0.2. No observation of an induction period indicated a strong aggregation force, based on the hydrogen-bonding attraction of the hydroxylamine in addition to the van der Waals interaction among the insoluble hydroxylamine hydrochloride.

The PHA-*b*-PSt micelles served as a reducing agent for oxygen [75], reverting to PVTEMPO-*b*-PSt.

13.2.3 Disproportionation-Induced Self-Assembly

Disproportionation-induced self-assembly of PVTEMPO-*b*-PSt was performed using hydrochloric acid in 1,4-dioxane (Fig. 13.9) [76, 77]. ESR demonstrated that the radical concentration of TEMPO decreased with an increase in HCl (Fig. 13.10), while UV analysis confirmed that the absorbance at 360 nm attributed to OAC increased as the disproportionation proceeded (Fig. 13.11). Figure 13.12 shows variation in the hydrodynamic diameter and scattering intensity of the copolymer by the disproportionation. The hydrodynamic diameter rapidly increased at a 0.8 molar ratio of HCl to the TEMPO, while the scattering intensity began to increase at 0.8. The micellization started at 0.8. The ratio at

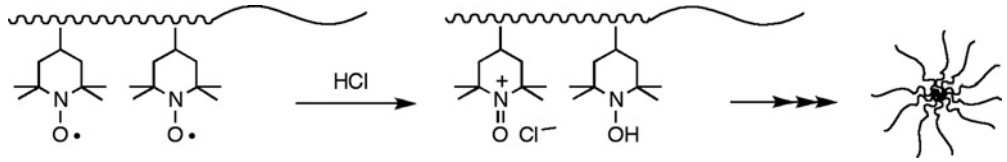


FIGURE 13.9 Self-assembly induced by the disproportionation of TEMPO.

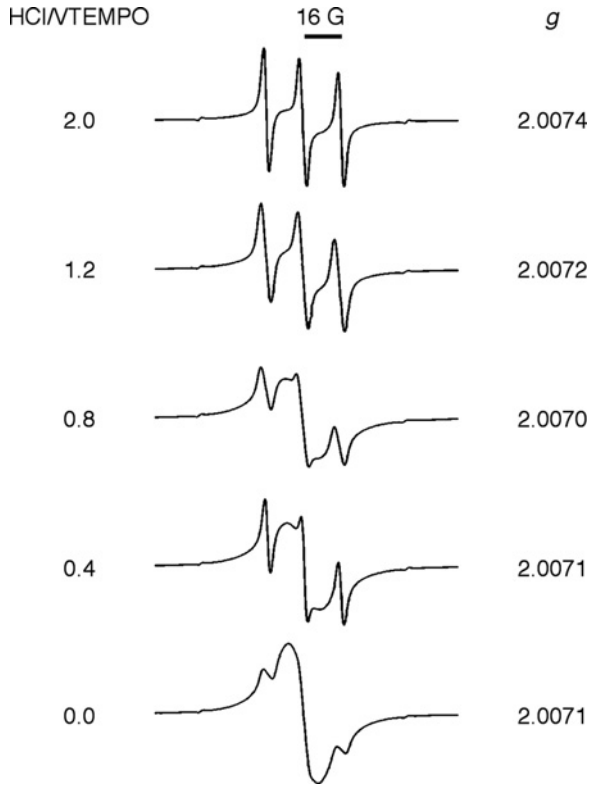


FIGURE 13.10 Variation in ESR spectra of PVTEMPO-*b*-PSt during the disproportionation-induced self-assembly; [PVTEMPO-*b*-PSt] = 1.71 g/L.

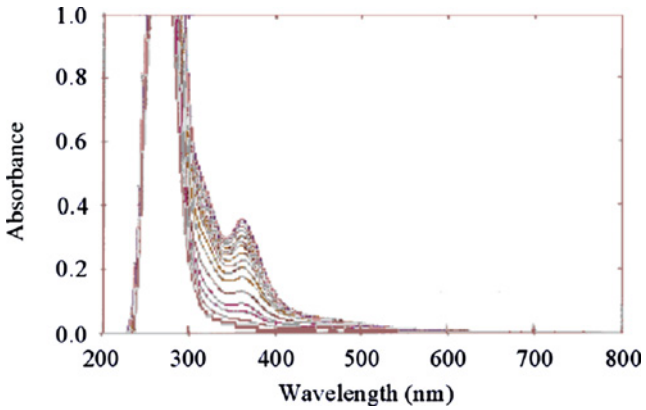


FIGURE 13.11 Variation in UV absorbance of PVTEMPO-*b*-PSt during micellization. HCl/TEMPO from the bottom = 0, 0.2, 0.4, 0.6, 0.8, 1.0, 1.1, 1.2, 1.3, 1.4, 1.5, 1.6, 1.7, 1.8, 1.9, and 2.0; [PVTEMPO-*b*-PSt] = 1.71 g/L.

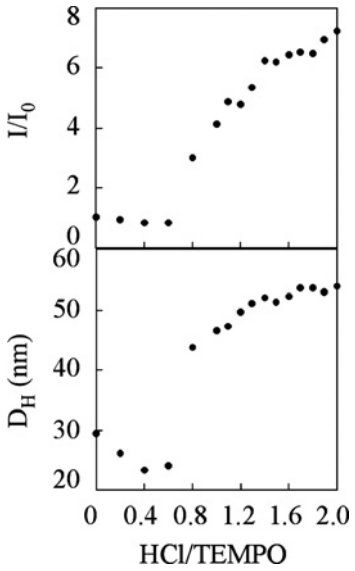


FIGURE 13.12 Variation in relative scattering intensity and hydrodynamic diameter of PVTEMPO-*b*-PSt versus HCl/TEMPO; [PVTEMPO-*b*-PSt] = 1.71 g/L.

which the micellization started was dependent on the acid strength. As the acid strength increased, the transition from unimers of the isolated copolymers to micelles occurred at a lower ratio of the acid (Fig. 13.13). The difference in micellization by the acid strength was accounted for by the difference in the solubility of the oxoaminium salts in 1,4-dioxane. The stronger acid provided a more soluble oxoaminium salt with a lower nucleophilic counteranion.

More recently, some applications of the TEMPO-containing micelles have been reported. A group of coworkers prepared the micelles supporting TEMPO on the core blocks by the self-assembly of an amphiphilic poly(4-amino-TEMPO acrylamide)-*block*-poly(ethylene glycol) diblock copolymer and poly(4-amino-TEMPO acrylamide)-*block*-poly(L-lactic acid)-*block*-poly(ethylene glycol) triblock copolymer and verified the utility of these micelles as EPR probes for bioimaging in vivo [78]. Another team demonstarted that the TEMPO-bearing micelles at the cores obtained by the self-assembly of PVTEMPO-*block*-poly(ethylene glycol) served as nanotherapeutic materials for diseases, such as cerebral and renal ischemia reperfusions and ulcerative colitis, due to their long blood circulation [79]. Another team of investigators prepared micelles

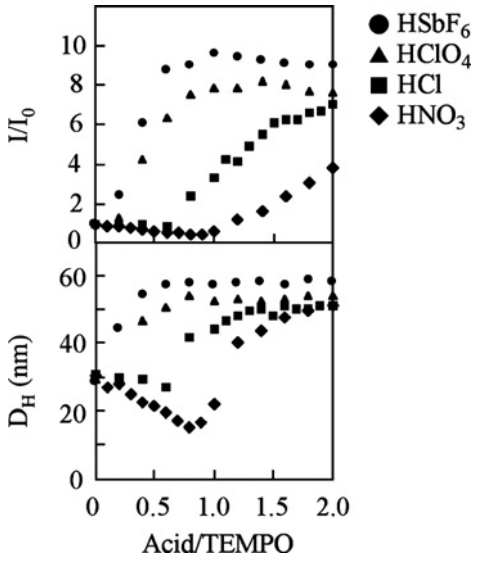


FIGURE 13.13 Variation in relative scattering intensity and hydrodynamic diameter of the copolymer during the micellization by four different acids; [PVTEMPO-*b*-PSt] = 1.71 g/L.

supporting TEMPO on the corona blocks by the self-assembly of poly(4-oxy-TEMPO methacrylate)-*block*-PSt and showed the potential as nanostructured organic radical batteries [80].

13.3 SELF-ASSEMBLY INDUCED BY IRREVERSIBLE PHOTOREACTIONS

Light reactions that occur during photosynthesis consist of irreversible photoreactions based on photooxidation. The irreversible reactions suppress the backward energy transfer and promote an efficient photon transfer. The fixation of the special structure formed by the irreversible photoreactions is also significant in holographic recordings for optical information–storage media because there is less volume shrinkage when recording holograms. Whereas there are a number of publications on the self-assembly induced by reversible photoreactions through the *cis–trans* isomerization and dimerization of azobenzene [81–83], spiropyran [84,85],

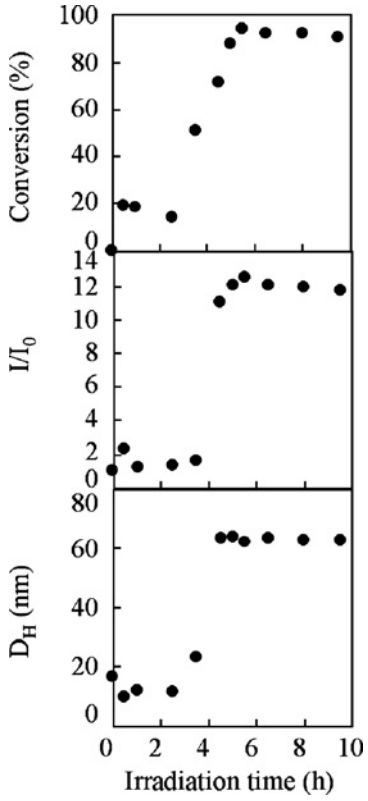
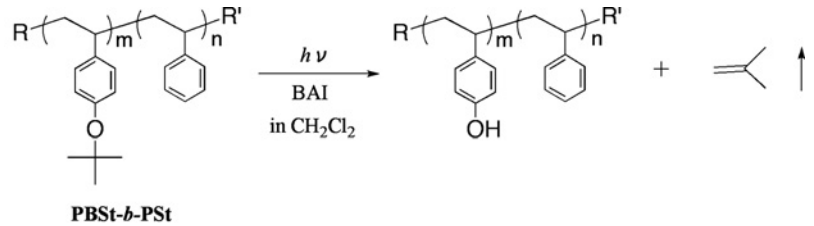


FIGURE 13.15 Variation in conversion, relative scattering intensity, and hydrodynamic diameter of the copolymer during irradiation using BAI; Mn(PBSt-*b*-PSt) = 15,000-*b*-97,000, $[\text{copolymer}]_0$ = 3.30 g/L.

stilbene [86–88], cinnamate [87], and triphenylmethane leukoresidues [89]. Because of the photoswitching function, only a few publications have reported the self-assembly by the irreversible photoreactions for small-molecule surfactants. Examples include the structure change by the photolysis of diazosulfonates [90–92], 1-iminopyridinium ylides [93], [4(4′-alkoxybenzoyl)phenylmethyl]phosphonic acids [94], and didecyl-2-methoxy-5-nitrophenyl phosphate [95]. The former three surfactants loose their surface-active ability by photolysis, resulting in the destruction of the micelles and vesicles. On the other hand, didecyl-2-methoxy-5-nitrophenyl phosphate formed vesicles by photolysis.



PBSt-*b*-PSt

R: PhCOO. R': 4-methoxy-TEMPO

FIGURE 13.14 Micellization induced by photolysis of PBSt-*b*-PSt.

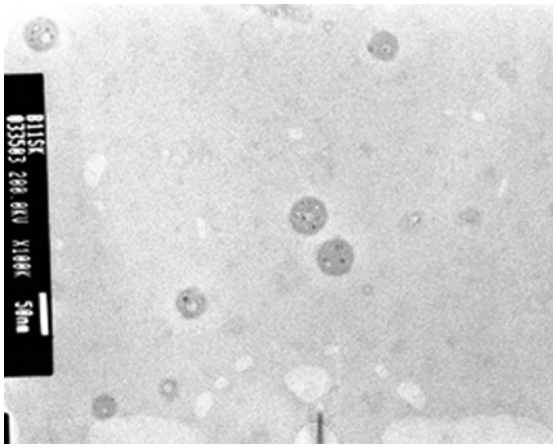


FIGURE 13.16 TEM image of the micelles; Mn(PBSt-*b*-PSt) = 15,000-*b*-97,000.

This section describes the self-assembly induced by the irreversible photoreactions of photolysis [96, 97], photo-Claisen rearrangement [98], and photoelectron transfer [99] for block copolymers supporting photoreactive groups.

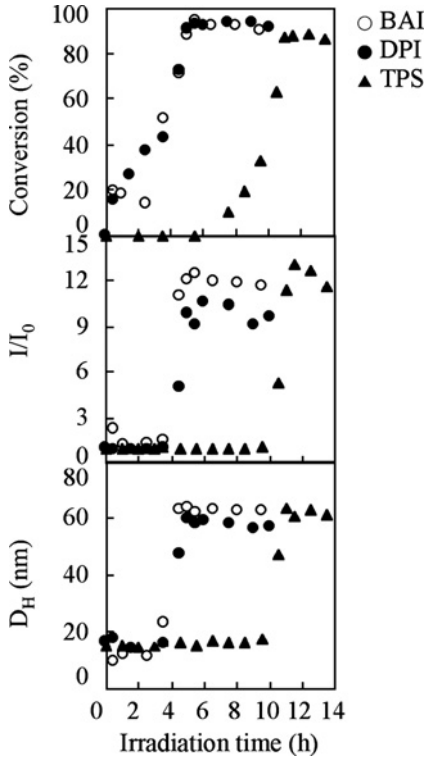


FIGURE 13.17 Variation in conversion, relative scattering intensity, and hydrodynamic diameter of the copolymer during irradiation in the presence of the photoacid generators; $[\text{copolymer}]_0$ = 3.30 g/L. Photoacid generator/BSt unit = 0.38.

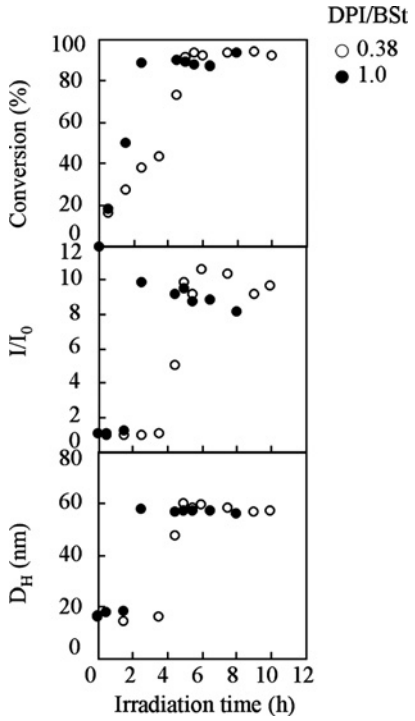


FIGURE 13.18 Variation in conversion, relative scattering intensity, and hydrodynamic diameter during irradiation at different DPI/BSt ratios; $[\text{copolymer}]_0$ = 3.30 g/L, Mn(PBSt-*b*-PSt) = 15,000-*b*-97,000.

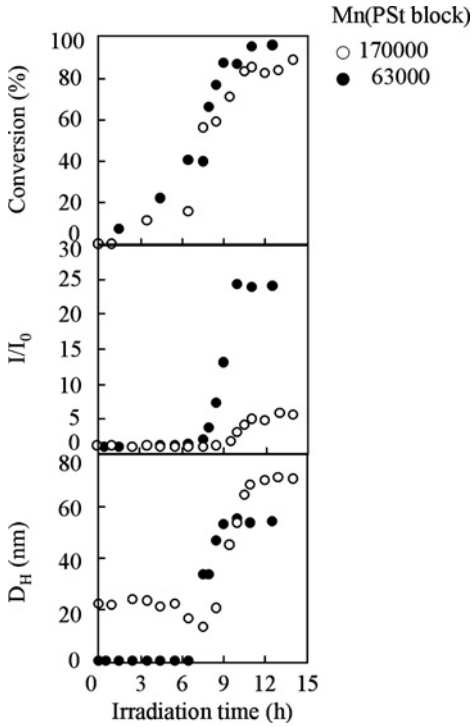


FIGURE 13.19 Variation in conversion, relative scattering intensity, and hydrodynamic diameter during irradiation using copolymers with different PSt block lengths; $[\text{copolymer}]_0$ = 3.30 g/L, DPI/BSt = 0.38.

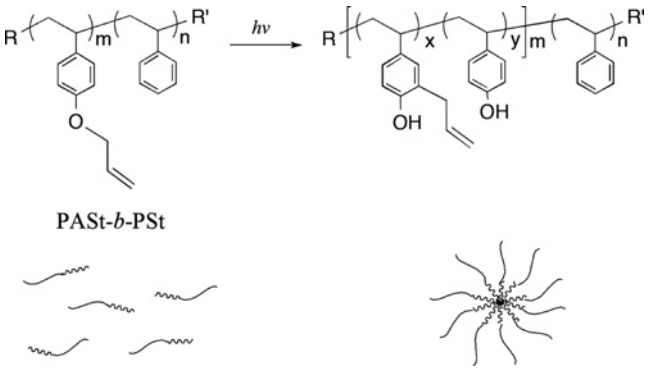


FIGURE 13.20 Photo-Claisen rearrangement-induced self-assembly of PASt-*b*-PSt.

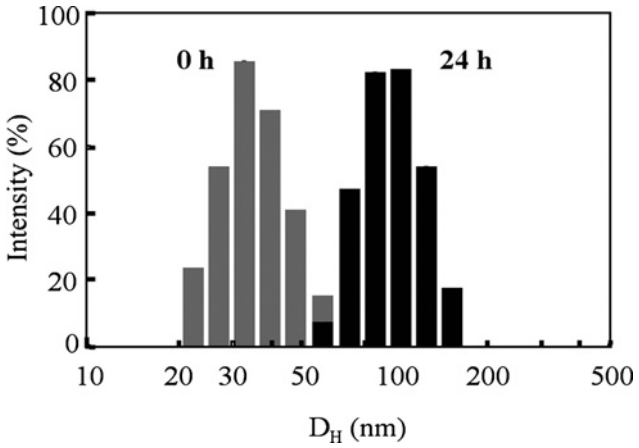


FIGURE 13.21 Scattering intensity distribution for the hydrodynamic diameter of the copolymer before and after irradiation. The irradiation time was 24 h; $[\text{copolymer}]_0 = 1.64$ g/L.

13.3.1 Photolysis-Induced Self-Assembly

Photolysis-induced self-assembly was established for a poly(4-*tert*-butoxystyrene)-*block*-polystyrene diblock copolymer (PBSt-*b*-PSt) that contained photodecomposable *tert*-butoxy groups [96, 97].

PBSt-*b*-PSt self-assembled into micelles in dichloromethane by irradiation in the presence of a photoacid generator of bis(alkylphenyl)iodonium hexafluorophosphate (BAI) (Fig. 13.14). Irradiation in the absence of BAI and the dark reaction in its presence produced no aggregates, indicating that the micellization was induced by the photolysis of *tert*-butoxy groups. The conversion of *tert*-butoxystyrene units into the vinyl phenol units [100] was confirmed by ^{1}H NMR. Figure 13.15 shows variation in the conversion of *tert*-butoxy groups to hydroxy groups, hydrodynamic diameter, and the

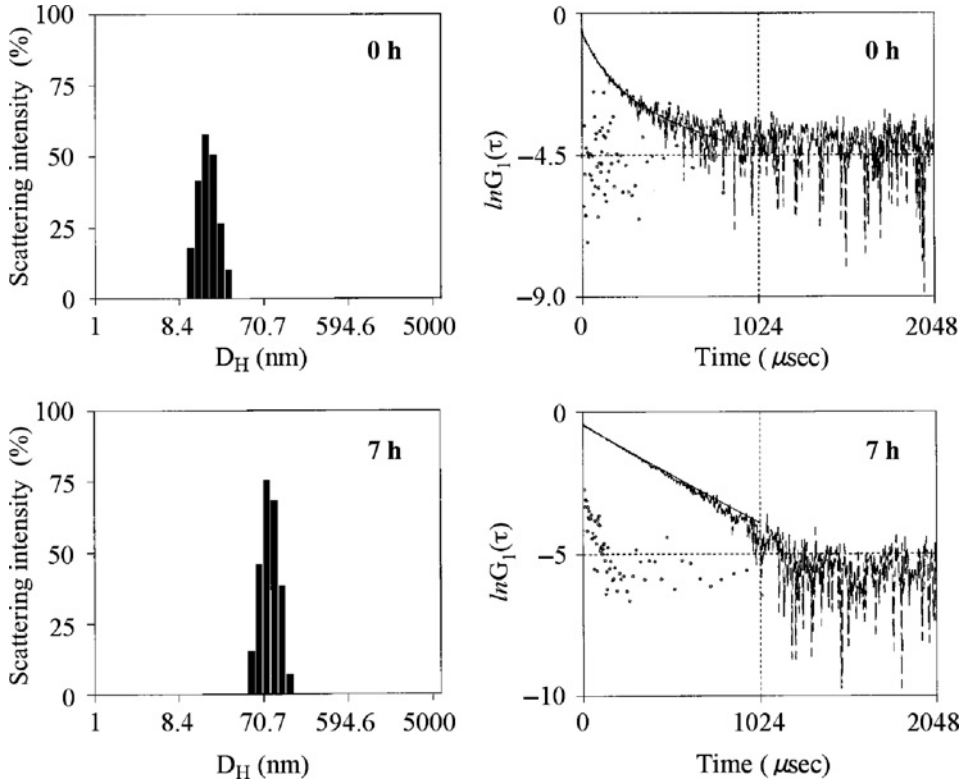


FIGURE 13.22 Scattering intensity distributions of the hydrodynamic diameter and plots of ln $G_1(\tau)$ versus τ for PPySt-*b*-PSt before (upper) and after irradiation for 7 h (lower); [PPySt-*b*-PSt] = 2.86 g/L

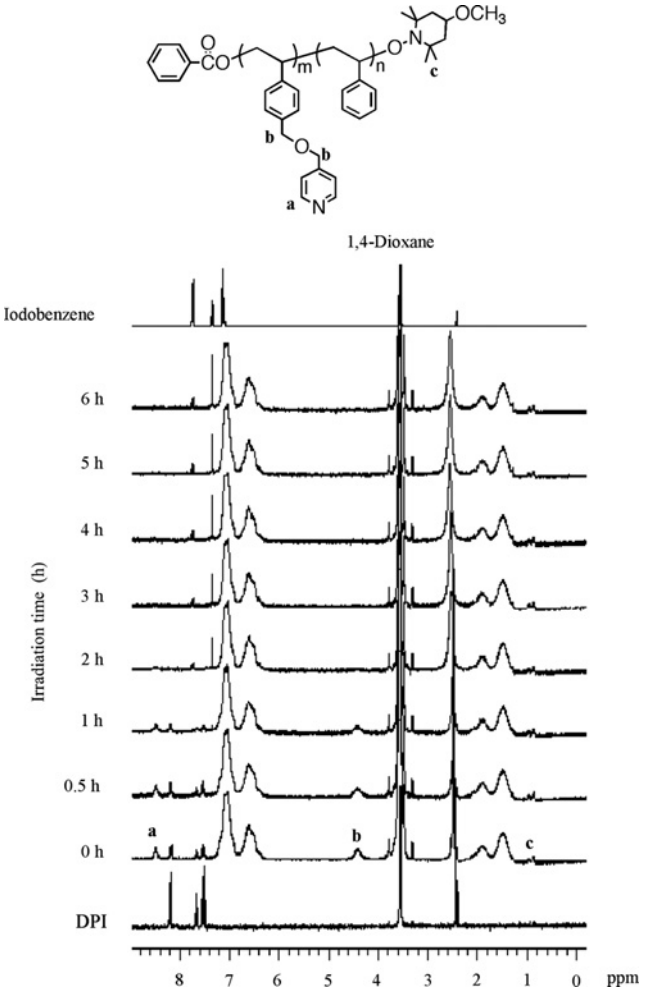


FIGURE 13.23 ^{1}H-NMR spectra of the copolymer during irradiation, DPI, and iodobenzene. Solvent: 1,4-dioxane-d_8; [PPySt-*b*-PSt] = 3.00 g/L.

relative scattering intensity of the copolymer during the irradiation in the presence of BAI. The good correlation of the plots of the hydrodynamic diameter and scattering intensity to the conversion indicated that the micellization occurred as photolysis of the *tert*-butoxy groups proceeded. The observation of the jump and the constant state within the short time period for the hydrodynamic diameter and scattering intensity suggests the rapid micellization due to the strong aggregation force of hydrogen bonding. The hydrodynamic diameter of the micelles averaged 63.0 nm, while that of the isolated copolymer was 16.6 nm. The TEM observations revealed that the photolysis-induced self-assembly provided spherical micelles (Fig. 13.16).

Micellization was also investigated using different kinds of photoacid generators, BAI, diphenyliodonium hexaflurophosphate (DPI), and triphenylsulfonium triflate (TPS) (Fig. 13.17). BAI and DPI produced a negligible difference in micellization, whereas TPS needed a longer irradiation time to promote micellization, in comparison. This difference among the photoacid generators in promoting micellization was based on their UV absorbance at 290 nm at which the photolysis proceeded; the photoacid generator that has a lower absorbance needed a longer irradiation time to initiate the micellization. It was found that the efficiency of the micellization was also dependent on the initial concentration of the photoacid generator. As shown in Fig. 13.18, the photoacid generator at a higher concentration provided a sharper and earlier transition during micellization, suggesting that the micellization was controlled by the concentration of the photoacid generator. The micellization was also controlled by the block length of the copolymer (Fig. 13.19). For the identical PBSt block length (Mn = 15,000), the copolymer with the shorter PSt block produced smaller micelles with a higher aggregation number.

More recently, the photolysis-induced self-assembly has also been determined using the photocleavage of *o*-nitrobenzyl esters contained in a poly(4,5-dimethoxy-2-nitrobenzyl acrylate)-*block*-PSt diblock copolymer [101]. They demonstarated that the micelles obtained by this self-assembly effectively encapsulated a fluorescent dye. Other coworkers found the self-assembly induced by photolysis involving the oxidation and reduction of an amphiphilic dendrimer consisting of oligo(*p*-phenylene vinylene) core branches and oligo(ethylene oxide) terminal chains [102]. This self-assembly was caused by the photooxidative cleavage of the double bond of the *p*-phenylene vinylene unit by oxygen, followed by the reduction of Au^{3+} ion into Au^0 by the hydroxy methyl radical generated by the photooxidation to produce the gold nanoparticles.

13.3.2 Photo-Claisen Rearrangement-Induced Self-Assembly

Photorearrangements have advantages in occurring without catalysts for a number of irreversible photochemical reactions. While a number of photorearrangements have been observed for *N*-aryl lactams [103, 104], the carboxylic acid derivatives of *N*-aryl amides [105,106], enol esters [107,108], enol lactones [109,110], and enamides [111,112] and the sulfonic acid derivative of *N*-aryl amides [113], the photo-Fries rearrangement [114–117], and photo-Claisen rearrangement [118, 119] have been investigated to determine the causes of the coloring of aromatic polyesters in sunlight and UV light [120].

Photo-Claisen rearrangement-induced self-assembly was performed using a poly(4-allyloxystyrene)-*block*-polystyrene (PASt-*b*-PSt) diblock copolymer. The allyloxystyrene units in PASt-*b*-PSt underwent photo-Claisen rearrangement in cyclohexane by irradiation at room temperature. However, it was revealed that the elimination of the allyl groups competitively occurred with the rearrangement (Fig. 13.20) [121]. No elimination occurred up to a ∼20%

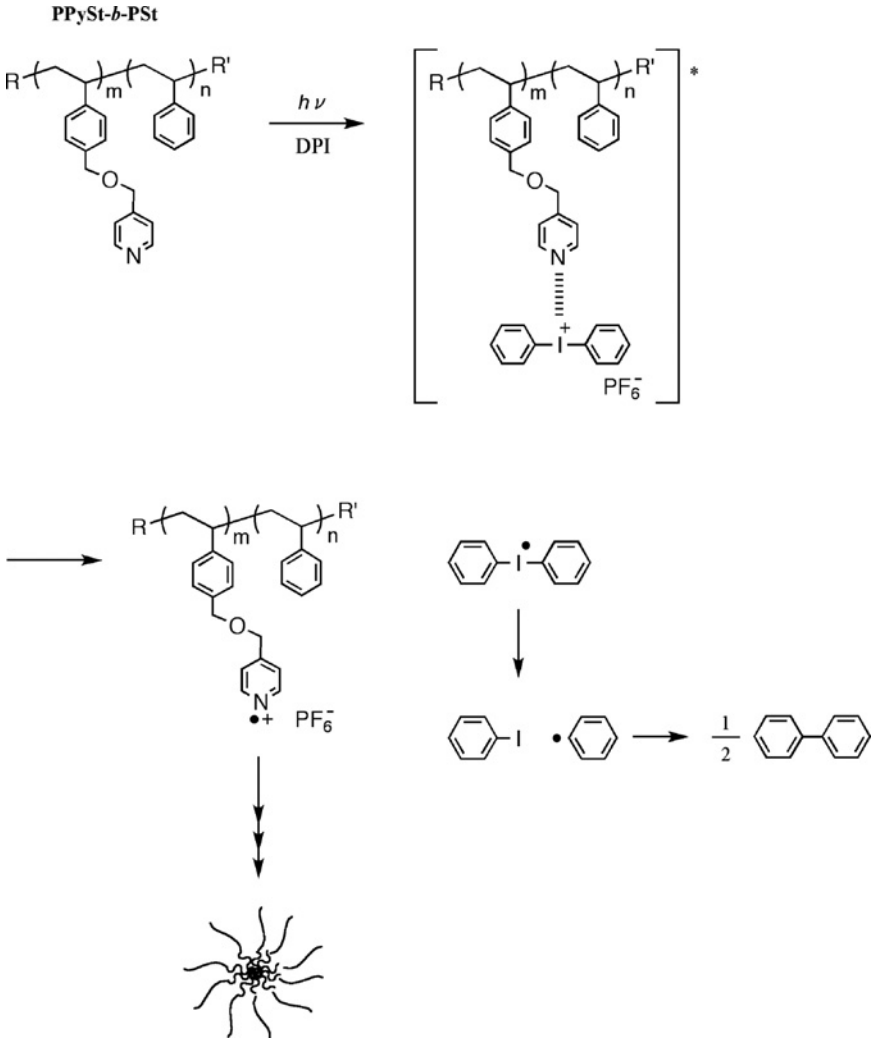


FIGURE 13.24 Photoreaction mechanism of PPySt-*b*-PSt and DPI.

conversion, and the quantitative rearrangement proceeded. However, over the 20% conversion, the elimination replaced the rearrangement and increased with the conversion. The rearrangement and elimination finally reached ∼50%. Light-scattering studies demonstrated that PASt-*b*-PSt formed micelles by this photoreaction. The scattering intensity distribution of the hydrodynamic diameter of the copolymer is shown in Fig. 13.21. Distribution of the hydrodynamic diameter of the isolated copolymers (35.3 nm) was shifted to that of the micelles (98.1 nm) by the reaction

13.3.3 Photoelectron Transfer–Induced Self-Assembly

The photoelectron transfer-induced self-assembly was attained through the photoreaction of the photoacid generator and electron donors. The diaryliodonium salt forms an exciplex with the electron donors and then undergoes photoelectron transfer from the electron donors to it to produce the cation radicals of the electron donors and the diaryliodine radical by the irreversible photodecomposition mechanism [122, 123].

A poly(4-pyridinemethoxymethylstyrene)-*block*-polystyrene (PPySt-*b*-PSt) diblock copolymer with the pyridine groups as the electron donors was irradiated at room temperature in 1,4-dioxane in the presence of DPI. The scattering intensity distributions and ln $G_1(\tau)$ versus τ for the copolymer solution before and after the reaction are shown in Fig. 13.22. $G_1(\tau)$ is the normalized time correlation function of the scattered field and is given by the following equation using $G_2(\tau)$, the time correlation function of the scattered intensity

$$G_2(\tau) = A(1 + \beta|G_1(\tau)|^2) \tag{13.1}$$

where A is a baseline that corresponds to the square of the average scattering intensity and β is an efficiency factor. The diameters of the micelles and isolated copolymers were estimated to be 68.9 nm and 27.2 nm, respectively. The copolymer was confirmed to form monodispersed spherical micelles based on the linear decay of the ln $G_1(\tau)$ value. For spherical particles with a monodispersity, $G_1(\tau)$ displays a single exponential decay curve and is represented by the following equations

$$G_1(\tau) = \exp(-\Gamma\tau) \tag{13.2}$$

$$\ln G_1(\tau) = (-\Gamma\tau) \tag{13.3}$$

where Γ is the decay constant and τ is the delay time [124]. ^{1}H-NMR analysis demonstrated that the micelles had cores formed by the PPySt blocks (Fig. 13.23). The signals originating from the pendant pyridinemethoxymethyl groups disappeared with the irradiation due to shielding of the PPySt core blocks by the PSt corona blocks. The signals of DPI also were replaced by signals of iodobenzene formed by the photodecomposition [122, 125, 126]. On the basis of the results that no micellization was induced by the irradiation of only DPI and by the dark reaction of the copolymer in the presence of DPI, the mechanism of the micellization was proposed (Fig. 13.24).

Variations in the signal intensity ratio of the methylene protons (b in Fig. 13.23) to the aromatic protons at 6.0–7.4 ppm in the ^{1}H NMR, hydrodynamic diameter, and scattering intensity during the micellization are shown in Fig. 13.25. The signal intensity reached zero at 4 h, while the hydrodynamic diameter and scattering intensity reached a steady state after 5 h, indicating that the micellization was completed within 5 h.

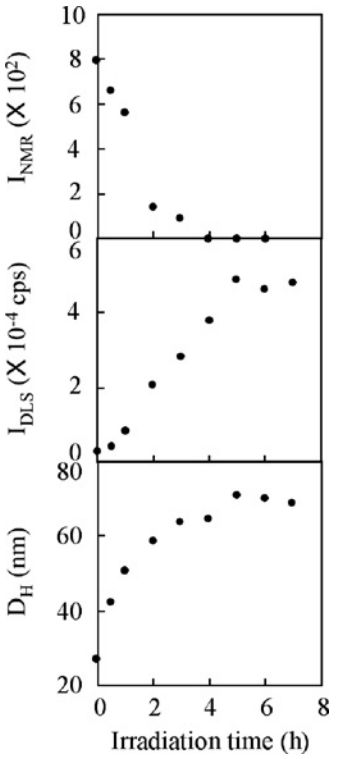


FIGURE 13.25 Variation in signal intensity ratio of methylene protons (**b** in Fig. 13.23) to the aromatic protons in ^{1}H NMR (I_{NMR}), scattering intensity (I_{DLS}), and hydrodynamic diameter of the copolymer during irradiation.

13.4 CONCLUSIONS

The biomimetic self-assembly induced by the chemical reactions occurring in vivo, such as electron transfer and irreversible photoreactions, was established using the block copolymers supporting the redox catalysts and photoreactive groups on the sidechains. These pendant groups were converted to solvophobic groups through these chemical reactions, resulting in the self-assembly of the copolymers. The reactions also involved the conversion of the pendant groups into other reactive groups to serve as an oxidant and reductant. The copolymers formed spherical micelles with some dozens of nanometers of hydrodynamic diameters by the self-assembly. Hence, the self-assembly induced by the chemical reactions provided nanoreactors of the spherical micelles with the functional groups supported on the core blocks. The chemical reactions employed as the trigger of the self-assembly in this study can be replaced by various reactions accompanied by the transfer of materials, electrons, photons, and energy. The significance and utility of the chemical reaction-induced self-assembly should increase as the applications of the functional nanoparticles formed by the self-assembly have expanded.

REFERENCES

[1] Anfinsen, C.B. (1973). *Science* **181**, 223–230.

[2] Bloomfield, V.A., Crothers, D.M.Tinoco, Jr., I. (1974). In *Physical Chemistry of Nucleic Acids*. Harper & Row, New York, pp. 83–102.

[3] Bar, R.S., Deamer, D.W., Cornwall, D.G. (1966). *Science* **153**, 1010–1012.

[4] Hofmann, A.F., Borgstrom, B. (1962). *Fed. Proc.* **21**, 43–50.

[5] Carlier, M.-F. (1988). *Cell Biophys*. **12**, 105–117.

[6] Didry, D., Carlier, M.-F., Pantaloni, D. (1998). *J. Biol. Chem.* **273**, 25602–25611.

[7] Chance, B. (1963). *Energy-Linked Functions of Mitochondria.* Academic Press, New York, pp. 51–73, 237–275.

[8] Hoffman, J.F. (1966). *Am. J. Med.* **41**, 666–680.

[9] Hoober, J.K. (1984). *Chloroplasts*. Plenum Press.

[10] Hochachka, P.W., Neely, J.R., Driedzic, W.R. (1977). *Fed. Proc.* **36**, 2009–2014.

[11] Griffiths, D.E. (1965). *Essays Biochem.* **1**, 9–120.

[12] Palczewski, K., Kumasaka, T., Hori, T., Behnke, C., Motoshima, B., Fox, A., Le Trong, I., Teller, T., Okada, T., Stenkamp, R.E., Yamamoto, M., Miyano, M. (2000). *Science* **289**, 739–745.

[13] Xie, J., Qin, M., Cao, Y., Wang, W. (2011). *Proteins* **79**, 2505–2516.

[14] Zhang, L., Eisenberg, A. (1995). *Science* **268**, 1728–1731.

[15] Ismael, M., Tondre, C. (1992). *Langmuir* **8**, 1039–1041.

[16] Yoon, K.A., Burgess, D.J. (1997). *J. Pharm. Pharmacol.* **49**, 478–484.

[17] Yin, H.Q., Zhou, Z.K., Huang, J.B., Zheng, R., Zhang, Y.Y. (2003). *Angew. Chem. Int. Ed.* **42**, 2188–2191.

[18] Majhi, P.R. Blume, A. (2011). *Langmuir* **17**, 3844–3851.

[19] Lowe, A.B., Billingham, N.C., Armes, S.P. (1997). *Chem. Commun.* 1035–1036.

[20] Yoshida, E., Ohta, M., Terada, Y. (2005). *Polym. Adv. Technol.* **16**, 183–188.

[21] Yoshida, E., Tanaka, M., Takata, T. (2005). *Colloid Polym. Sci.* **283**, 1100–1107.

[22] McClain, J.B., Canelas, D.A., Samulski, E.T., DeSimone, J.M., Londono, J.D., Cochran, H.D., Wignall, G.D., Chillura-Martino, G.D., Triolo, R. (1996). *Science* **274**, 2049–2052.

[23] Zhou, S., Chu, B. (1998). *Macromolecules* **31**, 5300–5308.

[24] Celso, L., Triolo, A., Triolo, F., Donato, D.I., Steinhart, M., Kriechbaum, M., Amenitsch, H., Triolo, R. (2002). *Eur. Phys. J. Soft Matter* **8**, 311–314.

[25] Yoshida, E., Nagakubo, A. (2007). *Colloid Polym. Sci.* **285**, 441–447.

[26] Yoshida, E., Mineyama, A. (2012). *Colloid Polym. Sci.* **290**, 183–187.

[27] Lee, A.S., Butun, V., Vamvakaki, M., Armes, S.P., Pople, J.A., Gast, A.P. (2002). *Macromolecules* **35**, 8540–8551.

[28] Liu, S., Weaver, J.V.M., Tang, Y., Billingham, N., Armes, S.P. (2002). *Macromolecules* **35**, 6121–6131.

[29] Hu, Y., Kramer, M.C., Boudreaux, C.J., McCormick, C.L. (1995). *Macromolecules* **28**, 7100–7106.

[30] Martin, T.J., Prochazka, K., Munk, P., Webber, S.E. (1996). *Macromolecules* **29**, 6071–6073.

[31] Gohy, J.F., Lohmeijer, G.G., Varshney, S.K., Decamps, B., Leroy, E., Boileau, S., Schubert, U.S. (2002). *Macromolecules* **35**, 9748–9755.

[32] Liu, S., Zhang, G., Jiang, M. (1999). *Polymer* **40**, 5449–5453.

[33] Gohy, J.F., Varshney, S.K. Jerome, R. (2001). *Macromolecules* **34**, 3361–3366.

[34] Brontein, L.M., Sidorov, S.N., Valetsky, P.M. (1999). *Langmuir* **15**, 6256–6262.

[35] Zhao, H., Douglas, E.P. (2002). *Mater. Res. Soc. Symp. Proc.* **2002**, 43–48.

[36] Yoshida, E., Kunugi, S. (2002). *Macromolecules* **35**, 6665–6669.

[37] Yoshida, E., Terada, Y. (2005). *Colloid Polym. Sci.* **283**, 1190–1196.

[38] Yoshida, E., Tanaka, M., Takata, T. (2005). *Colloid Polym. Sci.* **284**, 51–57.

[39] Lehninger, A.L., Reynafarje, B., Alexandre, A., Villalobo, A. (1980). *Ann. NY Acad. Sci.* **341**, 585–592.

[40] Erecinska, M., Wilson, D.F. (1982). *J. Membr. Biol.* **70**, 1–14.

[41] Capaldi, R.A. (1982). *Biochim. Biophys. Acta* **694**, 291–306.

[42] Chan, S.I., Li, P.M. (1990). *Biochemistry* **29**, 1–12.

[43] Alexandre, A., Reynafarje, B., Lehninger, A.L. (1978). *Proc. Natl. Acad. Sci.* **75**, 5296–5300.

[44] Slater, E.C. (1983). *Trends Biochem. Sci.* **8**, 239–242.

[45] Eitouni, H.B., Balsara, N.P. (2006). *J. ACS* **128**, 16248–16252.

[46] Rider, D.A., Winnik, M.A., Manners, I. (2007). *Chem. Commun.* **2007**, 4483–4485.

[47] Black, K.C.L., Liu, Z., Messersmith, P.B. (2011). *Chem. Mater.* **23**, 1130–1135.

[48] Xiong, W., Wang, H., Han, Y. (2011). *Soft Matter* **7**, 8516–8524.

[49] Golubev, V.A., Rozantsev, E.G., Neiman, M.B. (1965). *Bull. Acad. Sci. USSR Div. Chem. Sci.* **14**, 1898–1904.

[50] Hageman, HJ., Overeem, T. (1981). *Makromol. Chem. Rapid Commun.* **2**, 719–724.

[51] Hubbell, W.L., Metcalfe, J.C., Metcalfe, S.M., McConnell, H.M. (1970). *Biochim. Biophys. Acta* **219**, 415–427.

[52] Georges, M.K., Veregin, R.P.N., Kazmaier, P.M., Hamer, G.K. (1993). *Macromolecules* **26**, 2987–2988.

[53] Yoshida, E., Sugita, A. (1996). *Macromolecules* **29**, 6422–6426.

[54] Yoshida, E. (2009). *Colloid Polym. Sci.* **287**, 767–772.

[55] Yoshida, E. (2010). *Colloid Polym. Sci.* **288**, 239–243.

[56] Liu, Y.C., Wu, L.M., Chen, P. (1985). *Tetrahedron Lett.* **26**, 4201–4202.

[57] Golubev, V.A., Rozantsev, E.G., Neiman, M.B. (1965). *Izv. Akad. Nauk SSSR Ser. Khim.* **1965**, 1927–1936.

[58] Yoshida, E., Takata, T., Endo, T. (1992). *J. Polym. Sci. A: Polym. Chem.* **30**, 1193–1197.

[59] Yoshida, E., Takata, T., Endo, T. (1992). *Macromolecules* **25**, 7282–7285.

[60] Rozantsev, E.G., Golubev, V.A. (1966). *Izv. Akad. Nauk SSSR Ser. Khim.* **1966**, 891–896.

[61] Guranova, V.V., Kovarsksaya, B.M., Krinitzkaya, L.A., Neiman, M.B., Rozantsev, E.G. (1965). *Vysokomol. Soedin.* **7**, 1515–15191.

[62] Brik, M.E. (1990). *Synth. Commun.* **20**, 3283–3287.

[63] Paleos, C.M., Dais, P. (1977). *Chem. Commun.* **10**, 345–346.

[64] Zhdanov, R.I., Golubev, V.A., Gida, V.M., Rozantsev, E.G. (1971). *Dokl. Akad. Nauk SSSR* **196**, 856–857.

[65] Yoshida, E., Ishizone, T., Hirao, A., Nakahama, S., Takata, T., Endo, T. (1994). *Macromolecules* **27**, 3119–3124.

[66] Paper, I., Bobbitt, J.M., Cecile, M., Flores, L. (1988). *Heterocycles* **27**, 509–533.

[67] Yoshida, E., Nakamura, K., Takata, T., Endo, T. (1993). *J. Polym. Sci. A: Polym. Chem.* **31**, 1505–1512.

[68] Yoshida, E., Tanaka, T. (2006). *Colloid Polym. Sci.* **285**, 135–144.

[69] Miyazawa, T., Endo, T., Shiihashi, S., Ogawara, M. (1985). *J. Org. Chem.* **50**, 1332–1334.

[70] Yoshida, E., Takata, T., Endo, T. (1993). *Makromol. Chem.* **194**, 2507–2515.

[71] Yoshida, E., Yamaguchi, M., Takata, T., Endo, T. (1993). *Makromol. Chem.* **194**, 1307–1314.

[72] Yoshida, E., Takata, T., Endo, T., Ishizone, T., Hirao, A., Nakahama, S. (1994). *Chem. Lett.* 1827–1828.

[73] Rozenberg, V.I., Piotrovskii, V.K., Golubev, V.A., Gvon, K.I., Nikanorov, V.A., Bundel, Y.G., Reutov, O.A. (1975). *Russ. Chem. Bull. (Bull. Acad. Sci. USSR Div. Chem. Sci.)* **24**, 2508–2509.

[74] Yoshida, E., Tanaka, T. (2008). *Colloid Polym. Sci.* **286**, 827–830.

[75] Miyazawa, T., Endo, T., Okawara, M. (1985). *J. Org. Chem.* **50**, 5389–5391.

[76] Yoshida, E., Ogawa, H. (2007). *J. Oleo Sci.* **56**, 297–302.

[77] Yoshida, E. (2009). *Colloid Polym. Sci.* **287**, 1365–1368.

[78] Zhuang, X., Xiao, C., Oyaizu, K., Chikushi, N., Chen, X., Nishide, H. (2010). *J. Polym. Sci. A: Polym. Chem.* **48**, 5404–5410.

[79] Nagasaki, Y. (2012). *Ther. Deliv.* **3**, 165–179.

[80] Hauffman, G., Magiun, Q., Bourgeois, J.-P., Vlad, A., Gohy, J.-F. (2014). *Macromol. Rapid Commun*. **35**, 228–233.

[81] Lovrien, R. (1967). *Proc. Natl. Acad. Sci. USA* **57**, 236–242.

[82] Matejka, L., Dusek, K. (1981). *Makromol. Chem.* **182**, 3223–3236.

[83] Pieroni, O., Fissi, A. (1992). *J. Photochem. Photobiol. B: Biol.* **12**, 125–140.

[84] Menju, A., Hayashi, K., Irie, M. (1981). *Macromolecules* **14**, 755–758.

[85] Taguchi, M., Li, G., Gu, Z., Sato, O., Einaga, Y. (2003). *Chem. Mater.* **15**, 4756–4760.

[86] Meier, H. (1992). *Angew. Chem. Int. Ed. Engl.* **31**, 1399–1420.

[87] Szczubialka, K., Nowakoaska, M. (2003). *Polymer* **44**, 5269–5274.

[88] Eastoe, J., Sanchez, M., Dominguez, S., Wyatt, P., Beeby, A., Heenan, R. (2002). *Langmuir* **18**, 7837–7844.

[89] Irie, M., Hosoda, M. (1985). *Makromol. Chem. Rapid Commun.* **6**, 533–536.

[90] Dunkin, I.R., Gittinger, A., Sherrington, D.C., Whittaker, P. (1994). *J. Chem. Soc. Chem. Commun.* **1994**, 2245–2246.

[91] Mezger, T., Nuyken, O., Meindl, K., Wokaun, A. (1996). *Progress. Org. Coat.* **29**, 147–157.

[92] Nuyken, O., Voit, B. (1997). *Macromol. Chem. Phys.* **198**, 2337–2372.

[93] Haubs, M., Ringsdorf, H. (1987). *New J. Chem.* **11**, 151–156.

[94] Okamoto, Y., Yoshida, H., Takamuku, S. (1988). *Chem. Lett.* **1988**, 569–572.

[95] Veronese, A., Berclaz, N., Luisi, P.L. (1998). *J. Phys. Chem. B* **102**, 7078–7080.

[96] Yoshida, E., Kuwayama, S. (2007). *Colloid Polym. Sci.* **285**, 1287–1291.

[97] Yoshida, E., Kuwayama, S. (2008). *Colloid Polym. Sci.* **286**, 1621–1627.

[98] Yoshida, E., Kuwayama, S. (2009). *Colloid Polym. Sci.* **287**, 789–793.

[99] Yoshida, E., Kuwayama, S., Kawaguchi, S. (2010). *Colloid Polym. Sci.* **288**, 91–95.

[100] Conlon, D.A., Crivello, J.V., Lee, J.L., O'Brien, M.J. (1989). *Macromolecules* **22**, 509–516.

[101] Bertrand, O., Schumers, J.-M., Kuppan, C., Marchand-Brynaert, J., Fustin, C.-A., Gohy, J.-F. (2011). *Soft Matter* **7**, 6891–6896.

[102] Chang, D.W., Dai, L. (2007). *Nanotechnology* **18**, 365605.

[103] Fischer, M. (1968). *Tetrahedron Lett.* **9**, 4295–4298.

[104] Fischer, M., Mattheus, A. (1969). *Chem. Ber.* **102**, 342–350.

[105] Bellus, D.; Schaffner, K. (1968). *Helv. Chim. Acta* **51**, 221–224.

[106] Kan, R.O., Furey, R.L. (1966). *Tetrahedron Lett*. **7**, 2573–2578.

[107] Finnegan, R.A., Hagen, A.W. (1963). *Tetrahedron Lett*. **4**, 365–368.

[108] Gorodetsky, M., Mazur, Y. (1964). *J. ACS* **86**, 5213–5218.

[109] Yogev, A., Mazur, Y. (1965). *J. ACS* **87**, 3520–3521.

[110] Rigaudy, J., Derible, P. (1965). *Bull. Chem. Soc. Fr.* 3047–3054.

[111] Eschenmoser, A. (1963). *Pure Appl. Chem.* **7**, 297–316.

[112] Bertele, E., Boos, H., Dunitz, J.D., Elsinger, F., Eschenmoser, A., Felner, I., Gribi, H.P., Gschwend, H., Meyer, E.F., Pesaro, M., Scheffold, R. (1964). *Angew. Chem.* **76**, 393–399.

[113] Nozaki, H., Okada, T., Noyori, R., Kawanishi, M. (1966). *Tetrahedron* **22**, 2177–2180.

[114] Pitchumani, K., Warri, M., Ramamurthy, V. (1996). *J. ACS* **118**, 9428–9429.

[115] Anderson, J.C., Reese, C.B. (1960). *Proc. Chem. Soc*. 217.

[116] Arai, T., Tobita, S., Shizuka, H. (1994). *Chem. Phys. Lett.* **223**, 521–526.

[117] Magdy, M., Malik, A., Mayo, P. (1983). *Can. J. Chem.* **62**, 1275–1278.

[118] Pincock, A.L., Pincock, J.A., Stefanova, R. (2002). *J. ACS* **124**, 9768–9778.

[119] Sanchez, A.M., Veglia, A.V., Rossi, R.H. (1997). *Can. J. Chem.* **75**, 1151–1155.

[120] Miranda, M.A. (1995). In Horspool, W.M., Song, P.S. (eds.), *CRC Handbook of Organic Photochemistry and Photobiology.* CRC Press, Boca Raton, FL, p. 570.

[121] Pitchumani, K., Warrier, M., Ramamurthy, V. (1999). *Res. Chem. Intermed.* **25**, 623–631.

[122] Crivello, J.V. (1999). *J. Polym. Sci. A: Polym. Chem.* **37**, 4241–4254.

[123] Crivello, J.V., Lam, J.H.W. (1978). *J. Polym. Sci. Polym. Chem.* **16**, 2441–2451.

[124] Brown, W. (1996). *Light Scattering Principles and Development*. Clarendon Press, Oxford, UK, pp. 439–442.

[125] Crivello, J.V., Lam, J.H.W., Volante, C.N. (1977). *J. Radiat. Curing* **4**, 2–16.

[126] Kellmann, A. (1974). *Photochem. Photobiol.* **20**, 103–108.

14

MOLECULAR INTERACTION IN BIOMIMETICS AND BIOSYSTEMS: CHIRALITY AND CONFINEMENT AT NANODIMENSION

Nilashis Nandi and Saheb Dutta
Department of Chemistry, University of Kalyani, West Bengal, India

14.1 INTRODUCTION

Biological systems have intrigued scientists since the beginning of scientific development. Natural bioystems fascinated the human intellect, and knowledge gleaned from the scientific studies of fundamental and applied aspects of various natural systems always remained tremendously beneficial for the development of civilization. Biological systems are inherently complex. Here, the term *complex* signifies that biosystems, in their natural state, possess the features described below. A complex biosystem is heterogeneous and multicomponent, with each component interacting with the others, and where the overall properties of the biosystem are significantly different from those of individual components. Common examples are proteins, nucleic acids, and membranes in their functional form such as present in a living cell. These molecules are present in an aqueous environment and often act together to complement or complete a particular life process. For example, membrane proteins are often part of the biological membrane, and the amphiphilic membrane structure is coupled with an aqueous environment. Similarly, protein and nucleic acids (RNA and DNA) are often fully active in aqueous media as present in cell. The structure and function of protein and nucleic acid deviate from their native state without the presence of surrounding aqueous environment. Moreover, often protein and nucleic acid interact to complete a bioprocess such as protein synthesis. Consequently, these systems are inherently complex. A complete understanding of such complex systems is impossible without the understanding of the interactions driving the structure and functions of these systems. Although the origin of the intermolecular interaction in all systems is invariably electromagnetic in nature, its manifestations in diverse physicochemical systems are of bewildering variety. Because of several factors such as variation in the charge distribution from one system to the other, diverse spatial geometry or topology of atoms, proximity and orientation of the neighboring nonbonded atoms, and interactions between groups or individual molecules, the resulting properties are often remarkable. Hence, studies of intermolecular interactions in complex biological systems and in relatively simple model mimetic systems as well, continue to attract attention. Such studies are not only of fundamental interest but are also important in developing bioinspired materials.

The structural aspects of biomolecules such as their chirality or dissymmetry often lead to unusual distance and orientation dependence of the interaction and resulting properties of the biomolecules are exotic. The proximity of the molecules in biosystems is another important factor in controlling their functionality. Confinement at nanolength scale augments the orientation dependence of intermolecular interaction in biomimetic and biological systems. The present review in this chapter starts with a discussion on the recent computational and experimental studies in biomimetic and biological systems where chirality and confinement lead to novel phenomena. The scientific knowledge gained from the related studies has biotechnological implication that such knowledge may be useful in developing new bioinspired materials.

Encyclopedia of Biocolloid and Biointerface Science, Volume 1, First Edition. Edited by Hiroyuki Ohshima.
© 2016 John Wiley & Sons, Inc. Published 2016 by John Wiley & Sons, Inc.

Although chirality has ubiquitous presence in nature, its importance in intermolecular interaction is less frequently emphasized. It can be seen at the macroscopic length scale in plants and animal kingdoms, such as symmetry in patterns as well as shapes of leaves, respectively, and physiological features of various animals. It is a geometric property of various natural (as well as nonnatural) objects that renders them nonidentical and nonsuperimposable with their own mirror images. This broad definition of chirality includes diverse macroscopic objects such as hands (the word *chirality* originated from the Greek word *cheir*, meaning *hand*), animal organs, biological organisms, and macromolecules as well as microscopic objects such as various molecules as chiral entities [1–5]. If the object lacks an improper or alternating axis of symmetry, including both a center of symmetry and a plane of symmetry, then it is chiral [3, 4]. A necessary and sufficient condition for a molecule to be chiral is that it cannot be superimposed on its mirror image. A molecule possessing an asymmetrically substituted carbon atom is a common example of a chiral molecule. Thus objects of various length scales starting from macroscopic objects mentioned before, then mesoscopic objects (such as small to medium-sized aggregates of molecules) as well as small molecules could be chiral entities. Various molecules important for life such as protein, nucleic acid, lipids, and carbohydrates are chiral. Biochirality is thus all-pervasive in natural systems [6, 7]. A closer look at the structural hierarchy of biomolecules draws our attention to the fundamental and applied importance of chirality in life and qualitatively draws our attention to the structure function relationship in biology [8, 9].

The functionality of biomolecules is expected to depend on chirality. Naturally, biochirality is an intriguing aspect of life from various perspectives [1, 2, 6, 7, 10]. Since most of the functional biomolecules are chiral, the influence of chirality is observed at the molecular level in numerous biosynthetic pathways. However, the origin of biological homochirality has remained a fundamental unresolved problem [10]. Progress toward a quantitative understanding of the origin of the chiral preference or discrimination is challenging. Beyond the interest in developing a fundamental understanding of the origin and importance of overwhelming chiral discrimination observed in nature, knowledge about chirality-dependent interactions has practical significance as these interactions are important for catalysis, chiral polymer transition metal complexes, and asymmetric synthesis [11–14]. Understanding of chirality-dependent interactions in the reaction center of enzymes might play a tremendously important role in developing useful materials inspired by such biosystems. One well-known example of the importance of biochirality is noted in protein biosynthetic pathway. Although the relevance of chirality in this pathway seems obvious, considering the involvement of a number of chiral molecules in various steps, several questions remain unanswered concerning the role of biochirality in protein biosynthesis. It is to be noted that not only the proteinous active site but also the active site composed of nucleic acids (such as ribosomal transferase center) exhibit chirality dependent effects. Thus, chiral discrimination might be a general phenomenon exhibited by enzymes [1]. Active sites are cavities or clefts where the biological reaction takes place, and a number of active sites exhibit remarkable capacity of discrimination of noncognate substrates, including incorrect enantiomeric forms. Importantly, the confinement of substrates in the nanodimensional space of the active site plays an important role in the efficiency, accuracy, and speed of the biochemical reaction and the rejection of the non-cognate substrate.

Stringent chiral discrimination occurs within the enzymatic active site. Analyses of the molecular organization of the active-site structure and of the related interactions are useful in understanding the chiral specificity of enzymatic reactions. Crystallographic analysis provided clear insight into the microscopic organization of the enzymatic structures. Electronic-structure-based computations and molecular dynamics studies provided a unified perspective on the enzymatic reactions. The wealth of information provides a platform for analysis of the origin of the chiral preference exhibited by various enzymes. Enzymatic active sites are nanoflasks where vital biological reactions take place, and it is instructive to look into the molecular processes therein so that one can learn about the generic mechanisms used by these natural devices to utilize the cognate substrate and reject the others in a fast and accurate way. Although different enzymes and even enzymes in a given class can catalyze reactions of bewildering variety, studies so far offer great promise in identifying the role of chirality in the biological reactions and in following the fundamental correlation between chirality and life. Notably, the mechanism of discrimination between substrates is key to the ability of the enzymes to act as efficient biocatalysts. This mechanism is difficult to match by synthetic design, and this fact provides impetus for further study of the origin of enzymatic chiral discrimination. Interestingly, significant knowledge about chiral discrimination and interactions between molecules confined within a nanolength scale is gained from biomimetic systems, and hopefully this knowledge can be applied to understanding more complex systems.

Bilayers and monolayers are excellent models of biological membranes that exhibit fascinating chirality-dependent phenomena [15–20]. A number of biomimetic systems exhibit fascinating morphologies driven by the chiral structure of the constituent molecules. There has been significant progress toward understanding these systems through theoretical and computational studies. The constituents of the biological membranes such as lipids, cholesterols, and proteins are intrinsically chiral. It is no surprise that chirality plays an important role in the structure and function of biomembranes. The relationship between chirality and

morphology (as well as function) of biological membrane has fundamental importance. Mimics of biological membranes have technological implications, and detailed knowledge of the chirality-induced effects is essential for such future technological developments. The studies on simpler membrane-mimetic monolayer and bilayer membranes revealed that orientation-dependent interactions between molecules that are confined in a nanodimension exhibit interesting chiral discrimination effects. Diverse monolayer domain shapes formed from chiral amphiphiles draws our attention to the complicated interplay of intermolecular interactions and how these interactions lead to chiral discrimination. The origin of biological homochirality (predominance of only one enantiomeric form of amino acid and sugar rather than the corresponding racemic forms) is related to chiral discrimination and is a fundamental unresolved problem. This remained as a subject of intensive research [2,10]. Heteropairing of amino acid (L-enantiomer) and sugar (D-enantiomer) in today's living world is preferred by evolution. It is important to note that amino acids and sugars can racemize in aqueous medium, which could be a part of the prebiotic environment. This contradiction poses a problem in understanding the development of the enantiomeric excess of sugar and amino acids in either D or L form, respectively, as well as the retention of the same. One can define homochiral preference in biomimetic systems when interaction between same enantiomeric pairs (D–D or L–L) is favored over that between mirror-image pairs (D–L interaction). If homochiral interaction is strong, chiral phase separation may result from a racemic mixture, which is a chiral symmetry breaking or chiral segregation. On the other hand, heterochiral preference occurs where D–L interaction is preferred over D–D or L–L interaction. An understanding of the intermolecular interaction that controls the discrimination in biomimetic systems is expected to be useful in understanding the discrimination in biological systems.

The understanding gained from the recent computational studies described in the present review is that the restriction of free rotation of the amphiphile molecules at the air–water interface augments the orientation and distance dependence of intermolecular interaction. This ensures that the effect of chirality on the mesoscopic length scale organization of the amphiphilic aggregate is significant. These studies indicate that discrimination is manifested in confined spaces compared to that in the bulk phase and the restriction of dynamical motions (free rotation or translation) enhance the discrimination. Biological reactions occur in confined nanodimensional spaces. It involves L-amino acids and D-sugars (when natural chirality is relevant) and is significantly influenced by the chirality of the constituent molecules. Of the many examples of reactions, a few are relevant to protein biosynthesis, including transamination reaction, aminoacylation reaction, and peptide synthesis. Evidence of observable chiral discrimination in these reactions is available [2, 21–24]. These life processes (particularly the generation and retention of chiral structure of fundamental biological building blocks such as amino acids and peptides) is unlike the processes as observed in in vitro chemical reactions where the formation of racemic molecule is commonly favored over the enantiopure molecule.

As a specific example, we reiterate the progress of protein biosynthesis where influence of molecular chirality is significant. It is common wisdom that proteins are chiral at the primary level (length scale of the constituent amino acids), secondary (length scale of helix and β sheets) and higher (tertiary and quaternary) structural levels. In each case, both the basic building blocks and the architectures formed by such blocks are chiral. At the structural hierarchy of protein, only one enantiomer at the primary level renders the corresponding higher-level biological structure functional. Change in the enantiomeric form of the primary level is lethal for the functionality of the higher-level structure of protein. Protein biosynthesis is a multistep process and involves a number of small molecules such as amino acids, sugar, and adenosine triphosphate as well as large macromolecules such as synthetase, messenger mRNA, and transfer tRNA [8, 9]. Not only are protein molecules themselves chiral; most of the molecules involved in the process of protein synthesis are also chiral. It is tempting to conclude that chirality might have significance in the progress of the reaction. Molecular chirality influences the efficiency and accuracy of the process, rather than remaining as a structural feature developed randomly and without any specific purpose in nature. Rather, the chirality of the macromolecular protein structure and chirality of its constituent primary structural elements are assumed to influence its various functions such as molecular recognition and reactions performed by proteins. However, several lacunae of knowledge exist in understanding the recognition of other molecules, and reactions performed by them. The origin of the predominant homochirality in the protein structure and retention of enantiopurity (overwhelming L form of amino acid in the primary sequence) in protein structure and relationship of the chiral structure of protein with its functionality are less frequently explored.

With this end in view, we shall present a brief account of experimental works on chiral discrimination in biomimetic monolayers and protein biosynthesis systems. We present an overview of the recent computational studies that focus on influence of microscopic chirality on mesoscale structures in biomimetic systems such as monolayers and how the chirality of the reacting molecular segment influences the progress of protein biosynthesis. Studies have revealed that confinement at nanometer length scale enhances the chiral discrimination. Notably, these observations are related to the problem of understanding the correlation of chirality at various levels of structural hierarchy and the problem of understanding the retention of biological homochirality and the

heterochiral relationship between L-amino acid and D-sugar. In the following section we describe the scheme of the theoretical calculation applied to these systems.

14.2 METHODS OF THEORETICAL CALCULATION

We will discuss how the most notable feature of the domains formed from enantiomeric chiral amphiphiles is their curvature or handedness, and the absence of curvature is noted in the racemic state. Further, the domains are formed in the condensed phase where molecules are in close proximity. A focus of recent theoretical efforts in the case of biomimetic systems was to correlate the intermolecular interaction energy with the orientation and distance between neighboring chiral amphiphilic molecules [15–20]. The objective is to find the most favorable mutual orientation at various separations when a pair of molecules is in their minimal energy state and the individual molecules are in their most probable conformational state. For large molecules such as amphiphiles, the potential energy is a function of a large number of degrees of freedom. In principle, the intermolecular energy profile should be calculated as a function of all intra- as well as intermolecular degrees of freedom, which are relevant to the interface. However, the chirality induced effects are not significantly dependent on many of them. The theoretical calculations are performed at various degrees of consideration of molecular details, ranging from effective sphere, coarse-grained, to atomistic models [16]. Theory assumes that the intermolecular pair potential determines the mesoscopic chiral structure of the condensed-phase domain. This model has been successfully applied to monolayers and bilayers [15–20] and is described in this review.

The influence of the chirality on intermolecular interaction in biological reactions such as peptide synthesis and amino acylation reaction is studied based on the crystal structures of the active sites of the corresponding enzymes. The influence of chirality on the course of ribosomal peptide synthesis process is studied in a model of peptidyl transferase center in *Haloarcula marismortui* [25]. Similarly, the influence of chirality and electrostatic interaction in the first step of aminoacylation process is studied based on the crystal structure of the oligomeric complex of histidyl-tRNA synthetase from *Escherichia coli* complexed with ATP and histidinol and histidyl-adenylate [26]. The structural optimizations and the transition-state structure optimizations are performed using quadratic synchronous transient method 3 (QST3) [27–29], employing hybrid quantum-mechanical–semiempirical–molecular-mechanical theory (QM/MM). Transition states are identified using the frequency calculation and the presence of single imaginary frequency. The Gaussian suite [30] of programs is used in several calculations.

14.3 CHIRAL DISCRIMINATION IN BIOMIMETIC MONOLAYERS

In this section we present an overview of the recent results of the study of the chiral discrimination in amphiphilic monolayer using a combined hybrid quantum-mechanical–molecular-mechanical model. Earlier studies using classical theory–based computations using effective pair potential theory or coarse-grained models revealed that 1-*O*-hexadecyl glycerol (3-hexadecyl-oxy-propane-1,2-diol) monolayers exhibit an interesting crossover from heterochiral preference to homochiral preference and is consistent with the experimentally observed discrimination effects based on optical studies. It is interesting to note that both homochiral and heterochiral preferences can be observed in a particular monolayer system such as hexadecyl glycerol.

Significant orientation dependence of chiral discrimination is observed, which indicates that discrimination effects are dependent not only on intermolecular separation but also on their mutual orientation [31]. Monolayers of 1-stearoylamineglycerol [32] exhibit interesting chiral discrimination effects. The filigree-shaped domains of the *R*(+) enantiomers are curved clockwise, and those of the *S*(−)-enantiomers are curved anticlockwise (Fig. 14.1).

The appearance of curvatures in opposite directions indicates homochiral preference. On the other hand, the racemic mixtures form fractal-like domains without any specific curvature, suggesting heterochirality. The variation of the intermolecular interaction for the racemic pair as a function of the mutual tilt and azimuthal angles between the neighboring molecules shows a few deep minima at the shorter separation, and this feature remains unchanged at larger separations. Thus, the racemic domains are expected to have more favorable interactions at shorter separation. In contrast to the racemic pair potential, the corresponding plot of the enantiomeric pair shows that the minima occurring at the shorter separation are shallower than those at the larger separation of the same pair. The result indicates that the racemic pair will be energetically more favorable at shorter separation (compressed state in the condensed phase), which is suggestive of heterochiral preference. The corresponding state of the enantiomeric pair will be favorable at the larger separation, indicating that homochirality is favored in the enantiomeric system. It is revealed that the intermolecular energy profile of a pair of chiral molecules at nanoscale separation has specific orientation-dependent minima, differing for enantiomeric and racemic pairs. This difference is responsible for the chiral discrimination. When the molecules are widely separated, the dissymmetric nature of the orientation-dependent interaction is absent. No preferential mutual orientation is observed over the mesoscopic length scale, and the manifestation of chiral discrimination vanishes. This why the chirality-induced features are absent in liquid-expanded and gaseous phases of the monolayer [17]. The same trend is

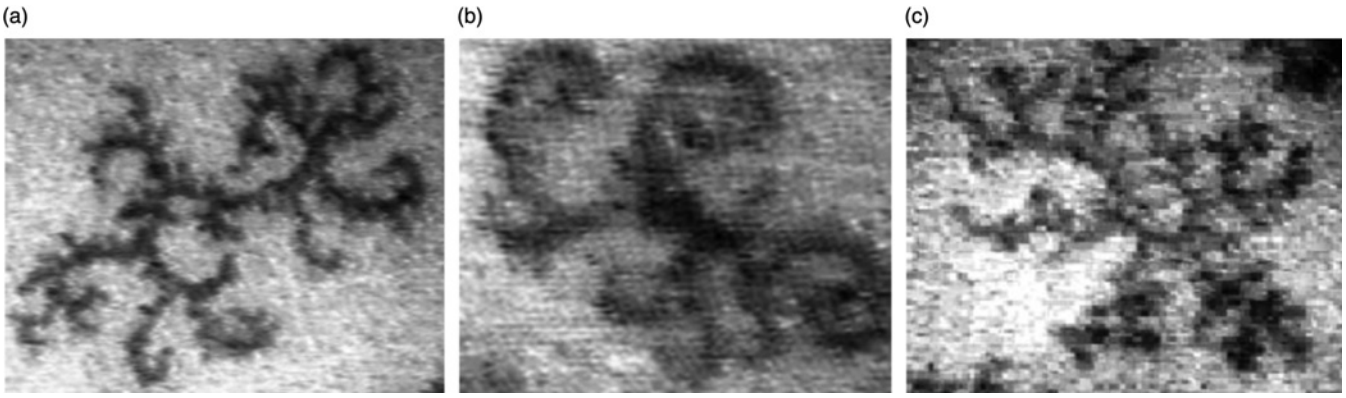


FIGURE 14.1 Fluorescence micrograph of homochiral discrimination in nonequilibrium domains of 1-stearylamine glycerol monolayers: (a) *S*(−)-enantiomer; (b) *R*(+)-enantiomer; (c) racemate. Image size 150 × 150 μm. (Reprinted [32] with permission from American Chemical Society. © American Chemical Society.)

noted in the case of a bilayer, where the helicity is observed at lower temperatures [19]. The reacting molecular segments in the active sites approach within nanoscale proximity in the course of a biological reaction. This proximity is important for chiral discrimination in biological reactions as discussed in the following section. Restriction of the orienational and translational degrees of freedom enhances the discrimination significantly when the molecule is restricted at the interface and surrounded by molecules in the condensed phase as noted in the present section for biomimetic monolayers. This is expected to be valid in biological nanosized cavities, which confine the reacting chiral segments. We are likely to conclude that similar principles can be operative in biological systems. Our computational studies support this view. In the following section, we present an overview of the recent studies on the influence of chirality of constituent molecules in the peptide synthesis and aminoacylation reaction, which are key reactions in the formation of peptides or proteins in cells.

14.4 EXPERIMENTAL STUDIES ON CHIRAL DISCRIMINATION IN PEPTIDE SYNTHESIS AND AMINOACYLATION REACTION

Protein biosynthesis occurs in successive stages in vivo. The major steps of protein synthesis are initiation, elongation, termination, release, folding, and posttranslational processing [8, 9]. The initiation step is the aminoacylation reaction, and this step is followed by the elongation step, which involves the peptide bond formation. The relationship between an amino acid (AA) and its cognate tRNA is established via the aminoacylation reaction. Once the aminoacyl tRNA is formed via the aminoacylation reaction, the polypeptide chain is lengthened by peptide bond formation between successive activated amino acid units. The aminoacylation reaction occurs in the active site of aminoacyl tRNA synthetase (Fig. 14.2). The elongation step takes place in the peptidyl transferase center, which is the active site (PTC). Subsequently, the termination codon of mRNA terminates the polypeptide chain synthesis and newly formed polypeptide is released. Finally, the newly formed polypeptide chain folds into its functional (biologically active) conformation [8, 9].

The aminoacylation reaction links the realm of the protein with the RNA world. Faithful translation of the genetic information is carried out in this step with surprising speed and accuracy [33–37]. The reaction occurs in two steps. The first step is the amino acid activation with the formation of aminoacyl adenylate and release of inorganic pyrophosphate. In the second step of the reaction, the 2′OH or 3′OH (hydroxyl group) (depending on the class to which the aaRS belongs) of the terminal adenosine of tRNA (A76) causes a nucleophilic attack at the carbonyl carbon atom of the aminoacyl-AMP. This result is the 2′- or 3′-esterification of the tRNA with the AA moiety and generation of AMP as the leaving group. Subsequently the product is released. Both activation and charging steps of 20 natural amino acids are catalyzed by 20 aaRSs. Subsequent step of protein synthesis after aminoacylation is the peptide bond formation occurring in the ribosome (a large and complex macromolecule). Pioneering studies revealed detailed organization at the molecular level of this functional molecular machine [38–47]. The active site of ribosome is termed the *peptidyl transferase center* (PTC). In this process, the α-amino group of the amino acid at A-site tRNA causes a nucleophilic attack at the carbonyl carbon of the ester bond connecting nascent peptide to P-site tRNA and forms an intermediate. The aminoacyl moiety attached to A76 of the tRNA in the A-site accepts the growing polypeptide from the tRNA in the P-site during peptidyl transfer. The new peptidyl-tRNA is subsequently translocated from the A-site to the P-site. The deacylated tRNA is translocated from the P-site to the exit (E)-site.

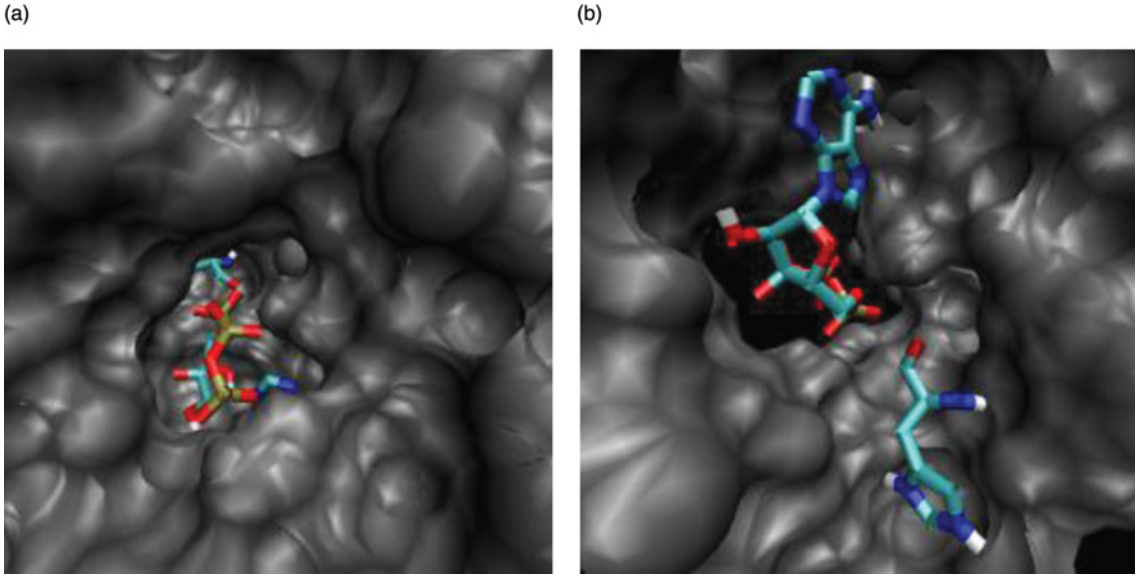


FIGURE 14.2 The active-site geometry of HisRS (1KMN.pdb) from *Escherichia coli* [26]. The ATP and histidinol are shown as bound substrate and substrate analog (analog of histidine), respectively. Two different views of the active site are shown: (a) from the perspective of the active site as viewed from the opening of the cavity; (b) as viewed from the amino acid binding site (few residues are omitted for clarity). The opening of the active site is ∼1.1 nm, and the tunnel length spanning the substrate and analogue is ∼1.7 nm. Images are prepared using VMD [108]. For a color version of this figure, see the color plate section.

Both concerted and stepwise mechanisms are proposed for the peptide synthesis. Two mechanisms are competitive and are studied in detail using experimental and computational methods. The stepwise mechanism takes place through a tetrahedral intermediate.

The residues composing the active-site wall within an enzyme not only enclose the reactants in a close separation but also confine them. This is a state of reduced degree of freedom for the reactants compared to the free state of the same moieties in the bulk, and this reduction in rotational and translational degrees of freedom enhances the stereoselectivity. Because of the reduction in rotational and translational degrees of freedom, reactant geometries with specific mutual orientations are more probable than their random mutual arrangements. The restriction of degrees of freedom is an important factor in steric recognition. However, the chiral discrimination is expected to be insignificant when the separation is rather large (several 10s of nanometers or larger separation). It has long been recognized that the enzymes, which are inherently chiral, are needed to orient both substrates and catalytic residues to preferentially stabilize one stereoisomeric transition state over another in the enzymatic reactions. The effectiveness of the catalytic activity of an enzyme in the rate enhancement significantly depends on the realization of tight binding, which is coupled with a high degree of steric recognition.

Both aminoacylation reaction and peptide bond formation exhibit strong chiral discrimination. The specificity of the aaRSs to incorporate a specific amino acid and its ability to discriminate between several competing substrates is well known. Synthetase ensures that only cognate substrates are selected from the large cellular pool of similar amino acids or tRNA to be incorporated within the active site. The ability to discriminate among amino acids is one of the major requirements for accurate translation of the genetic code because the structure of the cognate and noncognate amino acids may differ only in a subtle way in terms of charge distribution or spatial arrangements of groups attached to the chiral center. The frequency of misincorporation of noncognate amino acid is 1 in 10,000, which reflects a surprising accuracy of the mechanism. It was proposed that the acylation site rejects amino acids larger than the correct one because there is insufficient space for them. On the other hand, the smaller amino acids are cleaved by the hydrolytic editing site. However, this size- or volume-based mechanism is not capable of discriminatimg the enantiomeric species of the cognate amino acid as the D- and L-enantiomers that occupy identical total volumes.

Early studies indicated that when D-isomer is tested as substrates with particle-free supernatant of pancreas homogenate containing synthetase, no activity was observed [48]. Calendar and Berg observed that D-tyrosine could be esterified to $tRNA^{Tyr}$ and then could be incorporated into peptides [49, 50]. D-Tyrosine was incorporated into the peptide in an assay for a protein-synthesizing system. However, the L-tyrosine incorporation is much higher than the D-tyrosine incorporation. The reduced incorporation

of D-tyrosine indicates that the protein synthetic system is unfavorable toward the incorporation of D-amino acids into peptides. The overall rate of dipeptide formation is 30-fold higher for the L-enantiomer than the D-enantiomer. Yamane and coworkers studied stereoselectivity of peptide chain elongation [51]. Bergman and coworkers tested the specificity of L- and D-isomers of valine, isoleucine, and leucine for aminoacyl adenylate formation with valyl, isoleucyl, leucyl, and methionyl tRNA synthetases [52]. In all cases, formation of the D-aminoacyl adenylate is negligible or nil compared to the corresponding L-aminoacyl adenylate. Similar chiral specificity is noted for aspartyl tRNA synthetase of *Lactobacillus aerabinosus* [53]. Soutourina and coworkers concluded that in addition to D-tyrosine, D-enantiomers of other amino acids could be incorporated, based on an investigation of *E. coli* and *Saccharomyces cerevisiae* systems [54, 55]. Tamura and Schimmel studied the plausibility of chiral selectivity during the second step of aminoacylation using an RNA minihelix that recapitulates the amino acid attachment site within tRNA [56]. Formation of the [^{14}C]-L-Ala-minihelix is preferred over that of [^{14}C]-D-Ala-minihelix by a ratio of about 4:1. Stereoisomers of both Leu-*p*-dT_6dA_2 and Phe-*p*-dT_6dA_2 were also tested for chiral selectivity. A clear preference for L- over D-leucine (or phenylalanine) was observed. Chiral preference appears to occur during aminoacyl transfer from the 5′-phosphate to the minihelix. It might be noted that the mutual spatial orientation and distance between reacting molecular segments in the model system studied by the same two investigators [56] could differ from a corresponding biological system that might influence the observed ratio of selectivity. In a subsequent study, the same research group attempted to ascertain whether the free amino group attached to the asymmetric α-carbon of the amino acid played a role in the chiral selectivity of aminoacylation [22]. To address the question, the amino group of Ala was acetylated and *N*-acetyl-L- or D-Ala-aminoacyl oligonucleotide was used for the aminoacylation reaction. Nearly fourfold preference of L-Ala-minihelix^{Ala} over D-Ala-minihelix^{Ala} was observed. An energetic difference of <1 kcal/mol in the rate-determining step of the transition state is sufficient to give the observed fourfold preference for chiral specificity in the aminoacylation process. In a series of detailed studies Hecht and coworkers the extent of incorporation of D-amino acid into ribosome [57–60]. The result indicates that the D-isomer incorporation is severely inhibited compared to the natural isomer [58, 59]. The studies by Hecht and coworkers confirm that the incorporation of D-amino acids into a peptide is unfavorable relative to the incorporation of natural enantiomer. Several other examples of chiral discrimination in the protein biosynthetic pathway are available [61, 62].

It is important to remember that chirality is present also in the sugar ring of the nucleic acid structure. Significant influence of the chirality of the sugar ring involved in the CCA moiety is also noted [57]. This result is important in understanding the heterochiral relationship of D-sugar and L-amino acid in peptide synthesis, where the former is present as a part of the tRNA structure. While the *N*-acetyl-D-phenylalanyl–tRNA^{Phe} and *N*-acetyl-D-tyrosyl–tRNA^{Phe} produced only a small amount of dipeptide, the 2′- and 3′-deoxyadenosine analogs produced no detectable dipeptide formation. The result indicates that the effect of the sugar ring chirality is decisive over the peptide bond formation and alteration of the chirality of the same is unfavorable for the synthesis. Chiral discrimination is also studied in different model systems such as puromycine [9-{3′-deoxy-3′-[(4-methoxy-phenylalanyl)amino]-β-D-ribofuranosyl}-6(*N,N′*-dimethylamino) purine]. Note that the orientational degrees of freedom of A- and P-terminals in such analogs are in principle different from those within the ribosomal active site. Hence the mechanism and extent of discrimination might be different in these two cases. Another study employed a series of synthetic puromycin analogs to measure the activity of D-amino acid and β-amino acids in rabbit reticulocyte ribosome [21]. While the L-puromycin inhibits globin mRNA translation with an IC_{50} value of 1.8 μm, the corresponding D-puromycin or 9-{3′-deoxy-3′-[(4-methoxy-D-phenylalanyl)amino]-β-D-ribofuranosyl}-6(*N,N′*-dimethylamino) purine) inhibits globin translation, giving an IC_{50} value of 280 μm. The difference is 150-fold.

While the foregoing studies indicated that D-amino acid incorporation into proteins is practically impossible, Hecht and coworkers pointed out that alteration of the peptidyl transferase center might lead to enhanced D-amino acid incorporation [65]. Mutations in the 23SrRNA in the region of peptidyl transferase center (PTC) and helix 89 lead to conformational change in ribosome that alters its behavior in the protein synthesis. Modified ribosomes with mutations in regions 2447–2450 (belonging to the PTC region) and 2457–2462 (belonging to helix 89 region) of *E. coli* 23S rRNA and cell free protein synthesizing systems were prepared from mutant ribosomes. A high level of suppression in the presence of D-methionine and D-phenylalanine was observed. This indicates that the ribosome active-site structure is, at least partly, responsible for the discriminating mechanism and putative alterations may lead to enhanced incorporation of D-amino acid. The possibility of incorporation of D-isomer in a biosynthetic pathway or development of a racemic mixture cannot be ruled out, due to the presence of D-amino acid in several organisms [66]. The protein active site is complementary to substrate. With the proteins composed of L- and D-amino acids, it would be too cumbersome to maintain life. This could be a reason why evolution did not support the coexistence of protein composed of L- or D-amino acid. Equivalently, the development of protein structure composed of both L-and D-amino acids is unexpected. However, the foregoing view does not identify the mechanism of rejection of D-enantiomer when the

presence of the same are well known. The presence of D-amino acids in several biological organisms is known, for example, in the nonribosomal peptide synthesis and posttranslational modification therein [66–71]. A large number of biological molecules exhibit strong preference for either one of two enantiomeric forms (for each chiral center) of the nearly equal possible isomers. While the incorporation of D-amino acids is a hallmark of peptide-synthetase-based nonribosomal peptide synthesis [67, 68,71, 72] and post-translational modification [66, 69, 70], the RNA-dependent ribosomal synthesis of peptides and proteins exclusively incorporates only the 20 natural amino acids and selenocysteine with their natural chirality (L-form). Incorporation of D-amino acids into an organism can be toxic if it does not naturally occur in the same [71–81]. D-Amino acid occurs naturally in selected systems such as peptidoglycans of bacterial cell walls (D-Ala- and D-Glu-), in peptide antibiotics, and in the human brain (D-Asp and D-Ser are present at high concentrations). Several other examples of presence of D-amino acid in biological organism are noted. Dedkova and coworkers [65] pointed out that alteration of the peptidyltransferase center might lead to enhanced D-amino acid incorporation. The study indicates that the organization of PTC has a major influence on the process of synthesis and that alterations in PTC structure may lead to enhanced incorporation of D-amino acid.

The presence of D-enantiomers only in some specific organisms and its almost complete exclusion in the natural biosynthetic pathway of protein synthesis in today's world is now well established. This raises the question about the mechanism of chiral discrimination in biosynthetic pathways in different organisms [1]. Since the racemic compound in crystalline state is more stable than the corresponding enantiomeric form, it is unknown how the chances of racemization are avoided throughout the course of evolution in biological reactions. The answer to the question as to why the basic blocks of life are not being scrambled, and retain enantiomeric purity, is challenging as many biological systems incorporate D-amino acids as well as racemize in other cases as mentioned before. Computational analysis of the chiral discrimination in protein biosynthesis pathway is discussed in Section 14.5. These studies clarified the molecular aspects of the mechanism of chiral discrimination. In the following section, we discuss the mechanisms of retention of chirality and exclusion of noncognate enantiomer in protein biosynthesis reactions, particularly in aminoacylation and peptide bond formation steps as understood from computational analysis.

14.5 COMPUTATIONAL ANALYSIS OF CHIRAL DISCRIMINATION IN AMINOACYLATION REACTION

The aminoacyl tRNA synthetases (aaRSs) ensure that only cognate substrates as well as tRNA are selected from the large cellular pool of similar amino acids or other tRNAs. The frequency of misincorporation of noncognate amino acid is very low, which reflects a surprising accuracy of the mechanism. It is possible that a number of intricate contacts between aaRS and amino acid, which are favorable for cognate but unfavorable for noncognate amino acids, results in the successful recognition and concomitant discrimination. It might be assumed that the acylation site rejects amino acids larger than the correct one because there is insufficient space for them and the smaller amino acids are cleaved by the hydrolytic editing site. However, this size- or volume-based mechanism fails to discriminate the enantiomeric species of the cognate amino acid as the D- and L-enantiomers occupy identical total volumes.

In a series of studies, electronic-structure-based computations are carried out to understand the chiral discrimination in the first step of aminoacylation reaction (adenylation) [82–85]. A combined quantum-mechanical–semiempirical theory is applied to study the discrimination between L-His and D-His using a model of the corresponding active site of histidyl-tRNA synthetase (HisRS). The initial study showed that the substrate amino acid (His) is located within a network of interactions within the nanospace enclosed by the active-site residues [82]. The network of interaction is unfavorable when the D-amino acid is incorporated in the active-site geometry of the natural aaRS. The transition-state geometry corresponding to the activation by D-His is also unfavorable because of the lack of stabilizing interactions that are present in the transition-state structure corresponding to the activation by L-His [82]. Comparison of the reactant and the product geometry shows that the reacting moieties (amino acid and ATP) undergo a change in mutual separation and orientation during the course of the activation. The resulting variation in the energy is unfavorable for the D-His (as substrate) compared to L-His. All these results point out that the restriction of the degrees of freedom of the amino acid and confinement within a nanodimensional space enhances the chiral discrimination.

Chiral discrimination is described in further detail in a subsequent study [83]. The study shows that the variation of the interaction energies for the mutual approach of L-His and D-His toward ATP during nucleophilic attack are strikingly different. The result shows that the surrounding nanospace of synthetase confines the L-His and ATP in the global minima of the energy surface and proximally places the reactants in geometry suitable for the inline nucleophilic attack. The energy surface becomes highly unfavorable when the D-His is placed within the active site. The reorganization of the surrounding nanospace can somewhat improve the unfavorable nature of the intermolecular energy surface of D-His and surrounding residues. However, such a rearrangement requires large-scale structural reorganization of the synthetase structure and is unfavorable. In other words, the arrangement of the active site of synthetase to allow the incorporation of D-His is ruled out by the energy cost to be

paid for such misincorporation. The influence of active-site residues on the discrimination is also studied. Variation in the interaction energy as a function of relative separation between substrates (both L- and D-His) and important active-site residues are computed. The results emphasize the role of active-site residues in controlling the fidelity of the reaction. The interactions of both L-His and D-His with Glu83, Arg113, Arg259, and Tyr264 (all are active-site residues in proximity of the substrates) are studied using using *ab initio*/semiempirical theory. The result reveals the significant stability of the cognate amino acid (L-His) compared to D-His as a function of the separation between the active-site residues and His. The surrounding nanospace of synthetase confines the L-His and ATP to proximally place the reactants in geometry suitable for the inline nucleophilic attack. The confinement of reacting moieties placed within nanometer regime of an active site drives the corresponding reaction very precisely with remarkable discrimination capacity. The foregoing result shows that the set of active-site residues confine the amino acid and ATP in a potential well using an intricate interaction that is selective for the (natural) L-His for adenylation.

It is important to note that the significance of the surrounding active-site residues and the influence of confinement of substrates within the nanospace of active site on the chiral discrimination are not limited to the specific aaRS (HisRS) from a particular species (such as *E. coli*). Computational analyses have shown that the mechanism of chiral discrimination is common in other species studied [84, 85]. Crystallographic and biochemical studies revealed that a number of active-site residues are conserved in different species for a given aaRS. Comparison of the primary sequence and architecture of the active site of HisRS in three different species shows that the residues that are responsible for creating a network of important and favorable interactions with the substrate His and ATP are conserved in the active-site structures in different species studied such as *Escherichia coli, Thermus thermophilus*, and *Staphylococcus aureus* [84]. The relative arrangements of the conserved residues with respect to the substrates are conserved in these three organisms. The analysis suggests that the arrangement of residues in controlling the stringent chiral discrimination is developed through evolution and retained thereafter. In other words, the pattern of active-site organization and the concomitant network of interaction control the mechanism of the reaction. The accuracy of the reaction mechanism is developed through evolution to render the process of protein synthesis error-free. The active-site structure, so perfected, is possibly retained further. It is possible that the confinement of substrates within a nanodimensional space of active site and the resulting network of interaction are important guiding factors for the chiral discrimination exhibited by aaRSs in general [85]. The abovementioned electronic-structure-based computations indicate that the network of electrostatic interaction within the active site of aaRS has a decisive role in the chiral discrimination. The conclusions agree fairly well with the results from classical molecular dynamics simulations. Thompson and coworkers investigated the preference for acylation of L-Asp over D-Asp by aspartyl-tRNA synthetase (AspRS). Discrimination against D-Asp can be explained by the unfavorable binding with the D-Asp. Component analysis indicates that Coulomb interaction is the major favorable factor to the L-Asp binding [86].

A more recent computational study further shows that the network of substrate and active-site interaction has distinctive features for two classes of aaRSs and that few features are characteristic for each of the twenty aaRSs [87, 88]. For example, the molecular organization of the active-site nanospace of class I and class II aaRS are different. The difference is due principally to extended and bent states of ATP in the two classes. Computational studies show that the most feasible pathway for nucleophilic attack to αP is oppositely directed for classes I and II. It is also pointed out that the modes of nucleophilic attack by the oxygen atom of the carboxylic group of the substrate amino acid to the αP atom of adenosine triphosphate ATP are different. The *syn* oxygen atom of the carboxylic group attacks the αP atom of ATP in all class I aaRSs (except TrpRS) investigated, while the *anti* oxygen atom attacks in the case of class II aaRSs. The difference in mechanism is related to the fact that the relative arrangement of the ATP with respect to the AA is opposite in class I and class II aaRSs. Thus, the nucleophilic attack is energetically less favorable for class II aaRSs compared to the class I aaRSs (when the influence of the active site is excluded from consideration). However, this difference in the propensity of nucleophilic attack is counterbalanced by the bent state of ATP and the presence of Mg^{2+} ions and different sets of active site residues [87, 88]. The study shows that active site residues are not only involved in proper placement and orienting the substrates but also form a network of interaction with the substrates that is idiosyncratic for each aaRS. Thus, it is no surprise that the noncognate amino acids are excluded from entering the active site, leading to misincorporation. Obviously, the wrong enantiomer (such as D-amino acid) perturbs the network of interaction and is not favored. Another reason for the chiral specificity in aaRSs is noted [87]. The reduction of unfavorable electrostatic potential at the reaction center (between the attacking oxygen atom of the carboxylic acid group of substrate amino acid and αP atom of ATP) is an important prerequisite for the nucleophilic attack during the first step of aminoacylation reaction. The positively charged amino group of substrate amino acid (and the active-site residues close to the reaction center) plays a major role in reducing the aforesaid unfavorable electrostatic potential. Alteration of the chirality of substrate amino acid to the D-enantiomeric structure would change the spatial arrangement of the amino group. The resulting arrangement of groups is ineffective in reducing the potential. Thus, computational

analysis provides important insight into the factors responsible for chiral discrimination in the nanospace of the active site of aaRS.

14.6 COMPUTATIONAL STUDIES OF THE CHIRAL DISCRIMINATION IN PEPTIDE BOND FORMATION REACTION

Out of the several partial reactions of protein biosynthesis, peptidyl transferase reaction is one of the most intensively studied. Although ribosome is made up of RNA and proteins, the peptidyl transferase center is essentially composed of nucleic acid with no protein present within 1.5 nm distance of active site. The active site of the large subunit of the ribosome is composed of layers of conserved nucleotides. It is an important question as to how chiral discrimination is carried out by PTC and how the ribosomal pathway excludes amino acids other than the L-enantiomer. The mechanism of retention of enantiopurity is not straightforward to understand since D-amino acid is involved in nonribosomal peptide synthesis.

Few features of the reaction relevant to chiral discrimination are qualitatively understood from the experimental studies. First, the intermolecular energy profile of the reaction is expected to be orientation-dependent. Consequently, chiral discrimination may not be averaged out for all possible orientational degrees of freedom as in the case of same reaction in a solvent. Further, molecular segments involved in reaction (L-amino acid and D-sugar) being chiral, their chirality should influence the nature of the corresponding energy surface. Confinement within a nanospace must influence the discrimination exhibited by the reaction as also observed in biomimetic systems. It is pointed out in the literature that the preorganization of the active-site residues and their proximity is important for effective catalysis during the progress of the reaction [89]. All these factors are recently explored using computational methods to understand the molecular mechanism of the discrimination and are discussed as follows.

Peptide bond formation is studied using *ab initio* methods for L-alanine dipeptide formation considering both concerted and stepwise mechanisms [90]. In this study, the reacting amino acids are not covalently linked to any part of a larger structure, unlike those present in the CCA terminal in tRNA during peptide synthesis in PTC. The amino acid moieties are not surrounded by the active-site moieties. It is unlikely that chiral discrimination will be exhibited in such a system as the reacting moieties are free to assume various mutual arrangements without being constrained as they are not covalently linked to a larger structure (RNA) and neighboring residues (composing the PTC). As a result, discrimination is not expected to be observed, and the values obtained are averaged out over all possible mutual orientations. During the peptide bond formation, the $3'$ end of the A-site arrives at the P-site by a process of mutual rotation within active site [91,92]. The discrimination in the intermolecular energy surfaces of a pair of alanine molecules in the restricted orientational state (which is a simplified model of the A- and P-site terminals during their restricted rotation in PTC) is investigated [93]. The energy difference between the L–L pair and D-L-pair at given intermolecular orientation and separation for the same value of both variables for both pairs is defined as the chiral discrimination energy ($\Delta E_{\text{LL-DL}}$). When $\Delta E_{\text{LL-DL}}$ is negative, it is homochiral preference and when $\Delta E_{\text{LL-DL}}$ is positive, a heterochiral preference is dominant. It is ensured that the discrimination observed is not artificially generated by basis set superposition error (BSSE). The energy surface are calculated by MP2/6-311++G**, HF/6-311++G** and B3LYP/6-311++G** level of theories. The result shows that the interaction energy of the L–L pair and the corresponding interaction energy of the D–L pair are not identical with the variation in either the distance or the mutual orientation of two molecules. The plot of L–L pair is dissymmetric, revealing the underlying chirality of the molecules. In contrast, the plot for the D–L pair is symmetric around the 180° orientation, which reveals the racemic state of the neutral pair where the charge dissymmetry is also absent. Unlike the neutral case, the asymmetric charge distribution of the neighboring molecules (starting geometry) breaks the symmetry of the energy profile of the D–L zwitterionic pair, which can be observed in the corresponding dissymmetric nature of the energy profile.

It is pointed out that the very large difference between the energy surfaces of L–L and D–L pairs at specific orientations at same distances between the corresponding pairs is due to short-range repulsive interactions. In general, the short-range repulsive part of both van der Waals and electrostatic (Coulombic, dipolar or multipolar) interaction varies more sharply than does the corresponding long-range attractive part of the intermolecular interaction [94, 95]. The energy profile of L–L at a given short-range separation is less unfavorable than the corresponding energy profile of the D–L pair at the same intermolecular separation. However, the variations in intermolecular interaction energy are large at such short-range intermolecular distance, and this causes the large discrimination observed (which is the major source of the discrimination for neutral molecules). Favorable electrostatic interaction further contributes to the large homochirality of the $\Delta E_{\text{LL-DL}}$ for the zwitterionic pair in addition to the short-range steric repulsion. The basis set superposition error (BSSE)-corrected results show enhanced discrimination. Use of the higher-level Møller–Plesset perturbation theory (MP2) and further BSSE correction do not change the conclusions made at the Hartree–Fock (HF) level of theory. In other words, during the A-P rotatory movement, the L–L pair will pass through relatively low energy regions of the intermolecular energy surface compared to the D–L pair. The study suggests a possible method of D-amino acid exclusion.

The effect of confinement of substrates within the nanospace of PTC on the chiral discrimination is studied using hybrid quantum chemical studies [96]. The study shows that the interaction of the L–L pair can occur at significantly lower energy and without any steric constraint over the range of orientation. The interaction between the D–L pair is relatively unfavorable, and the corresponding energy profile has two minima only at limited range of orientations. The orientational space for the D–L pair is limited and experiences more steric clash with surrounding residues compared to the L–L pair. This is clear evidence of homochiral preference. In order to understand the origin of the observed discrimination, different surrounding residues are removed and the influence on the ease of the rotatory path is studied. Exclusion of the U2620 from the surrounding residues drastically diminishes the discrimination. This indicates that the U2620 has preferential nonbonded interaction with A- and P-terminals in the L–L form rather than the D–L form. However, homochiral preference remains significant. Entire preferred homochirality, as observed in experiment and calculated, is not due to U2620, and the residual discrimination is nonnegligible. All other residues are successively removed (A2485, A2486, C2487, A2488, A2637, G2540, U2451, and C2452) in order to identify the origin of residual discrimination, and this is noted to change little from that when U2620 was removed. It may be noted that the removal of backside residues such as A2485, A 2486, C2487, and A2488 gradually diminished the repulsive steric constraint but discrimination remained effectively unchanged. Finally, all residues are removed and two phenyl alanine groups are rotated without any surrounding residues in the same specified range of rotation. Interestingly, the discrimination is nonvanishing. Strong homochiral preference is still noted, which is entirely determined by the amino acid sidechains. Comparison of the relative energy gap of L–L and D–L pair plots including all surrounding residues except U2620 and the relative energy gap of L–L and D–L pairs with all surrounding residues removed clearly shows that the residual discrimination (as remained after removal of U2620) remained same in the specified range of orientation and is independent of other residues. This conclusion corroborates the results of previous study based on *ab initio* and DFT-based studies on interaction of alanine molecules where homochiral preference is noted as a function of mutual orientation [93]. The study quantitatively shows that the observed homochiral preference is due to U2620 residue as well as the amino acid sidechain at the A- and P-terminals. A major part of the discrimination comes from the variation of nonbonded interaction of rotating the A-terminal with U2620 during approach of the former toward the P-terminal. Significant discrimination is due to the difference in the sidechain interaction of A- and P-terminals themselves during the rotatory motion even when no surrounding residues are present.

It is important to address that how important is the chirality of the D-sugar in the context of the long-length-scale structural organization of the PTC. Explicitly, the question is whether the possible heteropairs and homopairs (other than the D-sugar and L-amino acid) can perform the peptide synthesis with similar efficiency in the natural biological surrounding (PTC). The influence of the D-sugar on the chiral discrimination in peptide synthesis has been investigated [97]. There could be several factors contributing to the discrimination: (1) the D-sugar ring might have favorable stereochemistry related to the structural organization of the tRNA itself, (2) the sugar ring might have the proper stereochemistry that can facilitate the rotatory path (through which the A-site tRNA $3'$-end flips into the P-site by rotating around the bond connecting the single strand $3'$-end) leading to the optimal orientation for peptide bond formation, and (3) the hydroxyl group attached to $2'$ can catalytically lower the transition-state barrier (related to the formation of the peptide bond) when positioned in a favorable stereochemical orientation.

Modeling studies show that the alterations in the chiral centers of the ribose sugar ring bring large scale structural changes in the tRNA structure. Such structural modifications are unfavorable for the peptide synthesis process [97]. It is observed that the presence of sugar ring in both terminals enhances the favorability of the rotatory path compared to the case when the sugar ring is removed. Since rotation of the A-terminal occurs around the $3'$ bond, the rotatory process is a mutual orientational motion of the amino terminal with respect to the A-site sugar ring. As a result, removal of the A-site sugar ring raises the energy due to the loss of favorable interaction. The ribose sugar ring and specifically that of the $2'$ chiral carbon of the A76 has also another influence on the peptide bond formation process. Experimental studies indicate that the hydroxyl group is responsible for the significantly high rate of the peptide synthesis in ribosome compared to that of an uncatalyzed one (in absence of ribosome). The role of $2'$ OH in the peptide synthesis was suggested [98–100]. The role of the $2'$ OH group into the rate enhancement produced by ribosome based on entropic contribution is proposed [101, 102]. The barrier heights of the transition states for the formation of peptide bond and the influence of the $2'$ OH group is studied for two different mechanisms (proton shuttle and anchoring mechanism), and the difference in the barrier heights is attributed to the absence of the $2'$ OH group, which results in removal of the chirality of the $2'$ carbon of the sugar ring [97]. It is noted that the reactant geometry contains a cycle of hydrogen bonds, and the hydrogen bond distances are further shortened in the transition state geometry. Several of these hydrogen bonds are absent when the $2'$ OH are removed. This result indicates that the change in the stereochemistry of the $2'$ center can alter the progress of the synthesis by several orders of magnitude. The observation corroborates the experimental data that the substitution of P-site tRNA $2'$ OH by $2'$ H and $2'$ F, results in 10^6 -fold reduction in the rate of peptide bond formation [24]. A

comparison of the transition states in the two cases indicates that the anchoring role of the 2′ OH group is responsible for lowering the barrier height compared to the case when the 2′ OH group is removed. The result strongly suggests that the chirality of the 2′ carbon is vital for the rate enhancement. Alteration of the stereochemistry at the 2′ center of sugar ring results in rise of the barrier height. Thus, the change in the stereochemistry of the 2′ OH makes the process as unfavorable. The computational study conclusively shows that the proper positioning of the group as well as the natural chirality (with respect to the 2′ center, at least) is vital for the reaction.

The residues present in the PTC surrounding the substrates (which are in proximity of nanometer length scale with the D-sugar) also influence the rotatory path and the discrimination. Although the bases are achiral, their interaction with the sugar ring can be orientation-dependent and can influence chiral discrimination. It was pointed out earlier that when achiral moieties have restricted orientational freedom, its interaction profile with a chiral moiety can have orientation dependence [104]. The orientation dependence can be different for L- and D-forms of the chiral moiety and might give rise to discrimination. The influence of various surrounding residues such as C2104, C2105, A2485, A2486, C2487, U2541, C2542, C2608, G2618, U2619, U2620, and A2637 on the rotatory path and their interaction with the sugar ring related to the A-site and P-site of the 50S ribosomal subunit of *Haloarcula marismortui* has been computationally investigated [97]. The removal of the surrounding residues affect the nonbonded interaction with the amino acid:sugar heteropair of natural chirality. It is concluded that while a set of surrounding residues have favorable influence on the peptide bond formation between A- and P-terminals within PTC, a number of other residues might have less influence on the same process.

The computational studies described earlier reveal that the molecular mechanism of the chiral discrimination involves the A- and P-amino acids, the D-sugar ring, and surrounding bases of the PTC. Several factors are noted to be responsible for discrimination and explain the high level of stereospecificity of the process. The factors can be summarized as follows. The chiralities of the amino acids at A- and P-terminals are most important. The rotatory path for the approach of D-amino acid toward the L-terminal is unfavorable because of steric hindrance between the amino acids themselves. Their nanoscale separation is important for discrimination, and at larger separation no discrimination is noted. The second factor is the restricted nature of the range of mutual orientation of the terminals during the rotatory path for the approach to form the peptide bond. This factor causes the resultant interaction profiles for L–L and D–L pairs to exhibit different forms of discrimination. The natural chirality (D-form) of the sugar ring has a favorable influence on the long-length-scale organization of the tRNA structure and is another factor for influencing discrimination. Alteration of the chirality of the sugar ring is unfavorable as it requires large structural rearrangements of tRNA. Favorable influence of the D-sugar ring is noted on the rotatory path for the process of approach to form the peptide bond. The removal of the sugar ring causes the rotatory path for approach to form the peptide bond as unfavorable, which indicates that the interaction of the D-sugar with the amino acids are more favorable than other homo- or heteropair combinations of the sugar amino acid pair. The stereochemistry of the 2′ center of the D-sugar has a vital influence as it catalyzes the peptide bond formation by making proper placement of the OH group that is involved in the catalysis. Analysis of the transition-state structure revealed that the alteration and removal of chirality of the 2′ center destabilize the transition state and renders the formation of peptide bond unfavorable. Finally, the nanoscale proximity of some of the surrounding bases present in PTC with the A- and P-terminals and their restricted orientation influence the discrimination. Thus, multiple factors control the discrimination in the peptide synthesis in PTC and allow accurate retention of the biological homochirality in the reaction.

14.7 CONCLUDING REMARKS

In the present review, we discussed recent experimental and computational analysis of the intermolecular interaction in the biomimetic and biological systems as influenced by chirality and confinement at nanodimension. Both the molecular chirality and confined geometries are found to be hallmarks of numerous biosystems and reactions therein. The confinement of neighboring amphiphiles in nanodimensional proximity in condensed state gives rise to interesting chiral discrimination and exotic morphology emerges as discussed in the present review. Similarly, chiral substrates confined in the active-site nanospace have significant influence on the course of vital biological reactions and exhibit stringent chiral discrimination, which plays a significant role in life processes. The microscopic understanding about the subject is beginning to emerge, and future research needed in order to understand the related principles of nature is identified. Recognition of the fact that the confinement of substrates in the active-site nanospace has significant influence on the course of vital biological reactions and chiral discrimination plays a significant role in the process of adding new dimensions to the *nanobiology* of respective biosystems. To recapitulate, *nanobiology* addresses biological and biophysical problems using tools, ideas, and materials of nanoscience and biology (biological systems are inherently nanodimensional) [105]. *Nanobiology* as a subject is outcome of an interplay between physics, chemistry, material science engineering, and biology and aims to devise ways to construct molecular machines by learning from nature. The ultimate goal is to be able to predictably manipulate and tailor them for targeted needs. If one needs to learn biological

systems at microscopic level, it is essential to know how to apply physical principles to the microscopic principles of the systems. Computational techniques play a great role in this direction. Several examples are available from the literature [1]. In one interesting study, Rothlisberger and coworkers used computational techniques to design eight enzymes that use two different catalytic motifs to catalyze the Kemp elimination reaction with measured rate enhancement of upto 10^5 and multiple turnovers [106]. The authors used quantum-mechanical transition-state calculation to create an idealized active site with protein functional groups positioned so as to maximize transition-state stabilization. Additional functional groups are included in the idealized active sites to further facilitate the catalytic activity. Density functional theory is applied to optimize the placement and orientation of the catalytic groups around the transition state for maximal stabilization. Using mutational analysis, authors confirmed that catalysis depends on computationally designed active site. X-Ray structures are used to determine the geometries. Increase in catalytic activity as well as in turnover was achieved. Other examples of utilization of computational methodology in designing biocatalyst are available in the literature [107]. The authors designed retroaldolases that use four different catalytic motifs to catalyze the breaking of a carbon–carbon bond in a nonnatural substrate. The study demonstrates a computation-based redesign of a novel retroaldolase activity in a scaffold that catalyzes an unrelated reaction. Many more examples are available [1] and indicate the promising future of the *nanobiology* as a subject that seems to be beneficial for humankind.

ACKNOWLEDGMENTS

Discussions with Dr. K. Thirumoorthy, Dr. S. Dutta Banik, Professor D. Vollhardt, and Professor B. Bagchi on various aspects of biomolecular system are gratefully acknowledged. Support by the Department of Science and Technology, India is also gratefully acknowledged. S.D. thanks the University of Kalyani for granting a research scholarship.

REFERENCES

[1] Nandi, N. (2011). *Chirality in Biological Nanospaces: Reactions in Active Sites.* CRC Press, Taylor & Francis Group, New York.

[2] Nandi, N. (2009). Chiral discrimination in the confined environment of biological nanospace: Reactions and interactions involving amino acids and peptides. *Int. Rev. Phys. Chem.* **28**, 111.

[3] Eliel, E.L., Wilen, S.H., Mander, L.N. (1994). *Stereochemistry of Organic Compounds.* Wiley, New York.

[4] Jacques, J., Collet, A., Wilen, S.H. (1981). *Enantiomers, Racemates, and Resolutions.* Wiley, New York.

[5] Flapan, E. (2000). *When Topology Meets Chemistry: A Topological Look at Molecular Chirality.* Cambridge Univ. Press, Cambridge, UK.

[6] Pály, G., Zucchi, C., Caglioti, L. (1999). *Advances in Biochirality.* Elsevier Science, Oxford, UK.

[7] Pályi, G., Zucchi, C., Caglioti, L. (2004). *Progress in Biological Chirality*. Elsevier Science, Oxford, UK.

[8] Nelson, D.L., Cox, M.M. (2002). *Lehninger Principles of Biochemistry*. Freeman, New York.

[9] Berg, J.M., Tymoczko, J.L., Stryer, S. (2002). *Biochemistry.* Freeman. New York.

[10] Dutta Banik, S., Nandi, N. (2013). Chirality and protein biosynthesis. *Top. Curr. Chem*, **333**, 255.

[11] Guerra, G., Cavallo, L., Corradini, P. (2003). Chirality of catalysts for stereospecific polymerizations. In Green, M., Nolte, R.J.M., Meijer, E.W. (eds.), *Materials Chirality*, Vol. 24, Topics in Stereochemistry Series. Denmark, S.E., Siegel, J. (Series eds) Wiley-Interscience, Hoboken, NJ, p. 1.

[12] (a) Rosa, C.D. (2003). Chain conformation, crystal structures, and structural disorder in stereoregular polymers; (b) Okamoto, Y., Yashima, E., Yamamoto, C. (2003). Optically active polymers with chiral recognition ability; (c) Fujiki, M., Nakashima, H., Toyoda, S. Koe, J.R. (2003). Chirality in polysilanes. In Green, M., Nolte, R.J.M., Meijer, E.W. (eds), *Materials Chirality*, Vol. 24, Topics in Stereochemistry Series. Denmark, S.E., Siegel, J. (Series eds) Wiley-Interscience, Hoboken, NJ, pp. 71 (a), 157–207 (b), 209 (c).

[13] Amouri, H., Gruselle, M. (2008). *Chirality in Transition Metal Chemistry: Molecules, Supramolecular Assemblies and Materials.* Wiley, Chichester.

[14] Capiro, V., Williams, M.J.J. (2009). *Catalysis in Asymmetric Synthesis.* Wiley, Chichester.

[15] Nandi, N., Vollhardt, D. (2003). Effect of molecular chirality on the morphology of biomimetic langmuir monolayers. *Chem. Rev.* **103**, 4033.

[16] Nandi, N., Vollhardt, D. (2007). Molecular interactions in amphiphilic assemblies: Theoretical perspective. *Accounts Chem. Res.* **40**, 351.

[17] Vollhardt, D. (1996). Morphology and phase behavior of monolayers. *Adv. Colloid Interface Sci.* **64**, 143.

[18] Nandi, N., Bagchi, B. (1996). Molecular origin of the intrinsic bending force for the helical morphology observed in chiral amphiphilic assemblies: Concentration and size dependence. *J. Am. Chem. Soc.* **118**, 11208.

[19] Nandi, N., Bagchi, B. (1997). Prediction of the senses of helical amphiphilic assemblies from effective intermolecular pair potential: Studies on chiral monolayers and bilayers. *J. Phys. Chem. A* **101**, 1343.

[20] Nandi, N., Vollhardt, D., (2006). Chirality and molecular recognition in biomimetics organized flims. in '*Bottoms up nano fabrication: Supramolecules, self assemblies and organized flims*', K. Ariga, H. S. Nalwa (eds), American scientific Publishers, Chapter 5, 1.

[21] Starck, S.R., Qi, X., Olsen B.N., Roberts, R.W. (2003). The puromycin route to assess stereo and regiochemical

constraints on peptide bond formation in eukaryotic ribosomes. *J. Am. Chem. Soc.* **125**, 8090.

[22] Tamura, K., Schimmel, P. (2004). Chiral-selective aminoacylation of an RNA minihelix. *Science* **305**, 1253.

[23] Dorner, S., Polacek, N., Schulmeister, U., Panuschka, C., Barta, A. (2002). Molecular aspects of the ribosomal peptidyl transferase. *Biochem. Soc. Trans.* **30**, 1131.

[24] Weinger, J.S., Parnell, K.M., Dorner, S., Green, R., Strobel, S. (2004). Substrate-assisted catalysis of peptide bond formation by the ribosome. *Nat. Struc. Mol. Biol.* **11**, 1101.

[25] Hansen, J.L., Schmeing, M.T., Moore, P.B., Steitz, T.A. (2002). Structural insights into peptide bond formation. *Proc. Natl. Acad. Sci. USA* **99**, 11670.

[26] Arnez, J.G., Augstine, J.G., Moras, D., Francklyn, C.S. (1997). The first step of aminoacylation at the atomic level in histidyl-tRNA synthetase. *Proc. Natl. Acad. Sci. USA* **94**, 7144.

[27] Jensen, F. (1999). *Introduction to Computational Chemistry.* Wiley, Weinheim.

[28] Peng, C., Schlegel, H.B. (1993). Combining synchronous transit and quasi methods to find transition states. *Israel J. Chem.* **33**, 449.

[29] Ayala, P.Y., Schlegel, H.B. (1997). A combined method for determining reaction paths, minima and transition state geometries. *J. Chem. Phys.* **107**, 375.

[30] Frisch, M.J., et al. (2004). *Gaussian 03, Revision C.02*. Gaussian, Inc., Wallingford, CT.

[31] Nandi, N., Vollhardt, D., Brezesinski, G. (2004). Chiral discrimination effects in langmuir monolayers of 1-*o*-hexadecyl glycerol. *J. Phys. Chem. B* **108**, 327.

[32] Nandi, N., Thirumoorthy, K., Vollhardt, D. (2008). Chiral discrimination in stearoyl amine glycerol monolayers. *Langmuir* **24**, 9489.

[33] Eriani, G., Delarue, M., Poch, O., Gangloff, J., Moras, D. (1990). Partition of tRNA synthetases into two classes based on mutually exclusive sets of sequence motifs. *Nature* **347**, 203.

[34] Moras, D. (1992). Structural and functional relationships between aminoacyl-tRNA synthetases. *Trends Biochem. Sci.* **17**, 159.

[35] Arnez, J.G., Moras, D. (1997). Structural and functional consideration of the amino acylation reaction. *Trends Biosci.* **22**, 211.

[36] Ibba, M., Söll, D. (2000). Aminoacyl-tRNA synthesis. *Annu. Rev. Biochem.* **69**, 617.

[37] Vasil'eva, I.A., Moor, N.A. (2007). Interaction of aminoacyl_tRNA synthetases with tRNA: General principles and distinguishing characteristics of the high-molecular-weight substrate recognition. *Biochemistry* (Moscow) **72**, 247.

[38] Yonath, A., Leonard, K.R., Wittmann, H.G. (1987). A tunnel in the large ribosomal subunit revealed by three-dimensional image reconstruction. *Science* **236**, 813.

[39] Ban, N., Nissen, P., Hansen, J., Moore, P.B., Steitz, T.A. (2000). The complete atomic structure of the large ribosomal subunit at 2.4 Å resolution. *Science* **289**, 905.

[40] Carter, A.P., Clemons, W.M., Jr., Brodersen, D.E., Morgan-Warren, R.J., Hartsch, T., Wimberly, B.T., Ramakrishnan, V. (2001). Crystal structure of an initiation factor bound to the 30*s* ribosomal subunit. *Science* **291**, 498.

[41] Bashan, A., Agmon, I., Zarivach, R., Schluenzen, F., Harms, J., Berisio, R., Bartels, H., Franceschi, F., Auerbach, T., Hansen, H.A.S., Kossoy, E., Kessler, M., Yonath, A. (2003). Structural basis of the ribosomal machinery for peptide bond formation, translocation, and nascent chain progression. *Mol. Cell* **11**, 91.

[42] Bashan, A., Yonath, A. (2008). Correlating ribosome function with high-resolution structures. *Trends Microbiol.* **16**, 326.

[43] Yonath, A., Mussig, J., Tesche, B., Lorenz, S., Erdmann, V.A., Wittmann, H.G. (1980). Crystallization of the large ribosomal subunit from B. stearothermophilus. *Biochem. Int.* **1**, 428.

[44] Clemons, W.M., Jr., Brodersen, D.E., McCutcheon, J.P., May, J.L., Carter, A.P., Morgan-Warren, R.J., Wimberly, B.T., Ramakrishnan, V. (2001). Crystal structure of the 30 S ribosomal subunit from thermus thermophilus: Purification, crystallization and structure determination. *J. Mol. Biol.* **310**, 827.

[45] Clemons, W.M., Jr., May, J.L., Wimberly, B.T., McCutcheon, J.P., Capel, M.S., Ramakrishnan, V. (1999). Structure of a bacterial 30S ribosomal subunit at 5.5Å resolution. *Nature* **400**, 833.

[46] Ban, N., Freeborn, B., Nissen, P., Penczek, P., Grassucci, R.A., Sweet, R., Frank, J., Moore, P.B., Steitz, T.A. (1998). A 9Å resolution x-ray crystallographic map of the large ribosomal subunit. *Cell* **93**, 1105.

[47] Weinger, J.S., Strobel, S.A. (2007). Exploring the mechanism of protein synthesis with modified substrates and novel intermediate mimics. *Blood Cells Mol. Diseases* **38**, 110.

[48] Davie, E., Konigsberger, V., Lipman, F. (1956). The isolation of a tryptophan activating enzyme from pancreas. *Arch. Biochem. Biophys.* **65**, 21.

[49] Calendar, R., Berg, P. (1966). The catalytic properties of tyrosyl ribonucleic acid synthetases from Escherichia coli and Bacillus subtilis. *Biochemistry* **5**, 1690.

[50] Calendar, R., Berg, P. (1967). D-tyrosyl RNA: Formation, hydrolysis and utilization for protein synthesis. *J. Mol. Biol.* **26**, 39.

[51] Yamane, T., Miller, L., Hopfield, J.J. (1981). Discrimination between D- and L-tyrosyl transfer ribonucleic acids in peptide chain elongation. *Biochemistry* **20**, 7059.

[52] Bergmann, F.H., Berg, P., Dieckmann, M. (1961). The enzymic synthesis of amino acyl derivatives of ribonucleic acid: II. The preparation of leucyl-, valyl-, isoleucyl-, and methionyl ribonucleic acid synthetases from *Escherichia coli*. *J. Biol. Chem.* **236**, 1735.

[53] Norton, S., Ravel, J., Lee, C., Shive, W. (1963). Purification and properties of the aspartyl ribonucleic acid synthetase of *Lactobacillus arabinosus*. *J. Biol. Chem.* **238**, 269.

[54] Soutourina, J., Plateau, P., Blanquet, S. (2000). Metabolism of D-aminoacyl-tRNAs in *Escherichia coli* and *Saccharomyces*. *J. Biol. Chem.* **275**, 32535.

[55] Soutourina, J., Blanquet, S., Plateau, P. (2000). Protein synthesis post-translation modification and degradation. *J. Biol. Chem.* **275**, 11626.

[56] Tamura, K., Schimmel, P. (2006). Chiral-selective aminoacylation of an RNA minihelix: Mechanistic features and chiral suppression. *Proc. Natl. Acad. Sci. USA* **103**, 13750.

[57] Hecht, S.M. (1992). Probing the synthetic capabilities of a center of biochemical catalysis. *Accounts Chem. Res.* **25**, 545.

[58] Heckler, T.G., Zama, Y., Naka, T., Hecht, S. (1983). Dipeptide formation with misacylated tRNAPhe's. *J. Biol. Chem.* **258**, 4492.

[59] Roesser, J.R., Xu, C., Payne, R.C., Surratt, C.K., Hecht, S. (1989). Preparation of misacylated aminoacyl-tRNAPhe's useful as probes of the ribosomal acceptor sit. *Biochemistry*, **28**, 5185.

[60] Heckler, T.G., Roesser, J.R., Xu, C., Chang, P.I., Hecht, S. (1988). Ribosomal binding and dipeptide formation by misacylated tRNAPhe's. *Biochemistry* **27**, 7254.

[61] Profy, A.T., Usher, D.A. (1984). Stereoselective aminoacylation of a dinucleoside monophosphate by the imidazolides of DL-alanine and N-(ter-butoxycarbonyl)-DL-alanine. *J. Mol. Evol.* **20**, 147.

[62] Bain, J.D., Diala, E.S., Glabe, C.G., Wacker, D.A., Lyttle, M.H., Dix, T.A., Chamberlin, A.R. (1991). Site-specific incorporation of nonnatural residues during in vitro protein biosynthesis with semi-synthetic aminoacyl-tRNAs. *Biochemistry* **30**, 5411.

[63] Nathans, D. (1964). Puromycin inhibition of protein synthesis: Incorporation of puromycin into peptide chains. *Proc. Natl. Acad. Sci. USA* **51**, 585.

[64] Nathans, D., Neidle, A. (1963). Structural requirments for puromycin inihibition of protein synthesis. *Nature* **197**, 1076.

[65] Dedkova, L.M., Fahmi, N.E., Golovine, S.Y., Hecht, S.M. (2003). Enhanced D-amino acid incorporation into protein by modified ribosomes. *J. Am. Chem. Soc.* **125**, 6616.

[66] Kreil, G. (1997). D-Amino acids in animal peptides. *Annu. Rev. Biochem.* **66**, 337.

[67] Marahiel, M.A., Stachelhaus, T., Mootz, H.D. (1997). Modular peptide synthetases involved in nonribosomal peptide synthesis. *Chem. Rev.* **97**, 2651.

[68] Döhren, H. Von., Keller, U., Vater, J., Zocher, R. (1997). Multifunctional peptide synthetases. *Chem. Rev.* **97**, 2675.

[69] Fujii, N. (2002). D-amino acids in living higher organisms. *Orig. Life Evol. Biosph.* **32**, 103.

[70] Torres, A.M., Tsampazi, M., Kennett, E.C., Belov, K., Geraghty, D.P., Bansal, P.S., Alewood, P.F., Kuchel, P.W. (2007). Characterization and isolation of L-to-D-amino-acid-residue isomerase from platypus venom. *Amino Acids* **32**, 63.

[71] Stachelhaus, T., Walsh, C.T. (2000). Mutational analysis of the epimerization domain in the initiation module pheate of gramicidin synthetase. *Biochemistry* **39**, 5775.

[72] Challis, G.L., Naismith, J.H. (2004). Structural aspects of non-ribosomal peptide biosynthesis. *Curr. Opin. Struct. Biol.* **14**, 748.

[73] Friedman, M. (1999). Chemistry, nutrition, and microbiology of D-amino acids. *J. Agric. Food Chem.* **47**, 3457.

[74] Ohnishi, E., Macleod, H., Horowitz, N.H. (1962). Mutants of neurospora deficient in D-amino acid oxidase. *J. Biol. Chem.* **237**, 138.

[75] Champney, W.S., Jensen, R.A. (1970). Molecular events in the growth inhibition of *Bacillus subtilis* by D-tyrosine. *J. Bacteriol.* **104**, 107.

[76] Cosloy, S.D., McFall, E. (1973). Metabolism of D-serine in *Escherichia coli* K-12: Mechanism of growth inhibition. *J. Bacteriol.* **114**, 685.

[77] Rytka, J. (1975). Positive selection of general amino acid permease mutants in Saccharomyces cerevisiae. *J. Bacteriol.* **121**, 562.

[78] Harris. C.L. (1981). Cysteine and growth inhibition of Escherichia coli: Threonine deaminase as the target enzyme. *J. Bacteriol.* **145**, 1031.

[79] Tsuruoka, T., Tamura, A., Miyata, A., Takei, T., Iwamatsu, K., Inouye, S., Matsuhashi, M. (1984). Second lytic target of β-lactam compounds that have a terminal d-amino acid residue. *J. Bacteriol.* **160**, 889.

[80] Caparros, M., Torrecuadrada, J.L.M., Pedro, M.A. de (1991). Effect of D-amino acids on *Escherichia coli* strains with impaired penicillin-binding proteins. *Res. Microbiol.* **142**, 345.

[81] Capparos, M., Pisabarro, A.G., Pedro, M.A. de (1992). Effect of D-amino acids on structure and synthesis of peptidoglycan in Escherichia coli. *J. Bacteriol.* **174**, 5549.

[82] Dutta Banik, S., Nandi, N. (2009). Orientation and distance dependent chiral discrimination in the first step of the aminoacylation reaction: Integrated molecular orbital and semi-empirica method (ONIOM) based calculation. *Colloid Surf. B: Biointerfaces* **74**, 468.

[83] Dutta Banik, S., Nandi, N. (2010). Aminoacylation reaction in the histidyl-tRNA synthetase: Fidelity mechanism of the activation step. *J. Phys. Chem. B* **114**, 2301.

[84] Dutta Banik, S., Nandi, N. (2011). Influence of the conserved active site residues of histidyl tRNA synthetase on the mechanism of aminoacylation reaction. *Biophys. Chem.* **158**, 61.

[85] Dutta Banik, S., Nandi, N. (2012). Architectonics of active sites: Life processes at nanodimension. In Ariga, K. (ed.), *Manipulation of Nanoscale Material: An Introduction to Nanoarchitectonics*. Royal Society Publication, p. 213.

[86] Thompson, D., Lazennec, C., Plateau, P., Simonson, T. (2007). Ammonium scanning in an enzyme active site. The chiral specificity of aspartyl-tRNA synthetase. *J. Biol. Chem.* **282**, 30856.

[87] Dutta Banik, S., Nandi, N. (2012). Mechanism of the activation step of the aminoacylation reaction: A significant difference between class I and class II synthetases. *Biomol. Struct. Dynamics* **1**, 15.

[88] Dutta, S., Choudhury, K., Dutta Banik, S., Nandi, N. (2014). Active site nanospace of aminoacyl tRNA synthetases: Differences between the class I and class II synthetases. *J. Nanosci. Nanotechnol.* **14**, 2280.

[89] Sharma P.K., Xiang, Y., Kato, M., Warshel, A. (2005). What are the roles of substrate-assisted catalysis and proximity effects in peptide bond formation by the ribosome? *Biochemistry* **44**, 11307.

[90] Thirumoorthy, K., Nandi, N. (2007). Water catalyzed peptide bond formation in L-alanine dipeptide: The role of weak hydrogen bonding. *J. Mol. Struct. (THEOCHEM)* **818**, 107.

[91] Zarivach, R., Bashan, A., Berisio, R., Harms, J., Auerbach, T., Schluenzen, F., Bartels, H., Baram, D., Pyetan, E., Sittner, A., Amit, M., Hansen, H.A.S., Kessler, M., Liebe, C., Wolff, A., Agmon, I., Yonath, A. (2004). Functional aspects of ribosomal architecture: Symmetry, chirality and regulation. *J. Phys. Org. Chem.* **17**, 901.

[92] Rodnina, M.V., Beringer, M., Bieling, P. (2005). Ten remarks on peptide bond formation on the ribosome. *Biochem. Soc. Transact.* **33**, 493.

[93] Thirumoorthy, K., Nandi, N. (2006). Comparison of the intermolecular energy surfaces of amino acids: Orientation-dependent chiral discrimination. *J. Phys. Chem. B* **110**, 8840.

[94] Israelachvili, J.N. (1985). *Intermolecular and Surface Forces: With Applications to Colloidal and Biological Systems*. Academic Press, London.

[95] Maitland, G.C., Rigby, M., Smith, E.B., Wakeham, W.A. (1981). *Intermolecular Forces: Their Origin and Determination*, Clarendon Press, Oxford, UK.

[96] Thirumoorthy, K., Nandi, N. (2007). Homochiral preference in peptide synthesis in ribosome: Role of amino terminal, peptidyl terminal, and U2620. *J. Phys. Chem. B* **111**, 9999.

[97] Thirumoorthy, K., Nandi, N. (2008). Role of chirality of the sugar ring in the ribosomal peptide synthesis. *J. Phys. Chem. B* **112**, 9187.

[98] Chamberlin, S.I., Merino, E.J., Weeks, K.M. (2002). Catalysis of amide synthesis by RNA phosphodiester and hydroxyl groups. *Proc. Natl. Acad. Sci. USA* **99**, 14688.

[99] Trobro, S., Åqvist, J. (2005). Mechanism of peptide bond synthesis on the ribosome. *Proc. Natl. Acad. Sci. USA* **102**, 12395.

[100] Schmeing, T.M., Huang, K.S., Kitchen, D.E., Strobel, S.A., Steitz, T.A. (2005). Structural insights into the roles of water and the $2'$ hydroxyl of the P site tRNA in the peptidyl transferase reaction. *Mol. Cell* **20**, 437.

[101] Gindulyte, A., Bashan, A., Agmon, I., Massa, L., Yonath, A., Karle, J. (2006). The transition state for formation of the peptide bond in the ribosome. *Proc. Natl. Acad. Sci. USA* **103**, 13327.

[102] Sievers, A., Beringer, M., Rodnina, M.V., Wolfenden, R. (2004). The ribosome as an entropy trap. *Proc. Natl. Acad. Sci. USA* **101**, 7897.

[103] Schweet, R.S., Allen, E. (1958). Purification and properties of tyrosine-activating enzyme of hog pancreas. *J. Biol. Chem.* **233**, 1104.

[104] Nandi, N. (2004). Role of secondary level chiral structure in the process of molecular recognition of ligand: Study of model helical peptide. *J. Phys. Chem. B* **108**, 789.

[105] Nussinov, N., Aleman, C. (2006). Nanobiology: From physics and enginnering to biology, *Phys. Biol.* **3** (doi:10.1088/1478-3975/3/1/E01).

[106] Rőthlisberger, D., Khersonsky, O., Wollacott, A.M., Jiang, L., DeChancie, J., Betker, J., Gallaher, J.L., Althoff, E.A., Zanghellini, A., Dym, O., Albeck, S., Houk, K.A., Tawfik, D.S., Baker, D. (2008). Kemp elimination catalysts by computational enzyme design. *Nature* **453**, 190.

[107] Jiang, L., Althoff, E.A., Clemente, F.R., Doyle, L., Rőthlisbeger, D., Zanghellini, A., Gallaher, J.L., Betker, J., Tanaka, F., Barbas, III, C.F., Hilvert, H., Houk, K.A., Stoddard, B.L., Baker, D. (2008). De novo computational design of retro-aldol enzymes. *Science* **319**, 1387.

[108] Humphrey, W., Dalke, A., Schulten, K. (1996). VMD: Visual molecular dynamics. *J. Mol. Graphics* **14**, 33.

15

SOFTINTERFACE ON BIOSENSING

YUKICHI HORIGUCHI[1] AND YUKIO NAGASAKI[1–3]

[1]*Graduate School of Pure and Applied Sciences, University of Tsukuba, Japan*
[2]*Master's School of Medical Sciences, University of Tsukuba, Japan*
[3]*Satellite Laboratory of International Center for Materials Nanoarchitectonics (WPI-MANA), National Institute of Materials Science (NIMS), Tsukuba, Japan*

15.1 INTRODUCTION

In order to maintain active society, it is important to keep all citizens in good health. To protect people from serious disorders such as cancer and Alzheimer's disease, excessively sensitive and accurate diagnosis from very early stages of the target diseases are required. Usually, specific proteins related to particular disease are detected as biomarkers by certain techniques. However, target proteins are not always generated in significant amounts; in particular, the target protein level in early stages of the disease is quite low. In addition, huge amounts of coexisting proteins often disturb a specific protein sensing. Two researchers developed the biosensing system using a radioactive labeling technique, which is known as *radioimmunoassay* (RIA) [1]. In this method, radiolabeled antigens bound to ligand (antibody) on the surface prior to the sensing. When this surface is exposed to sample fluid, the labeled antigens are replaced with unlabeled target protein (antigen). The liberated RI-labeled antigen can be quantified with an extremely low detection limit by an RI detector. Development of the RIA method realized the detection of insulin in picomolar range, which is sufficient for sensitive diagnosis of diabetes. Thus, the high-sensitivity protein detection system has been recognized as a promising diagnostic method for detection of various diseases. However, RIA has restrictions on this use, because it requires radiolabeled reagents, specially trained technicians, special licenses (the case in Japan), and special arrangements for storage and disposal. To detect a trace amount of target proteins without RI labeling, new amplification techniques using several other methods have been developed, such as latex immunoassay [2–4], Western blotting [5], and enzyme-linked immunosorbent assay (ELISA) [6]. For example, ELISA has been developed by amplification of enzymatic reaction instead of RI labeling and attained the same detection level as that of RIA. In most cases, a labeling process of target antigen or antibody is required for amplification of the detection signal, which makes the system complicated and leads to high production cost. More recently, label-free immunosensing systems have been developed to recognize the target biomolecules. In these methods, specific surface events are monitored in seconds by physical quantity changes such as quartz frequency and refractive index. Thus, these systems can substantiate rapid biosensing more simply, without any labeling process. For example, quartz crystal microbalance (QCM) [7] detects adsorption of biomolecules by change in frequency of a quartz crystal resonator derived from mass and viscosity changes on the sensor surfaces, which can detect large biomolecules sensitively [8, 9]. The surface plasmon resonance (SPR) sensor is also a specialized instrument used to detect biomolecules in femtomolar range by refractive index changes on the surface [10]. These label-free immunosensing systems can output the association and dissociation of biomolecules on the surface as signal in second resolution. These instruments are now commercially available. Furthermore, new sensors are also developing such as a shear horizontal surface acoustic wave (SAW) sensor [11]. The sensitivity of the SAW

Encyclopedia of Biocolloid and Biointerface Science, Volume 1, First Edition. Edited by Hiroyuki Ohshima.
© 2016 John Wiley & Sons, Inc. Published 2016 by John Wiley & Sons, Inc.

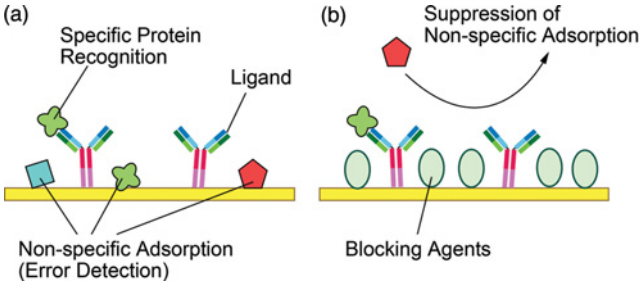


FIGURE 15.1 Protein adsorption behavior on hydrophobic and hydrophilic surfaces.

sensor is theoretically much higher than that of QCM, because that the frequency of the SAW (200−300 MHz) is much higher than that of conventional QCM (5−30 MHz). In addition, the SAW sensor surface is not limited to metal surfaces such as QCM and SPR sensors, which means that various types of surfaces such as carbon and titanium oxide are available for sensing.

Although the detection level can be improved by instrumental developments, an improvement of selective sensing is another important issue to be addressed. Because a nonlabeling sensing system cannot detect signals of a specific protein event but detects merely change in physical quantity of the surface by adsorbed whole molecules, nonspecific proteins disturb the specific protein recognition on the sensing surface. Thus, nonspecific protein adsorption should be minimized as much as possible in order to improve sensing performance (Fig. 15.1a). To suppress nonspecific adsorption on the sensor surface, blocking agents are generally employed after the immobilization of antibody. To fill up the nonspecific binding site, many kind of natural proteins such as bovine serum albumin (BSA), gelatin and casein have been employed as blocking agents (Fig. 15.1b). However, these blocking efficiencies are not sufficient, and there are two additional issues: (1) these kinds of natural polymer samples may contain dangerous bacteria, viruses, and prions, potentially inducing serious disease such as bovine spongiform encephalopathy (BSE); and (2) since performance varies somewhat between lots, it is difficult to maintain quality of the products.

For these reasons, synthetic products with high surface blocking performance are widely anticipated. Many synthetic polymers have been applied for surface modification of biosensors such as poly(vinyl alcohol), poly(ethylene glycol) (PEG), poly(2-hydroxyethyl methacrylate) (PHEMA) [12], poly(2-methacryloyloxyethyl phosphorylcholine) (PMPC) [13], and poly(2-methoxyethyl acrylate) (PMEA) [14]. For example, one team of investsigators reported that PEG immobilization in a tethered-chain configuration on the substrate surface effectively suppressed nonspecific protein adsorption [15]. We have also examined effective surface modification technology by our newly designed end-reactive PEG and applied them for high-performance biosensing surfaces. Here, we introduce PEGylation techniques to improve the specific molecular recognition efficacy on surfaces.

15.2 ADVANTAGES OF SUPPRESSING THE NONSPECIFIC ADSORPTION ON A SURFACE BY PEGylation

As stated above, nonspecific adsorption must be avoided for high-performance biosensing systems. Essential driving forces of protein adsorption on materials surface are derived from versatile interactions such as hydrophobic interaction, electrostatic interaction, the London dispersion force, and so on. In particular, hydrophobic hydration is one of the strongest interactions to promote the nonspecific protein adsorption on the surface. Thus, the surface modification techniques have focused on imparting hydrophilicity to the sensing surface for suppression of nonspecific protein adsorption. Poly(ethylene glycol) [PEG, also known as *poly(ethylene oxide)* (PEO) or *poly(oxyethylene)* (POE)] is one of the hydrophilic polymers most suitable for use as a modifier as it shows versatile functions in biotechnology and medicine. For instance, PEG is widely employed as a drug component such as a plasticizer, suppository base, and capsule [16–20]. PEG is an extremely low-toxicity polymer {e.g., PEG-750 (LD_{50} = 10 g/kg, intraperitoneally) [21], PEG-6000 (LD_{50} = 50 g/kg, orally) [22]}, which indicates that less interaction between PEG and biomolecules indicates relative lack of activity in a body. This unique character of PEG is derived from the hydrophilic chain with low interfacial free energy in water and high chain mobility. When PEG tethered layers are formed on a surface (PEGylation), steric stabilization by PEG prevents approach of protein on the surface (this is known as the *excluded-volume effect*). If we apply the PEGylation on the biosensing surfaces, the background noise by nonspecific adsorption of a large amount of coexisting proteins in the sample will be greatly suppressed. Hence, PEGylation techniques for biosensing surfaces have been investigated to improve the sensing performance.

15.3 PEG CHAIN BEHAVIOR ON SURFACES

In Section 15.2, we mentioned that PEGylation can impart a nonfouling characteristic on surfaces. To obtain maximum benefit from the PEGylation system, it is important to understand the PEG chain behavior on a surface. Modification techniques by terminally attaching polymer chains to surfaces have been widely used as biological applications; however, little was known about the kinetics of the tethered polymer chain on the surface at the molecular level in the early days. Hence, the physicochemical process of polymer chain attachment on the surface has been also investigated in recent

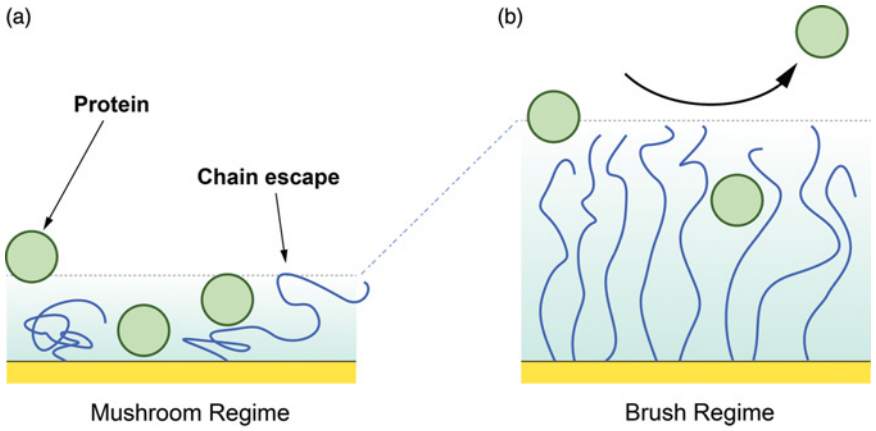


FIGURE 15.2 Behavior of PEG on surfaces: (a) mushroom regime (low density); (b) brush regime (high density).

decades. In a theoretical study, one researcher investigated the conformation of polymers attached on surface and suggested that there are different regimes for the grafted layer by density of grafted polymer on the surfaces [23]. The polymer chains forms a mushroomlike regime (well shrunken) on the surface when each chain is isolated and well separated; on the other hand, the polymer chains forms a brushlike regime (less shrunken) on the surface when the polymers are tethered densely on it [24]. It is also reported that the transition from the "mushroom regime" to the "brush regime" was monitored by measurement of the layer thickness on the grafted surface with gradient density [25,26]. The regime of the polymer as blocking agent on the surface is an important factor because the behavior of the polymer on the surface affects the blocking property derived from steric barrier of the surface. For example, the flexible polymer chains tethered on the surface transit from mushroom state to escape state when the polymer chains are compressed by proteins [27–29]; in other words, a steric barrier is not effective when the chain density is low (Fig. 15.2). Thus, the density of immobilized PEG on the surface is one of the most important factors for protein rejection property. A group of coworkers reported that the mass of absorbed protein decreased in a manner dependent on EG density [30]. This report showed that the density of the PEG chain affects the protein rejection on surfaces.

However, the nonfouling characteristic of PEG is derived from the spatial effect of PEG as well as the density of ethylene oxide units. It has been reported that PEG chain length affects the nonfouling characteristic [31] because steric sterilization by PEG random coils is strongly dependent on PEG layer thickness. Therefore, longer PEG chains with immobilized surfaces suppressed nonspecific protein adsorption more strongly. In contrast, this effect begins to decrease when PEG chain length exceeds 5 kDa. This means that reduction in PEG density on the surface allows space for nonspecific protein adsorption on that surface. Summarizing these observations, we concluded that 5 kDa of PEG is an appropriate length to ensure the highest level of nonfouling performance (Fig. 15.3).

The condition of the PEG immobilization process is also an important factor for construction of the PEGylated surface; specifically, concentration of PEG solution, ionic strength of the solution, flow time, and a number of immobilization cycles affect the density of the PEG on the surfaces [31, 32]. The combination of different lengths

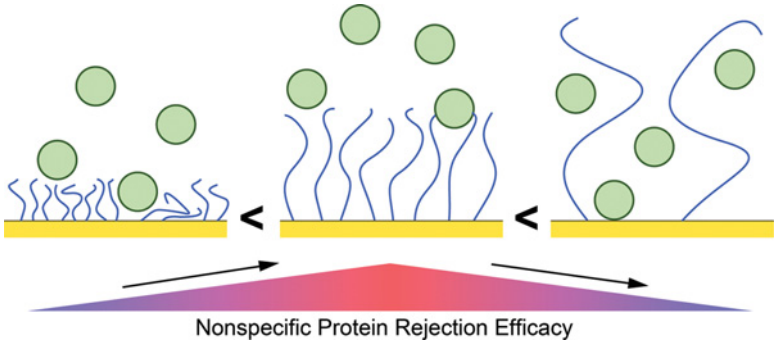


FIGURE 15.3 Correlation between PEG chain length and protein rejection efficacy.

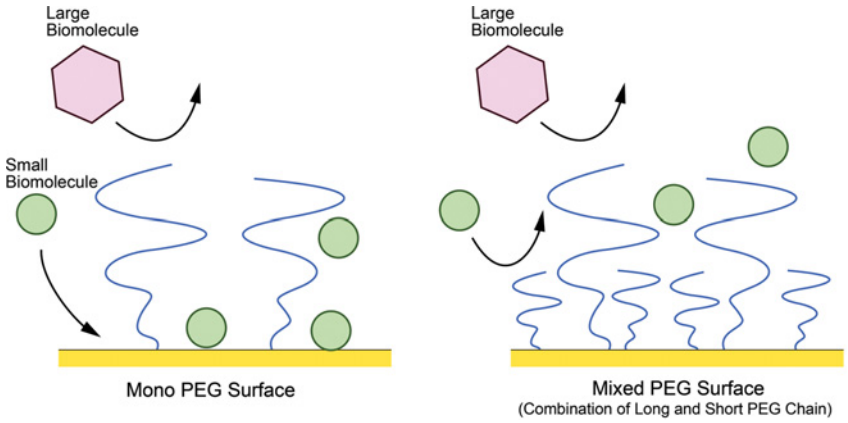


FIGURE 15.4 Difference in nonfouling character between mono-PEG surface and mixed-PEG surface.

of PEG immobilization on the surface is also an effective method for improving the nonfouling performance. We have reported that the combination of PEG (5k) and PEG (2k) tethered surface almost completely suppressed the nonspecific adsorption of low- as well as high-molecular-weight biomolecules [31–33], which indicated that two kinds of PEG chains suppress the nonspecific adsorption against different sizes of complementary biomolecules (Fig. 15.4). In this case, successive immobilization of longer PEG chain followed by shorter PEG chain is important point, because the density of the longer PEG chain is optimized first and shorter PEG chain fills the vacant spaces on the surface completely. This treatment improves the PEG chain density significantly.

15.4 FUNCTIONALIZATION OF PEG END FOR PEGylation ON SURFACE

In Section 15.3, we noted that the nonfouling characteristic of a steric barrier of PEG can be controlled by PEG density and thickness of the layer. To form the grafted PEG chains on a sensor surface, derivatization of one terminal of PEG should be required for tethering on a surface. At present, thiol-terminated PEG is widely used to immobilize the PEG chain on gold surfaces for biosensing systems such as SPR and QCM, because PEG chains were reported to be tethered on a gold surface strongly via S–Au bond (47 kcal/mol) [34]. We have been also employed this technique for the constructions of PEGylated surfaces [35–39]. Although immobilization by S–Au bond is quite a convenient technique for obtaining the densely packed PEG layer, this is not always a perfect method because of detachment of PEG chains from the surface. For example, S–Au bonds can be dissociated by oxidation of the thiol group [40–42]. Additionally, thiol-terminated compounds on gold surfaces can also be exchanged by other thiol-terminated compounds [43]. Thus, the structural stability of the S–Au bond depends on the surrounding environment. We have reported that the coordination method using a polyamine chain can be employed as an alternative technique for tethering. Although a coordination of amino group on a gold surface is not as strong (6 kcal/mol) as that in a S–Au bond [34], multipoint coordination by polyamine improves the immobilization stability. Actually, we have confirmed that the coordination of amino groups on gold surfaces was a primary factor when PEG-*b*-polyamine block copolymer was immobilized on a gold nanoparticle (GNP) surface [44]. Specifically, the size of GNPs prepared by poly(ethylene glycol)-*block*-poly((2-*N*,*N*-dimethylamino)ethyl methacrylate) (PEG-*b*-PAMA) under alkaline conditions was smaller (with high dispersion stability) compared with that prepared by neutral (or acidic) conditions. The results indicated that the polyamine is coordinated not by the electrostatic interaction between protonated amines and negatively charged gold surfaces but by chemisorption between lone pairs on nitrogen atoms and gold surfaces (Fig. 15.5). Actually, no detachment of PEG-*b*-polyamine was observed even under high-ionic-strength media [45]. We have also confirmed that three to six amino groups at the end of the PEG chain significantly improve the coordination stability compare with monoaminated PEG. On the contrary, the dispersion stability such as GNPs gradually decreases with further increase of the number of amino groups. The increase in amino repeating units at the end of PEG chain tends to decrease PEG brush density on the gold surface because of the exclusive area of polyamine segment on the surface.

From the information obtained, we have recently designed pentaethylenehexamine-terminated PEG (N6-PEG) for a surface modification agent. The performance of N6-PEG for immobilization on gold surface is very high because there is a multipoint gold–nitrogen bond of six amino groups. It is also confirmed that this PEG is useful for immobilization on carboxylated surfaces via covalent bond with active ester groups as well [33,46]. This technique can increase the PEGylation efficacy compared with monoaminated PEG

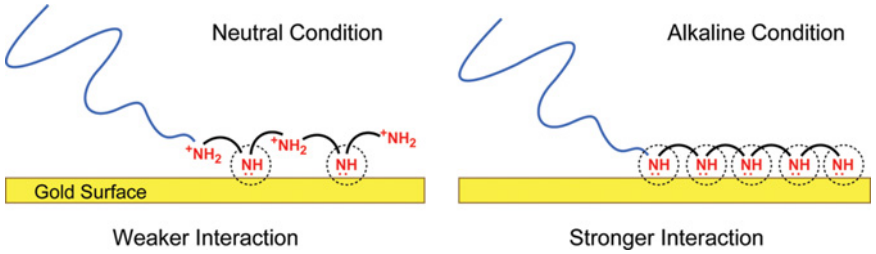


FIGURE 15.5 PEG-*b*-PAMA immobilization to gold surface in neutral condition and alkaline condition.

(N1-PEG), because part of the protonated amino groups can interact with anionic surfaces via electrostatic interaction to support esterification of the nonprotonated amino group (Fig. 15.6). N6-PEG is now commercially available from JSR Life Science, Japan as Blockmaster^{TM}.

For another example, PEG-*b*-polyanion such as poly(ethylene glycol)-*b*-poly(acrylic acid) (PEG-*b*-PAAc) is suitable for PEGylation of cationic surfaces, iron oxide surfaces, and so on [47–49]. However, PEG-*b*-PAAc is not always applicable, because the extremely hydrophilic PAAc segment decreases its interaction on positively charged substrate surface especially high ionic strength such as serum solution. We have reported that PEG-poly(4-vinylbenzylphosphonate) block copolymer (PEG-*b*-PVBP), which has a hydrophobic polystyrene chain in the polyanionic segment, showed strong affinity for the iron oxide surface. In this case, the interaction stability of multipoint anchoring of phosphate was enhanced via hydrophobic interaction between PVBP segment and iron oxide surface [50]. Recently, we have confirmed that the PEG-b-PVBP is also applicable to stainless surfaces to significantly improve their non-fouling characters.

Thus, PEGylation is a versatile system that imparts a nonfouling characteristic on various surfaces by suitably functionalized PEG. Design of the functionalization of PEG end plays an important role in PEGylation on various kinds of surfaces.

15.5 HYBRID IMMOBILIZATION OF PEG WITH LIGAND MOLECULES

The densely packed PEG tethered chain improves nonfouling performance on various kinds of surfaces. Multipoint anchoring is also an important factor in the stable immobilization of PEG chains on the surface under harsh environmental conditions. Coimmobilization of PEG tethered chain with ligand molecules is another important factor. In order to improve biosenesing performance, both specific protein recognition and suppression of nonspecific protein adsorption should be optimized at the same time. As stated above, the general blocking agents such as BSA are applied to the surface after immobilization of the ligand to fill any gaps on the surface for prevention of nonspecific protein adsorption. On the contrary, the PEGylation technique can be applied for not only blocking but also promoting ligand immobilization and specific recognition. We have reported that new construction of single-stranded DNA (ssDNA) and PEG coimmobilized surface using PEG-*b*-PAMA block copolymer showed high efficacy of hybridization. To form the coimmobilized surface, ssDNA chains were immobilized on the surface after

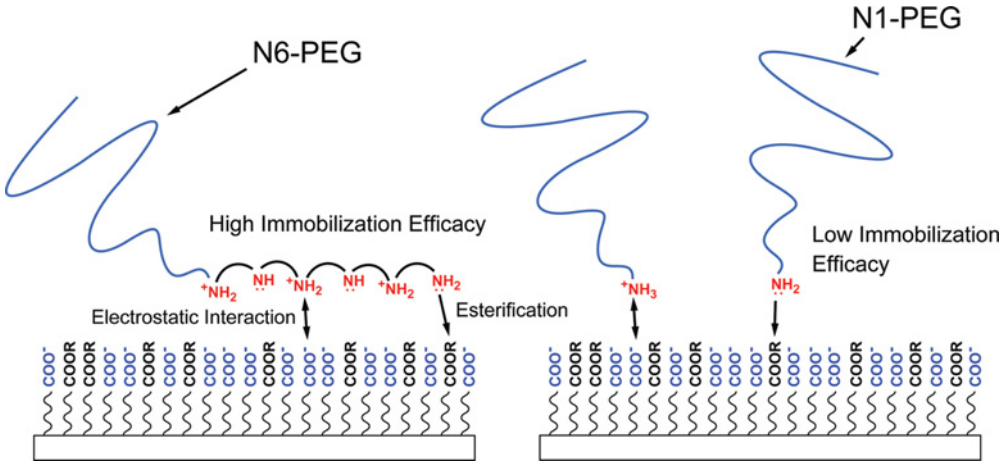


FIGURE 15.6 Immobilization of N6-PEG and N1-PEG on carboxylated surface. (Protonated N1-PEG interacts with negatively changed surface and hinders in accessing non-protonated N1-PEG to the surface.)

coating with PEG-*b*-PAMA. Under the suitable PAMA chain length, a high amount of ssDNA was immobilized under the standing fashion, which was supported by preimmobilized PEG-*b*-PAMA chain [51]. In this case, the amount of immobilized ssDNA was considerably improved by PEG-*b*-PAMA compared with bare gold surfaces, due to the electrostatic attractive force between a positively charged PAMA surface and negatively charged ssDNA. In addition, the recognition efficacy of a PEG-*b*-PAMA/ssDNA coimmobilized surface was also higher than that of the ssDNA surface, indicating that PEGylation improves the recognition efficacy of ssDNA on the surface. There is concern regarding the fact that coimmobilized PEG-*b*-PAMA controlled the ssDNA orientation on the coimmobilized surfaces in order to hybridize with complementary ssDNA effectively [51]. Thus, when we consider the design of a surface for the biosensing system, not only the nonfouling characteristic of the blocking agent but also the coimmobilization procedure should be addressed in forming highly sensitive immunosurfaces.

To understand this phenomenon in greater depth, we have also investigated the thrombin (TB) and thrombin binding aptamer (TBA) affinity on TBA/PEG-*b*-PAMA coimmobilized surface [52]. To control the coimmobilized surface condition, three kinds of PEG-*b*-PAMA with different chain lengths of PAMA were prepared to control the density of PEG (Fig. 15.7a). In addition, three kinds of TBAs with different numbers of thymine spacer units [TBA-T(*n*), where *n* = number of thymine) were also prepared to control the distance of TBA from the sensor surface (Fig. 15.7b). The result indicated that the amount of immobilized thiol-terminated TBA increased when the PAMA segment increased (20, 33, 50 AMA units), because exclusive area of PAMA segment tethered on the surface allowed further immobilization of TBA on the surface. However, TB binding efficacy on TBA/PEG-*b*-PAMA (20) coimmobilized surface is the highest among these surfaces even though the amount of immobilized TBA was the lowest (Fig. 15.7a). This result indicated that the molecular recognition efficacy could be controlled by coimmobilization of ligand and PEG in order to bind with the target more effectively. Furthermore, the distance of tethered TBA from the surface was also significantly affected to the TB binding efficacy. In the case of coimmobilization with PEG-*b*-PAMA (20), the TBA-T(40) showed the higher binding efficacy than TBA-T(20) and TBA-T(60) when the chain length of PEG was 5k. The result indicates that sufficient exposure of TBA from PEG layer is not obtained by using shorter spacers; in contrast, overexposure of the TBA from the dense PEG layer resulted from using longer spacers, which may induce folding or another unwanted orientation (Fig. 15.7b). Owing to these phenomena, we concluded that the surface for a biosensing system should be designed systematically to ensure high performance.

The PEG tethered chain on the biosensor surface also plays an important role in protection from denaturation of protein ligands such as antibody on surface. For example, we reported that the denaturation of the adsorbed protein on the surface was greatly suppressed by densely packed PEG tethered chains surrounding of the immobilized protein [39]. When the Fab′ of anti-CRP antibody (antibody fragment) was immobilized on the sensor chip surface, 90% of the CRP binding activity was lost on the constructed surface after 60 min, while the CRP binding activity did not decrease significantly when it was coimmobilized PEG chains at the

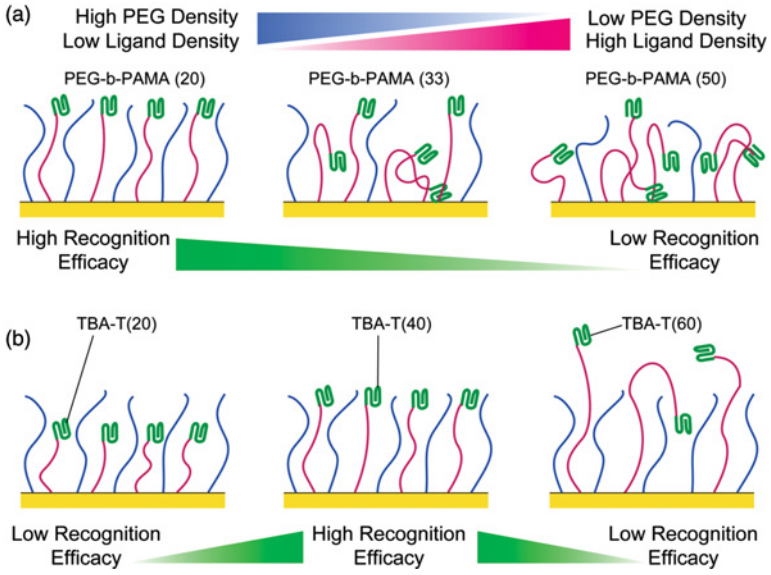


FIGURE 15.7 Schematic representations of various conditions of coimmobilization of PEG/ligand surfaces.

same time. Actually, more than 70% of the binding activity remained 60 min after construction of the CRP/PEG coimmobilized surface on gold sensor chip. This phenomenon indicated that densely packed PEGylation prevents denaturation immediately following protein immobilization.

To summarize, well-designed PEGylated surfaces greatly improve the specific recognition efficacy on the biosensor. The roles of PEG on the sensor chip surface were not only the suppression of nonspecific protein adsorption but also control of sensing performance of ligands. Investigation of PEG/ligand coimmobilized surface is one of the most important aspects in the design of the high-performance biosensing surface.

15.6 CONCLUSION

In this chapter, we introduced the basic interaction between biomolecules on the surface from the biosensor perspective. Suppression of nonspecific protein adsorption on the surface is one of the most important points in improving the property of the sensing surfaces. PEGylation techniques can improve nonfouling performance by the hydrophilic chain with low interfacial free energy in water and high chain mobility. The formation of hydrophilic and steric stabilized PEG layer can reject many complicated interactions such as hydrophobic interaction, electrostatic interaction, and intermolecular force. We introduced mainly the PEG immobilization techniques to improve the performance of nonspecific protein adsorption on surfaces as much as possible. The PEGylated surface shows not only suppression of nonspecific adsorption but also improvement of the immobilization efficacy of ssDNA, enhancement of the binding efficacy of specific protein binding, prevention of protein denaturation on the surface, and so on. Although an optimization of sensing performance depends on the targets, ligands, surfaces, and devices, PEGylation can be applied widely because suitable functionalization of the PEG end can accomplish the PEGylation on each kind of biosening surface. The tailor-made PEGylation technique is one promising ways to improve the biosening system.

REFERENCES

[1] Yalow, R.S., Berson, S.A. (1960). Immunoassay of endogenous PLASMA insulin in man. *J. Clin. Invest*. **39**, 1157–1175.

[2] Bernard, A.M., Lauwerys, R.R. (1982). Latex immunoassay of retinol-binding protein. *Clin. Chem.* **28**, 1167–1171.

[3] Bernard, A.M., Lauwerys, R.R. (1983). Continuous-flow system for automation of latex immunoassay by particle counting. *Clin. Chem.* **29**, 1007–1011.

[4] Song, M.I., Iwata, K., Yamada, M., Yokoyama, K., Takeuchi, T., Tamiya, E., Karube, I. (1994). Multisample analysis using an array of microreactors for an alternating-current field-enhanced latex immunoassay. *Anal. Chem.* **66**, 778–781.

[5] Towbin, H., Staehelin, T., Gordon, J. (1979). Electrophoretic transfer of proteins from polyacrylamide gels to nitrocellulose sheets: Procedure and some applications. *Proc. Natl. Acad. Sci. USA* **76**, 4350–4354.

[6] Engvall, E., Perlmann, P. (1972). Enzyme-linked immunosorbent assay, elisa. *J. Immunol.* **109**, 129–135.

[7] King, W.H. (1964). Piezoelectric sorption detector. *Anal. Chem.* **36**, 1735–1739.

[8] Lvov, Y., Ariga, K., Kunitake, T. (1994). Layer-by-layer assembly of alternate protein/polyion ultrathin films. *Chem. Lett.* **23**, 2323–2326.

[9] Rickert, J., Brecht, A., Göpel, W. (1997). Quartz crystal microbalances for quantitative biosensing and characterizing protein multilayers. *Biosens. Bioelectron.* **12**, 567–575.

[10] Kano, H., Kawata, S. (1994). Surface-plasmon sensor for absorption-sensitivity enhancement. *Appl. Optics* **33**, 5166–5170.

[11] Kondoh, J., Saito, K., Shiokawa, S., Suzuki, H. (1996). Simultaneous measurements of liquid properties using multichannel shear horizontal surface acoustic wave microsensor. *Jpn. J. Appl. Phys.* **35**, 3093.

[12] Wichterle, O., Lim, D. (1960). Hydrophilic gels for biological use. *Nature* **185**, 117–118.

[13] Ishihara, K., Aragaki, R., Ueda, T., Watenabe, A., Nakabayashi, N. (1990). Reduced thrombogenicity of polymers having phospholipid polar groups. *J. Biomed. Mater. Res.* **24**, 1069–1077.

[14] Tanaka, M., Motomura, T., Kawada, M., Anzai, T., Yuu, K., Shiroya, T., Shimura, K., Onishi, M., Akira, M. (2000). Blood compatible aspects of poly(2-methoxyethylacrylate) (PMEA)—relationship between protein adsorption and platelet adhesion on PMEA surface. *Biomaterials* **21**, 1471–1481.

[15] Nagaoka, S., Nakao, A. (1990). Clinical application of antithrombogenic hydrogel with long poly (ethylene oxide) chains. *Biomaterials* **11**, 119–121.

[16] Sothornvit, R., Krochta, J.M. (2001). Plasticizer effect on mechanical properties of β-lactoglobulin films. *J. Food Eng.* **50**, 149–155.

[17] Fang, J.-Y., Wu, P.-C., Huang, Y.-B., Tsai, Y.-H. (1995). In vitro permeation study of capsaicin and its synthetic derivatives from ointment bases using various skin types. *Int. J. Pharm.* **126**, 119–128.

[18] Uzunkaya, G., Bergişadi, N. (2003). In vitro drug liberation and kinetics of sustained release indomethacin suppository. *Il Farmaco* **58**, 509–512.

[19] Ishikawa, T., Watanabe, Y., Takayama, K., Endo, H., Matsumoto, M. (2000). Effect of hydroxypropylmethylcellulose (HPMC) on the release profiles and bioavailability of a poorly water-soluble drug from tablets prepared using macrogol and HPMC. *Int. J. Pharm.* **202**, 173–178.

[20] Heykants, J., Van Peer, A., Van de Velde, V., Van Rooy, P., Meuldermans, W., Lavrijsen, K., Woestenborghs, R., Van

Cutsem, J., Cauwenbergh, G. (1989). The clinical pharmacokinetics of itraconazole: An overview. *Mycoses* **32**, 67–87.

[21] Veronese, F. (ed.) (2009). *PEGylated Protein Drugs: Basic Science and Clinical Applications*. Birkhäuser Basel, pp. 127–146.

[22] Ren, S., Park, M.-J., Kim, A., Lee, B.-J. (2008). In vitro metabolic stability of moisture-sensitive rabeprazole in human liver microsomes and its modulation by pharmaceutical excipients. *Arch. Pharmacal. Res.* **31**, 406–413.

[23] de Gennes, P.G. (1980). Conformations of polymers attached to an interface. *Macromolecules* **13**, 1069–1075.

[24] Szleifer, I. (1996). Statistical thermodynamics of polymers near surfaces, *Curr. Opin. Colloid Interface Sci.* **1**, 416–423.

[25] Wu, T., Efimenko, K., Genzer, J. (2002). Combinatorial study of the mushroom-to-brush crossover in surface anchored polyacrylamide, *J. ACS* **124**, 9394–9395.

[26] Brittain, W.J., Minko, S. (2007). A structural definition of polymer brushes. *J. Polym. Sci. A: Polym. Chem.* **45**, 3505–3512.

[27] Milchev, A., Yamakov, V., Binder, K. (1999). Escape transition of a compressed polymer mushroom under good solvent conditions. *Europhys. Lett.* **47**, 675.

[28] Steels, B.M., Leermakers, F.A.M., Haynes, C.A. (2000). Analysis of compression of polymer mushrooms using self-consistent field theory. *J. Chromatogr. B: Biomed, Sci. Appl.* **743**, 31–40.

[29] Allen, C., Dos Santos, N., Gallagher, R., Chiu, G.N.C., Shu, Y., Li, W.M., Johnstone, S.A., Janoff, A.S., Mayer, L.D., Webb, M.S., Bally, M.B. (2002). Controlling the physical behavior and biological performance of liposome formulations through use of surface grafted poly(ethylene glycol). *Biosci. Reports* **22**, 225–250.

[30] Feller, L.M., Cerritelli, S., Textor, M., Hubbell, J.A., Tosatti, S.G.P. (2005). Influence of poly(propylene sulfide-block-ethylene glycol) di- and triblock copolymer architecture on the formation of molecular adlayers on gold surfaces and their effect on protein resistance: A candidate for surface modification in biosensor research. *Macromolecules* **38**, 10503–10510.

[31] Uchida, K., Otsuka, H., Kaneko, M., Kataoka, K., Nagasaki, Y. (2005). A reactive poly(ethylene glycol) layer to achieve specific surface plasmon resonance sensing with a high S/N ratio: The substantial role of a short underbrushed PEG layer in minimizing nonspecific adsorption. *Anal. Chem.* **77**, 1075–1080.

[32] Uchida, K., Hoshino, Y., Tamura, A., Yoshimoto, K., Kojima, S., Yamashita, K., Yamanaka, I., Otsuka, H., Kataoka, K., Nagasaki, Y. (2007). Creation of a mixed poly(ethylene glycol) tethered-chain surface for preventing the nonspecific adsorption of proteins and peptides. *Biointerphases* **2**, 126–130.

[33] Nagasaki, Y., Kobayashi, H., Katsuyama, Y., Jomura, T., Sakura, T. (2007). Enhanced immunoresponse of antibody/mixed-PEG co-immobilized surface construction of high-performance immunomagnetic ELISA system. *J. Colloid Interface Sci.* **309**, 524–530.

[34] Felice, R.D., Selloni, A. (2004). Adsorption modes of cysteine on Au(111): Thiolate, amino-thiolate, disulfide. *J. Chem. Phys.* **120**, 4906–4914.

[35] Otsuka, H., Akiyama, Y., Nagasaki, Y., Kataoka, K. (2001). Quantitative and reversible lectin-induced association of gold nanoparticles modified with α-lactosyl-ω-mercapto-poly(ethylene glycol). *J. ACS* **123**, 8226–8230.

[36] Satomi, T., Nagasaki, Y., Kobayashi, H., Otsuka, H., Kataoka, K. (2007). Density control of poly(ethylene glycol) layer to regulate cellular attachment. *Langmuir* **23**, 6698–6703.

[37] Yoshimoto, K., Hirase, T., Nemoto, S., Hatta, T., Nagasaki, Y. (2008). Facile construction of sulfanyl-terminated poly(ethylene glycol)-brushed layer on a gold surface for protein immobilization by the combined use of sulfanyl-ended telechelic and semitelechelic poly(ethylene glycol)s. *Langmuir* **24**, 9623–9629.

[38] Yoshimoto, K., Hirase, T., Madsen, J., Armes, S.P., Nagasaki, Y. (2009). Non-fouling character of poly[2-(methacryloyloxy)ethyl phosphorylcholine]-modified gold surfaces fabricated by the 'grafting to' method: Comparison of its protein resistance with poly(ethylene glycol)-modified gold surfaces. *Macromol. Rapid Commun.* **30**, 2136–2140.

[39] Yoshimoto, K., Nishio, M., Sugasawa, H., Nagasaki, Y. (2010). Direct observation of adsorption-induced inactivation of antibody fragments surrounded by mixed-PEG layer on a gold surface. *J. ACS* **132**, 7982–7989.

[40] Castner, D.G., Hinds, K., Grainger, D.W. (1996). X-ray photoelectron spectroscopy sulfur 2p study of organic thiol and disulfide binding interactions with gold surfaces. *Langmuir* **12**, 5083–5086.

[41] Cooper, E., Leggett, G.J. (1998). Static secondary ion mass spectrometry studies of self-assembled monolayers: Influence of adsorbate chain length and terminal functional group on rates of photooxidation of alkanethiols on gold. *Langmuir* **14**, 4795–4801.

[42] Bearinger, J.P., Terrettaz, S., Michel, R., Tirelli, N., Vogel, H., Textor, M., Hubbell, J.A. (2003). Chemisorbed poly(propylene sulphide)-based copolymers resist biomolecular interactions. *Nat. Mater.* **2**, 259–264.

[43] Hostetler, M.J., Green, S.J., Stokes, J.J., Murray, R.W. (1996). Monolayers in three dimensions: Synthesis and electrochemistry of ω-functionalized alkanethiolate-stabilized gold cluster compounds, *J. ACS* **118**, 4212–4213.

[44] Miyamoto, D., Oishi, M., Kojima, K., Yoshimoto, K., Nagasaki, Y. (2008). Completely dispersible PEGylated gold anoparticles under physiological conditions: Modification of gold nanoparticles with precisely controlled PEG-b-polyamine. *Langmuir* **24**, 5010–5017.

[45] Yoshimoto, K., Nozawa, M., Matsumoto, S., Echigo, T., Nemoto, S., Hatta, T., Nagasaki, Y. (2009). Studies on the adsorption property and structure of polyamine-ended poly(ethylene glycol) derivatives on a gold surface by surface plasmon resonance and angle-resolved X-ray photoelectron spectroscopy. *Langmuir* **25**, 12243–12249.

[46] Yuan, X., Fabregat, D., Yoshimoto, K., Nagasaki, Y. (2012). High PEGylation efficiency of pentaethylenehexamine-end poly(ethylene glycol) (mPEG-N6) for active-ester surface. *Colloids Surf. B: Biointerfaces* **92**, 25–29.

[47] Kamimura, M., Miyamoto, D., Saito, Y., Soga, K., Nagasaki, Y. (2008). Design of poly(ethylene glycol)/streptavidin coimmobilized upconversion nanophosphors and their application to fluorescence biolabeling. *Langmuir* **24**, 8864–8870.

[48] Kamimura, M., Miyamoto, D., Saito, Y., Soga, K., Nagasaki, Y. (2008). Preparation of PEG and protein co-immobilized upconversion nanophosphors as near-infrared biolabeling materials. *J. Photopolym. Sci. Technol.* **21**, 183–187.

[49] Lakshmipriya, T., Fujimaki, M., Gopinath, S.C.B., Awazu, K., Horiguchi, Y., Nagasaki, Y. (2013). A high-performance waveguide-mode biosensor for detection of factor IX using PEG-based blocking agents to suppress non-specific binding and improve sensitivity. *Analyst* **138**, 2863–2870.

[50] Ujiie, K., Kanayama, N., Asai, K., Kishimoto, M., Ohara, Y., Akashi, Y., Yamada, K., Hashimoto, S., Oda, T., Ohkohchi, N., Yanagihara, H., Kita, E., Yamaguchi, M., Fujii, H., Nagasaki, Y. (2011). Preparation of highly dispersible and tumor-accumulative, iron oxide nanoparticles: Multipoint anchoring of PEG-b-poly(4-vinylbenzylphosphonate) improves performance significantly. *Colloids Surf. B: Biointerfaces* **88**, 771–778.

[51] Yoshimoto, K., Matsumoto, S., Asakawa, R., Uchida, K., Ishii, T., Nagasaki, Y. (2007). Immobilization and hybridization behavior of DNA on poly(ethylene glycol)-block-poly[2-(N,N-dimethylamino)ethyl methacrylate]-modified gold surfaces. *Chem. Lett.* **36**, 1444–1445.

[52] Horiguchi, Y., Miyachi, S., Nagasaki, Y. (2013). High-performance surface acoustic wave immunosensing system on a PEG/aptamer hybridized surface. *Langmuir* **29**, 7369–7376.

16

BIOSEPARATION USING THERMORESPONSIVE POLYMERS

Kenichi Nagase and Teruo Okano

Institute of Advanced Biomedical Engineering and Science, Tokyo Women's Medical University (TWIns), 8-1 Kawadacho, Shinjuku, Tokyo 162-8666, Japan

16.1 INTRODUCTION

In recent decades, stimuli-responsive polymers have attracted much attention in materials science. One such polymer most widely used in biomedical applications is the thermoresponsive polymer poly(*N*-isopropylacrylamide) (PIPAAm). This polymer exhibits phase transition behavior across its lower critical solution temperature (LCST), 32°C, which is near the normal human body temperature [1]. The polymer also exhibits hydrophilic/hydrophobic changes, attributed to hydration and dehydration, respectively. The intrinsic properties of PIPAAm are used in thermally modulated drug delivery systems [2], thermoresponsive enzymes [3], biosensors [4], and thermoresponsive cell culture substrates [5,6]. Some investigators have demonstrated that this thermoresponsive polymer could be used in bioseparations, such as chromatography matrices or cell separation tools. In this chapter, various bioseparations using PIPAAm and its derivatives are summarized.

16.2 THERMORESPONSIVE CHROMATOGRAPHY WITH HYDROPHOBIC INTERACTIONS

Chromatography is an effective tool in bioseparations. The separation of bioactive compounds using reversed-phase chromatography requires the addition of organic solvents as a mobile phase to modulate interaction between the stationary phase and analytes. However, the use of organic solvents in the mobile phase can potentially deactivate bioactive compound analytes. To avoid this issue, thermoresponsive chromatography without any organic solvents has been developed. Figure 16.1 illustrates the concept of thermoresponsive chromatography. Modified PIPAAm is used as the chromatographic stationary phase, and the prepared beads are packed into a column. The hydrophobicity of the modified PIPAAm stationary phase changes with changing temperature. At low temperatures, the PIPAAm stationary phase is hydrophilic as a result of hydration. Hydrophobic interactions between PIPAAm and analytes are therefore relatively weak. However, at elevated temperatures, the modified PIPAAm becomes hydrophobic as a result of dehydration, and hydrophobic interactions between the modified PIPAAm and analytes are enhanced. In this way, hydrophobic interactions between the stationary phase and analytes can be modulated by changing the column temperature. This chromatographic system requires no organic solvents to modulate hydrophobic interactions between the stationary phase and analytes, leading to preservation of the activities of bioactive analytes and a reduction in pollution associated with waste organic solvents.

Various PIPAAm-modifying methods and PIPAAm graft configurations have been investigated to develop effective stationary phases for thermoresponsive chromatography matrices.

PIPAAm terminally grafted silica beads were prepared through coupling reactions between amino groups on silica surfaces and PIPAAm with activated ester groups. (Fig. 16.2a) [7]. The prepared PIPAAm-modified beads were

Encyclopedia of Biocolloid and Biointerface Science, Volume 1, First Edition. Edited by Hiroyuki Ohshima.
© 2016 John Wiley & Sons, Inc. Published 2016 by John Wiley & Sons, Inc.

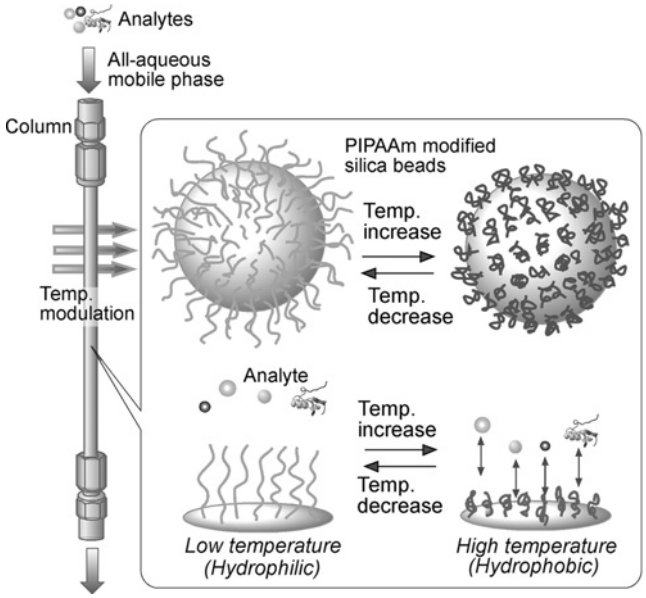


FIGURE 16.1 Concept of thermoresponsive chromatography using PIPAAm-grafted beads as packing material.

packed in columns, and their performance was evaluated by observing the elution profiles of five hydrophobic steroids at various temperatures. At low temperatures (e.g., 5°C), hydrophobic steroids were eluted in short retention times, and were not separated (Fig. 16.3). However, with increasing

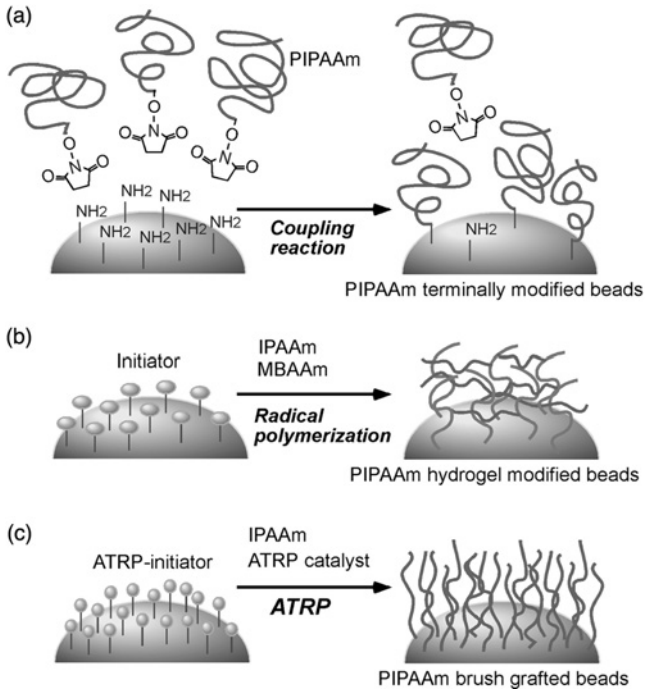


FIGURE 16.2 Various types of PIPAAm modification of bead surfaces for thermoresponsive chromatography matrices.

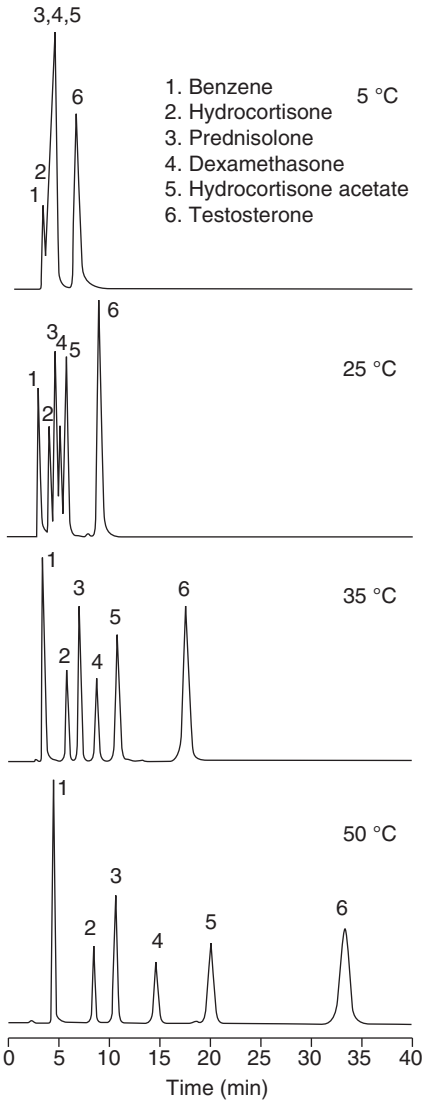


FIGURE 16.3 Chromatograms of hydrophobic steroids separated using column packed with PIPAAm-modified silica beads. (Adapted from Ref. 7. Copyright 1996, American Chemical Society.)

column temperature, the retention times of the hydrophobic steroids increased, because the hydrophobicity of the modified PIPAAm increases with increasing dehydration, leading to enhancement of hydrophobic interactions between the grafted PIPAAm and the steroids. At 50°C, baseline separation of the hydrophobic steroids was achieved.

PIPAAm-hydrogel-modified silica beads were prepared by radical polymerization using a premodified azo initiator on the surface and a cross-linker (Fig. 16.2b) [8]. The prepared beads were packed in a column, and the performance was evaluated by observing the elution behaviors of hydrophobic steroids. The retention times on the PIPAAm-hydrogel column were longer than those on PIPAAm terminally

modified beads, but the peaks in the chromatograms were wider for the PIPAAm-hydrogel-modified bead column than for the PIPAAm terminally grafted silica bead column. Steroid molecules tend to penetrate the PIPAAm-hydrogel layer and interact with PIPAAm, leading to wider peaks and longer retention times.

More recently, living radical polymerizations have been employed as useful and effective polymerization techniques. *Atom transfer radical polymerization* (ATRP), in particular, is a polymerization technique that enables accurate control of the polymerization and formation of densely packed polymer brushes on substrates [9, 10]. Modification of PIPAAm through surface-initiated ATRP has been used to prepare thermoresponsive chromatography matrices.

An ATRP initiator was immobilized on silica bead surfaces through a silane coupling reaction. ATRP was then performed using an ATRP catalyst, and densely packed PIPAAm brushes were grafted on the silica bead surfaces (Fig. 16.2c) [11]. Almost 10 times as much PIPAAm was grafted on the beads prepared by surface-initiated ATRP than on PIPAAm-hydrogel-modified beads or PIPAAm terminally grafted beads [12]. The prepared beads were evaluated as chromatographic matrices by observing the elution profiles of hydrophobic steroids at various temperatures. Significantly longer steroid retention times were observed compared with those obtained using PIPAAm terminally grafted beads or PIPAAm-hydrogel-modified beads, although the column length was only one-third that of the others. This is because there were more hydrophobic interactions between the steroids and the polymer as a result of the larger amount of PIPAAm on the beads. Also, in surface-initiated ATRP, the graft density can be modulated by changing the initiator density on the surface. The graft density of PIPAAm on the bead surfaces affected the thermally modulated dehydration properties and interactions between the PIPAAm graft interface and analytes [13, 14].

The hydrophobic interactions between grafted PIPAAm on beads and analytes were enhanced by incorporation of a hydrophobic monomer, *n*-butyl methacrylate (BMA), in PIPAAm, to improve the separation of relatively hydrophilic analytes.

A random copolymer of PIPAAm and BMA was prepared using a radical telomerization reaction, and the prepared P(IPAAm-*co*-BMA) was grafted on silica bead surfaces through a coupling reaction [15]. The prepared beads were evaluated by observing their hydrophobic steroid elution profiles at various temperatures. The retention times of the hydrophobic steroids increased with increasing BMA content of the copolymer, indicating that hydrophobic interactions between the steroids and copolymer increased with increasing BMA content. Also, the phase transition temperature decreased with increasing BMA content, and the temperature-dependent retention profiles of steroids are related to the phase transition temperature. On P(IPAAm-*co*-BMA)-modified beads, baseline separation of hydrophobic steroids was obtained at 30°C, whereas this steroid mixture was not separated on PIPAAm-homopolymer-modified beads. In addition, using a column packed with P(IPAAm-*co*-BMA)-modified beads, separation of a peptide mixture containing insulin chain A, β-endorphin fragment 1-27, and insulin chain B was performed [15], and phenylthiohydantoin amino acid analyses were performed using the same column [16].

BMA incorporation into PIPAAm brushes on silica beads was also performed to further enhance hydrophobic interactions between the polymer brushes and analytes. P(IPAAm-*co*-BMA)-brush-grafted beads were prepared by surface-initiated ATR copolymerization of BMA with IPAAm [17]. The separation efficiencies of benzoic acids and phenol, which are used as preservatives in fragrances, foods, and cosmetics, were evaluated using the prepared beads packed in a column. The retention time of the benzoic acids increased with increasing BMA content in the grafted copolymer brushes, because the copolymer brush hydrophobicity increased with increasing BMA content, leading to enhanced hydrophobic interactions between the copolymer brushes and analytes. High-resolution separation of benzoic acids was obtained using a column packed with copolymer-brush-grafted beads with a high BMA content. These results show that P(IPAAm-*co*-BMA)-brush-grafted beads can be used to separate relatively hydrophilic analytes [17].

16.3 THERMORESPONSIVE CHROMATOGRAPHY WITH ELECTROSTATIC INTERACTIONS

Ion exchange chromatography is an effective tool for separating ionic bioactive compounds such as peptides, and proteins, because almost all biological compounds have specific hydrophobic and ionic properties. However, ion exchange chromatography requires the addition of a large amount of salt to the mobile phase to modulate electrostatic interactions between the mobile phase and analytes. Excessive amounts of salts in the mobile phase can deactivate biologically active analytes. Desalting of the separated analytes is required in purification. To overcome these issues, thermoresponsive ion exchange chromatography matrices have been developed using thermoresponsive ionic copolymers.

Thermoresponsive cationic copolymers have been used as stationary-phase modifiers for separating acidic bioactive molecules. *N,N*-Dimethylaminopropylacrylamide (DMAPAAm) has been incorporated into thermoresponsive copolymers, and beads modified with a P(IPAAm-*co*-DMAPAAm-*co*-BMA) hydrogel have been used as thermoresponsive cationic chromatography matrices [18,19]. A column packed with the prepared beads was used to separate a mixture of adenosine nucleotides. The retention times decreased with

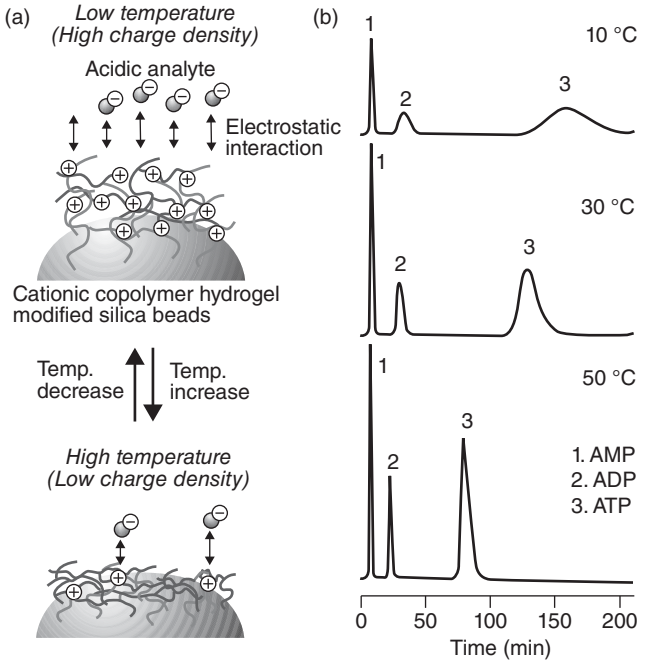


FIGURE 16.4 Thermoresponsive ion exchange chromatography: (a) temperature-modulated electrostatic interactions between thermoresponsive cationic copolymer and acidic biomolecules; (b) chromatogram of adenosine nucleotide mixture separated using column packed with beads modified with P(IPAAm-*co*-DMAPAAm-*co*-BMA) hydrogel. (Adapted from Ref. 19. Copyright 2004, Wiley.)

increasing temperature, because the basicity of the modified P(IPAAm-*co*-DMAPAAm-*co*-BMA) decreased with increasing temperature, as a result of the increased hydrophobicity of the dimethylamino group (Fig. 16.4). The results demonstrated that electrostatic interactions between a grafted cationic copolymer and analytes can be modulated by simply changing the temperature. Beads modified with the same copolymer hydrogel were used to analyze nonsteroidal anti-inflammatory drugs [20] and oligonucleotides [21].

For the separation of basic bioactive compounds, beads modified with a thermoresponsive anionic hydrogel were prepared by copolymerization of IPAAm and acrylic acid [22]. The elution behaviors of catecholamine derivatives on P(IPAAm-*co*-acrylic acid(AAc))-hydrogel-modified beads were observed at various temperatures. Four types of catecholamine derivatives were separated at high temperatures, whereas separation was not achieved using a column with PIPAAm-hydrogel-modified beads. The retention times of the catecholamine derivatives were in the same order as their hydrophobicities, indicating that hydrophobic interactions also contributed to the separation of catecholamine derivatives. The incorporation of a hydrophobic monomer into the thermoresponsive anionic copolymer P(IPAAm-*co*-AAc) therefore improved the separation efficiency.

A hydrophobic monomer, *tert*-butylacrylamide (tBAAm), was incorporated into a thermoresponsive anionic hydrogel to improve separation efficiency. A column packed with beads modified with a P(IPAAm-*co*-AAc-*co*-tBAAm) hydrogel was used to separate catecholamine derivatives; the retention times were higher and higher-resolution separation was achieved compared with those obtained using P(IPAAm-*co*-AAc)-hydrogel-modified beads [23]. In addition, angiotensin peptides were separated using a column packed with P(IPAAm-*co*-AAc-*co*-tBAAm)-hydrogel-modified beads; the separation time was shortened by changing the column temperature stepwise [24].

In thermoresponsive ion exchange chromatography, the graft configuration of the thermoresponsive polymer on the bead surface is important for the separation efficiency. Beads grafted with thermoresponsive ionic copolymer brushes were therefore prepared by surface-initiated ATRP.

A cationic monomer, 2-(dimethylamino)ethyl methacrylate (DMAEMA), was incorporated into PIPAAm brushes, and thermoresponsive beads with grafted cationic copolymer brushes were prepared as thermoresponsive anion exchange matrices [25]. A column packed with the prepared beads was used to investigate the elution behaviors of adenosine nucleotides at various temperatures. The adenosine nucleotide retention times were much higher than those observed using beads modified with thermoresponsive cationic hydrogels, in which large amounts of cationic copolymer were grafted on the bead surfaces, leading to strong electrostatic interactions between the stationary phase and the analytes. Also, when a step-temperature gradient was used, rapid changes in the retention times were observed compared with those for the column with thermoresponsive-hydrogel-modified beads. This is attributed to the graft configuration of the thermoresponsive cationic copolymer brush. On the thermoresponsive copolymer brush, each polymer chain moves freely, whereas the polymer chains are connected in the hydrogel, leading to a rapid temperature response [25].

For the effective separation of basic bioactive compounds, beads grafted with a thermoresponsive anionic copolymer, P(IPAAm-*co*-AAc-*co*-tBAAm), were prepared by surface-initiated ATRP [26]. A column packed with the beads was used for high-resolution separations of catecholamine derivatives and angiotensin peptides. The results were compared with those obtained using columns packed with copolymer-hydrogel-modified beads.

Beads modified with thermoresponsive ionic copolymer brushes adsorb proteins and can be used for protein purification. Silica beads grafted with thermoresponsive cationic copolymer, P(IPAAm-*co*-DMAPAAm-*co*-tBAAm), brushes were prepared by surface-initiated ATRP. The elution behaviors of an acidic protein [i.e., human serum albumin (HSA)] and a neutral protein (i.e., γ-globulin) were observed at various temperatures, using columns packed with the prepared

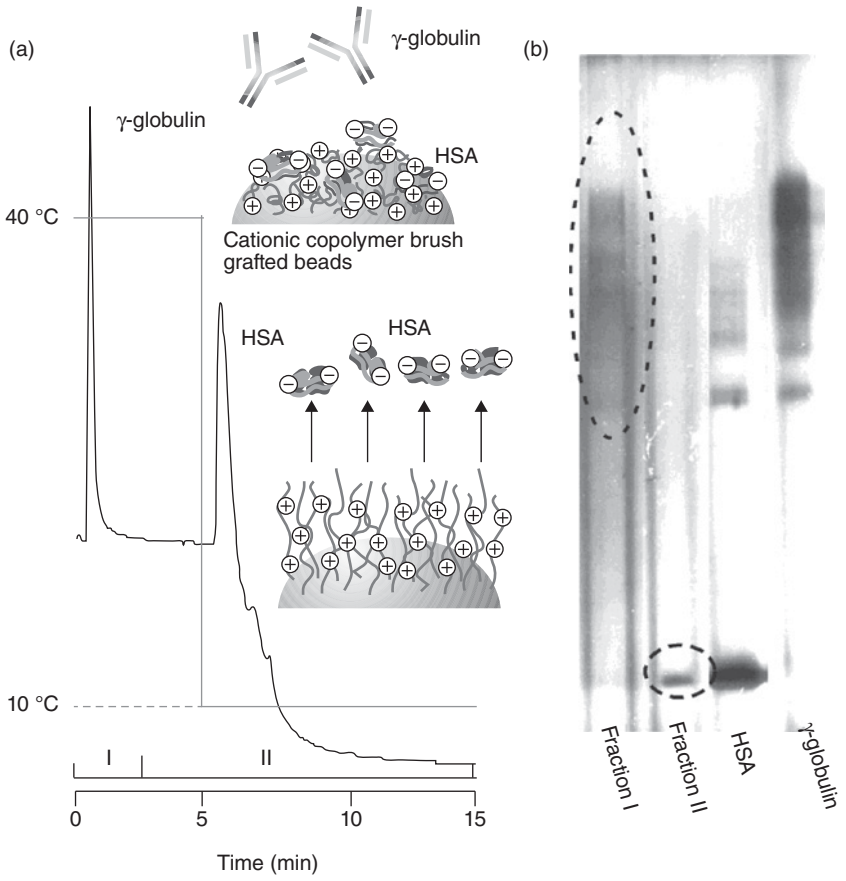


FIGURE 16.5 Separation of HSA and γ-globulin using thermoresponsive cationic copolymer brushes: (a) chromatograms with step-temperature gradients; (b) SDS-PAGE analysis of eluted proteins. (Adapted from Ref. 27. Copyright 2011, Elsevier.)

beads [27]. At high temperature, HSA was not eluted but γ-globulin was. This is because the acidic HSA was adsorbed on the cationic copolymer brushes through both electrostatic and hydrophobic interactions. The copolymer hydrophobicity increased with increasing temperature, as a result of dehydration of the grafted copolymer. However, a certain level of cationic charge remained even at high temperatures, although the charge density decreased with increasing temperature. The acidic HSA was therefore adsorbed on the copolymer brushes at elevated temperatures, but the neutral globulin was not. Because of this property, HSA and γ-globulin separation was performed using a step-temperature gradient (Fig. 16.5). A mixture of HSA and γ-globulin was loaded onto the column at 40°C; HSA was adsorbed on the copolymer brush surfaces and γ-globulin was eluted. The column temperature was then reduced to 10°C and the adsorbed HSA was recovered. Sodium dodecyl sulfate polyacrylamide gel electrophoresis (SDS-PAGE) analysis showed that the fractions at 40°C and 10°C contained purified γ-globulin and HSA, respectively.

Silica beads grafted with brushes of the thermoresponsive anionic copolymer P(IPAAm-*co*-AAc-*co*-tBAAm) were used as thermoresponsive protein adsorption materials for purification of basic proteins [28]. Lysozyme was absorbed on the thermoresponsive anionic copolymer brushes at high temperatures. This is also the result of hydrophobic and electrostatic interactions between the thermoresponsive anionic copolymer brushes and basic lysozyme. The protein adsorption properties of the copolymer-modified beads were used to purify egg-white lysozyme. At 30°C, whole egg-white proteins were loaded onto the bead-packed column; lysozyme was adsorbed on the copolymer brush surfaces, but the other proteins were eluted at this temperature. The temperature was then reduced to 10°C and the adsorbed lysozyme was recovered from the column. SDS-PAGE analysis showed that the fraction at 10°C contained only purified lysozyme [28].

16.4 THERMORESPONSIVE CHROMATOGRAPHY USING VOLUME EXCLUSION EFFECT OF PIPAAm

PIPAAm exhibits a temperature-dependent coil–globule transition. Below the LCST, PIPAAm chains swell and extend as a result of polymer hydration, but PIPAAm is dehydrated

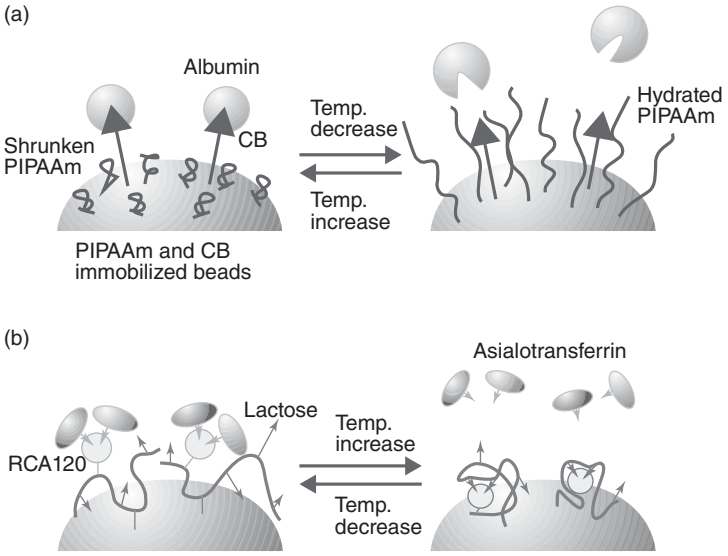


FIGURE 16.6 Affinity chromatography using thermoresponsive PIPAAm conformation changes: (a) selective adsorption and desorption of albumin; (b) selective adsorption and desorption of asialotransferrin. (Adapted from Refs. 30 and 31. Copyright 2002, 2003, American Chemical Society.)

and agglutinates above the LCST. On the basis of these properties, various types of thermoresponsive chromatography have been developed.

PIPAAm was grafted onto porous glass beads by a coupling reaction between the activated chain ends of PIPAAm and the amino groups on the glass bead surfaces [29]. A column was packed with the prepared PIPAAm-grafted glass beads as a gel permeation chromatography matrix. Below the LCST of PIPAAm (32°C), the elution times of dextrans of various molecular weights were shorter than those observed above the LCST. At lower temperatures, the grafted PIPAAm swells and extends, preventing dextran diffusion inside the glass bead pores. In contrast, above the LCST, the grafted PIPAAm on the glass beads dehydrates and shrinks, and dextran diffuses into the pores, leading to longer elution times. The elution times of dextran molecules can therefore be changed by changing the column temperature [29].

The PIPAAm modification site on porous beads is important for effective separation. Two types of PIPAAm-grafted polystyrene beads were prepared, using cyclohexanol and toluene as porogenic agents, in water [30]. When cyclohexanol was used, the PIPAAm was grafted on the outer surface and inside the pores, because radical polymerization occurred inside the pores. In contrast, when toluene was used, PIPAAm was grafted only on the external bead surfaces, because polymerization did not occur inside the pores. The elution profiles of dextran were observed using these prepared beads as gel permeation chromatography matrices. When the beads prepared with cyclohexanol were used, the dextran elution time was longer above the LCST than it was below the LCST. However, the opposite results were obtained using beads prepared with toluene. In other words, the elution time above the LCST was shorter than that below the LCST; the same results were observed using an unmodified column. These results show that temperature-dependent diffusion of analytes into the pores of porous beads can be achieved by grafting PIPAAm inside the pores [30].

Temperature-modulated PIPAAm extension and shrinkage have been used to develop new types of affinity chromatography. Cibacron blue F3G-A (CB), which is a specific ligand for HSA, and PIPAAm were immobilized on poly(glycidyl methacrylate-*co*-ethyleneglycol dimethacrylate) or poly(glycidyl methacrylate-*co*-triethyleneglycol dimethacrylate) beads (Fig. 16.6a) [31]. Albumin tended to adsorb on the beads, because the modified PIPAAm dehydrated and shrank, leading to exposure of albumin to coimmobilized CB. In contrast, at low temperatures, the adsorbed albumin was released, because the hydrated and expanded PIPAAm chains reduced the affinity between CB and albumin. These beads were used to purify albumin from human serum just by changing the temperature. Human serum was loaded onto the column at 37°C; albumin was adsorbed on the beads though the affinity between CB and albumin, whereas the other proteins were eluted. The temperature was then reduced to 20°C, and the adsorbed albumin was eluted, because the affinity between CB and albumin decreased as a result of PIPAAm chain extension [31].

Another type of thermoresponsive chromatography was used to purify asialotransferrin, using the affinity ligand *Ricinus communis* agglutinin (RCA120) and lactose, which competitively binds to RCA120 (Fig. 16.6b) [32]. PIPAAm chains, RCA120, and lactose were immobilized on sepharose beads. At low temperatures, the immobilized RCA120 was bound to asialotransferrin as a result of their affinity, but

lactose was unable to bind to RCA120, because of extension of the PIPAAm chains. However, at a higher temperature, the modified PIPAAm chains were hydrated, and they shrank, leading to an increase in the local concentration of lactose in the vicinity of RCA120. Lactose was bound to RCA120, and the bound asialotransferrin was released. The beads could therefore be used to purify asialotransferrin simply by changing the temperature.

16.5 THERMORESPONSIVE CHROMATOGRAPHY FOR HIGH-SPEED SEPARATION

In analytical chemistry, monolithic silica rod columns consisting of a single piece with a three-dimensionally interconnected structure have attracted attention as alternatives to bead-packed columns [33, 34]. Monolithic silica columns enable high-speed separation of analytes, because of the higher linear velocity of the mobile phase and reduced diffusion path lengths of analytes compared with those for bead-packed columns. The advantages of monolithic silica rod columns have been used in thermoresponsive chromatography matrices.

PIPAAm brushes were grafted on monolithic silica rod surfaces using surface-initiated ATRP, by flowing the reaction solution into a monolithic silica rod column (Fig. 16.7) [35]. The prepared PIPAAm-modified column was used to observe the elution behaviors of hydrophobic steroids. The steroid retention times were significantly shorter (<10 min) than those observed with a bead-packed column (>40 min). This is attributed to the reduced diffusion pathlengths of the analytes and higher linear velocity of the mobile phase in the monolithic silica rod. Additionally, introducing hydrophilic moiety on graft interface of PIPAAm brush on monolithic silica rod was performed for further

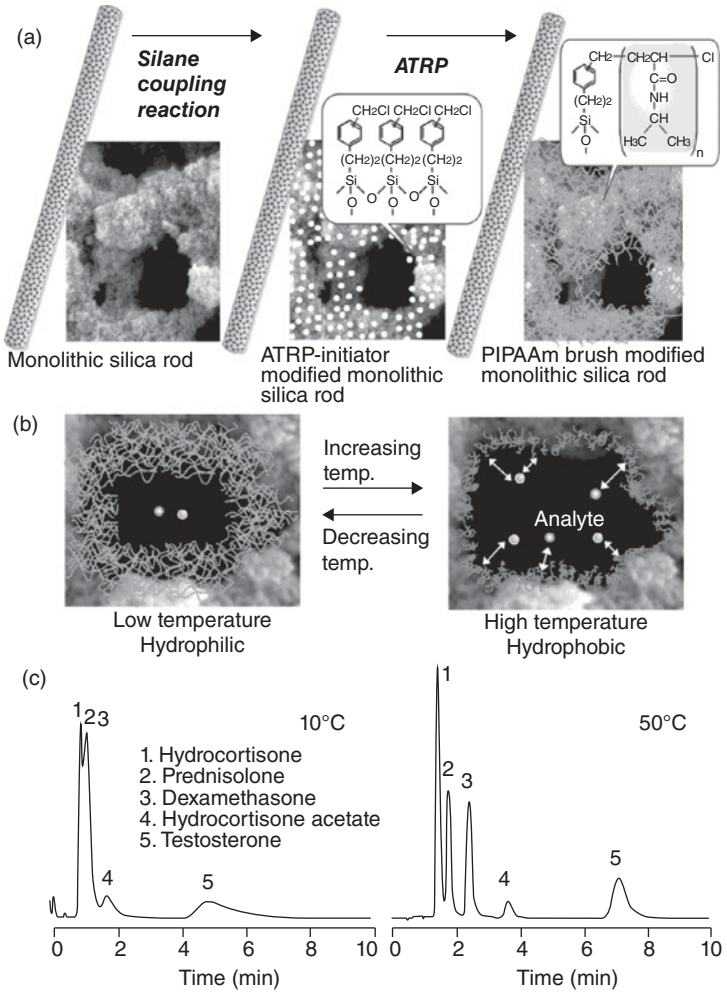


FIGURE 16.7 Thermoresponsive monolithic silica rod for high-speed separation: (a) scheme for preparation of monolithic silica rod; (b) thermally modulated interactions between PIPAAm brushes and analytes in monolithic silica rod; (c) chromatogram of hydrophobic steroids. (Adapted from Ref. 35. Copyright 2011, American Chemical Society.)

shortening of analysis time, because the polarity of PIPAAm graft interface affects elution behavior of analytes [14]. When the silica rod with grafted PIPAAm brushes was used, the separation of hydrophobic steroids was further shortened to within 5 min. These results indicate that thermoresponsive monolithic silica rods are alternatives to bead-packed columns for high-resolution separation of hydrophobic analytes with short retention times.

A thermoresponsive ion exchange monolithic silica rod column for high-speed separation of ionic biomolecules was prepared by modification of the silica rod with thermoresponsive cationic copolymer brushes. P(IPAAm-*co*-DMAEMA-*co*-tBAAm) brushes were grafted on the monolithic silica rod surface by surface-initiated ATRP [36]. The prepared monolithic silica rod column was used to investigate the temperature-dependent elution behaviors of adenosine nucleotides. The modified column separated an adenosine nucleotide mixture (AMP, ADP, and ATP) within 5 min, whereas a column packed with beads modified with the same copolymer brushes required approximately 100 min for separation. These results indicated that silica rods modified with thermoresponsive ionic copolymers are effective separation tools for ionic biomolecules.

16.6 THERMALLY MODULATED CELL SEPARATION USING PIPAAm

As progress has been made in biotechnology, the demand for cell separation technologies has increased. Fluorescence-activated cell sorting and magnetic cell sorting are widely used as precise cell separation methods. However, these cell separation methods require modification of cell surfaces using fluorinated antibodies or magnetic particles; this is undesirable when using original cells in their native state, such as in investigation of cell properties and in transplants in the human body. Also, these cell-sorting methods require expensive apparatus and incur high running costs. To overcome these issues, various cell separation systems using thermoresponsive polymers have been developed.

Cell separation using an aqueous two-phase system and PIPAAm-modified antibodies has been proposed as a concise cell separation procedure [37, 38]. Anti-CD34 antibodies for specific KG-1 cells were treated with itaconic anhydride and glucose to introduce vinyl groups into the antibodies. Then copolymerization of IPAAm and the antibodies with vinyl groups was performed, to produce PIPAAm-modified antibodies. The PIPAAm-modified antibodies were used for cell separation of KG-1 cells from Jurkat cells, using an aqueous two-phase system consisting of poly(ethylene glycol) (PEG) and dextran solutions. More than 80% of the KG-1 cells were obtained from the upper PEG solution phase, whereas few Jurkat cells were partitioned into the PEG phase, because the PIPAAm-modified antibodies tended to partition into the PEG solution phase. These results indicated that PIPAAm-modified antibodies enable partitioning of specific cells, using a simple method.

Cell separation using a PIPAAm cryogel, which was prepared by cross-linking polymerization under semifrozen conditions, has also been proposed [39, 40]. A Cu(II)–iminodiacetate ligand specific for *Escherichia coli* cells was bound to a PIPAAm cryogel, and *E. coli* cells were bound to the cryogel surface. At 25°C, 65% of the bound cells were eluted using 0.2 mol/L imidazole buffer solution. However, using the same buffer heated to 40°C, 85% of the bound cells were recovered, because the affinity between the cells and the ligand was reduced by disruption of the pore wall surfaces of the PIPAAm cryogel, induced by PIPAAm aggregation.

Other types of cell separation using a PIPAAm-grafted polypropylene (PP) membrane and adsorbed antibodies has been proposed [41]. A PIPAAm-grafted PP membrane was prepared by plasma-induced polymerization, and antimouse CD80 monoclonal antibodies (CD80mAb) or CD86 monoclonal antibodies (CD86 mAb) were adsorbed by incubation of the antibody solution. When the antibody CD80 mAb was adsorbed on the PP membrane, adsorption of CD80 cells was greater than that on a membrane with adsorbed CD86 mAb or an antibody-free PIPAAm-grafted PP membrane. When the temperature was reduced to 4°C, the adhered cells were recovered together with antibodies from the PIPAAm-grafted PP membrane, because the PIPAAm grafted on the PP membrane became hydrophilic and adhered cells were detached. CD80- or CD86-transfected cells were enriched to 72% or 66% from a 1:1 suspension using this method [41]. A similar method was used to adsorb anti-human CD34 monoclonal antibodies on a PIPAAm-grafted PP membrane to enrich CD34-positive KG-1a cells to 85% from a 1:1 cell suspension of KG-1a cells and Jurkat cells [42].

These methods enable simple separation of cells; however, they use antibodies, which are sometimes expensive and unstable, leading to high costs and low reproducibility. Additionally, the separated cells contain antibodies on the cell surfaces, which would lead to problems in research or in transplants in the human body. To avoid these issues, temperature-modulated cell separation methods without antibodies were investigated.

Lymphocyte subpopulations, B cells and T cells, were separated using a column packed with glass beads with grafted PIPAAm brushes [43]. PIPAAm brushes of various chain lengths were grafted on the glass bead surfaces by surface-initiated ATRP. The wettability of the PIPAAm brushes was determined using contact-angle measurements; the results showed that hydrophilicity increased with increasing PIPAAm brush length. Columns packed with glass beads with grafted PIPAAm brushes were used to investigate the retentions and recoveries of rat lymphocytes at 37°C and 5°C, respectively. Lymphocyte retention on the beads at 37°C decreased with increasing PIPAAm brush length,

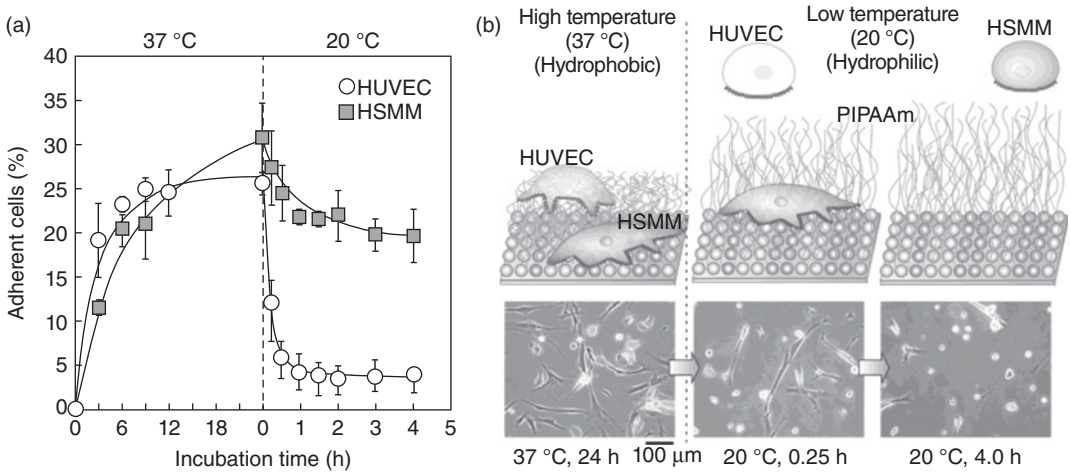


FIGURE 16.8 Temperature-modulated cell separation using PIPAAm brushes: (a) cell adhesion and detachment profiles; (b) cell morphologies on PIPAAm brushes. (Adapted from Ref. 44 with permission from The Royal Society of Chemistry.)

because the increased hydrophilic properties prevented lymphocyte retention on the PIPAAm brushes. However, at 5°C, the recovery rate increased with increasing PIPAAm brush length, because longer PIPAAm brushes tend to be hydrated and become hydrophilic, leading to lymphocyte desorption. Investigation of the subpopulation retention profiles showed that the B cells exhibited temperature-modulated retention and recovery, whereas low T-cell recovery rates were observed. This is probably because of the high adhesion properties of the T cells. These results indicated that a column packed with beads grafted with PIPAAm brushes could be used to modulate the ratio of B and T cells in lymphocytes simply by changing the temperature.

Human cells for cardiovascular tissue engineering can also be separated using PIPAAm brushes [44]. PIPAAm brushes were grafted onto a glass substrate by surface-initiated ATRP, and temperature-modulated adhesion and detachment of four types of human cells was observed. The cells all had similar adhesion rates to the PIPAAm brushes. However, different detachment rates from the PIPAAm brushes were observed. On the basis of these properties, human umbilical vein endothelial cells (HUVECs) and human skeletal muscle myoblast cells (HSMMs) were separated (Fig. 16.8). At 37°C, both types of cell adhered to the PIPAAm brushes. When the temperature was reduced to 20°C, the HUVECs were rapidly detached from the PIPAAm brushes, but the HSMMs were gradually detached from the PIPAAm brushes. In the initial incubation period at 20°C, concentrated HUVECs were obtained. In subsequent periods, a high ratio of HSMMs was recovered. These results indicated that adhesive cells can be separated using PIPAAm brushes, based on the different cell detachment rates.

Cell separation using the intrinsic detachment temperature of the cell has also been proposed [45]. Hydrophobized PIPAAm brushes were prepared on a glass substrate through surface-initiated ATRP by copolymerization with BMA as a hydrophobic comonomer. Cell adhesion at 37°C and detachment at 10°C and 20°C using the prepared P(IPAAm-*co*-BMA) brushes were observed. HUVECs were detached at 20°C, whereas normal human dermal fibroblast (NHDF) detachment was observed at 10°C; these results are attributed to the intrinsic metabolic activities of the cells [46]. On the basis of these properties, HUVECs and NHDFs were separated using multistep temperature changes. At 37°C, HUVECs and NHDFs both adhered to the copolymer brushes. The temperature was then reduced to 10°C, and the adhered NHDFs were recovered. The temperature was then elevated to 20°C, and the adhered HUVECs were recovered. These results suggested that each type of cell has an intrinsic temperature for detachment from thermoresponsive copolymer brushes, and the temperature difference could be used for cell separation.

These cell separation methods enable cell separation by simply changing the temperature, without modification of the cell surfaces. Such separated cells could be used in medical treatment.

16.7 CONCLUSIONS

In this chapter, various bioseparation techniques using thermoresponsive polymers were summarized. Thermoresponsive chromatography can be used to separate biomolecules simply by changing the temperature, without adding organic solvents or excessive amounts of salts to the mobile phase. Also, cell separation methods using thermoresponsive polymers are simple and do not require modification of the cell surfaces. These bioseparation techniques can be performed

by simply changing the external temperature, without using reagents that are harmful to biological compounds. These thermally modulated bioseparation methods are becoming increasingly important with progress in biomedical technology.

ACKNOWLEDGMENT

Part of the present research was financially supported by the "Funding Program for World-Leading Innovative R&D on Science and Technology (FIRST Program)," initiated by the Council for Science and Technology Policy from the Japan Society for the Promotion of Science (JSPS). This study was also facilitated and enhanced by the creation of innovation centers for advanced interdisciplinary research areas, through programs such as the Project for Developing Innovation Systems "Cell Sheet Tissue Engineering Center (CSTEC)" from the Ministry of Education, Culture, Sports, Science and Technology (MEXT), Japan; the Development of New Environmental Technology Using Nanotechnology Project of the National Institute of Environmental Science (NIES), commissioned from the Ministry of Environment, Japan; and Grants-in-Aid for Young Scientists (B) Grant 24760580 from the Ministry of Education, Culture, Sports, Science and Technology (MEXT), Japan.

REFERENCES

[1] Heskins, M., Guillet, J.E. (1968). *J. Macromol. Sci. A* **2**, 1441–1455.

[2] Cammas, S., Suzuki, K., Sone, C., Sakurai, Y., Kataoka, K., Okano, T. (1997). *J. Control. Release* **48**, 157–164.

[3] Hoffman, A.S., Stayton, P.S. (2007). *Progress Polym. Sci.* **32**, 922–932.

[4] Mori, T., Maeda, M. (2003). *Langmuir* **20**, 313–319.

[5] Yamada, N., Okano, T., Sakai, H., Karikusa, F., Sawasaki, Y., Sakurai, Y. (1990). *Makromol. Chem. Rapid Commun.* **11**, 571–576.

[6] Yamato, M., Akiyama, Y., Kobayashi, J., Yang, J., Kikuchi, A., Okano, T. (2007). *Progress Polym. Sci.* **32**, 1123–1133.

[7] Kanazawa, H., Yamamoto, K., Matsushima, Y., Takai, N., Kikuchi, A., Sakurai, Y., Okano, T. (1996). *Anal. Chem.* **68**, 100–105.

[8] Yakushiji, T., Sakai, K., Kikuchi, A., Aoyagi, T., Sakurai, Y., Okano, T. (1999). *Anal. Chem.* **71**, 1125–1130.

[9] Matyjaszewski, K., Xia, J. (2001). *Chem. Rev.* **101**, 2921–2990.

[10] Wu, T., Efimenko, K., Genzer, J. (2002). *J. ACS* **124**, 9394–9395.

[11] Nagase, K., Kobayashi, J., Kikuchi, A., Akiyama, Y., Kanazawa, H., Okano, T. (2007). *Langmuir* **23**, 9409–9415.

[12] Nagase, K., Kobayashi, J., Kikuchi, A., Akiyama, Y., Kanazawa, H., Okano, T. (2012). *ACS Appl. Mater. Interfaces* **4**, 1998–2008.

[13] Nagase, K., Kobayashi, J., Kikuchi, A., Akiyama, Y., Kanazawa, H., Okano, T. (2008). *Langmuir* **24**, 511–517.

[14] Nagase, K., Kobayashi, J., Kikuchi, A., Akiyama, Y., Annaka, M., Kanazawa, H., Okano, T. (2008), *Langmuir* **24**, 10981–10987.

[15] Kanazawa, H., Kashiwase, Y., Yamamoto, K., Matsushima, Y., Kikuchi, A., Sakurai, Y., Okano, T. (1997). *Anal. Chem.* **69**, 823–830.

[16] Kanazawa, H., Sunamoto, T., Matsushima, Y., Kikuchi, A., Okano, T. (2000). *Anal. Chem.* **72**, 5961–5966.

[17] Nagase, K., Kumazaki, M., Kanazawa, H., Kobayashi, J., Kikuchi, A., Akiyama, Y., Annaka, M., Okano, T. (2010). *ACS Appl. Mater. Interfaces* **2**, 1247–1253.

[18] Kikuchi, A., Kobayashi, J., Okano, T., Iwasa, T., Sakai, K. (2007). *J. Bioact. Compat. Polym.* **22**, 575–588.

[19] Kikuchi, A., Okano, T. (2004). *Macromol. Symp.* **207**, 217–228.

[20] Ayano, E., Nambu, K., Sakamoto, C., Kanazawa, H., Kikuchi, A., Okano, T. (2006). *J. Chromatogr. A* **1119**, 58–65.

[21] Ayano, E., Sakamoto, C., Kanazawa, H., Kikuchi, A., Okano, T. (2006). *Anal. Sci.* **12**, 539.

[22] Kobayashi, J., Kikuchi, A., Sakai, K., Okano, T. (2001). *Anal. Chem.* **73**, 2027–2033.

[23] Kobayashi, J., Kikuchi, A., Sakai, K., Okano, T. (2002). *J. Chromatogr. A* **958**, 109–119.

[24] Kobayashi, J., Kikuchi, A., Sakai, K., Okano, T. (2003). *Anal. Chem.* **75**, 3244–3249.

[25] Nagase, K., Kobayashi, J., Kikuchi, A., Akiyama, Y., Kanazawa, H., Okano, T. (2008). *Biomacromolecules* **9**, 1340–1347.

[26] Nagase, K., Kobayashi, J., Kikuchi, A., Akiyama, Y., Kanazawa, H., Annaka, M., Okano, T. (2010). *Biomacromolecules* **11**, 215–223.

[27] Nagase, K., Kobayashi, J., Kikuchi, A., Akiyama, Y., Kanazawa, H., Okano, T. (2011). *Biomaterials* **32**, 619–627.

[28] Nagase, K., Yuk, S.F., Kobayashi, J., Kikuchi, A., Akiyama, Y., Kanazawa, H., Okano, T. (2011). *J. Mater. Chem.* **21**, 2590–2593.

[29] Gewehr, M., Nakamura, K., Ise, N., Kitano, H. (1992). *Makromol. Chem.* **193**, 249–256.

[30] Hosoya, K., Sawada, E., Kimata, K., Araki, T., Tanaka, N., Frechet, J.M.J. (1994). *Macromolecules* **27**, 3973–3976.

[31] Yoshizako, K., Akiyama, Y., Yamanaka, H., Shinohara, Y., Hasegawa, Y., Carredano, E., Kikuchi, A., Okano, T. (2002). *Anal. Chem.* **74**, 4160–4166.

[32] Yamanaka, H., Yoshizako, K., Akiyama, Y., Sota, H., Hasegawa, Y., Shinohara, Y., Kikuchi, A., Okano, T. (2003). *Anal. Chem.* **75**, 1658–1663.

[33] Tanaka, N., Nagayama, H., Kobayashi, H., Ikegami, T., Hosoya, K., Ishizuka, N., Minakuchi, H., Nakanishi, K.,

Cabrera, K., Lubda, D. (2000). *J. High. Resolut. Chromatogr.* **23**, 111–116.

[34] Tanaka, N., Kobayashi, H., Nakanishi, K., Minakuchi, H., Ishizuka, N. (2001). *Anal. Chem.* **73**, 420A–429A.

[35] Nagase, K., Kobayashi, J., Kikuchi, A., Akiyama, Y., Kanazawa, H., Okano, T. (2011). *Langmuir* **27**, 10830–10839.

[36] Nagase, K., Kobayashi, J., Kikuchi, A., Akiyama, Y., Kanazawa, H., Okano, T. (2013). *ACS Appl. Mater. Interfaces* **5**, 1442–1452.

[37] Kamihira, M., Kumar, A. (2007). Development of separation technique for stem cells cell separation. In Kumar, A., Galaev, I., Mattiasson, B. (eds.), *Cell Separation-Fundamentals, Analytical and Preparative Methods.* Springer, Berlin/Heidelberg, pp. 173–193.

[38] Kumar, A., Kamihira, M., Galaev, I.Y., Mattiasson, B., Iijima, S. (2001). *Biotechnol. Bioeng.* **75**, 570–580.

[39] Dainiak, M.B., Kumar, A., Galaev, I.Y., Mattiasson, B. (2006). *Proc. Natl. Acad. Sci. USA* **103**, 849–854.

[40] Galaev, I.Y., Dainiak, M.B., Plieva, F., Mattiasson, B. (2006). *Langmuir* **23**, 35–40.

[41] Okamura, A., Itayagoshi, M., Hagiwara, T., Yamaguchi, M., Kanamori, T., Shinbo, T., Wang, P.-C. (2005). *Biomaterials* **26**, 1287–1292.

[42] Okamura, A., Hagiwara, T., Yamagami, S., Yamaguchi, M., Shinbo, T., Kanamori, T., Kondo, S., Miwa, K., Itagaki, I. (2008). *J. Biosci. Bioeng.* **105**, 221–225.

[43] Nagase, K., Mukae, N., Kikuchi, A., Okano, T. (2012). *Macromol. Biosci.* **12**, 333–340.

[44] Nagase, K., Kimura, A., Shimizu, T., Matsuura, K., Yamato, M., Takeda, N., Okano, T. (2012). *J. Mater. Chem.* **22**, 19514–19522.

[45] Nagase, K., Hatakeyama, Y., Shimizu, T., Matsuura, K., Yamato, M., Takeda, N., Okano, T. (2013). *Biomacromolecules* **14**, 3423–3433.

[46] Okano, T., Yamada, N., Okuhara, M., Sakai, H., Sakurai, Y. (1995). *Biomaterials* **16**, 297–303.

17

BIOSURFACTANTS

Etsuo Kokufuta

Faculty of Life and Environmental Sciences, University of Tsukuba, Tsukuba, Ibaraki 305-8572, Japan

17.1 INTRODUCTION

Surfactants (also known as *surface-active agents*) are amphiphilic molecules consisting of a polar headgroup and one or more hydrocarbon chains with hydrophobic character. Such molecules possess the ability to reduce the surface tension between liquid–liquid, liquid–solid, or liquid–gas phases. Biosurfactants (often called *microbial surfactants* or *bioemulsifiers*) are also amphiphilic molecules that are produced by a variety of microorganisms, such as bacteria, yeasts, and filamentous fungi. With respect to surfactant performance, such as emulsifying ability and solubilizing ability, many biosurfactants are comparable to synthetic surfactants. Rather, biosurfactants have several advantages over synthetic surfactants such as lower toxicity and higher biodegradability. Therefore, many studies have focused on the production, isolation, characterization, and application of biosurfactants. A computer-assisted literature search using Web of Science as a search engine provides research trends in this field over the past 38 years (see Fig. 17.1). Interestingly, the publications on glycolipids are greater in number than those in which the author(s) focused on the biosurfactants (compare red circles with blue squares in both "title" and "topics" in Fig. 17.1). This means that the glycolipids were studied beyond the scope of biosurfactants. Another remarkable feature is a jump in the number of publications, including the term *glycolipid*(*s*) in the keywords, which were observed between 1989 and 1991. This is due to a rapid increase in the publications in the research fields of biochemistry and molecular biology, chemistry, cell biology, microbiology, and biophysics, and, in particular, immunology. The field-dependent activities of biosurfactant research can be seen as the percentage against the total number (N_{tp}) of publications between 1975 and 2013. For example, for glycolipids (N_{tp} = 12,336 in topics), the order becomes chemistry (6.2%) > biophysics (7.5%) > materials science (1.5%) > physics (0.6%) > polymer science (0.4%); and for biosurfactants (N_{tp} = 3148 in topics), chemistry (20.8%) > materials science (5.4%) > biophysics (3.9%) > physics (0.9%) > polymer science (0.8%). It is likely that the activities in these research fields (other than in chemistry), which are closely related to *biocolloid and biointerface science*, are not as high as those in the biological and biochemical fields.

Taking the above observations into account, the author aims to provide the fundamentals of biosurfactants, in terms of (1) the classification based on chemical composition and structure, (2) the chemical and physical properties, and (3) the applications. The area of biocolloid and biointerface science is intended to become interdisciplinary, integrated with biosurfactant research, in the future. Although in a broad sense there are many surfactants produced by plants and animals, our focus is on microbial surfactants.

17.2 CLASSIFICATION

Biosurfactants are often classified by considering their chemical composition or their microbial origin. According to the chemical composition, microbial surfactants may be classified into five major groups: glycolipids, lipopeptides, phospholipids, fatty acids, and polymeric surfactants (see Fig. 17.1). They are further subdivided as shown in Table 17.1, which provides an overview of the variety of microbial surfactants.

Encyclopedia of Biocolloid and Biointerface Science, Volume 1, First Edition. Edited by Hiroyuki Ohshima.
© 2016 John Wiley & Sons, Inc. Published 2016 by John Wiley & Sons, Inc.

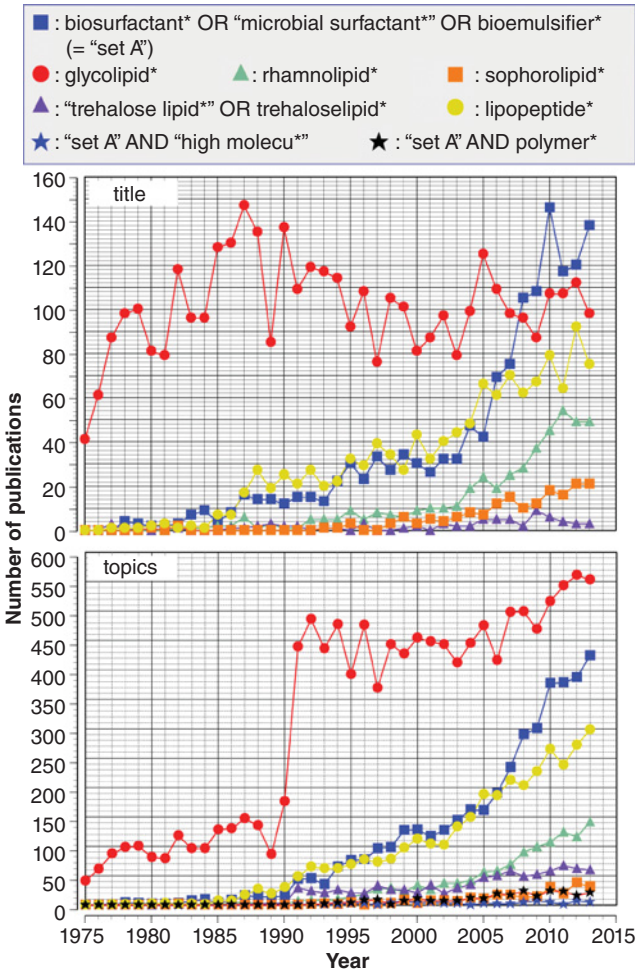


FIGURE 17.1 Annual change in the number of publications in the field of biosurfactants. The data were obtained by a year-by-year search for the terms (uppermost box) on the Thomson Reuters Web of Science (SCI-EXPANDED) research platform. The publications including the term(s) in the title are shown in "title," and those in which the term(s) appears in the keywords appear in "topics." An asterisk at the end of the term allows searches for all terms that begin with the word (e.g., "polymer*" retrieves the publications containing the terms such as polymer, polymeric, and polymerized). A phrase enclosed in double quotes was used to find exact matches; for example, "microbial surfactant*" for either microbial surfactant or microbial surfactants. Biosurfactants with high molar mass (i.e., polymeric biosurfactants) were searched from set A, which shows all the publications (red solid circles in "topics") dealing with biosurfactants.

Glycolipids, produced as extracellular or cell-wall-associated compounds by bacteria, yeasts, and fungi, are the most common and best studied. The major types of glycolipids are rhamnolipids, trehalolipids, and sophorolipids, among which a rhamnolipid (now commonly called *rhamnolipid 1*) was first discovered in metabolites of *Pseudomonas aeruginosa* strains [1]. Now it is well known that the rhamnolipids generally exist as one or two molecules of rhamnose, to which one or two molecules of β-hydroxydecanoic acid are bound, so that there are two major types: monorhamnolipids and dirhamnolipids (see Fig. 17.2). However, so many different rhamnolipids composed of one or two rhamnose and hydroxy fatty acids of different carbon numbers have been isolated and identified by such structural analysis methods as TLC, LC-MS, MS–MS, and NMR spectroscopy [2,3]. As a result, the nomenclature becomes longer and complex. Although the IUPAC names of two rhamnolipids are shown in Fig. 17.2, their synonyms are complicated from the beginning; for example, rhamnolipid 1 (or RHAMNOLIPID R-1) is Rhamnolipid R2, whereas rhamnolipid 2 is Rhamnolipid R1; see PubChem Depositor-Supplied Synonyms. To avoid such a complication, an expression as Rha-Ra-C10-C10 for Rhamnolipid 2 or Rha-C10 for R2 Ramnolipid 1 has been utilized (see Table 1 in Ref. 3).

Trehalolipids (or trehalose lipids) are a wide group of glycolipids, mainly constituted by the disaccharide trehalose linked at C6 and C6′ to mycolic acids, which are long α-chain branched-β-hydroxyl fatty acids. There is also another type in which a mycolic acid is bound to the trehalose molecule. Trehalose 6,6′-dimycolate (e.g., α,α'-trehalose 6,6′-bismycolate) and trehalose 6-monomycolate (e.g., α,α'-trehalose 6-mycolate) are typical of trehalose lipids (see Fig. 17.3). However, several microorganisms including the genera of *Rhodococcus*, *Mycobacterium*, *Arthrobacter*, *Nocardia*, and *Gordonia* produce different types of trehalolipids. The chemical structure of the main trehalose lipids along with the most commonly reported side chains has been summarized in a recent review [4], in which succinoyl trehalose lipids and trehalose tetraesters (see Fig. 17.4) are included together with trehalose mono- and dimycolates. However, note that the fatty acid carbon chains for each of the four main trehalose lipids described in Ref. 4 are not definite. To the best of the author's knowledge, most trehalose lipids, other than the two examples in Fig. 17.3, have neither PubChem Compound ID nor CAS number. For providing more insight into this puzzle, let us look at the case of trehalose tetraesters in Fig. 17.4. Although n = 5–9 [4] as well as $HOOCCH_2CH_2C(=O)$- at C2, $n = 6$ at C3, $n = 8$ at C4, and $n = 8$ at C2′ [5], another study [6] concluded that a trehalose tetraester produced by *Rhodococcus erythropoli*s 51T7 is a "mixture" containing 9–11 carbons (i.e., n = 8–10 in the structure in Fig. 17.4). Surprisingly, the lipid produced by the same microorganisms (*Rhodococcus erythropoli*s 51T7) appears in another report [7] as with a just "concrete" structure: heptanoate, instead of $HOOCCH_2CH2(=O)$- at C2; $n = 9$ at C3; $n = 7$ at C4; and $HOOCCH_2CH_2C(=O)$-, instead of fatty acid ester at C2′ [7, Fig. 1]. This is likely to be a rare case, but we must pay the greatest attention to the study at molecular level of the surfactant property and performance using succinoyl trehalose lipids or trehalose tetraesters.

Sophorolipids are a class of glycolipids constituted sophorose (2-*O*-ß-D-glucopyranosyl-D-glucose), to which a

TABLE 17.1 Classification of Biosurfactants Discussed in This Chapter

Biosurfactants	Subgroups	Examples shown in figures
Glycolipids	Rhamnolipids	Rhamnolipid 1, Rhamnolipid 2
	Trehalose lipids	Trehalose 6,6′-dimycolate
		Trehalose 6-monomycolate
		Succinoyl trehalose lipids
		Trehalose tetraesters
	Sophorolipids	Acidic sophorolipid and its lactonic form
	Others	Gingerglycolipids A, B, C
Lipopeptides	Surfactin	Surfactin A, B, C, D
Phospholipids	Phosphoglycolipids	General chemical structures are shown
	Glycophospholipids	for both lipids
Fatty acids	Microbial fatty acids	Corynomycolic acid
		Spiculisporic acid
		Secospiculisporic acid
Polymeric surfactants	Emulsan	Anionic polymer component isolated
	Biodispersan	from "native" emulsan (see text)
	Alasan	
	Liposan	

long-chain hydroxyl fatty acid is connected by a glycosidic bond. The first report [8] on sophorolipids produced by *Torulopsis magnolia* was published in 1961. The most common sophorolipids are composed of 9-octadecenoic acid ($CH_3(CH_2)_7CH{=}CH(CH_2)_7COOH$) and 6′,6″-diacetylated sophorose moieties. This compound forms a macrocyclic lactone, in which the COOH group of the hydroxyl fatty acid chain is esterified with the OH group at C4″ of sophorose. Figure 17.5 shows the chemical structures of the acidic and lactonic forms. Note that the lactonic structure appeased in several reports contains an error in the description of the position of esterification of sophorose [9]. Sophorolipids can be produced by yeasts, such as *Candida bombicola*, *Yarrowia lipolytica*, *Candida apicola*, and *Candida bogoriensis*, using carbohydrates and lipophilic substrates. However, microbial sophorolipids occur as mixtures of lactonic and nonlactonic structures. For, example, it was found that more than 95% of the analogs are lactonic sophorolipids and all the sophorolipids produced were either mono- or diacetylated form, when *Candida bombicola* (yeast) was cultivated

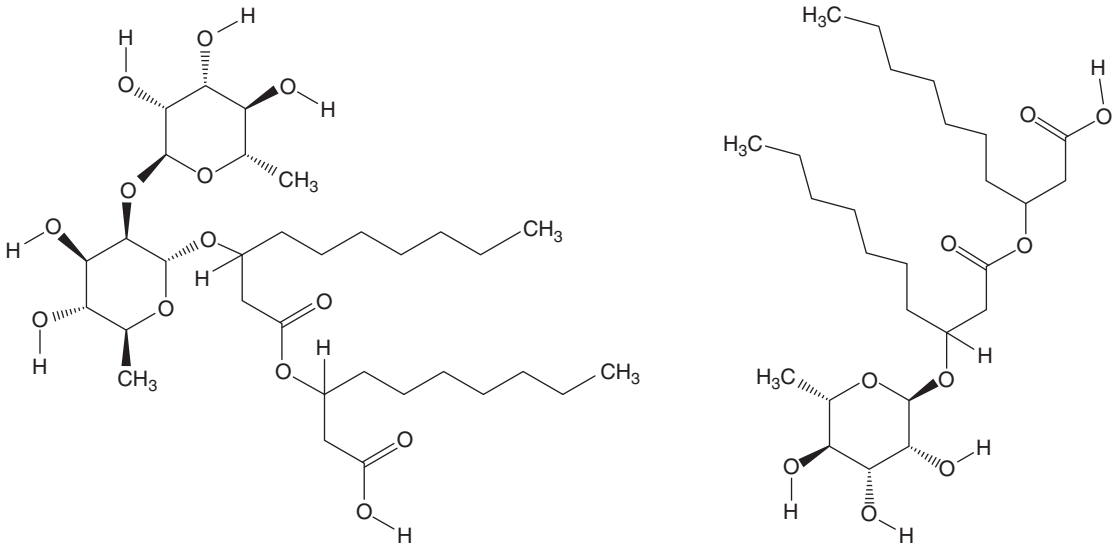
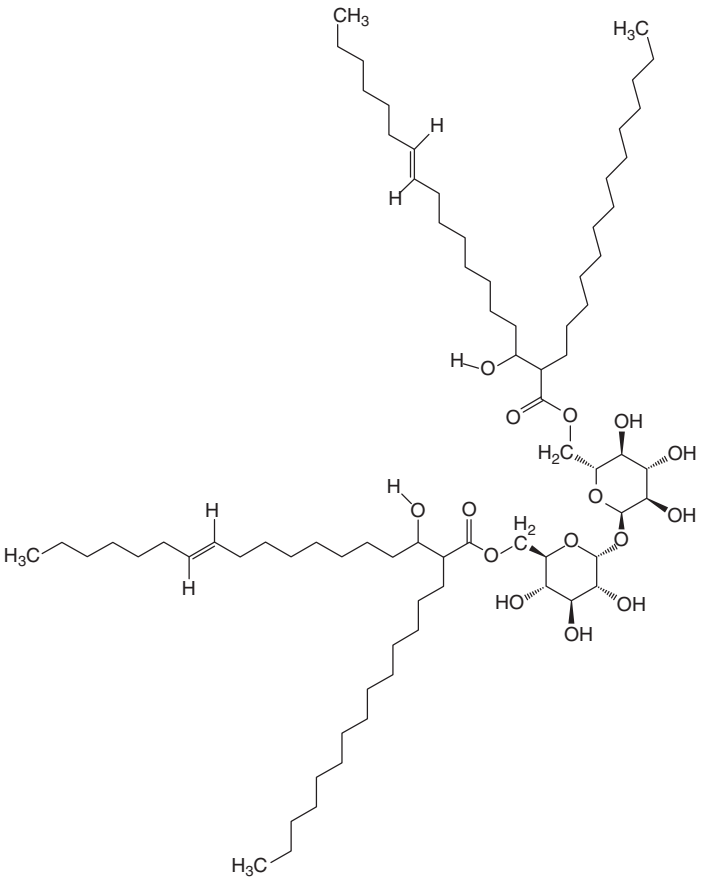
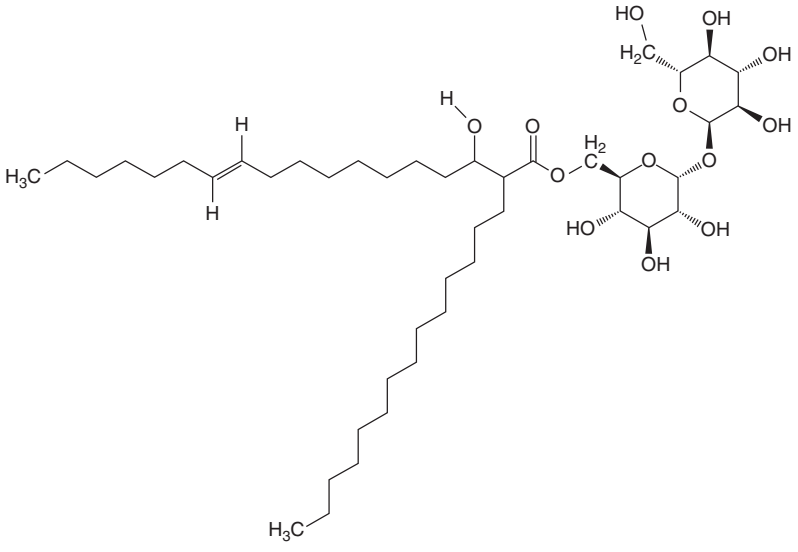


FIGURE 17.2 Two typical rhamnolipids: rhamnolipid 1 {IUPAC name: 3-[3-[(2*R*,4*R*,5*R*,6*S*)-4,5-dihydroxy-6-methyl-3-[(2*S*,3*R*,4*R*,5*R*,6*S*)-3,4,5-trihydroxy-6-methyloxan-2-yl]oxyoxan-2-yl]oxydecanoyloxy]decanoic acid}; rhamnolipid 2 {IUPAC name: 3-[3-[(2*R*,3*R*,4*R*,5*R*,6*S*)-3,4,5-trihydroxy-6-methyloxan-2-yl]oxydecanoyloxy]decanoic acid}.



(a)



(b)

FIGURE 17.3 Two typical examples of trehalose lipids: α,α'-trehalose 6,6′-bismycolate {IUPAC name: [(2*R*,3*S*,4*S*,5*R*,6*R*)-3,4,5-trihydroxy-6-[(2*R*,3*R*,4*S*,5*S*,6*R*)-3,4,5-trihydroxy-6-[[(*E*)-3-hydroxy-2-tetradecyloctadec-11-enoyl]oxymethyl]oxan-2-yl]oxyoxan-2-yl]methyl (*E*)-3-hydroxy-2-tetradecyloctadec-11-enoate}; α,α'-trehalose 6-mycolate {IUPAC name: [(2*R*,3*S*,4*S*,5*R*,6*R*)-3,4,5-trihydroxy-6-[(2*R*,3*R*,4*S*,5*S*,6*R*)-3,4,5-trihydroxy-6-(hydroxymethyl)oxan-2-yl]oxyoxan-2-yl]methyl (*E*)-3-hydroxy-2-tetradecyloctadec-11-enoate}.

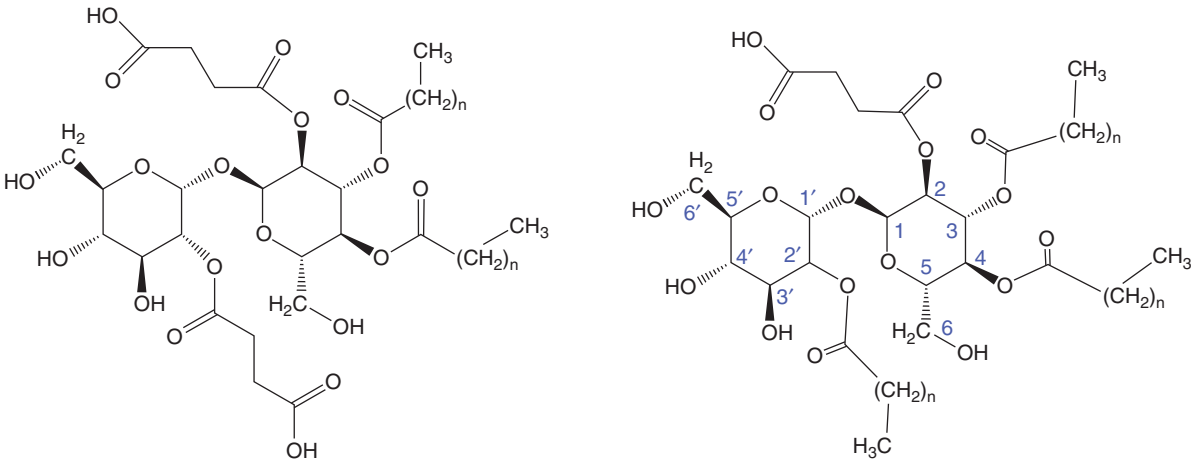
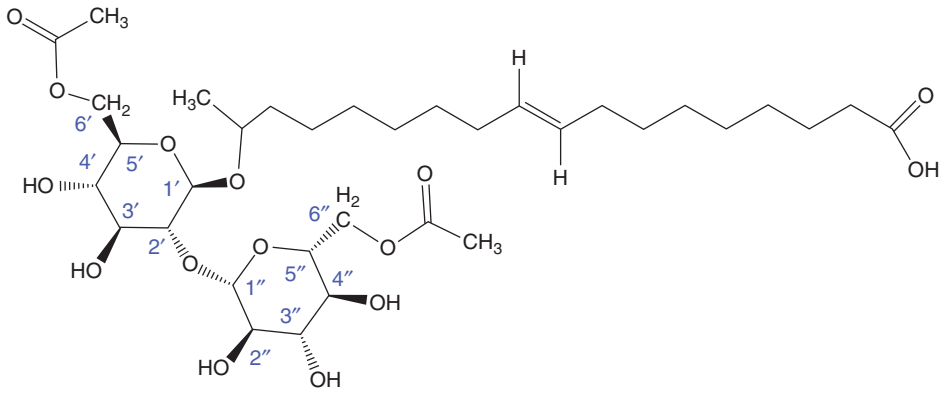


FIGURE 17.4 Structures of succinoyl trehalose lipids and trehalose tetraesters. For both lipids, $n = 5$–9 in Ref. 4 (for more details, see text). The structure of trehalose tetraesters was provided in Ref. 5, in which $n = 6$–8.



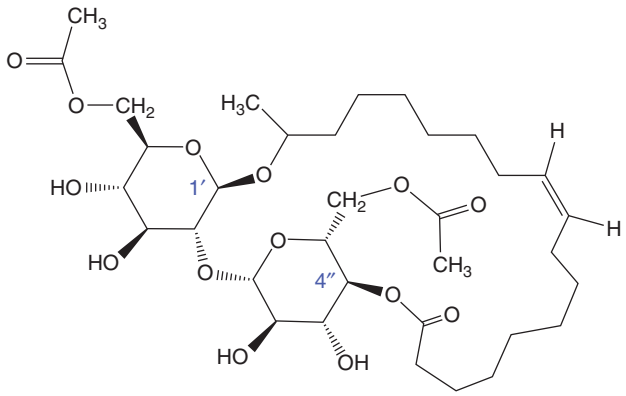


FIGURE 17.5 Acidic sophorolipid {IUPAC name: (*E*)-17-[(2*R*,3*R*,4*S*,5*S*,6*R*)-6-(acetyloxymethyl)-3-[(2*S*,3*R*,4*S*,5*S*,6*R*)-6-(acetyloxymethyl)-3,4,5-trihydroxyoxan-2-yl]oxy-4,5-dihydroxyoxan-2-yl]oxyoctadec-9-enoic acid} and its lactonic form. Note that the systematic name for acidic sophorolipid is (9*E*)-17-{[6-*O*-acetyl-2-*O*-(6-*O*-acetyl-*β*-D-glucopyranosyl)-*β*-D-glucopyranosyl]oxy}-9-octadecenoic acid, which is recorded in ChemSpider but not in PubChem. Also note that both acidic and lactonic forms have no CAS number.

in the presence of glucose and oleic acid under higher aeration [10]. In addition, a sophorolipid analog with a triunsaturated fatty acid was also obtained. Therefore, a method called *chemoenzymatic chemistry* has been developed to prepare a library of sophorolipid analogs from mixtures of natural sophorolipids [11].

At the end, a brief outlook of the plant glycolipids will be provided. In contrast to the microbial types, plant originated glycolipids attract interest in the pharmaceutical and medical areas. For example, three monoacyldigalactosylglycerols, gingerglycolipids A, B and C were isolated from *Zingiberis rhizoma*, and the structures were identified [12] (see Fig. 17.6). In addition, the structure dependence of three gingerglycolipids as an antiulcer agent was studied, so that these glycolipids have PubChem ID.

A number of bacterial species produce lipopeptides or peptide lipids, which consist of short linear chains or cyclic structures of amino acids, linked to a fatty acid via ester or amide bonds or both. Many of microbial lipopeptides are found to have surfactant properties, other than antibacterial or antifungal abilities, so that they are considered as a group of biosurfactants. The lipopeptide biosurfactants are further subdivided into iturin, fengycin, and surfactin, depending on their amino acid sequence and fatty-acid branching. Among these three, surfactin is one of the most effective biosurfactants. Surfactin was first discovered from the culture broth of *Bacillus subtilis* by Arima et al. [13]. Now it is well known that natural "surfactins" are a mixture of isoforms A, B, C, and D, the physiological properties of which are slightly different from each other [14]. An inherent structural aspect of these isoforms is a cyclic depsipeptide that contains one ester bond in addition to the amide bonds. As shown in Fig. 17.7, a peptide loop of seven amino acids (L-aspartic acid, L-leucine, glutamic acid, L-leucine, L-valine, and two D-leucines) is the same for each surfactin isoform, while the carbon number of a hydrophobic fatty acid is different from 13 to 16. Isoform C, with 15 carbons (3-hydroxy-13-methyl tetradecanoic acid), is commonly referred as to "Surfactin." In addition to the four surfactin isoforms, several linear surfactin analogs have been synthesized using solid phase peptide synthesis (SPPS) technique: for example, 3-hydroxy-13-methyltetradecanoyl-L-Glu-L-Leu-D-Leu-L-Val-L-Asp-D-Leu-L-Leu-OH [15]. Also, surfactinlike cyclic depsipeptides that have different molecular masses (1035, 1049, 1063, and 1077 g/mol), due to changes in the number of methylene groups in the lipid and/or peptide portions, were found to be produced by a marine bacterium (*Bacillus pumilus*) [16].

There are various analogs for the other lipopeptides, including iturin, and fengycin, and they are called "biosurfactant lipopeptides" in several articles [e.g., 17]. However, almost all reports focus on the biosynthesis of lipopeptides, without providing their surfactant properties and performance levels.

Most phospholipids are composed of a glycerol backbone, on which the C1 and C2 carbons are esterified with fatty acids and the C3 carbon is bound to a phosphate group via an ester bond. Although this is the most common explanation for phospholipids, a good classification involving compounds in which a sugar moiety is bound to the diacylglycerol and phosphate moieties would be desired when considering phospholipids as a class of biosurfactants. For this, William W. Christie, Technical Editor of AOCS Lipid Library [18], has made the following suggestions:

1. As the name suggests, "glycophospholipids" are lipid molecules that contain both phosphate and carbohydrate as integral structural components.
2. There are two main types of glycophospholipid based on a glycerol backbone, which are exclusively of microbial origin.
3. One type (phosphoglycolipids) is derived biosynthetically from *glycosyldiacylglycerols*, in which the sugar moiety is phosphorylated, that is, in which the carbohydrate moiety is linked to a diacylglycerol.
4. The second group (glycophospholipids) comprises more conventional phospholipids, with a phosphate moiety attached to a diacylglycerol and with the phosphate further glycosylated. According to his suggestions, it seems that phosphoglycolipids, such as 3-*O*-[6′-*O*-(1″, 2″-diacyl-3′-phospho-*sn*-glycerol)-α-D-glucopyranosyl]-1,2-diacyl-*sn*-glycerol types (see Fig. 17.8) isolated from *Mycoplasma laidlawii* falls into the broad class of biosurfactants. Also, this seems to be the case for such a glycophospholipid as 1′-(1,2-diacyl-*sn*-glycero-3-phosphoryl)-2′-*O*-(2′-amino-2-deoxy-D-glucopyranosyl)-*sn*-glycerol (see Fig. 17.9). However, a careful literature search using Web of Science showed that there are no publications dealing with both phosphoglycolipids and glycophospholipids. The main reason is probably that these phospholipid biosurfactants are isolated from the human pathogenic bacteria. Nevertheless, the reason why such phospholipids are included herein is to consider the future development of biotechnology, in particular of the gene engineering techniques.

Fatty acids consisting of long aliphatic chain(s) and carboxyl group(s) are typical compounds with surfactant properties. The classification of fatty acids is made according to how many carbons are in a chain, whether there is the double bond(s) in a chain, whether the chain is branched, and what functional group (e.g., OH) is attached to the chain. Fatty acids are usually derived from triglycerides or phospholipids in plants and animals. Also, several of microorganisms have been known to produce fatty acids of different sorts. As in a class of microbial biosurfactants, it has been claimed that the carbon number is the range of 12–14 for the saturated fatty acids [19]. However, corynomycolic acid ($C_{32}H_{64}O_3$; see Fig. 17.10) obtained as the extracellular product of

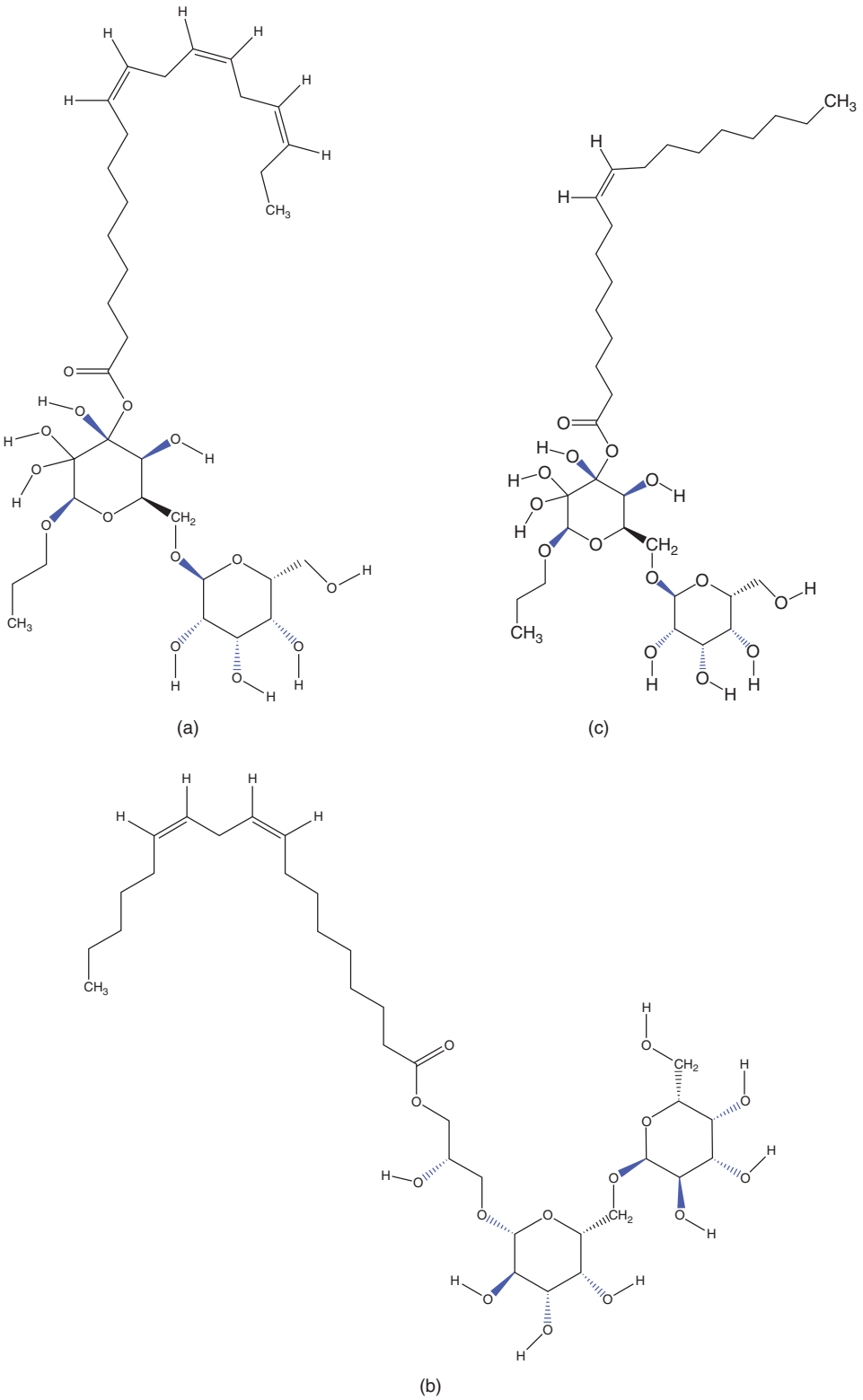


FIGURE 17.6 Gingerglycolipids A, B, and C as antiulcer agents. Gingerglycolipid A {IUPAC name: (2*R*,4*R*,5*S*,6*R*)-3,3,4,5-tetrahydroxy-2-propoxy-6-[[(2*S*,3*S*,4*S*,5*R*,6*R*)-3,4,5-trihydroxy-6-(hydroxymethyl)oxan-2-yl]oxymethyl]oxan-4-yl] (9*Z*,12*Z*,15*Z*)-octadeca-9,12,15-trienoate}; gingerglycolipid B {IUPAC name: [(2*S*)-2-hydroxy-3-[(2*R*,3*R*,4*S*,5*R*,6*R*)-3,4,5-trihydroxy-6-[[(2*S*,3*R*,4*S*,5*R*,6*R*)-3,4,5-trihydroxy-6-(hydroxymethyl)oxan-2-yl]oxymethyl]oxan-2-yl]oxypropyl] (9*Z*,12*Z*)-octadeca-9,12-dienoate}; gingerglycolipid C {IUPAC name: [(2*R*,4*R*,5*S*,6*R*)-3,3,4,5-tetrahydroxy-2-propoxy-6-[[(2*S*,3*S*,4*S*,5*R*,6*R*)-3,4,5-trihydroxy-6-(hydroxymethyl)oxan-2-yl]oxymethyl]oxan-4-yl] (*Z*)-octadec-9-enoate}.

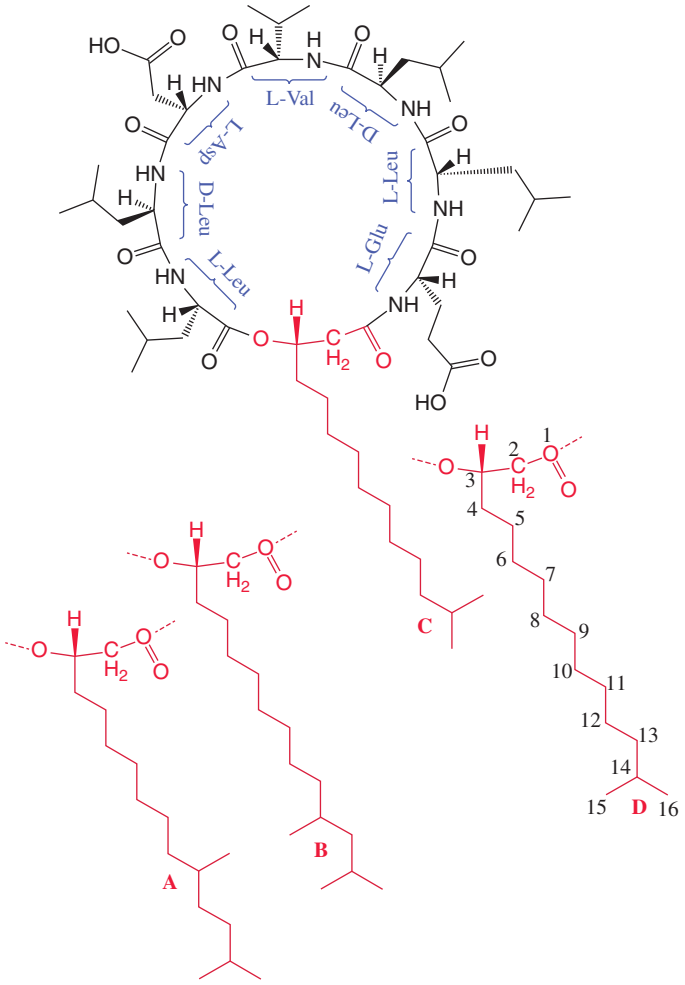


FIGURE 17.7 Four surfactin isoforms with different fatty-acid moieties highlighted in red: (a) 3-hydroxy-11-methyldodecanoic acid; (b) 3-hydroxy-12-methyltridecanoic acid; (c) see text; (d) 3-hydroxy-14-methylpentadecanoic acid.

Corynebacterium lepus grown on kerosene [20] has attracted much attention. Another interesting type is spiculisporic acid (see Fig. 17.11) from *Penicillium spiculosporum*, because the ring-opening form (secospiculisporic acid) of spiculisporic acid yields as a large amount of needle-like crystals in the culture broth [21]. For more detail classification of fatty acids, the AOCS Lipid Library [18] would be helpful, although almost all are products from animals and plants.

Although it is well known that biopolymers like xanthan gum (anionic polysaccharide) behave as an emulsifier or a surfactant, we focus here on microbially produced polymeric surfactants; in a stricter sense, polymeric surfactants are an extracellular product. The most typical example is *emulsan*, which is a potent extracellular polymeric bioemulsifier from *Acinetobacter calcoaceticus* RAG-1 [22]. However, this product was a complex consisting of the heteropolysaccharide and protein fractions, so that the chemical structure for the anionic polymer component, which was isolated from "native" emulsan, was reported very recently [23] (see Fig. 17.12). As the others, the following extracellular

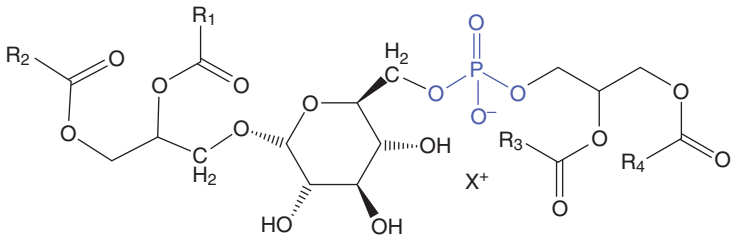


FIGURE 17.8 Typical example of phosphoglycolipids.

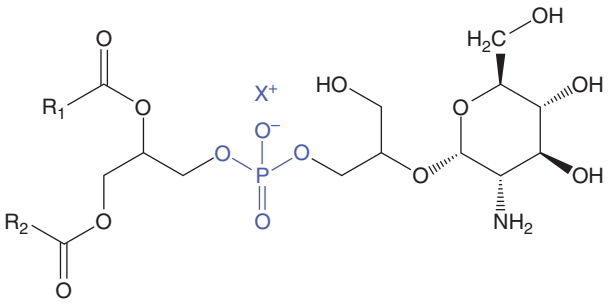
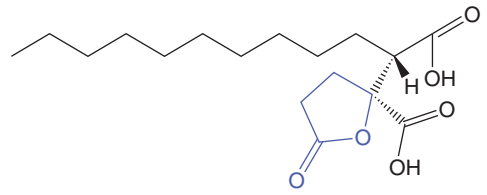
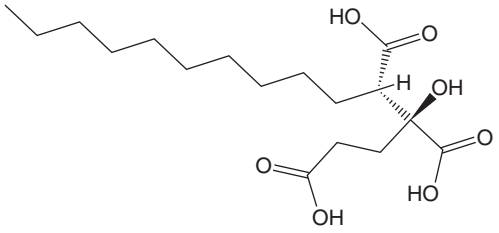


FIGURE 17.9 Typical example of glycophospholipids.



spiculisporic acid



secospiculisporic acid

FIGURE 17.11 Spiculisporic acid {IUPAC name: (2*S*)-2-[(1*S*)-1-carboxyundecyl]-5-oxooxolane-2-carboxylic acid} and secospiculisporic acid [IUPAC name: (3*S*,4*S*)-3-hydroxytetradecane-1,3,4-tricarboxylic acid]. The latter is the ring-opening form of spiculisporic acid in the lactone form.

polymeric bioemulsifiers have been known: (1) *biodispersan*, an extracellular dispersing substance from *A. calcoaceticus*, which is anionic heteropolysaccharide containing of four reducing sugars–glucosamine, 6-methylaminohexose, galactosamine, uronic acids, and an unidentified amino sugar [24]; (2) *alasan,* an alanine-containing anionic biosurfactant, which is produced by *A. radioresistens* KA-53 and composed of heteropolysaccharide and protein (called "AlnA") acting as the surface-active component [25, 26]; and (3) *liposan*, an extracellular water- soluble emulsifier from *C. lipolytica*, which is composed of protein and heteropolysaccharide (consisting of glucose, galactose, galactosamine, and galacturonic acid) [27]. In addition to the above, there are several studies for extracellular polymeric emulsifiers, whose chemical structures have remained unstudied for a long time, probably due to the complicated compositions; for example, emulsifying and surface active agents from *Corynebacterium hydrocarboclastus* [28].

17.3 CHEMICAL AND PHYSICAL PROPERTIES

Biosurfactants are synthetized by bacteria, yeasts, and fungi during cultivation with various carbon sources, and in special cases with hydrophobic substrates such as hydrocarbons. For the latter, the surfactant is produced as either an extracellular or cell-wall-associated matrix. The extracellular surfactant causes the emulsification of the hydrocarbon as the

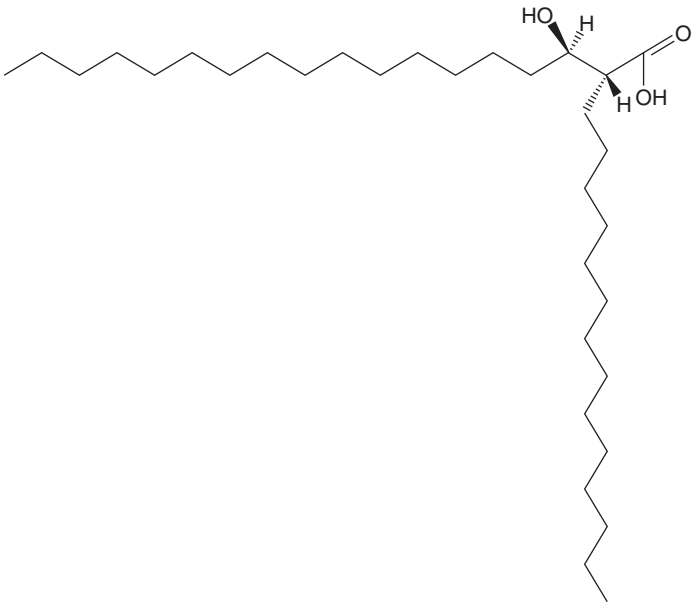


FIGURE 17.10 Structure of corynomycolic acid [IUPAC name: (2*R*,3*R*)-3-hydroxy-2-tetradecyloctadecanoic acid].

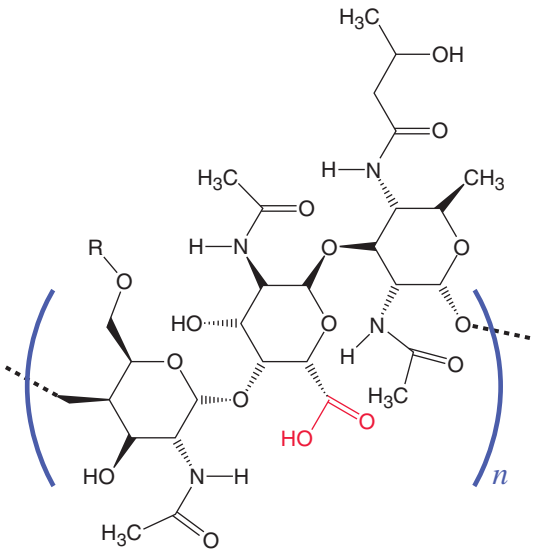


FIGURE 17.12 Structure of the anionic polysaccharide component isolated from the emulsan complex. R denotes acetyl or alcohol moiety.

substrate during the cultivation, while the cell-wall-associated surfactant facilitates the penetration of the hydrocarbon to the periplasmic space. Although there is a big difference between microbial and usual surfactants in the synthetic process, both surfactants are composed of the lipophilic (or hydrophobic) and the hydrophilic moiety. The common lipophilic moiety of biosurfactants is the hydrocarbon chain of fatty acids, which are bound to the polar or hydrophilic group, such as the alcohol groups of glycolipids, the COOH groups of lipopeptides or fatty acids. Many of biosurfactants have been known to exhibit normal stability (or instability) to chemical compounds. For example, the ester linkages of glycolipids are broken by saponification with alkaline hydroxides, and this is the case for the *O*-glycosidic bonds. Other chemical reactions, like oxidation or esterification, could be carried out without difficulties.

For more details about the solubility of biosurfactants, the general features are as follows. Nonpolar glycolipids such as trehalose 6,6′-dimycolate and trehalose 6-monomycolate (Fig. 17.3) are soluble in hydrophobic solvents such as chloroform, whereas more polar glycolipids such as anionic trehalose tetraesters (Fig. 17.4) are soluble in $CHCl_3/CH_3OH$ mixtures. Rhamnolipids with two fatty acids (Fig. 17.2) are soluble in methanol, chloroform, ethyl acetate, ethyl ether, and aqueous $NaHCO_3$ solutions, but not soluble in *n*-hexane. Sugar lipids are usually soluble in ether, *n*-hexane, and chloroform at room temperature and in warm acetone and methanol. This is the case for the other sugar lipids as shown in Figs. 17.5 and 17.6. Surfactin (Fig. 17.7) is soluble in alkaline water solutions, methanol, ethanol, acetone, ethyl acetate, chloroform, dichloromethane, and acetic acid, but not in pure water, petroleum ether, and hexane. Phospholipids are generally soluble in aliphatic hydrocarbons, aromatic hydrocarbons and halogenated hydrocarbons solvents, such as ether, benzene, chloroform and petroleum ether and particularly soluble in aliphatic alcohols (e.g., ethanol). However, it is not clear whether glycophospholipids shown in Figs. 17.8 and 17.9 show solubility similar to the common phospholipids.

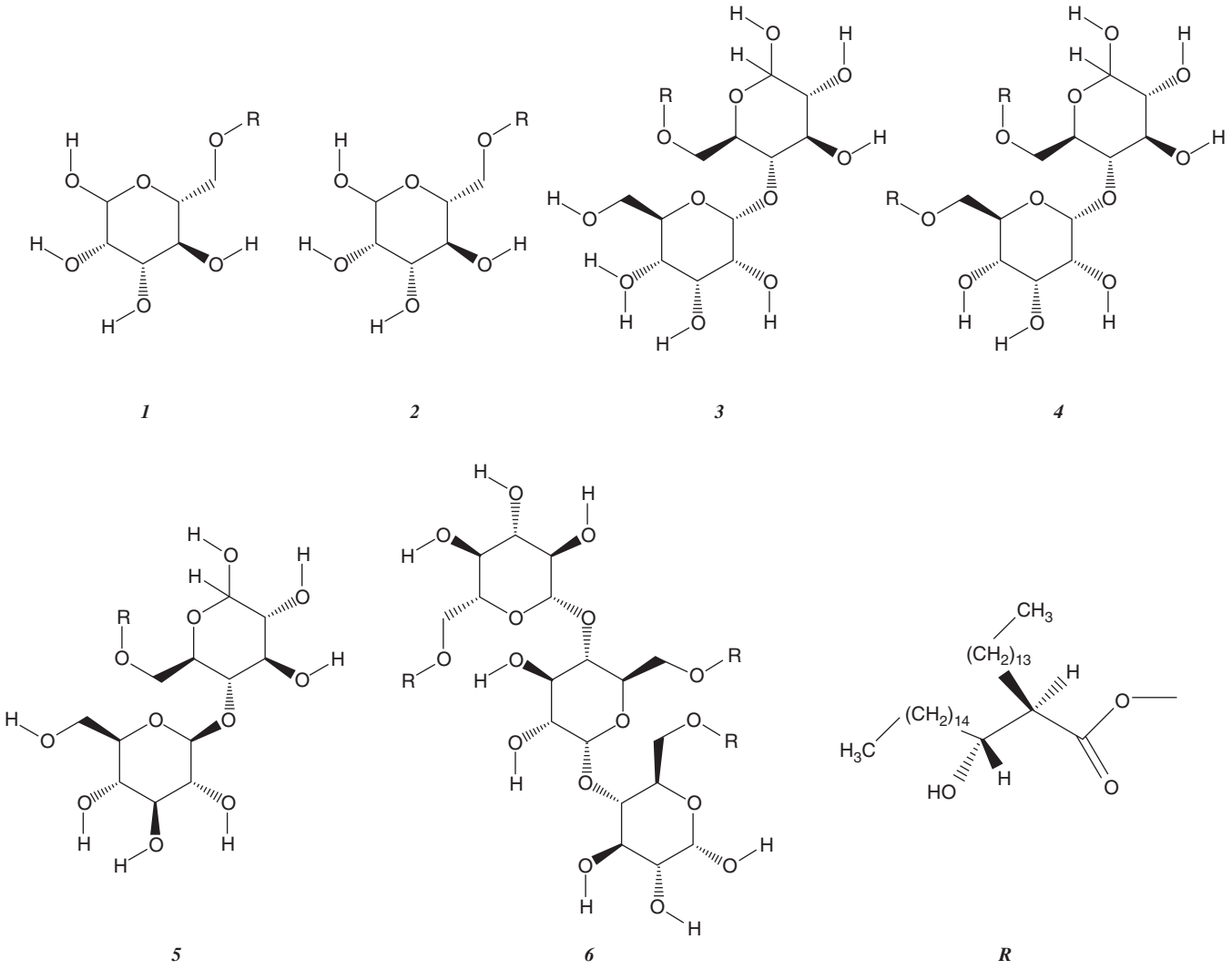
Spiculisporic acid (lactone form) and secospiculisporic acid (ring-opening form) (see Fig. 17.11) are complicated in their solubility behavior in water. Both acids are soluble in ether, but almost insoluble in water at room temperature. On heating, the solubility of the ring-opening form increases and reaches the level of 10 g/100 g solution at 60°C, at which the lactone form is almost insoluble. The solubility of the lactone form increases with increasing temperature > 70°C and reaches a similar level of the ring- opening form at 90°C. However, it should be noted that about 20% of the ring-opening form is still remaining in the water solution even at 90°C.

One of the most fundamental physical properties of biosurfactants is their surface tension (σ), interfacial tension (γ), and critical micelle concentration (CMC). Many studies dealing with different biosurfactants have reported these physical data. Most of the data were, however, obtained from "intact" products that mean "not complete" in the chemical structure. For example, it was reported that an unpurified polymer obtained from *C. hydrocarboclastu* reduces the surface tension of water (20°C) from 73 mN/m to 60 mN/m and the concentration dependence of σ shows two inflection points at 0.4 g/L and at 1.5 g/L, suggesting the acceptance of two CMC values [28]. Another example is a trehalose tetraester consisting of six components of fatty-acid chains [6] (see Fig. 17.4), whose water solution shows (against hexadecane) = 5 mN/m and CMC = 0.037 g/L at 25°C. Nevertheless, it is not the author's purpose to collect the data of this sort, so that a careful search has been performed to look for the physical data of biosurfactants with a definite structure. There have been only a very few studies in which a systematic comparison of biosurfactants was done. For example, six glycolipids with different structures from *Arthrobacter* sp. (strain DSM2567) have been compared with respect to their surface properties [29]. Table 17.2 shows the data from Ref. 29 with several modifications. Because the authors of that study [29] focused on the application of the biosurfactants into tertiary oil recovery, a high-concentration salt solution was used as the solvent, and the measurements were performed at 40°C. In addition, *n*-hexadecane ($C_{16}H_{34}$) as a model of diesel fuel was used for measuring the interfacial tension. Thus, we have to pay attention to these measuring conditions when comparing with the data of the usual surfactants. However, the following significant observations can be obtained:

1. Glycolipid **1**, composed of mannose and corynomycolic acid (see Fig. 17.10), and glycolipid **2**, containing glucose instead of mannose, reduce the σ (72 mN/m)

TABLE 17.2 Surfactant Properties at 40°C of Glycolipids 1–6 from *Arthrobacter* sp.

Glycolipid	σ [a] (mN/m)	CMC[b] (mg/L)	γ[c] (mN/m)	CMC[d] (mg/L)
1	40	5	19	50
2	40	10	9	20
3	33	1	1	20
4	46	10	13	10
5	35	3	1	4
6	44	20	19	10



1 ***2*** ***3*** ***4*** ***5*** ***6*** ***R***

[a] Obtained with aqueous glycolipid solutions containing (gL^{-1}) NaCl (100), $CaCl_2$ (28), $MgCl_2$ (10).
[b] Determined from the lipid concentration dependence of δ.
[c] Against *n*-hexadecane.
[d] Determined from the lipid concentration dependence of γ.

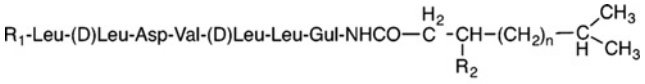
of the salt solution to 40 mN/m and the γ (41 mN/m) against *n*-hexadecane to 19 mN/m (glycolipid ***1***) and 9 mN/m (glycolipid **2**).

2. With glycolipid **3** (maltose monoester), the corresponding values decrease to 33 mN/m and 1 mN/m, respectively, and with glycolipid **4** (maltose diester) only to 46 mN/m and 13 mN/m, respectively.
3. Thus, glycolipids **3** and **5**, consisting of two carbohydrate moieties and one fatty-acid moiety (***R***), show stronger reduction in σ and γ than do glycolipids **4** (two sugars and two fatty acids) or **1** and **2** (one sugar and one fatty acid).
4. The monoesters of maltose (glycolipid **3**) and cellobiose (glycolipid **5**) possess the best surfactant

behavior (minimum σ and γ values, 34 ± 1 mN/m and 1 mN/m, respectively) of the glycolipids studied.

5. Also the CMC values ranging from 1 to 50 mg/L confirmed that the combination of two sugars with one corynomycolic acid (i.e., glycolipids **3** and **5**) was superior to the other combinations including the trisaccharide triester (glycolipid **6**). Although the interpretation at the molecular level was not shown in that study [29], these results are likely to address structural aspect of glycolipid surfactants.

Another example is the data in another study [15] in which the hemolytic activity of chemically synthesized linear surfactin analogs was evaluated in relation to their physicochemical properties. Linear surfactin analogs (LSA) synthesized are as follows:



LSA(1): R_1 = COOH, R_2 = OH, n = 8; LSA(2): R_1 = COOH, R_2 = H, n = 8;
LSA(3): R_1 = $CONH_2$, R_2 = H, n = 8; LSA(4): R_1 = COOH, R_2 = H, n = 5;
LSA(5): R_1 = COOH, R_2 = H, n = 13

where LAS(2) is a chemically linearized analog of cyclic natural surfactin C (see Fig. 17.7) and LSA(3) has an amide group as R_1. The σ values of LSA(1) ~ LSA(5) and cyclic natural surfactin C were measured in a 5 mM Tris buffer (pH 8.5) at 25°C and compared with each other. The minimum value of σ decreases in order of LSA(5) (~39 mN/m) > LSA(1) ≈ LSA(2) ≈ LSA(3) (~37 mN/m) > LSA(4) (~ 35 mN/m) ≫ surfactin C (30 mN/m). In addition, the CMC value decreases in order of LSA(4) (1113 μM) ≫ LSA(3) (401 μM) > LSA(1) (374 μM) > LSA(2) (301 μM) ≫ surfactin C (62 μM) ≫ LSA(5) (8 μM). Obviously, a long acyl chain bound to the peptide is effective in decreasing CMC but not in reducing the surface tension. In the case of surfactin C, the cyclic peptide decreases CMC and reduces the surface tension effectively. To facilitate the understanding of these results at the molecular level, the structure of a micelle in an aqueous solution is of importance. The fundamental adsorption and self-assembly properties of two glycolipids, rhamnolipids and sophorolipids; a lipopeptide; surfactin; and a protein, hydrophobin, and their mixtures with other amphiphiles and surfactants have been studied using neutron reflectivity and small-angle neutron scattering [30].

17.4 APPLICATIONS

A large number of experimental studies have suggested the uses of biosurfactants in oil recovery and oil pollution remediation. The potential applications of biosurfactants in medicine and food industrial processes are also suggested. Almost 60 review articles published over the past 35 years refer to the potentialities of biosurfactants for these applications. It is likely that some of them become more realistic from a review [31] in which a scan and mapping were performed for 255 patents on bioemulsifiers and biosurfactants. The highest number of patents is issued for use in the petroleum industry (33%), followed by cosmetics (15%) as an antimicrobial agent and medicine (12%), and in bioremediation (11%). It is emphasized that bioemulsifiers and biosurfactants have advantages over chemically synthesized surface active compounds as follows: (1) less or no toxicity, (2) biodegradability, (3) a broad range of novel structural characteristics, (4) physical properties such as low interfacial tension and critical micelle concentration, and (5) high temperature stability and activity at extreme salinity and pH conditions. Also emphasized is that biosurfactants or bioemulsifiers may be tailored to meet specific requirements, because they can be produced by gene modified microorganisms, and then further modified by using biological or biochemical techniques.

There are many publications in which the applications of biosurfactants are qualitatively or semiquantitatively evaluated in terms of their physical data as mentioned previously. For example, a qualitative evaluation of nine biosurfactants (rhamnolipids, sophorolipids, and glucose lipids) with different chemical compositions and structures was made through comparison of their surface tension and CMC values without consideration of the specific application field(s) [32]. A semiquantitative evaluation of rhamnolipids (and also several commercial biosurfactants) was also made in terms of the environmental applications, in particular in the removal of heavy metals or organic contaminants in the soil (bioremediation) [33]. Thus, the size and morphology of rhamnolipid micelles [34] estimated by the small-angle neutron scattering technique, and the metal stabilization by biosurfactants were considered, although the colloidal properties of the soil were not taken into account in the discussion. There is a more practical evaluation [35] in which rhamnolipid and sophorolipid biosurfactants and their mixtures were examined in terms of the emulsification of oil, and their detergency and vegetable oil extraction ability for biodiesel application was discussed. With respect to the potential applications in medicine, a detailed review has been published [36].

It is of particular importance to note the productivity of biosurfactants in their applications other than the use as medicines. In large-scale production, low production yield and high cost for recovery and purification are general problems. Although the use of culture broth without the isolation and purification of biosurfactants would be possible in some cases, this does not provide an answer to the question of how to develop an effective method for increasing productivity, which is a basic issue in fermentation technology. The authors of one review [37] examined the biochemical and genetic mechanisms of rhamnolipid production by

P. aeruginosa and proposed the application of quorum-sensing signal molecules in enhancing the rhamnolipid production. Rather, as a simplified way to increase the productivity during cultivation of filamentous fungus (*Aspergillus niger*), a polyelectrolyte complex-based technique for microorganism immobilization [38] has been reported [39, 40]. These examples clearly suggest the need for interdisciplinary integration in future developments in this field.

REFERENCES

[1] Jarvis, F.G., Johnson, M.J.A. (1949). *J. ACS* **71**, 4124–4126.

[2] Sharma, A., Jansen, R., Nimtz, M., Johri, B.N., Wray, V.J. (2007). *J. Nat. Prod*. **70**, 941–947.

[3] Abdel-Mawgoud, A.M., Lépine, F., Déziel, E. (2010). *Appl. Microbiol. Biotechnol*. **86**, 1323–1336.

[4] Andrea Franzetti, A., Gandolfi, I., Bestetti, G., Smyth, T.J.P., Banat, I.M. (2010). *Eur. J. Lipid Sci. Technol*. **112**, 617–627.

[5] Tuleva, B., Christova, N., Cohen, R., Stoev, G., Stoineva, I. (2008). *J. Appl. Microbiol*. **104**, 1703–1710.

[6] Marquésa, A.M., Pinazo, A., Farfan, M., Aranda, F.J., Teruel, J.A., Ortiz, A., Manresa, A., Espuny, M.J. (2009). *Chem. Phys. Lipids* **158**, 110–117.

[7] Zaragoza, A., Teruel, J.A., Aranda, F.J., Ortiz, A.J. (2013). *Colloid Interface Sci*. **408**, 132–137.

[8] Gorin, P.A.J., Spencer, J.F.T., Tulloch, A.P. (1961). *Can. J. Chem*. **39**, 846–855.

[9] Penfold, J., Chen, M., Thomas, R.K., Dong, C., Smyth, T.J.P., Perfumo, A., Marchant, R., Ibrahim, M., Banat, I.M., Stevenson, P., Parry, A., Tucker, I., Grillo, I. (2011). *Langmuir* **27**, 8867–8877.

[10] Ratsep, P., Shah, V. (2009). *J. Microbiol. Methods* **78**, 354–356.

[11] Gross, R.A., Rengathavasi, T., Koh, A., Peng, Y. *Modified Sophorolipids as Oil Solubilizing Agents*. United States Patent Application Publication US 20130331466 A1, Dec. 12, 2013.

[12] Yoshikawa, M., Yamaguchi, S., Kunimi, K., Matsuda, H., Okuno, Y., Yamahara, J., Murakami, N. (1994). *Chem. Pharm. Bull*. **42**, 1226–1230.

[13] Arima, K., Kakinuma, A., Tamura, G. (1968). *Biochem. Biophys. Res. Commun*. **31**, 488–494.

[14] Shaligram, N.S., Singhal, R.S. (2010). *Food Technol. Biotechnol*. **48**, 119–134.

[15] Dufour, S., Deleu, M., Nott, K., Wathelet, B., Thonart, P., Paquot, M. (2005). *Biochim. Biophys. Acta* **1726**, 87–95.

[16] Kalinovskaya, N.I., Kuznetsova, T.A., Ivanova, E.P., Romanenko, L.A., Voinov, V.G., Huth, F., Laatsch, H. (2002). *Marine Biotechnol*. **4**, 179–188.

[17] Niran Roongsawang, N., Washio, K., Morikawa, M. (2011). *Int. J. Mol. Sci*. **12**, 141–172.

[18] See AOCS Lipid Library website (http://lipidlibrary.aocs.org/index.html).

[19] Ramkrishna, S. (ed.) (2010). *Biosurfactants, Advances in Experimental Medicine and Biology*, Springer, New York, Vol. 672, p. 56.

[20] Cooper, D.G., Zajic, J.E., Gracey, D.E.F. (1979). *J. Bacteriol*. **137**, 795–801.

[21] Tabuch, T., Nakamura, I., Kobayashi, T. (1977). *J. Ferment. Technol*. **55**, 37–42.

[22] Rosenberg, E., Zuckerberg, A., Rubinovitz, C., Cutnick, D.L. (1979). *Appl. Environ. Microbiol*. **37**, 402–408.

[23] Barnhart, D., Kaplan, D.L., Winter, W.T., Panilaitis, B.J., Kiemle, D. (2012). *J. Carbohydr. Polym*. **88**, 257–262.

[24] Rosenberg, E., Rubinovitz, C., Legmann, R., Ron, E.Z. (1988). *Appl. Environ. Microbiol*. **54**, 323–326.

[25] Navon–Venezia, S., Zosim, Z., Gottieb, A., Legmann, R., Carmeli, S., Ron, E.Z., Rosenberg, E. (1995). *Appl. Environ. Microbiol*. **61**, 3240–3244.

[26] Toren, A., Navon-Venezia, S., Ron, E.Z., Rosenberg, E. (2001). *Appl. Environ. Microbiol*. **67**, 1102–1106.

[27] Cirigliano, M.C., Carman, G.M. (1984). *Appl. Environ. Microbiol*. **48**, 747–750.

[28] Zajic, J.E., Guignard, H., Gerson, D.F. (1977). *Biotechnol. Bioeng*. **19**, 1285–1301.

[29] Li, Z.-Y., Lang, S., Wagner, F., Witte, L., Wray, W. (1984). *Appl. Environ. Microbiol*. **43**, 610–617.

[30] Penfold, J., Thomas, R.K., Shen, H.-H. (2012). *Soft Matter* **8**, 578–591.

[31] Shete, A.M., Wadhawa, G., Banat, I.M., Chopade, B.A. (2006). *J. Sci. Industr. Res*. **65**, 91–115.

[32] Lang, S. (2002). *Curr. Opin. Colloid Interface Sci*. **7**, 12-–20.

[33] Mulligan, C.N. (2009). *Curr. Opin. Colloid Interface Sci*. **14**, 372–378.

[34] Dahrazma, B., Mulligan, C.N., Nieh, M.-P. (2008). *J. Colloid Interface Sci*. **319**, 590–593.

[35] Nguyen, T.T., Sabatini, D.A. (2011). *Int. J. Mol. Sci*. **12**, 1232–1244.

[36] Rodrigues, L., Banat, I.M., Teixeira, J., Oliveira, R. (2006). *J. Antimicrob. Chemother*. **57**, 609–618.

[37] Dusane, D.H., Zinjarde, S.S., Venugopalan, V.P., McLean, R.J.C., Weber, M.M., Rahman, P.K.S.M. (2010). *Biotechnol. Genet. Eng. Rev*. **27**, 159–184.

[38] Kokufuta, E., Matsumoto, W., Nakamura, I. (1982). *Biotechnol. Bioeng*. **24**, 1591–1603.

[39] Mizunuma, T., Kokufuta, E., Sato, S. (2007). *Colloids Surf. B* **56**, 155–160.

[40] Mizunuma, T., Kokufuta, E., Sato, S. (2007). *Colloids Surf. B* **57**, 56–60.

18

STRUCTURE AND REGULATION OF THE BLOOD–BRAIN BARRIER

YUNG-CHIH KUO,[1] CHIN-LUNG LEE,[1] AND JYH-PING HSU[2]

[1]*Department of Chemical Engineering, National Chung Cheng University, Chia-Yi, Taiwan 62102, ROC*
[2]*Department of Chemical Engineering, National Taiwan University, Taipei, Taiwan 10617, ROC*

18.1 INTRODUCTION

The central nervous system (CNS) is protected by the blood–brain barrier (BBB) and the blood–cerebrospinal fluid barrier (BCSFB). The BBB, a tissue site widely distributed in the cerebrum, is a specific biological barrier system, restraining and controlling the transports of endogenous and exogenous substances into the brain [1]. The primary roles of the BBB in physiology include maintenance of dynamic stability of the CNS, protection of extracellular microenvironment for brain cells, steady supply of nutrients into the brain via selective transport pathways, and the response of uncertain surrounding variations resulting from the activity of inflammatory cells [2]. The protein and ionic mediations in the BBB also sustain homeostasis for the CNS and regulate the drug delivery and efflux [3]. From the anatomic perspective, the components of the BBB contain brain microvascular endothelial cells (BMECs), astroglia, pericytes, and basement membrane [4]. Figure 18.1 is a schematic representation of the basic cellular structure in the BBB. In addition, interactions among the cerebral cells located between blood and the brain parenchyma lead to the particular configuration and biochemical characteristics of the BBB [5]. At the biomacromolecular level, BMECs display few pinocytotic vesicles, little fenestration, specific enzymes, factor VIII antigen, high transendothelial electrical resistance (TEER), low permeability, adenosine-5′-triphosphate (ATP)-binding cassette (ABC) transporters, and polarization of the membrane transporters, and can generate distinctive relations with the neighboring cells, rendering the unique trait of the BBB.

18.2 CELLULAR SYSTEM OF THE BBB

18.2.1 Tight Junctions

Tight junctions are the main infrastructure for separating molecules in the circulation system from the CNS and defending the external material invasion. This dense cell pattern is localized on the apical region between BMECs. With the function on compact closure for delivery, the tight junctions strictly confine the paracellular diffusion between apical and basolateral plasma membrane and restrict the mass transport between cells [7]. However, the tight junctions are not isolated and static fences in the BBB. Instead, the tight junctions are highly dynamic joints intimately regulated by ingredients in the CNS milieu [8]. One team of invesstigators found that the tight junctions can be regarded as a complex arrangement for transmitting signals between cells and are involved in the genetic expression, cell proliferation, and differentiation [9]. From the structural perspective, the tight junctions are parallel, interconnected, and transmembrane-protein-coupled seals. The transmembrane proteins can bind with cytoplasmic proteins in BMECs and interact with the basement membrane [2].

The extracellular proteins directly related to the tight junctions in the BBB are claudins and occludin [10]. The tight junction coproteins connecting with cytoskeletal actin comprise zonula occludens (ZOs), cingulin, 7H6, and AF-6. In addition, the cytoskeletal proteins can recruit signaling proteins and transcription factors. More than 40 proteins, including transmembrane proteins, cytoskeletal proteins, and

Encyclopedia of Biocolloid and Biointerface Science, Volume 1, First Edition. Edited by Hiroyuki Ohshima.
© 2016 John Wiley & Sons, Inc. Published 2016 by John Wiley & Sons, Inc.

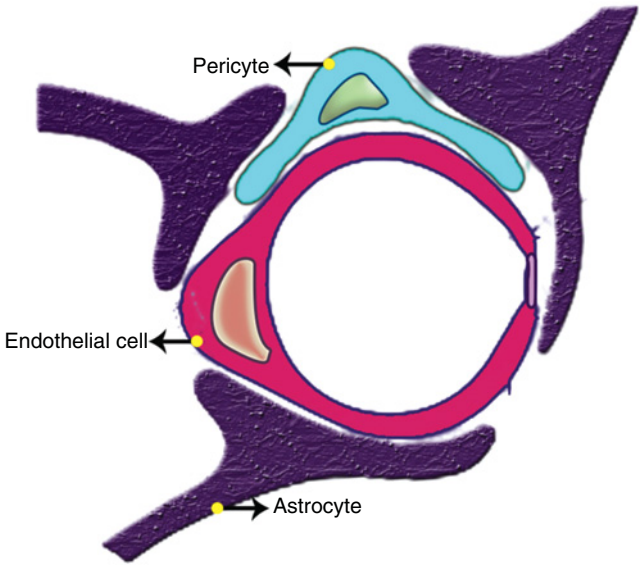


FIGURE 18.1 An illustrated anatomical structure of the BBB.

signaling proteins, are associated with the tight junctions and construct the protein complex for signal transmission and reception [11].

18.2.2 Neurovascular Unit

During cerebral development, aligned brain endothelia differentiate and evolve into microvessels with the BBB characteristics [12]. The brain microvessel walls dominate the feature of the BBB. It has been found that the effect of blood leakage enhances with an increasing diameter of the blood vessel, in general [13]. In addition, the biophysical and biochemical properties of BMECs determine the permeability of substances across the BBB [14]. However, the overall behavior of BMECs results from the cellular crosstalk among BMECs, neuroglia, pericytes, and the basement membrane [15]. Therefore, the brain astrocytes with their end feet touching BMECs, the microvessel-surrounding pericytes, and neurons can also affect the BBB permeability. The neurovascular unit (NVU) is composed of these brain cells and plays an essential role in the health and mediatory function of the CNS [16]. Moreover, the signal transmission among cells in the NUV strengthens the quality of the BBB and maintains the proper conditions for stabilizing the brain.

18.2.3 BMECs

Brain microvascular endothelial cells interact with cells in the NVU for regulating the selective transport between blood and the brain and metabolizing substances [17]. In addition, BMECs possess detoxifying functions by preventing poisons from infiltration into the brain [18]. The intrinsic difference between BMECs and other blood vessel endothelia is that the former possesses particular pathway molecules and conciliate the cells in the CNS [19]. The degree of impenetrability across the monolayer of BMECs is 50–100 times that of the microvessel endothelia in peripheral tissues [20]. This datum suggests severe limits to the transport of hydrophilic materials across BMECs. Moreover, the membrane thicknesses of BMECs are very much alike. The continuous basement membrane also contacts negatively charged BMECs, repelling molecules carrying negative charge into the brain. When compared with the endothelial cells in other organs, BMECs contain more and larger mitochondria. These mitochondria reinforce the energy system of BMECs, provide enzymes to destroy invading materials, activate various selective delivery systems, and assist the capture of required nutrients into the brain [21]. Furthermore, the complex proteins, such as the proteins at the tight junctions and the adherens junctions, fill up the interstices at the interface between BMECs and prohibit substances in the circulation system from entering the brain via the passive diffusion route. These mechanisms in BMECs can effectively shield the CNS to resist harmful hydrophobic substances. The BBB also includes the intercellular gap junctions [14]. However, the role of the gap junction proteins in the BBB permeability is not completely clear. In addition, the BBB is not merely a shelter for preventing the leakage of external blood molecules into the brain. Several membrane receptors and special transport systems in BMECs enable the brain to absorb essential hormones and to adjust ionic and metabolite concentration.

18.2.4 Astrocytes

Astrocytes are classified as neuroglial cells. The end feet of astrocytes form thin flat networks closely attached to the abluminal surface of BMECs and constitute one of the fundamental BBB morphologies (see Fig. 18.1) [22]. Astrocytes also possess several ionic channels and membrane receptors. The end feet of astrocytes contain a high surface density of the orthogonal arrays of particles (OAPs). The OAPs, such as water channel aquaporin 4 (AQP4) and K^+ channel Kir4.1, mediate the ionic level and volume of BMECs [23]. In addition, OAP/AQP4 is relevant to the expression of agrin in the basement membrane and intensifies the compactness of the BBB. Moreover, astrocytes play a significant role in the synthesis of proteoglycan, promote the charge selectivity and inductive ability of BMECs, and carry nutrients for neurons.

A certain part of microvessels in the CNS is deficient in astrocytes. However, these microvessels can still demonstrate the BBB traits. This is derived from the functions of soluble factors secreted by neighboring astrocytes. The astrocyte-secreted factors include transforming growth factor β (TGFβ), glia-derived neurotrophic factor (GDNF), basic fibroblast growth factor (bFGF), and angiopoietin 1 (Ang 1). Thus, the application of astrocyte-conditioning medium (ACM; the medium after cultivation of astrocytes) can improve the intensity of tight junctions between BMECs,

induce an appropriate expression of membrane protein transporters, and mimic the brain conditions in vivo for in vitro BBB models. Another team employed an ACM into the culture medium for growing human BMECs [24]. They found that the ACM can reduce 70% permeability across the BBB and enhance the expression of tight junction ZO-1.

18.2.5 Pericytes

When compared with peripheral blood vessels, the CNS vessels are surrounded by a relatively large quantity of pericytes [25]. Pericytes play a critical role in the formation of the BBB characteristics, particularly in the maintenance of the structural integrity at the cellular interface [26]. However, the importance of the brain microvascular pericytes is not limited to upholding of the BBB architecture. In fact, microvascular pericytes can assist angiogenesis in the brain and transmit signals to BMECs through several structural and molecular pathways such as the tight junctions, gap junctions, adhesion plaques, and soluble factors [27]. Therefore, the brain microvascular pericytes are significant in sustaining the brain homeostasis and holding the BBB unity.

The brain microvascular pericytes underlie the BMEC substratum, share the basement membrane with BMECs, and are necessary in the developmental process, biochemical signaling, and physical support of BMECs. For example, pericyte-secreted Ang 1 recognizes its receptor Tei-2 on BMECs for pertaining to the normal differentiation of BMECs [28]. A similar interaction is observed between BMEC-secreted platelet derived growth factor β (PDGFβ) and PDGF receptor β (PDGFRβ) on pericytes. It has been found that the mortality of newborn neonate, microvascular leakage, and hemorrhage probability increase in PDGFβ and PDGFRβ knockdown mice. Pericyte-secreted TGFβ is also a critical element for stabilizing and maturing blood microvessels. In mice without TGFβ and TGFβ type II receptor (TGFβR2), defective blood vessels are observed and can be attributed to the deficiency of TGFβ and TGFβR2, rendering the inhibition to endothelial proliferation and migration [29]. From the physiological perspective, the role of pericytes is comparable to that of astrocytes, in general. They secrete various factors to retain the dense paracellular junctions and the firm cellular wraps in the BBB. The intimate interaction between pericytes and astrocytes is also confirmed. Another group who investigated an *in vivo* BBB model of mice with/without pericytes [30] found that the presence of pericytes strongly affected the polarity of astrocyte end feet. The BBB model without pericytes leads to mislocalization of AQP4 and increases the BBB permeability. Therefore, the brain microvascular pericytes can directly stimulate BMECs, influence the function of astrocytes, and modify the BBB integrity.

The pathological situation can vary the percentage of pericytes covered on BMECs. Another team investigated the BBB structure of rats with traumatic brain injury [31]. They found that after the injury, the ratio of pericytes to BMECs decreases from 1:5 to 1:10 (or 1:12) within 2 h. In addition, the immovable pericytes on BMECs are degraded after the injury for 2 h. However, the relocation of astrocytes from the NVU is not observed. Another team investigated the BBB microstructure of cats under hypoxia [32]. They found that the hypoxemic condition induces the migration of 35% pericytes and thickens the basement membrane within 2 h. However, no obvious variation in BMECs is observed under hypoxia. Another team investigated the BBB structure of mice at sepsis via abdominal injection of lipopolysaccharide [33]. They found that the septicemia yields activated microglial cells, disrupted basement membrane, and detached pericytes from the basement membrane.

18.3 IN VITRO BBB MODEL

The in vitro BBB models belong to the category of cell models, which simplify the complicated circumstances in the brain in vivo and can standardize the related parameters, including the permeability. Therefore, the biomedical researchers have attempted to pursue an in vitro BBB model with a realistic feature of the BBB in vivo [34]. The replicated in vitro BBB models should be simple, reproducible, and reliable and imitate the brain to reflect the microvessels in vivo. The mimicking items of the in vitro BBB model include the anatomical similarity for normal and pathological conditions, the drug transfer route and the drug release mechanism into the CNS, the delivery pathways across the BMEC monolayer, and the proper expression of the membrane protein transporters.

Based on biological and philological observations, the primary objective of the *in vitro* BBB model is to reconstruct the BBB nature and simulate the transport mechanisms in vivo [35]. First, the in vitro BBB model should express sufficiently tight junctions to resist the penetration of substances across the BMEC monolayer via a paracellular pathway. A TEER value and/or permeability coefficient can be used as a typical evidence to judge the completeness and impenetrability of endothelial membrane in the in vitro BBB model. In addition, the appropriate expression of membrane protein transporters on BMECs in the in vitro BBB model indicates the homeostasis and the protection of the CNS [36, 37]. So far, the brain tissue from various mammalian species has been isolated for establishing the in vitro BBB model. These animals include rat, mouse, feline, canine, porcine, and bovine [38–46]. The discrepancy in the transport behavior among the in vitro BBB models from different animal species should be identified. In addition, the permeability obtained from the in vitro and in vivo (animal) BBB models should be assessed and distinguished.

18.3.1 Primary Culture

Joo and Kamushinain achieved the first *in vitro* BBB model by isolation of rat brain microvessels in 1973. Although human BMECs have been used in the in vitro BBB model and the related study, the human brains cannot be freely obtained [47]. In addition, the human brain tissue is often regarded as an improper source for research, although this aspect is under strong debate. Therefore, BMECs from porcine, bovine, and rodent sources are commonly used for the in vitro BBB model [48]. It has been confirmed that the primary culture of BMECs preserves the central feature of BMECs. However, several problems on the BBB characteristics arise in the primary culture using only BMECs. These include the cell purity such as the basement membrane containing an uncertain portion of pericytes. Moreover, BMECs may lose the function in vivo after isolation from tissue, due to the deficiency of mediation by the brain microenvironment. The cellular senescence after succeeding passage can also lead to the deprivation of the BBB traits and the feeble availability of the primary culture based merely on BMECs.

18.3.2 Coculture

The importance of the mechanisms in the cell-interacting NVU for the BBB characteristics, such as astrocyte-induced functions, is well recognized [10, 23, 44]. Therefore, it is inevitable to establish more complicated BBB models involving the other NVU elements except BMECs. The capability and diversity of the in vitro BBB models are thus promoted [49]. BMECs were cocultured with pericytes on porous membrane for studying the BBB permeability [50]. In addition, the cocultured BBB model can be applied to investigate the mass transport and the feedback behavior [51]. The cocultured BBB model can also be employed to evaluate the responsibility of various cells including astrocytes [52–55], pericytes [56], neurons [57], and microglia [58]. Moreover, a cocultured BBB model containing triple components of rat BMECs, astrocytes, and pericytes was recently established [59]. Rat BMECs, astrocytes, and neurons can also comprise a triple cocultured BBB model [60]. The fact that BMECs interconnect the NVU elements in vivo leads to accomplishment of the double and triple cocultured BBB models. These models benefit various BBB studies, including neuronal inflammation, disorder, and degeneration (Alzheimer's and Parkinson's diseases), disease evolution (infection of human immunodeficiency virus), drug abuse (alcohol and methamphetamine), and drug delivery into the CNS [61–65].

18.4 ABC TRANSPORTERS IN THE BBB

The ABC transporters belong to the transportation proteins on the membrane of BMECs. Through hydrolysis of ATP, the ABC transporters control the permeability of solutes across the BBB. In addition, the ABC transporters are regarded as the key mediators of drug distribution in and efflux from the CNS [66]. In fact, these efflux pumps in the BBB and the BCSFB obstruct the entrance of numerous chemicals into the CNS. The ABC transporters discovered include P-glycoprotein, multidrug resistance proteins (MRPs), and breast cancer resistance proteins (BCRPs). The multidrug resistance (MDR) is one of the major hindrances for delivering drug across BMECs. Therefore, the development of the non-ABC transporter substrates and the ABC transporter inhibitors can be an efficacious strategy to treat the brain-related diseases.

18.4.1 Mechanism of ABC Transporters

P-Glycoprotein, the phosphorylated glycoprotein, is a product of the MDR1 gene. P-glycoprotein is the first ABC transporter found from human BMECs. BMECs of monkeys, rats, mice, cats, dogs, cattle, and pigs can also express P-glycoprotein. This explains that P-glycoprotein is a common protective sentinel of the mammalian BBB [67]. P-Glycoprotein can also restrain harmful lipophilic chemicals from penetrating the BBB and protect the CNS. In clinical practice, it has been concluded that various therapeutic drugs with dissimilar molecular structure belong to the P-glycoprotein substrates [68]. For rodents, the genes to produce P-glycoprotein include mdr1a and mdr1b, which are analogous to MDR1 gene in human. In mdr1a knockout mice, the expression of P-glycoprotein in the BBB is inadequate and yields increases of 10–100 times in the permeability of drugs classified as the P-glycoprotein substrates [69]. Moreover, two other researchers investigated the effect of inhibitors on the blockage of P-glycoprotein efflux functions in the BBB [70]. They found an obvious enhancement in the concentration of various drugs in the brain. The rationale behind this observation is that P-glycoprotein plays an essential role in the transporter to expel drugs from penetrating through the BBB. Furthermore, it has been concluded that astrocytes can induce the expression of P-glycoprotein, MRP-3, MRP-4, and BCRP in rat BMECs [38]. In addition, the brain pericytes can stimulate the activity of P-glycoprotein on BMECs [71]. The brain pericytes also enhance the quantities of occludin, MRP-6, and mRNA on/in BMECs [72, 73].

18.5 SECRETED FACTORS FOR BBB REGULATION: MECHANISM AND INHIBITOR

Various components in the NVU regulate the BBB via the cellular secreted factors. The astrocyte-secreted factors include TGFβ, GDNF, bFGF, and Ang 1 [21]. These secreted factors from astrocytes mediate the compactness of the tight

junctions and the expression of the membrane proteins on BMECs [24]. In normal and pathological conditions, pericytes also generate secreted factors such as TGFβ1, matrix metalloproteinase (MMP), vascular endothelial growth factor (VEGF), bFGF, and Ang 1 [28]. These pericyte-secreted factors affect the activity of the ABC transporters, the brain physiology, and the integrity of the BBB [29].

18.5.1 TGFβ1

TGFβ belongs to a family of multifunctional peptide growth factors. TGFβ1, TGFβ2, TGFβ3, TGFβ4, and TGFβ5 are the subspecies of TGFβ. TGFβ type I and type II receptors are the two specific transmembrane receptors of TGFβ. Interactions between TGFβ and its receptors activate the intracellular signal transmission system, such as Smad protein and p38 mitogen-activated protein kinase, and the intercellular pathways of signal-regulating kinase [74]. In addition, TGFβ is an important endogenous molecule against the nerve diseases and disorders of the CNS [75]. Another group of investigators found that TGFβ1 secreted by brain pericytes can reduce the permeability across the BBB and stimulate the activity of P-glycoprotein on rat BMECs [71]. An application of SB431542, a competitive inhibitor of TGFβ1, decreases the efflux function of P-glycoprotein and increases the content of P-glycoprotein substrates, such as NaF and rhodamine 123, in rat BMECs. This demonstrates that TGFβ1 can upregulate the expression of P-glycoprotein in the BBB and may be closely related to the expression of the tight junction proteins. Others found that the pericyte-secreted TGF-β1 can induce the expression of VEGF receptor 1 under ischemic conditions to prevent the degeneration of blood vessels from oxygen suppression [76]. This explains the biochemical mechanism where pericytes regulate the vascular survival via TGFβ1.

18.5.2 VEGF

The VEGF family comprises six members: VEGF-A, VEGF-B, VEGF-C, VEGF-D, VEGF-E, and placenta growth factor. VEGF-A is the most important VEGF family member in the brain for vasculogenesis, angiogenesis, and regulation of the permeability across BMECs [77]. However, an overexpression of VEGF is related to various diseases and pathological situations such as the brain carcinoma, stroke, diabetic retinopathy, ischemia, brain injury, and BBB dysfunction [78–81]. VEGF is a water-soluble molecule residing in extracellular matrix (ECM) [82]. Before protease activation, VEGF is in an inactive state and can be regarded as one of the cellular inflammatory factors.

Another study revealed that BMECs under hypoxia secrete VEGF and phosphorylate vasodilator-stimulated phosphoprotein to suppress the expression of ZO-1 in the tight junctions, leading to an increase in the permeability across the BBB [83]. Another team investigated the effect of VEGF receptor flk-1 and Src inhibitors, SU5416 and PP2, on the function of P-glycoprotein [84]. They found that an increasing content of VEGF in the brain downregulates the activity of P-glycoprotein without altering the expressed quantity of P-glycoprotein. These findings confirm that an increase in the concentration of VEGF reduces the activity of P-glycoprotein in the BBB.

18.5.3 MMP-9

MMP is a kind of zinc- and calcium-dependent proteolytic enzyme, secreted by BMECs, astrocytes, and pericytes [85]. Zymogen and endogenous tissue inhibitors of metalloproteinases regulate the activation of MMP. In inflammatory states, MMP-2 and MMP-9 can disturb the physiology of the BBB. In addition, the various cellular components in the NVU can produce MMPs. BMECs secrete MMP-9, acreocytes MMP-2 and MT1-MMP, and pericytes MMP-3 and MMP-9. Moreover, MMPs can regulate the intercellular signaling mechanisms via remodeling of the relevant ECM molecules. Another study revealed that MMP-9 regulates the BBB by cleavage of occludin in the tight junctions [86]. In another study, the topical ischemia was found to increase the secretion of cerebral MMP-9 and yield a reduction in the quantity of ZO-1 in the tight junctions [87]. However, in the case of MMP-9 gene knockout, the mortality resulting from the rupture of the BBB decreases. Another team found that in rat stroke model, an application of BB1101, a general MMP inhibitor, can avoid the leakage of the BBB and reduce the BBB permeability [88].

18.6 NANOPARTICLES FOR DELIVERING PHARMACEUTICALS ACROSS THE BBB

There have been many investigations of applications of the colloidal drug delivery system, such as nanocarrier, to overcome the BBB and treat diseases and neurodegenerative disorders in the CNS. Figure 18.2 illustrates the typical structure of colloidal drug carrier with surface bioactive moieties. As indicated in this figure, the particle is coated with two antibodies for targeting. Another team of investigators modified sialic acid and similopioid peptide on poly(lactide-*co*-glycolide) (PLGA) nanoparticles (NPs) for improving the BBB permeability and the brain-targeting effect [89]. They found that sialic acid and similopioid peptide can prolong the central analgesic activity of loperamide for 24 h and extend the residence time for sustained release in the brain. Two other researchers concluded that after intravenous injection (IVI) of nanocarriers for 4 h, the order in the plasma concentration of coumarin 6 is polylactide (PLA)–tocopheryl polyethylene glycol succinate (TPGS) NPs > PLA–TPGS/transferrin NPs > PLGA NPs [90]. They also found that amphiphilic PLA–TPGS NPs can load a high

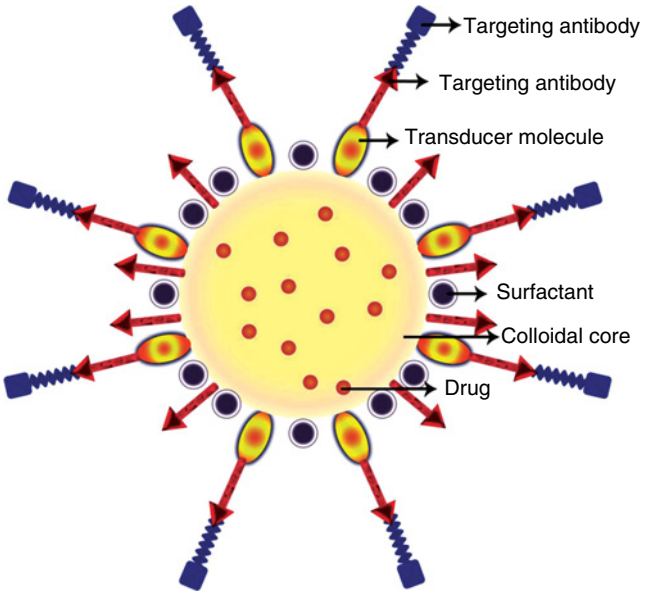


FIGURE 18.2 Schematic representation of colloidal drug delivery system with surface targeting antibodies.

content of coumarin 6 and maintain high particle stability. The main reason for the low plasma concentration of coumarin 6 by PLGA NPs is that hydrophobic PLGA NPs yields high affinity to monocytes, rendering a rapid elimination. In addition, the plasma concentration of coumarin 6 by PLA–TPGS NPs with surface transferrin is lower than that without surface transferrin. However, the former results in a higher concentration in the brain than the latter, demonstrating that surface transferrin can target the brain tissue. Another team found that a 12-amino-acid peptide (Pep TGN), displayed in bacteriophage Clone 12-2, generates a high brain-targeting effect [91]. They also concluded that the delivery efficiency of Pep TGN into the brain is higher than that of native M13 phage. In addition, a modification with Pep TGN on polyethylene glycol (PEG)-PLGA NPs improves the penetration across the BBB. Moreover, the uptake quantity of PEG-PLGA NPs with Pep TGN by bEnd.3 cells (immortalized mouse BMEC cell line) is higher than that without Pep TGN. Another group modified the transactivator of transcription (Tat) peptide and PEG on gelatin–siloxane (GS) NPs to escape the capture by reticuloendothelial system and transfer across the BBB [92]. They found that the modification with Tat peptide converts GS NPs from neutral surface charge into positive surface charge. In addition, Tat-PEG-GS NPs sustain a high brain concentration after IVI for 2 h. Another study revealed that a modification with trimethylated chitosan (TMC) on PLGA NPs promotes the BBB permeability [93]. From the analysis of brain tissue sections, large quantities of TMC-modified PLGA NPs accumulate in cortex, paracoele, the third ventricle, and choroid plexus epithelium. However, no brain uptake is observed in the case of PLGA NPs without TMC. In addition, the modification with TMC converts the particle surface charge from −20 mV to 20 mV and favors the adsorptive-mediated transcytosis (AMT) of TMC-PLGA NPs across the BBB. From the outcome of the Morris water maze behavioral test, coenzyme Q10-loaded TMC-PLGA NPs ameliorate the memory impairment of rats. Another study revealed that a modification with cationized bovine serum albumin (CBSA) reduces the negative charge on PEG–PLA NPs and benefits the particle uptake by negatively charged endothelia [94]. In addition, the tissue sections confirm that the surface charge is the main driving force for delivering PEG-PLA NPs with CBSA into the brain.Another group modified CBSA onto solid lipid nanoparticles (SLNs)–doxorubicin by replacing carboxyl groups with amines to obtain positively charged NPs [95]. They found that CBSA–SLN–doxorubicin can be endocytosed by endothelia and HNCG-1 tumor cells via the AMT. In addition, the uptake quantity of the particulate formulation by HNGC-1 tumor cells increases 6 times when compared with the doxorubicin solution dosage. Another group demonstrated that PEGylated polyamidoamine dendrimer conjugated fluorescein-doped magnetic silica NPs (PEGylated PFMSNs) can permeate the BBB via transcytosis [96]. They found that PEGylated PFMSNs can penetrate rat parenchyma and can be endocytosed by neurons after transport through endothelia and astrocytes. Intriguingly, PEGylation prevents PFMSNs from accumulation, reduces the adsorption of serum proteins, and enhances the probability of the BBB penetration. Another team applied human serum albumin NPs to adsorb HI 6 dimethanesulfonate and HI 6 dichloride monohydrate [97]. They found that from the adsorption isotherm, the Freundlich model is appropriate in these cases. In addition, from the BBB transport, the efficiencies of HI 6 dimethanesulfonate- and HI 6 dichloride monohydrate-coated human serum albumin NPs are, respectively, 1.5 and 2 times the efficiency of free oximes. Moreover, the inhibition efficacy of HI 6-loaded human serum albumin NPs to acetylcholinesterase is 2 times that of free oximes, suggesting a potential antidote for treating organophosphorus toxication. Another study revealed that β-hydroxybutyric acid–grafted docetaxel-loaded SLNs (HD-SLNs) assist the uptake by bEnd cells via monocarboxylic acid transporter [98]. In addition, the area under curve (AUC) of docetaxel in the brain by HD-SLNs is 12 times that by Taxotere. Another team found that penetratin-modified PEG-PLA NPs can infiltrate the BBB via lipid raft-mediated endocytosis or translocation processes via organelles such as Golgi apparatus, lysosome, and microtubule [99]. From pharmaceutical analysis, the penetratin modification is more effective in the uptake of PEG-PLA NPs in the brain than the low-molecular-weight protamine modification. In addition, penetratin can reduce the uptake quantity in non-targeting tissues. Another group of researchers investigated the influence of PEG chain length and particle size on the BBB penetration by PEGylated gold NPs [100]. They found that a

short PEG chain length yields small PEGylated gold NPs and the best BBB permeability occurs at the particle diameter of 4 nm. Another group prepared tacrine-loaded chitosan NPs by spontaneous emulsification [101]. They found that the release kinetics of tacrine follows the Fickian diffusion law. In addition, a modification with 1% polysorbate 80 advantages the BBB penetration and alters the tissue distribution in vivo. Another team investigated the effect of polysorbate 80-modified polybutylcyanoacrylate (PBCA) NPs on the integrity of porcine in vitro BBB model [102]. Based on the TEER value and the permeability of ^{14}C–sucrose and fluorescein isothiocyante–bovine serum albumin, a reversible disruption in the BBB is observed after incubation for 4 h. This suggests a temporal opening of the BBB by polysorbate 80-modified PBCA NPs.

ACKNOWLEDGMENTS

This work was supported by the Ministry of Science and Technology of the Republic of China.

ABBREVIATIONS

ABC	ATP-binding cassette
ACM	astrocyte-conditioning medium
AMT	adsorptive-mediated transcytosis
Ang 1	angiopoietin 1
ATP	adenosine-5′-triphosphate
BBB	blood–brain barrier
BCRP	breast cancer resistance protein
BCSFB	blood–cerebrospinal fluid barrier
bFGF	basic fibroblast growth factor
BMEC	brain microvascular endothelial cell
CBSA	cationized bovine serum albumin
CNS	central nervous system
ECM	extracellular matrix
GDNF	glial-derived neurotrophic factor
GS	gelatin–siloxane
HD-SLN	β-hydroxybutyric acid–grafted docetaxel-loaded solid lipid nanoparticle
IVI	intravenous injection
MMP	matrix metalloproteinase
MRP	multidrug resistance protein
NP	nanoparticle
NVU	neurovascular unit
PBCA	polybutylcyanoacrylate
PDGFβ	platelet derived growth factor β
PDGFRβ	platelet derived growth factor receptor β
PEG	poly(ethylene glycol)
pegylated PFMSN	pegylated polyamidoamine dendrimer-conjugated fluorescein-doped magnetic silica nanoparticle
Pep TGN	a 12-amino-acid peptide
PLA	polylactide
PLGA	poly(lactide-*co*-glycolide)
SLN	solid lipid nanoparticle
TAT	transactivator of transcription
TEER	transendothelial electrical resistance
TGFβ	transforming growth factor β
TMC	trimethylated chitosan
TPGS	tocopheryl poly(ethylene glycol)succinate
VEGF	vascular endothelial growth factor
ZO	zonula occluden

REFERENCES

[1] Jeffrey, P., Summerfield, S. (2010). Assessment of the blood–brain barrier in CNS drug discovery. *Neurobiol. Disorders* **37**, 33–37.

[2] Petty, M.A., Lo, E.H. (2002). Junctional complexes of the blood–brain barrier: Permeability changes in neuroinflammation. *Progress Neurobiol*. **68**, 311–323.

[3] Hawkins, B.T., Davis, T.P. (2005). The blood–brain barrier/neurovascular unit in health and disease. *Pharmacol. Rev*. **57**, 173–185.

[4] Cardoso, F.L., Brites, D., Brito, M.A. (2010). Looking at the blood–brain barrier: Molecular anatomy and possible investigation approaches. *Brain Res. Rev*. **64**, 328–363.

[5] Khan, E. (2005). An examination of the blood–brain barrier in health and disease. *Br. J. Nursing* **14**, 509–513.

[6] Ballabh, P., Braun, A., Nedergaard, M. (2004). The blood–brain barrier: An overciew: Structure, regulation, and clinical implications. *Neurobiol. Disorders* **16**, 1–13.

[7] Persidsky, Y., Ramirez, S.H., Haorah, J., Kanmogne, G.D. (2006). Blood–brain barrier: Structural components and function under physiologic and pathologic condition. *J. Neuroimm. Pharmacol*. **1**, 223–236.

[8] Wolburg, H., Noell, S., Mack, A.K., Wolburg-Buchholz, P., Fallier-Becker, H.P. (2009). Brain endothelial cells and the glio-vascular complex. *Cell Tissue Res*. **335**, 75–96.

[9] Gonzalez-Mariscal, L., Tapia, R., Chamorro, D. (2008). Crosstalk of tight junction components with signaling pathways. *Biochim. Biophys. Acta* **1778**, 729–756.

[10] Weiss, N., Miller, F., Cazaubon, S., Couraud, P.O. (2009). The blood–brain barrier in brain homeostasis and neurological diseases. *Biochim. Biophys. Acta* **1788**, 842–857.

[11] Terry, S., Nie, M., Matter, K., Balda, M.S. (2010). Rho signaling and tight junction functions. *Physiology* **25**, 16–26.

[12] Lee, S.W., Kim, W.J., Park, J.A., Choi, Y.K., Kwon, Y.W., Kim, K.W. (2006). Blood–brain barrier interfaces and brain tumors. *Arch. Pharm. Res*. **29**, 265–275.

[13] Marchi, N., Cavaglia, M., Fazio, V., Bhudia, S., Hallene, K., Janigro, D. (2004). Peripheral markers of blood–brain barrier damage. *Clin. Chim. Acta* **342**, 1–12.

[14] Zlokovic, B.V. (2008). The blood–brain barrier in health and chronic neurodegenerative disorders. *Neuron* **57**, 178–201.

[15] Zozulay, A., Weidenfeller, C., Galla, H.J. (2008). Pericyte–endothelial cell interaction increases MMP-9 secretion at the blood–brain barrier in vitro. *Brain Res*. **1189**, 1–11.

[16] Choi, Y.K., Kim, K.W. (2008). Blood–neural barrier: Its diversity and coordinated cell-to-cell communication. *BMB* (biochemistry and molecular biology) *Reports* **41**, 345–352.

[17] Calabria, A.R., Shusta, E.V. (2008). A genomic comparison of in vivo and in vitro brain microvascular endothelial cells. *J. Cereb. Blood Flow Metab*. **28**, 135–148.

[18] Ueno, M. (2007). Molecular anatomy of the brain endothelial barrier: An overview of the distributional features. *Curr. Med. Chem*. **14**, 1199–1206.

[19] Weksler, B.B., Subileau, E.A., Perriere, N., Charneau, P., Holloway, K., Leveque, M., Tricoire-Leignel, H., Nicotra, A., Bourdoulous, S., Turowski, P., et al. (2005). Blood–brain barrier-specific properties of a human adult brain endothelial cell line. *FASEB J*. **19**, 1872–1874.

[20] Abbott, N.J. (2002). Astrocyte-endothelial interactions and blood–brain barrier permeability. *J. Anat*. **200**, 629–638.

[21] de Boer, A.G., Gaillard, P.J. (2006). Blood–brain barrier dysfunction and recovery. *J. Neural Transm*. **113**, 455–462.

[22] Jeliazkova-Mecheva, V.V., Bobily, D.J. (2003). A porcine astrocyte/endothelia cell co-culture model of the blood–brain barrier. *Brain Res. Protocols* **12**, 91–98.

[23] Abbott, N.J., Ronnback, L., Hansson E. (2006). Astrocyte-endothelial interactions at the blood–brain barrier. *Nat. Rev. Neurosci*. **7**, 41–53.

[24] Siddharthan, V., Kim, Y.V., Liu, S., Kim, K.S. (2007). Human astrocytes/astrocyte-conditioned medium and shear stress enhance the barrier properties of human brain microvascular endothelial cell. *Brain Res*. **1147**, 39–50.

[25] Lai, C.H., Kuo, K.H. (2005). The critical component to establish in vitro BBB model: Pericyte. *Brain Res. Rev*. **50**, 258–265.

[26] Braun, A., Xu, H., Hu, F., Kocherlakota, P., Siegel, D., Chander, P., Ungvari, Z., Csiszar, A., Nedergaard, M., Ballabh, P. (2007). Paucity of pericytes in germinal matrix vasculature of premature infants. *J. Neurosci*. **27**, 12012–12024.

[27] Bagley, R.G., Weber, W., Rouleau, C., Teicher, B.A. (2005). Pericytes and endothelial precursor cells: Cellular interactions and contributions to malignancy. *Cancer Res*. **65**, 9741–9750.

[28] Anatomie, S. (2010). CNS pericytes: Concepts, misconceptions, and a way out. *Glia* **58**, 1–10.

[29] Gerhardt, H., Betsholtz, C. (2003). Endothelial-pericyte interactions in angiogenesis. *Cell Tissue Res*. **314**, 15–23.

[30] Armulik, A., Genove, G., Mae, M., Nisancioglu, M., Wallgard, E., Niaudet, C., He, L., Norlin, J., Lindblom, P., Strittmatter, K., Johansson, B., Betsholtz, C. (2010). Pericytes regulate the blood–brain barrier. *Nature* **468**, 557–562.

[31] Dore-Duffy, P., Owen, C., Balabanov, R., Murphy, S., Beaumont, T., Rafols, J.A. (2000). Pericyte migration from the vascular wall in response to traumatic brain injury. *Microvasc. Res*. **60**, 55–69.

[32] Gunel, E., Duz, B., Kahraman, S., Kayaly, H., Kubar, A., Timurkaynak, E. (2002). Early pericyte response to brain hypoxia in cats: An ultrastructural study. *Microvasc. Res*. **64**, 116–119.

[33] Nishioku, T., Dohgu, S., Takata, F., Eto, T., Ishikawa, N., Kodama, K.B., Nakagawa, S., Yamauchi, A., Kataoka, Y. (2009). Detachment of brain pericytes from the basal lamina is involved in disruption of the blood–brain barrier caused by lipopolysaccharide-induced sepsis in mice. *Cell. Mol. Neurobiol*. **29**, 309–316.

[34] Gumbleton, M., Audus, K.L. (2001). Progress and limitations in the use of in vitro cell cultures to serve as a permeability screen for the blood–brain barrier. *J. Pharm. Sci*. **90**, 1681–1698.

[35] Rubin, L.L., Staddon, M. (1999). The cell biology of blood–brain barrier. *Annu. Rev. Neurosci*. **22**, 11–28.

[36] Schinkel, A.H. (1999). P-glycoprotein, a gatekeeper in the blood–brain barrier. *Adv. Drug Deliv. Rev*. **36**, 179–194.

[37] Sun, H., Dai, H., Shaik, N., Elmquist, W.F. (2003). Drug efflux transporters in the CNS. *Adv. Drug Deliv. Rev*. **55**, 83–105.

[38] Perriere, N., Yousif, S., Cazaubon, S., Chaverot, N., Bourasset, F., Cisternino, S., Decleves, X., Hori, S., Terasaki, T., Deli, M., Scherrmann, J.M., Temsamani, J., Roux, F., Couraud, P.O. (2007). A functional in vitro model of rat blood–brain barrier for molecular analysis of effux transporters. *Brain Res*. **1150**, 1–13.

[39] Coisne, C., Dehouck, C.Faveeuw, F., Delplace, Y., Miller, F., Morissette, C., Fenart, L., Cecchelli, R., Tremblay, P., Dehouck, B. (2005). Mouse syngenic in vitro bolld–brain barrier model: A new tool to examine inflammatory events in cerebral endothelium. *Lab. Invest*. **85**, 734–746.

[40] Fletcher, N.F., Bexiga, M.G., Brayden, D.J., Brankin, B., Willett, B.J., Hosie, M.J., Jacque, J.M., Callanan, J.J. (2009). Lymphocyte migration through the blood–brain barrier (BBB) in feline immunodeficiency virus infection is significantly influenced by the pre-existence of virus and tumor necrosis factor (TNF)-α within the central nerbous system (CNS): studies using an in vitro feline BBB model. *Neuropathol. Appl. Neurobiol*. **35**, 592–602.

[41] Zhang, Y., Li, C.S., Ye, Y., Johnson, K., Poe, J., Johnson, S., Bobrowski, W., Garrido, R., Madhu, C. (2006). Porcine brain microvessel endothelial cells as an in vitro model to predict in vivo blood–brain barrier permeability. *Drug Metab. Dispos*., **34**, 1935–1943.

[42] Kuo, Y.C., Chen, H.H. (2006). Effect of nanoparticulate polybutylcyanoacrylate and methylmethacrylate–sulfopropylmethacrylate on the permeability of zidovudine and lamivudine across the in vitro blood–brain barrier. *Int. J. Pharm*. **327**, 160–169.

[43] Zhang, X., Alakhova, D.Y., Batrakova, E.V., Li, S., Yang, Z., Li, Y., Kabanov, A.V. (2009). Effect of pluronic p85 on amino acid transport in bovine brain microvessel endothelial cells. *J. Neuroimm. Pharmacol*. **4**, 35–46.

[44] Cecchelli, R., Berezowski, V., Lundquist, S., Culot, M., Renftel, M., Dehouck, M.P., Fenart, L. (2007). Modelling of the

blood–brain barrier in drug discovery and development. *Nat. Rev. Drug Discov*. **6**, 650–661.

[45] Smith, M., Omidi, Y., Gumbleton, M. (2007). Primary porcine brain microvascular endothelial cells: Biochemical and functional characterization as a model for drug transport and targeting. *J. Drug Target*. **15**, 253–268.

[46] Zenker, D., Begley, D., Bratzke, H., Rubsamen-Waigmann, H., von Briesen, H. (2003). Human blood-derived macrophages engance barrier function of cultured primary bovine and human brain capillary endothelial cells. *J. Physiol*. **551**, 1023–1032.

[47] Bernas, M.J., Cardoso, F.L., Daley, S.K., Weinand, M.E., Campos, A.R., Ferreira, A.G.J., Hoying, J.B., Witte, M.H., Brites, D., Persidsky, Y., Ramirez, S.H., Brito, M.A. (2010). Establishment of primary cultures of human brain microvascular endothelial cells to provide an in vitro cellular model of the blood–brain barrier. *Nat. Protocols* **5**, 1247–1254.

[48] Beck, D.W., Roberts, R.L., Olson, J.J. (1986). Glial cells influence membrane-associated enzyme activity at the blood–brain barrier. *Brain Res*. **381**, 131–137.

[49] Ramsauer, M., Krause, D., Dermietzel, R. (2002). Angiogenesis of the blood–brain barrier in vitro and the function of cerebral pericytes. *FASEB J*. **16**, 1274–1276.

[50] Nakagawa, S., Deli, M.A., Nakao, S., Honda, M., Hayashi, K., Nakaoke, R., Kataoka, Y., Niwa, M. (2007). Pericytes from brain microvessels strengthen the barrier integrity in primary cultures of rat brain endothelial cells. *Cell. Mol. Neurobiol*. **27**, 687–694.

[51] Megard, I., Garrigues, A., Orlowski, S., Jorajuria, S., Clayette, P., Ezan, E., Mabondzo, A. (2002). A co-culture-based model of human blood–brain barrier: application to active transport of indinavir and in vivo-in vitro correlation. *Brain Res*. **927**, 153–167.

[52] Al Almad, A., Gassman, M., Ogunshola, O.O. (2009). Maintaining blood–brain barrier integrity: Pericytes perform better than astrocytes during prolonged oxygen deprivation. *J. Cell. Physiol*. **218**, 612–622.

[53] Ghazanfari, F.A., Stewart, R.R. (2001). Characteristics of endothelial cells derived from the blood–brain barrier and of astrocytes in culture. *Brain Res*. **890**, 49–65.

[54] Gaillard, P.G., Voorwinden, L.H., Nielsen, J.L., Ivanov, A., Atsumi, R., Engman, H., Ringbom, C., de Boer, A.G., Breimer, D.D. (2001). Establishment and functional characterization of an in vitro model of the blood–brain barrier, comprising a co-culture of brain E endothelial cells and astrocytes. *Eur. J. Pharm. Sci*. **12**, 215–222.

[55] Kuo, Y.C., Lu, C.H. (2011). Effect of human astrocytes on the characteristics of human brain-microvascular endothelial cells in the blood–brain barrier. *Colloid Surf. B* **86**, 225–231.

[56] Kim, J.A., Tran, N.D., Li, Z., Yang, F., Zhou, W., Fisher, M.J. (2006). Brain endothelial hemostasis regulation by pericytes. *J. Cereb. Blood Flow Metab*. **26**, 209–217.

[57] Cestelli, A., Catania, C., D'Agostino, S., Di Liegro, I., Licata, L., Schiera, G., Pitarresi, G.L., Savettieri, G., De Caro, V., Giandalia, G., Giannola, L.I. (2001). Functional feature of a novel model of blood brain barrier: Studies on permeation of test compounds. *J. Control. Release*, **76**, 139–147.

[58] Sumi, N., Nishioku, T., Takata, F., Matsumoto, J.,Watanabe, T., Shuto, H., Yamauchi, A., Dohgu, S., Kataoka, Y. (2010). Lipopolysaccharide-activated microglia induce dysfunction of the blood–brain barrier in rat microvascular endothelial cells co-cultured with microglia. *Cell. Mol. Neurobiol*. **30**, 247–253.

[59] Nakagawa, S., Deli, M.A., Kawaguchi, H., Shimizudani, T., Shimono, T., Kittel, A., Tanaka, K., Niwa, M. (2009). A new blood–brain barrier model using primary rat brain endothelial cells, pericytes and astrocytes. *Neurochem. Int*. **54**, 253–263.

[60] Schiera, G., Sala, S., Gallo, A., Raffa, M.P., Pitarresi, G.L., Savettieri, G., Di Liegro, I. (2005). Permeability properties of a three-cell type in vitro model of blood–brain barrier. *J. Cell. Mol. Med*. **9**, 373–379.

[61] Liu, J., Johnson, T.V., Lin, J, Ramirez, S.H., Bronich, T.K., Caplan, S., Persidsky, Y., Gendelman, H.E., Kipnis, J. (2007). T cell independent mechanism for copolymer-1-induced neuroprotection. *Eur. J. Immunol*. **37**, 3143–3154.

[62] Haorah, J., Schall, K., Ramirez, S.H., Persidsky, Y. (2008). Activation of protein tyrosine kinases and matrix metalloproteinases causes blood–brain barrier injury: Novel mechanism for neurodegeneration associatedwith alcohol abuse. *Glia* **56**, 78–88.

[63] Ramirez, S.H., Heilman, D., Morsey, B., Potula, R., Haorah, J., Persidsky, Y. (2008). Activation of peroxisome proliferator-activated receptor gamma (PPARgamma) suppresses Rho GTPases in human brain microvascular endothelial cells and inhibits adhesion and transendothelial migration of HIV-1 infected monocytes. *J. Immunol*. **180**, 1854–1865.

[64] Ramirez, S.H., Potula, R., Fan, S., Eidem, T., Papugani, A., Reichenbach, N., Dykstra, H., Weksler, B.B., Romero, I.A., Couraud, P.O., Persidsky, Y. (2009). Methamphetamine disrupts blood–brain barrier function by induction of oxidative stress in brain endothelial cells. *J. Cereb. Blood Flow Metab*. **29**, 1933–1945.

[65] Zaghi, J., Goldenson, B., Inayathullah, M., Lossinsky, S.A., Masoumi, A., Avagyan, H., Mahanian, M., Bernas, M., Weinand, M., Rosenthal, M.J., Espinosa-Jeffrey, A., de Vellis, J., Teplow, D.B., Fiala, M. (2009). Alzheimer disease macrophages shuttle amyloid-beta from neurons to vessels, contributing to amyloid angiopathy. *Acta Neuropathol*. **117**, 111–124.

[66] Loscher, W., Potschka, H. (2005). Blood–brain barrier active efflux transporters: ATP-binding cassette gene family. *Neurotherapeutics* **2**, 86–98.

[67] Lin, J.H. (2004). How significant is the role of P-glycoprotein in drug absorption and brain uptake? *Drugs Today* **40**, 5–22.

[68] Fromm, M.F. (2003). Importance of P-glycoprotein for drug disposition in humans. *Eur. J. Clin. Invest*. **33**, 6–9.

[69] Schinkel, A.H., Jonker, J.W. (2003). Mammalian drug efflux transporters of the ATP binding cassette (ABC) family: An overview. *Adv. Drug. Deliv. Rev*. **55**, 3–29.

[70] Loscher, W., Potschka, H. (2002). Role of multidrug transporters in pharmacoresistance to antiepileptic drugs. *J. Pharmacol. Exp. Ther*. **301**, 7–14.

[71] Dohgu, S., Takata, F., Yamauchi, A., Nakagawa, S., Egawa, T., Naito, M., Tsuruo, T., Sawada, Y., Niwa, M., Kataoka, Y. (2005). Brain pericytes contribute to the induction and up-regulation of blood–brain barrier functions through transforming growth factor-β production. *Brain Res*. **1038**, 208–215.

[72] Berezowski, V., Landry, C., Dehouck, M.P., Cecchelli, R., Fenart, L. (2004). Contribution of glial cells and pericytes to the mRNA profiles of P-glycoprotein and multidrug resistance-associated proteins in an in vitro model of the blood–brain barrier. *Brain Res*. **1018**, 1–9.

[73] Hori, S., Ohtsuki, S., Hosoya, K., Nakashima, E., Terasaki, T. (2004). A pericyte-derived angiopoietin-1 multimeric complex induces occludin gene expression in brain capillary endothelial cells through Tie-2 activation in vitro. *J. Neurochem*. **89**, 503–513.

[74] Derynck, R., Zhang, Y.E. (2003). Smad-dependent and Smad-independent pathways in TGF-h family signaling. *Nature* **425**, 577–584.

[75] Flanders, K.C., Ren, R.F., Lippa, C.P. (1998). Transforming growth factor-hs in neurodegenerative disease. *Progress Neurobiol*. **54**, 71–85.

[76] Shih, S.C., Ju, M., Liu, N., Mo, J.R., Ney, J.J., Smith, L.E.H. (2003). Transforming growth factor β1 induction of vascular endothelial growth factor receptor 1: Mechanism of pericyte-induced vascular survival in vivo. *Proc. Natl. Acad. Sci. USA* **100**, 15859–15864.

[77] Kim, W.Y., Lee, H.Y. (2009). Brain angiogenesis in developmental and pathological processes: Mechanism and therapeutic intervention in brain tumors. *FEBS J*. **276**, 4653–4664.

[78] Machein, M.R., Plate, K.H. (2000). VEGF in brain tumors. *J. Neurooncol*. **50**, 109–120.

[79] Shibuya, M. (2009). Brain angiogenesis in developmental and pathological processes: Therapeutic aspects of vascular endothelial growth factor. *FEBS J*. **276**, 4636–4643.

[80] Aiello, L.P., Bursell, S.E., Clermont, A., Duh, E., Ishii, H., Takagi, C., Mori, F., Ciulla, T.A., Ways, K., Jirousek, M., Smith, L.E., King, G.L. (1997). Vascular endothelial growth factor-induced retinal permeability is mediated by protein kinase C in vivo and suppressed by an orally effective beta-isoform-selective inhibitor. *Diabetes* **46**, 1473–1480.

[81] Merrill, M.J., Oldfield, E.H. (2005). A reassessment of vascular endothelial growth factor in central nervous system pathology. *J. Neurosurg*. **103**, 853–868.

[82] Bergers, G., Brekken, R., McMahon, G., Vu, T.H., Itoh, T., Tamaki, K., Tanzawa, K., Thorpe, P., Itohara, S., Werb, Z., Hanahan, D. (2000). Matrix metalloproteinase-9 triggers the angiogenic switch during carcinogenesis. *Nat. Cell Biol*. **2**, 737–744.

[83] Davis, B., Tang, J., Zhang, L., Mu, D., Jiang, X., Biran, V., Vexler, Z., Ferriero, D.M. (2010). Role of vasodilator stimulated phosphoprotein in VEGF induced blood–brain barrier permeability in endothelial cell monolayers. *Int. J. Devel. Neurosci*. **28**, 423–428.

[84] Hawkins, B.T., Sykes, D.B., Miller, D.S. (2011). Rapid, reversible modulation of blood–brain barrier p-glycoprotein transport activity by vascular endothelial growth factor. *J. Neurosci*. **30**, 1417–1425.

[85] Candelario-Jalil, E., Yang, Y., Rosenberg, G.A. (2009). Diverse roles of matrix metalloproteinases and tissue inhibitors of metalloproteinases in neuroinflammation and cerebral ischemia. *Neuroscience* **158**, 983–994.

[86] Lohmann, C., Krischke, M., Wegener, J., Galla, H. (2004). Tyrosine phosphatase inhibition induces loss of blood–brain barrier integrity by matrix metalloproteinase-dependent and-independent pathways. *Brain Res*. **995**, 184–196.

[87] Asahi, M., Wang, X., Mori, T., Sumii, T., Jung, J.C., Moskowitz, M.A., Fini, M.E., Lo, E.H. (2001). Effects of matrix metalloproteinase-9 gene knock-out on the proteolysis of blood–brain barrier and white matter components after cerebral ischemia. *J. Neurosci*. **21**, 7724–7732.

[88] Sood, R.R., Taheri, T., Candelario-Jalil, E., Estrada, E.Y., Rosenberg, G.A. (2008). Early beneficial effect of matrix metalloproteinase inhibition on blood–brain barrier permeability as measured by magnetic resonance imaging countered by impaired long-term recovery after stroke in rat brain. *J. Cereb. Blood Flow Metab*. **28**, 431–438.

[89] Tosi, G., Vergoni, A.V., Ruozi, B., Bondioli, L., Badiali, L., Rivasi, F., Costantino, L., Forni, F., Vandelli, M.A. (2010). Sialic acid and glycopeptides conjugated PLGA nanoparticles for central nervous system targeting: In vivo pharmacological evidence and biodistribution. *J. Control. Release* **145**, 49–57.

[90] Gan, C.W., Feng, S.S. (2010). Transferrin-conjugated nanoparticles of poly(lactide)-D-α-tocopheryl polyethylene glycol succinate diblock copolymer for targeted drug delivery across the blood–brain barrier. *Biomaterials* **31**, 7748–7757.

[91] Li, J., Feng, L., Fan, L., Zha, Y., Guo, L., Zhang, Q., Chen, J., Pang, Z., Wang, Y., Jiang, X., Yang, V.C., Wen, L. (2011). Targeting the brain with PEG-PLGA nanoparticles modified with phage-displayed peptideXs. *Biomaterials* **32**, 4943–4950.

[92] Tian, X., Wei, F., Wang, T.X., Wang, D., Wang, J., Lin, X.N., Wang, P., Ren, L. (2012). Blood–brain barrier transport of Tat peptide and polyethylene glycol decorate.d gelatin–siloxane nanoparticle. *Mater. Lett*. **68**, 94–96.

[93] Wang, Z.H., Wang, Z.Y., Sun, C.S., Wang, C.Y., Jiang, T.Y., Wang, S.L. (2010). Trimethylated chitosan-conjugated PLGA nanoparticles for the delivery of drugs to the brain. *Biomaterials* **31**, 908–915.

[94] Parikh, T., Bommana, M.M., Squillante III, E. (2010). Efficacy of surface charge in targeting pegylated nanoparticles of sulpiride to the brain. *Eur. J. Pharm. Biopharm*. **74**, 442–450.

[95] Agarwal, A., Agrawal, H., Tiwari, S., Jain, S., Agrawal, G.P. (2011). Cationic ligand appended nanoconstructs: A prospective strategy for brain targeting. *Int. J. Pharm*. **421**, 189–201.

[96] Ku, S., Yan, F., Wang, Y., Sun, Y., Yang, N., Ye, L. (2010). The blood–brain barrier penetration and distribution of PEGylated fluorescein-doped magnetic silica nanoparticles in rat brain. *Biochem. Biophys. Res. Commun*. **394**, 871–876.

[97] Dadparvar, M., Wagner, Wien, S., Kufleitner, J., Worek, F., von Briesen, H., Kreuter, J. (2011). HI 6 human serum albumin nanoparticles—development and transport over an in vitro blood–brain barrier model. *Toxicol. Lett*. **206**, 60–66.

[98] Venishetty, V.K., Samala, R., Komuravelli, R., Kuncha, M., Sistla, R., Diwan, P.V. (2013). β-Hydroxybutyric acid grafted solid lipid nanoparticles: A novel strategy to improve drug delivery to brain. *Nanomedicine* **9**, 388–397.

[99] Xia, H., Gao, X., Gu, G., Liu, Z., Hu, Q., Tu, Y., Song, Q., Yao, L., Pang, Z., Jiang, X., Chen, J., Chen, H. (2012). Penetratin-functionalized PEG–PLA nanoparticles for brain drug delivery. *Int. J. Pharm*. **436**, 840–850.

[100] Etame, A.B., Smith, C.A., Chan, W.C.W., Rutka, J.T. (2011). Design and potential application of PEGylated gold nanoparticles with size-dependent permeation through brain microvasculature. *Nanomed. Nanotechnol. Biol. Med*. **7**, 992–1000.

[101] Wilson, B., Samanta, M.K., Santhi, K., Kumar, K.P.S., Ramasamy, M., Suresh, B. (2010). Chitosan nanoparticles as a new delivery system for the anti-Alzheimer drug tacrine. *Nanomed. Nanotechnol. Biol. Med*. **6**, 144–152.

[102] Rempe, R., Cramer, S., Hüwel, S., Galla, H.J. (2011). Transport of Poly(n-butylcyano-acrylate) nanoparticles across the blood–brain barrier in vitro and their influence on barrier integrity. *Biochem. Biophys. Res. Commun*. **406**, 64–69.

19

BORON TRACEDRUGS AS THERANOSTIC AGENTS FOR NEUTRON DYNAMIC THERAPY

Hitoshi Hori[1,2] and Hiroshi Terada[1]

[1]*Department of Pharmacology, Faculty of Pharmaceutical Sciences, Niigata University of Pharmacy and Applied Life Sciences, Niigata, Japan*
[2]*NDT Research Institute, Tokushima, Japan*

19.1 THE REAL CRISIS FOR TWENTY-FIRST-CENTURY MEDICINAL CHEMISTS IN PHARMACEUTICAL INDUSTRIES AND ACADEMIA

Most medicinal chemists in pharmaceutical companies and academia, such as universities and nonprofit institutes, continue to create new drug entities by using the conventional, traditional, and still reliable strategies and tactics of medicinal chemistry. Given that most diseases are currently usually diagnosed in well-developed symptomatic or terminal stages, that is, when multiple parts of a biological system are dysfunctional, it is little wonder that most of the molecularly targeted therapies have limited influence on the actual course of the disease. A recent article in *Nature Reviews Drug Discovery* [1] states: "Research and development (R&D) is the ultimate source of the economic value that the pharmaceutical industry creates. It is therefore not surprising that the evidence of a major decline in R&D productivity has led to a sense of crisis." The authors further comment that "Various solutions have been proposed, ranging from calls to re-engineer the R&D process to the radical suggestion that large pharmaceutical companies abandon internal R&D altogether. However, although decades of improvements to the R&D process and the introduction of new technologies, such as high-throughput screening, have substantially improved the efficiency of discrete steps in the R&D process, they have not been able to counteract the market and the institutional forces that underlie the decline in R&D productivity." We, as 'old-fashioned' medicinal chemists, think that the traditional medicinal chemistry dogma, that drugs should be designed to have specific chemical characteristics, contributes greatly to the real drug discovery crisis. Thus, a radically different way of thinking is needed, one that can lead to breakthroughs through chemical interaction-based drug discovery.

19.2 BORON TRACEDRUGS AS A CHALLENGE TO TRADITIONAL DRUG DESIGN METHODOLOGY

We recently proposed and pursued our concept of boron tracedrugs as "wonder drugs," based on our drug design of the ^{10}B carrier [2–5] for boron neutron capture therapy or BNCT [6, 7]. We proposed these not just as a new drug class with broad potential, but also as next-generation pharmaceutical drugs [8, 9]. We explain herein boron tracedrugs succinctly and clearly. We believe that frequently failed clinical trials over the last decade were due to intrinsic chemical characteristics rather than pharmacological characteristics of drugs designed by traditional drug design methodology. Since drugs, even molecularly targeted drugs, possess no intrinsic rational targeting mechanism associated with their chemical characteristics, they generally affect multiple molecular targets leading to multiple pharmacological effects. A further important point is that management of traceable data associated with the flow of goods, information, and other resources is integral to present logistics

Encyclopedia of Biocolloid and Biointerface Science, Volume 1, First Edition. Edited by Hiroyuki Ohshima.
© 2016 John Wiley & Sons, Inc. Published 2016 by John Wiley & Sons, Inc.

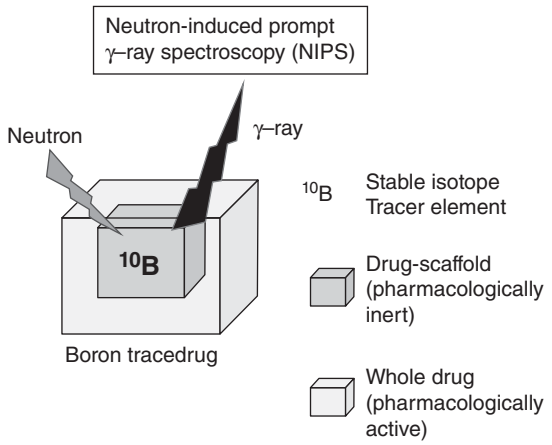


FIGURE 19.1 Conceptual design of boron tracedrugs.

information systems. However, many materials, such as drugs themselves, as yet have no general tags that enable their traceability. When these drugs need to be traced, the only option for tracking them is to analyze them by the appropriate analytical method or by using custom-made radioisotope-labeled synthetic compounds. For data management of tracking drugs, we propose our strategy and tactics for the use of boron tracedrugs.

The key design element of boron tracedrugs consists in their containing multiple (at least one) boron atoms firmly embedded in a molecular scaffold at a position that will have little or no influence on the functional group(s) and pharmacophore(s) of the drug to be traced. The traceability of boron tracedrugs is based on their neutron capture activity (followed by the generation of neutron-induced prompt γ rays) of the stable isotope boron-10 embedded in the drug. Thus, newly designed boron tracedrugs would be novel pharmaceuticals, the structures of which would always include natural boron (^{11}B, 80.4%; ^{10}B, 19.6%) as tracers, embedded in their scaffolds, as shown in Fig. 19.1.

There are many boron-containing compounds that have been used in drug development, including classes such as borinic esters and oxazaborolidines with antibacterial activity, as well as benzoxaborole for onychomycosis. Certain α-aminoboronic acids and related agents have anticancer, hypolipidemic, and antifungal activities; and diazaborines are antimalarial, whereas others, such as bortezomib, are protease and proteosome inhibitors [10, 11]. Thus, boron chemistry falls within the interest of synthetic organic chemists and medicinal chemists. Our concept of boron tracedrugs evolved from our previous drug design studies on the development of hypoxia-targeting ^{10}B carrier compounds described above. In particular, the pharmacokinetics of neutron-induced prompt γ-ray spectroscopy (NIPS) allows for the measurement of ^{10}B concentrations within a few minutes (see Fig. 19.1). We envisioned that if all pharmaceuticals contained ^{10}B embedded in their scaffold, research and developmental facilities would be simplified and "green chemistry" would be facilitated. Although boron is not an element commonly found in natural products or drugs, several bioactive boron-containing compounds are known. Although the creation of a boron tracedrug would seem to be a simple concept for researchers working on BNCT with NIPS, a search of the literature using PubMed and other tools revealed no previous reports of this application. Thus, such an application represents an unexplored area with much potential for next-generation neutron-related industrial development.

Here we should explain the difference between our boron tracedrugs and previously developed ^{10}B carrier drugs such as borocaptate sodium (BSH) and *p*-boronophenylalanine (BPA) used for BNCT. Boron tracedrugs seldom need to use ^{10}B-enriched boron reagents, which must be prepared custom-made and are very expensive. Thus boron tracedrugs can interact with a drug target both chemically (mainly by ^{11}B and partly by ^{10}B) and physically (only by ^{10}B with a natural abundance of $\sim$20%).

We suggest that boron tracedrugs will have a major impact on the developmental process of translational and clinical drugs for therapeutic and/or diagnostic use, and open a new era in medicinal chemistry without radioisotope technology. Research using such technology can be carried out in conventional laboratories without legal regulations (because of use of nonradioisotopes), except that related to the measurement of pharmacokinetics by prompt γ-ray analysis using neutrons in nuclear reactors and accelerators, including BNCT (^{18}F-BPA-positron emission tomography or ^{18}F-BPA-PET [12]), now under development. We also can use inductively coupled plasma atomic emission spectroscopy (ICPS) as a substitute for prompt γ-ray analysis when a neutron generator is not available in the laboratory. Boron tracedrugs can also be a good fit in the era of tailor-made or personalized medicine development, because of a less stringent requirement for the evaluation of absorption, distribution, metabolism, excretion, and toxicity (ADME/Tox) properties in early clinical drug development. Generally, at this stage of drug development, only a few drug candidates, selected on the basis of their preclinical investigation, should be applied to pharmacological assays. Boron tracedrugs have the added potential of being a new class of drugs, based on their physical destructive powers acquired by weak thermal neutrons used in BNCT. Possible applications include destruction of amyloid-β deposits (senile plaques) in the neocortex and τ inclusions as neurofibrillary tangles in neocortical neurons of patients with Alzheimer disease, of α-synuclein inclusions (Lewy bodies) in neocortical neurons of patients with Parkinson's disease/Lewy body dementia, and of other aberrant macromolecules in degenerative diseases frequently appearing in elderly patients [13].

Research on boron tracedrugs offers opportunities for research in engineering fields, in particular in nuclear engineering and neutron engineering, to develop human-friendly

atomic power reactors as neutron generators. In the chemical and chemical engineering fields, boron tracedrugs could help the pharmaceutical industry design diversity-oriented chemical libraries of boron-containing inorganic and organic compounds. The importance of traceability of synthetic materials, modified or natural products, biomolecules such as proteinaceous drugs/antibody drugs, interference RNAs for gene transfer systems, nanomaterials, and micromachines is apparent. However, there are no ethical discussions on the traceability of medicine(s) in patients except for a limited number of cases where drug accidents have occurred. Providing patients with drugs that guarantee high traceability is a priority for the entire field of pharmaceutical research and development in healthcare.

19.3 BORON TRACEDRUGS FOR NEUTRON DYNAMIC THERAPY (NDT), AS PHYSICIAN-FRIENDLY TOOLS

We now propose "new-fashioned" physics-based drugs, known as *boron tracedrugs*, for NDT, powered by neutron beams, as shown in Fig. 19.2. These tracedrugs are chemicals with characteristics different from those used as tracers.

After ^{10}B has captured a neutron, a nuclear reaction takes place to release two heavy particles, an α particle (^{4}He) and a lithium ion (^{7}Li). According to their high energies, these α particles and ^{7}Li nuclei can be regarded as short-range particles since they travel less than 10 μm in a microenvironment containing large numbers of macromolecules. When

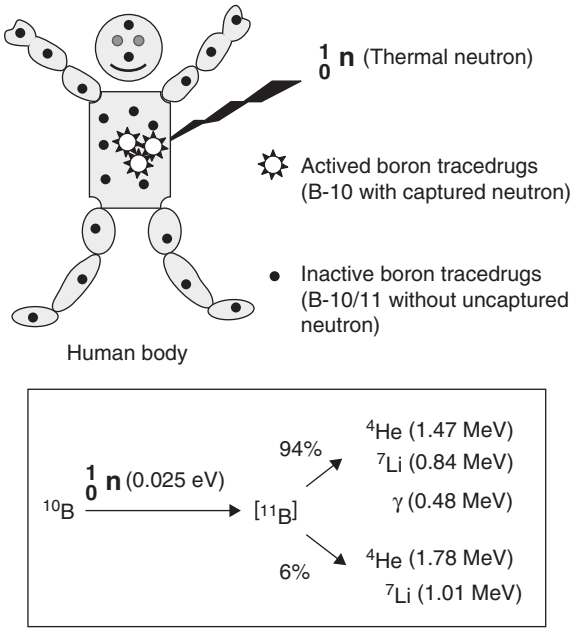


FIGURE 19.2 Conceptual design of a boron tracedrug for neutron dynamic therapy (NDT).

administered, these boron tracedrugs interact weakly with drug targets and endogenous molecules in the surrounding microenvironment, acting like prodrugs [14]. Only by capturing a neutron beam ("on-demand" or *honnête homme* signals) are they transformed to their active drug form to destroy drug targets by their great amount of energy (about 2.5 MeV generated from a thermal-neutron energy of 0.025 eV). Boron tracedrugs are designed to have on-demand traceability persistent during their lifetime. Such physics-based drugs are employed in radioimmunotherapy using radioisotopes for cancer treatment. Radioimmunotherapy involves the administration of radiolabeled monoclonal antibodies that are directed specifically against tumor-associated antigens. Clinical success has so far been achieved mostly with radiolabeled antibodies against CD20 (^{131}I-tositumomab and ^{90}Y-ibritumomab tiuxetan), for the treatment of lymphoma [15]. We are confident that NDT with the use of the stable isotope ^{10}B will have great advantage over radioimmunotherapy with radioisotopes especially with regard to convenience.

As the neutron source for BNCT, experimental nuclear reactors for clinical use have been commonly available. Installations of an accelerator-driven neutron source for BNCT are planned at some universities and institutes. In 2009, the Kyoto University Research Reactor Institute (Osaka, Japan) installed an accelerator-based intense neutron source for BNCT. Instead of nuclear reactors and in-room accelerators, we propose portable, mobile, desktop-type neutron generators as the neutron source for the clinical use of boron tracedrugs for NDT.

As mentioned earlier, the key structural feature of boron tracedrugs consists of their having multiple (at least one) boron atoms firmly embedded in a scaffold and located at a position that will have little or no influence on functional group moieties or pharmacophoric descriptors (i.e., be pharmacologically inert). Boron tracedrugs have unique characteristic physical effects due to their ^{10}B atoms; and their chemical and/or druglike effects are responsible for their pharmacodynamic characteristics. Marc Kirschner said the following in his vision for Initiative Systems Pharmacology at Harvard University: "In the past, the issues that caused drugs to fail were mainly off-target effects, but in many cases now, toxicity problems are on-target effects and the lack of efficacy in phase II and III trials is just unexplainable. So the question becomes: Could we develop a better way of predicting whether a drug will work or have an intolerable side-effect" [16]. Our answer is "yes," as we can supply boron tracedrugs for NDT as a better way to predict whether a drug will work or have intolerable side effects.

Shown schematically in Fig. 19.3, we present our recent results on boron tracedrugs for NDT [17]. In order to explore their destructive dynamic effect when bombarded by weak thermal neutrons, we performed thermal neutron irradiation of bovine serum albumin (BSA), a typical model biomacromolecule, treated with the boron tracedrugs.

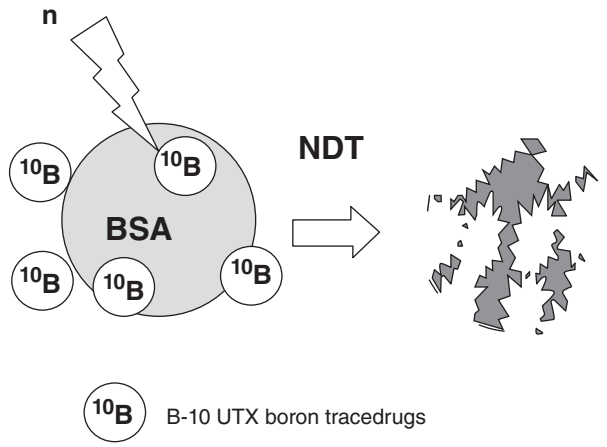


FIGURE 19.3 Schematic image of neutron dynamic therapy (NDT) using a boron tracedrug for bovine serum albumin (BSA) as a model macromolecule.

Boron tracedrugs, including the boron dipyrromethene (BODIPY)-containing compounds UTX-42, UTX-44, and UTX-47, and the curcuminoid compounds UTX-50 and UTX-51, were designed for NDT of BSA based on their molecular orbital calculations (Fig. 19.4).

Sodium dodecyl sulfate–polyacrylamide gel electrophoresis (SDS-PAGE) was performed to detect the decomposition of BSA by thermal neutron irradiation of this molecule treated with any of these boron tracedrugs. The combination of 1.0 μM BSA with a 100 μM concentration of any of these boron tracedrugs showed a decrease in the band density after irradiation. All tracedrugs tested caused destructive damage to BSA, the mechanism of which should be elucidated by further investigation. We speculate the mode of action of boron tracedrugs for NDT to be as follows. The nontoxic thermal neutron (0.025 eV), emitted by the neutron source in the nuclear reactor, reacts with the ^{10}B atom contained in the boron tracedrug (UTX-series drugs tested here), and is embedded in the environment of BSA. As was depicted in Fig. 19.2, after ^{10}B has captured a neutron, a nuclear reaction takes place, releasing high-energy α particles (^{4}He) and lithium ions (^{7}Li) that cause structural breakdown of the BSA macromolecule.

19.4 CONCLUSIONS

We describe here our concept of boron tracedrugs including their application for NDT. We consider such tracedrugs to be a potentially far-reaching new drug class that challenges the current predominance of conventional drugs that rely only on chemical interactions, particularly if this approach were to be extended to a wide range of drug types. Boron tracedrugs could be ideal medicines of the future, with applications as *diagnotherapeutics*, that is, drugs possessing properties of both diagnostics and therapeutics. Such application would derive from the information related to

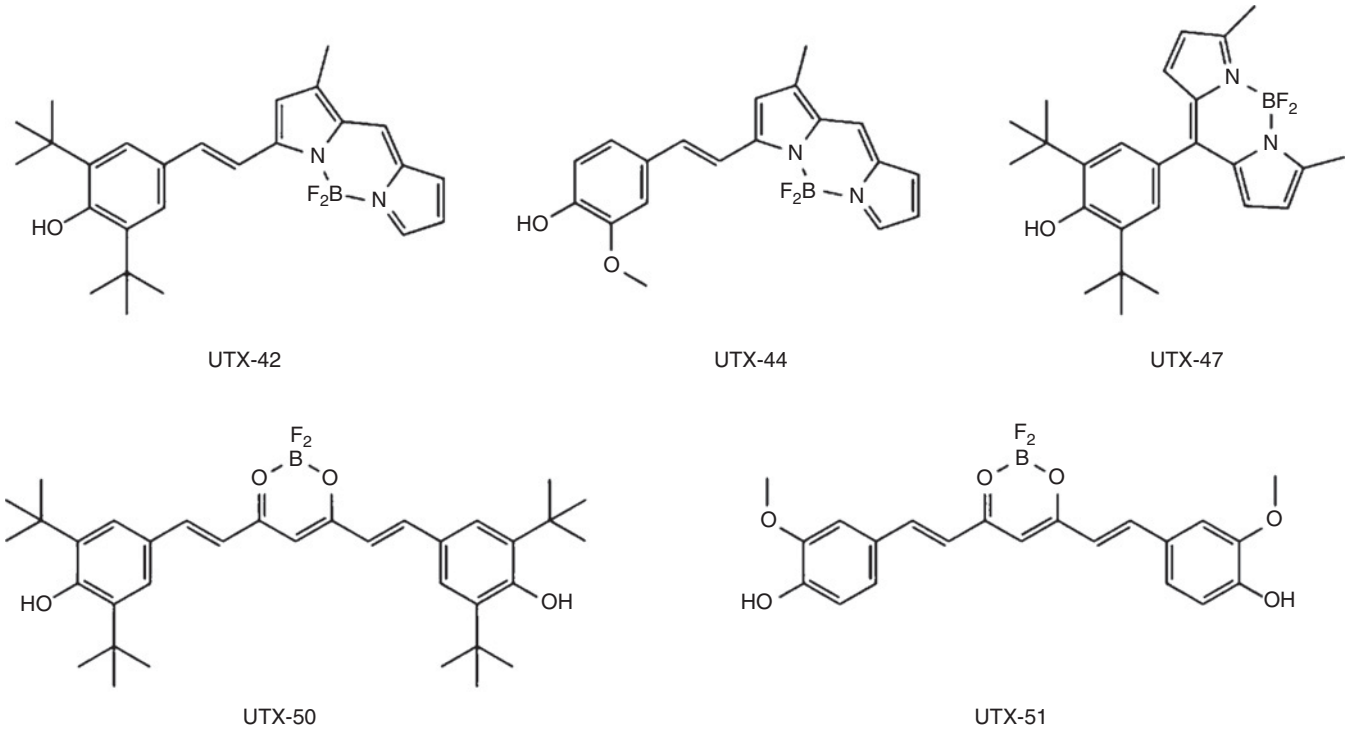


FIGURE 19.4 Designed boron tracedrugs for neutron dynamic therapy (NDT).

pharmacokinetics that would be available directly from the drugs themselves, without the need for additional treatments. These drugs could also be useful in the future when autopsy imaging and virtopsy (virtual biopsy) will become available for medical assessment of the cause of disease and death. In the near future, physics-based NDT using boron trace-drugs, as drugs possessing physical destructive power, could become applicable for all macromolecule-related diseases, against which conventionally pharmacodynamics-based or chemical interaction-based designed drugs have thus far been unsuccessful.

ACKNOWLEDGMENT

We thank Dr. Koji Ono and members of his group at the Research Reactor Institute, Kyoto University for their respective support, as well as all colleagues and coauthors of our previous reports. Finally, we gratefully acknowledge Dr. Kenneth L. Kirk (NIH) for his critical and valuable comments.

REFERENCES

[1] Tollman, P., Morieux, Y., Murphy, J.K., Schulze, U. (2011). Indentifying R&D outliers. *Nat. Rev. Drug Discov*. **10**, 653−654.

[2] Masunaga, S., Nagasawa, H., Hiraoka, M., Sakurai, Y., Uto, Y., Hori, H., Nagata, K., Suzuki, M., Maruhashi, A., Kinashi, Y., Ono, K. (2004). The usefulness of 2-nitroimidazole-sodium borocaptate-^{10}B conjugates as ^{10}B-carriers in boron neutron capture therapy. *Appl. Radiat. Isotopes* **61**, 953−958.

[3] Masunaga, S., Nagasawa, H., Hiraoka, M., Sakurai, Y., Uto, Y., Hori, H., Nagata, K., Suzuki, M., Maruhashi, A., Kinashi, Y., Ono, K. (2004). Applicability of the 2-nitroimidazole-sodium borocaptate-^{10}B conjugate, TX-2060, as a ^{10}B-carrier in boron neutron capture therapy. *Anticancer Res*. **24**, 2975–2984.

[4] Masunaga, S., Nagasawa, H., Gotoh, K., Uto, Y., Hori, H., Sakurai, Y., Nagata, K., Suzuki, M., Maruhashi, A., Kinashi, Y., Ono, K. (2006). Evaluation of hypoxia-specific cytotoxic bioreductive agent sodium borocaptate-^{10}B conjugates as ^{10}B-carriers in boron neutron capture therapy. *Rad. Med*. **24**, 98−107.

[5] Masunaga, S., Nagasawa, H., Sakurai, Y., Uto, Y., Hori, H., Nagata, K., Suzuki, M., Maruhashi, A., Kinashi, Y., Ono, K. (2006). The usefulness of mild temperature hyperthermia combined with a newly developed hypoxia-oriented ^{10}B conjugate compound, TX-2100, for boron neutron capture therapy. *Int. J. Hypertherm*. **22**, 287− 299.

[6] Yamamoto, T., Nakai, K., Matsumura, A. (2008). Boron neutron capture therapy for glioblastoma. *Cancer Lett*. **262**, 143−152.

[7] Suzuki, M., Tanaka, H., Sakurai, Y., Kashino, G., Yong, L., Masunaga, S., Kinashi, Y., Mitusmoto, T., Yajima, S., Tsutsui, H., Sato, T., Maruhashi, A., Ono, K. (2009). Impact of accelerator-based boron neutron capture therapy (AB-BNCT) on the treatment of multiple liver tumors and malignant pleural mesothelioma. *Radiother. Oncol*. **92**, 89−95.

[8] Hori, H., Uto, Y., Nakata, E. (2010). Medicinal electronomics bricolage design of hypoxia-targeting antineoplastic drugs and invention of boron tracedrugs as innovative future-architectural drugs. *Anticancer Res.* **30**, 3233−3242.

[9] Nakata, E., Koizumi, M., Yamashita, Y., Uto, Y., Hori, H. (2012). Boron tracedrug: Design, synthesis and pharmacological activity of phenolic BODIPY-containing antioxidants as traceable next generation drug model. *Adv. Exp. Med. Biol.* **737**, 301−306.

[10] Baker, S.J., Ding, C.Z., Akama, T., Zhang, Y.K., Hernandez, V., Xia, Y. (2009). Therapeutic potential of boron-containing compounds. *Future Med. Chem*. **1**, 1275−1288.

[11] Baker, S.J., Tomsho, J.W., Benkovic, S.J. (2011). Boron-containing inhibitors of synthetases. *Chem. Soc. Rev*. **40**, 4279−4285.

[12] Wittig, A., Michel, J., Moss, R.L., Stecher-Rasmussen, F., Arlinghaus, H.F., Bendel, P., Mauri, P.L., Altieri, S., Hilger, R., Salvadori, P.A., Menichetti, L., Zamenhof, R., Sauerwein, W.A. (2008). Boron analysis and boron imaging in biological materials for boron neutron capture therapy (BNCT). *Crit. Rev. Oncol./Hematol.* **68**, 66−90.

[13] Jucker, M., Walker, L.C. (2013). Self-propagation of pathogenic protein aggregates in neurodegenerative diseases. *Nature* **501**, 45−51.

[14] Tanabe, K., Ishizaki, J., Ando, Y., Ito, T., Nishimoto, S. (2012). Reductive activation of 5-fluorodeoxyuridine prodrug possessing azide methyl group by hypoxic X-irradiation. *Bioorg. Med. Chem*. **22**, 1682−1685.

[15] Pouget, J.P., Navarro-Teulon, I., Bardiès, M., Chouin, N., Cartron, G., Pèlegrin, A., Azria, D. (2011). Clinical radioimmunotherapy–the role of radiobiology. *Nat. Rev. Clin. Oncol*. **8**, 720−734.

[16] Kirschner, M. (2011). Marc Kirschner. Interview by Asher Mullard. *Nat. Rev. Drug Discov*. **10**, 894.

[17] Nakata, E., Koizumi, M., Yamashita, Y., Onaka, K., Sakurai, Y., Kondo, N., Ono, K., Uto, Y., Hori, H. (2011). Design, synthesis and destructive dynamic effects of BODIPY-containing and curcuminoid boron tracedrugs for neutron dynamic therapy. *Anticancer Res*. **31**, 2477−2481.

20

CARBOHYDRATES AS BIOCOLLOIDS IN NANOSCIENCE

Zaheer Khan,[1] Shokit Hussain,[2] Ommer Bashir,[2] and Shaeel Ahmed Al-Thabaiti[1]

[1]*Chemistry Department, Faculty of Science, King Abdulaziz University, P. O. Box 80203, Jeddah 21413, Saudi Arabia*
[2]*Department of Chemistry, Jamia Millia Islamia, Jamia Nagar, New Delhi -110025, India*

20.1 INTRODUCTION

A *colloid* or *colloidal mixture* of plant or animal origin is a buoyant particle that is composed mostly of water bound together by extracellular polymeric substances and populated by some microorganisms. Colloids, entities of linear size ranging from 10^{-9} to 10^{-5} m, have shapes ranging from simple ones such as spherical, cylindrical, and cubical to complicated ones such as biconcave disk and rouleau. Biocolloids can have complex and interesting shapes; among these, toroid is common to bacterial DNA, plasmid DNA of eukaryotic cells, and most viral DNA, all of which can be isolated as a single intact chromosome. For instance, when DNA is isolated as a single intact chromosome, it is of toroid shape. This includes all bacterial DNA, all plasmid DNA of eukaryotic cells, and most viral DNA. DNA is highly condensed in toroidal arrays inside living cells, where gene transcription is inactive [1], and the in vitro condensation of DNA has attracted much attention in gene therapy [2]. It was proposed that the toroidal shaped DNA appearing in living organisms relates to the organized form of the helix in proteins and the double helix in DNA [3]. Biochemists used microorganisms to the biological synthesis of inorganic materials or with a variety of substances of animal origin [4]. Much of the recent research efforts have focused on developing new strategies to fabricate nanoconstructs with carbohydrates [5] as capping ligands because of their potential applications in the design and development of nanoscale devices and nanosensors for biomedical applications [6]. Carbohydrates contain many hydroxyl and carbonyl groups; these groups offer sugar-coated nanoparticle a unique hydrogen bonding capabilities in constructing supramolecular architecture. On surface coating with nanoparticles, they provide attractive nanoconstruction abilities for building smart nanomaterials. For example, nanowires of platinum or tellurium have been constructed from glucose stabilized platinum nanoparticles or starch-stabilized tellurium nanoparticles [7]. Despite a large number of applications, there are only very few reports on direct generation of platinum nanoparticles in a sucrose matrix. A "green" method has been developed to synthesize and stabilize platinum nanoparticles in starch matrix using glucose as the reducing agent [8]. Platinum oxide composites with homogeneous size distributions were synthesised and then these materials are stabilized with sucrose. This structure provides a robust, highly porous, and self-sustaining structure with large surface area, which is essential to facilitate incorporation of the platinum ions in the metallization process to give a high platinum loading content.

The use of supramolecules (carbohydrates, *block-co*-polymers, ionic liquids, fatty acids, lipids, phospholipids, polymers, proteins, and surfactants) in the shape-controlled synthesis of nanoparticles, nanocrystals, and other nanometer-sized objects is an important requirement for permanent applications in the field of nanobiotechnology [9–15]. Out of these, supramolecules (biopolymers, carbohydtates, phospholipids, proteins, etc.) have been directly used in biomineralization to produce biofunctional materials. Carbohydrates-capped nanomaterials have more relevance to biological applications than do other supramolecule-capped nanobiomaterials because the surface activity of monosaccharide, structural monomer units of carbohydrates, at the

Encyclopedia of Biocolloid and Biointerface Science, Volume 1, First Edition. Edited by Hiroyuki Ohshima.
© 2016 John Wiley & Sons, Inc. Published 2016 by John Wiley & Sons, Inc.

liquid–solid biointerface plays a significant role. The main objective of this chapter is to summarise current knowledge of types, properties, and applications of biocolloids that influence nanoparticle–carbohydrate interactions and their implications on cellular uptake. In a biological medium, nanoparticles may interact with biomolecules such as carbohydrates, proteins, nucleic acids, lipids, and even biological metabolites, due to their nanoscale size and large surface-to-mass ratio. Controlling size and shape simultaneously remains an extremely difficult task, since the outcome of these syntheses is generally determined by a number of factors and is only partially characterized by the interplay of kinetics and thermodynamics. This difficulty increases when silver nanoparticles with a controlled size and shape are to be synthesized by green chemistry.

20.2 TYPES OF BIOCOLLOIDS

Many theoretical attempts have been made in the literature to electrophoresis analysis under various conditions. These include, for example, an isolated particle in an infinite medium [16], a particle near a boundary [17], and a particle near other particles [18]. However, available results are based mainly on uniformly structured, regular-shaped particles. A soft particle, or a particle having a porous structure, or comprising a rigid core and a porous layer, is often adopted to model biological cells [19] and particles such as humic substances [20], bacteria [21], and polyelectrolyte-coated particles [22] in their electrophoresis analysis. Under typical conditions, interestingly, the electrophoretic behavior of a soft particle can significantly differ from that of a rigid one. For a simpler mathematical treatment, previous electrophoresis analyses dealing with soft particles focused mainly on spherical particles of uniform structure [23] or nonuniform structure. Those for nonspherical soft particles are very limited. Two researchers [24] found that if the friction coefficient of its membrane layer is small, then the larger that coefficient, the larger its mobility, but this trend is reversed if that coefficient is sufficiently large.

Several types of biocolloids have been used as ultrasound contrast agents, including gas–liquid emulsions, liquid–liquid emulsions, liposomes, and other particles. The degree of acoustic backscatter depends on the intrinsic properties of the biocolloid. The compressibility of the biocolloid and the density difference between the biocolloid and surrounding tissue contribute to the acoustic backscatter. Nonlinear effects and resonance can also contribute considerably to the echo response. One advantage of the biocolloid is its payload capacity, making it amenable to multimodality imaging for the dual purposes of imaging and therapy. Another is the surface area for targeting. Biocolloids range in size between 10 nm to 10 μm in diameter and therefore can be engineered to present many ligands. Multiple ligand–receptor interactions can lead to firm adhesion, even in the face of hydrodynamic forces acting to dislodge the biocolloid.

Nanodrops are a type of liquid–liquid emulsion. The emulsion is formed by mechanical diminution of the fluorocarbon liquid into an aqueous phase. Droplet size can be controlled by sonication and extrusion techniques, as well as surfactant film curvature, to give diameters ranging between 10 and 1000 nm. The liquid fluorocarbon is dispersed in the form of small particles, nanodrops, within the aqueous phase. A surfactant layer on the fluorocarbon surface helps stabilize the tiny droplets from aggregating, coalescing, or coarsening. The surfactant layer also serves to passivate the surface from immunogenic and thrombogenic effects and provides a platform on which to attach targeting ligands and molecular contrast agents for other imaging modalities, such as magnetic resonance imaging. The fluorocarbon core can serve as a reservoir for hydrophobic drugs. Several different perfluorocarbon emulsions have been described as echo contrast agents. The liquid fluorocarbon phase is often highly hydrophobic, rendeering the particles stable against dissolution. Surface tension at the fluid–fluid interface drives the particle to adopt a spherical shape and limits its deformability. Thus, from a fluid mechanics perspective, the liquid droplets act very much like solid spheres. In general, liquid fluorocarbon nanoparticles scatter energy according to typical Rayleigh scattering theory [25]. For liquid or solid particles, the incompressibility of the interior phase prevents significant oscillation in the ultrasound field. While individual fluorocarbon nanoparticles in suspension are poorly reflecting, their aggregates can be echogenic [26]. Nanodrops therefore are suitable for applications involving high-frequency ultrasound and abundant target epitopes (to allow high accumulation by ligand receptor interactions), such as fibrin in thrombi [27]. Another fascinating imaging application of fluorocarbon nanoparticles has been the introduction of the *phase shift colloid*, where the liquid droplet vaporizes into a gas microbubble as a result of thermal activation [28]. The main benefit of such an agent is the combination of the high stability of the liquid–liquid emulsion with the high echogenicity of the gas–liquid emulsion. Problems, however, include lack of surfactant coverage after area expansion from the droplet to the bubble, leading to possible coalescence.

A *liposome* is a vesicle formed by a lipid bilayer membrane, enclosing an aqueous core. The interior and exterior compartments are separated by a semipermeable, hydrophobic membrane. Liposomes are fabricated by lipid self-assembly and postproduction processing. Typically, large multilamellar vesicles are formed by self-assembly during film hydration. High-power sonication with a cell disrupter at kHz frequencies creates localized shear stresses that break up these larger aggregates into smaller, unilamellar vesicles. Further size refinement can be achieved by forcing the liposomes through well-defined, microscale pores. Echogenic liposome formulations have been described [29]. Echogenic

particles have been found to produce detectable backscatter for ultrasound imaging. These include amorphous solid particles that contain gas pockets in their pores and fissures [30]. Similar to liposomes, gas pockets formed during rehydration may account for the detectable acoustic backscatter. The formation of these gas pockets depends strongly on the size and shape of surface features on the particle. Sizes of such particles can range within the submicrometer/nanometer order, and the gas pockets can be highly stable as a result of pinning of the interfacial contact lines within the solid crevices. Silica nanoparticles have also been tested as ultrasound contrast agents [31]. The *microbubble* is an ideal ultrasound contrast agent because it is extremely echogenic, as well as being biocompatible, multifunctional, and economical. Microbubbles are gas spheres ranging between 100 nm and 10 μm in diameter and are much smaller than the wavelength of diagnostic ultrasound, which is typically 100–1000 μm. The gas core has a low density and is highly compressible, allowing it to shrink and expand with the passage of an acoustic wave. The microbubble increases and decreases in diameter at a rapid velocity giving rise to a strong and unique echo. It is a fortuitous coincidence that the natural reaction time of a microbubble to a rapid pressure variation is on the order of microseconds. Thus, microbubbles resonate at frequencies typically used in ultrasound imaging, and resonance can be exploited to generate a very strong echo. Due to this high degree of backscatter in comparison to plasma and blood cells, a clinical ultrasound system is capable of detecting the signature from a single microbubble—a volume on the order of a femtoliter. Since microbubbles are too small to be resolved by current ultrasound instruments, microbubble imaging techniques are designed to differentiate their echoes from those arising from tissue based on changes in the echo spectrum and the response to changes in the amplitude or frequency of the wave. This provides an opportunity to detect a single microbubble adherent to a vascular target within the space of a single voxel and to distinguish the microbubble from the surrounding tissue. When a dilute microbubble suspension is driven by a harmonic pulse produced by a transducer element with a low peak negative ultrasound pressure, microbubble oscillation can be nearly sinusoidal with amplitude and shape that is a linear multiple of the transmitted wave. Increasing the pressure of the driving pulse or introducing a nearby boundary alters the oscillatory dynamics. The nonlinear dynamics and asymmetric profile result in echoes that contain harmonic multiples of the transmitted pulse. While tissue can also produce echoes that are rich in harmonic frequencies, substantial differences in the pressure and frequencies associated with harmonic spectra allow microbubble and tissue echoes to be differentiated. The advent of nonlinear imaging techniques has brought microbubbles to the forefront of ultrasound imaging agents. Pulsing schemes that exploit these nonlinear features involve trains of transmitted pulses with the amplitude scaled or the phase of the pulse changed between pulses.

20.3 PROPERTIES

A large number of infectious particles, including biocolloids, can be found in the subsurface suspended in the aqueous phase or adsorbed onto other colloid surfaces and/or the solid matrix [32]. The transport of biocolloids through saturated and unsaturated porous media is of significant interest, from the perspective of protection of groundwater supplies from contamination [33], assessment of risk from pathogens in groundwater [34], natural and enhanced bioremediation [35], and for the design of better water treatment systems to remove biocolloids from drinking-water supplies [36]. Microorganisms can also travel attached to abiotic particles [37]. Dispersion can be more important for colloids than for solutes, since it can lead to earlier breakthrough of the colloids. The biocolloids can attach to the soil–water interface, the air–water interface, or the triple contact of soil–water–air. Attachment/adsorption to these interfaces can be reversible or essentially irreversible under certain conditions, and is perhaps the most complex process, given the large number of colloid and grain surface characteristics that determine the probability of attachment, and the influence of the dissolved chemical species in the aqueous solution on attachment and detachment. There are processes that can result in the formation of clusters of biocolloids, either attached to an interface or mobile within the aqueous phase. Clusters can also be initiated via biological processes, to form biofilms [38]. Individual or clustered biocolloids can break off from the film, releasing them into the flowing aqueous medium [39]. To study the fate, transport of colloids and biocolloid at the pore scale, various investigators employed micromodels [40]. Resonance imaging has also been used [41, 42] to understand biocolloid transport at small scales. The main purpose of these microscale experiments has been to visualize biocolloid transport processes at the dimensions of a pore or collection of pores, validating or negating hypothesis that have been put forward with regard to processes that had not been actually observed; a secondary objective has been to quantify the importance of these processes.

20.4 CARBOHYDRATES IN NANOSCIENCE

To avoid the use of toxic organic solvents for the preparation of nanomaterials, researchers have explored the possibilities of preparing them in aqueous medium with the help of synthetic or commercial stabilizing or capping agents. With significant growth in the rather cross-disciplinary nanoscience research involving chemists, physicists, biologists, and engineers, researchers have become concerned about the need for developing more environmentally friendly and sustainable methods for the synthesis of nanomaterials. There is a current drive to integrate all the "green chemistry" approaches to design environmentally benign materials and processes.

Such an approach will also be of advantage for the integration of metal and alloy quantum dots into biologically relevant systems. Carbohydrates are by far the most abundant organic molecules found in nature, and nearly all organisms synthesize and metabolize carbohydrates [43]. The complex heterogeneity of carbohydrates in living systems is a direct result of several carbohydrate characteristics: the ability of different types and numbers of sugar residues to form glycosidic bonds with one another, the structural characteristics of these molecules, the type of anomeric linkage, the position, and the absence or presence of branching [44]. *Nanotechnology* is a field of science that is still under development and has a major influence on the industry from several years. Among variable nanomaterials and fields of their application, metal nanoparticles can be distinguished as the most popular in biology and medicine with gold and silver nanoparticles playing a prominent role. They were used as far as in fourth century for dyeing ceramics and stained glass [45]. Nowadays many methods of their syntheses have been elaborated in dependence on their shape and size to be obtained. Natural polymers like starch [46] and chitosan [47] have been used to stabilize silver nanoparticles by using different reducing agents. The concept of green nanoparticles preparation using β-D-glucose as the reducing agent was first reported by Raveendran et al. [46], and starch played the role of stabilizer. Soluble starch, the amylose component of starch, is a linear polymer formed by the-(1–4) linkages between D-glucose units and adopts a left-handed helical conformation in aqueous solution. Despite its slight branching, amylose behaves essentially like a linear polymer, forming films and complexes with ligands [48]. In the study reported in this chapter, the aldehyde terminal of soluble starch was used to reduce silver nitrate while the starch itself stabilized the silver nanoparticles. Heparin is a linear polysaccharide of glucose and a derivative of induronic acid. It is widely used in medicine as an anticoagulant. Studies show that nanocomposites synthesized with a use of heparin are more stable at physiological electrolyte concentrations than naked nanoparticles, because it binds to the particles, providing electrostatic repulsion from other particles [49]. The composites of nanosilver exhibit antibacterial activity against *Escherichia coli* and *Staphylococcus aureus*, and functionalized heparin exhibits anticoagulant properties [50]. Chitosan was described for the first time in 2004 as a stabilizing agent in nanoparticle synthesis. It was shown that the electrostatic attractive forces between amino groups in chitosan and $AuCl_4^-$ provide an effective driving force for the formation and stabilization of the gold and silver nanoparticles [51, 52]. Also, a method for the synthesis of nanoparticles of silver by incubation of its salts with the suspension of starch and *d*-glucose was described, in which glucose was used as the reducing agent and the starch as stabilizing agent. The starch can also act as a reducer of the silver salt. In this case the resulting silver nanoparticles are closed inside the helical structure of amylose [53]. Interestingly, honey was also used as reducing agent for the synthesis of silver nanoparticles having a size of 34 nm and showed stability in neutral or slightly alkaline solutions [54]. Carbohydrates perform numerous roles in living organisms, such as storage of energy; structural components; backbone of the genetic, immune system; fertilization; preventing pathogenesis; blood clotting, and development [55]. Carbohydrates contain many hydroxyl and carbonyl groups; these groups offer sugar-coated nanoparticle, unique H-bonding capabilities in constructing supramolecular architecture. On surface coating with nanoparticles, they provide attractive nanoconstruction abilities for building smart nanomaterials. One team of investigators [46] suggested an environmentally friendly method for the synthesis and stabilization of metal nanoparticles by suitable choice of materials and solvents. It was shown that by gently heating an aqueous solution of silver nitrate, soluble starch and glucose, one can synthesize "starched" silver nanoparticles in the 1–8-nm size range. While glucose serves as an environmentally benign reducing agent for the metal ions, starch provides stable surface passivation or protection to prevent the aggregation of these particles. These investigators also reported an environmentally benign method for the preparation of gold, silver, and gold–silver nanoparticles in water, using glucose as the reducing agent and starch as the protecting agent. The alloy nanoparticles are homogeneous, and their sizes are well within the quantum size domain (<10 nm) [56]. Stable silver nanoparticles were prepared by using soluble starch and iodometric titration confirmed the entrapment of silver nanoparticles inside the helical amylase chain [57]. Morphology and antibacterial activity of carbohydrate-stabilized silver nanoparticles were investigated [58], using carbohydrates (sucrose, soluble and waxy corn starch) as reducing as well as stabilizing agents. Chitosan is a transformed polysaccharide obtained by deacetylation of natural chitin, which is one of the most important natural polymers constituting the shells of crustaceans and the cell walls of many fungi. Chitosan is a potential polysaccharide and is used in the preparation of various films because of its excellent biocompatibility, biodegradability, nontoxicity, and adsorption properties [59–61]. Various chitosan nanocomposites of silver, gold, platinum, and palladium have been synthesized [62] in aqueous solutions. Metal nanoparticles were prepared by reduction with $NaBH_4$ in the presence of chitosan, which adsorbed onto the surface of metal nanoparticles and formed the metal–chitosan nanocomposites. Silver nanoparticles were synthesized in an alkaline aqueous solution of silver nitrate/hydroxypropyl starch using a chemical reduction method. *Hydroxypropyl starch* is a water-soluble/biocompatible starch derivative that plays a dual rule as reducing agent for silver ions and as stabilizing agent for the formed AgNPs. The effects of the reaction parameters, such as the concentrations of hydroxypropyl starch and $AgNO_3$, pH, temperature, and duration of the reaction

TABLE 20.1 Effects of Carbohydrates as Reducing and Stabilizing Agents on Morphology of Metal Nanoparticles

Carbohydrate/reagent	Stabilizer	λ_{max} (nm)	Morphology	Ref.
Glucose	HTAB	420	Nanocubes	86
Glucose	HTAB	378	Cubes, triangles, wires, and alignment of wires	87
Dendrimers				
Without NaOH		550		88
With NaOH		450		
Cotton	NaOH	425	Spherical	89
Glucose	NaOH	410	Cubic	90
Galactose	NaOH	420		
Maltose	NaOH	390		
Lactose NaOH		400		
β-D-Glucose		419	Monodisperse spherical	91
Chitosan		522	Red color	92
Heparin		401	Cluster to larger spherical	
Soluble starch		420	Spherical, pentagonal biprisms	93
D-Glucose	NaOH	410	Spherical	94
β-D-Glucose	$NaBH_4$	508	Ruby red	95
Dialdehyde–chitosan	HNO_3	416	Spherical	96
Guar gum (galactose, mannose)	NaOH	539	Spherical	97
D-Maltose without reagent		446	Spherical, monodispersed	98
NaCl, $NaNO_3$, CaC_{l2}			Aggregation	
Sucrose	Glucose	482	Spherical	99
Fructose		604	Cluster formation	
Sucrose		425		100
Sucrose	PVA	566	Nanoprisms or fibrils	81
Glucose		514	Spherical particles	101
Fructose and sucrose		404	Pink (Au), yellow (Ag)	
Sucrose	NaOH	415–425	Spherical	102
Glucose		410	Spherical	103
Fructose	SDS	425		
Sucrose		420		
Potato starch		375	Cubic	104
Cornstarch			Spherical	
Pueraria starch	NH_3	545	Spherical	105
Sago starch	NaOH, CTAB		Spherical, elongated fiber	106
Glucose		420	Fiberlike	107
Glucose	CTAB	400	Nanoplates, nanowires	108
Glucose	CTAB	400	Quantum dots	57

medium on the size and agglomeration of the formed silver nanoparticles were studied [63].

Another team [64] reported the synthesis of polysaccharide-stabilized gold and silver nanoparticles using naturally occurring polysaccharidesas as both the reducing and stabilizing agent. No other chemical reducing agent is needed. The gold nanoparticles prepared using chitosan as a protecting agent were of high monodispersity, and were comparable to citrate-stabilized gold nanoparticles. Among all of these agents, capping ligands play a vital role in transforming the spherical or triangular nanoparticles to nanodevices or nanosensors of any desired shape [65]. Much of the recent research has focused on developing new strategies to fabricate nanoconstructs with carbohydrates [66, 67] as capping ligands because of their potential applications in the design and development of nanoscale devices and nanosensors for biomedical applications [68]. Nanowires of platinum or tellurium have been constructed from glucose-stabilized platinum nanoparticles or starch-stabilized tellurium nanoparticles [69–72]. Current strategies for carbohydrate functionalization of Pt nanoparticles utilize thiol-tailored sugars as synthons [73–75]. Another group of coworkers have developed a "green" method to synthesize and stabilize carbohydrate-Pt nanocomposites in starch matrix using glucose as the reducing agent [76]. Another team [77] produced platinum oxide composites with homogeneous size distribution and then stabilized these materials with sucrose. The reduction was fastest in the case of sucrose followed by waxy corn and soluble starch, while stability of nanoparticles followed the order soluble

starch > waxy cornstarch > sucrose. The size and molecular weight were important for stabilization of the nanoparticles. This is required because the more hydrolyzed the carbohydrate, the better its ability to act as a reducing agent. The characteristic absorption peak due to the surface–plasmon resonance of platinum colloids was observed within the range of 415–425 nm. Glucose, fructose, or sucrose offers a weak reducer to produce Au^0 particles by $HAuCl_4$ in aqueous solution [78–80]. Another team reduced the $Au^{3+} \rightarrow Au^0$ reaction in the presence of sucrose in polyvinyl alcohol in hot water [81]. Chitosan has been employed to obtain different types of metal nanoparticle–polymer composites. Using chitosan as a polymeric matrix and $Na[BH_4]$ as reducing agent, relatively small silver nanoparticles have been reported [82]. Another group of coworkers used soluble starch and reported the synthesis of silver nanonanoparticles by using ascorbic acid as reducing agent [83]. Starch has also been used as a clean reducing agent of $AgNO_3$ [84]. Water-soluble starch containing the carbohydrate component amylose and other polymers have been employed as stabilizing agents [85]. Complete reduction of Ag^+ to Ag^0 occurred with change of color from colorless to golden yellow. Homogeneous spherical particles of 15 nm average size were obtained. Reduction in water-soluble starch by glucose and NaOH gave spherical particles [85]. Effects of carbohydrates and its monomers on the morphology of metal nanoparticles are summarized in Table 20.1.

REFERENCES

[1] Gosule, L.C., Schellman, J.A. (1976). Compact form of DNA induced by spermidine. *Nature* **259**, 333–335.

[2] Chim, Y.T.A., Lam, J.K.W., Ma, Y., Armes, S.P., Lewis, A.L., Roberts, C.J., Stolnik, S., Tendler, S.J.B., Davies, M.C. (2005). Structural study of DNA condensation induced by novel phosphorylcholine-based copolymers for gene delivery and relevance to DNA protection. *Langmuir* **21**, 3591–3598.

[3] Ward, W.S. (1993). Deoxyribonucleic acid loop domain tertiary structure in mammalian spermatozoa. *Biol. Reprod*. **48**, 1193–1201.

[4] Maliszewska, I. (2011). Microbial synthesis of metal nanoparticles, rozdział. In Rai, M., Duran, N. (eds.), *Metal Nanoparticles in Microbiology*. Springer-Verlag, Berlin/Heidelberg (doi: 10.1007/978-3-642-18312-6_7).

[5] Barrientos, A.G., de la Fuente, J.M., Rojas, T.C., Fernandez, A., Penades, S. (2003). Gold glyconanoparticles: Synthetic polyvalent ligands mimicking glycocalyx-like surfaces as tools for glycobiological studies. *Chemistry (Eur.)* **9**, 1909–1921.

[6] Rojas, T.C., de la Fuente, J.M., Barrientos, A.G., Penades, S., Ponsonnet, L., Fernandez, A. (2002). Gold glyconanoparticles as building blocks for nanomaterials design. *Adv. Mater*. **14**, 585–588.

[7] Reynolds, A.J., Haines, A.H., Russel, D.A. (2006). Gold glyconanoparticles for mimics and measurement of metal ion-mediated carbohydrate−carbohydrate interactions. *Langmuir* **22**, 1156–1163.

[8] De la Fuente, J.M., Eaton, P., Barrientos, A.G., Menendez, M., Penades, S. (2005). Thermodynamic evidence for Ca^{2+}-mediated self-aggregation of Lewis X gold glyconanoparticles. A model for cell adhesion via carbohydrate−carbohydrate interaction. *J. ACS* **127**, 6192–6197.

[9] Binder, W.H. (2005). Supramolecular assembly of nanoparticles at liquid–liquid interfaces. *Angew. Chem. Int. Ed*. **44**, 5172 – 5175.

[10] Park, Y., Hong, Y., Weyers, A., Kim, Y., Linhardt, R. (2011). Polysaccharides and phytochemicals: A natural reservoir for the green synthesis of gold and silver nanoparticles. *IRT Nanobiotechnol*. **5**, 69–78.

[11] Kemp, M., Kumar, A., Mousa, S., Park, T.J., Ajayan, P., Kubotera, N., Linhardt, R. (2009). Synthesis of gold and silver nanoparticles stabilized with glycosaminogly- cans having distinctive biological activities. *Biomacromolecules* **10**, 589–595.

[12] Huang, H., Yang, X. (2004). Synthesis of polysacharide stabilized gold and silver nanoparticles: A green method. *Carbohydr. Res*. **339**, 2627–2631.

[13] Sun, C., Qu, R., Chen, H., Ji, C., Wang, C., Sun, Y., Wang, B. (2008). Degradation behavior of chitosan chains in the green synthesis of gold nanoparticles. *Carbohydr. Res*. **343**, 2595–2599.

[14] Vigneshwaran, N., Nachane, R.P., Balasubramanya, R.H., Varadarajan, P.V. (2006). A novel one-pot green synthesis of stable silver nanoparticles using soluble starch. *Carbohydr. Res*. **341**, 2012–2018.

[15] Pal, T., Sau, T.K., Jana, N.R. (1998). Silver hydrosol, organosol, and reverse micelle-stabilized sol—a comparative study. *J. Colloid Interface Sci*. **202**, 30–36.

[16] Masliyah, J.H. (1994). *Electrokinetic Transport Phenomena*. AOSTRA, Edmonton, Alberta, Canada.

[17] Morrison, F.A., Stukel, J.J. (1970). Electrophoresis of an insulating sphere normal to a conducting plane. *J. Colloid Interface Sci*. **33**, 88–93.

[18] Lee, E., Chu, J.W., Hsu, J.P. (1997). Electrophoretic mobility of a spherical particle in a spherical cavity. *J. Colloid Interface Sci*. **196**, 316–320.

[19] Ohshima, H. (2010). *Biophysical Chemistry of Biointerfaces*. Wiley, Hoboken, ISBN: 978-0-470-16935-3, NJ.

[20] Yang, Z., Peng, X.F., Lee, D.J., Ay, S. (2007). Advective flow in spherical floc. *J. Colloid Interface Sci*. **308**, 451–459.

[21] Bos, R., van der Mei, H.C., Busscher, H.J. (1998). "Soft-particle" analysis of the electrophoretic mobility of a fibrillated and non-fibrillated oral streptococcal strain: Streptococcus salivarius. *Biophys. Chem*. **74**, 251–255.

[22] Donath, E., Voigt, A. (1986). Streaming current and streaming potential on structured surfaces. *J. Colloid Interface Sci*. **109**, 122–139.

[23] Hsu, J.P., Kuo, C.C. (2009). Electrophoresis of a soft toroid coaxially along the axis of a cylindrical pore. *Chem. Eng. Sci*. **64**, 5247–5254.

[24] Hsu, J.P., Chou, C.H., Tseng, S., Wu, R.M. (2009). 3D simulations of hydrodynamic drag on a nonhomogeneously structured permeable sphere and advective flow thereof. *J. Colloid Interface Sci*. **336**, 850–856.

[25] Couture, O., Bevan, P., Cherin, E. (2006). Investigating perfluorohexane particles with high-frequency ultrasound. *Ultrasound Med. Biol*. **32**, 73–82.

[26] Lanza, G.M., Wallace, K.D., Scott, M.J. (1996). A novel site-targeted ultrasonic contrast agent with broad biomedical application. *Circulation* **94**, 3334–3340.

[27] Lanza, G.M., Wallace, K.D., Fischer, S.E. (1997). High-frequency ultrasonic detection of thrombi with a targeted contrast system. *Ultrasound Med. Biol*. **23**, 863–870.

[28] Correas, J.M., Quay, S.D. (1996). EchoGen emulsion: A new ultrasound contrast agent based on phase shift colloids. *Clin. Radiol*. **51**, 11–14.

[29] Alkan-Onyuksel, H., Demos, S.M., Lanza, G.M. (1996). Development of inherently echogenic liposomes as an ultrasonic contrast agent. *J. Pharm. Sci*. **85**, 486–490.

[30] Parker, K.J., Tuthill, A., Lerner, R.M., Violante, M.R. (1987). A particulate contrast agent with potential for ultrasound imaging of liver. *Ultrasound Med. Biol*. **13**, 555–566.

[31] Liu, J., Levine, A.L., Mattoon, J.S., Yamaguchi, M., Lee, R.J., Pan, X., Rosol, T.J. (2006). Nanoparticles as image enhancing agents for ultrasonography. *Phys. Med. Biol*. **51**, 2179–2189.

[32] Jiang, D., Huang, Q., Cai, P., Rong, X., Chen W. (2007). Adsorption of Pseudomonas putida on clay minerals and iron oxide. *Colloids Surf. B: Biointerfaces* **54**, 217–221.

[33] Harvey, R.W., Kinner, N.E., Bunn, A., MacDonald, D., Metge, D. (1995). Transport behavior of groundwater protozoa and protozoan-sized microspheres in sandy aquifer sediments. *Appl. Environ. Microbiol*. **61**, 209–217.

[34] Adelman, D.D., Stansbury, J., Tabidian, M.A. (1998). A risk/cost analysis to manage viral contamination of groundwater. *Water Sci. Technol*. **38**, 1–6.

[35] Domy, A., Wenzel, W.W., Jaco, V., Bolan, N.S. (2004). Role of assisted natural remediation in environmental cleanup. *Geoderma* **122**, 2–4.

[36] Gerba, C.P., Goyal, S.M. (1985). *Pathogen Removal from Wastewater during Groundwater Recharge: Artificial Recharge of Groundwater*. Butterworth, Boston, p. 317.

[37] Craig, D.L., Fallowfield, H., Cromar, N. (2002). Enumeration of fecal coliforms from recreational coastal sites: Evaluation of techniques for the separation of bacteria from sediments. *J. Appl. Microbiol*. **93**, 557–565.

[38] Banning, N., Toze, S., Mee, B.J. (2003). Persistence of biofilm-associated Escherichia coli and Pseudomonas aeruginosa in groundwater and treated effluent in a laboratory model system. *Microbiology* **149**, 47–55.

[39] Choi, Y.C., Morgenroth, E. (2003). Monitoring biofilm detachment under dynamic changes in shear stress using laser-ba sed particle size analysis and mass fractionation. Biofilm monitoring. *Water Sci. Technol*. **47**, 69–76.

[40] Lanning, L.M., Ford, R.M. (2002). Glass micromodel study of bacterial dispersion in spatially periodic porous networks. *Biotechnol. Bioeng*. **78**, 556–566.

[41] Sherwood, J.L., Sung, J.C., Ford, R.M., Fernandez, E.J., Maneval, J.E., Smith, J.A. (2003). Analysis of bacterial random motility in a porous medium using magnetic resonance imaging and immunomagnetic labelling. *Environ. Sci. Technol*. **37**, 781–785.

[42] Olson, M.S., Ford. R.M., Smith, J.A., Fernandez. E.J. (2004). Quantification of bacterial cg magnetic resonance imaging. *Environ. Sci. Technol*. **38**, 3864–3870.

[43] Mody, R., Joshi, S., Chaney, W. (1995). Use of lectins as diagnostic and therapeutic tools for cancer. *J. Pharmacol. Toxicol. Methods* **33**, 1–10.

[44] Gorelik, E., Galili, U., Raz, A. (2001). On the role of cell surface carbohydrates and their binding proteins(lectins) in tumor metastasis. *Cancer Metast. Rev*. **20**, 245–277.

[45] Poliakoff, M., Anastas, P. (2001). A principled stance. *Nature* **413**, 257.

[46] Raveendran, P., Fu, J., Wallen, S.L. (2003). *J. ACS* **125**, 13940–13941.

[47] Huang, H., Yuan, Q., Yang, X. (2004). Preparation and characterization of metal–chitosan nanocomposites. *Colloids Surf. B: Biointerfaces* **39**, 31–37.

[48] Walter, R.H. (1998). *Polysaccharide Association Structures in Food.* Marcel Dekker, New York, p. 57.

[49] Shervani, Z., Ikushima, Y., Sato, M., Kawanami, H., Hakuta, Y., Yokoyama, T., Takako, N., Kuneida, H., Aramaki, K. (2008). Morphology and size-controlled synthesis of silver nanoparticles in aqueous surfactant polymer solutions. *Colloid Polym. Sci*. **286**, 403–410.

[50] Kemp, M., Kumar, A., Mousa, S., Park, T.J., Ajayan, P., Kubotera, N., Linhardt, R. (2009). Synthesis of gold and silver nanoparticles stabilized with glycosaminoglcans having distinctive biological activities. *Biomacromolecules* **10**, 589–595.

[51] Huang, H., Yang, X. (2004). Synthesis of polysacharide stabilized gold and silver nanoparticles: A green method. *Carbohydr. Res*. **339**, 2627–2631.

[52] Sun, C., Qu, R., Chen, H., Ji, C., Wang, C., Sun, Y., Wang, B. (2008). Degradation behavior of chitosan chains in the green synthesis of gold nanopartices, *Carbohydr. Res*. **343**, 2595–2599.

[53] Vigneshwaran, N., Nachane, R.P., Balasubramanya, R.H., Varadarajan, P.V. (2006). A novel one- pot green synthesis of stable silver nanoparticles using soluble starch. *Carbohydr. Res*. **341**, 2012–2018.

[54] Philip, D. (2010). Honey mediated green synthesis of silver nanoparticle. *Spectrochim. Acta A: Mol. Biomol. Spectrosc*. **75**, 1078–1081.

[55] Maton, A., Jean, H., Charles, W.M., Susan, J., Maryanna, Q.W., David, L.H., Jill, D.W. (1993). *Human Biology and Health*. Prentice-Hall, Englewood Cliffs, NJ, p. 52.

[56] Raveendran, P., Fu, J., Wallen, S.L. (2006). A simple and "green" method for the synthesis of Au, Ag, and Au–Ag alloy nanoparticles. *Green Chem*. **8**, 34–38.

[57] Hussain, J.I., Talib, A., Kumar, S., Al-Thabaiti, S.A., Hashmi, A.A., Khan, Z. (2011). Time dependence of nucleation and growth of silver nanoparticles. *Colloids Surf. A: Physicochem. Eng. Aspects* **381**, 23–30.

[58] Valodkar, N., Bhadoria, A., Pohnerkar, J., Mohan, M., Thakore, S. (2010). Morphology and antibacterial activity of carbohydrate-stabilized silver nanoparticles. *Carbohydr. Res*. **345**, 1767–1773.

[59] Fuentes, S., Retuert, P.J., Ubilla, A., Fernandez, J., Gonzalez, G. (2000). Relationship between composition and structure in chitosan-based hybrid films. *Biomacromolecules* **1**, 239–243.

[60] Tanabe, T., Okitsu, N., Tachibana, A., Yamauchi, K. (2002). Preparation and characterization of keratin–chitosan composite film. *Biomaterials* **23**, 817–825.

[61] Zhang, M., Li, X.H., Gong, Y.D., Zhao, N.M., Zhang, X.F. (2002). Properties and biocompatibility of chitosan films modified by blending with PEG. *Biomaterials* **23**, 2641–2648.

[62] Huang, H., Yuan, Q., Yang, X. (2004). Preparation and characterization of metal–chitosan nanocomposites. *Colloids Surf. B: Biointerfaces* **39**, 31–37.

[63] El-Rafie, M.H., El-Naggar, M.E., Ramadan, M.A., Fouda, M.M.G., Al-Deyab, S.S., Hebeish, A. (2011). Environmental synthesis of silver nanoparticles using hydroxypropyl starch and their characterization. *Carbohydr. Polym*. **86**, 630–635.

[64] Huang, H., Yang X. (2004). Synthesis of polysaccharide-stabilized gold and silver nanoparticles: A green method. *Carbohydr. Res*. **339**, 2627–2631.

[65] Dr Chane-Ching, J.-Y., Cobo, F., Aubert, D., Dr Harvey, H.G., Airiau, M., Prof Corma, A. (2005). General method for the synthesis of nanostructured large-surface-area materials through the self-assembly of functionalized nanoparticles. *Chemistry (Eur.)* **11**, 979–987.

[66] Kim, B.-S., Hong, D.-J., Bae, J., Lee, M. (2005). Controlled self-assembly of carbohydrate conjugate rod-coil amphiphiles for supramolecular multivalent ligands. *J. ACS* **127**, 16333–16337.

[67] Barrientos, A.G., de la Fuente, J.M., Rojas, T.C., Dr Fernandez, A., Penades, S. (2003). Gold glyconanoparticles: Synthetic polyvalent ligands mimicking glycocalyx-like surfaces as tools for glycobiological studies. *Chemistry (Eur.)* **9**, 1909–1921.

[68] Rojas, T.C, Fuente J.M., Barrientos, A.G., Penades, S., Ponsonnet, L., Fernandez, A. (2002). Gold glyconanoparticles as building blocks for nanomaterials design. *Adv. Mater*. **14**, 585–588.

[69] Zand, A.M., Khani, H., Imani, P., Rezaei, S., Rezaei-Zarchi, M.S. (2010). Determining the antibacterial effect of ZnO nanoparticle against the pathogenic bacterium, Shigella dysenteriae (type 1). *Int. J. Nano Dimension* **1**, 279–285.

[70] Reynolds, A.J., Haines, A.H., Russell, D.A. (2006). Gold glyconanoparticles for mimics and measurement of metal ion mediated carbohydrate-carbohydrate interactions. *Langmuir* **22**, 1156–1163.

[71] Halkes, K.M., de Carvalho, S.A., Elizabeth, C., Maliaars, P., Gerwig, G.J., Kamerling, J.P. (2005). Facile method for the preparation of gold glyconanoparticles from free oligosaccharides and their applicability in carbohydrate-protein interaction studies. *Eur. J. Org. Chem*. **12**, 3650–3659.

[72] De la Fuente, J.M., Eaton, P., Barrientos, A.G., Menendez, M., Penades, S. (2005). Thermodynamic evidence for Ca^{2+}–mediated self-aggregation of Lewis X gold glyconanoparticles. A model for cell adhesion via carbohydratecarbohydrate interaction. *J. ACS* **127**, 6192–6197.

[73] De la Fuente, J.M., Barrientos, A.G., Rojas, T.C., Rojo, J., Canada, J., Fernandez, A., Penades, S. (2001). Gold glyconanoparticles as water-soluble polyvalent models to study carbohydrate interactions. *Angew. Chem. Int. Ed*. **40**, 2258–2261.

[74] Ipe, B.I., Yoosaf, K., Thomas, K.G. (2006). Functionalized gold nanoparticles phosphorescent nanomaterials and sensors. *J. ACS* **128**, 1907–1913.

[75] Perez, J.M., Josephson, L., Weissleder, R. (2004). Use of magnetic nanoparticles as nanosensors to probe for molecular interactions. *Chem. Biol*. **5**, 261–264.

[76] Quinti, L., Weissleder, R., Tung, C.H. (2006). A fluorescent nanosensor for apoptotic cells. *Nano Lett*. **6**, 488–490.

[77] Rezaei-Zarchi, S., Imani, S., Zand, A.M., Saadati, M., Zaghari, Z. (2012). Study of bactericidal properties of carbohydrate-stabilized platinum oxide nanoparticles. *Int. J. Nano Lett.* (doi: 10.1186/2228-5326-2-21).

[78] Esumi, K., Hosoya, T., Suzuki, A., et al. (2000). Spontaneous formation of gold nanoparticles in aqueous solution of sugarpersubstituted poly(amidoamine) dendrimers. *Langmuir* **16**, 2978–2980.

[79] Gole, A., Kumar, A., Phadtare, S., et al. (2001). Glucose induced in-situ reduction of chloroaurate ions entrapped in a fatty amine film: Formation of gold nanoparticles–lipid composites. *Phys Chem Commun.* **19**, 1–4.

[80] Panigrahi, S., Kundu, S., Ghosh, S.K., et al. (2005). Sugar assisted evolution of mono- and bimetallic nanoparticles. *Colloids Surf. A: Physicochem. Eng. Aspects* **264**, 133–138.

[81] Tripathy, P., Ram, S., Fecht, H.-J. (2006). *Gold Nanoparticles from Induced Au^{3+} to Au^0 Reaction in Polyvinyl Alcohol Molecules in Presence of Sucrose in Hot Water*. Springer, Vol. 1, pp. 121–127

[82] Huang, H., Yuan, Q., Yang, W. (2004). Extractable substances from human hair: A discussion about the origin of the holes. *Colloids Surf. B: Biointerfaces* **39**, 31–37.

[83] Khan, Z., Singh, T., Hussain, J.I., Al-Thabaiti, S.A., El-Mossalamy, E.H., Obaid, A.Y. (2013). Starch-directed green synthesis, characterization and morphology of silver nanoparticles. *Colloids Surf. B: Biointerfaces* **102**, 578–584.

[84] Murugadoss, A., Chattopadhyay, A. (2008). A "green" chitosan–silver nanoparticle composite as a heterogeneous

as well as micro-heterogeneous catalyst. *Nanotechnology* **19**, 015603–015611.

[85] Shervani, Z., Ikushima, Y., Sato, M., Kawanami, H., Hakuta, Y., Yokoyama, T., Nagase, T., Kuneida, H., Aramaki, K. (2008). Morphology and size-controlled synthesis of silver nanoparticles in aqueous surfactant polymer solutions. *Springer* **286**, 403–410

[86] Yu, D., Yam, V.W.-W. (2004). Controlled synthesis of monodisperse silver nanocubes in water. *J. Am. Chem. Soc.* **126**, 13200–13201.

[87] Yu, D., Yam, V.W.-W. (2005). Hydrothermal-induced assembly of colloidal silver spheres into various nanoparticles on the basis of HTAB-modified silver mirror reaction. *J. Phys.Chem. B* **109**, 5497–5503.

[88] Esumi, K., Hosoya, T., Suzuki, A., Torigoe, K. (2000). Formation of gold and silver nanoparticles in aqueous solution of sugar-persubstituted poly(amidoamine) dendrimers. *J. Colloid Interface Sci*. **226**, 346–352.

[89] Montazera, M., Alimohammadib, F., Shameib, A., Rahimic, M.K. (2012). In situ synthesis of nano silver on cotton using Tollens' reagent. *Carbohydr. Polym*. **87**, 1706– 1712.

[90] Panacek, A., Kvıtek, L., Prucek, R., Kolar, M., Vecerova, R., Pizurova, N., Sharma, V.K., Nevecna, T., Zboril, R. (2000). Silver colloid nanoparticles: Synthesis, characterization, and their antibacterial activity. *J. Phys. Chem. B* **110**, 16248–16253.

[91] Raveendran, P., Fu, J., Wallen, S.L. (2003). Completely "green" synthesis and stabilization of metal nanoparticles. *J. ACS* **125**, 13940–13941.

[92] Huang, H., Yang, X. (2004). Synthesis of polysaccharide-stabilized gold and silver nanoparticles. *Carbohydr. Res*. **339**, 2627–2631.

[93] Vigneshwaran, N., Nachane, R.P., Balasubramanya, R.H., Varadarajan, P.V. (2006). A novel one-pot "green" synthesis of stable silver nanoparticles using soluble starch. *Carbohydr. Res*. **341**, 2012–2018.

[94] Vasilevaa, P., Donkovaa, B., Karadjovab, I., Dushkina, C. (2011). Synthesis of starch-stabilized silver nanoparticles and their application as a surface plasmon resonance-based sensor of hydrogen peroxide. *Colloids Surf. A: Physicochem. Eng. Aspects* **382**, 203–210.

[95] Liu, J., Anand, M., Roberts, C.B. (2006). Synthesis and extraction of â-D-glucose-stabilized Au nanoparticles processed into low-defect, wide-area thin films and ordered arrays using CO_2-expanded liquids. *Langmuir* **22**, 3964–3971.

[96] Lv,Y., Long, Z., Song, C., Dai, L., He, H., Wang, P. (2013). Preparation of dialdehyde chitosan and its application in green synthesis of silver nanoparticles. *BioResources* **8**, 6161–6172.

[97] Pandey, S., Goswami, G.K., NandaGreen, K.K. (2013). Synthesis of polysaccharide/gold nanoparticle nanocomposite: An efficient ammonia sensor. *Carbohydr. Polym*. **94**, 229–234.

[98] Li, X., Lenhart, J.J., Walker, H.W. (2010). Dissolution-accompanied aggregation kinetics of silver nanoparticles. *Langmuir* **26**, 16690–16698.

[99] Qi, Z.-M,; Zhou, H.-S., Matsuda, N., Honma, I., Shimada, K., Takatsu, A., Kato, K. (2004). Characterization of gold nanoparticles synthesized using sucrose by seeding formation in the solid phase and seeding growth in aqueous solution. *J. Phys. Chem. B* **108**, 7006–7011.

[100] Majid, M., Alimohammadi, F., Shamei, A., Rahimi, M.K. (2010). In situ synthesis of nano silver on cotton using Tollens' reagent. *Carbohydr. Polym*. **87**, 1706–1712.

[101] Panigrahi, S., Kundu, S., Ghosh, S.K., Nath, S., Pal, T. (2004). General method of synthesis for metal nanoparticles. *J. Nanopart. Res*. **6**, 411–414.

[102] Rezaei-Zarchi, S. (2011). Bactericidal properties of carbohydrate-stabilized platinum oxide nanoparticles. *World Acad. Sci. Eng. Technol*. **50**, 610–614.

[103] Mehta, S., Chaudhary, S., Gradzielski, M. (2010). Time dependence of nucleation and growth of silver nanoparticles generated by sugar reduction in micellar media. *J. Colloid Interface Sci*. **343**, 447–453.

[104] Adeli, M., Hosainzadegan, H., Pakzad, I., Zabihi, F., Alizadeh, M., Karimi. F. (2013). Preparing starchy foods containing silver nanoparticles and evaluating ntimicrobial Activity. *Jundishapur J. Microbiol*. **6**, 1–6.

[105] Xia, B., He, F., Li, L. (2013). Preparation of bimetallic nanoparticles using a facile green synthesis method and their application. *Langmuir* **29**, 4901−4907.

[106] Chin, S.F., Pang, S.C., Tay, S.H. (2011). Size controlled synthesis of starch nanoparticles by a simple nanoprecipitation method. *Carbohydr. Polym*. **86**, 1817–1819.

[107] Abdelgawada, A.M., Hudsona, S.M., Rojasb, O.J. (2014). Antimicrobial wound dressing nanofiber mats from multicomponent (chitosan/silver-NPs/polyvinyl alcohol) systems. *Carbohydr Polym*. **100**, 166–778.

[108] Khan, Z., Hussain, J.I., Kumar, S., Hashmi, A.A. (2011). Silver nanoplates and nanowires by a simple chemical reduction method. *Colloids Surf. B: Biointerfaces* **86**, 87–92.

21

HIGH-STRENGTH POLY(VINYL ALCOHOL) HYDROGELS FOR ARTIFICIAL CARTILAGE

Atsushi Suzuki[1] and Teruo Murakami[2]

[1]*Department of Materials Science and Research Institute of Environment and Information Sciences, Yokohama National University, Hodogaya-ku, Yokohama, Japan*

[2]*Research Center for Advanced Biomechanics, Kyushu University, Nishi-ku, Fukuoka, Japan*

21.1 INTRODUCTION

With the progress of a superaged society in Japan, the number of patients with osteoarthritis is increasing, and enormous pain and loss of motor skills can be caused by this disease [1]. As a result, the number of artificial joint replacements has been rapidly rising in recent years. In order to minimize both the physical and mental burden on patients, artificial joint replacement has come to provide several choices according to the severity of the disease, such as transposing a part of the joint rather than replacing the whole joint with an artificial joint. However, the application methods, effects, and risks of the respective techniques are still at the research-and-development (R&D) stage in terms of method selection. In this sense, it has been widely expected that alternative new materials for use as friction surfaces or partial cartilage replacement parts, which slides under high load in living tissue, would be made available. The use of *artificial hydrogel cartilage* with excellent lubricity is highly desired.

In the past few decades, most applications of total hip replacement have included ultra-high-molecular-weight polyethylene (UHMWPE), although metal-on-metal (MOM) or ceramic-on-ceramic (COC) articulations have also been used [2]. These joints have a UHMWPE cup against a metal or ceramic femoral head. To enhance the friction and wear properties of UHMWPE, there have been some attempts to modify the physicochemical structure of the surface. For example, the cross-linking of UHMWPE and the surface treatment with phospholipid polymeric brushlike layer could remarkably reduce wear [3–5]. These applications are basically applications of the materials harder than articular cartilage. On the other hand, there have been attempts to develop artificial cartilage made of soft materials with super lubricity based on a bionic design by elucidating the lubrication mechanisms of natural synovial joints [6–9]. Soft materials include elastomers, rubbers, and hydrogels. For example, poly(vinyl alcohol) (PVA) [10–13], one of the studied hydrogels most frequently for such applications, shows a very low friction coefficient under walking conditions lubricated with hyaluronate solution containing protein; however, the mechanical strength is not sufficient to be of practical use. To enhance the mechanical and tribological properties of PVA, the use of PVA powders with high molecular weight [11] and lubricant alterations [14, 15] have been reported. Some hydrogels show a low coefficient of friction under specific conditions and high water content comparable to natural articular cartilage. However, these hydrogels lack mechanical durability and wear resistance.

As candidates for practical use as artificial cartilage, new methods of preparing PVA hydrogels have been studied, such as combining different types of PVA gels with different structures, elastic moduli, and characteristics of permeability. This chapter presents a method for preparing biomimetic artificial PVA cartilage for use as artificial cartilage with superior lubricity based on bionic design [16, 17].

Encyclopedia of Biocolloid and Biointerface Science, Volume 1, First Edition. Edited by Hiroyuki Ohshima.
© 2016 John Wiley & Sons, Inc. Published 2016 by John Wiley & Sons, Inc.

21.2 FUNDAMENTAL PROPERTIES OF PHYSICAL PVA GELS

For the preparation of PVA gels, various methods have been reported up to now [18]. Among them, an aqueous solution of PVA can form a hydrogel through a repeated freeze–thawing (FT) process [19–21], in which PVA solutions are repeatedly frozen and then allowed to thaw. This method results in the formation of microcrystallites that serve as physical cross-links to render the materials insoluble in water. Recently, a new PVA gelation technique was reported, which is called the *cast-drying* (CD) method [22]. This method attempts to provide a simple process at room temperature (∼25°C) starting from an aqueous PVA solution without using additional chemical reagents. Briefly, this new method produces a physically cross-linked transparent polymer network from water and PVA powders, resulting in a swollen PVA CD gel in water.

The PVA powder used in the current study, which has been frequently used for the preparation of physical gels by our group [22–27], was supplied by Kuraray Co., Ltd., Japan. There are several types of PVA powder with different degrees of polymerization and hydrolysis. Among them, a powder, catalog number: PVA117, was used here; the average degree of polymerization was higher as ∼1700, and the average degree of hydrolysis was also higher between 98 and 99 mol%.

21.2.1 Network Structure: Swelling Ratio and Crystallinity

To study the molecular and network structures (e.g., the formation of hydrogen bonds) of PVA physical gels, Fourier transform infrared (FT-IR) spectroscopy, X-ray diffraction (XRD), and differential scanning calorimetry (DSC) can be applied. In the present study, an attenuated total reflection (ATR) FT-IR method was carried out at room temperature. The ATR FT-IR spectra were recorded on an FT-IR spectrophotometer (Jasco FTIR610) equipped with an ATR attachment with a horizontal ZnSe crystal (Jasco PRO400S). The IR absorbance spectra were normalized on the basis of CH_2 bending vibrations that appear at approximately 1500–1400 cm^{-1}. The components of the absorption band were deduced from the second derivative of the spectra and were resolved by applying the curve-fitting method. Small-angle X-ray scattering (SAXS) measurements were performed at room temperature using a SAXS system with a wavelength of 0.1488 nm at BL10C in the Photon Factory, High Energy Accelerator Research Organization (KEK) [25,27]. A small and wide-angle X-ray scattering (SWAXS) system with a wavelength of 0.1542 nm operated at 40 kV and 50 mA (SAXSess, Anton Paar, PANalytical) was additionally used. The crystallinity was measured using a differential scanning calorimeter (DSC, DSC8000, PerkinElmer) and a thermogravimetric analyzer (TGA, TGA4000, PerkinElmer). Two samples were cut from each dried sample. Using one sample, the weight ratio of the crystalline portion of the polymers was calculated by DSC. Using the other sample, the true weight of the total polymer was calculated by TGA. From these measurements, the crystallinity was calculated using the literature data of the heat required to melt 100% crystalline PVA [28].

From the results of the FT-IR and XRD measurements, the network of CD and FT gels on nanometer scale was found to be composed of microcrystallites and amorphous zones, as shown schematically in Fig. 21.1a. On the other hand, the network structures of the CD and FT gels on micrometer scale differed from each other, as shown in the schematic models in Fig. 21.1b. This schematic model is similar to that proposed for the thermoresponsive poly(*N*-isopropylacrylamide) (NIPA) gel [29]. The network consists of dense and dilute regions of polymers, which can be introduced permanently by the gelation process. The degree of inhomogeneity can be controlled from transparent to opaque by changing the gelation temperature as well as the crosslink density [29,30]. The fluid flows out rapidly in the opaque hydrogel, whereas it flows extremely slowly in the transparent hydrogels. Similar models of both networks, NIPA and PVA, can be proposed since the opacity of both samples is attributed to the aggregation of crosslinks, in spite of the different mechanisms of network formation. Since the flow of water affects the surface friction [17], the average pore size and pore size distribution of the hydrogels are extremely important.

In the case of CD gels, the swelling ratio and the crystallinity depend strongly on the gelation temperature T_{gel}. The swelling ratio is defined here as W_t/W_d, where W_t is the weight of the swollen sample and W_d is the dehydrated weight after measuring W_t. The swelling ratio decreased and the crystallinity increased with increasing T_{gel} [27]. This is attributed to the decrement in the water content bound to the polymers by the increase in T_{gel}, which enhanced the growth of microcrystallites. Considering that a larger amount of water was evaporated from the polymer during sample preparation at higher T_{gel}, it is easy to understand that the size of the microcrystallites increased with increasing T_{gel}. In the case of FT gel, on the other hand, the swelling ratio and the crystallinity depended on the number of the freeze–thawing repetitions, and the formation of the microcrystallites was enhanced whenever the freeze–thawing cycle was repeated.

It should be noted that the experiments were conducted using the dried gels; therefore, it is necessary to confirm that the insights obtained for the dried gels are applicable to the swollen gels. Here, the experiments were conducted for the swollen gels with different swelling ratios, which were prepared using PVA117. The XRD measurements of the PVA-cast gel film showed that the average size of microcrystallites D and the average distance between microcrystallites L are

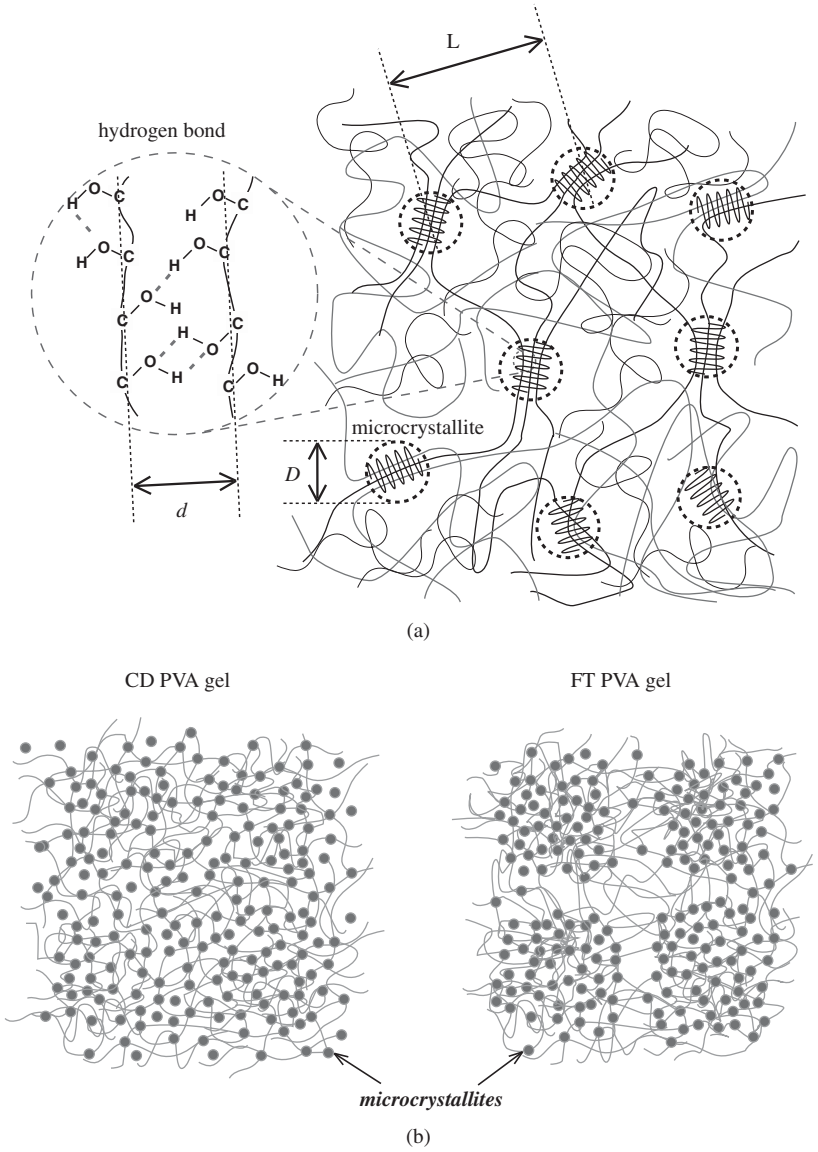


FIGURE 21.1 (a) Schematic illustration of network structure of physical PVA gels; (b) schematic models for two kinds of hydrogel structures.

not significantly different between the CD and FT gels. With an increase in W_t/W_d (from 1.05 to 3.33) in the swelling process, the peak position shifted to a lower wavelength and disappeared, which indicates that L increased, and became constant when W_t/W_d exceeded 1.8. Therefore, we can consider L of a gel with $W_t/W_d = 2$ to be L of the swollen gel [27]. Generally, the macroscopic size is not the same as the microscopic size because of defects of the polymer networks, such as the aggregation of network elements and distribution of the length between cross-links. However, the magnitude relationship of D and L between swollen and dried states is not affected, and therefore the network structures of the swollen gels can be qualitatively evaluated by the use of D and L of the dried states.

21.2.2 Conditions for Starting Raw Materials

To select the PVA powder used in the preparation of the CD gel, additional experiments were conducted using PVA powders as starting materials with different combinations of degrees of polymerization and hydrolysis [22,26,31]. The average degrees of polymerization and hydrolysis are high and high (sample A: PVA117), low and high (sample B), and high and low (sample C). Note that the low–low combination does not allow gelation. As shown in Fig. 21.2a, there was no difference in the FT-IR spectra of samples A and B, and the spectrum of sample C was quite different from both samples A and B. The absorption peaks could be assigned on the basis of literature reports [32–34]. The peak of O–H stretching is

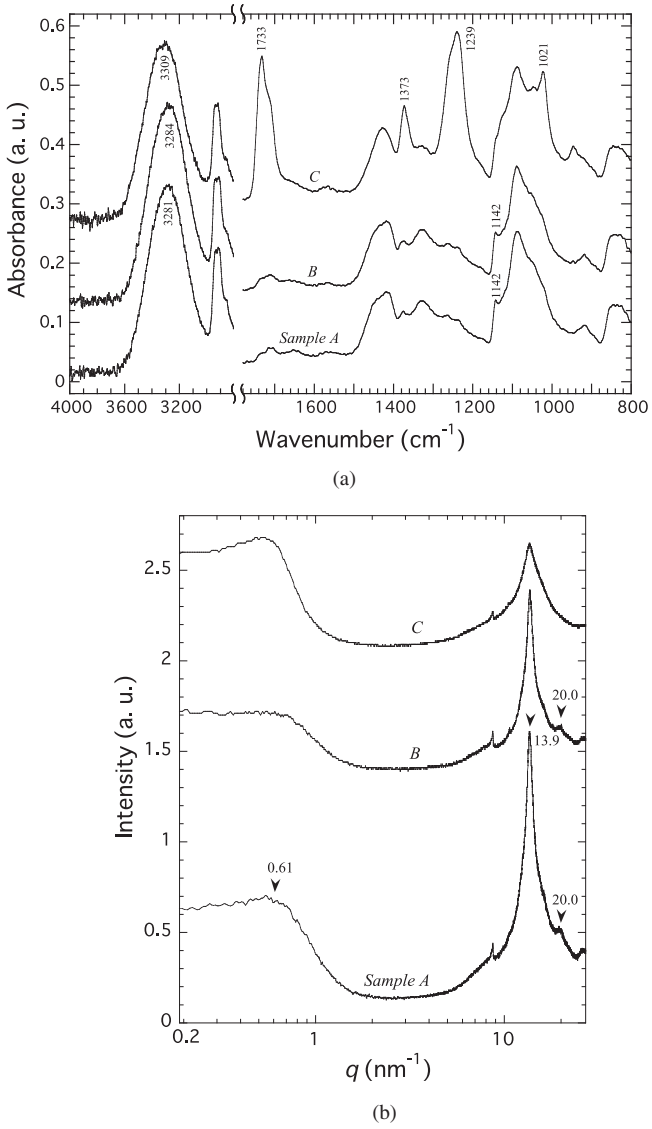


FIGURE 21.2 (a) ATR FT-IR; (b) SWAXS spectra of PVA cast films with different combinations of the degrees of polymerization and hydrolysis, the vertical axis (ordinate) of which is shifted for clarity.

observed at 3309 cm^{-1} for sample C, which is slightly larger than that of samples A and B at 3281 cm^{-1}. This evidence indicates that the acetic acid group in sample C prevented O–H groups from forming hydrogen bonds. As shown in Fig. 21.2b, the acetic acid group in sample C also increased C=O stretching at 1733 cm^{-1}, C–H stretching at 1373 cm^{-1}, and C–H deformation at 1239 cm^{-1}. Moreover, C–O stretching at 1142 cm^{-1} due to the formation of microcrystallites was not clearly observed in the spectrum of sample C. Although assignment of the peak at 1021 cm^{-1} is not clear, the appearance of this peak could have originated from the existence of acetic acid groups. As for the XRD spectra of as-prepared samples A, B, and C, on the other hand, a peak at $q = 13.9$ nm^{-1} ($d = 4.59$ Å) due to the hydrogen bonds between polymers was observed in all samples. However, the peak height of sample C was small, and D values of samples A, B, and C were, respectively, 2.6, 3.5, and 1.3 nm, which indicates that the acetic acid group in sample C prevented O–H groups from enhancing the crystal growth. Moreover, the peak intensity at approximately $q = 0.61$ nm^{-1} ($d = 10.3$ nm) of sample B was the broadest and the smallest of the three samples, which suggests that the microcrystallites were more randomly distributed without the specific structural modulation of L and that the network structure in the amorphous region was inhomogeneous. The slight shift of the peak position to a larger q indicates that L for sample B was slightly smaller than that for samples A and C. In addition, the small peak at $q = 20.0$ nm^{-1} ($d = 3.14$ Å) was not exclusively observed in sample C, which may be attributed to the high degree of hydrolysis in sample C. From these results, a high degree of polymerization is required to fortify an amorphous network by distributing the microcrystallite homogeneously, whereas a high degree of hydrolysis is required to make the large microcrystallites needed for crosslinking the amorphous region [22]. Therefore, it is important to use a starting material (PVA powder) with high degrees of polymerization and hydrolysis in order to obtain a swollen gel using the present cast-drying method.

21.3 TYPICAL EXAMPLES OF PHYSICAL PVA GELS: PREPARATIONS AND MECHANICAL PROPERTIES

From these measurements and analyses, it was confirmed that the CD gel obtained with high degrees of polymerization and hydrolysis was a three-dimensional network formed from an amorphous region cross-linked by microcrystallites (Fig. 21.1). It was also confirmed that the gel obtained had high water absorbence, good water retention, and excellent mechanical properties. Comparing the properties of CD gels to those of FT gels, it was confirmed that the swelling ratio (water content) and mechanical strength (stiffness, fracture toughness, and fatigue resistance) can be improved not only by increasing the crystallinity but also by adjusting the properties of microcrystallites, such as their size, number, and distribution. The properties are also determined by the macroscopic preparation conditions using simple treatments such as changes in temperature (freeze–thawing temperatures and drying temperatures) and humidity during the drying process, and postgelation treatment such as repeated water exchange with or without drying [23]. These factors could determine the network structures on multiple scales, and these factors in turn depend on the degrees of polymerization and hydrolysis of the PVA raw materials.

In the following text, we present the detailed preparation methods and mechanical properties for typical examples of

physical gels. Three different samples were prepared by the same PVA solution. The powder (PVA117) was mixed with pure water (deionized and distilled, Milli-Q water) at a concentration of 15 wt% and dissolved at a temperature above 90°C over a period of 2 h. The PVA pregel solution (15.0 g) was then decanted into a petri dish of polystyrene (with an inner diameter of 85 mm) at room temperature and dried at room temperature (or a specified temperature) to produce flat dense PVA films. Different types of physical crosslinked networks were obtained starting from this same PVA aqueous solution.

To fabricate FT gels, the solution in the petri dish was covered with a lid and sealed with Parafilm® to prevent evaporation for the water and left in a refrigerator at approximately −20°C for 7–24 h. It was then kept in a temperature-controlled container at 4°C. This freeze–thawing cycle was repeated 4 times. The gels were then immersed in a large amount of pure water until reaching their equilibrium states.

To fabricate FT-dry gels, the FT gels were sufficiently dried at room temperature and then immersed in pure water again.

To obtain CD gels, the solution in an uncovered petri dish was left to dry in air at room temperature until the weight became almost constant. This film was soaked in a large amount of pure water to obtain a PVA cast gel.

21.3.1 Swelling Ratio and Compression Stress

Figure 21.3 shows the swelling ratio and the 30% compression stress $\sigma_{30\%}$, which were measured at room temperature for the respective gels. The compression force was measured using a TA.XTPlus texture analyzer (Texture Technologies Co.) with a cylinder probe of 25 mm diameter [27]. The swollen samples were cut into 20-mm-diameter circles using a paper punch and then compressed by the cylindrical probe. The typical compression rate was 0.01 mm/s, and the sample was deformed by a 30% reduction. In this manner the compression stress $\sigma_{30\%}$, was obtained. The FT gel showed the largest W_t/W_d, and the FT-dry gel showed the largest $\sigma_{30\%}$. When $\sigma_{30\%}$ increased, W_t/W_d decreased correspondingly due to the decrease in the number of microcrystallites. The swelling ratio is correlated with the compression stress, i.e., $\sigma_{30\%}$ increases as W_t/W_d decreases.

According to the literature [9, 10], in the case of CD gels, the crystallinity increases and the swelling ratio decreases by repeated water exchange with drying. In the case of FT-dry gels, during a drying process, additional microcrystallites can be formed, resulting in a decrease in the swelling ratio and an increase in the compression stress as compared with FT gels. As shown in Fig. 21.3, the CD gel exhibited intermediate values of W_t/W_d and $\sigma_{30\%}$ between FT and FT-dry gels.

It has been reported that by water exchange with drying, the swelling ratio of CD gels decreases at first and becomes constant after several water exchanges (Fig. 21.4). The decrement of the swelling ratio resulted mainly from the formation of additional hydrogen bonds. The ATR FT-IR spectrum changed during the water exchange with drying due to the elution of noncross-linked polymers from the network and the formation of additional hydrogen bonds between the –OH groups of PVA. Among the characteristic properties of physically cross-linked gels, the elution behavior is particularly important mainly because elution is unavoidable in physical gels [23, 24]. As a result of elution, the number of free –OH groups increases, which are enhanced to form additional microcrystallites. Elution of polymers from PVA

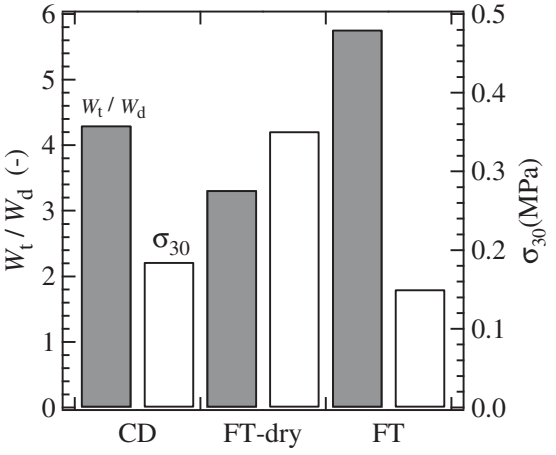


FIGURE 21.3 (a) Typical tearing curve of PVA cast gels prepared at room temperature (~25°C); (b) G_{av}, the average G in the flat region, was plotted against T_{gel}; (c) swelling ratio and compression stress for 30% reduction, σ_{30} of the respective gel.

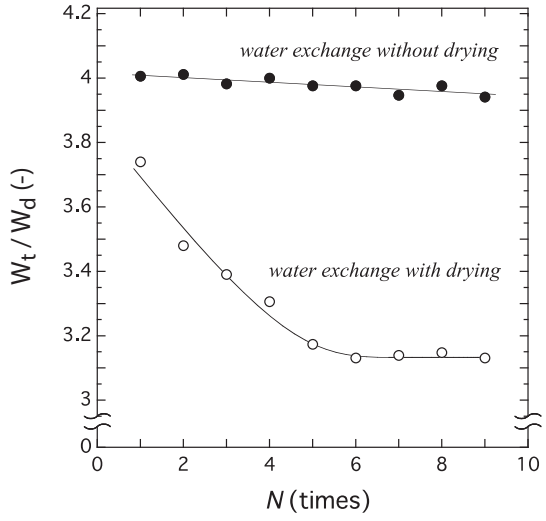


FIGURE 21.4 W_t/W_d of PVA cast gels during water exchange with or without drying. The solid lines are intended for visual guidance.

gels can be estimated by measuring quantitatively the total carbon in the outer water using a total organic carbon (TOC) analyzer, which will be described later. The non-crosslinked polymers elute during a simple swelling process, and the elution can be detected whenever the solvent water is exchanged. The amount of eluted polymers approaches zero after sufficient water exchange. The time revolution of the swelling ratio mentioned above corresponds to the change in elution amount.

It should be noted that the total change in W_t/W_d by water exchange with drying is ~15% (<5% by a single water exchange with drying) in the case of CD gel; W_t/W_d decreases more than 40% by a single water exchange with drying in the case of FT gel (Fig. 21.4).

21.3.2 Tearing Energy by a Trouser Tear Test

The tear energy G is defined as the fracture energy released per unit area of crack surface growth (J/m^2), which was obtained here by dividing the tear force by the gel thickness. The tear force was obtained by a trouser tear test in water [19]. The samples were cut into rectangle shape and an initial slit was made in one of the short sides, from which the tear was propagated. In this test, the rate of separation of the grips holding the gel was constant at 0.1 mm/s. As is seen in Fig. 21.5a, G of the CD gel exhibited a steady propagation after showing a peak at the initial stage. This large peak was attributed to the initial fracture energy needed to start the propagation in the vicinity of the end of the slit, where the polymer network was reinforced by the turbulence caused by cutting the slit. The average tearing energy G_{av} was obtained by averaging G in the flat region. When plotted against the cast-drying temperature T_{gel} shown in Fig. 21.5b, G_{av} increased with increasing T_{gel}. As shown in Fig. 21.6a, G of the CD gel is steady and time-homogeneous, whereas G of the FT gel shows stick–slip behavior due to the network inhomogeneity. G_{av} of the FT gel was much larger than that of the CD gel; G_{av} of the CD gel prepared at 60°C was still much lower than that of the FT gel.

Since G is not strongly dependent on the tearing speed, one can say that the CD gel is highly elastic. In the case of the CD gel, the crystallinity, which increases with increasing T_{gel}, is an essential factor for determining the tear resistance.

On the other hand, the crystallinity is of little relevance to G, suggesting that G is dependent not only on the size and number of the microcrystallites but also on their distribution [22]. The variation in G with time and the fracture surfaces of the CD and FT gels are shown in Fig. 21.6. The appearance of stick–slip behavior in the fracture pattern of the FT gel corresponds visually to the tearing curve, which resulted from the formation of fibrils of bundled polymers on micrometer scale. These results indicate that the microscopic network structure characterized by the presence of fibrils determines the tear energy for the FT gels.

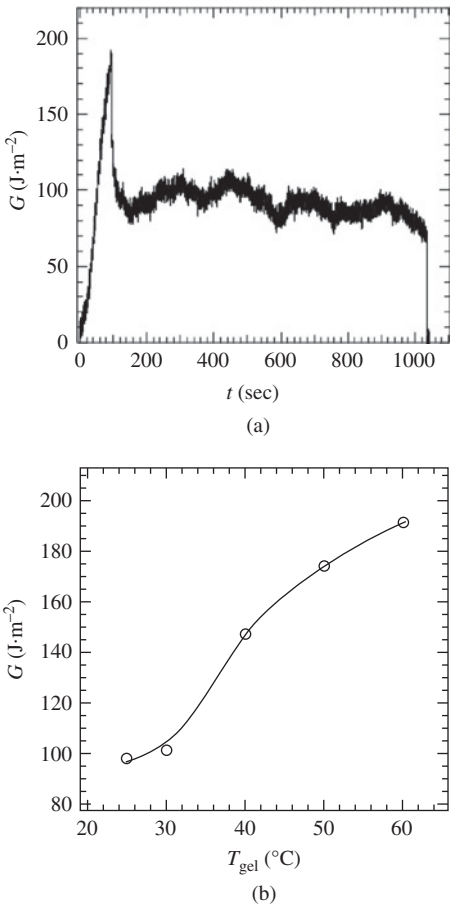


FIGURE 21.5 Fracture energy G of cast and FT gels during a tearing test with a pulling velocity of $v = 0.1$ mm/s: (a) fracture energy in tearing of T at a pulling velocity of $v = 0.1$ mm/s; (b) effects of tearing velocity and drying temperature on fracture energy of cast gels.

In order to further examine the differences of the fracture phenomena between CD and FT gels, the PVA solution was dried to some extent at room temperature before repeating the freeze–thawing process, which yielded gels mechanically intermediate between CD and FT gels [35]. The transparency of the gel increased with increased drying degree and G decreased rapidly. From these results, it was concluded that the large tear resistance was attributed to the macroscopic fibrils; therefore, much larger strength can be expected by controlling the structures of the fibrils.

21.3.3 Dynamic Friction Coefficient and Wear Ratio

To measure the mechanical properties of the physical PVA gels, reciprocating tests with ellipsoidal PVA specimens against a glass plate were conducted under conditions of continuous and constant loading [17]. The experimental conditions were as follows. The applied normal load was 2.94 N,

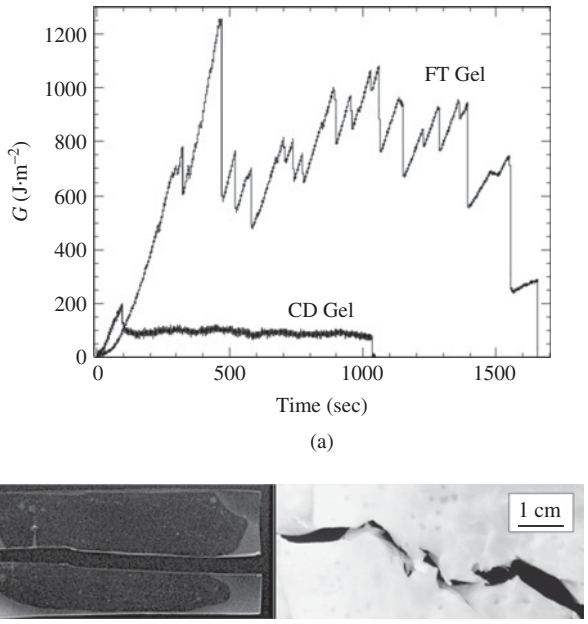


FIGURE 21.6 (a) Tear energy, G, of FT and CD gels during a tear test with a pulling velocity of $v = 0.1$ mm/s. (b) Fractured surfaces of CD (left) and FT (right) gels.

and the sliding speed and stroke length were 20 mm/s and 35 mm, respectively. The repetition number was 2000 cycles; therefore, the sliding distance for continuous testing was 140 m. The reciprocating tests were conducted in lubrication with saline at room temperature. As shown in Fig. 21.7, the FT gel showed larger initial friction with a gradual increase, a change that is similar to that of natural articular cartilage. In contrast, very low friction was maintained with the CD gel,

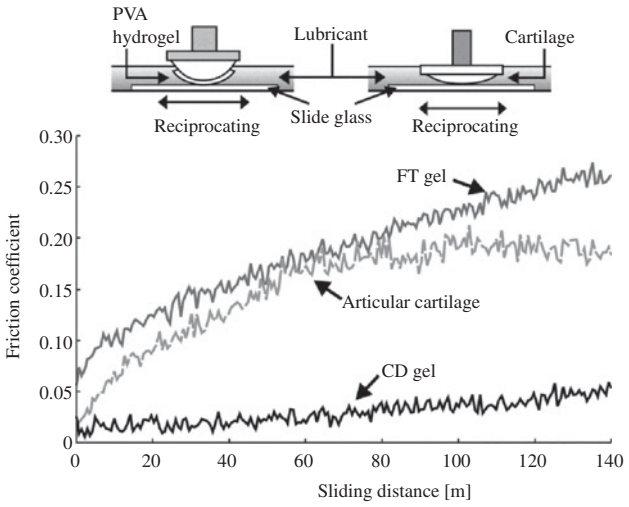


FIGURE 21.7 Time-dependent frictional behaviors of three types of PVA hydrogels in reciprocating tests in saline.

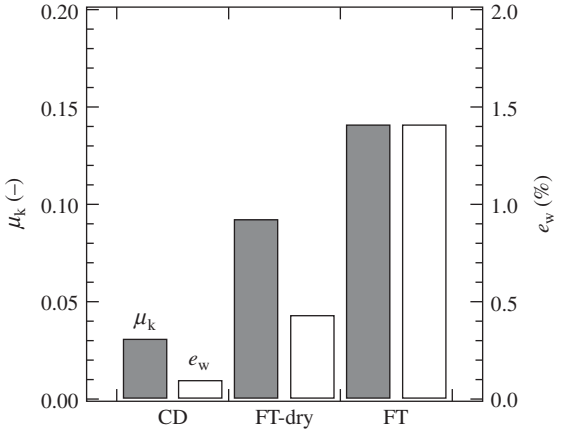


FIGURE 21.8 Coefficient of friction and wear ratio in reciprocating tests.

which exhibited a slight increase. The superior properties observed in the CD gel were evaluated using biphasic finite-element (FE) analysis. It was also shown that the friction and wear properties of the FT gel could be improved with the aid of boundary lubrication by adding simulated synovial fluid constituents.

The coefficient of kinetic friction μ_k was measured during linear reciprocating sliding (ball-on-plate mode) in water (no lubricant) using a ceramic femoral component ($\phi = 26$ mm, alumina ceramics) and plate gels. The test conditions were as follows: The normal load was 0.98–5.88 N, the sliding speed was 20 mm/s, the stroke was 25 mm, the cycle number was 2000, and the total sliding distance was 100 m.

Wearing of the polymers from the PVA gels was quantitatively estimated by measuring the total carbon (TC) in the solvents using a TOC analyzer (TOC-V_{CSN}, Shimadzu) that had a detection limit of 50 μg/L. The weight of the worn polymer W_e was then calculated from the TOC value, which was obtained by subtracting the total inorganic carbon (TIC) due to carbon dioxide from the TC. A reference sample of gel with water, the same sample set used for the wear measurements, was prepared. The weight ratio of sample to water was fixed at 1/50 (g/g). In order to obtain the real wear weight, both the TIC and the eluted TC were removed from the total TC after the wear measurement. The wear ratio e_W is defined as

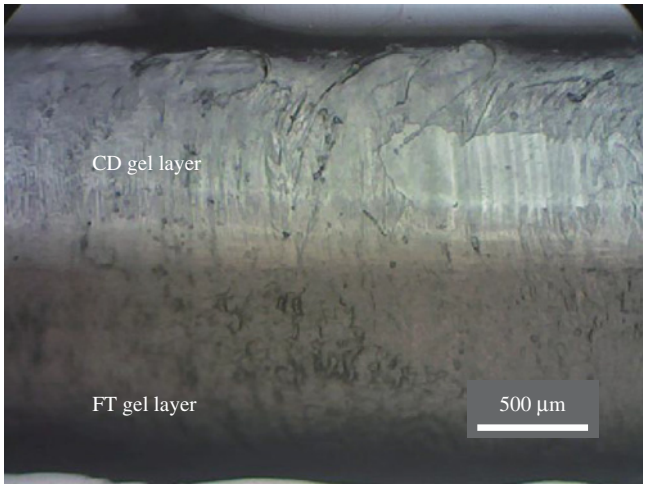
$$e_W = \frac{W_e}{W_0} \times 100$$

where W_0 indicates the initial weight of the dried film.

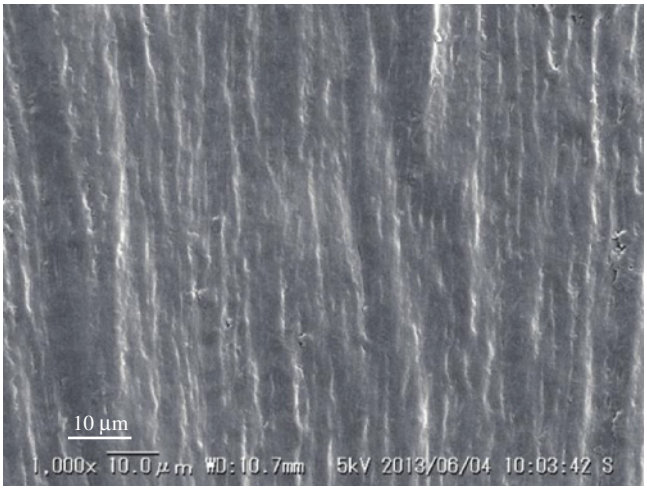
Figure 21.8 shows the friction and abrasion performance of the CD, FT, and FT-dry gels. The values of μ_k (averaged value between 1500 and 2000 cycle numbers) and e_W depended apparently on the gels. The CD gel showed the lowest μ_k and e_W. It was suggested that there is a correlation between e_W and μ_k and that low μ_k resulting in low e_W was possible.

21.4 MECHANICAL STRENGTHENING AND FUTURE VISIONS

For the application of hydrogels as artificial articular cartilage, several essential properties arerequired, such as biocompatibility, low friction, high wear resistance, suitable water content, and high mechanical strength (i.e., stiffness, fracture toughness, and fatigue resistance). PVA gels used for artificial cartilage are expected to combine superior mechanical strength and excellent lubricating properties comparable to natural synovial joints. Both CD and FT gels have high water absorbance and excellent mechanical properties as compared with other hydrogels. As shown in the present typical examples of physical gels, the CD gel showed the highest performance (high swelling ratio and low wear) among the three gels tested. However, CD gel alone cannot satisfy all required properties. Of the required properties, the mechanical strength and wear resistance of the FT and CD gels were poor as compared with natural synovial joints and further improvements are needed for practical uses.



(a)



(b)

FIGURE 21.9 (a) Cross section of a laminated gel of CD on FT gel in its swollen state; (b) SEM micrograph of an anisotropic dried FT gel. Fibrils are vertically oriented.

It may be difficult to significantly improve the mechanical properties using conventional fabrication methods. The conventional FT and CD fabrication methods are based on phase separation induced by the natural phenomenon of solidification and vaporization of water. In contrast to these simple and convenient methods, it is possible to improve the properties of gels by introducing artificial processes (Fig. 21.9). For example, there have been some attempts to control the polymer networks of FT and CD gels on multiple scales [17,35]. In the current study, a lamination method and hybrid techniques (Fig. 21.9a) using FT and CD gels were examined in order to improve the mechanical properties. The lamination allowed us to control the surface and bulk mechanical properties independently, which improved the mechanical and tribological properties. It was possible to realize higher mechanical performance by the synergistic interaction between the gels, which is partly attributed to the additional microcrystallites formed at the interface. Figure 21.10 shows the effects of the number of layers N on the mechanical properties while keeping the same total CD gel thickness. With increasing N, the breaking stress apparently increased, whereas the breaking strain did not evidently change. This is attributed to the different degrees of formation of the microcrystallites at the interface. Therefore, the swelling ratio, mechanical properties, and wear behavior can be controlled by laminating FT gel and CD gel.

A unidirectional freezing method is another example [35], by which a micrometer-scale fibril network structure can be formed in the network of FT gels (Fig. 21.9b). This

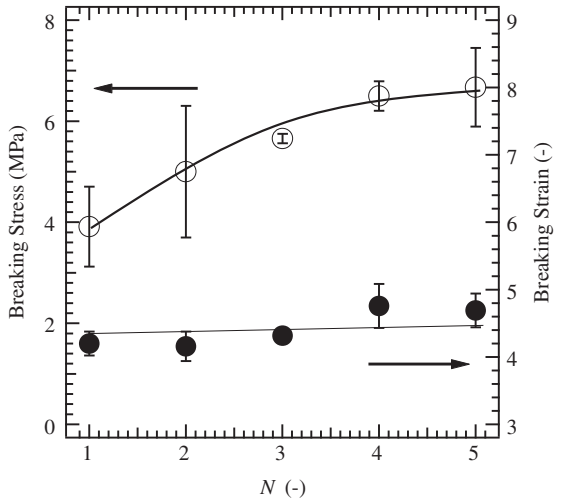


FIGURE 21.10 Breaking stress and strain of layered CD gels by a uniaxial loading test.

anisotropic network structure can lead to higher mechanical performance along the fibril direction. These techniques provide hierarchical network structures that could not be obtained by the conventional single process.

For the next step, the authors are currently developing hybrid hydrogels composed of cast-drying PVA on freeze–thawing PVA as another candidate material for artificial cartilage with superior lubricity. In fact, natural synovial joints have multiple layers, each layer of which has a respective function. Similarly, high performance is expected to emerge in hydrogels by hybridizing single layers with different properties. On the basis of the fundamental research, we are currently applying the hybrid techniques to the real system. The tribological properties were significantly improved within our preliminary experiments, which will be published elsewhere.

ACKNOWLEDGMENT

The authors express their thanks to Dr. S. Sasaki, Dr. S. Yarimitsu, Dr. K. Nakashima, and Dr. N. Sakai for their supports of experiments and many instructive comments. This work was supported by the Grant-in-Aid for Specially Promoted Research of Japan Society for the Promotion of Science (Kaken: 23000011).

REFERENCES

[1] Nakamura, K. (2011). *J. Orthop. Sci.* **16**, 489–491.

[2] Sato, M., Deguchi, S., Adachi, T., Murakami, T., Hirokawa, S. (2013). *Frontiers of Biomechanics* (in Japanese). Kyoritsu Shuppan Co., Ltd.

[3] Tomita, N., Kitakura, T., Onmori, N., Ikada, Y., Aoyama, E. (1999). *J. Biomed. Mater. Res. (Appl. Biomater.)* **48**, 474–478.

[4] Moro, T., Takatori, Y., Ishihara, K., Konno, T., Takigawa, Y., Matsushita, T., Chung, U.-il., Nakamura, K., Kawaguchi, H. (2004). *Nat. Mater.* **3**, 829–836.

[5] Williams, P.A., Yamamoto, K., Masaoka, T., Oonishi, H., Clarke, I.C. (2007). *Tribol. Transact.* **50**, 277–290.

[6] Murakami, T. (1990). *JSME* (Japan Society of Mechanical Engineers) *Int. J. III* **33**, 465–474.

[7] Murakami, T., Higaki, H., Sawae, Y., Ohtsuki, N., Moriyama, S., Nakanishi, Y. (1998). *Proc. Inst. Mech. Eng. H: J. Eng. Med.* **212**, 23–35.

[8] Oka, M., Ushio, K., Kumar, P., Ikeuchi, K., Hyon, S.H., Nakamura, T., Fujita, H. (2000). *Proc. Inst. Mech. Eng. H: J. Eng. Med.* **214**, 59–68.

[9] Arakaki, K., Kitamura, N., Fujiki, H., Kurokawa, T., Iwamoto, M., Ueno, M., Kanaya, F., Osada, Y., Gong, J.P., Yasuda, K. (2010). *J. Biomed. Mater. Res. A* **91**, 1160–1168.

[10] Sasada T. (1988). *Transact. 3rd World Biomater. Congr.* **11**, 6.

[11] Cha, W.-I., Hyon, S.-H., Oka, M., Ikada, Y. (1996). *Macromol. Symp.* **109**, 115–126.

[12] Oka, M., Ushio, K., Kumar, P., Ikeuchi, K., Hyon, S.H., Nakamura, T., Fujita, H. (2000). *Proc. Inst. Mech. Eng. H: J. Eng. Med.* **214**, 59–68.

[13] Kobayashi, M., Hyon, S.H. (2010). *Materials* **3**, 2753–2771.

[14] Nakashima, K., Sawae, Y, Murakami, T. (2007). *Tribol. Int.* **40**, 1423–1427.

[15] Yarimitsu, S., Nakashima, K., Sawae, Y., Murakami, T. (2007). *Tribol. Online* **2**, 114–119.

[16] Suzuki, A., Sasaki, S., Sasaki, S., Noh, T., Nakashima, K., Yarimitsu, S., Murakami, T. (2013). *Proc. World Tribology Congress*, Torino, Italy, Sept. 8–13, 2013.

[17] Murakami, T., Yarimitsu, S., Nakashima, K., Yamaguchi, T., Sawae, Y., Sakai, N., Suzuki, A. (2014). *Proc. Inst. Mech. Eng. J: J. Eng. Tribol.* **228**, 1099–1111.

[18] Alves, M.H., Jensen, B.E., Smith, A.A., Zelikin, A.N. (2011). *Macromol. Biosci.* **11**, 1293–1313.

[19] Hassan, C.M.Peppas, N.A. (2000). *Adv. Polym. Sci.* **153**, 37–65.

[20] Lozinsky, V.I., Galaev, I.Y., Plieva, F.M., Savina, I.N., Jungvid, H., Mattiasson B. (2003). *Trends Biotechnol.* **21**, 445–451.

[21] Tamura, K., Ike, O., Hitomi, S., Isobe, J., Shimizu, Y., Nambu, M. (1986). *ASAIO* (American Society for Artificial Internal Organs) *Transact.* **32**, 605–609.

[22] Otsuka E., Suzuki, A. (2009). *J. Appl. Polym. Sci.* **114**, 10–16.

[23] Otsuka E., Suzuki, A. (2009). *Progress Colloid Polym. Sci*. **136**, 121–126.

[24] Otsuka, E., Sasaki, S., Koizumi, K., Hirashima, Y., Suzuki, A. (2010). *Soft Matter* **6**, 6155–6159.

[25] Otsuka, E., Sugiyama, M., Suzuki, A. (2010). *J. Phys. Conf. Ser.* **247**, 012043.

[26] Sasaki, S., Otsuka, E., Hirashima, Y., Suzuki, A. (2012). *J. Appl. Polym. Sci.* **126**, E233–E241.

[27] Otsuka, E., Komiya, S., Sasaki, S., Xing, J., Bando, Y., Hirashima, Y., Sugiyama, M., Suzuki, A. (2012). *Soft Matter* **8**, 8129-8136.

[28] Peppas, N.A., Merrill, E.W. (1977). *J. Appl. Polym. Sci.* **21**,1763–1770.

[29] Suzuki, A., Yamazaki, M., Kobiki, Y., Suzuki, H. (1997). *Macromolecules* **30**, 2350–2354.

[30] Suzuki, A., Yoshikawa, M. (2006). *J. Chem. Phys.* **125**, 174901.

[31] Sasaki S., Suzuki, A. (2013). *React. Funct. Polym.* **73**, 878–884.

[32] Miya, M., Iwamoto, R., Mima, S.J. (1984). *Polym. Sci. Polym. Phys. Ed.* **22**, 1149–1151.

[33] Lee, J., Lee, K.J., Jang, J. (2008). *Polym. Test.* **27**, 360–367.

[34] Upadhyay, D.J., Bhat, N.V. (2004). *J. Membr. Sci.* **239**, 255–263.

[35] Noh, T., Bando, Y., Ota, K., Sasaki, S., Suzuki, A. (2015). *J. Appl. Polym. Sci.* **132**, 41356.

22

SUPERIOR TRIBOLOGICAL BEHAVIORS OF ARTICULAR CARTILAGE AND ARTIFICIAL HYDROGEL CARTILAGE

TERUO MURAKAMI[1] AND ATSUSHI SUZUKI[2]

[1]*Research Center for Advanced Biometrics, Kyushu University, Nishi-ku, Fukuoka, Japan*
[2]*Department of Materials Science and Research Institute of Environment and Information Sciences, Yokohama National University, Hodogaya-ku, Yokohama, Japan*

22.1 INTRODUCTION

The various natural biological systems have rational and robust mechanisms and sustain their function with effective protective systems with restoration mechanism. In healthy natural synovial joints, the superior lubrication mechanism appears to maintain very low friction and minimum wear for a whole lifetime. However, the deterioration of articular cartilage and synovial fluid can break down lubrication mechanism in synovial joints and lead to osteoarthritis with damage of articular cartilage, which restrict the daily activities and produce serious pain in severe cases. For more than a half century since the successful clinical application of total hip prosthesis composed of ultra-high-molecular-weight polyethylene (UHMWPE) cup and stainless-steel head [1], the application of joint replacements to patients with osteoarthritis or rheumatoid arthritis brings the recovery of walking ability and the relief from serious pain. However, in certain cases of artificial joints, the revision operations have been conducted, due to the loosening of joint prostheses, which is usually derived from wear debris-induced osteolysis [2]. Therefore, the reduction of wear is strongly required for improvement in longevity of artificial joints.

In contrast, healthy natural synovial joints maintain very low friction and minimum wear for long life. To establish low friction and low wear in artificial joints, we should elucidate the synergistic lubrication mechanism in natural synovial joints and then apply the effective lubrication mechanisms to artificial joint systems. This chapter begins with a description of the adaptive multimode lubrication mechanism [3, 4] in natural synovial joints, followed by discussion of biphasic finite element (FE) analyses for reciprocating sliding of articular cartilage, conducted under both on/off (sporadic; intermittent) and continuous loading conditions. Next, the effective method to inhibit an increase in friction for sliding pair of articular cartilage and glass plate in reciprocating tests under continuous loading condition is discussed in terms of biphasic and boundary lubrication. Subsequently, improvements of lubrication performance in joint prostheses with compliant artificial hydrogel cartilage [5] are described. The lowering of elastic modulus at ∼1 MPa as rubbing compliant materials from ∼800 MPa of UHMWPE not only can reduce the contact stress level but also enhance the fluid film formation due to the significant elastic deformation effect. Furthermore, biphasic and boundary lubrication are important for artificial hydrogel cartilage. Therefore, FE analyses and experimental evaluation for two kinds of poly(vinyl alcohol) (PVA) hydrogels are described.

22.2 VARIOUS LUBRICATION MODES IN NATURAL SYNOVIAL JOINTS

Healthy synovial joints maintain excellent load-carrying capacity and lubricating properties with extremely low friction and minimum wear even under heavy-load conditions at

Encyclopedia of Biocolloid and Biointerface Science, Volume 1, First Edition. Edited by Hiroyuki Ohshima.
© 2016 John Wiley & Sons, Inc. Published 2016 by John Wiley & Sons, Inc.

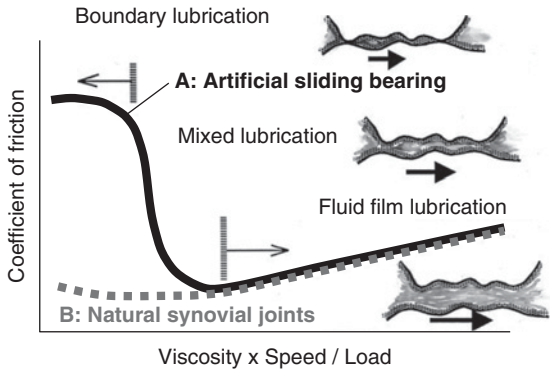
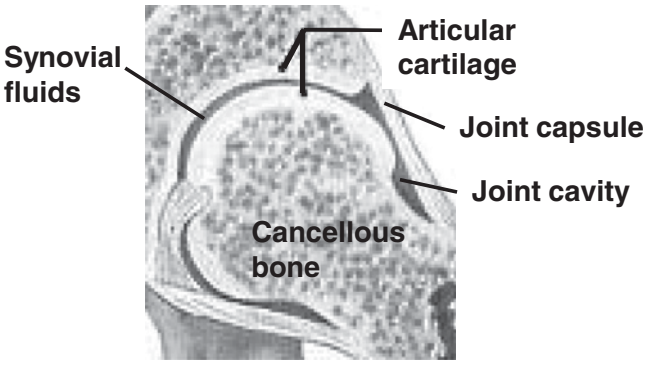


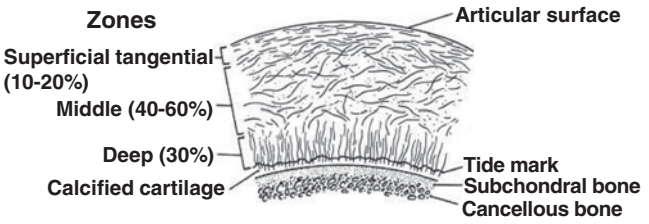
FIGURE 22.1 Stribeck curve and lubrication modes.

several times body weight in hip, knee, and ankle joints. The lubrication modes are usually differentiated on the basis of Stribeck curves as frictional behavior against the parameter for operating conditions as shown in Fig. 22.1. Most artificial rubbing systems such as sliding, bearing, and guiding are represented by nonlinear curves as indicated by curve *A* in Fig. 22.1. The friction varies with different lubrication modes, ranging from fluid film, mixed, and boundary lubrication, which vary according to the ratio of fluid film thickness to surface roughness. Usually, high friction and high wear are observed in boundary and mixed lubrication regimes as a result of direct contact between rubbing surfaces. On the contrary, the natural synovial joints appear to maintain low friction levels in a wider range of operating conditions (curve *B*).

In previous studies of fluid film lubrication versus boundary lubrication in major lubrication modes in natural synovial joints, other various lubrication mechanisms have been proposed. However, the variation in human daily activities is reflected in a wide range of operating conditions. Accordingly, it appears that the superior lubricating performance of natural joints is actualized not by a single lubrication mode but by a synergistic combination of various modes ranging from fluid film lubrication to boundary lubrication, corresponding to the severity of rubbing conditions [6]. The major lubrication mechanism would seem to be some form of elastohydrodynamic action determined by sliding or squeeze film action between porous surfaces, with boundary lubrication providing the surface protection in cases of severe loading and little movement [6]. Natural synovial joints have various geometric structures such as ball-and-socket, hinge, ellipsoidal, and other joint configurations, but in general are composed of epiphyseal parts covered with articular cartilage lubricated with synovial fluid (Fig. 22.2a [7]). The structure of articular cartilage is a depth-dependent complex fiber-reinforced structure (Fig. 22.2b [8]). Articular cartilage tissue consists of chondrocytes and an extracellular matrix (Fig. 22.3a [8]), which is composed mainly of proteoglycan and

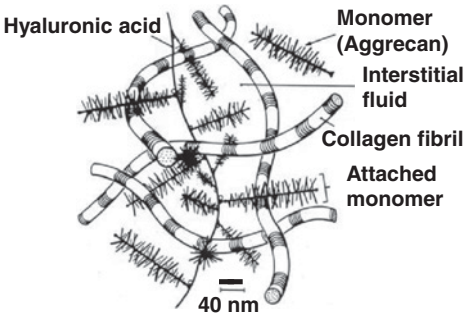


(a)

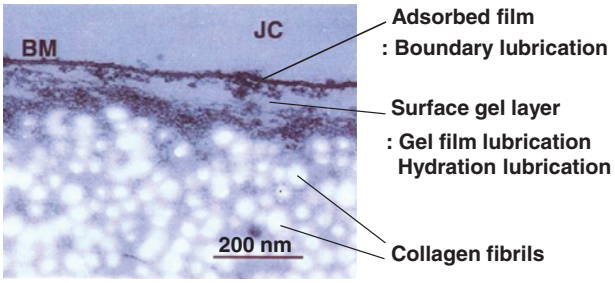


(b)

FIGURE 22.2 Human hip joint [7] (a) and structure of articular cartilage [8] (b).



(a) Extracellular matrix of articular cartilage [8]



(b) Adsorbed film and surface gel layer of cartilage surface (partly modified from [17])

FIGURE 22.3 Extracellular matrix (a) and surface structure (b) of articular cartilage.

collagen (type II). The collagen fibers are arranged in a configuration according to depth in three zones (Fig. 22.2b). Proteoglycan aggregate is composed of aggrecans noncovalently attached to hyaluronan (HA) with stabilizing link proteins. Aggrecan (Agg: aggregating proteoglycan) is composed of keratin sulfate and chondoroitin sulfate chains bound covalently to protein core molecules [8]. Thus, the proteoglycan is highly hydrophilic and therefore can store a large amount of water and support the compressive load with the aid of the confinement by collagen network. Thus, articular cartilage has high water content ranging from 70% to 80% and shows biphasic behavior in which both solid and fluid properties should be considered as indicated by the biphasic theory [9].

The compliant property of articular cartilage contributes to widening of the contact area as elastic deformation of the surface soft layer, with reduction of contact pressure and facilitation of fluid film formation by a soft elastohydrodynamic lubrication (soft EHL) mechanism. Therefore, such joints should be examined to evaluate the possibility of fluid film lubrication during walking. Various studies on minimum EHL film thickness for a smooth compliant surface predicted to be thinner than 1 μm during walking, and maximum height of the undeformed surface roughness of articular cartilage was estimated to be ≥1–2 μm. Thus problems with fluid film lubrication were evaluated, especially in cases where the film parameter in the ratio of minimum film thickness to composite roughness was <3. However, two investigators [10] evaluated the possibility of fluid film formation during normal walking by considering the elastic deformation of surface asperity in numerical EHL analysis. In their analysis, the flattening of surface asperity in the conjunction zone (load-carrying zone) was able to maintain fluid film thickness of ∼0.6 μm without interaction between rubbing surfaces during walking. This lubricating mechanism was called *micro-EHL*, which indicates the possibility of fluid film lubrication by effective hydrodynamic pressure as entraining and squeeze film action during normal walking.

Under slow movement conditions at which sliding speed is too low for hydrodynamic pressurization to sufficiently support a heavy load, the interstitial fluid pressurization in biphasic lubrication is expected to support most of the load and reduce friction [11–13]. The detailed biphasic lubrication mechanism in reciprocating motion is described in the following section.

Under further slower conditions or severe thin-film conditions such as at startup after standing for a long time, some local direct contacts appear to occur between rubbing cartilage surfaces. Under these thin-film conditions, mixed lubrication and/or boundary lubrication modes are likely to prevail. In the boundary lubrication regime, the adsorbed films composed of glycoproteins [14], proteins [15], and/or phospholipids [16,17] are likely to play roles in friction reduction and protection of surfaces. When these adsorbed films on cartilage surfaces were removed, a nonfibrillar proteoglycan gel-like surface layer is expected to maintain low friction, due to its low shearing resistance, and protects the cartilage bulk tissue [18]. Articular cartilage surfaces are covered with adsorbed films on underlying proteoglycan gel-like layer as shown in Fig. 22.3b [17]. This surface structure gives superior tribological properties.

The hydration lubrication mechanism is considered to become effective for these surfaces in aqueous environment of synovial joints. One author [19] indicated the importance of enhanced viscosity around hydrated surfaces and called this mechanism "surface gel hydration lubrication." Another investigator [20] defined the hydration lubrication as "water lubrication of surface layer with hydrophilic polymers fixed to the surface," and indicated the remarkable friction reduction brought by recovery of hydration in surface zone during unloading in intermittent rubbing test. Other researchers [21,22] described hydration lubrication in terms of molecular level and boundary lubrication. They also discussed lubrication by hydrated ions trapped between charged surfaces in aqueous media and by other hydrated boundary species, including charged and zwitterionic polymer brushes, surfactant monolayers, liposomes, and biological macromolecules of synovial joints. In their experiment using a surface force balance for HA and HA/Agg complex films on mica surfaces at boundary lubrication condition, HA exhibited friction increase at low contact pressure, but surfaces bearing HA/Agg complex showed a low coefficient of friction of ∼0.01 at <1 MPa. Lubricin showed a little high coefficient of friction 0.02 at <0.5–1 MPa. However, friction increased for both surfaces coated with HA/Agg or lubricin at higher contact pressure. In contrast, the phosphocholine group, which is zwitterionic, is overall neutral but contains both negative (PO_4^-) and positive [$N^+(CH_3)$] charged groups and has a high level of hydration, showed extremely low friction. The zwitterionic phosphocholic groups appear to show higher hydration than does the HA/Agg complex. HA has only negatively charged groups ($-COO^-$), and Agg has only negatively charged groups ($-COO^-$ and $-SO_3^-$), which may influence the intense hydration. The detailed hydration lubrication mechanism should be clarified in further study.

Thus, the various lubrication modes appear to synergistically play important roles in reduction of friction and wear, depending on the severity of operating condition, in the adaptive multimode lubrication mechanism. In the following section, we describe the effectiveness of biphasic lubrication and boundary lubrication.

22.3 BIPHASIC LUBRICATION IN NATURAL SYNOVIAL JOINTS

Articular cartilage has high water content, ranging within 70–80% in tissue, and thus exhibits a time-dependent biphasic behavior due to the simultaneous coexistence of solid

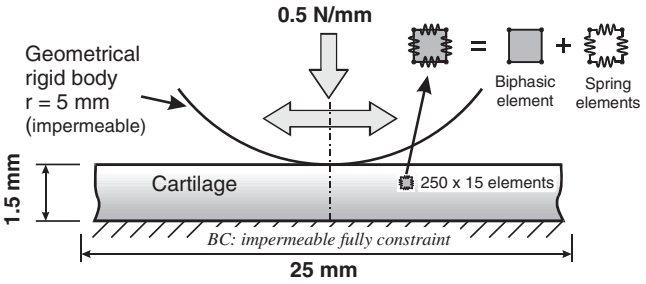
and liquid phases under compressive loading or deformation [11]. Since an experimental finding of the importance of fluid-phase load support in maintaining low friction in mixed and boundary lubrication regimes [14] and a proposed boundary friction model based on biphasic lubrication [15], the effectiveness of biphasic lubrication with interstitial fluid pressurization has been demonstrated on the basis of the biphasic FE analyses and experimental observations [16,23]. When articular cartilage as biphasic material with low permeability is applied by compressive load, the fluid content in the tissue is trapped within the contact area and the collagen matrix network resists interstitial fluid pressure in aggregate solid matrix. Thus, the interstitial fluid pressure supports a significant proportion of the total load in the contact area. The time-dependent change in load support by interstitial fluid pressure in biphasic cartilage depends on the extent of exudation from cartilage tissue and rehydration of cartilage. If the fluid load support is maintained at a high level for a long time, the low friction is maintained because of low-level solid–solid interaction [16].

For reciprocating sliding under constant load, one team [24] introduced a sliding motion into their FE model and indicated the importance of migrating contact area for the sustainability of the biphasic lubrication in their biphasic FE analysis.

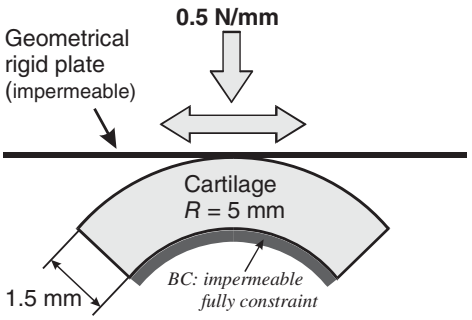
Another group [25] examined the compressive response of the articular cartilage using a high-precision testing machine with a feedback-controlled servomotor and estimated the material properties in physiological conditions for the biphasic FE model. For this model, the following three important features were adopted: (1) depth dependence of apparent Young's modulus of solid phase, (2) strain-dependent permeability as compaction effect, and (3) collagen reinforcement in tensile strain.

These properties were estimated by the curve fitting between the experimental time-dependent compressive behavior and simulation in indentation tests for cartilage specimens with cylindrical rigid indenter. Biphasic FE analysis was conducted using the commercial package ABAQUS (6.8-4). The biphasic tissue was modeled by CPE4RP (four-node bilinear displacement and pore pressure, reduced integration with hourglass control) elements, and a mesh was chosen as 0.1 mm thick with 0.1 mm breadth on surface. The bottom of the model was fixed and impermeable. The other surfaces were not fixed and were basically permeable except for the contact region.

To test the effects of joint contact, two simplified models were selected as on/off loading to cartilage (migrating contact) (model A; Fig. 22.4a) and continuous loading to cartilage (stationary contact) (model B; Fig. 22.4b) [26]. A load of 0.5 N/mm was applied at the center of the cylindrical indenter or against the center of cylindrical specimen in 1 s, and then the reciprocating motion was introduced at a speed of 4 mm/s over a stroke length of 8 mm.



(a) Model A: On-off loading to cartilage



(b) Model B: Continuous loading to cartilage

FIGURE 22.4 Cartilage models for biphasic FE analysis [26].

FE analyses for model A [25] showed that the tensile reinforcement by spring elements representing the collagen network and the depth-dependent elastic properties improved the proportion of the fluid load support, especially with sliding motion. The compaction effect on permeability in the solid phase was functional under conditions without migrating contact, whereas under sliding conditions the compaction effect was minimal.

In the simulation for two models [26], the reciprocation of a rigid cylinder or flat plate at 4 mm/s was started immediately after loading and continued for 508 s, for 127 cycles at a period of 4 s. Figure 22.5 shows the changes in interstitial fluid pressure. The initial fluid load support percentages are very high: 90% and 91% for models A and B, respectively. After 127 cycles, the high percentage of fluid load support (83%) was maintained even after 508 s in model A, but the percentage of fluid load support was remarkably decreased to 27% in model B under continuous loading.

The lowering in percentage of fluid load support indicates friction increase. On the basis of biphasic theory, time-dependent changes in friction coefficient μ_{eff} can be estimated for μ_{solid} as the coefficient of friction for solid–solid contact using the following formula.

$$\mu_{\text{eff}} = \mu_{\text{solid}} \left(1 - (1 - \Psi)\ W^{\text{p}}/W\right) \tag{22.1}$$

where W is the total load support, W^{p} is the load support by fluid pressure, and Ψ is the fraction of contact area of solid phase.

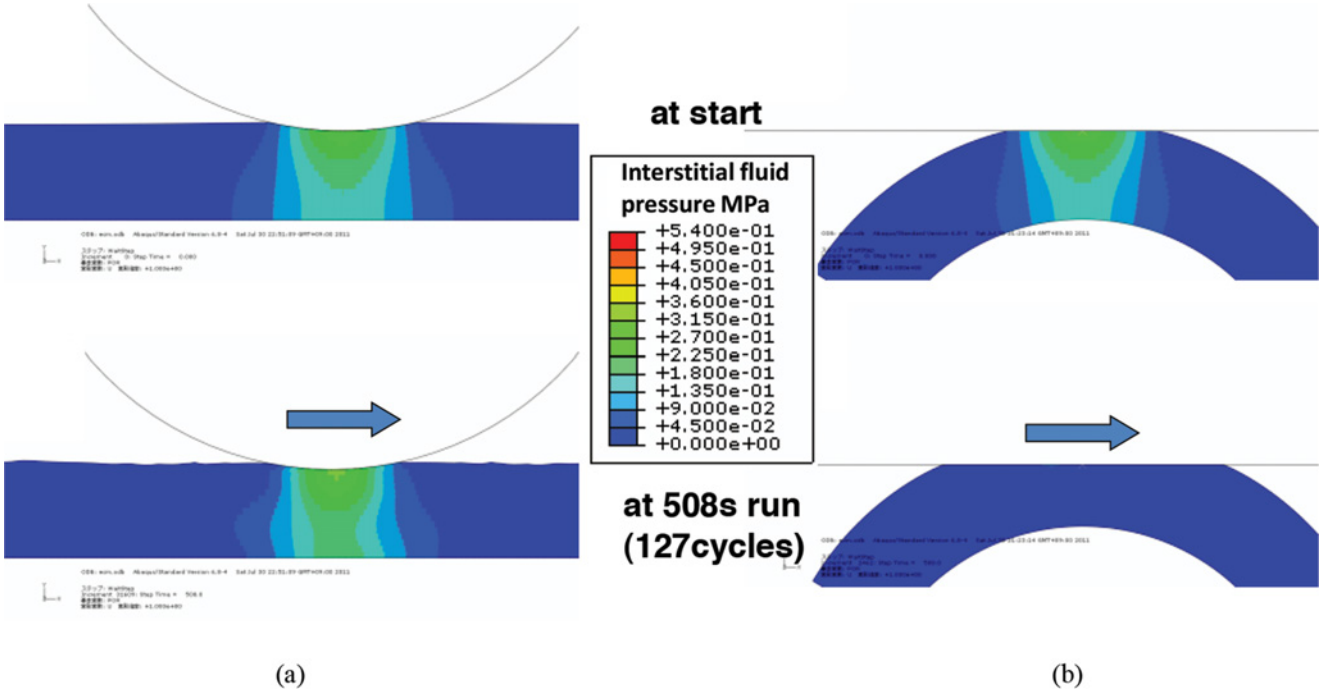


FIGURE 22.5 Changes in interstitial fluid pressure of articular cartilage: (a) on/off loading to cartilage; (b) continuous loading to cartilage (modified from Ref. 26). For a color version of this figure, see the color plate section.

In Fig. 22.6, the time-dependent changes in friction estimated from total traction force in biphasic FE analysis for assumption of $\mu_{solid} = 0$ or 0.01 and 0.2 are shown, where both adhesive and ploughing components are included as total traction force. It is worth noting for model A that the considerable low friction level is maintained as a result of the sustainability of interstitial fluid pressure depending on μ_{solid} in the reciprocating sliding. However, some ploughing resistance is included. In contrast, it is noteworthy that a significant gradual increase to a high friction level is observed in reciprocation for model B with $\mu_{solid} = 0.2$. Even under continuous loading conditions, low friction can be maintained if a low level of $\mu_{solid} = 0.01$ is sustained by effective boundary lubrication. For condition B, the ploughing action is negligible.

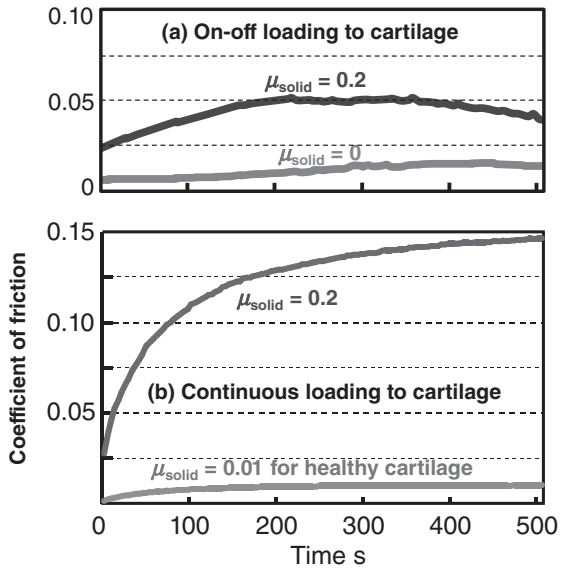


FIGURE 22.6 Changes in friction for reciprocating test of articular cartilage models.

Under operating conditions where the effectiveness of biphasic lubrication will be reduced, the roles of alternate lubrication mechanisms such as boundary lubrication and hydrated lubrication are examined in the following section.

22.4 BOUNDARY LUBRICATION IN NATURAL SYNOVIAL JOINTS

To maintain low friction and low wear in mixed or boundary lubrication regime where local direct contact occurs in natural synovial joints, adsorbed film formation on the articular cartilage surface appears to play an important role. Furthermore, the proteoglycan gel layer at the uppermost superficial zone in articular cartilage appears to play an important role in preserving low friction and low wear by the hydration lubrication mechanism even after removal of adsorbed film [18]. However, the interaction or synergistic action between adsorbed film and hydrated film/surface has not yet been

clarified. The importance of the role of charged polymer brushes, hydrated species, and lipidlike surfactant molecules in terms of molecular mechanisms of hydration lubrication in aqueous systems has been reported [21, 22].

In order to examine the effect of boundary lubrication, the frictional behaviors in a sliding pair of ellipsoidal articular cartilage specimens and reciprocating glass plate were examined in the sliding condition for model B without migration of contact zone for cartilage as the most severe case [28–30]. An upper intact cartilage specimen with subchondral layer was prepared from a femoral condyle in a porcine knee joint (6–7 months old). The lubricants are saline solution containing 0.15 M NaCl (Otsuka Pharmaceutical Factory Inc., Japan), saline solution of 0.5 wt% sodium hyaluronate (HA, molecular weight: 9.2×10^5), HA solutions containing 0.7 wt% or 1.4 wt% bovine serum albumin (Wako Pure Chemical Industries Ltd., Japan), 0.7 wt% human serum γ-globulin (Wako Pure Chemical Industries Ltd., Japan), and/or 0.01 wt% L,α-dipalmitoyl phosphatidylcholine (L,α-DPPC) as an phospholipid liposome. In order to prevent bacterial growth in protein solutions as lubricant, 0.3 wt% sodium azide was added for protein solutions.

The reciprocating test was conducted at a sliding speed of 20 mm/s for rectangular reciprocating mode and at a stroke of 35 mm at a constant load of 9.8 N. At room temperature, reciprocating sliding movement began immediately after loading, and interrupted after 514 cycles at sliding distance of 36 m for running time of 30 min, and then the unloading state was maintained for 5 min. Subsequently, the reciprocating test resumed immediately after reloading and continued for a further sliding distance of 36 m. The restarting processes after unloading were repeated 3 times. The number of tests under the same conditions was 3.

Figure 22.7 shows frictional behavior for intact cartilage [30]. In saline, the initial low friction was observed, but friction gradually increased to a high level during the rubbing process. However, when movement resumed after unloading for 5 min a remarkable reduction in friction was observed, down to a level only a little higher than the initial friction. This phenomenon was attributed to the recovery in hydration and deformation. After restarting, friction again gradually increased.

It is noteworthy that even the addition of 0.01 wt% DPPC alone to HA solution exhibited a remarkable reduction in friction. Furthermore, the addition of 0.01 wt% DPPC accompanied by 1.4 wt% albumin, 0.7 wt% γ-globulin in HA solution (as a simulated synovial fluid) demonstrated the lowest friction levels at about 0.01 CF (coefficient of friction) without gradual increase prior to each 36 m sliding. On the other hand, the addition of DPPC with albumin alone or γ-globulin alone in HA solution shows higher friction than DPPC alone in HA solution but lower than saline solution.

To sustain superior tribological properties of articular cartilage, not only low friction but also minimum wear are

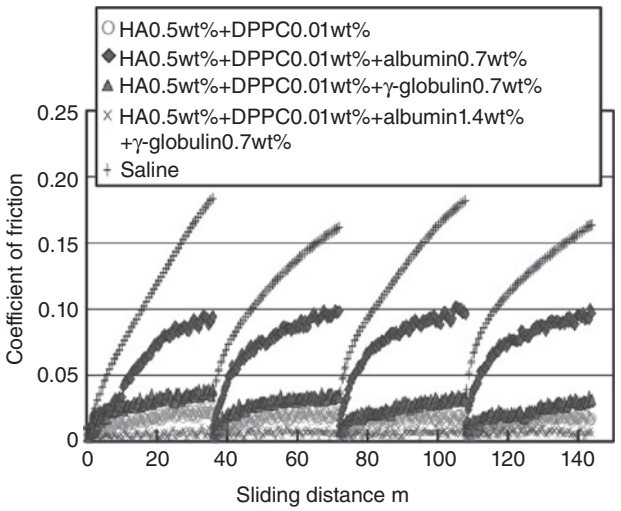
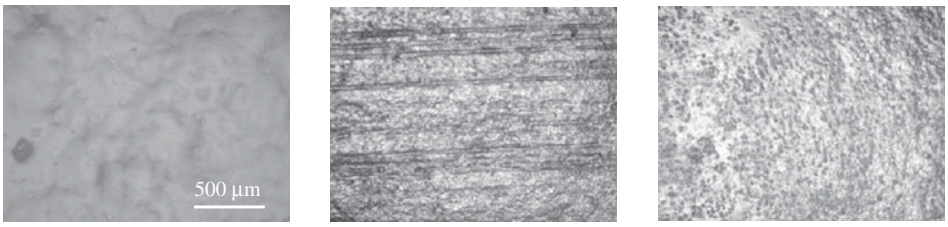


FIGURE 22.7 Changes in friction for reciprocating test of articular cartilage.

required in various daily activities. Therefore, the effect of wear on cartilage surfaces was evaluated. Representative photographs are shown in Fig. 22.8 [30]. Intact articular cartilage has a smooth surface with some irregularity. Tests with lubricants of HA solution containing 0.01 wt% DPPC exhibited low friction but mild wear with scratches on surfaces. However, minimum friction as low as 0.01 and little wear (Fig. 22.8c) were confirmed for simulated synovial fluid, where a superficial gel-like layer may have been slightly removed without scratching during rubbing.

We will now compare the effects of the addition of neutral phospholipid DPPC with and without protein. As shown in Fig. 7, the addition of DPPC alone in HA solution was highly effective in reducing friction for intact cartilage compared with the coexistence of DPPC and either albumin or γ-globulin in HA solution. This finding may suggest the formation of lubricating complex materials as membranelike and roller structures composed of DPPC and HA [31]. The detailed structure of the HA-DPPC complex has not yet been clarified, but the coexistence of DPPC and HA is likely to act synergistically as lamellar lubrication or related mechanism. Furthermore, for coexistence of DPPC and HA, an HA-DPPC composite boundary film was visually confirmed by in situ fluorescent observation [32] and friction was remarkably lowered, where the lubricating ability of the HA-DPPC complex as a gel-like film supposedly becomes effective because of the high water retention ability of HA. Thus, the HA solution containing DPPC showed an effective but limited protective property with local scratching as shown in Fig. 22.8. In contrast, the friction for HA solution with DPPC and albumin (steady-state CF $\sim$ 0.1) became higher than 0.07 for saline solution with DPPC and albumin [30] and about 0.02 for HA solution with DPPC. In this



(a) Before test

(b) After test with HA 0.5 wt% and DPPC 0.01 wt%

(c) After test with HA 0.5 wt%, DPPC 0.01 wt%, Albumin 1.4 wt% and γ-Globulin 0.7 wt%

FIGURE 22.8 Articular cartilage surfaces before and after reciprocating tests.

case, the albumin-DPPC composite was not found in composites containing DPPC, HA, and albumin [32], probably due to repulsive interaction between albumin and HA. In contrast, HA solution with DPPC and γ-globulin showed a lower CF ($\sim$0.03) than 0.07 for saline solution with DPPC and γ-globulin [30]. However, the supply of both albumin and γ-globulin at a defined ratio in HA solution containing DPPC could remarkably reduce the friction level (Fig. 22.7) and provide high wear resistance (Fig. 22.8).

One team of investigators attempted to determine why two kinds of proteins show different friction levels in HA solutions with DPPC [33]. In their study, HA solution with 1.4 wt% albumin and 0.7 wt% γ-globulin (albumin/globulin = A/G ratio of 2:1) or 0.7 wt% albumin and 1.4 wt% γ-globulin (A/G ratio of 1:2) showed very low wear during rubbing with PVA hydrogel. For low wear condition in the latter, the layered adsorbed film formation was observed by the fluorescent method. In such cases, it is suggested that the γ-globulin forms a protective adsorbed layer on the cartilage surface and that albumin is forms lower-shear layers. In contrast, in HA solution with 1.4 wt% albumin and 1.4 wt% γ-globulin (A/G ratio of 1:1) a heterogeneous adsorbed film was formed and higher wear occurred.

Fluorescent images showed that γ-globulin has stronger adsorption ability on cartilage than does albumin [28]. Furthermore, it was observed for binary protein solutions in the evanescent field within $\sim$200 nm from the surface, by total internal reflection fluorescence (TIRF) microscopy, that the bottom layer of stable protein-adsorbed film is composed mainly of γ-globulin and that the friction-induced enhancement of the formation of protein-adsorbed film occurs in lubricants with appropriate protein composition [34, 35].

The simulated synovial fluid of HA solution with 0.01 wt% DPPC, 0.14 wt% albumin, and 0.7 wt% γ-globulin is similar in composition to that in natural synovial fluid as HA solution containing lubricating constituents such as 1.25 wt% albumin and 0.75 wt% globulin (including $\alpha-$, $\beta-$ and γ-globulins) as medium values [36], 1.1 wt% albumin and 0.7 wt% globulin [37], or 1.9 wt% albumin, 1.1 wt% globulin and 0.01 wt% DPPC [17]. In this lubricant, the lubricating layered structure in adsorbed film is expected for low friction and minimal wear. In various daily activities, synovia constituents appear to play their appropriate roles depending on the severity of operating conditions. DPPC and albumin are likely to act as a low-shear layer, and γ-globulin functions as a protective film as strongly adsorbed on cartilage surface. HA can thicken the lubricating fluid film and form some lubricating gel-like layer. Regarding the role of lubricin as another lubricating constituent, another team [38] suggested that it anchors lipid layers on the cartilage. Elucidation of the synergistic mechanisms between lubricating constituents, on multiple scales, is expected with future studies.

22.5 LUBRICATION MODES IN ARTIFICIAL JOINTS

Most artificial joints are composed of UHMWPE and metallic or ceramic components. UHMWPE has a Young's modulus of $\sim$800 MPa, which is stiffer by two or three orders of magnitude than articular cartilage, and the minimum fluid film thickness is thinner than 0.1 μm for total hip and knee prostheses during stance phase of walking. The fluid film thickness is usually less than the surface roughness of rubbing materials. Therefore, mixed or boundary lubrication mode is the main lubrication mode and local direct contact occurs, resulting in medium friction and considerable wear. For hard-on-hard hip prostheses with high precision and high wear resistance, the possibility of fluid film formation is expected under normal walking conditions, but some problems such as stripe wear, streaking, and breakage of ceramic components may occur under severe operating conditions such as edge loading and/or malpositioning.

To improve the lubrication mode in artificial joints, the applications of compliant artificial cartilage materials have been proposed [5]. The application of compliant materials to the surface layer of the articular surface of total hip and knee replacements facilitates the formation of fluid film by a soft EHL mechanism accompanied by a wider contact area, but the film thickness during walking is not sufficiently thick. Previous studies showed that the values of minimum film

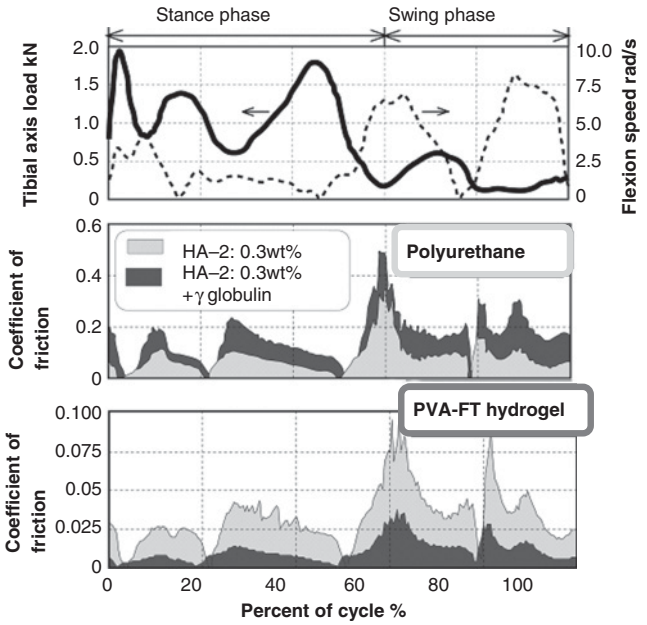


FIGURE 22.9 Frictional behavior of knee prostheses with soft layer in simulator [39].

thickness in simplified knee joint models with a 2-mm-thick soft layer of polyurethane (Young's modulus $E = 40$ MPa) and PVA hydrogel ($E = 1$ MPa) are 0.2 μm and 0.75 μm during stance phase of walking, respectively [39]. The surface roughness seemed to be greater than the minimum film thickness. To evaluate the lubrication modes, the frictional behaviors were examined for knee joint models composed of cylindrical femoral metallic components and flat tibial components with a soft layer of 2 mm thickness as artificial cartilage in a knee joint simulator [39]. The experimental results are shown in Fig. 22.9.

In Fig. 22.9, it should be noted that the knee prosthesis model with PVA hydrogel layer prepared by repeated freeze–thawing (FT) with high water content of 79 wt% and Young's modulus of 1.1 MPa exhibited lower friction in walking condition lubricated with HA solution containing serum protein than for the model with polyurethane layer with a *Young's* elastic modulus of 40 MPa. Maximum coefficient of friction for PVA hydrogel during stance phase was less than ∼0.01, but that for polyurethane increased to >0.2. The superiority of PVA hydrogel should be considered in terms of surface and biphasic properties in addition to differences in fluid film thickness.

In this simulator test, very low friction was confirmed for PVA hydrogel of high water content, but in reciprocating tests under thin-film conditions [33,41], even of high-water-content PVA hydrogel showed significant wear in HA solutions. Although various kinds of hydrogel as cartilage replacement have been developed, clinical application has not yet been completed. To extend the longevity of joint prostheses with artificial hydrogel cartilage, the improvement of tribological properties of artificial cartilage materials is required under various operating conditions in daily activities.

Therefore, in the following sections, the effectiveness of biphasic lubrication and boundary lubrication mechanisms in hydrogel in reciprocating motion are explored.

22.6 FRICTIONAL BEHAVIORS OF ARTIFICIAL HYDROGEL CARTILAGE

As stationary ellipsoidal specimens were placed on a reciprocating flat glass plate (a slide glass) in the reciprocating test, two kinds of artificial hydrogel cartilage specimens and the natural articular cartilage were prepared as described below [41].

22.6.1 Artificial Cartilage

The following two PVA hydrogel materials prepared by repeated freeze–thawing method and cast-drying method were used as specimens composed of a 2-mm-thick soft layer of PVA hydrogel adhered on acrylic ellipsoid (40 × 25 mm in diameter). Figure 22.10 [41] shows photographs, atomic force microscopy (AFM) surface images of their swollen states in water, and schema of microstructure for PVA hydrogels.

The PVA hydrogel preparations were as follows:

1. PVA hydrogel by repeated freeze–thawing (FT) method (Fig. 22.10a). The PVA (Kishida Chemical Co., Ltd., Japan) used in this method has a polymerization degree of 2000 and average degree of saponification of 98.4–99.8 mol%. PVA powder at 20 wt% was dissolved in pure water and heated at 120°C for 30 min in an autoclave and cast in a mold in air to control the specimen thickness, and then gelled by repeated freeze–thawing (FT) cycles (for periods ranging from 10 h at –20°C to 20 h at 4°C). The number of FT cycles was 5 times as optimum condition to establish maximum tensile strength and stiffness [42]. The elastic modulus of PVA hydrogel is 1.2 MPa, and the equivalent water content is 79%.
2. PVA hydrogel by cast-drying (CD) method (Fig. 22.10b) [43–45]. The PVA (Kuraray Co. Ltd., Japan) used in this method has a polymerization degree of 1700 and average degree of saponification of 98–99 mol%. An aqueous PVA solution was obtained by dissolving 15.0 wt% of the PVA powder into deionized and distilled water at 90°C for more than 2 h. The PVA solution was poured into a plastic dish of polyethylene and left in air at room temperature (∼25°C). The solution became very viscous within

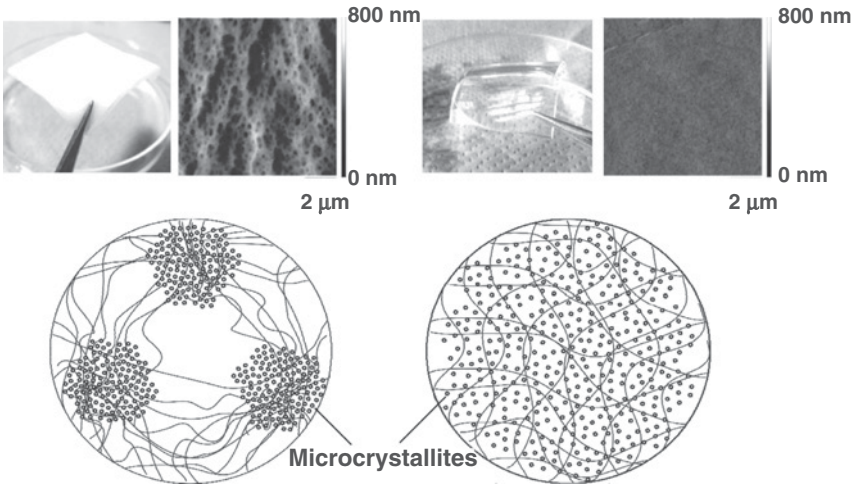


FIGURE 22.10 Photographs, AFM images, and schematic models for two PVA hydrogel structures (partly modified from Ref. 41).

several days and solidified within a week or more. The sample was usually prepared by the process of repeated water exchange with drying.

22.6.2 Articular Cartilage

The intact ellipsoidal articular cartilage specimens with subchondral layer were prepared from the femoral condyle of porcine knee joints as described above.

Reciprocating tests of stationary artificial hydrogel cartilage and articular cartilage specimens were conducted against reciprocating flat glass plate. In the reciprocating apparatus [28–30], the sliding speed and stroke length were 20 mm/s and 35 mm, respectively. Applied load was 2.94 or 9.8 N. The repeated test in interval of 36 m was conducted with the same conditions as mentioned above.

The friction levels of PVA hydrogel specimens and articular cartilage placed against a flat glass plate at continuous loading of 2.94 N in saline are shown in Fig. 22.11. The PVA-FT gel exhibited medium initial friction and time-dependent gradual increase similar to that for natural articular cartilage, where articular cartilage showed very low initial friction and gradual increase at a little lower level. In contrast, the PVA-CD gel exhibited very low friction with a more gradual increase. These differences are assumed to be related to the difference in biphasic lubrication as mentioned later.

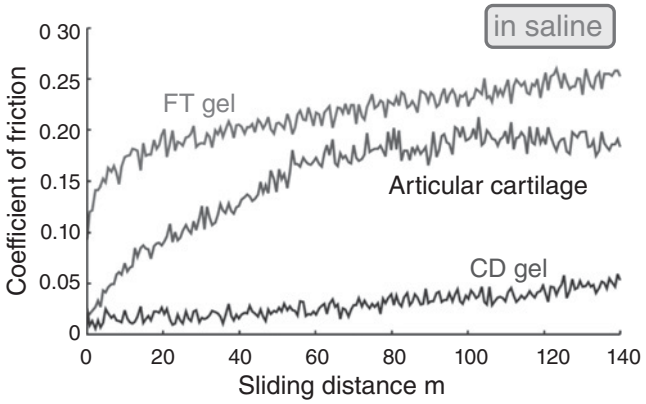


FIGURE 22.11 Frictional behaviors of PVA gels and cartilage in reciprocating tests [47].

22.7 BIPHASIC FINITE-ELEMENT ANALYSES FOR ARTIFICIAL HYDROGEL CARTILAGE

The biphasic FE analysis for two-dimensional models of PVA hydrogel cartilage similar to the cartilage model (model B) in Fig. 22.4 was conducted under continuous loading by an impermeable rigid plate in reciprocating motion. The biphasic element has uniform elastic modulus without spring and uniform permeability. A load of 0.2 N/mm was applied at the center of PVA hydrogel surface with a ramp time of 1 s, and then the load was held constant for a further 292 s during reciprocation motion at 4 mm/s and a period of 4 s.

The material properties of the PVA hydrogels were estimated from the stress–relaxation tests of cuboid ($10 \times 6 \times 4$ mm) under uniaxial compression at definite deformation after an average stress of 0.1 MPa had been attained [46]. The mechanical properties of two PVA hydrogel specimens are shown in Table 22.1 [41]. It is noteworthy that CD gel has a permeability that is two orders of magnitude lower than that of FT gel. The permeability of CD gel has a permeability level similar to that of natural articular cartilage.

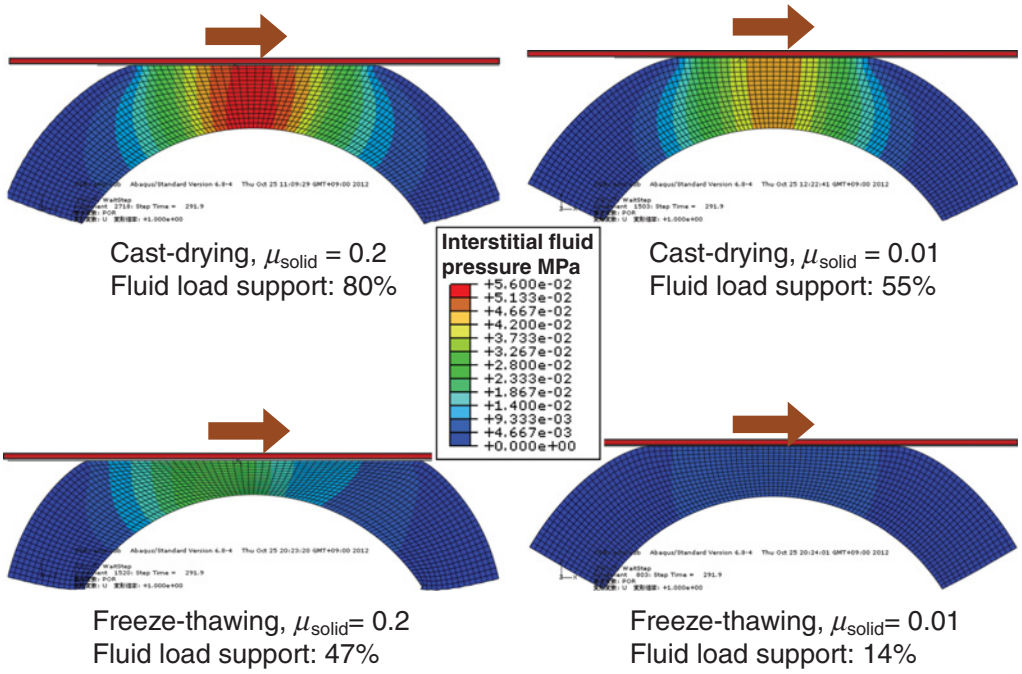


FIGURE 22.12 Changes in interstitial fluid pressure and fluid load support of PVA hydrogel [41]. For a color version of this figure, see the color plate section.

TABLE 22.1 Properties of PVA Hydrogels

Preparation method for PVA hydrogel	Permeability (m^4/Ns)	Young's modulus (kPa)	Poisson's ratio
Freeze–thawing (FT)	2.0×10^{-13}	110	0
Cast-drying (CD)	2.4×10^{-15}	190	0.41

Source: Ref. 41.

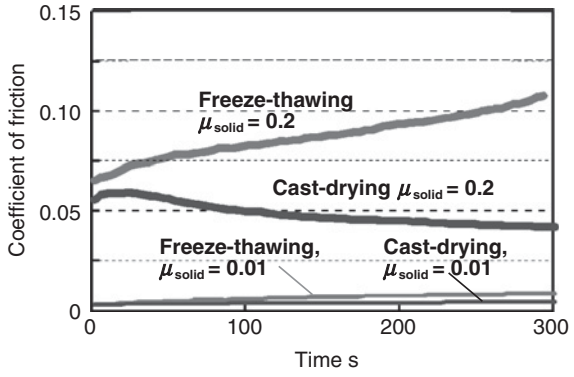


FIGURE 22.13 Frictional behaviors of two hydrogels estimated by biphasic FE analysis [41].

The interstitial fluid pressure with fluid load support after 292 s for two kinds of solid–solid friction conditions, as 0.01 and 0.2 in the reciprocating test, is shown in Fig. 22.12. The CD gel maintains significant pressure even after 292 s, but in FT gel the fluid pressure was remarkably reduced. For both PVA hydrogels, the high friction of solid–solid contact sustained fluid pressure levels that were higher than, and showed greater deformation than, those for low μ_{solid}. Therefore, caution is necessary because, contrary to expectation, the lower surface friction accelerates an increase in solid–solid contact.

The estimated frictional behaviors for PVA hydrogels in reciprocating tests are shown in Fig. 22.13. It is noticed that low friction property of surfaces (solid-to-solid) maintains a significantly low sliding friction level. Even for high μ_{solid}, use of a CD gel can result in a gradual decrease in friction, probably because of the rising fluid load support from the initial 74% to 80% levels in biphasic analysis (Fig. 22.12).

22.8 BOUNDARY LUBRICATION IN FREEZE-THAWING PVA HYDROGEL

The friction level for PVA-FT gel in saline is considered to be too high for clinical application. Therefore, to improve friction levels in FT gel, the effect of lubricant constituents was examined. We presented the detailed data in a previous paper [41]. As shown in Fig. 22.14, the combination of HA and DPPC with and without proteins could maintain a CF lower than ~0.01. Subsequently the wear resistance properties were examined. The simulated synovial fluid (0.5 wt% HA solution containing 0.01 wt% DPPC, 1.4 wt% albumin

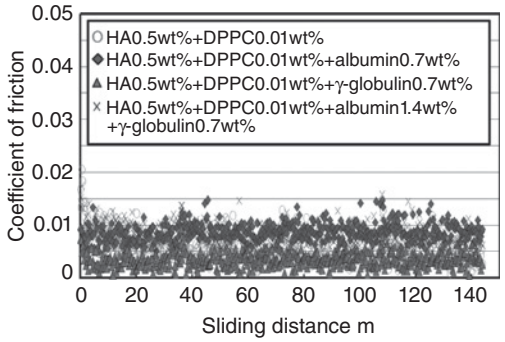


FIGURE 22.14 Influence of synovia constituents on changes in friction for PVA-FT hydrogel.

and 0.7 wt% γ-globulin) showed minimum wear (Fig. 22.15 [41]) similarly to articular cartilage. Thus, the reduction in both friction and wear for FT gel is possible with the aid of synovia in the human joint environment. However, biphasic lubrication has still important role in cases with changes in synovia constituents.

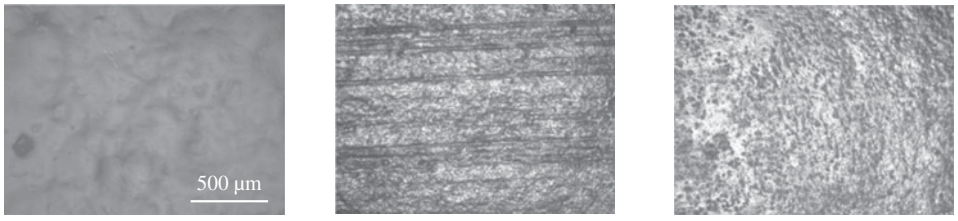
22.9 SUPERIOR TRIBOLOGICAL BEHAVIOR OF ARTIFICIAL HYDROGEL CARTILAGE

As artificial hydrogel cartilage containing high water content, two hydrogel showed quite different time-dependent frictional behaviors in reciprocating tests in saline (Fig. 22.11). In the measurement of time-dependent changes of the contact area in a static loading test [47], the FT gel showed an initial abrupt deformation and subsequent steady state. The CD gel showed a similarly initial abrupt deformation and maintained steady state, but its compressive deformation was lower than that of the FT gel. In contrast, natural articular cartilage showed gradual increase in deformation, as suggested by the usual biphasic model. These phenomena are likely to depend on the permeability, elastic (Young's) modulus, and structure of hydrogels. Detailed analysis for difference in deformation behaviors between PVA hydrogels and articular cartilage should be examined in further studies.

The high friction and constant compressive deformation of FT gel is considered to be due to biphasic properties with high permeability (Table 22.1). The interstitial fluid pressure in FT gel remarkably diminished after 292 s running as shown in Fig. 22.12, and therefore the fluid load support became small. The friction for FT gel in saline increased gradually as indicated by the curve for $\mu_{\text{solid}} = 0.2$ (Fig. 22.13). The frictional behavior for FT gel based on biphasic FE analysis with $\mu_{\text{solid}} = 0.01$ approximately corresponds to low friction in simulated synovial fluid.

In contrast, the low friction of CD gel with low permeability in saline is attractive because of the high interstitial fluid pressure sustained even after 292 s running. The measured coefficient of friction was lower than 0.05, and friction should be estimated by appropriate selection for $\mu_{\text{solid}} = 0.05$ or so to reflect the surface lubricity. Thus, the CD gel has considerably low friction property when pressed against a glass plate. In gel-on-gel combination, however, CD gels showed high friction and/or severe wear in saline and simulated synovial fluid [48]. Therefore, improvement of structure and properties of new hydrogels is necessary. We also [49,50] developed the hybridization of CD on FT gels, which showed better tribological performance in water lubrication. Related research on the hybrid gel indicated the superiority in tribological properties of promising hydrogels [51,52].

To summarize the important properties in optimum design of PVA hydrogels, it is pertinent to discuss the relation between the structures and properties of hydrogels. The material properties and structures in both PVA hydrogels appear to depend on the structure controlled by hydrogen bond. The schema for microstructure in PVA FT and CD hydrogels based on model proposed earlier [43,50] are shown in Fig. 22.10 [44]. The formation of hydrogen bonds and microcrystallites was identified using X-ray diffraction technique (XRD), Fourier transform infrared (FT-IR) spectroscopy, and measurements of the swelling ratio under repeated water exchanges [44]. Small-angle scattering indicates that the distance between microcrystallites in PVA-FT gel is shorter than in PVA-CD gel. As shown in Fig. 22.10, the milky white appearance of FT gel suggests the heterogeneous network



(a) Before test

(b) After test with HA 0.5 wt % and DPPC 0.01 wt%

(c) After test with HA 0.5 wt%, DPPC 0.01 wt%, Albumin 1.4 wt% and γ-Globulin 0.7 wt%

FIGURE 22.15 PVA-FT gel surfaces before and after reciprocating tests.

structure, and the transparency of CD gel indicates its uniform network structure. The network is generally composed of microcrystallites and amorphous zones. It is suggested that the fluid flows out rapidly from FT gel, which is composed of microcrystallites and considerable amorphous zones, as indicated by high permeability (Table 22.1), and porous texture in AFM image (Fig. 22.10). On the contrary, in the CD gel with low permeability, the fluid retained inside the gel flows out slowly, and thus the interstitial fluid pressure is maintained for a longer time under reciprocating tests. In reciprocating tests with an alumina ball placed against flat PVA hydrogel plates in pure water [49], the CD gel with low permeability showed lower wear and lower friction than did the FT gel with high permeability. The superiority of CD gel appears to be due to its better biphasic property in water.

Friction for biphasic materials under lubricated conditions is estimated from a combination of the friction for solid–solid contact and the negligibly low friction for fluid load support, as indicated in formula (22.1) for friction (above) [16,27], where high partitioning of load support by the fluid phase contributes to lowering of friction. Changes in load support in compliant hydrogels depend on not only permeability but also friction level for solid–solid contact. The lower friction for CD gel in saline (Fig. 22.11) appears to be caused by superior surface lubricity as $\mu_{\text{solid}} = 0.05$ or so as mentioned above. The smooth surface of CD gel may contribute to the reduction of friction in saline by suppressing interaction between rubbing surfaces. The rough and porous surface of FT gel may enhance interaction between rubbing surfaces in saline and increase friction, but improve the adsorbed film formation under lubricated conditions with a simulated synovial fluid resulting in low friction (Fig. 22.14) and minimum wear (Fig. 22.15 [41]). Elucidation of the exact lubrication mechanism for hydrogel should be continued in further studies.

Other improving methods for properties of PVA hydrogel are to additionally control the nanoscopic structure, to reinforce the structure with fibrous elements or other methods, and thus to enhance biphasic properties for efficient lubrication and load-carrying property. The PVA hydrogels based on the hydrogen-bonding network as physical bonding prepared without any additives or irradiative stimulus provides superior safety in the human body. The potential for restoration with hydrogen bonding in case of local fractures is an advantageous property.

For the clinical application of PVA hydrogel, durability, synergistic interaction with lubricants, ease of production, formability, appropriate fixation techniques, and other properties are required. In particular, the establishment of appropriate design in consideration of a multimode lubrication mechanisms not only for low friction but also for zero-wear and high fatigue resistance in the human body is required. To evaluate predictively the in vivo behaviors of two hydrogels, various studies such as those employing reciprocating tests and simulator tests should be conducted under biomechanically simulated environmental conditions. The desirable in vivo performance of PVA hydrogel implanted in rabbit knee joints in ongoing tests by a biomedical research group suggests the feasibility of clinical application. The optimization of tribological properties of hybrid gel will be actualized on the basis of the findings described above.

22.10 CONCLUSION

The superior lubricity of articular cartilage and artificial cartilage with high water content were described in reciprocating tests and biphasic FE analyses. The importance of adaptive multimode lubrication in both natural and artificial joints was discussed from the biotribological perspective under various operating conditions. In particular, friction and wear behaviors in reciprocating motion under continuous loading conditions were examined to clarify the effectiveness of biphasic lubrication and boundary lubrication. To mimic the performance of articular cartilage, two kinds of PVA hydrogels were prepared by repeated freeze–thawing and cast-drying methods. The application of biphasic finite-element analyses satisfactorily elucidated the time-dependent changes in load support ratio by fluid phase and friction. The roles of synovia constituents were discussed, accompanied by observation of adsorbed film formation in various experiments.

It was shown that the synergistic combination of biphasic lubrication and boundary lubrication becomes effective to sustain superior lubricity in articular cartilage and PVA hydrogels even at slow movement under continuous loading.

ACKNOWLEDGMENT

The authors express their thanks to Dr. S. Yarimitsu, Dr. K. Nakashima, Dr. T. Yamaguchi, Professor Y. Sawae of Kyushu University, and Dr. N. Sakai of Kyushu Institute of Technology for their contributions to this work. Most of recent research was supported by KAKENHI 23000011.

REFERENCES

[1] Charnley, J. (1979). *Low Friction Arthroplasty of the Hip*. Springer-Verlag.

[2] Ingham, E., Fisher, J. (2005). The role of macrophages in osteolysis of total joint replacement. *Biomaterials* **26**, 1271–1286.

[3] Murakami, T. (1990). The lubrication in natural synovial joints and joint prostheses. *JSME Int. J. III* **33**(4), 465–474.

[4] Murakami, T., Higaki, H., Sawae, Y., Ohtsuki, N., Moriyama, S., Nakanishi, Y. (1998). Adaptive multimode lubrication in

natural synovial joints and artificial joints. *Proc. Inst. Mech. Eng. H: J. Eng. Med.* **212**, 23–35.

[5] Murakami, T. (2013). Tribology of cartilage replacement. In Wang, Q.J., Chung, Y.-W. (eds.), *Encyclopedia of Tribology.* Springer, pp. 3854–3860.

[6] Dowson, D. (1966/67). Modes of lubrication in human joints. *Proc. Inst. Mech. Eng.* **181**(Pt. 3J), 45–54.

[7] Oka, M. (ed.) (1990). *Artificial Joints and Biomaterials.* Medical View.

[8] Mow, V.C., Hou, J.S., Owens, J.M., Ratcliffe, A. (1990). Biphasic and quasilinear viscoelastic theories for hydrated soft tissues. In Mow, V.C., et al. (eds.), *Biomechanics of Diarthrodial Joint*, Vol.1. Springer-Verlag, pp. 215–260.

[9] Mow, V.C., Kuei, S.C., Lai, W.M., Armstrong, C.G. (1980). Biphasic creep and stress relaxation of articular cartilage in compression theory and experiment. *J. Biomech. Eng*. **102**, 73–84.

[10] Dowson, D., Jin, Z.M. (1986). Micro-elastohydrodynamic lubrication of synovial joints. *Eng. Med.* **15**, 65–67.

[11] Forster, H., Fisher, J. (1996). The influence of loading time and lubricant on the friction of articular cartilage. *Proc. Inst. Mech. Eng. H: J. Eng. Med.* **210**, 109–119.

[12] Ateshian, G.A. (1997). Theoretical formulation for boundary friction in articular cartilage. *J. Biomech. Eng.* **119**(1), 81–86.

[13] Ateshian, G.A. (2009). The role of interstitial fluid pressurization in articular cartilage lubrication. *J. Biomech*. **42**, 1163–1176.

[14] Swann, D.A., Hendren, R.B., Radin, E.L., Sotman, S.L., Duda, E.A. (1981). The lubricating activity of synovial fluid glycoproteins. *Arthritis Rheum*. **24**, 22–30.

[15] Higaki, H., Murakami, T. (1996). Role of constituents in synovial fluid and surface layer of articular cartilage in joint lubrication (part 2) the boundary lubricating ability of proteins. *Jpn. J. Tribol.* **40**(7), 691–699.

[16] Hills, B.A. (1989). Oligolamellar lubrication of joints by surface active phospholipids. *J. Rheum.* **16**(1), 82–91.

[17] Higaki, H., Murakami, T., Nakanishi, Y., Miura, H., Mawatari, T., Iwamoto, Y. (1998). The lubricating ability of biomembrane models with dipalmitoyle phosphatidylcholine and γ-globulin. *Proc. Inst. Mech. Eng. H: J. Eng. Med.* **212**, 337–346.

[18] Murakami, T., Sawae, Y., Horimoto, M., Noda, M. (1999). Role of surface layers of natural and artificial cartilage. In Dowson, D., et al. (eds.), *Thin Film Lubrication in Lubrication at Frontier.* Elsevier, pp. 737–747.

[19] Sasada, T. (2000). Lubrication of human joints–nature of joint friction and "surface gel hydration lubrication" (in Japanese). *J. Jpn. Soc. Clin. Biomech.* **21**, 17–22.

[20] Ikeuchi, K. (2007). Origin and future of hydration lubrication. *Proc. Inst. Mech. Eng. J: J. Eng. Tribol.* **221**, 301–305.

[21] Klein, J. (2006). Molecular mechanisms of synovial joint lubrication. *Proc. Inst. Mech. Eng. J: J. Eng. Tribol.* **220**, 691–710.

[22] Klein, J. (2013). Hydration lubrication. *Friction* **1**, 1–23.

[23] Krishnan, R., Kopacz, M., Ateshian, G.A. (2004). Experimental verification of the role of interstitial fluid pressurization in cartilage lubrication. *J. Orthop. Res.* **22**, 565–570.

[24] Pawaskar, S.S., Jin, Z.M., Fisher, J. (2007). Modelling of fluid support inside articular cartilage during sliding. *Proc. Inst. Mech. Eng. J: J. Eng. Tribol.* **221**, 165–174.

[25] Sakai, N., Hagihara, Y., Furusawa, T., Hosoda, N., Sawae, Y., Murakami, T. (2012). Analysis of biphasic lubrication of articular cartilage loaded by cylindrical indenter. *Tribol. Int.* **45**, 225–236.

[26] Murakami, T. (2012). Importance of adaptive multimode lubrication mechanism in natural and artificial joints. *Proc. Inst. Mech. Eng. J: J. Eng. Tribol.* **226**, 827–837.

[27] Ateshian G.A., Wang, H., Lai, W.M. (1998). The role of interstitial fluid pressurization and surface porosities on the boundary friction of articular cartilage. *ASME J. Tribol.* **120**, 241–248.

[28] Murakami, T., Nakashima, K., Sawae, Y., Sakai, N., Hosoda, N. (2009). Roles of adsorbed film and gel layer in hydration lubrication for articular cartilage. *Proc. Inst. Mech. Eng. J: J. Eng. Tribol.* **223**, 287–295.

[29] Murakami, T., Nakashima, K., Yarimitsu, S., Sawae, Y., Sakai, N. (2011). Effectiveness of adsorbed film and gel layer in hydration lubrication as adaptive multimode lubrication mechanism for articular cartilage. *Proc. Inst. Mech. Eng. J: J. Eng. Tribol.* **225**, 1174–1185.

[30] Murakami, T., Yarimitsu, S., Nakashima, K., Sawae, Y., Sakai, N. (2013). Influence of synovia constituents on tribological behaviors of articular cartilage. *Friction* **1**(2), 150–162.

[31] Pasquali-Ronchetti, I., Quaglino, D., Mori, G., Bacchell, B. (1997). Hyaluronan-phospholipid interactions. *J. Struct. Biol.* **120**, 1–10.

[32] Yarimitsu, S., Nakashima, K., Sawae, Y., Murakami, T. (2010). Influences of synovia constituents on frictional behavior of artificial cartilage material and formation of boundary lubricating film (in Japanese). *Tribologist* **55**(7), 489–498.

[33] Nakashima, K., Sawae, Y., Murakami, T. (2005). Study on wear reduction mechanisms of artificial cartilage by synergistic protein boundary film formation. *JSME Int. J.* **48**(4), 555–561.

[34] Yarimitsu, S., Nakashima, K., Sawae, Y., Murakami, T. (2008). Effect of lubricant composition on adsorption behavior of proteins on rubbing surface and stability of protein boundary film. *Tribol. Online* **3**(4), 238–242.

[35] Yarimitsu, S., Nakashima, K., Sawae, Y., Murakami, T. (2009). Influences of lubricant composition on forming boundary film composed of synovia constituents. *Tribol. Int.* **42**, 1615–1623.

[36] Sasada, T., Tsukamoto. Y., Mabuchi, K. (1988). *Biotribology* (in Japanese). Sangyo Tosho.

[37] Oates, K.M.N., Krause, W.E., Jones, R.L., Colby, R.H. (2006). Rheopexy of synovial fluid and protein aggregation. *J. Roy. Soc. Interface* **3**, 167–174.

[38] Mirea, D.A., Trunfio-Sfarghiu, A.-M., Matei, C.I., Munteanu, B., Piednoir, A., Rieu, J.P., Blanchin, M.G., Berthie, Y. (2013). Role of the biomolecular interactions in the structure and tribological properties of synovial fluid, *Tribol. Int.* **59**, 302–311.

[39] Murakami, T., Sawae, Y., Higaki, H., Ohtsuki, N., Moriyama, S. (1997). Adaptive multimode lubrication in knee prostheses with artificial cartilage during walking. In Dowson, D., et al. (eds.), *Elastohydrodynamics'96: Fundamentals and Applications in Lubrication and Traction.* Elsevier Science, Amsterdam, pp. 371–382.

[40] Murakami, T., Sawae, Y., Nakashima, K., Fisher, J. (2000). In Dowson, D., et al. (eds.), *Thinning Films and Tribological Interfaces*, Vol. 38, Tribology and Interface Engineering Series. Elsevier Sciences, pp. 317–327.

[41] Murakami, T., Yarimitsu, S., Nakashima, K., Yamaguchi, T., Sawae, Y., Sakai, N., Suzuki, A. (2014). Superior lubricity in articular cartilage and artificial hydrogel cartilage. *Proc. Inst. Mech. Eng. J: J. Eng. Tribol.* **228**, 1099–1111.

[42] Nakashima, K., Murakami, T., Sawae, Y. (2000). Evaluation of tribological properties of polyvinyl alcohol hydrogel as artificial cartilage. *Proc. Int. Tribology Conf.* **2**, 1537–1540.

[43] Otsuka, E., Suzuki, A. (2009). A simple method to obtain a swollen PVA gel crosslinked by hydrogen bonds. *J. Appl. Polym. Sci.* **114**(1), 10–16.

[44] Otsuka, E., Suzuki, A. (2009). Swelling properties of physically cross-linked PVA gels prepared by a cast-drying method. *Progress Colloid. Polym. Sci*, **136**, 121–126.

[45] Otsuka, E., Sugiyama, M., Suzuki, A. (2010). Network microstructure of PVA cast gels observed by SAXS measurements. *J. Phys. Conf. Ser.* **247**, 012043.

[46] Yamaguchi, T., Murakami, T. (2013–2019). Surface friction and bulk transport properties in hydrogels. *Preprint JAST Conf*. (in Japanese), pp. 199–200.

[47] Murakami, T., Yarimitsu, Y., Nakashima, K., Sawae, Y., Sakai N, Araki, T., Suzuki, A. (2011). Time-dependent frictional behaviors in hydrogel artificial cartilage materials. *Proc. 6th Int. Biotribology Forum*, pp. 65–68.

[48] Yarimitsu, S., Nakashima, K., Sawae, Y., Murakami, T., Suzuki, A. (2014). Evaluation of friction and wear behavior of artificial hydrogel cartilage prepared by cast-drying method, *Abstract 2nd Int. Conf. Bio-Tribology*, Toronto.

[49] Suzuki, A., Sasaki, S., Sasaki, S, Noh, T., Nakashima, K., Yarimitsu, S., Murakami, T. (2013). Elution and wear of PVA hydrogels by reciprocating friction. *Extended Abstract for World Tribology Congress*, Torino, Italy.

[50] Suzuki, A., Murakami, T. (in press). High-strength poly(vinyl alcohol) hydrogels for artificial cartilage. In Ohshima, H. (ed.), *Encyclopedia of Biocolloid and Biointerface Science*. Wiley, Singapore.

[51] Murakami, T., Yarimitsu, S., Nakashima, K., Yamaguchi, T., Sawae, Y., Sakai, N., Suzuki, A. (2014). Evaluation of a superior lubrication mechanism with biphasic hydrogels for artificial cartilage. *Abstract for 2nd Int. Conf. Bio-Tribology*, Toronto.

23

SELF-ASSEMBLED CELL-MIMICKING VESICLES COMPOSED OF AMPHIPHILIC MOLECULES: STRUCTURE AND APPLICATIONS

Swati De and Ranju Prasad Mandal
Department of Chemistry, University of Kalyani, West Bengal, India

23.1 INTRODUCTION

The fundamental unit of life is the cell. For a long time, humans have been trying to mimic the cell and its functions by designing synthetic nanoreactors. Initial attempts to do so involved complicated synthesis. Self-assembled systems have been found to be easier to study than covalently linked systems. Among the most popular self-assembling substances are amphiphiles.

Amphiphile molecules have a hydrophobic part (tail) and a hydrophilic part (headgroup) (Fig. 23.1 and Table 23.1). Because of this dual nature, they self-assemble in aqueous solutions, assuming interesting structures [1–6]. The driving force for this self-aggregation is the *hydrophobic effect* [7], which arises mainly as a result of the entropic gain of the water structure as it is not in contact with the hydrophobic tails.

Phospholipids, such as DMPC and DPPC (Table 23.1), self-assemble in aqueous environments to form closed bilayer structures or vesicles. Usually lipids form lamellar bilayer structures but in dilute solutions they form vesicles (Latin *vesicula*, meaning "small bubbles"). The lipid building blocks of vesicles are often referred to as *tectons*. Vesicles are lamellar aggregates that curve to form a spherical structure that can enclose an inner aqueous compartment. This pioneering observation was first made by Bangham [8]. There is a close connection between vesicles and the constituting lipids, and so the terms *vesicle* and *liposome* (Greek *soma*, meaning "body"; i.e., body of lipids) are interchangeable. The importance of vesicles as potential membrane models was first noted by Gebicki and Hicks [9]. Later, Kunitake et al. [10] first showed that a completely synthetic amphiphile DDDAB (Table 23.1) can also form vesicles. In the present review, we will focus on vesicles formed by amphiphilic molecules and their varied applications.

23.2 PRINCIPLES OF VESICLE FORMATION

In this section, the factors guiding vesicle formation are discussed. The formation of vesicles can be viewed as a two-step process: (1) the amphiphile first forms a bilayer and then (2) the bilayer closes to form a vesicle.

23.2.1 Parameters

Broadly, the parameters described in the following sections guide vesicle formation.

23.2.1.1 Packing Parameter (p). The geometry assumed by an amphiphile-based self-assembly is described by the packing parameter (p) of the amphiphiles, which is defined as the ratio of hydrophobic volume (v_S) to the product of the headgroup area (a_S) and the chain length (l_S). This model of self-aggregation of phospholipids was developed by Israelachvili et al. [2].

$$p = \frac{v_S}{a_S \times l_S} \tag{23.1}$$

Encyclopedia of Biocolloid and Biointerface Science, Volume 1, First Edition. Edited by Hiroyuki Ohshima.
© 2016 John Wiley & Sons, Inc. Published 2016 by John Wiley & Sons, Inc.

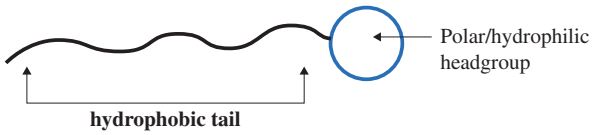


FIGURE 23.1 Amphiphile structure.

Table 23.2 shows the shapes of the predicted self-assembled structures, based on the value of p.

23.2.1.2 Interfacial Energy. The packing parameter (p) is based only on geometric considerations. However, there are free-energy factors that also drive self-assembly. The two main contributions to free energy are (1) interfacial energy of the hydrophobic–hydrophilic interface and (2) loss of entropy when the amphiphile tails are forced together to form a self-assembly.

When interfacial energy is large and entropy loss small, then the minimization of the interfacial area drives the self-assembly. Thus the self-assembly will be such that minimizes the interfacial area per unit volume (A_V) [11]:

$$A_V = \frac{d \times \Phi}{l_S} \tag{23.2}$$

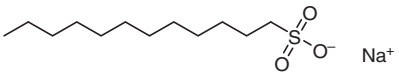
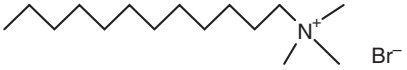
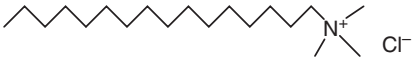
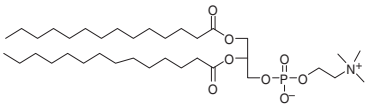
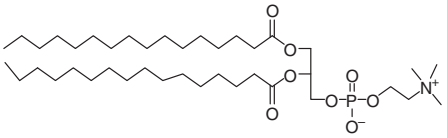
where

Φ = volume fraction of the hydrophobic domain
d = dimensionality
l_S = length of hydrophobic tail

Since dimensionality assumes the lowest value ($d = 1$) for planar interfaces, such interfaces will be preferably formed compared to cylindrical ($d = 2$) or spherical ($d = 3$) domains [11].

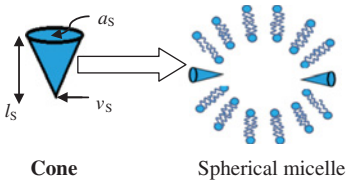
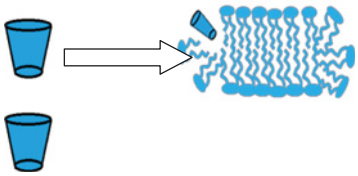
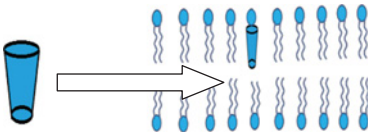
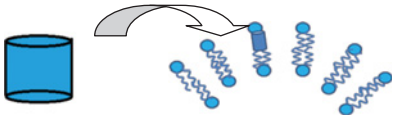
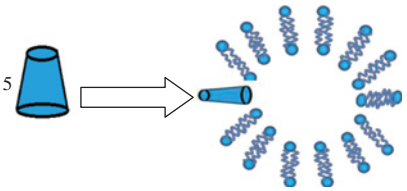
23.2.1.3 Bending Elasticity of Bilayer. Another factor that effects vesicle formation is the bending elasticity of the bilayer [11, 12] i.e. the resistance it offers to a deformation

TABLE 23.1 Some Common Amphiphilic Molecules

Full name (IUPAC)	Structure	Abbreviation
Sodium dodecyl sulfate		SDS
Dodecyltrimethyl ammonium bromide		DTAB
Cetyltrimethylammonium bromide		CTAB
Cetyltrimethylammonium chloride		CTAC
Dimethyldioctadecyl ammonium bromide		DDDAB
Dihexadecyldimethyl ammonium bromide		DHDAB
Dioctadecyldimethyl ammonium chloride		DODAC
Dimyristoylphosphatidyl choline		DMPC
Dipalmitoylphosphatidyl choline		DPPC

Source: From D.M. Vriezema et al., *Chem. Rev*. **105**, 1445–1489. Copyright © 2005 by American Chemical Society. Reprinted by permission of American Chemical Society.

TABLE 23.2 Effect of Packing Parameter (p) on Shape of Self-Assembled Amphiphilic Structures

Amphiphile	p	Shape	Structures formed
Single-chained amphiphiles with large headgroup area	$0 < p < \frac{1}{3}$		**Cone** Spherical micelle
Single-chained amphiphiles with small headgroup area	$\frac{1}{3} < p < \frac{1}{2}$		**Truncated cone** Cylindrical micelles
Double-chained lipids with large headgroup area	$\frac{1}{2} < p < 1$		**Truncated cone** bilayers
Double-chained lipids with small headgroup area	$p \sim 1$		**Cylinder** vesicles
Double-chained lipids with small headgroup areas, nonionic lipids	$p > 1$		**Inverted truncated cone** Inverted micelles

For $0 < p < \frac{1}{2}$, this model predicts the formation of micelles; for $\frac{1}{2} < p \leq 1$ vesicles are predicted and for $p > 1$, inverted micelles are predicted to form.

away from a spontaneous curvature of the bilayer. The circular rim of the bilayer disk gives rise to edge energy E_{disk}

$$E_{\text{disk}} = 2\pi R_{\text{V}}\gamma \tag{23.3}$$

where R_{V} = vesicle radius and γ = tension at the edge. This energy may be minimized by eliminating the edge if the bilayer closes to form a spherical vesicle [13] (Fig. 23.2).

However, there is an energy penalty, as bending of the bilayer to a closed vesicle requires a bending energy (E_{bend})

$$E_{\text{bend}} = 4\pi\chi \tag{23.4}$$

where χ = bending modulus. Thus the balance of edge tension and bending energy defines the *minimal vesicle size*; that is, when edge energy = bending energy, vesicle formation just begins

$$2\pi R_{\text{V}}\gamma = 4\pi\chi \tag{23.5}$$

so $R_{\text{V}} = 2\chi/\gamma$.

Thus vesicles easily form when the bilayer bending elasticity (χ) is low and the edge tension (γ) is high; in other words, hull closure to form a closed sphere provides adequate energy compensation (Fig. 23.2).

23.2.1.4 Rigidity of Bilayer and Transition Temperature (T_C). An important parameter in the formation of vesicular

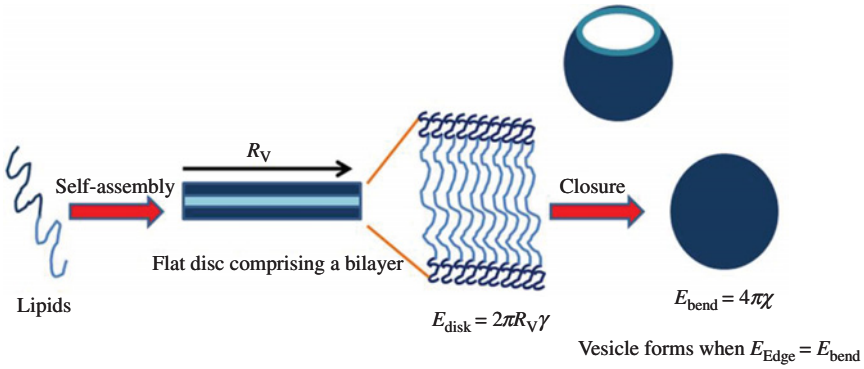


FIGURE 23.2 Energetics of curved vesicle formation from a planar bilayer. (From M. Antonietti et al., *Adv.Mater.* **15**, 1323–1333. Copyright © 2003 Wiley-VCH Verlag GmbH & Co. KGaA, Weinheim. Reprinted by permission of John Wiley & Sons.)

structures/liposomes is the rigidity of the bilayer. Phospholipid bilayers can exist in a liquid crystalline (*fluid*) state. or in a *gel* state. By increasing the temperature, the gel state bilayer "melts" at the transition temperature (T_C) and undergoes a transition from the gel into the liquid crystalline state. T_C depends on various factors, including lipid chain length, degree of saturation of lipid chain, and polar headgroup. Around T_C, bilayer permeability is very high. This is useful for triggered release of encapsulated matter.

Addition of a second component often changes bilayer characteristics. Addition of cholesterol to phosphatidylcholine bilayers alters the melting behavior of the bilayer since cholesterol prevents the phase transition. Usually, addition of cholesterol decreases bilayer permeability [14].

23.2.1.5 Formation of Nonequilibrium Vesicles. Often the shape and size of vesicles is guided by the preparation conditions (so-called nonequilibrium conditions). For such nonequilibrium vesicles, there is bilayer asymmetry [15], and many nonspherical shapes are possible [16].

These complex shapes arise only for nonequilibrium vesicles as equilibrium vesicles allow adjustment of V', that is, volume-to-area ratio by solvent permeation through the bilayer:

$$V' = \frac{6\pi^{1/2} \times V_S}{a_S^{3/2}} \tag{23.6}$$

Also the area differences (ΔA) are adjusted by rapid exchange of *tectons* between the inner and outer layers of the same vesicles or different vesicles:

$$\Delta A = A_{\text{inner leaflet}} - A_{\text{outer leaflet}} \tag{23.7}$$

23.3 CLASSICAL VESICLES

23.3.1 Classification

Vesicles can be classified according to their size and structure of the bilayer. Depending on the lipids used and the preparation conditions, the vesicles can vary widely in size and number of lamellae. Table 23.3 summarizes the classifications of vesicles based on size and bilayer structure. Figure 23.3 depicts the various types of vesicular structures.

Unilamellar vesicles comprise only one single bilayer (Fig. 23.3). Multilamellar vesicles (MLVs) consisting of many concentric shells of vesicles may also be formed [8,17]. These have an "onionlike" structure (Fig. 23.3) and are often termed "onion phases." Generally unilamellar vesicles are formed for dilute solutions of amphiphiles whereas MLVs are formed at high concentration.

23.3.2 Dynamic Processes Occurring in Vesicles

Vesicles are flexible and dynamic structures that exhibit Brownian motion in solution. Above T_C, vesicles can freely diffuse [18]. The diffusion rate of a vesicle is inversely proportional to size. The vesicles can also easily change shape (if the bilayer membrane is flexible). The amphiphiles making up the bilayer can diffuse laterally (Fig. 23.4). The

TABLE 23.3 Vesicle Classification Based on Size and Bilayer Structure

Type of vesicle	Abbreviation	Diameter (d)
Small unilamellar vesicles	SUV	20–100 nm
Large unilamellar vesicles	LUV	>100 nm
Giant unilamellar vesicles	GUV	>1 μm
Oligolamellar vesicles	OLV	0.1–1 μm
Multilamellar large vesicles	MLV	> 0.5 μm
Multivesicular vesicles	MVV	> 1 μm

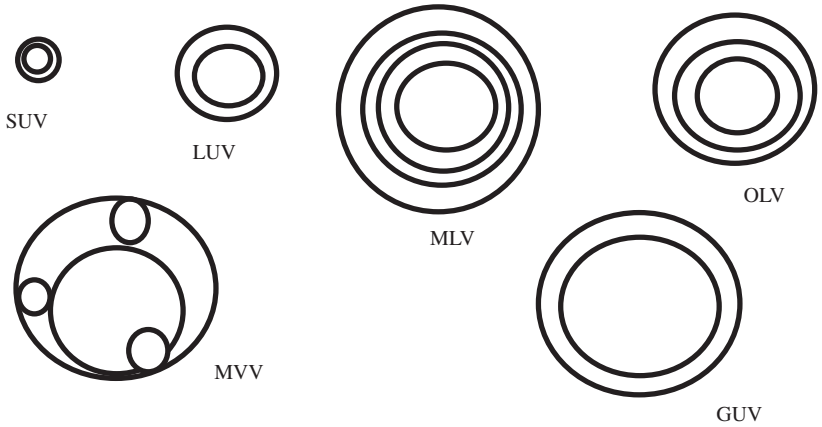


FIGURE 23.3 Morphology of different types of vesicles.

diffusion rate k_{diff} is high for shorter tails and higher temperatures. The amphiphiles can also undergo "flipflop" motion or transverse diffusion from the inner leaflet to the outer leaflet and vice versa (Fig. 23.4). This rate (k_{ff}) is high for short tails and at high temperatures. Amphiphiles can also temporarily leave the vesicle, diffuse in the surroundings and then finally come back to a vesicle. The rate of this exchange process is denoted by k_{ex} (Fig. 23.4).

Vesicles can also interact with one another to undergo aggregation, fusion and fission [18]. Aggregation is the formation of large clusters of vesicles while retaining the individual vesicular structure; that is, there is no mixing or leakage of the contents of the vesicles.

Fusion (Fig. 23.5) in the present context is the merging of smaller vesicles into larger ones. As a result, their membrane components and inner contents mix. *Fission* is the reverse of fusion; that is, smaller vesicles are formed from larger ones. These phenomena of aggregation, fusion and fission of vesicles bear strong resemblance to cellular processes such as endocytosis, exocytosis, and cell division [19].

23.3.3 Formation of Vesicles

Since the curvature energy of a bilayer in vesicles is higher than in the planar lamellar phase, energy is required to generate vesicles. Usually all the techniques employed for vesicle formation rely on some energy-providing mechanism. However, in some cases, spontaneous vesicle formation has also been observed.

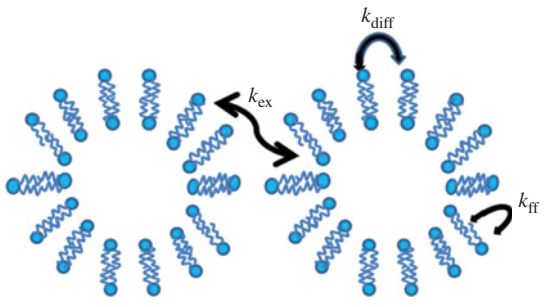


FIGURE 23.4 Dynamic processes occurring in vesicles.

23.3.3.1 Spontaneous Formation of Vesicles. In spontaneous formation process of vesicles, no external driving force is required. The classic example of spontaneous vesicle formation is for *catanionic* systems, where vesicles are obtained by mixing a cationic and an anionic surfactant [20, 21].

Spontaneous vesicle formation is also observed at low concentration in the binary phase diagrams of nonionic single-chain surfactants [22]. Such vesicles are stabilized by the addition of a rigid molecule such as cholesterol [23].

23.3.3.2 Energy-Driven Methods for Formation of Vesicles. There are several techniques for preparation of vesicles [13, 14,18,24–26]. All the different preparation procedures rely on two basic strategies: (1) hydration of lipid and (2) sizing of vesicles. In some methods, strategies 1 and 2 are combined together. Table 23.4 summarizes the common methods used for vesicle preparation.

1. *Lipid Film Hydration Method.* The phospholipid is dissolved in a suitable organic solvent in a round-bottomed flask. The solvent is then evaporated under reduced pressure using a rotary evaporator. The residual film consisting of the phospholipid bilayer is then hydrated with aqueous phase [25–27]. Although a large fraction of the vesicles obtained are MLVs, some GUVs may also be formed. The preferential formation of MLVs or GUVs is guided by the bilayer stacking during hydration stage (Fig. 23.6 summarizes this concept) [13].

   If the rate of bilayer separation is slow, MLVs are formed (Fig. 23.6a). If the rate of bilayer separation is high, GUVs are formed (Fig. 23.6b).

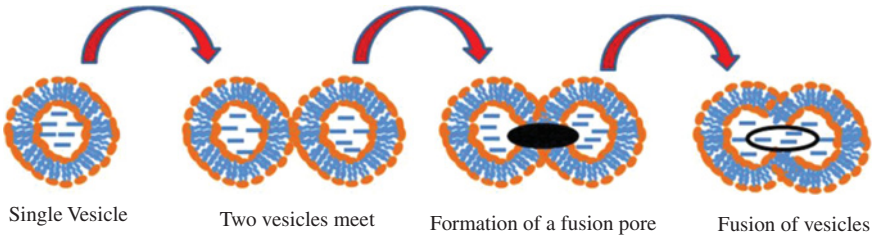


FIGURE 23.5 Vesicle fusion.

2. *Ether Injection Method*. This method was first reported by Bangham [17]. A lipid solution in diethyl ether is slowly injected into an aqueous solution at 50–60°C and under reduced pressure. Subsequently, ether vaporizes leading to the formation of unilamellar vesicles. Depending upon the condition employed, SUVs or LUVs are obtained. Two other investigators [28] developed a similar method but using ethanol instead of ether.
3. *Sonication Method.* The aqueous phase can be added to the surfactant/cholesterol mixture in organic solvent and the mixture then sonicated using a probe sonicator for a brief time period (3 min). This produces MLVs [29]. Sometimes, vigorous shaking or vortexing is required for homogenization.
4. *Reverse-Phase Evaporation*. Here a lipid-containing organic solvent (chloroform or ether) is emulsified with an aqueous phase by sonication [30]. This results in a water-in-oil (w/o) emulsion. Controlled removal of the organic phase using rotary evaporator results in LUVs as well as MLVs. Lower phospholipid concentrations yield a higher percentage of LUVs compared to MLVs. A critical step in this procedure is when most of the organic solvent has evaporated. A gel is then formed; this needs vigorous vortexing to be converted into a fluid state. One group of researchers have proposed many variations to this method [31].
5. *Solvent Spherule Method*. Rapid mixing of an organic phospholipid phase and an aqueous phase produces an oil-in-water (o/w) emulsion containing small spherules of lipid-containing solvents. This is followed by removal of organic phase thus resulting in the conversion of the spherules into MLVs [32].
6. *Hydration of Proliposomes*. Proliposomes are stable and dry powders containing a phospholipid and encapsulated material, such as a drug. These are formed by drying an organic solution of a phospholipid and drug resulting in particles consisting of a drug at the core encapsulated by a phospholipid shell. The organic phase can be removed in a rotary evaporator [33]. These proliposomes form MLVs when hydrated (Fig. 23.7).
7. *Detergent Dialysis*. This method is commonly used to produce LUVs. Here, phospholipids are solubilized in aqueous phase using surfactant micelles. Dialysis

TABLE 23.4 Methods of Vesicle Preparation and Type of Vesicle Formed

Method	Type of vesicle formed
Lipid film hydration	MLVs and GUVs
Ether injection method	SUVs, LUVs
Sonication	MLVs
Reverse-phase evaporation	LUVs, MLVs
Solvent spherule method	MLVs
Hydration of proliposome	MLVs
Detergent dialysis	LUVs
Reducing size and lamellarity of MLVs	LUVs, SUVs
Microfluidization	SUVs, LUVs
Electroformation	GUVs
Membrane contactor method	LUVs
Freeze drying of double emulsions	SUVs
Vesicle preparation by curvature tuning	SUVs
Hydration of phospholipids deposited on nanomaterials	SUVs, LUVs
Using supercritical fluids	LUVs

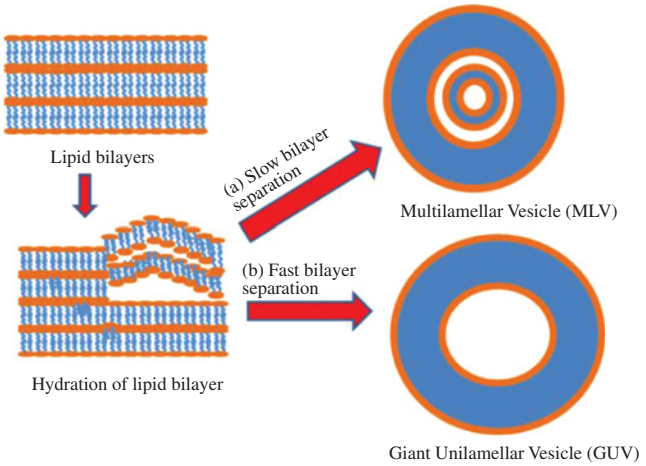


FIGURE 23.6 Formation of MLVs and GUVs by lipid film hydration method. (From Y.P. Patil et al., *Chem. Phys. Lipids* **177**, 8–18. Copyright © 2014 Elsevier. Reprinted by permission of Elsevier.)

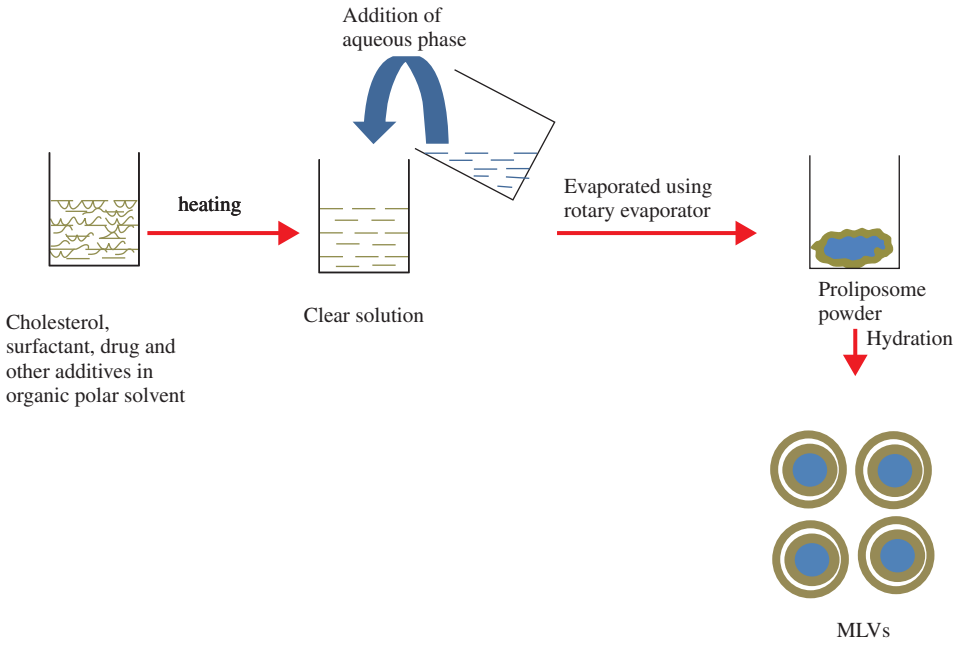


FIGURE 23.7 Formation of liposomes from proliposomes. For a color version of this figure, see the color plate section.

results in coalescence of the phospholipid rich micelles to form LUVs [34].

8. *Reducing Size and Lamellarity of MLVs*. MLVs can be easily formed. SUVs and LUVs ($d\sim$ 30–50 nm) can then be formed from MLVs by using French press [35, 36], sonication [29], homogenization [37], and membrane extrusion [38, 39]. The French press technique involves the extrusion of MLV suspensions at high pressure through a small orifice resulting in SUVs [35, 36]. Homogenization involves pumping of the vesicular suspension through an orifice and subsequent collision with a stainless steel wall at very high pressure to break down the MLVs. However, membrane extrusion is the most common method for converting MLVs to SUVs and LUVs [38, 39]. In this method, an MLV containing suspension is extruded several times through the pores of an etched polycarbonate membrane resulting in smaller vesicles. The minimum vesicle size attainable is governed by membrane pore size [40].
9. *Microfluidization*. This is one of the latest and most effective techniques for vesicle preparation. It involves fluid flow in narrow channels of cross section <500 μm. There is a detailed review on vesicle preparation using microfluidization [41]. The microhydrodynamic focussing (MHF) technique was first proposed by Jahn et al. [42] for preparing monodisperse SUVs and LUVs. This involves the counter diffusive flow of an aqueous buffer and solution of a phospholipid in isopropyl alcohol (Fig. 23.8).

This leads to some zones of low alcohol content where the phospholipids are forced to self-assemble into bilayers which finally close to form vesicles. In a variation of this technique, GUVs of diameter 4–20 μm form when two immiscible oil and water phases are made to flow in a single microchannel [43] using sorbitan monooleate and sterylamine as emulsifiers. Subsequently, the water droplets are frozen and removed from the oil phase by precipitation. The ice particles are then introduced into a hexane solution of a phospholipid. Evaporation of hexane followed by hydration results in the formation of GUVs. Water-in-oil-in-water (w/o/w) double emulsions containing a phospholipid in toluene–chloroform mixture, when subjected to a microfluidic process as above also results in GUVs [44] (Fig. 23.9).

10. *Electroformation*. Here, the phospholipid film deposited on electrodes is hydrated in presence of an electric field. This results in monodisperse GUVs. More GUVs can be formed, when thin films of phospholipids are obtained by spin coating the corresponding solutions on ITO slides [45] or on silicon wafers [46].
11. *Membrane Contactor Method*. Here a phospholipid solution in ethanol is extruded into an aqueous phase using a membrane contactor (Fig. 23.10) [47]. A tubular porous glass membrane with mean pore size 900 nm was initially used as the membrane contactor. Later polypropylene hollow fibers were used [48]. The main advantage of this method is the

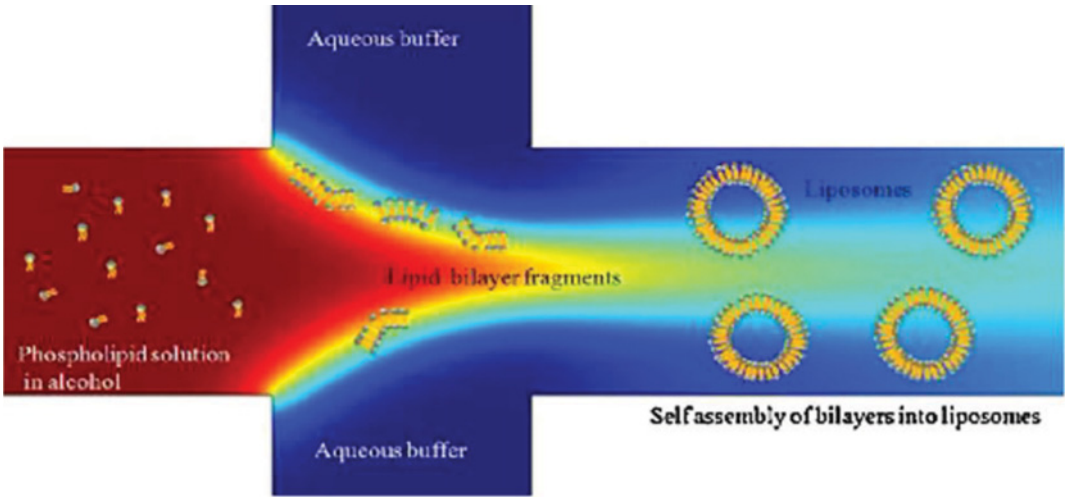


FIGURE 23.8 Formation of vesicles/liposomes by the MHF technique. (From Y.P. Patil et al., *Chem. Phys. Lipids* **177**, 8–18. Copyright © 2014 by Elsevier. Reprinted by permission of Elsevier.)

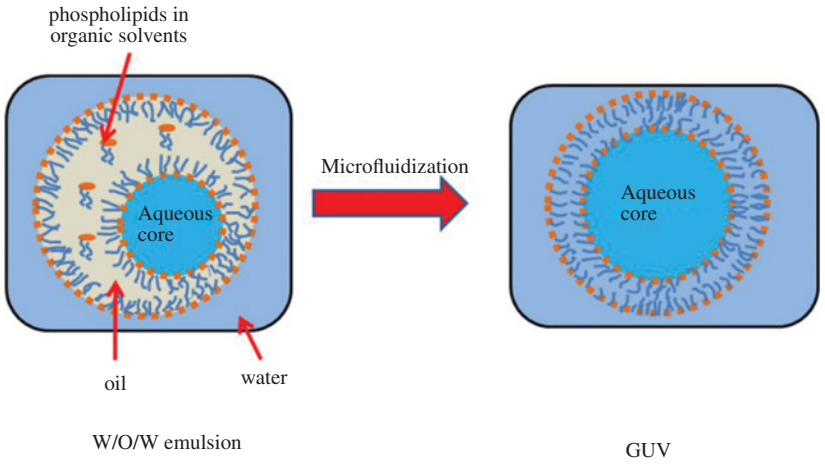


FIGURE 23.9 Formation of GUVs using w/o/w double emulsion. (From Y.P. Patil et al., *Chem. Phys. Lipids* **177**, 8–18. Copyright © 2014 by Elsevier. Reprinted by permission of Elsevier.)

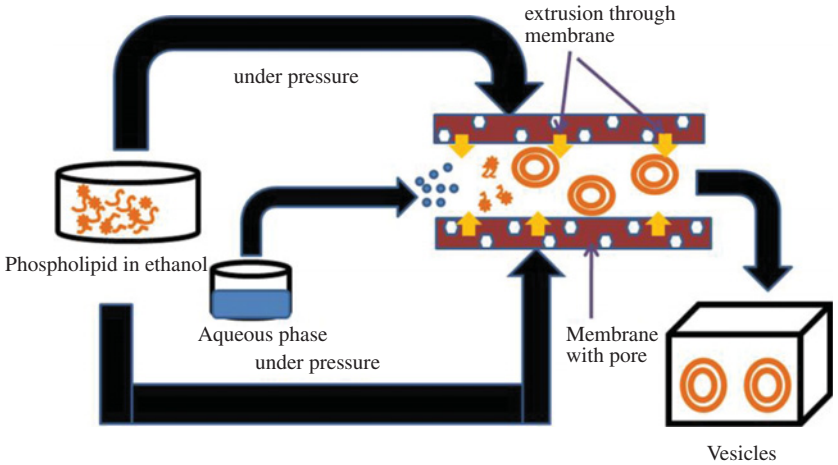


FIGURE 23.10 Formation of vesicles using a membrane contactor.

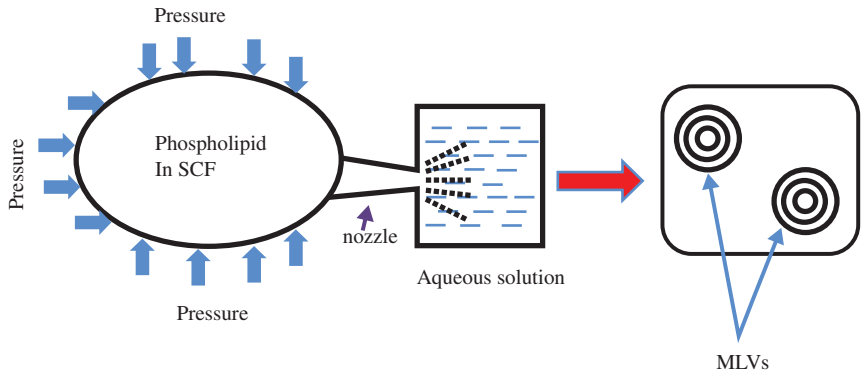


FIGURE 23.11 Preparation of MLVs using supercritical fluids.

possibility for continuous operation and large-scale applications.

12. *Freeze Drying of Double Emulsion*. Freeze drying of lipids dissolved in *t*-butyl alcohol/water system results in lipid cakes. Hydration of these cakes leads to MLVs that can be converted to LUVs/SUVs by extrusion [49].
13. *Vesicle Preparation by Curvature Tuning*. The contributions of various factors such as bilayer spontaneous curvature and curvature-induced stress to vesicle formation have been reviewed [50]. Spontaneous vesicle formation can be achieved using a rapid change of pH whereby MLVs can be converted to SUVs [51]. One team of investigators [52] introduced a novel modification to this using a *solventless* method. Charged lipids were mixed with lysopalmitoyl phosphatidylcholine and then subjected to rapid pH change to generate SUVs [52]. This obviates the need to prepare MLVs in the first step.
14. *Hydration of Phospholipids Deposited on Nanomaterials*. Vesicles can also be formed by hydration of phospholipids that have been previously deposited on electrospun amphiphilic nanofibers, composed of polymers [53]. Spontaneous vesiculation was observed on adding the nanofibers to water. The nanofibers acted as templates for self-assembly of lipids. The vesicular size is determined by the phospholipid: polymer ratio in the nanofiber, that is, by its hydrophilicity.
15. *Vesicle Preparation Using Supercritical Fluids*. Supercritical fluids (SCFs), such as carbon dioxide, are being increasingly used instead of organic solvents because of some of their useful properties. The use of SCFs for preparing vesicles has been reviewed [54]. MLVs can be prepared by taking a compressed mixture of the phospholipid, SCF, and an organic cosolvent and injecting this mixture through a nozzle into aqueous phase (Fig. 23.11).

A supercritical antisolvent (SAS) method was used to prepare small vesicles [55]. In this method, the organic cosolvent containing the phospholipid is sprayed into the supercritical fluid, which acts as the antisolvent leading to precipitation of the lipid particles. These particles on hydration in aqueous buffer form vesicles.

23.4 NOVEL VESICULAR SYSTEMS–GOING BEYOND LIPIDS

In the previous section, the classical vesicular systems solely based on phospholipids were discussed. The phospholipid based vesicles, although being very efficient drug delivery agents, suffer from two important drawbacks: (1) high formulation cost and (2) limited stability [56,57]. Because of the presence of ester bonds, phospholipids are easily hydrolyzed [56]. They are also prone to peroxidation processes [57]. These inherent disadvantages of the phospholipid vesicles were key factors that led to the development of other vesicular systems that can overcome these drawbacks. A number of such novel vesicular systems (discussed below) have been developed over the years (Table 23.5).

TABLE 23.5 Novel Vesicular Systems

Vesicular system	Principal components
Niosomes	Nonionic surfactant, cholesterol, and water
Ethosomes	Phospholipids, alcohol (high amount), and water
Transferosomes	Phospholipids, surfactants, alcohol, and aqueous buffer
Sphingosomes	Sphingolipids, cholesterol, and acidified water
Pharmacosomes	Colloidal dispersions of drugs covalently bound to lipids
e-Liposomes	A liposome encapsulating an emulsion nanodroplet
Polymerosomes	Polymer-based vesicles
Catansomes	Pair of oppositely charged surfactants forming a vesicle

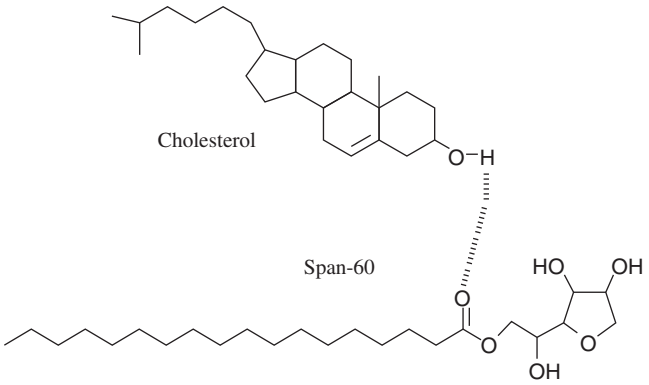


FIGURE 23.12 Noncovalent interactions between cholesterol and Span 60.

23.4.1 Niosomes

Niosomes are vesicles consisting mainly of nonionic surfactant and cholesterol. They were introduced by Handjani-Vila et al. in 1979 [58]. Niosomes have longer shelf life and stability than do conventional lipid vesicles, and they also possess the ability for targeted drug delivery in a controlled and sustained manner [59–64]. Niosomes were first introduced commercially for cosmetic applications by L'Oreal.

Vesicle formation is known to depend on *hydrophile–lipophile balance* (HLB). Thus HLB is a valuable guideline for choice of nonionic surfactants for niosome formulations. With the sorbitan esters of fatty acids (i.e., Spans), niosome formation occurs for HLB = 4–8 [60]. On the other hand, hydrophilic surfactants with HLB = 14–17 cannot form vesicles because of their high aqueous solubility [64]. Alkyl ether and ester surfactants can also be used for niosome formulation [59–62,65,66].

Cholesterol is added in niosomal formulations as it can interact with nonionic surfactants [67] (Fig. 23.12). Cholesterol modulates bilayer permeability, niosome fluidity, and vesicle rigidity [58,59,68]. Increasing the cholesterol content leads to a more homogeneous size distribution of niosomes and also smaller niosomes [69].

Often diacetyl phosphate is added as it is known to increase vesicle size, lead to vesicle charging, and also increase entrapment efficiency [66]. The niosomal bilayers (e.g., for phospholipid bilayers) are in either the gel or liquid state, depending on the temperature. The phase transition temperature (T_C) of the nonionic surfactant affects its entrapment efficiency. Span 60, which has a higher T_C (Table 23.6), forms "less leaky" niosomes at ambient temperature (~25°C) as it is in the ordered gel state. So Span 60 niosomes show higher entrapment efficiency than Span 20 or 80 niosomes [66]. Our work on gold nanoparticle synthesis is in concurrence with these findings [69].

Unlike phospholipid vesicles, niosomes are easier to prepare as nonionic surfactants are resistant to aerial oxidation.

TABLE 23.6 HLB Values and T_C of Some Sorbitan Esters

Surfactant	HLB	T_C (°C)	Chain length (number of carbons)
Span 20	8.6	16	C12 (monolaurate)
Span 40	6.7	42	C14 (monopalmitate)
Span 60	4.7	50	C18 (monostearate)
Span 80	4.3	~12	C18 (monooleate)

The same method as used for conventional vesicles can be used here. Often, in pharmaceuticals, the proniosome method is employed as a "ready to use" application [70]. The proniosome powders may be processed to form beads, tablets, or capsules. By this method aggregation, fusion and leaking can be prevented.

23.4.2 Ethosomes

Ethosomes are novel vesicular systems used for dermal and transdermal delivery of drugs to the skin [71–74]. Ethosomes are soft lipid vesicles that contain phospholipids, high concentration of alcohol (ethanol or isopropyl alcohol), and water. In comparison to phospholipid vesicles without ethanol, ethosomes have a more loosely packed bilayer. Differential scanning calorimetry indicates that ethosomal bilayers have a lower T_C compared to other bilayers [71]. The bilayers in ethosomes are thus highly fluid, facilitating deeper skin penetration. Ethosomes are generally unilamellar vesicles.

23.4.3 Transferosomes

Transferosomes overcome the shortcomings of the liposomal and niosomal systems for transdermal drug delivery, namely, poor skin permeability, leakage, and aggregation [75]. The transferosome consists of a lipid bilayer with specially tailored properties, due to the incorporation of *edge activators* into the bilayer [75]. Suitable edge activators are the bile salts, such as sodium cholate, sodium deoxycholate, and the nonionic surfactants Span 80 and Tween 80. A 3–10% alcohol (ethanol) solution is also added along with aqueous phase. Transferosomes can disrupt the organized structure of lipids in the stratum corneum of skin [77,78]. Transferosomes may be MLVs or LUVs.

23.4.4 Sphingosomes

Sphingosomes are clinically employed delivery systems for chemotherapy [79]. To overcome the instability of ester-based lipids, ether- or amide-linkage-containing lipids (sphingolipids) are used [80,81]. A *sphingosome* is a bilayered vesicle where the inner aqueous compartment is entirely enclosed by a natural or synthetic sphingolipid/cholesterol

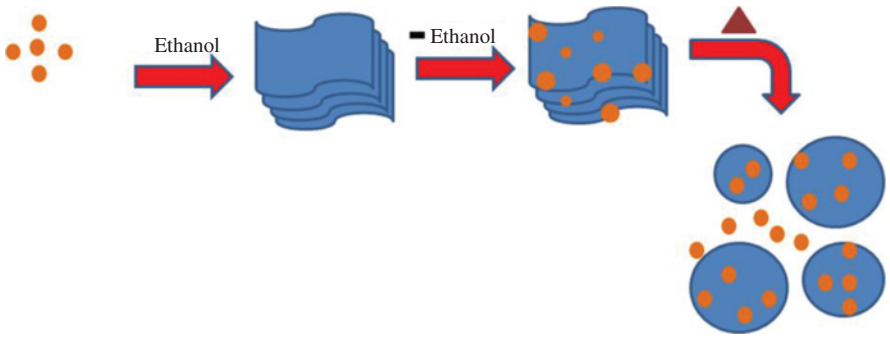


FIGURE 23.13 Mechanism for the formation of e-liposomes.

bilayer. The sphingolipids have longer circulation times and slower release rates compared to other lipids. Sphingosomes are usually prepared by the Bangham film method [17] forming MLVs. These MLVs can be reduced in size via extrusion through a polycarbonate membrane, through sonication, or using French press. Small unilamellar sphingosomes can interact with target cells via adsorption, endocytosis, and fusion (merging) of the sphingolipid bilayer with the plasma membrane of the cell to release the drug in the cytoplasm.

23.4.5 Pharmacosomes

When drugs linked to lipids form vesicles, they are called *pharmacosomes*. These can easily pass through biomembranes. Drugs having active functionalities such as –COOH, –OH, and $–NH_2$ can be linked to the lipid molecule producing an amphiphilic prodrug [82]. Pharmacosomes are site-specific, thus reducing drug toxicity. Pharmacosomes are prepared from the prodrug by ether injection or by hand-shaking.

23.4.6 e-Liposomes

An *echogenic liposome* or an *e-liposome* is a vesicle/liposome encapsulating an emulsion nanodroplet [83,84]. e-Liposomes are useful in drug delivery applications. Drugs are encapsulated inside the e-liposomes and on application of ultrasound, the emulsion changes from liquid to gas, thus increasing the volume inside the vesicle and causing vesicle rupture with subsequent drug release.

First small (< 100-nm) vesicles are formed and then ethyl alcohol is added. The alcohol interacts with polar region of the membrane and causes the spherical vesicles to unfold into sheets. Then alcohol is removed by centrifugal separation but the sheet remains stable at temperatures below the T_C of the lipids. Next, a nanoemulsion of a high-vapor-pressure liquid, such as perfluorohexane or perfluoroheptane, is added to the sheets and heated to $\leq$50°C (above T_C of the lipids). Now the e-liposome forms spontaneously, entrapping the emulsion (Fig. 23.13).

Dynamic light scattering indicates the e-liposomes to be 400–1200 nm in diameter (Fig. 23.14a). Cryo-TEM images of e-liposomes are shown in Fig. 23.14b.

The cryo-TEM images indicate an outer lipid membrane encapsulating the emulsion droplet.

23.4.7 Polymerosomes

To overcome the problems of using liposomes for drug delivery (mentioned earlier), various strategies have explored the use of polymers to reinforce the bilayer and prevent vesicle fusion. The polymerosome is formed from a block copolymer that is organized in a bilayer enclosing an aqueous internal cavity [85–87]. Polymerosomes are prepared by the film hydration method discussed earlier.

Because of the larger thickness of polymer bilayers (5–20 nm) compared to lipid bilayers (3–5 nm), the release rates from polymerosomes are slower. Also the stability of polymer vesicles are higher. Polymerosomes have been used for delivery of anticancer drugs such as paclitaxel (hydrophobic) and doxorubicin (hydrophilic) [88]. The latter is encapsulated in the internal cavity, whereas the former is incorporated into the bilayer during polymerosome formation to form a *polymer–drug cocktail* [88], which shows higher apoptosis in tumors than do the two drugs administrated separately.

To stabilize liposomes and achieve long circulation, poly(ethylene glycol) (PEG) can be been added to liposomes to produce "stealth liposomes" [89]. PEG provides steric hindrance and prevents fusion of the liposomes. This brings about an enhancement in the *in vivo* circulation times.

23.4.8 Catansomes

The spontaneous formation of vesicles from a mixture of single-chain cationic and anionic surfactants was first reported first by Kaler [21]. Since then a lot of work has been done [22].

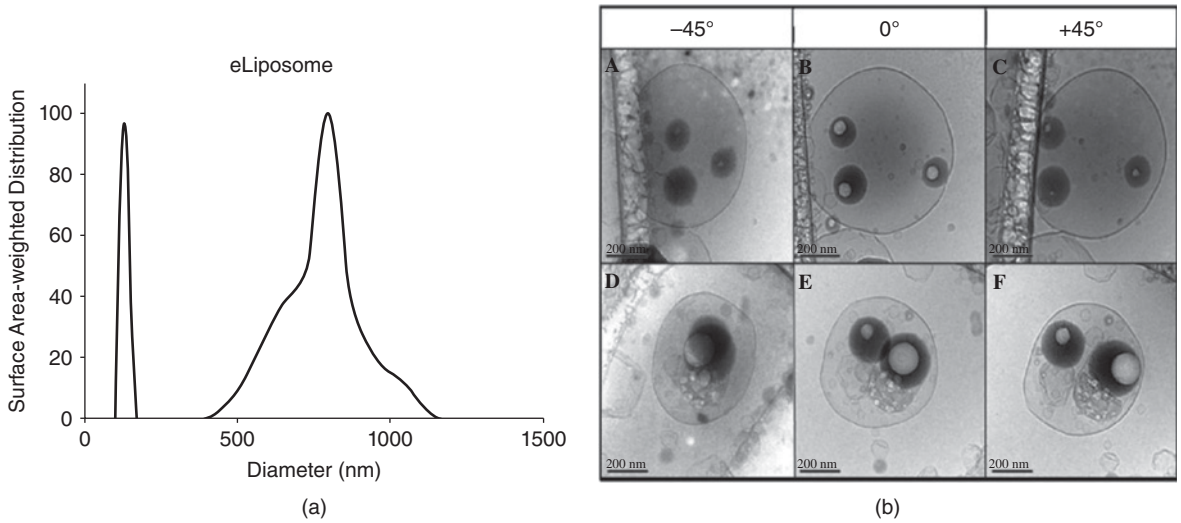


FIGURE 23.14 (a) Dynamic light scattering results for e-liposomes; (b) cryo-TEM images of e-liposomes. (Both images from J.R. Lattin et al., *Colloids Surf. B: Biointerfaces* **89**, 93–100. Copyright © 2012 by Elsevier. Reprinted by permission of Elsevier.)

23.5 VESICLE CHARACTERIZATION TECHNIQUES

Since the functioning of vesicles is strongly dependent on their properties such as size, shape, lamellarity, and surface charge, accurate characterization of vesicles is necessary. Table 23.7 lists the various characterization techniques for vesicles.

23.5.1 Morphology

Several electron microscopy techniques can be employed to study the size and morphology of vesicles. These include scanning electron microscopy (SEM), transmission electron microscopy (TEM), cryo-TEM, freeze–fracture transmission electron microscopy (FF-TEM), atomic force microscopy (AFM) [90], and scanning tunneling microscopy (STM). Optical microscopy is used to visualize the vesicles and also provide a rough estimate of their size.

TABLE 23.7 Some Popular Vesicle Characterization Techniques

Niosome parameter	Technique used
Morphology	SEM, TEM, freeze fracture electron microscopy, optical microscopy
Size distribution	Dynamic light scattering (DLS), SEC, AFFF, Coulter counter
Membrane thickness	SAXS
ξ- potential	Electrophoretic mobility
Stability	DLS, release studies
Entrapment efficiency	Centrifugation, dialysis, gel chromatography, HPLC, fluorescence, UV–visible spectroscopy
In vitro release	Dialysis using membranes
pH sensitivity assessment	Fluorescence spectroscopy

Abbreviations: AFFF–asymmetric field flow fractionation; HPLC—high-pressure liquid chromatography; SAXS—small-angle X-ray scattering; SEC–size exclusion chromatography; SEM–scanning electron microscopy; TEM–transmission electron microscopy.

23.5.2 Size Distribution

Size (diameter) of vesicles can be determined using dynamic light scattering (DLS) or photon correlation spectroscopy (PCS). DLS provides accurate information on the particle size and size distribution. One limitation of DLS is that it does not provide information on the shape of the system.

Size exclusion chromatography (SEC) may be used to fractionate vesicular population on the basis of their hydrodynamic size [91]. Another recent technique is *asymmetric field flow fractionation* (AFFF) [92]. This technique depends on the application of an external field (electric/magnetic/centrifugal force) in a direction perpendicular to the flow of a colloidal suspension. It can be used to measure size distribution of highly polydisperse samples.

23.5.3 Membrane Thickness, Lamellarity, and Fluidity

Vesicles can be morphologically classified according to the number of membrane bilayers (lamellae) into uni- and multilamellar vesicles. The number of lamellae can be determined by AFM, NMR, small-angle X-ray scattering (SAXS) [93], and electron microscopy [94]. The fluidity of the membrane can be assessed by fluorescence studies [95].

TABLE 23.8 Some Popular Liposomal Drug Formulations

Product	Drug	Company	Disease
Ambisome	Amphotericin B	Gilead	Fungal infection [101]
Doxil	Doxorubicin	Johnson & Johnson	Ovarian cancer [102],breast cancer
Daunoxome	Daunorubicin	Galen	Kaposi's sarcoma [103]
Marqibo	Vincristine	Talon	Acute lymphoblastic leukemia [104]

Source: From T.M. Allen et al., *Adv. Drug Deliv. Rev*. **65**, 36–48. Copyright © 2013 by Elsevier. Reprinted by permission of Elsevier.

The microviscosity of the membranes can be determined by fluorescence polarization studies [96].

23.5.4 Zeta-Potential and Surface Properties

The stability of vesicles is highly dependent on surface charge or ξ-potential. ξ-potential can be measured using a DLS instrument or by measuring electrophoretic mobility using laser Doppler velocimetry [97].

23.5.5 Stability

There is no direct method for estimating the stability of vesicles. However, DLS studies on a time-dependent basis can provide an idea about vesicular stability.

23.5.6 Entrapment Efficiency

The entrapment efficiency (EE) of vesicles is defined as the amount of active substances loaded within the vesicular structure and can be expressed as

$$\text{EE} = \frac{\text{amount entrapped}}{\text{total amount}} \times 100 \qquad (23.8)$$

where total amount = amount of the drug used in the preparation. The EE can be determined by various methods. One is by separating the unentrapped drug by dialysis or gel filtration. EE can also be determined fluorimetrically using a marker.

23.5.7 In Vitro Release Study

The *in vitro* drug release can be studied by using a dialysis tubing [98]. The vesicles containing encapsulated drugs are placed in prewashed dialysis tubing, which can be sealed. The dialysis sac is then dialyzed against a suitable dissolution medium. Samples are taken out at regular time intervals and centrifuged, and the supernatant is analyzed for drug content using UV spectroscopy, HPLC, and other techniques.

23.5.8 pH Sensitivity Assessment

Often vesicular drug delivery systems are targeted for internal delivery via endocytosis. They experience a gradual decrease in pH, and thus many vesicular formulations have been developed to exploit this factor. pH sensitivity assessment of vesicular drug delivery systems has also been used to evaluate bilayer thickness [99].

23.6 APPLICATIONS OF VESICLES

23.6.1 Drug Delivery

The concept of drug delivery using carrier molecules was first proposed by Paul Ehrlich in 1909, when he proposed the idea of "magic bullets." Later, it was established that liposomes can indeed entrap drugs and can be used as drug delivery systems (DDSs) [100]. Then followed extensive studies employing liposomal amphotericin [101] and liposomal doxorubicin [102], and these studies ultimately led to the first clinical trials for drugs based on liposomes. Since then, liposomal systems have served as the most clinically established DDSs to deliver drugs, genes, and vaccines [85]. (Table 23.8 summarizes a few of the popular clinically approved liposomal products.)

The recent past has witnessed the development of a new generation of liposomal DDS, specifically, those that respond to stimuli (i.e., temperature, pH, ultrasound, light, enzymes). More recently, other groups [105, 106] have published extensive reviews on triggered-release liposomal DDS. The first of these were the temperature sensitive liposomal DDS; for example, delivery of liposomal methotrexate was fourfold higher in heat-treated tumors than in nonheated ones [107]. This was followed by the formulations using pH-sensitive liposomes that are stable at physiological pH (i.e., pH $\sim$ 7.4). They destabilize under acidic conditions (e.g., in tumors), leading to pH-triggered release [108]. Phospholipid liposomes containing disulfur bridges are sensitive to the redox potential of the medium. On reduction of the S–S bond, the liposomes rupture, releasing their contents [109]. Ultrasound can trigger drug release from echogenic or e-liposomes [110]. Light can act as a trigger for photosensitive liposomes [111]. Enzyme-triggered liposomes have also been studied e.g. liposomes triggered by phospholipase C [112], alkaline phosphatase [113], and others. Virosomes are surface-functionalized toward specific targets (i.e., virus mimics). These have been widely used for vaccination by the delivery of antigens [114].

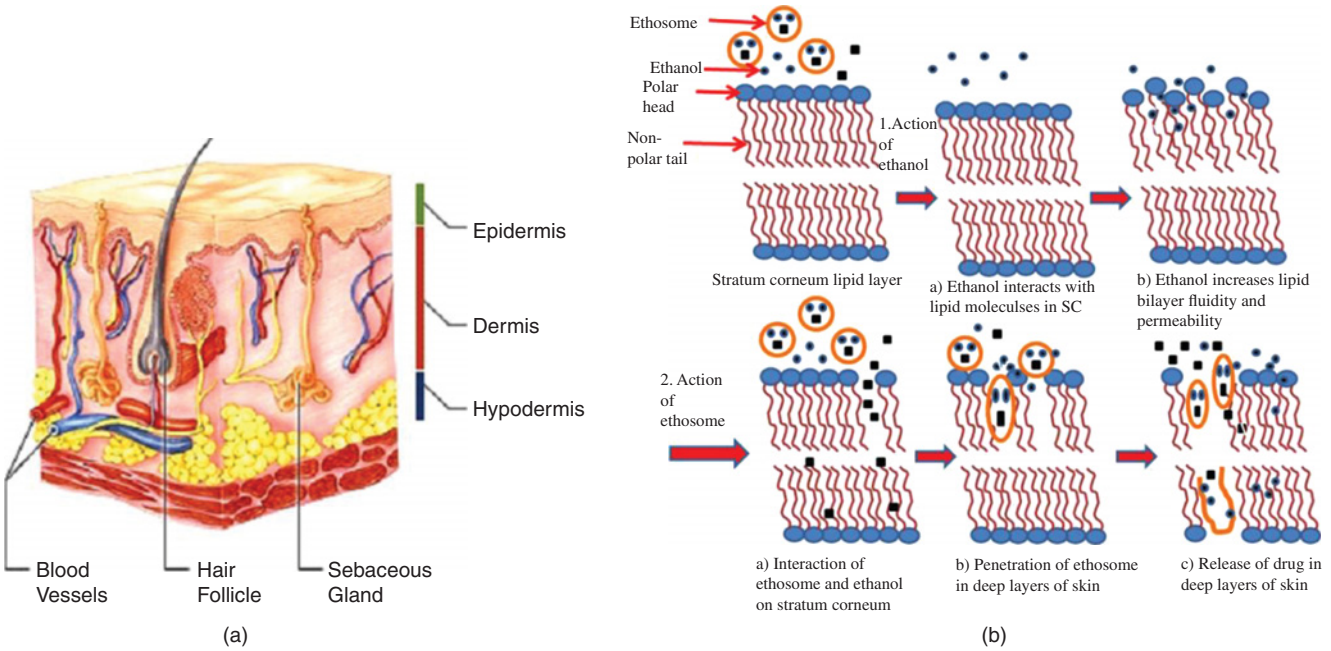


FIGURE 23.15 (a) Diagram of skin; (b) mechanism of action of ethosomes on human skin. (Both illustrations taken from open-access resource, *J. Adv. Pharm. Technol. Res*. **1**, 274–282.)

The polymer-based liposomes (i.e., polymerosomes) discussed earlier have been used for delivery of anticancer drugs such as paclitaxel (hydrophobic drug) and doxorubicin (hydrophilic drug) [88]. Liposomes have also been used as effective delivery systems for DNA [115] and siRNA [116]. Niosomes have also been used extensively as DDS for many applications [117, 118]. Niosome-based airjet nebulizers using the drug beclomethasone dipropionate (BDP) have also been prepared [119].

Theranostics is the development of specific therapies for various diseases combined with diagnostic capabilities, all combined into a single formulation [120]. Liposomes loaded with iron oxide nanoparticles were thus used [121]. Prolonged circulation time was noted and monitoring was done by studying the fluorescence of QDs.

23.6.2 Cosmetic Applications

Vesicular systems find widespread applications in the cosmetic industry. The stratum corneum (SC) of human skin is composed of insoluble keratins surrounded by the cell envelope (Fig. 23.15a).

The skin presents a formidable barrier for delivery of drugs and other materials. Cosmetic and drug formulations for the skin have focussed on efforts to overcome the skin barrier [122]. Deformable liposomes and transferomes were the first generation of elastic vesicles introduced that could penetrate skin and deliver material [123]. More recently, ethosomes (discussed earlier) [73,124] have been found to have improved skin penetration ability. The mechanism of action of ethosomes is as proposed as follows (Fig. 23.15b).

First, ethanol in ethosomes interacts with the lipid molecules via the polar headgroup region of the SC, hence increasing the bilayer fluidity. Subsequently, the ethosomes penetrate the lipid layer and fuse with lipids, resulting in release of the encapsulated material.

Another team of researchers formulated antioxidant ethosomes for topical delivery [125]. A US-based company, Osmotics Inc., recently reported a new type of cellulite cream called *lipoduction*, which uses ethosome technology to deliver ingredients directly into skin fat cells thus improving the appearance of cellulite.

Apart from ethosomes, niosomes have also been used for cosmetic formulations. Niosomes made from a Brij 52/cholesterol mixture using black tea extract were formulated as an active sunscreen agent [126]. US Patent 4,830,857, entitled *Cosmetic and Pharmaceutical Composition Containing Niosomes and a Water-Soluble Polyamide and a Process for Preparing This Composition*, was obtained C 1989 [127]. Another group obtained US patent 6,319,508 in 2001 [128], entitled *Anhydrous Cosmetic Composition Containing a Fatty Phase and Pro-liposomes*, where they prepared an anhydrous cosmetic makeup formulation containing a vesicular lipid phase and other used additives.

23.6.3 As Self-Assembled Nanoreactors

For a long time, vesicular systems have been explored as potential nanoreactors [129, 130]. The requirements for a

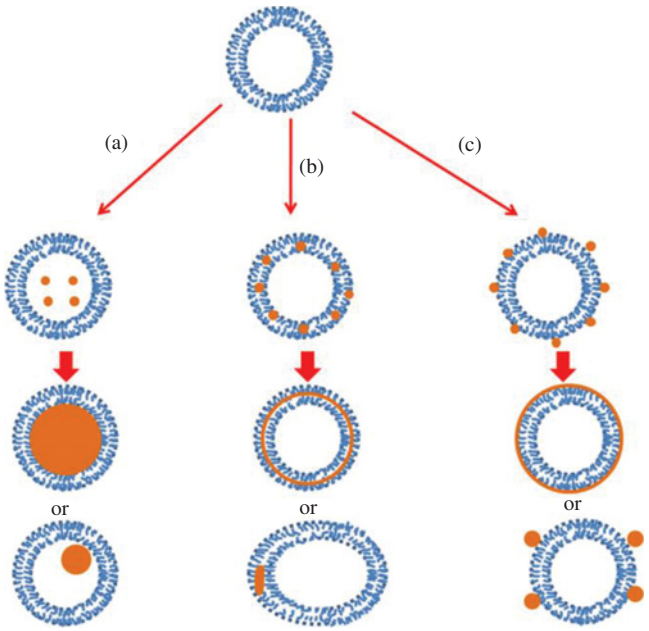


FIGURE 23.16 Synthetic strategies employed for the synthesis of materials using soft vesicles. (From R. Dong et al., *Accounts Chem. Res*. **45**, 504–513. Copyright © 2012 by American Chemical Society. Reprinted by permission of American Chemical Society.)

vesicle to act as nanoreactor have been listed in a review [130]. Briefly, they are (1) stable reactor membrane; (2) resistance offered by the vesicle to external destabilizing factors (e.g., pH, temperature, ionic strength), and (3) entrapment of reactants in the inner vesicular compartment. Others have studied a number of enzymatic reactions inside liposomes [131,132]. Green fluorescent protein (GFP) has been synthesized within liposomes [133].

Another group have provided an extensive review on the use of soft vesicles in the synthesis of hard materials [134]. They discussed such synthesis using three main strategies as depicted in Fig. 23.16: (a) reaction compartmentalization within the hydrophilic core; (b) membrane-restricted reaction within the bilayers, and (c) surface-reactive templating and synthesis at the outer surfaces of the vesicles.

Pioneering work on the synthesis of nanoparticles in the inner aqueous compartment of vesicles as per the logic depicted in Fig. 23.16a was done by Tricot and Fendler in the mid-1980s [135]. Rhodium-coated CdNPs were synthesized in situ in dihexadecyl phosphate vesicles. Subsequently core–shell metal sulfide nanocrystals were also synthesized employing this strategy [136]. Our group synthesized gold nanoparticles (GNPs) using span/cholesterol-based niosomes [69]. The surfactant HLB value, "leakiness" of the niosomes, and rigidity of the bilayer are important parameters that dictate the size and shape of the GNPs (Fig. 23.17).

The second strategy depicted in Fig. 23.16b utilizes the inner portion of the vesicle bilayer as a microreactor. By this strategy, hydrophobic nanoparticles (NPs) can be prepared in an aqueous environment. GNPs have been prepared in bilayers employing this strategy whereby $AuCl_4^-$ was incorporated in the bilayer as a counterion [137]. Hydrophobic quantum dots have also been prepared using this strategy [138].

According to the third strategy, the outer surface of the vesicles is the specific site for material synthesis. Initially, the precursors adsorb and react at the vesicle surface. Then the products nucleate, grow, and gradually cover the vesicle. Removal of the vesicle material leaves hollow micro- or nanocapsules. Hollow silica particles were synthesized by such vesicle-templating methods [139, 140]. Other workers have also used reactive catanionic vesicles as reactive precursors, not as templates to prepare ZnNPs [141, 142].

23.6.4 As Organized Assemblies for Fluorescence-Based Studies

For a long time, fluorescence probing was considered as a simple, convenient, and noninvasive tool to study vesicular systems. One team of investigators have carried out exhaustive fluorescence studies probing various aspects of lipid vesicles [143–145]. They have also probed the interaction of bile salts with vesicles using various fluorescence probes. Another group [146] have reviewed the main trends in the development of fluorescent probes for monitoring the structure, dynamics, and interactions in membrane-mimicking lipid bilayers.

Solvation dynamics studies in vesicles were carried out by several groups. These studies provide valuable insight into the polar solvent dynamics in vesicular systems. One group in particular have contributed significantly to solvation dynamics in phospholipid vesicles [147, 148]. Their study reveals two solvation components: the slow (>1-ns) response has been attributed to water bound at the vesicle interface, while the faster (∼600-ps) component is assigned to water in the inner aqueous core of the vesicles. Another group used time-resolved fluorescence and NMR to study solvent relaxation in lipids [149].

Niosomes have also been studied by fluorescence methods. Our group has performed fluorescence resonance energy transfer (FRET) studies in span/cholesterol niosomes and span-only micelles [150]. It was shown that FRET efficiency is more in niosomes compared to micelles. This is evidenced by a larger decrease in fluorescence of the donor in presence of the acceptor.

In recent times, *fluorescence correlation spectroscopy* (FCS) has emerged as a powerful technique to study biological systems at the single molecule level with high spatial resolution [151]. One team [152] studied the interactions of Nile red molecules with lipid vesicles using the on/off fluctuations in the fluorescence signal. FCS has been used [153] to determine the diffusion coefficient (D_t) of an organic molecule in

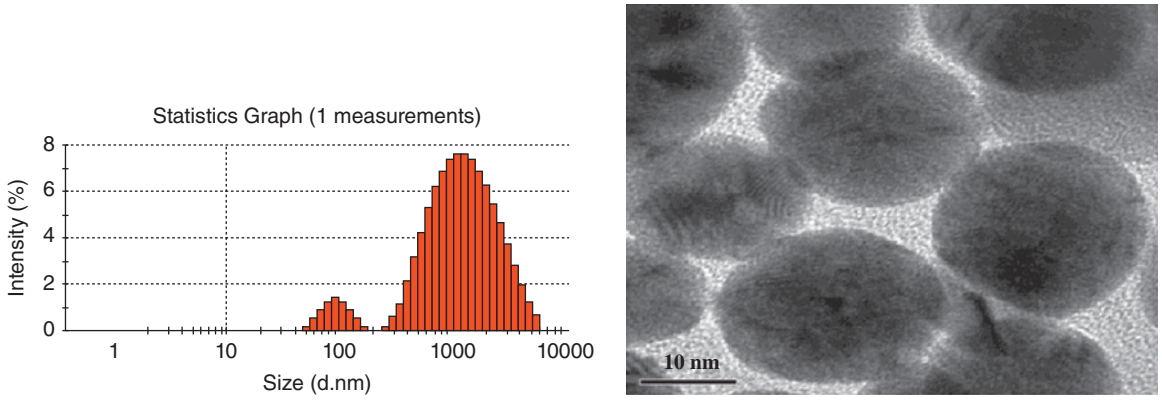


FIGURE 23.17 (a) Dynamic light-scattering data for GNPs synthesized in Span-based niosomes; (b) TEM image of GNPs synthesized in Span-based niosomes. (Both images from S. De, et al., *J. Colloid Inerface Sci*. **396**, 9–15. Copyright © 2012 by Elsevier. Reprinted by permission of Elsevier.)

giant unilamellar vesicles (> 25 μm). Others [154] have used FCS to study diffusion in GUVs and supported bilayers.

Another team of investigators used FCS to study dye diffusion in gel and fluid phases of a singl-lipid vesicle [155]. The D_t values determined were 5 $\mu m^2/s$ in the gel phase (for DPPC vesicle at 20°C) and 40 $\mu m^2/s$ in the fluid phase. The same group has studied dye diffusion in giant multilamellar niosomes of Triton X-100/ cholesterol [156] and catanionic vesicles of SDS/DTAB [157]. They found that the D_t values exhibit a much narrower distribution in niosomes compared to catanionic vesicles, indicating that the niosomes are quite homogeneous with small viscosity variation. This group has also performed time-resolved picosecond studies under a confocal microscope to study the solvation dynamics of Coumarin 153 (C-153) inside a single giant vesicle, the solvation time varying from 750 to 1000 ps [157]. Another team [159] used FCS to analyze binding of fluorescently labeled peptides to lipid vesicles. The peptides were labeled using Alexa 488, and the vesicles used were LUVs of phosphatidyl choline and phosphatidyl serine.

23.7 FUTURE PERSPECTIVES AND DIRECTIONS OF RESEARCH ON VESICLES

In the biological system, chemical reactions are often coupled in time and space. Nature, realizing this coupling, has designed well-defined reaction environments, the most sophisticated of which is the cell. Thus the cell is the primary source of inspiration for research in general. One step toward mimicking cells *in vitro* is the development and study of self-assembling nanoreactors. In the second half of the twentieth century, the use of lipid-based vesicles as potential biomimicking systems has received considerable attention.

In this chapter, we have focused on the principles of vesicle formation, the present *state-of-the-art* synthetic strategies, and the various types of vesicles and their characterization and applications. The most popular application of vesicular systems is as drug delivery vehicles. In medical science, vesicles constitute one of the most successfully translated drug delivery systems that are currently in clinical use for a variety of diseases such as cancer and inflammatory and dermatological diseases and also as vaccines. With the advent of novel vesicles (e.g., ethosomes and e-liposomes), drug delivery and cosmetic formulations have undergone a paradigm shift from the existing formulations. Such clinical profiles are important for the future development of vesicular systems with combined therapeutic–diagnostic (i.e., *theranostic*) capabilities. Vesicle–nanoparticle hybrids are a stepping stone in this direction. Liposomal vesicles have been used for synthesis of nanoparticles (QDs, magnetic NPs, GNPs, etc.). Vesicle templating is an important route for preparation of hollow nanospheres, which have manifold uses.

However, all success in vesicle-based applications depends on the stability of the vesicles. In this chapter, we have discussed how the stability of vesicles can be improved, for example, by using polymers (polymerosomes) and catanionic amphiphile pairs, that is, catansomes.

The future advancement of vesicular technology demands that smart and multifunctional vesicle hybrids be developed for biological, chemical, and catalytic applications. These hybrids must be stable and biocompatible. In this perspective, the evolution of vesicles is still ongoing. The future of vesicle research will witness the "survival of the fittest vesicle" for the manifold applications of vesicles.

ACKNOWLEDGMENTS

S.D. thanks the Department of Science and Technology, India; Council for Scientific and Industrial Research, India;

and Swedish Research Council, Stockholm for funding. The University of Kalyani is acknowledged for providing infrastructural facilities. R.P.M. acknowledges the University of Kalyani for a university research fellowship. We are both grateful to Professors S.P. Moulik and N. Nandi for helpful discussions and suggestions. Finally, we thank Professor Ohshima for his inspiration and encouragement throughout the process.

REFERENCES

[1] Laughin, R.G. (1996). *The Aqueous Behaviour of Surfactants*. Academic Press, London.

[2] Israelachvili, J. N., Mitchell, D.J., Ninham, B.W. (1976). Theory of self-assembly of hydrocarbon amphiphiles into micelles and bilayers. *J. Chem. Soc. Faraday Transact.* **72**, 1525–1568.

[3] Blokzijl, W., Engberts, J.B.F.N. (1993). Hydrophobic effects. Opinions and facts. *Angew. Chem. Int. Ed. Engl.* **32**, 1545–1579.

[4] Lowik, D.W.P.M., Van Hest, J.C.M. (2004). Peptide based amphiphiles. *Chem. Soc. Rev*. **33**, 234–245

[5] Velonia, K., Cornelisses, J.J.L.M., Feiters, M.C., Rowan, A.E., Notte, R.J.M. (2005). Aggregation of amphiphiles as a tool to create novel functional nano-objects, In Huck, W.T.S. (ed.), *Nanoscale Assemblies*. Kluwer Academic, New York.

[6] Fuhrhop, J.-H., König J. (1994). *Membrane and Molecular Assemblies: The Synthetic Approach*. The Royal Society of Chemistry, Cambridge, UK.

[7] Tanford, C. (1980). *The Hydrophobic Effect: Formation of Micelles and Biological Membranes*, 2nd ed. Wiley, New York.

[8] Bangham, A.D., Horne, R.W. (1964). Negative staining of phospholipids and their structural modification by surface-active agents as observed in the electron microscope. *J. Mol. Biol.* **8**, 660–668.

[9] Gebicki, J.M., Hicks, M. (1973). Ufasomes are stable particles surrounded by unsaturated fatty acid membranes. *Nature* **243**, 232–234.

[10] Kunitake, T., Okahata, Y. (1977). A totally synthetic bilayer membrane. *J. ACS* **99**, 3860–3861.

[11] Antonietti, M., Forster, S. (2003). Vesicles and liposomes: A self-assembly principle beyond lipids. *Adv. Mater.* **15**, 1323–1333.

[12] Gradzielski, M. (2003). Vesicles and vesicle gels-structure and dynamics of formation. *J. Phys. Condens. Matter* **15**, R655–R697.

[13] Patil, Y.P., Jadhav, S. (2014). Novel methods for liposome preparation. *Chem. Phys. Lipids* **177**, 8–18.

[14] Crommelin, D.J.A., Schreier, H. (1994). Liposomes. In Kreuter, J. (ed.), *Colloidal Drug Delivery Systems.* Marcel Dekker, New York.

[15] Lipowsky, R. (1991). The conformation of membranes. *Nature* **349**, 475–481.

[16] Mui, B.L., Döberiner, H.G., Madden, T.D., Cullis, P.R. (1995). Influence of transbilayer area asymmetry on the morphology of large unilamellar vesicles. *Biophys. J.* **69**, 930–941.

[17] Bangham, A.D., Standish, M.M., Watkins, J.C. (1965). Diffusion of univalent ions across the lamellae of swollen phospholipids. *J. Mol. Biol.* **13**, 238–252.

[18] Weissig, V., Torchilin, V. (eds) (2003). *Liposomes: A Practical Approach*. Oxford Univ. Press, Oxford, UK.

[19] Menger, F.M., Gabrielson, K.D. (1995). Cytomimetic organic chemistry: Early developments. *Angew. Chem. Int. Ed. Engl.* **34**, 2091–2096.

[20] Kaler, E.W, Murthy, A.K., Rodriguez, B.E., Zasadzinski, J.A. (1989). Spontaneous vesicle formation in aqueous mixtures of single-tailed surfactants. *Science* **245**, 1371–1374.

[21] Herrington, K.l., Kaler, E.W., Miller, D.D., Zasadzinski, J.A.N., Chiruvolu, S. (1993). Phase behavior of aqueous mixtures of dodecyltrimethylammonium bromide (DTAB) and sodium dodecyl sulfate (SDS). *J. Phys. Chem.* **97**, 13792–13802.

[22] Olsson, U., Nakamura, K., Kunieda, H., Strey, R. (1996). Normal and reverse vesicles with nonionic surfactant: solvent diffusion and permeability. *Langmuir* **12**, 3045–3054.

[23] Hofland, H.E.J., Bouwstra, J.A., Gouris, G.S., Spies, F., Talsma, H., Junginger, H.E. (1993). Nonideality of mixtures of pure nonionic surfactants both in solution and at silica/water interfaces. *J. Colloid Interface Sci.* **161**, 366–376.

[24] Gregoriadis, G. (ed.) (1993). *Liposome Technology.* CRC Press, Boca Raton, FL.

[25] Barenholz Y., Crommelin, D.J.A. (1994). Liposome as pharmaceutical dosage forms. In Swarbrick, J. (ed.), *Encyclopedia of Pharmaceutical Technology*. CRC Press, New York.

[26] Lichtenberg, D., Barenholz, Y. (1988). Liposomes: Preparation, characterization and preservation. In Glick, D. (ed.), *Methods of Biological Analysis.* Wiley, New York.

[27] Lasic, D.D. (1993). *Liposomes: From Physics to Application*. Elsevier Science B.V., Amsterdam.

[28] Batzri, S., Korn, E.D. (1973). Single bilayer liposomes prepared without sonication. *Biochim. Biophys. Acta* **298**, 1015–1019.

[29] Huang, C.H. (1969). Phosphatidylcholine vesicles: Formation and physical characteristics. *Biochemistry* **8**, 344–352.

[30] Szoka, F., Papahadjopoulos, D. (1981). In Knight, C.G. (ed.), *Liposomes: From Physical Structure to Therapeutic Applications.* Elsevier, Amsterdam, pp. 51–82.

[31] Handa, T., Takeuchi, H., Ohokubo, Y., Kawashima, Y. (1987). Lyophilized liposomes prepared by a modified reversed-phase evaporation method. *Chem. Pharm. Bull.* **35**, 748–755.

[32] Kim. S., Jacobs, R.E., White, S.H. (1972). Preparation of multilamellar vesicles of defined size-distribution by solvent-spherule evaporation. *Biochim. Biophys. Acta Biomembr.* **35**, 748–755.

[33] Chen, C.-M., Ali, D. (1987). Use of fluidized bed in proliposome manufacturing. *J. Pharm. Sci.* **76**, 419.

[34] Milsmann, M.H.W., Schwendener, R.A., Weder, H. (1978). The preparation of large single bilayer liposomes by a fast and controlled dialysis. *Biochim. Biophys. Acta Biomembr.* **512**, 147–155.

[35] Barenholzt, Y., Amselem, S., Lichtenberg, D. (1979). A new method for preparation of phospholipid vesicles (liposomes)–french press. *FEBS Lett.* **99**, 210–214.

[36] Hamilton, R.L., Jr., Goerke, J., Weinstein, J.N., Havel, R.J. (1980). Interaction of unilamellar liposomes with serum lipoproteins and apolipoproteins. *J. Lipid Res.*, **21**, 981–992.

[37] Brandl, M., Bachman, D., Drechsler, M., Bauer, K.H. (1990). Liposome preparation by a new high pressure homogenizer Gaulin Micron Lab 40. *Drug Devel. Industr. Pharm.* **16**, 2167–2191.

[38] Hope, M.J., Bally, M.B., Webb, G., Cullis, P.R. (1985). Production of large unilamellar vesicles by a rapid extrusion procedure. Characterization of size distribution, trapped volume and ability to maintain a membrane potential. *Biochim. Biophys. Acta* **812**, 55–65.

[39] MacDonald, R.C., MacDonald, R.I., Menco, B.P.M., Takeshita, K., Subbarao, N.K., Hu, L. (1991). Small-volume extrusion apparatus for preparation of large, unilamellar vesicles. *Biochim. Biophys. Acta Biomembr.* **1061**, 297–303.

[40] Frisken, B.J., Asman, C., Patty, P.J. (2000). Studies of vesicle extrusion. *Langmuir* **16**, 928–933.

[41] Van Swaay, D., deMello, A. (2013). Microfluidic methods for forming liposomes. *Lab Chip* **13**, 752–767.

[42] Jahn, A., Vreeland, W.N., Gaitan, M., Locascio, L.E. (2004). Controlled vesicle self-assembly in microfluidic channels with hydrodynamic focusing. *J. ACS* **126**, 2674–2675.

[43] Sugiura, S., Kuroiwa, T., Kagota, T., Nakajima M., Sato, S., Mukataka, S., Walde, P., Ichikawa, S. (2008). Novel method for obtaining homogeneous giant vesicles from a monodisperse water-in-oil emulsion prepared with a microfluidic device. *Langmuir* **24**, 4581–4588.

[44] Shum, H.C., Lee, D., Yoon, I., Kodger, T., Weitz, D.A. (2008). Double emulsion templated monodisperse phospholipid vesicles. *Langmuir* **24**, 7651–7653.

[45] Estes, D.J., Mayer, M. (2005). Electroformation of giant liposomes from spin-coated films of lipids. *Colloids Surf. B: Biointerfaces* **42**, 115–123.

[46] LeBerre, M., Yamada, A., Reck. L., Chen, Y., Baigl, D. (2008).Electroformation of giant phospholipid vesicles on a silicon substrate: Advantages of controllable surface properties. *Langmuir* **24**, 2643–2649.

[47] Jaafar-Malej, C., Charcosset, C., Fessi, H. (2011). A new method for liposome preparation using a membrane contactor. *J. Liposome Res.* **21**, 213–220.

[48] Laouini, A., Jaafar-Maalej, C., Sfar, S., Charcosset, C., Fessi, H. (2011). Liposome preparation using a hollow fiber membrane contactor—application to spironolactone encapsulation. *Int. J. Pharm.* **415**, 53–61.

[49] Wang, T., Deng, Y., Geng, Y., Gao, Z., Zou, J., Wang, Z. (2006). Preparation of submicron unilamellar liposomes by freeze-drying double emulsions. *Biochim. Biophys. Acta Biomembr.* **1758**, 222–231.

[50] Mouritsen, O.G. (2011). Lipids, curvature, and nanomedicine. *Eur. J. Lipid. Sci. Technol.* **113**, 1174–1187.

[51] Hauser, H. (1989). Mechanism of spontaneous vesiculation. *Proc. Natl. Acad. Sci. USA* **86**, 5351–5355.

[52] Genc, R., Oritz, M., O'Sullivan, C.K. (2009). Curvature-tuned preparation of nanoliposomes. *Langmuir* **25**, 12604–12613.

[53] Yu, D.G., Branford-White, C., Williams, G.R., Bligh, S.W.A., White, K., Zhu, L.M., Chatterton, N.P. (2011). Self-assembled liposomes from amphiphilic electrospun nanofibers. *Soft Matter* **7**, 8239–8247.

[54] Meure, L.A., Foster, N.R., Dehghani, F. (2008). Conventional and dense gas techniques for the production of liposomes: A review. *AAPS* (American Association of Pharmaceutical Scientists) *Pharm. Sci. Technol.* **9**, 798–809.

[55] Magnan, C., Badens, E., Commenges, N., Charbit, G. (2000). Soy lecithin micronization by precipitation with a compressed fluid antisolvent—influence of process parameters. *J. Supercrit. Fluids* **19**, 69–77.

[56] Kemps, J.M.A., Crommelin, D.J.A. (1988). Liposomes for drug delivery from physico-chemical studies to application. *Pharm. Weekblad* **123**, 355–363.

[57] Kemps, J.M.A., Crommelin, D.J.A. (1988). Cemische stabilitetit van fosfolipide in farmaceutische preparation-1 hydrolyse van fosfolipiden in watering milieu. *Pharm. Weekblad* **123**, 457–469.

[58] Handjani-Vila, R.M., Ribier, A., Rondot, B., Vanlerkerghie, G. (1979). Dispersion of lamellar phases of non ionic lipids in cosmetic products. *Int. J. Cosmet. Sci.* **1**, 303–314.

[59] Uchegbu, I.F., Vyas, S.P. (1998). Non-ionic surfactant based vesicles (niosomes) in drug delivery. *Int. J. Pharm.* **172**, 33–70.

[60] Uchegbu, I.F., Fluorence, A.T. (1995). Non-ionic surfactant vesicles (niosomes): Physical and pharmaceutical chemistry. *Adv. Colloid. Interface Sci.* **58**, 1–55.

[61] Florence, A.T., Cable, C. (1993). Non-ionic surfactant vesicles (niosomes) as vesicles for doxorubicin delivery. In Gregoriadis, G., Florence, A.T., Patel, H.M. (eds.), *Liposomes in Drug Delivery.* Taylor & Francis, Harwood Academic Publishers, Chur, Switzerland, pp. 239–254.

[62] Bouwstra, J.A., van Hai. D.A., Hofland, H.E.J. (1997). Preparation and characterization of nonionic surfactant vesicles. *Colloids Surf. A: Physicochem. Eng. Aspects* **123–124**, 71–80.

[63] Bouwstra, J.A., Hofland, H.E.J. (1994). In Kreuter, J. (ed.), *Colloidal Drug Delivery Systems.* Markel Dekker, New York, pp. 191–217.

[64] Mahale, N.B., Thakkar, P.D., Mali, R.G., Walunj, D.R., Chaudhari, S.R. (2012). Niosomes: Novel sustained release nonionic stable vesicular systems—an overview. *Adv. Colloid Interface Sci.* **183–184**, 46–54.

[65] Jousma, H., Joosten, J.G.H., Gooris, G.S., Junginger, H.E. (1989). Changes of mesophase structure of BRIJ 96/water mixtures on addition of liquid paraffin. *Colloid Polym. Sci.* **267**, 353–364.

[66] Yoshioka, T., Sternberg, B., Florence, A.T. (1994). Preparation and properties of vesicles (niosomes) of sorbitan monoesters (Span 20, 40, 60 and 80) and a sorbitan triester (Span 85). *Int. J. Pharm.* **105**, 1–6.

[67] Blickenstaff, R.T., Brandstadter, S.M., Reddy, S., Witt, R. (1994). Potential radioprotective agents 1. Homologs of melatonin. *J. Pharm. Sci.* **83**, 216–218.

[68] Liu, T., Guo, R., Hua, W., Qui, J. (2007). Structure behaviors of hemoglobin in PEG 6000/Tween 80/Span 80/H_2O niosome system. *Colloids Surf. A: Physiochem. Eng. Aspects* **293**, 255–261.

[69] De, S., Kundu, R., Biswas, A. (2012). Synthesis of gold nanoparticles in niosomes. *J. Colloid Interface Sci.* **386**, 9–15.

[70] Blazek-Welsh, A.I., Rhodes, D.G. (2001). Maltodextrin-based proniosomes. *AAPS Pharmsci.* **3**, 1–7.

[71] Touitou, E., Godin, B., Weiss, C. (2000). Enhanced delivery of drugs into and across the skin by ethosomal carriers. *Drug Devel. Res.* **50**, 406–415.

[72] Akiladevi, D., Basak, S. (2010). Ethosomes: A non-invasive approach for transdermal drug delivery. *Int. J. Curr. Pharm. Res.* **2**, 1–4.

[73] Touitou, E., Dayan, N., Bergelson, L., Godin, B., Eliaz, M. (2000). Ethosomes—novel vesicular carriers for enhanced delivery: Characterization and skin penetration properties. *J. Control. Release* **65**, 403–418.

[74] Knutson, K., Krill, S.L., Zhang, J. (1990). J. Solvent-mediated alterations of the stratum corneum. *J. Control. Release* **11**, 93–103.

[75] Cevc, G., Blume, G., Schätzlein, A. (1997). Transfersomes-mediated transepidermal delivery improves the regio-specificity and biological activity of corticosteroids in vivo. *J. Control. Release* **45**, 211–226.

[76] Cevc, G. (1996). Transferosomes, liposomes and other lipid suspensions on the skin: Permeation enhancement, vesicle penetration, and transdermal drug delivery. *Crit. Rev. Ther. Drug Carrier Syst.* **13**, 257–388.

[77] Jain, S., Jain, P., Umamaheshwari, R.B., Jain, N.K. (2003). Transfersomes—a novel vesicular carrier for enhanced transdermal delivery: Development, characterization, and performance evaluation. *Drug Devel. Industr. Pharm.* **29**, 1013–1026.

[78] Paul, A., Cevc, G., Bachhawat, B.K. (1998). Transdermal immunisation with an integral membrane component, gap junction protein, by means of ultradeformable drug carriers, transfersomes. *Vaccine* **16**, 188–195.

[79] Webb, M.S., Bally, M.B., Mayor, L.D. (1996). Inex Pharmaceutical Corporation. US Patent 5,543,152, June 8.

[80] Saraf, S., Paliwal, S. (2011). Sphingosomes–a novel appoach to vesicular drug delivery *Int. J. Curr. Sci. Res.* **1**, 63–68.

[81] Vyas, S.P., Khar, R.K. (2002). *Targeted and Controlled Drug Delivery*. CBS Publisher, New Delhi.

[82] Biju, S.S., Talegaonkar, S., Mishra, P.R., Khar, R.K. (2006) Vesicular systems: An overview. *Indian J. Pharm. Sci.* **68**, 141–153.

[83] Lattin, J.R., Belnap, D.M., Pitt, W.G. (2012). Formation of eLiposomes as a drug delivery vehicle. *Colloids Surf. B: Biointerfaces* **89**, 93–100.

[84] Javadi, M., Pitt, W.G., Belnap, D.M., Tsosie, N.H., Hartley, J.M. (2012). Encapsulating nanoemulsions inside eliposomes for ultrasonic drug delivery. *Langmuir* **28**, 14720–14729.

[85] Soussan, E., Cassel, S., Blazat, M., Rico-Lattes, I. (2009). Drug delivery by soft matter: Matrix and vesicular carriers. *Angew. Chem. Int. Ed.* **48**, 274–288.

[86] Gao, W., Hu, C.-M., Fang, J., Zhang, L. (2013). Liposome-like nanostructures for drug delivery. *J. Mater. Chem. B* **1**, 6569–6585.

[87] Lee, S.-M., Lee, O.-S., O'Halloran, T.V., Schatz, G.C., Nguyen, S.T. (2011). Triggered release of pharmacophores from [Ni(HAsO3)]-loaded polymer-caged nanobin enhances pro-apoptotic activity: A combined experimental and theoretical study. *ACS Nano* **5**, 3961–3969.

[88] Ahmed, F., Pakunlu, R.I., Brannan, A., Bates, F., Minko, T., Discher, D.E. (2006). Biodegradable polymersomes loaded with both paclitaxel and doxorubicin permeate and shrink tumors, inducing apoptosis in proportion to accumulated drug. *J. Control. Release* **116**, 150–158.

[89] Obermeier, B., Wurm, F., Mangold, D.-C., Frey, H. (2011). Multifunctional poly(ethylene glycol)s. *Angew. Chem. Int. Ed.* **50**, 7988–7997.

[90] Jass, J., Tjarnhage, T., Puu, G. (2003). Atomic force microscopy imaging of liposomes. In Nejat, D. (ed.), *Methods in Enzymology.* Academic Press, New York, pp. 199–213.

[91] Grabielle-Madelmont, C., Lesieur, S., Olivan, M. (2003). Characterization of loaded liposomes by size exclusion chromatography. *J. Biochem. Biophys. Methods* **56**, 189–217.

[92] Moon, M.H., Park, I., Kim, Y. (1998). Size characterization of liposomes by flow field-flow fractionation and photon correlation spectroscopy: Effect of ionic strength and pH of carrier solutions. *J. Chromatogr.* **813A**, 91–100.

[93] Jousma, H., Talsma, H., Spies, F., Jootsen, J.G.H., Junginger, H.F., Crommelin, D.J.A. (1987). Characterization of liposomes. The influence of extrusion of multilamellar vesicles through polycarbonate membranes on particle size, particle size distribution and number of bilayers. *Int. J. Pharm.* **35**, 263–274.

[94] Hauser, H. (1984). Some aspects of phase behaviour of charged lipids. *Biochim. Biophys. Acta Biomembr.* **772**, 37–50.

[95] Liu, T., Guo, R. (2007). Structure and transformation of the niosome prepared from PEG 6000/Tween 80/Span 80/H2O lamellar liquid crystal. *Colloids Surf. A: Physicochem. Eng. Aspects* **295**, 130–134.

[96] Manosroi, A., Chutoprapat, R., Abe, M. (2008). Characteristics of niosomes prepared by supercritical carbon dioxide ($scCO_2$) fluid. *Int. J. Pharm.* **352**, 248–255.

[97] Cevc, G. (1993). Electrostatic characterization of liposomes. *Chem. Phys. Lipids* **64**, 163–186.

[98] Hunter, C.A., Dolan, T.F., Coombs, G.H., Baillie, A.J. (1988). Vesicular systems (niosomes and liposomes) for

delivery of sodium stibogluconate in experimental murine visceral leishmaniasis. *J. Pharm. Pharmacol.* **40**, 161–165.

[99] Agrati, C., Marianecci, C., Sennato, S., Carafa, M., Bordoni, V., Cimini, E., et al. (2011). Multicompartment vectors as novel drug delivery systems: Selective activation of T$\gamma\delta$ lymphocytes after zoledronic acid delivery. *Nanomed. Nanotechnol. Biol. Med.* **7**, 153–161.

[100] Gregoriadis, G. (1973). Drug entrapment in liposomes. *FEBS Lett.* **36**, 292–296.

[101] Hann, I.M., Prentice, H.G. (2001). Lipid-based amphotericin B: A review of the last 10 years of use. *Int. J. Antimicrob. Agents* **17**, 161–169.

[102] Barenholz, Y. (2012). Doxil®—the first FDA-approved nano-drug: Lessons learned. *J. Control. Release* **160**, 117–134.

[103] Petre, C.E., Dittmer, D.P. (2007). Liposomal daunorubicin as treatment for Kaposi's sarcoma. *Int. J. Nanomed.* **2**, 277–288.

[104] Rodriguez, M.A., Pytilik, R., Kozak, J., Chhanabhai, M., Gascoyne, R., Biao, L., Deitcher, S.R., Winter, J.N. (2009). Vincristine sulfate liposomes injection (Marqibo) in heavily pretreated patients with refractory aggressive non-Hodgkin lymphoma *Cancer* **115**, 3475–3482.

[105] Bibi, S., Lattmann, E., Mohammed, A.R., Perrie, Y. (2012). Trigger release liposome systems: Local and remote controlled delivery. *J. Microencapsulation* **29**, 262–276.

[106] Allen, T.M., Cullis, P.R. (2013). Liposomal drug delivery systems: From concept to clinical applications. *Adv. Drug Deliv. Rev.* **65**, 36–48.

[107] Weinstein, J.N., Magin, R.L., Yatvin, M.B., Zaharko, D.S. (1979). Liposomes and local hyperthermia: Selective delivery of methotrexate to heated tumors. *Science* **204**, 188–191.

[108] Yatvin, M.B., Kreutz, W., Horwitz, B.A., Shintzky, M. (1980). pH-sensitive liposomes: Possible clinical implications. *Science* **210**, 1253–1255.

[109] Zhang, J.X., Zalipsky, S., Mullah, N., Pechar, M., Allen, T.M. (2004). Pharmaco attributes of dioleoylphosphatidylethanolamine/cholesterylhemisuccinate liposomes containing different types of cleavable lipopolymers. *Pharmacol. Res.* **49**, 185–198.

[110] Huang, S.L., MacDonald, R.C. (2004). Acoustically active liposomes for drug encapsulation and ultrasound-triggered release. *Biochim. Biophys. Acta* **1665**, 134–141.

[111] Yavlovich, A., Singh, A., Blumenthal, R., Puri, A. (2011). A novel class of photo-triggerable liposomes containing DPPC: $DC_{8,9}PC$ as vehicles for delivery of doxorubicin to cells. *Biochim. Biophys. Acta-Biomembranes* **1808**, 117–126.

[112] Kim, C.K., Park, K.M. (1994). Liposome immunoassay (LIA) for gentamicin using phospholipase C. *J. Immunol. Methods* **170**, 225–231.

[113] Kim, C.K., Lim, S.J. (1993). Liposome immunoassay (LIA) with antigen-coupled liposomes containing alkaline phosphatise. *J. Immunol. Methods* **159**, 101–106.

[114] Zurbriggen, R., Novak-Hofer, I., Seeling, A., Gluck, R. (2000). IRIV-adjuvanted hepatitis A vaccine: In vivo absorption and biophysical characterization. *Progress Lipid. Res.* **39**, 3–18.

[115] Fraley, R.M., Straubinger, R.M.; Rule, G., Springer, E.L., Papahadjopoulos, D. (1981). Liposome-mediated delivery of deoxyribonucleic acid to cells: Enhanced efficiency of delivery by changes in lipid composition and incubation conditions. *Biochemistry* **20**, 6978–6987.

[116] Straubinger, R.M., Papahadjopoulos, D. (1983). Liposomes as carriers for intracellular delivery of nucleic acids. *Methods Enzymol.* **101**, 512–527.

[117] Patel, K.K., Kumar, P., Thakkar, H.P. (2012). Formulation of niosomal gel for enhanced transdermal lopinavir delivery and its comparative evaluation with ethosomal gel. *AAPS Pharm. Sci. Technol.* **13**, 150–159.

[118] Abdelkader, H., Ismail, S., Kamal, A., Alany, R.G. (2011). Design and evaluation of controlled-release niosomes and discomes for naltrexone hydrochloride ocular delivery. *J. Pharm. Sci.* **100**, 1833–1846.

[119] Abd-Elbary, A., El-laithy, H.M., Tadros, M.I. (2008). Sucrose stearate-based proniosome-derived niosomes for the nebulisable delivery of cromolyn sodium. *Int. J. Pharm.* **357**, 189–198.

[120] Al-Jamal, W.T., Kostarelos, K. (2011). Liposomes: From a clinically established drug delivery system to a nanoparticle platform for theranostic nanomedicine. *Accounts Chem. Res.* **44**, 1094-1104

[121] Margolis, L.B., Namiot, V.A., Kljukin, L.M. (1983). Magnetoliposomes: Another principle of cell sorting. *Biochim. Biophys. Acta Biomembr.* **735**, 193–195.

[122] Elsayed, M.A., Abdalah, O.Y., Naggar, V.F., Khalafallah, N.M. (2006). Lipid vesicles for skin delivery of drugs: Reviewing three decades of research. *Int. J. Pharm.* **332**, 1–16.

[123] Essa, E.A., Bonner, M.C., Barry, B.W. (2003). Electroporation and ultradeformable liposomes; human skin barrier repair by phospholipid. *J. Control. Release* **92**, 163–172.

[124] Verma, P., Pathak, K. (2010). Therapeutic and cosmeceutical potential of ethosomes: An overview. *J. Adv. Pharm. Technol. Res.* **1**, 274–282.

[125] Koli, J.R., Lin, S. (2009). Development of anti oxidant ethosomes for topical delivery utilizing the synergistic properties of Vit A palmitate, Vit E and Vit C. *AAPS Pharm. Sci. Technol.* **11**, 1–8.

[126] Meng, I., Yeh, M.S., Hsiu-Chin, H., Jia-Horng, I., Min-Chuan, H., Kuei-Fen, H., Feng-Lin, I. (2013). Ethosomes in hair dye products as carriers of the major compounds of black tea extracts. *Int. J. Dermatol.* **52**, 239–245.

[127] Handjani-Vila, R.M., Ribier, A., Vanlerberghe, Z.G., Arlette, J.G. (1989). US Patent 4,830,857.

[128] Ribier, A., Simmonet, J., Thierry, M., et al. (2001). US Patent 6,319,508.

[129] Vrizema, D.M., Aragones, M.C., Elemans, J.A.A.W., Cornoelissen, J.J.L.M., Rowan, A.E., Notte, R.J.M. (2005). Self-assembled nanoreactors. *Chem. Rev.* **105**, 1445–1489.

[130] Monnard, P.A. (2003). Liposome-entrapped polymerases as models for microscale/nanoscale bioreactors. *J. Membr. Biol.* **191**, 87–97.

[131] Schmidli, P., Schurtenberger, P., Luisi, P.L. (1991). Liposome-mediated enzymatic synthesis of phosphatidylcholine as an approach to self-replicating liposomes. *J. ACS* **113**, 8127–8130.

[132] Bachmann, P.A., Luisi, P.L., Lang, J. (1992). Autocatalytic self-replicating micelles as models for prebiotic structures. *Nature* **357**, 57–59.

[133] Yu, W., Sato, K, Wakabayashi, M., Nakaishi, T., Ko-Mitamura, E.P., Shima, Y., Urabe, I., Yomo, T. (2001). Synthesis of functional protein in liposome. *J. Biosci. Bioeng*. **92**, 590–593.

[134] Dong, R., Liu, W., Hao, J. (2012). Soft vesicles in the synthesis of hard materials. *Accounts Chem. Res.* **45**, 504–513.

[135] Tricot, Y.M., Fendler, J.H. (1984). Colloidal catalyst-coated semiconductors in surfactant vesicles: In situ generation of rhodium-coated cadmium sulfide particles in dihexadecyl phosphate vesicles and their utilization for photosensitized charge separation and hydrogen generation. *J. ACS* **106**, 7359–7366.

[136] Korgel, B.A., Monbouquette, H.G. (2000). Controlled synthesis of mixed core and layered (Zn, Cd) S and (Hg, Cd) S nanocrystals within phosphatidylcholine vesicles. *Langmuir* **16**, 3588–3594.

[137] Du, J., Tang, Y., Lewis, A.L., Armes, S.P. (2005). pH-sensitive vesicles based on a biocompatible zwitterionic diblock copolymer. *J. ACS* **127**, 17982–17983.

[138] Al-Jamal, W.T., Al-Jamal, K.T., Tian, B., Lacerda, L., Bomans, P.H., Fredrik, P.M., Kostarelos, K. (2008). Lipid−quantum dot bilayer vesicles enhance tumor cell uptake and retention in vitro and in vivo. *ACS Nano* **2**, 408–418.

[139] Lou, X., Archer, L.A., Yang, Z. (2008). Hollow micro-/nanostructures: Synthesis and applications. *Adv. Mater.* **20**, 3987–4019.

[140] Hubert, D.H.W., Jung, M., Frederik, P.M., Bomans, P.H.H., Meuldijk, J., German, A.L. (2000). Vesicle-directed growth of silica. *Adv. Mater.* **12**, 1286–1290.

[141] Wang, J., Song, A., Jia, X., Hao, J., Liu, W., Hoffmann, H. (2005). Two routes to vesicle formation: Metal-ligand complexation and ionic interactions. *J. Phys. Chem. B* **109B**, 11126–11134.

[142] Gao, Y., Hao, J. (2009). Electrochemical synthesis of zinc nanoparticles via a metal−ligand-coordinated vesicle phase. *J. Phys. Chem.* **B113**, 9461–9471.

[143] Mohapatra, M., Mishra, A.K. (2011). Photophysical behavior of fisetin in dimyristoylphosphatidylcholine liposome membrane. *J. Phys. Chem.* **B115**, 9962–9970.

[144] Mohapatra, M., Mishra, A.K. (2013). Photophysical behavior of 8-anilino-1-naphthalenesulfonate in vesicles of pulmonary surfactant dipalmitoylphosphatidylcholine (DPPC) and its sensitivity toward the bile salt–vesicle interaction. *Langmuir* **29**, 11396–11404.

[145] Surya Prakash Rao, H., Desai, A., Sarkar, I., Mohapatra, M., Mishra, A.K. (2014). Photophysical behavior of a new cholesterol attached coumarin derivative and fluorescence spectroscopic studies on its interaction with bile salt systems and lipid bilayer membranes. *Phys. Chem. Chem. Phys.* **16**, 1247–1256.

[146] Demchenko, A.P., Mely, Y., Duportail, G., Klymchenko, A.S. (2009). Monitoring biophysical properties of lipid membranes by environment-sensitive fluorescent probes. *Biophys. J.* **96**, 3461–3470.

[147] Pal, S.K., Sukul, D., Mandal, D., Bhattacharyya, K. (1998). Solvation dynamics of coumarin 480 in vesicles. *J. Phys. Chem.* **B102**, 6114–6117.

[148] Datta, A., Pal, S.K., Mandal, D., Bhattacharyya, K. (1998). Solvation dynamics of 4-aminophthalimide in water-in-oil microemulsion of Triton X-100 in mixed solvents. *J. Phys.*

[149] Sykora, J., Kapusta, P., Fidler, V., Hof, M. (2002). On what time scale does solvent relaxation in phospholipid bilayers happen?. *Langmuir* **18**, 571–573.

[150] Girigoswami, A., Das, S., De, S. (2006). Fluorescence and dynamic light scattering studies of niosomes-membrane mimetic systems. *Spectrochim. Acta* **64A**, 859–866.

[151] Edman, L., Mets, U., Rigler, R. (1996). Conformational transitions monitored for single molecules in solution. *Proc. Natl. Acad. Sci. USA* **93**, 6710–6715.

[152] Gao, F., Mei, E., Lim, M., Hochstrasser, R.M. (2006). Probing lipid vesicles by bimolecular association and dissociation trajectories of single molecules. *J. ACS* **128**, 4814–4822.

[153] Korlach, J., Schwille, P., Webb, W.W., Feigenson, G.W. (1999). Characterization of lipid bilayer phases by confocal microscopy and fluorescence correlation spectroscopy. *Proc. Natl. Acad. Sci. USA* **96**, 8461–8466.

[154] Przybylo, M., Sykora, J., Humpolickova, J., Benda, A., Zan, A., Hof, M. (2006). Lipid diffusion in giant unilamellar vesicles is more than 2 times faster than in supported phospholipid bilayers under identical conditions. *Langmuir* **22**, 9096–9099.

[155] Ghosh, S., Adhikari, A., Sen Mojumdar, S., Bhattacharyya, K. (2010). A fluorescence correlation spectroscopy study of the diffusion of an organic dye in the gel phase and fluid phase of a single lipid vesicle. *J. Phys. Chem.* **114B**, 5736–5741.

[156] Ghosh, S., Mandal, A.K., Das, A.K., Mondal, T., Bhattacharyya, K. (2012). Diffusion of organic dyes in a niosome immobilized on a glass surface using fluorescence correlation spectroscopy. *Phys. Chem. Chem. Phys.* **14**, 9749–9757.

[157] Dey, S., Mandal, U., Sen Mojumdar, S., Mandal, A.K., Bhattacharyya, K. (2010). Diffusion of organic dyes in immobilized and free catanionic vesicles. *J. Phys. Chem.* **114B**, 15506–15511.

[158] Sen Mojumdar, S., Ghosh, S., Mondal, T., Bhattacharyya, K. (2012). Solvation dynamics under a microscope: Single giant lipid vesicle. *Langmuir* **28**, 10230–10237.

[159] Rusu, L., Gambhir, A., McLaughlin, S., Rädler, J. (2004). Fluorescence correlation spectroscopy studies of peptide and protein binding to phospholipid vesicles. *Biophys. J.* **87**, 1044–1053.

24

INTEGRIN-DEPENDENT CELL REGULATION AND ITS CLINICAL APPLICATION

Takuya Iyoda,[1,2,3] Takuya Matsunaga,[4] and Fumio Fukai,[1,2,3]

[1]*Department of Molecular Patho-Physiology, Faculty of Pharmaceutical Sciences, Tokyo University of Science, Noda, Chiba 274-8610, Japan*

[2]*Center for Drug Delivery Research, Tokyo University of Science, Noda, Chiba 274-8610, Japan*

[3]*Center for Physical Pharmacology, Research Institutes for Science and Technology, Tokyo University of Science, Noda, Chiba 274-8610, Japan*

[4]*Division of Endocrinology and Metabolism, Hematology Rheumatology and Respiratory Medicine, Department of Internal Medicine, Kagawa University, Kita-gun, Kagawa 761-0793, Japan*

24.1 INTRODUCTION

Most cells in the human body are commonly exposed to an extracellular environment. For cell survival and proliferation, cells require not only a signal from growth factor receptor but also an additional signal from adhesion receptor family molecules, integrins. Once normal cells detach from the extracellular matrix (ECM), they undergo programmed death termed *anoikis* [1, 2]. This process plays a fundamental role in preventing the dissemination of the cells to inappropriate site. In contrast, malignant cell types are often known to be independent of anchorage, which causes deregulated survival and growth [1, 2]. Cell-adhesion-mediated regulation of cell survival/death is not restricted in normal cells. It has also been demonstrated previously that leukemic cell adhesion to bone marrow fibronectin confers a multidrug resistance, commonly referred to *cell-adhesion-mediated drug resistance* (CAM-DR) [3], which could be a major cause of recurrence in acute leukemia [4–6]. These facts suggest that signals generated by aberrant interactions between adhesion molecules on cellular membrane and surrounding ECM environment are involved in cancer progression.

The ECM proteins often have concealed functional sites within their own structure. These cryptic active sites (matricryptic sites) are disclosed by proteolytic cleavage with ECM-degrading proteinases, which are secreted in pathological state such as inflammation and cancer. Exposure of matricryptic sites has been implicated in various diseases. We previously found that fibronectin harbors an antiadhesive site (YTIYVIAL) within the 14th FNIII repeat. A 22-mer peptide containing this active site, labeled FNIII14, has an ability to suppress cell adhesion to fibronectin substrate (Fig. 24.1a,b). The antiadhesive effect of FNIII14 is due to inactivation of β1-integrin [7, 8].

This matricryptic antiadhesive site could be exposed by degradation of fibronectin with inflammatory proteinases, including matrix metalloproteinases, MMP-2/9 [9]. Amino acid sequences similar to the YTIYVIAL of FNIII14 are presented in the other ECM proteins, such as collagens and tenascin (TN)-C. One of them, a sequence YTITIRGV, which is located in the FNIII repeat A2 domain of the alternative splicing region of TN-C, was found as another matricryptic site. A 22-mer peptide containing YTITIRGV, labeled TNIIIA2 (Fig. 24.2), enhances cell adhesion by inducing conformational and functional activation of β1-integrin [10]. The proadhesive effect of TNIIIA2 is also exposed by proteolytic degradation of TN-C. Moreover, it has been defined that TNIIIA2 specifically binds to cell surface heparan sulfate proteoglycans (HSPG), syndecan-4 (Fig. 24.3a–c), and the TNIIIA2/syndecan-4 complex laterally interacts with

Encyclopedia of Biocolloid and Biointerface Science, Volume 1, First Edition. Edited by Hiroyuki Ohshima.
© 2016 John Wiley & Sons, Inc. Published 2016 by John Wiley & Sons, Inc.

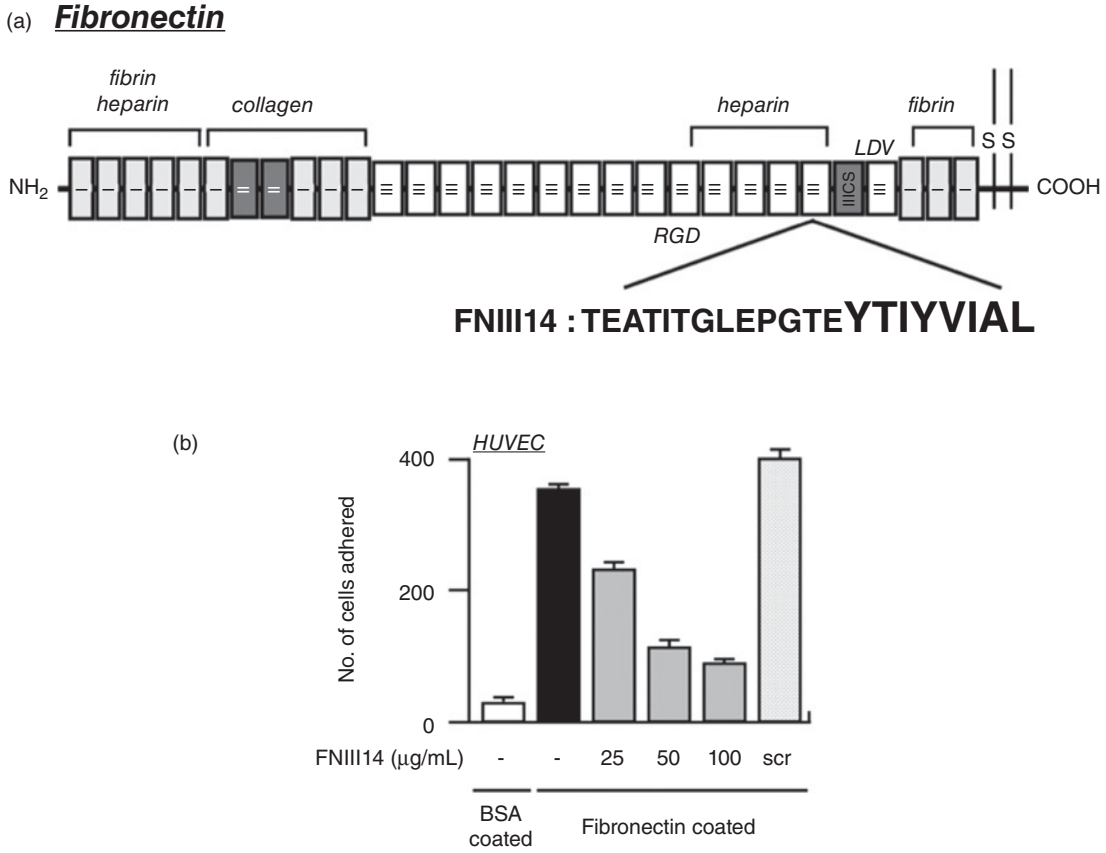


FIGURE 24.1 (a) Schematic illustration of the structure of fibronectin and FNIII14; (b) effect of peptide FNIII14 on adhesion of HUVEC to the fibronectin substrate.

β1-integrin to keep the conformation of integrin active (Fig. 24.4) [10]. Thus, we have obtained effective tools, FNIII14 and TNIIIA2, that enable us to control activation status of β1-integrins, either positively or negatively.

24.2 INACTIVATION OF β1-INTEGRIN BY FNIII14 INCREASES CHEMOSENSITIVITY OF ACUTE MYELOGENOUS LEUKEMIA (AML) CELLS

Although hematopoietic cells are usually nonadhered in blood vessels, integrin-mediated cell adhesion to fibronectin is fundamentally implicated in proliferation of hematopoietic stem and progenitor cells [11]. In contrast, hematopoietic tumor cells could proliferate without integrin ligation. Loss of *anchorage dependence* in cell proliferation is one characteristic of leukemic cells.

The majority of hematopoietic tumor cells are chemosensitive. For example, around 80% of patients with acute myelogenous leukemia (AML) might experience complete remission by anticancer drug prescription. Nevertheless, the percentage of long-term disease-free survival in AML patients is relatively low (30–50%). High relapse rate is a serious problem remaining in AML treatment. A number

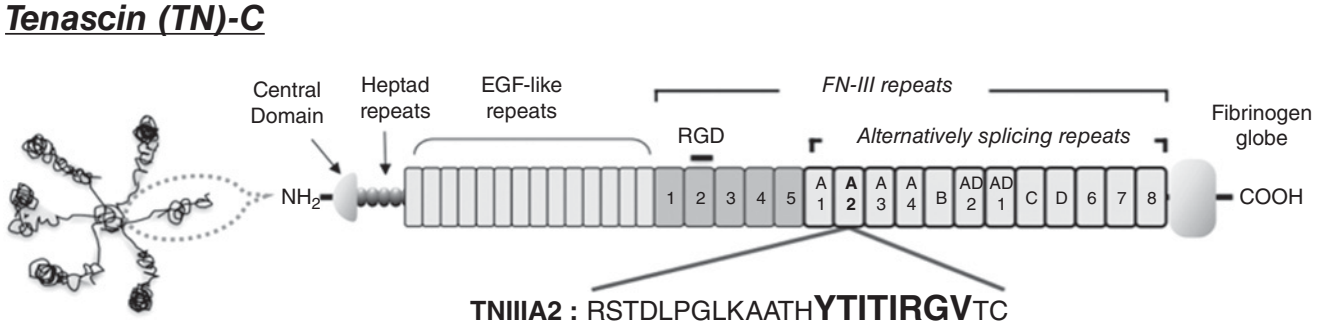


FIGURE 24.2 Schematic illustration of the structure of tenascin-C and TNIIIA2.

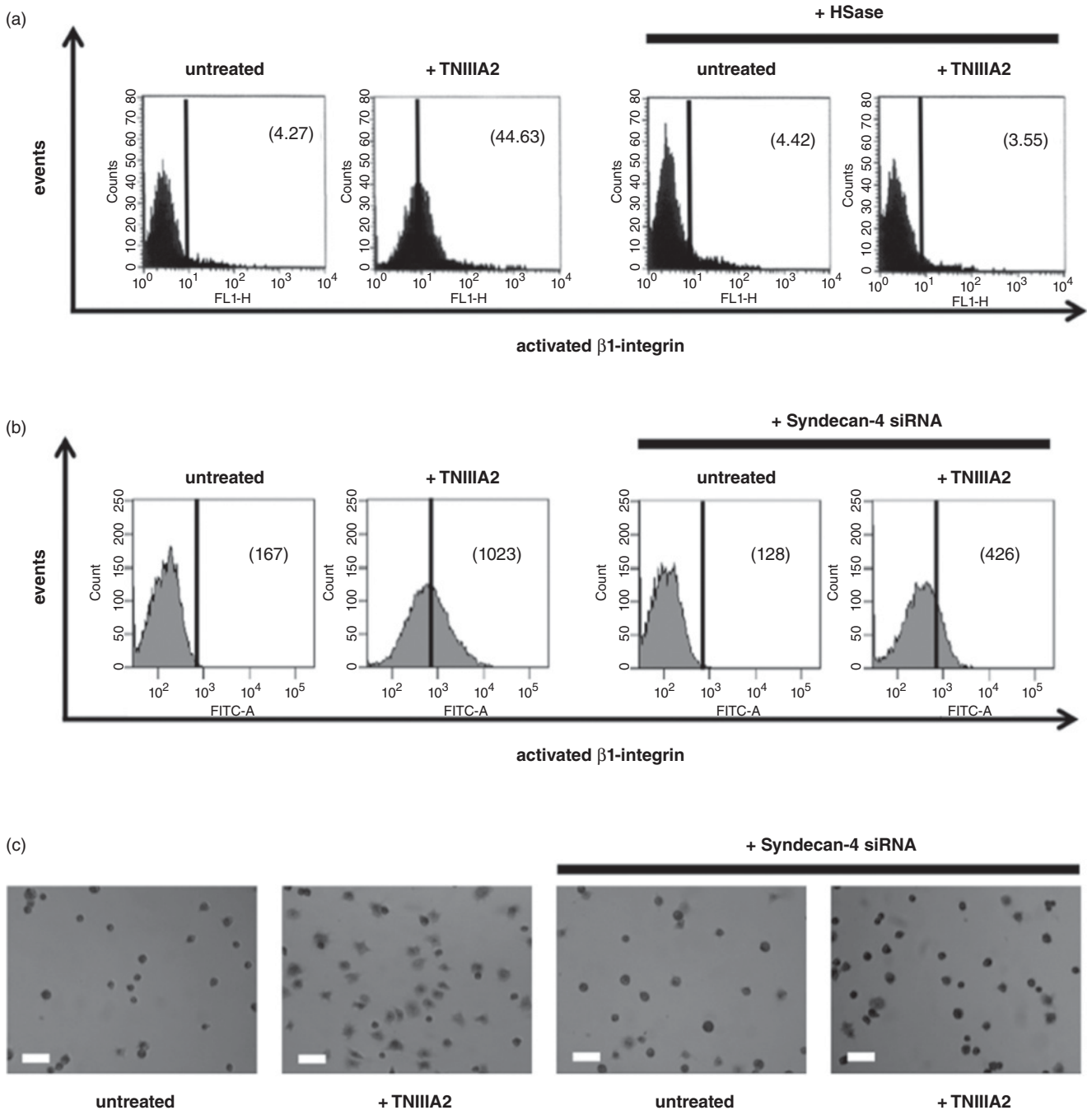


FIGURE 24.3 Implication of syndecan-4 in enhanced β1-integrin activation and the following acceleration in cell adhesion. (a) Requirement of HS chains for TNIIIA2-induced β1 integrin activation. Mean fluorescence intensity (MFI) is expressed in parentheses. (b,c) Effect of syndecan-4 knockdown on expression of TNIIIA2 activity: (b) WI38VA cells transfected with syndecan-4 siRNA were treated with TNIIIA2 and then examined for β1 integrin activation (c) or cell adhesion to fibronectin (d). (Scale bars, 100 μm.)

of studies demonstrated that the primary cause of this relapse is believed to be the minimal residual disease (MRD) in bone marrow [4,12,13]. As a mechanism of the MRD after chemotherapy, several groups have demonstrated that the AML cells acquire multidrug resistance when these cells adhere to fibronectin through $\alpha 4\beta 1$- or $\alpha 5\beta 1$-integrin, commonly referred to as *cell-adhesion-mediated drug resistance* (CAM-DR) [14]. These reports led us to presume that inactivation of β1-integrin might contribute to overwhelming the persistence of MRD in AML. As described above, we

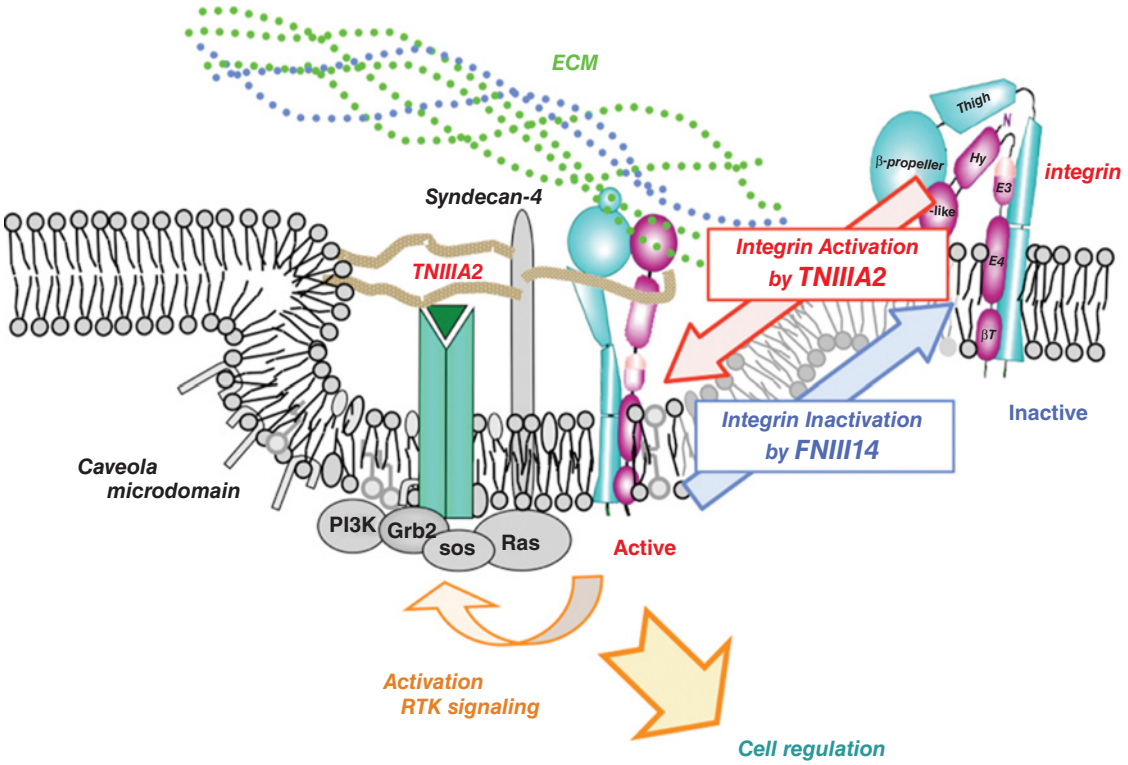


FIGURE 24.4 The intrinsic mechanism of cell regulation mediated through integrin activation and inactivation, induced by TNIIIA2 and FNIII14.

previously found antiadhesive peptide FNIIIA4 from fibronectin and reported that its antiadhesive effect is due to $\beta 1$-integrin inactivation. Therefore, it is expected that combined administration of antiadhesive peptide FNIII14 with anticancer drug administration might give a complete eradication of AML.

On the basis of this concept, we first examined the in vitro effect of FNIII14 on CAM-DR of hematopoietic tumor cells. When human AML cell line U937 cells were seeded on a fibronectin-coated plate and treated with the anticancer drug cytosine arabinoside (Ara-C), their viability was significantly higher than that of cells seeded on BSA-coated plate (Fig. 24.5). This suggests that U937 cells seeded to fibronectin-coated plate acquired CAM-DR through adhesion to fibronectin. The increased viability of cells on the fibronectin substrate was completely abrogated by addition of antiadhesive peptide FNIII14 (Fig. 24.5). Similar observations were obtained using other hematopoietic tumor cell line HL60 and fresh leukemic cells from six patients (data not shown). This in vitro experiment shows that the antiadhesive peptide FNIII14 might be effective in inhibition of CAM-DR.

We then examined the effect of this peptide in AML chemotherapy in an in vivo experimental system. An AML mouse model has been constructed by intravenous injection of human AML cell line U937 into the X-ray-irradiated SCID

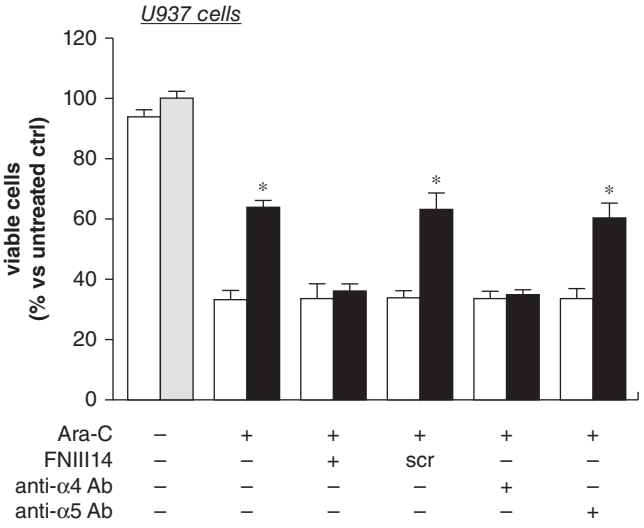


FIGURE 24.5 Effect of FNIII14 on the chemoresistance of leukemic cell lines induced by the interaction between integrin $\alpha 4\beta 1$ and fibronectin. U937 cells were seeded on 96-well plates coated with BSA (□) or fibronectin (■) and then incubated in the absence or presence of Ara C, FNIII14, FNIII14scr, anti-$\alpha 4$-integrin monoclonal antibody, and anti-$\alpha 5$-integrin monoclonal antibody. After 24 h, the viable cell number was evaluated by MTT assay. ($^*P < 0.05$.)

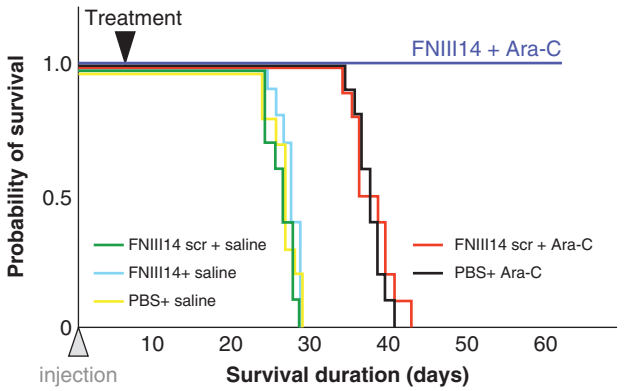


FIGURE 24.6 Combination therapy using FNIII14 and Ara C. Kaplan–Meier survival curves of mice treated with PBS and saline (yellow line), PBS and Ara-C (black line), FNIII14scr and saline (green line), FNIII14scr and Ara-C (red line), FNIII14 and saline (light blue), and FNIII14 and Ara-C (blue line) are shown. U937 cells were injected from tail vein, and Ara-C and peptide was administrated 7 days after U937 cell transplantation. (n = 6 for each group.)

mouse [15]. In this model mice, AML cells were detected only in bone marrow at days 7 after transplantation of AML cells, and all the mice consequently died by systemic dissemination of AML cells around day 25 (data not shown). As shown in figure 6, the mean survival of the mice administrated with vehicle, FNIII14, or FNIII14scr without Ara-C treatment, was around day 25. When the AML model mice were treated with anticancer drug Ara-C, their survival durations were prolonged, but all mice died around 35 days after U937 cell transplantation. In contrast, all of the mice treated with FNIII14+Ara-C survived even at the end of the observation period, day 62 (Fig. 24.6). In the FNIII14+Ara-C treated group, AML cells residing in bone marrow, which were detected at day 7 after transplantation, disappeared completely at day 62. Meanwhile, there were no differences in the number of white blood cells, neutrophils, lymphocyte, and platelets when the complete blood count was monitored for 11 days in the mice administrated with Ara-C alone or FNIII14+Ara-C (data not shown). Taken together, the combined administration of anticancer drug with β1-integrin inactivator "peptide FNIII14" might be a promising treatment to improve the prognosis of AML patients.

24.3 FORCED ADHESION TO FIBRONECTIN THROUGH SUSTAINED ACTIVATION OF β1-INTEGRIN BY TNIIIA2 CAUSED APOPTOSIS IN HEMATOPOIETIC TUMOR CELLS

One of extracellular matrix proteins, TN-C, is constitutively expressed in adult lymphoid tissues [16, 17]. Moreover, upregulation of TN-C expression in pathological states including tumorigenesis has been reported [18, 19]. These observations imply that the bone marrow of patients with hematopoietic malignancy probably show highly increased expression of TN-C. As described in Section 24.1, peptide TNIIIA2 derived from TN-C has the ability to enforce cell adhesion by activating β1-integrin. Therefore, we are interested in the effect of TNIIIA2 on hematopoietic tumor cells.

To elucidate this effect, we used Burkitt's lymphorma cell line Ramos cells, in which integrin $\alpha 4\beta 1$ is highly expressed as the major fibronectin receptor, but is incapable of contributing to cell adhesion because these receptors are ordinarily in the inactive state. When Ramos cells were enforced to adhere to the fibronectin by activating integrin $\alpha 4\beta 1$ with TNIIIA2, the number of viable cells was unexpectedly decreased without any antitumor drug administration (Fig. 24.7). This decrease in Ramos cell survival, induced by TNIIIA2, was almost completely blocked by concomitant administration of peptide CS1, an integrin-$\alpha 4\beta 1$ antagonist (Fig. 24.7). Addition of TS2/16, an anti-β1 integrin monoclonal antibody that has the ability to activate β1-integrin, also decreased Ramos cell survival (data not shown). Since this decrease in Ramos cell viability was accompanied by cell surface expression of phosphatidylserin (data not shown) [20], and since Z-VAD, a general caspase inhibitor, could completely cancel the effect of TNIIIA2 on Ramos cell viability (data not shown) [20], TNIIIA2 induced apoptosis in Ramos cells.

We next attempted to determine whether the induction of apoptotic cell death by enforced cell adhesion was specific in Ramos cells. When TNIIIA2 was added to U937 cell culture, these cells were forced to adhere to fibronectin substrates via activation of integrin $\alpha 4\beta 1$ (Fig. 24.8a,b). Under these experimental conditions, induction of adhesion and resulting decrease in viable cell number were observed in TNIIIA2-treated U937 cells. Moreover, we also employed several hematopoietic tumor cells with various expression levels of $\alpha 4\beta 1$ [20] and showed that TNIIIA2-mediated enforced cell adhesion through vigorous and sustained activation of β1-integrin leads apoptotic cell death in non-adherent hematopoietic tumor cells.

These observations seem to be inconsistent with the concept of CAM-DR as shown in Section 24.3. This discrepancy might be explained by the extent of cell adhesion to fibronectin substrate. In other words, "moderate adhesion" of tumor cells to fibronectin seems to confer their continuous survival. Actually, in a series of previous reports that mentioned CAM-DR, chemoresistance in tumor cells was induced by spontaneous cell adhesion to fibronectin, in which no artificial integrin activators were added in their experimental conditions [14,21–23]. In contrast, the peptide TNIIIA2 has the potent ability to induce β1-integrin activation and keep it for a long period [10], although cytokine-stimulated cell adhesion to fibronectin is rapid (reaching a maximum

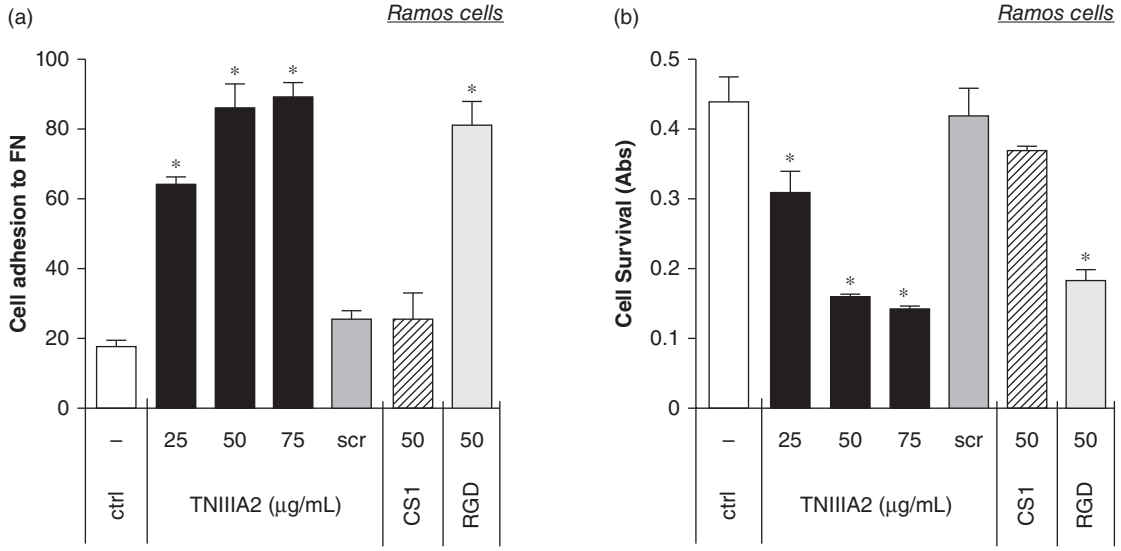


FIGURE 24.7 Effect on cell growth of forced adhesion of Ramos cells to FN. (a) Results of cell adhesion assay. The percentage of adherent cells is shown relative to the total number of cells seeded into the well. (b) Effect of induced adhesion to FN on Ramos cell survival is shown. (CS1 = connecting segment 1 peptide.)

within 30 min) but transient (returning to basal levels after several hours) [24]. From these facts, we presumed that this difference in the state of β1-integrin activation caused the difference in adhesion-induced cellular responses. It appears likely that CAM-DR may be induced through weak or moderate adhesion to fibronectin, and that tight and prolonged adhesion may turn on the proapoptotic signaling pathways, although it could not be ruled out the possibility that physiological amount of TNIIIA2 released in vivo may contribute to the induction of CAM-DR.

24.4 TNIIIA2-INDUCED ACTIVATION OF β1-INTEGRIN ENHANCES INTRACELLULAR DRUG ACCUMULATION IN HEMATOPOIETIC TUMOR CELLS

During cancer chemotherapy, development of multidrug resistance in tumor cells is a major complicating factor in tumor eradication. Acquisition of multidrug resistance might be induced by high-dose and long-term exposure to antitumor drugs. As mentioned above, TNIIIA2 could confer sensitivity

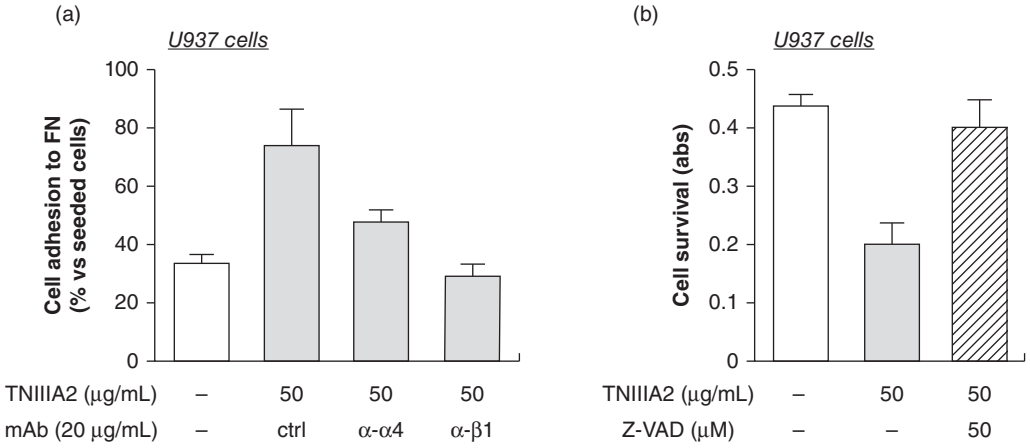


FIGURE 24.8 Peptide TNIIIA2-induced suppression in cell survival of U937 hematopoietic tumor cell. (a) U937 cells suspended in serum-free medium were seeded on fibronectin-coated plate in the presence or absence of TNIIIA2 and anti-integrin antibodies. Cell adhesion activity at 30 min after seeding was evaluated. (b) U937 cells were seeded as described above in the presence or absence of TNIIIA2 and Z-VAD. Viable cell number at 48 h after seeding was evaluated by WST assay.

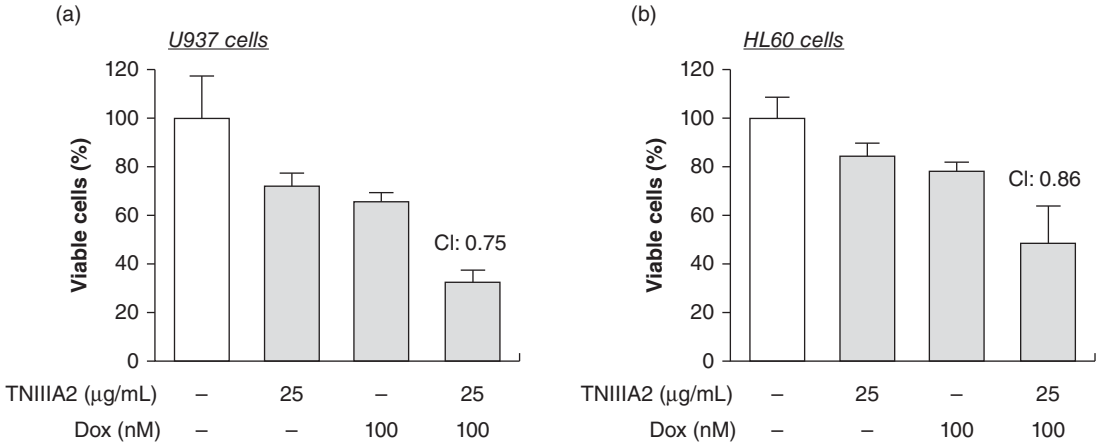


FIGURE 24.9 TNIIIA2-induced increase in chemosensitivity to Dox in hematopoietic tumor cells. U937 cells (a) and HL60 cells (b) were seeded in the presence or absence of TNIIIA2. Then Dox was added to culture medium. Viable cell number was evaluated by WST assay and then combination index (CI) was calculated (CI = [viability at Dox^+/$TNIIIA2^+$]/([viability at Dox^+] × [viability at $TNIIIA2^+$])). (According to C1, notations 1, >1, and <1 reveal additive, antagonistic, and synergistic, respectively.)

for apoptotic cell death to hematopoietic tumor cells through induction of tight and prolonged cell adhesion. Therefore, it is possible that the combined administration of TNIIIA2 with anticancer drug increases the efficacy of chemotherapy.

To test a possible clinical usefulness of TNIIIA2, U937 hematopoietic tumor cells were treated with the anticancer drug doxorubicin (Dox) in the presence or absence of TNIIIA2. When U937 cells were treated with Dox alone, around 30% decrease in their survival was observed (Fig. 24.9a). Approximately 70% decrease in the viable cells was observed by treatment with Dox in combination with TNIIIA2 (Fig. 24.9a). Almost the same results were obtained using another AML cell line HL60 (Fig. 24.9b). When synergism between TNIIIA2 and Dox was evaluated by calculation of "combination-index (CI)" [25], the effect of TNIIIA2 on the enhancement of anti-tumor activity of Dox was not additive, but synergistic. These observations indicate the possibility that TNIIIA2 could enhance the effect of an anticancer drug.

In order to clarify the mechanism underlying enhanced chemo-sensitivity in TNIIIA2-treated hematopoietic tumor cells, we next examined the level of intracellular drug accumulation in these cells. Flow cytometric analysis showed that the level of intracellular Dox was elevated when β1-integrins of U937 and HL60 cells were activated by TNIIIA2 (Fig. 24.10a,b). Increase in the Dox accumulation was dependent on the duration and dosage of TNIIIA2 administration (unpublished observation). Furthermore, elevation in the level of intracellular Dox was also elevated

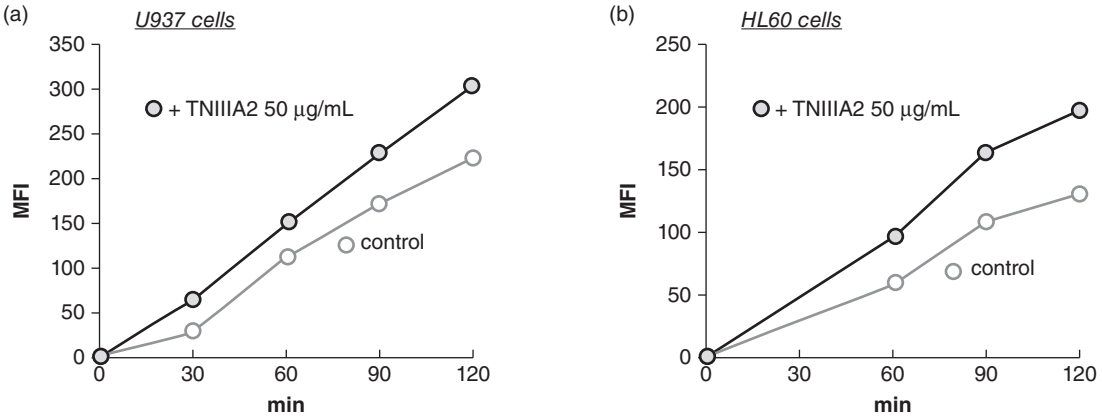


FIGURE 24.10 TNIIIA2-induced intracellular Dox accumulation in hematopoietic tumor cells. U937 cells (a) and HL60 cells (b) were seeded in the presence or absence of TNIIIA2. Then Dox was added to culture medium. Intracellular Dox level was analyzed by FACS.

by the β1-integrin-activating monoclonal antibody (unpublished observation). These results suggest that TNIIIA2-induced β1-integrin activation renders hematopoietic tumor cells chemosensitive through an intracellular accumulation of anticancer drug level. Although the mechanisms underlying TNIIIA2-mediated intracellular drug accumulation are still unclear, TNIIIA2 might be useful for tumor chemotherapy.

24.5 TNIIIA2-MEDIATED β1-INTEGRIN ACTIVATION ACCELERATES ERYTHROID DIFFERENTIATION OF HEMATOPOETIC TUMOR CELLS

Tumor cells are characterized not only by elevated proliferation and immortality. Poor differentiation is also accepted as one of intrinsic character of tumor cells. Therefore, differentiation-inducing therapy has attracted attention as a possible clinical approach of anticancer treatment.

Differentiation of hematopoietic stem and progenitor cells occurs ordinarily in bone marrow and fetal liver. Adhesive interactions between hematopoietic stem or progenitor cells and the surrounding microenvironment play a pivotal role in the regulation of appropriate proliferation and differentiation [11,26–30]. In the case of erythropoiesis, cell adhesion of erythroid progenitor cells via the fibronectin receptors integrin $\alpha4\beta1$ and $\alpha5\beta1$ has been reported as a key event for their differentiation [31–39]. However, the substantial function of these fibronectin receptors in erythroid differentiation was not fully understood.

As shown in Fig. 24.10a,c, we demonstrated that TNIIIA2 is able to accelerate hemin-induced erythroid differentiation in K562 leukemic cells, by the enhancement of cell adhesion. TNIIIA2-induced acceleration of erythroid differentiation was significantly revoked by antagonists such as anti-α5-integrin antibody and RGD peptide. Moreover, peptide FNIII14, which has an ability to reverse β1-integrin activation, abrogated an enhanced differentiation of K562 cells induced by concomitant administration of hemin with TNIIIA2 (Fig. 24.11a,c). These results suggest that the TNIIIA2 is able to work as an accelerator for hemin-induced erythroid differentiation, and this effect of TNIIIA2 is mediated through enhanced adhesion of K562 cells to fibronectin via β1-integrin activation.

K562 cells express only integrin-$\alpha5\beta1$ as fibronectin receptors [40]. In fact, TNIIIA2-mediated forced cell adhesion of K562 cells was suppressed only by the antagonist for integrin $\alpha5\beta1$ (Fig. 24.11b). No effect of the antagonists for integrin $\alpha4\beta1$ was observed in TNIIIA2-induced K562 cell adhesion (Fig. 24.11b). However, the TNIIIA2-mediated acceleration of hemin-induced erythroid differentiation was significantly blocked not only by an antagonist for integrin-$\alpha5\beta1$ (RGD peptide) but also by an antagonist for integrin-$\alpha4\beta1$ (CS1 peptide) (Fig. 24.11d). In order to resolve this contradiction, changes in the expression of α4-integrin during hemin-induced erythroid differentiation were evaluated. As a result, expression of α4-integrin became detectable 1 day after initiation of K562 differentiation, when these cells were concomitantly administrated with TNIIIA2 (data not shown) [41]. TNIIIA2-induced upregulation of α4-integrin was attenuated by α5-integrin agonist RGD. There was no difference in the level of α4-integrin expression when K562 cells were stimulated with hemin alone (data not shown) [41]. From these results, forced adhesion to fibronectin substrate through integrin-$\alpha5\beta1$ induces expression of integrin-$\alpha4\beta1$ in K562 erythroid progenitor cells, and this seems to be a prerequisite for acceleration of hemin-stimulated erythroid differentiation. Thus, modulation of the integrin activation status was implicated in regulation of erythroid differentiation. Further investigation would be necessary to ascertain if the proadhesive effect of TNIIIA2 could commonly play a role in hematopoiesis in vivo.

24.6 TNIIIA2-MEDIATED β1-INTEGRIN ACTIVATION LEADS DEREGULATED HYPERPROLIFERATION TO NONTRANSFORMED FIBROBLASTIC CELLS

Disruption of adhesive interaction between β1-integrin and fibronectin induces apoptosis, termed *anoikis*, in adherent nontransformed cells such as fibroblastic cells and epithelial cells [1, 2]. When NIH/3T3 cells were cultured in the serum-deprived conditions, their viability became decreased (Fig. 24.12a, gray line). Since this decrease in the number of viable cells was significantly abrogated by general caspase inhibitor Z-VAD (Fig. 24.12b, black line) and the β1-integrin-activating mAb, it was due to induction of anoikis elicited by the serum deprivation. Proadhesive peptide TNIIIA2 completely rescued NIH/3T3 cells from anoikis (Fig. 24.12a,b). This "cell-protective effect" of TNIIIA2 was abolished by antagonists for integrin-$\alpha5\beta1$, such as anti-α5-integrin antibody and RGD peptide (Fig. 24.12b). These results suggested that TNIIIA2 has a potential to render normal fibroblastic cells resistant to anoikis by its effect on β1-integrin activation.

On the other hand, platelet-derived growth factor (PDGF) acts as a potent mitogen stimulating cell survival and proliferation for both untransformed and transformed mesenchymal cells. PDGF ligation to its receptor PDGFR induces the activation of its intrinsic tyrosin kinase, which, in turn, activates the Ras/MAP kinase pathway [42]. It has been established that cell adhesion to ECM through integrins is also indispensable for cell proliferation [43]. We recently found that TNIIIA2 significantly accelerates PDGF-induced proliferation of NIH/3T3 cells adhered to fibronectin substrate (Fig. 24.13). PDGF could enhance cell proliferation in a dose-dependent manner, whereas excessive concentration of

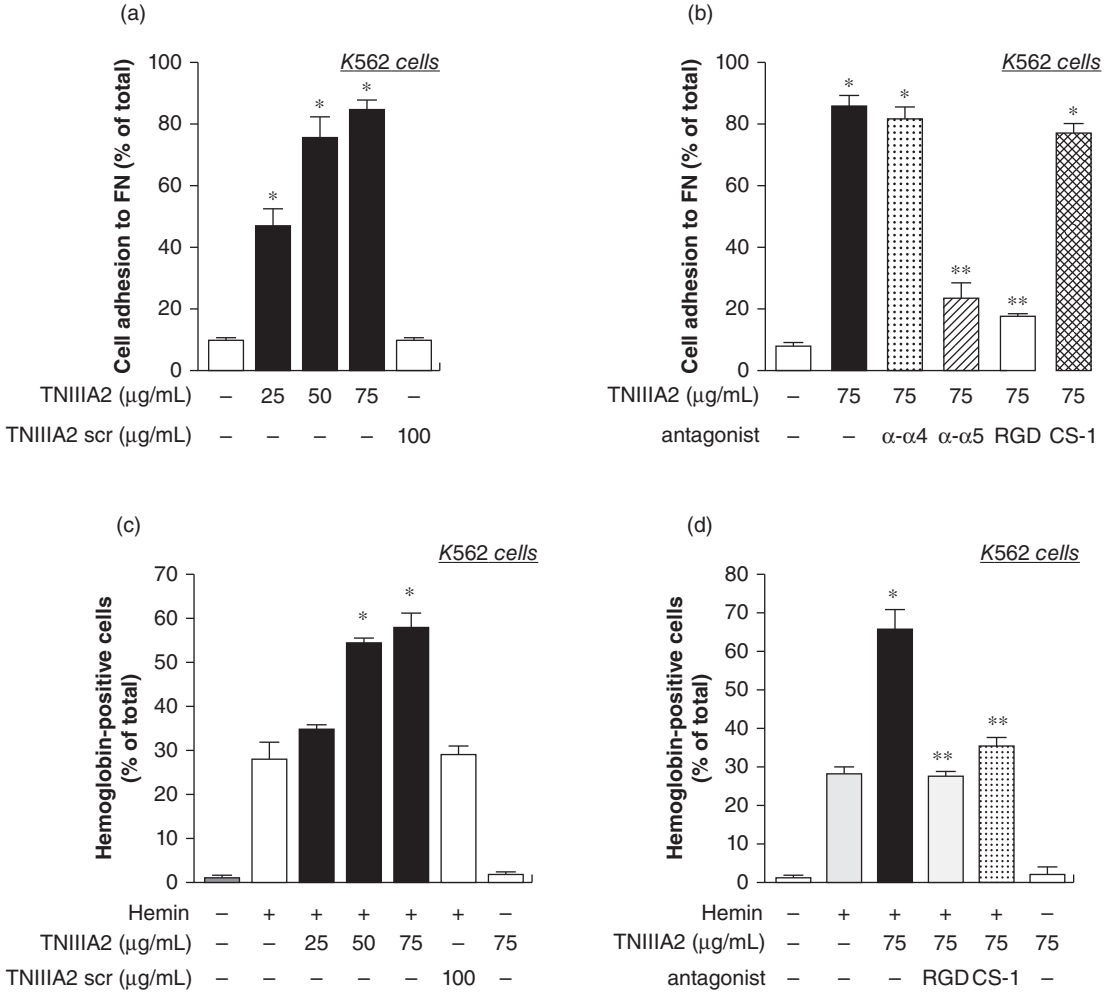


FIGURE 24.11 Adhesion-dependent acceleration of hemin-induced erythroid differentiation of K562 cells. (a) Dose dependence of TNIIIA2-induced adhesion of K562 cells. (b) Effects of antagonist for $\alpha 5\beta 1$-integrin (α-$\alpha 5$ Ab and RGD) and $\alpha 4\beta 1$-integrin (α-$\alpha 4$ Ab and CS1) on TNIIIA2-induced adhesion to FN in K562 cells. (c) Effect of TNIIIA2 on erythroid differentiation of K562 cells, induced by hemin. (d) Effects of antagonist for $\alpha 5\beta 1$-integrin (RGD) and $\alpha 4\beta 1$-integrin (CS1) on TNIIIA2-induced acceleration of erythroid differentiation.

PDGF (>10 ng/mL) showed no further enhancing effect on cell proliferation. However, once the cells face TNIIIA2, in the presence of PDGF, proliferation of PDGF-stimulated cells became more aggressive (Fig. 24.13). Almost the same results were also obtained even when TNIIIA2 was replaced by 9EG7, an anti-$\beta 1$-integrin monoclonal antibody that has the ability to activate $\beta 1$-integrin (Fig. 24.13). Combined administration of PDGF with Mg^{2+} that also has ability to activate $\beta 1$-integrin shows enhanced cell proliferation if compared with that of NIH/3T3 stimulated with PDGF solely (Fig. 24.13). In the series of experiments, both collocalization of PDGFR with $\beta 1$-integrin and enhancement of PDGFR autophosphorylation were also observed in NIH/3T3 cells stimulated with PDGF in combination with TNIIIA2 (data not shown). These results suggested that hyperproliferation of NIH/3T3 cells was caused by TNIIIA2-mediated potentiated and sustained activation of $\beta 1$-integrin. Since TNIIIA2 originates from tenascin-C that is highly expressed in tumor and tumor stromas, TNIIIA2-induced deregulated cell proliferation might be associated with tumorigenesis and/or tumor progression. Therefore, the active site of TNIIIA2 in the tenascin-C protein molecule might be a promising target for reducing cancer promotion.

24.7 CONCLUDING REMARKS

Adhesive interactions of cells with surrounding ECM through integrins are important to a variety of cellular events, although hormonal factors are known to function as a ligand

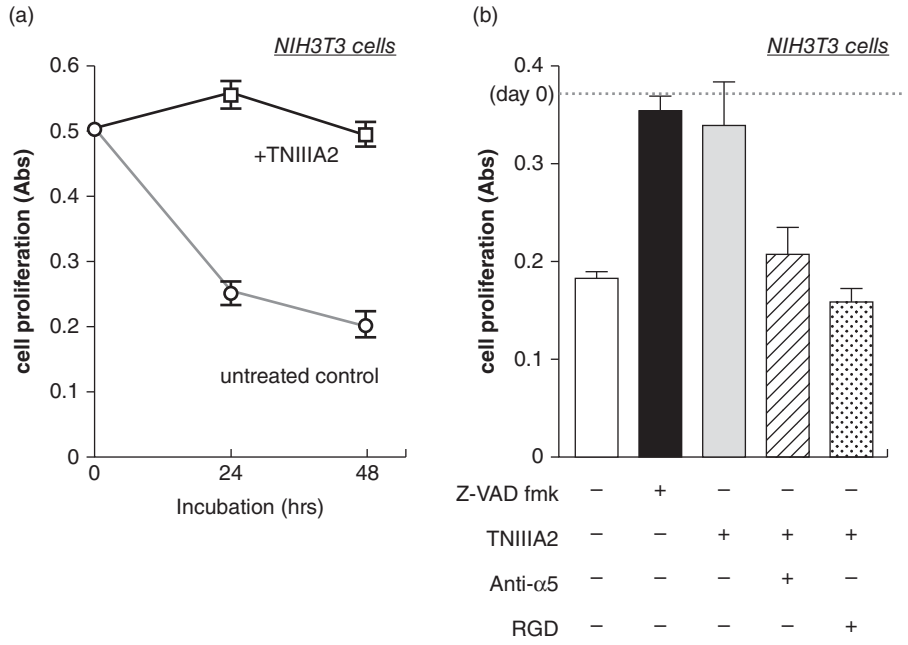


FIGURE 24.12 TNIIIA2 protects cells from anoikis by activating the β1-integrin. (a) Timecourse study of the effect of cell detachment on survival/proliferation of NIH3T3 cells. (b) Effect of inhibition of apoptosis (Z-VAD) or $\alpha 5\beta$1-integrin signal (anti-α5 Ab and RGD peptide) in detachment-induced cell death. (our unpublished observations)

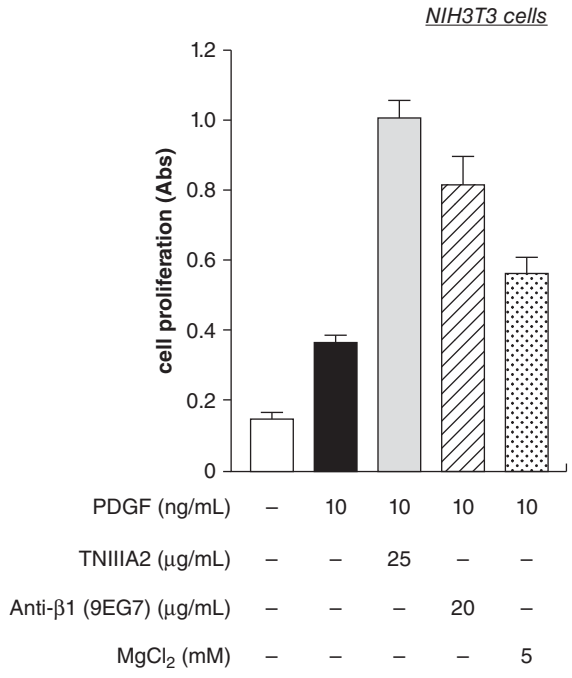


FIGURE 24.13 TNIIIA2 accelerates PDGF-induced cell proliferation. PDGF-induced cell growth was enhanced by addition of TNIIIA2, as well as administration with integrin activators (anti-β1 and $MgCl_2$) (our unpublished observations).

for cell surface receptors regulating cellular events. However, no reports referring to the "activation status" of β1-integrin in regulation of cellular responses have appeared in the literature. In this chapter, we mentioned the possibility that the changes in the state of β1-integrin activation contribute to the modulation of various cellular functions. Further investigations of the role of integrin activation status in disease outbreak and its progression might be attractive. Peptides FNIII14 and TNIIIA2, which enable us to control activation status of β1-integrins, either positively or negatively, might become beneficial tools.

It has generally been considered that the activation of integrins is regulated by *inside–out* signals from the cell interior. This signaling switch is triggered by an extracellular soluble agonist such as certain chemokines or growth factors. On the other hand, several artificial factors are known to activate β1-integrin. These include divalent cations such as Mn^{2+} and Mg^{2+} and anti-β1-integrin mAbs, which bind directly to the extracellular domain of β1-integrin. Cell surface molecules tetraspan/TM4SF, CD87/uPAR, and CD47/IAP are also known to modulate integrin activity via interaction with extracellular domains of β1-integrin. For example, CD151 constitutively associates with integrin-α3, and serves as a constitutive potentiator for $\alpha 3\beta$1-integrin activity through a direct association [44, 45]. We previously demonstrated that TNIIIA2 binds to cell surface syndecan-4 and that the formed TNIIIA2/syndecan-4 complex could activate β1-integrin by their lateral interaction to the ectodomain

of β1-integrin. This *outside–out* signaling might contribute to keep β1-integrin conformation active [10]. This relationship among TNIIIA2, syndecan-4, and β1-integrin may provide another example of the regulatory roles of extracellular domains in cell adhesion signaling [46–48].

In this chapter, we referred to the effect of two peptides containing matricryptic sites of fibronectin and tenascin-C, respectively. These bioactive regions might have been reexposed when parental ECM was degraded by inflammatory proteinases, which were reportedly secreted in pathological conditions including cancer. Therefore, at the site of cancer promotion and progression, these matricryptic sites possibly play important roles for inducing pathological cellular responses. Important implication of the "activation status of β1-integrin" in the modulation of cellular responses has been shown in this chapter. Thus, these matricryptic active sites in FNIII14 and TNIIIA2 might be a promising target for developing novel anticancer approaches.

REFERENCES

[1] Ilic, D., Almeida, E.A., Schlaepfer, D.D., Dazin, P., Aizawa, S., Damsky, C.H. (1998). *J. Cell Biol.* **143**, 547–560.

[2] Frisch, S.M., Screaton, R.A. (20091). *Curr. Opin. Cell Biol.* **13**, 555–562.

[3] Damiano, J.S., Hazlehurst, L.A., Dalton, W.S. (2001). *Leukemia* **15**, 1232–1239.

[4] Matsunaga, T., Takemoto, N., Sato, T., Takimoto, R., Tanaka, I., Fujimi, A., Akiyama, T., Kuroda, H., Kawano, Y., Kobune, M., Kato, J., Hirayama, Y., Sakamaki, S., Kohda, K., Miyake, K., Niitsu, Y. (2005). *Nat. Med.* **91**, 158–165.

[5] Hazlehurst, L.A., Dalton, W.S. (2001). *Cancer Metast. Rev.* **20**, 43–50.

[6] Matsunaga, T., Fukai, F., Miura, S., Nakane, Y., Owaki, T., Kodama, H., Tanaka, M., Nagaya, R., Tamayama, T., Niitsu, Y. (2008). *Leukemia* **22**, 353–360.

[7] Fukai, F., Hasebe, S., Ueki, M., Mutoh, M., Ohgi, C., Takahashi, H., Takeda, K., Katayama, T. (1997). *J. Biochem.* **121**, 189–192.

[8] Kamiya, S., Kato, R., Wakabayashi, M., Enami, I., Ishii, T., Takagi, J., Fukai, F. (2002). *Biochemistry* **41**, 3270–3277.

[9] Watanabe, K., Takahashi, H., Habu, Y., Kamiya-Kubushiro, N., Kamiya, S., Nakamura, H., Yajima, H., Ishii, T., Miyazaki, K., Fukai, F. (2000). *Biochemistry* **39**, 7138–7144.

[10] Saito, Y., Imazeki, H., Miura, S., Yoshimura, T., Okutsu, H., Harada, Y., Ohwaki, T., Nagao, O., Kamiya, S., Kodama, H., Handa, H., Yoshida, T., Fukai, F. (2007). *J. Biol. Chem.* **282**, 34929–34937.

[11] Williams, D.A., Rios, M., Stephens, C., Patel, V.P. (1991). *Nature* **352**, 438–441.

[12] Feller, N., van delPol, M.A., van Stijn, A., Weijers, G.W., Westra, A.H., Evertse, B.W., Ossenkoppele, G.J., Schuurhuis, G.J. (2004). *Leukemia* **8**, 1380–1390.

[13] Kern, W., Voskova, D., Schoch, C., Hiddemann, W., Schnittgr, S., Haferlach, T. (2004). *Blood* **104**, 3078–3085.

[14] Damiano, J.S., Hazlehurst, L.A., Dalton, W.S. (2001). *Leukemia* **15**, 1232–1239.

[15] Matsunaga, T., Fukai, F., Miura, S., Nakane, Y., Owak, T., Kodama, H., Tanaka, M., Nagaya, T., Takimoto, R., Takayama, T., Niitsu, Y. (2004). *Leukemia* **8**, 1380–1390.

[16] Chilosi, M., Lestani, M., Benedetti, A., Montaqna, L., Pedron, S., Scarpa, A., Menestrina, F., Hirohashi, S., Pizzolo, G., Semenzato, G. (1993). *Am. J. Pathol.* **143**, 1348–1355.

[17] Ocklind, G., Talts, J., Fässler, R., Mattsson, A., Ekblom, P. (1993). *J. Histochem. Cytochem.* **41**, 1163–1169.

[18] Atula, T., Hedström, J., Finne, P., Leivo, I., Markkanen-Leppänen, M., Haglund, C. (2003). *Anticancer Res.* **23**, 3051–3056.

[19] Leins, A., Riva, P., Lindstedt, R., Davidoff, M.F., Mehraein, P., Weis, S. (2003). *Cancer* **98**, 2430–2439.

[20] Saito, Y., Owaki, T., Matsunaga, T., Saze, M., Miura, S., Maeda, M., Eguchi, M., Tanaka, R., Taira, J., Kodama, H., Goto, S., Niitsu, Y., Terada, H., Fukai, F. (2010). *J. Biol. Chem.* **285**, 7006–7015.

[21] Hazlehurst, L.A., Dalton, W.S. (2001). *Cancer Metast. Rev.* **20**, 43–50.

[22] Wang, W.M., Consoli, U., Lane, C.M., Durett, A., Lauppe, M.J., Champlin, R., Andreeff, M., Deisseroth, A.B. (1998). *Cell Growth Differ.* **9**, 105–112.

[23] Damiano, J.S., Cress, A.E., Hazlehurst, L.A., Shtil, A.A., Dalton, W.S. (1999). *Blood* **93**, 1658–1667.

[24] Chigaev, A., Blenc, A.M., Braaten, J.V., Kumaraswamy, N., Kepley, C.L., Andrews, R.P., Oliver, J.M., Edwards, B.S., Prossnitz, E.R., Larson, R.S., Sklar, L.A. (2001). *J. Biol. Chem.* **276**, 48670–48678.

[25] Drewinko, B., Green, C., Loo, T.L. (1976). *Cancer Treat. Reports* **60**, 1619–1625.

[26] Coulombel, L., Vunillet, M.H., Leroy, C., Tchernia, G. (1988). *Blood* **71**, 329–334.

[27] Williams, D.A. (1994). *Pediatr. Res.* **36**, 557–560.

[28] Murti, K.G., Brown, P.S., Kumagai, M., Campana, D. (1996). *Exp. Cell Res.* **226**, 47–58.

[29] Clark, B.R., Gallagher, J.T.Dexter, T.M. (1992). *Baillieres Clin. Haematol.* **5**, 619–652.

[30] Wilson, A., Trumpp, A. (2006). *Nat. Rev. Immunol.* **6**, 93–106.

[31] Patel, V.P., Lodish, H.F. (1987). *J. Cell Biol.* **105**, 3105–3118.

[32] Vuillet-Gaugler, M.H., Breton-Gorius, J., Vainchenker, W., Guichard, J., Leroy, C., Tchernia, G., Coulombel, L. (1990). *Blood* **75**, 865–873.

[33] Tada, T., Widayati, D.T., Fukuta, K. (2006). *Anat. Histol. Embryol.* **35**, 235–240.

[34] Weinstein, R., Riordan, M.A., Wenc, K., Kreczko, S., Zhou, M., Dainiak, N. (1998). *Blood* **73**, 111–116.

[35] Eshghi, S., Vogelezang, M.G., Hynes, R.O., Griffith, L.G., Lodish, H.F. (2007). *J. Cell Biol.* **177**, 871–880.

[36] Papayannopoulou, T., Priestley, G.V., Nakamoto, B. (1998). *Blood* **91**, 2231–2239.

[37] van der Loo, J.C., Xiao, X., McMillin, D., Hashino, K., Kato, I., Williams, D.A. (1998). *J. Clin. Invest.* **102**, 1051–1061.

[38] Yanai, N., Sekine, C., Yagita, H., Obinata, M. (1994). *Blood* **83**, 2844–2850.

[39] Hamamura, K., Matsuda, H., Takeuchi, Y., Habu, S., Yagita, H., Okumura, K. (1996). *Blood* **87**, 2513–2517.

[40] Elices, M.J., Osborn, L., Takada, Y., Crouse, C., Luhowskyj, S., revised.

[41] Tanaka, R., Owaki, T., Kamiya, S., Matsunaga, T., Shimoda, K., Kodama, H., Hayashi, R., Abe, T., Harada, Y.P., Shimonaka, M., Yajima, H., Terada, H., Fukai, F. (2009). *J. Biol. Chem.* **284**, 19817–19825.

[42] Claesson-Welsh, L. (1994). *J. Biol. Chem.* **269**, 32023–32026.

[43] Chiarugi, P. (2008). *IUBMB (International Union of Biochemistry and Molecular Biology) Life* **60**, 301–307.

[44] Yauch, R.L., Kazarov, A.R., Desai, B., Lee, R.T., Hemler, M.E. (2000). *J. Biol. Chem.* **275**, 9230–9238.

[45] Nishiguchi, R., Sanzen, N., Nada, S., Sumida, Y., Wada, Y., Okada, M., Takagi, J., Hasegawa, H., Sekiguchi, K. (2005). *Proc. Natl. Acad. Sci. USA* **102**, 1939–1944.

[46] Adams, J.C., Kureishy, N., Taylor, A.L. (2001). *J. Cell Biol.* **152**, 1169–1182.

[47] Carey, D.J., Stahl, R.C., Cizmeci-Smith, G., Asundi, V.K. (1994). *J. Cell Biol.* **124**, 161–170.

[48] Liu, W., Litwack, E.D., Stanley, M.J., Langford, J.K., Lander, A.D., Sanderson, S.D. (1998). *J. Biol. Chem.* **273**, 22825–22832.

25

DEPTH PROFILE OF Kr^+-IRRADIATED CHITOSAN

Kazunaka Endo

Division of Colloid and Interface Science, Research Institute for Science and Technology, Tokyo University of Science, Japan

25.1 INTRODUCTION

Chitosan is especially known to be a most powerful adsorbent of natural origin and is widely used for the prevention of water pollution by highly toxic chlorinated aromatic compounds and metal ions [1]. Chitosan is inexpensive, environmentally benign, harmless to humans, and a hugely obtainable biomass, which makes it very promising and attractive for use in many applications. It is also found in many biomedical applications, including tissue engineering, owing to its biocompatibility, low toxicity, and degradation in the body by enzymes such as chitosanase and lysozyme, which has opened up avenues for modulating drug release in vivo in the treatment of various diseases. These chitosan-based delivery systems range from microparticles to nanoparticles to gels and films. Ion beam irradiation is also a useful method for modification of surface properties, such as wear resistance, corrosion resistance, and biopolymer compatibility. A composite film of the chitosan/carbon nanotube complex has been proposed as a material of blood biocompatibility, due to the advantage of ion beam irradiation [2].

On the other hand, the use of C13 NMR and X-ray photoelectron spectral analysis for chitosan has been studied in an attempt to clarify the electronic structure in the formation of properties of biological molecules from the DFT calculations [3], and to understand the changes in adsorption behavior of chemically modified biopolymer chitosan (cross-linked biopolymer) [4].

In the present study, we aim to analyze Raman and valence X-ray photoelectron spectra of chitosan film with Kr^+ ion beam irradiation. In order to simulate the experimental Raman and valence X-ray photoelectron spectra (VXPS) of the Kr^+ ion-irradiated film, we performed quantum-chemical calculations at B3LYP/6−31G** level using the GAUSSIAN 09 program [5].

25.2 COMPUTATIONAL METHOD

The first-geometry of model molecules {chitosan monomer [H-($C_6H_{11}NO_4$)-O-H] or dimer [H-($C_6H_{11}NO_4)_2$-O-H], adamantine derivative [$C_{10}H_{12}(CH_3)_4$] for diamondlike carbons, adamantine ($C_{10}H_{16}$) for amorphous carbons, pyrene ($C_{16}H_{10}$) for graphite} was optimized at AM1 method in MOPAC software. We optimized these molecules using a second-geometry method within hybrid density functional theory, which was Becke's three-parameter hybrid functional model [6], with the correlation functional model due to Lee et al. [7] (B3LYP), using 6-31G** bases. In the optimization, we adopted eigenvalues and eigenvectors of these molecules in order to simulate the valence X-ray photoelectron spectra, as considered by Koopmans' theoremlike method. The intensity of valence XPS was estimated from the relative photo-ionization cross section for Mg Kα radiation using the Gelius intensity model [8,9]. In the case of the relative atomic photoionization cross section, we used the theoretical values from Yeh [10].

To simulate the valence XPS, we started with a superposition of peaks centered on each vertical ionization potential (VIP). As described previously, each peak is represented by a Gaussian curve. In the case of the linewidth [i.e., $WH(k)$], we used $WH(k) = 0.10I_k$ (proportional to the ionization energy) for valence XPS.

Encyclopedia of Biocolloid and Biointerface Science, Volume 1, First Edition. Edited by Hiroyuki Ohshima.
© 2016 John Wiley & Sons, Inc. Published 2016 by John Wiley & Sons, Inc.

In order to account for and somewhat quantify solid-state effects in chitosan, diamondlike carbon, amorphous carbon, and graphite in our investigations, we defined a quantity *WD* in our earlier work [11–14]. The quantity *WD* denotes the sum of the workfunction of the sample (*W*) and other energy effects (with *D* as delta), such as the polarization energy and so on. The *WD* can be estimated from the difference between experimental or theoretical electron binding energy (I_c or I_k) of model molecules, and the experimental core and valence electron-binding energy of the solid chitosan, diamondlike carbon, amorphous carbon, and graphite. In order to compare the calculated binding energy for the model molecules and the experimental binding energy of the solid substances, one has to shift each computed value (I_c or I_k) by a quantity *WD* as $I'_c(= I_c - WD)$ [or $I'_k(= I_k - WD)$], to convert to I'_c (or I'_k) on a common binding energy axis (relative to the Fermi level).

After the geometry optimization, in order to take into account the anharmonicity effects in the calculation of vibrational frequencies, one uses the scaling factor for the calculated frequencies. As Scott and Random [15] showed the scaling factor as 0.9614 in the calculations of vibrational frequencies at B3LYP/6-31G** level for some small molecules under the room temperature, we also estimated the scaling factor as 0.9614.

To simulate Raman spectra of the carbonized chitosan film, we started with a superposition of peaks centered on each Raman shift for the four model components of chitosan, diamondlike C, amorphous C, and graphite. Each peak was represented by a Gaussian curve. In the case of the linewidth [*WH*(*k*)], we used $WH(k) = 50\ cm^{-1}$ for Raman shift, in order to simulate the Raman spectrum of carbonized chitosan film.

All calculations were performed by ab initio hybrid calculations in the GAUSSIAN 09 program on a Panasonic CF-N9 notebook personal computer.

25.3 EXPERIMENTAL METHOD

We used commercially available chitosan (Wako Chemical co., Inc). Krypton ion bombardment was carried out at an energy of 150 keV with fluences ranging from 1.0×10^{13} to 1.0×10^{15} ions cm^{-2} in the base pressure of $<4.0 \times 10^{-4}$ Pa at room temperature using a RIKEN 200-kV low-current implanter. The beam current density used was about 0.2 μA cm^{-2} to prevent the specimen from heating.

Experimental photoelectron spectra of the samples were obtained on a JEOL JPS-9010 MC spectrometer using Mg-Kα (1253.6 eV) radiation. The applied power was operated at 15 kV, and 20 mA. The base pressure of the analysis chamber was $<8.0 \times 10^{-7}$ Pa. Energy-scale calibration was achieved using the Au $4f_{7/2}$(83.8 eV) transition. Dispersion compensation yielded an instrumental resolution of 0.5 eV from full width at half-maximum for the Ag3*d* line of silver. Multiscan averaging on a multichannel analyzer was used for

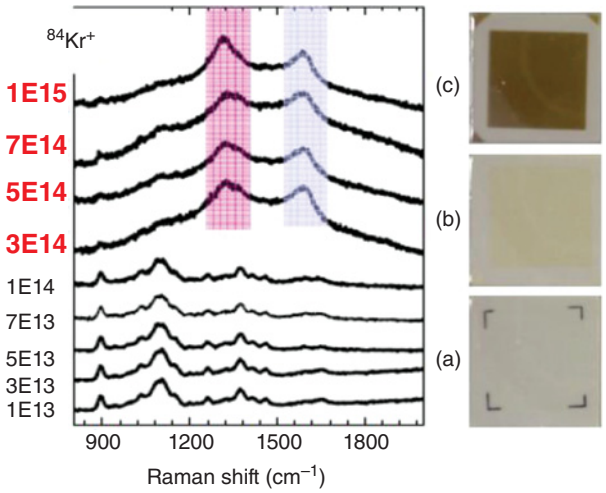


FIGURE 25.1 Raman shift of chitosan film modified by Kr^+ ion beam bombardments in the wavenumber range of 800–2000 cm^{-1} with surface color changes of a), b), and c) of chitosan films modified by Kr^+ ion beam bombardments at $1 \times 10^{13} - 1.0 \times 10^{14}$ (a), $3 \times 10^{14} - 5.0 \times 10^{14}$ (b), and $7 \times 10^{14} - 1.0 \times 10^{15}$ (c) ions cm^{-2}, respectively.

the valence band region, although a very low photoelectron emission cross section was observed in this range.

Raman shift measurements were performed on the samples in the wavenumber range from 800 to 2000 cm^{-1} using a Raman spectrometer (LabRAM, Jobin-Yvon, France) equipped with a HeNe ion laser (632.8 nm).

25.4 RESULTS AND DISCUSSION

We have studied the electronic state of chitosan from C13 NMR and X-ray photoelectron spectral analysis from the

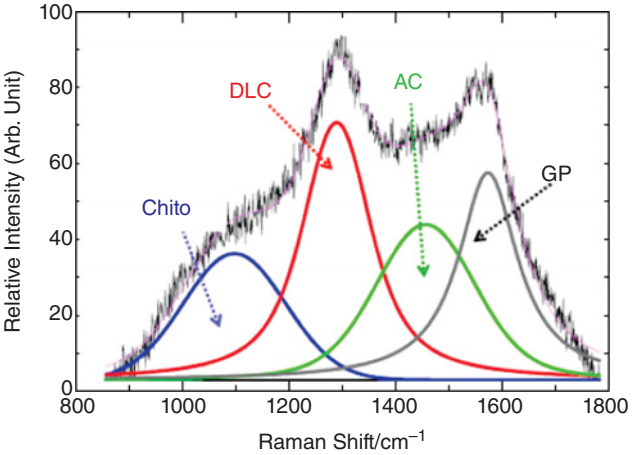


FIGURE 25.2 Experimental Raman spectra of carbonized chitosan film irradiated by Kr^+ ion beam at 1.0×10^{15} ions cm^{-2} (resolved spectra identified by four model components of chitosan, diamondlike C, amorphous C, and graphite).

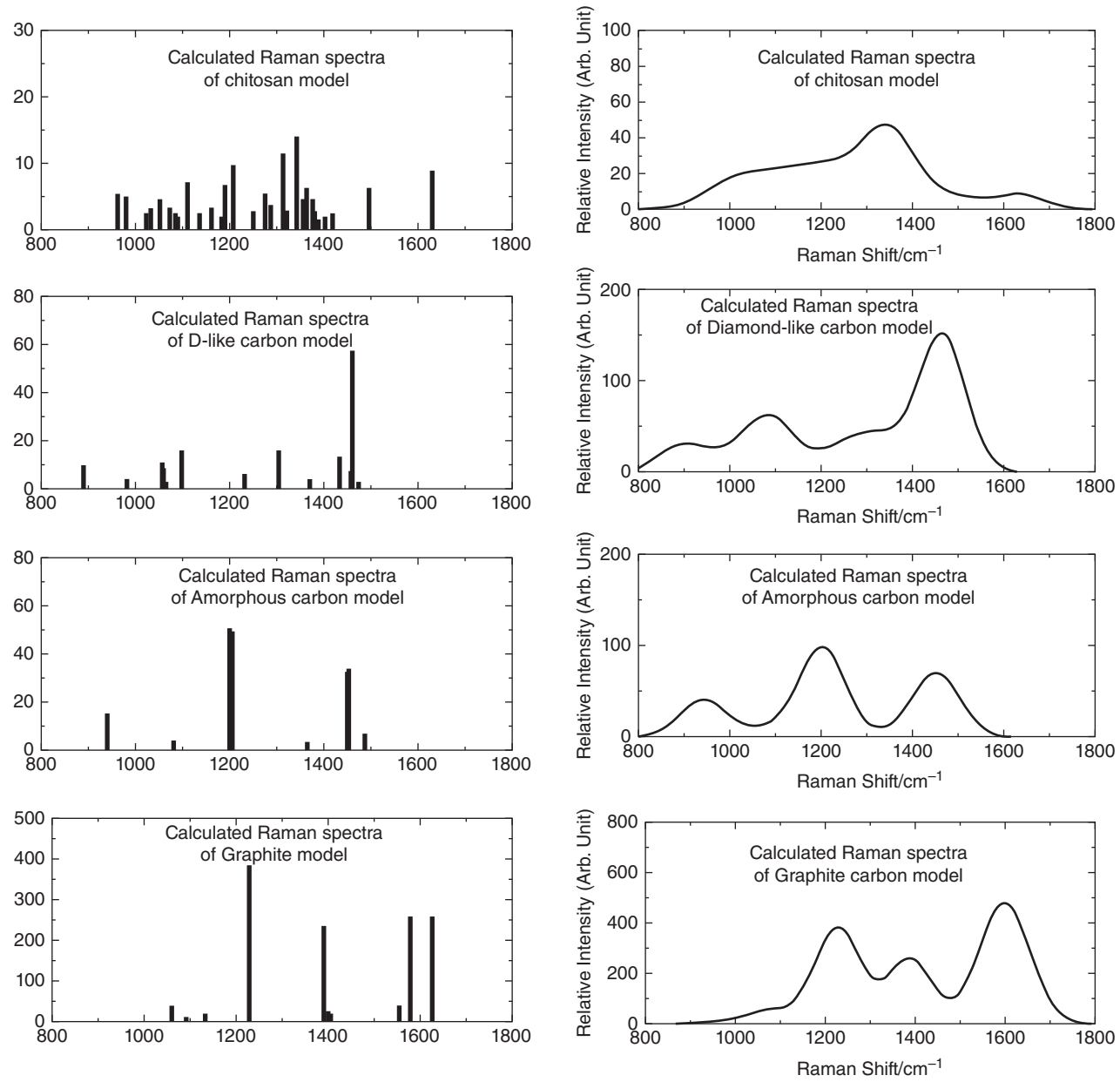


FIGURE 25.3 Simulated Raman spectra of chitosan ($C_6H_{13}NO_5$), diamondlike C [$C_{10}H_{12}(CH_3)_4$], amorphous C ($C_{10}H_{16}$), and graphite ($C_{16}H_{10}$) models for carbonized film.

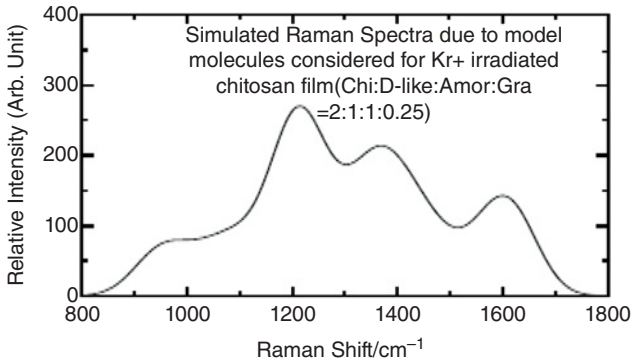
DFT calculations [3]. In this study, we focus on analysis of Raman and valence X-ray photoelectron spectra for carbonized chitosan film with Kr^+ ion irradiation to clarify the constitutional structure for the depth profile assignments of nm and μm orders.

25.4.1 Raman Shift Spectral Analysis

Figure 25.1 shows the Raman shift of chitosan films with Kr ion 150-keV energy bombardment at fluences ranging from 1.0×10^{13} to 1.0×10^{15} ions cm^{-2} in the base pressure of $<4.0 \times 10^{-4}$ Pa at room temperature. In the figure, the peak intensities of pure chitosan film appeared in the Raman shift range of 850–1700 cm^{-1} at 150 keV energy irradiation at fluences of 1.0×10^{13} –1.0×10^{14} ions cm^{-2}, while the strong double broader peaks at around 1300 and 1600 cm^{-1} are due to carbonized change [as seen in surface color changes of parts (b) and (c) of chitosan films on the right side in Fig. 25.1) with the 150 keV energy irradiation at fluences of 3.0×10^{14} ~1.0×10^{15} ions cm^{-2}.

In Fig. 25.2, we show the experimental Raman spectrum of carbonized film with Kr^+ ion bombardment at fluences of

(a) Simulated Raman Spectra of carbonized chitosan film



(b) Experimental Raman Spectra of carbonized chitosan film

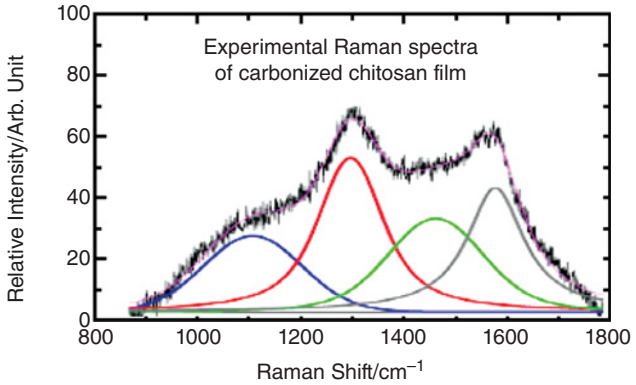


FIGURE 25.4 Simulated Raman spectrum of carbonized film on the upper side (a) with the experimental result on the lower side (b).

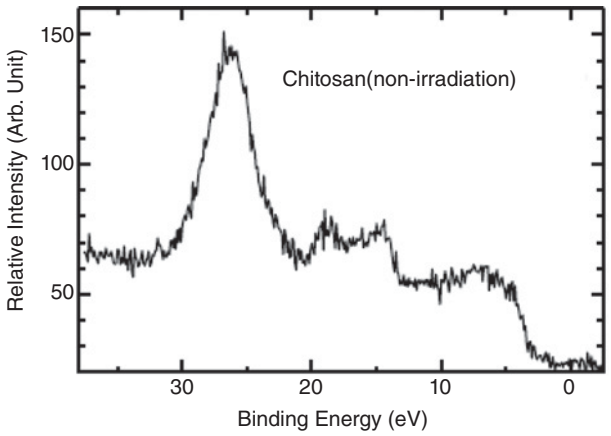
1.0×10^{15} ions cm^{-2}. We assumed the strong double broader peaks at around 1300 and 1600 cm^{-1} to be due to diamondlike carbon and graphite carbon, respectively, although the strong peak at around 1300 cm^{-1} was already analyzed as disordered carbons involved nanometer-scale cluster diamond crystalas [16]. In the figure, the Raman experimental spectrum of the carbonized film was shown to be due to four component contributions of chitosan (Chito), diamondlike carbon (DLC), graphite (GP), and amorphous carbon (AC). We thus performed the depth profile assignment at micrometer scale for the carbonized film from MO-DFT hybrid calculations at the B3LYP/6-31G** level using the model molecules {chitosan monomer [H-($C_6H_{11}NO_4$)-O-H] for chitosan, adamantane-derivative [$C_{10}H_{12}(CH_3)_4$] for diamondlike C, adamantane ($C_{10}H_{16}$) for amorphous C, pyrene ($C_{16}H_{10}$) for graphite} of the four components.

In order to analyze the experimental Raman spectrum of carbonized film in Fig. 25.2, we simulated four kinds of line spectra for Chito, DLC, AC, and GP models, respectively, on the left side in Fig. 25.3, while four kinds of broader simulated spectra enveloped with the Gaussian-line-shaped functions were given on the right side in the figure. Each Raman spectral intensity in Fig. 25.3 was obtained from Raman activity using the B3LYP/6-31G** method of four model molecules. This enabled us to obtain relative ratios of 2:1:0.5:0.375 for Chito:DLC:AC:GP of carbonization film from simulation Raman spectrum. In Fig. 25.4, we showed the simulated Raman spectrum of carbonized film on the upper side with the experimental result on the lower side. In the figure, the theoretical peak at around 1600 cm^{-1} due to graphite contribution corresponds well to the experimental one.

25.4.2 Valence Band X-Ray Photoelectron Spectral Analysis

It is well known that the XPS measurements are useful for examining the depth profile of materials at the nanometer level. In Fig. 25.5, we show experimental valence X-ray

(a) VXPS of chitosan film with nonirradiation.



(b) VXPS of chitosan film with 150 keV energy irradiation.

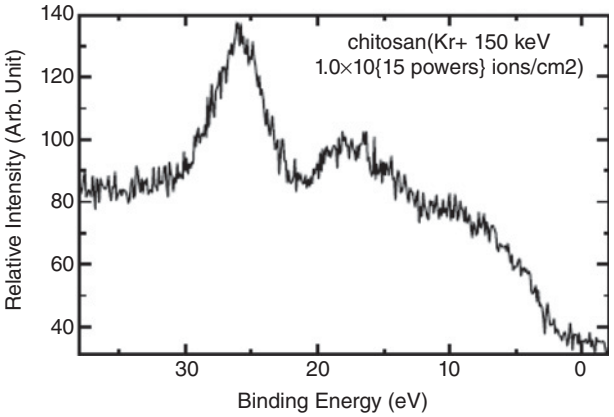


FIGURE 25.5 Experimental valence X-ray photoelectron spectra of chitosan films with non- and Kr^+ ion irradiation (1.0×10^{15} ions/cm^2) on the upper (a) and lower (b) sides, respectively.

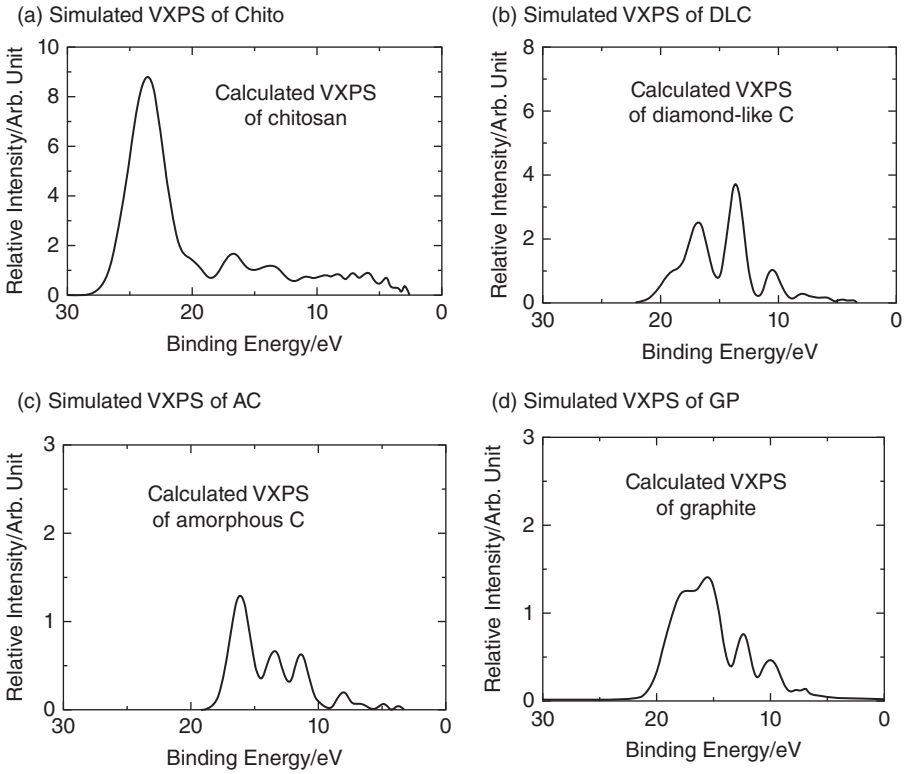


FIGURE 25.6 Simulated valence X-ray photoelectron spectra of chitosan ($C_{12}H_{242}N_2O_9$), diamondlike C ($C_{10}H_{12}(CH_3)_4$), amorphous C ($C_{10}H_{16}$), and graphite ($C_{16}H_{10}$) models for carbonized film.

photoelectron spectra of chitosan films with nonirradiation and Kr^+ ion irradiation (1.0×10^{15} ions/cm^2) on the upper (a) and lower (b) sides, respectively. The spectrum of the film with Kr^+ ion irradiation is seen to be lower broadening peak (at around 25 eV), due to presence of oxygen, than the spectrum with nonirradiation, so that carbonization of the Kr^+ ion-irradiated film can be predicted to have advanced by using the result of Raman spectral analysis for the irradiation film. Then, for the observed valence photoelectron spectrum of the carbonized film with the irradiation, we also determined that the spectrum is due to four component contributions of chitosan (Chito), diamondlike carbon (DLC), amorphous carbon (AC), and graphite (GP).

Figure 25.6 shows the simulated valence X-ray photoelectron spectra of chitosan ($C_{12}H_{242}N_2O_9$), diamondlike carbon [$C_{10}H_{12}(CH_3)_4$], amorphous carbon ($C_{10}H_{16}$), and graphite ($C_{16}H_{10}$) models as the four constitutional contributions for the carbonized film from B3LYP/6-31G**-level calculations. By considering the four component contributions, we obtained relative ratios of 1:0.5:0.5:1 at nanometer order for Chito:DLC:AC:GP of carbonization film, as shown in a simulated spectrum with the experimental one in Fig. 25.7.

We were thus able to analyze the carbonization of the chitosan film with Kr^+ ion bombardments as constitutional ratios of the depth profile from valence X-ray photoelectron and Raman spectral analysis at both nanometer and micrometer orders. Each constitutional ratio at micrometer order is chitosan:DLC:amorphous carbon: graphite carbon = 2:1:0.5:0.375, while the ratios at nanometer order are chitosan:DLC: amorphous carbon:graphite carbon = 2:1:1:2). The graphite constitution of the carbonized film is a small ratio of 0.375 in three kinds of carbon allotropes at micrometer order. On the other hand, the graphite ratio is around 2 times that of other carbon allotropes at nanometer order.

25.5 CONCLUSION

We analyzed valence X-ray photoelectron and Raman spectra of chitosan film modified by Kr^+ ion beam bombardments from B3LYP/6-31G**-level calculations. Experimental Raman spectra of the carbonized film with Kr^+ ion bombardment were found to be due to four component contributions of chitosan (Chito), diamondlike carbon (DLC), graphite (GP), and amorphous carbon (AC). By considering the four constitutional contributions, we performed depth profile assignments at nanometer and micrometer scales for the carbonized chitosan film in valence X-ray photoelectron spectroscopy and Raman shift experiments, respectively,

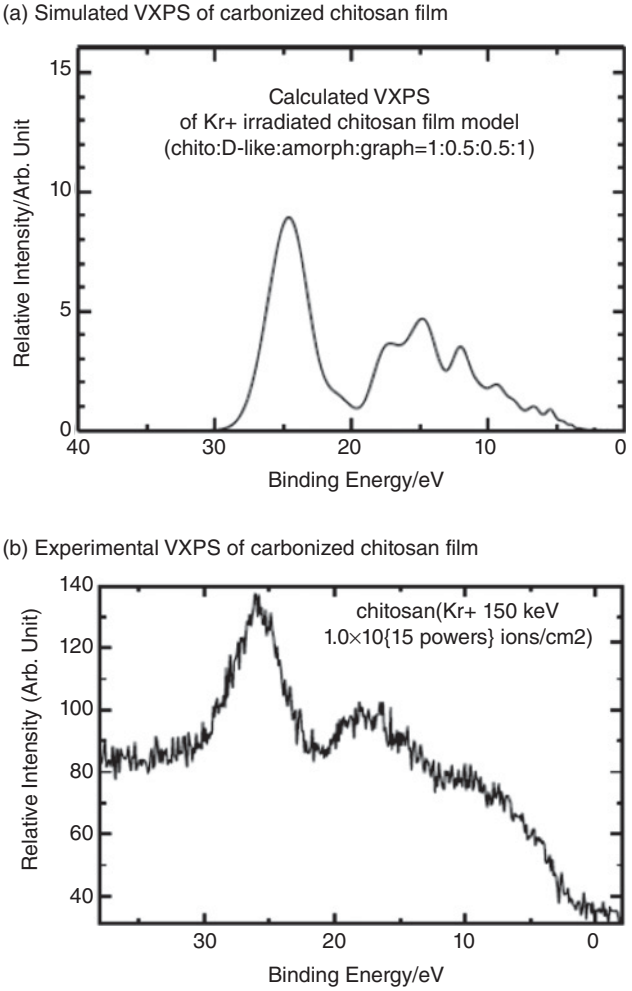


FIGURE 25.7 Simulated VXPS of carbonized film on the upper side (a) with the experimental result on the lower side (b).

from MO-DFT hybrid calculations in GAUSSIAN 09 using the model molecules. Carbonizations of the film by Kr^+ irradiation were obtained as Chito:DLC:AC :GP = 2:1:0.5:0.375 at micrometer order from Raman spectral analysis, while they were determined as Chito:DLC:AC:GP = 2:1:1:2 at nanometer order from valence X-ray photoelectron spectral analysis.

REFERENCES

[1] Muzzarelli, R.A.A. (1973). *Natural Chelating Polymers*, Pergamon, Oxford, UK.

[2] Takahashi, K., Shizume, R., Uchida, K., Yajima, H. (2009). *J. Biorheol*, **21**, 64.

[3] Danielache, S., Mizuno, M., Shimada, S., Endo, K., Ida, T., Takaoka, K., Kurmaev, E.Z. (2005). *Polym. J.* **37**, 21.

[4] Tamura, K., Endo, K., Takagi, Y., Kato, K., Matsumoto, D., Ida, T., Mizuno, M., Suzuki, Y., Takahashi, K., Uchida, K., Yajima, H. (2008). *J. Surf. Anal.* **14**, 344.

[5] Frisch, M.J., Trucks, G.W., Schlegel, H.B., Scuseria, G.E., Robb, M.A., Cheeseman, J.R., Scalmani, G., Barone, V., Mennucci, B., Petersson, G.A., Nakatsuji, H., Caricato, M., Li, X., Hratchian, H.P., Izmaylov, A.F., Bloino, J., Zheng, G., Sonnenberg, J.L., Hada, M., et al. (2009). *GAUSSIAN 09*, Revision A.02. Gaussian, Inc., Wallingford, CT.

[6] Becke, A.D. (1992). *J. Phys. Chem.* **97**, 9173.

[7] Lee, C., Yang, W., Parr, R.G. (1988). *Phys. Rev. B* **37**, 785.

[8] Gelius, U., Siegbahn, K. (1972). *Faraday Discuss. Chem. Soc.* **54**, 257 (1972).

[9] Gelius, U. (1974). *J. Electron. Spectrosc. Relat. Phenom.* **5**, 985.

[10] Yeh, J.-J. (1993). *Atomic Calculation of Photoionization Cross-Section and Asymmetry Parameters*. Gordon & Breach, New York.

[11] Endo, K., Kaneda, Y., Aida, M., Chong, D. P. *J. Phys. Chem. Solids*, **56**, 1131 (1995).

[12] Endo, K., Kaneda, Y., Okada, H., Chong, D.P., Duffy, P. (1996). *J. Phys. Chem.*, **100**, 19455.

[13] Endo, K., Maeda, S., Aida, M. (1997). *Polym. J.* **29**, 171.

[14] Endo, K., Maeda, S., Kaneda, Y. (1997). *Polym. J.* **29**, 255.

[15] Scott, A.P., Radom L. (1996). *J. Phys. Chem.* **100**, 16502.

[16] Ferraty, A.C., Robertson, J. (2004). *Phil. Trans. Roy. Soc. Lond. A* **362**, 2477.

26

ELECTRONIC STRUCTURE OF CHITOSAN

Kazunaka Endo

Division of Colloid and Interface Science, Research Institute for Science and Technology, Tokyo University of Science, Japan

26.1 INTRODUCTION

Chitosan is especially known as a most powerful adsorbent of natural origin and is widely used for the prevention of water pollution by highly toxic chlorinated aromatic compounds and metal ions [1]. It is inexpensive, environmentally benign, harmless to humans, and a hugely obtainable biomass, which makes it very promising and attractive for use in many applications. Chitosan is easily prepared from chitin by deacetylating its acetoamide groups with a strong alkaline solution. Chitin is a highly chemically stable natural biopolymer isolated from crustaceans (lobster, shrimp, crab, etc.), some invertebrates, and fungi [2]. It is produced in vast amounts ($\leq 10^{11}$ tons per year), second only to cellulose on a worldwide basis [3]. On the other hand, cellulose is an essential consistent in the assembly of plant cell walls. It has the significant biological functions of providing cells with mechanical strength and framework. As one of the most abundant natural polymers, it has found many important applications in areas such as food, drug delivery systems, and textile and pulp–paper industries. Elucidation of the structural and dynamic properties of cellulose is, therefore, fundamental to understanding its role in plant cell walls and its functionality in applications.

We have selected chitosan and cellulose for study of C13 NMR and X-ray photoelectron spectra (XPS) for the following reasons. Both compounds play a well-known and important role in the electronic structure involved in the formation of biological molecules. To understand the changes in adsorption behavior of chemically modified biopolymers, cellulose and chitosan (cross-linked biopolymers), it is necessary to first study the chemical bonding of unmodified cellulose and chitosan. On the other hand, cellulose and chitosan have a compact geometric structure that is convenient for molecular orbital (MO) calculations, and possess four different oxygen atom–based functional groups that make cellulose and chitosan suitable models for X-ray photoelectron spectroscopy (XPS) study.

26.2 EXPERIMENTAL METHOD

We used commercially available cellulose (Sigma Chemical Co., Inc.), and chitosan (Wako Chemical Co., Inc., respectively. They were pressed into the pellets before XPS measurements.

The XPS of the pellets for cellulose and chitosan were obtained on a PHI 5400MC ESCA spectrometer, using monochromatized Al Kα radiation. The spectrometer was operated at 600 W, 15 kV, and 40 mA. Photon energy was 1486.6 eV. A pass energy of 37.75 eV was used for high-resolution scans in a valence band analysis (range 50 eV). The angle between the X-ray source and analyzer was fixed at 45°. Spot size was 3 × 1 mm. Dispersion compensation yielded an instrumental resolution of 0.5 eV from full width at half-maximum for the Ag3*d* line of silver. Multiscan averaging on a multichannel analyzer was used for the valence band region, although a very low photoelectron emission cross section was observed in this range. Gold of 2.0 nm thick was deposited on the pellets of the samples using an ion sputter unit (Hitachi E 1030) for the scanning electron microscope. A low-energy electron floodgun was used in order to avoid any charging effect on the surface of the sample. We used the Au4*f* core level of the gold decoration on

Encyclopedia of Biocolloid and Biointerface Science, Volume 1, First Edition. Edited by Hiroyuki Ohshima.
© 2016 John Wiley & Sons, Inc. Published 2016 by John Wiley & Sons, Inc.

the samples as a calibration reference. The C1*s* line positions of $-CH_2OH$ groups in the samples could be fixed at 286.7 eV for cellulose and chitosan, respectively.

For the ^{13}C-NMR spectra, we referred to experimental results of (α-D-glucose, β-D-glucose, and β-D-glucosamine) [4–6], cellobiose [7], cellulose [7], and chitosan [8].

26.3 THEORETICAL BACKGROUND

26.3.1 NMR Chemical Shielding Tensor

We used the shielding tensor equation by the sum-over-states DFT perturbation theory. The shielding tensors [9] are given as follows:

$$\sigma_{uv} = \sigma_{uv}^{d} + \sigma_{uv}^{po} + \sigma_{uv}^{p1} \tag{26.1}$$

$$\sigma_{uv}^{d} = \alpha^2 \sum_{k} \left\langle k \left| h_{uv}^{11} \right| k \right\rangle \tag{26.2}$$

$$\sigma_{uv}^{po} = \alpha^2 \sum_{k} \sum_{j} \left\langle k \left| h_{u}^{01} \right| j \right\rangle \left\langle j \left| \left(\Lambda_j - \Lambda_k\right)_v \right| k \right\rangle \tag{26.3}$$

$$\sigma_{uv}^{p1} = 2\alpha^2 \sum_{k} \sum_{j} \left\langle k \left| h_{u}^{01} \right| a \right\rangle \beta_{ak}(v) \tag{26.4}$$

The Hamiltonians for the model molecule under a magnetic field are

$$h_u^{11} = \frac{\left(\vec{r} - \vec{R}_k\right)\left(\vec{r} - \vec{R}_N\right)\delta_{uv} - \left(\vec{r} - \vec{R}_N\right)_u \left(\vec{r} - \vec{R}_k\right)_u}{\left|\vec{r} - \vec{R}_N\right|^3} \tag{26.5}$$

$$h_u^{01} = \frac{cl_{Nu}}{\left|\vec{r} - \vec{R}_N\right|^3} \tag{26.6}$$

In this approach, an individual gauge for localized orbitals (IGLO) is implemented by the following transformation

$$B_{ak}(v) = \sum_{m} \left\{ \frac{\sum_{n} \left(-\frac{1}{2c}\langle a|l_{nv}|n\rangle + \sum_{i} \langle a|(\Lambda_n - \Lambda_j)_v|j\rangle\langle j|F^0|n\rangle \right) U_{nm}}{e_m - e_a - \Delta E_{m\to a}^{xc}} \right\} \times U_{km} \tag{26.7}$$

$$\left(\Lambda_j\right)_u = -\frac{1}{2c}\left(\vec{R}_j \times \vec{r}\right)_u \tag{26.8}$$

where F^{o} is the unperturbed DFT Hamiltonian operator, U_{km} is the unitary matrix of a transformation from the canonical to localized MOs, m corresponds to canonical MOs, and indices k, l, and n correspond to localized MOs.

26.3.2 XPS

For comparison between calculations for a single molecule of the model and experiments on a solid, we must shift each computed vertical ionization potential (VIP), I'_k by a quantity WD as $I_k = I'_k - WD$. To convert to ionization energy I_k relative to other energy effects, as stated in our previous studies [10, 11].

In order to obtain the accurate CEBEs, we used the generalized transition-state (GTS) method. In the GTS method, a team of coworkers [12] proposed the extension of Slater's transition-state method [13] and approximated the endothermicity ΔE=E(1)–E(0) by

$$\Delta E = [F(0) + 3F(2/3)]/4, \tag{26.9}$$

where $F(\lambda) = \partial E(\lambda)/\partial\lambda$, and λ ($0 < \lambda \leq 1$) is assumed to be a continuous variable, with $E(0)$ and $E(1)$ denoting the energies of the initial and final states, respectively. For example, for the ionization of an electron from molecular orbital (MO)ϕ_k of interest, λ represents the fraction of electron removed, and according to the Janak theorem [14], $F(\lambda)$ is the negative orbital energy $\varepsilon_k(\lambda)$. This procedure is applied in the following way. In the unrestricted generalized transition-state (uGTS) method, we removed $^2/_3\alpha$ electron from MO ϕ_k of interest.

For the VIPs of the valence regions, we used the so-called restricted diffuse ionizations (rDI) model, which was proposed for use with the HAM/3 method [15]. In the rDI model, half of the electron is removed evenly from the valence MOs and the negative charge of the resulting orbital energies correspond to calculated VIPs. This allows us to obtain all valence VIPs in a single calculation.

The intensity of valence XPS was estimated from the relative photoionization cross section for Al K radiation using the Gelius intensity model [16, 17]. For the relative atomic photoionization cross section, we used the theoretical values from Yeh [18].

26.4 CALCULATIONS

26.4.1 NMR Chemical Shielding Tensor

In the case of solving the nonlinear equations involving a Hartree–Fock-like DFT equation, we think it is the best way to select a better initial condition. We considered molecular models from X-ray diffraction data for α-D-glucose, β-D-glucose, β-D-glucosamine, and cellobiose, respectively.

First- and second-geometry optimizations for saccharide and monoaminosugar molecules were performed by the semiempirical AM1 method, and at HF/6-31G(*d*,*p*) level with the program GAUSSIAN 09 [19], respectively. In the case of the optimizations for the model molecules from the X-ray diffraction data, we fixed the positions of the atoms except for H atoms and optimized the positions of H atoms. For cellulose and chitosan, we adopted the model tetramer from X-ray diffraction data. We also performed the geometry optimization for the tetramer model of the biopolymers by using the AM1 method, and at the HF/6-31G(*d*,*p*) level. In the optimization of the molecules, we fixed the positions of the atoms except for H atoms in a glucose unit, and all proton positions were optimized. We performed the ^{13}C shielding calculations of the dimer model due to a deMon NMR program, after we removed the dimer model, cutting both glucose edges off from the tetramer. Reference standard tetramethyl silane (TMS) was optimized also under a similar calculation level. Figure 26.1 shows the model molecules of saccharide, monoaminosugar, cellulose, and chitosan, respectively.

Chemical shift calculations were carried out with the program deMon NMR [9]. We used the Perdew-Wang-91 (PW91) [20–22] exchange correlation potential, the approximation Loc.1 SOS-DFTP, and polarized valence double-ζ(DZVP) basis [23] of (621/41/1*) for C and N, and (41) for H with auxiliary fitting functions labeled (5,2;5,2) for C, N and O, and (5,1;5,1) for H, respectively.

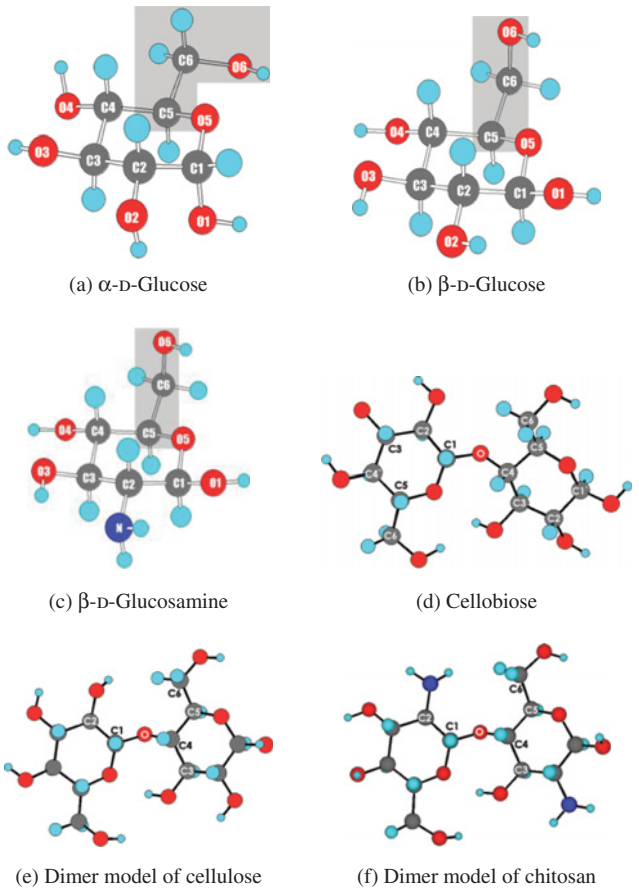


FIGURE 26.1 Model molecules of saccharide, monoaminosugar, cellulose, and chitosan.

26.4.2 XPS

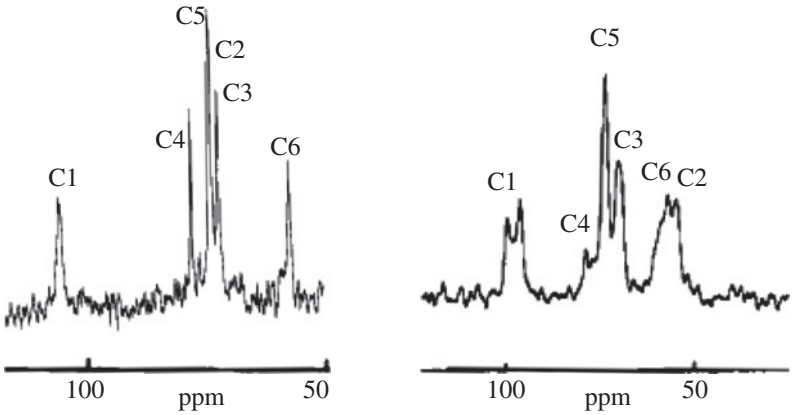
The model dimer molecules of cellulose and chitosan obtained in NMR calculations were calculated by deMon DFT programs [24, 25]. DeMon calculations were also performed with the Perdew-Wang-91 (PW91) [20–22] exchange correlation potential. In running the deMon program, we used a nonrandom grid and polarized valence double-ζ(DZVP) basis [20] of (6121/41/1*) for C and N, and (41) for H with auxiliary fitting functions labeled (5,2;5,2) for C, N and O, and (5,1;5,1) for H.

26.5 RESULTS AND DISCUSSION

As shown in the monomer models (α-D-glucose, β-D-glucosamine) for cellulose and chitosan, respectively, in Fig. 26.1, the structure of both biopolymers is similar except for the substitution of one OH group in cellulose by the NH_2 group in chitosan. In both compounds one can select six nonequivalent carbon atoms (C1–C6) and four nonequivalent oxygen atoms from different functional groups: –O– (O5), which belongs to the glucose ring; –O– (O1, O4), which links the adjacent glucose rings; OH (O3); and CH_2OH (O6). According to the experimental results, ^{13}C-NMR signals [11, 12] show six nonequivalent carbons of C1–C6 for both cellulose and chitosan polymers in Fig. 26.2. For the XPS of the cellulose, experimental CEBEs of O1s consist of two different –O– and –OH peaks centered at 532.9 and 533.5 eV, respectively, and the C1s is also due to two kinds of –O–CH–O– and –CH(OH) peaks at 288.1 and 286.7 eV. Therefore we will analyze the spectra for the biopolymers by deMon DFT [9,24,25] calculations using the model dimers.

26.5.1 ^{13}C-NMR Chemical Shielding Tensor

26.5.1.1 Saccharides and Aminosugar. In Table 26.1, we show the calculated carbon shielding constants (σ^d, σ^{p0}, σ^{p1}, σ^{total}), and chemical shift (δ_{calc}) for α-D-glucose, β-D-glucose, and β-D-glucosamine, respectively, with the experimental chemical shift (δ_{exp}) referring to the shielding constant of TMS. These compounds were selected to reflect the monomer units in cellulose and chitosan. It can be seen in Table 26.1 that the calculated chemical shifts (δ_{calc}) of C1–C6 carbons for α-D-glucose, β-D-glucose, and β-D-glucosamine are in considerably good accordance in the experimental ^{13}C values (δ_{exp}) in solution in the average absolute deviation (AAD) of $\pm$ 3.1 ppm. We can see from the calculation result



(a) Cellulose (b) Chitosan

FIGURE 26.2 Solid-state ^{13}C-NMR spectra of (a) cellulose and (b) chitosan.

TABLE 26.1 ^{13}**C Chemical Shielding Constants of α-Glucose, β-Glucose, and β-Glucosamine with Experimental Shifts in Reference to Shielding Constant of TMS**

	C1	C2	C3	C4	C5	C6
			α-Glucose			
σ^d	252.0	254.2	254.5	254.5	254.5	253.0
σ^{p0}	35.7	49.6	50.8	50.0	52.0	50.9
Total diamagnetic	287.7	303.8	305.3	304.5	306.5	303.8
σ^{p1}	−143.2	−138.1	−139.4	−139.4	−140.0	−127.6
Total shielding	144.4	165.7	165.9	165.2	166.5	176.2
Chemical shift	97.6	76.3	76.2	76.9	75.5	65.8
Experimental	93.4	72.9	73.3	70.8	71.8	63.8
			β-Glucose			
σ^d	252.0	254.7	254.5	254.4	254.0	253.0
σ^{p0}	34.3	51.0	49.3	51.3	49.1	52.2
Total diamagnetic	286.2	305.7	303.7	305.8	303.1	305.2
σ^{p1}	−144.5	−142.1	−141.6	−132.9	−142.2	−126.1
Total shielding	141.7	163.6	162.1	172.9	160.9	179.1
Chemical shift	100.3	78.4	79.9	69.1	81.1	62.9
Experimental	97.6	75.4	76.5	70.3	76.2	61.9
			β-Glucosamine			
σ^d	251.9	255.9	254.5	254.5	254.1	253.0
σ^{p0}	33.5	57.9	49.4	51.3	49.3	52.2
Total diamagnetic	285.4	313.8	303.9	305.8	303.4	305.2
σ^{p1}	−145.3	−133.1	−140.8	−134.1	−142.1	−126.1
Total shielding	140.1	180.7	163.1	171.7	161.3	179.1
Chemical shift	101.9	61.3	78.9	70.3	80.8	62.9
Experimental	95.3	59.5	74.5	72.2	78.6	63.1

TABLE 26.2 ^{13}C Chemical Shielding Constants of Cellobiose with Experimental Shifts in Reference to Shielding Constant of TMS

	Cellobiose					
	C1	C2	C3	C4	C5	C6
σ^d	252.2	254.5	254.4	254.2	254.1	253.0
σ^{p0}	34.3	50.8	49.3	49.9	49.4	51.4
Total diamagnetic	286.5	305.3	303.7	304.1	303.5	304.4
σ^{p1}	−152.0	−141.4	−141.9	−135.5	−144.2	−129.0
Total shielding	127.0	163.8	161.9	168.6	159.4	175.5
Chemical shift	104.5	75.2	77.2	70.4	79.7	63.6
Experimental	104.6	76.5	78.7	72.4	79.7	63.8
	C1′	C2′	C3′	C4′	C5′	C6′
σ^d	251.6	254.0	253.9	254.0	254.3	254.5
σ^{p0}	34.0	50.3	49.8	49.2	49.9	50.4
Total diamagnetic	285.6	304.4	303.8	303.3	304.2	304.8
σ^{p1}	−146.8	−139.2	−140.3	−151.0	−139.3	−132.3
Total shielding	138.8	165.2	163.4	152.3	164.9	172.5
Chemical shift	100.3	73.9	75.6	86.8	74.1	66.5
Experimental	97.5	76.5	78.7	85.5	79.7	63.8

that the chemical shielding of C1–C6 carbons depends on the total paramagnetic shielding constants (σ^{p0} and σ^{p1}), since the diamagnetic term (σ^d = 252−254 ppm) of six carbons is almost constant. The shielding orders of carbon nuclei for saccharides and aminosugar in Table 26.1 follow C1 [–O–$\underline{C}$H(OH)–] > C2–C5 [–$\underline{C}$H(OH)– or –O–$\underline{C}$H–C] > C6 [–$\underline{C}H_2$(OH)], and C1 [–O–$\underline{C}$H(OH)–] > C5 (–O–$\underline{C}$H–C) > C3, C4 [–$\underline{C}$H(OH)–] > C6[–$\underline{C}H_2$(OH)] > C2 [–$\underline{C}$H(NH_2)], respectively. In order to compare the calculated carbon chemical shifts of the typical disaccharide molecule for cellulose with the experimental values in solid, we used the cellobiose compound shown in Fig. 26.1d. Table 26.2 also shows the calculated 12 carbon shielding constants and chemical shifts with the experimental ^{13}C chemical shift values referring to the shielding constant of TMS. The 12 carbon chemical shifts are classified into five species, due to the differences among the neighbor oxygen functional groups: C1 carbon, which bonded to two ether (–O–) groups is at the lowest field (δ_{exp} = 104.6 ppm); C1′ carbon, which has –O– and –OH groups and exists at the next lower field (δ_{exp} = 97.5 ppm); and C4, which, bonded to one –O– group, is observed at the second next lowest field (δ_{exp} = 85.5 ppm). Carbons in the –CH(OH) group are in the range of δ_{exp} = 72.4−79.7 ppm, and carbons in the –CH_2(OH) group are at the highest field (δ_{exp} = 63.8 ppm). The calculated results correspond well to the order of the experimental values in solids in AAD of ±1.9 ppm. For cellobiose results, the chemical shielding of 12 carbons is also seen to be determined dominantly with the total paramagnetic shielding constants.

26.5.1.2 Cellulose and Chitosan. In Table 26.3, we showed the calculated 12 carbon shielding constants and chemical shifts of the dimer models for cellulose and chitosan with the six experimental ^{13}C shift values referring to the shielding constant of TMS. In the table, we adopted experimental ^{13}C values of C4′ and C4 for cellobiose and β-D-glucosamine, respectively, for comparison of the calculated C4′ values of the model molecules, because the C4′ carbon of the model molecules bonds to the –OH group. Then, the calculated values exist in the AAD range of ± 3.1 ppm for both cellulose and chitosan, and are also in good accordance with experimental ones. Carbon NMR chemical shielding is also dominated by the total paramagnetic shielding constants, since the diamagnetic shielding constants are very similar.

In Table 26.3, the shifts of C1 and C1′ carbons bonded to two oxygen atoms are much lower-field than all other carbons in cellulose and chitosan. For C4 and C6 carbons of both models, the former carbon shift bonded to an ether group is at the lower field, while the latter carbon in the –$\underline{C}H_2$(OH) group exists in the higher field. These results correspond to a tendency of C1, C1′, C4, and C6 for cellobiose.

In the case of C2 and C2′ carbons for both polymers, the carbon nuclei in the –$\underline{C}$H(NH_2) group of chitosan are at the highest field of all carbons. This is so because the total paramagnetic terms of C2, C2′ carbons in the chitosan model have much higher values than those terms in the cellulose model, since the diamagnetic term has an almost constant value (σ^d = 251−255 ppm).

TABLE 26.3 ^{13}C Chemical Shielding Constants of Cellulose and Chitosan with Experimental Shifts in Reference to TMS Constant

			Cellulose			
	C1	C2	C3	C4	C5	C6
σ^d	252.0	254.2	254.4	253.7	254.3	253.4
σ^{p0}	34.2	50.6	50.0	49.5	49.7	53.2
Total diamagnetic	286.2	304.7	304.4	303.1	304.0	306.6
σ^{p1}	–159.2	–143.3	–143.2	–135.8	–146.3	–128.9
Total shielding	127.0	161.5	161.2	167.4	157.8	177.7
Chemical shift	112.1	77.6	77.9	71.7	81.2	61.4
Experimental	107.1	73.4	76.0	88.9	77.7	64.0
	C1′	C2′	C3′	C4′	C5′	C6′
σ^d	251.4	254.1	254.4	254.2	254.3	253.5
σ^{p0}	33.9	49.6	50.0	48.5	49.8	52.6
Total diamagnetic	285.3	303.7	304.4	302.7	304.1	306.0
σ^{p1}	–147.6	–144.4	–143.2	–153.0	–146.0	–129.1
Total shielding	137.7	159.3	161.1	149.7	158.1	176.9
Chemical shift	101.4	79.7	77.9	89.3	80.9	62.1
Experimental	107.1	73.4	76.0	88.9	77.7	64.0
			Chitosan			
	C1	C2	C3	C4	C5	C6
σ^d	251.0	254.5	253.2	253.4	253.4	251.7
σ^{p0}	31.9	56.7	47.4	48.7	49.4	50.0
Total diamagnetic	282.9	311.3	300.7	302.2	302.8	301.7
σ^{p1}	–159.5	–131.1	–143.7	–140.9	–143.8	–130.9
Total shielding	123.4	180.2	157.1	161.2	159.0	170.8
Chemical shift	115.6	58.8	81.9	77.8	80.0	68.2
Experimental	110.0	62.4	80.8	86.6	80.8	65.6
	C1′	C2′	C3′	C4′	C5′	C6′
σ^d	250.7	254.6	253.5	253.6	253.1	251.7
σ^{p0}	32.7	56.2	48.6	47.7	49.2	49.6
Total diamagnetic	283.3	310.8	302.1	301.3	302.3	301.3
σ^{p1}	–149.4	–135.0	–141.1	–153.6	–141.7	–130.8
Total shielding	133.9	175.9	160.9	147.7	160.6	170.5
Chemical shift	105.1	63.1	78.1	91.3	78.4	68.5
Experimental	110.0	62.4	80.8	86.6	80.8	65.6

26.5.2 XPS

26.5.2.1 Valence XPS. It is interesting to discuss the experimental spectrum in detail from a theoretical viewpoint. We showed the theoretical valence spectra of cellulose and chitosan by deMon DFT calculations using the dimer models with experimental ones in Fig. 26.3 panels (a) and (b), respectively. The simulated results for cellulose and chitosan are in considerably good accordance with the experimental ones in the figure. Tables 26.4 and 26.5 summarize the experimental peaks, calculated VIPs, main atomic orbital (AO) photoionization cross sections (PICSs), orbital nature, and functional group. In Figure 26.3a,b, the intense peaks at around 26 eV are due mainly to $s\sigma$(O2s–C2s) bonding of the –O–C group for the biopolymers. From the simulation spectra in Fig. 26.3 we can discern an energy range of 21–23 eV in the difference between cellulose and chitosan. In the case of chitosan,

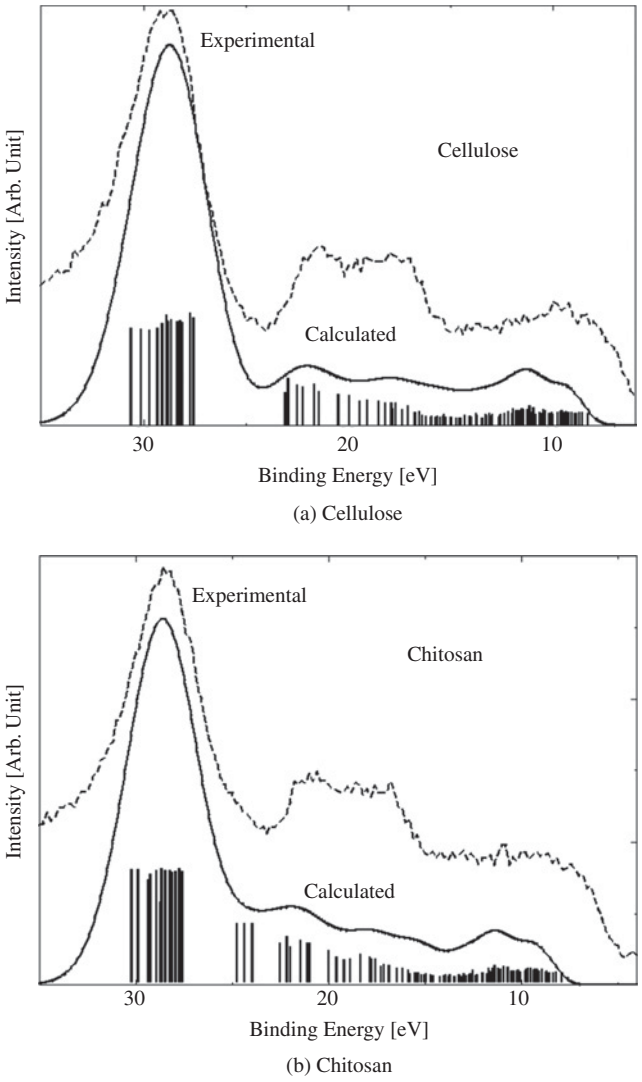


FIGURE 26.3 Valence XPS of (a) cellulose and (b) chitosan.

the shoulder peak at ∼22 eV results from the $s\sigma$(N2s–C2s) bonding of the H_2N–C group. Broader and shoulder peaks in the range of 13–20 and 3–13 eV result dominantly from $p\sigma$ bonding and $p\pi$ (lone-pair) nonbonding, respectively, for both polymers. Furthermore, we examined contribution of each atom for the simulated spectra in Fig. 26.4a,b, where we can see that the intense peak at ∼26 eV is due to the O and O + N atoms for cellulose and chitosan, respectively. For both polymers, the carbon contribution is a little larger than the oxygen one for a broader peak in the range of 13−20 eV. In the case of a broader peak between 3.0 (or 5.0) and 13 eV, the oxygen contribution also seems to dominate.

26.5.2.2 CEBEs of the Biopolymers. Table 26.6 shows the CEBEs of the model monomers for the biopolymers using the uGTS method with scaled-pVDZ basis. In the table, we showed the *WD* values of the polymers from the differences between calculated CEBE values for the model molecules and experimental ones for the solid polymers. We thus estimated an energy range of 5.9 and 5.7 eV for averaged *WD* values of cellulose and chitosan, respectively. The *WD* values from the CEBEs are the most reliable, as described in our previous work [10, 11].

26.6 CONCLUSION

We have analyzed ^{13}C-NMR chemical shielding and valence XPS of cellulose and chitosan by deMon DFT calculations using the model dimers. For ^{13}C-NMR chemical shielding, the calculated chemical shifts of (α-D-glucose, β-D-glucose, and β-D-glucosamine) and cellobiose with DZVP basis are in considerably good accordance with the experimental values in the average absolute deviations (AAD) of ± 3.1 and 2.0 ppm, respectively. The calculated ^{13}C shifts of the dimer models correspond well to the experimental ones of both solid polymers in the AAD of ± 3.1 ppm. The carbon NMR

TABLE 26.4 Observed Peaks, VIP,[a] Main Atomic Orbital (AO) PICS, Orbital Nature, and Functional Group for Valence XPS of Cellulose

Peak (eV)	VIP (eV)	Main AO PICS	Orbital nature [b]	Functional group
29	30.8–28.4	O2s	$s\sigma$(O2s–C2s)–B	–O–C
(33–25) [c]				
22	23.5–22.5	C2s	$s\sigma$ (C2s–C2s)–B	–C–C
(24–21)		O2s		
19	21.0–13.0	O2s	$p\sigma$ (C2s–O2p)–B	–C–O
(21–17) [c]		O2p	$p\sigma$ (O2s–C2p)–B	–O–C
12	14.0–13.0	C2p O2p	$p\sigma$ (O2p–C2p)–B	–O–C
	12.5–11.7	C2p O2p	$p\sigma$(O,C2p–O,C2p)–B	–C–O, –C–C
(16–8) [c]	10.5–9.1	O2p	$p\pi$(lone pair)–NB	–O–

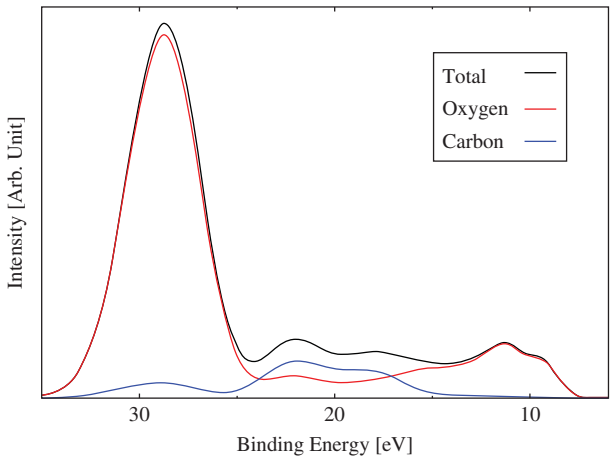
[a] Shift between observed and calculated VIP = 3.0 eV.
[b] B and NB mean bonding and nonbonding, respectively.
[c] Peak range.

TABLE 26.5 Observed Peaks, VIP,[a] Main AO PICS, Orbital Nature, and Functional Group for Valence XPS of Chitosan

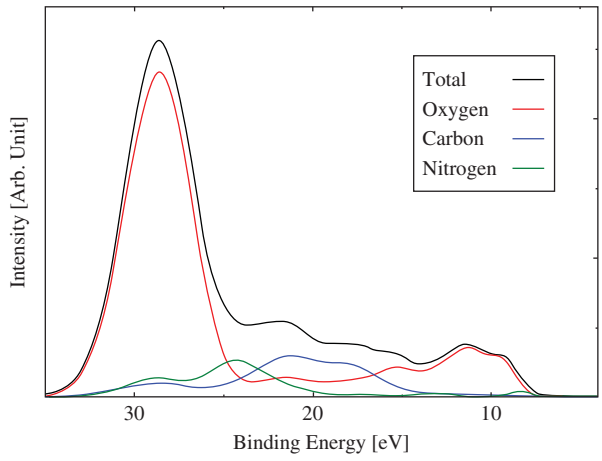
Peak (eV)	VIP (eV)	Main AO PICS	Orbital nature [b]	Functional group
29	30.4–28.1	O2*s*	*sσ*(O2*s*–C2*s*)-B	–O–C
(35–24)[a]	25.0–24.6	N2*s*	*sσ*(C2*s*–N2*s*)-B	–N–C
22	22.9–21.8	C2*s*	*sσ*(C2*s*–C2*s*)-B	–C–C
(24–20)[a]			*pσ*(C2*s*–O2*p*)-B	–C–O
19	20.5–17.6	O2*p*	*pσ*(C2*s*–O2*p*)-B	–C–O
(20–17) [c]		C2*p*		
11	12.5–11.5	C2*p* O2*p*	*pσ*(O,C2*p*–O,C2*p*) B	–C–O,–C–C
(12.5–8) [c]	10.3–8.8	O2*p*	*pπ*(lone pair)-NB	–O–
	8.1–8.5	N2*p*	*pπ*(lone pair)-NB	–N–

[a] Shift between observed and calculated VIP = 3.0 eV.
[b] B and NB mean bonding and nonbonding, respectively.
[c] Peak range.

chemical shielding is also dominated by the total paramagnetic shielding constants, since the diamagnetic shielding constants are almost similar values. The simulated valence



(a) Cellulose



(b) Chitosan

FIGURE 26.4 Each atom contribution for valence XPS of (a) cellulose and (b) chitosan.

TABLE 26.6 CEBEs (in eV) of Biopolymers by deMon Calculations Using Model Dimers

	Model Molecule		
Polymer	Obs.	Calc.	*WD*
	Cellulose		
C1*s* [O–CH–O]	288.1	294.3	6.2
C1*s* [–CH(OH)–]	286.7	292.5	5.8
O1*s* [–O–]	533.5	539.3	5.8
O1*s* [–OH]	532.9	538.5	5.6
	Chitosan		
C1*s* [O–CH–O]	288.0	294.2	6.2
C1*s* [–CH(OH)–]	286.6	292.5	5.9
O1*s* [–O–]	533.5	538.8	5.3
O1*s* [–OH]	533.0	538.6	5.6
N1*s* [–NH_2–]	399.3	404.6	5.3

spectra of the dimer models using the restricted diffuse ionization (rDI) method showed good agreement with the experimental ones of cellulose and chitosan. We obtained reasonable *WD* values for cellulose and chitosan as 5.9 and 5.7 eV, respectively, from the differences between calculated CEBE values for the monomer model molecules and experimental ones for the solid polymers.

REFERENCES

[1] Muzzarelli, R.A.A. (1977). *Chitin.* Pergamon Press, Oxford, UK.
[2] Tracy, M.V. (1957). *Rev. Pure Appl. Chem.* **7**, 1.
[3] Muzzarelli, R.A.A. (1973). *Natural Chelating Polymers*. Pergamon Press, Oxford, UK.
[4] Piron, E., and Domard, A. (1998). *Int. J. Biol. Macromol.* **22**, 33–40.
[5] Horii, F., Hirai, A., and Kitamaru, R. (1983). *Polym. Bull.* **10**, 357.

[6] Guibal, E., Milot, C., Eterradossi, O., Gauffier, C., Domard, A. (1999). *Int. J. Biol. Macromol.* **24**, 49–59.

[7] Dudley, R.L., Fyfe, C.A., Stepheson, P.J., Deslamdes, Y., Hamer, G.K., Marchessault., R.H. (1983). *J. ACS* **105**, 2469–2472.

[8] Saito, H., Tabeta, R., Ogawa, K. (1987). *Macromolecules* **20**, 2424.

[9] Malkin, V.G., Malkina, O.L., Casida, M.E., Salahub, D.R. (1994). *J. ACS* **116**, 5898.

[10] Endo, K., Kaneda, Y., Aida, M., Chong, D.P. (1995). *J. Phys. Chem. Solids* **56**, 1131.

[11] Endo, K., Kaneda, Y., Okada, H., Chong, D.P., Duffy, P. (1996). *J. Phys. Chem.* **100**, 19455.

[12] Williams, A.R., deGroot, R.A., Sommers, C.B. (1975). *J. Chem. Phys.* **63**, 628.

[13] Slater, J.C. (1972). *Adv. Quantum Chem.* **6**, 1.

[14] Janak., J.F. (1978). *Phys. Rev*. **A18**, 7165.

[15] Lindholm, E., Asbrink, L. (1985). *Molecular Orbitals and Their Energies Studied by the Semiemprical HAM Method.* Springer, Berlin.

[16] Gelius, U., Siegbahan, K. (1972). *Faraday Discuss. Chem. Soc.* **54**, 257.

[17] Gelius, U. (1974). *J. Spectrosc. Relat. Phenom.* **5**, 985.

[18] Yeh, J.J. (1993). *Atomic Calculation of Photoionization Cross Section and Asymmetry Parameters*. Gordon & Breach, New York.

[19] Frisch, M.J., Trucks, G.W., Schlegel, H.B., Scuseria, G.E., Robb, M.A., Cheeseman, J.R., Scalmani, G., Barone, V., Mennucci, B., Petersson, G.A., Nakatsuji, H., Caricato, M., Li, X., Hratchian, H.P., Izmaylov, A.F., Bloino, J., Zheng, G., Sonnenberg, J.L.Hada, M., et al. (2009). *GAUSSIAN 09*, Revision A.02. Gaussian, Inc., Wallingford, CT.

[20] Perdew, J.P., Wang, Y. (1992). *Phys. Rev. B* **45**, 13244.

[21] Perdew, J.P. (1991). In Ziesche, P., Eischrig, H. (eds.), *Electronic Structure of Solids*. Akademie Verlag, Berlin.

[22] Perdew, J.P., Chevary, J.S., Vosko, S.H., Pederson, M.R., Singh, D.J., Foilhais, C. (1992). *Phys. Rev. B* **46**, 6671.

[23] Dunning, T.H., Jr., Hay, P.J. (1977). In Schaefer, H.F. (ed.), *Methods of Electronic Structure Theory.* Plenum Press, New York.

[24] St.-Amant, A., Salahub, D.R. (1991). *Chem. Phys. Lett.* **169**, 387 (1990).

[25] St.-Amant A. (1992). *deMon, un programme LCGTO-MCP-DF, et une etude théorique de l'adsorption de l'hydrogène sur les monomères et dimères de Ni, Rh, et Pd*, Ph.D. Thesis, Université de Montréal.

27

ALIGNED FIBRILLAR COLLAGEN MATRICES

Ralf Zimmermann,[1] Jens Friedrichs,[1] Babette Lanfer,[1] Uwe Freudenberg,[1,2] and Carsten Werner[1,2]

[1] *Leibniz Institute of Polymer Research Dresden, Max Bergmann Center of Biomaterials Dresden, Hohe Strasse 6, D-01069 Dresden, Germany*

[2] *Technische Universität Dresden, Center for Regenerative Therapies Dresden, Tatzberg 47, 01307 Dresden, Germany*

27.1 INTRODUCTION

Collagen represents the most abundant protein in mammals, accounting for up to 35% of the protein content in the body [1]. At present 28 different types of collagens [2] are known to be involved in shaping and maintaining the extracellular matrix (ECM) by forming fibrillar or other large-scale assemblies [3]. Collagen builds up tissue-specific geometries of stable architecture that impart mechanical strength and stability to the ECM and mediate cell attachment, morphology, proliferation, and migration [4–7].

Collagen type I is the main collagen of skin and bone and the major constituent of most ECM variants. Three left-handed supercoiled polypeptide chains [two α1(I) and one α2(I)] of a polyproline-II-like conformation form a right-handed triple helix with a diameter of 1.5 nm and a length of 300 nm [3,8,9]. The collagen molecules form fibrils with diameters in the range of 20–70 nm in a multistep, entropy-driven self-assembly process termed *fibrillogenesis* [3,10,11]. Turbidimetric analysis of the fibril formation in vitro showed an initial lag phase followed by a growth phase with sigmoidal increase of the fibril formation rate [12,13]. It has been suggested that the formation of dimers and trimers takes place during the lag phase while rapid lateral aggregation involving five trimers (*microfibril*) occurs in the following growth phase. Further growth occurs by linear and lateral addition of the trimeric units, which results in the formation of collagen fibrils [14, 15]. When inspected by electron microscopy [16] or AFM [17], collagen fibrils present a repeating pattern of ∼67 nm (D-band periodicity) perpendicular to their axes.

In vivo, collagen fibrils are arranged in complex three-dimensional (3D) arrays, very often in an aligned manner to fulfill biomechanical functions such as resisting high-tensile forces in tendons. Collagens can be found as parallel fiber bundles in tendons and ligaments [18], as concentric waves in bone [19], or as orthogonal lattices in corneas [20]. The spatial organization of collagen fibers in vivo is believed to play an important role in directing cell behavior and fate decisions. For example, it has been reported that fibroblasts align along oriented collagen fibril matrices via contact guidance [21–24]. The direction of cell repopulation and the distribution of newly synthesized collagen was determined by the alignment of collagen fibrils [22]. Thus, in order to mimic the ECM structure of tissues and, in particular, to investigate the influence of the shape of ECM structures on cell behavior, it is of great interest to create aligned collagen fibril matrices for cell culture studies. However, the reconstitution of collagen matrices in vitro results in isotropic structural networks with arbitrarily oriented collagen fibrils [25].

Several methods have been developed to reconstitute aligned collagen matrices in vitro. Elsdale and Bard introduced a technique that involved draining of a supporting coverslip in one direction during gelation of a collagen solution [21]. Torbet and Ronzière exposed a gelling collagen solution to a strong magnetic field [26]. Under this condition the fibrils were aligned as a result of the diamagnetic properties of collagen molecules [24,26–28]. Two other researchers

Encyclopedia of Biocolloid and Biointerface Science, Volume 1, First Edition. Edited by Hiroyuki Ohshima.
© 2016 John Wiley & Sons, Inc. Published 2016 by John Wiley & Sons, Inc.

[29] made use of magnetic beads to align the collagen fibers by moving the beads in the gelling solution toward the poles of an external magnet. The effect of collagen fibril alignment was also observed in microfluidic channels (<100 μm width) as result of a short initial pressure-driven flow and subsequent static gelation of a collagen solution [30].

However, the previously reported methods require rather complex technical equipment and do not provide broad application in cell biology because of the limited size of the area covered by the artificial matrices. Importantly, none of the abovementioned techniques enables the variation of the collagen fibril alignment, density, and morphology.

We therefore introduced new techniques based on a microfluidic system (Section 27.2) and on collagen self-assembly on mica surfaces (Section 27.3) to create well-aligned and "native" collagen fibril matrices covering large areas. These methods also allow control of the density and orientation of the collagen fibrils by different means.

27.2 SHEAR FLOW DEPOSITION OF COLLAGEN MATRICES

27.2.1 Fibers in Shear Flow

In a simple shear flow, ellipsoidal particles usually align in the flow direction but change their orientation by 180° in a tumbling motion. This effect was first described by Jefferey [31], who calculated the motion of a single ellipsoid in a shear flow independent of inertia of fluid and particle. According to Ref. 31, the motion of an ellipsoid in an unbounded simple shear flow is given by the following equations

$$\tan\theta = \frac{Cr_e}{\left(r_e^2\cos^2\phi + \sin^2\phi\right)^{\frac{1}{2}}} \tag{27.1}$$

$$\tan\phi = r_e \tan\left(\frac{2\pi t}{T} + k\right) \tag{27.2}$$

where the angles φ and θ describe the orientation of the fiber with respect to the flow direction (in spherical coordinates), r_e is the effective aspect ratio of the particle (length/diameter), C is the orbit constant, and k is the initial value of φ. The spheroid will rotate with a period

$$T = \frac{2\pi}{\gamma}\left(r_e + r_e^{-1}\right) \tag{27.3}$$

under the actions of the shear rate γ. The particle is aligned with the vorticity axis for $C = 0$ and located in the plane of flow for C approaching infinity [31].

The motion of a fiber near a wall was reported to result in smaller angular velocities of the particles and larger periods between fiber rotations [32–35], whereas another team [36] claimed shorter periods of rotation. In regions closer to the wall than a half-fiber length, fibers were observed to follow a "pole vaulting" motion or a "springy rotation" during which the mass center of the fiber moved away from the wall [34,37]. With increasing flexibility of the fibers, the rotation changed toward snake-and-helix rotation and coil formation [37]. Additionally, fibers performing a "rolling–sliding motion" perpendicular to the flow direction were described [38]. With increasing aspect ratio and distance to the wall, the number of perpendicularly oriented fibers decreased. In the near-wall regions fibers with particle aspect ratio (length/diameter of particle) $r_p = 40$ stayed aligned with the flow direction whereas those with $r_p = 10$ moved toward an orientation perpendicular to the flow direction [39].

27.2.2 Experimental Approach

In Figure 27.1 we illustrate the experimental approach for the shear flow deposition of collagen matrices with adjustable orientation, density, and morphology by variation of the collagen solution, shear rate and substrate properties. The key element of the corresponding experimental setup is a microfluidic system with two parallel channels (length 8 mm, width 1 mm, height 73.6 μm) as well as inlet and outlet ports. The channels were fabricated by mirocasting of polydimethylsiloxane (PDMS) and the ports were integrated into a polycarbonate manifold. For detailed information concerning the technology, we refer the reader to Ref. 40. The open side of the channels can be placed on coverslips of different surface modifications, thus allowing for studies on the impact of surface hydrophilicity/hydrophobicity on the properties of the collagen matricies obtained. To improve the contact between the microfluidic system and the coverslips,

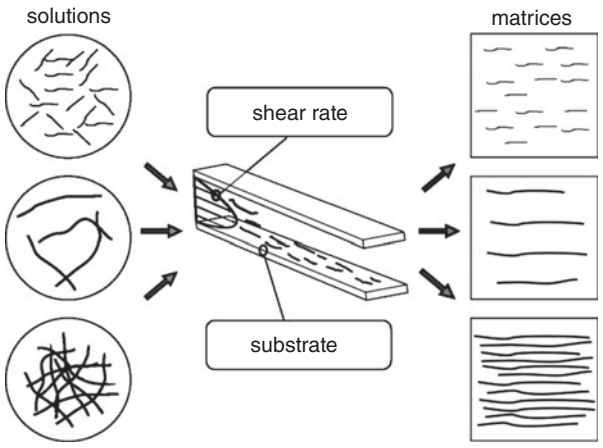


FIGURE 27.1 Scheme of the experimental approach for preparation of collagen fibril matrices that are adjustable in orientation, density, and morphology by variation of collagen solution, shear rate, and substrate.

additional channels for the application of vacuum were integrated into the PDMS.

The hydrodynamic flow (flow rate) of the collagen solutions in the microchannels can be controlled by a syringe pump that is connected via poly(ether–ether–ketone) (PEEK) tubing to external valves and to the microfluidic system [41]. Deposition of the collagen fibrils is performed under conditions of laminar flow. In all experiments reported, the Reynolds number (as a criterion for laminar flow) was <1.

The collagen matrices obtained can be analyzed by applying optical or atomic force microscopy in combination with image analysis for quantification of fibril alignment and coverage. For details on the analysis performed to obtain the results presented in this section, we refer the reader to Ref. 41. Two fibril deposition methods are described below.

27.2.2.1 Method A: Deposition of Collagen Fibrils during Fibril Formation. The method described here allows the deposition of aligned collagen matrices consisting of in situ formed fibrils onto planar surfaces. The microfluidic system is placed in an incubator at 37°C whereas the syringe pump for flow generation is kept below 4°C. To avoid early fibrillogenesis, the collagen solution is prepared at a temperature of 4°C and is drawn into chilled syringes, which then are directly installed into the syringe pump. Afterward the streaming process begins with pumping the chilled collagen solution from the syringe through the heated tubing. The length of the tubing towards the microfluidic channel can be varied, thereby influencing the conditioning time the collagen solution remains within the heated tubing before entering the channel.

Figure 27.2a shows confocal reflection microscopy (CRM) and atomic force microscopy (AFM) images of the collagen matrices prepared at three different concentrations on poly(octadecene-*alt*-maleic acid) (POMA) surfaces [42]. The flow rate was set to 11 μL/min and corresponds to a conditioning time of 5 min. The increase of the collagen solution concentration resulted in a significant increase of collagen fibril coverage (6.9% for 0.2 mg/mL, 29% for 0.4 mg/mL, and 83% for 0.8 mg/mL, at the middle position). Furthermore, visual inspection reveals an increase of the fibril length for the higher collagen concentrations. Collagen matrices deposited at a solution concentration of 0.2 mg/mL consist of single, short, and bent collagen fibrils that increase in length at a solution concentration of 0.4 mg/mL and further at 0.8 mg/mL. Furthermore, the increase of the collagen solution concentration also caused an increase in the fibril orientation (FWHM 41.4° for 0.2 mg/mL, 31.1° for 0.4 mg/mL, and 30° for 0.8 mg/mL; see Figure 27.2b and Table 27.1).

As described above, collagen fibrillogenesis is a multistep process whose dynamics depends on the starting solution concentration [25,43]. With increasing starting concentration the process of fibril formation is accelerated and higher numbers of fibrils are formed [25], which could explain why there are shorter and fewer fibrils for lower concentrations in contrast to longer fibrils and more dense matrices for higher starting concentrations. Turbiditiy measurements showed lag times for solution concentrations around 0.2 mg/mL exceeding the conditioning time of 10 min [25]. Thus, it could be assumed that fibril formation does not take place under these conditions. However, it was reported that the lag time disappeared when the neutralized collagen solution was kept at 4°C for a period of >5 min. Since the collagen solution in the experiments reported above was stored at 4°C for ≤1 h before streaming [41], it can be expected that a lag time as described above is not relevant anymore. Thus, fibrils might begin to form as early as in the chilled storage reservoir or while streaming through the tempered tubing.

In order to reveal correlations between the conditioning time of the collagen solution in the tempered tubing before entering the channel and the morphology of the resultant collagen fibril matrices, streaming experiments were performed at varied lengths of tubing between the syringe and the microfluidic channel. The length of the tubing was varied for a constant flow rate of 11 μL/min according to calculated conditioning times of 5, 10, and 30 min of the collagen solution in the tempered tubing. After 5 min of conditioning, dense and aligned fibrillar matrices consisting of long and short collagen fibrils are formed, whereas after 30 min mainly long, aligned, and more individual collagen fibrils appear (see Figure 27.3). The reproducibility of the experiments decreased with increasing conditioning time, due to the formation and adsorption of rather large fibril aggregates. Image analysis was not possible on matrices from solutions with 30 min conditioning time. However, differences between the matrices referring to morphology and structure are directly obvious from the CRM images (Figure 27.3).

27.2.2.2 Method B: Deposition of Fully Developed Collagen Fibrils. The method described here was developed to create highly aligned matrices consisting of long and "mature" collagen fibrils. Solutions containing appropriate low concentrations of this type of fibril can be obtained by homogenization and centrifugation of collagen gels [41]. Subsequently, the readily processed supernatant is pumped through the microfluidic channel. The orientation and density of the resulting collagen matrices can be varied with the flow rate, concentration of the collagen solution, and the type of surface coating [41]. In the following subsections we discuss the influence of these parameters on the collagen matrices obtained.

Influence of Flow Rate. In Figure 27.4a we show CRM and AFM images of collagen matrices prepared on POMA surfaces at different positions along the microfluidic channel. The collagen solution concentration was adjusted to 3 μg/mL, and the flow rate was set to 11 μL/min. The resultant matrices

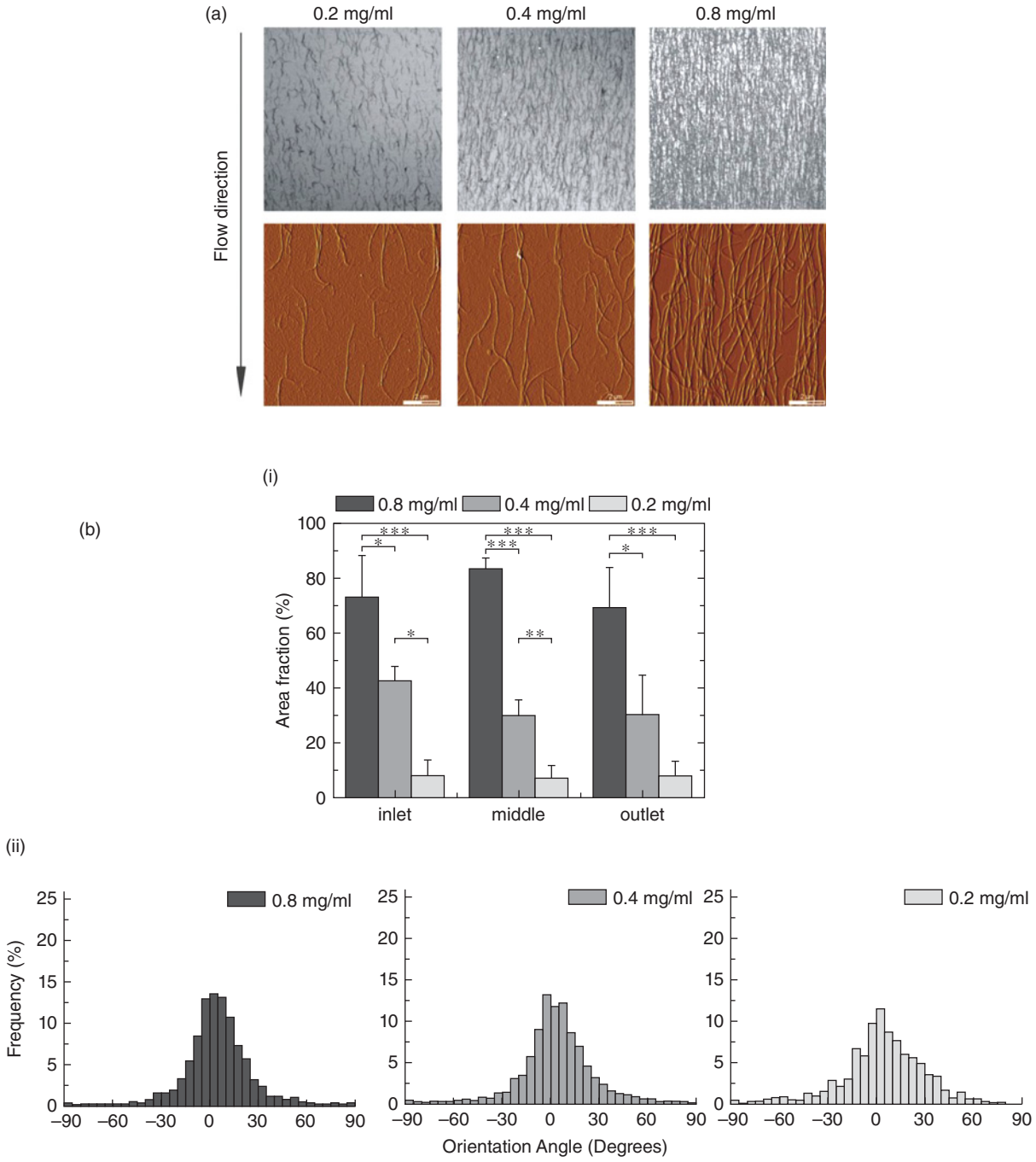


FIGURE 27.2 CRM (first row) and AFM (second row) images of aligned collagen fibril matrices prepared according to method A at collagen solution concentrations of 0.2, 0.4, and 0.8 mg/mL on POMA-coated substrates with a flow rate of 11 mL/min and a conditioning time of 5 min (a) and quantitative influence of the collagen solution concentration on the density and orientation of the obtained collagen fibril matrices (b): (i) relative area fraction (y axis) of collagen fibril coverage at three different positions (x axis) is plotted ($n \pm 3$, ±SD, $^{*}p < 0.05$, $^{**}p < 0.01$, $^{***}p < 0.001$); (ii) distribution of collagen fiber angles for different concentrations at middle position of the channel. The histograms show the relative frequency (y axis) of fiber angles in 5° bins (x axis) with 0° set as parallel to the channel axis. [Reprinted from *Biomaterials* **29** (2008), B. Lanfer, U. Freudenberg, R. Zimmermann, D. Stamov, V. Körber, C. Werner, Aligned fibrillar collagen matrices obtained by shear flow deposition, 3888–3895. Copyright 2008, with permission from Elsevier.]

TABLE 27.1 Influence of Process Parameters on Fibril Orientation (FWHM) in Collagen Matrices Prepared According to Methods A and B

Method A	FWHM (°)	Method B	FWHM (°)
Concentration		Flow rate	
0.2mg/mL	41.4	0.45 μL/min	30.1
0.4 mg/mL	31.1	4 μL/min	16.3
0.8 mg/mL	30	11 μL/min	14.4
		Concentration	
		3±0.1 μg/mL	14.4
		14±2.5 μg/mL	17
		Substrate	
		POMA	14.4
		PEMA	18.1
		Glass	13.9

consisted of long, highly aligned, and individual collagen fibrils. The density of the collagen matrices decreased along the channel axis. A possible reason for this observation might be a depletion of collagen across the channel length [44] since very low-concentration solutions were employed.

Figure 27.4b shows how the applied flow rate influences the alignment and coverage of fully developed collagen fibrils on POMA surfaces. The best alignment could be achieved for 11 μL/min (FWHM 14.4°; see Figure 27.4b and Table 27.1). Parallel alignment of the fibrils was consistent across the whole length and width of the microfluidic channel, whereas the decrease of the collagen fibril coverage along the channel from inlet to outlet was observed for all matrices prepared according to method B. With decreasing flow rate, the amount of adsorbed collagen fibrils increased independently of the channel position (17% for 11 μL/min, 38% for 4 μL/min, and 65% for 0.45 μl/min, at inlet position; see Figure 27.4b). For higher flow rates, less fibril coverage across width and length of the channel was observed. The fibril alignment remained almost constant (FWHM: 14.4° for 11 μL/min and 16.3° for 4 μL/min; see Figure 27.4b and Table 27.1). For the lowest flow rate (0.45 μL/min), an increasing amount of nonaligned aggregates at the inlet and outlet of the channel was observed. Consequently the orientation of the fibrils significantly decreased under these conditions (FWHM = 30.1°). The appropriate adjustment of the flow rate thus enables the generation of highly aligned matrices, which are at the same time adjustable in density.

Influence of Collagen Concentration. Results obtained for matrices prepared at collagen concentrations of 3 ± 0.1 μg/mL and 14 ± 2.5 μg/mL are compared in Figure 27.5a and Table 27.1. The increase of the solution concentration to 14 ± 2.5 μg/mL resulted in an increase of fibril coverage from 18% at 3 ± 0.1 μg/mL to 35% at 14 ± 2.5 μg/mL at (at the inlet position), whereas the fibril orientation slightly decreased (FWHM 14.4°–17°) at higher collagen solution concentration. The decrease of alignment cannot be attributed to the relative lack of orientation of the collagen fibrils as such but to an increase of aggregates of nonaligned collagen fibrils. Nevertheless, the results demonstrate that the density of matrices prepared according to method B is also adjustable by choosing appropriate solution concentrations.

Influence of Substrate. In order to investigate the fibril–surface interactions and to possibly increase the density and alignment of the collagen fibrils, the authors of Ref. 41 employed substrates that differed in the degree of hydrophobicity/hydrophilicity. Beyond POMA, also poly(ethylene-*alt*-maleic-acid) (PEMA)-coated glass as well as freshly cleaned glass coverslips were used [41]. The experiments were performed at a flow rate of 11 μL/min. For POMA-modified surfaces, higher coverage (14%) of collagen fibrils could be achieved as compared to PEMA-modified (7%) and bare glass slides (6%) (see Figure 27.5b). The alignment

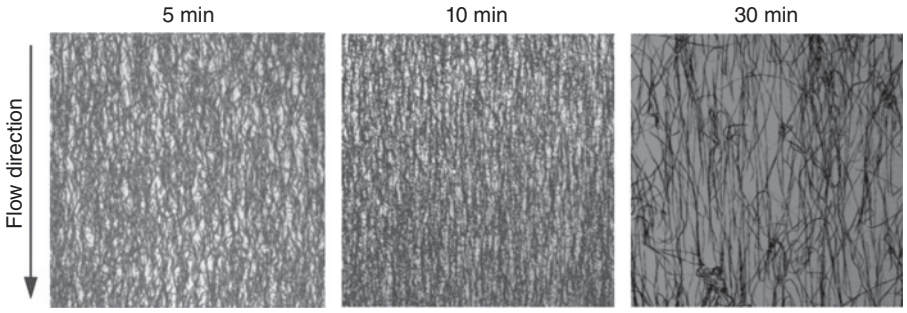


FIGURE 27.3 CRM images of collagen fibril matrices prepared according to method A from collagen solutions (0.8 mg/mL) pumped through heated tubing for varying conditioning time periods of 5, 10, and 30 min before entering the channel (on POMA surfaces, flow rate of 11 mL/min). Dimensions of images are 62.5 × 62.5 μm. [Reprinted from *Biomaterials* **29** (2008), B. Lanfer, U. Freudenberg, R. Zimmermann, D. Stamov, V. Körber, C. Werner, Aligned fibrillar collagen matrices obtained by shear flow deposition, 3888–3895. Copyright 2008, with permission from Elsevier.]

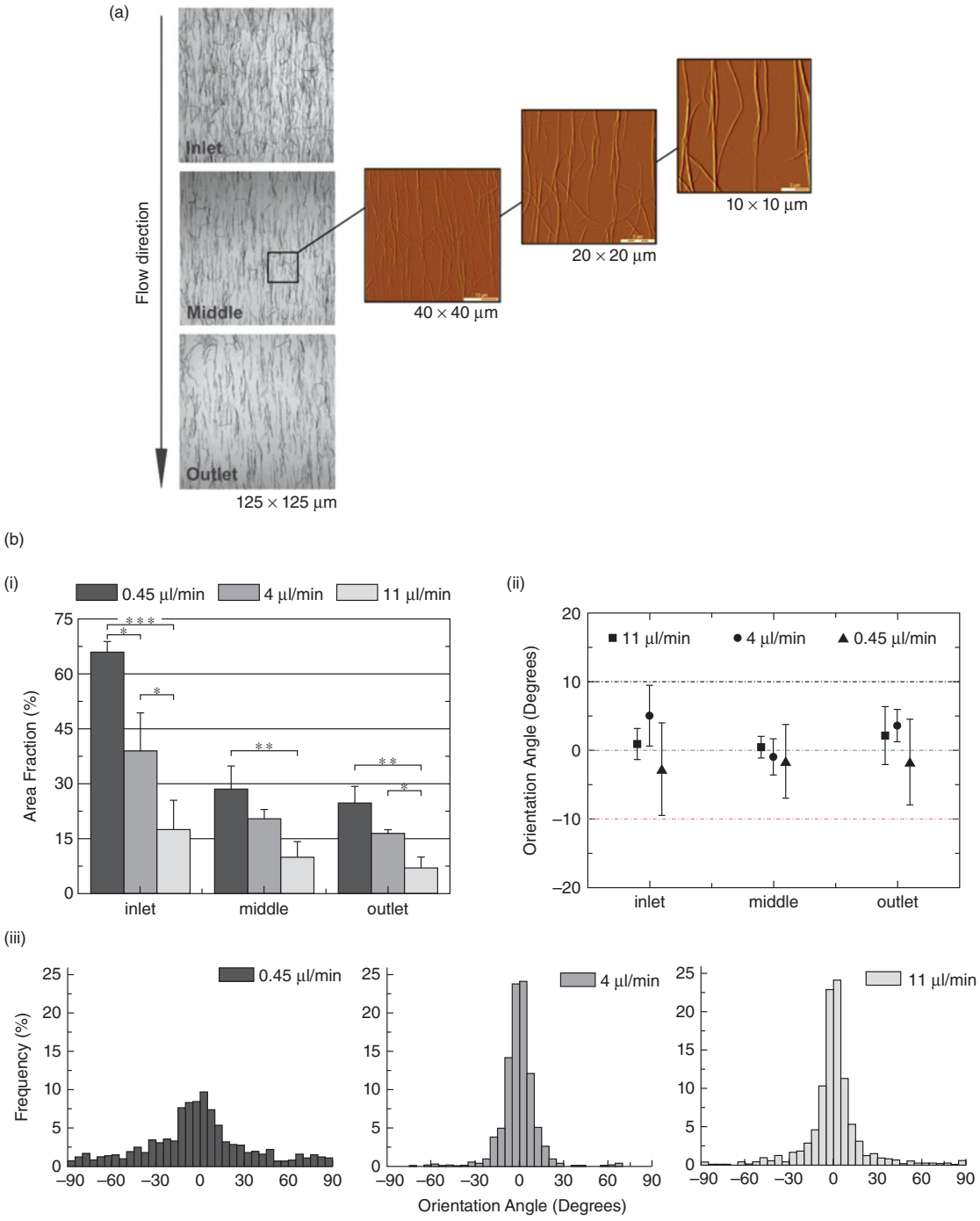


FIGURE 27.4 CRM and AFM images of aligned collagen fibril matrices prepared according to method B (solution concentration 3 ± 0.1 mg/mL, flow rate 11 mL/min, substrate POMA) along the length (inlet, middle, and outlet) of the microfluidic channel (a) and influence of different flow rates on the collagen fibril coverage and orientation (b): (i) collagen fibril coverage as area fraction in percentage at different channel positions ($n = 3$, ±SD, $^{*}p < 0.05$, $^{**}p < 0.01$, $^{***}p < 0.001$); (ii) mean orientation angle of collagen fibrils along channel length (n = 3, ±SD); (iii) distribution of collagen fiber angles at middle position of channel. The histograms show the relative frequency (y axis) of fiber angles in 5° bins (x axis) with 0° set as parallel to the channel axis. [Reprinted from *Biomaterials* **29** (2008), B. Lanfer, U. Freudenberg, R. Zimmermann, D. Stamov, V. Körber, C. Werner, Aligned fibrillar collagen matrices obtained by shear flow deposition, 3888–3895. Copyright 2008, with permission from Elsevier.]

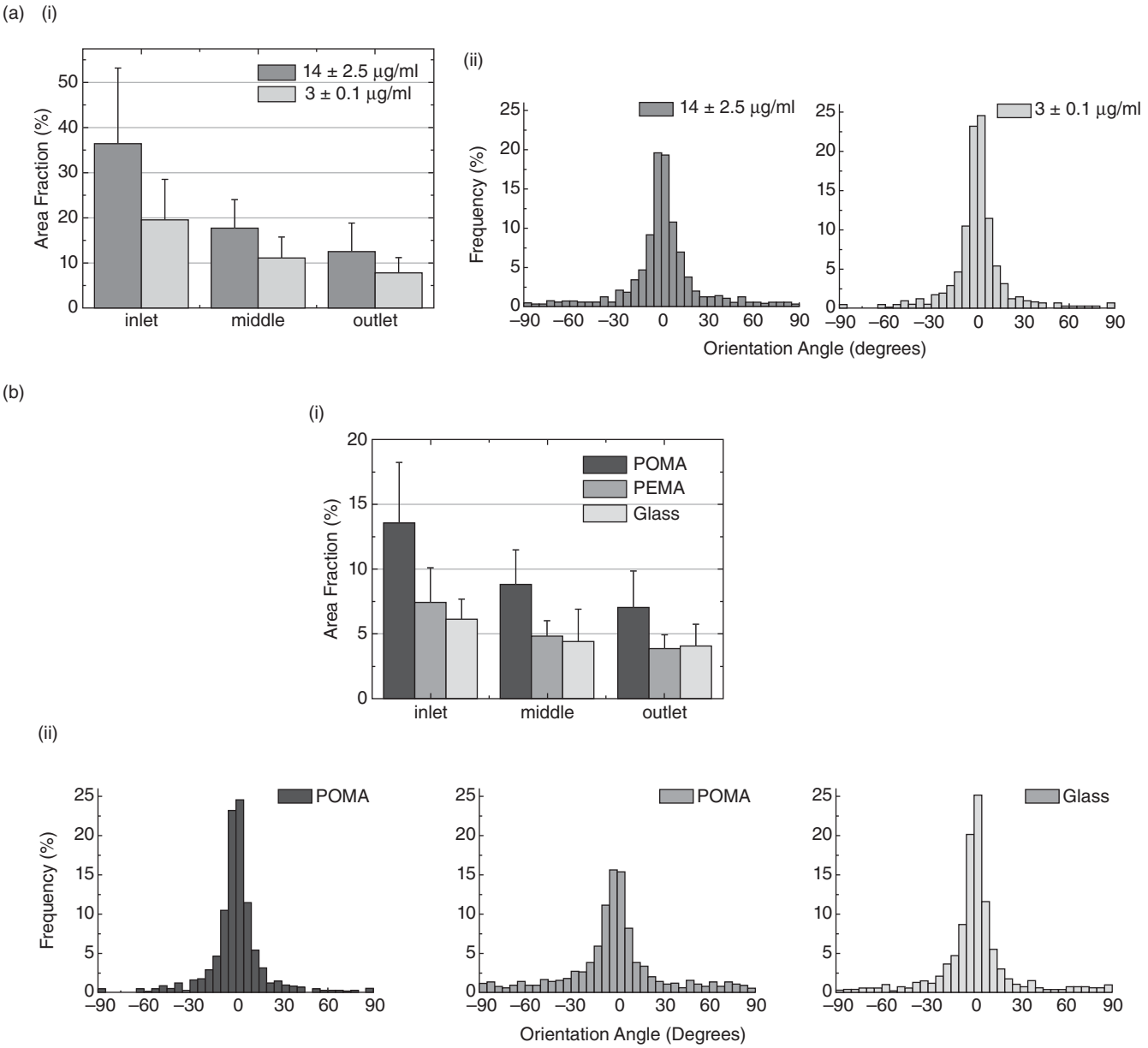


FIGURE 27.5 Influence of collagen solution concentration on density and orientation of collagen fibril matrices prepared according to method B at a flow rate of 11 mL/min on POMA films (a): (i) relative area fraction (y axis) of collagen fibril coverage at three different positions (x axis) at both concentrations is plotted ($n = 3$, ±SD); (ii) distribution of collagen fiber angles for both concentrations at middle position of e channel. The histograms show the relative frequency (y axis) of fiber angles in 5° bins (x axis) with 0° set as parallel to the channel axis. Influence of substrate on density and orientation of collagen fibril matrices prepared according to variant B (flow rate 11 mL/min, solution concentration: 3 ± 0.1 mg/mL) (b). (i) The relative area fraction (y axis) of collagen fibril coverage for the three substrates at three different positions (x axis) is plotted ($n = 3$, ±SD). (ii) Distribution of collagen fiber angles for the three substrates at middle position of channel. The histograms show the relative frequency (y axis) of fiber angles in 5° bins (x axis) with 0° set as parallel to the channel axis. [Reprinted from *Biomaterials* **29** (2008), B. Lanfer, U. Freudenberg, R. Zimmermann, D. Stamov, V. Körber, C. Werner, Aligned fibrillar collagen matrices obtained by shear flow deposition, 3888–3895. Copyright 2008, with permission from Elsevier.]

of collagen fibrils on POMA-coated and glass substrates was higher than on PEMA-modified substrates (FWHM 14.4° for POMA; 18.1° for PEMA, 13.9° for glass; see Figure 27.5b and Table 27.1).

The copolymers POMA and PEMA consist of alternating units of maleic acids and alkyl chains [42]. However, the comonomer octadecene in POMA is rather big compared to the small ethylene residue in PEMA [42]. Consequently, thin films of these copolymers show differences in hydrophobicity and structural characteristics ranging from a nearly nonswollen, hydrophobic film for POMA to highly swollen copolymer brushes for PEMA [42]. Covalent attachment of the collagen to the copolymers could be excluded, since the other comonomer of both copolymers (POMA and PEMA) was in the nonreactive diacid form. Instead, the higher coverage on POMA-coated substrates was attributed to hydrophobic interactions between the collagen and the alkyl chains of the POMA-coated substrate surface. The hydrophilic gel-like structure of PEMA and the smooth and nonswollen glass surface apparently do not favor adsorption of the hydrophobic collagen. Moreover, the soft nature of the swollen PEMA film possibly impedes the alignment of the collagen fibrils, due to the hindrance of the hydrodynamic flow by the polymer chains in the interfacial region [45].

27.2.3 Possible Mechanism of Fibril Alignment

Because *prealignment* effects [46] appear to play a minor role in this system and as the viscosity only slightly influences the fibril alignment–as matrices produced according to method B showed the highest degree of alignment despite the low viscosity of the utilized solutions–the formation of longer fibrils (besides the flow rate) seems to critically determine the alignment (Table 27.1) pointing at the underlying mechanism of a mechanical alignment. Fibers in a simple shear flow usually align in the direction of flow; however, their orientation can change by 180° in a tumbling motion [31]. This motion was observed in a low-Reynolds-number regime for pulp fibers that reveal rigidities in the same range as collagen fibrils (pulp fibers, 5.4 GPa [47]; collagen fibers, 5.5 GPa [48]). Thus it is likely that the collagen fibrils interact with the wall during the tumbling motion. If one end of the fibril attaches to the surface, the remaining part can be aligned by the streaming fluid in a position of low hydrodynamic resistance, that is, parallel to the flow direction. However, due to additional interaction of the fibril with the surface, not all fibrils align parallel to the flow. Near the wall, the number of fibers aligning in the flow direction was reported to be higher for higher aspect ratios ($r_p > 40$) [39,49]. Since aspect ratios of the long fibrils in our system are comparable to those of reported in Ref. 49, inertia effects may contribute to the increase of fibril alignment with increasing length. Thus, it can be concluded that fibril alignment is dependent on (1) the flow rate (which influences the shear stress/force in the system (tubing and channel)) and (2) the length of the fibrils, and to a lesser degree (3) the viscosity of the solution (which also influences shear force, but in a much lower order than the flow rate).

27.2.4 Comparison with Other Methods

Compared to microfluidic approaches [30] with narrow flow channels (channel width <30 μm), the methods described above allow the preparation of homogeneously aligned collagen matrices covering an area of several square millimeters. Therefore, these matrices are more suitable for cell culture studies since the average cell diameter is much smaller than the lateral dimensions of the covered area. Furthermore, in comparison to other current techniques, the degree of fibril alignment is very high and can be varied with the flow rate in the channel. Highest alignment was achieved with 47% and 68% of the collagen fibrils within 5° of the channel axis for method A and method B, respectively. In comparison, Lee et al. reported 40% of the collagen fibrils to be within 5° of the channel axis, whereas for increasing channel width this percentage decreased. The examples presented thus indicate that the method introduced in Ref. 41 produces highly aligned matrices that are of comparable or better quality than those obtained by other current techniques and that are at the same time tunable in morphology.

27.3 COLLAGEN SELF-ALIGNMENT ON MICA

27.3.1 Directing Collagen Self-Assembly into Ultrathin Matrices

Recently, a method was developed to create structurally well-defined and nanoscopically reproducible two-dimensional (2D) matrices of highly aligned type I collagen molecules [17,50,51]. In a first step, a layered crystal of muscovite mica is cleaved, exposing an atomically flat surface. Subsequently, a drop of buffer solution is placed onto the freshly cleaved mica [52]. A buffer solution containing the collagen molecules is then injected into the buffer solution covering the mica surface. This initiates the adsorption and self-assembly of highly aligned fibrillar collagen structures on the supporting mica surface. The direction of collagen alignment is determined by the crystallographic orientation of the mica substrate [53]. The pH value, electrolyte content, and electrolyte concentration of the buffer solution play a crucial role in guiding the self-assembly process of the collagen molecules into higher-ordered structures [50] (Figure 27.6). The assembly time of the collagen matrix ranges from minutes to a few hours and depends on the collagen concentration, the pH value, the electrolyte content, and the temperature of the buffer solution [17,50]. Depending on the self-assembly conditions, this collagen matrix could establish

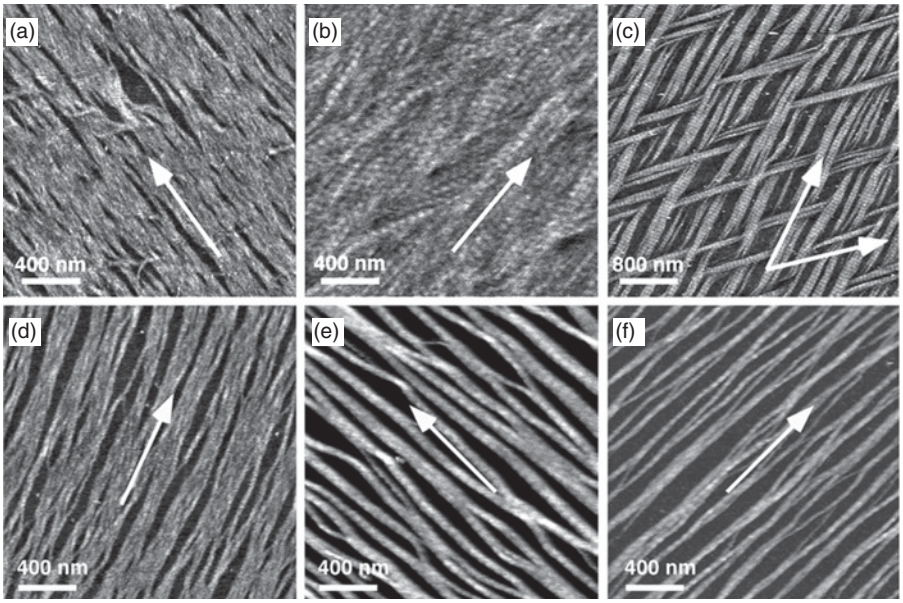


FIGURE 27.6 Directed self-assembly of ultrathin nanoscopic collagen matrices in physiological buffers. (a–c) Demonstration of influence of electrolytes on collagen self-assembly. (a) Collagen matrix self-assembled from collagen molecules in 200 mM NaCl at pH 7.5 buffered with 50 mM Tris-HCl. The aligned fibrils did not show any periodical structure along their axes. (b) Collagen matrix self-assembled in 200 mM KCl at pH 7.5 buffered with 50 mM Tris-HCl. (c) Collagen matrix self-assembled in 200 mM KCl at pH 8.5 buffered with 50 mM Tris-HCl. Along their axes the fibrils (arrows) showed a D-band periodicity of ≈66 nm, typical for collagen assembled in vivo. (d–f) Self-assembly of collagen matrices in physiological buffers. (d) Collagen matrix self-assembled in PBS; the collagen molecules assembled into fibrils that aligned (arrows) into similar patterns such as observed for fibrils assembled with NaCl (a). (e) Collagen matrix self-assembled from collagen molecules in a buffer mimicking the eukaryotic cytoplasmic environment (130 mM monopotassium glutamate, 8.5 mM monosodium glutamate, 10 mM Hepes, 2 mM $MgCl_2$, 1 mM Na_2ATP, 1 mM EGTA, 0.5 mM NaH_2PO_4, 0.5 mM Na_2HPO_4, 0.5 mM $CaCl_2$, pH 7.2 adjusted with KOH). (f) Collagen matrix self-assembled in a buffer mimicking the eukaryotic extracellular environment (109.2 mM NaCl, 4.1 mM KCl, 1.7 mM $CaCl_2$, 0.65 mM $MgCl_2$, 7.9 mM monosodium glutamate, 0.4 mM NaH_2PO_4, 0.3 mM Na_2HPO_4, 27 mM $NaHCO_3$, 20 mM Hepes, pH 7.4 adjusted with NaOH). Both the extracellular and intracellular buffers promoted collagen fibrils to establish the D-band periodic structure. Topographs exhibit a color scale corresponding to a vertical range of 5 nm. [Reprinted from *Small* 3 (2007), D.A. Cisneros, J. Friedrichs, A. Taubenberger, C.M. Franz, D.J. Muller, Creating ultrathin nanoscopic collagen matrices for biological and biotechnological applications, 956–963. Copyright 2007, with permission from John Wiley & Sons.]

characteristic structural features observed for native collagen fibrils [17]. The self-assembled collagen matrix consists of highly ordered collagen fibrils and exhibits a thickness of ≈3 nm, which corresponds to the average diameter of one collagen microfibril.

27.3.2 Adjusting the Collagen Matrix Density by pH Change

Assembling the collagen matrix in buffer solutions having identical electrolyte compositions but different pH values guided the assembly of the collagen molecules into different 2D matrices [50]. At low pH values of 2.5 and 3.5, the collagen molecules adsorbed as globular structures onto the mica surface. This observation correlates well with the low tendency of collagen fibrils to self-assemble at low pH values [3]. Most probably, the globular structures observed represent monomeric collagen or aggregates of a few collagen molecules. Between pH 4.5 and 8.9, the collagen molecules assembled into fibrillar structures that formed structurally well-defined matrices, indicating that the assembly of collagen molecules into the matrices readily occurred at pH values as low as 4.5. However, increasing the pH value of the buffer solution toward the pI of collagen (≈9.3 [54]) decreased the density of collagen fibrils forming the 2D matrix. At pH 9.3 the density of collagen fibrils adsorbed onto the mica was about half that obtained within the pH range 4.5–8.9. Increasing the pH above 9.3 further decreased the density of fibrils

forming the collagen matrices. These results demonstrate that the density of collagen fibrils forming the final 2D matrix can be precisely controlled by the pH value of buffer solution.

27.3.3 Role of Electrolytes in Determining Final Collagen Matrices

In addition to pH changes, it was observed that the electrolyte type and the electrolyte concentration of the buffer solution could influence the assembly of collagen molecules into nanoscopic matrices [50]. When assembled in the absence of K^+, the collagen fibrils exhibited a high degree of parallel alignment (Figure 27.6a). The collagen fibrils mainly associated laterally, thereby forming flat (≈3-nm) elongated structures called *microribbons* [50]. Remarkably, the fibrillar structures assembled under these conditions did not display the characteristic D band (Figure 27.6a), such as observed for collagen fibrils assembled in vivo [16]. This situation changed when K^+ was present during the self-assembly process. In this case the collagen molecules assembled into fibrillar structures that exposed their native 67-nm periodic structure (Figure 27.6b). When assembled in the presence of K^+ at a higher pH value, collagen fibrils displayed a crossed pattern (Figure 27.6c) such as observed for the self-assembly of α-synuclein fibrils [55].

The supramolecular assembly of collagen molecules was also studied in buffers mimicking physiologically relevant conditions. Assembled in phosphate-buffered solution (Figure 27.6d), the collagen matrices were structurally similar to matrices assembled at high NaCl concentrations but in absence of K^+ (Figure 27.6a). This indicated that the K^+ concentration of ≈ 4.1 mM within the PBS buffer was not sufficiently high to promote the D-band formation of the self-assembled collagen fibrils. However, when assembled in a buffer mimicking the intracellular environment of eukaryotic cells [56], the collagen matrices showed a well-pronounced formation of the D band (Figure 27.6e). The formation of the D-band periodicity may be assigned to the much higher K^+ concentration of the buffer solution in which the self-assembly of the collagen fibrils took place. Although they contained a K^+ concentration of only 4.1 mM, buffer solutions mimicking the extracellular environment of eukaryotes [56] also promoted D-band formation (Figure 27.6f). This suggests that other electrolytes may assist K^+ in promoting D-band formation of collagen. It may be assumed that certain electrolyte compositions may promote the formation of D-band periodicity, even in the absence of K^+. However, further experimental work is needed to prove this.

27.3.4 Structural Features of Self-Assembled Collagen Fibrils Resembling In Vivo Fibrils

At increased spatial resolution, substructural details within the D band of the fibrils self-assembled into the 2D matrix could be resolved. The multi banded sub-structures of D-banded collagen fibrils resembled those observed by transmission electron microscopy of positively stained collagen fibers extracted from rat tail tendon [16]. From this structural correlation it could be concluded that the collagen structures self-assembled in vitro established similar structural details as collagen fibrils assembled in vivo [17].

27.3.5 Reshaping Collagen Matrices on Nanoscale

After assembly of the collagen matrix, single fibrils could be realigned in a controlled manner using the AFM stylus as nanotweezers [50,57]. After initiation of the self-assembly of collagen molecules (Figure 27.7a), the final matrix structure was imaged by AFM in the tapping mode, where the maximum force applied by the stylus was sufficiently small

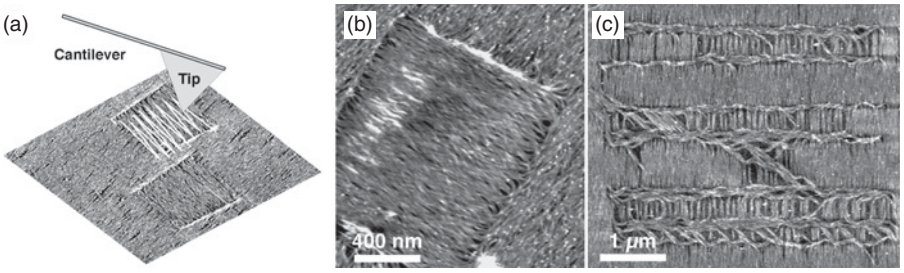


FIGURE 27.7 Designing nanoscopic collagen matrices using an AFM cantilever as a nanotool. (a) After preparation of the collagen matrix, the stylus of the AFM cantilever is pushed onto the matrix to design new patterns and structures (white lines). This induces the collagen molecules to reassemble into the fast-scanning direction of the stylus. (b,c) AFM topographs of patterns created with the method described. Note how collagen molecules are sometimes knotted into complex nanostructures. Experiments were performed on native collagen molecules in buffer solution at pH 7.5 (200 mM NaCl, 50 mM TrisHCl). Full gray levels of topographs correspond to a vertical scale of 4 nm. [Reprinted from *Small* **3** (2007), D.A. Cisneros, J. Friedrichs, A. Taubenberger, C.M. Franz, D.J. Muller, Creating ultrathin nanoscopic collagen matrices for biological and biotechnological applications, 956–963. Copyright 2007, with permission from John Wiley & Sons.]

to prevent reversible or irreversible structural distortions [58]. Predefined regions of the matrix were scanned using contact-mode AFM in order to manipulate the collagen fibrils. Reimaging of the manipulated region in tapping mode showed that the collagen fibrils realigned in the fast-scanning direction of the AFM stylus (Figure 27.7a). In this way, it was possible to create highly organized patterns on the nanometer scale (Figure 27.7b,c).

27.3.6 Collagen Matrices Showing Enhanced Stability after Maturation

The collagen fibrils of the matrix could be realigned only within the first 5 h after the self-assembly of the collagen matrix took place. After this time, the individual fibrils could not be reoriented. Thus, it was concluded that the collagen fibrils strengthened their bonds or enhanced the number of these bonds within the matrix. It could be further suggested that these bonds, increasing the mechanical stability of the matrix, formed relatively slowly. The maturation time of ≈5 h observed here for the collagen matrix stabilization is very similar to the time of 6–8 h during which collagen gels begin to lose their ability to be reorganized by fibroblasts in cell culture [59]. This suggests that the maturation process that takes place in the 2D matrices of self-assembled collagen fibrils is similar to that in 3D networks of collagen fibrils, and that a similar process may take place in tissues. After this setting period, the structured collagen matrices were mechanically stable. When the matrices were reinvestigated after a few months of storage at room temperature in a buffer solution, it was found that both the orientation and mechanical stability of the collagen matrices had not changed [57].

27.3.7 Insight into Collagen Self-Assembly through Time-Lapse AFM

As described in the previous sections, the D-band periodicity of self-assembled collagen fibrils forming 2D matrices matches that of collagen fibrils and fibers found in vivo. These findings were, however, obtained from static AFM topographs. To gain insight into the dynamic process of collagen self-assembly, time-lapse high-resolution AFM imaging was applied. Figure 27.8 shows time-lapse AFM topographs of collagen fibrils adsorbed and aligned onto the supporting mica surface (Figure 27.8a,b). The longitudinal and lateral growth of these fibrils could be followed over the timecourse of the time-lapse AFM (Figure 27.8c–e). As the recording of AFM topographs continued, several other fibrils adsorbed onto the mica and aligned in the same direction as the previously adsorbed fibrils (Figure 27.8d–f). Independent of the time of their adsorption, all fibrils continuously grew laterally and longitudinally until they covered the entire support with a ≈3-nm-thick matrix. On approaching, it was possible for adjacent fibrils to fuse laterally (Figure 27.8h,i). Sometimes, this lateral fusion of two fibrils left local defects, such as gaps or slight mismatches of the D-band periodicity. About 50% of these defects, which occurred at the initial stages of the self-assembly process, disappeared over time. This self-healing process may be promoted by collagen molecules from the buffer solution and represents a self-organization process that significantly contributes to the toughness and strength of collagen fibrils from tendons. During wound healing, fibroblasts increase the synthesis of the ECM and decrease its degradation [5, 6]. Such self-organizing capabilities of collagen to heal out defects could contribute to faster and more efficient tissue repair.

27.3.7.1 Early Fibrils and Fibril Flexibility. The self-assembly kinetics of collagen molecules into fibrils forming the 2D matrix depended on the collagen concentration of the solution [17]. The smallest isolated fibrillar structures observed exhibited dimensions of $\approx 800 \times 20$ nm. Considering that only the width of the isolated fibrils imaged appears wider due to nonlinear AFM stylus–sample convolution effects [60], the widths taken from the thinnest collagen fibrils of ≈5 nm embedded in the collagen matrix are not broadened through convolution effects [61]. The dimensions of 800×5 nm corresponded well to those of early fibrils [62] observed to occur during the development of chicken tendon. It has been proposed that early fibrils could represent the building blocks of collagen fibril assembly [63]. Time-lapse AFM could also monitor the fusion of the tips of two collagen fibrils growing toward each other [64]. The fusion of fibrillar tips requires intrinsic flexibilities, which allows both fibril ends to match each other. After tip fusion, the fibril continuously grew in longitudinal and lateral directions. This ability of fibrils to match each other for fusion enabled the formation of a uniform collagen matrix coating the entire supporting mica surface.

27.3.7.2 Collagen Fibrils Grow in Steps. Increasing the temporal resolution of time-lapse AFM provided further insights into the molecular mechanisms of fibril growth. To initiate collagen self-assembly, single collagen molecules were injected into the buffer solution at a low concentration. Recording the width of a growing collagen fibril over time revealed discrete jumps (Figure 27.8l, vertical arrows between horizontal lines). This indicates that single fibrils changed their widths in average step sizes of 3.7 ± 1.3 nm. This step size corresponds well to the average diameter ≈ 3.3 nm of a single microfibril [65, 66]. From this observation it followed that collagen fibrils assemble in two steps: In the first step, presumably five collagen molecules fused laterally and collapsed. This collapse initiated the formation of a microfibril, which assembled with the larger collagen fibrils, as indicated by the growing steps of fibril.

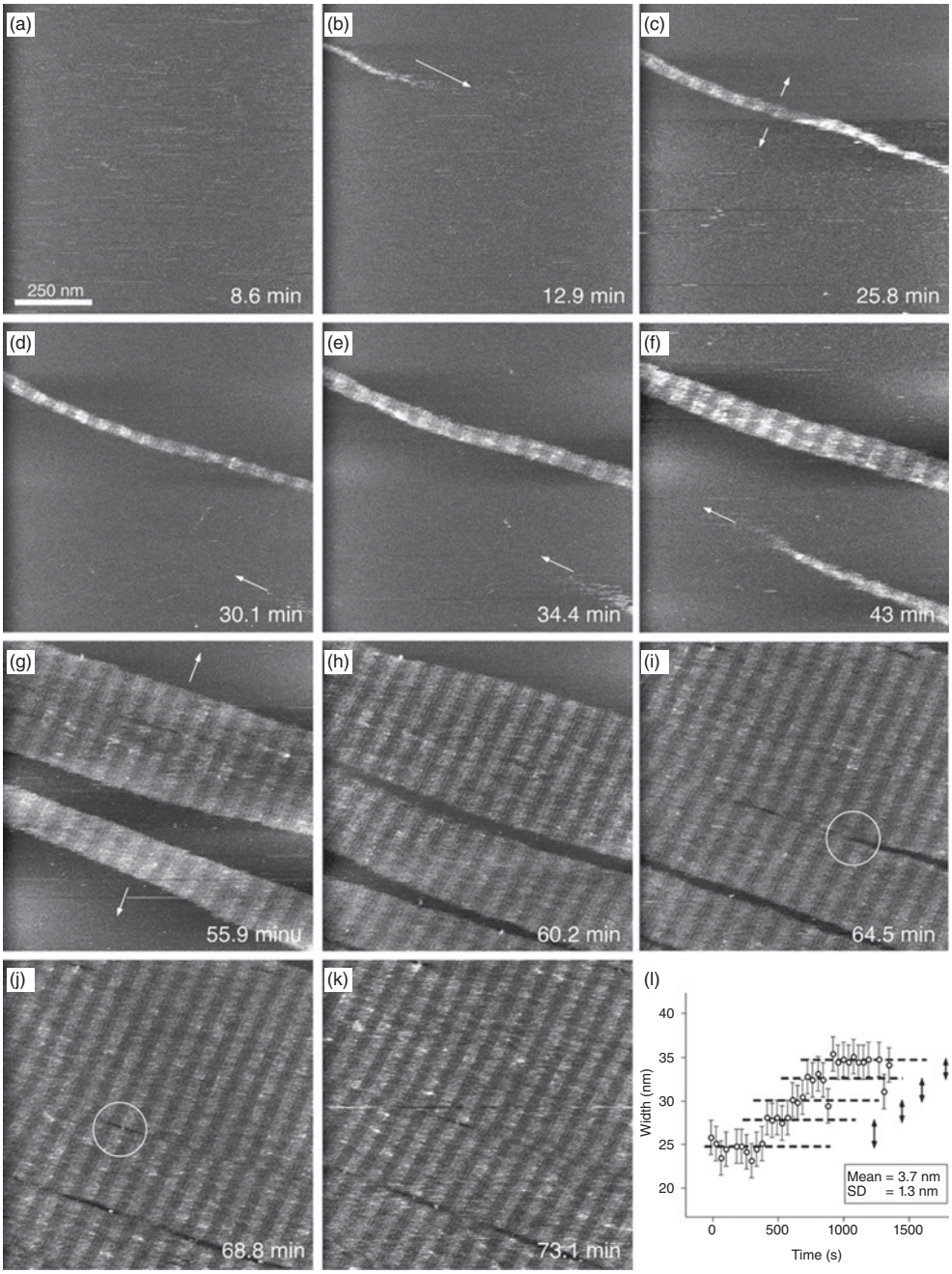


FIGURE 27.8 Self-assembly of collagen matrices observed by time-lapse AFM: (a–e) Collagen molecules of the buffer solution assemble into fibrils that grow laterally and longitudinally (arrows) onto a mica support. The typical D-band periodicity known from collagen fibrils grown in vivo can be clearly resolved in the self-assembled fibrils. (f–k) AFM topographs of a fibril growing longitudinally toward the center of the topograph while another fibril grows laterally. The growing collagen fibrils assemble into a 2D matrix covering the entire mica support. The height of the matrix corresponds to ≈3 nm. Most defects formed by growing fibrils that collide [see circle in panel (i)] disappear after the fibrils have fused (i–k). Tapping-mode AFM topographs were recorded in buffer solution (pH 9.2, 50 mM glycine, 200 mM KCl, 27°C, at a collagen concentration of 12 mg/mL) and exhibit a full gray level corresponding to a vertical scale of 5 nm. (l) Width of a single collagen fibril plotted over a certain growth time followed with time-lapse AFM. Note how the width changes by discrete steps (horizontal lines and vertical arrows), which have an average width of 3.7 ± 1.3 nm. [Reprinted from *Small* **3** (2007), D.A. Cisneros, J. Friedrichs, A. Taubenberger, C.M. Franz, D.J. Muller, Creating ultrathin nanoscopic collagen matrices for biological and biotechnological applications, 956–963. Copyright 2007, with permission from John Wiley & Sons.]

27.4 SUMMARY

Recent developments in the preparation of aligned collagen fibril matrices by shear flow and by using the collagen self-assembly on mica have been reviewed. We demonstrated and discussed in detail the options of both methods and compared them with other techniques.

The shear flow deposition method introduced by the authors of Ref. 41 allows one to create collagen matrices differing in alignment, density, and morphology. These matrix properties can be varied by choosing appropriate process parameters. The versatility of this method allows for the easy and quick preparation of fine-tuned biofunctionalized matrices to enable advanced strategies in cell biology and tissue engineering. In particular, the well-defined matrices provide the opportunity to characterize and control the adhesion, orientation, and migration of cells. Using the resulting options, the surface-engineered collagen substrates were used to guide neurite outgrowth and elongation in vitro [67]. Since the collagen fibril architecture in vivo is tissue-specific and cellular fate decisions critically depend on the surrounding ECM [68, 69], cell biology experiments to investigate the effect of collagen fibril length and density on stem cell differentiation are of great interest. For that purpose, the formation of aligned collagen fibrils will be further elaborated to incorporate glycosaminoglycans such as heparin and heparan sulfate [70], which mediate growth factor and protein binding [71]. This method is also applicable for building up 3D matrices through layer-by-layer deposition and for the coating hollow tubular structures to be used as conduit in nerve repair.

In the second part of the chapter we demonstrated that collagen molecules can be processed into an ultrathin (≈3-nm) collagen matrix. Collagen fibrils of this 2D matrix can be precisely aligned at the nanometer scale. Adjusting the buffer conditions controls the spacing and structural orientation of collagen fibrils to highly reproducible matrices. These buffer conditions also determine whether the fibrils establish their native D-band periodic structure. Currently, the self-assembly of collagen matrices is conducted using muscovite mica as the supporting surface. In the future, self-assembly of the matrices should be carried out on other surfaces. Alternative approaches may involve floating theses layers from the supporting surface and using them for coating nonbiological and biological materials. Experiments extending these matrices to other materials and applications are in progress. Collagen matrices may be further mechanically and physically stabilized by the introduction of crosslinks between the fibrils using the enzyme lysyl oxidase [72]. This would allow biotechnologically promising applications to functionalize the matrices by almost any given type of protein fused to collagen-binding domains. These matrices would provide a native environment for proteins, eliminating nonspecific protein interactions with the supporting surface [73, 74]. Most importantly, such an approach would provide a matrix to cover biosensors. In future, functionalization of this ultrathin matrix with other proteins may allow the development of a toolbox for biosensors or biomaterials. In nature, cells adapt and modify the surrounding ECM by mechanical or chemical means [75]. It is of tremendous cell biological and medical interest to be able to create biomaterials that regulate cellular functions. Artificial environments may be developed for cells that include essential natural substrates that lead cells to desired states of differentiation or activation. Existing applications of collagen as a biomaterial include their use as drug delivery systems, for skin replacements, and as matrices for cell culture [76]. The collagen matrices described provide nanostructured patterns, which may in the future be functionalized with ECM proteins or biochemical signals to regulate cell functions [77].

ACKNOWLEDGMENT

We gratefully thank Elsevier and Wiley for permitting the reuse of material from Refs. 41 and 51 for the preparation of this chapter.

REFERENCES

[1] Meisenberg, G., Simmons, W.H. (2011). *Principles of Medical Biochemistry*; 3rd ed. Elsevier Health Sciences.

[2] Kadler, K.E., Baldock, C., Bella, J., Boot-Handford, R.P. (2007). *J. Cell Sci.* **120**, 1955–1958.

[3] Kadler, K.E., Holmes, D.F., Trotter, J.A., Chapman, J.A. (1996). *Biochem. J.* **316**(Pt.1), 1–11.

[4] Akiyama, S.K., Nagata, K., Yamada, K.M. (1990). *Biochim. Biophys. Acta* **1031**, 91–110.

[5] Grinnell, F. (2000). *Trends Cell Biol.* **10**, 362–365.

[6] Grinnell, F. (2003). *Trends Cell Biol.* **13**, 264–269.

[7] Thakar, R.G., Ho, F., Huang, N.F., Liepmann, D., Li, S. (2003). *Biochem. Biophys. Res. Commun.* **307**, 883–890.

[8] Rich, A., Crick, F.H. (1961). *J. Mol. Biol.* **3**, 483–506.

[9] Canty, E.G., Kadler, K.E. (2005). *J. Cell Sci.* **118**, 1341–1353.

[10] Ottani, V., Martini, D., Franchi, M., Ruggeri, A., Raspanti, M. (2002). *Micron* **33**, 587–596.

[11] Engel, J., Bächinger, H.P. (2005). *Structure, Stability and Folding of the Collagen Triple Helix*. Springer, Berlin/Heidelberg, pp. 7–33.

[12] Wood, G.C., Keech, M.K. (1960). *Biochem. J.* **75**, 588–598.

[13] Williams, B.R., Gelman, R.A., Poppke, D.C., Piez, K.A. (1978). *J. Biol. Chem.* **253**, 6578–6585.

[14] Silver, F.H., Langley, K.H., Trelstad, R.L. (1979). *Biopolymers* **18**, 2523–2535.

[15] Silver, F.H. (1981). *J. Biol. Chem.* **256**, 4973–4977.

[16] Chapman, J.A., Tzaphlidou, M., Meek, K.M., Kadler, K.E. (1990). *Electron Microsc. Rev.* **3**, 143–182.

[17] Cisneros, D.A., Hung, C., Franz, C.M., Muller, D.J. (2006). *J. Struct. Biol.* **154**, 232–245.

[18] Elliott, D.H. (1965). *Biol. Rev.* **40**, 392–421.

[19] Weiner, S., Traub, W. (1992). *FASEB J.* **6**, 879–885.

[20] Holmes, D.F., Gilpin, C.J., Baldock, C., Ziese, U., Koster, A.J., Kadler, K.E. (2001). *Proc. Natl. Acad. Sci. USA* **98**, 7307–7312.

[21] Elsdale, T., Bard, J. (1972). *J. Cell Biol.***54**, 626–637.

[22] Matsumoto, N., Horibe, S., Nakamura, N., Senda, T., Shino, K., Ochi, T. (1998). *Arch. Orthop. Trauma Surg.* **117**, 215–221.

[23] Ng, C.P., Swartz, M.A. (2006). *Ann. Biomed. Eng.* **34**, 446–454.

[24] Guido, S., Tranquillo, R.T. (1993). *J. Cell Sci.***105**(Pt. 2), 317–331.

[25] Salchert, K., Streller, U., Pompe, T., Herold, N., Grimmer, M., Werner, C. (2004). *Biomacromolecules* **5**, 1340–1350.

[26] Torbet, J., Ronzière, M.C. (1984). *Biochem. J.* **219**, 1057–1059.

[27] Kotani, H., Iwasaka, M., Ueno, S., Curtis, A. (2000). *J. Appl. Phys.* **87**, 6191.

[28] Torbet, J., Malbouyres, M., Builles, N., Justin, V., Roulet, M., Damour, O., Oldberg, A., Ruggiero, F., Hulmes, D.J.S. (2007). *Biomaterials* **28**, 4268–4276.

[29] Guo, C., Kaufman, L.J. (2007). *Biomaterials* **28**, 1105–1114.

[30] Lee, P., Lin, R., Moon, J., Lee, L.P. (2006). *Biomed. Microdevices* **8**, 35–41.

[31] Jeffery, G.B. (1922). *Proc. Roy. Soc. A: Math. Phys. Eng. Sci.* **102**, 161–179.

[32] Dabros, T. (1985). *J. Fluid Mech.* **156**, 1–21.

[33] Gavze, E., Shapiro, M. (1997). *Int. J. Multiphase Flow* **23**, 155–182.

[34] Stover, C.A., Cohen, C. (1990). *Rheol. Acta* **29**, 192–203.

[35] Pozrikidis, C. (2003). *J. Fluid Mech.* **496**, 105–127.

[36] Moses, K.B., Advani, S.G., Reinhardt, A. (2001). *Rheol. Acta* **40**, 296–306.

[37] Forgacs, O.L., Mason, S.G. (1959). *J. Colloid Sci.* **14**, 473–491.

[38] Holm, R., Söderberg, D. (2007). *Rheol Acta* **46**, 721–729.

[39] Carlsson, A. (2007). Orientation of fibres in suspensions flowing over a solid surface. Mechanics, KTH, School of Engineering Sciences (SCI), Stockholm.

[40] Gast, F.U., Dittrich, P.S., Schwille, P., Weigel, M., Mertig, M., Opitz, J., Queitsch, U. (2005). *Microfluid. Nanofluid.* **2**, 21–36.

[41] Lanfer, B.; Freudenberg, U.; Zimmermann, R.; Stamov, D.; Körber, V.; Werner, C. (2008). *Biomaterials* **29**, 3888–3895.

[42] Pompe, T., Zschoche, S., Herold, N., Salchert, K., Gouzy, M.-F., Sperling, C., Werner, C. (2003). *Biomacromolecules* **2003**, 4, 1072–1079.

[43] Gelman, R.A., Poppke, D.C., Piez, K.A. (1979). *J. Biol. Chem.* **254**, 11741–11745.

[44] Norde, W., Rouwendal, E. (1990). *J. Colloid Interface Sci.* **139**, 169–176.

[45] Zimmermann, R., Dukhin, S.S., Werner, C., Duval, J.F.L. (2013). *Curr. Opin. Colloid Interface Sci.* **18**, 83–92.

[46] Giraud-Guille, M.M. (1992). *J. Mol. Biol.* **224**, 861–873.

[47] Nilsson, B., Wågberg, L., Gray, D. (2000). Conformability of wet pulp fibres at small length scales. Mid Sweden Univ., Sundsvall.

[48] Yang, L., van der Werf, K.O., Koopman, B.F.J.M., Subramaniam, V., Bennink, M.L., Dijkstra, P.J., Feijen, J. (2007). *J. Biomed. Mater. Res.* **82**, 160–168.

[49] Subramanian, G., Koch, D.L. (2005). *J. Fluid Mech.* **535**, 383–414.

[50] Jiang, F., Hörber, H., Howard, J., Müller, D.J. (2004). *J. Struct. Biol.* **148**, 268–278.

[51] Cisneros, D.A., Friedrichs, J., Taubenberger, A., Franz, C.M., Muller, D.J. (2007). *Small* **3**, 956–963.

[52] Müller, D.J., Amrein, M., Engel, A. (1997). *J. Struct. Biol.* **119**, 172–188.

[53] Sun, M., Stetco, A., Merschrod, S.E. (2008). *Langmuir* **24**, 5418–5421.

[54] Hattori, S., Adachi, E., Ebihara, T., Shirai, T., Someki, I., Irie, S. (1999). *J. Biochem.* **125**, 676–684.

[55] Heise, H., (2005). *Proc. Natl. Acad. Sci. USA* **102**, 15871–15876.

[56] Patton, B.J., Fuchs, A.F., Steiner, R., Patton, H.E. (1988/89). *Textbook of Physiology*, Vols. 1,2. Saunders, Philadelphia.

[57] Jiang, F., Khairy, K., Pool, K., Howard, J., Müller, D. J. (2004). *Microsc. Res. Technol.* **64**, 435–440.

[58] Müller, D.J., Büldt, G., Engel, A. (1995). *J. Mol. Biol.* **249**, 239–243.

[59] Sawhney, R.K., Howard, J. (2002). *J. Cell Biol.* **157**, 1083–1091.

[60] Schwarz, U.D., Haefke, H., Reimann, P., Güntherodt, H.J. (2011). *J. Microsc.* **173**, 183–197.

[61] Engel, A., Schoenenberger, C.A., Müller, D.J. (1997). *Curr. Opin. Struct. Biol.* **7**, 279–284.

[62] Graham, H.K., Holmes, D.F., Watson, R.B., Kadler, K.E. (2000). *J. Mol. Biol.* **295**, 891–902.

[63] Canty, E.G., Kadler, K.E. (2002). *Compar. Biochem. Physiol. A: Mol. Integrat. Physiol.* **133**, 979–985.

[64] Cisneros, D.A., Muller, D.J., Daud, S.M., Lakey, J.H. (2006). *Angew. Chem. Int. Ed. Engl.* **45**, 3252–3256.

[65] Orgel, J.P.R.O., Irving, T.C., Miller, A., Wess, T.J. (2006). *Proc. Natl. Acad. Sci. USA* **103**, 9001–9005.

[66] Orgel, J.P., Miller, A., Irving, T.C., Fischetti, R.F., Hammersley, A., Wess, T.J. (2001). *Structure* **9**, 1061–1069.

[67] Lanfer, B., Seib, F.P., Freudenberg, U., Stamov, D., Bley, T., Bornhauser, M., Werner, C. (2009). *Biomaterials* **30**, 5950–5958.

[68] Yang, F., Murugan, R., Wang, S., Ramakrishna, S. (2005). *Biomaterials* **26**, 2603–2610.

[69] Rajnicek, A., Britland, S., McCaig, C. (1997). *J. Cell Sci.* **110**(Pt. 23), 2905–2913.

[70] Stamov, D., Grimmer, M., Salchert, K., Pompe, T., Werner, C. (2008). *Biomaterials* **29**, 1–14.

[71] Casu, B., Lindahl, U. (2001). *Adv. Carbohydr. Chem. Biochem.* **57**, 159–206.

[72] Kim, M.S., Kim, S.-S., Jung, S.T., Park, J.-Y., Yoo, H.-W., Ko, J., Csiszar, K., Choi, S.-Y., Kim, Y. (2003). *J. Biol. Chem.* **278**, 52071–52074.

[73] Wong, T.S., Schwaneberg, U. (2003). *Curr. Opin. Biotechnol.* **14**, 590–596.

[74] Ivanov, Y.D., Govorun, V.M., Bykov, V.A., Archakov, A.I. (2006). *Proteomics* **6**, 1399–1414.

[75] Vogel, V., Sheetz, M. (2006). *Nat. Rev. Mol. Cell Biol.* **7**, 265–275.

[76] Lee, C.H., Singla, A., Lee, Y. (2001). *Int. J. Pharm.* **221**, 1–22.

[77] Stevens, M.M., George, J.H. (2005). *Science* **310**, 1135–1138.

28

COLLOIDAL CRYSTALLIZATION

TSUNEO OKUBO

Institute for Colloidal Organization, Hatoyama 3-1-112, Uji, Kyoto 611-0012, Japan

28.1 INTRODUCTION

More recent research has focused on colloidal crystals, that is, the crystal-like distribution of colloidal particles in suspensions of aqueous and organic solvents [1–13]. Many researchers have studied structural colors, interparticle reactions, crystal structure, morphology of single crystals, phase transition, crystallization kinetics of nucleation and crystal growth, physicochemical properties (rigidity, viscosity, etc.), structural changes induced by external fields (e.g., gravity, centrifugal and electric fields, shearing forces), and technical applications (photonic crystals, colloidal lithograpy, etc.).

As is well known, all kinds of substances or materials are composed of a huge number (on the order of Avogadro's number, ideally) of elementary particles (atoms, molecules, colloidal particles, etc.). There exist three states of substances–gas, liquid (normal and ordered liquids), and solid (crystals and amorphous solids), depending on the distribution of the elementary particles as a function of time. In *gas* state, all the elementary particles move freely by the thermal energy $k_{\mathrm{B}}T$ given to each elementary particle in the modes of translation and rotation. Here, k_B is the Boltzmann constant and T is the absolute temperature. When an elementary particle collides with other particles or with a container wall, it is simply reflected. In *liquid* state, all the elementary particles also move freely but maintain short nearest-neighbor interparticle distances. The elementary particles in *solid* state also move in the vibrational and rotational modes with thermal energy but keep their equilibrium points. It is easy to distinguish between a crystal and an amorphous solid; the former distributes *in order* and the latter, *in disorder*. Irrespective of the kind of elementary particles, all the substances have three states depending on the abovementioned conditions. Thus, *colloidal gases*, *colloidal liquids*, and *colloidal crystals* are sound scientific terms that refer to substances whose elementary particles are colloidal particles themselves. It should be noted here that many researchers have used the term *colloidal glasses* for highly concentrated suspensions of polydisperse colloidal particles. This author, however, proposes the *amorphous solid* instead, which is much better than the *glass*, following the simplified definition of states of substances.

Two groups of colloidal crystals have been studied intensively hitherto: those in (1) diluted and deionized aqueous suspensions (*soft* systems) [14–33] and (2) concentrated suspensions mainly in the refractive index (RI)-matched organic solvents (*hard* systems) [34–39]. Soft crystals are very convenient models for studying both *soft*- and *hard*-sphere systems, depending on the ionic concentrations of suspension; examples are *soft* crystals in the exhaustively deionized state and *hard* crystals in the presence of a rather large amount of salt, such as sodium chloride. The hard crystal is best for study of crystallization only by the interparticle repulsive interaction due to the thermal movement of particles, excluding volume effects (or steric stability effects). On the other hand, soft crystals also result from *repulsive interaction* between particles; these phenomena are termed *electrostatic repulsion* and *excluded-volume effects*. We should note here that in the usual crystals, such as metals, proteins, and ice, *attractive interactions* between elementary particles play an important role in the crystallization process, as will be described below.

We should note that most colloidal particles in water acquire *negative charges* on their interfaces with water in order to lower the enlarged Gibbs free-energy interface by

Encyclopedia of Biocolloid and Biointerface Science, Volume 1, First Edition. Edited by Hiroyuki Ohshima.
© 2016 John Wiley & Sons, Inc. Published 2016 by John Wiley & Sons, Inc.

two mechanisms: by the (1) *dissociation of ionizable groups* and (2) *preferential adsorption of ions* from suspension. These ionic groups leave their counterions, and these excess charges accumulate near the interface, forming an electrical double layer. The counterions in the diffuse region are distributed according to a balance between the thermal diffusive forces and the forces of electrical attraction with colloidal particles. The importance of the electrical double layers for the colloidal crystallization of soft system has been clarified by many researchers [1–33]. The giant size of single crystals is the result of the exhaustively deionized and diluted suspension of colloidal spheres, where the number of nuclei available for crystallization is drastically reduced [23–33]. Colloidal crystals are very visually appealing, with their strong structural colors, because the interparticle distance is often just in the order of the light wavelength, with each single crystal reflecting light in different colors, due to *Bragg diffraction*.

In this chapter, general features of colloidal particles and their crystallization in terms of their structural, kinetic, and dynamic properties such as morphology, crystallization kinetics, physicochemical properties, and electrooptical phenomena, especially in aqueous media, are reviewed and discussed.

28.2 PREPARATION AND CHARACTERIZATION OF BIOLOGICAL AND SYNTHETIC COLLOIDAL PARTICLES

28.2.1 Biological Colloidal Particles

There exist several biological colloidal particles. Tobacco mosaic virus (TMV) (cylinderlike, 18 nm in diameter and 300 nm in length) is typical as rodlike colloidal particles [40–443]. Further large assembling of TMV was also studied [44]. Cowpea mosaic virus (CPMV) is also rod-shaped [45]. Purified samples of bacterial cellulose (*nata de coco*) is rod-shaped, 1–2 μm in length and 10 × 50 nm in cross section, and their suspension shows heavy iridescent birefringence [46]. Various kinds of 2D assemblies of H-shaped streptavidin mutants form, depending on the pH values [47]. Filamentous bacteriophage *fd* virus is also interesting as one of the rodlike biological polymers [48]. Microcrystalline cellulose is rodlike but rather polydisperse ellipsoidal [49, 50]. Microcrystalline cellulose was stabilized in aqueous media by grafting the cellulose with poly(ethylene glycol) or carboxylation [51]. Typical collagen is a rodlike polymer with a 280 nm length and 1.2 nm diameter and is composed of three amino acid chains wound into coaxial helices [52–54]. The temperature-induced gel–sol transition of the small chains of collagens is a very interesting phenomenon. The shape of *Lypocodium* spore is determined by the combination of hemisphere and tetrahedron, but close to sphere totally (30 μm in size) [55]. Pollen particles (10–50 μm in size) from many kinds of flowers are typical examples of biological colloidal particles. However, many of them are not so stable and not dispersed homogeneously in water. Diatoms are typical examples of inorganic and naturally occurring colloidal particles [56]. Their shape and surface structure are beautiful–spherical, ellipsoidal, linear, triangle, crescentlike, violinlike, and so on. Fossil colloidal spheres of radiolarian are rather monodisperse in size [57]. Diatoms and radiolarians originate from algae and plankton, respectively. However, their main chemical components are the same: *silica*. Oceanic colloidal particles such as Palau white clay will be also grouped into a biological colloidal particle.

28.2.2 Polymer Colloidal Particles

Monodispersity in size of spherical particles plays an important and basic role for in colloidal organization. Highly monodisperse polystyrene and poly(methyl methacrylate) spheres (PMMA, size ranging from ∼20 nm to several mm in diameter) are now available commercially. In particular, polystyrene spheres such as Dow polystyrene and Duke Scientific sulfonated polystyrene spheres have been used so often among researchers as the standard samples [58–65]. Anionic and cationic polystyrene spheres are synthesized by using anionic and cationic initiators, respectively. However, we should note that the cationic ones are generally unstable, as described below in detail. Various kinds of core–shell spheres, where the hard core is coated with a soft shell and vice versa, have been prepared by the copolymerization method, for example [1,60,63]. PMMA stabilized by thin layers (∼10 nm) of poly-12-hydroxystearic acid spheres were used in a mixture of decalin and tetralin (or carbon disulfide) to match the refractive index of the spheres in the field of the hard colloidal crystallization [66–71]. Monodisperse poly(1*H*,1*H*-heptafluorobutyl methacrylate) spheres (138 nm in diameter) were synthesized [72]. Several kinds of fluorine-containing polymer spheres, poly(tetrafluoro ethylene), PTFE, copolymer of tetrafluoroethylene and perfluorovinylether, and copolymer of perfluoroethylene and perfluoropropylene, were also used to study colloidal organization [73, 74]. Colloidal spheres having cores rich in polystyrene and shells rich in hydrated poly(2-hydroxyethyl methacrylate) were synthesized [75–77]. Heterocoagulation of large cationic spheres with small anionic polyacrylate beads followed by heat annealing produced core–shell particles [78]. Hollow polyelectrolyte capsules were prepared by means of stepwise adsorption of polyelectrolytes followed by dissolution of the templating core [79]. Furthermore, vesicle-templated polymer hollow spheres were synthesized [80]. Polyelectrolyte multilayer coatings on the colloidal particles have been studied extensively [81–84].

Anisotropically shaped colloidal particles are most interesting for study of the organization including crystallization. Anisotropy-shaped polymer particles, such as symmetric doublets [85], asymmetric doublets [85], and egg-shaped [86], ellipsoidal [85], beadlike [87], snow dole-like, dumbbell-like, raspberrylike [88, 89], clenchlike, comfitlike (*framboidal*) [90], golfball-like [91], red-blood corpuscle-like [92, 93], disklike, and polyhedral [94, 95] particles are now available at laboratory scale. Monodisperse ellipsoidal polystyrene particles have been prepared by the unique method of stretching the polystyrene spheres dispersed in the film of poly(vinyl alcohol) [96, 97]. Bowl-shaped particles were used for study of the orientation and inclusion phenomena [98–100]. Monodispersed colloidal gel spheres have been synthesized. Gel spheres of poly(*N*-isopropylacrylamide) are famous as typical samples of thermosensitive hydrogels [101].

28.2.3 Inorganic Colloidal Particles

Monodispersed colloidal particles of metals [102], metal oxide [103], and metal sulfides [104] have been synthesized intensively. Colloidal silica spheres have been used often for study of colloidal organization phenomena such as colloidal crystallization and drying patterns for >20 years [105, 106]. Highly monodisperse colloidal silica spheres ranging from 5 nm to 10 mm in diameter are now available commercially. Colloidal silica spheres coated with other functional groups, dyes, fluorescent probes, and so on using the reactive silanol groups have been studied [107–110]. Colloidal silica spheres modified with linear-type polymers and their colloidal crystallization have been studied intensively [111–116]. The dispersion property of colloidal silica spheres coated with a layer of end-grafted poly(dimethylsiloxane) was studied in heptanes [117]. Titania (TiO_2) colloidal spheres are synthesized in a diffusion flame reactor and by others [118–122]. Spherical (polyhedral in the strictly sense) gold particles ranging from 2 nm to several μm in diameter are famous as the hydrophobic colloidal spheres and their aggregates by the addition of salts following the Shultz–Hardy rule [123, 124]. Similar-sized aggregates (∼1 μm) from gold preparticles are obtained [125]. Gold spheres have been also synthesized [126, 127]. Studies using silver spheres were also reported [128, 129]. Small silver spheres capped with dodecanethiol were prepared and formed ordered arrays after drying [130]. Syntheses and their organization of the similar-sized agglomerates (1.5 μm in diameter) from the diamond preparticles (4–6 nm in diameter) have been reported [131, 132]. Spherical particles of unique morphology of boehmite, α-AlOOH, were obtained by aging acidic solutions of alminum perchlorate [133–135]. Colloidal spheres of CdS and ZnS have been prepared [136–138]. Charge reversals of CdS colloidal spheres under the Langmuir–Blodgett membrane were reported [139]. Molybdenum sulfide particles were synthesized in microemulsion [140]. Colloidal copper dispersion was studied [141]. Copper oxide(I) spheres (∼200 nm in diameter) were synthesized [142]. Colloidal spheres of PbI_2 were prepared [143]. Core–shell-type (CdSe)ZnS particles (2.3–5.5 nm) have been studied [144]. Core–shell microspheres consisting of single-walled carbon nanotubes and $CaCO_3$ were synthesized [145].

Symmetric polyhedron-shaped particles are prepared mainly from metals. Cubic colloidal particles (20–50 nm in size) composed of MgO, CdO, PbSe, PbTe, and αFe_2O_3 have been synthesized [146, 147]. Cube-shaped platinum particles have been prepared [148]. Hexahedron-shaped particles of WO_3, InS_3, and SnO_2 were also obtained [130]. Octahedrons of In_2O_3 were prepared [121]. Octahedron-shaped alnite $Fe_3(SO_4)_2(OH)_5.2H_2O$ was crystallized on heating acidic solutions of ferric sulfate [134, 135]. Flowerlike particles formed from $FeCl_2$ and bipyridine are beautiful. Whisker-shaped particles (5 μm in wing length) were synthesized by Matsushita Sangyo Co. (Osaka). Hexahedral copper oxide (CuO) particles were obtained [103]. Furthermore, Au, Ag, Ni, and Al are known to produce octahedron-shaped particles [130].

Spindle-shaped colloidal silica particles have been prepared [149]. Rod-shaped [150–153] and platelike particles of gold [154, 155] are available at laboratory scale. Stacking aggregates of platelike gold particles are also interesting [154]. Platelike particles of nickel(II) hydroxide coated with polyacrylate were stable in aqueous suspension [156]. Platinum colloidal particles of different shapes were synthesized [157]. Rod-shaped (or ellipsoidal) particles of β-FeOOH are obtained from $FeCl_3$ after 6–10 months at room temperature as a red suspension at the bottom of the container [158]. Rodlike boehmite (γ-AlOOH) particles have been used for study of phase transition [159]. α-Alumina, α-Al_2O_3 particles (average size ∼200 nm) with an irregular shape are available commercially. Silica- coated boehmite rods (e.g., 230 nm in length, 9 nm in diameter) [160] were synthesized according to the method of Buining [161]. Sterically stabilized gibbsite, $Al(OH)_3$ platelets are also used for the crystallization phenomena [162]. Ellipsoidal TiO_2 [163] and rodlike rutite-type particles [164]were prepared. Bentonite (or montmorilonite) particles are platelike in shape, but their monodispersity is not extensive [49]. However, rather monodispersed bentonite particles were obtained by the fractional repeated centrifugation technique [165–168]. Ellipsoidal plate-shaped particles of tungstic acid, $H_2WO_4{\cdot}H_2O$, are highly monodispersed [169–172]. Howevere, these particles disappear after several weeks in the deionized state with coexistence of ion exchange resins, since the tungstic acid particle is one of the sparingly water-soluble electrolytes in water (like silver chloride) and is ion-exchanged for a long period. Rod-shaped or spindle-shaped V_2O_5 particles have been prepared [173]. Disklike manganese oxide particles were synthesized and their ordered arrays were studied [174].

Monodisperse cylindrical (or rod-shaped) particles of nickel dimethylglyoxime were obtained, and an ordered array of the particles was observed [175]. Disklike pseudocubic [52], ellipsoidal [176], peanut-shaped [177], and hexagonal plate-shaped hematite (αFe_2O_3) particles [177] were prepared by the sol–gel method. Spindle-shaped hematite particles coated with polymer brush were synthesized and their crystallization was studied [178]. A disk-like particle (3 nm in diameter and 0.1 nm thick) of a synthetic trioctahedric hectorite has been studied [179–181]. Laponite, synthetic hectorite clay, is a disklike particle [182, 183].

28.2.4 Basic Characteristics of Colloidal Particles

Characterization of the surface charges is very important for study of colloidal crystallization, especially in aqueous media. The stoichiometric charge density of colloidal particles can be determined conveniently by conductometric titration [184]. The titration curves have been shown in several papers, for example [49,185–187]. Potentiometric (pH) determination of charge density has been reported [188].

For colloidal particles, irrespective of shape, the *counterion* association, that is, the strong associative interaction between the charges on the particles and their counterions, which deprives some of the counterions of freedom of thermal motion, has been a subject of extensive theoretical and experimental study. The effective charge number as a fraction of the stoichiometric one (β), which is determined from conductance [1,149,189], electrophoretic mobility [190], dielectric [191], and osmotic pressure measurements [192], decreases as the analytical (stoichiometric) charge number of a particle (Z) increases. The relationship between β and Z is shown in Eq. (28.1) [185].

$$\log \beta = 2.61 - 0.87 \log Z, \quad \text{for } Z > 3000 \qquad (28.1)$$

Note that the β values for colloidal spheres with very large Z values become extremely small. For example, 99.9 % of total counterions are associated with the charges on the sphere surface when Z is 10^6. The charge renormalization effect has been discussed in the literature [193–195]. Counterion binding of colloidal spheres has also been discussed [196]. We should note here that 1-β corresponds to the counterion binding at the surface of the Helmholtz layer in electrical double layers.

28.3 WHY CRYSTAL STRUCTURES FORM

Many researchers have clarified that the colloidal crystals form by Brownian movement of colloid-sized particles and by interparticle *repulsion* according to the principle of deadspace minimization [11,20,25–31]. In other words, particles form crystal-like distribution *spontaneously* with the help of Brownian thermal movement of particles by maximizing packing density [197]. Kepler's proposal that the volume density of the most densely packed 3D sphere, with face-centered cubic (fcc) lattices, is $\pi/18^{1/2}$ ($= 0.90689\ldots$) has been approved by Hales [198, 199]. The volume density of the most dense 2D packing (hexagonal structure) was found to be $\pi/12^{1/2}$ ($=0.906899\ldots$.) [200, 201]. For 2D ellipses, it proves to be very difficult to calculate the volume density of the most dense packing. Densities of the seven kinds of packing have been calculated hitherto [202]. For 3D ellipsoids, density is rarely discussed theoretically. It should be noted here that some of protein molecules opt to form close-packed 2D ordering. For example, spherical molecular chaperone and rectangular catalase molecules form hexagonal and rectangular 2D sheet structures in solid state [203].

A team of investigators [3,64] clarified that colloidal crystallization takes place by Kirkwood–Alder transition. When extrarepulsive interaction (such as electrostatic repulsion) is in effect among colloidal particles in addition to the repulsion forces from their *Brownian movement*, colloidal crystallization takes place easily even at the very low particle concentrations. The thickness of the *electrical double layers* is estimated approximately with the Debye screening length l_D as given by Eq. (28.2). Debye length corresponds to the distance from the colloidal surface, where the electrostatic potential decreases to be 1/2.7 compared to that at the slipping zone:

$$l_D = \left(4\pi e^2 n / \epsilon k_B T\right)^{-1/2} \qquad (28.2)$$

Here, e is the electronic charge, ϵ is the dielectric constant of the solvent, and n is the concentration of *diffusible* or *free-state* cations and anions in suspension. Thus, n is the sum of the concentrations of diffusible counterions and "foreign salt," and of both H^+ and OH^- from the dissociation of water. Maximum value of l_D in water is $\sim$1 μm, which is estimated from Eq. (28.2) by taking $n = 2 \times 10^{-7}$ (M) $\times N_A \times 10^{-3}$ cm^{-3}, where N_A is the Avogadro number. It should be noted that the electrical double layers form always, without exception, in the colloidal dispersions of a solid in a polar liquid.

In the deionized state, the electrical double layer is very thick, and the interparticle repulsive forces prevail over long distances, as long as *micrometers*, although the forces become very weak. Formation of the crystal-like ordering is explained nicely with the *effective soft-sphere model*. The effective diameter d_{eff} of spheres includes the Debye screening length l_D and is given by the diameter plus twice the Debye length. When d_{eff} is shorter than the observed intersphere distance l, a gaslike distribution is observed. When d_{eff} is comparable to or a bit shorter than the intersphere distance, the distribution of spheres is usually liquidlike. When the effective diameter is close to or greater than the

observed intersphere distance, crystal-like ordering forms. The effective soft-sphere model has been supported by many researchers from the systematic comparison of d_{eff} with l values [11,20,25,28–31]. We should note again that the *colloidal* crystals, liquids, and gases are analogous to and models of the structures of actual molecules and atoms in the state of crystals, liquids, and gases [3,66].

The lattice spacing of colloidal crystals changes according to the particle concentration *exclusively*, which definitely supports the importance of the interparticle *repulsion* induced by Brownian movement of particles themselves and also the electrostatic interparticle *repulsive* forces. The formation of Coulomb crystals for the trapped spherical plasma with a single sign (plus) of charge has been reported [204]. This observation also strongly supports the important role of *electrostatic repulsion forces* for the crystallization in addition to the *Brownian movement* of the respective plasmas. Quite a few researchers have proposed the occurrence of intersphere *attraction* forces instead of *repulsion* for colloidal crystallization. However, this idea has been proved to be absolutely erroneous [11,205]. Colloidal crystallization takes place by interparticle repulsion *exclusively* irrespective of particle concentration ranging from very diluted to concentrated suspensions. We should note here that typical crystals in nature such as ice, metals, and proteins form by the *attraction*, not *repulsion*, of like colloidal crystals.

The critical concentration of melting of colloidal crystals in the deionized aqueous suspension ϕ_c in volume fraction is very sensitive to the degree of deionization of the suspensions. According to the author's experience, stock suspension must be deionized with the coexistence of the mixed beads of cation and anion exchange resins for more than *one month*, ideally, for 1–10 years. Furthermore, the sample suspensions prepared by dilution of the stock suspension with pure water must be deionized further >3 weeks before measurement. Most reliable ϕ_c values have been obtained for exhaustively deionized suspensions of monodisperse polystyrene spheres and colloidal silica spheres having diameters of 80–200 nm located around 0.0003 in volume fraction irrespective of sphere diameter [20]. The sharp increase in ϕ_c was observed, however, for spheres of <60 nm diameter [20]. Colloidal spheres that are not large enough compared with the sizes of solvent water, hydronium ions and other simple ions, can not contribute to the formation of electrical double layers.

28.4 MORPHOLOGY AND PHASE DIAGRAM OF COLLOIDAL SINGLE CRYSTALS

The close-up color images in Fig. 28.1 show typical examples of the single crystals of monodispersed silica spheres appearing in aqueous dispersions. The stock suspensions were deionized exhaustively by the coexistence of cation and anion exchange resins for >10 years. Cells were placed

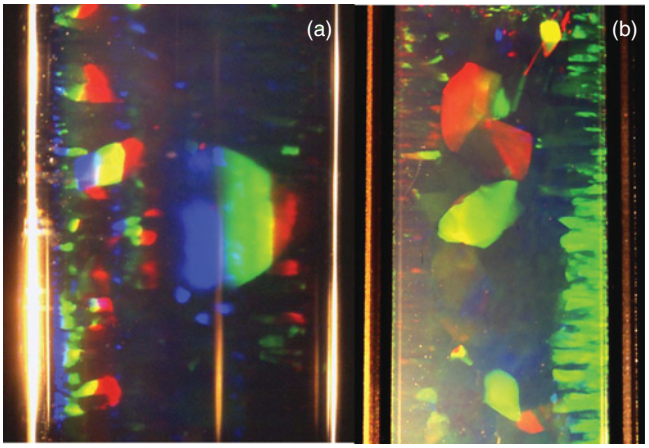


FIGURE 28.1 Close-up images of colloidal crystals in test tube (a) and in a plain cell (b) at 25°C. (a) CS91, ϕ; = 0.00083, 18 days after preparation and 1 h after mixing; (b) CS81, $\phi = 0.00095$, 7 days after preparation and 40 min after mixing. For a color version of this figure, see the color plate section.

in a test tube (Fig. 28.1a) and a quartz glass optical container for fluorescence measurements, 10 mm in width, 10 mm in depth, and 40 mm in height (Fig. 28.1b). The resins coexisted in the bottom of the cell (the parts of the bottom are cut here). The pictures were taken 18 days and 7 days after suspension preparation, and 1 h and 40 min after upturn mixing, respectively. Sphere concentrations were 0.00083 and 0.00095, respectively, in volume fraction. In these experimental conditions, very few nuclei form and the single crystals become very large. These colloidal single crystals can be observed with the naked eye, and they are quite large and beautiful. Influence of the polydispersity of colloidal spheres on the critical concentration of *crystal–liquid* phase transition has been discussed [206–211]. It should be noted here that the effective polydispersity of colloidal spheres decreases sharply in the deionized aqueous suspension, since the effective diameter $d_0 + 2 \times l_D$ comes to be very large compared with the real diameter. Here l_D is given by Eq. (28.2). The critical concentration of melting or crystallization (ϕ_c) in deionized suspensions increased sharply with increasing polydispersity of the spheres. It should be noted that morphology of colloidal crystal is essentially the same as that of other typical crystals. Most metal crystals are composed of single crystals surrounded by grain boundaries. Lattice spacings of colloidal crystals, studied by reflection spectroscopy in detail [28–31,33], are very long, several thousand times greater compared with that of metals, and just in the range of light wavelengths. There are two basic kinds of single crystals (observable in Fig. 28.1): (1) red, blue, yellow, and blocklike crystals, are formed by the *homogeneous nucleation mechanism* in the bulk phase far from the cell wall; and (2) green and pillarlike crystals grow by the *heterogeneous nucleation mechanism* along the cell wall. It should be noted

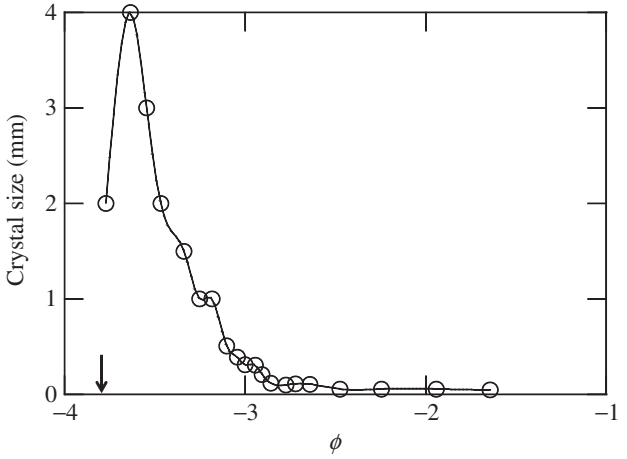


FIGURE 28.2 Mean single-crystal sizes as a function of sphere concentration. Polystyrene spheres (D1B76), 109 nm in diameter, critical concentration of melting: 0.00016 (ϕ).

that each single crystal is surrounded by grain boundaries and that the crystals are densely packed [212,213]. When the incident light angle is changed slowly, the packing state of the single crystals is observable.

The single crystals suddenly became much larger when the sphere concentration decreased in the exhaustively deionized suspensions [11,20,23]. A typical example of the mean size of the single crystals relative to sphere concentration is shown in Fig. 28.2. This observation is quite understandable, because crystal size should increase with decreasing nucleation rate, and also with decreasing number of nuclei. Nucleation rate, of course, decreases as sphere concentration decreases. When the sphere concentration is comparatively high, size of colloidal crystals is very small, and single crystals are not observed with the naked eye. Colloidal single crystals have been observed by polarizing microscopy [214].

Another group of investigators have measured the melting temperature of colloidal crystals, for the first time, as a function of sphere concentration [4]. Heat of melting and entropy change were 16–21 kJ/mol and 42–67 J/K, respectively. This author [18,105,215, 216] measured melting temperatures of exhaustively deionized colloidal crystals. The crystalline sediments of monodisperse stearylated silica spheres formed by gravity [217]. Phase diagrams and dynamics of colloidal crystals and colloidal liquids were discussed experimentally and theoretically in detail [10,16,218–225].

28.5 LATTICE STRUCTURE OF COLLOIDAL CRYSTALS

Generally speaking, structures of colloidal crystals are face-centered cubic (*fcc*) or body-centered cubic (*bcc*) lattices. Square-ordered structures, however, were observed when two plates of a cell were oriented in a wedge geometry [7]. Abundant data on the colloidal lattice structures indicate that *fcc* lattices are most stable and transform into *bcc* lattices when (1) particle concentration is very low, (2) a small amount of salt is added, (3) the suspension temperature is raised, (4) the particle charge density is high, or (5) high pressure is applied [11,20]. The coexistence of *fcc* and *bcc* crystal lattices is closely related to the increased free space for particles forming lattice structures; in other words, the *fcc* form is more dense than the *bcc* one. The *fcc* and *bcc* structures are observable visually by a metallurgical microscope, especially in sedimentation equilibrium, and the interparticle distances can be determined from microscopic observation. However, it is usually difficult to observe the 3D lattice structures microscopically, even by scanning microscopy. Amorphous solid (or glass) structures are observed for highly polydispersed colloids, especially in rather concentrated suspensions. The lattice spacing of colloidal crystals can be studied conveniently by reflection and transmission optical spectroscopy. The shape of a spectrum pattern is a single peak, a double peak, or a single peak with a shoulder. The peak wavelengths originating from *fcc* and *bcc* are always close together, with a difference of only 1.03 in the ratios of their peak wavelengths. The author's group clarified that the cationic charged colloidal crystals formed, although the spheres were not as chemically stable as in the deionized condition [226]. Furthermore, core–shell-type spheres formed colloidal crystals in deionized aqueous media [227, 228].

Several types of asymmetric colloidal crystals have been studied, especially in sedimentation equilibrium in deionized suspensions of anisotropic particles. Cylindrical colloids of nickel dimethylglyoxime (9.6 μm in length, 0.12 μm in diameter) were ordered in a hexagonal array [175]. It is now clear that the particles are oriented to reduce the deadspace as effectively as possible. Bowl-shaped polystyrene particles were also oriented in deionized suspension (see Fig. 28.3a) [98, 99,229]. Interestingly, these particles included spheres of various sizes in their cavities (see Fig. 28.3b). Both the host and guest particles were not in direct contact, but remained separated by the electrical double layers formed around the particles. The particle distribution of ellipsoidal poly(tetrafluoroethylene) on transformation from unsymmetric to symmetric crystals has been observed, with dilution accompanied by thickening of the electrical double layers [99]. Asymmetrically ordered structures, similar to paved bricks, have been formed in rectangular tungstic acid colloids. Ordered phases of platelike particles were observed in rather concentrated dispersions [98, 99].

It is well known that the rodlike and/or disklike colloidal particles form nematic, smectic (or lamellar), and columnar ordering. One researcher [230] studied the nematic ordering of tobacco mosaic virus (TMV) and found that this ordering

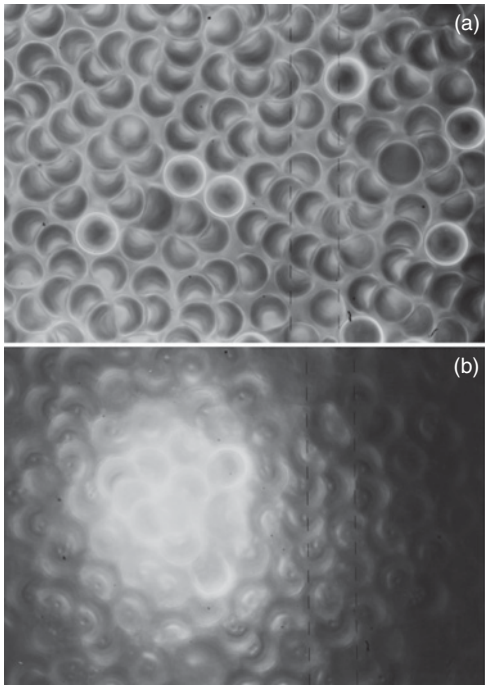


FIGURE 28.3 Microscopy of arrangement of bowl-shaped colloidal particles (DR728) (a) and their inclusion with colloidal spheres (N1000) (b). (a) $\phi^* = 0.000199$; (B) $d_0 = 1.02$ mm, $\phi^* = 0.00241$, length of the full scale: 10 μm.

takes place because the loss in orientational entropy is compensated by the gain in packing entropy. The nematic suspensions of rodlike boehmite (AlOOH) [159,231], Li_2Mo_6 wires [232], V_2O_5 ribbons [233], and imogolite nanotubes [234, 235] have been studied intensively. A magnetically oriented microcrystal array was obtained for $LiCoPO_4$ microrods, mesocrystals of L-alanine and lysozyme [236–240].

28.6 ALLOY CRYSTALS OF COLLOIDAL MIXTURES

Opal is one of the typical examples of colloidal alloys fixed in solid state, which may form during the course of sedimentation of the mixtures in suspension having different but rather monodisperse-sized colloidal spheres [241, 242]. Colloidal alloy structures are very interesting because most of the structures of metal alloys also appear in colloidal suspensions of binary mixtures of spheres. The superlattice structures observed hitherto in colloidal systems are of the AlB_2, $NaZn_{13}$, $CaCu_5$, $MgCu_2$, NaCl, and AB_4 types [243–251]. Note that these alloy structures are explained by changes in the effective size ratio, that is, the effective size of small spheres, including the electrical double layers versus that of large spheres [241,245], and the segregation effect [252].

28.7 COLLOIDAL CRYSTALLIZATION KINETICS

Most kinetic measurements on colloidal crystallization showed an induction period, after which the crystal growth starts, especially in diluted suspensions (see Fig. 28.4a). This observation supports the theory that the kinetics of colloidal crystallization is explainable by the classical diffusive crystallization theory, including nucleation and crystal growth processes [253–256].

The number of nuclei that germinate per unit of time, the nucleation rate v_n, is given by

$$v_n = \phi l^3 \Big/ \left[\left(4\sqrt{2}/3 \right) \pi (d_0/2)^3 L^3 t_i \right] \qquad (28.3)$$

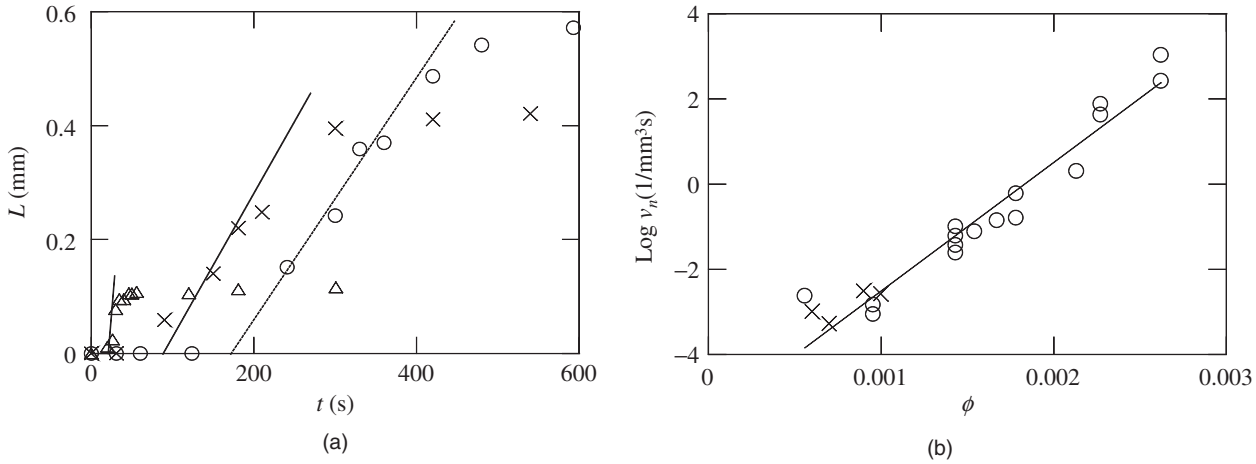


FIGURE 28.4 (a) Crystal size estimated from the half-width during course of crystallization of CS91 spheres at 23°C. Circles, $\phi = 0.00143$; crosses, 0.00179; triangles, 0.00262; (b) nucleation rates of CS91 spheres at 25°C. Circles, taken from Ref. 254; crosses, Ref. 253.

where ϕ is the volume fraction of sphere particles and L and l are the mean size of single crystals formed and the nearest-neighbor intersphere distance, respectively; d_o is the diameter of sphere particles. t_i is the induction period and corresponds to the time of nucleation process.

Colloidal crystallization processes consist in rapid growth of a metastable crystal (step 1) and slow reorientation toward the stable crystal (step 2). The first crystal growth rate of a metastable crystal v_1 is given by [256]

$$v_1 = v_{1\infty}\left[1 - \exp(-\sigma)\right] \tag{28.4}$$

Here, σ is the relative supersaturation given by $(\phi - \phi_c)/\phi_c$, ϕ_c is the critical concentration of melting, and $v_{1\infty}$ is the maximum crystal growth rate. Equation (28.4) is further simplified as follows:

$$v_1 = v_{1\infty} - v_{1\infty}\phi_c/\phi \tag{28.5}$$

Equation (28.5) shows that the growth rate decreases linearly as the reciprocal sphere concentration increases; this observation has been supported experimentally, but only in a very low sphere concentration range [256].

The peak profile in reflection spectroscopy became sharp with time during the course of crystallization, which corresponds to an increase in crystal size. The background intensity decreased in the course of crystallization, which is ascribed to the diminution in the multiple scattering of the suspension. The nearest-neighbor intersphere distance l is determined from the peak wavelength [257]. The calculated value of the nearest-neighbor intersphere distance is obtained from the sphere size and concentration [257].

As was described earlier, an excellent agreement between l and l_0 has been obtained, which demonstrates that the lattice spacing of the colloidal crystal changes according to the sphere concentration exclusively, and furthermore, that the crystals form by intersphere repulsion due to Brownian movement of the spheres themselves and also by the electrostatic intersphere repulsive forces.

The nucleation rate v_n increased substantially as sphere concentration increased, as is shown in Fig. 28.4b. This rate increased by 10^{10}-fold when ϕ increased by 10^2-fold. An increase in sphere concentration is followed by an increase in v_n, and number of nuclei, and resulted in a decrease in the size of single crystals formed, as discussed in one report [36]. It should be mentioned here that the size of single crystals, observed with by the naked eye, is polydisperse, as has often observed (see Fig. 28.1 for examples) [23]. Therefore, any clear separation of the nucleation step from the crystallization process will be difficult, and the nucleation reaction may remain operative even in the crystal growth period.

The fast and slow crystal growth rates, v_1 and v_2, were evaluated for colloidal crystallization. The v_1 values in the diluted suspensions decrease linearly as the reciprocal concentration of spheres increases [254]. It should be noted that the importance of the dynamic phase transition has been reported for colloidal crystals and for other crystals such as metals and polymers. v_2-value decreases as sphere concentration increases. The slow crystallization step is ascribed to the *reorientation* of the metastable crystals formed in the first step toward the stable ones matched with the other crystals mediated by the grain boundaries and the cell wall. When sphere concentration is high, the number of the metastable crystals formed is huge and their size becomes quite small. Then, a very long time will be required for matching of the crystals with other crystals and with the cell wall. The occurrence of *Ostwald ripening* is also highly plausible in the slow process, though direct observation was not successful until one team [258] observed the ripening for colloidal crystallization processes.

The kinetics of colloidal crystallization in alcoholic organic solvents and their aqueous mixtures have been studied by reflection spectroscopy [259]. Kinetic study of colloidal crystallization in acetonitrile has been performed for silica spheres modified with polymers on their surfaces [260, 261]. Kinetic analysis of the crystallization of ellipsoidal particles under an alternating electric field was also undertaken [262]. The authors studied the kinetics of crystallization in shear flow [263]. Kinetic analyses conducted by one team of investigators [264, 265] to elucidate the mechanisms of colloidal crystallization must be cited here. Dynamics of crystallization in hard-sphere suspensions has been studied intensively by several research groups [266–271]. Crystallization kinetics has been studied and reviewed for both soft- and hard-sphere systems [272, 273].

28.8 STATIC AND DYNAMIC LIGHT SCATTERING AND SMALL-ANGLE NEUTRON SCATTERING

Figure 28.5 shows the static light-scattering intensity $I(q)$ and the effective diffusion coefficients, estimated from the dynamic light scattering D_{eff}, as a function of scattering vector q for the colloidal silica spheres (diameter 103 nm) at $\phi = 0.0049$ [274]. Circles and crosses (tickmarks) indicate the data for the suspensions with and without coexisting ion exchange resins. The suspensions are "crystal" and "liquid," respectively. Surprisingly, very sharp peaks appeared for the crystals. The measurements have been taken at very short intervals of half a degree (0.5°). However, this interval was not always narrow enough for the determination of the reliable values of the peak scattering vector q_m. Static and dynamic light-scattering measurements have been performed mainly for various sizes of colloidal silica spheres [275, 276] and polystyrene spheres [277–279]. Backscattering of light

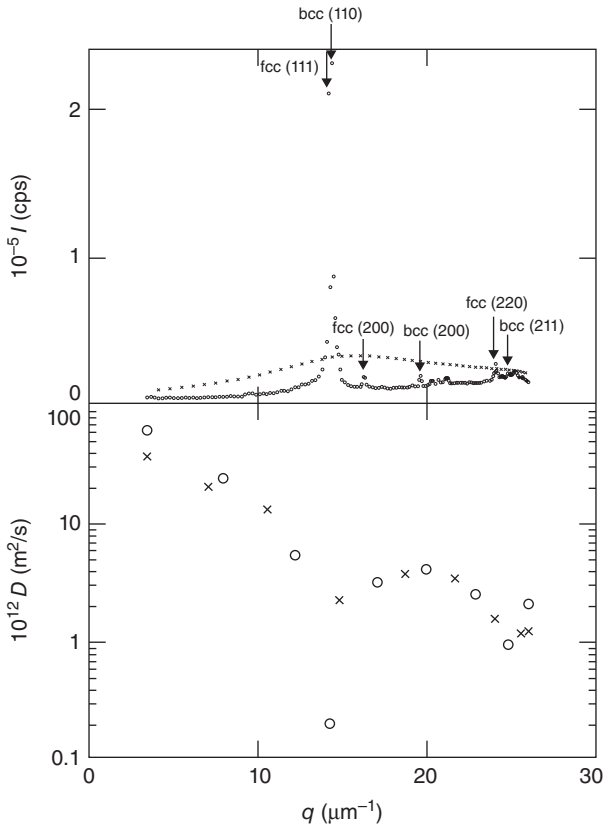


FIGURE 28.5 Static and dynamic light-scattering measurements of CS81 spheres at 24°C, $\phi = 0.0049$.

measurements on the several colloidal crystal systems was also reported [280].

The diffusion coefficients D evaluated from the cumulative analysis are also shown in Fig. 28.5. The D values decreased as the scattering vector increased, whereas the background intensity of scattered light for the crystals increased as q increased. Furthermore, the diffusion coefficients from the suspensions showing peaks in the light-scattering curve were substantially low. According to two authors [281], the *effective diffusion coefficient* D_{eff} is given by

$$D_{\text{eff}} = D_0 / S(q) \tag{28.6}$$

where D_0 is the diffusion coefficient of spheres in "gas" suspension and $S(q)$ is the structure factor. The constancy of $D_{\text{eff}} \times S(q)$ has been satisfactory for colloidal liquids, within experimental error. The interparticle structure factor $S(Q)$, which is important to know for insight into the dynamic particle distribution and the particle interaction, has been observed from light-, X-ray-, and neutron-scattering measurements for deionized and salt-containing colloidal suspensions [67,282–291]. The effect of polydispersity of colloidal spheres on the structural factor was discussed in detail [292].

28.9 STRUCTURAL RELAXATION TIMES OF COLLOIDAL CRYSTALS

Fluctuation of colloidal spheres in the crystal structure is discussed with respect to the structural relaxation time (τ). Two kinds of τ values, in fast (τ_{f}) and slow steps (τ_{s}), are observed by the stopped-flow technique. The former is expressed as follows:

$$\tau_{\text{f}} = D_0^2 / 6D_{\text{tr}} \tag{28.7}$$

Here, D_0 is the mean intersphere distance and D_{tr} is the cooperative translational diffusion constant in strongly interacting structures. The D_{tr} value of spheres is given by the Einstein–Stokes equation for self-diffusion:

$$D_{\text{tr}} = k_{\text{B}} T / (3\eta\pi d_{\text{eff}}) \tag{28.8}$$

Here, η is the viscosity of the solvent. The essential point in the fluctuation of spheres is that the D_{tr} and τ_{f} values observed in the colloidal crystals agree with the calculated values from Eqs. (28.7) and (28.8) when d_{eff} is used instead of d [true diameter of colloidal sphere in Eq. (28.8)] [293, 294]. Agreement between the calculation and observation in the deionized suspensions of monodisperse polystyrene spheres was excellent. It should be noted here that the Debye screening length does not correspond to the hydrodynamic length quantitatively. The hydrodynamic length will be shorter than the Debye length because many of the solvent molecules flow freely through the simple ion clouds of the electrical double layers. One investigative team observed particle motion directly by a microscopy and concluded that the observed translational diffusion constants agreed with the value calculated from Eq. (28.8) using the real value of the sphere diameter [295]. However, the tendency of $D_{\text{obs}} < D_{\text{calc}}$ is not denied in their paper, especially for small spheres, specifically, $D_{\text{obs}} = 3.6 \times 10^{-9}$ cm^2 s^{-1} and $D_{\text{calc}} = 4.0 \times 10^{-9}$ cm^2 s^{-1} for $d = 0.458$ μm.

The τ_{f} value is given by the simple relation [61,296]

$$\tau_{\text{f}} \sim \eta / G \tag{28.9}$$

where G denotes the rigidity or dynamic (local shear) elastic modulus of the suspension. G ranges from 0.01 to 10 Pa for colloidal crystals, and these values are not far from those of previous reports by the dynamic method [6,297–300].

The effect of the electrical double layers on the translational diffusion constant of colloidal spheres has been discussed using photon correlation spectroscopy [301, 302] and also theoretically [303]. The diffusion constant showed a minimum value when the double-layer thickness was comparable to the radius of the particle [10]. Dynamic light-scattering measurements have been carried out in detail for colloidal crystals [304–311]. Particle motion was studied

by the tracer diffusion method for concentrated colloidal suspensions [312].

28.10 RIGIDITY OF COLLOIDAL CRYSTALS

The elastic modulus is one of the most fundamental properties of colloidal crystals and has been measured by various techniques. The static elastic moduli of crystals of monodisperse polystyrene spheres were evaluated from reflection spectrum measurements at sedimentation equilibrium [313]. This author has measured *static* moduli of colloidal crystals by several methods: microscopic observation [49,99,125,175,186,283,314–317] and reflection spectrum methods in sedimentation equilibrium [187,248,318], reflection spectroscopy under centrifugal compression [319], and a direct-current (DC) electric field method [320].

On the other hand, the *dynamic* (shear) elastic modulus has been measured [321] by shear wave propagation experiments. Those researchers measured elastic moduli of flocculated suspensions of colloids in the presence of foreign salt [322–324]. The dynamic moduli of colloidal crystals, especially in the deionized suspensions, have been studied by several teams of investigators [5, 6,296–298,325–330]. This author has measured the dynamic elastic moduli by the structural relaxation method [293, 294] and rotator viscometry [331–333].

The experimental results on the rigidity of colloidal crystals are summarized as follows [11]. *First*, the dynamic elastic modulus is always smaller than the static one. The metastable colloidal crystals are formed rapidly, with structural relaxation times ranging from 10 ms to 1 s. However, formation of the stable crystals in an equilibrium state requires a long time. The elasticity of the metastable crystals is low. Thus the dynamic moduli are smaller than the static rigidity in most cases. Figure 28.6 shows the plots of log G (rigidity) against log N (sphere number per unit volume) reported so far for some colloidal crystals of monodispersed polystyrene spheres with diameters ranging from 91 to 109 nm. G values are denoted by open circles; crosses (tickmarks) and open triangles represent the static ones, which we evaluated at sedimentation equilibrium. The filled circles, filled squares, and filled triangles denote dynamic rigidities.

Second, log G of colloidal crystals, including amorphous solids, increases linearly with a slope of unity as log N increases. The order of magnitude of the modulus may be expressed in terms of the magnitude of the thermal fluctuation δ of a sphere as [3]

$$G \sim f/l \sim \left(k_{\mathrm{B}}T\big/< \delta^2 >\right)\big/l \qquad (28.10)$$

where f is the force constant, l is the intersphere distance, δ is the thermal fluctuation of a sphere in the effective potential valley, $k_{\mathrm{B}}T$ denotes the product of the Boltzmann constant

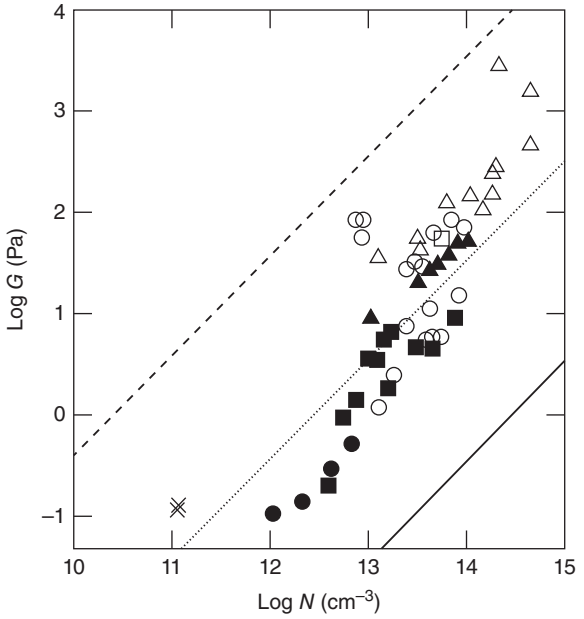


FIGURE 28.6 Rigidities of colloidal crystals as a function of number density of colloidal spheres. Open circles, reflection spectroscopy [187]; crosses (tickmarks), microscopy [315]; open triangles, rotator viscometry [331]; open squares, DC electric fields [320]; solid circles, see Ref. 313; solid triangles, see Refs. 5, 325; solid squares, see Ref. 6. (Redrawn using data from Ref. 182.)

and the temperature. Introducing a nondimensional parameter g for $<\delta^2>^{1/2}/l$, the modulus is obtained as a linear function of N, as follows:

$$G \sim Nk_{\mathrm{B}}T\big/g^2 \qquad (28.11)$$

For $g = 1$, Eq. (28.11) gives the rigidity of an ideal gas having the same sphere concentration. Lindemann's law of crystal melting tells us that $g < 0.1$ holds for a stable crystal.

Third, rigidity of the colloidal crystals, including an amorphous solid, is larger than that of colloidal liquid when comparisons are made at the same sphere concentration. *Fourth*, the rigidity of colloidal crystals increases substantially as the deionization of the suspension proceeds. *Fifth*, the rigidity of the amorphous solid increases as the polydispersity of spheres increases, and the G value of the crystal is smaller than that of amorphous solids at the same particle concentration. *Sixth*, the rigidity of the structured suspensions increases as the particle charge density decreases, which is due to the extended electrical double layers formed with the counterions of the particles. *Seventh*, rigidity at a certain concentration of particles initially increases further. A maximum value of G was observed around 85 nm in diameter. It is interesting to note here that Eq. (28.11) holds for all kinds of substances, including metals, proteins, ice, and colloidal crystals. Rough values of the substances are estimated using Eq. (28.11).

Rigidities of colloidal alloys [334] and the colloidal crystals in alcoholic organic solvents [235, 236] have been studied.

28.11 VISCOSITY AND VISCOELASTICITY OF COLLOIDAL CRYSTALS

This author has measured viscosities of colloidal liquids and colloidal crystals in exhaustively deionized aqueous suspensions, for the first time, with the use of Ostwald-type and rotational viscometers [331,337–341]. The viscosity of the deionized suspension was very sensitive to the degree of deionization of the suspension and decreased substantially when the suspension was contaminated with ionic species. The reduced viscosity η_{sp}/c (specific viscosity η_{sp} divided by particle concentration c) of colloidal liquids was much higher than that predicted by Einstein's equation and decreased sharply with increasing ion concentration. The specific viscosity of colloidal spheres can be expressed as follows:

$$\eta_{sp} = \eta/\eta_0 - 1 = k_1\phi + k_2\phi_2 + \cdots \qquad (28.12)$$

Here, η and η_0 are the viscosities of the colloidal suspension and the solvent; ϕ is the concentration of the colloids (volume fraction); k_1 is the Einstein coefficient, 2.5; and k_2 denotes the electrostatic interaction parameter, which is very large for the deionized suspensions. The deviation of the observed η_{sp} values from Einstein's equation was very significant in the deionized liquids. However, the $\eta_{sp} - \phi$ relationship agreed very well with the Einstein equation in the presence of an excess amount of sodium chloride. Qualitatively speaking, the large k_2 observed implies that the electrostatic repulsion interaction is significant and the shells of the electrical double layers around the spheres are very thick. Furthermore, η_{sp}/c increased as the charge density decreased and/or the polydispersity index increased.

Viscometric properties of colloidal crystals are very peculiar. A peak in the relative viscosity against concentration curves showing the phase transition between colloidal crystals and liquids was observed for the deionized spheres (see Fig. 28.7). A sharp increase in shear stress with increasing shear rate was observed for the colloidal crystals, from which the rigidity was evaluated as described in the preceding section. Furthermore, log η of colloidal crystals decreased linearly with a slope close to -1 as log(*shear rate*) increased. This strongly supports the solidlike nature of the suspensions. The log η – log(*shear rate*) plots for the colloidal liquids showed non-Newtonian flow with constant viscosity irrespective of shear rate. Viscosities of colloidal crystals were studied by other groups [296,330,342].

Viscoelastic properties of colloidal liquids and crystals in the deionized aqueous suspension have been studied in detail [333,343–348]. The slopes of the log(*shear stress*) versus log(*shear rate*) and/or log(*storage modulus*) versus log(*angular frequency*) plots for the colloidal crystals were zero, and increased to unity as the structure transformed to liquids.

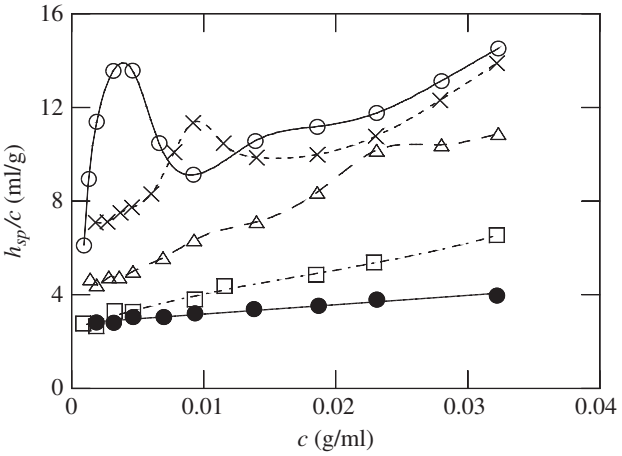


FIGURE 28.7 Plots of η_{sp}/c against c for polystyrene spheres at 25°C. Open circles, [NaCl] = 0 M; crosses, 6.67×10^{-6} M; triangles, 2×10^{-5} M; squares, 6.67×10^{-5} M; solid circles, 2×10^{-4} M.

28.12 EXTERNAL FIELD EFFECTS ON COLLOIDAL CRYSTALS

The rigidity of colloidal crystals is very small, ranging from 10^{-2} to 10^3 Pa. On the other hand, rigidity values of metals range from 10^{10} to 10^{12} Pa. Thus, colloidal crystal is distorted very easily by the weak external fields, such as the gravitational field, shearing forces, elevated pressure, presence of an electric field, or centrifugal compression. The gravitational compression of colloidal crystals occurs easily. From the height dependence of the lattice spacing determined from reflection spectroscopy, the rigidity of the colloidal crystals has been determined. Furthermore, from the concentration dependence of the intersphere distance, at the bottom layer in the observation cell, the static elastic modulus can be determined in the sedimentation equilibrium as was described in Section 5.1.

Colloidal crystals in a rotating disk are also compressed in the centrifugal field (see Fig. 28.8) [310]. Beautiful color bands appeared under the centrifugal field. The elastic moduli at various sphere concentrations can be obtained from variation in the reflection peak wavelengths as a function of the distance from the center in the centrifugal equilibrium. These color bands clearly show that the intersphere reactions are repulsive, and that the repulsive forces are counterbalanced by the centrifugal fields.

Electric-force-induced change in the lattice structure of colloidal crystals has been studied by several researchers

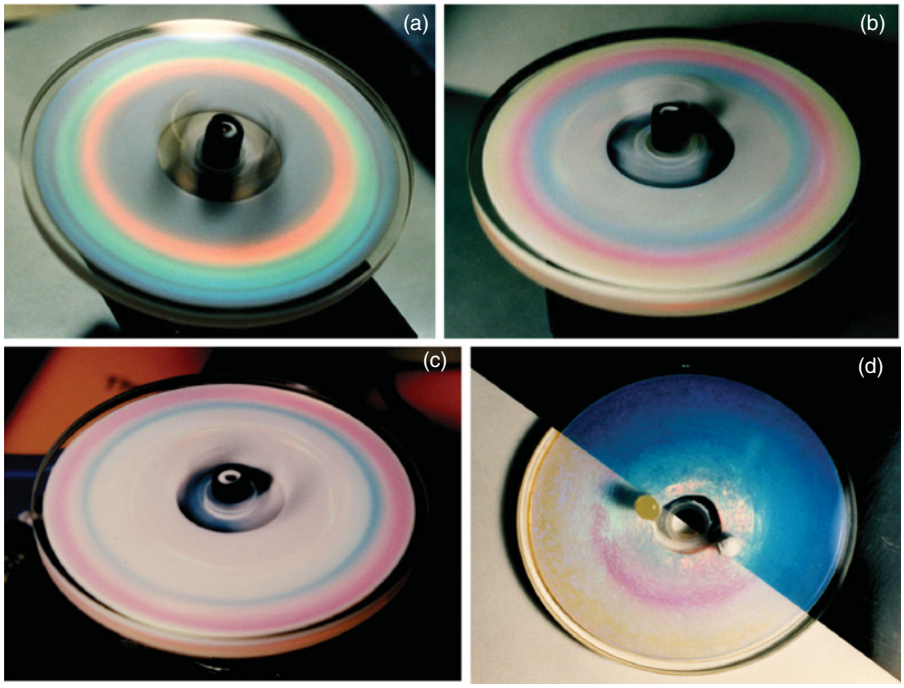


FIGURE 28.8 Close-up color images of colloidal single crystals of D1K88 (a,b) and D1B72 spheres (c,d) in a rotating cell. $\phi_{D1K88} = 0.0617$, $\phi_{D1B72} = 0.0820$. Images captured with (a) obtuse-angle illumination and (b,c) acute-angle illumination, and (d) photograph showing the observation cell on black and white papers. For a color version of this figure, see the color plate section.

[11,20,349] and by the author's group [350–363]. The beautiful effect of waveform transformation from square to triangle has been observed [350–363]. This effect is explained by the fact that the translational motion of the charged spheres is too slow to allow us to follow up changes of the electric field. Our research group observed second-order harmonics in the electrooptic effects of colloidal crystals (see Fig. 28.9). The frequency of the output was just twice that of the input field. In order to study the causes of the generation of the second-order

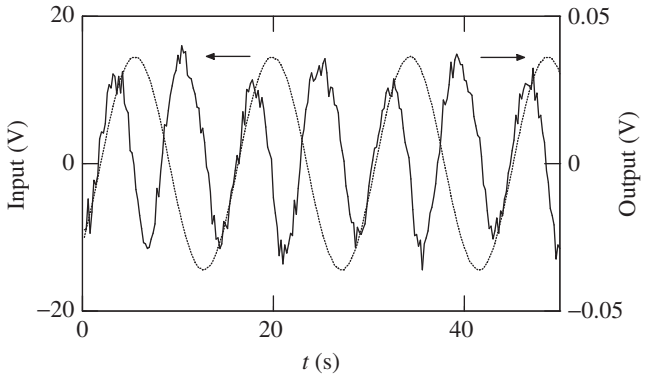


FIGURE 28.9 Waveform of the applied field (dotted-line curve) and reflection (solid-line curve) signals of colloidal crystals of CS82 spheres at 25°C. $\phi = 0.048$, $E = 3.7$ V/cm, $f = 0.07$ Hz, T-type cell. (Redrawn using data from Ref. 353.)

harmonics, time-resolved reflection spectra were measured in a sine-wave electric field. The peaks shifted shorter and then longer wavelengths periodically. Changes in the peak profiles, including the peak intensities and half-widths, were also observed clearly under a sine-wave electric field. The peak wavelengths were plotted against time. The frequency observed was the same as that applied. However, the integrated intensities of the reflection peak profile for the whole gamut of wavelength changes were modulated drastically, and the frequency was just twice the one applied. In other words, second-order harmonics were obtained for the integrated intensity. The calculation of the integrated intensities is quite consistent with observation using the photomultiplier. The observed harmonics were caused by the nature of colloidal crystals themselves.

The amplitudes, alternating-current (AC) components of the electrically induced shear waves as a function of the frequency applied, showed several peaks in the curves. The peak shifted to higher frequencies as sphere concentration increased. The appearance of the peaks demonstrates the existence of some characteristic frequencies for the viscoelastic colloidal crystals. We observed the harmonic oscillation on the shear waves of colloidal crystals from electrooptical effects using electric light-scattering measurements. At 90° scattered light is detected from incident white light. One research team studied the electrooptics of colloidal crystals in organic solvents and gels [360]. Another group clarified

the nonlinear effect for the modulation signal from the optical measurements in the AC electric field [327,364]. *Synchronous oscillation* remained even after the sine-wave electric current was turned off. This is due to the sheared waves of the crystals. The photonic trapping effect of colloidal crystals has been studied [362, 363]. Two-dimensional ordering induced by the electric field has been reported by several research groups [365–367]. The magnetic field effects on the orientation of anisotropic colloidal particles are now well known [237–240,368]. Crystal–liquid phase transition induced by ultraviolet light irradiation was reported for colloidal suspension containing malachite green [369].

Colloidal crystal structures have been studied at high pressure ($\leq$200 MPa) [370]. Formation of *bcc* lattices from liquid and/or transformation from *fcc* to *bcc* lattices was observed under elevated pressure. These observations were explained by the increase in effective charge number on the colloidal surface and the decrease in the Debye screening length as pressure increases.

Shearing deformation of colloidal crystals has been studied by several researchers. One pair of investigators reported that the Bragg diffraction spots diffused as the shear rate increased, and turned into diffraction rings characteristic of liquid structures at high shear rates [14,61,371]. Two other researchers observed a shear melting at high shear rates [6,14]. On the other hand, another pair of linvestigators reported that their suspension did not exhibit disappearance of order at any shear rate, but showed changes in the lattice structure at moderate volume fraction (0.05–0.50) [372]. Another team proposed that the shear-induced melting was due to screw dislocation [342]. Yet another group conducted small-angle neutron scattering measurements of colloidal crystals undergoing shear [373]. Small G values have been obtained under shear [14,61,374–377]. This author found that fcc and bcc lattices coexisted under flow, although the lattices were more or less deformed and melted at high shear rates [378]. Deformation of the electrical double layer from a spherical shape was deduced at low sphere concentrations under shear, and the sliding-layer model proposed by two other investigators [372] was supported especially at high sphere concentrations. Structural changes under shearing flow have been further studied by several researchers [379–383].

The intersphere distances in the crystal of monodisperse polystyrene spheres in the deionized suspension are sensitive to the coexisting water-soluble polymers in the following order [384]:

$$\text{PEG} > \text{PVA} > \text{none} > \text{PVP} \cong \text{HPC} > \text{PAA}_\text{m} \quad (28.13)$$

Here, PEG, PVA, PVP, HPC, and PAA_m indicate poly(ethylene glycol), poly(vinyl alcohol), poly(vinyl pyrrolidone), hydroxypropyl cellulose, and poly(acrylamide), respectively. On the other hand, the order is observed microscopically in the sedimentation equilibrium [384]:

$$\text{PVA} > \text{PEG} > \text{PVP} > \text{HPC} > \text{PAA}_\text{m} \quad (28.14)$$

These orders are explained by the strength of the intersphere repulsion forces through the electrical double layers, which is sensitive to the polymer adsorption on the colloidal surfaces by the hydrophobic and/or dipole–dipole interactions. The scheme of the adsorption mechanism has been proposed by another team [12]. Furthermore, crystal structures in organic solvents and water–organic solvent mixtures have been studied by several groups [2,64,314,315,317,318,385].

Thermosensitive colloidal crystals have been made using the hydrogels of *N*-isopropylacrylamide [101,386–396]. Details on the gel sphere crystals are described in Chapter 41.

28.13 COLLOIDAL CRYSTALLIZATION IN MICROGRAVITY

Another team [397] reported morphological properties of the colloidal crystals of hard-sphere systems in microgravity using Space Shuttle *Columbia*. Colloidal crystallization has been studied kinetically in microgravity, produced by parabolic flights of an aircraft [398–401]. Crystal growth rates decreased in microgravity by about 25% compared with those in normal gravity. One of the main causes for the retardation in microgravity was suggested to be elimination of the downward diffusion of spheres, which may enhance intersphere collisions. The absence of convection of the suspensions in microgravity was also much more important than the elimination effect of downward diffusion. Crystal growth rates of the colloidal alloys of binary mixtures of monodispersed polystyrene and/or silica spheres have been studied in microgravity [402]. The rates increased substantially up to $\sim$1.7-fold in microgravity compared with those in normal gravity. We should note that the *segregation* effect is familiar for binary mixtures of colloid and powder science; large spheres are segregated upward and small ones downward in normal gravity. In microgravity such segregation disappears and the homogeneous mixing takes place favorably, which leads to rapid alloy crystallization. Gravitational effects on the alloy crystallization from bimodal colloidal dispersions were discussed by two other investigators [403].

28.14 TWO-DIMENSIONAL COLLOIDAL CRYSTALS

Two-dimensional distributions of polystyrene spheres at the air/water interface have been studied by measurement of surface pressure–surface area isotherms [404, 405]. Two-dimensional ordering of polystyrene spheres has also been

studied [406–409]. Another author noted that electrostatic repulsion between charged particles is enhanced at an interface between an aqueous phase and air, especially at large particle separation [7]. At the interface a particle has an asymmetric counterion distribution, which results in a dipole moment normal to the water interface. It has also been shown that the interaction near a water–air interface became repulsive and long-ranged [410,411]. The interaction energy decayed in inverse proportion to the salt concentration. Another team [409] observed a transition from the original hexagonal shape to a rhombohedral configuration when the monolayers at the air–water surfaces were compressed on a Langmuir trough. Furthermore, they observed that the particle structure at air–water interfaces was very sensitive to the salt concentration in the aqueous phase. At low salt concentration ordered structure formed as a result of interparticle repulsion, while at high salt concentration the spheres formed 2D clusters [409]. 2D colloidal crystals also form by cooperative intercolloidal electrostatic repulsion such as with 3D colloidal crystals. Melting of 2D crystals and solids have been studied in detail [62,412–417]. 2D colloidal crystals were studied at the electrode interface. ABC-type triblock terpolymer films formed highly oriented and ordered double-helical rodlike structures by solvent evaporation [418]. 2D phase transition of colloidal crystals has been discussed theoretically [419].

28.15 BIOLOGICAL COLLOIDAL CRYSTALS

In general, the result of crystal-like ordering of colloidal particles *in suspension state* is called as *colloidal crystal formation* as described in Section 28.1. Colloidal crystal ordering in solid state is often observed in biological systems such as insects, birds, and fishes. Sea mice is the polychaete *Aphroditae* and one of the marine worms, found along oceanic continental shelves. They have a brightly iridescent furry appearance. The fur consists of hairs, which are packed with arranged little tubules as found in a hexagonal honeycomb. The TEM image of the ordered structure within the spines closely resembles the hexagonal 2D colloidal crystal [420,421].

The peacock (*Pavo* spp.) is famous for its brightly colored tail feathers. The structure of these feathers has been studied and measured by SEM and TEM microscopy [422]. Structural colors of the wings of the *Morpho* butterflies were also studied in detail by [423,424]. The synergism between regularity and irregularity in the structures was the main cause of the characteristic blue color of *Morpho* wings. It was also found that the pigments close to the iridescent structure enhance the blue coloring by reducing background light. The Japanese jewel beetle, *Chysochroa fulguidissima*, emits beautiful iridescent colors. Detailed optical analyses of the colors of dorsal surface were performed [425]. The color change in the fish *Motile iridophores*, that inhabits tropical areas is due to the reflection of light from multilayered thin-film interference [426,427].

28.16 NEW COLLOIDAL CRYSTAL SYSTEMS

Typical colloidal spheres are hard solid spheres. Recently new types of colloidal crystals have been developed. Gel spheres will locate in between linear-type polymers and hard colloidal spheres from the perspective of colloidal chemistry. Most gel spheres are whitish turbid in aqueous media, implying the existence of interfaces with refractive indices different from those of solvent molecules. Thus, fundamental structures and properties of most gel crystals are quite similar to those of colloidal crystals. Gel crystals are reviewed and discussed in Chapter 41.

The author's group (Fujii S., Nakamura, Y., Okubo, T., unpublished results) observed strong iridescent colors during drying of an aqueous suspension of poly(*n*-butyl acrylate) particles. Glass transition temperature of this polymer is $-54°C$, and the rubber liquid state at room temperature. The colors are due to formation of emulsion crystals. When the suspension was dried, however, the iridescent colors disappear, since the suspension becomes unstable as water content decreases. The final state of the particles is rubberlike liquids.

Strongly colorful and angle-independent liquidlike structures formed in ionic liquids [428–431]. Poly(methyl methacrylate)-grafted colloidal silica spheres were dispersed in 1-ethyl-3-methyl imidazolium bis(trifluoro methane sulfonyl)amide at room temperature. The iridescent colors changed with particle concentration.

Another team reported a new type of diamondlike colloidal crystal formed from oppositely charged and equally sized gold and silver particles [432]. Furthermore, core–shell-type clusters, where the shell is formed by the particles in excess, were prepared from oppositely charged silver and gold particles [433,434]. These regulated aggregates are a highly interesting finding, since most researchers assumed that only polydisperse aggregates should form from cationic and anionic colloidal spheres by electrostatic interparticle attraction. The important role of electrical double layers was also proposed for crystallization.

Oil-in-water-type emulsions containing 10% surfactant showed the iridescent colors ascribed to the lyotropic liquid crystal structures [435]. One team [436] prepared brightly colored emulsion crystals composed of mixtures of aqueous $Na_2S_2O_3$ solution and THF solution of hydroxylpropyl cellulose. The color changed from deep purple to pink as the concentration of $Na_2S_2O_3$ changed from 45 to 50 wt%. The color change was explained by Mie's scattering theory in combination with the Christiansen effect.

As was described in Section 28.3, spherical plasma with positive charges formed crystal structures [204]. This

"plasma crystal" supports the important role of interparticle electrostatic repulsion. Recently, keen interest has focused on the gas-, liquid-, and crystal-like distributions of dusty plasmas in space, that is, low-temperature plasmas containing charged macroparticles [437]. The main cause for the plasma crystallization interparticle electrostatic repulsions, which are quite similar to colloidal crystallization.

Another group of coworkers [438, 439] found stable micrometer-sized water droplets in polar oils without any additives. Under appropriate conditions the oil-dispersed water droplets formed a body-centered cubic (*bcc*) lattice with a lattice spacing of the order of 10 μm, and some of the crystals remained stable for ∼2 years without droplet coalescence. This crystallization has been explained by the electrostatic repulsion between charged water droplets [438–443].

28.17 MISCELLANEOUS

A colloidal particle in suspension state is assumed to be a type of polyelectrolyte existing on colloidal surfaces, since a large number of charges always distribute on the colloidal surfaces. This assumption prompted physicochemical studies of colloidal suspensions such as mean activity coefficient, osmotic coefficient, heat of dilution, and partial molal volume. One team [444] measured the mean activity coefficients, osmotic coefficients, and single- ion activities of monodisperse polystyrene spheres in the colloidal crystal state, although the proposal of intersphere *attraction* in the study was denied strongly and intersphere *repulsion* was clarified to be essential for colloidal crystallization exclusively by the author himself [11]. There is no experimental evidence to support the idea of *attraction*. One investigator [192] measured the osmotic pressure and then the osmotic coefficient of gaslike and liquidlike colloidal dispersions of carboxyl-group-containing spheres, a copolymer of butyl acrylate and styrene, by a membrane osmometer against pure water. Very small osmotic coefficients ranging from 0.02 to 0.04 have been observed, which supported the theory of significant counterion binding in a colloidal sphere. Note here that a simple method to measure osmotic pressure was proposed [445, 446]. Two other researchers [447] derived an equation of state for colloidal crystal and liquid by direct osmotic pressure measurements of colloidal dispersions. A theoretical approach to an equation of state has been formulated mainly by computer simulation, and the results supported the effective soft-sphere model [7,448–451].

Dielectric dispersion may afford important information on the dynamic properties of colloidal crystals. However, most of work has been done in the presence of sodium chloride salt, for example [12,452–454]. Thus, the systems were always gaslike or liquidlike. The author measured conductivity dispersion of colloidal crystals, for example [20]. The characteristic frequency increased sharply as the sphere size decreased, sphere concentration increased, and/or salt concentration increased.

Refractive indices of colloidal dispersions and films, which are important for study of physicochemical properties such as light-scattering analyses, were measured [455–461]. The author measured refractive indices of colloidal crystals [462]. The reduced RI increments of colloidal liquid were higher than those of corresponding colloidal gas in the presence of sodium chloride. A sharp peak was observed in the reduced RI increments in the colloidal crystal–sphere concentration curve. The peak corresponds to the phase transition between colloidal crystals and liquids.

28.18 APPLICATION OF COLLOIDAL CRYSTALS

Fixation of colloidal crystal structures in solid state has been the first step in most of colloidal crystal application studies. Poly(methyl acrylate) films containing crystal arrays of colloidal silica spheres were prepared successfully by two different teams [463,464]. In general, the lithography process is divided into two steps: (1) providing a master or composite pattern for pattern replication and (2) the actual replication, where the pattern transferred is made quickly and precisely. In the standard techniques of lithography, replication shorter than several the 10s of nm scale is difficult [465]. For the fabrication of nanometer-scale structures, electron and ion beam lithography techniques are appropriate. However, these methods require a long processing time and incur higher costs [466]. To overcome these difficulties, colloidal lithography has been developed [465]. Two investigators [467] evaporated colloidal suspension (spheres 300 nm in diameter) on a glass plate and obtained the regions of hexagonally packed spheres. After platinum deposition they obtained ordered arrays of triangular areas. Later, deposition over the entire surface of a macroscopic substrate was achieved [468]. Furthermore, the coating techniques such as spin coating and the Langmuir–Blodgett method were developed [469, 470]. Recent development on the colloidal lithography is amazing [471, 472].

Preparation of photonic crystals includes the addition of structured solid materials composed of two components having different refractive indices and having periodically ordered structures in the scale of light wavelengths. Using these materials, a photonic bandgap (PBG) filter is formed. This technique is quite interesting for the design and construction of new types of devices. Production of the first photonic bandgap was reported in 1991 [473]. Structures exhibiting full PBG in the microwave, millimeter, and submillimeter regimes were initially fabricated in 2004 or earlier. Now, submicrometer-length-scale photonic crystal has been developed rapidly using colloidal crystals as the starting material [474–486]. Another team [487] synthesized monodisperse

hollow polymer spheres and studied the photonic crystal function including magnetic field effects. Theoretical predictions were also shown, based on energy considerations. A 2D crystal of monodisperse magnetic particles was formed as a liquid surface [488]. Another team [489] observed 2D and 3D self-assembly of magnetic particles by interparticle magnetic repulsion forces on liquid surfaces using the layer-by-layer technique. The possibility of using spheres in photonic bandgap applications was also reported. Furthermore, tunable paramagnetic colloidal photonic crystals were developed [490]. Another team [491] prepared photonic rubber sheets with tunable color by elastic deformation, and also studied the tunable structural color in colloidal photonic crystals [492]. In order to obtain large single crystals, another team studied template-directed colloidal crystallization [493]. Frankly speaking, there are still many difficulties to be solved before practical use of colloidal crystals is possible.

Semiconductor crystals with radii smaller than the bulk exciton Bohr radius show the highly effective bandgap of the material. ZnS growth on CdSe crystals was prepared to provide very high fluorescent quantum yield of 50% [489, 490,493, 494].

28.19 CONCLUDING REMARKS

Colloidal crystals are the suspensions in which colloidal particles distribute regularly as atoms and molecules do in metals and protein crystals. Giant colloidal crystals were found to emit brilliant iridescent colors by the Bragg diffraction method and are visually spectacular. In this chapter, recent research on the structural colors, morphology, crystallization kinetics, structural and dynamic properties, electrooptic effects, and other aspects of colloidal crystals have been discussed. Formation of giant colloidal crystals is due to the electrostatic intersphere *repulsion* and to the highly expanded *electrical double layers* surrounding colloidal spheres. Morphology, lattice structure, and physicochemical properties have been described as being quite similar to those of typical crystals found in nature, such as those in metals, protein, and ice, when different lineal scales are correctly taken into account.

Several concerns are recommended for experimental study of colloidal crystallization. First, ionic contamination of the sample suspension must be avoided as carefully as possible, especially in aqueous suspension. Most of the author's experiments were made for exhaustively deionized aqueous suspensions. Colloidal crystallization is substantially influenced by the ionic concentration of the suspension because of the significant contribution of the electrical double layers formed around colloidal particles in aqueous suspension. Accurate determination of the ionic concentration of the aqueous colloidal suspensions is extremely difficult, since ionic contamination of the suspensions takes place always and easily from the suspension container and air. In the author's laboratory, most sample suspensions coexisted for a long time with an excess amount of mixtures of cation and anion exchange resins. In this case, the salt concentration should be on the order of 10^{-7} mol/L. Very careful experiments must be made to avoid the ionic contamination in order to obtain the reliable data. We should note that exhaustive deionization is achieved only by ion exchange resins that have coexisted for a long time, typically more than one year.

We should focus on why *repulsive*—rather than *attractive*–interparticle interaction is important in colloidal crystallization. The latter is quite common for most crystals in nature, including metals, proteins, and ice. For typical crystals in nature, the elementary particles described in Section 28.1 are very small, and the contribution of both the transitional and rotational diffusion constants given in Eqs. (28.15) and (28.16) are so large that the ordering including crystallization will be quite difficult without very strong interparticle attractive forces:

$$D_{\mathrm{tr}} = k_{\mathrm{B}}T/3\pi\eta d \tag{28.15}$$

$$D_{\mathrm{r}} = k_{\mathrm{B}}T/\pi\eta d^3 \tag{28.16}$$

Here, D_{tr} and D_{r} are the translational and rotational diffusion constants of a sphere (where d = diameter), $k_{\mathrm{B}}T$ is thermal energy, and η is the viscosity of solvent. On the other hand, the diffusive forces of very large colloidal particles are too weak to form ordering without the presence certain other interparticle repulsion forces. Without additive repulsion interactions the colloidal particles will associate easily with each other. Maintaining balance or equilibrium between attractive and repulsive interparticle reactions is very important for effective ordering.

REFERENCES

[1] Vanderhoff, W., van de Hul, H.J., Tausk, R.J.M., Overbeek, J.Th.G. (1970). In Goldfinger, G. (ed.), *Clean Surfaces: Their Preparation and Characterization for Interfacial Studies*. Marcel Dekker, New York, pp. 15–44.

[2] Hiltner, P.A., Papir, Y.S., Krieger, I.M. (1971). *J. Phys. Chem.* **75**, 1881–1886.

[3] Kose, A., Ozaki, M., Takano, K., Kobayashi, Y., Hachisu, S. (1973). *J. Colloid Interface Sci.* **44**, 330–338.

[4] Williams, R., Crandall, R.S., Wojtowicz, P.J. (1976). *Phys. Rev. Lett.* **37**, 348–351.

[5] Mitaku, S., Ohtsuki, T., Kishimoto, A., Okano, K. (1980). *Biophys. Chem.* **11**, 411–416.

[6] Lindsay H.M., Chaikin, P.M. (1982). *J. Chem. Phys.* **76**, 3774–3781.

[7] Pieranski, P. (1983). *Contemp. Phys.* **24**, 25–73.

[8] Ottewill, R.H. (1985). *Ber. Bunsenges. Phys. Chem.* **89**, 517–525.

[9] Aastuen, D.J.W., Clark, N.A., Cotter, L.K., Ackerson, B.J. (1986). *Phys. Rev. Lett.* **57**, 1733–1736.

[10] Pusey, P.N., van Megen, W. (1986). *Nature* **320**, 340–342.

[11] Okubo, T. (1988). *Accounts Chem. Res.* **21**, 281–286.

[12] Russel, W.B., Saville, D.A., Schowalter, W.R. (1989). *Colloidal Dispersions*. Cambridge Univ. Press, Cambridge, UK, pp. 329–365.

[13] Sood, A.K. (1991). *Solid State Phys*. **45**, 1–73.

[14] Ackerson, B.J., Clark, N.A. (1981). *Phys. Rev. Lett.* **46**, 123–126.

[15] Okubo, T. (1988). *J. Chem. Soc. Faraday Transact.* 1 **84**, 1163–1169.

[16] Monovoukas, Y., Gast, A.P. (1989). *J. Colloid Interface Sci.* **128**, 533–548.

[17] Aastuen, D.J.W., Clark, N.A., Swindall, J.C., Muzny, C.D. (1990). *Phase Transit.* **21**, 139–155.

[18] Okubo, T. (1991). *J. Chem. Phys.* **95**, 3690–3697.

[19] Okubo, T. (1992). *Naturwissenschaften* **79**, 317–320.

[20] Okubo, T. (1993). *Progress. Polym. Sci.* **18**, 481–517.

[21] Simon, R., Palberg, T., Leiderer, P. (1993). *J. Chem. Phys.* **99**, 3030–3036.

[22] Okubo, T. (1993). *Colloid Polym. Sci.* **271**, 190–196.

[23] Okubo, T. (1994). *Langmuir* **10**, 1695–1702.

[24] Okubo, T. (1994). *Langmuir* **10**, 3529–3535.

[25] Fujita, H., Ametani, K. (1977). *Jpn. J. Appl. Phys.* **16**, 1091–1096.

[26] Tobochnik, J., Chapin, P.M. (1988). *J. Chem. Phys.* **88**, 5824–5830.

[27] Thirumalai, D. (1989). *J. Phys. Chem.* **93**, 5637–5644.

[28] Okubo, T. (1994). In Schmitz, K.S. (ed.), *Macro-ion Characterization. From Dilute Solutions to Complex Fluids*. American Chemical Society, Washington, DC, pp. 364–380.

[29] Okubo, T. (1996). *Colloids Surf. A* **109**, 77–88.

[30] Okubo, T.Tsuchida, A. (2002). *Forma* **17**, 141–153.

[31] Okubo, T. (2005). In Yoshioka, S. (ed.), *Structural Colors in Biological Systems*. Osaka Univ. Press, pp. 267–286.

[32] Okubo, T., Yoshimi, H., Shimizu, T., Ottewill, R.H. (2000). *Colloid Polym. Sci.* **278**, 469–474.

[33] Okubo, T. (2008). *Polym. J.* **40**, 882–890.

[34] Russel, W.B. (1990). *Phase Transit.* **21**, 127–137.

[35] Harkless, C.R., Singh, M.A., Nagler, S.E., Stephenson, G.B., Jordan-Sweet, J.L. (1990). *Phys. Rev. Lett.* **64**, 2285–2288.

[36] Dhont, J.K.G., Smits, C., Lekkerkerker, H.N.W. (1992). *J. Colloid Interface Sci.* **152**, 386–401.

[37] Schatzel, K., Ackerson, B.J. (1993). *Phys. Rev. E* **48**, 3766–3777.

[38] Wurth, N., Schwarz, J., Culis, F., Leidener, P., Palberg, T. (1995). *Phys. Rev. E* **52**, 6415–6423.

[39] van Megen, W. (1995). *Transport Theor. Stat. Phys.* **24**, 1017–1051.

[40] Parsegian, V.A., Brenner, S.L. (1976). *Nature* **259**, 632–635.

[41] Butler, P.J.G., Lomonossoff, G.P. (1980). *Biophys J.* **32**, 295–312.

[42] Jeng, T. W.; Growther, R. A.; Stubbs, G.; Chiu, W. *J. Mol. Biol.* **205**, 251–257.

[43] Maier, E.E., Krause, R., Deggelmann, M., Hagenbuchle, M., Weber, R., Fraden, S. (1992). *Macromolecules* **25**, 1125–1133.

[44] Niu, Z., Li, S., Bruckman, M.A., Lee, L.A., Lee, B., Pingali, S.V., Thiagarajan, P., Wang, Q. (2008). In Nagarajan, R., Hatton, T.A. (eds.), *Nanoparticles: Synthesis, Stabilization, Passivation, and Functionalization*, Vol. 996, ACS Symp. Series, American Chemical Society, Washington, DC, pp. 369–385.

[45] Ratna, B.R., Soto, C.M., Danner, L., Blum, A.S., Fang, J., Lin, T., Johnson, J.E. (2003). *Langmuir* **19**, 489–490.

[46] Araki, J., Kuga, S. (2001). *Langmuir* **17**, 4493–4496.

[47] Wang, S.W., Robertson, C.R., Gast, A.P. (1999). *J. Phys. Chem. B* **103**, 7751–7761.

[48] Adams, M., Dogic, Z., Keller, S.L., Fraden, S. (1998). *Nature* **393**, 349–352.

[49] Okubo, T. (1990). *Colloid Polym. Sci.* **268**, 1159–1166.

[50] Araki, J., Wada, M., Kuga, S., Okano, T. (2000). *Langmuir* **16**, 2413–2415.

[51] Araki, J., Wada, M., Kuga, S. (2001). *Langmuir* **17**, 21–27.

[52] Ramachandran, G.N., Kartha, G. (1954). *Nature* **174**, 269–270.

[53] Hall, C.E., Doty, P. (1958). *J. ACS* **80**, 1269–1274.

[54] Hulmes, D.J.S., Miller, A. (1979). *Nature* **282**, 878–880.

[55] Okubo, T., Kokufuta, E., Nakamuro, M., Yoshinaga, K., Mizutani, M., Tsuchida, A. (2010). *Colloids Surf. B* **80**, 193–199.

[56] Roun, F.E., Crawford, R.M., Mann, D.G. (1990). *The Diatoms.* Cambridge Univ. Press, Cambridge, UK.

[57] Haeckel, E. (2005). *Art Forms from the Ocean*. Prestel, Munich/London.

[58] Ottewill, R.H., Shaw, J.N. (1966). *Kolloid Z. Z. Polym.* **218**, 34–40.

[59] Hiltner, P.A., Krieger, I.M. (1969). *J. Phys. Chem.* **73**, 2386–2389.

[60] Fitch, R.M. (ed.) (1971). *Polymer Colloids*, Plenum Press, New York.

[61] Clark, N.A., Ackerson, B.J. (1980). *Phys. Rev. Lett.* **44**, 1005–1008.

[62] Murray, C.A., Wenk, R.A. (1989). *Phys. Rev. Lett.* **62**, 1643–1646.

[63] Fitch, R. M. (ed.) (1997). *Polymer Colloids: A Comprehensive Introduction*. Academic Press, San Diego.

[64] Kose, A., Hachisu, S. (1974). *J. Colloid Interface Sci.* **46**, 460–469.

[65] Okubo, T. (2008). *Colloid Polym. Sci.* **286**, 1307–1315.

[66] Ottewill, R.H. (1989). *Langmuir* **5**, 4–9.

[67] Goodwin, J.W., Ottewill, R.H. (1991). *J. Chem. Soc. Faraday Transact.* **87**, 357–369.

[68] van Megen, W., Underwood, S.M., Pusey, P.N. (1991). *Phys. Rev. Lett.* **67**, 1586–1589.

[69] He, Y., Ackerson, B.J., van Megen, W., Underwood, S.M., Schatzel, K. (1996). *Phys. Rev. E* **54**, 5286–5297.

[70] Harland, J.L., van Megen, W. (1997). *Phys. Rev. E* **55**, 3054–3067.

[71] Moussaid, A., Pusey, P.N. (1999). *Phys. Rev. E* **60**, 5670–5676.

[72] Guisheng, P., Kesavamoorthy, R., Asher, S.A. (1998). *J. AC S* **120**, 6518–6524.

[73] Lutterbach, N., Versmold, H., Reus, V., Belloni, L., Zemb, Th. (1999). *Langmuir* **15**, 337–344.

[74] Okubo, T., Yoshimi, H., Shimizu, T., Ottewill, R.H. (2000). *Colloid Polym. Sci.* **278**, 469–474.

[75] Okubo, M., Yamamoto, Y., Kamei, S. (1989). *Colloid Polym. Sci.* **267**, 861–865.

[76] Cardoso, A.H., Leite, C.A.P., Galembeck, F. (1999). *Langmuir* **15**, 4447–4453.

[77] Chen, Y., Ford, W.T., Materer, N.F., Teeters, D. (2000). *J. ACS* **122**, 10472–10473.

[78] Li, H., Kumacheva, E. (2003). *Colloid Polym. Sci.* **281**, 191–205.

[79] Sukhorukov, G.B., Brumen, M., Donath, E., Mohwald, H. (1999). *J. Phys. Chem. B* **103**, 6434–6440.

[80] Hotz, J., Meier, W. (1998). *Langmuir* **14**, 1031–1036.

[81] Caruso, F., Donath, E., Mohwald, H. (1998). *J. Phys. Chem. B* **102**, 2011–2016.

[82] Decher, G., Schmitt, J. (1992). *Progress Colloid Polym. Sci.* **89**, 160–164.

[83] Ferreira, M., Rubner, M.F. (1995). *Macromolecules* **28**, 7107–7114.

[84] Dai, Z., Mohwald, H., Tiersch, B., Dahne, L. (2002). *Langmuir* **18**, 9533–9538.

[85] Sheu, H.R., Tseng, C.M., El-Aasser, M.S., Micale, F.J., Vanderhoff, J.W. *Grad. Res. Program Rep.* **24**, 6–7; ibid. **25**, 7–8.

[86] Vanderhoff, J.W., El-Aasser, M.S., Fitch, R.M. (eds.) (1987). *Future Directions in Polymer Colloids*. Martinus Nijhoff, Dordrecht, pp. 23–46.

[87] Saadat, Y., Hosseinzadeh, S., Abdolbaghi, S., Afshar-Taromi, F. (2013). *Colloid Polym. Sci.* **291**, 1113–1120.

[88] Huang, H., Liu, H. (2010). *J. Polym. Sci. A Polym. Chem.* **48**, 5198–5205.

[89] Okubo, M., Katsuta, Y., Matsumoto, T. (1980). *J. Polym. Sci. Polym. Lett. Ed.* **18**, 481–486.

[90] Okubo, M., Fujibayashi, T., Yamada, M., Minami, H. (2005). *Colloid Polym. Sci.* **283**, 1041–1045.

[91] Okubo, M., Takekoh, R., Suzuki, A. (2002). *Colloid Polym. Sci.* **280**, 1057–1061.

[92] Okubo, M., Minami, H. (1997). *Colloid Polym. Sci.* **275**, 992–997.

[93] Okubo, M., Minami, H. (2000). *Macromol. Symp.* **150**, 201–210.

[94] Okubo, M., Fujibayashi, T., Terada, A. (2005). *Colloid Polym. Sci.* **283**, 793–798.

[95] Fujibayashi, T., Okubo, M. (2007). *Langmuir* **23**, 7958–7962.

[96] Nagy, M., Keller, A. (1989). *Polym. Commun.* **30**, 130–132.

[97] Ho, C.C., Keller, A., Odell, J.A., Ottewill, R.H. (1993). *Colloid Polym. Sci.* **271**, 469–479.

[98] Okubo, T., Aotani, S. (1988). *Naturwissenschaften* **75**, 145–146.

[99] Okubo, T., Aotani, S. (1988). *Colloid Polym. Sci.* **266**, 1049–1057.

[100] Riegel, I.C., Eisenberg, A., Petzhold, C.L., Samios, D. (2002). *Langmuir* **18**, 3358–3363.

[101] Pelton, R. (2000). *Adv. Colloid Interface Sci.* **85**, 1–33.

[102] Zsigmondy, R. (1906). *Z. Physik. Chem.* **56**, 65–69.

[103] Matijevic, E. (1981). *Accounts Chem. Res.* **14**, 22–29.

[104] Matijevic, E., Wilhelmy, D.M. (1982). *J. Colloid Interface Sci.* **86**, 476–484.

[105] Okubo, T. (1991). *J. Chem. Phys.* **96**, 2261–2268.

[106] Guez, H.M., Meseguer, F., Lopez, C., Mifsud, A., Moya, J.S. (1997). *Langmuir* **13**, 6009–6011.

[107] van Helden, A.K., Jansen, J.W., Vrij, A. (1981). *J. Colloid Interface Sci.* **81**, 354–368.

[108] Emmett, S., Lubetkin, S.D., Vincent, B. (1989). *Colloids Surf.* **42**, 139–153.

[109] Veihaegh, N.A.M., van Blaaderen, A. (1994). *Langmuir* **10**, 1427–1438.

[110] Imhof, A., van Blaaderen, A., Dhont, J.K.G. (1994). *Langmuir* **10**, 3477–3484.

[111] Yoshinaga, K., Nakanishi, K. (1994). *Compos. Interfaces* **2**, 95–103.

[112] Yoshinaga, K., Chiyoda, M., Yoneda, A., Nishida, H., Komatsu, M. (1999). *Colloid Polym. Sci.* **277**, 479–482.

[113] Yoshinaga, K., Fujiwara, K., Mouri, E., Ishii, M., Nakamura, H. (2005). *Langmuir* **21**, 4471–4477.

[114] Yoshinaga, K., Shigeta, M., Komune, S., Mouri, E. (2007). *Colloids Surf. B: Biointerfaces* **54**, 108–113.

[115] Ma, Z., Watanabe, M., Mouri, E., Yoshinaga, K. (2010). *Colloid Polym. Sci.* **288**, 519–525.

[116] Ma, Z., Watanabe, M., Mouri, E., Yoshinaga, K. (2011). *Colloid Polym. Sci.* **289**, 85–91.

[117] Nommensen, P.A., Duits, M.H.G., Lopulissa, J.S., van den Ende, D., Mellema, J. (1998). *Progress Colloid Polym. Sci.* **110**, 144–149.

[118] Pratsinis, S.E., Zhu, W., Vemury, S. (1996). *Powder Technol.* **86**, 87–93.

[119] Zhu, W., Pratosinis, S.E. (1996). In Chow, G.M., Gonzalves, K.E. (eds.), *Nanotechnology*, Vol. **622**, ACS Symp. Series, American Chemical Society, Washington DC, pp. 64–78.

[120] Lee, J.H., Beaucage, G., Pratsinis, S.E., Vemury, S. (1998). *Langmuir* **14**, 5751–5756.

[121] Zang, L., Qu, P., Zhao, J., Shen, T., Hidaka, H. (1997). *Chem. Lett.* **26**, 791–792.

[122] Qu, P., Zhao, J., Zang, L., Shen, T., Hidaka, H. (1998). *Colloids Surf. A*, **138**, 39–50.

[123] Uyeda, N., Nishino, M., Suito, E. (1973). *J. Colloid Interface Sci.* **43**, 264–276.

[124] Liz-Marzan, L.M., Glersig, M., Mulvaney, P. (1996). *Langmuir* **12**, 4329–4335.

[125] Okubo, T. (1987). *Colloid Polym.* **265**, 522–527.

[126] Mayya, K.S., Patil, V., Sastry, M. (1997). *Langmuir* **13**, 2575–2577.

[127] Santhanam, V., Liu, J., Agarwal, R., Andres, R.P. (2003). *Langmuir* **19**, 7881–7887.

[128] Patil, V., Mayya, K.S., Pradhan, S.D., Sastry, M. (1997). *J. ACS* **119**, 9281–9282.

[129] Kim, S.H., Medeiros-Ribeiro, G., Ohlberg, D.A.A., Williams, R.S., Heath, J.R. (1999). *J. Phys. Chem. B* **103**, 10341–10347.

[130] Korgel, B.A., Fullam, S., Connolly, S., Fitzmaurice, D. (1998). *J. Phys. Chem. B* **102**, 8379–8388.

[131] Okubo, T. (2013). *Colloid Polym. Sci.* **291**, 1623–1629.

[132] Okubo, T. (2013). *Colloid Polym. Sci.* **291**, 1887–1893.

[133] Scott, W.B., Matijevile, E. (1978). *J. Colloid Interface Sci.* **66**, 447–581.

[134] Matijevic, E., Sapieszko, R.S., Melvilb, J.B. (1975). *J. Colloid Interface Sci.* **50**, 567.

[135] Sapieszko, R.S., Patel, R.C., Matijevic, E. (1977). *J. Phys. Chem.* **81**, 1061–1068.

[136] Sugimoto, T., Wang, Y., Itoh, H., Muramatsu, A. (1998). *Colloids Surf. A* **134**, 265–279.

[137] Sugimoto, T., Dirige, G.E., Muramatsu, A. (1996). *J. Colloid Interface Sci.* **180**, 305–308.

[138] Sondi, I., Siiman, O., Koester, S., Matijevic, E. (2000). *Langmuir* **16**, 3107–3118.

[139] Mayya, K.S., Patil, V., Kumar, P.M., Sastry, M. (1998). *Thin Solid Films* **312**, 300–305.

[140] Boakye, E., Radovic, L.R., Osseo-Asare, K. (1994). *J. Colloid Interface Sci.* **163**, 120–129.

[141] Pileni, M.P. (1997). *Langmuir* **13**, 3266–3276.

[142] Muramatsu, A., Sugimoto, T. (1997). *J. Colloid Interface Sci.* **189**, 167–173.

[143] Sandroff, C.J., Hwang, D.M., Chung, W.M. (1986). *Phys. Rev. B* **33**, 5953.

[144] Dabbousi, B.O., Viejo, J.R., Mikulec, F.V., Heine, J.R., Mattoussi, H. (1997). *J. Phys. Chem. B* **101**, 9463–9475.

[145] Tajima, T., Tsutsui, A., Fujii, T., Takada, J., Takaguchi, Y. (2012). *Polym. J.* **44**, 620–624.

[146] Sugimoto, T., Sakata, K. (1992). *J. Colloid Interface Sci.* **152**, 587–590.

[147] Ueda, R. (1987). In Sunagawa, I. (ed.), *Morphology of Crystals* Pt. B. Terra, Tokyo, p. 364.

[148] Petroski, J.M., Green, T.C., El-Sayed, M.A. (2001). *J. Phys. Chem.* **105**, 5542–5547.

[149] Ogino, K., Kuronuma, I. (1976). *J. Colloid Interface Sci.* **56**, 629–630.

[150] Hachisu, S., Kose, A., Kobayashi, Y., Takano, K. (1976). *J. Colloid Interface Sci.* **55**, 499–509.

[151] Yu, Y.Y., Chang, S.S., Lee, C.L., Wang, C.R.C. (1997). *J. Phys. Chem. B* **101**, 6661–6664.

[152] Link S.; Burda, C.; Mohamed, M. B.; Nikoobakht, B.; El-Sayed, M. A. *J Phys Chem A*, 1999, **103**, 1165–1170

[153] Chang, S.S., Shih, C.W., Chen, C.D., Lai, W.C., Wang, C.R.C. (1999). *Langmuir* **15**, 701–709.

[154] Okamoto, S., Hachisu, S. (1973). *J. Colloid Interface Sci.* **43**, 30–35.

[155] van de Zande, B.M.I., Dhont, J.K.G., Bohmer, M.R., Fokkink, L.G.J., Schonenberger, C. (2000). *Langmuir* **16**, 451–458.

[156] Brown, A.B.D., Clarke, S.M., Rennie, A.R. (1998). *Langmuir* **14**, 3129–3132.

[157] Ahmadi, T.S., Wang, Z.L., Green, T.C., Henglein, A., El-Sayed, M.A. (1996). *Science* **272**, 1924–1927.

[158] Watson, J.H.L., Jr., Cardel, R.R., Heller, W. (1962). *J. Phys. Chem.* **66**, 1757–1763.

[159] Buining, P.A., Philipse, A.P., Lekkerkerker, H.N.W. (1994). *Langmuir* **10**, 2106–2114.

[160] Koenderink, G.H., Vliegenthart, G.A., Kluijtmans, S.G.J.M., van Blaaderen, A., Philipse, A.P., Lekkerkerker, H.N.W. (1999). *Langmuir* **15**, 4693–4696.

[161] Buining, P.A., Patmamanoharan, C., Jansen, J.H.B., Lekkerkerker, H.N.W. (1991). *J. Am. Ceram. Soc.* **74**, 1303–1307.

[162] van der Kooij, F.M., Lekkerkerker, H.N.W. (1998). *J. Phys. Chem. B* **102**, 7829–7832.

[163] Sugimoto, T., Okada, K., Itoh, H. (1997). *J. Colloid Interface Sci.* **193**, 140–143.

[164] Sedlacik, M., Mrlik, M., Kozakova, Z., Pavlinek, V., Kuritka, I. (2013). *Colloid Polym. Sci.* **291**, 1105–1111.

[165] Matsumoto, M. (1996). *Biophys. Chem.* **58**, 173–183.

[166] Matsumoto, M. (1999). *Colloids Surf. A* **148**, 75–81.

[167] Gong, T., Wu, D.T., Marr, W.M.M. (2002). *Langmuir* **18**, 10064–10067.

[168] Rowan, D.G., Hansen, J.P. (2002). *Langmuir* **18**, 2063–2068.

[169] Zocher, V.H., Jacobsohn, K. (1929). *Kolloid. Beih.* **28**, 167–206.

[170] Okubo, T. (1987). *J. ACS* **109**, 1913–1916.

[171] Okubo, T. (1987). *J. Phys. Chem.* **91**, 1977–1980.

[172] Okubo, T. (1988). *J. Chem. Soc. Faraday Transact. 1* **84**, 703–712.

[173] Hachisu, S., Furusawa, K. (1963). *Sci. Light* **12**, 1–8.

[174] Brock, S.L., Sanabria, M., Suib, S.L., Urban, V., Thiyagarajan, P., Potter, D.I. (1999). *J. Phys. Chem. B* **103**, 7416–7428.

[175] Okubo, T. (1987). *Angew. Chem. Int. Ed. Engl.* **26**, 765–767.

[176] Sugimoto, T., Khan, M.M., Muramatsu, A. (1993). *Colloids Surf. A* **70**, 167–169.

[177] Sugimoto, T., Waki, S., Itoh, H., Muramatsu, A. (1996). *Colloids Surf. A* **109**, 155–165.

[178] Ohno, K., Tsuchida, A., Okubo, T. (in press). *Colloid Polym. Sci.* (doi:10.1007/s00396 -013-3136-1).

[179] Mourchid, A., Delville, A., Lambard, J., Lecolier, E., Levitz, P. (1995). *Langmuir* **11**, 1942–1950.

[180] Grillo, I., Levitz, P., Zemb, Th. (2000). *Langmuir* **16**, 4830–4839.

[181] Kimura, H., Sakurai, M., Sugiyama, T., Tsuchida, A., Okubo, T., Masuko, T. (2011). *Rheol. Act.* **50**, 159–168.

[182] Morvan, M., Espinat, D., Lambard, J., Zemb, T. (1994). *Colloids Surf. A* **82**, 193–203.

[183] Kroon, M., Vos, W.L., Wegdam, G.H. (1998). *Phys. Rev. E* **57**, 1962–1970.

[184] Vanderhoff, J.W., van den Hul, H.J. (1973). *J. Macromol. Sci. Chem.* **A7**, 677–707.

[185] Okubo, T. (1988). *J. Colloid Interface Sci.* **125**, 380–385.

[186] Okubo, T., Aotani, S. (1988). *Colloid Polym. Sci.* **266**, 1042–1048.

[187] Okubo, T. (1989). *J. Chem. Soc. Faraday Transact. 1* **85**, 455–466.

[188] Bolt, G.H. (1957). *J. ACS* **61**, 1166–1169.

[189] Schaffer, D.W. (1977). *J. Chem. Phys.* **66**, 3980–3984.

[190] Okubo, T. (1987). *Ber. Bunsenges. Phys. Chem.* **91**, 1064–1069.

[191] Midmore, B.R., Diggins, D., Hunter, R.J. (1989). *J. Colloid Interface Sci.* **129**, 153–161.

[192] Rymden, R. (1988). *J. Colloid Interface Sci.* **124**, 396–402.

[193] Alexander, S., Chaikin, P.M., Grant, P., Morales, G.J., Pincus, P., Hone, D. (1984). *J. Chem. Phys.* **80**, 5776–5781.

[194] Palberg, T., Kottal, J., Bitzer, F., Simon, R., Wurthard, M., Leiderer, P. (1995). *J. Colloid Interface Sci.* **169**, 85–89.

[195] Garbow, N., Evers, M., Palberg, T., Okubo, T. (2004). *J. Phys. Condens. Matter* **16**, 3835–3842.

[196] Gilanyi, T. (1988). *J. Colloid Interface Sci.* **125**, 641–648.

[197] Conway, J.H., Sloane, N.J.A. (1998). *Sphere Packing, Lattices and Groups*, 3rd ed. Springer-Verlag.

[198] Hales, T.C. (1997). *Discrete Comput. Geom.* **17**, 1–51.

[199] Hales, T.C. (1997). *Discrete Comput. Geom.* **18**, 135–149.

[200] Fejes Toth, L. (1972). *Lagerungen in der Ebene, auf der Kugel und im Raum*, 2nd ed. Springer, Heidelberg.

[201] Thue, A. (1910). *Christiania Vid. Selsk. Skr.* **1**, 3–9.

[202] Tanemura, M., Matsumoto, T. (1997). *Z. Kristallograph.* **212**, 637–647.

[203] Aoyama, K., Ogawa, K., Kimura, Y., Fujiyoshi, Y. (1995). *Ultramicroscopy* **57**, 345–354.

[204] Itano, W.M., Bolinger, J.J., Tan, J.N., Jelenkovic, B., Huang, X.P., Wineland, D.J. (1998). *Science* **279**, 686–689.

[205] Overbeek, J.Th.G. (1987). *J. Chem. Phys.* **87**, 4406–4408.

[206] Dickinson, E. (1978). *Chem. Phys. Lett.* **57**, 148–150.

[207] Dickinson, E. (1978). *Faraday Discuss. Chem. Soc.* **65**, 127–129.

[208] Dickinson, E. (1979). *J. Chem. Soc. Faraday Transact. 2* **75**, 466–473.

[209] Dickinson, E., Parker, R., Lai, M. (1981). *Chem. Phys. Lett.* **79**, 578–582.

[210] Dickinson, E., Parker, R. (1985). *J. Phys. Lett.* (Paris) **46**, L229–L232.

[211] Barat, J.U.L., Hansen, J.P. (1986). *J. Phys.* **47**, 1547–1553.

[212] Okubo, T. (1987). *Ber. Bunsenges. Phys. Chem.* **91**, 516–519.

[213] Okubo, T. (2006). *Colloid Polym. Sci.* **285**, 245–250.

[214] Monovoukas, Y., Gast, A.P. (1991). *Langmuir* **7**, 460–468.

[215] Okubo, T. (1992). *Colloid Polym. Sci.* **270**, 1018–1026.

[216] Okubo, T. (1994). *Colloid Polym. Sci.* **272**, 440–446.

[217] Emmett, S., Lubetkin, S.D., Vincent, B. (1989). *Colloids Surf.* **42**, 139–153.

[218] Robbins, M.O., Kremer, K., Grest, G.S. (1988). *J. Chem. Phys.* **88**, 3286–3312.

[219] Voegtli, L.P., Zukoski, C.F., IV (1991). *J. Colloid Interface Sci.* **141**, 79–91.

[220] Shih, W.Y., Aksay, I.A., Kikuchi, R. (1987). *J. Chem. Phys.* **86**, 5127–5132.

[221] Kremer, K., Robbins, M.O., Pincus, P. (1983). *J. Chem. Phys.* **79**, 1474–1479.

[222] Hone, D., Alexander, S., Chaikin, P.M., Pincus, P. (1983). *J. Chem. Phys.* **79**, 1474–1479.

[223] Chaikin, P.M., Pincus, P., Alexander, S., Hone, D. (1982). *J. Colloid Interface Sci.* **89**, 555–563.

[224] Barnes, C.J., Chan, D.Y.C., Everett, D.H., Yates, D.E. (1978). *J. Chem. Soc. Faraday Transact. 2* **1978**, 136–148.

[225] Kaldasch, J., Laven, J., Stein, H.N. (1996). *Langmuir* **12**, 6197–6201.

[226] Okubo, T., Kimura, H., Hase, H., Yamaguchi, K., Nagai, K. (2004). *Colloid Polym. Sci.* **282**, 250–255.

[227] Okubo, T., Kimura, H., Hase, H., Lovell, P.A., Erington, N., Thongnoi, P. (2005). *Colloid Polym. Sci.* **283**, 393–401.

[228] Okamoto, J., Kimura, H., Tsuchida, A., Okubo, T., Ito, K. (2007). *Colloids Surf. B: Biointerface* **56**, 231–235.

[229] Brown, A.B.D., Clarke, S.M., Rennie, A.R. (1998). *Langmuir* **14**, 3129–3132.

[230] Onsager, L. (1949). *Ann. NY Acad. Sci.* **51**, 627–659.

[231] van Bruggen, M.P.B., Dhont, J.K.G., Lekerkerker, H.N.W. (1999). *Macromolecules* **32**, 2256–2264.

[232] Davidson, P., Gabriel, J.C., Levelu, A.M., Batail, P. (1993). *Adv. Mater.* **5**, 665–668.

[233] Davidson, P., Gabriel, J.C.P., Pileni, M.P. (eds.) (2005). *Nanocrystals Forming Mesoscopic Structures*. Wiley-VCH, Weinheim, pp. 173–212.

[234] Kajiwara, K., Donkai, N., Hiragi, Y., Inagaki, H. (1986). *Makromol. Chem.* **187**, 2883–2894.

[235] Donkai, N., Hoshino, H., Kajiwara, K., Miyamoto, T. (1993). *Makromol. Chem.* **194**, 559–580.

[236] Genoud, J.Y., Staines, M., Mawdsley, A., Manojlovic, V., Quinton, W. (1999). *Supercond. Sci. Technol.* **12**, 663–671.

[237] Kimura, T., Kimura, F., Yoshino, M. (2006). *Langmuir* **22**, 3464–3466.

[238] Kimura, T., Chang, C., Kimura, F., Maeyama, M. (2009). *J. Appl. Crystallogr.* **42**, 535–537.

[239] Kimura, F., Kimura, T., Oshima, W., Maeyama, M., Aburaya, K. (2010). *J. Appl. Crystallogr.* **43**, 151–153.

[240] Kimura, F., Mizutani, K., Mikami, B., Kimura, T. (2011). *Cryst. Growth Design* **11**, 12–15.

[241] Murray, M.J., Sanders, J.V. (1980). *Phil. Mag. A* **42**, 721–740.

[242] Sanders, J.V., Murray, M.J. (1978). *Nature* **275**, 201–203.

[243] Hachisu, S., Yoshimura, S. (1980). *Nature* **283**, 188–189.

[244] Yoshimura, S., Hachisu, S. (1983). *Progress Colloid Polym. Sci.* **68**, 59–70.

[245] Yoshimura, S., Hachisu, S. (1985). *J. Phys.* (Paris) **46**(C3), 115–126.

[246] Hachisu, S. (1990). *Phase Transit.* **21**, 243–249.

[247] Okubo, T. (1987). *J. Chem. Phys.* **87**, 5528–5533.

[248] Okubo, T. (1990). *J. Chem. Phys.* **93**, 8276–8283.

[249] Shih, W.Y., Smith, W.H., Aksay, I.A. (1989). *J. Chem. Phys.* **90**, 4506–4512.

[250] Bartlett, P., Ottewill, R.H. (1992). *J. Chem. Phys.* **96**, 3306–3318.

[251] Bartlett, P., Ottewill, R.H., Pusey, P.N. (1992). *Phys. Rev. Lett.* **68**, 3801–3804.

[252] Hachisu, S., Kose, A., Kobayashi, Y., Takano, K. (1976). *J. Colloid Interface Sci.* **55**, 499–509.

[253] Okubo, T., Okada, S., Tsuchida, A. (1997). *J. Colloid Interface Sci.* **189**, 337–347.

[254] Okubo, T., Okada, S. (1997). *J. Colloid Interface Sci.* **192**, 490–496.

[255] Okubo, T., Tsuchida, A., Kato, T. (1999). *Colloid Polym. Sci.* **277**, 191–196.

[256] Okubo, T., Ishiki, H. (2000). *J. Colloid Interface Sci.* **228**, 151–156.

[257] Okubo, T. (1986). *J. Chem. Soc. Faraday Transact.* 1 **82**, 3163–3173.

[258] Wong, E.M., Bonevich, J.E., Pearson, P.C. (1998). *J. Phys. Chem.* **B102**, 7770–7775.

[259] Okubo, T., Okada, S. (1998). *J. Colloid Interface Sci.* **204**, 198–204.

[260] Okubo, T., Ishiki, H., Kimura, H., Chiyoda, M., Yoshinaga, K. (2002). *Colloid Polym. Sci.* **280**, 290–295.

[261] Yoshinaga, K., Chiyoda, M., Ishiki, H., Okubo, T. (2002). *Colloids Surf.* **A204**, 285–293.

[262] van de Ven, T.G.M., Baloch, M.K. (1990). *J. Colloid Interface Sci*. **136**, 494–508.

[263] Tsuchida, A., Takyo, E., Taguchi, K., Okubo, T. (2004). *Colloid Polym. Sci.* **282**, 1105–1110.

[264] Aastuen, D.J.W., Clark, N.A., Cotter, L.K., Ackerson, B.J. (1986). *Phys. Rev. Lett.* **57**, 1733–1736.

[265] Aastuen, D.J.W., Clark, N.A., Swindal, J.C., Muzny, C.D. (1990). *Phase Transit.* **21**, 139–155.

[266] He, Y., Ackerson, B.J., van Megen, W., Underwood, S.M., Schatzel, K. (1996). *Phys. Rev. E* **54**, 5286–5297.

[267] Ackerson, B.J., Schatzel, K. (1995). *Phys. Rev. E* **52**, 6448–6460.

[268] Schatzel, K., Ackerson, B.J. (1993). *Phys. Scripta* **T49**, 70–73.

[269] Schatzel, K., Ackerson, B.J. (1993). *Phys. Rev. E* **48**, 3766–3777.

[270] Harland, J.L., van Megen, W. (1997). *Phys. Rev. E* **55**, 3054–3067.

[271] Henderson, S.I., Mortensen, T.C., Underwood, S.M., van Megen, W. (1996). *Physica A* **233**, 102–116.

[272] Wurth, M., Schwarz, J., Culis, F., Leiderer, P., Palberg, T. (1995). *Phys. Rev. E* **52**, 6415–6423.

[273] Palberg, T. (1999). *J. Phys. Condens. Matter* **11**, R323–R360.

[274] Okubo, T., Kiriyama, K., Nemoto, N., Hashimoto, H. (1996). *Colloid Polym. Sci.* **272**, 93–104.

[275] Okubo, T., Kiriyama, K. (1997). *J. Mol. Liquids* **72**, 347–364.

[276] Okubo, T., Tsuchida, A. (2002). *Colloid Polym. Sci.* **280**, 438–445.

[277] Hartl, W., Versmold, H. (1987). *Z. Phys. Chem.* **153**, 1–14.

[278] Okubo, T., Kiriyama, K. (1996). *Ber. Bunsenges. Phys. Chem.* **100**, 849–856.

[279] Okubo, T., Kiriyama, K., Yamaoka, H., Nemoto, N. (1995). *Colloids Surf.* **A103**, 47–58.

[280] von Berlepsch, H., Strey, R. (1994). *Colloid Polym. Sci.* **272**, 577–583.

[281] Pusey, P.N., Tough, R.J.A. (1985). In Pecora, R. (ed.), *Particle Interactions. Dynamic Light Scattering*, Plenum, London, pp. 85–179.

[282] Ottewill, R.H. (1985). *Ber. Bunsenges. Phys. Chem.* **89**, 517–525.

[283] Okubo, T. (1989). *J. Chem. Phys.* **90**, 2408–2415.

[284] Bartlet, P., Ottewill, R.H., Pusey, P.N. (1990). *J. Chem Phys.* **93**, 1299–1312.

[285] Ackerson, B.J., Clark, N.A. (1983). *Faraday Discuss. Chem. Soc.* **76**, 219–228.

[286] Brown, J.C., Pusey, P.N., Goodwin, J.W., Ottewill, R.H. (1975). *J. Phys. (Paris)* **A8**, 664–682.

[287] Cebula, D.J., Goodwin, J.W., Jeferey, G.C., Ottewill, R.H., Parentich, A., Richardson, R.A. (1983). *Faraday Discuss. Chem. Soc.* **76**, 37–52.

[288] Philipse, A.P., Vrij, A. (1988). *J. Chem. Phys.* **88**, 6459–6470.

[289] Smith, G.S., Sirota, E.B., Satinya, C.R., Plano, R.J., Clark, N.A. (1990). *J. Chem. Phys.* **92**, 4519–4529.

[290] Ashdown, S., Markovic, I., Ottewill, R.H., Lindner, P., Obertur, R.C., Rennie, A.R. (1990). *Langmuir* **6**, 303–307.

[291] Reus, V., Belloni, L., Zemb, T., Lutterbach, N., Versmold, H. (1997). *J. Phys. France* **7**, 603–626.

[292] D'Aguanno, B., Klein, R. (1991). *J. Chem. Soc. Faraday Transact.* **87**, 379–390.

[293] Okubo, T. (1987). *J. Colloid Interface Sci.* **117**, 165–171.

[294] Okubo, T. (1987). *J. Chem. Phys.* **87**, 3022–3028.

[295] Cornel, R.1., Goodwin, J.W., Ottewill, R.H. (1979). *J. Colloid Interface Sci.* **71**, 254–266.

[296] Lindsay, H.M., Dozier, P.W.D., Chaikin, M., Klein, P. (1986). *J. Phys.* **A19**, 2583–2589.

[297] Mitaku, S., Ohtsuki, T., Enari, K., Kishimoto, A., Okano, K. (1978). *Jpn. J. Appl. Phys.* **17**, 305–313.

[298] Ohtsuki, T., Mitaku, S., Okano, K. (1978). *Jpn. J. Appl. Phys.* **17**, 627–635.

[299] Ohtsuki, T., Kishimoto, A., Mitaku, S., Okano, K. (1981). *Jpn. J. Appl. Phys.* **20**, 509–518.

[300] Joanicot, H.M., Jorand, M., Pieranski, P., Rothen, F. (1984). *J. Phys.* (Paris) **45**, 1413–1421.

[301] Schmacher, G.A., van de Ven, T.G.M. (1987). *Faraday Discuss. Chem. Soc.* **83**, 75–81.

[302] Schmacher, G.A., van de Ven, T.G.M. (1991). *J. Chem. Soc. Faraday Transact.* **87**, 971–976.

[303] Ohshima, H., Healy, T.W., White, L.R., O'Brien, R.W. (1984). *J. Chem. Soc. Faraday Transact. 2* **80**, 1299–1317.

[304] van Veluwen, A., Lekerkerker, H.N.W., de Kruif, L.G., Vrij, A. (1987). *J. Chem. Phys.* **87**, 4873–4880.

[305] Brown, J.C., Pusey, P.N., Goodwin, J.W., Ottewill, R.H. (1975). *J. Phys.* (Paris) **A8**, 664–682.

[306] Gruner, F., Lehmann, W. (1979). *J. Phys.* (Paris) **A12**, L303–L307.

[307] Hansen, J.P., Hayter, J.B. (1982). *Mol. Phys.* **46**, 651–656.

[308] Hess, W., Klein, R. (1983). *Adv. Phys.* **32**, 173–283.

[309] Klein, R., Hess, W. (1983). *Faraday Discuss. Chem. Soc.* **76**, 137–150.

[310] van Megen, W., Snook, I. (1983). *Faraday Discuss. Chem. Soc.* **76**, 151–163.

[311] Hartl, W., Vertsmold, H. (1987). *Z. Phys. Chem.* (Neue Folge) **153**, 1–4.

[312] Ottewill, R.H., Williams, N.St.J. (1987). *Nature* **325**, 232–234.

[313] Crandall, R.S., Williams, R. (1977). *Science* **198**, 293–295.

[314] Okubo, T. (1987). *J. Chem. Phys.* **86**, 2394–2399.

[315] Okubo, T. (1987). *J. Chem. Phys.* **86**, 5182–5187.

[316] Okubo, T. (1988). *J. Chem. Phys.* **88**, 6581–6584.

[317] Okubo, T. (1988). *J. Chem. Phys.* **88**, 2083–2086.

[318] Okubo, T. (1990). *J. Chem. Soc. Faraday Transact. 1* **86**, 151–156.

[319] Okubo, T. (1990). *J. ACS* **112**, 5420–5424.

[320] Okubo, T. (1987). *J. Chem. Soc. Faraday Transact. 1* **83**, 2487–2495.

[321] Goodwin, J.W., Smith, R.W. (1974). *Faraday Discuss. Chem. Soc.* **57**, 126–129.

[322] Buscal, R., Goodwin, J.W., Hawkins, M.W., Ottewill, R.H. (1982). *J. Chem. Soc. Faraday Transact. 1* **78**, 2873–2887.

[323] Goodwin, J.W., Gregory, T., Miles, J.A., Warren, B.C.H. (1984). *J. Colloid Interface Sci.* **97**, 488–495.

[324] Goodwin, J.W., Hughes, R.W., Patridge, S J., Zukoski, C.F. (1986). *J. Chem. Phys.* **85**, 559–566.

[325] Mitaku, S., Ohtsuki, T., Okano, K. (1980). *Jpn. J. Appl. Phys.* **19**, 439–448.

[326] Joanny, J.F. (1979). *J. Colloid Interface Sci.* **71**, 622–624.

[327] Fujita, H., Ametani, K. (1979). *Jpn. J. Appl. Phys.* **18**, 753–758.

[328] van Megen, W.J., Snook, I.K.Watts, R.O. (1980). *J. Colloid Interface Sci*. **77**, 131–137.

[329] Benzing, D.W., Russel, W.B. (1981). *J. Colloid Interface Sci.* **83**, 178–190.

[330] Joanicot, H.M., Jorand, M., Pieranski, P., Rothen, F. (1984). *J. Phys.* (Paris) **45**, 1413–1421.

[331] Okubo, T. (1988). *Ber. Bunsenges. Phys. Chem.* **92**, 504–511.

[332] Okubo, T. (1990). *J. Colloid Interface Sci.* **135**, 259–262.

[333] Matsumoto, T., Okubo, T. (1991). *J. Rheol.* **35**, 135–148.

[334] Okubo, T., Ishiki, H. (2001). *Colloid Polym. Sci.* **279**, 571–578.

[335] Okubo, T. (1990). *J. Chem. Soc. Faraday Transact. 1* **86**, 151–156.

[336] Okubo, T., Ishiki, H., Chiyoda, M., Yoshinaga, K. (2002). *Colloid Polym. Sci.* **280**, 446–453.

[337] Okubo, T. (1987). *J. Chem. Phys.* **87**, 6733–6739.

[338] Okubo, T. (1988). *Naturwissenschaften* **75**, 91–93.

[339] Okubo, T. (1988). *Colloid Polym. Sci.*, **266**, 1049–1057.

[340] Okubo, T. (1990). *J. Phys. Chem.* **94**, 1962–1966.

[341] Okubo, T. (1993). *Colloid Polym. Sci.* **271**, 873–883.

[342] Jorand, M., Koch, A.J., Rothen, F. (1986). *J. Phys.* **47**, 217–227.

[343] Okubo, T., Kimura, H., Hatta, T., Kawai, T. (2002). *Phys. Chem. Chem. Phys.* **4**, 2260–2263.

[344] Kimura, H., Okubo, T. (2002). *Colloid Polym. Sci.* **280**, 579–583.

[345] Okubo, T., Kimura, H., Kawai, T., Niimi, H. (2003). *Langmuir* **19**, 6014–6018.

[346] Kimura, H., Niimi, H., Tsuchida, A., Okubo, T. (2005). *Colloid Polym. Sci.* **283**, 1079–1084.

[347] Kimura, H., Nakayama, Y., Tsuchida, A., Okubo, T. (2007). *Colloids Surf. B: Biointerfaces* **56**, 236–240.

[348] Kimura, H., Sakurai, M., Sugiyama, T., Tsuchida, A., Okubo, T., Masuko, T. (2011). *Rheol. Acta* **50**, 159–168.

[349] Tomita, M., van de Ven, T.G.M. (1985). *J. Phys. Chem.* **89**, 1291–1296.

[350] Stoimenova, M., Okubo, T. (1995). *J. Colloid Interface Sci.* **176**, 267–271.

[351] Stoimenova, M., Dimitrov, V., Okubo, T. (1996). *J. Colloid Interface Sci.* **184**, 106–111.

[352] Okubo, T., Tsuchida, A., Okada, S., Kobata, S. (1998). *J. Colloid Interface Sci.* **199**, 83–91.

[353] Okubo, T., Tsuchida, A., Takahashi, T., Iwata, A. (1998). *J. Colloid Interface Sci.* **207**, 130–136.

[354] Okubo, T., Tsuchida, A., Iwata, A., Takahashi, T. (1999). *Colloids Surf.* **A148**, 87–94.

[355] Stoimenova, M., Alekov, A., Okubo, T. (1999). *Colloids Surf.* **A148**, 83–86.

[356] Stoimenova, M., Okubo, T. (1999). In Schwarz, J.A., Contescu, C.I. (eds.), *Surfaces of Nanoparticles and Porous Materials.* Marcel Dekker, New York, pp. 103–124.

[357] Okubo, T., Tsuchida, A., Takahashi, T., Iwata, A., Okada, S., Kobata, S., Kobayashi, K., Okubo, T. (1999). *Langmuir* **15**, 4203–4207.

[358] Okubo, T. (2003). *Progress Colloid Polym. Sci.* **124**, 112–115.

[359] Tsuchida, A., Shibata, K., Okubo, T. (2003). *Colloid Polym. Sci.* **281**, 1104–1108.

[360] Shibata, K., Kimura, H., Tsuchida, A., Okubo, T., Sato, S., Yoshinaga, K. (2006). *Colloid Polym. Sci.* **284**, 372–379.

[361] Tsuchida, A., Okubo, T. (2006). In Stoylov, S., Stoimenova, M. (eds.), *Molecular and Colloidal Electro-optics*, CRC Press, pp. 447–456.

[362] Shibata, K., Yamamoto, T., Kurita, M., Kimura, H., Tsuchida, A., Okubo, T. (2006). *Colloid Polym. Sci.* **284**, 688–693.

[363] Shibata, K., Kimura, H., Tsuchida, A., Okubo, T. (2006). *Colloid Polym. Sci.* **285**, 127–133.

[364] Fujita, H., Ametani, K. (1979). *Jpn. J. Appl. Phys.* **11**, 1907–1917.

[365] Trau, M., Saville, D.A., Aksay, I.A. (1996). *Science* **272**, 706–709.

[366] van der Zande, B.M.I., Koper, G.J.M., Lekkerkerker, H.N.W. (1999). *J. Phys. Chem. B* **103**, 5754–5760.

[367] Gong, T., Marr, D.W.M. (2001). *Langmuir* **17**, 2301–2304.

[368] Fujiwara, M., Oki, E., Hamada, M., Tanimoto, Y., Mukuda, I., Shimomura, Y. (2001). *J. Phys. Chem. A* **105**, 4383–4386.

[369] Gu, Z.Z., Fujishima, A., Sato, O. (2000). *J. ACS* **122**, 12387–12388.

[370] Okubo, T. (1988). *J. Chem. Soc. Faraday Transact. 1* **84**, 1949–1959.

[371] Clark, N.A., Hurd, A.J., Ackerson, B.J. (1979). *Nature* **281**, 57–60.

[372] Tomita, M., van de Ven, T.G.K. (1984). *J. Colloid Interface Sci.* **99**, 374–386.

[373] Ackerson, B.J., Hayter, J.B., Clark, N.A., Cotter, L. (1986). *J. Chem. Phys.* **84**, 2344–2349.

[374] Weitz, D.A., Dozier, W.D., Chaikin, P.M. (1985). *J. Phys. Colloq.* **46**, 257–268.

[375] Di Meglio, J.M., Weitz, D.A., Chaikin, P.M. (1987). *Phys. Rev. Lett.* **58**, 136–139.

[376] Ackerson, B.J., Clark, N.A. (1983). *Physica* **A118**, 221–249.

[377] Ackerson, B.J., Clark, N.A. (1984). *Phys. Rev*. **A30**, 906–918.

[378] Okubo, T. (1988). *J. Chem. Soc. Faraday Transact. 1* **84**, 1171–1180.

[379] Hoffman, R.L. (1987). *Future Directions in Polymer Colloids*. Martinus Nijhoff, Dordrecht, pp. 151–165.

[380] Mathis, C., Bossis, G., Brady, J.F. (1988). *Progress Colloid Polym. Sci.* **76**, 16–19

[381] Lindner, P., Markovic, I., Oberthur, R.C., Ottewill, R.H., Rennie, A.R. (1988). *Progress Colloid Polym. Sci.* **76**, 47–50.

[382] Bossis, G., Brady, J.F., Mathis, C. (1988). *J. Colloid Interface Sci.* **126**, 1–15.

[383] Mathis, C., Bossis, G., Brady, J.F. (1988). *J. Colloid Interface Sci.* **126**, 16–25.

[384] Okubo, T. (1987). *J. Chem. Soc. Faraday Transact. 1* **83**, 2497–2504.

[385] Cornell, R.M., Goodwin, J.W., Ottewill, R.H. (1979). *J. Colloid Interface Sci.* **71**, 254–266.

[386] Senff, H., Richtering, W. (1999). *J. Chem. Phys.* **111**, 1705–1711.

[387] Hu, Z., Lu, X., Gao, J. (2001). *Adv. Mater.* **13**, 1708–1712.

[388] Okubo, T., Hase, H., Kimura, H., Kokufuta, E. (2002). *Langmuir* **18**, 6783–6788.

[389] Okubo, T., Mizutani, T., Okamoto, J., Kimura, K., Tsuchida, A., Tauer, K., Khrenov, V., Kawaguchi, H., Tsuji, S. (2006). *Colloid Polym.* **285**, 351–358.

[390] Okubo, T., Suzuki, D., Yamagata, T., Katsuno, A., Sakurai, M., Kimura, H., Tsuchida, A. (2011). *Colloid Polym. Sci.* **289**, 291–299.

[391] Okubo, T., Suzuki, D., Yamagata, T., Horigome, K., Shibata, K., Tsuchida, A. *Colloid Polym. Sci.* **289**, 1273–1281.

[392] Suzuki, D., Horigome, K., Yamagata, T., Shibata, K., Tsuchida, A., Okubo, T. (2011). *Colloid Polym. Sci.* **289**, 1799–1808.

[393] Suzuki, D., Yamagata, T., Horigome, K., Shibata, K., Tsuchida, A., Okubo, T. (2012). *Colloid Polym.* **290**, 107–117.

[394] Okubo, T., Suzuki, D., Shibata, K., Tsuchida, A. (2012). *Colloid Polym. Sci.* **290**, 1403–1412.

[395] Okubo, T., Suzuki, D., Tsuchida, A. (2013). *Colloid Polym. Sci.* **291**, 661–668.

[396] Okubo, T., Suzuki, D. (2013). *Colloid Polym. Sci.* **291**, 1721–1727.

[397] Zhu, J., Li, M., Reger, R., Meyer, W., Ottewill, R.H., STS-73 Space Shuttle Crew, Russel, W.B., Chaikin, P.M. (1997). *Nature* **387**, 883–885.

[398] Okubo, T., Tsuchida, A., Okuda, T., Fujitsuna, K., Ishikawa, M., Morita, T., Tada, T. (1999). *Colloids Surf.* **A160**, 311–320.

[399] Okubo, T., Tsuchida, A., Kobayashi, K., Kuno, A., Morita, T., Fujitsuna, M., Kohno, Y. (1999). *Colloid Polym. Sci.* **277**, 474–478.

[400] Tsuchida, A., Taguchi, K., Takyo, E., Yoshimi, H., Kiriyama, S., Okubo, T., Ishikawa, M. (2000). *Colloid Polym. Sci.* **278**, 872–877.

[401] Okubo, T., Tsuchida, A. (2002). *Ann. NY Acad. Sci.* **974**, 164–175.

[402] Okubo, T., Tsuchida, A., Takahashi, S., Taguchi, K., Ishikawa, M. (2000). *Colloid Polym. Sci.* **278**, 202–210.

[403] Bartlett, P., Ottewill, R.H. (1994). *Adv. Colloid Interface Sci.* **50**, 39–50.

[404] Schuller, H. (1967). *Kolloid Z. Z. Polym*. **216/217**, 380–383.

[405] Sheppard, E., Tcheurekdjian, N. (1968). *J. Colloid Interface Sci.* **28**, 481–486.

[406] Aveyard, R., Clint, J.H. (1995). *J. Chem. Soc. Faraday Transact.* **91**, 2681–2697.

[407] Aveyard, R., Binks, B.P., Fletcher, P.D.I., Rutherford, C.E. (1994). *J. Dispers. Sci. Technol.* **15**, 251–271.

[408] Aveyard, R., Cooper, P., Fletcher, P.D.I., Rutherford, C.E. (1993). *Langmuir* **9**, 604–613.

[409] Aveyard, R., Clint, J.H., Nees, D., Paunov, N. (2000). *Langmuir* **16**, 1969–1979.

[410] Hurd, A.J. (1985). *J. Phys. A* **8**, L1055–L1060.

[411] Goulding, D., Hansen, J.P. (1998). *Mol. Phys.* **95**, 649–655.

[412] Glaser, M.A., Clark, N.A. (1990). *Phys. Rev. A* **41**, 4585–4588.

[413] Weider, T., Glaser, M.A., Hanley, H.J.M., Clark, N.A. (1993). *Phys. Rev. B* **47**, 5622–5628.

[414] Pouligny, B., Malzbender, R., Ryan, P., Clark, N.A. (1990). *Phys. Rev. B* **42**, 988–991.

[415] Murray, C.A., van Winkle, D.H. (1987). *Phys. Rev. Lett.* **58**, 1200–1203.

[416] Trau, M., Saville, D.A., Aksay, I.A. (1997). *Langumuir* **13**, 6375–6381.

[417] Solomentsev, Y., Bohmer, M., Anderson, J.L. (1997). *Langmuir* **13**, 6058–6068.

[418] Hong, S., Higuchi, T., Sugimori, H., Kaneko, T., Abetz, V., Takahara, A., Jinnai, H. (2012). *Polym. J.* **44**, 567–572.

[419] Naidoo, K.J., Schnitker, J. (1994). *J. Chem. Phys.* **100**, 3114–3121.

[420] Mc Phedran, R.C., Nicorovici, N.A., Mc Kenzie, D.R., Botten, L.C., Parker, A.R., Rouse, G.W. (2001). *Austral. J. Chem.* **54**, 241–244.

[421] Welch, V.C. (2005). In Kinoshita, S., Yoshioka, S. (eds.), *Structural Colors in Biological Systems. Principles and Applications.* Osaka Univ. Press, pp. 53–71.

[422] Yoshioka, Y., Kinoshita, S. (2002). *Forma* **17**, 169–153.

[423] Kinoshita, S., Yoshioka, S. (2005). In Kinoshita, S., Yoshioka, S. (eds.), *Structural Colors in Biological Systems. Principles and Applications.* Osaka Univ. Press, pp. 113–140.

[424] Kinoshita, S., Yoshioka, S. (2005). In Kinoshita, S., Yoshioka, S. (eds.), *Structural Colors in Biological Systems. Principles and Applications*. Osaka Univ. Press, pp. 141–152.

[425] Hariyama, T., Hironaka, M., Horiguchi, H., Stavenga, D.G. (2005). In Kinoshita, S., Yoshioka, S. (eds.), *Structural Colors in Biological Systems. Principles and Applications*. Osaka Univ. Press, pp. 153–176.

[426] Kasukawa, H., Oshima, N. (1987). *Pigment Cell Res*. **1**, 152–157.

[427] Fujii, R., Kasukawa, H., Miyaji, K., Oshima, N. (1989). *Zool. Sci.* **6**, 477–486.

[428] Ueno, K., Inaba, A., Sano, Y., Kondoh, M., Watanabe, M. (2009). *Chem. Commun.* **2009**, 3603–3605.

[429] Ueno, K., Sano, Y., Inaba, A., Kondoh, M., Watanabe, M. (2010). *J. Phys. Chem. B* **114**, 13095–13103.

[430] Ueno, K., Inaba, A., Ueki, T., Kondoh, M., Watanabe, M. (2010). *Langmuir* **26**, 18031–18038.

[431] Ueno, K., Watanabe, M. (2011). *Langmuir* **27**, 9105–9115.

[432] Kalsin, A.M., Fialkowski, M., Paszewski, M., Smoukov, S.K., Bishop, K.J.M., Grzybowski, B.A., Schatz, G.C. (2006). *Science* **312**, 420–424.

[433] Kalsin, A.M., Pinchuk, A.O., Smoukov, S.K., Paszewski, M., Schatz, G.C., Grzybowski, B.A. (2006). *Nano Lett.* **6**, 1896–1903.

[434] Kalsin, A.M., Kowalczyk, B., Smoukov, S.K., Klajn, R., Grzybowski, B.A. (2006). *J. ACS* **128**, 15046–15047.

[435] Friberg, S.E., Al-Bawab, A., Bozeya, A., Aikens, P.A. (2009). *J. Colloid Interface Sci.* **336**, 345–351.

[436] Watanabe, J., Okoshi, K., Sano, N., Edo, S. (2005). In Kinoshita, S., Yoshioka, S. (eds.), *Structural Colors in Biological Systems. Principles and Applications*. Osaka Univ. Press, pp. 319–327.

[437] Fortov, V.E., Khrapak, A.G., Khrapak, S.A., Molotkov, V.I., Petrov, O.F. (2004). *Phys. Uspekhi* **47**, 447–492.

[438] Leunissen, M.E., van Blaaderen, A., Hollingworth, A.D., Sullivan, M.T. (2007). *Proc. Natl. Acad. Sci. USA* **104**, 2585–2590.

[439] Leunissen, M.E., Zwanikken, J., van Roij, R., Chaikin, P.M., van Blaaderen, A. (2007). *Phys. Chem. Chem. Phys.* **9**, 6405–6414.

[440] Zwanikken, J., van Roij, R. (2007). *Phys. Rev. Lett.* **99**, 178301.

[441] Born, M. (1920). *Z. Phys.* **1**, 45–48.

[442] Verwey, E.J.W., Niessen, K.F. (1939). *Phil. Mag.* **28**, 435–446.

[443] Israelachvili, J.N. (1992). *Intermolecular and Surface Forces*, 2nd ed. Academic Press, London.

[444] Sugimura, M., Okubo, T., Ise, N., Yokoyama, S. (1984). *J. AC S* **106**, 5069–5072.

[445] Rohrsetzer, S., Kovacs, P., Nagy, M. (1986). *Colloid Polym. Sci.*, **264**, 812–816.

[446] Costello, B.A., Kim, I.T., Luckham, P.F. (1990). *J. Chem. Soc. Faraday Transact.* **86**, 3693–3694.

[447] Takano, K., Hachisu, S. (1977). *J. Chem. Phys.* **67**, 2604–2608.

[448] Alder, B.J., Wainwright, T.E. (1957). *J. Chem. Phys.* **27**, 1208–1209.

[449] Alder, B.J., Hoover, W.G., Toung, D.A.Y. (1968). *J. Chem. Phys.* **49**, 3688–3696.

[450] Hoover, W.G., Gray, S.C., Johnson, K.W. (1971). *J. Chem. Phys.* **55**, 1128–1136.

[451] Hopkins, A.J., Woodcook, L.V. (1990). *J. Chem. Soc. Faraday Transact.* **86**, 3419–3428.

[452] Schwan, H.P., Schwarz, G., Macznk, J., Pauly, H. (1962). *J. Phys. Chem.* **66**, 2626–2635.

[453] De Lacey, E.H.B., White, L.R. (1981). *J. Chem. Soc. Faraday Transact. 2* **77**, 2007–2039.

[454] Rosen, L.R., Saville, D.A. (1991). *Langmuir* **7**, 36–42.

[455] Nakagaki, M., Heller, W. (1956). *J. Appl. Phys.* **27**, 975–979.

[456] Robillard, F., Patistsas, A.J. (1973). *Can. J. Chem.* **51**, 2395–2401.

[457] Robillard, F., Patistsas, A.J. (1974). *Can. J. Chem.* **52**, 1571–1582.

[458] Champion, J.V., Meeten, G.H., Senior, M.J. (1978). *J. Chem. Soc. Faraday Transact. 2* **74**, 1319–1329.

[459] Champion, J.V., Meeten, G.H., Senior, M.J. (1979). *J. Colloid Interface Sci.* **72**, 471–482.

[460] Meeten, G.H. (1980). *J. Colloid Interface Sci.* **77**, 1–5.

[461] Sano, Y., Nakagaki, M. (1984). *J. Phys. Chem.* **88**, 95–99.

[462] Okubo, T. (1990). *J. Colloid Interface Sci.* **135**, 294–296.

[463] Jethmalani, J.M., Ford, W.T., Beaucage, G. (1997). *Langmuir* **13**, 3338–3344.

[464] Yoshinaga, K., Mouri, E., Ogawa, J., Nakai, A., Ishii, M., Nakamura, H. (2004). *Colloid Polym. Sci.* **283**, 340–342.

[465] Xia, Y., Rogers, J.A., Paul, K.E., Whitesides, G.M. (1999). *Chem. Rev.* **99**, 1823–1848.

[466] Smith, H.I. (2001). *Physica E* **11**, 104–109.

[467] Fischer, U.C., Zingsheim, H.P. (1981). *J. Vacuum Sci. Technol.* **19**, 881–885.

[468] Deckman, H.W., Dunsmuir, J.H. (1983). *J. Vacuum Sci. Technol. B* **1**, 1109–1112.

[469] Deckman, H.W., Dunsmuir, J.H., Garoff, S., McHenry, J.A., Pfeiffer, D.G. (1988). *J. Vacuum Sci. Technol.* **6**, 333–336.

[470] Hayness, C.L., Van Duyne, R.P. (2001). *J. Phys. Chem. B* **105**, 5599–5611.

[471] Ingert, D., Pileni, M.P. (2005). In Pileni M.P. (ed.), *Nanocrystals Forming Mesoscopic Structures*. Wiley-VCH, Weinheim, pp. 295–305.

[472] Choi, F.G., Jang, S.G., Kim, S., Lee, E., Han, C.S., Yang, S.M. (2006). *Adv. Funct. Mater.* **16**, 33–40.

[473] Yablonovitch, E., Gmitler, T.J., Meade, R.D., Rapper, A.M., Brammer, K.D., Joannopoulos, J.D. (1991). *Phys. Rev. Lett.* **67**, 3380–3383.

[474] Pradhan, R.D., Bloodgood, J.A., Watson, G.H. (1997). *Phys. Rev.* **B55**, 9503–9507.

[475] Wijnhoven, J.E.G., Vos, W.L. (1998). *Science* **281**, 802–804.

[476] Zakhidov, A.A., Baughman, R.H., Igbal, Z., Culi, C., Khayrullin, I., Dantas, S.O., Marti, J., Ralchenko, V.G. (1998). *Science* **282**, 897–901.

[477] Levi, B.G. (1999). *Phys. Today* **52**, 17–18.

[478] Megen, M., Wijnhoven, J.E.G.J., Lagendijk, A., Vos, W.L. (1999). *J. Opt. Soc. Am.* **B16**, 1403–1408.

[479] Park, S.H., Xia, Y. (1999). *Langmuir* **15**, 266–273.

[480] Debord, J.D., Lyon, L.A. (2000). *J. Phys. Chem.* **B104**, 6327–6331.

[481] Freemantle, M. (1998). *Chem. Eng. News*, **76**, 32–37.

[482] Shim, M., Wang, C., Guyot-Sionnest, P. (2001). *J. Phys. Chem.* **B105**, 2369–2373.

[483] Yang, S.M., Ozin, G.A. (2000). *Chem. Commun.* **2000**, 2507–2508.

[484] Yin, Y., Lu, Y., Gates, B., Xia, Y. (2001). *J. ACS* **123**, 8718–8729.

[485] Yin, Y., Xia, Y. (2002). *Adv. Mater.* **14**, 605–608.

[486] Matsuo, S., Fujine, T., Fukuda, K., Juodkazis, S., Misawa, H. (2003). *Appl. Phys. Lett.* **82**, 4283–4285.

[487] Xu, X., Asher, S.A. (2004). *J. ACS* **126**, 7940–7945.

[488] Wen, W., Zhang, L., Sheng, P. (2000). *Phys. Rev. Lett.* **85**, 5464–5467.

[489] Saad, Y., Golosovsky, T., Ji, M., Davidov, D., Avni, Y., Frenkel, A. (2001). *Opt. Mater.* **17**, 1–6.

[490] Davidson, P., Gabriel, J.C.P. (2006). In Pileni, M.P. (ed.), *Nanocrystals Forming Mesoscopic Structures*. Wiley-VCH, Weinheim, pp. 173–212.

[491] Fudouzi, H., Sawada, T. (2006). *Langmuir* **22**, 1365–1368.

[492] Furumi, S., Fudouzi, H., Sawada, T. (2012). *J. Mater. Chem.* **22**, 21519–21528.

[493] van Blaaderen, A., Ruel, R., Wiltzius, P. (1997). *Nature* **385**, 321–324.

[494] Hines, M.A.Guyot-Sionnest, P. (1996). *J. Phys. Chem.* **100**, 468–471.

29

DIELECTRIC PROPERTIES OF BIOLOGICAL MACROMOLECULES AND BIOMOLECULE–WATER INTERFACES

Brandon Campbell, Lin Li, and Emil Alexov

Computational Biophysics and Bioinformatics, Physics Department, Clemson University, Clemson, SC 29634, USA

29.1 BACKGROUND

In order to understand the electrostatic and dielectric properties of biological systems, one should take into account that at normal conditions all biological macromolecules exist in water and are surrounded by other macromolecules, ions, and ligands [1] (Fig. 29.1a) [2, 3]. Such a complex system is characterized by the constant motion of the entities within it as they interact with each other and undergo collisions in the crowded environment of the cell. Some of these entities, such as ions, are objects that have a spherically symmetric shape and do not change during a considered reaction. Others, such as water molecules, do not greatly change their shape, but are quite mobile and change both their position and orientation. Finally, macromolecules and ligands are complex objects made of many atoms, which, despite being chemically connected, are not rigid but constantly undergo conformational changes. Taking all of these together, the system made of macromolecules and water, if considered at the atomic level of detail, exhibits an enormous degree of freedom. Typically explicit modeling of such systems is done via molecular dynamics simulations [4, 5]. However, the explicit sampling of all essential states, those required for a given process, may not be an easy task or may not even be possible for systems consisting of millions and more atoms.

To reduce the complexity of explicit modeling, one can adopt an implicit approach and model the biological macromolecules and water molecules via continuum electrostatics [6] (Fig. 29.1b) [2, 3]. However, this should be done without losing much of the detail of the explicit approaches, which, in turn, requires description of dielectric properties via a function that mimics the effects of explicit atom considerations. The difficulties stem from several sources. Macromolecules and ligands are very inhomogeneous. While they are typically very polar, they may not be very polarizable because of constraints posed by the chemical bonds and compactness of the 3D structure. In addition, they constantly sample different conformation states, and thus affect the interior and the molecular surface of the system. The water phase is equally complex because water molecules possess the ability to propagate inside macromolecules [7] or bind tightly to the molecular surface [8, 9]. The ability of water molecules to form hydrogen bonds with the atoms of macromolecules [10], especially in cavities and macromolecular interiors, greatly restricts their ability to reorient and respond to the local electrostatic field, thus affecting their dielectric properties. Ions can bind to molecular surfaces or even inside the macromolecule and drastically change the local electrostatic field [11]. In this chapter, we describe these specific effects reflecting the complex nature of macromolecule–water systems and provide conceptual approaches to capture these atomic details via continuous electrostatics and structure-based dielectric functions.

Encyclopedia of Biocolloid and Biointerface Science, Volume 1, First Edition. Edited by Hiroyuki Ohshima.
© 2016 John Wiley & Sons, Inc. Published 2016 by John Wiley & Sons, Inc.

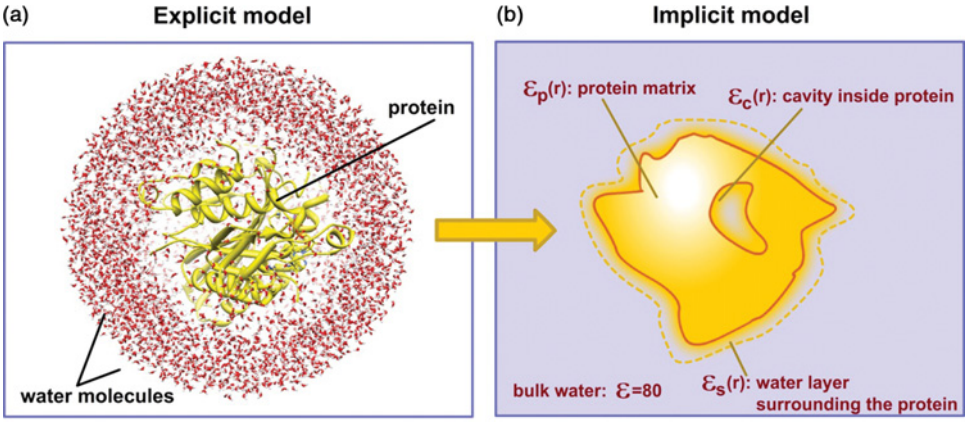


FIGURE 29.1 Solvent models: (a) explicit solvent model of human kinesin Kif7 (PDB ID 2XT3) within a water environment; (b) implicit solvent model of the same molecule as in (a). [Molecular graphics and analyses were performed with the UCSF Chimera package. Chimera is developed by the Resource for Biocomputing, Visualization, and Informatics at the University of California, San Francisco (supported by NIGMS P41-GM103311).]

29.2 MACROMOLECULAR DYNAMICS AND ITS EFFECT ON THE MACROMOLECULAR INTERIOR AND MOLECULAR SURFACE

Biological macromolecules are flexible inhomogeneous objects. The intrinsic motions can be grouped into several distinctive categories: (1) thermal fluctuations of atoms, amino or nucleic acids, or entire domains; (b) conformational changes induced by a function (such as binding a ligand or undergoing catalytic reaction); (3) intrinsically disordered macromolecules; and (4) conformational changes caused by a change of the environment such as pH or salt concentration. Below we briefly outline these effects in separate sections.

29.2.1 Thermal Fluctuations of Atoms, Amino or Nucleic Acids, or Entire Domains

At nonzero temperature all atoms fluctuate around their equilibrium positions. Most biological macromolecules function at room temperature (293.15 K), and at this temperature thermal fluctuations can be on various scales ranging from negligibly small changes [12] to relatively large-scale [13] structural changes [14, 15]. Small structural fluctuations of individual atoms in a highly packed macromolecular interior, perhaps, have very little effect on the electrostatics and the corresponding dielectric constant. This statement is reinforced by the fact that most of the atoms in the macromolecular core are apolar, carrying no or little partial charge, and thus have no direct effect to the local electrostatic field. In contrast, if these atoms are located at the molecular surface, they are typically polar, carrying significant partial charge. Therefore, their fluctuations affect both the local electrostatic field at and nearby the molecular surface and at the same time change the geometry of the macromolecule–water boundary, altering the interactions with individual water molecules [16].

Atoms within a macromolecule are connected with their neighbors via chemical bonds and other nonbonded interactions. Thus any structural fluctuation of a given atom, in principle, should affect the other atoms within the macromolecule. This connectivity results in collective motions involving groups of atoms (amino or nucleic acids) or entire structural domains [17–20]. Obviously these structural fluctuations will have a greater effect on the macromolecular interior and macromolecular surface than will the fluctuation of a single atom. The structural changes can be as large as almost doubling the original dimension of the macromolecule [21]. However, the density of the macromolecular interior is typically affected much less than the molecular surface (i.e., the density remains almost unchanged), but large structural domains change their mutual positions greatly affecting the shape of the molecular surface. If such an ensemble of structures is about to be modeled, one should consider that the molecular surface (and to a less extent the molecular interior) cannot be described by a simple geometric function.

29.2.2 Conformational Changes Induced by Macromolecular Function

Any macromolecule interacts with something else, may it be a small substrate, a ligand, a membrane, or another macromolecule [22]. Such interactions are expected to affect the local and global conformation of the interacting partners as indicated by numerous experiments [23–26]. A particular example are enzymes that bind their ligand in a typically well-defined active-site pocket, which, in turn, closes after recognition to provide a supporting environment for the

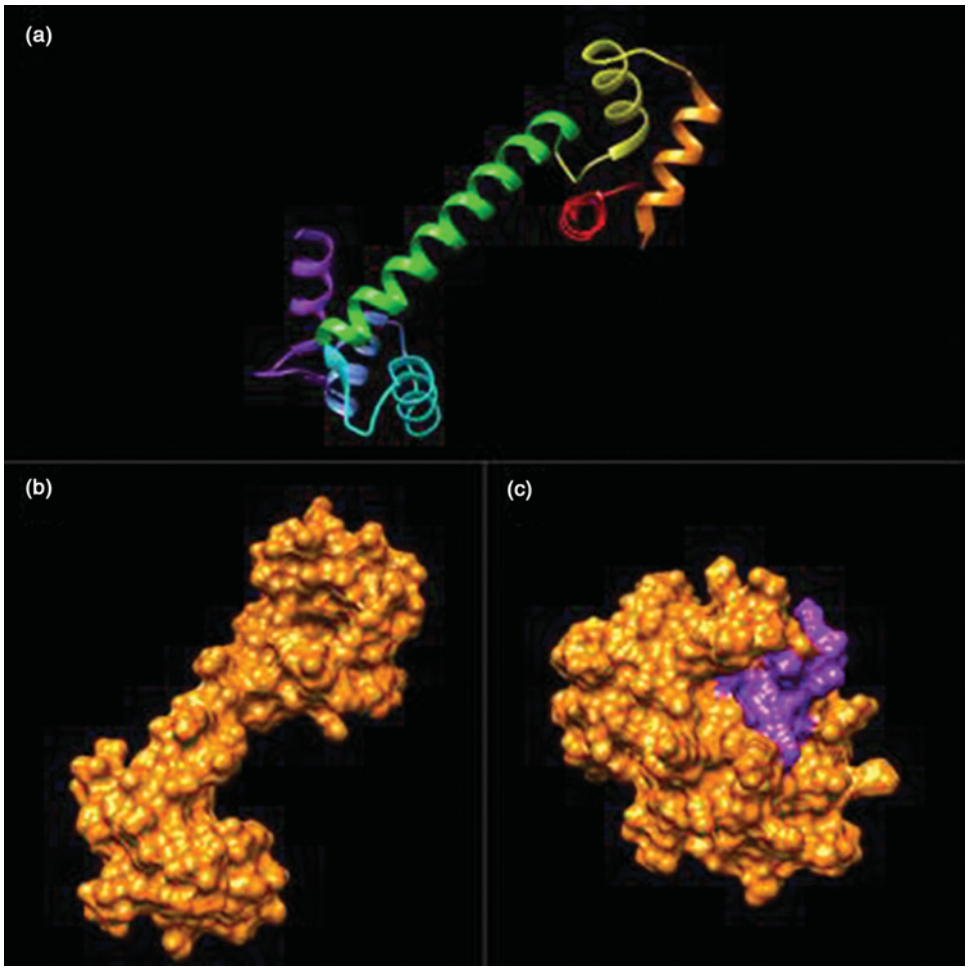


FIGURE 29.2 (a) Ribbon structure of apo calmodulin (PDB ID 4BW7), colored to illustrate the various tertiary structural components of the protein; (b) molecular surface of apo state of calmodulin; (c) structural changes of calmodulin (PDB ID 2LGF) after it has complexed with the peptide L-selectin, a glycoprotein receptor. [Molecular graphics and analyses were performed with the UCSF Chimera package. Chimera is developed by the Resource for Biocomputing, Visualization, and Informatics at the University of California, San Francisco (supported by NIGMS P41-GM103311).]

corresponding reaction [27–29]. Such cases represent the class of reactions that affect the local macromolecular interior and macromolecular surface, but have little or no effect on the rest of the macromolecular–water system.

On the opposite end of the spectrum are so-termed allosteric reactions, reactions that are promoted by the binding of a ligand at a distance from the active-site region [30, 31]. There are two basic explanations for the uniqueness of such reactions: (1) the reaction involves changes of a significant part of the molecular surface, not just the region around the active site; and (2) the reaction causes the signal to propagate from the allosteric site to the active site, and this involves a chain of conformational changes throughout the entire macromolecule.

Perhaps the most extreme effects are observed in reactions involving the rearrangement of structural domains. A typical example is calmodulin (Fig. 29.2a) [3, 32], which in the apo form (before the reaction) adopts an extended conformation (Fig. 29.2) [3, 32], but after binding the cognate peptide, undergoes a large conformational change to adopt a compact form (Fig. 29.2c) [3, 33]. In terms of ensemble modeling of electrostatic and dielectric properties of such a diverse conformational space, one should develop a specific approach to account for the population of different conformational states [34].

29.2.3 Intrinsically Disordered Macromolecules

In parallel with conformational changes occurring as a function of time (during the corresponding biological reaction or experimental duration), many macromolecules exist as a multitude of conformations. Typically such macromolecules

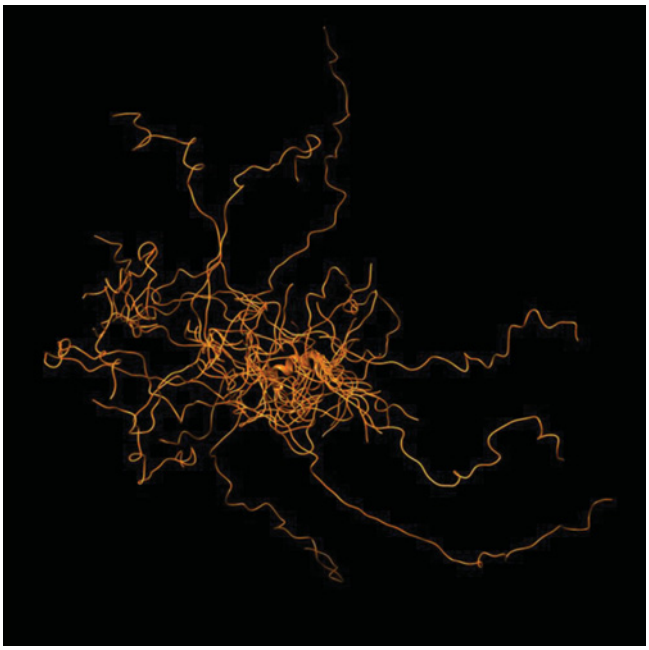


FIGURE 29.3 Image of the intrinsically disordered phosphoprotein TSP9. [Molecular graphics and analyses were performed with the UCSF Chimera package. Chimera is developed by the Resource for Biocomputing, Visualization, and Informatics at the University of California, San Francisco (supported by NIGMS P41-GM103311).]

are referred to as *intrinsically disordered molecules* [35–37]. The disorder may be local, involving a loop or small structural segment, or the entire macromolecule may exist in numerous alternative conformations (Fig. 29.3) [3, 38]. Such phenomena affect both the molecular surface definition and the properties of the molecular interior. Typically the macromolecule or parts of the macromolecule are disordered before the reaction, which is thought of as the macromolecule possessing the ability to respond to different ligands and adopt appropriate configurations for each particular partner [39–42]. However, opposite cases do exist where parts of the macromolecular structure become unstructured after the reaction or binding [43].

29.2.4 Conformational Changes Caused by a Change in Environment Due to pH or Salt Concentration

Biological macromolecules are located in different subcellular compartments and different organs/tissues, with each of them having characteristic pH and salt concentrations [44–46]. Their pH optimum of stability is correlated with the pH optimum of the corresponding reaction [47]. Thus the macromolecules sense different pH and salt concentrations when being transferred from one compartment to another or simply because the reaction involves changes of the environment. The effect of pH can be relatively small, inducing local conformational changes caused by protonation or deprotonation of a particular titratable group. Such conformational changes typically do not affect the macromolecular interior and have a small effect on the molecular surface as well. However, exceptions do occur as indicated in a recent study on coupling between local conformational fluctuations, ligand binding, and structural transitions in staphylococcal nuclease [48]. Protein–protein interactions can be greatly affected by the local pH [49–51] as well as protein stability [52, 53]. At the same time, pH- induced changes can be very large, changing the equilibrium between monomeric and dimeric states of macromolecules [54–56]. Perhaps the most drastic change is expected to occur when the entire structure of a macromolecule changes shape from one suitable for the water phase to a shape suitable for insertion into a biological membrane as in the case of the CLIC protein family [57, 58]. Obviously the effect on the electrostatics of such large-scale conformational changes cannot be mimicked with any dielectric function.

29.3 WATER MOLECULE DYNAMICS AND ITS EFFECT ON PROTEIN INTERIOR AND MOLECULAR SURFACE

The water phase, which consists of indistinguishable water molecules, is sometimes considered the simplest phase to model electrostatically, but may also be the most complicated. Water molecules in the liquid phase are quite free to diffuse and to change their orientation [59]. These changes in bulk water are reduced because of the water molecule's tendency to form hydrogen bonds with its neighbors, resulting in water clusters. However, these clusters are not static, since water molecules frequently exchange their hydrogen bonds and change their affiliation and orientation. The situation is completely different at the macromolecule–water interface. Depending on the physical nature of the macromolecular surface, mostly hydrophilic or partially hydrophobic, the ability of water molecules to diffuse and to reorient will be minimally or drastically affected. In addition, frequently the water molecules at the molecular surface can be involved in specific interactions, mostly via hydrogen bonds, with atoms of the macromolecule, thus further affecting their flexibility [60]. The most significant change of bulk water properties happens when water molecules are buried inside the macromolecular interior [61]. Such waters, if their residential time is long enough, are referred to as *structured waters* [62–64]. There are also many experimentally documented cases of structured waters being crucial for various reactions. The examples include *proton wires*, where chains of structured waters serve as a conduit for proton transport [65–68], water-mediated reactions [69, 70], structure waters acting as a *placeholders* for ligands in apo conformations [71–73], and cases where structured waters are an inherent part of the protein structure and aid in the stability [74–76] or flexibility [77, 78] of the proteins.

29.4 MODELING MACROMOLECULAR INTERIOR AND MACROMOLECULE–WATER INTERFACES

Typically the electrostatics, the potential distribution or polar solvation energy, in a system consisting of biological macromolecules and water is calculated via the Poisson–Boltzmann equation [79–81] or generalized Born approaches [82, 83]. Many methods and tools exist for modeling electrostatics in biological systems [84–90]. At the first level of approximation, the space of the system must be divided into two (or three) regions with distinctive dielectric properties. These regions are divided into the space occupied by the macromolecule by the rest of the space occupied by the water phase. While this is quite a straightforward approach, it faces a major challenge in determining the molecular surface of the macromolecule. Various methods exist for building the boundary between a macromolecule and water. The simplest and perhaps most illustrative approach is the van der Waals (vdW) molecular surface method. In this approach the molecular boundary is delivered as a surface made from vdW spheres, representing atoms within the macromolecule [91]. The radius of these spheres is force field-dependent and the aggregate of these spheres represents the molecular boundary, or vdW surface (vdWS). While this approach is simple, it suffers from the presence of many small cavities at the surface created by neighboring spheres. These cavities cannot be accessed by water molecules.

A second approach that attempts to alleviate these artificial cavities is the *solvent accessible surface* (SAS) approach, which utilizes a rolling spherical probe that travels across the vdWS. The radius of the probe corresponds to the average radius of a water molecule and the center of the probe traces out the molecular surface. Another similar approach to SAS is the *solvent excluded surface* (SES) method, which uses probes that roll across a molecular boundary [92]. In this approach the molecular boundary is determined from the volume difference calculated between a probe accessible to the molecular boundary and one that is inaccessible. While these approaches are considered simple, there are many other approaches that require more complicated mathematical procedures for determining the molecular surface, such as the *blobby* surface, *skin* surface, and methods that map the molecular surface onto a virtual three-dimensional grid for calculations [93]. Each of the various methods has its benefits and deficiencies, and often the best choice may lie in the intended use, either visualization or calculation.

29.5 ROLE OF IONS

Typically ions are considered to be part of the water phase, which provides screening of electrostatic interactions via redistribution of their local density [94]. However, ions can bind to the macromolecular surface or macromolecular interior and thus drastically affect the local electrostatic potential [95, 96]. If the ion position can be detected experimentally [97, 98], then the ion can be treated as a part of the macromolecular structure and no further considerations are needed. However, especially for surface-bound ions, the positions frequently cannot be experimentally resolved and have to be predicted [99, 100].

29.6 DIELECTRIC PROPERTIES OF BIOLOGICAL MACROMOLECULES AND BIOMOLECULE–WATER INTERFACES

In this section we describe approaches to account for all or some of these effects occurring at the atomic level of detail into the modeling of electrostatic potential using a single structure. Three important and distinctively different regions of space should be considered: (1) the water molecules within the immediate water shell surrounding the protein, (2) the cavities inside the protein, and (3) the inhomogeneous protein matrix [16].

As mentioned previously, the water molecules in the immediate vicinity of the protein interface may not be as mobile and flexible [101, 102] as the water molecules in the bulk phase [103], and the molecular surface may undergo constant changes. Obviously the dielectric properties of these water molecules cannot be modeled with the bulk dielectric constant of 80. Perhaps a lower dielectric constant should be used. In addition, the dielectric constant should depend on the topology of the protein surface; for instance, the immediate water shell around a convex surface should be assigned a lower dielectric constant (water reorganization is more restricted) than for cases over concave protein surfaces [104, 105]. The extra complexity comes from the structural changes occurring at the molecular surface, which from an ensemble-averaged perspective, should result in a smooth transition from macromolecular to water phases. Such a smooth transition can be captured via a smooth dielectric function [16], rather than by a sharp dielectric boundary. The larger the structural fluctuations are, the smoother the macromolecule–water transition should be. In this regard, unstructured macromolecules or macromolecules undergoing extremely large conformational changes, such as calmodulin, should be approximated with a custom-designed dielectric function that depends on the overall shape of the transition.

Additional complexity arises when describing dielectric properties of a macromolecule–water interface due to the treatment of ions, especially surface- bound ions. While various approaches of the modified Poisson–Boltzmann equation do exist in order to account for the finite size of ions and other physical effects, the best treatment is to include ions explicitly when modeling by making ions part of the macromolecular structure [100]. Such an approach does not require modification of the dielectric function.

The second region requiring special attention involves the cavities inside macromolecules. The water molecules in small cavities are likewise small in number, in some cases just a single water molecule, and typically their mobility is highly restricted. In contrast, in large cavities the water molecules may form clusters and may act collectively [106]. In addition, the residence time of water molecules can vary significantly [107], as some water molecules are almost permanent in the macromolecular interior while others spend just a fraction of their time there. Thus, for a correct description of these effects on the dielectric properties of the internal cavities, one needs to assess the size, shape, and accessibility of the cavity and to assign an appropriate dielectric constant. Having in mind that the size and shape of the cavities is subject to structural fluctuations as well, the dielectric function should also provide a smooth transition from the macromolecular matrix to the macromolecular cavity [16].

The third region, and the most difficult to address, is the space occupied by the macromolecule. As discussed above, macromolecules are quite inhomogeneous entities, and atoms in biomolecules have different charges and flexibilities depending on their packing and their mutual interactions. The dielectric function describing such complex environments should reflect the physical nature of the macromolecule. The most straightforward approach is delivered from atomic densities of the corresponding atoms [16]. It is expected that the space occupied by loosely packed and charged atoms will have a significant tendency to reorganize and to respond of the local electrostatic field. This should be modeled as a region of high dielectric constant. Such regions are the protein surfaces, which are loosely packed and rich in charged and polar residues. In contrast, regions of tightly packed uncharged atoms, as in the hydrophobic core, have little ability to respond to the local electrostatic field and should be modeled with a low dielectric constant. All of these features can be captured with the so-termed Gaussian method of representing atomic densities by using it to deliver a smooth dielectric function as described in Ref. 16. Essentially, one uses atomic coordinates and forcefield parameters to convert the atomic densities into a local dielectric constant as originally described by Nicholls and Pickup [108] and further developed by Li et al. [16]. Given a macromolecule with N atoms, the density of an atom i is represented by a Gaussian distribution

$$\rho_i(r) = e^{\frac{r_i^2}{\sigma_i^2 R_i^2}} \tag{29.1}$$

where $\rho_i(r)$ is the density at position r, r_i is the distance between the center of the atom i and position r, R_i is the van der Waals (vdW) radius of atom i, and σ_i is the relative variance. After the density of each atom within the macromolecule is generated, the density in the overlapping areas occupied by multiple atoms is calculated by

$$\rho_{\text{mol}}(r) = 1 - \Pi_i[1 - p_i(r)] \tag{29.2}$$

where the $\rho_{\text{mol}}(r)$ denotes the density at position r by multiple atoms, and $\rho_i(r)$ is the density of a single atom i, which can be obtained from Eq. (29.1). This product function guarantees that the density at the overlapping region is higher than the density generated by any involved single atom, but the density $\rho_{\text{mol}}(r)$ should not be greater than 1. Finally, the smooth dielectric function is delivered from the density distribution using the linear function

$$\varepsilon = \rho \cdot \varepsilon_{\text{in}} + (1 - \rho) \cdot \varepsilon_{\text{out}} \tag{29.3}$$

where ε on the left denotes the dielectric distribution, ε_{in} denotes the reference dielectric values in the molecule when the density is 1, ε_{out} denotes the dielectric value for the water phase, and ρ is the density, which can be obtained from Eq. (29.3).

The resulting dielectric constant distribution is illustrated in Fig. 29.4 [3, 109], where the Gaussian-based smooth

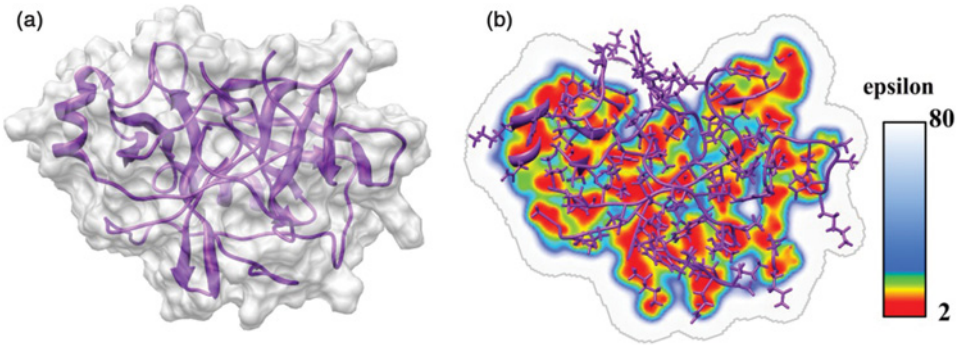


FIGURE 29.4 (a) Structure of the Bovine Eglin protein (PDB ID 1ACB); (b) dielectric distribution of the Gaussian smooth method for this protein. [Molecular graphics and analyses were performed with the UCSF Chimera package. Chimera is developed by the Resource for Biocomputing, Visualization, and Informatics at the University of California, San Francisco (supported by NIGMS P41-GM103311).] For a color version of this figure, see the color plate section.

dielectric constant is delivered for a particular macromolecule, the bovine α-chymotrypsin-eglin protein. One can appreciate that the dielectric constant is indeed a smooth function and there are no sharp dielectric jumps across the space. It can also be seen that the macromolecular interior, the internal cavities, and the macromolecule–water interface are modeled differently from the bulk water phase.

29.7 CONCLUDING REMARKS

It should be clarified that this chapter does not deal with the "optimal" value of the macromolecular homogenous dielectric constant, which is an ongoing debate in current scientific literature [110–118]. Instead, we emphasize that the dielectric constant of macromolecules is not constant at all [16]. This is the reason why various studies use numerous "optimal" dielectric constant values [119–123]. This is also the reason why, if one uses a homogeneous dielectric constant, the optimal value depends on the reaction modeled [124, 125]. The smooth Gaussian-based dielectric function [16] addresses many of these issues by providing a structure-based approach of mimicking the ability of different regions to react to the local electrostatic field.

ACKNOWLEDGMENTS

This work was supported by a grant from the Institute of General Medical Sciences, National Institutes of Health, Award 1R01GM093937.

REFERENCES

[1] Alberts, B., Wilson, J.H., Hunt, T. (2008). *Molecular Biology of the Cell*. Garland Science, New York, xxxiii, 1601.

[2] Klejnot, M., Kozielski, F. (2012). Structural insights into human Kif7, a kinesin involved in Hedgehog signalling. *Acta Crystallogr. D: Biol. Crystallogr*. **68**, 154–159.

[3] Pettersen, E.F., Goddard, T.D., Huang, C.C., Couch, G.S., Greenblatt, D.M., et al. (2004). UCSF Chimera–a visualization system for exploratory research and analysis. *J. Comput. Chem.* **25**, 1605–1612.

[4] Karplus, M. (2003). Molecular dynamics of biological macromolecules: A brief history and perspective. *Biopolymers* **68**, 350–358.

[5] Van Gunsteren, W.F., Berendsen, H.J. (1982). Molecular dynamics: Perspective for complex systems. *Biochem. Soc. Transact*. **10**, 301–305.

[6] Honig, B., Nicholls, A. (1995). Classical electrostatics in biology and chemistry. *Science* **268**, 1144–1149.

[7] DeFlores, L.P., Tokmakoff, A. (2006). Water penetration into protein secondary structure revealed by hydrogen-deuterium exchange two-dimensional infrared spectroscopy. *J. ACS* **128**, 16520–16521.

[8] Baratova, L.A., Fedorova, N.V., Dobrov, E.N., Lukashina, E.V., Kharlanov, A.N., et al. (2004). *N*-Terminal segment of potato virus X coat protein subunits is glycosylated and mediates formation of a bound water shell on the virion surface. *Eur. J. Biochem*. **271**, 3136–3145.

[9] Kuhn, L.A., Siani, M.A., Pique, M.E., Fisher, C.L., Getzoff, E.D., et al. (1992). The interdependence of protein surface topography and bound water molecules revealed by surface accessibility and fractal density measures. *J. Mol. Biol.* **228**, 13–22.

[10] Sharrow, S.D., Edmonds, K.A., Goodman, M.A., Novotny, M.V., Stone, M.J. (2005). Thermodynamic consequences of disrupting a water-mediated hydrogen bond network in a protein:pheromone complex. *Protein Sci*. **14**, 249–256.

[11] Bonthuis, D.J., Netz, R.R. (2013). Beyond the continuum: How molecular solvent structure affects electrostatics and hydrodynamics at solid-electrolyte interfaces. *J. Phys. Chem. B* **117**, 11397–11413.

[12] Sauer, M., Neuweiler, H. (2014). PET-FCS: Probing rapid structural fluctuations of proteins and nucleic acids by single-molecule fluorescence quenching. *Methods Mol. Biol.* **1076**, 597–615.

[13] Shiozawa, M., Yoda, M., Kamiya, N., Asakawa, N., Higo, J., et al. (2001). Evidence for large structural fluctuations of the photobleached intermediate of photoactive yellow protein in solution. *J. ACS* **123**, 7445-7446.

[14] Parak, F.G. (2003). Proteins in action: The physics of structural fluctuations and conformational changes. *Curr. Opin. Struct. Biol.* **13**, 552–557.

[15] Gagne, D., Doucet, N. (2013). Structural and functional importance of local and global conformational fluctuations in the RNase A superfamily. *FEBS J.* **280**, 5596–5607.

[16] Li, L., Li, C., Zhang, Z., Alexov, E. (2013). On the dielectric "constant" of proteins: Smooth dielectric function for macromolecular modeling and its implementation in DelPhi. *J. Chem. Theory Comput.* **9**, 2126–2136.

[17] McCammon, J.A., Gelin, B.R., Karplus, M., Wolynes, P.G. (1976). The hinge-bending mode in lysozyme. *Nature* **262**, 325–326.

[18] Brooks, B., Karplus, M. (1985). Normal modes for specific motions of macromolecules: Application to the hinge-bending mode of lysozyme. *Proc. Natl. Acad. Sci. USA* **82**, 4995–4999.

[19] Barber, A.F., Carnevale, V., Raju, S.G., Amaral, C., Treptow, W., et al. (2012). Hinge-bending motions in the pore domain of a bacterial voltage-gated sodium channel. *Biochim. Biophys. Acta* **1818**, 2120–2125.

[20] Schultz-Heienbrok, R., Maier, T., Strater, N. (2005). A large hinge bending domain rotation is necessary for the catalytic function of Escherichia coli 5′-nucleotidase. *Biochemistry* **44**, 2244–2252.

[21] Evenas, J., Forsen, S., Malmendal, A., Akke, M. (1999). Backbone dynamics and energetics of a calmodulin domain

mutant exchanging between closed and open conformations. *J. Mol. Biol.* **28**, 603–617.

[22] Alexov, E. (2008). Protein-protein interactions. *Curr. Pharm. Biotechnol.* **9**, 55–56.

[23] Hofrichter, J., Ansari, A., Jones, C.M., Deutsch, R.M., Sommer, J.H., et al. (1994). Ligand binding and conformational changes measured by time-resolved absorption spectroscopy. *Methods Enzymol*. **232**, 387–415.

[24] Suzuki, M., Loakes, D., Yagi, N. (1996). DNA conformation and its changes upon binding transcription factors. *Adv. Biophys.* **32**, 53–72.

[25] Son, J., Lee, E.H., Park, M., Kim, J.H., Kim, J., et al. (2013). Conformational changes in human prolyl-tRNA synthetase upon binding of the substrates proline and ATP and the inhibitor halofuginone. *Acta Crystallogr. D: Biol. Crystallogr.* **69**, 2136–2145.

[26] Mangialavori, I.C., Ferreira-Gomes, M.S., Saffioti, N.A., Gonzalez-Lebrero, R.M., Rossi, R.C., et al. (2013). Conformational changes produced by ATP binding to the plasma membrane calcium pump. *J. Biol. Chem.* **288**, 31030–31041.

[27] Hammes, G.G. (2002). Multiple conformational changes in enzyme catalysis. *Biochemistry* **41**, 8221–8228.

[28] Sytina, O.A., Heyes, D.J., Hunter, C.N., Alexandre, M.T., van Stokkum, I.H., et al. (2008). Conformational changes in an ultrafast light-driven enzyme determine catalytic activity. *Nature* **456**, 1001–1004.

[29] Ofiteru, A., Bucurenci, N., Alexov, E., Bertrand, T., Briozzo, P., et al. (2007). Structural and functional consequences of single amino acid substitutions in the pyrimidine base binding pocket of Escherichia coli CMP kinase. *FEBS J*. **274**, 3363–3373.

[30] Goodey, N.M., Benkovic, S.J. (2008). Allosteric regulation and catalysis emerge via a common route. *Nat. Chem. Biol.* **4**, 474–482.

[31] Pellicena, P., Kuriyan, J. (2006). Protein-protein interactions in the allosteric regulation of protein kinases. *Curr. Opin. Struct. Biol.* **16**, 702–709.

[32] Kursula, P. (2014). Crystallographic snapshots of initial steps in the collapse of the calmodulin central helix. *Acta Crystallogr. D: Biol. Crystallogr*. **70**, 24–30.

[33] Gifford, J.L., Ishida, H., Vogel, H.J. (2012), Structural insights into calmodulin-regulated L-selectin ectodomain shedding. *J. Biol. Chem.* **287**, 26513–26527.

[34] Isvoran, A., Craescu, C.T., Alexov, E. (2007). Electrostatic control of the overall shape of calmodulin: Numerical calculations. *Eur. Biophys. J.* **36**, 225–237.

[35] Dunker, A.K., Lawson, J.D., Brown, C.J., Williams, R.M., Romero, P., et al. (2001). Intrinsically disordered protein. *J. Mol. Graph. Model.* **19**, 26–59.

[36] Uversky, V.N., Oldfield, C.J., Dunker, A.K. (2008). Intrinsically disordered proteins in human diseases: Introducing the D2 concept. *Annu. Rev. Biophys*. **37**, 215–246.

[37] Tompa, P. (2012). Intrinsically disordered proteins: A 10-year recap. *Trends Biochem. Sci.* **37**, 509–516.

[38] Song, J., Lee, M.S., Carlberg, I., Vener, A.V., Markley, J.L. (2006). Micelle-induced folding of spinach thylakoid soluble phosphoprotein of 9 kDa and its functional implications. *Biochemistry* **45**, 15633–15643.

[39] von der Malsburg, A., Abutbul-Ionita, I., Haller, O., Kochs, G., Danino, D. (2011). Stalk domain of the dynamin-like MxA GTPase protein mediates membrane binding and liposome tubulation via the unstructured L4 loop. *J. Biol. Chem.* **286**, 37858–37865.

[40] Slutzki, M., Jaitin, D.A., Yehezkel, T.B., Schreiber, G. (2006). Variations in the unstructured C-terminal tail of interferons contribute to differential receptor binding and biological activity. *J. Mol. Biol.* **360**, 1019–1030.

[41] Sigalov, A.B., Aivazian, D.A., Uversky, V.N., Stern, L.J. (2006). Lipid-binding activity of intrinsically unstructured cytoplasmic domains of multichain immune recognition receptor signaling subunits. *Biochemistry* **45**, 15731–15739.

[42] Verkhivker, G.M., Bouzida, D., Gehlhaar, D.K., Rejto, P.A., Freer, S.T., et al. (2003). Simulating disorder-order transitions in molecular recognition of unstructured proteins: Where folding meets binding. *Proc. Natl. Acad. Sci. USA* **100**, 5148–5153.

[43] Turjanski, A.G., Gutkind, J.S., Best, R.B., Hummer, G. (2008). Binding-induced folding of a natively unstructured transcription factor. *PLoS Comput. Biol.* **4**, e1000060.

[44] Alexov, E. (2004). Numerical calculations of the pH of maximal protein stability. The effect of the sequence composition and three-dimensional structure. *Eur. J. Biochem.* **271**, 173–185.

[45] Chan, P., Warwicker, J. (2009). Evidence for the adaptation of protein pH-dependence to subcellular pH. *BMC Biol*. **7**, 69.

[46] Garcia-Moreno, B. (2009). Adaptations of proteins to cellular and subcellular pH. *J. Biol.* **8**, 98.

[47] Talley, K., Alexov, E. (2010). On the pH-optimum of activity and stability of proteins. *Proteins* **78**, 2699–2706.

[48] Whitten, S.T., Garcia-Moreno, E.B., Hilser, V.J. (2005). Local conformational fluctuations can modulate the coupling between proton binding and global structural transitions in proteins. *Proc. Natl. Acad. Sci. USA* **102**, 4282–4287.

[49] Mitra, R.C., Zhang, Z., Alexov, E. (2011). In silico modeling of pH-optimum of protein-protein binding. *Proteins* **79**, 925–936.

[50] Onufriev, A.V., Alexov, E. (2013). Protonation and pK changes in protein-ligand binding. *Q. Rev. Biophys.* **46**, 181–209.

[51] Aguilar, B., Anandakrishnan, R., Ruscio, J.Z., Onufriev, A.V. (2010). Statistics and physical origins of pK and ionization state changes upon protein-ligand binding. *Biophys. J.* **98**, 872–880.

[52] Liu, B., Westhead, D.R., Boyett, M.R., Warwicker, J. (2007). Modelling the pH-dependent properties of Kv1 potassium channels. *J. Mol. Biol.* **368**, 328–335.

[53] Chan, P., Lovric, J., Warwicker, J. (2006). Subcellular pH and predicted pH-dependent features of proteins. *Proteomics* **6**, 3494–3501.

[54] Jaudzems, K., Askarieh, G., Landreh, M., Nordling, K., Hedhammar, M., et al. (2012) pH-dependent dimerization of spider silk *N*-terminal domain requires relocation of a wedged tryptophan side chain. *J. Mol. Biol*. **422**, 477–487.

[55] Bose, K., Clark, A.C. (2005). pH effects on the stability and dimerization of procaspase-3. *Protein Sci*. **14**, 24–36.

[56] Sorgen, P.L., Duffy, H.S., Spray, D.C., Delmar, M. (2004). pH-dependent dimerization of the carboxyl terminal domain of Cx43. *Biophys. J.* **87**, 574–581.

[57] Tulk, B.M., Schlesinger, P.H., Kapadia, S.A., Edwards, J.C. (2000). CLIC-1 functions as a chloride channel when expressed and purified from bacteria. *J. Biol. Chem.* **275**, 26986–26993.

[58] Littler, D.R., Harrop, S.J., Goodchild, S.C., Phang, J.M., Mynott, A.V., et al. (2010). The enigma of the CLIC proteins: Ion channels, redox proteins, enzymes, scaffolding proteins? *FEBS Lett.* **584**, 2093–2101.

[59] Sedlmeier, F., Horinek, D., Netz, R.R. (2011). Spatial correlations of density and structural fluctuations in liquid water: A comparative simulation study. *J. ACS* **133**, 1391–1398.

[60] Ha, J.H., Capp, M.W., Hohenwalter, M.D., Baskerville, M., Record, M.T., Jr. (1992). Thermodynamic stoichiometries of participation of water, cations and anions in specific and nonspecific binding of lac repressor to DNA. Possible thermodynamic origins of the "glutamate effect" on protein-DNA interactions. *J. Mol. Biol.* **228**, 252–264.

[61] Ihm, C., In, Y., Park, Y., Paek, K. (2004). Small cavitands specifically binding a water molecule. *Org. Lett.* **6**, 369–372.

[62] Bottoms, C.A., Smith, P.E., Tanner, J.J. (2002). A structurally conserved water molecule in Rossmann dinucleotide-binding domains. *Protein Sci.* **11**, 2125–2137.

[63] Likic, V.A., Juranic, N., Macura, S., Prendergast, F.G. (2000). A "structural" water molecule in the family of fatty acid binding proteins. *Protein Sci*. **9**, 497–504.

[64] Zhou, D., Bryant, R.G. (1996). Water molecule binding and lifetimes on the DNA duplex d(CGCGAATTCGCG)2. *J. Biomol. NMR* **8**, 77–86.

[65] Wood, M.L., Schow, E.V., Freites, J.A., White, S.H., Tombola, F., et al. (2012). Water wires in atomistic models of the Hv1 proton channel. *Biochim. Biophys. Acta* **1818**, 286–293.

[66] Cardenas, D.J., Cuerva, J.M., Alias, M., Bunuel, E., Campana, A.G. (2011). Water-based hydrogen-atom wires as mediators in long-range proton-coupled electron transfer in enzymes: A new twist on water reactivity. *Chemistry* **17**, 8318–8323.

[67] Gu, W., Helms, V. (2009). Tightly connected water wires facilitate fast proton uptake at the proton entrance of proton pumping proteins. *J. ACS* **131**, 2080–2081.

[68] Narayan, S., Wyatt, D.L., Crumrine, D.S., Cukierman, S. (2007). Proton transfer in water wires in proteins: Modulation by local constraint and polarity in gramicidin a channels. *Biophys. J.* **93**, 1571–1579.

[69] Wei, D., Wilson, W.D., Neidle, S. (2013). Small-molecule binding to the DNA minor groove is mediated by a conserved water cluster. *J. ACS* **135**, 1369–1377.

[70] Zhou, Q., Zhai, Y., Lou, J., Liu, M., Pang, X., et al. (2011). Thiabendazole inhibits ubiquinone reduction activity of mitochondrial respiratory complex II via a water molecule mediated binding feature. *Protein Cell* **2**, 531–542.

[71] Wiesner, S., Kurian, E., Prendergast, F.G., Halle, B. (1999). Water molecules in the binding cavity of intestinal fatty acid binding protein: Dynamic characterization by water 17O and 2H magnetic relaxation dispersion. *J. Mol. Biol.* **286**, 233–246.

[72] Likic, V.A., Prendergast, F.G. (2001). Dynamics of internal water in fatty acid binding protein: Computer simulations and comparison with experiments. *Proteins* **43**, 65–72.

[73] Koellner, G., Kryger, G., Millard, C.B., Silman, I., Sussman, J.L., et al. (2000). Active-site gorge and buried water molecules in crystal structures of acetylcholinesterase from Torpedo californica. *J. Mol. Biol.* **296**, 713–735.

[74] Szep, S., Park, S., Boder, E.T., Van Duyne, G.D., Saven, J.G. (2009). Structural coupling between FKBP12 and buried water. *Proteins* **74**, 603–611.

[75] Takano, K., Yamagata, Y., Yutani, K. (2003). Buried water molecules contribute to the conformational stability of a protein. *Protein Eng.* **16**, 5–9.

[76] Park, S., Saven, J.G. (2005). Statistical and molecular dynamics studies of buried waters in globular proteins. *Proteins* **60**, 450–463.

[77] Leioatts, N., Mertz, B., Martinez-Mayorga, K., Romo, T.D., Pitman, M.C., et al. (2014). Retinal ligand mobility explains internal hydration and reconciles active rhodopsin structures. *Biochemistry* **53**, 376–385.

[78] Fischer, S., Verma, C.S. (1999). Binding of buried structural water increases the flexibility of proteins. *Proc. Natl. Acad. Sci. USA* **96**, 9613–9615.

[79] Li, C., Li, L., Petukh, M., Alexov, E. (2013). Progress in developing Poisson-Boltzmann equation solvers. *Mol. Based Math. Biol.* **1**.

[80] Grochowski, P., Trylska, J. (2008). Continuum molecular electrostatics, salt effects, and counterion binding–a review of the Poisson-Boltzmann theory and its modifications. *Biopolymers* **89**, 93113.

[81] Baker, N.A. (2004). Poisson-Boltzmann methods for biomolecular electrostatics. *Methods Enzymol*. **383**, 94–118.

[82] Bashford, D., Case, D.A. (2000). Generalized born models of macromolecular solvation effects. *Annu. Rev. Phys. Chem.* **51**, 129–152.

[83] Onufriev, A., Case, D.A., Bashford, D. (2002). Effective Born radii in the generalized Born approximation: The importance of being perfect. *J. Comput. Chem*. **23**, 1297–1304.

[84] Lu, B., Cheng, X., Huang, J., McCammon, J.A. (2010). AFMPB: An adaptive fast multipole Poisson-Boltzmann solver for calculating electrostatics in biomolecular systems. *Comput. Phys. Commun.* **181**, 1150–1160.

[85] Baker, N.A., Sept, D., Joseph, S., Holst, M.J., McCammon, J.A. (2001). Electrostatics of nanosystems: Application to microtubules and the ribosome. *Proc. Natl. Acad. Sci. USA* **98**, 10037–10041.

[86] Ren, P., Chun, J., Thomas, D.G., Schnieders, M.J., Marucho, M., et al. (2012). Biomolecular electrostatics and solvation: A computational perspective. *Q. Rev. Biophys.* **45**, 427–491.

[87] Zhou, Y.C., Feig, M., Wei, G.W. (2008). Highly accurate biomolecular electrostatics in continuum dielectric environments. *J. Comput. Chem.* **29**, 87–97.

[88] Zheng, Q., Wei, G.W. (2011). Poisson-Boltzmann-Nernst-Planck model. *J. Chem. Phys*. **134**, 194101.

[89] Wang, C., Wang, J., Cai, Q., Li, Z., Zhao, H.K., et al. (2013). Exploring accurate Poisson-Boltzmann methods for biomolecular simulations. *Comput. Theor. Chem.* **1024**, 34–44.

[90] Li, L., Li, C., Sarkar, S., Zhang, J., Witham, S., et al. (2012). DelPhi: A comprehensive suite for DelPhi software and associated resources. *BMC Biophys*. **5**, 9.

[91] Decherchi, S., Colmenares, J., Catalano, C.E., Spagnuolo, M., Alexov, E., et al. (2013). Between algorithm and model: Different molecular surface definitions for the Poisson-Boltzmann based electrostatic characterization of biomolecules in solution. *Commun. Comput. Phys.* **13**, 61–89.

[92] Lee, B., Richards, F.M. (1971). The interpretation of protein structures: Estimation of static accessibility. *J. Mol. Biol.* **55**, 379–400.

[93] Rocchia, W., Sridharan, S., Nicholls, A., Alexov, E., Chiabrera, A., et al. (2002). Rapid grid-based construction of the molecular surface and the use of induced surface charge to calculate reaction field energies: Applications to the molecular systems and geometric objects. *J. Comput. Chem.* **23**, 128–137.

[94] Bertonati, C., Honig, B., Alexov, E. (2007). Poisson-Boltzmann calculations of nonspecific salt effects on protein-protein binding free energies. *Biophys. J.* **92**, 1891–1899.

[95] Lund, M., Vrbka, L., Jungwirth, P. (2008). Specific ion binding to nonpolar surface patches of proteins. *J. ACS* **130**, 11582–11583.

[96] Linse, S., Brodin, P., Johansson, C., Thulin, E., Grundstrom, T., et al. (1988). The role of protein surface charges in ion binding. *Nature* **335**, 651–652.

[97] Ralle, M., Verkhovskaya, M.L., Morgan, J.E., Verkhovsky, M.I., Wikstrom, M., et al. (1999). Coordination of CuB in reduced and CO-liganded states of cytochrome bo3 from Escherichia coli. Is chloride ion a cofactor? *Biochemistry* **38**, 7185–7194.

[98] Lafontaine, D.A., Ananvoranich, S., Perreault, J.P. (1999). Presence of a coordinated metal ion in a trans-acting antigenomic delta ribozyme. *Nucleic Acids Res*. **27**, 3236–3243.

[99] Petukh, M., Zhenirovskyy, M., Li, C., Li, L., Wang, L., et al. (2012). Predicting nonspecific ion binding using DelPhi. *Biophys. J.* **102**, 2885–2893.

[100] Petukh, M., Kimmet, T., Alexov, E. (2013). BION web server: Predicting non-specifically bound surface ions. *Bioinformatics* **29**, 805–806.

[101] Montagna, M., Sterpone, F., Guidoni, L. (2012). Structural and spectroscopic properties of water around small hydrophobic solutes. *J. Phys. Chem. B* **116**, 11695–11700.

[102] Sterpone, F., Stirnemann, G., Laage, D. (2012). Magnitude and molecular origin of water slowdown next to a protein. *J. ACS* **134**, 4116–4119.

[103] Pal, S., Balasubramanian, S., Bagchi, B. (2004). Anomalous dielectric relaxation of water molecules at the surface of an aqueous micelle. *J. Chem. Phys.* **120**, 1912–1920.

[104] Oleinikova, A., Brovchenko, I. (2012). Thermodynamic properties of hydration water around solutes: Effect of solute size and water-solute interaction. *J. Phys. Chem. B* **116**, 14650–14659.

[105] Cheng, Y.K., Rossky, P.J. (1998). Surface topography dependence of biomolecular hydrophobic hydration. *Nature* **392**, 696–699.

[106] Vaitheeswaran, S., Yin, H., Rasaiah, J.C., Hummer, G. (2004). Water clusters in nonpolar cavities. *Proc. Natl. Acad. Sci. USA* **101**, 17002–17005.

[107] Yin, H., Feng, G., Clore, G.M., Hummer, G., Rasaiah, J.C. (2010). Water in the polar and nonpolar cavities of the protein interleukin-1beta. *J. Phys. Chem. B* **114**, 16290–16297.

[108] Grant, J.A., Pickup, B.T., Sykes, M.J., Kitchen, C.A., Nicholls, A. (2007). The Gaussian Generalized Born model: Application to small molecules. *Phys. Chem. Chem. Phys.* **9**, 4913–4922.

[109] Frigerio, F., Coda, A., Pugliese, L., Lionetti, C., Menegatti, E., et al. (1992). Crystal and molecular structure of the bovine alpha-chymotrypsin-eglin c complex at 2.0 A resolution. *J. Mol. Biol.* **225**, 107–123.

[110] Genheden, S., Ryde, U. (2012). Comparison of end-point continuum-solvation methods for the calculation of protein-ligand binding free energies. *Proteins* **80**, 1326–1342.

[111] Patargias, G.N., Harris, S.A., Harding, J.H. (2010). A demonstration of the inhomogeneity of the local dielectric response of proteins by molecular dynamics simulations. *J. Chem. Phys.* **132**, 235103.

[112] Simonson, T. (2008). Dielectric relaxation in proteins: The computational perspective. *Photosynth. Res.* **97**, 21–32.

[113] Lund, M., Jonsson, B., Woodward, C.E. (2007). Implications of a high dielectric constant in proteins. *J. Chem. Phys.* **126**, 225103.

[114] Chamorovsky, S.K., Cherepanov, D.A., Chamorovsky, C.S., Semenov, A.Y. (2007). Correlation of electron transfer rate in photosynthetic reaction centers with intraprotein dielectric properties. *Biochim. Biophys. Acta* **1767**, 441–448.

[115] Karp, D.A., Gittis, A.G., Stahley, M.R., Fitch, C.A., Stites, W.E., et al. (2007). High apparent dielectric constant inside a protein reflects structural reorganization coupled to the ionization of an internal Asp. *Biophys. J.* **92**, 2041–2053.

[116] Cerutti, D.S., Wong, C.F., McCammon, J.A. (2003). Brownian dynamics simulations of ion atmospheres around polyalanine and B-DNA: Effects of biomolecular dielectric. *Biopolymers* **70**, 391–402.

[117] Kato, M., Pisliakov, A.V., Warshel, A. (2006). The barrier for proton transport in aquaporins as a challenge for electrostatic models: The role of protein relaxation in mutational calculations. *Proteins* **64**, 829–844.

[118] Teixeira, V.H., Cunha, C.A., Machuqueiro, M., Oliveira, A.S., Victor, B.L., et al. (2005). On the use of different dielectric constants for computing individual and pairwise terms in poisson-boltzmann studies of protein ionization equilibrium. *J. Phys. Chem. B* **109**, 14691–14706.

[119] Gilson, M.K., Honig, B. (1988). Calculation of the total electrostatic energy of a macromolecular system: Solvation energies, binding energies, and conformational analysis. *Proteins* **4**, 7–18.

[120] Gunner, M.R., Zhu, X., Klein, M.C. (2011). MCCE analysis of the pKas of introduced buried acids and bases in staphylococcal nuclease. *Proteins* **79**, 3306–3319.

[121] Warwicker, J. (2011). pKa predictions with a coupled finite difference Poisson-Boltzmann and Debye-Huckel method. *Proteins* **79**, 3374–3380.

[122] Antosiewicz, J., McCammon, J.A., Gilson, M.K. (1994). Prediction of pH-dependent properties of proteins. *J. Mol. Biol.* **238**, 415–436.

[123] Spassov, V.Z., Yan, L. (2008). A fast and accurate computational approach to protein ionization. *Protein Sci*. **17**, 1955–1970.

[124] Warshel, A., Papazyan, A. (1998). Electrostatic effects in macromolecules: Fundamental concepts and practical modeling. *Curr. Opin. Struct. Biol.* **8**, 211–217.

[125] Warshel, A., Sharma, P.K., Kato, M., Parson, W.W. (2006). Modeling electrostatic effects in proteins. *Biochim. Biophys. Acta* **1764**, 1647–1676.

30

NMR OF DRUG DELIVERY COUPLED WITH LIPID MEMBRANE DYNAMICS

EMIKO OKAMURA

Faculty of Pharmaceutical Sciences, Himeji Dokkyo University, 7-2-1, Kamiohno, Himeji 670-8524, Japan

30.1 INTRODUCTION

Molecular mechanisms of drug–biomembrane interactions are of great significance as a primary stage of bioactivity in the cell. The lipid bilayer membrane, as a platform of vital functions, is a dynamic structure where molecules are always fluctuating under physiological conditions [1]. The mechanism of drug delivery is related to the molecular dynamics in this soft, fluid membrane interface. In situ observation to capture dynamic aspects of membranes and drugs is important because it can provide the molecular picture of drug delivery to the membrane without undesirable perturbation.

Nuclear magnetic resonance (NMR) spectroscopy is a versatile method for studying drug delivery from water to membranes [2]. It is noninvasive and tells us about the structures and dynamics of both drugs and membranes at the molecular level. High-resolution solution NMR is informative, and also suitable for drug delivery studies, to shed light on molecules of drugs and membrane lipids always moving and fluctuating in abundant water. Multinuclear NMR often provides site-selective information about drugs and membranes simultaneously and independently. Now the development of instrumentation and computational techniques enables us to determine static and dynamic properties of both drugs and membranes in situ.

In this chapter, the NMR research of drug deliveries is reviewed mainly on the basis of our recent studies. A small-sized anticancer 5-fluorouracil (5FU), an anesthetics sevoflurane (SF), an endocrine disruptor, bisphenol A (BPA) and its fluorinated derivative (FBPA), and a neuropeptide, leucine-enkephalin (L-Enk) are addressed as a model drug; for the structures, see Fig. 30.1. Special focus is on the dynamic feature of deliveries of these molecules related to the lipid membrane dynamics. Prior to the survey of delivery study, the dynamic aspects of lipid bilayer membranes, as a platform of delivery processes, are briefly summarized. It is emphasized how the dynamic feature of drug deliveries is coupled with such membrane dynamics.

30.2 DYNAMICS OF MEMBRANES AS A PLATFORM OF VITAL FUNCTIONS

The lipid bilayer membrane is a fluid, soft interface that separates the inside from the outside of a living cell. The boundaries of membranes are not smooth but rough at the molecular level [3]; molecules are always fluctuating in a membrane environment. Because molecular movements in membranes are closely related to vital functions, it has been an issue of great attention how molecular dynamics is modified in such confined but fluid geometries.

Lipid molecules that form biomembrane matrices are mostly in a liquid-crystalline state. Under physiological conditions, the lipids exhibit two-dimensional liquidlike properties in the lateral direction to the membrane surface. The idea was introduced as the fluid mosaic model by Singer and Nicolson more than four decades ago [4]. Since then, the dynamic aspects of lipid membrane matrices have been

Encyclopedia of Biocolloid and Biointerface Science, Volume 1, First Edition. Edited by Hiroyuki Ohshima.
© 2016 John Wiley & Sons, Inc. Published 2016 by John Wiley & Sons, Inc.

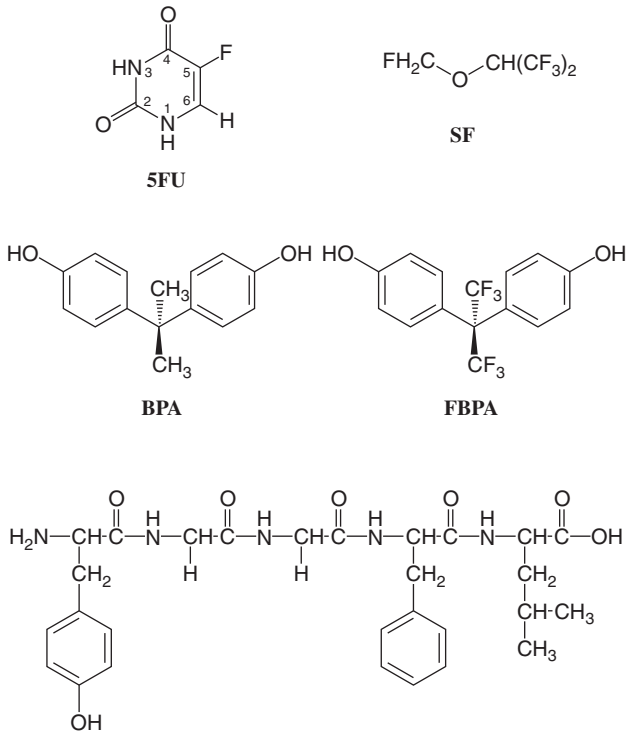


FIGURE 30.1 Molecular structures of drugs described in the delivery study.

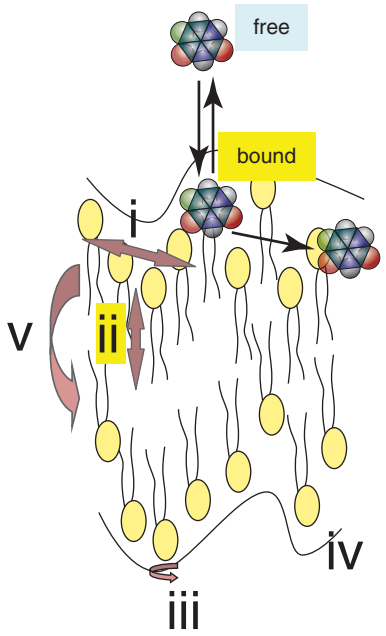


FIGURE 30.2 Lipid motion in fluid bilayer membranes and drug delivery. The characters i–v represent (i) lateral diffusion of lipids in plane of the bilayer, (ii) protrusion along the bilayer normal, (iii) rotational diffusion and wobbling of lipids, (iv) undulation, and (v) flipflop of lipid molecules between the two monolayers (see text for details).

unveiled at a molecular level, by the use of many physicochemical techniques involving spectroscopies and computer calculations.

At present, the lipid motions in fluid membranes are categorized by a variety of dynamical modes with wide range of timescale [3, 5, 6]. As illustrated in Fig. 30.2, the motions include (1) lateral diffusion of lipids in the plane of the bilayer; (2) protrusion, the movement of individual lipids or lipid segments along the bilayer normal; (3) rotational diffusion and wobbling of lipids; (4) undulations, the collective movements of membrane patches; and (5) flipflop of lipid molecules between the two monolayers of bilayer, as well as bond oscillations and *gauche–trans* isomerization of lipid alkyl chains. The approximate correlation times of the respective modes are in the wide range from picoseconds to hours [5]. It is expected that drug deliveries are concerted with such dynamic behaviors of membrane lipid molecules (Fig. 30.2).

In real cell membranes, the dynamical features are more complex because of the heterogeneous distribution of lipid microdomains called the "raft" [7, 8], and the presence of membrane proteins and a system of filaments called the *cytoskeletons* [1]. Generally, the presence of macromolecular proteins and the raft-forming cholesterol makes the membrane less fluid [9, 10].

30.2.1 Diffusion

Lateral *diffusion* of lipids in the parallel direction to the membrane surface is the typical index of molecular dynamics in membranes. Pulsed-field-gradient (PFG) NMR spectroscopy [11] is a noninvasive technique to directly measure the molecular diffusion not only in the three-dimensional (3D) isotropic solution but also in a two-dimensional (2D) anisotropic membrane. It tells us about how the movement of every membrane component is modified in a two-dimensional confined but soft space without perturbing the system. Although its application to the membrane system has been limited because of the low signal resolution and slow diffusion of molecules, more recent PFG studies have obtained well-resolved NMR signals in highly viscous membrane environments, using labeling or magic-angle spinning technique [12, 13].

One team of investigators have observed and compared the self-diffusion of lipid molecules in size-controlled micelles and vesicles as freestanding model of fluid membranes without labeling or using the spinning technique [14]. The success is due to the application of high-resolution solution-state NMR in combination with the PFG technique. The extent of boundary restriction has been controlled by employing the micelles and vesicles with average diameters of 3 nm (micelle), 30 nm [small unilamellar vesicle (SUV)], and 100

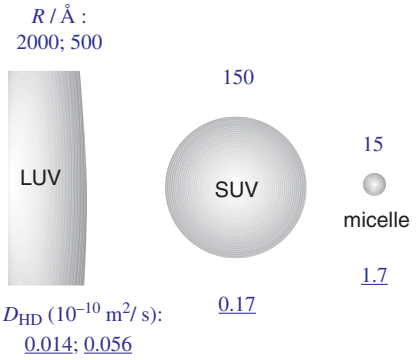


FIGURE 30.3 Schematic illustration of size-controlled vesicles and micelles as model of confined fluid membrane. The radii of the respective particles are given by R in Å units. Underlined values represent D_{HD}, the self-diffusion coefficient of each particle estimated from the hydrodynamic (HD) diffusion in H_2O at 303 K.

and 400 nm [large unilamellar vesicle (LUV)]. It is noted that LUV is characterized by almost negligible surface curvature effect [15], in contrast to the highly curved micellar surface (Fig. 30.3).

In recent decades, a specially designed high-field-gradient probe has been developed for a high-resolution solution NMR apparatus [14], to obtain a reliable signal of molecular motion in a highly viscous membrane environment. The probe can exert a field gradient of ≤13.5 T/m. Generally, the self-diffusion coefficient D is determined as the slope of the Stejskal–Tanner plot [16], by using the echo signal attenuation as a function of the field gradient strength G. The Stejskal–Tanner equation is given by

$$\ln \frac{I(G)}{I(0)} = -D(\gamma\delta)^2 \left(\Delta_{\text{diff}} - \frac{\delta}{3}\right) G^2 \qquad (30.1)$$

where $I(G)$ and $I(0)$ are the echo signal intensities where the field gradient is present and absent, respectively; γ, the gyromagnetic ratio; δ, the gradient pulsewidth; and Δ_{diff}, the diffusion time interval, respectively. As listed in Table 30.1, the high-field-gradient NMR shows that the lipid diffusion in membrane is enhanced in the order of micelle > SUV > 100-nm LUV ≈ 400-nm LUV [14], in accordance with the surface curvature dependence of the dynamical structure in such lipid aggregates [15].

It is interesting that the slowdown of lipid motions in membranes is leveled off in 100- and 400-nm LUVs, although the hydrodynamic (HD) continuum model [17] shows that the lipid aggregate diffusion is slowed down in inverse proportion to the aggregate size. In fact, it is also found that the lateral diffusion coefficient of the fluid lipid in 800-nm LUV is as large as $\sim 1 \times 10^{-11}$ m^2 s^{-1} [18], more than one order of magnitude as fast as the rotational and the translational diffusion of LUV by the HD continuum model (both of the order of 10^{-13} m^2 s^{-1}). Even in a cell-sized giant vesicle (of 10–20 μm diameter), the lateral diffusion coefficient is reported to be 0.8×10^{-11} m^2 s^{-1} at relevant temperature [19, 20]; not so much decreased as compared to the 800-nm LUV, although the vesicle size is more than one order of magnitude

TABLE 30.1 Self-Diffusion Coefficient of Lipids in Lysophosphatidylcholine Micelle, EPC SUV and LUV Determined by High-Field-Gradient NMR Method

		Self-diffusion coefficient (10^{-10} m^2 s^{-1})		
	Method	Headgroup	Chain core	Ref.
In micelle (3 nm)[a]	PFG NMR	0.65 ± 0.02	0.63 ± 0.02	14
		0.5–1.3[b]		55
In SUV (30 nm)	PFG NMR	0.24 ± 0.01	0.28 ± 0.01	14
	PFG NMR	0.23–0.24[c]		56
In LUV (100 nm)	PFG NMR	0.12 ± 0.01	0.14 ± 0.01	14
In LUV (400 nm)	PFG NMR	0.13 ± 0.01	0.15 ± 0.01	14
	FRAP	0.124–0.134[d]		57
		0.12[e]		58

[a] Average diameters of the particles determined from quasielastic light scattering are given in parentheses.
[b] Summarized values for ionic surfactants at 303 K.
[c] For dioleoyl-PC (DOPC) SUV at 298 K.
[d] For planar DOPC bilayer at 296 K.
[e] For dipalmitoyl-PC (DPPC) bilayer at 333 K.
General notes: The lipid concentrations are fixed to 30 mM. Diffusion coefficients are independently determined from the choline methyl signal and the chain methylene or methyl signal, respectively. Diffusion coefficients of lipids, estimated from the fluorescence recovery after photobleaching (FRAP) and molecular dynamics (MD) simulation, are also listed.
Source: Reprinted with permission from Ref. 14. Copyright 2004 The American Physical Society.

larger in the giant vesicle. Therefore, we can say that the lipid lateral diffusion in the giant vesicle is considerably large, as compared with the rotational and translational diffusion by the HD estimate, $\sim 10^{-14}$ m^2 s^{-1}.

30.2.2 Protrusion

Protrusion, the movement of individual lipids or lipid segments in the vertical direction to the membrane surface, is expected to relate closely to the mechanism of drug transport processes through the cell membrane. The vertical fluctuation or the out-of-plane vibration of the lipid molecules in membranes has been a subject of interest for more than two decades, and studied by using physicochemical techniques involving 2D NMR [21–24] and incoherent quasielastic neutron scattering [3, 25].

Most recently, the solution NMR has been applied to the cell-sized giant vesicle (CSV) of $\sim$10 μm diameter, to shed light on how lipid motions and fluctuations are modified in giant cell-sized membranes [26]. 2D nuclear Overhauser enhancement spectroscopy (NOESY) and the one-dimensional (1D) transient NOE spectra of CSVs have been systematically compared to the results of LUVs from 100 to 800 nm in diameter. Although no alteration is found in the chemical shifts and the longitudinal relaxation times (T_1) of phospholipid segments in CSV and LUV, the broad bandwidth of the ^{1}H-NMR signal and the large ^{31}P-NMR chemical shift anisotropy of CSV show a remarkable slowdown of the lipid tumbling motion in CSV with the rotational correlation time (τ_c) from subsecond to second order. In addition, the ^{1}H-^{1}H NOE enhancement (η) of the CSV lipid signal demonstrates the proximity between the hydrophilic headgroup and alkyl chains of the lipid [26]. The proximity is the result of the large protrusion in the vertical direction of the CSV surface, despite the slight curvature of the membrane. It is possible, however, that the protrusion motion is limited by the incorporation of hydrophobic molecules in CSV, although almost little effect is found in the presence of cations around the membrane surface [27].

30.3 DRUG DELIVERY RELATED TO MEMBRANE DYNAMICS

A large number of drugs, especially those containing small molecules, are transferred to the inside of living cells by passing through the plasma membrane based on the passive transport without the help of membrane transport proteins [28]. In these cases, drug binding from water to lipid bilayer membranes is of great importance as a preliminary stage of the biological action in the cell. As described in the previous section, lipid bilayer membranes are dynamic structures where the molecules are always moving and fluctuating in a confined geometry. Drug delivery mechanisms are expected to follow such dynamics in the fluid membrane. In particular, the drug permeation is expected to be closely related to the drug motion in the vertical direction to the membrane surface.

In this section, the dynamic aspects of drug deliveries are described. Our attention focuses on (1) the diffusivity of drugs in the membrane, (2) the kinetics of membrane binding and dissociation, and (3) the *dynamic* binding probability to quantify the efficiency of drug delivery from water to the membrane. The dynamic scheme of the delivery process is illustrated in Fig. 30.4. The solution NMR enables us to quantify (1) how much, how fast, and how efficiently the drug is bound to membrane; and (2) how rapidly the drug is moving within the membrane.

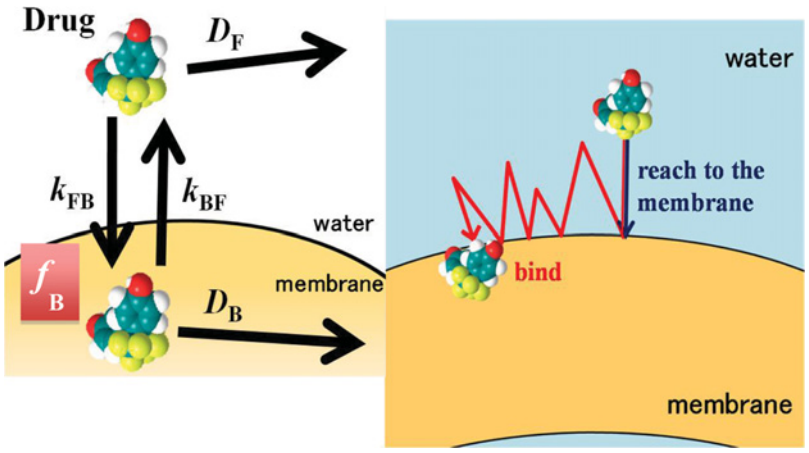


FIGURE 30.4 Dynamic model of drug delivery from water to the membrane. Left panel illustrates the diffusivity of the drug in water (D_F) and the membrane (D_B), the bound fraction (f_B), and the rate constants of membrane binding (k_{FB}) and dissociation (k_{BF}). Right panel shows "the *dynamic* binding probability" to quantify how efficiently the drug is bound to the membrane (see text).

30.3.1 Diffusion of Drugs in the Membrane

PFG NMR spectroscopy is powerful in terms of its ability to directly capture the molecular diffusion of drugs as well as lipids in a confined, anisotropic membrane. In the early 2000s, the diffusion of lipids and trapped drugs has been simultaneously observed in the freestanding membrane system, by using high-field-gradient high-resolution solution NMR at 600 MHz [14]. The self-diffusion of an endocrine disruptor, bisphenol A (BPA; 4,4′-isopropylidenediphenol; Fig. 30.1) is directly monitored, and was compared to the result for lipid molecules in size-controlled micelles and vesicles as described in Section 30.2.1.

As listed in Table 30.2, the BPA diffusion slows down in large-sized LUVs as compared to that in SUVs and micelles. It is also emphasized that the slowdown of lipid motions in membranes is leveled off in 100- and 400-nm LUVs, although the hydrodynamic (HD) continuum model gives the slowdown in diffusion in inverse proportion to lipid particle size. Recall that the surface curvature effect in LUV can be neglected at the molecular level. The situation is quite analogous to the membrane lipid motion in micelles and vesicles described in Section 30.2.1.

The above result implies that BPA mobility is related to membrane lipid dynamics. In fact, the simultaneous observation of the lipid diffusion in membranes shows that the BPA mobility is comparable to the respective lipid movement (Table 30.2); it is synchronized or concerted with the lipid matrix motion [14]. Thus it is rational to consider that the BPA diffusion in membrane is dominated by the dynamic property of the membrane matrices. It is clearly shown in Table 30.2 that the *intra*aggregate motion plays a significant role when the confined system is fluid and soft [14]. Because BPA has a high affinity for the membrane interface [29], the motion is decelerated by the site-specific, strong binding to the membrane lipid. The situation is in clear contrast to the movements of benzene and toluene [14], these movements are relatively independent of the membrane lipid motions as a result of the weak interaction with the membrane lipids.

The diffusion motion of a fluorinated BPA derivative, FBPA [$(CF_3)_2C(C_6H_4OH)_2$] (Fig. 30.1) has also been analyzed by ^{19}F NMR in combination with the PFG technique [30]. It is found that the diffusion coefficient of FPBA bound to 100-nm LUV is almost analogous to the value of nonfluorinated BPA; the mobility of FBPA in LUV is two orders of magnitude smaller than the mobility in water, and corresponds well to the movement of the membrane lipid, egg phosphatidylcholine (EPC) in LUV. Another team of investigators have reported that the mobility of cholesterol and the mobility of dimyristoylphosphatidylcholine (DMPC) in the membrane are shown to be equal, by using solid-state PFG NMR at 303–333 K [31]. The translational motions of cholesterol seem to be governed by the *intra*membrane fluidity. In contrast, the magic-angle spinning (MAS) solid-state PFG NMR [32, 33] shows that indole and an anti-inflammatory drug, ibuprofen, are moving faster than the membrane lipid, which is similar to the mobility of benzene and toluene [14]. A recent molecular dynamics (MD) simulation has also pointed out that an anesthetic, halothane, can move more than one order of magnitude faster than the membrane lipid [34].

With regard to an anticancer drug, 5-fluorouracil (5FU, Fig. 30.1), it is also found that the mobility of 5FU in EPC LUV is concerted with the EPC movement, although the molecular size of 5FU is much smaller than the EPC molecule [35]. This finding comes from the success in the simultaneous observation of membrane-bound and unbound (free) components as well as the membrane lipid, by the use of multinuclear ^{19}F and ^{1}H NMR in situ. In ^{19}F NMR, the self-diffusion coefficients of membrane-bound and free 5FU can be independently determined by combining the PFG technique. The method relies on the mobility difference between

TABLE 30.2 Self-Diffusion Coefficients of BPA in Water and in Model Confined Fluid Membrane

	Self-diffusion coefficient (10^{-10} m^2 s^{-1})			
		Lipid		
	BPA	Headgroup	Chain core	HD rigid sphere[a]
In bulk water	6.01 ± 0.03	–	–	–
In micelle	0.55 ± 0.01	0.65 ± 0.02	0.63 ± 0.02	1.7
In SUV	0.26 ± 0.01	0.25 ± 0.01	0.27 ± 0.01	0.17
In 100-nm LUV	0.12 ± 0.01	0.12 ± 0.01	0.14 ± 0.01	0.056
In 400-nm LUV	0.12 ± 0.01	0.13 ± 0.01	0.15 ± 0.01	0.014

[a] The hydrodynamic (HD) estimate of the overall translational diffusion D_T is inversely proportional to the HD radius d as $D_T = k_BT/6\pi\eta d$, where k_B represents the Boltzmann constant; T, the absolute temperature; and η, the solvent viscosity. The HD estimate to the overall rotational diffusion D_R is $D_R = k_BT/8\pi\eta d^3$. This corresponds to an additional translational diffusion of $\sim k_BT/8\pi\eta d$ and does not change the magnitude order of the HD estimate listed.
General notes: The diffusivity of the membrane lipid molecule is also shown. For the experimental conditions, see Table 30.1. The hydrodynamic (HD) diffusion coefficients [17] of the whole particle itself are listed in the right column.
Source: Reprinted with permission from Ref. 14. Copyright 2004 The American Physical Society.

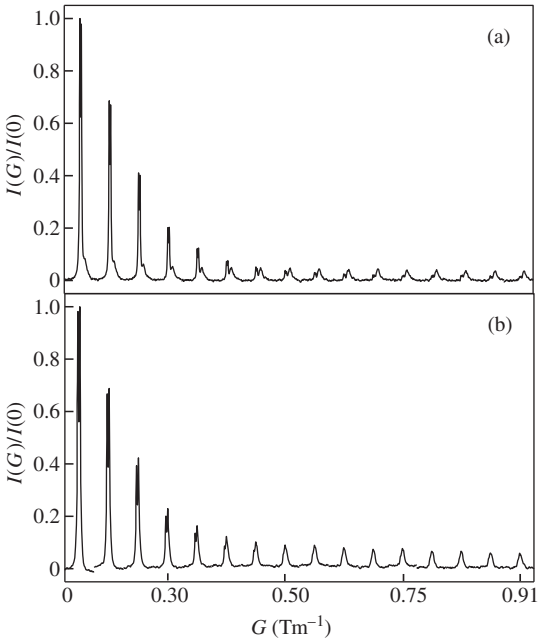


FIGURE 30.5 Plots showing attenuation of (a) ^{19}F- and (b) ^{1}H-NMR signals of 2 mM 5FU in the presence of LUV under the magnetic field gradient (G) of 0.05, 0.15, 0.225, 0.30, 0.35, 0.40, 0.45, 0.50, 0.55, 0.60, 0.65, 0.70, 0.75, 0.80, 0.85, and 0.91 T/m (from left to right). Here the rectangular FG pulses were applied with a time interval (Δ_{diff}) of 100 ms, with the gradient pulsewidth (δ) of 2 ms. (Reprinted with permission from Ref. 35. Copyright 2008 AIP Publishing LLC.)

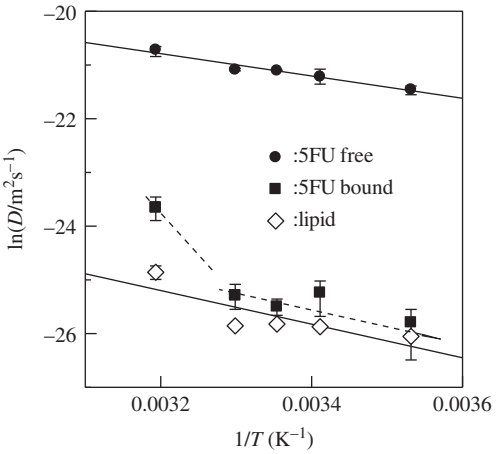


FIGURE 30.6 Temperature dependence of the self-diffusion rates of membrane-bound and free 5FU together with the mobility of the membrane lipid. For free 5FU and the lipid, the temperature dependences of the diffusion are of the Arrhenius type with activation energies of 21 kJ/mol (free 5FU) and 26 kJ/mol (lipid), respectively. Note that the dependence of the bound 5FU diffusion deviates from the Arrhenius type at 313 K (see text). (Reprinted with permission from Ref. 35. Copyright 2008 AIP Publishing LLC.)

the bound and the free components, where the signal decays can be treated as a biexponential function of the field gradient strength, G (Fig. 30.5) [35]. In Fig. 30.6, the diffusion coefficients of free and bound 5FU molecules are plotted as a function of the reciprocal temperature, together with the mobility of the membrane lipid. As compared to the free 5FU, the mobility of the membrane-bound 5FU is found to slow down by almost two orders of magnitude. At 283–303 K, the 5FU mobility in the membrane is almost comparable to that of the membrane lipid molecules. This means that the molecular motion in the fluid membrane environment is closely related to the *intra*membrane fluidity. The temperature dependence of the 5FU diffusion in the membrane is found to be of Arrhenius type, with the activation energy of diffusion motion, 26 kJ/mol [35]. In addition, the activation energy of 5FU is very close to the value of the membrane lipid [35, 36].

Although 5FU is moving as rapidly as the lipid matrix motion, the mobility is enhanced at high temperature. This is shown in Fig. 30.6 at 313 K. The enhancement of the 5FU mobility in the membrane is probably due to the fact that the lateral diffusion of 5FU is accelerated within the lipid membrane, or the fact that the membrane-bound 5FU rapidly exchanges with the free 5FU molecule as a result of the loose binding in the lipid matrices at high temperature [35].

30.3.2 Kinetics of Membrane Binding and Dissociation

As demonstrated in Fig. 30.4, the translational motion of drugs in the vertical direction to the membrane surface is closely related to the drug entry into the cell across the lipid membrane. The authors have focused on the drug motion in the *normal* direction to the lipid membrane, from the viewpoint of the exchange kinetics of free and bound drug molecules between bulk water and lipid membranes. The rate constants of membrane binding k_{FB} and dissociation k_{BF} of 5FU, a pentapeptide L-Enk (Fig. 30.1), and FPBA have been quantified by high-resolution solution NMR in combination with the PFG technique [30, 37, 38]. To evaluate the rate constants k_{FB} and k_{BF}, both ^{19}F- and ^{1}H-NMR signals have been analyzed by using the analytical formula of the Bloch equation with exchange terms. In this section, the focus is on how to quantify the exchange rate constants k_{FB} and k_{BF} of the drug by analyzing the NMR signal, and how the drug exchange motions differ from each other and how the diffusivities of the respective motions are differs from the diffusivity described in Section 30.3.1.

30.3.2.1 Hydrophilic Drugs. As mentioned in Section 30.3.1, the application of PFG NMR to the membrane system enables us to separate the signals of free and membrane-bound drugs in situ. In such cases, the exchange rate constants

of drug molecules can be obtained by (1) completely decomposing the drug signal into free and bound components, (2) evaluating the diffusion coefficients of the respective components by using the Stejskal–Tanner plot [16], and (3) fitting the analytical formula of the Bloch equation to the experimental signal intensities of each component.

A typical example is the case of 5FU [37]. When the 5FU exchange motion between the bulk water and lipid membrane is under equilibrium as

$$\text{Free (F)} \underset{k_{BF}}{\overset{k_{FB}}{\rightleftharpoons}} \text{bound (B)}, \tag{30.2}$$

the analytical signal intensity formulas are derived by using the Bloch equation in combination with the diffusion and exchange terms as [39]

$$I_F(G) = \left\{ \frac{I_{F0}}{2} + \frac{\lambda I_{F0} + k_{BF} I_{B0}}{2\Delta} \right\} \exp\{(-\sigma + \Delta)\tau\} + \left\{ \frac{I_{F0}}{2} - \frac{\lambda I_{F0} + k_{BF} I_{B0}}{2\Delta} \right\} \exp\{(-\sigma - \Delta)\tau\} \tag{30.3}$$

and

$$I_B(G) = \left\{ \frac{I_{B0}}{2} - \frac{\lambda I_{B0} - k_{FB} I_{F0}}{2\Delta} \right\} \exp\{(-\sigma + \Delta)\tau\} + \left\{ \frac{I_{B0}}{2} + \frac{\lambda I_{B0} + k_{FB} I_{F0}}{2\Delta} \right\} \exp\{(-\sigma - \Delta)\tau\} \tag{30.4}$$

where $I_F(G)$ and $I_B(G)$ are the PFG NMR signal intensities of free (F) and bound (B) components. λ, σ, and Δ are

$$\lambda = \frac{1}{2}\left\{k_{BF} - k_{FB} + D_B(\gamma\delta G)^2 - D_F(\gamma\delta G)^2\right\}, \tag{30.5}$$

$$\sigma = \frac{1}{2}\left\{k_{BF} + k_{FB} + D_B(\gamma\delta G)^2 + D_F(\gamma\delta G)^2\right\}, \tag{30.6}$$

and

$$\Delta = \sqrt{\lambda^2 + k_{BF}k_{FB}}, \tag{30.7}$$

where D_F and D_B are the diffusion coefficients of free and bound 5FU. The exchange rate constants, k_{FB} and k_{BF}, can be determined by fitting Eqs. (30.3) and (30.4) to the signal intensities, $I_F(G)$ and $I_B(G)$ [37].

It is found that k_{FB} and k_{BF} of 5FU are 0.2 ± 0.1 and $4.1 \pm 1.5\ s^{-1}$ at 303 K where the membrane lipids are in the fluid liquid-crystalline state [37]. This corresponds to the half-value periods of binding and dissociation, t_{FB} and t_{BF}, of 3.5 and 0.17 s, respectively. The timespan of the membrane binding and dissociation of 5FU are found to be on second and a subsecond timescales, respectively. The temperature dependence shows that the exchange rate constants, k_{FB} and k_{BF}, are of Arrhenius type with the activation energy of the exchange motion, ~57 kJ/mol [37]. The activation energy is more than twice as high as that of the translational diffusion in the lipid membrane (26 kJ/mol) mentioned in Section 30.3.1. This indicates that the 5FU motion in the vertical direction to the membrane surface is restricted as compared with the translational diffusion in the membrane.

Molecular dynamics of peptide binding to the membrane is crucial for a better understanding of the primary stage of the bioactivities in the cell. In situ NMR is expected to be powerful to gain insight into the mechanistic view of peptide functions in a natural manner. The proton NMR is effective because ^{1}H is abundant in the natural system. Recently, the PFG ^{1}H NMR method has been also applied to explore the dynamics of peptide binding to fluid lipid membranes [38]. The kinetics of binding of a neuropeptide, leucine-enkephalin (L-Enk, Fig. 30.1) to lipid bilayer membranes has been quantified by PFG ^{1}H NMR in situ. The peptide signal has been analyzed by solution of the Bloch equation with exchange terms in the presence of EPC LUV of 100 nm diameter as confined, but fluid model cell membranes [38]. Even when membrane-bound and free states of L-Enk cannot be distinguished in the one-dimensional (1D) ^{1}H-NMR spectrum, the PFG technique unveils the bound component of L-Enk after the preferential decay of the free component at the high field gradient. The rate constants of the peptide binding and dissociation are 0.040 and 0.40 s^{-1} at 303 K [38]. The values correspond to the lifetime of the peptide binding of the order from 1 to 10 s.

30.3.2.2 Hydrophobic Drugs. As described in Section 30.3.2.1, PFG ^{19}F and ^{1}H NMR allow us to quantify how fast 5FU and L-Enk are bound to the membrane and dissociate from the membrane. The method is based on the simultaneous detection of bound and free (unbound) states of the drug in situ. The bound and free states are distinguishable in case of rather hydrophilic drug such as 5FU and L-Enk because of the relatively slow exchange of the drug molecules between these two states [37, 38]. In contrast, the permeation of a hydrophobic drug across the membrane is generally too rapid [1] to permit easy distinction between bound and free states. In fact, the ^{19}F-NMR signal of the hydrophobic FBPA is still observed as a singlet even in the presence of EPC LUV, as illustrated in Fig. 30.7. This means that the bound component of FBPA is exchanging so rapidly with the free component that we cannot distinguish these two states on the NMR timescale. When molecules are in rapid exchange between the bound and free states, the NMR spectra consist of a single set of peaks whose chemical shifts are averaged between these the two states [2]. Although the

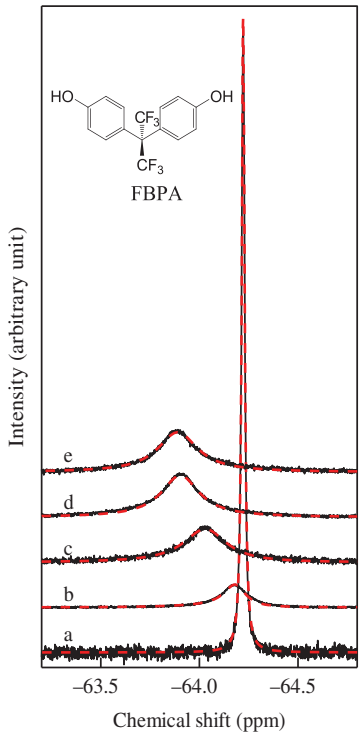


FIGURE 30.7 One-dimensional ^{19}F-NMR spectra of FBPA in the absence (a) and presence of (b) 0.4, (c) 1, (d) 4, and (e) 40 mM EPC LUV at 303 K. The solid lines show the observed spectra and the dashed lines show the fitting results of Eq. (30.15) to the respective NMR signals. (Reprinted with permission from Ref. 30. Copyright 2011 American Chemical Society.)

bound and free components are averaged in the NMR spectra, the exchange rate constants are nonetheless obtainable from an analysis of the spectra that relies on the expression of 1D NMR signal intensity by a set of Bloch equations with exchange terms [30].

When a hydrophobic FBPA molecule is exchanging between the bound (B) and the free (F) states, a set of Bloch equations with exchange terms can be written as

$$\frac{dM_{\mathrm{B}}}{dt} = -\left(\frac{1}{T_{2\mathrm{B}}^{0}} + \frac{i\omega_{B}^{0}}{2\pi} + k_{\mathrm{BF}}\right) M_{\mathrm{B}} + k_{\mathrm{FB}} M_{\mathrm{F}} \qquad (30.8)$$

and

$$\frac{dM_{\mathrm{F}}}{dt} = -\left(\frac{1}{T_{2\mathrm{F}}^{0}} + \frac{i\omega_{\mathrm{F}}^{0}}{2\pi} + k_{\mathrm{FB}}\right) M_{\mathrm{F}} + k_{\mathrm{BF}} M_{\mathrm{B}}, \qquad (30.9)$$

where M_{B} and M_{F} are the signal intensities of B and F components, and T_{2i}^{0} and ω_{i}^{0} (i = B or F) are respectively the transverse relaxation time and the resonance frequency of the pure B or F states of FBPA. The analytical solution of Eqs. (30.8) and (30.9) is, therefore, expressed as a function of the frequency ω

$$M_{\mathrm{B}}(\omega) = \frac{M_0}{\pi} \frac{\beta_{\mathrm{F}} f_{\mathrm{B}} + k_{\mathrm{FB}} f_{\mathrm{F}}}{\beta_{\mathrm{B}}\beta_{\mathrm{F}} - k_{\mathrm{BF}} k_{\mathrm{FB}}} \qquad (30.10)$$

and

$$M_{\mathrm{F}}(\omega) = \frac{M_0}{\pi} \frac{\beta_{\mathrm{B}} f_{\mathrm{F}} + k_{\mathrm{BF}} f_{\mathrm{B}}}{\beta_{\mathrm{B}}\beta_{\mathrm{F}} - k_{\mathrm{BF}} k_{\mathrm{FB}}} \qquad (30.11)$$

where

$$\beta_{\mathrm{B}} = \frac{1}{T_{2\mathrm{B}}^{0}} + \frac{i\omega_{\mathrm{B}}^{0}}{2\pi} + k_{\mathrm{BF}} - \frac{i\omega}{2\pi} \qquad (30.12)$$

and

$$\beta_{\mathrm{F}} = \frac{1}{T_{2\mathrm{F}}^{0}} + \frac{i\omega_{\mathrm{F}}^{0}}{2\pi} + k_{\mathrm{FB}} - \frac{i\omega}{2\pi} \qquad (30.13)$$

and f_j is the fraction of the j (= B or F) state. Under the equilibrium condition

$$k_{\mathrm{BF}} f_{\mathrm{B}} = k_{\mathrm{FB}} f_{\mathrm{F}}, \qquad (30.14)$$

the observed 1D NMR signal intensity is finally given as

$$M(\omega) = M_{\mathrm{B}}(\omega) + M_{\mathrm{F}}(\omega) = \frac{M_0}{\pi} \frac{\beta_{\mathrm{F}} f_{\mathrm{B}} + k_{\mathrm{FB}} f_{\mathrm{F}} + \beta_{\mathrm{B}} f_{\mathrm{F}} + k_{\mathrm{BF}} f_{\mathrm{B}}}{\beta_{\mathrm{B}}\beta_{\mathrm{F}} - k_{\mathrm{BF}} k_{\mathrm{FB}}} \qquad (30.15)$$

As the transverse relaxation times $T_{2\mathrm{B}}^{0}$ and $T_{2\mathrm{F}}^{0}$ and the frequencies ω_{B}^{0} and ω_{F}^{0} are evaluated from the 1D ^{19}F NMR spectra in both presence and absence of LUV [30], the parameters k_{BF}, k_{BF}, f_{B}, and f_{F} can be finally determined by fitting Eq. (30.15) to the observed signal intensity and reduced by using the relations $f_{\mathrm{B}} + f_{\mathrm{F}} = 1$ and Eq. (30.14).

It is found that the rate constant of FBPA-binding k_{FB} is enhanced from 22 to 280 s^{-1} by increasing the lipid concentration in LUV [30]. The k_{FB} is much larger than that of hydrophilic 5FU (0.2 s^{-1}) described in Section 30.3.2.1 [37]. The dissociation rate constant k_{BF} of FBPA is in the range from 68 to 107 s^{-1}. The rate constants obtained correspond to the half-value periods of the FPBA binding and dissociation, t_{FB} and t_{BF}, of 3–32 and 5–10 ms, respectively [30]. The timespan of the membrane binding and dissociation of FBPA is found to be a 10^{-3}–10^{-2} -s timescale, which is two to three orders of magnitude as fast as the 5FU binding of a 10^{-1}–10^{0} -s timescale.

30.3.3 Thermodynamic Stability

30.3.3.1 5FU and L-Enk. The success in distinguishing the bound and free 5FU signals enables us to quantify in what amount of the drug is bound to the membrane in situ. This is accomplished by integrating the respective components of the 5FU signal. The quantification is achieved after the signal decomposition of the 1D NMR spectrum or the PFG NMR application. In the 1D ^{19}F-NMR spectrum of 5FU at 303 K, the membrane-bound fraction is found to be ∼0.1 relative to the total signal intensity of 5FU in water [35]. This is consistent with the bound fraction obtained by the PFG ^{1}H-NMR measurement; note that the PFG analysis is effective because the decomposition of the 1D ^{1}H-NMR spectrum is not successful because of the overlap of the bound and free components [35, Fig. 4B]. Both ^{19}F and ^{1}H NMR results of the 5FU bound fraction about 0.1 at 283–313 K give the binding free energy, ranging from −4 to −2 kJ/mol; the magnitude is very close to the thermal fluctuation, 2.4–2.6 kJ/mol.

The binding amount of L-Enk is not so large; it ranges, for example, from 0.09 for 5 mM L-Enk to 40 mM lipid LUV from the PFG ^{1}H-NMR analysis [38]. This indicates that 0.45 mM of L-Enk is bound to the LUV that corresponds to the peptide/lipid molar ratio of 0.011. The binding free energy ΔG of L-Enk is estimated as −2.9 kJ/mol at 303 K, the magnitude close to the thermal fluctuation, 2.5 kJ/mol. The value is analogous to the result of 5FU mentioned above, and it is reasonable in terms of the rather hydrophilic nature of L-Enk and 5FU.

30.3.3.2 FBPA. The thermodynamic stability of hydrophobic FBPA molecules in membranes can also be quantified in situ, by fitting Eq. (30.15) to the observed 1D ^{19}F-NMR spectra. It is found that the bound fraction f_B gradually increases with increase of the lipid concentration in LUV, and it finally comes to almost unity at high lipid/FBPA molar ratio [30]. It is noted that the result is consistent with the chemical shift, the transverse relaxation time, and the diffusivity variations as a function of the lipid concentration [30]. The f_B values are also comparable with the fraction ${f_B}^{\omega}$, which is estimated from the observed chemical shift ω_{obs} at the FBPA peak maximum, in accordance with the two-site model where ω_{obs} is equal to the weighted average of the chemical shifts of pure free and bound components ω_F^0 and ω_B^0:

$$\omega_{obs} = \left(1 - f_B^{\omega}\right)\omega_F^0 + f_B^{\omega}\omega_B^0 \qquad (30.16)$$

For FBPA, the difference in the free energy ΔG between the bound and the free states is calculated to be −20 ± 2 kJ/mol at 303 K, the value independent of the molar ratio of lipid/FBPA. The ΔG of −20 kJ/mol indicates that the hydrophobic FBPA prefers the membrane interior to the bulk water. This is consistent with the previous NMR result of non-fluorinated BPA that it is located between the lipid headgroup and hydrocarbon chain region most adjacent to the interface, with the two methyl groups oriented toward the inside of the bilayer [29]. The situation is in contrast to rather hydrophilic 5FU and L-Enk described in Section 30.3.3.1, where the magnitude of the binding free energy is very close to the thermal fluctuation [35, 38].

The temperature dependence of ΔG informs us of the differences in the entropy ΔS and in the enthalpy ΔH between the free and the bound states of FBPA. The ΔS of FBPA binding is (157 ± 10) J/(mol K), about 2.5 times as large as that of 5FU, (63 ± 29) J/(mol K) [30]. The large ΔS value of FBPA indicates that FBPA avoids the hydrophobic hydration in bulk water and is remarkably stabilized in the membrane. ΔH of FBPA [(28 ± 3) kJ/mol] and 5FU [(15 ± 9) kJ/mol] are both positive [30], indicating the endothermic binding of both drugs to the membrane. For FBPA, $T\Delta S$ is much larger than ΔH ($\Delta H < T\Delta S$), whereas $\Delta H \simeq T\Delta S$ for 5FU [30]. The binding of the FBPA is found to be entropy-driven.

30.3.4 Dynamic Binding Probability

The efficiency of drug transfer from water to membranes (right panel in Fig. 30.4) is of significance to consider the drug delivery mechanism. One group of investigators have introduced a *dynamic* binding probability P to quantify the efficiency, which is defined by a ratio t_R/t_B, where t_R is the mean time interval for a drug to reach at first to the membrane surface, and t_B is the interval for the drug to bind to the membrane, as illustrated in Fig. 30.8 [30]. t_R is evaluated by the analytical formula of the reaction time of diffusion-controlled reaction [40], and t_B is calculated from the observed k_{FB} as $t_B = {k_{FB}}^{-1}$. Regarding the spherical system of radius r_s where the spherical vesicle of radius r_v is

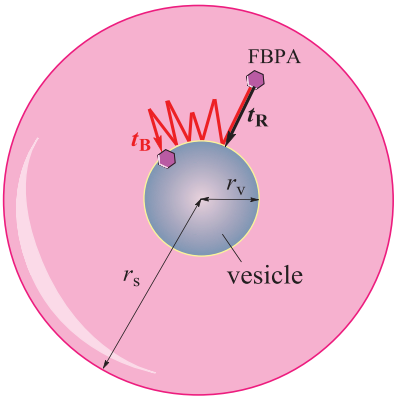


FIGURE 30.8 Model for evaluating the efficiency of FBPA transfer from water to vesicle. (Reprinted with permission from Ref. 30. Copyright 2011 American Chemical Society.)

TABLE 30.3 Mean Time Intervals t_R and t_B, and Dynamic Binding Probability P of FBPA Molecules

	FBPA					5FU[a]
c_{EPC} (mM)[b]	0.4	0.7	1.0	2.0	2.5	40
t_R (ms)	0.92	0.50	0.34	0.15	0.12	1.8×10^{-3}
t_B (ms)	27	45	6.5	7.2	3.6	5.0×10^{3}
P	3.4×10^{-2}	1.1×10^{-2}	5.2×10^{-2}	2.1×10^{-2}	3.3×10^{-2}	4.1×10^{-7}

[a] 5FU at 10 mM.
[b] EPC concentration.
General notes: The values for 5FU are also listed in the right column. All values are at 303 K.
Source: Reprinted with permission from Ref. 30. Copyright 2011 American Chemical Society.

placed on the center (Fig. 30.8), the mean time interval t_R is given as

$$t_R = \frac{r_s^2}{D} \frac{(1-x^2)(5+6x+3x^2+x^3)}{15x(1+x+x^2)} \qquad (30.17)$$

where $x = r_v/r_s$ [30]. D, the diffusion coefficient of FBPA in the bulk, is evaluated by using the movement of the drug molecule relative to the center of the vesicle. The calculated results of t_R, t_B, and P ($= k_{FB}\, t_R$) are listed in Table 30.3. For FBPA, it is found that the dynamic binding probability P is in the range of 0.030 ± 0.022. This means that the ratio (N_{FBPA} to reach memebrane)/(N_{FBPA} to bind to membrane) (where N_{FBPA} = number of FBPA molecules) is ~40. The binding probability P of the hydrophilic 5FU is, in contrast, almost five orders of magnitude smaller than FBPA. The difference in hydrophobicity between FBPA and 5FU is found to affect the efficiency of drug transfer to the membrane.

30.3.5 Effect of Cholesterol

Cholesterol plays a significant role in regulating structure, dynamics, and functions of biological membranes [7–10,41–44]. Under physiological conditions where molecules are fluctuating at soft membrane interfaces [2, 5], cholesterol stiffens the membrane lipids; the lipid molecules reduce the freedom of motion in the membrane [9, 10]. The delivery process is likely to be limited in such rigid membrane environments. In fact, it has been reported that the permeability of small molecules is inhibited by the presence of cholesterol [45–47]. Cholesterol also suppresses the permeability of water via the auaporin-4 channel in the membrane [48] and permeability of Ca^{2+} mediated by the ionophore A23187 [49]. It is reported that the presence of cholesterol decreases the drug binding affinity to the membrane [50, 51].

Most recently, the high-resolution solution NMR has been applied in a study of the delivery of a fluorinated anesthetic, sevoflurane (SF, fluoromethyl 2,2,2-trifluoro-1-[trifluoromethyl]ethyl ether; Fig. 30.1), to cholesterol-containing LUV from water at a clinically relevant concentration [52]. SF is a hydrophobic molecule with its solubility in water, several hundred μM at ambient temperature. The low solubility in water results in SF preference for the hydrophobic membrane interior. Utilizing that SF contains fluorine nuclei, both ^{19}F and ^{1}H NMR are used to monitor SF molecules in the membrane. The NMR chemical shift, the longitudinal relaxation time (T_1), and the diffusion coefficient are analyzed to quantify how the SF uptake is modified by the presence of cholesterol in the membrane.

It is found that the uptake of SF is limited in the cholesterol-rich membrane. The limited uptake of SF is related to the rigidity of the membrane where the molecular movements are restricted by the presence of cholesterol. This is demonstrated by the slowdown of the lipid diffusion at high cholesterol fraction in the membrane [52].

30.4 CONCLUDING REMARKS AND FUTURE PERSPECTIVES

High-resolution solution-state NMR spectroscopy is a powerful method to gain insight into the molecular picture of membrane fluctuation and drug transport processes in membranes. In this chapter, two kinds of in situ NMR methods used to observe the molecular dynamics in model cell membranes are described. One is to apply multinuclear NMR spectroscopy in combination with the pulsed-field-gradient (PFG) spin-echo technique. The criterion is that the signals assigned to membrane-bound molecules are insensitive to the PFG application because of the motional slowdown in the membrane environment, whereas the signal assigned to free (unbound) species is attenuated preferentially with increasing the field-gradient (FG) strength. The simultaneous observation of the membrane-bound and free signals enables one to quantify the amount of drug that is bound to the membrane and how rapidly the drug is moving within the membrane in relation to the thermal fluctuation of the soft, fluid environment. The other method is to analyze 1D NMR spectra by using the solution of the Bloch equation with exchange terms. The method is particularly useful where the bound and the free components of the drug are indistinguishable because of the rapid exchange on the NMR timescale. The

TABLE 30.4 Dynamic Parameters of Drug Deliveries Quantified by 1D and PFG NMR In Situ

Drug	c_{drug} (mM)	c_{lipid} (mM)	f_B	ΔG (kJ mol^{-1})	D_F (10^{-10} m^{2}s^{-1})	D_B (10^{-10} m^{2}s^{-1})	k_{FB} (s^{-1})	k_{BF} (s^{-1})
5FU[a]	10	40	0.13 ± 0.01	-4.2 ± 0.1	7.7 ± 0.4	0.16 ± 0.04	0.2 ± 0.1	4.1 ± 1.5
FBPA[b]	0.063	0.4	0.32 ± 0.01	–	5.2 ± 0.2	0.075 ± 0.035	37 ± 1	79 ± 2
		2.5	0.73 ± 0.01	-20 ± 2	–	–	282 ± 13	107 ± 2
		40	1.0	–	–	–	–	–
L-Enk[c]	5	40	0.09 ± 0.01	-2.9 ± 0.1	2.9 ± 0.1	0.050 ± 0.014	0.040 ± 0.004	0.40 ± 0.01

[a] From Ref. 37.
[b] From Ref. 30.
[c] From Ref. 38.
General notes: All values are at 303 K. The terms c_{drug} and c_{lipid} represent the drug and lipid concentrations, respectively (see text for details).

diffusivity, the kinetics of membrane binding and dissociation, the dynamic binding probability, and the thermodynamic stability of hydrophilic and hydrophobic drugs are quantified by NMR in situ without any perturbation of the system. The results are summarized in Table 30.4.

It is reasonable to consider application of the in situ NMR method to the living system. Permeation of the drug to the internal part of the cell via the cell membrane is an issue of great significance not only as the primary stage of bioactivities but also for the purpose of rational drug design. Although endocytosis is thought to be a typical mechanism for drug entry into the cell, it is still unknown, in some cases, how the passive transport of the drug proceeds through the biological membrane. Fluorescence labeling is a commonly used technique. Although it is sensitive, it sometimes modulates the intracellular delivery of the drug [53]. In this sense, the label-free, in-cell NMR method is advantageous. The in situ technique is effective for observing real-time processes of cellular uptake of drugs without perturbing the system. Actually, the transport of a hydrophobic ion across the *Escherichia coli* membrane has been most recently analyzed with time resolution, by using nonlinear optical second-harmonic generation (SHG) [54]. Real-time in-cell NMR is to be realized to quantify the kinetics of drug delivery to natural human cells, in relation to the cell membrane dynamics.

ACKNOWLEDGMENTS

The author's work is supported by JSPS KAKENHI Grants 14540531, 17550153, 20550027, and 24550035; MEXT KAKENHI Grant 21107527; and Hyogo Science and Technology Association Grant 25073, Japan.

REFERENCES

[1] Alberts, B., et al. (2008). *Molecular Biology of the Cell*, 5th ed. Garland Science, New York.

[2] Okamura, E., Nakahara, M. (2001). In Volkov, A.G. (ed.), *Liquid Interfaces in Chemical, Biological, and Pharmaceutical Applications*. Marcel Dekker, New York, pp. 775–805 and references cited therein.

[3] Sackmann, E. (1995). In Lipowsky, R., Sackmann, E. (eds.), *Handbook of Biological Physics*, Vol. 1. Elsevier, pp. 213–304.

[4] Singer, S.J., Nicolson, G.L. (1972). *Science* **175**, 720–731.

[5] Gawrisch, K. (2004). In Yeagle, P. L. (ed.), *The Structure of Biological Membranes*. CRC Press, Boca Raton, FL, pp. 147–171.

[6] Scheidt, H.A., Huster, D. (2008). *Acta Pharmacol. Sinica* **29**, 35–49.

[7] Simons, K., Ikonen, E. (1997). *Nature* **387**, 569–572.

[8] Boesze-Battaglia, K. (2004). In Yeagle, P.L. (ed.), *The Structure of Biological Membranes*. CRC Press, Boca Raton, FL, pp. 309–327.

[9] Yeagle, P.L. (ed.) (2004). *The Structure of Biological Membranes.* CRC Press, Boca Raton, FL, pp. 243–254, and references cited therein.

[10] Rog, T., et al. (2009). *Biochim. Biophys. Acta* **1788**, 97–121.

[11] Stilbs, P. (1987). *Progress NMR Spectrosc.* **19**, 1–45.

[12] Filippov, A., Orädd, G., Lindblom, G. (2003). *Biophys. J.* **84**, 3079–3086.

[13] Gaede, H.C., Gawrisch, K. (2003). *Biophys. J.* **85**, 1734–1740.

[14] Okamura, E., et al. (2004). *Phys. Rev. Lett.* **93**, 248101.

[15] Okamura, E., et al. (1997). *Chem. Lett.* **26**, 1061–1062.

[16] Stejskal, E.O., Tanner, J.E. (1965). *J. Chem. Phys.* **42**, 288–292.

[17] Wakai, C., Nakahara, M. (1997). *J. Chem. Phys.* **106**, 7512.

[18] Yoshii, N., Emoto, T., Okamura, E. (2013). *Colloids Surf. B: Biointerfaces* **106**, 22–27.

[19] Doeven, M.K., et al. (2005). *Biophys. J.* **88**, 1134–1142.

[20] Przybylo, M., et al. (2006). *Langmuir* **22**, 9096–9099.

[21] Xu, Z.-C., Cafiso, D.S. (1986). *Biophys. J.* **49**, 779–783.

[22] Huster, D., Gawrisch, K. (1999). *J. Phys. Chem. B* **103**, 243-251.

[23] Huster, D., Gawrisch, K. (1999). *J. Am. Chem. Soc.* **121**, 1992–1993.

[24] Giordani, C., et al. (2008). *J. Phys. Chem. B* **112**, 2622–2628.

[25] Koenig, S., et al. (1992). *J. Phys.* **2**, 1589–1615.

[26] Takechi, Y., Saito, H., Okamura, E. (2013). *Chem. Phys. Lett.* **570**, 136–140.

[27] Takechi, Y., et al. (2015). Membrane, 40, 38–45.

[28] Balaz, S. (2000). *Perspect. Drug Discov. Design* **19**, 157–177.

[29] Okamura, E., Kakitsubo, R., Nakahara, M. (1999). *Langmuir* **15**, 8332–8335.

[30] Yoshii, N., Okamura, E. (2011). *J. Phys. Chem. B* **115**, 11074–11080.

[31] Orädd, G., Lindblom, G., Westerman, P.W. (2002). *Biophys. J.* **83**, 2702–2704.

[32] Gaede, H.C., Gawrisch, K. (2003). *Biophys. J.* **85**, 1734–1740.

[33] Gaede, H.C., Yau, W.-M., Gawrisch, K. (2005). *J. Phys. Chem. B* **109**, 13014–13023.

[34] Pickholz, M., Saitz, L., Klein, M.L. (2005). *Biophys. J.* **88**, 1524–1534.

[35] Okamura, E., Yoshii, N. (2008). *J. Chem. Phys.* **129**, 215102.

[36] Filippov, A., Orädd, G., Lindblom, G. (2003). *Biophys. J.* **84**, 3079–3086.

[37] Yoshii, N., Okamura, E. (2009). *Chem. Phys. Lett.* **474**, 357–361.

[38] Yoshii, N., Emoto, T., Okamura, E. (2011). *Biophysics* **7**, 105–111.

[39] Johnson, C.S., Jr. (1993). *J. Magn. Reson. A* **102**, 214–218.

[40] Szabo, A., Schulten, K., Schulten, Z. (1980). *J. Chem. Phys.* **72**, 4350.

[41] Forbes, J., et al. (1988). *J. Chem. Soc. Faraday Transact.* **1 84**, 3821–3849.

[42] Pan, J., et al. (2008). *Phys. Rev. Lett.* **100**, 198103.

[43] Mills, T.T., et al. (2008). *Biophys. J.* **95**, 669–681.

[44] Mills, T.T., et al. (2008). *Biophys. J.* **95**, 682–690.

[45] Subczynski, W., et al. (1994). *Biochemistry* **33**, 7670–7681.

[46] Demel, R.A., Bruckdorfer, K.R., Van Deenen, L.L.M. (1972). *Biochim. Biophys. Acta* **255**, 321–330.

[47] Papahadjopoulos, D., Nir, S., Ohki, S. (1972). *Biochim. Biophys. Acta* **266**, 561–583.

[48] Tong, J., Briggs, M.M., McIntosh, T.J. (2012). *Biophys. J.* **103**, 1899–1908.

[49] Bittman, R., et al. (1984). *Biochim. Biophys. Acta* **772**, 117–126.

[50] Nguyen, T.T., Conboy, J.C. (2011). *Anal. Chem.* **83**, 5979–5988.

[51] Schote, U., et al. (2002). *J. Pharm. Sci.* **91**, 856–867.

[52] Okamura, E., Takechi, Y., Aki, K. (2014). *J. Oleo Sci.* **63**, 1149–1157.

[53] Okamura, E., et al. (2005). *Chem. Lett.* **34**, 1064–1065.

[54] Zeng, J., et al. (2013). *Biophys. J.* **104**, 139–145.

[55] Bossev, D.P., Matsumoto, M., Nakahara, M. (in press). In Abe, M. (ed.), *Mixed Surfactant Systems.* Marcel Dekker, New York.

[56] Stilbs, P., Arvidson, G., Lindblom, G. (1984). *Chem. Phys. Lipids* **35**, 309–314.

[57] Ladha, S., et al. (1996). *Biophys. J.* **71**, 1364–1373.

[58] Lindahl, E., Edholm, O. (2001). *J. Chem. Phys.* **115**, 4938.

31

STIMULUS-RESPONSIVE INTELLIGENT DRUG DELIVERY SYSTEM BASED ON HYDROXYAPATITE-RELATED MATERIALS

MAKOTO OTSUKA

Research Institute of Pharmaceutical Sciences, Faculty of Pharmacy, Musashino University, Nishi-Tokyo 202-8585, Japan

31.1 INTRODUCTION

For the treatment of intractable diseases, slow-release drug delivery systems could provide the required dose at the required time to the targeted site. Such systems reduce undesirable side effects and achieve a long-term therapeutic concentration at a specific site [1]. Slow-release systems are often coupled with biodegradable solid devices, which gradually degrade in the body and continue to release the drug for a long period [2]. Solid-type slow-release systems are mainly implanted surgically, which is often invasive and difficult depending on the site [3]. Microspheres composed of a biodegradable microgel have been explored as an injectable device [4], which allow the drug to be released over a period of several weeks. Injectable materials that self-assemble into a solid in the body would be another solution to avoid surgical implantation. The slow-release drug delivery systems are useful for practical therapeutics without concern about a patient's compliance. However, the biggest drawback of this dosage form is that, once applied, stopping the application of the drug is difficult. When the disease condition changes, it is not possible to change the dose.

On the other hand, intelligent drug delivery systems are capable of adjusting drug release rates in response to the physiological need of the patient [5,6]. Intelligent drug delivery systems are based mostly on stimulus-responsive polymers that sense a change in a specific variable and activate the delivery, as this phenomenon is reversible [7]. It is important to develop intelligent drug delivery systems to understand physiological systems and mechanisms of the human body and related diseases.

In order to develop a stimulus-responsive intelligent drug release system for skeleton hard tissues, it is vital that the characteristics of bone graft remodeling by osteoclasts and osteoblasts be fully understood. Since bone resorption and formation occur repeatedly in the functional units called *bone multicellular units*, which maintain the dynamic equilibrium of mineral density in normal bone [8], uncoupling between bone resorption by osteoclasts and bone formation by osteoblasts causes an absolute decrease in the amount of bone in osteoporosis. We have, therefore, developed a stimulus-responsive intelligent drug release system to improve bioaffinity and drug delivery ability to skeleton hard tissues by enhancing the interaction between the composites and bone cells for applications as cell scaffold devices [7].

This review focuses on the process of developing an intelligent drug release system for biological stimulus-responsive drug release for skeletal hard tissues. It consists of hydroxyapatite-related compounds that mimic natural bone, and the system shows stimulus-responsive drug release for a long period of time to hard tissues or the whole body.

31.2 SLOW DRUG RELEASE FROM SELF-SETTING APATITE CEMENTS

The conventional bioactive ceramics on the market, such as hydroxyapatite (HAp), β-tricalcium phosphate, and bioglass

Encyclopedia of Biocolloid and Biointerface Science, Volume 1, First Edition. Edited by Hiroyuki Ohshima.
© 2016 John Wiley & Sons, Inc. Published 2016 by John Wiley & Sons, Inc.

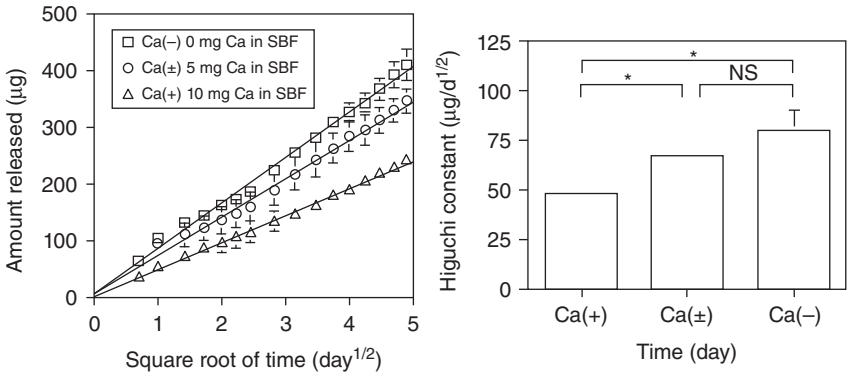


FIGURE 31.1 Calcium-level-responsive in vitro drug release from AP cement containing estradiol.

ceramics, have good bioaffinity, and can directly connect with bone [9]. However, these materials could remain in bone for an extended period and alter its mechanical strength because their chemical composition and geometric structure are very different from those of natural bone and they exhibit lower bioaffinity [9]. Two investigators [10] developed an injectable apatite cement formulation (AP) consisting of an equimolar mixture of tetracalcium phosphate [TECP; $Ca_4(PO_4)_2O$] and dicalcium phosphate dihydrate (DCPD; $CaHPO_4.2H_2O$], which had the capacity of self-setting in vivo, within the bone cavity. The development of the cement established good prospects for minimally invasive surgical techniques developed in recent years, which are less aggressive than the classical surgical methods [11]. Drug delivery systems for several drugs [12,13] have been developed on the basis of biocompatible self-setting AP cement [10, 14] that is transformed into hydroxyapatite with lower crystallinity in the body. After implantation of the AP cement, initial drug release from the cement was found to be greater than that at a later stage [13]. The rate-limiting step of drug release from the matrix system was basically the drug diffusion process in the micropores of the matrix. The drug release from drug-loaded cement matrix systems follows the Higuchi equation [15]

$$M_t = A\sqrt{C_s \frac{D_i \varepsilon}{\tau}(2C_d - \varepsilon C_s)t} \qquad (31.1)$$

where M_t is the amount of drug released after time t, A is the surface area of the device, D_i is the diffusion coefficient of the drug, C_s is the solubility, C_d is the concentration of drug in the matrix, τ is the tortuosity, and ε is the porosity.

31.3 EFFECT OF CALCIUM LEVEL ON IN VITRO DRUG RELEASE FROM APATITE CEMENT [16]

It is well known that fine calcium phosphate fine crystals are precipitated after soaking in simulated body fluid (SBF), since SBF has a high degree of supersaturated concentration with respect to the solubility of hydroxyapatite [17]. In order to clarify the calcium concentration dependences of the in vitro drug release from apatite cement containing estradiol, their drug release rates were measured in different dissolution media with high or low calcium concentrations. The in vitro estradiol levels released from the AP cement systems in 0, 5, and 10 mg of calcium/100 mL SBF were 410, 346, and 241 μg after 24 days, respectively, indicating that the estradiol release rate from the apatite cement decreased with increasing calcium concentration in dissolution media (Fig. 31.1). The result of in vitro estradiol release in SBF suggested that change in the geometric structure of the device surface depends on the degree of calcium concentration in SBF. The cement surface was covered with precipitated fine hydroxyapatite crystals during the drug release test as a result of the high degree of supersaturation of SBF with respect to the solubility of hydroxyapatite, and inhibited drug release. Conversely, in SBF at unsaturated calcium levels, the hydroxyapatite in the cement matrix dissolved and/or eroded, accelerating drug release. Therefore, in vitro estradiol release from the cement matrix was reflected decreasing or increasing effective diffusivity of estradiol in the pores, indicating that the release rates depended on calcium levels in SBF, which explains the calcium-level-responsive drug release from the matrix.

31.4 CALCIUM-LEVEL-RESPONSIVE DRUG RELEASE OF APATITE CEMENTS CONTAINING ANTIOSTEOPOROSIS DRUG IN HEALTHY AND DISEASED RATS AND THERAPEUTIC EFFECTS [16]

After subcutaneous implantation of AP cements containing estradiol into osteoporotic rats, the plasma calcium levels and the drug release from the cements [18, 19] were measured [16]. Healthy model rats have a constant plasma calcium concentration of around 10 mg/100 mL (Fig. 31.2, left).

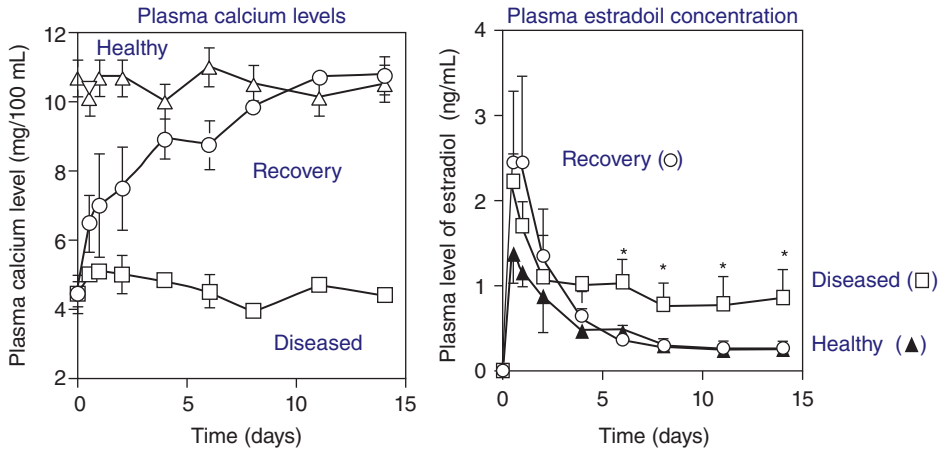


FIGURE 31.2 Calcium-level-responsive drug release from AP cement containing estradiol in ostseoporotic rats.

However, the diseased model rats maintained a low calcium level of ~5 mg/100 mL during drug release. In contrast, the plasma calcium level of the recovery model rats was increased by feeding them calcium, and reached healthy level of around 10 mg/100 mL after 7 days.

The plasma estradiol concentrations in the diseased model rats increased rapidly (Fig. 31.2, right), attaining a maximum level (C_{max}) of 2.23 ng/mL, and then decreased gradually, yet after 5 days were still significantly higher than those in the healthy group. In the recovery model rats, the plasma estradiol concentrations increased rapidly, attaining C_{max} of 2.55 ng/mL. These levels, however, decreased gradually, and after 5 days were almost the same as those of healthy rats. In contrast, C_{max} of the healthy rats (1.43 ng/mL) was much lower than that of the diseased and recovery model rats. The in vivo estradiol release of the recovery model rats supported the hypothesis that the drug release behavior of the apatitic cement drug delivery system was responsive to plasma calcium levels.

The bone mineral density (BMD) of the diseased and the recovery model rats was measured by bone mineral densitometry (Fig. 31.3). The BMD of the recovery model (IR) and control diseased (CR) groups was significantly increased compared with that before the experiment in the control group (CD) and implanted group (ID) without calcium feeding, indicating that calcium feeding was an important factor and estradiol-loaded cement implantation was effective for the therapeutic improvement in diseased model rats. In terms of the BMD, the diseased rats ranked as follows: IR > CR > ID > CD, indicating that the increase of BMD was a combination effect of the estradiol release from the cement and plasma calcium concentration. These results suggest that plasma estradiol levels are regulated by the characteristics of apatite cements, and the degree of osteoporosis is improved

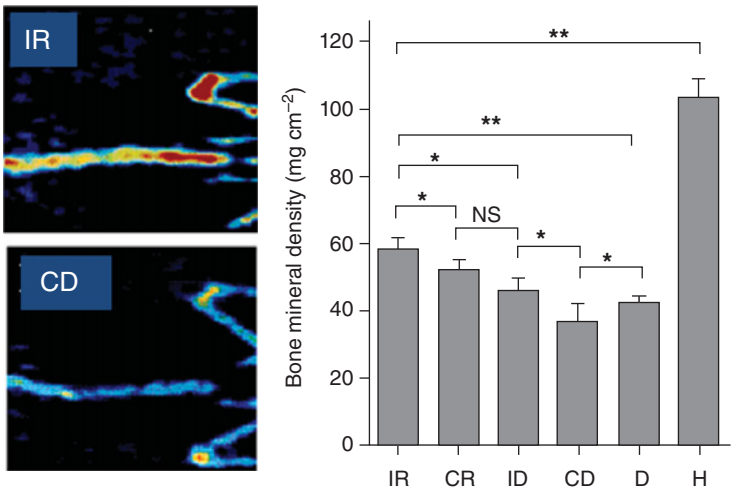


FIGURE 31.3 BMD of implanted apatite cement containing estradiol in osteoporotic rats. For a color version of this figure, see the color plate section.

by implantation of estradiol-loaded apatite cement with sufficient calcium supplementation.

31.5 DRUG DELIVERY SYSTEM CONTAINING VK2 BASED ON SELF-SETTING APATITE/COLLAGEN COMPOSITE CEMENTS (AC) [20]

Several researchers [21, 22] reported an HAp/collagen composite with a nanostructure that is similar to natural bone. They also reported that the molecular interaction between apatite and collagen induced the formation of nanostructure particles, which have characteristics and biocompatibility similar to those of natural bone. The results indicated that the biomimic materials had significantly high bioaffinity with natural bone after implantation, and the molecule-level structure of inorganic and organic composites is a very important factor for the biocompatibility of artificial bone in vivo. To develop artificial self-setting bone cement with almost the same chemical formulation as natural bone, the AC bulk powder was obtained by grinding the AP cement powder (TECP and DCPD) with 20% type I bovine collagen in a vibration mixer mill. The X-ray powder diffraction (XRD) profiles of the sample cements (Fig. 31.4, left) were measured to evaluate the test material characteristics as an index of bioaffinity. The fresh fixed physicalmixed AC (PAC) cements showed typical diffraction peaks of HAp at $2\theta = 31.8$ and 32.8° with additional peaks at $2\theta = 28.9$ and 29.5° due to TECP and at $2\theta = 26.5°$ due to DCPD. The XRD results indicated that the majority of metastable calcium phosphates, DCPD and TECP, transformed into low-crystallinity HAp, but some parts of DCPD and TECP did not transform, and remained in the cements. In contrast, the XRD profiles of AC had broad peaks at 31–33° due to bonelike HAp and no peaks due to TECP and DCPD (Fig. 31.4, left). These results also suggested that crystalline transformation of AP is accelerated by the addition of collagen and mechanical treatment. The transformed apatite structure in the AC was similar to natural bone apatite with low crystallinity reported by another team [21, 22] because the bonelike nanoapatite crystals precipitated out on collagen matrices during the setting time after mixing of the solution.

Scanning electron microscopy (SEM) and electron probe microanalysis (EPMA) (Fig. 31.4, right) were performed to characterize the element dispernsability in the AC [20]. The SEM of PAC without grinding showed a rough surface and large particles (>20-μm-diameter), indicating that the cement was a heterogeneous system. In contrast, AC with grinding showed a smooth surface consisting of particles of <1–2 μm in diameter.

In order to develop bone regenerative artificial bone systems based on the AC cement, it is necessary that bone growth factors be loaded in bioactive artificial bone matrices and slowly released over time. One team of investigators [23] reported that metacarpal bone mineral density was increased in osteoporosis through the administration of menatetrenone, [vitamin K_2 (VK2), an antiosteoporosis drug]. Therefore, VK2 was selected as a model drug and loaded in the bone cement matrices to develop a drug delivery system. Three types of the AC and AP cement (500 mg) containing 10 mg of VK2 were developed as follows: APK: VK2 loaded in the AP; PACK: VK2 loaded in the PAC without grinding; and ACK: VK2 loaded in the AC with grinding. The AC cements containing VK2 were implanted into the backs of rats and the density was measured using bone mineral densitometry. Microradiograms of AP and AC were obtained by dual-energy X-ray absorptiometry after implantation in the rats, and the cement mineral content (BMC) was evaluated based on these microradiograms.

The effects of VK2 on the BMC of AC cements implanted in osteoporotic rats were investigated (Fig. 31.5, left). The BMC profile of ACK was significantly higher than those of

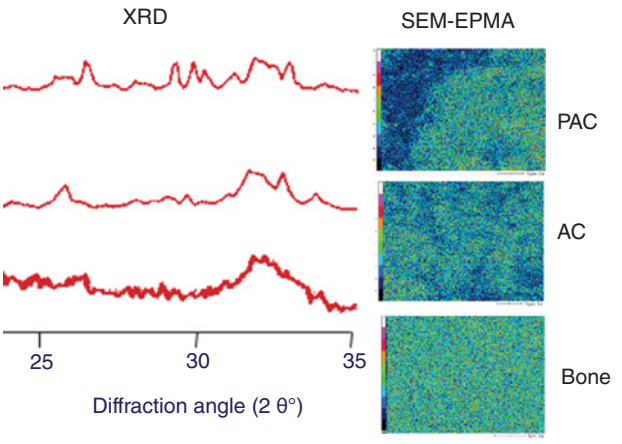


FIGURE 31.4 Effects of grinding of element dispersibility of AC and PAC by electron probe microanalyzer. For a color version of this figure, see the color plate section.

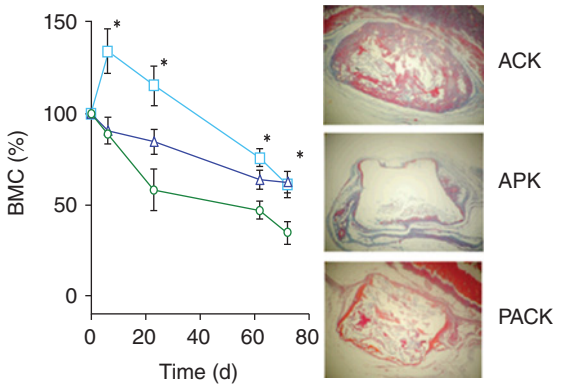


FIGURE 31.5 BMC profiles of implanted apatite/collagen composite cement containing VK2 in osteoporotic rats and their cross-sectional micrographs after 72 days.

PACK and APK. In contrast, the microstructure of ACK was significantly different from that of APK, and that difference was drastically affected by the duration of the experiment. For ACK, BMC reached its peak at day 7. PACK and APK recorded the highest and lowest degradation rates of BMC, respectively. At day 21, the amount of BMC present was ranked as follws: ACK > APK > PACK.

Micrographs of the cross sections of the apatite/collagen cements containing VK2 were taken after 72 days of implantation (Fig. 31.5, right). After implantation, it was discovered that the APK cement had undergone deformation, but there was no evidence to suggest penetration of organic components into the cement material. Like for the PACK cement with a reduction in diameter but an increase in thickness, the shape of the ACK cement had been completely distorted after 72 days. The BMC result of the cements loaded with VK2 suggests that their formulation has a significant effect on the rate of biodegradation. After 72 days, the ACK cement exhibited an increase in BMC, which was also higher than that of the PACK cement. The organic components had penetrated deeply into the center of the ACK. These results suggested that the changes in BMC were more dynamic for the ACK than for the PACK cement. As shown in the XRD results (Fig. 31.4, left), grinding the apatite/collagen composite cement can lead to a crystalline structure that is more or less the same as natural bone, which could have an influence on the release of bone growth factors such as VK2 and the regeneration and absorption of bone during the experimental period.

31.6 BIODEGRADATION OF THE AC BLOCK WITH INTERCONNECTING PORES AS A SKELETAL BONE CELL SCAFFOLD [24]

Since interconnective pores in bonelike materials are therapeutically effective for bone regeneration in the body through the introduction of bone cells and blood vessels [26], interconnective porous biomaterials are useful as a scaffold for bone cell cultures for implant. One team of researchers [26] discovered that the various types of interconnective void and pore in artificial bone enhanced the transition from artificial material to natural bone. These voids played a key role in stimulating tissue invasion and biocompatibility. On the basis of the test results, it can be suggested that continuous voids supported the formation of new bone by allowing the bone cells and/or tissues to penetrate into the voids more readily and the growth of new blood vessels to commence. Since artificial bone is fabricated with favorable properties using AC with connective voids, these devices could be utilized as a bone cell scaffold to culture bone marrow extracted from patients for bone regenerative medicine. Artificial bone materials with interconnecting pores (ACC) as a cell scaffold device were therefore prepared, and their biocompatibility was investigated after implantation into rats. The ACC blocks [25] were prepared on the assumption that the AC cement in a mold ($10 \times 10 \times 7.5$ mm) contained 60 organized stainless-steel needle-like male dies 600 μm in diameter (Fig. 31.6, left). The XRD result indicated that the calcium phosphates of ACC transformed into biological HAp with no peak due to the presence of raw materials, as previously reported [21]. The total porosity of the ACC cement was 64% by combining the micro- and macropores, which were 40% and 23%, respectively.

After the artificial bone blocks were implanted subcutaneously into female SD rats, their BMC profiles were determined by dual-energy X-ray absorptiometry (Fig. 31.6, right). The analysis revealed that the BMC of ACC increased rapidly to around 120% after 28 days but dropped to 105% after 56 days. A similar trend was also observed for the AC block (ACN) cement as its BMC rose to approximately 110% after weeks 1–3, and at day 56 the BMC was around 98%. In contrast, the BMC of the AP block (APN) decreased steadily throughout the entire experiment and at day 56 it was recorded to be approximately 90%. On the basis of these results, it is clear that the cement system will ultimately



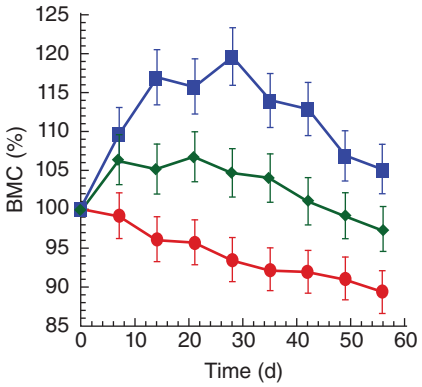


FIGURE 31.6 Plot of time versus changes in BMC of cement blocks implanted in rats (■, ACC; ♦, ACN; ●, APN) and photograph of ACP block.

determine the changes in the BMC profile. A decrease in the BMC from all implanted blocks was observed during the latter stages of the experiment, at 40–56 days, owing to the abdomen and phagocytosis on the surface of macropores by osteoclastlike cells, bearing a resemblance to bone remodeling. Photographs of removed implants also indicated that the deformation of the cement blocks can be considered as an indication of biological activity; the order of this activity was ACC > CAN > APN.

31.7 DRUG RELEASE FROM BIODEGRADABLE APATITE/COLLAGEN COMPOSITE CEMENTS WITH INTERCONNECTIVE MACROPORES [27]

To improve biocompatibility during cell culture in bone regenerative medicine, three-dimensional (3D) perforated porous apatite/collagen composite cement, ACC with drug delivery capability was developed. The ACC drug delivery device was prepared to pour the AC cement paste containing 3% indomethacin (IMC) into a mold ($10.0 \times 10.0 \times 7.5$ mm) containing 0, 20, 40 or 60 stainless needles to generate interconnective macropores [27].

The in vitro drug release tests of the ACC devices were carried out in SBF at pH 7.25. Since the rate-limiting step of drug release from the drug-loaded matrix systems was basically the drug diffusion process in the micropores in the matrix, the drug release from the matrix systems follows the Higuchi equation [Eq. (31.1)]. The in vitro IMC release from ACC with various numbers of macropores showed straight lines at the initial drug release stage (Fig. 31.7, left) on the Higuchi plot. The Higuchi release constant (HC) was evaluated using the initial slope of the Higuchi plot as the drug release rate. The relationship between HC and A of ACC (Fig. 31.7, right) had a straight line, suggesting the adequacy of the Higuchi equation. The result therefore suggested that the rate of drug release can be controlled by the number of macro-pores for culturing bone cells.

31.8 IN VITRO BONE CELL ACTIVITY–RESPONSIVE DRUG RELEASE FROM BIODEGRADABLE APATITE/COLLAGEN BONE CELL SCAFFOLD WITH INTERCONNECTIVE MACROPORES [28]

Since the crystalline structure of AC was almost the same as that of natural bone [18], the material was phagocytized at the surface of macropores by bonelike cells, similar to the remodeling of bone. Therefore, the rapid bioabsorption of AC may be considered to be similar to the biological action of active bone cells [29]. In order to clarify the role of osteoclasts during drug release from the apatite/collagen nanocomposite, the influence of the dissolution medium on the drug release capabilities of the device based on a physicochemical model for the nanoscale biointeface between bone matrices and bone cells was investigated. AP, AC, and ACC blocks containing 2.5% VK2 were obtained in the mold ($10.0 \times 10.0 \times 7.5$ mm) to form interconnective macropores (0–60 stainless-steel needles).

To clarify the role of bone remodeling in the drug delivery system based on AC matrices, a physical in vitro dissolution model was established. The drug release profile was investigated in an SBF solution with a pH of 7.25 to simulate osteoblastlike conditions (SOB) and in an acetate buffer with a pH of 4.5 to simulate osteoclastlike conditions (SOC) [28].

The effect of the dissolution medium on the in vitro release of VK2 from AP, AC, and ACC60 indicated (Fig. 31.8) that virtually no drugs were being released from the AC block

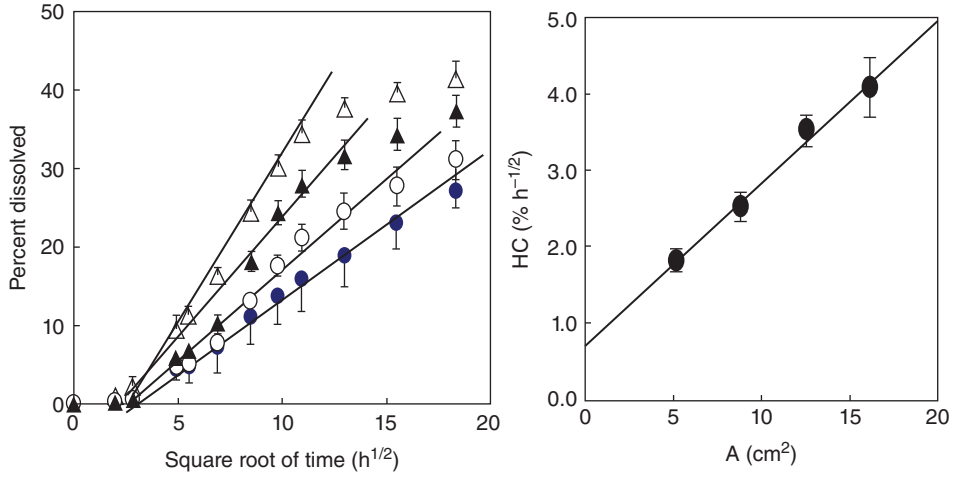


FIGURE 31.7 Effect of macropore number on IMC release of ACC block (●, $n = 0$; ○, $n = 20$; ▲, $n = 40$; △, $n = 60$; A, block surface area; HC, Higuchi content).

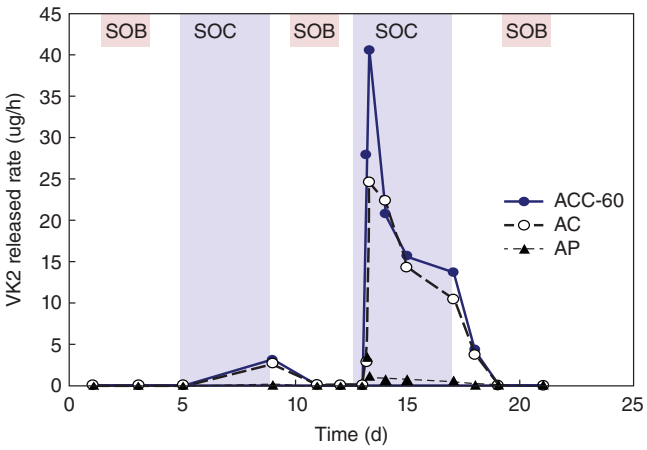


FIGURE 31.8 Effect of dissolution medium on in vitro release of VK2 from AP, AC, and ACC.

and ACC60 in SOB, but the situation was quite the opposite in SOC, with significant improvements in the drug release rates. The drug release and calcium phosphate dissolution results suggested that the HAp matrices in the device were dissolved in SOC, and the drug release was accelerated with increasing porosity. In SOB, however, the device was covered with precipitated HAp particles, inhibiting the release of drugs from the micropores. The drug release from AC and ACC blocks was dependent on the dissolution medium. However, this was not the case for the AP block.

31.9 IN VIVO BONE CELL ACTIVITY–RESPONSIVE DEOXYRIBONUCLEIC ACID (DNA) RELEASE FROM INJECTABLE SELF-SETTING APATITE CEMENT AND APPLICATION TO GENE THERAPY [30]

The therapeutic effect of plasmid DNA complexes in current gene therapy is not satisfactory because of the short duration of their gene expression. Gene delivery systems that release the plasmid complex for long periods are thus required. However, an efficient DNA slow-release system has not been established owing to the low dispersion stability of the DNA/polycation complexes. Since hyaluronan (HA) could be deposited onto the DNA/polycation complexes, stabilize their dispersion, and be used to prepare very small particles, DNA/polycation/HA complex particle-releasing systems could be developed using injectable materials that self-set in the body in a biodegradable solid device. This section describes the development of DNA/polyethyleneimine (PEI)/HA ternary complex-releasing systems based on biocompatible, biodegradable apatite cement with inorganic components similar to bone and teeth. Injectable self-setting apatite cement containing pDNA-*GM-CSF*/PEI/HA [encoding granulocyte macrophage colony-stimulating factor (GM-CSF)] was prepared, and the efficacy of the durable DNA complex release system was examined [31]. An injectable apatite cement slurry was prepared as follows. The apatite/atelo-collagen composite cement bulk powder was ground with 20% atelocollagen in a vibration mixer mill. The AC cement bulk powder was mixed with 25 mM phosphoric acid, and a condensed suspension of DNA/PEI/HA complex small particles was then mixed with the apatite cement slurry. When the apatite cement is implanted into the body, it is expected to be degraded by osteoclasts to release the DNA complex, since it is known that osteoclasts dissolve and resorb bone by secreting an acidic liquid [32].

In order to simulate this, DNA-releasing ability was evaluated with MLC6 cells, an osteoclast-like cell line with the same function as osteoclasts [32]. B16 melanoma cells were used as nondegrading control cells.

Release of the DNA complexes from the apatite cement was faster with MLC6 cells than with B16 cells (Fig. 31.9). The DNA complexes were continuously released from the apatite cement including collagen, which showed an XRD pattern similar to that of natural bone. Higher affinity of the collagen-containing cement with MLC6 cells than that with other polymers was also confirmed microscopically (Fig. 31.9).

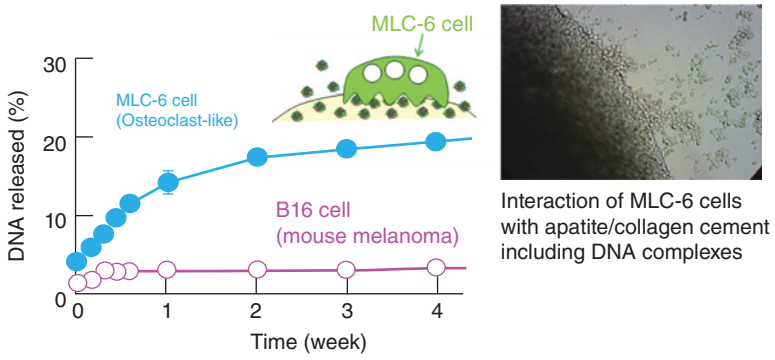


FIGURE 31.9 Effect of bone cell types of DNA complexes released from apatite/collagen composite cements.

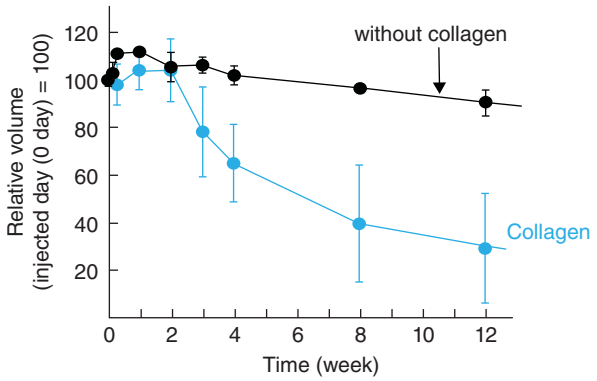


FIGURE 31.10 Effect of collagen content on biodegradation rate of apatite/collagen composite contents containing DNA complexes.

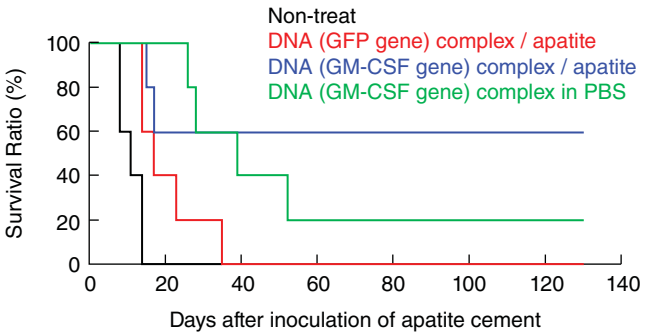


FIGURE 31.12 Therapeutic effects of slow-release apatite system on solid tumor of rats.

Osteoclasts also resorb excessive apatite, such as an ectopic bone, in the body [33]. Thus, the apatite cement inoculated into tumor-bearing mice was expected to be degraded by the cells. Apatite cement slurry including DNA/PEI/HA ternary complex particles was inoculated into the femurs of mice using an injection syringe, and the volume of the inoculated apatite cement was evaluated by X-ray computed tomography (CT). The solidified cement gradually degraded, and the degradation rate was dependent on the quality of the cement. Apatite cements with collagen again showed much faster degradation (Fig. 31.10) than did those without collagen. The crystal structure of the cement similar to that of natural bone was readily recognized by osteoclasts.

The therapeutic effect of the bone cell activity–responsive slow-releasing apatite system was then examined in tumor model mice. DNA/PEI/HA complex particles were prepared with the pDNA encoding mouse granulocyte macrophage-colony-stimulating factor (GM-CSF) or green fluorescent protein (GFP) (Fig. 31.11). The DNA complex particles were mixed with apatite cement slurry including 5% collagen. B16 cells were subcutaneously inoculated under the abdominal skin of mice. When the tumor size increased to 4 mm, apatite cement slurry including DNA complex was injected once around the tumor. The volume of apatite cement solidified in the body was also evaluated.

The tumors grew rapidly in the control mice. In contrast, in one of five mice that received a single dose of pDNA (GM-CSF)/PEI/HA complex particles without apatite cement, complete disappearance of the tumors was observed (Fig. 31.11). An apparent therapeutic effect was also seen in the other four mice, in which tumor growth remained suppressed for 10 days after the injection, but tumor growth then restarted. A significant effect was seen in mice injected with pDNA (GM-CSF)/PEI/HA complex particles in the apatite cement, and a complete response was seen in three of the five mice, without any tumor regrowth for ≤100 days (Fig. 31.11). X-Ray CT was performed to evaluate the reduction rate of apatite cement volume in the mice. The volume reuction rate in the three mice in which the tumor disappeared was higher than that in the other two mice that showed tumor regrowth. The therapeutic result (Fig. 31.12) suggested that

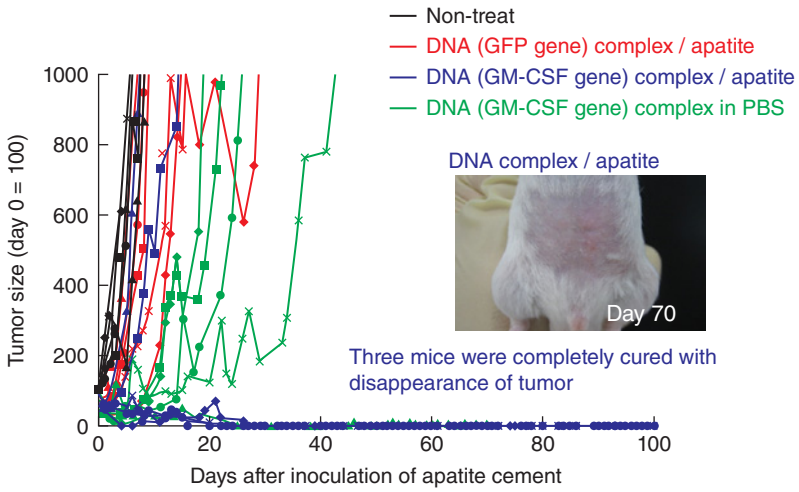


FIGURE 31.11 Therapeutic effects of slow-release apatite system on solid tumor of rats.

the rat group with pDNA (GM-CSF)/PEI/HA complex particles in the apatite cement had the best survival score. This indicates the importance of successive release and the potential of the injectable apatite cement as a durable gene transfection device.

ACKNOWLEDGMENTS

The author is deeply grateful to Professor William I. Higuchi, University of Utah, for his leadership in our international collaboration research. The author also thanks Dr. Tomoko Ito, Shin-Yamanote Hospital and Dr. Atsuo Ito, NIAIST, for their scientific advice. Finally, the author thanks to Mr. Kazuki Yoneoka, Mr. Ryuhei Hirano, Mr. Hidenori Nakagawa and Mr. Tomoaki Kuninaga for their experimental work.

REFERENCES

[1] Langer, R. (1980). *Chem. Eng. Commun.* **6**, 1–48.

[2] Middleton, J.C., Tipton, A.J. (2000). *Biomaterials* **21**, 2335–2346.

[3] Jeong, B., Bae, Y.H., Lee, D.S., Kim, S.W. (1997). *Nature* **388**, 860–862.

[4] Lin, C.C., Metters, A.T. (2006). *Adv. Drug Deliv. Rev.* **58**, 1379–1408.

[5] Patel, D.M., Patel, B.K., Patel, C.N. (2011). *Int. J. Adv. Pharm. Res.* **2**(2), 57–63.

[6] Mary, C.M., Nicholas, A.P. (2009). *Adv. Drug Deliv. Rev.* **61**, 1391–1401.

[7] Berry, R.F., McKinney, F.E., Parr, N. (2008). *IBM Syst. J.* **47**(2), 197–206.

[8] Baron, R., Vignery, A., Horowitz, M. (1987). Lymphocytes, macrophages and the regulation of bone remodeling. In Peck, W.A. (ed.), *Bone and Mineral Research.* Elsevier, Amsterdam, pp. 209–279.

[9] Aoki, H. (1994). Medical applications of hydroxyapatite. *Ishiyaku-Euro America* **156**.

[10] Brown, W.E., Chow, L.C. (1983). *J. Dent. Res.* **62**, 672.

[11] Ginebra, M.P., Traykova, T., Planell, J.A. (2006). *J. Control. Release* **113**, 102–110.

[12] Otsuka, M., Matsuda, Y., Suwa, Y., Fox, J.L., Higuchi, W.I. (1995). *J. Pharm. Sci.* **84**, 733–736.

[13] Otsuka, M., Nakahigashi, Y., Matsuda, Y., Fox, J.L., Higuchi, W.I., Sugiyama, Y. (1997). *J. Control. Release* **43**, 115–122.

[14] Corltz, B.R., Ison, I.C., Fulmer, M.T., Poser, R.D., Smith, S.T., VanWagoner, M., Ross, J., Goldstein, S.A., Jupiter, J.B., Rosenthal, D.I. (1995). *Sciences* **267**, 1796–1799.

[15] Higuchi, T. (1963). *J. Pharm. Sci.* **52**, 1145–1150.

[16] Otsuka, M., Yoneoka, K., Matsuda, Y., Fox, J.L., Higuchi, W.I. (1999). *J. Pharm. Pharmacol.* **51**, 475–481.

[17] Kokubo, T., Kushitani, H., Sakka, S., Kitsugi, T., Yamamuro, T. (1990). *J. Biomed. Mater. Res.* **24**, 721–734.

[18] Mclean, F., Urist, M., Bone, R. (1968). *Fundamentals of the Physicology of Skeletal Tissue*. Univ. Chicago Press, p. 119.

[19] Eriksen, E.F., Mosekilde, L. (1990). *Bone Mineral Res*. **7**, 273–312.

[20] Otsuka, M., Kuninaga, T., Otsuka, K., Higuchi, W.I. (2006). *J. Biomed. Mater. Res. B: Appl. Biomater*. (2006), **79B**, 176–184.

[21] Kikuchi, M., Itoh, S., Ichinose, S., Shinomiya, K., Tanaka, J. (2001), **22**, 1705–1711.

[22] Itoh, S., Kikuchi, M., Koyama, Y., Takakuda, K., Shinomiya, K., Tanaka, J. (2002). *Biomaterials* **23**, 3919–3926.

[23] Shiomi, S., Nishiguchi, S., Kubo, S., Tamori, A., Habu, D., Takeda, T., Ochi, H. (2002). *Am. J. Gastroenterol.* **97**(4), 978–981.

[24] Otsuka, M., Nakagawa, H., Otsuka, K., Ito, A., Higuchi, W.I. (2013). *J. Biomed. Mater. Res. B: Appl. Biomater.* **101B**(2), 338–345.

[25] Delloye, C., Cnockaert, N., Cornu, O. (2003). *Acta Orthop. Belg.* **69**, 1–8.

[26] Kuboki, Y., Jin, Q., Kikuchi, M., Mamood, J., Takita, H. (2002). *Connect. Tissue Res.* **43**, 529–534.

[27] Otsuka, M., Nakagawa H., Ito A., Higuchi W.I. (2010). *J. Pharm. Sci.* **99**(1), 286–292.

[28] Otsuka, M., Hirano, R. (2011). Bone cell activity responsive drug release from biodegradable apatite/collagen nanocomposite cements. In vitro dissolution medium responsive vitamin K2 release. *Colloids Surf. B: Biointerfaces* **85**(2), 338–342.

[29] Väänänen, H.K., Zhao, H., Mulari, M., Halleen, J.M. (2000). *J. Cell Sci*. **113**(Pt.3), 377–381

[30] Ito, T., Koyama, Y., Otsuka, M. (2012). *J. Genet. Med.* **14**, 251–261.

[31] Ginebra, M.P., Traykova, T., Planell, J.A. (2006). *J. Control. Release* **113**, 102–110.

[32] Teitelbaum, S.L. (2000). *Science* **289**, 1504–1508.

[33] Asou, Y., Rittling, S.R., Yoshitake, H., Tsuji, K., Shinomiya, K., Nifuji, A., Denhardt, D.T., Noda M. (2001). *Endocrinology* **142**, 1325–1332.

32

DRYING STRUCTURE

TSUNEO OKUBO

Institute for Colloidal Organization, Hatoyama 3-1-112, Uji, Kyoto 611-0012, Japan

32.1 INTRODUCTION

Most structural patterns in nature form via *self-organization* accompanied by the *dissipation* of free energy and in the nonequilibrium state. In order to understand the very complex mechanisms of the dissipative self-organization of the simple model systems, instead of the complex nature itself, study of the *evaporating*, *convectional*, *sedimentary,* and *drying* dissipative patterns during dryness of suspensions and solutions is important, although these four kinds of structures are correlated cooperatively and overlap each other [1–3]. Studies of the drying patterns of colloidal suspensions and solutions also provide important knowledge in both biological and industrial fields.

Evaporation of the solution and suspension takes place first at the air–liquid interface during the course of liquid drying [4, 5].

Lowering of temperature of liquid close to the interface takes place heterogeneously depending on the location, which will induce the convectional flow of solvent by the effects of Marangoni and gravitational convection. Degree of lowering of water temperature at the surface area comes to be more than 1 degree even at room temperature, and evaporation of water from the liquid surface is not inhibited completely without thorough shielding of the liquid from atmosphere.

Typical *convectional* patterns are *Benard cells* [6, 7], the hexagonal circulating pattern, and *Terada cell* [8–10], the spokelines spreading throughout the entire the liquid surface accompanied by a high number of cell convections in the normal direction of the spokelines. More recently, whole processes of the convectional patterns have been identified experimentally [11–15]. Theoretical studies of the convectional patterns have been reported mainly using Navier–Stokes equations [16–20]. However, these are not always successful, even when the theories are compared with the actual observation, since the actual drying processes are not so simple.

Sedimentary dissipative patterns during the course of drying suspensions have been studied in detail on a coverglass, a watchglass, a glass dish, and other surfaces, for the first time, in the author's laboratory [13, 21–28]. Broad ringlike patterns were formed in suspension state. It was clarified that the sedimentary particles were suspended in suspension by the electrical double layers around the particles and always moved by the balancing of the force fields between the convectional flow and the gravitational sedimentation. Dynamic cluster and bundle-like sedimentary patterns form synergistically from the spokelike convectional structures of coffee [14] and black tea [15].

Drying dissipative patterns have been studied for many kinds of colloidal particles, linear-type synthetic and biopolyelectrolytes, water-soluble neutral polymers, ionic and nonionic surfactants, gels, colloidal polymer complexes, and dyes by many researchers hitherto [1–3, 29–35]. The macroscopic *broad ring* patterns of the hill accumulated with the solutes formed. Macroscopic *spokeline* patterns, specifically, spokelike cracks or fine hills including flickering spokelike ones, were also observed for many solutes. Beautiful *fractal* patterns such as branchlike, arclike, blocklike, starlike,

Encyclopedia of Biocolloid and Biointerface Science, Volume 1, First Edition. Edited by Hiroyuki Ohshima.
© 2016 John Wiley & Sons, Inc. Published 2016 by John Wiley & Sons, Inc.

crosslike, and stringlike confiigurations were often observed at the microscopic scale, especially in the thin and central areas of the dried film.

We should note several important findings in the drying processes: (1) primitive, vague sedimentary patterns are formed in concentrated suspensions or solutions before dryness and grow toward fine structures during the processes of solidification [27]; (2) *information* on the suspensions and solutions, shape, and size of solute and atmospheric humidity and temperature, for example, is *transferred* into the drying patterns (some of this information is transferred to the drying patterns accompanied by the selection and amplifying effects by the static and dynamic interaction of solutes with other solutes and/or substrate surfaces; nowadays, detailed molecular and colloidal information is available in part from the drying patterns themselves . . . as is well known, the three major groups of biopolymers are *polypeptides*, *polysaccharides*, and *polynucleotides*; the chemical structures of these mainchains are quite different from each other; it is very interesting to discuss how these structures influence the drying patterns; and (3) *dissipative crystallization* of synthetic and biological polyelectroytes has been clarified [36–42]. Accumulation, uneven distribution, symmetric distribution, ordering of polymer single crystals, coupling of single crystals with dissipative broad ring patterns, and other distribution patterns have been clarified.

We should note that all theoretical studies of the drying patterns made thus far have been quite unsatisfactory because any theoretical studies have derived from the final drying patterns only a part of so many integrated processes. Deegan et al. [43, 44] have reported traces of spokelike patterns in the suspensions of polystyrene spheres under a microscope. They introduced the *capillary flow theory* accompanied by the *pinning effect* of the contact line of the drying drop. This theory states that the broad ring size should remain at the outside edge of the initial liquid. The pinning effect seems to have been researched quite heavily. From our series of the drying experiments of suspensions and solutions, however, this effect is not always supported experimentally, because the broad ring size decreases sharply as solute concentration decreases, especially in the low concentration range [1–3]. The broad ring size changes mainly because of the excluded volume of each solute and/or structural formation among the solutes [1–3]. Theoretical discussion of the *cooperativity* itself, including the information transfer among the cooperative and consecutive drying processes, namely, evaporation, convection, sedimentation, and solidification is desired in near future.

32.2 CONVECTIONAL PATTERNS

The most famous *convectional* pattern is the *hexagonal circulating* one. The *Bernard cell* has been observed when liquids contain platelike colloidal particles as monitors and are heated homogeneously in a plain pan [6, 7]. Another typical convectional dissipative pattern consists in spokelines, which were observed in the whole area at the liquid surface and also appeared in various substrates sometimes accompanied by a vast number of small *cell convections*. The spoke patterns with cell convections were observed formerly for the membranes of Chinese black ink on water [8–11, 45]. The author likes to call the spoke pattern the *Terada cell*. Convectional patterns, especially Terada cells, were observed directly in the initial drying process of Chinese black ink in a glass dish [11], the 100% ethanol suspensions of colloidal silica spheres [12], a cup of Miso soup [13], coffee [14], black tea [15], and colloidal crystals of poly(methyl methacrylate) (PMMA) spheres on a coverglass and a watchglass [46, 47]. Distorted Bernard cells were often observed for Miso soup, coffee, and black tea. For the 100% ethanol suspensions of colloidal silica spheres, Terada cell–type convectional flow was observed clearly with the naked eyes, and the convectional patterns changed dynamically with time. Deegan et al. [43, 44] reported the traces of spokelike patterns in the suspensions of polystyrene spheres (1 μm in diameter) under a microscope.

Coffee with cream shows very clear convectional patterns, especially at the initial stage during the course of dryness [14]. Mean sizes of coffee and coffee plus cream colloidal particles were 460 and 210 nm, respectively, and the former was twice as large as the latter. This strongly supports the theory that coffee particles tend to aggregate in suspension state. On the other hand, each coffee particle is coated with cream layers (composed mainly of oils and fats) and forms small and stable dispersions. Zeta-potentials of coffee both without and with cream were negative, at −24 and −52 mV, respectively. These values in the zeta-potential also support the theory that cream-coated coffee particles are more stable than bare coffee particles in suspension state, since the colloidal particles having large absolute values of zeta-potential are more stably dispersed in general. Actually, significant sedimentation of coffee without and with cream in a test tube did not take place for about 1 day and 3 days at 8°C, respectively.

Figure 32.1 shows the change in patterns of iced coffee during the drying processs in the presence of cream on a coverglass. The stock suspension of coffee plus cream was diluted with the same amount of pure water before the observation was made. The formation of *clusters* from the spokelines and then further growth of *bundles* from the clusters from the outside edge toward the central area at the liquid surface is observed, although the distinction between clusters and bundles is difficult. Twenty-five minutes after setting, the vague blocklike or broad ringlike patterns appeared from the central area to the outside region of the air–liquid interface. Furthermore, a large number of short spokelines were observed at the outer edge of the liquid. The integrated

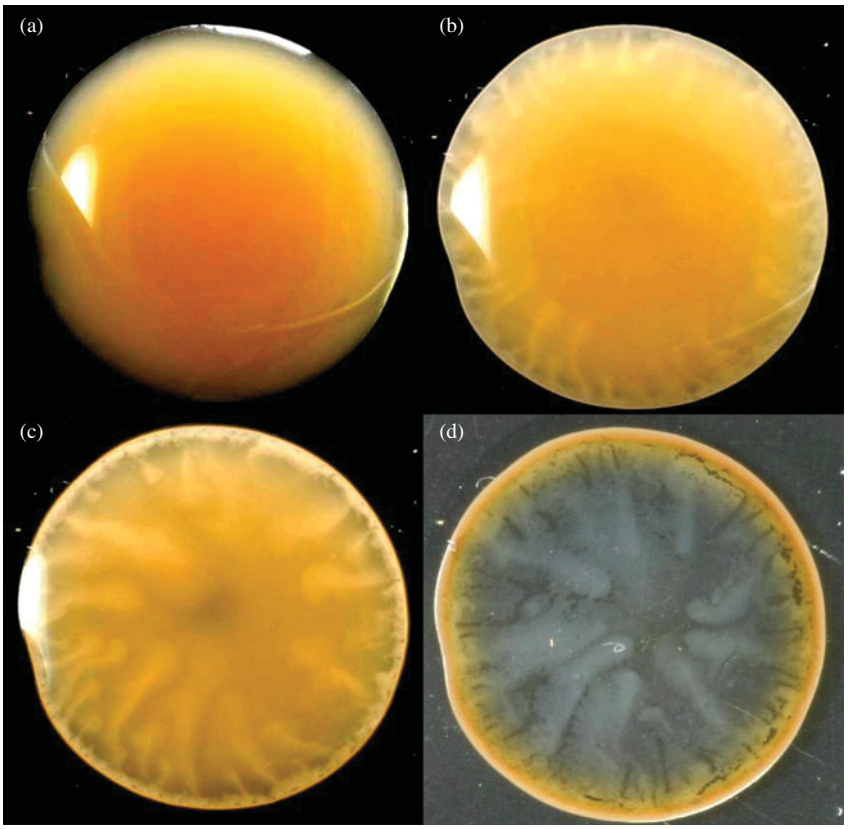


FIGURE 32.1 Convectional, sedimentary, and drying patterns of coffee (for iced coffee) with cream on a coverglass at 27°C, 1.26 wt%, 0.1 mL: (a) 10 min; (b) 50 min; (c) 1 h 40 min; (d) 3 h 25 min after setting. For a color version of this figure, see the color plate section.

convectional patterns of the spokelines form. In one study, after 50 min, integrated clustering of several spokelines began and although their number decreased, they became thick and clear. Furthermore, bundles of the cluster were recognized in the inner area of the liquid surface. The number of clusters and/or bundles decreased, from 35, 20, 16, and 12 to 12 after 50 min, 1 h 40 min, 2 h 40 min, 3 h 15 min, and 3 h 25 min, respectively. Quite similar convectional patterns have been observed for colloidal crystal suspension of PMMA spheres in a watchglass [47]. Furthermore, vigorous changes in convectional flow of colloidal silica spheres in ethanol also support the formation of the clusters and bundles [12]. Figure 32.1d illustrates a scenario in which the drying proccess was almost completed at the broad ring area, with the inner area still in liquid state, athough the drying cycle was completed very soon. In other words, the bundle-like patterns already represent a typical sedimentation pattern in the final stage of convection. It should be noted that the clusters and then bundles originated in the spokelines and always change their forms *dynamically* and *cooperatively*.

When a large amount of coffee-plus-cream suspension was set in a watchglass, then (1) the circulating line patterns were observed within 30 min, (2) between 4 and 30 min total flow of suspension at the liquid surface was in the direction from center to outside edge, (3) the total flow was reversed from the outside edge toward the center after 30 min, (4) growth of the spokelines toward the central area and formation of the clusters and bundles were observed, and (5) after about 7 h, the large bundles further grew into approximately three blocks of bundles. At the initial stage within 4 min, appearance and disappearance of the circulating lines took place in random directions. However, several regularly oriented circulating lines and circles appeared soon. Interestingly, two circles on the right side moved together toward the right outer edge while maintaining their relative positions. This observation supports the theory that the direction of the total flow of the suspension at the liquid surface is induced toward outer edge from the center by the integration of all convectional circulating lines from ~13 to 26 min.

Growth processes of the spokelines are further observed in detail using the extended illustrations as is shown in Fig. 32.2. Around 20 minutes after setting, few and short spokelines appeared at the outside edge. Then the number of the spokelines increased. These spokelines further grew toward the central area accompanied by the dynamical fusion and separation between the neighboring spokelines and clusters (see

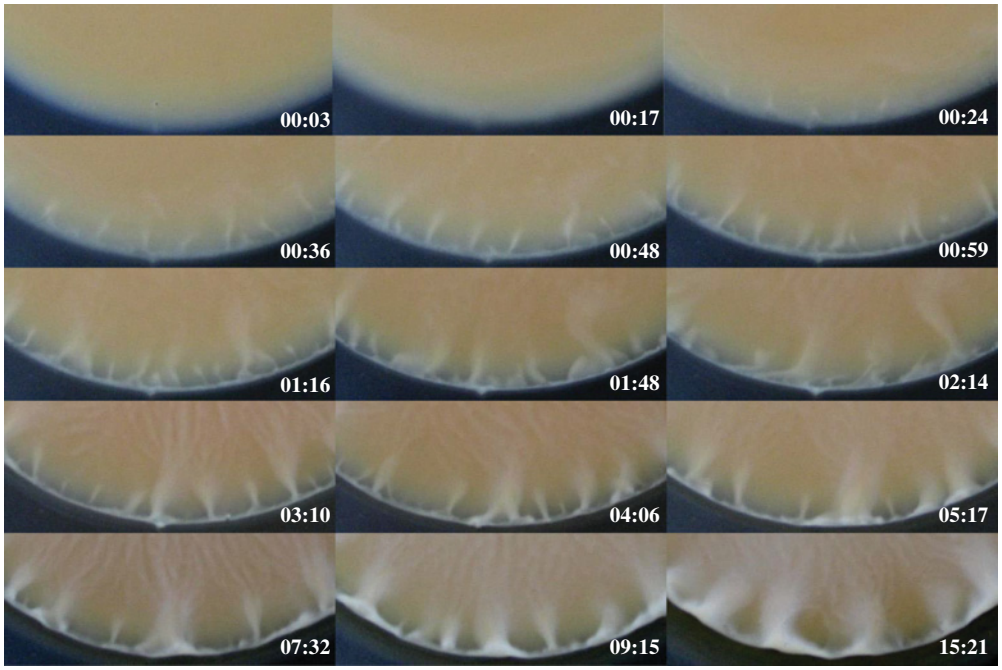


FIGURE 32.2 Time dependence of convectional patterns of coffee with cream in a large watchglass; extended areas of lower outside region. Liquid temperature changes from ~70°C to 20°C.

images ranging from 48 min to 15 h 21 min). Both of long and short spokelines increased sharply with time between 20 and 40 min. However, this number began to decrease after one hour. It should be noted that the decrease in number is accompanied by the formation of clusters and bundles. Quite similar changes in number were observed also for the convectional patterns of suspensions of poly(methyl methacrylate) (PMMA) on a coverglass [46] and a watchglass [47].

Summarizing our observations of convectional patterns of coffee with cream in a large watchglass, (1) at the initial stage within 4 min, the appearance and disappearance of the circulating lines took place at random directions; (2) between 4 and 20 min, total flow of convection at the surface layers was from the center toward the outside edge; (3) around 20–30 min after setting, few and short spokelines appeared at the outer edge, and then the number of spokelines began to increase; (4) at the same time as spokeline formation, total flow of convection was reversed from the outer edge to the central area and the outward flow remained until solidification started; (5) growth of the spokelines and formation of the clusters and bundle took place between 48 min and 15 h.

Here, the vigorous convectional flow of alcohol suspension of monodisperse colloidal silica spheres should be mentioned [12]. A series of the convectional, sedimentary and drying patterns of ethanol suspension of colloidal silica spheres (110 nm in diameter) were studied on a watchglass. Vigorous convectional flow was reflected in a beautiful dynamic change in convectional patterns. In the initial state within 50 min after the suspension was set for an initial volume fraction of 0.006, the spokelike patterns formed in the outer area of the monomer suspension. The suspensions of the spokeline area drop in the outer region of the central liquid pool, sometimes bridged by the mother suspension pool and disappearing when most of the drop suspensions flow down to the mother suspension. Again the suspension flow took place from the mother suspension pool toward the outside edge, resulting in the appearance of the spokelike suspension drops. Surprisingly, these dynamic changes in patterns took place simultaneously and in integrated fashion. Between 60 and 75 min, the mother suspension area decreased with time and the initial convectional patterns changed drastically in response to the different patterns, similar in configuration to a lotus-root section. After 90 min the suspension remained in the central area only, and broad rings formed in the final course of dryness, which is quite similar to the sedimentary patterns observed for aqueous suspensions. Interestingly, colloidal particles disappeared just at the central deepest point of the drying pattern.

Typical convectional patterns observed hitherto are spokelines (Terada cells) [11, 14, 15, 46–51], hexagonal circulating cells (Benard cells) [7, 13, 14], circulating cells [11, 14] in a smokelike configuration [11], with integrative circulation [12] and microscopic cell convection (Terada cells) [11]. It should be noted that the convectional patterns have been observed only for colloidal suspensions and not for typical solutions. Anisotropic colloidal particles did work as an optically good indicator of the convectional flow, according to the flow birefringence effect. However, we should note that

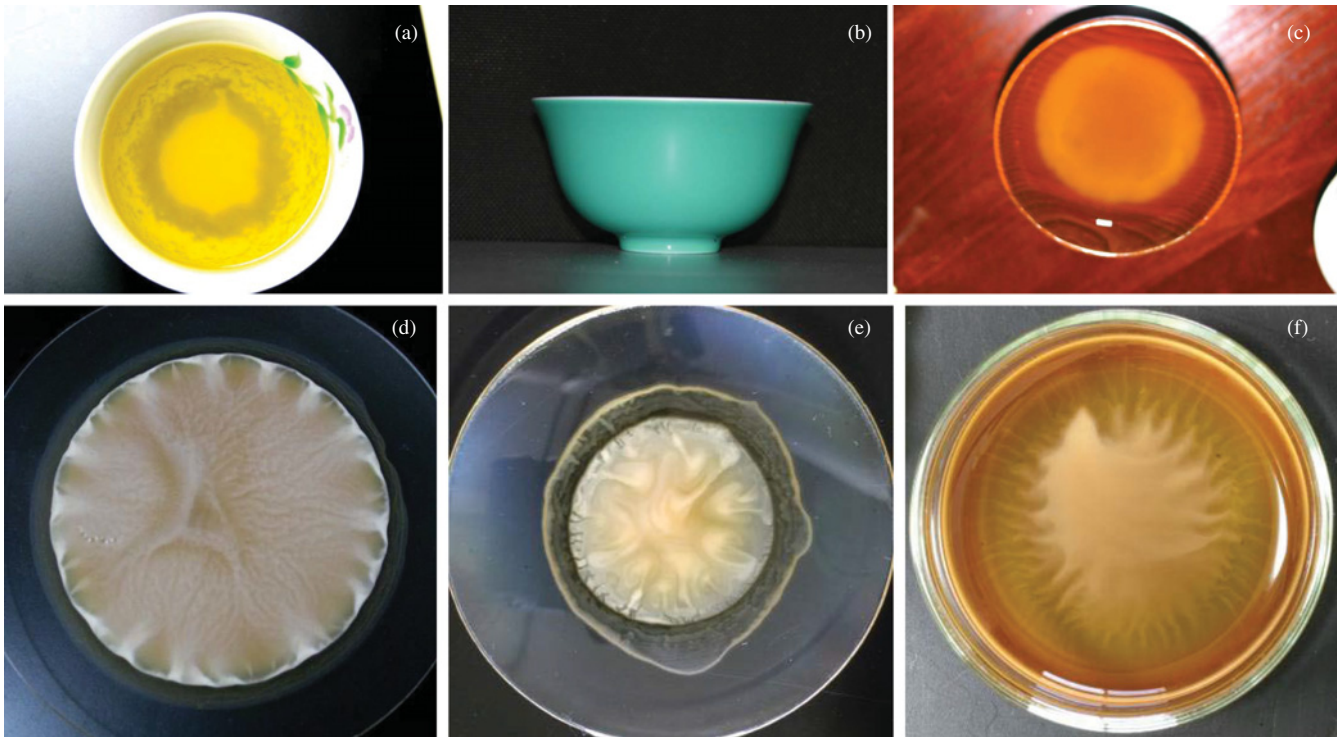


FIGURE 32.3 Typical examples of broad ringlike (a–c), cluster (d), bundle (e), and flamelike (f) sedimentation patterns of (a,b) green tea, (c) miso soup, and (d–f) coffee. (a) In a teacup at 24°C; (b) side view of a teacup; (c) in a bowl at 24°C; (d) in a watchglass (150 mm), 10 mL, 2.3 wt%, with cream, from 70°C to 20°C, after 12 h 25 min; (e) in a watchglass (50 mm), 1 mL, 0.7 wt%, with cream, after 9 h 20 min; (f) in a glass dish (42 mm), 3 mL, 2.3 wt%, with cream, after 20 h 5 min. For a color version of this figure, see the color plate section.

the convections, which are quite similar to those observed for the colloidal suspensions, should exist even in solution systems such as polymers and simple solute solutions.

The convectional flow of solvent and solutes is most important among the evaporation, convection, sedimentation, and solidification processes during the drying process. It should be noted further that information on the size, shape, conformation, and/or flexibility of particles and polymers is transformed from the initial convectional process toward the succeeding sedimentation and then solidification proceeds integratively and is accompanied by the amplification and selection processes. The important role of Marangoni convection in the metal colloidal crystallization process was proposed [52]. Experimental and theoretical studies on the convectional flow of colloidal particles have been reported, although these studies have not yet proved satisfactory [20, 52–62].

32.3 SEDIMENTATION PATTERNS

In most Japanese hotels, a guest will find in his or her room a set of green tea, which is composed of green tea granules in a paper filtering bag, a teacup, and hot water. The green tea is prepared conveniently by shaking the teabag dipped into hot water in a cup. The author was pleased to find that the broad ring always formed within <10 min in green tea in a cup left unattended on a disk. Figure 32.3a shows typical examples of the broad-ring patterns of green tea [28]. The broad ring, which is the hill accumulated with green tea colloidal particles, was formed in the inclined inner wall of the cup, and not in the deepest central area. In order to clarify the reasons for this broad-ring pattern in standing green tea, the authors have reviewed the literature on the sedimentation patterns and also the drying dissipative patterns of the monodisperse colloidal silica spheres and other particle systems on a coverglass, in a glass dish, polystyrene dish, and several sizes of watchglasses during the course of drying aqueous and ethanol suspensions [12–15,21–28,35,46–48,63,64]. The broad-ring patterns always formed unexpectedly rapidly in the suspension state irrespective of the cells used. The broad-ring structures were confirmed to be formed by the delicate balancing of the upward (and/or outerward) convectional flow of the colloidal particles in an inner wall and downward gravitational sedimentation (and/or innerward convectional flow). The important role of the microscopic cell convection in the liquid phase was supported for the broad-ring formation of suspensions and solutions.

The broad rings of the sedimentation patterns became sharp with time in many cases. Sharpness of the broad rings was sensitive to changes in room temperature and/or humidity [23]. Interesting sedimentation and then drying patterns were also formed during the course of dryness of binary and ternary colloidal crystal mixtures among the colloidal silica spheres of 183 nm, 305 nm, and 1.21 μm diameter in aqueous suspensions on a watchglass, a glass dish, and a coverglass [25, 26]. Colorful macroscopic broad-ring-like drying patterns appeared on the basis of the sedimentation structures. In a watchglass, for example, macroscopic sedimentation and then drying patterns were composed of the outer and inner layers of small and large spheres, respectively, for the binary mixtures by the segregation effects [25].

Most of the sedimentation patterns observed thus far have broad rings. However, vague but wrinkled microscopic sedimentation patterns were observed even in the suspension phase for bentonites [27]. These patterns became clearer and finer close to the solidification process. It has since been clarified that the drying patterns form integratively on the basis of the sedimentation patterns, which, of course, also originated from the convectional patterns in suspension state. The typical sedimentation patterns observed are broad-ring [14, 15, 46, 47, 50, 51], flamelike (clusters and bundles) [12, 14, 15], and vague wrinkled patterns [27], and some of them are shown in Fig. 32.3.

32.4 DRYING PATTERNS OF COLLOIDAL DISPERSIONS AND COLLOIDAL CRYSTALS

Drying patterns observed by a close-up camera and an optical microscope are called *macroscopic* and *microscopic patterns* in the present context. In the drying patterns65, stratified *s*tructures of solutes formed from micro- to macroscales. Most extended microscale patterns of colloidal crystals of polystyrene spheres were fractal patterns [65]. The *stratified* pattern formation is observed in general for many kinds of colloidal particles in suspension state.

Figure 32.4 shows the typical patterns formed in the drying of a series of the colloidal crystal suspensions of silica spheres, with their diameters ranging from 56 nm (a) to 1090 nm (d) at 0.0333 of the sphere concentration [63]. The spokelike cracks formed from the outside edge toward the center. Interestingly, the cracks were introduced in the final stage of dryness along the outer edges first, where the dryness proceeded in advance. New cracks developed successively and cooperatively keeping the same angle with the adjacent older cracks [66]. Dried film is transparent, and many cracks are observed for small spheres. When sphere size increases, film becomes whitey and the crack number decreases sharply. Increase in size will result in increase in the elastic modulus of the film, followed by decrease in crack number. The cracks originated from the convectional patterns formed typically for spherical colloidal particles as described above. It should be noted here that many potential cracks formed in the suspension state by the cell convections and the convectional flow of spheres and solvents. Broad rings are also observed at the outer edges, especially for small spheres. A main cause of broad rings is the convection flow of solvent and colloidal spheres. In particular, the flow of colloidal spheres from the center toward the outer edges in the lower layer of the liquid drop is important, which was observed directly from the movement of the temporally aggregates formed in the aqueous suspensions of Chinese black ink particles [11] and PMMA spheres [47, 48], for example. Interestingly, broad rings tend to shift toward the central area as sphere size increases, with the appearance of a hill of the spheres in the center region for the largest spheres as shown in Fig. 32.4. Furthermore, it is impressive to observe a hole in the central area where quite a few spheres are distributed. The spokelike cracks and broad ring patterns are quite familiar for so many kinds of colloidal spheres. Shape of colloidal particles is also reflected in the drying patterns. The spokelike cracks disappear for the nonspherical (anisotropically shaped) particles [27, 67] in addition to the very large spheres [68]. Figure 32.4 demonstrates that information such as the size and shape of colloidal particles is transferred via sedimentation processes to the drying patterns of spokelike cracks and broad rings. In other words, size and shape of the colloidal particles is estimated qualitatively from the drying patterns.

One of the typical examples of the transfer processes from the sedimentation to the solidification is shown in Fig. 32.5. The drying frontier of the fractionated bentonite suspensions moves from right to left with time in the pictures.[27] Border between the liquid and solid regions is the frontier zone of dryness. After setting the bentonite suspensions, vague wrinkled sedimentation patterns appeared. As time elapsed, the drying frontier moved to the left side, and the vague sedimentation patterns formed in the liquid phase became clearer and finer during the course of solidification. These observations strongly support the notion that the primitive and vague sedimentation patterns previously formed in liquid phase become sharper based on the sedimentation patterns toward solid phase.

Figure 32.6 shows typical examples of the cooperative drying pattern formation between colloidal silica spheres (1.2 μm in diameter) and sodium chloride [22]. Colorful crosslike patterns of NaCl, which are surrounded with the dendritic silica spheres of 183 nm [48], 305 nm [23], and 560 nm in diameter were observed [24].

Binary [25] and ternary mixtures [26] of colloidal silica spheres having different sizes showed an interesting *segregation effect* in their drying patterns. The semiquantitative estimation of sphere size and the mixing ratio in the original suspensions was made successfully from the drying patterns. From the peak profiles in the reflection spectroscopy, AFM

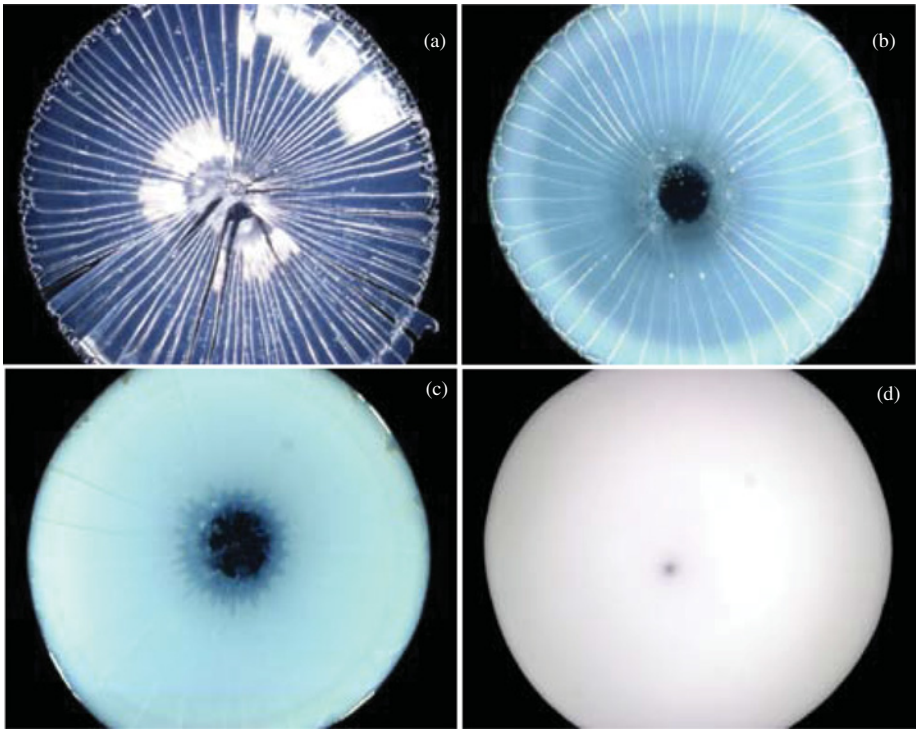


FIGURE 32.4 Macroscopic drying patterns of colloidal silica spheres on a coverglass at 25°C: (a) CS45 (56.3 nm in diameter); (b) CS82 (103 nm); (c) CS161 (183 nm); (d) CS1001 (1090 nm) ($\phi = 0.0333$, 0.1 mL, length of the bar = 5 mm).

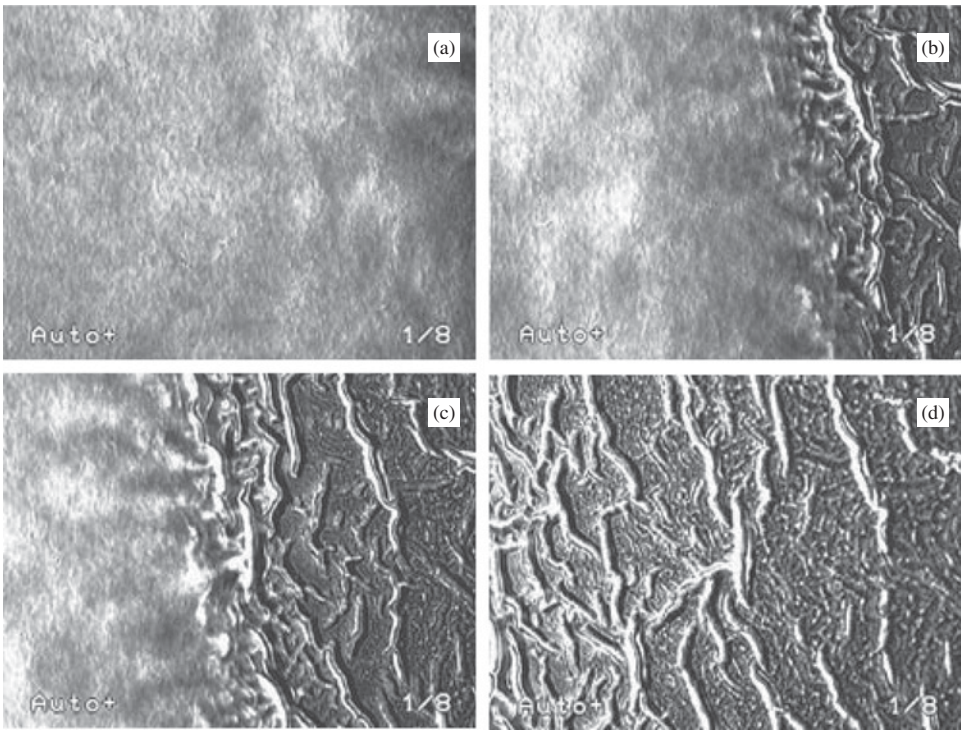


FIGURE 32.5 Change in patterns of bentonite suspension at the boundary regions of sedimentation and solidification processes with time on a coverglass at 25°C (4.6 mg/mL, 0.05 mL): (a) 46 min 30 s, (b) 48 min, (c) 48 min 45 s, (d) 49 min 50 s after setting (length of bar = 10 μm).

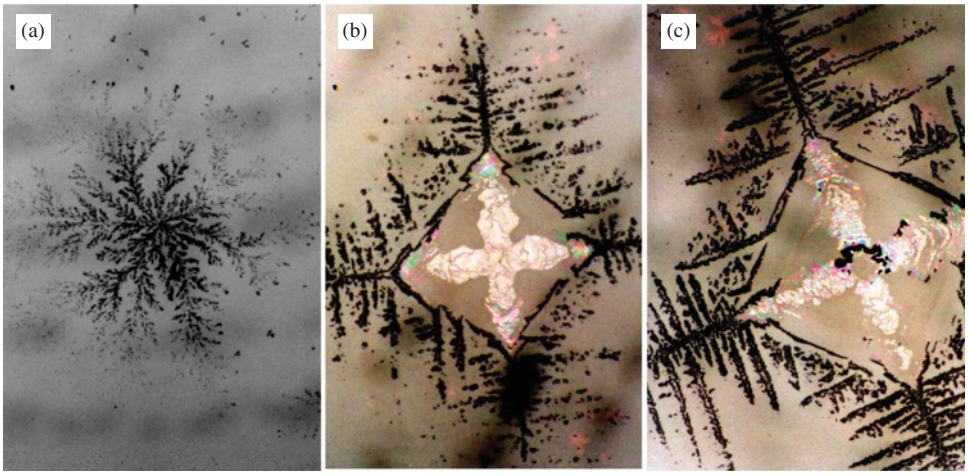


FIGURE 32.6 Microscopic drying patterns of silica spheres (1.2 μm in diameter) in the presence of sodium chloride in a glass dish at 24°C ($\phi = 0.00129$, 10 ml): (a) [NaCl] = 0.0003 M; (b) 0.001 M; (c) 0.003 M.

measurements, and the thickness profiles of the dried film, the segregation took place during the course of dryness; that is smaller spheres distribute outward and orient broad rings separately and independently to each other. Blue, pink, and white color bands corresponding to the accumulation areas of small (183-nm-diameter), medium (300-nm-diameter), and large colloidal silica spheres appeared in close-up color pictures of macroscopic patterns of the binary and ternary mixtures. Widths of the color bands changed quantitatively with the mixing ratio. Linearity between the widths of the pink bands and the mixing ratio was excellent. Semiquantitative analyses of mixing ratio and sphere size are clarified to provide information on drying patterns.

The drying patterns of biological colloids, lycoposium spore particles (31 μm in average diameter) were also studied [68].The vague broad-ring structure was observed, and the size of the particles on a coverglass decreased with a corresponding decrease in particle concentration. Microscopic drying patterns almost disappeared except for the short chain-like patterns. These observations support the theory that the convectional contribution to drying patterns is still effective in the lycoposium suspension, although the convectional forces are very weak compared to the sedimentary forces.

The mechanism of a multibranched and honeycomb network drying pattern formation of gold suspension on substrates has been discussed in the literature [69, 70]. Dissipative patterns during dryness of colloidal suspension ejected by inkjet printing have been studied [71].

32.5 DRYING PATTERNS OF POLYMER GEL SPHERES

In general, polymer solution, which is composed of linear-type polymers and their solvents, is *transparent*. The main cause of the transparency is the fact that the unit's size in the dynamic thermal motion of the polymers, which is close to the size of their monomer units, is very small compared with light wavelengths and rather close to size of solvents. Furthermore, there are *no interfaces* between the polymer solutes and solvent phases, since polymers and solvents are able to change their location rather freely because of their own thermal motion. On the other hand, size of the typical colloidal spheres is close to or larger than light wavelengths, and 100–1000-fold greater than that of the medium (solvent) molecules. Thus colloidal dispersion is *turbid* except for those in the refractive-index (RI)- matched condition between spheres and medium. In other words, turbid dispersion supports the existence of the *interfaces* in a sense of colloid chemistry. We should note here that most of gel dispersions are also turbid, and their nature seems to be just in between polymer solution and colloidal dispersion. Study of the macroscopic and microscopic drying patterns of gel spheres is, therefore, highly attractive.

Several years ago, the authors studied the drying patterns of small size poly (*N*-isopropylacrylamide), pNIPAm(70-5) gels (72 nm in hydrodynamic diameter at 20°C and 28 nm at 50°C, and 5% in the degree of cross-linking) on a coverglass [72]. The principal macroscopic patterns at 25°C were the small size of single or multiple broad rings of the hill accumulated with the gels. As the temperature rose to 50°C, the drying pattern area extended to the beautiful *flickering spoke-like patterns* transitionally. These observations supported the theory that the extended gels at low temperatures tend to associate weakly with each other, whereas gels at high temperatures shrink and move rather freely by the convectional flow of water medium molecules, although a weak intergel attraction on a substrate still remains.

Drying dissipative patterns of monodisperse thermosensitive gel spheres of poly(*N*-isopropylacrylamide),

TABLE 32.1 Characteristics of pNIPAm Gel Spheres

Gel spheres	d_0 (nm)		ρ		T_t (°C)	ζ-Pot. (mV)	Refs.
	20°C	45°C	25°C	45°C		25°C	
pNIPAm(200-0.5)	344	116	0.030	0.61	32	−10.1	73,78
pNIPAm(200-2)	260	103	0.035	0.59	32.5	−14.8	74,79
pNIPAm(200-5)	238	113	0.088	–	33	−13.5	73,77
pNIPAm(200-10)	213	121	0.122	0.62	35	−16.7	74,79
pNIPAm(400-5)	412	220	0.11*	0.68	33	−14.4	75,80
pNIPAm(600-5)	546	294	0.127	0.72	33	−17.9	75,80
pNIPAm(1500-5)	1530	505	–	0.80	31	−13.4	This work

*at 20°C

pNIPAm(200-10) [73], pNIPAm(200-5) [74], pNIPAm(200-2) [68], pNIPAm(200-0.5) [75], pNIPAm(400-5) [76], pNIPAm(600-5) [77], and pNIPAm(1500-5) [76] were studied systematically. Table 32.1 shows the fundamental properties of pNIPAm gel spheres. Zeta-potential (ζ-pot.) values derived from the electrophoretic mobility measurements are always *negative*. The absolute values are small compared with those of the typical hard spheres, −30 to −60 mV, but far from zero. These ζ-values of pNIPAm gels are consistent with the formation of the electrical double layers around the gel–water interfaces [77–80]. The ρ-values in the table show the *effective density* of the gel spheres' inner hydrodynamic diameter, given by the ratio of gel concentrations in weight percent (wt%) against volume percent (vol%) (100ϕ). Evaluation of vol% was made uniquely from the reflection spectroscopy of gel crystals in the deionized aqueous suspension [77–80]. The ρ-values at low temperatures were quite small, whereas those at high temperatures were large (see Table 32.1). The ρ-values increased sharply as the degree of cross-linking increased, especially at low temperatures. The ρ-values increased slightly as the sphere size increased at any temperatures, when comparison was made among the gels having the same degree of cross-linking as is seen in Table 32.1.

Formation of the monodispersed agglomerated particles of pNIPAm spheres and their ordered arrays were observed, for the first time, in the drying patterns. Figure 32.7 demonstrates the typical drying patterns showing the oriented arrays of the agglomerates of pNIPAm gel spheres on each substrate. Microscopic ordered-structures on the substrates were (a) flickering ordered spokelines, (b) ordered rings, (c) net structures, and (d) latticelike structures of the agglomerated particles. The net and lattice structures formed more favorably at high degree of cross-linking, at high gel concentrations, and/or at high temperatures. It was found that the ordered spokelines (a) and rings (b) formed first during the course of dryness, and then the net (c) and lattice ordering (d) formed integratively from (a) and (b). We should note here that the suspensions of pNIPAm gel spheres emit the Bragg diffraction light at any temperatures examined between 20°C and 50°C and form the *colloidal crystal* structure especially in the deionized suspension state with coexistence of the

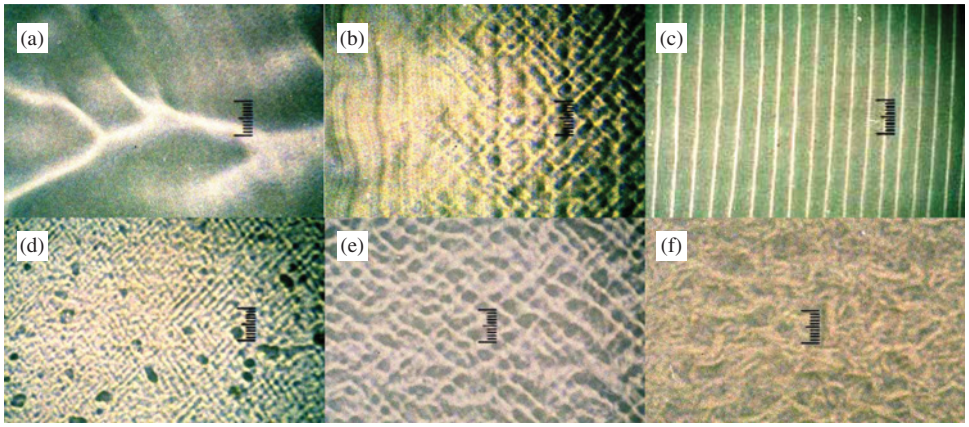


FIGURE 32.7 Typical examples of microscopic drying patterns of (a,b) pNIPAm(200-0.5): (c) pNIPAm(200-2); (d) pNIPAm(200-10); (e) pNIPAm(400-5); (f) pNIPAm(1500-5) at 45°C (humidity 35%, full scale at 100 μm): (a) 1.01 wt%, on a watchglass; (b)1.01, watchglass; (c) 0.039, glass dish; (d) 2.4, glass dish; (e) 0.97, glass dish; (f) 3.1, coverglass. For a color version of this figure, see the color plate section.

TABLE 32.2 Characteristics of AIBA-P2VP and PEGMA-P2VP Gel Spheres at 25°C

Gel spheres	d_0 (nm)	ρ	ζ-Pot. (mV)	Refs.
AIBA-P2VP(0.1)	170	0.51	+60	51,91
AIBA-P2VP(0.5)	170	0.70	+58	51,91
AIBA-P2VP(1)	180	0.81	+47	51,91
PEGMA-P2VP(0.1)	400	0.83	+16	52,92
PEGMA-P2VP(0.5)	390	0.73	+22	52,92
PEGMA-P2VP(1)	385	0.93	+23	52,92

cation and anion exchange resins [77–83]. The ordering was clarified to form by the extended *electrical double layers* in addition of the *excluded volume effect* of the gels themselves, although most researchers have believed thus far that pNIPAm gels crystallize by the *excluded volume effect* exclusively [84–90].

Several investigators prepared cationic hydrogel spheres, AIBA-P2VP [91] and PEGMA-P2VP [92], and studied their crystallization [91, 92] and drying patterns in detail [51, 52]. The characteristic properties of these spheres are compiled in Table 32.2. The high ρ-values and ζ-potentials support the theory that cationic gels are rather dense with polymers but contain small amounts of water in gel domain. Microscopic drying patterns quite similar to those of pNIPAm gels were observed for these cationic gel spheres. Thus, the net and lattice structures of agglomerates form always for gel systems and not for typical colloidal hard-sphere systems.

The drying patterns form by the successive and cooperated processes of the *evaporation*, *convection*, *sedimentation*, and *solidification*, although these four processes are correlated strongly and overlap each other. *Agglomeration* of the single gel spheres is similar to *aggregation* of the gel spheres. However, in the authors' opinion, agglomeration and aggregation are different. *Agglomeration* takes place by *weak* and *integrative* affinitive interactions among the monomer gel components, resulting in monodisperse associates, whereas *aggregation* forms by the *strong* intersphere attraction forces resulting in the presence of polydisperse associates. We should pay attention to the impact of the ordered convectional flow of the single agglomerated particles and also weak interaction between the single spheres and the substrate on the formation of the monodispersed agglomerates. Several agglomeration phenomena have been reported thus far. As is well known, monodispersed colloidal silica spheres produced by the Stoeber method form via the agglomeration of the monodispersed prespheres of several nanometers in their size [93]. The processes of the formation of monodispersed colloidal silica spheres and their orientation on the substrates are similar to those of the agglomeration of the thermosensitive gel spheres and their orientation in this study.

Polymer complexation will be another example of a phenomenon similar to the present agglomeration of gels. As is well known, most of the polyion complexation between macrocations and macroanions proceeds by the strong electrostatic attraction and resulting in the polydispersed aggregates [78]. However, the polymer complexes formed from the weak hydrogen-bonding attraction represented by the complexation between poly(acrylic acid) and poly(ethylene glycol) led to formation of the monodisperse colloidal spheres and further their colloidal crystallization in both suspension- and dried film states [49].

32.6 DRYING PATTERNS OF SYNTHETIC AND BIOLOGICAL POLYMERS

Figure 32.8 shows the microscopic drying patterns of polyethylene glycol (PEG500K and PEG200K) observed by

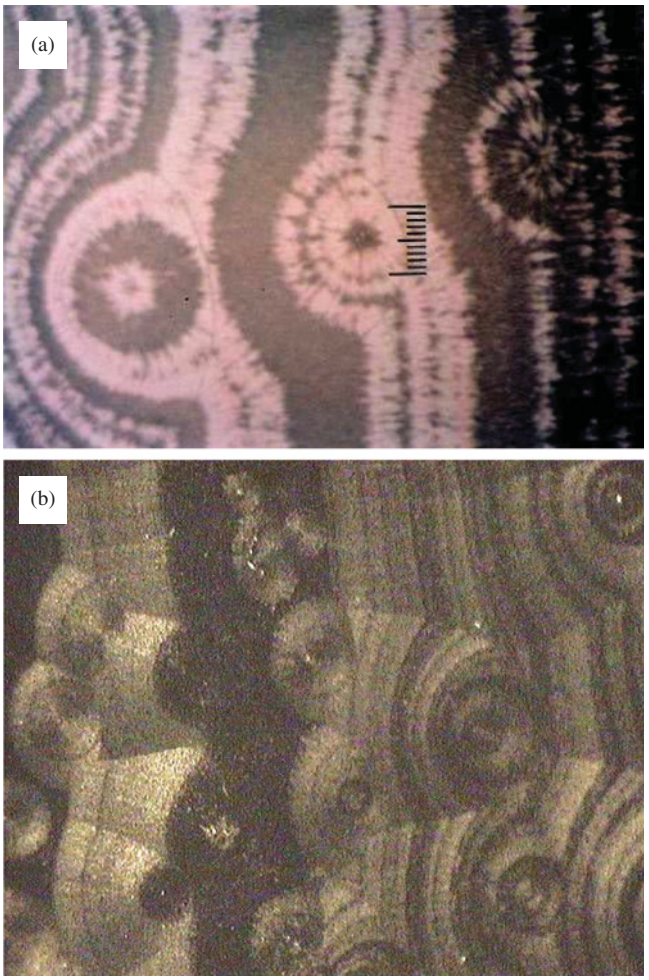


FIGURE 32.8 Microscopic (a) and polarizing microscopic drying dissipative patterns (b) of PEG500K (a) and PEG2000K solution (b) on a watchglass at 24°C: (a) 0.01 monoM, 4 mL, 45 h 25 min after setting, full scale at 100 μm; (b) 0.1 monoM, frame size 2.6 × 3.4 mm.

the optical microscopy and polarizing microscopy, respectively [37]. Clearly, of the coupled structures of *spherulites* and *lamellae*, with the latter originating from the ring-drying pattern, are observed. Morphology of PEG crystals was influenced greatly during the drying, process, although the lattice structure should not be changed at all during the dissipative processes. The *coupling effect* is a typical example of dissipative crystallization of polymers. One investigator studied drying patterns of PEG polymer with salt on Teflon plate [38].

Characteristic coupling dissipative effects of spherulites (or hedrites) were also observed for one of the anionic polyelectrolytes, sodium polymethacrylate [39]. The ringlike arrays of the large spherulites along the broad ring area, a very large single spherulite, and the bundle of the spherulites at the central area formed on a coverglass, a watchglass, and a glass dish, respectively. The fine structure of a single spherulite crystal at the central area (a) and the outer edge (b) formed, respectively, on a watchglass.

Drying patterns of poly(allylamine hydrochloride), one of the cationic polyelectrolytes, were studied on a coverglass [36]. The fractal patterns of 1.2–1.6 in dimension were observed as is shown in Fig. 32.9. Surprisingly, shape of the polymer crystals changed from crosslike to curved patterns as initial polymer concentration increased. Furthermore, crystal size increased with increasing concentration, which is reverse in tendency with the change in crystal size in solution state. It should be recalled that conformation of polyelectrolytes changes from *rod* to *coil* as polymer concentration increases. Thus, it is highly plausible that the shape information of the polymer at the initial solution state was transferred to the drying patterns. Drying patterns of a series of poly(*N*-alkylpyridinium halide) were observed [95]. The patterns were influenced substantially by the hydrophobicities of the polyelectrolytes. Several researchers discussed the drying fractal patterns with the use of fractal theory [96–99]. Drying processes of highly concentrated polymer solution have been studied, where buckling of the surface membrane during dryness takes place [84–86].

Drying patterns of several biological polyelectrolytes, grouped into polypeptides [40, 103, 104], polysaccharides [41, 105–108], and polynucleotides [42, 109, 110] were studied in the author's laboratory. Typical microscopic patterns are shown in Fig. 32.10 for polypeptides (a–c), polysaccharides (d–f), and polynucleotides (g–i). For polypeptites, rodlike, spherulite (or hedrite), and street roadlike crystals formed. Rodlike, dendritic rods, swordlike and hedrite crystals were observed for polysaccharides. For polynucleotides, dendritic, rodlike, dendritic long rods, swordlike, and spherulite crystals were observed. Microscopic patterns are similar in part and unique with respect to each other among intra- and inter-segmental groups. The conformations of these polymers are differentiated by the kind of polymer, for example, helical, stretched rod, β-sheet, or twisted ribbon; also, by the chemical structures of the mainchains are also quite different to each other among the groups. However, it is interesting and suggestive to observe the rather common type of drying patterns among the biological polyelectrolytes. Furthermore, we should note that these microscopic patterns appeared at the specified places, at the central areas, and/or close to the outside edges, for example. The macroscopic patterns of the biological polyelectrolytes showed clearly the dissipative crystallization effects such as accumulation, segregation and orientation. For the diluted NaDNA solution [42], for example, the orientation of the long dendritic rods formed along the spokelines, which supports the important role of the convectional flow processes of the polymer molecules during the course of dryness.

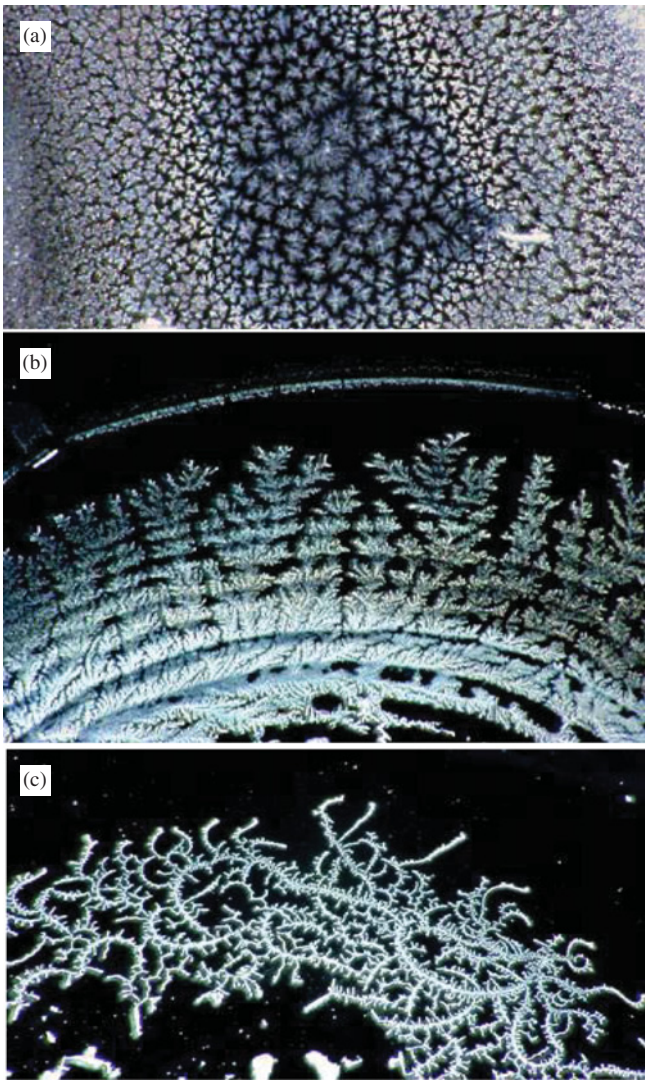


FIGURE 32.9 Microscopic patterns of PAL on a coverglass at 25°C. In water, 0.1 mL (a) 1×10^{-5} monoM, (b) 1×10^{-4} momoM, and (c) 1×10^{-3} monoM (length of bar = 200 μm).

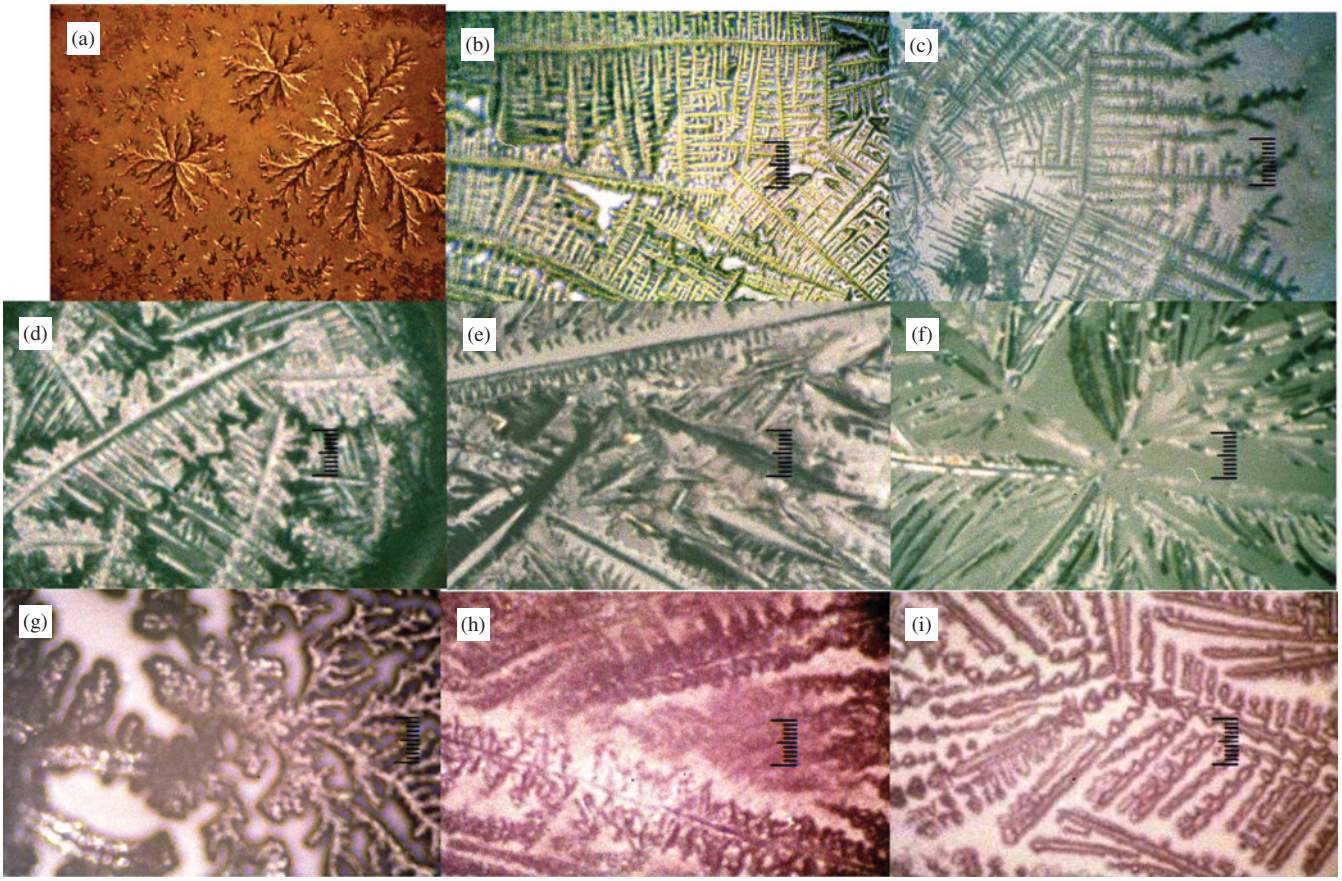


FIGURE 32.10 Typical examples of microscopic patterns of biopolymers: (a) NaPDGA + NaPLGA (1:1) [103], [NaPGA] = 0.01 monoM, on a coverglass, 0.1 mL, at 25°C; (b) NaPLGA + NaCl [103], [NaPLGA2] = 0.008 monoM, [NaCl] = 4 mM, on a watchglass, 0.7 mL, 25°C; (c) PDLHBr + PLLHBr [40], [PDLHBr] = [PLLHBr] = 0.00005 monoM, on a watchglass, 0.7 mL, 24°C; (d) NaHLA [108], [NaHLA] = 0.004 monoM, [NaCl] = 0.06 mM, on a coverglass, 0.1 mL, at 25°C; (e) NaCMC2 [106], [NaCMC2] = 0.008 monoM, [NaCl] = 0.04 M, on a coverglass, 0.1 mL, 25°C; (f) βCD [107], [βCD] = 0.01 M, on a glass dish, 0.7 mL, at 20°C; (g) NaDNA [42], [NaDNA] = 0.01 monoM, on a watchglass, 0.7 mL, at 25°C; (h) KPolyA [109], [KPolyA] = 0.00414 monoM, [KCl] = 0.06 M, pH = 6.6, at 20°C; (i) PolyA + PolyU [110], [PolyA] = [PolyU] = 0.002 monoM, [KCl] = 0.01 M, on a coverglass, 0.1 mL, pH = 6.6, at 25°C. Full scale is at 100 μm (a–g) and 50 μm (h,i). For a color version of this figure, see the color plate section.

Influence of double-stranded and/or triple-stranded complex formation of KPolyA and KPolyU on the drying patterns has been studied [110]. Macroscopic broad ring size decreased by complexation. It was difficult to determine whether microscopic patterns of dendritic long rods originated from single-stranded or double-stranded helices. The inclusional association constants were determined from the bent points in the curves of the broad ring size versus surfactant concentration when a finite amount of cyclodextrin was presents [111]. The short and thick rodlike microscopic drying patterns were observed for the inclusional complexes. Recently, drying crack and ring patterns in spherulites of poly(*L*-lactic acid) were studied in detail [112]. One researcher studied the crystal structure of collagen solution [113,114]. Drying patterns of β-cyclodextrin (βCD) and their inclusional complexes with sodium *n*-alkylsulfates have also been studied [107, 115, 116]. Association constants of the inclusion associates were estimated from the macroscopic drying patterns.

32.7 DRYING PATTERNS OF IONIC AND NEUTRAL SURFACTANTS

The microscopic patterns of cationic surfactant, *n*-dodecyltrimethylammonium chloride, were observed [117]. Basic structures were crosslike. However, crystal size and shape changed as a function of the distance from the film center. Drying patterns of a series of *n*-alkyltrimetylammonium bromides (alkyl: *n*-decyl, *n*-dodecyl, *n*-tetradecyl, and

n-hexadecyl) were studied [118]. Microscopic drying patterns such as rodlike, dendritic, and granule-like patterns were observed, and they changed as a function of the carbon number of the alkyl group, surfactant concentration, and the distance from thecenter of the pattern. Drying patterns of aqueous solution of sodium *n*-alkylsulfates (alkyl: *n*-hexyl, *n*-octyl, *n*-decyl, *n*-dodecyl, and *n*-hexadecyl) on a coverglass were observed [119]. Branched stringlike microscopic patterns appeared to increase irrespective of number.

Film surfaces of polyoxyethylene alkyl ethers changed from the *rough* to *smooth* as the HLB (hydrophile–liophile balance) values of the surfactants increased [120]. Furthermore, film thickness profiles as a function of the distance from the center of the film shifted from the center-accumulated hill shape to the broad ringlike structure as is shown in Fig. 32.11. Macroscopic and microscopic drying patterns of surfactant molecules were found to give important information on the association and dissociation phenomena.

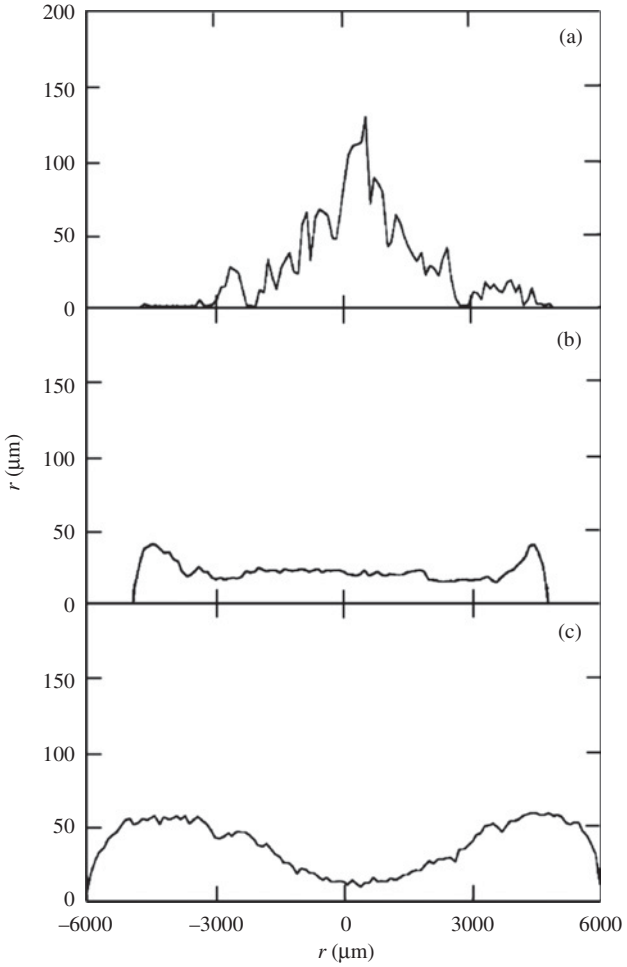


FIGURE 32.11 Thickness profiles of dried films of polyoxyethylene(5) stearyl ether (a), polyoxyethylene(10) stearyl ether (b), and polyoxyethylene(20) stearyl ether (c) at 25°C. In water, 0.06 M, 0.05 mL.

32.8 DRYING PATTERNS OF SIMPLE ELECTROLYTES

Drying patterns of simple electrolytes such as KCl, NaCl, $CaCl_2$, and $LaCl_3$ were studied [121]. Macroscopic broad rings formed at the outside edge of the drying film area, which shrank from the initial solution area, especially at low salt concentrations. The microscopic blocklike and dendritic crosslike patterns were observed for all the salt examined. Size of single crystals dried on a coverglass increased as salt concentration increased. The drying patterns of the binary mixtures of the salts were also observed. Size of the broad ring increased sharply by mixing, whereas the microscopic patterns were insensitive to the mixing.

32.9 DRYING PATTERNS OF OTHER SOLUTES

Droplets of the aqueous caffeine solutions were dried on various substartes (glass, polystyrene, and polyester) [122]. Coexistence of α- and β-caffeine was observed and the alpha and beta forms were locally separated. Drying patterns of porphyrin derivatives were observed on silica [123].

Professor D. Jishiashvil of Georgian Tech University performed interesting drying experiments (D. Jishiash, J. Okamoto, A. Tsuchida, and T. Okubo, unpublished results). A drop of water was placed on the Ge:GeO_2 film, where Ge and GeO_2 are crystal state and amorphous matrix. Then, water-soluble GeO_2 was solved, and the drying patterns appeared at the dried spot, when the liquid-drop was dried. Two examples of the microscopic pictures are shown from the central to the outside edge in Fig. 32.12. Macroscopic broad rings also formed. Furthermore, colorful microscopic patterns appeared. Interestingly, aqueous GeO_2 solution did not show similar microscopic patterns on any substrates including Si wafer.

Drying patterns of fluorescence dyes, rhodamine 6G, uranine, 7-hydroxy coumarin, and 7-amino-4-(trifluoromethyl) coumarin, for example [124]. The macroscopic broad ring patterns formed for all the ethanol solutions examined. Size of the ring increased with increasing dye concentration, but sharply above the certain critical dye concentration. Microscopic fine patterns including the streetlike, needle-like, and flowerlike crystals formed.

32.10 TRANSFERRING INFORMATION ON SOLUTIONS AND SUSPENSIONS TOWARD THE DRYING PATTERNS

As described in the Introduction section one of the main purposes of the author's drying experiments is to obtain *information* on solutes, solvent, and atmosphere from the drying patterns. It has now been clarified that information on solutions and suspensions, shape and size of solutes and

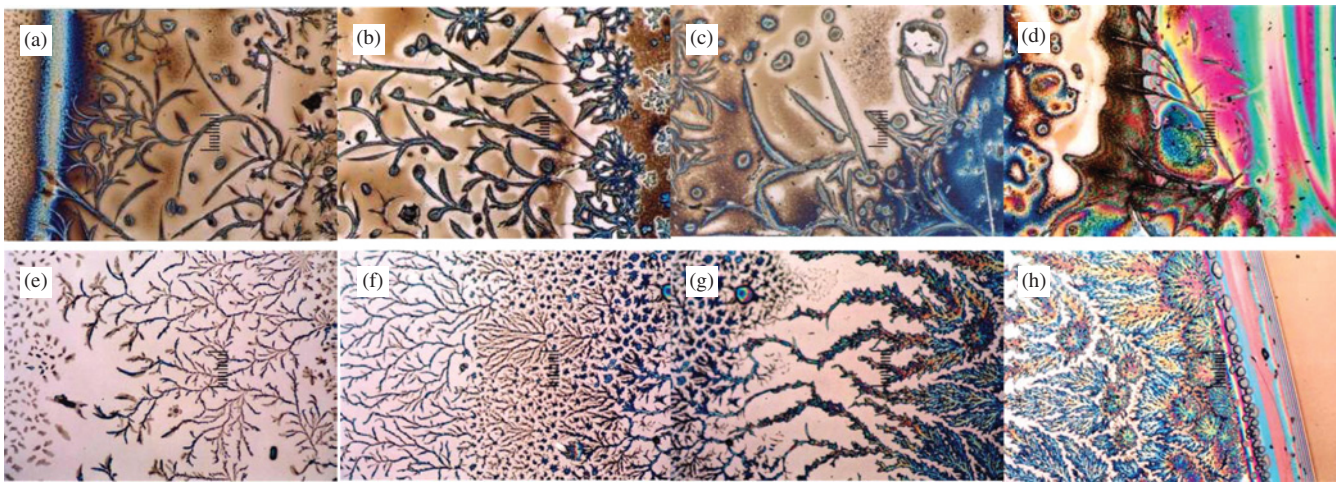


FIGURE 32.12 Microscopic drying patterns of Ge:GeO_2 film. (a–d) code 23b, on Si, 5×, full scale at 200 μm; (e–h) code 24b, on Si, 40×, full scale at 25 μm, from the central area to the right edge. For a color version of this figure, see the color plate section.

TABLE 32.3 Transfer of Information on Suspensions and Solutions toward Drying Patterns on a Glass Substrate

Information		Drying patterns	
Concentration	Up	Broad-ring size	Up
		Broad-ring shape	Broaden
		Broad-ring height	Up
		Spoke-line number	Down
		Fractal dimension	Up or insensitive
		Single-crystal size	Up
Molecular weight, polymer	Up	Broad-ring size	Up
Particle size	Up	Broad-ring size	Down
		Spoke-line number	Down
Hydrophobicity	Up	Broad-ring size	Down
HLB, surfactant	Up	Broad-ring shape, from round hill	
Salt	Up	Broad ring	Up or down
		Bumpy-shaped broad ring	
		Round hill, from broad ring	
		Spoke-line number	Down
Temperature	Up	Broad-ring shape	Sharpen
		Broad-ring size	Up
		Spoke-line number	Down
Humidity	Up	Broad-ring size	Down
		Broad-ring shape	Broaden
		Spoke-line number	Down
Surface tension	Down	Pattern area, broad-ring size	Up
Polarity of solvent	Up	Pattern area	Down
		Drying time	Up
Polymer extended, from coil		Cross, star, from arc, string	
Ordered structure (helix or β-sheet)		Broad-ring size	Up
Anisotropic-shaped, from sphere		Round hill, from broad ring	
Gel sphere		Flamelike (flickering), spoke line	
		Ordering of agglomerates	
Mixture of different-sized spheres		Multiple broad rings,	
		Segretation; small outer, large inner	

temperature and humidity, for example, is transferred to the drying patterns by the cooperative and successive processes of evaporation, convection, sedimentation, and solidification. Therefore, it is highly plausible that a part of the information is available from the macroscopic and microscopic drying patterns. The relationships between the *information* and *drying patterns* are summarized in Table 32.3 mainly by applying the data of the drying patterns found in the author's group.

For example, increase in the solute concentration of the initial solutions and suspensions has resulted in increase of the size and height of the broad ring and decrease of number of spokelines. Interestingly, single crystal size in the broad ring area increase with increasing solute concentration, which is opposite in tendency to crystallization of the solution and suspension in the bulk phase. We should note here that the macroscopic and microscopic drying patterns originated from the integrated *information* of solutes and atmosphere. The assignment of the solutes and atmosphere from the drying patterns will be made correctly, when the specific drying patterns appeared. For example, when the *ordering of the agglomerates* was observed, the solutes are highly plausible to be *gel spheres*.

32.11 MISCELLANEOUS

Film formation mechanisms from polymer colloidal dispersions have been studied extensively for more than 50 years, and are correlated closely with the drying patterns [125–141]. Three processes are proposed here: (1) close-packing processes of polymer colloids by evaporation of solvent; (2) deformation of the particles followed by disappearing voids, although the original particles are still distinguishable; and (3) continuous film formation by the diffusion of polymer across particle boundaries. Cracking patterns of the films induced by the shrinkage during dryness were also investigated for the paste layers of clay, sand, and water deposited on rigid substrates [142–144]. Characteristic pattern formation in the dried thin film on a substrate has been reported. Wormlike and hexagonally packed domains were obtained from asymmetric organic–organometallic diblock copolymers [145]. Honeycomb patterns of polymers were studied intensively by one group of investigators [146]. Self-organization of a chromophore-labeled double chain amphiphile was reported [147]. Superhelix-to-tubule transformation of J-aggregates was studied by TEM [148]. Adsorbed and dried patterns of ionic surfactants were studied by several researchers [149–152].

32.12 CONCLUDING REMARKS

Most of the self-organization phenomena in nature are known to take place accompanied by dissipation of free energy and in the nonequilibrium state. Among a huge number of the dissipative self-organization events, study on the drying processes will be one of the most convenient and simple. This author studied the drying processes of (1) evaporation, (2) convection, (3) sedimentation, and (4) solidification as systematically as possible. Several important factors that determine the drying patterns will be discussed here. *First*, we will discuss the importance of *integrativity* among processes 1–4 during the course of dryness. We should note that the primitive patterns having information on solutions and suspensions will have formed already in the evaporation and convection processes. Furthermore, the primitive patterns are further transferred to the sedimentation and then solidification structures with *selection* and *amplification* of the initial information of solution and suspension. *Second*, the important role of the *interaction between solutes and substrates* must be

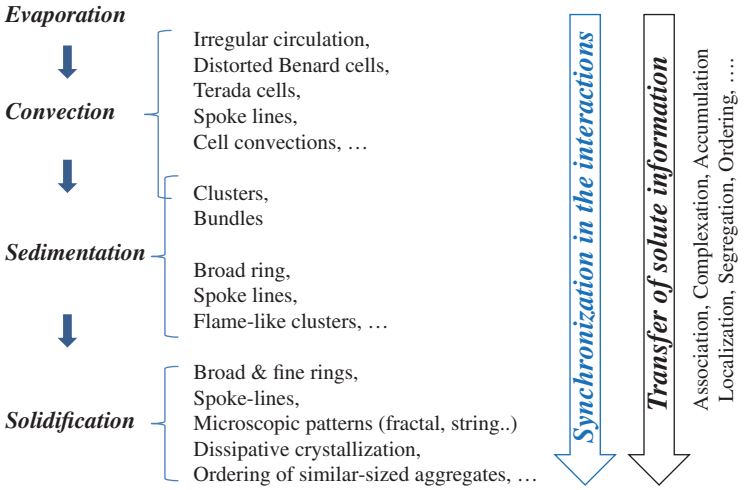


FIGURE 32.13 Synchronized pattern formation processes during the course of dryness of suspensions and solutions.

discussed. For example, extended conformation of macroions will be retained during the drying process through the interaction of the solutes and substrate. The stretched conformation of the macroions will change rather easily in the bulk solution state during the course of concentration toward coil conformation. However, when the stretched polymer chains interact with the substrate, change of their conformation will be delayed throughout the drying process. Thus, the initial conformation will be transferred to the drying pattern. *Third*, the important role of the *concentration* of solutes by the evaporation of solvent during dryness must be discussed for the organization of solutes. Solute concentration will correspond to enhancement the intersolute repulsion forces, which are inevitable for the organization of colloidal systems as understood easily from colloidal crystallization. *Fourth*, the important role of the *gravitational effect* for convectional flow of solvents and solutes has been clarified. Marangoni convection is also important. *Fifth*, the most important factor in self-organization during dryness will be the *translational thermal movements* of all the relating elementary substances, including solutes, solvents, and components of the substrate surfaces. Each component has its own thermal energy $k_B T$. Analyses of *information* included in the initial solutions and suspensions from the drying dissipative patterns are still quite unsatisfactory at present. Further experimental and theoretical detailed studies are desired for understanding of the dissipative structural formation mechanisms in nature.

The total drying processes of solutions and suspensions are compiled in Fig. 32.13. It should be noted that synchronization of each processes will be one of the most important factors determining the actual drying patterns.

REFERENCES

[1] Okubo, T. (2006). In Stoylov, S.P., Stoimenova, M.V. (eds.), *Molecular and Colloidal Electro-optics.* Taylor & Francis, New York, pp. 573–589.

[2] Okubo, T. (2008). In Nagarajan, R., Hatton, T.A. (eds.), *Nanoparticles: Syntheses, Stabilization, Passivation, and Functionalization.* American Chemical Society, Washington, DC, pp. 256–270.

[3] Okubo, T. (2010). *Macromol. Symp.* **288**, 67–77.

[4] Hisatake, K., Tanaka, S., Aizawa, Y. (1993). *J. Appl. Phys.* **73**, 7395–7401.

[5] Shahidzadeh-Bonn, N., Rafai, S., Azouni, A., Bonn, D. (2006). *J. Fluid Mech.* **549**, 307–313.

[6] Gribbin, G. (1999). *Almost Everyone's Guide to Science. The Universe, Life and Everything.* Yale Univ. Press, New Haven, CT.

[7] Ball, P. (1999). *The Self-Made Tapestry. Pattern Formation in Nature.* Oxford Univ. Press, Oxford, UK.

[8] Terada, T., Yamamoto, R., Watanabe, T. (1934). *Sci. Paper Inst. Phys. Chem. Res. Jpn.* **23**, 173–184.

[9] Terada, T., Yamamoto, R., Watanabe, T. (1935). *Sci. Paper Inst. Phys. Chem. Res. Jpn.* **27**, 75–92.

[10] Nakaya, T. (1947). *Memoirs of Torahiko Terada (in Japanese)*. Kobunsya, Tokyo.

[11] Okubo, T., Kimura, H., Kimura, T., Hayakawa, F., Shibata, T., Kimura, K. (2005). *Colloid Polym. Sci.* **283**, 1–9

[12] Okubo, T. (2006). *Colloid Polym. Sci*, **285**, 225–231.

[13] Okubo, T. (2009). *Colloid Polym. Sci.* **287**, 167–178.

[14] Okubo, T., Okamoto, J., Tsuchida, A. (2009). *Colloid Polym. Sci.* **287**, 351–365.

[15] Okubo, T. (2009). *Colloid Polym. Sci.* **287**, 645–657.

[16] Palmer, H.J. (1976). *J. Fluid Mech.* **75**, 487–511.

[17] Anderson, D.M., Davis, S.H. (1995). *Phys. Fluids* **7**, 248–265.

[18] Pouth, A.F., Russel, W.B. (1998). *AIChE (American Institute of Chemical Engineers) J.* **44**, 2088–2098.

[19] Burelbach, J.P., Bankoff, S.G. (1998). *J. Fluid Mech.* **195**, 463–494.

[20] Fischer, B.J. (2002). *Langmuir* **18**, 60–67.

[21] Okubo, T. (2006). *Colloid Polym. Sci.* **284**, 1191–1196.

[22] Okubo, T. (2006). *Colloid Polym. Sci.* **284**, 1395–1401.

[23] Okubo, T., Okamoto, J., Tsuchida, A. (2007). *Colloid Polym. Sci.* **285**, 967–975.

[24] Okubo, T. (2007). *Colloid Polym. Sci.* **285**, 1495–1503.

[25] Okubo, T., Okamoto, J., Tsuchida, A. (2008). *Colloid Polym. Sci.* **286**, 385–394.

[26] Okubo, T., Okamoto, J., Tsuchida, A. (2008). *Colloid Polym. Sci.* **286**, 941–949.

[27] Yamaguchi, T., Kimura, K., Tsuchida, A., Okubo, T., Matsumoto, M. (2005). *Colloid Polym. Sci.* **283**, 1123–1130.

[28] Okubo, T. (2006). *Colloid Polym. Sci.* **285**, 331–337.

[29] Vanderhoff, J.W. (1973). *J. Polym. Sci. Symp.* **41**, 155–174.

[30] Nicolis, G., Prigogine, I. (1977). *Self-Organization in Non-equilibrium Systems*. Wiley, New York.

[31] Ohara, P.C., Heath, J.R., Gelbart, W.M. (1997). *Angew. Chem.* **109**, 1120–1122.

[32] Maenosono, S., Dushkin, C.D., Saita, S., Yamaguchi, Y. (1999). *Langmuir* **15**, 957–965.

[33] Nikoobakht, B., Wang, Z.L., El-Sayed, M.A. (2000). *J. Phys. Chem.* **104**, 8635–8640.

[34] Ung, T., Litz-Marzan, L.M., Mulvaney, P. (2001). *J. Phys. Chem. B* **105**, 3441–3452.

[35] Okubo, T., Okamoto, J., Tsuchida, A. (2010). *Colloid Polym. Sci.* **288**, 189–197.

[36] Okubo, T., Kanayama, S., Ogawa, H., Hibino, M., Kimura, K. (2004). *Colloid Polym. Sci.* **282**, 230–235.

[37] Okubo, T., Okamoto, J., Takahashi, S., Tsuchida, A. (2009). *Colloid Polym. Sci.* **287**, 933–942.

[38] Choi, B.K. (2004). *Solid State Ionics* **168**, 123–129.

[39] Okubo, T., Hagiwara, A., Kitano, H., Okamoto, J., Takahashi, S., Tsuchida, A. (2009). *Colloid Polym. Sci.* **287**, 1155–1165.

[40] Okubo, T., Okamoto, J., Tsuchida, A. (2010). *Colloid Polym. Sci.* **288**, 981–989.

[41] Okubo, T., Mizutani, M., Takahashi, S., Tsuchida, A. (2010). *Colloid Polym. Sci.* **288**, 1551–1559.

[42] Okubo, T., Mizutani, M., Takahashi, S., Tsuchida, A. (2010). *Colloid Polym. Sci.* **288**, 1435–1444.

[43] Deegan, R.D., Bakajin, O., Dupont, T.F., Huber, G., Nagel, S.R., Witten, T.A. (1997). *Nature* **389**, 827–829.

[44] Deegan, R.D., Bakajin, O., Dupont, T.F., Huber, G., Nagel, S.R., Witten, T.A. (2000). *Phys. Rev. E* **62**, 756–765.

[45] Terada, T., Yamamoto, R. (1935). *Proc. Imp. Acad. Tokyo* **11**, 214.

[46] Okubo, T., Okamoto, J., Tsuchida, A. (2006). *Colloid Polym. Sci.* **286**, 1123–1133.

[47] Okubo, T. (2008). *Colloid Polym. Sci.* **286**, 1307–1315.

[48] Okubo, T. (2008). *Colloid Polym. Sci.*, **286**, 1411–1423.

[49] Okubo, T., Okamoto, J., Tsuchida, A. (2010). *Colloid Polym. Sci.* **288**, 189–197.

[50] Okubo, T., Fujii, S., Aono, K., Nakamura, Y. (2013). *Colloid Polym. Sci.* **291**, 1019–1030.

[51] Okubo, T., Fujii, S., Nakamura, Y. (2013). *Colloid Polym. Sci.* **291**, 2805–2813.

[52] Maillard, M., Motte, L., Ugo, A.T., Pileni, M.P. (2000). *J. Phys. Chem. B* **104**, 11875–11877.

[53] Matar, O.K., Craster, R.V. (2001). *Phys. Fluids* **13**, 1869–1883.

[54] Schatz, M.F., Neitzel, G.P. (2001). *Annu. Rev. Fluid Mech.* **33**, 93–129.

[55] Martincigh, B.S., Simoyi, R.H. (2002). *J. Phys. Chem.* **106**, 482–489.

[56] Hu, H., Larson, R.G. (2002). *J. Phys. Chem. B* **106**, 1334–1344.

[57] Truskett, J.N. (2003). *Langmuir* **19**, 8271–8279.

[58] Savino, R., Fico, S. (2004). *Phys. Fluids* **16**, 3738–3754.

[59] Hu, H., Larson, R.G. (2005). *Langmuir* **21**, 3963–3971.

[60] Girard, F., Antoni, M., Faure, S., Steinchen, A. (2006). *Langmuir* **22**, 11085–11091.

[61] Ristenpart, W.D., Kim, P.G., Domingues, C., Wan, J., Stone, H.A. (2007). *Phys. Rev. Lett.* **99**, 234502 (1–4).

[62] Girard, F., Antoni, M., Faure, S., Steinchen, A. (2008). *Colloids Surf. A* **323**, 36–49.

[63] Okubo, T., Yamada, T., Kimura, K., Tsuchida, A. (2005). *Colloid Polym. Sci.* **283**, 1007–1015.

[64] Okubo, T. (2008). *Colloid Polym. Sci.* **286**, 1527–1531.

[65] Okubo, T., Kimura, K., Kimura, H. (2002). *Colloid Polym. Sci.* **280**, 1001–1008.

[66] Okubo, T., Nozawa, M., Tsuchida, A. (2007). *Colloid Polym. Sci.* **285**, 827–832.

[67] Okubo, T., Otake, A., Tsuchida, A. (2009). *Colloid Polym. Sci.* **287**, 1435–1444.

[68] Okubo, T., Kokufuta, E., Nakamuro, M., Yoshinaga, K., Mizutani, M., Tsuchida, A. (2010). *Colloids Surf. B: Biointerfaces* **80**, 193–199.

[69] Mougin, K., Haidara, H. (2002). *Langmuir* **18**, 9566–9569.

[70] Stowell, C., Korgel, B.A. (2001). *Nano Lett.* **1**, 595–600.

[71] Park, J., Moon, J. (2006). *Langmuir* **22**, 3506–3513.

[72] Okubo, T., Itoh, E., Tsuchida, A., Kokufuta, E. (2006). *Colloid Polym. Sci.* **285**, 339–349.

[73] Okubo, T., Suzuki, D., Yamagata, T., Katsuno, A., Mizutani, M., Kimura, H., Tsuchida, A. (2011). *Colloid Polym. Sci.* **289**, 807–816.

[74] Okubo, T., Suzuki, D., Tsuchida, A. (2012). *Colloid Polym. Sci.* **290**, 411–421.

[75] Okubo, T., Suzuki, D., Tsuchida, A. (2012). *Colloid Polym. Sci.* **290**, 867–877.

[76] Okubo, T., Suzuki, D., Tsuchida, A. (2012). *Colloid Polym. Sci.* **290**, 1901–1911.

[77] Okubo, T., Suzuki, D., Yamagata, T., Katsuno, A., Sakurai, M., Kimura, H., Tsuchida, A. (2011). *Colloid Polym. Sci.* **289**, 291–299.

[78] Okubo, T., Suzuki, D., Yamagata, T., Horigome, K., Shibata, K., Tsuchida, A. (2011). *Colloid Polym. Sci.* **289**, 1273–1281.

[79] Suzuki, D., Yamagata, T., Horigome, K., Shibata, K., Tsuchida, A., Okubo, T. (2011). *Colloid Polym. Sci.* **289**, 1799–1808.

[80] Suzuki, D., Yamagata, T., Horigome, K., Shibata, K., Tsuchida, A., Okubo, T. (2012). *Colloid Polym. Sci.* **290**, 107–117.

[81] Okubo, T., Suzuki, D., Shibata, K., Tsuchida, A. (2012). *Colloid Polym. Sci.* **290**, 1403–1412.

[82] Okubo, T., Suzuki, D., Tsuchida, A. (2013). *Colloid Polym. Sci.* **291**, 661–668.

[83] Okubo, T., Suzuki, D. (2013). *Colloid Polym. Sci.* **291**, 1721–1727.

[84] Holtz, J.H., Asher, S.A. (1997). *Nature* **389**, 829–832.

[85] Pelton, R. (2000). *Adv. Colloid Interface Sci.* **85**, 1–33.

[86] Xia, Y., Gates, B., Yin, Y., Lu, Y. (2000). *Adv. Mater.* **12**, 693–713.

[87] Hellweg, T., Dewhurst, C.D., Bruckner, E., Kratz, K., Eimer, W. (2000). *Colloid Polym. Sci.* **278**, 972–978.

[88] Debord, J.D., Lyon, L.A. (2000). *J. Phys. Chem. B* **104**, 6330–6331.

[89] Xia, Y. (2001). *Adv. Mater.* **13**, 369.

[90] Gao, J., Hu, Z. (2002). *Langmuir* **18**, 1360–1367.

[91] Okubo, T., Fujii, S., Aono, K., Nakamura, Y. (2013). *Colloid Polym. Sci.* **291**, 2569–2577.

[92] Okubo, T., Fujii, S., Aono, K., Nakamura, Y., Tsuchida, A. (2013). *Colloid Polym. Sci.* **291**, 1201–1210.

[93] Stoeber, W., Fink, A., Bohn, E. (1968). *J. Colloid Interface Sci.* **26**, 62–69.

[94] Okubo, T., Hongyo, K., Enokida, A. (1984). *J. Chem. Soc. Faraday Transact. 1* **80**, 2087–2098.

[95] Okubo, T., Ogaw, H., Tsuchida, A. (2010). *Colloid Polym. Sci.* **288**, 245–256.

[96] Doulia, D., Tzia, K., Gekas, V. (2000). *Int. J. Food Prop.* **3**, 1–14.

[97] Mehrafarin, M., Faghihi, M. (2001). *Physica A* **301**, 163–168.

[98] Chai, L.H. (2007). *Int. J. Thermal Sci.* **46**, 802–811.

[99] Xu, P., Mujumdar, A.S., Yu, B. (2008). *Drying Technol*. **26**, 640–650.

[100] Pauchard, L., Allain, C. (2003). *Phys. Rev. E* **68**, 052801.

[101] Kajiya, T., Nishitani, E., Yamaue, T., Doi, M. (2006). *Phys. Rev. E* **73**, 011601.

[102] Jung, Y., Kajiya, T., Yamaue, T., Doi, M. (2009). *Jpn. J. Appl. Phys.* **48**, 031502.

[103] Okubo, T., Takahashi, S., Tsuchida, A. (2011). *Colloid Polym. Sci.* **289**, 1729–1737.

[104] Okubo, T., Onoshima, D., Tsuchida, A. (2007). *Colloid Polym. Sci.* **285**, 999–1007.

[105] Okubo, T. (2011). *Colloid Polym. Sci.* **289**, 159–167.

[106] Okubo, T. (2011). *Colloid Polym. Sci.* **289**, 1205–1213.

[107] Okubo, T. (2013). *Colloid Polym. Sci.* **291**, 2447–2454.

[108] Okubo, T., Tsuchida, A. (in press). *Colloid Polym. Sci.* (doi:10.1007/s00396-013-3082-y).

[109] Okubo, T., Takahashi, S., Tsuchida, A. (2011). *Colloids Surf. B: Biointerfaces* **87**, 11–17.

[110] Okubo, T. (2011). *Colloids Surf. B: Biointerfaces* **87**, 430–446.

[111] Okubo, T. (2013). *Colloid Polym. Sci.* **291**, 2599–2605.

[112] Nurkhamidah, S., Woo, E.M. (2012). *Colloid Polym. Sci.* **290**, 275–288.

[113] Maeda, H. (1999). *Langmuir* **15**, 8505–8513.

[114] Maeda, H. (2000). *Langmuir* **16**, 9977–9982.

[115] Okubo, T. (2013). *Colloid Polym. Sci.* **291**, 2455–2462.

[116] Okubo, T. (2013). *Colloid Polym. Sci.* **291**, 2599–2605.

[117] Okubo, T., Kanayama, S., Kimura, K. (2004). *Colloid Polym. Sci.* **282**, 486–494.

[118] Okubo, T. *Colloid Polym. Sci.* **291**, 2455–2462.

[119] Kimura, K., Kanayama, S., Tsuchida, A., Okubo, T. (2005). *Colloid Polym. Sci.* **283**, 898–904.

[120] Okubo, T., Shinoda, C., Kimura, K., Tsuchida, A. (2005). *Langmuir* **21**, 9889–9895.

[121] Okubo, T., Tsuchida, A., Togawa, H. (2009). *Colloid Polym. Sci.* **287**, 443–454.

[122] Leiterer, J., Emmerling, F., Panne, U., Christen, W., Rademann, K. (2008). *Langmuir* **24**, 7970–7978.

[123] Latterini, L., Blossey, R., Hofkens, J., Vanoppen, P., deSchryver, F.C., Rowan, A.E., Nolte, R.J.M. (1999). *Langmuir* **15**, 3582–3588.

[124] Okubo, T., Yokota, N., Tsuchida, A. (2007). *Colloid Polym. Sci.* **285**, 1257–1265.

[125] Dillon, R.E., Matheson, L.A., Bradford, E.B. (1951). *J. Colloid Sci.* **6**, 108–117.

[126] Henson, W.A., Taber, D.A., Bradford, E.B. (1953). *Industr. Eng. Chem.* **45**, 735–739.

[127] Brown, G.L. (1956). *J. Polym. Sci.* **22**, 423–434.

[128] Sheetz, D.P. (1965). *J. Appl. Polym. Sci.* **9**, 3759–3773.

[129] Vanderhoff, J.W., Tarkowski, H.L., Jenkins, M.C., Bradford, E. (1966). *J. Macromol. Chem.* **1**, 361–397.

[130] Vanderhoff, J.W., Bradford, E.B., Carrington, W.K. (1973). *J. Polym. Sci. Symp.* **41**, 155–174.

[131] Croll, S.G. (1986). *J. Coat. Technol.* **58**, 41–49.

[132] Eckersley, S. T., Rudin, A. (1990). *J. Coat. Technol.* **62**, 89–100.

[133] Dobler, F., Holl, Y. (1996). *Trends Polym. Sci.* **4**, 145–151.

[134] Winnik, M.A., Feng, J. (1996). *J. Coat. Technol.* **68**, 39–50.

[135] Winnik, M.A. (1997). *Curr. Opin. Colloid Interface Sci.* **2**, 192–199.

[136] Winnik, M.A. (1997). *Emulsion Polymerization and Emulsion Polymers.* Wiley, New York, pp. 467–517.

[137] Routh, A.F., Russel, W.B. (1998). *AIChE J.* **44**, 2088–2098.

[138] Routh, A.F.Russel, W.B. (1998). *Langmuir* **15**, 7762–7773.

[139] Petersen, C., Heldmann, C., Johannsmann, D. (1998). *Langmuir* **15**, 7745–7751.

[140] Routh, A.F., Russel, W.B., Tang, J., El-Aasser, M.S. (2001). *J. Coat. Technol.* **73**, 41–48.

[141] Shmuylovichi, L., Shen, A.Q., Stone, H.A. (2002). *Langmuir* **18**, 3441–3445.

[142] Hutchinson, J.W., Suo, Z. (1992). *Adv. Appl. Mech.* **29**, 63–191.

[143] Colina, H., Roux, S. (2000). *Eur. Phys. J. E* **1**, 189–194.

[144] Tirumkudulu, M.S., Russel, W.B. (2005). *Langmuir* **21**, 4938–4948.

[145] Lammertink, R.G.H., Hempenius, M.A., Vancso, G.J. (2000). *Langmuir* **16**, 6245–6252.

[146] Karthaus, O., Maruyama, N., Cieren, X., Shimomura, M., Hasegawa, H., Hashimoto, T. (2000). *Langmuir* **16**, 6071–6076.

[147] Luo, G., Liu, T., Ying, L., Zhao, X.S., Huang, Y., Wu, D., Huang, C. (2000). *Langmuir* **16**, 3651–3659.

[148] von Berlepsch, H., Boettcher, C., Ouart, A., Regenbrecht, M., Akari, S., Keiderling, H., Schnablegger, H., Dahne, S., Kirstein, S. (2000). *Langmuir* **16**, 5908–5916.

[149] Patrick, H.N., Warr, G.G., Manne, S., Aksay, I.A. (1999). *Langmuir* **15**, 1685–1692.

[150] Wall, J.F., Zukoski, C.F. (1999). *Langmuir* **15**, 7432–7437.

[151] Velegol, S.B., Fleming, B.D., Biggs, S., Wanless, E.J., Tilton, R.D. (2000). *Langmuir* **16**, 2548–2556.

[152] Li Bai, C. (2002). *Langmuir* **18**, 657–660.

33

ELECTROPHORETIC MOBILITY OF COLLOIDAL PARTICLES

HIROYUKI OHSHIMA

Faculty of Pharmaceutical Sciences, Tokyo University of Science, 2641 Yamazaki Noda, Chiba 278-8510, Japan

33.1 INTRODUCTION

Electrophoresis is a phenomenon in which charged colloidal particles move in an electrolyte solution under an external electric field. The particles in the stationary state move with a constant velocity as a result of the balance between the applied electric field and a viscous resistance exerted by the liquid on the particles. We treat the case where the magnitude of the applied electric field $\boldsymbol{E}$ is not very large. In such cases the particle velocity $\boldsymbol{U}$, which is called the *electrophoretic velocity*, is proportional to $\boldsymbol{E}$ in magnitude. The ratio of the magnitude of the velocity $\boldsymbol{U}$ to that of the applied field $\boldsymbol{E}$ is called the electrophoretic mobility μ, which is defined by $\mu = U/E$ (where $U = |\boldsymbol{U}|$ and $E = |\boldsymbol{E}|$).

In the case of hard particles without surface structures the electrophoretic mobility μ depends on the zeta-potential ζ of the particle. The *ζ-potential* is defined as the potential at the slipping plane, at which the liquid velocity relative to the particle is zero. If the slipping plane is located at the particle surface, ζ becomes equal to the surface potential ψ_0. In the following, we treat the case where $\zeta = \psi_0$ and where particles are of spherical or cylindrical shape.

On the other hand, in the case of soft particles, that is, hard particles covered with an ion-penetrable surface layer of polyelectrolytes, the zeta-potential concept loses its meaning and the *Donnan potential* in the surface layer plays an essential role in electrophoresis of soft particles.

In this chapter we derive equations for the electrophoretic mobility of hard and soft colloidal particles.

33.2 SMOLUCHOWSKI'S, HÜCKEL'S, AND HENRY'S EQUATIONS

Theories of the electrophoretic mobility of hard colloidal particles were developed by Smoluchowski [1], Hückel [2], and Henry [3]. Overbeek [4] , Booth [5], and Dukhin et al [6, 7]. Wiersema et al. [8] solved numerically the full kinetic equations, describing the electrophoresis of spherical hard particles. The computer calculation of the electrophoretic mobility of a spherical particle was considerably improved by O'Brien and White [9]. Approximate analytic mobility expressions, on the other hand, have been proposed by various authors [1–5, 7, 8, 10, 12, 17, 20–29]. In this section we deal with early electrophoresis theories of Smoluchowski [1], Hückel [2], and Henry [3].

We consider a spherical particle of zeta potential ζ in an electrolyte solution. If the particle radius a is much greater than the Debye length κ^{-1}, that is, $\kappa a \gg 1$, then the electrophoretic mobility μ is given by Smoluchowski's equation [1]

$$\mu = \frac{\varepsilon_{\mathrm{r}}\varepsilon_{\mathrm{o}}}{\eta}\zeta \tag{33.1}$$

where ε_{r} and η are, respectively, the relative permittivity and the viscosity of the electrolyte solution and ε_0 is the permittivity of a vacuum. Equation (33.1) can be derived from the balance of two forces acting on the particle surface per unit area carrying a charge density σ, that is, the electric force σE and the frictional force. Since the liquid velocity

Encyclopedia of Biocolloid and Biointerface Science, Volume 1, First Edition. Edited by Hiroyuki Ohshima.
© 2016 John Wiley & Sons, Inc. Published 2016 by John Wiley & Sons, Inc.

decays from $\boldsymbol{U}$ at the particle surface to zero over distances of the order of the Debye length κ^{-1}, the frictional force is given by $\eta U/\kappa^{-1}$. Thus the force balance condition gives $\sigma E = \eta U/\kappa^{-1}$. We replace the surface charge density σ with the particle surface potential $\psi_0 = \sigma/\varepsilon_r\varepsilon_0\kappa$, which expresses the fact that at the particle surface the potential slope ψ_0/κ^{-1} is equal to the electric field strength $\sigma/\varepsilon_r\varepsilon_0$. Further, by equating ψ_0 and ζ, we obtain E [Eq. (33.1)].

In the opposite limit case where the particle radius a is much smaller than the Debye length κ^{-1}, that is, $\kappa a \ll 1$, μ is given by Hückel's equation [2].

$$\mu = \frac{2\varepsilon_r\varepsilon_o}{3\eta}\zeta \tag{33.2}$$

Equation (33.2) can be derived from the balance between the Stokes resistance $6\pi\eta aU$ and the electric force QE acting on the particle carrying the total surface charge $Q = 4\pi a^2\sigma$ and the zeta-potential ζ, which may be replaced by the Coulomb potential $\psi_o = Q/4\pi\varepsilon_r\varepsilon_0 a$.

For the case of arbitrary values of κa and low ζ, the mobility μ is given by the following Henry's equation [3], which bridges Smoluchowski's equation (33.1) and Huckel's equation (33.2)

$$\mu = \frac{\varepsilon_r\varepsilon_o}{\eta}\zeta f(\kappa a) \tag{33.3}$$

with

$$f(\kappa a) = 1 - e^{\kappa a}\{5E_7(\kappa a) - 2E_5(\kappa a)\} \tag{33.4}$$

where $E_n(\kappa a)$ is the exponential integral of order n and is defined by

$$E_n(\kappa a) = (\kappa a)^{n-1}\int_{\kappa a}^{\infty}\frac{e^{-t}}{t^n}dt = a^{n-1}\int_a^{\infty}\frac{e^{-\kappa r}}{r^n}dr \tag{33.5}$$

where $f(\kappa a)$ is Henry's function. An accurate approximate expression for Eq. (33.5) has been derived [24]:

$$f(\kappa a) = \frac{2}{3}\left[1 + \frac{1}{2\left(1 + \dfrac{2.5}{\kappa a\{1 + 2\exp(-\kappa a)\}}\right)^3}\right] \tag{33.6}$$

As $\kappa a \to \infty$, $f(\kappa a) \to 1$ and Eq. (33.6) gives Smoluchowski's equation (33.1), while if $\kappa a \to 0$, then $f(\kappa a) \to {}^2/_3$ [Hückel's Eq. (33.2)].

For the case of a cylindrical particle of radius a and zeta-potential ζ, the electrophoretic mobility depends on the orientation of the particle with respect to the applied electric field. When the cylinder is oriented parallel to the applied electric field, its electrophoretic mobility $\mu_{//}$ is given by Smoluchowski's equation [1]:

$$\mu_{//} = \frac{\varepsilon_r\varepsilon_o}{\eta}\zeta \tag{33.7}$$

If, on the other hand, the cylinder is oriented perpendicularly to the applied field, then the mobility $\mu_{//}$ depends not only on ζ but also on the value of κa and is given by

$$\mu_{\perp} = \frac{\varepsilon_r\varepsilon_o}{\eta}\zeta f(\kappa a) \tag{33.8}$$

with

$$f(\kappa a) = 1 - \frac{4(\kappa a)^4}{K_0(\kappa a)}\int_{\kappa a}^{\infty}\frac{K_0(t)}{t^5}dt + \frac{(\kappa a)^2}{K_0(\kappa a)}\int_{\kappa a}^{\infty}\frac{K_0(t)}{t^3}dt \tag{33.9}$$

where $K_0(x)$ is the zero-order modified Bessel function of the second kind. Equation (33.9), which is Henry's function for cylindrical particles, was first derived by Henry [3]. The following approximate expression for Eq. (33.9) has been derived [23]:

$$f(\kappa a) = \frac{1}{2}\left[1 + \frac{1}{\left(1 + \dfrac{2.55}{\kappa a\{1 + \exp(-\kappa a)\}}\right)^2}\right] \tag{33.10}$$

As $\kappa a \to \infty$, $f(\kappa a) \to 1$ and Eq. (33.10) gives Smoluchowski's equation (33.7), while if $\kappa a \to 0$, then $f(\kappa a) \to {}^1/_2$ (Hückel's limit).

For a cylindrical particle oriented at an arbitrary angle between its axis and the applied electric field, its electrophoretic mobility averaged over a random distribution of orientation is given by [26, 27]

$$\mu_{av} = \frac{1}{3}\mu_{//} + \frac{2}{3}\mu_{\perp} \tag{33.11}$$

Figure 33.1 summarizes Henry's functions for spheres and cylinders.

33.3 GENERAL THEORY OF THE ELECTROPHORETIC MOBILITY OF SPHERICAL HARD PARTICLES

Consider a spherical hard particle of radius a moving with a velocity $\boldsymbol{U}$ in a liquid containing a general electrolyte composed of N ionic species with valence z_i and bulk concentration (number density) n_i^{∞}, and drag coefficient λ_i ($i = 1, 2, \ldots, N$). The origin of the spherical polar coordinate system (r, θ, ϕ) is held fixed at the center of the particle, and the polar axis ($\theta = 0$) is set parallel to $\boldsymbol{E}$ (Fig. 33.2). For

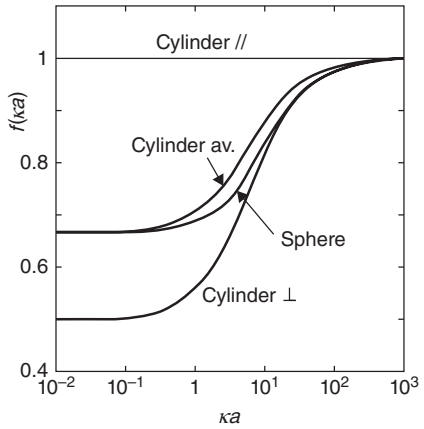


FIGURE 33.1 Henry's function $f(\kappa a)$ for a sphere and a cylinder of radius a as a function of scaled radius κa. The cylinder is oriented parallel ($\mu_{//}$) or perpendicularly ($\mu_{//}$) to the applied electric field. For a cylindrical particle oriented at an arbitrary angle between its axis and the applied electric field, its electrophoretic mobility averaged over a random distribution of orientation is given by $\mu_{av} = (\mu_{//} + 2\mu_{//})/3$. (From Ref. 19.)

a spherical particle, $\boldsymbol{U}$ takes the same direction as $\boldsymbol{E}$. The main assumptions are as follows: (1) the Reynolds number of the liquid flow is small enough to ignore inertial terms in the Navier–Stokes equation and the liquid can be regarded as incompressible, (2) the applied field $\boldsymbol{E}$ is weak so that the particle velocity $\boldsymbol{U}$ is proportional to $\boldsymbol{E}$ and terms of higher order in $\boldsymbol{E}$ may be neglected, (3) the slipping plane (at which the liquid velocity relative to the particle becomes zero) is located on the particle surface (at $r = a$), (4) no electrolyte ions can penetrate the particle surface.

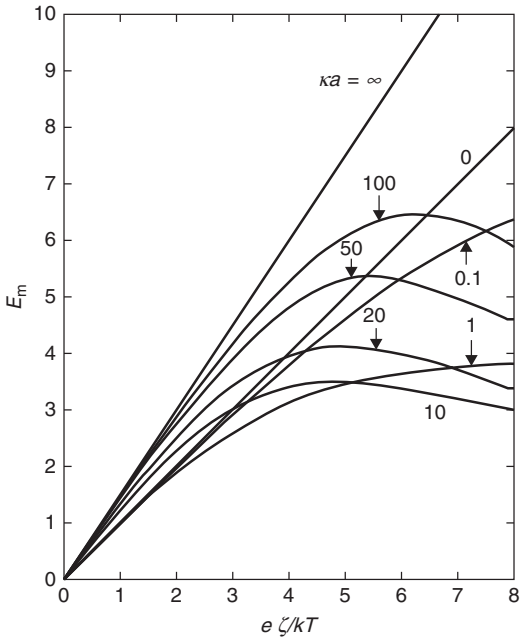


FIGURE 33.2 The scaled electrophoretic mobility E_m of a positively charged spherical colloidal particle of radius a in an aqueous KCl solution at 25°C as a function of scaled zeta-potential $e\zeta/kT$ for various values of κa. Calculated by the method of O'Brien and White [9]. E_m is defined by Eq. (33.24). (From Ref. 19.)

The motion of charged colloidal particles in a liquid containing an electrolyte caused by an externally applied electric field can be described by the Navier–Stokes equation for the liquid flow around the particle, continuity equations for the liquid flow and the flow of the ionic species, and the Poisson equation connecting the electric potential and the concentrations of the ionic species. The Navier–Stokes equation for the liquid flow $\boldsymbol{u}(\boldsymbol{r})$ around the particle is given by

$$\eta \nabla \times \nabla \times \boldsymbol{u}(\boldsymbol{r}) + \nabla p(\boldsymbol{r}) + \rho_{el}(\boldsymbol{r}) \nabla \psi(\boldsymbol{r}) = \boldsymbol{0}, \; r > a \qquad (33.12)$$

where η is the viscosity of the electrolyte solution, $p(\boldsymbol{r})$ is the pressure at position $\boldsymbol{r}$, $\rho_{el}(\boldsymbol{r})$ is the charge density resulting from the mobile charged ionic species, $\psi(\boldsymbol{r})$ is the electric potential, and $r = |\boldsymbol{r}|$.

Ohshima et al. [12] derived the general expression for the electrophoretic mobility of a sphere.

$$\mu = \frac{a^2}{9} \int_a^\infty \left(1 - \frac{3r^2}{a^2} + \frac{2r^3}{a^3}\right) G(r) dr \qquad (33.13)$$

with

$$y = \frac{e\psi^{(0)}}{kT}$$

$$G(r) = -\frac{e}{\eta r} \frac{dy}{dr} \sum_{i=1}^{N} z_i^2 n_i^\infty e^{-z_i y} \phi_i \qquad (33.14)$$

where $\psi^{(0)}$ is the equilibrium potential, y is the corresponding scaled quantity, and ϕ_i is related to the deviation $\delta\mu_i$ of the electrochemical potential of ith ionic species by

$$\delta\mu_i(\boldsymbol{r}) = -z_i e \phi_i(r) E \cos\theta \qquad (33.15)$$

With

$$\varphi_i(r) = r + \frac{a^3}{2r^2} + f_i(r) \qquad (33.16)$$

where the first term r on the right-hand side corresponds to the potential of the applied external field $\boldsymbol{E} \cdot \boldsymbol{r}$; the second term $a^3/2r^2$, to deviation of the external field due to the presence of the particle core; and the third term $f_i(r)$, to the contribution of the relaxation effect of electrolyte ions.

It can be shown that Smoluchowski's equation (33.1) can be derived for the case where Eq. (33.16) is approximated by

$$\phi_i(r) = \frac{3a}{2} \qquad (33.17)$$

If Eq. (33.16) is approximated by

$$\phi_i(r) = r \tag{33.18}$$

then Hückel's equation (33.2) is derived. Finally, Henry's equation (33.3) can be derived when

$$\phi_i(r) = r + \frac{a^3}{2r^2} \tag{33.19}$$

For a cylinder oriented perpendicularly to the applied field, the general expression for $\mu_{//}$ is given by [23]

$$\mu_\perp = \frac{a^2}{8}\int_a^\infty \left[1 - \frac{r^2}{a^2}\left\{1 - 2\ln\left(\frac{r}{a}\right)\right\}\right] G(r)dr \tag{33.20}$$

with

$$\varphi_i(r) = r + \frac{a^2}{r} + f_i(r) \tag{33.21}$$

where r is the distance from the cylinder axis. Henry's equation (9) for $\mu_{//}$ can be derived when Eq. (33.21) is approximated by

$$\varphi_i(r) = r + \frac{a^2}{r} \tag{33.22}$$

33.4 RELAXATION EFFECT

Henry's mobility Eq. (33.3) assumes that the double-layer potential distribution around a spherical particle remains unchanged during electrophoresis, assuming $\phi_i(r) = 0$. For high zeta-potentials, however, the double layer is no longer spherically symmetric. This effect is called the *relaxation effect* (the double-layer polarization or the surface conduction). Henry's Eq. (33.3) does not take into account the relaxation effect, and thus, this equation is correct to the first order of zeta-potential ζ. If the relaxation effect is taken into account, then the electrophoretic mobility μ becomes dependent on the ionic drag coefficient λ_i. We introduce the scaled ionic drag coefficient m_i defined by

$$m_i = \frac{2\varepsilon_r\varepsilon_o kT}{3\eta z_i^2 e}\lambda_i \tag{33.23}$$

For an aqueous KCl solution at 25°C, $m = 0.176$ for K^+ ions and $m = 0.169$ for Cl^- ions. In Fig. 33.2 we plot the electrophoretic mobility μ of a positively charged sphere in an aqueous KCl solution at 25°C ($\varepsilon_r = 78.5$ and $\eta = 0.891$ mPa • s) as a function of scaled zeta-potential $e\zeta/kT$ for several values of κa calculated by the method of O'Brien and White [9]. Here E_m is the scaled electrophoretic mobility defined by

$$E_m = \frac{3\eta e}{2\varepsilon_r\varepsilon_o kT}\mu \tag{33.24}$$

The cases of $\kappa a = \infty$ and $\kappa a = 0$, which are both straight lines, correspond to Smoluchowski's Eq. (33.1) and Hückel's Eq. (33.2), respectively. It is seen that there exists a mobility maximum due to the relaxation effect.

The following approximate mobility expression for a sphere of radius a and zeta-potential ζ, which is correct to order $1/\kappa a$, is applicable for $\kappa a \geq 10$ and arbitrary ζ [12]:

$$\begin{aligned}\mu = {} & \mathrm{sgn}(\zeta)\frac{\varepsilon_r\varepsilon_o}{\eta}\left\{|\zeta| - \frac{2F}{1+F}\left(\frac{kT}{ze}\right)H\right\} \\ & + \mathrm{sgn}(\zeta)\frac{2\varepsilon_r\varepsilon_o kT}{3\eta e}\left[\frac{1}{\kappa a}\left\{-18\left(t + \frac{t^3}{9}\right)K\right.\right. \\ & + \frac{15F}{1+F}\left(t + \frac{7t^2}{20} + \frac{t^3}{9}\right) - 6(1+3\overline{m})(1-e^{-\overline{\zeta}/2})G \\ & + \frac{12F}{(1+F)^2}H + \frac{9\overline{\zeta}}{1+F}(\overline{m}G + mH) \\ & \left.\left. - \frac{36F}{1+F}\left(\overline{m}G^2 + \frac{m}{1+F}H^2\right)\right\}\right]\end{aligned} \tag{33.25}$$

with

$$\begin{aligned}&\overline{\zeta} = \frac{ze|\zeta|}{kT},\ F = \frac{2}{\kappa a}(1+3m)(e^{\overline{\zeta}/2}-1),\ G = \ln\left(\frac{1+e^{\overline{\zeta}/2}}{2}\right) \\ &H = \ln\left(\frac{1+e^{\overline{\zeta}/2}}{2}\right),\ m = \frac{2\varepsilon_r\varepsilon_o kT}{3\eta z^2e^2}\lambda,\ \overline{m} = \frac{2\varepsilon_r\varepsilon_o kT}{3\eta z^2e^2}\overline{\lambda} \\ &K = 1 - \frac{25}{3(\kappa a+10)}\exp\left[-\frac{\kappa a}{6(\kappa a-6)}\overline{\zeta}\right],\ t = \tanh(\overline{\zeta}/4)\end{aligned} \tag{33.26}$$

A mobility expression for a sphere correct to order ζ^3 and applicable for $ze\zeta/kT \leq 3$ and arbitrary κa is given below [24]:

$$\begin{aligned}\mu = {} & \frac{2\varepsilon_r\varepsilon_o\zeta}{3\eta}\left(1 + \frac{1}{2[1+2.5/\{\kappa a(1+2e^{-\kappa a})\}]^3}\right) \\ & - \frac{2\varepsilon_r\varepsilon_o\zeta}{3\eta}\left(\frac{ze\zeta}{kT}\right)^2\left[\frac{\kappa a\{\kappa a + 1.3\exp(-0.18\kappa a) + 2.5\}}{2\{\kappa a + 1.2\exp(-7.4\kappa a) + 4.8\}^3}\right. \\ & \left. + \left(\frac{m+\overline{m}}{2}\right)\frac{9\kappa a\{\kappa a + 5.2\exp(-3.9\kappa a) + 5.6\}}{8\{\kappa a - 1.55\exp(-0.32\kappa a) + 6.02\}^3}\right]\end{aligned} \tag{33.27}$$

Simple approximate mobility expressions for a sphere of radius a correct to order 1 applicable for with $\kappa a \geq 30$ have been derived for various cases [25]:

1. Charged particles in a symmetric electrolyte solution of valence z

$$\mu = \mathrm{sgn}(\zeta)\frac{\varepsilon_r\varepsilon_o}{\eta}\left\{|\zeta| - \frac{2F}{1+F}\left(\frac{kT}{ze}\right) \times \ln\left[\frac{1+\exp(ze|\zeta|/2kT)}{2}\right]\right\} \quad (33.28)$$

with

$$F = \frac{2}{\kappa a}(1+3m)\left\{\exp\left(\frac{ze\,|\zeta|}{2kT}\right) - 1\right\} \quad (33.29)$$

$$m = \frac{2\varepsilon_r\varepsilon_o kT}{3\eta z^2 e^2}\lambda \quad (33.30)$$

2. Positively charged particles ($\zeta > 0$) in a 2–1 electrolyte

$$\mu = \frac{\varepsilon_r\varepsilon_o}{\eta}\left\{\zeta - \frac{2F}{1+F}\left(\frac{kT}{e}\right)\ln\left[\frac{1}{2} + \frac{1}{2}\sqrt{\frac{2}{3}\exp\left(\frac{e\zeta}{kT}\right) + \frac{1}{3}}\right]\right\} \quad (33.31)$$

$$F = \frac{\sqrt{6}}{\kappa a}(1+3m_-)\left\{\exp\left(\frac{e\zeta}{2kT}\right) - 1\right\} \quad (33.32)$$

$$m_- = \frac{2\varepsilon_r\varepsilon_o kT}{3\eta e^2}\lambda_- \quad (33.33)$$

3. Negatively charged particles ($\zeta < 0$) in a 2–1 electrolyte

$$\mu = \frac{\varepsilon_r\varepsilon_o}{\eta}\left\{\zeta + \frac{2F}{1+F}\left(\frac{kT}{e}\right) \times \ln\left[\frac{1}{2}\exp\left(-\frac{e\zeta}{2kT}\right) + \frac{1}{2}\sqrt{\frac{1}{3}\exp\left(-\frac{e\zeta}{kT}\right) + \frac{2}{3}}\right]\right\} \quad (33.34)$$

$$F = \frac{\sqrt{3}}{\kappa a}(1+3m_+)\left\{\exp\left(\frac{e\,|\zeta|}{kT}\right) - 1\right\} \quad (33.35)$$

$$m_+ = \frac{\varepsilon_r\varepsilon_o kT}{6\eta e^2}\lambda_+ \quad (33.36)$$

4. Positively charged particles ($\zeta > 0$) in a 1–2 electrolyte

$$\mu = \frac{\varepsilon_r\varepsilon_o}{\eta}\left\{\zeta - \frac{2F}{1+F}\left(\frac{kT}{e}\right) \times \ln\left[\frac{1}{2}\exp\left(\frac{e\zeta}{2kT}\right) + \frac{1}{2}\sqrt{\frac{1}{3}\exp\left(\frac{e\zeta}{kT}\right) + \frac{2}{3}}\right]\right\} \quad (33.37)$$

with

$$F = \frac{\sqrt{3}}{\kappa a}(1+3m_-)\left\{\exp\left(\frac{e\zeta}{kT}\right) - 1\right\} \quad (33.38)$$

$$m_- = \frac{\varepsilon_r\varepsilon_o kT}{6\eta e^2}\lambda_- \quad (33.39)$$

5. Negatively charged particles ($\zeta < 0$) in a 1–2 electrolyte

$$\mu = \frac{\varepsilon_r\varepsilon_o}{\eta}\left\{\zeta + \frac{2F}{1+F}\left(\frac{kT}{e}\right)\ln\left[\frac{1}{2} + \frac{1}{2}\sqrt{\frac{2}{3}\exp\left(\frac{e\,|\zeta|}{kT}\right) + \frac{1}{3}}\right]\right\} \quad (33.40)$$

with

$$F = \frac{\sqrt{6}}{\kappa a}(1+3m_+)\left\{\exp\left(\frac{e\,|\zeta|}{2kT}\right) - 1\right\} \quad (33.41)$$

$$m_+ = \frac{2\varepsilon_r\varepsilon_o kT}{3\eta e^2}\lambda_+ \quad (33.42)$$

In these equations F corresponds to Dukhin's number, expressing the relaxation effect. It can also be shown that mobility expressions $\mu_\perp$ for cylinders of radius a oriented perpendicular to the applied field correct to order 1 coincides with the mobility expressions for a sphere of radius a [see Eqs. (33.28)–(33.42)] [28].

Similarly, approximate mobility expressions for a sphere of radius a and zeta- potential ζ in a mixed electrolyte solution can be derived. For a sphere moving in a mixed solution of 1:1 electrolyte of concentration n_1 and 2:1 electrolyte of concentration n_2, we obtain for a positively charged sphere ($\zeta > 0$)

$$\mu = \frac{\varepsilon_r\varepsilon_o}{\eta}\left\{\zeta - \frac{2F_{-1}}{1+F_{-1}}\left(\frac{kT}{e}\right)\ln\left(\frac{1+\beta}{2}\right)\right\} \quad (33.43)$$

with

$$F_{-1} = \frac{2(1+3m_{-1})}{\kappa a\sqrt{1-\alpha/3}}\left\{\exp\left(\frac{e\zeta}{2kT}\right)-1\right\},$$
$$m_{-1} = \frac{2\varepsilon_r\varepsilon_o kT}{3\eta e^2}\lambda_{-1} = \frac{2N_A\varepsilon_r\varepsilon_o kT}{3\eta\Lambda^o_{-1}}$$

$$\alpha = \frac{3n_2}{n_1+3n_2}, \beta = \sqrt{\frac{\alpha}{3}+\left(1-\frac{\alpha}{3}\right)\exp\left(\frac{e\zeta}{kT}\right)} \qquad (33.44)$$

where λ_{-1} and Λ^o_{-1} are, respectively, the drag coefficient and the limiting conductance of the counterions (anions) of valence -1 and m_{-1} is the corresponding scaled drag coefficient. The electrophoretic mobility μ is thus given by the following equation. For a negatively charged sphere, we obtain

$$\mu = \frac{\varepsilon_r\varepsilon_o}{\eta}\left[\zeta+\left(\frac{1}{1+F_{+1}}+\frac{1}{1+F_{+2}}-2\right)\left\{\frac{\zeta}{2}-\left(\frac{kT}{e}\right)\ln\right.\right.$$
$$\left.\left.\times\left(\frac{1+\beta}{2}\right)\right\}+\left(\frac{1}{1+F_{+1}}-\frac{1}{1+F_{+2}}\right)H(\zeta,\alpha)\right] \qquad (33.45)$$

with

$$H(\zeta,\alpha) = \frac{(1-\alpha)}{2}\sqrt{\frac{3}{\alpha}}\left\{\left(\frac{e\zeta}{kT}\right)\ln\left[\left(\frac{1+\sqrt{\alpha/3}}{1-\sqrt{\alpha/3}}\right)\left(\frac{1-\beta}{1+\beta}\right)\right]\right.$$
$$-2\ln\left(\frac{\beta+\sqrt{\alpha/3}}{1+\sqrt{\alpha/3}}\right)\cdot\ln\left(\frac{1-\beta}{1+\beta}\right)$$
$$-\mathrm{Li}_2\left(\frac{\beta+\sqrt{\alpha/3}}{1+\sqrt{\alpha/3}}\right)+\mathrm{Li}_2\left(\frac{\beta-\sqrt{\alpha/3}}{1-\sqrt{\alpha/3}}\right)$$
$$-\mathrm{Li}_2\left(-\frac{\beta-\sqrt{\alpha/3}}{1+\sqrt{\alpha/3}}\right)+\mathrm{Li}_2\left(-\frac{\beta+\sqrt{\alpha/3}}{1-\sqrt{\alpha/3}}\right)$$
$$\left.-\mathrm{Li}_2\left(-\frac{1+\sqrt{\alpha/3}}{1-\sqrt{\alpha/3}}\right)+\mathrm{Li}_2\left(-\frac{1-\sqrt{\alpha/3}}{1+\sqrt{\alpha/3}}\right)\right\}$$
$$-\frac{e\zeta}{2kT}+\ln\left(\frac{1+\beta}{2}\right)$$

$$F_{+1} = \frac{2}{\kappa a}(1+3m_{+1})\left\{\exp\left(\frac{e|\zeta|}{2kT}\right)-1\right\},$$
$$F_{+2} = \frac{\sqrt{3}}{\kappa a}(1+3m_{+2})\left\{\exp\left(\frac{e|\zeta|}{kT}\right)-1\right\},$$
$$m_{+1} = \frac{2\varepsilon_r\varepsilon_o kT}{3\eta e^2}\lambda_{+1} = \frac{2N_A\varepsilon_r\varepsilon_o kT}{3\eta\Lambda^o_{+1}}, \quad m_{+2} = \frac{\varepsilon_r\varepsilon_o kT}{6\eta e^2}\lambda_{+2}$$
$$= \frac{N_A\varepsilon_r\varepsilon_o kT}{3\eta\Lambda^o_{+2}} \qquad (33.46)$$

where $\mathrm{Li}_2(z)$ is a dilogarithm function [defined by $Li_2(z) = \sum_{k=1}^{\infty}(z^k/k^2)$], which can easily be evaluated via Mathematica,

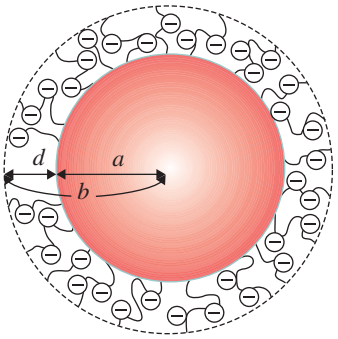


FIGURE 33.3 A spherical soft particle in an external applied electric field $\boldsymbol{E}$; a = radius of the particle core and d = thickness of the polyelectrolyte layer coating the particle core. $b = a+d$.

for example, and where λ_{+1} and Λ^o_{+1} are, respectively, the drag coefficient and limiting conductance of counterions (cations) of valence $+1$, λ_{+2} and Λ^o_{+2} are those of counterions (cations) of valence $+2$, and m_{+1} and m_{+2} are the corresponding scaled drag coefficients.

33.5 ELECTROPHORETIC MOBILITY OF SOFT PARTICLES

The electrophoretic mobility of soft particles, that is, a hard particle covered with an ion-penetrable surface layer of polyelectrolytes (Fig. 33.3) is quite different from that of hard particles without surface structures in that the mobility of hard particles is determined by the particle zeta-potential, but the concept of zeta-potential loses its meaning for soft particles and the mobility of soft particles depends on the Donnan potential in the surface layer.

Consider now a spherical soft particle moving with a velocity $\boldsymbol{U}$ in a symmetric electrolyte solution of valence z and bulk concentration (number density) n in an applied electric field $\boldsymbol{E}$ [30–48]. We suppose that the uncharged particle core of radius a is coated with an ion-penetrable layer of polyelectrolytes of thickness d and that ionized groups of valence Z are distributed within the polyelectrolyte layer at a uniform density N so that the polyelectrolyte later is uniformly charged at a constant density $\rho_{\mathrm{fix}} = ZeN$. The polymer-coated particle thus has an inner radius a and an outer radius $b = a + d$ (Fig. 33.3). Let the drag coefficient of coions be λ_+ and that of counterions be λ_-. We adopt the model of Debye–Bueche [49] that the polymer segments are regarded as resistance centers distributed uniformly in the polyelectrolyte layer, exerting frictional forces on the liquid flowing in the polyelectrolyte layer.

The fundamental electrokinetic equations for the liquid velocity $\boldsymbol{u}(\boldsymbol{r})$ at position $\boldsymbol{r}$ are [19, 20, 30, 34]

$$\eta\nabla\times\nabla\times\boldsymbol{u}+\nabla p+\rho_{e1}\nabla\psi=\boldsymbol{0}, \quad r>b \qquad (33.47)$$
$$\eta\nabla\times\nabla\times\boldsymbol{u}+\gamma\boldsymbol{u}+\nabla p+\rho_{e1}\nabla\psi=\boldsymbol{0}, \; a<r<b \qquad (33.48)$$

Equation (33.47) is the usual Navier–Stokes equation. The term $\gamma \boldsymbol{u}$ on the left-hand side of Eq. (33.48) represents the frictional forces exerted on the liquid flow by the polymer segments in the polyelectrolyte layer, and γ is the frictional coefficient. If it is assumed that each resistance center corresponds to a polymer segment, which, in turn, is regarded as a sphere of radius a_p and the polymer segments are distributed at a uniform volume density of N_p in the polyelectrolyte layer, then each polymer segment exerts the Stokes resistance $6\pi\eta a_\mathrm{p}\boldsymbol{u}$ on the liquid flow in the polyelectrolyte layer so that

$$\gamma = 6\pi\eta a_\mathrm{p} N_\mathrm{p} \tag{33.49}$$

The general mobility expression for a soft sphere is given by [34]

$$\begin{aligned}\mu = {} & \frac{b^2}{9}\int_b^\infty \left[3\left(1-\frac{r^2}{b^2}\right) - \frac{2L_2}{L_1}\left(1-\frac{r^3}{b^3}\right)\right] G(r)dr \\ & + \frac{2L_3}{3\lambda^2 L_1}\int_a^\infty \left(1+\frac{r^3}{2b^3}\right) G(r)dr \\ & - \frac{2}{3\lambda^2}\int_a^b \left[1 - \frac{3a}{2\lambda^2 b^3 L_1}\left\{(L_3+L_4\lambda r)\cosh\left[\lambda(r-a)\right]\right\}\right. \\ & \left. - \left\{-(L_4+L_3\lambda r)\sinh\left[\lambda(r-a)\right]\right\}\right] G(r)dr \end{aligned} \tag{33.50}$$

where $G(r)$ is given by Eq. (33.14) and

$$\lambda = (\gamma/\eta)^{1/2} \tag{33.51}$$

$$\begin{aligned} L_1 = {} & \left(1 + \frac{a^3}{2b^3} + \frac{3a}{2\lambda^2 b^3} - \frac{3a^2}{2\lambda^2 b^4}\right)\cosh\left[\lambda(b-a)\right] \\ & - \left(1 - \frac{3a^2}{2b^2} + \frac{a^3}{2b^3} + \frac{3a}{2\lambda^2 b^3}\right)\frac{\sinh\left[\lambda(b-a)\right]}{\lambda b} \end{aligned} \tag{33.52}$$

$$\begin{aligned} L_2 = {} & \left(1 + \frac{a^3}{2b^3} + \frac{3a}{2\lambda^2 b^3}\right)\cosh\left[\lambda(b-a)\right] \\ & + \frac{3a^2}{2b^2}\frac{\sinh\left[\lambda(b-a)\right]}{\lambda b} - \frac{3a}{2\lambda^2 b^3} \end{aligned} \tag{33.53}$$

$$L_3 = \cosh\left[\lambda(b-a)\right] - \frac{\sinh\left[\lambda(b-a)\right]}{\lambda b} - \frac{a}{b} \tag{33.54}$$

$$L_4 = \sinh\left[\lambda(b-a)\right] - \frac{\cosh\left[\lambda(b-a)\right]}{\lambda b} + \frac{\lambda a^2}{3b} + \frac{2\lambda b^2}{3a} + \frac{1}{\lambda b} \tag{33.55}$$

If we neglect the relaxation effect, we approximate $\phi_\pm(r)$, where $\phi_+(r)$ and $\phi_-(r)$ are, respectively, the ϕ_i function for coions and counterions in Eq. (33.14), by

$$\phi_\pm(r) = \phi_\pm(b) = b + \frac{a^3}{2b^3} \tag{33.56}$$

We thus obtain the following approximate expression for the electrophoretic mobility of a soft particle:

$$\mu = \frac{2\varepsilon_\mathrm{r}\varepsilon_\mathrm{o}}{3\eta}\left(1+\frac{a^3}{2b^3}\right)\frac{\psi_\mathrm{o}/\kappa_\mathrm{m} + \psi_\mathrm{DON}/\lambda}{1/\kappa_\mathrm{m} + 1/\lambda} + \frac{ZeN}{\eta\lambda^2} \tag{33.57}$$

with

$$\psi_\mathrm{DON} = \left(\frac{kT}{ze}\right)\ln\left[\frac{ZN}{2zn} + \left\{\left(\frac{ZN}{2zn}\right)^2 + 1\right\}^{1/2}\right] \tag{33.58}$$

$$\begin{aligned} \psi_o = {} & \frac{kT}{ze}\left(\ln\left[\frac{ZN}{2zn} + \left\{\left(\frac{ZN}{2zn}\right)^2 + 1\right\}^{1/2}\right]\right. \\ & \left. + \frac{2zn}{ZN}\left[1 - \left\{\left(\frac{ZN}{2zn}\right)^2 + 1\right\}^{1/2}\right]\right) \end{aligned} \tag{33.59}$$

$$\kappa_m = \kappa\left[1 + \left(\frac{ZN}{2zn}\right)^2\right]^{1/4} \tag{33.60}$$

where ψ_DON and ψ_o=$\psi(b)$ are, respectively, the Donnan potential and the surface potential of the surface layer, and κ_m is the Debye–Hückel parameter in the surface layer that involves the contribution of the fixed charges *ZeN*. Equation (33.57) consists of two terms: the first term is a weighted average of the Donnan potential ψ_DON and the surface potential ψ_o. It should be stressed that only the first term is subject to the shielding effects of electrolytes, tending toward zero as the electrolyte concentration n increases, while the second term does not depend on the electrolyte concentration. In the limit of high electrolyte concentration, all the potentials vanish and only the second term of the mobility expression remains:

$$\mu \to \mu^\infty = \frac{ZeN}{\eta\lambda^2} \tag{33.61}$$

Equation (33.61) shows that as $\kappa \to \infty$, μ tends to a nonzero limiting value μ^∞. This is a characteristic of the electrokinetic behavior of soft particles, in contrast to the case of the electrophoretic mobility of hard particles, which should reduce to zero as a result of the shielding effects, since the mobility expressions for rigid particles do not have μ^∞, as schematically shown in Fig. 33.4.

Also we note that Eq. (33.57) does not depend on the potential $\psi^{(0)}(a)$ at the slipping plane at $r = a$. This means that the mobility of soft particles is insensitive to the precise position of the slipping plane. In other words, for such cases, the zeta-potential loses its meaning.

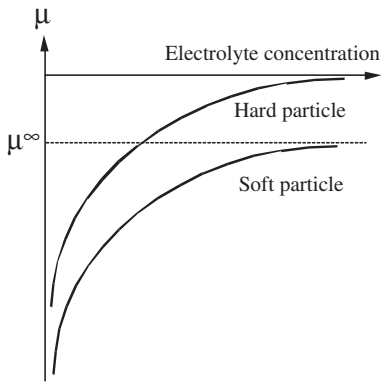


FIGURE 33.4 Schematic representation of the electrophoretic mobilites of soft and hard particles plotted as functions of electrolyte concentration.

In order to take into account the relaxation effect outside the surface charge layer, we approximate $\phi_{\pm}(r)$ by [46]

$$\phi_{+}(r) = \phi_{+}(b) = b + \frac{a^3}{2b^2} \tag{33.62}$$

$$\phi_{-}(r) = \phi_{-}(b) = \left(b + \frac{a^3}{2b^2}\right) \cdot \frac{1}{1+F} \tag{33.63}$$

with

$$F = \frac{2}{\kappa b}(1 + 3m_{-})\left(e^{y_o/2} - 1\right) \tag{33.64}$$

Here F corresponds to Dukhin's number. By using Eqs. (33.62) and (33.63), we finally obtain

$$\begin{aligned}\mu = {} & \frac{2\varepsilon_r\varepsilon_o}{3\eta}\left(1 + \frac{a^3}{2b^3}\right)\frac{\psi_o/\kappa_m + \psi_{DON}/\lambda}{1/\kappa_m + 1/\lambda} + \frac{ZeN}{\eta\lambda^2} \\ & \times \left(1 - \frac{F}{1+F}\cdot\frac{1}{1+e^{-y_{DON}}}\right) \\ & - \frac{F}{1+F}\cdot\frac{2\varepsilon_r\varepsilon_o}{3\eta}\left(1 + \frac{a^3}{2b^3}\right)\left(\frac{kT}{ze}\right)\left[2\ln\left(\frac{1+e^{y_o/2}}{2}\right)\right. \\ & \left. + \frac{\kappa}{\lambda}\left(e^{y_o/2} - 1\right) - \frac{\kappa^2}{2\lambda(\lambda+\kappa_m)}\cdot\frac{e^{y_{DON}} - 1}{1+e^{-y_{DON}}}\right] \end{aligned} \tag{33.65}$$

where y with subscripts o and Don are the scaled surface and Donnan potentials, respectively. For other electrokinetics of hard and soft particles, the reader should refer to the literature [19–21].

REFERENCES

[1] von Smoluchowski, M. (1921). In Greatz, L. (ed.), *Handbuch der Elektrizität und des Magnetismus*, Vol. 2. Barth, Leipzig, p. 366.

[2] Hückel, E. (1924). *Phys. Z.* **25**, 204.

[3] Henry, D.C. (1931). *Proc. Roy. Soc. Lond. A* **133**, 106.

[4] Overbeek, J.Th.G. (1943). *Kolloid-Beihefte* 54 (1943) 287.

[5] Booth, F. (1950). *Proc. Roy. Soc. Lond. A* **203**, 514.

[6] Wiersema, P.H., Loeb, A.L., Overbeek, J.Th.G. (1966). *J. Colloid Interface Sci.* **22**, 78.

[7] Dukhin, S.S., Semenikhin, N.M. (1970). *Kolloid Zh.* **32**, 360.

[8] Dukhin, S.S., Derjaguin, B.V. (1974). In Matievic, E. (ed.), *Surface and Colloid Science*, Vol. 7. Wiley, New York.

[9] O'Brien, R.W., White, L.R. (1978). *J. Chem. Soc. Faraday Transact. 2* **74**, 1607.

[10] O'Brien, R.W., Hunter, R.J. (1981). *Can. J. Chem.* **59**, 1878.

[11] Hunter, R.J. (1981). *Zeta Potential in Colloid Science*. Academic Press, New York.

[12] Ohshima, H., Healy, T.W., White, L.R. (1983). *J. Chem. Soc. Faraday Transact. 2* **79**, 1613.

[13] van de Ven, T.G.M. (1989). *Colloid Hydrodynamics*, Academic Press, New York.

[14] Dukhin, S.S. (1993). *Adv. Colloid Interface Sci.* **44**, 1.

[15] Lyklema, J. (1995). *Fundamentals of Interface and Colloid Science, Solid-Liquid Interfaces*, Vol. 2. Academic Press, New York.

[16] Ohshima, H., Furusawa, K. (eds.) (1998). *Electrical Phenomena at Interfaces*, *Fundamentals, Measurements, and Applications*, 2nd ed., revised and expanded, Marcel Dekker, New York.

[17] Delgado, A.V. (ed.) (2000). *Electrokinetics and Electrophoresis.* Marcel Dekker, New York.

[18] Spasic, A., Hsu, J.-P. (eds.) (2005). *Finely Dispersed Particles. Micro-. Nano-, Atto-Engineering.* CRC Press, Boca Raton, FL.

[19] Ohshima, H. (2006). *Theory of Colloid and Interfacial Electric Phenomena*. Elsevier, Amsterdam.

[20] Ohshima, H. (2010). *Biophysical Chemistry of Biointerfaces.* Wiley, Hoboken, NJ.

[21] Ohshima, H. (ed.) (2012). *Electrical Phenomena at Interfaces and Biointerfaces, Fundamentals and Applications in Nano-, Bio- and Environmental Sciences.* Wiley, Hoboken, NJ.

[22] Ohshima, H. (1994). *J. Colloid Interface Sci.* **168**, 269.

[23] Ohshima, H. (1996). *J. Colloid Interface Sci.* **180**, 299.

[24] Ohshima, H. (2001). *J. Colloid Interface Sci.* **239**, 587.

[25] Ohshima, H. (2005). Colloids Surf. A: Physicochem. Eng. Aspects **267**, 50.

[26] van der Drift, W.P.J.T., de Keizer, A., Overbeek, J.Th.G. (1979). *J. Colloid Interface Sci.* **71**, 67.

[27] de Keizer, A., van der Drift, W.P.J.T., Overbeek, J.Th.G. (1975). *Biophys. Chem.* **3**, 107.

[28] Ohshima, H. (2014). *Colloid Polym. Sci.* 292, 1227.

[29] Ohshima, H. (2014). *Colloid Polym. Sci*. 292, 1457.

[30] Ohshima, H. (1994). *J. Colloid Interface Sci.* **163**, 474.

[31] Ohshima, H. (1995). *Colloids Surf. A: Physicochem. Eng. Aspects* **103**, 249.

[32] Ohshima, H. (1995). *Adv. Colloid Interface Sci.* **62**, 189.

[33] Ohshima, H. (1995). *Electrophoresis* **16**, 136.

[34] Ohshima, H. (2000). *J. Colloid Interface Sci.* **228**, 190.

[35] López-García, J.J., Grosse, C., Horno, J. (2003). *J. Colloid Interface Sci*. **265**, 327.

[36] Hill, R.J., Saville, D.A. (2005). *Colloids Surf. A: Physicochem. Eng. Aspects* **267**, 31.

[37] Dukhin, S.S., Zimmermann, R., Werner, C. (2006). *Adv. Colloid Interface Sci*. **122**, 93.

[38] Duval, J.F.L., Ohshima, H. (2006). *Langmuir* **22**, 3533.

[39] Ohshima, H. (2006). *Electrophoresis* **27**, 526.

[40] Ohshima, H. (2006). *Colloid Polym. Sci.* **285**, 1411.

[41] Ohshima, H. (2009). *Sci. Technol. Adv. Mater.* **10**, 063001.

[42] Ahualli, S., Jiménez, M.L., Carrique, F., Delgado, A.V. (2009). *Langmuir* **25**, 1986.

[43] Grosse, C., Dergado, A.V. (2010). *Curr. Opin. Colloid Interface Sci*. **15**, 145.

[44] Duval, J.F.L., Gaboriaud, F. (2010). *Curr. Opin. Colloid Interface Sci*. **15**, 184.

[45] Ohshima, H. (2010). *J. Colloid Interface Sci.* **349**, 641.

[46] Ohshima, H. (2011). *Colloids Surf. A: Physicochem. Eng. Aspects* **376**, 72

[47] Ohshima, H. (2013). *Curr. Opin. Colloid Interface Sci*. **18**, 73 (2013).

[48] Ohshima, H. (2014). *Colloids Surf. A: Physicochem. Eng. Aspects* **440**, 151 (2014).

[49] Debye, P., Bueche, A. (1948). *J. Chem. Phys.* **16**, 573.

34

ELECTROSTATIC INTERACTION BETWEEN COLLOIDAL PARTICLES

HIROYUKI OHSHIMA

Faculty of Pharmaceutical Sciences, Tokyo University of Science, 2641 Yamazaki Noda, Chiba 278-8510, Japan

34.1 INTRODUCTION

When two charged particles approach each other in an electrolyte solution, the electrical double layers around the particles overlap each other, resulting in electrostatic interaction between them [1–10]. In this chapter we derive expressions for the potential energy of the electrostatic interaction between charged particles for various cases. We treat not only hard particles without surface structures but also soft particles, that is, hard particles covered with an ion-penetrable surface layer of polyelectrolytes. In the latter case we consider before and after contact of the surface layers of interacting particles.

34.2 INTERACTION BETWEEN HARD PARTICLES

34.2.1 Interaction between Two Parallel Plates: Low-Potential Case

Consider first two parallel dissimilar plates 1 and 2, separated by a distance h immersed in a liquid containing N ionic species with valence z_i and bulk concentration (number density) n_i^∞ ($i = 1,2, \ldots, N$). We take an x axis perpendicular to the plates with its origin at the right surface of plate 1, as in Fig. 34.1.

We assume that the electric potential $\psi(x)$ outside the plates ($0 < x < h$) obeys the following one-dimensional planar Poisson–Boltzmann equation (see Chapter 78):

$$\frac{d^2\psi(x)}{dx^2} = -\frac{1}{\varepsilon_r\varepsilon_0}\sum_{i=1}^{N} z_i e n_i^\infty \exp\left(-\frac{z_i e\psi(x)}{kT}\right) \quad \text{for } 0 < \times < h \tag{34.1}$$

The boundary conditions at the plate surface depend on the type of the double-layer interaction between plates 1 and 2. If the surface potentials of plates 1 and 2 remain constant at their unperturbed surface potentials ψ_{01} and ψ_{02} during interaction, respectively (interaction at constant surface potential), then

$$\psi(0) = \psi_{01},\ \psi(h) = \psi_{02}, \tag{34.2}$$

On the other hand, if the surface charge densities of plates 1 and 2 remain constant at σ_1 and σ_2 (electrostatic interaction at constant surface charge density), respectively, then

$$\left.\frac{d\psi}{dx}\right|_{x=0^+} = -\frac{\sigma_1}{\varepsilon_r\varepsilon_0},\quad \left.\frac{d\psi}{dx}\right|_{x=h^-} = \frac{\sigma_2}{\varepsilon_r\varepsilon_0}, \tag{34.3}$$

where we have assumed that the influence of the external fields within the plates can be neglected.

The interaction force P can be calculated by integrating the excess osmotic pressure and the Maxwell stress over an arbitrary closed surface Σ enclosing either one of the two interacting plates. As Σ, we choose two planes located at $x = -\infty$ (in the bulk solution far from the plates) and $x = x'$

Encyclopedia of Biocolloid and Biointerface Science, Volume 1, First Edition. Edited by Hiroyuki Ohshima.
© 2016 John Wiley & Sons, Inc. Published 2016 by John Wiley & Sons, Inc.

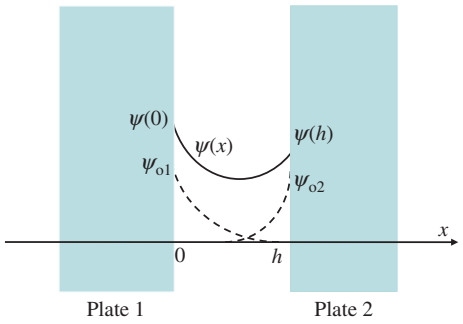


FIGURE 34.1 Potential distribution $\psi(x)$ across two interacting parallel dissimilar plates 1 and 2 carrying unperturbed surface potentials ψ_{01} and ψ_{02}, respectively, at separation h.

$(0 < x' < h)$ enclosing plate 1. Here x' is an arbitrary point in the region $0 < x < h$ between plates 1 and 2. Thus the force $P(h)$ of the double layer interaction per unit area is given by

$$P_{\text{pl}}(h) = \sum_{i=1}^{N} n_i^{\infty} kT \left[\exp\left(-\frac{z_i e\psi(x')}{kT}\right) - 1\right] - \frac{1}{2}\varepsilon_r\varepsilon_0 \left(\left.\frac{d\psi}{dx}\right|_{x=x'}\right)^2 \tag{34.4}$$

which, for the low-potential case, can be linearized to

$$P_{\text{pl}}(h) = \frac{1}{2}\varepsilon_r\varepsilon_0 \left\{\kappa^2\psi^2(x') - \left(\left.\frac{d\psi}{dx}\right|_{x=x'}\right)^2\right\} \tag{34.5}$$

Here $P(h) > 0$ corresponds to repulsion and $P(h) < 0$ to attraction. The corresponding interaction energy $V_{\text{pl}}(h)$ between two parallel plates per unit area can be obtained by integrating $P_{\text{pl}}(h)$ with the result that

$$V_{\text{pl}}(h) = \int_h^{\infty} P_{pl}(h)dh \tag{34.6}$$

34.2.2 Derjaguin's Approximation for Calculation of Interactions between Two Spheres or Cylinders

Once the interaction energy $V_{\text{pl}}(h)$ between two parallel plates at separation h is obtained, one can derive the following expressions (Fig. 34.2).

We give below Derjaguin's approximation to calculate the sphere–sphere interaction energy [11] and the cylinder–cylinder interaction energy [12, 13]:

$$V_{\text{sp}}(H) = \frac{2\pi a_1 a_2}{a_1 + a_2}\int_H^{\infty} V_{\text{pl}}(h)dh \quad \text{for two spheres} \tag{34.7}$$

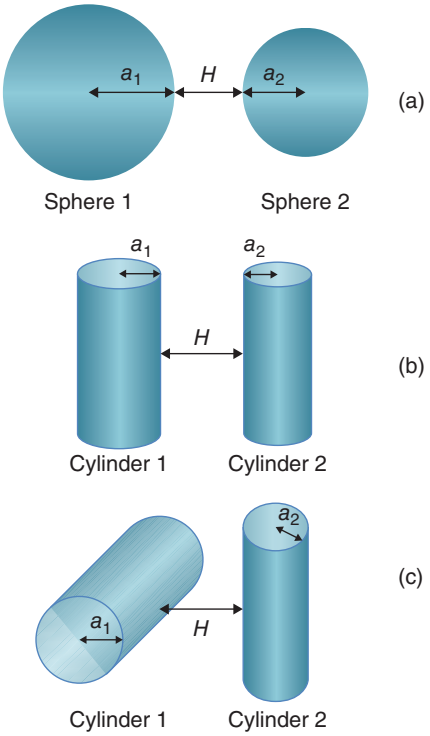


FIGURE 34.2 Interaction between two spheres or cylinders 1 and 2 of radii a_1 and a_2, respectively, at separation H: (a) two spheres; (b) two parallel cylinders; (c) Two crossed cylinders.

$$V_{\text{cy}//}(H) = \sqrt{\frac{2a_1a_2}{a_1 + a_2}}\int_H^{\infty} V_{\text{pl}}(h)\frac{dh}{\sqrt{h - H}}$$

for two parallel cylinders (34.8)

$$V_{\text{cy}\perp}(H) = 2\pi\sqrt{a_1a_2}\int_H^{\infty} V_{\text{pl}}(h)dh$$

for two crossed cylinders (34.9)

34.2.3 Low-Potential Case

For the low-potential case, expressions for the interaction energy between two parallel plates, two spheres, and two parallel or crossed cylinders are easily derived. The results are given below. In the following expressions, superscript ψ stands for the interaction at constant surface potential, σ for the interaction at constant surface charge density, and ψ–σ for the interaction for the case where the surface potential and the surface charge density of pates 1 and 2 are, respectively, kept constant during interaction.

1. Interaction energy $V_{\text{pl}}(h)$ per unit area between two parallel plates 1 and 2 carrying unperturbed surface

potentials ψ_{01} and ψ_{02}, respectively, at separation h between their surfaces [14–16]:

$$V_{\rm pl}^{\psi}(h) = \varepsilon_{\rm r}\varepsilon_0\kappa\left[\left(\frac{\psi_{01}+\psi_{02}}{2}\right)^2\left\{1-\tanh\left(\frac{\kappa h}{2}\right)\right\} - \left(\frac{\psi_{01}-\psi_{02}}{2}\right)^2\left\{\coth\left(\frac{\kappa h}{2}\right)-1\right\}\right] \quad (34.10)$$

$$V_{\rm pl}^{\sigma}(h) = \varepsilon_{\rm r}\varepsilon_0\kappa\left[\left(\frac{\psi_{01}+\psi_{02}}{2}\right)^2\left\{\coth\left(\frac{\kappa h}{2}\right)-1\right\} - \left(\frac{\psi_{01}-\psi_{02}}{2}\right)^2\left\{1-\tanh\left(\frac{\kappa h}{2}\right)\right\}\right] \quad (34.11)$$

$$V_{\rm pl}^{\psi-\sigma}(h) = \varepsilon_{\rm r}\varepsilon_0\kappa\left[\frac{\psi_{01}\psi_{02}}{\cosh(\kappa h)} + \frac{1}{2}\left(\psi_{01}^2-\psi_{02}^2\right)\{1-\tanh(\kappa h)\}\right] \quad (34.12)$$

2. Interaction energy between two spheres 1 and 2 of radii a_1 and a_2 carrying unperturbed surface potentials ψ_{01} and ψ_{02}, respectively, at separation H between their surfaces

$$V_{\rm sp}^{\psi}(H) = \pi\varepsilon_{\rm r}\varepsilon_0\frac{a_1a_2}{a_1+a_2}\left\{(\psi_{01}+\psi_{02})^2\ln(1+e^{-\kappa H}) + (\psi_{01}-\psi_{02})^2\ln(1-e^{-\kappa H})\right\} \quad (34.13)$$

$$V_{\rm sp}^{\sigma}(H) = \pi\varepsilon_{\rm r}\varepsilon_0\frac{a_1a_2}{a_1+a_2}\left\{-(\psi_{01}+\psi_{02})^2\ln(1-e^{-\kappa H}) - (\psi_{01}-\psi_{02})^2\ln(1+e^{-\kappa H})\right\} \quad (34.14)$$

$$V_{\rm sp}^{\psi-\sigma}(H) = 4\pi\varepsilon_{\rm r}\varepsilon_0\frac{a_1a_2}{a_1+a_2}\left\{\psi_{01}\psi_{02}\arctan(e^{-\kappa H}) + \frac{1}{4}\left(\psi_{01}^2-\psi_{02}^2\right)\ln(1+e^{-2\kappa H})\right\} \quad (34.15)$$

3. Interaction energy per unit length between two parallel infinitely long cylinders 1 and 2 of radii a_1 and a_2 carrying unperturbed surface potentials ψ_{01} and ψ_{02}, respectively, at separation H between their surfaces:

$$V_{\rm cy//}^{\psi}(H) = -2\varepsilon_{\rm r}\varepsilon_0\sqrt{\kappa}\sqrt{\frac{2\pi a_1a_2}{a_1+a_2}}\left[\left(\frac{\psi_{01}+\psi_{02}}{2}\right)^2 \mathrm{Li}_{1/2}(-e^{-\kappa H}) + \left(\frac{\psi_{01}-\psi_{02}}{2}\right)^2\mathrm{Li}_{1/2}(e^{-\kappa H})\right] \quad (34.16)$$

$$V_{\rm cy//}^{\sigma}(H) = 2\varepsilon_{\rm r}\varepsilon_0\sqrt{\kappa}\sqrt{\frac{2\pi a_1a_2}{a_1+a_2}}\left[\left(\frac{\psi_{01}+\psi_{02}}{2}\right)^2 \mathrm{Li}_{1/2}(e^{-\kappa H}) - \left(\frac{\psi_{01}-\psi_{02}}{2}\right)^2\mathrm{Li}_{1/2}(-e^{-\kappa H})\right] \quad (34.17)$$

$$V_{\rm cy//}^{\psi-\sigma}(H) = \sqrt{2}\varepsilon_{\rm r}\varepsilon_0\sqrt{\kappa}\sqrt{\frac{2\pi a_1a_2}{a_1+a_2}}\left[\psi_{01}\psi_{02}e^{-\kappa H}\times\Phi\left(-e^{-\kappa H},\frac{1}{2},\frac{1}{2}\right) - \frac{1}{2}\left(\psi_{01}^2-\psi_{02}^2\right)\mathrm{Li}_{1/2}(-e^{-2\kappa H})\right] \quad (34.18)$$

where $\mathrm{Li}_s(z) = \sum_{k=1}^{\infty} z^k/k^s$ and $\Phi(z,s,a) = \sum_{k=0}^{\infty} z^k/(k+a)^s$ are, respectively, a polylogarithm function and a Lerch transcendent.

4. Interaction energy between two crossed infinitely long cylinders 1 and 2 of radii a_1 and a_2 carrying unperturbed surface potentials ψ_{01} and ψ_{02}, respectively, at the closest separation H between their surfaces:

$$V_{\rm cy\perp}^{\psi}(H) = 4\pi\varepsilon_{\rm r}\varepsilon_0\sqrt{a_1a_2}\left[\left(\frac{\psi_{01}+\psi_{02}}{2}\right)^2\ln(1+e^{-\kappa H}) + \left(\frac{\psi_{01}-\psi_{02}}{2}\right)^2\ln\left(\frac{1}{1-e^{-\kappa H}}\right)\right] \quad (34.19)$$

$$V_{\rm cy\perp}^{\sigma}(H) = 4\pi\varepsilon_{\rm r}\varepsilon_0\sqrt{a_1a_2}\left[\left(\frac{\psi_{01}+\psi_{02}}{2}\right)^2\ln\left(\frac{1}{1-e^{-\kappa H}}\right) - \left(\frac{\psi_{01}-\psi_{02}}{2}\right)^2\ln(1+e^{-\kappa H})\right] \quad (34.20)$$

$$V_{\rm cy\perp}^{\psi-\sigma}(H) = 4\pi\varepsilon_{\rm r}\varepsilon_0\sqrt{a_1a_2}\left[\psi_{01}\psi_{02}\arctan(e^{-\kappa H}) + \frac{1}{4}\left(\psi_{01}^2-\psi_{02}^2\right)\ln(1+e^{-2\kappa H})\right] \quad (34.21)$$

It can be shown that the unperturbed surface potentials ψ_{01} and ψ_{02} of particles 1 and 2 are, respectively, related to the surface charge densities σ_1 and σ_2 by

$$\psi_{0i} = \frac{\sigma_i}{\varepsilon_{\rm r}\varepsilon_0\kappa} \quad (i=1,2) \quad (34.22)$$

34.2.4 Linear Superposition Approximation: Arbitrary Potential Case

Although it is generally difficult to derive the interaction energy between two particles with arbitrary surface potential, a simple approximation method [the linear superposition approximation (LSA)] is available to derive the interaction energy between particles at large particle separations $\kappa h \gg 1$ or

$\kappa H \gg 1$. Expressions for the interaction energy obtained with the help of the linear superposition approximation, which do not depend on the type of the double-layer interaction, can be applied both to the constant surface potential and constant surface charge density cases as well as their mixed case. In addition, the results obtained on the basis of the linear superposition approximation can be applied not only to hard particles. The interaction energy based on LSA involves the effective surface potentials $\psi_{\text{eff }1}$ and $\psi_{\text{eff }2}$ of two interacting particles, which are derived as follows.

Consider the interaction energy between two parallel plates 1 and 2 at separation h with arbitrary (unperturbed) surface potentials ψ_{01} and ψ_{02}, respectively, in a symmetric electrolyte solution of valence z and bulk concentration n. We take an x axis perpendicular to the plates with its origin at the surface of plate 1. The unperturbed potential distributions $\psi_1(x)$ and $\psi_2(x)$ for plates 1 and 2 in the absence of interaction, respectively, can be derived from by solving Eq. (34.1) for the present case with the result that

$$\psi_1(x) = \frac{2kT}{ze} \ln\left(\frac{1+\gamma_1 e^{-\kappa x}}{1-\gamma_1 e^{-\kappa x}}\right) \tag{34.23}$$

$$\psi_2(x) = \frac{2kT}{ze} \ln\left(\frac{1+\gamma_2 e^{-\kappa(h-x)}}{1-\gamma_2 e^{-\kappa(h-x)}}\right) \tag{34.24}$$

with

$$\gamma_1 = \tanh\left(\frac{ze\psi_{01}}{4kT}\right), \gamma_2 = \tanh\left(\frac{ze\psi_{02}}{4kT}\right) \tag{34.25}$$

The asymptotic forms of the unperturbed potentials $\psi_1(x)$ and $\psi_2(x)$ produced at large distances by plates 1 and 2, respectively, in the absence of interaction can be derived from Eqs. (34.23) and (34.24)

$$\psi_1(x) = \psi_{\text{eff1}} e^{-\kappa x} \tag{34.26}$$

$$\psi_2(x) = \psi_{\text{eff2}} e^{-\kappa(h-x)} \tag{34.27}$$

where ψ_{eff1} and ψ_{eff2} are, respectively, the effective surface potentials of plates 1 and 2

$$\psi_{\text{eff1}} = 4\gamma_1 = 4\tanh\left(\frac{ze\psi_{01}}{4kT}\right), \psi_{\text{eff2}} = 4\gamma_2 = 4\tanh\left(\frac{ze\psi_{02}}{4kT}\right) \tag{34.28}$$

The potential distribution $\psi(x)$ around the midpoint between plates 1 and 2 can thus be approximated by

$$\psi(x) = \psi_1(x) + \psi_2(x) = \psi_{\text{eff1}} e^{-\kappa x} + \psi_{\text{eff2}} e^{-\kappa(h-x)} \tag{34.29}$$

By noting that for large separation h, $\psi(x)$ is small so that Eq. (6) can be employed, we substitute Eq. (34.29) into Eq. (34.5) to obtain

$$P(h) = 2\varepsilon_r \varepsilon_0 \kappa^2 \psi_{\text{eff1}} \psi_{\text{eff2}} e^{-\kappa h} \tag{34.30}$$

The interaction energy $V(h)$ per unit area of plates 1 and 2 is thus

$$V_{\text{pl}}(h) = \int_h^\infty P_{\text{pl}}(h)dh = 2\varepsilon_{\text{r}} \varepsilon_0 \kappa \psi_{\text{eff1}} \psi_{\text{eff2}} e^{-\kappa h} \tag{34.31}$$

From Eq. (34.31) as combined with Derjaguin's approximation, the interaction energy between two spheres or cylinders of radii a_1 and a_2 at large separations can be derived. The results are given below.

1. Interaction energy per unit area between two parallel plates at separation h:

$$V_{\text{pl}}(h) = 2\varepsilon_{\text{r}} \varepsilon_0 \kappa \psi_{\text{eff1}} \psi_{\text{eff2}} e^{-\kappa h} \tag{34.32}$$

2. Interaction energy between two spheres of radii a_1 and a_2 at separation H:

$$V_{\text{sp}}(H) = \frac{4\pi a_1 a_2}{a_1 + a_2} \varepsilon_{\text{r}} \varepsilon_0 \psi_{\text{eff1}} \psi_{\text{eff2}} e^{-\kappa H} \tag{34.33}$$

3. Interaction energy per unit length between two parallel cylinders of radii a_1 and a_2 at separation H:

$$V_{\text{cy}//}(H) = 2\sqrt{\frac{2\pi a_1 a_2}{a_1 + a_2}} \sqrt{\kappa} \varepsilon_r \varepsilon_0 \psi_{\text{eff1}} \psi_{\text{eff2}} e^{-\kappa h} \tag{34.34}$$

4. Interaction energy between two crossed cylinders of radii a_1 and a_2 at separation H:

$$V_{\text{cy}\perp}(H) = 4\pi\sqrt{a_1 a_2} \varepsilon_{\text{r}} \varepsilon_0 \psi_{\text{eff1}} \psi_{\text{eff2}} e^{-\kappa H} \tag{34.35}$$

In the arbitrary potential case, tt can be shown that the unperturbed surface potentials ψ_{01} and ψ_{02} of particles 1 and 2 are, respectively, related to the surface charge densities σ_1 and σ_2 by

$$\psi_{0i} = \frac{\sigma_i}{\varepsilon_{\text{r}} \varepsilon_0 \kappa} \ (i = 1, 2) \tag{34.36}$$

which reduces to Eq. (23) for the low-potential limit.

34.3 INTERACTION BETWEEN SOFT PARTICLES

For the case of interaction between soft particles, one must solve the Poisson–Boltzmann equations for both regions inside and outside the surface layer [17–26]. Consider two parallel dissimilar soft plates 1 and 2 of thicknesses d_1 and d_2, respectively, separated by a distance h immersed in a liquid containing N ionic species with valence z_i and bulk concentration (number density) n_i^∞ ($i = 1, 2, \ldots, N$). We treat the case where fixed charges are distributed in the surface layers of plates 1 and 2 at uniform densities of ρ_{fix1} and ρ_{fix2}, respectively. We take an x axis perpendicular to the plates with its origin at the right surface of plate 1, as in Fig. 34.3

We assume that the electric potential $\psi(x)$ outside the plates ($0 < x < h$) obeys the following one-dimensional planar Poisson–Boltzmann equation:

$$\frac{d^2\psi(x)}{dx^2} = -\frac{1}{\varepsilon_r\varepsilon_0}\sum_{i=1}^{N} z_i e n_i^\infty \exp\left(-\frac{z_i e\psi(x)}{kT}\right) - \frac{\rho_{\text{fix1}}}{\varepsilon_r\varepsilon_0} \quad \text{for } -d_1 < x < 0 \tag{34.37}$$

$$\frac{d^2\psi(x)}{dx^2} = -\frac{1}{\varepsilon_r\varepsilon_0}\sum_{i=1}^{N} z_i e n_i^\infty \exp\left(-\frac{z_i e\psi(x)}{kT}\right) \quad \text{for } 0 < x < h \tag{34.38}$$

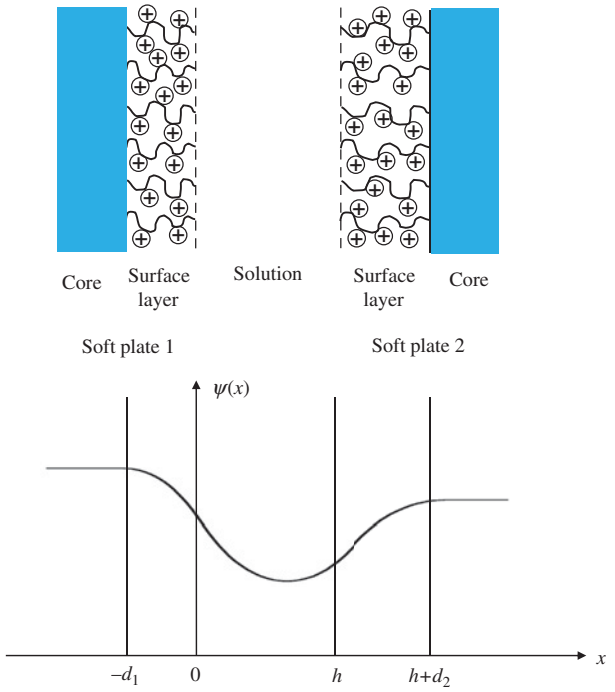


FIGURE 34.3 Interaction between two parallel dissimilar soft plates 1 and 2 covered with surface layers of thicknesses d_1 and d_2, respectively, at separation h and potential distribution $\psi(x)$ across them.

$$\frac{d^2\psi(x)}{dx^2} = -\frac{1}{\varepsilon_r\varepsilon_0}\sum_{i=1}^{N} z_i e n_i^\infty \exp\left(-\frac{z_i e\psi(x)}{kT}\right) - \frac{\rho_{\text{fix2}}}{\varepsilon_r\varepsilon_0} \quad \text{for } h < x < h + d_2 \tag{34.39}$$

By solving these equations subject to the appropriate boundary conditions, we can obtain the interaction energy between soft particles. The results for the low-potential case are given below.

1. Interaction energy per unit area between two parallel soft plates 1 and 2 carrying fixed charge densities ρ_{fix1} and ρ_{fix2}, respectively (Fig. 34.3):

$$V_{\text{pl}}(h) = \frac{1}{4\varepsilon_r\varepsilon_0\kappa^3}\left[\{\rho_{\text{fix1}}\sinh(\kappa d_1) + \rho_{\text{fix2}}\sinh(\kappa d_2)\}^2 \left\{\coth\left(\frac{\kappa(h+d_1+d_2)}{2}\right) - 1\right\} - \{\rho_{\text{fix1}}\sinh(\kappa d_1) - \rho_{\text{fix2}}(\kappa d_2)\}^2 \left\{1 - \tanh\left(\frac{\kappa(h+d_1+d_2)}{2}\right)\right\}\right] \tag{34.40}$$

2. Interaction energy between two soft spheres of inner radii a_1 and a_2 and outer radii $b_1 = a_1 + d_1$ and $b_2 = a_2 + d_2$ carrying fixed charge densities $\rho_{\text{fix 1}}$ and $\rho_{\text{fix 2}}$, respectively (i.e., the thicknesses of the surface layers of soft spheres 1 and 2 are d_1 and d_2, respectively) (Fig. 34.4a):

$$V_{\text{sp}}(H) = \frac{1}{\varepsilon_r\varepsilon_0\kappa^4}\left(\frac{\pi b_1 b_2}{b_1 + b_2}\right)\left[\{\rho_{\text{fix1}}\sinh(\kappa d_1) + \rho_{\text{fix2}}\sinh(\kappa d_2)\}^2 \ln\left(\frac{1}{1 - e^{-\kappa(H+d_1+d_2)}}\right) - \{\rho_{\text{fix1}}\sinh(\kappa d_1) - \rho_{\text{fix2}}\sinh(\kappa d_2)\}^2 \ln(1 + e^{-\kappa(H+d_1+d_2)})\right] \tag{34.41}$$

3. Interaction energy per unit length between two parallel soft cylinders of inner radii a_1 and a_2 and outer radii $b_1 = a_1 + d_1$ and $b_2 = a_2 + d_2$ carrying fixed charge densities $\rho_{\text{fix 1}}$ and $\rho_{\text{fix 2}}$, respectively (i.e., the thicknesses of the surface layers of soft spheres 1 and 2 are d_1 and d_2, respectively) (Fig. 34.4b):

$$V_{\text{cy//}}(H) = \frac{1}{2\varepsilon_r\varepsilon_0\kappa^{7/2}}\sqrt{\frac{2\pi b_1 b_2}{b_1 + b_2}}\left[\{\rho_{\text{fix1}}\sinh(\kappa d_1) + \rho_{\text{fix2}}\sinh(\kappa d_2)\}^2 \text{Li}_{1/2}(e^{-\kappa(H+d_1+d_2)}) + \{\rho_{\text{fix1}}\sinh(\kappa d_1) - \rho_{\text{fix2}}\sinh(\kappa d_2)\}^2 \text{Li}_{1/2}(-e^{-\kappa(H+d_1+d_2)})\right] \tag{34.42}$$

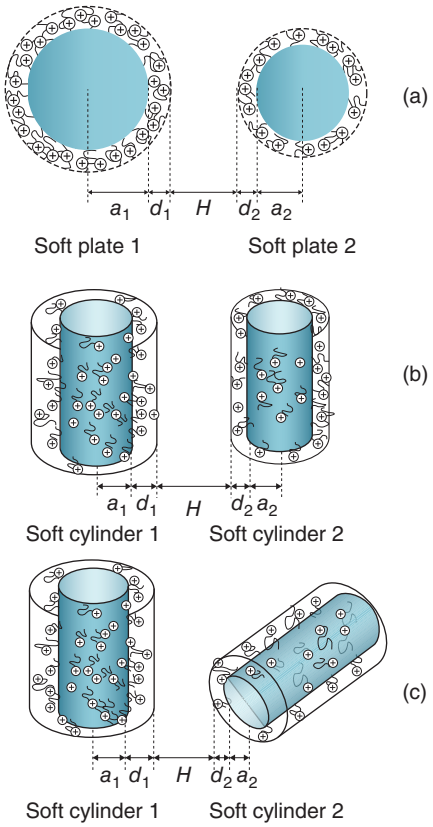


FIGURE 34.4 Interaction between two soft spheres or cylinders 1 and 2 of radii a_1 and a_2 covered with surface layers of thicknesses d_1 and d_2, respectively, at separation H: (a) two soft spheres; (b) two parallel soft cylinders; (c) two crossed soft cylinders.

4. Interaction energy between two crossed soft cylinders of inner radii a_1 and a_2 and outer radii $b_1 = a_1 + d_1$ and $b_2 = a_2 + d_2$ carrying fixed charge densities $\rho_{\text{fix }1}$ and $\rho_{\text{fix }2}$, respectively (i.e., the thicknesses of the surface layers of soft spheres 1 and 2 are d_1 and d_2, respectively) (Fig. 34.4c):

$$V_{\text{cy}\perp}(H) = \frac{\pi\sqrt{b_1 b_2}}{\varepsilon_r\varepsilon_0\kappa^4}\left[\{\rho_{\text{fix1}}\sinh(\kappa d_1) + \rho_{\text{fix2}}\sinh(\kappa d_2)\}^2 \ln\left(\frac{1}{1-e^{-\kappa(H+d_1+d_2)}}\right) - \{\rho_{\text{fix1}}\sinh(\kappa d_1) - \rho_{\text{fix2}}\sinh(\kappa d_2)\}^2 \ln(1+e^{-\kappa(H+d_1+d_2)})\right] \tag{34.43}$$

For the arbitrary potential case, it can be shown that the interaction energy takes the same form as Eqs. (34.32)–(34.35) for hard particles, but the effective potential takes the different form from that for hard particles. It can be shown that the unperturbed surface potentials ψ_{01} and ψ_{02} of soft particles 1 and 2 are, respectively, related to the fixed charge densities ρ_{fix1} and ρ_{fix2} by

$$\psi_{0i} = \left(\frac{kT}{ze}\right)\left(\ln\left[\frac{\rho_{\text{fixi}}}{2zen} + \left\{\left(\frac{\rho_{\text{fixi}}}{2zen}\right)^2 + 1\right\}^{1/2}\right] + \frac{2zen}{\rho_{\text{fixi}}}\left[1 - \left\{\left(\frac{\rho_{\text{fixi}}}{2zen}\right)^2 + 1\right\}^{1/2}\right]\right) \quad (i = 1, 2) \tag{34.44}$$

which, for the low-potential limit, reduces to

$$\psi_{0i} = \frac{\rho_{\text{fixi}}}{2\varepsilon_r\varepsilon_0\kappa^2} \quad (i = 1, 2) \tag{34.45}$$

Note that if the ionized group of valence Z and number density N_i are distributed within the surface layer of particle i (i =1, 2), then we have $\rho_{\text{fix }i} = ZeN_i$. It is also to be noted that the unperturbed surface potential $\psi_{0\,i}$ of soft particle i (i = 1,2) with a thick surface layer ($d_i \gg 1/\kappa$) is related to the Donnan potential $\psi_{\text{DON }i}$ in the surface layer of particle i by

$$\psi_{0i} = \psi_{\text{DON}i} - \left(\frac{kT}{ze}\right)\tanh\left(\frac{ze\psi_{\text{DON}i}}{2kT}\right) \quad (i = 1, 2) \tag{34.46}$$

where the Donnan potential $\psi_{\text{DON }i}$ is given by

$$\psi_{\text{DON}i} = \left(\frac{kT}{ze}\right)\text{arcsin h}\left(\frac{\rho_{\text{fix}i}}{2zen}\right) = \left(\frac{kT}{ze}\right)\ln\left[\frac{\rho_{\text{fix}i}}{2zen} + \sqrt{\left(\frac{\rho_{\text{fix}i}}{2zen}\right)^2 + 1}\right] \tag{34.47}$$

Equation (34.47) reduces to $\psi_{0\text{i}} = \psi_{\text{DON}i}/2$ (i = 1, 2) in the low-potential limit.

34.4 INTERACTION BETWEEN TWO SOFT PARTICLES AFTER CONTACT

In this section we consider two theoretical models for the interaction between two parallel soft plates, that is, a two-stage model and a three-stage model

34.4.1 Two-Stage Model

de Gennes [27] proposed a theory of the interaction between two colloidal particles covered with graft polymers (i.e., polymer brush layers), assuming that when the two brushes come into contact, they are squeezed against each other but they do not interdigitate. If brushes are charged, then electrostatic repulsion between brushes must also be taken into

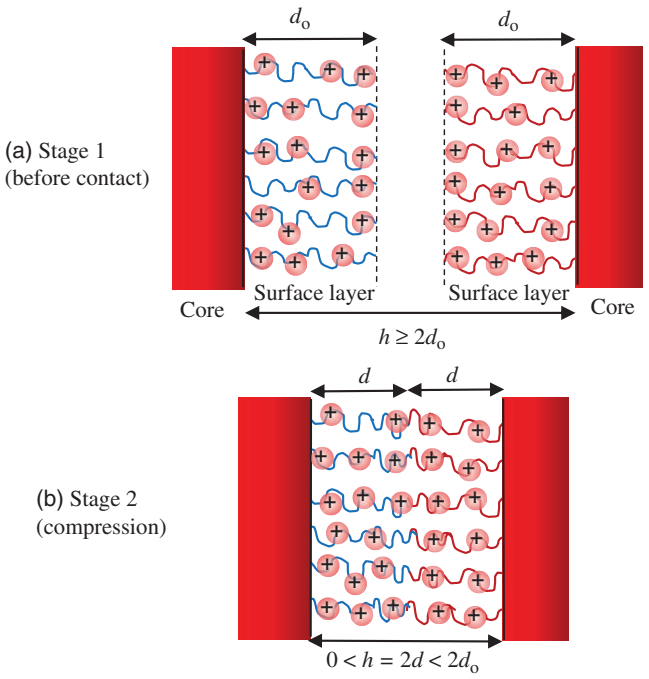


FIGURE 34.5 A two-stage model [28] for the interaction between two parallel plates covered with polyelectrolyte brush layers at separation h, where d_0 is the thickness of the intact brush layer. (a) *Stage 1*–interaction at $h \geq 2d_0$ before the two brushes come into contact. (b) *Stage* 2–after the two brush layers come into contact, compression of the interacting brush layers occurs with decreasing h for $0 < h = 2d < 2d_0$. The thickness d of the interacting brush layers, which is always equal to $h/2$, decreases as compression proceeds with decreasing h.

account in addition to the steric repulsion. Ohshima [28] extended the model of de Gennes [27] to the case of charged polymer brushes (polyelectrolyte brushes) and obtained an expression for the electrostatic repulsion between brushes after they come into contact. In this theory we restricted ourselves to the case where the brushes are squeezed against each other but they do not interdigitate. This model consists of two stages: (1) interaction before contact and (2) interaction between two compressed brush layers (Fig. 34.5).

34.4.1.1 Stage 1: Interaction before Contact. First we consider the electrostatic interaction between two parallel similar plates covered with a layer of polyelectrolyte brushes of intact thickness d_0 at separation h immersed in a solution of infinitely large volume containing an electrolyte of valence z and bulk concentration (number density) n. We first treat the case where the brush layers on the interacting plates at separation h are not in contact ($h \geq 2d_0$). We assume that dissociated groups of valence Z are uniformly distributed in the intact brush layer at a number density of N_0. It can be shown that the repulsion per unit area between two parallel soft plates before contact is approximately given by

$$P(h) = 64nkT \tanh^2(y_0/4) \exp[-\kappa(h - 2d_0)] \quad h \geq 2d_0, \tag{34.48}$$

where y_0 is the scaled unperturbed potential at the front edge of the intact brush layer (i.e., the potential at the boundary between the brush layer and the surrounding electrolyte solution before the two brushes come into contact) and is given by

$$\begin{aligned} y_0 &= y_{\text{DON}} - \tanh(y_{\text{DON}}/2) \\ &= \ln\left[\frac{ZN_0}{2zn} + \sqrt{\left(\frac{ZN_0}{2zn}\right)^2 + 1}\right] \\ &\quad + \frac{2zn}{ZN_0}\left[1 - \sqrt{\left(\frac{ZN_0}{2zn}\right)^2 + 1}\right] \end{aligned} \tag{34.49}$$

34.4.1.2 Stage 2: Repulsion between Compressed Brush Layers. Next we consider the situation after the two brushes come into contact. In this case the thickness of each compressed brush layer, which we denote by d ($\leq d_0$), is always half the separation h:

$$h = 2d \leq 2d_0 \tag{34.50}$$

Since the density of dissociated groups increases as h decreases, it is now a function of h. We denote by $N(h)$ the density of dissociated groups after contact. Following de Gennes [27], we assume that when the two brushes come into contact, they are squeezed against each other but they do not interdigitate. We also assume that the brushes are contracted in such a way that the density of dissociated groups is always uniform over the compressed brush layers. In other words, the product of $N(h)$ and d is constant and always equal to $N_0 d_0$:

$$N(h)d = N(h) \cdot \frac{h}{2} = N_0 d_0 \tag{34.51}$$

The interaction force $P_e(h)$ per unit area between the two brush layers after contact is thus given by

$$P(h) = 2nkT\left[\sqrt{1 + \left(\frac{ZN_0 d_0}{znh}\right)^2} - 1\right], 0 < h \leq 2d_0 \tag{34.52}$$

Equation (34.52) is the required expression for the interaction force $P(h)$ per unit area between two charged brush layers after they come into contact.

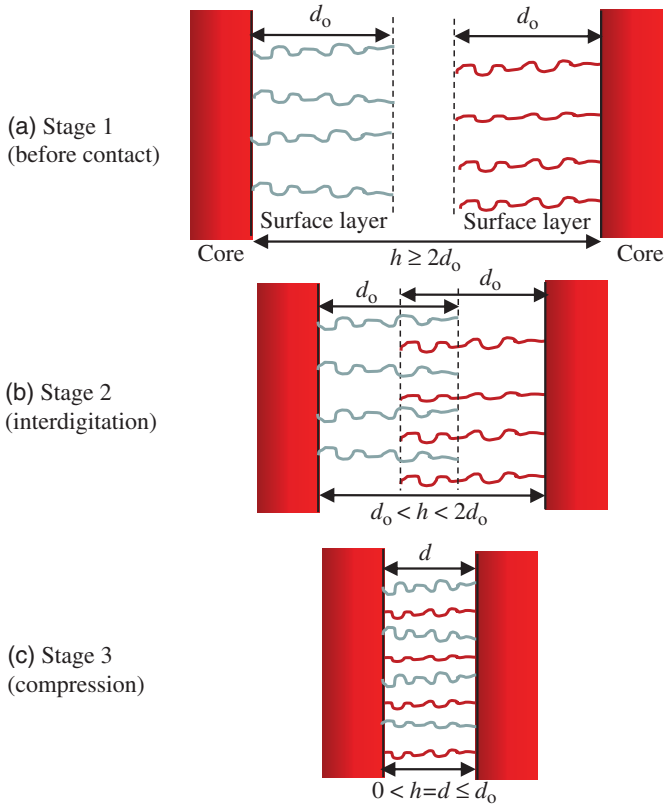


FIGURE 34.6 A three-stage model [29] for the interaction between two parallel plates covered with polyelectrolyte brush layers at separation h, where d_0 is the thickness of the intact brush layer. (a) *Stage 1*–interaction at $h \geq 2d_0$ before the two brush layers come into contact. (b) *Stage 2*–after the two brush layers come into contact, interdigitation of the two interacting brush layers proceeds with decreasing h for $d_0 \leq h < 2d_0$ until full interdigitation occurs at $h = d_0$ (stage 2). The thickness of the interacting brush layer remains constant at d_0. (c) *Stage 3*–compression of the interacting brush layers occurs with further decreasing h for $0 < h = d < d_0$. The thickness d of the interacting brush layers, which is always equal to h, decreases as compression proceeds with decreasing h.

34.4.2 Three-Stage Model

This model assumes that the interaction process consists of three stages: 1–3 [29] (Fig. 34.6).

Stage 1 corresponds to interaction before contact of the brushes of the interacting plates. In stage 2 interdigitation proceeds until the front edge of the polymer brush on either one of the interacting plates reaches the surface of the opposing plate core, that is, until full interdigitation occurs. In stage 3, after full interdigitation, compression of the polyelectrolyte brushes starts.

34.4.2.1 Stage 1: Interaction before Contact. The interaction force per unit area between two parallel soft plates before contact is approximately given by Eq. (34.49).

34.4.2.2 Stage 2: Repulsion between Interdigitated Brushes. Consider the interaction between two parallel interdigitated brushes as shown in Fig. 34.6 (stage 2). In this figure, the regions $0 < x < h–d_0$ and $d_0 < x < h$ correspond to intact brushes and the region $h–d_0 < x < d_0$ to interdigitated brushes. Note that the density of ionized groups is N_0 for the regions $0 < x < h–d_0$ and $d_0 < x < h$ and $2N_0$ for the region $h–d_0 < x < d_0$ due to interdigitation. Thus the scaled Donnan potential y_{DON1} in the regions $0 < x < h–d_0$ and $d_0 < x < h$ is given by

$$y_{DON1} = \text{arcsin h}\left(\frac{ZN_0}{2zn}\right) = \ln\left[\frac{ZN_0}{2zn} + \sqrt{\left(\frac{ZN_0}{2zn}\right)^2 + 1}\right] \tag{34.53}$$

and the scaled Donnan potential y_{DON2} in the region $h–d_0 < x < d_0$ is given by

$$y_{DON2} = \text{arcsin h}\left(\frac{ZN_0}{zn}\right) = \ln\left[\frac{ZN_0}{zn} + \sqrt{\left(\frac{ZN_0}{zn}\right)^2 + 1}\right] \tag{34.54}$$

Further we introduce

$$\kappa_1 = \kappa\sqrt{\cosh(y_{DON1})}, \kappa_2 = \kappa\sqrt{\cosh(y_{DON2})} \tag{34.55}$$

where κ_1 and κ_2 can be interpreted as the Debye-Hückel parameters in the regions $0 < x < h- d_0$ and $d_0 < x < h$ and in the region $h-d_0 < x < d_0$, respectively. It can be shown that the electrostatic force $P(h)$ per unit area between two parallel interdigitated brushes at separation h is given by

$$\begin{aligned} P(h) = 4nkT \Bigg\{ & \sinh^2\left[\frac{y_{DON2}}{2} - \frac{(y_{DON2} - y_{DON1})}{2G(h)}\right. \\ & \left.\sinh(\kappa_1(h-d_0)) \cdot \cosh\left(\kappa_2\left(\frac{h}{2} - d_0\right)\right)\right] \\ & -\frac{1}{4}\left(\frac{\kappa_2}{\kappa}\right)^2\left(\frac{y_{DON2} - y_{DON1}}{G(h)}\right)^2 \\ & \sinh^2[\kappa_1(h-d_0)] \cdot \sinh^2\left[\kappa_2\left(\frac{h}{2} - d_0\right)\right]\Bigg\} \\ & \text{for } d_0 < h < 2d_0 \end{aligned} \tag{34.56}$$

where $G(h)$ is defined by

$$\begin{aligned} G(h) = & \sinh[\kappa_1(h-d_0)]\cosh\left[\kappa_2\left(\frac{h}{2} - d_0\right)\right] \\ & -\left(\frac{\kappa_2}{\kappa_1}\right)\cosh[\kappa_1(h-d_0)]\sinh\left[\kappa_2\left(\frac{h}{2} - d_0\right)\right] \end{aligned} \tag{34.57}$$

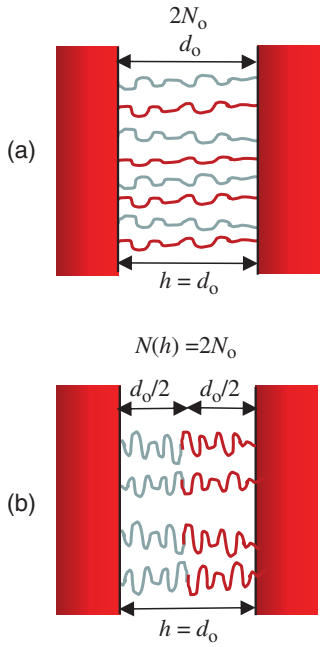


FIGURE 34.7 Interaction at $h = d_0$ for a three-stage model (a) and a two-stage model (b). The densities of ionized groups have the same value of $2N_0$ for two cases (a) fully interdigitated brushes of thickness d_0 at separation $h = d_0$ (at transition from stage 2 to stage 3 in a three-stage model) and (b) half-compressed brush layers of thickness $d/2$ at separation $h = d_0$ (at stage 2 in a two-stage model).

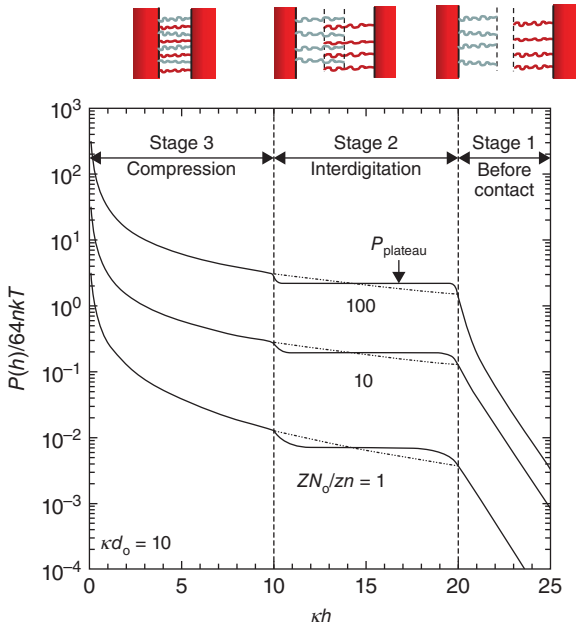


FIGURE 34.8 Scaled repulsion $P/64nkT$ per unit area between two parallel plates covered with a polymer brush layer as a function of scaled separation κh for $ZN_0/zn = 1$, 10, and 100 (i.e., $y_{DON1} = 0.4812, 2.312, 4.605$; $y_{DON2} = 0.8814, 2.998, 5.298$, respectively) at $\kappa d_0 = 10$. Solid lines represent stage 1 (interaction before contact) ($h \geq 2d_0$), stage 2 (interdigitation proceeds for $d_0 \leq h < 2\,d_0$), and stage 3 (compression proceeds for $0 \leq h < d_0$) [29]. Dotted lines correspond to the two stage-model [28].

34.4.2.3 Stage 3: Repulsion between Compressed Brushes. Consider the interaction between two brushes at separation $h = d_0$, where the front edge of each of the brush layer just reaches the surface of the opposing core. As is illustrated in Fig. 34.7a, the density of ionized groups becomes twice ($2N_0$) as large as that of the intact brush layer (N_0). This situation is the same as the situation when the same brush layers (carrying the intact thickness d_0 and the density N_0 of ionized groups) are half compressed so that the density of ionized groups becomes twice ($2N_0$) as large as that of the intact brush layer (N_0) (Fig. 34.7b).

With further decreasing h, compression of the brush layers in the present model (*with* stage 2) and that in the previous model (*without* stage 2) both proceed in the same way. Thus as long as stage 3 ($0 < h < d_0$) is concerned, the three-stage model and the two-stage model become equivalent, both giving the same force expression $P(h)$. The interaction force $P(h)$ per unit area between the two brush layers is thus given by Eq. (34.52):

$$P(h) = 2nkT\left[\sqrt{1 + \left(\frac{ZN_0 d_0}{znh}\right)^2} - 1\right] \quad \text{for } 0 < h \leq d_0 \tag{34.58}$$

It is seen that Eq. (34.58) is the same as the result for the previous model without stage 2.

In Fig. 34.8 we give some results of the calculation of the interaction force $P(h)$ acting between two parallel polyelectrolyte brush layers as a function of reduced separation κh for several values of ZN_0/zn at scaled brush thickness $\kappa d_0 = 10$ (Fig. 34.8).

In Fig. 34.8 we also plot the result of the two-stage model (dotted lines). We see that the interaction force is always repulsive before and after the two brushes come into contact. We see that for large ZN_0/zn and thus high y_{DON1} and y_{DON2}, in stage 2 the interaction force $P(h)$ becomes almost constant independent of plate separation h. This plateau value $P_{plateau}$ is obtained from Eq. (34.56)

$$P_{plateau} = 4nkT\left\{\sinh^2\left[\frac{y_{DON1} + \sqrt{2}y_{DON2}}{2(1+\sqrt{2})}\right] - \left(\frac{y_{DON1} - y_{DON2}}{2(1+\sqrt{2})}\right)^2 \cosh(y_{DON2})\right\} \tag{34.59}$$

which is independent of h and d_0.

34.5 ELECTROSTATIC INTERACTION BETWEEN TWO INTERPENETRATING SOFT PARTICLES

In this section we give a three-stage model of the electrostatic interaction between two interpenetrating charged spherical soft particles with no particle core (space-charged porous spheres) in an electrolyte solution [30] (Fig. 34.9).

In other words, there are three stages: (1) interaction before contact between the two spheres, (2) partial interpenetration, and (3) full interpenetration, that is, engulfing of one sphere by the other. This is an extension of the work of Dähnert and Rödenbeck [31], who considered the interaction between two interpenetrating vesicle-like surface-charged particles, to the case of the interaction of space charge porous spheres. Analytic expressions for the interaction energy and force between two interpenetrating weakly charged porous spheres as a function of particle separation are derived for the respective stages on the basis of the linearized Poisson–Boltzmann equations for the electric potential distribution.

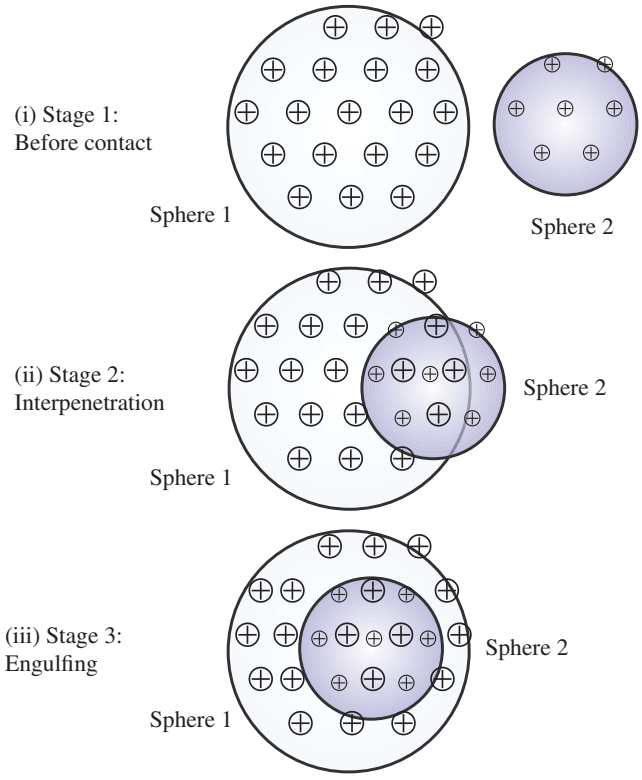


FIGURE 34.9 Three-stage model for the electrostatic interaction between two charged soft spheres 1 and 2: (a) before contact, (b) interpenetration, (c) engulfing.

34.5.1 Linearized Poisson–Boltzmann Equations for Two Interacting Charged Porous Spheres

Consider two charged porous spheres of radii a_1 and a_2 carrying fixed charges of constant volume densities ρ_1 and ρ_2, respectively, at separation R between their centers O_1 and O_2 in an electrolyte solution containing N ionic species with valence z_i and bulk concentration (number density) n_i ($i = 1,2, \ldots, N$) (in units of m^{-3}) in three stages: (1) interaction before contact, (2) interpenetration, and (3) engulfing [30]. Without loss of generality, we may treat the case in which the radius a_1 of sphere 1 is larger than or equal to the radius a_2 of sphere 2:

$$a_1 \geq a_2 \tag{34.60}$$

We assume that the relative permittivity in spheres 1 and 2 take the same value ε_r as that of the electrolyte solution and that the electrical potential ψ is low enough to allow the linearization of the Poisson–Boltzmann equations for ψ.

The linearized Poisson–Boltzmann equation in the respective regions can generally be given by

$$\Delta\psi = \kappa^2\psi - \frac{\rho}{\varepsilon_r\varepsilon_0} \tag{34.61}$$

where ρ is the fixed charge density in the respective regions in three stages. For example, in stage 2 (Fig. 34.10),

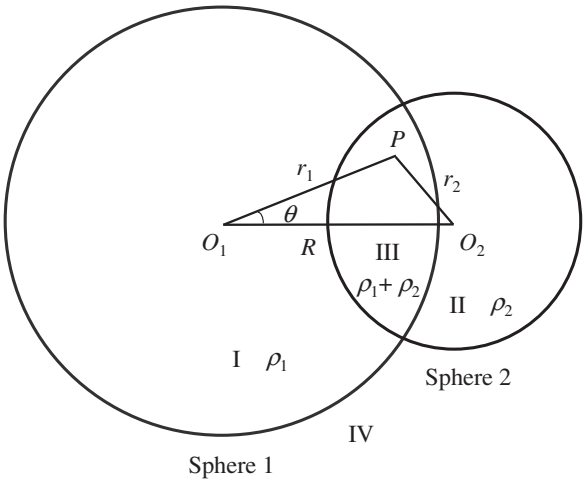


FIGURE 34.10 Interaction between two interpenetrating spheres 1 and 2 at separation R between their centers. $a_1 - a_2 < R < a_1 + a_2$. Region I: inside sphere 1 and outside sphere 2. Region II: inside sphere 2 and outside sphere 1. Region III: inside both spheres 1 and 2. Region IV: outside both spheres 1 and 2. A reference point P lies in region III.

we have

$$\rho = \begin{cases} \rho_1 & \text{for region I} \\ \rho_2 & \text{for region II} \\ \rho_1 + \rho_1 & \text{for region III} \\ 0 & \text{for region IV} \end{cases} \tag{34.62}$$

The solution to Eq. (34.61) can be expressed as the sum

$$\psi = \psi_1 + \psi_2 \tag{34.63}$$

where ψ_1 and ψ_2 are, respectively, the unperturbed potentials for spheres 1 and 2 in the absence of the interaction between the two spheres. It can be shown that the interaction energy $V(R)$ between two charged porous spheres 1 and 2 at separation R is given as follows.

34.5.1.1 Stage 1: Interaction between Two Porous Spheres before Contact.

$$V(R) = \frac{4\pi a_1 a_2 \rho_1 \rho_2}{\varepsilon_r \varepsilon_0 \kappa^4} \left\{ \cosh(\kappa a_1) - \frac{\sinh(\kappa a_1)}{\kappa a_1} \right\} \left\{ \cosh(\kappa a_2) - \frac{\sinh(\kappa a_2)}{\kappa a_2} \right\} \frac{e^{-\kappa R}}{R} \quad \text{for } R \geq a_1 + a_2 \tag{34.64}$$

34.5.1.2 Stage 2: Interaction between Two Partially Interpenetrating Charged Porous Spheres.

$$\begin{aligned} V(R) = \frac{2\pi a_1 a_2 \rho_1 \rho_2}{\varepsilon_r \varepsilon_0 \kappa^4 R} \Bigg[& \frac{1}{\kappa^2 a_1 a_2} \left\{ 1 + \frac{\kappa^2}{2} \left(R^2 - a_1^2 - a_2^2 \right) \right\} \\ & + \frac{\kappa^2}{24 a_1 a_2} (R - a_1 - a_2)^2 \{ R^2 + 2(a_1 + a_2) R - 3(a_1 - a_2)^2 \} \\ & + \left(1 - \frac{1}{\kappa^2 a_1 a_2} \right) e^{-\kappa R} \cosh(\kappa(a_1 - a_2)) \\ & - \left(\frac{1}{\kappa a_1} - \frac{1}{\kappa a_2} \right) e^{-\kappa R} \sinh(\kappa(a_1 - a_2)) \\ & - \left(1 + \frac{1}{\kappa a_1} \right) \left(1 + \frac{1}{\kappa a_2} \right) e^{-\kappa(a_1 + a_2)} \sinh(\kappa R) \Bigg] \\ & \text{for } a_1 - a_2 \leq R \leq a_1 + a_2 \end{aligned} \tag{34.65}$$

34.5.1.3 Stage 3: Interaction for Case Where Sphere 2 Is Engulfed by Sphere 1.

$$V(R) = \frac{4\pi a_1 a_2 \rho_1 \rho_2}{\varepsilon_r \varepsilon_0 \kappa^4 R} \left[\frac{(\kappa a_2)^2 R}{3 a_1} - \left(1 + \frac{1}{\kappa a_1} \right) e^{-\kappa a_1} \left\{ \cosh(\kappa a_2) - \frac{\sinh(\kappa a_2)}{\kappa a_2} \right\} \sinh(\kappa R) \right] \quad \text{for } 0 \leq R \leq a_1 - a_2 \tag{34.66}$$

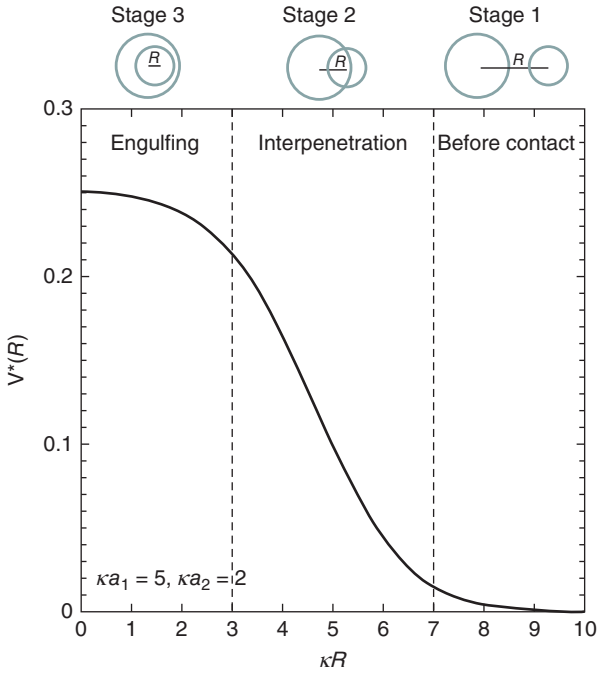


FIGURE 34.11 Scaled potential energy $V^*(R) = V(R)/(4\pi a_1 a_2 \rho_1 \rho_2/\varepsilon_r \varepsilon_0 \kappa^3)$ between two dissimilar charged soft particles with no particle core (porous spheres) 1 and 2 at separation R between their centers for three stages of interaction, that is, interaction before contact, interpenetration, and engulfing. Calculated with $\kappa a_1 = 5$ and $\kappa a_2 = 2$ [30].

Some results of the calculation of the interaction energy between two charged porous spheres are given in Fig. 34.11, which shows the results for the interaction between two dissimilar spheres with $\kappa a_1 = 5$ and $\kappa a_2 = 2$.

We see that the electrostatic interaction between two interpenetrating spheres is repulsive if the fixed volume charges ρ_1 and ρ_2 of the two spheres are of the same sign and attractive if they are of the opposite sign in all stages 1, 2, and 3 and that the interaction force $P(R)$ exhibits a maximum in magnitude in stage 2 and becomes zero at $R = 0$. At $R = 0$, at which the centers of spheres 1 and 2 coincide with each other, the potential energy $V(R)$ of the electrostatic interaction between two spheres 1 and 2 reaches a maximum in magnitude so that the interaction force $P(R)$ between the two spheres becomes zero. Note that the zero separation $R = 0$ corresponds to an unstable equilibrium for two likely charged spheres.

REFERENCES

[1] Derjaguin, B.V., Landau, L. (1941). *Acta Physicochim.* **14**, 633.

[2] Verwey, E.J.W., Overbeek, J.Th.G. (1948). *Theory of the Stability of Lyophobic Colloids.* Elsevier, Amsterdam.

[3] Derjaguin, B.V. (1989). *Theory of Stability of Colloids and Thin Films*. Consultants Bureau, New York/London.

[4] Lyklema, J. (1995). *Fundamentals of Interface and Colloid Science, Solid-Liquid Interfaces*, Vol. 2. Academic Press, New York.

[5] Ohshima, H., Furusawa, K. (eds.) (1998). *Electerical Phenomena at Interfaces, Fundamentals, Measurements, and Applications*, 2nd ed. (revised and expanded). Marcel Dekker, New York.

[6] Ohshima, H. (2006). *Theory of Colloid and Interfacial Electric Phenomena*. Elsevier/Academic Press, Amsterdam.

[7] Tadros, T.F. (ed.) (2007). *Colloid Stabolity, The Role of Surface Forces*–Part 1. Wiley-VCH, Weinheim.

[8] Ohshima, H. (2010). *Biophysical Chemistry of Biointerfaces.* Wiley, Hoboken, NJ.

[9] Israelachvili, J.N. (2010). *Intermolecular and Surface Forces*, 3rd ed. Academic Press, Amsterdam.

[10] Ohshima, H. (2012). *Electrical Phenomena at Interfaces and Biointerfaces, Fundamentals and Applications in Nano-. Bio-, and Environmental Sciences.* Wiley, Hoboken, NJ.

[11] Derjaguin, B.V. (1934). *Kolloid Z.* **69**, 155.

[12] Sparnaay, M.J. (1959). *Recueil* **712**, 6120.

[13] Ohshima, H., Hyono, A. (2009). *J. Colloid Interface Sci.* **333**, 202.

[14] Hogg, R., Healy, T.W., Fuerstenau, D.W. (1966). *Transact. Faraday Soc.* **62**, 1638.

[15] Wiese, G.R., Healy, T.W. (1970). *Transact. Faraday Soc.* **66**, 490.

[16] Kar, G., Chander, S., Mika, T.S. (1973). *J. Colloid Interface Sci.* **44**, 347.

[17] Ohshima, H., Kondo, T. (1987). *Theor. Biol.* **128**, 187.

[18] Ohshima, H., Makino, K., Kondo, T. (1987). *J. Colloid Interface Sci.* **116**, 196.

[19] Ohshima, H., Kondo, T. (1988). *J. Colloid Interface Sci.* **123**, 136.

[20] Ohshima, H., Kondo, T. (1993). *J. Colloid Interface Sci.* **155**, 499.

[21] Hsu, J.P., Hsu, W.C., Chang, Y.I. (1994). *J. Colloid Interface Sci.* **165**, 1.

[22] Zharkih, N.I., Dukhin, S.S. (1994). *Colloid J*. **56**, 680.

[23] Ohshima, H. (2008). *J. Colloid Interface Sci.* **328**, 3.

[24] Duval, J.F.L., Merlin, J., Narayana, P.A.L. (2011). *Phys. Chem. Chem. Phys*. **13**, 1037.

[25] Ohshima, H. (2012). *Soft Matter* **8**,3511.

[26] Ohshima, H. (2013). *Curr. Opin. Colloid Interface Sci*. **18**, 73.

[27] de Gennes, P.G. (1987). *Adv. Colloid Interface Sci*. **27**, 189.

[28] Ohshima, H. (1999). *Colloid Polym. Sci.* **277**, 535.

[29] Ohshima, H. (2014). *Colloid Polym. Sci.* **292**, 431.

[30] Ohshima, H. (in press). *Colloids Surf. A: Physicochem. Eng. Aspects.*

[31] Dähnert, K., Rödenbeck, M. (1994). *J. Colloid Interface Sci.* **163**, 229.

35

PHYSICOCHEMICAL PROPERTIES AND CLINICAL APPLICATIONS OF SURFACTANT-FREE EMULSIONS PREPARED WITH ELECTROLYTIC REDUCTION ION WATER (ERI)

KEN-ICHI SHIMOKAWA AND FUMIYOSHI ISHII

Department of Pharmaceutical Sciences, Meiji Pharmaceutical University, Tokyo, Japan

To facilitate the application of ERI lotion (surfactant-free emulsions containing ERI) as a component of medical drugs, we evaluated the healing effects of this water on burn wounds. A 15-month-old boy had a burn injury caused by boiling water that extended from the left forearm to the hand. An extensive skin defect was observed from the left forearm to the dorsum of the hand, and a II_b/III-degree burn was diagnosed. The burn was treated by applying ERI lotion, antibiotic/steroid combination ointment, and vitamin A/E ointment with wrap therapy. Skin color was almost normal after 74 days, and no functional impairment was observed, showing a favorable course. The burn wound completely healed without the formation of a hypertrophic or keloid scar or pigmentation. These results suggested that extensive II/III burns may be treated adequately with this topical therapy.

Since surfactant agents markedly damage skin tissue sensitized by, for example, burn wounds and atopic dermatitis, surfactant-free emulsions are expected to be the new bases of drugs for external use.

35.1 INTRODUCTION

The electrolysis of water containing a small amount of salt produces a form of water that is useful and generally known as *functional electrolyzed water*. Various types of functional water can be produced depending on the electrolysis conditions used, and these types of water have been classified into two major categories. One is functional electrolyzed acidic water, which is generated at the anode and is used mainly for sterilization. The other is functional electrolyzed alkaline water, which is generated at the cathode and is used primarily for drinking and washing [1,2]. Many studies have examined electrolyzed acid water, and revealed that it has strong bactericidal activity and is safe and environmentally friendly. Therefore, this water has been used in various fields [3–5] such as washing food [6, 7] and medicine [8–11].

Functional electrolyzed alkaline water is used as drinking water, as a supplement to sustain and promote health, and as a treatment. However, few studies have examined functional electrolyzed alkaline water, and its usefulness has not been adequately confirmed.

We previously conducted several studies on ERI [12–21]. The resulting ERI produced using the general method of producing functional electrolyzed water was physically electron-rich water that was obtained after the application of electric current–voltage to water containing a small amount of salt using a special diaphragm system. This water was found to have cleansing, deodorizing, antimicrobial, and antidust actions because its potent alkalinity and negatively charged ions detached and removed dirt and bacteria that cause odor [12]. Since ERI prevents oxidation, it also has rust-preventing and antiseptic actions. Furthermore, stable emulsions of various types of oils have been prepared using ERI with no emulsifiers, thereby demonstrating its emulsifying action [13, 14]. Capitalizing on these properties, ERI

Encyclopedia of Biocolloid and Biointerface Science, Volume 1, First Edition. Edited by Hiroyuki Ohshima.
© 2016 John Wiley & Sons, Inc. Published 2016 by John Wiley & Sons, Inc.

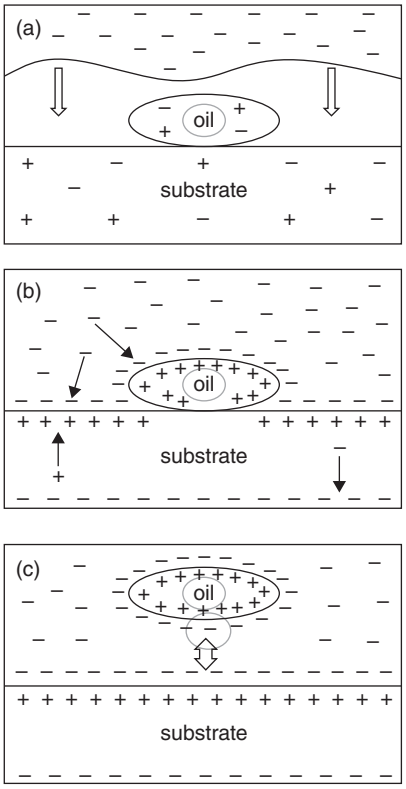


FIGURE 35.1 The mechanism of cleansing by ERI. (a) When ERI comes into contact with oil, the surface of oil becomes positively charged because of the large amount of negatively charged ions. (b) The oil surface with cations attracts anions, and these anions envelop the oil surface and simultaneously cover the oil surface. (c) The anions as a group on the oil surface and those on the oil surface electrostatically repel each other, and their separation promotes the detachment phenomenon.

is widely used as a cleansing agent in various industrial products [12].

The mechanism of cleansing with ERI is as follows. ERI is anionic water that contains a large amount of negatively charged electrons obtained from ion exchange membranes and electrodes by electrolysis. Therefore, when ERI comes into contact with oil, the surface of the oil becomes positively charged, due to the large amount of negatively charged ions (Fig. 35.1a). The oil surface with cations attracts anions, and these anions envelop the oil surface and simultaneously cover the substrate surface (Fig. 35.1b). The anions as a group on the oil surface and those on the substrate surface electrostatically repel each other, and their separation promotes the detachment phenomenon (Fig. 35.1c) [12].

Surfactant-free stable emulsions have been prepared using these properties, and their function has been reported in detail [12]. Emulsions prepared using emulsifier-free electrolytic reduction ion water coagulate less, are more stable, and have a shorter particle diameter than do emulsions prepared using an emulsifier (egg lecithin). Therefore, utilizing the emulsification effect of electrolytic reduction ion water, surfactant-free stable emulsions can be prepared to reduce skin reactions to surfactant stimulation or allergic reactions. This electrolytic reduction ion water is expected to be particularly applicable to medical drugs, cosmetics [13, 14], and foods that are used for a prolonged period.

Magnesium aluminum silicate is a sheet-type clay mineral and a saponite in the smectite group. Magnesium aluminum silicate markedly increases viscosity and is thixotropic when dispersed in various types of solvents; therefore, they can be used as agents to improve the textures of cosmetics, prevent pigment sedimentation in paints, catalyze specific reactions, add adsorptive properties to functional films, and prevent the dripping of adhesives [22]. Smectites have a basic three-layered structure (tetrahedral–octahedral–tetrahedral layers) in which an octahedral layer with an Mg atom in the center and six apical oxygen atoms is present between regular tetrahedral layers with an Si atom in the center and four apical oxygen atoms. The surface layer of saponite is negatively charged because of the isomorphous substitution of parts of Si and Mg in the smectite structure with Al. Therefore, saponite increases its volume more than 10-fold when dispersed in water due to ion adsorption and water entry into the interlayer areas, thereby forming a highly viscous gel.

We previously prepared magnesium aluminum silicate solutions using various solvents including ERI, and reported their rheology characteristics by measuring oscillation with a stress control-type rheometer [15]. Using ERI as a dispersion medium, the gel–sol conversion occurred at a low frequency (external factor). In addition, gel was prepared using ERI containing magnesium aluminum silicate, and gel characteristics for various types of salt were evaluated in detail [16]. The findings obtained revealed that the presence of Ca^{2+} rendered the system unstable, whereas uni- and multivalent cations excluding Ca^{2+} markedly improved gel stability.

Emulsions for medicine such as creams are generally prepared with lecithin as an amphoteric surfactant or polysorbate as a nonionic surfactant. Some surfactants excluding lecithin are known to induce stimulant dermatitis, and may sometimes cause allergic symptoms [5]. Surfactant-free emulsions are optimal for biological safety. However, emulsification itself is difficult in the absence of surfactants, and temporal stability is poor. Therefore, surfactant-free stable emulsions were prepared using the cleansing effects of ERI, and their functionalities were reported [13]. Surfactant-free emulsions prepared with ERI were more stable and had a smaller mean diameter than did those containing egg yolk lecithin as a surfactant. These findings suggested that skin-irritating reactions and allergic symptoms due to surfactants could be reduced by preparing surfactant-free stable emulsions using the emulsification effect of ERI. Therefore, we prepared magnesium aluminum silicate gel using ERI as a dispersion medium, and reported its physiochemical characteristics [15, 16].

In addition, to evaluate its application to medical drugs, we evaluated the healing-promoting effects of ERI on burns and atopic dermatitis, and demonstrated its effectiveness in alleviating these symptoms [17–20].

Taken together, the above findings indicate that ERI can be used to prepare drugs with a drug delivery system (DDS) that can better maintain the gel state than those prepared with purified water. ERI with emulsification characteristics and a gel drug-maintaining function are useful for preparing controlled release transdermal therapeutic drugs.

In this review, we described surfactant-free emulsions prepared by the addition of various types of oils to ERI containing magnesium aluminum silicate, and evaluated their physiochemical characteristics [21]. Surfactant-free emulsions may be used as the new bases for drugs for external use because surfactant agents have been shown to markedly damage skin tissue sensitized by, for example, burn wounds and atopic dermatitis. Therefore, we discussed the possibility of the clinical application of surfactant-free emulsions with a case report [18–20].

35.2 PREPARATION AND PHYSICOCHEMICAL PROPERTIES OF SURFACTANT-FREE EMULSIONS PREPARED WITH ERI CONTAINING MAGNESIUM ALUMINUM SILICATE

The surfaces of smectites are negatively charged by the isomorphous substitution of some silicate and magnesium ions by aluminum ions in the smectite structure, and this results in the formation of cardhouse structures. These cardhouse structures produce viscosity. The dispersion forms a gel with progression of cardhouse structures but forms a sol after the application of a shear force, thereby showing thixotropic properties. Smectites are widely used as rheology modifiers and texture enhancers, and particularly as a cosmetic material because they markedly increase viscosity and are highly thixotropic, spread well over the skin, and are non-greasy [23].

Therefore, various types of oils were added to ERI containing 3% magnesium aluminum silicate (GE100), and the physiochemical characteristics of the emulsions were evaluated [21]. Changes in the thixotropy of GE100 are shown in Fig. 35.2 and Table 35.1. In Fig. 35.2, the dotted and solid lines indicate thixotropy before and after ultrasonication, respectively. Shearing stress clearly increased after ultrasonication, and may have been because the honeycomb structure of magnesium aluminum silicate was more finely dispersed, resulting in denser binding.

In addition, as shown in Table 35.1, a comparison of thixotropy before and after ultrasonication showed a 60% increase in the hysteresis loop area rate after ultrasonication.

Oil concentrations of 0.1, 1 and 10% (jojoba oil, squalane, olive oil, or MCT) were subsequently added to GE100, and the mixtures were ultrasonicated. Changes in thixotropy are shown in Fig 35.3 and Table 35.2. Figure 35.3 shows that the shearing stress decreased as the concentration of each type of oil increased, and this was attributed to the suppressed formation of the card-house structures of magnesium aluminum silicate with an increase in the percentage of oil.

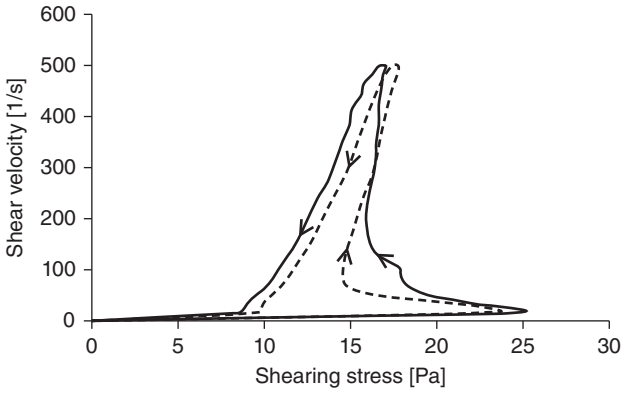


FIGURE 35.2 Thixotropic changes in magnesium aluminum silicate gels prepared using ERI (GE100) sonicated by ultrasonication. Dotted line, before ultrasonication; solid line, after ultrasonication. Each linear arrow shows the direction of the hysteresis loop.

The hysteresis loop area also decreased with an increase in the oil concentration, as shown in Table 35.2 and Fig. 35.3. The rate (%) of the hysteresis loop area of GE100 containing each type of oil to that of GE100 alone (2042 Pa/s) was the highest for MCT (143%) at a concentration of 0.1%, and the lowest also for MCT (58%) at a concentration of 10% (Fig. 35.4). On the other hand, GE100 containing olive oil showed high rates (134% and 103% at concentrations of 0.1% and 10%, respectively). In Table 35.2, thixotropy was compared among GE100 emulsions containing various types of oils at a concentration of 0.1% or 1% in terms of the rate (%) of the hysteresis loop area of GE100 containing each type of oil expressed as a percentage of that of GE100 alone (2042 Pa/s). The results obtained showed that the hysteresis loop area rate was more than 100% at a low oil concentration, which indicated that thixotropy was increased. An increase

TABLE 35.1 Effects of Ultrasonic Treatment on Hysteresis Loop Areas of Magnesium Aluminum Silicate Gels Prepared Using GE100

	Hysteresis loop area (Pa·1/s)	Area ratio (%)
GE100 before ultrasonication	1278 ± 33	100
GE100 after ultrasonication	2042 ± 67	160

Notes: GE100 = electrolytic reduction ion water (ERI) containing 3% magnesium aluminum silicate. Mean ± SD, $n = 3$.

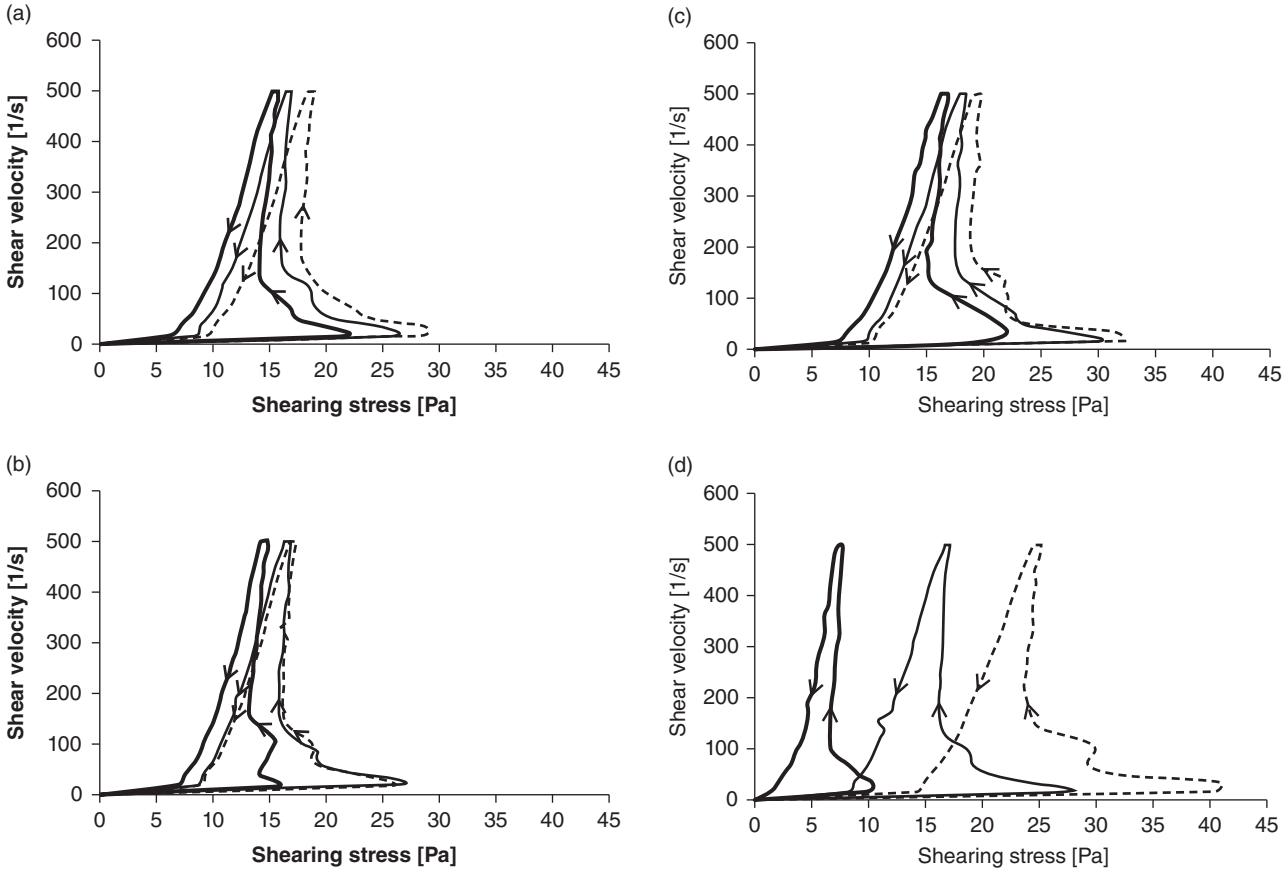


FIGURE 35.3 Thixotropic changes in different gels containing various oils. Dotted line, GE100 + 0.1% oil; thin solid line, GE100 + 1% oil; thick solid line, GE100 + 10% oil. (a) Jojoba oil; (b) squalene; (c) olive oil; (d) MCT. Each linear arrow shows the direction of the hysteresis loop.

in thixotropy reflected high viscosity in the static state and low viscosity after the application of a shear force. When an emulsion is topically applied to the skin, oil added to GE100 may allow a highly viscous state to be maintained, thereby providing moisturizing effects, and also improve viscosity and malleability. However, the hysteresis loop area rate was less than 100% in GE100 containing each type of oil at a concentration of 10%. This suggested that the formation of the cardhouse structures of magnesium aluminum silicate may have been prevented when the oil concentration in GE100 was increased. The hysteresis loop area rate was the lowest for MCT (58%), which may have been because MCT is a medium chain fatty-acid triglyceride of caprylic acid (8-carbon straight-chain fatty acid) and its viscosity is lower than that of the other long chain fatty acids. The hysteresis loop area rate of 10% olive oil was higher (103%) than that of the other types of oils at a concentration of 10%. This may have been because olive oil is a longchain fatty acid that

TABLE 35.2 Thixotropic Values of Emulsions Containing Various Oils

	Hysteresis loop area (Pa/s)		
GE100 + oil (%)	0.1%	1%	10%
GE100 only	–	–	2042 ± 67 (100)
GE100 + jojoba oil	2419 ± 138 (118)	2219 ± 152 (109)	1842 ± 62 (90)
GE100 + squalane	2039 ± 142 (100)	2178 ± 129 (107)	1485 ± 170 (73)
GE100 + olive oil	2741 ± 319 (134)	2496 ± 64 (122)	2101 ± 257 (103)
GE100 + MCT	2916 ± 377 (143)	2301 ± 76 (113)	1184 ± 124 (58)

Notes: Mean ± SD, $n = 3$.

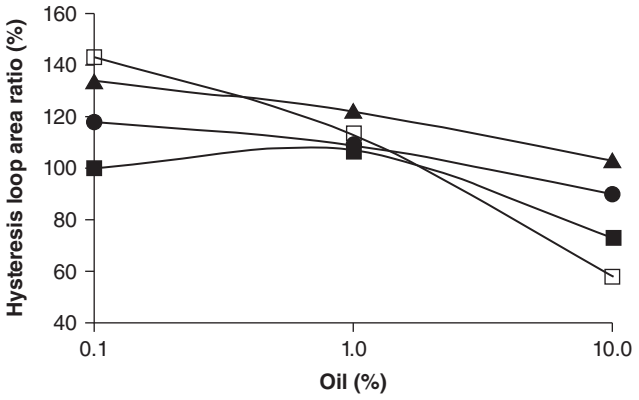


FIGURE 35.4 Relationship between content rate (%) of various oils and hysteresis loop area (• GE100 + jojoba oil; ■ GE100 + squalene; ▲ GE100 + olive oil; □ GE100 + MCT).

consists mainly of oleic acid (monounsaturated 18-carbon fatty acid), and the higher viscosity of this oil than MCT affects thixotropy. The dynamic viscosity of olive oil is known to be approximately 85 mPa · s at 20°C, whereas that of MCT is approximately 23 mPa · s [24].

The rate (%) of the hysteresis loop area of GE-100 containing each type of oil to that of GE-100 alone (2042 Pa/s) was the highest for MCT (143%) at a concentration of 0.1%, and the lowest also for MCT (58%) at a concentration of 10% (Fig. 35.3). On the other hand, GE-100 containing olive oil showed high rates (134 and 103% at concentrations of 0.1% and 10 %, respectively).

Table 35.3 shows the zeta-potential of the oil droplets in each emulsion. The zeta-potential of GE100 containing jojoba oil at concentrations of 0.1 and 1% was low (−38.3 and −37.3 mV, respectively). However, no significant differences were observed in the zeta potential among the other types of emulsions (range: −23.4 - −26.8 mV). A comparison of zeta potentials revealed that samples of GE-100 containing 0.1 or 1% jojoba oil had low values (Table 35.3).

Based on the Derjaguin–Landau–Verwey–Overbeek theory (DLVO theory) [25, 26], these results suggested that the emulsion containing jojoba oil at a low concentration may be more stable than the other emulsions.

The mean particle diameters of the oil droplets in each emulsion are shown in Table 35.4. The mean particle diameters were small for olive oil and MCT. According to the Stokes equation [I], the smaller the particle diameter, the lower the particle rise velocity. Therefore, emulsions of olive oil and MCT with small particle diameters may be more stable.

TABLE 35.3 Zeta-Potentials of Oil Droplets in Various Emulsions (mV)

GE100 + oil (%)	0.1	1	10
GE100 + jojoba oil	−38.3	−37.3	−22.3
GE100 + squalane	−26.9	−31.0	−26.4
GE100 + olive oil	−26.1	−26.5	−25.2
GE100 + MCT	−23.4	−30.5	−26.8

TABLE 35.4 Mean Diameters of Oil Droplets in Various Emulsions (nm)

GE100 + oil (%)	0.1%	1%	10%
GE100 + jojoba oil	363 ± 329	573 ± 278	452 ± 244
GE100 + squalane	355 ± 610	376 ± 832	471 ± 401
GE100 + olive oil	250 ± 204	271 ± 267	327 ± 475
GE100 + MCT	238 ± 182	266 ± 179	295 ± 299

Notes: Mean ± SD, $n = 220$.

$$v = \frac{d^2|\rho_0 - \rho|g}{18\eta} \tag{35.1}$$

where v = particle fall or rise velocity; d = particle diameter in the dispersed phase; ρ,ρ_0 = densities of the dispersed phase and dispersion medium, respectively; g = acceleration due to gravity; η = viscosity of dispersion medium.

These results on thixotropy and particle diameter indicate that when oil is added at a low concentration (0.1%), the MCT emulsions produced may have a better texture and be more stable, and when oil is added at a low (0.1%)–high (10%) concentration, the olive oil emulsions produced may have a better texture and be more stable (Tables 35.2 and 35.4).

Oil is added to GE100 because it moisturizes the skin when emulsions are applied [27]. In addition, fat-soluble drugs can be added to the oil layer and used as bases for drugs for external use. Potent steroids are initially used as a general treatment method for atopic dermatitis, and are changed to weaker steroids with the alleviation of symptoms [28]. However, synthetic surfactants such as sorbitan sesquioleate and glyceryl monostearate are used as emulsifiers, and have been shown to markedly damage sensitive skin tissue. In addition, drugs and cosmetics contain antiseptics such as paraoxybenzoic acid, which can cause allergic contact dermatitis and contact urticarial; therefore, concerns have been expressed regarding the influences of their long-term use on the skin [29].

The GE100 used in this study was ERI containing magnesium aluminum silicate, which is frequently used in cosmetics and improves the texture of the emulsion for topical application to the skin. Oil was added to this GE100 for moisturizing effects, and emulsions were prepared. The various types of oils evaluated in this study are currently used in drugs, cosmetics, and foods. The emulsions obtained by the addition of each oil can prevent the adverse effects associated with long-term use on the skin because of the absence

of surfactants, antiseptics due to the bactericidal effects of ERI (S100) as the main solvent of GE100, and antioxidative agents, such as dibutylhydroxytoluene, tocopherol [12], or ascorbic acid, due to the reductive effects of ERI itself. Oil-in-GE100 emulsions are expected to be used as new bases for external drugs.

35.3 EFFECTS OF ELECTROLYTIC REDUCTION ION WATER (ERI) LOTION PREPARED WITH SURFACTANT-FREE EMULSIONS ON BURN WOUND HEALING (CASE REPORT)

The main surgical primary emergency disorders observed in children include injuries, burns, inflammatory diseases, and the accidental ingestion of foreign bodies [30, 31]. Of these, the number of burn cases is high, and burns are often severe in infants. Local therapy with disinfectants and ointments containing steroids or antibiotics has conventionally been performed to inhibit infection of the wound surface when treating degree II/III burns. However, this conventional therapy has gradually changed to occlusive dressing therapy with wound dressings (such as polyurethane films, hydrocolloids, polyether foam, and hydrogels), which maintains the moist environment in the burn area and optimizes the repair function of the body [32–34]. Previous studies reported that plastic films for food wrapping (wrap films) can be inexpensive materials that are appropriate for dressings, and therapy using wrap films (wrap therapy) is an effective burn treatment method [35, 36].

In this case report, wrap therapy was performed as a conservative treatment with an ERI lotion, antibiotic/steroid combination ointment, and vitamin A/E ointment, and favorable results were obtained [19].

Case Report A 15-month-old male sustained a burn injury to the dorsum of the hand and was treated on an outpatient basis in another hospital. He was referred to our hospital 4 days after the injury. An extensive skin defect was observed over the entire dorsum of the hand. He was diagnosed with a II_b/III burn. The treatment course from the first consultation day to 130 days after the initiation of treatment is shown in Fig. 35.5.

Figure 35.5a shows the state of the damaged area on the first consultation day. Marked redness and swelling of the fingers and dorsum of the left hand and left wrist were observed. The central area of the dorsum of the hand was whitish in color. The skin was detached from the lower half of the fingers to the entire dorsum of the hand. Therefore, an ERI lotion (ERI containing 10% squalane, 5% jojoba oil, 4% glycerin, 3% algisium C, and 0.1%hyaluronic acid, A.I. System Products Corp., Aichi, Japan), antibiotic/steroid combination ointment (Hysetin-P® ointment containing chloramphenicol, fradiomycin sulfate, and prednisolone, Fuji Pharma Co., Ltd., Tokyo), and vitamin A/E ointment (Juvela® ointment containing tocopherol and vitamin A oil, Eisai Co., Ltd., Tokyo) were applied to the burn area, and wrap therapy was

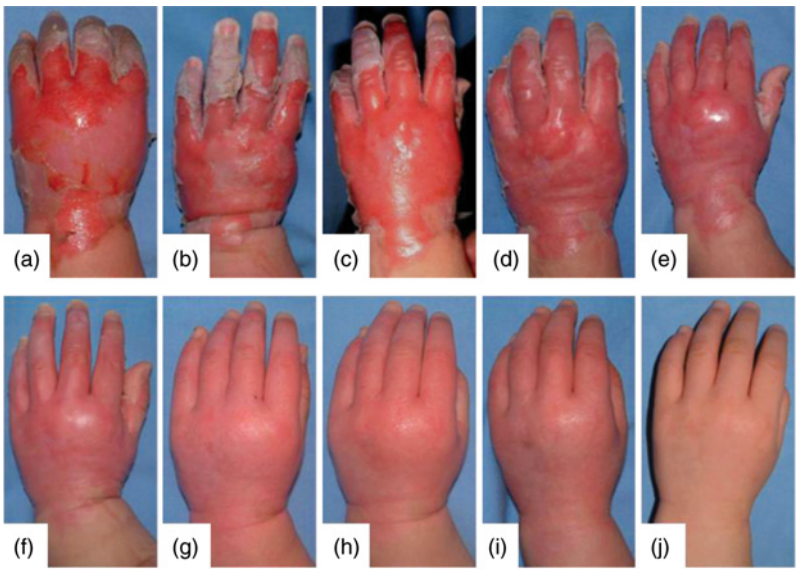


FIGURE 35.5 A case involving treatment of the dorsum of the left hand with ERI lotion, antibiotic/steroid combination ointment, and vitamin A/E ointment employing wrap therapy. (a) Before treatment; (b) day 2 after treatment; (c) day 3 after treatment; (d) day 5 after the treatment; (e) day 7 after treatment; (f) day 10 after treatment; (g) day 21 after treatment; (h) day 32 after treatment; (i) day 74 after treatment; (j) day 130 after treatment.

initiated. Figure 35.5b shows the state of the damaged area 2 days after the initiation of therapy. Redness and swelling were still observed, but swelling was slightly reduced. Redness and swelling were still present after 3–5 days (Fig. 35.5c,d). After 7 days, Hysetin-P ointment as the antibiotic/steroid ointment was changed to Dexan-G® ointment containing betamethasone valerate and gentamicin sulfate (Fuji Pharma Co., Ltd., Tokyo), and burn treatment was continued employing a similar method (Fig. 35.5e). Figure 35.5f shows the state of the damaged area after 10 days. Redness and swelling persisted despite a slight reduction in redness. Figure 35.5g shows the state of damaged area after 21 days. Skin redness further decreased, and there was no functional impairment. After 32 days, epithelialization of the dorsum of the hand was completed (Fig. 35.5h). Figure 35.5i shows the state of the hand after 74 days. Despite slight skin redness, no functional impairment was observed, showing a favorable course. Redness was negligible 130 days after the initiation of therapy (Fig. 35.5j). There was neither scar formation nor pigmentation, and skin color was normal in appearance. Therefore, the burn wound was considered to have completely healed.

Burn injuries often require surgical skin grafting depending on their depth in addition to conventional topical therapy. Our patients had II/III burns. However, since their parents hoped for treatment on an outpatient basis, wrap therapy was performed as a conservative treatment with an ERI lotion, antibiotic/steroid combination ointment, and vitamin A/E ointment. Hysetin-P ointment was changed to Dexan-G ointment 7 days after the initiation of therapy in this patient because ointments exhibiting the stronger anti-inflammatory activity of topical steroids are considered to be more effective.

In this case report, the tissue repair course for burn healing advanced smoothly, resulting in complete healing without the formation of a hypertrophic or keloid scar or pigmentation. These results suggest that extensive II/III burns can be adequately treated by topical therapy with an ERI lotion, antibiotic/steroid combination ointment, and vitamin A/E ointment.

REFERENCES

[1] Ozawa, T., Arai T. (2009). *J. Tokyo Dent. Assoc.* **57**, 4–10.

[2] Sato, T. (2010). *Nippon Dent Rev.* **70**, 33–39.

[3] Shiba, A., Kanaishi, A. (2011). *J. Jpn Soc. Dent. Mater. Devel.* **30**, 5–8.

[4] Asano, S., Iwasaki, H., Shimada, K., Nishida, T., Ito, K. (2008). *J. Jpn Soc. Oral Funct. Water* **9**, 3–6.

[5] Minamoto, K. (2010). *Jpn J. Hygiene* **65**, 20–29.

[6] Hricova, D., Stephan, R., Zweifel, C. (2008). *J. Food Protect.* **71**, 1934–1947.

[7] Wang, H., Feng, H., Luo, Y. (2007). *J. Food Sci.* **72**, M001–M007.

[8] Nelson, D.B. (2005). *Curr. Opin. Infect. Diseases* **18**, 326–330.

[9] Lee, J.H., Rhee, P.L., Kim, J.H., Kim, J.J., Paik, S.W., Rhee, J.C., Song, J.H., Yeom, J.S., Lee, N.Y. (2004). *J Gastroenterol. Hepatol*. **19**, 897–903.

[10] Lee, S.H., Choi, B.K. (2006). *J. Microbiol.* **44**, 417–422.

[11] Kashiwabara, T., Goto, T., Sato, Y., Tomotake, Y., Nagao, K., Ichikawa, T. (2010). *J. Prosthodont. Res.* **54**, 147–149.

[12] Okajima, M. (2002). *Proc. Jpn. Soc. Applied Research in Negative Ion*, pp. 1–12.

[13] Konomatsu, A., Sugibayashi, K., Okajima, M., Ishii, F. (2003). *Mater. Technol.* **21**, 273–285.

[14] Kitamura, T., Koike, M., Todo, H., Okajima, M., Ishii, F., Sugibayashi, K. (2008). *Nippon Koshohin Gakkaishi* **32**, 1–9.

[15] Takigawa, T., Okajima, M., Shimokawa, K., Ishii, F. (2008). *Mater. Technol.* **26**, 50–54.

[16] Okajima, M., Shimokawa, K., Ishii, F. (2009). *Colloid Surf. B: Biointerfaces* **72**, 284–288.

[17] Okajima, M., Shimokawa, K., Ishii, F. (2010). *BioSci. Trends* **4**, 31–36.

[18] Shu, T., Okajima, M., Shimokawa, K., Ishii, F. (2010). *BioSci. Trends* **4**, 1–3.

[19] Shu, T., Okajima, M., Wada, Y., Shimokawa, K., Ishii, F. (2010). *BioSci. Trends* **4**, 213–217.

[20] Shu, T., Okajima, M., Wada, Y., Shimokawa, K., Ishii, F. (2010). *BioSci. Trends* **4**, 499–503.

[21] Okajima, M., Wada, Y., Hosoya, T., Hino, F., Kitahara, Y., Shimokawa, K., Ishii, F. (2013). *Drug Discov. Ther.* **7**, 90–94.

[22] Kunimine Kogyo Co., Ltd. *Smectone*® SA, a technical documentation (http://www.kunimine.co.jp/english/index.htm).

[23] Co-op *Chemical* Co., Ltd., Chiyoda-ku, Tokyo, Japan. *Explanation of the product* (http://www.jade.dti.ne.jp/∼coopchem/newsmectite.html).

[24] Bonnet, J.P., Devesvre, L., Artaud, J., Moulin, P. (2011). *Eur. J. Lipid Sci. Technol.* **113**, 1019–1025.

[25] Derjaguin, B.V., Landau, L. (1941). *Acta Physicochim. URSS* **14**, 633–662.

[26] Verwey, E.J.W., Overbeek, J.T.G. (1952). *Theory of the Stability of Lyophobic Colloids*. Elsevier, Amsterdam, Vols. 1 and 2.

[27] Sagiv, A.E., Dikstein, S., Ingber, A. (2001). *Skin Res. Technol.* **7**, 32–35.

[28] Saeki, H., Furue, M., Furukawa, F., Hide, M., Ohtsuki, M., Katayama, I., Sasaki, R., Suto, H., Takehara, K. (2009). *J. Dermatol.* **36**, 563–577.

[29] Cork, M.J., Danby, S.G., Vasilopoulos, Y., Hadgraft, J., Lane, M.E., Moustafa, M., RichGuy, R.H., MacGowan, A.L., Tazi-Ahnini, R., Ward, S.J. (2009). *J. Invest. Dermatol.* **129**, 1892–1908.

[30] Hettiaratchy, S., Dziewulski, P. (2004). *Br. Med. J.* **328**, 1427–1429.

[31] Koike, Y., Honda, S., Tsuda, I., Nakagawa, T., Ito, Y., Une, Y., Onishi, S., Imai, A. (2003). *J. Clin. Pediatr. Sapporo* **51**, 19–22.

[32] Kujath, P., Michelsen, A. (2008). *Dtsch. Arztebl. Int.* **105**, 239–248.

[33] Brett, D.W. (2006). *J. Wound Ostomy Continence Nurs.* **33**, 3–8.

[34] Ogawa, Y. (2003). *Jpn. J Acute Med.* **27**, 74–76.

[35] Natui, M. (2003). *J. Wound Care* **12**, 63–66.

[36] Kubota, T., Kaneko, W. (2007). *Jpn Soc. Emerg. Pediatr.* **6**, 177–180.

36

STEADY-STATE COUPLING IN ENZYME MEMBRANE

KAZUO NOMURA

Department of Chemistry, Faculty of Science, Kyushu University, Fukuoka, Japan

36.1 INTRODUCTION

The enzymatic reaction across an enzyme membrane is a coupled membrane phenomenon. Immobilization of an enzyme on the membrane enables its activity to be retained for a long time period; therefore, many types of membrane reactors using an enzyme as a catalyst have been designed to remove different kinds of residual organic compounds from water in the environment. Across the enzyme membrane, the artificially synthesized compounds can be decomposed by virtue of the enzyme from natural sources, where the reaction product is separated, concentrated and collected.

It has been pointed out that in the membrane system under a stationary-state condition, coupling phenomena between the material flows and the chemical reactions can be observed [1–3]. Steady-state coupling between the diffusion of the reaction participants and the velocity of the chemical reaction in an artificial enzyme membrane has been described in this chapter.

In the membrane systems consisting of a membrane with a bound enzyme and aqueous solutions, the enzymatic reaction and the diffusion of the reaction participants occur simultaneously [4,5], in which recovery of the reaction product concentrated into the aqueous phase on one side can be performed. Based on the distinct difference in membrane permeability to 4-nitrophenol and that to 4-nitrophenylphosphate, a membrane reactor system of an acid phosphatase–immobilized enzyme membrane, which is capable of separating and concentrating the product of the enzymatic hydrolysis without any other externally applied forces, has been designed, as described in a previous paper [6]. The observed steady-state recovery flux of the product has been found to obey the Michaelis-Menten equation.

On the other hand, based on the nonequilibrium thermodynamics, a general expression for the distribution depth of the reaction affinity within a membrane can be derived as the relaxation length of the reaction affinity, starting with the phenomenological equations for the reaction rate and diffusional fluxes of the reactants and products [2].

In this chapter, we describe how this theoretical approach has been applied to the membrane system with immobilized acid phosphatase to evaluate the degree of the steady-state coupling between the enzymatic reaction rate and the diffusional fluxes, determining the relaxation length, which is a function of the maximum reaction rate, the Michaelis constant, and the diffusion constants of the solutes [7].

36.2 THEORETICAL BACKGROUND

Based on linear nonequilibrium thermodynamics, a general expression for the distribution of the affinity of the chemical reaction within a membrane can be derived from the phenomenological equations given for the reaction rate and diffusional flows of the reactants and products under steady-state conditions [2,3]. In this study, this theoretical approach has been applied to a membrane with an immobilized enzyme to evaluate the degree of the steady-state coupling between the enzymatic reaction rate and the diffusional fluxes across the membrane in the linear region, determining the relaxation length, which is a function of the maximum reaction rate and

Encyclopedia of Biocolloid and Biointerface Science, Volume 1, First Edition. Edited by Hiroyuki Ohshima.
© 2016 John Wiley & Sons, Inc. Published 2016 by John Wiley & Sons, Inc.

the Michaelis constant for the enzymatic reaction and the diffusion coefficients of the reaction participants.

We consider the membrane system in which a chemical reaction catalyzed by an enzyme, acid phosphatase, is taking place. For our system, the following reaction is included

$$\mathrm{S} \rightarrow \mathrm{P} + \mathrm{p} \tag{36.1}$$

where S, P, and p denote the substrate (4-nitrophenyl phosphate), the main product of the hydrolysis (4-nitrophenol), and phosphoric acid, respectively. In the enzyme membrane, the transports of the reactant and the products and the chemical reaction occur simultaneously.

According to nonequilibrium thermodynamics [1,8,9], the dissipation function Φ for the enzyme membrane system can be written in terms of a set of flows that includes the chemical reaction rate and the conjugate forces as

$$\Phi = T\sigma = \sum_i J_i \nabla(-\mu_i) + vA \ (i = \mathrm{S}, \mathrm{P}, \mathrm{p}) \tag{36.2}$$

where σ denotes the internal entropy production (rate); T, J_i, and μ_i are the absolute temperature, the flux of solute i, and the chemical potential (total chemical potential) of solute i, respectively; and v and A are the chemical reaction rate and the chemical affinity for the chemical reaction, respectively. For the chemical reaction [Eq. (36.1)], the chemical affinity is expressed as

$$A = -\sum_i \nu_i \mu_i \ (i = \mathrm{S}, \mathrm{P}, \mathrm{p}) \tag{36.3}$$

where ν_i denotes the stoichiometric coefficient of species i, that is, $\nu_{\mathrm{S}} = -1$, $\nu_{\mathrm{P}} = 1$, $\nu_{\mathrm{p}} = 1$. In terms of the dissipation function given by Eq. (36.2), flows can be described as a linear function of forces by a set of phenomenological equations

$$J_i = \sum_j l_{ij} \nabla(-\mu_j), \ v = l_{chem} A \ (i,j = \mathrm{S}, \mathrm{P}, \mathrm{p}) \tag{36.4}$$

where the l_{ij} values and l_{chem} are the phenomenological coefficients. According to the Curie–Prigogine principle [1,2,8,9], a vector flow and a scalar flow cannot be coupled in the isotropic medium, so all the crossterms for the reaction rate and the diffusional fluxes of the solutes disappear in Eq. (36.4). An alternative set of phenomenological equations can be expressed in terms of the resistance coefficients, r_{ij} values, and r_{chem}, as

$$\nabla(-\mu_i) = \sum_j r_{ij} J_j, \ A = r_{chem} v \ (i,j = \mathrm{S}, \mathrm{P}, \mathrm{p}) \tag{36.5}$$

The balance equation (continuity equation) for solute i can be expressed in terms of the molar concentration c_i as

$$\frac{\partial c_i}{\partial t} = -\nabla J_i + \nu_i v \ (i = \mathrm{S}, \mathrm{P}, \mathrm{p}) \tag{36.6}$$

where ν_i denotes the stoichiometric coefficient of chemical species i in the chemical reaction. Accordingly, under the condition of the steady state ($\partial c_i / \partial t = 0$), the following relation holds:

$$\nabla J_j = \nu_j v \ (i = \mathrm{S}, \mathrm{P}, \mathrm{p}) \tag{36.7}$$

Differentiating Eq. (36.5) and applying the condition of steady state [i.e., Eq. (36.7)], we obtain

$$\nabla^2(-\mu_i) = \left(\sum_j \nu_j r_{ij} \right) v \ (i,j = \mathrm{S}, \mathrm{P}, \mathrm{p}) \tag{36.8}$$

or

$$\nabla^2(-\mu_i) = \left(\sum_j \nu_j r_{ij} \right) l_{chem} A \ (i,j = \mathrm{S}, \mathrm{P}, \mathrm{p}) \tag{36.9}$$

We have assumed that summation of the resistance coefficients is independent of the position within the membrane. Consider that the diffusional flux is only in the direction perpendicular to the membrane surface (direction along the x axis). Multiplying both sides of the equation by ν_i and carrying out the summation over i, we obtain a differential equation by virtue of Eq. (36.3) as

$$\frac{d^2 A}{dx^2} = (\lambda^{-2}) A \tag{36.10}$$

where the coefficient λ^{-2} (λ is the relaxation length [2]) is a function of l_{chem} and r_{ij} values as

$$\lambda^{-2} = l_{chem} \sum_{i,j} \nu_i \nu_j r_{ij} \ (i,j = \mathrm{S}, \mathrm{P}, \mathrm{p}) \tag{36.11}$$

The solution of Eq. (36.10) gives the distribution of the chemical affinity of the reaction within the enzyme membrane, $A(x)$, in general, as

$$A(x) = \frac{A(a)\sinh(x/\lambda) + A(0)\sinh[(a-x)/\lambda]}{\sinh(a/\lambda)} \tag{36.12}$$

where the membrane is assumed to be bound by two planes normal to the x axis at $x = 0$ and $x = a$.

Next, the phenomenological coefficients included in the expression of the relaxation length [Eq. (36.11)] will be considered for the case of the enzymatic reaction in the membrane system.

Based on the Michaelis-Menten reaction mechanism, in general, the enzymatic reaction scheme for the hydrolysis of the phosphoric acid monoester is expressed as

$$\mathrm{E} + \mathrm{S} \underset{k_2}{\overset{k_1}{\rightleftharpoons}} \mathrm{X} \underset{k_4}{\overset{k_3}{\rightleftharpoons}} \mathrm{E} + \mathrm{P} + \mathrm{p} \tag{36.13}$$

where E, S, X, P, and p denote the enzyme (acid phosphatase), the substrate (4-nitrophenyl phosphate), the enzyme–substrate complex, the main product (4-nitrophenol), and phosphoric acid, respectively; $k_1, k_2, k_3,$ and k_4 are rate constants. Because the enzyme catalyzes the hydrolysis of the substrate, the total reaction can be regarded as a first order reaction

$$\mathrm{S} \underset{k_-}{\overset{k_+}{\rightleftharpoons}} \mathrm{P} + \mathrm{p} \tag{36.14}$$

where k_+ and k_- are the rate constants.

First, we consider the phenomenological coefficient l_{chem} according to the rate law of the first-order reaction with respect to the substrate [Eq. (36.14)], as

$$v = k_+ c_\mathrm{S} - k_- c_\mathrm{P} c_\mathrm{p} \tag{36.15}$$

where c denotes the concentration for each species. The rate equation can be expressed in terms of the chemical affinity for the reaction [Eq. (36.14)], as

$$v = k_+ c_\mathrm{S} \left[1 - \exp\left(-\frac{A}{RT}\right)\right] \tag{36.16}$$

where A can be given as a function of the concentrations and the standard chemical potentials, μ^0, as

$$A = -(\mu_\mathrm{P} + \mu_\mathrm{p} - \mu_\mathrm{S}) = -\Delta\mu^0 + RT \ln \frac{c_\mathrm{S}}{c_\mathrm{P} c_\mathrm{p}} \tag{36.17}$$

$$\Delta\mu^0 = \mu_\mathrm{P}^0 + \mu_\mathrm{p}^0 - \mu_\mathrm{S}^0 \tag{36.18}$$

where the activity coefficients for the solutes (reactants and products) are assumed to be unity. In the range of the steady state, it can be assumed that $A/RT \ll 1$ holds for the chemical affinity of the reaction. In this linear region, provided that $\exp(-\Delta\mu^0/RT) \equiv K = k_+/k_-$, the following expression for the reaction rate can be obtained from Eq. (36.16) [K is the equilibrium constant for the reaction, Eq. (36.14)]:

$$v = k_+ c_\mathrm{S} \left(\frac{A}{RT}\right) \tag{36.19}$$

Comparing Eq. (36.19) with the last equation in the phenomenological equation, Eq. (36.4), we obtain

$$l_{chem} = \frac{k_+ c_\mathrm{S}}{RT} \tag{36.20}$$

Taking into account the Michaelis-Menten mechanism as represented by Eq. (36.13), the rate equation can be obtained under a steady-state condition, $dc_\mathrm{X}/dt = 0$:

$$v = \frac{dc_\mathrm{P}}{dt} = \frac{k_1 k_3 c_\mathrm{S} c_\mathrm{E}^0 - k_2 k_4 c_\mathrm{P} c_\mathrm{p} c_\mathrm{E}^0}{k_2 + k_3 + k_1 c_\mathrm{S} + k_4 c_\mathrm{P} c_\mathrm{p}} \tag{36.21}$$

$$= \frac{\dfrac{k_3 c_\mathrm{S} c_\mathrm{E}^0}{K_\mathrm{M}} - \dfrac{k_2 c_\mathrm{P} c_\mathrm{p} c_\mathrm{E}^0}{K_\mathrm{P}}}{1 + \dfrac{c_\mathrm{S}}{K_\mathrm{M}} + \dfrac{c_\mathrm{P} c_\mathrm{p}}{K_\mathrm{P}}} \tag{36.22}$$

where c_E^0 is the initial concentration of the enzyme:

$$K_\mathrm{M} = \frac{k_2 + k_3}{k_1} \quad K_\mathrm{P} = \frac{k_2 + k_3}{k_4} \tag{36.23}$$

By making the right side of Eq. (36.21) equal to zero, the ratio of the rate constants for the total reaction of the enzymatic reaction [Eq. (36.14)], k_+/k_-, can be confirmed to be a function of only the rate constants in the Michaelis-Menten mechanism as [10]

$$\frac{k_+}{k_-} = \frac{k_1 k_3}{k_2 k_4} \tag{36.24}$$

Since the most important case for our enzyme–membrane system as a membrane reactor device for the residual organic compounds in water is the low concentration range of the reactant in external water, we consider the limited region of the substrate concentration, $c_\mathrm{S} \ll K_\mathrm{M}$. This substrate concentration condition leads the following equation [Eq. (36.25)] provided that $c_\mathrm{P} c_\mathrm{p} \ll K_\mathrm{P}$. The latter condition generally holds for the Michaelis-Menten mechanism; in other words, the rate of the backward reaction for the products is negligible:

$$v = \frac{k_3 c_\mathrm{S} c_\mathrm{E}^0}{K_\mathrm{M}} - \frac{k_2 c_\mathrm{P} c_\mathrm{p} c_\mathrm{E}^0}{K_\mathrm{P}} \tag{36.25}$$

On the basis of this equation, it turns out that the phenomenological coefficient l_{chem} can be expressed in terms of the kinetic parameters for the enzymatic reaction as

$$l_{chem} = \frac{k_3 c_\mathrm{E}^0 c_\mathrm{S}}{K_\mathrm{M} RT} = \frac{V_\mathrm{max} c_\mathrm{S}}{K_\mathrm{M} RT} \tag{36.26}$$

where V_max and K_M are the maximum value of the enzymatic reaction rate and the Michaelis constant for the enzyme membrane, respectively, which can be obtained from analysis of the substrate concentration dependence of the reaction rate.

The other factor that determines the relaxation length λ is the resistance for the transport of reaction participants, as represented by Eq. (36.11). The resistance for the transport is related to the friction for transport through the membrane.

We assume that two participants, substrate S and the reaction product P, diffuse within the membrane. According to Spiegler's treatment [11], the diffusion coefficient of species i, namely, D_i, is expressed in terms of the friction coefficients provided that the friction between two solutes is negligible as

$$D_i = RT/(f_{iw} + f_{im}) \ (i = \mathrm{S}, \mathrm{P}) \tag{36.27}$$

where f_{iw} and f_{im} denote the friction coefficients between i and the solvent, and i and the membrane matrix, respectively. The linear relation between the diffusional flux $J_i = c_i v_i$ and its conjugate driving force $\nabla(-\mu_i)$ is given as follows:

$$\nabla(-\mu_i) = (f_{iw} + f_{im})\frac{J_i}{c_i} \ (i = \mathrm{S}, \mathrm{P}) \tag{36.28}$$

Therefore, in this membrane system, it is evident from the first equation of Eq. (36.5) that the resistance coefficients are expressed as

$$v_i v_S r_{iS} + v_i v_P r_{iP} = RT/D_i c_i \quad (i = \mathrm{S}, \mathrm{P}) \tag{36.29}$$

We have assumed that the effect of the small ion, that is, phosphate anion (p), can be neglected. Finally, summation of the resistance coefficients in Eq. (36.11) leads to the following equation:

$$\sum_{i,j} v_i v_j r_{ij} = RT\left(\frac{1}{D_\mathrm{S} c_\mathrm{S}} + \frac{1}{D_\mathrm{P} c_\mathrm{P}}\right) \tag{36.30}$$

Substituting Eqs. (36.26) and (36.30) into Eq. (36.11), we obtain the expression for the relaxation length that has the dimension of length:

$$\lambda = \left[\frac{K_\mathrm{M}}{V_{\max} c_\mathrm{S}}\left(\frac{1}{D_\mathrm{S} c_\mathrm{S}} + \frac{1}{D_\mathrm{P} c_\mathrm{P}}\right)^{-1}\right]^{1/2} \tag{36.31}$$

36.3 RESULTS AND DISCUSSION

36.3.1 Membrane Permeation across the Ionomer Membrane

Under the same conditions concerning solution pH values, the stirring speeds in the internal and external solutions and temperature for the measurements for the immobilized enzyme membrane, the flux measurements were carried out separately [6] for the product, 4-nitrophenol (PNP), and the reactant, 4-nitrophenyl phosphate (PNPP), across the perfluorocarboxylate ionomer membrane of the sodium form that was used as the supporting membrane for the enzyme immobilization. A perfluorocarboxylate polymer membrane

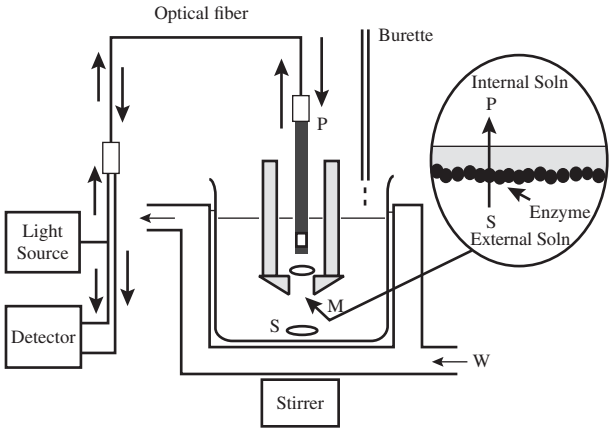


FIGURE 36.1 Schematic diagram of assembled system for measurements of flux across the perfluorocarboxylate ionomer membrane with or without the immobilized enzyme. Time dependence of the absorption spectrum was followed using an immersed probe (P) connected to a fiberoptic UV spectrophotometer. Arrows (→) show the path of the ultraviolet radiation. The membrane, magnetic spin bar, and thermostatically controlled water are designated by M, S, and W, respectively. (Adapted from Ref. 6.)

(Flemion 230, kindly supplied by the Asahi Glass Co., Tokyo, with an ion exchange capacity of 1.4 mmol univalent ion/dry [12]) was used as the supporting material for the enzyme. Initially, both the external and internal solutions contained only 0.1 moldm^{-3} NaCl. The pH values of both compartments were adjusted with a 0.1 moldm^{-3} sodium acetate buffer (pH = 4.8). The flux measurement was started by injecting a small volume of the 4-nitrophenyl phophate solution or 4-nitrophenol solution into the external solution. The timecourse of the concentration was followed by the fiberoptic spectrometer setup shown in Fig. 36.1 at 25.0°C. Each compartment was stirred at a speed of 650 rpm.

A higher permeability has been observed for 4-nitrophenol in contrast to 4-nitrophenyl phosphate, to which this membrane exhibits no significant permeability under the conditions of the experiments. An example of the time course for the amount of each compound transported across the membrane without the enzyme is shown in Fig. 36.2. The steady-state flux of 4-nitrophenol J_P has been obtained from the slope of the linear portion after a transient region in the timecourse curve.

According to the time lag method, the diffusion coefficient was obtained from the timecourse curve of the amount transported across the ionomer membrane. The time lag was obtained from the point where the straight line in a range of steady state and the baseline intersect, as demonstrated in Fig. 36.2. The time lag θ is expressed in terms of the diffusion coefficient D and the membrane thickness, a, as [13]

$$\theta = \frac{a^2}{6D} \tag{36.32}$$

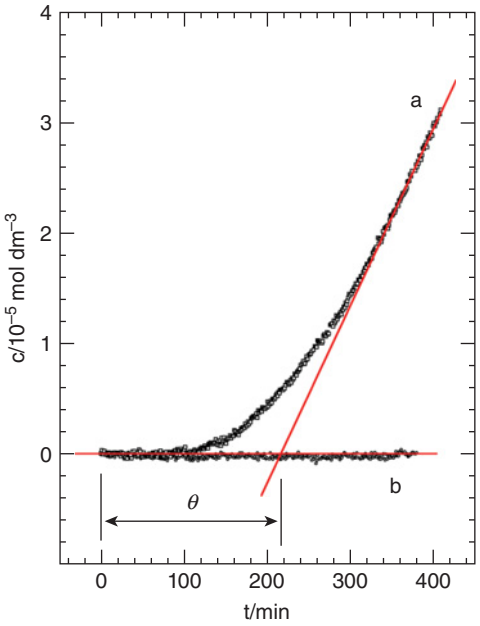


FIGURE 36.2 Typical time dependence of concentration of 4-nitrophenol in internal solution obtained from change in optical absorbance at 317 nm (a) and that of 4-nitrophenyl phosphate in the internal solution obtained from change at 310 nm (b). Initially, both the external and internal solutions contained a 0.1 mol dm^{-3} acetate buffer solution (pH 4.8) and 0.1 mol dm^{-3} NaCl. A small amount of the aqueous solution of 4-nitrophenol (or 4-nitrophenyl phosphate) was injected into the external solution at time zero. The initial concentration of 4-nitrophenol (or 4-nitrophenyl phosphate) just after the injection in the external solution was 1×10^{-2} mol dm^{-3}. Time lag θ is shown by the point where the straight line in the steady state and the base line intersect. (Adapted from Ref. 7.)

According to this equation, the diffusion coefficient D for the ionomer membrane was obtained as 8.0×10^{-9}cm^{2}s^{-1}.

36.3.2 Immobilization of Enzyme

As described in a previous paper [6], 30 μL of a mixture of 25 μL of the enzyme solution (10 mg/mL acid phosphatase, EC 3.1.3.2, from potato, CalBiochem) and 25 μL of the aqueous buffer solution (0.1 mol dm^{-3} sodium acetate buffer pH 4.8 with 0.1 mol dm^{-3} NaCl) was placed on the surface of the one side of the perfluorinated carboxylate ionomer membrane (Flemion 230, Asahi Glass Co.). After leaving it at 25°C for one hour, the membrane with the enzyme was stored at 5°C overnight. After the membrane covered with the enzyme suspension was restored at room temperature, 50 μL of the mixed solution of the cross-linking reagent (2.5 wt% glutaraldehyde solution) [14–16] with an equivalent volume of the phosphate buffer solution (pH 7.4) was placed into the enzyme suspension on the membrane surface. After one hour, one side of the membrane, over which the enzyme was immobilized in the micropores, was washed with 0.1 mol dm^{-3} NaCl solution. The immobilized enzyme membrane mounted in the cell assembly was stored at 5°C before the flux measurement.

36.3.3 Hydrolysis of 4-Nitrophenylphosphate across Immobilized Enzyme Membrane

The assembled measuring system for the flux of the hydrolysis product is schematically illustrated in Fig. 36.1. The area of the membrane surface adjacent to the solution (diffusion area) was 0.20 cm^2. Initially, both the external and internal solutions contained only 0.1 mol dm^{-3} NaCl. The measurement was started by injecting the substrate solution into the external solution. On the basis of the distinct difference between the membrane permeability to the reaction product and that to the reactant (substrate), a membrane reactor system has been designed. Acid phosphatase (EC 3.1.3.2) from potato was immobilized on the perfluorocarboxylate ionomer membrane by placing the enzyme solution on the supporting membrane without suction. Disodium 4-nitrophenyl phosphate was used as the substrate for the enzyme-catalyzed reaction. The pH of either solution in the membrane system for the measurements was adjusted to 4.8 using a 0.1 mol dm^{-3} sodium acetate buffer.

Because the ionomer membrane exhibits a high permeability only to the reaction product (4-nitrophenol), the liberation of 4-nitrophenol in the enzyme membrane produces the diffusional flux of the product to the internal solution. After the flux measurement, the pH of the internal solution was adjusted to pH 8.5, then the UV absorption spectrum of the solution was measured to confirm that the absorbance of the 4-nitrophenyl phosphate near its absorption maximum, 310 nm, was not entirely detected, while the absorption due to 4-nitrophenol at 400 nm was observed. The flux of the reaction product J_P at the steady state was obtained from the slope of the linear portion of the timecourse curve for the amount of the reaction product in the internal solution. All the measurements were carried out at 25.0°C. The internal and external compartments were stirred at a speed of 650 rpm.

From the dependence of J_P on the initial substrate concentration c_S of the external solution, the Michaelis constant for the immobilized acid phosphatase K_M^* and the maximum flux of the reaction product J_P^{max} were determined [6,17,18]. The dependence of J_P on the substrate concentration has been found to follow the relation of the Michaelis-Menten type (Fig. 36.3a):

$$J_P = \frac{J_P^{max} c_S}{K_M^* + c_S} \tag{36.33}$$

From the double reciprocal plot of $1/J_P$ vs. $1/c_S$, the Lineweaver–Burk plot, (correlation coefficient; $R = 0.999$) as shown in Fig. 36.3b, we have obtained K_M^* and J_P^{max}. These

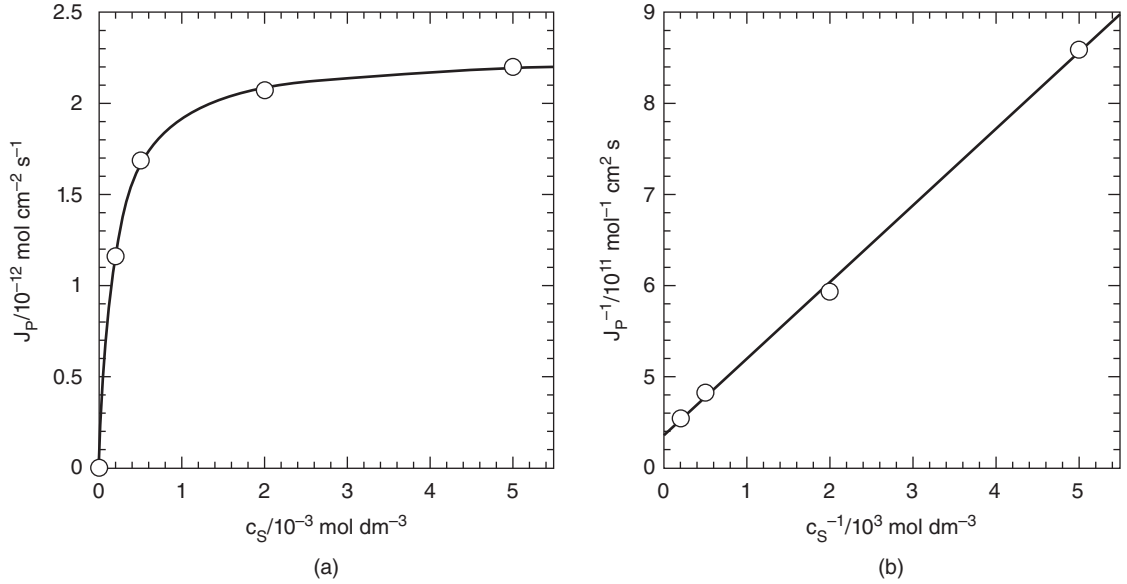


FIGURE 36.3 (a) Substrate concentration dependence of flux of hydrolysis product across enzyme membrane at pH 4.8. The steady-state flux of 4-nitrophenol produced during the hydrolysis of 4-nitrophenyl phosphate in the enzyme membrane system J_P was determined by following the absorption spectra of the internal solution. (Adapted from Ref. 6.) (b) Plot of $1/J_P$ versus $1/c_S$ for the enzyme membrane system [panel (a)].

values of K_M^* and J_P^{max} are listed in Table 36.1 together with the maximum velocity and the Michaelis constant K_M for the free enzyme reaction in an aqueous solution. For the acid phosphatase from potato, K_M values reported in the literature are 4.9×10^{-4} mol dm^{-3} in maleate buffer, pH 6.0, at 37°C [19], 4.3×10^{-4} mol dm^{-3} in acetate buffer, pH 4.9, at 38°C [20], and 6.2×10^{-4} mol dm^{-3} in acetate buffer, pH5.5, at 38°C [21].

The relation between the diffusional flux and the reaction rate of the enzymatic reaction for the enzyme membrane under the steady state condition will be given in the next section.

36.3.4 Degree of Coupling between Reaction Rate and Diffusional Flux in the Enzyme Membrane System

According to the theoretical consideration in the preceding section, the relaxation length λ for the enzyme membrane can be evaluated as a parameter for the region (depth in the x-axis direction from the membrane surface) where the enzymatic reaction proceeds accompanied by diffusion of the reaction participants.

TABLE 36.1 Michaelis-Menten Parameters for Fluxes across Enzyme Membrane (Immobilized Acid Phosphatase from Potato) and for Free Enzyme (Acid Phosphatase from Potato)

	K_M (mol dm^{-3})	J_P^{max} (mol cm^{-2}s^{-1})	V_{max} (mol dm^{-3}s^{-1})
Enzyme membrane	1.92×10^{-4}	2.29×10^{-12}	
Free enzyme	8.1×10^{-5}		3.7×10^{-8}

We first consider a limiting case in which the resistance coefficients for the product (PNP) and those for the substrate (PNPP) are equal (i.e., $r_{SS} - r_{SP} = -r_{SP} + r_{PP}$), then $1/D_S c_S = 1/D_P c_P$. The effects of the ratio of the two terms, $1/D_S c_S$ and $1/D_P c_P$, on the value of λ will be investigated later. For this limiting case, the following equation for the relaxation length can be obtained from Eq. (36.31):

$$\lambda = \left(\frac{2K_M}{V_{max}} D_P\right)^{1/2} \tag{36.34}$$

Under the steady-state condition, we obtain the following relation from Eq. (36.7)

$$\left(\frac{\partial J_S}{\partial x}\right) = -\left(\frac{\partial J_P}{\partial x}\right) = -v \tag{36.35}$$

where subscripts S and P refer to the substrate (PNPP) and the reaction product (PNP), respectively. The enzymatic reaction rate, v, denotes the local velocity of the reaction. Integrating Eq. (36.35) from the membrane surface on the external substrate solution side, $x = 0$, to the other membrane surface on the internal solution side, $x = a$, we obtain

$$J_S(a) - J_S(0) = -\{J_P(a) - J_P(0)\} = -J_R \tag{36.36}$$

where

$$J_R \equiv \int_0^a v dx \tag{36.37}$$

Since we consider the situation where the substrate concentration at the membrane surface on the opposite side ($x = a$) is equal to zero, $J_S(a) = 0$. On the other hand, we consider the case when the external buffered solution contains only the substrate molecules so that $J_P(0) = 0$. Therefore, from Eq. (36.36), we obtain

$$J_S(0) = J_P(a) = J_R \tag{36.38}$$

The flux $J_P(a)$ is equivalent to the experimentally observed flux of P under the steady-state condition. It should be noted that Eq. (36.38) expresses the relation between the flux of the substrate from the external solution outside the membrane and the rate of the reaction through which the substrate molecules are consumed within the enzyme membrane, and that between the reaction rate and the flux of the product toward opposite-side solution, which is observed. This supports the experimentally observed fact that the flux of P is expressed in terms of a Michaelis-Menten-type equation [Eq. (36.33)]. By using the averaged reaction rate of the enzymatic reaction within the membrane, $\bar{v}$ ($= \{\int v dx\}/a$), we can rewrite Eq. (36.38) as

$$\bar{v} = \frac{J_P}{a} \tag{36.39}$$

Accordingly, the maximum velocity of the enzymatic reaction, V^*_{max}, and the maximum flux, J_P^{max}, which has been obtained from the reciprocal plot for the product flux across the enzyme membrane (listed in Table 36.1) can be related as

$$V^*_{max} = \frac{J_P^{max}}{a} \tag{36.40}$$

The maximum velocity for the enzyme membrane has been obtained according to Eq. (36.40). As a result, for this case, the relaxation length λ was obtained using Eq. (36.34) to be 29.0 μm.

The distribution of the affinity of the reaction in the enzyme membrane can be obtained from Eq. (36.12). Since we consider the case where the concentration of the substrate at the surface, $x = a$, is zero, then

$$A(a) = 0 \tag{36.41}$$

so that we obtain

$$\frac{A(x)}{A(0)} = \frac{\sinh[(a-x)/\lambda]}{\sinh(a/\lambda)} \tag{36.42}$$

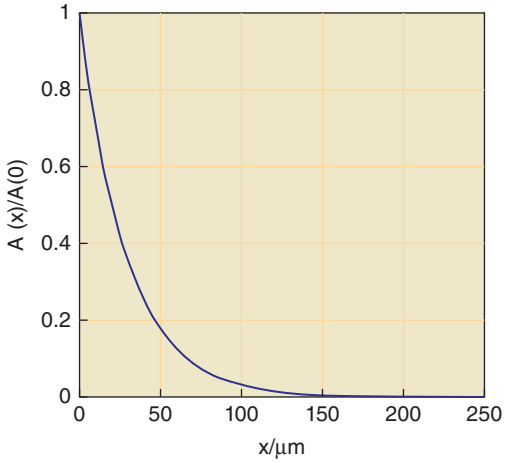


FIGURE 36.4 Affinity distribution $A(x)$ within acid phosphatase–immobilized membrane for case 1: $\lambda = 29$ μm. (Ref. 7)

Figure 36.4 shows the affinity distribution calculated using Eq. (36.42) (case 1). The value of a was 250 μm (membrane thickness [6]).

When the bound enzyme is not uniformly distributed throughout the membrane, it is likely that the inert layer in which the enzyme is not immobilized exists with a certain thickness. For preparation of the enzyme membrane, immobilization of the enzyme was carried out spontaneously by placing the enzyme solution on the external solution-side surface of the supporting membrane without suction. Therefore, the enzyme immobilized onto the surface region is not likely to be fully distributed into the core region of the membrane far from the membrane surface [22]. As the next example, consider the case where the enzyme is immobilized only in the active layer within which the enzyme's distribution is uniform (case 2).

The distribution of the affinity was calculated according to Eq. (36.42). The thickness of the inert layer is denoted by δ ($a + \delta = 250$ μm). As seen from the balanced equation [Eq. (36.6) for P], Eq. (36.43) holds in the inert layer under the steady-state condition:

$$\frac{dJ_P}{dx} = 0 \tag{36.43}$$

Therefore, the flux of the product is independent of the position within the inert layer and at the interface on the internal solution side. The calculated results for case 2 are plotted for each value of the active layer thickness a in Fig. 36.5.

So far, it has been assumed that the contributions of the frictional term for the product and that for the substrate are comparable in the expression of λ. The influence of the frictional terms on the affinity distribution is being investigated. The results of the calculations are shown in Fig. 36.6. It is

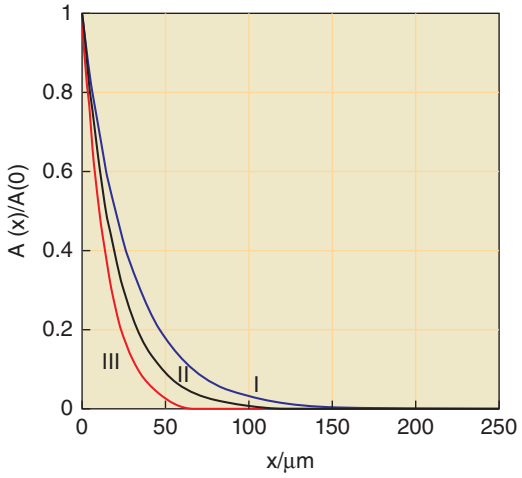


FIGURE 36.5 Affinity distribution $A(x)$ for acid phosphatase–immobilized membrane for case 2. Curve I: inert layer's thickness, $\delta = 0$ μm. Curve II: $\delta = 125$ μm. Curve III: $\delta = 182.5$ μm. (Ref. 7)

seen from the comparison in this figure that the influence of the relative value of the frictional terms, $1/D_S c_S$ and $1/D_P c_P$, is not very significant.

In boundary regions including membranes as a barrier for mass transports, an invariant concentration distribution for each chemical species is formed under the stationary-state condition. In the case where chemical reactions occur within the boundary region, the concentration distribution is changed depending on the reaction rate. The reaction layer thickness due to the acetaldehyde oxidation catalyzed by alcoholdehydrogenase has been evaluated from the steady-state pH distribution in the unstirred layer near the bilayer lipid membrane, which was measured by the microelectrode method, by one group of

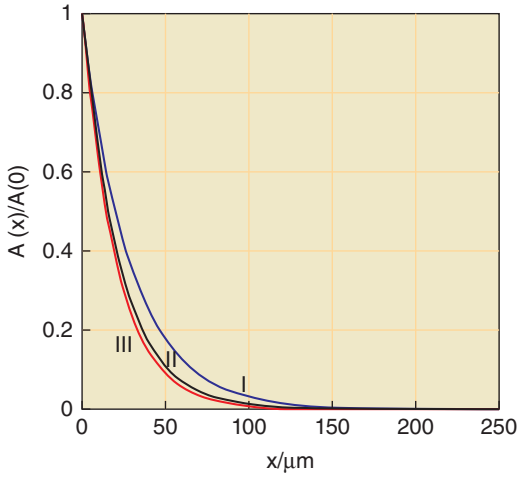


FIGURE 36.6 Influence of frictional terms $(1/D_i c_i)$ on $A(x)$ in case 1 ($\delta = 0$ μm). Curve I: $1/D_S c_S = 1/D_P c_P$ i.e., case 1. Curve II: $1/D_S c_S = 5/D_P c_P$. Curve III: $1/D_S c_S \gg 1/D_P c_P$. (Ref. 7)

TABLE 36.2 Amount of Immobilized Acid Phosphatase from Sweet Potato onto Cation Exchange Membrane

	E (U) [a]	E_1 (U) [b]	E_2 (U) [c]	E_3 (U) [d]	E_{total} (U) [e]
Membrane a	2.13	0.848	0.016	0.021	0.88
Membrane b	10.04	2.627	0.036		2.66

[a] Amount of enzyme placed on surface of cation exchange membrane.
[b] Amount of enzyme immobilized by first immobilization.
[c] Amount of enzyme immobilized by second immobilization.
[d] Amount of enzyme immobilized by third immobilization.
[e] The sum of E_1, E_2, and E_3.
Source: Adapted from Ref. 25.

investigators [23]. In their membrane system, the enzyme exists in the aqueous phase in the membrane vicinity. On the other hand, the concentration distribution of the reacting species or the product in the enzyme layer of the biosensor in operation was investigated for the glucose oxidation catalyzed by glucose oxidase, where a platinum microtip was used for the scanning electrochemical microscopic measurements [24].

36.3.5 Quantity of Immobilized Acid Phosphatase

Two enzyme membranes with different amounts of the immobilized enzyne were prepared separately [25]. Acid phosphatase (EC 3.1.3.2) from sweet potato with a protein concentration of 57 mg/mL was obtained as a suspension with 1.8 mol dm^{-3} aqueous $(NH_4)_2SO_4$ (Sigma, St. Luis). The perfluorocarboxylate ion-exchange membrane (Flemion 230, kindly supplied by the Asahi Glass Co., Tokyo, with an ion exchange capacity of 1.4 mmol univalent ion/g dry) was mounted in the cell for the flux measurements. The mixed suspension of the enzyme and aqueous acetate buffer solution was placed on the surface of the external solution side of the ion exchange membrane. After leaving it at 25°C for one hour, the enzyme suspension on the membrane was removed and diluted with 0.1 mol dm^{-3} acetate buffer to analyze the enzyme activity. Two enzyme membranes of different enzyme amounts were prepared. For these enzyme membranes, the immobilization process mentioned above was carried out 2 or 3 times. The cell for the measurement with approximately 2 mL of an internal solution of acetate buffer was stored at 5°C, while the flux measurements were not carried out. The amount of the enzyme placed on the membrane for the immobilization E and that of the immobilized enzyme on the membrane E_n, are shown in Table 36.2. Thus, this immobilization procedure for acid phosphatase from sweet potato involves only a process of incorporating the enzyme into the micropores of the perfluorinated ionomer membrane without any cross-linking reagent.

For free enzyme in aqueous solution of a 0.1 mol dm^{-3} acetate buffer (pH 4.8), the enzymatic reaction rate of hydrolysis of PNPP was investigated. From the Hanes–Woolf plot

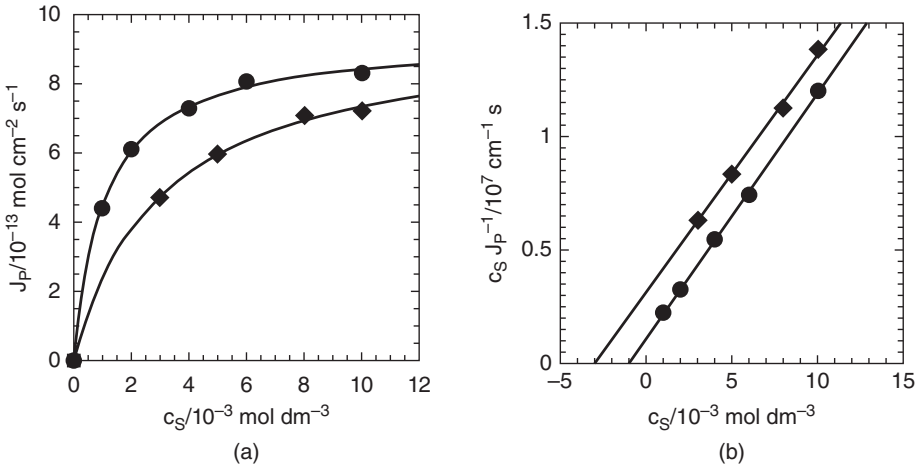


FIGURE 36.7 (a) Substrate concentration dependence of flux of reaction product across immobilized enzyme membranes at pH 4.8. Quantity of immobilized acid phosphatase from sweet potato for each membrane was determined: ♦ 0.88 enzyme U (M-a), ● ; 2.66 enzyme U (M-b). (Adapted from Ref. 25.) (b) Plot of Hanes–Woolf type for immobilized enzyme membranes [panel (a)], ♦ M-a, ● ; M-b. (Adapted from Ref. 25.)

for the initial reaction rate, the Michaelis constant K_M was determined to be 6.14×10^{-5} mol dm^{-3}. The values of K_M reported in the literature are 6.8×10^{-5} mol dm^{-3} (in 0.2 mol dm^{-3} acetate buffer, pH 5.8, at 35°C) [26] and 1.4×10^{-4} mol dm^{-3} (in 0.1 mol dm^{-3} acetate buffer, pH 5.6, at 40°C) [27]. The dependence of the enzyme activity on the enzyme unit in bulk solution was investigated at a fixed high concentration of PNPP in the saturated region of the initial rate versus the substrate concentration curve. The initial concentration of PNPP was 5×10^{-4} mol dm^{-3}. A linear relationship exists between the reaction rate and the enzyme unit. Using this calibration curve, the change in the amount of the enzyme placed on the membrane after each immobilization step was determined.

Flux measurements were carried out using the same apparatus as illustrated in Fig. 36.1. The layer of immobilized acid phosphatase was on the external solution side of the membrane. Initially, external and internal solutions contained only 50 mL and 2 mL of 0.1 mol dm^{-3} acetate buffer (pH = 4.8), respectively. The reaction was started by injecting a small volume of 0.1 mol dm^{-3} PNPP into the external solution. The amount of PNP transported into the internal solution was followed by measuring the timecourse of the optical absorbance at 317 nm. In Fig. 36.7a, the dependence of the PNP flux in a stationary state on the initial substrate concentration is shown for the two enzyme membranes.

In Fig. 36.7b, the flux divided by the initial substrate concentration is plotted against the initial substrate concentration (Hanes–Woolf-type plot). In this plot, the x intercept and the slope give K_M, and $1/J_{max}$, reespectively. The determined value of K_M and J_{max} are shown in Table 36.3.

In both enzyme membranes, the enzyme–substrate affinity was apparently lower than that in the solution. The amount of the immobilized enzyme is thought to have an effect on the enzyme–substrate affinity. The value of the maximum flux J_{max}, divided by the amount of the immobilized enzyme on the membrane E_{total}, can be regarded as the enzyme activity per unit. Compared to the free state of the enzyme, the immobilized enzyme on the membrane would be in a dense state. In the enzymatic reaction, the enzyme forms a complex with the substrate. Thus, the reaction proceeds through a intermediate state formed by the interaction of the substrate with the active site of the enzyme. This suggests a possible effect of the dense state of the enzyme on the formation of the enzyme–substrate complex.

TABLE 36.3 Michaelis Constant and Maximum Flux for Immobilized Enzyme Membrane

	K_M (10^{-3} mol dm^{-3})	J_{max} (10^{-13} mol cm^{-2} sec^{-1})	$J_{max}\ E_{total}^{-1}$ (10^{-13} mol cm^{-2} sec^{-1} U^{-1})
Membrane a	3.00	9.99	11.35
Membrane b	1.00	9.25	3.48

Source: Adapted from Ref. 25.

REFERENCES

[1] Prigogine, I. (1967). *Introduction to Thermodynamics of Irreversible Processes*, 3rd ed. Interscience Publishers, New York, pp. 40–54.

[2] Katchalsky, A., Oster, G. (1969). In Tosteson, D.C. (ed.), *The Molecular Basis of Membrane Function.* Prentice-Hall, Englewood-Cliffs, NJ, pp. 1–44.

[3] Volkenshtein, M.V. (1983). *Biophysics.* Mir Publishers, Moscow, pp. 313–345.

[4] Goldman, R., Kedem, O., Katchalski, E. (1968). *Biochemistry* **7**, 4518–4532.

[5] Horvath, C., Engasser, J.M. (1974). *Biotechnol. Bioeng.* **16**, 909–923.

[6] Nomura, K., Liu, M. (2006). *Bull. Chem. Soc. Jpn.* **79**, 343–347.

[7] Nomura, K., Miyawaki, H. (2014). *Bull. Chem. Soc. Jpn.* **87**, 809–815.

[8] Katchalsky, A., Curran, P.F. (1965). *Nonequilibrium Thermodynamics in Biophysics*. Harvard Univ. Press, Cambridge, MA, pp. 85–97.

[9] Caplan, S.R., Essig, A. (1983). *Bioenergetics and Linear Nonequilibrium Thermodynamics*. Harvard Univ. Press, Cambridge, MA, pp. 24–53.

[10] Alberty, R.A., Silbey, R.J. (1992). *Physical Chemistry.* Wiley, New York, pp. 730–735.

[11] Spiegler, K.S. (1958). *Trans. Faraday Soc.* **54**, 1408–1428.

[12] Nomura, K., Koga, T. (2001). *J. Colloid Interface Sci.* **241**, 428–433.

[13] Crank, J. (1975). *The Mathematics of Diffusion*, 2nd ed. Clarendon Press, Oxford, UK, pp. 47–64.

[14] Gilbault, G.G. (1984). *Analytical Uses of Immobilized Enzymes.* Marcel Dekker, New York, pp. 77–111.

[15] Mulchandani, P., Mulchandani, A., Kaneva, I., Chen, W. (1999). *Biosens. Bioelectron.* **14**, 77–85.

[16] Sacks, V., Eshkenazi, I., Neufelt, T., Dosoretz, C., Rishpon, J. (2000). *Anal. Chem.* **72**, 2055–2058.

[17] Giorno, L., Drioli, E., Carvoli, G., Cassano, A., L. Donato, L. (2001). *Biotechnol. Bioeng.* **72**, 77–84.

[18] Uragami, T., Ueguchi, K., Watanabe, M., Miyata, T. (2006). *Catal. Today* **118**, 158–165.

[19] Marzadori, C., Gessa, C., Ciurli, S. (1998). *Biol. Fertil. Soils* **27**, 97–103.

[20] Alvarez, E.F. (1962). *Biochim. Biophys. Acta* **59**, 663–672.

[21] Bingham, W.E., Farrell, H.M. Jr., Dahl, K.J. (1976). *Biochim. Biophys. Acta* **429**, 448–460.

[22] Liu, Z.-M., Dubremetz, J.-F., Richard, V., Yang, Q., Xu, Z.-K., Seta, P. (2005). *J. Membr. Sci.*, **267**, 2–7.

[23] Antonenko, Y.N., Pohl, P., Rosenfeld, E. (1996). *Arch. Biochem. Biophys.* **333**, 225–232.

[24] Csóka, B., Kovács, B., Nagy, G. (2003). *Biosens. Bioelectron.* **18**, 141–149.

[25] Takeda, H., Tanaka, H., Nomura, K. (2010). *Chem. Lett.* **39**, 1102–1103.

[26] Uehara, K., Fuzimoto, S., Taniguchi, T., Nakai, K. (1974). *J. Biochem.* **75**, 639–649.

[27] Yamato, S., Kawakami, N., Shimada, K., Ono, M., Idei, N., Itoh, Y. (2000). *Anal. Chim. Acta* **406**, 191–199.

37

EVALUATION OF ZETA-POTENTIAL OF INDIVIDUAL EXOSOMES SECRETED FROM BIOLOGICAL CELLS USING A MICROCAPILLARY ELECTROPHORESIS CHIP

Takanori Akagi and Takanori Ichiki
Department of Bioengineering, Graduate School of Engineering, University of Tokyo

37.1 INTRODUCTION

Biological cells are known to secrete membrane vesicles, which are called *exosomes* and *microvesicles*, with specific characteristics including size and composition [1]. Exosomes are small vesicles (30–100 nm) released by exocytosis from multivesicular bodies (MVBs) of the endosomes of cells and contain an array of proteins, lipids, and nucleic acids derived from the parent cells. More recent studies have revealed that regardless of the distance between cells, exosomes participate in intercellular communication in the immune system, cancer development, and cancer metastasis, for example, by stabilizing the circulating microRNA (miRNAs) and mRNAs in the ribonuclease (RNase)-rich environment of body fluids [2]. Furthermore, exosomes have the potential for use in therapeutic and diagnostic applications including tumor-derived exosome-based cancer vaccines [3] and exosomal RNA-based diagnostic and prognostic markers [4]. However, there is little knowledge concerning their physical properties, such as the surface charge.

Electrostatic interaction is a strong interaction between an exosome and a cell; hence, evaluating zeta-potential, measures of surface electric charge, of exosomes is necessary for understanding the mechanisms of intercellular communications. Zeta-potential, which can be estimated from the electrophoretic mobility (EPM), is one of the electrical properties of exosomal surfaces. For evaluating zeta-potential of particles or cells, several automated zeta-potential analyzers can be used to measure the electrophoretic velocity of a number of particles or cells moving in a stationary plane within a short timeframe have been developed and are now commercially available [5]. However, they are not suitable for obtaining the precise distribution of the zeta-potential profile, especially when the samples are mixtures of heterogeneous particles because they cannot perform particle-by-particle measurement [6]. Hence, particle-by-particle measurement is also required for the electrrokinetic evaluation of exosomes.

On the basis of the abovementioned background, we have investigated the electrokinetic evaluation of exosomes using an on-chip microcapillary electrophoresis (μCE) system equipped with a laser darkfield microscope to realize the sensitive tracking of individual exosomes [7, 8].

37.2 EXOSOME PREPARATION

Exosome samples secreted from six types of cell, normal prostate epithelial PNT2 cells, prostate cancer PC3 and PC-3Mluc-C6 (PC-3ML) cells (Xenogen), normal breast epithelial MCF10A cells, and breast cancer MDA-MB-231 (MM231) and MDA-MB-231-luc-D3H2LN cells (MM231LN) (Xenogen) cells cultivated in vitro were collected and used in this study. The cells were grown to confluence in medium supplemented with 10% fetal bovine serum (FBS), 100 μg/mL kanamycin, 100 units/ml penicillin, and 100 μg/mL streptomycin in a humidified atmosphere of 95% air and 5% CO_2 at 37°C. Exosomes were prepared from the culture medium as described previously [9]. The culture

Encyclopedia of Biocolloid and Biointerface Science, Volume 1, First Edition. Edited by Hiroyuki Ohshima.
© 2016 John Wiley & Sons, Inc. Published 2016 by John Wiley & Sons, Inc.

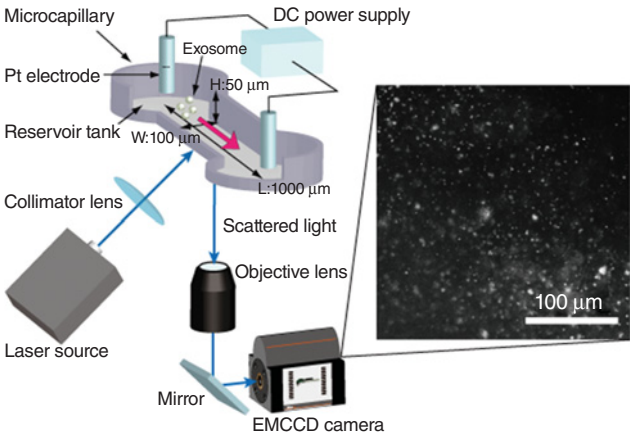


FIGURE 37.1 Schematic diagram (a) and photograph (b) of the on-chip microcapillary electrophoresis (μCE) system equipped with a laser darkfield microscope. This system enables the sensitive imaging of individual exosomes in a darkfield by detecting laser light scattered by exosomes using an EM-CCD camera.

medium was replaced with serum-free RPMI medium and the cells were incubated for 24 h. Exosomes were extracted from the supernatant of the serum-free cell culture medium by differential ultracentrifugation performed as follows. The cell culture was centrifuged twice at 2000 × *g* for 15 min using a centrifuge (Tomy LC-220) and the resulting supernatant was recentrifuged at 12,000 ×*g* for 35 min using an ultracentrifuge (Beckman Coulter Optima L-90K). Then, the clarified supernatant was subsequently ultracentrifuged at 110,000 × *g* for 70 min. The resulting pellets were washed in a large volume of phosphate buffered saline (PBS) and finally centrifuged at 110,000 × *g* for 70 min. The washed pellets containing exosomes were then suspended in PBS.

37.3 ELECTROPHORESIS SYSTEM FOR EXOSOMES

Figure 37.1 is a schematic diagram of the on-chip μCE system equipped with a laser darkfield microscope. The system comprises a μCE chip, a pair of platinum electrodes, a high-voltage DC power supply [Matsusada Precision HVL-1.1P(A)], a 488-nm laser source (50 mW, Melles Griot 85-BCD-030-053), an inverted microscope (Nikon Ti-U), and an electron multiplying charge-coupled device (EM-CCD) camera (Andor iXon3 897). The poly(dimethylsiloxane) (PDMS) μCE chip was fabricated using a method described previously [10].

Samples suspended in PBS (1.06 mM KH2PO4, 155.17 mM NaCl, 2.97 mM Na_2HPO_4•$7H_2$, pH = 7.4, ionic strength 0.16) were introduced into the flow channel of the μCE chip, and electrodes were placed in the reservoir tanks. After the μCE chip was mounted on the microscope, electrophoretic migration was recorded under an electric field of 50 V/cm. This on-chip μCE system enables the sensitive imaging of individual exosomes in a darkfield by detecting laser light scattered by exosomes using an EM-CCD camera. The electroosmosis velocity induced inside the microchannel was measured by suspending charge-free beads of 500 nm diameter (Otsuka Electronics) in the electrophoresis buffer in a control experiment conducted before and after each electrophoresis experiment. Since the measured velocity of the migrating samples includes the electroosmosis velocity weakly observed in the microchannel, the true EPM, μ_{ep} was calculated as follows

$$\mu_{ep} = (U_{em} - U_{eo})/E \tag{37.1}$$

where U_{em} is the apparent electrophoretic velocity, U_{eo} is the electroosmotic flow velocity, and E is the electric field strength (V/cm). Furthermore, the zeta-potentials ζ of exosomes were calculated from the measured EPM using the Smoluchowski equation

$$\mu_{ep} = \frac{\varepsilon_r \varepsilon_0}{\eta}\zeta \tag{37.2}$$

where η is the viscosity coefficient of the buffer solution, and ε_r and ε_0 are the relative permittivity of the solution and the permittivity of vacuum, respectively. Note that, strictly speaking, factors with some degree of uncertainty are unfortunately included in the Smoluchowski equation used to analyze the electrophoresis of biological particles such as exosomes. Hence, in this chapter, we use both zeta-potential and EPM as parameters to provide information about the surface charge of exosomes.

37.4 RELATION BETWEEN ZETA-POTENTIALS OF EXOSOMES AND THEIR ORIGINATING CELLS

The EPM distributions of both cells and exosomes derived from the parent cells are shown in Figs. 37.2 and 37.3 [7]. Figure 37.2a shows the zeta-potential distributions of exosomes derived from MCF10A, MM231, and MM231LN cells. The averages ± standard deviations of the zeta-potential distributions of exosomes were −8.8 ± 2.5 mV (MCF10A), −10.2 ± 2.4 mV (MM231), and −10.9 ± 2.3 mV (MM231LN). The zeta-potential distributions of exosomes derived from MM231and MM231LN cells showed negative shifts compared with those of exosomes derived from MCF10A. Figure 37.2b shows the zeta-potential distributions of MCF10A, MM231, and MM231LN cells. The averages ± standard deviations of these zeta-potential distributions were −9.2 ± 2.1 mV (MCF10A), −10.9 ± 1.9 mV (MM231), and −11.6 ± 2.1 mV (MM231LN). Interestingly, the zeta-potentials of exosomes from tumor cells tend to show a negative shift compared with those of exosomes from normal cells (p <0.05,

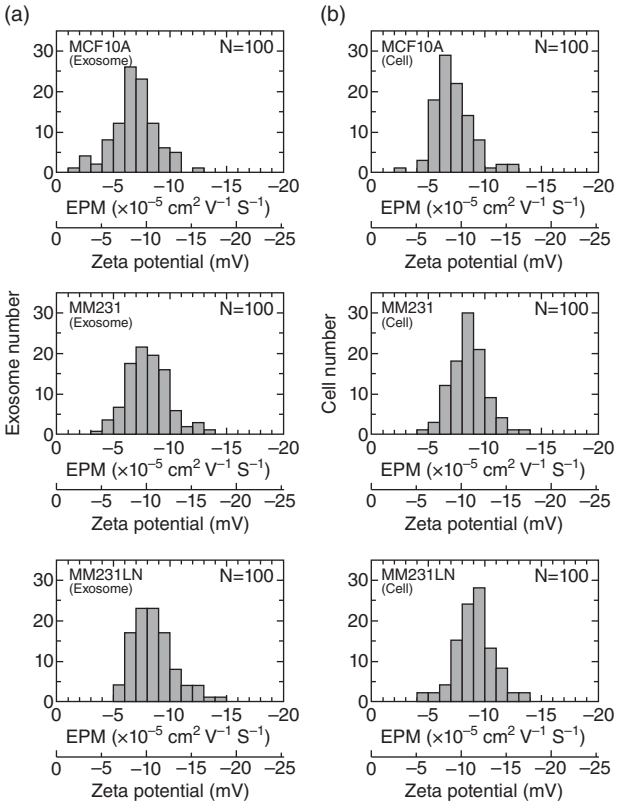


FIGURE 37.2 (a) Zeta-potential distributions of exosomes derived from normal breast epithelial cells (MCF10A), and breast cancer cells (MM231 and MM231LN). (b) Zeta-potential distributions of MCF10A, MM231, and MM231LN cells.

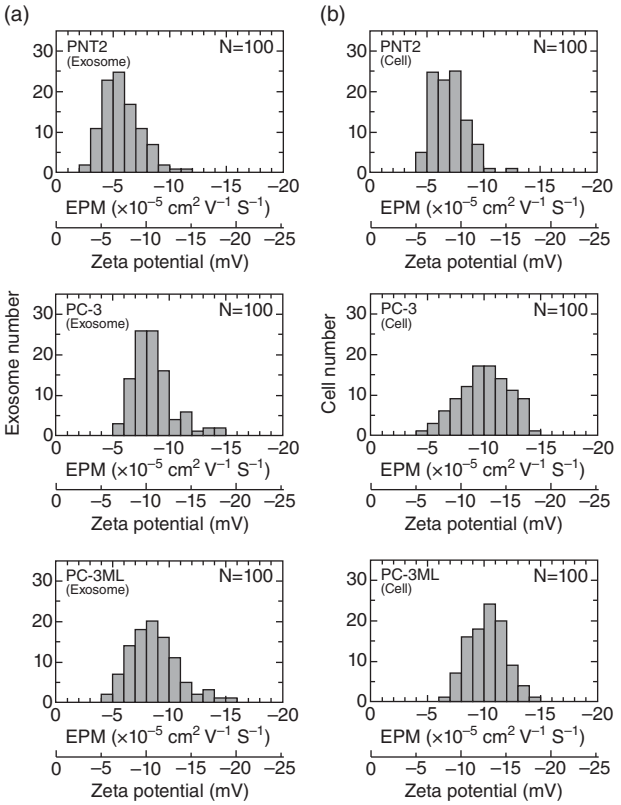


FIGURE 37.3 (a) Zeta-potential distributions of exosomes derived from normal prostate epithelial cells (PNT2) and prostate cancer cells (PC3 and PC3ML). (b) Zeta-potential distributions of PNT2, PC3, and PC3ML cells.

Dunnett's test). In contrast, there was no large difference between the relative standard deviation of the zeta-potential of exosomes and that of their cells of origin, which was approximately 10% at the most.

Moreover, a similar tendency was observed for human prostate cells. Figure 37.3a shows the zeta-potential distributions of exosomes derived from PNT2, PC3, and PC3ML cells. The average ± standard deviations of zeta-potential of exosomes were −7.4 ± 2.2 mV (PNT2), −11.0 ± 2.3 mV (PC3), and −11.1 ± 2.7 mV (PC3ML). Figure 37.3b shows the zeta-potential distributions of PNT2, PC3, and PC3ML cells. The average ± standard deviations of zeta-potentials of the corresponding cells were −8.9 ± 1.9 mV (PNT2), −12.8 ± 2.8 mV (PC3), and −13.1 ± 2.1 mV (PC3ML). The zeta potential of exosomes secreted from tumor cells shows a negative shift compared with that of exosomes from normal cells ($p < 0.05$, Dunnett's test).

To further examine the correlation between the zeta-potentials of exosomes and their cells of origin, the average zeta-potential of six types of exosome and their cells of origin are plotted in Fig. 37.4. There is a strong correlation between the average zeta-potential of exosomes and that of their cells

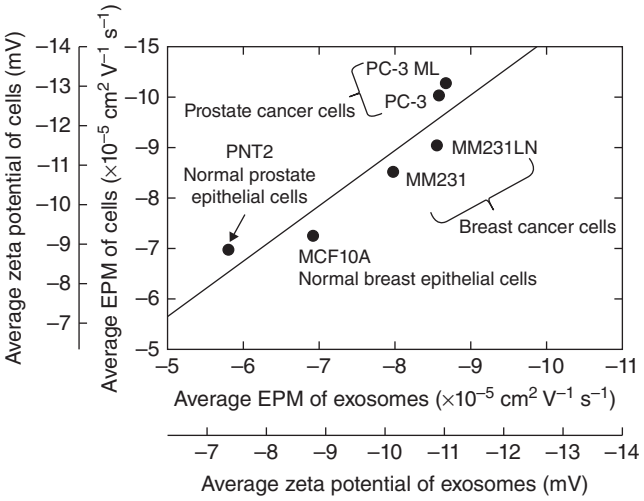


FIGURE 37.4 Comparison of average zeta-potentials of six types of exosome and their cells of origin measured using on-chip microcapillary system. The correlation coefficient between the average EPMs of cells and exosomes is 0.92.

of origin (correlation coefficient: 0.92). This fact means that the zeta-potential of exosomes strongly reflects that of their parent cells.

The zeta-potential of cancer cells changes owing to abnormal expression of sugar chains with malignant transformation [11]. Therefore, exosomes may well reflect changes in the sugar chains in their parent cells due to malignant transformation. Indeed, it has recently been reported that exosomes also bear saccharide groups such as mannose, polylactosamine, α-2,6 sialic acid, and complex *N*-linked glycans.

37.5 EFFECT OF SIALIDASE ON THE ZETA-POTENTIAL OF EXOSOMES

To investigate the relationship between the level of sialic acids and the electrical properties of the exosomal surface of normal prostate PNT2 and prostate cancer PC3 cells, the zeta-potential of desialylated exosomes was measured using the on-chip μCE system equipped with a laser dark-field microscope [8]. Figure 37.5 shows the zeta-potential distributions of exosomes derived from PNT2 and PC3 cells before and after treatment with sialidase. The means and standard deviations of the zeta-potential distributions of the exosomes derived from PNT2 and PC3 cells were -7.4 ± 2.2 and -11.0 ± 2.3 mV, respectively. The zeta-potential of exosomes secreted from PC3 cells was significantly more negative than that from PNT2 cells ($p < 0.05$, Tukey's test). In contrast, the means and standard deviations of the zetapotential distributions of exosomes derived from PNT2 and PC3 cells after treatment with sialidase were -4.1 ± 2.6 and -4.6 ± 3.3 mV, respectively. There was no significant difference between the zeta-potentials of the exosomes (p=0.668, Tukey's test). The variations of the mean zeta potential of exosomes of PNT2 and PC3 cells were +3.3 and +6.4 mV, respectively. The shift in the zeta-potential of exosomes of PC3 cells after sialidase treatment was about twice as large as that of the exosomes of PNT2 cells.

On the basis of these results, schematic images of the surface of exosomes secreted from cancer and normal cells are shown in Fig. 37.6. According to Ohshima's model [12], the EPM of a particle covered with a polymer, such as a cell or an exosome, can be determined using the electrical and mechanical properties of the polymer and the physical properties of the buffer solution. Therefore, sialic acids on the exosome surface can be considered as one of the factors contributing to the net negative charge of exosomes.

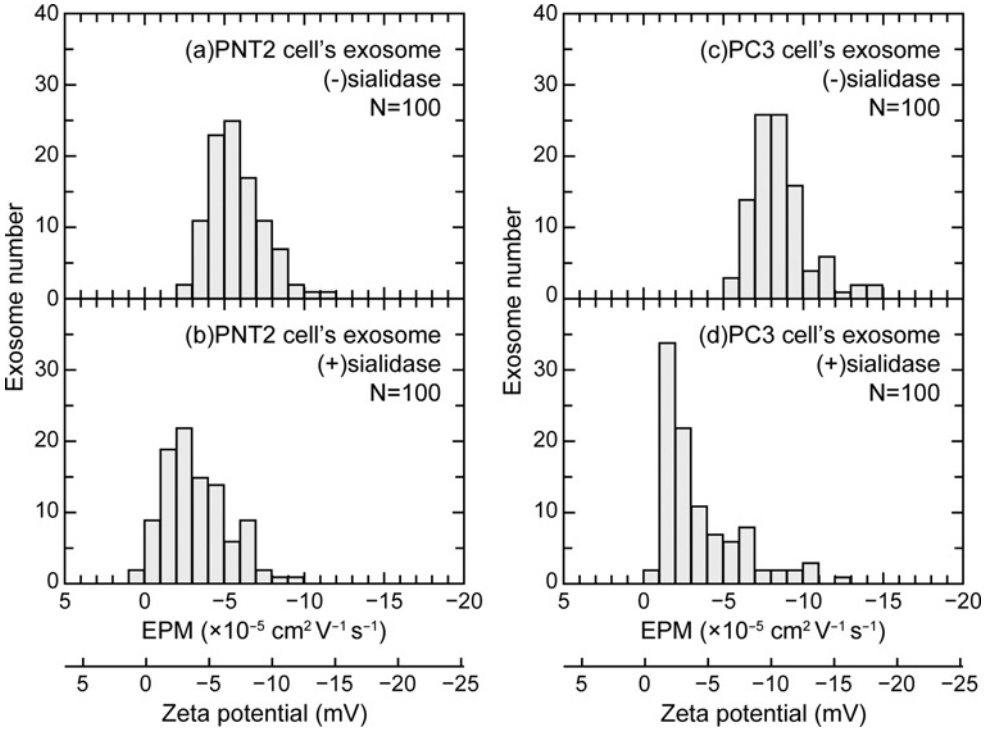


FIGURE 37.5 Effect of sialidase treatment on zeta-potential distributions of exosomes secreted from human normal prostate epithelial PNT2 cells (left) and human prostate cancer PC3 cells (right) evaluated using the on-chip μCE measurement system.

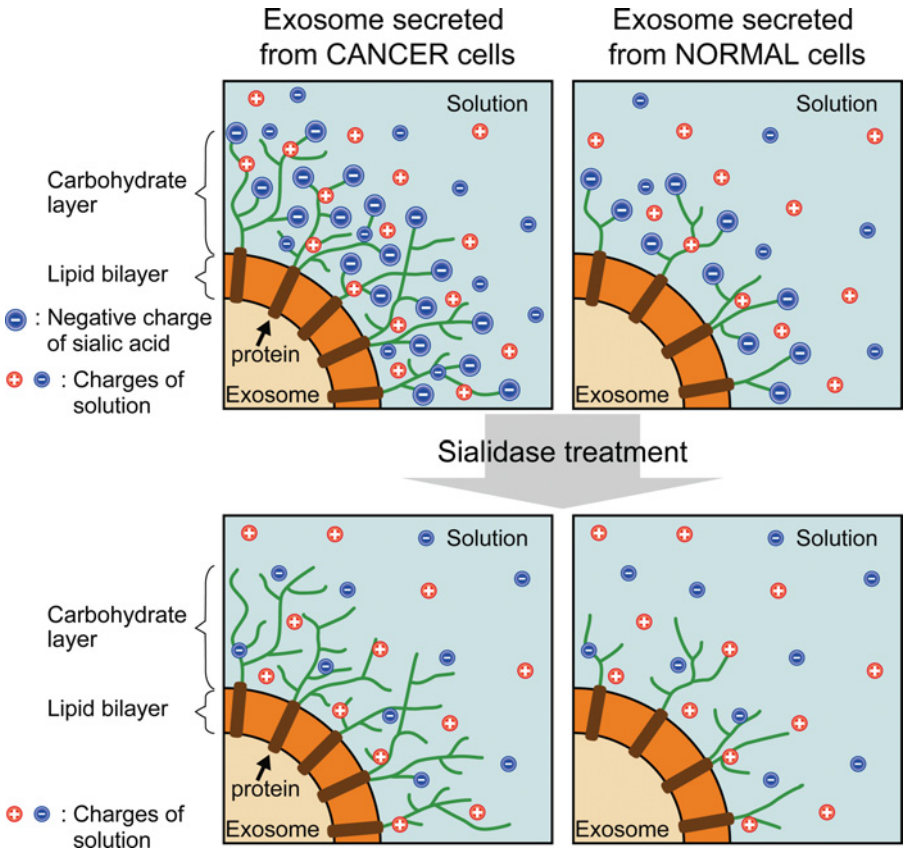


FIGURE 37.6 Schematic illustrations of charge distribution on the surface of exosomes secreted from cancer (left) and normal (right) cells before and after treatment with sialidase.

37.6 CONCLUSION

The EPM measurement system using a μCE chip was demonstrated to be suitable for analyzing events on the surface of individual exosomes. The difference in EPMs between exosomes secreted from normal and cancer cells and one of the mechanisms were revealed. Unfortunately, EPM cannot provide the disease-specific information. Hence, this methodology is expected to be useful for the prescreening of exosomes derived from prostate cancer without the need for labeling.

REFERENCES

[1] Valadi, H., Ekstrom, K., Bossios, A., Sjostrand, M., Lee, J.J., Lotvall, J.O. (2007). *Nat. Cell Biol.* **9**, 654–659.

[2] Thery, C., Ostrowski, M., Segura, E. (2009). *Nat. Rev. Immunol.* **9**, 581–593.

[3] Soo, C.Y., Song, Y., Zheng, Y., Campbell, E.C., Riches, A.C., Gunn-Moore, F., Powis, S.J. (2012). *Immunology* **136**, 192–197.

[4] Taylor, D.D., Gercel-Taylor, C. (2008). *Gynecol. Oncol.* **110**, 13–21.

[5] Yu, L., Shen, Z., Mo, J., Dong, X., Qin, J., Lin, B. (2007). *Electrophoresis* **28**, 4741–4747.

[6] Hood, J.L., San, R.S., Wickline, S.A. (2011). *Cancer Res.* **71**, 3792–3801.

[7] Kato, K., Kobayashi, M., Hanamura, N., Akagi, T., Kosaka, N.; Ochiya, T., Ichiki, T. (2013). *Jpn. J. Appl. Phys.* **52**, 06GK10.

[8] Akagi, T., Kato, K., Hanamura, N., Kobayashi, M., Ichiki, T. (2014). *Jpn. J. Appl. Phys.* **53**, 06JL01.

[9] Lamparski, H.G., Metha-Damani, A., Yao, J.Y., Patel, S., Hsu, D.H., Ruegg, C., Le Pecq, J.B. (2002). *J. Immunol. Methods* **270**, 211–226.

[10] Akagi, T., Ichiki, T. (2008). *Anal. Bioanal. Chem.* **391**, 2433–2441.

[11] Makino, K., Taki, T., Ogura, M., Handa, S.; Nakajima, M.; Kondo, T.; Ohshima, H. (1993). *Biophys. Chem.* **47**, 261–265.

[12] Ohshima, H., Kondo, T. (1989). *J. Colloid Interface Sci.* **130**, 281–282.

38

FLOCCULATION DYNAMICS ON THE BASIS OF COLLISION-LIMITED ANALYSIS

YASUHISA ADACHI

Faculty of Life and Environmental Science, University of Tsukuba, Ibaraki, Japan Tsukuba, Ibaraki, Japan

38.1 INTRODUCTION

Colloidal suspensions are unstable in nature, as a result of the effect of attractive interactions due to the universal van der Waals forces and specific electrostatic or chemical attraction exerted between heterogeneous surfaces of colloidal particles [1]. Therefore, in principle, when a colloidal suspension is placed for a long period of time, all particles will stick to each other to form an aggregate as a result of collisions. Collisions are induced by the influence of Brownian motion, the velocity difference in the flow field of shear and extension flow, turbulence, or field force such as gravity [2–5]. However, collisions usually will be hindered by the repulsive force induced by the presence of electric double layer or the steric interference of adsorbed molecules such as surfactants or macromolecules on the colloidal surface [6, 7]. If these repulsive interactions are reduced or removed, flocculation will begin to take place upon collision between two particles. Sequence of collision will result in the growth of flocs. The important factors involved in this process are as follows:

1. The rate of flocculation [8]
2. The geometric structure of resulting flocs [9]
3. The relation between the structure of flocs and other properties; such as the rate of sedimentation and the rheology of suspension [10, 11].

These factors are controlled by the chemical and hydrodynamic condition of the suspension schematically illustrated in Fig. 38.1. Therefore, the rate is controlled by the condition of hydrodynamic transportation and chemical reaction. Additiionally, the geometric structure of flocs reflects their formation process controlled by the rate of flocculation. For a description of sedimentation and the rheological process, information on geometric structure is essential. Scheme of analysis is given mainly by hydrodynamic conditions, and the difference in substances is related to chemical conditions. Here, our main interest is in using a model system. An application of the model suspension initially formed of uniform monodispersed spheres is useful for analysis of these factors and their relations. Thus, analysis of flocculation rate based on the colloidal interaction and transport phenomena can be based on spherical geometry of particles. Many numerical simulations for the reproduction of fractal geometry are reported for flocs formed of monodisperse spheres [29]. Experimental efforts to confirm these predictions are also reported using monodispersed suspension. It should be noted, however, that the formed structure also influences the rate of flocculation [12, 13]. In this chapter, the rate theory of flocculation is summarized followed by the result on the structure of flocs. An emphasis on the enhancement of collision process by the application of polymer flocculants will be treated in the last part of this chapter [14].

38.2 POPULATION BALANCE EQUATION

In an unstable suspension, the size distribution of flocs will change in accordance with the progress of flocculation

Encyclopedia of Biocolloid and Biointerface Science, Volume 1, First Edition. Edited by Hiroyuki Ohshima.
© 2016 John Wiley & Sons, Inc. Published 2016 by John Wiley & Sons, Inc.

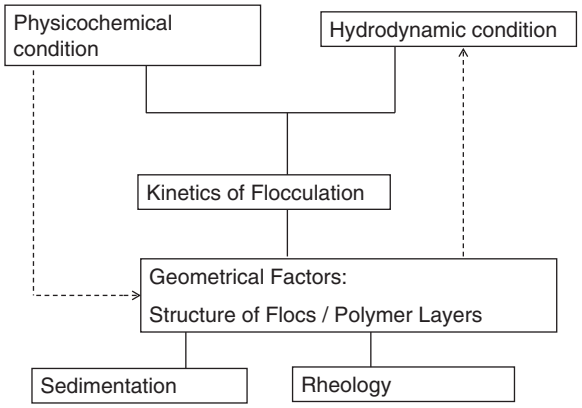


FIGURE 38.1 A correlation diagram of physical properties of a floc. The broken line represents influence at geometric factors on the collision process.

as illustrated in Fig. 38.2. Smoluchowski expressed the temporal evolution of size distribution of flocs, assuming that the flocculation process is a sequence of binary collision Cwithout any breakups of flocs. He proposed the following equation for the population balance of floc size distribution:

$$\frac{dn_k}{dt} = \frac{1}{2}\sum_{\substack{i=1\\ i+j=k}}^{i=k-1} \beta(a_{i,}a_j)n_i n_j - n_k \sum_{j=1}^{\infty} \beta(a_k, a_j)n_j. \qquad (38.1)$$

In other words, the rate of change in the concentration of the k-fold cluster (a floc composed of k primary particles) n_k is equal to the sum of the rate of formation of the k-fold cluster by the collision pair between i-fold and j-fold clusters satisfying $k = i + j$ and the rate of distinction of k-fold clusters by the collision with other clusters. The flocculation kernel, called a *collision frequency function* in case the flocculation process is controlled by collision, $\beta(a_i, a_j)$, is determined as a function of radius of the pair of two colliding particles reflecting the mechanism of collision process. In case the rate of collision is equal to that of coagulation, that is, the coagulation process is limited by the rate of collision, the process is termed *rapid*.

38.3 BROWNIAN COAGULATION

38.3.1 Collision Process under Brownian Motion

When interacting forces acting between colloid particles are removed, the rate of flocculation is determined by the rate of collision between colloid particles. Colloid suspension in such condition will flocculate spontaneously even when placed in a static condition by the effect of Brownian motion. The rate of collision between colloid particles immersed in a stagnant fluid can be derived by analyzing the diffusion process between colloidal particles (Fig. 38.3). If we take J_B as the value of rate of collision of i-fold clusters to the j-fold cluster, the value can be expressed by the application of Fick's first law as follows:

$$J_B = 4\pi r^2 D_{ij}\frac{\partial n_i}{\partial r}, \qquad (38.2)$$

where D_{ij} denotes the relative diffusion constant between the i-fold cluster and the j-fold cluster. If we assume that

$$n_i(r) = 0 \quad \text{at } r = R_{ij} = a_i + a_j \qquad (38.3)$$

and

$$n_i(r) \to n_{ib} \quad when\ r \to \infty \qquad (38.4)$$

we obtain J_B as

$$J_B = 4\pi R_{ij} D_{ij} n_{ib} \qquad (38.5)$$

where subscript b denotes the value at bulk solution. If we remember that there are n_j j-fold clusters in unit volume, the following equation for the total number of collisions in unit volume is derived:

$$\beta_B(a_{i,}a_j)n_i n_j = 4\pi R_{ij} D_{ij} n_i n_j. \qquad (38.6)$$

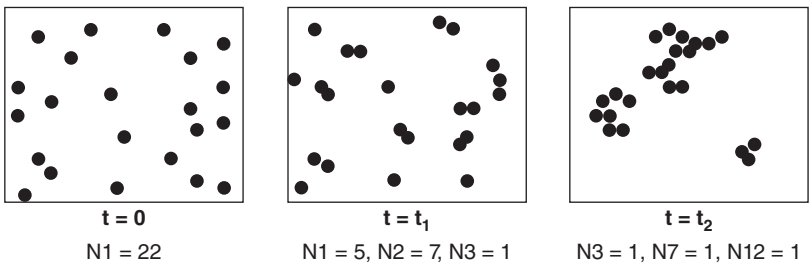


FIGURE 38.2 Temporal evolution of floc size distribution.

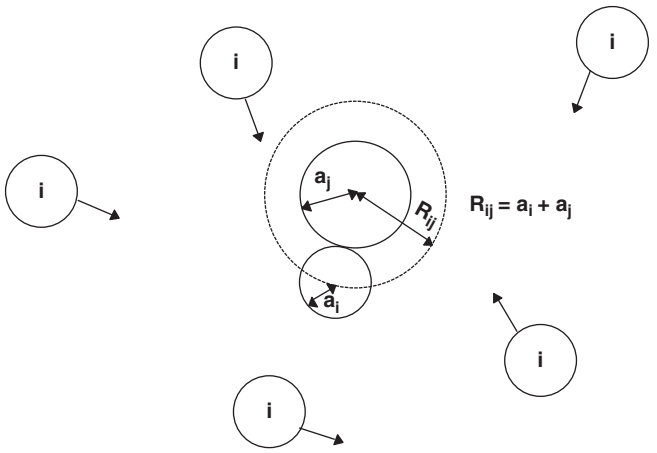


FIGURE 38.3 Diffusion of i-fold clusters relative to j-fold cluster.

In this expression, subscript b indicating the bulk is omitted. An expression of Einstein relation on the relative displacement between the i-fold and j-fold clusters can be written

$$\begin{aligned} 2D_{ij}t &= \overline{(\Delta X_i - \Delta X_j)^2} \\ &= \overline{\Delta X_i^2} - 2\overline{\Delta X_i \Delta X_j} + \overline{\Delta X_j^2} \\ &= \overline{\Delta X_i^2} + \overline{\Delta X_j^2} \\ (\therefore \overline{\Delta X_i \Delta X_j} &= 0 \quad (\textit{independence of Brownian motion of two clusters})) \\ &= 2D_i t + 2D_j t = 2(D_i + D_j)t. \end{aligned} \tag{38.7}$$

Thus, the relative diffusion constant of two clusters is the sum of diffusion constant if the independency of the Brownian motion of the two clusters is maintained.

Furthermore, substituting an expression of the Stokes–Einstein relation will yield,

$$\begin{aligned} \beta_B(a_i, a_j) &= 4\pi(a_i + a_j)\left(\frac{k_B T}{6\pi a_i \mu} + \frac{k_B T}{6\pi a_j \mu}\right) \\ &= \frac{2k_B T}{3\mu}(a_i + a_j)\left(\frac{1}{a_i} + \frac{1}{a_j}\right) \\ &= \frac{2k_B T}{3\mu}\left(2 + \frac{a_j}{a_i} + \frac{a_i}{a_j}\right). \end{aligned} \tag{38.8}$$

In other words, the collision frequency function of the Brownian coagulation is determined by the ratio of the size of colliding particles.

38.3.2 Smoluchowski Solution

In this case, coagulation begins in the early stage with monodispersed suspension of spherical particles, where we can assume that

$$a_i \approx a_j \tag{38.9}$$

the following approximation

$$(a_i + a_j)\left(\frac{1}{a_i} + \frac{1}{a_j}\right) \cong 4 \quad \text{(Smoluchowski approximation)} \tag{38.10}$$

will lead to the constant value of collision frequency function as follows:

$$\beta_B(a_i, a_j) = \frac{8k_B T}{3\mu}. \tag{38.11}$$

On the basis of this assumption, Smoluchowski derived the following solution for the temporal evolution of the total number concentration of clusters and their size distributions. Thus, substitution of Eq. (38.11) into Eq. (38.1) will yield

$$\frac{dN(t)}{dt} = -\frac{4k_B T}{3\mu}N(t)^2 \tag{38.12}$$

where

$$N(t) = \sum_{k=1}^{\infty} n_k. \tag{38.13}$$

The integrated expression with initial concentration of $N(t) = N(0)$ at $t = 0$ is derived as

$$\frac{1}{N(t)} - \frac{1}{N(0)} = \frac{4k_B T}{3\mu}t. \tag{38.14}$$

Substitution of this result into Eq. (38.1) will yield

$$\frac{n_k(t)}{N(t)} = P^{k-1}(1 - P) \tag{38.15}$$

where

$$P = \frac{\left(\frac{t}{\tau}\right)}{\left(1 + \frac{t}{\tau}\right)}, \tau = \frac{3\mu}{4k_B T N(0)}. \tag{38.16}$$

Equation (38.15) demonatrates that the size distribution on the basis of Smoluchowski approximation is a geometric progression with a common ratio of P and the first term of (1-P); τ is the coagulation time, denoting the time required for the number of particles reduce to half of $N(0)$.

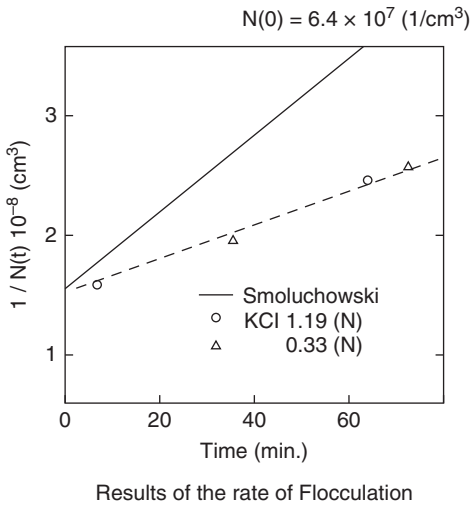


FIGURE 38.4 Exprimental result of kinetics of Brownian coagulation. Solid lines represent the prediction on the basis Smoluchowski theory [8].

Experimental data on the kinetics of rapid coagulation were obtained by numerous researchers using the dispersion of polymer latices (PSL) [16–21]. All the results supported the linear relation between $1/N(t)$ versus t. However, the measured rates are 40–70% smaller than the theoretical prediction (Fig. 38.4). This effect is usually described by the collection factor α_B, termed the *coagulation coefficient*. One investigator [22] analyzed this factor by ascribing it to the effect of hydrodynamic interaction between colliding particles. Since the Hamaker constant calculated in accordance with Spielman's theory gives a reasonable value, this result has been accepted by many researchers. However, there still remains the mysterious result of experiment. More specifically, the experimental data obtained for the dependence of the reduction in the initial particle concentration in the region of very dilute suspension cannot be explained by the theory of Spielman. More recently, another team [23] verified that the effect of volume fraction on the hydrodynamic interaction in the case of rapid Brownian coagulation is effective for only two or three orders of magnitude higher-concentration regions. It may be worthwhile to examine the original assumption of the mean field approximation adopted by Smoluchowski.

38.3.3 Self-Similar Solution

Since the derivation of Smolukowski approximation is based on the assumption limited to the early stage of coagulation, it seems difficult to apply the relation in the analysis of flocculation at a later stage. However, support for the theory of Brownian coagulation was originally obtained from experiment with polydisperse aerosols [24]. It has been reported that the functional forms of size distributions of aerosol observed in different places are the same, implying the presence of a universal function for the size distribution function [25]. This observation leads to the insight of Smoluchowski population equation at a later stage. In the case of Brownian coagulation, two other investigators [26] demonstrated the consistent presence of a self-preserving size distribution function of coagulated flocs with Smoluchowski population equation. Thus, if a sufficiently long time has elapsed after the onset of coagulation, the size distribution will converge to a certain functional form [27]. In this case, floc size distribution can be expressed by a product of the size of sample and a self-preserving function. Variability of the function is reduced by a representative value of the sample. Therefore, the number concentration of floc with volume of v is expressed as:

$$n(v,t) = \frac{N(t)^2}{\phi}\Psi(\eta), \tag{38.17}$$

where η is the dimensionless volume, defined as,

$$\eta = \frac{v}{\bar{v}} = \frac{N(t)v}{\phi}, \tag{38.18}$$

$$N(t) = \int_0^\infty n dv \tag{38.19}$$

and

$$\phi = \int_0^\infty n v dv. \tag{38.20}$$

Two investigators [28] calculated the asymptotic form of $\Psi(\eta)$ for the case of Brownian coagulation in Eq. (38.8). Using their results, temporal variation of the total number concentration of clusters, is obtained as,

$$\frac{dN(t)}{dt} = -\frac{4.26\, k_B T}{3\mu} N(t)^2. \tag{38.21}$$

This result is noteworthy, since the obtained factor 4.26 is close to 4.0, which is the theoretical value predicted on the basis of Smolukowski approximation Eq. (38.10). Thus, it was concluded that in the case of Brownian coagulation the predicted rate of coagulation taking into account the size distribution increases by only ~5% from the rate constant obtained for uniform spheres. The rate of Brownian coagulation is nearly constant from the beginning to later stages, where we expect self-preserving size distribution of flocs.

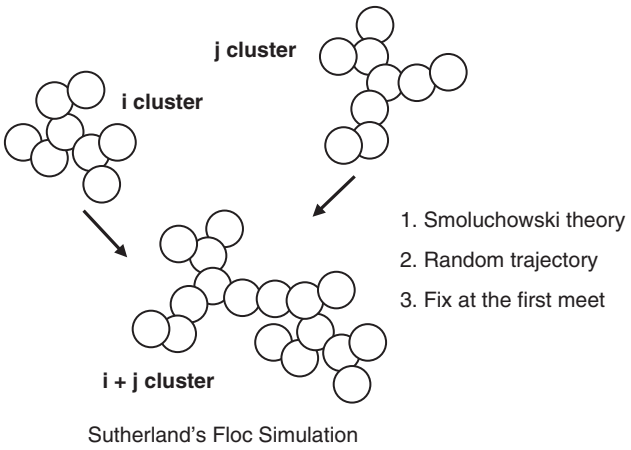


FIGURE 38.5 Sutherland's floc simulation of cluster–cluster collision model.

38.3.4 Effect of Fractal Structure of Flocs on Flocculation Rate

The conclusion in the previous section is questioned in terms of the effect of the formation of fractal structure of flocs. Thus, in the later stage, the concept of cluster–cluster aggregation in accordance with the collision sequence of Smoluchowski theory with an assumption of rigid adhesion of colliding cluster pairs will result in the formation of extremely bulky structure of flocs. The density decreases with an increase of size of floc. This relation is usually expressed as

$$a_f = a_0 i^{1/D} \tag{38.22}$$

where a_0 is the diameter of primary particle, a_f is the radius of floc, and D is the fractal dimension. This relation is numerically predicted by the cluster–cluster addition model proposed in the literature [29,30] (Fig. 38.5) and expanded [31]. The result was confirmed by floc structure composed of PSL particles [32]. The shapes of resulted flocs are obviously far from sphere remaining the ambiguity of collision radius and Stokes diameter. Analysis of the effect of this factor on the population equation was reported [32]. However, in this case, because the effect of structure development in collision radius and Stokes radius counterbalance each other, the influence of the development of floc structure on the rate of coagulation was not detectably large.

One of the most important characteristics of fractal aggregate is, however, that the development of fractal structure is followed by the increase of occupied volume by floc structure. In other words, the free space that can be used for diffusion will be substantially decreased in accordance with the progress of coagulation [13]. Through this effect, the number concentration will be increased, reflecting the decrease of free volume as illustrated in Fig. 38.6. With this picture,

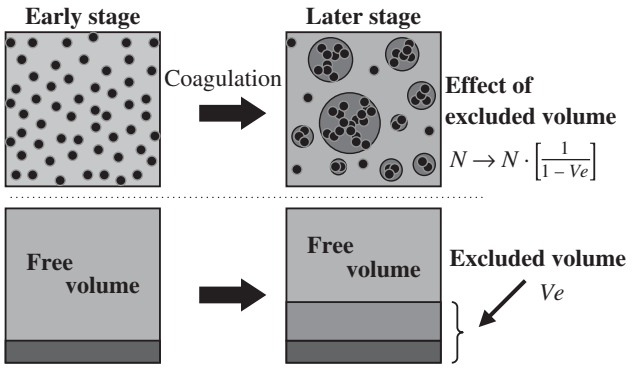


FIGURE 38.6 Increase of excluded volume and decrease of free volume with development of floc structure in Brownian flocculation [13].

the rate of coagulation is modified as

$$\frac{dN(t)}{dt} = -\alpha_B \frac{4k_B T}{3\mu} N(t)^2 \left(\frac{1}{1-V_e}\right)^2 \tag{38.23}$$

where V_e denotes the effective excluded volume of floc structure defined as

$$V_e = \sum_{i=1}^{N} \frac{\pi}{6} d_{f_i}^3 \tag{38.24}$$

This scenario was verified by a careful measurement on the rate of Brownian flocculation under optical microscope (Fig. 38.7). As for the definition of d_f, the lengths of the major axes of the best-fit ellipses for corresponding flocs were adopted. As shown in Fig. 38.8, the rate of coagulation gradually

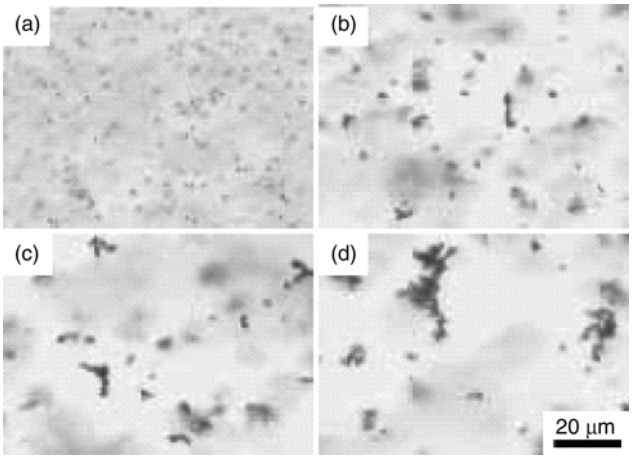


FIGURE 38.7 Typical snapshot of the state of coagulation for rapid Brownian coagulation. Date represents (a) 0 min., (b) 10 min., (c) 20 min. and (d) 30 min. After the onset of coagulation, $N_0 = 1.5 \times 10^9$ (1/cm^3); 1040 nm. PSL dispersion was coagulated in a 1.24 M KCl [13].

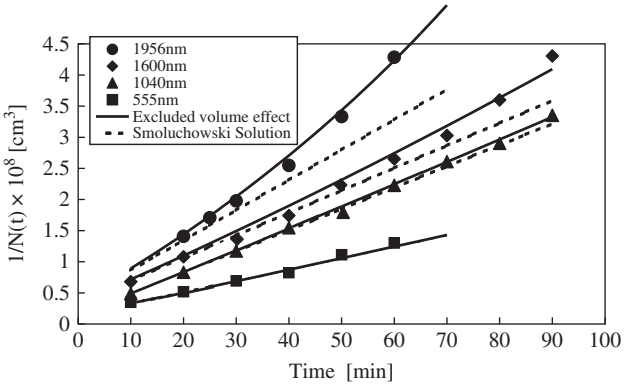


FIGURE 38.8 Temporal variation of the number concentration of flocs including later stage of coagulation where fractal structure of flocs are developed; $N_0 = 1.5 \times 10^9$ (1/cm^3) [13].

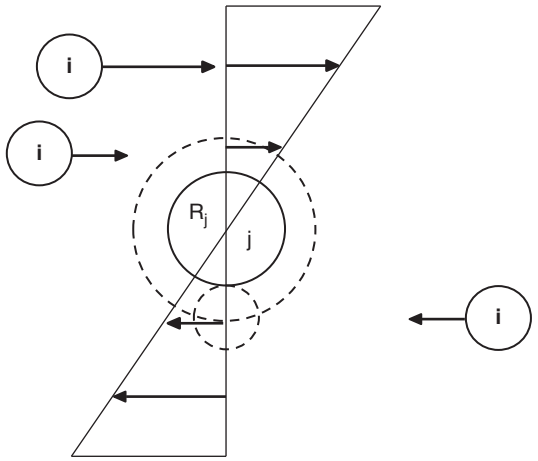


FIGURE 38.9 Coagulation in shear flow.

increases in the later stage. The prediction on the basis of Eq. (38.23) agrees well with these results.

38.4 COAGULATION IN SHEAR FLOW

38.4.1 Collision Frequency in Shear Field

In many situations of practical application, the operation of flocculation is carried out in a mixing flow. Therefore, analysis of flocculation in a flow field can be regarded as an issue of engineering subject in addition to its scientific appeal. The most simple problem is that the rate of flocculation in a simple shear flow, which was initially formulated by Smoluchowski [15], is the starting basis of this regime; however, the treatment and solution obtained for the simple situation is also important when flocculation in turbulent flow is considered.

Imagine that a viscous Newtonian fluid is placed in a gap between two parallel plates moving oppositely at the same velocity to the direction parallel to the surface of the plates. A simple shear flow field with velocity distribution of

$$u(y) = Gy \tag{38.25}$$

will be generated as shown in Fig. 38.8. Here G denotes the shear rate or velocity gradient. When colloidal particles are immersed in this field, they will cause collisions subject to the motion of fluid. Smoluchowski [15] derived the theory of rate of coagulation by assuming the number of collisions per unit time to be in a unit volume. Let us place a sphere with radius a_i (which represents an i-fold cluster) at the origin and assume that the number of collisions with another spheres of radius a_j (which represents a j-fold cluster) distributed with number concentration of n_j (Fig. 38.9). The number of collisions experienced by the first sphere, J_s, can be obtained by calculating the fluid volume crossing the collision sphere with radius $R_{ij} = a_i + a_j$ as follows:

$$\begin{aligned} J_s &= 2\int_0^{R_{ij}} Gy \cdot 2\sqrt{R_{ij} - y^2}\,dy \cdot n_j \\ &= \frac{4}{3}R_{ij}^3 G n_j. \end{aligned} \tag{38.26}$$

Therefore, the collision frequency function can be derived as,

$$\beta_s(a_i, a_j) = \frac{4}{3}R_{ij}^3 G. \tag{38.27}$$

In the early stage of coagulation starting from monodispersed spheres with radius a_0, the rate of coagulation can be derived as,

$$\frac{dN(t)}{dt} = -\frac{16}{3}a_0^3 G N(t)^2. \tag{38.28}$$

If we can assume that

$$\phi = \frac{4\pi}{3}a_0^3 N(0) = \text{Const.} \tag{38.29}$$

Equation (38.28) is reduced to,

$$\frac{dN(t)}{dt} = -\frac{4}{\pi}\phi G N(t). \tag{38.30}$$

The solution of Eq. (38.30) can be easily obtained as

$$\ln\left(\frac{N(t)}{N(0)}\right) = -\frac{4\phi G}{\pi}t \tag{38.31}$$

Equation (38.31) indicates that the value of ϕGt is an essential factor in controlling and evaluating the degree of flocculation in shear flow. In accordance with Eq. (38.27), we

should also note that the collision frequency in a shear flow is proportional to the third power of the particle diameter. Later, we will see that this conclusion can be extended to the case where coagulation takes place in a turbulent flow.

38.4.2 Interaction between Colloid Particles in Laminar Shear Flow

The treatment in the previous section does not factor in the effect of interaction between two approaching particles. In reality, in addition to colloidal interaction (electrostatic repulsion and Van der Waals attraction), the relative motion between colloidal particles immersed in a viscous liquid is hydrodynamically influenced by the presence of other particles. This factor is essentially important when the rate of coagulation in the flow field is considered. In the absence of attractive forces, approaching particles will never encounter each other because of this effect. The relative trajectory of two spheres in a shear field was first obtained by Lin et al. [33]. More general expressions for the flow field of two sphere interaction in the linear flow field were derived by other investigators [34]. Their results were combined with colloidal interaction to calculate the relative trajectory of two approaching spheres in a flow field [36, 37]. When the discussion is limited to the binary collisions between two equal-sized spheres in the absence of electrostatic repulsion, the following approximate form using a collection factor for collision frequency function [21]

$$\beta_s = \alpha_s \frac{16}{3} a_0^3 G \tag{38.32}$$

$$\alpha_s = C_A^{0.18}, C_A = \frac{A}{36\pi\mu a_0^3 G} \tag{38.33}$$

can be used to predict the rate of coagulation.

38.4.3 Effect of Formation of Floc Structure on Shear Coagulation Rate

The treatment of coagulation in flow field described so far is limited to the initial stage of coagulation where binary collision between singlets is dominant. However, it is obvious that, in the later period, the formation and developments of fractal structure of floc can be a considerable factor in the rate of coagulation [12]. If we replace the assumption of uniform primary spheres by flocs of the same size, the temporal evolution of floc number concentration $N(t)$ can be expressed as follows:

$$\frac{dN(t)}{dt} = -\alpha_s \frac{16}{3} a_f^3 G N(t)^2 \tag{38.34}$$

Remember that the value of a_f is a function of the number of primary particles described in Eq. (38.22);

$$a_f = a_0 i^{1/D} \tag{38.22}$$

and i can be expressed as,

$$i = \frac{N(0)}{N(t)}. \tag{38.35}$$

Substituting Eqs. (38.22) and (38.35) into Eq. (38.34) yields,

$$\frac{dN_f}{dt} = -\alpha_s \frac{16}{3} a_0^3 G \left(\frac{N(0)}{N(t)}\right)^{3/D} N(t), \tag{38.36}$$

where α_s is the capture efficiency between flocs, which is obtained by hydrodynamic trajectory analysis of approaching flocs in a shear field, assuming that (1) shapes and size of flocs are equal-sized spheres, (2) effects of permeability on the collision trajectory is ignored, and (3) the attractive force is estimated as the van der Waals force of two primary particles (Fig. 38.10). The resulting value of α_s can be approximated as follows:

$$\alpha_s = C_A^{0.18}, C_A = \frac{Aa_0}{36\pi\mu a_f^4 G} = \frac{A}{36\pi\mu(\frac{N(0)}{N(t)})^{4/D} G}. \tag{38.37}$$

Substituting Eq. (38.37) into Eq. (38.36) yields

$$\frac{N(t)}{N(0)} = (1 - \frac{3 - 4\times 0.18 - D}{D} \cdot \frac{16}{3} \cdot \alpha_s a_0^3 N(0) G t)^{\frac{D}{3-4\times 0.18-D}} \tag{38.38}$$

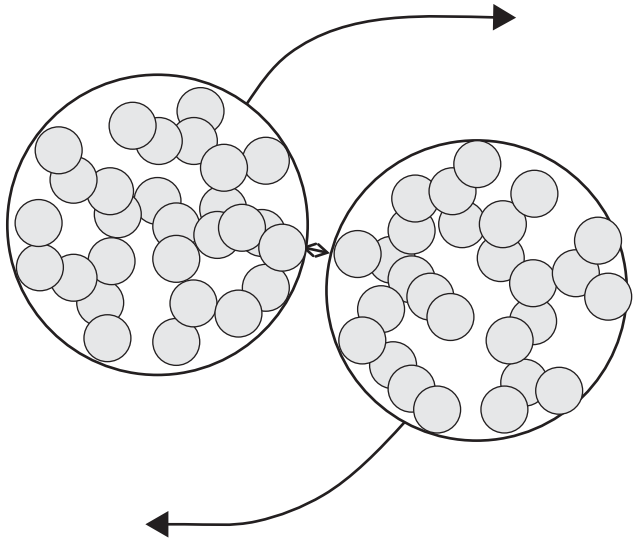


FIGURE 38.10 Collision process of two flocs in shear flow. Hydrodynamic interaction is calculated for two impermeable spheres enclosing floc, while Van der Waals attraction is that of two primary particles.

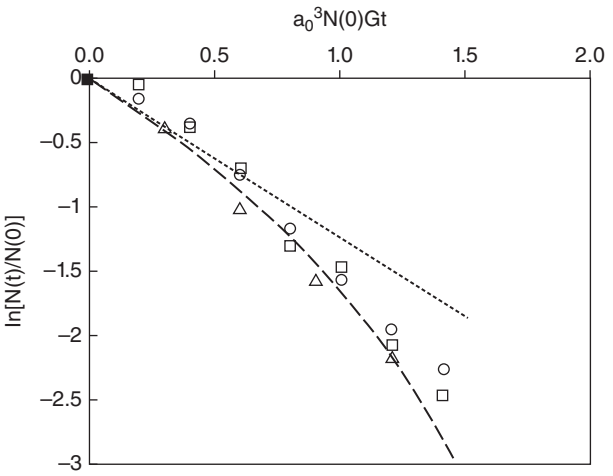


FIGURE 38.11 Temporal variation of the number concentration of flocs including later stage of coagulation where fractal structure of flocs are developed in shear flow [12].

The validity of Eq. (38.38) was confirmed by a careful measurement of the temporal variation of the total number concentration of flocs coagulated in a laminar shear flow generated in a gap between two concentric cylinders. The data thus obtained were plotted in Fig. 38.11. As demonstrated in this figure, the prediction on the basis of Eq. (38.38) yields a good agreement with the experimental data of the progress of flocculation in the later stage. It should be noted that one investigator [38] pointed out the importance of the effect of permeability in reducing the contribution due to the hydrodynamic infection. However, our experimental result did not confirm this prediction.

38.5 INITIAL STAGE OF BRIDGING FLOCCULATION IN A TURBULENT MIXING

38.5.1 Schematic Picture of Flocculation with Polymer Flocculants in a Practical System

In most practical applications, flocculation operation is carried out in turbulent flow. However, as can be easily imagined, the process of flocculation in the usual application is very complicated. If we assume the normal operation of water treatment where flocculation of coll veroidal dispersion is initiated on the addition of polymer flocculants, we will recognize that the process of flocculation consists of several elementary processes taking places simultaneously as illustrated in Fig. 38.12:

1. Dilution of flocculants into homogeneous solution
2. Collision between colloidal particles
3. Stretching of polymer chain
4. Collision of polymer chain and colloidal particles
5. Reconformation of adsorbed polymer chain on the surface of colloidal particles
6. Formation of polymer bridge between colloidal particles
7. Rearrangement and breakup of floc structure

All these processes take place simultaneously in the flow field of turbulent mixing. Therefore, analysis of turbulence from the perspective of the flocculation process can be regarded as an important issue for better control of colloidal flocculation. In the last section of this chapter, an analysis of collision process between colloidal particles in a turbulent flow is introduced to normalize the mixing flow condition, which will be ultimately useful for the evaluation of the effect of polymer flocculants applied in the same mixing condition.

38.5.2 Collision Process in Turbulent Flow

Turbulent flow can be regarded as a superposition of eddies with different sizes. The kinetic energy of turbulent fluctuations generated by unstable hydrodynamic condition of the main flow is transmitted from larger eddies, which will produce a number of intermediate-sized eddies, sequentially resulting in the generation of enormous numbers of small energy-dissipating eddies, and eventually dissipating into heat. This is the so-called cascade process of energy transfer of turbulence. Kolmogoroff [39] proposed a hypothesis of local isotropy of turbulence for small-scale eddies. In other words, in fully developed turbulence, the anisotropic character of the main flow will be lost through the cascade process, and consequently the statistical properties of small- scale eddies can be determined independently of the directional information of the main flow. On the basis of this argument, Kolmogoroff introduced an important length scale λ, which characterizes the size of an energy-dissipating eddy and termed it the *microscale of turbulence*

$$\lambda = \left(\frac{\nu^3}{\varepsilon}\right)^{1/4} \tag{38.39}$$

where ν and ε denote the kinematic viscosity of fluid and the rate of energy dissipation per unit mass, respectively. If the length scale of the region of interest is smaller than λ, the fluctuating field of turbulence can be treated as homogeneously isotropic. The magnitude of λ is roughly 30–100 μ m, which is sufficiently larger than the collision radius of the colloidal particle, and because of their higher shear rates, which essentially dominate the collision rates between colloidal particles, the assumption of local isotropy is applicable to estimation of the rate of coagulation, and the turbulent coagulation can

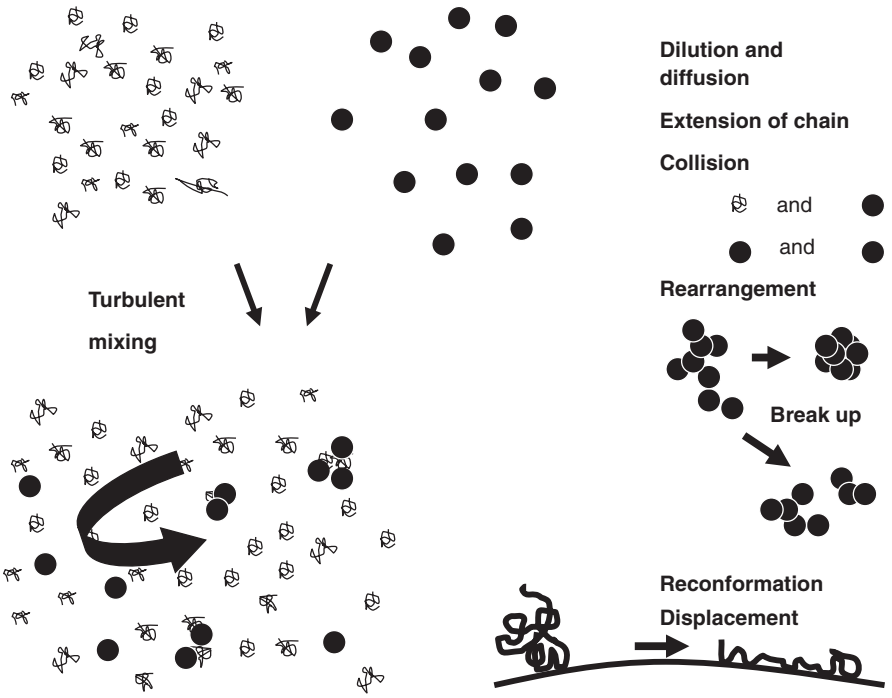


FIGURE 38.12 Schematic drawing of bridging flocculation in turbulent mixing.

be treated as a sort of shear coagulation. A treatment of turbulent coagulation was first carried out by Camp and Stein [40] in a practical manner assuming that the collision mechanism of colloidal particles in a turbulent flow is analogous to that in laminar shear flow. In order to estimate the rate of coagulation in a turbulent flow, they simply used the effective velocity gradient $\sqrt{\varepsilon/\nu}$, in place of the shear rate G, in the collision frequency function in a shear flow [Eq. (38.27)]. This simple idea constitutes a starting point for the study of turbulent coagulation. A more rigorous derivation of the rate of turbulent coagulation was formulated later by investigators [4] who obtained the collision frequency of j-fold clusters experienced by an i-fold cluster by calculating the inward flux of mean flow crossing the surface of collision sphere with collision radius of R_{ij} as

$$J_T = 2\pi R_{ij}^2 \cdot \overline{\left|\frac{\partial u_r}{\partial r}\right|} R_{ij} n_j \tag{38.40}$$

where u_r denotes the radial component of velocity fluctuation. Using the results of the statistical analysis of isotropic turbulence by another author [41] and assuming a normal distribution of $\partial u_r/\partial r$ that was experimentally supported [40], other investigators determined the collision frequency function as

$$\beta_T(a_i, a_j) = \sqrt{\frac{8\pi\varepsilon}{15\nu}} R_{ij}^3 \tag{38.41}$$

If we compare this result with that obtained for a laminar shear flow expressed by Eq. (38.27), the collision process of a colloidal particle in a turbulent flow can be treated essentially the same as that in a laminar shear field.

In the case of colloidal particles immersed in a viscous liquid, however, collision frequency function is modified by a factor of α_T, which takes into account the hydrodynamic interaction. The effect hydrodynamic interaction is emphasized by the coagulation experiment of latex particles by several workers [43–45]. For rapid coagulation in the initial stage starting from monodispersed spheres, the temporal variation of the total number concentration of clusters can be expressed by

$$\frac{dN(t)}{dt} = -\frac{1}{2}\alpha_T \sqrt{\frac{8\pi\varepsilon}{15\nu}} (2a_0)^3 N(t)^2 \tag{38.42}$$

In the case of rapid coagulation, α_T can be approximated by

$$\alpha_T = \left(\frac{A}{36\pi\mu a_0^3 \sqrt{\frac{4\varepsilon}{15\pi\nu}}} \right)^{0.18} \tag{38.43}$$

If we apply the initial-stage approximation, then

$$\phi = \frac{4\pi}{3} a_o^3 N(0) = \frac{4\pi}{3} R^3 N(t) = \text{Const.} \tag{38.44}$$

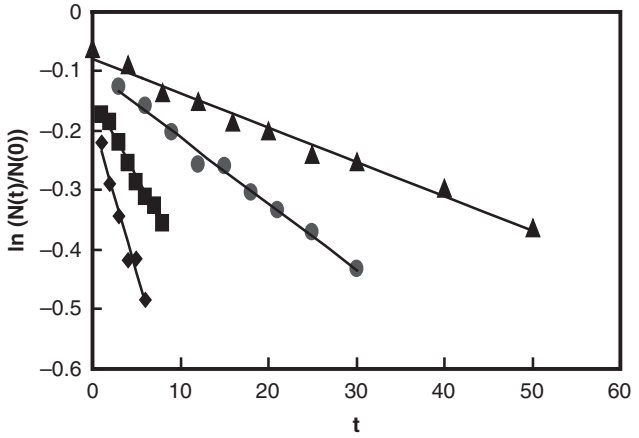


FIGURE 38.13 Temporal variation of total number of clusters per unit volume in the case of salt-induced coagulation as a function of the number of mixing steps (t), where [KCl] = 1.12 M. The total number concentration of PSL particle: (♦) 4.83×10^8 1/cm^3; (■) 2.52×10^8 1/cm^3; (●) 1.07×10^8 1/cm^3 ; (▲) 5.11×10^7 1/cm^3 [59].

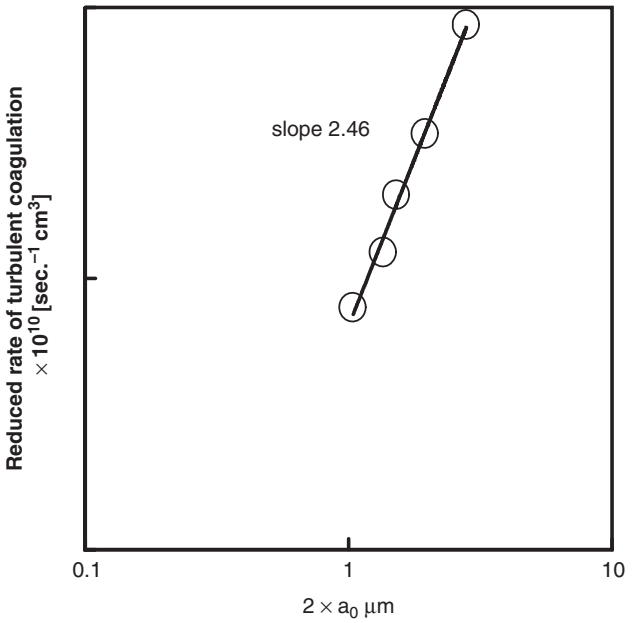


FIGURE 38.14 Reduced rate of turbulent coagulation as a function of the diameter of primary particles [59].

We can solve Eq. (38.42) approximately as

$$\ln \frac{N(t)}{N(0)} = -\alpha_T \sqrt{\left(\frac{24\varepsilon}{5\pi\nu}\right)}\phi t \tag{38.45}$$

In a fixed condition of the mixing, the value of ε can be regarded constant. Therefore, it should be noted that the rate of coagulation is proportional to the 2.46th power of the size of primary particles under certain mixing conditions.

In Fig. 38,13, the temporal variation of $N(t)$ for the case of coagulation of latex particles induced under the condition of rapid coagulation is plotted against t. This experiment was carried out using a homemade mixing device of end-over-end rotation of two small bottles. As indicated by the plotted data, the linear relation between $\ln(N(t))$ and t is confirmed. The slope, denoting the rate of coagulation, is proportional to $N(0)$. Coagulation rates of latex particles obtained for different particle diameters are divided by each N(0) and compared as a function of diameter of primary particles in Fig. 38.14 [59]. Although control of the mixing operation is rather crude, as demonstrated in this figure, the progress of coagulation are found to obey the prediction of Eqs. (38.43)–(38.45) well. Another previous trial in comparison of different mixing procedures confirmed the same tendency [21,44]. This finding forms a basis for establishment of the evaluation of turbulent mixing on the basis of collision process of colloidal particles.

38.5.3 Historical Review of Concept of Nonequilibrium Flocculation

Currently, various types of polymer flocculants have been developed for application to many industrial process, mining operations, papermaking, and water treatment procedures to enhance solid–liquid separation and to control the rheological state of colloidal dispersion. Although such applications have long developmental histories [46,47], the dynamic process explaining exactly how polymer flocculants will induce flocculation is still unclear. Previous studies demonstrate the concept of optimum dosage in inducing colloid flocculation and indicate that colloids will stabilized by the excess or overdosage rather permanently. The experimental results of optimum dosage have generated speculation regarding the concept of polymer bridging. A pioneering study [48] pointed out the varying degree of colloidal stability that can be obtained simply by changing the mixing method. Two investigators [49] showed that higher-molecular-weight polymers will act as more effective flocculants as well as stabilizers. The stabilizing mechanism is recognized as a steric effect of the adsorbed polymer layer to avoid the approach of colloidal particles on collision. In case of either flocculation or stabilization, the adsorption of polymer is critically important in understanding the mechanism of change of colloidal dispersion. Another major effort was made to study the conformation of polymer at interfaces [50,51]. One author demonstrated the importance of the role of charge [52] and also demonstrated the dynamic concept of nonequilibrium flocculation [53]. Specifically, in practical situations, polyelctrolytes, that is, polymer chains with charged groups, are more effectively utilized as flocculants. Two authors [54] demonstrated that in concentrated suspension, pellet floc, that is, large, high-density flocs with excellent dewaterability, can be formed under the condition that the charge of colloidal

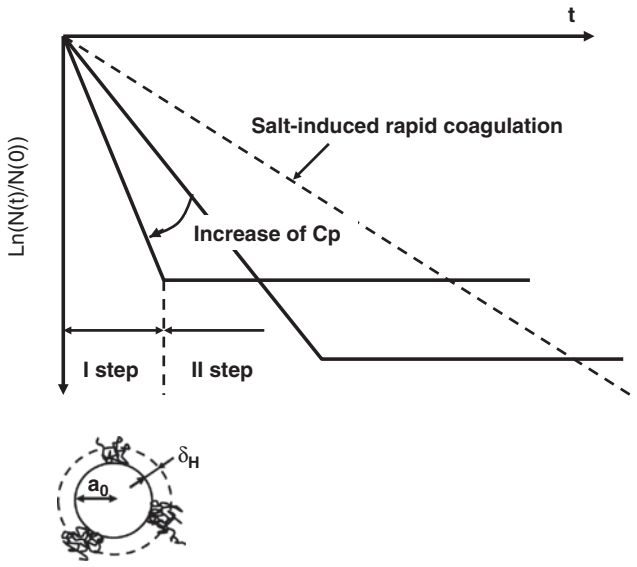


FIGURE 38.15 Illustration of concept of the progress of flocculation induced by polymer flocculant at overdosage [58].

particles will be neutralized by the adsorption of oppositely charged polyelectrolyte. It should be noted that the picture of pelletization is consistent with the concept of nonequilibrium flocculation [55]. Those authors [55] attempted systematic analysis of the role of polyelectrolytes in the relation between adsorption of polyelectrolytes and their effect on colloidal stability, however, they have not stressed the dynamic aspect, which is critically important. Probably one of the most important events of flocculation takes places immediately after the onset of mixing operation where the system is placed far from equilibrium.

38.5.4 Initial-Stage Dynamics of Bridging Flocculation of PSL Particles Induced by Polyelectrolytes under High Ionic Strength

In the last part of the previous section, the principle of the normalizing method of turbulent mixing in terms of collision rate of colloidal particles was explained. The established procedure has been used to evaluate the protruding length of polymers attached to the surface of colloidal particles. Thus, if we apply the polymer flocculants to the colloidal dispersion, the collision radius will be effectively increased to enhance the rate of flocculation.

Clear results can be obtained, if sufficient amount of polymer flocculants is supplied to the colloidal surface. In Fig. 38.15, we illustrate a concept of the progress of flocculation at the overdosage of polymer flocculants. Important information can be obtained on comparison of the progress of flocculation with excess addition of flocculants and that of salt-induced rapid coagulation (without polymer). From the

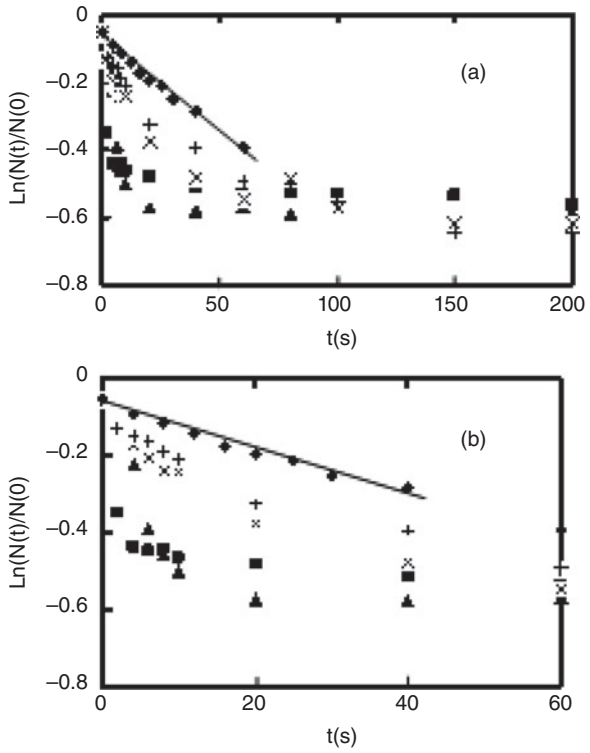


FIGURE 38.16 Plot of $\ln(N(t)/N(0))$ versus t for flocculation induced with an application of polyelectrolyte. The background solution of KCl is 1.0 M; $N(0) = 5.11 \times 10^7$ 1/cm^3. (a) The results for higher molecular weight of polyelectrolyte (MW = 4.9×10^6 g/mol). (b) Figure scaled up to 60 s. The solid line represents the regression line of the result of salt-induced coagulation taken from Fig. 38.13. Symbols: (□) 0.2 ppm, (+) 0.5 ppm, (▲) 1 ppm, (■) 3 ppm [14].

ratio of the rate of polymer flocculation and that of salt-induced rapid coagulation η, the effective layer thickness δ_H of adsorbed polymer flocculants can be evaluated by the following equation:

$$\eta = \frac{(a_0 + \delta_H)^3}{\alpha_T \cdot a_0^3} \tag{38.46}$$

The value of η is noteworthy. It was found to increase with an increase in polymer dosage [56–59]. Surprisingly, in some time, the value was found to be close to 100. At the same time, flocculation will cease immediately at high dosage. Our earlier studies revealed that the state of a polymer in a solution, rather than the equilibrium state of adsorption, is critical. Our recent work using polyelectrolyte with molecular weight of 4900 kDa demonstrated in Fig. 38.16 implies the possibility of stretching polymer by mixing will also contribute to the formation of floc. Thus, the estimated value of δ_h is much larger than the size of the same polymer obtained by viscosity and dynamic light scattering [14] as illustrated in Fig. 38.17.

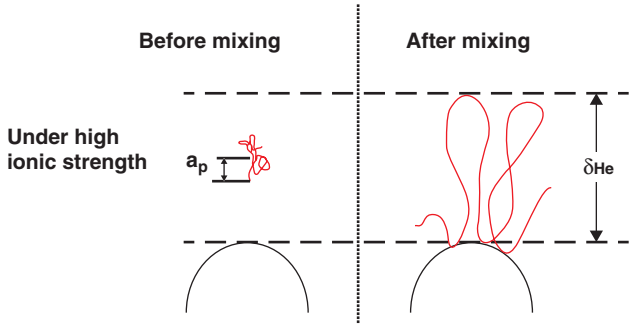


FIGURE 38.17 Image drawing of the change IN conformation of polyelectrolyte flocculant in the presence of mixing flow obtained from the result of a flocculation experiment [14].

38.6 CONCLUSION AND FUTURE PERSPECTIVES

One can immediately imagine that geometry of collisions will be an effective factor in the dynamics of flocculated suspension. However, it is not easy to obtain clear data. In this chapter, we introduced results obtained mainly in our laboratory.

Actually, the genetic structure is not merely the result of kinetics but will affect the kinetics profoundly. In the present chapter we assumed that flocs are monodispersed. Analysis of the effect of polydispersity and permeability is still in a primitive stage and future studies are needed to confirm these early theories.

Another major issue awaiting future research will be concentrated suspension.

ACKNOWLEDGMENT

The author expresses his gratitude to Dr. Motoyoshi Kobayashi and Mr. Takuya Sugimoto for fruitful discussion of collision dynamics. The work is partly founded by Kakenhi (Grant 222408025).

REFERENCES

[1] Israelachvili, J.N. (2011). *Intermolecular and Surface Forces*. Academic Press.

[2] Russel, W.B., Saville, D.A.Schowalter, W.R. (1991). *Colloidal Dispersions.* Cambridge Univ. Press.

[3] Van de Ven, T.G.M. (1989). *Colloidal Hydrodynamics*. Academic Press.

[4] Saffman, P.G., Turner, J.S. (1956). On the collision of drops in turbulent clouds. *J. Fluid Mech.* **1**, 16–30.

[5] Li, X., Loagan, B. (1997). Collision frequencies of fractal aggregates with small particles by differential sedimentation. *Environ. Sci. Technol*, **31**, 1229–1236.

[6] Verwey, E.J., Overbeek, J.T.G. (1948). *Theory of the Stability of Lyophobic Colloids*. Elsevier.

[7] Napper, D. (1983). Polymeric stabilization of colloidal dispersions. Academic Press.

[8] Adachi, Y. (1995). Dynamic aspects of coagulation and flocculation. *Adv. Colloid Interface Sci.* **56**, 1–31.

[9] Adachi, Y., Ooi, S. (1990). Geometrical structure of a floc. *J.Colloid Interface Sci.* **135**, 374–384.

[10] Kobayashi, M., Adachi, Y., Ooi., S. (2001). Effect of particle size on breakup of flocs in a turbulent flow. *Annu. J. Hydraul. Eng. JSCE* **45**, 133–137.

[11] Adachi, Y., Kamiko, M. (1994). Sedimentation of a polystyrene latex floc. *Powder Technol.* **78**, 129–135.

[12] Sato, D.,Kobayashi, M., Adachi, Y. (2004). Effect of floc structure on the rate of shear coagulation. *J. Colloid Interface Sci.* **272**, 345–351.

[13] Fukasawa, T., Adachi, Y. (2006). Effect of floc structure on the rate of Brownian coagulation. *J.Colloid Interface Sci.* **304**, 115–118.

[14] Adachi, Y., Xiao, J. (2013). Initial stage of bridging flocculation of PSL particles induced by an addition of polyelectrolyte under high ionic strength. *Colloids Surf. A: Physicochem. Eng. Aspects* **435**, 127–131.

[15] Von Smoluchowski, M. (1917). Versuch einer Mathematische Theorie der Koagulationskinetik Kolloider Lusngen. *Z.Phys. Chem.* **92**, 129–168.

[16] Higuchi, W.I.Okada, R., Stelter, G.A., Lemberger, A.P. (1963). Kinetics of rapid aggregation in suspensions. Comparison of experiments with the Smoluchowski theory. *J. Pharm. Sci.* **52**, 49–54.

[17] Swift. D.L., Friedlander, S.K. (1964). The coagulation of hydrosols by Brownian motion and laminar shear flow. *J.Colloid Sci.* **19**, 621–647.

[18] Higashitani, K., Matsuno, Y. (1979). Rapid Brownian coagulation of colloid dispersions. *J. Chem. Eng. Jpn.* **12**, 460–465.

[19] Hatton, P., Mcfadyen, P., Smith, A.L. (1974). Rapid flocculation rates of polystyrene latex dispersions. *J. Chem. Soc. Faraday Transact.* **70**, 655–660.

[20] Lips, A.,Willis, E. (1973). Low angle light scattering technique for the study of coagulation. *J. Chem. Soc. Faraday Transact.* **69**, 1226–1236.

[21] Adachi, Y., Chohen Stuart, M.A. (1994). Kinetics of turbulent coagulation studied by means of end-over-end rotation. *Colloid Interface Sci*. **165**, 310–317.

[22] Spielam, L.A. (1970). Viscous interactions in Brownian coagulation. *J. Colloid Interface Sci.* **334**, 562–571.

[23] Matsuoka, Y., Fukasawa, T., Higashitani, K., Ymamoto, R. (2012). Effect of hydrodymamic interactions on rapid Brownian coagulation of colloidal dispersions. *Phys. Rev. E.* **86**, 051403-1-9.

[24] Whytlaw-Gray, R., Peterson, H.S. (1932). Smoke: A study of aerial dispersed systems. London: Edward Arnold and Co.

[25] Friedlander, S.K. (1960). Similarity consideration for the particle-size spectrum of a coagulating and settling aerosols. *J. Meteol.* **17**, 479–483.

[26] Swift, D.L., Friedlander, S.K. (1964). The coagulation of hydrosols by Brownian motion and laminarshear flow. *J.Colloid Interface Sci.* **19**, 621–647.

[27] Friedlander, S.K. (2000). *Smoke,Dust, and Haze: Fundamentals of Aerosol Dynamics*, 2nd ed. Oxford Univ. Press.

[28] Friedlander, S.K., Wang, C.S. (1966). The self-preserving particle size distribution for coagulation by brownian motion. *J. Colloid Interface Sci.* **19**, 126–132.

[29] Suterland, D.N. (1967). A theoretical model of floc structure. *J. Colloid Sci.* **25**, 373–380.

[30] Sutherland, D.N., Goodarz-Nia, I. (1971). Floc simulation: the effect of collision sequence. *J. Chem. Eng. Sci.* **26**, 2071–2085.

[31] Meakin, P. (1988). Fractal aggregates. *Adv. Colloid Interface Sci.* **28**, 249–331.

[32] Schaeter, D.W., Martin, J.E., Wiltzuis, P., Cammel, D.S. (1984). Fractal geometry of colloidal aggregates. *J. Phys. Rev. Lett.* **52**, 2371–2374.

[33] Mountain, R.D., Mulholland, G.W., Baum, H. (1986). Simulation of aerosol agglomeration in the free molecular and continuum flow regimes. *Colloid Interface Sci.* **1141**, 67–81.

[34] Lin, C.J., Lee, K.J., Sather, N.F. (1970). Slow motion of two spheres in a shear field. *J. Fluid Mech.* **43**, 35-47.

[35] Batchelor, G.K., Green, J.T. (1972). The hydrodynamic interaction of two small freely-moving spheres in a linear flow field. *J. Fluid Mech.* **56**, 375–400.

[36] Zeichnerj, G.R., Schowalter, W.R. (1977). Use of trajectory analysis to study stability of colloidal dispersions in flow fields. *AIChE J*. **23**, 243–254.

[37] Van de Ven, T.G.M., Mason, S.G. (1977). The microrheology of colloidal dispersions VII. Orthokinetic doublet formation of spheres. *Colloid Polym. Sci*. **255**, 468–479.

[38] Torres, F.E., Russel, W.B., Schowalter, W.R. (1991). Floc structure and growth kinetics for rapid shear coagulation of polystyrene colloids. *J. Colloid Interface Sci.* **142**, 554–574.

[39] Kolmogoroff, A. (1941). The local structure of turbulence in incompressible viscous fluid for very large Reynolds' numbers. *Dokl. Akad. Nauk SSSR* **30**, 301–305; Dissipation of energy in the locally isotropic turbulence, ibid. **32**, 16–21.

[40] Camp, T.R., Stein, P.C. (1943). Velocity gradients and internal work in fluid motion. *J. Boston Soc. Civil Eng. Sec. Am. Soc. Civil Eng.* **30**, 219–237.

[41] Taylor, G.I. (1935). Statistical theory of turbulence. *Proc. Roy. Soc. A* **151**, 421–478.

[42] Townsend, A.A. (1974). The measurement of double and triple correlation derivatives in isotropic turbulence. *Proc. Chem. Phylogen. Sci.* **43**, 560–570.

[43] Higashitani, K., Yamauchi, Y., Matsuno, Y., Hosokawa, G. (1983). Turbulent coagulation of particles dispersed in a viscous fluid. *J. Chem. Eng. Jpn.* **16**, 299–304.r

[44] Kobayasi, M., Ishibashi, D. (2011). Turbidity measurement for the absolute rate of coagulation in a turbulent flow. *Colloid Polym. Sci.* **289**, 831–836.

[45] De Boer, G.B.J., Hoedemakers, G.F.M., Thoenes, D. (1989). Coagulation in turbulent flow, Part I. *Chem. Eng. Res. Design* **67**, 301–307.

[46] Ruehrwein, R.A., Ward, D.W. (1952). Mechanism and clay aggregation by polyelectrolytes. *Soil Sci.* **73**, 485–492.

[47] La Mer, V.K., Healy, T.W. (1963). Adsorption-flocculation reactions of macromolecules at solid-liquid interface. *Rev. Pure Appl. Chem*. **13**, 112.

[48] Fleer, G.J., Lyklema, J. (1976). Polymer adsorption and its effect on the stability of hydrophbic colloids III. Kinetics of the flocculation of silver iodide sols. *J. Colloid Interface Sci.* **55**, 228–238.

[49] Ash, S.G., Clayfield, E.J. (1976). Effect of polymers on the stability of ccolloids. *J. Colloid Interface Sci.* **55**, 645–657.

[50] P.G.DeGennes, (1987). Polymer at an Interface; a simplified view. *Adv. Colloid Interface Sci.* **27**, 189–209.

[51] Fleer, G.J.M.A., Cohen Stuart, J.M.H.M. (1993). Scheutiens, polymers at interfaces. In Cosgrove, T., Vincent, B. (eds.), *Polymers at Interfaces*. Chapman & Hall.

[52] Gregory, J. (1973). Rates of flocculation of latex particles by cationic polymes. *J. Colloid Interface Sci.* **42**, 448–456.

[53] Gregory, J. (1988). Polymer adsorption and flocculation in sheared suspensions. *Colloid Surf.* **31**, 231–253.

[54] Higashitani, K.,Kubota, T. (1987). Pelleting flocculation of colloidal latex particles. *Powder Technol*. **51**, 61–69.

[55] Eriksson, L., Alm, B., Stenius, P. (1993). Formation and structure of polystyrene latex aggregates obtained by flocculation with cationic polyelectrolytes. *Colloid Surf. A*, **70**, 47–60.

[56] Adachi Y., Cohen Stuart, M.A., Fokkink, R. (1994). Dynamic aspects of bridging flocculation studied using standardized mixing. *J.Colloid Interface Sci.* **167**, 346–351.

[57] Matsumoto, T., Adachi, Y. (1998). Effect of ionic strength on the initial dynamics of flocculation of polystyrene latex with polyelectrolyte. *J.Colloid Interface Sci.* **204**, 328–335.

[58] Adachi, Y., Wada, T. (2000). Initial stage dynamics of bridging flocculation of polystyrene latex spheres with polyethylene oxide. *J.Colloid Interface Sci.* **229**, 148–154.

[59] Aoki, K., Adachi, Y. (2006). Kinetics of polyelectrolyte adsorption onto polystyrene latex particle studied using electrophoresis: Effects of molecular weight and ionic strength. *J. Colloid Interface Sci.* **300**, 69–77.

[60] Adachi, Y. (2012). Dynamics of polymers and polyelectrolytes at colloidal interface and subsequent flocculation. In Ohshima, H. (ed.), *Electrical Phenomena at Interfaces and Biointerfaces: Fundamentals and Applications in Nano-, Bio-, and Environmental Sciences*., Wiley, Hoboken, NJ, pp. 299–314.

39

ANISOTROPIC GEL FORMATION INDUCED BY DIALYSIS

Toshiaki Dobashi and Takao Yamamoto
Graduate School of Science and Technology, Gunma University, Gunma, Japan

39.1 INTRODUCTION

Gels consist of a polymer network swollen by their medium. The cross-linking sites of a polymer network are usually dispersed randomly in gels, resulting in a macroscopically isotropic and homogeneous structure. This is because the maximum entropy of easily deformed polymer segments between cross-linking sites is obtained when the number of conformational states is maximum, specifically, in the isotropic and homogeneous states. In materials science and technology, however, it is sometimes important to control the anisotropic properties of materials. The anisotropy of gels is even more important in biological organisms, since gels in organisms such as those in muscles and blood vessels are anisotropic, having an advantage of function in organisms [1]. A crystal lens has anisotropy with an even gradient [2]. Therefore, anisotropy is often one of the required factors for artificial tissues and organs [3]. If polymer molecules in gels are rigid and strictly aligned in a particular direction, however, the entropy gain becomes smaller and the gel state becomes unstable. Therefore, various attempts to achieve a good balance between the abovementioned competitive effects, that is, an energetic penalty for an isotropic arrangement and an entropic penalty for molecular alignment, have been performed to obtain anisotropic gels [4–13].

Among the methods for preparing anisotropic gels, dialysis-induced gelation [14] has the advantage that the balance between the two effects is automatically obtained by self-organization and the gel formation, which is closely related to the appearance of anisotropy, can be analyzed by means of nonequilibrium thermodynamics [15]. In this method, polymer solutions are brought in contact with cross-linker solutions at an interface that is not permeable to polymer molecules but permeable to the solvent and medium, a solution of low-molecular-weight molecules including cross-linkers. Cross-linking starting from the interface enables us to obtain anisotropic gels. In Section 39.2, we describe the preparation of gels in detail and the resulting characteristics of the gels, focusing on the gelation process. In Section 39.3, a theoretical treatment of the analysis of gel formation process is provided. In Section 39.4, some of the applications reported previously and their potential uses are summarized.

39.2 DIALYSIS-INDUCED GELATION

39.2.1 Boundary Conditions

Dialysis-induced gelation is realized under various boundary conditions, as shown in Fig. 39.1. Figure 39.1a shows the most common means of dialyzing polymer solutions into a medium, where the boundary between the polymer solution and the medium is determined by the dialysis tube. Unless the resultant gel is too swollen or shrunk to detach itself from the dialysis tube, the boundary between the gel phase and medium is almost fixed during gelation. In Fig. 39.1b, a polymer solution is placed in a cell consisting of a set of circular parallel plates surrounded by a dialysis tube, and immersed in the medium. In this case, the boundary between the polymer solution and the resultant gel is partly fixed by the two plates and partly determined by the dialysis tube. In Fig. 39.1c, a polymer solution is sandwiched between a set of circular

Encyclopedia of Biocolloid and Biointerface Science, Volume 1, First Edition. Edited by Hiroyuki Ohshima.
© 2016 John Wiley & Sons, Inc. Published 2016 by John Wiley & Sons, Inc.

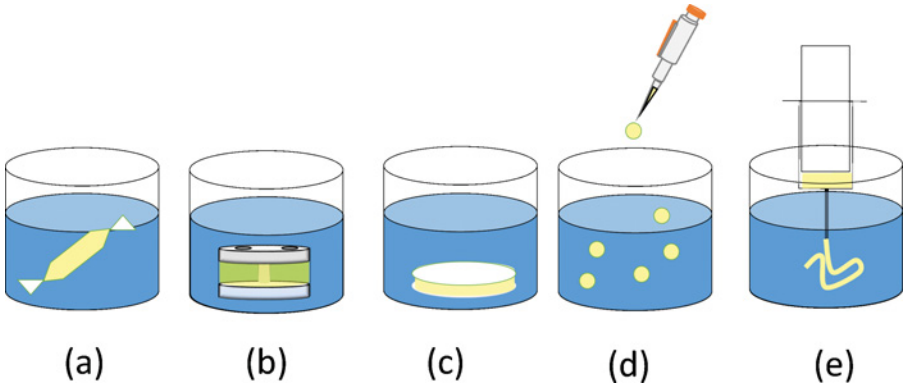


FIGURE 39.1 Illustration of dialysis-induced gelation by various methods under different boundary conditions.

parallel plates and immersed in the medium. Although there is no separation between polymer solutions and the medium, a thin gel membrane produced with the first contact of the polymer solution and the medium at the contact surface can serve as a dialysis tube, resulting in dialysis-induced gelation. The gelation shown in Fig. 39.1a–c is regarded as a process involving the growth of a gel layer toward the center. We also note that the geometry in (a) – (c) in Fig. 39.1 is cylindrically symmetrical. In Fig. 39.1c, we can use two parallel plates with various shapes to design different boundary conditions. For example, using square parallel plates, we obtain a geometrical condition having a fourfold rotation axis. If we drip a polymer solution into a medium, polymer molecules at the surface of the droplet cross-link on contact and the resulting thin concentric gel membrane serves as a spherical dialysis membrane [16], as shown in Fig. 39.1d. The geometry in this case is spherically symmetric. If we keep adding a polymer solution into the medium, we obtain a threadlike gel, as shown in Fig. 39.1e. In Figs. 39.1d,e, the position of the boundary surface between the initially yielded gel and the medium is maintained only when the cross-linking rate and cross-linking density at the surface are sufficiently large to maintain the shape. Otherwise, the polymer solutions dissolves in a large amount of the medium or the boundary largely deforms with time.

39.2.2 Birefringence of Dialysis-Induced Gel

Various combinations of rodlike or semiflexible polymer solutions, such as collagen, Curdlan, carboxymethylcellulose (CMC), chitosan, gelatin, polyglutamic acid, polylysine, arginic acid, and κ-carrageenan, and their appropriate media yield anisotropic gels, as shown in Fig. 39.2, under the boundary condition shown in Fig. 39.1a or c [17–24]. In all figures, black crossed lines are observed under crossed nicols. From optics [25], the symmetric axis of molecular alignment is in the radial direction. Among the combinations, the direction of molecular alignment was determined to be circumferential for the collagen and arginic acid systems [19,23]. A clear birefringence gradient is observed for all the gels. The turbid stripes observed in Figs. 39.2i and iii are attributed to the coupling of gelation and other physical phenomena such as phase separation. All the images observed under different boundary conditions, denoted as (a)–(e) in Fig. 39.1, exhibit

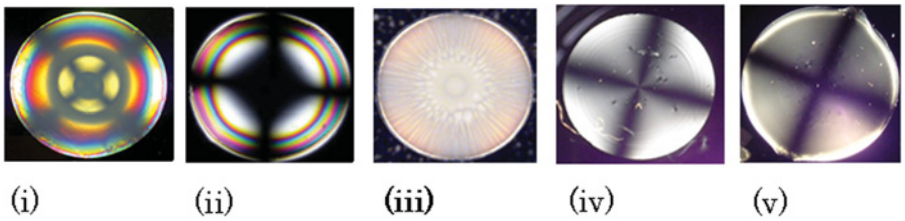


FIGURE 39.2 Gels observed under crossed nicols for polymer solution/medium systems using the boundary condition (a) or (c) in Fig. 39.1. The gels prepared under condition (a) were excised perpendicularly to the long axis of the dialysis tube, and the gels prepared under condition (c) were stripped off the plates. The photographs were taken from the top view: (i) Curdlan in NaOH solution/$CaCl_2$ solution (from Ref. 14, Fig. 2); (ii) DNA in buffer of pH 9.2/$CoCl_2$ solution (from Ref. 17, Fig. 1); (iii) CMC in pure water/$CaCl_2$ solution (from Ref. 18, Fig. 1); (iv) chitosan in acetic acid solution/NaOH solution (from Ref. 24, Fig. 1a); (v) myosin in pure water/glutaraldehyde solution. For a color version of this figure, see the color plate section.

clear birefringence (not shown). Therefore, the appearance of birefringence induced by dialysis should be a universal phenomenon. On the other hand, when we lower the concentrations of cross-linkers in the medium, the birefringence of the gels becomes weaker and finally disappears. These results suggest that a large chemical potential difference of polymer molecules at the interface between the polymer solutions and the medium is a necessary condition for yielding anisotropic gels.

39.2.3 Trigger for Gelation

Although the appearance of anisotropy is a common feature of dialysis-induced gelation, the cross-linking mechanism depends on the system. For example, the gelation of the solutions of DNA [17] and CMC [18] in Fig. 39.2ii and iii is induced by the cross-linking of polymer molecules by multivalent cations. Thus, the inflow of multivalent cations in the medium triggers gelation. In contrast to these systems, the gelation of the solution of chitosan in Fig. 39.2iv is induced by changing the pH of the solution to decrease the charge of polymer molecules to allow cross-linking due to hydrogen bonding. In this case, both the inflow and outflow of H^+ and OH^- from the polymer solution induce gelation. In Fig. 39.2i, the gelation mechanism is even more complex. Curdlan, (1→3)-β-D-glucan, is dissolved in an alkaline solution with a high pH. By lowering the pH of the solution, the Curdlan solution gels because the charge of Curdlan molecules is reduced, resulting in the disappearance of ionic binding sites and in a conformational change of Curdlan to induce cross-linking due to hydrogen bonding. The Curdlan solution also gels with cross-linkers of multivalent cations such as calcium cations. Therefore, when the Curdlan solution with a high pH is dialyzed into calcium chloride solution, both the inflow of calcium cations and the outflow of hydroxide ions induce gelation. The gelations by calcium-ion-induced cross-linking and hydrogen-bonding-induced cross-linking are competitive. As shown in Section 39.3, calcium-ion-induced cross-linking in the initial process and hydrogen-bonding-induced cross-linking in the late process are suggested from the results of a series of experiments and comparison with a theoretical argument. Interestingly, no calcium ions were detected in the polymer solution in the initial gelation, indicating that all the calcium ions in the inflow are used for cross-linking Curdlan to grow the gel layer. A dual cross-linking mechanism similar to that of the above-mentioned Curdlan system is also observed for DNA in a buffer of pH 9.2 dialyzed into a multivalent cation solution (Fig. 39.2ii) [9]. In this case, the pH of the solvent of DNA decreases, resulting in a decrease in the charge of DNA molecules and ultimately in the number of cross-linking sites during gelation. Although the mechanism of cross-linking is complex and depends on the system, gelation always consists of (1) irreversible molecular diffusion in both the polymer solution and the medium, (2) irreversible trans-interface molecular diffusion, (3) a reversible change in the conformation and charge of polymer molecules resulting from a change in the solvent composition, and (4) a reversible or irreversible molecular alignment starting from the interface between the polymer solution and the medium and the reversible or irreversible cross-linking of polymer molecules under the condition that the polymer solution is confined in a limited space.

39.2.4 Dynamics of Gelation

Figure 39.3 shows a typical example (chitosan in a low-pH solution dialyzed in a high-pH solution, as shown in Fig. 39.2iv, using square coverglasses as parallel plates) of the timecourse of anisotropic gelation. The front lines of the turbid gel layer and birefringent layer are traced under observation with open nicols and crossed nicols, respectively. To monitor the pH change, a small amount of litmus reagent is added to the chitosan solution, and the interface between the pink zone (acidic) and sky-blue zone (alkaline) is also traced during gelation. Clear boundaries between the layers with and without birefringence, between the turbid gel layer and the transparent sol, and between the pink zone and the sky-blue zone develop during dialysis. Figure 39.4 shows that during gel formation by the sandwich method, all the front lines of gelation, orientation, and pH change proceed simultaneously [24]. The mechanism of the synchronization of the motion of the front lines may be related to the gradient of the chemical potential of chitosan near the boundary layer. The results also indicate that anisotropic gelation can be traced by examining only the gel layer thickness x against the dialysis time t. Figure 39.5 shows the time course of x plotted using the scaled variables $\tilde{x} = x/R$ and $\tilde{t} = t/R^2$, where R is the radius of the parallel plates in Fig. 39.1c. The perfect superposition irrespective of the radius in the scaling plot and initial proportional relationship between $\tilde{x}^2$ versus $\tilde{t}$ (not shown) suggest a diffusion-limited process. Such a scaling relationship and the initial proportional behavior were observed for all systems previously reported. Thus, these characteristic behaviors are universal for dialysis-induced anisotropic gelation. On the other hand, the dynamics in the late process are different from each other and depend on the system.

39.3 THEORETICAL TREATMENT OF ANALYSIS OF DIALYSIS-INDUCED GELATION

The gelation mechanisms for the systems investigated so far are classified into four types; (1) gelation induced by the inflow of cross-linking agent, (2) gelation induced by a pH change due to both the inflow and outflow of ions, (3) gelation accompanied by a transition in mechanism, and (4) gelation induced by a dual mechanism.

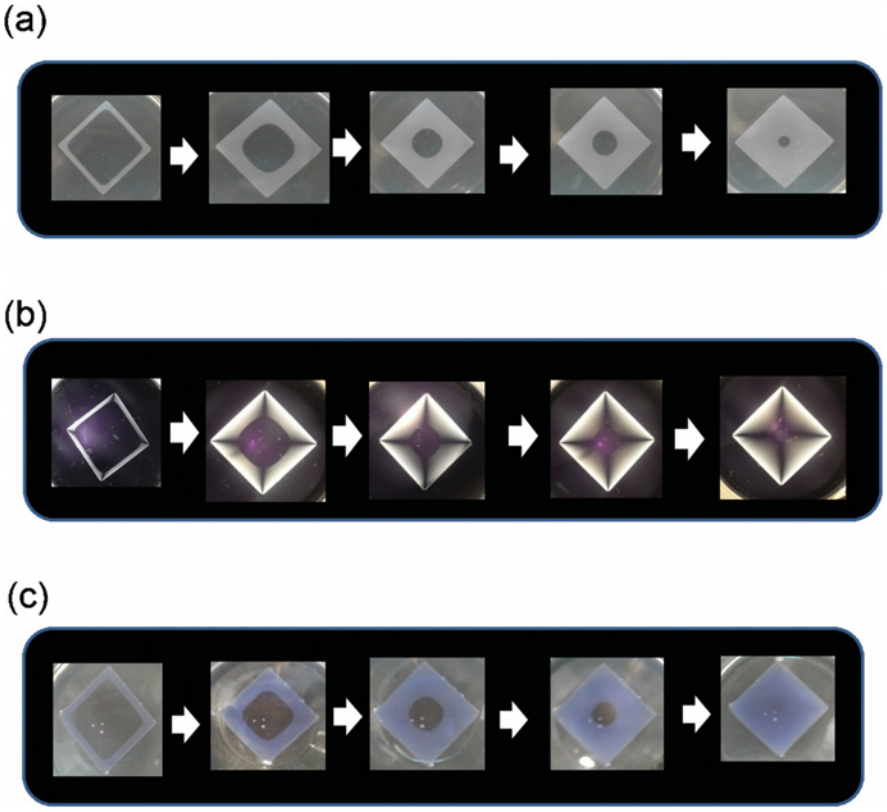


FIGURE 39.3 Development of birefringent, turbid, and sky-blue layers for the system of chitosan in acetic acid solution/NaOH solution under the square boundary condition in Fig. 39.2iv.

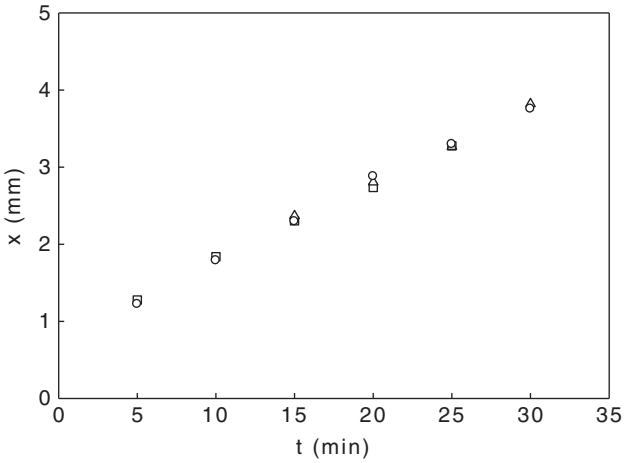


FIGURE 39.4 Timecourse of distance from edge of coverglass to interface between gel layer and sol core observed under open nicols (gel thickness) (∘), to interface between oriented layer and amorphous core observed under crossed nicols (oriented layer thickness) (□), and to interface between pink layer and sky-blue core dyed by litmus agent (△) (high-pH layer thickness) in immersion process of 200 μL of chitosan solution (1 wt% chitosan in 1 wt% aqueous acetic acid with 0.05 g/dL litmus agent) in 40 mL of 0.3 M NaOH for the system shown in Fig. 39.2iv. (From Ref. 27, Fig.2.) Reprinted with permission from the Material Research Society of Japan.

39.3.1 Dynamics of Gelation Induced by a Cross-Linking Agent

The gelation of the solutions of DNA, CMC, and Curdlan (early stage) is induced by cations flowing from the medium into the inner polymer solution. The inflowing cations cross-link the polymers and serves as a cross-linking agent. Let

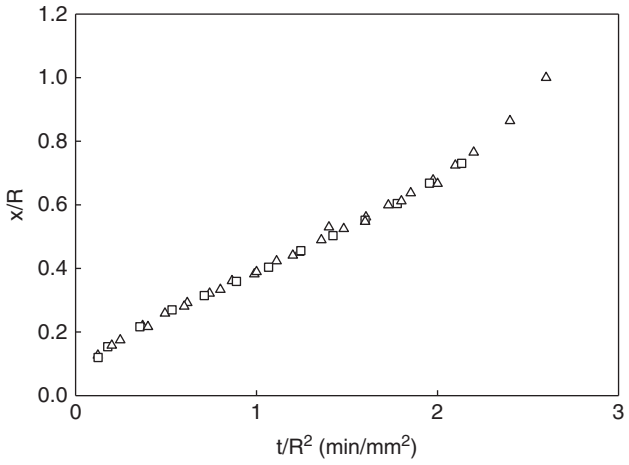


FIGURE 39.5 Timecourse of gel thickness in a scaled plot for system shown in Fig. 39.2iv. The diameters of the coverglasses are 12 mm (□), 15 mm (△), and 18 mm (∘).

us call the ion inducing the gelation by inflowing from the medium to the inner polymer solution the *inflow-ion*. The dynamics of the gelation is quantitatively explained by nonequilibrium thermodynamics based on the following assumptions [15]:

1. All the inflow-ions arriving at the inner polymer solution instantly cross-link with the polymers to produce a new gel layer.
2. The gel layer does not capture the inflow-ions as a sink, i.e., all the inflow-ions arrive at the inner polymer solution through the gel layer to realize a steady state.
3. The medium, gel and inner polymer solution are in local thermodynamic equilibrium at the boundary.

Assumption 1 ensures that the boundary between the gel layer and the inner solution is macroscopically sharp and that the gel formation dynamics can be visualized by tracking the motion of the boundary. The method in which the timecourse of the gelation is expressed by the boundary motion is called the *moving-boundary picture*.

Here, let us choose a system with cylindrical symmetry, specifically, the system sandwiched between two parallel circular glass plates with radius R. For a cylindrically symmetric system, the boundary is also cylindrically symmetric; the boundary is expressed as a circle concentric with the circular glass. The gel layer width x denotes the difference between the radii of the two circles. The relationship between the immersion time t and the gel layer width x is derived on the basis of nonequilibrium thermodynamics and assumptions 1–3.

As shown in Fig. 39.6, ρ_s, ρ_s', and ρ_0' denote the inflow-ion concentrations in the medium and in the gel layer at the boundaries with the medium and with the inner polymer solution, respectively. These concentrations are independent of the immersion time. The inflow-ion concentration ρ_0 in the inner polymer solution is zero because of assumption 3. The inflow-ion concentration at a distance r from the center of the cylinder is denoted by $\rho'(r)$, where $R - x \le r \le R$, $\rho'(R - x) = \rho_0'$, and $\rho'(R) = \rho_s'$.

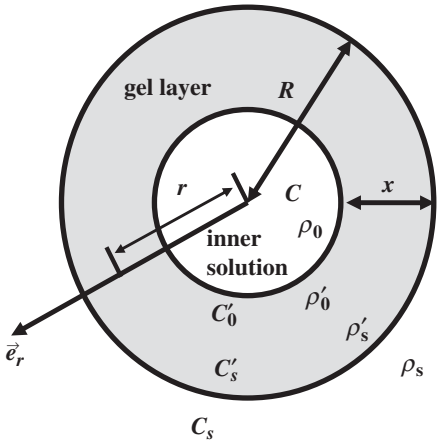


FIGURE 39.6 Upper view of dialysis system. The variables used to describe the theory are shown.

At the boundaries between the gel and the medium and between the gel and the inner polymer solution, the chemical potentials of the inflow-ion are balanced because of assumption 3:

$$\begin{cases} \mu_s^{\text{in}}(\rho_s) = \mu_G^{\text{in}}(\rho_s') \\ \mu_G^{\text{in}}(\rho_0') = \mu_0^{\text{in}}(0) \end{cases} \tag{39.1}$$

where μ_s^{in}, μ_0^{in}, and μ_G^{in} are respectively the chemical potentials of the inflow-ion in the medium, inner polymer solution, and gel layer. The cylindrical symmetry allows us to assume that the inflow-ion flux $\vec{j}^{\text{in}}$ is always along the radial direction and depends on only the distance r. Thus, we have

$$\vec{j}^{\text{in}} = -j^{\text{in}}\vec{\text{e}}_r \tag{39.2}$$

where j^{in} is the flux density and $\vec{\text{e}}_r$ is the unit vector along the radial direction. According to Fick's law, the velocity of the inflow-ion in the radial direction at a distance r is given by

$$v^{\text{in}} = -k^{\text{in}}\frac{\partial \mu_G^{\text{in}}(r)}{\partial r} \tag{39.3}$$

where k^{in} is the mobility of the inflow-ion and is assumed to be independent of the position in the gel layer. The flux density is given by

$$j^{\text{in}} = v^{\text{in}}\rho'(r) = -k^{\text{in}}\rho'(r)\frac{\partial \mu_G^{\text{in}}(r)}{\partial r}. \tag{39.4}$$

Assumption 2 requires that

$$\text{div}\vec{j}^{\text{in}} = -\frac{1}{r}\frac{\partial r j^{\text{in}}}{\partial r} = 0. \tag{39.5}$$

From the above equation, we obtain

$$j^{\text{in}}(r) = \frac{A}{r} \tag{39.6}$$

where A is a constant of integration determined by the boundary condition [Eq. (39.1)]. Using Eq. (39.4), we can rewrite Eq. (39.6) as follows:

$$-k^{\text{in}}\rho'(r)\frac{\partial \mu_G^{\text{in}}(r)}{\partial r} = \frac{A}{r} \tag{39.7}$$

Integrating both sides of the above equation from $r = R - x$ to $r = R$, we have

$$k^{\text{in}}[g^{\text{in}}(\rho'_s) - g^{\text{in}}(\rho'_0)] = A \ln \frac{R}{R-x} \tag{39.8}$$

where $g^{\text{in}}(\rho')$ is the partial pressure of the inflow-ion in the gel layer and is expressed in terms of the free energy satisfying

$$\mu_G^{\text{in}}(\rho') = \frac{\partial f_G^{\text{in}}(\rho')}{\partial \rho'} \tag{39.9}$$

as

$$g^{\text{in}}(\rho') = \rho' \mu_G^{\text{in}}(\rho') - f_G^{\text{in}}(\rho'). \tag{39.10}$$

Equation (39.8) gives the constant of integration as follows:

$$A = \frac{k^{\text{in}}[g^{\text{in}}(\rho'_s) - g^{\text{in}}(\rho'_0)]}{\ln \frac{R}{R-x}} \tag{39.11}$$

Therefore, the flux density j^{in} is given by

$$j^{\text{in}}(r) = \frac{k^{\text{in}}[g^{\text{in}}(\rho'_s) - g^{\text{in}}(\rho'_0)]}{\ln \frac{R}{R-x}} \frac{1}{r} \tag{39.12}$$

By denoting the number of inflow-ions required to produce a unit volume of the gel by ρ_G, we find that assumption 1 gives the relationship between the time interval dt and the width of the newly produced gel layer dx

$$2\pi R j^{\text{in}}(R) dt = \rho_G 2\pi (R - x) dx \tag{39.13}$$

From Eqs. (39.12) and (39.13), the time development equation of the gel width x is given by

$$\frac{dx}{dt} = K \frac{1}{(R-x) \ln \frac{R}{R-x}} \tag{39.14}$$

where

$$K = \frac{k^{\text{in}}[g^{\text{in}}(\rho'_s) - g^{\text{in}}(\rho'_0)]}{\rho_G} \tag{39.15}$$

Note that ρ_G is an increasing function of the concentration of the polymer in the inner solution since the number of cross-linking agent molecules required to cross-link the polymer increases with increasing number of polymer molecules in the inner solution. Thus, the coefficient K decreases with increasing concentration of the polymer in the inner solution.

In terms of the scaled time $\tilde{t} = t/R^2$ and the scaled width $\tilde{x} = x/R$, we have the following "universal" expression independent of the radius of the parallel plates, R:

$$\frac{d\tilde{x}}{d\tilde{t}} = K \frac{1}{(1-\tilde{x}) \ln \frac{1}{1-\tilde{x}}} \tag{39.16}$$

The solution to the above equation is given by

$$\frac{1}{2}(1-\tilde{x})^2 \ln(1-\tilde{x}) - \frac{1}{4}\tilde{x}^2 + \frac{1}{2}\tilde{x} = K\tilde{t} \tag{39.17}$$

The right-hand side (RHS) in the above equation, namely

$$\tilde{y}(\tilde{x}) \equiv \frac{1}{2}(1-\tilde{x})^2 \ln(1-\tilde{x}) - \frac{1}{4}\tilde{x}^2 + \frac{1}{2}\tilde{x} \tag{39.18}$$

is a universal function irrespective of the details of the system. Only the parameter K indicates the individuality of the gelation dynamics. The gelation dynamics of the DNA solution plotted in terms of the scaled time and the function $\tilde{y}$ is shown in Fig. 39.7. All the data for the low-pH DNA solutions (pH 6.8, 72, and 7.8) sit on the lines as shown in Fig. 39.7a.

In the initial stage of the gelation process, $\tilde{x} \approx 0$, we have $\tilde{y}(\tilde{x}) \approx \frac{1}{2}\tilde{x}^2$. Then, the square-root-type time development equation

$$\tilde{x} = \sqrt{2K\tilde{t}} \tag{39.19}$$

is obtained.

The square-root behavior appears since the gelation dynamics is inflow-ion-diffusion-limited. Diffusion process is governed by Fick's law, given by Eq. (39.3). The diffusion constant D conventionally characterizing diffusion is defined by the relationship between the flux and the concentration gradient as

$$D = D(\rho') = k^{\text{in}} \rho' \frac{\partial \mu_G^{\text{in}}(\rho')}{\partial \rho'} \vec{e}_r \tag{39.20}$$

Comparing the above equation with the flux expression [Eq. (39.4)], we have the concentration-dependent diffusion constant

$$D = D(\rho') = k^{\text{in}} \rho' \frac{\partial \mu_G^{\text{in}}(\rho')}{\partial \rho'} \tag{39.21}$$

For simplicity, instead of the above "precisely defined" diffusion constant, we focus on the "mean" diffusion constant

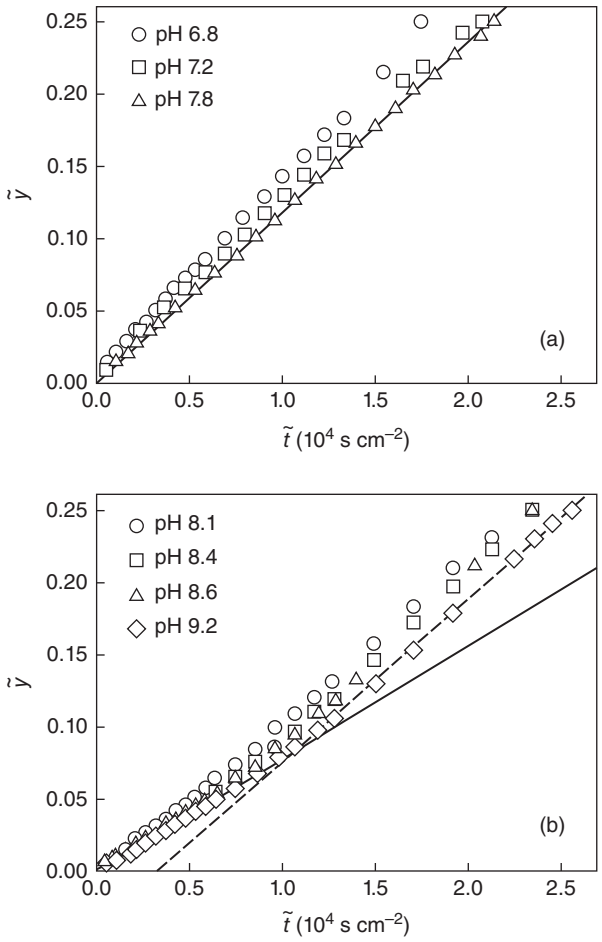


FIGURE 39.7 Gel formation process of DNA solution immersed in $AlCl_3$ solution expressed by the function $\tilde{y}(\tilde{x})$ against the scaled time $\tilde{t}$. The results for DNA solutions with various pH in the range of pH 6.8–9.2 are shown. (From Ref. 9, Fig. 6.) Reprinted with permission from the American Chemical Society.

defined by

$$\bar{D} = \frac{1}{\rho_s' - \rho_0'} \int_{\rho_0'}^{\rho_s'} D(\rho) d\rho \tag{39.22}$$

This equation is rewritten as follows:

$$\bar{D} = \frac{1}{\rho_s' - \rho_0'} \int_{\rho_0'}^{\rho_s'} D(\rho) d\rho = \frac{1}{\rho_s' - \rho_0'} \int_{\rho_0'}^{\rho_s'} k^{\text{in}} \rho \frac{\partial \mu_G^{\text{in}}(\rho)}{\partial \rho} d\rho$$

$$= k^{\text{in}} \frac{1}{\rho_s' - \rho_0'} [g^{\text{in}}(\rho_s') - g^{\text{in}}(\rho_0')]$$

$$= \frac{\rho_G}{\rho_s' - \rho_0'} K \approx \frac{\rho_G}{\rho_s'} K \approx \frac{\rho_G}{\rho_s} K \tag{39.23}$$

From the above equation and the definition of K, we have the following relationship:

$$\bar{D} \approx \frac{\rho_G}{\rho_s} K \tag{39.24}$$

39.3.2 Dynamics of Gelation Induced by pH Change

The gelation of chitosan solution is induced by a pH change. The gelation dynamics induced by a pH change involves ions (e.g., H^+) flowing out of the inner polymer solution to the medium as well as inflow-ions (e.g., OH^-) since both the inflow of ions in the medium and the outflow of ions in the inner polymer solution can change the pH of the inner polymer solution. Let us call the ion inducing gelation by outflowing from the inner polymer solution the *outflow-ion*. The ion outflow reduces the number of inflow-ions ρ_G required to produce a unit volume of gel. Combining the time development equation of ρ_G with the time development equation of the boundary [Eq. (39.16)], we derive the pH-change-type gelation dynamics [26].

New assumptions, namely, that (4) the gel layer does not capture the outflow-ions as a sink, that is, that all the outflow-ions arrive at the medium through the gel layer to realize a steady state; (5) the inner polymer solution is always in thermodynamic equilibrium; and (6) the flows of the inflow-ion and the outflow-ion do not affect each other, are added to assumptions 1–3. Assumption 5 implies that the concentration of the outflow-ion in the inner polymer solution is uniform. The concentration of the outflow-ion in the inner solution is denoted by $C(t)$. As shown in Fig. 39.6, C_s' and C_0' denote the outflow-ion concentrations in the gel layer at the boundaries with the medium and inner polymer solution, respectively. Since the volume of the medium is quite large, the concentration of the outflow-ion C_s in the medium is expected to always be zero. The outflow-ion concentration at a distance r from the center of the cylinder is denoted by $C'(r)$, where $R - x \le r \le R$.

At the boundaries between the gel and the medium and between the gel and the inner polymer solution, the chemical potentials of outflow-ions are balanced because of assumption 3

$$\begin{cases} \mu_s^{\text{out}}(0) = \mu_G^{\text{out}}(C_s') \\ \mu_G^{\text{out}}(C_0') = \mu_0^{\text{out}}(C(t)) \end{cases} \tag{39.25}$$

where μ_s^{out}, μ_0^{out}, and μ_G^{out} are, respectively, the chemical potentials of outflow-ions in the medium, the inner polymer solution, and the gel layer. Note that these chemical potentials are expected to be independent of the inflow-ion concentration from assumption 5. The outflow-ion flux $\vec{j}^{\text{out}}$ is also along the radial direction and depends only on the distance r

$$\vec{j}^{\text{out}} = j^{\text{out}} \vec{e}_r \tag{39.26}$$

where j^{out} is the flux density. The velocity of the outflow-ion in the radial direction at a distance r is given by

$$v^{\text{out}} = -k^{\text{out}} \frac{\partial \mu_G^{\text{out}}(r)}{\partial r} \tag{39.27}$$

where k^{out} is the mobility of the outflow-ion and is assumed to be independent of the position in the gel layer. The flux density is given by

$$j^{\text{out}} = v^{\text{out}} C'(r) = -k^{\text{out}} C'(r) \frac{\partial \mu_G^{\text{out}}(r)}{\partial r} \tag{39.28}$$

Assumption 4 requires that

$$\text{div}\vec{j}^{\text{out}} = \frac{1}{r} \frac{\partial r j^{\text{out}}}{\partial r} = 0. \tag{39.29}$$

From the above equation, we obtain

$$j^{\text{out}}(r) = \frac{B}{r} \tag{39.30}$$

where B is constant of integration determined by the boundary condition. Following the procedure by which the constant A is derived, we have

$$B = \frac{k^{\text{one}}[g^{\text{one}}(C_s') - g^{\text{one}}(C_0')]}{\ln \frac{R}{R-x}} \tag{39.31}$$

where $g^{\text{one}}(C')$ is the partial pressure of the outflow-ion in the gel layer and is given by

$$g^{\text{out}}(C') = C' \mu_G^{\text{out}}(C') - f_G^{\text{out}}(C') \tag{39.32}$$

with the free energy satisfying

$$\mu_G^{\text{out}}(C') = \frac{\partial f_G^{\text{out}}(C')}{\partial C'} \tag{39.33}$$

Here, we use assumption 5, from which the chemical potential of the outflow-ion can be assumed to depend on only the concentration of the outflow-ion and not on that of the inflow-ion. Since the concentration of the outflow-ion in the medium is zero, we can expect that C_0' is also zero. This means that $g_G^{\text{out}}(C_0') \approx g_G^{\text{out}}(0) \approx 0$ and

$$B = -\frac{k^{\text{out}} g^{\text{out}}(C_0')}{\ln \frac{R}{R-x}} \tag{39.34}$$

Then, the flux density j^{out} is obtained as

$$j^{\text{out}}(r) = \frac{-k^{\text{out}} g^{\text{out}}(C_0')}{\ln \frac{R}{R-x}} \frac{1}{r} \tag{39.35}$$

Since the concentration of the outflow-ion in the inner polymer solution is reduced by flow of the outflow-ion and the gel layer does not capture the outflow-ions, we have

$$\pi(R-x)^2 dC = -j^{\text{out}}(R) 2\pi R dt \tag{39.36}$$

Then, using Eqs. (39.35) and (39.36), we have the time development equation for $C(t)$;

$$\frac{dC(t)}{dt} = -2 \frac{k^{\text{out}} g^{\text{out}}(C_0')}{(R-x)^2 \ln \frac{R}{R-x}} \tag{39.37}$$

In terms of the scaled variables $\tilde{t}$ and $\tilde{x}$, the above equation is rewritten as

$$\frac{dC(\tilde{t})}{d\tilde{t}} = -2 \frac{k^{\text{out}} g^{\text{out}}(C_0')}{(1-\tilde{x})^2 \ln \frac{1}{1-\tilde{x}}} \tag{39.38}$$

Note that the scaled gel width $\tilde{x}$ is changing with time, as shown by Eq. (39.16).

The pH change is induced by neutralization by inflowing of the inflow-ions. The number of the inflow-ions required to neutralize the inner solution is proportional to the concentration of the outflow-ions in the inner solution. Hence, ρ_G is expressed as [26]

$$\rho_G = \alpha C \tag{39.39}$$

where α is a positive constant. The above equation indicates that the number of the inflow-ions required to produce a unit volume of gel decreases with increasing immersion time since the concentration C decreases owing to the outflow of ions in the inner solution.

To discuss the dynamics of the gelation induced by a pH change, we take the time development of ρ_G into account. The gelation dynamics is expressed by the simultaneous equations Eqs. (39.16), (39.25), (39.38), and (39.39). To obtain the solution to these equations, we must obtain the thermodynamic functions, the partial pressures g^{in} and g^{out}, and the chemical potentials, μ_0^{in}, μ_G^{in} μ_s^{in}, μ_0^{out}, μ_G^{out}, and μ_s^{out}. In the simplest case, we adopt the ideal gas picture for the inflow-ions and the outflow-ions. Then, the partial pressures are given by

$$\begin{cases} g^{\text{in}}(\rho') = k_B T \rho' \\ g^{\text{out}}(C') = k_B T C' \end{cases}, \tag{39.40}$$

and the relationships between the concentrations at the boundaries are given by

$$\begin{cases} \rho_s' = \rho_s, & C_s' = C_s = 0 \\ \rho_0' = \rho_0 = 0, & C_0' = C \end{cases} . \tag{39.41}$$

From Eqs. (39.39)–(39.41), since the coefficient K given by Eq. (39.15) is expressed as

$$K = K(\tilde{t}) = \frac{\gamma \rho_s}{\alpha C(\tilde{t})} \tag{39.42}$$

with

$$\gamma = k^{\text{in}} k_B T \tag{39.43}$$

and

$$-k^{\text{out}} g^{\text{out}}(C_0') = -\beta C(\tilde{t}) \tag{39.44}$$

with

$$\beta = k^{\text{out}} k_B T \tag{39.45}$$

the simultaneous equations expressing the gelation dynamics [Eqs. (39.16) and (39.38)], are rewritten as

$$\begin{cases} \dfrac{d\tilde{x}}{d\tilde{t}} = \dfrac{\gamma \rho_s}{\alpha C(\tilde{t})} \dfrac{1}{(1-\tilde{x}) \ln \dfrac{1}{1-\tilde{x}}} \\ \dfrac{dC(\tilde{t})}{d\tilde{t}} = -\dfrac{2\beta C(\tilde{t})}{(1-\tilde{x})^2 \ln \dfrac{1}{1-\tilde{x}}} \end{cases} . \tag{39.46}$$

For the initial conditions

$$\begin{cases} C(0) = C_{\text{init}} \\ \tilde{x}(0) = 0 \end{cases} \tag{39.47}$$

the solution to $\tilde{x}(\tilde{t})$ is given by

$$\tilde{z}\left(\tilde{x}; \frac{2\beta}{K_{\text{init}}}\right) = K_{\text{init}} \tilde{t} \tag{39.48}$$

where

$$K_{\text{init}} = \frac{\gamma \rho_s}{\alpha C_{\text{init}}} \tag{39.49}$$

and

$$\tilde{z} = \tilde{z}(\tilde{x}; h) = \int_0^{\tilde{x}} \frac{(1-u) \ln \dfrac{1}{1-u}}{1 - h \ln(1-u)} du \tag{39.50}$$

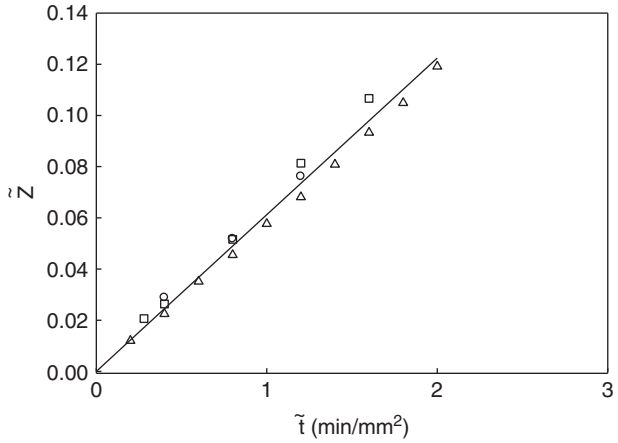


FIGURE 39.8 Gel formation process of chitosan solutions with chitosan concentrations 0.5 % (∘), 1.0% (□), and 1.5% (△) expressed by the function $\tilde{z}(\tilde{x})$ against the scaled time $\tilde{t}$. (From Ref. 27, Fig. 5.) Reprinted with permission from the American Chemical Society.

Equation (39.46) or the solution [Eq. (39.48)] is expressed in terms of only the scaled variables $\tilde{t}$ and $\tilde{x}$. Hence, the scaling relation with respect to the radius R holds even in the pH-change-induced gelation dynamics. The scaling relation showing that the gelation dynamics is expressed in terms of the scaled variables $\tilde{t}$ and $\tilde{x}$ is expected to hold universally since the scaling relation is unaffected by details of the thermodynamic functions for the ions. One significant feature of the time development equation [Eq. (39.48)] is that the equation is independent of the polymer concentration in the inner solution. This is a characteristic feature of the gelation dynamics of pH-change-induced gelation, and, generally, of the thermodynamic-state-change-induced gelation. The independence was experimentally verified by analyzing the gelation of chitosan solution, as shown in Fig. 39.8 [27].

The timecourse of the gelation dynamics induced by a pH change expressed by Eq. (39.48) is different from that induced by inflowing cross-linking agents expressed by Eq. (39.17). The deviation from the cross-linking-agent-induced gelation dynamics is characterized by the parameter h in the function $\tilde{z}$; $\tilde{z}(\tilde{x}; 0) = \tilde{y}(\tilde{x})$. For small values of $\tilde{x}$, the $h \ln(1-u)$ term in the denominator of the integral in Eq. (39.50) is negligible; $\tilde{z}(\tilde{x}; h) \approx \tilde{y}(\tilde{x})$ for $\tilde{x} \approx 0$. Therefore, the timecourse in the early stage is the same as that for the cross-linking-agent-induced gelation:

$$\tilde{y}(\tilde{x}) = K_{\text{init}} \tilde{t}. \tag{39.51}$$

Experimentally, the coefficient K_{init} is obtained from the slope of the initial line of the plot of $\tilde{t}$ versus $\tilde{y}$. The coefficient K_{init} is proportional to the concentration of the inflow-ion in the medium and to the reciprocal of the initial concentration

of the outflow-ion in the inner polymer solution. These features were experimentally verified by analyzing the gelation of chitosan solution [26,27]. Note that $K_{\rm init}$ is independent of the concentration of the polymer in the inner solution, unlike in the case of cross-linking-agent-induced gelation.

In the late stage, where $\tilde{x} \approx 1$, the function $\tilde{z}$ asymptotically behaves as

$$\tilde{z} \approx a + \frac{K_{\rm init}}{2\beta}\left(\tilde{x} - \frac{1}{2}\tilde{x}^2\right), \tag{39.52}$$

where a is a constant. Then, the time course of gelation in the late stage is expressed as

$$\tilde{x} - \frac{1}{2}\tilde{x}^2 = 2\beta\tilde{t} + b \tag{39.53}$$

where b is a constant. The $\tilde{t}$ -linear behavior of $\tilde{x} - \frac{1}{2}\tilde{x}^2$ is a characteristic feature of the late stage. β is obtained from the slope of the linear relationship.

39.3.3 Dynamics of Gelation Accompanied by Transition in Mechanism

Although in the cross-linking-agent-induced gelation, ions in the inner solution also flow out to the medium, the outflow does not affect gelation. However, the outflow of ions in some cases changes the gelation mechanism. During the dialysis of Curdlan solution, the pH decreases with the outflow of ions in the inner solution. This decrease in the pH changes the gelation mechanism from the cross-linking-agent-induced type to the pH-change-induced type. Let us denote the scaled time at which the gelation mechanism changes by $\tilde{t}_c$, and C and $\tilde{x}$ at $\tilde{t}_c$ by C_c and $\tilde{x}_c$ respectively.

In the early stage, i.e., $0 \le \tilde{t} \le \tilde{t}_c$, the dynamics of the gelation is expressed by

$$\tilde{y}(\tilde{x}) = K\tilde{t}. \tag{39.54}$$

The concentration C varies with the elapsed time in accordance with the differential equation

$$\frac{dC(\tilde{t})}{d\tilde{t}} = -\frac{2\beta C(\tilde{t})}{(1-\tilde{x})^2 \ln\dfrac{1}{1-\tilde{x}}}. \tag{39.55}$$

From Eqs. (39.54) and (39.55), we derive the relationship between $\tilde{C}$ and $\tilde{x}$ as

$$\tilde{x} = 1 - \left(\frac{C}{C_{\rm init}}\right)^{\frac{K}{2\beta}}. \tag{39.56}$$

Then, in terms of the transition concentration C_c of the gelation dynamics, the scaled transition width $\tilde{x}_c$ is expressed as

$$\tilde{x}_c = 1 - \left(\frac{C_c}{C_{\rm init}}\right)^{\frac{K}{2\beta}} \approx 1 - \left(\frac{C_c}{C_{\rm init}}\right)^{\frac{\gamma\rho_s}{2\beta\rho_G}}. \tag{39.57}$$

For the transition width, the scaling holds. The transition width increases with increasing initial concentration $C_{\rm init}$ of the outflow-ion and with increasing concentration ρ_s of the inflow-ion.

In the late stage, namely, $\tilde{t}_c \le \tilde{t}$, the dynamics of the gelation is expressed by $\tilde{z}$. Since in this case, the elapsed time is long, the late-stage behavior of $\tilde{z}$ appears; the time development of $\tilde{x}$ is given by the asymptotic form

$$\tilde{x} - \frac{1}{2}\tilde{x}^2 = 2\beta\tilde{t} + b \tag{39.58}$$

39.3.4 Dynamics of Gelation Induced by Dual Mechanisms

In the case of the gelation of DNA solution by aluminum ions, the pH change is induced by ions flowing from the inner solution to the medium and it decreases the number of cross-linking sites of DNA. The decrease in the number of cross-linking sites changes ρ_G from a large value in the early stage to a small value in the late stage. The plot of $\tilde{t}$ vs $\tilde{y}$ is linear in each stage, but its slope differs. Denoting the scaled crossover time from the early stage to the late stage by $\tilde{t}_c$, we obtain the gelation dynamics as [9]

$$\begin{cases} \tilde{y}(\tilde{x}) = K_1\tilde{t} & (0 \le \tilde{t} \le \tilde{t}_c) \\ \tilde{y}(\tilde{x}) = K_2\tilde{t} + (K_1 - K_2)\tilde{t}_c & (\tilde{t}_c \le \tilde{t}) \end{cases}, \tag{39.59}$$

where K_1 and K_2 are respectively the slopes in the early and late stages, and $K_1 < K_2$. As shown in Fig 39.7b, the two-stage gelation behavior appears for the high-pH DNA solution [9].

The time development of the concentration of outflow-ions in the inner solution is governed by Eq. (39.55). Then, the scaled width $\tilde{x}_c$ at the crossover time is expressed by

$$\tilde{x}_c = 1 - \left(\frac{C_c}{C_{\rm init}}\right)^{\frac{K_1}{2\beta}} \tag{39.60}$$

where C_c is the outflow-ion concentration when ρ_G changes. Then, the crossover time is given by

$$\tilde{t}_c = \frac{1}{K_1}\tilde{y}(\tilde{x}_c) = \frac{1}{K_1}\tilde{y}\left(1 - \left(\frac{C_c}{C_{\rm init}}\right)^{\frac{K_1}{2\beta}}\right) \tag{39.61}$$

39.4 APPLICATIONS OF DIALYSIS-INDUCED ANISOTROPIC GELS

Gels showing anisotropy are useful in various applications. Dialysis-induced gelation has been applied for both industrial and biological uses. One team of investigators prepared double-network hydrogels with extremely high mechanical strength containing a synthetic liquid crystalline polyelectrolyte, poly(2,2′-disulfonyl-4,4′-benzidine terephthalamide) (PBDT), using a similar methodology [8,28]. Another group used dialysis-induced anisotropic gelation to control the hierarchical structure of cell scaffolds as a template for constructing artificial tissues that mimic for native tissues [29]. Microfluidic devices have been used to precisely regulate the shape and size of cell scaffolds and to construct engineered tissues in which the arrangement of cells and cell scaffolds was controlled. That group also found that an anisotropic collagen scaffold is useful for bone cell growth.

It is challenging to develop materials consisting of biomolecules without damaging their unique biofunctions, since toxic materials can be selectively adsorbed on them. As a typical example, carcinogenic agents and environmental hormones having planar aromatic groups intercalate with DNA double helices [30,31], thereby inhibiting the interpretation of the hereditary code [32]. This specific property of DNA can be used as for developing the most efficient selective adsorbents for such specific toxic agents. For this application, DNA must be in a water-insoluble state [33, 34]. The water-insoluble anisotropic gel prepared from double-helical DNA by simple dialysis is considered to be an adsorbent with which toxic agents can be extracted effectively (an advantageous gel property) and detected even when agents produce no color in the visible wavelength range (an advantagous birefringent property).

REFERENCES

[1] Oka, S. (1981). *Cardiovascular Hemorheology.* Cambridge Univ. Press, New York.

[2] Piatigorsky, J. (2007). *Gene Sharing and Evolution*. Harvard Univ. Press.

[3] Wong, J.Y., Bronzino, J.D., Peterson, D.R. (eds.) (2013). *Biomaterials: Principles and Practices.* CRC Press.

[4] Kamla, R., Aswal, V.K., Bohidar, H.B. (2012). *J. Phys. Chem.B* **116**, 14805–14816

[5] McConney, M.E., White, T.J., Tondiglia, V.P., Natarajan, L.V., Yang, D.-k., Bunning, T.J. (2012). *Soft Matt.* **8**, 318–323

[6] Guo, Z.-X., Zhang, M., Zhao, L.-B., Guo, S.-S., Zhao, X.-Z. (2011). *Biomicrofluidics* **5**, 026502/1–026502/6.

[7] Bhargavi, R., Nair, G.G., Prasad, S.K., Prabhu, R., Yelamaggad, C.V. (2011). *J. Appl. Phys.* **109**, 083537/1–083537/7.

[8] Wu, Z.L., Kurokawa, T., Saw, D., Hu, J., Furukawa, H., Gong, J.P. (2011). *Macromolecules* **44**, 3535–3541.

[9] Furusawa, K., Narazaki, Y., Tomita, N., Dobashi, T., Sasaki, N., Yamamoto, T. (2010). *J. Phys. Chem. B* **114**, 13923–13932.

[10] Elazzouzi-Hafraoui, S., Putaux, J.-L., Heux, L. (2009). *J. Phys. Chem. B* **113**, 11069–11075.

[11] Alcazar, D., Wang, F., Swager, T.M., Thomas, E.L. (2008). *Macromolecules* **41**, 9863–9868.

[12] Deindoefer, P., Davis, R., Zentel, R. (2007). *Soft Matt.* **3**, 1308–1311.

[13] Casolaro, M., Bottari, S., Ito, Y. (2006). *Biomacromolecules* **7**, 1439–1448.

[14] Konno, A., Tsubouchi, M. (1998). *Kinran Tanki Daigaku Kenkyushi* **29**, 89–95 (in Japanese); Dobashi, T., Nobe, M., Yoshihara, H., Yamamoto, T., Konno, A. (2004). **20**, 6530–6534.

[15] Nobe, M., Dobashi, T., Yamamoto, T. (2005). *Langmuir* **21**, 8155–8160.

[16] Thiele, H. (1954). *Discuss. Faraday Soc.* **18**, 294–301.

[17] Dobashi, T., Furusawa, K., Kita, E., Minamisawa, Y., Yamamoto, T. (2007). *Langmuir* **23**, 1303–1306.

[18] Lin, S.C., Minamisawa, Y., Furusawa, K., Maki, Y., Takeno, H., Yamamoto, T., Dobashi, T. (2010). *Colloid Polym. Sci.* **288**, 695–701.

[19] Furusawa, K., Sato, S., Masumoto, J., Hanazaki, Y., Maki, Y., Dobashi, T., Yamamoto, T., Fukui, A, Sasaki, N. (2012). *Biomacromolecules* **13**, 29–39.

[20] Narita T., Tokita, M. (2006). *Langmuir* **22**, 349–352.

[21] Furusawa, K., Saito, H., Tsugueda, A., Narazaki, Y., Yamamoto, T., Dobashi, T. (2008). *Transact. Mater. Res. Soc. Jpn.* **33**, 467–469.

[22] Okajima, M.K., Miyazato, S., Kaneko, T. (2009). *Langmuir* **25**, 8526–8531.

[23] Maki, Y., Ito, K., Hosoya, N., Yoneyama, C., Furusawa, K., Yamamoto, T., Dobashi, T., Sugimoto, Y., Wakabayashi, K. (2011). *Biomacromolecules* **12**, 2145–2152.

[24] Dobashi, T., Tomita, N., Maki, Y., Chang, C.P., Yamamoto, T. (2011). *Carbohydr. Polym.* **84**, 709–712.

[25] Born, M., Wolf, E. (1974). *Principles of Optics*, version 5. Pergamon Press, Oxford, UK.

[26] Yamamoto, T., Tomita, N., Maki, Y., Dobashi, T. (2010). *J. Phys. Chem. B* **114**, 10002–10009.

[27] Tomita, N., Yamamoto, T., Dobashi, T. (2010). *Transact. Mater. Res. Soc. Jpn.* **35**, 299–302.

[28] Yang, W., Furukawa, H., Gong, J.P. (2008). *Adv. Mater.* **20**, 4499–4503.

[29] Hanazaki, Y., Masumoto, J., Sato, S., Furusawa, K., Fukui, A., Sasaki, N. (2013). *ACS Appl. Mater. Interfaces* **5**, 5937–5946.

[30] Lerman, L S. (1961). *J. Mol. Biol.* **3**, 18–30.

[31] Saenger, W. (1987). *Principles of Nucleic Acid Structure.* Springer-Verlag, Berlin.

[32] Brookers, P., Lawley, P. D. (1964). *Nature* **202**, 781.

[33] Iwata, K., Sawadaishi, T., Nishimura, S., Tokura, S., Nishi, N. (1996). *Int. J. Biol. Macromol.* **18**, 149–150.

[34] Kitamura, H., Matsuura, E., Nagata, A., Sakairi, N., Tokura, S., Nishi, N. (1997). *Int. J. Biol. Macromol*. **20**, 75–77.

40

GELS

ETSUO KOKUFUTA

Faculty of Life and Environmental Sciences, University of Tsukuba, Tsukuba, Ibaraki 305-8572, Japan

40.1 INTRODUCTION

The study of gels was one of the most advanced areas in polymer science in the 1990s. According to the terminology of polymers and polymerization processes in dispersed systems (IUPAC Recommendations 2011) [1], a *gel* is defined as "nonfluid colloidal network or polymer network that is expanded throughout its whole volume by a fluid." Along this definition, we can visualize a variety of gels, so that at first the most familiar gels are taken as examples to outline the general characteristics of gels. Here let us look at silica gel, agarose gel, and polyacrylamide gel with respect to their structural characteristics. As shown in Fig. 40.1, silica gel is formed of a colloidal network in which small silica particles are three-dimensionally connected with each other. Perhaps the siloxane bond (≡Si—O—Si≡) plays an important role in forming network junction points on the surface of each particle. The dispersed phase of silica gel is a gas (air), and this type of gel is referred to as *aerogel*. Both agarose and polyacrylamide gels have a covalent polymer network and are defined as *polymer gels*. However, there is a difference in the formation of the network junction points. In the case of agarose gel, the polymer network forms through the physical aggregation of polymer chains, caused by helix formation, which results in regions of local order acting as the network junction points. Agarose is soluble in water at temperatures above 65°C, and the solution (sol) is gelated by cooling during which the helix formation takes place. On further heating the gel becomes sol, indicating that the regions of local order are thermally reversible. Thus, in this case the resulting swollen network may be termed a *thermoreversible gel*. The network of polyacrylamide (PAAm) is formed by cross-linking polymer chains. *N*,*N*′-Methylenebisacrylamide (Bis) is a cross-linker that connects the polymer chains via the covalent bond; thus PAAm gel is not thermoreversible. Agarose and PAAm gels, in which the swelling agent is water, therefore both are defined as *hydrogels.* Although the IUPAC recommendation [1] has provided the definition of a wide range of gels (e.g., soap gels, phospholipids, clays, V_2O_5 gels, and globular or fibrillar protein gels), this chapter focuses on the hydrogels in which the network is formed via cross-linking of synthetic polymer chains with a suitable cross-linking agent. The reason is that many gels of this sort undergo a *volume phase transition* (VPT) in response to an external stimulus, studies of which have contributed to a great advance in our knowledge of polymer gels. The author aims to provide a good understanding of VPT in synthetic polymer gels from different perspectives.

40.2 OUTLINE OF VOLUME PHASE TRANSITION (VPT)

The swelling of polymer gels, such as that observed when rubber is placed in benzene, has long been a well-known phenomenon. As early as 1948, researchers [2] performed a detailed study of the swelling behavior of cellulose xanthate gels in dilute salt solutions. Others [3,4] also made great contributions to understanding the swelling behavior of ionic and neutral gels. In early studies by these pioneers, however, little attention paid to the existence of a critical endpoint in the phase equilibria, although in 1968 two authors [5] published a theoretical paper on this subject. The earliest report of the VPT in a gel was in 1978 by Tanaka [6], who discovered a

Encyclopedia of Biocolloid and Biointerface Science, Volume 1, First Edition. Edited by Hiroyuki Ohshima.
© 2016 John Wiley & Sons, Inc. Published 2016 by John Wiley & Sons, Inc.

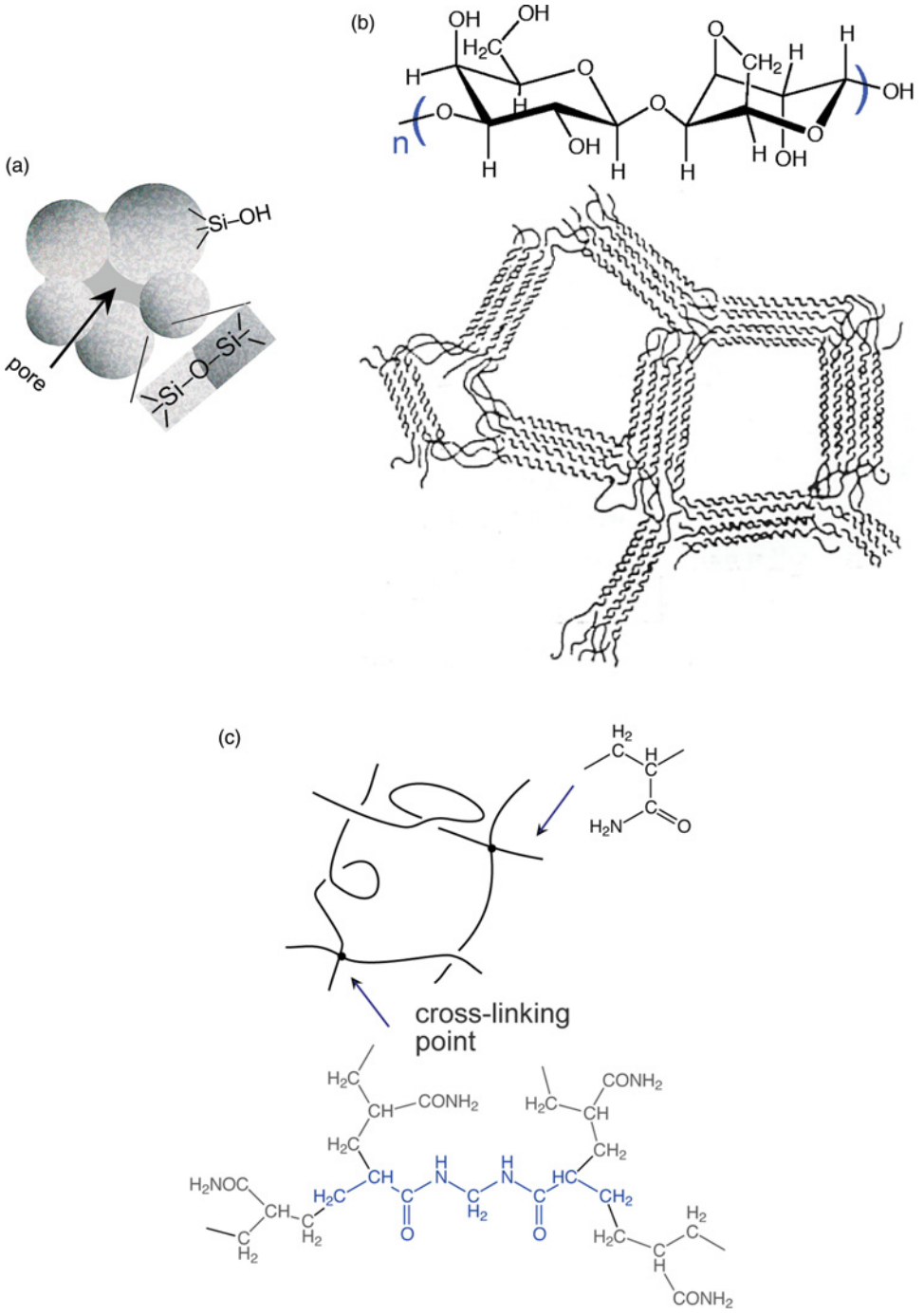


FIGURE 40.1 Schematic illustration of silica gel (a), agarose gel (b), and polyacrylamide gel (c). In (c) the polyacrylamide (PAAm) chains are covalently crosslinked with *N*,*N*′-methylenebisacrylamide (Bis) (see chemical structure of cross-linking point).

discontinuous volume collapse of PAAm gels in acetone–water mixtures when varying the temperature or the composition of the mixture. This phenomenon is now referred to by the acronym VPT (or simply as *phase transition*) of gels and is observed in many gels of synthetic and natural polymers. The VPT is accompanied by reversible, discontinuous (or in some cases, continuous) volume changes, often as large as several hundred times, in response to small variations in the solution conditions surrounding a gel. Variables that trigger the VPT include solvent composition, salt concentration, pH, temperature, and small electric fields. Figure 40.2 outlines the VPT of a gel cylindrical in shape [7], which was prepared in

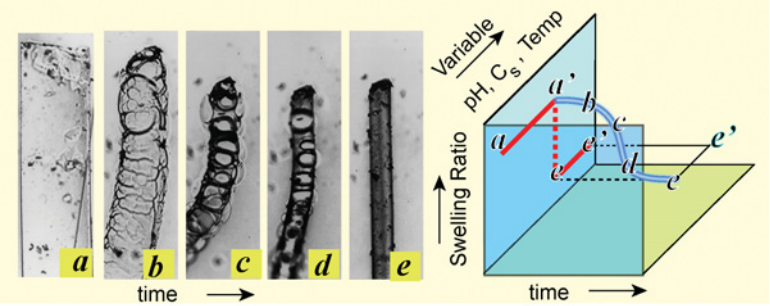


FIGURE 40.2 Volume phase transition (VPT) of a gel in response to a small change of the valuables that are the solution conditions surrounding the gel. Heavy line passing through points a, a', e and e' denotes the equilibrium swelling curve (equilibrium swelling ratio versus valuable). Thin line shows the kinetics curve of the shrinking transition process, in which points a ($\approx a'$) to e ($\approx e'$) correspond to the pictures on the left. (Adapted from Kokufuta 2005 [7].)

a glass capillary with an inner diameter of d_0 (0.29 mm in this case). The gel sample was removed from the capillary, cut into an appropriate size, and purified via repetition of swelling and shrinking in a large volume of the solution for measurement. In this figure, component a shows the gel in the swollen state, which continues until point a', where the gel starts the VPT (shrinking transition in this case). Segments b–d show the process of the VPT, and e is the gel in the fully collapsed state where the size or volume of the gel no longer changes when the surrounding condition such as temperature or pH (i.e., variables) is changed. A heavy line in the 3D graph denotes the equilibrium swelling curve, in which a broken line shows the VPT. A thin line shows the kinetic curve of the VPT. Note that in this chapter, unless otherwise noted, the equilibrium swelling ratio is given as d/d_0 or V/V_0 ($\equiv (d/d_0)^3$), where d denotes the equilibrium diameter of the gel, d_0 is the diameter of the gel when it was prepared, and V and V_0 are the gel volume in the equilibrium state and at the preparation, respectively. Also note that the gel diameters (d_t) during the VPT cannot be precisely determined when bubbles appear on the surface of the gel. At that time, an average value, obtained from the diameters at many positions (usually >10) of the gel, was used as the diameter at time t if we have to investigate the swelling and shrinking kinetics of gels.

40.3 THEORIES OF VPT

For theoretical interpretation of the swelling behavior of gels, it is convenient to imagine that there exists an analogy between swelling equilibrium and osmotic equilibrium. Then it is assumed that the polymer network might play multiple roles as a solute, osmotic membrane, and also pressure-generating device through polymer–solvent mixing effects, network elasticity, and electrostatic interactions of the fixed charges with counterions. According to this consideration, Flory proposed an equation to describe the osmotic pressure (Π) of a gel as a sum of three contributions [3]: $\Pi = \Pi_{\text{mix}} + \Pi_{\text{elas}} + \Pi_{\text{ion}}$, where Π_{mix} represents the contribution from polymer–solvent mixing, Π_{elas} is the elastic contribution due to deforming the network chain from its reference state, and Π_{ion} is the contribution arising from the difference in mobile ion concentrations between the gel and bulk phases. Although Flory's description did not suggest that gels undergo a VPT, Tanaka and his coworkers [7, 8] made several modifications of it to explain their experimental results demonstrating the phase transition in the polymer gels in which the network has a slight amount of charge. Their mathematical description is

$$\Pi = -\frac{N_A kT}{\upsilon_s}\left[\varphi + \ln(1-\varphi) + \frac{\Delta F}{2kT}\varphi^2\right] + \nu kT\left[\frac{\varphi}{2\varphi_0} - \left(\frac{\varphi}{\varphi_0}\right)^{1/3}\right] + \nu f kT\left(\frac{\varphi}{\varphi_0}\right) \tag{40.1}$$

where N_A = Avogadro's number, k = Boltzmann's constant, T = absolute temperature, υ_s = molar volume of the solvent, φ = volume fraction of the network, φ_0 = volume fraction of the network under the theta condition in which the cross-linked chain takes a random walk configuration, ΔF = free-energy change associated with formation of a contact between polymer segments in the network, ν = number of effective chains per unit volume at $\varphi = \varphi_0$, and f = number of counterions per effective chains in the network. It is clear that the first, second, and third terms in Eq. (40.1) are related to Π_{mix}, Π_{elas}, and Π_{ion}, respectively [e.g., 10].

Osmotic pressure Π must be zero when the gel is in equilibrium with the surrounding solvent. Zero osmotic pressure is also necessary for the free energy (F_g) of the gel to be minimized, since $\Pi = -\partial F_g/\partial V$, where V is the volume of the gel and is proportional to φ_0/φ. Using Eq. (40.1), such

conditions may be expressed as

$$\tau \equiv 1 - \frac{\Delta F}{kT} = \frac{\nu v_s}{N_A \varphi^2}\left[(2f+1)\left(\frac{\varphi}{\varphi_0}\right) - 2\left(\frac{\varphi}{\varphi_0}\right)^{1/3}\right] + 1 + \frac{\varphi}{2} + \frac{2\ln(1-\varphi)}{\varphi^2} \tag{40.2}$$

where parameter τ ($= 1 - \Delta F/kT$) is called the *reduced temperature*, which changes with temperature and solvent composition. The equation then determines the equilibrium network concentration as a function of τ. For certain values of τ, however, Eq. (40.2) is satisfied by three values of φ, corresponding to two minima and one maximum of the free energy. The value of φ corresponding to the lower minimum represents the equilibrium value. A discrete volume transition occurs when the two free-energy minima have the same value. Figure 40.3 shows typical swelling curves calculated for an ionic gel as a function of f. In calculations of the equilibrium swelling ratio (φ_0/φ) by Eq. (40.2), Tanaka et al. used $\varphi_0 = 0.5$ and $\nu v_s/N_A\varphi^3 \approx 10$ (i.e., $\nu v_s = 7.5 \times 10^{24}$) [8]. The former value was obtained by assuming that monomers and cross-linkers would be polymerized during gelation in a random-walk fashion to form a network, while the latter was chosen so as to fit the theoretical curves with the experimental data that are obtained from partially hydrolyzed PAAm gels. As can be seen from Fig. 40.3, an increase in f causes a drastic change in both V/V_0 and τ at the transition.

A more detailed comparison of experimental results with the theoretical description was undertaken using a gel composed of *N*-isopropylacrylamide (NIPAAm) and sodium

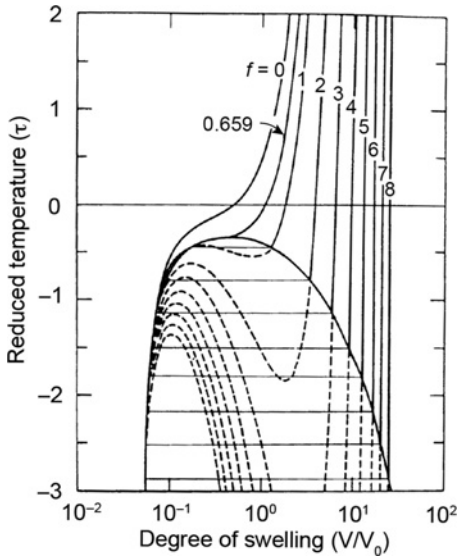


FIGURE 40.3 Relationship between equilibrium degree of swelling ($V/V_0 \approx \varphi_0/\varphi$) and reduced temperature as a function of the numbers (f) of ionized groups per effective chains. (Adapted from Kokufuta 2001 [10] in which the original drawing in [8] was modified with the permission of Prof. T. Tanaka.)

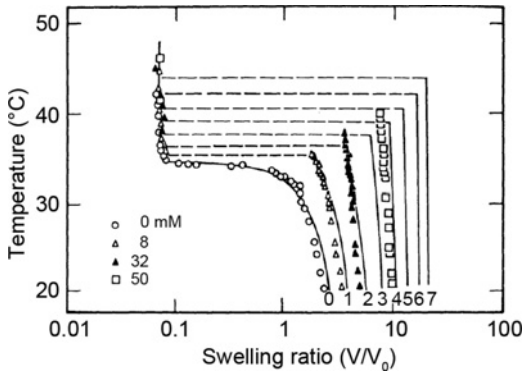


FIGURE 40.4 Temperature dependence of swelling ratio for ionic NIPAAm gels with different amounts of COONa groups. Numbers in the figure denote the f value that is the number of counterions per chain. The curve of $f = 0$ was obtained so as to fit the calculation to the experimental dada (circles) through freely choosing the parameters in Eq. (40.3), which were then used in the calculation of the other curves ($f > 1$). Plots with different symbols are experimental results for the COONa concentrations in mM. (Adapted from Kokufuta 2001 [10] in which the original drawing in [9] was modified with the permission of Prof. T. Tanaka.)

acrylate (NaAAc) [9]. As will be mentioned later, NIPAAm yields thermosensitive polymers or gels; the former undergoes a phase separation, and the latter experiences a volume collapse (shrinking transition) in water on heating to about 32°C. Thus, as shown in Fig. 40.4, the hydrogel without NaAAc (i.e., pure NIPAAm gel) undergoes a continuous VPT at around 34°C. However, an increase in the amount of copolymerized NaAAc causes a large volume change at the transition. At the same time, an increase in transition temperature (T_V) is observed. To compare these results with the theoretical description, term $\Delta F/kT$ (i.e., χ parameter) in Eq. (40.2) was rewritten as $\chi = \Delta F/kT = (\Delta H - T\Delta S)/2kT$. Thus, Eq. (40.2) becomes

$$\frac{1}{T} = \frac{\Delta S}{\Delta H} + \frac{k}{\Delta H}\left\{\frac{\nu v_s}{N_A\varphi^2}\left[(2f+1)\left(\frac{\varphi}{\varphi_0}\right) - 2\left(\frac{\varphi}{\varphi_0}\right)^{1/3}\right] + 1 + \frac{\varphi}{2} + \frac{2\ln(1-\varphi)}{\varphi^2}\right\} \tag{40.3}$$

In calculating the swelling ratio as a function of temperature, the following approach was used in [9]. The equilibrium swelling ratio was calculated using the relation $V/V_0 = \varphi_0/\varphi = (d/d_0)^3$, where d is equilibrium gel diameter and d_0 (1.35 mm) is the inner diameter of the capillary utilized in the gel preparation. Parameter φ_0 (~ 0.07) was obtained from the experimental asymptotic value of V/V_0 at high temperatures (see V/V_0 at temperatures above 35°C). Also, ν (1.0×10^{22} L^{-1}) was from the amount of cross-linker by considering that one cross-linker provides two effective chains in the network at maximum, and ΔH (-8.7×10^{-14} erg) was the literature value [9]. It should

be noted that, because (1) NIPAAm gels in water exhibit an endothermic shrinking on heating ($\Delta H > 0$), but (2) an exothermic swelling on cooling ($\Delta H < 0$) (for example, see Ref. 11, in which references to earlier work may be found), the calculation focuses on the swelling transition. Also note that the ΔH value is based on "one unit" of NIPAAm chains in the gel network; therefore, ΔH becomes 5.3 kJ per unit mole. In addition, it was assumed in [9] that since the transition temperature T_V is determined principally by the $\Delta H/\Delta S$ ratio, ΔS is approximately equal to $\Delta H/T_V$ and the curvature of a swelling curve is determined mainly by the value of ΔH. Taking these observations into account, they obtained the theoretical swelling curve for the NIPAAm gel. However, the estimated theoretical fit was rather poor; for example, the calculated curve predicts much smoother change than the measured curve near the transition region (data not shown). Thus, as the second approach, an attempt was made to estimate the parameters from the experimental dada for the neutral NIPAAm gel by a curve-fitting technique. The results of the best fit gave the following values: $\Delta H = -5.4 \times 10^{-11}$ erg, $\Delta S = -1.8 \times 10^{-13}$erg.K^{-1}, $\nu = 1.2 \times 10^{24}$ L^{-1}, and $\varphi_0 = 0.07$. Using these parameters, the swelling curves for ionic NIPAAm gels with COONa (8–50 mM in preparation) were calculated (see the solid curves in Fig. 40.3). The calculated curves well reproduced the experimental data for the ionic gels; however, the values obtained from the two-parameter fit for ΔH and ν were significantly greater than the values determined from independent measurements. For this discrepancy, Tanaka et al. mentioned the following reasons. In modeling, the effects of loops, free branches, non-Gaussian properties of chains (due to self-avoiding random walk, and stretching limit due to finite length of the chains), polydispersity of chains, and other factors were not considered. Moreover, in this author's opinion, for ionic gels, it also neglected the charge–charge interaction and counterion condensation, which may affect the actual value of osmotic pressure [7,10].

After publication of the Tanaka team's papers (mainly Refs. 6, 8, and 9), there have been many arguments concerning Flory's description. At the same time, several authors proposed modified models for the VPT in gels. A team of coworkers [12] have developed a theory with a quasi—chemical lattice mode for the mixing term Π_{mix}; however, Guassian chains are still assumed, and therefore it is difficult to fit experimental results with a single set of parameters over the entire range of swelling. Another group of coworkers [13] employed a lattice–fluid model to overcame difficult use of the lattice-based mixing term. They derived interaction energy from the various cohesive energy densities in the system that fits the experimental results. But their model, although sensitive to the fact that gels swell under pressure in an attempt to increase entropy, overestimates this effect. Another team [14] used a virial-type expression for mixing term Π_{mix} according to two investigators [15] who studied the temperature dependence of the hydrophobic interaction between molecules in water. Also, an elastic expression that accounts for the limits of elongation was employed. They can predict continuous transitions that become discontinuous upon ionization (see Fig. 40.4), but as yet several adjustable parameters are needed. More details for these modifications are presemted in the literature [10].

Before discussing the disagreement between prediction and observation in terms of the above models including Tanaka's descriptions, we have to determine why ionic gels collapse with rising temperature. In general, osmotic pressure increases not only with increasing concentration of counterions, but also with rising temperature. In order to resolve this conflict, one may assume that *hydrophobic interaction* is competitive with osmotic pressure arising from counterions. Nevertheless, it is preferable to discuss whether the concept of osmotic pressure is adequate. With respect to this subject, another team [4] argued that the Donnan distribution could not give even a rough approximation. Then they proposed a theory based on random coil model in which the charge interaction along a chain was calculated by the Debye–Hückel theory. This was taken over by Hasa–Ilavsky–Dusek (HID) theory [16], in which the elastic term was modified by considering the influence of charges on the deformation of the network. A mathematical description of the HID theory [17] was

$$\begin{aligned}\Pi = &-\frac{RT}{v_s}\left[\ln(1-\varphi)+\varphi+\chi\varphi^2\right] - RT\varphi_o \\ &\times\left[\varphi^{1/3} - \frac{\varphi}{2} + \frac{3}{5n\varphi^{1/3}} + \frac{99}{175n^2\varphi^{1/3}} + \frac{513}{875n^3\varphi^{5/3}}\right] \\ &+ \frac{RTf_m\rho\varphi}{M_0} - \frac{N_A\nu Z^2 e^2 f_m^2}{3D\varphi_0\left\langle R_0^2\right\rangle^{1/2}\varphi^{4/3}}\left[\frac{2.5A}{1+A} - \ln(1-A)\right]\end{aligned} \tag{40.4}$$

and

$$A = \left[\frac{9DkTM_0}{\pi N_A e^2\left\langle R_0^2\right\rangle f_m\rho}\right] \tag{40.5}$$

Here, f_m is the mole fraction of ionic monomer unit in the network, ρ the density of the dry gel, Z the degree of polymerization of the chain in the network, e the electronic charge, D the dielectric constant of solvent, $\left\langle R_0^2\right\rangle$ the mean-square end-to-end distance, and M_0 the average molecular weight of copolymer unit [i.e., $M_0 \approx f_m M_i + (1-f_m)M_n$, where M_i and M_n are the molecular weight of the ionic and the neutral monomer unit in the network, respectively]. It is clear that Eq. (40.4) includes the term due to the electrostatic interaction between the fixed charges that was ignored in Tanaka's description based on Flory's theory. In addition,

the elastic term in Eq. (40.1) was modified in Eq. (40.4). Therefore, one may expect that the prediction of swelling degree ($1/\varphi$) as a function of f_m from Eq. (40.4) would be better than that from Eq. (40.3). However, it was concluded that neither the Flory nor the HID theory could provide a reasonable approach for predicting the swelling degree for polyelectrolyte gels in which the network is composed of different ratios of *N,N*-dimethylacrylamide (DMAAm) (neutral monomer) and 2-acrylamide-2-methylpropanesulfonic acid (AMPS) (ionic monomer). Nevertheless, we must remember the essential difference between the approaches of Flory and Katchalsky for the swelling of polymer gels. Flory considered that a lightly cross-linked ionic gel closely resembles a Donnan membrane system, while such a gel in the Katchalsky treatment was considered to be an extension of the corresponding polyion (see Fig. 40.5). The latter allows us to discuss the swelling and shrinking behaviors of polymer gels in terms of attractive and repulsive interactions between segments or functional groups in the network.

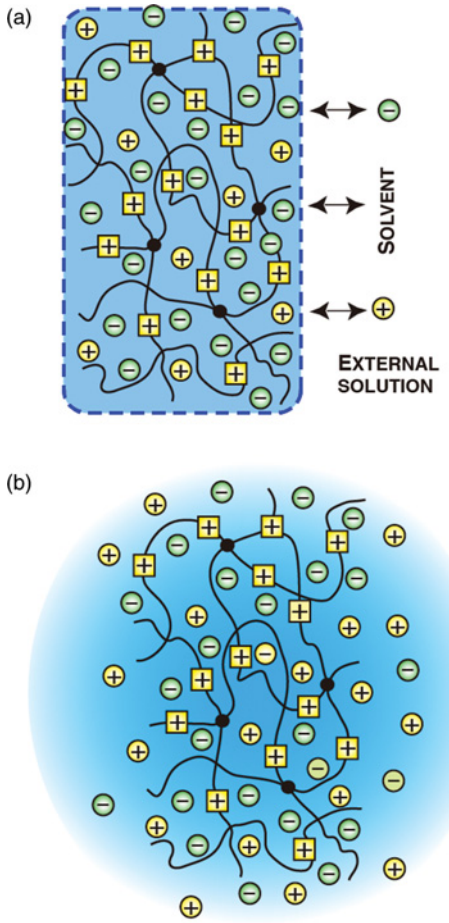


FIGURE 40.5 Schematic representations of a cationic gel based on Flory's model (a) and Katchalsky's model (b). The fixed charge is represented by a square with a plus sign, while circles with minus and plus signs denote counterion and byion, respectively. (Adapted from Kokufuta 2005 [7].)

40.4 UNDERSTANDING VPT AT THE MOLECULAR LEVEL

Although there is much debate about a theoretical explanation of the VPT in gels, a large number of data have been accumulated in experiments with various gel systems. It is therefore important to draw a generalized perspective about the phase transition from experimental data. This may be achieved through classification of the experimental swelling curves. We have tried to present a "unified" model of gel transitions, with an addition of an example for volume transition in a gel driven by hydrogen bonding [18]. Then, the gel volume phase transitions were classified into four types (see Fig. 40.6) by considering the following attractive forces that act to shrink the polymer network: ionic, hydrophobic, van der Waals, and hydrogen bonding. When a repulsive force,

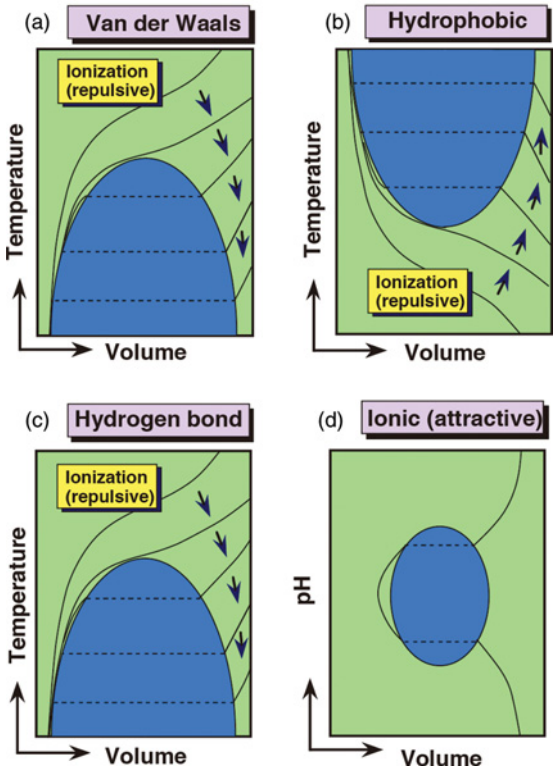
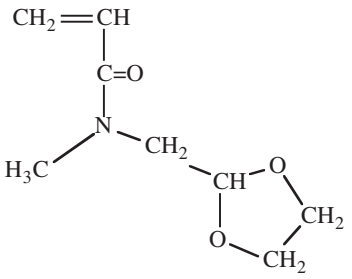


FIGURE 40.6 Four types of intermolecular forces that play an important role in the VPT of gels. When such attractive forces as van der Waals interaction (a), hydrophobic interaction (b), hydrogen bonding (c), and electrostatic interaction (d) become stronger than the repulsive electrostatic force, the gels start the transition. An increase in the ionization degree causes the increase in the gel volume at the transition. For more details, see text. (Adapted from Ilmain et al. 1991 [18].)

usually electrostatic in nature, overcomes an attractive force such as hydrogen bonding or the hydrophobic interaction between the network chains, gel volume should increase discontinuously in some cases and continuously in others. The variables triggering the VPT influence these intermolecular forces and thereby the "balanced state" of the attractive and repulsive forces. One study [18] erred several times in citing references as well as in giving an example for a gel system in which the van der Waals force becomes dominant as the attractive force. However, this classification serves as a good guide for discussing whether the main factor consists in swelling or collapsing a gel. For example, the polyampholyte network in a bulk gel [19,20] or in a microgel [21] collapses at a pH (isoelectric point) at which the network-bound positive and negative charges balance each other (see Fig. 40.6d). For the VPT of this sort, it has been pointed out that Flory's theory is not available [19]. Another example is that the VPT of a poly(ethylenimine) (PEI) gel is well explained in terms of a balance between the attractive hydrogen bonding and the cationic charge repulsion [7,22]. In addition, anionic surfactants such as sodium dodecyl sulfate (SDS) effectively collapsed the PEI gel due not only to the neutralization of the cationic charges but also to hydrophobic interaction.

In Fig. 40.6 the hydrophobic interaction must be defined in a category different from the other three intermolecular attractive forces. Since the studies on the thermodynamics of nonpolar solvation in the mid-1940s [23], the standard model for the hydration of nonpolar solute species has emphasized enhancement of the solvent water structure hydrating the solute. The exact nature of this structural ordering has remained unclear, but it is not disputed that the nonpolar solvation process results in a net loss of entropy. This entropic mechanism for association of nonpolar moieties subsequently became central to models of protein folding and stability following the seminal work of Kauzmann in 1959 [24], who argued that a structural interpretation of the thermodynamic data could be developed by considering the hydration of the polar and nonpolar molecular groups that constitute proteins. In the area of polymer gels, the main issue regarding hydrophobic interaction, which initially attracted the most attention, seems to be in understanding the phase transition of NIPAAm gels. In general, gels swell on heating, an example of which is shown in Fig. 40.3. In contrast, the NIPAAm gels undergo the swelling transition on "cooling" (Fig. 40.4), the process of which is an exothermic ($\Delta H < 0$), but $\Delta S < 0$. Such negative enthalpy and entropy changes may be rationalized by assuming that an "icelike structure" is stabilized in the neighborhood of nonpolar solutes—thus the heat evolved may be attributed to the latent heat of freezing of "icebergs" that represent regions of crystalline order and whose formation, therefore, leads to a loss of entropy. The tendency of nonpolar solutes to aggregate in aqueous media reduces the number of water molecules in their immediate vicinity and leads to "melting icebergs." This provides the driving force toward such aggregation and has been referred to as the *hydrophobic bond* [24]. These considerations are elementary, as mentioned above, but allow us to understand the difference between diagrams (b) and (a), as well as (b) and (c) in Fig. 40.6. For the NIPAAm gel network whose monomer unit is composed of a hydrophilic amide moiety and hydrophobic isopropyl and methylene moieties, it is not so simple to understand and interpret the phase transition mechanism at the molecular level. Indeed, the phase transition of gels and the phase separation of polymers, based on *N*-propylacrylamides and *N*-propylmethacrylamides, are dependent on the structure of the constituent monomers (see Fig. 40.7) [11,25]. These results indicate that we must consider (1) amide–amide and amide–water hydrogen bonding and (2) a possible hydrogen bonding of solvent water with the H–C bond of the alkyl groups, in terms of water clustering around both the alkyl and the amide groups. In addition, it has been suggested that the effects of R and R′ on the *electronic structure* of $R{-}C(=O)NH{-}R'$ seem to play an important role in these hydrogen bond formations [25]. In the case of a gel based on *N*-(1,3-dioxolan-2-ylmethyl)-*N*-methylacrylamide (DIOMMA) whose chemical structure is given by



a rise in temperature leads to the volume collapse in water but the swelling in alcohols [26]. This opposite trend in the thermal properties in water and in alcohols was discussed in terms of polymer–polymer, polymer–solvent, and solvent–solvent interactions. However, in more detail, the two oxygen atoms in the dioxolane moiety seem to cause clustering of water molecules, which hinders hydrophobic association in the network. Indeed, with increasing temperature, the degree of swelling of DIOMMA gel in water quasi-monotonically decreases up to near 60 °C and gradually levels off to a constant value at about 70°C, the results of which are clearly different from the volume changes of the other *N*-alkyl acrylamide gels such as NIPAAm gels. In alcohols such as methanol and ethanol, the DIOMMA gel network is under a collapsed sate, probably due to the solvent-mediated hydrogen bounding at a low temperature range (<25°C). However, such hydrogen bonds are broken on heating, and at the same time the network is solvated via hydrogen bonding between the OH and amide groups. All the above discussions were based on the results obtained

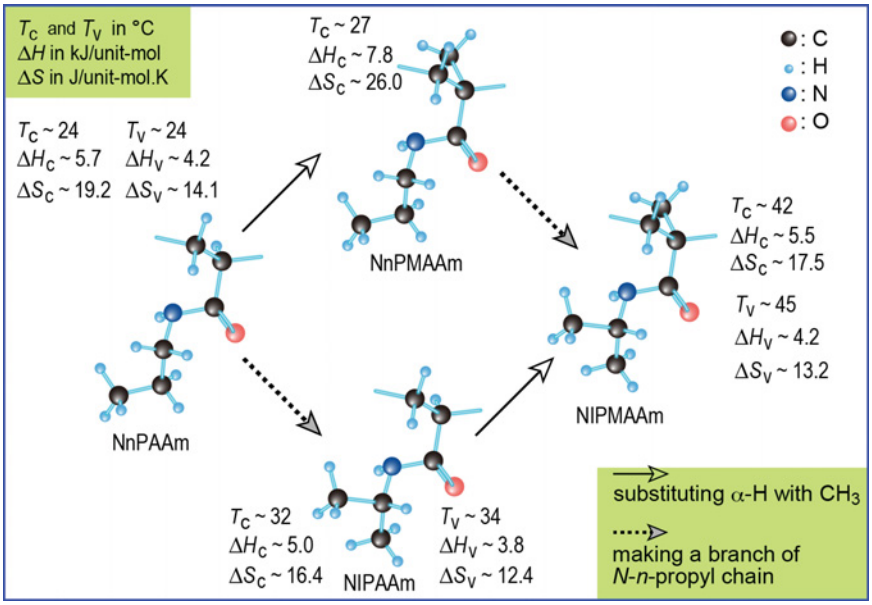


FIGURE 40.7 Systematic comparison of the effects of α-methyl group and sidechain branching on the phase separation of polymers, as well as on the VPT of gels, based on *N*-propylacrylamide or methacrylamide monomers: *N*-isopropylacrylamide (NIPAAm), *N*-isopropylmethacrylamide (NIPMAAm), *N*-*n*–propylacrylamide (NnPAAm), and *N*-*n*-propylmethacrylamide (NnPMAAm). T_c denotes the phase separation temperature, and ΔH_c and ΔS_c ($= \Delta H_c/T_c$) are the enthalpy and entropy change during the phase separation, respectively. Similarly, T_v is the volume phase transion temperature, ΔH_v and ΔS_v ($= \Delta H_v/T_v$) are the enthalpy and entropy change during the VPT, respectively. Note that the phase separation of the polymer or the collapse transition of the gel in water on heating is the endothermic process, so that $\Delta H > 0$ and $\Delta S > 0$. All the data were determined by heating DSC measurements of the polymers or the gels so as to avoid the effect of the concentration. In the case of NnPMAAm, the data for the gel are not shown because the gel could not be prepared because of a low water solubility of the monomer [11]. (Adapted from Kano & Kokufuta 2009 [11] and Kokufuta et al. 2012 [25].)

with techniques such as Fourier transform infrared (FTIR) or attenuated total reflectance (ATR)-FTIR spectroscopy, ^{1}H-NMR spectroscopy, and differential scanning calorimetry (DSC). Almost all the important studies are included in the literature [11,25,26].

40.5 EFFECTS OF DISTRIBUTION OF IONIC OR HYDROPHILIC MONOMER UNITS WITHIN THE NETWORK

It was previously mentioned that there are two models for understanding ionic gel transitions: (1) Flory theory based on classical Donnan method and (2) Katchalsky theory based on random-coil model in which the charge interaction along a chain was considered. However, it is difficult to determine which model is realistic, as can be seen from certain experiments [17]. Here, it is shown that studies on the effect of charge distribution within the network provide an answer to this question. For this, we synthesized four ionic gels composed of NIPAAm and AAc residues (NIPAAm:AAc ratio of the feed ≈10:1 by moles the monomers or repeating units) using the following approaches [27]: (1) for gel I, the redox polymerization of an aqueous solution containing NIPAAm, AAc, and Bis which can be initiated by a pair of ammonium persulfate (APS, initiator) and *N,N,N′,N′*-tetramethylethylenediamine (TMED; accelerator); (ii) for Gel II, the physical entrapment of poly(AAc) by Bis-crosslinked NIPAAm gel, the preparation method of which is the same as that in (i) except for the use of poly(AAc) instead of the AAc monomer; (iii) for Gel III, the gelation of an aqueous solution containing poly(NIPAAm) and poly(AAc) by γ-rays from ^{60}Co under conditions where no complexation occurs between poly(NIPAAm) and poly(AAc); and (iv) for Gel IV, the γ-ray irradiation of an aqueous solution of poly(NIPAAm–co–AAc). Figure 40.8 shows the temperature dependence of the normalized equilibrium diameters (d/d_0) at pHs 3 and 10 for Gels I and II as the example. At pH 10 at which the COOH groups of the AAc units are fully ionized ($COOH + NaOH \rightarrow COO^- + Na^+ + H_2O$), a marked difference due to the AAc distribution was observed between G I and G II. The localized COO^- ions in G II are

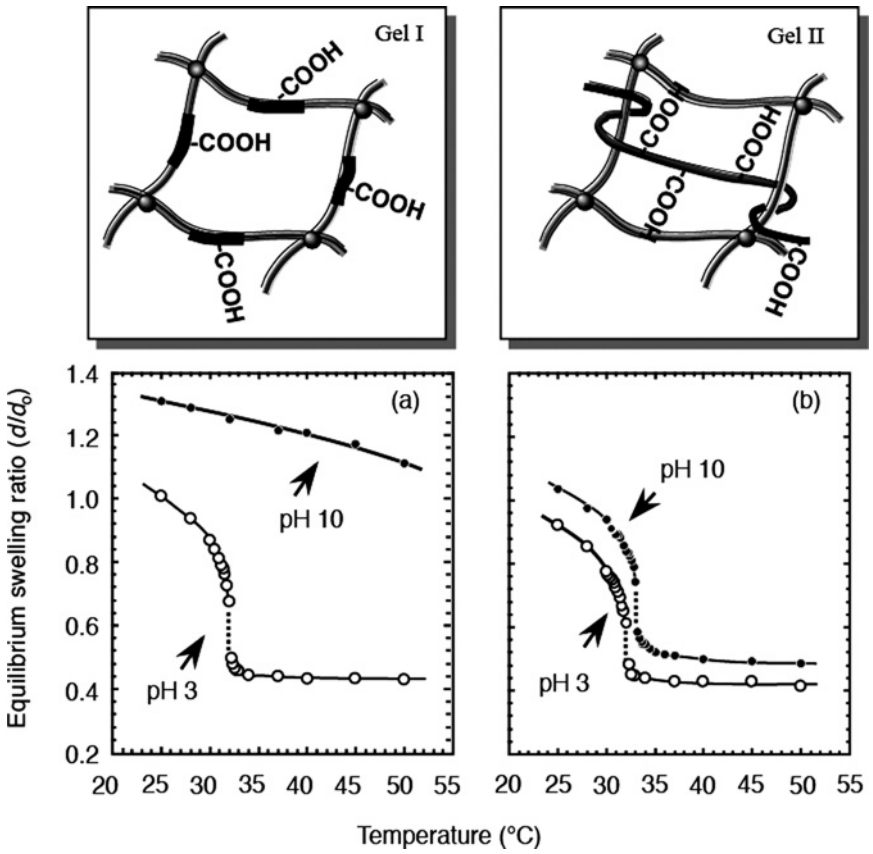


FIGURE 40.8 Temperature dependence of normalized equilibrium diameters (d/d_0) at pH 3 and 10 for Gel I (a) and Gel II (b). Poly(AAc) with MW = 450,000 was used for the preparation of gel II. (Adapted from Kano & Kokufuta 2009 [11] and Kokufuta et al. 2012 [25].)

not effective in preventing the thermally induced gel collapse at temperatures above T_v. This clearly indicates the effect of microscopically created charge inhomogeneity on the VPT. Since there is little disagreement between the T_c and T_v values for the polymers and gels of NIPAAm (see Fig. 40.7), a similar molecular mechanism may be predicted in the phase separation and the volume transition. For Gel II composed of ca. 90 % of Bis-crosslinked "pure" NIPAAm chains, it is predictable that its VPT behavior is not so different from those of poly(NIPAAm) and NIPAAm gel, even at pH 10 where the incorporated poly(AAc) chains (ca. 10 % in unit mole base) are fully ionized. Indeed, at pH 10 Gel II underwent a VPT at a temperature near to the T_c or T_v (~33°C) of the NIPAAm polymer and gel. The same result has been obtained by a comparison of Gels III and IV (see [27]). In addition, when the swelling curves of Gel II were studied at pHs 3 and 10 as a function of the molecular weight of the entrapped poly(AAc), the following results have been obtained: (i) The increase in the molecular weight at pH 10 brought about an increase in the gel volume over the temperature range of 25 °C to 50 °C; and (ii) at pH 3 and at temperatures $< T_v$, the gel volume decreased with increasing molecular weight of the entrapped poly(AAc). Therefore, it has been clear at the molecular level that the charge distribution has a marked effect on the swelling of NIPAAm-based polyelectrolyte gels.

In the above example, we looked at the case where the charges that cause a repulsive force are localized in the network. Now, it is interesting to see what is happening in the network into which neutral polymer chains that do not undergo hydrophobic association are physically immobilized. For this, two NIPAAm-based gels were prepared: One consists of the copolymer of NIPAAm and vinyl pyrrolidone (VP), and the other is the NIPAAm gel with immobilized poly(VP) [7]. The amount of VP monomer or repeating VP unit was varied from 0 to 50 mol %. As can be seen from Fig. 40.9, the copolymerization of a hydrophilic VI monomer causes a rise in T_v, and simultaneously extends a range of temperatures at which a large volume change takes place. By the immobilization of poly(VP), however, there is little change in T_v, although an increase in the gel volume under a fully collapse state is observed. This is the case, even when 50 % of poly(VP) was immobilized. These results clearly indicate that the distribution of "neutral but hydrophilic" chain

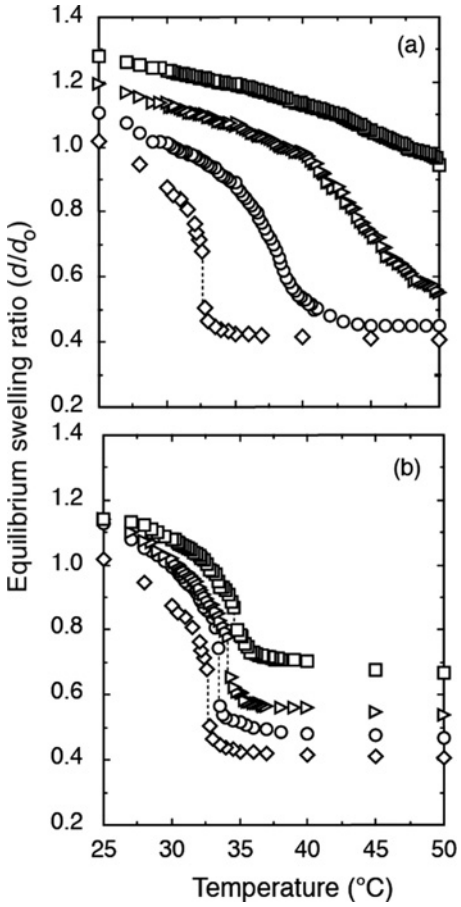


FIGURE 40.9 Temperature dependence of normalized equilibrium diameters (d/d_0) for NIPAAm gels with copolymerized VP (a) as well as with immobilized poly(VP) with MW = 360,000 (b). Contents of VP monomer or VP unit in the pregel solution: (rhombus) 0 mol%, (circle) 10 mol%, (right-pointing triangle) 30 mol%, and (square) 50 mol%. The measurements were carried out in pure water. (Adapted from Kokufuta 2005 [7].)

segments within the NIPAAm network plays an important role in the association of hydrophobic chain segments. Then, it is natural to conclude that the charged segments affect the VPT in polyelectrolyte gels through both the long-range Coulombic interaction and the hydrophilic nature.

40.6 EFFECTS OF COIL-TO-HELIX TRANSITION IN POLYPEPTIDE GELS

We have attempted to see the VPT in gels through force balance approach (FBA) that is based on the balanced state of the attractive and repulsive forces between the constituent polymer chains in the network. In other words, this is to draw analogies between the behavior of uncross-linked and cross-linked polymers in a solvent. Here it is demonstrated that the FBA successfully accounts for the VPT of polypeptide hydrogels [28]. Polypeptides in aqueous solutions are known to adopt three different conformations (α-helix, random coil and β-sheet structures) depending on pH, temperature and additives. Circular dichroism (CD), optical rotatory dispersion (ORD) and ^{1}NMR techniques are often used for investigating the polypeptide conformations in solutions. However, such techniques are less helpful for the gels that are prepared via cross-linking of polypeptides with a suitable agent such as glutaraldehyde (GA). This is mainly due to the difficulty to handle them in the measurements. In particular, CD and ORD are unable to use for the gels that become opaque in their preparations or measurements. Even in such a case, however, the FBA allows us to discuss the gel volume transition in terms of the conformation change of the peptide chain in solutions. For example, as shown in Fig. 40.10, a hydrogel obtained from poly(α-L-lysine) (α-PLL) by cross-linking with GA shows little change of the volume at the pH range (see Fig. 40.10c) at which the polymer undergoes a coil-to-helix transition. However, α-PLL gel undergoes a VPT at pH at which the polymer had adopted α-helix conformation (Fig. 40.10e). The gel after the transition further collapses upon heating even in the temperature region (Fig. 40.10g) where the polymer adopts the β-sheet structure. In the case of racemic poly(α-DL-lysine) (α-PDLL) that does not adopt any secondary structure in the pH and temperature ranges studied, the gel shows the VPT similar to those of α-PLL gel. However, the pH range causing the gel collapse is wider than that for α-PLL gel (Fig. 40.10d–f). Moreover, the magnitude of the volume changes with temperature is larger for α-PDLL gel than for α-PLL gel, although the fully collapsed volume for former at high temperatures (e.g., 60°C) is larger than that for the latter. These results indicate that the formation of the helical segments in the cross-linked chain has little effect in the gel collapse, but their association by attractive force causes the gel to shrink. The attractive interactions are mainly due to the hydrogen bonding, but hydrophobic interactions between the lysine sidechains should be considered [28].

40.7 EFFECTS OF SURFACTANT BINDING

It has been mentioned that the distribution of network charges strongly affects the VPT of ionic NIPAAm gels. This can be observed in the case of ionic surfactant–bound NIPAAm gels [7,29]. Ionic surfactants such SDS and sodium dodecylbenzene sulfonate (NaDBS) are bound to neutral NIPAAm polymers and gels, by which they are converted into a polyelectrolyte [30–32]. To the polymer the binding takes place at critical aggregation concentration (CAC). This causes an elevation of lower critical solution temperature (LCST $\equiv T_c$) as a result of electrostatic repulsion between the charges of the polymer-bound surfactant micelles. Similarly, an increase in T_v as well as in the swelling ratio at T_v can be observed

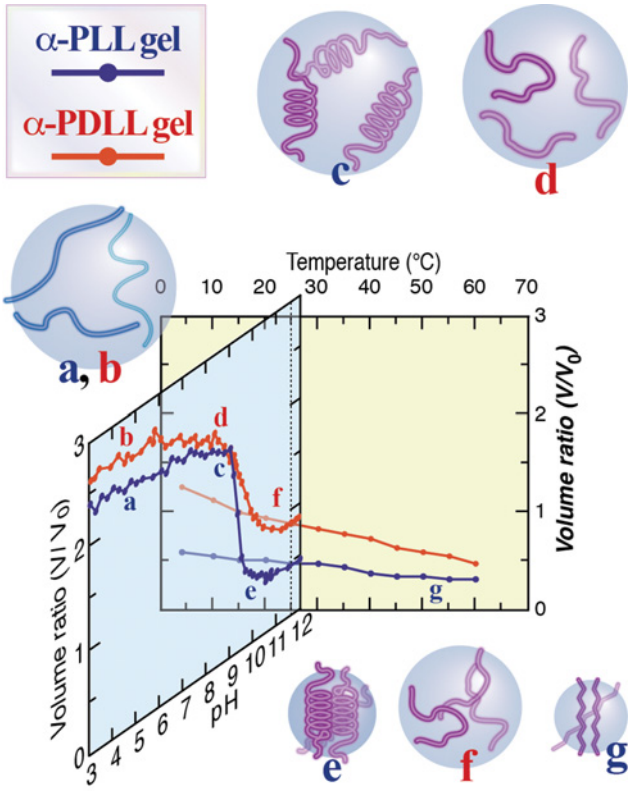


FIGURE 40.10 Schematic representation of poly(lysine) gel collapse in response to pH and temperature. The volume ratio (V/V_0) was calculated by $V/V_0 = (d/d_0)^3$ from the data obtained by initially increasing the pH or temperature of the outer solution. Sample: α-PLL gel (dashed line) and α-PDLL gel (gray solid line). The predicted conformations in the cross-linked polymer chains are as follows: for α-PLL gel, random coils (a), partially formed helices before their association (c), associated helices (e), and β-structure (g); and for racemic α-PDLL gel, random coils (b), collapsed coils before their association (d), and associated collapsed coils (f). (Adapted from Kokufuta et al. 2011 [28].)

in surfactant-bound NIPAAm gel systems. A few studies [33, 34] attempted to describe the VPT behavior in connection with the formation of surfactant micelles in the gel. However, quantitative analysis for the amount of bound surfactants, followed by a careful comparison of the surfactant-bound NIPAAm gel and the AAc-copolymerized NIPAAm gel, both of which have almost the same charge density (0.16 ± 0.02), has raised the questions as to why (1) the volumes of the surfactant-bound gels are much smaller than those of the copolymer gel and (2) the T_v of the former is higher than that of the latter (see Fig. 40.11a). A rise in temperature causes a slight increase in the network charges, which can be accurately determined from surfactant uptake by the gel [35]; however, the differences that are mentioned in questions 1 and 2 above cannot be understood in the common knowledge of ionic gel transitions. Therefore, answers to these questions would help clarify the nature of swelling forces in ionic gels, including the surfactant-bound gels. Now, let us assume that surfactant molecules bind only to the polymer networks within a layer of the gel near the surface but not to all of the networks in the body of the gel (Fig. 40.11b). The reason is that charges of the surfactant-bound layer seem to hinder further diffusion into internal parts of the gel of the surfactant molecules with charges of the same sign. Thus, a NIPAAm gel with bound surfactants is seemed to resemble a sort of "composite" polyelectrolyte gel consisting of cross-linked polymer chains with different amounts of ionizable groups. Since, as shown in Fig. 40.11a, the T_v of the pure NIPAAm gel is lower than those of three ionic NIPAAm gels, part *c* (in Fig. 40.11b) without bound surfactants should collapse at temperatures slightly higher than T_v, but parts *a* and *b* remain in the swollen state. We usually define T_v as the temperature at which a gel discontinuously and completely collapses; therefore, the experimentally determined T_v of a surfactant-bound gel is governed primarily by the degree of ionization in part *a*, but not in parts *b* and *c*. However, the swelling ratio as the overall gel volume is strongly affected by changes in the degree of ionization in part *b*. Even if part *a* is maintained at the same level of ionization in both the SDS- and NaDBS-bound gels, in this case the level in part *b* for the former is higher than that for the latter. Then, we can see from the features in Fig. 40.11a that (1) the SDS-bound gel exhibits a high degree of swelling compared with the NaDBS-bound gel, and (2) the total change in the gel volume at T_v for both surfactant-bound gels is smaller than that for the copolymer gel with a homogeneous charge distribution as a result of random copolymerization of AAc monomers.

Measurement of the spatial distribution of surfactant concentration within the gel phase should provide direct evidence for the local surfactant binding as assumed above. For this purpose NaDBS is an appropriate surfactant because it has the phenyl group, which exhibits an absorption band in the UV range. Figure 40.11c shows typical examples of the position dependence of transmittance (PDT), the results of which were obtained with the sample gel disks with bound NaDBS. The gel disks with a thickness of ~0.2 μm were obtained by cutting a cylindrical gel rod using a microtome, after confirming that the surfactant binding had attained equilibrium. The scanning was performed from the right-hand end to the left-hand end of each gel disk. Two wavelengths, 261 nm and 400 nm, were used to measure the PDT. Since NaDBS has no absorption at 400 nm, the transmittance at this wavelength varies depending on the sample thickness. Therefore, the PDT at 400 nm should be used as a control. PDTs (segments *a* and *b* in Fig. 40.11c) are the results obtained using wet and dry gels with an initial diameter (d_0) of 2 mm, respectively. The wet gel sample was fully swollen in pure water prior to contact with the NaDBS solution, whereas the dry gel was directly treated with the surfactant solution without swelling procedure (for more details, see

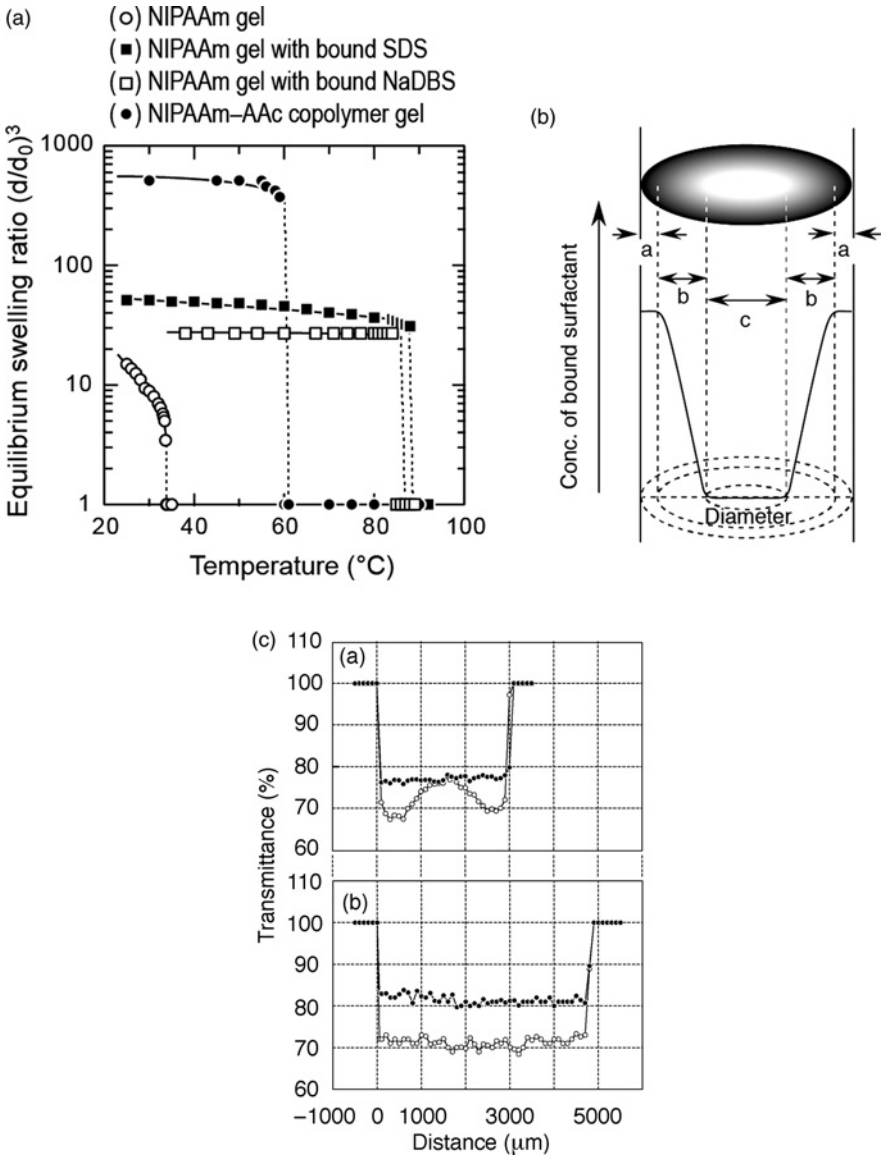


FIGURE 40.11 Several important features of surfactant-bound NIPAAm gels. (a) Comparison of equilibrium swelling curve for pure NIPAAm gel with those for ionic NIPAAm gels with bound NaDBS and SDS as well as with copolymerized AAc. The charge densities based on moles of ionized groups (sulfate, sulfonate, and carboxylate ions) per mole of NIPAAm plus Bis (cross-linker) are 0.16 ± 0.02 for both surfactant-bound gels; and 0.18 for NIPAAm-AAc copolymer gel as a control sample. The former was determined from the surfactant uptake by the pure NIPAAm gel at 25°C and at initial surfactant concentrations >20 mM. (b) Schematic representation for a cylindrical gel with inhomogeneously bound surfactant molecules. A horizontal sectional view of a cylindrical gel after attainment of a saturated level of surfactant binding is illustrated together with a concentration profile of bound surfactant: *a*, part with a saturated level of bound surfactants; *b*, part in which the surfactant concentration gradually decreases toward the center; and *c*, part in which there is no bound surfactant (i.e., corresponding to neutral gel). (c) Position dependence of transmittance (PDT) for cylindrical wet gel disk (*a*) and dry gel disk (*b*) with a saturated level of NaDBS binding. The diameter (d_0) before the surfactant binding was 2 mm each for both gels. Wavelengths used for the measurements: 261 nm (open circles) and 400 nm (filled circles). (Adapted from Kokufuta 2005 [7] and Kokufuta et al. 1997 [29].)

Experimental Section in Ref. 29). In PDT (*a* in Fig. 40.11c), a rapid decrease in transmittance at both ends was observed when using the wavelength at 261 nm. However, the transmittance increased gradually and became constant when the scanning point approached the central core of the gel disk. On the other hand, the transmittance at 400 nm was almost constant, independent of the position. Therefore, it is evident that the surfactant molecules bound strongly only around the gel walls. This conclusion can be supported by PDT (*b* in Fig. 40.11c) for the dry gel in which we did not observe specific position-dependent changes in transmittance at 261 nm. In the case of the dry gel, the surfactant solution permeated throughout the gel phase, such as by taking up water by a sponge, thus allowing the surfactant molecules to bind to the network without distribution, at least within the resolution (30 μm) of our microscopic spectroscopy, the value of which is dependent on the size of the beam going through the gel disks. Thus, a marked difference can be observed in the diameters of the surfactant-bound wet and dry gels; specifically, the distance between the right- and left-hand ends, which is larger for the dry gel than for the wet gel, although their diameters in the preparation were identical with each other. As a result, it becomes apparent that the VPT in surfactant-bound ionic NIPA gels is obviously affected by the inhomogeneously distributed charges. The same conclusion has been obtained from experiments with NIPAAm microgels to which NaDBS had been bound [36]. If the osmotic pressure due to mobile counterions plays an important role in the VPT of polyelectrolyte gels, one would expect there to be little influence on the inhomogeneity of charge distributions within the gel. Thus, the results presented here may provide a key to consider whether or not the VPT of polyelectrolyte gels is governed by osmotic pressure. Then it is logical to consider that the nature of NIPAAm gels with ionic surfactants is explained well in terms of the Katchalsky model not based on the osmotic pressure arising from counterions.

40.8 NETWORK INHOMOGENEITY AND SWELLING–SHRINKING KINETICS

We have looked at the influence of the homogeneity of the ionic or strongly hydrophilic monomer units in the network on the VPT in gels. Here let us consider in a wide sense the structural inhomogeneity of the network, namely, network inhomogeneity. According to the definition of gels, many sorts of gels are inhomogeneous in the structure of their networks; for example, see agarose gel in Fig. 40.1. However, in the case of polymer gels it seems that network homogeneity is governed mainly by the distribution of cross-linking points within the network. Indeed, a microscope laser light-scattering study [37] showed a fluctuating speckle pattern due to highly nonuniform spatial distributions of polymer network concentration and cross-linking density in a Bis-cross-linked NIPAAm gel. These inhomogeneities were then considered to have two origins: (1) the dynamic critical fluctuations of the polymer solution at the onset of gelation and (2) the domain formation due to the microphase separation, both of which are directly related to the phase equilibrium properties of the gel during the gelation process. Such fluctuations of polymer density are permanently frozen in the gel structure. In addition to these permanent spatial fluctuations, a polymer network undergoes thermal dynamic concentration fluctuations. Therefore, the nature of gel inhomogeneities can be accounted for in terms of three (two static and one dynamic) types of fluctuation. The conventional technique of dynamic light scattering (DLS) can now be used to study the structural inhomogeneity of gels [38]. The DLS data may be analyzed by the partial heterodyne method [39].

It is obvious from the above that the network homogeneity affects the VPT in gels. However, a question remains regarding a correlation of the swelling–shrinking kinetics of gels with their microscopic structures. Before discussing this issue, we must know the swelling and shrinking kinetics of gels. One group of coworkers [40–42] have studied a theory of the swelling-shrinking kinetics of gels and compared it with their experiment results. Then, the characteristic time (τ) taken for a gel to swell or shrink was given by

$$\tau \propto l^2/D \tag{40.6}$$

where l denotes the characteristic linear dimension of the gel and D is the collective diffusion coefficient of the networks. This equation means that the time for a gel to swell or shrink depends on its size, such as the radius of a spherical gel. Thus, the gels seem to undergo a fast volume change as the term l in Eq. (40.6) is reduced. A candidate falling into this criterion would be gel particles with diameters in the range of several tens to several hundreds of nanometers, often referred to as *microgels* or *nanogels*. However, the swelling–shrinking kinetics of such gel particles has not yet been studied in detail through the direct measurement of particle sizes as a function of time, probably because of the lack of experimental techniques. Indeed, the fast kinetics of microgels has been predicted from the studies of (1) the diffusion rate of solutes into or out of the gel particles (e.g., [43]) and (2) the permeation rate of solvents through the pore formed among the gel particles [44]. Another candidate seems to be macroporous gels having a large pore size, a high pore volume, and a high specific surface area, a good example of which is the opaque gels obtained via the gelation of NIPAAm at temperatures above the LCST or T_v [45–48]. The observed rapid volume change of such macroporous gels was then interpreted by assuming that their bodies are made up of minute domains of densely and sparsely cross-linked gel networks; therefore, the term l in Eq. (40.6) should be reduced.

A technique for achieving fast deswelling kinetics of NIPAAm gels without relying on reduction of l in Eq. (40.6) has been reported [49]. This was based on the use of a macromonomer that is composed of a NIPAAm mainchain and a vinyl group at one end; thus cross-linking with Bis yields a gel network to which many graft NIPAAm chains are bound, that is, a comb-type grafted NIPAAm gel. The gel obtained was transparent in appearance, like conventional Bis-crosslinked NIPAAm gels, but exhibited a very rapid rate of shrinking in response to a change in temperature of 10–40°C. Since the shrinking rate was found to vary depending on the length of graft chains, it was concluded that the thermal collapse of graft chains "bound to the network" plays a key role in the overall gel collapse. This should be distinct from the dynamic property of conventional gels, which is dominated by the diffusion-limited transport of polymeric components of the network in a solvent as characterized by the term D in Eq. (40.6). Then, it is logical to assume that the network homogeneity causes fast deswelling kinetics. This assumption was confirmed by using chemical and radiation cross-linked gels [50]. More specifically, four gels cylindrical in shape were prepared by two different methods: (1) γ-ray irradiation to aqueous solutions of poly(NIPAAm) or poly(NnPAAm) (for their structures, see Fig. 40.7) and (2) redox polymerization of NIPAAm or NnPAAm monomer using Bis as the cross-linker. There were a few differences in the swelling kinetics among these gels. However, a marked difference was observed in the shrinking processes, the rate of which was faster in the order of radiation cross-linked NIPAAm gel > radiation cross-linked NnPAAm gel > chemically cross-linked NnPAAm > chemically cross-linked PNIPAAm gel. This difference was discussed in terms of the microscopic structure of the gels, which was studied by DLS. It was found that the static inhomogeneities frozen in the chemically and radiation cross-linked gels play a key role in their shrinking kinetics.

40.9 MICROGELS

The terms *microgels* and *nanogels* have been used in the previous sections [36,43,44]. Both terms were also used in many papers dealing with the gel particles with diameters in the range of several tens to several hundreds of nanometers, as was mentioned previously. However, in IUPAC Recommendations 2012, nanoparticle is defined as "particle of any shape with dimensions in the 1×10^{-9} and 1×10^{-7} m range (i.e., 1 nm $\sim$ 100 nm)" and this is the case for "nanogel" (see pp. 393–394 in Ref. 51). According to this, some of the important features of microgels will be discussed at the end of this chapter. The contents are mainly limited to microgels based on NIPAAm because almost all of the previous sections have focused on the VPT in "bulk" gels of this sort.

In 1987 Tanaka et al. prepared microgels with a swollen diameter of 0.4 μm (400 nm) by cross-linking NIPAAm with Bis in a sorbitan monolaurate/water mixture as the polymerization medium [52]. To the best of the present author's knowledge, this is the first report on NIPAAm microgels. While different polymerization mediums were used to prepare NIPAAm microgels, two other researchers [53] reported a simple technique for synthesizing monodisperse aqueous NIPAAm latex particles. They demonstrated that the latex dispersions can be obtained by "tumbling" a 5-mL vial containing aqueous solutions consisting of different amounts of NIPAAm, Bis, and an initiator such as potassium persulfate. The polymerization was done at temperatures (e.g., 70°C) that are higher than the LCST or T_v. The latex particles obtained were swollen to about 1 μm in diameter at low temperatures but were contracted by a factor of ~10 in volume, when the temperature was raised above the LCST. It seems that this work facilitates further studies on NIPAAm based-microgels, mainly because of its simple preparation method, as well as the thermal behavior of latexes similar to those of bulk NIPAAm gels and NIPAAm polymers in water. In addition, it should be noted that NIPAAm microgels have slight positive or negative charges arising from polymerization initiators. Therefore, microgel dispersions allow us to use the techniques such as DLS, static light scattering (SLS), electrophoretic light scattering (ELS), and potentiometic and colloid titrations, which are important tools in the study of colloid dispersions. Therefore, many studies have been performed with NIPAAm-based microgels with and without other comonomer units, almost all of which were reviewed in 2000 by Pelton [54], who attempted to discuss the temperature dependence of particle size in terms of the theories of VPT based on the Flory theory, but not on the Katchalsky theory. Also, it was mentioned that the electrophoretic behavior of NIPAAm gel particles is well accounted for in terms of a"charged surface model" established by Pelton and his coworkers, but not of "free-draining model" for polyelectrolyte coils. However, more recent studies [55,56] with ionic or amphoteric NIPAAm microgels clearly demonstrated that their electrophoretic behavior must be discussed in terms of free-draining model, at least in a swollen state. In addition, it seems that "charged hairy surface-layer model" proposed by Ohshima [57, 58] provide a good discussion of the electrophoretic results of NIPA microgels that are in the collapsed state.

In several studies in the 2000s, geometric characteristics of NIPAAm-based microgel particles were investigated. For example, we carefully compared the DLS and SLS results of various microgels based on NIPAAm and concluded that the surfaces of swollen microgel particles were decorated with attached dangling chains, while the microgels with the surface to which oppositely charged polyions are bound are spherical in shape and there are no dangling surface chains [59] (see Fig. 40.12). The structure of microgel particles as

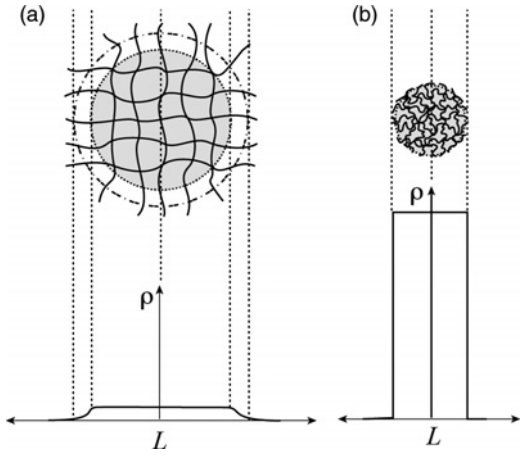


FIGURE 40.12 Schematic representations for a microgel particle in a swollen state (a) and a fully collapsed state (b). The degree of collapse pictured is 0.5 in diameter (L). The polymer density (ρ) was assumed to be constant within the main body (gray circles) of the gel particle, that is, random distribution of cross-linked polymer chains. Ratio of radius of gyration (mean-square radius; R_g from SLS) to hydrodynamic radius (R_h from DLS) is larger than 0.775 for (a), but equal or close to 0.775 for (b). Note that the theoretical R_g/R_h ratio for densely packed spheres becomes 0.775. (Adapted from Kokufuta et al. 2007 [59].)

shown in Fig. 40.12b has also been suggested by the studies [60, 61] of poly(vinyl alcohol) microgels obtained by γ-ray irradiation. Therefore, the size or volume changes of microgel particles in response to small variations in the solution conditions (temperature, pH, salt concentration, etc.) may be discussed in terms of the Katchalsky model (see Fig. 40.5). Then, the complex formation between NIPAAm-based ionic microgels with opposite charges, as well as between an anionic or cationic microgel and oppositely charged linear polyions, provide the key to understanding the mechanism of polyelectrolyte complex formation in water [62–64]. The main reason is that the charges within the internal part of microgels can prevent the aggregation of gel particles, on addition of oppositely charged microgels or polyions. This is the case even when a 1:1 stoichiometric polyelectrolyte complex forms in water, in which the linear polyion complexes are aggregate with each other. As a result, we may study the 1:1 stoichiometric microgel complexes by using techniques such as SLS, DL,S and ELS.

40.10 CONCLUSIONS

This chapter has covered a relatively mature area of polymer gels; however, the fruits of the studies on the VPT in the gels have brought to developments in stimuli-responsive materials. On the other hand, there are extremely many kinds of gels according to the IUPAC definition [1], so that gels composed of materials with self-assembled fibrillar networks were not covered in this chapter. Nevertheless, the understanding of the VPT with such a way as FBA (force balance approach) would provide a key for "controlling" molecular self-assembly, in particular in aqueous systems. Hopefully, the discussions in this chapter can lead to an understanding of the scientific principles governing response driven functions leading to future technologies.

REFERENCES

[1] Slomkowski, S., Alemán, J.V., Gilbert, R.G., Hess, M., Horie, K., Jones, R.G., Kubisa, P., Meisel, I., Mormann, W., Penczek, S., Stepto, R.F.T. (2011). *Pure Appl. Chem.* **83**, 2229–2259.

[2] Vermaas, D., Hermans, J.J. (1948). *Recueil* **67**, 983–997.

[3] Flory, P.J. (1953). *Principle of Polymer Chemistry.* Cornell Univ. Press, New York, pp. 576–594.

[4] Katchalsky, A., Michaeli, I. (1955). *J. Polym. Sci.* **15**, 69–86.

[5] Dusek, K., Patterson, D. (1968). *J. Polym. Sci. A-2* **6**, 1209–1216.

[6] Tanaka, T. (1978). *Phys. Rev. Lett.* **12**, 820–823.

[7] Kokufuta, E. (2005). *Langmuir* **21**, 10004–10015.

[8] Tanaka, T., Fillmore, D.J., Sun, S-T., Nishio, I., Swislow, G., Shah, A. (1980). *Phys. Rev. Lett.* **45**, 1636–1639.

[9] Hirotsu, S., Hirokawa, Y., Tanaka, T. (1987). *J. Chem. Phys.* **87**, 1392–1395.

[10] Kokufuta, E. (2001). Phase transitions in polyelectrolyte gels. In Radeva, T. (ed.), *Physical Chemistry of Polyelectrolytes*, Surfactant Science Series, Vol. 99. Marcel Dekker, New York, pp. 591–685.

[11] Kano, M., Kokufuta, E. (2009). *Langmuir* **25**, 8649–8655.

[12] Prange, M.M., Hooper, H.H., Prausnitz J.M. (1989). *AIChEJ* **35**, 803–813.

[13] Marchetti, M., Prager, S., Cussler, E.L. (1990). *Macromolecules* **23**, 1760–1765.

[14] Otake, K., Inomata, H., Konno, M., Saito, S. (1989). *J. Chem. Phys.* **91**, 1345–1350.

[15] Nemẽthy, G., Sheraga, H.A. (1962). *J. Phys. Chem.* **66**, 1773–1789.

[16] Hasa, J., Ilavsky, M., Dusek, K. (1975). *J. Polym. Sci. Polym. Phys. Ed.* **13**, 253–262.

[17] Tong, Z., Liu, X. (1994). *Macromolecules* **27**, 844–848.

[18] Ilmain, F., Tanaka, T., Kokufuta, E. (1991). *Nature* **349**, 400–401.

[19] Nisato, G., Munch, J.P., Candau, S.J. (1999). *Langmuir* **15**, 4236–4244.

[20] Ogawa, Y., Ogawa, K., Kokufuta, E. (2004). *Langmuir* **20**, 2546–2552.

[21] Ogawa, K., Nakayama, A., Kokufuta, E. (2003). *Langmuir* **19**, 3178–3184.

[22] Kokufuta, E., Suzuki, H., Yoshida, R., Yamada, K., Hirata, M., Kaneko, F. (1998). *Langmuir* **14**, 788–795.

[23] Frank, H.S., Evans, M.W. (1945). *J. Chem. Phys.* **13**, 507–532.

[24] Kauzmann, W. (1959). *Adv. Protein Chem.* **14**, 1–57.

[25] Kokufuta, M K., Sato, S., Kokufuta, E. (2012). *Colloid Polym. Sci*. **290**, 1671–1681.

[26] Tokuhiro, T., Ito, S., Kokufuta, E. (1998). *Macromolecules* **31**, 8549–8557.

[27] Kokufuta, E., Wang, B., Yoshida, R., Khokhlov, A.R., Hirata, H. (1998). *Macromolecules* **31**, 6878–6884.

[28] Kokufuta, M.K., Sato, S., Kokufuta, E. (2011). *Colloid. Surf. B: Biointerfaces* **87**, 299–309.

[29] Kokufuta, E., Suzuki, H., Sakamoto, D. (1997). *Langmuir* **13**, 2627–2632.

[30] Schild, H.G., Tirrell, D.A. (1991). *Langmuir* **7**, 665–671.

[31] Inomata, H., Goto, S., Otake, K., Saito, S. (1992). *Langmuir* **8**, 1030–1031.

[32] Tam, K.C., Ragaram, S., Pelton, R.H. (1994). *Langmuir* **10**, 418–422.

[33] Wada, N., Kajima, Y., Yagi, Y., Inomata, H., Saito, S. (1993). *Langmuir* **9**, 46–49.

[34] Kokufuta, E., Zhang, Y.-Q., Tanaka, T., Mamada, A. (1993). *Macromolecules* **26**, 1053–1059.

[35] Kokufuta, E., Nakaizumi, S., Ito, S., Tanaka, T. (1995). *Macromolecules* **28**, 1704–1708.

[36] Suzuki, H., Kokufuta, E. (1999). *Colloids Surf. A* **147**, 233–240.

[37] Sato-Matsuo, E., Orkisz, M., Sun, S.T., Li, Y., Tanaka, T. (1994). *Macromolecules* **27**, 6791–6796.

[38] Norisuye, T., Kida, Y., Masui, N., Tran-Cong-Miyata, Q., Maekawa, Y., Yoshida, M., Shibayama, M. (2003). *Macromolecules* **36**, 6202–6212.

[39] Joosten, J.G.H., McCarthy, J.L., Pusey, P.N. (1991). *Macromolecules* **24**, 6690–6699.

[40] Tanaka, T., Fillmore, D.J. (1979). *J. Chem. Phys.* **70**, 1214–1218.

[41] Tanaka, T., Sato, E., Hirokawa, Y., Hirotsu, S., Peetermans, J. (1985). *Phys. Rev. Lett.* **55**, 2455–2458.

[42] Sato-Matsuo, E., Tanaka, T. (1988). *J. Chem. Phys.* **89**, 1695–1703.

[43] Kato, T., Fujimoto, K., Kawaguchi, H. (1994). *Polym. Gels Netw.* **2**, 307–313.

[44] Ogawa, K., Wang, B., Kokufuta, E. (2001). *Langmuir* **17**, 4704–4707.

[45] Kabra, B.G., Gehrke, S.H. (1991). *Polym. Commun.* **32**, 322–323.

[46] Wu, X.S., Hoffman, A.S. (1992). *J. Polym. Sci. A* **30**, 2121–2129.

[47] Kokufuta, E., Matsukawa, S. (1996). *Ber. Bunsenges. Phys. Chem.* **100**, 1073–1078.

[48] Kishi, R., Hirasa, O., Ichijo, H. (1997). *Polym. Gels Netw.* **5**, 145–151.

[49] Kaneko, Y., Sakai, Y., Kikuchi, A., Yoshida, R., Sakurai, Y., Okano, T. (1995). *Macromolecules* **28**, 7717–7723.

[50] Takekawa, M., Kokufuta, E. (2009). *Colloid. Polym. Sci.* **287**, 323–334.

[51] Vert, M., Doi, Y., Hellwich, K.-H., Hess, M., Hodge, P., Kubisa, P., Rinaudo, M., Schué, F. (2012). *Pure Appl. Chem.* **84**, 377–410.

[52] Hirose, Y., Amiya, T., Hirokawa, T., Tanaka, T. (1987). *Macromolecules* **20**, 1342–1344.

[53] Pelton, R.H., Chibante, P. (1986). *Colloids Surf.* **20**, 247–256.

[54] Pelton, R. (2000). *Adv. Colloid Interface Sci.* **85**, 1–33.

[55] Ogawa, K., Nakayama, A., Kokufuta, E. (2003). *J. Phys. Chem. B* **107**, 8223–8227.

[56] Kokufuta, E., Sato, S., Kokufuta, M.K. (2013). *Langmuir* **29**, 15442–15449.

[57] Ohshima, H., Makino, K., Kato, T., Fujimoto, K., Kondo, T., Kawaguchi, H. (1993). *J. Colloid Interface Sci.* **159**, 512–514.

[58] Ohshima, H. (2013). *Curr. Opin. Colloid Interface Sci.* **18**, 73–82.

[59] Kokufuta, E., Ogawa, K., Doi, R., Kikuchi, R., Farinato, R.S. (2007). *J. Phys. Chem. B* **111**, 8634–8640.

[60] Wang, B., Mukataka, S., Kodama, M., Kokufuta, E. (1997). *Langmuir* **13**, 6108–6114.

[61] Schmitz, K.S., Wang, B., Kokufuta, E. (2001). *Macromolecules* **34**, 8370–8377.

[62] Miyake, M., Ogawa, K., Kokufuta, E. (2006). *Langmuir* **22**, 7335–7341.

[63] Doi, R., Kokufuta, E. (2010). *Langmuir* **26**, 13579–13589.

[64] Doi, R., Kokufuta, E. (2011). *Langmuir* **27**, 392–398.

41

GEL CRYSTALS

TSUNEO OKUBO

Institute for Colloidal Organization, Hatoyama 3-1-112, Uji, Kyoto 611-0012, Japan

41.1 INTRODUCTION

Gel crystals are grouped into three systems: (I) crystal-like ordering of gel spheres (particles) in suspension state, (II) gels containing interior crystal arrays of colloidal particles, and (III) crystal-like arrays of gel spheres formed at the plane and curved interfaces (see Fig. 41.1). All of these systems are quite interesting because of their structure and function are similar to those of biological assemblies such as skin and crystalline lens. Furthermore, most gels are highly sensitive to the external fields and atmospheres. Typical gel spheres in type I are cross-linked linear-type polymers. Recently, many kinds of core–shell-type gel spheres have been prepared. Mixtures of the gel spheres and colloidal hard spheres are also interesting. Spheres of type II gel crystals will be distributed in the gas, liquid, or solid state. Many kinds of interfaces of type III gel crystals are also available on the gas-, liquid- or solid-state spheres (particles) or plates. Here, most studies have focused on type I gel crystals formed from spherical gel particles. However, anisotropic and also monodisperse particles are very exciting to study because of their specific functions and propertird in gel crystals.

First, let's discuss type I gel crystals: the gel particle crystals. In general, polymer solution, which is composed of linear-type polymers and their solvents, is *transparent*. The main cause for the transparency is the fact that the size of the unit's polymer dynamic thermal motion, which is close to the size of these type I gel crystal monomer units, is very small compared with the light wavelengths and is rather close to the size of solvents (see Fig. 41.2). There exist no *interfaces* between the polymer solutes and solvents, since the monomer units and solvent molecules exchange their locations rather freely by their thermal motion. On the other hand, colloidal dispersions of hard spheres are composed of the large solid particles and very small of medium-sized molecules. The sizes of typical colloidal particles are dimensionally close to or larger than those of the light wavelengths, and 100–1000-fold larger than those of the medium molecules. Thus, colloidal dispersion is *turbid* except for those in the refractive-index-matched condition between particles and medium. In other words, turbid dispersion supports the existence of the *interfaces* in a sense of colloid chemistry.

Most colloidal particles in water, on the other hand, get negative charges on their interfaces by two mechanisms: (1) *dissociation of ionizable groups* introduced to the interfaces from the initiators during polymerization of monomers, and (2) the *preferential adsorption of ions* from suspension in order to reduce the high free-energy level at the particle–water interfaces. Typical examples of the latter are the colloidal crystallization of monodispersed gold and silver particles. They acquire negative charges *spontaneously*, when they disperse in water, and then they always show negative ζ-potential in suspension state. However, these particles should have no charges on the sphere surfaces when the spheres do not come in contact with water [1]. The charges on a colloidal sphere are introduced spontaneously when the amount of charge is not sufficient for the stabilization of dispersion, whereas the charges are bound with their counterions when the charge amount on a colloidal sphere is excessive. This *charge renormalization effect* has been discussed by various researchers [2–5].

The ionic groups at the interfaces leave their counterions in the medium phase, and these excess charges accumulate near the interface, forming an *electrical double layer*. The

Encyclopedia of Biocolloid and Biointerface Science, Volume 1, First Edition. Edited by Hiroyuki Ohshima.
© 2016 John Wiley & Sons, Inc. Published 2016 by John Wiley & Sons, Inc.

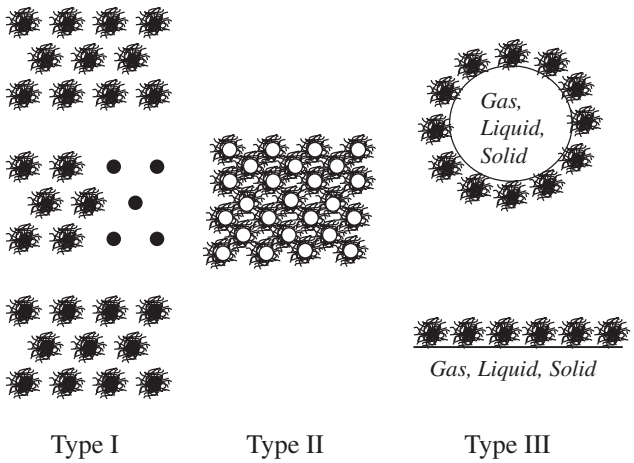


FIGURE 41.1 Types of gel crystals.

counterions and coions in the diffuse region are distributed according to a balance between the thermal diffusive forces and the forces of electrical interaction with colloidal particles. The impact of the electrical double layers on colloidal crystallization has been clarified by many researchers [1–28]. Giant sizes of colloidal single crystals [20–29] have been formed in the exhaustively deionized and diluted suspension of colloidal spheres [20,29–31]. Colloidal crystals are beautiful and fantastic with respect to their iridescent structural colors, since the interparticle distance is just in the range of light wavelengths and each single crystal reflects light in different colors as a result of Bragg diffraction. From our experience, the colloidal spheres smaller than ~40 nm in diameter hardly form crystal structures even though the spheres are monodisperse and the suspensions are deionized exhaustively because of the very vigorous Brownian thermal motion of such small spheres and the difficulty in the formation of the electrical double layers. Colloidal crystals were not formed for the monodisperse and 29-nm spheres at any sphere concentrations, despite the formation of the typical liquid-like structures, *ordered liquid* [32]. The electrical double layers might not be formed firmly when the sphere size is not large enough relative to the size of simple electrolytes and/or medium-sized molecules, since the interfaces between the spheres and the solvent molecules are not formed firmly.

Now, most gel dispersions are also turbid, and characteristically they appear to be just in between *linear-type polymer solution* and *colloidal dispersion* as schematically represented in Fig. 41.2. When the degree of cross-linking is quite low, then the gels will behave like polymer solutions, whereas the gels will behave as colloidal particles as their degree of cross-linking increases. Crystallization of thermosensitive gel spheres of poly(*N*-isopropylacrylamide), pNIPAm and their mixtures with other colloidal spheres has been studied in aqueous media by several research groups hitherto (see also Table 41.1) [33–51]. Especially in the authors' previous papers [48–51], the important role of the electrical double layers on the crystallization of gel spheres has been demonstrated, for the first time, using the monodisperse thermosensitive gel spheres of poly(*N*-isopropylacrylamide) ranging from 0.5 mol% to 10 mol% in the degree of cross-linking and also ranging from 200 to 600 nm in gel size in their hydrated and swollen states.

Type I gel crystals are really crystal, where the gel spheres move with the translational and rotational modes by the thermal energy $k_B T$ but retain their equilibrium positions. On the other hand, thermal movement of type II gel crystals is greatly restricted. Type II gel crystals, gels containing crystal structure, however, may be much more useful in order to build up the external field responsible optical devices, because the contraction and/or extension of gels, which is one of the most interesting function, is significant compared with other types of gel crystals.

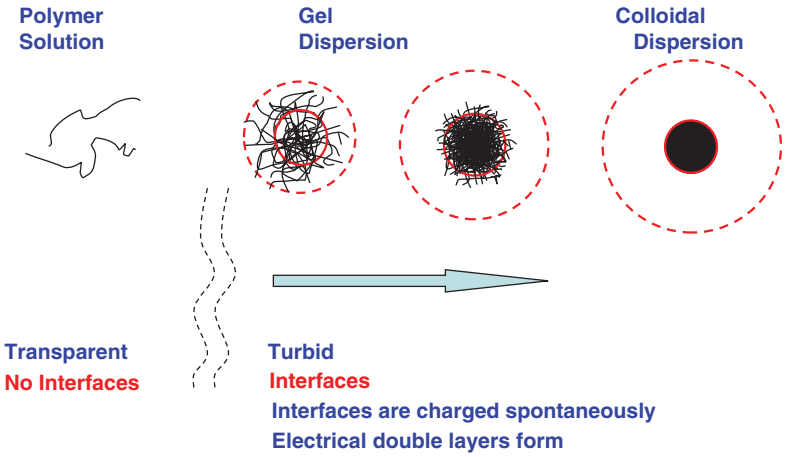


FIGURE 41.2 Schematic representation of the comparative characteristics of polymer solution, gel dispersion, and colloidal dispersion.

TABLE 41.1 Characteristics of Colloidal Crystals of pNIPAm Gel Systems

	$d0$ (nm)		ρ (wt%/vol%)		Critical conc. of crystallization (wt%) With resins			T_t Without resins		l_D at 1wt% (nm)		l_D/d_o at 1wt%			ζ-pot	
Gel spheres	25°C (20°C)	45°C	25°C (20°C)	45°C	20°C (25°C)	33°C	45°C	20°C (25°C)	33°C		25°C (20°C)	45°C	25°C	45°C (25°C)	25°C	Ref. (mV)
pNIPAm(200-0.5)	320	120	0.030	0.61	0.015	0.17	0.3	0.8	2	32	48	150	0.15	1.29	−10.1	49
pNIPAm(200-2)	260	100	0.035	0.59	0.015	0.05	0.3	0.4	0.3	33	48	130	0.19	1.26	−14.8	50
pNIPAm(200-5)	225	110	0.088	—-	[0.01]	—-	—-	[0.8]	—	33	97	—-	0.43	—-	−13.5	48
pNIPAm(200-10)	200	120	0.122	0.62	0.01	0.03	0.06	0.15	0.6	35	110	155	0.54	1.28	−16.7	50
pNIPAm(400-5)	[410]	220	[0.11]	0.68	0.02	0.04	0.07	0.3	—	33	[210]	295	[0.51]	1.34	−14.4	51
pNIPAm(600-5)	520	290	0.127	0.72	0.03	0.12	0.35	0.8	2	33	290	405	0.56	1.38	−17.9	51
pNIPAm(1500-5)	[1500]	505	—	0.80	—-	—-	—-	—-	—-	31	—-	—-	—	—-	−13.4	This work

41.2 GEL SPHERES USED FOR TYPE I GEL CRYSTALS

One of the most familiar gel spheres of type I gel crystals is thermosensitive polymer gel spheres, pNIPAm gels. Table 41.2 shows several characteristics of a series of poly(*N*-isopropylacrylamide) gel spheres, pNIPAm(200-0.5), pNIPAm(200-2), pNIPAm(200-5), pNIPAm(200-10), pNIPAm(400-5), pNIPAm(600-5), and pNIPAm(1500-5). Here, the first and second numbers in parentheses indicate the rough values of sphere size at 20°C in nanometer scale and the degree of cross-linking in mol%, respectively. The sphere size, d_0 estimated from the dynamic light-scattering measurements, decreased sharply as the suspension temperature increased. The temperatures of the transition were around 33°C for each sphere. Deionized stock suspensions, with their concentrations ranging from ∼2 to 4 wt%, emitted strong iridescent colors at 25°C. The densities of the gel spheres in the suspension state (ρ) were estimated from the reflective spectroscopy by the author's group, for the first time. The ρ-value is obtained from the ratio of the gel concentration in weight percent divided by that in volume percent. The density increased sharply as the suspension temperature increased. At an elevated temperature the gel spheres must be highly compact with the polymer chains and colloidal interfaces forming firmly. The ρ-value of the gel spheres increased as the degree of cross-linking and/or size of spheres increased. The ζ-potentials were negative and decreased slightly as the degree of the cross-linking and/or sphere size increased. These results are consistent with the colloidal nature of the gel spheres; specifically, the water–gel interfaces form more firmly as the sphere density increases. The negative charges on the gel interfaces originate mainly from the charges from the initiator used, potassium persulfate in the polymerization processes and also from the spontaneous charging at the interfaces between the gel spheres and water as was described in Section 41.1.

The volume fraction of gel spheres, ϕ-values, are estimated from the l-values using Eq. (41.1) [52]:

$$l = 0.904 \times d_0 \times \phi^{-1/3} \tag{41.1}$$

The characteristic values of *cationic* gel spheres, lightly cross-linked poly(2-vinyl pyridine) spheres, AIBA-P2VP [53], and lightly cross-linked poly(2-vinyl pyridine) stabilized with poly (ethylene glycol), PEGMA-P2VP [54], are given in Table 41.2. The diameters were measured using various techniques, including scanning electron microscopy (SEM), laser diffraction particle size analyzer method (LDPS), electrophoretic light-scattering measurements (ELS), and dynamic light-scattering measurements (DLS). The mean size of PEGMA-P2VP gel spheres d_0 decreased slightly when the degree of cross-linking increased from 0.1 to 1 mol%, which is consistent with the dependence of the degree of cross-linking of pNIPAm gel spheres. Zeta-potentials of AIBA-P2VP increased as degree of cross-linking decreased, whereas those of PEGMA-P2VP decreased. One cause will be due to the fact that AIBA-P2VP is softer and contain a more amount of water molecules within a gel sphere compared with PEGMA-P2VP, since the effective density of AIBA-P2VP gel spheres (ρ) is small compared with that of the corresponding PEGMA-P2VP, especially at low degree of cross-linking. When the gel spheres are soft, the ionic groups contacting with water molecules and then number of the ionized groups should increase.

The ρ-values of AIBA-P2VP and PEGMA-P2VP increased with increasing degree of cross-linking and were insensitive to the sphere concentration as is shown in Tables 41.1 and 41.2. The ρ-values of PEGMA-P2VP gel spheres were slightly larger than those of AIBA-P2VP and also increased with increasing degree of cross-linking. The ρ-values of pNIPAm gel crystals were quite insensitive to the sphere concentration. The density of AIBA-P2VP in the dried state should be close to that of PEGMA-P2VP, since most of the content of both gel spheres is P2VP polymer. The specific density of PEGMA-P2VP was measured to be 1.1 in mean value [53,54]. Thus, the volume fractions of the AIBA-P2VP gel polymers and water in suspension state are evaluated to be 0.74 (=0.81/1.1) and 0.26, 0.64 (=0.7/1.1) and 0.36, and 0.45 (=0.51/1.1) and 0.55, for AIBA-P2VP(1), AIBA-P2VP(0.5), and AIBA-P2VP(0.1), respectively [53]. Furthermore, the volume fractions of the PEGMA-P2VP gel polymers and water in suspension state are estimated to be 0.75 (=0.83/1.1) and 0.25, 0.66 (=0.73/1.1) and 0.34, and 0.85 (0.93/1.1)

TABLE 41.2 Characteristics of AIBA-P2VP and PEGMA-P2VP Gel Spheres at 25°C

				Critical conc. Melt. (wt%)		l_D (nm)	
Gel spheres	d_0 (nm)	ζ-Pot. (mV)	ρ	With resins		Without resins	Ref.
AIBA-P2VP(0.1)	170	+60	0.51	0.2	0.8	44.6	53
AIBA-P2VP(0.5)	170	+58	0.70	0.18	0.5	64.0	53
AIBA-P2VP(1)	180	+47	0.81	0.7	1.5	81.5	53
PEGMA-P2VP(0.1)	400	+16.0	0.83	1.1	1.2	260	54
PEGMA-P2VP(0.5)	390	+21.9	0.73	0.7	1.0	230	54
PEGMA-P2VP(1)	385	+22.7	0.93	0.7	1.0	260	54

and 0.15, respectively, for PEGMA-P2VP(0.1), PEGMA-P2VP(0.5), and PEGMA-P2VP(1) [54]. This means that the quarter volume of a gel sphere is filled with water in suspension state. Clearly, AIBA-P2VP and PEGMA-P2VP are very hard and close to the typical colloidal hard spheres. pNIPAm gel spheres and the core–shell-type gel spheres, for example, have been studied intensively in deionized water and at room temperature [55–67].

41.3 PHASE DIAGRAM AND MORPHOLOGY OF TYPE I GEL CRYSTALS

Close-up color pictures of colloidal single crystals of pNIPAm(200-5) gels in a test tube are shown in Fig. 41.3 [48]. Images (a) and (b) identify deionized and salt-containing suspensions, respectively. The giant single crystals of several 10s of millimeters, which are composed of gel spheres, were observed especially in the low gel concentrations and in the deionized state with the coexistence of the ion exchange resins. There are two kinds of single crystals, which were recognized macroscopically, by the naked eye: (1) red, blue, yellow and blocklike crystals and (2) pillarlike ones. (1) The formers form from the *homogeneous nucleation mechanism* in the bulk phase far from the cell wall. The color change from the reddish to bluish or bluish (or greenish) to reddish in a single crystal is due to the change in the incident angles of light through the curved wall of the test tube. When a test tube is rotated slowly, the single crystals exhibiting the strong iridescent colors disappeared suddenly, but the other single crystals appeared in the other places. These iridescent colors are clearly ascribed to Bragg diffraction of the incident light through the crystals. The single crystals are packed densely separated with the grain boundaries, and the appearance and disappearance of the crystals take place depending on the Bragg diffraction conditions. On the other hand, the pillarlike crystals grow from the *heterogeneous nucleation mechanism* along the cell wall. It should be noted here that each single crystal of the typical colloidal spheres is surrounded by grain boundaries and packed densely [16,20,29,30,68]. The morphology of the single crystals of the gel spheres is quite similar to that of the typical colloidal spheres [3,16,20–23,29–31,69–74]. Large single crystals were observed in the rather diluted gel suspensions *in the presence of salt*, for the first time. For typical colloidal hard spheres, large single crystals are not formed with salt systems. In other words, gel crystals are rather insensitive to the salt addition compared with typical colloidal sphere system.

Figure 41.4 is a phase diagram of the crystallization of pNIPAm(200-5) at 25°C [48]. The figure also shows the size of single crystals very roughly corresponding to the size of the open circles. Solid circles show the colloidal liquid state. Concentrations of the diffusible simple ions (most of them will be hydronium and hydroxide ions in aqueous media) in suspension with and without ion exchange resins in the figure are estimated to be approximately 2×10^{-7} M and 1×10^{-6} M, respectively, from the conductance measurements and the authors' experience [30, 31]. Clearly, the critical concentration of melting (or crystallization) increased by the addition of a small amount of sodium chloride. The phase diagram of the gel spheres is also very similar to those of typical colloidal spheres, polystyrene, colloidal silica, and PMMA spheres, for example [20,22,31,72,73], although the absolute values of the corresponding volume percents (vol%) of pNIPAm(200-5) are 10-fold higher than those of typical colloidal spheres. This difference in the critical concentrations supports the idea that the crystallization takes place by the

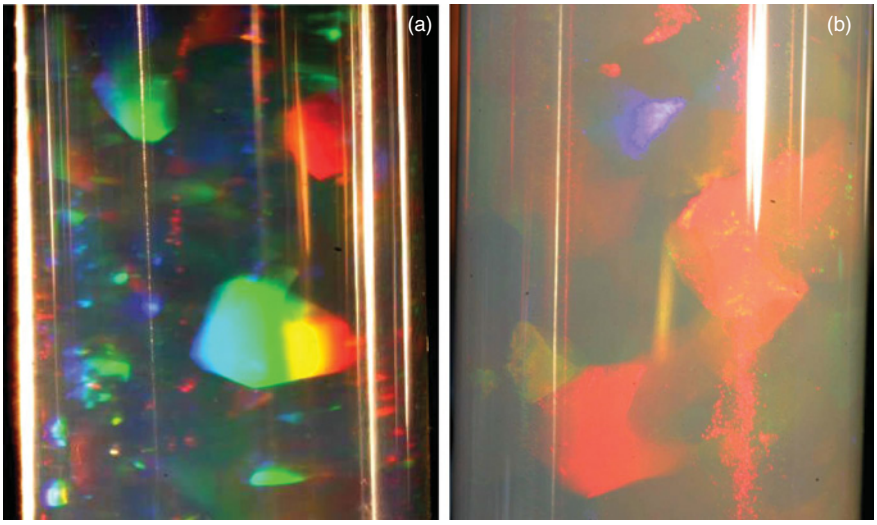


FIGURE 41.3 Close-up color images of PNIPAM(200-5) in a test tube: (a) [PNIPAM(200-5)] = 0.116 wt%, with resins, at 25°C; (b) 2.82 wt%, [NaCl] = 3.5×10^{-5} M, at 25°C. For a color version of this figure, see the color plate section.

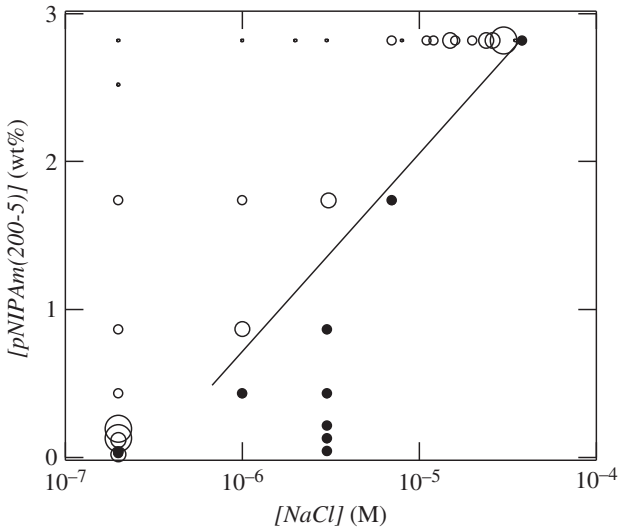


FIGURE 41.4 Phase diagram of colloidal crystal of PNIPAM(200-5) gel spheres as a function of salt concentration at 25°C. White circles–crystal, size of circles shows rough values of crystal size; black circles—liquid. (Adapted from Okubo 2002 [43].)

incomplete electrical double layers from the *vague interfaces* of gel spheres compared with the firm interfaces of the typical colloidal spheres.

The mean size of the single crystals observed macroscopically changed as a function of the concentration of pNIPAm gel spheres. Several important findings are summarized [48–51]. *First*, size of single crystals of pNIPAm(200-10) from the homogeneous nucleation mechanism decreased sharply as gel concentration increased. *Second*, the very large single crystals formed at the gel concentration slightly higher than the critical concentration of crystallization at 20°C especially for pNIPAm(200-10), which is quite similar to the observation of typical colloidal spheres. This is due to the fact that the sphere–solvent interfaces form firmly when the degree of cross-linking is large. *Third*, crystal size versus concentration profiles of pNIPAm(200-10) were almost completely insensitive to the suspension temperature between 20 °C and 45°C, whereas the profiles of pNIPAm having low degree of cross-linking were sensitive to the suspension temperature. This result also supports the theory that the intergel repulsion of pNIPAm(200-10) is strong compared with that of gels having lower degrees of cross-linking.

Size of single crystals of pNIPAm(400-5) from the homogeneous nucleation mechanism increased gently as gel concentration increased, and the largest single crystals formed at the gel concentration around 2 wt% at 20°C and then the crystal size decreased again gently. At high temperatures the crystals' maximum size was not observed in the range of concentrations examined. These gentle concentration dependences of crystal size of pNIPAm(400-5) are different from those of the typical colloidal dispersions and also those of small gel spheres, where very large single crystals formed at the sphere concentration slightly higher than the critical concentration of melting and crystal size decreased sharply as the sphere concentration increased. Concentration dependences of pNIPAm(600-5) spheres are complex. At 20°C and 33°C the largest crystals appeared at the gel concentration close to the critical concentration of melting, but their size decreased gently as sphere concentration increased. At 45°C, crystal size increased gently with sphere concentration, and the maximum size of crystals usually forms around ≥4 wt%. Thus, the concentration dependences of the crystal size of pNIPAm(400-5) and pNIPAm(600-5) are gentle and different from the other small gel spheres such as pNIPAm(200-5). These results support the assumption that the crystals of large gel spheres are not so stable compared with the small gel spheres. In general, the relative contribution of the electrical double layers (l_D) against the sizes of gel spheres (d_o) decreases as the gel size increases.

Another team of investigators [75] proposed the reentrant order–disorder transition from their theoretical study as a function of gel sphere concentration. Two other investigators [76] reported the supporting data using static (SLS) and dynamic light-scattering (DLS) technique. This author believes the polydispersity index of the gel spheres to be most important for phase transitions.

41.4 LATTICE STRUCTURE OF TYPE I GEL CRYSTALS

SLS measurements of deionized suspensions of the thermosensitive gels of poly(*N*-isopropylacrylamide) with various degrees of cross-linking and sizes were made at 20°C and 40°C [77]. Sharp scattering peaks are observed in the scattering curve and they were assigned to the face-centered cubic (fcc) and/or body-centered cubic (bcc) lattices in the distribution of gel spheres. The fcc and bcc crystal structures formed in the stable and unstable conditions respectively; thus, the former formed more favorably at high sphere concentrations and/or low temperatures. The closest intersphere distances were much longer than the hydrodynamic diameters of the gel spheres, especially at low sphere concentrations. These experimental results emphasize the important role of the extended electrical double layers in the crystallization of gel spheres, although the contribution of double layers in gel systems is weak compared with that in the typical colloidal spheres.

Figure 41.5 shows examples of the static light-scattering intensities, with $I(q)$ as a function of scattering vector q for pNIPAm(200-5) at 0.3 wt% and at 40 °C [77]. Sharp blue and the broad red curves indicate data for the coexistence of suspensions with and without ion exchange resins. These suspensions are *crystal* and *liquid*, respectively. Very sharp peaks appeared for the crystals. The light-scattering

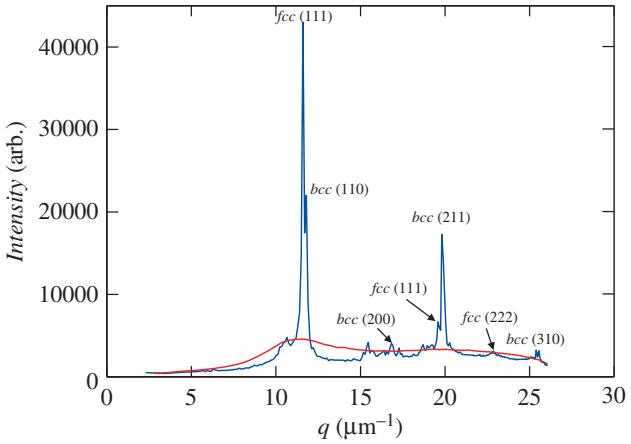


FIGURE 41.5 Scattering intensity of aqueous suspensions of pNIPAm(200-5) as a function of scattering vector at 40°C, 0.30 wt%. Blue curve–with ion exchange resins; red curve–without resins.

intensity measurements were made at intervals of half of a degree (0.5°). However, this interval was not always narrow enough for the determination of very reliable values of the peak scattering vector q_m. Similar profiles in the intensity of scattered light showing the peaks have been reported for typical colloidal crystals of hard spheres in deionized aqueous suspensions. However, most of the experiments of hard spheres were made for the much lower sphere concentrations than the gel systems [78–81].

Assignment of the respective peaks q_m to the crystal planes was made from comparison of the observed peak vectors with the calculation from $q_{h,k,l} = 2\pi/a(h^2+k^2+l^2)^{1/2}$, where h, k, and l are Miller's indices and a is the unit cell size. During crystallization and the aging process it is highly plausible that several kinds of single crystals having the same crystal lattice structures but slightly different lattice spacing values form. The quite low rates of crystallization of pNIPAm gels were compared with those of typical colloidal spheres such as colloidal silica spheres (see Section 41.5). Only the high and main peaks were assigned to be the reflections of face-centered cubic (fcc) and body-centered cubic (bcc), lattices as is shown in Fig. 41.5. The Bragg distances (d_B) were evaluated from the q_m values using Bragg equations, $d_B = 2\pi/q_m$. The nearest-neighbored intersphere distance (l), which is given by $(3/2)^{1/2}d_B$, agreed satisfactorily with the corresponding l_0-values calculated from the sphere concentration. In this work, l_0-values were calculated assuming the simple cubic lattice in the sphere distribution, although the real crystals of gel spheres are fcc and/or bcc lattices. Differences in the l_0-values among the simple cubic fcc and bcc lattices at the same sphere concentration are within 3%, corresponding to the experimental errors in SLS measurements. The peaks are sharp and the background intensity is low. Thus, there should not be a significant difference between the profiles in the structure factor $S(q)$ and the intensity of scattered light $I(q)$:

$$I(q) = P(q)\,S(q) \tag{41.2}$$

Here, $P(q)$ is the single-particle form factor, and can be estimated experimentally from the $I(q)$ measurements on the same suspension but in the presence of salt, for example.

The scattering curve of the gel suspensions without resins shown in red in Fig. 41.5 showed rather broad main and further broad second peaks. The fcc and bcc crystals coexisted. Clearly, very sharp double peaks appeared at low q in the figure, and were assigned to the (111) and (110) reflections of fcc and bcc lattices, respectively. Most other peaks were then assigned rather accurately as is shown in Fig. 41.5. The difference in peak scattering vectors between the (111) reflection of fcc and (110) of bcc was only 1–2° in scattering angle. The agreement between the observed distance and the calculation from the sphere concentration is satisfactory when the experimental errors of the SLS measurements are taken into account. The red scattering curve in Fig. 41.5 demonstrates, on the other hand, that the suspension without resins is the typical *liquid* or *disordered liquid* structure.

Sharp reflection peaks were observed for pNIPAm gel suspensions especially at high gel concentrations and high suspension temperature. The primary peak wavelength (λ_p) in the reflection spectroscopy of colloidal crystals at the scattering angle of 90° is estimated from the nearest-neighbor intersphere distance (l) of the face-centered- and/or body-centered-cubic lattices, which are most familiar types of lattice structures in colloidal crystals [52]:

$$\lambda_p = nl/0.6124 \tag{41.3}$$

Here, the refractive index (RI) of the liquid (n) is given as follows:

$$n = \phi \times (\text{RI of gel sphere}) + (1-\phi) \times (\text{RI of water}) \tag{41.4}$$

In our experiments gel sphere concentrations are not so high, and n is safely assumed to be that of water, 1.33. Thus, l-values are estimated from reflection spectroscopy.

The nearest-neighbor intergel sphere distance (l) is in a linear relationship with the reflection peak wavelengths given by Eq. (41.3). The lattice spacing of gel sphere crystals does not change with variation of suspension temperature, because the lattice spacing is determined by sphere concentration or sphere number in suspension, and *not by gel size*. Insensitivity of the lattice spacing of the thermosensitive gel sphere crystals on suspension temperature was supported experimentally by others [67] as well as the present authors. Temperature

dependence of the lattice spacing of type II gel crystals is substantial [82], since the lattice spacing changes following variation in gel size.

41.5 KINETICS OF TYPE I GEL CRYSTALLIZATION

The size of the colloidal single crystals from the homogeneous nucleation L is estimated by Scherrer's equation from the half-width of the reflection spectrum [83, 84]

$$L \propto n\,(\Delta q)^{-1} \tag{41.5}$$

where n is the number of the order in the Bragg equation. q is the scattering vector, and Δq denotes $q_l - q_s$, with q_l and q_s referring the largest and smallest wavelengths corresponding to the half-width of the reflection peak. It should be noted here that Eq. (41.5) is derivable by assuming the existence of a powderlike random distribution of a large number of colloidal crystals in the reflection volume. However, this assumption is difficult to maintain, since the most dense planes of the colloidal single crystals tend to orient parallel to the cell plane.

The peak intensity I of the reflection spectra is approximated by Eq. (41.6) [26,81]

$$I \propto N_{\text{cryst}} L^3 \propto L^3 \tag{41.6}$$

where N_{cryst} is the number of single crystals in the reflection volume, which is directly proportional to the number concentration of crystals in the final stages of crystallization, being equal to the total number of nuclei that were formed in the whole course of crystallization. The crystal growth rate v is evaluated from the cube-root plot of the reflection intensity using Eq. (41.6) or the half-width of the reflection peak using Eq. (41.5).

Most kinetic measurements on colloidal crystallization, including gel sphere crystallization, have included observation of an induction period, after which the crystal growth started especially in the diluted suspensions. This observation supports the assumption that the kinetics of colloidal and gel crystallization is explainable by the classical diffusive crystallization theory, including nucleation and crystal growth processes. The number of nuclei that germinate per unit time, the nucleation rate v_n is given by

$$v_n = N_n / t_i \tag{41.7}$$

where N_n is the total number of nuclei that are formed during the nucleation process and t_i is the induction period. Here, we assume that the number of nuclei equals the number of single crystals formed. The number of spheres per mean size of single crystals N_c is given for the cubic lattice by

$$N_c = 2^{1/2} L^3 / l^3 \tag{41.8}$$

where L and l are the mean size of single crystals formed and the closest intersphere distance, respectively. The total number of colloidal spheres (N_T) in a unit volume is $\phi/[(4/3)\pi(d_0/2)^3]$. Then, v_n is given as follows:

$$v_n = N_T / N_c t_i \tag{41.9}$$

The size of a single crystal is highly polydisperse, as has been observed previously [20]. Therefore, clear-cut separation of the nucleation step from the crystallization process will be difficult, and the nucleation reaction may remain even in the crystal growth period. Furthermore, Ostwald ripening of the crystals, that is, further growth of large crystals and disappearance of small ones, has not been observed for many colloidal crystallization systems.

According to two investigators [83,84], the crystal growth rate v is given by

$$v = v_\infty \left[1\text{-}\exp(-\Delta\mu / k_B T)\right] \tag{41.10}$$

Here, $\Delta\mu$ is the chemical potential difference between the crystal and liquid phases and is given by Eq. (41.11)

$$\Delta\mu = \mu_{\text{cryst}} - \mu_{\text{liq}} \tag{41.11}$$

$\Delta\mu > 0$ means that the crystallization will proceed. We should note that Eq. (41.12) holds [71]:

$$\Delta\mu / k_B T = \ln(\phi / \phi_c) \sim \sigma \tag{41.12}$$

where σ is the relative supersaturation given by $(\phi - \phi_c)/\phi_c$. From Eqs. (41.10) and (41.12), we can derive the following equation:

$$v = v_\infty [1\text{-}\exp(-\sigma)] \tag{41.13}$$

Equation (41.13) is further simplified as follows:

$$v = v_\infty - v_\infty \phi_c / \phi \tag{41.14}$$

Equation (41.14) often holds in our experiments for typical colloidal hard spheres [81,85–92]; v_∞ is given by Eq. (41.15):

$$v_\infty = 4D_0 / \xi \tag{41.15}$$

Here, D_0 is the diffusion coefficient of spheres and ξ is the mean diffusion length (path) in the crystallization suspension. The unit of gel concentration in the kinetic study should be a volume fraction (or volume percent) instead of a weight percent as is shown in Eqs. (41.12) and (41.14), for example.

Crystal growth rate coefficients, k ($= v/L_\infty$) of the crystallization of a series of thermosensitive gel spheres of pNIPAm are shown in Fig. 41.6 [93]. Crystallization of colloidal silica

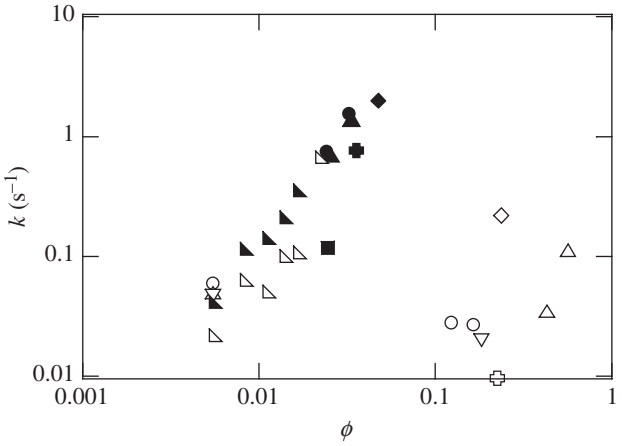


FIGURE 41.6 Rate coefficients, k in the crystallization of PNIPAM and CS83 spheres at 20°C (open symbols) and 45°C (solid symbols). (200-10) circles, (200-5) broad crosses, (200-2) triangles, (200-0.5) squares, (400-5) reversed triangles, (600-5) diamonds, CS83 triangle flags.

spheres are also compared. The k-values of gel and silica systems increased sharply as the sphere concentration and suspension temperature increased. The k-values of gel system were insensitive to the degree of cross-linking in the range from 2 to 10 mol% of cross-linker against amount of the monomer in mole, and decreased sharply when the degree of cross-linking decreased further to 0.5 mol%. The k-values increased as gel size increased. The k-values of gel systems at 20°C were small and observed only at very high sphere concentrations in volume fractions, whereas those at 45°C were high and close to those of silica systems. Induction time t_i, after which crystallization starts, increased as the degree of cross-linking increased and/or the gel size decreased at any temperatures, when comparison was made at the same gel concentration. The t_i-values at 45°C were high and decreased sharply with increasing sphere concentration, whereas those at 20°C were high only at very high sphere concentrations. These kinetic results support the theory that the electrical double layers play an important role in gel crystallization in addition to the excluded volume of gel spheres. It is deduced further that the electrical double layers of the gel system form from the vague interfaces (between gel and water phases) compared with those of typical colloidal hard-sphere system.

41.6 ROLE OF ELECTRICAL DOUBLE LAYERS ON TYPE I GEL CRYSTALLIZATION

Colloidal crystallization of typical colloidal hard spheres in aqueous and polar organic solvents takes place by the thermal fluctuation of the spheres and the extended electrical double layers. In other words, electrostatic repulsive intersphere interactions exist. In the deionized state, the electrical double layer is very thick and the intersphere repulsive forces prevail over a long distance as much as micrometers, although the forces become weak. Formation of the crystal-like ordering is nicely explained with the *effective soft-sphere model*. The effective diameter d_{eff} of the spheres includes the Debye screening length l_D and is given by the diameter d_0 plus twice the Debye length in Eq. (41.16). Here, d_0 of gel spheres is assumed to be very close to the hydrodynamic diameter measured by the dynamic light-scattering spectroscopy:

$$d_{\text{eff}} = d_0 + 2 \times l_D \tag{41.16}$$

Debye screening length is given by Eq. (41.17)

$$l_D = (4\pi e^2 n / \varepsilon k_B T)^{-1/2} \tag{41.17}$$

where e is the electronic charge, ε is the dielectric constant of the solvent, and n is the concentration of "diffusible" or "free-state" cations and anions in suspension. Thus, n is the sum of the concentrations of diffusible counterions, foreign salt, and both hydronium and hydroxide ions from the dissociation of water. The maximum value of l_D in water is ~1 μm, which is estimated from Eq. (41.17) by taking $n = 2 \times 10^{-7}$ (mol dm^{-3}) $\times N_A \times 10^{-3}$ cm^{-3}, where N_A is Avogadro's number. When d_{eff} is shorter than the intersphere distance l, a gaslike distribution is observed. When d_{eff} is comparative to, or a bit shorter than, the intersphere distance, the distribution of spheres is usually liquidlike. When the effective diameter is close to, or larger than, the observed intersphere distance, crystal-like ordering is formed. This effective soft-sphere model has been supported by systematic comparison between d_{eff} and l values. According to the effective soft-sphere model, l is close to d_{eff} in crystal suspensions.

The ratio of the Debye screening length (l_D) against the hydrodynamic diameter (d_0) size l_D/d_0 is given in Table 41.1 [48–51]. This ratio is an important parameter to know for the relative contribution of the Debye screening effect against the excluded-volume effect. The l_D/d_0-values increased sharply as gel concentration decreased and/or temperature increased. The ratio l_D/d_0 at 1 wt% increased as gel size increased at any temperature. The main cause for these tendencies is due to the fact that the density of the gel spheres increased with increasing size as is seen in Table 41.1. The colloidal interfaces should be formed more easily for more compact gel spheres. Interfaces between the gel spheres and medium-sized molecules will be located slightly inward from the outside edge of the gel spheres. The crystallization of pNIPAm gels takes place by the significant contribution of the extended electrical double layers in addition to the excluded-volume effect, especially at low gel concentrations, at low temperatures, at high degrees of cross-linking of gel spheres, and further at large gel spheres. This indicates further that

the gel spheres share interfaces with bulk water phase. In other words, simple ions inside a gel sphere are placed under restraint from free diffusion in part, although most simple ions and water molecules are able to diffuse rather freely inside the gels.

The l_D/d_0 ratios are calculated to be 0.45, 0.38, and 0.26 for the crystals of AIBA-P2VP(1), AIBA-P2VP(0.5), and AIBA-P2VP(0.1), respectively, at approximately 8–10 wt%, from Table 41.2 [53]. The ratios are calculated to be 0.65, 0.59, and 0.68 for the suspensions of PEGMA-P2VP(0.1), PEGMA-P2VP(0.5), and PEGMA-P2VP(1) at approximately 5 wt%, respectively [54]. These results support the theory that the cationic gel spheres AIBA-P2VP and PEGMA-P2VP have *interfaces* with water phases but the thickness of the electrical double layers are not so large compared with the anionic charged gel and colloidal hard spheres even in the deionized suspension. The other reason for the smaller the electrical double layers is due to the fact that both cationic gel spheres AIBA-P2VP and PEGMA-P2VP are still large in size compared with typical pNIPAm gel spheres. Furthermore, the fact that the calculation of the l_D/d_0 of AIBA-P2VP and PEGMA-P2VP was made at rather high sphere concentrations, must be another important cause. In conclusion, it is clear that the crystallization of the cationic gel spheres takes place by the important contribution of the *extended electrical double layers* in addition to the *excluded-volume effect* of the gel spheres themselves, although the interfaces of gel spheres with water come to be vague, especially when the degree of cross-linking is low. Two coworkers [94] measured simultaneous static and dynamic three-dimensional cross-correlated light scattering of concentrated pNIPAm microgels in dimethyl formamide. They found that the microgel structure is different from that of hard spheres as the cross-link density decreases, leading to a fuzzy particle surface with dangling polymer chains.

41.7 RIGIDITY OF TYPE I GEL CRYSTALS

According to a discussion in one study [95], the nearest-neighbor intersphere distance l is given by Eq. (41.18) in the sedimentation equilibrium

$$(l - l_m)/l_m = (\sigma_{\text{eff}}\, g\, \phi_m/G)(h - h_m) \qquad (41.18)$$

where l_m and ϕ_m indicate the lattice spacing (nearest-neighbor intersphere distance) and the sphere concentration (in volume fraction) at the midplane of the suspension column in the sedimentation equilibrium, respectively; h and h_m are the heights of the arbitrary layer and midplane; g is the gravitational constant; σ_{eff} is the difference in the specific densities of pNIPAm gel spheres minus that of water in the suspension state; and G is the rigidity (Young's elastic modulus) of gel crystal.

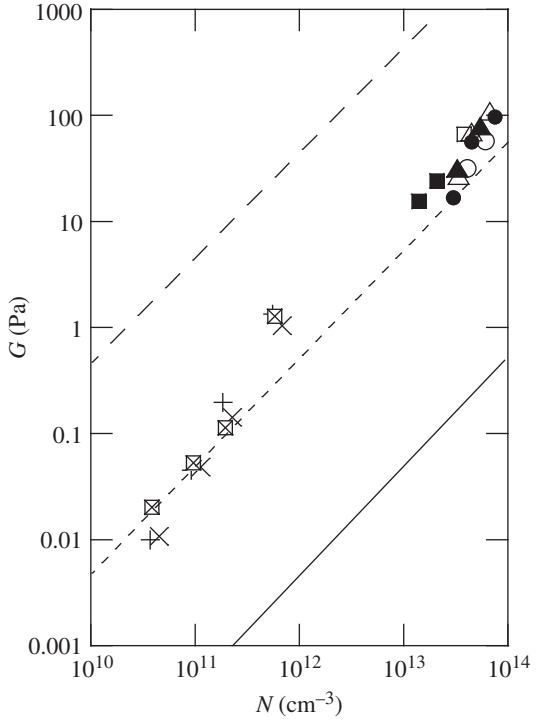


FIGURE 41.7 Log G versus log N plots of pNIPAm(200-2) (open circle), pNIPAm(200-5) (triangle), pNIPAm(200-10) (square), AIBA-P2VP(0.1) (solid circle), AIBA-P2VP(0.5) (solid triangle), AIBA-P2VP(1) (solid square), PEGMA-P2VP(0.1) (plus sign), PEGMA-P2VP(0.5) (cross sign), and PEGMA-P2VP(1) (cross sign in square), $b = 1$ (solid line), 0.1 (short broken line), 0.01 (long broken line).

The G-values thus estimated are shown in Fig. 41.7 as a function of number density of the gel spheres N. As have been discussed in the literature [95,96], the order of magnitude of the modulus G is approximated in terms of the magnitude of the thermal fluctuation δ of a sphere as

$$G \cong f/l \cong (k_B T/ < \delta^2 >)/l \qquad (41.19)$$

where f is the force constant, l is the intersphere distance, δ is the thermal fluctuation of a sphere in the effective potential valley, k_B is the Boltzmann constant, and T is the absolute temperature. Introducing a nondimensional fluctuation parameter b for $<\delta^2>^{1/2} / l$, the modulus is obtained as a linear function of N [96,97]:

$$G \cong N k_B T/b^2 \qquad (41.20)$$

When $b = 1$, Eq. (41.20) gives the elastic modulus of an ideal gas having the same sphere concentration. Lindemann's law of crystal melting tells us that $b < 0.1$ holds for a stable crystal. Short and long dashed lines in Fig. 41.7 represent $b = 0.1$ and 0.01, respectively. It is clear that all the G-values of pNIPAm gel spheres shown by open symbols are located around the short dashed line. The solid symbols in Fig. 41.7

show the *G*-values of the cationic gel spheres, lightly cross-linked poly(2-vinylpyridine) stabilized with poly(ethylene glycol), PEGMA-P2VP measured by the microscopy in the sedimentation equilibrium [54]. Most *G*-values of PEGMA-P2VP spheres also located around short dashed lines, and the slope of the observed log *G* values against log *N* plots seems slightly larger than that of the short dashed line. Thus, there exists no difference in the elastic properties between anionic pNIPAm and cationic AIBA-P2VP and PEGMA-P2VP gel spheres. Most of *G*-values of the typical colloidal crystals are located between the short dashed and long dashed lines [21–23]. The *b*-values of pNIPAm gel spheres estimated from the *G*-values using Eq. (41.20) were $0.05 \sim 0.07$, $0.05 \sim 0.09$, and $0.05 \sim 0.15$, repectively. These results on *G*- and *b*-values of pNIPAm gel crystals support the notion that the elastic properties of gel crystals is not essentially different from those of typical colloidal crystals and further metals, polymers, and other materials [96, 97]. These experimental results also emphasize that the gel crystals are soft compared with those of typical hard-sphere systems and that the role of the extended electrical double layers for the crystallization of gel spheres is important but weak compared with that of hard colloidal spheres.

41.8 TYPE II GEL CRYSTALS

One team of investigators [98] have studied this field for a long time. They prepared crystal arrays of polystyrene spheres (150 nm in diameter) first in aqueous media and then polymerized the suspension with 50% *N*-vinylpyrrolidone, 17% acrylamide, 4.5% *N*,*N*-methylene bisacrylamide, and 1% benzoin methylether [98]. The gels maintained the crystal structure of spheres and the extinction peak wavelength did not change as a result of gelation. The peak wavelength shifted toward a shorter one by a uniaxial strain in the plane of the film, and extinction spectra recovered again when stress was relieved. The same team prepared the thermosensitive gels containing crystal arrays of polystyrene spheres in the interior of the gel [99]. Lattice spacing changed with gel temperature quite sharply. Inverse opal structure was observed to have a periodically ordered porosity, endowing type II hydrogels with structural colors based on Bragg diffraction of light. We should note that the porous hydrogels exhibit a rapid change in volume in response to environmental variations [100–110], pH, ionic concentration, and temperature, for example. Type II gel crystals in organic solvents were prepared by another team [66, 67].

41.9 TYPE III GEL CRYSTALS

Studies of adsorbed and stabilized emulsions or forms by solid colloidal particles were reported [111, 112], for example, more than a century ago. Silica sols, carbon black, and polystyrene particles were used as emulsifiers to preparestable oil-in-water and water-in-oil emulsions [113,114]. Studies on stabilizing forms by the mixtures of solid particles with surfactants and/or surface-active polymers have been performed [113,115,116], but few reports of foams stabilized only by solid particles have appeared in the literature [111,113,117–120]. One team [111,112] found the formation of highly stable foams adsorbed and stabilized gel spheres with *ordered* polystyrene spheres in water. The suspensions emitted light induced by Bragg diffraction of the incident white light and were stable for more than one year. In another study pH-sensitive liquid marbles were prepared by adsorption of poly(2-vinylpyridine) spheres on the liquid water [123]. Adsorption of cross-linked poly(2-vinylpyridine) on the surfaces of gold particles was studied [124].

41.10 TYPE III GEL CRYSTALLIZATION OF GEL AGGLOMERATES DURING DRYNESS

Drying patterns of gel sphere suspensions of pNIPAm [125–128], AIBA-P2VP [129], and PEGMA-P2VP [130] were studied on a coverglass, a watchglass, and a Petri glass dish. Formation of the monodispersed agglomerated particles and their ordered arrays were observed. Figure 2.8 shows typical examples of the following microscopic drying structure patterns: (a) flickering *ordered spokelines*, (b) *ordered rings*, (c) *net* structure, and (d) *lattice* like ordered structures of the agglomerated particles. The net and lattice structures formed more favorably at high degrees of cross-linking, at high gel concentrations, and/or at high temperatures. By the addition of sodium chloride, very large dendritelike and net structures of the large agglomerated particles formed at 20°C and 45°C, respectively. The importance of the coordinated convectional flow of the agglomerated particles during the drying processes is supported for the ordered array formation. The role of the electrical double layers around the agglomerated particles and the interaction of the particles with the substrate surfaces during dryness are also important for the ordering. These microscopic drying patterns of gel spheres were very characteristic to the gel systems and differ from those of linear-type polymers and also from typical colloidal spheres.

41.11 CONCLUSIONS AND FUTURE PERSPECTIVES

The critical concentration of melting of type I gel crystals is quite sensitive to the ionic concentration of the gel suspension, as is clear in the sharp change in the critical concentration of melting both with and without the resins. Furthermore, the morphology of the single crystals of gel spheres surprisingly resembles those of typical colloidal spheres such as

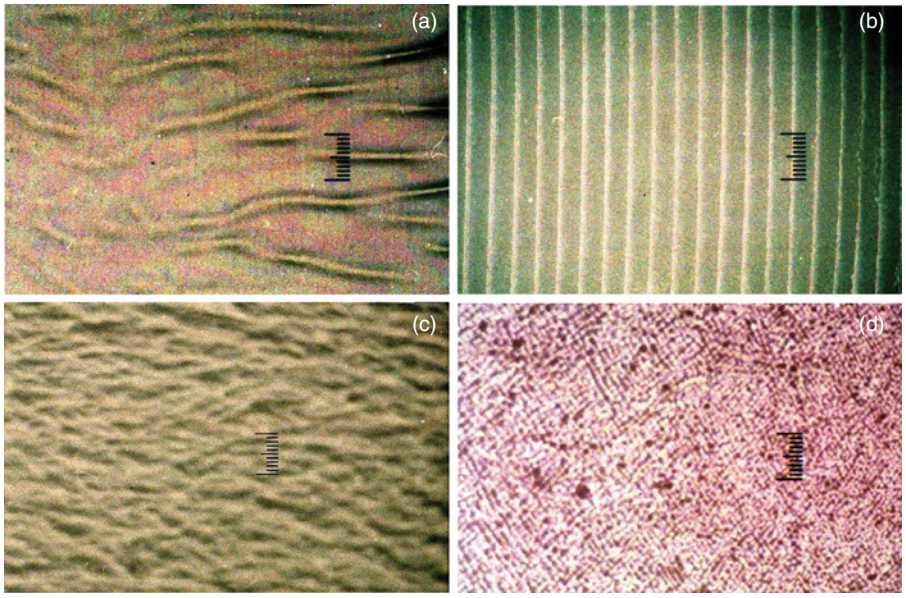


FIGURE 41.8 Typical microscopic drying structures of (a) *ordered spokelines*, (b) *ordered rings*, (c) *net* structure, and (d) *lattice* like ordered structures of the agglomerated particles of gel spheres. (a) pNIPAm(200-10), 0.119 wt%, on a coverglass, 20°C; full scale is 200 μm, (b) pNIPAm(200-0.5), 0.0336 wt%, on a glass dish, 45°C; full scale is 100 μm. (c) AIBA-P2VP(1), 3.45 wt%, on a watchglass, 22°C; full scale is 100 μm. (d) pNIPAm(200-5), 1.55 wt%, on a glass dish, 45°C; full scale is 200 μm. For a color version of this figure, see the color plate section.

polystyrene and colloidal silica spheres, for example. Turbidity of the liquid-state suspensions of the gel spheres was high and similar in extent compared to that of the typical colloidal spheres having hydrodynamic size similar to that of the gels. Turbidity itself of the gel supports the theory that there exists a certain interface separating two phases, namely, gel spheres and medium-sized molecules having different refractive indices, respectively. This work clearly demonstrates that the crystallization of the gel spheres especially in the deionized aqueous system takes place by the excluded-volume effect of the gels, and also by the contribution of the extended electrical double layers formed around each gel spheres.

Most researchers, including the present authors, have believed that the gel spheres of pNIPAm do not form interfaces with water phase because of the significant diffusion of water and ionic species through the gels. We should note here that a group of researchers [45, 46] found that the nearest-neighbor intergel distances in the crystal structures of core–shell spheres, having pNIPAm as a shell at rather high sphere concentration without resins, were slightly larger than the hydrodynamic size of the gels. They attributed this difference to the existence of the local charges on the gel spheres, which originated from the charges of initiators used during polymerization of the core–shell spheres. Their explanation is correct, the current authors believe. Additionally, their experiments also support the importance of the electrical double-layer effect on the crystallization, although the extent of the contribution of double layers is small from their experimental condition *without deionization* of the suspension. The present authors' most recent experiments have been made in the deionized condition, where the contributions of electrical double layers are substantially high. The important contribution of the electrical double layers to crystallization is clearly demonstrated by the crystallization at 45°C, where the excluded diameter of the gel spheres (d_0) is very small compared with the intersphere distance (l).

Crystallization phenomena of the mixtures of pNIPAm gels and colloidal silica spheres were studied in the deionized state by the authors' group [43, 44]. The crystallization was discussed by the coupling effects of the extended electrical double layers around the colloidal silica spheres and the excluded-volume effects of the pNIPAm gels. Contribution of the electrical double layers around the gels was not discussed in this chapter. However, the contribution of the electrical double layers must be discussed anew for these systems too. The pNIPAm gel spheres contain many water molecules in the inner region of the sphere, especially at low temperature as described above. Then, the gel spheres in the suspension state will be assumed to be in *liquid phase*, which is distinguished from the bulk water phase. It is highly plausible that the gel spheres and water molecules interact strongly with each other by the solvation and polar–polar interaction between gels and water, for example, and behave as a kind of *liquid* different from the bulk water. In other words, the gel suspensions will be a *microemulsion* system, where

the electrical double layers extend from the liquid-phase spheres.

In this work, the excluded diameter of the gel sphere is assumed to be equal to the hydrodynamic diameter estimated from the dynamic light-scattering measurements. If the excluded diameter were sensitive to the ionic concentration of the suspensions, especially at low temperatures (e.g., 25°C), the possibility of crystallization caused by the extension of the gel spheres themselves still remains, even in the deionized state. In other words, the possibility of crystallization taking place only by the excluded-volume effect still remains at low temperatures. However, at high temperatures (e.g., 45°C), gel size is fairly small compared with the intergel distances by the substantial shrinking of the gels, and the contribution of the excluded-volume effect becomes quite small. Thus, crystallization at high temperatures should not take place without the contribution of the electrical double layers. Measurements of the hydrodynamic diameter of gel spheres in deionized state and at very low concentrations, where no two (or more) gel spheres interact with each other, are, therefore, important for further clarification of the gel crystallization process.

REFERENCES

[1] Okubo, T. (1996). *Colloid Surf. A* **109**, 77–88.

[2] Alexander, S., Chaikin, P.M., Grant, P., Morales, G.M., Pincus, P., Hone, D. (1984). *J. Chem. Phys.* **80**, 5776–5781.

[3] Okubo, T. (1993). *Progress Polym. Sci.* **18**, 481–517.

[4] Palberg, T., Kottal, J., Bitzer, F., Simon, R., Wurtham, M., Leiderer, P. (1995). *J. Colloid Interface Sci.* **169**, 85–89.

[5] Garbow, N., Evers, M., Palberg, T., Okubo, T. (2004). *J. Phys. Condens. Matt.* **16**, 3835–3842.

[6] Vanderhoff, W., van de Hul, H.J., Tausk, R.J.M., Overbeek, J.Th.G. (1970). In Goldfinger, G. (ed.), *Clean Surfaces: Their Preparation and Characterization for Interfacial Studies*. Marcel Dekker, New York, pp. 15–44.

[7] Hiltner, P.A., Papir, Y.S., Krieger, I.M. (1971). *J. Phys. Chem.* **75**, 1881–1886.

[8] Kose, A., Ozaki, M., Takano, K., Kobayashi, Y., Hachisu, S. (1973). *J. Colloid Interface Sci.* **44**, 330–338.

[9] Williams, R., Crandall, R.S., Wojtowicz, P.J. (1976). *Phys. Rev. Lett.* **37**, 348–351.

[10] Mitaku, S., Ohtsuki, T., Enari, K., Kishimoto, A., Okano, K. (1978). *Jpn. J. Appl. Phys.* **17**, 305–313.

[11] Lindsay, H.M., Chaikin, P.M. (1982). *J. Chem. Phys.* **76**, 3774–3781.

[12] Pieranski, P. (1983). *Contemp. Phys.* **24**, 25–73.

[13] Ottewill, R.H. (1985). *Ber. Bunseng. Phys. Chem.* **89**, 517–525.

[14] Aastuen, D.J.W., Clark, N.A., Cotter, L.K., Ackerson, B.J. (1986). *Phys. Rev. Lett.* **57**, 1733–1736.

[15] Pusey, P.N., van Megen, W. (1986). *Nature* **320**, 340–342.

[16] Okubo, T. (1988). *Acc. Chem. Res.* **21**, 281–286.

[17] Sood, A.K. (1991). *Solid State Phys*. **45**, 1–73.

[18] Okubo, T. (1988). *J. Chem. Soc. Faraday Tranact. 1* **84**, 1163–1169.

[19] Lowen, H., Palberg, T., Simon, R. (1993). *Phys. Rev. Lett.* **70**, 1557–1560.

[20] Okubo, T. (1994). In Schmitz, K.S. (ed.), *Macro-ion Characterization. From Dilute Solutions to Complex Fluids*, ACS Symp. Series Vol. 548, American Chemical Society, Washington, DC, pp. 364–380.

[21] Okubo, T., Tsuchida, A. (2002). *Forma* **17**, 141–153.

[22] Okubo, T. (2002). In Hubbard, A. (ed.), *Encyclopedia of Surface and Colloid Science.* Marcel Dekker, New York, pp. 1300–1309.

[23] Okubo, T. (2005). In Kinoshita, S., Yoshioka, S. (eds.), *Structural Colors in Biological Systems*, Osaka Univ. Press, pp. 267–286.

[24] Okubo, T. (2008). *Polym. J.* **40**, 882–890.

[25] Russel, WB. (1990). *Phase Transition* **21**, 127–137.

[26] Dhont, J.K.G., Smits, C., Lekkerkerker, H.N.W. (1992). *J. Colloid Interface Sci.* **152**, 386–401.

[27] Verhaeghe, N.A.M., van Blaaderen, A. (1994). *Langmuir* **10**, 1427–1438.

[28] Butler, S., Harrowell, P. (1995). *Phys. Rev. E* **52**, 6424–6430.

[29] Okubo, T. (1992). *Naturwissenschaften* **79**, 317–320.

[30] Okubo, T. (1993). *Colloid Polym. Sci.* **271**, 190–196.

[31] Okubo, T. (1994). *Langmuir* **10**, 1695–1702.

[32] Okubo, T., Tsuchida, A. (2002). *Colloid Polym Sci*. **280**, 438–445.

[33] Pelton, R.H., Chibante, P. (1986). *Colloids Surf.* **20**, 247–256.

[34] Shibayama, M., Tanaka, T. (1993). *Adv. Polym. Sci.* **109**, 1–62.

[35] Shibayama, M. (1998). *Macromol. Chem. Phys.* **199**, 1–30.

[36] Holtz, J.H., Asher, S.A. (1997). *Nature* **389**, 829–832.

[37] Pelton, R. (2000). *Adv Colloid Interface Sci*. **85**, 1–33.

[38] Xia, Y., Gates, B., Yin, Y., Lu, Y. (2000). *Adv Mater*. **12**, 693–713.

[39] Hellweg, T., Dewhurst, C.D., Bruckner, E., Kratz, K., Eimer, W. (2000). *Colloid Polym Sci*. **278**, 972–978.

[40] Debord, J.D., Lyon, L.A. (2000). *J. Phys. Chem. B* **104**, 6330–6331.

[41] Xia, Y. (2001). *Adv. Mater.* **13**, 369.

[42] Gao, J., Hu, Z. (2002). *Langmuir* **18**, 1360–1367.

[43] Okubo, T., Hase, H., Kimura, H., Kokufuta, E. (2002). *Langmuir* **18**, 6783–6788.

[44] Okubo, T., Mizutani, T., Okamoto, J., Kimura, K., Tsuchida, A., Tauer, K., Khrenov, V., Kawaguchi, H., Tsuji, S. (2006). *Colloid Polym. Sci.* **285**, 351–358.

[45] Crassous, J.J., Ballauff, M., Drechsler, M., Schmidt, J., Talmon, Y. (2006). *Langmuir* **22**, 2403–2406.

[46] Crassous, J.J., Wittemann, A., Siebenburger, M., Schrinner,

M., Drechsler, M., Ballauff, M. (2008). *Colloid Polym. Sci.* **286**, 805–812.

[47] Crassous, J.J., Rochette, C.N., Wittemann, A., Schrinner, M., Ballauff, M., Drechsler, M. (2009). *Langmuir* **25**, 7862–7871.

[48] Okubo, T., Suzuki, D., Yamagata, T., Katsuno, A., Sakurai, M., Kimura, H., Tsuchida, A. (2011). *Colloid Polym. Sci.* **289**, 291–299.

[49] Okubo, T., Suzuki, D., Yamagata, T., Horigome, K., Shibata, K., Tsuchida, A. (2011). *Colloid Polym. Sci.* **289**, 1273–1281.

[50] Suzuki, D., Horigome, K., Yamagata, T., Shibata, K., Tsuchida, A., Okubo, T. (2011). *Colloid Polym. Sci.* **289**, 1799–1808.

[51] Suzuki, D., Yamagata, T., Horigome, K., Shibata, K., Tsuchida, A., Okubo, T. (2012). *Colloid Polym. Sci.* **290**, 107–117.

[52] Okubo, T. (1986). *J. Chem. Soc. Faraday Transact. 1* **82**, 3163–3173.

[53] Okubo, T., Fujii, S., Aono, K., Nakamura, Y. (2013). *Colloid Polym. Sci.* **291**, 2569–2577.

[54] Okubo, T., Fujii, S., Aono, K., Nakamura, Y., Tsuchida, A. (2013). *Colloid Polym. Sci.* **291**, 1201–1210.

[55] Weissman, J.M., Sunkara, H.B., Tse, A.S., Asher, S.A. (1996). *Science* **274**, 959–960.

[56] Debord, J.D., Lyon, L.A. (2000). *J. Phys. Chem. B* **104**, 6327–6331.

[57] Hu, Z., Lu, X., Gao, J. (2001). *Adv. Mater.* **13**, 1708–1712.

[58] Debord, J.D., Eustis, S., Debord, S.B., Lofye, M.T., Lyon, L.A. (2002). *Adv. Mater.* **14**, 658–662.

[59] Debord, S.B., Lyon, L.A. (2003). *J. Phys. Chem. B* **107**, 2927–2932.

[60] Jones, C.D., Lyon, L.A. (2003). *J. ACS* **125**, 460–465.

[61] Jones, C.D., Serpe, M.J., Schroeder, L., Lyon, L.A. (2003). *J. ACS* **125**, 5292–5293.

[62] Lyon, L.A., Debord, J.D., Debord, S.B., Jones, C.D., Serpe, M.J. (2004). *J. Phys. Chem. B* **108**, 19099–19108.

[63] Reese, C.E., Mikhonin, A.V., Kamenjicki, M., Tikhonov, A., Asher, S.A. (2004). *J. ACS* **126**, 1493–1496.

[64] Kumoda, M., Watanabe, M., Takemoto, Y. (2006). *Langmuir* **22**, 4403–4407.

[65] Suzuki, D., Mc Grath, J.G., Kawaguchi, H., Lyon, L.A. (2007). *J. Phys. Chem. C* **111**, 5667–5672.

[66] Yoshinaga, K., Fujiwara, K., Tanaka, Y., Nakanishi, M., Takesue, M. (2003). *Chem. Lett.* **32**, 1082–1083.

[67] Yoshinaga, K., Satoh, S., Mouri, E., Nakai, A. (2006). *Colloid Polym. Sci.* **285**, 694–698.

[68] Okubo, T. (2006). *Colloid Polym. Sci.* **285**, 245–250.

[69] Okubo, T. (1994). *Langmuir* **10**, 3529–3535.

[70] Okubo, T. (1995). *J. Colloid Interace Sci.* **171**, 55–62.

[71] Okubo, T., Fujita, H. (1996). *Colloid Polym. Sci.* **274**, 368–374.

[72] Okubo, T., Fujita, H., Kiriyama, K., Yamaoka, H. (1996). *Colloid Polym. Sci.* **274**, 73–80.

[73] Okubo, T., Yoshimi, H., Shimizu, T., Ottewill, R.H. (2000). *Colloid Polym. Sci.* **278**, 469–474.

[74] Okubo, T., Kimura, H., Hase, H., Lovell, P.A., Errington, N., Thongnoi, S. (2005). *Colloid Polym. Sci.* **283**, 393–401.

[75] Gottwald, D., Likos, C.N., Kahl, G., Lowen, H. (2004). *Phys. Rev. Lett.* **92**, 068301 (1-4).

[76] Mohanty, P.S., Richtering, W. (2008). *J. Phys. Chem. B* **112**, 14692–14697.

[77] Okubo, T., Suzuki, D., Tsuchida, A. (2013). *Colloid Polym. Sci.* **291**, 661–668.

[78] Okubo, T., Kiriyama, K., Nemoto, N., Hashimoto, H. (1996). *Colloid Polym. Sci.* **274**, 93–104.

[79] Okubo, T., Kiriyama, K. (1996). *Ber. Bunsenges. Phys. Chem.* **100**, 849–856.

[80] Okubo, T., Kiriyama, K. (1997). *J. Mol. Liquids* **72**, 347–364.

[81] Okubo, T., Okada, S., Tsuchida, A. (1997). *J. Colloid Interface Sci.* **189**, 337–347.

[82] Weissman, J.M., Sunkara, H.B., Tse, A.S., Asher, S.A. (1996). *Science* **274**, 959–960.

[83] Wilson, H.W. (1900). *Phil. Mag.* **50**, 238–250.

[84] Frenkel, J. (1932). *Phys. Z. Sowjetunion* **1**, 498–500.

[85] Okubo, T. (1997). *Curr. Topics Colloid Interface Sci.* **1**, 169–193.

[86] Okubo, T., Okada, S. (1997). *J. Colloid Interface Sci.* **192**, 490–496.

[87] Okubo, T., Okada, S. (1998). *J. Colloid Interface Sci.* **204**, 198–204.

[88] Okubo, T., Ishiki, H. (1999). *J. Colloid Interface Sci.* **211**, 151–159.

[89] Okubo, T., Tsuchida, A., Okada, S., Fujitsuna, K., Ishikawa, M., Morita, T., Tada, T. (1999). *Colloid Surf. A* **160**, 311–320.

[90] Okubo, T., Ishiki, H. (2000). *J. Colloid Interface Sci.* **228**, 151–156.

[91] Okubo, T., Tsuchida, A., Kato, T. (1999). *Colloid Polym. Sci.* **277**, 191–196.

[92] Okubo, T., Ishiki, H., Chiyoda, M., Yoshinaga, K. (2002). *Colloid Polym. Sci.* **280**, 290–295.

[93] Okubo, T., Suzuki, D., Shibata, K., Tsuchida, A. (2012). *Colloid Polym. Sci.* **290**, 1403–1412.

[94] Eckert, T., Richtering, W. (2008). *J. Chem. Phys.* **129**, 124902 1-6.

[95] Crandall, R.S., Williams, R. (1977). *Science* **198**, 293–295.

[96] Mitaku, S., Ohtsuki, T., Okano, K. (1980). *Jpn. J. Appl. Phys.* **19**, 439–448.

[97] Mitaku, S., Ohtsuki, T., Kishimoto, A., Okano, K. (1980). *Biophys. Chem.* **71**, 411–416.

[98] Asher, S.A., Holtz, J., Liu, L., Wu, Z. (1994). *J. ACS* **116**, 4997–4998.

[99] Weissman, J.M., Sunkara, H.B., Tse, A.S., Asher, S.A. (1996). *Science* **274**, 959–960.

[100] Zhao, B., Moore, J.S. (2001). *Langmuir* **17**, 4758–4763.

[101] Zhang, X.Z., Yang, Y.Y., Chung, T.S., Ma, K.X. (2001). *Langmuir* **17**, 6094–6099.

[102] Takeoka, Y., Watanabe, M. (2002). *Langmuir* **18**, 5977–5980.

[103] Takeoka, Y., Watanabe, M. (2003). *Adv. Mater.* **15**, 199–201.

[104] Lee, Y.J., Braun, P.V. (2003). *Adv. Mater.* **15**, 563–566.

[105] Saito, H., Takeoka, Y., Watanabe, M. (2003). *Chem. Commun.* **2003**, 2126–2127.

[106] Takeoka, Y., Watanabe, M. (2003). *Langmuir* **19**, 9104–9106.

[107] Matsubara, K., Watanabe, M., Takeoka, Y. (2007). *Angew. Chem. Int. Ed.* **46**, 1688–1692.

[108] Ueno, K., Matsubara, K., Watanabe, M., Takeoka, Y. (2007). *Adv. Mater.* **19**, 2807–2912.

[109] Ueno, K., Sakamoto, J., Takeoka, Y., Watanabe, M. (2009). *J. Mater. Sci.* **19**, 4778–4783.

[110] Nakayama, D., Takeoka, Y., Watanabe, M., Kataoka, K. (2003). *Angew. Chem. Int. Ed.* **42**, 4197–4200.

[111] Ramsden, W. (1903). *Proc. Roy. Soc.* **72**, 156–164.

[112] Pickering, S.U. (1907). *J. Chem. Soc.* **91**, 2001–2021.

[113] Binks, B.P. (2002). *Curr. Opin. Colloid Interface Sci.* **7**, 21–41.

[114] Aveyard, R., Binks, B.P., Clint, J.H. (2003). *Adv. Colloid Interface Sci.* **100–102**, 503–546.

[115] Aveyard, R., Binks, B.P., Fletcher, P.D.I., Peck, T.G., Rutherford, C.E. (1994). *Adv. Colloid Interface Sci.* **48**, 93–136.

[116] Pugh, R.J. (1996). *Adv. Colloid Interface Sci.* **64**, 67–142.

[117] Du, Z., Bilbao-Montoya, M., Binks, B.P., Dickinson, E., Ettelaie, R., Murray, B.S. (2003). *Langmuir* **19**, 3106–3108.

[118] Dickinson, E., Ettelaie, R., Kostakis, T., Murray, B.S. (2004). *Langmuir* **20**, 8517–8525.

[119] Alargova, R.G., Warhadpande, D.S., Paunov, V.N., Velev, O.D. (2004). *Langmuir* **20**, 10371–10374.

[120] Binks, B.P., Horozov, T.S. (2005). *Angew. Chem. Int. Ed.* **44**, 3722–3725.

[121] Fujii, S., Ryan, A.J., Armes, S.P. (2006). *J.ACS* **128**, 7882–7886.

[122] Fujii, S., Iddon, P.D., Ryan, A.J., Armes, S.P. (2006). *Langmuir* **22**, 7512–7520.

[123] Fujii, S., Kameyama, S., Armes, S.P., Dupin, D., Suzaki, M., Nakamura, Y. (2010). *Soft Matt*. **6**, 635–640.

[124] Akamatsu, K., Shimada, M., Tsuruoka, T., Nawafune, H., Fujii, S., Nakamura, Y. (2010). *Langmuir* **26**, 1254–1259.

[125] Okubo, T., Suzuki, D., Yamagata, T., Katsuno, A., Mizutani, M., Kimura, H., Tsuchida, A. (2011). *Colloid Polym. Sci.* **289**, 807–816.

[126] Okubo, T., Suzuki, D., Tsuchida, A. (2012). *Colloid Polym. Sci.* **290**, 411–421.

[127] Okubo, T., Suzuki, D., Tsuchida, A. (2012). *Colloid Polym. Sci.* **290**, 867–877.

[128] Okubo, T., Suzuki, D., Tsuchida, A. (2012). *Colloid Polym. Sci.* **290**, 1901–1911.

[129] Okubo, T., Fujii, S., Nakamura, Y. (2013). *Colloid Polym. Sci.* **291**, 2805–2813.

[130] Okubo, T., Fujii, S., Aono, K., Nakamura, Y. (2013). *Colloid Polym. Sci.* **291**, 1019–1030.

42

OLEIC ACID-BASED SURFACTANTS AS COST-EFFECTIVE GEMINI SURFACTANTS

KENICHI SAKAI AND MASAHIKO ABE

Department of Pure and Applied Chemistry, Faculty of Science and Technology, Tokyo University of Science

42.1 INTRODUCTION

Gemini surfactants, consisting of two monomeric surfactants linked by a spacer, are an important class of functionalized amphiphilic molecules with remarkable physicochemical properties. The physicochemical aspects of the aqueous solution properties of gemini surfactants have been reviewed in the literature [1–3]. Generally, when compared with conventional monomeric surfactants, the corresponding gemini surfactants give (1) a lower critical micelle concentration (cmc), (2) a lower surface tension measured at the cmc, (3) spontaneous formation of vesicles and/or wormlike micelles even at relatively low concentrations, and (4) a lower Krafft temperature and good water solubility in the case of ionic gemini surfactants. These physicochemical properties allow for the reduction of total consumption of chemicals in waterborne industrial products, and therefore, gemini surfactants are called "environmentally friendly materials." Nevertheless, the number of commercially available gemini surfactants is very limited. We note that, as far as we are aware, only four gemini surfactants are commercially available in Japan at present. Their chemical structures are shown in Fig. 42.1. This difficulty in providing a wide variety of gemini surfactants to the markets arises from their high selling price. In order to facilitate the widespread use of gemini surfactants in a variety of applications, the development of low-cost strategies for the synthesis and purification of gemini surfactants is essential.

On the basis of this background, oleic acid–based gemini surfactants have been developed by our research group. Oleic acid is the basis of human sebum and stratum corneum cell lipids, and hence, it is a biocompatible, ecological, and relatively low-cost material. Indeed, from the standpoint of its chemical structure, we hypothesize the following two points: (1) it is possible to modify the *cis* double bond with various kinds of headgroups through relatively simple chemical reactions to achieve cost-effective syntheses, and (2) it is possible to introduce a hydrophobic chain at the terminal carbonyl group via the amide or ester bonding. These two synthetic strategies allow for the design of a wide variety of gemini surfactants, as well as for control of the hydrophilic/hydrophobic balance of the surfactants by variations in the hydrophobic chain length and the type of headgroup. Both of these features are advantageous to the development of environmentally friendly surfactants for a wide variety of industrial products. In this chapter, we review recent developments of oleic acid–based gemini surfactants and their physicochemical properties.

42.2 SYNTHESES AND MOLECULAR STRUCTURES

The chemical structures of the oleic acid–based gemini surfactants developed by our research group are shown in Fig. 42.2. These include anionic phosphate-type [4], sulfonate-type [5], carboxylate-type [6, 7], cationic quaternary ammonium-type [8], nonionic sugar-type [9], and polyoxyethylene-type [10] surfactants. These surfactants are also categorized into three groups from their synthetic

Encyclopedia of Biocolloid and Biointerface Science, Volume 1, First Edition. Edited by Hiroyuki Ohshima.
© 2016 John Wiley & Sons, Inc. Published 2016 by John Wiley & Sons, Inc.

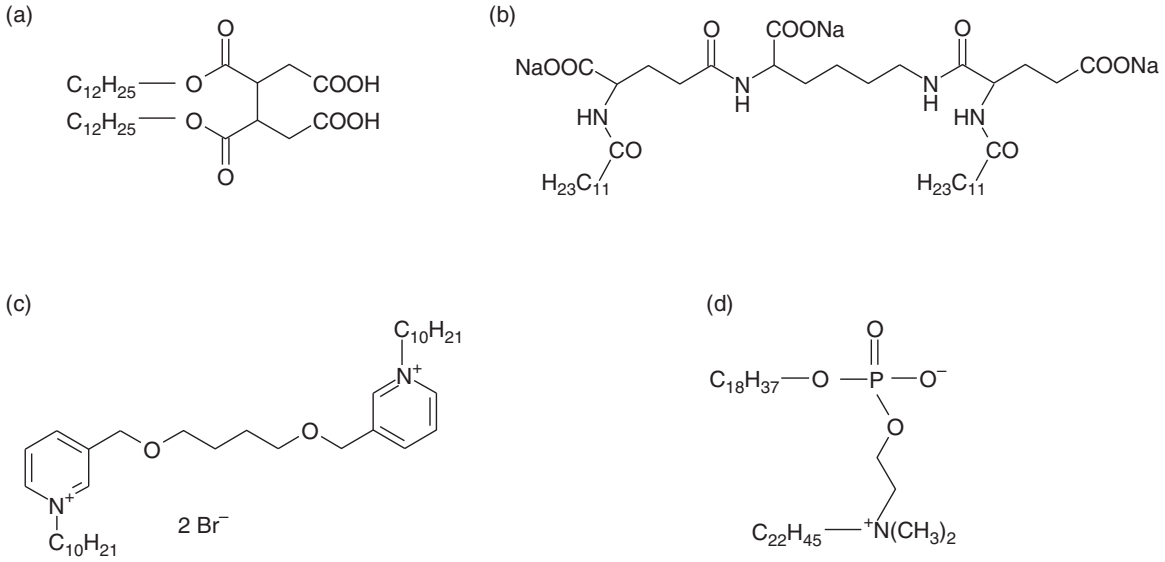


FIGURE 42.1 Chemical structures of commercially available gemini surfactants: (a) dicarboxylic acid–type anionic gemini surfactant (Gemsurf, Chukyo Yushi); (b) glutamic acid–based anionic gemini surfactant with a lysine spacer (Pellicer, Asahi Kasei Chemicals); (c) dipyridinium-type cationic gemini surfactant (Hygenia, Tama Kagaku Kogyo); (d) phosphate–quaternary ammonium-type zwitterionic gemini amphiphile (Vinoveil, NOF).

aspects, as shown in Fig. 42.3. The three synthetic routes are as follows: (1) the oxidation of the *cis* double bond to yield dihydroxy compounds (phosphate-, carboxylate-, and polyoxyethylene-types), (2) the one-step oxidation of the *cis* double bond to introduce a sulfonate headgroup, and (3) the reaction of the *cis* double bond with a peroxide to yield epoxy compounds (quaternary ammonium and sugar types).

These surfactants exhibit the following general features relevant to their chemical structures:

1. With the exception of the carboxylate-type gemini surfactants, it is not possible to introduce two identical headgroups to the *cis* double bond of oleic acid (9 and 10 positions). The introduction of two nonidentical headgroups into the 9 and 10 positions proceeds unselectively, resulting in a mixture of two regioisomers. For example, in the case of the phosphate-type gemini surfactant, the phosphate group is unselectively introduced to either the 9 or 10 position, and the final product obtained is a mixture of these regioisomers.
2. In view of the reaction mechanisms, one of the symmetric/asymmetric headgroups is generally in an *anti* position with respect to the other headgroup. This means that the final product is a mixture of enantiomers of each regioisomer. For example, the phosphate-type gemini surfactant is composed of two regioisomers and their respective enantiomers (9*R*,10*R* and 9*S*,10*S*). We have used such mixtures when studying the physicochemical properties of these surfactants.
3. The change in length of the hydrophobic chain covalently bound to the terminal carbonyl group results in a change in the geometric symmetry of the surfactant molecules.

42.3 DILUTE AQUEOUS SOLUTION PROPERTIES

We have studied dilute aqueous solution properties of oleic acid–based gemini surfactants by means of, for example, static surface tension, conductivity, pyrene fluorescence, dynamic light scattering (DLS), and cryogenic transmission electron microscope (cryo-TEM) measurements. Here, as a typical example, static surface tension data obtained for the aqueous solutions of the carboxylate-type gemini surfactants (abbreviated as "CC-9,9-Es*n*," where *n* is the length of the hydrocarbon chain covalently bound to the terminal carbonyl group of oleic acid) are shown in Fig. 42.4 [6]. These measurements were performed at pH 9 in the presence of 10 mmol dm^{-3} NaCl. Neither precipitation nor phase separation was seen in these aqueous solutions because two carboxylic acid headgroups are expected to be fully deprotonated at this pH. In the region of low surfactant concentrations, the surface tension decreases sharply with increasing concentration and attains a breakpoint. The surfactant concentration corresponding to this breakpoint is assumed to be the cmc or the critical association concentration (cac) of each surfactant. This is a general behavior we can see in aqueous surfactant systems.

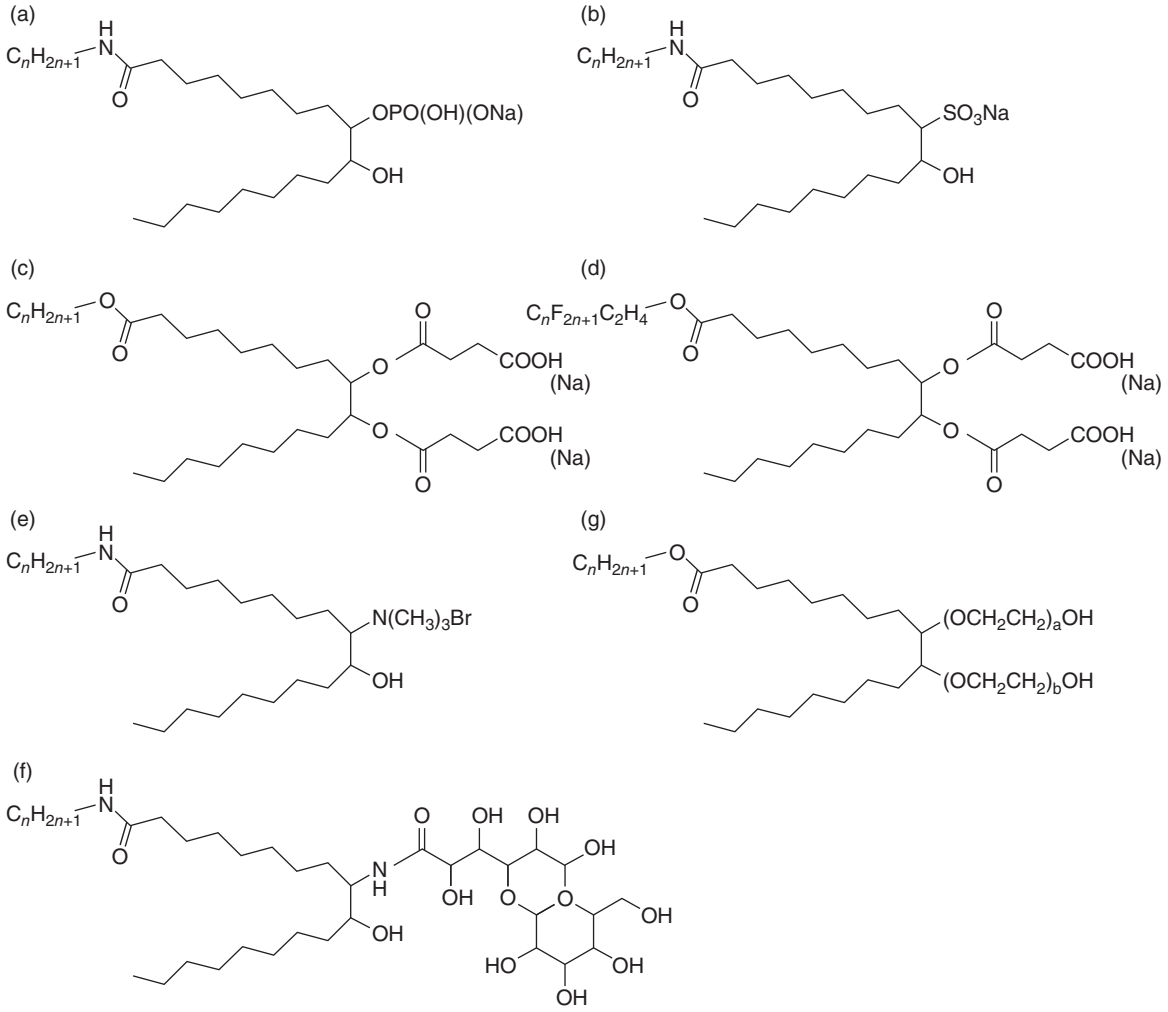


FIGURE 42.2 Chemical structures of oleic acid–based gemini surfactants developed by our research group: (a) phosphate-type anionic surfactant (POH-9,9-Am*n*, n = 6,8,10); (b) sulfonate-type anionic surfactant (SOH-9,9-Am*n*, n = 8,10); (c) carboxylate-type hydrogenated anionic surfactant (CC-9,9-Es*n*, n = 6,8,10); (d) carboxylate-type partially fluorinated anionic surfactant (CC-9,9-EsH2F*n*, n = 4,6,8); (e) quaternary ammonium-type cationic surfactant (NOH-9,9-Am*n*, n = 8,10,12); (f) sugar-type nonionic surfactant (LacOH-9,9-Am*n*, n = 10); (g) polyoxyethylene-type nonionic surfactant (EO*m*-9,9-Es*n*, $m = a + b$ = 10,20,30, n = 10).

The surface tension data allow us to calculate some physicochemical parameters: the surface excess concentration estimated at the cmc (or cac) (Γ_{cmc} or Γ_{cac}) and the occupied area per molecule adsorbed at the air-aqueous solution interface (A_{cmc} or A_{cac}) are calculated from the following equations [11]:

$$\Gamma_{\text{cmc(cac)}} = -\frac{1}{2.303iRT}\left(\frac{d\gamma}{d\log C}\right)_T \tag{42.1}$$

$$A_{\text{cmc(cac)}} = \frac{1}{N_A\Gamma_{\text{cmc(cac)}}} \tag{42.2}$$

where γ is the equilibrium surface tension measured at a surfactant concentration of C, T is the absolute temperature, N_A is the Avogadro constant, and R is the gas constant. In this particular case, the number of adsorption species [i in Eq. (42.1)] is assumed to be 1 in the presence of 10 mmol dm^{-3} NaCl. We also calculated pC_{20} for each surfactant. Here the C_{20} is defined as the surfactant concentration that produces a reduction of 20 mN m^{-1} in the surface tension of an aqueous solution of 10 mmol dm^{-3} NaCl ($pC_{20} = -\log C_{20}$), and therefore, this value is indicative of an efficiency in lowering the surface tension [11].

The physicochemical parameters calculated for the aqueous CC-9,9-Es*n* systems are summarized in Table 42.1. The corresponding data reported for the other series of oleic acid–based gemini surfactants are also shown in this table. It is clear that an increased hydrophobic chain

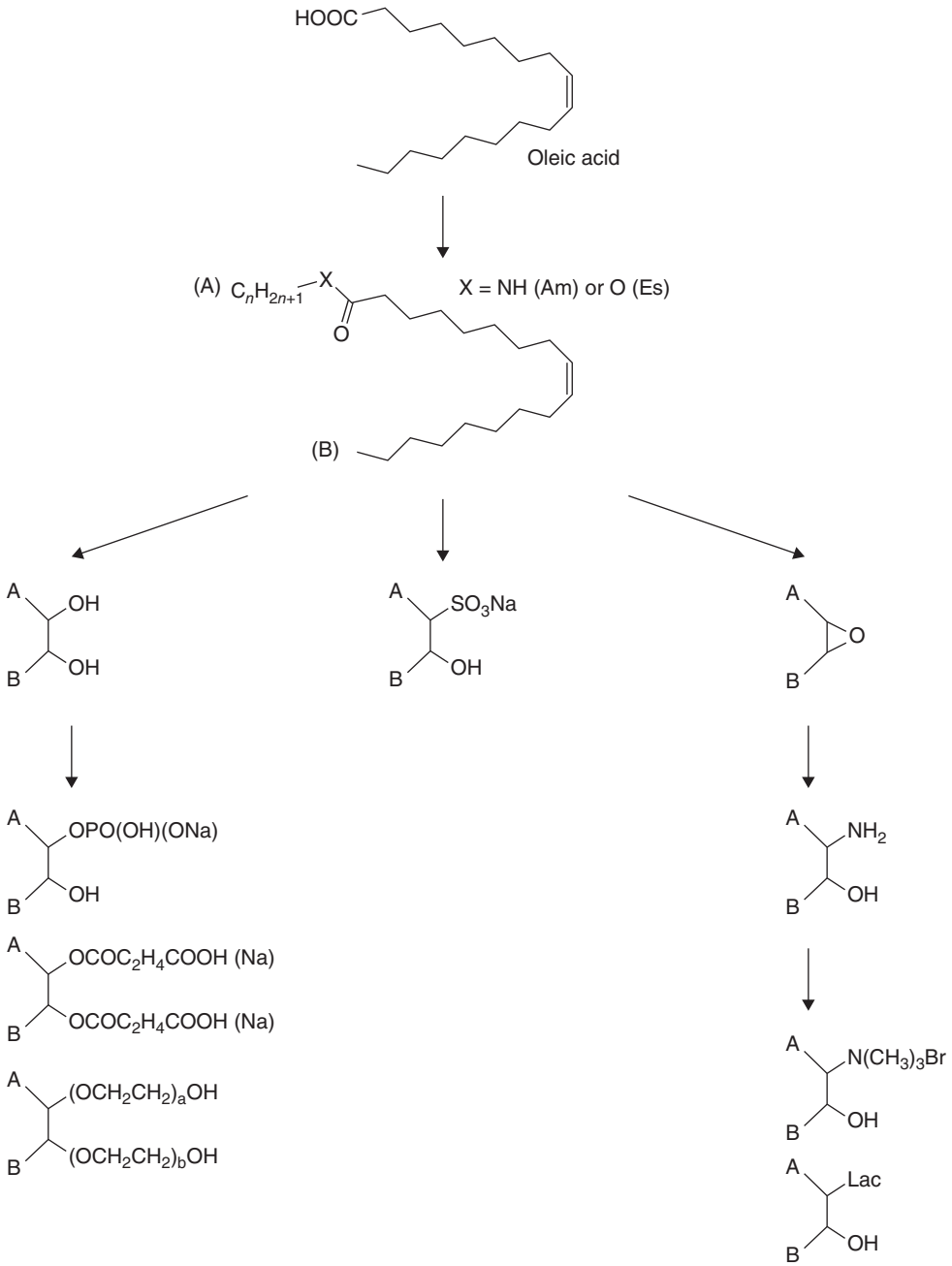


FIGURE 42.3 Synthetic routes of oleic acid–based gemini surfactants.

length results in lower cmc (cac) and larger pC_{20} values for all of the surfactant series. In addition, except the quaternary ammonium-type cationic surfactants (NOH-9,9-Am*n*), the increased hydrophobic chain length also results in larger Γ_{cmc} (Γ_{cac}) and hence smaller A_{cmc} (A_{cac}) values. These results are reflective of the increased hydrophobic character of the gemini surfactants with increasing their hydrophobic chain length. This logically leads to the formation of a closely packed monolayer film at the air–aqueous solution interface, although within our experimental resolution the resulting γ_{cmc} (γ_{cac}) data are almost unchanged as a function of their chain length. The decreased Γ_{cmc} (and increased A_{cmc}) observed for the aqueous NOH-9,9-Am*n* systems may result from the occurrence of steric hindrance between longer-chain molecules adsorbed at the air–aqueous solution interface [8].

It has been reported that molecular symmetry of gemini surfactants plays a significant role in their aqueous solution properties [12]. In order to assess this effect, we have synthesized a petroselinic acid–based sulfonate-type gemini

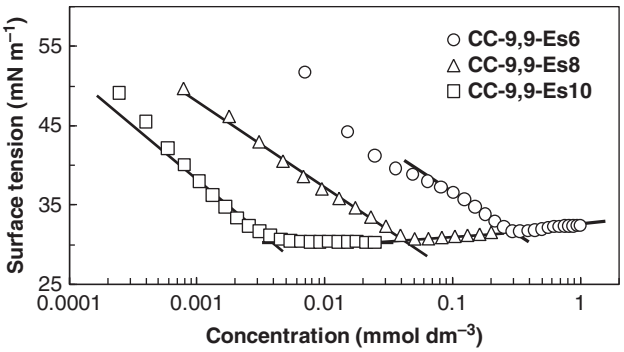


FIGURE 42.4 Static surface tension of aqueous CC-9,9-Es*n* (n = 6,8,10) solutions as a function of their concentrations. The surfactant solutions contained 10 mmol dm^{-3} NaCl as a background electrolyte, and the solution pH was fixed at 9. (This figure is reproduced from Ref. 6 with copyright permission from the Japan Oil Chemists' Society.)

surfactant (abbreviated as SOH-12,6-Am10 in Table 42.1) and compared the aqueous solution properties with those for the corresponding oleic acid–based surfactant (SOH-9,9-Am10) [5]. The hydrocarbon chain length of petroselinic acid is the same as oleic acid, but the *cis* double bond lies at the 6–7 position, which is different from that for oleic acid (9–10 position). As a result, the total number of methylene units is identical for the two surfactants ($\alpha + \beta = 28$, where α and β are the chain lengths from the headgroups), but the degree of molecular symmetry differs (i.e., $\alpha/\beta = 19/9 = 2.1$ for SOH-9,9-Am10 and $\alpha/\beta = 16/12 = 1.3$ for SOH-12,6-Am10, respectively). Cleary, the increased molecular symmetry results in (1) lower cac, (2) lower γ_{cac}, (3) greater Γ_{cac} (and hence smaller A_{cac}), and (4) greater pC_{20} values. These results suggest that SOH-12,6-Am10 exhibits greater surface activity as compared with SOH-9,9-Am10. We assume that the more symmetric analog (SOH-12,6-Am10) provides greater hydrophobic environments within the molecule.

The combination of DLS and cryo-TEM measurements has provided the information about the molecular assemblies spontaneously formed in dilute aqueous solutions of the oleic acid–based gemini surfactants. In most cases, relatively small micellar assemblies are suggested to be formed in such aqueous solutions (CC-9,9-Es*n* (n = 6,8) [6], CC-9,9-EsH2F*n* (n = 4,6,8) [7], and NOH-9,9-Am*n* (n = 8,10,12) [8]), but larger assemblies are also observed in some cases. For example, one of the phosphate-type surfactants (POH-9,9-Am8) forms vesicular assemblies under certain experimental conditions (see a cryo-TEM image; Fig. 42.5) [4]. Generally, gemini surfactants give a larger packing parameter than monomeric ones [13], and hence molecular assemblies with lesser positive curvature tend to be formed even just above the cmc (or cac). We also note that the formation of premicelles is suggested for the cationic oleic acid–based gemini surfactants (NOH-9,9-Am*n*) at concentrations below their cmc [8].

42.4 TEMPERATURE–CONCENTRATION PHASE BEHAVIOR WITH WATER

We have studied the temperature–concentration phase diagrams of binary mixtures of oleic acid–based gemini surfactants with water [7]. The surfactants used here were carboxylate-type gemini surfactants with disodium salts; one is the series of partially fluorinated surfactants (abbreviated as "CC-9,9-EsH2F*n*", where n is the fluorocarbon chain length = 4,6,8) and the other is CC-9,9-Es8 as an example of the corresponding hydrogenated surfactants. The number of studies focusing on the phase diagrams of partially fluorinated gemini surfactants in a wide range of temperatures and concentrations is very limited because of the synthetic

TABLE 42.1 Physicochemical Parameters Calculated for Aqueous Solutions of Oleic Acid–Based Gemini Surfactants

	cmc (or cac) (mmol dm^{-3})	γ_{cmc} (or γ_{cac}) (mN m^{-1})	Γ_{cmc} (or Γ_{cac}) (μmol m^{-2})	A_{cmc} (or A_{cac}) (nm^2)	pC_{20}	Conditions	Ref.
POH-9,9-Am6	0.32	30	2.1	0.80	5.4	100 mmol dm^{-3} NaCl, pH 7	4
POH-9,9-Am8	0.044	30	2.3	0.72	6.1	100 mmol dm^{-3} NaCl, pH 7	4
POH-9,9-Am10	0.011	29	2.6	0.65	6.5	100 mmol dm^{-3} NaCl, pH 7	4
SOH-9,9-Am8	0.24	34	1.0	1.7	5.4	No added electrolytes, No pH control	5
SOH-9,9-Am10	0.025	32	1.2	1.3	6.0	No added electrolytes, No pH control	5
SOH-12,6-Am10	0.0068	27	1.4	1.2	6.8	No added electrolytes, No pH control	5
CC-9,9-Es6	0.41	30	1.8	0.94	5.2	10 mmol dm^{-3} NaCl, pH 9	6
CC-9,9-Es8	0.040	31	1.9	0.88	6.1	10 mmol dm^{-3} NaCl, pH 9	6
CC-9,9-Es10	0.0037	31	2.6	0.63	6.6	10 mmol dm^{-3} NaCl, pH 9	6
CC-9,9-EsH2F4	0.025	28	–	–	–	10 mmol dm^{-3} NaCl, pH 9	7
CC-9,9-EsH2F6	0.0034	24	–	–	–	10 mmol dm^{-3} NaCl, pH 9	7
CC-9,9-EsH2F8	0.00073	23	–	–	–	10 mmol dm^{-3} NaCl, pH 9	7
NOH-9,9-Am8	0.72	38	0.88	1.9	4.9	No added electrolytes, No pH control	8
NOH-9,9-Am10	0.16	37	0.71	2.3	5.2	No added electrolytes, No pH control	8
NOH-9,9-Am12	0.036	37	0.51	3.3	5.7	No added electrolytes, No pH control	8

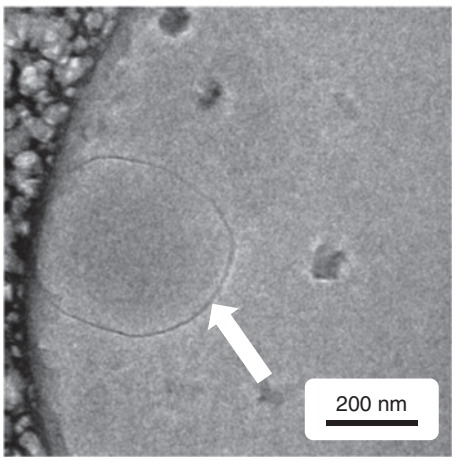


FIGURE 42.5 A cryo-TEM image obtained for the aqueous solution of POH-9,9-Am8. The surfactant concentration was set at 64 × cac in the presence of 100 mmol dm^{-3} NaCl at pH 7. (This figure is reproduced from Ref. 4 with copyright permission from Elsevier.)

difficulties of such surfactant samples. The aqueous phase behavior was characterized with a combination of visual appearance, polarized optical microscopy (POM), and small-angle X-ray scattering (SAXS) data.

The resulting temperature–concentration phase diagrams of CC-9,9-EsH2F*n* and CC-9,9-Es8 are shown in Fig. 42.6. Several phase states, including micellar solution phase (W_m), hexagonal phase (H_1), bicontinuous cubic phase (V_1), and lamellar phase (L_α), were observed along with coexistence of these phases in certain regions. A middle phase (M) is also seen in the phase diagram of CC-9,9-Es8. We found the following features in these diagrams [7]:

1. The increased surfactant concentration yields molecular assemblies with lesser positive curvature. The increased surfactant concentration leads to an increased counterion concentration, a decreased repulsion between ionic headgroups, and hence a decreased cross-sectional area of the headgroups [14, 15]. This change leads to an increased packing parameter of the surfactants [13], and hence we see molecular assemblies with lesser positive curvature at high concentrations.
2. Assemblies with lesser positive curvature tend to be formed at higher temperatures. This is rationalized by the fact that the increased temperature results in a decreased hydrophilicity of the headgroups, leading

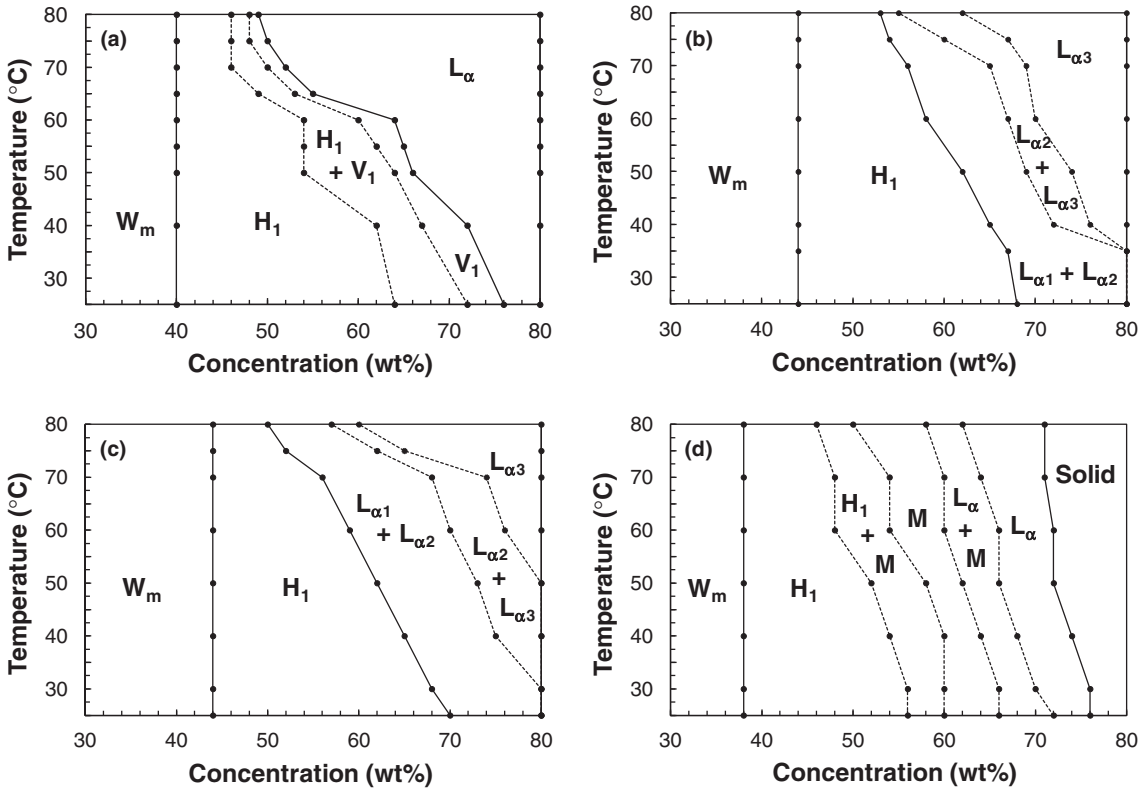


FIGURE 42.6 Temperature–concentration phase diagrams of (a) CC-9,9-EsH2F4, (b) CC-9,9-EsH2F6, (c) CC-9,9-EsH2F8, and (d) CC-9,9-Es8. The surfactant samples used in this study were disodium salts. (This figure is reproduced from Ref. 7 with copyright permission from the Japan Oil Chemists' Society.)

to a decreased cross-sectional area of the surfactants. Similar temperature-induced phase transitions have been observed in the amino acid–based monomeric and gemini surfactant systems [15].

3. The shorter fluorocarbon chain analog tends to form assemblies with greater positive curvature such as H_1 and V_1 phases, whereas the longer fluorocarbon chain analog tends to form assemblies with lesser positive curvature such as L_α phase.
4. The hydrogenated surfactant can form liquid crystals more effectively than the partially fluorinated surfactants. For example, the W_m–H_1 phase transition concentration is observed to be lower for CC-9,9-Es8 than for the three CC-9,9-EsH2F*n* samples. It seems likely that this property results from the ease of molecular packing of the hydrogenated surfactant. In other words, close molecular packing is inhibited in the CC-9,9-EsH2F*n* systems because of the limited miscibility between fluorocarbon and hydrocarbon units. The following two results are also rationalized by this interpretation: (1) two-phase separation of white solids from a solution phase is observed only in the CC-9,9-EsH8 system; and (2) the temperature-induced phase transition occurs more drastically for CC-9,9-EsH2F*n* than for CC-9,9-EsH8 because of the ease of molecular motion of the partially fluorinated surfactants within their assemblies.

42.5 CHARACTERIZING INSOLUBLE MONOLAYER FILMS FORMED AT THE AIR–WATER INTERFACE

The oleic acid–based carboxylate-type gemini surfactants (CC-9,9-Es*n*) exhibit pH-dependent protonation–deprotonation behavior in aqueous media [6]. In alkaline solutions, the surfactants can lower the surface tension as well as form molecular assemblies, as mentioned in Sections 42.3 and 42.4. Under acidic or neutral conditions, the surfactants are intrinsically insoluble in aqueous media and form a monolayer film at the air–water interface when they are spread on the water surface from volatile solvents (e.g., chloroform).

Figure 42.7 shows the surface pressure–area (π–A) isotherm data obtained for the three analogs of CC-9,9-Es*n* at pH 6–7 [6]. The surface pressure increases gradually with decreasing molecular area. No phase transition points are seen in these π–A isotherm data. Interestingly, each π–A isotherm attains a critical point in the range of the molecular area of 0.5–0.7 nm^2, and then the surface pressure becomes constant, even when the molecular area is further decreased from the critical point. On the basis of these data, the following two points are suggested. *First*, at a given surface pressure, the molecular area increases with an increase in the chain length (n). This is an opposite trend from that for the data shown in Table 42.1, where the occupied area (A_{cmc} or A_{cac}) estimated from the static surface tension data at pH 9 decreases with n. This suggests that the geometric molecular volume is a critical factor in determining the degree of molecular packing in the intrinsically insoluble pH region, whereas the intermolecular hydrophobic interaction plays a crucial role at pH 9. *Second*, the absolute slope of the π–A isotherm in the vicinity of the critical point is larger for the longer-chain analog than for the shorter one. This may indicate that, although the molecular area increases with increasing chain length at a given surface pressure, the degree of homogeneity of the monolayer film increases with increasing chain length.

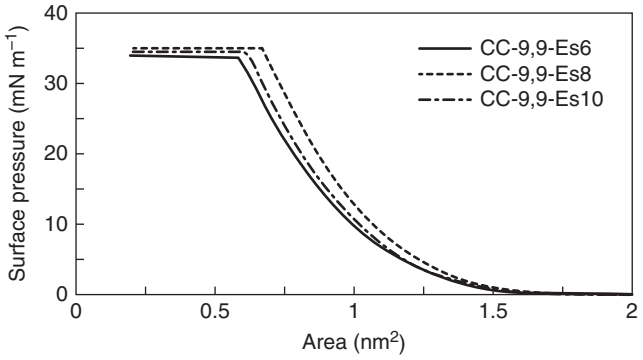


FIGURE 42.7 π–A isotherms of CC-9,9-Es*n* (n = 6,8,10) at pH 6–7 in the absence of added electrolytes. (This figure is reproduced from Ref. 6 with copyright permission from the Japan Oil Chemists' Society.)

Infrared external reflection (IER) measurements provide further insights regarding the chain conformation of the surfactant molecules adsorbed at the air–water interface [16]. The typical IER spectra for CC-9,9-Es8 are given in Fig. 42.8 [6]. The characteristic absorption peak appears in the range of 2920–2930 cm^{-1}, which originated from the CH_2 asymmetric stretching vibration of the hydrocarbon chains. The wavelength gradually shifts toward lower values with an increase in the sample volume spread on the water surface. This primarily suggests that the increased molecular density results in a change of the hydrocarbon chains from *gauche*-to-*trans* conformations.

42.6 ADSORPTION CHARACTERISTICS AT SOLID–AQUEOUS SOLUTION INTERFACES

The adsorption of gemini surfactants at solid–liquid interfaces has been reported by a number of researchers through measurement of adsorption isotherms [17–20] and the study of adsorbed layer morphologies [19–23]. Key findings include the facts that (1) the adsorption plateau region (i.e., saturation) appears at much lower concentrations when compared with the corresponding monomeric surfactants [17],

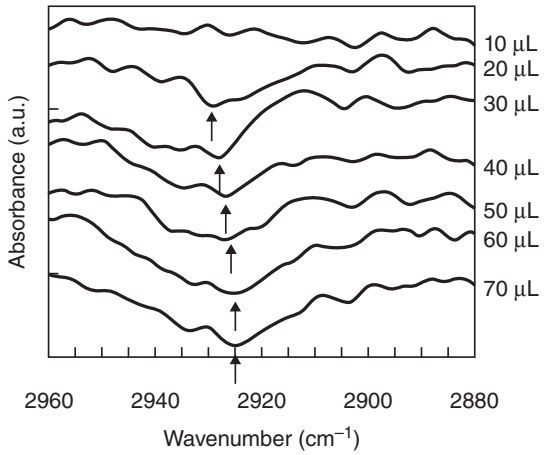


FIGURE 42.8 Infrared external reflection spectra of monolayer films of CC-9,9-Es8 formed at the air–water interface. The effects of molecular packing on the chain conformation were studied by changing the sample volume of the CC-9,9-Es8 chloroform solution (0.1 mmol dm^{-3}) spread on the water surface in the range 10–70 μL. The aqueous solution pH was set at 6–7 in the absence of added electrolytes. (This figure is reproduced from Ref. 6 with copyright permission from the Japan Oil Chemists' Society.)

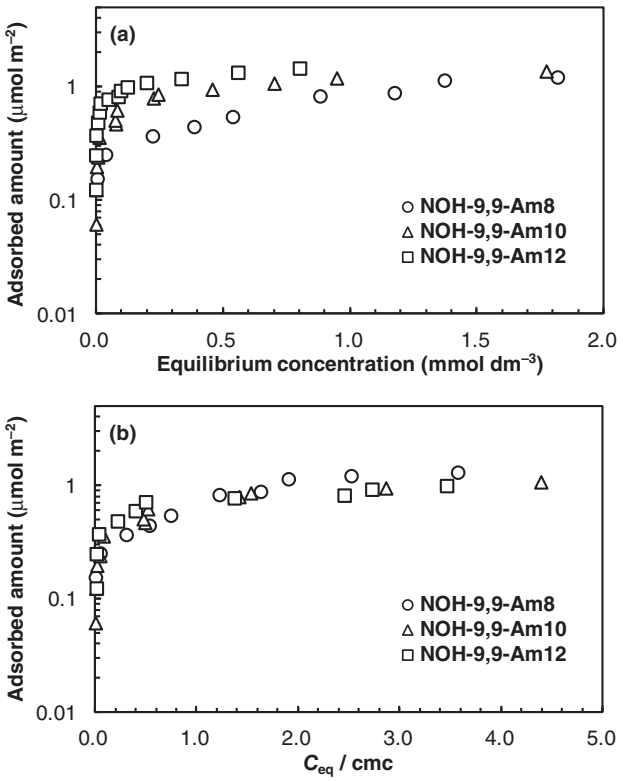


FIGURE 42.9 Adsorption isotherms of NOH-9,9-Am*n* (*n* = 8,10,12) on colloidal silica particles as a function of (a) equilibrium concentration of NOH-9,9-Am*n* (= C_{eq}) and (b) C_{eq}/cmc. (This figure is reproduced from Ref. 8 with copyright permission from the Japan Oil Chemists' Society.)

which reflects their remarkably lower cmc; (2) a higher adsorption density in the saturation region can be expected for gemini surfactants (in particular those having a short spacer unit such as C_2H_4) as compared to monomeric ones when we compare the adsorption data (in mol m^{-2}) normalized by the number of hydrocarbon chains [17]; and (3) as a result of their increased packing parameter, gemini surfactants yield surface aggregates with reduced positive curvature when compared to the corresponding monomeric surfactants [21].

We have characterized the adsorption of the oleic acid–based quaternary ammonium-type gemini surfactants (NOH-9,9-Am*n*, where *n* is the length of the hydrocarbon chain bound to the terminal carbonyl group of oleic acid) at the silica–aqueous solution interface [8]. The adsorption isotherms of these surfactants on colloidal silica particles are shown in Fig. 42.9. When the amount of surfactant adsorbed is replotted as a function of the equilibrium surfactant concentration (C_{eq}) normalized by the cmc, it is obvious that the shape of the adsorption isotherms of the three surfactants is qualitatively similar. Briefly, at relatively low concentrations (in the region of C_{eq}/cmc < 0.1), an increase in C_{eq} results in a steep increase in the amount of surfactants adsorbed, after which adsorption becomes more gradual at relatively high concentrations (in the region of C_{eq}/cmc > 0.1). An increased NOH-9,9-Am*n* chain length results in a shift to a lower equilibrium concentration at which adsorption starts to increase sharply, clearly being reflective of the lower cmc of the longer-chain analogs. The adsorption isotherms suggest that two adsorption processes are present. At low equilibrium concentrations the cationic surfactants are electrostatically adsorbed onto the negatively charged colloidal silica particles, while at high equilibrium concentrations, hydrophobic intermolecular interactions play a dominant role in surfactant adsorption.

The adsorption isotherms also allow us to calculate the occupied area per surfactant molecule adsorbed at the silica–aqueous solution interface. The adsorbed amount estimated at the cmc is in the range of 0.7–0.8 μmol m^{-2} for all of the NOH-9,9-Am*n* samples. This corresponds to an occupied area of 2.1–2.4 nm^2. Assuming that the surfactants form a complete flat bilayer at the silica–aqueous solution interface, the "actual" occupied area is estimated at 4.2–4.7 nm^2. These values are significantly higher than the occupied area per surfactant molecule adsorbed at the air–aqueous solution interface (Table 42.1), indicating that the adsorption density of NOH-9,9-Am*n* on colloidal silica parties is lower than that at the air-aqueous solution interface.

We have assessed the morphology of surfactant assemblies formed at the silica–aqueous solution interface [8], by means of soft-contact atomic force microscopy (AFM) imaging technique [24]. As a result, no significant surface features could be discerned in this case, indicating the formation of

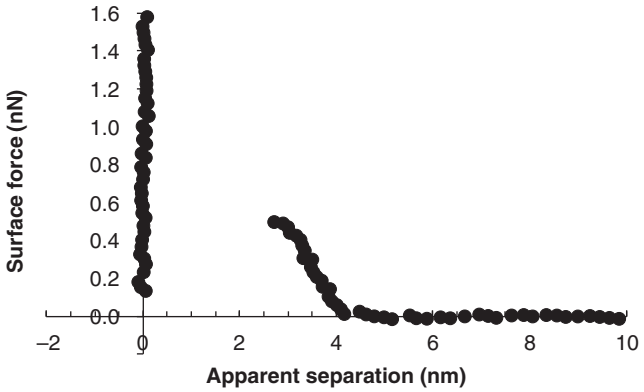


FIGURE 42.10 Force–distance data obtained for the NOH-9,9-Am10 aqueous system. The surfactant concentration was set at 10 × cmc. A flat silica plate was used as a solid substrate. (This figure is reproduced from Ref. 8 with copyright permission from the Japan Oil Chemists' Society.)

planar aggregates (i.e., a bilayer). This is consistent with the general trend observed for gemini surfactants [21].

AFM force curve measurements further provide structural information on the molecular assemblies formed at solid-solution interfaces. A typical force–distance curve obtained for the NOH-9,9-Am10 system is shown in Fig. 42.10 [8]. The shape of the force–distance curve suggests the repulsive interaction to originate from steric interactions arising from the NOH-9,9-Am10 molecular aggregates formed on the silica surface. The push-through distance (∼2.7 nm in this case) provides a measure of the adsorbed layer thickness under application of normal pressure. This distance is smaller than the hydrodynamic diameter of the NOH-9,9-Am10 micelles (∼5–7 nm). This suggests that, assuming bilayer formation, the hydrocarbon chains of the opposing molecules are interpenetrated to a certain degree as a result of the pressure applied normal to the surface.

It should be noted that the force–distance curve shown in Fig. 42.10 differs significantly from those reported in the previous paper [20], where force curves in aqueous solutions of the cationic gemini surfactant 1,2-bis(dodecyldimethylammonio)ethane dibromide in the presence of 10 mmol dm^{-3} NaBr were measured. In that case, compression of the surfactant layer resulted in a two-step repulsive interaction, where one stage was a relatively long-range repulsion and the other was a steeply increasing short-range repulsion. The first push-through, observed after the long-range repulsion, was ascribed to collapse of the weakly adsorbed surfactant layer on the tip, whereas the second push-through, observed at shorter separations, resulted from collapse of the surfactant layer formed on the solid substrate. The absence of the steep short-range repulsion in the NOH-9,9-Am10 system suggests, therefore, that steric repulsion against normal pressure is reduced as compared to the conventional gemini surfactant system. In addition, it was not possible to detect any long-range electrostatic repulsion in the current system, which may be due to collapse of the NOH-9,9-Am10 layer on the cantilever tip under normal pressure. It seems likely that this phenomenon reflects the lower adsorption density and/or the looser molecular packing arrangement of NOH-9,9-Am10, which is attributed to the asymmetric structure.

42.7 CONCLUDING REMARKS

In this chapter, we have presented the physicochemical properties of the oleic acid–based gemini surfactants recently developed in our research group. Basically, these surfactants exhibit excellent surface activities in aqueous solutions and tend to form molecular assemblies with less positive curvature. This molecular association occurs not only in aqueous bulk solutions but also at solid-aqueous solution interfaces. These behaviors follow general trends we can see in typical gemini surfactant systems. We can also see notable differences between our oleic acid–based surfactant systems and typical gemini surfactant systems. For example, we found the lower adsorption density and the looser molecular packing arrangement of our oleic acid–based surfactants adsorbed at the solid–aqueous solution interface. Such differences arise from the asymmetric headgroup and tail structures of our surfactants.

The oleic acid–based gemini surfactants have been synthesized using the reduced cost strategy; however, their selling prices are still higher than those of conventional monomeric surfactants. We anticipate, therefore, that these surfactants will find application in the formulation of high-performance chemical products in fields such as cosmetics, personal care, and medical applications. Our preliminary experiments have demonstrated that some of the oleic acid–based gemini surfactant samples exhibit excellent biodegradability and low (or no) skin irritant effects. This feature will also help us to find suitable applications of these surfactants.

REFERENCES

[1] Zana, R., Xia, J. (eds.) (2003). *Gemini Surfactants, Synthesis, Interfacial and Solution-Phase Behavior, and Applications*. Marcel Dekker, New York, Chapter 1.

[2] Zana, R. (2003). In Esumi, K., Ueno, M. (eds.), *Structure-Performance Relationships in Surfactants*, 2nd ed. Marcel Dekker, New York, Chapter 7.

[3] Zana, R., Alami, E. (2003). In Holmberg, K. (ed.), *Novel Surfactants: Preparation, Applications, and Biodegradability.* Marcel Dekker, New York, Chapter 12.

[4] Takamatsu, Y., Iwata, N., Tsubone, K., Torigoe, K., Endo, T., Sakai, K., Sakai, H., Abe, M. (2009). *J. Colloid Interface Sci.* **338**, 229–235.

[5] Sakai, K., Sangawa, Y., Takamatsu, Y., Kawai, T., Matsumoto, M., Sakai, H., Abe, M. (2010). *J. Oleo Sci.* **59**, 541–548.

[6] Sakai, K., Umemoto, N., Matsuda, W., Takamatsu, Y., Matsumoto, M., Sakai, H., Abe, M. (2011). *J. Oleo Sci.* **60**, 411–417.

[7] Sakai, K., Umemoto, N., Aburai, K., Takamatsu, Y., Endo, T., Kitiyanan, B., Matsumoto, M., Sakai, H., Abe, M. (2014). *J. Oleo Sci.* **63**, 257–267.

[8] Sakai, K., Saito, Y., Uka, A., Matsuda, W., Takamatsu, Y., Kitiyanan, B., Endo, T., Sakai, H., Abe, M. (2013). *J. Oleo Sci.* **62**, 489–498.

[9] Matsuda, W., Takamatsu, Y., Sakai, K., Sakai, H., Abe, M. (2009). *Abstracts of the 62nd Division Meeting on Colloid and Surface Chemistry.* The Chemical Society of Japan, Tokyo.

[10] Furukawa, Y., Takamatsu, Y., Sakai, K., Sakai, H., Abe, M. (2010). *Abstracts of Annual Meeting of Japan Society of Colour Material.* Japan Society of Colour Material, Tokyo.

[11] Rosen, M. J. (2004). *Surfactants and Interfacial Phenomena*, 3rd ed. Wiley, Hoboken, NJ.

[12] Wang, X., Wang, J., Wang, Y., Ye, J., Yan, H., Thomas, R.K. (2003). *J. Phys. Chem. B* **107**, 11428–11432.

[13] Israelachvili, J.N. (1992). *Intermolecular and Surface Forces*, 2nd ed. Academic Press, San Diego, Chapter 17.

[14] Kunieda, H., Masuda, N., Tsubone, K. (2000). *Langmuir* **16**, 6438–6444.

[15] Shrestha, R.G., Nomura, K., Yamamoto, M., Yamawaki, Y., Tamura, Y., Sakai, K., Sakamoto, K., Sakai, H., Abe, M. (2012). *Langmuir* **28**, 15472–15481.

[16] Kawai, T. (2010). *J. Jpn. Soc. Colour Mater.* (Shikizai) **83**, 505–510.

[17] Esumi, K., Goino, M., Koide, Y. (1996). *J. Colloid Interface Sci.* **183**, 539–545.

[18] Chorro, C., Chorro, M., Dolladille, O., Partyka, S., Zana, R. (1998). *J. Colloid Interface Sci.* **199**, 169–176.

[19] Atkin, R., Craig, V.S.J., Wanless, E.J., Biggs, S. (2003). *J. Phys. Chem. B* **107**, 2978–2985.

[20] Sakai, K., Matsuhashi, K., Honya, A., Oguchi, T., Sakai, H., Abe, M. (2010). *Langmuir* **26**, 17119–17125.

[21] Manne, S., Schäffer, T.E., Huo, Q., Hansma, P.K., Morse, D.E., Stucky, G.D., Aksay, I.A. (1997). *Langmuir* **13**, 6382–6387.

[22] Fielden, M.L., Claesson, P.M., Verrall, R.E. (1999). *Langmuir* **15**, 3924–3934.

[23] Duval, F.P., Zana, R., Warr, G.G. (2006). *Langmuir* **22**, 1143–1149.

[24] Manne, S., Cleveland, J.P., Gaub, H.E., Stucky, G.D., Hansma, P.K. (1994). *Langmuir* **10**, 4409–4413.

44

FUNCTIONAL HYDROGEL MICROSPHERES

Daisuke Suzuki, Takuma Kureha, and Koji Horigome
Graduate School of Textile Science & Technology, Shinshu University, Ueda, Nagano, Japan

44.1 INTRODUCTION

Polymer hydrogel microspheres (known as *microgels*) are spherical objects comprising cross-linked polymeric networks swollen by water. Typical microgels are approximately 10–1000 nm in size, and are dispersed in a solvent. Microgels have been extensively researched in previous decades, as their "smart material" properties are beneficial in numerous technologies such as drug and gene delivery [1–4]; chemical and biological separation [5, 6]; sensors [7, 8]; templates or stabilizers for inorganic nanoparticles [9–12]; photonic crystals [13–16]; and smart particulate emulsifiers [17–19]. Most microgels share a number of properties with macrogels; specifically, their physicochemical properties respond to external stimuli such as pH, temperature, light, presence of biomolecules, and salt concentration. This stimuli-responsive property of microgels enables many of the abovementioned applications. In addition, the colloidal nature of microgels confers tremendous advantages over macrogels. For example, microgels rapidly respond to external environmental changes because of of their high surface:volume ratios.

Probably the best known and most widely studied microgels are the poly(*N*-isopropylacrylamide) or pNIPAm microgels. Chains of pNIPAm demonstrate a thermoresponsive property, altering from coiled to globular at the lower critical solution temperature (LCST) of around 32°C in pure water [20, 21]. Thus, pNIPAm microgel undergoes a volume phase transition (VPT) at around the LCST of pNIPAm linear chains [22]. In contrast, pH-responsive microgels have been synthesized from polyelectrolyte microgels, and many researchers have already copolymerized charged monomers in microgels. For instance, by precipitation polymerization in several alcohols, researchers have fabricated monodispersed and pH-responsive microgels from acrylamide, methacrylic acid, and the cross-linker methylenebisacrylamide (BIS) [23, 24]. Naturally, because the presence of electrolytes in microgel dispersions affects the electrostatic interactions among the microgels, polyelectrolyte microgels also depend on salt concentration. This chapter introduces functional microgels and overviews their synthesis, characterization, and applications.

44.2 MICROGEL SYNTHESIS

An important consideration in microgel synthesis is to ensure their monodispersity and prevent their coagulation. Microgels can be synthesized in three ways: (1) from monomer, (2) from polymer, and (3) from macrogel. In general, monodispersed microgels cannot be obtained by methods 2 and 3; thus, microgels are usually prepared from monomers, which permits monodispersed microgels if the polymerization is sufficiently precise. Thermosensitive microgels are most commonly fabricated by precipitation polymerization. Briefly, microgel formation requires that the synthesized polymer is insoluble under the polymerization conditions, whereas the monomer is soluble. For instance, pNIPAm microgels form when precipitation polymerization is performed in water at 70°C, since pNIPAm is water-insoluble at high temperatures [20, 21]. Microgels of pNIPAm chains cross-linked by BIS were first reported in 1986 [25]. In this method, the monomers and cross-linkers are completely dissolved in water. The mixture is usually bubbled with nitrogen gas to purge oxygen from the solution, and then heated to a

Encyclopedia of Biocolloid and Biointerface Science, Volume 1, First Edition. Edited by Hiroyuki Ohshima.
© 2016 John Wiley & Sons, Inc. Published 2016 by John Wiley & Sons, Inc.

temperature above the LCST of pNIPAm. Finally, polymerization is initiated by adding a water-soluble initiator such as potassium persulfate (KPS) to the reactor.

Thermosensitive microgels prepared by precipitation polymerization become aggregated by homogeneous nucleation. Besides pNIPAm microgels, precipitation polymerization is applicable to other acrylamide derivatives such as *N*-isopropylmethacrylamide (NIPMAm) whose LCST is ~44°C in aqueous media [26–28]. The polymerization is usually conducted at high temperature, which liberates sulfate radicals from compounds such as ammonium persulfate or KPS. The sulfate radicals attack monomers such as NIPAm, initiating radical propagation and chain growth. Once the polymer chain reaches a critical length, it collapses onto itself, producing precursor particles. The chain collapses because the polymerization temperature exceeds the LCST of the polymer. The precursor particles grow by aggregation with other precursor particles. As the aggregated precursor particles coalesce, the charged chain ends become concentrated at the surface. Therefore, the charge imparted by the initiator stabilizes the microgels once they have reached a critical size. The size of the resultant microgels can be controlled by polymerization temperature, surfactant addition, and copolymerization. Cross-linkers are required to prevent microgels from dissolution as the mixture is cooled below the LCST. In particular, multiresponsive microgels can be formed by copolymerizing ionic monomers with NIPAm or NIPMAm.

Even the simplest pNIPAm microgel contains two chemical species (NIPAm and cross-linker), and many of the fascinating microgels contain multiple monomers. The presence of more than one monomer introduces complexity in any free-radical copolymerization because each monomer exhibits a unique reactivity. For example, it is commonly accepted that the cross-linker BIS polymerizes faster than NIPAm during precipitation polymerization. Consequently, the cross-link density is higher in the polymer that forms first than in the last, and the exterior of the microgel is less cross-linked than the microgel core [29].

The desired functionality of microgels is achieved by correct design and control of microgel structure. Among the most widely studied structures are the core–shell microgels, which are broadly divisible into two classes: (1) the *solid core*, which is surrounded by a hydrogel shell [30–34], and (2) the *entire structure*, which consists of hydrogel [35–41]. In class 1, the core usually comprises solid materials such as polystyrene and silica particles. The hydrogel shell is then introduced by seeded precipitation polymerization. One team of investigators synthesized polystyrene core–pNIPAm hairy particles by living radical graft polymerization [34]. The hydrogel shell of the hairy particles is not cross-linked; thus, the thermoresponsive behavior of the particles is uniquely different from that of conventional solid core–hydrogel shell microgels.

The second class of core–shell microgels contains hydrogel in both the core and the shell. Core–shell microgels synthesized by precipitation polymerization were first reported by Lyon et al. [35]. During this polymerization, preformed deswollen hydrogel cores are surrounded by hydrogel shell with a structure or functionality that is the same as or different from that of the core. This technique enables control of the radial distribution of the functional groups in the microgels, and the display of interesting properties. Because the shell can be synthesized by introducing different comonomers to the core, core–shell microgels can undergo multiple phase transition behaviors with increasing temperature [35]. Furthermore, core–shell microgels form the basis of hollow hydrogel capsules [36]. In this case, the core and shell are prepared with a degradable and nondegradable cross-linker, respectively. Following core degradation, the microgels are extensively purified by centrifugation to remove the degraded linear polymer chains from the core.

Recently, our group reported different types of composite microgels containing solid material. Polymer particles are commonly produced by dispersion polymerization. In principle, the conditions for successful dispersion polymerization are simple, requiring a steric stabilizer and solvent that dissolves the monomer but precipitates the polymer. First, we used pNIPAm microgels as stabilizers during alcoholic dispersion polymerization of styrene (Fig. 44.1) [42]. The size, size distribution, and morphology of the

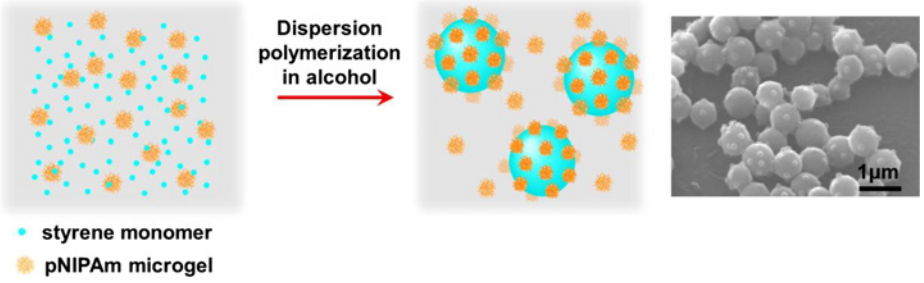


FIGURE 44.1 Dispersion polymerization of styrene in pNIPAm microgels. SEM image shows the composite microgels. pNIPAm microgels (370 nm) were used as stabilizers. [Reprinted with permission from Ref. 42. Copyright (2012) American Chemical Society.]

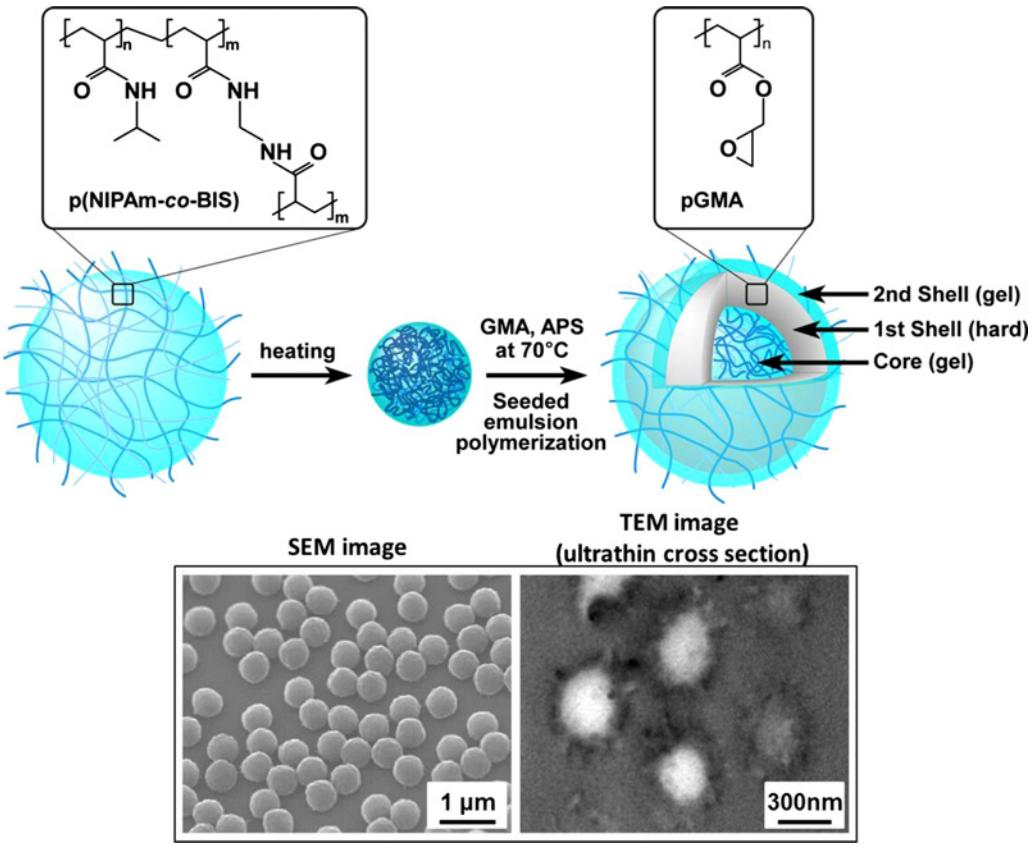


FIGURE 44.2 Approach for synthesizing multilayered composite microgels. The composite microgels can be confirmed by SEM and TEM. [Reprinted with permission from Ref. 43. Copyright (2013) American Chemical Society.]

resultant polystyrene particles depend on the size and concentration of the microgels. In particular, polystyrene particles coated with PNIPAm-based microgels were observed using scanning electron microscopy (SEM; see Fig. 44.1). Multilayered composite microgels have also been synthesized by surfactant-free seeded emulsion polymerization [43]. Electron microscopic observations of these composite microgels reveal a distinct solid shell of oil-soluble chemical species (glycidyl methacrylate, in this case), while surface analysis reveals a hydrogel layer surface (Fig. 44.2).

44.3 MICROGEL CHARACTERIZATION

This section briefly overviews the frequently used techniques for characterizing microgels. Since microgels are colloidal in nature, they can be characterized according to their size, polydispersity, and shape and state of dispersion/flocculation. Moreover, microgels also possess gel properties; therefore, equally important features are degree of swelling and network structure.

The size, size distribution, and shape of microgels are usually determined from optical microscopy. Microgels with diameters approximating or largely exceeding 1 μm are generally considered suitable for observation by optical microscopy. Improved spatial resolution for smaller microgels is achieved by confocal microscopy. In this technique, microgels are labeled by fluorescence dyes such as rhodamine or by quantum dots incorporated into the microgel's network [44]. Notably, the behavior of microgels dispersed in water can be studied by the same optical methods [26].

If higher resolution is required, the applied microscopies require radiation of much smaller wavelengths. Thus far, dried (solid) microgels have usually been characterized by electron microscopy. For example, SEM and transmission electron microscopy (TEM) can identify the size, polydispersity, and shape of microgels in the dry state. Furthermore, depending on the sample preparation and the resolution of the microscope, information on the surface structure is obtainable. In particular, TEM has often been used to investigate microgels hybridized with metal nanoparticles. Because of the large electron density differences between metal nanoparticles and polymer components, even comparatively small metal nanoparticles embedded in rather large microgels can be imaged with high resolution [45]. A typical SEM image

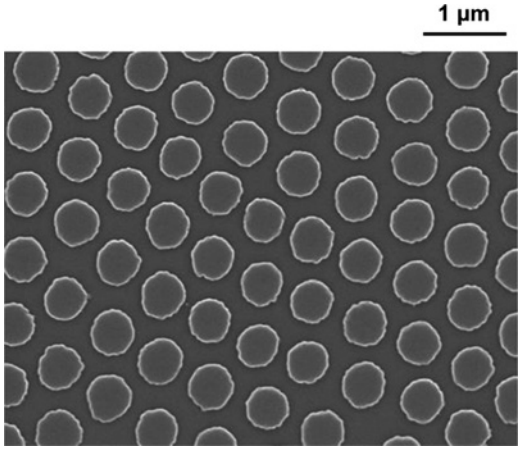


FIGURE 44.3 SEM image of pNIPAm microgels dried on polystyrene substrate at 25°C. [Reprinted with permission from Ref. 46. Copyright (2011) American Chemical Society.]

of pNIPAm-based hydrogel spheres is shown in Fig. 44.3 [46].

One drawback of electron microscopy is that it reveals the nearly deswollen state of microgels. For many purposes, the collapse of microgels under the high vacuum of the microscope is undesirable, and the microgels should be imaged in the swollen state. In such cases, cryo-TEM offers a valuable alternative. In this technique, microgel dispersions are quickly frozen at low temperatures (e.g., with liquid butane or propane cooled with liquid nitrogen). If the cooling rates are sufficiently high, the structure in the solution is frozen and the water in the microgel samples is vitrified. Since the temperature, pH, and ionic strength of the initial microgel dispersion are alterable, cryo-TEM allows microgel imaging under different conditions determined by the initial state.

Another frequently used microscopy method is atomic force microscopy (AFM). In contrast to optical and electron microscopes, the sample is imaged by AFM in a purely mechanical way. Microgel height is determined from the repulsive and attractive interactions between the sample surface and the resulting cantilever displacement. Similar to electron microscopy, AFM conducted in air provides images of nearly collapsed microgels. However, solubilized samples can be studied using AFM in a liquid cell. Recently, the VPT of thermoresponsive microgels was monitored by AFM [47, 48].

Microgels have also been characterized by light scattering and spectroscopy. Because the available information depends on the light wavelengths, microgels in water can be characterized from various perspectives. For example, the size and polydispersity of microgels dispersed in water may be studied by dynamic light scattering (DLS). Since parameters such as temperature, pH, and ionic strength of the dispersion medium can be readily varied, DLS is ideally suited to investigate the behavior of responsive microgels. For instance, DLS obtains the swelling curves of thermoresponsive microgels. First, the microgel size is calculated as the hydrodynamic diameter (or radius). The hydrodynamic diameters D_h of microgels are determined from the measured diffusion coefficients using the Stokes–Einstein equation. Subsequently, the swelling capacity of responsive microgels is quantified by the swelling ratio α:

$$\alpha = \frac{V(T)}{V_0} = \left(\frac{R_h(T)}{R_{h,0}} \right)^3 \tag{44.1}$$

In this equation, $V(T)$ and V_0 are the microgel volumes at temperature T and in the fully swollen state, respectively. Because microgels are nearly spherical [49], α can be determined from the respective hydrodynamic radius R_h rather than from the volume V.

In contrast, small-angle scattering (SAS) of X rays and neutrons enable structures to be studied on a local length scale [50–52]. This localization relates to the enhanced range of scattering vectors available in experiments involving X rays and neutrons, whose de Broglie wavelength is much smaller than the wavelength of lasers used in light-scattering setups. Therefore, light-scattering experiments yield the overall microgel size, while SAS provides structural parameters at the nanometer scale. For instance, the network correlation length ξ is determined from SAS measurements of microgels [53–55].

The electrostatic properties of colloids influence their colloidal stability and interactions with dissolved polymers and surfaces. The fascinating electrical properties of microgels arise from covalently bonded electrically charged groups contributed by the polymerization initiator. The electrical properties of microgel dispersions have been characterized from their electrophoretic mobility, which determines the zeta-potential replaced with the surface potential of the particles. Although constructed from cross-linked and hydrated polymers, microgels possess no definite solid–liquid interfaces; thus, they cannot be characterized by the ζ-potential. Hence, Ohshima's theory has been applied to the electrophoretic mobility of microgels [56–59]. In addition, microgels are soft, ion-penetrable particles, and their electrophoretic mobility also provides morphological information. Ohshima and colleagues theoretically described the electrophoretic mobility of latex particles covered by ion-penetrable surface layers [60–62]. This theory was initially developed for biocolloids. The total particle potential is contributed by both the surface charge layer and Donnan potential. Ohshima's model has been successfully applied to core–shell composite particles such as polystyrene latex covered by pNIPAm hydrogel layers [60–62]. The theory yields two important parameters: the volume density of fixed ionic groups bound within the surface charge layer (N) and

the softness parameter ($1/\lambda$). The model is governed by the following equations:

$$\mu = \frac{\varepsilon_r \varepsilon_0}{\eta}\left(\frac{\psi_0/\kappa_m + \psi_{DON}/\lambda}{1/\kappa_m + 1/\lambda}\right) + \frac{ZeN}{\eta^{\lambda^2}} \tag{44.2}$$

$$\psi_0 = \frac{kT}{ve}\left(ln\left[\frac{ZN}{2\nu n} + \left\{\left(\frac{ZN}{2\nu n}\right)^2 + 1\right\}^{1/2}\right] + \frac{2\nu n}{ZN}\left[1 - \left\{\left(\frac{ZN}{2\nu n}\right)^2 + 1\right\}^{1/2}\right]\right) \tag{44.3}$$

$$\psi_{\mathrm{DON}} = \frac{kT}{ve} ln\left[\frac{ZN}{2\nu n} + \left\{\left(\frac{ZN}{2\nu n}\right)^2 + 1\right\}^{\frac{1}{2}}\right] \tag{44.4}$$

$$\kappa_m = k\left[1 + \left(\frac{ZN}{\nu n}\right)^2\right]^{1/4} \tag{44.5}$$

where ε_r, ε_0, η, and e are the relative permittivity, permittivity in vacuum, viscosity, and electronic charge, respectively; κ_{m} is the reciprocal of the double-layer thickness within the surface charge layer. The Donnan potential of the surface charge layer and the potential at the boundary between the surface layer and the surrounding solution are given by ψ_{DON} and ψ_0, respectively. Z and ν are the charge numbers and valencies of the ionized groups within the surface layer and the electrolyte, respectively. λ denotes the friction experienced by the liquid flowing through the surface layer. The softness parameter λ^{-1} approaches zero as the particles become more rigid. N and n are the number densities (m^{-3}) of charged groups in the surface charge layer and electrolyte ions, respectively, and k is the Boltzmann constant.

44.4 FUNCTIONAL MICROGELS

This section summarizes some important functional microgels, which have been developed mainly by our group and synthesized by precipitation polymerization.

44.4.1 Hybrid Microgels

Hybrid microgels comprise metal nanoparticles embedded in polymer microgels. Monodispersed inorganic nanoparticles are synthesized in situ by reduction of precursor ions immobilized in the polymer networks of the microgel. Under these conditions, pNIPAm-based microgels containing functional groups behave as reactors for synthesizing inorganic nanoparticles [9–11]. By changing the microgel composition, metal nanoparticles of varying size are obtained [9]. Hybrid microgels are attractive functional material candidates, since they combine the features of soft microgels (such as high colloidal stability and stimuli-responsiveness) with the optical, electronic, and magnetic properties of metal nanoparticles. The synthesis of metal nanoparticles (CdS, fluorescent and nonfluorescent Ag, and Fe_3O_4) in poly(NIPAm-acrylic acid-2-hydroxyethyl acrylate) microgels has been comprehensively investigated [9,63]. Others [11,64] discussed how the volume transition of the pNIPAm shell modulates the catalytic activity of metallic nanoparticles in polystyrene core–pNIPAm shell particles. They also demonstrated the catalytic efficacy of thermosensitive Au-pNIPAm yolk shell hybrid particles in the reduction of aqueous 4-nitrophenol and nitrobenzene, and that temperature enhances catalysis sensitivity [65]. We have reported on microgels hybridized with in situ synthesized inorganic nanoparticles, where microgels of different structure templates exhibit tunable properties [10,66–69]. The thermosensitivity of such hybrid microgels manifests as color change. By controlling the interparticle interactions between the nanoparticles embedded in the microgel, we can alter the surface plasmon resonance absorption of Au and Au/Ag nanoparticles (Fig. 44.4) [10,67]. Another template enabled the fabrication of a hybrid microgel wherein a stable Au nanoshell was formed in situ at a rigid core surface [66]. We have also demonstrated the formation of colloidal crystals of core–shell hybrid microgels by thermal annealing [69]. Here, the hybrid microgel architecture was constructed in multiple synthetic steps to homogenously localize the Au nanoparticles within the microgels (Fig. 44.5). Novel assemblages that exploit this hybrid structure will be useful for creating complex, tunable optical materials with periodic refractive index over multiple length scales.

In addition to the abovementioned reports, microgels hybridized with metal nanoparticles have been extensively applied to tuning optical properties [70–74] and catalysis [75–80].

44.4.2 Janus Microgels

Janus particles are particles with chemically different hemispherical surfaces [81]. The synthesis of rigid Janus particles has markedly progressed, and we believe that the synthetic method is now established [82]. Therefore, future research will focus on applications rather than production of these particles. As mentioned above, microgels are soft agglomerates of cross-linked polymer networks, and highly swollen in appropriate solvent. Recently, our group has created its first Janus microgels [83, 84], which are cationic on one side and anionic on the other. The hydrophilicity of the entire microgel is tunable by external stimuli such as pH and temperature. We are currently engaged in controlling the shape of microgel assemblies by their stimulus-responsive

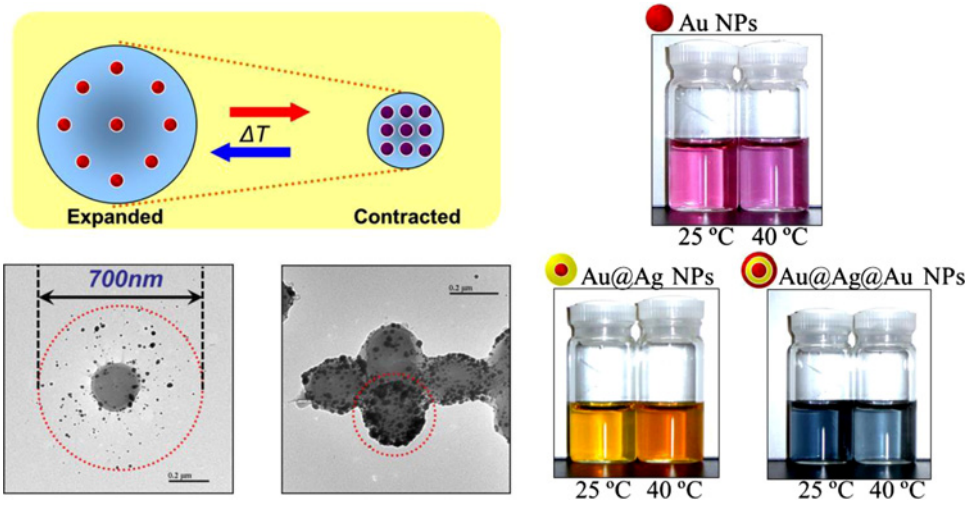


FIGURE 44.4 As the temperature changes, the microgel swells and shrinks, altering the relative distance between metallic nanoparticles suspended in the polymer matrix, the interaction of their surface plasmons, and thus their optical properties. The rightmost frames show the color differences at 25°C and 40°C (left and right, respectively, in each frame) for samples loaded with gold nanoparticles (top), gold–silver core–shell nanoparticles (bottom left), and gold–silver–gold multishell nanoparticles (bottom right). [Reprinted with permission from Refs. 10 and 67. Copyright (2005 and 2006) American Chemical Society.]

properties; our Janus microgels can assemble into A-B_A-B_A-B-type strings via attraction between cationic and anionic hemispheres. This arrangement is crucially different from the A-B_B-A-type clusters formed by non-charged/onesided charged amphiphilic Janus particles. First, temperature- and pH-responsive microgels were constructed from NIPAm and acrylic acid (AAc) monomers. NIPAm-*co*-AAc microgels were prepared by aqueous free-radical precipitation polymerization. Oil-in-water (o/w)-type Pickering emulsions were formed by stirring a mixture of aqueous microgel dispersion and hexadecane at room temperature. Here, the microgels behaved as particulate stabilizers. Subsequently, one hemisphere of the microgels was modified with ethylenediamine at the oil–water interface. At pH 5, almost all of the carboxyl groups in the microgel were highly deprotonated, and the charge was distributed

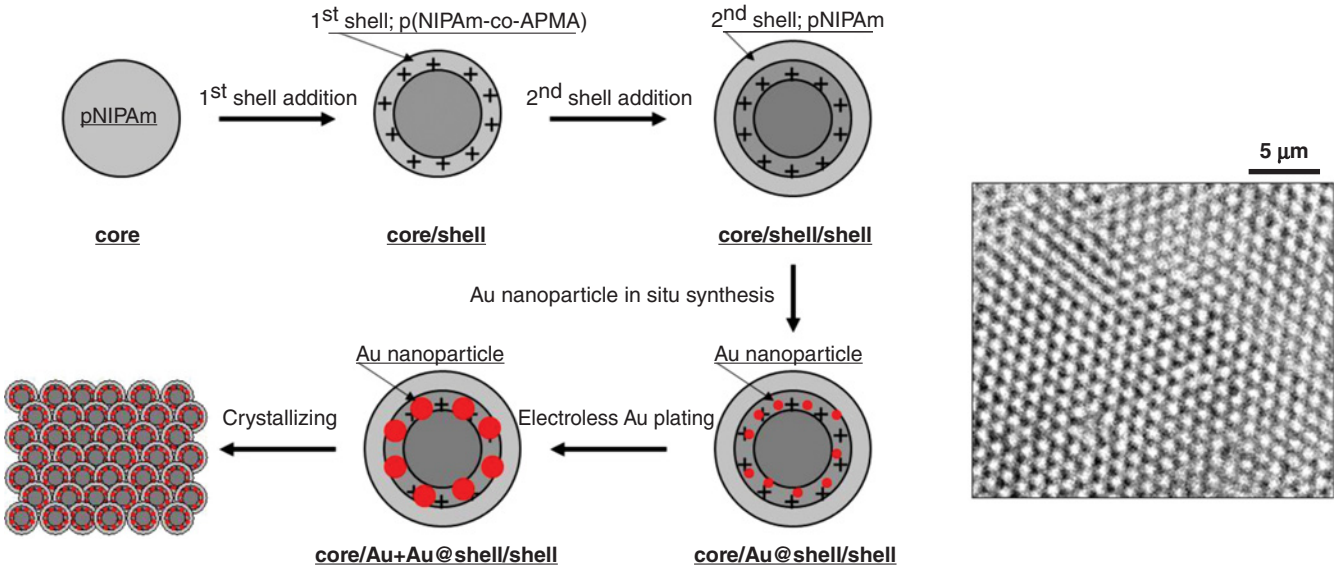


FIGURE 44.5 Synthesis of multiple core–shell hybrid microgels and their colloidal crystals. [Reprinted with permission from Ref. 69. Copyright (2007) American Chemical Society.]

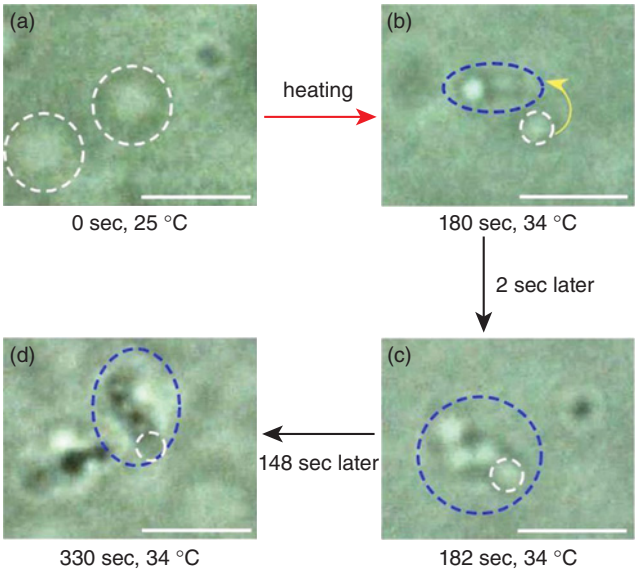


FIGURE 44.6 Temperature-induced assembly of Janus microgels traced by optical microscopy. All scale bars are 5 μm. (a) At 25°C, pH = 3, and salt concentration = 10 mM, Janus microgels exist in a swollen state. (b) Dispersion immediately jumped from 25°C to 34°C. The microgels contracted as they dehydrated. Thus, the deswollen microgels have assembled into strings 180 s after the temperature jump. Here, the microgel (delineated by the white circle) is just attaching to the microgel trimer (delineated by the blue circle). (c) A microgel tetramer forms 2 s later. (d) A microgel pentamer forms 148 s following microgel tetramer formation in (c). (Reprinted from Ref. 84 with permission from Springer Science + Business Media. Copyright (2011).)

homogeneously across the microgel surface. However, at pH 3, although the vast majority of AAc carboxyl groups were protonated, anionic sulfate groups released from the initiator were active throughout the microgel, and the amine groups became positively charged over a single hemisphere. Thus, dipolar Janus structures were fabricated by changing the pH. Generally, microgels are colloidally stabilized by steric hindrance; however, they are influenced by electrostatic attractive forces. Our Janus microgels were colloidally stable at 25°C and pH 3, but they were flocculated above 34°C at the same pH. These behaviors were revealed by DLS. Interestingly, the flocs showed a stringlike structure under optical microscopy (Fig. 44.6). The advantages of Janus microgels are as follows:

1. *Variable Stimulus-Responsive Properties*. Radical precipitation polymerization yields many types of stimulus-responsive microgels.
2. *Reversible Dispersion/Flocculation Behavior*. pNIPAm microgels are known to reversibly disperse and flocculate [46]. The colloidal stability of such microgels can be controlled by varying the external stimuli such as temperature and pH.
3. *Biocompatibility*. To date, several types of biocompatible microgels have been fabricated from natural polymers. These advantages suggest a role for Janus microgels in precisely controlled particle clusters, microfluidic devices, microactuators, and model colloids for molecular science.

44.4.3 Oscillating Microgels

Different from conventional stimuli-responsive microgels, novel oscillating microgels with periodically changing physicochemical properties have been developed by our group and others. Oscillations are automatic; specifically, the microgels periodically swell/deswell in the absence of externally stimulated on/off switches [85–87]. This section summarizes some recent advances in this new class of microgels.

Oscillating microgels are fabricated by anchoring functional species with periodically changeable properties to the microgels. If the microgel is to synchronize with pH-oscillating reactions, the functional group should be a carboxyl or amine group. For example, poly(NIPAm-*co*-AAc) microgels synthesized by precipitation polymerization are synchronized with the bromate–sulfite pH–oscillating reaction [85].

In our research, microgels were synchronized with the redox oscillation of the Belousov–Zhabotinsky (BZ) reaction by covalently bonding the metal ion catalyst of the BZ reaction to the microgel [86, 87]. Aqueous free-radical precipitation polymerization, by which stimuli-responsive microgels are synthesized, is also beneficial for synthesizing monodispersed microgels. To this end, ruthenium (4-methyl-4′-vinyl-2,2′-bipyridine)bis(2,2′-bipyridine)bis(hexafluorophosphate) monomer [denoted as $Ru(bpy)_3$ monomer], NIPAm, and cross-linker BIS are dissolved in water, and polymerization is initiated by injecting a cationic initiator solution (e.g., V50) into the mixture at 70°C [86, 87]. Polymerization usually requires about 6 h to complete. During the polymerization, 50–60% of the $Ru(bpy)_3$ monomer is incorporated into the resultant microgels with the $Ru(bpy)_3$ moieties fixed in the reduced $Ru(bpy)_3^{2+}$ state [88]. The loss of $Ru(bpy)_3$ monomer during polymerization is attributable mainly to the hydrophilicity of the monomer. The LCST of highly charged pNIPAm linear chains is much higher than that of pure pNIPAm. Consequently, the poly(NIPAm-*co*-$Ru(bpy)_3$) chains are forced into the coiled state during polymerization, even at 70°C, and are not incorporated by microgels. The $Ru(bpy)_3$ monomer also faces shrinkage of the hydrodynamic diameters of the microgels during polymerization; the effect is similar to that of ionic surfactants in precipitation polymerization [88]. Moreover,

by changing the ionic strength, monomer concentration, and initiator concentration, we can control the microgel size. To date, monodispersed microgels of hydrodynamic diameter 100–800 nm have been prepared in their swollen states. Currently, to achieve the swelling/deswelling volume oscillation, the metal catalyst of the BZ reaction must be immobilized within polymer chains of microgels.

How the oscillatory behavior of microgels is regulated must be clarified. Oscillatory behavior is governed by the conditions of the involved chemical reactions. The reaction temperature and the concentrations of the reacting chemical substrates essentially determine the oscillatory characteristics of the chemical reaction itself (such as the induction period, oscillation amplitude, oscillation period, and waveform). The state of the microgel network structure (i.e., whether the polymer chain is coiled or globular) should also dynamically affect the chemical reactions via a feedback effect. In the next three subsections, the features of oscillating microgels are clarified by summarizing the effects of the abovementioned primary influencers of oscillatory behavior by focusing on the BZ reaction. To simplify the discussion, we assume that all reaction solutions are mechanically stirred, although mechanical stirring is another important mediator of oscillatory behavior.

In general, the oscillations in the BZ reaction are preceded by an induction period, as shown in Fig. 44.7. In practical applications, the induction period of the oscillating microgels must be controlled as precisely as possible. This induction period depends on the types and concentrations of the chemical substrates (i.e., metal ion catalysts, oxidizing and reducing reagents, strong acids), and on the temperature and stirring rate [89]. The induction period of the BZ reaction is most likely explained by a critical concentration of the organic brominated species [mainly bromomalonic acid

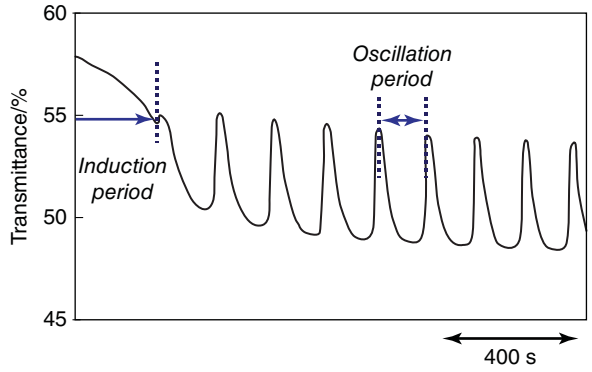


FIGURE 44.7 Typical profile of cyclic optical transmittance by oscillating microgels. To observe transmittance changes originating from microgel oscillation, measurements were made relative to an isosbestic point (570 nm) of the Ru^{II} and Ru^{III} states. [Reprinted with permission from Ref. 88. Copyright (2008) American Chemical Society.]

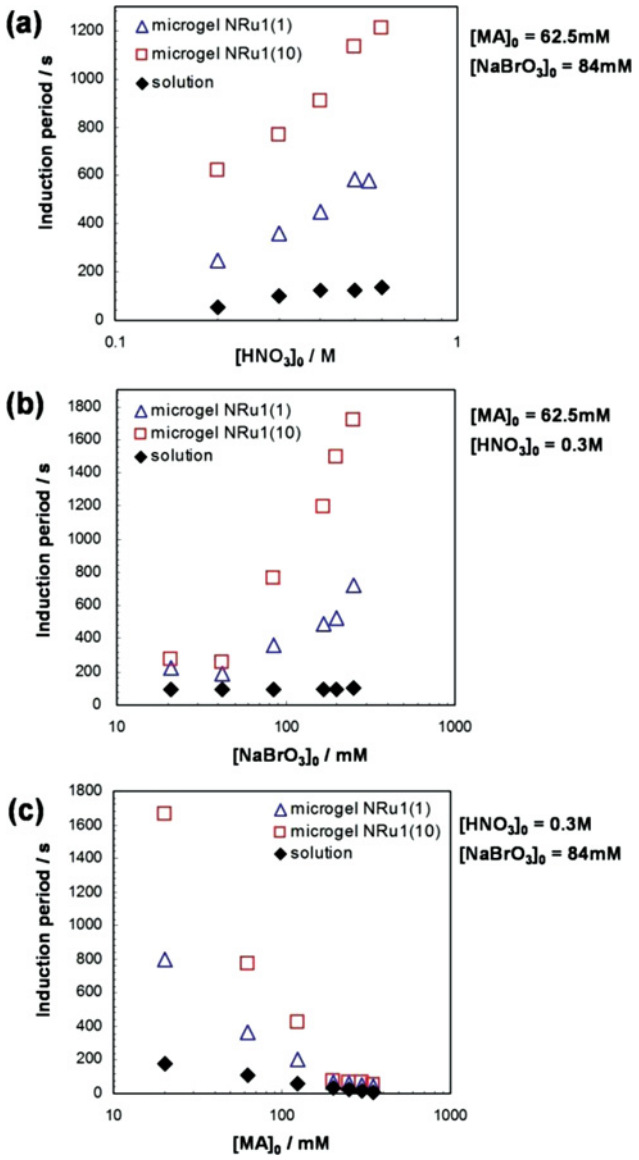


FIGURE 44.8 Effect of initial substrate concentrations on induction period in the bulk solution system (black diamonds), 1 mol.% BIS cross-linked oscillating microgels (blue triangles), and 10 mol% BIS cross-linked oscillating microgels (red squares). [Reprinted with permission from Ref. 91. Copyright (2008) American Chemical Society.]

(BrMA)] that triggers oscillation [89, 90]. The effect of initial substrate concentrations on the induction period of the oscillating microgels is less easily clarified, but has been investigated by varying substrate concentration while other parameters are fixed [91]. For oscillating microgels containing immobilized metal ion catalysts, the induction period also strongly depends on the microgel network structure [88]. Figure 44.8 plots the induction periods of microgel oscillations, and those of the conventional BZ reaction without microgels, at 25°C. In all cases, the chemical reagents in the BZ

reaction are malonic acid (MA), sodium bromate ($NaBrO_3$), and nitric acid (HNO_3), and the oscillating microgels represent 1 mol% and 10 mol% cross-linked (by BIS cross-linker) polymer. As the cross-link density increases, the induction period of the microgels markedly lengthens, as is evident from Fig. 44.8. From a hypothesis proposed earlier [90], we relate the induction period of the oscillating microgel system to the immobilization of the metal ion catalysts in the microgels. BrMA must be produced at lower rate than in the BZ reaction with nonimmobilized catalysts, because the diffusion constants of the chemical substrates and intermediates are reduced in the microgel networks. Moreover, increasing $[NaBrO_3]_0$ extends the induction period of the oscillating microgels, but does not affect the induction period in bulk solution (Fig. 44.8b). Again, the induction period is related mainly to the critical BrMA concentration, which is known to depend on $[NaBrO_3]_0$ [89,90]. The differing induction period between the oscillating microgels and the bulk solution might be related to additional factors such as the concentrations of metal ion catalyst and MA. In fact, as $[NaBrO_3]_0$ increases, the tendency for the induction period to lengthen strengthens with decreasing concentration of metal catalyst in the BZ reaction with nonimmobilized cerium ions [90]. The relationship between induction period and temperature has also been clarified [88]. The induction period is longer in the oscillating microgels than in the conventional BZ reaction at all temperatures below the VPTT (volume phase transition temperature) of the microgels. In addition, at all temperatures, the induction period of the microgels is extended with increasing cross-link density. All of these results can be attributed to $Ru(bpy)_3$ immobilization within the cross-linked network structures [91]. The mechanism underlying the induction period of oscillating microgels is complex, and requires further investigation.

The short swelling/deswelling oscillation period of microgels is very difficult to follow by DLS. Thus, oscillation amplitudes at different hydrodynamic diameters were estimated from diameter changes between the reduced Ru^{II} state and the oxidized Ru^{III} state at the same temperature [86,88,91]. The hydrodynamic diameters of poly(NIPAm-*co*-$Ru(bpy)_3$) microgels as functions of temperature were measured by DLS, and are plotted in Fig. 44.9. Since the BZ reaction proceeds only at high salt concentration, the HNO_3 concentration exceeded 0.3 M in all solutions. The deswelling curves almost coincide when small quantities (<0.12 mol%) of $Ru(bpy)_3$ are immobilized, as shown in Fig. 44.9a. In contrast, when 0.34 mol.% of the $Ru(bpy)_3$ monomer is incorporated into microgels, the transition temperature is higher for the oxidized Ru^{III} state than for the reduced Ru^{II} state. Comparing parts (b) and (c) of Fig. 44.9, we note that the shift in transition temperature enlarges as the amount of $Ru(bpy)_3$ monomer immobilized in the microgels increases from 0.56 mol% to ~1 mol%. From these data, we can roughly estimate the volume changes in the oscillations.

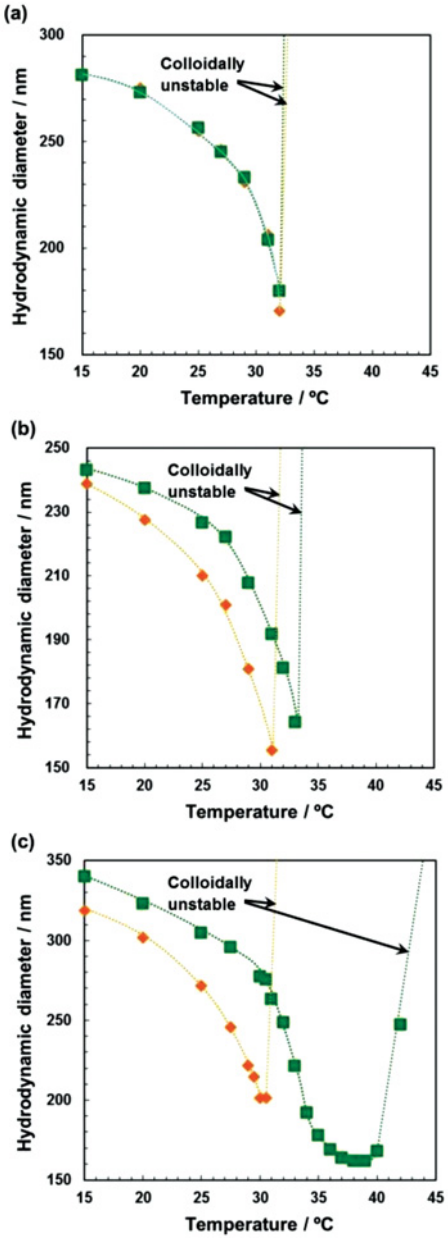


FIGURE 44.9 Relationship between hydrodynamic diameter of microgels and temperature, measured by DLS. BIS cross-linked poly(NIPAm-*co*-$Ru(bpy)_3$) microgels in the reduced Ru^{II} state are suspended in solution with 1 mM Ce^{III} and 0.3 M HNO_3 (orange diamonds), and in the oxidized Ru^{III} state in solution with 1 mM Ce^{IV} and 0.3 M HNO_3 (green squares). Samples contain (a) ~0.1 mol.%, (b) ~0.6 mol.%, and (c) ~1.0 mol.% $Ru(bpy)_3$ monomer. [Reprinted with permission from Refs. 88 and 99. Copyright (2008 and 2010) American Chemical Society.]

For instance, at a constant temperature of 30°C, the volume of the oscillating microgels changes by ~40% (Fig. 44.9c).

Since hydrodynamic diameters are not easily measured by real-time DLS, oscillation amplitudes are monitored by

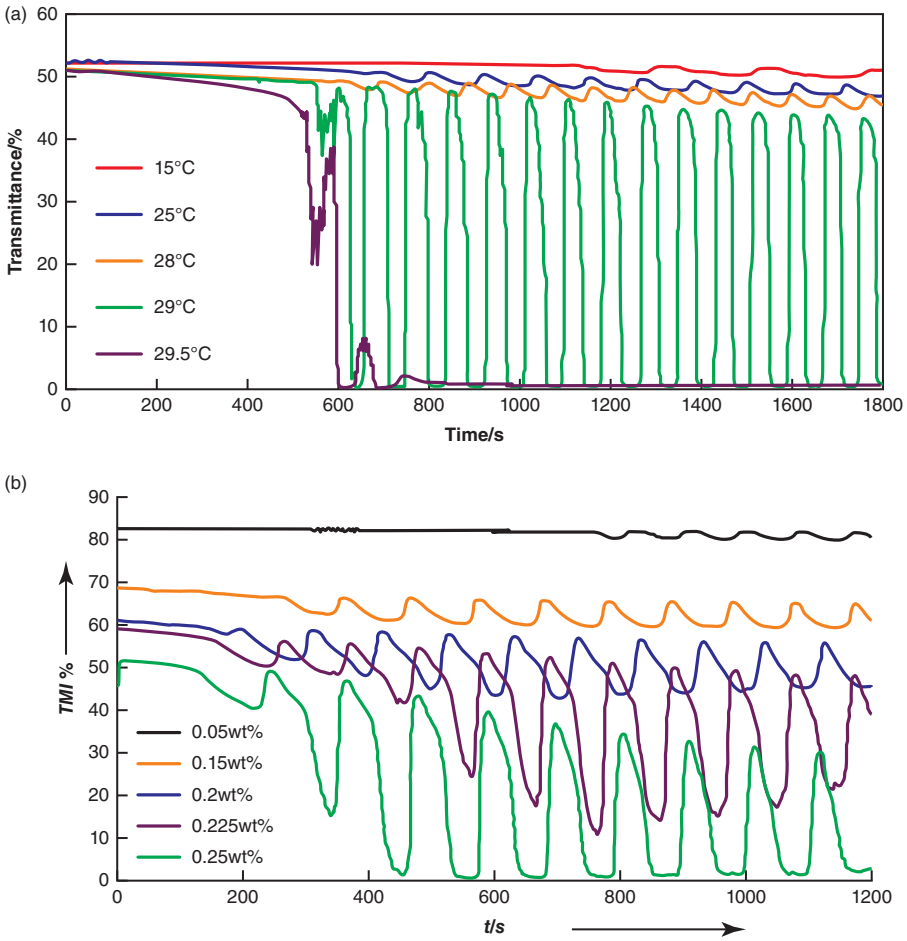


FIGURE 44.10 Profiles of cyclic optical transmittance of BIS cross-linked oscillating microgel dispersions. Profiles are measured at (a) different temperatures and (b) different microgel concentrations. [Reprinted with permission from Refs. 86 and 88. Copyright © 2008 Wiley-VCH. Copyright (2008) American Chemical Society.]

changes in the optical transmittance of dispersed microgels. The results are plotted in Fig. 44.10. The oscillation amplitudes in the microgel volume and optical transmittance are related, because the swelling determines the scattering intensity and the optical transmittance. Below the transition temperature (15–28°C; Fig. 44.10a), the oscillation amplitude of the optical transmittance slightly increases with increasing temperature, mainly because the hydrodynamic diameter shift between the Ru^{II} and Ru^{III} states increases, as shown in Fig. 44.9b,c.

Note that the oscillation amplitude of the redox potential in the bulk solution of the BZ reaction depends on the concentrations of initial substrates and the $Ru(bpy)_3$ catalyst [92]; thus, the $Ru(bpy)_3$ catalyst exists partially in the reduced Ru^{II} state and partially in the oxidized Ru^{III} state at the same time. Moreover, using isothermal titration calorimetry and ultrasensitive differential scanning calorimetry, one team of investigators [93] reported that less heat was released by the oscillating microgel system than by a bulk solution of the BZ reaction, because the chemical reaction in the former is restricted by the hydrogel network structure. Consequently, the DLS-derived results of Fig. 44.9 might overestimate the amplitude of the volume oscillation.

Although the overall BZ reaction involves more than 80 elementary reactions, understanding how the overall oscillation period P_{osc} is affected by the chemical reaction conditions is a worthwhile pursuit. Similar to the induction period mentioned above, the P_{osc} of the BZ reaction depends on the initial substrate concentrations, temperature, and stirring rate. Moreover, when oscillating microgels are involved, the P_{osc} should also be affected by metal–catalyst–immobilization. To investigate this effect, we compared the P_{osc} of microgel oscillations with those of the bulk solution of the BZ reaction. First, with the temperature fixed at 25°C, the dependence of P_{osc} on initial substrate concentration was determined. As shown in Fig. 44.11, the P_{osc} clearly differs between

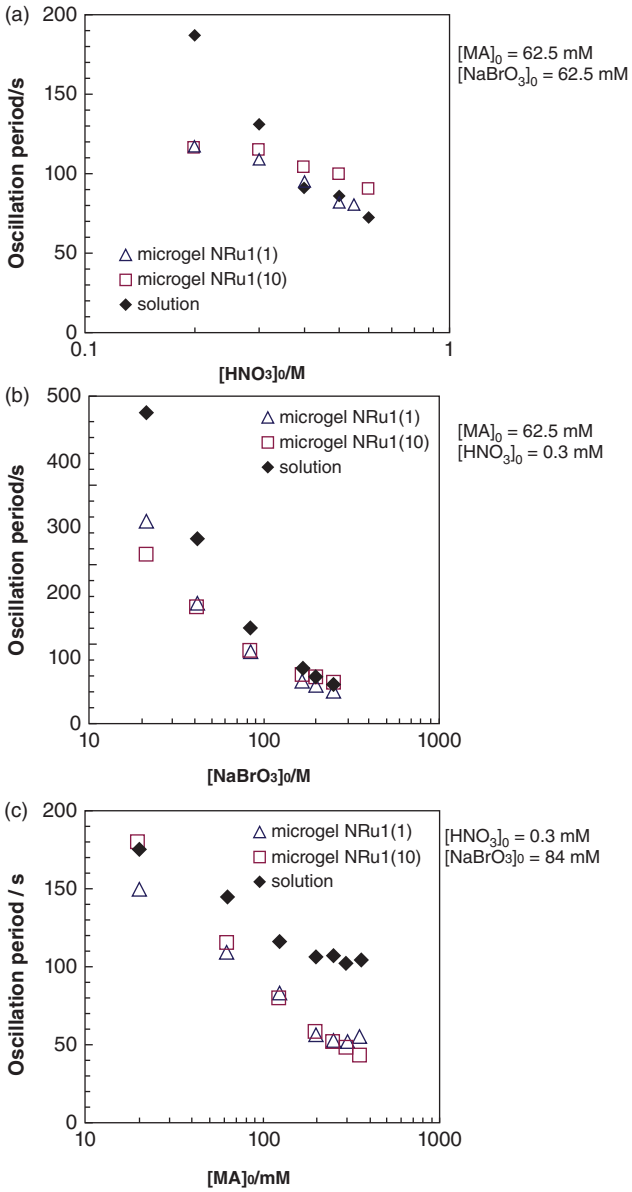


FIGURE 44.11 Effect of initial substrate concentration on oscillation period of the bulk solution system (black diamonds), 1 mol.% BIS cross-linked oscillating microgels (blue triangles), and 10 mol.% BIS cross-linked oscillating microgels (red squares). [Reprinted with permission from Ref. 91. Copyright (2008) American Chemical Society.]

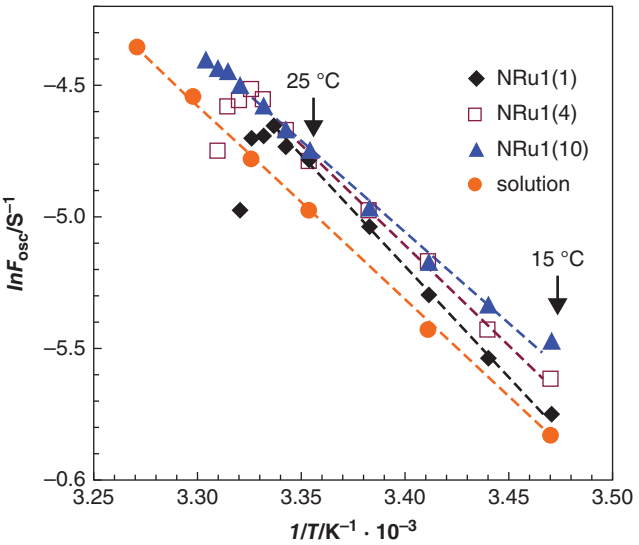


FIGURE 44.12 Arrhenius dependence of oscillation frequency (F_{osc}) of BIS cross-linked oscillating microgels: 1 mol.% (black diamonds), 4 mol.% (red squares), and 10 mol.% (blue triangles). Control measurements of the BZ reaction without microgels are also shown (orange circles). [Reprinted with permission from Ref. 88. Copyright (2008) American Chemical Society.]

the bulk solution and the microgel dispersion. In all cases, P_{osc} reduces as the initial substrate concentration increases. Unlike the situation in the bulk solution, the relationship between P_{osc} and substrate concentration in the dispersed oscillating microgels is strengthened for MA, but weakened for HNO_3 and $NaBrO_3$. Large differences in P_{osc} between the bulk solution and the oscillating microgels also appear at high $[MA]_0$ and low $[HNO_3]_0$ or $[NaBrO_3]$, but not at higher $[HNO_3]_0$ or $[NaBrO_3]_0$. Although the aforementioned results cover only a subset of the possible phenomena, they may be useful for qualitatively controlling the P_{osc}.

Next, we describe how the cross-link density of oscillating microgels alters the P_{osc}. For this purpose, we analyze three types of oscillating microgels with different cross-link densities. For convenience, the analyzed variable is the oscillation frequency, F_{osc} (= $1/P_{osc}$). As shown in Fig. 44.12, the F_{osc} of the bulk solution of the BZ reaction increases with increasing temperature according to Arrhenius' law [94,95]. Below the transition temperature, the oscillating microgels also follow the Arrhenius law [88]. In contrast, the F_{osc} decreases near the transition temperature, and the corresponding plots deviate from the Arrhenius equation. The reasons for this phenomenon will be explained later. The F_{osc} of the oscillating microgels apparently exceeds that of the bulk solution. Moreover, at low temperatures (e.g., 15°C), the F_{osc} increases with increasing cross-link density of the microgels, but remains almost unchanged near the transition temperature (around 25°C). This phenomenon reflects the thermoresponsive properties of oscillating microgels, specifically, at 15°C when all microgels are highly swollen, the mesh size of the microgel network structure may monotonically decrease as the BIS feed increases. In contrast, near the transition temperature, changes in BIS feed may scarcely alter the mesh size. Thus, the oscillation period of the microgels clearly depends on their cross-linked network structure. Notably, the network structure also changes during swelling/deswelling

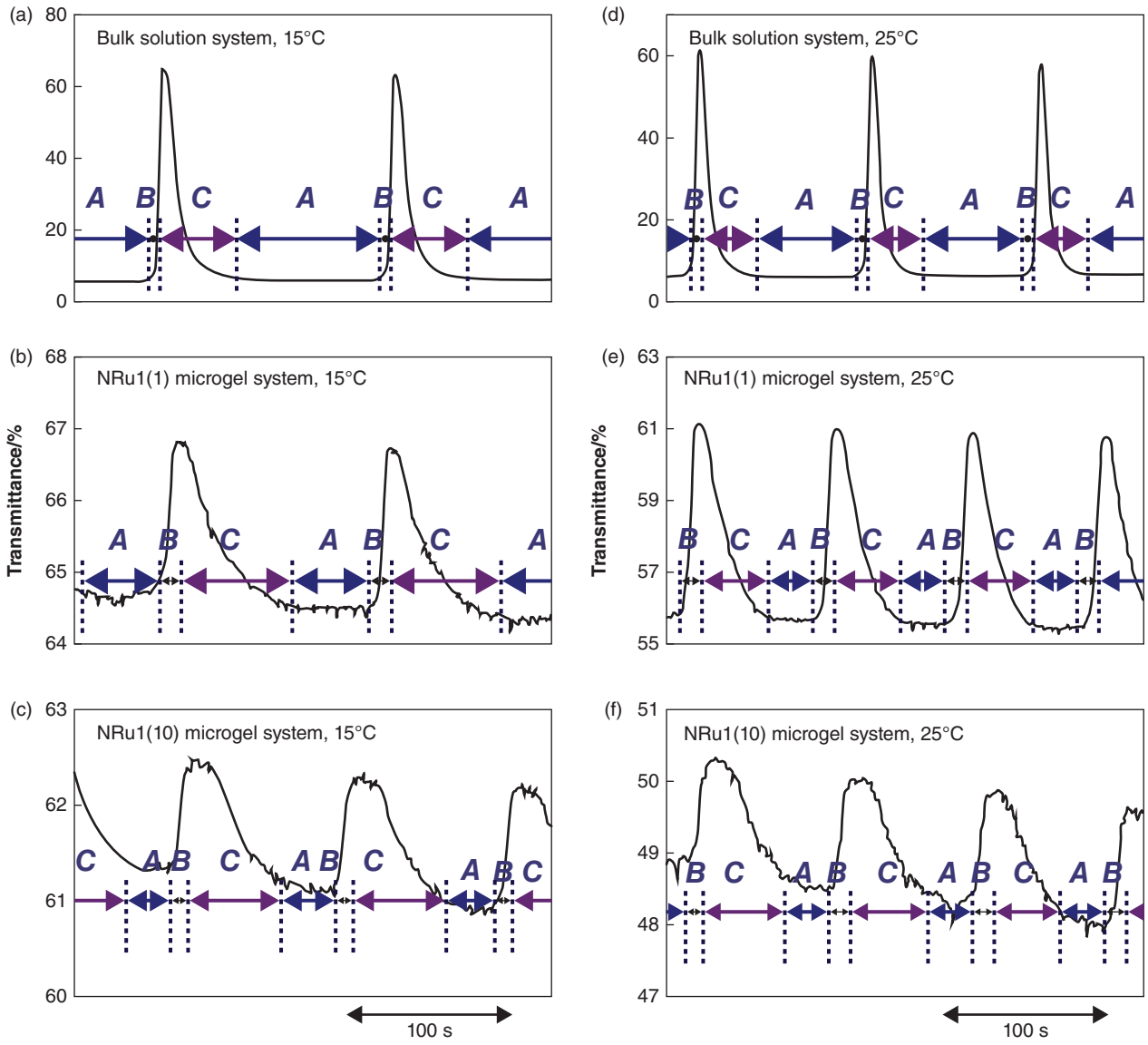


FIGURE 44.13 Typical oscillation waveforms of bulk solution (a,d), 1 mol.% BIS cross-linked oscillating microgels (b,e), and 10 mol.% BIS cross-linked oscillating microgels (c,f). The profiles were measured at 15°C (a–c) and 25°C (d–f). [Reprinted with permission from Ref. 88. Copyright (2008) American Chemical Society.]

volume oscillations of the microgels, suggesting that chemical changes respond to feedback from mechanical changes. Although this effect has yet to be clarified, the network structure undoubtedly plays an important role in controlling the F_{osc} of the oscillating microgels.

To better understand the mechanisms that alter the period of oscillating microgels, the waveforms observed in bulk solution were compared with those obtained from microgels. The oscillations were compared by dividing their waveforms according to the three main processes of the FKN mechanism: consumption of bromide ion (process A), autocatalytic reaction of bromous acid accompanied by catalyst oxidation (process B), and organic reaction accompanied by catalyst reduction (process C) [96, 97]. This division of the typical waveforms is depicted in Fig. 44.13. At a given temperature, the durations of processes B and C relative to the oscillation period (i.e., B/P_{osc}, and C/P_{osc}) are longer for the oscillating microgels than in bulk solution. In addition, at 15°C these ratios enlarge with increasing cross-link density of the oscillating microgels, but remain almost constant at 25°C. Since processes B and C involve catalytic reactions, these findings reflect the immobilization of the $Ru(bpy)_3$ catalyst in the microgels. For the same amount of catalyst, the rate of an immobilized catalytic reaction is lower than that of a

soluble catalytic reaction. In contrast, the A/P_{osc} values of the oscillating microgels are smaller than those in bulk solution, although the reason for the smaller values is unclear. The abovementioned pair of contrasting events alters the P_{osc} of the oscillating microgels. The waveforms of the volume oscillation and the bulk solution of the BZ reaction are also affected by initial substrate concentration [91]. In particular, the prolongation of process C imposed by the abovementioned cross-linking effect [88] reduces with increasing initial MA concentration, resulting in a different dependence for each substrate.

This section has described how the swelling/deswelling oscillation (i.e., volume oscillation) of oscillating microgels synchronizes with chemical reactions such as the BZ reaction. We now explore another oscillating behavior, namely, the flocculating/dispersing oscillation of microgels [86, 87]. This oscillatory behavior has been previously reported in a pH-oscillating system [85].

As shown in Fig. 44.10a, the oscillation amplitude of the optical transmittance increases with increasing temperature within the range 15–28°C [88]. This amplitude increase arises from the increased deviation in hydrodynamic diameter between the $Ru(bpy)_3^{2+}$ and $Ru(bpy)_3^{3+}$ states at constant temperature (Fig. 44.9). At 29°C, a dramatic change in amplitude and waveform appears, and oscillations disappear at 29.5°C. Considering the hydrodynamic diameters plotted in Fig. 44.9, these dramatic changes must be associated with colloidal stability differences between the $Ru(bpy)_3^{2+}$ and $Ru(bpy)_3^{3+}$ states. Under these conditions, the high salt concentration negates the electrostatic repulsion, and the microgels in the reduced $Ru(bpy)_3^{2+}$ state become flocculated. The microgels exist in a deswollen state and lack the repulsive interaction of steric hindrance that originates at the exterior of hydrated polymer chains.

Next, recognizing that colloidal stability is sensitive to microgel concentration, we investigated the effect of microgel concentration on the oscillations at constant temperature [86]. The results are plotted in Fig. 44.10b. From this figure, the optical transmittance apparently depends on microgel concentration. The amplitude and waveform of the optical transmittance dramatically change only at higher microgel concentrations, indicating that the microgels are repeatedly flocculated and redispersed under these conditions.

Moreover, the optical transmittance and redox potential of the microgel dispersion were measured simultaneously [88]. Here, increased redox potential implies increased concentration of oxidized $Ru(bpy)_3^{3+}$ catalyst. As shown in Fig. 44.14a, the transmittance curve overlaps the redox potential curve at low temperatures, indicating that the swelling/deswelling volume oscillation of the microgels is synchronized with the cyclic chemical reaction. In contrast, as shown in Fig. 44.14b,c, the transmittance curve deviates from the redox potential curve at higher temperatures, indicating a flocculating/dispersing oscillation of the microgels.

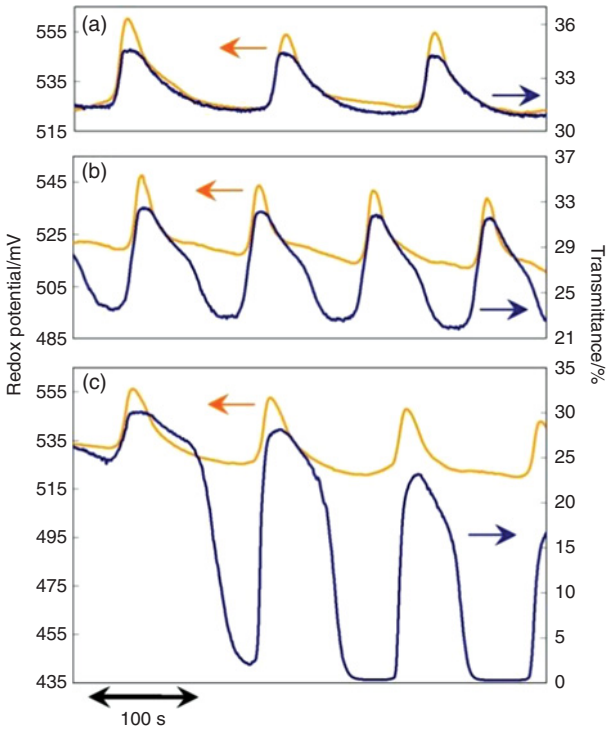


FIGURE 44.14 Simultaneous measurements of redox potential (orange) and transmittance (blue) of 1 mol.% BIS cross-linked oscillating microgel at different temperatures: (a) 25°C, (b) 27°C, and (c) 27.5°C. [Reprinted with permission from Ref. 88. Copyright (2008) American Chemical Society.]

Note that the transmittance decreases sharply when a high proportion of the catalyst exists in the reduced $Ru(bpy)_3^{2+}$ state, further indicating that the large decreases manifest from microgel flocculations. Here, the flocculations are redispersed because the microgel does not lie in a deep potential minimum; hence the flocculations are weak and reversible [98].

Furthermore, as shown in Fig. 44.15, the microgels oscillate in both volume and flocculation/dispersal behavior [87,99]. At low temperature (20°C), the waveform is shaped similar to that of typical BZ reactions detected by optical transmittance and redox potential changes. Thus, the oscillating viscosity in the microgel dispersion is due to swelling/deswelling oscillation of the microgels. As shown in Fig. 44.15a, the viscosity is high when the microgels exist in a swollen state at point (i) and low in the deswollen state at point (ii). In contrast, the waveform shape dramatically alters at higher temperature (23°C; Fig. 44.15b). Considering the abovementioned optical transmittance and redox potential data, the oscillating viscosity in the dispersion may be reasonably attributed to the flocculating/dispersing oscillations of the microgels. In this case, the smaller peak is attributed to a simple volume oscillation of each microgel from point (i) to point (ii) in Fig. 44.15b. The succeeding amplitude spike

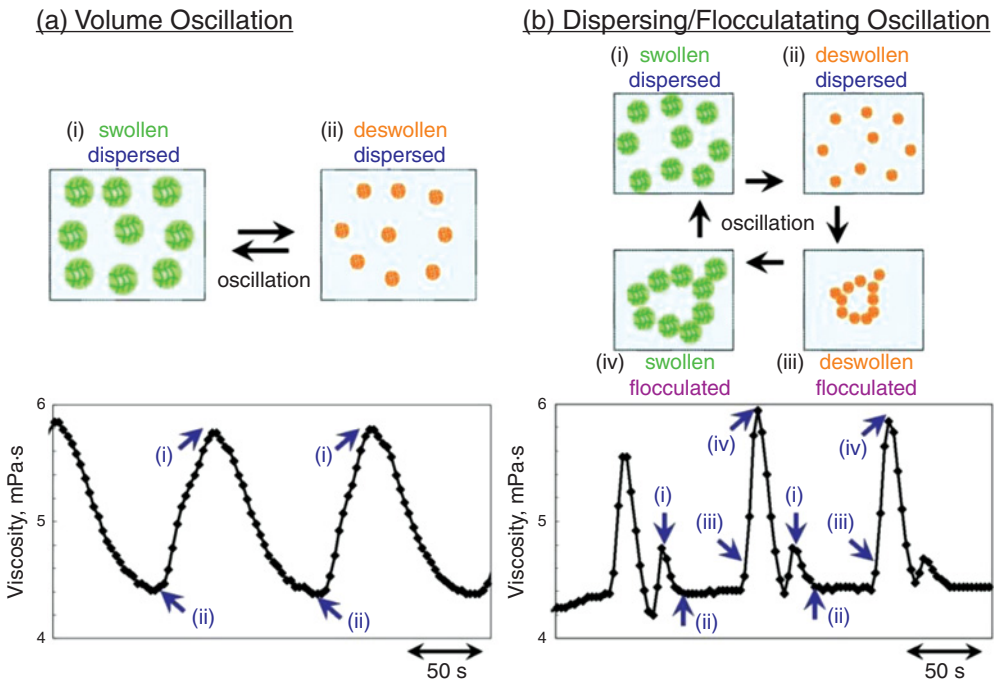


FIGURE 44.15 Profiles of cyclic viscosity in oscillating microgel dispersions: (a) swelling/deswelling (volume) oscillation of microgels at 20°C; (b) dispersing/flocculating oscillation of microgels at 23°C. [Reprinted with permission from Ref. 87. Copyright (2009) American Chemical Society.]

arises from flocculation of the microgels at point (iii), where the flocs become sufficiently large for detection by optical transmittance. Flocculation persists until colloidal stability is recovered through hydrating and swelling at point (iv). The viscosity of the dispersion is then decreased as the flocs redisperse. At minimum viscosity, redispersal may be complete. The swelling/deswelling cycle of the microgels then repeats. Consequently, the behavior of the flocculating/dispersing oscillation is better revealed by rheological measurements than by transmittance measurements [87]. Large amplitudes of viscosity oscillation have also followed the induction of large swelling/deswelling volume oscillations in microgels incorporating many $Ru(bpy)_3$ complexes [99].

More recently, we obtained high-amplitude swelling/deswelling oscillations by introducing a hierarchical structure into an artificial muscle constituting a high-volume fraction of swollen microgels [100]. The microgels used in this analysis were fabricated by copolymerizing NIPAm, $Ru(bpy)_3$, *N*-(3-aminopropyl) methacrylamide hydrochloride (APMA), and cross-linker by free-radical precipitation polymerization. Reversible high-amplitude oscillations were induced in the macrogel by dispersing/flocculating oscillations of the constituent microgels. Although microgel motions are restricted in macrogels, slight cross-linking in the macrogel should permit some movement. The amplitude of the macrogel is much larger than that of unstructured gel. We believe that the autonomously oscillating soft actuators prepared by this simple fabrication process are suitable for practical use in micropumps.

44.5 CONCLUDING REMARKS

This chapter has summarized the behaviors of stimulus-responsive microgels with particular focus on hybrid microgels, Janus microgels, and oscillating microgels. We consider that research into these emerging functional microgels has taken its initial steps. As fundamental research progresses and the technology develops, hydrogels will make valuable theoretical and practical contributions to colloid, polymer, and materials chemistry.

REFERENCES

[1] Nayak, S., Lee, H., Chmielewski, J., Lyon, L.A. (2004). *J. Am. Chem. Soc.* **126**, 10258–10259.

[2] Bae, Y., Jang, W.D., Nishiyama, N., Fukushima, S,; Kataoka, K. (2005). *Mol. Biosyst.* **1**, 242–250.

[3] Tamura, A., Oishi, M., Nagasaki, Y. (2009). *Biomacromolecules* **10**, 1818–1827.

[4] Guan, Y., Zhang, Y. (2011). *Soft Matt.* **7**, 6375–6384.

[5] Morris, G.E., Vincent, B., Snowden, M.J. (1997). *J. Colloid Interface Sci.* **190**, 198–205.

[6] Kawaguchi, H., Kisara, K., Takahashi, T., Achiha, K., Yasui, M., Fujimoto, K. (2000). *Macromol. Symp.* **151**, 591–598.

[7] Kim, J., Serpe, M.J., Lyon, L.A. (2005). *Angew. Chem. Int. Ed.* **44**, 1333–1336.

[8] Sorrell, C.D., Carter, M.C.D., Serpe, M.J. (2011). *Adv. Funct. Mater.* **21**, 425–433.

[9] Zhang, J., Xu, S., Kumacheva, E. (2004). *J. Am. Chem. Soc.* **126**, 7908–7914.

[10] Suzuki, D., Kawaguchi, H. (2005). *Langmuir* **21**, 8175–8179.

[11] Lu, Y., Mei, Y., Drechsler, M., Ballauff, M. (2006). *Angew. Chem. Int. Ed.* **45**, 813–816.

[12] Palioura, D., Armes, S.P., Anastasiadis, S.H., Vamvakaki, M. (2007). *Langmuir* **23**, 5761–5768.

[13] Weissman, J.M., Sunkara, H.B., Tse, A.S., Asher, S.A. (1996). *Science* **274**, 959–960.

[14] Hellweg, T., Dewhurst, C.D., Brúckner, E., Kratz, K., Eimer, W. (2000). *Colloid Polym. Sci.* **278**, 972–978.

[15] Lyon, L.A., Debord, J.D., Debord, S.B., Jones, C.D., McGrath, J.G., Serpe, M.J. (2004). *J. Phys. Chem. B* **108**, 19099–19108.

[16] Okubo, T., Suzuki, D., Yamagata, T., Katsuno, A., Sakurai, M., Kimura, H., Tsuchida, A. (2011). *Colloid Polym. Sci.* **289**, 291–299

[17] Fujii, S., Read, E.S., Binks, B.P., Armes, S.P. (2005). *Adv. Mater.* **17**, 1014–1018.

[18] Brugger, B., Richtering, W. (2008). *Langmuir* **24**, 7769–7777.

[19] Ngai, T., Behrens, S.H., Auweter, H. (2005). *Chem. Commun.* **3**, 331–333.

[20] Heskins, M., Guillet, J.E. (1968). *J. Macromol. Sci. Chem.* **A2**, 1441–1455.

[21] Schild, H.G. (1992). *Progress Polym. Sci.* **17**, 163–249.

[22] Wu, C., Zhou, S. (1997). *Macromolecules* **30**, 574–576.

[23] Kawaguchi, H., Yamada, Y., Kataoka, S., Morita, Y., Ohtsuka, Y. (1991). *Polym. J.* **23**, 955–962.

[24] Kawaguchi, H., Fujimoto, K., Saito, M., Kawasaki, T., Ohtsuka, Y. (1993). *Polym. Int.* **30**, 225–232.

[25] Pelton, R.H., Chibante, P. (1986). *Colloids Surf.* **20**, 247–256.

[26] Meng, Z., Smith, M.H., Lyon, L.A. (2009). *Colloid Polym. Sci.* **287**, 277–285.

[27] Guillermo, A., Cohen Addad, J.P., Bazile, J.P., Duracher, D., Elaissari, A., Pichot, C. (2000). *J. Polym. Sci. B: Polym. Phys.* **38**, 889–897.

[28] Suzuki, D., Horigome, K. (2013). *J. Phys. Chem. B* **117**, 9073−9082.

[29] Wu, X., Pelton, R.H., Hamielec, A.E., Woods, D.R., McPhee, W. (1994). *Colloid Polym. Sci.* **272**, 467–477.

[30] Dingenouts, N., Seelenmeyer, S., Deike, I., Rosenfeldt, S., Ballau, M., Lindner, P., Narayanan, T. (2001). *Phys. Chem. Chem. Phys.* **3**, 1169–1174.

[31] Xiao, X.C., Chu, L.Y., Chen, W.M., Wang, S., Xie, R. (2004). *Langmuir* **20**, 5247–5253.

[32] Zha, L., Zhang, Y., Yang, W., Fu, S. (2002). *Adv. Mater.* **14**, 1090–1092.

[33] Kim, J.H., Lee, T.R. (2004). *Chem. Mater.* **16**, 3647–3651.

[34] Tsuji, S., Kawaguchi, H. (2004). *Langmuir* **20**, 2449–2455.

[35] Jones, C D., Lyon, L.A. (2000). *Macromolecules* **33**, 8301–8306.

[36] Nayak, S., Gan, D., Serpe, M.J., Lyon, L.A. (2005). *Small* **1**, 416–421.

[37] Nayak, S., Lyon, L.A. (2004). *Angew. Chem. Int. Ed.* **43**, 6706–6709.

[38] Jones, C.D., Lyon, L.A. (2003). *Macromolecules* **36**, 1988–1993.

[39] Berndt, I., Richtering, W. (2003). *Macromolecules* **36**, 8780–8785.

[40] Zeiser, M., Freudensprung, I., Hellweg, T. (2012). *Polymer* **53**, 6096–6101.

[41] Suzuki, D., Yoshida, R. (2010). *Polym. J.* **42**, 501–508.

[42] Suzuki, D., Yamakawa, S. (2012). *Langmuir* **28**, 10629–10634.

[43] Suzuki, D., Yamagata, T., Murai, M. (2013). *Langmuir* **29**, 10579–10585.

[44] Bradley, M., Bruno, N., Vincent, B. (2005). *Langmuir* **21**, 2750–2753.

[45] Schrinner, M., Ballauff, M., Talmon, Y., Kauffman, Y., Thun, J., Möller, M., Breu, J. (2009). *Science* **323**, 617–620.

[46] Suzuki, D., Horigome, K. (2011). *Langmuir* **27**, 12368–12374.

[47] Tagit, O., Tomczak, N., Vancso, G.J. (2008). *Small* **4**, 119–126.

[48] Wiedemair, J., Serpe, M.J., Kim, J., Masson, J.F., Lyon, L.A., Mizaikoff, B., Kranz, C. (2007). *Langmuir* **23**, 130–137.

[49] Bolisetty, S., Hoffrnann, M., Lekkala, S., Hellweg, T., Ballauff, M., Harnau, L. (2009). *Macromolecules* **42**, 1264–1269.

[50] Crowther, H., Saunders, B.R., Mears, S.J., Cosgrove, T., Vincent, B., King, S.M., Yu, G.E. (1999). *Colloids Surf. A* **152**, 327–333.

[51] Dingenouts, N., Nordhausen, C., Ballauff, M. (1998). *Ber. Bunsenges. Phys. Chem.* **102**, 1594–1596.

[52] Seelenmeyer, S., Deike, I., Rosenfeldt, S., Norhausen, C., Dingenouts, N., Ballauff, M., Narayanan, T., Lindner, P. (2001). *J. Chem. Phys.* **114**, 10471–10478.

[53] Mears, S.J., Deng, Y., Cosgrove, T., Pelton, R. (1997). *Langmuir* **13**, 1901–1906.

[54] Kratz, K., Lapp, A., Eimer, W., Hellweg, T. (2002). *Colloids Surf. A* **197**, 55–67.

[55] Stieger, M., Ped ersen, J.S., Lindner, P., Richtering, W. (2004). *Langmuir* **20**, 7283–7292.

[56] Rasmusson, M., Vincent, B., Marston, N. (2000). *Colloid Polym. Sci.* **278**, 253–258.

[57] Garcia-Salinas, M.J., Romero-Cano, M.S., de las Nieves, F.J. (2001). *J. Colloid Interface Sci.* **241**, 280–285.

[58] Daly, E., Saunders, B.R. (2000). *Phys. Chem. Chem. Phys.* **2**, 3187–3193.

[59] Hoare, T., Pelton, R. (2005). *Polymer* **46**, 1139–1150.

[60] Ohshima, H., Kondo, T. (1989). *J. Colloid Interface Sci.* **130**, 281–282.

[61] Ohshima, H., Makino, K., Kato, T., Fujimoto, K., Kondo, T., Kawaguchi, H. (1993). *J. Colloid Interface Sci.* **159**, 512–514.

[62] Makino, K., Yamamoto, S., Fujimoto, K., Kawaguchi, H., Ohshima, H. (1994). *J. Colloid Interface Sci.* **166**, 251–258.

[63] Zhang, J., Xu, S., Kumacheva, E. (2005). *Adv. Mater.* **17**, 2336–2340.

[64] Lu, Y., Ballauff, M. (2011). *Progress Polym. Sci.* **36**, 767–792.

[65] Wu, S., Dzubiella, J., Kaiser, J., Drechsler, M., Guo, X., Ballauff, M., Lu, Y. (2012). *Angew. Chem. Int. Ed.* **51**, 2229–2233.

[66] Suzuki, D., Kawaguchi, H. (2005). *Langmuir* **21**, 12016–12024.

[67] Suzuki, D., Kawaguchi, H. (2006). *Langmuir* **22**, 3818–3822.

[68] Suzuki, D., Kawaguchi, H. (2006). *Colloid Polym. Sci.* **284**, 1443–1451.

[69] Suzuki, D., McGrath, J.G., Kawaguchi, H., Lyon, L.A. (2007). *J. Phys. Chem. C* **111**, 5667–5672.

[70] Karg, M., Pastoriza-Santos, I., Perez-Juste, J., Hellweg, T., Liz-Marzan, L.M. (2007). *Small* **3**, 1222–1229.

[71] Contreras-Cáceres, R., Pacifico, J., Pastoriza-Santos, I., Pérez-Juste, J., Fernández-Barbero, A., Liz-Marzán, L.M. (2009). *Adv. Funct. Mater.* **19**, 3070–3076.

[72] Karg, M., Hellweg, T. (2009). *Curr. Opin. Colloid Interface Sci.* **14**, 438–450.

[73] Karg, M., Hellweg, T., Mulvaney, P. (2011). *Adv. Funct. Mater.* **21**, 4668–4676.

[74] Akamatsu, K., Shimada, M., Tsuruoka, T., Nawafune, H., Fujii, S., Nakamura, Y. (2010). *Langmuir* **26**, 1254–1259.

[75] Biffis, A., Cunial, S., Spontoni, P., Prati, L. (2007). *J. Catal.* **251**, 1–6.

[76] Wunder, S., Polzer, F., Lu, Y., Yu, M., Ballauff, M. (2010). *J. Phys. Chem. C* **114**, 8814–8820.

[77] Wunder, S., Lu, Y., Abrecht, M., Ballauff, M. (2011). *ACS Catal.* **1**, 908–916.

[78] Hain, J., Schrinner, M., Lu, Y., Pich, A. (2008). *Small* **4**, 2016–2024.

[79] Okeyoshi, K., Suzuki, D., Kishimura, A., Yoshida, R. (2011). *Small* **7**, 311–315.

[80] Okeyoshi, K., Suzuki, D., Yoshida, R. (2012). *Langmuir* **28**, 1539–1544.

[81] Perro, A., Reculusa, S., Ravaine, S., Bourgeat-Lamic, E., Duguet, E. (2005). *J. Mater. Chem.* **15**, 3745–3760.

[82] Walther, A., Müller, A.H.E. (2013). *Chem. Rev.* **113**, 5194–5261.

[83] Suzuki, D., Tsuji, S., Kawaguchi, H. (2007). *J. Am. Chem. Soc.* **129**, 8088–8089.

[84] Umeda, Y., Kobayashi, T., Hirai, T., Suzuki, D. (2011). *Colloid Polym. Sci.* **289**, 729–737.

[85] Varga, I., Szalai, I., Mészaros, R., Gilányi, T. (2006). *J. Phys. Chem. B* **110**, 20297–20301.

[86] Suzuki, D., Sakai, T., Yoshida, R. (2008). *Angew. Chem. Int. Ed.* **47**, 917–920.

[87] Suzuki, D., Taniguchi, H., Yoshida, R. (2009). *J. Am. Chem. Soc.* **131**, 12058–12059.

[88] Suzuki, D., Yoshida, R. (2008). *Macromolecules* **41**, 5830–5838.

[89] Field, R.J., Burger, M. (1985). *Oscillations and Traveling Waves in Chemical Systems*. Wiley, New York.

[90] Cadena, A., Pérez, N., Ágreda, J.A., Barragán, D. (2005). *J. Braz. Chem. Soc.* **16**, 214–219.

[91] Suzuki, D., Yoshida, R. (2008). *J. Phys. Chem. B* **40**, 12618–12624.

[92] Yoshida, R., Tanaka, M., Onodera, S., Yamaguchi, T., Kokufuta, E. (2000). *J. Phys. Chem. A* **104**, 7549–7555.

[93] Zhao, F., Ding, Y., Lu, Y., Liu, X., Zhang, G. (2009). *J. Phys. Chem. B* **113**, 6661–6665.

[94] Ruoff, P. (1995). *Physica D* **84**, 204–211.

[95] Nagy, G., Körös, E., Oftedal, N., Tjelflaat, K., Ruoff, P. (1996). *Chem. Phys. Lett.* **250**, 255–260.

[96] Field, R.J., Körös, E., Noyes, R.M. (1972). *J. Am. Chem. Soc.* **94**, 8649–8664.

[97] Field, R.J., Noyes, R.M. (1974). *J. Chem. Phys.* **60**, 1877–1884.

[98] Rasmusson, M., Routh, A., Vincent, B. (2004). *Langmuir* **20**, 3536–3542.

[99] Taniguchi, H., Suzuki, D., Yoshida, R. (2010). *J. Phys. Chem. B* **114**, 2405–2410.

[100] Suzuki, D., Kobayashi, T., Yoshida, R., Hirai, T. (2012). *Soft Matt.* **8**, 11447–11449.

45

HYDROPHILIC–LIPOPHILIC BALANCE (HLB): CLASSICAL INDEXATION AND NOVEL INDEXATION OF SURFACTANT

YUJI YAMASHITA AND KAZUTAMI SAKAMOTO

Department of Pharmaceutical and Life Sciences, Faculty of Pharmacy, Chiba Institute of Science, Choshi, Chiba 288-0025, Japan

45.1 INTRODUCTION

In the last few decades, many polyoxyethylene (POE)-type surfactants have been investigated for their fundamental properties such as melting point and solubility in water or oil, and their practical properties such as clouding temperature, solubilization, liquid crystal formation, and emulsification. These properties were studied systematically and classified with respect to the hydrophilic–lipophilic balance (HLB) of the surfactant. Development of this "HLB concept" would be one of the greatest contributions possible with the advancement of practical usage of POE surfactants in the industrial fields. Table 45.1 lists applications corresponding to the HLB number range.

The HLB number is an index of the affinity of a surfactant toward a solvent; for example, a high HLB number indicates that the surfactant is more attracted to water (is water-soluble). It is well known as a practical example of the HLB number that the type and appropriate amount of POE surfactant can be estimated to emulsify a kind of oil-in-water (o/w) solution. In addition, the HLB number shows a good correlation with the clouding temperature and phase inversion temperature (PIT), and has provided significant benefit to the development of advanced emulsification technology. The HLB number scale, introduced by Griffin, was the first successful attempt at quantitative characterization of the POE surfactants, while classification of surfactants by HLB number in some instances does not help one to predict the optimum emalsification.

Initially, Griffin established the HLB number by his extensive experiments using POE surfactants; therefore, HLB calculation cannot be assumed to work for general surfactants other than those of the POE type. It is understood that the POE chain has a unique interaction with water molecules, characterized by a decrease in temperature with conformational change and dehydration. Furthermore, use of the HLB number in practical applications can be fraught with difficulty as there are no accountable adjustments of POE–water interactions relating to the effects of additives, temperature, self-organization, and so on in the HLB number calculated by the equations provided. The HLB number and its calculation are certainly convenient and applicable to mixture properties exclusively for POE surfactants but do not always provide a correct HLB value for non-POE surfactants. Consequently, a surfactant suitable for application cannot become widespread in the marketplace even if it has excellent properties.

From this perspective, we attempted to review the classical HLB number and the substantial issues involving basic properties and applications. By reconsidering the HLB number, we introduced our most recent studies on the hydrophilic–lipophilic nature of the surfactant.

45.2 CALCULATIONS OF HLB NUMBER

Various equations used to calculate the HLB number have been proposed over the past 50 years. The first and still most commonly used equation was proposed by Griffin

Encyclopedia of Biocolloid and Biointerface Science, Volume 1, First Edition. Edited by Hiroyuki Ohshima.
© 2016 John Wiley & Sons, Inc. Published 2016 by John Wiley & Sons, Inc.

TABLE 45.1 HLB Numbers and Corresponding Applications

HLB number range	Corresponding application
1.5–3	Antifoaming agent
1–4	Emulsifier for w/o emulsions
6–8	Wetting agent
10–13	Emulsifier for o/w emulsions
13–15	Detergent
15–18	Solubilizer

[1]. This equation expresses the structural balance between hydrophilic and lipophilic groups in a surfactant molecule as numeric index from 0 to 40 on the basis of emulsification examination using trial POE surfactants. This equations is useful for POE surfactants; specifically, the HLB numbers of the POE alkyl ethers (C_mEO_n) are given by the following equation, where the HLB number equals the weight fraction of oxyethylene (POE) moiety in the molecule:

$$\text{HLB} = \frac{\text{POE(wt\%)}}{5} \tag{45.1}$$

As mentioned above, these numbers are obtained from empirically emulsifying examinations, and thus this equation can be utilized as a reliable and convenient tool for industrial applications. On the other hand, Griffin also obtained another equation to calculate the HLB number for fatty-acid esters chemically bonded with polyalchohols as follows [2]

$$\text{HLB} = 20 \times \left(1 - \frac{S}{A}\right) \tag{45.2}$$

where S and A are the saponification and acid numbers of the ester, respectively. The HLB number given to polyglycerol fatty-acid ester as a representative for this equation frequently shows different solution properties from C_mEO_n, even though their HLB numbers appeared to be equivalent. So that it is difficult to apply HLB numbers for that mixed-surfactant system as their values are assigned from different equations.

Davies' method [3, 4], which is one of the traditional methods used to calculate HLB, is based on the unit value given to the each functional group as either a hydrophilic or a hydrophobic element, and HLB of the molecule can be calculated as a summation of whole unit values:

$$\text{HLB} = 7 + \sum(\text{unit value of hydrophilic group}) + \sum(\text{unit value of lipophilic group}) \tag{45.3}$$

The representative unit values are shown in Table 45.2. This versatile equation is able to calculate the HLB number even for ionic surfactants, although the resulting HLB value might not predict the properties of the surfactant solution.

TABLE 45.2 Representative Unit Values Used in Davies Equation

Hydrophilic group	Unit value	Lipophilic group	Unit value
$-SO_4Na$	38.7	CH_3-	−0.475
–COONa	19.1	$-CH_2-$	−0.475
$-(CH_2-CH_2-O)-$	0.33	–	–
–OH	1.9	–	–

Another important equation commonly used for HLB calculation is based on the *organic conceptual diagram* [5]. Initially, the primary objective of this method was to identify the complex properties of organic compounds via intermolecular interactions. The conceptual diagram consists mainly of an *organic value* (OV) and an *inorganic value* (IV), which respectively relate to the intermolecular force generated by van der Waals interactions and electrostatic interactions, and the combination of two values corresponds to the HLB number:

$$\text{HLB} = \frac{\Sigma\,\text{IV}}{\Sigma\,\text{OV}} \times 10 \tag{45.4}$$

The representative organic and inorganic values are shown in Table 45.3.

Let us compare the HLB numbers of $C_{12}EO_n$ calculated by Eqs. (45.1), (45.3), and (45.4). Figure 45.1 shows the change in HLB number as a function of the EO chain length (n). As expected, the HLB number monotonically increases with n, suggesting that the hydrophilicity of $C_{12}EO_n$ increases. However, there are discrepancies of HLB values between equations which disperse further by increasing EO numbers. Namely for $C_{12}EO_5$, the Griffin's HLB value is 10.8, whereas the Davies's equation (3) gives 4.9 which underestimates in comparison to the Griffin's equation. On the other hand, the HLB value calculated from the organic conceptual diagram's equation (4) is 21.1 contrastively overestimating. No matter what correct HLB value is, it is a fact that these different equations resulted to the different answers. This is a crucial problem when industrial applications are exercised, because more or less we rely on the HLB number of the surfactant regardless of their origin.

TABLE 45.3 Representative IV and OV Used in Organic Conceptual Diagram [6]

Functional group	IV	OV
C	0	20
$-(CH_2-CH_2-O)-$	60	−10
–OH	100	0
–O–	20	0
–COOH	150	0
$-NH_2$	70	0

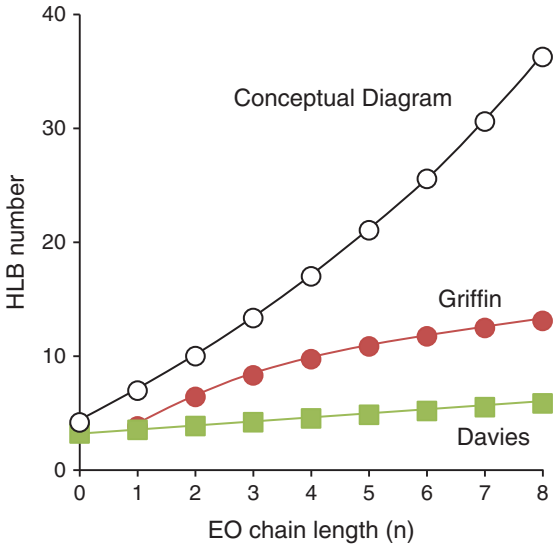


FIGURE 45.1 Comparison of HLB numbers calculated by Eqs. (45.1), (45.3), and (45.4). The HLB number is plotted agains the EO chain length (n) for $C_{12}EO_n$.

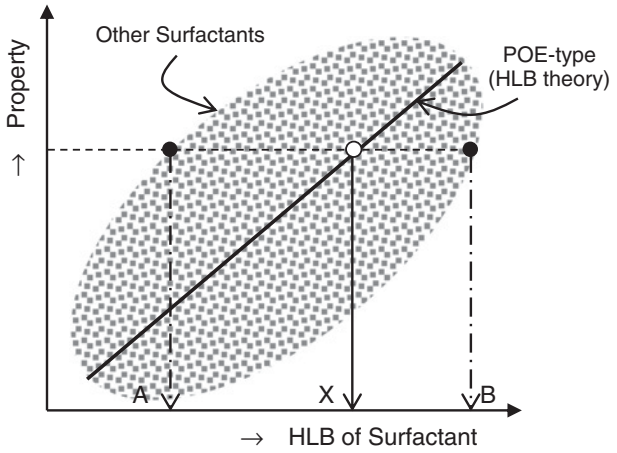


FIGURE 45.2 Correlation diagram of HLB number and property of surfactant. POE-type surfactants have mutual linear relationships, while the ellipsoidal region corresponds to the relationship with the other surfactants. Even if a specific property is required, several surfactants can be adapted (A or B and so on).

45.3 PRACTICAL SIDE OF HLB THEORY

Despite the recent market trend favoring ecofriendly (environmentally friendly) surfactants to replace petroleum-derived materials, POE surfactants are still predominant. One reason is that there is no sufficiently accurate index (corresponding to the HLB number for POE surfactants) to define the intrinsic properties of prospective surfactants, and therefore it should be difficult to obtain the intended properties and state of the solution. Careful thought and constructive examination will be needed to fill this gap. As an example, there is an interesting phenomenon in which polyglycerol fatty-acid esters in diluted solutions show a specific clouding point (CP) within the limited range of hydrophilic–lipophilic balance, which is incompatible with POE surfactants [7]. Furthermore, there have been two reports of phase inversion temperature (PIT) found in a polyglycerol-type surfactant–w/o ternary system, where the HLB of the polyglycerol-type surfactant was tunable by temperature [8, 9]. This implies that polyglycerol-type surfactants possess similar basic properties such as CP and PIT but differ from POE surfactants in this way. In summary, the HLB concept was established for POE surfactants that function within the family of POE structures, but there must be a way to correlate the HLB concept with the surfactants of different chemical species in order to compare or combine functions altogether.

Figure 45.2 shows a conceptual representation of the HLB concept. The horizontal axis (X; abscissa) represents the HLB number of a surfactant and the vertical one (Y; ordinate) represents a property of the surfactant solution such as clouding point, phase inversion temperature, phase state, and so on. The proportional line in the figure represents a relationship between Y and X for POE surfactants. This line can enable one to predict properties of the POE surfactant solution if the respective HLB values are given. On the other hand, for most (non-POE) surfactants, HLB numbers corresponding to the specific properties of their solutions deviate from the pattern shown as A, B, and so on in Fig. 45.2. Thus it would be difficult to predict the properties on the basis of the HLB number. In such cases, to obtain the desired property of the surfactant solution, one could choose a specific surfactant from among the POE-type surfactants (HLB=X in Fig. 45.2) and still have several choices for the other surfactants (HLB=A or B or another option). Although conceptually explained here, the phrase "HLB dependence" possibly fails to adequately assess the HLB aspect in order to utilize the surfactant in developing a real formulation.

45.4 EVALUATION OF HYDROPHILICITY AND LIPOPHILICITY

A surfactant consists of hydrophilic and lipophilic groups that are covalently bonded. Therefore it is conceivable that using a single method might not ensure accurate characterization of the nature of every functional group. Chromatography has been applied for evaluation of the surfactant, and there have been many studies on the polarity [10–12] and hydrophilicity–lipophilicity [13] of surfactants using reversed-phase chromatography. However, this method was unable to establish a practical index because of the limited number of surfactants used, as this was a labor-intensive and time-consuming task. However, we have proposed a novel

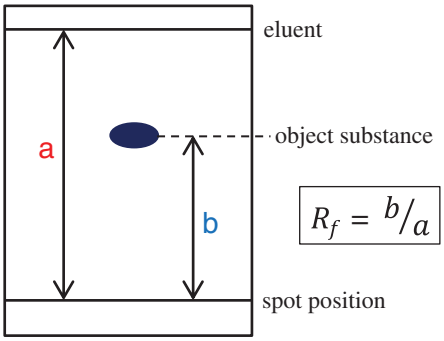


FIGURE 45.3 R_f measurement using TLC plate.

method using thin-layer chromatography (TLC), and systematically evaluated ionic and nonionic surfactants [14]. In addition, we ensured that this TLC method was consistent with the HPLC method. Another team of investigators [15] examined our TLC method for POE alkyl ethers and confirmed it to be compatible with the calculated HLB numbers of these surfactants.

On the basis of these studies, we have attempted to develop this TLC method theoretically. The originality and ingenuity in our study have enabled us to use two TLC plates with different polarities, normal and reverse phases, to obtain the individual R_f values as seen in Fig. 45.3. The intrinsic capacity constant (k) of a surfactant is calculated by use of the following equation:.

$$k = \frac{1}{R_f} - 1 \tag{45.5}$$

Thus, each k value is obtained for the normal and reverse phases, and their ratio (k_N/k_R : k_N for normal phase, k_R for reverse phase) is regarded as a *correlation index of hydrophilicity–lipophilicity*. The selection and combinatorial approach of the TLC plate (stationary phase) and the mobile phase lead to a comprehensive index that includes contributions of every functional group of the surfactant molecule partitioning in the mobile phase and interacting with the stationary phase. By using a given eluent as the mobile phase, in addition, we can estimate the effect of solvation of the object substance. Eventually, the following new index, *integrated surfactant potency* (ISP), representing surfactant properties, will be introduced as functions of k_N and k_R:

$$\text{ISP} = f\left(\frac{k_N}{k_R}\right) \tag{45.6}$$

This expression seems to be similar to the HLB calculation using the organic conceptual diagram [5], whereas our proposed method enables the empirical analysis of a substance itself.

TABLE 45.4 HLB Numbers of Various Lauroyl Amino Acids

Amino Group	Abbre.	HLB (Davies)
Glycine	L-Gly	12.5
Alanine	L-Ala	11.7
Vaine	L-Val	10.6
Leucine	L-Leu	10
Isoleucine	L-lle	10
Phenylalanine	L-Phe	8.7
Tryptophan	L-Trp	9.6
Serine	L-Ser	15
Proline	L-Pro	10.6
Aspartic acid	L-Asp	15.6
Glutamic acid	L-Glu	14.7

45.5 TLC EVALUATION OF AMINO ACID-DERIVED SURFACTANTS

To confirm the validity of this TLC method, the new index, k_N/k_R, was examined using the amino acid–derived surfactants in comparison to the HLB number calculated from Davies' theory [Eq. (45.3)]. The surfactants used consist of lauroyl (C_{12}) group as lipohilic group and different kinds of amino acids as hydrophilic group (Table 45.4), and the TLC measurements were carried out at room temperature using a methanol/water mixture [80/20 (v/v)] as eluent.

The hydrophilicity of the surfactant is remarkably sensitive to the type of amino acid used, resulting in the different HLB numbers as seen in Table 45.4. The hydrophilic–lipophilic property of the surfactant is well defined by Davies' theory for the homolog of the amino acid surfactants. Figure 45.4 shows a plot of k_N/k_R against the HLB number, where the k_N/k_R tends to increase with higher HLB numbers.

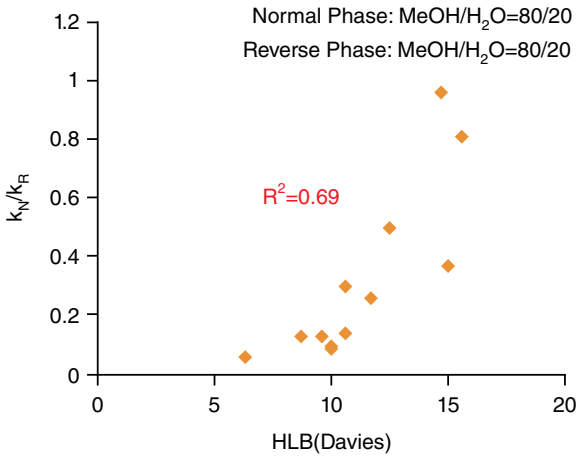


FIGURE 45.4 Relationship between HLB number calculated by Davies' theory [Eq. (45.3)] and the empirical new index, k_N/k_R. The eluent is a methanol/water mixture (80/20 in volume) for both TLC plates.

The correlation coefficient is 0.69, indicating a fair correlation. Although this evaluation system was not sufficiently verified in terms of the eluent, stationary-phase dissociation of ionic amino acid moieties, this TLC method can be a useful tool in determining the surfactant property, and further development must be done to establish as a novel indexation system.

45.6 CONCLUSIONS

In this chapter, we reviewed the classical HLB number theory and its calculations, and pointed out the problems that might be encountered in real manufacturing processing. In particular, the different equations lead to different HLB numbers, which must place the desired properties of the formulation at risk. To resolve such an unnoticed or overlooked misfit between the HLB number and the solution properties, and applications such as emulsification, a new method has been proposed by using the chromatography technique. Instead of the HLB number, we proposed an original and useful index, termed *integrated surfactant potency* (ISP). The appropriate formula of ISP is being investigated in detail and will be standardized for all surfactants by modifying the eluent and the stationary phase. In addition, ISP will potentially be able to predict properties of the surfactant solution such as critical micellar concentration (cmc), clouding temperature, and liquid crystal structures associated with the hydrophilic–lipophilic balance of the surfactant. It is our objective to establish this TLC method to be utilized in many industrial fields to offer solutions with proper selection of surfactants.

REFERENCES

[1] Griffin, W.C. (1949). *J. Soc. Cosmet. Chem.* **1**, 311.

[2] Griffin, W.C. (1954). *J. Soc. Cosmet. Chem.* **5**, 249.

[3] Davies, J.T. (1957). *Proc. Int. Congress Surface Activity*, 2nd ed., London, Vol. 1, p. 426.

[4] Davies, J.T., Rideal, E.K. (1961). *Interfacial Phenomena.* Academic Press, New York, p. 371.

[5] Suzuki, H. (1990). *Interface and Surface Active Agent*, Sangyotosho, p. 38.

[6] Nihon Emulsion Co., Ltd., *Formulation Design with Organic Conceptual Diagram*, p. 16 (http://www.ihon-emulsion.co.jp/pdf/ocdbook_e.pdf).

[7] Kunieda, H. et al. (2002). *J. Colloid Interface Sci.* **245**(2), 365.

[8] Kunieda, H. et al. (2002). *J. Oleo Sci.* **51**(6), 379.

[9] Sagitani, H., et al. (1989). *J. Am. Oil Chem. Soc.* **66**(1), 146.

[10] Nace, V.M., et al. (1995). *J. Am. Oil Chem. Soc.* **72**, 89.

[11] Trapani, G., et al. (1995). *Int. J. Pharm.* **116**(1), 95.

[12] Plaza, M., et al. (1998). *Colloids Surf. A* **137**, 287.

[13] Hahn, L., et al. (1989). *Tenside Surf. Deterg.* **26**(3), 192.

[14] Sakamoto, K. (1986). *Society of Cosmetic Chemists, Proc. Annual Scientific Meeting*, Dec. 4–5.

[15] Solans, C., et al. (2002). *Colloid Surf. A; Physicochem. Eng. Aspects* **189**, 85.

46

INSULIN FIBRILLATION AND ROLE OF PEPTIDES AND SMALL MOLECULES IN ITS INHIBITION PROCESS

VICTOR BANERJEE AND K.P. DAS

Department of Chemistry, Laboratory of Protein Chemistry, Bose Institute, Kolkata, West Bengal, India

46.1 INTRODUCTION

46.1.1 Protein Fibrillation

Proteins are the key members of complex molecular networks of the living organism, controlling the processes taking place in the cell. To carry out their task, proteins must remain in their folded conformation that usually corresponds to the thermodynamically most stable state. During their lifecycle, proteins experience stress conditions, which may perturb the folded native conformation. When these natively folded proteins are converted into nonnative *cross-β-sheet*-fold fibrous structures in different stress conditions, their functional properties are lost forever. This process is called *protein fibrillation* or, more commonly, *amyloid* like aggregation. Matthias Schleiden first coined the term *amyloid* in 1838 to describe an amylaceous component of a plant. Later, in 1854, Rudolph Virchow used the term to describe the high-nitrogen-content deposits seen in liver autopsy [1]. Since then the term *amyloid* has been used to refer to high proteinaceous deposits.

Under normal aggregating conditions, proteins usually form amorphous structures. However, protein fibrillation leads to protein aggregates having a well-defined organized structure. So far numerous proteins are found to form fibrous structure despite the lack of any amino acid sequence homology among them and thus, it is said to be an intrinsic property of a protein [2, 3]. Interestingly, fibrils of all these proteins share a common structural trait [4–6] and go through a common pathway for adaptation of such an ordered structure. A typical fibrillation process involves nucleation phase followed by fibril growth and formation of matured fibrils [7, 8]. In the nucleation phase only minute amounts of fibrils form, which eventually act as catalyst for development of fibrils in the elongation phase. When most of the proteins converted into fibrils, the process reaches equilibrium. The length of the nucleation and the elongation phase depends on the stress conditions and the proteins under study [8–10]. The presence of preformed fibrils or foreign surfaces, such as nanoparticles, can influence the fibrillation kinetics by catalyzing the nucleation phase at these interfaces [11–13]. Unfolded and aggregated proteins are usually evacuated from the cell by the quality control management system of the body through proteolytic cleavage by enzymes. Nonetheless, the aggregated fibrous forms of proteins are often resistant to these enzymes and thus a burden to the system. These aggregates elicit toxicity to the cellular environment [14].

46.1.2 Diseases Associated with Protein Fibrillation

In humans, more than 40 diseases are known to be related to protein fibrillation [4, 14, 15]. A selected list of some of these diseases is given in Table 46.1, along with the names of the specific proteins as the predominant components of the deposits. Each disease is synchronized to the fibrillation of a specific protein at a specific location. For example, amyloid β-peptide (Aβ) fibril in the brain is closely linked to Alzheimer's disease. Among the amyloid diseases,

Encyclopedia of Biocolloid and Biointerface Science, Volume 2, First Edition. Edited by Hiroyuki Ohshima.
© 2016 John Wiley & Sons, Inc. Published 2016 by John Wiley & Sons, Inc.

TABLE 46.1 Some Amyloid Related Diseases and Their Respective Precursors and Amyloid Fibril Forming Proteins

Amyloid diseases	Precursor proteins	Amyloid proteins
Alzheimer's disease	Amyloid precursor protein	Aβ peptides
Spongiform encephalopathies	Prion protein (PrPc)	PrPsc
Primary systemic amyloidosis	Immunoglobulin light and heavy chains	AL and AH
Senile systemic amyloidosis	Wild-type transthyretin	ATTR
Hemodialysis-related amyloidosis	β2-microglobulin	Aβ2M
Hereditary nonneuropathic systemic amyloidosis	Lysozyme	ALys
Type 2 diabetes	Pro-IAPP	IAPP or "amylin"
Injection-localized amyloidosis	Insulin	AIns
Secondary systemic amyloidosis	(Apo) serum amyloid A	Serum amyloid A
Familial amyloid polyneuropathy I	Transthyretin variants	ATTR
Familial amyloid polyneuropathy II	Apolipoprotein A1	AApoA1
Familial amyloidosis	Fibrinogen $\alpha\alpha$A-chain)	AFib

Parkinson's disease and Alzheimer's disease rank among the most weakening and socially troublesome diseases of the modern world [16]. So far, no definitive treatment plan exists for amyloid diseases, although Alzheimer's disease drug candidates aiming to reduce the amount of protofibrillar aggregates of Aβ are reported to be under clinical trial [17]. Disease caused by fibrillation of a given protein may show variations in terms of phenotypes and incubation periods and is assumed to be connected to the structural isoforms, also known as *morphologies* [18].

46.1.3 Fibrillation of Insulin

Insulin is a 51-residue protein hormone, produced naturally in the islets of Langerhans in the pancreas. It forms fibrillar structures in different stress conditions, such as low pH, high temperature, and low concentration of denaturants [9]. Insulin is a major α-helical protein composed of two chains, A and B, which are interconnected by two disulfide linkages. Chain A of insulin consists of two helical segments, A2–A8 and A13–A20, and chain B includes a region of extended structure B1–B8. The α-helical region between residues B9–B19 and B20–B23 is a β-turn region, and B24–B28 residues form another extended strand [19]. The key step in the fibrillation process of this protein is the conversion of its α-helical secondary structure into β-sheet configuration [10]. Insulin exists as a hexamer, tetramer, trimer, or monomer depending on the solution condition [10, 20, 21]. Dissociation of the native oligomer into monomer is the primary stage of insulin amyloidosis. Afterward, monomeric insulin partially unfolds and triggers the fibril formation. Insulin fibril formation may depend on many factors. Even different batches of insulin isolated from the same source may show variation in fibrillation propensity [19]. This variation is attributed to the presence of different amount of preformed fibril nuclei in the insulin samples [19]. Ionic strength, viscosity, pH of the solution, and external temperature also influence the process [19]. The specific residues, which are involved in interaction in this process, have been extensively researched [19, 22]. Conformational displacement of the *C*-terminal portion of the B chain partially exposes the hydrophobic residues, including A2, A3, B11, and B15, which play a critical role in this process [22]. Like other fibrils, the core structures of insulin fibrils contain *cross-β-sheets*, where β-strands run perpendicular to the fibril axis. Details of the mechanism of insulin fibrillation and the structure of insulin fibrils are described in Sections 46.1.3.3 and 46.1.3.4, respectively.

46.1.3.1 Problems Associated with Insulin Fibrils. Insulin plays a crucial role in carbohydrate metabolism in the human body. Many diseases have been linked to the nonregulatory production of insulin and its nonfunctionality due to formation of fibrils. Literature shows increasing evidence of insulin amyloids in clinical situations [23–26]. Fibril formation of insulin poses a problem as it reduces the therapeutic efficiency of injectable insulin used to treat type 2 diabetes. Insulin fibrils could also be found in the body of patients taking repeated insulin injections to fight against type 2 diabetes [24, 27]. Such patients are susceptible to have insulin fibril deposits in various body parts such as shoulders [26], arms [28], thighs [24, 25], and abdominal walls [28, 29] at or around the site of injections. These fibrils were also observed to be formed irrespective of the source and type of insulin [23–27].

46.1.3.2 Study of Insulin Fibrillation. Congo red and Thioflavin T (ThT) are the most widely used probes to detect the presence of insulin fibrils under in vitro conditions [30]. These two probes are specific to amyloid like fibrils. On binding to fibrils, fluorescence emission intensity of ThT enhanced significantly. Kinetics of insulin fibrillation is also monitored by measuring the fluorescence emission intensity enhancement of ThT. Time course of insulin fibrillation observed using ThT fluorescence usually shows a sigmoidal

profile (Fig. 46.1a). This profile consists of a lag phase followed by an exponential growth phase, which eventually levels off (Fig. 46.1a). The lag phase signifies the nucleation step of insulin fibrillation where a number of temporal conformers of insulin appeared. In the latter (exponential growth) phase, the rapid increase in fluorescence emission intensity indicates growth of fibrils, and the saturation in intensity level represents equilibrium in fibril growth. The time profile fits nicely to Eq. (46.1), which leads to the computation of the lagtime and the apparent fibril growth rate constant [10]:

$$Y = \frac{A_2 - A_1}{1 + \exp\left[\dfrac{(t_0 - t)}{\mathrm{x}}\right]} + A_2 \qquad (46.1)$$

In this equation, A_1 is the initial fluorescence, A_2 is the maximum fluorescence, t_0 is the time when fluorescence has reached the half- maximum; $1/x = k$ is the apparent rate constant of the fibril growth; and lagtime is approximated by $t_0 - 2x$.

Secondary structure of insulin during fibrillation has been monitored using CD and FTIR spectroscopy. Since insulin is a major α-helical protein, it shows a characteristic W-shaped spectrum in CD measurement with two negative ellipticities at $\sim$ 210 nm and $\sim$ 224 nm (Fig. 46.1b). In the course of fibrillation, these two negative ellipticities converge into one point that is around $\sim$ 218 nm, and the shape of the spectrum changes to U (Fig. 46.1b). The change in the CD spectrum is due to formation of a β-sheet structure. In case of FT-IR, a peak shift is observed in the amide I region from 1654 to $\sim$ 1630 cm^{-1} on conversion into fibrils (Fig. 46.1c) [20, 31]. Scanning electron microscopy, transmission electron microscopy, atomic force microscopy, and other microscopic methods are now used to study the insulin fibril morphology [10, 20, 32]. Atomic force microscopy is used to measure the tensile strength of insulin fibrils appearing in different conditions [33]. A representative TEM image of insulin fibril is shown in Fig. 46.1d.

46.1.3.3 Mechanism of Insulin Fibrillation. The ordered aggregation process of insulin proceeds through multiple steps with different temporal and length scales of conformational changes. When the concentration of intermediates with partially unfolded structures exceeds the critical value, the nucleation process starts. These intermediate conformers are similar to the premolten globule states [4]. Insulin in fibrillation condition shows a novel partial fold, which is similar to those observed in the NMR studies of two disulfide insulin analogs [34,35]. The fibrillation proceeds via dissociation of the native oligomer to monomer followed by partial unfolding to initiate the formation of fibrillation nucleus. Hence, unfolding of the monomer triggers the association process. In 2004 two authors proposed that the exposure of hydrophobic residues of the disordered regions of A and B chains of the insulin is the cause of aberrant self-association of the monomerc insulin [22]. The *C*-terminal segment of chain B is disordered, and partial opening of this region opens up the hydrophobic aromatic amino residues of B24–B26. These residues are further involved in the formation fibril nucleus of nonnative β-sheet structure.

It is very difficult to determine the size of the nucleus as it is a transient intermediates in the aggregation pathway. Hence, different biophysical techniques have been used to trap and identify the fibril nucleus. On the basis of aggregation kinetics, some of the nucleus sizes were determined and it was found that there might be variation in size and shape of the nucleus depending on the protein sequence and conditions. These nucleus sizes range from monomer to hexamer. For polyglutamine protein, the nucleus is monomeric and that of β2-microglobulin is of hexameric in nature [36, 37]. In 2005, Ahmad et al. characterized the soluble insulin oligomers, which may be the fibril nucleus [38]. They used H/D exchange kinetics to explore the solvent exposed regions of those soluble oligomers. They probed the surface hydrophobicity of these early oligomers with ANS fluorescence. This study highlighted the presence of at least two major populations of oligomeric forms in between native monomer and the mature fibrils. Nonetheless, the shape of this oligomeric nucleus remained elusive. In 2007, another group, using the SAX technique, characterized those oligomers [39]. They showed it is helical in shape. This study was very important in terms of rational design of drugs. Nayak et al. [40] proposed a model for insulin fibril nucleus based on their SANS study and the previous study by Vestergaard. They proposed that the fibril nucleus is the end-on association of three cylindrical insulin dimers, which then associated inside on orientation to form larger fibrils. It is interesting to note that insulin exists as a zinc-coordinated circular hexamer in vivo as compared to linear hexameric nucleus in vitro [40].

46.1.3.4 Structure of Insulin Fibrils. Structural studies of amyloid have involved several biophysical techniques, such as X-ray fiber diffraction, electron microscopy, atomic force microscopy, and more recently solid-state nuclear magnetic resonance and electromagnetic resonance [41, 42]. These studies showed that fibrils are long, straight, and unbranched. These are composed of smaller protofilaments, which are subunits consisting of amyloid fibrils. The number of protofilaments may vary in a fibril structure depending on the precursor protein [43, 44]. These protofilaments are often twisted around one another to form mature fibril [45–47]. The internal structure of protofilaments of amyloid fibrils showed a "cross-β" pattern in an X-ray diffraction study [48]. This was further confirmed by studying fiber diffraction of synthetically designed peptide fibrils [49, 50]. The pattern indicates that these fibrous molecules share a core structure consisting of a β-sheet conformation where the hydrogen bonding

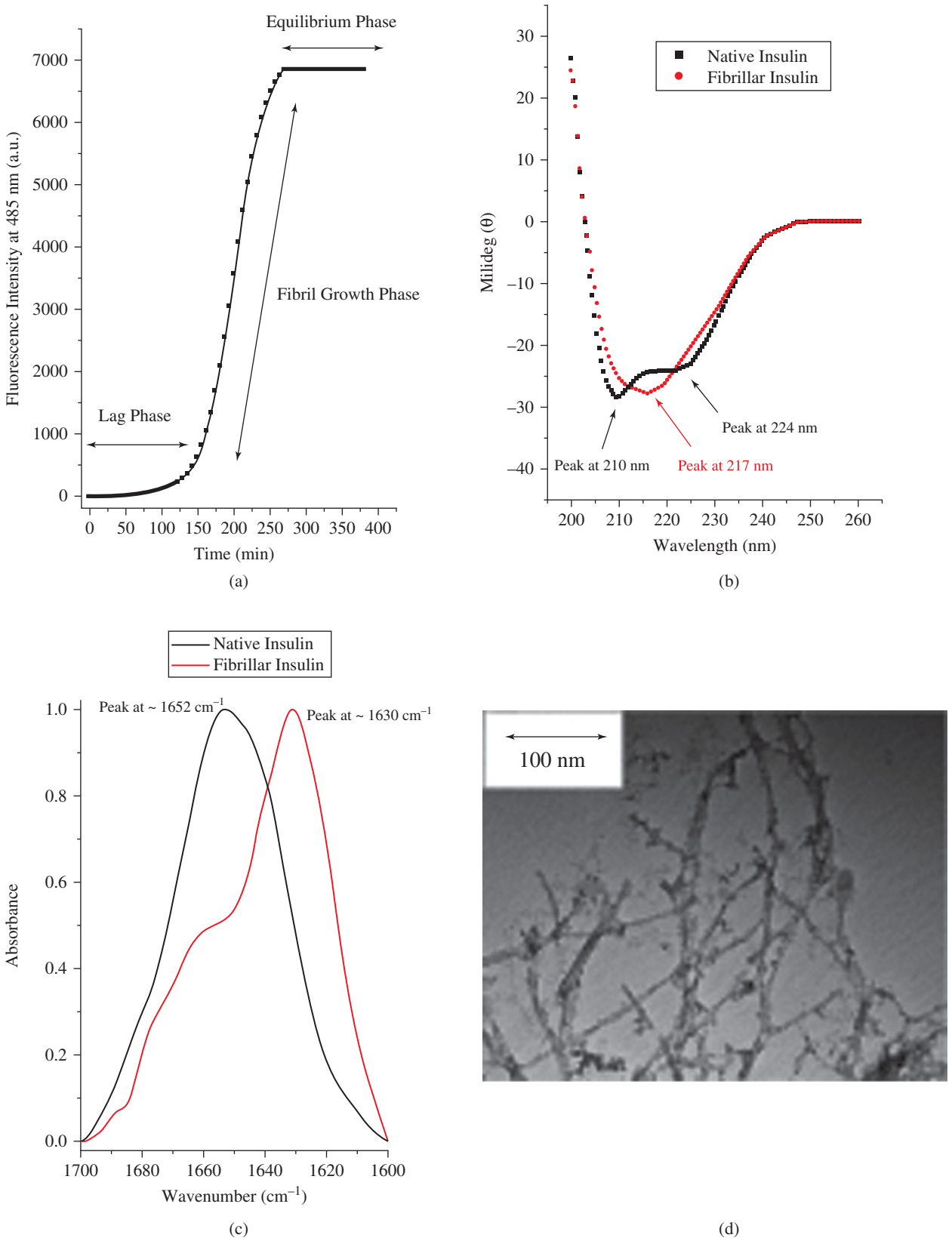


FIGURE 46.1 (a) Timecourse of insulin fibrillation monitored using ThT fluorescence (λ_{ex} = 450 nm, λ_{em} = 485 nm); (b) far-UV-CD spectra of native insulin and fibrillar insulin; (c) FT-IR spectra of native insulin and fibrillar insulin; (d) transmission electron microscopy (TEM) image of fibrillar insulin.

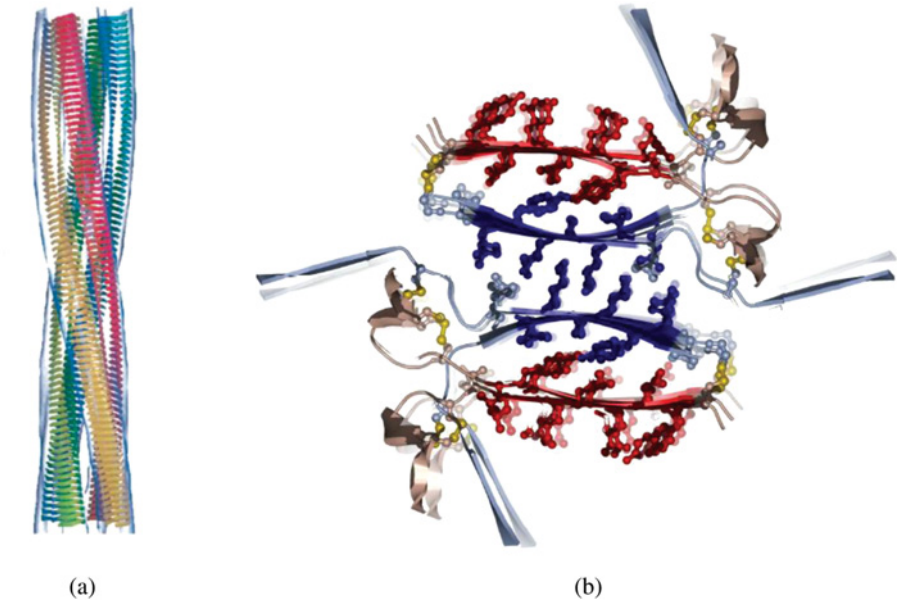


FIGURE 46.2 (a) A possible β-strand model docked into the EM density of the compact fibril (transparent gray surface). The four protofilaments are colored separately. (Adapted from Jimenez et al. 2002 [43], p. 9196. © The National Academy of Science; reproduced with permission.) (b) Fibril model of insulin A and B chains of insulin molecule are shown in pale red and pale blue, respectively. The LVEALYL segment, which forms the spine of the fibril, is in dark blue. The SLYQLENY segment, from the A chain, which forms auxiliary sheets to the spine of the fibril, is in dark red. Disulfide bonds are shown in yellow. (Adapted from Ivanova et al. 2009 [53], p. 18990. © The National Academy of Science; reproduced with permission.)

direction runs parallel to the fiber axis and the β-strands are perpendicular, much like the steps of a ladder.

On the basis of this cross-β pattern, Jimenez et al. proposed a model of insulin fibril using 3D-cryo-EM reconstruction [43]. The probable schematic model of four protofilament form of insulin is presented in Fig. 46.2. Mass-spectrometric analysis of the insulin fibrils showed that the disulfide bonds of the native insulin remain intact in its fibrillar form [43]. The interchain disulfide bond requires the strand to run in parallel, and the intrachain disulfide bond initiates curvature into the strand. The basic shape of the protofilament remains the same irrespective of any polypeptide chain. Volume calculations advocate that each insulin occupies two β-strand layers. For simplicity, all chains are shown in parallel packing, although alternate molecules could be antiparallel. The twist of the fibrils reported is left-handed [51,52]. To pack insulin protofilaments together in a consistent interface, the protofilament twist must follow the overall twist of the fibril. Hence, protofilaments also have left-handed helical twist.

Later, Ivanova et al. proposed the insulin fibril structure based on X-ray fiber diffraction and mass per unit length and the crystal structure of LVEALYL [53]. They found that this single segment could nucleate and inhibit the insulin fibrillation in a mole-ratio-dependent manner. Thus, it must be the central core of the cross-β spine of the insulin fibrils. The X-ray diffraction pattern of insulin fibrils showed that fibrils were β-sheet in nature and parallel to the fiber axis. There are two pairs of sheets with different sheet-to-sheet distance. The chain B segment LVEALYL was used as the molecular basis of the steric zipper spine of insulin fibrils. This segment is in helical conformation in the native insulin and thus converts into extended β-strand. The disulfide bonds that connect chains A and B force the A chain to convert into an extended β-strand. LVEALYL segment also gives a structural template to the extended segment LYQLENY of chain A. The spine of this model makes up four β-sheets (Fig. 46.2b). The structures of the inner two β-sheets, which form the streic zippers, overlay on the crystal structure of LVEALYL (Fig. 46.2b). The outer two β-sheets formed from the extended segment LYQLENY of chain A (Fig. 46.2b). The *N*- and *C*-termini retain the native like structure. This model is in good agreement with the earlier model proposed by Jimenez et al. and Ionescu-Zanetti et al. [43, 52]. The model provides a high-resolution structural basis of insulin fibrils, which cannot be obtained by low-resolution density map analysis. However, these models are limited to the structure of matured fibrils only.

Small-angle X-ray scattering gave insights into the structure and assembly of amyloid fibrils formed by insulin

in its early stage of fibrillation [39]. For the first time, the study reveals the oligomeric assembly of insulin fibrils. The SAX study proposed that insulin fibrils are assembled from a helical fibrillation precursor composed of five to six insulin monomers, which corresponds to the fibril nucleus. The mature amyloid fibril is composed of three individual filaments that wrap around one another [39]. However, the SAX study of the fibrils formed by α-synuclein revealed a contrasting structure in which a single filament appeared to make up the mature fiber. Nayak et al. also proposed a model of insulin fibril nucleus, which is basically an end-on associated form of three dimmers of insulin [40]. More recently, Kurouski et al. probed an insulin fibril surface by tip-enhanced Raman spectroscopy (TERS) [32]. The insulin fibril surface consists of 34% β-sheet and 66% α-helix and unordered structure [32]. Residues C, F and W are found to be frequent in the β-sheet region, whereas P was only found in the α-helix and unordered region of the fibril. The study corroborates well with the existing model proposed by Jimenez et al. in 2002 [32].

46.2 PREVENTION OF INSULIN FIBRILLATION

46.2.1 General Strategies to Prevent Insulin Fibrillation

Various small molecules have been used to prevent insulin fibrillation. The rationales behind the use of those small molecules are different in each case. One early strategy was to promote the self-association of insulin. Since insulin must be transformed into a monomer before the onset of fibrillation, the self-association of insulin was promoted by the addition of Zn^{2+} or Ca^{2+} to stabilize its hexameric structure [54, 55]. Polyhydroxy compounds, such as carbohydrates, glycerol, and amphiphilic block copolymers, attenuate the penetration of water into the hydrophobic core by forming a protective layer around the surface of the insulin. They also reduce the number of unwanted hydrophobic interactions and thus act as amyloid inhibitors [56, 57]. Betaine, trehalose, and citrulline also inhibited insulin fibrillation, presumably by a similar mechanism [58]. These strategies were very general and have their shortcomings. The hexameric insulin has a low rate of adsorption in the bloodstream. Its larger size impedes its adsorption. Hence, insulin must dissociate to a dimeric or a monomeric state for effective transport and activity [59, 60]. Therefore, addition of metal ions may have increased the stability of insulin but at the same time, they also decrease the functional activity of the protein. Polyhydroxy compounds require a high-molar-excess concentration to execute inhibitory activity, which may elicit unwanted immune responses. Consequently, these are not suitable for a drug candidate. Biocompatible peptides are suited for this job. However, they do have limitations, the most common one is their instability in hydrolysable conditions. In Section 46.2.2 we discuss the design of peptide-based inhibitors and the role of other small molecules in insulin fibrillation.

46.2.2 Peptide-Based Inhibitors of Insulin Fibrillation

Since peptides can be nontoxic, they may not turn on the unwanted immune response and thus have a good potential to become suitable drug candidate. Now many research groups are exploring peptide-based inhibitors [20, 61, 62].

46.2.2.1 Hybrid Peptides Designed as Inhibitors of Insulin Fibrillation. Gibson and Murphy used hybrid peptide to prevent the insulin aggregation [61]. The hybrid peptide consisted of one recognition domain and one disrupting domain [61]. The recognition domain preferentially binds to insulin, and the disrupting domain inhibits the fibril formation. In order to prepare a recognition domain, they initially identified the short insulin fragments that preferentially bind to insulin. They produced a mixture of insulin fragments by limited proteolysis and incubated it with native insulin. The mixture was then separated by reversed-phase HPLC and analyzed by MALDI-TOF spectrometry. Among the different fragments of insulin, ALYLV, GSHLVEAL, and VEALYL selectively bind to insulin. Since the LVEALYLE domain is proposed to be associated with insulin misfolding, it was hypothesized that this domain could also be effective as recognition domain in hybrid peptides [9, 61]. However, none of these peptides was able to inhibit insulin fibrillation. Numerous studies showed the suppression of protein aggregation by arginine [63, 64]. Hence, they used hexameric R as a disrupting region. This hexameric R was then added at either the *N*- or at *C*-terminal side of those three insulin fragments. Nonetheless, only RRRRRR LVEALYLV, above a critical concentration of 2 mM, was able to alter insulin fibrillation. Other combinations were ineffective. Therefore, a precise recognition domain with a properly oriented disrupting domain will be effective as inhibitor (Fig. 46.3). They hypothesized that the inhibitory effect was may be due to micelle-like property of the hybrid peptide, which can decrease solvent surface tension above a critical concentration and thereby decrease the unwanted hydrophobic interactions. However, cetyltrimethylammonium chloride (CTAC), a cationic surfactant, was not able to prevent insulin fibrillation, indicating that the micelle theory may not have direct influence on the inhibitory effect of the hybrid peptide. The inhibitory effect could also be attributed to the specific binding of the LVEALYLV region, which is in close proximity to F25 and Y26 residues, which play a critical role in insulin fibrillation. Thus, the local concentration of the disrupting domain becomes very high at the active site of fibrillation and prevents the unwanted hydrophobic association.

Gibson and Murphy [65] also used a hybrid peptide to influence the Aβ aggregation. The recognition domain

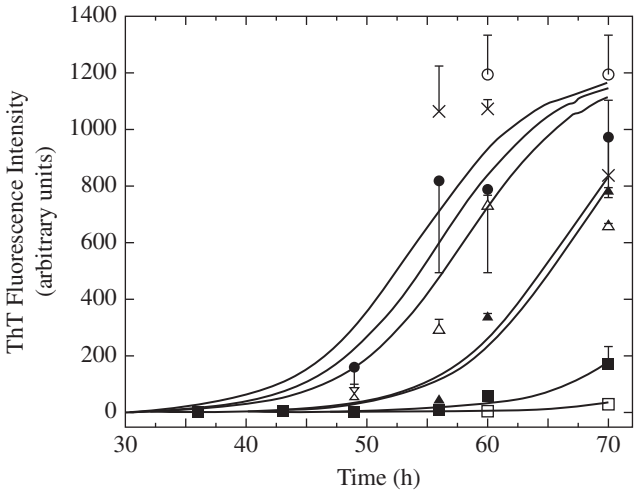


FIGURE 46.3 Kinetics of insulin fibrillogenesis in the presence of various peptides. Insulin was dissolved at 0.52 mM in 1 M acetic acid (pH 2.0), and mixed with indicated peptides at 2 mM. Samples were kept at 37°C during the duration of the experiment. ThT of insulin alone (3) or mixed with RRRRRR (s), ALYLVRRRRRR (d), GSHLVEALRRRRRR (m), RRRRRRGSHLVEAL (D), LVEALYLVRRRRRR (j), or RRRRRRLVE ALYLV (u) was measured over time. Lines represent fitting of the data to a two-step kinetic model. (Adapted from Gibson and Murphy 2006 [61], p. 1133. © The Protein Society; reproduced with permission.)

contains 15–25 amino acid residues of Aβ-peptide linked to oligolysine-disrupting element. However, the inhibitor did not alter the aggregation rate of the Aβ-peptide. The hybrid peptide attenuated the toxicity of the fibrillation process by reducing the appearance of early soluble oligomeric phases. Later other researchers modified the disrupting region by replacing the linear oligolysine with branched compounds [65]. The L-lysines were also replaced by their D analogs. The purpose of this replacement was a success. The rate of Aβ aggregation was reduced to a significant amount by the introduction of new hybrid peptides.

46.2.2.2 Naturally Occurring Peptides as Insulin Fibril Inhibitors. The main challenge in the development of potential inhibitors of fibrillation is to retain the functional activity of the target protein. Since most of the inhibitors developed so far bind to the active site of the proteins, their functional activity has been weighed down. Insulin is a natively occurring inhibitor of islet amyloid polypeptide (IAPP) [66]. IAPP and insulin are cosecreted from pancreatic β-cells together [67]. IAPP is a glucose regulatory protein that shares sequence homology with insulin. However, IAPP is susceptible to aggregation, and its aggregates are found in the pancreatic amyloid in type 2 diabetes [68]. Since IAPP strongly interacts with insulin, it was hypothesized that a nonamyloidogenic analog of IAPP may reduce the aggregation of insulin [66, 69]. Yan et al. developed a nontoxic and nonamyloidogenic conformationally constrained IAPP analog (IAPP-GI) that blocked the cytotoxic self assembly of IAPP (Fig. 46.4) [70]. Velkova et al. used this analogue to test its inhibitory effect on the insulin fibrillation [66]. Incubation of insulin with 5–10-fold molar excess of IAPP-GI under low-pH and high-temperature conditions showed suppression of insulin fibrillation. It is well known that in the course of fibrillation, insulin forms a series of soluble oligomeric species that are toxic in nature [10,71]. To address the question of whether IAPP-GI intervenes in the formation of soluble toxic oligomers of insulin, Velkova's team used nonreducing Nu-PAGE and Western Blot and monitored the fibrillation kinetics [66]. The data showed that the IAPP-GI completely blocked the formation of nonnative soluble oligomers and thus reduced the overall toxicity of the process [66]. Cell viability assay also supported the finding. Insulin-induced IR autophosphorylation assay was executed using cultured human breast cancer cells to determine whether insulin retains its activity on binding to the inhibitor. Insulin and the insulin IAPP-GI conjugate induced same amounts phosphorylated IRβ. Thus, insulin function remains unaffected on binding to IAPP conjugate. The proposed mechanism of interaction of insulin with IAPP-GI and nontoxic IAPP conformer is illustrated in Fig. 46.5. This

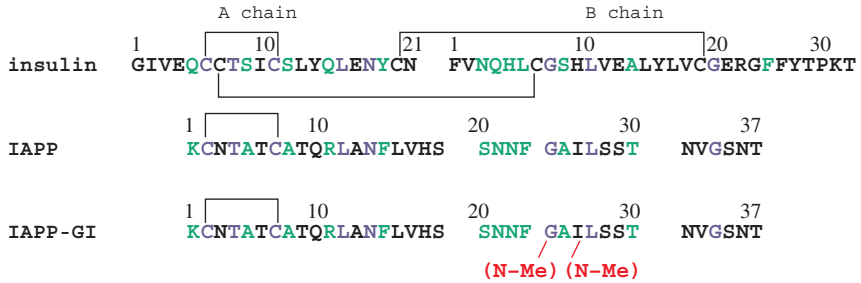


FIGURE 46.4 Primary structures of insulin, IAPP, and the IAPP mimic IAPP-GI. Residues common to all three sequences are shown in blue, and similar residues are shown in green. (Adapted from Velkova et al. 2008 [66], p. 7114. © Wiley-VCH Verlag GmbH & Co. KGaA, Weinheim; reproduced with permission.)

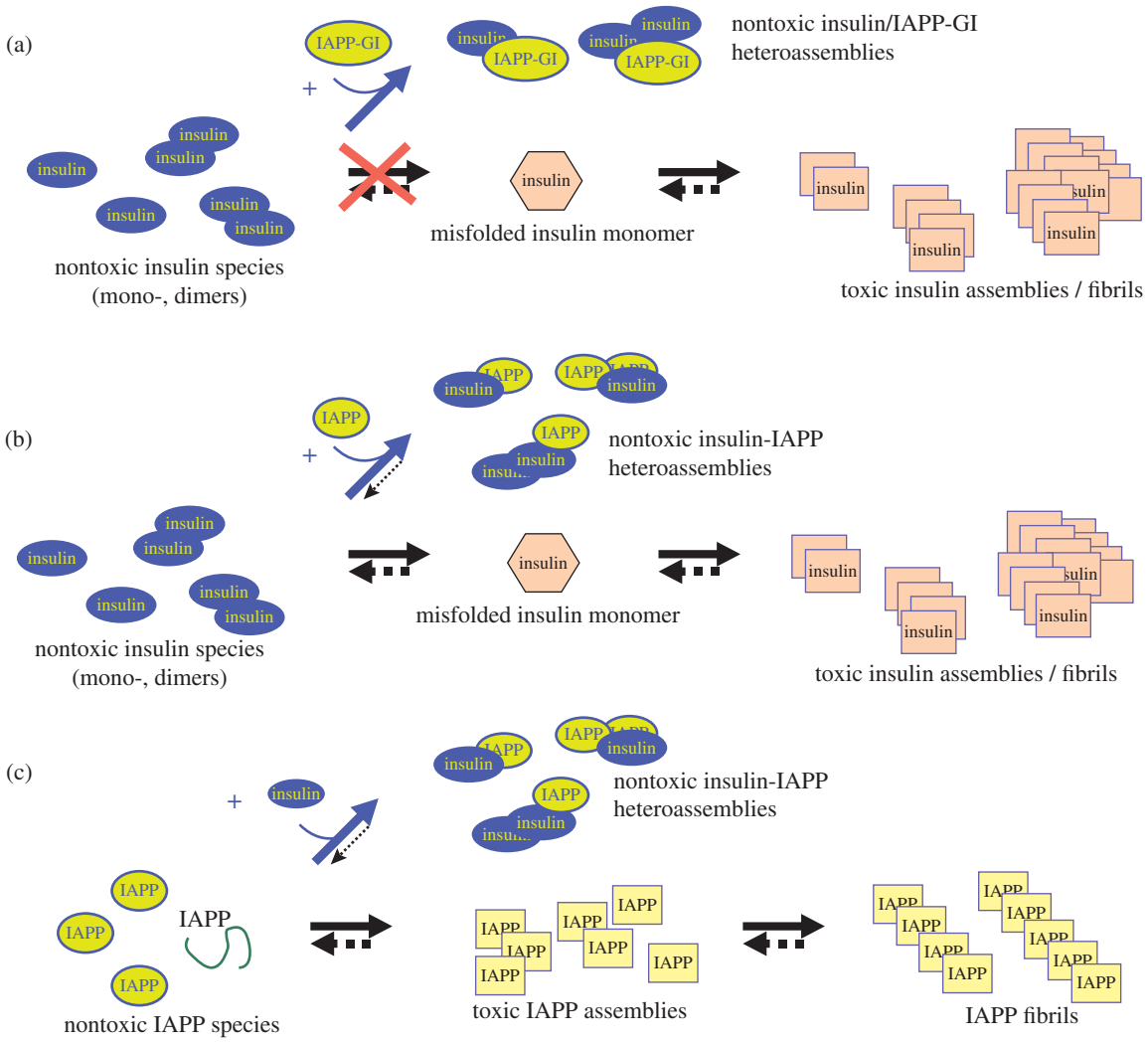


FIGURE 46.5 Proposed of interaction of insulin with IAPP-GI and a nontoxic IAPP conformer. (a) IAPP-GI is proposed to bind with high affinity early, nonfibrillar, and nontoxic insulin species—likely natively folded monomers and/or dimers—and thus to block insulin misfolding and self-assembly. (b) A nonfibrillar and nontoxic IAPP conformer, likely a monomer, is proposed to bind with high affinity early, nonfibrillar, and nontoxic insulin species—likely natively folded monomers and/or dimers—and thus to attenuate insulin misfolding and aggregation. (c) Interaction of early nonfibrillar and nontoxic insulin and IAPP species—likely monomers and/or dimers—is suggested to attenuate cytotoxic self-assembly and fibrillogenesis of IAPP. (Adapted from Velkova et al. 2008 [66], p. 7114. © Wiley-VCH Verlag GmbH & Co. KGaA, Weinheim; reproduced with permission.)

study was very important, not only for the strategy but also for the insightful message of cross-amyloid interaction. If this interaction existed in vivo, then there would be a molecular link between Alzheimer's disease and type 2 diabetes [66, 72, 73].

A more recent study showed that the proinsulin C-peptide is a natural inhibitor of insulin fibrillation [74]. Proinsulin C-peptide is a 31-residue peptide that is cleaved from the proinsulin by different peptidases to release insulin. Insulin and the C-peptide are then secreted into the bloodstream [75]. Although C-peptide is mostly unordered, it is required for the correct folding of the proinsulin [76, 77]. Early studies showed that the C-peptide alters the aggregation of IAPP [69, 78]. However, two reports showed that the C-peptide does not influence insulin aggregation at pH 2 and 7.3 [79, 80]. These reports are in contradiction with a more recently published article [74]. Insulin fibrillation kinetics depends on a critical concentration [39]. Beyond this concentration, there is not much change in the lag phase of the process. Huang et al. and Noormagi et al. both used very low insulin concentrations, which were lower than the critical concentration [79, 80]. However, another team used

a 1 mM concentration of insulin, which is well above the critical range [74]. This might be the cause of the differences in the results between these studies. The aggregation prevention was executed by the formation of stable insulin C-peptide complex. H/D exchange study of aggregates containing insulin and the C-peptide showed the presence of two populations: one with the completely fibrillated insulin and the other with lower backbone accessibility, which can be achieved by the formation of stable insulin C-peptide complex [74]. Thus, two naturally occurring peptide variants IAPP and C-peptide have the potential to be a supporting drug in insulin therapy of type 2 diabetes.

46.2.2.3 Hydrophobic Peptides as Inhibitors of Insulin Fibrillation. Insulin fibrillation was initiated with the partial opening of the charged *C*-terminal domain followed by unfolding of the *N*-terminal B-chain helix [22]. The residues F (B24), F (B25), and Y (B26) support the formation of an antiparallel β-sheet [81]. Thus, fibrillation is the interplay of electrostatic and hydrophobic interaction. Another team used Trp–Trp–Tau-based tripeptide conjugates containing both charged and hydrophobic residues to counteract the possible hydrophobic and hydrophilic interactions in the insulin fibrillation [81]. They explored the interaction of two designed peptides 1 and 3 and their dimeric forms 2 and 4 with insulin in fibrillating condition (Fig. 46.6). They found that all of the peptide conjugates inhibit the fibrillation process and the maximum inhibition observed for peptide 4. The secondary structure of both bovine and human insulin was retained even after the 20 h of incubation in presence of substoichiometric concentration of peptide 4. To ascertain whether peptide 4 interfered in the nucleation phase of the fibrillation process, it was added to the incubating solution of insulin at different times and the fibrillation kinetics was monitored by Thioflavin T fluorescence measurement. As the time of incubation increased, the inhibitory effect of peptide 4 declined. Beyond 6h incubation there was hardly any effect observed. Thus, peptide 4 interacted with the early conformers of insulin in fibril-forming condition. Since these early conformers elicit more toxic effects in the cellular environment compared to the matured fibrils, it was surmised that peptide 4 may actually reduce the overall toxicity of the process by interacting with those conformers. The molecular interaction was probed by the solution ^{1}H NMR that showed a downfield shift of amide (NH), indolic and aromatic proton of the 4, followed by an upfield shift with peak broadening of the aromatic protons of the insulin. This might be the cause of ring current shift due to the π–π interaction of the inhibitor and the insulin. As stated earlier, the F (B24), F (B25), and Y (B26) residues play a critical role in insulin fibrillation, and it was assumed that peptide 4 interacted with these residues to quench the process.

We also explored the interaction of different hydrophobic peptides with insulin in fibril-forming condition. We found that a nine-residue peptide, NK9 (NIVNVSLVK), which was adopted from the middle of SARS corona virus E-protein primary sequence, initially chosen serendipitously, delays the insulin fibrillation process [20]. The maximum inhibition was observed for 1:1 molar ratio of NK9 to insulin. Beyond this concentration, there was minimal change in the lag phase (Fig. 46.7a). However, the amount of fibril mass declined as the molar ratio of NK9 to insulin increased (Fig. 46.7a). To investigate whether NK9 intervenes in the nucleation phase, we added NK9 into an incubating solution of insulin at different times of incubation (Fig. 46.7b). The results were similar to what Mishra's team observed with the inhibitor peptide 4. Thus, NK9 also interfered in the nucleation phase of insulin fibrillation (Fig. 46.7b) [20,81]. Therefore, it could be surmised that NK9 prevents the appearance of soluble toxic oligomeric phases of insulin. NK9 prevented the

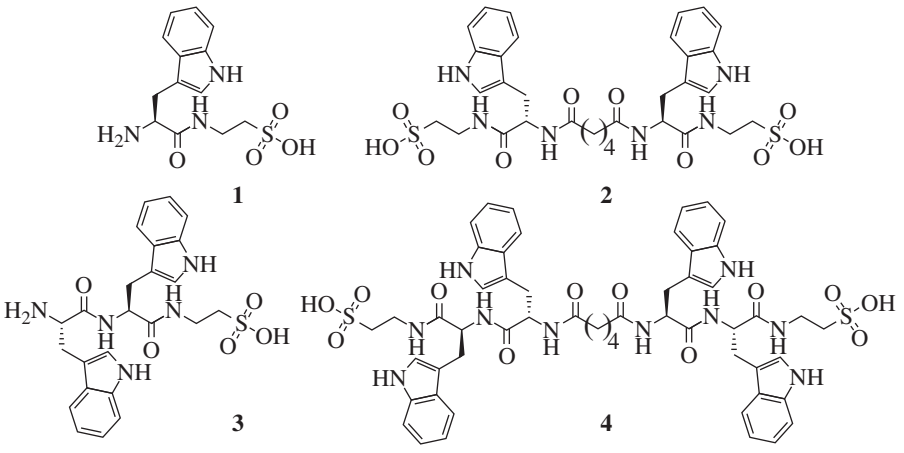


FIGURE 46.6 Chemical structures of water-soluble tryptophan and taurine containing inhibitors of insulin aggregation. (Adapted from Mishra et al. 2013 [81], p. 3903. © American Chemical Society; reproduced with permission.)

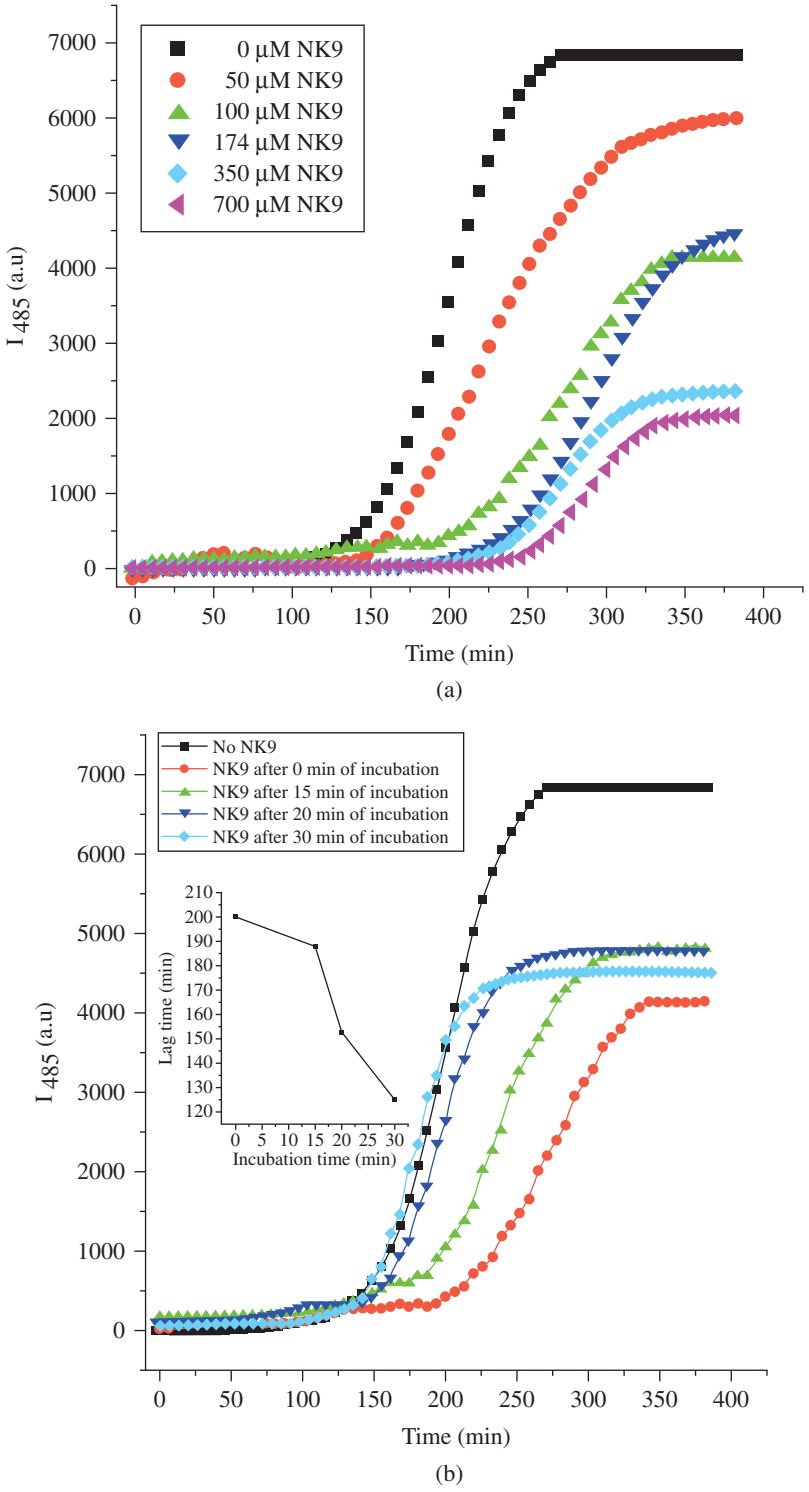


FIGURE 46.7 Timecourse of insulin fibrillation in the presence and absence of NK9, monitored using ThT fluorescence. (a) Temporal evolution of the ThT fluorescence intensity during incubation of insulin (350 μM) in fibrillation condition (pH 2.6, 62°C) in presence and absence of NK9 at different concentrations. ThT curves of insulin in respective NK9 concentrations are shown in the figure. (b) Effect of NK9 on fibrillation kinetics of insulin. NK9 (100 μM) was added to the buffer solutions (pH 2.6) of insulin (350 μM) at 62°C at 0, 15, 20, and 30 min of incubation. Molar ratio of NK9 to insulin is 0.28:1. Inset shows a plot of lagtime of insulin fibrillation in presence of 100 μM NK9 against incubation time. (Adapted from Banerjee et al. 2013 [20], p. e72318.)

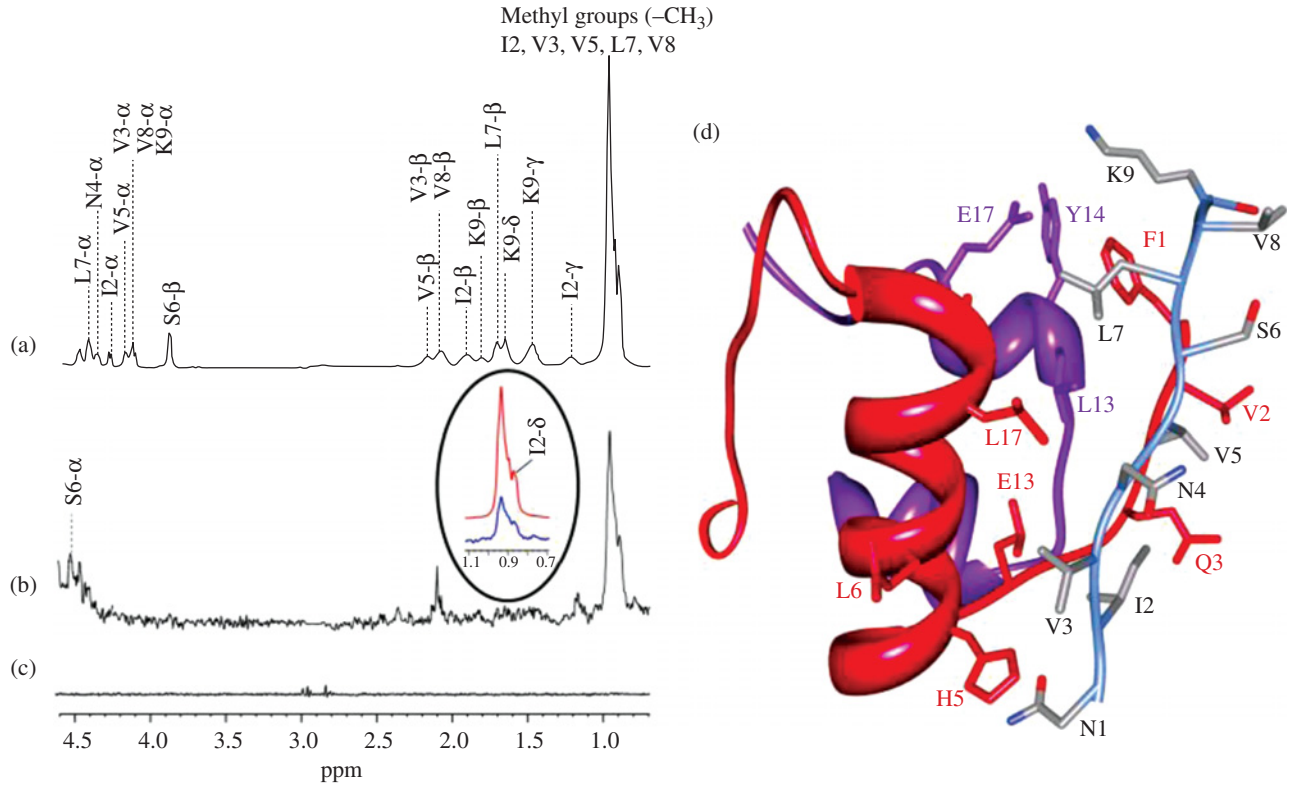


FIGURE 46.8 STD NMR spectra. (a) Reference spectrum of NK9 in presence of insulin at a molar ratio of insulin:NK9 = 1:100. (b) STD NMR spectrum of same sample showing the resonance transfer within the binding epitope of insulin. The experiments were performed at 298 K with 2 s of saturation time (on resonance = 7.3 ppm; off resonance = 40 ppm). (c) STD spectrum of NK9 alone (on resonance = 7.3 ppm; off resonance = 40 ppm). (d) The docking model of insulin-NK9 complex correlated of the STD NMR data. (Adapted from Banerjee et al. 2013 [20], p. e72318.)

dissociation of native insulin oligomer to its monomeric form with micromolar binding affinity. With the help of a docked model and ^{1}H-STD-NMR study, NK9 was found to be in close proximity with F (B1), V (B2), Q (B3), L (B6), H (B10), L (B17), L (A13), Y (A14), and E (A17) residues of insulin (Fig. 46.8). The result showed that unordered portion of the chain B also contributed to the nucleation phase of the fibrillation process.

Thus, NK9 and peptide 4 have different binding sites for insulin [20, 81]. Still, both of these peptides intervene in the nucleation phase of the process. Hence, it could be assumed that the unordered portion and the *N*-terminal helical portion of chain B mutually assist each other to form the fibril nucleus. Blockage of either site will slow down the nucleation phase and thus inhibit the fibrillation process.

46.2.3 Small Molecule Inhibitors of Insulin Fibrillation

Various class of small molecules have been used as inhibitors of the protein fibrillation. Aromatic compounds, fluoroalcohols, trehalose, amphiphilic surfactants, metal complexes, and nanoparticles attenuate the fibrillation propensity of insulin [10, 82–85].

46.2.3.1 Polycyclic Aromatic Compounds. Polycyclic aromatic compounds are well-known fibril inhibitors as both contain a recognition domain as well as a blocking domain [82]. Among these polycyclic compounds, phenolsulfonphthaleine, epigallocatechin gallate, and curcumin inhibit insulin fibrillation [82,86,87]. (–)-Epigallocatechin-3-gallate (EGCG) inhibits the insulin fibrillation under two different conditions [86]. However, the optimum concentration for EGCG to exert an inhibitory effect varies under these two conditions. At low pH and high temperature, the fibrils appear in the presence of EGCG to be shorter and thinner, whereas under physiological conditions, insulin forms globular aggregates in the presence of EGCG, which indicates that EGCG inhibits insulin fibrillation in two different pathways. Curcumin interacts with native, intermediate oligomeric forms and the final fibril forms of insulin and inhibits the process in a dose-dependent manner [87]. Curcumin has the ability to break β-sheets of the fibril form and thus reduce the amount of fibril formed [87]. A molecular docking study

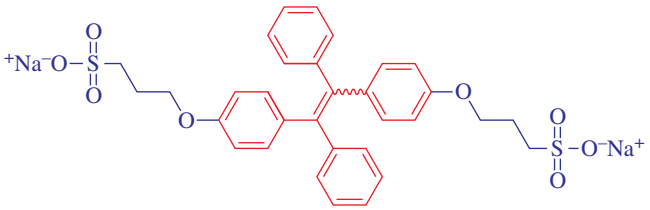


FIGURE 46.9 Structure of 1,2-bis[4-(3-sulfonatopropoxyl) phenyl]-1,2-diphenylethene sodium salt (BSPOTPE), which plays dual roles (ex situ monitor and in situ inhibitor) in the insulin fibrillogenesis process. (Adapted from Hong et al. 2011 [88], p. 1680. © American Chemical Society; reproduced with permission.)

proposed that chain B is the most likely region of interaction of insulin [87].

1,2-Bis[4-(3-sulfonatopropoxyl)phenyl]-1,2-diphenylethene sodium salt (BSPOTPE), a derivative of tetraphenylethene (TPE), is an efficient inhibitor of insulin fibrillation (Fig. 46.9) [88]. As low as 10 μM concentration of BSPOTPE extends the nucleation phase of insulin fibrillation to 2 h. The biocompatible inhibitor BSPOTPE binds to the partially unfolded conformers of insulin and inhibited the nucleation phase. The compound does not disintegrate the protofibrils of insulin and thus will be ineffective if added after the nucleation phase. Molecular docking studies proposed that the compound binds to the hydrophobic residues near the B-chain helix of 11–19. This helix portion partially unfolds in the nucleation phase and exposes the hydrophobic residues to the solvent. This persuades the binding of the BSPOTPE to these exposed residues and prevents unwanted hydrophobic interaction. Interestingly, this compound not only acts as in situ inhibitor of insulin fibrillation but also is an ex situ probe used to detect fibrils. The compound binds to the partially unfolded states and aggregated states of insulin, and thus the rotation of phenyl rings of the probe is physically restricted. This blocks the nonradiative relaxation channels and populates the radiative decays of the excitons. This renders the partially unfolded conformers and aggregates highly luminescent.

Interestingly, some monocyclic benzene derivatives also act as insulin fibril inhibitors [89]. Two monocyclic aromatic compounds, aspirin and nitrophenol, were found to inhibit A-β aggregation [90, 91]. However, aromatic monocyclic compounds such as insulin fibril inhibiter have also been reported [89]. That same study [89] showed that the substituent of the benzene ring signicantly influences the inhibitory effect. Stronger electron-withdrawing groups showed a pronounced effect on the rate of fibrillation. Those researchers [89] proposed that Y16 and the electron-deficient aromatic compound may act as a donor–acceptor pair and that inhibition is executed by this π–π stacking interaction. These aromatic compounds also stabilize the helical conformation of insulin and thereby prevent its conversion into cross-β structure formation.

46.2.3.2 Trifluoroethanol as Insulin Fibril Inhibitor. 2,2,2-Trifluoroethanol (TFE) stabilizes the α-helical structure in proteins and also induces α-helical structure in unordered proteins at high concentration [92, 93]. As stated earlier, insulin fibril consists of a parallel β-sheet structure. Hence, stabilization of the native α-helix may reduce the propensity of insulin to assume its fibrillar form. We have tested the role of TFE in the fibrillation pathway of insulin [10]. TFE promotes fibrillation of αA,αB-crystallin and peptide LYS (11–36) derived from the T4 lysozyme, whereas, in cases with prion and Aβ, TFE inhibits their fibrillation propensity. Therefore, TFE has a controversial role in the fibrillation process of proteins and is highly system-dependent [40, 94–96]. We monitored the kinetics of insulin fibrillation in presence and absence of TFE using ThT fluorescence intensity (Fig. 46.10). The sigmoidal curves were fitted into the equation [Eq. (46.1)] for determination of kinetic parameters. The kinetic parameters, such as lag phase and apparent rate of fibril growth, are presented in Table 46.2. The kinetic data clearly show that TFE dose dependently increases the lag phase of the process, indicating the possible occurrence of an interaction within the nucleation phase. Interestingly, the apparent rate constant for fibril growth has increased in the presence of TFE, showing a cooperative transition from fibril nucleus to matured fibrils (Table 46.2). TEM micrographs in Fig. 46.11 showed that in the presence of TFE, insulin fibrils are shorter in length and are discrete. Shorter fibrils have more edges compared to longer fibrils and thus, have more surfaces to act as seeds in the process. This will eventually increase the fibril growth rate. This may be the reason of high cooperativity in the elongation phase of fibrils in the presence of TFE. Monitoring the hydrodynamic radius of insulin during its fibrillation process by using dynamic light scattering showed that TFE inhibited the formation of early soluble oligomers that is reported to be the toxic element in the fibrillation pathway (Fig. 46.12a,b), thereby modulating the pathway of insulin fibrillation. Generally, it is assumed that TFE displaces the water molecules from the protein surface and strengthens the intramolecular H bonding. Thus, unwanted hydrophobic interactions are reduced, and so is the propensity of fibrillation. Another fluoroalcohol, HFIP, also modulates the structure of the protofibrils of a model protein Barster [97]. However, HFIP-induced

TABLE 46.2 Kinetic Parameters of Insulin Fibrillation

Solution	Lagtime (h)	Apparent rate constant of fibril growth (h^{-1})
Insulin	0.41 ± 0.01	3.2 ± 0.1
Insulin + 5% TFE	0.78 ± 0.01	6.2 ± 0.3
Insulin + 15% TFE	1.21 ± 0.01	9.5 ± 0.3
Insulin + 25% TFE	2.78 ± 0.003	9.8 ± 0.3

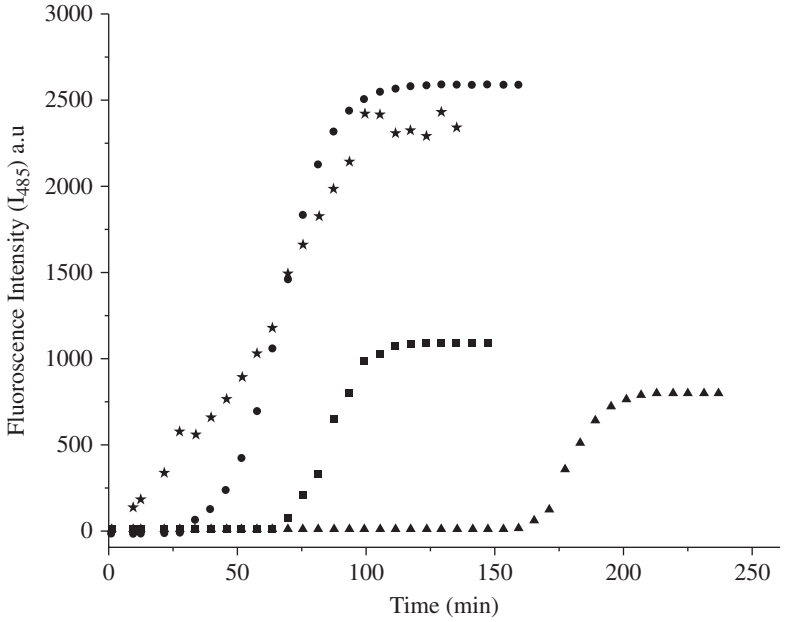


FIGURE 46.10 Aggregation kinetics of bovine insulin ($\lambda_{ex} = 450$ nm, $\lambda_{em} = 485$ nm) was monitored by ThT fluorescence after the addition of different concentrations of TFE to samples preincubated at 50 mM citrate phosphate buffer, 0.1 M NaCl, of pH 2.6 and at 62°C. The ThT fluorescence is shown as a function of incubation time at different TFE concentrations. Final concentrations of ThT and insulin in the solution are 20 μM and 17.44 μM, respectively. 0% (v/v) TFE (★), 5% (v/v) TFE (•), 15% (v/v) TFE (■), 25% (v/v) TFE (▲). (Adpated from Banerjee and Das 2011 [10], p. 142. © Elsevier B.B.; reproduced with permission.)

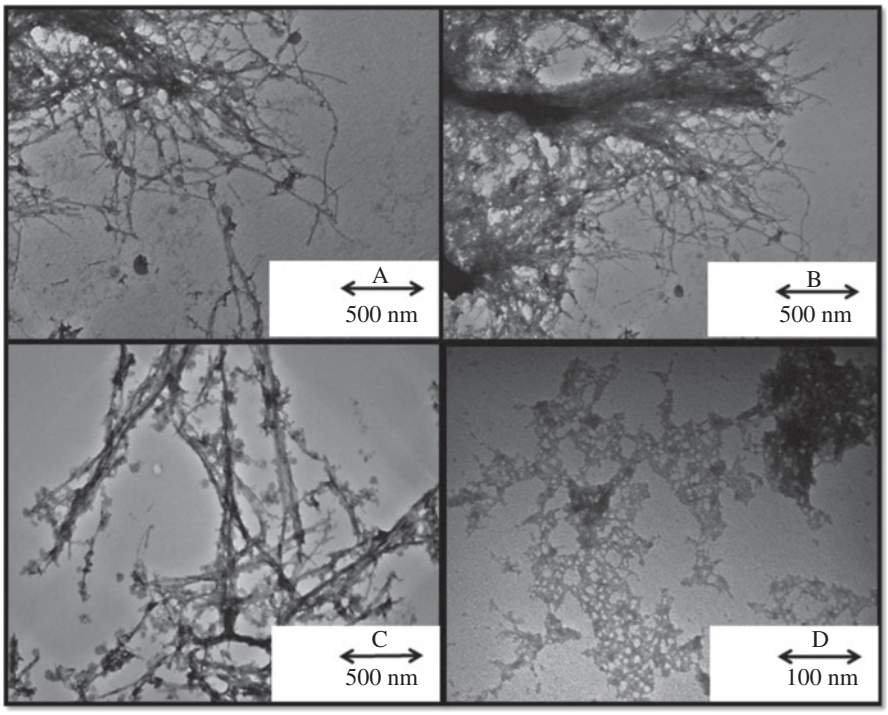


FIGURE 46.11 Selected images of electron micrographs of an insulin fibril sample incubated for 12 h in 50 mM citrate phosphate buffer at pH 2.6 in presence of (a) 0% TFE, (b) 5% TFE, (c) 15% TFE. (d) 25% TFE. (Adapted from Banerjee and Das 2011 [10], p. 142. © Elsevier B.V.; reproduced with permission.)

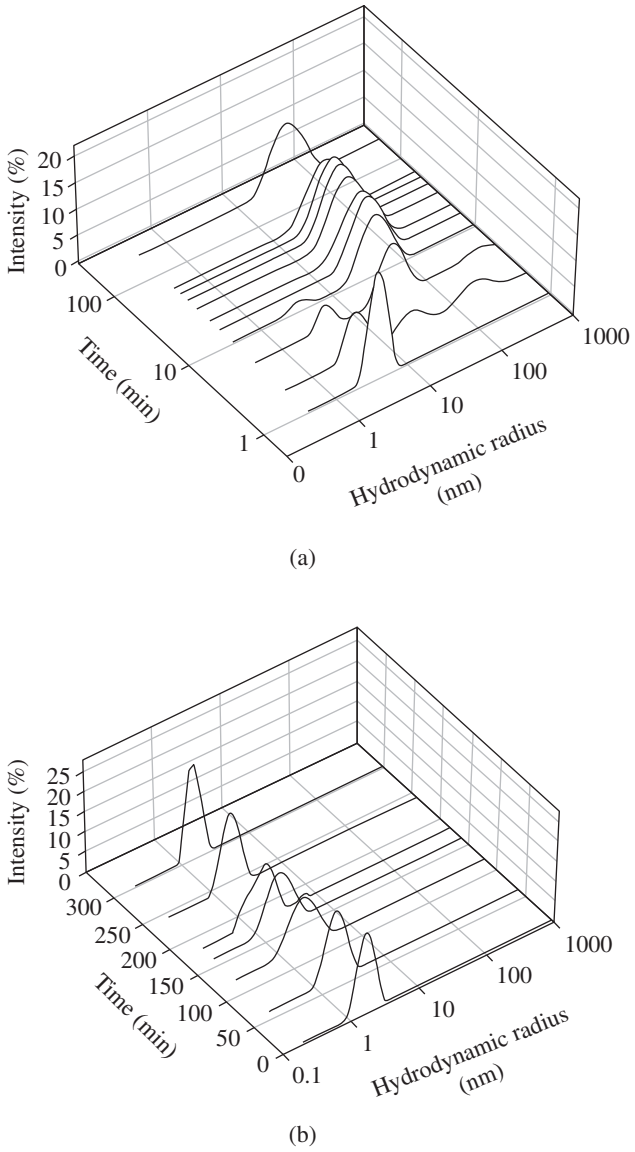


FIGURE 46.12 Intensity particle size distribution spectra of bovine insulin in 10(a) 0% (v/v) and (b) 25 % (v/v) concentrations of TFE at 25°C. Since insulin is monodispersed in this concentration and temperature range, particle size above 100 nm was excluded. (Adapted from Banerjee and Das 2011 [10], p. 142. © Elsevier B.V.; reproduced with permission.)

protofibrils are longer than the TFE-induced fibrils of Barster. Hence, these fluoroalcohols may not follow a similar mechanism of interaction with the fibrillating proteins.

46.3 SUMMARY AND CONCLUSION

Insulin is a relatively small α-helical protein, which can undergoes structural transition to produce insulin fibrils having a preponderance of cross-β-sheets. Fibrillation under physiological conditions is a slow process and often takes a very long time to evolve. However, fibrillation of insulin can pose a serious threat to its therapeutic uses against type 2 diabetes. Insulin exists in various multimeric forms under physiological conditions. The key step in the formation of insulin fibrils is its dissociation of the insulin oligomer into the monomer, which is the precursor for the nucleation phase of the fibrillation process. Small molecules, which can interfere with the insulin dissociation process, can delay the fibrillation process. On the basis of this principle, several small molecules and peptides have been developed that can slow down the fibrillation process. Of these, the designed hybrid peptides have been found to be quite promising. The role of hydrophobic peptide NK9 was studied in detail to understand the structural basis of the mechanism of delaying the fibrillation process. Among other small molecules, some aromatic polycyclic compounds and trifluoroethanol were found to be quite effective. These studies may constitute the basis for designing small molecules to control protein fibrillation in general.

REFERENCES

[1] Friedreich, N., Kekulé, A. (1859). Zur Amyloidfrage. *Archiv. Pathol. Anat.* **16**, 50–65.

[2] Guijarro, J.I.; Sunde, M.; Jones, J.A.; Campbell, I.D.; Dobson, C.M. (1998). Amyloid fibril formation by an SH3 domain. *Proc. Natl. Acad. Sci.* **95**, 4224–4228.

[3] Chiti, F., Webster, P., Taddei, N., Clark, A., Stefani, M., Ramponi, G., Dobson, C.M. (1999). Designing conditions for in vitro formation of amyloid protofilaments and fibrils. *Proc. Natl. Acad. Sci. USA* **96**, 3590–3594.

[4] Uversky, V.N., Fink, A.L. (2004). Conformational constraints for amyloid fibrillation: The importance of being unfolded. *Biochim. Biophys. Acta Proteins Proteom.* **1698**, 131–153.

[5] Toyama, B.H., Weissman, J.S. (2011). Amyloid structure: Conformational diversity and consequences. *Annu. Rev. Biochem.* **80**, 557–585.

[6] Surmacz-Chwedoruk, W., Malka, I., Bożycki, Ł., Nieznańska, H., Dzwolak, W. (2014). On the heat stability of amyloid-based biological activity: Insights from thermal degradation of insulin fibrils. *PLoS ONE* **9**, e86320.

[7] Harper, J.D., Lansbury, P.T. (1997). Models of amyloid seeding in Alzheimer's disease and scrapie: Mechanistic truths and physiological consequences of the time-dependent solubility of amyloid proteins. *Annu. Rev. Biochem.* **66**, 385–407.

[8] Morel, B., Varela, L., Azuaga, A.I., Conejero-Lara, F. (2010). Environmental conditions affect the kinetics of nucleation of amyloid fibrils and determine their morphology. *Biophys. J.* **99**, 3801–3810.

[9] Brange, J., Andersen, L., Laursen, E.D., Meyn, G., Rasmussen, E. (1997). Toward understanding insulin fibrillation. *J. Pharm. Sci.* **86**, 517–525.

[10] Banerjee, V., Das, K.P. (2012). Modulation of pathway of insulin fibrillation by a small molecule helix inducer 2,2,2-trifluoroethanol. *Colloids Surf. B: Biointerfaces* **92**, 142–150.

[11] Sluzky, V., Tamada, J.A., Klibanov, A.M., Langer, R. (1991). Kinetics of insulin aggregation in aqueous solutions upon agitation in the presence of hydrophobic surfaces. *Proc. Natl. Acad. Sci. USA* **88**, 9377–9381.

[12] Fei, L., Perrett, S. (2009). Effect of nanoparticles on protein folding and fibrillogenesis. *Int. J. Mol. Sci.* **10**, 646–655.

[13] Cabaleiro-Lago, C., Quinlan-Pluck, F., Lynch, I., Dawson, K.A., Linse, S. (2010). Dual effect of amino modified polystyrene nanoparticles on amyloid β protein fibrillation. *ACS Chem. Neurosci.* **1**, 279–287.

[14] Chiti, F., Dobson, C.M. (2006). Protein misfolding, functional amyloid, and human disease. *Annu. Rev. Biochem.* **75**, 333–366.

[15] Monsellier, E., Chiti, F. (2007). Prevention of amyloid-like aggregation as a driving force of protein evolution. *EMBO Rep.* **8**, 737–742.

[16] Dobson, C.M. (2002). Protein-misfolding diseases: Getting out of shape. *Nature* **418**, 729–730.

[17] Lansbury, P.T., Lashuel, H.A. (2006). A century-old debate on protein aggregation and neurodegeneration enters the clinic. *Nature* **443**, 774–779.

[18] Collinge, J., Clarke, A.R. (2007). A general model of prion strains and their pathogenicity. *Science* **318**, 930–936.

[19] Blundell, T.L., Cutfield, J.F., Cutfield, S.M., Dodson, E.J., Dodson, G.G., Hodgkin, D.C., Mercola, D.A., Vijayan, M. (1971). Atomic positions in rhombohedral 2-zinc insulin crystals. *Nature* **231**, 506–511.

[20] Banerjee, V., Kar, R.K., Datta, A., Parthasarathi, K., Chatterjee, S., Das, K.P., Bhunia, A. (2013). Use of a small peptide fragment as an inhibitor of insulin fibrillation process: A study by high and low resolution spectroscopy. *PLoS ONE* **8**, e72318.

[21] Ahmad, A., Millett, I.S., Doniach, S., Uversky, V.N., Fink, A.L. (2004). Stimulation of insulin fibrillation by urea-induced intermediates. *J. Biol. Chem.* **279**, 14999–15013.

[22] Hua, Q.-x., Weiss, M.A. (2004). Mechanism of insulin fibrillation: The structure of insulin under amyloidogenic conditions resembles a protein-folding intermediate. *J. Biol. Chem.* **279**, 21449–21460.

[23] Störkel, S., Schneider, H., Müntefering, H., Kashiwagi, S. (1983). Iatrogenic, insulin-dependent, local amyloidosis. *Lab. Invest. J. Tech. Methods Pathol.* **48**, 108–111.

[24] Dische, F., Wernstedt, C., Westermark, G., Westermark, P., Pepys, M., Rennie, J., Gilbey, S., Watkins, P. (1988). Insulin as an amyloid-fibril protein at sites of repeated insulin injections in a diabetic patient. *Diabetologia* **31**, 158–161.

[25] Swift, B., Hawkins, P., Richards, C., Gregory, R. (2002). Examination of insulin injection sites: An unexpected finding of localized amyloidosis. *Diabet. Med.* **19**, 88–882.

[26] Sahoo, S., Reeves, W., DeMay, R.M. (2003). Amyloid tumor: A clinical and cytomorphologic study. *Diagn. Cytopathol.* **28**, 325–328.

[27] Muzaffar, M., Ahmad, A. (2011). The mechanism of enhanced insulin amyloid fibril formation by NaCl is better explained by a conformational change model. *PLoS ONE* **6**, e27906.

[28] Yumlu, S., Barany, R., Eriksson, M., Röcken, C. (2009). Localized insulin-derived amyloidosis in patients with diabetes mellitus: A case report. *Human Pathol.* **40**, 1655–1660.

[29] Albert, S.G., Obadiah, J., Parseghian, S.A., Yadira Hurley, M., Mooradian, A.D. (2007). Severe insulin resistance associated with subcutaneous amyloid deposition. *Diabet. Res. Clin. Pract.* **75**, 374–376.

[30] Nilsson, K.P.R. (2009). Small organic probes as amyloid specific ligands–past and recent molecular scaffolds. *FEBS Lett.* **583**, 2593–2599.

[31] Bouchard, M., Zurdo, J., Nettleton, E.J., Dobson, C.M., Robinson, C.V. (2000). Formation of insulin amyloid fibrils followed by FTIR simultaneously with CD and electron microscopy. *Protein Sci.* **9**, 1960–1967.

[32] Kurouski, D., Deckert-Gaudig, T., Deckert, V., Lednev, I.K. (2012). Structure and composition of insulin fibril surfaces probed by TERS. *J. ACS* **134**, 13323–13329.

[33] Velikov, K.P., Koenderink, G., Bonn, M. (2013). Amyloids: From molecular structure to mechanical properties. *Polymer* **30**, e16.

[34] Hua, Q.-X., Hu, S.-Q., Frank, B.H., Jia, W., Chu, Y.-C., Wang, S.-H., Burke, G.T., Katsoyannis, P.G., Weiss, M.A. (1996). Mapping the functional surface of insulin by design: Structure and function of a novel A-chain Analogue. *J. Mol. Biol.* **264**, 390–403.

[35] Weiss, M.A., Hua, Q.-X., Jia, W., Chu, Y.-C., Wang, R.-Y., Katsoyannis, P.G. (2000). Hierarchical protein "un-design": Insulin's intrachain disulfide bridge tethers a recognition α-helix. *Biochemistry* **39**, 15429–15440.

[36] Chen, S., Ferrone, F.A., Wetzel, R. (2002). Huntington's disease age-of-onset linked to polyglutamine aggregation nucleation. *Proc. Natl. Acad. Sci.* **99**, 11884–11889.

[37] Xue, W.-F., Homans, S.W., Radford, S.E. (2008). Systematic analysis of nucleation-dependent polymerization reveals new insights into the mechanism of amyloid self-assembly. *Proc. Natl. Acad. Sci.* **105**, 8926–8931.

[38] Ahmad, A., Uversky, V.N., Hong, D., Fink, A.L. (2005). Early events in the fibrillation of monomeric insulin. *J. Biol. Chem.* **280**, 42669–42675.

[39] Vestergaard, B., Groenning, M., Roessle, M., Kastrup, J.S., Van De Weert, M., Flink, J.M., Frokjaer, S., Gajhede, M., Svergun, D.I. (2007). A helical structural nucleus is the primary elongating unit of insulin amyloid fibrils. *PLoS Biol.* **5**, e134.

[40] Nayak, A., Sorci, M., Krueger, S., Belfort, G. (2009). A universal pathway for amyloid nucleus and precursor formation for insulin. *Proteins Struct. Funct. Bioinform.* **74**, 556–565.

[41] Tycko, R. (2003). Insights into the amyloid folding problem from solid-state NMR. *Biochemistry* **42**, 3151–3159.

[42] Makin, O.S., Sikorski, P., Serpell, L.C. (2006). Diffraction to study protein and peptide assemblies. *Curr. Opin. Chem. Biol.* **10**, 417–422.

[43] Jiménez, J.L., Nettleton, E.J., Bouchard, M., Robinson, C.V., Dobson, C.M., Saibil, H.R. (2002). The protofilament structure of insulin amyloid fibrils. *Proc. Natl. Acad. Sci.* **99**, 9196–9201.

[44] Fowler, D.M., Koulov, A.V., Alory-Jost, C., Marks, M.S., Balch, W.E., Kelly, J.W. (2005). Functional amyloid formation within mammalian tissue. *PLoS Biol.* **4**, e6.

[45] Jiménez, J.L., Tennent, G., Pepys, M., Saibil, H.R. (2001). Structural diversity of ex vivo amyloid fibrils studied by cryo-electron microscopy. *J. Mol. Biol.* **311**, 241–247.

[46] Jimenez, J.L., Guijarro, J.I., Orlova, E., Zurdo, J., Dobson, C.M., Sunde, M., Saibil, H.R. (1999). Cryo-electron microscopy structure of an SH3 amyloid fibril and model of the molecular packing. *EMBO J.* **18**, 815–821.

[47] Goldsbury, C., Kistler, J., Aebi, U., Arvinte, T., Cooper, G.J.S. (1999). Watching amyloid fibrils grow by time-lapse atomic force microscopy. *J. Mol. Biol.* **285**, 33–39.

[48] Eanes, E.D., Glenner, G.G. (1968). X-ray diffraction studies on amyloid filaments. *J. Histochem. Cytochem.* **16**, 673–677.

[49] Inouye, H., Fraser, P.E., Kirschner, D.A. (1993). Structure of beta-crystallite assemblies formed by Alzheimer beta-amyloid protein analogues: Analysis by x-ray diffraction. *Biophys. J.* **64**, 502–519.

[50] Sunde, M., Blake, C. (1997). The structure of amyloid fibrils by electron microscopy and x-ray diffraction. In Richards, F.M., Peter, S.K. (eds.), *Advances in Protein Chemistry*. Academic Press, San Diego, Vol. Vol. 50, pp. C11–C12, 123–124, 125–159.

[51] Bauer, H.H., Aebi, U., Häner, M., Hermann, R., Müller, M., Arvinte, T., Merkle, H.P. (1995). Architecture and polymorphism of fibrillar supramolecular assemblies produced by in vitro aggregation of human calcitonin. *J. Struct. Biol.* **115**, 1–15.

[52] Ionescu-Zanetti, C., Khurana, R., Gillespie, J.R., Petrick, J.S., Trabachino, L.C., Minert, L.J., Carter, S.A., Fink, A.L. (1999). Monitoring the assembly of Ig light-chain amyloid fibrils by atomic force microscopy. *Proc. Natl. Acad. Sci. USA* **96**, 13175–13179.

[53] Ivanova, M.I., Sievers, S.A., Sawaya, M.R., Wall, J.S., Eisenberg, D. (2009). Molecular basis for insulin fibril assembly. *Proc. Natl. Acad. Sci.* **106**, 18990–18995.

[54] Thurow, H., Geisen, K. (1984). Stabilisation of dissolved proteins against denaturation at hydrophobic interfaces. *Diabetologia* **27**, 212–218.

[55] Grau, U., Saudek, C.D. (1987). Stable insulin preparation for implanted insulin pumps. Laboratory and animal trials. *Diabetes* **36**, 1453–1459.

[56] Brewster, M.E., Hora, M.S., Simpkins, J.W., Bodor, N. (1991). Use of 2-hydroxypropyl-beta-cyclodextrin as a solubilizing and stabilizing excipient for protein drugs. *Pharm. Res.* **8**, 792–795.

[57] Rabiee, A., Ebrahim, A., Navidpour, L., Morshedi, D., Ghasemi, A., Sabbaghian, M., Nemati, M., Nemat, M. (2011). Benzofuranone derivatives as effective small molecules related to insulin amyloid fibrillation: A structure-function study. *Chem. Biol. Drug Design* **78**, 659–666.

[58] Arora, A., Ha, C., Park, C.B. (2004). Inhibition of insulin amyloid formation by small stress molecules. *FEBS Lett.* **564**, 121–125.

[59] DeFelippis, M.R., Chance, R.E., Frank, B.H. (2001). Insulin self-association and the relationship to pharmacokinetics and pharmacodynamics. *Crit. Rev. Ther. Drug Carrier Syst.* **18**.

[60] Giger, K., Vanam, R.P., Seyrek, E., Dubin, P.L. (2008). Suppression of insulin aggregation by heparin. *Biomacromolecules* **9**, 2338–2344.

[61] Gibson, T.J., Murphy, R.M. (2006). Inhibition of insulin fibrillogenesis with targeted peptides. *Protein Sci.* **15**, 1133–1141.

[62] Luo, J., Abrahams, J.P. (2014). Cyclic peptides as inhibitors of amyloid fibrillation. *Chem. Eur. J.* **20**, 2410–2419.

[63] Buchner, J., Rudolph, R. (1991). Renaturation, purification and characterization of recombinant Fab-fragments produced in Escherichia coli. *Nat. Biotechnol.* **9**, 157–162.

[64] Taneja, S., Ahmad, F. (1994). Increased thermal stability of proteins in the presence of amino acids. *Biochem. J.* **303**, 147–153.

[65] Gibson, T.J., Murphy, R.M. (2005). Design of peptidyl compounds that affect β-amyloid aggregation: Importance of surface tension and context. *Biochemistry* **44**, 8898–8907.

[66] Velkova, A., Tatarek-Nossol, M., Andreetto, E., Kapurniotu, A. (2008). Exploiting cross-amyloid interactions to inhibit protein aggregation but not function: Nanomolar affinity inhibition of insulin aggregation by an IAPP mimic. *Angew. Chem. Int. Ed.* **47**, 7114–7118.

[67] Johnson, K., O'Brien, T., Hayden, D., Jordan, K., Ghobrial, H., Mahoney, W., Westermark, P. (1988). Immunolocalization of islet amyloid polypeptide (IAPP) in pancreatic beta cells by means of peroxidase-antiperoxidase (PAP) and protein A-gold techniques. *Am. J. Pathol.* **130**, 1.

[68] Westermark, P., Andersson, A., Westermark, G.T. (2011). Islet amyloid polypeptide, islet amyloid, and diabetes mellitus. *Physiol. Rev.* **91**, 795–826.

[69] Westermark, P., Li, Z.-C., Westermark, G.T., Leckström, A., Steiner, D.F. (1996). Effects of beta cell granule components on human islet amyloid polypeptide fibril formation. *FEBS Lett.* **379**, 203–206.

[70] Yan, L.-M., Tatarek-Nossol, M., Velkova, A., Kazantzis, A., Kapurniotu, A. (2006). Design of a mimic of nonamyloidogenic and bioactive human islet amyloid polypeptide (IAPP) as nanomolar affinity inhibitor of IAPP cytotoxic fibrillogenesis. *Proc. Natl. Acad. Sci. USA* **103**, 2046–2051.

[71] Jayaraman, M., Kannayiram, G., Rajadas, J. (2008). Amyloid toxicity in skeletal myoblasts: Implications for inclusion-body myositis. *Arch. Biochem. Biophys.* **474**, 15–21.

[72] Sun, M.-K., Alkon, D.L. (2006). Links between Alzheimer's disease and diabetes. *Drugs Today* **42**, 481.

[73] Yan, L.-M., Velkova, A., Tatarek-Nossol, M., Andreetto, E., Kapurniotu, A. (2007). Ein IAPP-Mimetikum blockiert die zytotoxische Aggregation von Aβ – die Kreuzunterdrückung der Amyloidtoxizität von Aβ und IAPP deutet auf einen molekularen Zusammenhang zwischen Alzheimer-Krankheit und Typ-II-Diabetes hin. *Angew. Chem.* **119**, 1268–1274.

[74] Landreh, M., Stukenborg, J.-B.; Willander, H., Söder, O., Johansson, J., Jörnvall, H. (2012). Proinsulin C-peptide interferes with insulin fibril formation. *Biochem. Biophys. Res. Commun.* **418**, 489–493.

[75] Steiner, D.F., Cunningham, D., Spigelman, L., Aten, B. (1967). Insulin biosynthesis: Evidence for a precursor. *Science* **157**, 697–700.

[76] Qiao, Z.-S., Min, C.-Y., Hua, Q.-X., Weiss, M.A., Feng, Y.-M. (2003). In vitro refolding of human proinsulin kinetic intermediates, putative disulfide-forming pathway, folding initiation site, and potential role of C-peptide in folding process. *J. Biol. Chem.* **278**, 17800–17809.

[77] Min, C.Y., Qiao, Z.S., Feng, Y.M. (2004). Unfolding of human proinsulin. *Eur. J. Biochem.* **271**, 1737–1747.

[78] Janciauskiene, S., Eriksson, S., Carlemalm, E., Ahrén, B. (1997). B cell granule peptides affect human islet amyloid polypeptide (IAPP) fibril formation in vitro. *Biochem. Biophys. Res. Commun.* **236**, 580–585.

[79] Huang, K., Dong, J., Phillips, N.B., Carey, P.R., Weiss, M.A. (2005). Proinsulin is refractory to protein fibrillation: Topological protection of a precursor protein from cross-β assembly. *J. Biol. Chem.* **280**, 42345–42355.

[80] Noormagi, A., Gavrilova, J., Smirnova, J., Tõugu, V., Palumaa, P. (2010). Zn(II) ions co-secreted with insulin suppress inherent amyloidogenic properties of monomeric insulin. *Biochem. J.* **430**, 511–518.

[81] Mishra, N.K., Joshi, K.B., Verma, S. (2013). Inhibition of human and bovine insulin fibril formation by designed peptide conjugates. *Mol. Pharm.* **10**, 3903–3912.

[82] Frydman-Marom, A., Rechter, M., Shefler, I., Bram, Y., Shalev, D.E., Gazit, E. (2009). Cognitive-performance recovery of Alzheimer's disease model mice by modulation of early soluble amyloidal assemblies. *Angew. Chem.* **121**, 2015–2020.

[83] Vilasi, S., Iannuzzi, C., Portaccio, M., Irace, G., Sirangelo, I. (2008). Effect of trehalose on W7FW14F apomyoglobin and insulin fibrillization: New insight into inhibition activity. *Biochemistry* **47**, 1789–1796.

[84] Wang, S.S.S., Liu, K.-N., Han, T.-C. (2010). Amyloid fibrillation and cytotoxicity of insulin are inhibited by the amphiphilic surfactants. *Biochim. Biophys. Acta Mol. Basis Disease* **1802**, 519–530.

[85] Hadas, S., Georges, B., Shlomo, M. (2009). Synthesis and characterization of fluorinated magnetic core–shell nanoparticles for inhibition of insulin amyloid fibril formation. *Nanotechnology* **20**, 225106.

[86] Wang, S.-H., Dong, X.-Y., Sun, Y. (2012). Effect of (−)-epigallocatechin-3-gallate on human insulin fibrillation/aggregation kinetics. *Biochem. Eng. J.* **63**, 38–49.

[87] Rabiee, A., Ebrahim-Habibi, A., Ghasemi, A., Nemat-Gorgani, M. (2013). How curcumin affords effective protection against amyloid fibrillation in insulin. *Food Funct.* **4**, 1474–1480.

[88] Hong, Y., Meng, L., Chen, S., Leung, C.W.T., Da, L.-T., Faisal, M., Silva, D.-A., Liu, J., Lam, J.W.Y., Huang, X., Tang, B.Z. (2011). Monitoring and inhibition of insulin fibrillation by a small organic fluorogen with aggregation-induced emission characteristics. *J. Am. Chem. Soc.* **134**, 1680–1689.

[89] Levy-Sakin, M., Shreberk, M., Daniel, Y., Gazit, E. (2009). Targeting insulin amyloid assembly by small aromatic molecules: Toward rational design of aggregation inhibitors. *Islets* **1**, 210–215.

[90] Thomas, T., Nadackal, T.G., Thomas, K. (2001). Aspirin and non-steroidal anti-inflammatory drugs inhibit amyloid-β aggregation. *Neuroreport* **12**, 3263–3267.

[91] De Felice, F.G., Houzel, J.-C., Garcia-Abreu, J., Louzada Jr., P.R.F., Afonso, R.C., Meirelles, M.N.L., Lent, R., Neto, V.M., Ferreira, S.T. (2001). Inhibition of Alzheimer's disease β-amyloid aggregation, neurotoxicity, and in vivo deposition by nitrophenols: implications for Alzheimer's therapy. *FASEB J.* **15**, 1297–1299.

[92] Sonnichsen, F.D., Van Eyk, J.E., Hodges, R.S., Sykes, B.D. (1992). Effect of trifluoroethanol on protein secondary structure: An NMR and CD study using a synthetic actin peptide. *Biochemistry* **31**, 8790–8798.

[93] Hirota, N., Goto, Y., Mizuno, K. (1997). Cooperative α-helix formation of β-lactoglobulin and melittin induced by hexafluoroisopropanol. *Protein Sci.* **6**, 416–421.

[94] Ecroyd, H., Carver, J. (2009). Crystallin proteins and amyloid fibrils. *Cell. Mol. Life Sci.* **66**, 62–81.

[95] Liu, W., Prausnitz, J.M., Blanch, H.W. (2004). Amyloid fibril formation by peptide LYS (11-36) in aqueous trifluoroethanol. *Biomacromolecules* **5**, 1818–1823.

[96] Vieira, E.P., Hermel, H., Möhwald, H. (2003). Change and stabilization of the amyloid-beta](1-40) secondary structure by fluorocompounds. *Biochim. Biophys. Acta Proteins Proteom.* **1645**, 6–14.

[97] Sekhar, A., Udgaonkar, J.B. (2010). Fluoroalcohol-induced modulation of the pathway of amyloid protofibril formation by Barstar. *Biochemistry* **50**, 805–819.

47

INTERFACIAL WATER BETWEEN CHARGE-NEUTRALIZED POLYMER AND LIQUID WATER

Hiromi Kitano and Makoto Gemmei-Ide

Department of Applied Chemistry, Graduate School of Science and Engineering, University of Toyama, Toyama, Japan

47.1 INTRODUCTION

The structure of water at polymer material–liquid water interfaces reflects chemical and physical properties of the polymer. Therefore, the structure analysis of interfacial water gives us invaluable information about usability of polymer materials in biomedical fields.

Zwitterionic polymer is the general term for an ampholytic polymer containing identical numbers of cationic and anionic species, commonly on the same monomer units [1]. Zwitterionic polymers have been designed to mimic phosphatidylcholine (lecithin, PC), which is abundant in cell membranes [2, 3], and their applicability to biomedical fields has been extensively investigated. For example, polymer films composed of apolar monomers such as *n*-butyl methacrylate (BMA) and zwitterionic monomers such as 2-methacryloyloxyethyl phosphorylcholine (MPC, phosphobetaine), 3-sulfo-*N,N*-dimethyl-*N*-(3-methacrylamidopropyl)propanaminium hydroxide inner salt (SPB, sulfopropylbetaine), and 1-carboxy-*N*,*N*-dimethyl-*N*-(2-methacryloyloxyethyl)methanaminium hydroxide inner salt (CMB, caboxymethylbetaine; Scheme 47.1a) [4–8] were found to be highly biocompatible [4, 6–9]. The amount of proteins adsorbed and the number of platelets adhering to a film of a random copolymer of CMB and BMA were found to be much less than those onto a PolyBMA film [7, 8].

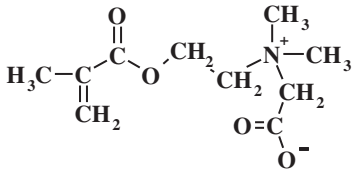
The sorbing processes of water to polymeric materials or distinction of the water sorbed to the polymers from that incorporated within the polymer matrix were examined with difference spectra obtained by attenuated total reflection (ATR) infrared spectroscopy [10, 11], and it was found that the structure of water incorporated in the matrix of polymer thin films composed of BMA and zwitterionic monomers such as MPC, SPB, and CMB was similar to that of bulk water [7, 8]. Raman spectroscopy also indicated that the hydrogen-bonded network structure of water in the vicinity of zwitterionic polymers and copolymers is not largely disturbed, in contrast to the electrostatically hydrated ordinary polyelectrolytes [12, 13]. However, the structure of "interfacial" water cannot directly be observed by these methods, and therefore, the *sum frequency generation* (SFG) method, which can detect molecules that lose centrosymmetry [14], was adopted to investigate the structure of water at various polymer–liquid water interfaces. The polymer materials examined were (1) a thin film of a zwitterionic copolymer, poly(CMB-*r*-BMA); (2) a brush of polyCMB; and (3) an amphoteric brush of poly(MA-*r*-DMAEMA)(1:1).

47.2 POLYMER FILM SYSTEMS

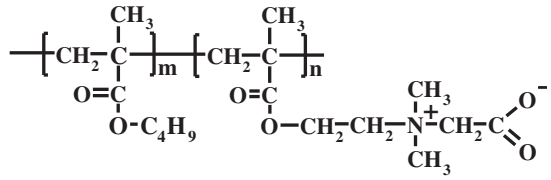
For the deposition of copolymer films, a flat face of fused-quartz semicylindrical prism was modified with octacdecyltrichlorosilane (ODS). Copolymers [poly(CMB-*r*-BMA), poly(MA-*r*-BMA), and poly(DMAEMA-*r*-BMA)] having ∼70 mol% of BMA residues were prepared in ethanol using 2,2′-azobisinsobutyronitrile (AIBN), and their thin films

Encyclopedia of Biocolloid and Biointerface Science, Volume 2, First Edition. Edited by Hiroyuki Ohshima.
© 2016 John Wiley & Sons, Inc. Published 2016 by John Wiley & Sons, Inc.

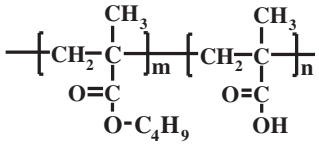
(a)



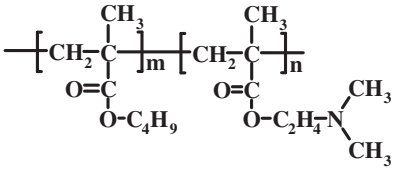
(b)



(c)



(d)



Scheme 47.1 Chemical structures of (a) 1-carboxy-*N*,*N*-dimethyl-*N*-(2-methacryloyloxyethyl)-methanaminium hydroxide inner salt (CMB), (b) a copolymer of CMB and *n*-butyl methacrylate (BMA) [poly(CMB-*r*-BMA)], (c) a copolymer of methacrylic acid (MA) and BMA [poly(MA-*r*-BMA)], and (d) a copolymer of 2-(dimethylamino)ethyl methacrylate (DMAEMA) and BMA [poly(DMAEMA-*r*-BMA)].

were prepared by the cast method on a flat face of the prism [15].

The sum frequency generation (SFG) spectra of water at the polymer–water interfaces were obtained using the apparatus reported elsewhere [16, 17]. Namely, a picosecond Nd:YAG laser was employed to pump an (OPG/OPA/DFG) system, which generates tunable infrared radiation from 2.3 to 8.5 μm. The second-harmonic output (532 nm) from the laser was used as a visible light. The flat face of a quartz prism was in contact with various media, and infrared and visible beams were overlapped at the interfaces. The incident angles of the visible and IR beams were 70° and 50°, respectively. The polarization conditions in the present experiment were all *s*, *s*, and *p* for SFG, visible, and IR laser beams, respectively. This polarization combination (*ssp*) is sensitive only to the vibrational mode normal to the surface of isotropic media. The SFG light generated from the sample surface was detected by a monochromator and Photomultiplier Tube.

Figure 47.1a shows SFG spectra of various polymer-coated prisms in the region 2800–3800 cm^{-1} in contact with liquid water. Peaks corresponding to O–H stretching (>3000 cm^{-1}) were observed for interfaces between the prisms and liquid water. The intensity of O–H stretching was in the following order: poly(MA-*r*-BMA) > polyBMA > poly(CMB-*r*-BMA) > poly(DMAEMA-*r*-BMA). SFG spectra in the region of 2800–3800 cm^{-1} for prisms soaked in liquid water for 48 h are shown in Fig. 47.1b. The intensity of O–H stretching was in the following order: poly(MA-*r*-BMA) > polyBMA > poly(DMAEMA-*r*-BMA) > poly(CMB-*r*-BMA). The total peak area for the same wavenumber region is compiled in Table 47.1. A slight *increase* in the peak area corresponding to O–H stretching was observed for the prisms covered with polyBMA, poly(MA-*r*-BMA), and poly(DMAEMA-*r*-BMA) films. In contrast, that for the poly(CMB-*r*-BMA)-covered quartz prism *decreased* with time.

The contact angles of the air-in-water system for three kinds of copolymer films and a polyBMA film are shown in Fig. 47.2. The figure indicates that the surface of poly(CMB-*r*-BMA) was most promptly equilibrated on contact with liquid water, whereas the surfaces of poly(MA-*r*-BMA) and poly(DMAEMA-*r*-BMA) were equilibrated more slowly, and even 48 h after onset of the contact with liquid water, the copolymer surfaces were not completely equilibrated yet.

These results indicated prompt appearance of hydrophilic and zwitterionic CMB residues on the surface of the film and disappearance of BMA residues on contact with liquid water to minimize free energy of the surface. As a result, the SFG signal of hydrophobically hydrated water (clathrate-formed water) decreased and the CMB inert to the water molecules dominated the SFG spectra (drastic reduction of oriented water layer).

On the other hand, the MA residue in the poly(MA-*r*-BMA) film was not greatly deprotonated, and its hydrophilicity was much smaller than that of CMB. Therefore, the exposure of MA residues at the film surface might not be significant in comparison with that of CMB residues. A similar tendency existed in the film of poly(DMAEMA-*r*-BMA). MA and DMAEMA residues gradually appeared at the surface, resulting in electrostatically hydrated water, and the SFG signal of the O–H stretching region increased correspondingly.

The contact angles (air-in-water) for poly(MA-*r*-BMA) and poly(DMAEMA-*r*-BMA) films 48 h after onset of immersion in liquid water were around 125° and 140°, respectively, whereas that for poly(CMB-*r*-BMA) was around 150°. Therefore, the poly(CMB-*r*-BMA) film was more hydrophilic than the poly(MA-*r*-BMA) and poly(DMAEMA-*r*-BMA) films at the equilibrated state with water. However, the hydrophilicity does not significantly contribute to the biocompatibility of the materials concerned. For example, a self-assembled monolayer having a sulfonate or tertiary ammonium headgroup adsorbed both lysozyme

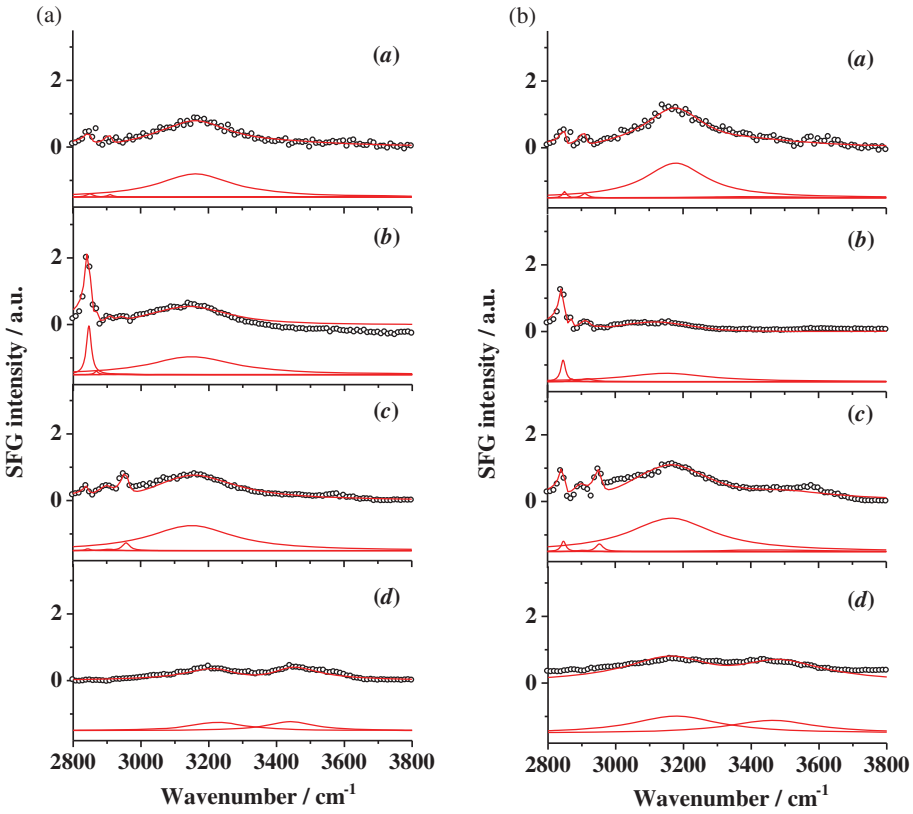


FIGURE 47.1 SFG spectra of O–H stretching region (>3000 cm^{-1}) and C–H stretching region (>3000 cm^{-1}) of various polymer films: (*a*) polyBMA; (*b*) poly(CMB-*r*-BMA) (CMB 29 mol%); (*c*) poly(MA-*r*-BMA) (MA 29 mol%); (*d*) poly(DMAEMA-*r*-BMA) (DMAEMA 28 mol%). (a) 0 h and (b) 48 h on immersion in water.

and fibrinogen to a large extent, whereas the zwitterionic group–carrying SAM showed significant suppression of protein adsorption [18]. The tendencies seen in Fig. 47.1b and Table 47.1 are in accordance with results of previous studies obtained by using Raman and infrared spectroscopies [12, 13].

As for the polyBMA system, the SFG signal was slightly increased 48 h after onset of the immersion in liquid water (Fig. 47.1b). The contact angle of polyBMA-modified quartz in the air-in-water system slightly decreased at the beginning, probably due to the gradual detachment of the film from the ODS-modified quartz in water.

TABLE 47.1 Intensity of SFG Signal for O–H Stretching Region at Interfaces of Water and Copolymer Films

	Total[a]	
Sample	0 h	48 h
PolyBMA	130.2 (0.58)	166.0 (0.74)
Poly(CMB-*r*-BMA)	108.4 (0.48)	50.4 (0.22)
Poly(MA-*r*-BMA)	151.4 (0.67)	225.1 (1.00)
Poly(DMAEMA-*r*-BMA)	72.6 (0.32)	158.4 (0.71)

[a]The values in parentheses are peak areas normalized by the peak area for a bare fused-quartz prism.

In SFG spectra for the interfaces of various prisms with liquid water, the O–H signal of strongly hydrogen-bonded water molecules appeared at around 3200 cm^{-1}, and that of weakly hydrogen-bonded ones appeared at around 3400 cm^{-1}. These peaks were very broad because of the strong coupling of neighboring water molecules and Fermi resonance with H–O–H deformation [17].

The electrostatic interaction between any compounds concerned and surrounding water molecules determines the orientation of the water molecules. Previously, the structure of water was investigated at the quartz–water interface in the presence of supported lipid bilayers (SLBs) by the SFG method [19]. The O–H oscillator strengths were most affected by the charged SLBs, rather than bilayers that did not contain a net charge [egg yolk phosphatidylcholine (PC)]. More recently, phase-sensitive SFG spectroscopy has revealed that water molecules at phospholipid–water interfaces are oriented preferentially by the electrostatic potential imposed by phospholipids [20]. Zwitterionic PC and phosphatidylethanolamine showed weaker water-orientating capability relative to negative phospholipids.

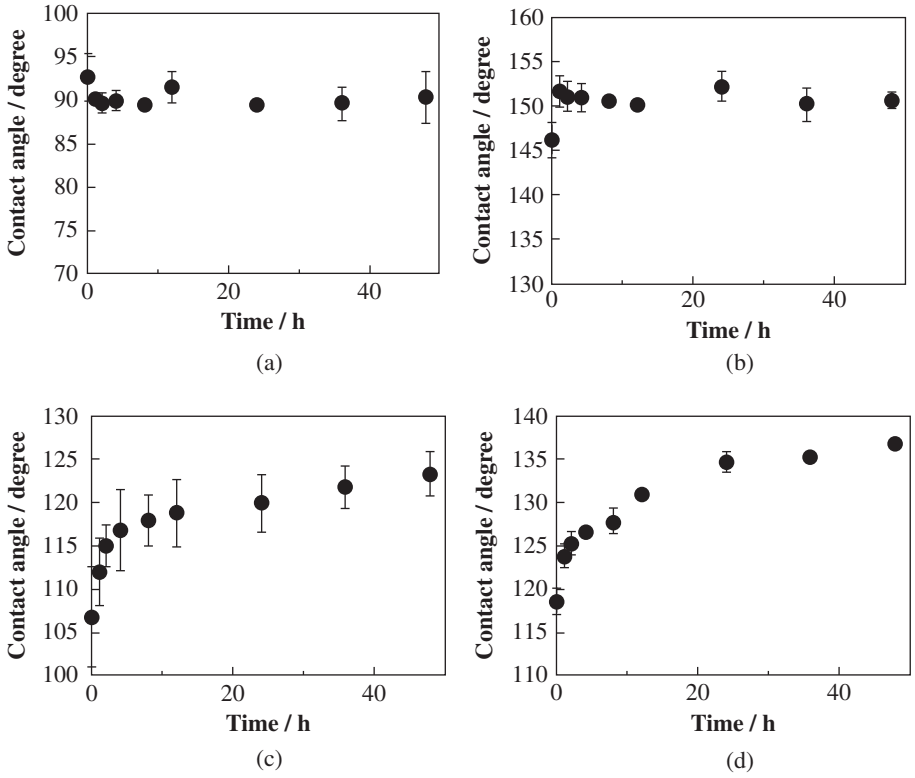


FIGURE 47.2 Time evolution of contact angles (air-in-water) of various surfaces: (a) polyBMA; (b) poly(CMB-*r*-BMA); (c) poly(MA-*r*-BMA); (d) poly(DMAEMA-*r*-BMA). Each θ value is the average value of five measurements, and the error bars denote standard deviation.

Using the same technique, the orientation of water at the PC–water interfaces was investigated in detail [21]. The water associated with the negatively charged phosphate is strongly H-bonded and has a net H-up orientation, whereas the water around the positively charged choline forms weaker H-bonds and has a net H-down orientation, and the water weakly interacting with the hydrophobic region of the lipid has a net H-up orientation.

The water molecules at the shortest distance from the phosphoryl choline groups might be affected by the ionic groups. The huge number of water molecules from the secondary hydration layer would be affected by both positively and negatively charged groups, resulting in orientation weaker than that of primary hydrating water. Phase-sensitive (heterodyne-detected) SFG can provide invaluable information about the "direction" of orientation (hydration), whereas conventional (homodyne-detected) SFG discussed in this chapter can give information about the "degree" of orientation. It should be mentioned here that the heterodyne-detected SFG method cannot easily be applied to liquid-solid interfaces in comparison with the homodyne-detected SFG method.

These results strongly suggested that the water molecules at the zwitterionic copolymer–water interfaces were not greatly oriented in comparison with the water molecules on the surfaces of polyBMA film-, poly(MA-*r*-BMA) film-, and poly(DMAEMA-*r*-BMA) film-modified quartz prisms. The order of the peak area of O–H stretching indicates that the zwitterionic polymer was the least perturbative to the structure of vicinal water (Table 47.1).

47.3 ZWITTERIONIC POLYMER BRUSH SYSTEM

A zwitterionic PCMB brush was prepared on a fused-quartz prism by the surface-initiated atom transfer radical polymerization (SI-ATRP) of CMB monomer [22]. The conformation of PCMB brush and the state of water at the surface of the brush were examined using the SFG technique. The C–H stretching band of the brush, indicating the *gauche* defect of the brush, was affected by the contact medium such as dry nitrogen, water vapor–saturated nitrogen, and liquid water. The water molecules at the PCMB–water interfaces were not largely oriented in comparison with the interfacial water of both bare and ATRP–initiator-modified quartz prisms. The electrical neutralization between neighboring positive and negative charges might diminish the electrostatic adsorption of water molecules to the vicinity of zwitterionic polymer brushes.

47.4 AMPHOTERIC POLYMER BRUSH SYSTEM

A polyampholyte brush was prepared on the surface of a quartz prism by surface-initiated reversible addition–fragmentation chain transfer (RAFT) polymerization of MA and DMAEMA at a monomer ratio of 1:1 [23]. The sum frequency generation method indicated that water molecules at the amphoteric polymer brush–water interfaces were not greatly oriented in comparison with those at the surfaces of bare quartz prisms, and negatively charged polyMA and positively charged polyDMAEMA brushes. The small perturbation effect of an amphoteric polymer brush on the structure of vicinal water was in accordance with the tendency of aqueous solution and thin films of amphoteric polymers observed by using Raman and infrared spectroscopies, respectively.

47.5 CONCLUSION

Water molecules at the surface of charge-neutralized polymer materials are not strongly oriented in comparison with those at the surfaces of nonpolar polymer film and positively or negatively charged polymer films and polymer brushes. Since zwitterionic polymer materials have excellent biocompatibilities in general [24, 25], it is highly probable that a small perturbation on the structure of vicinal water is a factor of biocompatibility of the materials concerned.

On contact of polymer materials with blood, for example, adsorption of proteins occurs, and, subsequently, cells adhere to the polymers via the adsorbed proteins. On contact of the proteins with the polymers, water molecules in the contacting region on the surface of the proteins and the polymers are repelled, and the partly dehydrated proteins are adsorbed to the polymers and denatured. Since the water molecules above zwitterionic polymers are not so strongly oriented, an increase in entropy on dehydration of the polymer surface at the collision of the protein molecule might not be as large as that in the case of a lopsidedly charged polymer surface and a hydrophobically hydrated polymer surface, providing the antibiofouling properties to zwitterionic polymers. Whether they are zwitterionic or amphoteric, charge-balanced polymer materials might satisfy these conditions.

REFERENCES

[1] Kudaibergenov, S., Jaeger, W., Laschewsky, A. (2006). *Adv. Polym. Sci.* **201**, 157.

[2] Yamauchi, J., Masuhara, E., Kadoma, N., Nakabayashi, N. (1977). Jpn. Patent JP 54063025.

[3] Lewis, A.L. (2000). *Colloids Surf. B: Biointerfaces* **18**, 261.

[4] Ishihara, K., Aragaki, R., Ueda, T., Watanabe, A., Nakabayashi, N. (1990). *J. Biomed. Mater. Res.* **24**, 1069.

[5] Yuan, J., Mao, C., Zhou, J., Shen, J., Lin, S.C., Zhu, W., Fang, J. F. (2003). *Polym. Int.* **52**, 1869.

[6] Kitano, H., Mori, T., Tada, S., Takeuchi, Y., Gemmei-Ide, M., Tanaka, M. (2005). *Macromol. Biosci*. **5**, 314.

[7] Kitano, H., Tada, S., Mori, T., Takaha, K., Gemmei-Ide, M., Tanaka, M., Fukuda, M., Yokoyama, Y. (2005). *Langmuir* **21**, 11932.

[8] Tada, S., Inaba, C., Mizukami, K., Fujishita, S., Gemmei-Ide, M., Kitano, H., Tanaka, M., Mochizuki, A., Matsunaga, T. (2009). *Macromol. Biosci*. **9**, 63.

[9] Lobb, E.J., Ma, I.Y., Billingham, N., Armes, S.P., Lewis, A.L. (2001). *J. ACS* **123**, 7913.

[10] Ide, M., Yoshikawa, D., Maeda, Y., Kitano, H. (1999). *Langmuir* **15**, 926.

[11] Kitano, H., Ichikawa, K., Ide, M., Mizuno, W., Fukuda, M. (2001). *Langmuir* **17**, 1889.

[12] Kitano, H., Sudo, K., Ichikawa, K., Ide, M., Ishihara, K. (2000). *J. Phys. Chem. B* **104**, 11425.

[13] Kitano, H., Imai, M., Mori, T., Gemmei-Ide, M., Yokoyama, Y., Ishihara, K. (2003). *Langmuir* **19**, 10260.

[14] Shen, Y.R. (1984). *The Principles of Non-linear Optics.* Wiley, New York.

[15] Kondo, T., Nomura, K., Gemmei-Ide, M., Kitano, H., Noguchi, H., Uosaki, K., Saruwatari, Y. (2014). *Colloids Surf. B: Biointerfaces* **113**, 361.

[16] Noguchi, H., Taneda, K., Minowa, H., Naohara, H., Uosaki, K. (2010). *J. Phys. Chem. C* **114**, 3958.

[17] Nihonyanagi, S., Ye, S., Uosaki, K. (2001). *Electrochim. Acta* **46**, 3057.

[18] Holmlin, R.E., Chen, X., Chapman, R.G., Takayama, S., Whitesides, G.M. (2001). *Langmuir* **17**, 2841.

[19] Kim, J., Kim, G., Cremer, P.S. (2001). *Langmuir* **17**, 7255.

[20] Chen, X., Hua, W., Huang, Z., Allen, H.C. (2010). *J. ACS* **132**, 11336.

[21] Mondal, J.A., Nihonyanagi, S., Yamaguchi, S., Tahara, T. (2012). *J. ACS* **134**, 7842.

[22] Kondo, T.Nomura, K., Murou, M., Gemmei-Ide, M., Kitano, H., Ohno, K., Saruwatari, Y., Noguchi, H., Uosaki, K. (2012). *Colloids Surf. B: Biointerfaces* **100**, 126.

[23] Kondo, T., Gemmei-Ide, M., Kitano, H., Ohno, K., Noguchi, H., Uosaki, K. (2012). *Colloids Surf. B: Biointerfaces* **91**, 215.

[24] Kitano, H., Suzuki, H., Matsuura, K., Ohno, K. (2010). *Langmuir* **26**, 6767.

[25] Kitano, H., Suzuki, H., Kondo, T., Sasaki, K., Iwanaga, S., Nakamura, M., Ohno, K., Saruwatari, Y. (2011). *Macromol. Biosci.* **11**, 557.

48

LANGMUIR MONOLAYER INTERACTION OF PERFLUOROOCTYLATED LONG-CHAIN ALCOHOLS WITH BIOMEMBRANE CONSTITUENTS

Hiromichi Nakahara and Osamu Shibata

Department of Biophysical Chemistry, Graduate School of Pharmaceutical Sciences, Nagasaki International University, Sasebo, Nagasaki, Japan

48.1 INTRODUCTION

Fluorinated amphiphiles have attracted significant interest largely owing to their unique properties including their hydrophobicity and lipophobicity [1], high gas-dissolving capacity [1, 2], chemical and biological inertness, low surface tension, and high fluidity [1, 3]. The potential applications of these compounds in medicine, disease diagnosis, and therapy have promoted numerous investigations on materials substituted with fluorine [1,4–6]. Indeed, it has been reported that fluorinated amphiphiles are potentially applicable as blood substitutes [4, 7–10] and effective additives to lung surfactant preparations [11–14]. However, highly fluorinated compounds [especially perfluorooctanoic acid (PFOA)] tend to accumulate in the environment and in the human body [15–18]. The key to the accumulation of PFOA is its anionic type and the sorption of the anionic PFOA by soils and sediments is quite smaller compared to the undissociated PFOA. In another sense, perfluorooctyl bromide (PFOB) has been shown to have short organ retention times and to have a potential for use for oxygen delivery [1, 2]. Thus, it is important to gain a more in-depth understanding of the effect of fluorinated chemicals on the human body and of their interaction with biomembranes lipids.

Perfluorinated chains (*F*-chains) differ markedly from hydrogenated chains (*H*-chains) in terms of bulkiness, helical conformation, and stiffness [2]. The properties of *F*-chains are described well in the review articles [2–4, 6, 19]. Among numerous techniques used to investigate the properties of fluorinated amphiphiles, Langmuir monolayers at the air–water interface represent a considerably simple and optimal model in mimicry of biomembranes. The monolayer technique provides a clue to understanding the interfacial behavior of amphiphiles and the mutual interaction between them. With Brewster angle microscopy (BAM), fluorescence microscopy (FM) [20–22], and atomic force microscopy (AFM), such behavior and interaction can be visualized on the micro- and nanoscales.

This chapter describes more recent efforts devoted to understanding the interaction and miscibility of two-component monolayers of long-chain alcohols [$CF_3(CF_2)_7(CH_2)_mOH$, or *F*8*Hm*OH] and biomembrane constituents [in particular, dipalmitoylphosphatidylcholine (DPPC)]. The thermodynamical and morphological elucidation of the binary miscibility in the monolayer state has been performed by using isotherm data of surface pressure (π) and surface potential (ΔV) against molecular area (A), and topological images with BAM, FM, and AFM.

48.2 THERMAL PROPERTIES OF *F*8*Hm*OH

An effect of fluorination of a tail group of saturated long-chain carboxylic acids on their physicochemical property such as melting point (T_m) has been documented well in a review article [19]. The whole fluorination of the acids

Encyclopedia of Biocolloid and Biointerface Science, Volume 2, First Edition. Edited by Hiroyuki Ohshima.
© 2016 John Wiley & Sons, Inc. Published 2016 by John Wiley & Sons, Inc.

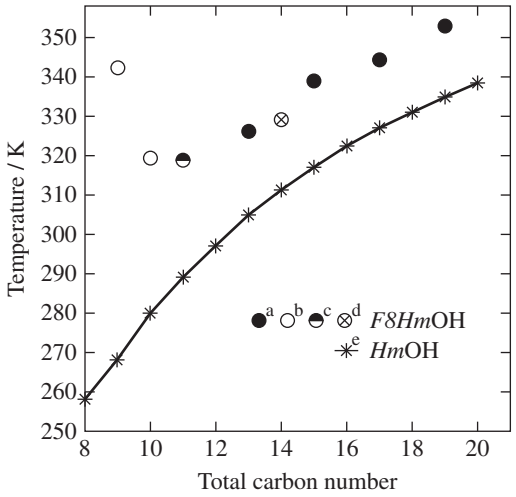


FIGURE 48.1 Change in melting point of *F*8*Hm*OH and *Hm*OH against carbon number. [Data (see symbols in diagram): (a) data from Nakahara et al. 2013 [23]; (b) from Tokyo Chemical Industry Co., Ltd.; (c) from Matrix Scientific; (d) from Apollo Scientific Ltd.; (e) from *CRC Handbook of Chemistry and Physics* 2010 [63].]

results in more than twice larger increments in a plot of melting-point slopes versus carbon number. This means that the high fluorination provides original compounds with thermal stability or resistance. In this regard, partially fluorinated amphiphiles are also expected to be endowed with such properties. The melting point of ω-(perfluorooctyl)alkanol (or *F*8*Hm*OH) and the corresponding hydrogenated alcohol (or *Hm*OH) is plotted against the total carbon number of the alcohols in Fig. 48.1. The relationship between the melting point of *F*8*Hm*OH and the carbon number ($11 \leq m \leq 19$) is almost linear. A slope of the line ($\partial T_m/\partial m$) is ~4.4 K. The melting point of *Hm*OH also increases with increasing carbon numbers, with a gradient of $\partial T_m/\partial m = 5.7$ K ($11 \leq m \leq 19$). The slopes for both the alcohols mean the contribution to an increase in melting point per methylene group ($-CH_2-$). Thus, it is found that perfluorooctylation in the terminal aliphatic chain of *Hm*OH generates thermal resistance (~1 K) for the elongation of a methylene group. Considering the larger T_m of *F*8*Hm*OH in Fig. 48.1, the behavior apparently seems to conflict with the weak van der Waals interactions between *F*-chains. However, we must reconsider the fact that the weak van der Waals interaction is closely related to molecular weight (MW). Here, focusing our attention on the melting points of *F*8*H*7OH (T_m = 338.8 K, MW = 534.25) and *H*20OH (T_m = 338.6 K, MW = 298.55), it is understandable that the larger molecular weight of *F*8*H*7OH reflects the weak van der Waals interaction between *F*8-chains. In the smaller carbon number region below $m = 10$ in Fig. 48.1, the melting points (especially *F*8*H*1OH) show irregular values. This is considered to be due to the low purity (>97%; Tokyo Chemical Industry Co., Ltd.) of the measured *F*8*H*1OH samples or the structural instability of *F*8*H*1OH. To our knowledge, several reagent companies generally supply *F*8*H*1OH (CAS 423-56-3) at the similar grade (purity = ~97%). On the other hand, *F*8*Hm*OH ($m \geq 5$) can be highly purified by repeated recrystallizations (purity > 99.5%) [23]. Furthermore, it is widely accepted that the fluorination in α-carbon of aliphatic alcohols includes difficulties in the synthetic process. Combinations of these observations may produce the irregular values, which needs to be investigated in more detail.

48.3 LANGMUIR MONOLAYER BEHAVIOR OF *F*8*Hm*OH

The surface pressure (π) molecular area (A) and the surface potential (ΔV)–A isotherms of *F*8*Hm*OH (m = 5,7,9,11) monolayers on 0.15 M NaCl are shown in Fig. 48.2. The other alcohols with $m \leq 4$ are, in common, difficult to form a insoluble (or stable) monolayer at the air–water interface because of their high solubility in water. The *F*8*H*5OH monolayer (curve 1) initially has a π-value of >1 mN m^{-1} at large molecular areas, where the monolayer is in a disordered phase corresponding to the liquid-expanded (LE) phase of typical hydrogenated lipid monolayers. The isotherm has a kink at ~5 mN m^{-1} (indicated by a dashed arrow), which means a phase transition of the disordered state to an ordered state corresponding to liquid-condensed (LC) phase of the lipid monolayers. The kink is

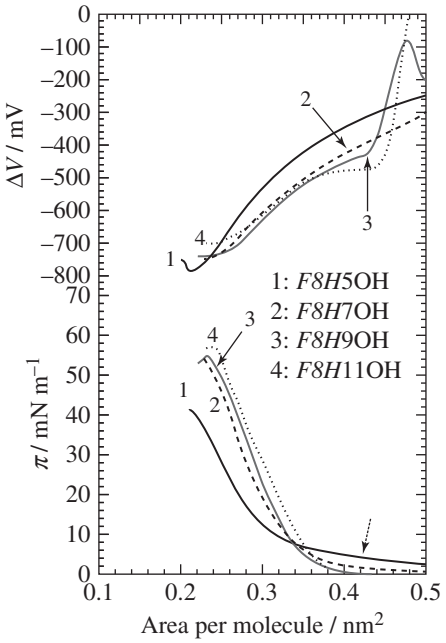


FIGURE 48.2 The π–A and ΔV–A isotherms of *F*8*Hm*OH [m = 5 (curve 1), 7 (curve 2), 9 (curve 3), 11 (curve 4)] monolayers on 0.15 M NaCl. The isotherms except for m = 5 (at 293.2 K) were measured at 298.2 K.

much more obscure in comparison to typical hydrogenated lipids such as myristic acid [24], dipalmitoylphosphatidylcholine (DPPC) [25–28], dipalmitoylphosphatidylglycerol (DPPG)[28–30], and dimyristoylphosphatidylethanolamine (DMPE) [31, 32]. Indeed, the fluorinated amphiphiles often undergo a phase transition, which is difficult to distinguish on π–A isotherms [26, 33]. However, the break has been confirmed by temperature dependence of the transition pressure (π^{eq}) [23]. The π^{eq} values of *F*8*H*5OH monolayers increase linearly with increasing temperatures. The π^{eq} inclination against temperature ($\partial\pi^{eq}/\partial T$) for *F*8*H*5OH monolayers is $\sim$0.4 mN m^{-1} K^{-1} [23]. On the other hand, the slope for the *Hm*OH monolayers ($11 \leq m \leq 14$) is reported to be $\sim$1.0 mN m^{-1} K^{-1} regardless of aliphatic chain lengths [34]. It is well known that the $\partial\pi^{eq}/\partial T$ value for the monolayers of fluorinated amphiphiles is smaller than that for hydrogenated ones, due to the thermal resistance of *F*-chains [9, 19, 35]. Actually, perfluorocarboxylic acid monolayers have the inclination of 0.2–0.3 mN m^{-1} K^{-1}, which means that perfluorination of hydrocarbon chains in monolayers generates three- to fivefold thermal resistance [19]. Herein, the slopes of *F*8*H*5OH monolayers are very similar to perfluorinated amphiphiles.; thus, it can be assumed that *F*8*H*5OH of partially fluorinated alcohol faithfully inherits the thermal resistance from perfluorinated *F*-chains.

The other *F*8*Hm*OH monolayers exhibit an isotherm of the typical ordered phase without the transition. The collapse pressure (π^{c}) at which the monolayer is transformed into a bilayer or other three-dimensional (3D) structures, increases slightly with increasing chain length. The limiting (or extrapolated) areas of *F*8*Hm*OH monolayers are concentrated in 0.33−0.35 nm^2 and are similar to the cross-sectional area of an *F*-chain ($\sim$0.30 nm^2) [1]. Considering the cross-sectional area of an *H*-chain ($\sim$0.20 nm^2), it is found that the *F*8 moiety in *F*8*Hm*OH molecules dominates over the monolayer ordering and orientation at the close-packed state for *F*8*Hm*OH monolayers.

The ΔV–A isotherms of *F*8*Hm*OH monolayers indicate changes in molecular orientation on lateral compression. It is widely accepted that the ΔV–A isotherm of lipid monolayers consisting of *H*-chains or *F*-chains exhibits positive or negative variation with decreasing A. The negative ΔV value of *F*-chains is attributed to the electronegativity of a fluorine, which has been discussed thoroughly [25, 33, 36–40]. The ΔV value decreases with decreasing molecular areas and finally approaches a minimum ΔV value (ΔV_{min}) at the close-packed state, where monolayers begin to collapse. The ΔV_{min} values reach around −750 mV independent of total chain lengths. This means that the orderings of *F*8*Hm*OH monolayers at the close-packed state are similar. The convergence of ΔV_{min} value and the negative ΔV variation on compression support the *F*8 moiety (or, more accurately, terminal CF_3 group) to be exposed to the air, similarly to typical lipid monolayers.

48.4 BINARY MONOLAYERS OF DPPC AND *F*8*Hm*OH

48.4.1 The π–A and ΔV–A Isotherms

The miscibility of binary monolayers can be assessed from the π–A and ΔV–A isotherms measured by varying the monolayer composition. The isotherms of binary monolayers often lie in compositional order between the isotherms of each pure monolayer. The binary monolayers, including both a hydrogenated amphiphile and a fluorinated amphiphile, indicate the distinct and large variation in ΔV–A isotherms due to their opposite ΔV signs [30, 40–42]. The criteria for miscibility of binary monolayers are based on a variation in π^{eq} as well as π^{c} with regard to composition [43]. Determination of the pressures (π^{eq} and π^{c}) can be precisely performed by considering the inflection point in the corresponding ΔV–A isotherm appears. The π–A isotherms for the binary DPPC/*F*8*Hm*OH monolayers are shown in Fig. 48.3. DPPC monolayers (curve 1) have a LE/LC phase transition at $\sim$11 mN m^{-1}, which has been discussed widely [25, 27, 28, 31]. In all the binary systems, the π^{eq} value is found to change with mole fraction of *F*8*Hm*OH (or X_{F8HmOH}), which suggests the miscibility of the two components. The slope of $\partial\pi^{eq}/\partial X_{F8HmOH}$ is the point to understand how the two components are miscible with each other. The positive and negative slopes are respectively indicative of fluidization and solidification of DPPC monolayers by the *F*8*Hm*OH addition. The binary DPPC/*F*8*Hm*OH monolayers exhibit a fluidizing ($m = 5$) or solidifying ($m = 7, 9, 11$) effect. It depends on a mismatch of the hydrophobic chain lengths of the two components. Thus, the influence of *F*8*Hm*OH addition on DPPC monolayers varies at the boundary of total carbon number of 15 in *F*8*Hm*OH, which agrees nearly with the chain length of DPPC. Detailed discussions on the effect will be made quantitatively in the latter section. At high surface pressures, the π^{c} value for all the systems also changes with X_{F8HmOH}, which provides further evidence of the binary miscibility within a monolayer. These variations of surface pressures (π^{eq} and π^{c}) against X_{F8HmOH} strongly suggest thermodynamical miscibility between DPPC and *F*8*Hm*OH irrespective of the number of methylene groups (m).

48.4.2 Excess Gibbs Free Energy

The lateral interactions between DPPC and *F*8*Hm*OH within a monolayer can be analyzed in terms of the excess Gibbs free energy of mixing (ΔG^{exc}_{mix}), which is calculated with the following equation [43]

$$\Delta G^{exc}_{mix} = \int_0^{\pi} (A_{12} - X_1 A_1 - X_2 A_2) \mathrm{d}\pi \qquad (48.1)$$

where A_i and X_i are the molecular area and mole fraction of component i, respectively, and A_{12} is the mean molecular area

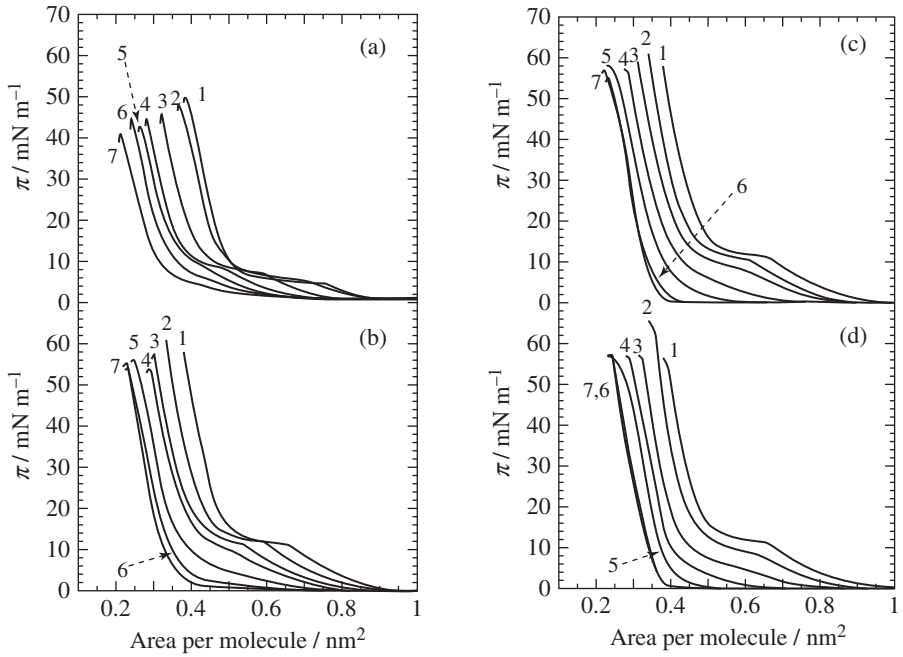


FIGURE 48.3 The π–A isotherms of the two-component DPPC/*F*8*Hm*OH monolayers on 0.15 M NaCl at $X_{F8HmOH} = 0$ (curve 1), 0.1 (curve 2), 0.3 (curve 3), 0.5 (curve 4), 0.7 (curve 5), 0.9 (curve 6), and 1 (curve 7): (a) $m = 5$, (b) $m = 7$, (c) $m = 9$, and (d) $m = 11$. The isotherms except for $m = 5$ (at 293.2 K) were measured at 298.2 K.

of the binary monolayer. For identical interactions between the two components, ΔG^{exc}_{mix} is zero. In this state, they are either ideally mixed in the monolayer or are not mixed completely, resulting in a patchlike packing state [44,45]. A negative ΔG^{exc}_{mix} value indicates that an attractive interaction exists between the two components. The $\Delta G^{exc}_{mix} - X_{F8HmOH}$ plot for DPPC/*F*8*Hm*OH at representative surface pressures is shown in Fig. 48.4. The ΔG^{exc}_{mix} value decreases with an increase in surface pressure greater than 15 mN m^{-1} for all the systems. At 5 mN m^{-1}, however, complicated behavior is observed especially for m = 5,7. This is attributed to the different phases of the monolayers (disordered and ordered), which

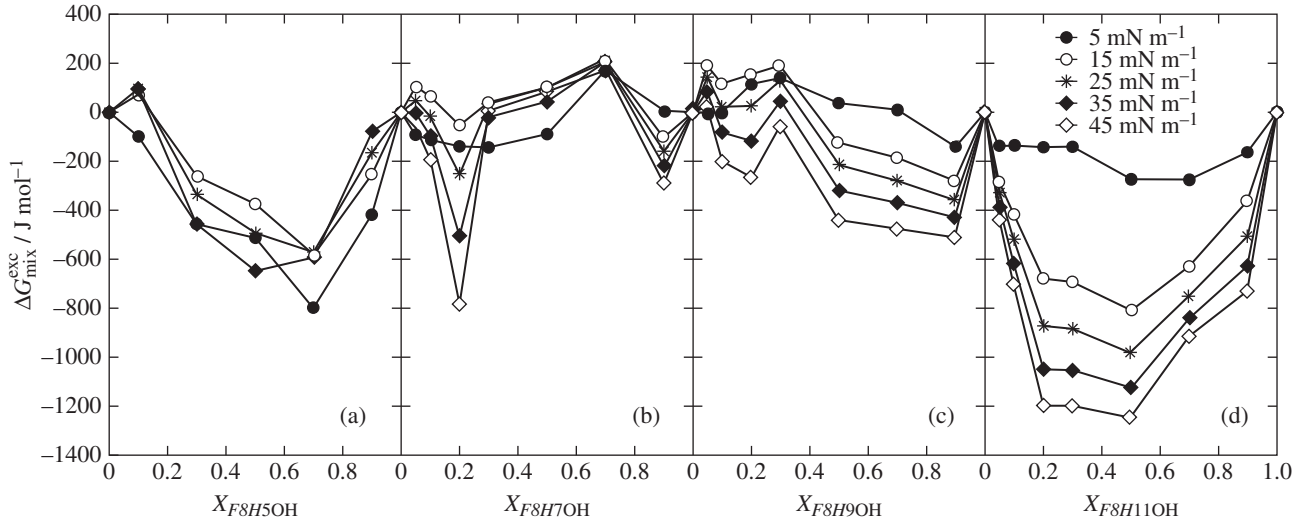


FIGURE 48.4 Excess Gibbs free energy of mixing (ΔG^{exc}_{mix}) of the binary DPPC/*F*8*Hm*OH monolayers as a function of X_{F8HmOH} at typical surface pressures on 0.15 M NaCl: (a) $m = 5$, (b) $m = 7$, (c) $m = 9$, and (d) $m = 11$. The isotherms except for $m = 5$ (at 293.2 K) were measured at 298.2 K.

are caused by the changes in π^{eq} with regard to X_{F8HmOH} (see Fig. 48.3). For example, the monolayers at 5 mN m^{-1} for $X_{F8H7OH} = 0.2$ and 0.9 are in the disordered phase and the ordered phase respectively. Thus, the ΔG^{exc}_{mix} analysis for surface pressures greater than 15 mN m^{-1} provides a better understanding of the mutual interactions between the components because the monolayers are entirely in the ordered phase irrespective of surface pressure and composition. All the systems show negative ΔG^{exc}_{mix} signs, which suggests the existence of attractive interactions between the two components. In particular, the plots for DPPC/*F*8*H*11OH indicate most significant variations (Fig. 48.4d). As the surface pressure increases, the ΔG^{exc}_{mix} value reaches the minimum (~ -1200 J mol^{-1}) at 45 mN m^{-1} for $0.2 \leq X_{F8H11OH} \leq 0.5$. This behavior suggests that the attractive force between the palmitoyl chains of DPPC and the hydrocarbon moieties of *F*8*H*11OH increases on compression and that the affinity between the two components is the highest for $0.2 \leq X_{F8H11OH} \leq 0.5$. In other words, the shorter methylene group ($m \leq 9$) in *F*8*Hm*OH does not indicate strong interactions with hydrophobic chains in DPPC.

48.4.3 Two-Dimensional Phase Diagram

Two-dimensional (2D) phase diagrams (π vs. X_{F8HmOH}) exhibit the phase distributions of disordered and ordered phases at low surface pressures, and monolayer (2D) and bulk (3D) phases at high surface pressures. These diagrams are constructed by plotting the π^{eq} and π^{c} values for the binary monolayers against composition at a fixed temperature (see Fig. 48.5). In the DPPC/*F*8*H*5OH system, the π^{eq} value increases with increasing X_{F8H5OH} smaller than 0.7. Then, it decreases to the π^{eq} value of pure *F*8*H*5OH ($\sim$5 mN m^{-1}). On the other hand, for the $m \geq 7$ systems, the reduction in π^{eq} is caused by an increase in X_{F8HmOH}. The magnitude of the reduction is improved as the total chain length of *F*8*Hm*OH increases. The slope of $\partial\pi^{eq}/\partial X_{F8HmOH}$ provides information on the degree of the solidification (negative) or fluidization (positive) [19, 35]. The π^{eq} values for the $m = 9,11$ systems vary linearly with respect to X_{F8HmOH}. The indices of $\partial\pi^{eq}/\partial X_{F8HmOH}$ for $m = 9$ ($0 \leq X_{F8H9OH} \leq 0.3$) and 11 ($0 \leq X_{F8H11OH} \leq 0.2$) are around -14 [42] and -33 mN m^{-1} [30], respectively; that is, the magnitude of the solidification for the DPPC/*F*8*H*11OH system is more than twice that for the *F*8*H*9OH system. On the other hand, the binary DPPC/*F*8*H*7OH system indicates negative but nonlinear variations in π^{eq} with respect to X_{F8H7OH} [41]. From the small X_{F8HmOH} region for the $m \geq 7$ systems, it is found that the solidification degree becomes larger for longer m: *F*8*H*7OH < *F*8*H*9OH < *F*8*H*11OH. On the contrary, *F*8*H*5OH exerts the fluidizing effect on DPPC monolayers. It is suggested that the extension of methylene group ($-CH_2-$) in a partially fluorinated chain significantly contributes to the solidifying effect. In this regard, all the systems described here indicate the miscibility with DPPC in

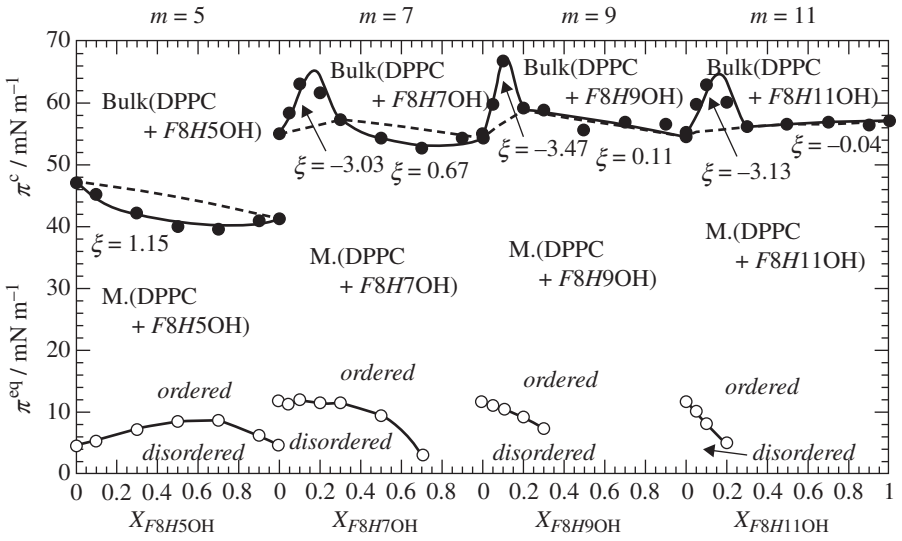


FIGURE 48.5 Two-dimensional phase diagrams based on the variation in transition pressure (π^{eq}: open circle) and collapse pressure (π^{c}: solid circle) on 0.15 M NaCl at 298.2 K (293.2 K for $m = 5$) as a function of X_{F8HmOH}. The dashed lines were calculated according to Eq. (48.2) for $\xi = 0$. The solid line at high surface pressures was obtained by curve fitting of experimental collapse pressures to Eq. (48.2). "M" indicates a mixed monolayer formed by DPPC and *F*8*Hm*OH species, whereas "Bulk" denotes a solid phase of DPPC and *F*8*Hm*OH ("bulk phase" may be called "solid phase" not in monolayer state).

the monolayer state, although there is considerable variation in the manner of miscibility (fluidization and solidification) among the systems.

The coexistence of the phase boundary of the 2D and 3D phases of the molecules spread on a surface can be theoretically simulated using the Joos equation [46, 47] under the assumption of a regular surface mixture:

$$1 = x_1^{\mathrm{s}} \exp\left\{\left(\pi_{\mathrm{m}}^{\mathrm{c}} - \pi_1^{\mathrm{c}}\right)\omega_1/kT\right\} \exp\left\{\xi\left(x_2^{\mathrm{s}}\right)^2\right\} + x_2^{\mathrm{s}} \exp\left\{\left(\pi_{\mathrm{m}}^{\mathrm{c}} - \pi_2^{\mathrm{c}}\right)\omega_2/kT\right\} \exp\left\{\xi\left(x_1^{\mathrm{s}}\right)^2\right\} \quad (48.2)$$

Here, x_1^{s} and x_2^{s} denote the respective molar fractions of components 1 and 2 in the two-component monolayers; π_1^{c} and π_2^{c}, the respective collapse pressures of components 1 and 2; $\pi_{\mathrm{m}}^{\mathrm{c}}$, the collapse pressure of the two-component monolayer at a given composition of x_1^{s} (or x_2^{s}); ω_1 and ω_2, the corresponding molecular areas at the collapse; and ξ, the interaction parameter. The solid curve at higher surface pressures was drawn by adjusting ξ in Eq. (48.2) to obtain the best fit for the experimental values of collapse pressures. The profiles of the phase diagrams of the DPPC/*F*8*Hm*OH systems are presented in Fig. 48.5. In the collapse pressure region, the $m \geq 7$ systems in the small X_{F8HmOH} region are of the positive azeotropic type, where the maximum in curves of the phase boundary corresponds to the 2D positive azeotropic point. On the other hand, the phase diagram for DPPC/*F*8*H*5OH is assigned to the negative azeotropic type.

The interaction energy can be calculated as the following equation

$$\Delta\varepsilon = \xi RT/z \quad (48.3)$$

where z is the number of nearest neighbors, equal to 6, in a close-packed monolayer, and the interaction energy is $\Delta\varepsilon = \varepsilon_{12} - (\varepsilon_{11} + \varepsilon_{22})/2$ [46]; ε_{ij} denotes the potential energy of interaction between components i and j. The calculated ξ and $\Delta\varepsilon$ are listed in Table 48.1. The ξ value for all the systems except for $m = 5$ is quite larger in magnitude in the small X_{F8HmOH} region. In contrast, in the large X_{F8HmOH} region, the two components nearly cause the ideal interaction (especially m = 9,11). As for the DPPC/*F*8*H*7OH system, the phase diagram in the large X_{F8H7OH} is of the negative azeotropic type. This behavior is similar to that for the DPPC/*F*8*H*5OH system, although the degree of ξ values is smaller. Thus, the mode of mutual interactions is different at the boundary between m = 5,7. Moreover, as mentioned above, the variation in π^{eq} against X_{F8HmOH} also supports the boundary; convex variations (fluidization) for $m = 5$ and linear or nonlinear negative ones (solidification) for $m \geq 7$. However, in comparison to the π^{eq} behavior, the magnitude of the effect is not found to be reflected in the ξ value. This may be due to the fact that the monolayer is in the closest packing (the lowest compressibility) at π^{c}. Thus, it is suggested that the mode of the binary interaction at low surface pressures is different from that at high surface pressures. In fact, such opposite mode of interactions was remarkably observed for the DPPC/*F*8*H*7OH system [41]. For $0 \leq X_{F8H7OH} \leq 0.3$, the two components do not favorably interact with each other at low surface pressures because of the almost constant π^{eq} value with respect to X_{F8H7OH}. However, the large negative ξ value ($\xi = -3.03$) is indicative of the strong interaction between them. On the other hand, the phase diagram for $0.3 \leq X_{F8H7OH} \leq 1$ exhibits the opposite behavior to the case of $0 \leq X_{F8H7OH} \leq 0.3$. Nevertheless, these results evidence the monolayer miscibility between DPPC and *F*8*Hm*OH.

TABLE 48.1 Interaction Parameters and Energies for the DPPC/*F*8*Hm*OH Systems on 0.15 M NaCl [30, 40–42]

m	T (K)	X_{F8HmOH}	ξ	$\Delta\varepsilon$ (kJ/mol)
5	293.2	$0 \leq X_{F8H5OH} \leq 1$	1.15	0.47
7	298.2	$0 \leq X_{F8H7OH} \leq 0.3$	−3.03	−1.26
		$0.3 \leq X_{F8H7OH} \leq 1$	0.67	0.28
9	298.2	$0 \leq X_{F8H9OH} \leq 0.2$	−3.47	−1.43
		$0.2 \leq X_{F8H9OH} \leq 1$	0.11	0.05
11	298.2	$0 \leq X_{F8H11OH} \leq 0.3$	−3.13	−1.29
		$0.3 \leq X_{F8H11OH} \leq 1$	−0.04	−0.02

48.4.4 Brewster Angle Microscopy (BAM)

Brewster angle microscopic observations at the air–water interface can directly provide morphological information on the phase behavior of monolayers at the air–water interface. In the BAM observation, the dark and bright contrasts are respectively assigned to LE (or disordered) and LC (or ordered) phases of lipid monolayers, which is based on the difference in refractive index of monolayer phases caused by a change in the molecular density or packing at the surface [48, 49]. As for DPPC monolayers (column 1 in Fig. 48.6a), the domain nucleation of LC phases is brought out at $\pi^{\mathrm{eq}} = \sim 5$ (at 293.2 K) and ~ 11 mN m^{-1} (at 298.2 K), and then the LC domains grow in size and number with increasing surface pressures. Further compression changes the LE/LC coexistence phases into homogeneous LC phases. A detailed analysis on the morphology of DPPC monolayers has already been reported elsewhere [14, 30]. On the other hand, *F*8*Hm*OH monolayers exhibit optically homogeneous images over the entire surface pressures [30,40–42]. The BAM images for the binary monolayer shown in Fig. 48.6 indicate morphologies different from those for DPPC alone. A small amount addition of *F*8*H*5OH ($X_{F8H5OH} = 0.1$) makes the LC domain of DPPC more branched, and thus it becomes elongated and forms a whirlpool (a so-called triskelion) that grows in a counterclockwise fashion. With the further addition ($X_{F8H5OH} = 0.3$), the domains with the whirled arms change into the round domains. On the other hand, a small addition

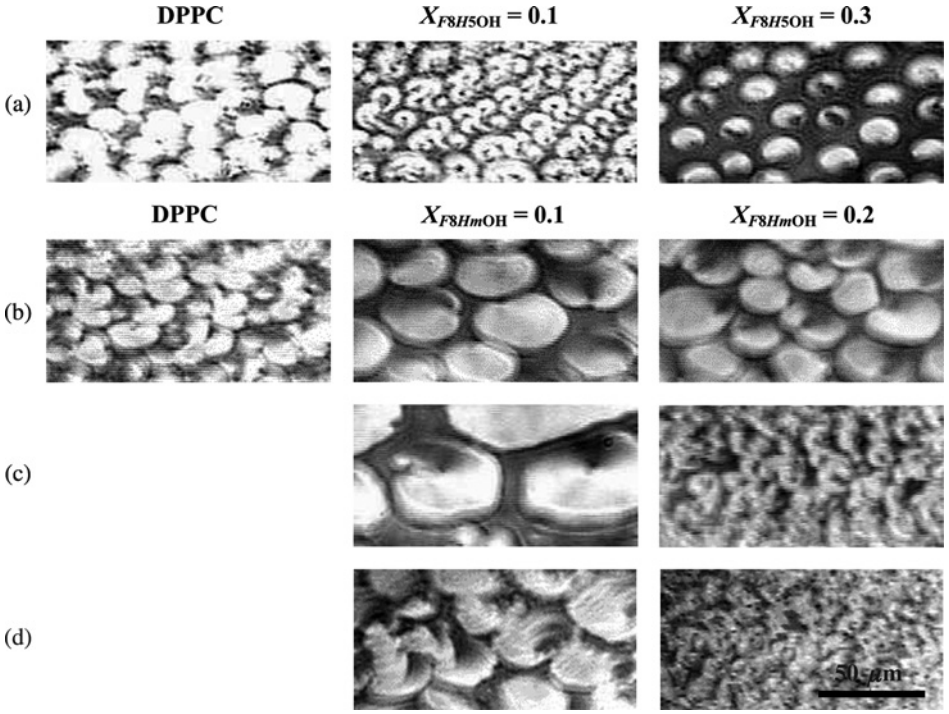


FIGURE 48.6 BAM images of the binary DPPC/*F*8*Hm*OH monolayers on 0.15 M NaCl at 298.2 K (293.2 K for $m = 5$): (a) $m = 5$ at 8 mN m^{-1}, (b) $m = 7$ at 15 mN m^{-1}, (c) $m = 9$ at 15 mN m^{-1}, and (d) $m = 11$ at 15 mN m^{-1}. The scale bar in the lower right represents 50 μm.

of *F*8*Hm*OH ($m \geq 7$) to DPPC monolayers ($X_{F8HmOH} = 0.1$) induces a size increment of the ordered domains, where the domain shape becomes round. At $X_{F8HmOH} = 0.2$, however, the domain size becomes much smaller and the domain shape changes to be branched similar to the LC domain of DPPC for $m = 9,11$. In the case of $m = 7$, the domain shape and size are kept almost constant despite the increment from $X_{F8H7OH} =$ 0.1–0.2. Above $X_{F8HmOH} = 0.2$, the BAM images are homogeneously dark over the entire surface pressures [30,41,42]. It is widely accepted that a domain formation is controlled by the balance of line tension at the phase boundary between the disordered and ordered domains and long-range dipole–dipole interactions between the ordered domains [50–53]. Therefore, the variations in domain shape and size describe the change of the composition at disordered/ordered phase boundary and the interaction between ordered domains for the two-component monolayers.

48.4.5 Fluorescence Microscopy (FM)

The phase behavior of monolayers is often observed with fluorescence microscopy (FM) as functions of composition and surface pressure. FM measurements require a fluorescent probe, which is incorporated into the monolayer. Contrast in the FM image is generated by the difference in solubility of fluorescent probes in the disordered (or LE) and ordered (or LC) monolayers [20–22]. This is based on the fact that the probe generally forms disordered monolayers at the interface as a result of its spatially bulky moiety (or fluorescent part). This induces strong affinity for the disordered phase of the monolayers. The FM observation provides powerful information on the phase growth and variation in higher resolution and magnification than the BAM observation. However, there is a possible risk that the probe (or dye) might affect the original phase behavior of monolayers. Thus, the validity of the resulting FM image should be checked in terms of whether the incorporation of FM probes has no influence on the original isotherm and the original domain shape in BAM images. It is widely accepted that the addition of <1 mol% FM probes produces few effects on the monolayer behavior [28, 54]. The FM micrographs of the binary DPPC/*F*8*Hm*OH monolayers (see Fig. 48.7) show the presence of different phase morphologies in the disordered/ordered coexistence region above π^{eq}. The phase morphologies (or domain shape and distribution) agree well with the corresponding BAM images (Fig. 48.6), which supports the validity of FM observations for the present systems. At $X_{F8HmOH} = 0.1$, the line tension at the phase boundary is dominated for $m \geq 7$, whereas the dipole–dipole repulsive force contributes more to the domain shape for $m = 5$. The further addition improves the contribution of the line tension to domain morphologies for DPPC/*F*8*H*5OH. As opposed to the system of $m = 5$, the domain sizes become smaller for the systems of $m = 9,11$ ($X_{F8HmOH} = 0.2$). This means that

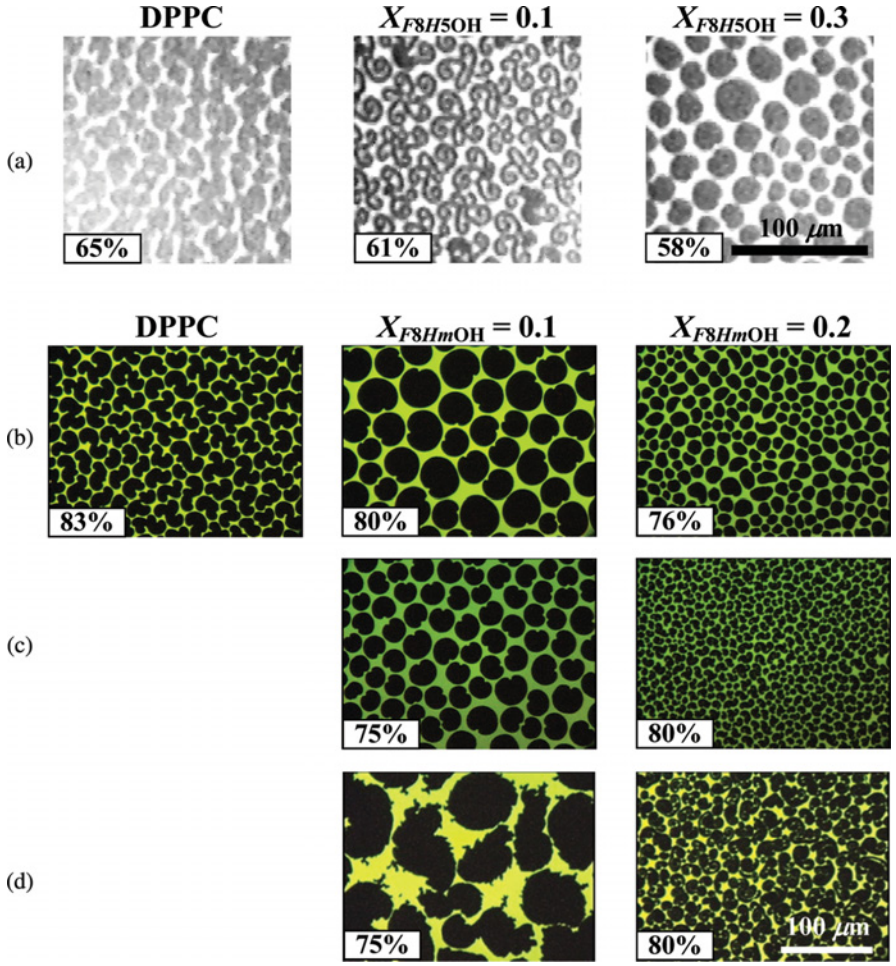


FIGURE 48.7 Fluorescent micrographs of the binary DPPC/*F*8*Hm*OH monolayers on 0.15 M NaCl at 15 mN m^{-1} at 298.2 K (293.2 K for $m = 5$) : (a) $m = 5$, (b) $m = 7$, (c) $m = 9$, and (d) $m = 11$. Percentages (%) refer to the ratio of ordered domains in the micrograph. The monolayers contain 1 mol% of fluorescent probe (R18 for $m = 5$ and NBD-PC for the others). The scale bar in the lower right represents 100 μm.

the contribution of the line tension decreases by the further addition. It is not yet understood how the composition of each domain is related to the balance of the line tension and dipole–dipole interaction. Nevertheless, a change in domain shape of the ordered domains is substantial evidence of the two-component miscibility.

48.4.6 Atomic Force microscopy (AFM)

The phase behavior and distribution of monolayers at the air–water interface can be visualized at the nanometer scale by AFM. Prior to the AFM observation, the monolayer located at the interface needs to be transferred onto a solid substrate using the Langmuir–Blodgett (LB) technique, where the monolayer is kept at the desired surface pressure. However, the LB technique includes a possibility of changes of the native monolayer structures by the electric charge between the samples and substrates, and by the physical factors during the deposition procedure. AFM images may therefore not provide completely accurate information on the phase behavior at the air–water interface but nevertheless allow us to understand phase morphologies that cannot be caught with in situ microscopic techniques (BAM and FM) due to the limited optical resolution and magnification of the microscopes. The AFM topographic images for the DPPC/*F*8*Hm*OH monolayers shown in Fig. 48.8 are apparently different from each other. The LB film of DPPC at high surface pressures indicates a homogeneous image [26]. In the DPPC/*F*8*H*5OH system (Fig. 48.8a), phase separation of the high (for DPPC) and low (for *F*8*H*5OH) domains is observed, which coincides with the positive ξ value (Fig. 48.5 and Table 48.1). Considering the BAM and FM images at micrometer scale, it is concluded that the two components are partially miscible within a monolayer. On the other hand,

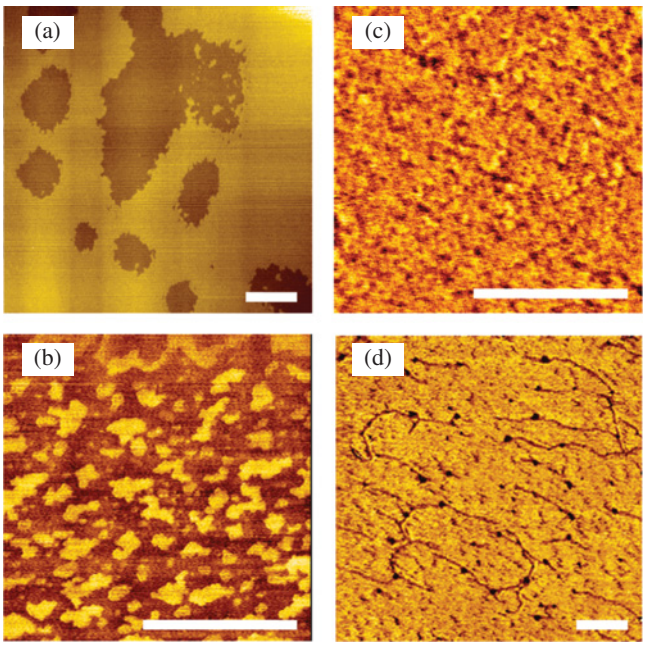


FIGURE 48.8 Typical AFM topographic images of the binary DPPC/*F*8*Hm*OH monolayers for $X_{F8HmOH} = 0.3$ at 35 mN m^{-1}: (a) $m = 5$, (b) $m = 7$, (c) $m = 9$, and (d) $m = 11$. The scale bar in the lower right represents 500 nm.

in the other systems, the domains are finely dispersed. In particular, for DPPC/*F*8*H*7OH (Fig. 48.8b), the dispersion or the fragmentation of DPPC monolayers is induced by the surface pressure [41]. In the DPPC/*F*8*H*9OH system (Fig. 48.8c), the dispersion is further enhanced and then the image becomes almost homogeneous in terms of height difference. The AFM image at $X_{F8H11OH} = 0.3$ show several dark "cracks" with low thickness (Fig. 48.8d). The cracks are formed predominantly by *F*8*H*11OH [30]. This means that the *F*8*H*11OH monolayers are less oriented because the hydrophobic chain of *F*8*H*11OH is longer than that of DPPC. The poor orientation is considered to be strongly affected by the further reclining *F*8 moieties at the linkage (CF_2–CH_2) in *F*8*Hm*OH. As a result, the dispersion of DPPC domains may be caused by combination of the poor orientation and the relatively weak van der Waals interaction or cohesive force between the *F*8 moieties.

The criteria for the monolayer miscibility is still disputable. The existence of the phase-separated domain in the micrographs does not necessarily imply the immiscibility between components, because the domain morphologies vary in shape and size with respect to monolayer composition as mentioned above. Assuming the completely immiscible monolayers, the domain shapes should be a circle form due to the minimization of surface free energy at the boundary among heterogeneous components; that is, if the circular and phase-separated domain is observed fully in BAM, FM, and AFM images, the components forming monolayers can be entirely immiscible at micro- as well as nanoscale [29, 32]. Therefore, herein, it is concluded that all the binary DPPC/*F*8*Hm*OH monolayers are (partially) miscible thermodynamically and morphologically.

48.5 MISCIBILITY OF *F*8*Hm*OH WITH LIPIDS

It is well known that *F*-chains and *H*-chains are immiscible with each other in both liquid and solid states, where they are dissolved in the aqueous medium. The immiscibility is attributed mainly to the weak van der Waals force of the *F*-chains. However, *F*-chains and *H*-chains can interact more in a monolayer state spread at the air-exposed surface than in a bulk solution [26, 55–57]. This is considered to be due to no hydrophobic interaction between hydrophobic chains in the air side. Indeed, the monolayers of perfluorinated long-chain carboxylic acids have a limited affinity for hydrocarbon-based lipids such as DPPC [26], DMPE [32], DPPG [29], and fatty acids [19]. In the case of partially fluorinated amphiphiles (here *F*8*Hm*OH), they indicate the miscibility with a variety of lipids composing biomembranes within a monolayer (see Table 48.2). In addition, *F*8*Hm*OH has the monolayer miscibility with other types of partially fluorinated amphiphiles such as *F*8*H*5PC and PBD. On the other hand, the corresponding fatty alcohols (*Hm*OH) are expectedly miscible well with the hydrocarbon-base lipids but are immiscible with a fluorinated alkane (*F*8*H*11) (see Table 48.3). This means that perfluorooctylation in lipids endows them with affinity for both *H*-chains and *F*-chains. Thus, the perfluorooctylated lipids in the monolayer state can exert the original physicochemical properties as well as the unique properties of *F*-chains mentioned in Section 48.1. Biological membranes (or biomembranes) comprise many kinds of lipids and proteins. Especially, double long-chain phospholipids such as phosphatidylcholines and phosphatidylethanolamine are their major components. In comparison to typical single-chain lipids, the molecular motion

TABLE 48.2 Monolayer Miscibility of *F*8*Hm*OH with Biomembrane Constituents or Synthetic Lipids

	DPPC	DPPG	MA	Ch	*F*8*H*5PC	PBD	Ref(s).
***m* = 5**	M	–	M	–	M	–	24,33,40
***m* = 7**	M	–	–	–	–		41
***m* = 9**	M	–	–	–	–	–	42
***m* = 10**	–	–	–	–	–	M	37
***m* = 11**	M	M	–	M	–	–	30

Abbreviations: Ch = cholesterol; *F*8*H*5PC = (perfluorooctyl) pentylphosphocholine; M = (partially) miscible monolayers; MA = myristic acid; PBD = 11,11-difluoro-11-(pentafluorophenyl)undecan-1-ol.

TABLE 48.3 Monolayer Miscibility of *Hm*OH with Biomembrane Constituents or Synthetic Lipids

	DPPC	$m = 16$	MA	PA	SA	*F*8*H*11	refs.
***m* = 12**	–	–	–	–	–	I	58
$m = 14$	–	M	M	M	M	I	58,59
$m = 16$	M	–	M	–	–	I	58–61
$m = 18$	M	–	–	–	–	–	61,62
$m = 20$	M	–	–	–	–	–	62

Abbreviations: *F*8*H*11 = 1-perfluorooctyl-tetradecane; M,I = (partially) miscible and immiscible monolayers, respectively; PA = palmitic acid; SA = stearic acid.

and behavior of the phospholipids are much more complicated because of the intramolecular and intermolecular attractions between *H*-chains, which are usually restricted to spatially bulky hydrophilic groups. Even in the monolayer state, where the intermolecular interaction is simplified by the 2D treatment, the complex behavior generates unexpected influence on the monolayer properties such as ordering, packing, and phase transition. An in-depth deep understanding of phospholipid monolayers at the interface is quite important for elucidation of biomembrane functions as well as pulmonary surfactants, in particular. However, the available literature on the monolayer interaction between lipids and fluorinated amphiphiles is not yet sufficient. Further investigation on the interaction is successively necessary for use and application of materials substituted with fluorine.

48.6 CONCLUSIONS AND PERSPECTIVES

The two-component monolayers of partially fluorinated alcohols such as *F*8*Hm*OH and the lipids in biomembranes indicate lateral miscibility with each other. However, the miscibility behavior for the binary DPPC/*F*8*Hm*OH monolayers is significantly different in interaction parameter and energy. The system for $m = 5$ shows a positive interaction parameter (a negative azeotropic type), whereas the parameters for $m \geq 7$ are negative (a positive azeotropic type). In addition, it is found that *F*8*Hm*OH can be miscible with a wide range of lipid species, including fluorinated amphiphiles in the monolayer state. The accumulation effect of *F*8*Hm*OH on the human body and the environment is commonly smaller, compared to perfluorinated and highly fluorinated amphiphiles. Therefore, perfluorooctylated compounds have a potential for use and application in medical and pharmaceutical fields as well as in industrial and materials science. With the aim of such applications, partially (or hybrid-type) fluorinated compounds are currently under extensive investigation. It is hoped that a further understanding of interaction of fluorinated compounds breaks through the subject of intensive research on signal transfer via biomembranes (especially lipid rafts) and respiratory disease related to pulmonary surfactants.

REFERENCES

[1] Riess, J.G. (2002). Fluorous micro- and nanophases with a biomedical perspective. *Tetrahedron* **58**, 4113–4131.

[2] Krafft, M.P., Riess, J.G. (2009). Chemistry, physical chemistry, and uses of molecular fluorocarbon–hydrocarbon diblocks, triblocks, and related compounds–unique "apolar" components for self-assembled colloid and interface engineering. *Chem. Rev.* **109**, 1714–1792.

[3] Kissa, E. (2001). *Fluorinated Surfactants and Repellents*, 2nd ed., revised and expanded. Marcel Dekker, Basel/New York, pp. 1–615.

[4] Krafft, M.P., Riess, J.G. (1998). Highly fluorinated amphiphiles and colloidal systems, and their applications in the biomedical field. A contribution. *Biochimie* **80**, 489–514.

[5] Krafft, M.P. (2001). Fluorocarbons and fluorinated amphiphiles in drug delivery and biomedical research. *Adv. Drug Deliv. Rev.* **47**, 209–228.

[6] Riess, J.G. (2001). Oxygen carriers ("blood substitutes")–raison d'etre, chemistry, and some physiology. *Chem. Rev.* **101**, 2797–2920.

[7] Krafft, M.P., Rolland, J.P., Vierling, P., Riess, J.G. (1990). New perfluoroalkylated phosphocholines. Effect on particle size and stability of fluorocarbon emulsions. *New J. Chem.* **14**, 869–875.

[8] Lane, T.A. (1995). Perfluorochemical-based artificial oxygen carrying red cell substitutes. *Transfus. Sci.* **16**, 19–31.

[9] Riess, J.G., Krafft, M.P. (1998). Fluorinated materials for in vivo oxygen transport (blood substitutes), diagnosis and drug delivery. *Biomaterials* **19**, 1529–1539.

[10] Lowe, K.C. (2001). Fluorinated blood substitutes and oxygen carriers. *J. Fluorine Chem.* **109**, 59–65.

[11] Gerber, F., Krafft, M.P., Vandamme, T.F., Goldmann, M., Fontaine, P. (2005). Preventing crystallization of phospholipids in monolayers: A new approach to lung-surfactant therapy. *Angew. Chem. Int. Ed. Engl.* **44**, 2749–2752.

[12] Gerber, F., Krafft Marie, P., Vandamme Thierry, F., Goldmann, M., Fontaine, P. (2006). Fluidization of a dipalmitoyl phosphatidylcholine monolayer by fluorocarbon gases: Potential use in lung surfactant therapy. *Biophys. J.* **90**, 3184–3192.

[13] Gerber, F., Krafft, M.P., Vandamme, T.F. (2007). The detrimental effect of serum albumin on the re-spreading of a dipalmitoyl phosphatidylcholine Langmuir monolayer is counteracted by a fluorocarbon gas. *Biochim. Biophys. Acta* **1768**, 490–494.

[14] Nakahara, H., Lee, S., Krafft, M.P., Shibata, O. (2010). Fluorocarbon-hybrid pulmonary surfactants for replacement therapy–a Langmuir monolayer study. *Langmuir* **26**, 18256–18265.

[15] Riess, J.G. (2009). Highly fluorinated amphiphilic molecules and self-assemblies with biomedical potential. *Curr. Opin. Colloid Interface Sci.* **14**, 294–304.

[16] Goss, K.U. (2008). The pKa values of PFOA and other highly fluorinated carboxylic acids. *Environ. Sci. Technol.* **42**, 456–458.

[17] Burns, D.C., Ellis, D.A., Li, H., McMurdo, C.J., Webster, E. (2008). Experimental pKa determination for perfluorooctanoic acid (PFOA) and the potential impact of pKa concentration dependence on laboratory-measured partitioning phenomena and environmental modeling. *Environ. Sci. Technol.* **42**, 9283–9288.

[18] Higgins, C.P., Luthy, R.G. (2006). Sorption of perfluorinated surfactants on sediments. *Environ. Sci. Technol.* **40**, 7251–7256.

[19] Nakahara, H., Shibata, O. (2012). Langmuir monolayer miscibility of perfluorocarboxylic acids with biomembrane constituents at the air-water interface. *J. Oleo Sci.* **61**, 197–210.

[20] von Tscharner, V., McConnell, H.M. (1981). An alternative view of phospholipid phase behavior at the air-water interface. Microscope and film balance studies. *Biophys. J.* **36**, 409–419.

[21] von Tscharner, V., McConnell, H.M. (1981). Physical properties of lipid monolayers on alkylated planar glass surfaces. *Biophys. J.* **36**, 421–427.

[22] Peters, R., Beck, K. (1983). Translational diffusion in phospholipid monolayers measured by fluorescence microphotolysis. *Proc. Natl. Acad. Sci. U.S.A.* **80**, 7183–7187.

[23] Nakahara, H., Nakamura, S., Okahashi, Y., Kitaguchi, D., Kawabata, N., Sakamoto, S., Shibata, O. (2013). Examination of fluorination effect on physical properties of saturated long-chain alcohols by DSC and Langmuir monolayer. *Colloids Surf. B* **102**, 472–478.

[24] Nakahara, H., Tsuji, M., Sato, Y., Krafft, M.P., Shibata, O. (2009). Langmuir monolayer miscibility of single-chain partially fluorinated amphiphiles with tetradecanoic acid. *J. Colloid Interface Sci.* **337**, 201–210.

[25] Hiranita, T., Nakamura, S., Kawachi, M., Courrier, H.M., Vandamme, T.F., Krafft, M.P., Shibata, O. (2003). Miscibility behavior of dipalmitoylphosphatidylcholine with a single-chain partially fluorinated amphiphile in Langmuir monolayers. *J. Colloid Interface Sci.* **265**, 83–92.

[26] Nakahara, H., Nakamura, S., Kawasaki, H., Shibata, O. (2005). Properties of two-component Langmuir monolayer of single chain perfluorinated carboxylic acids with dipalmitoylphosphatidylcholine (DPPC). *Colloids Surf. B* **41**, 285–298.

[27] Nakahara, H., Nakamura, S., Hiranita, T., Kawasaki, H., Lee, S., Sugihara, G., Shibata, O. (2006). Mode of interaction of amphiphilic α-helical peptide with phosphatidylcholines at the air-water interface. *Langmuir* **22**, 1182–1192.

[28] Nakahara, H., Lee, S., Shibata, O. (2009). Pulmonary surfactant model systems catch the specific interaction of an amphiphilic peptide with anionic phospholipid. *Biophys. J.* **96**, 1415–1429.

[29] Yokoyama, H., Nakahara, H., Shibata, O. (2009). Miscibility and phase behavior of DPPG and perfluorocarboxylic acids at the air-water interface. *Chem. Phys. Lipids* **161**, 103–114.

[30] Nakahara, H., Krafft, M.P., Shibata, A., Shibata, O. (2011). Interaction of a partially fluorinated alcohol (*F*8*H*11OH) with biomembrane constituents in two-component monolayers. *Soft Matt.* **7**, 7325–7333.

[31] Hoda, K., Ikeda, Y., Kawasaki, H., Yamada, K., Higuchi, R., Shibata, O. (2006). Mode of interaction of ganglioside Langmuir monolayer originated from echinoderms: Three binary systems of ganglioside/DPPC, ganglioside/DMPE, and ganglioside/cholesterol. *Colloids Surf. B* **52**, 57–75.

[32] Yokoyama, H., Nakahara, H., Nakagawa, T., Shimono, S., Sueishi, K., Shibata, O. (2009). Miscibility behavior of two-component monolayers at the air-water interface: Perfluorocarboxylic acids and DMPE. *J. Colloid Interface Sci.* **337**, 191–200.

[33] Shibata, O., Krafft, M.P. (2000). Mixed Langmuir monolayers made from single-chain perfluoroalkylated amphiphiles. *Langmuir* **16**, 10281–10286.

[34] Vollhardt, D., Emrich, G., Siegel, S., Rudert, R. (2002). Phase transition in monolayers of straight chain and 2-methyl branched alcohols at the air-water interface. *Langmuir* **18**, 6571–6577.

[35] Matsumoto, Y., Nakahara, H., Moroi, Y., Shibata, O. (2007). Langmuir monolayer properties of perfluorinated double long-chain salts with divalent counterions of separate electric charge at the air-water interface. *Langmuir* **23**, 9629–9640.

[36] Broniatowski, M., Dynarowicz-Łatka, P. (2006). Semifluorinated chains at the air/water interface: Studies of the interaction of a semifluorinated alkane with fluorinated alcohols in mixed Langmuir monolayers. *Langmuir* **22**, 2691–2696.

[37] Broniatowski, M., Dynarowicz-Łatka, P. (2006). Interactions of a fluoroaryl surfactant with hydrogenated, partially fluorinated, and perfluorinated surfactants at the air/water interface. *Langmuir* **22**, 6622–6628.

[38] Broniatowski, M., Miñnes, J., Dynarowicz-Łatka, P. (2004). Semifluorinated chains in 2D-(perfluorododecyl)-alkanes at the air/water interface. *J. Colloid Interface Sci.* **279**, 552–558.

[39] Broniatowski, M., Sandez Macho, I., Miñnes, J., Jr., Dynarowicz-Łatka, P. (2004). Langmuir monolayers characteristic of (perfluorodecyl)-alkanes. *J. Phys. Chem. B* **108**, 13403–13411.

[40] Nakamura, S., Nakahara, H., Krafft, M.P., Shibata, O. (2007). Two-component Langmuir monolayers of single-chain partially fluorinated amphiphiles with dipalmitoylphosphatidylcholine (DPPC). *Langmuir* **23**, 12634–12644.

[41] Nakahara, H., Hirano, C., Fujita, I., Shibata, O. (2013). Interfacial properties in langmuir monolayers and LB films of DPPC with partially fluorinated alcohol (*F*8*H*7OH). *J. Oleo Sci.* **62**, 1017–1027.

[42] Nakahara, H., Hirano, C., Shibata, O. (2013). Two-component Langmuir monolayers and LB films of DPPC with partially fluorinated alcohol (*F*8*H*9OH). *J. Oleo Sci.* **62**, 1029–1039.

[43] Gaines Jr., G.L. (1966). *Insoluble Monolayers at Liquid-Gas Interfaces*. Interscience Publishers, New York, pp. 281–288.

[44] Shah, D.O., Schulman, J.H. (1967). *J. Lipid Res.* **8**, 215–226.

[45] Marsden, J., Schulman, J.H. (1938). *Transact. Faraday Soc.* **34**, 748–758.

[46] Joos, P., Demel, R.A. (1969). The interaction energies of cholesterol and lecithin in spread mixed monolayers at the air-water interface. *Biochim. Biophys. Acta* **183**, 447–457.

[47] Savva, M., Acheampong, S. (2009). The interaction energies of cholesterol and 1,2-dioleoyl-sn-glycero-3-phosphoethanolamine in spread mixed monolayers at the air-water interface. *J. Phys. Chem. B* **113**, 9811–9820.

[48] Hénon, S., Meunier, J. (1991). Microscope at the Brewster angle: Direct observation of first-order phase transitions in monolayers. *Rev. Sci. Instrum.* **62**, 936–939.

[49] Hönig, D., Möbius, D. (1991). Direct visualization of monolayers at the air-water interface by Brewster angle microscopy. *J. Phys. Chem.* **95**, 4590–4592.

[50] Weis, R.M., McConnell, H.M. (1985). *J. Phys. Chem.* **89**, 4453–4459.

[51] Möhwald, H. (1990). *Annu. Rev. Phys. Chem.* **41**, 441–476.

[52] Weis, R.M., McConnell, H.M. (1984). Two-dimensional chiral crystals of phospholipid. *Nature* **310**, 47–49.

[53] Thirumoorthy, K., Nandi, N., Vollhardt, D. (2007). Role of dipolar interaction in the mesoscopic domains of phospholipid monolayers: dipalmitoylphosphatidylcholine and dipalmitoylphosphatidylethanolamine. *Langmuir* **23**, 6991–6996.

[54] Wang, C., Li, C., Ji, X., Orbulescu, J., Xu, J., Leblanc, R.M. (2006). Peptidolipid as binding site of acetylcholinesterase: Molecular recognition of paraoxon in Langmuir films. *Langmuir* **22**, 2200–2204.

[55] Courrier, H.M., Vandamme, T.F., Krafft, M.P., Nakamura, S., Shibata, O. (2003). Mixed monolayers made from dipalmitoyl phosphatidylcholine and a fluorinated amphiphile. *Colloids Surf. A* **215**, 33–41.

[56] Lehmler, H.J., Bummer, P.M. (2004). Mixing of perfluorinated carboxylic acids with dipalmitoylphottphatidylcholine. *Biochim. Biophys. Acta* **1664**, 141–149.

[57] Lehmler, H.-J., Jay, M., Bummer, P.M. (2000). Mixing of partially fluorinated carboxylic acids and their hydrocarbon analogues with dipalmitoylphosphatidylcholine at the air-water Interface. *Langmuir* **16**, 10161–10166.

[58] Broniatowski, M., Nieto-Suarez, M., Vila-Romeu, N., Hac-Wydro, K., Dynarowicz-Łatka, P. (2004). Two-dimensional miscibility between a semifluorinated hydrocarbon and hydrogenated alcohols. *Colloids Surf. A* **249**, 3–9.

[59] Matuo, H., Hiromoto, K., Motomura, K., Matuura, R. (1978). Mixed monolayers of long normal chain fatty acids with long normal chain fatty alcohols. *Bull. Chem. Soc. Jpn.* **51**, 690–693.

[60] Lawrie, G.A., Gentle, I.R., Barnes, G.T. (2000). The structure of mixed monolayer films of DPPC and hexadecanol. *Colloids Surf. A* **171**, 217–224.

[61] Chen, K.B., Chang, C.H., Yang, Y.M., Maa, J.R. (2000). On the interaction of dipalmitoyl phosphatidylcholine with normal long-chain alcohols in a mixed monolayer: A thermodynamic study. *Colloids Surf. A* **170**, 199–208.

[62] Romão, R.I.S., Gonçalves da Silva, A.M. (2004). Phase behaviour and morphology of binary mixtures of DPPC with stearonitrile, stearic acid, and octadecanol at the air-water interface. *Chem. Phys. Lipids* **131**, 27–39.

[63] *CRC Handbook of Chemistry and Physics*, 91st ed. (2010). CRC Press. Boca Raton, London, p. 2610.

49

AFFINITY LATEX

HARUMA KAWAGUCHI

Department of Chemistry, Faculty of Engineering, Kanagawa University, Yokohama, Japan

49.1 INTRODUCTION

49.1.1 Bioseparation

One of the most frequently used routine operations for biochemists and bioengineers is separation and purification of specific biomolecules from a mixture of various biomolecules. There are many bioseparation techniques, such as centrifugation, electrophoresis, filtration, and phase separation. Among them, chromatography is the most popular one. Chromatography is defined as a technique for separation of a specific molecule from a mixture by passing it through a material through which some parts of the mixture travel farther than others. It includes several systems, that is, adsorption chromatography, partition chromatography, gas–liquid chromatography, ion exchange chromatography, size exclusion chromatography, and affinity chromatography.

49.1.2 Affinity Chromatography

The principle of affinity chromatography is something different from those of other chromatographic methods. The general chromatography relies on differences in the physical properties of the molecules to be separated. However, affinity chromatography exploits the unique property of extremely specific biological interactions to accomplish separation.

The affinity chromatography system is constructed by the following process: (1) a ligand or probe is attached to gel beads, (2) the gel beads are packed into a column, (3) a mixture of biomolecules is forced into the column, and (4) affinity-dependent flowdown behavior enables the separation of target molecules.

Affinity chromatography has been used to identify ligand-binding proteins, nucleotides, nucleic membrane receptors, and so on. For example, a pair of investigators demonstrated the separation of a transcription factor by using a column in which sequence-specific DNA/agarose beads were packed [1].

Affinity chromatography seems to be an established technique. But it has a fatal fault due to the nature of gel beads. Efficiency of affinity chromatography needs to bind as many ligands as possible. Therefore, gel beads are chosen as a carrier of ligands because they have huge number of sites to bind ligands on the surface and in the interior. But the microenvironment in the interior network structure is not uniform. This means that the ligands are located at different microenvironments and thus their target-catching activities vary, resulting in inefficient purification of the target.

It was expected that a ligand carrier having neither micronor macropores would avoid this disadvantage. But the carrier particle of flat surface with no pores has a smaller surface area than do porous particles. In order to ensure a large surface area to the carrier particle, the size of particle should be decreased. One gram of agarose gel beads has a surface of about 6 m^2. One gram of particles with a flat surface should be 0.2 μm in diameter in order to possess the same surface area as gel beads. Because such particles of submicrometer size cannot be packed in a column, they are used in the dispersion. The dispersed particles carrying the ligand on their flat surface can meet their target molecules frequently and be expected to exhibit high efficiency in bioseparation.

Purification/separation of biomolecules by affinity latex can be done as follows: (1) adding the affinity latex to a protein mixture solution, (2) incubating them for a certain

Encyclopedia of Biocolloid and Biointerface Science, Volume 2, First Edition. Edited by Hiroyuki Ohshima.
© 2016 John Wiley & Sons, Inc. Published 2016 by John Wiley & Sons, Inc.

time, (3) separating the latex particles that caught specific proteins from the solution, and (4) releasing the proteins from the latex particles by changing the medium. In the following section, the design of affinity latex is discussed.

49.2 IMMUNOLATEX

Before reporting affinity latex, a history of immunolatex is presented. An *immunolatex* is a latex on which an antigen or an antibody is bound. The first immunolatex appeared as a latex diagnostics for protein A in 1956 [2[. Antiprotein A antibody was immobilized on poly(vinyltoluene) particles, and the presence or absence of protein A in the patient's body was confirmed by observing the absence or presence of aggregates that resulted from the formation of antibody–antigen agglutination. In 1970, a team of researchers developed an immunolatex for cell labeling, that is, used it to find the location of its antigen on a cell surface [3, 4]. They used poly(acrolein-*co*-hydroxyethyl methacrylate) particles preferentially as a carrier of antibody due to their bioinertness [5]. Another investigator immobilized anticancer antibody on a magnetic microspheres, the size of which was comparable with that of the cells. The immune beads selectively caught cancer cells and collected by magnetic force [6]. These would be pioneer studies for affinity latex.

Other pioneer work was done using DNA-carrying microspheres. Another team developed oligothymidine (oligo[dT], degree of polymerization = 30)-carrying microspheres, which proved to be an efficient separator of mRNA from the mixture of all kinds of RNA and other substances [7]. This could be done because only mRNA has an adenine sequence at the chain ends. Single-stranded DNA-carrying microspheres were also used for solid-phase DNA sequencing [8].

49.3 MATERIALS COMPOSING AFFINITY LATEX

49.3.1 Latex Particle as a Ligand Carrier

Polymer particles are generally formed by particle-forming polymerization such as emulsion polymerization, suspension polymerization, and precipitation polymerization. Among these polymerizations, soap-free emulsion polymerization is preferred because it gives monodispersed and submicrometer-sized particles with a clean surface. The material for the polymer was carefully selected. The key criterion for the polymer particle material is its hydrophilicity–hydrophobicity balance. Latex particles with a hydrophobic surface are apt to adsorb proteins nonspecifically and, consequently, they are unsuitable for affinity latex. Several hydrophilic monomers are copolymeized with styrene in soap-free emulsion polymerization. Styrene contributes to the formation of monodisperse, spherical core particles and hydrophilic monomers do to the coating of the core with hydrophilic shell layer which keeps nonspecific proteins away in general.

TABLE 49.1 Requirements for Carrier Particles

- reject any nonspecific adsorption,
- have a site to bind a ligand,
- not disturb the specific interaction between ligand and target,
- Be easily collectable from the dispersion,

The comonomer finally chosen was glycidyl methacrylate (GMA) [9]. The polymerization was first carried out using styrene (St) with a small amount of GMA (5 wt% to St) and, at the final stage of the polymerization, additional GMA (10 wt% to St) was charged to the reaction vessel in order to form a shell layer on each particle. A part of GMA units was converted to glycelol methacrylate due to hydrolysis of glycidyl group of GMA during the polymerization.

The reason for choosing GMA as the comonomer was not only its moderate hydrophilicity to avoid nonspecific adsorption. As shown in Table 49.1, the particles have to have binding site for ligand, and GMA satisfied the requisite. Glycidyl groups in GMA units chemically bind amine groups of ligand. After binding ligands, the remaining glycidyl groups were hydrolyzed to convert them to diol groups. The P(St-*co*-GMA) core–PGMA shell particles with a diameter of ~0.2 μm thus obtained exhibited satisfactory performance in rejecting nonspecific adsorption of proteins.

49.3.2 Procedure for Binding Ligands to a Latex Particle Surface

The process to bind ligands is a crucial one for affinity latex preparation. If the ligand is bound badly to the particle, as shown in Fig. 49.1, domains *A* and *C*, the ligand has a poor ability to catch its target.

Direct binding of ligand to the particle surface sometimes gives no successful results. It was because the target molecule could not approach the ligand close to the particle surface due to steric hindrance. The example discussed below demonstrated this situation clearly.

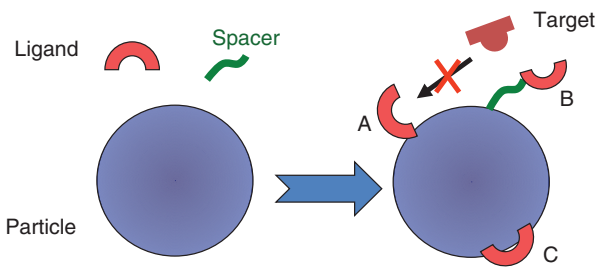


FIGURE 49.1 Mode of ligand attachment. Segments *A* and *C* are not good, but *B* is OK for catching the target.

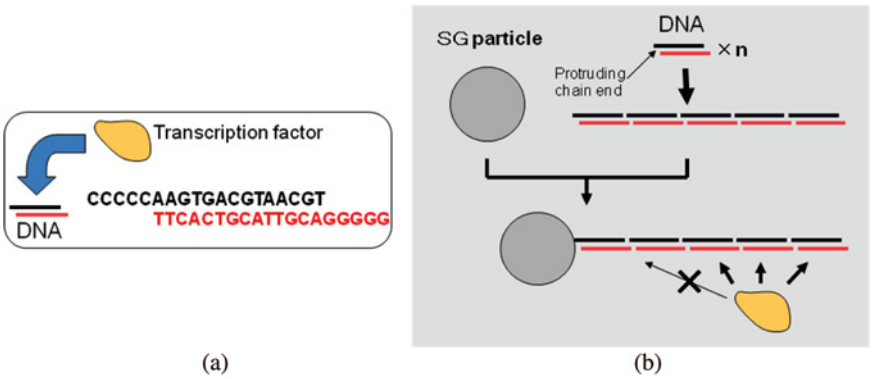


FIGURE 49.2 Preparation of sequence-specific DNA-carrying affinity particle for separation of transcription factor.

A transcription factor ATF/E4TF3 attaches specifically to a DNA with a specific base sequence (Fig. 49.2a), and the attachment switches the transcription on. Purification and concentration of the transcription factor was attempted using an affinity latex carrying the abovementioned fragment, taking advantage of the mechanism described above [9, 10]; however, it failed. The failure was attributed to steric hindrance near the ligand by a particle surface. Therefore, the DNA sequence was joined in tandem and attached to the particle surface as shown in Fig. 49.2b. This affinity latex resulted in the successful separation of pure and concentrated transcription factor from the serum. The result indicated that at least three sets of the DNA units from the surface of particles contributed as a spacer.

The recommendable spacers were oligoethyleneoxide, ethylene glycol diglycidyl ether, and glycil glysine for general targets.

49.3.3 Binding Site of Ligand Molecule

The choice of binding site of the ligand is another important consideration. The first event of some drugs injected into the body is to attach to their receptors on cell surfaces. This scheme is applicable for detection of the drug's receptor using drug-carrying affinity particles. The examined drug was naltrindole (NTI; Fig. 49.3, center) [11]. NTI was bound to a latex particle through three directions, *A*, *B*, and *C*. Use of affinity latices on which the drug was attached to the particles at *B* and *C* resulted in unsuccessful capture of target protein, but use of affinity latex carrying the drug at *A* brought about efficient capture of the target. These results imply that *B* and *C* domains in NTI are essential for pharmacologic activity.

Screening of biomolecules for a specific compound is one of the major purposes of affinity latex. Successful results were obtained and the mechanism and kinetics of their binding reaction [12, 13] For example, an affinity latex carrying a DNA-binding transcription factor caught eight polypeptides, which were found to be bound to the same DNA sequence and regarded as a family concerning to transcription.

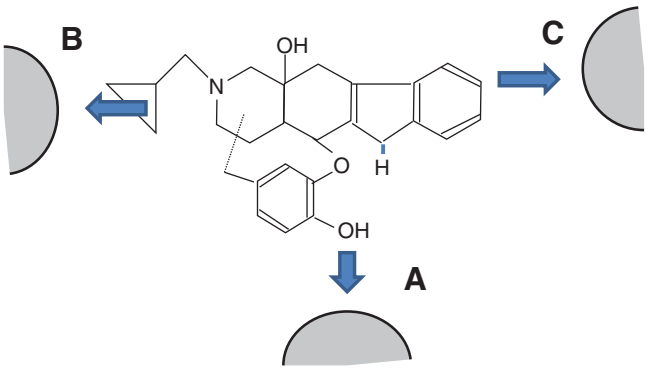


FIGURE 49.3 Choice of binding site of drug onto latex particle.

49.4 COMPARISON BETWEEN AFFINITY COLUMN CHROMATOGRAPHY AND AFFINITY LATEX

As presented in the previous section, affinity latex exhibited an excellent ability to separate its receptor protein from a mixture of proteins. Here, the ability of the affinity latex is compared with that of affinity column chromatography. Table 49.2 shows the differences of two systems in terms of the location of ligands, the chance of ligands to encounter the targets, recovery of separated targets, and so on.

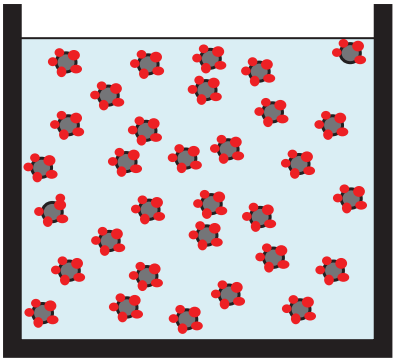
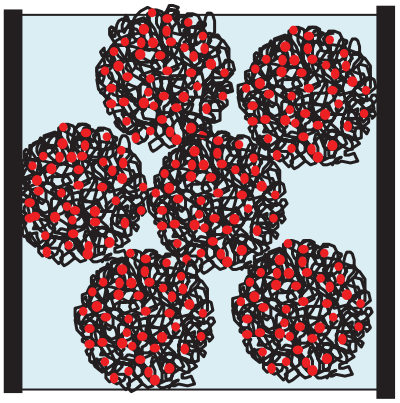
Differences in the homogeneity of the microenvironment surrounding a ligand and the action of the ligand seem to indicate that the affinity latex method is more efficient than affinity column chromatography.

49.5 FEATURES OF AFFINITY LATEX

49.5.1 Specific Base Sequence ssDNA-Carrying Affinity Latex

A complementary DNA pair in its solution forms a double-stranded DNA spontaneously below its specific melting temperature. A pair of one-point mismatch DNA also forms a

TABLE 49.2 Comparison between Affinity Latex and Affinity Column Chromatography

	Affinity latex	Affinity column chromatography
		
Reaction site	particle surface	pores in gel particle
Homogeneity of the site	high	miscellaneous
Action of ligand	approaching to target	waiting for targets
Dead volume	small	large
Recovery of targets	release of them from gathered particles	collection of flow

moderate amount of double-stranded DNA under the same conditions if the DNA is composed of more than 20 bases. But this was not the case in the affinity latex system in one study [14]. The experiment was carried out using the following procedure [14]: (1) DNA-S was bound to a particle, (2) a dispersion of particle S was mixed with a solution of DNA-A or DNA-B, and (3) the amount of hybrid (A/S or B/S) was measured as a function of time.

In that study [14], 50% of A hybridized with particle S within 1 h whereas the amount of B/S hybrid was almost 0; this means that the hybridization efficiency was almost zero at room temperature (see Fig. 49.4).

Another experiment was done by mixing both solutions of DNA-A (labeled) and DNA-B simultaneously with the dispersion of particle L. In this competitive hybridization, the amount of A/L hybrid was measured by the label. It was confirmed that the coexistence of DNA-B with 300 times DNA-A did not disturb the hybridization of A with particle L.

Both experiments strongly indicated that the DNA bound on a particle surface had a strong affinity to capture its complement DNA and, on the other hand, strongly refuted



FIGURE 49.4 DNA used for determination of hybridization efficiency.

hybridization with mismatched DNA. This was attributed to the relative inflexibility of the DNA bound to the particle surface. Such DNA would not be efficient at fitting the conformation with mismatch DNA:

$$\left(\frac{\text{dsDNA of mismatch pair}}{\text{dsDNA of complementally pair}}\right)_{\text{in solution}} \gg \left(\frac{\text{dsDNA of mismatch pair}}{\text{dsDNA of complementally pair}}\right)_{\text{on latex}}$$

49.5.2 Speedy Recovery of Target-Capturing Affinity Particles

The first-generation affinity latex was recovered from the medium by centrifugation after hybridization. Because the particles were small (<1 μm), centrifugation at >12,000 × g for >30 min was necessary to sediment them out of the medium. However, such a severe condition could potentially damage the target molecules and reduce the efficiency of the separation process. To overcome this disadvantage, another method to recover the affinity particles was examined and magnetic force was chosen as an alternative option [15]. First, composite particles, including magnetic nanoparticles, were prepared. Various methods are used to entrap magnetic nanoparticles in polymer particles; these fall into two basic categories: (1) direct entrapment of nanoparticles and introduction of precursor and (2) introduction of precursor of magnetic nanoparticles followed by in situ nanoparticle formation. The suitable size of magnetic particles embedded in affinity latex particles was estimated to be around 20 nm.

49.6 NOVEL AFFINITY LATEX

49.6.1 Capture and Cutting Affinity Latex

An affinity latex with dual functions was developed. It is P(St-*co*-GMA) core/PGMA shell particle carrying mismatch binding protein (MutS) and an anthraquinone derivative (AQ). AQ is a light-activated agent that photocleaves dsDNA [16]. This novel affinity latex can catch and cleave mismatched DNA selectively and propose a new mismatch detection system. Use of the affinity latex made it possible to discriminate complementary and mismatched DNA and photocleave only mismatched DNA. The efficiency of photocleavage increased with UV irradiation time.

49.6.2 Affinity Latex for the Detection of Telomerase

Highly sensitive detection of telomerase enables us to detect many kinds of cancers in early stage, and also gives us much important information about cell biology. This was made possible by an affinity latex that detected G4-DNA generated from elongation of telomere by telomerase [17]. The measurement using SPR biosensor increased the sensitivity drastically.

49.7 CONCLUDING REMARKS AND FUTURE PROSPECTS

Since the first immunolatex was proposed as a latex diagnostics, submicrometer-sized particles have been used for biomedical applications. Affinity latices should be inert particles to nonspecific biomolecules but have high affinity with specific target molecules. Such an affinity latex could be obtained by careful binding of ligand molecules on well-designed polymer particles. Affinity latices are applied not only to various bioseparations but also to identification of drug receptors, to activation of cells, and so on.

The ability of biomolecules to bind to a particle surface but the feature that causes them to thereby become less flexible and increase the recognition ability might be applicable to the control of biomolecules functions.

REFERENCES

[1] Singer, J.M., Plotz, C.M. (1956). The latex fixation test: 1. Application to the serologic diagnosis of rheumatoid arthritis. *Am. J. Med.* **21**, 888.

[2] Kadonaga, J.T., Tijian, R. (1986). Affinity purification of sequence-specific DNA binding proteins. *Proc. Natl. Acad. Sci. USA* **83**, 5889–5893.

[3] Rembaum, H., Yen, S.P.S., Volksen, W. (1978). Labeled cells. *ChemTECH.* (March) 182.

[4] Rembaum, A., Yen, S.P.S., Cheong, E., Wallace, S., Molday, R.S., Gorden, I.L., Dreyer, W.J. (1976). Functional polymeric microspheres based on 2-hydroxyethyl methacrylate for immunochemical studies. *Macromolecules* **9**, 328.

[5] Molday, R.S. (1984). Cell labeling and separation using immunospecific microspheres. In *Cell Separation: Methods and Selected Applications*, Vol. 3. Academic Press, New York, p. 237.

[6] Ugelstad, J., et al. (1982). *Progress Polym. Sci.* **17**, 87.

[7] Kuribayashi, K., Hikata, M., Hiraoka, O., Miyamoto, C., Furuichi, Y. (1988). A rapid and efficient purification of poly(A)-mRNA by oligo(dT)30-latex. *Nucleic Acids Res. Symp. Ser.* **19**, 61

[8] Uhlen, M. (1989). Magnetic separation of DNA. *Nature* **340**, 733.

[9] Kawaguchi, H., Asai, A., Ohtsuka, Y., Wada, T., Handa, H. (1989). Purification of DNA binding transcription factors by their selective adsorption on the affinity latex particles. *Nucleic Acids Res.* **17**, 6229–6240.

[10] Inomata, Y., Kawaguchi, H., Hiramoto, M., Wada, T., Handa, H. (1992). Direct urification of multiple ATF/E4TF3 polypeptides from HeLa cell clude nuclear extracts using DNA affinity latex particles. *Anal. Biochem*. **206**, 109.

[11] Hasegawa, M., Ohno, H., Tanaka, H., Hatakeyama, M., Kawaguchi, H., Takahashi, T., Handa, H. (2006). Affinity identification of δ-opoid resceptors using latex nanoparticles. *Bioorg. Med. Chem. Lett.* **16**, 158–161.

[12] Zenkoh, T., Hatori, H., Tanaka, H., Hasegawa, M., Hatakeyama, M., Kabe, Y., Setoi, H., Kawaguchi, H., Handa, H., Takahashi, T. (2004). Design and synthesis of a solid-supported FR225659 derivative for its receptor screening, *Org. Lett.* **6**, 2477.

[13] Yamaguchi, Y., Wada T., Suzuki F., Takagi, T., Hasegawa, J., Handa, H. (1998). Casein kinase II interacts with the bZIP domains of several transcription factors. *Nucleic Acids Res.* **26**, 3854.

[14] Hatakeyama, M., Iwato, S., Fujimoto, K., Handa, H., Kawaguchi, H. (1998). DNA-carrying latex particles for DNA diagnosis. 1. Separation of normal and point mutant DNAs according to the difference in hybridization efficiency. *Colloids Surf.* **10**, 161–169.

[15] Nishio, K., Abe, M., Handa, H., et al. (2008). Development of novel magnetic nanocarriers for high-performance affinity purification. *Colloids Surf. B: Biointerfaces* **64**, 162–169.

[16] Oba, S., Hatakeyama, M., Handa, H., Kawaguchi, H. (2005). Development of polymer latex particles for selective cleavage of mismatched DNA and their application for DNA diagnosis. *Bioconjug. Chem*. **16**, 551–558.

[17] Hara, R., Kawaguchi, H. (2012) Highly Sensitive Detection of Telomerase by Using G-Quartet DNA binder Conjugated Polymeric Microspheres. *Kobunshi Ronbunshu*, **69**, 122-128 (in Japanese)

50

LATEX DIAGNOSIS

HARUMA KAWAGUCHI
Department of Chemistry, Faculty of Engineering, Kanagawa University, Yokohama, Japan

50.1 INTRODUCTION

Early detection of disease is necessary to ensure high quality of life. Many diagnostic methodologies such as fluorescence-, radio-, enzyme-linked, and chemiluminescence immunoassays, enzyme-linked immunosorbent assay, Western blotting, and agglutination testing, were developed and their advantages have been increasingly evident. Among them, latex diagnostics cut a conspicuous figure because of its unique process in which latex particles carrying antigen or antibody, called *immunolatex*, are ingeniously used for a variety of assays [1]. There are three major types of immunolatex: an agglutination test caused by antigen–antibody interaction, particle-enhanced immunoassay, and multiplex assay.

50.2 MATERIALS COMPOSING IMMUNOLATEX

The basic event in latex diagnostics is enabled by cooperation between antigen, antibody, and latex particles, the features of which are introduced below.

50.2.1 Antigen and Antibody

An *antigen* is a substance that generates the respective antibody (e.g., the Y-shaped protein shown in Fig. 50.1) and binds to it specifically by means of its variable region interaction. Antigens are usually proteins and polysaccharides, less frequently also lipids, that originated from within the body or from the external environment. The latter, such as bacteria and viruses, are recognized as invaders and are attacked by the antibody. The binding reaction between antigen and antibody produces aggregates with high specificity and precision. Therefore, if the body fluid of a patient generates aggregates when mixed with a solution containing a tiny amount of antibody, we can recognize the existence of an antigen in that patient's body.

50.2.2 Latex Particle

A *latex* is the aqueous dispersion of polymer particles. Latices are generally prepared by procedures such as emulsion polymerization, soap-free emulsion polymerization, and miniemulsion polymerization. The reaction medium is water in most cases. These polymerizations produce mostly monodispersed, submicrometer-sized polymeric particles with huge specific surface areas. The stability of particles in dispersion should be controlled by considering the long-term storage and the quick assay. A moderate degree of stability is attained by achieving balance between electrostatic repulsive force and van der Waals attractive force.

The surface of particles can be modified, if necessary, to accept the binding or adsorption of immunocompounds.

50.3 DESIGN OF IMMNOLATEX

50.3.1 Hemagglutination

As mentioned above, antigen and antibody coagulate specifically and, in some cases, the size of aggregates reaches the one observable macroscopically. The diagnostics obtained via such observation is referred to as a *direct* (or *active*)

Encyclopedia of Biocolloid and Biointerface Science, Volume 2, First Edition. Edited by Hiroyuki Ohshima.
© 2016 John Wiley & Sons, Inc. Published 2016 by John Wiley & Sons, Inc.

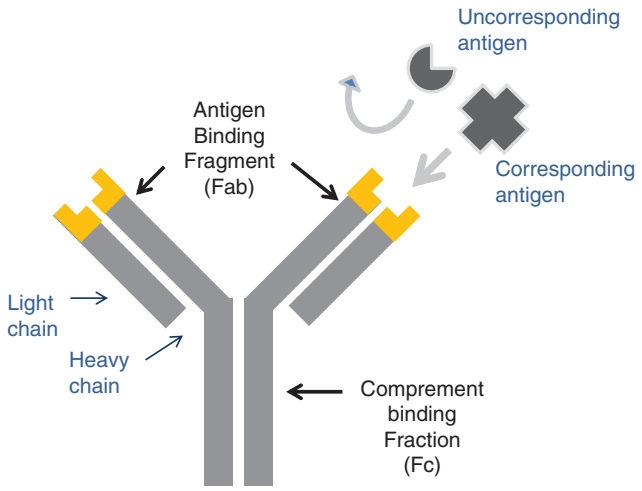


FIGURE 50.1 Structure of antibody.

agglutination test. But usually the products of agglutination are too small to confirm their presence or absence or to measure their size quantitatively. To detect the antigen–antibody agglutination more clearly, the antibody molecules were attached to a red cell in order to convert independent antibody molecules to multiple valence antibodies [2]. The multiple valence antibodies contributed to the formation of massive aggregates, as illustrated in Fig. 50.2. This diagnostic methodology using antibody-sensitized red cells is referred to as *reversed passive hemagglutination* (RPHA). The term *passive* indicates that the agglutination occurs with the aid of a carrier, in this case, a red cell, that is sensitized with immunocomponent. The system in which a red cell carries antigen is called simply a *passive hemagglutination system*, where *reversed* indicates that the particle (red cell) is sensitized with antibody but not antigen. If a red cell holds any antigen by nature, the system is classified as a direct agglutination system.

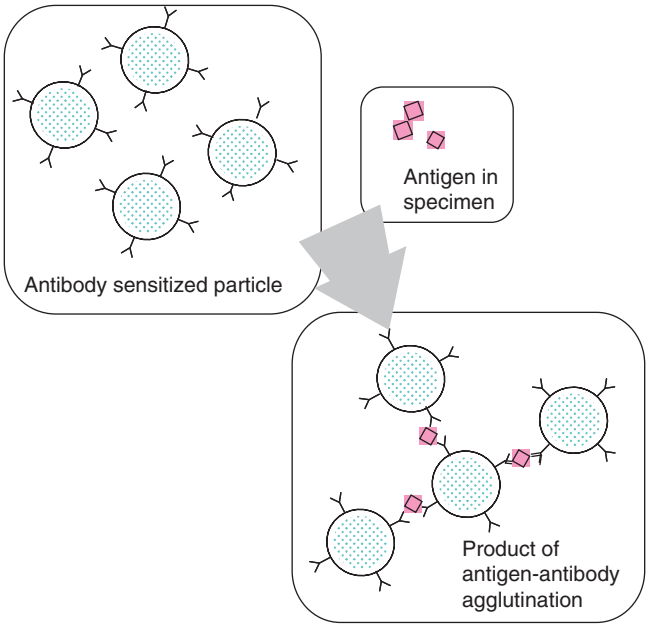


FIGURE 50.2 Typical agglutination using sensitized particle.

50.3.2 Use of Latex Particle as Carrier of Immunocomponents

A red cell is a suitable carrier for antigen or antibody, but it includes some drawbacks. For instance, a red cell itself is sometimes antigenic, with diameter size limited to around 7 μm. It is fragile and is not suited for long-term storage. In contrast to a red cell, a latex particle has the following merits: (1) no antigenicity, (2) high productivity, (3) controllable size and surface chemistry, and (4) high storage stability. Because of these advantages, latex particles are preferred to red cells as carriers of immunocomponents.

The first immunolatex was reported in the literature in 1956 [3]. It consisted of a dispersion of poly(vinyltoluene-*co*-styrene) microspheres carrying antirheumatoid antibody. Aggregates formed when the latex was mixed with the blood sample of a patient who was positive for the rheumatoid factor, due to antigen–antibody binding as shown in Fig. 50.2. Thus, the extent of aggregate formation is regarded as the measure of rheumatism.

Singer's immunolatex yielded successful results to some extent. But it had some disadvantages, namely, unavoidable nonspecific adsorption and low efficiency of aggregate formation.

50.3.3 Improvement of Immunolatex in Terms of Sensitization Mode

There are two strategies for the selection of particle material, that is, to use hydrophobic particles or hydrophilic particles.

50.3.3.1 Hydrophobic Particle as a Carrier. The surface of latex particle is generally hydrophobic. Such surface is favorable to adsorb an antigen or an antibody so that the hydrophobic particle surface can be sensitized easily by a simple adsorption process. Adsorption is generally done in a phosphate buffer saline at room temperature for 1–2 h.

The adsorption of proteins to a hydrophobic surface is not limited to that of targeted immunomolecules but also takes place for nonspecific molecules. Therefore, the surface must be converted to hydrophilic one after sensitization. Generally the surface modification can be done by covering the hydrophobic surface with albumin or poly(ethylene glycol) adsorbed spontaneously [1]. The particles thus obtained have a sterically stabilized surface. The extent of steric stabilization must be controlled properly because colloidal stability

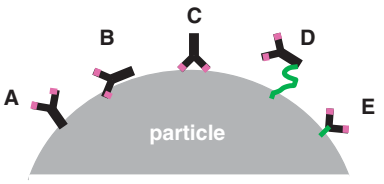


FIGURE 50.3 Style of immobilized antibody.

that is either too low or too high can reduce the sensitivity of latex diagnostics.

Biomolecules have their specific conformation. In particular, the conformation around the functional domain is important. Each antibody has a specific domain, a fragment of antigen binding site called *Fab*, that recognizes and binds its counterpart antigen at the edge of a Y-shaped molecule (Fig. 50.1). Fab fragment should be exposed to the medium (Fig. 50.3 pattern A) but B and C must be avoided. The pH at which an antibody molecule is attached is an important factor in controlling the orientation of antibody on the particle surface. Fc fragment was preferentially adsorbed to the surface at pH > 8 because the hydrophobic attractive force between Fc fragment and the particle surface overcame the electrorepulsive force between them, but this was not the case for less hydrophobic Fab [4]. As mentioned above, Fc does not directly contribute to antigen–antibody agglutination and even obstructs it in some cases. Therefore, $(Fab)_2$ is sometimes separated from Fc by pepsin and only V arms [$(Fab)_2$] can be bound to the particle surface (Fig. 50.3, pattern *E*) [5].

50.3.3.2 Hydrophilic Particle as a Carrier. Aiming to avoid nonspecific adsorption in the course of agglutination test, a particle with a hydrophilic surface can be used as a carrier of antigen or antibody, In this case, spontaneous adsorption of an antigen or an antibody to hydrophilic particles does not take place. Therefore, sensitization of hydrophilic particle can be done by chemical bonding of immunocompounds. In this case, carboxy, hydroxy, amino, epoxy, and aldehyde groups on the particle surfaces are commonly used for binding with amino groups in antibody molecules. Among binding reagents, carbodiimide is the most popular one. The carbodiimide method requires the inclusion of an activation process of carboxy groups of particles prior to reaction with amino groups of antibody. Undesirable side reactions caused by carbodiimide may result in denaturing and/or cross-linking. Glutalaldehyde is commonly used to bind the amino groups of the particle and antibody molecules. CNBr and sulfonyl chloride are used to activate glycol groups and hydroxy groups, respectively, on the particle to bind antibody at its amino group

50.3.3.3 Use of Spacer. To separate Fab from the particle surface and avoid the steric hindrance of antigen–antibody reaction, antibody is bound to the particle not directly but through a linker or spacer as shown in pattern *D* in Fig. 50.3. The linker would be hydrophilic chains of 6–10 atoms such as ethyleneglycol diglycidyl ether and glycil glycine.

50.4 MEASUREMENT OF AGGLUTINATION

50.4.1 Patterns of Agglutination Test

The extent of antigen–antibody agglutination is detected by several means, from qualitative to highly quantitative ones. The simplest one is observation of the products of agglutination on a petri dish, although it is only a qualitative check. Semiquantitative measurement is done using a titer in which samples with different dilutions are charged and the figure of agglutinated precipitates on the bottom of each well is observed. Carrier particles with large diameter and high density are used in order to shorten the time for aggregate formation.

The extent of agglutination is quantitatively detectable by spectroscopy as shown in Table 50.1.

Transmitted light through the sample presented the change in turbidity caused by antigen–antibody agglutination. This refers to as immunoturbidmetric test and the detectable concentration of antigen is 10^{-9}–10^{-4} mol/L. The turbidity of dispersion depends not only on the particle size but also on the wavelength of incident light. In a latex photometric immunoassay (LPIA), the initial rate of turbidity change at 940 nm on mixing a specimen with immunolatex of relatively small particle size, is measured to quantitatively determine the antigen or antibody (10^{-11}–10^{-7} mol/L) [6]. The near-nfrared wavelength was chosen for the determination because the turbidity at 940 nm highly depends on the size of aggregates.

The turbidity is a result of scattering. Therefore, the intensity of scattered light is another measure of the extent of agglutination. This is nephelometric immunoassay (NIA), in which the detectable concentration is 10^{-10}–10^{-5} mol/L. The size of particles used for these measurements ranges from 100 to 500 nm in general. The large particles present high sensitivity in agglutination test, but such particles lack the dispersion stability.

The principle of particle-counting immunoassay (PACIA) is different from those of the abovementioned methods. In

TABLE 50.1 Optical Measurements for Agglutination Testing

Method	Detected light
Turbimetric	Transmitted light
Nephelometric	Forwardscattered light
Scanning laser microscopy	Backscattered light
Particle counting	—

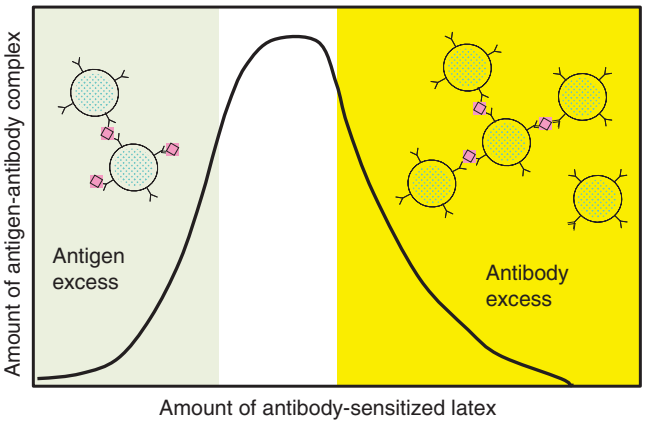


FIGURE 50.4 Dependence of agglutination on amount of titrant (antibody-sensitized latex).

PACIA the distribution of individual particles and two- and three-particle aggregates or the amount of unreacted individual particles can be measured. It counts the latex aggregates (P) and single latex particles (M) and the value of P/(P+M) is applied to a calibration curve to estimate the concentration of antigen [7].

The small increments in average diameter caused by weak agglutination can be measured by photon correlation spectroscopy (PCS), capillary hydrodynamic fractionation, laser photoacoustic spectroscopy, and similar methods. The latex particles used for these highly sensitive tests must be extremely monodisperse, and any aggregates must be eliminated in the original dispersion.

50.4.2 Antigen Excess Zone

The antibody or antigen excess zone is an important consideration. In the titration of antibody to a sample solution including antigen, the turbidity increases with increasing titrant (see Fig. 50.4) but then gradually levels off. Further addition of antibody results in a decrease in the turbidity. This is the antibody excess zone in which the aggregates, once formed, redissolves, due to the poor antigen–antibody balance.

A drawback of these latex systems is the narrow concentration range of detectable target compounds, antigen or antibody. To overcome this drawback, a latex composed of a wide distribution of size of particles is used.

50.5 LATEX DIAGNOSTICS INDEPENDENT FROM AGGLUTINATION

A particle capture enzyme-linked immunosorbent assay (PC-ELISA) is discussed here. It includes two methods: a "sandwich" method and a competitive method, which are illustrated in Fig. 50.5. The immunolatex is first captured on

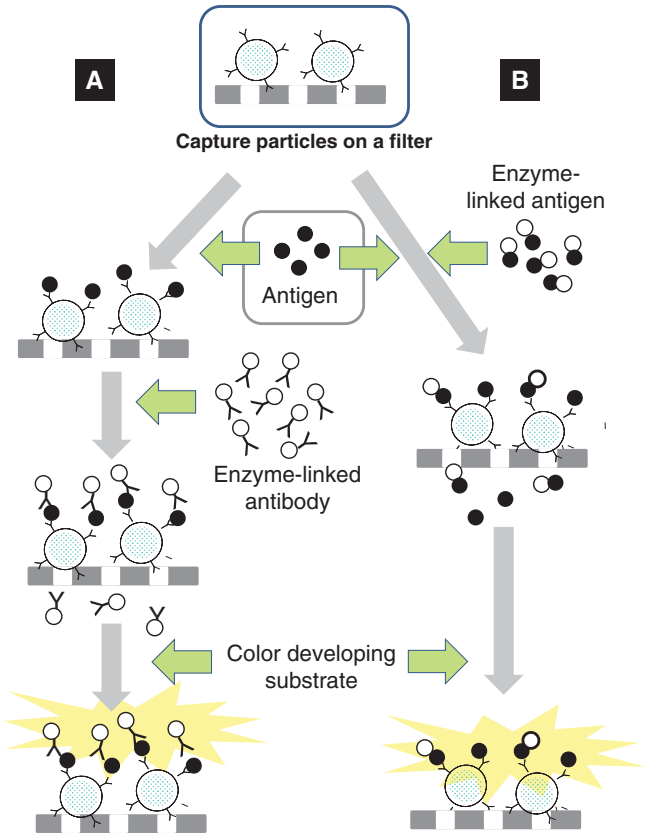


FIGURE 50.5 Particle capture enzyme-linked immunosorbent assays: (a) sandwich method; (b) competitive method.

a filter in both methods. A specimen is added on it. In the sandwich method, an antibody –antigen – antibody sandwich forms if the specimen includes antigen. In the competitive method, an enzyme-linked antigen is added simultaneously with the specimen and competitive adsorption takes place between antigen and enzyme-linked antigen to the antibody on the particle surface.

All of unbound antigen and enzyme-linked antigen are filtered out and the color intensity on the filter is measured to determine the antigen. The color-developing process can be omitted if enzyme is replaced with any colorant.

Another method is used to carry out ELISA with no particle trapping on a filter. In this method, antibody-carrying particles react with antigen molecules followed by sandwich formation with enzyme-linked antibody in the dispersion. Then the particles are recovered from the dispersion. The determination of the antigen is carried out in the same manner as that for ELISA. This method is referred to as *chemiluminescence enzyme immunoassay* (CLEIA). A similar assay using fluorescence instead of enzyme is becoming popular [chemiluminescence immunoassay (CLIA)]. Magnetic immunoparticles are used for these assay system because of enhancement of particle recovery.

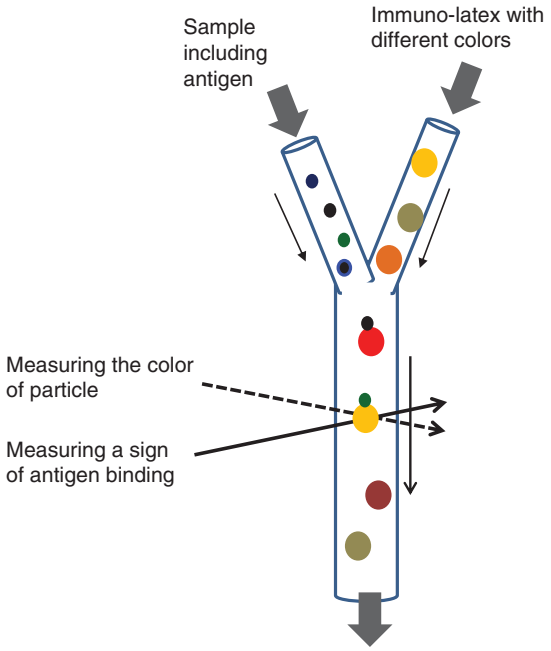


FIGURE 50.6 Multiplex assay using bead array.

50.6 MULTIPLEX ASSAY USING AFFINITY LATEX

Multiplex assay is defined as the assay for simultaneous detection of multiple targets by using multiple ligands. This assay needs only very small amount of samples and, therefore, patients suffer little pain. Speed is another merit of the multiplex assay. There are two types of multiplex assay systems: one that is composed of chips and another one that is composed of dispersing particles. In the former, each ligand is identified by the position on a chip. In contrast, in multiplex assay using affinity particles, called *suspension array* or *bead array*, each particle in the dispersion carries its own sign, or barcode, to indicate its identity as presented in Fig. 50.6 [8,9].

Color, size, density, electric charge, and other parameters have been used for the barcode. A series of multicolored particles were obtained by mixing multiple dyes or quantum dots (QD) with different mixing ratio [10]. For example, 100 kinds of microbe were prepared by combining different amounts of two kinds of fluorescent dyes with 10 concentrations per dye into the beads with a diameter of 5 μm. Such beads are identified in a flow cell by the specific fluorescence emitted from each dye embedded in the beads. In some QD-assisted multiplex assay systems, leakage of QD caused problems. To prevent leakage of QDs, silica nanoparticles were deposited on the polymer particles to form silica shell [11].

50.7 CONCLUDING REMARKS AND FUTURE PROSPECTS

Latex particles provide an excellent carrier for bioassays because of their bioinertness, uniformity, abundant lineup, controllable dispersion stability, and other factors. In addition, development of instruments participates in further progress of latex diagnostics to raise the sensitivity, reduce the amount of specimen, and shorten the measurement time.

REFERENCES

[1] Bangs, L.B. (1999). Microspheres for medical diagnostics, Part 2: Specific tests and assays. In Arshady, R. (ed.), *Microspheres, Microcapsules & Liposomes. Vol. 2: Medical & Biotechnology Applications*. Citus Books, London.

[2] Burnet, F.M. (1946). *Br. J. Exp. Pathol.* **27**, 244.

[3] Singer, J.M., Plotz, C.M. (1956). The latex fixation test. I. Application to the serologic diagnosis of rheumatoid arthritis. *Am. J. Med.* **21**, 888–892.

[4] Kawaguchi, H., Sakamoto, K., Ohtsuka, Y., Ohtake, T., Sekiguchi, H., Iri, H. (1989). *Biomaterials* **10**, 25.

[5] Bangs, L.B. (1999). Microspheres for medical diagnostics. Part 1: General principles and criteria. In Ashady, R. (ed.), *Microspheres, Microcapsules & Liposomes*. Citus Books, London.

[6] Okamura, S. (1987). Rapid quantification of α-fetoprotein in serum with a latex piotometric immunoassay system. *Clin. Chem.* **33**, 2306–2307.

[7] Cambiaso, C.L. (1999). Particle counting immunoassay (PACIA). 1. A general method for the determination of antibodies, antigen, and hapten. *J. Immunol. Methods* **18**, 33–44.

[8] Hadfield, S.G., Lane, A., Mellmurray, M.B. (1987). A novel coloured latex test for the detection and identification of more than one antigen. *J. Immunol. Methods* **97**, 153–158.

[9] Kawaguchi, H. (2008). In Elaissari, A. (ed.), *Colloidal Nanoparticles in Biotechnology.* Wiley, Hoboken, NJ, pp. 117–131.

[10] Fulton, R.J., McDade, R.L., Smith, P.L., Kienker, L.J., Kettman, J.R., Jr. (1997). Advanced multiplexed analysis with the FlowMetrixTM system. *Clin. Chem.* **43**, 1749–1756.

[11] Cao, Y.C., Huang, Z.L., Liu, T.C., Wang, H.Q., Zhu, X.X., Wang, Z. (2006). Preparation of silica encapsulated quantum dot encoded beads for multiplex assay and its properties. *Anal. Biochem.* **351**, 193–200.

51

LIGHT SCATTERING AND ELECTROPHORETIC LIGHT SCATTERING OF BIOPOLYMERS

ETSUO KOKUFUTA

Faculty of Life and Environmental Sciences, University of Tsukuba, Tsukuba, Ibaraki, Japan

51.1 INTRODUCTION

In general, the term *biopolymer* refers to proteins, polysaccharides, polynucleotides, and bacterial aliphatic polyesters. In 2012 the IUPAC recommended the use of the term *biomacromolecule* when molecular characteristics are considered [1]. The light-scattering methods, usually separated into static light scattering (SLS) and dynamic light scattering (DLS), are a useful experimental tool to explore characteristics of macromolecules in solutions, so most of the discussion focuses on the SLS and DLS of biomacromolecules. This is case for electrophoretic light scattering (ELS), by which the electrophoretic mobility of macromolecules bearing charges can be determined and if necessary, the mobility can be converted into zeta-potential.

51.2 STATIC LIGHT SCATTERING

Static light scattering (SLS) is founded on the principle of Rayleigh scattering, which is the scattering of light by particles and molecules that are much smaller than the wavelength of the light [2]. The scattered intensity is then characterized by the *Rayleigh ratio* $R(\theta)$, which is defined as $R(\theta) = (i_\theta r^2)/(IfV)$, where I is the intensity of the incident light, i_θ is the total intensity of scattered light observed at an angle θ and a distance r from the point of scattering, and V is the scattering volume. The factor f is dependent on the polarization of the incident light: $f = 1$ for vertically polarized light, $f = \cos^2\theta$ for horizontally polarized light, and $f = (1 + \cos^2\theta)/2$ for unpolarized light. In Rayleigh light scattering, it is well known that $R(\theta)$ is proportional to the product of molar mass (M) and weight concentration (c) of particles or molecules. The proportional constant is often regarded as an optical constant (K), and for vertically polarized light it can be given as $K = (4\pi^2 n_0^2/N_A\lambda^4)(\partial n/\partial c)^2$, where n_0 is the refractive index of the pure solvent, N_A is the Avogadro number, λ is the incident light wavelength, and $\partial n/\partial c$ denotes the refractive-index increment. Thus, $R(\theta)$ expressed by $R(\theta) = KMc$, but this is true for only very small rigid objects.

When the scattering objects are polymers, we must consider the effects of polymer–solvent interactions. Also, the effects arising from their shape anisotropy must be considered. The former can be treated by the virial expansion of the osmotic pressure, and the latter is accomplished by introduction of the particle-scattering function $P(\theta)$, which is often called the *particle form factor*. As a result, the fundamental equation for SLS, which is useful for determining the weight-average molecular weight M_w, the z-average radius of gyration $\langle R_g\rangle_z$ (hereafter simply denoted as R_g), and the second virial coefficient A_2, can be given as follows [3–5]:

$$\frac{Kc}{R_\theta} = \frac{1}{M_w P(\theta)} + 2A_2 c + \cdots = \tag{51.1a}$$

$$\frac{1}{M_w}\left(1 + \frac{16\pi^2}{3\lambda^2}R_g^2 \sin^2\left(\frac{\theta}{2}\right) + \cdots\right) + 2A_2 c + \cdots \tag{51.1b}$$

Note that $P(\theta)$ is defined as the ratio of the intensity of radiation scattered at an observation angle θ to the intensity of radiation scattered at an angle zero and can be related to R_g by $P(\theta) = 1 - (16\pi^2 R_g^2/3\lambda^2)\sin^2(\theta/2) + \cdots$. Also note that

Encyclopedia of Biocolloid and Biointerface Science, Volume 2, First Edition. Edited by Hiroyuki Ohshima.
© 2016 John Wiley & Sons, Inc. Published 2016 by John Wiley & Sons, Inc.

this equation is combined with Eq. (51.1a) using the relation of $1/(1-x) \cong 1+x$.

In actual SLS measurements, the calibration of SLS instruments is required with standard pure liquids whose Rayleigh ratios are known [6–8]. For this, toluene is frequently used because the Rayleigh ratios of toluene are suitably high for precise measurements and are known over a range of wavelengths and temperatures. Now we consider the excess Rayleigh ratio $\Delta R_\theta (= R(\theta)_{solution} - R(\theta)_{solvent})$, although R_θ in Eq. (51.1a) should have been written as ΔR_θ in the strict sense. When calibration is performed with toluene as the reference with a known absolute scattering intensity, ΔR_θ can be given as

$$\Delta R_\theta = \left(\frac{\Delta I_\theta}{I_{tol}}\right)\left(\frac{n_0}{n_{tol}}\right)^2 R_{tol} \tag{51.2}$$

where $\Delta I_\theta (= I_{solution} - I_{solvent})$ is the excess light-scattering intensity (i.e., the difference between the scattering intensities at angle θ for a solution and for a pure solvent), I_{tol} is the scattering intensity of toluene at θ, n_0 is the refractive index of the solvent (used for sample preparation), n_{tol} is the refractive index of toluene, and R_{tol} is the Rayleigh ratio of toluene. In Eq. (51.2), the term $(n_0/n_{tol})^2$ is the factor used to correct the scattering volume [9, 10]. Combination of Eqs. (51.1b) and (51.2) gives

$$\frac{Kc}{\Delta R_\theta} \equiv \frac{1}{M_w}\left(1 + \frac{R_g^2 q^2}{3}\right) + 2A_2 c \tag{51.3}$$

In Eq. (51.3), the scattering vector q, defined as $q = 4\pi n \sin(\theta/2)/\lambda$ (where n is the refractive index of the solution), is used. Also, the contribution of terms higher than the third one, shown by dots in Eq. (51.1b), is neglected in common practice.

Equation (51.3) becomes $Kc/\Delta R_\theta = M_w^{-1} + 2A_2 c$ at $q = 0$ (or $\theta = 0$) and $Kc/\Delta R_\theta = M_w^{-1} + R_g^2 (3M_w)^{-1} q^2$ at $c = 0$. When the ΔR_θ values obtained at different concentrations and at different angles are plotted against $q^2 + kc$ (where k is an arbitrary constant used to adjust the scale), the extrapolation allows us to determine the $\lim_{q\to 0}(Kc/R_\theta)$ values at different c and the $\lim_{c\to 0}(Kc/R_\theta)$ values at different q (see Fig. 51.1). As a result, we can obtain (1) M_w from the intercept of the $\lim_{c\to 0}(Kc/R_\theta)$ versus $q^2 + kc$ curve and of the $\lim_{q\to 0}(Kc/R_\theta)$ versus $q^2 + kc$ curve, (2) R_g from the slope of the $\lim_{q\to 0}(Kc/\Delta R_\theta)$ versus $q^2 + kc$ curve, and (3) A_2 from the slope of the $\lim_{c\to 0}(Kc/\Delta R_\theta)$ versus $q^2 + kc$ curve.

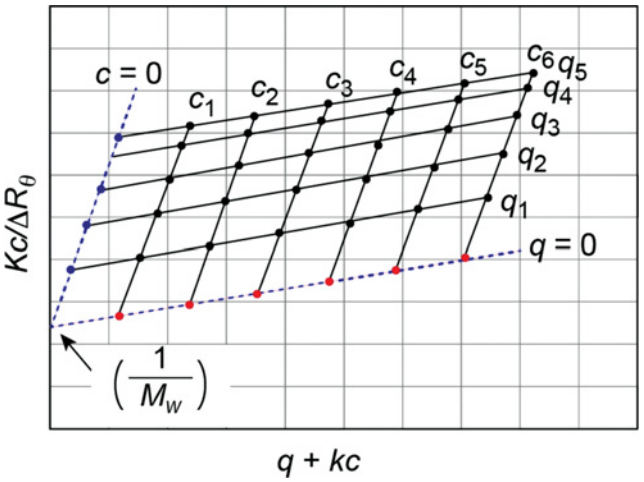


FIGURE 51.1 Schematic Zimm plot. See text on how to determine M_w, R_g, and A_2.

51.3 DYNAMIC LIGHT SCATTERING

While in SLS the time average of the scattering intensity (i.e., the absolute mean intensity) is measured, *dynamic light scattering* (DLS) analyzes the fluctuations of the scattering intensity caused by the Brownian motion of particles or molecules in solution. DLS is also known as *photon correlation spectroscopy* (PCS) or *quasielastic light scattering* (QELS). Methodologically, the DLS measurements performed in the 1950s and 1960s utilized optical *heterodyne* detection techniques [11, 12], which will be described later in this chapter. According to the author's literature survey, it seems that the principle of measuring the time-dependent fluctuation in the scattering intensity was established in the late 1960s [13]. The *homodyne* DLS measurements, which are now common, were likely to be started in the 1970s [14–18]. To understand the measuring principle, let us consider the case in which the particles in solution are illuminated by a coherent light source, typically a laser. The movement of the particles causes either constructive or destructive interference of the scattered light. The sum of these interferences generates a "speckle" pattern consisting of bright spots (due to constructive interference) and dark spots (due to destructive interference). Because the speckle pattern fluctuates in time, due to the mutual movements of the particles, the time-dependent change in the intensity of one speckle would provide their dynamic information.

As shown in Fig. 51.2, in DLS the time dependence of the scattering intensity is first measured. The time correlation of the intensity is then examined with the intensity $I(t)$ detected at a time t and the intensity $I(t+\tau)$ after a delay of τ. In practice, the second-order autocorrelation function $g_2(\tau)$ is obtained directly from the software of the correlator during the measurement.

$$g_2(\tau) = \frac{\langle I(t) \cdot I(t+\tau)\rangle}{\langle I(t)\rangle^2} \tag{51.4}$$

Here, the brackets denote an average over the duration of the intensity measurement. In some cases, $g_2(\tau)$ is referred

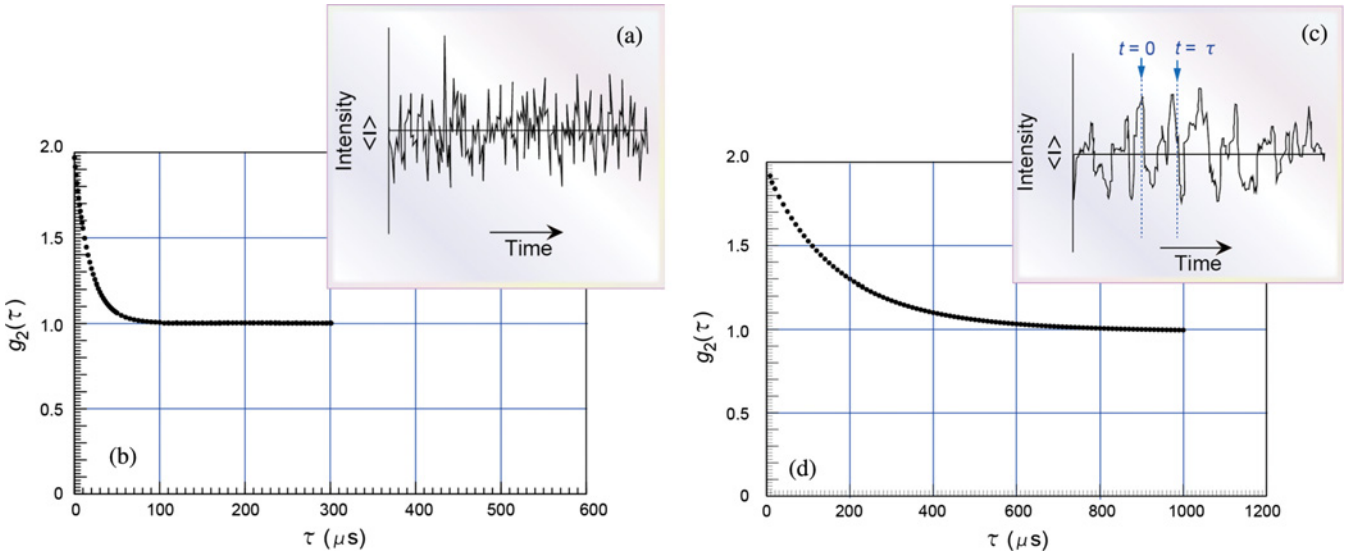


FIGURE 51.2 Typical examples of time dependence of scattering intensity (a,c) and for second-order autocorrelation function $g_2(\tau)$ (b,d). (a,b) Monodisperse gold particles with a diameter of 10 nm; (c,d) polystyrene latex particles with an average diameter of 100 nm. Note that parts (a) and (c) contain the illustration, whereas the $g_2(\tau)$ curves are raw data obtained from the correlator.

to as the *normalized intensity autocorrelation function* and written as $G(\tau)$, instead of $g_2(\tau)$. Because $g_2(\tau)$ or $G(\tau)$ is a function of the scattering vector q, expression $g_2(q, \tau)$ or $G(q, \tau)$ is also used. In addition, by considering the intensity $I(0)$ at a time $t = 0$ and the intensity $I(t)$ after a delay time of t, the second-order autocorrelation function in normalized form can also be written as $g_2(t)$ or $G(t)$ or $g_2(q, t)$ or $G(q, t) = \langle I(0) \cdot I(t) \rangle / \langle I \rangle^2$.

As can be seen from Fig. 51.2, $g_2(\tau)$ at short delay times is usually large, indicating a high correlation because of a few movements of particles from the initial state. However, $g_2(\tau)$ decays exponentially with an increase in τ, and becomes unity at the final state. This means that there is no correlation between the scattered intensity of the initial and final states after the elapse of long periods. Large particles diffuse more slowly than small particles, so that $g_2(\tau)$ decays at a slower rate (compare Fig. 51.2c,d). As a result, $g_2(\tau)$ in Eq. (51.4) provides the raw DLS data for analyzing the correlated movement of the particles, from which the size and size distribution of particles or molecules in solution can be calculated.

To analyze the DLS data, $g_2(\tau)$ is related to the first-order autocorrelation function $g_1(\tau)$, which is often referred to as the *electric field autocorrelation function*, using the Siegert relation [19]

$$g_2(\tau) = 1 + \beta |g_1(\tau)|^2 \tag{51.5}$$

where $\beta (\leq 1)$ is a constant, which depends an apparatus and measuring conditions, such as the number of coherence areas that generate the signal. In other words, β is an indication that we must factor in deviations from ideal correlation, so that we may perform DLS measurements under the most suitable conditions through examination of β. It should be noted that when $g_2(\tau)$ is not normalized, that is, when $g_2(\tau) = \langle I(t) \cdot I(t + \tau) \rangle / \langle I(t) \rangle^2$, the Siegert relation is given as $g_2(\tau) = B[1 + \beta |g_1(\tau)|^2]$, where B is the experimental baseline and should be equal to unity. However, in practice, a small amount of noise in the measurement can result in values that differ from unity by small ($\leq 10^{-4}$) amounts.

Once the $g_1(\tau)$ data have been obtained, different mathematical approaches can be employed to determine the size distribution profile of particles or molecules in solution. The simplest approach is to treat the center-of-mass diffusion of identical, monodisperse particles, because $g_1(\tau)$ can be given as

$$g_1(\tau) = \exp(-\Gamma\tau) \tag{51.6a}$$

$$\Gamma = q^2 D \tag{51.6b}$$

Here, Γ is the decay or relaxation rate, D is the diffusion coefficient of the particles, and q is as above. When using the Stokes–Einstein relation, we may calculate the hydrodynamic radius R_h from

$$R_h = \left(\frac{kT}{6\pi\eta} \cdot \frac{1}{D} \right) \tag{51.7}$$

where k is the Boltzmann constant, T is the absolute temperature, and η is the viscosity of the solvent. For identical particles, there is no angular dependence of D, so that R_h from Eq. (51.7) is of real value for a spherical particle in solution.

Indeed, the plot of $\ln[g_2(\tau) - 1]$ against τ from Fig. 51.2b can be fitted by a relation of $y = -0.0560x - 0.0356$ with the squared correlation coefficient (r^2) of 0.999, provided that $\Gamma = 2.80 \times 10^{-2}\ \mu s^{-1}$ and $\beta = 0.965$. Consequently, we obtain $R_h = 5.3_{(5)}$ nm by Eqs. (51.6b) and (51.7). However, in the case where the plot of Γ/q^2 against q^2 shows an angular dependence, particles are not spherical in shape. Thus, a high-quality DLS analysis must be performed at several angles, in particular for a polydisperse sample with an unknown particle size distribution.

For polydisperse systems, the correlation function $g_1(\tau)$ can be expressed as an integral of the exponential decays weighted over the distribution of relaxation rates $G(\Gamma)$

$$g_1(\tau) = \int_0^\infty G(\Gamma) \exp(-\Gamma\tau)\, d\Gamma \qquad (51.8)$$

The distribution $G(\Gamma)$ contains information about the diffusion characteristics of each particle in the population; therefore, it is of importance to extract $G(\Gamma)$ from $g_1(\tau)$ in Eq. (51.8). In principle, inversion of $g_1(\tau)$ is possible, but this is regarded as an ill-posed problem. Several numerical methods developed so far are devoted to the calculation of $G(\Gamma)$. One of the most common methods is a cumulant expansion [20] of $g_1(\tau)$ in Eq. (51.8), from which we obtain

$$g_1(\tau) = \exp\left(-\bar{\Gamma}\tau\right)\left(1 + \frac{\mu_2}{2!}\tau^2 - \frac{\mu_3}{3!}\tau^3 + \cdots\right) \qquad (51.9)$$

Here, $\bar{\Gamma}$ is the first cumulant (average decay rate) and μ_2 and μ_3 are the second and third cumulants. The relation of $\bar{\Gamma}$ and q is given by

$$\bar{\Gamma}/q^2 = D_{m,z}(1 + Cq^2R_g^2 + \cdots) \qquad (51.10)$$

where $D_{m,z}$ is the z-averaged mutual diffusion coefficient, and R_g is as above and becomes $L/(12)^{1/2}$ for a thin rod of length L. The coefficient C of the second term is the initial dependence of the first cumulant on q^2 and is found to increase with an increase in polydispersity, as well as in rotation for rods. We must remember that the cumulant method is valid for small τ and sufficiently narrow $G(\Gamma)$. An attempt to fit $g_2(\tau)$ in Fig. 51.2d with Eq. (51.9) provides a relation of $ln[g_2(\tau) - 1] = 2.67 \times 10^{-6}\tau^2 - 5.58 \times 10^{-3}\tau - 0.0357$ ($r^2 = 0.999$, within the second cumulant), from which we obtain $\bar{\Gamma} = 2.95 \times 10^{-3}\ \mu s^{-1}$, $\beta = 0.965$ and $\mu_2/\bar{\Gamma}^2$ (as the polydispersity index) = 0.189. Thus, the size of the particle in Fig. 51.2d is found to be almost 10 times larger than that in Fig. 51.2b.

An alternative method is used to analyze the autocorrelation function $g_1(\tau)$ for either heterodisperse or polydisperse, and multimodal distribution systems that cannot be resolved with the cumulant method; for example, note the bimodal $g_2(\tau)$ curve in Fig. 51.3a. This analytical method is a Laplace inversion program, which is called as CONTIN and was developed by Provencher [21]. A peak constrained analysis CONTIN allows us to provide a distribution function (spectrum) of Eq. (51.8), because we can modify Eq. (51.8) as

$$g_1(\tau) = \int_{-\infty}^{\infty} \Gamma G(\Gamma) \exp(-\Gamma\tau) d \log(\Gamma/q^2) \qquad (51.11)$$

so as to plot $\Gamma G(\Gamma)$ in an ordinate and $\log(\Gamma/q^2)$ in an abscissa (see Fig. 51.3b). The area under the each peak corresponds to the weight of each peak. Consequently, we may obtain the average decay rates $\langle\Gamma\rangle$ for each particle in solution. It should be noted that the R_h calculated from $\langle\Gamma\rangle$ with Eqs. (51.6b) and (51.7) is the averaged value for a hydrodynamically equivalent spherical particle or molecule.

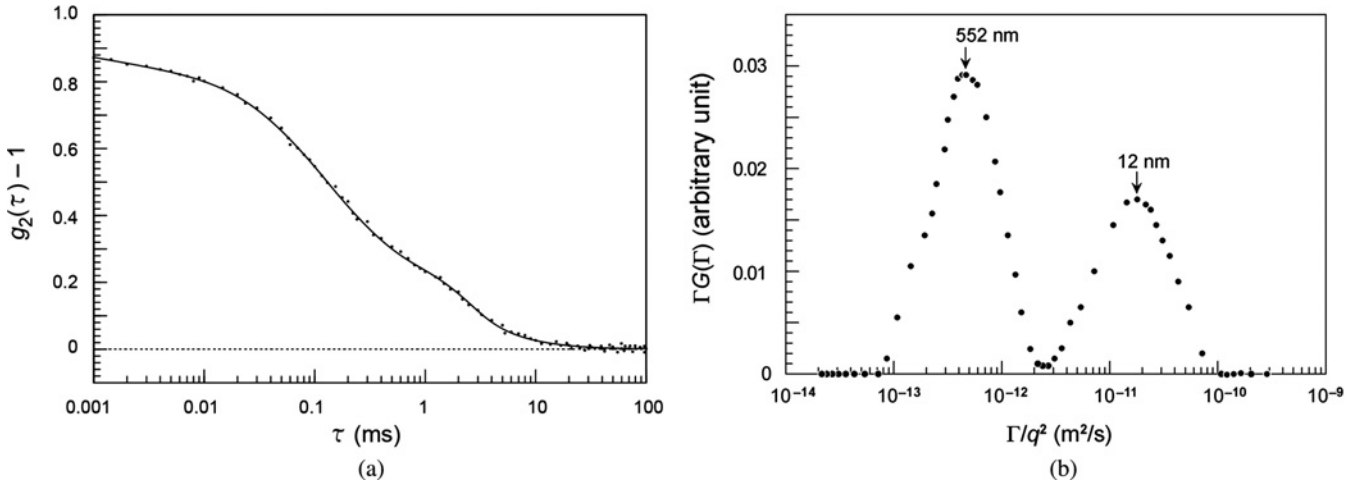


FIGURE 51.3 Typical example for a bimodal system in which protein molecules with an apparent R_h of 12 nm aggregate to form larger particles ($R_h \approx 552$ nm on average). (a) $g_2(\tau)$ curve; (b) result of CONTIN for the $g_2(\tau)$ in (a).

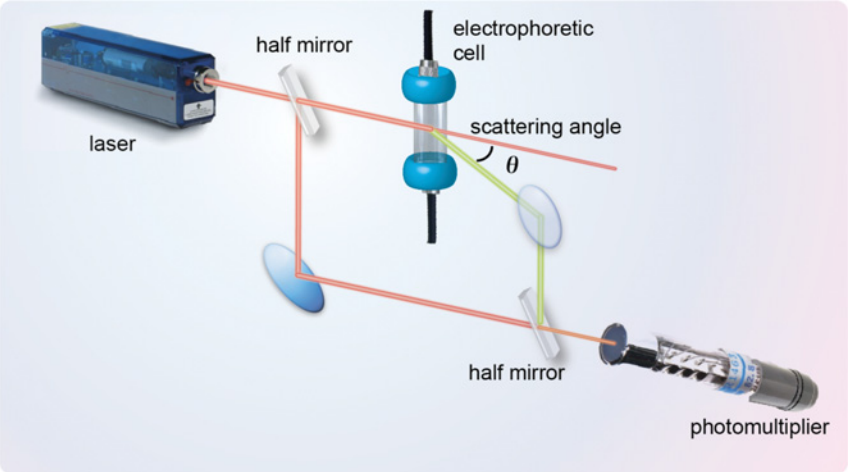


FIGURE 51.4 Simple heterodyne optical system for ELS. Note that the scattering light beam (dashed line) is mixed with the incident beam (solid line) via the half-mirror placed in the front of the photomultiplier.

51.4 ELECTROPHORETIC LIGHT SCATTERING

In *electrophoretic light scattering* (ELS) the motion of charged particles or molecules in solution is measured under an applied oscillating electric field. This is the main difference from DLS that relies on the Brownian motion as mentioned previously. Conventional DLS techniques employ *homodyne* scattering principles, in which all of the photons of light that reach a detector (photomultiplier) are scattered from the sample. In the case of ELS, however, the scattered light from the sample is mixed with unscattered reference light (usually the incident light) at the detector (see Fig. 51.4). This method is referred to as *heterodyne detection*, from which we can obtain a beat signal proportional to the Doppler shift or phase change in the scattered light (see Fig. 51.5a,b).

When the scattered light is mixed within a strong component of the incident radiation, we can obtain a spectrum that contains only the low-frequency beats between the incident frequency of the radiation and the frequency of scattered light. The resultant spectrum in the absence of the electric field is a Lorentzian curve centered at zero frequency, and the corresponding autocorrelation function is an exponential decay. In the presence of an electric field, the current spectrum is shifted from zero frequency by an amount equal to the original Doppler shift from the incident frequency, and the corresponding autocorrelation function is a damped cosine wave whose frequency is equal to the Doppler shift and whose decay constant is the same as that in the absence of the field. As a result, we may obtain the electrophoretic mobility of charged particles or molecules in solution. However, as shown in Fig. 51.5c, the heterodyne power spectrum

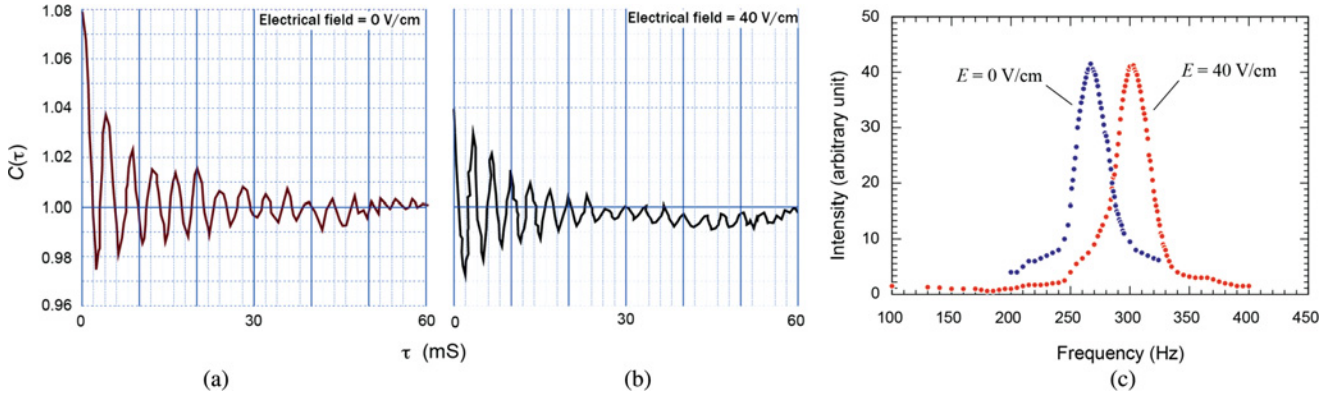


FIGURE 51.5 Determination of Doppler frequency shift due to motion of charged particles under an applied electric field. Graphs (a) and (b) show damping autocorrelation functions $C(\tau)$ with and without electric field. Graph (c) shows the power spectra obtained by fast Fourier transform of the correlation functions in graphs (a) and (b).

obtained by Fourier transform of the correlation function in the absence of the electric field (i.e., $E = 0$ V/cm) does not manifest a peak at zero frequency. This means that the heterodyne correlation functions include the contribution due to the Brownian motion of particles (see discussion below); thus a difference between the frequencies of spectra at $E = 0$ V/cm and 40 V/cm corresponds to the Doppler shift in this case. References 22–29 provide more details.

In practice, the first-order autocorrelation function $C(\tau)$, often referred to as the *photon-counting heterodyne correlation function*, for a solution with an electrophoretically monodisperse solute, can be written as [27]:

$$C(\tau) = \beta_0\delta(\tau) + \alpha_0 + \alpha_1 \exp(-2\Gamma\tau) + [\alpha_2 \exp(-2\Gamma\tau) \times \cos(\Delta\omega\tau)] \quad (51.12)$$

Here β_0, α_0, α_1, and α_2 are constants dependent on the optical system but independent of correlation time τ, and $\delta(\tau)$ is the delta function. The first two terms consist of the intensities of the reference light and the scattered light and are independent of the frequency. The next term includes the normalized electric field autocorrelation function because $\Gamma(= Dq^2)$ has the same definition as in DLS; see Eq. (51.6b). The fourth term in brackets, in which $\Delta\omega$ is a frequency shift of the heterodyne signal, as mentioned above, is due to simultaneous electrophoresis and diffusion. The Fourier transform of Eq. (51.12) with respect to time, as stipulated by the Weiner–Khinchine theorem [30], gives the power spectrum

$$S(\omega) = \beta_0 + \alpha\delta(\omega) + \frac{2(\alpha_1/\pi)\Gamma}{(\omega + \Delta\omega)^2 + \Gamma^2} + \frac{\alpha_2\Gamma}{2\pi}\left(\frac{1}{(\omega + \Delta\omega)^2 + \Gamma^2} + \frac{1}{(\omega - \Delta\omega)^2 + \Gamma^2}\right) \quad (51.13)$$

where α is a constant independent of the incident light frequency ω. In both Eqs. (51.12) and (51.13), $\Delta\omega$ is expressed as $\Delta\omega = |\omega_s - \omega_r| = |(\omega - \omega_D) - (\omega - \omega_M)|$, where ω_s is the angular frequency of the scattered light, ω_r is the angular frequency of the reference beam and is the same as that of the incident beam (i.e., $\omega_r = \omega$), ω_D is the Doppler frequency, and ω_M is the modulation frequency. Since the frequency of the incident beam is modulated in the scattered light by the amount of ω_D, $\Delta\omega$ is given as

$$\Delta\omega = \frac{2\pi n}{\lambda} EU \sin\theta \quad (51.14)$$

where E (V/cm) and U (μm/s)/(V/cm) are the applied electric field strength and electrophoretic mobility, respectively. Therefore, U can be directly evaluated from frequencies of the power spectrum.

In actual ELS measurements, $\Delta\omega$ varies depending on the position within the measuring cell, due mainly to the electroosmotic flow. Thus, the mobility obtained from Eq. (51.14) without considering electroosmotic effects is only an apparent value. Many efforts have been made to improve ELS instrument, mainly in optical system and cell geometry, as well as to develop computer software for analyzing the autocorrelation function and for displaying the power spectrum. As a result, it is possible to see how the mobility varies with the electroosmotic effect; for example, see Fig. 51.6, which illustrates the power spectra at different positions in a rectangular ELS cell. Now, highly precise measurements of electrophoretic mobility can be performed with ELS instruments commercially available from several manufacturers. Once the mobility is obtained, the zeta-potential (ζ) can be calculated by the Smoluchowski equation: $\zeta = 4\pi\eta u/\varepsilon$, where ε is the dielectric constant of the solvent. However, it should be noted that charged macromolecules (polyelectrolytes), which behave in sedimentation or diffusion as an impermeable coil, should behave in electrophoresis as if they were free draining. In such cases, the calculation of ζ from the mobility is scientifically meaningless. Also noted is the electrophoretic behavior of a particle composed of a hard core plus a shell of charged hairy surface-layer, the theory of which has been proposed by Ohshima [31]. A more recent publication [32] provides more detailed information about free draining or partially free-draining behavior in the electrophoresis.

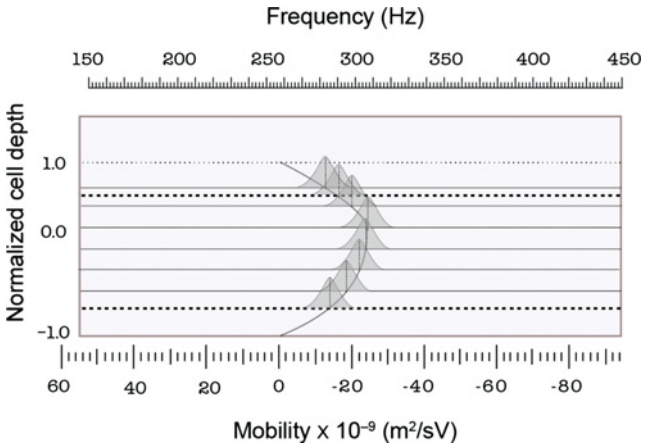


FIGURE 51.6 Electroosmotic flow profile obtained from ELS of bovine serum albumin (pH = 7.0; ionic strength = 0.015) using a rectangular cell (17 mm in length, 10 mm in width, and 2 mm in depth). Two broken lines show the positions of the stationary layer at which the electroosmotic flow is eliminated.

51.5 DISCUSSION AND CONCLUSION

Both SLS and DLS, as well as ELS, have been common tools in the characterization of a variety of colloid and polymer systems including biomacromolecules. Our recent interest is how to explore colloid–colloid and colloid–polymer interactions, as well as polymer–polymer interactions, in the absence or presence of additives via a "clever" combination of light-scattering techniques. As a simple example, let us

consider the aggregation of pure and monodisperse proteins with or without additives. Both M_w (absolute molar mass in this case) and R_g can be determined by SLS. A single exponential fit of the DLS data would provide an "apparent" R_h value. Also, examination of the plot of Γ/q^2 against q^2 at different scattering angles provides information about whether the protein is spherical in shape. In addition, the protein charges at given solution conditions become apparent from the ELS data. Even when the protein molecules aggregate, DLS and ELS can also be used because both techniques are applicable to the sample of known concentration. For example, a multimodal system consisting of the native protein and its aggregates may be examined by the CONTIN analysis of the DLS data. Also, ELS tells us the ionization states of protein particles leading to their aggregation. The problem is the use of SLS. In principle, the SLS measurement is impossible when the CONTIN analysis shows bimodal or more complex distributions. In addition, there is a restriction on the size of particles or molecules to be measured, called the *Rayleigh–Debye–Gans approximation* (RDGA).

To clarify particle size limits for SLS measurements, we have to go back to two theories of light scattering, which were proposed by Rayleigh and Mie. In Rayleigh scattering, the size of the particles is assumed to be much smaller than the wavelength of light, so that the particles act as point sources of scattered light. In practice, it is often estimated to be less than $\lambda/10$ (or $\lambda/20$), corresponding to ~60 (or 30) nm in diameter when He-Ne laser ($\lambda = 632.8$ nm) is a light source. If the particle sizes exceed this limit, we must consider Mie scattering [33], in which the particles are relatively large (diameter $\approx \lambda$), and the refractive index of the dispersed phase is significantly different from the dispersion medium. However, such simple discussions do not provide a clear answer as to how particle sizes and what geometries of particles are suitable for SLS, because in actual SLS measurements we have to consider various types of particles, such as multilayer spheres, clustering spheres, core–shell particles, and so on. Thus, a more real example [34] is shown below, in order to facilitate a discussion about how to combine SLS, DLS, and ELS to study the complex formation of protein with water-soluble polymers.

The complex formation of human serum albumin (HSA) with poly(*N*-isopropylacrylamide) (PNIPA) was studied in an aqueous acidic solution (pH 3) containing 0.01 M NaCl as a supporting salt [34]. Three PNIPA samples of different molar mass were used: PNIPA(L), $M_w = 1.72 \times 10^6$; PNIPA(M), $M_w = 4.82 \times 10^5$; and PNIPA(S), $M_w = 2.10 \times 10^4$. The HSA–PNIPA mixtures were prepared over a wide range of mixing ratio (r_m) given by $r_m = (C_{PNIPA}/C_{HSA})(M_{HSA}/M_{PNIPA})$, where C_{PNIPA} and C_{HSA} are the concentrations (in mg/mL) of PNIPA and HAS, respectively, and M_{HSA} is the molar mass (66,436 g/mol) of HAS and M_{PNIPA} is the M_w of each PNIPA. DLS and ELS were first performed to examine the complex formation. In DLS all of the $g_2(\tau)$ functions were analyzed by the CONTIN program.

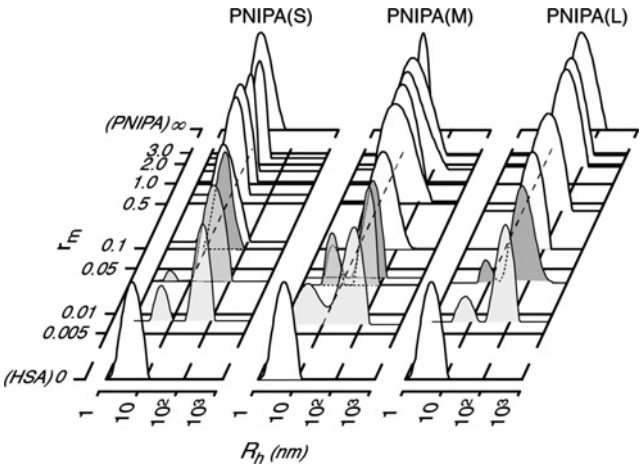


FIGURE 51.7 Results of DLS for HSA mixtures with three PNIPA samples as a function of r_m. Complexation was studied at 25°C, ionic strength = 0.01 (NaCl), pH = 3.0 and $C_{HSA} = 0.1$ mg/mL. Some distributions are distinguished in different shades of gray. Bimodal distributions due to the coexistence of the uncomplexed HAS and the HAS-PNIPA complex can be observed at $r_m < 0.1$ (protein-rich mixtures). (This drawing was reproduced from Ref. 34 with several modifications.)

It was found that DLS shows the presence of excess HSA in a low r_m range (see Fig. 51.7), whereas ELS detected excess PNIPA in a high r_m range (see Fig. 51.8). These results indicate the formation of water-soluble complexes in the HAS-PNIPA mixtures. However, unfortunately, the resulting complexes cannot be isolated from the mixture, due to weak protein–polymer interactions. Therefore, one may consider that SLS cannot be used in this case. Nevertheless, several modifications of Eq. (51.1b) allow us to use the SLS for examining the HAS-PNIPA mixtures containing water-soluble complexes. First, the concentration C_x and molar mass M_x of the complex were expressed as $C_x = C_{PNIPA}(1 + \beta)$ and $M_x = \alpha M_{PNIPA}(1 + \beta)$, according to mass balance requirements. Here, β represents the mass ratio of bound protein to the polymer and α is the number of polymer chains within one complex particle, that is, the number of aggregated *intrapolymer* complexes. Next, it was assumed that "unmeasurable" refractive-index increments $(dn/dc)_x$ of the complex can be expressed as $(dn/dc)_x = [1/(1 + \beta)](dn/dc)_{PNIPA} + [\beta/(1 + \beta)](dn/dc)_{HSA}$, where $(dn/dc)_{PNIPA}$ and $(dn/dc)_{HSA}$ are the "measurable" refractive index increments of PNIPA and HAS, respectively. Then, Eq. (51.1b) can be rewritten as

$$\frac{K'C_{PNIPA}}{R_\theta} = \frac{1}{\alpha M_{PNIPA}B^2}\left(1 + \frac{16\pi^2}{3\lambda^2}R_g^2 \sin^2\left(\frac{1}{\theta}\right)\right) + 2A_2C_{PNIPA}\left(\frac{1+\beta}{B}\right)^2 \quad (51.15)$$

where $K' = (4\pi^2 n_0^2/N_A\lambda^4)$ and $B = (dn/dc)_{PNIPA} + \beta(dn/dc)_{HSA}$.

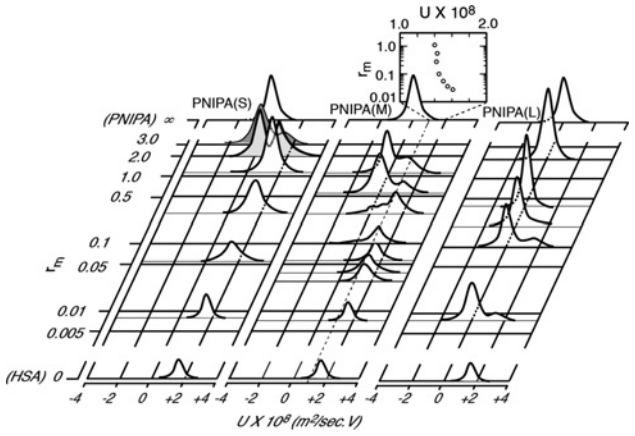


FIGURE 51.8 Results of ELS for HSA mixtures with three PNIPA samples as a function of r_m. Complexation was studied under the same conditions as mentioned in Fig. 51.7. Some distributions are distinguished in different shades of gray. From several PNIPA-rich mixtures ($r_m > 1.0$), a peak appears at mobility (U) = 0 m^2/sV, due to the presence of uncomplexed PNIPA, which is a neutral polymer. This trend is contingent on the M_w of PNIPA, because the scattering intensity strengthens with increasing M_w even when the polymer has no charge. (For more detail, see the original paper [34], from which this figure was reproduced with several modifications.)

Figure 51.9 shows typical examples of a "modified" Zimm plot for the HSA complexes with PNIPA(M) at $r_m = 1.10$ and with PNIPA(L) at $r_m = 0.00773$. For SLS measurements, C_{NIPA} was varied so as to remain constant r_m, because a marked r_m dependence of R_h was observed from Fig. 51.7 In addition, DLS was always performed over the range of 30° $\leq \theta \leq$ 140° before SLS to determine the best-suited power of the incident light at which the $g_2(\tau)$ gives a monomodal profile with the CONTIN program. As a result, the double extrapolations of $K'C_{PNIPA}/R_\theta$ versus $\sin^2(\theta/2) + kC_x$ plots to $\theta \to 0$ and $C_{PNIPA} \to 0$ gave two straight lines with correlation coefficients $r^2 > 0.99$, simultaneously intersecting the Y axis. However, M_x, A_2, and R_g cannot be estimated unless α is known. Thus, the second assumption was made, which is $\alpha \equiv 1$, meaning the formation of an intramolecular complex in the present case. This allows us to calculate β from an intersection on the Y axis of Fig. 51.9 Then, the following data are obtained: $M_x = 7.48 \times 10^5$ g/mol, $A_2 = -2.38 \times 10^{-5}$ $cm^3 \cdot mol/g$, and $R_g = 79$ nm for the HSA-PNIPA(M) complex; and $M_x = 2.40 \times 10^6$ g/mol, $A_2 = -1.38 \times 10^{-5}$ $cm^3 \cdot mol/g$ and $R_g = 203$ nm for the PNIPA(L) complex. Since the number (n) of the HAS molecules bound per chain of PNIPA can be given by $n = \beta(M_{PNIPA} + M_{HSA})$, we can obtain $n \approx 4$ for the complex at $r_m = 1.10$ and $n \approx 10$ for the complex at $r_m = 0.00773$. In the SLS analysis used here the two assumptions were made, so that the data must be confirmed by the other experimental method. For this, dialysis experiments were performed to estimate the β value, from which the n value was calculated. It was found that the n values obtained from SLS and dialysis experiments agree within ± 1, meaning that the analytical approach used here is proper.

Now let us go back to the discussion about particle size limits for SLS measurements. DLS provides $R_h = 35.9$ nm for PNIPA(L) with $M_w = 1.72 \times 10^6$ and $R_g = 63.4$ nm, both of which were determined by SLS. Because SLS was performed with the Ar–ion laser ($\lambda = 488$ nm), $\lambda/10$ becomes approximately 49 nm in diameter. Thus, it seems that SLS is not suitable for the characterization of PNIPA(L). In the case of polymer coils, however, the point sources of scattered light can be considered as "segments" of a polymer chain. According to Flory [35], the size limit for SLS measurements of polymers is within $0.1 < \sqrt{r^2}/\lambda < 1$, where $\sqrt{r^2}$ is the root-mean-square distance and is given by $\sqrt{r^2} = \sqrt{6} \times R_g$.

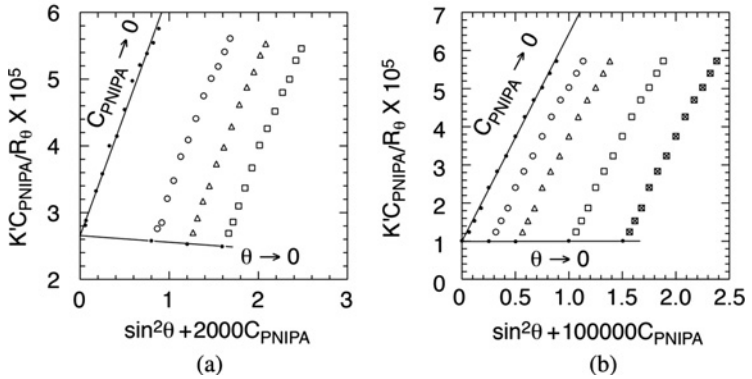


FIGURE 51.9 Modified Zimm plots for HSA mixtures with PNIPA(M) at $r_m = 1.10$ (a) and PNIPA(L) at $r_m = 0.00773$ (b). To retain constant r_m, both PNIPA and HAS concentrations (in g/mL) were varied: $C_{PNIPA} = 4 \times 10^{-4}$ and $C_{HSA} = 5 \times 10^{-5}$ (open circle), $C_{PNIPA} = 6 \times 10^{-4}$ and $C_{HSA} = 7.5 \times 10^{-5}$ (open triangle), $C_{PNIPA} = 8 \times 10^{-4}$ and $C_{HSA} = 10 \times 10^{-5}$ (open square) for PNIPA(M); $C_{PNIPA} = 2.5 \times 10^{-6}$ and $C_{HSA} = 1.25 \times 10^{-5}$ (open circle), $C_{PNIPA} = 5 \times 10^{-6}$ and $C_{HSA} = 2.5 \times 10^{-5}$ (open triangle), $C_{PNIPA} = 10 \times 10^{-6}$ and $C_{HSA} = 5 \times 10^{-5}$ (open square), $C_{PNIPA} = 15 \times 10^{-6}$ and $C_{HSA} = 7.5 \times 10^{-5}$ (open square with a cross) for PNIPA(L). (This illustration was reproduced from Ref. 34 with several modifications.)

For PNIPA(L), $\sqrt{r^2}/\lambda \approx 0.3$, suggesting that the SLS can be performed within the size limit. For the HAS–PNIPA(L) complex at $r_m = 0.00773$, $\sqrt{r^2}/\lambda \approx 1.02$, so that there remains the question of whether the SLS data are correct. However, as shown in Fig. 51.9, the Zimm plot is normal. Also, the negative A_2 is interpreted as a result of the attractive interaction between the complex particles. Far more important than these is the fact that there is a good agreement between the n values from the SLS and dialyzing experiments. On the other hand, the complex is considered to be a cluster of spheres, consisting of a PNIPA chain and the bound HAS particles. Consequently, the elements within the protein (as a hard particle) and the segments within the polymer chain act as scattering points, which cause the elastic scattering without loss of energy. A more detailed discussion of this issue can be found in a particular report [36] in which the complex formation between oppositely charged microgels ($R_h \approx 120$–160 nm) was studied by SLS and DLS.

Finally, we have to consider multiple scattering, because the light-scattering methods assume that each detected photon has been scattered by the sample exactly once. When examining various sorts of particles or molecules by the light-scattering techniques (mainly DLS and SLS, but also ELS), however, we will encounter multiple scattering, wherein photons are scattered multiple times by the sample before being detected. This is a very difficult issue, particularly for the reasons as mentioned above. In DLS experiments, a *cross-correlation* technique to suppress undesired contributions from multiple scattering has been reported [37–39]. This technique can be used to correct SLS data for multiple scattering contributions [40]. However, it is likely that such a light-scattering apparatus is not commercially available at the present, so that we need to be conscious of current needs and future trends in this field.

REFERENCES

[1] Vert, M., Doi, Y., Hellwich, K.-H., Hess, M., Hodge, P., Kubisa, P., Rinaudo, M., Schué, F. (2012). *Pure Appl. Chem.* **84**, 377–410.

[2] Strutt, J.W. (Lord Rayleigh) (1899). *Scientific Papers.* Cambridge Univ. Press, Cambridge, UK, Vol. 1, pp. 104–111.

[3] Debye, P. (1944). *J. Appl. Phys.* **15**, 338–342.

[4] Zimm, B.H. (1945). *J. Chem. Phys.* **13**, 141–145.

[5] Zimm, B.H. (1948). *J. Chem. Phys.* **16**, 1093–1099.

[6] Pike, E.R., Pomeroy, W.R.M., Vaughan, J.M. (1975). *J. Chem. Phys.* **62**, 3188–3192.

[7] Moreels, E., Ceuninck, W.D., Finsy, R. (1987). *J. Chem. Phys.* **86**, 618–623.

[8] Wu, H. (2010). *Chem. Phys.* **367**, 44–47.

[9] Hermans, J.J., Levinson, S. (1951). *J. Opt. Soc. Am.* **41**, 460–465.

[10] Coumou, D.J. (1960). *J. Colloid Sci.* **15**, 408–417.

[11] Benoit, H. (1951). *Ann. Phys. Paris* **6**, 561–609.

[12] Cummins, H.Z., Knable, N., Yeh, Y. (1964). *Phys. Rev. Lett.* **12**, 150–153.

[13] Jakeman, E., Pike, E.R. (1969). *J. Phys. A: Gen. Phys.* **2**, 411–412.

[14] Chu, B. (1970). *Annu. Rev. Phys. Chem.* **21**, 145–174.

[15] Schurr, J.M. (1977). *CRC Crit. Rev. Biochem.* **4**, 371–431.

[16] Burchard, W. (1983). *Adv. Polym. Sci.* **48**, 1–124.

[17] Schurr, J.M., Schmitz, K.S. (1986). *Adv. Annu. Rev. Phys. Chem.* **37**, 271–305.

[18] Berne, B.J., Pecora, R. (2000). *Dynamic Light Scattering: With Applications to Chemistry, Biology, and Physics*, 2nd ed. Dover Publications, New York.

[19] Siegert, A.J.F. (1986). *MIT Radiation Lab. Report*, No. **46.**

[20] Koppel, D.E. (1972). *J. Chem. Phys.* **57**, 4814–4820.

[21] Provencher, S.V. (1982). *Comput. Phys. Commun*. **27**, 213–227, 229–242.

[22] Ware, B.R. Flygare, W.H. (1971). *Chem. Phys. Lett.* **12**, 81–85.

[23] Ware, B.R., Flygare, W.H. (1972). *J. Colloid Interface Sci.* **39**, 670–675.

[24] Ware, B.R. (1974). *Adv. Colloid Interface Sci.* **4**, 1–44.

[25] Josefowlcz, J., Hallett, F.R. (1975). *FEBS Lett.* **60**, 62–65.

[26] Mohan, R., Steiner, R., Kaufmann, R. (1976). *Anal. Biochem.* **70**, 506–525.

[27] Shaafi, R.I., Fernandez, S.M. (eds.) (1983). *Fast Methods in Physical Biochemistry and Cell Biology*. Elsevier, Amsterdam.

[28] Miller, J.F. (1992). *J. Colloid Interface Sci.* **153**, 266–271.

[29] Medebach, M. (2012). *J. Chem. Phys.* **136**, 044201(1–9).

[30] McQuarrie, D.A. (1976). *Statistical Mechanics.* Harper & Row, New York.

[31] Ohshima, H., Makino, K., Kato, T., Fujimoto, K., Kondo, T., Kawaguchi, H. (1993). *J. Colloid Interface Sci*. **159**, 512–514.

[32] Kokufuta, E., Sato, S., Kokufuta, M.K. (2013). *Langmuir* **29**, 15442−15449.

[33] Mie, G. (1908). *J. Ann. Phys.* **330**, 377–445.

[34] Matsudo, T., Ogawa, K., Kokufuta, E. (2003). *Biomacromolecules* **4**, 728–735.

[35] Flory, P.J.E. (1953). *Principles of Polymer Chemistry*. Cornell Univ. Press, New York, p. 297.

[36] Miyake, M., Ogawa, K., Kokufuta, E. (2006). *Langmuir* **22**, 335–7341.

[37] Schätzel, K., Drewel, M., Ahrens, J. (1990). *J. Phys.: Condens. Matt.* **2**, SA393–SA398.

[38] Urban, C., Schurtenberger, P. (1998). *J. Colloid Interface Sci.* **207**, 150–158.

[39] Block, I.D., Scheffold, F. (2010). *Rev. Sci. Instrum.* **81**, 123107(1–7).

[40] Pusey, P.N. (1999). *Curr. Opin. Colloid Interface Sci.* **4**, 177–185.

52

IMPACT OF LINE TENSION ON COLLOIDAL SYSTEMS

Hiroki Matsubara, Takanori Takiue, and Makoto Aratono
Department of Chemistry, Faculty of Sciences, Kyushu University, Fukuoka, Japan

52.1 INTRODUCTION

Line tension τ is the excess energy associated with the unit length of a contact line between either (1) two or (2) three coexisting interfaces. For case 1, the line tension is regarded as a natural analog of the surface tension between two bulk phases and therefore, in this case, the line tension takes only positive values. For case 2, with three coexisting interfaces, the line tension can be negative because of the interplay between these interfaces.

In both cases, theoretical estimates for the magnitude of the line tension lie in the range from 10^{-10} to 10^{-12} N, and therefore it has been considered that the effect of line tension is negligible compared to that of interfacial tension unless the system of interest has macroscopic size. However, it is also true that τ plays an increasingly important role in the stability of microscopic systems as the radius of contact line perimeter r decreases. In practice, the line tension becomes comparable to the interfacial tension when r is less than 10^{-6} m. Therefore, renewed interest in line tension has been generated recently by the advent of nanotechnology.

However, despite its technological importance, there is a still great scarcity of experimental information on line tension, primarily because line tension as measured by different researchers is still quite variable and controversial. In this review, we tried to choose reliable experiments of both types 1 and 2 line tension. Determination as to whether a literature presented good data is obtained line tension behavior can be explained reasonably by theory and/or by macroscopic observation such as domain deformation, budding of bilayer membrane, and spontaneous lens splitting. Hence, we focused on the theoretical interpretation of line tension data in this review as well as the methodology of line tension measurements.

This review is organized as follows. Section 52.2 describes the techniques used to determine type 1 line tension for condensed domains in Langmuir monolayers. How to control the domain line tension is explained in Section 52.3. The relation between the domain line tension and stability of vesicles is then discussed in Section 52.4. Type 2 line tension is the focus of Sections 52.5–52.7. The basic concept of this line tension is introduced in Section 52.5 in terms of wetting transition. Then, this is extended to understand the physicochemical behavior of other related systems, namely, fine particles at fluid–liquid interfaces (Section 52.6) and thin liquid films in foam systems (Section 52.7). Section 52.8 summarizes the main conclusions and proposes some interesting future topics.

52.2 DOMAINS IN LANGMUIR MONOLAYERS

Langmuir monolayers at the air–water interface often exhibit a first-order transition between a fluidlike lower-ensity phase (liquid-expanded state: LE) to a condensed phase (liquid-condensed state: LC) [1]. An essential feature of this transition is the existence of the gentle plateau region(s) in the surface pressure and area isotherm. In such systems, the line tension first produces an energy barrier for nucleation of the LC phase domain. However, once the coexistence of several LC domains is achieved, line tension promotes growth of the LC domains to reduce the total length of the phase boundary. In this second process, the electric repulsion between

Encyclopedia of Biocolloid and Biointerface Science, Volume 2, First Edition. Edited by Hiroyuki Ohshima.
© 2016 John Wiley & Sons, Inc. Published 2016 by John Wiley & Sons, Inc.

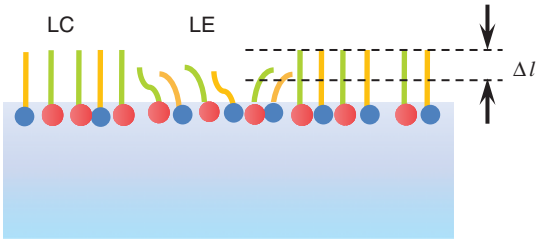


FIGURE 52.1 A schematic illustration of the generation of domain line tension between LE and LC phases.

hydrophilic groups of amphiphile molecules in each domain counteracts the domain growth.

In the simple expression, the line tension of the domain perimeter is given by [2]

$$\tau = \gamma \Delta l \tag{52.1}$$

where γ denotes the surface tension of the domain walls in the air and Δl is the difference in the height between the domain and surroundings (Fig. 52.1). One team of investigators considered the effect of electrostatic repulsion between molecules within an isolated condensed film domain and derived an expression for the edge energy E of a circular domain given by [3,4]

$$E = 2\pi R \left[\tau - \left(m^2/4\pi\varepsilon_0\epsilon\right) \ln(4R/e^2\delta)\right] \tag{52.2}$$

where R is the radius of domain, m (C m^{-1}) is the dipole moment density difference between the domain and the surrounding area, ε_0 (C^2 J^{-1} m^{-1}) is the permittivity of vacuum, ϵ is the dielectric constant of water, δ is a closest approach cutoff distance with an order of magnitude of an intermolecular distance. In Eq. (52.2), it is assumed that the condensed phase is isotropic and the molecular dipoles are perpendicular to the plane of monolayer (equivalent dipole model). From Eq. (52.2), one can realize that the optimal size of the 2D domains under consideration is determined by the competition between these two terms; the line tension term favors one large domain in order to minimize the energy penalty of the perimeter, whereas the electric repulsion favors coexistence of smaller domains. It is also revealed that elongated or striped domains can be observed in real experiments when strong electrostatic repulsion exists between hydrophilic groups [5,6].

Structuring in Langmuir monolayers has been a topic of longstanding interest [7–10]. In particular, from the perspective of domain line tension, the mixed monolayer of sphingolipid, phospholipid, and cholesterol has been studied widely because of its close relation to the raft formation in biomembranes [11, 12]. In such a ternary system, sphingolipid and cholesterol form a solidlike domain called *liquid-ordered phase* L_o, surrounded by phospholipid-rich fluid like phase (*liquid-disordered phase* L_d) because of tight molecular packing between them. It is believed that sphingolipid/cholesterol-rich domains, called *lipid raft*, have a strong affinity to certain proteins and are attributable for some important cell functions such as cell signaling [13]. Langmuir monolayers of these lipids are therefore useful model membrane to understand the structure–function relation of real biomembranes. The abovementioned McConnell theory was also based on the fluorescence microscopy studies on the domain formation in lipid Langmuir films.

A more recent development of the theoretical treatment of this issue was given by a team of researchers [2] who extended the standard thermodynamic theory of self-assembly of amphiphile molecules in 3D systems to the 2D domains in a lipid– cholesterol binary system. The free-energy balance between headgroup repulsion and hydrocarbon tail attraction in micellar systems was replaced by that between line tension and dipole repulsion, and the entropy of mixing in solid domains was also introduced to calculate the free energy as a function of domain aggregation number. From their model, it was revealed that lipid domains with finite size distribution can be allowed as thermodynamic equilibrium state under limited conditions.

In most cases, the line tension of domains in Langmuir films was determined indirectly by means of theoretical analysis of shape relaxation process of artificially deformed circular domains [14–16]. Both fluorescence microscopy and Brewster angle microscopy (BAM) are utilized to visualize lipid domains. The former method uses fluorescent phospholipid analysis, which preferentially partitions in the cholesterol-poor phase; therefore, the lipid condensed domains appear dark. On the contrary, in the latter case, the *p*-polarized light reflected from the air–water interface is detected at the Brewster angle of pure water. The condensed film domain reflects incident *p*-polarized light because of its large difference in dielectric constant from pure water; thus, in this case, the domain itself appears bright in obtained images.

One of the examples of such relaxation is shown in Fig. 52.2 The bola-shaped domain created by flow shear of water subphase shrinks toward the circular domain by line tension that is opposed by the viscous drag of the water subphase. In the low Reynolds number limit, the velocity of bola shrinking is given by [14]

$$V = 3\tau/8\eta R \tag{52.3}$$

where η is the viscosity of the subphase and R is the radius of a single bola. The line tension extracted from this relation was up to several hundreds pN. These values roughly coincided with theoretical estimation, but the error of measurements were no better than ±20%. Another team pointed out that the difficulty to measure perturbations that deform original circular domain and proposed original hydrodynamic model to describe domain relaxation [16].

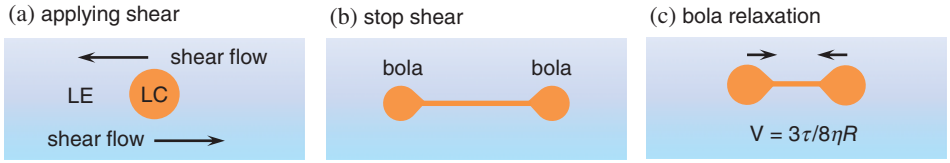


FIGURE 52.2 Principle of line tension measurement by the domain shape relaxation technique.

Figure 52.3 shows more direct method to obtain domain line tension in Langmuir films [17]. Here optical tweezers apply forces in the range of pN on the silica particle adsorbed at the edge of circular LC domain of methyl octadecanoate and the hydrodynamic flow of surrounding LE phase deformed domain edge into a wedgelike shape. For stationary state, a force balance the viscous drag F_η and effective line tension τ_{eff} at the wedge of angle θ is

$$F_\eta = -2\tau_{\text{eff}}\cos\theta/2 \tag{52.4}$$

In theory, the deformation of domain shape changes local molecular density in the domain and then τ_{eff} via the dipole repulsion term in Eq. (52.2). However, the authors claimed that the difference between the real and effective line tension is less than 10% and the optical tweezers method can give the line tension very close to its equilibrium value. They also took into account of the viscosity of surrounding LE phase η_s by the coefficient f and expressed F_η as

$$F_\eta = f\eta RV \tag{52.5}$$

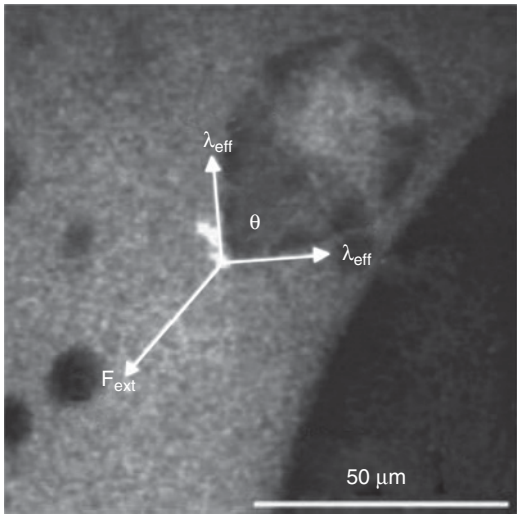


FIGURE 52.3 An LC domain captured by optical tweezers. A silica bead adsorbed at the domain boundary is held by the tweezers fixing the position of the domain and the flow deforming the domain. Here $F_{\text{ext}} = -F_\eta$ and $\lambda_{\text{eff}} = \tau_{\text{eff}}$. (Adapted from Wurlitzer et al. 2000 [17], pp. 3822–3828, Fig. 2. © AIP Publishing LLC; reproduced with permission.)

The coefficient f depends on the dimensionless Boussinesq number $B = \eta_s/\eta R$ and is

$$f = \frac{4\pi B}{\ln(2B) - 0.577 + 4/\pi B - \ln(2B)/2B^2} \tag{52.6}$$

when $B > 2$. The limitation assumed in Eq. (52.3) corresponds to $B \ll 1$, indicating that hydrodynamics is dominated by drag from the water. Considering that there are no well-established direct measurements of domain line tension, this report is deemed to be important for future line tension study. One of the unsolved problems of domain line tension measurement is how to determine line tension if the domain has elongated or striped shapes. To solve this issue, the theoretical fitting of domain shapes will be a powerful tool again.

52.3 MODIFICATION OF DOMAIN LINE TENSION

There are only a few studies that intentionally target the modification of line tension of the system. This is probably because the researchers had to spend their efforts for the measurement of the pN-order force in order to achieve satisfactory accuracy. However, just as surfactants can reduce surface tension and stabilize dispersed phases in 3D systems, one may expect that some sort of molecules act as line-active agents (or linactants) and stabilize 2D domains. Another group of researchers showed in a mixed Langmuir monolayer of pentadecanoic acid (PDA) and perfluoroundecanoic acid (PFUDA) that partially fluorinated phosphonic acid (linactant) partitioned at the phase boundaries between hydrocarbon-rich and fluorocarbon-rich phases and reduced line tension as the concentration of linactant increased [18, 19]. They abbreviated their linactants, namely, $CF_3(CF_2)_{n-1}(CH_2)_mPO_3H$, as $F_nH_mPO_3$ and ranked their linactant efficiency in the order $F_8H_8PO_3 < F_{10}H_6PO_3 < F_8H_{11}PO_3 < F_{10}H_9PO_3$ from the data shown in Fig. 52.4 The most efficient linactant reduced the line tension by more than 20% at a mole fraction of only 0.8%. They also showed that these linactants drive modification of preformed amphiphile domains [18]. The most remarkable shape deformation was observed in the $F_8H_{11}PO_3$ system, where the peanut-shaped domain was induced in the mixed monolayer of PDA (96.5%) and PFUDA (3.5%) if the linactant concentration was successively increased up to 0.08%.

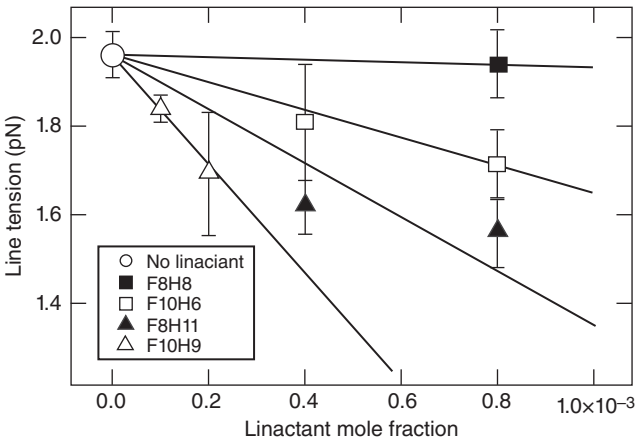


FIGURE 52.4 Line tension as a function of linactant concentration for a monolayer composed of PDA (96.5%) and PFUDA (3.5%). The origin of line tension measurement is set for the PDA-PFUDA monolayer without linactant at surface pressure of 6 mN m^{-1}. (Adapted from Trabelsi et al. 2009 [19], pp. 8056–8061. © American Chemical Society; reproduced with permission.)

Another pair of researchers suggested from MD simulation results that hybrid saturated–unsaturated chain lipids can bind to the liquid-ordered L_o domain composed of saturated lipid and cholesterol and reduce line tension of the domain against unsaturated lipid surroundings [20]. They insisted that these molecules are potential candidates of natural linactants for biomembranes. Another team examined the influence of nonlipid amphiphiles, vitamin E, Triton-X 100, and benzyl alcohol, on the phase separation of binary and ternary lipid mixtures by combination of MD simulation and microscope observation of corresponding giant unilamellar vesicles (GUVs) [21]. Their MD simulations suggested that vitamin E was preferentially partitioned boundaries between L_d and L_o phases and decreased tendency to form domains in GUV systems. On the other hand, it was expected for benzyl alcohol that they were partitioned to L_d phase then decreased lipid order there. This behavior may increase chain length mismatch Δl at domain boundary and explain why benzyl alcohol induced phase separation in GUV systems. Triton-X 100 was almost equally partitioned to both phases but promoted ordering in L_o phase. This also increased Δl and the phase separation again observed. These results indicate that nonlipid amphiphiles can be influential to domain line tension through their preferential partitioning into the one of coexisting phases. A similar argument can be found in our more recent paper concerning the condensed film formation of cationic surfactant at the air–water interface in the presence of long-chain alkanes [6], where the mixing of shorter chain alkanes in the condensed domain leads to smaller Δl then induces elongated or striped shape domains by increasing electric repulsion between surfactant ions relatively. We will explain how to realize the

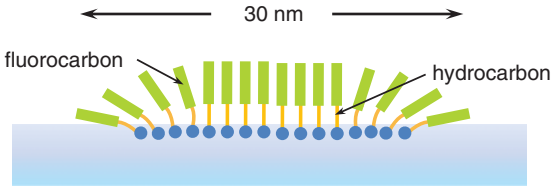


FIGURE 52.5 An expected structure of 2D micelle of $F_nH_mPO_3$.

condensed film of cationic surfactant later in Section 52.5 of this review.

Another team also showed that $F_nH_mPO_3$ formed 2D micelles of as their concentration increased in a neat one-component monolayer. When the concentration of linactant is further increased, these micelles were hexagonally packed analogous to a lyotropic liquid crystal phase in 3D system. The diameter of 2D micelle, $d \sim 30$ nm, is much larger than the extended chain length of $F_nH_mPO_3$, which is up to 3 nm. To understand the driving force for the 2D micelle formation, the earlier studies performed by Krafft et al. were informative [22, 23]. They applied X-ray reflectometry (XR) to the 2D micelle of semifluorinated alkaneF_8H_{16} at the air–water interface that also showed hexagonal packing structure in the high-surface-pressure region. The XR data suggested that the structure of 2D micelle is a bilayer in which the fluorinated segments outward to the air and hydrocarbon segments occupy inside of contacts with water phase. The difference in cross-sectional area between fluorocarbon (0.28 nm^2) and hydrocarbon (0.18 nm^2) bends the bilayer structure to optimize chain packing in the hydrocarbon segments and, as a result, the 2D micelle has a hemispherical shape as shown in Fig. 52.5 The diameter of 2D micelle is therefore determined by the balance of length (i.e., volume) of hydrocarbon and fluorocarbon segments.

There are various kinds of colloidal assemblies in 3D systems such as micelles, vesicles, bilayers, and lyotropic liquid crystals [24]; however, only the micelles and their hexagonally arranged structure were observed experimentally in 2D systems. In 3D systems, the optimal shape of surfactant aggregates changes not only by the interaction between surfactants in each aggregate but also by the interaction between aggregates. Therefore, to realize more complex pattern formation in 2D systems, the structural design of linactant molecules should be reconsidered to have a proper interaction between 2D aggregates.

52.4 VESICLES

GUVs are closed form of bilayer membrane and those composed of ternary mixtures of sphingolipid, phospholipid, and cholesterol, have been widely used as a model of biological cells. Another team first considered hypothetically what would happen if phase separation were to occur in such

a bilayer membrane [25, 26]. The starting point of their thoughts is that the edge energy of the domain is linearly increased with the length of the phase boundary. This condition gives rise to an outward bending of the domain when its radius reaches a finite critical value. They call this process the "domain-induced budding of vesicles," which is balanced by the bending energy of the bud determined by the bending rigidity of the film. The total energy of vesicle separated into phase α and β is therefore given by

$$E = E_b^{(\alpha)} + E_b^{(\beta)} + E_l^{(\alpha\beta)} \tag{52.7}$$

The bending energies are taken to be [27]

$$E_b^{(i)} = \int dA^{(i)} \frac{\kappa^{(i)}}{2} \left(C_1 + C_2 - 2C_{sp}^{(i)} \right)^2 \tag{52.8}$$

where $\kappa^{(i)}$ is the bending rigidity and $C_{sp}^{(i)}$ is the spontaneous curvature of α and β phases. C_1 and C_2 denote the principal curvature of the membrane surface. The edge energy is given by the line integral

$$E_l^{(\alpha\beta)} = \oint dl\tau \tag{52.9}$$

along the phase boundary. The total energy is minimized for a given set of the domain area A^α and A^β, the pressure difference P between the inside and outside of vesicle, the enclosed volume V, and the line tension τ. If the bending rigidity $\kappa^{(\beta)}$ of the growing domain is smaller than $\kappa^{(\alpha)}$, or the spontaneous curvature $C_{sp}^{(\beta)}$ is larger than $C_{sp}^{(\alpha)}$, the budding occurs for smaller values of domain area ratio $x = A^\beta/(A^\alpha + A^\beta)$ and thus leads to transition for smaller buds of phase β. For sufficiently large τ and x, the bud can have a neck with a finite diameter such as that shown in Fig. 52.6 This neck formation finally leads to breakup of the original vesicle into two vesicles consisting of components α and β.

An experimental verification of the abovementioned theory was demonstrated by Baumgart and coworkers for GUVs composed of sphingomyelin, dioleoylphosphatidylcholine (DOPC), and cholesterol [28]. Figure 52.7 shows images of equatorial sections of GUVs obtained using two-photon microscopy. The phase coexistence of the sphingomyelin and cholesterol enrich L_o phase (blue) and DOPC enrich L_d phase (red) are exhibited for various film compositions. The panels c, g, and h correspond to complete buds with necks and others show incomplete buds. They applied a refined Lipowsky theory [29] and obtained mechanical parameters for these vesicles. For example, for the vesicle in the panel a, $\tau \approx 9 \pm 0.3 \times 10^{-13}$N was obtained. However, the obtained line tension is one order of magnitude smaller than the estimation from Eq. (52.1) which is simply based on the energy penalty arose from height mismatch at domain boundary. Akimov et al. suggested an mechanical model that minimizes the height mismatch by the elastic deformation of

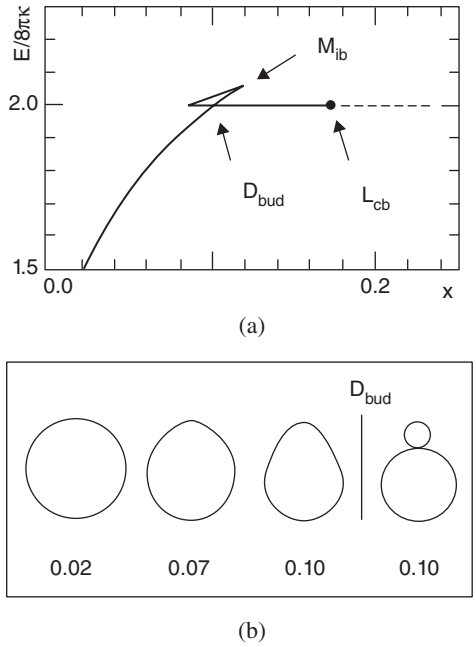


FIGURE 52.6 (a) Energy of the vesicle as a function of the relative domain area x for reduced line tension $\lambda \equiv \tau R_0/\kappa^{(\beta)} = 7$, and (b) some of the corresponding vesicle shapes. R_0 stands for the radius of the original vesicle. The incomplete bud is stable up to D_{bud} at $x = 0.10$, is metastable beyond it, and becomes unstable at M_{ib}. The vesicle separates into two smaller ones from the neck at L_{cb}. (Adapted from Jülicher and Lipowski 1993 [26], pp. 2964–2967. © American Physical Society; reproduced with permission.)

hydrophobic chains near the domain boundary [30]. They claimed that the line tension can be reduced to ∼1 pN if the height mismatch is reduced to ∼3 Å by tilting and stretching of lipid chains.

The Lipowsky theory also suggests the existence of critical domain radius for the initiation of budding, therefore, the components which stabilize small size domains, typically linactants, are disadvantageous to induce budding. García-Sáez et al. modified the height mismatch between L_o and L_d phases by controlling the thickness of the L_d phase using phosphatidylcholines with different chain length [31]. Their experiments showed that the phase separation temperature and the budding tendency of GUV increases as a function of chain length of lipids. The calculated line tension based on the elastic deformation model is in the range of 0.06-6 pN depending on the height mismatch. Furthermore, Staneva et al. found that budding can be induced also by the addition of nonlipid amphiphiles such as Triton-X 100 [32]. This is coincided with the finding mentioned in the previous section: Triton X-100 increases height mismatch by the promotion of ordering in the L_o phase [21]. These results confirmed that the line tension strongly influenced on physicochemical properties of lipid domains.

Some researchers found that the line tension also plays crucial role in pore-closing dynamics of GUVs [33–35].

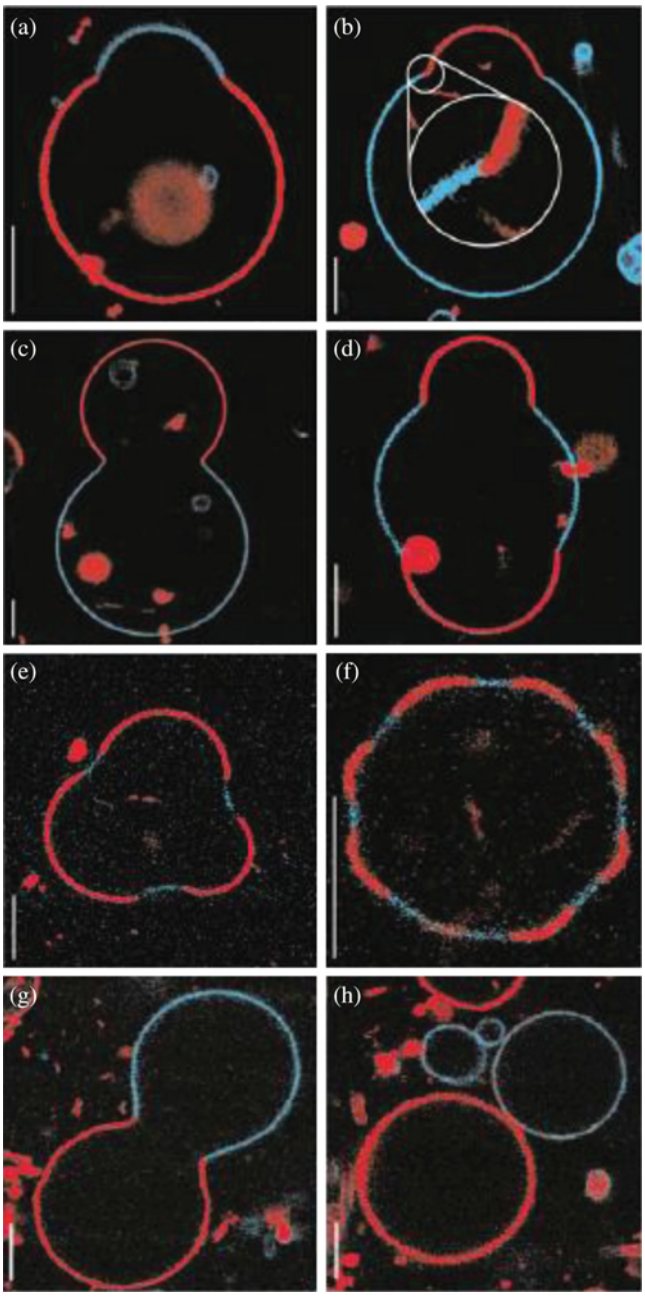


FIGURE 52.7 Two-photon microscopy images showing equatorial sections of GUVs with L_0 (blue)–L_d (red) phase coexistence. Scale bar shows 5 mm. (Adapted from Baumgart et al. 2003 [28], pp. 821–824, Fig. 1. © Nature Publishing Group; reproduced with permission.)

In their studies, UV irradiation and laser ablation were employed to generate transient pores on GUVs. Assuming that the rate of pore-closing is determined by the competition between line tension and surface tension γ at the membrane surface, one has [33, 34]

$$\frac{dr(t)}{dt} = \frac{r(t)}{2\eta}\left[\gamma(t) - \frac{\tau}{r(t)}\right] \tag{52.10}$$

where η is the viscosity of the medium and $r(t)$ is the radius of the transient pore. This experiment is performed to keep vesicle radius R constant during pore-opening and -closing processes. In such situation, the surface tension becomes constant and Eq. (52.10) is reduced to

$$R^2 \ln r(t) \approx -\frac{2\tau}{3\pi\eta}t \tag{52.11}$$

therefore, the line tension working at the edge of membrane pores can be obtained by determining $r(t)$. Srividya et al applied laser ablation method to GUVs formed by saturated lipids with 12, 14, 16, and 18 carbon acyl chains, and found that their line tension ranges from 1-12 pN, exhibiting an increase with acyl chain length. They also found that the natural lipid Egg-PC, which is a mixture of saturated and unsaturated lipids, increased the line tension of GUV up to 32 pN [35]. It was also discussed by Brochard-Wyart et al. [33] that the line tension increased with increasing the amounts of cholesterol in the bilayer.

52.5 LINE TENSION AT WETTING TRANSITIONS

From section 5, we will consider the line tension generated by three coexisting interfaces. When a liquid droplet is placed on a substrate, there are three possible outcomes which are called partial wetting, pseudo-partial wetting and complete wetting [36]. In the partial wetting state, the liquid does not spread on the substrate but instead remains in the form of a macroscopic lens. In contrast to this behavior, for complete wetting, the liquid spreads out to form a uniform film on the substrate. The pseudo-partial wetting state is an intermediate state between partial and complete wetting where a film of molecular thickness is in equilibrium with a macroscopic liquid lens. The microscopic structure of the three-phase contact line is also changed drastically when the transition between these three wetting states occurs. Therefore, the wetting transition is in principal accompanied with aprupt change in the line tension at the three-phase contact.

The theoretical connection between line tension and wetting transition was first proposed by Indekeu et al [37, 38]. According to his theory, the force acting through the thin film connected to the lens displaces the lens profile near the three-phase contact line from the idealized one that obeys the Young–Laplace equation, as schematically shown in Fig. 52.8 The excess free energy required for this deformation is the line tension. Thus, the line tension is considered to be the following functional:

$$\tau = \int_{-\infty}^{\infty}\left[\frac{\gamma}{2}\left(\frac{dl}{dx}\right)^2 + V(l) + \text{const.}\right]dx \tag{52.12}$$

where γ is the surface tension, l the interface displacement which is a function of x, and $V(l)$ the interface potential. The

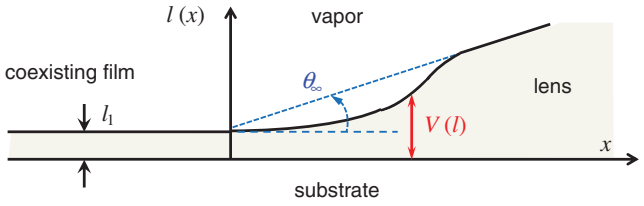


FIGURE 52.8 Interface displacement model for a droplet on solid substrate. θ_∞ indicates the ideal contact angle derived from the Young equation. The real contact angle θ becomes smaller than θ_∞ by the attractive surface force $V(l)$.

first term in the integrand of Eq. (52.12) is attributable to the increase in the interfacial area, while the second term is attributable to the free energy per unit area when a uniform film of thickness l is present. By minimizing Eq. (52.12) and taking the potential at $l \to \infty$ as a reference state, the following equation for the line tension can be derived:

$$\tau = (2\gamma)^{1/2}\,\xi \int_{l_1}^{\infty} \left[V(l)^{1/2} - S^{1/2}\right] dl \qquad (52.13)$$

where ξ is the bulk correlation length, l_1 the film thickness in equilibrium with the lens, and S the spreading coefficient. This equation suggests that the equilibrium line tension is calculated by estimating the interface potential $V(l)$ and integrating Eq. (52.13) from the thickness l_1 to infinity.

For a first-order wetting transition to complete wetting, two minima should exist at a finite and an infinite film thickness on the interfacial potential as shown in Fig. 52.9a. Before the wetting transition, the negative contribution J_1 in the integral of Eq. (52.13) exceeds the positive contribution J_2. However, the magnitude of J_1 reduces as the transition point is approached, and finally, only the positive contribution remains in the integral. Hence, the line tension should be positive at the complete-wetting transition. On the other hand, when the wetting transition occurs between two microscopic films of different thicknesses, the line tension changes sign from positive to negative, as expected from Fig. 52.9b. For a second-order transition from a film of finite thickness to a thick film, the line tension is negative and approaches zero at the wetting transition.

Experimentally, the line tension in three-phase systems can be estimated from the dependence of the contact angle on the contact line perimeter, i.e. on the lens radius. There are two methods available for determining contact angles and/or profiles of microscopic lenses. One method is based upon high-resolution scanning force microscopy (SFM) imaging in tapping mode which is applicable for liquid-vapor interfaces of stable lenses on solid substrates [39–41]. The measured interfacial profile is fitted with appropriate surface energies and then the line tension is theoretically calculated from the data.

For droplets on liquid surfaces lenses readily migrate across the surface, hence, the optical interference method [42–45] is more convenient to use for this situation. In this method, droplet lenses are illuminated by a monochromatic light source from above and the resultant interference fringes

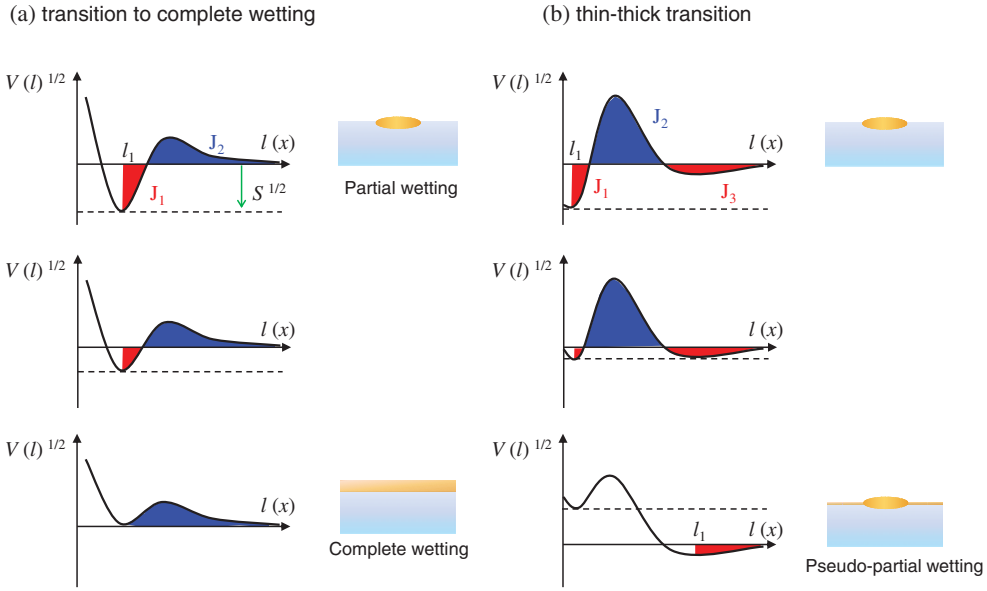


FIGURE 52.9 (a) A schematic interface potential for the first-order transition to the complete wetting and (b) that between wetting films with different thickness. l_1 represents the equilibrium thickness of the wetting film where the integral of Eq. (52.13) starts. If the thinner film in case (b) is considered as nonwetting state, the same conclusion can be obtained for the transition between partial wetting and pseudo–partial wetting.

are recorded on a CCD camera and converted to the lens contact angle, θ. The lens radius is also obtained from the CCD image. From the mechanical balance between the interfacial tensions and the line tension at the three-phase contact line, one can show that [43]

$$\gamma^{AO}\cos\left(\frac{\gamma^{OW}\theta}{\gamma^{AO}+\gamma^{OW}}\right)+\gamma^{AO}\cos\left(\frac{\gamma^{AO}\theta}{\gamma^{AO}+\gamma^{OW}}\right)=\gamma^{AW}-\frac{\tau}{r} \tag{52.14}$$

Here γ^{AW}, γ^{AO}, and γ^{OW} are the interfacial tensions between air-water, air-oil, and oil-water interfaces, respectively, and r is the radius of the lens. Hence, the slope of a straight line drawn from a plot of the left-hand side of Eq. (52.14) against r^{-1} yields the line tension at given experimental condition. This method is restricted to small θ where Eq. (52.14) is valid.

Law and co-workers measured the contact angle of octane and octene droplets on a silicon wafer as a function of temperature [40, 46]. The silicon wafer was coated with hexadecyltrichlorosilane to control the wettability of the surface. They demonstrated that the line tension changes sign from negative to positive with a diverging slope near the first-order wetting transition. If the long-range surface force decays slowly as a function of the thickness, the line tension would be allowed to diverge at the transition point. Pompe measured the line tension of hexaethylene glycol on a silicon wafer and obtained positive values below a contact angle of 6° and negative values above [47]. The measured interfacial profile was fitted with a nonretarded van der Waals and exponentially decaying interactions.

There are a few experimental verifications of the interfacial displacement model for wetting transitions on liquid surfaces. However, we have recently confirmed the reversal of the line tension sign associated with the wetting transition for a hexadecane lens on aqueous solutions of cationic surfactant with various chain length [48–50]. The surfactant molecules adsorbed at the air-water interface decreases required enthalpy for transferring oil molecules from oil lens to the film by lateral van der Waals dispersion interaction and simultaneously increases mixing entropy in the film. As a result, hexadecane, which is not spread on pure water by itself, undergoes wetting transition to a mixed monolayer of surfactant and oil at a certain surfactant concentration. From the formalism mentioned above, this is a wetting transition between partial wetting to pseudo-partial wetting and qualitatively its interface potential obeys the scenario for thin-thick transition shown in Fig. 52.9b. The detailed treatment of interface potential in this system can be found in the literature [49–51]. The reversal of line tension sign was also confirmed by splitting and merging behavior of hexadecane lenses in each wetting regimes (Fig. 52.10). Small lenses formed by stirring merge spontaneously into a large lens as the equilibrium is approached, however, after the wetting transition, large lenses break into small lenses

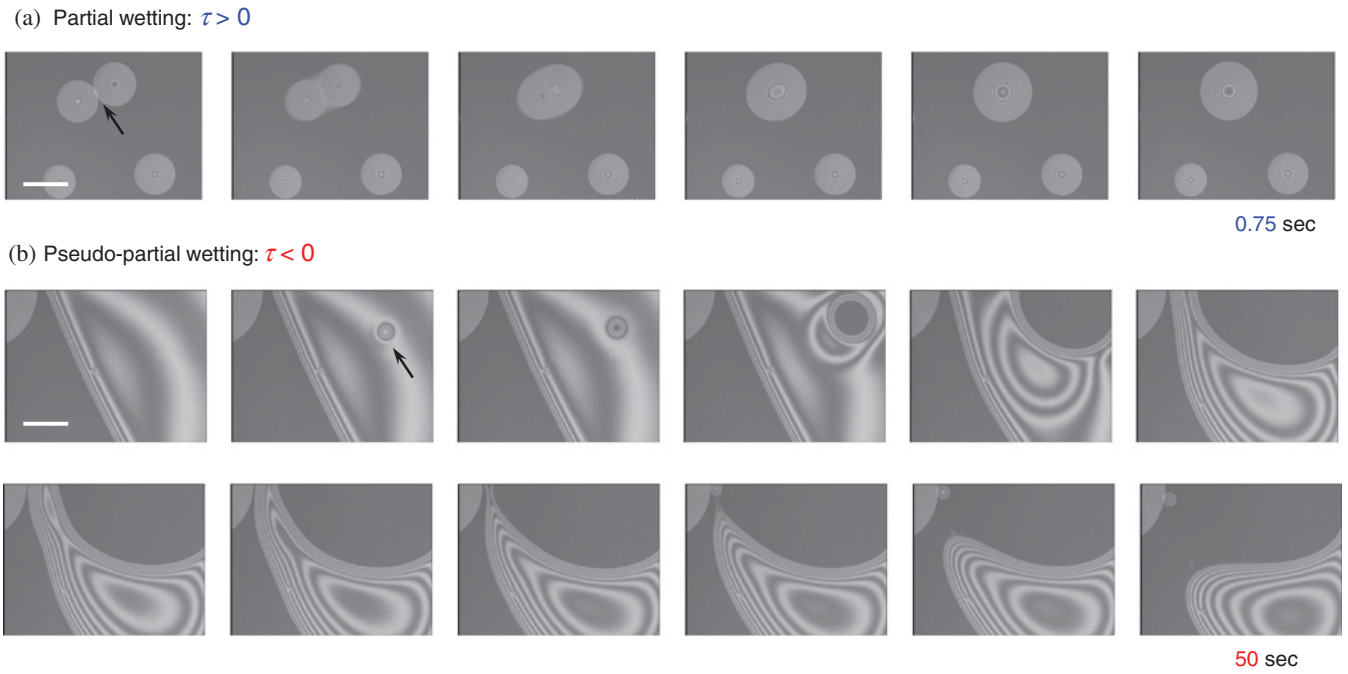


FIGURE 52.10 Microscopic images of alkane lenses on cationic surfactant solutions; (a) the coalescence of lenses in partial wetting state and (b) the spitting process in pseudo–partial wetting. Yellow arrows show places where the merging and splitting start. Scale bar shows 50 μm.

without stirring to increase the total length of three-phase contact.

Interestingly, in the mixed monolayer, cationic surfactants can form condensed film since the penetrated oil molecules into the surfactant adsorbed film enhanced lateral hydrophobic interaction between chains without increasing electric repulsion between hydrophilic groups [52]. Furthermore, it was also revealed that the freezing film can take a bilayer form depending on the combination of surfactant and oil [53]. We also utilized these freezing transitions to control line tension sign of coexisting oil lenses. At present, it was found that cooling of pseudo-partial wetting film leads to a reversal of line tension sign from negative to positive at both freezing transitions [54, 55]. The relation between line tension sign and physical states of the air-water interface was recently summarized in [55].

When small gas bubbles or liquid droplets are nucleated on a solid surface, there also exists three-phase contact lines. If positive line tension was expected for a bubble or droplet at the interface in question, this nucleation requires energy that exceeds potential barrier generated by the line tension as well as the interfacial energies between nucleated phase and its surroundings. Therefore, in the similar manner discussed in this section, the effect of line tension on heterogeneous nucleation has been studied. One of recent researches on this issue can be found in [56] for bubbles and in [57] for liquid droplets.

52.6 PARTICLES AT LIQUID SURFACES

Fine particles tend to be strongly trapped on fluid-liquid interfaces because of the reduction in the interfacial energy due to adsorption [58–60]. The structure of the particle monolayers depends on the particle contact angle [61, 62]. Hydrophobic particles with large contact angles provide well-ordered monolayers at interparticle distances of a few particle diameters by the long-range dipole repulsion between particles in the water phase whereas the monolayers of less-hydrophobic particles are totally disordered and aggregated. The difference between the monolayer structures also leads to different stabilization mechanisms for the Pickering emulsions; the steric-barrier mechanism for the oil in water emulsion and the bridging-particle-monolayer mechanism for the water in oil emulsion [63].

The sign of line tension of fine particles at fluid-liquid interface determines if the contact angle θ decreases or increases with increasing particle size. To determine contact angle of particle at fluid-liquid interface, the gel-trapping technique is one of the useful techniques [64]. In this technique, a hydrocolloid polymer is poured to gel the aqueous phase after the particle adsorption is equilibrated. Then the top phase is replaced with a poly (dimethylsiloxane) (PDMS) which allows us to peel particle layer off the aqueous phase after it is cured. The contact angle of particles is finally measured by using scanning electron microscope (SEM).

McBride et al. determined the line tension of dodecyltrichlorosilane coated silica spheres at the liquid PS-air interface by similar methodology [65]. They adsorbed particle at the interface well above the glass transition temperature of PS then cool the system below it to immobilize particles. Atomic force microscopy (AFM) was then used to image particles. They used silica particles with wide range of radius to show the presence of the minimum radius of silica particle, r_m, and minimum contact angle, θ_m, below which single particles are unstable at the liquid-vapor interface and submerged into the bulk liquid. The connection between these parameters was given by

$$r_m = \frac{\tau}{\gamma \sin\theta_m \left(1 - \frac{\cos\theta_\infty}{\cos\theta_m}\right)} \tag{52.15}$$

with

$$\cos\theta_m = \left[\cos\theta_\infty\right]^{1/3} \tag{52.16}$$

This equation was obtained by comparing the energy of single particle at the interface

$$E_s = \gamma_{SV} A_1 + \gamma_{SL} A_2 + 2\pi b\tau \tag{52.17}$$

and that of completely submerged one

$$E_b = \gamma_{SL}(A_1 + A_2) + \pi b^2 \gamma \tag{52.18}$$

where γ_{SV} and γ_{SL} denote the interfacial tension at the solid-vapor and solid-liquid interfaces and A_1 and A_2 are the upper and lower spherical cap area of the adsorbed particle. They averaged the experimental results for 147 individual spheres with radius ranging from 88 to 498 nm and yielded $\tau = 0.93 \pm 0.01$ nN from the modified Young-equation [66]

$$\cos\theta = \frac{\cos\theta_\infty}{1 - \frac{\tau}{\gamma b}} \tag{52.19}$$

Here θ_∞ express the contact angle of flat surface, γ is the surface tension of the air-water interface, b is the radius of contact line which calculated by particle radius r as $b = r\sin\theta$ for particles with ideally smooth surface. The horizontal and vertical dashed lines in Fig. 52.11 represent $\theta_m \sim 40.4^{\circ}$ and $r_m \sim 78$ nm, respectively, deduced from the theory. The excellent agreement between experimental θ_m and r_m data and the theory suggests the adsorption behavior of fine particles in reality changes $r < r_m$, by the effect arises from the line tension.

Lewandowski et al. proposed an strategic usage of line tension to control the orientation of a cylindrical particles at the aqueous-gas interface [67]. They calculated the phase diagram of cylindrical particles at air–water and oil–water

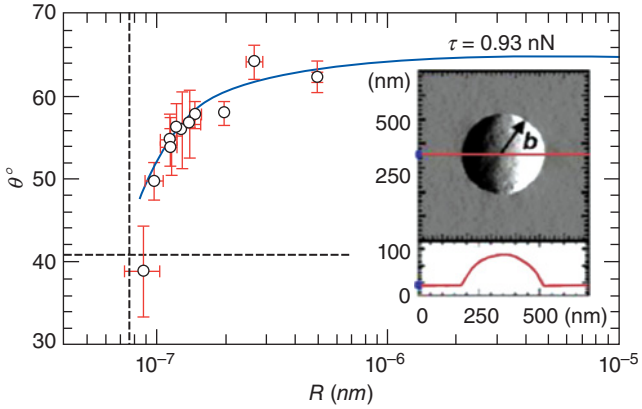


FIGURE 52.11 Contact angle θ versus particle radius R plots. Solid line indicates the estimation from Eq. (52.19) with $\tau = 0.93 \pm 0.01$ nN, and the vertical and horizontal dotted lines are those from Eqs. (52.15) and (52.16). The inset shows the AFM image of Stöber silica sphere of $R \sim 184$ nm. (Adapted from McBride and Law 2012 [66], p. 196101. (© American Physical Society; reprinted with permission.)

interfaces which included the side-on, end-on, and submerged states as a function of the scaled aspect ratio $x = 2L/\pi r$ and contact angle θ_∞, where L and r denoted the cylinder length and radius, respectively. Line tension can also influence the orientations by changing the equilibrium contact angle θ and by increasing the energetic cost of the contact line. They found that cylindrical particle can be driven from side-on to end-on orientations with increasing line tension over some range of x and θ_∞. This transition terminates for high enough τ where the energy of submerged particle overwhelms other two orientations similar to that noted for spherical particles. They confirmed the theory by using disk-shaped nanowires with $x = 0.28$ and longer nanowires with $x = 3.0$. The former always takes end-on orientation whereas the latter takes side-on orientation in SEM images taken for nanowires embedded in PDMS replicas of the air-aqueous solution interfaces.

There is only a few studies concerning with negative line tension or change in line tension sign for fine particles at fluid-liquid interfaces. Maestro et al. found that contact angle of polystyrene (PS) particle at the air-water interface decreases with increasing the particle diameter [68]. They obtained $\tau \sim 0.5$ nN when methanol was used as spreading solvent. From the fact that the τ increased to 5 nN if the spreading solvent was changed to 2-propanol, they considered that the spreading solvent adsorbed on particle surface due to its roughness and change its surface property. The rough surface magnifies the line tension effect so this hypothesis also explains high τ values obtained in this study. If the surface of PS was covered with 2-propanol, the particle becomes more hydrophobic and the excess line energy may increase. They also found that contact angle increases with particle diameter at the octane-water interface for PS particles spread by methanol, indicating the line tension becomes negative if the upper bulk phase changes from air to octane. They could not propose clear explanation for this observation, however, they implied that the preferential adsorption of spreading solvent on particle surface is probably also crucial for the occurrence of negative line tension because the contact angle of PS at the octane-water interface is independent on particle diameter when they spread from 2-propanol.

52.7 FOAM FILMS

The plateau border is the liquid junction connecting thin aqueous films which separates bubbles in a foam. In such a system, the presence of pressure difference between the inside and the outside of the plateau border drives film thinning. Therefore, to prevent the foam film from rapture, there are some proper repulsions between the interfaces on both sides of the film. The forces acting in foam film is called the disjoining pressure, π, which is considered as the sum of three interfacial forces [69];

$$\pi = \pi_{el} + \pi_{vdw} + \pi_{st} \tag{52.20}$$

In most cases, surfactant molecules adsorbed at the air-water interfaces generates the electric repulsion, π_{el}, between interfaces. The π_{vdw} is the van der Waals interaction between gas phases and is always attractive. Fig. 52.12 is a schematic

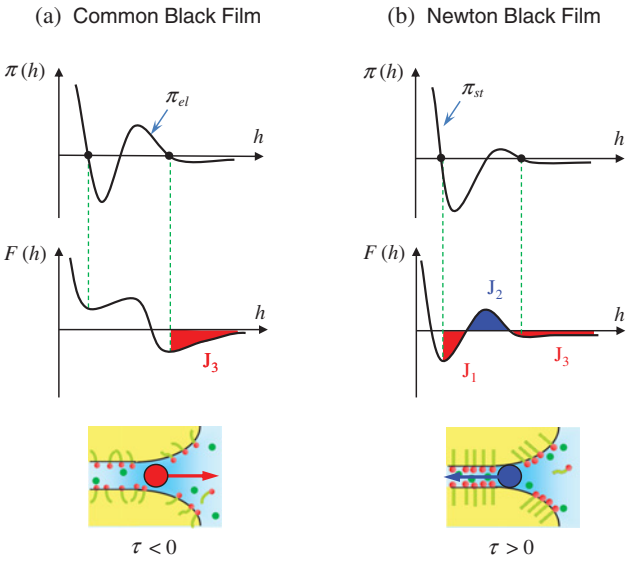


FIGURE 52.12 A schematic diagram of the disjoining pressure curve and free-energy of foam film of (a) common black film and (b) Newton black film. The sign of line tension at the boundary of foam film is determined by the sum of J_1, J_2, and J_3. If J_2 is large enough in panel (b), the line tension of NBF film could be positive whereas that of CBF is principally negative.

diagram of the disjoining pressure curve and free-energy of foam film obtained by integrating π against the film thickness h. The right panel shows the case that a strong π_{el} kinetically stabilizes the system at the secondary minimum of the free energy curve. The thickness of this minimum is less than the wavelength of visible lights (normally around several tens of nanometers), hence, the film stabilized by the electrostatic repulsion is called common black film (CBF). It is well known that the electric repulsion can be reduced easily by increasing electrolyte concentration. In foam film systems, this leads to the reduction of potential barrier between the primary and secondary minima and the occurrence of the thin-thick transition as shown in the left panel. In molecular dimension, the overlapping of hydration shell of hydrophilic groups, π_{st}, becomes dominant. The Newton black film (NBF) is the film stabilized by this steric repulsion and its thickness is normally less than 5 nm.

The line tension works in the transition zone where the foam film is connected to bulk aqueous phase in the liquid junction. Platikanov et al. developed the "diminishing bubble method" to determine the line tension of foam film systems [70, 71]. In this method, a small gas bubble is placed on the solution surface to form a circular NBF on its top. The bubble grows smaller due to the gas diffusion through the film as time passes. The experimentally measurable quantities are the radii of the bubble, R, and that of the film, r. They are related to the line tension as

$$\frac{1}{\cos\theta} = \frac{2\gamma}{\Delta} - \frac{\tau}{\Delta r} \tag{52.13}$$

where γ is the surface tension of the solution and $\Delta = 2\gamma\cos\theta_\infty$. The θ_∞ is the contact angle of the large black film ($r \to \infty$). They applied this method to 0.05 % sodium dodecyl sulfate (SDS) solution by varying the concentration of NaCl. The most important finding of these experiments is that line tension changes sign from positive to negative as NaCl concentration increases. For 0.32 M NaCl aqueous solution, the contact angle decreases with decreasing r, suggesting positive τ. The contact angle becomes almost independent on r at 0.36 M and increases with decreasing r at 0.45 M.

The line tension of CBF reported as well for 0.05 % SDS + 0.1 M NaCl aqueous solution [72]. Kolarov et al. found that the contact angle of the foam film in the porous plate cell increases with decreasing film radius by using the interference pattern in reflected light. This indicates the line tension is negative for the CBF.

The relation between line tension and interaction free-energy in the film was first derived by de Feijter et al. [73] and then applied to the experimental observations by Princen [74]. The final conclusion was quantitatively the same as discussed for the wetting films by using Eq. (52.13); the line tension τ is proportional to the integral of the free-energy curve from the thickness of the existing film, CBF or NBF in the present case, to infinity. For example, the line tension of CBF should take a finite negative value because the line tension was solely determined by the contribution J_3 that comes from the long-range van der Waals attraction. On the other hand, the line tension of NBF films can change its sign depending on the relative relation between $J_1 + J_3$ and J_2. The addition of electrolyte reduce the height of the potential barrier J_2 and leads to the reversal of line tension sign from positive to negative as observed in accordance with the experimental observation.

Figure 52.13 shows a comparison of equilibration processes of CBF and NBF stabilized by cationic surfactant–alkane mixed adsorbed film with different concentrations of

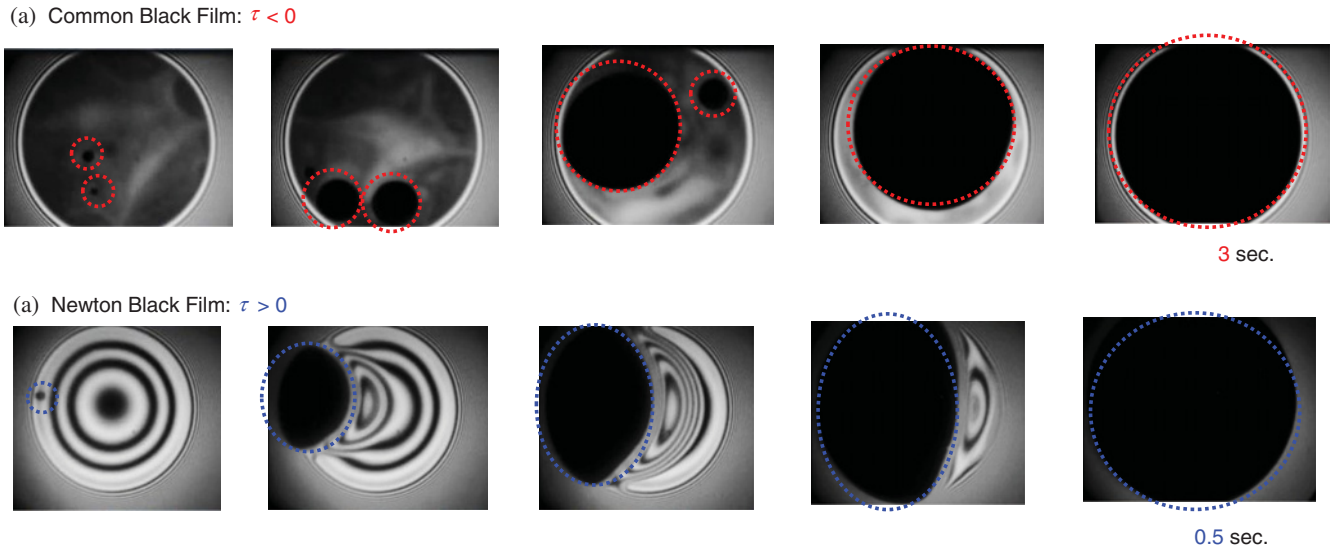


FIGURE 52.13 Equilibrium processes of (a) CBF and (b) NBF films in the porous plate cell.

NaCl [75]. The dotted regions are the black films nucleated from the surrounding thicker aqueous film. The nucleation of CBF occurs in different places at the same time, indicating that the creation of the contact line is energetically favourable due to the negative line tension. On the other hand, for NBF, the first nucleation takes longer time compared to CBF nucleation and the NBF film expands rapidly to cover the whole area of the film once its nucleation is happened. This behavior is corresponding to the fact that the nucleation of NBF is prevented by the energy barrier due to positive line tension.

De Feijter et al. [73] and Churaev et al. [76] also discussed the line tension between bulk liquid and its thin film from the shape of the transition zone. See original papers for details.

52.8 SUMMARY

In this review, we summarized line tension studies provided in recent publications. Because of the difficulties in measuring tiny forces in micron scale objects, the discrepancies of line tension data between researchers has yet to be resolved. However, as we have seen in this review, some of line tension data are supported by macroscopic observations and, we believe, worth to be trusted.

Among them, the domain line tension in Langmuir monolayers has been studied widely due to its technological importance (ex. structuring of 2D system) and experimental accessibility of the air-water interface. Therefore, the methods for measuring domain line tension were well-established compared to the other systems. Now the interest of researchers in this field is being shifted to the discovery of linactants. Most succeeded example of linactants is partially fluorinated compounds $F_nH_mPO_3$, which reduce the domain line tension of the condensed domain in the PDA - PFUDA mixed monolayers. In these cases, the bulkiness and lower surface energy of fluorocarbon moiety granted a head-group character to linactant molecules. However, this molecular design is exactly the same as that of surfactant from the view point that there is two chemical groups favoring different bulk phases, as a result, these linactants only form hemispheres in quasi-2D space when they are solely added at the air-water interface. Therefore, introducing a functional group which generates lateral interactions between linactant aggregates is one of the future candidate of linactant design.

The budding and breaking up of GUVs are one of the high-lights of domain line tension studies. These processes require high enough line tension value, hence, the additives influential to GUV budding had a character to dissolve preferentially to L_d or L_o phases and consequently enhance the Δl. Some researchers suggested other driving forces for GUV budding. For example, the calcium ions are considered to induce budding through the change in osmotic pressure [77]. The relation between a pore forming peptide and budding was also found in [78]. More experimental and theoretical efforts are probably necessary to obtain a collective view of domain budding mechanism. Schwartz et al. recently wrote a good review on the domain line tension which included the recent developments of their linactant studies [79].

The type (b) line tension can be understood by interaction free-energy between interfaces in three-phase contact zone. This theory has been verified extensively for line tension behavior at wetting transitions. The surfactant induced wetting transition is unique approach which is only available method to switch line tension sign by external thermodynamic variables such as surfactant concentration and temperature. The line tension also changes the phase diagram of fine particle adsorbed at fluid-liquid interfaces and, in principal, leads to the transition between side-on and end-on orientations for cylindrical particles. The self-assembly of particles is promising research field in bottom-up nanotechnology. However, there is only a few study on how chemical property of particle surface influences the line tension. Therefore, for practical use, the relation between particle wettability and line tension values should be established more in detail. The line tension effect on foam film stability was studied only qualitatively and therefore have a possibility to open new research field in the future.

REFERENCES

[1] Vollhardt, D. (1996). *Adv. Colloid Interface Sci.* **64**, 143–171.

[2] Hu, Y., Meleson, K., Israelachvili, J. (2006). *Biophys. J.* **91**, 444–453.

[3] McConnell, H.M. (1991). *Annu. Rev. Phys. Chem.* **42**, 171–195.

[4] McConnell, H.M., Moy, V.T. (1988). *J. Phys. Chem.* **92**, 4520−4525.

[5] Iimura, K., Shiraku, T., Kato, T. (2002). *Langmuir* **18**, 10183–10190.

[6] Matsubara, H., Takaichi, T., Takiue, T., Aratono, M., Bain, C.D., Toyoda, A., Iimura, K. (2013). *J. Phys. Chem. Lett.* **4**, 844–848.

[7] Gains, L.G. (1969). *Insoluble Monolayers at Liquid-Gas Interfaces.* Interscience Publishers, New York.

[8] Roberts, G.G. (ed.) (1990). *Langmuir-Blodgett Films.* Plenum Press, New York.

[9] Petty, C.M. (1996). *Langmuir-Blodgett Films, An Introduction.* Cambridge Univ. Press, Cambridge, UK.

[10] Birdi, K.S. (1999). *Self-Assembly Monolayer Structures of Lipids and Macromolecules at Interfaces.* Kluwer Academic/Plenum Publishers, New York.

[11] London, E. (2012). *Curr. Opin. Struct. Biol.* **12**, 480–486.

[12] Veatch, S.L., Keller, S.L. (2003). *Biophys. J.* **85**, 3074–3083.

[13] Simons, K., Ikonen, E. (1997). *Nature* **387**, 569–572.

[14] Benvegnu, D.J., McConnell, H.M. (1992). *J. Phys. Chem.* **96**, 6820–6824.

[15] Läuger, J., Robertson, C.R., Frank, C.W., Fuller, G.G. (1996). *Langmuir* **12**, 5630–5635.

[16] Wintersmith, J.R., Zou, L., Bernoff, A.J., Alexander, J.C., Mann, J.A., Jr., Kooijman, E.E.; Mann, E.K. (2007). *Phys. Rev. E* **5**, 061605.

[17] Wurlitzer, S., Steffen, P., Wurlitzer, M., Khattari, Z., Fischer Th. M. (2000). *J. Chem. Phys.* **113**, 3822–3828.

[18] Trabelsi, S., Zhang, S., Lee, T.R., Schwartz, D.K. (2008). *Phys. Rev. Lett.* **100**, 037802.

[19] Trabelsi, S., Zhang, Z., Zhang, S., Lee, T.R., Schwartz, D.K. (2009). *Langmuir* **25**, 8056−8061.

[20] Schäfer, L.V., Marrink, S.J. (2010). *Biophys. J.* **99**, L91–L93.

[21] Muddana, H.S., Chiang, H.H., Butler, P.J. (2012). *Biophys. J.* **102**, 489–497.

[22] Fontaine, P., Goldmann, M., Muller, P., Fauré, M.-C., Konovalov, O., Krafft, M.P. (2005). *J. ACS* **127**, 512–513.

[23] Maaloum, M., Muller, P., Krafft, M.P. (2002). *Angew. Chem. Int. Ed.* **41**, 4331–4334.

[24] Evans, D.F., Wennerström, H. (1999). *The Colloidal Domain.* Wiley-VCH, New York, Chapter 1.

[25] Lipowsky, R. (1993). *Biophys. J.* **64**, 1133–1138.

[26] Jülicher, F., Lipowsky, R. (1993). *Phys. Rev. Lett.* **70**, 2964–2967.

[27] Helfrich, W. (1973). *Z. Naturforsch. Teil C* **28**, 693.

[28] Baumgart, T., Hess, S.T., Webb, W.W. (2003). *Nature* **425**, 821–824.

[29] Jülicher, F., Lipowsky, R. (1996). *Phys. Rev. E* **53**, 2670–2683.

[30] Akimov, S.A., Kuzmin, P.I., Zimmerberg, J., Cohen, F.S., Chizmadzev, Y.A. (2004). *J. Electroanal. Chem.* **564**, 13–18.

[31] García-Sáez, A.J., Chiantia, S., Schwille, P. (2007). *J. Biol. Chem.* **282**, 33537–33544.

[32] Staneva, G., Seigneuret, M., Koumanov, K., Trugnan, G., Angelova, M.I. (2005). *Chem. Phys. Lipids* **136**, 55–66.

[33] Puech, P.-H., Borghi, N., Karatekin, E., Brochard-Wyart, F. (2003). *Phys. Rev. Lett.* **90**, 128304.

[34] Rodriguez, N., Cribier, S., Pincet, F. (2006). *Phys. Rev. E* **74**, 061902.

[35] Srividya, N., Muralidharan, S. (2008). *J. Phys. Chem. B* **112**, 7174–7152.

[36] Brochard-Wyart, F., Di Meglio, J.M., Quéré, D., De Gennes, P.G. (1991). *Langmuir* **7**, 335–338.

[37] Indekeu, J.O. (1992). *Physica A* **183**, 439–461.

[38] Dobbs, H.T., Indekeu, J.O. (1992). *Physica A* **210**, 457–481.

[39] Herminghaus, S., Fery, A., Reim, D. (1997). *Ultramicroscopy* **69**, 211–217.

[40] Wang, J.Y., Betelu, S.,) Law, B.M. (2001). *Phys. Rev. E* **63**, 31601.

[41] Pompe, T. (2002). *Phys. Rev. Lett.* **89**, 076102.

[42] Aveyard, R., Clint, J.H. (1997). *J. Chem. Soc. Faraday Transact.* **93**, 1397–1403.

[43] Aveyard, R., Clint, J.H., Nees, D., Paunov, V. (1999). *Colloids Surf. A* **146**, 95–111.

[44] Chen, P., Susnar, S.S., Mak, C., Amirfazli, A., Neumann, A.W. (1997). *Colloids Surf. A* **129–130**, 45–60.

[45] Stöckelhuber, K.W., Radoev, B., Schulze, H.J. (1999). *Colloids Surf. A* **156**, 323–333.

[46] Wang, J.Y., Betelu, S., Law, B.M. (1999). *Phys. Rev. Lett.* **83**, 3677–3680.

[47] Pompe, T., Heminghaus, S. (2000). *Phys. Rev. Lett.* **85**, 1930–1933.

[48] Takata, Y., Kikuchi, Y., Matsubara, H., Takiue, T., Aratono, M. (2005). *Langmuir* **21**, 8594–8596.

[49] Takata, Y., Matsubara, H., Kikuchi, Y., Takiue, T., Law, B.M., Aratono, M. 2008) *Colloid Polym. Sci.* **286**, 647–654.

[50] Matsubara, H., Ikebe, Y., Takata, Y., Takiue, T., Aratono, M. (2010). *Bull. Chem. Soc. Jpn.* **83**, 1198–1202.

[51] Matsubara, H., Aratono, M., Wilkinson, K.M., Bain, C.D. (2006). *Langmuir* **22**, 982–988.

[52] Ohtomi, E., Takiue, T., Aratono, M., Matsubara, H. (2010). *Colloid Polym. Sci.* **288**, 1333–1339.

[53] Matsubara, H., Ohtomi, E., Aratono, M., Bain, C.D. (2008). *J. Phys. Chem. B* **112**, 11664–11668.

[54] Ushijima, Y., Ushijima, B., Ohtomi, E.,Takata, Y., Takiue, T., Aratono, M., Matsubara, H. (2011). *Colloids Surf. A* **390**, 33–39.

[55] Matsubara, H., Ushijima, B., Law, B.M., Takiue, T., Aratono, M. (in press). *Adv. Colloid Interface Sci.*

[56] Van Limbeek, M.A.J., Seddon, J.R.T. (2011). *Langmuir* **27**, 8694–8699.

[57] Zhou, D., Mi, J., Zhong, C. (2012). *J. Phys. Chem. B* **116**, 14100–14106.

[58] Pieranski, P. (1980). *Phys. Rev. Lett.* **45**, 569–572.

[59] Robinson, D.J., Earnshaw, J.C. (1993). *Langmuir* **9**, 1436–1438.

[60] Binks, B.P., Lumsdon, S.O. (2000). *Langmuir* **16**, 8622–8631.

[61] Horozov, T.S., Aveyard, R., Clint, J.H., Binks, B.P. (2003). *Langmuir* **19**, 2822–2829.

[62] Horozov, T.S., Aveyard, R., Bins, B.P., Clint, J.H. (2005). *Langmuir* **21**, 7405–7412.

[63] Horozov, T.S., Binks, B.P. (2006). *Angew. Chem.* **118**, 787–790.

[64] Paunov, V.N. (2003). *Langmuir* **19**, 7970–7976.

[65] Aveyard, R., Clint, J.H. (1996). *J. Chem. Soc. Faraday Transact.* **92**, 85–89.

[66] McBride, S.P., Law, B.M. (2012). *Phys. Rev. Lett.* **109**, 196101.

[67] Lewandowski, E.P., Searson, P.C., Stebe, K.J. (2006). *J. Phys. Chem. B* **110**, 4283–4290.

[68] Maestro, A., Bonales, L.J., Ritacco, H., Rubio, R.G., Ortega, F. (2010). *Phys. Chem. Chem. Phys.* **12**, 14115–14120.

[69] Exerowa, D., Kruglyakov, P.M. (1998). *Foam and Foam Films.* Elsevier, Amsterdam.

[70] Platikanov, D., Nedyalkov, M., Nasteva, V. (1980). *J. Colloid Interface Sci.* **75**, 620–628.

[71] Exerowa, D., Kashchiev, D., Platikanov, D., Toshev, B.V. (1994). *Adv. Colloid Interface Sci.* **49**, 303–339.

[72] Kolarov, T., Zorin, Z.M. (1979). *Colloid Polym. Sci.* **257**, 1292–1293.

[73] Feijter, J.A., Vrij, A. (1972) *J. Electroana. Chem.* **37**, 9–22.

[74] Princen, H.M. (1984). *Colloids Surf.* **9**, 67–77.

[75] Matsubara, H. (unpublished data).

[76] Churaev, N.V., Starov, V.M., Derjaguin, B.V. (1982). *J. Colloid Interface Sci.* **89**, 16–24.

[77] Shimokawa, N., Hishida, M., Seto, H., Yoshikawa, K. (2010). *Chem. Phys. Lett.* **496**, 59–63.

[78] Yu, Y., Vroman, J.A., Bae, S.C., Granick, S. (2010). *J. ACS* **132**, 195–201.

[79] Sriram, I., Schwartz, D.K. (2012). *Surf. Sci. Rep.* **67**, 143–159.

53

LIQUID STRUCTURES AND PROPERTIES OF LIPIDS

Makio Iwahashi

Department of Chemistry, School of Science, Kitasato University, Sagamihara, Kanagawa-ken, Japan

53.1 INTRODUCTION

Lipids include hydrocarbons, alcohols, fatty acids, fatty-acid esters, steroids, soaps, detergents, and more complex molecules such as triacylglycerols, phospholipids, gangliosides, and lipopolysaccharides. These lipids are essential for human life as foods, pharmaceuticals, cosmetics, biodiesel for automobile engines and boilers, and dielectric insulating oil for transformers. The physicochemical properties of lipids have been introduced widely and in detail [1–3]. In general, lipids melt from their highest melting form (the most stable form) to an apparently isotropic liquid state. However, some short-range order is conceivably maintained even in the liquid state because only a small change (∼10%) in the volume occurs when the materials go from crystal to liquid. The short range order (microstructure) in liquid most probably affects the properties of lipids, especially in the liquid state and ultimately in the solid state; it would play important roles in the overall functions of lipids. However, the liquid structure of lipids, as opposed to crystal structure, has been scarcely investigated since the experimental determination of the liquid structure of lipids is very difficult. The experiments needed to clarify the liquid structure require a large amount of highly pure samples and a combination of different investigation methods. Namely, the true feature of the liquid structure does not rise to the surface with only one method.

Today, highly purified samples of several kinds of lipids have been sufficiently supplied and their structures and physical properties in the liquid state are being clarified by combining various experiment methods. In this chapter the liquid structures and properties of lipids such as alkanes, alcohols, fatty acids, and fatty-acid esters, inclusive mono-, di-, and triacyglycerols, are introduced as follows:

(1) comparison of alcohols with their corresponding fatty acids in their aggregated structures and property (the aggregation number of alcohols and the stability of fatty acid dimer); (2) inter- or intramolecular movements of alkanes, alcohols, fatty acids, and fatty-acid esters (segmental and translational movements of molecules); (3) structure of cluster composed of fatty-acid dimers in the pure liquid state and in CCl_4 solution; (4) effect of cluster structures of fatty acids on their properties such as density, viscosity, and self-diffusion coefficient; (5) effect of additivities on the cluster structure and the liquid properties of oleic acid; (6) aggregated structures and properties of acylglycerols; and (7) application of fatty-acid esters as an insulating oil and a medical agent for a hepatoma operation using microcatheters.

53.2 COMPARISON OF ALCOHOLS WITH THEIR CORRESPONDING FATTY ACIDS IN THEIR AGGREGATED STRUCTURES AND PROPERTIES

53.2.1 Density and Molar Volume

Figure 53.1 shows the density ρ of normal fatty acid (open circle) and normal alcohol (solid circle) possessing one to nine carbon atoms at 20°C as an example [1]. The density of fatty acid is evidently larger than that of the corresponding alcohol. Then let us calculate the molar volumes V for fatty acid and alcohol, using their ρ values and the following equation:

$$V = \frac{M}{\rho} \tag{53.1}$$

where M is the molar weight of fatty acid or alcohol.

Encyclopedia of Biocolloid and Biointerface Science, Volume 2, First Edition. Edited by Hiroyuki Ohshima.
© 2016 John Wiley & Sons, Inc. Published 2016 by John Wiley & Sons, Inc.

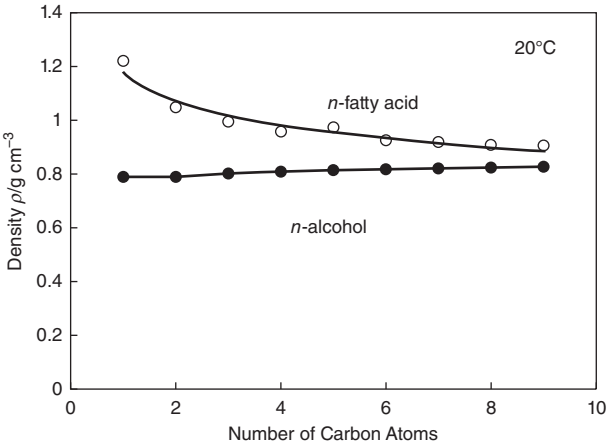


FIGURE 53.1 The relationship between density ρ and number of carbon atoms for normal fatty acid (○) and alcohol (●) at 20°C (293 K). (Original data are from Ref. 1.)

As shown in Fig. 53.2, the molar volume of fatty acid (open circle) except formic acid is almost equal to that of the corresponding alcohol (solid circle). Fatty-acid and alcohol molecules, which have a same number of carbon atoms, occupy almost an equivalent space in the liquid state.

53.2.2 Viscosity of Fatty Acids and Alcohols

Most readers would expect that fatty acid has a higher viscosity than the corresponding alcohol since the hydrogen bonding of carboxyl group of fatty acid is stronger than that of the OH group of alcohol. Figure 53.3 shows the temperature dependence of viscosity η of formic acid and methanol and also that of acetic acid and ethanol, respectively. Formic acid has higher viscosity than methanol at the same temperatures; acetic acid also has slightly higher viscosity than ethanol [1].

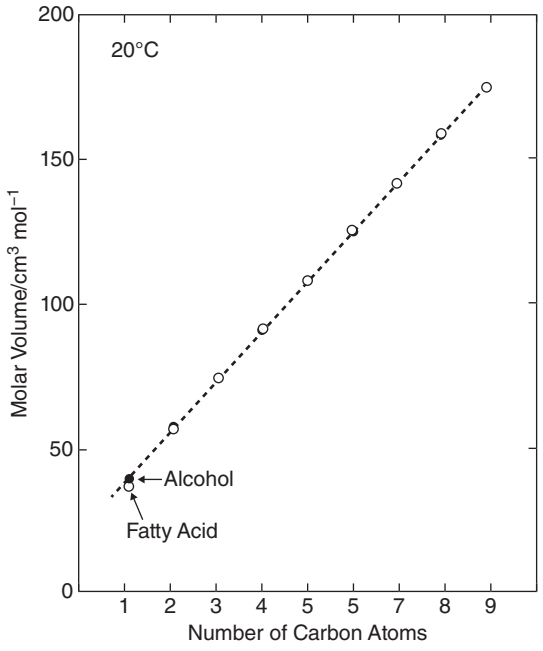


FIGURE 53.2 Relationship between molar volume and number of carbon atoms for normal fatty acid (○) and alcohol (●) at 20°C (293 K).

Interestingly, the viscosity of formic acid is higher than that of acetic acid in spite of its smaller molecular size. X-ray diffraction measurements indicated that formic acid in its crystalline phase forms large polymers through its strong hydrogen bonding. The proton, which is directly attached to C1-carbon atom of formic acid, would contribute to the formation of hydrogen bonding among the formic acid molecules [4].

The viscosity of propanoic or butanoic acid is, however, lower than that of the corresponding alcohol as shown in Fig. 53.4 This suggests that, in spite of relatively low hydrogen-bonding ability of alcohol compared to that of fatty acid, the alcohol molecules in the liquid phase easily aggregate to form larger polymers than fatty acid molecules owing to the appropriate direction of hydrogen bonding among alcohol molecules. On the contrary, the carboxylic acids form only cyclic, hydrogen-bonded dimers by the strong hydrogen bonding between the two fatty-acid molecules. Consequently, the viscosity of alcohol having three or four carbon atoms in its hydrocarbon chain is larger than that of the corresponding fatty acid.

The viscosity profiles for octanoic acid and octan-1-ol (Fig. 53.5) are different from those for propanoic acid and propanol or those for butanoic acid and butan-1-ol (Fig. 53.4). Namely, the viscosity of octan-1-ol decreases steeply as temperature increases, while that of octanoic acid decreases gradually; above 330 K (57°C) the viscosity of octan-1-ol becomes lower than that of octanoic acid [1,5]. This suggests that at high temperature the hydrogen bonding among the OH groups of octan-1-ol becomes weak and that the polymers of octan-1-ol become small in size and decrease in their number, while octanoic acid still maintains its dimer structure even at high temperature.

In the case of *cis*-9-octadecenoic acid (oleic acid) and *cis*-9-octadecen-1-ol (oleyl alcohol), the viscosity of oleic acid is always larger than that of oleyl alcohol as shown in Fig. 53.6 [6]. This suggests that the polymer of oleyl alcohol is small in its size and few in its number even at room temperature. Consequently, it is concluded that the long hydrocarbon part in an alcohol molecule plays as a solvent and dilutes the concentration of OH group. The longer hydrocarbon chain would decrease the association number of alcohol and the number of the aggregates since the hydrogen bonding among OH groups of alcohols is not so strong. On the contrary, owing to the strong hydrogen bonding, fatty acids, except formic and acetic acids, are thought to exist always as cyclic dimers regardless of the hydrocarbon chain length

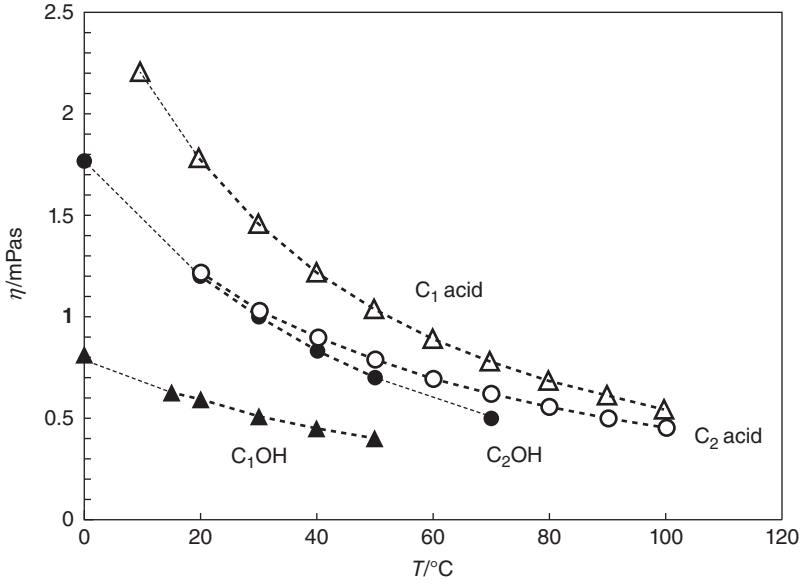


FIGURE 53.3 Temperature dependence of viscosity η for fatty acids and alcohols in the liquid state. △ denotes formic acid (C1-acid); ▲, methanol (C1-OH); (○) acetic acid (C2-acid); ●, ethanol (C2-OH). [Original data are from Ref. 1.)

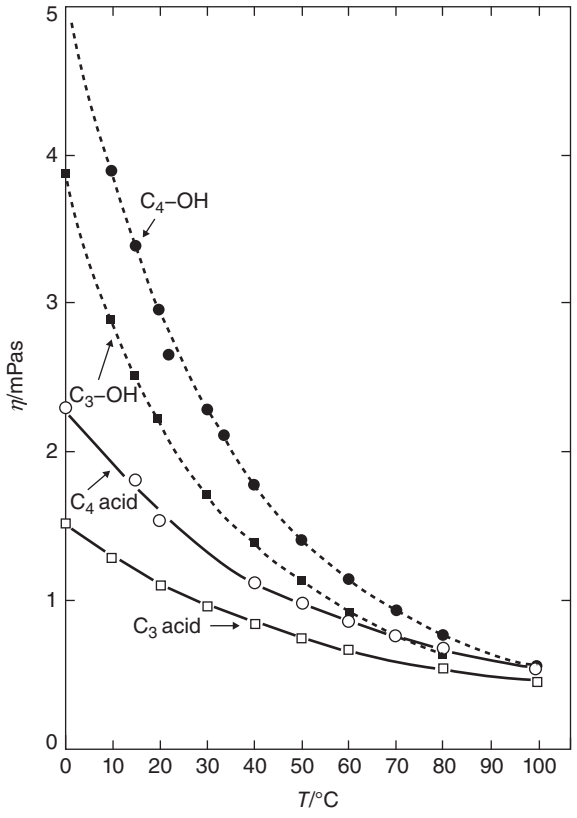


FIGURE 53.4 Temperature dependence of viscosity η for fatty acids and alcohols in the liquid state: □, propanoic acid (C3-acid); ■, propanol (C2-OH); ○, butanoic acid (C4-acid); ●, butan-1-ol (C4-OH). (Original data are from Ref. 1.)

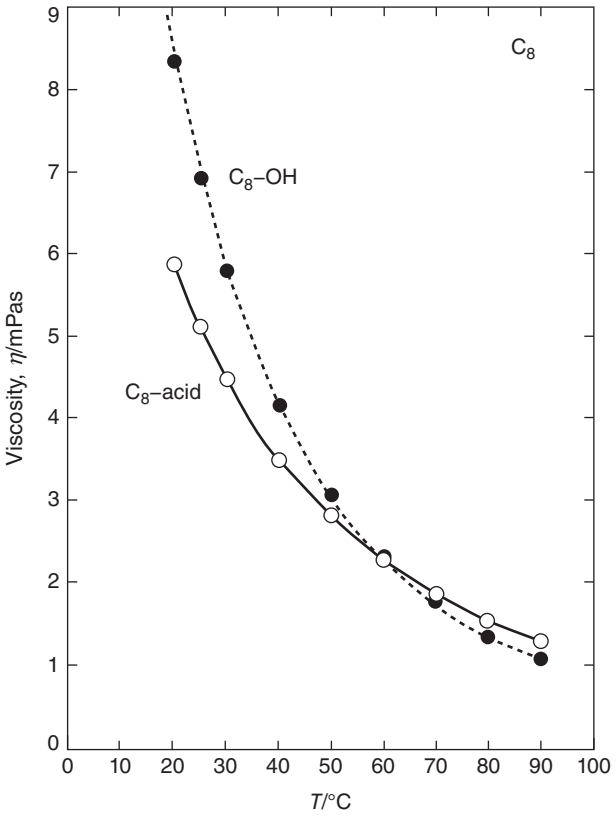


FIGURE 53.5 Temperature dependence of viscosity η for octanoic acid (C8-acid, ○) and octan-1-ol (C8-OH, ●) in the liquid state. (Original data are from Ref. 1.)

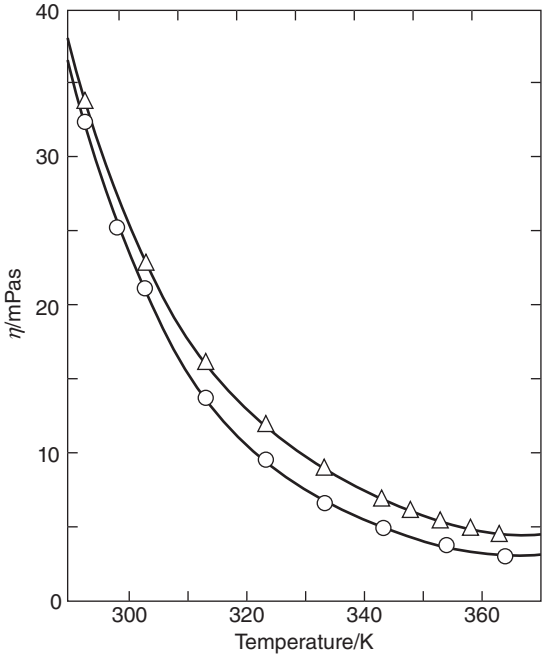


FIGURE 53.6 Temperature dependence of viscosity η for oleic acid (△) and oleyl alcohol (○) in the liquid state. (Adapted from Iwahashi et al. 1995 [6], pp. 4155–4164. © American Chemical Society; reproduced with permission.)

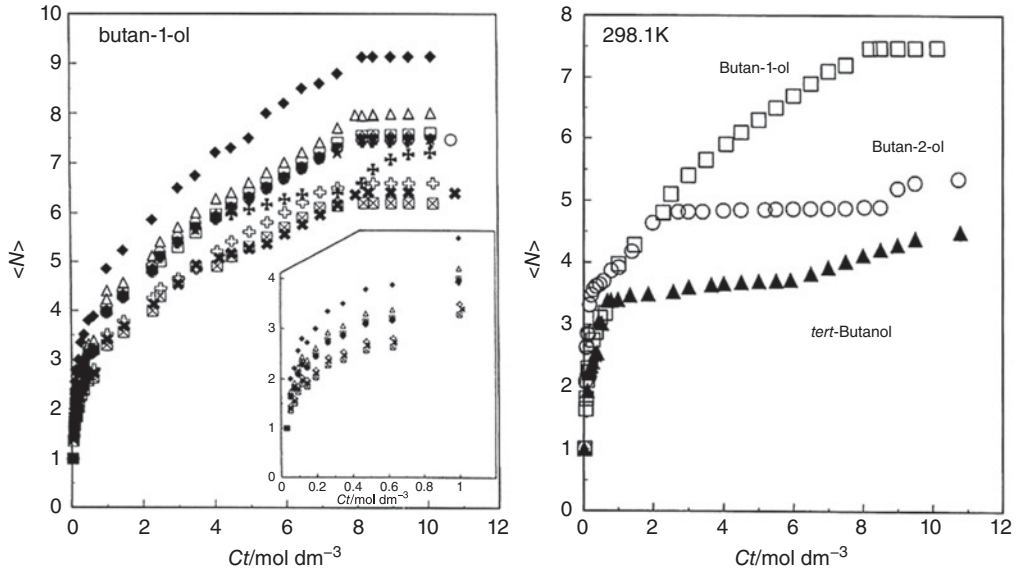
even at high temperature, as to be described in the following section.

53.3 AGGREGATION NUMBER OF ALCOHOL AND STABILITY OF FATTY ACID DIMER

53.3.1 Effect of Molecular Structure on Aggregation Number of Alcohol in CCl_4 and in Its Pure Liquid

The effect of molecular structure on the self-association of alcohol in its pure liquid state and in carbon tetrachloride was quantitatively investigated through the near-infrared spectroscopic (NIR) observation for butan-1-ol, butan-2-ol, and 2-methylpropan-2-ol (*tert*-butanol), which are structural isomers to each other [7]. A successive association process was assumed for the aggregation of alcohol molecules; the analysis based on this process was applied to the sharp band around 1410 nm (the first-overtone band of the OH stretching vibration mode attributed to free OH monomer and partly to OH polymer).

Figure 53.7a shows, as a typical example, the degree of association (the size of the multimer in monomeric units), <*N*>, for the aggregate of butan-1-ol at various constant temperatures. The <*N*> value increases with increasing concentration and decreases with increasing temperature [7]. Figure 53.7b shows a comparison of the concentration



(a) (b)

FIGURE 53.7 (a) Effect of concentration on the aggregation number <*N*> for butan-1-ol at temperatures ranging from 278.2 K (25.1°C) (◆) to 338.1 K (65°C) (×) at 5 K intervals. Inserted small graph also indicates the <*N*> versus concentration relationship below 1.0 mol dm^{-3}. (b) Comparison of <*N*> for three kinds of butanols at 298.1 K (25°C): □ denotes butan-1-ol; ○, butan-2-ol; ▲, 2-methylpropan-2-ol (*tert*-butanol). (Adapted from Iwahashi, M., Suzuki, M., Katayama, N., Matsuzawa, H., Czarnecki, M. A., Ozaki, Y., Wakisaka A. (2000). *Appl. Spectrosc*. 54, 268–276. © Society for Applied Spectroscopy; reproduced with permission.)

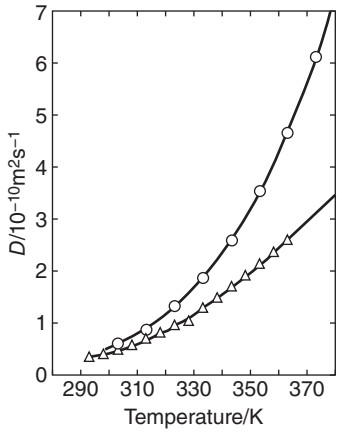


FIGURE 53.8 Temperature dependence of self-diffusion coefficient D for *cis*-9-octadecen-1-ol (oleyl alcohol) (○) and *cis*-9-octadecenoic acid (oleic acid) (Δ). (Adapted from Iwahashi et al. 1995 [6], pp. 4155–4161. © American Chemical Society; reproduced with permission.)

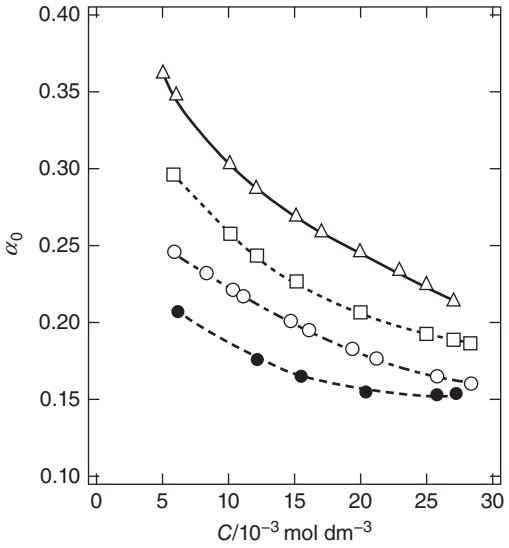


FIGURE 53.9 Concentration dependence of dissociation α_0 of oleic acid dimer in CCl_4 at 35°C (●), 40°C (○), 45°C (□), and 50°C (Δ). (Adapted from Iwahashi et al. 1995 [10], pp. 697–701. © Royal Society of Chemistry; reproduced with permission.)

dependence of <*N*> for the above three kinds of butanols at 298.1 K (25°C), the association ability is in the following order: butan-1-ol > butan-2-ol > *tert*-butanol.

The <*N*> value for octan-1-ol in the temperature range 298.1-348.1 K (25-65°C) was *ca*. four both in the pure liquid state and in decane [5]. That for *cis*-9-octadecen-1-ol (oleyl alcohol), which has a longer hydrocarbon chain, was 2.37-3.78 (average 2.95) both in the pure liquid state and in decane in the temperature range 298.1–348.1 K [6]; the <*N*> value had also a tendency to decrease with an increase in temperature. The apparent association constant K for oleyl alcohol was relatively low and also decreased with an increase in temperature. The low K value, which means small portions of polymerized molecules in the liquid state, is most likely responsible for the lower viscosity (Fig. 53.6) and the higher self-diffusion coefficient (Fig. 53.8) of oleyl alcohol than those of oleic acid, which exists almost entirely as cyclic dimers.

53.3.2 Stability of Fatty-Acid Dimers in CCl_4 and in the Pure Liquid State (Melt)

The IR spectra of octanoic acid in the liquid state in the temperature range 296–346 K (23–73°C) indicated that the acid molecules are always self-associated to form dimers by the hydrogen bond between the two carboxyl groups [8]. Namely, the strong absorption band at 1710 cm^{-1} due to the C=O stretching vibration and the relatively broad band at 920 cm^{-1} due to the OH out-of-plane bending vibration of the carboxyl group (assigned to the cyclic hydrogen-bonded dimer) were completely unaltered throughout the temperature range. Another researcher [9] designated, from the magnitude of the mutual diffusion coefficient and its concentration dependence, that the carboxylic acids in CCl_4 at 298 K were present almost entirely as dimers and gave no indication of further association.

To determine more quantitatively the degree of dissociation, α_0, of dimer of oleic acid into its free molecules in CCl_4 at its low concentration region, vapor pressure osmosis measurements were carried out [10].

Figure 53.9 shows the concentration dependence of α_0 at various constant temperatures. The α_0 value increases slightly with decreasing its concentration and increasing temperature: In its concentration from 5×10^{-3} to 2.6×10^{-2} mol dm^{-3} at 50°C, α_0 ranges from 0.35 to 0.22 molar fraction of dimer concentration. Thus, even in the dilute solutions the dissociation of the acid dimers into the monomeric species is not significant: Most fatty acid molecules exist as dimers in a non-polar solvent such as CCl_4 [10].

The degree of dissociation α of oleic acid dimers into monomers in the pure liquid state was also quantitatively determined through the NIR spectroscopic observations [10, 11], in which the temperature dependence of the absorbance intensity of the 1445-nm band assigned to the first overtone of the stretching mode of the free OH of the carboxyl group of oleic acid was observed. To evaluate α, the molar absorption coefficient, ε_{OH}, of the 1445-nm OH band for fatty acid is absolutely essential. However, the Lambert–Beer law was not applicable even to the extremely low concentrated samples of oleic acid in CCl_4. This is because the hydrogen bonding between the two carboxyl groups is too strong. To obtain the ε_{OH} value, the reciprocal apparent molar absorption coefficient for the 1445-nm OH band was extrapolated

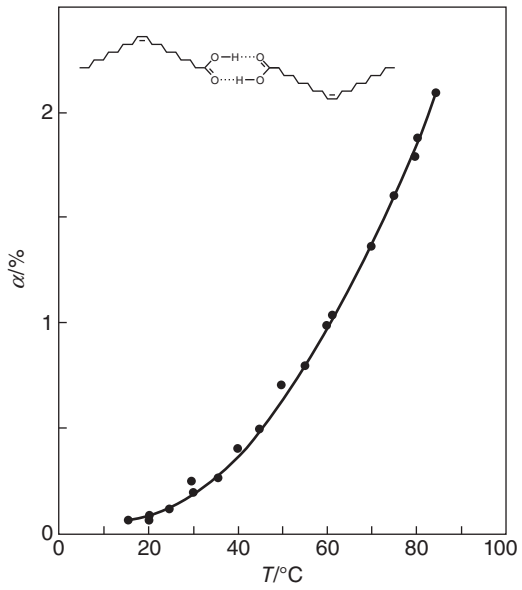


FIGURE 53.10 Temperature dependence of dissociation (α) of oleic acid dimer into its monomers in the melt. A schematic drawing of oleic acid dimer is inserted. (Adapted from Iwahashi et al. 1995 [10], pp. 697–701. © Royal Society of Chemistry; reproduced with permission.)

to that at zero concentration [11]. The obtained ε_{OH} value, however, gave a ten times larger degree of dissociation than its reliable value for oleic acid [9]: This is a typical failed case in the analysis of spectra of the samples having strong self-association ability.

Combination of NIR absorbance for a sample of oleic acid in CCl_4 and degree of dissociation, α_0, obtained through the vapor-pressure osmosis measurements gave a reliable ε_{OH} value for the 1445-nm band of oleic acid. Using this ε_{OH} value, reliable α values in the pure liquid state were determined as a function of T [10] as shown in Fig. 53.10

The dissociation of oleic acid dimer is not so large, although it slightly increases with increasing temperature: α is almost zero at room temperature and ~2% even at 80°C [10]. Other normal fatty acids (C8–C18) gave also similar results [12]. Thus, it is concluded that the fatty-acid dimers are the units in the molecular transfer and segmental movements in the pure liquids and even in nonpolar solvent within these temperature and concentration regions.

53.4 INTRA- OR INTERMOLECULAR MOVEMENTS OF LIPIDS

53.4.1 Segmental Movements (Intramolecular Movements)

^{13}C-NMR spin–lattice relaxation time T_1 for the different carbon atoms along the hydrocarbon chain of lipids is related to the segmental motion (specially, rotational tumbling motion) in the lipid molecules [13, 14]. In addition, as the ^{13}C-NMR spin–lattice relaxation of a protonated carbon is overwhelmingly dominated by dipole–dipole interactions with the attached protons, T_1 for the carbon atom in a segment is related to the number of directly bonded hydrogens N and the effective correlation time τ_c for the rotational movement of the segments in the sample molecule [13, 14]. T_1 is given in terms of N and $1/\tau_c$ as follows:

$$T_1 = \frac{r_{CH}^6}{N\left(\frac{h}{2\pi}\right)^2 \gamma_c^2 \gamma_H^2}\left(\frac{1}{\tau_c}\right) \tag{53.2}$$

where h is Planck's constant, and γ_C and γ_H are the gyromagnetic ratios of ^{13}C and ^{1}H, respectively. r_{CH} is the C–H distance usually about 0.109 nm. Specfically, the reciprocal of τ_c represents the net magnitude of the segmental motion of the carbon.

For alkanes it was reported that the $1/\tau_c$ value for each carbon atom increases with an increase in temperature [13, 14]. At a constant temperature, the movement of the carbon atom at each methyl end of alkane is large, while that at the gravitational center of the molecule is small. The $1/\tau_c$ value for the carbon atom located at the same position, counted from the methyl group for the alkanes at each constant temperature, decreases with an increase in the molecular length of alkane. For alcohols that form polymer through the hydrogen bonding among OH groups, the movement of the carbon atom at methyl end is also large and that adjacent to the hydrogen bonded atom is small [14]. For fatty acids, which exist as dimers, the movement of the carbon atom at the methyl end is large, while that of the carbon atom neighboring the carboxylic group is small [12,14,15].

For example, Fig. 53.11 shows the relationships between $1/\tau_c$ and the position of carbon atoms for octanoic acid (C8), dodecanoic acid (C12), and hexadecanoic acid (C16) at 80°C (353 K). The segmental movements of the methyl groups at the ends of fatty acids are large and almost equal to each other regardless of their hydrocarbon chain length, while the movements of the other same-positioned carbon atoms counted from the methyl end slightly decrease with an increase in the hydrocarbon chain length.

Figure 53.12 shows the relationship between $1/\tau_c$ and the position of carbon atoms for *cis*-9-octadecenoic acid (oleic acid) having a double bond in its molecule at various temperatures. The $1/\tau_c$ value for each carbon atom increases with increasing temperature. Interestingly, the segmental movements of the carbon atoms at the double-bond position are small; the movements of the carbon atoms neighboring the double bond are larger than those of the carbon atoms at the double bond position. Similar results were obtained for *cis*-6-octadecenoic acid (*cis*-6) and *cis*-11-octadecenoic acid

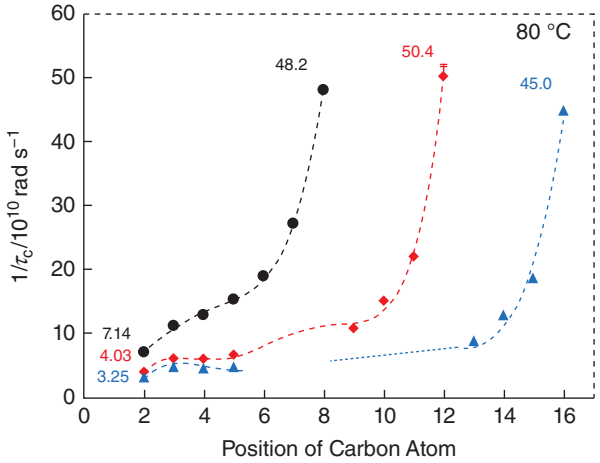


FIGURE 53.11 Relationship between $1/\tau_c$ (indicator of segmental movement) versus position of carbon atoms for octanoic acid (●), dodecanoic acid (◆) and hexadodecanoic acid (▲) at 80°C.

(*cis*-11) [15]. The segmental movements of the carbon atoms of *trans*-9-octadecenoic acid (elaidic acid: *trans*-9) neighboring its double bond are smaller than those of *cis*-type unsaturated fatty acids. Stearic acid, as a whole, exhibited movements similar to those of *trans*-9. Thus, the segmental movements of the fatty-acid dimer would resemble a dumbbell. These fatty-acid dimers gather together and construct their liquids.

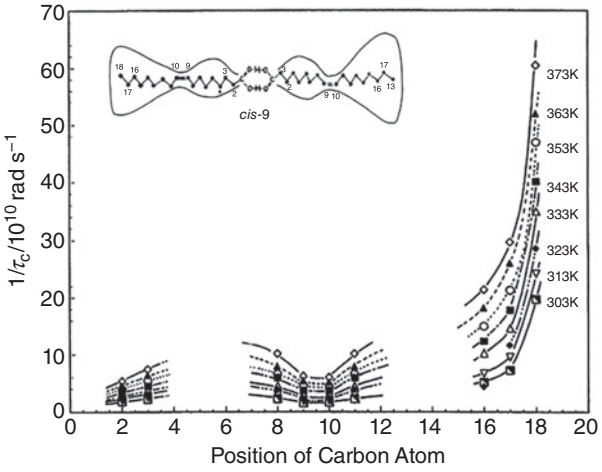


FIGURE 53.12 Relationship between $1/\tau_c$ (indicator of segmental movement) versus position of carbon atom for *cis*-9-ocatdecenoic acid at various constant temperatures: 303 (□), 313 (▽), 323 (◆), 333 (△), 343 (■), 353 (○), 363 (▲), and 373 K (◇). Inserted is a schematic drawing of the segmental movement of oleic acid dimer. The segmental movements of the fatty-acid dimer resemble a dumber. (Adapted from Iwahashi et al. 2000 [15], pp. 6186–6194. © American Chemical Society; reproduced with permission.)

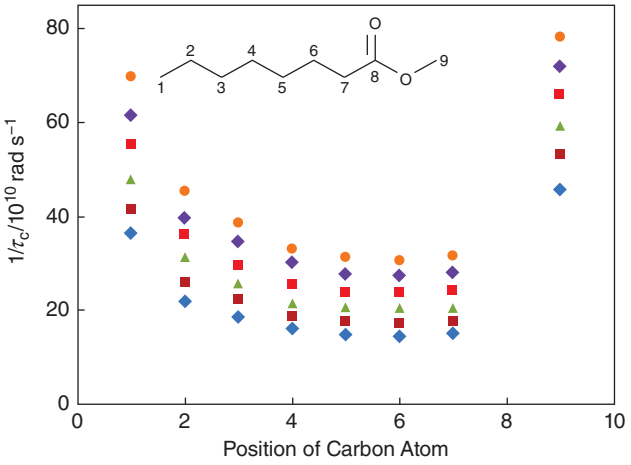


FIGURE 53.13 Relationship between $1/\tau_c$ versus position of carbon atom of methyloctanoate at various constant temperatures: 303 (◆), 313 (■), 323 (△), 333 (■), 343 (◆), and 353 K (●). Position of each carbon atom is counted from the methyl group of main acyl group as shown in the inserted model.

Figure 53.13 and 53.14 show the relationships between $1/\tau_c$ versus position of carbon atoms of methyloctanoate and 2-ethtylhexyloctanoate molecules at various temperatures, respectively. As a whole, the segmental movements increase also with increasing temperature. The movement of methyl group positioned at each end of ester molecules is large, while the movements of the carbon atom near the gravitational center and at the branched position are extremely small compared to that of the carbon atom at other positions [16]. This implies that the fatty acid esters do not form self-associated aggregates in the liquid state.

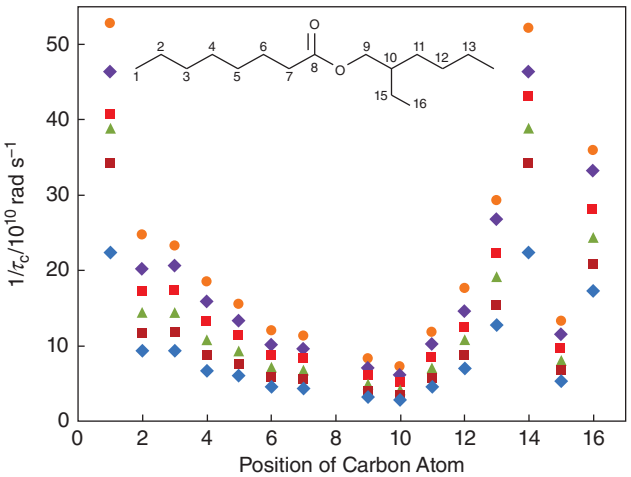


FIGURE 53.14 Relationship between $1/\tau_c$ versus position of carbon atom of 2-ethylhexyoctanoate at various constant temperatures: 303 (◆), 313 (■), 323 (▲), 333 (■), 343 (◆), 353 K (●). Position of each carbon atom is counted from the methyl group of main acyl group as shown in the inserted model.

53.4.2 Intermolecular (Transfer) Movements and Apparent Hydrodynamic Radius for Alkane, Alcohol, Fatty Acid, and Fatty-Acid Ester

As derived by Stokes, the ordinary frictional coefficient (f_0) for the spherical object contacting with fluid layer is given by $f_0 = 6\pi\eta a$, where a is radius of a spherical object moving in a fluid continuum, π the ratio of the circular constants, and η the viscosity of the solvent. The movement of the object is impelled by a force due to the pressure built up in front of it ($= 4\pi\eta a$) and a frictional force parallel to its surface ($= 2\pi\eta a$); these two forces add up to the value given for the above ordinary frictional coefficient. Even through the fluid does not stick to the surface of the spherical object (the slip boundary condition), some fluid in front of the object has to be displaced when the object moves [17]. On the other hand, the side surface of the object does not displace any fluid since the frictional force parallel to the surface of the spherical object is very small. Thus, the overall frictional force (f) becomes $4\pi\eta a$. Thus, for a moving spherical particle almost equal in size to surrounding solvent molecules under slip boundary condition, the Stokes' equation for frictional coefficient f is given by [18–20].

$$f = 4\pi\eta a \tag{53.3}$$

On the other hand, from the Einstein's equation for diffusion, the frictional coefficient is expressed by

$$f = kT/D \tag{53.4}$$

where k is the Boltzmann constant, T the absolute temperature, and D the diffusion coefficient. By combining Eqs. (53.3) and (53.4), the apparent hydrodynamic radius (Stokes–Einstein radius) a is given by

$$a = \frac{kT}{4\pi\eta D} \tag{53.5}$$

This is the Stokes–Einstein formula under the slip boundary condition [17–23]. Using this Stokes–Einstein formula, the dynamic conformation of a normal alkane molecule (C5–C14) in the pure liquid state was estimated [8].

In Figure 53.15 the apparent hydrodynamic radii a at 298.1 K for the normal alkanes (C5–C14) (open circles) are plotted against the number of carbon atoms. The a value seems to increase slightly with an increase in the number of carbon atoms. However, as a whole, these a values for alkanes are almost constant (*ca.* 2.5×10^{-10} m on average), which is comparable to van der Waals radius of the cross section of the hydrocarbon chain (2.4×10^{-10} m). The almost constant hydrodynamic radius suggests that alkane molecules in the pure liquid state take a flexible rodlike conformation, randomly orientate, and entangle with one another; the free rotational (end-over-end) motion as well as transverse

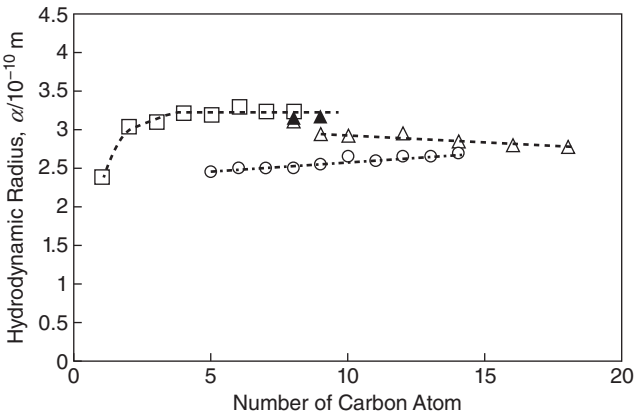


FIGURE 53.15 Apparent hydrodynamic radius a for alkanes (C5–C14), alcohols (C1–C8) and *n*-fatty acids (C8 and C9) at 298.1 K: ○ denotes alkanes; □, alcohols; ▲, fatty acids. In addition, △ denotes fatty acids (C8–C18) at 343 K. (The figure for alkane and alcohol are adapted from Iwahashi et al. 1990 [8], pp. 2154–2158; the figure for fatty acid is from Iwahashi et al. 2002 [12], pp. 157–164. © Chemical Society of Japan; reproduced with permission.)

motion of the alkane molecule would be severely restricted owing to the lack of enough space; the alkanes would translate only longitudinally along the axes of the flexible rod-like molecules. Specifically, the apparent hydrodynamic radius a obtained for alkanes reflects the radius of the cross section of the methyl parts at the terminal positions of alkane molecule and scarcely relates to its molecular length.

In the same graph, a value for normal alcohol (open square) at 25°C (298.1 K) is plotted against the number of carbon atoms in the hydrocarbon chain. The a value increases up to 1-propanol and saturates at 1-butanol to be constant ($\sim 3.2 \times 10^{-10}$ m). This also indicates that the alcohol molecule longer than 1-butanol molecule also takes a rodlike conformation with a constant cross section [24]. This would be supported by the results for octanoic and nonanoic acids.

The a value of octanoic or nonanoic acid at 25.0°C (298.1 K) (solid triangle) is approximately 3.1×10^{-10} m, which is close to that of normal alcohol. Of course, fatty acid exists as dimers, while alcohol usually exists as polymers. Thus it is presumed that alcohol molecules move not as large polymers but as linearly self-associated dimers as well as fatty-acid molecules at least in the translational motion because of their relatively low hydrogen-bonding ability [8]. As an additional example, the a values for fatty acids (C8–C18) (open triangle) at 70°C (343 K) are plotted against the number of carbon atoms in the same graph. Although the a value decreases slightly with increasing number of carbon atoms, as a whole, it is almost constant.

In general, the Stokes–Einstein formula under a slip boundary condition is applicable only for a spherically shaped molecule having a similar size to that for the surrounding solvent molecules [25]. However, the results for

the normal alkanes, alcohols, and fatty acids indicate that the formula is sufficiently applicable even to rodlike molecules having a relatively long hydrocarbon chain.

In the case of a rodlike molecule in its pure liquid, the free rotational (end-over-end), as well as transverse motion of the rodlike molecule, is severely restricted [26] even with slip between the molecules since the object molecule has to displace many other molecules in its transversal motion or end-over-end rotation. This is because the liquid has very little space for motion, as assumed by the fact that only ~10% increases in volume at a solid-melt transition for a long-chained fatty acid [4]. Thus, only a longitudinal translation is allowed. In the longitudinal motion of a flexible rodlike molecule, as the object molecule should displace some other molecules only in front of its molecules surrounding the object molecule, the resistance force comes to be only $4\pi\eta a$.

Other authors [27] also suggested that the elementary diffusion process for normal alkanes, alcohols and fatty acids involves the translation of extended molecule parallel to its chain axis, based on the fact that the activation energies of self-diffusion increase with increasing molecular weight of the alkanes.

In Fig. 53.16, a values for methylesters of fatty acid (C8–C16), butyldodecanoate, isobutyldodecanoate, 2-ethylhexylesters of fatty acid (C8–C16) at 353 K (80°C) are plotted as a function of the number of carbon atoms in their main acyl groups [16]. Obviously the a values of esters of the same kind are almost equal to each other regardless of the chain length of the acyl group in the ester molecule. The a values for fatty acid esters are larger than those for the corresponding normal fatty acids (open circles). By comparison of the a values for the various fatty acid esters having 12 carbon atoms in their main acyl groups, it has become apparent that the fatty-acid ester possessing the larger sidechain has the larger a value. Namely, the sidechain in the fatty-acid ester presumably determines the overall apparent hydrodynamic radius in the longitudinal translation of the fatty-acid ester.

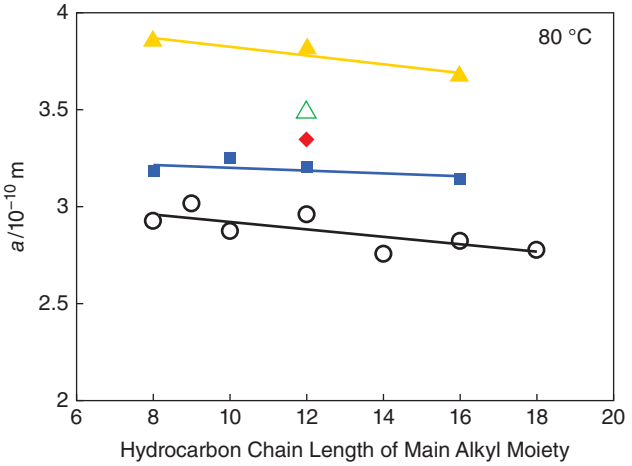


FIGURE 53.16 Apparent hydrodynamic radius a for various fatty-acid esters at 80°C (353.1 K): ▲ denotes 2-ethylhexyl esters (C8–C16); △, isobutyl ester (C12); ◆, butyl ester (C12); ■, methyl esters (C8–C16). As reference standard, a for fatty acid (C8–C18) at 80°C (open circle) is also plotted.

53.5 LIQUID STRUCTURES OF FATTY ACIDS

53.5.1 Fatty Acid Having a Longer Hydrocarbon Chain

The self-organization of fatty acids in the liquid state has been thoroughly studied by using near-infrared spectroscopy and vapor pressure osmosis on various fatty acids [2]. Fatty acids exist mostly as dimers, even at high temperature, where the dimers are the units in their intra- and intermolecular movements. These were found to aggregate to form clusters possessing the structure of a quasismectic liquid crystal, where the long-chained fatty acid dimers arrange longitudinally and alternately to form an interdigitated structure in the clusters. This has been determined based on measurements of viscosity, density, and NMR and X-ray diffraction [2]. The clusters most likely determine the liquid property of the fatty acid. [12,15,28–30].

As a typical example, Fig. 53.17 shows the temperature dependence of density for five kinds of fatty acids [*cis*-6-, *cis*-9- (oleic), *cis*-11-, *trans*-9-ocatdecenoic (elaidic) and octadecanoic (stearic) acids] in the pure liquid state [15]. From this graph, two questions are raised:

1. Why are the densities of three kinds of *cis*-type unsaturated fatty acids almost equal to each other?
2. Why does stearic acid possess the lowest density?

The lowest density of stearic acid is contract to our expectance based on chemical conformations, melting temperatures, and heats of fusion. The stearic acid molecules having fewer *gauche* structures should easily aggregate with each other and orient more tightly than the molecules of the unsaturated fatty acids.

X-Ray diffraction measurements for the liquid samples of the five kinds of fatty acids have solved the above questions and riddles.

In Table 53.1, the short and long spacings for the five kinds of fatty acids are listed. The short and long spacings are $\sim 4.6 \times 10^{-10}$ m and *ca.* 24-26 $\times 10^{-10}$ m, respectively. The long spacing seems to be too small, because two fatty acid molecules always form a dimer, which is $\sim 50 \times 10^{-10}$ m in length.

The incomprehensive value for the long spacing can be explained by assuming the existence of clusters possessing a unique arrangement of the dimerized molecules in the liquid of fatty acid.

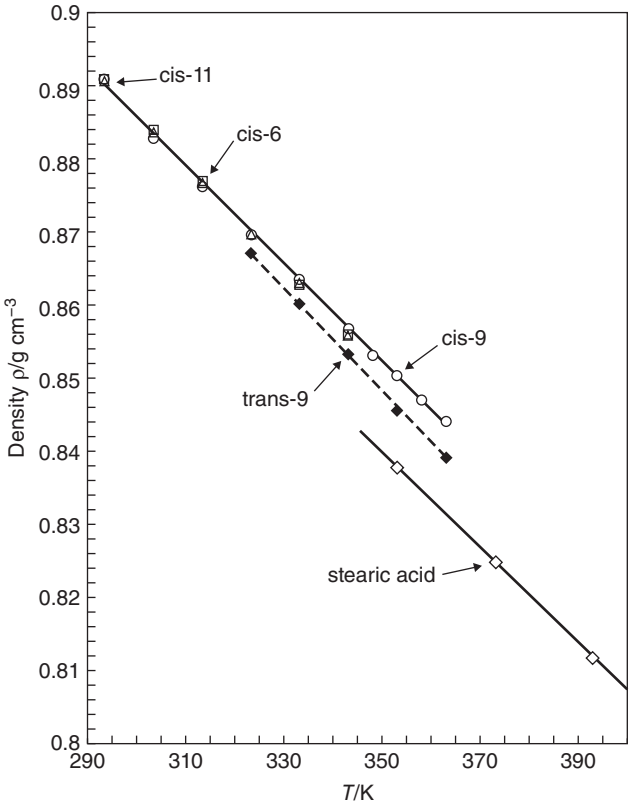


FIGURE 53.17 Temperature dependence of density ρ for various fatty acids: □ denotes *cis*-6; ○, *cis*-9; △, *cis*-11; ◆, *trans*-9; ◇, stearic acid. (Adapted from Iwahashi M., Kasahara Y. (2011). Dynamic molecular movements and aggregation structures of lipids in a liquid state. *Curr. Opin. Colloid Interface Sci.* **16**, 359–366. ©: Elsevier Ltd.; reproduced with permission.)

As represented in the schematic drawings for *cis*-9 and *cis*-11 in Fig. 53.18, the dimerized acid molecules arrange longitudinally and alternately to make an interdigitated structure. The dimerized carboxyl groups in one dimer and the methyl groups at the terminal of the neighboring dimers are aligned alternately in the same lateral plane. If the dimerized acid molecules take this intergitated structure, the methyl and methylene groups near the terminal positions of the acid molecules are able to move largely, because the movements of the carbonyl groups in the neighboring dimers are restricted. This structure allows the most compact packing for the dimerized molecules of the fatty acids. *cis*-6 would have almost a same cluster structure and a liquid structure as *cis*-9 and *cis*-11 [15]. This is the reason why the three kinds of *cis*-type unsaturated acids have a similar density *vs*. temperature profile to each other as shown in Fig. 53.17.

TABLE 53.1 Short and Long Spacings for *cis*-6, *cis*-9, *cis*-11, *trans*-9, and Stearic Acid Having 18 Carbon Atoms Near Their Melting Points

	T (K)	Short Spacing (10^{-10}m)	Long Spacing ($^{-10}$m)
cis-6	304	4.58	24.2
cis-9	298	4.57	23.8
cis-11	298	4.57	24.1
trans-9	319	4.59	25.0
Stearic acid	343	4.66	25.7

"Short spacing" means the distance among the neighboring fatty-acid molecules.

Source: Adapted from Iwahashi et al. 2000 [15], pp. 6186–6194. © American Chemical Society; reproduced with permission.

The long spacings for stearic acid and elaidic acid are larger than those for the *cis*-type unsaturated fatty acids, as listed in Table I. Additional X-ray diffraction experiments at various temperatures also revealed that the long spacing for stearic acid exceeds those for *cis*-type acids, while the short spacing for stearic acid was less than those for the *cis*-type acids [15]. Namely, stearic acid molecules are more extended and have a shorter lateral distance than the *cis*-type acid molecules. This indicates that stearic acid molecules also have an interdigitated lamellar structure in the liquid state and that the straight, rod-like molecules of stearic acid aggregate tightly with each other to form rigid clusters.

The rigid clusters aggregate randomly to produce many spaces among the clusters as shown in Fig. 53.19. The liquid structure may resemble the "house of cards" structure often found in bulky clay [31]. The spaces produce low density for the liquid of stearic acid. However, the real distance between the interacting molecules in the cluster of stearic acid is so small that the molecules in the cluster cannot move easily because of the large attractive forces (i.e., mainly by van der Waals forces) among the molecules. This causes the low self-diffusion coefficient of stearic acid compared to those of *cis*-type unsaturated fatty acids [15]. On the other hand, the flexible molecules of the *cis*-type unsaturated fatty acid make similar clusters, which seem to be soft, aggregate randomly with each other to construct a liquid. The softness of the clusters prevents the formation of the spaces among them. Thus, as a whole, the *cis*-type unsaturated fatty acids seemingly have higher density than stearic acid. As the interaction among the molecules in the cluster of the *cis*-type acid is not strong, the molecules of the *cis*-type acid can move more easily than those of stearic acid [15].

53.5.2 Fatty Acid Having a Medium Hydrocarbon Chain

In Fig. 53.20 the density of normal fatty acid (C2–C18) at 80°C (353K) is plotted against the number of carbon atoms (Cn). Extremely high density of formic acid (C1-acid) would result from the formation of polymer even in the liquid state. The density of fatty acid, except formic acid, decreases gradually with increasing chain length (Cn) of fatty acid. Interestingly, however, the inclination of the density curve apparently changes at C12. This relatively steep change in

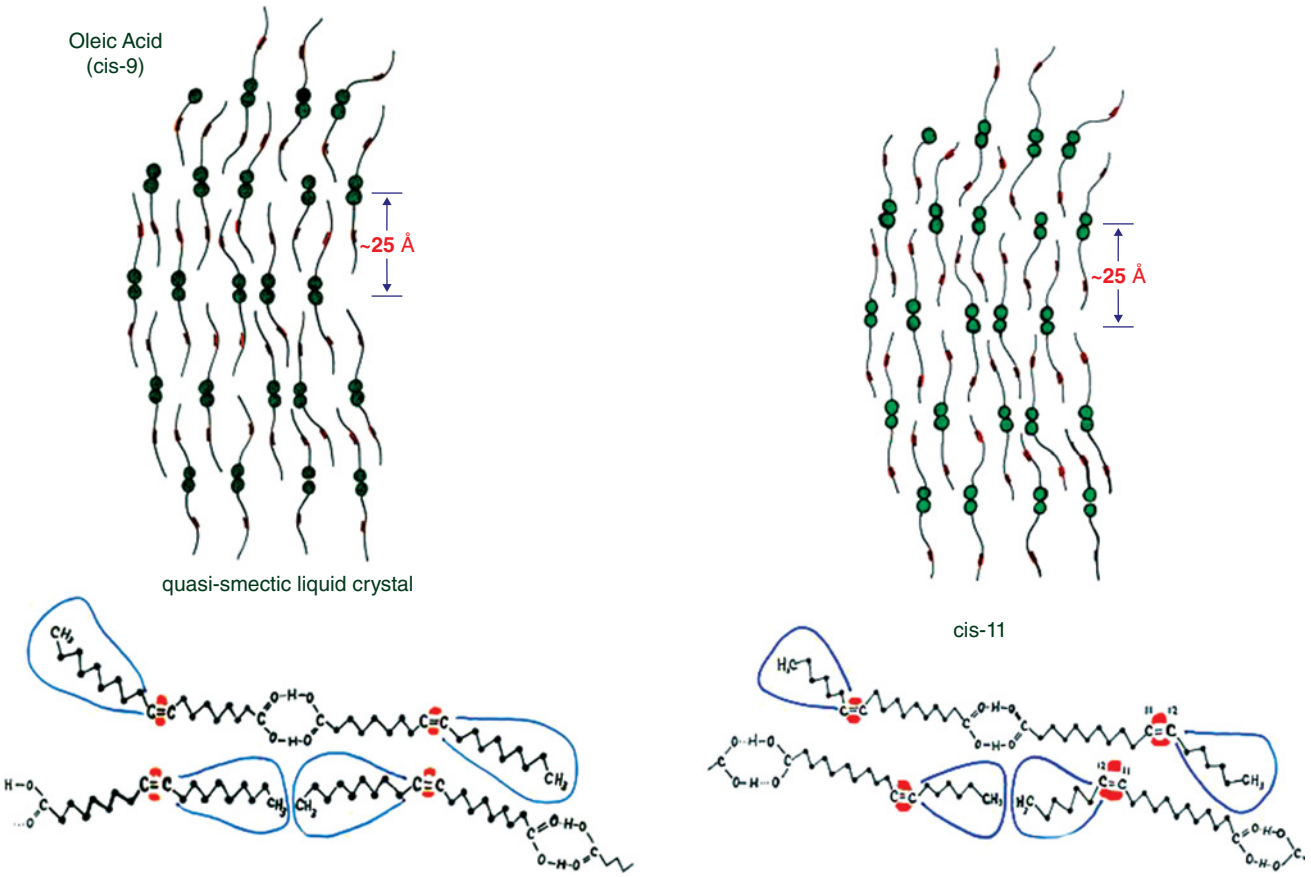


FIGURE 53.18 Cluster models, proposed for the dimers of *cis*-9 or *cis*-11 having 18 carbon atoms, in the liquid state. The clusters take the structure of a quasismectic liquid crystal. This structure allows the most compact packing for the dimer molecules of fatty acids. Below drawings are arrangements proposed for the dimers of *cis*-9 or *cis*-11 molecules in the cluster, respectively; *cis*-6 would take a similar cluster structure. (Adapted from Iwahashi 2000; 104:6186–6194, © American Chemical Society; reproduced with permission.)

inclination suggests that the microliquid structure (cluster structure) of the normal fatty acid is different below and above C12. Above C12 the long-chained fatty acid dimers would arrange longitudinally and alternately to make an interdigitated structure in the clusters, as being described for the fatty acids having 18 carbon atoms. Then what structure does the fatty acid having a medium length hydrocarbon chain take?

X-Ray diffraction, self-diffusion coefficient, ^{13}C-NMR spin–lattice relaxation time, near-infrared (NIR) spectroscopy, and ^{1}H-NMR chemical shift measurements for the samples of octanoic acid in its melt and in its CCl_4 solution were carried out; it became clear that the dimers of fatty acid having a moderate-length hydrocarbon chain construct also the clusters having a smectic liquid crystal-like structure in the melt and also in a non-polar solvent [32].

For example, Fig. 53.21 shows the temperature dependence of the long spacing for the neat sample of octanoic, oleic, or stearic acid. The long spacing for octanoic acid being longer than its molecular length increases gradually up to 350 K and then steeply with increasing temperature, while those for stearic and oleic acids maintain almost constant value regardless of temperature.

Figure 53.22 represents the schematic drawings of the clusters for octanoic acid (a) and stearic acid (b), respectively. The dimers of stearic acid are completely interdiginated in the cluster, while the dimers of octanoic acid are half-interdiginated. Thus the cluster of octanoic acid is thought to be not so stable compared to that of longer chained fatty acid such as oleic acid or stearic acid [32].

53.6 EFFECT OF CHOLESTEROL AND OTHER ADDITIVES ON THE CLUSTER STRUCTURE AND PROPERTIES OF OLEIC ACID

It is known empirically that cholesterol, one of lipids, increases the viscosity of oleic acid. The effect of cholesterol

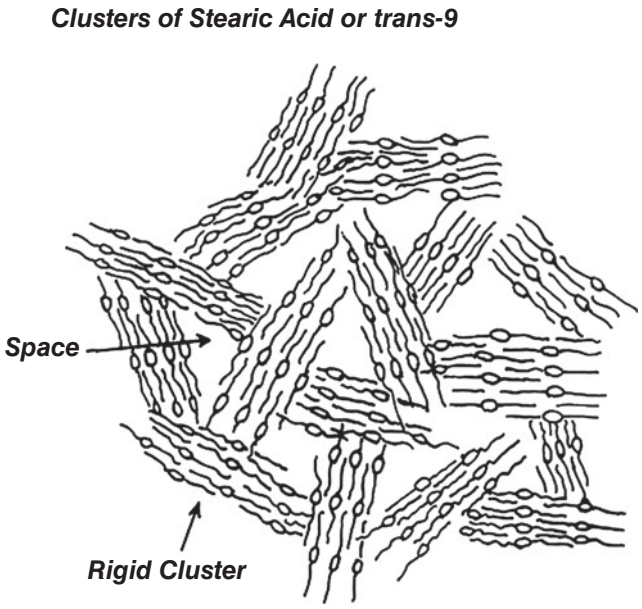


FIGURE 53.19 Schematic drawing of the clusters composed of stearic acid dimers. The straight, rodlike molecules of stearic acid aggregate tightly to form rigid clusters. These rigid clusters aggregate randomly to form a liquid having many spaces. The spaces produce low density and, consequently, a large apparent volume for the liquid of stearic acid.

and other additives on viscosity, self-diffusion coefficient, and intramolecular movements of oleic acid was investigated to clarify the mechanism of the effect of cholesterol on the intermolecular and intramolecular (segmental) movements of oleic acid in the liquid state [30].

Figures 53.23 and 53.24 show the effects of additives on the viscosity and self-diffusion coefficient of oleic acid,

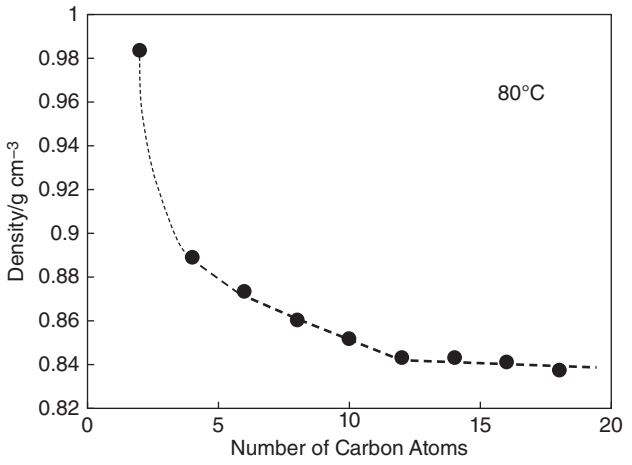


FIGURE 53.20 Density versus number of carbon atoms of normal fatty acids (C2–C18) at 80°C. (Original data are from Ref. 1.) Formic acid is an exception because it is thought to form polymer even in the liquid state.

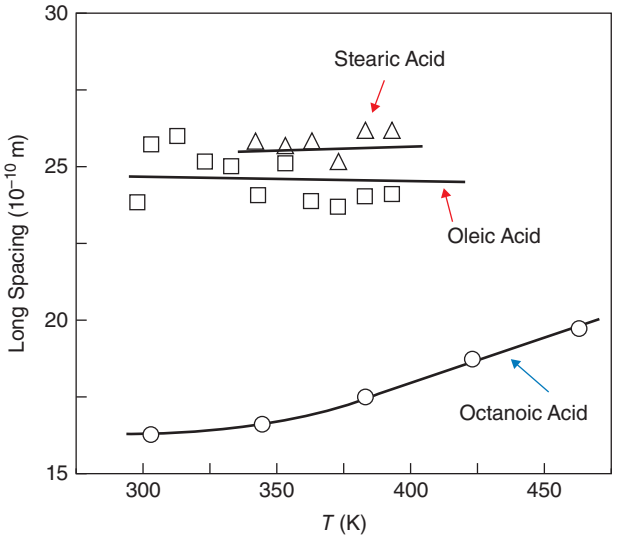


FIGURE 53.21 Temperature dependences of long spacing for octanoic acid (○), oleic acid (□), and stearic acid (Δ). (Adapted from Matsuzawa et al. 2013 [32], pp. 25–32. © Scientific Research Publishing, Inc.; reproduced with permission.)

respectively. The additives containing a steroid ring increase the viscosity of oleic acid, while the small additives such as ethanol and benzene decrease it; the former additives also decrease the self-diffusion coefficient, while the latter additives increase it. In particular, cholesterol significantly increases the viscosity and reduces the self-diffusion coefficient, while ethanol decreases the viscosity and increases the self-diffusion and intramolecular movements of oleic acid.

Here, two experimental findings exist for cholesterol and ethanol: (1) both cholesterol and ethanol possessing one OH

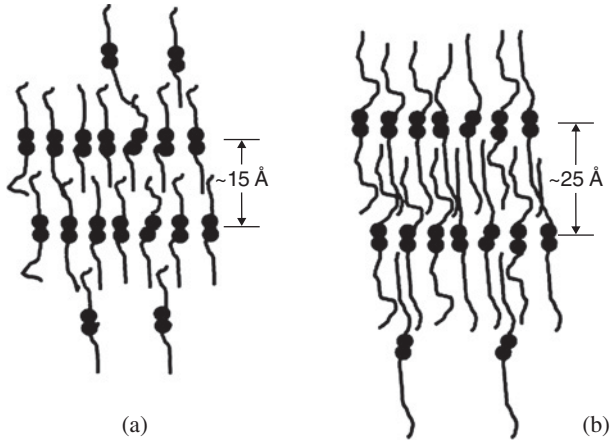


FIGURE 53.22 Cluster models for (a) octanoic acid and (b) stearic acid. Dimers in the cluster of stearic acid are completely interdiginated, while the dimers of octanoic acid are half-interdiginated. (Adapted from Matsuzawa et al. 2013 [32], pp. 25–32. © Scientific Research Publishing, Inc.; reproduced with permission.)

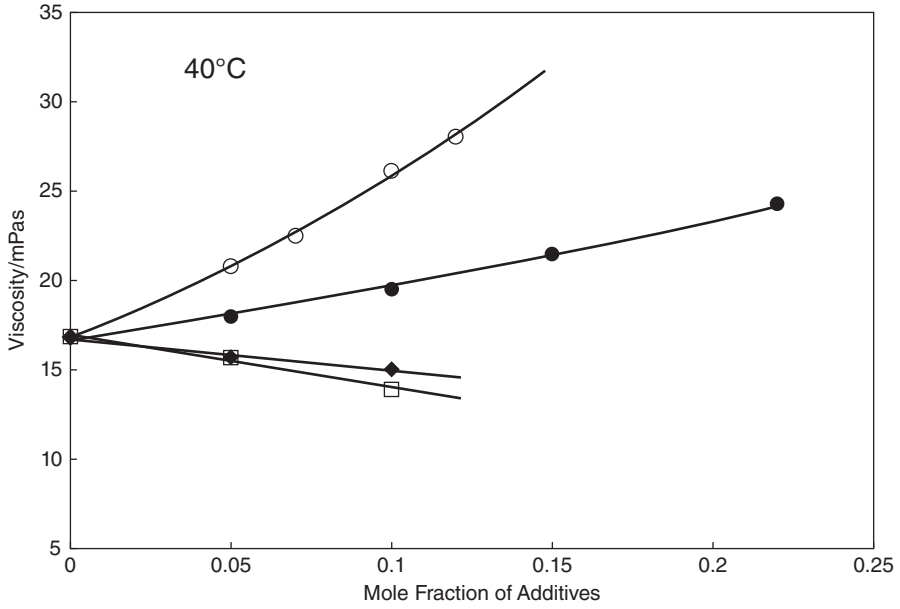


FIGURE 53.23 Effect of various additives on viscosity of oleic acid at 40°C (313 K): ○ denotes cholesterol; ●, cholestane; ◆, ethanol; □, benzene. (Adapted from Iwahashi et al. 2007 [30], pp. 740–747. © American Chemical Society; reproduced with permission.)

group promote similarly the upfield shift of the ^{1}H-NMR signal of the carboxyl group of oleic acid [30] and (2) the difference spectra obtained for the samples of oleic acid–cholesterol mixtures really resemble those for oleic acid–ethanol mixtures. The IR difference spectra were obtained by subtracting the spectrum relatively corrected for each pure component (oleic acid, cholesterol or ethanol) from the spectrum for the mixture (composed of oleic acid/cholesterol or oleic acid/ethanol). The IR difference spectra obtained indicate only the situation of hydrogen bonding [30].

The above two observations indicate that oleic acid makes a complex with cholesterol as well as with ethanol [30].

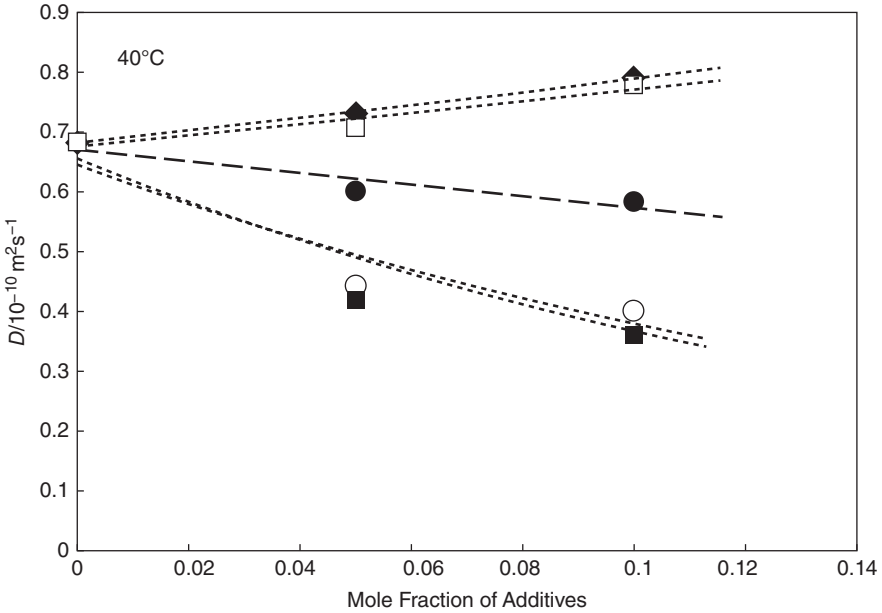


FIGURE 53.24 Effect of various additives on self-diffusion coefficient D of oleic acid at 40°C (313 K): ○ denotes cholesterol; ■, cholestanol; ●, cholestane; ◆, ethanol; □, benzene. (Adapted from Iwahashi et al. 2007 [30], pp. 740–747. © American Chemical Society; reproduced with permission.)

Then, why does cholesterol, as opposed to ethanol, decrease the inter- and intramolecular movements of oleic acid? This question can be addressed as follows.

The complex formed from cholesterol and oleic acid, whose structure may resemble cholesteryl oleate, most likely penetrates into clusters composed of oleic acid dimers. Such complexes improve the packing of dimers inside the clusters by attraction between their hydrophobic moieties of cholesterol and oleic acid molecules. The improvement of packing would increase the viscosity and decrease the self-diffusion coefficient and the intramolecular movements of oleic acid; the formation of the oleic acid–cholesterol complex would be the origin of the lowering of the molecular movements of oleic acid. On the other hand, the complex composed of oleic acid and ethanol also penetrates into the cluster consisting of oleic acid dimers. However, it does not condense the arrangement of the oleic acid dimers in the cluster; instead, it disturbs the arrangement because the hydrophobic moiety of ethanol is too small, even if the position of the oleic acid/ethanol complex in the cluster is same as that of the oleic acid/cholesterol complex [30].

53.7 AGGREGATED STRUCTURES AND PROPERTIES OF ACYLGLYCEROLS

53.7.1 Triacylglycerols

To date, three models for liquid-state ordering in triacylglycerols (TGs) have been proposed. By X-ray diffraction, one investigator [33, 34] proposed that TGs were present as domains approximately 20 nm in diameter and maintained a structure similar to that in the crystalline state, except that the chains were melted. Specifically, the structure for liquid TGs is small pseudolamellar domains (smectic liquid crystal); the lamellar domain remains 20–40°C above the melting point of TG and the domains decrease in size with an increase in temperature. In the domain TG molecules have a chairlike conformation (h-conformation).

By neutron diffraction, another author [35] proposed a nematic liquid crystal model for the TG melt. In this model, TG molecules have also a chair-like conformation (h-conformers) whose three hard aliphatic chains are orientated to form domains having a nematic liquid crystal structure. Another investigator [36] proposed that TG molecules have splayed, disordered chains in the liquid state. Namely, the TG molecules take a Y-shaped conformation (Y-conformers), in which the three soft hydrocarbon chains have an angle of 120°between them; the Y-conformer disks loosely attach to each other and stack into flexible, short cylindrical rods. They also suggested that the h-conformers exist at low temperature, and Y-conformers exist at high temperature. The Y-conformer model was supported by using molecular dynamics simulation [37]. In conclusion, the true liquid structure or the aggregation structure of TGs in the melt needs still further investigation.

53.7.2 Diacylglycerols

Regrettably, the liquid structure for diacylglycerols has not yet been clarified.

In general binary mixture (*RS*-form) of enantiopure compounds (*R*- and *S*-form) in the solid state can be classified, in terms of the interaction of *R*- and *S*-form molecules in the crystal, into three types of modification: a racemic compound, a solid solution, or a eutectic mixture of *R*- and *S*-crystallites. The three types of modification depend on the strength of interaction between *R*- and *S*-form molecules [38].

The phase diagram of binary mixture of enantiopure and racemic 1,2-diacylglycerol (1,2-DAG) containing palmitic or stearic acid was reported [39]. Racemic mixtures of 1,2-diacylglycerol formed a eutectic mixture (conglomerate) in the highest melting form (β') and a solid solution in the metastable (α) form [3,40]. Transformation from metastable α to highest melting form (β') of racemic 1,2-DAG is extremely slow compared to that of enantiopure even through the liquid state. This is because the racemic β'-form crystal is a mixture of *R*-form and *S*-form crystallites; on the other hand, metastable α-form crystal is a solid solution composed of *R*- and *S*-molecules, which freely mix to each other. Consequently, it is very difficult for *R*- or *S*-molecules in the solid solution to transfer separately and then aggregate to make β'-form crystals composed of only *S*- or *R*-species.

53.7.3 Monoacylglycerol

1-Monoacylglycerols have been used in many fields as harmless detergents. *RS*-1-monoacylglycerols containing even carbon-chain lengths from C12 to C18 are expected to be racemic compounds, as they appear at higher melting temperatures than their optically active *S*-forms do [38]. To confirm this presumption, the thermodynamic and spectrographic properties such as melting temperature, latent heat of fusion, solubility, heat of solution, and infrared and NMR spectra were investigated for the stable β-forms of the optically active *S*- and the corresponding racemic *RS*-1-monostearol in the solid state [41]. The phase diagram for the binary mixture and the IR spectra of *S*- and *RS*-crystals indicated that the *RS*-form is racemic molecular compound consisting of *R*- and *S*-1-monostearol molecules. The latent heats of fusion for *S*- and *RS*-1-monostearol crystals were 82.4 and 75.4 kJ mol^{-1}, respectively. On the other hand, the heats of solution in benzene for *S*- and *RS*-crystals were 86.3 and 99.9 kJ mol^{-1}, respectively. The difference in the heat of solution between the *S*- and *RS*-crystals, 13.6 kJ mol^{-1}, is thought to be attributable to the difference in the extent of hydrogen bonding. This indicates that *R*- and *S*- molecules

in the *RS*-form strongly interact to form a racemic pair not only in the solid state but also in the molten state. Such a racemic pair would dissociate into the free molecules when they are dissolved in a nonpolar solvent. This was supported by comparisons in IR and NMR spectra for both *S*- and *RS*-1-monoacylglycerols in dissolved states and melt.

53.8 NEW APPLICATION OF FATTY-ACID ESTERS

53.8.1 Application of Fatty-Acid Ester as Insulating Oil in Transformers

Ever since the prohibition of the use of polychlorinated biphenyl (PCB), mineral oils have been commonly used again as electrical insulating oil in transformers because of its relatively high electrical insulating ability and fluidity: Fluidity of insulating oil is essential for the exclusion of generated heat. Considering the depletion of resources and environmental problems, natural oils produced by plants are expected to be good electrical insulators in terms of a high dielectric breakdown voltage and environmental safety [42–44]. However, natural plant oils have higher viscosity than do the generally used mineral oils. Now then, fatty-acid esters synthesized from natural plant oils are attracting attention as an environmentally friendly insulating oil having low viscosity. Fatty-acid esters such as methyl octanoate (C8-Me), methyl dodecanoate (C12-Me), 2-ethylhexyl octanoate, and 2-ethylhexyl dodecanoate having high fluidity show excellent moisture tolerance against dielectric breakdown compared to mineral oil [45].

As shown in Fig. 53.25, the electrical breakdown for mineral oil (solid diamonds) occurs below 50 ppm of moisture content, while that for these fatty-acid esters occurs at higher moisture content. In particular, C8-Me (solid square) has the highest protective ability against the electrical breakdown.

To clarify the mechanism for the superior moisture tolerance of fatty-acid esters, the status of dissolved water in the esters was investigated with IR spectroscopic measurements and the computer calculation using the density functional theory (DFT) [45] for the normal vibration frequencies of water existing in fatty-acid ester. The IR spectroscopy and the calculation revealed that water molecules in fatty-acid ester are fairly trapped as a solitary molecule by the ester moiety of fatty acid ester. On the other hand, water molecules in mineral oil may exist as clusters [46], which are assumed to be a trigger in the electrical breakdown of insulating oil [45]. Consequently, fatty-acid esters have a higher tolerance against electrical breakdown than mineral oil. As shown in Fig. 53.26, however, when the moisture content in fatty-acid esters increases and reaches to the ratio of 200/1 (the ratio of the number of ester molecules to one water molecule), the breakdown voltage steeply decreases. This indicates that at the ratio of 200/1, water molecules probably start to aggregate and create the clusters composed of water molecules even in the fatty-acid esters.

53.8.2 An Application of Fatty-Acid Ester for Hepatoma Operation Using a Microcatheter

Hepatoma cells grow and multiply by obtaining nourishment and oxygen from arteries, while ordinary hepatocells,

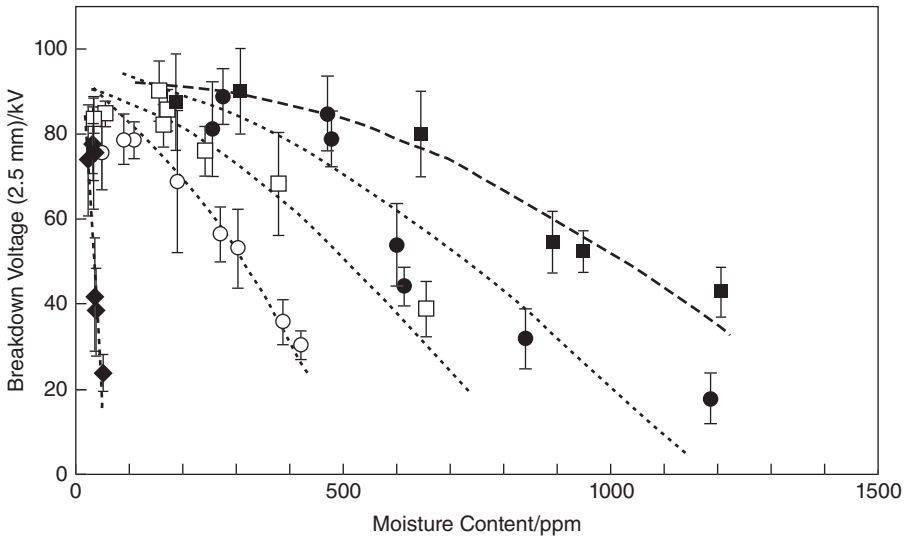


FIGURE 53.25 Breakdown voltage at 2.5-mm gap versus moisture content in mineral oil (◆) and in various fatty acid esters at room temperature (~25°C): ■ denotes C8-Me; ●, C12-Me; □, C8-2EH; ○, C12-2EH. (Adapted from Kasahara et al. 2013 [45], pp. 1223–1229. © American Oil Chemical Society; reproduced with permission.)

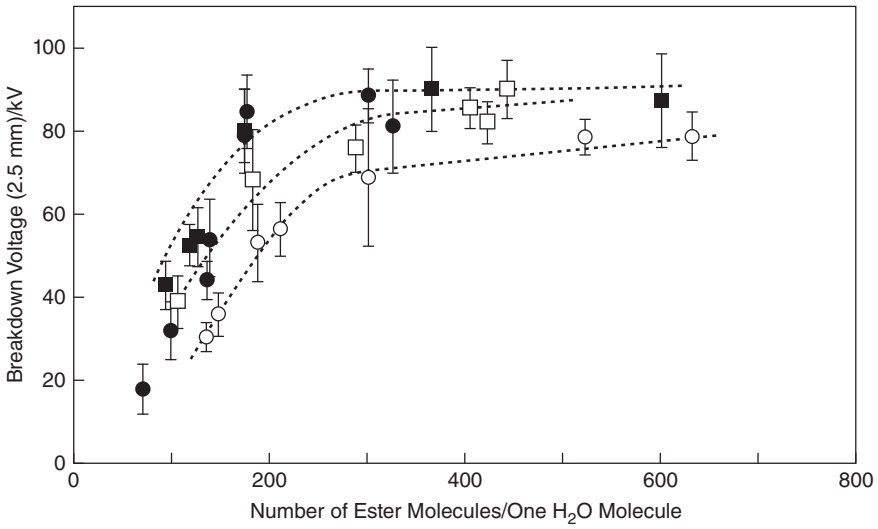


FIGURE 53.26 Relationship between breakdown voltage at 2.5-mm gap for various fatty acid esters including water and the number of fatty-acid ester molecules per one H_2O molecule: ■ denotes C8-Me; ●, C12-Me; □, C8-2EH; ○, C12-2EH. The breakdown voltage for each fatty-acid ester gradually decreases as the number of ester molecules per one H_2O molecule decreases, and then decreases sharply below ~200 ester molecules per one H_2O molecule. (Adapted from Kasahara et al. 2013 [45], pp. 1223–1229. © American Oil Chemical Society; reproduced with permission.)

which receive nourishment and oxygen not only from arteries but also from portal veins (i.e., 25% from arteries and 75% from portal veins). Based on this character of the hepatoma cells, transcatheter arterial chemoembolization (TACE) is an effective treatment for patients with advanced hepatocellular carcinoma (HCC) [47, 48]. In TACE, the final chemoembolization is usually carried out with a piece of gelatin that would disappear within 2 weeks. For TACE, a joint use of a dispersion liquid of anticancer agent in ethylester of iodized fatty acid obtained from poppy seed oil [trivial name *lipiodol* (LPD)] is also recommended to enhance its anticancer effect: LPD has a tendency to gather to hepatoma cells and maintain its position. The fatty acid obtained from poppy seed oil consists mainly of linoleic acid. The iodized ethyl ester of the fatty acid plays as not only a solvent for the lipophilic anticancer agent but also as a liquid contrast medium for X-ray photographic imaging because iodine atom has many electrons.

As one of the anticancer agents, [(1*R*,2*R*)-cyclohexane-1, 2-diamine-*N*,*N*′]bis (tetradecanoate-*O*) platinum [trivial name *miriplatin* (MPT)] has been designed as a lipophic platinum complex that can be easily suspended in LPD [49–51].

Figure 53.27 shows the chemical structure of MPT. In vitro studies have shown that platinum compounds gradually released from MPT suspending in LPD were incorporated into rat hepatoma cells and bound to nuclear DNA to form platinum DNA adducts [52,53]. In several animal models, MPT/LPD suspension had sufficient antitumor effects on hepatic after intrahepatic arterial administration [54,56].

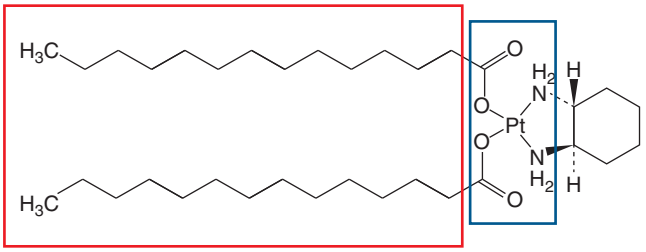
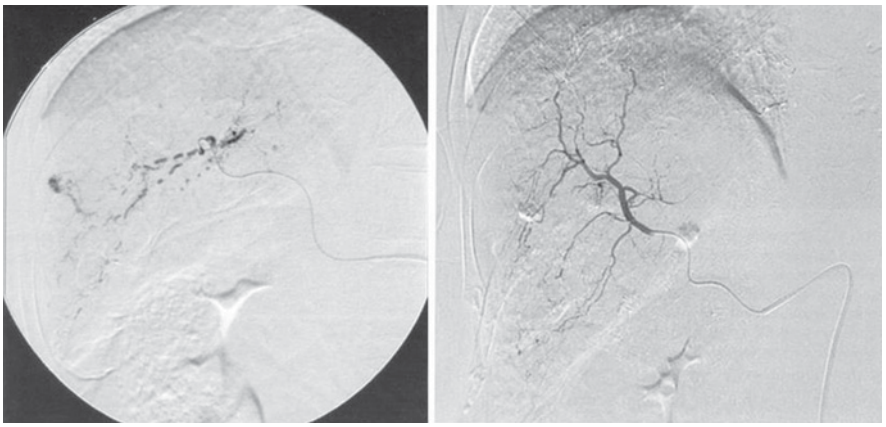


FIGURE 53.27 Structural formula of [(1*R*,2*R*)-cyclohexane-1,2-diamine-*N*,*N*′]bis (tetradecanoate-*O*)platinum. Its trivial name is miriplatin (MPT), which is used as one of the anticancer agents that can be suspended in iodized ethyl ester of fatty acid obtained from poppy seed oil [trivial name lipiodol (LPD)]. Note that the structure of MPT resembles a surfactant having two hydrophobic chains. Two alkyl groups surrounded by a thin square are hydrophobic, and the part surrounded by a thick square is hydrophilic. (Adapted from Tanaka et al. 2011 [50], pp. 39–48. © Dainippon Sumitomo Pharma Co., Ltd.; reproduced with permission.)

The TACE using MPT/LPD suspension is expected to have enhanced therapeutic effect on human HCC. However, in actual clinical practice, the injection of MPT/LPD suspension through a catherter requires high pressure owing to the high viscosity of the suspension. In addition, this high viscosity of MPT/LPD suspension was thought to lead to uneven distribution within HCC, as shown in Fig. 53.28a, which eventually hampers its therapeutic effect. Another team [56] proposed a warming method to reduce the viscosity of MPT/LPD suspension and to improve antitumor effect of



(a) (b)

FIGURE 53.28 The appearance of MPD/LPD suspension within the arteries immediately after its injection in patients who underwent TACE: (a) with MPD/LPD at room temperature and (b) with warmed MPD/LPD. In photo (a), globular or beaded appearance exists; in photo (b), smooth and continuous appearance exists. (Images from Kora et al. 2013 [56], pp. 1023–1029. © Springer; reproduced with permission.)

TACE. By an vitro study, it became clear that warming actually reduced the viscosity and also the injection pressure of MPT/LPD suspension through microcatheters. For example, warming the MPT/LPD suspension up to 40°C significantly reduced its viscosity to almost half that at room temperature (25°C) and injection pressure through microcatheters. Furthermore, the warmed MPT/LPD suspension exhibited a more smooth and continuous appearance within the vascular lumen (Fig. 53.28b) compared to that at room temperature (Fig. 53.28a).

Thus, the warming MPT/LPD suspension method is thought to be superior on its injection and improving antitumor effect. However, the mechanism of reducing pressure on injecting MPT/LPD suspension through a microcatherter and the reason for its continuous flow appearance have not been fully elucidated.

However, on the base of the surface and interfacial chemistry, the reducing pressure and the continuous distribution of the warmed MPT/LPD suspension within vascular lumen are explicable as follows:

LPD is oil (ethylester of iodized fatty acid), while blood is water, although it includes many substances; MPD is a kind of surfactant having two long hydrophobic hydrocarbon chains as shown in Fig. 53.27 As the solubility of MPD in LPD is very low, MPD in LPD usually exists as a dispersion of small, solvated solids.

On injection of MPT/LPD suspension (oil) into blood (water) at room temperature, oil–water interface is newly created. At this moment, MPD molecules (a kind of surfactant) adsorbing at the interface are extremely few because of the extremely low solubility of MPT in LPD (i.e., the low concentration of free MPT molecules in LPD) and their hard translations to the interface because of the high viscosity of MPT/LPD suspension at room temperature. Thus, on injection of MPT/LPD suspension into blood, a large droplet of MPT/LPD suspension (oil), which has a high interface tension, is formed at the end of a microcatherter. The high interface tension produces a high resistance against the injection of MPT/LPD suspension.

On the other hand, on injecting MPT/LPD suspension at a high temperature, the MPT molecules would easily absorb to the newly formed interface since the concentration of the free MPT molecules in LPD is large and the viscosity of the MPT/LPD suspension is low. Thus, on injection of MPT/LPD suspension at a high temperature, the absorption of the free MPT molecules onto the interface newly formed would easily and largely occur. Consequently, the interface tension becomes lower and the resistance against the injection would reduce. Furthermore, owing to the low interface tension the droplet easily becomes small droplets (small emulsions), which appear to be continuous. The small droplets can reach even to thin blood vessels.

In this chapter, the liquid structures of alkanes, alcohols, fatty acids, and fatty-acid esters including TGs are introduced. In practice, in the food industry, cosmetics, and other fields, the liquid contains various acylglycerols and fatty acids simultaneously and has special structures and functions. Therefore, study of the mixed liquid of lipids should be the main objective in future research.

REFERENCES

[1] Small, D.M. (1986). The physics and chemistry of lipids from alkanes to phospholipids. In Hanahan, D.M. (ed.), *Handbook of Lipid Research*, Plenum Press, New York.

[2] Iwahashi, M., Kasahara, Y. (2011). Dynamic molecular movements and aggregation structures of lipids in a liquid state. *Curr. Opin. Colloid Interface Sci.* **16**, 359–366.

[3] Craven, R.J., Lencki, R.W. (2013). The polymorphism of acylglycerols: A stereochemical perspective. *Chem. Rev.* **113**, 7402–7420 (doi:10.1021/cr400212r).

[4] Ralson, A.W. (1948). *Fatty Acids and Their Derivatives*. Wiley, New York, p. 330.

[5] Iwahashi, M., Hayashi, Y., Hachiya, N., Matsuzawa, H., Kobayashi, H. (1993). Self-association of octan-1-ol in the pure liquid state and in decane solutions as observed by viscosity, self-diffusion, nuclear magnetic resonance and near infrared spectroscopy measurements. *J. Chem. Soc. Faraday Transact.* **89**, 707–712.

[6] Iwahashi, M., Hachiya, N., Hayashi, Y., Matsuzawa, H., Liu, Y., Czarnecki, M.A., Ozaki, Y., Horiuchi, T., Suzuki, M. (1995). Self-association of *cis*-9-octadecen-1-ol in the pure liquid state and in decane solutions as observed by viscosity, self-diffusion, nuclear magnetic resonance, electron spin resonance, and near-infrared spectroscopic measurements. *J. Phys. Chem.* **99**, 4155–4161.

[7] Iwahashi, M., Suzuki, M., Katayama, N., Matsuzawa, H., Czarnecki, M.A., Ozaki, Y., Wakisaka, A. (2000). Molecular self-assembling of butan-1-ol, butan-2-ol, and 2-methylpropan-2-ol in carbon tetrachloride solutions as observed by near-infrared spectroscopic measurements. *Appl. Spectrosc.* **54**, 268–276.

[8] Iwahashi, M., Yamaguchi, Y., Ogura, Y., Suzuki, M. (1990). Dynamical structures of normal alkanes, alcohols, and fatty acids in their liquid state as determined by viscosity, self-diffusion coefficient, infrared spectra, and ^{13}C-NMR spin-lattice relaxation time measurements. *Bull. Chem. Soc. Jpn.* **63**, 2154–2158.

[9] Longsworth, L.G. (1966). Diffusion of hydrogen bonding solutes in carbon tetrachloride. *J. Colloid Interface Sci.* **22**, 3–11.

[10] Iwahashi, M., Suzuki, M., Czarnecki, M.A., Liu, Y., Ozaki, Y. (1995). Near-IR molar absorption coefficient for the OH-stretching mode of *cis*-9-octadecenoic acid and dissociation of the acid dimers in the pure liquid state. *J. Chem. Soc. Faraday Transact.* **91**, 697–701.

[11] Iwahashi, M., Hachiya, N., Hayashi, Y., Matsuzawa, H., Suzuki, M., Fujimoto, Y., Ozaki, Y. (1993). Dissociation of dimeric *cis*-9-octadecenoic acid in pure liquid and observed by near-infrared spectroscopic measurement. *J. Phys. Chem.* **97**, 3129–3233.

[12] Iwahashi, M., Kasahara, Y., Minami, H., Matsuzawa, H., Suzuki, M., Ozaki, Y. (2002). Molecular behaviors of *n*-fatty acids in liquid state. *J. Oleo Sci.* **51**, 157–164.

[13] Hertz, H.G. (1984). The problem of intramolecular rotation in liquids and nuclear magnetic relaxation. *Progress Nuclear Magn. Reson. Spectrosc.* **16**, 115–162.

[14] Freeman, R., Hill, H.D.W. (1970). Spin–lattice relaxation in high-resolution NMR spectra of carbon-13. *J. Chem. Phys.* **53**, 4103–4105.

[15] Iwahashi, M., Kasahara, Y., Matsuzawa, H., Yagi, K., Nomura, K., Terauchi, H., Ozaki, Y., Suzuki, M. (2000). Self-diffusion, dynamical molecular conformation and liquid structures of *n*-saturated and unsaturated fatty acids. *J. Phys. Chem. B* **104**, 6186–6194.

[16] Iwahashi, M., Kasahara, Y., Watanabe, S., Wakamatsu, R., Suzuki, T., Kanetani, A., Kano, T., Tamura, T. (unpublished results).

[17] Hu, C.M., Zwanzig, R. (1974). Rotational friction coefficients for spheroids with the slipping boundary condition. *J. Chem. Phys.* **60**, 4354–4357.

[18] Kato, T. (1985). Determination of velocity correlation coefficients in aqueous solutions of 2-butoxyethanol by quasi-elastic light scattering, pulsed-gradient FT-NMR and Rayleigh-Brillouin scattering. *J. Phys. Chem.* **89**, 5750–5755.

[19] Perrin, F. (1934). Brownian movement of an ellipsoid. I. Dielectric dispersion of an ellipsoidal molecule. *J. Phys. Radium.* **5**, 497–511.

[20] Steel, W. (1969). In Hanley, H.J.M. (ed.), *Transport Phenomena in Fluids*. Marcel Dekker, New York, p. 230.

[21] Li, J.C.M., Chang, P. (1955). Self-diffusion coefficient and viscosity in liquids. *J. Chem. Phys.* **23**, 518–520.

[22] Espinosa, P.J., Garcia de la Torre, J. (1987). Theoretical prediction of translational diffusion coefficients of small rigid molecules from their molecular geometry. *J. Phys. Chem.* **91**, 3612–3616.

[23] Aims, G.R, Bauer, D.R., Brwuman, J.I., Pecora, R. (1973). Depolarized Rayleigh scattering and orientational relaxation of molecules in solution. I. Benzene, toluene, and *p*-xylene. *J. Chem. Phys.* **58**, 5570–5578.

[24] Iwahashi, M., Ohbu, Y., Kato, K., Suzuki, Y., Yamaguchi, Y., Muramatsu, M. (1986). The dynamical structure of normal alcohols in their liquids as determined by the viscosity and self-diffusion measurements. *Bull. Chem. Soc. Jpn.* **59**, 3771–3774.

[25] Edward, J.T. (1970). Molecular volumes and the Stokes-Einstein equation. *J. Chem. Educ.* **47**, 261–270.

[26] Doi, M., Edwards, S.F. (1978). Dynamics of rod-like macromolecules in concentrated solution. Part 1. *J. Chem. Soc. Faraday Transact.* **74**, 560–570.

[27] Douglass, D.C., McCall, D.W. (1958). Diffusion in paraffin hydrocarbons. *J. Phys. Chem.* **62**, 1102–1107.

[28] Iwahashi, M., Takebayashi, S., Umehara, A., Kasahara, Y., Minami, H., Matsuzawa, H., Inoue, T., Takahashi, H. (2004). Dynamical dimer structure and liquid structure of fatty acids in their binary liquid mixture: Dodecanoic and 3-phenylpropionic acids system. *Chem. Phys. Lipids* **129**, 195–208.

[29] Iwahashi, M., Takebayashi, S., Taguchi, M., Kasahara, Y., Minami, H., Matsuzawa, H. (2005). Dynamical dimer structure and liquid structure of fatty acids in their binary liquid mixture: Dodecanoic/octanoic acid and decanoic/dodecanoic acid systems. *Chem. Phys. Lipids* **133**, 113–124.

[30] Iwahashi, M., Umehara, A., Wakisaka, K., Kasahara, Y., Minami, H., Matsuzawa, H., Shinzaawa, H., Ozaki, Y., Suzuki, M. (2007). Effect of cholesterol and other additives on viscosity, self-diffusion coefficient, and intramoleecular movements of oleic acid. *J. Phys. Chem. B* **111**, 740–747.

[31] Everett, D.H. (1988). *Basic Principles of Colloid Science*. Royal Society of Chemistry, London.

[32] Matsuzawa, H., Tsuda, M., Minami, H., Iwahashi, M. (2013). Dynamic molecular behavior and cluster structure of octanoic acid in its liquid and CCl_4 solution, *Food Nutr. Sci.* **4**, 25–32.

[33] Larsson, K. (1972). Molecular arrangement in glycerides. *Fette Seifen Anstrichm* **74**, 136–143.

[34] Larsson, K. (1992). On the structure of the liquid state of triglycerides. *J. Am. Oil Chem. Soc.* **69**, 835–836.

[35] Cebula, D.J., McClements, D.J., Povey, M.J.W., Smith, P.R. (1992). Neutron diffractionstudies of liquid and crystalline trilaurin. *J. Am. Oil Chem. Soc.* **69**, 130–136.

[36] Corkery, R.W., Rousseau, D., Smith, P., Pink, D.A., Hanna, C.B. (2007). A case for discotic liquid crystals in molten triglyderides. *Langmuir* **23**, 7241–7246.

[37] Hall, A., Repakova, J., Vattulainen, I. (2008). Modeling of the triglyceride-rich core in lipoprotein particles. *J. Phys. Chem. B* **112**, 13772–13782.

[38] Polleck, J.R.A., Stevens, R. (eds.) (1965). *Dictionary of Organic Compounds.* Eyre & Spottishwoode Publishers, London, Vol. 4, p. 2350.

[39] Iwahashi, M., Ashizawa, K., Ashizawa, M., Kaneko, Y., Muramatu, M. (1984). Optically active and racemic glycerides. II. Thermodynamic studies on the polymorphic transition of (*R*)- and (*RS*)-1,2-diglycerides. *Bull. Chem. Soc. Jpn*. **57**, 956–959

[40] Hsu, W.-D., Violi, A. (2009). Order-disorder phase transformation of triacylglycerols: Effect of the structure of the aliphatic chains. *J. Phys. Chem. B* **113**, 887–893.

[41] Iwahashi, M., Watanabe, Y., Watanabe, T., Muramatu, M. (1984). Optically active and racemic glycerides. I. Thermodynamic and structural relationship between optically active and the corresponding racemic α-monostarins in their crystalline, molten, and dissolved states. *Bull. Chem. Soc. Jpn.* **57**, 1446–1448.

[42] Martin, D., Wang, ZD. (2008). Statistical analysis of the AC breakdown voltages of ester based transformer oils. *IEEE Transact. Dielectr. Insul.* **15**, 1044–1050.

[43] Watkins, C. (2008). Transforming the transformer industry. *Inform* **19**, 524–526.

[44] Tangsathitkulchai, C., Sittichaitaweekul, Y., Tangsathitkulchai, M. (2004). Temperature effect on the viscosities of palm oil and coconut oil blended with diesel oil. *J. Am. Oil Chem. Soc.* **81**, 401–405

[45] Kasahara, Y., Kato, M., Watanabe, S., Iwahashi, M., Wakamatsu, R., Suzuki, T., Kanetani, A., Kano, T., Tamura, T. (2012). Consideration on the relationship between dielectric breakdown voltage and water content in fatty acid esters, *J. Am. Oil Chem. Soc.* **89**, 1223–1229

[46] Takaoka, K., Kobayashi, K., Takahashi, M., Sone, M. (1999). State analysis and thermal changes of dissolved water in decane, dibutyl ether, 3-decanone and methyl decanoate as determined by FT IR spectroscopy. *NIKKA* (in Japanese) **1**, 25–31.

[47] Kokudo, N., Makuuchi, M. (2009). Evidence-based clinical practice guidelines for hepatocellular carcinoma in Japan: The J-HCC guidelines. *J Gastroenterol.* **44**, 119–121.

[48] Arii, S., Sata, M., Sakamoto, M., Shimada, M. (2010). Management of hepatocellular carcinoma: report of consensus meeting in the 45th annual meeting of the Japan Society of Hepatology. *Hepatol. Res.* **40**, 667–685.

[49] Maeda, M., Uchida, N.A., Sasaki, T. (1986). Liposoluble platinum(II) complexes with antitumor activity. *Jpn J. Cancer Res.* **77**, 523–525.

[50] Tanaka, K., Kunimatsu, T., Shimakura, J., Hanada, M. (2011). Development of miriplatin, a novel antitumor platinum for hepatocellular carcinoma. *Sumitomo Kagaku* **39–48** (www.sumitomo-chem.co.jp/rd/report/theses/docs/2011-1I_4.pdf).

[51] Ono, Y., Yoshika, H., Ohkusa, A., Okafiji, T., Kawakami, A., Ishida, O., Suzuki, T., Fukui, M. (1992). The effect of liposoluble *cis*-platinum(II) complex administered via hepatic artery on rat hepatic carcinoma. *J. Jpn Soc. Cancer Ther.* **27**, 49–58

[52] Hanada, M., Baba, A., Tsutsumishita, Y., Noguchi, T., Yamaoka, T., Chiba, N., Nishikaku, F. (2009). Intra-hepatic arterial administration with miriplatin suspended in an oily hymphographic agent inhibits the growth of tumors implanted in rat livers by inducing platinum-DNA adducts to form and massive apoptosis. *Cancer Chemother Pharmacol*. **64**, 473–483.

[53] Hanada, M., Baba, A., Tsutsumishita, Y., Noguchi, T., Yamaoka, T. (2009). Intra-hepatic arterial administration with miriplatin suspended in an oily hymphographic agent inhibits the growth of human hepatoma cells orthotopically implanted in nude rats. *Cancer Sci*. **100**, 189–194.

[54] Kishimoto, S., Miyazawa, K., Fukushima, S., Takeuchi, Y. (2000). In vitro antitumor activity, intracellular accumulation, and DNA adduct formation of *cis*-[((1*R*, 2*R*)-1,2-cycrohexanediamine-*N*,*N*′) bis(myristato)] platinum(II) suspended in lipiodol. *Jpn J. Cancer Res.* **91**, 99–104.

[55] Kishimoto, S., Miyazawa, K., Terakawa, Y., Ashikari, H., Ohtani, A., Fukushima, S., Takeuchi, Y. (2000). Cytotoxicity of *cis*-[((1*R*,2*R*)-1,2-cycrohexanediamine-*N*,*N*′) bis (myristato)] platinum(II) suspended in liodol in a newly established cisplatin-resistant rat hepatoma cell line. *Jpn J. Cancer Res.* **91**, 1326–1332.

[56] Kora, S., Urakawa, H., Mitsufuji, T., Osame, A., Higashihara, H., Yoshimitsu, K. (2013). Warming effect on miriplatin-lipiodol suspension as a chemotherapeutic agent for transarterial chemoembolization for hepatocellular carcinoma: preliminary clinical Eexperience, *Cardiovasc. Intervent. Radiol.* **36**, 1023–1029 (doi 10.1007/s00270-012-0537-3).

54

BIREFRINGENCE IN LIPID BILAYER MEMBRANES

KIYOSHI MISHIMA

Yorozu Kohboh, Dome, 2-2804-1 Makuhari Hanumigawa-ku, Chiba-shi, Chiba 262-0032, Japan

54.1 INTRODUCTION

Much of the current knowledge about the structural and dynamic properties of lipid bilayers and biological membranes was gained by many techniques such as X-ray diffraction, differential scanning calorimetry (DSC), NMR, and electron microscopy [1–7]. However, recent findings suggest that our knowledge about the membrane structure and dynamics is still superficial in many respects [8]. For instance, bilayers vary considerably in thickness and orientation of molecules in the bilayer is not as simple as previously expected. Hydrophobic helices with hydrophilic endings are not necessarily arranged perpendicular to the membrane plane [9], and dynamic rearrangement of geometrical distribution is believed to be of even higher importance [10, 11]. Although structural biophysical techniques, such as X-ray and neutron scattering techniques, have been used to investigate structure of lipid bilayers, many of them provide information about the steady-state condition of the structure, rather than the dynamic information. To gain better understanding about the function of biological membranes, more specific information is required regarding the structure and dynamics of bilayer membranes.

Recent developments in optical technology and spectroscopy have raised hopes of addressing such issues [12]. Lipid bilayers are optically anisotropic materials because of the orientational assembly with rodlike polar molecules in the bilayer. The optical properties parallel are very different from those perpendicular to the bilayer plane, which leads to birefringence (double refraction). The birefringence is highly sensitive to the orientational order of lipid molecules in bilayer membranes. Thus, it is possible to detect changes in the orientational order by measuring birefringence. Several experimental techniques to reveal such optically anisotropic structure have been recently developed. These birefringence techniques are simple and powerful tools for investigating the structural and dynamic properties of lipid bilayers without any kind of labeling. The techniques are extended to a time-resolved technique where changes in the bilayer structure and dynamics can be observed in real time [13, 14]. In this chapter, we first give a general explanation for refractive indices in optically anisotropic materials. Then, we describe theoretical expressions of refractive indices in lipid bilayer membranes, and of interference resulting from birefringence in the bilayer membranes. Finally, we introduce some birefringence techniques that recently have been developed, and provide some experimental results obtained by these techniques.

54.2 BIREFRINGENCE IN UNIAXIAL CRYSTALS

First we describe basic properties of electromagnetic wave propagation in optically anisotropic materials [15, 16]. We consider materials whose electrical excitations depend on the direction of the electric field. In contrast to defining a single dielectric constant for an isotropic medium, the dielectric constant of an anisotropic medium depends on the direction of the electric field. The electric displacement vector $\mathbf{D}$ will then no longer be parallel to the electric field $\mathbf{E}$. The two vectors are related with a dielectric tensor $\boldsymbol{\varepsilon}$ as $\mathbf{D} = \boldsymbol{\varepsilon} \cdot \mathbf{E}$. If an electric field $\mathbf{E} = (E_1, E_2, E_3)$ is applied to the material, each component of the resultant displacement vector $\mathbf{D} = (D_1, D_2, D_3)$ is linearly related to the components of $\mathbf{E}$

Encyclopedia of Biocolloid and Biointerface Science, Volume 2, First Edition. Edited by Hiroyuki Ohshima.
© 2016 John Wiley & Sons, Inc. Published 2016 by John Wiley & Sons, Inc.

as $D_i = \varepsilon_{i1}E_1 + \varepsilon_{i2}E_2 + \varepsilon_{i3}E_3$ $(i = 1, 2, 3)$. Since the tensor is symmetric $(\varepsilon_{ij} = \varepsilon_{ji})$ in transparent dielectric materials, the number of independent components in the tensor is six instead of nine components. There exists a coordinate system fixed in the material such that the expression of the tensor take the diagonal form:

$$\boldsymbol{\varepsilon} = \begin{pmatrix} \varepsilon_x & 0 & 0 \\ 0 & \varepsilon_y & 0 \\ 0 & 0 & \varepsilon_z \end{pmatrix} \tag{54.1}$$

Where ε_x, ε_y and ε_z are called the *principal dielectric constants*. In this system of principal dielectric axes the relation between two vectors **D** and **E** takes the simple form: $D_i = \varepsilon_i E_i$ $(i = x, y, z)$. For some materials, two of the principal dielectric constants are equal. Such materials are said to be optically uniaxial. If $\varepsilon_x = \varepsilon_y \neq \varepsilon_z$, the z axis is called the *optical axis of the uniaxial material*.

When a plane light wave falls on to a boundary between two homogeneous media of different optical properties, it is partially refracted and partially reflected. The phenomenon is ruled by the continuous boundary conditions imposed by Maxwell's equations at the interface. The refracted wave proceeds into the second medium with a different direction because of the change in the wave velocity. Relation between the angle of incidence θ_i and angle of refraction θ_r is described by the law of refraction:

$$\frac{\sin\theta_i}{\sin\theta_r} = \frac{v_1}{v_2} = n_{12} \tag{54.2}$$

where v_1 and v_2 are the phase velocities of propagation in media 1 and 2, respectively, and n_{12} the relative index of refraction from the first into the second medium (Fig. 54.1).

An absolute refractive index of a medium is defined as the refractive index for refraction from vacuum into that medium. If n_1 and n_2 are the absolute refractive indices of two media, the relative index of refraction n_{12} is equal to the ratio n_2/n_1.

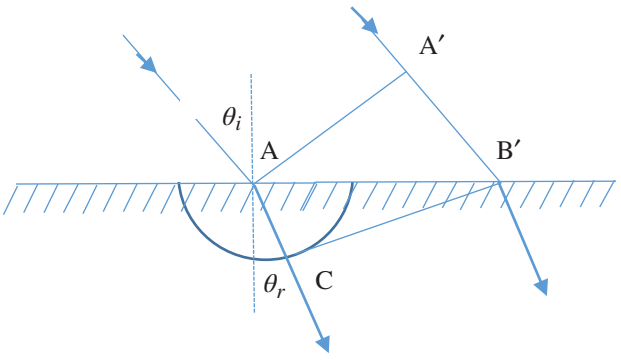


FIGURE 54.1 Refraction of a plane wave in homogeneous media $A'B'/AC = v_1/v_2$.

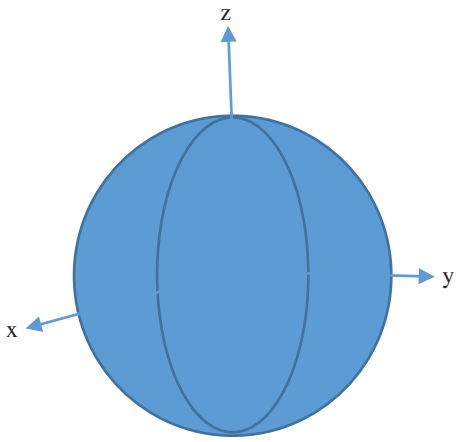


FIGURE 54.2 Phase velocities of ordinary wave (sphere) and extraordinary wave (ellipsoid) in a uniaxial medium. The z axis is the optical axis of the medium.

The absolute refractive index relates to the square root of the dielectric constant (Maxwell's formula). For a medium that does not adsorb light energy, the index equals to the square root of the dielectric constant. Since the dielectric constant of uniaxial materials differs in the direction, the refractive index also differs in the direction. So that the phase velocity is affected by the polarization and propagation direction of the light wave. In general two waves with different velocity travel in the uniaxial material. One of the two waves that corresponds to any particular wave-normal direction is an ordinary wave with a velocity independent of the direction of propagation, the other an extraordinary wave with velocity depending on the angle between the direction of propagation and the optic axis. The electric field of the ordinary light is polarized perpendicular to the optic axis, while the field of the extraordinary light is polarized parallel to the optic axis. The velocities of these two waves are only equal when the wave normal is in the direction of the optic axis. Figure 54.2 shows the velocities of these two waves. In this figure the velocity of the ordinary wave (sphere) v_{o} is larger than that of the extraordinary wave (ellipsoid) v_{e}. Such material is said to be a positive uniaxial crystal. If $v_{\mathrm{o}} < v_{\mathrm{e}}$, the material is called a negative uniaxial crystal.

As shown in Fig. 54.3a, the ordinary light obeys the low of refraction, while the extraordinary light, in general, dose not because of dependence of the velocity on the direction of propagation. When light propagates perpendicularly to the optic axis, the extraordinary wave travels with a velocity independent to the propagation directions (Fig. 54.3b). In this case we can define the refractive index for extraordinary light. The difference in refractive indices of extraordinary (n_e) and ordinary (n_o) light is called the *birefringence* of the material:

$$\Delta n = n_e - n_o \tag{54.3}$$

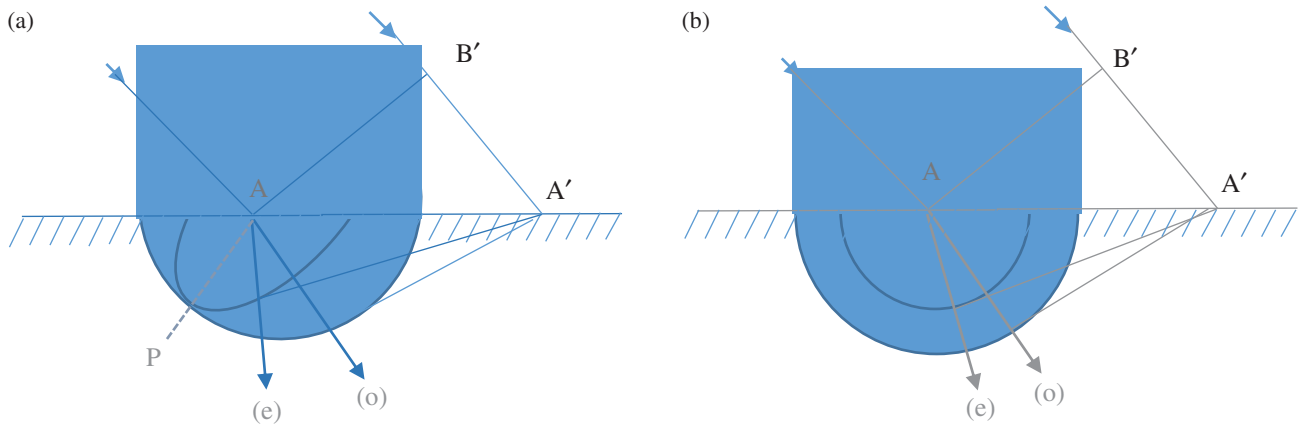


FIGURE 54.3 Propagation of a plane wave into a uniaxial medium: (a) the plane of incidence contains the optical axis; (b) the optical axis is perpendicular to the plane of incidence as well as parallel to the surface of refraction (o = ordinary wave; e = extraordinary wave).

It is noted that the electric vector of extraordinary light is polarized parallel to the optical axis, while the electric vector of the ordinary one is polarized perpendicular to the optical axis. The birefringence is one of principal parameters describing optical properties of anisotropic materials.

54.3 BIREFRINGENCE IN LIPID BILAYERS

Birefringence does not occur only in solid crystals but also in liquid crystals such as lipid bilayers or some surfactant aggregates. Nonrandom orientation of lipid molecules in a bilayer membrane creates an anisotropic system with a uniaxial optical axis with two principal refractive indices, namely, the extraordinary refractive index n_e and the ordinary refractive index n_o. In general, the birefringence Δn $(= n_e - n_o)$ observed in the system is the sum of an intrinsic birefringence of the molecule itself and the form birefringence [17]. *Intrinsic birefringence* results mainly from the anisotropic properties of the molecules itself, whereas *form birefringence* results mainly from anisotropy of a layered structure composed of isotropic or anisotropic molecules because of the continuo boundary conditions imposed by Maxwell's equations at the interfaces of layers [18]. Form birefringence arises on scales much larger than the molecular dimensions but smaller than the wavelength of incoming light. Many studies have attempted to calculate theoretically the effect of form birefringence on the optics of lipid membranes and biological cells [18–28].

One group of researchers has demonstrated relations between anisotropic refractive indices of a single lipid bilayer and the molecular properties such as polarizability tensor, shape, and orientation from spectroscopic measurements using coupled plasmon–waveguide resonance [17]. The relationship of the anisotropic refractive indices to the molecular properties is expressed as described in the following paragraph [17].

A local electric field is induced at the molecule of interest (E^{local}) by an averaged macroscopic electric field (E), which accompanies light propagation in a dielectric environment. Such a local field is a sum of the averaged macroscopic field and an additional component that is produced by the molecule itself. Thus the local field in a dielectric environment can be written as [24, 29]

$$E_i^{local} = E_i + L_i P_i \quad (i = x, y, z) \tag{54.4}$$

where P_i is the polarization per unit volume and L_i is a form factor that describes the influence of asymmetry in the shape of the molecule on the creation of the local electric field. In the case of isotropic media, $L_i = 4\pi/3$ and Eq. (54.4) becomes the Lorentz formula for the local field. The polarization is written by the dielectric constant and the averaged electric field as

$$P_i = (\varepsilon_i - 1)E_i/4\pi \tag{54.5}$$

where ε_i is the dielectric constant along the i axis. The polarization is also written by the molecular polarizability tensor and the local electric field as

$$P_i = \alpha_i E_i^{local}/V \tag{54.6}$$

where α_i is the ii-component of the molecular polarizability tensor whose principal axes are assumed to coincide with x, y, and z, and V is the molecular volume. For a dielectric materials that does not absorb light energy, the dielectric constant equals to the square of the refractive index: $\varepsilon_i = n_i^2$. Combining Eqs. (54.4)–(54.6) results in

$$n_i^2 - 1 = 4\pi\alpha_i/(V - \alpha_i L_i) \tag{54.7}$$

This equation implies that optical anisotropy can be due either to the anisotropy of the molecular polarizability tensor or to the asymmetry of the shape factors.

Another team provided the shape factor for a single lipid bilayer using the cavity field theory in a continuous dielectric medium [17, 30]. They considered that the lipid acyl chain can be represented as a cylindrical cavity. If the optical axis of the uniaxially anisotropic medium coincides with the cylinder axis and the electric field is applied in the i direction, either parallel to the cylinder axis or normal to it, the shape factors L_i can be written as

$$L_z = 4\pi(1 - l/\sqrt{d^2 + l^2}) \tag{54.8}$$

and

$$L_x = L_y = 2\pi\, l/\sqrt{d^2 + l^2} \tag{54.9}$$

where l is the average length of the acyl chain and d the diameter of the cylinder.

Equation (54.7) describes an ideal case when there is no spatial distribution of molecular orientation and the principal axes of the molecular polarizability tensor coincide with the x, y, and z axes. In the more practical case of a spatial distribution of molecular orientation, one should replace α_i and L_i with their average values, respectively. If $\alpha_x = \alpha_y = \alpha_t$ and $\alpha_z = \alpha_l$, which is the case for rodlike molecules, values of the average polarizability are written as

$$\alpha_z^{av} = \alpha^{av} + 2/3(\alpha_l - \alpha_t)S \tag{54.10}$$

$$\alpha_x^{av} = \alpha^{av} - 1/3(\alpha_l - \alpha_t)S \tag{54.11}$$

where

$$\alpha^{av} = 1/3(\alpha_l + 2\alpha_t) \tag{54.12}$$

and α_l and α_t are the longitudinal and transverse polarizabilities.

The average value of the shape factor can be obtained by projecting the long axis of the molecule onto the optical axis (z axis), and by projecting the cross section of the cylinder onto the membrane plane (the x–y plane). This will result in the replacement of the l and d parameters in Eqs. (54.8) and (54.9) with $l' = l\cos\theta$ and $d'^2 = d^2/\cos\theta$, where θ is the angle that the long axis of the molecule makes with the optical axis of an anisotropic system. In principle, this angle represents an average value that can be obtained from the angular distribution of the long axes of the molecules. In practice, this average value can be very well approximated by the degree of orientational order (S), which is defined as [31]:

$$S = 1/2(3\langle\cos^2\theta\rangle - 1) \tag{54.13}$$

where the brackets denote an average over all abundant orientations.

By replacing the l and d parameters by l' and d', and knowing the value of the S parameter, one can evaluate the average values of the shape factors. Furthermore, these values can then be used in Eq. (54.7), which also has to be modified by substituting individual polarizabilities with their averaged values. This will result in the following modified equation

$$n_z^2 - 1 = 4\pi\alpha_z^{av}/\left(V - \alpha_z^{av}L_z^{av}\right) \tag{54.14}$$

and

$$n_x^2 - 1 = 4\pi\alpha_x^{av}/\left(V - \alpha_x^{av}L_x^{av}\right) \tag{54.15}$$

from which one can evaluate the molecular polarizabilities along the principal axes of the molecule, knowing the value of the degree of orientational order (S) and the experimental values of the refractive index obtained by exciting light with the electric vector polarized parallel (yielding n_x) and perpendicular (yielding n_z) to the membrane plane. It should be noted that the birefringence is a measure of the order in in the bilayer membrane. By measuring birefringence, changes in the membrane structure can be monitored with high sensitivity.

54.4 INTERFERENCE WITH BIREFRINGENT MATERIALS

Interference between ordinary and extraordinary beams often occurs as a result of their phase difference. A birefringent plane plate placed between a polarizer and an analyzer is first considered. When a beam of linearly polarized light emerging from a polarizer incidents normally onto the plate, the beam is divided into two rays with different velocities of propagation, and with their electric displacement vectors vibrating in two mutually orthogonal directions to the plate normal. They emerge from the plate with a certain phase difference δ. Components of two vibrations in a certain direction are then singled out through the analyzer and may be brought to interference in the focal plane of a lens placed behind the analyzer (Fig. 54.4).

Intensity of the interference light is obtained as follows [15]. When D' and D'' are the two mutually orthogonal directions of vibration in the plate, and OP and OA are the directions of vibration that are passed by the polarizer and the analyzer respectively in Fig. 54.4, the amplitude of the light incident on the plate is represented by the vector OE. The components in the directions of D' and D'' are $OB = E\cos\varphi$ and $OC = E\sin\varphi$, respectively, where ψ is the angle of OP vector to the D' axis. The amplitude of the light passed by the analyzer is represented by the vector OA; its components are $OF = E\cos\varphi\cos(\varphi - \chi)$ and $OG = E\sin\varphi\sin(\varphi - \chi)$,

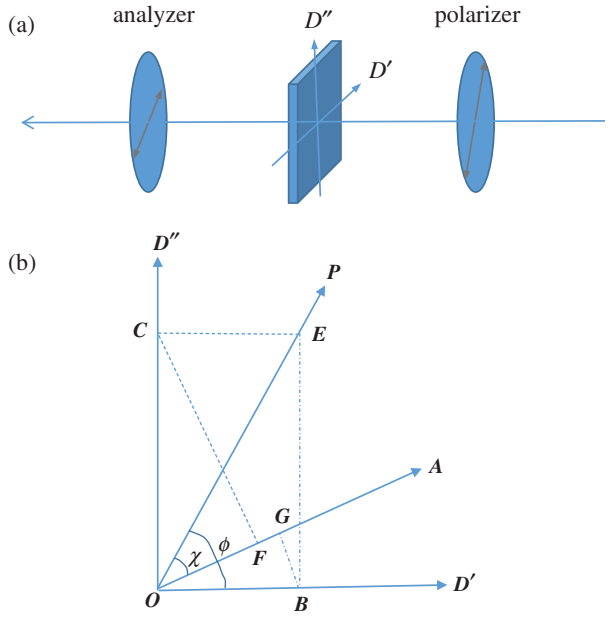


FIGURE 54.4 (a) Interference with a birefringent plane plate placed between a polarizer and an analyzer; (b) **c**onstruction of the vibration components transmitted by the polarizer and the analyzer.

where χ is the angle between OA and OP. On leaving the plate, two components differ in phase by the amount

$$\delta = \frac{2\pi}{\lambda}(n'' - n')\rho \tag{54.16}$$

where n'' and n' are refractive indices for two emerging rays, λ is the wavelength of the incident light, and ρ is the mean geometric path of the two beams. Difference in the refractive indices is written by the birefringence of the uniaxial crystal plate

$$n'' - n' = \Delta n \sin^2\theta \tag{54.17}$$

where θ is the angle between the optical axis of the crystal plate and the mean path of the two beams. The intensity obtained from interference of the two beams with phase difference δ is given by

$$I = I_1 + I_2 + 2\sqrt{I_1 I_2}\cos\delta \tag{54.18}$$

where I_1 and I_2 are the intensities (squared amplitudes) of the two beams. The intensity is written by using the amplitudes as

$$I = a\{\cos^2\chi - \sin 2\varphi \sin 2(\varphi - \chi)\sin^2(\delta/2)\} \tag{54.19}$$

where $a = E^2$, which is the intensity of the incident light on the plate per unit area

In the case where polarizer and analyzer are parallel ($\chi = 0$; parallel polarizers), the interference light intensity is written as

$$I = a\{1 - \sin^2 2\phi \sin^2(\delta/2)\} \tag{54.20}$$

When polarizer and analyzer are perpendicular ($\chi = \pi/2$; crossed polarizers), the interference light intensity is given by

$$I = a\sin^2 2\phi \sin^2(\delta/2)\} \tag{54.21}$$

In an earlier study we calculated the light intensity of interference with a hollow sphere placed between a polarizer and an analyzer [32]. The shell of the hollow sphere is considered to be a uniaxial crystal with the birefringence of Δn, and the optical axis of the crystal is radially oriented in the shell. Furthermore, it is assumed that the birefringence is far smaller than the refractive indices of the crystal n_o and n_e ($\Delta n \ll n_o, n_e$). This suggests that the refractive indices of two emerging rays n' and n'' are approximately equivalent. Direction of beams propagated in the shell changes when the direction of the optical axes is varied. However, this change is negligible, if $n' = n''$ is held. On this assumption, for the case of two beams propagated through only the shell (Fig. 54.5a), the mean geometric path of the beams with varying electric vibration can be easily expressed as

$$\rho = 2R_o\cos\beta \tag{54.22}$$

and for the case of the beams propagated from the shell to the inside medium (Fig. 54.5b)

$$\rho = 2(R_o\cos\beta - R_i\cos\beta') \tag{54.23}$$

where R_o and R_i are the outer and the inner radii of the shell, respectively, and β is the refractive angle between the optical axis and the light path. β' is the incident angle at the interface for the case of the propagation (Fig. 54.5b). In the limiting case of $\beta' = \pi/2$, Eq. (54.23) reduces to Eq. (54.22). Averaging over the light path for the factor $\sin^2\theta$ in Eq. (54.17), the difference in the refractive indices $n'' - n'$ for the case shown in Fig. 54.5b is given as

$$\begin{aligned} n'' - n' &= \Delta n\langle\sin^2\theta\rangle_{AV} \\ &= \frac{\Delta n}{2}\left(1 - \frac{\sin 2\beta - \sin 2\beta'}{2(\beta - \beta')}\right) \end{aligned} \tag{54.24}$$

The difference in the refractive indices $n'' - n'$ for the case shown in Fig. 54.5a is obtained by replacing β' with $\pi/2$ in Eq. (54.24). It is noted that the birefringence Δn is approximately equivalent to that of a plate composed of same uniaxial crystal, when the shell has a large curvature. If the optical

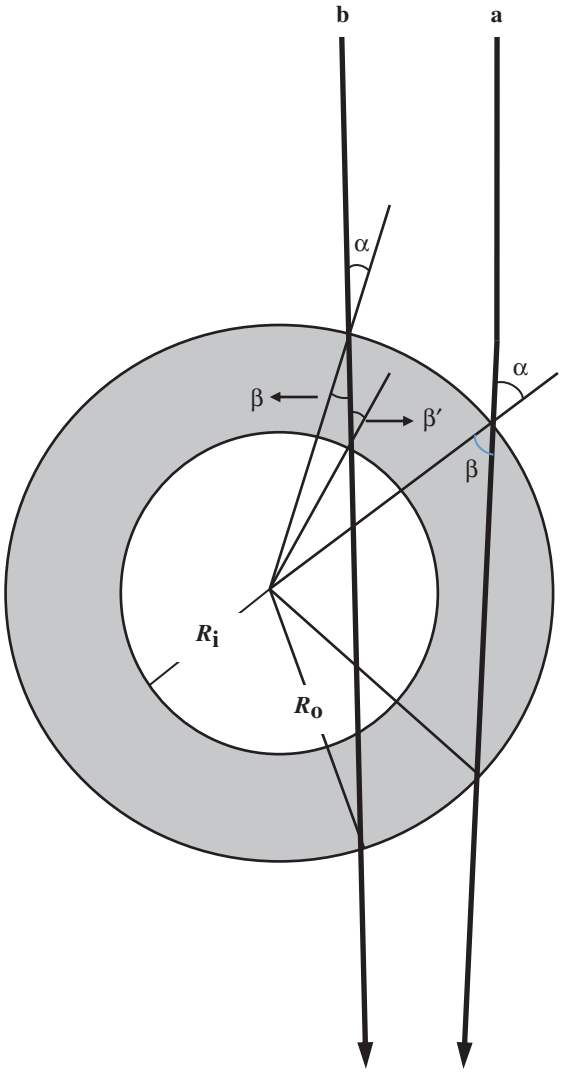


FIGURE 54.5 Mean geometric paths of ordinary and extraordinary beams propagated through (a) a shell and (b) both a shell and the inside medium.

axis of the crystal is not radially oriented, it is not easy to express the difference $n'' - n'$. However, when the direction of the optical axis is radial on average, Eq. (54.24) is valid. In this case, Δn is the mean birefringence. Then the phase difference δ for the hollow sphere is given as

$$\delta = \frac{2\pi}{\lambda}\Delta n\left(R_o\cos\beta - R_i\cos\beta'\right)\left(1 - \frac{\sin 2\beta - \sin 2\beta'}{2\left(\beta - \beta'\right)}\right) \tag{54.25}$$

where $\beta' = \pi/2$ for the case of the propagation shown in Fig. 54.5a.

Intensity of the interference light by the sphere is given by integration with the incoming angle α over the illuminated area of the sphere. In the case of crossed polarizers, the interference light intensity is expressed as

$$i = \int a\sin^2 2\phi\ \sin^2(\delta/2)\}dS \tag{54.26}$$

where adS is the intensity of the incident light flux with the cross-sectional area of dS. When the incident light flux illuminates an area of the shell surface dS' with the incoming angle α, the area dS is expressed as

$$dS = dS'\cos\alpha = R_o^2 d\phi\sin(2\alpha)d\alpha/2 \tag{54.27}$$

Thus, the interference light intensity is

$$i = \int_0^{2\pi}(a/2)R_o^2\sin 2\,\phi\ d\phi\int_0^{\pi/2}\sin^2(\delta/2)\sin 2\alpha\,d\alpha \tag{54.28}$$

Since the total intensity of the illuminated light i_o is $i_o = \pi aR_o^2$, the first integral is equal to $i_o/2$. The second integral is divided into two terms for the cases of propagation shown in (a) and (b) of Fig. 54.5 Therefore the interference light intensity per unit incident light with crossed polarization is expressed as

$$A = \frac{i}{i_o} = \frac{1}{2}\left(\int_0^{\alpha_o}\sin^2\left(\frac{\delta}{2}\right)\sin 2\alpha\,d\alpha + \int_{\alpha_o}^{\pi/2}\sin^2\left(\frac{\delta}{2}\right)\sin 2\alpha\,d\alpha\right) \tag{54.29}$$

where α_o is the incoming angle of the beam propagated on the interface between the shell and the inside medium of the hollow sphere. The angle is represented by $\alpha_o = \arcsin(mR_i/R_o)$ in which m is the relative refractive index of the shell to the medium. In the second term of Eq. (54.29), the phase difference is taken as Eq. (54.25) with $\beta' = \pi/2$. The interference light intensity A was numerically calculated by the Simpson method. Also, the interference intensity by a single vesicle was experimentally measured using a polarized microscopy with crossed polarizers with varying the wavelength of the incident light. Eq. (54.29) is used to analyze experimental data obtained by polarized transmitted-light spectroscopy.

54.5 BIREFRINGENCE TECHNIQUES FOR ANALYZING LIPID BILAYER MEMBRANES

Although much of our knowledge about structural and dynamic properties of lipid bilayer membranes was gained by many kinds of techniques, many fundamental questions about the structure and dynamics of these membranes have

not yet been answered. Many of structural biophysical techniques provide information about the steady-state condition of the membranes, rather than the dynamic information. To understand the function of biological membranes, more specific information is required regarding the interplay between lipid structure and protein function in the membranes. Recently, in order to reply such requests, several optical techniques based on the optical anisotropy in lipid membranes have been developed. These are the waveguide spectroscopy techniques as dual-polarization interferometry (DPI) [33–36], optical waveguide lightmode spectroscopy (OWLS) [14, 37–41], and coupled plasmon–waveguide resonance (CPWR) [42–44], and polarized transmitted light spectroscopy (PTL) [32, 45]. In the waveguide spectroscopic measurements, planar lipid bilayers formed on a solid support are used, while liposomes are used in the transmitted-light measurement. In contrast to the structural techniques, such as X-ray and neutron scattering, these birefringence techniques can indicate dynamic changes in the lipid bilayer structure in real time. In addition, most of the birefringence techniques are label-free methods.

54.5.1 Dual-Polarization Interferometry (DPI)

Dual-polarization interferometry (DPI) was developed for analyzing supported lipid bilayers using a dual optical waveguide interferometric technique [33–36]. The *supported lipid bilayer* (SLB) is a planar lipid membrane supported on a solid substrate such as silicon oxynitride. SLBs are commonly prepared by adsorption of liposomes to the surface and by inducing rupture and fusion of the liposomes to a coherent planar bilayer [46,47]. Although formation of SLBs has been extensively investigated by many workers [48–56], understanding the mechanism of the SLB formation is not yet thorough [36]. The DPI technique provides information about several properties such as refractive index, density, thickness, mass, and birefringence of supported lipid bilayers. The details of the experimental arrangement and methods of data analysis have been described in the literature [36, 57]. We will give a brief summary. DPI consists of a dual-slab waveguide sensor chip with an upper sensing waveguide that supports the lipid bilayer, and a lower optical reference waveguide illuminated by an alternating polarized beam (HeNe laser). The sensor chip consists of a four layer dielectric stack of deposited silicon oxynitride on a silicon wafer surface and works as an integrated Young's interferometer, generating interference fringes at its output. Two orthogonal polarizations are passed through the sensor chip creating two different waveguide modes, called *transverse electric* (TE) and *transverse magnetic* (TM) waveguide modes. Each mode generates an evanescent field from the top sensing waveguide surface interacting with materials coming into contact with the sensor surface and resulting in a change in refractive index. When this occurs, the phase difference between the sensing waveguide and the buried reference waveguide is altered and the position of the interference fringes changes. In this way the sensor is capable of measuring very subtle molecular changes that occur on the sensor surface. The interference fringe pattern for each TM and TE waveguide mode shown as the diffraction fringe image, illuminates an element-imaging device in the far field, the output of which is passed to the digital signal processing unit. The relative phase position is updated every 2 ms using a spatial Fourier transform method. Two separate measurements of fringe shift TM and TE data are transferred to computer for further analysis to provide a real-time data display and to further resolve the data into thickness and refractive-index values for the growing layer.

Birefringence of the layer Δn $(= n_e - n_o)$ can be obtained by calculating the difference between the two effective refractive indices, namely, refractive index of transverse magnetic waveguide mode (n_{TM}) and refractive index of transverse electric waveguide mode (n_{TE}). The analysis can be replicated by instead fixing one of the two refractive indices, thickness of the layer, or $n_{TM} - n_{TE}$ to determine the other two from the measured change in propagation constants for the two modes. The n_{TM} refractive index is affected by the layer thickness and by both n_e and n_o as $n_{TM} = \sqrt{n_e^2 \sin^2\theta + n_o^2 \cos^2\theta}$, where θ, the mode angle, denotes the angle between the optical axis of the bilayer and the mean path of the two-wave mode, while the n_{TE} is affected only by the layer thickness and n_o as $n_{TE} = n_o$.

According to the equations above and the propagation constants for the two modes in the device, both n_e and n_o can be calculated from n_{TM} and n_{TE}. The respective effective indices n_{TM} and n_{TE} corresponding to the measured TM and TE phase changes are calculated by fitting the data to a waveguide equation. When a correct thickness is used for an anisotropic layer, the difference between the n_{TM} and n_{TE} will be the true effective birefringence of the layer [59]. For deposition of a lipid bilayer, a constant thickness is assumed for the entire process, corresponding to the steric thickness obtained by neutron scattering and X-ray reflectivity. When the thickness is fixed for an anisotropic lipid bilayer, changes in refractive index and therefore density and mass can be further calculated for the supported lipid bilayer. Similarly, changes in the thickness of the deposited bilayer can also be resolved by fixing the refractive index at a predetermined value. The effective birefringence $(n_{TM} - n_{TE})$ can be determined only by calculating the two different refractive indices, n_{TM} and n_{TE} for each waveguide mode by fixing the thickness or the refractive index of the deposited layer and assuming a uniform layer coverage. In practice, the refractive index n_e is approximately equal to the refractive index of transverse magnetic mode (n_{TM}) because the contribution of n_o to the TM mode is small. There is only a discrepancy of about 2% between the calculated effective birefringence $(n_{TM} - n_{TE})$ and the layer birefringence $(n_e - n_o)$.

TABLE 54.1 Properties of Supported Lipid Bilayers Obtained by DPI

Lipid	Density (g/cm^3)	Thickness (Å)	Mass (ng/mm^2)	Birefringence	Area/lipid (Å^2)
20°C: gel phase					
DMPC[a]	1.002±0.002	47.2±0.8	4.73±0.08	0.0223±0.0003	47.6±0.82
30°C: fluid phase					
DMPC	1.003±0.003	45.1±0.6	4.52±0.06	0.0193±0.0007	49.9±0.7

[a]DMPC = 1,2-dimyristoyl –sn-glycero-3-phosphocoline.

Mass of the adsorbed layer formed on the solid support m can be calculated from DPI measurements using de Feijter formula [60]

$$m = d(n_{iso} - n_{\text{buffer}}) \left(\frac{dn}{dc}\right)_{\text{lipid}} \tag{54.30}$$

where d is the thickness of the layer, n_{buffer} is the refractive index of the buffer used for the experiments, and n_{iso} denotes the average or corresponding isotopic refractive index of the layer as

$$n_{iso} = \sqrt{\left(n_{\text{TM}}^2 + 2n_{\text{TE}}^2\right)/3} \tag{54.31}$$

Assume that $(dn/dc)_{\text{lipid}}$ is the specific refractive-index increment of the lipid layer. The de Feijter formula assumes that $(dn/dc)_{\text{lipid}}$ remains constant throughout the experiment. The value is, however, not well known, and an equivalent alternative model is used for convenience, assuming a commonly used approximate fixed isotropic refractive index of the lipid layer of 1.47 [36]. The DPI technique has been applied to investigate bilayer structure and formation [61–63], membrane insertion of protein and peptide [33,34, 57,58, 64], and so on. DPI is of great advantage to monitor changes in membrane structure in real time during binding of biomolecules such as peptide. As an example, birefringence values of SLBs obtained by DPI technique are listed in Table 54.1 [65].

54.5.2 Optical Waveguide Lightmode Spectroscopy (OWLS)

Optical waveguide lightmode spectroscopy (OWLS) is one of the waveguide spectroscopy techniques using SLBs. The technique was also developed for analyzing kinetics of protein association with lipid membranes [66–69] and applied to study structure of lipid membrane and interaction of various kinds of biomolecules with lipid membranes [37–41, 70–73]. The OWLS instrument is capable of recording effective refractive indices of the waveguide modes [74–76] with a precision of 10^{-6} [14]. We will briefly describe a procedure and analysis of OWLS measurement for analyzing the interaction of detergent with SLB [71]. A small flowthrough cuvette sealed to the waveguide with an O-ring is used as a sample cell. This ensures that the free detergent concentration is constant and equal to the bulk dissolved concentration. The assembly is then transferred to the goniometer head of an integrated optical scanner. In this instrument a monochromatic, polarized lightbeam (HeNe laser) is directed to the grating coupler area of the chip [77] and the angle α between the grating normal, and the incident laser beam is varied with microradian precision by a computer-driven stepping motor. At certain angles the light is coupled into the waveguide and can be detected with photodiodes positioned at the ends of the waveguide. The angles corresponding to the incoupling maxima are then used to calculate the effective refractive indices N of the transverse electric TE. and transverse magnetic TM. modes, according to the incoupling relation [75]

$$N = n \sin\alpha + \ell\,\lambda/\Lambda \tag{54.32}$$

where n is the refractive index of air and ℓ is the diffraction order.

Pure buffer was allowed to flow through the cuvette in order to determine the parameters of the waveguiding film in the absence of an adlayer, for example, n_{F}, the refractive index of the waveguiding film and d_{F}, the thickness of the film, from the measured N by solving the three-layer-mode equations [75]. Subsequently the chip is removed from the instrument in order to deposit a Langmuir–Blodgett (LB) bilayer. The lipids deposited on the surface form an adlayer whose thickness d_{A} and mean refractive index n_{A} can be found by solving the four-layer mode equations [75]. The amount L of lipid deposited on the surface is determined using the de Feijter formula of Eq. (54.30). Finally the detergent solution is allowed to flow over the membrane. Throughout the experiments a constant flow rate is maintained. The mass of the lipid bilayer–detergent mixture was calculated according to Eq. (54.30). The absolute mass can be determined by a precision of 1 ng/cm^2 [46].

54.5.3 Coupled Plasmon–Waveguide Resonance (CPWR)

Coupled plasmon–waveguide resonance (CPWR) spectroscopy was also developed to analyze kinetic and structural characterization of membrane–protein systems using supported lipid membranes [42, 78]. Resonant excitation by photons of collective electronic oscillations (plasmons) in a

TABLE 54.2 Average Values of Refractive Indices, Form Factor, and Polarizabilities Obtained with Supported POPC Bilayers Containing 10 mol% BODIPY, Using CPWR

Refractive indices[a]		Orientation angle[b]	Form factors[c]		Polarizabilities[d] (Å^3)			
n_p	n_s	θ	L_z	L_x	α_z	α_x	α_1	α_t
1.530	1.475	38°	1.38	5.57	68	46	85	37

[a] n_p and n_s are p- and s-polarized refractive indices, respectively.
[b] Angle between the molecular long axis and the optical axis of the membrane (z axis).
[c] Form factor is defined in Eq. (54.4). The membrane is parallel to the x–y plane.
[d] α_1 and α_t are the longitudinal and transverse polarizabilities of the molecule.
Abbreviations: BODIPY = dipyrromethene boron difluoride; POPC = 1-palmitoyl-2-oleoyl-*sn*-glycero-3-phosphocoline.

thin metallic film provides a source of an evanescent electromagnetic field, which can probe the optical properties of materials in direct contact with the plasmon-generating medium [43].

The principle of CPWR spectroscopy is explained [17] as follows. Plasma oscillations in metals are collective longitudinal excitations of the conductive electron gas, and plasmons are the quanta corresponding to these charge–density oscillations. Such oscillations can be localized on an interface between metallic and dielectric surfaces, along which they propagate as electromagnetic waves with the electric field normal to this interface and decay exponentially with penetration distance from the interface. Surface plasmons can be excited only with certain metallic materials (gold and silver are the best examples) and only by evanescent waves when the wavevector of the evanescent wave is in resonance with that of the surface plasmon wave. Furthermore, plasmon excitation can be achieved only by an evanescent wave generated by polarized incident light with the electric vector perpendicular to the film surface, namely, transverse magnetic (TM-) or p-polarized light [43, 44, 79]. However, when the metal film is covered with a thin dielectric layer that supports waveguide modes, there is the possibility of coupling the incident light into both the plasmon mode of the metal film and the guided mode of the dielectric adlayer. This allows resonance excitation using polarized light with the electric vector parallel to the film surface, called *transverse electric* (TE-) or s-polarized light, because exciting the guided mode reverses the phase shift of the light and the metal sees it as if it were a p-polarized excitation. By precisely adjusting the thickness and refractive index of the dielectric film, the guided mode conditions and surface plasmon conditions can be made coincident for both polarizations at two different incident angles, resulting in two very sharp resonances [42, 80, 81].

The CPWR technique combines advantages of both plasmon resonance and waveguide spectroscopies. Such a combination uses a simple light detection system that involves measurement of the intensity of totally reflected p- and s-polarized light and that is characterized by a high sensitivity due to the resonance phenomenon on which the measurement is based. These properties, taken together with a proper analysis of resonance spectra, allow evaluation of the refractive index, the adsorption coefficient, and the thickness of anisotropic lipid membranes [43, 44, 78, 82–84]. These parameters of the sample reflect three parameters of CPWR spectra: the light incident angle (or light wavelength), the spectral width, and the resonance depth. Thin-film electromagnetic theory based on Maxwell's equations provides an analytical relationship between the spectral parameters and the sample properties [78], where the sample is modeled as a uniform layer (or layers) of anisotropic dielectric material. This allows a unique evaluation of these parameters by fitting theoretical curves to the experimental ones. Table 54.2 lists refractive indices of supported lipid membranes measured by CPWR technique [17].

54.5.4 Polarized Transmitted Light Spectroscopy (PTL)

Polarized transmitted light spectroscopy (PTLS) was developed for analyzing molecular orientation order of liposomal bilayer membranes in bulk solution [32], and has been applied to study the effects of hydrophilic and hydrophobic additives on the molecular order of liposomal membranes [85–90]. As shown in Eq. (54.29), the interference light with crossed polarization strongly depends on the birefringence of liposomal membranes. In PTL measurements, intensity of the interference light with crossed polarization is obtained from transmitted light intensities with parallel and crossed polarization. The details of the procedures of PTL measurements and the method of data analysis have been described in the literature [45]. Here we will provide a brief summary.

We consider lipid dispersion containing various vesicles in size. Since the interference light with crossed polarization also depends on the vesicle size, intensity of the interference light observed by the lipid dispersion is a sum of the individual interference light by the vesicles. The mean intensity of the interference light $\langle A \rangle$ is written as

$$\langle A \rangle = \sum_j \sum_k A(R_{oj}, R_{ik}) f(R_{\mathrm{oj}}, R_{\mathrm{ik}}) \qquad (54.33)$$

where $A(R_{oj},R_{ik})$ is the interference light by a vesicle with an inner radius of R_{ik} and an

outer radius of R_{oj}, and $f(R_{oj},R_{ik})$ the number fraction of the vesicle. Using the mean intensity of the interference light, the total interference light per unit area is given by $\langle A\rangle N\ell$ for the dispersion with the number density of N and the light pathlength of ℓ. Also, the total scattered light is $\langle S\rangle N\ell$, where $\langle S\rangle$ is the mean intensity of scattered light as defined by a similar way as Eq. (54.33). We consider the polarized light transmitted through the dispersion with a small pathlength of $d\ell$. Deviation of the light intensity with crossed polarization I_1 to the polarized incoming light is written as

$$\frac{dI_1}{d\ell} = \langle A\rangle NI_2 - \langle A\rangle NI_1 - \langle S\rangle NI_1 \tag{54.34}$$

where I_2 is the light intensity with parallel polarization. The first term is an increase by the interference light crossly polarized to the incoming light, the second term is a reduction by the interference light polarized in parallel, and the last term is a reduction by scattering light. Since the light intensity of parallel polarization is far larger than that of crossed polarization, namely, $I_2 \gg I_1$, the second term is neglected comparing with the first term:

$$\frac{dI_1}{d\ell} = \langle A\rangle NI_2 - \langle S\rangle NI_1 \tag{54.35}$$

Deviation of the light intensity with parallel polarization is similarly written as Eq. (54.34). However the effect of the scattered light rather than that of the interference light is dominant, so that the deviation is written as

$$\frac{dI_2}{d\ell} = -\langle S\rangle NI_2 \tag{54.36}$$

The light intensity transmitted through the light path of ℓ is given by

$$I_2 = I_0 \exp(-\tau\, l) \tag{54.37}$$

where I_o is the incident light intensity and $\tau = \langle S\rangle N$ is the turbidity.

The transmitted light intensity with crossed polarization is obtained by combining Eqs. (54.35) and (54.37) as

$$I_1 = I_0\,(\varphi + \langle A\rangle N\, l)\exp(-\tau\, l) \tag{54.38}$$

where φ is a ratio I_1/I_0 in the absence of vesicles, namely, a background of the optical system. Ratio of the transmitted-light intensities I_1/I_2 is related only to the interference light as

$$\frac{I_1}{I_2} = \varphi + \langle A\rangle N\, l \tag{54.39}$$

The mean interference light intensity $\langle A\rangle$ can be determined from the slope of a linear dependence on the number density of vesicles and the light pathlength.

However, when the interference light intensity is much larger than the scattered light intensity, such as $\langle A\rangle I_2 \gg \langle S\rangle I_1$, the intensity ratio becomes a nonlinear dependence. In this case, Eq. (54.35) is reduced to

$$\frac{dI_1}{d\ell} = \langle A\rangle NI_2 \tag{54.40}$$

Combining Eqs. (54.37) and (54.40), we can express the transmitted light intensity with crossed polarization as

$$I_1 = I_0\left(\varphi + \frac{\langle A\rangle}{\langle S\rangle}(1 - \exp(-\tau\ell))\right) \tag{54.41}$$

The ratio of the transmitted light intensities I_1/I_2 is

$$\frac{I_1}{I_2} = \left(\varphi + \frac{\langle A\rangle}{\langle S\rangle}\right)\exp(-\tau\ell) - \frac{\langle A\rangle}{\langle S\rangle} \tag{54.42}$$

The intensity ratio deviates positively from a linear dependence.

Experimentally, it is easy to determine the interference light intensity from the ratio of transmitted light intensities with a linear dependence. To obtain a linear dependence of the intensity ratio I_1/I_2 on $N\ell$, vesicles with appropriate size and incident light with a larger wavelength should be employed. It is necessary to test whether the linear relation actually holds. In addition, use of incident light with a larger wavelength is helpful to analyze data of the interference light. As seen in Eq. (54.25), the phase difference δ is in proportion with the birefringence Δn, and becomes small with increasing the wavelength. For the small phase difference, the interference light intensity is approximately proportional to the square of δ[Eq. (54.29)]. This leads to a linear dependence between the interference light intensity and the square of the birefringence Δn. In fact, this square relation is experimentally observed for the small birefringence at a range of large wavelength, as shown in the literature [45, Fig. 4].

As mentioned above, the birefringence of lipid bilayers relates not only to the acyl chain order but also to the molecular orientation order in the bilayers. Let's consider the relation between the birefringence and the molecular order. According to the theory of an uniaxial liquid crystal, the ordinary and extraordinary refractive indices n_o and n_e are related to the principal polarizabilities α_o and α_e as [91]

$$\frac{n_e^2 - 1}{n_e^2 + 2} = \frac{4\pi}{3}\frac{N\alpha_e}{1 + A_1\alpha_e} \tag{54.43}$$

$$\frac{n_o^2 - 1}{n_o^2 + 2} = \frac{4\pi}{3}\frac{N\alpha_o}{1 + A_2\alpha_o} \tag{54.44}$$

TABLE 54.3 Birefringence Values of Liposomal Bilayer Membrane Measured by PTL

Lipid	Birefringence
DPPC (23–25°C; gel phase)	0.020±0.002
DPPC[a] (37°C; ripple phase)	0.028±0.002

[a]DPPC = 1,2-dipalmitoyl –sn-glycero-3-phosphatidylcholine.

where N is the number density of molecules, and A_1 and A_2 are constants by which the Clausius–Mosotti relation is adapted to the uniaxial crystal. Since the birefringence of lipid bilayers is small, at $n_o \approx n_e$, these adapted factors can be neglected and $(n_e + 1)/(n_e^2 + 2) \approx (n_o + 1)/(n_o^2 + 2)$. Thus, the birefringence Δn is obtained from the following equation

$$\Delta n = \left(\tilde{n} - 1 - \frac{\Delta n}{3}\right)\left(\frac{\alpha_e - \alpha_o}{\alpha_o}\right) \tag{54.45}$$

with the mean refractive index $\tilde{n}$

$$\tilde{n} = \frac{n_e + 2n_o}{3} \tag{54.46}$$

The birefringence calculated using Eq. (54.45) is a large value of 0.079 on the assumption that lipid molecules with fully extended chains are uniformly arrayed [32]. In this assumption, the polarizabilities of the bilayer α_e and α_o are equal to polarizabilities of the lipid molecule, $\alpha_\parallel$ and $\alpha_\perp$, specifically, $\alpha_e = \alpha_\parallel$ and $\alpha_o = \alpha_\perp$, where the indices $\parallel$ and $\perp$ denote the principal direction of the molecule and a direction perpendicular to it, respectively. As shown in Table 54.3, birefringence values of bilayer membranes are far smaller than the calculated values. These smaller values arise from disorders of chains and molecular orientation in the bilayer. In particular, the birefringence of the multilamellar bilayers is strongly affected by a disorder in the longitudinal orientation. The degree of order of the uniaxial liquid crystal is defined by the ratio of the polarizabilities of the crystal to the molecular polarizabilities as [91]

$$S = \frac{\alpha_e - \alpha_o}{\alpha_\parallel - \alpha_\perp} \tag{54.47}$$

In the case of lipid bilayers, the term $\Delta n/3$ in Eq. (54.45) is approximately neglected compared with $\tilde{n} - 1$ since the $\Delta n/3$ value is about 2.5% of the $\tilde{n} - 1$ value. In this case, the degree of order S is written as

$$S = \left(\frac{\Delta n}{\tilde{n} - 1}\right)\left(\frac{\alpha_\perp}{\alpha_\parallel - \alpha_\perp}\right) \tag{54.48}$$

where it is assumed that $\alpha_o \approx \alpha_\perp$. This equation indicates that the order S is in proportion with the birefringence. Considering the square relation of the birefringenceΔn with the interference light intensity ($A \propto \Delta n^2$), the order S is proportional to the square root of the interference light intensity, that is, $S \propto \sqrt{A}$.

Polarized transmitted light measurements are performed using a spectrophotometer or a laser diode optical system equipped with two polarizers. The polarizers used are Glan–Thompson prisms with extinction ratio of 5×10^{-5} or polarization filters with a ratio of 10^{-4}. The incident light is reduced by use of a *ND* filter at the measurement of transmitted light with parallel polarization. The sample cell made of quartz was used in order to reduce the effect on the optical background at the crossed polarization measurement. There are two types of measurements of the transmitted light with crossed polarization I_1 and parallel polarization I_2, since the ratio I_1/I_2 depends on the light pathlength ℓ and the number density of vesicles N: (1) measurement by varying the light pathlength ℓ using a sample cell of a syringe type and (2) measurement by varying the number density of vesicles N by diluting the lipid dispersion using a square cell. It is convenient to express the number density N in terms of more directly measurable parameter. Using the lipid concentration c, the number density is given by $N = c/M$, where M is the mean anhydrous mass of a single vesicle. The mean anhydrous mass is a constant value when no vesicle disruption occurs at the dilution.

Experimental results show the linear dependence on the lipid concentration and the cell length at low values [45]. The interference light intensity is determined from the slopes of the lines. To obtain a linear dependence of the intensity ratio I_1/I_2 on $N\ell$, multilamellar vesicles with appropriate size were prepared. Small unilamellar vesicles (SUVs) are not suitable for measuring the interference light because of their weak intensity. Sometimes, a SUV was removed by filter to avoid vesicle aggregation by addition of additives. The suitable size is roughly more than $\lambda/\tilde{n}$, where λ is the wavelength of the incident light and $\tilde{n}$ is the mean refractive index of lipids. Since the interference light strongly depends on vesicle size, the vesicle aggregation and disruption are usually monitored by the turbidity obtained from the transmitted light with parallel polarization. Occasionally, the size distribution of vesicles in the dispersion should be measured by dynamic light scattering. The PTL technique was applied mainly to study the effects of hydrophilic and hydrophobic additives on the molecular order of liposomal membranes using the square- root relation between the order S and the interference light intensity A, namely, S $\propto \sqrt{A}$ [85–90]. Finally we show the birefringence values of liposomal membranes obtained by PTL using a spectrophotometer in Table 54.3 [32].

REFERENCES

[1] Tardieu, A., Luzzati, V., Reman, F.C. (1973). *J. Mol. Biol.* **75**, 711–733.

[2] Seelig, J., Niederberger, W. (1974). *J. ACS* **96**(7), 2069–2072.

[3] Niederberger, W., Seelig, J. (1976). *J. ACS* **98**(12), 3704–3706.

[4] Sturtevant, J.M. (1987). *Annu. Rev. Phys. Chem.* **38**, 466-476.

[5] Small, D.M. (ed.) (1986). *The Physical Chemistry of Lipids*. In Hanahan, D.J. (series ed.), Handbook of Lipid Research, Vol. 4, Plenum Press, New York.

[6] Katsaras, J., Gutberlet, T. (eds.) (1999). *Lipid Bilayers Structure and Interactions*, Springer-Verlag, Heidelberg.

[7] Tien, H.T., Ottova, A. (eds.) (2003). *Planar Lipid Bilayers (BLMs) and Their Applications*. Elsevier Science, Amsterdam/New York.

[8] Engelman, D.M. (2005). *Nature* **438**, 578–580.

[9] von Heijine, G. (2006). *Nat. Rev. Mol. Cell Biol.* **7**, 909–918.

[10] Mossman, K., Groves, J. (2007). *J. Chem. Soc. Rev.* **36**, 46–54.

[11] Mossman, K.D., Campi, G., Groves, J.T., Dustin, M.L. (2005). *Science* **310**, 1191–1193.

[12] Edidin, M. (2003). *Nat. Rev. Mol. Cell Biol.* **4**, 414–418.

[13] Lee, T.-H., Heng, C., Swann, M.J., Gehman, J.D., Separovic, F., Aguilar, M.I. (2010). *Biochim. Biophys. Acta* **1798**, 1977–1986.

[14] Horvath, R., Kobzi, B., Keul, H., Moeller, M., Kiss, É. (2013). *Int. J. Mol. Sci.* **14**, 9722–9736.

[15] Born, M., Wolf, E. (1970). *Principles of Optics*, 4th ed. Pergamon Press, Oxford, UK, pp. 695–708.

[16] Lipson, S.G., Lipson, H. (1981). *Optical Physics*, 2nd ed. Cambridge Univ. Press, Cambridge, UK, pp. 87–119.

[17] Salamon, Z., Tollin, G. (2001). *Biophys J.* **80**, 1557–1567.

[18] Roberts, N.W. (2006). *Vision Res.* **46**, 3259–3266.

[19] Moody, M.F. (1964). *Biol. Rev.* **39**, 43–86.

[20] Weale, R.A. (1971). *Vision Res.* **11**, 1373–1385.

[21] Laughlin, S.B., Menzel, R., Snyder, A.W. (1975). Membranes, dichroism and receptor sensitivity. In Snyder, A.W., Menzel, R. (eds.), *Photoreceptor Optics.* Springer, Berlin, p. 237.

[22] Israelachvili, J.N., Sammut, R.A., Snyder, A.W. (1975). *Vision Res.* **16**, 47–52.

[23] Snyder, A.W., Laughlin, S.B. (1975). *J. Compar. Physiol.* **100**, 101–116.

[24] den Engelsen, D. (1976). *Surf. Sci.* **56**, 272–280.

[25] De Jeu, W.H. (1978). Physical properties of liquid crystalline materials. In Gray, G. (ed.), *Liquid Crystal Monographs*. Gordon & Breach, Amsterdam, Vol. 1, pp. 34–48.

[26] Harosi, F.I. (1981). Microspectrophotometry and optical phenomena: Birefringence, dichroism and anomalous dispersion. In Enoch, J.M., Tobey, F.L., Jr. (eds.), *Vertebrate Photoreceptor Optics.* Springer, Berlin, p. 337.

[27] Harosi, F.I. (1978). *Vision Res.* **18**, 353–354.

[28] Beche, B., Gaviot, E. (2003). *Opt. Commun.* **219**, 15–19.

[29] Bottcher, C.J.F. (1952). *Theory of Electric Polarisation.* Elsevier, Amsterdam.

[30] Onsager, L. (1936). *J. ACS* **58**(8), 1486–1493.

[31] Saupe, A., Teil, I.Z. (1964). *Naturfoschung* **19A**, 161–171.

[32] Mishima, K., Satoh, K., Ogihara, T. (1987). *Biochim. Biophys. Acta* **898**, 231–238.

[33] Cross, G.H., Reeves, A.A., Brand, S., Popplewell, J., Peel, L.L., Swann, M.J., Freeman, N.J. (2003). *Biosens. Bioelectron.* **19**, 383–390.

[34] Swann, M.J., Peel, L.L., Carrington, S., Freeman, N.J. (2004). *Anal. Biochem.* **329**, 190–198.

[35] Cross, G.H., Reeves, A., Brand, S., Swann, M.J., Peel, L.L., Freeman, N.J., Lu, J.R. (2004). *J. Phys. D: Appl. Phys.* **37**, 74–80.

[36] Mashaghi, A., Swann, M., Popplewell, J., Textor, M., Reimhult, E. (2008). *Anal Chem.* **80**, 3666–3676.

[37] Horvath, R., Fricsovszky, G., Papp, E. (2003). *Biosens. Bioelectron.* **18**, 415–428.

[38] Michielin, O., Ramsden, J.J., Vergeres, G. (1998). *Biochim. Biophys. Acta* **1375**, 110–116.

[39] Ramsden, J.J. (1993). *Phys. Chem.* **97**, 4479–4483.

[40] Ramsden, J.J. (1999). *Phil. Mag. B* **79**, 381–386.

[41] Sugihara, K., Delai, M., Szendrő, I., Guillaume-Genti, O., Vörös, J., Zambelli, T. (2012). *Sens. Actuator B* **161**, 600–606.

[42] Salamon, Z., Macleod, H.A.G., Tollin, G. (1997). *Biophys. J.* **73**, 2791–2797.

[43] Salamon, Z., Brown, M.F., Tollin, G. (1999). *Trends Biochem. Sci.* **24**, 213–219.

[44] Salamon, Z., Tollin, G. (1999). Surface plasmon resonance: Theoretical principles. In Lindon, J.C., Tranter, G.E.J., Holmes, L. (eds.), *Encyclopedia of Spectroscopy and Spectrometry.* Academic Press, New York, Vol. 3, pp. 2311–2319.

[45] Mishima, K. Birefringence studies on effects of additives on bilayer lipid membranes. In Leimannova Liu, A. (ed.), *Advances in Planar Lipid Bilayers and Liposomes.* Elsevier, Amsterdam, Vol. 3, pp. 55–83.

[46] McConnell, H.M., Watts, T.H., Weis, R.M., Brian, A.A. (1986). *Biochim. Biophys. Acta* **864**, 95–106.

[47] Tamm, L.K., McConnell, H.M. (1985). *Biophys. J.* **47**, 105–113.

[48] Keller, C.A., Kasemo, B. (1998). *Biophys. J.* **75**, 1397–1402.

[49] Keller, C.A., Glasmastar, K., Zhdanov, V.P., Kasemo, B. (2000). *Phys. Rev. Lett.* **84**, 5443–5446.

[50] Reimhult, E., Hook, F., Kasemo, B. (2005). *J. Phys. Chem. B* **109**, 21755–21765.

[51] Rossetti, F.F., Bally, M., Michel, R., Textor, M., Reviakine, I. (2005). *Langmuir* **21**, 6443–6450.

[52] Reimhult, E., Zach, M., Hook, F., Kasemo, B. (2006). *Langmuir* **22**, 3313–3319.

[53] Richter, R.P., Berat, R., Brisson, A.R. (2006). *Langmuir* **22**, 3497–3505.

[54] Castellana, E.T., Cremer, P.S. (2006). *Surf. Sci. Rep.* **61**, 429–444.

[55] Merz, Ch., Knoll, W., Textor, M., Reimhult, E. (2008). *Biointerphases* **3**, FA41–FA50.

[56] Cho, N.-J., Frank, C.W., Hook, F. (2010). *Nat. Protocols* **5**, 1096–1106.

[57] Lee, T., Hall, K., Swann, M., Popplewell, J., Unabia, S., Park, Y., Hahm, K., Aguilar, M. (2010). *Biochim Biophys Acta* **1798**, 544–557.

[58] Hirst, D., Lee, T.-H., Swann, M., Unabia, S., Park, Y., Hahm, K., Aguilar, M. (2011). *Eur. Biophys. J.* **40**, 503–514.

[59] Horvath, R., Ramsden, J. (2007). *Langmuir* **23**, 9330–9334.

[60] de Feijter, F.N., Benjamins, J., Veer, F.A. (1978). *Biopolymers* **17**, 1759–1772.

[61] Popplewell, J.F., Swann, M.J., Freeman, N.J., McDonnell, C., Ford, R.C. (2007). *Biochim. Biophys. Acta* **1768**, 13–20.

[62] Terry, C.J., Popplewell, J.F., Swann, M.J., Freeman, N.J., Fernig, D.G. (2006). *Biosens. Bioelectron.* **22**, 627–632.

[63] Popplewell, J.F., Freeman, N.J., Carrington, S., Ronan, G., McDonnell, C., Ford, R.C. (2005). *Biochem. Soc. Transact*. **33**, 931–933.

[64] Yu, L., Guo, L., Ding, J.L., Ho, B., Feng, S.S., Popplewell, J.F., Swann, M.J., Wohland, T. (2009). *Biochim. Biophys. Acta* **1788**, 333–344.

[65] Fernandez, D.I., Lee, T.-H., Sani, M.-A., Aguilar, M.-I., Separovic, F. (2013). *Biophys. J.* **104**, 1495–1507.

[66] Ramsden, J.J., Schneider, P. (1993). *Biochemistry* **32**, 523–529.

[67] Ramsden, J.J. (1994). *Q. Rev. Biophys.* **27**, 41–105.

[68] Ramsden, J.J., Wright, C.S. (1995). *Glycoconjugate J.* **12**, 113–121.

[69] Ramsden, J.J., Bachmanova, G.I., Archakov, A.I. (1994). *Phys. Rev. E.* **50**, 5072–5076.

[70] Csúcs, G., Ramsden, J.J. (1998). *Biochim. Biophys. Acta Biomembr.* **1369**, 61–70.

[71] Csúcs, G., Ramsden, J.J. (1998). *Biochim. Biophys. Acta Biomembr.* **1369**, 304–308.

[72] Ramsden, J.J., Bachmanova, G.I., Archakov, A.I. (1996). *Biosens. Bioelectron.* **11**, 523–528.

[73] Vörös, J., Ramsden, J.J., Csúcs, G., Szendrő, I., de Paul, S.M., Textor, M., Spencer, N.D. (2002). *Biomaterials* **23**, 3699–3710.

[74] Ramsden, J.J. (1993). *Statist. Phys.* **73**, 853–877.

[75] Tiefenthaler, K., Lukosz, W.J. (1989). *Opt. Soc. Am. B* **6**, 209–220.

[76] Ramsden, J.J. (2006). Proteins at solid-liquid interfaces. In Déjardin, P. (ed.), *Principles and Practice.* Springer-Verlag, Heidelberg, pp. 23–49.

[77] Tiefenthaler, K. (1992). *Adv. Biosensors* **2**, 261–289.

[78] Salamon, Z., Macleod, H.A., Tollin, G. (1997). *Biochim. Biophys. Acta* **1331**, 117–129

[79] Salamon, Z., Tollin, G. (1999). Surface plasmon resonance: Applications. In Lindon, J.C., Tranter, G.E., Holmes, J.L. (eds.), *Encyclopedia of Spectroscopy and Spectrometry.* Academic Press, New York, Vol. 3, pp. 2294–2302.

[80] Macleod, H.A. (1986). *Thin Film Optical Filters*. Hilger, Bristol, Macmillan, New York.

[81] Macleod, H.A. (1921). Unconventional coatings. In Moore, D.T. (ed.), *Tutorials in Optics.* Optical Society, Washington, DC, pp. 121–135.

[82] Alves, I.D., Salgado, G.F.J., Salamon, Z., Brown, M.F., Tollin, G., Hruby, V.J. (2005). *Biophys. J.* **88**, 198–210.

[83] Salamon, Z., Cowell, S., Varga, E., Yamamura, H.I., Hruby, V.J., Tollin, G. (2000). *Biophys. J.* **79**, 2463–2474.

[84] Salamon, Z., Lindblom, G., Rilfors, L., Linde, K., Tollin, G. (2000). *Biophys. J.* **78**, 1400 –1412.

[85] Mishima, K., Satoh, K., Suzuki, K. (1996). *Colloids Surf. B: Biointerfaces* **7**, 83–89.

[86] Mishima, K., Satoh, K., Suzuki, K. (1997). *Colloids Surf. B: Biointerfaces* **9**, 9–15.

[87] Mishima, K., Satoh, K., Suzuki, K. (1997). *Colloids Surf. B: Biointerfaces* **10**, 113–117.

[88] Mishima, K., Watanabe, H., Kaneko, S., Ogihara, T. (2003). *Colloids Surf. B: Biointerfaces* **28**, 307–312.

[89] Mishima, K., Nakajima, M., Ogihara, T. (2004). *Colloids Surf. B: Biointerfaces* **33**, 185–189.

[90] Mishima, K., Watanabe, H., Kaneko, S., Ogihara, T. (2002). *Colloids Surf. B: Biointerfaces* **25**, 219–224.

[91] Kelker, H., Hatz, R. (1980). *Handbook of Liquid Crystal.* Verlag Chemie, pp. 254–262.

55

SURFACE STATES OF LIPID MONOLAYERS CONTAINING GANGLIOSIDES

SHOKO YOKOYAMA

School of Pharmaceutical Sciences, Kyushu University of Health and Welfare, Miyazaki, Japan

55.1 INTRODUCTION

Biological membranes are composed of phospholipids, glycolipids, cholesterol, and glycoproteins. Several models of biological membranes have emerged since Singer and Nicolson [1] proposed the fluid mosaic model. Simons and coworkers [2, 3] proposed "rafts" and "caveolae" at the cell surface, which are rich in glycolipid, phospholipid, and cholesterol. Another team [4] proposed that gangliosides form microdomains at the cell surface, through which signal transduction occurs. The role of membrane organization and the structure of rafts are interesting subjects in membrane structural biology.

We have studied the surface states of ganglioside G_{M1} (GM1) monolayer and mixed GM1–phospholipid monolayers using atomic force microscopy [5–7]. *Atomic force microscopy* (AFM) is a surface imaging technique capable of nanometer-scale resolution, which operates by measuring the forces acting between a probe and the sample [8]. The surface states of the monolayers containing GM1 changed as the surface pressure was varied, suggesting that GM1 participates in specific cell recognition or signal transduction. The surface pressure-responsive change in morphology of GM1 was affected by the surrounding environment, suggesting that the GM1 localized in each organ has a specific role [5–7]. Another group [9] reported the distribution of GM1 in model membranes of lipidrafts.

In this chapter, I report the surface states of lipid monolayers containing ganglioside G_{D1a} (GD1a), ganglioside G_{T1b} (GT1b) and cholesterol (Chol), as a raft model. The results for ternary, quaternary and five-component systems of monolayers are mainly shown in this chapter, while single and binary systems of ganglioside monolayers are briefly described.

55.2 EXPERIMENTAL MATERIALS

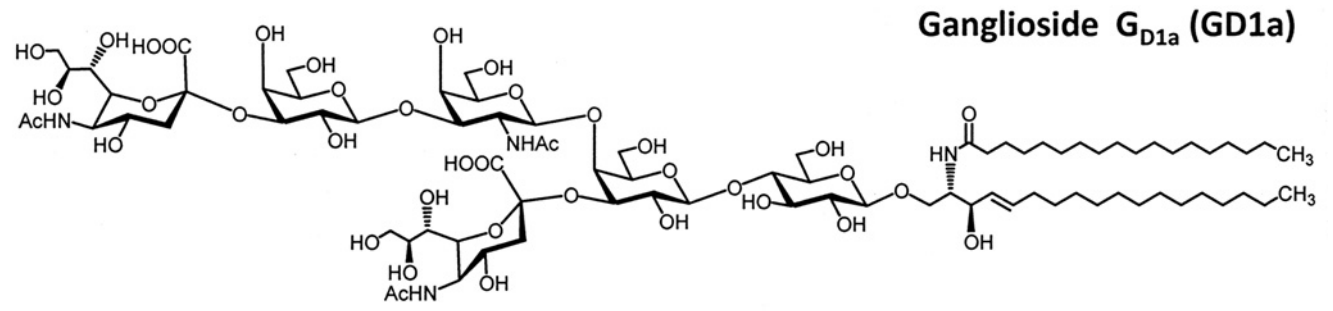
Ganglioside G_{D1a} (GD1a), ganglioside G_{T1b} (GT1b), L-α-dipalmitoylphosphatidylcholine (DPPC), dioleoylphosphatidylcholine (DOPC), and cholesterol (Chol) were purchased from Sigma Chemical Co. In this experiment, superpure water (Super-Q system) was used. Chemical structures of GD1a and GT1b are shown in Scheme 55.1

55.3 MEASUREMENT OF SURFACE PRESSURE

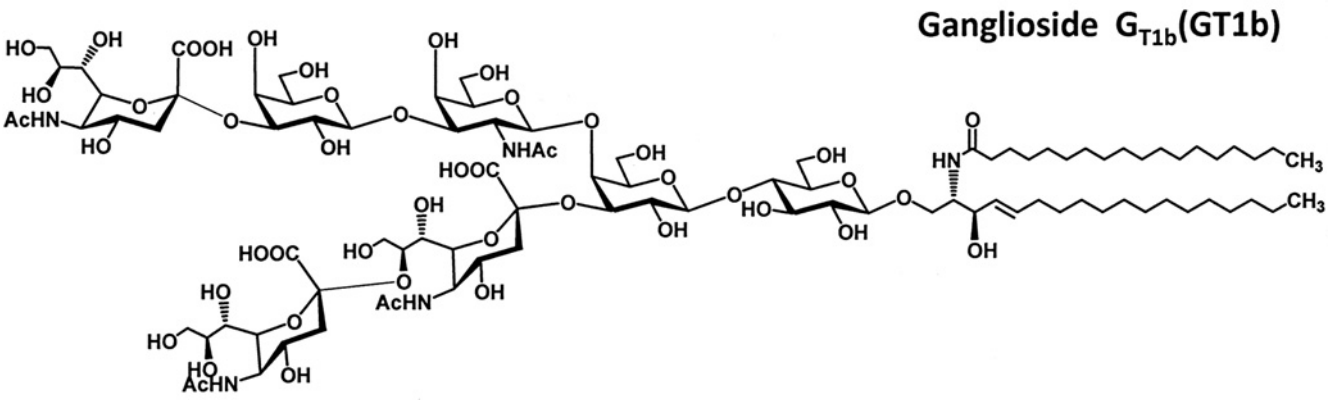
The surface pressures of monolayers for gangliosides, phospholipids, and mixed ganglioside–phospholipid at the air–water interface were determined at 25 ± 0.5°C (or 25–50 ± 0.5°C) by the Wilhelmy plate method using a surface pressure meter of type HBM-A (Kyowa Interface Science Co. Ltd.) with a bar made of Teflon. The speed of compression on the monolayer was 20 mm/min.

The surface pressure (π) *vs*. area (A) isotherms and the collapse pressures for DPPC [10], DOPC [7], GM1 [10], GD1a [11–13], and GT1b [11,14] monolayers have been presented. The phase transition from the liquid-expanded film to the liquid-condensed film was observed for DPPC,

Encyclopedia of Biocolloid and Biointerface Science, Volume 2, First Edition. Edited by Hiroyuki Ohshima.
© 2016 John Wiley & Sons, Inc. Published 2016 by John Wiley & Sons, Inc.



L-α-Neu*p*(2→3)-D-β-Gal*p*(1→3)-D-β-Gal*p*NAc(1→6)[L-α-Neu*p*(2→3)]-D-β-Gal*p*(1→4)-D-β-Glc*p*(1→)-Cer



L-α-Neu*p*(2→3)-D-β-Gal*p*(1→3)-D-β-Gal*p*NAc(1→6)[L-α-Neu*p*(2→9)-L-α-Neu*p*(2→3)]-D-β-Gal*p*(1→4)-D-β-Glc*p*(1→)-Cer

Scheme 55.1 Chemical structures of GD1a and GT1b.

DOPC, GM1, GD1a, and GT1b monolayers, while only the liquid-expanded film was observed for DOPC monolayer.

55.4 PREPARATION OF LB FILM

Single-layer Langmuir–Blodgett (LB) films for AFM were obtained as follows. The monolayers were transferred at 25°C using a vertical dipping method onto freshly cleaved mica. Deposition proceeded at 5 mm/min, under various surface pressures.

55.5 AFM OBSERVATION

A model JSPM-5200 atomic force microscope (JEOL Ltd.) was used for AFM observations. The AFM probe used was a Micro Cantilever CSC38 (JEOL Ltd.) made of silicon and coated with Au, which had a spring constant of 0.08 N/m, a length of 250 μm, and a thickness of 1.0 μm. AFM observation was carried out with the contact mode in the air. In this study, observation of monolayer was carried out by varying the surface pressure, since surface pressure at the biological membrane should rise when cells or signals approach the membrane.

55.6 RESULTS AND DISCUSSION

55.6.1 Single System of Ganglioside Monolayer

The surface states of GD1a and GT1b monolayers, as a model of glycolipid microdomain, were observed using AFM. Changes in morphology were found in GD1a and GT1b monolayers when the surface pressure was raised. A swelling pattern and a ripple pattern were observed for the GD1a and GT1b monolayers, respectively [15]. The morphology and the responsive surface pressure were different among GD1a, GT1b, and GM1.

55.6.2 Binary System of Ganglioside–Phospholipid

Surface states of binary GD1a/DPPC, GT1b/DPPC, GD1a/DOPC, and GT1b/DOPC monolayers were measured.

55.6.2.1 Binary GD1a/DPPC Monolayer [12]. AFM images of the GD1a/DPPC (6:4) monolayer showed DPPC domains in flat matrix at 10 mN/m. The flat state of the matrix changed to a percolation pattern by varying the surface pressure from 10 to 28 mN/m. A similar percolation pattern was observed in GM1/DPPC (1:9) monolayer [10]. The amount of GD1a forming a percolation pattern in the monolayer was larger than GM1. This phenomenon may be related to the higher content of GD1a than GM1 in the biological membrane: 13 % GM1 and 38 % GD1a in human brain tissue [16]; 2% GM1 and 45 % GD1a in the synapse membrane of rats [17].

55.6.2.2 Binary GT1b/DPPC Monolayer [18]. AFM images of the GT1b/DPPC (4:6) monolayer showed GT1b domains (50–100 nm) together with DPPC domains (2 μm) in the matrix at a surface pressure of 15 mN/m, the GT1b domains disappeared and the DPPC domains (0.5–1 μm) embedded in the matrix at 20 mN/m. When surface pressure further increased to 28 mN/m, the DPPC domains disappeared and the monolayer became flat and uniform.

55.6.2.3 Binary GD1a/DOPC Monolayer [19]. The rafts are surrounded by unsaturated phospholipid [2, 3]. Thus, surface states of ganglioside/DOPC binary monolayer were measured before studying ternary ganglioside/DPPC/DOPC monolayer.

AFM images of the GD1a/DOPC (4:6) monolayer showed flowerlike and petal-like domains of GD1a embedded in DOPC-rich matrix, where the matrix was uniform and flat, at a surface pressure of 10 mN/m. When surface pressure increased to 15 mN/m, the uniform and flat matrix changed to a spotted pattern. At surface pressures above 20 mN/m, flowerlike and petal-like domains disappeared and the membrane became almost flat at 30 mN/m.

55.6.2.4 Binary GT1b/DOPC Monolayer [20]. AFM images of the GT1b/DOPC (4:6) monolayer showed flowerlike domains of GT1b and a spotted pattern in the matrix at a surface pressure of 10 mN/m. When surface pressure increased to 20 mN/m, the spotted pattern in the matrix almost disappeared, and the flowerlike domains were embedded in the flat matrix. When surface pressure further increased to 25 mN/m, the flowerlike domains changed to the spotted pattern.

The pattern for both of GT1b and GD1a systems was similar. However, the order of pattern with increasing surface pressure was different between them.

55.6.3 Ternary System of Ganglioside/DPPC/DOPC

The rafts are surrounded by unsaturated phospholipid [2, 3]. Thus, surface states of ternary ganglioside/DPPC/DOPC monolayer were studied before studying quaternary ganglioside/DPPC/DOPC/Chol monolayer.

55.6.3.1 Ternary GD1a/DPPC/DOPC Monolayer. AFM images of the GD1a/DPPC/DOPC (4:6:6) monolayer [21] are shown in Fig. 55.1, where bright areas in the images indicate topographic highs.

At a surface pressure of 25 mN/m (Fig.55.1a), largely circular domains of DPPC with a flat surface are embedded in the matrix. Furthermore, the matrix shows two phases, namely snow crystal-like domains, which consist of GD1a and a small amount of DOPC, embedded in the DOPC matrix.

At a surface pressure of 30 mN/m (Fig. 55.1b), DPPC domains are found, however, the morphology of the matrix drastically changed by varying the surface pressure from 25 to 30 mN/m. A percolation pattern was formed in the matrix. This behavior of the GD1a ternary monolayer is quite contrary to the previous GM1 ternary monolayer; a

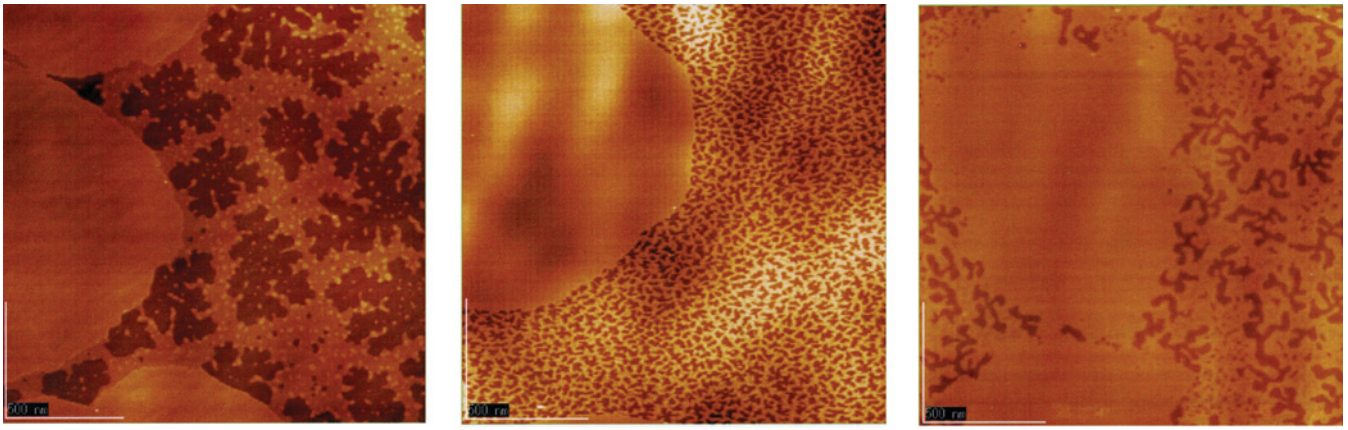


FIGURE 55.1 AFM images of ternary GD1a/DPPC/DOPC (4:6:6) monolayer, with surface pressure (a) 25, (b) 30, and (c) 35 mN/m and scan area 1.5×1.5 μm.

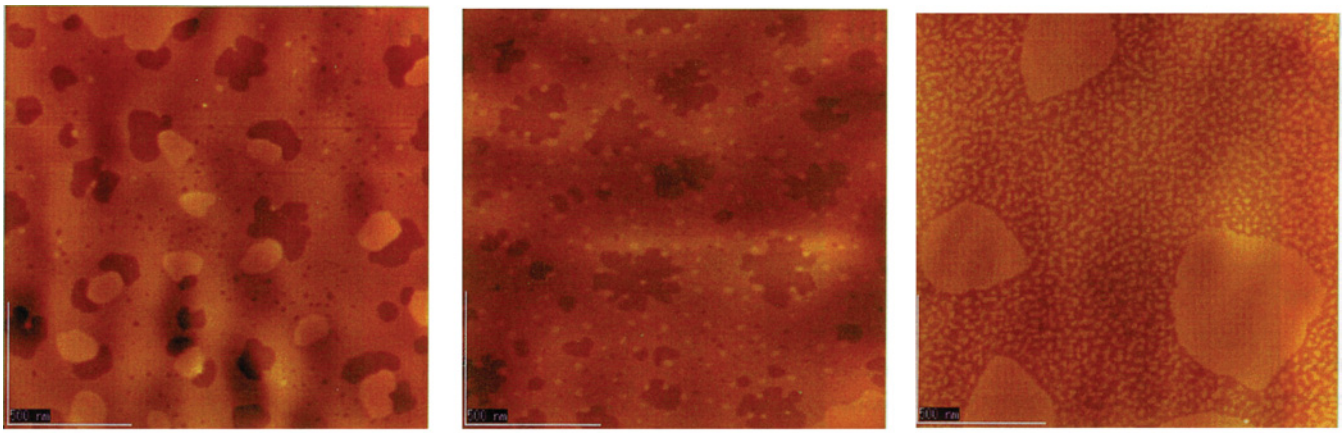


FIGURE 55.2 AFM images of ternary GD1a/DPPC/DOPC (6:4:4) monolayer, with surface pressure (a) 10, (b) 15, and (c) 20 mN/m and scan area 1.5 × 1.5 μm.

percolation pattern was formed in the DPPC-rich domain for the GM1/DPPC/DOPC ternary system [7], while a percolation pattern was formed in the DOPC-rich matrix for the GD1a/DPPC/DOPC ternary system.

When surface pressure increased to 35 mN/m (Fig. 55.1c), the percolation pattern disappeared and the matrix changed to a waterweedlike pattern.

A ternary system containing a higher ratio of GD1a was then chosen to examine the effect of membrane composition on the surface state of the GD1a ternary monolayer. AFM images of the GD1a/DPPC/DOPC (6:4:4) monolayer [19] are shown in Fig. 55.2.

At a surface pressure of 10 mN/m (Fig. 55.2a), brightly elliptical domains of DPPC and dark domains of GD1a were embedded in the matrix. When surface pressure increased to 15 mN/m (Fig. 55.2b), the elliptical domains of DPPC disappeared, and flowerlike and petal-like domains of GD1a were embedded in the matrix. The membrane morphology changed markedly by varying the surface pressure from 15 to 20 mN/m. The flowerlike and petal-like domains of GD1a disappeared and elliptical domains of DPPC appeared again. Furthermore, the matrix formed a percolation pattern. The morphology shown in Fig. 55.2c was maintained at surface pressures of 20∼35 mN/m. Similar morphology, as shown in Fig. 55.2c, was observed not only in the ternary GD1a/DPPC/DOPC (4:6:6) monolayer (Fig. 55.1b) but also in the binary GD1a/DPPC monolayer ($X_{GD1a} = 0.4$ and 0.6 [12]). The change in morphology of the GD1a/DPPC/DOPC (6:4:4) monolayer with increasing surface pressure was more complicated than the GD1a/DPPC/DOPC (4:6:6) monolayer.

Next, a ternary system with a lower ratio of GD1a was examined. AFM images of the GD1a/DPPC/DOPC (2:6:6) monolayer [19] at surface pressures of 15∼35 mN/m are shown in Fig. 55.3.

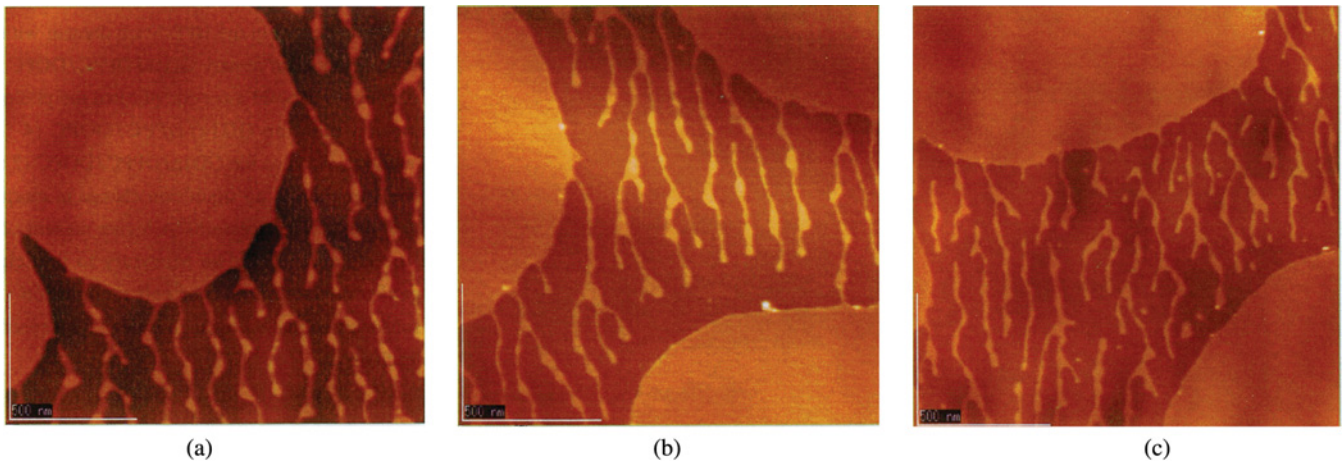


FIGURE 55.3 AFM images of ternary GD1a/DPPC/DOPC (2:6:6) monolayer, with surface pressure (a) 15, (b) 20, and (c) 35 mN/m and scan area 1.5 × 1.5 μm.

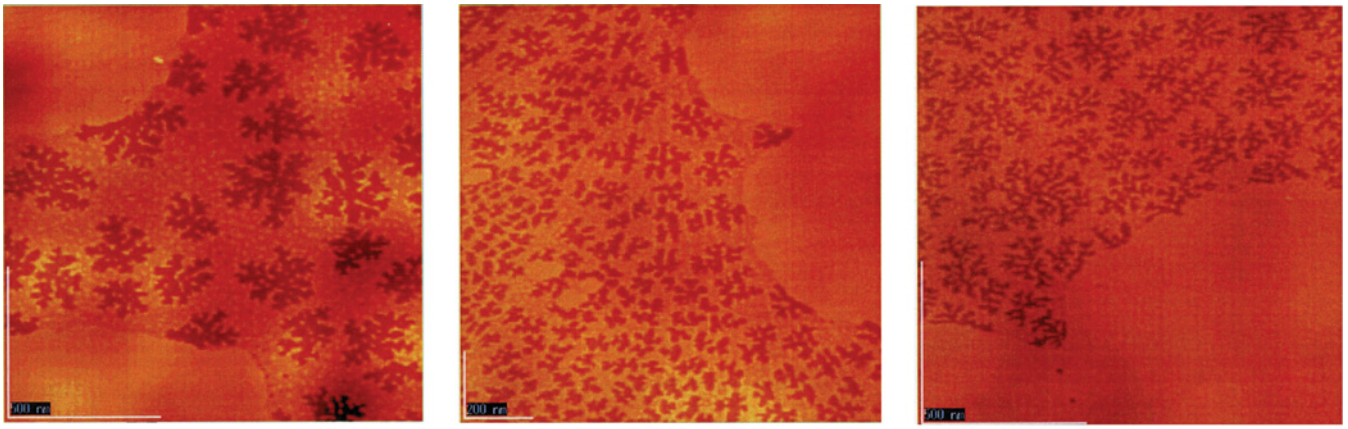


FIGURE 55.4 AFM images of ternary GT1b/DPPC/DOPC (4:6:6) monolayer, with surface pressure (a) 25, (b) 30, and (c) 35 mN/m and scan area 1.5 × 1.5 μm.

Largely circular domains of DPPC are embedded in the matrix. The matrix composed of DOPC and GD1a shows a dripping pattern, which indicates higher fluidity of the matrix. No significant change in the morphology of the GD1a/DPPC/DOPC (2:6:6) monolayer was found by varying surface pressure. A higher content of GD1a in membrane may be necessary to participate in signal transduction compared with GM1, since the content of GD1a in the biological membrane is higher than GM1: 45% GD1a and 2% GM1 in the synapse membrane of rats [17].

55.6.3.2 Ternary GT1b/DPPC/DOPC Monolayer [20]. AFM images of the GT1b/DPPC/DOPC (4:6:6) monolayer are shown in Fig. 55.4.

Largely circular domains of DPPC with a flat surface are embedded in the matrix. Furthermore, snow crystal-like domains of GT1b were formed in the DOPC matrix at 25 mN/m (Fig. 55.4a). When surface pressure increased to 30 mN/m, the snow crystal-like pattern in the matrix changed to a sleety pattern (Fig. 55.4b). Then the sleety pattern in the matrix returned to the snow crystal-like pattern again at 35 mN/m (Fig. 55.4c). The change in morphology of the GT1b/DPPC/DOPC (4:6:6) monolayer with increasing surface pressure was a little compared with the GD1a/DPPC/DOPC (4:6:6) monolayer. Furthermore, the GT1b ternary monolayer showed no percolation pattern as observed for the GD1a ternary monolayer (Fig. 55.1b).

A ternary system containing a lower ratio of GT1b was then chosen to examine the effect of membrane composition on the surface state of the GT1b ternary monolayer. AFM images of the GT1b/DPPC/DOPC (2:6:6) monolayer are shown in Fig. 55.5.

At a surface pressure of 20 mN/m, largely circular (1-μm) domains of DPPC and dark flowerlike domains of GT1b were embedded in the matrix. The membrane morphology

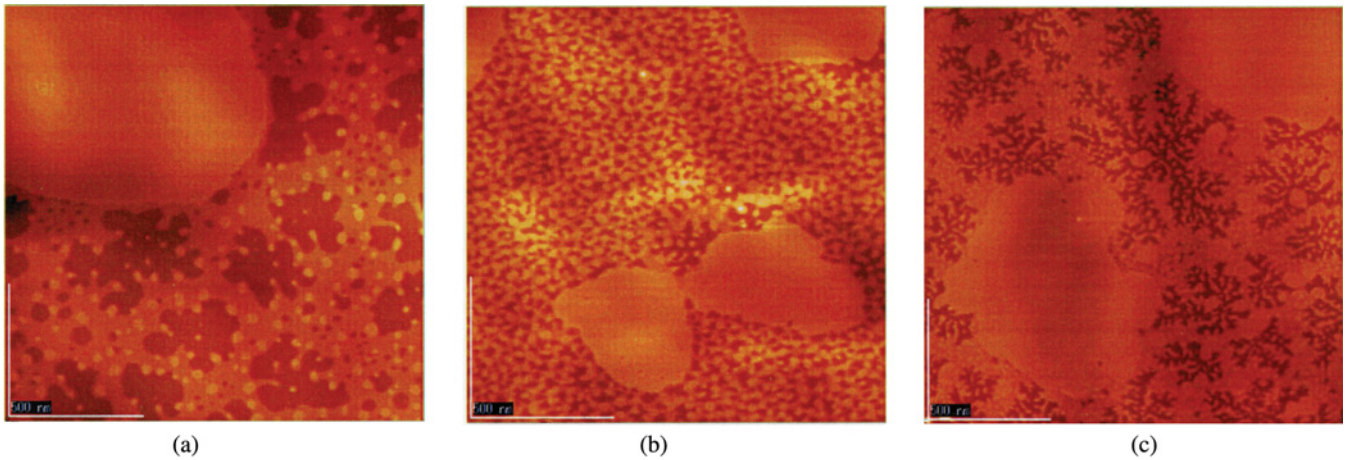


FIGURE 55.5 AFM images of ternary GT1b/DPPC/DOPC (2:6:6) monolayer, with surface pressure (a) 20, (b) 25, and (c) 30 mN/m and scan area 1.5 × 1.5 μm.

changed markedly by varying the surface pressure from 20 to 25 mN/m. The flowerlike domains completely disappeared, and a percolation pattern was formed in the matrix (Fig. 55.5b). When surface pressure further increased to 30 mN/m, the membrane morphology changed again; the percolation pattern disappeared and snow crystal-like domains appeared in the matrix (Fig. 55.5c).

The membrane morphology of the GT1b/DPPC/DOPC (2:6:6) monolayer (Fig. 55.5) was quite different from that of the GD1a/DPPC/DOPC (2:6:6) monolayer (Fig. 55.3). The GD1a ternary (2:6:6) monolayer showed the dripping pattern in the matrix, while the GT1b ternary (2:6:6) monolayer showed no dripping pattern but the more complicated patterns at various surface pressures. Furthermore, the GD1a ternary monolayer showed no significant change in the morphology by varying the surface pressure, while the GT1b ternary monolayer changed markedly the membrane morphology by varying the surface pressure.

A percolation pattern, as observed for the GD1a/DPPC/DOPC (4:6:6) monolayer, was not shown for the GT1b/DPPC/DOPC (4:6:6) monolayer but was shown for the GT1b/DPPC/DOPC (2:6:6) monolayer. Specifically, a percolation pattern seems to be formed in the GT1b ternary monolayer with a lower ratio of GT1b, while a percolation pattern was formed in the GD1a ternary system with a higher ratio of GD1a. A lower content of GT1b in the membrane seems to be convenient to participate in signal transduction compared with GD1a. The content of GT1b in the biological membrane is lower than GD1a: 38% GD1a and 16% GT1b occur in the brain tissue [13]. The specific morphology of the GT1b/DPPC/DOPC (2:6:6) monolayer may be related to the lower content of GT1b in the biological membrane.

55.6.4 Ternary System of Ganglioside/DPPC/Chol

The rafts are rich in Chol. Thus, surface states of ganglioside/DPPC/Chol ternary monolayer were studied before studying gaglioside/DPPC/DOPC/Chol quaterrnary monolayer.

55.6.4.1 Ternary GD1a/DPPC/Chol Monolayer [22]. AFM images of the GD1a/DPPC/Chol (0.5:6:3) monolayer are shown in Fig. 55.6. At a surface pressure of 20 mN/m, a dendritic cell-like domain, which have never been seen, appeared in the matrix. Dendritic cell-like domains increased at 28 mN/m, and then the domains disappeared when surface pressure further increased to 35 mN/m.

A small amount of GD1a contributed to form the specific morphology in the ternary monolayer containing Chol. Whereas ternary systems with higher ratio of GD1a showed no dendritic cell-like domains: the GD1a/DPPC/Chol (4:6:3) monolayer showed dotted pattern at surface pressures of 20–35 mN/m; the GD1a/DPPC/Chol (2:6:3) monolayer showed flowerlike domains at 25 mN/m and spotted pattern at 30 mN/m.

55.6.4.2 Ternary GT1b/DPPC/Chol Monolayer [23]. AFM images of the GT1b/DPPC/Chol (0.5:6:3) monolayer are shown in Fig. 55.7.

At surface pressures of 15–28 mN/m, amebiform domains appeared in the matrix. When surface pressure further increased to 30 mN/m, the amebiform domains disappeared. A small amount of GT1b contributed to form the specific morphology, as well as GD1a, in the ternary monolayer

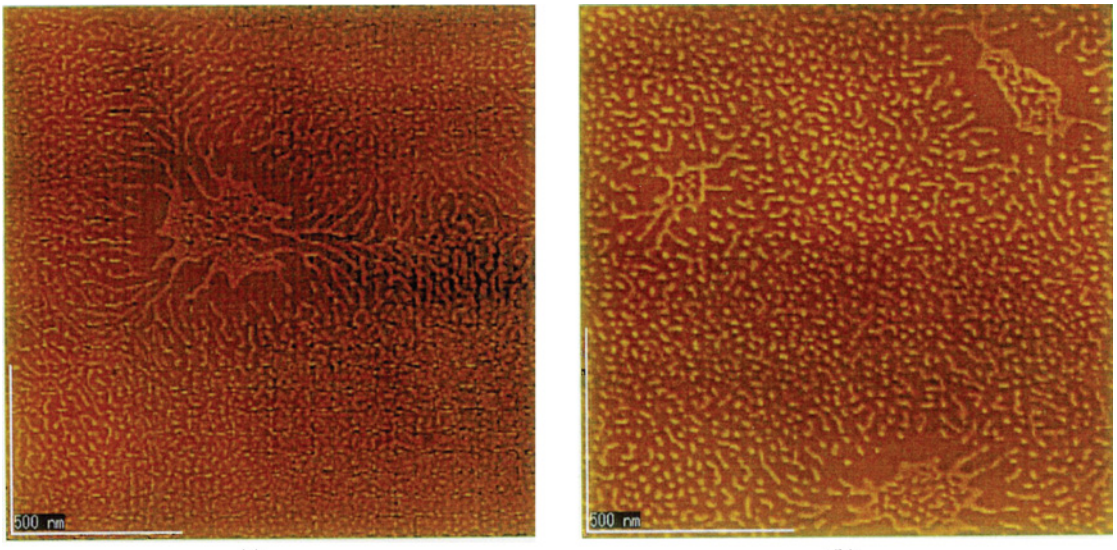


FIGURE 55.6 AFM images of the GD1a/DPPC/Chol (0.5:6:3) monolayer, with surface pressure (a) 20 and (b) 28 mN/m and scan area 1.5 × 1.5 μm.

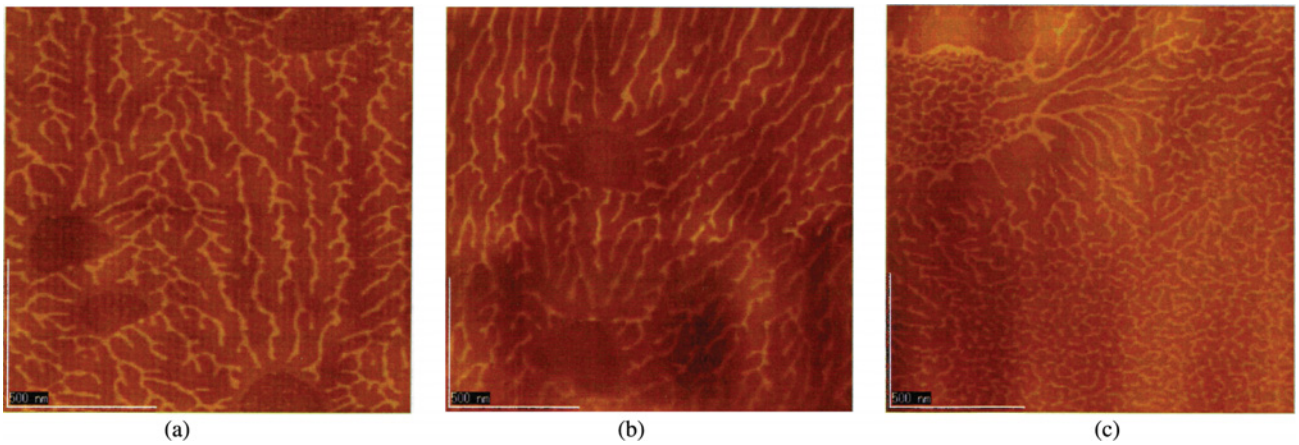


FIGURE 55.7 AFM images of ternary GT1b/DPPC/Chol (0.5:6:3) monolayer, with surface pressure (a) 15, (b) 20, and (c) 28 mN/m and scan area 1.5 × 1.5 μm.

containing Chol. Whereas ternary systems with higher ratio of GT1b showed no amebiform domains. AFM images of the GT1b/DPPC/Chol (2:6:3) monolayer showed a spotted pattern at 25 mN/m and flowerlike domains at 28 mN/m. The AFM image of the GT1b/DPPC/Chol (4:6:6) monolayer showed no specific morphology and no significant change in morphology by varying the surface pressure from 15 to 35 mN/m.

55.6.5 Quaternary System of Ganglioside/DPPC/DOPC/Chol

The rafts are rich in Chol and are surrounded by unsaturated phospholipid [2, 3]. Surface states of quaternary ganglioside/DPPC/DOPC/Chol monolayer as a raft model were studied.

55.6.5.1 Quaternary GD1a/DPPC/DOPC/Chol Monolayer [22]. First, the GD1a/DPPC/DOPC/Chol (0.5:6:6:3) monolayer was chosen for measurement, since the GD1a/DPPC/Chol (0.5:6:3) monolayer showed specific morphology (Fig. 55.6). AFM images of the GD1a/DPPC/DOPC/Chol (0.5:6:6:3) are shown in Fig. 55.8.

At a surface pressure of 15 mN/m, mononuclear cell-like domains, which have never been seen, appeared in the matrix (Fig. 55.8a). When surface pressure increased to 35 mN/m, the domain developed a more complicated morphology: spotted and dotted patterns coexisted in the domains (Fig. 55.8b). Furthermore, a percolation pattern appeared in the matrix.

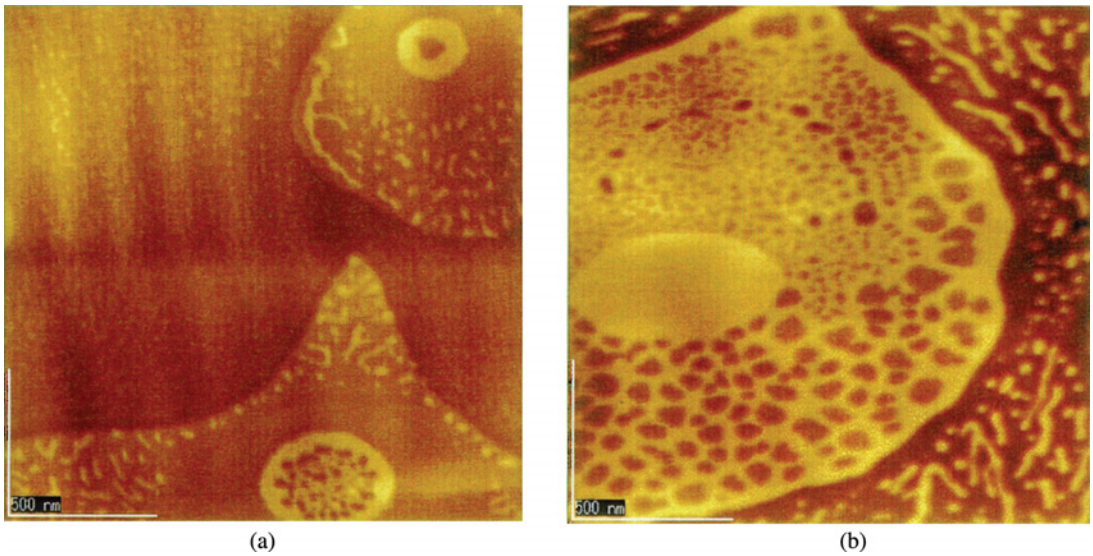
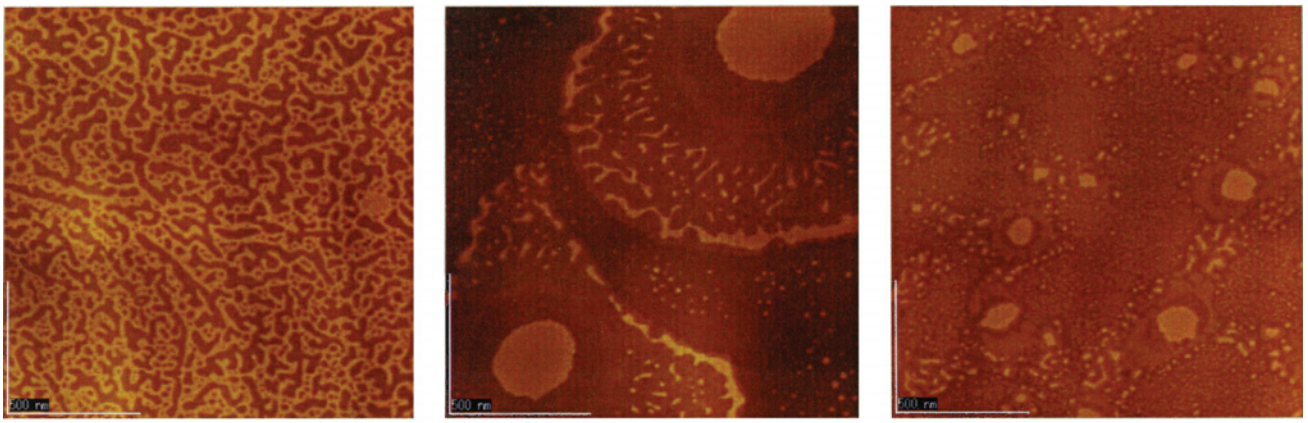


FIGURE 55.8 AFM images of quaternary GD1a/DPPC/DOPC/Chol (0.5:6:6:3) monolayer, with surface pressure (a) 15 and (b) 35 mN/m and scan area 1.5 × 1.5 μm.



(a) (b) (c)

FIGURE 55.9 AFM images of quaternary GT1b/DPPC/DOPC/Chol (0.5:6:6:3) monolayer, with surface pressure (a) 15, (b) 28, and (c) 30 mN/m and scan area 1.5 × 1.5 μm.

On the other hand, the GD1a/DPPC/DOPC/Chol (2:6:6:3) moonolayer, containing a higher ratio of GD1a, showed no mononuclear cell-like domain [20].

In the previous ternary systems without Chol, the GD1a/DPPC/DOPC (4:6:6) monolayer showed specific morphology (Fig. 55.1). In contrast, a small amount of GD1a contributed to form the extremely specific morphology in the quaternary monolayer containing Chol. These results suggest that a small amount of GD1a plays a specific role in rafts.

55.6.5.2 Quaternary GT1b/DPPC/DOPC/Chol Monolayer [23]. AFM images of the GT1b/DPPC/DOPC/Chol (0.5:6:6:3) monolayer are shown in Fig. 55.9.

At a surface pressure of 15 mN/m, a percolation pattern is shown (Fig. 55.9a). When surface pressure increased to 28 mN/m, the percolation pattern disappeared, and mononuclear cell-like domains appeared in the matrix (Fig. 55.9b). When surface pressure further increased to 30 mN/m, the mononuclear cell-like domains deformed (Fig. 55.9c).

The mononuclear cell-like domain was found in systems of both GT1b and GD1a; however, it was observed within a narrow range of surface pressure in the GT1b quaternary system. Furthermore, the GT1b quaternary system showed a percolation pattern. These results suggest that GT1b plays a more specific role in rafts than GD1a.

The GT1b/DPPC/DOPC/Chol (2:6:6:3) monolayer containing a higher ratio of GT1b showed no mononuclear cell-like domain [23]. A small amount of GT1b contributed to form the mononuclear cell-like domain.

55.6.6 Five-Component System of Gangliosides/ DPPC/DOPC/Chol [24]

Surface states of five-component GD1a/GT1b/DPPC/DOPC/Chol monolayers as a biological membrane were investigated. In the previous quaternary systems, the GD1a/DPPC/DOPC/Chol (0.5:6:6:3) monolayer showed a mononuclear cell-like domain, while the GD1a/DPPC/DOPC/Chol (2:6:6:3) monolayer showed no mononuclear cell-like domain and no significant change in morphology by varying the surface pressure. Thus, we chose 0.5 the total molar ratio of GD1a and GT1b in this measurement. First, the GD1a/GT1b/DPPC/DOPC/Chol (0.25:0.25:6:6:3) monolayer was chosen for measurement. AFM images of the monolayer are shown in Fig. 55.10.

At a surface pressure of 15 mN/m, a mononuclear cell-like domain was embedded in the matrix (Fig. 55.10a) as in the previous GD1a quaternary monolayer (Fig. 55.8). When surface pressure increased to 20 mN/m, the nucleus disappeared in the cellular domain (Fig. 55.10b). When surface pressure further increased to 25 mN/m, a nucleus began to appear in the cellular domain (Fig. 55.10c), and the mononuclear cell-like domain pattern recovered at surface pressures above 30 mN/m (Fig. 55.10d).

The quaternary GD1a/DPPC/DOPC/Chol (0.5:6:6:3) monolayer without GT1b indicated mononuclear cell-like domains at surface pressures of 15-35 mN/m (Fig. 55.8). Thus, addition of a small amount of GT1b may contribute to control the disappearance and appearance of the nucleus in the cellular domain, which seems to be related to an on/off function.

A five-component system containing a lower ratio of GT1b was then examined. AFM images of the GD1a/GT1b/DPPC/DOPC/Chol (0.4:0.1:6:6:3) monolayer are shown in Fig. 55.11.

Mononuclear cell-like domains and cellular domains without a nucleus alternately appeared every additional 5 mN/m of surface pressure, which seemed to be an on/off function.

A five-component system containing a lower ratio of GD1a was then examined. AFM images of the GD1a/GT1b/DPPC/DOPC/Chol (0.1:0.4:6:6:3) monolayer are shown in Fig. 55.12.

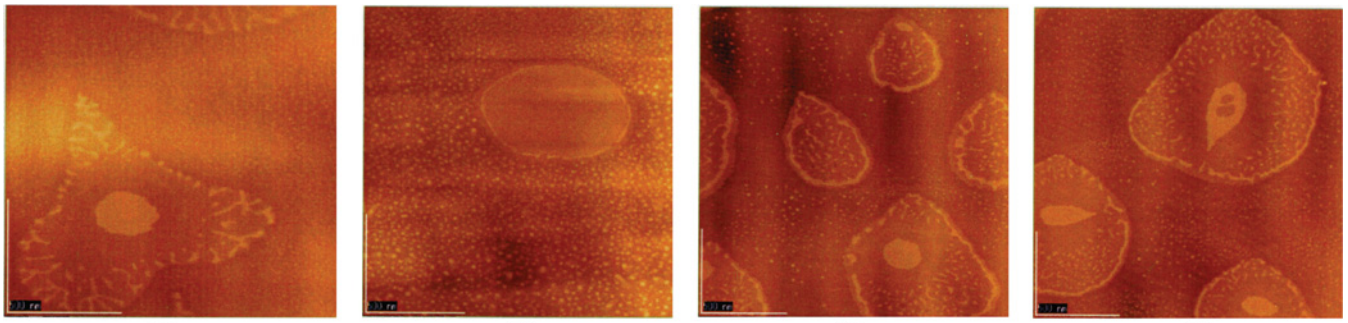


FIGURE 55.10 AFM images of the GD1a/GT1b/DPPC/DOPC/Chol (0.25:0.25:6:6:3) monolayer, with surface pressure (a) 15, (b) 20, (c) 25, and (d) 30 mN/m and scan area 1.5 × 1.5 μm.

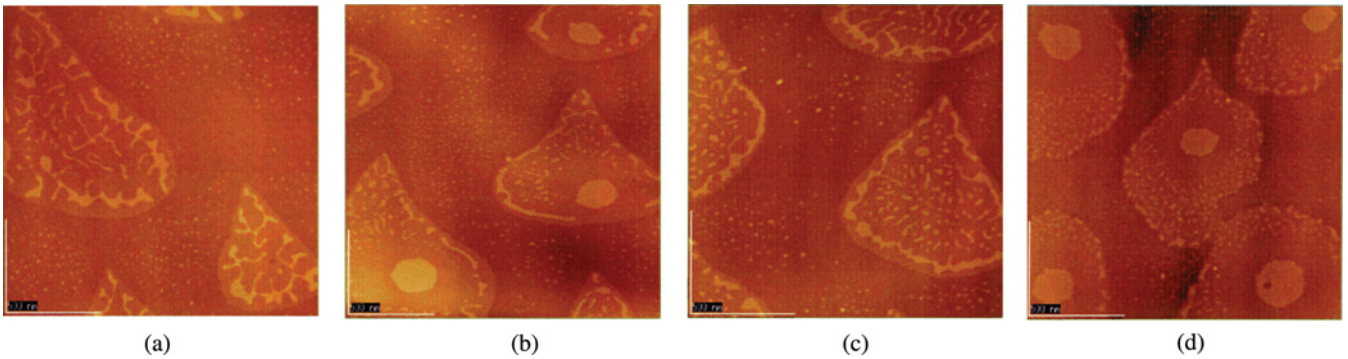


FIGURE 55.11 AFM images of the GD1a/GT1b/DPPC/DOPC/Chol (0.4:0.1:6:6:3) monolayer, with surface pressure (a) 15, (b) 20, (c) 25, and (d) 30 mN/m and scan area 1.5 × 1.5 μm.

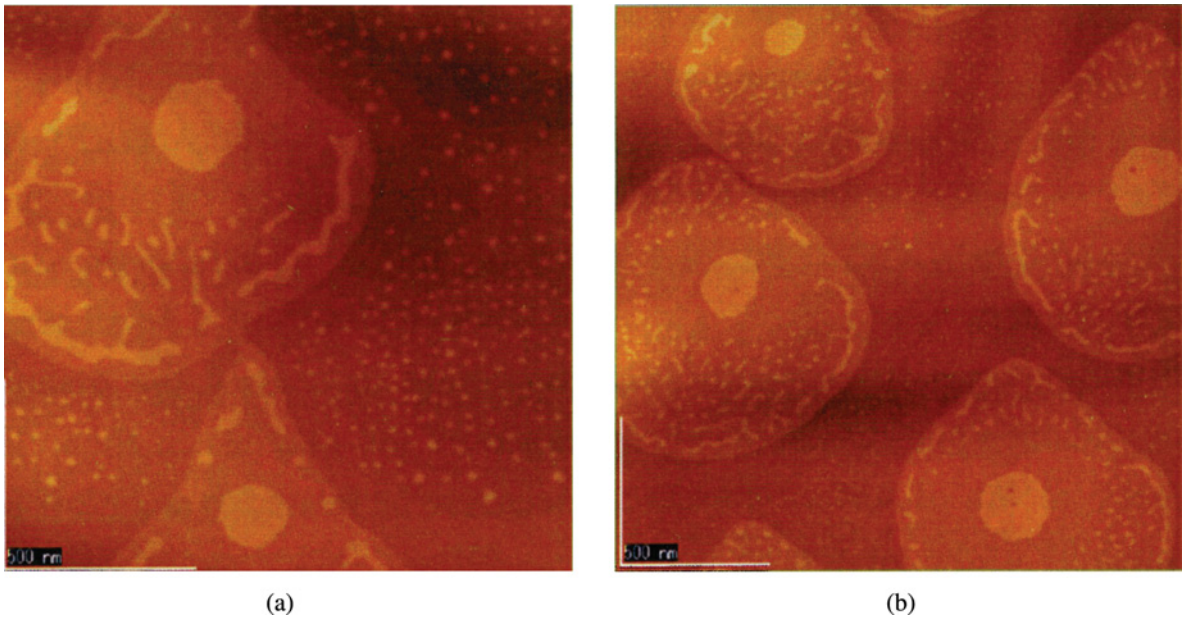


FIGURE 55.12 AFM images of GD1a/GT1b/DPPC/DOPC/Chol (0.1:0.4:6:6:3) monolayer, with surface pressure (a) 15 and (b) 30 mN/m and scan area 1.5 × 1.5 μm.

Mononuclear cell-like domains are found at surface pressures of 15–30 mN/m. The quaternary GT1b/DPPC/DOPC/Chol (0.5:6:6:3) monolayer without GD1a showed a mononuclear cell-like domain at 28 mN/m, and the domains deformed at 30 mN/m (Fig. 55.9). Furthermore, the quaternary monolayer showed a percolation pattern at 15 mN/m (Fig. 55.9). The addition of a small amount of GD1a to the quaternary GT1b/DPPC/DOPC/Chol (0.5:6:6:3) monolayer contributed to the formation of mononuclear cell-like domains at all surface pressures of 15–30 mN/m.

These results suggest that a small amount of each ganglioside plays a specific role in another ganglioside-rich monolayer; a small amount of GD1a functions as a structure maker of the mononuclear cell-like domain, while a small amount of GT1b functions as a structure breaker of the mononuclear cell-like domain. GT1b occurs in higher amounts in the cerebellum. The cerebellum plays a central role in athletic motor functions, where frequent switching on and off of signals is required. When signals or cells approach the ganglioside domains, the surface pressure at the domain should rise. We reported [5] that the conformational change of GM1 at the membrane surface with increasing surface pressure is thought to be related to specific cell recognition or signal transduction. Therefore, the change in morphology of the five-component monolayer by varying the surface pressure and the composition may contribute to the promotion of various physiological events in biological membranes, one of which may be an on/off function, although the role of ganglioside in the biological membrane has not yet been made so clear in the biochemical field.

55.7 CONCLUSION

Surface states of monolayer containing ganglioside changed in morphology by varying the surface pressure. The morphology and the responsive surface pressure of monolayers containing ganglioside were affected by the surrounding environment, suggesting that ganglioside localized in each organ has a specific role.

The GD1a/DPPC/Chol (0.5:6:3) monolayer and the GT1b/DPPC/Chol (0.5:6:3) monolayer showed a dendritic cell-like domain and an amoebiform domain, respectively. The GD1a/DPPC/DOPC/Chol (0.5:6:6:3) monolayer and the GT1b/DPPC/DOPC/Chol (0.5:6:6:3) monolayer, as a raft model, showed a mononuclear cell-like domain, suggesting that ganglioside plays a specific role in rafts.

The GD1a/GT1b/DPPC/DOPC/Chol (0.4:0.1:6:6:3) monolayer showed two patterns of mononuclear cell-like domain and cellular domain without a nucleus every additional 5 mN/m of surface pressure, while the GD1a/GT1b/DPPC/DOPC/Chol (0.1:0.4:6:6:3) monolayer showed mononuclear cell-like domains at all surface pressures of 15–30 mN/m. These results suggested that a small amount of each ganglioside played a specific role in another ganglioside-rich monolayer; a small amount of GD1a functioned as a structure maker of the mononuclear cell-like domain, while a small amount of GT1b functioned as a structure breaker of the mononuclear cell-like domain, which seemed to be related to an on/off function.

REFERENCES

[1] Singer, S.J., Nicolson, G.L. (1972). *Science* **175**, 720–731.

[2] Parton, R.G., Simons, K. (1995). *Science* **269**, 1398–1399.

[3] Simons, K., Ikonen, E. (1997). *Nature* **387**, 569–572.

[4] Iwabuchi, K., Yamamura, S., Prinetti, A., Handa, K., Hakomori, S. (1998). *J. Biol. Chem.* **273**, 9130–9138.

[5] Yokoyama, S., Takeda, T., Ohta, Y., Imura, T., Yamaguchi, A., Sakai, H., Abe, M. (2001). *J. Oleo Sci.* **50**, 917–920.

[6] Yokoyama, S., Ohta, Y., Takeda, T., Imura, T., Sakai, H., Abe, M. (2004). *J. Oleo Sci.* **53**, 97–100.

[7] Ohta, Y., Yokoyama, S., Sakai, H., Abe, M. (2004). *Colloids Surf. B.: Biointerfaces* **34**, 147–153.

[8] Morita, S. (2000). *Scanning Probe Microscope*. Maruzen, Japan, p. 21.

[9] Yuan, C., Furlong, J., Burgos, P., Johnston, L.J. (2002). *Biophys. J.* **82**, 2526–2535.

[10] Ohta, Y., Yokoyama, S., Sakai, H., Abe, M. (2004). *Colloids Surf. B: Biointerfaces* **33**, 191–197.

[11] Probst, W., Mobius, D., Rahmen, H. (1984). *Cell Mol. Neurobiol.* **4**, 157–176.

[12] Ohtsuka, I.; Yokoyama, S. *Mater. Technol.* 2007, **25**, 215-219.

[13] Bordi, F., Luca, F., Cametti, C., Naglier, A., Misasi, R., Sorice, M. (1999). *Colloids Surf. B : Biointerfaces* **13**, 135–142.

[14] Luckham, P., Wood, J., Froggatt, S., Swart, R. (1993). *J. Colloid Interface Sci.* **156**, 164–172.

[15] Ohtsuka, I., Yokoyama, S. (2005). *Mater. Technol.* **23**, 191–194.

[16] Steck, T.L., Dawson, G. (1974). *J. Biol. Chem.* **249**, 2135–2142.

[17] Ando, S. (1997). *Brain Functions and Gangliosides.* Kyoritsu Press, Japan, p. 48.

[18] Ohtsuka, I., Yokoyama, S. (2007). *Mater. Technol.* **25**, 271–273.

[19] Ohtsuka, I., Yokoyama, S. (2008). *Mater. Technol.* **26**, 191–196.

[20] Ohtsuka, I., Yokoyama, S. (2008). *Mater. Technol.* **26**, 229–235.

[21] Yokoyama, S., Ohtsuka, I. (2008). *Mater. Technol.* **26**, 7–9.

[22] Yokoyama, S., Ohtsuka, I. (2009). *Mater. Technol.* **27**, 3–5.

[23] Ohtsuka, I., Toizumi, F., Yokoyama, S. (2010). *Mater. Technol.* **28**, 1–7.

[24] Ohtsuka, I., Toizumi, F., Yokoyama, S. (2011). *Mater. Technol.* **29**, 197–201.

56

LIPONANOCAPSULE: A NANOCAPSULE BUILT FROM A LIPOSOMAL TEMPLATE

YUUKA FUKUI AND KEIJI FUJIMOTO

The Center for Chemical Biology, School of Fundamental Science and Technology, Graduate School of Science and Technology, Keio University, Yokohama, Japan

56.1 INTRODUCTION

In this introductory section, we describe liposome as a template for nanocapsules.

In diverse biological systems, amphiphilic phospholipid molecules are assembled into a bilayer structure to form cell membranes where they are coated with various biomolecules such as polysaccharides and proteins. Cell membranes are fluid and thereby allow for lateral and rotational diffusion of biomolecules embedded in the lipid bilayer. Cytoplasmic organelles are also enclosed by the lipid bilayer, which provides a barrier that determines their boundary and allows for compartmentalization of many biological entities into each organelle. For the molecular transport in the cell and the intercommunication among cells, lipid vesicles are known to serve as a delivery vehicle of functional biomolecules. In this regard, the bilayer structures play important roles to induce many biological reactions and maintain robustness and the total integrity of a cell.

Inspired by such lipid bilayer structures, a nanometer-sized phospholipid vesicle, namely, a liposome, has been developed and utilized as a biocompatible and versatile tool to encapsulate and deliver molecules of interest with possible applications in cosmetics [1] and pharmaceutics [2, 3]. However, liposomes are fluid and fragile against external stimuli such as temperature, pH, shear, adsorption, and enzymatic reactions. Therefore, development of an innovative technique to provide the liposome with robustness has been of considerable interests among many researchers. There have been numerous studies to develop reliable techniques to stabilize the liposome [4–6], such as polymerization inside the bilayer for solidifying the capsule, insertion of polymer chains into the lipid bilayer for stilling the ruffled membrane, adsorption or coating of polymer chains over the lipid surface via the intermolecular interactions for providing steric stabilization [7, 8] and formation of inorganic shells for reinforcing the capsule [9–11]. As another possible way, we here propose a strategy to create a "capsule wall" over the liposome surface with the layer-by-layer assembly of polyelectrolytes. The layer-by-layer assembly is a sophisticated approach to fabricate a thin multilayer of polyelectrolytes, which is based on the alternate deposition of anionic polymers and cationic polymers [12]. This is believed to be driven by the complex formation via electrostatic attractions between anionic and cationic polymers. To produce capsules, the polymer deposition has been carried out onto organic or inorganic cores [13–15], biological cells [16], and even to liquid crystals and emulsions [17]. In our approach, the layer-by-layer deposition of polyelectrolytes over the liposome made it possible to create a bioderived nanocapsule (liponanocapsule) with a variety of polymeric capsule walls. We expected that the multilayer coating over the liposomes would not only make the nanocapsule robust but also endow it with diverse structures and functions thanks to synergistic effects of functional polymer shells and dynamic lipid membranes. In addition, a multilayer shell produced over the liposomal template could serve as a locus for diverse reactions such as mineralization, polymerization, and enzymatic reactions.

Encyclopedia of Biocolloid and Biointerface Science, Volume 2, First Edition. Edited by Hiroyuki Ohshima.
© 2016 John Wiley & Sons, Inc. Published 2016 by John Wiley & Sons, Inc.

56.2 MULTILAYER COATING TO PRODUCE *LIPONANOCAPSULE*

Many of polyelectrolytes are applicable to construct the multilayer shell and Fig. 56.1 summarizes the alternate deposition of polyelectrolytes over the liposomal template [18, 19]. Polyelectrolytes were selected from bioderived polymers where cationic polymers of poly-L-lysine (PLL), polyarginine (PArg), chitosan (CHI) and anionic polymers of poly-L-aspartic acid (PAsp), dextran sulfate (DXS), and DNA were used to prepare bioderived nanocapsules.

The first polymeric layer was generated by the adsorption of cationic polymers onto the negatively charged liposomes, which were prepared from a mixture of dilauroyl phosphatidic acid (DLPA) with a negative charge and dimyristoylphosphatidylcholine (DMPC). It was found that the amount of adsorbed polymers was dependent on lipid ratios, pH values, salt concentrations, and temperatures. PLL is a cationic polypeptide and undergoes unique conformational changes in response to pH and temperature. There have been reports on conformational changes of PLL from random coil to β-sheet on adsorption [20, 21]. It was observed that adsorbed PLL was transformed from random coil into β-sheet structure. This is probably because the positive charge of the adsorbed PLL chain was canceled out by the negative charge of the liposome surface, and thereby the adsorbed PLL chain could adopt the extended conformation sufficiently to form the β-sheet structure.

Next, the second layer could be produced over the first cationic layer by depositing anionic polymers to improve the mechanical robustness of nanocapsule. In this manner, the alternative adsorptions of cationic polymers and anionic polymers were carried out. The ζ-potentials of liponanocapsules changed between positive and negative values at each deposition. TEM images revealed that the shape and the structure of nanocapsules remained intact even after the construction of several polymeric layers. Durability of nanocapsules against surfactants was improved by the layer-by-layer deposition over the lipid membrane. By the addition of Triton-X 100, bare liposomes were ruptured while the liponanocapsule remained suspended without rupturing. Fluorescent substances were incorporated inside the inner cavity of the liponanocapsule prepared with CHI and DXS, and the leakage was measured to investigate the effect of the treatment with the surfactant on the lipid membrane [19]. As a result, the leakage was gradually reduced with increasing the number of layers, indicating that the layer-by-layer coating is an effective way to improve the mechanical robustness of nanocapsules.

56.3 RELEASE BEHAVIOR OF LIPONANOCAPSULES

Liposomes have been utilized as a carrier to encapsulate and deliver many substances, including drugs, proteins, and nucleic acids. As described above, liposomes are fluid and fragile against external stimuli. Furthermore, it is of great importance to improve the release behavior of substances for applications in the biomedical field, especially the drug delivery system. A negatively charged fluorescent probe, 1-hydroxypyrene-3,6,8-trisulfonic acid (HPTS) was encapsulated into bare liposomes and liponanocapsules. Liposomes showed 30–40% release of the encapsulated HPTS after 72 h, whereas the release from liponanocapsules was suppressed by means of layer-by-layer multilayer formation over the liposome [18, 19, 22]. It was found that the release rate was tunable by the surface coverage and the layer number of the polymer deposition. Then, an amphoteric alendronate, a commonly known bone-targeting drug and a nonionic glucose, were encapsulated in liponanocapsules and the release behavior was investigated in the same manner as HPTS. Figure 56.2 shows the result of alendronate. Irrespective of the charge of the encapsulated substance, the release was greatly suppressed compared with bare liposomes. At the same time, the polymer deposition reduced the membrane fluidity of the lipid bilayer. It is thought that the release of the encapsulated substances is greatly influenced by the fluidity. Therefore, it can be concluded that the release proceeds in the diffusion-limited manner, resulting in low permeability of substances through the capsule wall.

In addition, it is expected that the release is tunable by the selection of the capsule wall. For instance, when DNA was chosen to prepare a polymeric layer, the liponanocapsule exhibited a switching release in response to temperature. It is known that DNA is denatured into the random-coil structure

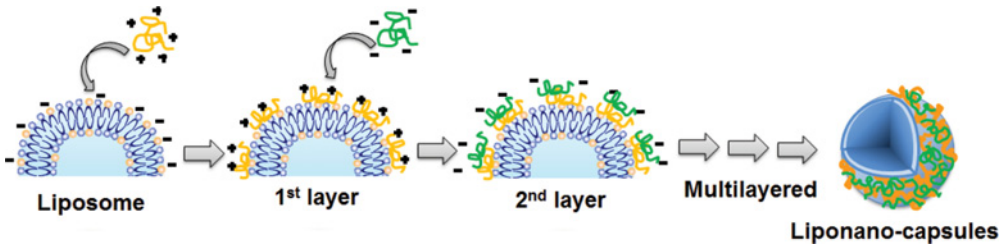


FIGURE 56.1 Schematic illustration of layer-by-layer deposition of polyelectrolytes over a liposome to prepare liponanocapsule.

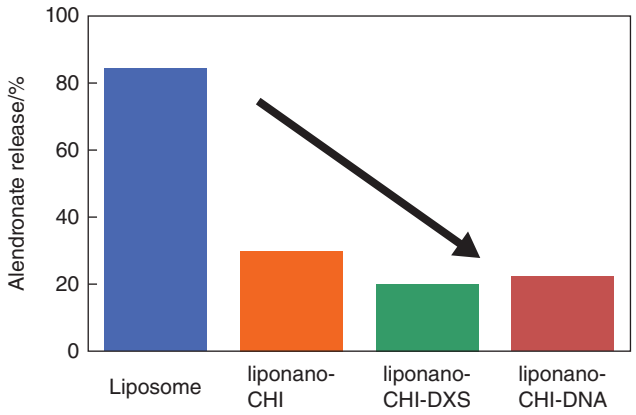


FIGURE 56.2 Percentage release of alendronate from a liposome and liponanocapsules after 85 h incubation (pH 4.5, 20°C).

by heating. As expected, the release from DNA-deposited nanocapsules was clearly increased by raising temperature from 25°C to 60°C. As denatured DNA was partially desorbed and removed from the surface of the liponanocapsule, it is thought that the capsule wall was greatly perturbed by desorption of DNA and consequently the release was triggered in a temperature-dependent manner [19].

56.4 INTERACTION OF LIPONANOCAPSULES WITH CELLS

As described above, the polymer layer formed over the liposomal template would render diverse properties to the capsule surface. When we intend to apply the liponanocapsules as a tool in the pharmaceutical and medical fields, it is important to consider their interactions with an external system such as proteins and cells. Here, we selected CHI and DNA as the outermost layer because they are known to exhibit good inertness on the interaction with cells [22]. We also carried out the surface deposition of PArg to provide the liponanocapsule with abilities to overcome the permeability barrier of the plasma membrane and transfect encapsulated substances into the cytosol. Arginine oligopeptides are well known to possess a cell-penetrating activity, which serve a function in delivering various substances [23–28]. Cellular uptake assays demonstrated that all of liposomes and liponanocapsules were internalized at 37°C. When experiments were carried out at 4°C, bare liposomes showed a suppressed uptake and the CHI-deposited nanocapsules with a positive charge underwent binding onto the cell surface rather than internalization. The cell penetration of arginine peptides occurs in a temperature-independent manner [29]. In fact, PArg-coated nanocapsules could be internalized at 4°C, indicating that the internalization is attributed to the cell-penetrating activity of the PArg layer. It was also found that cell-penetrating activity remained even after the deposition of DNA over the PArg-deposited nanocapsule and cellular uptake of liponanocapsules decreased with increasing the surface coverage of DNA.

56.5 ASSEMBLY OF LIPONANOCAPSULES TO CREATE FREESTANDING BIOSCAFFOLD

Freestanding thin films such as a nanosheet and a nanocarpet have attracted considerable attention in diverse applications including electronics, separation technology, pharmaceutical science, and biomedical engineering. In particular, it is expected that they will be utilized as a bioscaffold for wound healing, cardiovascular stent coating, and tissue engineering [30]. The fabrication of freestanding membranes has been achieved by various methods, including detachment of membranes built on the solid surface and formation of membranes at the air–liquid and the liquid–liquid interfaces [31]. Also, freestanding membranes can be obtained by assembling of nanoparticles through confinement of nanoparticles in microdroplets and further drying-mediated assembly of nanoparticles and microdroplets [32]. The use of liponanocapsules as a building block to create a bioscaffold is advantageous because individual bioderived liponanocapsules possess versatility, for example, biocompatibility and bioresorbability, abilities for controlled release, and cell penetration. They will be able to serve not only as a scaffold for tissue repair and regeneration but also as a supplier for the controlled release of drugs and growth factors. Therefore, we carried out the microhole-confined assembly to prepare a freestanding membrane from nanocapsules (Fig. 56.3). An aqueous suspension of nanocapsules was blotted over a metal mesh with the microholes [22]. As water evaporation proceeded

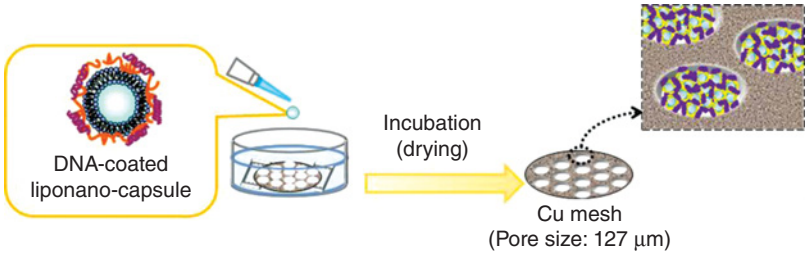


FIGURE 56.3 Schematic illustration of fabrication of freestanding membranes from DNA-coated liponanocapsules by drying-mediated assembly over the microholes of the mesh grid.

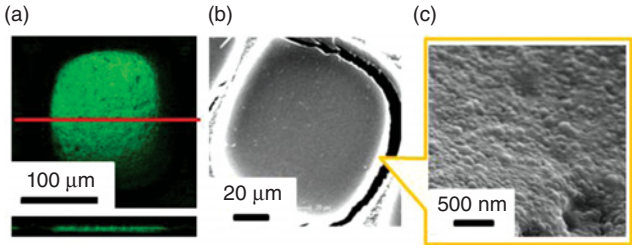


FIGURE 56.4 Confocal laser microscopic (a) and scanning electron microscopic images (b,c) of membranes produced from DNA-coated liponanocapsules.

from the suspension, dewetting took place so as to trap nanocapsules into each individual microhole.

We could not prepare membranelike structures from bare liposomes, and a partially ruptured membrane was obtained by the assembly of PArg-coated nanocapsules. In such a bottom–up assembly, DNA often acts as a "dry ligand" to produce a freestanding nanosheet of nanoparticles [32–34]. The organization of DNA coronas makes it possible to build up freestanding nanoparticle superlattices through the ordering of nanoparticles and nonspecific DNA–DNA interactions. Therefore, we prepared liponanocapsules displaying the DNA layer and intended to fabricate a freestanding membrane by the drying-mediated DNA organization. As a result, we could obtain the freestanding membrane. After drying, the shape and the structure of each nanocapsule remained the same and the fluorescent-labeled dextran was kept inside each nanocapsule (Fig. 56.4). Although other polyelectrolytes were tested, DNA was the best dry ligand among them. DNA-assisted assembly of nanoparticles is an effective method to create a bioscaffold from liponanocapsules.

56.6 COATING WITH MINERALS TO PREPARE ORGANIC–INORGANIC HYBRID LIPONANOCAPSULE

Mineralization found in nacre and bone is highly controlled within closed compartments, such as vesicles and insoluble extracellular organic matrices under mild conditions, resulting in the formation of hierarchical architectures that provide multifunctional properties [35–37]. Inspired by such a system, there have been numerous studies on mineralization using a liposomal template to give rise to organic-inorganic hybrid nanocapsules. Here, we focused on calcium phosphate (CaP) as a mineral, which is the main constituent of hard tissues in vertebrates, such as bones and teeth, and is the most abundant inorganic material in living organisms. In terms of materials design, the pH-dependent dissolution of CaP is advantageous to render pH-responsivity to carriers for drug or gene delivery [38]. CaP formation over the liposomal surface has often been conducted by adding both calcium and phosphate ions to the outer water phase and subsequently controlling reaction conditions such as pH and temperature [39]. In our approach, we utilized liponanocapsules with various polymeric layers as templates for mineralization [40]. Figure 56.5 summarizes the strategy for preparation of hybrid organic–inorganic liponanocapsules. In order to conduct a spatial control of CaP formation, calcium ions and phosphate ions were compartmentalized into the outer phase and the inner cavity of the capsule, respectively. This can allow for phosphate ions and calcium ions to mutually diffuse across the capsule wall (counterdiffusion-driven mineralization). The release of phosphate ions from a bare liposome was so fast that CaP formation could not be observed on the surface. Therefore, it is required to conduct the slow and mutual diffusion for the formation of hybrid nanocapsules; that is, the control of the ion diffusion with the polysaccharide layer of the capsule wall is a key to tune mineralization.

In addition, it is expected that ions captured by ionic moieties of the polymeric layer could facilitate the precipitation of CaP on the surface. There have been numerous studies on the template effect of organic or polymeric compounds on CaP growth from aqueous media. In this regard, sophisticated approaches based on bioinspired and biomimetic mineralization have been employed to control crystal properties and determine the site for CaP formation [41–46]. We focused on polyelectrolytes containing functional groups such as phosphate and carboxyl, which are implicated in CaP

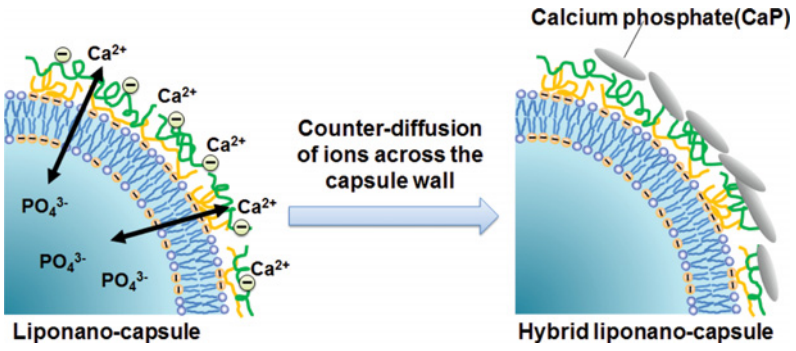


FIGURE 56.5 Schematic illustration of preparation of hybrid organic–inorganic liponanocapsules via counterdiffusion of ions across the capsule wall.

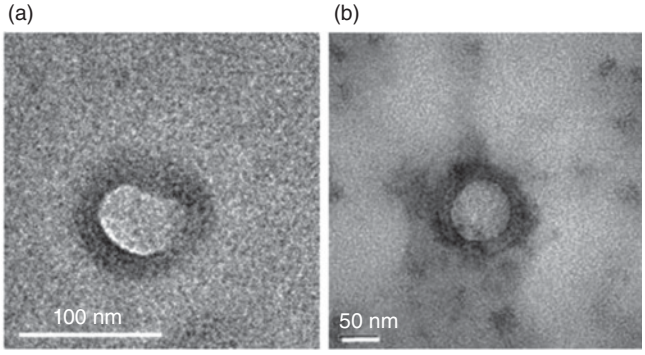


FIGURE 56.6 TEM images of hybrid nanocapsules after deposition of CaP over a liposome (a) and DNA-coated liponano-capsule (b). Reaction was carried out at 37°C for 1 h using $Ca(NO_3)_2$ and $(NH_4)HPO_4$ as ion species.

crystallization. Carboxyl groups of collagen are supposed to be responsible for nucleation of hydroxyapatite (HAp) on collagen from a simulated body fluid (SBF). Phosphate groups, which are displayed on bare liposomes and DNA-coated nanocapsules, are expected to function as a site for CaP nucleation. TEM observations showed that CaP was precipitated selectively over both surfaces as a result of the mutual diffusion of calcium ions and phosphate ions and the high affinity of the phosphate moiety for calcium ions (Fig. 56.6). The thickness of the CaP layer changed with the reaction time. From the results of electron diffraction and infrared analysis, CaP precipitated over the DNA-coated nanocapsules showed high crystallinity compared with bare liposomes. These suggest that the high affinity for calcium ions and the locus suitable to promote CaP nucleation and crystallization in addition to the control of the release of ions are needed to create the hybrid nanocapsule. Finally, it is also noted that the combination of mineralization with liponanocapsules could provide multifunctional hybrid nanocapsules with bioinertness, biocompatibility, and resorbability derived from biominerals.

56.7 CONCLUSIONS

We have described a facile and useful approach for design and synthesis of bioderived nanocapsules, liponanocapsules, based on the concept of layer-by-layer assembly of polyelectrolytes over a liposomal template. This approach allowed for diverse selections of the polymer ranging from synthetic polymers to bioderived polymers such as polypeptides, polysaccharides, and DNA. The resultant liponanocapsules exhibited excellent properties, including mechanical robustness, controlled release of substances, and enhanced cell membrane permeability. Furthermore, the liponanocapsules were assembled into a freestanding membrane by linking with the outermost DNA layer as a dry ligand. Such a hierarchical structure is advantageous in use as a bioscaffold for gene transfection, cell culture, and tissue regeneration because various substances, including drugs and growth factors, can be encapsulated and their release is also controllable. Finally, we presented a novel strategy in creating hybrid nanocapsule via mineralization of calcium phosphate over the surface of liponanocapsules.

The liponanocapsule is a designable material and will open a promising opportunity for potential applications in a variety of fields, especially cosmetics and pharmaceutics.

REFERENCES

[1] Moussaoui, N., Cansell, M., Denziot, A. (2002). *Int. J. Pharm.* **242**, 361–365.

[2] Weiner, N., Lieb, L., Niemiec, S., Ramachandran, C., Hu, Z., Egbaria, K. (1994). *J. Drug Target.* **2**, 405–410.

[3] Lasic, D.D. (1997). *J. Control. Release* **48**, 203–222.

[4] Ruysschaert, T., Germain, M., Gomes, J.F.P.D., Fournier, D., Sukhorukov, G.B., Meier, W., Winterhalter, M. (2004). *IEEE Transact. Nanobiosci.* **3**, 49–55.

[5] Hubert, D.H.W., Jung, M., German, A.L. (2000). *Adv. Mater.* **12**, 1291–1294.

[6] Ringsdorf, H., Schlarb, B., Venzmer, J. (1988). *Angew. Chem. Int. Ed.* **27**, 113–158.

[7] Yaroslavov, A.A., Rakhnyanskaya, A.A., Yaroslavova, E.G., Efimova, A.A., Menger, F.M. (2008). *Adv. Colloid Int. Sci.* **142**, 43–52.

[8] Tribet, C., Vial, F. (2008). *Soft Matt.* **4**, 68–81.

[9] Schmidt, H.T., Gray, B.L., Wingert, P.A., Ostafin, A.E. (2004). *Chem. Mater.* **16**, 4942–4947.

[10] Xu, Q., Tanaka, Y., Czernuszka, J.T. (2007). *Biomaterials* **28**, 2687–2694.

[11] Schmidt, H., Ostafin, A.E. (2002). *Adv. Mater.* **14**, 532–535.

[12] Decher, G. (1997). *Science* **277**, 1232–1237.

[13] Angelatos, A.S., Katagiri, K., Caruso, F. (2006). *Soft Matt.* **2**, 18–23.

[14] Caruso, F., Caruso, R.A., Mohwald, H. (1998). *Science* **282**, 1111–1114.

[15] Antipov, A.A., Sukhorukov, G.B., Donath, E., Mohwald, H. (2001). *J. Phys. Chem. B* **105**, 2281–2284.

[16] Diaspro, A., Silvano, D., Krol, S., Cavalleri, O., Gliozzi, A. (2002). *Langmuir* **18**, 5047–5050.

[17] Tjipto, E., Cadwell, K.D., Quinn, J.F., Johnston, A.P.R., Abbott, N.L., Caruso, F. (2006). *Nano Lett.* **6**, 2243–2248.

[18] Fujimoto, K., Toyoda, T., Fukui, Y. (2007). *Macromolecules* **40**, 5122–5128.

[19] Fukui, Y., Fujimoto, K. (2009). *Langmuir* **25**, 10020–10025.

[20] Fukushima, K., Muraoka, Y., Inoue, T., Shimozawa, R. (1989). *Biophys. Chem.* **34**, 83–90.

[21] Fukushima, K., Muraoka, Y., Inoue, T., Shimozawa, R. (1988). *Biophys. Chem.* **30**, 237–244.

[22] Yamamoto, S., Fukui, Y., Kaihara, S., Fujimoto, K. (2011). *Langmuir* **27**, 9576–9582.

[23] Takechi, Y., Yoshii, H., Tanaka, M., Kawakami, T., Aimoto, S., Saito, H. (2011). *Langmuir* **27**, 7099–7107.

[24] Chugh, A., Eudes, F., Shim, Y. (2010). *IUBMB Life* **62**, 183–193.

[25] Vives, E., Richard, J.P., Rispal, C., Lebleu, B. (2003). *Curr. Protein Peptide Sci.* **4**, 125–132.

[26] El-Andaloussi, S., Jarver, P., Johansson, H.J., Langel, U. (2007). *Biochem. J.* **407**, 285–292.

[27] Brooks, N.A., Pouniotis, D.S., Tang, C., Apostolopoulos, V., Pietersz, G.A. (2010). *Biochim. Biophys. Acta Rev. Cancer* **1805**, 25–34.

[28] Tsogas, I., Tsiourvas, D., Nounesis, G., Paleos, C.M. (2005). *Langmuir* **21**, 5997–6001.

[29] Conner, S.D., Schmid, S.L. (2003). *Nature* **422**, 37–44.

[30] Caridade, S.G., Monge, C., Gilde, F., Boudou, T., Mano, J.F., Picart, C. (2013). *Biomacromolecules* **14**, 1653–1660.

[31] Cheng, W., Campolongo, M.J., Tan, S.J., Luo, D. (2009). *Nano Today* **4**, 482–493.

[32] Cheng, W., Campolongo, M.J., Cha, J.J., Tan, S.J., Umbach, C.C., Muller, D.A., Luo, D. (2009). *Nature Mater.* **8**, 519–525).

[33] Jakobsen, U., Simonsen, A.C., Vogel, S. (2008). *J. ACS* **130**, 10462–10463.

[34] Licata, N.A., Tkachenko, A.V. (2008). *Europhysics Letters.* **84**, 20010.

[35] Hayashi, A., Nakamura, T., Watanabe, T. (2010). *Crystal Growth Design* **10**, 5085–5091.

[36] Garimella, R., Bi, X.H., Anderson, H.C., Camacho, N.P. (2006). *Bone* **38**, 811–817.

[37] Mann. S. (2001). *Biomineralization. Principles and Concepts in Bioinorganic Materials Chemistry*. Oxford Univ. Press, Oxford, UK.

[38] Sugawara, A., Yamane, S., Akiyoshi, K. (2006). *Macromol. Rapid Commun.* **27**, 441–446.

[39] Xu, Q., Tanaka, Y., Czernuszka, J.T. (2007). *Biomaterials* **28**, 2687–2694.

[40] Fukui, Y., Fujimoto, K. (2011). *Chem. Mater*. **23**, 4701–4708.

[41] Girija, E., Yokogawa, Y., Nagata, F. (2004). *J. Mater. Sci. Mater. Med.* **15**, 593–599.

[42] Spanos, N., Klepetsanis, P.G., Koutsoukos, P.G. (2001). *J. Colloid Interface Sci.* **236**, 260–265.

[43] Tsortos, A., Nancollas, G.H. (2002). *J. Colloid Interface Sci.* **250**, 159–167.

[44] Takeuchi, A., Ohtsuki, C., Kamitakahara, M., Ogata, S., Tanihara, M., Miyazaki, T. (2006). Bioceramics, Trans Tech Publications Ltd., Switzerland, **18**, 489–492.

[45] Takeuchi, A., Ohtsuki, C., Miyazaki, T., Kamitakahara, M., Ogata, S., Yamazaki, M., Furutani, Y., Kinoshita, H., Tanihara, M. (2005). *J. Roy. Soc. Interface Sci.* **2**, 373–378.

[46] Wang, J., Zhou, W., Hu, W., Zhou, L., Wang, S., Zhang, S. (2011). *J. Biomed. Mater. Res*. **A 99**, 327–334.

57

PHYSICAL PHENOMENA OF MAGNETIC SUSPENSIONS FOR APPLICATION TO BIOENGINEERING

Akira Satoh

Faculty of Systems Science and Technology, Akita Prefectural University, Honjo City, Akita Prefecture, Japan

57.1 INTRODUCTION

A representative application of magnetic suspensions to the bioengineering field is a magnetic drug delivery system (magnetically targeted drug) employing a gradient magnetic field [1–3]. As schematically shown in Fig. 57.1, the concept of the magnetic delivery system is that composite particles composed of thermo-sensitive polymeric material loading (anticancer) drugs and magnetic materials (particles) are administered to a targeted region such as a tumor or cancer cells intensively and effectively by means of a gradient applied magnetic field. There are two main approaches to synthesize magnetic composite particles for transporting anticancer drugs in a magnetically targeted drug delivery system. The first approach for synthesizing these functional composite particles is to use a particle with a magnetic core or a composite magnetic core that is coated with polymeric materials that function to adsorb and load (store) the drugs [4–13]. The second approach is to coat the surface of a non-magnetic core particle with small magnetic particles in addition to the polymeric materials that adsorb and load drugs [14–17]. On the application of a nonuniform magnetic field, both types of composite particle will experience a body force acting in the direction of the field gradient, so that it is possible to use this effect to administer drug agents to a specific site (tumor or cancer cells) in the human body intensively and effectively by means of an appropriate arrangement of magnets [18–21].

Surface modification technology plays an important role in successful synthesis of composite particles for magnetic drug delivery. Moreover, according to the synthesis method, diffusion and sedimentation phenomena in the gravity field may have a significant effect on the final quality of these functional particles. In particular, the sedimentation behavior of the magnetic composite particles has a significant relationship with the drug concentration on the surface properties of biological membranes [22]. Furthermore, it is necessary to develop the technology for controlling self-assembled layers, aggregation structures, and orientational features of magnetic particles on a material surface after sedimentation, by means of an applied magnetic field. From the above consideration, it is clear that, in developing functional composite particles for the magnetic drug delivery system, physical phenomena such as aggregation phenomena, orientional distribution, and phase change of magnetic particles on a material surface have a significant relationship with the synthesis procedure.

From this background, in the present chapter we address suspensions of magnetic spherical and axisymmetric particles in order to focus on the following two physical phenomena for discussion; we consider (1) the dependence of the magnetic particle behavior on a material surface on various factors such as the magnetic field and the magnetic particle–particle interaction strength [23–26] and (2) sedimentation characteristics of magnetic particles in the gravity field and also the integrated structures on a material surface after sedimentation, which are dependent on various factors such as the magnetic field strength [27].

Monte Carlo, molecular dynamics, and Brownian dynamics methods [28–31] are powerful simulation techniques for the detailed microscopic analysis of the above-mentioned physical phenomena. In the present chapter, we treat

Encyclopedia of Biocolloid and Biointerface Science, Volume 2, First Edition. Edited by Hiroyuki Ohshima.
© 2016 John Wiley & Sons, Inc. Published 2016 by John Wiley & Sons, Inc.

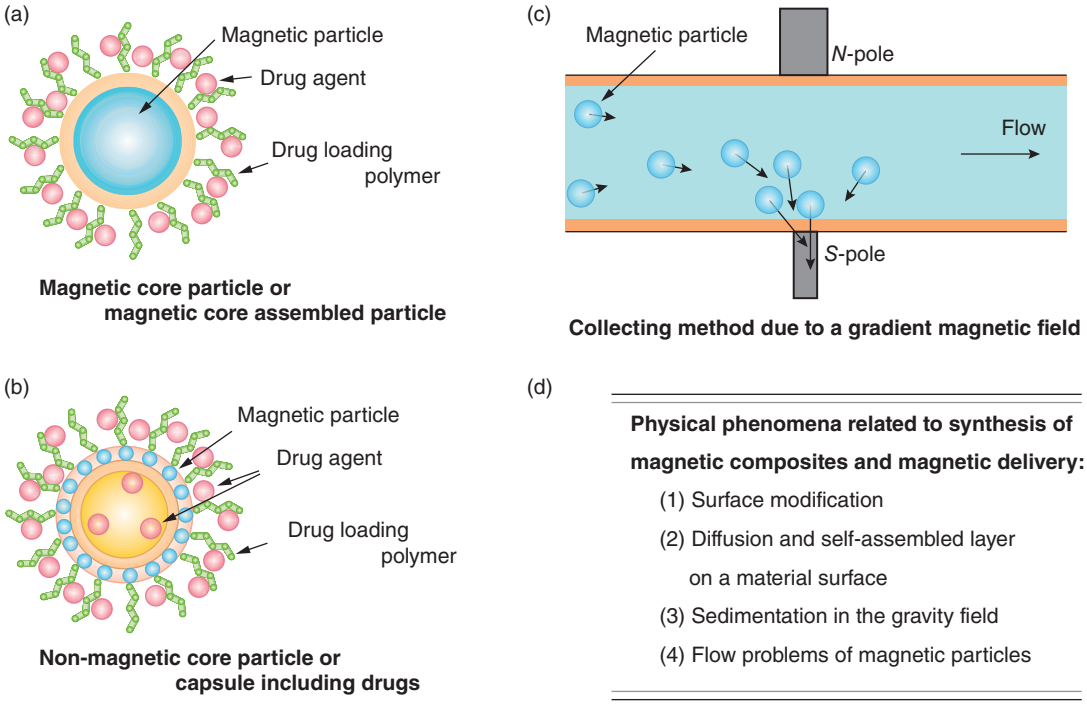


FIGURE 57.1 Concept of a magnetic drug delivery system and related physical phenomena: (a) magnetic core particle coated with drug loading polymers; (b) nonmagnetic core particle or capsule including drugs coated with drug-loading polymers; (c) collecting method due to a magnetic body force acting on magnetic particles; (d) physical phenomena related to the synthesis of magnetic composites and a magnetic delivery.

suspensions composed of magnetic particles for which Monte Carlo and Brownian dynamics are significantly useful simulation techniques. Hence, in the following text we first outline these simulation methods and then discuss the above-mentioned physical phenomena. Finally, we expect that the present discussion on the application examples of molecular simulations to the physical phenomena of interest yields a significant guide for the microscopic analysis of the physical problems that will be encountered in generating new magnetic composite particles for the loading of drugs in a magnetic delivery system.

57.2 SIMULATION METHODS FOR COLLOIDAL SUSPENSIONS

57.2.1 Monte Carlo Method

The Monte Carlo method generates a series of microscopic states conforming to a certain stochastic law, irrespective of the equations of motion of particles (or molecules), and this method is suitable mainly for phenomena in thermodynamic equilibrium [28–30]. In the following text, we explain the important concepts of the Monte Carlo method.

We consider how microscopic states are stochastically derived. We here treat a system composed of N interacting spherical particles with temperature T and volume V of the system; these quantities are values given and are assumed to be constant. If the position vector of an arbitrary particle i ($i = 1,2,\ldots,N$) is denoted by $\boldsymbol{r}_i$, the total interaction energy U of the system can be expressed as a function of the particle positions, that is, can be expressed as $U = U(\boldsymbol{r}_1, \boldsymbol{r}_2, \ldots, \boldsymbol{r}_N)$. For the present system specified by given values of N, T and V, the appearance of a microscopic state that particle i ($i = 1,2,\ldots,N$) exits within the small range of $\boldsymbol{r}_i \sim(\boldsymbol{r}_i + \Delta\boldsymbol{r}_i)$ is governed by the probability density function $\rho(\boldsymbol{r}_1, \boldsymbol{r}_2, \ldots, \boldsymbol{r}_N)$, and this may be expressed from statistical mechanics as

$$\rho(\boldsymbol{r}_1, \boldsymbol{r}_2, \ldots, \boldsymbol{r}_N) = \frac{\exp\{-U(\boldsymbol{r}_1, \boldsymbol{r}_2, \ldots, \boldsymbol{r}_N)/kT\}}{\int_V \cdots \int_V \exp\{-U(\boldsymbol{r}_1, \boldsymbol{r}_2, \ldots, \boldsymbol{r}_N)/kT\} d\boldsymbol{r}_1 d\boldsymbol{r}_2 \cdots d\boldsymbol{r}_N} \tag{57.1}$$

If a series of microscopic states are generated with an occurrence according to this probability, a simulation may have a physical meaning. However, this approach is impracticable, since there is considerable difficulty in the analytic evaluation of the definite integral of the denominator in

Eq. (57.1). It is the Metropolis method [32] that is able to overcome this difficulty for Monte Carlo simulations.

In the Metropolis method, the transition probability from microscopic states i to j, p_{ij}, is expressed as

$$p_{ij} = \begin{cases} 1 & (\text{for } \rho_j/\rho_i \geq 1) \\ \dfrac{\rho_j}{\rho_i} & (\text{for } \rho_j/\rho_i < 1) \end{cases} \tag{57.2}$$

in which ρ_i and ρ_j are the probability density functions for microscopic states i and j appearing, respectively. The ratio of ρ_j/ρ_i is obtained from Eq. (57.1) as

$$\begin{aligned} \frac{\rho_j}{\rho_i} &= \exp\left[-\frac{1}{kT}(U_j - U_i)\right] \\ &= \exp\left[-\frac{1}{kT}\left\{U(\boldsymbol{r}^j_1, \boldsymbol{r}^j_2, \ldots, \boldsymbol{r}^j_N) - U(\boldsymbol{r}^i_1, \boldsymbol{r}^i_2, \ldots, \boldsymbol{r}^i_N)\right\}\right] \end{aligned} \tag{57.3}$$

In the above equations, U_i and U_j are the interaction energies of microscopic states i and j, respectively, and the superscripts attached to the position vectors denote the same meaning in regard to the microscopic states. Equation (57.2) implies that, in the transition from microscopic state i to j, the new microscopic state j is adopted if the system energy decreases, and if the system energy increases, it is adopted with the probability ρ_j/ρ_i (<1). It is clearly seen from Eq. (57.3) for ρ_j/ρ_i that the denominator in Eq. (57.1) is not required in Eq. (57.3) since ρ_j is divided by ρ_i and the term is canceled through this operation. This is the main reason of great success of the Metropolis method for Monte Carlo simulations. That a new microscopic state is adopted with the probability ρ_j/ρ_i even in the case of the increase in the interaction energy, verifies the accomplishment of the minimum free-energy condition for the system. In other words, the adoption of microscopic states yielding an increase in the system energy corresponds to an increase in the entropy.

The above discussion is directly applicable to a system composed of nonspherical particles. The situation of nonspherical particles in thermodynamic equilibrium is specified by the particle position of the mass center, $\boldsymbol{r}_i$ ($i = 1,2,\ldots,N$), and the unit vector $\boldsymbol{e}_i$ ($i = 1,2,\ldots,N$) denoting the particle direction. The transition probability from microscopic state i to j, p_{ij}, can be written in similar form to Eq. (57.2), and the expression for ρ_j/ρ_i becomes

$$\begin{aligned} \frac{\rho_j}{\rho_i} &= \exp\left[-\frac{1}{kT}(U_j - U_i)\right] \\ &= \exp\left[-\frac{1}{kT}\left\{U_j\left(\boldsymbol{r}^j_1, \boldsymbol{r}^j_2, \ldots, \boldsymbol{r}^j_N, \boldsymbol{e}^j_1, \boldsymbol{e}^j_2, \ldots, \boldsymbol{e}^j_N\right)\right.\right. \\ &\quad \left.\left. - U_i\left(\boldsymbol{r}^i_1, \boldsymbol{r}^i_2, \ldots, \boldsymbol{r}^i_N, \boldsymbol{e}^i_1, \boldsymbol{e}^i_2, \ldots, \boldsymbol{e}^i_N\right)\right\}\right] \end{aligned} \tag{57.4}$$

For a strongly interacting particle system, the addition of a cluster-moving algorithm may be necessary for correctly simulating a magnetic spherical particle suspension [30]. This is because the usual Metropolis MC algorithm [32] does not take into account the cooperative behavior between the groups of particles that form clusters. In the case of a conventional MC algorithm, should a number of clusters be formed, they will remain scattered because there is no facility for them to join with each other. The cluster-moving MC algorithm regards such scattered clusters as temporary unitary particles, and moves the clusters according to a transition probability similar to the conventional Metropolis method, so that an additional mechanism for particle aggregation can be achieved.

57.2.2 Brownian Dynamics Method for Axisymmetric Particles

When we treat a colloidal dispersion or a polymeric solution, the Stokesian dynamics [33, 34] and Brownian dynamics methods [28] are usually employed as a microscopic or mesoscopic analysis tool. Since the translational and rotation motion has to be simulated simultaneously in the case of nonspherical particles, the simulation is much more complex than for a spherical particle system. We here summarize the theory of the Brownian dynamics method for an axisymmetric particle system [31], which is more useful for the numerous simulations based on realistic materials.

Dispersed particles or polymers are modeled as idealized spherical or dumbbell particles [35], and the motion of these particles will be pursued by the equation of motion. In a particle suspension, the base liquid is usually assumed to be a continuum medium, and its effect is included in the equations of motion of the particles or the polymers only as friction terms [28]. If particle size approximates to or is smaller than micrometer order, the inertia terms may be considered as negligible. In the present section, we treat this type of small particle and neglect the inertia terms.

We consider the translational and rotational Brownian motion of rodlike particles in a simple shear flow field $\boldsymbol{U}$ with angular velocity vector $\boldsymbol{\Omega}$ and rate-of-strain tensor $\boldsymbol{E}$, as shown in Fig. 57.2. The theory shown below is applicable to a dilute dispersion where the multi-body hydrodynamic interactions among particles are negligible, but it may also be relevant as a first approximation in the case of a nondilute suspension.

For an axisymmetric particle, the translational motion can be decomposed into the motion in the long-axis direction and the motion in a direction normal to the particle axis. Similarly, the rotational motion can be decomposed into the rotation about the particle axis and the rotation about a line normal to the particle axis through the center of mass.

An arbitrary vector is decomposed into the two vectors parallel and normal to the particle axis, and these vectors are

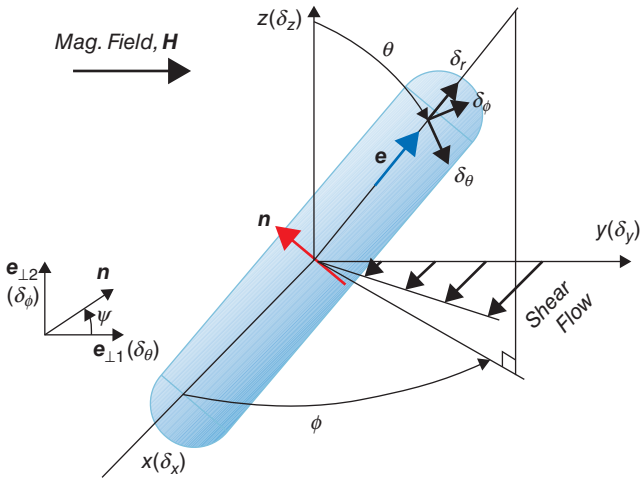


FIGURE 57.2 Magnetic spherocylinder particle in a simple shear flow under the circumstance of an applied magnetic field.

denoted by subscripts || and⊥, respectively. The equation of translational motion, providing the particle position $\boldsymbol{r}(t)$, is then expressed as [30]:

$$\boldsymbol{r}_{||}(t+\Delta t) = \boldsymbol{r}_{||}(t) + \boldsymbol{U}_{||}\Delta t + \frac{1}{kT} D^T_{||} \boldsymbol{F}^P_{||}(t)\Delta t + \Delta r^B_{||}\boldsymbol{e}(t) \tag{57.5}$$

$$\boldsymbol{r}_{\perp}(t+\Delta t) = \boldsymbol{r}_{\perp}(t) + \boldsymbol{U}_{\perp}\Delta t + \frac{1}{kT} D^T_{\perp} \boldsymbol{F}^P_{\perp}(t)\Delta t + \Delta r^B_{\perp 1}\boldsymbol{e}_{\perp 1}(t) + \Delta r^B_{\perp 2}\boldsymbol{e}_{\perp 2}(t) \tag{57.6}$$

in which k is Boltzmann's constant, T is the system temperature, $\boldsymbol{F}^p_{||}$ and $\boldsymbol{F}^p_{\perp}$ are the forces acting on the particle of interest, $\boldsymbol{e}(t)$ is the unit vector denoting the particle direction, the vectors $\boldsymbol{e}_{\perp 1}$ and $\boldsymbol{e}_{\perp 2}$ are the unit vectors normal to each other in the plane normal to the particle axis, and $D^T_{||}$ and $D^T_{\perp}$ are the translational diffusion coefficients [30,36,37]. The quantities $\Delta r^B_{||}$, $\Delta r^B_{\perp 1}$, and $\Delta r^B_{\perp 2}$ are the random displacements inducing the translational Brownian motion and have the following stochastic characteristics:

$$\left\langle \Delta r^B_{||} \right\rangle = \left\langle \Delta r^B_{\perp 1} \right\rangle = \left\langle \Delta r^B_{\perp 2} \right\rangle = 0,$$
$$\left\langle \left(\Delta r^B_{||}\right)^2 \right\rangle = 2D^T_{||}\Delta t,\ \left\langle \left(\Delta r^B_{\perp 1}\right)^2 \right\rangle = \left\langle \left(\Delta r^B_{\perp 2}\right)^2 \right\rangle = 2D^T_{\perp}\Delta t \tag{57.7}$$

For the case of a particle with a magnetic moment normal to the particle axis such as the rodlike hematite particle, it is required to specify the spin Brownian motion about the particle axis in addition to the ordinary rotational motion about a line normal to the particle axis [38]. The equation for the particle direction $\boldsymbol{e}(t)$ and the magnetic moment direction $\boldsymbol{n}(t)$ are expressed as

$$\boldsymbol{e}(t+\Delta t) = \boldsymbol{e}(t) + \boldsymbol{\Omega}_{\perp}\times\boldsymbol{e}\Delta t + \frac{1}{kT} D^R_{\perp}\boldsymbol{T}^P_{\perp}(t)\times\boldsymbol{e}\Delta t - \frac{Y^H}{Y^C}\left((\boldsymbol{\varepsilon}\cdot\boldsymbol{ee}):\boldsymbol{E}\right)\times\boldsymbol{e}\Delta t + \Delta\phi^B_{\perp 1}\boldsymbol{e}_{\perp 1} + \Delta\phi^B_{\perp 2}\boldsymbol{e}_{\perp 2} \tag{57.8}$$

$$\boldsymbol{n}(t+\Delta t) = \boldsymbol{n}(t) + \boldsymbol{\Omega}_{||}\times\boldsymbol{n}\Delta t + \frac{1}{kT} D^R_{||}\boldsymbol{T}^P_{||}(t)\times\boldsymbol{n}\Delta t + \Delta\phi^B_{||}\boldsymbol{e}\times\boldsymbol{n} \tag{57.9}$$

in which Y^C and Y^H are the resistance functions [36], and $\boldsymbol{\varepsilon}$ is the third-rank tensor, called *Eddington's epsilon*, and $D^R_{||}$ and $D^R_{\perp}$ are the rotational diffusion coefficients. Also, $\boldsymbol{T}^P$ is the torque acting on the particle of interest and is evaluated from summation of the torques due to, for example, magnetic and steric repulsive forces.

The quantities $\Delta\phi^B_{||}$, $\Delta\phi^B_{\perp 1}$, and $\Delta\phi^B_{\perp 2}$ are the random displacements inducing the rotational Brownian motion and have the following stochastic characteristics:

$$\left\langle \Delta\phi^B_{||} \right\rangle = \left\langle \Delta\phi^B_{\perp 1} \right\rangle = \left\langle \Delta\phi^B_{\perp 2} \right\rangle = 0,\ \left\langle \left(\Delta\phi^B_{||}\right)^2 \right\rangle = 2D^R_{||}\Delta t,$$
$$\left\langle \left(\Delta\phi^B_{\perp 1}\right)^2 \right\rangle = \left\langle \left(\Delta\phi^B_{\perp 2}\right)^2 \right\rangle = 2D^R_{\perp}\Delta t \tag{57.10}$$

The quantities in the parallel and the normal directions to the particle axis are expressed using the unit vector $\boldsymbol{e}$, denoting the particle axis direction, as

$$\left.\begin{aligned} &\boldsymbol{F}^{||} = (\boldsymbol{F}\cdot\boldsymbol{e})\,\boldsymbol{e}, \quad \boldsymbol{F}^{\perp} = \boldsymbol{F} - \boldsymbol{F}^{||}, \quad \boldsymbol{T}^{||} = (\boldsymbol{T}\cdot\boldsymbol{e})\,\boldsymbol{e}, \\ &\boldsymbol{T}^{\perp} = \boldsymbol{T} - \boldsymbol{T}^{||}, \quad \boldsymbol{\Omega}^{||} = (\boldsymbol{\Omega}\cdot\boldsymbol{e})\,\boldsymbol{e} \quad \boldsymbol{\Omega}^{\perp} = \boldsymbol{\Omega} - \boldsymbol{\Omega}^{||} \end{aligned}\right\} \tag{57.11}$$

57.3 SURFACE MODIFICATION

57.3.1 Magnetic Spherical Particle System

57.3.1.1 Introductory Remarks. If ferromagnetic nanoparticles are dispersed on a nonmagnetic substrate, these nanostructured films acquire very attractive magnetic properties. One simple method for preparing self-organized monolayers of particles is to dry a colloidal dispersion. When a droplet of the dispersion is deposited on a substrate, reduction in size of the droplet due to evaporation of the solvent produces ordered microstructures of monolayers through the phenomenon of self-organization.

Molecular simulation is a powerful method for investigating in detail the influence of the governing parameters such as the areal density of particles and the external magnetic

field strength. Various two-dimensional (2D) and quasi-two-dimensional (Q2D) simulations have been conducted on a monolayer composed of ferromagnetic spherical particles [39]. If the magnetic field is applied in the direction normal to the plane of a Q2D monolayer, it can be expected that the formation of chainlike structures will be prevented by a repulsive magnetic interaction between particles [40]. This fact suggests that properties of the monolayer can be changed significantly by adjusting the direction and/or the strength of an applied magnetic field. Hence, investigation of the influence of both the magnetic field strength and the areal density on the microstructures is quite important for developing new nanogranular magnetic thin films.

In this section, therefore, we consider a Q2D system of a monolayer composed of ferromagnetic particles under an external magnetic field applied in the direction normal to the monolayer plane. Monte Carlo simulations were carried out in order to clarify the influence of the magnetic field strength and the areal density on the microstructures in the state of thermodynamic equilibrium [23].

57.3.1.2 Particle Model and Quasi-Two-Dimensional Monte Carlo Simulation. We consider a Q2D system composed of N monodispersed spherical particles that have a magnetic dipole at their center. This system is assumed to be in thermodynamic equilibrium with system temperature T. The particle is modeled as a sphere with a magnetic moment $\boldsymbol{m}_i$ at the particle center, of diameter d and coated with a uniform steric surfactant layer of thickness δ. Employing the notation r_{ij} for the separation between particles i and j, $\boldsymbol{n}_i$ ($=\boldsymbol{m}_i/m$) for the magnetic moment direction of particle i and $\boldsymbol{H}$ ($=H\boldsymbol{h}$, $H = |\boldsymbol{H}|$) for the applied magnetic field, the magnetic particle-field interaction energy $u_i^{(H)}$ and the magnetic particle-particle interaction energy $u_{ij}^{(m)}$ are expressed as [23]

$$u_i^{(H)} = -kT\xi \boldsymbol{n}_i \cdot \boldsymbol{h},$$
$$u_{ij}^{(m)} = kT\lambda \frac{d^3}{r_{ij}^3}(\boldsymbol{n}_i \cdot \boldsymbol{n}_j - 3(\boldsymbol{n}_i \cdot \boldsymbol{t}_{ij})(\boldsymbol{n}_j \cdot \boldsymbol{t}_{ij})) \quad (57.12)$$

in which ξ and λ are the dimensionless parameters, representing the strength of particle–field and particle–particle interactions, respectively, relative to the thermal energy. These parameters are written as

$$\xi = \mu_0 mH/kT, \quad \lambda = \mu_0 m^2/4\pi d^3 kT \quad (57.13)$$

in which k is Boltzmann's constant, μ_0 is permeability of free space, and $\boldsymbol{t}_{ij}$ is the unit vector denoting the direction of the relative position of particle i to j, given by $\boldsymbol{t}_{ij} = \boldsymbol{r}_{ij}/r_{ij}$ ($r_{ij} = |\boldsymbol{r}_{ij}|$).

If the steric layers of the two particles of interest overlap, a repulsive interaction arises between the two particles. This repulsive interaction $u_{ij}^{(V)}$ is expressed as [23]

$$u_{ij}^{(V)} = kT\lambda_V \left\{ 2 - \frac{2r_{ij}/d}{2\delta/d} \ln\left(\frac{d+2\delta}{r_{ij}}\right) - \frac{r_{ij}/d - 1}{\delta/d} \right\} \quad (57.14)$$

in which λ_V is the dimensionless parameter representing the strength of the repulsive interaction due to the particle overlap relative to thermal energy.

The particles can move only within the xy plane, but their magnetic moment can incline in any direction in 3D space. A uniform external magnetic field $\boldsymbol{H}$ is applied in the direction normal to the material surface (or in the z direction). The results shown below were obtained for $\lambda = 8$ and $\lambda_V = 150$ for comparison with the previous results.

57.3.1.3 Results and Discussion. Figure 57.3 shows the influence of the magnetic field strength on the microstructure of the monolayer for the case of the areal density of particles, $\phi_a = 0.3$. A numerous number of chainlike structures are formed in the absence of the magnetic field (not shown as a figure), and these chain-like structures still remain even in the case of the relatively weak magnetic field $\xi = 10$, shown in Fig. 57.3a. This is because the magnetic particle–particle interaction is more dominant than the effect of the magnetic field, so that the magnetic moments can remain inclining in directions in the xy plane. As the influence of the magnetic field increases further to $\xi = 20$ and 30, the chainlike microstructures gradually disappear (Fig. 57.3b) and random liquidlike structures appear (Fig. 57.3c).

Figure 57.4 shows the dependence of the orientational distribution function Ψ on the magnetic field strength in order to investigate quantitatively the influence of the magnetic field strength on the orientation of the magnetic moment. The abscissa of the figure indicates the polar angle θ from the field direction. In the case of $\xi = 10$, the orientational distribution has a wide and relatively flat profile with a peak at $\theta \simeq 73°$. As the magnetic field is increased to $\xi = 20$, a broad peak profile appears in the magnetic field direction ($\theta = 0°$) and the peak becomes higher. This implies that, although the magnetic moment still has a weak tendency to incline in the magnetic field direction, it can incline in neighboring directions relatively freely. For the case of $\xi = 30$, the orientation of the magnetic moments is strongly restricted toward the field direction, so that the peak of the profile becomes much higher.

Figure 57.5 shows the dependence of the radial distribution function on the magnetic field strength where r in the figure is the particle–particle distance. For the cases of $\xi = 0$ and 10 (Fig. 57.5a,b), sharp peaks appear at $r/(d+2\delta) \simeq 1.0$, 2.0, and so on, which implies that chain-like clusters are significantly formed. As the magnetic field is increased to $\xi = 20$

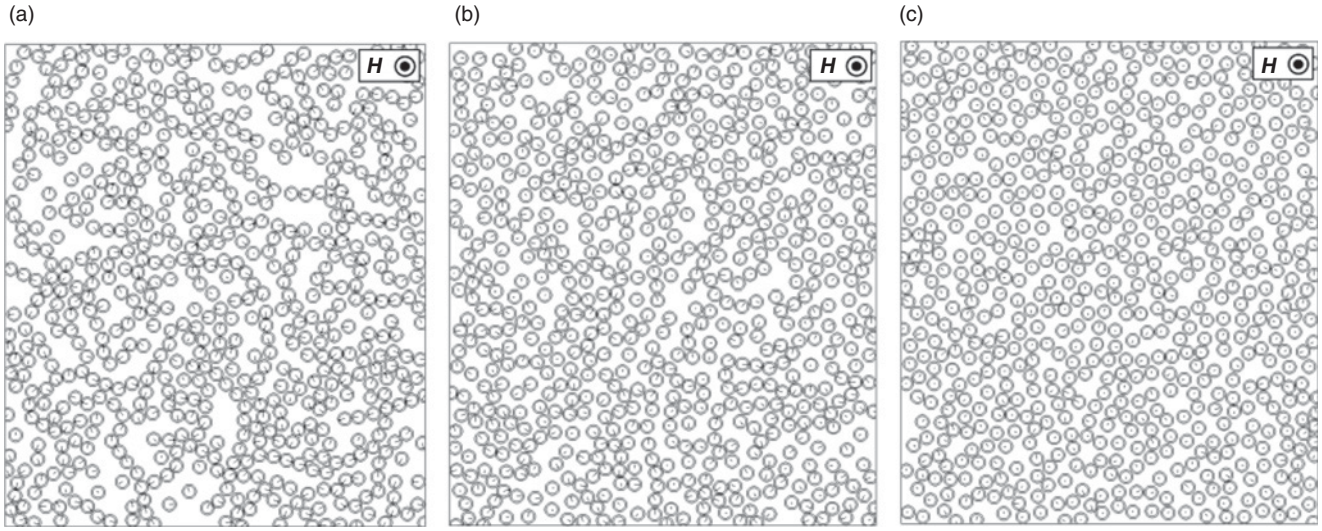


FIGURE 57.3 Influence of the magnetic field strength on microstructures for $\phi_a = 0.3$: (a) $\xi = 10$; (b) $\xi = 20$; (c) $\xi = 30$.

(Fig. 57.5c), the second peak becomes much lower and therefore this implies that chainlike clusters become much shorter. For the case of a further stronger magnetic field, $\xi = 30$ (Fig. 57.5d), the magnetic repulsive interaction due to the dipole–dipole interaction between particles is much more dominant, and the chainlike formation is no longer found. This leads to liquidlike characteristics in the radial distribution function.

57.3.2 Rodlike Particle System

57.3.2.1 Introductory Remarks. New functional materials may be developed by artificially controlling the particle microstructure in order to give rise to desired functional properties. If magnetic rodlike particles are sedimented in the gravitational field, the particle orientational distribution may be controlled by an applied magnetic field, and on the evaporation of the base liquid we may obtain a surface modified material, frequently via a process of self-organization.

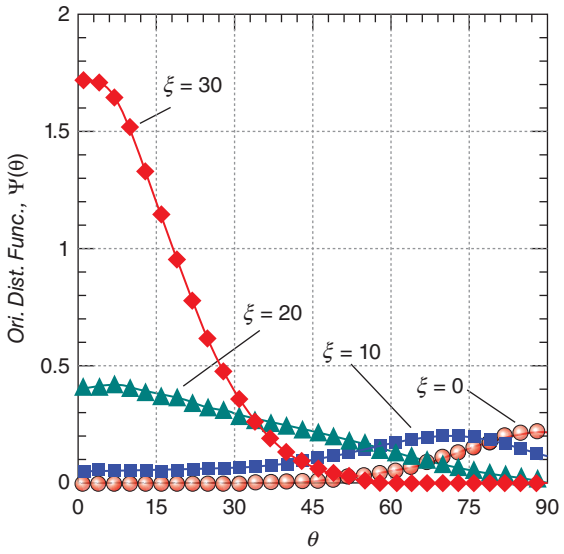


FIGURE 57.4 Dependence of the orientational distribution function on the magnetic field strength ξ.

Ferromagnetic rodlike particles are ordinarily magnetized in the major-axis direction and the different types of magnetic rodlike particles are also an attractive subject from an application perspective. A suspension composed of hematite particles with a magnetic moment normal to the particle axis has already been synthesized [41, 42]. Several theoretical work relating to this type of suspension show that under a simple shear flow a rodlike particle can rotate freely to a certain degree but with the magnetic moment remaining inclined toward the magnetic field direction [43, 44]. This behavior is completely different from that of a suspension composed of rodlike particles magnetized in the direction of the particle axis. In addition to the magnetorheological perspective, these suspensions are an attractive research subject from the viewpoint of developing the techniques for controlling the orientational features of magnetic rodlike particles.

In this present section, we discuss the dependence of the aggregate structures and the orientational distribution on various factors such as the magnetic particle–particle and particle–field interactions. The results shown below were obtained by means of the cluster-moving Monte Carlo method explained in Section 57.2.1, for a two-dimensional system [24].

57.3.2.2 Particle Model and Simulation Method. Experimental observation shows that rodlike hematite particles have the shape of a spheroid [41, 42]. However, it is quite difficult to assess whether the spheroidal particles overlap during a simulation procedure; therefore, we use the simpler approach

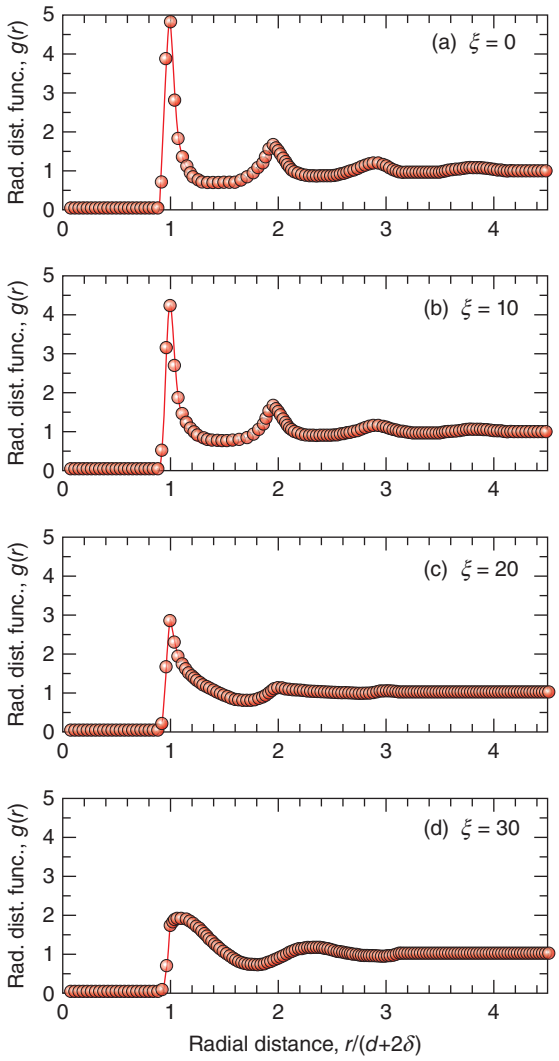


FIGURE 57.5 Influence of the magnetic field strength on the radial distribution function for $\phi_a = 0.3$: (a) $\xi = 0$; (b) $\xi = 10$; (c) $\xi = 20$; (d) $\xi = 30$.

of a linear sphere-connected model. In this particle model, a rodlike particle is modeled by a number of linearly connected spheres. The length of the rod-like particle is expressed by the number N_P of constituent particles and is covered by a surfactant layer (steric layer) with constant thickness δ. Hence, the present phenomenon is characterized by the particle length N_p, the areal fraction ϕ_a, and the three nondimensional parameters ξ, λ, and λ_V, shown in Eq. (57.13), where ξ, λ, and λ_V imply the strength of the magnetic particle-field, the particle–particle interactions, and the streic interaction relative to the thermal energy, respectively.

57.3.2.3 Results and Discussion. Figure 57.6 shows snapshots for the particle length $N_P = 3$ and the areal fraction $\phi_a = 0.2$. For the case of $\lambda = 5$ (Fig. 57.6a), there are numerous short clusters composed of two or three particles that are observed to move independently. This is because the magnetic interaction between particles is not sufficiently strong to allow the formation of longer clusters. On the other hand, for the case of $\lambda = 10$ (Fig. 57.6b), numerous long raftlike clusters are observed to be formed. In this case, the magnetic interaction between particles is sufficiently strong to promote the short clusters to aggregate to form longer raftlike clusters that are generally observed to have a relatively nonlinear form.

Figure 57.7 shows snapshots for a strong magnetic field for the case such as $\xi = 20$. The magnetic field is applied in the upward direction of the paper. For the case of $\lambda = 5$ (Fig. 57.7a), the magnetic particle–particle interaction is relatively weak so that significantly long clusters are not formed over the whole region; nevertheless, relatively long clusters are partially observed. This is because a strong applied magnetic field enhances the alignment of the magnetic moments in the field direction and this alignment induces the cluster formation. For a strong magnetic particle–particle interaction in the case of $\lambda = 10$ (Fig. 57.7b), there is a significant tendency for numerous long raftlike clusters to be formed in the field direction, however, it is not observed that these long raftlike clusters aggregate further to form thicker columnlike clusters. This is in significantly contrast to the behavior observed in a spherical particle system [45] where thick chainlike clusters are formed in the case of a relatively strong magnetic interaction. This is because, in a rodlike particle system, sufficiently strong forces do not act between two raftlike clusters that are in a parallel arrangement.

Figure 57.8 shows the cluster size distribution for $\xi = 20$, $\lambda = 10$, and $\phi_a = 0.2$, and the results were obtained for the three cases of the particle length, $N_p = 3,5,7$. It is seen that for the same conditions the number of longer clusters decreases with increasing particle length, but this tendency is not so significant. The curve of $N_P = 7$ almost coincides with that for $N_P = 5$, and even the curve for $N_P = 3$ does not deviate significantly from the other two curves. These characteristics may be explained as follows. The magnetic interaction strength between the neighboring particles in the same cluster does not change for different particle lengths, but the influence of Brownian displacements appears to be strongly dependent on the particle length. That is, the rotational motion of a longer particle induces a more severe overlap effect between the neighboring particles of the same cluster, which leads to a more stable cluster formation for the cluster composed of shorter particles.

57.3.3 Disklike Particle System

57.3.3.1 Introductory Remarks. A suspension composed of disklike or platelike fine particles shows interesting behavior in regard to the phase transition from a disordered isotropic to a nematic phase [46], magnetic-field-induced

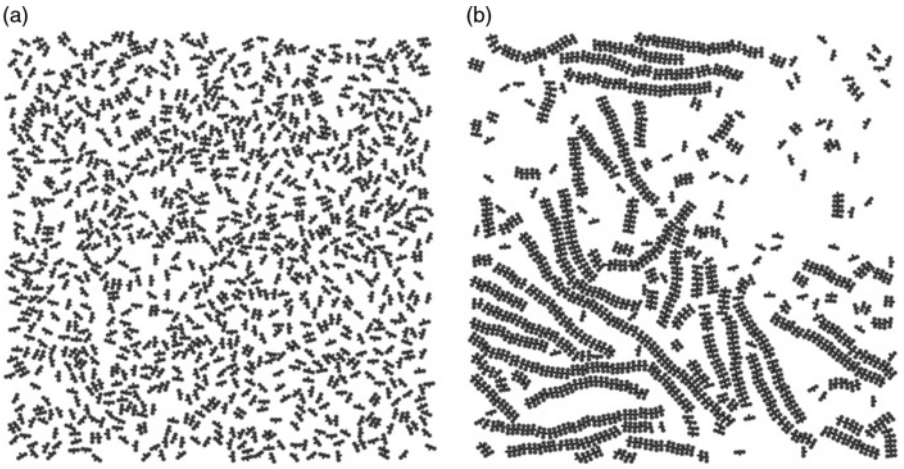


FIGURE 57.6 Influence of the magnetic particle–particle interaction on aggregate structures for $N_P = 3$ and $\phi_a = 0.2$: (a) $\lambda = 5$; (b) $\lambda = 10$.

orientational characteristics [47], and isotropic–nematic interfacial phenomena [48]. Also, the aggregation phenomena of platelike particles have been shown to be controlled by changing the surface roughness of such particles [49, 50]. Moreover, the structure and thermodynamics of nonmagnetic platelike particles has been discussed widely concerning the influence of the particle shape and the polydispersity in size on the internal structures (interparticle pair correlation), the equation of state, the static structure factor, the isothermal compressibility, the orientational order properties, and so on [51]. This type of platelike nanoparticle has been successfully synthesized by the sonochemical method [52, 53]. On the other hand, hematite particles exhibit a characteristic feature in that the particles are magnetized in a direction normal to the particle axis direction.

In this section, we address a dispersion composed of oblate hematite particles magnetized in a direction normal to the particle axis direction, and discuss the dependence of aggregation phenomena on various factors such as the magnetic particle-field and the magnetic particle-particle interactions [26].

57.3.3.2 Particle Model and Simulation Method. We use for the particle model a platelike particle that has the cross-section shape of a spherocylinder and with a magnetic moment oriented normal to the particle axis at the particle center. The disklike particle is composed of a short cylinder with diameter d and thickness b_1, with the cylinder surrounded by a torus with a semicircular cross section; this particle is assumed not to be coated with a surfactant layer. The present phenomenon is characterized by the two nondimensional parameters ξ and λ, expressed in Eq. (57.13). An external magnetic field is assumed to be applied in the direction normal to the material surface.

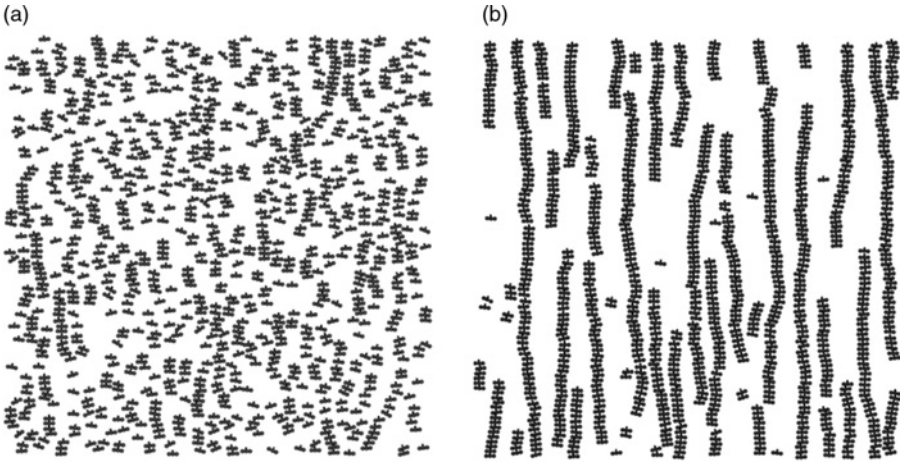


FIGURE 57.7 Influence of the magnetic particle–particle interaction on aggregate structures for $\xi = 20$, $N_P = 3$, and $\phi_a = 0.2$: (a) $\lambda = 5$; (b) $\lambda = 10$.

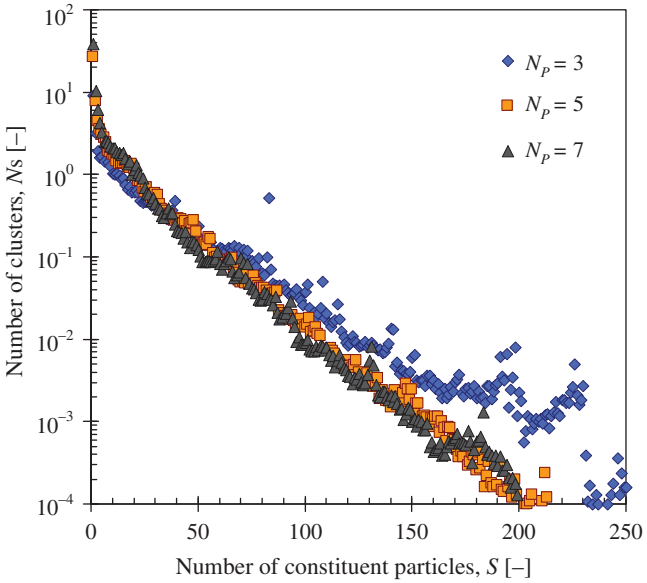


FIGURE 57.8 Cluster size distribution for $\xi = 20$, $\lambda = 10$, and $\phi_a = 0.2$.

We consider a quasi-2D model system for a dispersion composed of platelike particles in thermodynamic equilibrium, and Monte Carlo simulations were carried out in order to investigate the orientational phenomena [26]. A quasi-2D system implies that platelike particles are limited to move in a two-dimensional plane, but are free to incline with an unrestricted orientation.

57.3.3.3 Results and Discussion. Figure 57.9 shows snapshots obtained for the volumetric fraction $\phi_V = 0.56$ and the magnetic interaction between particles, $\lambda = 5$. For the case of $\xi = 5$ (Fig. 57.9a), the particles form long columnlike clusters, although the influence of an external magnetic field is of the same order of that of the magnetic particle–particle interaction with $\xi = 5$ and $\lambda = 5$. This is because the distance between particles becomes shorter as the volumetric fraction increases, as for $\phi_V = 0.56$, so that the translational and rotational movement are restricted. For the strong magnetic field $\xi = 10$ (Fig. 57.9b), it can be seen that only short columnlike clusters are formed and long clusters are not observed in the system. Moreover, the particles are located in an edge-to-edge contact formation that gives rise to brick-wall-like aggregates. In this formation, the particles on the upper and lower sides are separated by approximately $d_1/2$ ($d_1 = d+b_1$) along the direction normal to the particle axis, relative to the particle of interest. For the case of a significantly strong magnetic field, $\xi = 15$ (Fig. 57.9c), columnlike clusters are not observed. In contrast, brick-wall-like aggregates are formed and extended over the whole area of the system. This can be explained as follows. In a strong applied magnetic field, the magnetic moments are restricted to the magnetic field direction, and the repulsive interactions among the magnetic moments become stronger as the magnetic field strength increases. In this situation the particles cannot form columnlike clusters. If the particles form aggregates in the face-to-face formation with their magnetic moment inclining in the magnetic field direction, the repulsive interactions become dominant. Hence the particles are located at the separation distance of approximately $d_1/2$ along the direction normal to the particle axis in order to reduce the repulsive interaction, which yields the brick-wall-like aggregates.

We now discuss the influence of the volumetric fraction on the internal structures under the situation of a significantly strong magnetic field strength $\xi = 15$. For $\phi_V = 0.54$ shown in Fig. 57.10a, the magnetic moment of the particles tends to incline in the magnetic field direction while the particle axes point in various directions within the xy plane; that is, the system shows an isotropic structure. For $\phi_V = 0.55$ shown in Fig. 57.10b, the snapshot exhibits different characteristics compared with that in Fig. 57.10a. Thus, in some areas the particles are located in the edge-to-edge contact formation and also form brick-wall-like aggregates. For $\phi_V = 0.60$ shown in Fig. 57.10c, these brick-wall-like structures are formed over the whole area of the system, and the particles

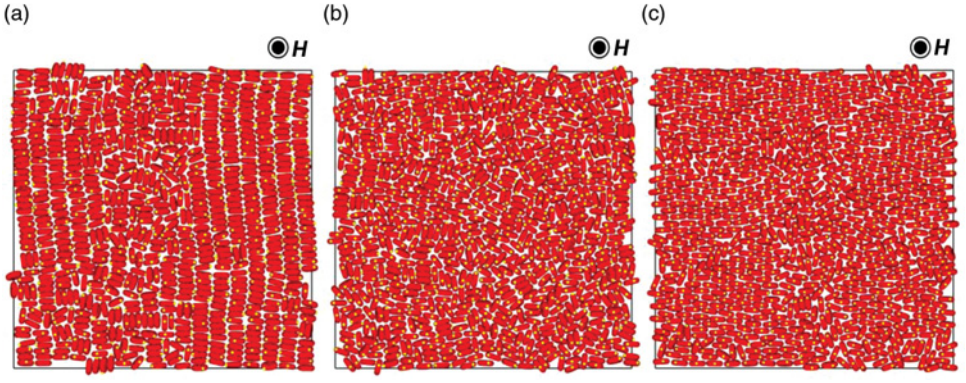


FIGURE 57.9 Aggregate structures of magnetic disklike particles in an applied magnetic field for $\phi_V = 0.56$ and $\lambda = 5$: (a) $\xi = 5$; (b) $\xi = 10$; (c) $\xi = 15$.

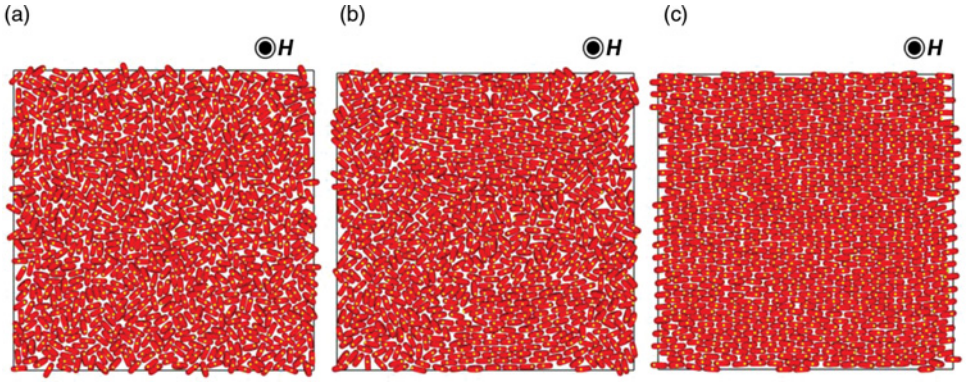


FIGURE 57.10 Aggregate structures of magnetic disklike particles in an applied magnetic field for $\xi = 15$ and $\lambda = 5$: (a) $\phi_V = 0.54$; (b) $\phi_V = 0.55$; (c) $\phi_V = 0.60$.

have a more significant tendency to incline in a single direction than in the case of $\phi_V = 0.55$. This is because the particle–particle distances are smaller and therefore the translational and rotational movements become significantly restricted as the volumetric fraction increases. Thus the particle axes come to exhibit this specific directional characteristic.

In order to discuss the orientational order of particles quantitatively in detail, it is desirable to address the nematic order parameter. The nematic order parameter S is a measure of the orientational correlation between the direction of the particle axis and the nematic director, which, in the present case, is the magnetic field direction (y direction $\boldsymbol{\delta}_y$). The influence of the volumetric fraction on the nematic order parameter is shown in Fig. 57.11 for the case of a strong magnetic field, $\xi = 15$. In the region of small volumetric fractions, the nematic order parameter shows a value of approximately $S \simeq 0.2$ that does not significantly increase with the volumetric fraction. In contrast, the curve shows a significantly steep increase converging to unity during the very small region of volumetric fraction change from $\phi_V = 0.54$ to 0.60.

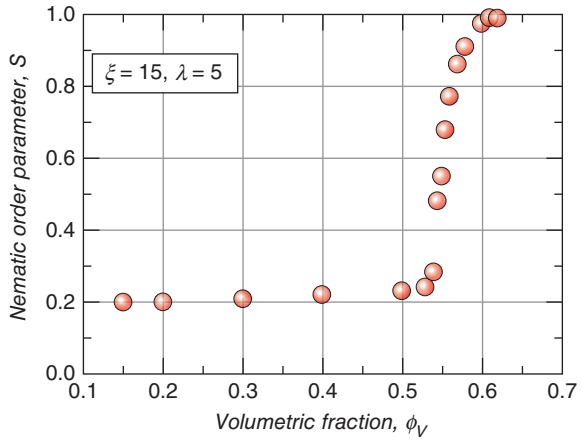


FIGURE 57.11 Nematic order parameter for $\xi = 15$ and $\lambda = 5$.

This indicates that the brick-wall-like structures abruptly appear during a very small change in the volumetric fraction. From these results concerning the behavior of the order parameter, it is suggested that a phase transition occurs between $\phi_V = 0.54$ and 0.60 for the case of $\xi = 15$ and $\lambda = 5$.

57.4 SEDIMENTATION

57.4.1 Introductory Remarks

Ultra-high-density recording materials based on FePt particles have been studied from various perspectives in the context of developing new devices [54–56]. One representative method for preparing self-organized monolayers of particles is to dry a colloidal dispersion on the material surface. As already mentioned in Section 57.3.1.1, in this method a droplet of the dispersion is deposited on a substrate, the solvent is evaporated to reduce the size of the droplet, and thereby ordered microstructures may be obtained. It is clear from this example that it is significantly important to control the sedimentation and the crystallization of the colloidal particles deposited on the surface of the substrate. If the orientational characteristics of the magnetic particles can be controlled by an applied magnetic field after the sedimentation, we may have sufficient possibility for developing an effective surface modification technique. We have therefore investigated the influence of the magnetic field strength and the particle areal density on the microstructure of a quasi-two-dimensional (Q2D) monolayer composed of ferromagnetic particles by means of Monte Carlo simulations [23]. In order to develop a precise technique for generating a uniform monolayer on a substrate surface under the gravitational field, a significant requirement is necessitated to investigate the behavior of fine particles in this situation.

In the present section, we discuss the sedimentation phenomena of a colloidal dispersion composed of ferromagnetic spherical particles in the gravitational field, by means of Brownian dynamics simulations [57].

57.4.2 Particle Model and Simulation Method

As mentioned above, a particle is modeled as a spherical particle with central point dipole and is coated with a uniform surfactant layer (or a steric layer) with thickness δ. The magnetic force between particles i and j, $\boldsymbol{F}_{ij}^{(\mathrm{m})}$, the magnetic torque $\boldsymbol{T}_{ij}^{(\mathrm{m})}$, and the torque $\boldsymbol{T}_i^{(H)}$ acting particle i due to the deviation of the magnetic moment from an applied magnetic field $\boldsymbol{H}$ ($H = |\boldsymbol{H}|$), are straightforwardly obtained from the interaction energies expressed in Eq. (57.12). Moreover, the force due to the overlap of the steric layers $\boldsymbol{F}_{ij}^{(V)}$ is also obtained from Eq. (57.14). In addition, since we consider sedimentation phenomena, it is also necessary to take into account the gravitational force $\boldsymbol{F}_i^{(G)}$. Hence, the net force acting on particle i, $\boldsymbol{F}_i$, and the net torque acting on particle i, $\boldsymbol{T}_i$, are obtained by summation.

The present particle is spherical and geometrically point-symmetric, but requires a degree of freedom for the magnetic moment in addition to the particle position, so that it is necessary to treat both the translational and the rotational motion as in the case of the rod-like particles; that is, during the simulation the particle position $\boldsymbol{r}_i$ and the orientation of the magnetic moment $\boldsymbol{n}_i$ will be treated simultaneously. The equations for simulating the translational and the rotational Brownian motion are straightforwardly derived from Eqs. (57.5) to (57.9) as

$$\boldsymbol{r}_i(t+\Delta t) = \boldsymbol{r}_i(t) + \frac{1}{kT} D^T \boldsymbol{F}_i(t)\Delta t + \Delta r_{||}^B \boldsymbol{n}_i(t) + (\Delta r_{\perp 1}^B \boldsymbol{n}_{\perp 1(i)}(t) + \Delta r_{\perp 2}^B \boldsymbol{n}_{\perp 2(i)}(t)) \tag{57.15}$$

$$\boldsymbol{n}_i(t+\Delta t) = \boldsymbol{n}_i(t) + \frac{1}{kT} D^R \boldsymbol{T}_i(t) \times \boldsymbol{n}_i(t)\Delta t + \left\{ \Delta \phi_{||}^B \boldsymbol{n}_i(t) + (\Delta \phi_{\perp 1}^B \boldsymbol{n}_{\perp 1(i)}(t) + \Delta \phi_{\perp 2}^B \boldsymbol{n}_{\perp 2(i)}(t)) \right\} \times \boldsymbol{n}_i(t) \tag{57.16}$$

The particle direction $\boldsymbol{e}_i$ is equal to the magnetic moment direction $\boldsymbol{n}_i$ for the present spherical magnetic particle. The random displacements $\Delta r_{||}^B$, $\Delta \phi_{||}^B$, and so on have to satisfy the stochastic characteristics in Eqs. (57.7) and (57.10). The vectors $\boldsymbol{n}_{\perp 1(i)}$ and $\boldsymbol{n}_{\perp 2(i)}$ are the unit vectors normal to each other in the plane normal to the particle axis (or the magnetic moment direction), as explained in Section 57.2.2. Nondimensionalization of quantities provides three nondimensional parameters R_B, R_H, and R_m that characterize the present sedimentation phenomenon. R_B is the ratio of the representative Brownian motion, R_H is the ratio of the representative torque due to an applied magnetic field, and R_m is the ratio of the representative magnetic force, to the representative gravity. Specification of the values of the nondimensional parameters, the volumetric fraction ϕ_V of particles, and so on, enables us to conduct the present Brownian dynamics simulations.

57.4.3 Results and Discussion

Figure 57.12 shows results of the snapshots after a macroscopic steady state had been attained to. For the case of $R_m = 1$ (Fig. 57.12a), magnetic forces between particles are weak and particles cannot aggregate to form complex clusters but rather form many simple chainlike clusters from the substrate surface that align in the opposite direction to the gravity field. The formation of these chainlike clusters can be explained in the following. Since the magnetic field is very strong for $R_H = 10$, during the first stage of the sedimentation the magnetic particles sediment with their magnetic moment inclined toward the field direction and attain to the substrate surface without forming aggregates. During the second stage, due to the field alignment of the magnetic moments, the particles tend to sediment directly onto the presedimented particles, leading to the growth of almost linear chainlike clusters as this sedimentation process is repeated. For the case of $R_m = 6$ shown in Fig. 57.12b, the magnetic forces between particles are relatively strong, and consequently the direction of their magnetic moments is as not strongly restricted to the magnetic field direction. In this situation, the particles tend

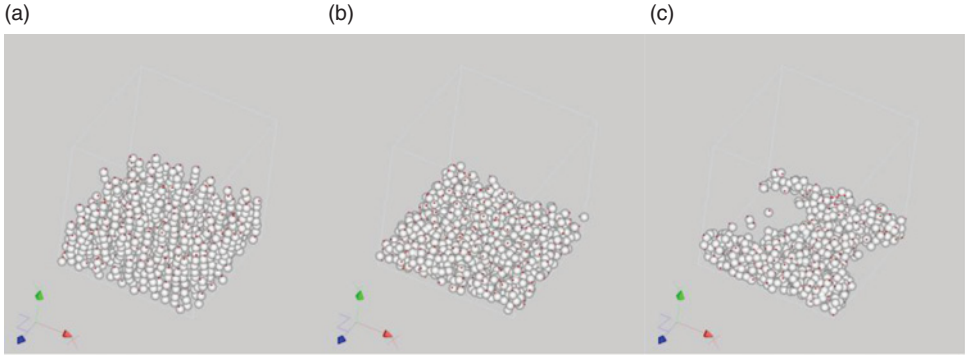


FIGURE 57.12 Aggregate structures for the volumetric fraction $\phi_V = 0.1$ and the magnetic field strength $R_H = 10$ for the three cases of the magnetic particle–particle interaction strength: (a) $R_m = 1$; (b) $R_m = 6$; (c) $R_m = 10$.

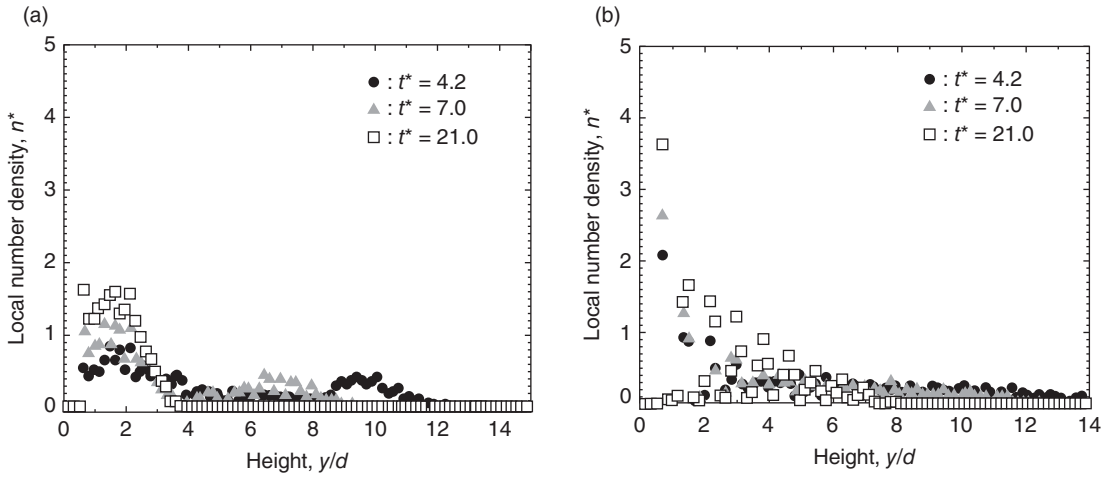


FIGURE 57.13 Time change in the local number density n^* for $\phi_V = 0.1$ and for (R_H, R_m) = (a) (1,10) and (b) (10,1).

to aggregate to form clusters during the sedimentation process, although these clusters are not necessarily linear chainlike aggregates because the particle–particle interaction is relatively strong. For the case of $R_m = 10$ shown in Fig. 57.12c, the magnetic particle–particle force is now more dominant than the Brownian random force, so that larger clusters are formed during the sedimentation process. These clusters do not significantly change their aggregate formation after the attainment to the substrate surface because the particle–particle interaction is significantly strong. This behavior gives rise to some large void spaces among the aggregated particles, as clearly shown in Fig. 57.12c.

In order to discuss the sedimentation process quantitatively, we focus on the time change in the local number density of each layer that is made by slicing the simulation region in a direction normal to the plane of the substrate material: t^* in the figure is the nondimensionalized time. For the case of larger magnetic forces between particles such as $R_m = 10$ in Fig. 57.13a, the magnetic force between particles is relatively strong, so that particles can aggregate during the initial stage of the sedimentation. Hence, at the earlier time of 4.2, relatively large clusters are already observed in the regions around at $y/d = 2.0$ and 9.5. After this initial aggregate formation, all particles sediment and combine with the already-sedimented particles to form larger aggregates. In Fig. 57.13b, where the magnetic force between particles is relatively weak, particles usually sediment without significant aggregates forming during the initial stage until around until $t^* = 7.0$. At a further advance in time $t^* = 21.0$, sharp peaks appear in the distribution at approximately the positions of integer times the distance of $y/d \simeq 0.85$. This is a quantitative proof for the observation that clusters are formed to stand in the upright formation along the direction of the gravity field. This characteristic clearly demonstrates the internal feature that was observed in snapshot in Fig. 57.13a. The reason why peaks appear at the positions of integer times the distance of $y/d \simeq 0.85$ is that the steric layers of particles partially overlap due to effects of the gravitational and magnetic interactions, and also that the chainlike clusters are not formed in perfectly linear formation. Additionally, we can see that particles exist in the upper region, which clearly shows that longer chainlike are formed in the magnetic field direction.

57.5 CONCLUSION

In addition to the application of magnetic suspensions to the magnetic drug delivery system, surface-modified magnetic particles (e.g., silica-coated magnetic particles) may be used for recovering specific substances such as hazardous heavy-metal molecules (environmental waste and pollutants) or valuable noble metal molecules from water (sea, lake, etc.) by processes that make use of a gradient external magnetic field (based on magnetic separation) [58–60]. Attempts are being made to synthesize multifunctionalized composite particles for developing a more effective drug delivery system and a bioadsorption system [14,61,62]. Since the application of an alternating magnetic field on magnetic composite particles induces a heating effect, this heat dissipation phenomenon may be used as a mechanism for releasing the drugs transported by the composite particles [63–66]. The development of a technology for transporting magnetic composite particles in blood vessels and collecting them at specific sites (cancer cells) in the body requires analysis of the flow behavior of magnetic particles in blood vessels or tracheae [67–70]. In order to analyze this kind of flow problem for a suspension, it is necessary to simulate both the behavior of particles and the ambient flow field simultaneously. The methods of lattice Boltzmann [71–73], dissipative particle dynamics [74–76],

and multiparticle collision dynamics [77] are potential simulation techniques in order to address the important problem of taking into account the multi-body hydrodynamic interactions among particles.

REFERENCES

[1] Häfeli, U., S.chütt, W., Teller, J., Zborowski, M. (eds.) (1997). *Scientific and Clinical Applications of Magnetic Carriers*. Springer, Berlin.

[2] Kuznetsov, A.A., Filippov, V.I., Kuznetsov, O.A., Gerlivanov, V.G., Dobrinsky, E.K., Malashin, S.I. (1999). *J. Magnetism Magn. Mater.* **194**, 22–30.

[3] Weingart, J., Vabbilisetty, P., Sun, X. (2013). *Adv. Colloid Interface Sci*. **197–198**, 68–84.;

[4] Zhang, J.L., Srivastava, R.S., Misra, R.D.K. (2007). *Langmuir* **23**, 6342–6351.

[5] Liu, T., Hu, S., Hu, S., Tsai, S., Chen, S. (2007). *J. Magnetism Magn. Mater.* **310**, 2850–2852.

[6] Yang, J., Lee, J., Kang, J., Lee, K., Suh, J., Yoon, H., Huh, Y., Haam, S. (2008). *Langmuir* **24**, 3417–3421.

[7] Balakrishnan, S., Bonder, M.J., Hadjipanayis, G.C. (2009). *J. Magnetism Magn. Mater.* **321**, 117–122.

[8] Abdalla, M.O., Aneja, R., Dean, D., Rangari, V., Russell, A., Jaynes, J., Yates, C., Turner, T. (2010). *J. Magnetism Magn. Mater.* **322**, 190–196.

[9] Tomitaka, A., Koshi, T., Hatsugai, S., Yamada, T., Takemura, Y. (2011). *J. Magnetism Magn. Mater*. **323**, 1398–1403.

[10] Cao, Z., Yue, X., Li, X., Dai, Z. (2013). *Langmuir* **29**, 14976–14983.

[11] Tomitaka, A., Ueda, K., Yamada, T., Takemura, Y. (2012). *J. Magnetism Magn. Mater.* **324**, 3437–3442.

[12] Wang, N., Guan, Y., Yang, L., Jia, L., Wei, X., Liu, H., Guo, C. (2013). *J. Colloid Interface Sci.* **395**, 50–57.

[13] Zhang, X., Xue, L., Wang, J., Liu, Q., Liu, J., Gao, Z., Yang, W. (2013). *Colloids Surf. A* **431**, 80–86.

[14] Liu, G., Hu, D., Chen, M., Wang, C., Wu, L. (2013). *J. Colloid Interface Sci.* **397**, 73–79.

[15] Jankiewicz, B.J., Jamiola, D., Choma, J., Jaroniec, M. (2012). *J. Colloid Interface Sci.* **170**, 28–47.

[16] Ambrogio, M.W., Frasconi, M., Yilmaz, M.D., Chen, X. (2013). *Langmuir* **29**, 15386–15393.

[17] Richert, H., Surzhenko, O., Wangemann, S., Heinrich, J., Görnert, P. (2005). *J. Magnetism Magn. Mater.* **293**, 497–500.

[18] Mishima, F., Fujimoto, S., Takeda, S., Izumi, Y., Nishijima, S. (2007). *J. Magnetism Magn. Mater*. **310**, 2883–2885.

[19] Cao, Q., Han, X., Li, L. (2011). *J. Magnetism Magn. Mater*. **323**, 1919–1924.

[20] Takeda, S., Mishima, F., Fujimoto, S., Izumi, Y., Nishijima, S. (2007). *J. Magnetism Magn. Mater.* **311**, 367–371.

[21] Shapiro, B. (2009). *J. Magnetism Magn. Mater.* **321**, 1594–1599.

[22] Vargha-Butler, E.I., Foldvari, M., Mezei, M. (1989). *Colloids Surf*. **42**, 375–389.

[23] Aoshima, M., Satoh, A., Chantrell, R.W. (2008). *J. Colloid Interface Sci*. **323**, 158–168.

[24] Satoh, A., Sakuda, Y., Katayama, Y. (2009). *Int. J. Emerging Multidisc. Fluid Sci.* **1**, 127–139.

[25] Satoh, A., Sakuda, Y. (2009). *Mol. Phys.* **107**, 1621–1627.

[26] Satoh, A., Sakuda, Y. (2010). *Mol. Phys*. **108**, 2105–2113.

[27] Hayasaka, R., Satoh, A. (2008). *Brownian Dynamics Simulations of Sedimentation Phenomena of Ferromagnetic Spherical Particles in a Colloidal Dispersion*; *Proc. 2008 ASME International Mechanical Engineering Congress and Exposition*, Boston, Oct. 31–Nov. 6, 2008.

[28] Allen, M.P., Tildesley, D.J. (1987). *Computer Simulation of Liquids*. Clarendon Press, Oxford.

[29] Binder, K., Heermann, D.W. (1988). *Monte Carlo Simulation in Statistical Physics: An Introduction*. Springer, Berlin.

[30] Satoh, A. (2003). *Introduction to Molecular-Microsimulation of Colloidal Dispersions*. Elsevier, Amsterdam.

[31] Satoh, A. (2010). *Introduction to Practice of Molecular Simulation (Molecular Dynamics, Monte Carlo, Brownian Dynamics, Lattice Boltzmann and Dissipative Particle Dynamics)*. Elsevier, Amsterdam.

[32] Metropolis, N., Rosenbluth, A.W., Rosenbluth, M.N., Teller, A. (1953). *J. Chem. Phys.* **21**, 1087–1092.

[33] Bossis, G., Brady, J.F. (1984). *J. Chem. Phys*. **80**, 5141–5154.

[34] Brady, J.F., Bossis, G. (1985). *J. Fluid Mech.* **155**, 105–129.

[35] Bird, R.B., Armstrong, R.C., Hassager, O. (1987). *Dynamics of Polymeric Liquids, Vol. 1, Fluid Mechanics*. Wiley, New York.

[36] Brenner, H. (1974). *Int. J. Multiphase Flow* **1**, 195–341.

[37] Kim, S., Karrila, S.J. (1991). *Microhydrodynamics: Principles and Selected Applications*. Butterworth-Heinemann, Stoneham, UK.

[38] Satoh, A. (2014). Application of the Brownian dynamics method to a rod-like hematite particle dispersion. *Mol. Phys.* **112**, 1002–1011.

[39] Weis, J.J. (2003). *J. Phys. Condensed Matt*. **15**, S1471–S1495.

[40] Ando, T., Hirota, N., Satoh, A., Beaugnon, E. (2006). *J. Magnetism Magn. Mater.* **303**, 39–48.

[41] Ozaki, M. (1996). *Magnetic Properties of Hematite Suspensions.* Report of the Graduate School of Science, Yokohama City Univ. **47**, 19–47 (in Japanese).

[42] Ishikawa, T., Ozaki, M. (2004). *Magnetic Properties of Hematite Micro-Particles in Aqueous Suspensions*; *Proc. 57th Divisional Meeting on Colloidal and Interface Chemistry.* The Chemical Society of Japan 105 (in Japanese).

[43] Satoh, A., Ozaki, M., Ishikawa, T., Majima, T. (2005). *J. Colloid Interface Sci*. **292**, 581–590.

[44] Satoh, A., Ozaki, M. (2006). *J. Colloid Interface Sci*. **298**, 957–966.

[45] Satoh, A., Chantrell, R.W., Kamiyama, S., Coverdale, G.N. (1996). *J. Colloid Interface Sci*. **178**, 620–627.

[46] Van der Beek, D., Davidson, P., Wensink, H.H., Vroege, G.J., Lekkerkerker, H.N.W. (2008). *Phys. Rev. E* **77**, 031708.

[47] Van der Beek, D., Petukhov, A.V., Davidson, P., Ferre, J., Jamet, J.P., Wensink, H.H., Vroege, G.J., Bras, W., Lekkerkerker, H.N.W. (2006). *Phys. Rev. E* **73**, 041402.

[48] Van der Beek, D., Reich, H., Van der Schoot, P., Dijkstra, M., Schilling, T., Vink, R., Schmidt, M., Van Roij, R., Lekkerkerker, H. (2006). *Phys. Rev. Lett.* **97**, 087801.

[49] Zhao, K., Mason, T.G. (2008). *Phys. Rev. Lett.* **101**, 148301.

[50] Zhao, K., Mason, T.G. (2007). *Phys. Rev. Lett.* **99**, 268301.

[51] Harnau, L. (2008). *Mol. Phys.* **106**, 1975–2000.

[52] Li, J., Qin, Y., Kou, X., Huang, J. (2004). *Nanotechnology* **15**, 982–986.

[53] Li, J., Qin, Y., Kou, X., Huang, J. (2005). *J. Nanosci. Nanotechnol.* **5**, 1699–1706.

[54] Harrell, J.W., Kang, S., Jia, Z., Nikles, D.E., Chantrell, R.W., Satoh, A. (2005). *Appl. Phys. Lett.* **87**, 202508.

[55] Verdes, C., Chantrell, R.W., Satoh, A., Harrell, J.W., Nikles, D. (2006). *J. Magnetism Magn. Mater.* **304**, 27–31.

[56] Zu, R.D., Shouheng, S., Zhong, L.W. (2002). *Surf. Sci.* **505**, 325–335.

[57] Hayasaka, R., Satoh, A. (2008). *Brownian Dynamics Simulations of Sedimentation Phenomena of Ferromagnetic Spherical Particles in a Colloidal Dispersion*; *Proc. 2008 ASME International Mechanical Engineering Congress and Exposition*, Boston, Oct. 31–Nov. 6, 2008.

[58] Girginova, P.I., Daniel-da-Silva, A.L., Lopes, C.B., Figueira, P., Otero, M., Amaral, V.S., Pereira, E., Trindade, T. (2010). *J. Colloid Interface Sci.* **345**, 234–240.

[59] Lan, S., Wu, X., Li, L., Li, M., Guo, F., Gan, S. (2013). *Colloids Surf. A* **425**, 42–50.

[60] Bruce, I.J., Sen, T. (2005). *Langmuir* **21**, 7029–7035.

[61] Xie, M., Shi, H., Ma, K., Shen, H., Li, B., Shen, S., Wang, X., Jin, Y. (2013). *J. Colloid Interface Sci.* **395**, 306–314.

[62] Huang, S., Li, C., Cheng, Z., Fan, Y., Yang, P., Zhang, C., Yang, K., Lin, J. (2012). *J. Colloid Interface Sci.* **376**, 312–321.

[63] Müller-Schulte, D., Schmitz-Rode, T. (2006). *J. Magnetism Magn. Mater.* **302**, 267–271.

[64] Kim, D., Nikles, D.E., Johnson, D.T., Brazel, C.S. (2008). *J. Magnetism Magn. Mater.* **320**, 2390–2396.

[65] Shamim, N., Hidajat, L., Hong, K., Uddin, M.S. (2006). *J. Colloid Interface Sci.* **304**, 1–8.

[66] Liu, T., Hu, S., Liu, K., Shaiu, R., Liu, D., Chen, S. (2008). *Langmuir* **24**, 13306–13311.

[67] Furlani, E.J., Furlani, E.P. (2007). *J. Magnetism Magn. Mater.* **312**, 187–193.

[68] Nacev, A., Beni, C., Bruno, O., Shapiro, B. (2011). *J. Magnetism Magn. Mater.* **323**, 651–668.

[69] Habibi, M.R., Ghassemi, M., Hamedi, M.H. (2012). *J. Magnetism Magn. Mater.* **324**, 1473–1482.

[70] Ally, J., Martin, B., Khamesee, M.B., Roa, W., Amirfazli, A. (2005). *J. Magnetism Magn. Mater.* **293**, 442–449.

[71] Succi, S. (2001). *The Lattice Boltzmann Equation for Fluid Dynamics and Beyond*. Clarendon Press, Oxford, UK.

[72] Rothman, D.H., Zaleski, S. (1997). *Lattice Gas Cellular Automata, Simple Models of Complex Hydrodynamics*. Cambridge Univ. Press, Cambridge, UK.

[73] Ladd, A.J.C. (1994). *J. Fluid Mech.* **271**, 285–309.

[74] Hoogerbrugge, P.J., Koelman, J.M.V.A. (1992). *Europhys. Lett.* **19**, 155–160.

[75] Español, P., Warren, P. (1995). *Europhys. Lett.* **30**, 191–196.

[76] Espanñol, P. (1995). *Phys. Rev. E* **52**, 1734–1742.

[77] Gompper, G., Ihle, T., Kroll, D.M., Winkler, R.G. (2009). In Christian, H., Kremer, K. (eds.), *Multi-Particle Collision Dynamics: A Particle-Based Mesoscale Simulation Approach to the Hydrodynamics of Complex Fluids* (*Advanced Computer Simulation Approaches for Soft Matter Sciences III Advances in Polymer Science*). Springer, Berlin, Vol. 221, pp. 1–87.

58

ION-SENSING MEMBRANE ELECTRODES IN STUDY OF SURFACTANT–BIOPOLYMER INTERACTION

SUDESHNA M. CHATTERJEA,[1] KOUSTUBH PANDA,[1] AND SATYA P. MOULIK[2]

[1]*Department of Biotechnology and Dr. B.C. Guha Centre for Genetic Engineering and Biotechnology, University of Calcutta, West Bengal, India*

[2]*Department of Chemistry, Center for Surface Science, Jadavpur University, Kolkata, India*

58.1 INTRODUCTION

Surface-active agents or *surfactants* are compounds that lower interfacial tension at different interfaces and are a fascinating area of research in different fields such as chemistry, biology, and engineering because of their important practical applications. Surfactants are usually amphiphilic organic compounds containing a hydrophilic polar headgroup and a lipophilic part consisting of hydrocarbonated chains generally with a $(CH_2)_n$ motif. Most commonly, they are classified into four groups according to the charge on the hydrophilic group: anionic, cationic, zwitterionic, or nonionic. Surfactants are produced in large amounts and are widely used for industrial and domestic purposes [1]. For a long time they have been among the most versatile of process chemicals in industry and biotechnology [2].

Anionic surfactants are widely used in modern households in products such as soaps, toothpastes, cosmetics, washing liquids, laundry detergents, textiles, and also in mining [3]. Cationic surfactants also have widespread use in the manufacture of commercial products and pharmaceutical formulations including textile softeners, anticorrosion agents, disinfectants, cosmetics, and household cleaning products [4]. Detergents are also routinely used in research laboratories. Sodium dodecyl sulfate (SDS), cetyltrimethylammonium bromide (CTAB), Triton-X 100 and 114, 3-[(3-cholamidopropyl)dimethylammonio]-1-propanesulfonate (CHAPS), sodium deoxycholate (NaDC), NP40, and other compounds are used to solubilize chemical species by dissociating aggregates, disrupting lipid bilayers, and by solubilizing proteins. SDS used during electrophoresis denature proteins by disrupting their secondary and tertiary structures allowing separation of proteins according to their molecular weights. For solubilizing proteins keeping their structures intact, nonionic surfactants like octylthioglucoside can be used and are preferred for studying protein conformation and function [5].

Several microorganisms such as bacteria and yeast synthesise surface-active agents. When grown on hydrocarbon sources, these microorganisms synthesize a wide range of chemicals with surface activity such as those of glycolipids and phospholipids. These chemicals emulsify the hydrocarbon substrates and facilitate their transport into cells [6, 7]. Pulmonary surfactants consisting mostly of dipalmitoylphosphatidylcholine are secreted by the type II cells of the lung alveoli in mammals [8]. These types of surfactants synthesized by living cells are called *biosurfactants*. They can be diverse and environment friendly, and have potential applications in environment protection [9]. By enhancing emulsification of hydrocarbons, they accelerate bioremediation of hydrocarbon-contaminated sites [10]. They can also be used in enhanced oil recovery, herbicide and pesticide formulations, detergents, healthcare and cosmetics, pulp and paper, coal, textiles, and other applications [11].

Because of their anthropogenic origin and extensive use, surfactants are considered a common environmental

Encyclopedia of Biocolloid and Biointerface Science, Volume 2, First Edition. Edited by Hiroyuki Ohshima.
© 2016 John Wiley & Sons, Inc. Published 2016 by John Wiley & Sons, Inc.

pollutants [1]. The diversity of existing surfactants and their widespread presence in both industrial products and the environment has created a need for analytical tools to accurately determine and monitor their concentrations in aqueous environments [3]. Initially, the most widely used technique for surfactant analysis was the standard method of two-phase titration. This however, had several drawbacks and a number of alternative analytical methods have been developed based on ion pair formation such as titrimetry [12], flow injection analysis [13], spectrophotometry [14], chromatography [15], and optical sensing [16]. None of these methods are however suitable for *in situ* or at-site quantitative determination.

As an alternative, ion-selective electrodes (ISEs), namely potentiometric ion sensors have been developed for determining ions in aqueous environment [17]. Since their invention in 1906 [18], they have become one of the most important forms of chemical sensors [19]. ISEs applied to surfactants in solution are called *surfactant ion-selective electrodes* (SISEs), which have become a major tool for analyzing surfactants in environmental wastewater, industrial process control, and pharmaceutical domains [20–23]. Compared to other analytical methods, SISEs are simple to use, environment friendly, robust, durable, and suitable for use in field environments. Other advantages include automation of routine sample analysis. Complying with good laboratory practice, low consumption of reagents, results that are independent of sample turbidity or coloring, minimum sample preparation, continuous monitoring of surfactant ion concentrations, and response to cationic and anionic surfactants depending on the nature of the electroactive material used [3,23,24]. Major limitations include inability to detect concentrations in the μM or nM range (real matrices) and the short lifetime of these devices due to gradual loss of response characteristics.

Biopolymer–surfactant interaction is an important field of study due to its relevance in many biological, pharmaceutical, and industrial applications. Protein–surfactant interactions also provide models for studying lipid–protein interactions existing in cell membranes. Since proteins interact mostly with ionic surfactants, interactions with SDS has been most widely studied. Interactions with other surfactants such as bile salts CTAB, and cetylpyridinium chloride (CPC) have also been investigated [25, 26] to some extent. Among proteins, serum albumins have been mostly studied. Other proteins studied include gelatin, lysozyme, hemoglobin, and myoglobin [27]. Research on development and application of SISEs have been carried out for more than three decades and they are found to be more suitable for determining the binding isotherm of surfactant–polymer interactions and determining surfactant concentration in dilute solution [28]. The main purpose of this chapter is to provide a systematic summation of the development of SISEs and their uses and applications in studying surfactant interactions with biopolymers.

58.2 DEVELOPMENT OF SURFACTANT ION-SELECTIVE ELECTRODES (SISEs)

Potentiometric surfactant sensors are used to either determine the endpoint of titration or directly determine surfactant concentration. The most popular sensors of this group are the poly(vinyl chloride) (PVC)-based solid membranes, coated wire-type sensors, and ISFET (ion-selective field effect transistor) sensors. These sensors are suitable for determining cationic, anionic, or nonionic surfactants [2] and are used primarily to determine monomer concentration of surfactants, in environmental samples such as wastewater, in food and cosmetic formulations, phase transfer catalysts, etc. [3, 29–31].

At first, potentiometric sensors determined surfactants by indirect measurements such as interference on calcium ion-selective electrodes [32] or by titrating with sodium salt of tetraphenylborate (TPB^-) [33]. Liquid membrane electrodes selective toward multiple anionic surfactants were first developed using ion pairs as exchange systems [34].

The development of liquid and solid (PVC) membranes specifically designed to estimate surfactant ion concentrations came in the second stage of development featuring preparation of many different kinds of sensors, and the first commercial ISEs were prepared.

58.2.1 Liquid Membrane Electrodes (LMEs)

To form a liquid membrane system, a water insoluble carrier complex (comprising the ionophore) is dissolved in a low-polarity solvent (toluene, nitrobenzene, etc.) taken in a U-tube and partitioned between water and the solvent in the two limbs. The carrier complex can be changed to sense different surfactant ions as needed.

The first potentiometric sensors selective for anionic surfactants were developed by describing the principle for liquid membrane electrodes specific for dodecylsulfate (DS^-), tetrapropylenebenzenesulfonate ($TPBS^-$), and dioctylsulfosuccinate ($DOSS^-$) ions and were used to determine the critical micelle concentrations (CMC) of each [35]. This was followed by an electrode developed by Birch and Clarke [36], who used the carrier complex cetyltrimethyl–dodecyl sulfate (CTA-DS) in nitrobenzene. This electrode responded to DS^- and was used for monitoring DS^- adsorption over numerous polymers and proteins, and for potentiometric titration of various commercial detergents [37, 38]. LMEs responsive to anionic surfactants containing cationic colorants such as crystal violet [39] as ion exchanger were also developed.

Two other researchers prepared liquid membranes for DS^- using Co^{3+} complexes that could be used for titrating various alkylsulfates (between C8 and C18) separately, or in binary mixtures [40]. Similarly, using other metallic complexes anionic detergents in oil residues could be determined [41]. Another researcher developed a different kind

of a polymeric sensor (mercurated polystyrene) for titrating and to study physicochemical properties of commonly occurring anionic surfactants [42]. Cation-selective LMEs were developed on the basis of their complex formation with TPB^- [43].

Although easy to build, liquid membrane electrodes had several disadvantages. The major problems encountered were drifting of potentiometric signal with time, lack of robustness, and risk of membrane dissolution in the aqueous phase near the CMC of the surfactant. Because of temporal variability, LMEs require continuous recalibration, making them unsuitable for direct potentiometric techniques [3,44].

Liquid membranes are discussed further in the context of bile-salt-selective electrodes in Section 58.2.2.6.

58.2.2 PVC-Based ISEs

Liquid membranes were superseded by solid membranes when Moody and Thomas first showed the possibility of keeping liquid membrane immobilized on PVC [45, 46]. Since then, liquid membranes have been replaced by plasticized polymeric membranes, where PVC serves as the matrix for holding the dispersed carrier complex. These membranes are robust, less soluble in aqueous media, and simple in design. The most widely used formulation comprises three components: ionophore, plasticizer, and PVC. The analytical response depends on a suitable combination of the plasticizer and the ionophore. Membrane selectivity can be altered by modifying the relative proportions of membrane components. Figure 58.1 compares the electrode assemblies for determination of surfactant ion concentrations using liquid and solid membrane electrodes.

Plasticizers are organic compounds that improve a membrane's elasticity and mechanical properties. When added to PVC, they also help in designing and improving membrane selectivity by fixing its dielectric constant. Choosing an appropriate plasticizer, an adequate membrane component, and sometimes an additive is essential for constructing an ion-selective electrode with high analytical performance and longer lifetime [47]. The proportion of plasticizer, however, must be optimized to minimize electrical asymmetry of the membrane, to keep the sensor clean, and to prevent it from leaching into the aqueous phase [48]. The nature of the plasticizer used affects sensitivity, linear range of electrodes, and possibly also selectivity. It should also be compatible with both the polymer and the ionophore [49]. The most popular plasticizers for PVC membranes are *o*-nitrophenyl octyl ether (NPOE) and *o*-nitrophenylphenyl ether (NPPE).

58.2.2.1 Conventional ISEs. These devices are prepared by dissolving PVC, plasticizer, and the carrier complex in an appropriate organic solvent (tetrahydrofuran or cyclohexanone) by gentle heating. The organic solvent is then allowed to evaporate at room temperature, leaving a dry membrane. The membrane then can be sliced and mounted on the body of an electrode filled with a reference system, normally Ag/AgCl. These electrodes are known as *conventional ISEs*.

The first PVC-based electrodes for titrating surfactants were actually ISEs selective to nitrate and calcium ions [43]. Although these electrodes could also sense anionic and cationic surfactants, the major drawback however was interference from anions for the nitrate electrodes, and from bivalent cations for calcium electrodes [50, 51].

The first PVC electrode prepared specifically for anionic surfactants was designed by Tanaka [52, 53]. A mixture comprising of a ferroin cation and the anions alkylbenzenesulfonate and perchlorate was used as the ionophore.

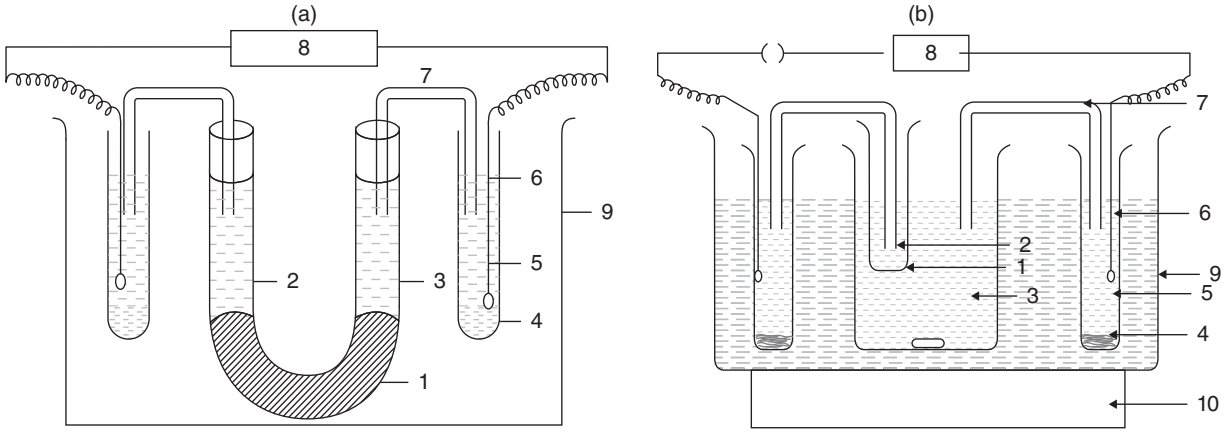


FIGURE 58.1 Electrode assembly for surfactant ion detection by SISEs: (a) liquid membrane electrode; (b) PVC-based membrane electrode (1–membrane; 2–internal reference solution; 3– test solution; 4—KCl; 5–saturated KCl solution; 6–calomel electrode; 7–salt bridge; 8–voltmeter; 9–water bath, 10–magnetic stirrer).

Membranes prepared by another team [54] had cations or anions bound chemically to the polymeric chain. Although these stable permselective membrane electrodes could be used to determine surfactant ion activities above and below their CMC, they showed little selectivity between surfactants of similar charge [54].

A different idea for membrane preparation was tried using only a polymer and a plasticizer, based on the principle that the ion pair being formed in solution by titration becomes the carrier complex that is gradually incorporated in the matrix. This gradual incorporation protects overconcentration of the complex in the membrane, which negatively affects the detection limit [55].

Two other researchers prepared another sensor membrane using NPOE as plasticizer and a suitable ionophore, and showed that these types of electrodes could be used to detect amphoteric and cationic surfactants [56]. At low pH, the amphoteric surfactant becomes cationic and could be titrated with TPB^-. Using this method, zwitterrionic surfactants could also be detected [56].

A number of reports on electrodes sensitive to nonionic surfactants also exist in the literature [56–58]. The basic principle is the formation of a complex by associating the ethoxylated part of the nonionic surfactants with Ba^{2+} and titrating the positively charged complex with TPB^-. Although a detection limit of 10^{-7} was reported for Antarox 880 [57], the analysis took more than an hour. To prepare more stable, reproducible and long-lived devices, another team [59] used PVC membranes containing TPB^- complexes with Ba^{2+} and polyethoxylate-based nonionic surfactant as sensing material.

To investigate a variety of ionic surfactants, a sensor membrane plasticized with NPOE and containing an additive to improve electrical conductivity was developed [60]. This membrane needed no preconditioning and yielded good results during potentiometric titrations with SDS and hyamine as anionic and cationic standards, respectively.

For estimating anionic surfactants in solution, DS^- or TPB^- is used as standard, and for cationic surfacatnts, *N*-benzyl-*N*,*N*-dimethyl-*N*-[4,1,3,3-tetramethylbutyl)-phenoxyethyl]ammonium chloride (commercial name Hyamine 1622), cetylpyridinium chloride (CPC), or 1,3-dodecyl-2-methyl imidazolium [61–64] (commercial name TEGOtrant A100; Metrohm) are used as standards. On the basis of this principle, several commercial electrodes were prepared that were specially constructed for analyzing surfactants; examples are electrodes by Orion [65, 66], "high-sensitivity tenside" electrodes by Metrohm [67], which is stable for several months and yielded results with relative standard deviation between 0.2% and 1.3% for anionic surfactants. Other advantages are its stability over a wide pH range and linear response over a large range of surfactant concentration.

More recent advances in preparation of membrane electrodes for better selectivity and lower detection limit involved preparation of a variety of carrier complexes. A ligand 7-methyl-7,13-di-octyl-1,4,10-trioxa-13-aza-7-azoniacyclopentadecane was synthesized and used as an ionophore for detecting anionic surfactants [23]. The membrane prepared using this ligand and NPOE as plasticizer showed Nernstian response to DS^- had a detection limit of 6×10^{-7} M, showed reasonable response toward alkyl sulfates and alkylbenzene sulfonates, but showed no response toward carboxylates, cationic, or nonionic surfactants. In another report, a cyclam derivative 1,4,8,11-tetra(*n*-octyl)-1,4,8,11-tetraazacyclotetradecane was used as carrier complex [1]. The most effective membrane composition involved 56% dibutyl phthalate, 3.4% ionophore, 3.8% tetra-*n*-octylammonium bromide (a cationic additive), and 36.8% PVC. This electrode showed Nernstian response toward DS^- with a detection limit of 4×10^{-6} M. Calculation of selectivity coefficients showed poor response toward commonly occurring inorganic cations and anions. Except for bicarbonate, electrode selectivity followed the Hoffmeister series. With the exception of linear alkylsulfates, response toward other anionic and nonionic surfactants was poor. In addition, it showed nonlinear response toward certain cationic and zwitterionic surfactants.

A DS^- selective electrode containing CTA^+-DS^- as ionophore showed Nernstian response, 2.9×10^{-6} M detection limit, wide pH range, small response time, and low selectivity toward common inorganic anions [68]. Another team of investigators used the same ionophore for preparing CTAB-selective SISEs for studying CTAB interactions with various biopolymers [69, 70].

A membrane electrode using CPC based Sn(IV) phosphate (CPC-SnP) as the electroactive material was prepared showing a linear response for CPC [71]. Although the response slope was sub-Nernstian (29.1 mV/decade), determination of CPC concentration using this electrode compared favorably with those obtained by the two-phase titration method. The electrode has a pH range of 2–6 and a response time of 30 s.

Another group prepared two conventional plastic membrane electrodes selective toward tetradecyltrimethylammonium cation (TTA^+) [4]. The ion exchangers were the ion associate TTA-PT, and the aggregate TTA-PSS, where PT and PSS are phosphotungstate and polystyrene sulfonate, respectively. Electrodes showed Nernstian response and had pH ranges of 4–10.5 and 3.8–10.7. Electrodes with the ion aggregate as exchanger had lifespans of 28 weeks, while electrodes with the ion associate as exchanger had lifespans of 20 weeks. Surface analysis using electron microscopy and X-ray photoelectron spectroscopy showed that the limited lifespans of plastic electrodes was due to topographical changes at the electrode surface and leaching of active ingredient from the surface.

A sensor based on 1,3-didecyl-2-methylimidazoliumtetraphenylborate (DMI^+-TPB^-) as the ionophore, and *o*-NPOE as plasticizer was used to titrate SDS and sodium dodecyl benzene sulfonate (SDBS) using DMI and CPC. Usable titration curves could be obtained in a concentration range of 10 μM [72].

58.2.2.2 Modified PVC-Based Electrodes. A decrease in the performance ability of these surfactant ion-sensing electrodes due to loss of sensitivity, electrode response slope, and aging, restrict their long-term use. To overcome this, a number of new methods and new materials were designed. A series of them were prepared using long and flexible open-chain polyethers that could be used for determining quaternary ammonium cationic surfactants [73].

Although most membranes described in the literature are PVC-based, other approaches mainly to improve membrane selectivity were also tried. Thus membranes based on silicon rubber matrix using CTA^+-DS^- as ionophore were prepared. They could detect millimolar concentrations of DS^- when titrated with cetylpyridinium bromide (CPB), due to their response toward cationic surfactants [74].

An extensive study compared PVC with other polymers such as polybutadiene, polymethylmetacrylate, and polystyrene by preparing membranes with same ionophores and plasticizers. Relatively acceptable results were obtained only when vinyl polychloride was substituted with vinyl polybromide [54].

In a separate attempt to fix the electroactive material to the membrane to reduce its solubilization, PVC chains were functionalized. Hayakawa [75] synthesized modified PVC copolymerizing vinyl chloride with 3-acrylamido-*N*,*N*-dimethylpropylamine in different ratios followed by alkylation of the amine segments with methyl iodide. Membrane electrodes showed near-Nernstian response and could be used to determine SDS concentrations reasonably accurately below CMC. In mixtures of SDS and other surfactants, however, the concentration of the secondary surfactant could not be determined without large errors [75]. A PVC-based electrode reversible to SDS was prepared [76] in which a fraction of chlorine atoms bound to the poly(vinyl chloride) backbone was functionalized by nucleophilic substitution using trimethylamine. A number of studies have been published describing the use of mixed membranes comprising PVC and polypyrrole. Another team [77] prepared dodecylbenzenesulfonate ($DDBS^-$)-doped polypyrrole electrochemically and used this as the ionophore for constructing the sensor. This electrode showed Nernstian behavior and was stable for 6 months.

A solid-contact sensor for cationic surfactants using CP^+-TPB^- as the ion exchanger was developed and characterized. It was found that the surface of the sensor could be modified with PVC molecular sieves, and the modified electrodes could separately determine alkylpyridinium homologs with different lengths of hydrocarbon radicals (C10–C18) [78]. Another team prepared two neutral sensing materials SDS-SWCNT (single-walled carbon nanotubes) and SWCNT-CTAB, and incorporated them into a plasticized PVC membrane. Electrodes exhibited Nernstian response for SDS and near-Nernstian response for CTAB below their CMC, and showed acceptable selectivity over common anions. Results obtained were comparable to those obtained using classical methods [79]. For potentiometric flow injection analysis of anionic and polyethoxylate nonionic surfactants, PVC-based ISEs were constructed with an all-solid-state tubular flow-through design. Ion exchangers appropriate for detection of surfactant ions were incorporated into the plasticized PVC membranes [80, 81].

58.2.2.3 Coated-Wire Electrodes (CWEs). In 1970s surfactant titration using ion-selective electrodes with no inner solution was developed using a coated-wire electrode. Preparations involved introducing a conductive material (a Pt, Ag, Cu, or Al wire or a graphite rod) inert toward the membrane components into a sensor cocktail containing the ionophore repeatedly, and allowing the membrane forming solution to evaporate until a polymeric film of desired thickness was formed. If the coating was nonuniform, the wire interfered with electrode response [82, 83]. Because of their simplicity and low preparation costs, they were widely used in laboratories. The first coated-wire electrode for anionic surfactants was prepared by Fujinaga et al. [84], but Vytras first reported a device coated with a two-component membrane [85]. Vytras tested a PVC membrane plasticized with 2,4-dinitrophenyloctyl ether that enabled the possibility of titrating various kinds of surfactants, even in mixed systems [83]. Like conventional electrodes, Vytras prepared CWEs for titrating [86, 87] cationic and zwitterionic surfactants by TPB^-, and nonionic surfactants by adding Ba^{2+} in the membrane.

The major drawback of CWEs is shorter lifetime, higher potential drift, and low reproducibility compared to conventional PVC electrodes. Hence these are more suited for flow injection analysis where contact between the sample plug and the electrode surface is brief and for detecting endpoints in titrations that are guided by jumps in the electrode potential. In all other cases conventional membrane electrodes are more suitable [3].

58.2.2.4 Ion-Selective Electrode Field-Effect Transistors (ISFETs). To design sensors that can be mass-produced and retain reproducibility during use, ISFETs have been developed. These are cost-effective miniature devices with very low response times [88] and hence are more suitable for *in vivo* applications with small sample volumes. An added advantage over conventional membrane electrodes is that several ISEFETs can be integrated in a single chip and produce single-piece multiparametric sensors [89].

The first ISFET measurements of anionic surfactants were reported by Masadome et al. [90]. Subsequently, an ISFET of a PVC membrane was developed for the cholate ion by a design known as *ChemFET* (chemically modified field effect transistor). These devices showed super-Nernstian behavior with an improved detection limit [91]. ChemFETs specifically designed for measuring anionic surfactants were prepared and used in potentiometric titrations of different anionic detergents and commercial samples containing them. The results were consistent with the standard two-phase method [92]. These sensors were stable for 4 months, showed Nernstian response to the primary ion, had detection limits of about 10^{-6} M, and showed linear response. Three ChemFETs for measuring cationic surfactants were also fabricated and characterized. These devices used a PVC-sebacate matrix containing benzyldimethyl–hexadecylammonium reineckate, dodecyltrimethylammonium reineckate, and hexadecylpyridinium phosphotungstate as exchangers and were used not only to estimate cationic surfactants' concentration but also to evaluate their CMCs [93].

Limitations of ISFETs include manual application of membranes, low adherence to transistor gates, drifts in potential response, and limited working life. One of the strategies used to overcome these limitations and make large-scale preparations possible, involved reformulations for automatic implantations by designing membranes based on photocurable polymers. These could be manipulated via photolithography procedures. Thus photocurable membranes for anionic surfactants were prepared, characterized, and optimized [88,94]. Comparison with conventional electrPodes showed similar results.

58.2.2.5 Screen-Printed Electrodes (SPEs). More recently, SPEs have been developed for detecting surfactant ion concentration in solution. One team reported SPEs for determining CPC concentrations in solution directly or by potentiometric titrations using TPB^- [95]. They involve in situ modified and unmodified screen-printed ion-selective electrodes that were stable, had low response times, showed near-Nernstian response in the concentration range from 10^{-2} to 10^{-6} M, and had a pH range of 2–8. Analytical performances of these electrodes were similar to those of carbon paste electrodes (CPEs) and conventional PVC electrodes, and the results were comparable to those obtained using classical methods. In another report SPEs were used for potentiometric titration and determination of CTAB in different pharmaceuticals and water samples [96]. Results were comparable with those obtained for carbon paste, coated-wire, coated-graphite, and pol(yvinyl chloride) electrodes.

58.2.2.6 Membranes Reversible to Biological Surfactants: The Bile Salts. In 1977, Gilligan et al. [97] reported a liquid membrane electrode capable of measuring activity of the bile salts, sodium taurocholate (NaTC) and sodium taurodeoxycholate (NaTDC). This electrode could also detect SDS in solution. The ion-sensing complex comprised a 1:1 mixture of hexadecyltributylammonium ion and either of the tauro salts. CMC obtained for SDS using this electrode was comparable to that obtained using conventional SDS-selective electrodes. This electrode could also be used to measure bile ions in presence of phosphatidylcholine (mixed micellar solution).

A cholate (C^-) ion-selective liquid membrane electrode was prepared [98] using benzyldimethylcetylammonium cholate in 1-decanol as sensor. This electrode was used to estimate the pool of cholic acid in human bile [98]. In addition to detecting C^-, this electrode could also detect other anionic surfactants such as DS^-, $DDBS^-$, and $DOSS^-$ [99]. Campanella et al. then used the same ion exchanger to prepare a PVC-based bile-salt-selective electrode. Bile salt estimations by both types of membrane electrodes were similar [100]. Another pair of investigators [101] prepared liquid membrane electrodes reversible to five bile salts: sodium cholate (NaC), deoxycholate (NaDC), chenodeoxycholate NaCDC), ursodeoxycholate (NaUDC), and dehydrocholate (NaDHC). The ion exchanger in each case was hexadecyl tributylammonium bromide and the corresponding bile salt dissolved in 1-octanol. Electrode responses were near-Nernstian in the premicellar region, and the CMC values determined were in the range obtained by other methods. The electrodes were used to study binding interaction of bile salts with bovine serum albumin (BSA). Nitrobenzene-based liquid membrane electrodes were prepared containing CTAB-NaDC or CTAB-NaCDC as carrier complexes. To prepare NaC-selective membranes, however, dimethyldioctadecyl ammonium bromide (DDOAB)-NaC was used instead to resolve solubility constraints. These electrodes were used to determine the CMC of the bile salts in pure and in mixed states [102].

There are also some reports on preparation of bile ion-selective microelectrodes. Kunz and Lindenbaum [103] prepared NaC, NaDC, and NaCDC sensitive microelectrodes, and compared their Nernstian behavior under different conditions of temperature and pH. These microelectrodes showed selectivity over the physiologically important inorganic anions in bile. Another team [104,05] tested several organic compounds for preparing microelectrode sensitive to cholic acid. A mixture of benzyldimethylhexadecylammonium cholate/decanol with hexadecyltributylammonium taurocholate/5% hexachlorobenzene +0.5% bromoacetanilide in *o*-dichlorobenzene was used for preparing a double-barrel microelectrode because of overall low detection limit (10^{-4} M), low interference from common anions, and low drifts. This electrode was also sensitive toward NaDC, NaCDC, and NaUDC.

A PVC-based NaDC-sensitive electrode was prepared using CTA^+-DC^- as the sensing material [106]. Another

group [107] prepared PVC membranes containing CTA^+ and a mixture of anions (DS^-, $DDBS^-$, $DOSS^-$, DC^-, and $TCDC^-$) in 1:1 molar ratio using cyclohexanone as the solvent. This membrane showed selectivity separately toward all component anions and was stable for 3 months, although it showed sub-Nernstian behavior. Later Chatterjea et al. developed a multiple-bile ion-sensing membrane electrode [108] selective toward NaC, NaDC, and NaCDC, and their glycine and taurine conjugates, which could change selectivity following appropriate conditioning. This electrode had a low response time, was stable for 5 months, had a detection limit of ~10 nM, and showed low selectivity toward interfering bile ions and SDS. Selectivity toward commonly occurring anions followed the Hoffmeister series except phosphate. This electrode could be used to kinetically follow bile salt interactions with macromolecules.

58.3 STUDY OF SURFACTANT BIOPOLYMER SYSTEMS USING SISEs

Surfactant interaction with polymers has been the subject of investigation since the early 1950s. Apart from academic interests, studying these type of interactions are important because of their applications in pharmaceutical, biomedical, and food industries; enhanced oil recovery; mineral processing; and so on [28,109].The dominant forces involved in these interactions are charge–dipolar interactions, hydrophobic interactions, hydrogen bonding, and van der Waals forces.

It is known that polyelectrolytes induce aggregation of oppositely charged surfactants [110]. When a surfactant is gradually added to a polyelectrolyte (biopolymer) in solution, the formation of surfactant–biopolymer complexes can generally be described in terms of two critical concentrations. The first is the concentration at which small surfactant assemblies start binding to the polymer, normally called the *critical aggregation concentration* (CAC). With increasing surfactant concentration, micellar aggregates of similar or different forms become attached to the polymer sites and saturate them. This state is called the *polymer saturation concentration* (C_s) representing the surfactant concentration at which the polymer becomes saturated with bound surfactants. In the surfactant concentration region CAC-C_s, micelle-like aggregates develop [111]. At higher surfactant concentrations, free (nonbound) surfactant monomers associate at a critical concentration C_e to form free larger micelles. C_e is also called the *extended critical micelle concentration*. Normally, CAC is appreciably lower than C_e. Other reports [112,113] have shown that the surfactant aggregates are similar to free micelles. A "necklace bead" model has been recognized for the depiction of a polymer–surfactant complex where the polymer induced micellar aggregates begin to form at CAC, decorate the polymer strand up to C_s, and then begin to form free micelles at C_e. Stagewise interaction of surfactant molecules with a polymer with gradual increase in surfactant ion concentration in aqueous medium is pictorially illustrated in Fig. 58.2. SISEs, tensiometry, and *isothermal titration calorimetry* (ITC) can be used to determine CAC, C_s, and C_e (111,114,115). Figure 58.3 shows representative tensiometric and ITC profiles of surfactant–polymer interaction in arbitrary scale. These techniques have been used to investigate a number of polymer–surfactant systems [116].

Polymer–surfactant interactions can occur between neutral polymers and surfactants, between charged polymers (polyelectrolytes) and surfactants, or between biopolymers and surfactants. All of these interactions could be studied using SISE. In this chapter, we focus on the interactions of surfactants with biopolymers and biologically active polyelectrolytes.

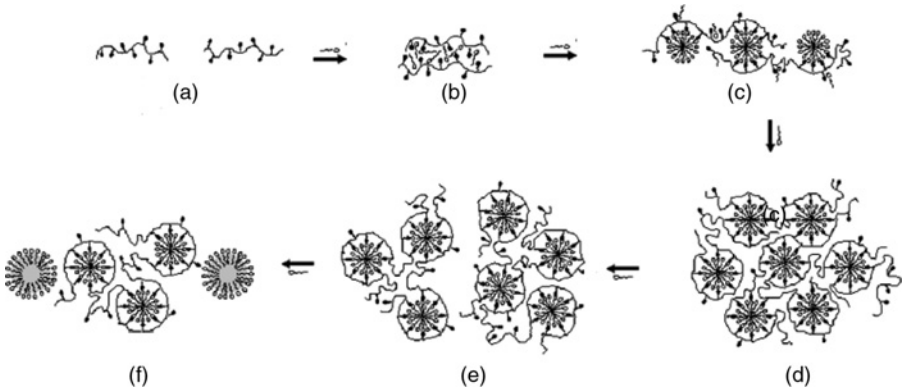


FIGURE 58.2 Pictorial representation of different stages of polymer–surfactant interaction with gradual addition of surfactant to a polymer in aqueous medium: (a) surfactant-monomer-loaded polymer; (b) CAC-forming state; (c) induced micelles formed on the polymer strands; (d) aggregation to coacervation above C_S; (e) deaggregation of coacervate; (f) "necklace beads" with free micelles at and above C_M.

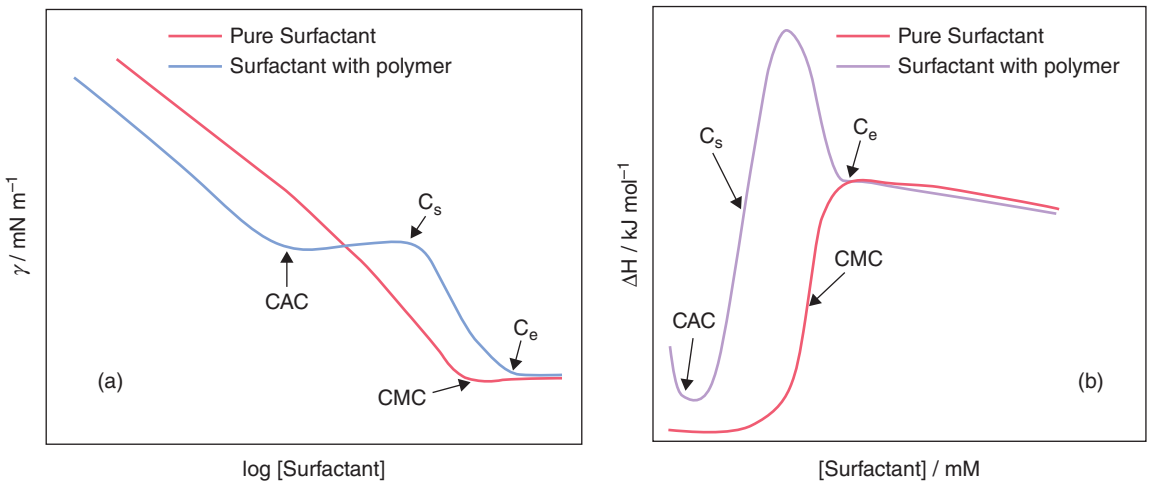


FIGURE 58.3 Representative plots for polymer–surfactant interactions (arbitrary scale): (a) tensiometric results; (b) calorimetric results (CMC–critical micelle concentration of pure surfactant; CAC–critical aggregation concentration; C_s–maximum surfactant-binding concentration; C_e–extended critical micelle concentration).

Interactions between ionic surfactants and biopolymers, for example proteins, have been widely investigated because of their biological importance. Interactions of surfactant-synthetic polymer systems showed physicochemical similarities with surfactant-biopolymer systems. Binding of charged surfactants to protein can be viewed as occurring in two distinct stages. In the first stage, the surfactant binds to a specific site on the protein surface known as the *high-energy binding region* guided by both electrostatic and hydrophobic interactions. In the second stage, the protein unfolds, exposing its hydrophobic interior and additional potential binding sites [117]. The binding of cationic surfactants to biopolymers of low charge density occurs by way of combination of noncooperative and cooperative binding [118]. Structural investigation of protein–surfactant complexes by NMR and neutron scattering showed that formation of protein–surfactant aggregates could also be described by the "necklace bead" [119, 120] model. The model assumed that the unfolded polypeptide chain is flexible in solution and that micelle-like clusters of surfactants are distributed along the unfolded polypeptide chain. Another team [121] carried out a series of small-angle neutron-scattering (SANS) investigations of BSA-SDS and ovalbumin-SDS complexes. From the quantitative interpretations of SANS intensity distributions, they came up with a well-defined structural model for these complexes and renamed the model the 'correlated necklace model." It is noted that the aggregate sizes are always smaller than the micellar aggregation number under the same solvent conditions.

Formation of biopolymer-surfactant aggregates in dilute solutions have been extensively investigated using different techniques such as surface tension, conductivity, viscosity, fluorescence microscopy, light scattering, neutron scattering, and NMR [122–124]. Results obtained using all these techniques consistently showed these interactions to be cooperative in nature. Although surface tension and electrical conductivity are used mostly for determining concentrations, they are not suitable for unambiguous determination of CAC, C_s, and C_M in presence of salts. SISEs were able to monitor continuous changes in surfactant concentrations, thus providing a versatile and alternative technique to determine monomeric surfactant concentration in dilute polymer–surfactant mixtures in presence of salts [125]. Earlier studies focused mainly on surfactant polymer systems at relatively higher polymer or surfactant concentrations. Introduction of SISEs have allowed extension of these studies to very low surfactant concentrations [126].

Binding constants and cooperativity parameters for an interaction can be estimated by studying their binding isotherms. Analysis of binding isotherms of surfactant–biopolymer interactions (curves representing amount of bound surfactant ion as a function of concentration of nonbound surfactant ion) provide insights into how binding interactions are influenced by surfactant chain length, polyelectrolyte linear charge density, and ionic strength. Although other methods are available [127, 128], potentiometric methods involving SISEs have been found to be the method of choice for studying binding isotherms and the degree of micellar counterion ionization of ionic surfactant–biopolymer systems.

58.3.1 Interactions between Ionic Surfactants and Biopolymers

Studies of surfactant interaction with biopolymers mostly involved proteins and biologically active polyelectrolytes.

The nature of the interaction depended mainly on the type of biopolymer, surfactant, pH, ionic strength, and temperature. A number of biopolymer–surfactant systems have so far been studied using SISEs, of which the most frequently studied surfactant is SDS. Other anionic surfactants including some bile salts and a few cationic surfactants like CTAB and CPC were also studied.

Since the introduction of SDS-selective liquid membrane electrodes by Birch et al., these have been used to study binding interactions of SDS with polymers such as poly(vinyl alcohol), poly(vinyl pyrrolidone), and biopolymers such as dextran, and BSA in premicellar solutions. Results obtained showed that the electrode gave rapid and reliable data in solutions containing polymer–surfactant complexes [37].

Binding properties of dextran sulfate (DS) with surfactants could be investigated using SISEs. This biocompatible polyanionic dextran derivative mimics natural mucopolysaccharides like chondroitin sulfates and have applications in the healthcare sector. Binding of DTAB determined using a DTA-DS carrier complex was found to be highly cooperative [129]. Binding interactions were also studied in presence of multivalent cations such as Mg^{2+}, Ca^{2+}, Zn^{2+}, and La^{3+} [130]. Dependence of chain length on binding of alkylpyridinium cations (undecyl-, dodecyl-, tridecyl-, and tetradecylpyridinium ions) to dextran sulfate was studied using solid membrane electrodes selective for each surfactant ion. Binding isotherms showed high cooperativity indicating a significant effect of hydrophobic interactions [131]. Studies of temperature dependence of DTA^+ binding to dextran sulfate in the range 278–323 K showed small but significant temperature dependence. Equilibrium thermodynamic parameters (free energy, entropy, and enthalpy) were also calculated from this study [132]. The results were comparable with that obtained from binding of dodecylpyridinium ions (DoP^+) with DNA as a function of temperature [133]. Values obtained for the thermodynamic parameters indicated the importance of hydrophobic interactions in the polyion–surfactant binding process. Another team reported binding isotherms of sodium dextran sulfate to DoP^+ [134].

Binding isotherms of SDS bound to biologically active polyelectrolytes poly(L-ornithine), poly(D,L-ornithine), and poly(L-lysine) at neutral pH were determined using SISEs. All three binding curves showed high cooperativity suggesting micelle-like clustering of the surfactant ions onto the polypeptide side groups [135]. Another team used DTA^+ - and TTA^+ -selective electrodes to study binding isotherms of DTAB and TTAB interactions with carboxylic polyelectrolytes such as alginate, pectate, and (carboxy)methyl cellulose in presence and absence of NaCl [136]. Interactions of (carboxy)methylcellulose (sodium salt) with salts, dyes, and surfactants have been studied by viscometry, conductometry, spectrophotometry, and CTAB-selective SISEs [137]. Binding of CTAB with the polyelectrolyte was Langmuirian in absence of KCl, and strongly cooperative in its presence. Thermodynamic parameters were calculated using Langmuir and Scatchard equations. (Carboxy)methyl cellulose interaction with a mixture of cationic surfactants [DTAB, DTA-chloride, TTAB, CTAB, triphenylphosphonium bromide, and tetradecylpyridinium bromide (TeP)] have been examined by tensiometry, viscosimetry, SISEs, and dynamic light scattering. The effect of varying surfactant chain length, headgroup size, counterion, and ionic strength on the CAC of mixed polymer surfactant systems and the collapse of the polymer molecule under different solution conditions were studied [138].

The interaction of CTAB and CPC with *Aspergillus niger* cellulose (ANC) has been studied using SISEs, fluorescence, and turbidimetric techniques [139, 140]. Using the Wyman binding potential model, the binding was found to be entropy-controlled. Another team [141] investigated the interaction of CTAB with α-amylase from *Bacillus subtilis* at 25°C at different pH, ionic strength, and concentrations of urea using CTAB-selective membrane electrodes. The binding isotherms obtained were also analyzed using the Wyman binding potential concept.

Chitosan, a cationic biopolymer, has a number of applications in food and pharmaceutical industries because of its unique nutritional and physicochemical properties. Many of these properties depend on its ability to interact with anionic surface-active molecules such as phospholipids, surfactants, and bile acids. Thongngam et al. [142] characterized the interaction of chitosan with SDS using ITC, SISEs, and turbidity measurements. Binding interaction was found to be highly exothermic. Another study provided information that can be used to design chitosan-based products with specific nutritional and functional characteristics, such as lowering of cholesterol [143]. SISEs, surface tension, ITC, turbidity, and zeta-potential measurements were used to study SDS binding with chitosan to obtain information on the structure of the surfactant-polyelectrolyte complexes in the bulk phase. At optimal ionic ratio, the SDS-chitosan system is suitable for the encapsulation of hydrophobic molecules [144].

Another team described the interaction of TeP^+ and DoP^+ with sodium poly(aspartate) at different molecular weights and found that with decreasing molecular weights CAC increased while the binding cooperativity decreased. Polyaspartates resemble real proteins in several respects [145].

Interaction of gelatin with surfactants has also been extensively investigated. SISEs have been used to provide information regarding the effect of surfactant on the gelling capacity of the protein. Binding isotherms of SDS to alkali-processed and acid-processed bone gelatin were determined using DS^- reversible electrodes. Results obtained were comparable to that obtained using viscosity [146]. A surfactant-selective LME comprising the carrier complex CTA^+-DS^-

in *o*-nitrotoluene was used by Fruhner et al. [147] to construct binding isotherms of gelatin interactions with alkyl sulfates and alkyltrimethylammonium ions in dilute aqueous solutions. At pH $\geq$ 7 the degree of binding was independent of pH. At pH $\leq$ 6 the extent of binding increased steeply with decreasing pH. Extent of binding also increased strongly with increasing chain length. Octyl sulfate showed low binding even at low pH. Cationic surfactants showed weaker interactions than anionic surfactants of comparable alkyl chain length. The photobehavior of pyrene in both fluid and gel states of gelatin in absence and presence of SDS and DTAB was studied [148]. SISEs were used to determine binding capacities of SDS and DTAB to gelatin in both states. Results obtained from these studies complemented with viscosity and gel strength measurements could be used to relate surfactant–gelatin interactions with macroscopic or microscopic properties of gels. Other investigators[149] studied interactions between SDS and gelatin using a wide variety of physicochemical methods such as turbidity, conductometry, surface tension, ITC, and potentiometry to better understand the bulk behavior of SDS-gelatin systems and to obtain optimal ionic ratio of these complexes for forming capsules using the coacervation process. Binding isotherms obtained using SDS selective electrodes correlated with surface tension measurements.

Maulik et al. studied binding isotherms of BSA, β-lactoglobulin, hemoglobin, gelatin, lysozyme, and deoxyribonucleic acid with both CTAB and SDS by using SISEs at different pH, ionic strength, and temperature [150]. Reversibility of binding was established by studying the association and dissociation process. Another group used SISEs to study sodium alkyl sulfate ($C_nH_{2n+1}OSO_3Na$, where n = 8,10,12) binding to human erythrocytes [151] to clarify the mechanism of shape changes induced by the anionic surfactants.

Mokus et al. [152] described the construction of a DS^- sensitive electrode with CTA^+-DS^- complex as the ionophore in a siloxane polymer membrane and used it to measure the activity of SDS in biological samples. By comparing with results obtained from equilibrium dialysis, they showed that the electrode could be used to detect both the high-affinity binding sites of human serum albumin (HSA) for SDS and to follow its cooperative binding to serum albumin, ovalbumin, and β-lactoglobulin. Binding of CTAB with HSA at various ionic strengths [153] and that of CPC with HSA at different pH were studied using SISEs and fluorescence spectroscopy. Binding isotherms were analyzed to determine the Hill parameters. Results indicated two sets of binding sites under all experimental conditions and suggested a role of hydrophobic interactions in binding [154]. The interaction of a fluorinated surfactant sodium perfluorooctanoate with HSA was studied using potentiometry and a combination of ultraviolet (UV)–circular dichroism (CD) spectroscopy [155]. Results indicated that the surfactant molecules had a high affinity for HSA and stabilized the protein structure. Aggregates formed by HSA interaction with sodium perfluorooctanoate–sodium octanoate, and sodium perfluorooctanoate–sodium dodecanoate systems were investigated by conductance, SISEs, electrophoresis, and spectroscopy measurements [156]. Interactions between a homologous series of cationic surfactants [DTAB, TTAB, hexadecyltrimethyl ammonium bromide (HTAB)] and BSA were studied using SISEs at various temperatures [157]. The method was fast and accurate and data analysis revealed two sets of binding sites. Binding of *n*-hexadecylpyridinium bromide to BSA was also studied [158].

Binding isotherms of hemoglobin interaction with TTAB and CTAB were obtained [157] using ion-selective electrodes and apparent binding constants were calculated using the Wyman binding potential model. It was found that the binding of surfactant molecules induced unfolding of hemoglobin, resulting in exposure of the heme pocket facilitating heme oxidation. The binding process was endothermic since affinity increased with temperature. CTAB binding to, oxyhemoglobin, and carbaminohemoglobin were also studied [159]. Binding of CPC with glucose oxidase was studied as a function of ionic strength, concentrations of urea, and pH using CPC-selective membrane electrodes, UV-visible absorption spectroscopy, and enzymatic activity assay method. Binding parameters revealed two sets of binding sites and were used to calculate intrinsic Gibbs free energy of binding [160].

Interaction of CTAB with large T4 DNA was studied using CTAB selective electrode combined with fluorescence microscopy. Using potentiometric techniques, the binding equilibrium was studied, while a globule-to-coil reversible transition was established using fluorescence microscopy. The cooperativity of binding was attributed to bimodality in the distribution between the elongated coil and the compact globule states of T4 DNA chains [161].

Other investigators [101] studied binding interactions of bile salts NaC, NaDC, NaCDC, NaUDC, NaDHC with BSA using bile-salt-selective electrodes. From the Scatchard plots using nonlinear least-squares fit, binding constants and the number of binding sites were estimated. The relative order of binding was NaDC $\approx$NaCDC>NaUDC $\gg$NaC >NaDHC. Estimation of thermodynamic parameters showed that bile salts bound to hydrophobic sites on BSA.

Theoretical models for potentiometric titration curves of some ionic and nonionic surfactants were proposed by Sak-Bosner et al. [162]. They estimated response parameters for a few surfactant sensors using data generated by previously described liquid membrane surfactant-sensing electrodes. The models were optimized using *Solver* (Microsoft Excel) and Wolfram Research *Mathematica v*. 7.1.

58.3.2 Kinetic Studies of Surfactant–Biopolymer Interactions Using SISEs

Interaction between surfactants and biopolymers proceed through intrinsic mechanistic stages to reach equilibrium. The mechanistic courses of a reaction can be understood by following its kinetics. Kinetic courses of such interactions have been studied by Maulik et al. [69] using SISEs. Using a CTAB-selective membrane electrode, they have followed the kinetics of binding of CTAB with sodium salt of carboxymethyl cellulose. The binding process followed a first-order kinetics and yielded three rate constants. Binding affinity increased with increasing CTAB concentration, and decreased with ionic strength. Thermodynamic parameters evaluated for activation, showed the reactions to be entropy-controlled. The same authors also studied the kinetics of interaction of CTAB with BSA [70]. Least-square curve fitting gave three rate constants of binding. Parameters of activation showed that the entropy and enthalpy of activation closely compensated each other. Kinetic interactions of CTAB with gelatin, hemoglobin β-lactoglobulin, and lysozyme were also studied [163]. Reaction occurred in three stages for the denatured protein gelatin, but in two stages for the native proteins hemoglobin, β-lactoglobulin, and lysozyme under the same conditions. In each case, reaction rates increased with temperature following the trend $k_1 \gg k_2 > k_3$. CTA^+ interactions with proteins were both electrostatic and hydrophobic. All reactions were entropy-controlled, and the phenomenon of isokinetic entropy–enthalpy (164) compensation was also observed.

The study was extended to the binding interactions of CTAB with DNA [165], which also followed first-order kinetics. Reactions occurred in three stages for native DNA and in two stages for denatured DNA. In another study, kinetic interaction of CTAB with DNA was carried out in water and in sodium chloride solution. The results can be explained in terms of a reaction mechanism involving two consecutive reversible steps. The first step corresponds to the union/separation of the surfactant with/from the DNA, and the second step corresponds to a conformational change of the surfactant-DNA complex [166]. The equilibrium constant calculated from the forward and reverse rate constants of these steps agreed with the results obtained by another team [165].

The representative values of rate constants obtained with CTAB interactions with different biopolymers are shown in Table 58.1. It may be observed that under the same conditions of ionic strength, pH, CTAB concentrations and temperature, different amounts of biopolymers were needed to obtain rate constants of similar magnitudes reflecting differences in their reaction propensities.

Very recently, Chatterjea et al. [108] developed a multiple-bile ion-sensing membrane electrode using which rate constants of binding of NaC, NaDC, and NaCDC with a biocompatible polymer polyethylene, glycol were found. Single-stage first-order reaction kinetics was observed. Preparation and use of this multiple-ion-sensing electrode is a unique development and immensely promising for the study of polymer–surfactant/biosurfactant interactions. Further work involving kinetics of bile salt interactions with other proteins and biopolymers is in progress.

TABLE 58.1 Representative Rate Constants of CTAB interactions with Different Biopolymers Determined Using CTAB-Selective SISE at [CTAB] = 50 μM dm^{-3}, pH = 5, μ = 0.05, T = 310 K

Biopolymer	k_1 (h^{-1})	k_2 (h^{-1})	k_3 (h^{-1})
Carboxymethyl cellulose (0.056% w/v)	327	46.8	18.0
Gelatin (0.08% w/v)	345	46.8	18.3
BSA (0.2% w/v)	367	47.9	12.6
Hemoglobin (0.01% w/v)	356	50.4	-
Lysozyme (0.02% w/v)	302	13.3	-
β-Lactoglobulin (0.015% w/v)	360	55	-
DNA (0.001% w/v)	414	48.9	10.8

58.4 CONCLUSION

Surfactant interactions with biopolymers is an important field of study where determination of surfactant concentration at different stages, particularly at low concentration (μM), may be required. For this purpose, among different available techniques, electrochemical methods using SISEs are potentially useful. Both liquid and solid membrane electrodes have been developed with different ionophores resulting in reversibility of a membrane towards a surfactant. The exchange of ions between solutions and the ionophore develops a potential across the membrane making them successful ion sensors. Monitoring of this membrane potential measures the activity (or concentration) of the surfactant ions which helps probe the process of interaction with polyelectrolytes, synthetic polymers, or biopolymers. Although the development of such electrodes has a long history, they are still in the process of improvement in terms of sensitivity, stability, durability, interference, detection limits, to make them feasible for multiple use that could make them commercially viable. Although different types of ISEs have been developed, reports on electrodes selective to multiple surfactant ions are rare. There has been a recent development in this direction [108], opening up the scope of developing SISEs capable of monitoring multiple ions with high selectivity and detection limit in the range in the nM range. Although there has been several reports on different ISEs detection limit in the nM range has not yet been reported for any.

An important use of SISEs apart from equilibrium studies is the investigation of kinetics of interaction, which is not which is not easily accomplishable using other methods. Although there are reports on reaction rates and associated thermodynamic parameters for a few synthetic surfactant–biopolymer systems, reports on biosurfactant/biopolymer systems are very rare.

The information gathered and discussed in this chapter should hopefully help researchers and practitioners become updated in this field, enabling them to advance the field by further development and use of SISEs.

ACKNOWLEDGMENT

S.M.C and K.P. thank the Department of Science and Technology, Government of India for financial support for this work with a Woman Scientist position to the former (Sanction Order SR/WOS-A/LS-201/2010 C). S.P.M. acknowledges with thanks the Indian National Science Academy, New Delhi for an Honorary Scientist Position, and Jadavpur University, Kolkata for an Emeritus Professorship, and infrastructural facilities.

REFERENCES

[1] Lizondo-Sabater, J., Martínez-Máñez, R., Sancenón, F., Seguí, M.J., Soto, J. (2008). Ion-selective electrodes for anionic surfactants using a cyclam derivative as ionophore. *Talanta* **75**, 317–325.

[2] Sak-Bosnar, M., Grabaric, Z., Grabaric, B.S. (2004). Surfactant sensors in biotechnology Part 1-electrochemical sensors. *Food Technol. Biotechnol.* **42**, 197–206.

[3] Sanchez, J., Del Valle, M. (2005). Determination of anionic surfactants employing potentiometric sensors-a review. *Crit. Rev. Anal. Chem.* **35**, 15–29.

[4] Marafie, H.M., Al-Shammari, T.F., Shoukry, A.F. (2012). New tetradecyltrimethylammonium-selective electrodes: Surface composition and topography as correlated with electrode's life span. *Talanta* **91**, 26–32.

[5] Asada, A., Sonoyama, M. (2011). Solubilization and structural stability of bacteriorhodopsin with a mild nonionic detergent, n-octyl-β-thioglucoside. *Biosci. Biotechnol. Biochem.* **75**, 376–378.

[6] Kim, S.H., Lim, E.J., Lee, S.O., Lee, J.D., Lee, T.H. (2000). Purification and characterization of biosurfactants from Nocardia sp. L-417. *Biotechnol. Appl. Biochem.* **31**, 249–253.

[7] Muriel, J.M., Bruque, J.M., Olías, J.M., Jiménez-Sánchez, A. (1996). Production of biosurfactants by Cladosporium resinae. *Biotechnol. Lett.* **18**, 235–240.

[8] Creuwels, L.A.J.M., Van Golde, L.M.G., Haagsman, H.P. (1997). The pulmonary surfactant system: Biochemical and clinical aspects. *Lung* **175**, 1–39.

[9] Banat, I.M., Makkar, R.S., Cameotra, S.S. (2000). Potential commercial applications of microbial surfactants. *Appl. Microbiol. Biotechnol.* **53**, 495–508.

[10] Del'Arco, J.P., De Franca, F.P. (2001). Influence of oil contamination levels on hydrocarbon biodegradation in sandy sediment. *Environ. Pollut.* **112**, 515–519.

[11] Ron, E.Z., Rosenberg, E. (2001). Natural roles of biosurfactants. *Environ. Microbiol.* **3**, 229–236.

[12] Alegret, S., Alonso, J., Bartrolí, J., Baró-Romà, J., Sànchez, J., Del Valle, M. (1994). Application of an all-solid-state ion-selective electrode for the automated titration of anionic surfactants. *Analyst* **119**, 2319–2322.

[13] Young, T.E., Synovec, R.E. (1996). Enhanced surfactant determination by ion-pair formation using flow-injection analysis and dynamic surface tension detection. *Talanta* **43**, 889–899.

[14] Liu, H., Dasgupta, P.K. (1994). Flow-injection extraction without phase separation based on dual-wavelength spectrophotometry. *Anal. Chim. Acta* **288**, 237–245.

[15] Ye, M.Y., Walkup, R.G., Hill, K.D. (1994). Determination of surfactant sodium lauryl ether sulfate by ion pairing chromatography with suppressed conductivity detection. *J. Liquid Chromatogr. Rel. Technol.* **17**, 4087–4097.

[16] Shakhsher, Z.M., Seitz, W.R. (1990). Optical detection of cationic surfactants based on ion pairing with an environment-sensitive fluorophor. *Anal. Chem.* **62**, 1758–1762.

[17] Bakker, E., Bühlmann, P., Pretsch, E. (1997). Carrier-based ion-selective electrodes and bulk optodes. 1. General characteristics. *Chem. Rev.* **97**, 3083–3132.

[18] Cremer, M. (1906). Über die Ursache der elektromotorischen Eigenschaften der Gewebe, zugleich ein Beitrag zur Lehre von den polyphasischen Elektrolytketten. *Z. Biol.* **47**, 562–607.

[19] Bühlmann, P., Pretsch, E., Bakker, E. (1998). Carrier-based ion-selective electrodes and bulk optodes. 2. Ionophores for potentiometric and optical sensors. *Chem. Rev.* **98**, 1593–1687.

[20] Morelli, J.J., Szajer, G. (2000). Analysis of surfactants: Part I. *J. Surfact. Deterg.* **3**, 539–552.

[21] Morelli, J.J., Szajer, G. (2001). Analysis of surfactants: Part II. *J. Surfact. Deterg.* **4**, 75–83.

[22] Madunić-Čačić, D., Sak-Bosnar, M., Galović, O., Sakač, N., Matešić-Puač, R. (2008). Determination of cationic surfactants in pharmaceutical disinfectants using a new sensitive potentiometric sensor. *Talanta* **76**, 259–264.

[23] Seguí, M.J., Lizondo-Sabater, J., Benito, A., Martínez-Máñez, R., Pardo, T., Sancenón, F., Soto, J. (2007). A new ion-selective electrode for anionic surfactants. *Talanta* **71**, 333–338.

[24] Birch, B.J., Cockcroft, R.N. (1981). Analysis of ionic surfactants in the detergent industry using ion-selective electrodes. *Ion Select. Electrode Rev.* **4**, 1–41.

[25] Moriyama, Y., Takeda, K. (2005). Protective effects of small amounts of bis (2-ethylhexyl) sulfosuccinate on the helical

structures of human and bovine serum albumins in their thermal denaturations. *Langmuir* **21**, 5524–5528.

[26] Honda, C., Kamizono, H., Matsumoto, K.I., Endo, K. (2004). Studies on bovine serum albumin–sodium dodecyl sulfate complexes using pyrene fluorescence probe and 5-doxylstearic acid spin probe. *J. Colloid Interface Sci.* **278**, 310–317.

[27] Tanford, C. (1972). Hydrophobic free energy, micelle formation and the association of proteins with amphiphiles. *J. Mol. Biol.* **67**, 59–74.

[28] Li, G., Ma, H., Hao, J. (2012). Surfactant ion-selective electrodes: A promising approach to the study of the aggregation of ionic surfactants in solution. *Soft Matt.* **8**, 896–909.

[29] Mahajan, R.K., Nandni, D., Puri, R.K. (2010). Novel perchlorate selective electrode based on neutral surfactant ion-pair complex of dodecyltrimethylammonium-perchlorate. *Anal. Lett.* **43**, 2114–2124.

[30] Jimenez-Jorquera, C., Orozco, J., Baldi, A. (2009). ISFET based microsensors for environmental monitoring. *Sensors* **10**, 61–83.

[31] Abbas, M.N., Mostafa, G.A.E., Homoda, A.M.A. (2000). Cetylpyridinium–iodomercurate PVC membrane ion selective electrode for the determination of cetylpyridinium cation in Ezafluor mouth wash and as a detector for some potentiometric titrations. *Talanta* **53**, 425–432.

[32] Craggs, A., Moody, G.J., Thomas, J.D.R., Birch, B.J. (1980). Effect of anionic surfactants on calcium ion-selective electrodes. *Analyst* **105**, 426–431.

[33] Buschmann, N., Schulz, R. (1993). Comparison of different ion sensitive electrodes for the titrimetric determination of ionic surfactants. *Tenside Surfact. Deterg.* **30**, 18–23.

[34] Coetzee, C.J., Freiser, H. (1968). Anion-responsive electrodes based on ion association extraction systems. *Anal. Chem.* **40**, 2071.

[35] Gavach, C., Bertrand, C. (1971). Electrodes specifiques d'anions a longue chaine hydro-carbonee: Application au dosage potentiométriqué de détergents anioniques. *Anal. Chim. Acta* **55**, 385–393.

[36] Birch, B.J., Clarke, D.E. (1972). An electrode selective to the dodecyl sulfate anion: Comments on the application of direct potentiometry to cmc measurements. *Anal. Chim. Acta* **61**, 159–162.

[37] Birch, B.J., Clarke, D.E., Lee, R.S., Oakes, J. (1974). Surfactant-selective electrodes: Part III. Evaluation of a dodecyl sulfate electrode in surfactant solutions containing polymers and a protein. *Anal. Chim. Acta* **70**, 417–423.

[38] Birch, B.J., Clarke, D.E. (1973). Surfactant-selective electrodes: Part I. An improved liquid ion-exchanger. *Anal. Chim. Acta* **67**, 387–393.

[39] Ishibashi, N., Kohara, H., Horinouchi, K. (1973). Aromatic sulphonate ion-selective electrode membrane with crystal violet as ion-exchange site. *Talanta* **20**, 867–874.

[40] Ciocan, N., Anghel, F.D. (1978). An ion-extractive liquid-membrane anionic surfactant sensitive electrode and its analytical applications. *Fresenius Z. Anal. Chem.* **290**, 237–240.

[41] Anghel, D.F., Popescu, G. (1981). *Potentiometric Methods of Determining the Concentration of Ionic Surfactant Substances of Micellar Solutions Used in Recovery of Petroleum from Deposits*. Romanian Patent 71873.

[42] Szczepaniak, W., Ren, M. (1994). Selectivity of liquid membrane electrode based on mercurated polystyrene as ion-exchanger to anionic surfactants and soaps. *Electroanalysis* **6**, 341–347.

[43] Schmitt, T.M. (1992). *Analysis of Surfactants.* Marcel Dekker, New York.

[44] Gerlache, M., Kauffmann, J.M., Quarin, G., Viré, J.C., Bryant, G.A., Talbot, J.M. (1996). Electrochemical analysis of surfactants: An overview. *Talanta* **43**, 507–519.

[45] Moody, G.J., Oke, R.B., Thomas, J.D.R. (1970). A calcium-sensitive electrode based on a liquid ion exchanger in a poly (vinyl chloride) matrix. *Analyst* **95**, 910–918.

[46] Craggs, A., Moody, G.J., Thomas, J.D.R. (1974). PVC matrix membrane ion-selective electrodes. Construction and laboratory experiments. *J. Chem. Educ.* **51**, 541–544.

[47] Mihali, C., Vaum, N. (2012). *Use of Plasticizers for Electrochemical Sensors, Recent Advances in Plasticizers*, InTech, Croatia, pp. 125–140.

[48] Senturk, Z., Gerlache, M., Kauffmann, J.M. (1997). Potentiometric analysis of surfactants. *FABAD Farm. Bilimler Derg*, **22**, 131.

[49] Attiyat, A.S., Christian, G.D., Hallman, J.L., Bartsch, R.A. (1988). A comparative study of the effect of *o*-nitrophenyl octyl ether and *o*-nitrophenyl pentyl ether as plasticizers on the response and selectivity of carrier-based liquid membrane ion-selective electrodes. *Talanta* **35**, 789–794.

[50] Davies, J.E.W., Moody, G.J., Thomas, J.D.R. (1972). Nitrate ion selective electrodes based on poly (vinyl chloride) matrix membranes. *Analyst* **97**, 87–94.

[51] Griffiths, G.H., Moody, G.J., Thomas, J.D. (1972). An investigation of the optimum composition of poly (vinyl chloride) matrix membranes used for selective calcium-sensitive electrodes. *Analyst* **97**, 420–427.

[52] Tanaka, T., Hiiro, K., Kawahara, A. (1974). Alkylbenzenesulfonate ion selective electrode using ferroin salt in polyvinyl chloride matrix. *Anal. Lett.* **7**, 173–176.

[53] Tanaka, T., Hiiro, K., Kawahara, A. (1975). *Determining Activities of Ions of Alkylbenzene Sulfonic Acids in Wastewaters or Rivers*. Jpn. Patent 50051397.

[54] Cutler, S.G., Meares, P., Hall, D.G. (1977). Surfactant-sensitive polymeric membrane electrodes. *J. Electroanal. Chem. Interfacial Electrochem.* **85**, 145–161.

[55] Vytřas, K. (1985). Potentiometric titrations based on ion-pair formation. *Ion Select. Electrode Rev.* **7**, 77–164.

[56] Buschmann, N. (1992). *Tenside Surf. Deterg.* **29**, 128.

[57] Jones, D.L., Moody, G.J., Thomas, J.D.R., Birch, B.J. (1981). Barium-polyethoxylate complexes as potentiometric sensors and their application to the determination of non-ionic surfactants. *Analyst* **106**, 974–984.

[58] Sak-Bosnar, M., Madunic-Cacic, D., Matesic-Puac, R., Grabaric, Z. (2007). Nonionic surfactant-selective electrode

and its application for determination in real solutions. *Anal. Chim. Acta* **581**, 355–363.

[59] Martıínez-Barrachina, S., Alonso, J., Matia, L., Prats, R., del Valle, M. (2001). All-solid-state potentiometric sensors sensitive to nonionic surfactants based on ionophores containing ethoxylate units. *Talanta* **54**, 811–820.

[60] Buschmann, N., Schulz, R. (1992) Development of an ion sensitive electrode for the titration of surfactants, in VI Jornadas de la detergencia (AID), Barcelona. *Jorn Com. Esp. Deterg.* **23**, 323–328.

[61] Buschmann, N. (1994). Personal communication.

[62] Schulz, R., Gerhards, R. (1994). Optimization of the potentiometric titration of ionic detergents. *Am. Lab.* **26**, 40–44.

[63] Wang, J., Du, Z., Wang, W., Xue, W. (2011). Ion-selective electrode for anionic surfactants using hexadecyl trimethyl ammonium bromide-sodium dodecylsulfate as an active ionophore. *Int. J. Electrochem.* **2011**, 1–8.

[64] Baró-Romà, J., Sánchez, J., Del Valle, M., Alonso, J., Bartrolí, J. (1993). Construction and development of ion-selective electrodes responsive to anionic surfactants. *Sensors Actuators B: Chem.* **15**, 179–183.

[65] *Model 93-42 Surfactant Electrode, Instruction Manual* (1989). Orion Research, Cambridge, MA.

[66] Gallegos, R.D. (1993). Titrations of non-ionic surfactants with sodium tetraphenylborate using the Orion surfactant electrode. *Analyst* **118**, 1137–1141.

[67] Schulz, R. (1999) Titrimetric determination of surfactants and pharmaceuticals. *Modern Methods Anal. Practice*. Metrohm Ltd., Herisau.

[68] Szczepaniak, W. (1990). Mercurated polystyrene as a sensor for anionic surfactants in ion-selective polymeric membrane electrodes. *Analyst* **115**, 1451–1455.

[69] Maulik, S., Jana, P.K., Moulik, S.P., Chattoraj, D.K. (1995). Biopolymer–surfactant interaction. I. Kinetics of binding of cetyltrimethyl ammonium bromide with carboxymethyl cellulose (Na salt). *Biopolymers* **35**, 533–541.

[70] Maulik, S., Moulik, S.P., Chattoraj, D.K. (1996). Biopolymer–surfactant interaction 2: Kinetics of binding of cetyltrimethylammonium bromide with bovine serum albumin. *Bull. Chem. Soc. Japan* **69**, 2911–2918.

[71] Devi, S., Chattopadhyaya, M.C. (2012). A new PVC membrane ion selective electrode for determination of cationic surfactant in mouthwash. *J. Surfact. Deterg.* **15**, 387–391.

[72] Galović, O., Samardžić, M., Derežić, D., Madunić-Čačić, D., Sak-Bosnar, M. (2012). Potentiometric titration of micromolar levels of anionic surfactants in model effluents using a sensitive potentiometric sensor. *Int. J. Electrochem. Sci.* **7**, 1522–1531.

[73] Shvedene, N.V., Shishkanova, T.V., Torocheshnikova, I.I., Baulin, V.E., Pletnev, I.V. (1998). Phosphoryl containing podands as carriers in plasticized membrane electrodes selective to quaternary ammonium surfactants. *J. Inclus. Phenom. Mol. Recogn. Chem.* **32**, 9–21.

[74] Fogg, A.G., Pathan, A.S., Burns, D.T. (1974). A silicone-rubber surfactant electrode. *Anal. Chim. Acta* **69**, 238–242.

[75] Fukui, H., Kaminaga, A., Maeda, T., Hayakawa, K. (2003). Preparation of surfactant anion-selective electrodes with different selectivity coefficients and a trial to determine each *component in* binary surfactant mixtures. *Anal. Chim. Acta* **481**, 221–228.

[76] Varga, I., Mészáros, R., Szakács, Z., Gilányi, T. (2005). Novel method for the preparation of anionic surfactant-selective electrodes. *Langmuir* **21**, 6154–6156.

[77] Alizadeh, N., Khodaei-Tazekendi, H. (2001). Linear alkylbenzenesulfonate (LAS) ion-selective electrode based on electrochemically prepared polypyrrole and PVC. *Sensors Actuators B: Chem*. **75**, 5–10.

[78] Kulapin, A.I., Chernova, R.K., Nikol'skaya, E.B., Kulapina, E.G. (2003). Modified potentiometric sensors for the separate determination of cationic surfactants. *J. Anal. Chem*. **58**, 282–286.

[79] Najafi, M., Maleki, L., Rafati, A.A. (2011). Novel surfactant selective electrochemical sensors based on single walled carbon nanotubes. *J. Mol. Liquids* **159**, 226–229.

[80] Alonso, J., Baró, J., Bartrolí, J., Sànchez, J., Del Valle, M. (1995). Flow-through tubular ion-selective electrodes responsive to anionic surfactants for flow-injection analysis. *Anal. Chim. Acta* **308**, 115–121.

[81] Martıínez-Barrachina, S., del Valle, M., Matia, L., Prats, R., Alonso, J. (2001). Potentiometric flow injection system for the determination of polyethoxylate nonionic surfactants using tubular ion-selective electrodes. *Anal. Chim. Acta* **438**, 305–313.

[82] Cattrall, R.W., Freiser, H. (1971). Coated wire ion-selective electrodes. *Anal. Chem*. **43**, 1905–1906.

[83] Vytřas, K. (1991). Coated wire electrodes in the analysis of surfactants of various types: An overview. *Electroanalysis* **3**, 343–347.

[84] Fujinaga, T., Okazaki, S., Freiser, H. (1974). Ion selective electrodes responsive to anionic detergents. *Anal. Chem*. **46**, 1842–1844.

[85] Vytřas, K., Dajkova, M., Mach, V. (1981). Coated-wire organic ion-selective electrodes in titrations based on ion-pair formation: Part 2. Determination of ionic surfactants. *Anal. Chim. Acta* **127**, 165–172.

[86] Gerlache, M., Sentürk, Z., Viré, J.C., Kauffmann, J.M. (1997). Potentiometric analysis of ionic surfactants by a new type of ion-selective electrode. *Anal. Chim. Acta* **349**, 59–65.

[87] Vytřas, K., Dvořáková, V., Zeman, I. (1989). Titrations of non-ionic surfactants with sodium tetraphenylborate using simple potentiometric sensors. *Analyst* **114**, 1435–1441.

[88] Sànchez, J., del Valle, M. (2001). Photocurable ISFET for anionic surfactants. Monitoring of photodegradation processes. *Talanta* **54**, 893–902.

[89] Janata, J. (1994). Historical review. Twenty years of ion-selective field-effect transistors. *Analyst* **119**, 2275–2278.

[90] Masadome, T., Wakida, S.I., Kawabata, Y., Imato, T., Ishibashi, N. (1992). Contribution of plasticizer to response of surfactant-selective plasticized poly (vinyl chloride) membrane electrode by using ion-sensitive field-effect transistor. *Anal. Sci*. **8**, 89–91.

[91] Campanella, L., Battilotti, M., Borraccino, A., Colapicchioni, C., Tomassetti, M., Visco, G. (1994). A new ISFET device repsonsive to anionic detergents. *Sensors Actuators B: Chem*. **19**, 321–328.

[92] Sanchez, J., Beltran, A., Alonso, J., Jiménez, C., Del Valle, M. (1999). Development of a new ion-selective field-effect transistor sensor for anionic surfactants: Application to potentiometric titrations. *Anal. Chim. Acta* **382**, 157–164.

[93] Campanella, L., Aiello, L., Colapicchioni, C., Tomassetti, M. (1997). Analysis of cationic surfactants in environmental aqueous matrices by new ISFET devices. *Anal. Lett.* **30**, 1611–1629.

[94] Sànchez, J., del Valle, M. (2001). A new potentiometric photocurable membrane selectiveto anionic surfactants. *Electroanalysis* **13**, 471–476.

[95] Mohamed, G.G., Ali, T.A., El-Shahat, M.F., Al-Sabagh, A.M., Migahed, M.A., Khaled, E. (2010). Potentiometric determination of cetylpyridinium chloride using a new type of screen-printed ion selective electrodes. *Anal. Chim. Acta* **673**, 79–87.

[96] Mohamed, G.G., Ali, T.A., El-Shahat, M.F., Al-Sabagh, A.M., Migahed, M.A. (2010). New screen-printed ion-selective electrodes for potentiometric titration of cetyltrimethylammonium bromide in different civilic media. *Electroanalysis* **22**, 2587–2599.

[97] Gilligan III, T.J., Cussler, E.L., Evans, D.F. (1977). Liquid membrane electrodes for bile salts. *Biochim. Biophys. Acta General Subjects* **497**, 627–630.

[98] Campanella, L., Tomassetti, M., Cordatore, M. (1986). Application of a new cholate liquid membrane electrode to the determination of the cholic acids pool in human bile. *J. Pharm. Biomed. Anal.* **4**, 155–162.

[99] Campanella, L., Mazzei, F., Tomassetti, M. (1987). Determinazione di tensioattivi anionici nelle acque mediante l'uso di un elettrodo iono-selettivo. *Inquinamento* **6**, 44–46.

[100] Campanella, L., Mazzei, F., Tomassetti, M., Sbrilli, R. (1988). Polymeric membrane cholate-selective electrode. *Analyst* **113**, 325–328.

[101] Vadnere, M., Lindenbaum, S. (1982). Surfactant-selective electrode study of bile salt—protein binding. *Int. J. Pharm.* **11**, 57–69.

[102] Jana, P.K., Moulik, S.P. (1994). Employment of a useful liquid membrane electrode system to characterise the micelles of bile salts and other detergents in pure and mixed states. *Colloid Polym. Sci.* **272**, 837–845.

[103] Kunze, L.J., Lindenbaum, S. (1989). An ion-selective microelectrode for bile salts. *J. Pharm. Biomed. Anal.* **7**, 947–954.

[104] Yu, B., Hong, W. (1990). Two-barrel bile-acids-sensitive microelectrodes based on liquid ion exchanger. *Biotechnol. Progress* **6**, 62–66.

[105] Bi, Y., Yi-qun, Z., Wen-bin, H. (1990). Miniaturization of a liquid membrane sensor for the determination of bile acids. *Biosens. Bioelectron.* **5**, 215–222.

[106] Gyimesi, J., Kovács, B. (1991). Deoxycholate-sensitive PVC membrane electrode. *Electroanalysis* **3**, 585–586.

[107] Panda, A.K., Possmayer, F., Petersen, N.O., Nag, K., Moulik, S.P. (2005). Physico-chemical studies on mixed oppositely charged surfactants: Their uses in the preparation of surfactant ion selective membrane and monolayer behavior at the air water interface. *Colloids Surf. A: Physicochem. Eng. Aspects* **264**, 106–113.

[108] Chatterjea, S.M., Panda, K. (2013). Development of a multiple-bile-ion-sensing membrane electrode. *Anal. Biochem.* **441**, 218–224.

[109] Goddard, E.D. (1993). *Interactions of Surfactants with Polymers and Proteins*. CRC Press, Boca Raton, FL.

[110] Abuin, E.B., Scaiano, J.C. (1984). Exploratory study of the effect of polyelectrolyte surfactant aggregates on photochemical behavior. *J. ACS* **106**, 6274–6283.

[111] Naskar, B., Ghosh, S., Moulik, S.P. (2014). Interaction of normal and reverse pluronics (L44 and 10R5) and their mixtures with anionic surfactant sodium N-dodecanoylsarcosinate. *J. Colloid Interface Sci.* **414**, 82–89.

[112] Hansson, P., Almgren, M. (1995). Large C12TAB micelles formed in complexes with polyvinylsulfate and dextran sulfate. *J. Phys. Chem.* **99**, 16694–16703.

[113] Hansson, P., Almgren, M. (1996). Interaction of C nTAB with sodium (carboxymethyl) cellulose: Effect of polyion linear charge density on binding isotherms and surfactant aggregation number. *J. Phys. Chem.* **100**, 9038–9046.

[114] Mukherjee, S., Dan, A., Bhattacharya, S.C., Panda, A.K., Moulik, S.P. (2011). Physicochemistry of interaction between the cationic polymer poly (diallyldimethylammonium chloride) and the anionic surfactants sodium dodecyl sulfate, sodium dodecylbenzenesulfonate, and sodium N-dodecanoylsarcosinate in water and isopropyl alcohol−water media. *Langmuir* **27**, 5222–5233.

[115] Kogej, K., Skerjanc, J. (1999). Binding of cetylpyridinium cation by poly (acrylic acid). Effect of polymer charge density. *Acta Chim. Slov.* **46**, 269–280.

[116] Thurn, T., Couderc, S., Sidhu, J., Bloor, D.M., Penfold, J., Holzwarth, J.F., Wyn-Jones, E. (2002). Study of mixed micelles and interaction parameters for ABA triblock copolymers of the type EO m-PO n-EO m and ionic surfactants: Equilibrium and structure. *Langmuir* **18**, 9267–9275.

[117] Kötz, J., Kosmella, S., Beitz, T. (2001). Self-assembled polyelectrolyte systems. *Progress Polym. Sci.* **26**, 1199–1232.

[118] Hayakawa, K., Kwak, J.C.T. (1991). *Cationic Surfactants. Physical Chemistry*. Marcel Dekker, New York.

[119] Ghosh, S., Banerjee, A. (2002). A multitechnique approach in protein/surfactant interaction study: Physicochemical aspects of sodium dodecyl sulfate in the presence of trypsin in aqueous medium. *Biomacromolecules* **3**, 9–16.

[120] Sun, C., Yang, J., Wu, X., Huang, X., Wang, F., Liu, S. (2005). Unfolding and refolding of bovine serum albumin induced by cetylpyridinium bromide. *Biophys. J.* **88**, 3518–3524.

[121] Guo, X.H., Chen, S.H. (1990). The structure and thermodynamics of protein—SDS complexes in solution and the mechanism of their transports in gel electrophoresis process. *Chem. Phys.* **149**, 129–139.

[122] Cabane, B. (1977). Structure of some polymer-detergent aggregates in water. *J. Phys. Chem.* **81**, 1639–1645.

[123] Gao, Z., Wasylishen, R.E., Kwak, J.C. (1990). NMR studies in surfactant and polymer-surfactant systems: Micelle

formation of sodium ω-phenyldecanoate and interaction with poly (ethylene oxide). *J. Colloid Interface Sci.* **137**, 137–146.

[124] Winnik, F.M., Regismond, S.T., Goddard, E.D. (1997). Interactions of an anionic surfactant with a fluorescent-dye-labeled hydrophobically-modified cationic cellulose ether. *Langmuir* **13**, 111–114.

[125] Rizzatti, I.M., Zanette, D.R., Zanette, D. (2004). Construction of surfactant-membrane electrodes selective for sodium dodecyl sulfate in poly (ethylene oxide)-surfactant mixtures. *J. Braz. Chem. Soc.* **15**, 491–495.

[126] Luan, Y.X., Xu, G.Y., Chen, A.M. (2003). Applications of surfactant-selective membrane electrode in the study of the interactions between surfactants and polymers. *Acta Physicochim. Sinica* **19**, 185–192.

[127] Bouchemal, K. (2008). New challenges for pharmaceutical formulations and drug delivery systems characterization using isothermal titration calorimetry. *Drug Discov. Today* **13**, 960–972.

[128] Tam, K.C., Wyn-Jones, E. (2006). Insights on polymer surfactant complex structures during the binding of surfactants to polymers as measured by equilibrium and structural techniques. *Chem. Soc. Rev.* **35**, 693–709.

[129] Hayakawa, K., Kwak, J.C. (1982). Surfactant-polyelectrolyte interactions. 1. Binding of dodecyltrimethylammonium ions by sodium dextransulfate and sodium poly (styrenesulfonate) in aqueous solution in the presence of sodium chloride. *J. Phys. Chem.* **86**, 3866–3870.

[130] Hayakawa, K., Kwak, J.C. (1983). Study of surfactant-polyelectrolyte interactions. 2. Effect of multivalent counterions on the binding of dodecyltrimethylammonium ions by sodium dextran sulfate and sodium poly (styrene sulfonate) in aqueous solution. *J. Phys. Chem.* **87**, 506–509.

[131] Malovikova, A., Hayakawa, K., Kwak, J.C. (1984). Surfactant-polyelectrolyte interactions. 4. Surfactant chain length dependence of the binding of alkylpyridinium cations to dextran sulfate. *J. Phys. Chem.* **88**, 1930–1933.

[132] Santerre, J.P., Hayakawa, K., Kwak, J.C. (1985). A study of the temperature dependence of the binding of a cationic surfactant to an anionic polyelectrolyte. *Colloids Surf.* **13**, 35–45.S

[133] Shirahama, K. (1982). Paper presented at 35th Colloid and Surface Chemistry Symp., Kiryu, Japan.

[134] Shirahama, K, Watanabe, T., Harada, H. (1990). *The Structure, Dynamics, and Equilibrium Properties of Colloid Systems*. Kluwer, London, p. 161.

[135] Satake, I., Yang, J.T. (1976). Interaction of sodium decyl sulfate with poly (L-ornithine) and poly (L-lysine) in aqueous solution. *Biopolymers* **15**, 2263–2275.

[136] Hayakawa, K., Santerre, J.P., Kwak, J.C. (1983). Study of surfactant-polyelectrolyte interactions. Binding of dodecyl- and tetradecyltrimethylammonium bromide by some carboxylic polyelectrolytes. *Macromolecules* **16**, 1642–1645.

[137] Gupta, S., Moulik, S.P., Das, A.R. (1991). Physicochemical behaviour of the sodium salt of carboxymethylcellulose in dye, salt and surfactant environments. *Makromol. Chem.* **192**, 447–460.

[138] Mata, J., Patel, J., Jain, N., Ghosh, G., Bahadur, P. (2006). Interaction of cationic surfactants with carboxymethylcellulose in aqueous media. *J. Colloid Interface Sci.* **297**, 797–804.

[139] Rafati, A.A., Etesami, M., Razavizadeh, B.M. (2007). Study of interaction between Aspergillus niger cellulase (ANC) and cetyltrimethylammonium bromide (CTAB) using surfactant membrane selective electrode. *J. Mol. Liquids* **136**, 44–49.

[140] Rastegari, A.A., Bordbar, A.K., Mehnati-Najafabadi, V. (2010). Conformational changes and sequence analysis in cellulase from Aspergillus niger with cationic surfactant. *Cellulose* **17**, 1213–1225.

[141] Bordbar, A.K., Omidiyan, K., Hosseinzadeh, R. (2005). Study on interaction of α-amylase from Bacillus subtilis with cetyl trimethylammonium bromide. *Colloids Surf. B: Biointerfaces* **40**, 67–71.

[142] Thongngam, M., McClements, D.J. (2004). Characterization of interactions between chitosan and an anionic surfactant. *J. Agric. Food Chem.* **52**, 987–991.

[143] Thongngam, M., McClements, D.J. (2005). Influence of pH, ionic strength, and temperature on self-association and interactions of sodium dodecyl sulfate in the absence and presence of chitosan. *Langmuir* **21**, 79–86.

[144] Onesippe, C., Lagerge, S. (2008). Study of the complex formation between sodium dodecyl sulfate and chitosan. *Colloids Surf. A: Physicochem. Eng. Aspects* **317**, 100–108.

[145] Liu, J., Takisawa, N., Shirahama, K., Abe, H., Sakamoto, K. (1997). Effect of polymer size on the polyelectrolyte-surfactant interaction. *J. Phys. Chem. B* **101**, 7520–7523.

[146] Fruhner, H., Kretzschmar, G. (1992). The interaction of anionic surfactants with gelatin. *Colloid Polym. Sci.* **270**, 177–182.

[147] Fruhner, H., Kretzschmar, G. (1989). Effect of pH on the binding of alkyl sulfates to gelatin. *Colloid Polym. Sci.* **267**, 839–843.

[148] Henriquez, M., Abuin, E., Lissi, E. (1993). Interactions of ionic surfactants with gelatin in fluid solutions and the gel state studied by fluorescence techniques, potentiometry, and measurements of viscosity and gel strength. *Colloid Polym. Sci.* **271**, 960–966.

[149] Onesippe, C., Lagerge, S. (2008). Study of the complex formation between sodium dodecyl sulfate and chitosan. *Colloids Surf. A: Physicochem. Eng. Aspects* **317**, 100–108.

[150] Maulik, S., Dutta, P., Chattoraj, D.K., Moulik, S.P. (1998). Biopolymer–surfactant interactions: 5: Equilibrium studies on the binding of cetyltrimethyl ammonium bromide and sodium dodecyl sulfate with bovine serum albumin, β-lactoglobulin, hemoglobin, gelatin, lysozyme and deoxyribonucleic acid. *Colloids Surf. B: Biointerfaces* **11**, 1–8.

[151] Inoue, K., Sekido, T., Sano, T. (1996). Binding of sodium alkyl sulfates to human erythrocyte studied with a surfactant ion selective electrode. *Langmuir* **12**, 4644–4650.

[152] Mokus, M., Kragh-Hansen, U., Letellier, P., le Maire, M., Møller, J.V. (1998). Construction and use of a detergent-sensitive electrode to measure dodecyl sulfate activity and binding. *Anal. Biochem.* **264**, 34–40.

[153] Bordbar, A.K., Sohrabi, N., Gharibi, H. (2004). Binding set analysis for interaction of human serum albumin with cethyl trimethylammonium bromide. *Bull. Korean Chem. Soc.* **25**, 791–795.

[154] Bordbar, A.K., Taheri-Kafrani, A. (2007). Binding and fluorescence study on interaction of human serum albumin (HSA) with cetylpyridinium chloride (CPC). *Colloids Surf. B: Biointerfaces* **55**, 84–89.

[155] Messina, P., Prieto, G., Dodero, V., Ruso, J. M., Schulz, P., Sarmiento, F. (2005). Ultraviolet–circular dichroism spectroscopy and potentiometric study of the interaction between human serum albumin and sodium perfluorooctanoate. *Biopolymers* **79**, 300–309.

[156] Blanco, E., Messina, P., Ruso, J.M., Prieto, G., Sarmiento, F. (2006). Regarding the effect that different hydrocarbon/fluorocarbon surfactant mixtures have on their complexation with HSA. *J. Phys. Chem. B* **110**, 11369–11376.

[157] Rafati, A.A., Bordbar, A.K., Gharibi, H., Amini, M.K., Safarpour, M.A. (2004). The interactions of a homologous series of cationic surfactants with bovine serum albumin (BSA) studied using surfactant membrane selective electrodes. *Bull. Chem. Soc. Japan* **77**, 1111–1116.

[158] Naderimanesh, H., Alizadeh, N., Shamsipoor, M. (1996). *Proc. Int. Conf. Protein Structure-Function Relationship*, pp. 167–174.

[159] Rafati, A.A., Ghasemian, E. (2009). Thermodynamic and binding study of hemoglobin, oxy-hemoglobin and carbamino-hemoglobin upon interaction with cationic surfactants, using surfactant membrane selective electrodes. *J. Mol. Liquids* **144**, 131–137.

[160] Bordbar, A.K., Hosseinzadeh, R. (2006). Binding of cetylpyridinum chloride to glucose oxidase. *Colloids Surf. B: Biointerfaces* **53**, 288–295.

[161] Mel'nikov, S.M., Sergeyev, V.G., Yoshikawa, K. (1995). Transition of double-stranded DNA chains between random coil and compact globule states induced by cooperative binding of cationic surfactant. *J. ACS* **117**, 9951–9956.

[162] Sak-Bosnar, M., Madunic-Cacic, D., Sakac, N., Samardzic, M., Kurtanjek, Z. (2011). Estimation and optimization of potentiometric sensor response parameters from surfactant titration data using Microsoft Excel Solver and Mathematica. *Sensor Lett.* **9**, 491–498.

[163] Maulik, S., Moulik, S.P., Chattoraj, D.K. (1996). Biopolymer-surfactant interaction: 4 Kinetics of binding of cetyltrimethyl ammonium bromide with gelatin, hemoglobin, β-lactoglobulin and lysozyme. *J. Biomol. Struct. Dynamics* **13**, 771–780.

[164] Liu, L., Guo, Q.X. (2001). Isokinetic relationship, isoequilibrium relationship, and enthalpy-entropy compensation. *Chem. Rev.* **101**, 673–696.

[165] Maulik, S., Chattoraj, D.K., Moulik, S.P. (1998). Biopolymer–surfactant interaction: 3: Kinetics of binding of cetyltrimethyl ammonium bromide to deoxyribonucleic acid. *Colloids Surf. B: Biointerfaces* **11**, 57–65.

[166] Grueso, E., Roldan, E., Sanchez, F. (2009). Kinetic study of the cetyltrimethylammonium/DNA interaction. *J. Phys. Chem. B* **113**, 8319–8323.

59

MEMBRANE POTENTIAL AS A FUNCTION OF DIELECTRIC CONSTANT

Akihiko Tanioka and Hidetoshi Matsumoto

Department of Organic and Polymeric Materials, Tokyo Institute of Technology, Tokyo, Japan

59.1 INTRODUCTION

There has been increasing interest in analyzing the ion transport phenomena in a charged membrane in electrolyte aqueous organic solution systems [1] or low-water-content systems [2] across a charged membrane for industrial and medical applications. The measure of membrane potential is a significant method for characterizing transport phenomena across a charged membrane [3, 4]. Theoretically the membrane potential in a charged membrane–electrolyte aqueous solution system developed by Teorell, Meyer, and Sievers (TMS) [5–7] can be treated by Donnan equilibrium theory [8, 9] and the Nernst–Planck equation [10–13], if it is assumed that the fixed-charge groups are homogeneously distributed in the membrane [14] and the effect of the mean activity coefficient of electrolyte in external solution is negligible.

The ion transport phenomena across a charged membrane in an aqueous solution system have been studied by many authors [15–23]. Usually in the theoretical treatment the membrane is considered to be a gel material that is filled with enough water to allow ions and fixed-charge groups to behave as if they were in aqueous solution. On the other hand, if organic solvent is added or the membrane water content is significantly decreased, it is highly unlikely that the system is in aqueous solution. The studies and experimental data, however, available for electrolyte aqueous organic solution and low-water-content systems are limited [24, 25]; thus the transport phenomena in the systems are not very clear.

Ionic transport phenomena through a charged membrane are strongly affected by the fixed-charge groups in the membrane. All of the fixed-charge groups in the membrane do not function perfectly. The fixed-charge density of the membrane estimated by the ionic transport procedure (membrane potential method) is less than that estimated by equilibrium analysis (titration method) [22,26,27]. This phenomenon has been attributed to a decrease in the activity of fixed-charge groups in the membrane due to ion pair formation between the fixed-charge group and the counterion in the membrane [28–34].

One research team proposed a theoretical model considering the ion-pairing effect between the fixed-charge group and the counterion in the membrane [16]. According to their model, the ion-pairing effect is more significant under low-dielectric-constant conditions (e.g., a nonaqueous solution system or a low-water-content membrane system). Another team studied the ion-pairing effect in a nonaqueous solution system and revealed that theoretical predictions agreed well with the experimental results, based on the membrane potential and permeability measurements [17–20]. Another group indicated that the effect of ion-pair formation was significant in low-water-content cation exchange membranes with inhomogeneous fixed-charge distribution. They also systematically verified the ion-pairing effect in low-water-content membranes by preparing cation and anion exchange membranes with various water content levels and homogeneous fixed-charge distribution by radical copolymerization and examined the ion-pairing effect with respect to membrane potential measurements. This is the first comprehensive study

Encyclopedia of Biocolloid and Biointerface Science, Volume 2, First Edition. Edited by Hiroyuki Ohshima.
© 2016 John Wiley & Sons, Inc. Published 2016 by John Wiley & Sons, Inc.

on the ion-pairing effect in low-water-content charged membranes.

59.2 THEORETICAL BACKGROUND

According to the TMS studies [5–7], the potential across a membrane separating two cells having different concentrations of aqueous solutions can be expressed by the sum of the Donnan potential between the membrane surface and the external solution, and a diffusion potential in the membrane. We will confirm that their idea is applicable to the pure organic solution or aqueous organic solution system, and the low-water-content membrane.

59.2.1 Donnan Potential

The electrochemical potentials of the ith ion in an external solution and in a charged membrane filled with solution are given by μ_i and $\bar{\mu}_i$, respectively

$$\mu_i = \mu_i^0 + RT \ln \gamma_i C_i + z_i F \phi \quad i = +, - \tag{59.1}$$

$$\bar{\mu}_i = \bar{\mu}_i^0 + RT \ln \bar{\gamma}_i \bar{C}_i + z_i F \bar{\phi} \quad i = +, - \tag{59.2}$$

where μ_i^0 and $\bar{\mu}_i^0$ are the standard electrochemical potentials, z_i is the valence of ion, R is the gas constant, T is the absolute temperature, γ_i and $\bar{\gamma}_i$ are the ion activity coefficients, C_i and $\bar{C}_i$ are the ion concentrations, F is the Faraday constant, and ϕ and $\bar{\phi}$ are the electrical potentials; the overbar denotes the values in the charged membrane. At the interface between the membrane and the external solution, the electrochemical potentials in the two phases are equilibrated:

$$\mu_i = \bar{\mu}_i \quad i = +, - \tag{59.3}$$

The Donnan potential $\Delta\phi_{\text{Don}}$ between the membrane surface and the solution is given from Eqs. (59.1)–(59.3) by

$$\Delta\phi_{\text{Don}} = \bar{\phi} - \phi = -\frac{RT}{z_i F} \ln \frac{\bar{\gamma}_i \bar{C}_i}{k_i \gamma_i C_i} \quad i = +, - \tag{59.4}$$

where k_i is the distribution coefficient of the ion i defined as

$$\bar{\mu}_i^0 - \mu_i^0 = -RT \ln k_i \quad i = +, - \tag{59.5}$$

Under the condition $z_+ = -z_-$, the relationship between the concentrations of ions in the membrane and in external solution can be obtained

$$\bar{C}_+ \bar{C}_- = \frac{\gamma_\pm^2 C_s^2}{Q^2} \tag{59.6}$$

where C_s is the electrolyte concentration in external solution equated as $(C_+ C_-)^{1/2}$, $\gamma_\pm$ is the mean activity coefficient of electrolyte equated as $(\gamma_+ \gamma_-)^{1/2}$, and Q is defined by

$$Q = \left(\frac{\bar{\gamma}_+ \bar{\gamma}_-}{k_+ k_-} \right)^{1/2} \tag{59.7}$$

On the other hand, the condition of electroneutrality in the membrane is given by

$$\sum_{i=+,-} z_i \bar{C}_i + z_x C_x = 0 \tag{59.8}$$

where z_x is the valence of fixed charge groups, and C_x is the fixed-charge density. Inserting Eq. (59.6) into Eq. (59.8) and solving a quadratic equation, we can express the concentrations of ions in membrane as follows:

$$\bar{C}_+ = \sqrt{\left(\frac{z_x C_x}{2 z_+} \right)^2 + \left(\frac{\gamma_\pm C_s}{Q} \right)^2} - \frac{z_x C_x}{2 z_+} \tag{59.9}$$

$$\bar{C}_- = \sqrt{\left(\frac{z_x C_x}{2 z_+} \right)^2 + \left(\frac{\gamma_+ C_s}{Q} \right)^2} + \frac{z_x C_x}{2 z_+} \tag{59.10}$$

The most important point in Eqs. (59.9) and (59.10) is that the mean activity coefficient of electrolyte in external solution $\gamma_\pm$ is multiplied by the electrolyte concentration C_s. The effect of mean activity coefficient of electrolyte is usually neglected in solution. The Donnan potential on the left- and right-hand sides of the interface between the membrane and the surrounding solution are given by inserting Eq. (59.9) into Eq. (59.4). If it is assumed that the activity coefficients of ions are not a function of the ion concentrations in the membrane [14], the total Donnan potential through the membrane can be expressed by the sum of the Donnan potentials at the left- and right-hand sides for an aqueous organic solution system cited above

$$\Delta\phi_{\text{Don}(1\to\text{r})} = -\frac{RT}{z_+ F} \ln \left[\frac{\gamma_+'' C_s'' \bar{C}_+'}{\gamma_+' C_s' \bar{C}_+''} \right] \tag{59.11a}$$

where C_s' and C_s'' are the concentrations of the solution in left- and right-hand sides and $\bar{C}_+'$ and $\bar{C}_+''$ are the cation concentrations at the left- and right-hand sides of the charged membrane, which are given by Eq. (59.9). The value of γ_+''/γ_+' cannot be obtained individually, thus we approach it by $\gamma_\pm''/\gamma_\pm'$ and will not make obvious errors. Therefore Eq. (59.11a) becomes

$$\Delta\phi_{\text{Don}(1\to\text{r})} = -\frac{RT}{z_+ F} \ln \left[\frac{\gamma_\pm'' C_s'' \bar{C}_+'}{\gamma_\pm' C_s' \bar{C}_+''} \right] \tag{59.11b}$$

59.2.2 Membrane Diffusion Potential

The ionic flux across the membrane is given by the Nernst–Planck equation, which can be applied to the phase of the membrane

$$J_i = -\bar{\omega}_i RT \frac{d\bar{C}_i}{dx} - z_i F \bar{\omega}_i \bar{C}_i \frac{d\bar{\phi}}{dx} \quad i = +, - \tag{59.12}$$

where $\bar{\omega}_i$ is the ionic mobility of the ion i in the membrane. The electroneutrality condition in a membrane requires that

$$J_+(x) = J_-(x) \tag{59.13}$$

By differentiating Eq.(59.8), we can obtain

$$\frac{d\bar{C}_+}{dx} = \frac{d\bar{C}_-}{dx} \tag{59.14}$$

Inserting Eqs. (59.12) and (59.14) into Eq. (59.13), we can express the diffusion potential $\Delta\phi_{\text{diff}}$ as

$$\Delta\phi_{\text{diff}} = \bar{\phi}'' - \bar{\phi}' = -\frac{RT}{z_+ F}\frac{r-1}{r+1}\ln\left[\frac{(r+1)\,\bar{C}''_+ + \dfrac{z_x}{z_+}C_x}{(r+1)\,\bar{C}'_+ + \dfrac{z_x}{z_+}C_x}\right] \tag{59.15}$$

where r is the cation-to-anion mobility ratio in the membrane defined by

$$r = \frac{\bar{\omega}_+}{\bar{\omega}_-} \tag{59.16}$$

where $\bar{\omega}_+$ and $\bar{\omega}_-$ are the cation and anion mobilities in the membrane, respectively.

59.2.3 Mean Activity Coefficient in Mixed Solvent–Salt Systems [38–45]

The mean activity coefficient of electrolyte in external aqueous organic solution can be predicted by combining the Tan's modified Wilson model though it is convenient one, the vapor pressure model of electrolyte solutions and the Gibbs–Duhem equation. In previous papers, this observation has not been considered. Therefore the error resulting from this treatment has always been included in calculation of the effective charge density. The model calculation presented in this section should reduce such an error. According to our work, the ionic mean activity coefficient $\gamma_\pm$ in a ternary system (containing two solvents and one salt) at constant temperature and pressure is given by the following equation:

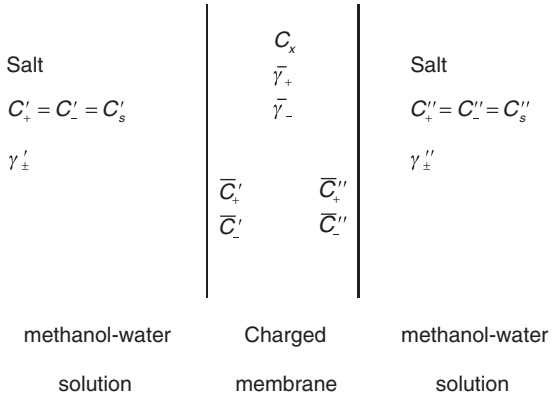


FIGURE 59.1 Solution system studied in this chapter.

$$\ln\left(\gamma_\pm\right)\Big|_{m=m} = \int_{m=0}^{m=m} \frac{1}{m}\mathrm{d}\left\{m\left[\alpha\bar{\phi}_1 + (1-\alpha)\,\bar{\phi}_2 - 1\right]\right\} \tag{59.17}$$

Here, m is the molality of the solution, $\bar{\phi}_n$ is the partial osmotic coefficient for solvent n, and α is a constant.

59.2.4 Membrane Potential

The membrane potential $\Delta\phi$ is the sum of the Donnan and the membrane diffusion potentials, which are given by Eqs. (59.11b) and (59.15), respectively

$$\Delta\phi = \Delta\phi_{\text{Don}(1\to\text{r})} + \Delta\phi_{\text{diff}} \tag{59.18}$$

The solution system of this work is shown in Fig. 59.1, and Eq. (59.18) will be applied to calculation the membrane potential in this kind of system.

59.2.5 Effective Membrane Charge Density

Ion-pairing theories have been studied by some authors [46, 47]. To explicitly evaluate the interaction of ion pairs between the counterion and fixed-charge group in the membrane phase, we have used a very simple model that is based on the Fuoss approach to ion pairing in electrolyte solutions [47, 48] as shown in Fig. 59.2. The theoretical basis of the Fuoss approach to ion pairing is the linear Poisson–Boltzmann equation. Linearization of the Boltzmann factor might not be justified when the electrostatic potential energy is greater than kT. However, it is likely that the screened Coulomb potential may be used in this case over a range of concentrations greater than that for which the linearization of the Poisson–Boltzmann equation can be justified [35]. We have resorted to this approach because of its simplicity. Some

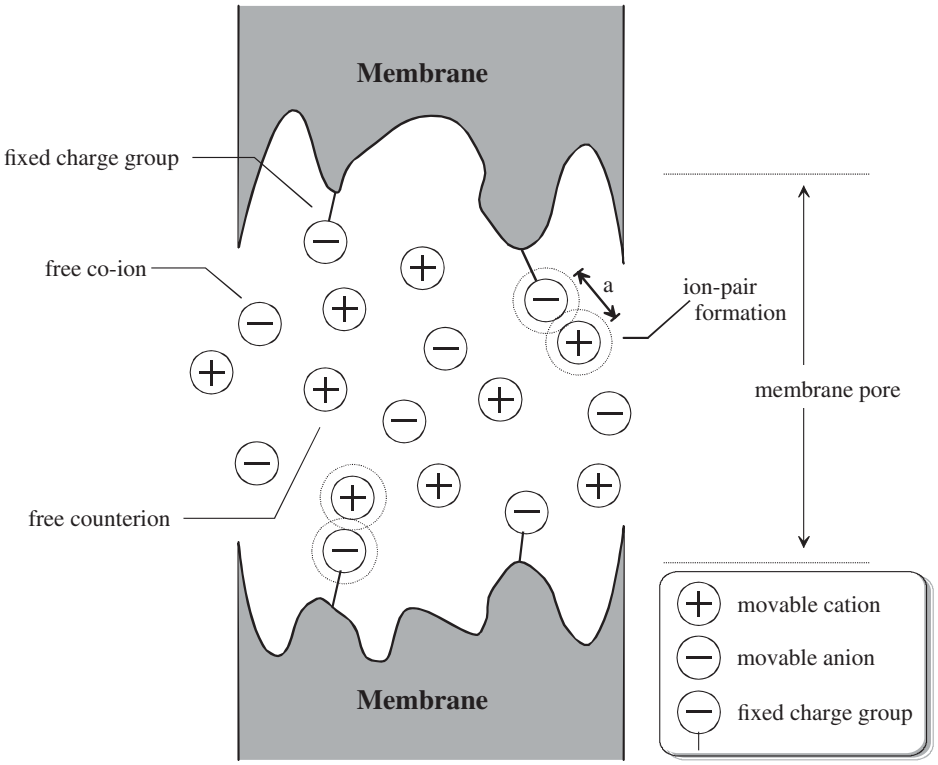


FIGURE 59.2 Simplified view of ion pairing in a negatively charged membrane.

of the assumptions introduced by Fuoss may also be questionable, since in our case, one of the ions in the ion pair is fixed [49]. The deviation which is caused by this problem can be compensated by the regressing process of two parameters in the new model. Application of the Fuoss formalism to the ion pair in a membrane would lead to the association constant [47,48]

$$K_A = \frac{4\pi N_A}{3 \times 10^{-3}} a^3 \exp(b) \tag{59.19}$$

$$b = \frac{e^2}{4\pi\varepsilon_0\varepsilon_s akT} \tag{59.20}$$

where N_A is Avogadro's number, e is the electronic charge, ε_s is the dielectric constant of the solvent, ε_0 is the vacuum permittivity, k is the Boltzmann constant, and a is the contact distance. If the interaction by which the immobilized reactant is formed proceeds very rapidly compared with the diffusion process, a local equilibrium can be assumed to exist between the free and immobilized components of the diffusing substance. As the first approximation, it is assumed that the rate of immobilization is proportional to the concentration of nonimmobilized position and association constant and that the rate of separation is proportional to the concentration of immobilized components. Therefore, according to these assumptions, the relationship between the effective membrane charge density QC_x and the association constant K_A is derived as follows

$$QC_x = \frac{1}{k'K_A + 1} C_x \tag{59.21}$$

where k' is a constant that indicates the effect of the association constant on the membrane charge density. Clearly the effect of the ion pairing will decrease the effective membrane charge density. In the limited case, K_A will tend to infinity if the ion pair strongly associates together, and then QC_x will become zero. On the other hand, K_A will tend to zero if the ion pair interaction is very weak, and QC_x will become C_x. The dielectric constant of a mixed solvent can be estimated from Oster's mixing rule [50]

$$\varepsilon_s = \varepsilon_1 + [(\varepsilon_2 - 1)(2\varepsilon_2 + 1)/2\varepsilon_2 - (\varepsilon_1 - 1)]x_2V_2/V \tag{59.22}$$

where ε_1 and ε_2 are the dielectric constants of solvents 1 and 2, respectively, and V is the partial molar volume of a mixed solvent that can be simply estimated by

$$V = x_1V_1 + x_2V_2 \tag{59.23}$$

where V_1 and V_2 are the partial molar volume of solvents 1 and 2, respectively. Inserting Eqs. (59.19) and (59.20) into

Eq. (59.21), and applying Eqs. (59.22) and (59.23), we can obtain the theoretical formalism for estimating QC_x as follows

$$QC_x = \frac{C_x}{\frac{4\pi N_A}{3\times 10^{-3}} k' a^3 \exp\left\{\frac{e^2}{4\pi\varepsilon_0 akT\left\{\varepsilon_1 + \Delta\varepsilon x_2' V_2/V\right\}}\right\} + 1} \tag{59.24}$$

where

$$\Delta\varepsilon = (\varepsilon_2 - 1)(2\varepsilon_2 + 1)/2\varepsilon_2 - (\varepsilon_1 - 1) \tag{59.25}$$

59.2.6 Permeability Coefficient

The ionic flux across the membrane J_i can be obtained by the Nernst–Planck equation, which can be applied to the phase of the membrane without considering the associated effect of ions in the external solution as shown in Eq. (59.12). Also the electroneutrality condition in a membrane is required as shown in Eqs. (59.8) and (59.13). By inserting Eqs. (59.12) and (59.14) into Eq. (59.13), we can obtain the term of $d\bar{\phi}/dx$ in Eq. (59.12) as follows:

$$\frac{d\bar{\phi}}{dx} = -\frac{RT}{z_+ F}\frac{\bar{\omega}_+ - \bar{\omega}_-}{\bar{\omega}_+\bar{C}_+ + \bar{\omega}_-\bar{C}_-}\frac{d\bar{C}_+}{dx} \tag{59.26}$$

Finally, the electrolyte flux across the membrane J can be estimated by inserting Eq. (59.26) into Eq. (59.12)

$$J = J_+ = -\frac{\bar{\omega}_+ RTC_x}{(r+1)\,d} \times\left[\frac{2}{C_x}\left(\bar{C}_+'' - \bar{C}_+'\right) + \frac{r-1}{r+1}\frac{z_x}{z_+}\ln\frac{(r+1)\,\bar{C}_+'' + \frac{z_x}{z_+}C_x}{(r+1)\,\bar{C}_+' + \frac{z_x}{z_+}C_x}\right] \tag{59.27}$$

where d is the thickness of the membrane, r is the cation-to-anion mobility ratio in the membrane, and $\bar{C}_+'$ and $\bar{C}_+''$ are the cation concentrations on the left- and right-hand sides of the charged membrane, respectively, which are as given in Eq. (59.9) [38]:

$$\bar{C}_+ = \sqrt{\left(\frac{z_x C_x}{2z_+}\right)^2 + \left(\frac{\gamma_\pm C_s}{Q}\right)^2} - \frac{z_x C_x}{2z_+} \tag{59.28}$$

Here, $\gamma_\pm$ is the mean activity coefficient of the electrolyte in an external solution and can be calculated by application of certain theories [41,43,45]. The nonideality caused by the associating effect of ions in organic solution systems can be estimated by the mean activity coefficient of the electrolyte. The same method has been adopted to calculate the vapor pressure and the mean ionic activity coefficient in organic solution systems by some authors [51–53]. The permeability coefficient P can be easily obtained by the original definition

$$P = -\frac{J}{C_s'' - C_s'} \tag{59.29}$$

where C_s' and C_s'' are the concentrations of the solution on the left- and right-hand sides, respectively.

59.2.7 Mobility of Ions in a Membrane

If the interaction by which the immobilized reactant is formed proceeds very rapidly compared with the diffusion process, a local equilibrium can be assumed to exist between the free and immobilized components of the diffusing substance. As the first approximation, the concentration of immobilized substance C_{im} is directly proportional to the concentration of a substance free to diffuse C_f:

$$C_{\text{im}} = RC_f \tag{59.30}$$

According to the diffusion theory with chemical reaction, the relationship between the apparent diffusion constant D_a and the actual diffusion constant D' can be expressed as follows [54–56]

$$D_a = \frac{1}{R+1}D' \tag{59.31}$$

where R has a similar physical meaning with the association constant K_A of ion pairing in the membrane phase if the reactant corresponds to the fixed-charge group [57–63]. Therefore, the following relationship can be obtained between R and K_A

$$R = \beta K_A \tag{59.32}$$

where β is a constant that indicates the effect of the association constant on the mobility of the counterion in the membrane. Taking into account Eq. (59.31), the relationship between the counterion mobility in the membrane $\bar{\omega}_{\text{counterion}}$ and the association constant K_A is

$$\bar{\omega}_{\text{counterion}} = \frac{1}{\beta K_A + 1}\frac{\omega_{\text{counterion}}}{q^2} \tag{59.33}$$

where θ is the tortuosity factor [64, 65] and $\omega_{\text{counterion}}$ is the mobility of a counterion in an external solution. Clearly the effect of the ion pairing is to decelerate the mobility of the counterion. In the limited case, K_A will tend to infinity if the ion pair strongly associates together, and then $\bar{\omega}_{\text{counterion}}$ will become zero. On the other hand, K_A will tend to zero if the ion pair interaction is very weak, and $\bar{\omega}_{\text{counterion}}$ will become

$\omega_{\text{counterion}}/q^2$ as the behavior appearing in the charged gel membrane [65]. If it is assumed that $\omega_{\text{counterion}}$ in a mixed solvent linearly changes with the consistency of the pure solvent, then the mobility of the counterion in an external solution can be estimated by

$$\omega_{\text{counterion}} = \omega_{\text{counterion},1}x_1 + \omega_{\text{counterion},2}x_2 \qquad (59.34)$$

where x_1 and x_1 are the salt-free mole fractions of solvents 1 and 2, respectively. Inserting Eqs. (59.19), (59.20), and (59.34) into Eq. (59.33), and applying the relationships of Eqs. (59.22) and (59.23), we can obtain the theoretical formalism for estimating $\bar{\omega}_{\text{counterion}}$ as follows:

$$\bar{\omega}_{\text{counterion}} = \frac{(\omega_{\text{counterion},1}x_1 + \omega_{\text{counterion},2}x_2)/q^2}{\dfrac{4\pi N_A}{3\times 10^{-3}}\beta a^3 \exp\left\{\dfrac{e^2}{4\pi\varepsilon_0 akT\{\varepsilon_1 + \Delta\varepsilon x_2 V_2/V\}}\right\} + 1} \qquad (59.35)$$

The mobility of coion in a membrane $\bar{\omega}_{\text{co-ion}}$ can then be obtained from Eq. (59.16).

59.3 MATERIALS AND EXPERIMENTAL PROCEDURES

59.3.1 Materials

59.3.1.1 Commercial Ion Exchange Membrane for Organic Solution System. A cation exchange membrane (K171, Asahi Chemicals), which is composed of poly(divinylbenzene-*co*-styrene) containing sulfonic acid groups, and an anion-exchange membrane (A201, Asahi Chemicals), which is composed of poly(butadiene-*co*-styrene) containing quaternary amine groups in a polymer matrix, were used for the measurements. The thickness, water content, and ion exchange capacity of these membranes are given in Table 59.1. Before measurements were carried out, both membranes were immersed in 3 mol/L LiCl for 3 days to ensure that counterions were exchanged for the same species. After both membranes were thoroughly washed with ion-exchanged water, they were immersed in ion-exchanged water for 3 days to remove the excess ions in the membrane matrix [23].

TABLE 59.1 Physicochemical Properties of Ion Exchange Membranes

Membrane	Thickness (mm)	Water content (wt%)	Ion exchange capacity (mol/L)
K171	0.11–0.13	20–23	5.5–5.8
A201	0.22–0.24	26–27	3.9–4.4

TABLE 59.2 Physicochemical Properties of Charged Membranes

Membrane	w_w (w/w%)	IEC [meq/g (dry membr.)]	C_X (mol/L)	Thickness (μm)
CEM1	6.7	0.62	8.6	50
CEM2	15	1.5	8.5	50
CEM3	40	2.9	4.2	50
K501	30	1.5	5.5	170
AEM1	9.0	0.58	5.9	50
AEM2	11	0.71	5.6	50
AEM3	22	0.77	2.7	50
A501	26	1.4	5.4	140

Symbols: C_X–fixed-charge density; K501/A501–commercial CEM and AEM, respectively, from Asahi Kasei Corporation, Japan; IEC—ion exchange capacity; w_w–water content.

59.3.1.2 Prepared Ion Exchange Membranes for Low-Water-Content System. Three kinds of cation exchange membranes (CEMs) with different water contents, composed of poly(styrene-*co*-divinylbenzene) [poly(St-*co*-DVB)] containing sulfonic acid groups, and three kinds of anion exchange membranes (AEMs) with different water contents, composed of poly(styrene-*co*-4-vinylpyridine-*co*-divinylbenzene) [poly(St-*co*-4VP-*co*-DVB)] containing quaternary pyridinium groups were prepared by radical copolymerization [66–68]. The PE porous membranes were used as reinforcement for the charged membranes. The PE membranes (area = 4 × 4 cm^2) were soaked in MeOH for 24 h and vacuum-dried at room temperature. They were immersed in the monomer solutions, which were composed of St, DVB, and polymerization initiator (*t*-butylperoxy-2-ethylhexanoate) for CEMs, and St, 4VP, DVB, and the initiator for AEMs, under reduced pressure. The membranes containing monomer solution were placed between two polyethylene terephthalate (PET) films and heated in a hot press at 70°C for 32 h to form the base membranes. The poly(St-*co*-DVB) membranes were soaked in NMP for 30 min at room temperature and then sulfonated with 95% H_2SO_4. The poly(St-*co*-4VP-*co*-DVB) membranes were quaternized with 40 wt% CH_3I/*n*-hexane solution shielded from light at 40°C for 20 h. The prepared membranes were washed thoroughly with MeOH and deionized water.

The physicochemical properties of the prepared membranes are summarized in Table 59.2. Aciplex K501/A501 (Asahi Kasei Corporation, Japan), commercial hydrocarbon ion exchange membranes, were used for comparison. We succeeded in preparing charged membranes with various water content levels by radical copolymerization, particularly low-water-content charged membranes, whose water contents are <10 wt%.

59.3.2 Potentiometric Titration and Measurement of Equilibrium Water Content

The potentiometric titration was performed with an automatic titrator (DMS Titrino 716, Metrohm, Switzerland) as previously described [66, 67]. A combined pH glass electrode (#6.0218.010, Metrohm, Switzerland) and a combined Ag electrode (#6.0450.100, Metrohm, Switzerland) were used for the titration of CEMs and AEMs, respectively. Two pieces of CEMs and AEMs (each membrane area was 4×4 cm^2) were immersed in 2 mol/L HCl and 2 mol/L KCl for 12 h in order to convert the counterion to the H^+ and Cl^- form, respectively. They were then washed sufficiently with deionized water. Thereafter, the CEMs were immersed in 50 mL of 2 mol/L KCl with stirring under N_2 gas flow for 1 h, and the AEMs were immersed in 50 mL of 2 mol/L $NaNO_3$ with stirring for 1 h. These treatments were repeated 4 times in order to elute H^+ or Cl^- thoroughly from the membranes, and all eluents were collected. The collected solutions were titrated with 0.1 mol/L KOH and 0.1 mol/L $AgNO_3$, respectively. The titers of KOH and $AgNO_3$ correspond to the amount of fixed-charge groups in the CEM and AEM, respectively, N_X (mol). The weight of the equilibrium swollen membrane w_{wet} (g), was measured after carefully removing the surface water with filter paper; and the weight of dried membrane w_{dry} (g) was measured after vacuum drying at 100°C for 6 h. The equilibrium water content of the membranes w_w (%) is given by

$$w_w = \frac{w_{wet} - w_{dry}}{w_{wet}} \times 100 \tag{59.36}$$

The ion exchange capacity IEC (mol/g-dry membrane), and the fixed-charge density C_X(mol/L) are determined by the following equations

$$IEC = \frac{N_X}{w_{dry}} \tag{59.37}$$

$$C_X = \frac{\rho N_X}{w_{wet} - w_{dry}} \tag{59.38}$$

where ρ is density of water at 25°C ($=0.99704 \times 10^3$ g/L). All measurements were carried out at 25±1°C.

59.3.3 Membrane Potential Measurements

The membrane potentials of both membranes used in this study were measured to obtain the effective membrane charge densities and the cation-to-anion mobility ratios in the membrane. A charged membrane was installed at the center of the measuring cell, which had two glass containers, one on either side of the membrane. The volume of each container was 200 cm^3, and the membrane area was 7.55 cm^2. Electrolyte solutions of different concentrations were poured into these containers; the concentration in the left container was varied from 0.001 to 4.0 mol/L, and that in the right one was kept constant at 0.001 mol/L. The weight fractions of methanol in mixed solvents were 0%, 20%, 50%, 80%, and 100%. An electrometer (TOA HM-20E) connected to glass electrodes (TOA HS-205C) was used for measurement of the electrical potential. Two glass electrodes were placed in saturated KCl solutions that were connected to the containers by salt bridges. The solutions in both containers were stirred by magnetic stirrers to minimize the effect of the boundary layers on the membrane potential.

59.3.4 Measurement of Modified Degree of Hydration

The modified degree of hydration H, similarly defined as the degree of hydration presented by other authors [18,65], was the volume fraction of the mixed solvent in a wet membrane. It could be estimated from the following equation

$$H = \frac{(W_w - W_d)/\rho_s}{(W_w - W_d)/\rho_s + W_d/\rho_m} \tag{59.39}$$

where W_w and W_d are the weights of a membrane at the equilibrium wet and dry states, respectively, and ρ_s and ρ_m are the densities of the mixed solvent and membrane, respectively. For simplicity, the density of the mixed solvent was calculated using the following empirical equation

$$\rho_s = \frac{1}{\sum_n x'_n/\rho_n} \tag{59.40}$$

where x'_n and ρ_n are the salt-free weight fraction and density of solvent n, respectively.

59.3.5 Measurement of Permeability Coefficient

The permeability coefficients of both membranes used in this study were measured to obtain the mobilities of ions in the membrane. A charged membrane was installed at the center of the measuring cell, which had two glass containers, one on either side of the membrane. The volume of each container was 200 cm^3, and the membrane area was 7.55 cm^2. Electrolyte solutions of different concentrations were poured into these containers; the concentration in the left container was varied from 0.01 to 2.0 mol/L, and the container on the right side was filled with the non-electrolyte-containing solvent. The data were measured by using a digital conductivity meter (TOA CM-20E) connected to a conductivity cell (TOA CG-511B). The solutions in both containers were stirred by magnetic stirrers to minimize the effect of the boundary layers on the flux of ions. The permeability coefficient P was

estimated from the ion concentration change with time on the right-hand side using the following equation

$$P = -\frac{V\Delta C_s'}{\left(C_s'' - C_s'\right) SH\Delta t} \tag{59.41}$$

where V is the volume of the right container, $\Delta C_s'$ is the ion concentration change on the right side at time interval Δt, and S is the membrane area. If the value of C_s' were kept smaller than $0.01C_s''$ at time interval Δt, then the value of $C_s'' - C_s'$ could be adopted as C_s'' without leading to any obvious errors.

59.4 RESULTS AND DISCUSSION

59.4.1 Organic Solution System

The results for the membrane potentials of K171 and A201 are shown in Figs. 59.3 and 59.4, respectively, where the theoretical results for the LiCl methanol–water solutions are shown as lines, and the experimental data agree well with the calculated results. For the cation exchange membrane, the membrane potential experiences a maximum as the electrolyte concentration increases, and the maximum of membrane potential decreases with increase in the weight fraction of methanol. On the other hand, for the anion exchange membrane, the membrane potential undergoes a minimum as the electrolyte concentration increases, and the minimum of membrane potential increases with increase in the weight fraction of methanol.

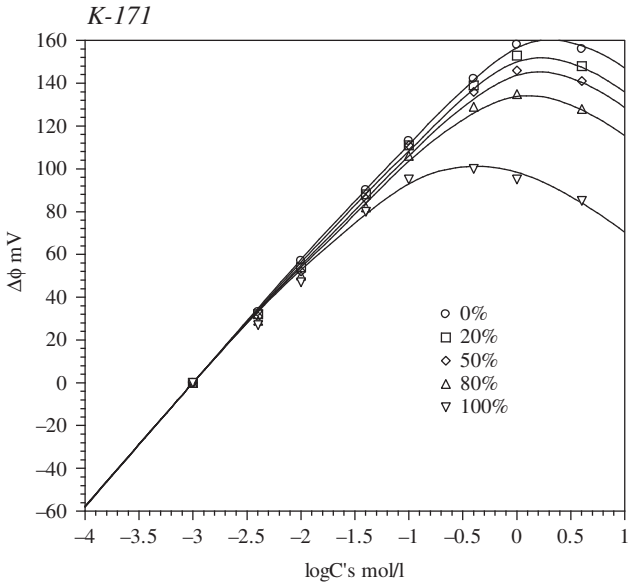


FIGURE 59.3 Membrane potential of cation exchange membrane for various weight fractions of methanol from 0% to 100%. Solid lines represent the theoretical results obtained by fitting the experimental data to Eq. (59.18).

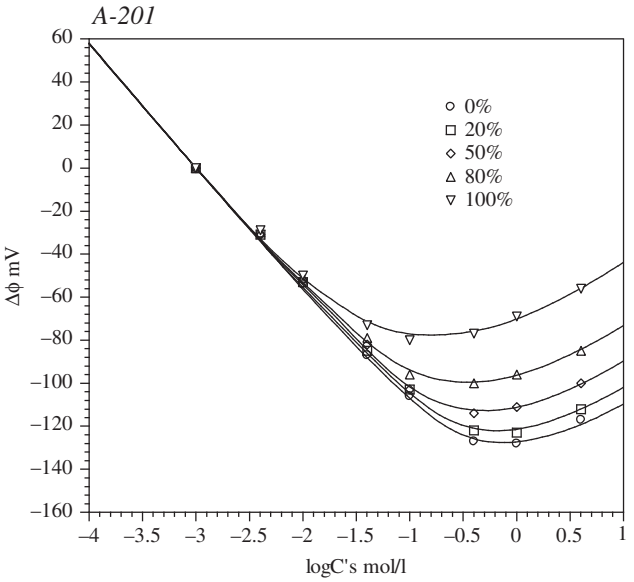


FIGURE 59.4 Membrane potential of anion exchange membrane for various weight fractions of methanol from 0% to 100%. Solid lines represent the theoretical results obtained by fitting the experimental data to Eq. (59.18).

The effective membrane charge density QC_x and the cation-to-anion mobility ratio in the membrane r can be estimated by fitting the experimental data to the transport theory based on the Donnan equilibrium and the Nernst–Planck equation considering the effect of the mean activity coefficient of electrolyte in external solution. A nonlinear parameter estimation program UNCMIN [69] is used to fit the experimental data. In the process of estimation, C_s' and C_s'' are the experimental results QC_x and r are the unknown parameters. The values of QC_x and r in various weight fractions of methanol solutions are given in Table 59.3. The calculated results of Q in various weight fractions of methanol are shown in Fig. 59.5. The solid lines in Fig. 59.5 represent the theoretical results obtained by fitting the effective membrane charge density to Eq. (59.24). This can well describe the

TABLE 59.3 Values of Effective Membrane Charge Densities and cation-to-anion Mobility Ratios in Membrane for Various Weight Fractions of Methanol from 0% to 100%

	Cation exchange membrane		Anion exchange membrane	
Weight fractions of methanol (%)	QC_x (mol/L)	r	QC_x (mol/L)	r
0	−1.6	0.39	0.35	1.9
20	−1.1	0.41	0.28	1.9
50	−0.86	0.42	0.20	2.0
80	−0.53	0.42	0.12	2.0
100	−0.14	0.43	0.049	2.0

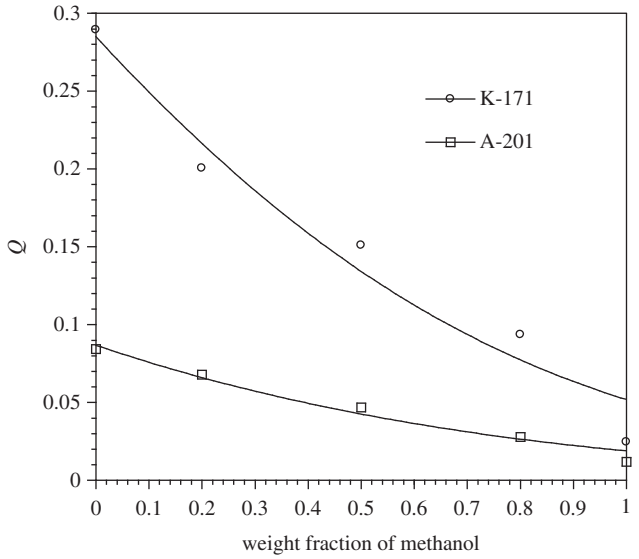


FIGURE 59.5 Values of Q in cation exchange and anion exchange membranes with various weight fractions of methanol. Solid lines represent the theoretical results obtained by fitting the data to Eq. (59.24).

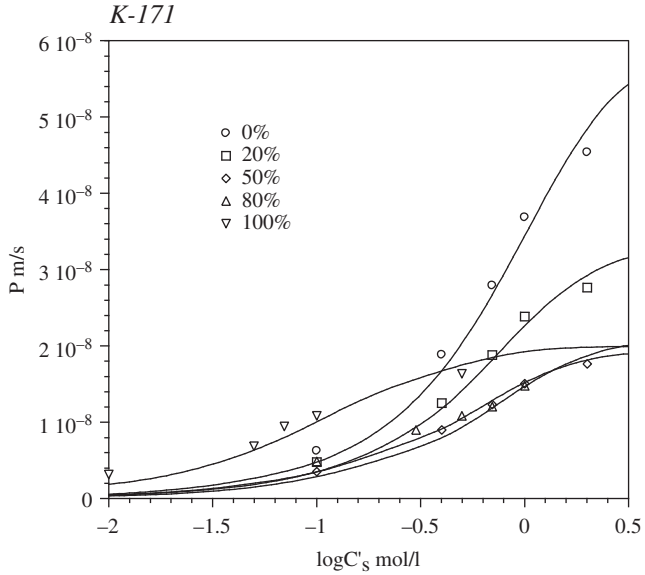


FIGURE 59.6 Permeability coefficient of cation exchange membrane for various weight fractions of methanol from 0% to 100%. Solid lines represent the theoretical results obtained by fitting the experimental data to Eqs. (59.27) and (59.29).

variation tendency of the effective membrane charge density with the weight fraction of methanol. The parameters a and k' obtained by fitting to Eq. (59.24) are listed in Table 59.4. From Fig. 59.5, it can be found that the effective membrane charge density decreases with the increase in weight fraction of methanol. It is assumed that most of the fixed-charge groups are occupied by the counterion due to the formation of the ion pairs, and the effect will decrease the amount of the effective fixed-charge groups. This is one reason why the effective membrane charge density decreases with the increase of the weight fraction of methanol.

It is shown in Eq. (59.18) that the ion mobility ratio in membranes have a greater influence on the membrane diffusion potential than on the Donnan potential. In general, the ion mobility ratio is kept constant when the solute and the fixed-charge groups in the membrane are both strong electrolytes, even if their signs change from negative to positive. On the other hand, if the fixed-charge group is the weak electrolyte and the solute is a strong one, a large shift in the ion mobility ratio is observed, as has been reported previously [23,70]. It is very important to clarify which ionic mobility, that of the counterion or of the coion, is more variable.

TABLE 59.4 Parameters a and k' Obtained by Fitting to Eq. (59.24)

	$a \times 10^{10}$m	$k' \times 10^{-6}$
Cation exchange membrane	5.3	0.58
Anion exchange membrane	6.6	1.7

It is generally known that charged groups in the membrane have a greater influence on the counterion than on the coion [14]. The ion mobility ratios of LiCl in pure water and pure methanol are 0.507 and 0.757, respectively. From Table 59.3, we can find that the values of the ion mobility ratio in cation exchange membranes are smaller than those in pure water or pure methanol, and are larger in anion exchange membrane. The results are the same as those obtained by other authors [16,19,23]. The ionic mobility will be discussed further with respect to the data obtained by electrolyte permeation measurements.

The results for the permeability coefficients of K171 and A201 are shown in Figs. 59.6 and 59.7, respectively, where the theoretical results for the LiCl methanol–water solutions calculated by Eqs. (59.27) and (59.29) are shown as lines, and the experimental data were in good agreement with the calculated results. In both membranes, the permeability coefficient slightly increases with the concentration on the left side in the low-concentration range. When the concentration on the left side is around that of the effective membrane charge density, a sharp increase in the permeability coefficient appears. After that, with the increase in concentration on the left side, the increasing rate of the permeability coefficient decelerates again and finally reaches a maximum. From Figs. 59.6 and 59.7, it can be found that the maximum of the permeability coefficient will decrease as the weight fraction of methanol increases.

The mobility of a cation in a membrane $\bar{\omega}_+$ can be estimated by fitting the experimental data of the permeability coefficient to Eqs. (59.27) and (59.29). A nonlinear parameter

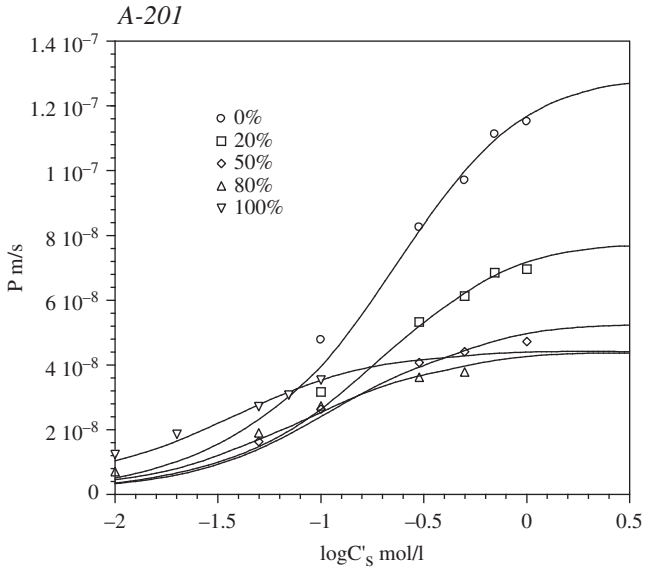


FIGURE 59.7 Permeability coefficient of anion exchange membrane for various weight fractions of methanol from 0% to 100%. Solid lines represent the theoretical results obtained by fitting the experimental data to Eqs. (59.27) and (59.29).

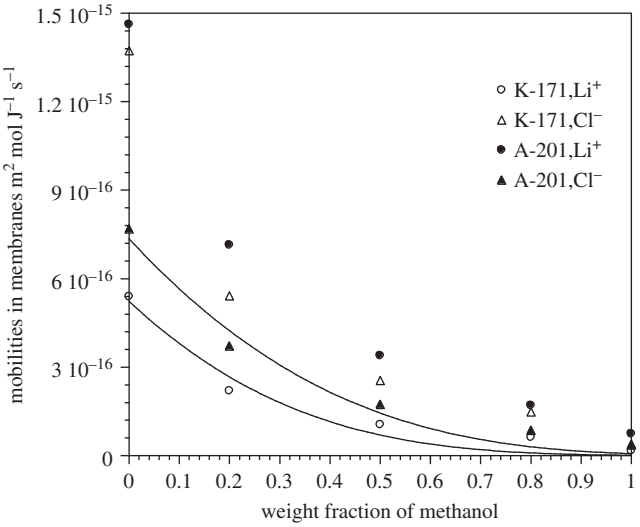


FIGURE 59.8 Mobility of ions in cation exchange and anion exchange membranes with various weight fractions of methanol. Solid lines represent the theoretical results obtained by fitting the data to Eq. (59.35).

estimation program (UNCMIN [69]) is used to fit the experimental data. In the estimation process, C_s' and C_s'' are the experimental results, while the effective membrane charge density and the cation-to-anion mobility ratio are obtained from a previous paper [24] and are listed in Table 59.2, and $\bar{\omega}_+$ is the unknown parameter. The mobility of the anion in a membrane $\bar{\omega}_-$ can be calculated by Eq. (59.16). The calculated results of $\bar{\omega}_+$ and $\bar{\omega}_-$ in various weight fractions of methanol are shown in Fig. 59.8. The solid lines in Fig. 59.8 are the theoretical results obtained by fitting the mobilities of the counterion in a membrane to Eq. (59.35) using the nonlinear parameter estimation program UNCMIN [53]. This can accurately describe the variation tendency of mobility of a counterion in a membrane with the weight fraction of methanol. According to one definition [64], the tortuosity factor θ can be expressed by

$$q = \frac{2 - H}{H} \tag{59.42}$$

In the case of a commercial ion exchange membrane, the modified degree of hydration H is approximately 0.2–0.4, which corresponds to a q value of 9–4. For simplicity, we fixed the tortuosity factor at $q = 5$, for the general charged membranes without causing any obvious errors, and the parameters a and β obtained by fitting to Eq. (59.35) are listed in Table 59.5. From Fig. 59.8, it can be found that the mobilities of a counterion in a membrane are smaller than those of a coion in a membrane, and that the mobilities of a counterion in a membrane are smaller than their corresponding values in a mixed solvent. It is assumed that most of the counterions are adsorbed by the fixed-charge groups, and the entrapped counterions have difficulty in moving to the adjoining sites. This is one reason why the mobilities of counterions are very low. One team also suggested [35] that the mobility of a coion in a membrane is the same as that in pure solvent, and that the mobility of a counterion in a membrane is a function of the fixed-charge groups in the membrane for a very low-water-content membrane system. The equations by that team [35] are modified and adapted to the systems in this study as follows:

$$\frac{\bar{\omega}_{\text{co-ion}}}{\omega_{\text{co-ion}}} = \alpha \tag{59.43}$$

$$\frac{\bar{\omega}_{\text{counterion}}}{\omega_{\text{counterion}}} = \alpha \frac{\bar{C}_{\text{co-ion}} + \phi C_x}{\bar{C}_{\text{co-ion}} + C_x} \tag{59.44}$$

Here, α is a parameter for reducing the effect that results from the difference of the structure, and ϕ is a parameter that is a function of the ion concentration. The ratios of ionic mobility for both membranes, which is the in membrane-to-mixed solvent ratio, $\bar{\omega}_i/\omega_i$, are shown in Table 59.6. Because $\phi < 1$ in

TABLE 59.5 Parameters a and β Obtained by Fitting to Eq. (59.35)

	$a \times 10^{10}$ m	$\beta \times 10^{-7}$
Cation exchange membrane	2.6	1.5
Anion exchange membrane	3.5	1.8

TABLE 59.6 Ratios of Ionic Mobility Denoted as in Membrane-to-Mixed Solvent, $\bar{\omega}_i/\omega_i$, for Both Membranes

	Cation exchange membrane		Anion exchange membrane	
Solvent	$\bar{\omega}_+/\omega_+ \times 10^3$	$\bar{\omega}_-/\omega_- \times 10^3$	$\bar{\omega}_+/\omega_+ \times 10^3$	$\bar{\omega}_-/\omega_- \times 10^3$
Water[a]	1.3	1.7	3.5	0.94
Methanol[b]	0.040	0.069	0.17	0.065

[a]In water: $\omega_{Li^+} = 4.154 \times 10^{-13}$ m^2 mol J^{-1} s^{-1} and $\omega_{Cl^-} = 8.201 \times 10^{-13}$ m^2 mol J^{-1} s^{-1}.
[b]In methanol: $\omega_{Li^+} = 4.254 \times 10^{-13}$ m^2 mol J^{-1} s^{-1} and $\omega_{Cl^-} = 5.618 \times 10^{-13}$ m^2 mol J^{-1} s^{-1}.

all regions of the ion concentration, the ratio of $\bar{\omega}_i/\omega_i$ for the coion will be larger than that for the counterion. The results in Table 59.3 agreed with this conclusion. From Table 59.6, it can also be found that the ratio of $\bar{\omega}_i/\omega_i$ in methanol is much smaller than that in water in both membranes of K171 and A201 (see also Table 59.6). One reason is that the counterions tend to form ion pairs with the fixed-charge groups in a mixed-solvent system since the dielectric constant of methanol is smaller than in water. Thus the ion pairs between counterions and fixed-charge groups will increase with the increase in methanol concentration, and the mobilities of the counterion will decrease.

59.4.2 Low-Water-Content System

59.4.2.1 Membrane Potential. A theoretical prediction of membrane potentials was performed on the basis of our theoretical model (details of calculation are described in the Section 59.2). Before the calculation of membrane potentials, we estimated (1) the partition coefficients of ions between the membrane phase and the external electrolyte solution phase and (2) the diffusion coefficient of ions in the membranes. The partition coefficients of the ions could not be obtained experimentally; therefore, we adapted Ferry's statistical calculation of partition coefficients k_i, based on the assumptions that (1) the solutes are spherical and the pores are cylindrical and (2) the interaction between the membrane matrix and a solute molecule is negligible [71]:

$$k_i = (1 - r_i/r_{pore})^2 \tag{59.45}$$

Here, r_i is the ionic radius of the ith species (we used the crystallographic radius in Table 59.7 [72] as the ionic radius) and r_{pore} is the pore radius of the membrane, and we estimated the pore radius of the membrane by water permeability measurements using the Hagen–Poiseuille equation (actually the prepared membranes appear to have a dense structure; however, another author adapted this treatment for fine-pore synthetic membranes and estimated the mean pore radii within several nm [73]):

$$J_v = \frac{\theta r_{pore}^2}{8\eta\tau}\frac{\Delta P}{\Delta x} \tag{59.46}$$

Here, J_v is the flux of water, η is the viscosity of water, ΔP is the pressure difference, Δx is the membrane thickness, θ is the porosity of the membrane [θ = (*water volume*)/(*membrane volume*)], and τ is the tortuosity factor of the membrane [$\tau = (2 - \theta)/\theta$ [64]]. The mean pore radius and the partition coefficient of the membranes are listed in Table 59.8. The diffusion coefficient of ions in the membranes was given by

$$\bar{D}_{\text{im}} = \frac{D_i}{\tau^2} \tag{59.47}$$

where $\bar{D}_{\text{im}}$ and D_i represent the diffusion coefficient of the ith species in the membrane and that in the solution [74], respectively. The diffusion coefficients in the membranes are summarized in Table 59.9.

The theoretical calculations of membrane potentials were fitted to the experimental data. Here, the dielectric constant in the membrane ε_r and the center-to-center distance of ion pair a are the fitting parameters with the following conditions

$$2 < \varepsilon_r < 78 \tag{59.48}$$

$$r_c^c < a < r_h^c + r_h^f \tag{59.49}$$

where r_c^c, r_h^c, and r_h^f are the crystallographic radius of the counterion, hydrated radius of the counterion, and hydrated radius of the fixed-charge group, respectively. The values of

TABLE 59.7 Crystallographic and Hydrated Radius of Ions

	K^+	Na^+	Li^+	Mg^{2+}	Ca^{2+}	$N(CH_3)_4{}^+$	Cl^-	Br^-	I^-	$NO_3{}^-$	$SO_4{}^{2-}$
r_c (Å)	1.33	0.95	0.6	0.99	0.65	3.47	1.81	1.95	2.16	2.64	2.9
r_h (Å)	3.3	3.6	3.8	4.1	4.3	3.7	3.3	3.3	3.3	3.4	3.8

TABLE 59.8 Mean Pore Radius and Partition Coefficient of Membranes

Membrane	r_{pore} (nm)	k_{K+} (−)	k_{Na+} (−)	k_{Li+} (−)	$k_{Ca^{2+}}$ (−)	$k_{Mg^{2+}}$ (−)	k_{Cl-} (−)
CEM1	NO	0.56	0.51	0.49	0.45	0.43	0.49
CEM2	1.6	0.64	0.61	0.59	0.56	0.55	0.59
CEM-3	2.4	0.74	0.72	0.71	0.69	0.67	0.71
	r_{pore} (nm)	k_{Cl-} (−)	k_{Br-} (−)	k_{I-} (−)	k_{NO_3-} (−)	$k_{SO_4^{2-}}$ (−)	k_{Na+} [−]
AEM1	1.3	0.57	0.57	0.57	0.56	0.51	0.53
AEM2	1.4	0.58	0.58	0.58	0.57	0.53	0.55
AEM-3	1.8	0.67	0.67	0.67	0.66	0.62	0.64

TABLE 59.9 Diffusion Coefficient of Ions in Bulk Water

	K^+	Na^+	Li^+	Mg^{2+}	Ca^{2+}	Cl^-	Br^-	I^-	NO_3^-	SO_4^{2-}
D ($\times 10^5$ cm^2/s)	1.957	1.334	1.030	0.7922	0.7063	2.033	2.081	2.046	1.903	1.065

the dielectric constants, 2 and 78, correspond to that of the bulk polymer of the membrane matrix, poly(St-*co*-DVB), and bulk water, respectively. We assumed that the center-to-center distance of the ion pair changed from the crystallographic radius of the counterion to the sum of the hydrated radii of the fixed-charge group and counterion. The sizes of ions used in the calculation are summarized in Table 59.7 [72]. We used the hydrated radii of SO_4^{2-} and $N(CH_3)_4^+$ as that the of fixed-charge group of the CEMs and AEMs, respectively, for approximation. In the calculations, the ion activity coefficient in the membrane $\bar{\gamma}_{im}$ was used as the concentration of the external electrolyte solution.

Figure 59.9 shows typical experimental results for the membrane potential for (a) CEM and (b) AEM. The points and solid lines represent the experimental data and the theoretical results, respectively. All the calculated results of membrane potential agreed well with the experimental values. This supported the belief that the ion-pairing effect was significant in a low-water-content membrane system. In the following section, we examine the fitting parameters ε_r and a, obtained from our theoretical analysis.

59.4.2.2 Dielectric Constant in Membranes and Center-to-Center Distance of an Ion Pair. Figure 59.10 and Table 59.10, respectively demonstrate the water content dependence of the dielectric constant ε_r in the membranes and the center-to-center distance of an ion pair a, based on our theoretical analysis. As can be seen in Figure 59.10,

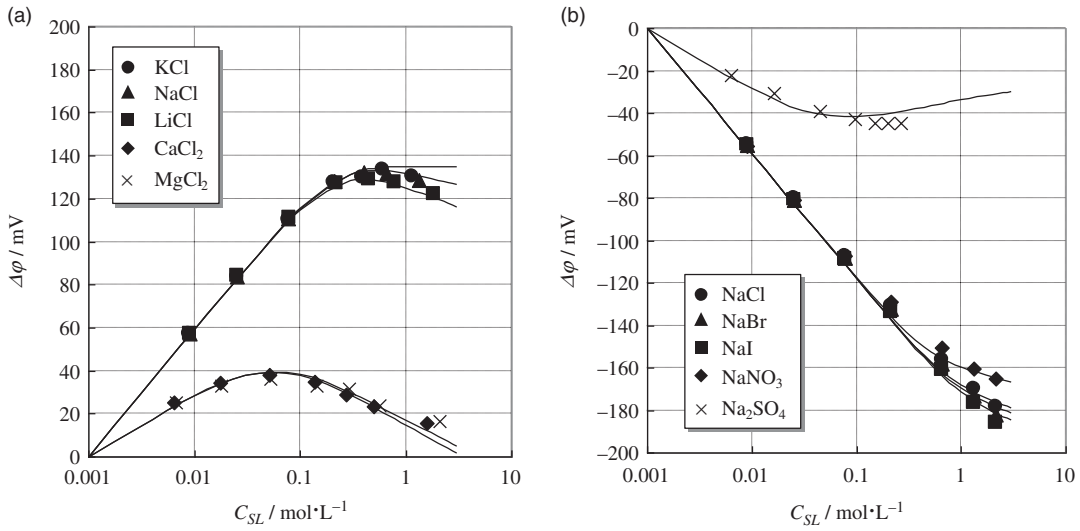


FIGURE 59.9 Membrane potential across the membranes as a function of electrolyte concentration in bulk solutions (C_{SL}): (a) CEM2; (b) AEM2. Solid lines indicate the theoretical results obtained by fitting our theory considering ion pair formation between fixed-charge groups and counterions to the experimental data.

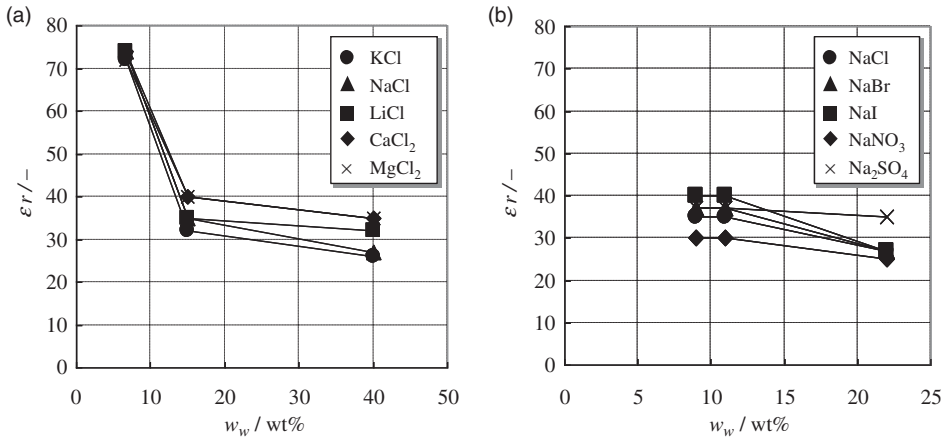


FIGURE 59.10 Dielectric constants in membranes ε_r as a function of water content obtained by theoretical analysis: (a) CEM; (b) AEM.

the dielectric constant in the membranes is smaller than the value in the bulk water ($\varepsilon_r = 78$). Table 59.10 indicates that the center-to-center distance of an ion pair is independent of the water content of the membranes and within the range from the crystallographic radius to the hydrated radius of a counterion (see Table 59.7). These results suggested that fixed-charge groups in the membrane were neutralized by associated counterions. This is attributed to dielectric saturation. Water content dependences of the dielectric constant behaved differently between CEMs and AEMs; the dielectric constant in a CEM remarkably increased with a decrease in the water content of ~10 wt%, while that in an AEM did not show a water content dependence. This interesting discrepancy of the dielectric constant for a CEM contradicts the general prediction that the dielectric constant in a low-water-constant membrane would be low as a result of dielectric saturation [75]. For the sulfonated poly(St-*co*-DVB) membranes, however, another team of investigators reported that the amount of nonfreezing water in the membrane, whose mobility is strongly restricted by the interactions between the polymer matrixes and water molecules, decreased with a decrease in the water content, according to their differential scanning calorimetry measurements [76]. Under such conditions, it is presumed that the dielectric constant in the membrane increased with a decrease in water content.

TABLE 59.10 Center-to-Center Distance of Ion Pair in Membranes from Theoretical Calculations

	a (Å)				
Membrane	K^+	Na^+	Li^+	Ca^{2+}	Mg^{2+}
CEM1	1.8	1.6	2.2	3.3	3.4
CEM2	1.8	1.7	1.7	3.6	3.7
CEM3	1.8	1.7	1.5	3.7	3.7
	a (Å)				
	Cl^-	Br^-	I^-	$NO3^-$	SO_4^{2-}
AEM1	3	2.9	3.0	2.8	3.3
AEM2	3	2.9	3.0	2.8	3.5
AEM3	2.6	2.6	3.0	2.8	3.5

59.4.2.3 Charge Effectiveness of the Membranes. All of the fixed-charge groups in the membrane do not function perfectly, as a result of the neutralization by the counterion. Therefore, the effectiveness of fixed-charge groups in the membrane is an important index for the discussion on the ionic transport phenomenon across charged membranes. The charge effectiveness of the membrane Q represents the effectiveness of the fixed-charge groups in the membranes and is defined as follows:

$$Q = \frac{\frac{1}{d}\int_0^d \bar{C}_{Xm}(x)dx}{C_{Xm}} \tag{59.50}$$

Figure 59.11 shows the charge effectiveness of the membranes as a function of water content of the membranes. The charge effectiveness of the membranes was small (< 0.35). The water content dependence of the charge effectiveness of the membrane obeyed that of the dielectric constants in the membranes; the charge effectiveness of the CEM showed a critical point around the 10 wt% water content (this result implies that charged membranes may show large charge effectiveness and high permselectivity even under low-water-content conditions). The charge effectiveness of the membrane in a divalent counterion system ($MgCl_2$ and $CaCl_2$ for CEMs; Na_2SO_4 for AEMs) was much lower than that in a monovalent counterion system. This phenomenon can also be explained by the ion-pairing effect; the electrostatic interaction between a fixed-charge group and a counterion depends on the valence of the counterions [75].

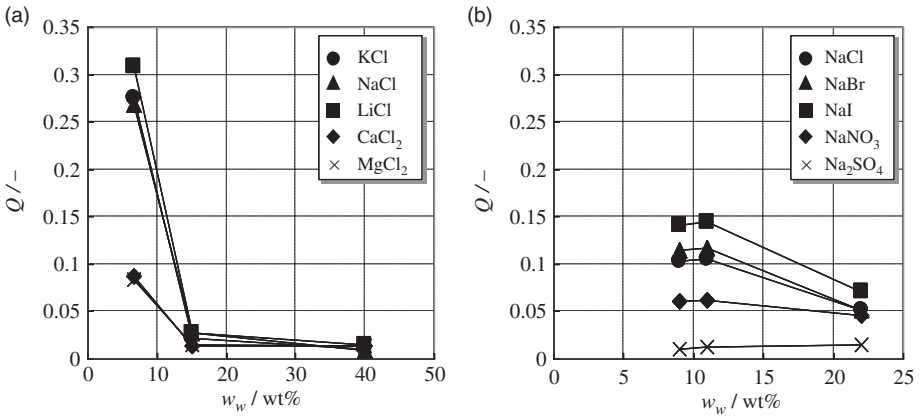


FIGURE 59.11 Charge effectiveness of membranes Q as a function of water content: (a) CEM; (b) AEM.

In the present study, we verified the ion-pairing effect in low-water-content charged membranes on the basis of membrane potential measurements. Analysis of the experimental results was based on the Donnan equilibrium, the Nernst–Planck equation for ion flux, and the Fuoss formalism for ion pair formation between the fixed-charge groups and counterions in the membranes. The theoretical predictions agreed well with the experimental results, demonstrating that the ion-paring effect was significant in the low-water-content membrane system. Our first-approximation theoretical approach also revealed the following findings:

1. Dielectric constants in the membrane were smaller than the value in bulk water. The dielectric constant in the CEM showed a critical point near the 10 wt% water content level, while that in the AEM did not show a water content dependence.
2. The center-to-center distance of an ion pair was independent of the water content of membranes.
3. The charge effectiveness of the membrane was small (< 0.35). The water content dependence of the charge effectiveness of the membranes obeyed that of the dielectric constants in the membrane.

These results provide fundamental knowledge for the development of not only polyelectrolyte membranes for fuel cells but also high-performance membranes for other applications. Another group of investigators has also studied the local structure of counterions in ion exchange resins by X-ray absorption fine structures (XAFS) [77]. They evaluated the direct ion pairs between the fixed-charge groups and counterions. A more detailed discussion on ion pairing in the membranes based on both membrane potential measurements and other spectroscopic measurements (e.g., XAFS, NMR, dielectric relaxation measurements in the GHz region [78]) will be required.

REFERENCES

[1] Tanioka, A., Chou, T.-J., Hamada, M. (2002). Transport in membranes: Ionic transport across charged membrane in aqueous organic solutions. *Encyclopedia of Surface and Colloid Science*, pp. 5418–5429, CRC Press, Boca Raton, FL.

[2] Matsumoto, H., Yamamoto, R., Tanioka, A. (2005). Membrane potential across low-water-content charged membranes: Effect of ion pairing. *J. Phys. Chem. B* **109**, 14130.

[3] Helfferich, F. (1962). *Ion Exchange*. McGraw-Hill, New York.

[4] Lakshminarayanaiah, N. (1969). *Transport Phenomena in Membranes*. Academic Press, New York.

[5] Teorell, T. (1935). An attempt to formulate a quantitative theory of membrane permeability. *Proc. Soc. Exp. Biol.* **33**, 282.

[6] Teorell, T. (1953). Transport processes in ionic membranes. *Progress Biophys. Biophys. Chem.* **3**, 305.

[7] Meyer, K.H., Sievers, J.F. (1936). La perméabilité des membranes. *Helv. Chim. Acta* **19**, 649.

[8] Donnan, F.G. (1911). Theorie der Membrangleichgewiche und Membranpotentiale bei Vorhandensein von nicht Dialysierenden Elektrolyten. Ein beitrag zur Physikalisch-chemischen Physiologie. *Z. Electrochem.* **17**, 572.

[9] Donnan, F.G. (1934). Die genaue Thermodynamik der Membrangleichgewichte. II. *Z. Phys. Chem. A* **168**, 369.

[10] Nernst, W. (1888). Zur Kinetik der in Lösung befindlichen Körper. *Z. Phys. Chem.* **2**, 613.

[11] Planck, M. (1890), Über die Erregung von Electricitat und Warme in Electrolyten. *Annu. Phys. Chem.* **39**, 161.

[12] Planck, M. (1890). Über die Potentialdifferenz zwishen zwei verdunnten Losungen binarer Electrolyte. *Annu. Phys. Chem.* **40**, 561.

[13] Lakshminarayanaiah, N. (1984). *Equations of Membrane Biophysica*. Academic Press, Orlando, FL.

[14] Kimura, Y., Lim, H., Iijima, T. (1984). Membrane potentials of charged cellulosic membranes. *J. Membr. Sci.* **18**, 285.

[15] Kimura, Y., Lim, H., Iijima, T. (1986). Permeability of alkali chlorides through charged cellulosic membranes. *Die Ang. Makromol. Chem.* **138**, 151.

[16] Higa, M., Tanioka, A., Miyasaka, K. (1988). Simulation of the transport of ions against their concentration gradient across charged membranes. *J. Membr. Sci.* **37**, 251.

[17] Higa, M., Tanioka, A., Miyasaka, K. (1990). A study of ion permeation across a charged membrane in multicomponent ion systems as a function of membrane charge density. *J. Membr. Sci.* **49**, 145.

[18] Elmidaoui, A., Molenat, J., Gavach, C. (1991). Competitive diffusion of hydrochloric acid and sodium chloride through an acid dialysis membrane. *J. Membr. Sci.* **55**, 79.

[19] Higa, M., Tanioka, A., Miyasaka, K. (1991). An experimental study of ion permeation in multicomponent ion systems as a function of membrane charge density. *J. Membr. Sci.* **64**, 255.

[20] Higa, M., Kira, A., Tanioka, A., Miyasaka, K. (1993). Ionic partition equilibrium in a charged membrane immersed in a mixed ionic solution. *J. Chem. Soc. Faraday Transact.* **89**, 3433.

[21] Gastilla, J., García-Hernández, M.T., Hayas, A., Horno, J. (1996). Simulation of non-stationary electrodiffusion processes in charged membranes by the network approach. *J. Membr. Sci.* **116**, 107.

[22] Kawaguchi, M., Murata, T., Tanioka, A. (1997). Membrane potentials in charged membranes separating solutions of weak electrolytes. *J. Chem. Soc. Faraday Transact.* **93**, 1351.

[23] Westermann-Clark, G.B., Christoforou, C.C. (1984). Note nonaqueous electrokinetic transport in charged porous media. *J. Membr. Sci.* **20**, 325.

[24] Hamann, C.H., Theile, V., Koter, S. (1993). Transport properties of cation-exchange membranes in aqueous and methanolic solutions. Diffusion and osmosis. *J. Membr. Sci.* **78**, 147.

[25] Chou, T.-J., Tanioka, A. (1998). Ionic behavior across charged membranes in methanol-water solutions. 1. Membrane potential. *J. Membr. Sci.* **144**, 275.

[26] Saito, K., Tanioka, A., Miyasaka, K. (1994). A study of effective charge density of swollen poly(vinyl alcohol) membrane mixed with poly(styrenesulfonic acid). *Polymer* **35**, 5098.

[27] Matsumoto, H., Tanioka, A., Murata, T., Higa, M., Horiuchi, K. (1998). Effect of proton on potassium ion in countertransport across fine porous charged membrane. *J. Phys. Chem. B* **102**, 5011.

[28] Glueckauf, E., Watts, R.E. (1962). *Proc. Roy. Soc. Lond. Ser. A* **268**, 339.

[29] Glueckauf, E. (1962). *Proc. Roy. Soc. Lond. Ser. A* **268**, 350.

[30] Reiss, H., Bassignana, I.C. (1982). *J. Membr. Sci.* **11**, 219.

[31] Selvey, C., Reiss, H. (1985). *J. Membr. Sci.* **23**, 11.

[32] Petropoulos, J.H., Tsimboukis, D.G., Kouzeli, K. (1983). *J. Membr. Sci.* **16**, 379.

[33] Petropoulos, J.H. (1990). *J. Membr. Sci.* **52**, 305.

[34] Larter, R. (1986). *J. Membr. Sci.* **28**, 165.

[35] Mafé, S., Ramírez, P., Tanioka, A., Pellicer, J. (1997). Model for counterion-membrane-fixed ion pairing and Donnan equilibrium in charged membranes. *J. Phys. Chem. B* **101**, 1851.

[36] Chou, T.-J., Tanioka, A. (1998). Membrane potential across charged membranes in organic solutions. *J. Phys. Chem. B* **102**, 7198.

[37] Chou, T.-J., Tanioka, A. (1998). Current-voltage curves of composite bipolar membrane in alcohol-water solutions. *J. Phys. Chem. B* **102**, 7866.

[38] Chou, T.-J., Tanioka, A. (1998). Ionic behavior across charged membranes in methanol-water solutions. 2. Ionic mobility. *J. Phys. Chem.* **102**, 129.

[39] Chou, T.-J., Tseng, H.-C., Tanioka, A. (1998). Salting effect on the liquid-liquid equilibria for the partially miscible systems of *n*-propanol-water and *i*-propanol-water. *Industr. Eng. Chem. Res.* **37**, 2039.

[40] Tan, T.C. (1987). Model for predicting the effect of dissolved salt on the vapour fluid equilibrium of solvent mixtures. *Chem. Eng. Res. Design* **65**, 355.

[41] Chou, T.-J., Tanioka, A. (1998). Predicting the effect of dissolved salt on the vapor-liquid equilibria for alcohol-water-salt systems. *Transact. IChemE. Pt. A* **77**, 329.

[42] Macedo, E.A., Skovborg, P., Rasmussen, P. (1990). Calculation of phase equilibria for solutions of strong electrolytes in solvent-water mixtures. *Chem. Eng. Sci.* **45**, 875.

[43] Chou, T.-J., Tanioka, A. (1997). A vapor pressure model for aqueous and non-aqueous solutions of single and mixed electrolyte systems. *Fluid Phase Equilibr.* **137**, 17.

[44] Lin, C.-L., Lee, L.-S., Tseng, H.-C. (1993). Thermodynamic behavior of electrolyte solutions. Part II. Prediction of vapor-liquid equilibria for mixed-solvent electrolyte systems. *Fluid Phase Equilibr.* **90**, 81.

[45] Reiss, H. (1956). Refined theory of ion pairing. I. *Equilibrium aspects. J. Chem. Phys.* **25**, 400.

[46] Fuoss, R.M. (1958). Ionic association. III. The equilibrium between ion pairs and free ions. *J. ACS* **80**, 5059.

[47] Bockris, J. O'M., Reddy, A.K.N. (1970). *Modern Electrochemistry*. Plenum Press, New York.

[48] Manning, G.S., Zimm, B.H. (1965). Cluster theory of polyelectrolyte solution. I. Activity coefficients of the mobile ions. *J. Chem. Phys.* **43**, 4250.

[49] Franks, F. (1973). *Water, a Comprehensive Treatise*, Vol. 2. Plenum Press, New York.

[50] Tomasula, P., Czerwienski, G.J., Tassios, D. (1987). Vapor pressures and osmotic coefficients: Electrolyte solutions of methanol. *Fluid Phase Equilibr.* **38**, 129.

[51] Cisternas, L.A., Lam, E.J. (1991). An analytic correlation for the vapour pressure of aqueous and non-aqueous solutions of single and mixed electrolytes. Part II. Application and extension. *Fluid Phase Equilibr.* **62**, 11.

[52] Lin, C.-L., Lee, L.-S., Tseng, H.-C. (1993). Thermodynamic behavior of electrolyte solutions. Part I. Activity coefficients and osmotic coefficients of binary systems. *Fluid Phase Equilibr.* **90**, 57.

[53] Crank, J. (1975). *The Mathematics of Diffusion*, 2nd ed. Clarendon Press, Oxford, UK.

[54] Michaels, A.S., Vieth, W.R., Barrie, J.A. (1963). Diffusion of gases in polyethylene terephthalate. *J. Appl. Phys.* **34**, 13.

[55] Vieth, W.R., Howell, J.M., Hsieh, J.H. (1976). Dual sorption theory. *J. Membr. Sci.* **1**, 177.

[56] Weisz, P.B. (1976). Sorption-diffusion in heterogeneous systems. Part 1. General sorption behaviour and criteria. *Transact. Faraday Soc.* **63**, 1801.

[57] Weisz, P.B., Hicks, J.S. (1967). Sorption-diffusion in heterogeneous systems. Part 2. Quantitative solutions for uptake rates. *Transact. Faraday Soc.* **63**, 1807.

[58] Weisz, P.B., Zollinger, H. (1967). Sorption-diffusion in heterogeneous systems. Part 3. Experimental models of dye sorption. *Transact. Faraday Soc.* **63**, 1815.

[59] Vieth, W.R., Wang, S.S., Gilbert, S.G. (1972). Urea hydrolysis on collagen-urease complex membrane. *Biotechnol. Bioeng. Symp.* **3**, 285.

[60] Komiyama, J., Iijima, T. (1974). Diffusion of monoanionic dyes in Nylon. *J. Polym. Sci. Pt. A-2* **12**, 1465.

[61] Demisch, H.-U., Pusch, W. (1979). Electric and electrokinetic transport properties of homogeneous weak ion exchange membranes. *J. Colloid Interface Sci.* **69**, 247.

[62] Demisch, H.-U.Pusch, W. (1980). Electrical and electroosmotic transport behavior of asymmetric cellulose acetate membranes. *J. Colloid Interface Sci.* **76**, 445.

[63] Pusch, W. (1986). Measurement techniques of transport through membranes. *Desalination* **59**, 105.

[64] Mackie, J.S., Meares, P. (1955). The diffusion of electrolytes in a cation-exchange resin membrane. *Proc. Roy. Soc. Lond.* **A232**, 498.

[65] Kahaner, D., Moler, C., Nash, S. (1989). *Numerical Methods and Software*. Prentice-Hall, Englewood Cliffs, NJ.

[66] Yamamoto, R., Matsumoto, H., Tanioka, A. (2003). Membrane potentials across cation-exchange membranes with a low water content. *J. Phys. Chem. B* **107**, 10506.

[67] Tanioka, A., Matsumoto, H., Yamamoto, R. (2004). Charge effectiveness of sulfonated polymer membranes under low-water-content condition. *Sci. Technol. Adv. Mater.* **5**, 461.

[68] Mizutani, Y. (1962). *J. Chem. Soc. Jpn. Industr. Chem. Sec. (Kogyo Kagaku Zasshi)* **65**, 1124.

[69] Sieber, M., Motamedian, S., Minoura, N., Tanioka, A. (1997). Mathematical analysis of membrane potentials for polypeptide membranes. *J. Chem. Soc. Faraday Transact.* **93**, 2533

[70] Elmidaoui, A., Cherif, A.T., Molenat, J., Gavach, C. (1995). Transfer of H_2SO_4, Na_2SO_4 and $ZnSO_4$ by dialysis through an anion exchange membrane. *Desalination* **101**, 39.

[71] Ferry, J.D. (1936). *J. Gen. Physiol.* **20**, 95.

[72] Nightingale, E. R. *J. Phys. Chem.* 1959, **63**, 1381.

[73] Pusch, W. (1988). In Flanks, F. (ed.), *Water Science Reviews 3: Water Dynamics.* ; Cambridge Univ. Press, Cambridge, UK, p. 297.

[74] Robinson, R.A., Stokes, R.H. (1959). *Electrolyte Solutions*, 2nd ed. Butterworths, London, pp. 513–515.

[75] Yamamoto, R., Matsumoto, H., Tanioka, A. (2003). Ionic transport behavior across charged membranes with low water content. I. Theoretical aspect of membrane potentials in membranes having inhomogeneously distributed fixed-charge groups. *J. Phys. Chem. B* **107**, 10615.

[76] Tasaka, M., Suzuki, S., Ogawa, Y., Kamaya, M. (1988). *J. Membr. Sci.* **38**, 175.

[77] Harada, M., Okada, T., Watanabe, I. (2002). *J. Phys. Chem. B* **106**, 34.

[78] Paddison, S.J., Bender, G., Kreuer, K.D., Nicoloso, N., Zawodzinski, T.A.Jr. (2000). *J. New Mater. Electrochem. Syst.* **3**, 291.

60

BIOPHYSICAL STUDIES OF A MICELLAR PROTEIN α-CRYSTALLIN BY FLUORESCENCE METHODS

ARITRA CHOWDHURY,[1] RAJAT BANERJEE,[2] AND K.P. DAS[3]

[1]*School of Chemistry, University of Manchester, Manchester, United Kingdom*
[2]*Department of Biotechnology and Dr. B.C. Guha Centre for Genetic Engineering and Biotechnology, University of Calcutta, Kolkata, India*
[3]*Department of Chemistry, Bose Institute, Kolkata, India*

60.1 α-CRYSTALLIN

α-Crystallin is a member of the small heatshock protein (sHSP) superfamily and a key component of the mammalian eye lenses. It consists of two highly homologous chains, α,A- and α,B-chains, containing 173 and 175 amino acids, respectively, with a molecular mass of ∼20 kDa [1–3]. In the eye lens, α,A- and α,B-crystallins assemble into large oligomeric complex of molecular mass ∼800 kDa with a 3:1 stoichiometry. Recombinant α-crystallins also show extensive oligomerization leading to a rather homogenous 24mer aggregate for α,B-crystallin and heterogeneous aggregates for α,A-crystallin varying from 300 – 700 kDa [3–6]. Although initially considered to be a lenticular protein, α-crystallin was eventually detected in several other tissues, and implicated in different neurological pathophysiologies; thus its function has been redefined from that of a mere structural protein [7,8]. α-Crystallin is a potent chaperone. It prevents nonspecific hydrophobic interaction mediated protein aggregation and helps to refold unfolded states leading to folded functional forms. This chaperone function of α-crystallin is thus essential for maintaining transparency and integrity of the lens [9].

60.2 A BRIEF INTRODUCTION TO FLUORESCENCE IN PROTEINS

Fluorescence spectroscopy has been a key element of a biophysicist's toolset in terms of exploring protein structure and function. It can provide a host of valuable information about structural stability, ligand binding, conformational changes, and allostery.

The fluorescent probes used for protein structure characterization can be either extrinsic or intrinsic. Intrinsic fluorophores consist of fluorescent amino acids such as phenylalanine, tyrosine, and tryptophan and sometimes fluorescent cofactors such as NADP [10]. Tryptophan is most widely used for structural studies because of its environment sensitivity, making it useful for unfolding, ligand binding, or any other structural transition studies. Tyrosine, while not as widely used as tryptophan, still remains the intrinsic probe of choice in tryptophan-less proteins. Although it is not as sensitive as tryptophan, tyrosine fluorescence can still give important structural information. Phenylalanine has weak fluorescence and is not of much value from a biophysical perspective. Unlike intrinsic probes, extrinsic probes can be extremely diverse [11]. They can be either covalent or noncovalent. Covalent fluorophores conjugate with sidechain functionalities of the amino acid residues in protein. Covalent labeling can be site-selective and can provide crucial regiospecific information of the immediate microenvironment. Noncovalent probes, on the other hand, bind via noncovalent interactions such as H-bonding, electrostatic, hydrophobic, and Van-der Waals interaction. Noncovalent probes can be used as markers for hydrophobic or charged pockets and as ligand analogues.

Fluorescent techniques used to study protein structure can be varied. Steady-state fluorescence is a rather simple

Encyclopedia of Biocolloid and Biointerface Science, Volume 2, First Edition. Edited by Hiroyuki Ohshima.
© 2016 John Wiley & Sons, Inc. Published 2016 by John Wiley & Sons, Inc.

and inexpensive yet very powerful technique that can provide information such as solvent accessibility from emission maximum and Stern–Volmer plots, ligand binding from quenching or enhancement studies, and protein–protein interaction using polarization studies. Fluorescence lifetime is a more advanced technique that gives more specific details about microenvironment such as salvation and local polarity. Time-resolved fluorescence anisotropy may be used to assess the dynamics of a domain [10–12]. Another recent yet powerful technique is single-molecule fluorescence spectroscopy, where signals from single molecules are detected. Single-molecule fluorescence detection can be realized on several platforms, such as a confocal microscope, total internal reflection fluorescence (TIRF) microscope, or near-field scanning optical microscope (NSOM). Such studies provide information about the dynamics of a protein at single-molecule level instead of information of an en masse average obtained from ensemble techniques [13].

Often the high-resolution structure of a protein remains inaccessible in situations when crystals cannot be obtained and often the large size of the protein limits the use of NMR. In this chapter we demonstrate the use of fluorescence techniques to decipher key structural and biophysical aspects of protein structure and function even in absence of high-resolution structure, with the case of the oligomeric lens chaperonin α-crystallin. Interestingly, most of the data fit well with high-resolution structure obtained rather recently using a combination of solid state NMR, SAXS, and cryo-EM.

60.3 CHALLENGES IN DETERMINING α-CRYSTALLIN STRUCTURE AND PRELIMINARY STRUCTURAL MODELS BASED ON MICELLAR ARCHITECTURE

Initially α-crystallin was regarded as a structural lens protein, and its extensive oligomerization has been an element of curiosity. However, despite persistent efforts, its high-resolution structure remained elusive for a long time. The oligomeric heterogeneity and possible flexible structural motifs were thought to be the causes of failures to crystallize the protein. Such a huge oligomeric assembly was beyond the scope of conventional protein NMR techniques. Hence several models were proposed on the basis of some experimental findings to understand the oligomeric structure [14].

Studies in 1981 involved cross-linking α-crystallin oligomers with bifunctional imido esters [15]. Earlier studies using SAXS had already shown α-crystallin to have a semispherical structure. Its hydrodynamic diameter and the stiochiometry of α,A and α,B were also determined [16]. The study suggested random orientations of all the subunits indicating equivalent positions within the oligomer.

One research team proposed a layered micellar model where each subunit was treated as an ampliphile and the entire oligomer had a hydrophobic micelle-like core and presented hydrophilic facets on the surface (Fig 60.1a) [17]. Pyrene fluorescence was used to support the model. Pyrene shows strong excimer fluorescence when one pyrene molecule is in close proximity to the other one. Taking in consideration that only αA can react with the pyrene derivative as αB has no cysteine residues and that high pyrene excimer fluorescence indicates close proximity of αA subunits, they proposed possible compositions of the three layers of the micelle. Changes in excimer fluorescence with temperature were related to disassociation/reassociation of the different micellar layers associated with temperature-induced conformational change [17].

Based on oligomerization patterns of *N*-terminal and *C*-terminal fragments of α-crystallin, a rhombic decahedron-based model involving tetrameric α-crystallin building blocks (Fig. 60.1b) was proposed [18]. Another team then proposed a pitted flexiball model taking into account the robust nature of α-crystallin's oligomer (Fig. 60.1c). It combined the idea of tetrameric building blocks developed by Wistow [18] as well as some micellar features [19]. Despite having many failures and being extrapolative at times with no actual correlation with the experimental data, these early models led to certain key findings, including the equivalence of the subunits and the fact that α-crystallin oligomers are formed using different levels of intersubunit interaction involving smaller building blocks, which holds true even to this day [20].

60.4 HYDROPHOBICITY OF α-CRYSTALLIN AND ITS CHAPERONE FUNCTION

Similarity of α-crystallin with HSP members on a sequence level was identified as early as 1982 [21]. However, there was a paradigm shift in α-crystallin research when Horwitz showed that α-crystallin functions as molecular chaperone and prevented protein aggregation [22]. Soon several studies followed that reinstated its chaperone function [23–25].

However, due to lack of a detailed structural insight, understanding the basis of this chaperone function became a key focus of α-crystallin research. Another team showed α-crystallins to have several surface-exposed hydrophobic pockets using two hydrophobic fluorophores 1,8-ANS (1-anilinonaphthalene-8-sulfonic acid) and DPH (1,6-diphenyl 1,3,5-hexatriene) (Fig. 60.2) [26]. Fluorophores, like 1,8-ANS and DPH, have minimal emission in aqueous solutions, which increase several fold in apolar microenvironments such as membrane bilayers, and hydrophobic pockets in proteins, and hence such probes are widely used for protein characterization [11]. Hence, hydrophobic interactions, which are responsible for chaperone activity, were a reasonable line of

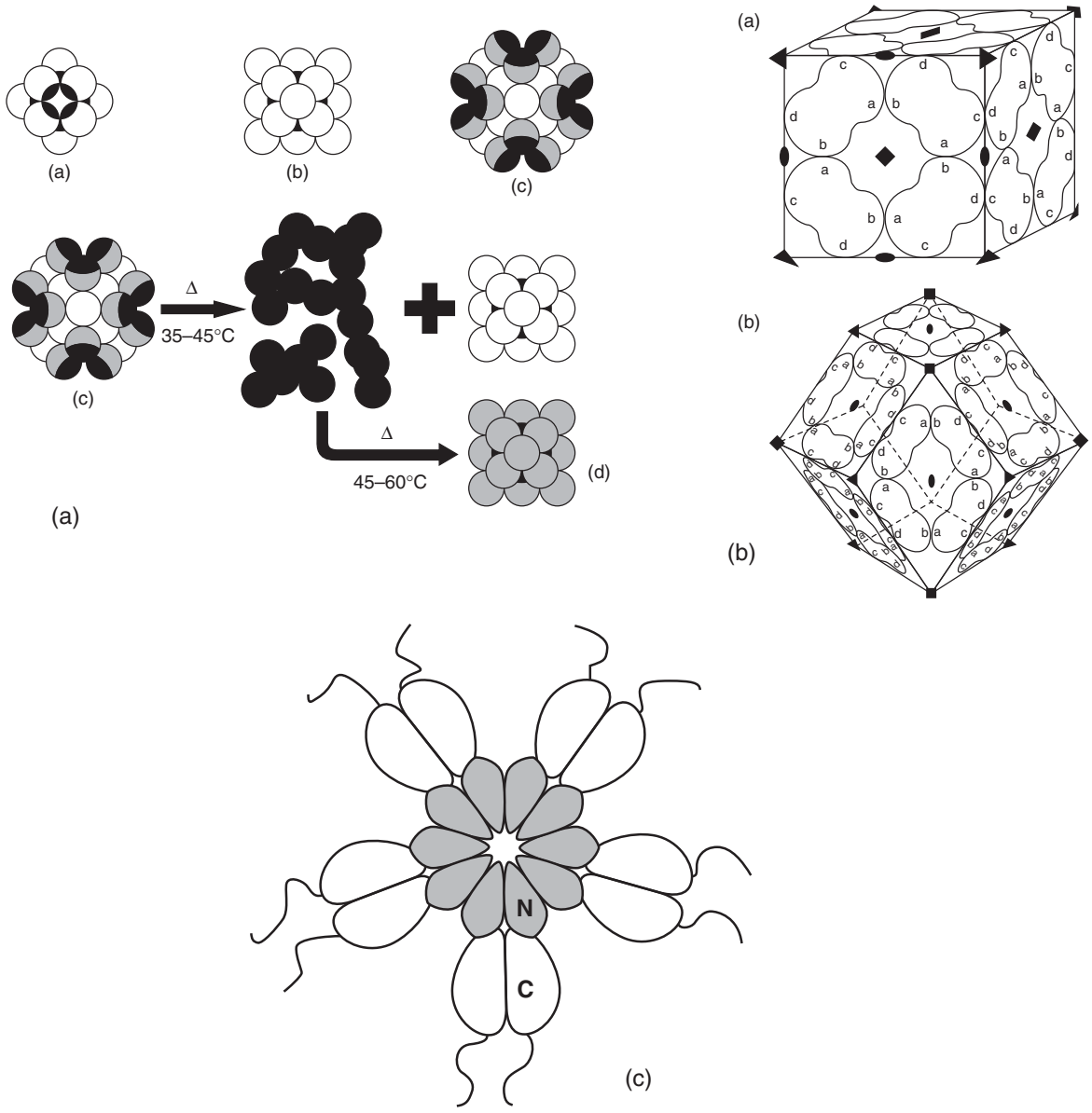


FIGURE 60.1 (a) Schematic representation of the three-layer red micelle model showing thermal transition between the different intermediates. (*a*) First (innermost) layer consists of 12 subunits: cuboctahedron. (*b*) First and second layers constitute a total of 18 subunits: octahedron. (*c*) First, second, and third layers make up a total of 42 subunits: cuboctahedron type. The hydrophobic portion is shown in black. (*d*) A two-layer structure, similar but not identical to that shown in subpart (*b*), found on heating of the original three-layer structure [subpart (*c*)]. (b) A diagrammatic representation of the quaternary structure of α-crystallin, showing the *C* terminal with a peanut shape and four contact points, *a*,*b*,*c*,*d*. Top (*a*) and bottom (*b*) show cubic and rhombic decahedron models, respectively. Symmetry axes are shown with oval (C_2), triangle (C_3), and square (C_4) conformations. (c) Micelle-like pitted–flexiball model for α-crystallin. The α,A- and α,B-crystallin subunits occupy equivalent positions. Each subunit is composed of two domains. The *N*-terminal domains (gray) constitute the center of the complex, while the larger *C*-terminal domains (open) are spaced at the periphery, providing a polar pitted coating around a hydrophobic core. The hydrophilic *C*-terminal extensions flex freely from the surface. Specific interactions between the *C*-terminal domains of the subunits result in the formation of tetrameric building blocks. Hydrophobic interactions between the *N*-terminal domains provide a micelle-like cohesion between the building blocks. The fivefold radial symmetry in this figure is arbitrarily chosen, and the arrangement of tetrameric building blocks may well be less regular than depicted. ((a) Adapted from Walsh et al. 1991 [17], pp. 20079–20084. © American Society for Biochemistry and Molecular Biology; reproduced with permission. (b) Adapted from Wistow 1993 [18], pp. 729–732. © Elsevier. (c) Adapted from Smulders et al. 1998, pp. 187–196. © Elsevier. Parts (b) and (c) reproduced with permission from Elsevier, Inc.)

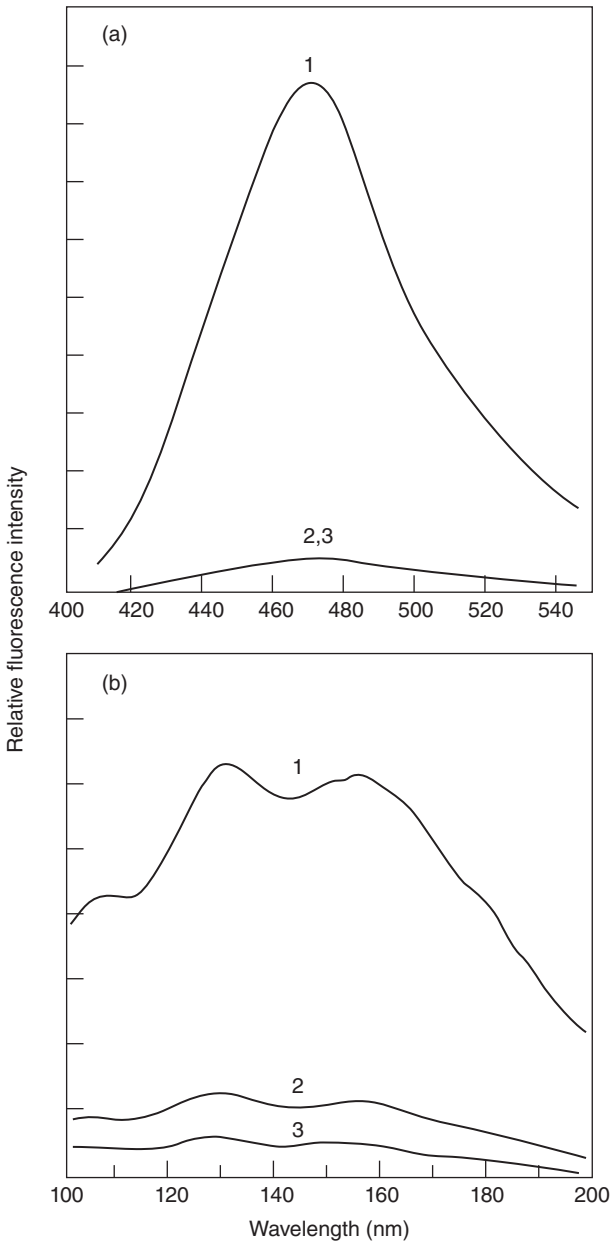


FIGURE 60.2 ANS fluorescence (a) and DPH fluorescence (b) spectra in various α-crystallins: (1) α-crystallin; (2) β-crystallin: (3) γ-crystallin. ANS concentration is 50 μM, and DPH is 7μM; protein concentration is 0.1 mg /mL in ANS measurements and 0.2 mg /mL in DPH measurements. Only α-crystallin shows significantly enhanced ANS and DPH fluorescence and is thus very hydrophobic. (Adapted from Liang and Li 1991 [26], pp. 61–66. © Elsevier, Inc.; reproduced with permission.)

thought. However, mere presence of hydrophobic pockets does not definitively prove the role of hydrophobic interaction in chaperone activity. One report used the hydrophobic fluorophore pyrene and ANS to characterize chaperone function of α-crystallin [27]. Pyerene fluorescence is characterized by a structured emission spectrum consisting of at least five distinct vibrionic bands. A ratio of the first and third vibrionic bands is a marker of microenvironment polarity [28,29]. This ratio increased with increasing temperature showing distinct transitions, suggesting decreased microenvironment polarity arising from more hydrophobic pockets opening up as a result of a temperature-dependent structural transition. The exposure of hydrophobic pockets was also observed with ANS fluorescence increasing with temperature. Interestingly, the chaperone function of α-crystallin as probed by its ability to protect photoaggregation of γ_L- crystallin, increased with temperature. This was for the first time a direct correlation between increased hydrophobocity and enhanced chaperone function, supporting the hypothesis that surface hydrophobic patches are responsible for α-crystallin's chaperone function.

60.5 EFFECT OF TEMPERATURE ON CHAPERONE FUNCTION OF α-CRYSTALLIN

A detailed systematic study of α-crystallin's change in surface hydrophobocity and chaperone function was carried out [30]. In this study, as a marker of hydrophobic patches, bis-ANS was used as the fluorescence probe. ANS, despite being used widely as a marker for hydrophobic pockets, does not bind proteins through hydrophobic interactions alone. It is an anionic small molecule, and electrostatic interactions play a key role in its binding with proteins. On the contrary, bis-ANS, which is a dimer of ANS as it is a much larger molecule, interacts with proteins predominantly through hydrophobic interactions, and charge plays a nominal role; so it possibly is a better marker of hydrophobic pockets in proteins than ANS due to lack of nonspecific electrostatic/charge-driven interaction with proteins. Bis-ANS fluorescence showed a temperature-dependent transition increasing after ~40°C (Fig. 60.3). Interestingly α-crystallin samples preincubated at elevated temperatures and then cooled down still showed greatly increased bis-ANS binding, suggesting an irreversible temperature-induced conformational change that opens up more hydrophobic sites. The chaperone activity of α-crystallin samples assessed by its ability to prevent insulin B-chain aggregation increased with preincubation temperature, with the trend showing a direct correspondence to the bis-ANS fluorescence [30]. This provides conclusive evidence that chaperone activity of α-crystallin primarily involved surface-exposed hydrophobic pockets.

Another team also found similar correspondence between temperature-dependent ANS fluorescence and chaperone activity [31]. Although these temperature-dependent studies of surface hydrophobocity using hydrophobic fluorophore clearly indicated the implication of hydrophobic patches in α-crystallins function, they also raised controversy as to whether thermal activation was required for α-crystallin to become functional. The authors argued that the temperature-dependent structural transition in α-crystallin,

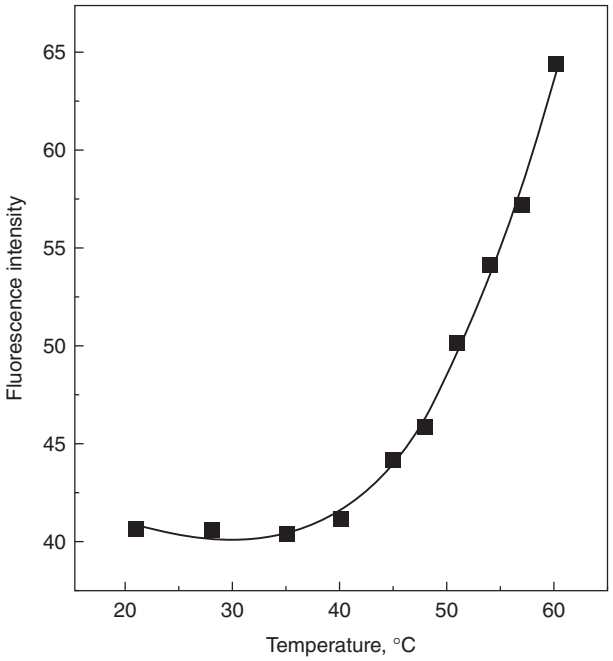


FIGURE 60.3 Fluorescence emission intensity at 22°C of bis-ANS (l 3 μM) in the presence of α-crystallin as a function of preincubation temperature. Samples of α-crystallin (0.06 mg/mL in 50 mM phosphate buffer) were preincubated at different temperatures for 15 min and cooled down to room temperature; bis-ANS (13 μm final concentration) was then added and fluorescence intensity measured at 490 nm at room temperature. (Adapted from Das and Surewicz [30], pp. 321–325. © Elsevier, Inc.; reproduced with permission.)

which exposes more hydrophobic patches, acts as a thermal switch between nonfunctional and functional states, drawing parallels with such structural transition-mediated activation of the classic chaperonin GroEL [31]. However, from a detailed temperature-dependent investigation of α-crystallin's chaperone ability to prevent aggregation of both natural and unnatural substrates, that is, γ_L-crystallin and insulin B chain respectively, it was concluded that even at temperatures well below 30°C, which Raman and Rao suggested as the activation temperature of α-crystallin, its chaperone activity was quite apparent [32]. Nonetheless, its activity increased at elevated temperatures. Hence the current opinion is that α-crystallin does not require a thermal activation for its chaperone function, which prevails even at low temperature, although it increases with temperature as a result of increased hydrophobic exposure.

60.6 IDENTIFICATION OF CHAPERONE SITES OF α-CRYSTALLIN USING HYDROPHOBIC FLUOROPHORES

α-Crystallin's interaction with bis-ANS not only was useful in demonstrating the role of hydrophobic interactions for its function but also led to crucial evidence for the region of the protein involved in binding substrate proteins. An obvious corollary of the correlation of bis-ANS binding with chaperone activity is that the same sites in the protein are responsible for binding bis-ANS and the client proteins. The first experimental evidence of this notion came from the work involving α-crystallin photolabeled with bis-ANS [33]. Bis-ANS under strong UV light forms covalent adducts with proteins. The photolabeled α-crystallin had significantly reduced chaperone function, as one might expect if bis-ANS binds and thus occupies the sites responsible for the chaperone function, impeding the docking of the substrate proteins (Fig. 60.4). On this idea, that same team subsequently developed an approach to identify the sequences involved in client protein recognition [34].The idea was simple; when the client protein-binding sites of α-crystallin are occupied by bis-ANS, photolabeling will fix the fluorophore to the binding site. Identification of the peptides containing the fluorophore after proteolysis will lead to the identification of the binding region. Figure 60.4 also shows the SDS, which demonstrates that the photolabeling is reduced after substrate binding. Using this approach, two peptide fragments in α,A crystallin lying in the *N*-terminal and α-crystallin domain and one fragment in α,B-crystallin from the α-crystallin domain were identified that contained the client protein-binding site. This investigation supplemented and confirmed previous notions about the identity of the chaperone actie sites [35].

60.7 SUBSTRATE CONFORMATION RECOGNIZED BY α-CRYSTALLIN: COMPARISON WITH OTHER CHAPERONES

With α-crystallin's role as a chaperone established and having obtained some insights into the structural basis of its function, it was crucial to compare α-crystallin's molecular recognition with other known sHSP members and classical chaperones such as GroEL/GroES. Hence, it was essential to identify conformational states of client proteins recognized by α-crystallin. For DnaJ and GroEL, intrinsic tryptophan fluorescence of the client proteins was used to characterize their conformation [36–38]. This was possible because DnaJ and GroEL did not have any tryptophan residues. However, α-crystallin had a single tryptophan residue, and its fluorescence overlapped with those of the substrate proteins posing problems. One team of investigators circumvented this problem by using tryptophan-free mutant W9F of α-crystallin, which was structurally and functionally very similar to the wild-type protein [39]. Tryptophan fluorescence of the substrates γ_L- crystallin and rhodanase was used to assess their structure after forming complexation with α-crystallin by heat treatment (Fig. 60.5). Tryptophan emission is a good marker of solvent polarity arising from the polarity-sensitive

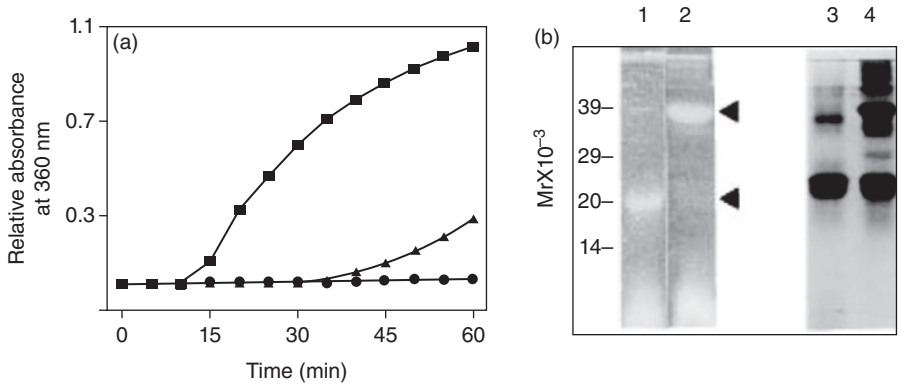


FIGURE 60.4 (a) Effect of bis-ANS binding on chaperonelike activity of α-crystallin. The assays were monitoring heat-induced aggregation of ADH and its suppression by α-crystallin, using apparent absorbance at 360 nm as a probe. [(■) ADH; (•) ADH + 25 μg of α-crystallin; (▲) ADH+ 25 μg bis-ANS- α-crystallin.] (b) Bis-ANS labeling of α-crystallin in the presence and absence of alcohol dehydrogenase. Lanes 1 and 3, bis-ANS + α-crystallin after photolysis; lanes 2 and 4, α-crystallin + ADH + bis-ANS after photolysis. Bis-ANS was added to sample in lanes 2 and 4 after 1-h incubation of the proteins at 48°C. The 20- and 39-kDa bands in lanes 1 and 2 are bis-ANS-labeled α-crystallin and ADH, respectively. (Adapted from Sharma et al. 1998 [33], pp. 8965–8970 and [34], pp. 15474–15478. © American Society for Biochemistry and Molecular Biology; reproduced with permission.)

fluorescence of the indole moiety. As a protein gets structurally compromised/unfolded, its core becomes progressively solvated, and this is reflected in the redshift of its tryptophan emission. Both rhodanase and γ_L- crystallin in complex with α-crystallin showed very little redshift of emission maxima from that of their native states. The denatured protein in presence of 6 M GdnHCl, however, showed significant redshifts due to full exposure of the tryptophan to the solvent, indicating complete collapse of structure. Stern–Volmer quenching plots with soluble quenchers acrylamide and iodide is another way to assess solvent accessibility of a fluorophore; from the parameter Stern–Volmer constant (K_{sv}) that increases with greater exposure to solvent. The K_{sv} values for the proteins bound to α-crystallin showed nominal increase from those of the native values when compared to the enhancement of K_{sv} value for the denatured protein. This reconfirmed that α-crystallin recognizes substrate conformers with core solvation very much like that in the native. Further experiments with bis-ANS indicated hydrophobic patches to be present on the α-crystallin-bound client protein. Another interesting observation was that the fluorescence of the α-crystallin-bound proteins remained unchanged even at high temperatures, much higher than temperatures at which the proteins unfold, suggesting remarkable stability of the protein/α-crystallin complex. Such mechanism of chaperone action is very different from GroEL/GroES system. *First*, the GroEL recognizes more extended/unfolded conformers of proteins while the α-crystallin identifies and binds the compact early unfolding intermediates with some hydrophobic surface pockets; this was demonstrated by a 10-nm redshift of rhodanese emission bound to GroEL compared to the native state [36,39]. In contrast, the redshift for rhodanese bound to α-crystallin is only 5 nm. *Second*, the GroEL/ GroES system involves three distinct steps of substrate protein binding, refolding, and release coupled with nucleotide hydrolysis, while after arresting early unfolding intermediates α-crystallin forms very stable complexes and does not release them [40]. This may have enormous implication in a cellular scenario, where GroEL/ GroES may be employed to initiate functional recovery of structurally compromised proteins while α-crystallin might arrest aggregation prone early unfolding conformers forming stable soluble complexes and maintains transparency of the refractive media.

Another key aspect of α-crystallin's chaperone function was its attenuation by nucleotide binding and the exact role of nucleotide in this process. ATP had been known to interact with α-crystallin from previous NMR studies [41]. However, one team had extended those reports by investigating the ATP binding through intrinsic fluorescence quenching studies [42]. The disassociation constant was in the millimolar molar range; nevertheless, despite such weak binding, ATP α-crystallin interaction is very crucial considering that lens ATP concentration may go up to 6 mM [43]. More recently it was shown that α,B-crystallin has a putative ATP binding sequence, and the binding was confirmed with by FRET between a fluorescent analog of ATP and covalently attached external fluorophor eosin to the thiol of a cysteine introduced by mutation of α,B-crystallin (Fig. 60.6) [44]. For the GroEL/GroES system, ATP hydrolysis is a key step for its function. However, whether α-crystallin

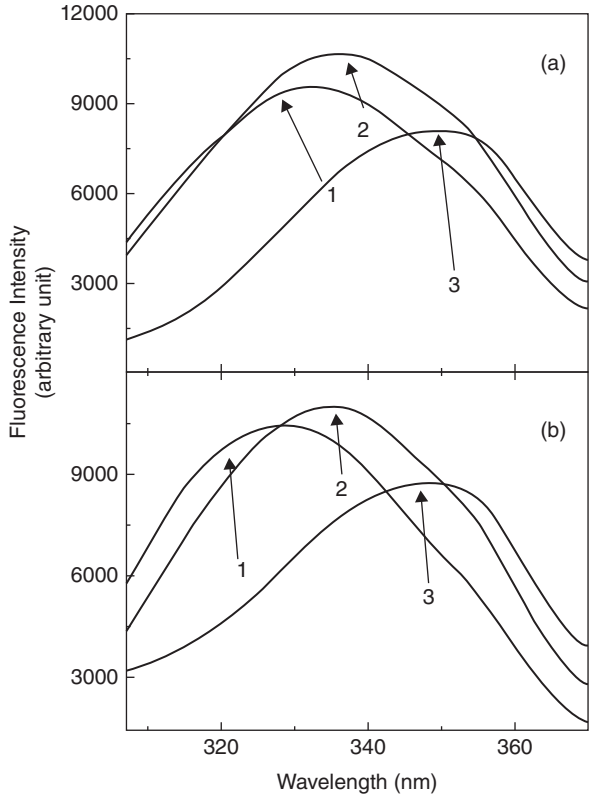


FIGURE 60.5 Fluorescence emission spectra of rhodanese (a) and γ-crystallin (b). Curve point 1, native protein; curve point 2, protein bound to W9F α,A-crystallin; curve point 3, protein unfolded in 6 M guanidine HCl. Spectra were recorded at 25°C. (Adapted from Das et al. 1996 [39], pp.10449–10452. © American Society for Biochemistry and Molecular Biology; reproduced with permission.)

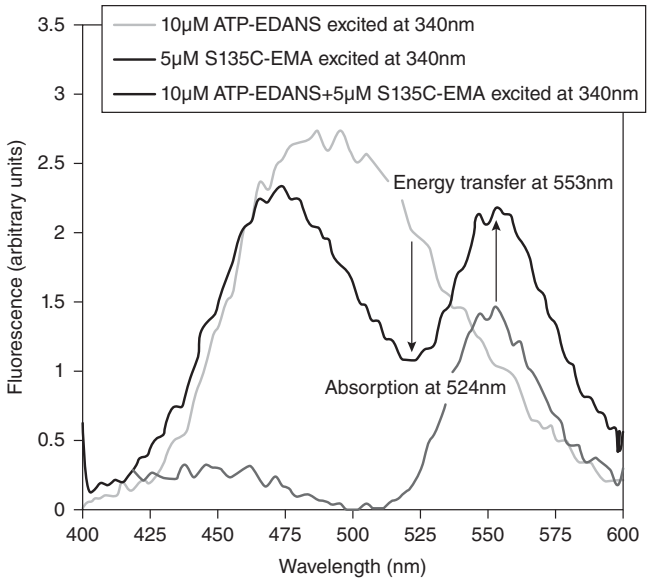


FIGURE 60.6 FRET analysis of interactions between fluorescent ATP analog azido-ATP-EDANS and the α,B-crystallin β8 mutant S135C-EMA. In the absence of an acceptor molecule, azido-ATP-EDANS had an emission maximum at 487 nm when excited at 340 nm (thick gray line). In the absence of a donor molecule, the fluorescent acceptor S135C-EMA had an emission maximum at 553 nm when excited at 340 nm (thin black line). When S135C-EMA was added to the solution containing the fluorescent donor azido-ATP-EDANS (thick black line), the emission of azido-ATP-EDANS at 524 nm decreased by 44% and the emission of the fluorescent acceptor, S135C-EMA at 553 nm, increased by ∼50%. The decrease in the emission fluorescence of the donor at 524 nm was due to energy transfer to the acceptor S135C-EMA, indicating close proximity of the donor and acceptor molecules. (Adapted from Ghosh et al. 2006 [44], pp. 364–375. © Elsevier, Inc.; reproduced with permission.)

has ATPase function remains controversial. Another group reported autokinase activity of α-crystallin [48]; however, other groups failed to find ATPase activity [14]. Hence the key questions involving ATP-α-crystallin interaction were the mechanism of α-crystallin's chaperone function after ATP binding and whether ATP hydrolysis is needed for the enhancement of its chaperone activity. In a study by our group we attempted to resolve these enigma [49]. We hypothesized that since α-crystallin's chaperone function arises from its hydrophobic pockets, its enhancement of chaperone function must be associated with increase in the number of hydrophobic pockets or better access to these hydrophobic pockets [49]. We found that bis-ANS fluorescence increased on interaction of ATP and α-crystallin. Further investigation of the binding parameters from fluorescence titration showed decreased disassociation constant for the binding, suggesting that α-crystallin has increased affinity for bis-ANS in presence of ATP (Fig. 60.7) [49]. We then used ATP, a nonhydrozable ATPγS analog, and the increased chaperone activity of α-crystallin was still reproduced in presence of ATP or ATPγS. Moreover, ATPγS, just like ATP, augmented α-crystallin's affinity for bis-ANS. Hence it was unambiguous demonstration that ATP played a structural or precisely an allosteric role in enhancing α-crystallin's chaperone function. It allosterically [49] promotes substrate interaction by increasing α-crystallin's affinity for protein substrates. Such role of a nucleotide as an allosteric modulator ligand in chaperone function was novel and distinctly different from GroEL/GroES chaperone systems. While the ATPase activity of α-crystallin still remains a controversy, our study was able to prove conclusively that ATP hydrolysis is not needed for enhancing α-crystallin's chaperone function [49].

60.8 SUBUNIT EXCHANGE OF α-CRYSTALLIN AND ITS DIVERSE ROLE

While discussing the preliminary models, we showed how the subunits in the oligomeric assembly of α-crystallin

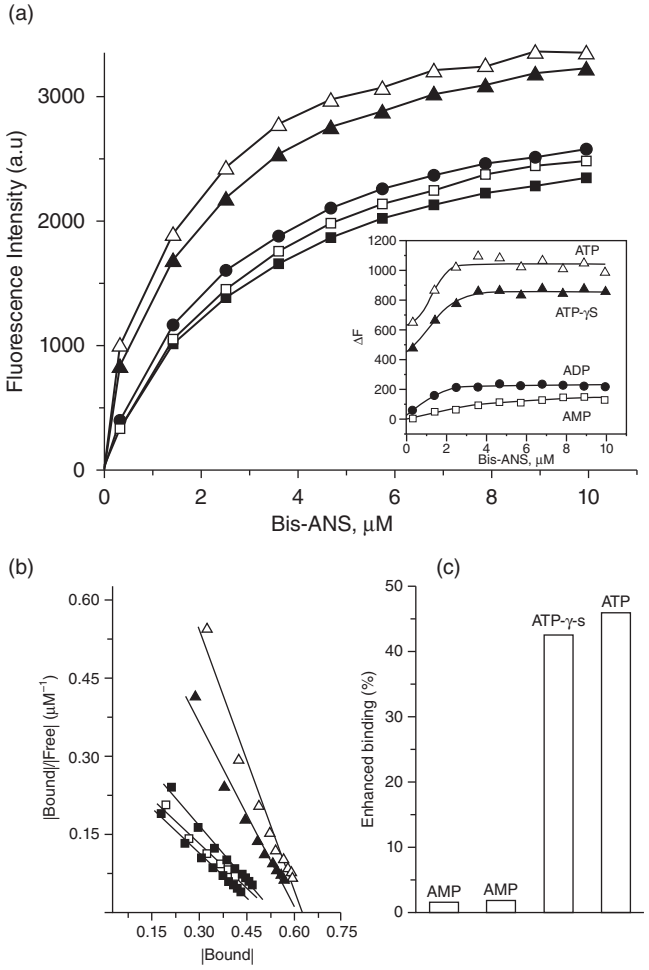


FIGURE 60.7 Effect of adenosine mono-, di-, and triphosphates on the bis-ANS binding to bovine α_L-crystallin and enhanced binding of γ-crystallin with α_L-crystallin at 37°C. (a) Bis-ANS fluorescence intensity as functions of bis-ANS concentration in the absence (■) and presence of 3 mM each of AMP (□), ADP (•), ATPγS (▲), and ATP (△). Inset shows increase in fluorescence intensity (ΔF) due to the addition of nucleotides as functions of bis-ANS concentration. (b) Scatchard plot for determination of the bis-ANS-binding parameters. (c) Binding enhancement of γ-crystallin to α_L-crystallin in presence of various nucleotides (3 mM).The data clearly show that ATPγS and ATP produce nearly equal enhancement of bis-ANS binding. (Adapted from Biswas and Das 2004 [49], pp. 42648–42657. © American Society for Biochemistry and Molecular Biology; reproduced with permission.)

appeared to be equivalent. This had two possible interpretations; either α-crystallin has a geometric arrangement where all the subunits had equivalent local symmetry or it has a dynamic oligomeric assembly. From structural perspectives the second idea seemed to be more viable. Experimental evidences of interaction between α-crystallin subunits and exchange between reconstituted α,A-crystallin and α B oligomers using gel-based assays were available [50]. However, since these studies used α-crystallin purified using denaturation renaturation cycles, the structural integrity of the protein was questionable. Another team showed in a 1994 paper that using a direct FRET-based approach provided the strongest experimental evidence in favor of subunit exchange [51]. They labeled two aliquots of α,A-crystallin with thiol reactive fluorophores AIAS (4-acetamido-4′-[(iodoacetyl)amino] stilbene-2,2′disulfonic acid) and LYI (Lucifer yellow iodoacetamide), which were good FRET donor–acceptor pairs [51]. When these two aliquots were mixed, a FRET signal was increased exponentially before it was saturated (Fig. 60.8). It is well known that FRET can occur only when the donor–acceptor pairs are in close proximity as the efficiency of FRET falls off with sixth power of distance. Hence, FRET in this case of α-crystallin labeled with AIAS and LYI is possible only when the donor and acceptor are located within the same oligomer via subunit exchange process. The FRET signal was saturated when all the hybrid oligomers formed had equal proportions of donor- and acceptor-labeled subunits. The change in FRET signal was described by a simple exponential model, and hence kinetic parameters such as first-order rate constant were deduced (Fig. 60.8) [51]. α-Crystallin showed marked increase in exchange kinetics with temperature, and this was used to evaluate the activation energy of the process by construction of Arrhenius plots. Dependence of subunit exchange kinetics with increasing ionic strength was also reported, suggesting the role of both hydrophobic and polar residues [51].

However, the role of subunit exchange in α-crystallin function was quite diverse. Several reports correlated subunit exchange kinetics with its chaperone function, and such studies were used to decipher several aspects of the α-crystallin biochemistry, including variation of its function in cataract causing or phosphorylation mimicking α-crystallin mutants [52, 53]. A reasonable way to interpret this correlation is to consider the equivalence of all the α-crystallin subunits despite the fact that all of them do not have the same local symmetry because of the subunit exchange. Thus, if the oligomers were static, all the subunits could not have interacted favorably with the client proteins, due to geometric restraints. Since the oligomers are dynamic, it is thus reasonable to assume that the oligomer substrate disassociation either is irreversible or occurs on a slower timescale than subunit exchange. Subunits bound to a client protein might exchange position with an unbound subunit that was previously in a position where substrate interaction was not favorable. This process will continue until all subunits associate with the client proteins, when the subunit and client protein stiochiometry become the limiting factor. Hence any change that impedes subunit exchange would decrease chaperone function. α-Crystallin is extremely efficient in suppressing aggregation of its natural substrates such as other members of the α-crystallin family, including β- and γ-crystallins. Based

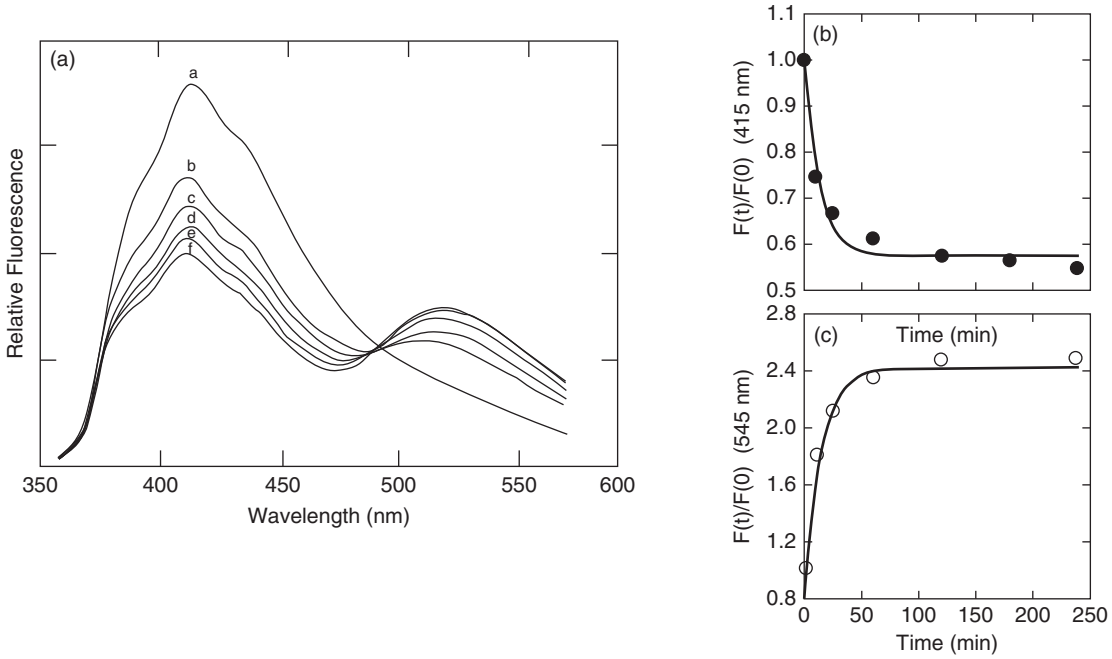


FIGURE 60.8 (a) Time-dependent changes in emission spectrum of AIAS-labeled α,A-crystallin due to subunit exchange. The emission spectra of α,A-crystallin excited at 335 nm were recorded at times equal to 0 (*a*), 10 (*b*), 25 (*c*), 60 (*d*), 120 (*e*), and 240 min (*f*) after mixing an equal amount of AIAS-labeled and LYI-labeled α,A-crystallin at 37°C. The decrease in fluorescence intensity at 415 nm of AIAS-labeled α,A-crystallin and the concomitant increase in fluorescence intensity at 525 nm of LYI-labeled α,A-crystallin are indicative of energy transfer due to subunit exchange of subunits between the two labeled populations. (b,c) Time-dependent changes in emission intensity due to subunit exchange. (b) Decrease in relative fluorescence intensity at 415 nm as a function of time after mixing an equal amount of AIAS-labeled and LYI-labeled α,A-crystallin. (c) Increase in relative fluorescence intensity at 545 nm due to fluorescence resonance energy transfer from AIAS-labeled α,A-crystallin to LYI-labeled α,A-crystallin. The *curves* represent the best statistical fit of the data to the exponential function $F(t) = C_1 + C_2\, e\, -kt$. The rate constants determined by curve fitting were 0.075 min^{-1} for data shown in (b) and 0.069 min^{-1} for data shown in (c). (Adapted from Bova et al. 1997 [51], pp. 29511–29517. © American Society for Biochemistry and Molecular Biology; reproduced with permission.)

on the idea that slow subunit exchange is associated with poorer chaperone function, we investigated the possibility of whether there is any preferential recognition of natural substrates over nonnatural substrates by α-crystallin and what role, if any, subunit exchange has in it [54]. Subunit exchange kinetics and the associated activation energy barrier, for α-crystallin bound to both natural and unnatural substrates, were measured (Fig. 60.9). We found that α-crystallin has a striking preference for natural substrates over nonnatural substrates such as ADH [54]. Interestingly, increased retardation of subunit exchange and higher activation energy in α-crystallin bound to nonnatural substrates compared to α-crystallin bound to natural substrates was also observed [54]. We rationalized this observation by taking into account the secondary structure propensities of the client proteins. While the natural substrates were all β-sheet major proteins, the unnatural substrate used had mainly helical structure. It is possible that for α-crystallin subunit bound with α-helical protein it is less favorable to undergo subunit exchange than for a subunit bound with β-sheet proteins. To get an in depth understanding of α-crystallin's substrate discrimination, detailed studies with several client proteins having different secondary structure need to be performed. Subunit exchange also helped us deduce a noncanonical mode of zinc ion binding by α-crystallin [55]. In an earlier study, we observed that α-crystallin bound to zinc ions with micromolar affinity and enhanced the chaperone function by increasing the number of hydrophobic patches [56]. Considering that α-crystallin does not have any putative zinc finger sequence, in a subsequent study we investigated the mode of this interaction [55]. MALDI and DLS data pointed toward the possibility of intersubunit bridging by zinc ions. Our hypothesis was confirmed when we found that zinc binding almost completely halted subunit exchange, as this

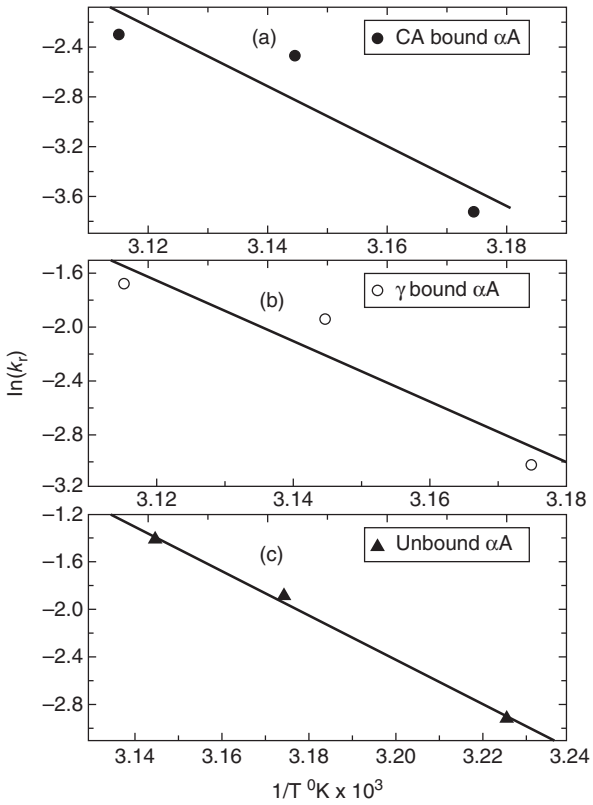


FIGURE 60.9 Determination of activation energy of subunit exchange of α,A-crystallin in absence and presence of different bound substrates. Arrhenius plot of the subunit exchange reaction of native α,A-crystallin (a), γ-crystallin-bound α,A-crystallin (b), and CA-bound α,A-crystallin (c). The complex was allowed to form by incubating different concentrations separately of each substrate protein with both 0.4 mg/mL AIAS-tagged and LYI-tagged α,A-crystallin at 65°C for 1 h. The solutions were cooled back to 25°C for 1 h. Then, equal amounts of AIAS-labeled and LYI-labeled α,A-crystallin were mixed containing the bound substrate, and the subunit exchange rate was measured at 42°C, 45°C, and 48°C, respectively. The rate constants at respective temperature were obtained by $\ln(k_r) = \ln A - E_a/RT$. The activation energy (E_a) was determined from the slope. (Adapted from Biswas et al. 2007 [54], pp. 189–197. © John Wiley & Sons. Inc.; reproduced with permission.)

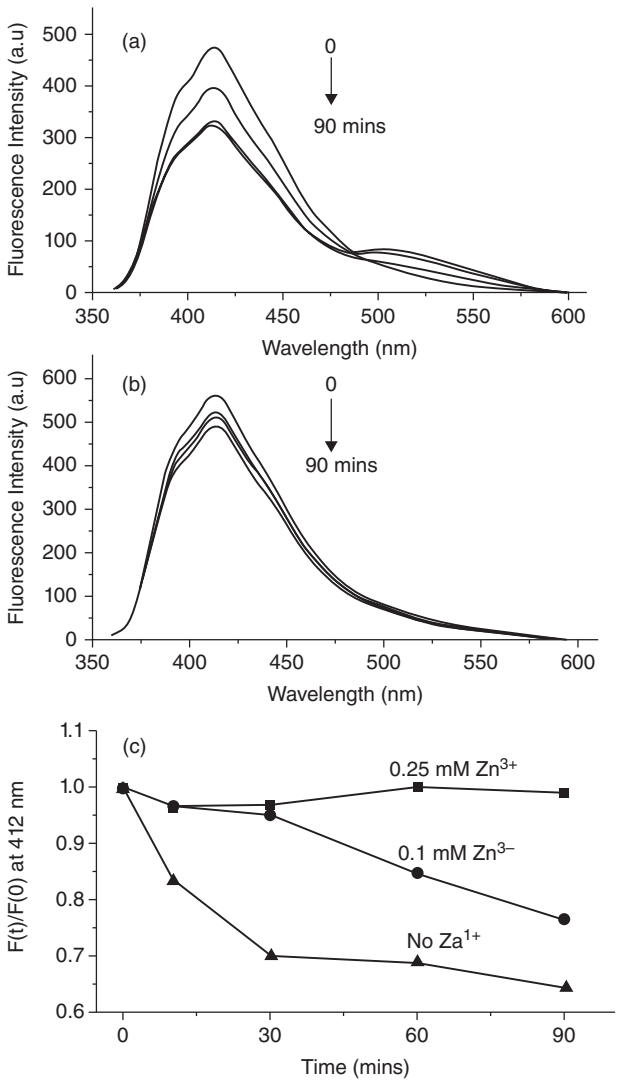


FIGURE 60.10 Effect of Zn^{2+} ions on subunit exchange of α,A-crystallin. Time-dependent changes in emission spectrum of LYI- and AIAS-tagged α,A-crystallin in absence (a) and presence (b) of 100 μM Zn^{2+}. After mixing equal volume of the LYI- and AIAS-tagged α,A-crystallin at 37°C in absence and presence of 100 μM Zn^{+2}, the emission spectra were measured at different times: 0 min, 10 min, 30 min, 60 min and 90 min. Fluorescence spectra were recorded between 360 and 600 nm after 100-fold dilution, using 335 nm as excitation wavelength. (c) Relative changes in the fluorescence intensity at 412 nm as a function of time for different Zn^{2+} concentrations: (▲) no Zn^{2+}; (•) 100 μM Zn^{2+}; (■) 250 μM Zn^{2+}. (Adapted from Karmakar and Das 2011 [55], pp. 105–116. © John Wiley & Sons. Inc.; reproduced with permission.)

could be rationalized only if the subunits were cross-linked by zinc (Fig. 60.10). The fact that zinc binding enhanced the chaperone activity while decreasing su-unit exchange may seem contrary to our previous discussion; however, this apparently anomalous exception can be explained by exposure of additional hydrophobic pockets that compensates the loss of chaperone activity from hindered subunit exchange.

60.9 OLIGOMERIC ASSEMBLY AND UNFOLDING OF α-CRYSTALLIN

In this last section we will focus on two very recent studies by our group that shed some light on the stability of the oligomer and unfolding properties of α-crystallin [58, 59]. Several attempts had been made to disrupt α-crystallin's oligomerization using small molecules, surfactants, or chemical modifications [60–62]. A key question was whether α-crystallin's oligomerization was necessary for function. Another team reported that sodium deoxycholate, a bile salt and mild

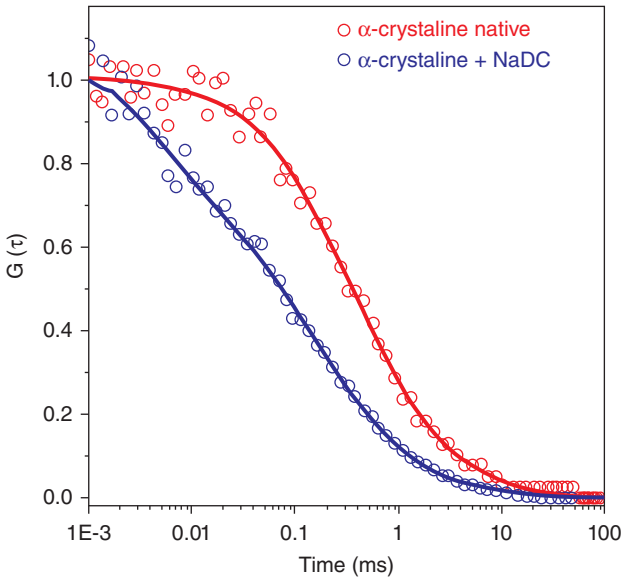


FIGURE 60.11 Normalized autocorrelation functions of acrylodan-α,A-crystallin system in the absence (red) and presence (blue) of 1 wt% NaDC. Actual autocorrelation curves are shown in the inset.The quicker decay of the correlation function and the increase in the number of particles all suggested tetramerization. (Adapted from Chowdhury et al. 2012 [58], p. 155101. © American Institute of Physicists; reproduced with permission.)

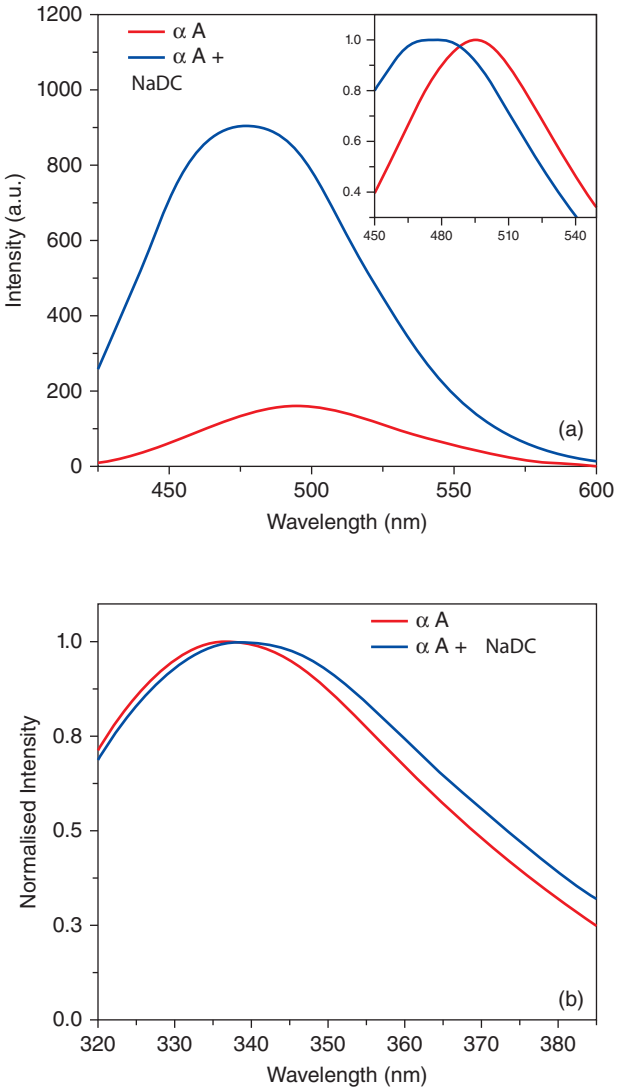


FIGURE 60.12 (a) Emission spectra (at λ_{ex} = 405 nm) of acrylodan-labeled α,A-crystallin (~10 μM)-labeled protein in 50 mM Tris-HCl, pH 7.4) in native state (red) and in presence of NaDC (blue). The inset represents intensity normalized emission. The blueshift in emission shows that the α-crystallin domain is buried in presence of deoxycholate. (b) Normalized tryptophan emission spectra (at λ_{ex} = 295 nm) of α,A-crystallin in native state (red) and in presence of NaDC (blue). The protein (20 μM) was in 50 mM Tris-HCl, pH 7.4. The redshift in emission shows that the *N*-terminal domain is exposed in presence of deoxycholate. (Adapted from Chowdhury et al. 2012 [58], p. 155101. © American Institute of Physicists; reproduced with permission.)

surfactant, formed α-crystallin tetramers that showed increased autophosphorylation [63]. We confirmed the tetramerization using fluorescence correlation spectroscopy of α-crystallin labeled with acrylodan (Fig. 60.11) [58]. Using site-selective fluorescence studies, we demonstrated that the *N*-terminal domain gets exposed while the α-crystallin domain gets buried [58] (Fig. 60.12). We also showed, using ultrafast fluorescence of acrylodan, that solvation dynamics at the α-crystallin domain was slowed (or retarded) (Fig. 60.13). Exposure of the *N*-terminal domain explains why the tetrameraization as *N* terminal is known to promote higher-level oligomerization of smaller building blocks such as dimmers. We could also explain the phosphorylation pattern in presence of deoxycholate in terms of the region-specific conformation changes that we had observed without the need to account for the change in quaternary structure, suggesting that the increased phosphorylation was due largely to the subtle conformation change than tetramerization itself [58].

Another key question about α-crystallin is how it unfolds from such a massive structured architecture and the mechanism of breakdown at different levels of its structure, that is, secondary, tertiary, and quaternary elements. Previous studies showed that during unfolding α-crystallin passes through several intermediates along with incremental dissolution of oligomeric structure [64–68]. However, the steps of oligomer breakdown and the oligomeric status of the intermediates were unknown. We attempted to observe the effects of minimal perturbation of structure using a low concentration of denaturant leading to partial dissociation of the subunit assembly [59]. A detailed fluorescence study exploiting intrinsic tryptophan and extrinsic polarity probe acrylodan showed a degree of core solvation comparable to

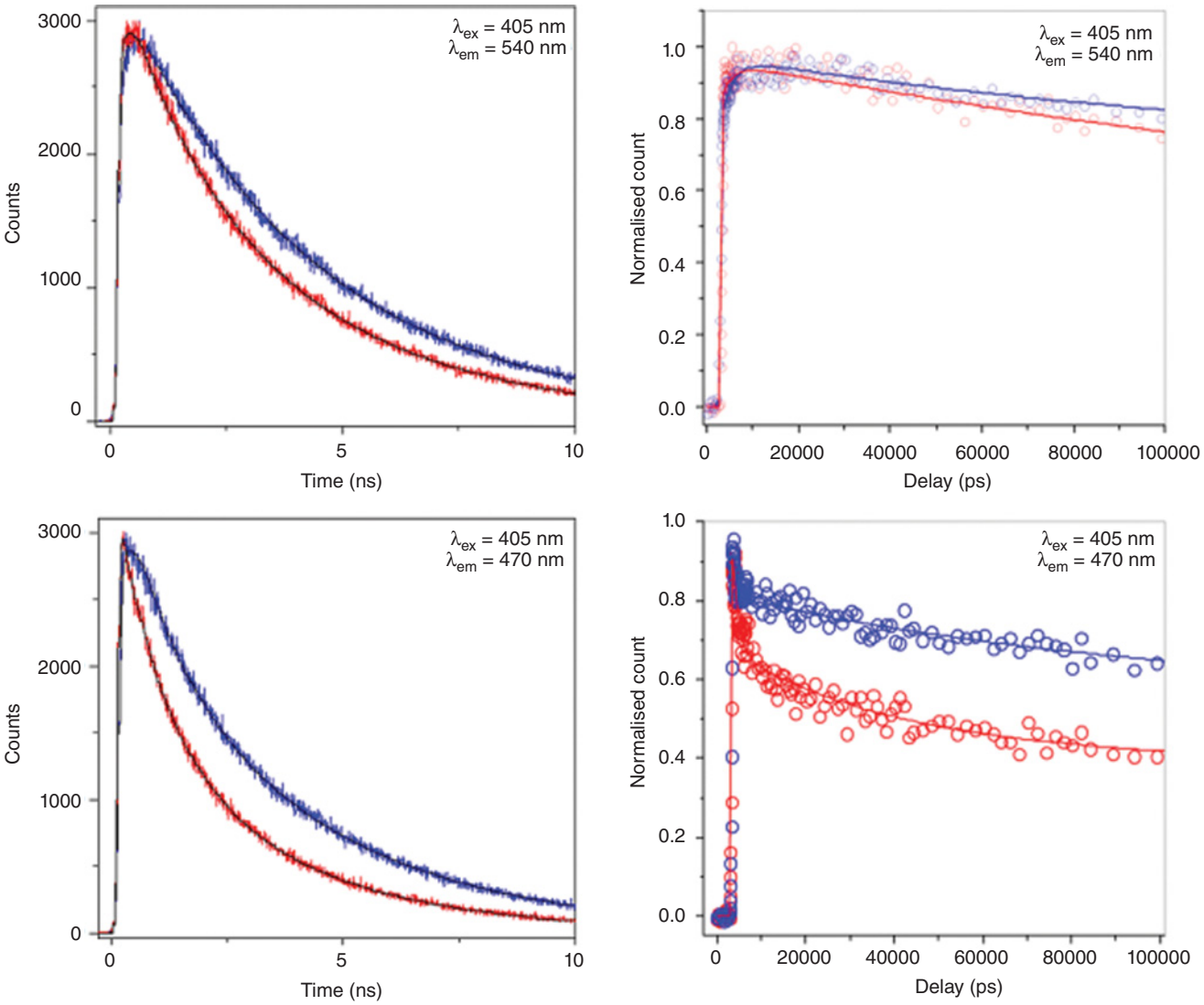


FIGURE 60.13 Left column: Picosecond transients of acrylodan -αA-crystallin system (at λ_{ex}= 405 nm) in the absence and presence of NaDC at λ_{em} = 540 nm (upper panel) and λ_{em} = 470 nm (lower panel). Right column: Femtosecond transients of acrylodan–α,A-crystallin system (at λ_{ex} = 405 nm) in the absence and presence of NaDC at (a) λ_{em} = 540 nm (upper panel) and (b) λ_{em} = 470 nm (lower panel). In all four panels, the lower and upper curves correspond to native alpha crystallin in absence and presence of NaDC respectively. The ultrafast data show that fluorescence relaxation kinetics of acrylodan is slowed in presence of deoxycholate, suggesting slower solvation. (Adapted from Chowdhury et al. 2012 [58], p. 155101. © American Institute of Physicists; reproduced with permission.)

the native state, initially leading us to assume there is no structural breakdown at such low denaturant concentration as we had expected (Fig. 60.14). However, a bis-ANS fluorescence study showed a small but reproducible increase of fluorescence at this low denaturant concentration (Fig. 60.15) [59]. We also witnessed acceleration of subunit exchange [59], which was interpreted as a significant loss of tertiary structure. To our surprise, we also found that this intermediate state had unperturbed oligomerization [59]. A structural intermediate having such extensive oligomerization formed during unfolding had not been known before to the best of our knowledge. The identification of this intermediate was possible because of the extremely high sensitivity of bis-ANS fluorescence as this transition was silent to most of the other biophysical probes. We also identified another intermediate, which showed significant secondary structure loss and was formed at higher denaturation concentration and retained about two-thirds of its oligomeric size.

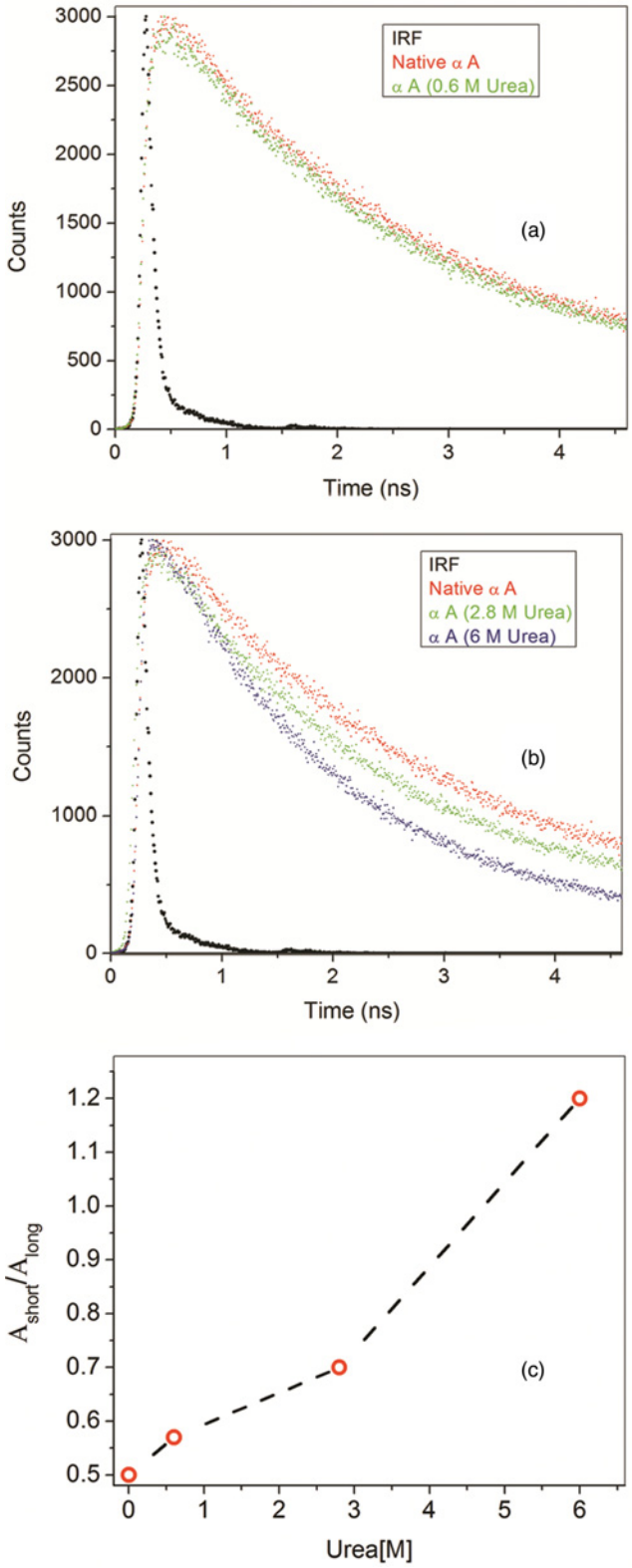


FIGURE 60.14 (a) Picosecond-resolved transients of acrylodan-labeled α-crystallin (at $\lambda_{ex} = 405$ nm) in native state (red) and in presence of 0.6 M urea (green) at 510 nm; (b) picosecond-resolved transients of acrylodan-labeled α-crystallin (at $\lambda_{ex} = 405$ nm) in native state (red) and in presence of 2.8 M urea (green) and 6 M urea (red) at 510 nm; (c) ratio of relative contributions (α) of the short (picosecond) and long (nanosecond) components of the transients; used as a marker of solvation. The time-resolved data show that in 0.6 M urea crystallin is as solvated as the native, suggesting minimal structure loss. (Adapted from Chowdhury et al. 2014 [59], pp. 549–560. © John Wiley & Sons, Inc.; reproduced with permission.)

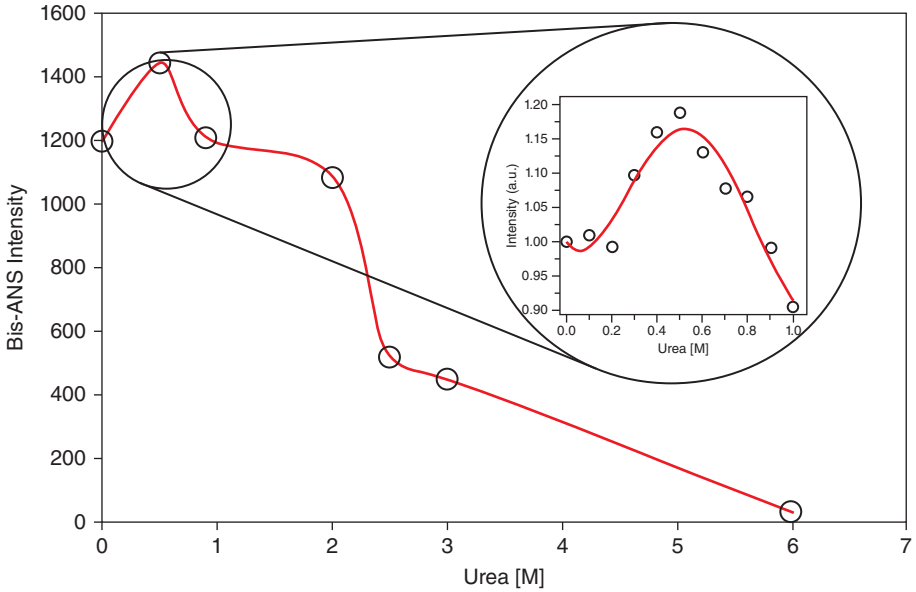


FIGURE 60.15 Bis-ANS fluorescence of α,A-crystallin at various denaturant concentrations. Inset shows bis-ANS binding at denaturant concentrations from 0 to 1 M. Data points were fitted to a polynomial. The increased fluorescence around 0.6 M indicates presence of an intermediate. (Adapted from Chowdhury et al. 2014 [59], pp. 549–560. © John Wiley & Sons, Inc.; reproduced with permission.)

α-Crystallin's unfolding was clearly a case of nonhierarchical structure loss where tertiary structure loss preceded oligomer breakdown. From this we also concluded that the α-crystallin oligomeric structure is very robust and this can be justified considering the several layers of interactions that are responsible for oilgomerization in α-crystallin (Fig. 60.16). An implication of this is that oligomer formation may be a rather early folding event for α-crystallin where an amphiphile-like interaction drives the self -ssembly that propagates folding. However, this needs to be confirmed by experimentation.

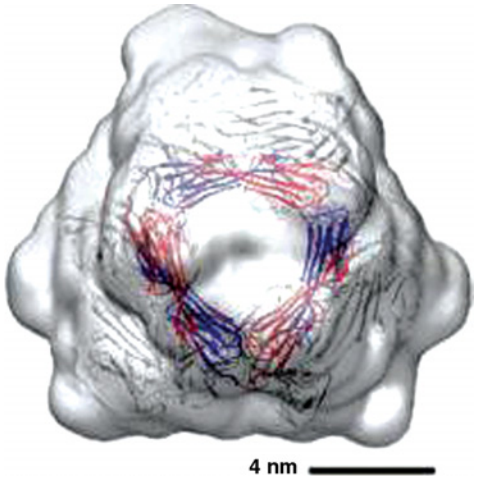


FIGURE 60.16 A model of 24mer α,B-crystallin. α-Crystallin dimer, (red and blue) fitted into the volumetric map of the SAXS data. This figure clearly shows the existence of dimeric building blocks. The oligomer is formed by *N*-terminal domain interaction of these building blocks. (Adapted from Jehle et al. 2010 [20], pp. 1037–1042. © Macmillan Publishers; reproduced with permission.)

60.10 SUMMARY AND CONCLUSIONS

Fluorescence-based techniques can provide useful structural information on proteins. In this chapter we have demonstrated how such techniques have been utilized to derive detailed structural and functional insight into a large oligomeric protein α-crystallin having micelle-like architecture. Using extrinsic hydrophobic probes, the surface hydrophobicity of α-crystallin was characterized. Temperature-dependent chaperone activity was correlated with exposure of surface hydrophobic pockets of α-crystallin. Covalent photolabeling of extrinsic fluorophore helped identify the client protein binding site on the surface of α-crystallin. Use of tryptophan-free mutant of α-crystallin helped us identify the conformation of substrate proteins recognized by α-crystallin. It has been shown that α-crystallin recognizes early folding intermediates of client proteins compared to extended conformation of the substrate proteins by other chaperone such as GroEL. Sununit exchange in α-crystallin could be demonstrated by covalently labeling α-crystallin separetly with fluorescent donor-acceptor pair, mixing them together, and following the FRET. Such FRET

studies have led to crucial understanding of the mechanism of discrimination between natural and nonnatural substrates by α-crystallin. Subunit exchange studies also provided important evidence of intersubunit bridging by Zn^{2+} ions. Using fluorescence correlation spectroscopy, site-selective fluorescence labeling, and ultrafast fluorescence decay, we were able to throw light on the mechanism of hyperphosphorylation of α-crystallin in its tetrameric form in presence of Na-deoxycholate. We were also able to identify crucial structural intermediates, one with compromised tertiary structure retaining full oligomeric assembly at low denaturant concentration and one with compromised secondary, tertiary, and quaternary structure at higher denaturant concentration. The study revealed that in the course of unfolding of α-crystallin, various levels of organization do not lose their structure in hierarchical order.

REFERENCES

[1] van der Ouderaa, F.M., de Jong, W.W., Bloemendal, H. (1973). *Eur. J. Biochem.* **39**, 207–222.

[2] de Jong, W.W., Terwindt, E.C., Bloemendal, H. (1975). *FEBS Lett.* **58**, 310–313.

[3] Kramps, J.A., de Man, B.M., de Jong, W.W. (1977). *FEBS Lett.* **74**, 82–84.

[4] Horwitz, J. (2009). *Exp. Eye Res.* **88**, 190–194.

[5] Horwitz, J., Bova, M.P., Ding, L., Haley, D.A., Stewart, P.L. (1999). *Eye* **13**, 403–408.

[6] Peschek, J., Braun, N., Franzmann, T.M., Georgalis, Y., Haslbeck, M., Weinkauf, S., Buchner, J. (2009). *Proc. Natl. Acad. Sci. USA* **106**, 13272–13277.

[7] Srinivasan, A.N., Nagineni, C.N., Bhat, S.P. (1992). *J. Biol. Chem.* **267**, 23337–23341.

[8] Iwaki, T., Kume-Iwaki, A., Liem, R.K.H., Goldman, J.E. (1989). *Cell* **57**, 71–78.

[9] Derham, B.K., Harding, J.J. (1999). *Progress Retinal Eye Res.* **18**, 463–509.

[10] Lakowicz, J. (ed.) (2006). *Principles of Fluorescence Spectroscopy.* Springer, New York, pp. 529–575.

[11] Lakowicz, J. (ed.) (2006). *Principles of Fluorescence Spectroscopy.* Springer, New York, pp. 63–95.

[12] Lakowicz, J. (ed.) (2006). *Principles of Fluorescence Spectroscopy*. Springer, New York, pp. 97–155.

[13] Lakowicz, J. (ed.) (2006). *Principles of Fluorescence Spectroscopy*. Springer, New York, pp. 757–795.

[14] Horwitz, J. (2003). *Exp. Eye Res.* **76**, 145–153.

[15] Siezen, R.J., Bindels, J.G., Hoenders, H.J. (1980). *Eur. J. Biochem.* **107**, 243–249.

[16] Siezen, R.J., Berger, H. (1978). *Eur. J. Biochem.* **91**, 397–405.

[17] Walsh, M.T., Sen, A.C., Chakrabarti, B. (1991). *J. Biol. Chem.* **266**, 20079–20084.

[18] Wistow, G. (1993). *Exp. Eye Res.* **56**, 729–732.

[19] Smulders, R.H.P.H., van Boekel, M.A.M., de Jong, W.W. (1998). *Int. J. Biol. Macromol.* **22**, 187–196.

[20] Jehle, S., Rajagopal, P., Bardiaux, B., Markovic, S., Kuhne, R., Stout, J.R., Higman, V.A., Klevit, R.E., van Rossum, B.J., Oschkinat, H. (2010). *Nat. Struct. Mol. Biol.* **17**, 1037–1042.

[21] Ingolia, J.D., Craig, E.A. (1982). *Proc. Natl. Acad. Sci.* **79**, 2360–2364.

[22] Horwitz, J. (1992). *Proc. Natl. Acad. Sci.* **89**, 10449–10453.

[23] Rawat, U., Rao, M. (1998). *J. Biol. Chem.* **273**, 9415–9423.

[24] Raman, B., Ramakrishna, T., Rao, C.M. (1997). *FEBS Lett.* **416**, 369–372.

[25] Hook, D.W.A., Harding, J.J. (1997). *Eur. J. Biochem.* **247**, 380–385.

[26] Liang, J.N., Li, X.-Y. (1991). *Exp. Eye Res.* **53**, 61–66.

[27] Raman, B., Rao, C.M. (1994). *J. Biol. Chem.* **269**, 27264–27268.

[28] Nakajima, A. (1976). *J. Mol. Spectrosc.* **61**, 467–469.

[29] Nakajima, A. (1976). *J. Luminesc.* **11**, 429–432.

[30] Das, K.P., Surewicz, W. (1995). *FEBS Lett.* **369**, 321–325.

[31] Raman, B., Ramakrishna, T., Mohan Rao, C. (1995). *FEBS Lett.* **365**, 133–136.

[32] Bhattacharyya, J., Das, K.P. (1998). *IUBMB Life* **46**, 249–258.

[33] Sharma, K.K., Kaur, H., Kumar, G.S., Kester, K. (1998). *J. Biol. Chem.* **273**, 8965–8970.

[34] Sharma, K.K., Kumar, G.S., Murphy, A.S., Kester, K. (1998). *J. Biol. Chem.* **273**, 15474–15478.

[35] Sharma, K.K., Kaur, H., Kester, K. (1997). *Biochem. Biophys. Res. Commun.* **239**, 217–222.

[36] Martin, J., Langer, T., Boteva, R., Schramel, A., Horwich, A.L., Hartl, F.U. (1991). *Nature*, **352**, 36–42.

[37] Mendoza, J.A., Butler, M.C., Horowitz, P.M. (1992). *J. Biol. Chem.* **267**, 24648–24654.

[38] Langer, M., Lu, C., Echols, H., Flanagan, J., Hayer, M.K., Hartl, F.U. (1992). *Nature* **356**, 683–689.

[39] Das, K.P., Petrash, J.M., Surewicz, W.K. (1996). *J. Biol. Chem.* **271**, 10449–10452.

[40] Tyagi, N.K., Fenton, W.A., Horwich, A.L. (2009). *Proc. Natl. Acad. Sci.* **106**, 20264–20269.

[41] Reddy, M.C., Palmisano, D.V., Groth-Vasselli, B., Farnsworth, P.N. (1992). *Biochem. Biophys. Res. Commun.* **189**, 1578–1584.

[42] Palmisano, D.V., Groth-Vasselli, B., Farnsworth, P.N., Reddy, M.C. (1995). *Biochim. Biophys. Acta Protein Struct. Mol. Enzymol.* **1246**, 91–97.

[43] Greiner, J.V., Kopp, S.J., Glonek, T. (1985). *Investig. Ophthalmol. Visual Sci.* **26**, 537–544.

[44] Ghosh, J.G., Houck, S.A., Doneanu, C.E., Clark, J.I. (2006). *J. Mol. Biol.* **364**, 364–375.

[45] Rawat, U., Rao, M. (1998). *J. Biol. Chem.* **273**, 9415–9423.

[46] Muchowski, P.J., Clark, J.I. (1998). *Proc. Natl. Acad. Sci.* **95**, 1004–1009.

[47] Wang, K., Spector, A. (2000). *Eur. J. Biochem.* **267**, 4705–4712.

[48] Kantorow, M., Piatigorsky, J. (1994). *Proc. Natl. Acad. Sci.* **91**, 3112–3116.

[49] Biswas, A., Das, K.P. (2004). *J. Biol. Chem.* **279**, 42648–42657.

[50] Van den Oetelaar, P.J.M., Van Someren, P.F.H.M., Thomson, J.A., Siezen, R.J., Hoenders, H.J. (1990). *Biochemistry* **29**, 3488–3493.

[51] Bova, M.P., Ding, L.-L., Horwitz, J., Fung, B.K.-K. (1997). *J. Biol. Chem.* **272**, 29511–29517.

[52] Li, H., Li, C., Lu, Q., Su, T., Ke, T., Li, D.-W.C., Yuan, M., Liu, J., Ren, X., Zhang, Z., Zeng, S., Wang, Q.K., Liu, M. (2008). *Biochim. Biophys. Acta Mol. Basis Disease* **1782**, 303–309.

[53] Ahmad, M.F., Raman, B., Ramakrishna, T., Rao, C.M. (2008). *J. Mol. Biol.* **375**, 1040–1051.

[54] Biswas, A., Das, K.P. (2007). *Biopolymers* **85**, 189–197.

[55] Karmakar, S., Das, K.P. (2011). *Biopolymers* **95**, 105–116.

[56] Biswas, A., Das, K.P. (2007). *Biochemistry* **47**, 804–816.

[57] Roe, R.R., Pang, Y.-P. (1999). *J. Mol. Model* **5**, 134–140.

[58] Chowdhury, A., Mojumdar, S.S., Choudhury, A., Banerjee, R., Das, K.P., Sasmal, D.K., Bhattacharyya, K. (2012). *J. Chem. Phys.* **136**, 155101–155109.

[59] Chowdhury, A., Choudhury, A., Banerjee, V., Banerjee, R., Das, K.P. (2014). *Biopolymers* **101**, 549–560.

[60] Srinivas, V., Raman, B., Rao, K.S., Ramakrishna, T., Rao, C.M. (2003). *Protein Sci.* **12**, 1262–1270.

[61] Biswas, A., Das, K.P. (2004). *Protein J.* **23**, 529–538.

[62] Horwitz, J., Huang, Q., Ding, L. (2004). *Exp. Eye Res.* **79**, 817–821.

[63] Kantorow, M., Horwitz, J., van Boekel, M.A.M., de Jong, W.W., Piatigorsky, J. (1995). *J. Biol. Chem.* **270**, 17215–17220.

[64] Saha, S., Das, K.P. (2007). *Protein J.* **26**, 315–326.

[65] Sun, T.-X., Akhtar, N.J., Liang, J.J.-N. (1999). *J. Biol. Chem.* **274**, 34067–34071.

[66] Siezen, R.J., Bindels, J.G. (1982). *Exp. Eye Res.* **34**, 969–983.

[67] van den Oetelaar, P.J.M., Hoenders, H.J. (1989). *Biochim. Biophys.Acta Protein Struct. Mol. Enzymol.* **995**, 91–96.

[68] Doss-Pepe, E.W., Carew, E.L., Koretz, J.F. (1998). *Exp. Eye Res.* **67**, 657–679.

61

MODELING MUSCLE CONTRACTION MECHANISM IN ACCORDANCE WITH SLIDING-FILAMENT THEORY

TOSHIO MITSUI[1] AND HIROYUKI OHSHIMA[2]

[1]*Graduate School of Engineering Science, Osaka University, 1-3 Toyonaka, Osaka, 560-8531, Japan*
[2]*Faculty of Pharmaceutical Sciences, Tokyo University of Science, 2641 Yamazaki, Noda, Chiba 278-8510, Japan*

61.1 INTRODUCTION

The early history of muscle research was surveyed by A. Huxley in 1980 [1]. As described in Chapter II in Part II of Ref. 1, H. Huxley [2] found an overlapping double array of thick and thin filaments in striated muscle by electron microscope. On the basis of their electronmicroscopic observations, H. Huxley and Hanson [3] proposed the sliding-filament theory, which states that muscle contraction occurs by mutual sliding between the thick and thin filaments. Independently A. Huxley and Niedergerke [4] proposed the sliding theory based on their optical microscopic studies. Chapters III and the following chapters in Part II of Ref. 1 discuss the molecular model proposed by A. Huxley and his colleagues, which is usually called a *power stroke model*.

More recently Mitsui et al. [5–7] proved that the power stroke model is not consistent with the sliding-filament theory and proposed a model from a quite different perspective. Their model is in accordance with the sliding-filament theory and accurately explains major experimental results. Mathematical details of their study are described in the literature [5, 6] and are reviewed in one article [7]. The aim of the present chapter is to introduce their ideas, trying to make their contents [7] more readable.

Muscle structures and the sliding-filament theory are illustrated as an introduction in Section 61.2. The thermodynamic relationship that any models based on the sliding- filament theory should fulfill is derived in Section 61.3. Difficulties of the power stroke model are explained in Section 61.4. Requirements for any models based on the sliding- filament theory are listed in Section 61.5. A model that satisfies those requirements is presented in Section 61.6. Characteristics of the model that are helpful for numerical calculations are mentioned in Section 61.7. Section 61.8 demonstrates how the model explains major experimental data on muscles. Summary and discussion are given in Section 61.9.

61.2 MUSCLE STRUCTURES AND THE SLIDING-FILAMENT THEORY

As an introduction to the following discussion, the structure of muscle and the sliding-filament theory are illustrated in Figs. 61.1–61.4.

Figure 61.1 shows the structure of vertebrate skeletal muscle; part (a) shows the whole muscle, which is connected to bone by tendon. The whole muscle consists of many long muscle cells (single fibers). Part (b) shows a part of the cell. The cell is a bundle of many myofibrils. Part (c) shows a part of myofibril, which consists of many sarcomeres in series. Part (d) shows the sarcomere, which consists of thick filaments indicated as part € and thin filaments indicated as part (f). Part (e) shows that the thick filament has many myosin projections in microscopy. The lower illustration is the cross section at the myosin projection position. Part (f) shows that the thin filament consists of actin, troponin, and tropomyosin. Actin molecules produces force in cooperation with myosin molecules. Actin and myosin are called *contractile protein*. Part (g) shows the filament arrangement at the cross

Encyclopedia of Biocolloid and Biointerface Science, Volume 2, First Edition. Edited by Hiroyuki Ohshima.
© 2016 John Wiley & Sons, Inc. Published 2016 by John Wiley & Sons, Inc.

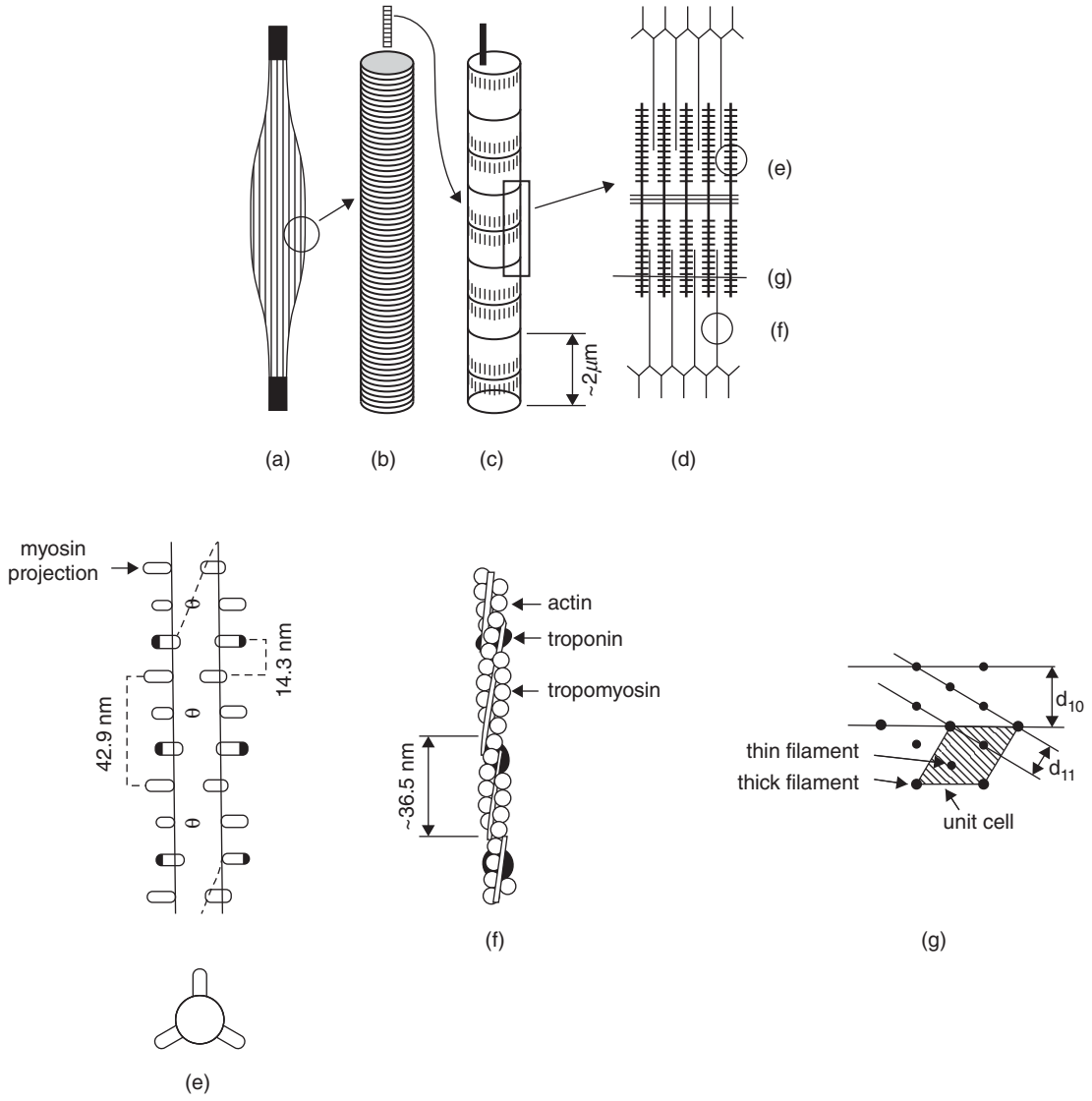


FIGURE 61.1 Structure of vertebrate skeletal muscle: (a) whole muscle; (b) unit cell (single-fiber); (c) myofibril; (d) sarcomere; (e) thick filament (lower cross-sectional view); (f) thin filament; (g) hexagonal array of filaments on the cross section indicated in (d).

section of the sarcomere indicated by g in (d). It has hexagonal symmetry.

The muscle contraction occurs by increasing overlap between the thick and thin filaments according to the sliding-filament theory. This is illustrated in Figure 61.2.

Figure 61.3 illustrates the structure of myosin molecule, which has two globular parts indicated as S-1 at the end. The part S-1 is called the *myosin head.*

Figure 61.4 illustrates how the contractile proteins interact for force production. The thick filament is a bundle of LMM. In microscopy, the myosin heads in Fig. 61.4 are observed as the myosin projections in Fig. 61.1e. It is generally accepted that the force for the filament sliding is produced only when myosin heads bind to the actin molecule as shown by the myosin heads *b* and *c*. The link between the thick and thin filaments formed by the myosin head *b* or *c* is called a crossbridge.

61.3 THERMODYNAMIC RELATIONSHIP THAT ANY MODELS BASED ON SLIDING-FILAMENT THEORY SHOULD FULFILL

Generally the first step in constructing a molecular model in material physics is to look for a thermodynamic relationship among parameters to appear in models. The relationship imposes restrictions on construction of models. Let us follow this procedure for a study of muscle contraction.

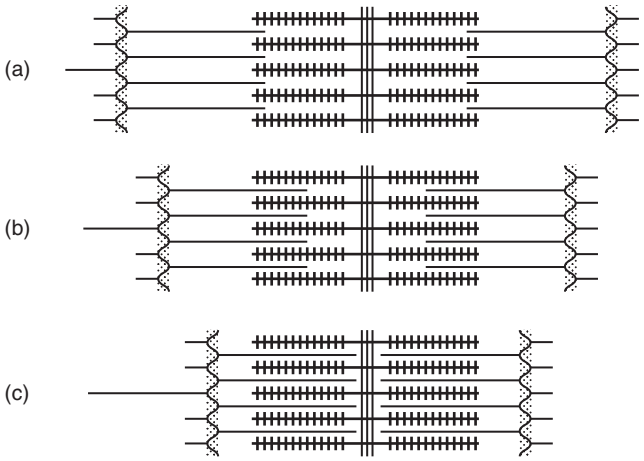


FIGURE 61.2 Illustration of the sliding-filament theory; contraction of muscle is caused by increasing overlap between the thick and thin filaments in sarcomere: (a) no overlap; (b) partial overlap; (c) full overlap.

61.3.1 Work Done by One Crossbridge Using ATP Hydrolysis energy

It is assumed that the myosin head exerts force on actin filament only when it is attached to actin as shown by the heads *b* and *c* in Figure 61.4. The force that causes the filament sliding is produced by spending ATP. The ATP hydrolysis energy per one molecule is denoted as e_A. In one cycle spending e_A, the mean force exerted on the actin filament by one attached myosin head is denoted as p and the translation distance of the attached head as D. Then pD gives the work done by the myosin head utilizing e_A. Measured macroscopic quantities during muscle contraction are the tension T, contraction velocity V, and the rate of heat production H. Unit of T is N/m^2. V is defined for unit length of muscle and its unit is 1/s. H is defined for unit volume of muscle and its units is

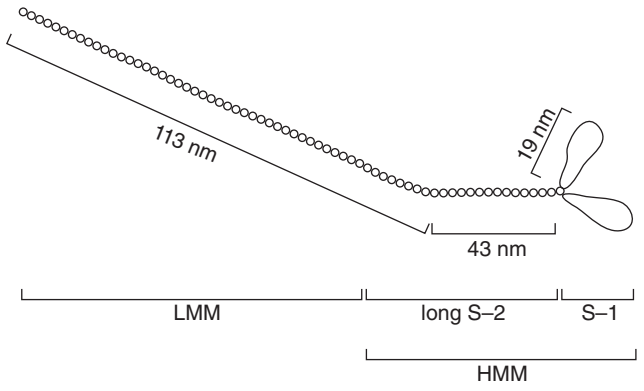


FIGURE 61.3 Structure of a myosin molecule (LMM, light meromyosin; HMM, heavy meromyosin; S-1, subfragment 1 (myosin head); S-2, subfragment 2).

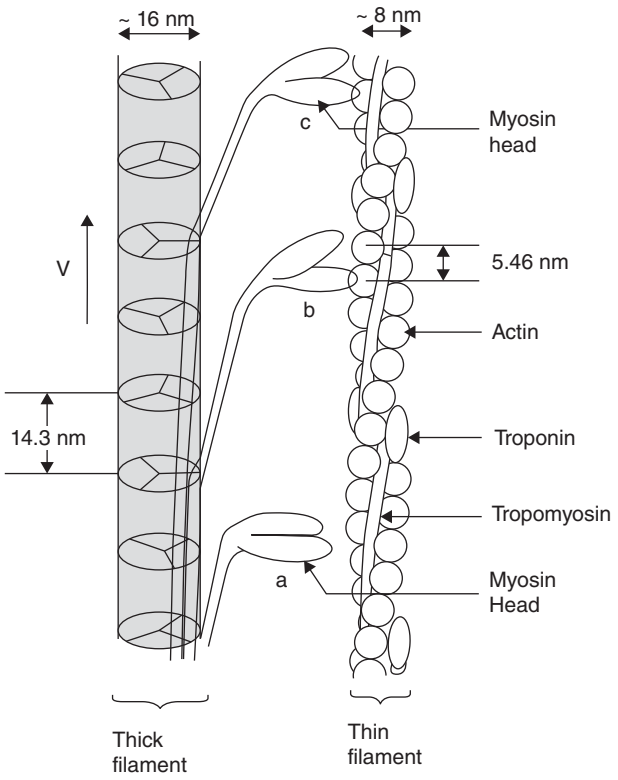


FIGURE 61.4 Thick and thin filaments in interaction. Myosin head a does not attach to the thin filament and does not produce force. Myosin heads *b* and *c* attach to the thin filament and produce force.

$W/m^3 = (N \bullet m)/sm^3 = N/(m^2 \bullet s)$. The rate of work done by unit volume of muscle W is given by TV:

$$W = TV \tag{61.1}$$

The unit of TV is $N/(m^2 \bullet s)$, the same as H. The rate of total energy production per unit volume is $W + H$. The portion of e_A used for work is given by $e_A\ W/(W + H)$. Hence, by the first law of thermodynamics, we have

$$pD = e_A W/(W + H) \tag{61.2}$$

61.3.2 Relation between p and T in Sliding-Filament Theory

Figure 61.5 schematically shows a portion of the sarcomere producing the tension T at full filament overlap: (a) side view and (b) projection of the sarcomere along the filament axis. The projection consists of hexagons or rhombus cells of edge a. The rhombus area contains one myosin filament and has the same area as the hexagon cell.

In Fig. 61.5a, the vertical thin rods are actin filaments. The thick vertical rods are backbones of myosin filament and

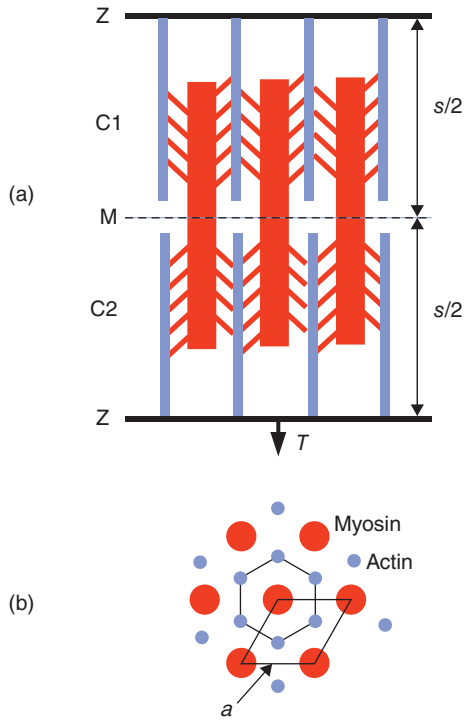


FIGURE 61.5 A portion of the sarcomere at the full filament overlap. (a) Side view. Myosin filaments are shown by thick vertical bars with branches and the actin filament by vertical thin rods. The thickness of half sarcomere is $s/2$. See text for more details. (b) Projection of the sarcomere along the filament axis. The projection consists of rhombus cells of edge a or of hexagons.

the oblique thin rods symbolically represent myosin heads, including the heads attached and not attached to the myosin filaments. Although only nine oblique rods are depicted per myosin backbone per half sarcomere for simplicity in (a), actually about 300 heads exists as calculated below. Z and M planes are perpendicular to the filaments. Since the tension T is given in units of N/m^2, let us consider a flat cylinder between the planes Z and M, whose base is 1 m^2 wide and thickness is the half sarcomere length $s/2$, as indicated by C1 and C2. The upper Z plane is considered fixed, and thus the tension T is downward. Then the actin filaments in C1 exert upward force on myosin filaments balancing the tension T, while the myosin filaments in C2 exert upward force on actin filaments balancing T. In this way, each flat cylinder produces the tension T in the sliding-filament theory. Below we shall consider C1.

The number of myosin heads in C1 is denoted as $N_{\rm hs}$, whose numerical value can be obtained as follows. The edge of the rhombus unit cell is indicated as a in Fig. 61.5b. It is known that a varies depending on T but, as an approximation, a is set equal to 42 nm following [8]. Then the area of the unit cell is $a^2\sin 60° = 1528 \times 10^{-18}$ m^2. Microscopic photographs of muscle suggest that the ratio of sarcomere area in the base of C1 is not very far from 1, and the ratio is set as 0.9 as an approximation, following one study [8]. Then the number of myosin filaments in C1 is $0.9/(a^2\sin 60°) = 5.89 \times 10^{14}$ m^{-2}. As shown in Fig. 61.1e, the myosin projections (myosin heads) are arranged with spacing of about 14.3 nm on the actin filament with threefold rotation symmetry. The spacing is denoted as d and is set equal to 14.3 nm as in another study [8]. Because of the threefold rotation symmetry, the myosin filament has six myosin heads per d. The length of myosin filament minus that of the bare zone is about 1.43 μm. Thus the number of myosin heads on one myosin filament per half sarcomere is $6 \times (1.43 \times 10^{-6}/2)/14.3 \times 10^{-9} = 300$. Thus we have an approximate value of $N_{\rm hs}$ as

$$N_{\rm hs} = 300 \times 5.89 \times 10^{14}{\rm m}^{-2} = 1.76 \times 10^{17}{\rm m}^{-2} \qquad (61.3)$$

The symbol r is defined as the ratio of the number of myosin heads attached to an actin filament per total number of myosin heads at the same moment. Then the relation between the mean force p produced by one attached head and the tension T is given by

$$p = T/(rN_{\rm hs}) \qquad (61.4)$$

61.3.3 Thermodynamic Relationship

Combining Eqs. (61.1), (61.2), and (61.4) gives

$$D/r = e_{\rm A}N_{\rm hs}V/(W+H) \qquad (61.5)$$

This is the required thermodynamic relationship that any model based on the sliding-filament theory should satisfy.

If the units of the quantities in Eq. (61.5) are presented in parentheses, they are D(m), $e_{\rm A}$(J), $N_{\rm hs}$(1/m^2), V(1/s), and $(W+H)$(J/m^{3}s), so that the unit of the right-hand term is (J)(1/m^2)(1/s)(m^{3}s)/J = m, the same as the unit of D/r.

As T approaches to 0, $W = TV$ becomes negligible compared to H, and Eq. (61.5) becomes

$$D/r = e_{\rm A}N_{\rm hs}V/H \qquad (61.6)$$

Let us use $e_{\rm A} = 8.0 \times 10^{-20}$ J/molecule, $V_{\rm max} = 2.25$ (1/s) (V under no load) [9], $H = 35.2$ kW/m^2 at $T = 0$ at 0°C [10], as was done in Section 2.1 of Ref. 5. Then Eq. (61.6) gives

$$D/r = 900 \text{ nm, for } T = 0 \text{ at } 0°{\rm C} \qquad (61.7)$$

This value of D/r is large, but those of similar order of magnitude can be obtained from other experimental data as described in the next section.

61.3.4 Values of D/r Estimated from Literature Data [11]

Harada et al. [11] observed the motion of actin filaments on a glass strip covered by myosin molecules, and measured the velocity of the actin filament and rate of hydrolysis of ATP. They estimated from their data that D is larger than 60 nm at 30 and larger than 200 nm at 20°C. As mentioned by several authors, however, their method for estimating D seems too speculative. Nevertheless, the order of magnitude of D/r can be estimated from their data as follows.

According to Harada et al. [11], the mean sliding velocity of the actin filaments does not depend on the filament length. They determined the rate of hydrolysis of ATP by the Pi production rate per 1 nm of the actin filament. Here let us simplify their system by supposing the following model. Myosin molecules are arranged on a straight line with the mutual separation of d_{H} on the glass strip. The length of the line is more than 1 m. A straight actin filament of 1 m is on the myosin line and moves along it. Now the stress T is regarded as a friction force against the actin filament movement. Then relations similar to Eqs. (61.2), (61.4), and (61.5) can be derived. If the quantities concerning the experiment by Harada et al. are expressed with suffixes H, Eq. (61.5) becomes

$$D_{\mathrm{H}}/r_{\mathrm{H}} = e_{\mathrm{A}} N_{\mathrm{H}} V_{\mathrm{H}}/(H_{\mathrm{H}} + W_{\mathrm{H}}) \tag{61.8}$$

Harada et al. [11] determined the average distance between myosin molecules on the glass strip by electron microscope as about 12 nm. Hence we set

$$d_{\mathrm{H}} = 12 \text{ nm} \tag{61.9}$$

Since the length of the actin filament is 1 m and the myosin molecule is two-headed, we have

$$N_{\mathrm{H}} = 2/d_{\mathrm{H}} = 2/12 \times 10^{-9} = 0.17 \times 10^{9} \tag{61.10}$$

In Table 1 of the paper by Harada et al. [11], values of v(μm/s) and (pi/s per nm) are given. With our notations, V_{H} (m/s) = $v \times 10^{-6}$ and $H_{\mathrm{H}} + W_{\mathrm{H}}$ (J/s per m) = e_{A}(pi/s per nm)×10^9. Then Eq. (61.8) becomes

$$D_{\mathrm{H}}/r_{\mathrm{H}} \text{ (nm)} = 170v/(\text{Pi/s per nm}) \tag{61.11}$$

By using the values given in Table 1 of Harada et al. [11] and N_{H} in Eq. (61.10), we have

$$D_{\mathrm{H}}/r_{\mathrm{H}} = 850 \text{ nm} \quad \text{for actin filament at } 22°\text{C} \tag{61.12a}$$
$$D_{\mathrm{H}}/r_{\mathrm{H}} = 350 \text{ nm} \quad \text{for actin filament at } 30°\text{C} \tag{61.12b}$$
$$D_{\mathrm{H}}/r_{\mathrm{H}} = 1280 \text{ nm} \quad \text{For thin filament at } 22°\text{C} \tag{61.12c}$$

These values of $D_{\mathrm{H}}/r_{\mathrm{H}}$ are as large as D/r = 900 nm in Eq. (61.7).

61.4 DIFFICULTIES OF THE POWER STROKE MODEL

61.4.1 Difficulty Concerning Magnitude of r

According to Eq. (61.7), the order of magnitude of D/r is 900 nm for free shortening at 0°C. This value of 900 nm is derived from the sliding-filament theory according to the first law of thermodynamics irrespective of modeling on muscle contraction mechanism. Hence any model based on the sliding-filament theory should give this order of magnitude. In the power stroke model, the power stroke (or working stroke), which corresponds to D in our notation, is approximately 10 nm [12]. Then the relation D/r = 900 nm gives r as 0.011.

The stiffness of a muscle varies depending on the stress and is assumed to be a measure of r in the power stroke model [13]. According to one report [13], the ratio of the stiffness of the crossbridge at $T = 0$ to that at $T = T_0$ is about 0.35, where T_0 is the isometric tension (see Fig. 61.13, given later). Therefore, if $r = 0.011$ is for $T = 0$, the ratio r for $T = T_0$ becomes $r = 0.011/0.365 = 0.031$. This means that 3.1 % of all the myosin heads in muscle contribute to force production at the maximum. The value of 0.011 or 0.031 seems too small to be realistic. This is an essential difficulty of the power stroke model.

61.4.2 Values of r and D Estimated from Experimental Data

In the isometric state, Eq. (61.4) becomes $p_0 = T_0/(r_0 N_{\mathrm{hs}})$, where p_0, T_0 and r_0 are values of p, T and r in the isometric tetanus state. Then

$$r_0 = T_0/(N_{\mathrm{hs}} p_0) \tag{61.13}$$

$T_0 = 4.1 \times 10^5$ N/m^2 according to Edman [9] and $N_{\mathrm{hs}} = 1.76 \times 10^{17}$ m^{-2} by Eq. (61.3). The experimental results of one team [14] indicate that p_0 is close to 5.7 pN. We adopt this value in the following calculations:

$$p_0 = 5.7 \text{ pN} \tag{61.14}$$

Using these values, Eq. (61.13) gives

$$r_0 = 0.41, \text{ for } T = T_0 \tag{61.15}$$

X-Ray data are favorable to $r_0 = 0.41$. By X-ray diffraction study of the [1,0] and [1,1] equatorial reflections from a sartorius muscle, another team [15] estimated that about 80% of myosin heads migrate around the thin filament in isometric tetanus muscle. This percentage is higher (approximately 92–99%) according to one report [16]. Since these percentages are about twice r_0 = 41%, it seems reasonable to suppose

that approximately one of two heads of a myosin molecule attaches to actin filament and produces force while the other exists in the vicinity of the thin filament as nonattached relief.

In shortening muscles, several teams of investigators [16–19] observed that the intensity ratio of the [1,0] and [1,1] equatorial reflections increases only minimally as shortening velocity increases, indicating that the total number of myosin heads in the vicinity of the actin filament decreases only slightly. These experimental data strongly suggest that the ratio r in shortening muscles is about the same as r_0 in Eq. (61.15), and we incorporate $r = r_0$ in the following discussion:

$$r = 0.41, \text{ for any } T \tag{61.16}$$

This value of 0.41 is much larger than 0.011 or 0.031 of the power stroke model.

In the power stroke model, the constant r indicated by X-ray studies is explained by assuming that weakly attached crossbridges exist in addition to strongly attached crossbridges and that the muscle stiffness and the force are determined by the strongly attached crossbridges. This explanation implies that 1.1% or 3.1% of all myosin heads are strongly attached heads and produce tension while (41 – 1.1)% or (41 – 3.1)% are weakly attached heads. Such situation does not seem realistic if muscle is a machine of high efficiency.

By Eq. (61.16), Eq. (61.7) gives

$$D = 370 \text{ nm, for } T = 0 \text{ at } 0°\text{C} \tag{61.17}$$

This D value is large but estimated from the thermodynamic relationship and the experimental data regardless modeling of the muscle contraction mechanism. As mentioned in Section 61.4.1, the working stroke (D in our notation) is about 10 nm in the power stroke model. The value 370 nm is much larger than 10 nm, indicating need of a new model.

61.5 REQUIREMENTS FOR ANY MODELS BASED ON SLIDING-FILAMENT THEORY

Requirements that any models based on the sliding-filament theory should fulfill may be listed as follows.

1. Large D/r or D in shortening muscles. The value of $D/r = 900$ nm [Eq. (61.7)] for free shortening is derived solely from the sliding-filament theory and the first law of thermodynamics with macroscopic experimental data. Also the value of $D = 370$ nm [Eq. (61.17)] is strongly suggested by the experimental data as discussed in Section 61.4.2. These values are very large but are determined irrespective of modeling of the muscle contraction mechanism. Accordingly, any model based on the sliding-filament theory should give the order of magnitude of D/r or D.
2. Small D observed in experiments with single myosin molecule in vitro. One team [20] studied the movement and force generation produced by a single myosin head and found the movement during one ATP hydrolysis cycle to be about 4 nm. Another team [21] developed a new assay for direct manipulation of S-1, making visualization possible with a fluorescent label. Their results show that a myosin head moves along the actin filament with 5.3-nm steps, often producing displacement of 11– 30 nm for each ATP hydrolysis cycle.
3. Crossbridges independently produce force in the isometric tetanus state. As noted in Section 61.1, early history of muscle research is surveyed by A. Huxley [1]. Chapter III in Part II of Ref. 1 concerns experimental data by two investigators [22] and analysis of their data [23]. They [22] measured tension developed by isolated frog muscle fibers when stimulated at various degrees of stretch in the isometric tetanus state. Their length–tension curve indicates that there is a linear fall as length is increases above the optimum [11, Fig. 9]. This is what to be expected if the tension that the fiber is able to generate is directly proportional to the extent of overlap between thick and thin filaments in each sarcomere. Then it is reasonable to conclude that the myosin heads produce force independently of each other in the isometric tetanus state as discussed in [23].
4. Reasonable explanation should be given on the coupling between the force production and energy liberation by chemical reaction.
5. The model should explain major experimental data on muscle properties or behaviors.

61.6 CONSTRUCTION OF A NEW MODEL

61.6.1 Formation of Complex MA_3 by a Myosin Head and Three Actin Molecules

Let us consider interaction between an ATP-activated single myosin head and an actin filament by using distribution of potential wells for the head on the actin filament as shown in Fig. 61.6.

In Fig. 61.6a the activated myosin head is indicated as M, which sits at a position apart from the actin filament. The actin filament is represented by the periodic array of potential wells that correspond to the possible binding sites for M. As shown in Fig. 61.1f, an actin filament consists of two strands. The wells are arranged with the period L of actin strand

$$L = 5.46 \text{ nm} \tag{61.18}$$

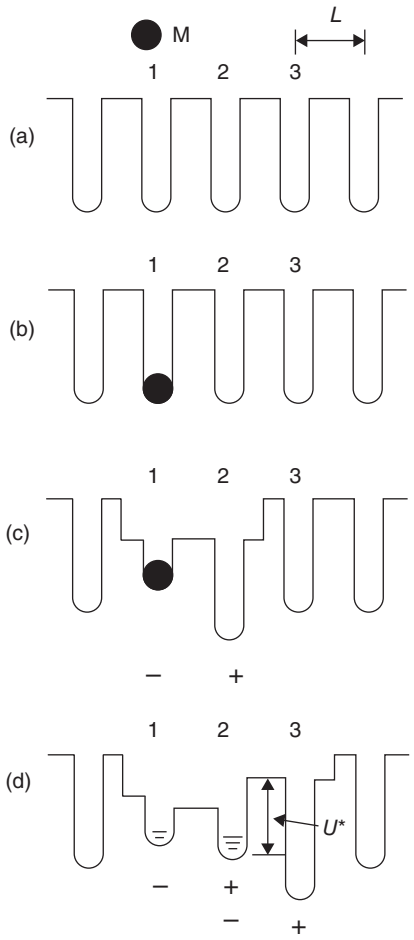


FIGURE 61.6 Diagram showing sequential changes in the potential of force acting on ATP-activated single myosin head M (subfragment 1) when M binds to an actin filament. The numbers 1, 2, and 3 are assigned to the potential wells at the binding sites of actin molecules on the same strand. (a) Periodic potential distribution when M is sitting at a position apart from the actin filament. (b) Just after M attaches to actin 1. (c) Molecules deform and potential distribution changes. (d) Final potential distribution. Generally M is statistically distributed in wells 1 and 2.

The helical structure of the actin filament will disturb the periodic potential arrangement, but its effect does not seem essential and is neglected here.

Two other teams [24, 25] studied the binding pattern of a myosin head to an actin filament by using tryptic digestion of myofibrils and measuring optical polarization and dichroism. One team [25] concluded that in the rigor rabbit psoas muscle each myosin head binds to two actin monomers in a thin filament, indicating the possibility that the myosin head firstly binds to one and then to two monomers in the actin filament. Figure 61.6b–d shows an example of possible mechanism of how such binding change occurs. Figure 61.6b shows the state at the moment M when attaches to actin 1. Attachment of the myosin head may cause large strain in actin molecules. Protein molecules are structurally polar. (Note, for instance, that G-actin has the permanent dipole moment of 600 Debyes [26].) Hence the actin filament is piezoelectric. Consequently, it is a possibility that the strain produces an electric polarization as symbolically indicated by the electric charges – in actin 1 and + in actin 2 in Fig. 61.6c. The myosin head is negatively charged and the Coulomb interaction between the head charge and the induced polarization charges raises the potential well for the head at actin molecule 1 and lower the well at actin 2 as shown in part (c) of Fig. 61.6. Also it is assumed that the change lowers the potential barrier between 1 and 2 (c), so that M can jump over the barrier as a result of the thermal fluctuation and is statistically distributed in the wells 1 and 2 as schematically drawn in (d). Then the head at well 2 will produce the polarization charge – in well 2 and + in well 3 similarly to the case of (c) but somewhat differently from (c), due to the different prehistory. The induced charges in this case are symbolically shown by small – and + in (d). The structural changes from (c) to (d) will be similar to that from (b) to (c) but somewhat different from (c) because of the different prehistory. The resultant potential distribution is supposed to be such as shown in (d). Presumably the myosin head bound to actin 1 and 2 is observed [24,25]. Figure 61.6d shows the potential barrier U^* that the myosin head M has to cross over to move from well 2 to 3. U^* will be discussed in Section 61.6.3.

61.6.2 Molecular Model for MA_3

Figure 61.7 illustrates the change of molecular structures associated with the change in potential distribution in Fig. 61.6. Figure 61.7a shows a myosin head just after attachment to actin filament (the shape is speculated), which corresponds to the state in (b). Then the potential changes occur from (b) to (c) and (d), causing the shift of the binding site of the head from (a) to (b) in Fig. 61.7. The shape of the head in (b) is depicted by referring to the shape in Fig. 6 of Ref. 27. It is assumed that the molecular deformation occurs mainly in the shadowed three actin molecules together with the head in Fig. 61.7b, associated with the potential variation in Fig. 61.6d. The shadowed complex in Fig. 61.7b is denoted as MA_3. Figure 61.7c is a model of Fig. 61.7b. The tilting angle of the neck domain relative to the vertical z axis is denoted as θ_{eq} in the case of a single myosin head.

61.6.3 Cooperative Interaction among Crossbridges

As mentioned regarding requirement 3 in Section 61.5, one can conclude that the myosin heads produce force independently of each other in the tetanus state. One team [23] extended this conclusion to the case of shortening muscle

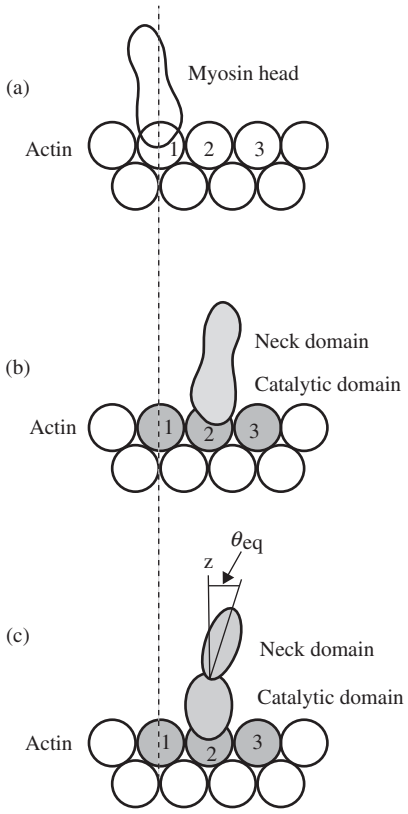


FIGURE 61.7 Formation of a complex MA_3 of myosin head and actin molecules. (a) Just after attachment of myosin head to actin molecule 1 corresponding to Fig. 61.6b. Molecules are not deformed yet. (b) The shadowed myosin head and actin molecules 1, 2, and 3 are deformed and the complex MA_3 is formed, corresponding to Fig. 61.6d. (c) Modeling of (b). The myosin head is represented as neck domain plus catalytic domain. The angle θ_{eq} is the bending angle of neck domain at equilibrium.

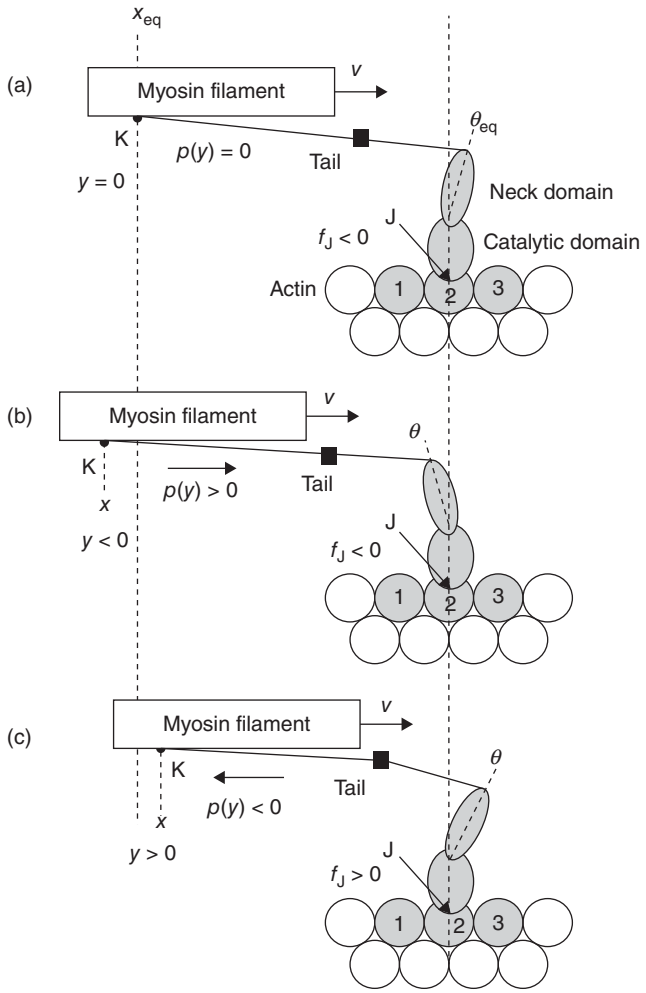


FIGURE 61.8 Three states (a), (b), and (c) of the MA_3 complex indicated by shadowing. Ends of the crossbridges are indicated as *J* and *K*. Ends *J* are set on the dotted line *z* and *K* at different positions referring to the dashed line x_{eq} in (a), (b), and (c). *y* represents shortening of the crossbridge. (a) The myosin head is at its equilibrium angle, θ_{eq} and $y = 0$. (b) The myosin head is pulling the myosin filament forward. The crossbridge is elongated and $y < 0$. (c) The myosin head is pushing the myosin filament backward. The crossbridge is shortened and $y > 0$.

and assumed that the myosin heads produce force independently of each other also in shortening muscles, and proposed an "independent force-generator theory." Construction of the power stroke model was based on this theory, as discussed in chapters following Chapter III in Part II of Ref. 1. It seems, however, too speculative to assume that myosin heads produce force independently of each other also in shortening muscles. The power stroke model encounters various difficulties as mentioned in Section 61.4. The difficulties, however, can be avoided by assuming cooperative interaction among crossbridges in shortening muscles as discussed elsewhere [5–7]. The cooperative interaction disappears in the isometric tetanus state [5–7] in accordance with the conclusion in another study [23]. The discussion in Refs. 5–7 is outlined below.

According to Eq. (61.16), 41% of the myosin heads are bound to actin filaments forming the complex MA_3 in shortening muscle. In Fig. 61.8, the complex MA_3 is shadowed and connected to a myosin filament by the thin bar denoted as tail, forming the crossbridge.

The right direction corresponds to the sliding direction of the myosin filament against the actin filament and is called *forward* and the left direction, *backward*. The end of the crossbridge at the myosin filament is indicated as *K* and the end at the actin filament, as *J*. The tail has bending freedom [5, Section 3.4], which is represented by one hinge depicted as a black square for simplicity. Figure 61.8 shows three states of the crossbridge, where the actin filaments are fixed at the same position and *J* are placed on the line *z*. In part (a), the tilting angle of the neck domain is equal to the

equilibrium angle θ_{eq}. The shortening of the crossbridge is defined in reference to the state at θ_{eq} and denoted as y. The force that the crossbridge exerts on the myosin filament is a function of y and denoted as $p(y)$. In (a), $y = 0$ and $p(y) = 0$. In (b), K is set to left from K in (a) and the neck domain tilts to left from θ_{eq}. The myosin filament is pulled forward [$p(y) > 0$]. The crossbridge is elongated ($y < 0$). The tail is straightened and the elastic force by the myosin head will be straightforwardly transmitted to the myosin filament. In (c), K is set to right from (a) so that the tail is shortened ($y > 0$), and the crossbridge pushes the myosin filament backward [$p(y) < 0$]. The tail is bent, and the effect of the backward force by the crossbridge will be weakly transmitted to the myosin filament.

The basic idea of theoretical treatments elsewhere [5,6] is outlined below. As shown in Fig. 61.6d, the myosin molecule has to cross over the potential barrier U^* to move from well 2 to well 3 in MA_3. The probability Q that the myosin head crosses over U^* is discussed based on Eyring theory of the rate process described in Ref. 28, as was done in another study [29]. (It should be noted that our model is quite different from the model discussed in Ref. 29, although Eyring theory is used during formulation in both models.) U^* and Q are functions of $p(y)$ and written as $U^*(y)$ and $Q(y)$. Then, as in Eq. (3-5-1) in Ref. 5, $Q(y)$ is given by

$$Q(y) = A \exp(-U^*(y)/kT) \tag{61.19}$$

Here, A is a constant, k is the Boltzmann constant, and T is the absolute temperature. In Ref. 5, $U^*(y)$ is expressed by $U^*(y) = U^*_0 - af_J(y)$ [5, Eq. (3-5-2)] and $f_J(y) = -p(y)$ [5, Eq. (3-4-2)], where U^*_0 and a are constants. Thus we have

$$U^*(y) = U^*_0 + ap(y) \tag{61.20}$$

Because of the bending freedom, the stiffness of the crossbridge (i.e., myosin head plus tail) depends on y. The stiffness is denoted as κ_f in the case shown in Fig. 61.8b, where the tail is straightened and $y < 0$. The stiffness is denoted as κ_b in part (c), where the tail is bent and $y > 0$. Following Eq. (3-4-6) in Ref. 5, $p(y)$ is approximately given by

$$p(y) = -k_f y, \quad \text{for } y < 0 \tag{61.21a}$$

$$p(y) = -k_b y, \quad \text{for } y > 0 \tag{61.21b}$$

Values of the stiffness are given by Eqs. (4-1-13) and (4-1-14) in Ref. 5:

$$k_f = 2.80 \text{ pN/nm} \tag{61.22a}$$

$$k_b = 0.26 \text{ pN/nm} \tag{61.22b}$$

Equation (61.22) indicates that the crossbridge is elastically nonlinear.

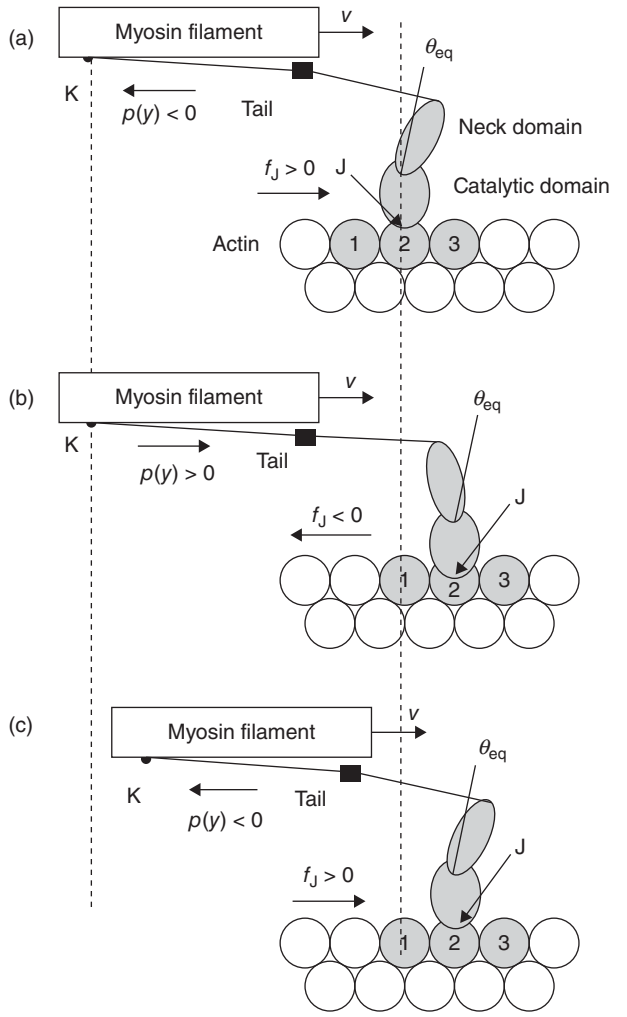


FIGURE 61.9 Step motion of complex MA_3 (shadowed) along an actin filament. (a) The neck domain tilts to the right from θ_{eq}. The myosin filament is pushing the neck domain forward and MA_3 is just before translation to the right position. (b) Just after the MA_3 has moved to the new position. The crossbridge is pulling the myosin filament forward. (c) The myosin filament moves to the right by the filment sliding and MA_3 is ready for translation to the right position.

We leave mathematical discussion based on these equations to Refs. 5 and 6, and explain only implication of the above equations here. Figure 61.9 illustrates what happens with the model during the filament sliding. Figure 61.9a shows the state that the neck domain tilts to right from the equilibrium angle θ_{eq} and pushes the myosin filament backward. The crossbridge is shortened, and thus $y > 0$, the stiffness is κ_b and $p(y) < 0$ by Eq. (61.21b). (The head corresponds to the weakly attached head in terms of the power stroke model since $\kappa_b < \kappa_f$.) When the myosin filament moves forward, $p(y)$ decreases and the potential barrier $U^*(y)$ decreases according to Eq. (61.20), so that the transition probability $Q(y)$ increases according to Eq.

(61.19). Let us denote the critical y at which the head most frequently crosses over U^* during filament sliding as y_c, and simplify the discussion by assuming that all the transitions crossing over U^* occur at y_c. If Fig. 61.9a shows the state at y_c, the head will cross over U^* in the next moment and will form a new complex MA_3 as shown in (b), where the neck domain tilts to the left from θ_{eq} and pulls the myosin filament forward. Now $y < 0$, $p(y) > 0$ [Eq. (61.21a)], and the stiffness is κ_f. (The head corresponds to the strongly attached head in term of the power stroke model since $\kappa_f > \kappa_b$.) $U^*(y)$ is large according to Eqs. (61.20), (61.21a), and (61.22a), and $Q(y)$ is small per Eqs. (61.19) and (61.20). Hence the head has practically no chance to cross over U^* and continually pulls the myosin filament forward. Then the myosin filament slides forward and the end of the crossbridge K moves forward from (b) to (c). The situation in (c) is identical to that in (a) except for binding actin mates, and the U^* transition occurs. Filament sliding takes place repeating such steps. The parameter y_c is a function of the tension as will be discussed in Section 61.7.2.

The filament sliding is a result of force production by all MA_3. On the other hand, the filament sliding induces the U^* transition of each MA_3 so that the MA_3 produces the force. Thus the force production of each crossbridge is enhanced by other crossbridges. In this sense, there is a mutual cooperation among crossbridges. Generally cooperative system is mathematically discussed by using a feedback loop that output of each element is affected by output of all elements in the system [e.g., 30, Section 22]. Equations (61.19)–(61.22) imply such a feedback loop.

As mentioned in Section 61.5, one research team [21] developed a new assay for direct manipulation of S-1, making visualization possible with a fluorescent label. Their results show that a myosin head moves along the actin filament in 5.3-nm steps, often producing displacement of 11–30 nm for each ATP hydrolysis cycle. In their experiment, the single myosin molecule has no partner of cooperation and the force on the head is close to 0 after the movement, corresponding to the case of practically zero $p(y)$ in the expression of $U^*(y) = U^*_0 + ap(y)$ [Eq. (61.20)]. Thus their results seem to indicate that U^*_0 is relatively large so that the probability for the myosin head to cross over U^* is small. Presumably, there was some fluctuation of the force depending on the experimental conditions, and D was observed as about 5.46 nm [Eq. (61.18)] a few times. This is an answer to requirement 2 in Section 61.5.

As mentioned in Section 61.3.4, Harada et al. [11] studied the motion of actin filaments on a glass strip covered by myosin molecules. They observed that the actin filaments longer than ~40 nm moved on the myosin-covered glass strip, and that the actin filaments of ~40 nm sometimes stopped the movement. It is plausible that usually two or three myosin heads attach to the moving actin filament of 40 nm and occasionally only one myosin head remains to attach to the actin filament so that there is no cooperatively working mate and the actin filament stops.

The change of the form of MA_3 from Fig. 61.9 (b) to (c) does not occur without the filament sliding. Thus the filament sliding is a necessary condition for the cooperative interaction among crossbridges. In the isometric tetanus state, there is no filament sliding and hence no cooperativity among crossbridges. Accordingly, crossbridges produce force independently in the isometric tetanus state as observed by several investigators [22, 23]. This is an answer to requirement 3 in Section 61.5.

61.6.4 Chemical Reactions and Energy Liberation Associated with Force Production

The authors of one study [31] proposed the chemical cycle associated with the force production in the power stroke model. In their scheme, dissociations of pi and ADP play the important role in force production. In our model, the way of energy flow and chemical reaction is quite different from theirs, and dissociations of pi and ADP do not play any important role in connection with force production.

The energy liberated by hydrolysis of one ATP molecule is denoted as e_A. The ATP-activated myosin head M in Figure 61.6a has e_A. A portion of e_A is used to form the complex MA_3 in Fig. 61.6d. The remains of e_A are used for the force production. The head detaches from the actin filament when e_A is exhausted. Each cycle of force generation is connected with the chemical reactions, which consist of dissociation from one actin molecule and binding to the neighboring actin molecule. Figure 61.10 illustrates the steps. On the right, a myosin head is depicted as a box with the energy G stored in it. On the left, an actin filament is depicted as a box with many shelves where the shelf A_i corresponds to ith actin molecule. The force f_J from the myosin filament to the head

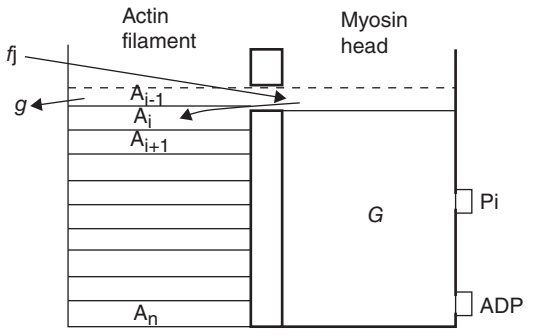


FIGURE 61.10 Energy flow and chemical reaction associated with the force production. Chemical reaction is a series of detachment from actin A_{i-1} and attachment to A_i. The fraction g of the free energy of a myosin head is used for force production at each chemical reaction. The energy stored in the myosin head after the ith step is denoted by G. The initial value of G is e_A given to the head by the ATP hydrolysis.

lowers the potential barrier U^* and lets the head dissociate from $A_{i\text{-}1}$ and bind to A_i. The myosin head produces force associated with this step. The level of G is lowered by g by the chemical reaction and the force generation. Energy liberation rate calculated on this scheme is in good agreement with experimental observation as shown later in Fig. 61.15. The step energy liberation seems to be related with thermal fluctuations as discussed in next subsection.

61.6.5 Role of Thermal Fluctuations

On the basis of Eyring theory with respect to the rate process described in Ref. 28, the probability Q for a myosin head to cross over U^* is given by $Q = A \exp(-U^*/kT)$ [Eq. (61.19)]. In most textbooks, Eyring theory is discussed in the case where a single material particle crosses over a potential barrier U^*. Then, the energy for the particle to cross over U^* is supplied by the thermal energy of the surroundings. In the case of a myosin head, however, the head has much internal freedom for structural and thermal fluctuation. Then it becomes possible for adiabatic fluctuation to occur in a limited timeframe in such a way that the decrease of structural fluctuation energy of the head is compensated by increase of the thermal fluctuation energy of constituent atoms, and vice versa. Thus the internal energy of the head can be used to excite the mode of motion of center of gravity of the head and to help the head cross over U^* in Fig. 61.6d. The difference between the potential energies at wells 2 and 3 in Fig. 61.6d is converted into the elastic energy of the crossbridge to be used to pull the myosin filament in the process from Fig. 61.9 (b) to (c). In this way the internal energy of the head originally supplied by ATP hydrolysis is used by parts to pull the myosin filament. The thermal fluctuation plays an important role for force production but it is not contradictory to the second law of thermodynamics because contribution from thermal fluctuation of surroundings to force production is zero as time average. This idea is similar to the model proposed by Huxley in 1957 [32] in the sense that the thermal energy plays an important role to produce force. In his model, however, it is assumed that thermal fluctuation having energy comparable to the ATP hydration energy e_A (about $21kT$ at 0°C) is excited to produce the power stroke. Then the probability for such excitation is approximately proportional to $\exp(-e_A/kT) = \exp(-21) = 7.6 \times 10^{-10}$, which seems too small to be realistic. In our model, a fraction of e_A is used in each cycle of force production and there is no such difficulty.

61.7 CHARACTERISTICS OF THE MODEL THAT ARE HELPFUL FOR NUMERICAL CALCULATIONS

Major experimental data can be explained based on the proposed model as demonstrated in the next section. In this section, factors that are very helpful for numerical calculations are mentioned, leaving details of the calculations to Refs. 5 and 6.

61.7.1 Relation between p and T

Combining Eqs. (61.4) and (61.16) gives

$$p/p_0 = T/T_0, \quad \text{for any } T \tag{61.23}$$

This relation means that we can obtain an expression of any quantity as a function of macroscopic parameter T/T_0 when we derive an expression of the quantity as a function of microscopic parameter p/p_0. This is a very useful relationship for numerical calculations.

61.7.2 Cyclic Force Generation and Parameter y_c

The shortening y of the crossbridge is defined in reference to Fig. 61.8. The parameter y_c is defined in Section 61.6.3 as a critical y at which the U^* transition occurs during the filament sliding. Since y is considered as the critical value y_c in Fig. 61.9a, the U^* transition occurs in next moment and the myosin head changes its partner actin molecules from (a) to (b) with shift of the crossbridge end J by $L = 5.46$ nm. Thus the crossbridge length increases by L and the shortening y changes from y_c to $y_c - L$. In the change from (b) to (c), the myosin filament moves forward by L and the molecular shape of MA_3 becomes the same as (a). Thus y changes from $y_c - L$ to y_c. In the steady filament sliding, y repeats the cycle from (a) to (b) to (c). Figure 61.11 illustrates the cycles on the y axis: y changes from y_c to $y_c - L$ by the U^* transition and from $y_c - L$ to y_c through filament sliding. In the steady sliding, y increases at the constant rate and thus y of all the crossbridges are distributed uniformly between

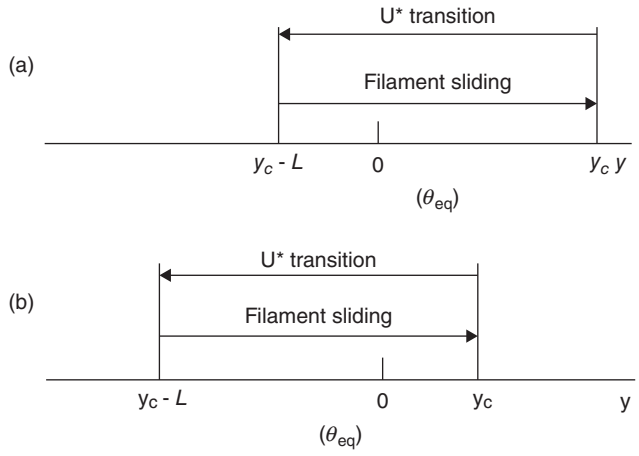


FIGURE 61.11 Cycle of variation of y. The filament sliding velocity is determined by y_c. (a) Fast filament sliding. (b) Slow filament sliding.

$y_c - L$ and y_c at any moment. Accordingly, the force p produced by a crossbridge during one cycle is given by integration of the force $p(y)$ from $y_c - L$ to y_c. Per Eq. (61.21), $p(y)$ is proportional to -y and thus p becomes small as y_c becomes large. Figure 61.9a shows the case of fast sliding for small p and (b) the case of slow sliding for large p.

The tension T is determined by p [Eq. 61.23)] and thus determined by y_c. The filament sliding velocity v is determined by the transition probability $Q(y_c)$ putting $y = y_c$ in Eqs.(61.19) and (61.20). Thus v can be calculated as a function of y_c. The parameter y_c is very useful to discuss also other quantities, as can be seen in Refs. 5 and 6.

61.8 COMPARISON OF CALCULATION RESULTS WITH EXPERIMENTAL DATA

Calculations are done on muscle properties or behaviors on the model proposed model in Refs. 5 and 6. This section illustrates how well the calculation results explain experimental observations. In Section 61.8.1, we comment on postulation in the calculations in Refs. 5 and 6, leaving the details of calculations to those studies [5, 6]. Section 61.8.2 discusses for steady filament sliding as discussed in Ref. 5. Section 61.8.3 covers transition phenomena discussed in Ref. 6.

61.8.1 Existence Probability of Myosin Molecule in Wells in MA_3

Figure 61.6d schematically shows distribution of the existence probability of myosin molecules in wells 1 and 2 in the MA_3 complex. In shortening muscle the myosin head in well 2 moves over the potential barrier U^* and produces force, while the head in well 1 does not directly contribute to force production. Hence, if the muscle is designed as an effective machine, the depth of well 2 will be made suitably deep so that the existence probability in well 2 becomes 1, as shown in Fig. 61.12a. The existence probability is affected also by the tension T. The crossbridges having $y < 0$ pull the myosin filament forward. Then, by reaction, the myosin filament pulls the myosin head of the crossbridge backward and tends to increase the existence probability of the head in well 2. Hence it is a possibility that the existence probability in well 1 become finite when T is large, as shown schematically in Fig. 61.12b.

In Ref. 5, calculations are based on the assumption that the existence probability in well 2 is 1 as shown in Fig. 61.12a. General behaviors of steady filament sliding are clearly explained on this assumption61., as illustrated in Section 8.2. There is, however, disagreement between the calculated result and the experimental data in the force–velocity relation for $T/T_0 > 0.66$ as shown later in Fig. 61.14.

In Ref. 6, finite probability is considered in well 1 as schematically shown in Fig. 61.12b, and the above-mentioned disagreement in the force–velocity relation becomes understandable. The transition phenomena are discussed in relation with the finite probability in well 1. Calculation results clearly explain various experimental data on the transition phenomena as illustrated in Section 61.8.3.

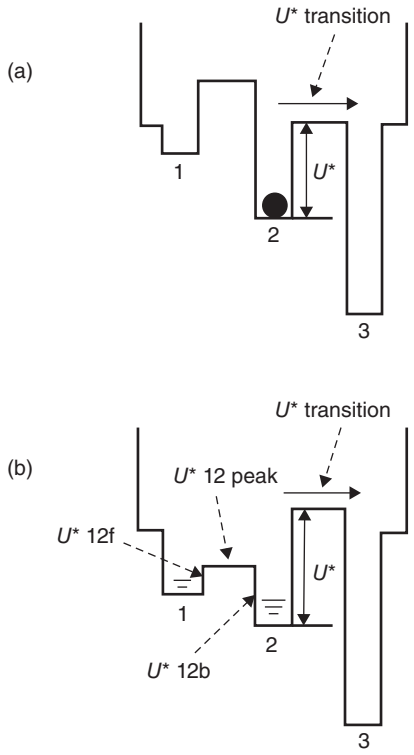


FIGURE 61.12 Existence probability of myosin head in wells of the MA_3 complex. (a) The case of $T < T_{dev}$. The black circle indicates that the myosin head exists solely in well 2. The force–velocity relation is Hill-type in this case. (b) The case of $T_{dev} < T < T_{0obs}$, where the existence probability of the myosin head becomes finite in wells 1, causing deviation of the force–velocity relation from Hill-type.

61.8.2 Steady Filament Sliding

This subsection introduces calculation results in Ref. 5 on muscle behaviors in steady filament sliding. Those calculations [5] are based on the scheme shown in Fig. 61.12a.

The ratio of the stiffness of the muscle at $T = 0$ to that at $T = T_0$ is about 0.35, where T_0 is the isometric tension [13]. This T dependence of stiffness was attributed to the variation of the number of the attached myosin heads in the power stroke model. In our model, the T dependence is explained in terms of the difference between the stiffness κ_f of the crossbridge having the straightened tail and κ_b related with the bent tail [see Eq. (61.22)]. Calculation is done on relative stiffness $S/S(T_0)$ as a function of T/T_0 in Section 4.1 of Ref. 5. Figure 61.13 shows that the calculation results reproduce the general feature of the experimental data.

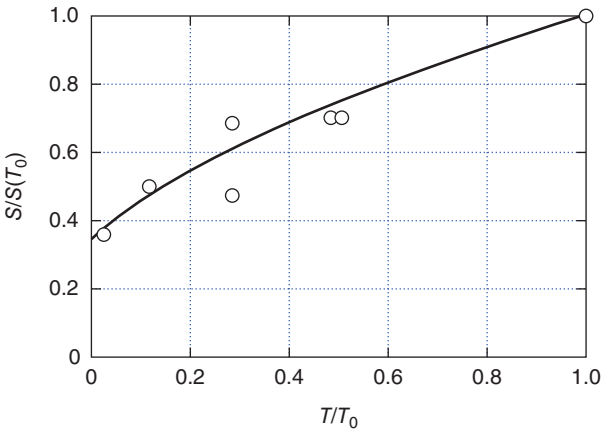


FIGURE 61.13 Relative stiffness $S/S(T_0)$ of muscle as a function of T/T_0, after Fig. 9 of Ref. 5. Open circles represent experimental data cited from Fig. 10B of the paper by Ford et al. [13]. Solid line indicates calculation results in Ref. 5. (Data from Mitsui et al. 2008 [5], Fig. 5 and Ford et al. 1985 [13], Fig. 10B.)

The filament sliding velocity v is calculated for a muscle of unit length as a function of T/T_0 in Section 4.2 of Ref. 5. The unit of v is converted to the value for half sarcomere (μm/s) by using the sarcomere length 2.10 μm reported by Edman [9]. Figure 61.14 shows the result by the curve in comparison with the experimental data given by Edman [9]. The curve coincides with the hyperbolic force–velocity relation reported by Hill [33], and is called *Hill-type curve below*.

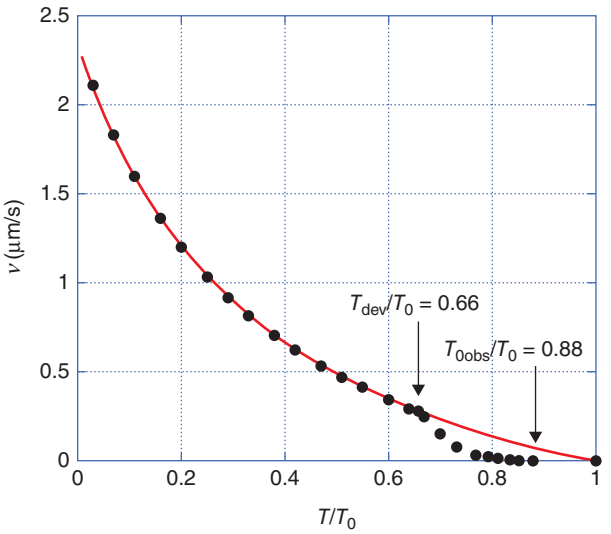


FIGURE 61.14 Force–velocity relation and definition of T_{dev} and T_{0obs}, after Fig. 11 of Ref. 5. The ordinate v is the filament sliding velocity per half sarcomere. The curve is after the calculation result in Ref. 5. Circles correspond to experimental results given in Fig. 6A of the paper by Edman [9]. (Data from Mitsui et al. 2008 [5], Fig. 11 and Edman 1988 [9], Fig. 6A.)

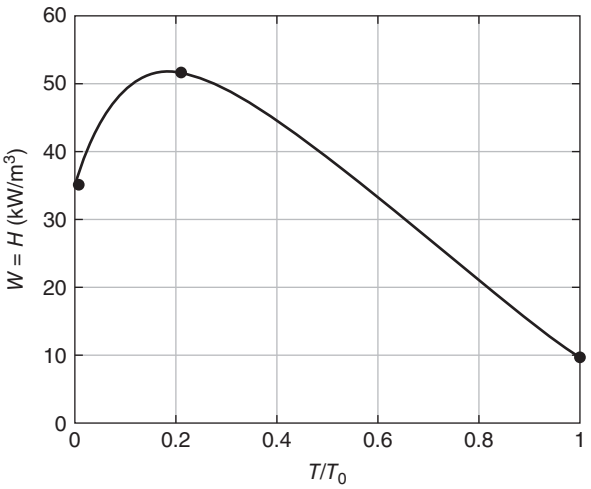


FIGURE 61.15 Energy liberation rate $W + H$ in contracting muscle as a function of T/T_0, after Fig. 12 of Ref. 5. Black circles represent experimental data by Homsher et al. [10]. Curve represents results of calculation [5]. (Data from Mitsui et al. 2008 [5], Fig. 12 and Homsher et al. 1984 [10].)

The distribution of data points, however, deviates from the red curve as the tension increases beyond $T_{dev}/T_0 = 0.66$. The origin of this deviation is discussed later with Fig. 61.18.

In Section 61.3.1, the rates of total energy liberation rate per unit volume of muscle are denoted as $W + H$. In Section 4.3 of Ref. 5, the expression for $W + H$ is derived and given as Eq. (4-3-13). The functional form of the expression is quite similar to the empirical equation given by Hill [34]. Figure 61.15 shows calculation result given in Ref. 5 in comparison with the experimental data.

Figure 61.16 shows the distance D over which a myosin head translates using $e_{A,}$ after Fig. 61.14 of Ref. 5. In the calculation there [5], Eqs. (61.3), (61.5), (61.16), and (61.23) are used with the values given by the curves in Figs. 61.14 and 61.15. Theb D becomes 370 nm for $T = 0$ as expected from Eq. (61.17).

Large values of D can be estimated also from the experiment by Harada et al. [11] mentioned in Section 61.3.4. They observed that most actin filaments shorter than about 40 nm dissociated from the myosin-coated surface, while longer ones remained bound to the surface. This fact suggests that two or three myosin heads are bound to an actin filament of 40 nm so that at least one of the myosin heads remains attached to the filament, although the others occasionally detach. In Section 61.3.4, the mean distance between neighboring myosin molecules d_H is set equal to 12 nm [Eq. (61.9)]. Then the mean number of the myosin heads that can bind to the actin filament of 40 nm is $2 \times 40/12 = 6.7$, considering the two-headed structure of myosin molecule. The ratio of the number of myosin heads attached to the actin filament is denoted as r_H. Then $6.7r_H = 2 \sim 3$. Thus

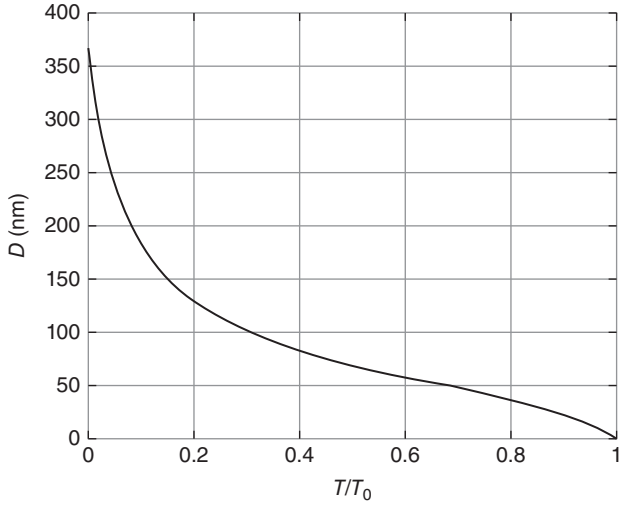


FIGURE 61.16 Calculated D as a function of T/T_0, after Fig. 14 of Ref. 5. D is the distance over which a myosin head translates using the ATP hydrolysis energy e_A. Temperature is about 0°C. (Data from Mitsui et al. 2008 [5], Fig. 14.)

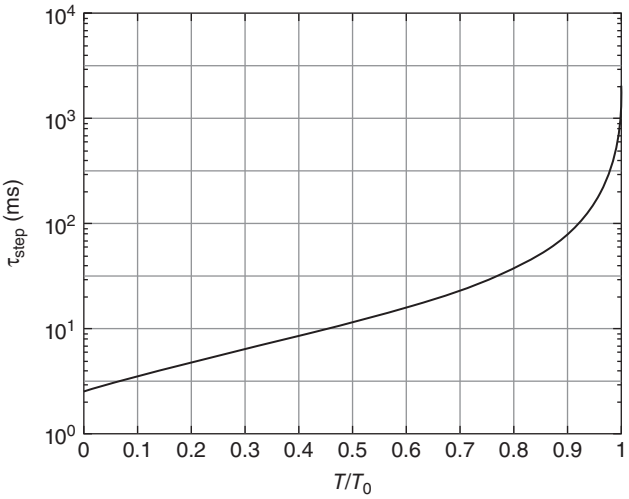


FIGURE 61.17 7 Mean time τ_{step} needed for occurrence of the U^* transition as a function of T/T_0, calculated by Eq. (61.24).

$r_H = 0.30 \sim 0.45$. By using values of $D/r_H = 850$, 350, 1280 nm in Eq. (61.12), we have $D = 260$–380, 110–160, and 380–580 nm at $T/T_0 = 0$. They are as large as 370 nm at $T/T_0 = 0$ in Fig. 61.16. Also Harada et al. [11] observed that an actin filament of about 40 nm sometimes stopped the motion. Presumably in this case only one myosin head remains attached to an actin filament so that there is no cooperatively working mate and the actin filament stops.

To discuss the transition phenomena in the next section, it is important to have an idea about mean time τ_{step} for occurrence of the U^* transition as a function of T/T_0. In the steady filament sliding, τ_{step} corresponds to the time in which a myosin head moves from one actin molecule to the neighboring one. Then τ_{step} is given by

$$\tau_{step} = L/v \tag{61.24}$$

Here $L = 5.46$ nm [Eq. (61.18)] is the distance between the centers of potential wells 2 and 3 in Fig. 61.6d, and v is the sliding velocity, which is given by the curve in Fig. 61.14. Values of τ_{step} calculated by Eq. (61.24) are shown as a function of the relative tension in Fig. 61.17, where τ_{step} is ~2 ms at $T/T_0 = 0$, increasing to ~10 ms at $T/T_0 = 0.5$, and increasing to >100 ms as T/T_0 increases. Hence the U^* transition is a relatively slow process and practically does not contribute to early processes in the transition phenomena, as will be discussed later concerning Fig. 61.20.

61.8.3 Transition Phenomena

Transient phenomena were studied by various workers. Especially, detailed studies were done on the isometric tension transient by Ford et al. [35] and on the isotonic velocity transient by Civan and Podolsky [36]. Calculations are done to explain the experimental data on these transition phenomena in Ref. 6. Results are introduced in this section.

Figure 61.14, on the force–velocity relation, shows that the experimental data deviate from the calculation result (the red curve) for $T/T_0 > T_{dev}/T_0 = 0.66$. The curve coincides with the hyperbolic force–velocity relation reported by Hill [33]. As mentioned in Section 61.8.1, finite existence probability is considered in well 1 as shown schematically in Fig. 61.12b to explain the deviation.

Section 7 of Ref. 6 discusses how U^* varies when the existence probability of the myosin head becomes finite in well 1 in the case of $T > T_{dev}$. A parameter $({y_c}^H - {y_c}^*)$ is derived to represent the structural modulation of MA_3 due to finite existence probability of the myosin head in well 1. As a result, $U^*(y) = {U^*}_0 + ap(y)$ [Eq. (61.20)] has an additional factor $c({y_c}^H - {y_c}^*)$:

$$U^*(y) = U^*0 + ap(y) + c\left(y_c^H - y_c^*\right) \tag{61.25}$$

Here, c is a constant. Calculated $({y_c}^H - {y_c}^*)$ is given as a function of T/T_0 by the curve in Fig. 61.18a. The filament sliding velocity v^* to be observed is given in relation with the Hill-type velocity v^H by

$$v^* = v^H \exp\left(-b_v \left(y_c^H - y_c^*\right)\right) \tag{61.26}$$

Calculation is done by setting

$$b_v = c/kT = 7.9\ (1/\text{nm}) \tag{61.27}$$

Obtained v^* is shown by the curve in Fig. 61.18b, which agrees well with the experimental data by Edman [9].

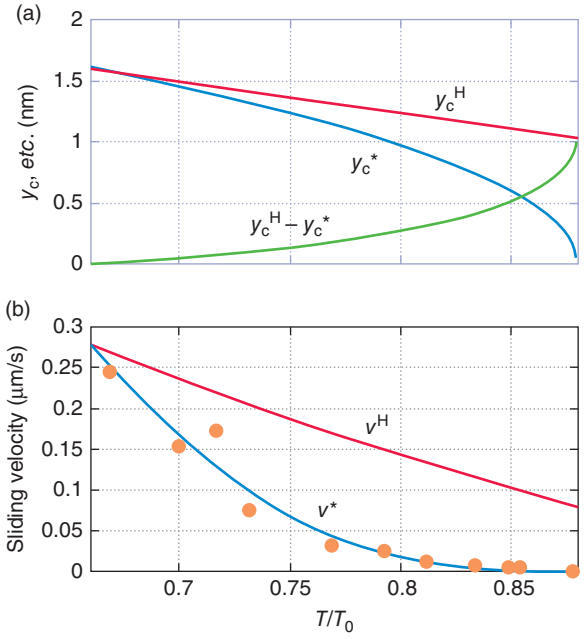


FIGURE 61.18 Deviation of the force–velocity relation from Hill-type, after Fig. 19 of Ref. 6. (a) The curve $y_c^H - y_c^*$ gives values of the same in Eq. (61.25). (b) Circles indicate experimental data of the sliding velocity per half sarcomere obtained referring to Fig. 3A of the paper by Edman [9]. Curve: v^H, the Hill-type filament sliding velocity, the same as the curve in Fig. 61.13. Curve: v^*, the velocity calculated by Eqs. (61.26) and (61.27). (Data from Mitsui and Ohshima [6], Fig. 19 and Edman 1988 [9], Fig. 3A.)

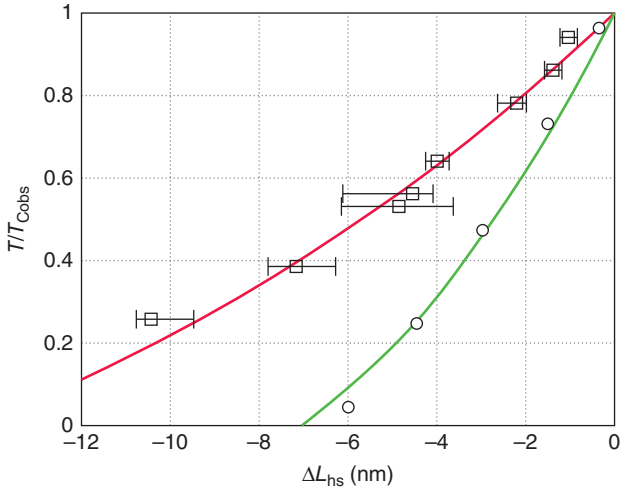


FIGURE 61.19 T/T_{0obs} versus ΔL_{hs} relations in the first phases in the transient phenomena, after Fig. 9 of Ref. 6. Circles indicate experimental data in the isometric tension transient cited from Fig. 13 of Ford et al. [35] Squares represent experimental data in the isotonic velocity transient obtained from Fig. 3 of Civan and Podolsky [36]. The error bar indicates error of readout from Fig. 3 of Ref. 36. The thin curve: T/T_{0obs} calculated for the first phase of the isometric tension transient in Ref. 6. The thick curve: ΔL_{hs} calculated for the first phase of the isotonic velocity transient in Ref. 6. (Data from Mitsui and Ohshima 2011 [6], Fig. 9; Ford et al. 1977 [35], Fig. 13; and Civan and Podolsky 1966 [36], Fig. 3.)

Huxley [37] divided the transient responses to the sudden reduction of length or of load into four phases. The first phase of the isometric tension transient is the step change of tension due to sudden length change. The first phase of the isotonic velocity transient is the step change of muscle length due to the sudden load change. The initial state in these changes is the isometric tetanus state, in which the existence probability of the myosin head is finite in well 1 as shown in Fig. 61.12b. Calculation is done assuming that the existence probability does not change during the first phases in Ref. 6.

Figure 61.19 shows calculation results reported in Section 4 of Ref. 6. Here the length change per half sarcomere is denoted as ΔL_{hs} in both transients and the relative tension is given by T/T_{0obs} (Fig. 61.14 for T_{0obs}). The experimental data by Ford et al. [35] are shown by circles for the isometric tension transient and the data by Civan and Podolsky [36] by squares for the isotonic velocity transient.

In the calculation Ref. 6, it is assumed that there is a time lag in length change of the thin filament against the length changes of crossbridge and the myosin filament, taking the results by Julian and Sollins [38] into account. Also it is assumed that extensibility ratios of the crossbridge, myosin filament and actin filament are 0.22, 0.26, and 0.52. These values roughly agree with the extensibility ratios 0.31, 0.27, and 0.42 estimated through X-ray diffraction [39]. Calculation is done by using the values of stiffness given by Eq. (61.22), which implies that the elasticity of crossbridge is largely nonlinear. The curvatures of the curves in Fig. 61.19 reflect the nonlinearity.

As mentioned above, the results shown in Fig. 61.19 are obtained assuming that the existence probability of the myosin head in well 1 of Fig. 61.12b does not change during the first phases. Thus the initial existence probability becomes unstable after the first phases. The complex muscle behaviors in the following phases are considered as the process that the existence probability in well 1 decreases toward a stable probability at the new state.

Ford et al. [35] studied in detail the relative tension T/T_{0obs} as functions of time t for various length change steps ΔL_{hs} after the first phase in the isometric tension transient. In Fig. 61.20, the green circles represent experimental data cited from Ref. 35, and the red curves show calculated values reported in Section 5 of Ref. 6. The curves are approximately in agreement with the experimental data. The curves become flat as t increases. Since the maximum t in the abscissa is 9 ms, the gap between the flat line and the line of $T/T_{0obs} = 1$ means that there is a very slow process of tension increase with time constant more than 9 ms. As shown in Fig. 61.17, the time τ_{step} needed for the U^* transition increases with T/T_0 and becomes more than 40 ms for $T/T_0 > 0.8$. In Fig. 61.20,

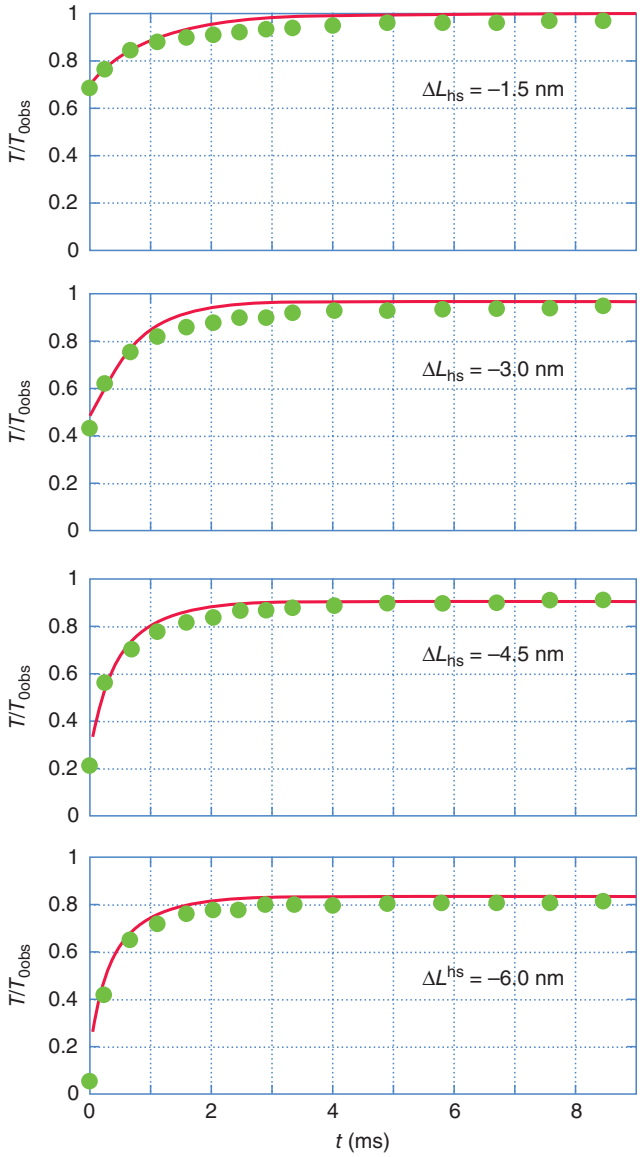


FIGURE 61.20 T/T_{0obs} as functions of time t for various length change steps ΔL_{hs} in the isometric tension transient, after Fig. 14 of Ref. 6. The origin of t is set as the moment that the first phase finishes. Circles indicate experimental data cited from Fig. 23 of Ford et al. [35]. Curves represent calculation results in Ref. 6. (Data from Mitsui and Ohshima 2011 [6], Fig. 14 and Ford et al. 1977 [35], Fig. 23.)

the flat parts appear for $T/T_0 > 0.8$. Accordingly, the U^* transition does not contributes to variation of T/T_{0obs} in the time range in Fig. 61.20.

Civan and Podolsky [36] studied in detail the timecourse of length change ΔL_{hs} after the first phase in the isotonic velocity change. In Fig. 61.21, green circles represent experimental data cited in Ref. 36. Red curves represent calculation results reported in Section 6 of Ref. 6, which show similar tendency as the experimental data.

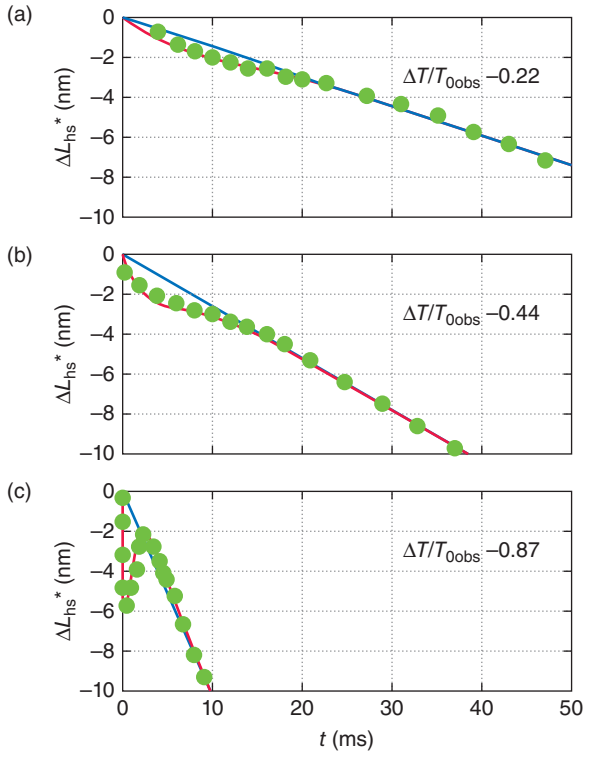


FIGURE 61.21 Length change $\Delta L'_{hs}$ versus t relations for three values of $\Delta T/T_{0obs} = (T_{0obs} - T)/T_{0obs}$, after Fig. 18 of Ref. 6. (a) $\Delta T/T_{0obs} = 0.22$; (b) $\Delta T/T_{0obs} = 0.44$; (c) $\Delta T/T_{0obs} = 0.87$. Data points are obtained from Fig. 3 of the paper by Civan and Podolsky [36]. Straight lines indicate steady filament sliding. Curves: $\Delta L_{hs}'$ calculation results in Ref. 6. (Data from Mitsui and Ohshima 2011 [6], Fig. 18 and Civan and Podolsky 1966 [36], Fig. 3.)

61.9 SUMMARY AND DISCUSSION

61.9.1 Requirements for Models

In Section 61.5, requirements for any models based on the sliding-filament theory are listed. They are discussed with the same item numbers below.

1. Large D/r or D in shortening muscles. Our model is constructed to give the large values of D/r as explained in Section 61.6. The value of r is estimated as 0.41 for any T [Eq. 61.16)], and calculated values of D become as large as shown in Fig. 61.16.
2. Small D observed in experiments with single myosin molecule in vitro. The myosin molecule has to cross over the potential barrier $U^*(y)$ to move from well 2 to well 3 in Fig. 61.12. In our model, U^*_0 is relatively large in the expression $U^*(y) = U^*_0 + apy$ [Eq. (61.20)], and the probability $Q(y) = A\exp(-U^*(y)/kT)$ [Eq. (61.19)] for the myosin head to cross over $U^*(y)$ is small when the force $p(y)$ on

the head is small. In two single-molecule experiments [20, 21], the single myosin molecule has no partner of cooperation and the force on the head $p(y)$ is close to 0, and thus $Q(y)$ is small and D is expected to be about L = 5.46 nm [Eq. (61.18)]. D may be a few times L since there may be some fluctuation of the force depending on the experimental conditions.

3. Crossbridges independently produces force in the isometric tetanus state. As mentioned at the end of Section 61.6.3, the filament sliding is a necessary condition in the cooperative interaction among crossbridges. Since there is no filament sliding in the isometric tetanus state, crossbridges produce force independently in the isometric tetanus state, in agreement with two observations [22, 23].
4. Reasonable explanation should be given to the coupling between the force production and energy liberation by chemical reaction. In our model, the ATP hydrolysis energy stored in a myosin molecule is used by fraction for force production as illustrated in Fig. 61.10. There are repeated chemical reactions between the myosin head and actin filament per the ATP energy. The myosin head has many modes of structural and thermal fluctuations, which makes the fractional use of the ATP energy possible as discussed in Section 61.6.5. This scheme clearly explains the energy liberation rate versus T/T_0 relation as shown in Fig. 61.15.
5. The model should explain major experimental data on muscle properties or behaviors.

   Figures 61.13–61.15 and 61.18–61.21 demonstrate good agreement between calculation results based on the model and the experimental data.

61.9.2 Discussion

It seems quite difficult for the power stroke model to fulfill requirement 1 as discussed in Section 61.4. In the power stroke model, the ATP hydrolysis energy e_A is used in one power stroke. This does not seem efficient use of e_A. As explained with Fig. 61.10, e_A is used in fraction in our model as is done in most biological systems. In the power stroke model, the actin filament is treated as a relatively passive element such as a ladder for a myosin head. In general, protein molecules play a more active role in biological systems.

Extensibility ratios of the crossbridge, myosin filament, and actin filament are assumed to be 0.22, 0.26, and 0.52 to obtain good agreement between the calculation results and experimental data in Fig. 61.19. These values are approximately in agreement with the extensibility ratios 0.31, 0.27, and 0.42 estimated through X-ray diffraction [39]. The ratio is assumed to be 1, 0, and 0 in the power stroke model [40].

Merits of the two-headed structure of myosin molecule are discussed in Section 5.2 in Ref. 5.

Cooperativity among myosin moleules is discussed with respect to cytoplasmic streaming in Characean algae in Section 5.3 of Ref. 5.

Presumably, one can get valuable information on the mechanism of myosin sliding on the actin filament by extending the ingenious experiment by Harada et al. [11], changing experimental parameters and using muscles of different kinds.

Our model has some similarity with the ratchet model [cf., e.g., 41]. In the ratchet model, however, concrete picture seems lacking on chemical reaction and energy liberation process during the force production as posed by requirement 4 in Section 61.5.

Chemical reaction and energy liberation process in our model are illustrated in Fig. 61.10.

As discussed in terms of Fig. 61.6, piezoelectric effect is important to construct the present model. In general, protein molecules are structurally polar, and hence any biological system should be treated as a system of four variables (stress, strain, electric field, and polarization) from the physical perspective, as mentioned also in the discussion on the flagellar rotary motion [42, Section 6.1].

REFERENCES

[1] Huxley, A.F. (1980). *Reflections on Muscle*. Liverpool Univ. Press, Liverpool, UK.

[2] Huxley, H.E. (1953). Electron microscope studies of the organization of the filaments in striated muscle. *Biochim. Biophys. Acta* **12**, 387–394.

[3] Huxley, H.E., Hanson, J. (1954). Changes in the cross-striations of muscle during contraction and stretch and their structural interpretation. *Nature* **173**, 973–976.

[4] Huxley, A.F., Niedergerke, R. (1954). Interference microscopy of living muscle fibres. *Nature* **173**, 971–973.

[5] Mitsui, T., Ohshima, H. (2008). Remarks on muscle contraction mechanism. *Int. J. Mol. Sci.* **9**, 872–904.

[6] Mitsui, T., Takai, N., Ohshima, H. (2011). Remarks on muscle contraction mechanism II. Isometric tension transient and isotonic velocity transient. *Int. J. Mol. Sci.* **12**, 1697–1726.

[7] Mitsui, T., Ohshima, H. (2011). Theory of muscle contraction mechanism with cooperative interaction among crossbridges. *Biophysics* **8**, 27–39.

[8] Mitsui, T., Ohshima, H. (1988). A self-induced translation model of myosin head motion in contracting muscle. I. Force-velocity relation and energy liberation. *J. Muscle Res. Cell Motility* **9**, 248–260.

[9] Edman, K.A.P. (1988). Double-hyperbolic force-velocity relation in frog muscle fibres. *J. Physiol.* **404**, 301–321.

[10] Homsher, E., Irving, M., Yamada, T. (1984). The effect of shortening on energy liberation and high energy phosphate hydrolysis in frog skeletal muscle. In Pollack, G.H., Sugi, H. (eds.), *Contractile Mechanism in Muscle*. Plenum Press, New York, pp. 865–876.

[11] Harada, Y., Sakurada, K., Aoki, T., Thomas, D.D., Yanagida, T. (1990). Mechanochemical coupling in actomyosin energy transduction studies by *in vitro* movement assay. *J. Mol. Biol.* **219**, 49–68.

[12] Geeves, M.A., Holmes, K.C. (2005). The molecular mechanism of muscular contraction. *Adv. Protein Chem.* **71**, 161–193.

[13] Ford, L.E., Huxley, A.F., Simmons, R.M. (1985). Tension transients during steady shortening of frog muscle fibers. *J. Physiol.* **361**, 131–150.

[14] Ishijima, A., Harada, Y., Kojima, H., Funatsu, T., Higuchi, H., Yanagida, T. (1994). Single-molecule analysis of the actomyosin motor using nano-manipulation. *Biochem. Biophys. Res. Commun*. **199**, 1057–1063.

[15] Matsubara, I., Yagi, N., Hashizume, H. (1975). Use of an X-ray television for diffraction of the frog striated muscle. *Nature* **255**, 728–729.

[16] Yagi, N., Takemori, S., Watanabe, M. (1993). An X-ray diffraction study of frog skeletal muscle during shortening near the maximum velocity. *J. Mol. Biol.* **231**, 668–677.

[17] Podolsky, R.J., Onge, S. St., Yu, L., Lymn, R.W. (1976). X-ray diffraction of actively shortening muscle. *Proc. Natl. Acad. Sci. USA* **73**, 813–817.

[18] Huxley, H.E. (1979). Time resolved X-ray diffraction studies in muscle. In Sugi, H., Pollack, G.H. (eds.), *Cross-bridge Mechanism in Muscle Contraction.* Univ. Tokyo Press, Tokyo, pp. 391–405.

[19] Huxley, H.E., Kress, M. (1985). Crossbridge behaviour during muscle contraction. *J. Muscle Res. Cell Motility* **6**, 153–161.

[20] Molloy, J.E., Burns, J.E., Kendrick-Jones, J., Tregear, R.T., White, D.C.S. (1995). Movement and force produced by a single myosin head. *Nature* **378**, 209–212.

[21] Kitamura, K., Tokunaga, M., Hikikoshi-Iwane, A., Yanagida, T. (1999). A single myosin head moves along an actin filament with regular steps of 5.3 nanometres. *Nature* **397**, 129–134.

[22] Ramsey, R.W., Street, S.F. (1940). The isometric length-tension diagram of isolated skeletal muscle fibers of the frog. *J. Cell. Compar. Physiol.* **15**, 11–34.

[23] Gordon, A.M., Huxley A.F., Julian, F.J. (1966). The variation in isometric tension with sarcomere length in vertebrate muscle fibers. *J. Physiol.* **184**, 170–192.

[24] Andreeva, A.L., Andreev, O.A., Borejdo, J. (1993). Structure of the 265- kilodalton complex formed upon EDC cross-linking of subfragment 1 to F-actin. *Biochemistry* **32**, 13956–13960.

[25] Xiao, M., Andreev, O.A., Borejdo, J. (1995). Rigor cross-bridges bind to two actin monomers in thin filaments of rabbit psoas muscle. *J. Mol. Biol.* **248**, 294–307.

[26] Oosawa, F., Asakura, S. (1975). *Thermodynamics of the Polymerization of Proteins*. Academic Press, New York, pp. 66–67.

[27] Rayment, I., Holden, H.M., Whittaker, M., Yohn, C.B., Lorenz, M., Holmes, K.C., Milligan, R.A. (1993). Structure of the actin-myosin complex and its implications for muscle contraction. *Science* **261**, 58–65.

[28] Eyring, H. (1936). Viscosity, plasticity, and diffusion as examples of absolute reaction rate. *J. Chem. Phys.* **4**, 283–291 [see also Section 27.4, The Eyring equations, in Atkins, P.W. (1998). *Physical Chemistry*, 6th ed., Freeman & Co. and Sumanas, New York, 1998].

[29] Huxley, A.F., Simmons, R.M. (1971). Proposed mechanism of force generation in striated muscle. *Nature* **233**, 533–538.

[30] Mitsui, T., Tatsuzaki, I., Nakamura, E. (1976). *An Introduction to the Physics of Ferroelectrics*. Gordon & Breach, New York.

[31] Lymn, R.W., Taylor, E.W. (1971). Mechanism of adenosin triphosphate hydrolysis by actomyosin. *Biochemistry* **10**, 4617–4624.

[32] Huxley, A.F. (1957). Muscle structure and theories of contraction. *Progress Biophys. Biophys. Chem.* **7**, 255–318.

[33] Hill, A.V. (1938). The heat of shortening and the dynamic constants of muscle. *Proc. Roy. Soc.* **B126**, 136–195.

[34] Hill, A.V. (1964). The effect of load on the heat of shortening muscle. *Proc. Roy. Soc. B* **159**, 297–318.

[35] Ford, L.E., Huxley, A.F., Simmons, R.M. (1977). Tension responses to sudden length change in stimulated frog muscle fibres near slack length. *J. Physiol.* **269**, 441–515.

[36] Civan, M.M., Podolsky, R.J. (1966). Contraction kinetics of striated muscle fibres following quick changes in load. *J. Physiol.* **184**, 511–534.

[37] Huxley, A.F. (1974). Muscular contraction. *J. Physiol.* **243**, 1–43.

[38] Julian, F.J., Sollins, M.R. (1975). Variation of muscle stiffness with force at increasing speed of shortening. *J. Gen. Physiol.* **66**, 287–302.

[39] Wakabayashi, K., Sugimoto, Y., Tanaka, H., Ueno, Y., Takazawa, Y., Amemiya, Y. (1994). X-ray diffraction evidence for the extensibility of actin and myosin filaments during muscle contraction. *Biophys. J.* **67**, 2422–2435.

[40] Irving, M. (1995). Give in the filament. *Nature* **374**, 14–15.

[41] Juelicher, F., Ajdari, A., Prost, J. (1997). Modeling molecular motors. *Rev. Mod. Phys.* **69**, 1269–1281.

[42] Mitsui, T., Ohshima, H. (2012). Proposed model for the flagellar rotary motor with shear stress transmission. *Biophysics* **8**, 151–162.

62

NANOCARRIERS OF FUNCTIONAL MATERIALS FROM AMINO ACID SURFACTANTS

Geetha Baskar, S. Angayarkanny, and Asit Baran Mandal
CSIR–Central Leather Research Institute (CLRI), Adyar, Chennai 600 020, India

62.1 INTRODUCTION

Nanocarriers, which typically range within 1–100 nm in size, are excellent reservoirs and vehicles of functional materials. Because of their high surface area:volume ratio, nanocarriers provide incredible scope in the manipulation of structures at nanometer scale, and exhibit remarkable characteristics. They provide encapsulation of functional materials with retention of inherent characteristics. They act as smart vehicles and aid in site-specific delivery of functional materials [1–3]. Nanocarriers are emerging as promising materials in drug delivery systems for challenging diseases such as cancer [4]. The important characteristics of nanocarriers have implications on the economy, efficiency, and environment in terms of applied materials and industries. The "smart" nanocarriers, which exhibit characteristics in response to external stimuli such as temperature and pH, are in demand in various applications. In fact, nanocarriers have brought about revolutionary green approaches in various industries [5–7]. Nanocarriers occupy an intense area of research, and there is growing interest in designing nanocarriers to meet the increasing demand. Amphiphiles, simple and polymeric types, and nanoparticles from organic and inorganic polymers are the well-identified substrates that produce nanocarriers [8–11]. The substrates consist of regions that have large variations in polarity; for example, nonpolar core and polar shell structures are the most suitable architectures for nanocarriers. They enable stable dispersions in size ranging within a few nanometers of functional materials such as drugs. Here, in view of the small size of the dispersed structures and the density difference between the continuous and dispersed phases, the colloidal dispersions are stable. Some of the important physicochemical characteristics of the nanocarriers, the principles of which are drawn from emulsion-phase structures, play a significant role on the stability of the colloidal dispersions [12, 13].

The main focus in the field of nanocarriers is to develop low-cost simple methodology for the tailormade nanocarriers for cosmetics, diagnostic tools, and drugs [14] for which the self-assembled structures form one of the best options. Self-assembled structures such as micelles, vesicles, and liposomes, ranging with a few nanometers in size, are formed in solutions of low-molecular-weight surfactants, also known as *amphiphiles.* Macromolecules of molecular weight generally $\geq 10^4$ Da, also form self-aggregated structures such as polymeric micelles and polymerosomes, 5–100 nm in size. A pictorial representation of nanocarriers from self-assembled structures of simple and polymeric amphiphiles and the inorganic polymer nanoparticle is presented in Fig. 62.1.

It is essential to understand the fundamental aspects underlying the process of self-assembly and the formation of self-aggregated structures for the design of nanocarriers. With growing concern for energy and environment, there is an obvious demand for the design of high-performance nanocarriers derived from biodegradable resources. For this, the ideal source materials are proteins, peptides, amino acids, natural oils, and sugar. These surfactants from such natural sources are broadly classified as *biosurfactants*. The most popular application of nanocarriers from biosurfactants is in the field of drug delivery systems. They are being widely exploited in medicine from the context of diagnostics and targeted

Encyclopedia of Biocolloid and Biointerface Science, Volume 2, First Edition. Edited by Hiroyuki Ohshima.
© 2016 John Wiley & Sons, Inc. Published 2016 by John Wiley & Sons, Inc.

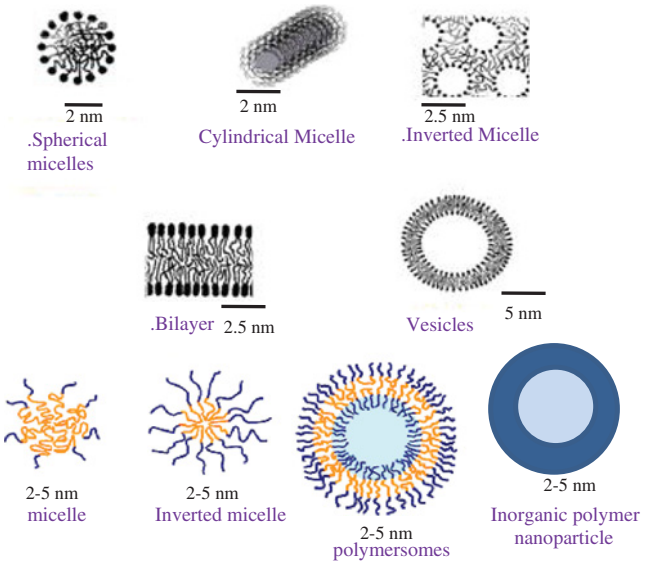


FIGURE 62.1 Pictorial representation of nanocarriers from self-assembled structures of simple and polymeric amphiphiles, and the inorganic polymer nanoparticle.

delivery of drugs, as seen from literature reports [15]. Nanocarriers from polymeric nanopartilces are produced adopting template assisted strategy involving self-assembled structures of amino acid surfactants. By virtue of structures, nanocarriers facilitate the colloidal dispersions of drugs, and facilitate travel in the body fluid consisting of water as the major component, and targeted delivery of the drugs. They can be considered for potential applications that include herbicides, pesticide formulations, detergents, healthcare, cosmetics, paper, coal, textiles, ceramic processing, food industries, and/or processing [16–19].

In this chapter, a brief report of self-assembled structures of simple and polymeric amphiphiles, followed by an elaborate account of biosurfactants, especially those derived from amino acid derivatives, is presented. Applications of nanocarriers from amino acid surfactants, polypeptides, and polymers consisting of amino acid or peptide segments, especially in drug delivery, are discussed. The scope for producing nanocarriers from polymeric nanoparticles employing the self-assembled structures of simple and polymeric amino acids surfactants is also discussed.

62.2 SELF-ASSEMBLY AND AGGREGATED STRUCTURES

The self-assembly process eventually leading to formation of aggregated structures occurs in simple and polymeric amphiphiles. Amphiphiles are compounds consisting of hydrophilic and lipophilic or, in other words, hydrophobic groups. From the terminology, one can understand that

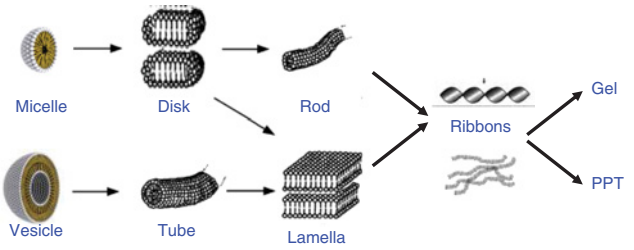


FIGURE 62.2 Intercoversion of self-aggregated structures.

hydrophilic groups are those having affinity for water and therefore are generally polar. Hydorphobic or lipophilic groups interact with air or nonpolar solvents. In water, amphiphiles self-assemble to form different structures such as micelles, vesicles, or gels [20–24]. Inverse micelles are formed in nonaqueous solvents as demonstrated in a report by Mandal et al. [25]. An excellent account of the hierarchy of self-aggregated structures in simple and polymeric amphiphiles was given by another team [26]. The interconversion of aggregated structures ultimately leading to formation of gel or precipitate from the simple assembled structures such as micelles is ilustrated in Fig. 62.2. The microstructure of self-organized assemblies on an infinitesimal scale underlies the comprehensive performance in various applications [27–31].

62.2.1 Self-Aggregated Structure Formation in Simple Amphiphiles

The molecular interactions due to electrostatic, hydrophobic, and van der Waals forces are the driving forces in the self-assembly. The chemical architecture of the surfactants plays a significant role in determining the formation of self-assembled structures [32–35]. On the basis of the charge carried by the polar group attached to the hydrophobic segment, surfactants are classified as anionic, cationic, nonionic, and/or zwitterionic; the details on the self-assembly in surfactants of different charge characteristics can be found in the work of Rosen [36]. Basically, the formation of self-assembled structure is governed by the packing parameter (p) that is dependent on the length of the hydrophobic group and the surface area of the headgroup/molecule at the interface [37]. A general understanding is that surfactants consisting of single headgroup and tailgroup prefer to organize as micelle assemblies and those with double tail and single head, as lamellae or vesicles. There are, of course, exceptions to these tendencies.

A typical micelle aggregate in water consists of the hydrophilic "head" regions in contact with the surrounding solvent and the hydrophobic “tail” regions in the micelle center. This type of micelle is known as a *normal-phase micelle* (oil-in-water micelle). Inverse micelles have headgroups at the center with the tails extending outward

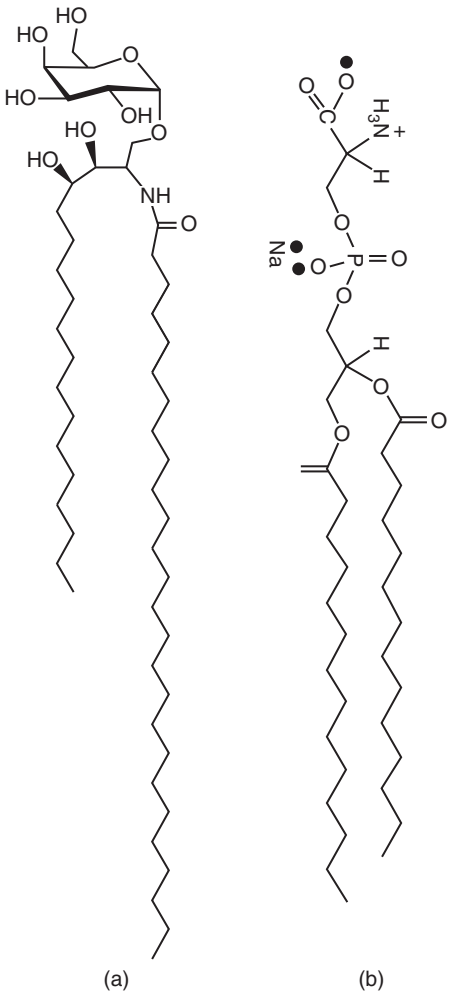


FIGURE 62.3 Structural representation of (a) glycolipid and (b) phospholipid.

(water-in-oil micelle). Figure 62.3 may be referred to for structures. Micelles are approximately spherical in shape. The chemical architecture and the microenvironment play a significant role in the formation of unusual micelle structures such as ellipsoids and cylindrical and inverse micelles. The size and shape of these assemblies depend on the chemical architectures of surfactants, and may vary with concentration, temperature, and solvent. In ionic surfactants it is possible to change the surfactant behavior from a hydrophilic to lipophilic compound. The transformations in solution structures from globular (spherical) to flexible rodlike micelle assemblies occur as a result of increase in concentration. The variations in temperature and number of ethylene oxide groups affect modulations in solution structures in nonionic surfactants from ethoxylated alcohols [38]. Vesicles consist of bilayer organization of the surfactant molecules in a spherical architecture. The important architecture requirement for the formation of bilayer is presence of double tail and single headgroup; classic examples are phospholipids and glycolipids (Fig. 62.3). By virtue of bilayer organization, vesicles exhibit extraordinary characteristics. They provide a waterpool inside the aggregates that facilitates encapsulation of polar functional compounds such as dyes and drugs. Vesicles exhibit excellent microfluidity and stability characteristics that are required in the design of stable nanocarriers. Cell membranes consist of vesicles and act as carriers transporting proteins and nucleic acids between cells [39].

The formation of vesicles or, in other words, bilayer structures from single-chain amphiphiles, attracts significant attention. The mechanism operating in the reversible transformation of structures varying between micelles and vesicles in phospholipids has been described [40]. Several strategies such as tuning the packing parameter, design of amphiphiles, and selection of external stimuli are adopted to form bilayer assemblies from single-chain amphiphiles [41–43]. The tuning of the intermolecular forces affords programmed transformations of aggregated structures. They are desirable in the design of smart materials [44, 45]. The formation of vesicles and micelle structures in mixtures of cationic and anionic surfactants [46], and fatty- acid soaps [47], has been demonstrated. Interestingly, these amphiphiles are preferred in view of reversible switching between micelles and vesicles.

62.2.2 Different Chemical Architectures in Surfactants

In low-molecular-weight surfactants, based on the chemical architecture, amphiphiles are classified as simple geminis and bola amphiphiles. Please note that low-molecular-weight surfactants are also referred as simple surfactants. In simple surfactants, as determined by the packing parameter, different structures such as micelles, vesicles, and membranes are formed.

Gemini surfactants are characterized by two hydrophilic and hydrophobic groups that are linked by the spacer group (Fig. 62.4). Thus, Geminis exhibit extraordinary surface activity and aggregation behavior. A review on geminis may be found in the literature [48,49]. In geminis, the modulation in aggregated structures is afforded through symmetric and asymmetric variations in the alkyl chain length and the spacer groups. In this way, different types of aggregated structures, namely, micelles, bilayers, vesicles, and membranes, could be generated. The optimization of electrostatic interaction

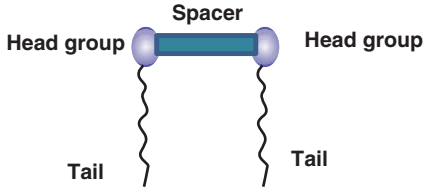


FIGURE 62.4 Chemical structural representation of gemini surfactant.

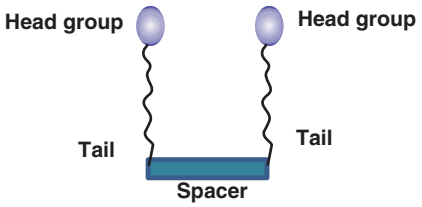


FIGURE 62.5 Chemical structural representation of bola amphiphile.

and the intramolecular hydrophobic association as dictated by the spacer groups, account for the formation of various types of aggregated structures. The structure–property correlation in geminis has been reviewed in the literature [50–52]. In view of the industrial significance, the popular cationic geminis with methylene spacer groups have been investigated in detail with respect to the adsorption and aggregation characteristics under various conditions [53–55].

Bola amphiphiles (also known as *bolaform surfactants*, *bolamphiphiles*, or *alpha–omega-type surfactants*) are amphiphilic molecules that have hydrophilic groups at both ends of a long hydrophobic hydrocarbon chain (Fig. 62.5) [56, 57] or, in other words, two surfactants connected at their tails. Compared to simple surfactants, the bola amphiphiles have higher solubility in water, which may be due to the introduction of a second headgroup. The second headgroup also induces an increase in the critical micelle concentration (cmc), and a decrease in aggregation number. The bola amphiphiles form self-aggregates such as spheres, cylinders, disks, and vesicles. Therefore, bola amphiphiles are considered as hydrophobic skeletons with two water-soluble headgroups on both ends [58–65]. Bolaform amphiphiles exhibit high thermal resistance and are identified in the cell membranes of thermophilic bacteria. The formation of controlled self-assembly by bolaamphiphiles has been understood according to the concepts of supraamphiphiles with noncovalent interactions [66–69].

62.3 POLYMERIC AMPHIPHILES

The concept of self-assembly in simple surfactants is extended to polymeric amphiphiles to generate self-assembled structures of remarkable stability and structural diversity [70–73]. The self-assembled structures such as micelles of low-molecular-weight surfactants are dynamic, as continuous exchange occurs between the aggregated and nonaggregated structures within them. On the contrary, in view of covalent bond force between the molecules in the aggregated structures and the entanglement of chains, the aggregated structures that from polymeric amphiphiles show extraordinary stability. Furthermore, they provide a large structural diversity due to variations in the chemical architectures and distribution of different segments, and exhibit smart behavior responding to external stimuli such as pH and temperature.

The hydrophilic-lipophilic balance (HLB) in polymeric amphiphiles is modified by adopting a simple method, through variation in ratio of chain length of different components. Polymeic amphiphiles are, in fact, recognized as one of the potential nanocarriers. One team has presented an excellent review on the polymer nanocarriers [74]. Polymeric amphiphiles form different aggregated structures determined by the hydrophilic lipophilic balance and the architectures.

62.3.1 Architectures and Formation of Self-Aggregated Structures in Polymeric Amphiphiles

Polymeric amphiphiles exhibit different architectures such as block, random, comblike, and brushlike, as determined by the chemical characteristics and distribution of the segments (Fig. 62.6). Polymeric amphiphiles with block copolymer architecture are synthesized by employing synthetic strategies such as cationic, anionic, atom transfer radical polymerization (ATRP), and reversible addition fragmentation chain transfer (RAFT) reactions. For example, pluronics, one of the best-known block copolymer amphiphiles, consist of hydrophilic and hydrophobic blocks derived from poly(ethylene oxide) (PEO) and poly(propylene oxide) (PPO), respectively. They form direct and indirect micelles depending on the HLB as determined by the PEO and PPO blocks, respectively, and also microenvironment as detailed in studies by Mandal et al. [75–78].

62.3.2 Self-Organisation in Graft Polymers and Other Polymeric Amphiphiles

Polymeric amphiphiles from graft polymers are popular, especially in view of simple synthetic methodologies. The

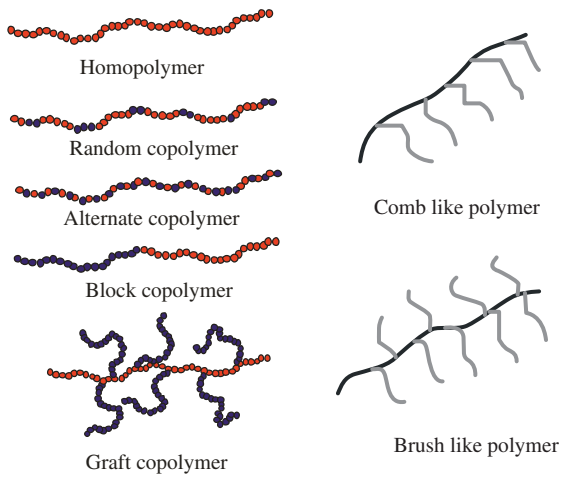


FIGURE 62.6 Pictorial representation of polymeric amphiphiles of different architectures (red, hydrophilic; blue, hydrophobic).

approaches are (1) grafting of preformed polymer onto suitable backbone through chemical reactions [typical examples are grafting amino-terminated poly(styrene) (PS) on the poly(acrylic acid) (PAA) backbone chain [79] and PAA-*g*-poly(*N*-isopropyl acrylamide) (PNIPAM) [80]] and (2) graft polymerization of a monomer on a suitable polymeric backbone through free-radical and ionic polymerization methods as in the case of cholestryl-grafted poly(propyl amino methacrylate) copolymers [81]. The structural architecture of polymeric amphiphiles and the microenvironment provided at different interfaces both dictate formation of self-assembled structures that vary among monolayers, vesicles, and micelles. The influence of structural features on the adsorption characteristics and scope for modulation of these characteristics through changes in chain architecture of the polymer, hydrophilic and hydrophobic chain length, introduction of spacer group [82], and additives are well documented in the literature [83]. The influence of polymer architecture on the behavior of polymers has also been well documented in a more recent report [84]. It is understood that secondary bond forces arising from H-bonding, electrostatic, and hydrophobic interactions control the formation of self-assembled structures. Water-soluble polymeric amphiphiles with comblike structures are in high demand from the perspectives of synthetic strategies and functional characteristics. They can generate functional latex that forms novel cross-linked structures [85]. They perform as effective steric stabilizers at the interface and could form stable colloidal dispersions or emulsion-phase structures. It is noteworthy that emulsion-phase structures are gaining popularity as templates in the generation of nanomaterials [86].

Water-dispersible ionic polymers with comblike architectures form different kinds of associated structures varying between polyelectrolytes to polysoaps. The predominance of electrostatic interaction promotes polyelectrolyte structures in aqueous medium, as shown for in polyacrylic and related acids [87], whereas polysoap structures resembling micelle-like nanostructures are promoted in polymers with long hydrocarbon sidechains, through hydrophobic association [88, 89]. The efficient use of comblike copolymers from acrylic acid and octadecyl acrylates in miniemulsion polymerization reactiond to produce poly(styrene) latex has been established [90].

Polymeric amphiphiles consisting of biodegradable segments drawn from biologically related and biocompatible species have been reported. Polymers consisting of sugars or steroids units provide rigid headgroups that can be functionalized using different reagents. For example, 2-amino-2-deoxy-D-glucopyranose, the building block of chitin [91], can be ionized specifically at the amino and hydroxyl terminals to form interesting starting materials for sugar- based surfactants. Several anionic, cationic, and nonionic 2-aminoglucose-based surfactants are known. Synthesis and solution properties of two new glucose-based series, namely, sodium methyl-2-acylamido-3-deoxy-6-*O*-sulfo-D-glucopyranosides, were recently studied. The chemical modification of self-aggregated structures of surface-active polymers or, in other words, polymerizable amphiphiles, is a promising approach to forming stabilized structures as reported [92, 93].

62.4 AMINO ACID SURFACTANTS

62.4.1 Highlights of Unique Characteristics of Amino Acid Surfactants

The biodegradability, facile green methodologies in the generation of amino acids, the chemical architecture consisting of chiral centers, functional groups such as carboxyl, amino groups that undergo facile chemical modifications, the wide structural diversity, and response to external stimuli like pH, all account for choice of amino acid surfactants as nanocarriers [94–100]. The superior properties of amino acid surfactants to form rods, fibers, and tubes as a result of one-dimensional growth of the aggregated structures have been comprehensively described in one review [101]. The structure–property correlation; the reversible manipulation of structures among micelles, vesicles, and fibers through change in pH and temperature; and the role of chirality in the aggregated structures have been demonstrated in the literature [102–105]. Simple, gemini, and bola amphiphiles that exhibit different chemical architectures can be designed from amino acids. They self-organize in presence of solvents to form different types of aggregated structures similar to those established through classic surfactants.

The most popular and well-known example of amino acid surfactants is the *N*-fatty acyl amino acid surfactant, known for quite a long time and derived from the renewable sources of amino acids and vegetable oils [106–110]. The widespread applications of these surfactants in pharmaceuticals, antimicrobial agents, food emulsifiers, and cleaning agents are well established [111]. There is an excellent scope for the synthesis of *N*-fatty acyl amino acids surfactants from leather waste and silkworm industries [112]. The ordered structures from amino acids, peptides, and proteins find diverse advanced applications [113].

62.4.2 Types of Amino Acid Surfactants

Amino acids belonging to different types (viz., acidic, basic, and neutral) form the starting materials for the synthesis of amino acid surfactants. Examples of some amino acids are glycine, alanine, leucine, valine, serine (neutral), aspartic acid, glutamic acid (acidic), proline, and lysine (basic) (see Table 62.1).

The chemical structures of amino acids facilitate the design of anionic, cationic, and zwitterionic surfactants

TABLE 62.1 Classification of Amino Acids

Characteristics	Amino acids
Hydrophilic, acidic	Aspartic acid, glutamic acid
Hydrophilic, basic	Lysine, arginine, and histidine
Hydrophilic, nonionic	Glycine, serine, cysteine, tyrosine, threonine, asparagin, and glutamine
Hydrophobic	Alanine, leucine, isoleucine, proline, phenyl alanine, tryptophan, methionine

through selective chemical modifications of the carboxyl and the amino groups. Furthermore, the side chain structures in the acidic, basic, and neutral amino acids play a significant role in the self-assembly process. Amino acid surfactants are versatile nanocarriers, and, in fact, it is possible to fine-tune the properties of the aggregates to suit almost every application. In these surfactants, the amino acids and long aliphatic chains have been combined with each other to generate three main structures: (1) linear or single-chain, (2) dimeric or gemini, and (3) glycerolipidlike structures. Linear structures consist of an amino acid bearing at least one hydrophobic tail derived from fatty acids, alcohols, or amines [114–117]. It is to be noted that single-chain lipo–amino acid surfactants exhibit diversity in structures with the common chiral centers, and therefore, afford nanocarriers with large variations in the characteristics [118–122]. The remarkable varieties of structures from lysine amino acids, in view of availability of one carboxyl group and two amino groups, have been studied in detail. Lysine-derived surfactants cover anionic, cationic, and nonionic types depending on chemical modification to form ester or amide linkage [123].

The disulfide amino acid cystine is one of the best starting amino acids for the synthesis of geminis. This amino acid, the major component of keratin present in hair, is known for the inherent characteristics to form fiberlike structures. Cationic geminis from *N* -alkyl derivatives and anionic, from fatty esters, from cysteine, exhibit superior aggregation behavior. Geminis derived from cystine dimethyl ester, cystamine dichydrochloride [124], and *N*- alkyl cystine esters [125] have been reported.

62.4.3 Self-Assembled Structure Formation in Amino Acid Surfactants

Amino acid amphiphiles, when dissolved in water, self-assemble to form various supramolecular assemblies that give rise to primary, secondary, and tertiary structures. The primary structure (angstrom to nanometer scale) is determined by the molecular level recognition of the aggregate. The secondary structure (nano- to micrometer scale) is defined as the morphology of the aggregates, that is, micelles, vesicles, fibers, ribbons, or sheets. They are directly influenced by the molecular structure. Secondary structures give rise to tertiary structures such as disks and fibers. The fibers could precipitate, or form gel depending on the electrostatic and H-bonding interactions [126].

The assembled structures of different morphology and the influence of chemical structural features, especially in the micellization process, are presented here to help the reader understand the spectacular self-assembling process of the amino acid amphiphiles.

The length of alkyl chain essentially controls the hydrophobic interaction. The influence of odd- and even-number carbons in the alkyl chain on the type of aggregated structures could be seen in the series of bolaamphiphiles. Shimizu and colleagues synthesized a new family of oligopeptide-based bolaamphiphiles, glycylglycine-, glycylglycylglycine-, sarcosylsarcosine-, L-prolyl-L-proline-, glycylsarcosylsarcosine-, and glycyl-L-prolyl-L-proline-based bolaamphiphiles with a dicarboxylic headgroup at each end [127]. It was observed that only sodium or potassium salts (acid soap) of the bola amphiphiles, with an even-number alkyl chain ($n = 6,8,10$), produced well-defined microtubes of 1–3 μm diameter with closed ends. All tubes encapsulated a number of vesicular assemblies inside the aqueous compartment. The odd-number alkyl chain surfactants form relatively stronger hydrogen bonds between amide groups and are not suitable for the formation of intralayer anion dimmers and hence microtubes. Nanoscale fibers with widths of 10–30 nm, via proton triggered self-assembly of bola amphiphiles consisting of L-valyl-L-valine moiety in water [127]. The dependence of pK_a on chain length in bola amphiphile was also demonstrated. On increasing chain length of the bola amphiphile from 6–10 carbon atoms, the pH for complete protonation of the bola amphiphile increased from 3.40 to 4.90. Similar alkyl-chain-length-dependent pK_a in amino- acid-based amphihiples was reported [128]. The alkyl-chain-length-dependent hydration and the micellisation process are demonstrated in the homologues series of anionic surfactants from alanine, namely, sodium-*N*-(alkyloxycarbonyl) alanine, varying alkyl chain as octyl, dodecyl, hexadecyl, and octadecyl. One team showed significant differences in the micellisation process of nonionic surfactants derived from lysine [129]. These amphiphiles consist of two different fatty-acid chains in the hydrophobic part and one or two polyoxyethylene methoxy–capped chains in the hydrophilic headgroup. It was shown that the asymmetry surfactants exhibit better surface activity and micellization characteristics. Another team demonstrated the effect of alkyl chain length on the conformation of aggregated structures in aqueous medium [130]. It was shown that the conformation adopted by two optically active cationic surfactants with different sidechains from phenylalanine and leucine was different in aqueous medium. Nuclear magnetic resonance (NMR) studies indicate that the phenyl ring is directed into the micellar core, while the isopropyl group is directed outward from the micellar

core. Interestingly, the area per molecule occupied by the surfactants at the air–water interface (43.6 $Å^2$ for and 54.6 $Å^2$) is similar to that of related cationic surfactants and the aggregation number is much smaller. The results are explained on the basis of probable influence of the size or homochiral nature of the head group in the packing of the micelle.

Another team demonstrated the effect of chain length in aqueous aggregation properties in diacyl lysine salts, wherein the alkyl chain length varied as $n = 5,7,9,11,13$. From X-ray studies, it was shown that the long alkyl chain favors a lamellar arrangement; intermediate-length, cubic bicontinuous structures; and the short derivative, a reverse hexagonal structure [131]. Another group demonstrated alkyl-chain-length-dependent tertiary structures in peptide oligomer surfactants [132]. It was shown that the oligomers exhibited conformation similar to β-poly(L-alanine) in the solid state, and the long acyl chains, induced a sheet structure due to H-bonding between the peptide skeleton. The stabilization of helical structure on micellization was established with respect to potassium salts of the related surfactants.

In the gemini surfactants from cystine, the octyl chain was established to be the optimum length of alkyl chain to form micelles in water. The introduction of decyl or dodecyl, in these gemins, confers lipophilic character. They show very low solubility in water at pH 7.0. The chemical architecture of octyl ester in cationic geminis from cystine favors tilted orientation at the interface and thereby favors elongated morphology and fibril-like structures [125]. The sidechain structure of amino acid plays a significant role on the microstructures of self-assembled structures, as established, for example, in the lauryl esters of tyrosine (LET) and phenyl alanine (LEP). The phenol OH in tyrosine favors packing in the polar shell in contrast to the phenyl ring of (LEP), in the core of the micelles [102, 103], and thereby impacts the dimensions of micellar core and thickness of the shell (Fig. 62.7).

The chiral structures of amino acid amphiphiles influence the aggregated structures and the micellization process as established [133] in proline surfactants. Amino acid amphiphiles also favor gel-like assemblies. The formation of a gel requires right primary, secondary, and tertiary

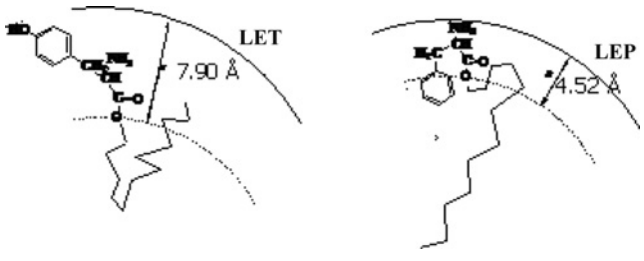


FIGURE 62.7 Conformation of amino acid surfactants from tyrosine (LET) and phenyl alanine (LEP): phenolic group of LET in the shell, thickness 7.90 Å, phenyl of LEP in the core, thickness, 4.52 Å.

structures. It is hypothesized that rodlike micelles are responsible for gelation. The example of low-molecular-weight organogelators could be found in serine-based amphiphiles [134]. Aromatic rings that provide π–π stacking provides more facile gelation process.

The formation of vesicles using mixtures of anionic and cationic surfactants is dictated by electrostatic interactions, the hydrophobic interactions between the alkyl chain of the ionic surfactants, and the type of counterions [135, 136]. Another team [137] studied the conditions for formation of vesicles in the mixture of lysine-derived anionic gemini and cationic single- chain surfactant from serine. The lysine-derived pseudoanionic gemini surfactant and cationic single-chain surfactant from serine of different chain lengths were studied in detail. It was demonstrated that the mixtures of these cationic and anionic surfactants formed vesicles when the overall charge of the vesicle was cationic.

The formation of vesicles and subsequent transformation into tubelike morphology by altering the composition was demonstrated in the mixtures of histidine-derived bolaamphiphile, 1,12-dihistidine diaminododecane (H_2D), and dodecyl trimethyl ammonium bromide (DTAB). Another team synthesized a cationic surfactant from arginine that formed a vesicle at a concentration as low as 0.005 mM and was subsequently transformed to ribbonlike morphology at a high concentration [138].

The maleyl derivatives of LET (MTH) and LEP (MPH) also showed sidechain- dependent self-aggregated structures. The sodium salts of MTH formed micelles in water as against MPH, vesicles [139]. These amphiphiles exhibit pH-responsive aggregated structures. MTH transforms from micelles to vesicles on reducing the pH as against MPH, from vesicles to large aggregates, leading to precipitates [140]. Another team [141] demonstrated formation of vesicles using single-chain valine-based surfactant, namely, *N*-(2-hydroxydodecyl)-L-valine, at pH∼13. They demonstrated that the surfactant exhibits stepwise aggregate formation. At low concentration, only spherical vesicles were formed, which partially transformed to tubular structures with an increase in concentration. It was shown that the tubelike structures have a packing parameter of $0.7 < P < 1$ whereas vesicles have a packing parameter in the $0.5 < P < 0.7$ region [141].

62.4.4 Polymeric Amphiphiles from Amino Acids

Poly(L-amino acid)s (PAAs) are biodegradable ionic polymers often employed for the design of nanocarriers. By virtue of hydrolysable peptide bonds, they can form polyelectrolyte complexes with DNA and hence have immense potential in theuraptics. They are involved in the synthesis of amphiphilic block copolymers that form self-assembled structures such as micelles or polymersomes. Polymerosomes have the unique property of encapsulation of hydrophilic components in the

aqueous cavities and hydrophobic molecules within their membranes. By suitable molecular design and the choice of environment, such as a solvent, the polymerosomes can be generated. Another team demonstrated that the polymeric amphiphile from amino acids segments and consisting of two hydrophilic segments linked through hydrophobic alkyl chain form vesicles in water and inversted micelles in toluene [142].

Synthetic PAA nanocarriers are usually obtained from the polymerization of *N*-carboxyanhydride (NCA) initiated by primary amino compounds. Poly(aspartate), poly(benzyl-L-glutamate) (PBLG), poly(L-lysine) (PLL), and poly(histidine) (PHis) are the best-known PAA nanocarriers. The hydrophilic blocks in the block copolymers from PAA are mainly PEG, heparin, hyaluronan, and polygalactose. [143]. The more hydrophilic molecules form nanosized micellar aggregates, molecules of intermediate hydrophobicity, polymeric vesicles, and the more hydrophobic variants, amorphous polymeric nanoparticles of 100–1000 nm in diameter. By strategic design through synthetic methodologies, it is possible to generate different aggregated structures from polymeric amphiphiles. The formation of controllable and versatile self-assembled nanostructures is demonstrated in the copolymers, for example, in glutamic acid derivatives [144].

Another team synthesized a series of pH-responsive random copolymer poly(l-glutamic acid-co-l-lysine) [P(Glu-co-Lys)] through the ring-opening polymerization (ROP) of γ-benzyl-l-glutamate *N*-carboxyanhydride (BLG-NCA) and 3-benzyloxycarbonyl-l-lysine *N*-carboxyanhydride (ZLys-NCA) and the subsequent deprotection. They were established to act as intelligent drug delivery systems for cancer therapy [145].

Another team designed a series of polyanionic nanocarriers based on biodegradable and biocompatible poly(aspartic acid)s for oral administration. Adopting a series of synthetic methodologies, partially esterified poly(aspartic acids), which afford an amphiphilic polyanion, poly(sodium aspartate-g-hexadecyl aspartate) (Na-PASP-g-C-16-PASP), was produced [146].

Another team synthesized a series of PCL-pluronic-PCL-biodegradable block copolymers by ring-opening polymerization of ε-caprolactone (ε-CL) initiated by pluronic (PEG–PPG–PEG) macromonomer. The self-assembled structures from these block polymers were employed as hydrophobic drug carriers [147]. The gel–sol transition temperature range could be altered in these polymer according to practical applications, which would be very useful as injectable drug delivery system.

Amino acid sidechain-based block polymeric amphiphiles were developed as smart nanocarriers and as vehicles for both drugs and genes [148]. Here, the amino acids, l-phenyl alanine and l-alanine containing vinyl monomers, were polymerized via reversible addition fragmentation chain transfer (RAFT) process in the presence of monomethoxy poly(ethylene glycol)-based macrochain transfer agents (mPEGn-CTA) [148].

Poly(ethylene glycol) (PEG2000) polymers containing one or two amine residues are linked to α-lipoamino acids (LAA) to produce mono- and homo-disubstituted PEG–LAA conjugates as new materials. The PEF-LAA congugates provide dual functions, and form vesicles with different surface properties [149].

Another team reported novel PEGtide dendrons of generations 1 through 5 (G1.0–5.0) containing alternating discrete poly(ethylene glycol) (dPEG) and amino acid/peptide moieties. The dendrons were modified with mannose derivatives to establish the targeting utility of the nanocarriers [150]. Selected examples of polymeric amphiphiles from amino acids derivatives are listed in Table 62.2.

62.5 POLYMERIC NANOCARRIERS IN PHARMACEUTICAL AND OTHER APPLICATIONS

In a recent review one team investigated the drug delivery of polymeric amphiphiles from amino acids [143]. Amino acid containing polymeric amphiphile such as 7-carboxymethoxy coumarin monoend-functionalized methoxy poly(ethylene glycol) (mPEG-Lys-DCOU) micelles have been established as promising carriers for antitumor drug delivery [155]. By ring-opening polymerization reaction, disulfide-linked block copolymers of methoxy poly(ethylene glycol) (mPEG) and

TABLE 62.2 Selected Examples of Nanocarriers from Polymers with Amino Acid Sidechains

Serial No.	Amino acid	Nanocarrier	Ref.
1	L-Lysine	(a) Poly(l-glutamic acid-*co*-l-lysine)	148
		(b) [P(Glu-*co*-Lys)], poly(ε-benzyloxycarbonyl-L-lysine),	151
2	Arginine	(a) Polyarginine,	152
4	Aspartic acid	Poly(sodium aspartate-*g*-hexadecyl aspartate)	146
6	L-Aspargine	(a) Poly(asparagine) grafted with octadecylamine (PAsn-*g*-C18)	153
		(b) Poly-l-asparagine	154
7	l-Phenylalanine and l-alanine	Poly(ethylene glycol)-*b*-poly(Boc-l-phenyl alanine/alanine amino acids methacryloyloxyethyl ester)	148

poly(ε-benzyloxycarbonyl-L-lysine) (PZLL) were synthesized. They showed excellent hemocompatibilities, and cell and tissue compatibilities, and hence potential drug delivery systems. The enhancement in the effectiveness of the drug was established in the poly(amino acid) amphiphiles modified with immunomodulatory agent.

A novel transepidermal drug carrier system was produced from phospholipids and amphiphilc poly(amino acid)s grafted with alkyl amines [153]. Novel poly-l-asparagine (PASN) nanocapsules were found to act as potential anticancer drug delivery systems. PASN nanocapsules showed sizes of around 170–200 nm and negative zeta-potential values (around −20 to −40 mV). The nanocapsules enabled a high level of encapsulation and efficiency of the anticancer drug. Another team established the superior properties of nanocarriers from poly-L-asparagine (PASN) nanocapsules, as the anticancer-targeted drug delivery system [154]. Smart block copolymers containing a poly(ε-caprolactone) (PCL) hydrophobic block with a poly(triethylene glycol) block that were copolymerized with an amino acid-functionalized monomer have been synthesized. The block copolymers formed micellar structures in aqueous solutions. The polymer that was functionalized with 6-aminocaproic acid (ACA) possessed pH-sensitive phase transitions at mildly acidic pH and body temperature. Doxorubicin-loaded micelles formed from these polymers were stable at blood pH (∼7.4) and showed increased drug release at acidic pH.

A series of pH-responsive random copolymer poly(l-glutamic acid-*co*-L-lysine) [P(Glu-*co*-Lys)] were synthesized through the ring-opening polymerization (ROP). Critical aggregation concentration and transmission electronmicroscopy measurements indicated that the P(Glu-*co*-Lys)s could self-assemble into aggregates. The surface charge of P(Glu-*co*-Lys) aggregates was greatly affected by the pH of the solutions and L-glutamic acid/L-lysine ratio. These polymer nanoparticles are smart and exhibit characteristics as determined by the surface charge. The charge reversal and the toxicity characteristics of these nanoparticles were established in presence of the anticancer drug cisplatin [143].

The design and development of water-dispersible, pH-responsive peptides that mimic shell cross-linked magnetic nanocarriers (PMNCs) using a facile soft chemical approach has been reported. These nanocarriers have an average size of ∼10 nm, are resistant to protein adsorption in physiological medium, and transform from a negatively charged to a positively charged form in the acidic environment [156].

62.5.1 Polymeric Nanoparticles

Nanoparticles (NPs) are solid colloidal systems composed of the dispersion of functional materials, such as drugs [157]. Organic and inorganic polymers are the best-known substrates and are generally described as polymeric nanoparticles. The engineering of self-aggregated structures of amphiphiles with polymer nanoparticles is one of the most promising approaches in the design of high-performance nanocarriers from nanoparticles. Here, the self-assembled structures provide dual functions of acting as templates and surface modifiers. The synthetic methodologies determine the morphopolgy, varying between nanospheres and nanocapsules of the nanoparticles, and control the dispersion properties. To elaborate, in nanospheres, the functional material-like drug is dispersed in the polymeric chain. On the contrary, in nanocapsules, the drug solubilized inside the pool of water inside is surrounded by the polymeric chain membranes and thereby acts as more efficient reservoirs of functional materials [158]. The functional materials show enhanced dispersion properties in the colloids of nanoparticles. Furthermore, the polymer nanoparticles are versatile structures, providing scope for modifications of the surface structures and compositions, and hence, high-efficiency nanocarriers [159–173].

62.5.2 Amino Acid Templates for Synthesis of Nanoparticles

The self-assembled structures of amino acids are employed as templates in the design of polymer nanoparticles. Here, the emulsion-phase structures as determined by the organization of the amino acids and their derivatives at the liquid–liquid interface enable the templates to produce nanoparticles of desired size, morphology, and microstructures. It is noteworthy to mention here that emulsion-phase structures find remarkable potential in design of advanced materials, formulations, and controlled polymerization reactions. The surfactants employed in the emulsions act as templates and also surface modifiers, and thereby provide scope for the design of high-performance nanocarriers. The preparation of silica nanoparticles employing the self-aggregated structures from amino acid surfactants as templates has been established [174]. The scope for the design of silica spheres of size 12–23 nm, with well-ordered structures, from tetraethoxysilicate (TEOS) employing the well-known Stober method using L-lysine was shown [175]. By the same procedure, hollow silica spheres were prepared using the amino acid surfactant, lauryl ester of tyrosine. The maleamic acid derivatives of glycine perform as cosurfactant for SDS micelles, and afford polymer nanoparticles by the emulsion template methodology [176, 177]. The micelle structures of amino acid surfactants, LET and LEP, showed extraordinary emulsification characteristics for industrially significant monomers such as styrene and butyl acrylate, and this property was utilized to produce polymeric nanoparticle dispersions [178]. The micelle templates of these surfactants enabled polymerization under controlled conditions and formed nanoparticles of poly(styrene) homopolymer and copolymer with low polydispersity index in the molecular weight and size distribution. The significance of micellar structures and the emulsion phases, as

determined by the chemical architecture of the surfactant, has been established. The polymer nanoparticle–coated micelle assemblies of LET act as potential nanocarriers for the model solid lipid stearyl alcohol [178].

62.6 SUMMARY

Nanocarriers are promising materials and, in fact, have potential to revolutionize various industries. Among various substrates, amphiphiles derived from simple and polymeric surfactants are clearly identified as the potential substrates for the nanocarriers. The growing demand for environment conservation necessitates the ecofriendly source materials for amphiphiles. Among various sources, amino acids offer one of the best choices in view of several unique characteristics such as ease of production through chemical and biochemical pathways, facile chemical modifications of carboxyl, amino and sidechain reactive groups in their structures, biodegradability, and nontoxicity. Further, amino acids, in combination with other natural sources such as lipids, can form lipoamino acids. Amino acids can form an integral part of the macromolecules as mainchain as in proteins or sidechain, as in synthetic polymers. The diversity in structures is offered by simple low-molecular-weight amino acid surfactants and the polymers consisting of amino acid segments and thereby facilitate surface modifications, binding, and site-specific delivery of functional materials such as drugs, dyes, and lubricants. With these extraordinary features, nanocarriers directly impact the economy, the prime factor of various industries. By virtue of their small size, ranging within 1–100 nm, and their high aspect ratio, nanocarriers facilitate the encapsulation and design of nanomaterials. The principles and the fundamental aspects of the self-assembly process in simple and polymeric amphiphiles, the science and technology of emulsions, all underlie the design of new series of nanocarriers. Current and future research in the area of nanocarriers, especially those from amino acid surfactants, embrace the multidisciplinary areas of synthetic and physical chemistry, biology, and physics. Nanocarriers are expected to emerge as indispensable materials in a wide range of photonics, catalysts, and diagnostic tools.

ACKNOWLEDGMENTS

The authors thank CSIR CLRI for the grant through X11 V year plan, STRAIT, CSC0201.

REFERENCES

[1] Meng, H., Liong, M., Xia, T., Li, Z., Ji, Z., Zink, J.I., Nel, A.E. (2010). *ACS Nano* **4**, 4539−4550.

[2] Tang, Y., Lei, T., Manchanda, R., Nagesetti, A., Fernandez-Fernandez, A., Srinivasan, S., McGoron, A. (2010). *Pharm. Res.* **27**, 2242−2253.

[3] Heidel, J., Davis, M. (2011). *Pharm. Res.* **28**, 187−199.

[4] Peer1, D., Kar, J., Hong, S., Farokhzad, O., Margalit, L.R. (2007). *Nature* **2**, 751-760.

[5] Landsiedel, R., Kapp, M.D., Schulz, M., Wiench, K., Oesch, F. (2009). *Mutat. Res. Rev. Mutat. Res.* **681**, 241−258.

[6] Gwinn, M.R. (2011). In Jerome, O.N. (ed.), *Encyclopedia of Environmental Health*. Elsevier, Burlington, pp. 1–11.

[7] Peng, Y.X., Zheng, Z.H., Ding, X.B., Zhang, W.C.; Ye, Z.H. (2003). *Progress Org. Coating* **48**, 161−163

[8] Yu, M., Zhao J., Feng, S. (2012). *Int. J. Pharm.* **438**(1–2), 98-106

[9] Simovic, S., Barnes, T.J., Tan, A., Prestidge, C.A. (2012). *Nanoscale* **4**, 1220−1230

[10] Volodkin, D., Arntz, Y., Schaaf, P., Moehwald, H., Voegel, J.C., Ball, V. (2008). *Soft Matt.* **4**, 122−130.

[11] Ding, J., Chen, J., Li, D., Xiao, C., Zhang, J., He, C., Zhuang, X., Chen, X. (2013). *J. Mater. Chem. B* **1**, 69−81.

[12] Wilking, J.N., Meleson, K., Chang, C.B., Graves, S.M., Mason, T.G. (2006). *J. Phys. Condens. Matt.* **18**, 635–666.

[13] Garti, N., Benichou, A. (2001). *Encyclopedic Handbook of Emulsion Technology*, Marcel Dekker, New York.

[14] Guimarães, K., Ré, M. (2011). Lipid nanoparticles as carriers for cosmetic ingredients: The first (SLN) and the second generation (NLC). In Beck, R., Guterres, S.Pohlmann, A. (eds.), *Nanocosmetics and Nanomedicines.* Springer, Berlin/Heidelberg, pp. 101–122 .

[15] Mura, M., Nicolas, J., Couvreur, P. (2013). *Nature Mater*. **12**, 991–1003

[16] Banat, I.M., Makkar, R.S., Cameotra, S.S. (2000). *Appl. Microbiol. Biotechnol.* **53**, 495–508.

[17] Kitamoto, D.A.I., Isoda. H., Nakahara, T. (2002). *J. Biosci. Bioeng*. **94**, 187–201.

[18] Makkar, R.P.S., Monga, S.M.A., Gupta, A.K. (2002). *Braz. J. Infect. Diseases* **6**, 263–265.

[19] Henkel, M., Müller, M.M., Kügler, J.H., Lovaglio, R.B., Contiero, J., Syldatk, C., Hausmann, R. (2012). *Process Biochem.* **47**, 1207–1219.

[20] Ringsdorf, H., Schlarb, B., Venzmer, J. (1988). *Angew. Chem. Int. Ed.* **27**, 113–158.

[21] Wan, L.J. (2006). *Acc. Chem. Res*. **39**, 334–342.

[22] Kunitake, T., Okahata, Y.J. (1977). *J. ACS* **99**, 3860–3861.

[23] Kimizuka, N., Kawasaki, T., Kunitake, T. (1993). *J. ACS* **115**, 4387–4388.

[24] Evans, D.F., Wennerstrom, H. (2001). *The Colloidal Domain: Where Physics, Chemistry, Biology, and Technology Meet*. Wiley-VCH, New York.

[25] Krishnan, R.S.G., Thennarasu, S., Mandal, A.B. (2004). *J. Phys. Chem B* **108**, 8806.

[26] Wang, C., Wang, Z., Zhang, X. (2012). *Acc. Chem. Res.* **45**, 608–618

[27] Ikkala, O., Brinke, G.T. (2002). *Science* **295**, 2407.

[28] Zhang, D., Qi, L., Ma, J., Cheng, H. (2002). *Adv. Mater.* **14**, 1499–1502.

[29] Allen, T.M., Cullis, P.R. (2004). *Science* **303**, 1818.

[30] Krister, H. (2003). *J. Colloid Interface Sci.* **8**, 187–196.

[31] Merritt, M.V., Chang, I.W., Flannery, C.A., Jon Hsieh, S., Lee, K., Yung, J. (1995). *J. ACS* **117**, 9791–9799.

[32] Ringsdorf, H., Schlarb, B. (1988). *Angew. Chem. Int. Ed.* **27**, 113–158.

[33] Wan, L.J. (2006). *Acc. Chem. Res.* **39**, 334–342.

[34] Kunitake, T., Okahata, Y. (1977). *J. ACS* **99**, 3860–3861.

[35] Kimizuka, N., Kawasaki, T., Kunitake, T. (1993). *J. ACS* **115**, 4387–4388.

[36] Rosen, M.J. (1978). *Surfactants and Interfacial Phenomena*. Wiley, New York.

[37] Israelachvili, J.N., Mitchell, D.J., Ninham, B.W. (1976). *J. Chem. Soc., Faraday Transact.* **72**, 1525–1568.

[38] Schick, M.J. (1987). *Nonionic Surfactants: Physical Chemistry*, Surfactant Science Series, Marcel Dekker, New York.

[39] van Dommelen, S.M., Vader, P., Lakhal, S., Kooijmans, S.A.A.van Solinge, W.W., Wood, M.J.A., Raymond M.Schiffelers, R.M. (2012). *J. Control. Release* **161**, 635–644.

[40] Stuart, M.C.A., Boekema, E.J. (2007). *Biophys. Acta* **1768**, 2681–2689.

[41] Kawasaki, H., Imahayashi, R., Tanaka, S., Almgren, M., Karlsson, G., Maeda, H. (2003). *J. Phys. Chem. B* **107**, 866–8668.

[42] Roy, S., Dey, J. (2005). *Langmuir* **21**, 10362–10369.

[43] Davies, T.S., Ketner, A.M., Raghavan, S.R. (2006). *J. ACS* **128**, 6669–6675.

[44] Philp, D., Stoddart, J.F. (1996). *Angew. Chem. Int. Ed.* **35**, 1154–1196.

[45] Tanford, C. (1978). *Science, New Series.* American Association for the Advancement of Science, Vol. 200, pp. 1012–1018.

[46] Jiang L., Wang, K., Deng, M., Wang, Y., Huang, J. (2008). *Langmuir* **24**, 4600–4606

[47] Namani, T., Walde, P. (2005). *Langmuir* **21**, 6210–6219.

[48] Menger, F.M., Keiper, J.S. (2000). *Angew. Chem. Int. Ed.* **39**, 1906–1920.

[49] Han, Y., Wang, Y. (2011). *Phys. Chem. Chem. Phys.* **13**, 1939–1956.

[50] Zana, R. (2002). *Adv. Colloid Interface Sci.* **97**, 205–253.

[51] Brito, R.O., Marques, E.F., Gomes, P., Maria João Araújo, M.J., Pons, R. (2008). *J. Phys. Chem. B* **112**, 14877–14887.

[52] Tehrani-Bagha, A.R., Oskarsson, H., van Ginkel, C.G., Holmberg, K. (2007). *J. Colloid Interface Sci.* **312**, 444–452.

[53] Din, K.U., Sheikh, M.S, Dar, A.A. (2010). *J. Phys. Chem. B* **114**, 6023–6032.

[54] Kabirud, D., Ajmal Koya, P. (2010). *Langmuir* **26**, 7905–7914.

[55] Angayarkanny, S., Baskar, G., Mandal, A.B. (2012). *J. Colloid Interface Sci.* **367**, 319–326.

[56] Fuhrhop, A.H., Wang, T.Y. (2004). *Chem. Rev.* **104**, 2901–2937.

[57] Meister, A., Bastrop, M., Koschoreck, S., Garamus, V.M., Sinemus, T., Hempel, G., Drescher, S., Dobner, B., Richtering, W., Huber, K., Blume, A. (2007). *Langmuir* **23**, 7715–7723.

[58] Fuoss, R.M., Edelson, D. (1951). *J. ACS* **73**, 269–273.

[59] Menger, F., Wrenn, S. (1974). *J. Phys. Chem. B* **78**, 1387–1390.

[60] Yiv, S., Kale, K.M., Lang, J., Zana, R. (1976). *J. Phys. Chem. B* **80**, 2651–2655.

[61] Fuhrhop, J.H. Fritsch, D. (1986). *Acc. Chem. Res.* **19**, 130–137.

[62] .Nagarajan, R. (1987). *Chem. Eng. Commun.* **55**, 251–273.

[63] Fuhrhop, J.H., Wang, T. (2004). *Chem. Rev.* **104**, 2901–2938.

[64] Benvegnu, T., Brard, M., Plusquellec, D. (2004). *Science* **8**, 469–479.

[65] Meister, A., Blume, A. (2007). *Curr. Opin. Colloid Interface Sci.* **12**(3), 138–147.

[66] Song, B., Liu, G., Xu, R., Yin, S., Wang, Z., Zhang, X. (2008). *Langmuir* **24**, 3734–3739.

[67] Liu, K., Wang, C., Li, Z., Zhang, X. (2011). *Angew. Chem Int. Ed.* **50**, 4952–4956.

[68]

[69] Wang, C., Wang, Z.X. (2011). *Small* **7**, 1379–1383.

[70] Moffitt, M., Khougaz, K., Eisenberg, A. (1996). *Acc. Chem. Res.* **29**, 95–102.

[71] Alexandridis, P. (1996). *J. Colloid Interface Sci.* **1**, 490–501.

[72] Chen, D.Y., Jiang, M. (2005). *Acc. Chem. Res.* **38**, 494–502.

[73] Cabral, H., Nishiyama, N., Kataoka, K. (2011). *Acc. Chem. Res.* **44**, 999–1008.

[74] Nicolas, J., Mura, S., Brambilla, D., Mackiewicz, N., Couvreur, P. (2013). *Chem. Soc. Rev.* **42**, 1147–1235.

[75] James, J., Vellaichami, S., Krishnan, R.S.G., Samikannu, S., Mandal, A.B. (2005). *Chem. Phys.* **312**, 275–287.

[76] James, J., Ramalechume, C, Mandal, A.B. (2005). *Chem. Phys.* **405**, 84–89.

[77] James, J., Ramalechume, C., Mandal, A.B. (2007). *J. Polym. Sci. B: Polym. Phys.* **45**, 2410–2420.

[78] James, J., Mandal, A.B. (2011). *Colloids Surf. B: Biointerfaces* **84**, 172–180

[79] Ma, Y., Cao, T., Webber, S.E. (1998). *Macromolecules* **31**, 1773–1778.

[80] Chen, G., Hoffman, A.S. (1995). *Nature* **373**, 49–52.

[81] Liu, X.M., Pramoda, K.P., Yang, Y., Chow, S.Y., He, C. (2004). *Biomaterials* **25**, . 619–2628.

[82] Kjellin, U.R.M., Claesson, P.M., Linse, P. (2002). *Langmuir* **18**, 6745–6763.

[83] Mouri, E., Kaewsaiha, P., Matsumoto, K., Matsuoka, H., Torikai, N. (2004). *Langmuir*, **20**, 10604–104611.

[84] Harrisson, S., Wooley, K.L. (2005). *Chem. Commun.* **2005**, 3259–3261.

[85] Kanouni, M., Rosano, H.L., Naouli, N. (2002). *Adv. Colloid Interface Sci.* **99**, 229–254.

[86] Romoscanu, A.I., Mezzenga, R. (2006). *Langmuir* **22**, 8770–8776

[87] Wang, C., Ravi, P., Tam, K.C., Gan, L.H. (2004). *J. Phys. Chem. B* **108**, 1621–1627.

[88] Cochin, D., Candau, F., Zana, R. (1993). *Macromolecules* **26**, 5755–5764.

[89] Kramer, M.C., Steger, J.R., Hu, Y., Mc Cormick, C.L. (1996). *Macromolecules* **29**, 1992–1997.

[90] Bskar, G., Landfester, K., Antonietti, M. (2000). *Macromolecules* **33**, 9228–9232.

[91] Bazito, R., Seoud, O.A. (2002). *Langmuir* **18**, 4362–4366.

[92] Hupfer, B., Ringsdorf, H., Schupp, H. (1981). *Makromol. Chem.* **182**, 247–253.

[93] Fendler, J.H., Tundo, P. (1984). *Acc. Chem. Res.* **17**, 3–8.

[94] Pere, C., Infante, I., Maria, R. (2002). *Biocatal. Biotransform.* **20**, 215–233.

[95] Presenz, P. (1996). *Pharmazie* **51**, 755–758.

[96] Infante, M.R., Pinazo, A., Seguer, J. (1997). *Colloids Surf. A* **123**, 49–69.

[97] Takehara, M. (1989). *Colloids Surf. A* **38**, 149–167.

[98] Rodriguez, E. (2004). *J. Appl. Microbiol.* **96**, 903–912.

[99] Morán, P., Clapés, F., Comelles, T., García, L., Pérez, P., Vinardell, M., Mitjans, M., Infante, M.R. (2001). *Langmuir* **17**, 5071–5075.

[100] Vulfson, E. (2004). *Novel Surfactants. Enzymatic Synthesis of Surfactants*. In Holberg, K. (ed.), Surfactant Science Series. Marcel Dekker, New York.

[101] Pinazo, A., Pons, R., Prez, L., Infante, M.R. (2011). *Industr. Eng. Chem. Res.* **50**, 4805–4817.

[102] Vijay, R., Angayarkanny, S., Baskar, G. (2008). *Colloids Surf. A* **317**, 643–649.

[103] Vijay, R., Singh, J., Baskar, G., Ranganathan, R. (2009). *J. Phys. Chem. B* **113**, 13959–13970.

[104] Huang, R., Qi, W., Su, R., Zhao, J., He, Z. (2011). *Soft Matt*. **7**, 6418–6421.

[105] Angayarkanny, S., Vijay, R., Baskar, G., Mandal, A.B. (2012). *Langmuir* **28**, 9378–9386.

[106] Furutani, T., Ooshima, H., Kato, J. (1997). *Enzyme Microbiol. Technol.* **20**, 214–220.

[107] Gallot, B., Hassan, H.H. (1989). *Mol. Cryst. Liquid Cryst.* **170**, 195–214.

[108] Nagao, A., Kito, M. (1989). *J. Am. Oil Chem. Soc.* **66**, 710–713.

[109] Nnanna, I.A., Xia, J. (2001). *Protein-Based Surfactants*. In Holberg, K. (ed.), Surfactant Science Series. Marcel Dekker, New York.

[110] Valivety, R., Jauregui, P. (1997). *J. Am. Oil Chem. Soc.* **74**, 879–886 .

[111] Hayes, D.G., Kitamoto, D., Solaiman, D., Ashby, R.D. (eds.) (2009). *Biobased Surfactants and Detergents: Synthesis, Properties, and Applications*. AOCS Press, Urbana, IL.

[112] Jiding, X., Junhong, Q., Ifendu, A. (1996). *J. Agric. Food Chem.* **44**, 975–979.

[113] Gazita, E. (2007). *Chem. Soc. Rev.* **36**, 1263–1269.

[114] Morán, M.C., Pinazo, A., Pérez, L., Clapés, P., Angelet, M., García, M.T., Vinardellb, M.P., Infante, M.R. (2004). *Green Chem*. **6**, 233–240.

[115] Takehara, M. (1989). *Colloids Surf. A* **38**, 149–167.

[116] Zhang, X.M., Adachi, S., Watanabe, Y., Matsuno, R. (2005). *Food Res. Int.* **38**, 297–300.

[117] Gerova, M., Rodrigues, F., Lamere, J.F., Dobrev, A., Fery-Forgues, J. (2008). *Colloid Interface Sci*. **319**, 526–533.

[118] Roy, S.Dey, J. (2006). *J. Chem. Soc. Jpn.* **79**, 59–66.

[119] Das, D., Dasgupta, A., Roy, S., Mitra, R.N., Debnath, S., Das, P.K. (2006). *Chem. Eur.* **12**, 5068–5074.

[120] Varka, E.M., Heli, M.G., Coutouli-Argyropoulou, E., Pegiadou, S.A. (2006). *Chem. Eur. J.* **12**, 8305–8311.

[121] Ohta, A., Toda, K., Morimoto, Y., Asakawa, T., Miyagishi, S. (2008). *Colloids Surf. A* **317**, 316–322.

[122] Capone, S., Walde, P., Seebach, D., Ishikawa, T., Caputo, R. (2008). *Chem. Biodivers.* **5**, 16–30.

[123] Pons, R., Morn, M.C., Infante, M.R., Pinazo, A. (2010). In Fanum, M. (ed.), *Colloids in Biotechnology.* CRC Press, Boca Raton, FL, Vol. 152, pp. 125–138.

[124] Pinazo, A., Diz, M., Solans, C., Erra, P., Infante, M.R. (1993). *J. Am. Oil Chem. Soc.* **70**, 37–42.

[125] Angayarkanny, S., Baskar, G., Mandal, A.B. (2012). *J. Colloid Interface Sci.* **367**, 319–326.

[126] Imae, T., Hayashi, N., Matsumoto, T., Tada, T., Furusaka, M. (2000). *J. Colloid Interface Sci.* **225**, 285–290.

[127] Kogiso, S., Ohnishi, K., Yase, M., Masuda, T. (1998). *Langmuir* **14**, 4978–4986.

[128] Imae,T., Takahashi, Y., Muramatsu, H. (1992). *J. ACS* **114**, 3414–3419.

[129] Infante, M.R., Seguer, J., Pinazo, A., Vinardell, M.P. (1999). *J. Dispers. Sci. Technol.* **20**, 621–642.

[130] Diego, M.J., Castro, H.C., Hailes, M.J., Lawrence, J. (2001). *Colloid Interface Sci.* **234**, 122–126.

[131] Pinazo, A., Perez, L., Lozano, M., Angelet, M., Infante, M.R., Vinardell, M.P., Pons, R. (2008). *J. Phys. Chem. B* **112**, 8578–8585.

[132] Okabayashi, H., Etori, H., Yamada, Y., Taga, K., Yoshida, T. (1996). *Vibrat. Spectrosc.* **13**, 51–63.

[133] Borocci, G., Mancini, G., Cerichelli, L., Luchetti, S. (1999). *Langmuir* **15**, 2627–2644.

[134] Estroff, L.A., Hamilton, A.D. (2004). *Chem. Rev.* **104**, 1201–1208.

[135] Hao, J., Hoffmann, H.J. (2004). *Colloid Interface Sci.* **9**, 279–293.

[136] Israelachvili, J.N., Mitchell, D.J., Ninham, B.W. (1976). *J. Chem. Soc. Faraday Transact.* **272**, 1525–1568.

[137] Marques, E.F., Brito, R.O., Silva, S.G., Enrique, J., Borges, R., Vale, M.L., Gomes, P., Araújo, M.J., Söderman, O. (2008). *Langmuir* **24**, 11009–11017.

[138] Pinazo, A., Pérez, L., Infantea, M.R., Pons, R. (2004). *Phys. Chem. Chem. Phys.* **6**, 1475–1481.

[139] Angayarkanny, S., Baskar, G., Mandal, A.B. (2012). *Langmuir* **28**, 9378–9386.

[140] Singh, J., Ranganathan, R., Angayarkanny, S., Baskar, G., Mandal, A.B. (2013). *Langmuir* **29**, 5734–5741.

[141] Ghosh, A., Dey, J. (2008). *J. Phys. Chem. B* **112**, 6629–6635.

[142] Elamprakash, N., Sivakumar, S., Aathimanikandan, V., Thayumanavan, S. (2006). *J. ACS* **128**, 16224–16230.

[143] Lalatsa, A., Schaetzlein, A.G., Mazza, M., Le, T.B.H., Uchegbu, I.F. (2012). *J. Control. Release* **161**, 523–536.

[144] Zhu, X.M., Liu, M. (2011). *Langmuir* **27**, 12844–12850.

[145] Men, L., Huang, W., Wang, D., Huang, X., Zhu, X., and Yan, D. (2013), *Biomacromolecules*, **14**, 2601–2610.

[146] Hsu, S.P., Chu, I.M. (2012). *J. Polym. Res.***19**, 9913–9916.

[147] Gong, C.Y., Wang, Y.J., Wang, X.H., Wei, X.W., Wu, Q., Wang, B., Dong, P.W., Chen, L., Luo, F., Qian, Z.Y. (2011). *J. Nanopart. Res.* **13**, 721–731

[148] Kumar, S., Acharya, R., Chatterji, U., De, P. (2013). *Langmuir* **29**, 15375–15385.

[149] Pignatello, R., Pantò, V., Impallomeni, G., Carnemolla, G.M., Carbone, C., Puglisi, G. (2013). *Macromol. Chem. Phys.* **214**, 46–55.

[150] Gao, J., Chen, P., Singh, Y., Zhang, X., Szekely, Z., Stein, S., Patrick, J. (2013). *Bioconjug. Chem.* **24**, 1332–1344.

[151] Ding, J., Chen, J., Li, D., Xiao, C., Zhang, J., He, C., Zhuang, X., Chen, X.J. (2013). *Mater. Chem. B* **1**, 69–81.

[152] Kanwar, J.R.G., Verma, J., Anita, K.B., Rupinder, K. (2012). *Anti-Cancer Drugs* **23**, 471–482.

[153] Park, S., Lee, E., Yang, H.M., Park, C.W., Kim, J.D. (2013). *Colloids Surf. B*: *Biointerfaces* **110**, 333–338.

[154] Rivera-Rodriguez, G.R., Alonso, M.J., Torres, D. (2013). *Official J. Arbeitsgemeinschaft fur Pharmazeutische Verfahrenstechnik e.V.* **85**, 481–487.

[155] Lai, Y., Long, Y., Lei, Y., Deng, X., He, B., Sheng, M., Gu, Z. (2012). *J. Drug Target.* **20**, 246–254.

[156] Barick, K.C., Jadhav, N.V., Bahadur, D., Pandey, B.N., Hassan, P.A. (2012). *Adv. Funct. Mater*. **22**, 4975–4984.

[157] Hillaireau, H., Couvreur, P. (2006). In Uchegbu, I.F., Schatzlein, A.G. (eds.), *Polymers in Drug Delivery.* Taylor & Francis, New York, p. 101.

[158] Letchford, K., Burt, H. (2007). *Eur. J. Pharm. Biopharm.* **65**, 259–266.

[159] Elsabahy, M., Wooley, K.L. (2012). *Chem. Soc. Rev.* **41**, 2545.

[160] Landsiedel, R., Kapp, M.D., Schulz, M., Wiench, K., Oesch, F. (2009). *Mutat. Res. Rev. Mutat. Res.* **681**, 241–258.

[161] Gwinn, M.R. (2011). Nanomaterials: Potential ecological uses and effects. In Jerome, O.N. (ed.), *Encyclopedia of Environmental Health.* Elsevier, Burlington, pp. 1–11.

[162] Peng, Y.X., Zheng, Z.H., Ding, X.B., Zhang, W.C., Ye, Z.H. (2003). *Progress Org. Coating* **48**, 161–163.

[163] Barner-Kowollik, C., Heuts, J.P.A., Davis, T.P.J. (2001). *Polym. Sci. A* **39**, 656–664.

[164] Cardenas, M., Schillen, K., Nylander, T., Jansson, J. (2004). *Phys. Chem. Chem. Phys.* **6**, 1603–1607.

[165] Antonietti, M., Lohmann, S., Van Niel, C. (1992). *Macromolecules* **25**, 1139–1143.

[166] Antonietti, M., Bremser, W., Mueschenborn, D., Rosenauer, C., Schupp, B., Schmidt, M. (1991). *Macromolecules* **24**, 6636–6643.

[167] Hager, M., Currie, F., Holmberg, K. (2004). A nucleophilic substitution reaction in microemulsions based on either an alcohol ethoxylate or a sugar surfactant. *Colloids Surf. A* **250**(1–3), 163–170.

[168] von Corswant, C., Engstrom, S., Soderman, O. (1997). *Langmuir* **13**(19), 5061–5070.

[169] Glatter, O., Orthaber, D., Stradner, A., Scherf, G., Fanun, M., Garti, N., Clement, V., Leser, M.E. (2001). *J. Colloid Interface Sci.* **241**(1), 215–225.

[170] Solans, C., Izquierdo, P.J., Nolla, J., Azemar, N., Garcia-Celma, M.J. (2005). *Curr. Opin. Colloid Interface Sci.* **10**(3–4),102–110.

[171] Carteau, D., Pianet, I., Brunerie, P., Guillemat, B., Bassani, D.M. (2007). *Langmuir* **23**(7), 3561–3565.

[172] Ricci, M., Blasi, P., Giovagnoli, S., Perioli, L., Vescovi, C., Rossi, C. (2004). *Int. J. Pharm.* **275**(1–2), 61–72.

[173] Bouchemal, K., Briançon, S., Perrier, E., Fessi, H., Bonnet, I., Zydowicz, N. (2004). *Int. J. Pharm.* **269**(1), 89–100.

[174] Melvin, A., Vijay, R., Chaudhari, V.R., Gupta, B., Prakash, R., Haram, S., Baskar, G., Khushalani, D. (2010). *J. Colloid Interface Sci.* **346**, 265–269.

[175] Yokoi, T., Sakamoto, Y., Terasaki, O., Kubota, Y., Okubo, T., Tatsumi, T. (2006). *J. ACS* **128**, 13664–13665.

[176] Gaspar, L.M., Baskar, G., Reddy, B.S.R. (2004). *Langmuir* **20**, 9029–9035.

[177] Gaspar, L.M., Baskar, G. (2006). *Langmuir* **22**, 2795–2801.

[178] Angayarkanny, S., Baskar, G., Mandal, A.B. (2013). *Langmuir* **29**, 6805–6814.

63

SYNTHESES OF METALLIC NANOCOLLOIDS AND THE QUENCHING ABILITIES OF REACTIVE OXYGEN SPECIES

YUKIHIDE SHIRAISHI AND NAOKI TOSHIMA

Department of Applied Chemistry, Tokyo University of Science Yamaguchi, Sanyo Onoda-shi, Yamaguchi 756-0884, Japan

63.1 INTRODUCTION

Recently much attention has been paid to metallic nanocolloids, important building blocks of nanostructures to achieve nanotechnology, which has been demonstrated by the US government as one of the most important technologies of this century. *Metallic nanocolloids* are defined as the dispersed state of fine metallic particles ranging in size from 1 nm to 1 μm [1–3]. Metallic nanocolloids such as nanoparticles are now creating a new class of materials different from either conventional bulk materials or atoms, providing one of the smallest building blocks of matter. Metallic nanocolloids have various properties based on high surface area and quantum size effects, and are promising as catalysts. Many preparation methods have been proposed, and detailed characterizations have been carried out on various preparations of metallic c nanocolloids. Here we focus on the synthesis of monometallic and bimetallic nanocolloids, which are mainly stabilized by polymers, and the application to reactive oxygen species (ROS) scavengers.

Addition of water-soluble natural or synthetic polymers [4, 5], surfactants [6], and organic ligands [7, 8] can stabilize the colloidal dispersion of metals as well. These stabilizers are called *protective colloids* or *surrounding ligand*. In this case, the surrounding ligand can be absorbed on the surface of metallic nanocolloids, and steric repulsion between the surrounding ligand stabilizes the metallic nanocolloids. Figure 63.1 depicts a schematic stabilization structure of a metallic colloid by soluble polymers in an aqueous solution. Stabilizing polymers can be adsorbed on the surface of hydrophobic metallic nanocolloids. Hydrophobic "train" segments are directly adsorbed on the surface of solid metal, and hydrophilic "loop" or "tail" segments are spread out into the hydrophilic solvent. The diameter d of core metallic nanocolloids can be easily measured by transmission electron microscopy. The thickness δ of surrounding ligand or the total diameter D including the surrounding ligand can be measured by various methods depending on the nature of the surrounding ligand. In solution, the hydrodynamic radius provides $D/2$. When the hydrodynamic radius is large enough, it can be measured by a light-scattering method. However, when the hydrodynamic radius is small, it can still be measured by a Taylor dispersion method if the size is homogeneous or uniform enough [9]. When the surrounding ligand is composed of soluble polymers, the direct measurement of D is not so easy. The thickness δ was proposed to be measured by the amount of polymers adsorbed on the surface of metallic nanocolloids [10]. Because it is not easy to measure D in solution, measurement using scanning tunnel microscopy (STM) was performed in the dry state [11].

Recently much attention has focused on polymer-protected metallic nanocolloids as nanocolloids based on rapid improvement of analytical technology on fine materials. Such nanocolloids, defined by a diameter of 1–10 nm and a narrow size distribution, are creating a new category of materials, which is different from either conventional

Encyclopedia of Biocolloid and Biointerface Science, Volume 2, First Edition. Edited by Hiroyuki Ohshima.
© 2016 John Wiley & Sons, Inc. Published 2016 by John Wiley & Sons, Inc.

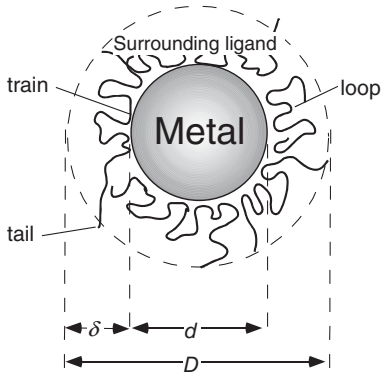


FIGURE 63.1 Structure model of polymer-protected metallic nanocolloids.

bulk materials or atoms, the smallest units of matter. Much attention has focused on their special properties in physical, biological, and chemical fields. The quantum size effect [12] is a major problem for physicists. Gold nanocolloids, for example, are interesting as materials of nonlinear optics for third harmonic generation. In the biological field, gold nanocolloids have been used for labeling specific positions of cells for observation by transmission electron micrography (TEM). Silver nanocolloids are very popular for detection of specific proteins in electrophoresis.

The most intensive investigations of applications of metallic nanocolloids are focused on catalyses. Many reports have been published on the application to catalysts [13]. Since some noble metallic nanocolloids are reducing catalysts, they may be usable as antioxidants, which reduce reactive oxygen species (ROS) in a living body. However, there are only a few studies reporting antioxidant effects of gold nanocolloids [14–16]. Typical ROS in animals, including human beings, are superoxide anion radicals, hydrogen peroxide, and hydroxyl radicals produced in normal metabolic process [17]. The dominant pathway to generate ROS is the mitochondrial electron transport chain, by which 98% oxygen inhaled by animals is reduced to water for energy production. In the electron transport process, a small number of electrons leak out and react with oxygen to generate superoxide anion radicals [18]. The superoxide anion radical is reduced to hydrogen peroxide by superoxide dismutase (SOD), and subsequently hydrogen peroxide crosses the mitochondrial membranes and diffuses inside and even outside of cells. The hydroxyl radical is generated from superoxide anion radical and hydrogen peroxide by Haber–Weiss and Fenton reactions, respectively. These ROS oxidize biomolecules found in the body such as nucleic acids, proteins, and lipids. There are many defensive systems against oxidative stress in the body. As the first defence, ROS are reduced by antioxidant enzymes such as SOD, catalase, and glutathione peroxidase as well as endogenous and exogenous small molecules, including glutathione and vitamins C and E. When biomolecules are oxidized, they are repaired or replaced by biological protective systems. Nevertheless, biomolecules are irreversible and gradually become oxidized, and oxidized biomolecules accumulate over long time periods and impair biological functions, eventually leading to aging and age-related diseases [19].

In this chapter we would like to present a preparation procedure and characteristic aspects of monometallic and bimetallic nanocolloids, and then show special structures and application to ROS scavengers of the metallic nanocolloids as examples.

63.2 MONOMETALLIC NANOCOLLOIDS

63.2.1 Preparation of Monometallic Nanocolloids

Monometallic nanocolloids can be prepared by two distinct methods: (1) by subdivision of bulk metals (a physical method) and (2) by growth of particles starting from metal atoms, which are obtained from molecular or ionic precursors (a chemical method). The latter preparative method (method 2) is more suitable for obtaining small and uniform nanocolloids than is method 1. In method 2, control of atom aggregation is the most important step in controlling the size and uniformity of the monometallic nanocolloids.

Faraday found that the addition of gelatin to gold nanocolloids protected them from the aggregation [20]. Another team advanced this idea and used synthetic polymers, such as poly(vinyl alcohol), as a surrounding ligand for platinum and palladium nanocolloids and applied them to catalysts [21,22]. Another group of researchers introduced gold and platinum nanocolloids, produced by citrate reduction, for use as supported catalysts [23, 24]. Ligands and polymers, with some affinity for metals, are often used as stabilizers of metallic nanocolloids. These substances also control both the reduction rate of metal ions and the aggregation process of metal atoms. Preparation of polymer-stabilized nanocolloids by a chemical method involves two processes: reduction of metal ions to 0-valence atoms and coordination of the stabilizing polymer to monometallic nanocolloids.

One of the most reproducible methods for preparation of monometallic nanocolloids is alcohol reduction of precious metal ions in alcohol–water in the presence of water-soluble polymers such as poly(*N*-vinyl-2-pyrrolidone) (PVP) [25]. The precious-metal ions form complexes with polymers at first. The metal ions can be reduced by alcohol to produce polymer–metal atom complexes accompanying aldehyde formation from alcohol. Other chemical reductants, such as hydrazine, molecular hydrogen, glycol, and sodium borohydride, can be used instead of alcohol. Energy, such as photoenergy, X-ray and γ-ray energy, electron beams, microwaves, ultrasonic waves, and electrolysis, can also be used in solution in the presence of stabilizers to break the

bond or reduce the metal ions to 0-valence metal atoms resulting in monometallic nanocolloids.

63.2.2 Characterization of Metallic Nanocolloids

Metallic nanocolloids can be characterized as follows.

1. *Ultraviolet and Visible Adsorption Spectroscopy*. The color change is a convenient and useful method to identify the chemical change from the solution of metal ions to the dispersion of metallic nanocolloids. The dispersions of Au, Ag, and Cu nanocolloids have a reddish yellow color because of their plasmon absorption, the peak position of which varies depending on the particle size and the extent of coagulation.
2. *Transmission Electron Microscopy (TEM).* This is the most reliable method for measuring the size and shape of metallic nanocolloids. The average size is usually calculated by counting the sizes of ~200 particles. High-resolution TEM can provide information not only on particle size and shape but also on the crystalline structure of metallic nanocolloids. When energy-disperse X-ray microanalysis (EDS) is used in conjunction with TEM, elemental information of metallic nanocolloids can be obtained. The localized elemental information is acquired by energy-loss spectroscopy in conjunction with energy-filtering TEM.
3. *X-Ray Photoelectron Spectroscopy*. This methhod is used to obtain information on the state of metal, such as the oxidation state of metal on the surface. Metal on the surface is often oxidized by air. So the 0-valence of surface metal must be confirmed by using X-ray photoelectron spectroscopy.
4. *X-Ray Diffraction*. For monometallic nanocolloids, X-ray diffraction can provide information on the phase changes depending on the particle size. X-ray diffraction can determine whether the bimetallic nanocolloids are composed of the mixtures of two kinds of monometallic nanocolloids or of single bimetallic nanocolloids in which two elements are included in one particle.

63.2.3 Application to Reactive Oxygen Species (ROS) Scavengers by Monometallic Nanocolloids

Noble metal is often used as ROS scavengers. Cyclodextrin (CyD)-protected noble metallic nanocolloids were prepared by photoreduction method. Figure 63.2 shows a transmission electron micrograph and the corresponding histogram indicating the particle size distributions of γCyD-protected Pt nanocolloids. The most γCyD-protected Pt nanocolloids were distributed in the range of 1–4 nm, suggesting that the size of CyD-protected Pt nanocolloids is homogeneous. The

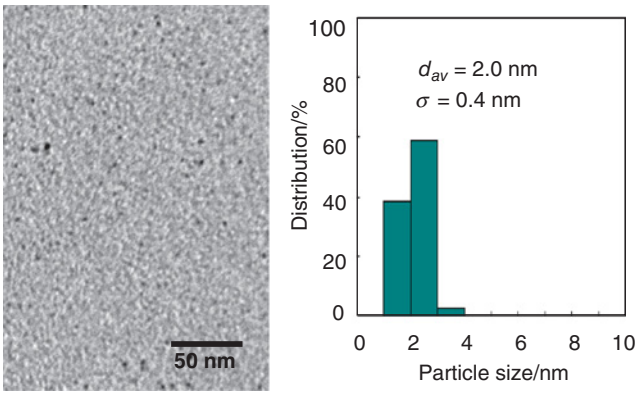


FIGURE 63.2 Transmission electron micrographs and particle size distribution histograms of γCyD-protected Pt nanocolloids (d_{av} = average diameter; σ = standard deviation).

average diameters of γCyD-protected Pt nanocolloids are 2.0 nm, with a narrow size distribution.

γCyD-protected noble metallic nanocolloids were applied to the catalyst for quenching of reactive oxygen species. Figure 63.3 exhibits UV–Vis absorption spectra of an aqueous solution of hydrogen peroxide in the absence and presence of γCyD-Pt nanocolloids. Table 63.1 summarizes the quenching ability of hydrogen peroxide by γCyD-protected noble metallic nanocolloids. The γCyD-protected Pt, Pd, and Au nanocolloids quenched 65%, 13%, and 3%, respectively, of hydrogen peroxide. Kajita et al. reported the quenching ability of hydrogen peroxide by Pt-black and pectin-protected Pt nanocolloids, as shown in Fig. 63.4 [26]. The Pt-black, which was composed of relatively larger particles (the average diameter of 100 nm) and their aggregates, did not quench hydrogen peroxide at all. The high catalytic activity of

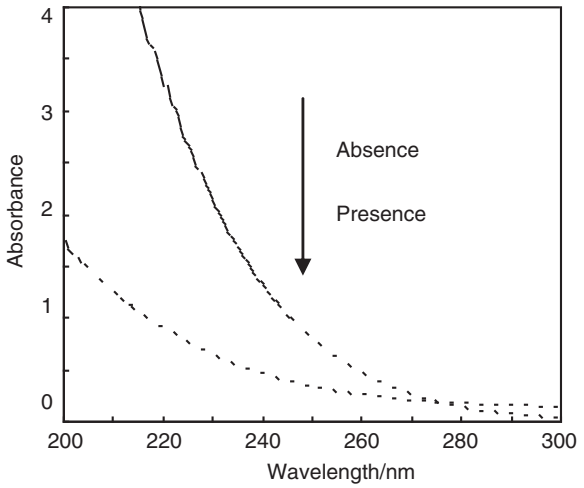


FIGURE 63.3 UV–Vis absorption spectra of an aqueous solution of hydrogen peroxide in the absence and presence of γCyD-Pt nanocolloids.

TABLE 63.1 Quenching ability of hydrogen peroxide by γCyD-protected noble metallic nanocolloids.

Nanocolloids	H_2O_2 removal ratio (%)
γCyD-Au	3.0
γCyD-Pd	13
γCyD-Pt	65

γCyD-Pt nanocolloids may be due to the effect of surface area. On the other hand, the pectin-protected Pt nanocolloids with average diameters in the range of 4.7 nm have higher catalytic activity (residual ratio 17%, removal ratio 83%) than that of γCyD-Pt nanocolloids. Polymers that weakly coordinate to the surface of metallic nanocolloids at many points are especially effective for stabilizing the metallic nanocolloid catalyst [27]. In the process of catalytic reaction, when the substrate is added to the reaction mixture, a weakly coordinating polymer can be easily replaced in part with the substrate molecule, resulting in the reaction of substrates on the surface of metallic nanocolloids. Strongly coordinating organic ligands cannot be easily replaced by substrate molecules, making it difficult for the substrate to make the catalytic reaction proceed on the surface of metal nanocolloids. This kind of reversible capping of the polymer on the metal surface cannot occur in organic ligands with low molecular weight, although organic ligands or ionic species play an important role to control the shape of metallic nanocolloids [28].

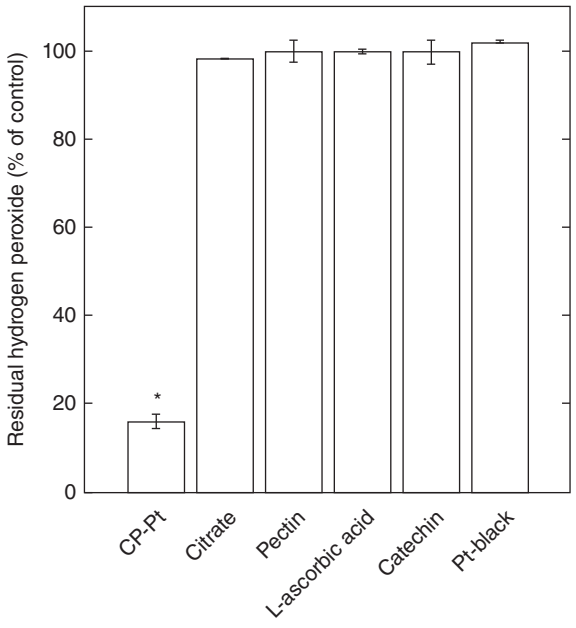


FIGURE 63.4 Comparison of quenching activity of hydrogen peroxide by pectin-protected Pt nanocolloids and Pt-black. (Adapted from Kajita et al. 2007 [26], p. 66, Fig. 5. © Informa UK Ltd.; reproduced with permission.)

63.3 BIMETALLIC NANOCOLLOIDS

63.3.1 Preparation of Bimetallic Nanocolloids

Bimetallic nanocolloids, in which each particle contains two metal elements, are very important and interesting in terms of catalysis of metallic nanocolloids because catalytic performance is very often affected by the addition of another element to the metal. In addition, the structure of bimetallic nanocolloids is strongly related to catalytic performance. Polymer-protected bimetallic nanocolloids have been prepared by simultaneous reduction of two corresponding metal ions with refluxing alcohol in the presence of PVP. For example, PVP-protected Pt-core/Pd-shell bimetallic nanocolloids can be prepared by refluxing the alcohol/water (1/1, v/v) mixed solution of palladium(II) chloride and hexachloroplatinic(IV) acid in the presence of PVP at about 90–95°C for 1 h [29]. The special structure has been proposed on the basis of extended X-ray absorption fine structure (EXAFS) analyses [30]. The PVP-protected Pt-core/Pd-shell model for Pt/Pd (1/4, mole ratio) is shown in Fig. 63.5, where 13 platinum atoms are preferentially located in the central part (core) of the bimetallic nanocolloids, and where 42 palladium atoms surround the core forming a shell with an atomic layer. The formation process of core–shell structure may be due to orders of reduction potential of metal ions and coordination ability of the protective polymer to reduced atoms.

Au/Pd, Au/Pt, and Pt/Rh bimetallic nanocolloids have been prepared by the same method [31]. One team prepared Ag/Pd bimetallic nanocolloids by photoreduction of silver(I) bis(oxalato)palladate(II) in water [32]. Ag/Pt bimetallic nanocolloids were obtained by sodium tetrahydroborate reduction of silver(I) bis(oxalato)platinate(II) in ethylene glycol [33]. Colloidal dispersions Au/Ag bimetallic nanocolloids were prepared by γ-irradiation of the mixed solution for study of electrochemical reaction [34].

The inverted core/shell, for example, Pd-core/Pt-shell-structured bimetallic nanocolloids, are difficult to synthesize. Addition of platinum(IV) ions to palladium nanocolloids resulted in a redox reaction to form platinum nanocolloids and palladium(II) ions. In order to avoid this unfavorable reaction, the colloidal dispersions of palladium cores were treated with hydrogen and then solutions of the second element, platinum(II) ions, were slowly added to the dispersions. This novel method, based on sacrificial hydrogen strategy,

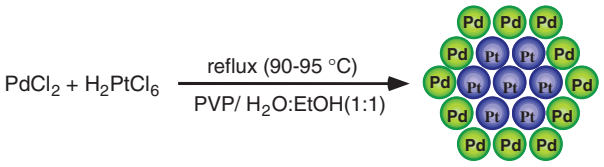


FIGURE 63.5 Schematic illustration of formation of Pt-core/Pd-shell bimetallic nanocolloids.

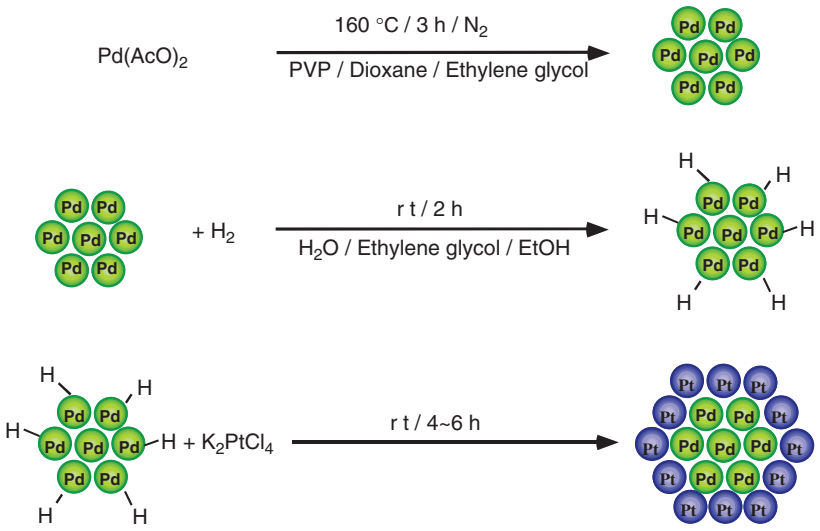


FIGURE 63.6 Schematic illustration of formation of Pd-core/Pt-shell bimetallic nanocolloids.

gave the inverted core—shell-structured bimetallic nanocolloids as shown in Fig. 63.6. The PVP-protected Pd-core/Pt-shell structure was confirmed by FT-IR spectrum of adsorbed carbon monoxide [35].

Reduction of two different precious-metal ions by UV irradiation in the presence of Poly(γ-cyclodextrin) (PγCyD) gave a colloidal dispersion of so-called core–shell-structured bimetallic nanocolloids. In the case of Au and Pt ions, the colloidal dispersions of bimetallic nanocolloids with an Au-core/Pt-shell structure are produced. PγCyD- protected Au/Pt bimetallic nanocolloids were applied to the catalyst for quenching of hydrogen peroxide [36].

63.3.2 Application to ROS Species Scavengers by Bimetallic Nanocolloids

Figure 63.7 exhibits the relationship between catalytic activity and the metal composition of PγCyD-protected Au-core/Pt-shell bimetallic nanocolloids. Since gold have low activity and platinum have high activity for the quenching of hydrogen peroxide, PγCyD-protected Au-core/Pt-shell bimetallic nanocolloids were assumed to exhibit activities somewhere between the corresponding monometallic nanocolloids. PγCyD-protected Au-core/Pt-shell (1/4) bimetallic nanocolloids show higher catalytic activity than do the monometallic nanocolloids. Previous reports had shown that platinum nanocolloids containing a certain amount of additional other metals such as gold and palladium exhibit higher catalytic activity in hydrogen evolution and hydrogenation than do platinum monometallic nanocolloids [37]. In the series of the PVP-protected Au/Pt bimetallic nanocolloids, the relation between catalytic activity and Pt content is expressed by a sigmoidal curve. High catalytic activity was achieved at the position of 40% Au and 60% Pt. The same tendency was observed on PγCyD-protected Au-core/Pt-shell bimetallic nanocolloids. The high catalytic activity can be explained by an electronic effect of neighboring Au on the surface Pt.

On the other hand, the next question is how the catalytic activity of Pt-core/Au-shell (inverted core/shell) structured bimetallic nanocolloids is. Figure 63.7 also depicts the relationship between the metal composition and the catalytic activity of PγCyD-protected Pt-core/Au-shell bimetallic nanocolloids for the quenching of hydrogen peroxide.

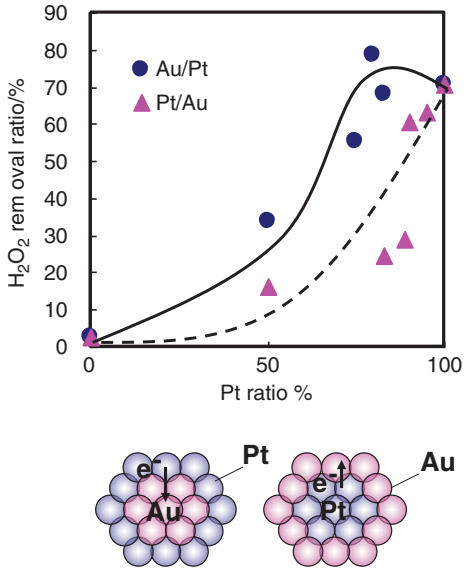


FIGURE 63.7 Plots of quenching activity of hydrogen peroxide versus the metal composition of PγCyD-protected Au-core/Pt-shell and Pt-core/Au-shell bimetallic nanocolloids.

Since gold has low activity and platinum has high activity for the quenching of hydrogen peroxide as described above, PγCyD-protected Pt-core/Au-shell bimetallic nanocolloids were believed to possess the activities just between the two corresponding monometallic nanocolloids. However, the catalytic activities of PγCyD-protected Pt-core/Au-shell bimetallic nanocolloids are lower than those expected at a molar ratio of <100 mol% of Pt. The transition of catalytic activity from the linear correlation can be explained by an electronic effect of the neighboring Au on the surface Pt. When the Pt core particles is covered mostly by Au atoms, the number of surface Pt atoms decreases, resulting in decrease of the catalytic activity.

ACKNOWLEDGMENTS

The authors thank not only all the coauthors of the cited references but also the coworkers who have worked with them, especially Miss M. Hashimura and Miss M. Nakao for their wide-ranging contributions to the present work. This work was partially supported by a Grant-in-Aid for Scientific Research (C) (Grant 24510158, to Y.S.) and a Grant-in-Aid for Challenging Exploratory Research (Grant 23656158, to Y.S. and N.T.) from the Ministry of Education, Culture, Sports, Science, and Technology (MEXT), Japan.

REFERENCES

[1] Ohshima, H. (ed.) (2012). *Electrical Phenomena at Interfaces and Biointerfaces*. Wiley, Hoboken, NJ.

[2] Toshima, N., Yonezawa, T. (1998). *New J. Chem.* **22**, 1179–1201.

[3] Schmid, G. (ed.) (1994). *Clusters and Colloids: From Theory to Applications*. VCH, Weinheim.

[4] Rampino, L.D., Nord, F.F. (1941). *J. ACS* **63**, 2745–2749.

[5] Hirai, H., Chawanya, H., Toshima, N. (1985). *Reactive Polym.* **3**, 127–141.

[6] Petit, C., Taleb, A., Pileni, M.P. (1999). *J. Phys. Chem. B* **103**, 1805–1810.

[7] Schmid, G., Maihack, V., Lantermann, F., Peschel, S. (1996). *J. Chem. Soc. Dalton Transact.* **1996**, 589–595.

[8] Toshima, N., Nakata, K., Kitoh, H. (1997). *Inorg. Chim. Acta* **265**, 149–153.

[9] Yonezawa, T., Tominaga, T., Toshima, N. (1995). *Langmuir* **11**, 4601–4606.

[10] Hirai, H., Yakura, N. (2001). *Polym Adv. Technol.* **12**, 724–733.

[11] Reetz, M.T., Helbig, W., Quaiser, S.A., Stimming, U., Breuer, N., Vogel, R. (1995). *Science* **267**, 367–369.

[12] Volokitin, Y., Sinzig, J., Jongh, L.J., Schmid, G., Vargaftik, M.N., Moiseev, I.I. (1996). *Nature* **384**, 621–623.

[13] Fendler, J.H. (ed.). *Nanoparticles and Nanostructured Films : Preparation, Characterization and Applications.* Wiley-VCH, Weinheim.

[14] Esumi, K., Takei, N., Yoshimura, T. (2003). *Colloids Surf. B* **32**, 117–123.

[15] Esumi, K., Houdatsu, H., Yoshimura, T. (2004). *Langmuir* **20**, 2536–2538.

[16] Akiyama, S., Yoshimura, T., Yoshimura, Esumi K. (2005). *J. Jpn Soc Colour Mater.* **78**, 112–121.

[17] Halliwell, B., Gutteridge, J.M.C. (1999) (ed.). *Free Radicals in Biology and Medicine*. Oxford Univ. Press, New York, pp. 36–104.

[18] Raha, S., Robinson, B.H. (2000). *Trends Biochem Sci.* **25**, 502–508.

[19] Bokov, A., Chaudhuri, A., Richardson, A. (2004). *Mech. Age. Devel.* **125**, 811–826.

[20] Faraday, M. (1857). *Phil. Transact. Roy. Soc. Lond.* **147**, 145–181.

[21] Rampino, L.D., Nord, F.F. (1941). *J. ACS* **63**, 2745–2749.

[22] Rampino, L.D., Nord, F.F. (1941). *J. ACS* **63**, 3268.

[23] Turkevich, J., Stevenson, P.C., Hillier, J. (1951). *Discuss. Faraday Soc.* **11**, 55–75.

[24] Turkevich, J., Kim, G. (1970). *Science* **169**, 873–879.

[25] Hirai, H., Nakao, Y., Toshima, N., Adachi, K. (1976). *Chem. Lett.* **1976**, 905–906.

[26] Kajita, M., Hikosaka, K., Iitshka, M., Kanayama, A., Toshima, N., Miyamaoto, Y. (2007). *Free Radical Res.* **41**, 615–626.

[27] Ueyama, N., Harada, A. (eds.) (2004). *Macromolecular Nanostructured Materials*. Kodansha, Tokyo, pp. 182–196.

[28] Toshima, N. (2004). *Encyclopedia of Nanoscience and Nanotechnology*. Marcel Dekker, New York, pp. 1869–1880.

[29] Toshima, N., Kushihashi, K., Yonezawa, T., Hirai, H. (1989). *Chem. Lett.* **1989**, 1769–1772.

[30] Toshima, N., Harada, M., Yonezawa, T., Kushihashi, K., Asakura, K. (1991). *J. Phys. Chem.* **95**, 7448–7453.

[31] Toshima, N. (1990). *J. Macromol. Sci. Chem.* **A27**, 1225–1238.

[32] Torigoe, K., Esumi, K. (1993). *Langmuir* **9**, 1664–1667.

[33] Torigoe, K., Nakajima, Y., Esumi, K. (1993). *J. Phys. Chem.* **97**, 8304–8309.

[34] Mulvaney, P., Giersig, M., Henglein, A. (1993). *J. Phys. Chem.* **97**, 7061–7064.

[35] Wang, Y., Toshima, N. (1997). *J. Phys. Chem. B* **101**, 5301–5306.

[36] Shiraishi, Y., Hashimura, M., Nakao, M., Ishizu, T., Kajita, M., Miyamaoto, Y. (2011). *Supramol. Chem.* **23**, 195–198.

[37] Yonezawa, T., Toshima, N. (1993). *J. Mol. Catal.* **83**, 167–181.

64

SILVER AND GOLD NANOCOMPOSITES: AMINO ACID SIDECHAIN EFFECT ON MORPHOLOGY

ZOYA ZAHEER* AND RAFIUDDIN

**Department of Chemistry, Faculty of Science, King Abdulaziz University, P.O. Box, 80203, Jeddah, 21589, Saudi Arabia*
Department of Chemistry, Aligarh Muslim University, Aligarh-202002, UP, India

64.1 INTRODUCTION

The motivation for biointerface science stems from the urgent need to increase the understanding of interactions between biomolecules and surfaces. The behavior of complex macromolecular systems at material interfaces are important in the fields of biology, biotechnology, diagnostics, and medicine. Molecularly designed interfaces, colloidal and/or nanoparticle interfaces has been the subject of various authors from the 1857. Faraday reported the formation of deep red solutions of colloidal gold by reduction of an aqueous solution of chloroaurate using phosphorus in a two-phase system. He investigated the optical properties of thin films prepared from dried colloidal solutions and observed reversible color changes of the films upon mechanical compression [1]. Topics of interest include, but are not limited to neural interfaces, cells in engineered microenvironments and regenerative medicine, computational and modeling approaches to biointerfaces, membranes and membrane-based biosensing, peptides, carbohydrates, and DNA at biointerfaces. The interfaces are omnipresent in Nature and can be used broadly as ideal means for the self-assembly of nanoparticles. The chemistry of nanosized and colloidal metal particles in terms of their physicochemical properties in solution has come a long way, and their importance in various fields of chemistry and physics are unlimited [2–10]. The reason for using colloidal metal solutions was to apply these materials as catalysts for free-radical reactions initiated by light or ionizing radiation. In these reactions, electrons are transferred across the particle–solution interface similar to electrode reactions in electrochemistry. The small particles are therefore referred to as *microelectrodes*. Various theories have been applied for the preparation and characterization of small particles [11–15]. In colloid preparation, the hydrated electrons and reducing organic radicals that are generated in the radiolysis of aqueous solutions reduce dissolved metal ions, thus producing unusual valence states.

One team of researchers [16] observed an absorption at 310 nm after application of a 0.1-μs pulse of high-energy electrons to a 10^{-4} mol dm^{-3} solution of silver sulfate and attributed it to the free silver atom produced in the reaction for the first time

$$Ag^{+} + e^{-}_{aq} \longrightarrow Ag^{0} \qquad (64.1)$$

which subsequently coalesce to form larger particles [6]. Most studies on the surface chemistry of metal particles have been performed with silver, because the position and shape of the plasmon absorption band of this metal is strongly influenced by chemical modification to the surface. Whereas these changes can be used as sensitive indicators for the occurrence of an interaction between the metal particles and a dissolved substrate, the changes themselves are not yet understood in detail [6]. The silver atom formed in the reaction in Eq. (64.1) reacts rapidly with an Ag^{+} ion to yield Ag^{2+} [Eq. (64.2)], and the Ag^{2+} ions dimerize [Eq. (64.3)]. $Ag_4{}^{2+}$ undergoes

Encyclopedia of Biocolloid and Biointerface Science, Volume 2, First Edition. Edited by Hiroyuki Ohshima.
© 2016 John Wiley & Sons, Inc. Published 2016 by John Wiley & Sons, Inc.

further reaction to yield larger aggregates until Ag_8 is formed in solution [17–19]:

$$Ag^+ + Ag^0 \longrightarrow Ag_2^+ \quad (64.2)$$

$$2Ag_2^+ \longrightarrow Ag_4^{2+} \quad (64.3)$$

$$2Ag_4^{2+} \longrightarrow Ag^+ + Ag_7^{3+} \quad (64.4)$$

$$2Ag_7^{3+} \longrightarrow Ag_8 + 6Ag^+ \quad (64.5)$$

$$2Ag_7^{3+} \longrightarrow Ag_9^+ + 5Ag^+ \quad (64.6)$$

In absence of a stabilizing polymer, the rate constants for reactions (64.5) and (64.6) are 8×10^9 and 2.6×10^9 mol^{-1} dm^3 s^{-1}, respectively [6]. In absence of a polyanion, the growth stops at the stage of $Ag_4{}^{2+}$ [20]. The cluster $Ag_6{}^{4+}$ and other highly charged silver clusters have been detected in zeolites. In aqueous solution, the stabilizing effect, exerted by the anionic charges in a zeolite cage, is not present. It has been established that exposure of zeolite-stabilized $Ag_6{}^{n+}$ clusters to water results in fragmentation [21]. For the gold reduction, reaction can be summarized as follows:

$$AuCl_4^- + 3e^- \longrightarrow Au^0 + 4Cl^- \quad (64.7)$$

Metal nanoparticles (monometallic and bimetallic) have exhibited their diversity and potential applications in, for instance, information technology, optoelectronics, sensing, biocatalyst and plasmonics [22–28]. There has been a great deal of efforts applied to the development of new methodologies for preparing a range of metal nanoparticles having uniform sizes and aspect ratios; such approaches include the use of rigid and soft templates, seed mediated growth, polymers, and surfactants and co-surfactants for crystal growth of nanomaterials [29–32].

Amino acids (the basic structural units of proteins; facilitate a wide range of physiological functions) are biologically important substances whose activities depend largely on their redox behavior. Amino acids are known to provide different coordination sites: at the N, O, and S centers that can coordinate with silver ions and with metallic nanoparticles. Amino acids play a significant role in the preparation of advanced nanomaterials of silver. It has been recognized that amino and carboxyl functional groups of amino acids undergo chemical transformations while the side chain remains intact. Another team [33] reported that the sidechain –OH group of tyrosine residues and –COOH groups of aspartic acid and/or glutamic acid residues are responsible for the reduction of Ag^+ ions and for the anisotropic growth of silver nanocrystals into nanoplates, respectively. The process of silver nanoplates formation was kinetically controlled and depending on the ratio of –COOH groups to tyrosine per peptide molecule and silver surface. Different-shaped and different-sized Au–Ag nanocomposites from gold nanorods in presence of various amino acids such as arginine, cysteine, glycine, glutamate, glutamine, histidine, lysine, and methionine have been synthesized [34]. The –SH group of cysteine was responsible for the formation of quantum dots of silver [35]. Extensive research in finely dispersed metallic particles has clearly established that size, combination, and internal structure strongly affect their properties in both dispersed and condensed states [36]. Numerous methods have been used for the preparation of ultrasmall metal nanoparticles, such as molecular beam epitaxy [37], chemical vapor deposition [38], reduction by ionizing radiation [6], thermal decomposition in organic solvents [39], chemical or photoreduction in reverse micelles [40], and chemical reduction with [41] or without stabilizing polymers [42]. The colors of the silver colloidal sols vary depending on the method of preparation and the state of aggregation. Silver nanocrystallities, mostly hydrosols, are widely studied because of their applicability in surface-enhanced Raman scattering [43–45] and their use in the photographic process [46]. Prolate spheroids and bispherical particles are particularly effective in surface-enhanced Raman scattering [47, 48].

The main objective of this chapter is to summarize the role of amino acid sidechains that influence morphology of nanoparticles and their implications in cellular uptake. In a biological medium, nanoparticles may interact with biomolecules such as carbohydrates, proteins, nucleic acids, lipids, and even biological metabolites because of their nanosize and large surface-to-mass ratio. Of particular importance is the adsorption of amino acids on the nanoparticle surface. Controlling size and shape simultaneously remains an extremely difficult task, since the outcome of these syntheses is generally determined by a number of factors and is only partially characterized by the interplay of kinetics and thermodynamics. This difficulty increases when silver nanoparticles with a controlled size and shape must be synthesized by green chemistry. Sulfur-containing amino acids have three possible reactions and/or coordination sites: at the S, O, and N centers. Sulfur has been established as the most susceptible element to gain electrons from the oxidizing agents. In methionine [2-amino-4-(methylthio)butanoic acid], the reactive site is partially blocked by a methyl (–CH_3) group. Recognizing the importance of amino acids in the synthesis of silver nanomaterials as reducing and nucleophilic reagents, we have chosen to discuss the role of amino acids, especially methionine in this chapter.

64.2 ROLE OF SIDECHAIN

The chemical literature contains abundant reports aimed at clarifying the role of α- amino acids in the synthesis of different-shaped/-sized silver–gold nanocomposites and their nanoparticles [49–54]. One team of investigators [50] reported the surface chemistry of gold colloids in presence

of different amino acids (neutral, acidic, and basic) and suggested that basic sidechain of amino acids (glutamine, arginine, lysine, histidine, cysteine, methionine, and tyrosine) can act as cross-linking agent for pairs of gold particles, whereas the amino acids with nonpolar (alanine) and acidic sidechains (aspartic and glutamic acids) produced no change in the spectra of gold nanoparticles. These investigators also suggested the connection between gold nanoparticles via amino acids, in the absence/presence of glutaraldehyde as a molecular "bridge," over a wide range of pH values.

Lysine, a basic sidechain amino acid, has been used in the synthesis of gold nanowires [50]. Length of the nanowires (5 nm and length varying from 80 to 200 nm) might be controlled at a specific pH (∼8.4–9.5) and at a constant molar ratio of gold and lysine.

The key factor for the formation of linear nanowires is believed to be a subtle attractive (cross-linking) force, provided by the basic sidechain of lysine. Gold nanoplates (with thicknesses of <30 nm) have been synthesized in large quantities using aspartate-mediated reduction of gold salt [55], suggesting that specific interactions between the amino acid and the crystal lattice structure alter the surface distribution with amino acid concentrations and reduction processes.

The reaction pathways and the final oxidation products depend on the experimental conditions and the nature of the amino acid sidechain. Aromatic sidechain amino acids were oxidized more rapidly than the alkyl sidechain amino acids [56, 57]. Amino acids are known to provide different coordination sites at the N, O, and S centers that can coordinate with a variety of metal ions. Sulfur has been established as the most susceptible element to gain electrons from oxidizing agents [58]. The reactions of silver and gold ions with sulfur-containing amino acids (methionine and cysteine) have been investigated for several reasons [50,53,54]. Methionine has rich applications in redox and surface chemistry as a reductant and a stabilizer [59]. The literature describing the preparation of silver nanoparticles is especially broad, since classical colloid methods are combined with modern nanotechnology leading to many procedures for particle preparation, control of particle size, and surface modification. Silver nanoparticles have been the subject of great interest for decades because of their use in catalysis, photography, photonics, electronics, labeling, imaging, sensing, and surface-enhanced Raman scattering. Silver nanoparticles capped with various stabilizers (surfactants or polymers) have been widely studied [60–64]. Silver atoms that are reduced from silver ions by ascorbate deposit onto the surfaces of the gold nanoparticles to form dumbbell-shaped silver–gold nanoparticles whose morphologies differ depending on the pH and the concentration of silver ions and glycine. By controlling the value of pH as well as the amount of glycine in the growth solutions, I-shaped, dumbbell-shaped, and/or peanut-shaped gold core/gold–silver shell nanoparticles from gold nanoparticles seeds can be achieved [65]. Glycine, used to control the pH of the solutions, also plays a role in controlling the reduction of silver and gold ions. In the presence of high concentrations of glycine, AgCl and AgBr do not precipitate, mainly because of the formation of glycine–silver complexes. These investigators also pointed out that the as-prepared silver and gold nanoparticles were stable for >3 months in glycine solution after removal of CTAB; this result suggests that glycine acts as a capping agent that stabilizes the silver–gold nanoparticles. The silver and gold nanoparticles having different morphologies (shape, size, and the size distribution) prepared simply by controlling the nature of the amino acid species and its concentration, the pH, and the incubation time were summarized in Table 64.1. Functionalized nanoparticles were conjugated with protein molecules through electrostatic attraction between the surface-terminated negatively charged carboxylate groups of glutamic acid and the positively charged amino groups of the protein [70].

The reduction of $HAuCl_4$ by acidic amino acid (i.e., glutamic acid) occurred through the transfer of electrons from the $-NH_2$ group to the Au^{3+} ion leading to the formation of Au^0. This metallic gold then nucleates and grows to form gold nanoparticles, and is subsequently capped and stabilized by the amino acid. The amino group of the amino acid is oxidized to a positive radical, due to the transfer of an electron from the amine to the gold ion. The visible spectrum of the resulting gold nanoparticles showed one sharp peak. The shape of the spectra markedly changed from sharp to much broader, indicating that aggregation of the gold nanoparticles occurred by increasing the concentration of glutamic acid. The color of the colloidal solutions changed from reddish, dark red, to blue. The change in color of colloidal gold solutions from red to blue as a consequence of aggregation is a well-understood phenomenon. Glutamic acid acted as a reducing as well as stabilizing and/or capping agent in the synthesis of silver and gold nanoparticles, which might be due to the association and adsorption of acidic sidechain ($HOOCCH_2CH_2$-) onto the surfaces of metal nanoparticles [67,70].

64.3 MECHANISM IN THE FORMATION OF SILVER NANOPARTICLES

When $AgNO_3$ is allowed to react with methionine in presence of CTAB and sodium hydroxide, a yellow color appears as the reaction proceeds, indicating the formation of silver nanoparticles. To confirm the nature of the yellow color and determine the size of the nanoparticles, spectra of the resulting color were recorded by using a Spectronic 21D spectrophotometer. Spectrophotometric and transmission electron microscopic (TEM) measurements were carried out using a JEOL, JEM-1011 model, operating at 300 kV, respectively. For the TEM, samples were prepared by placing

TABLE 64.1 Effects of Sidechain on Morphologies of Silver and Gold Nanoparticles

Sidechain	Color of sol	Morphology; media	Ref.
Silver Nanoparticles			
$HSCH_2$	Golden yellow	λ_{max} = 410 nm, quantum dots; CTAB	35
CH_3SCH_2	Purple	λ_{max} = 550 nm, corn; CTAB	66
$HOOC(CH_2)_2$	Yellow	λ_{max} = 325 nm, spherical; CTAB	67
$HOOCCH_2$	Yellow	λ_{max} = 400 nm, spherical; CTAB	68
$HOPhCH_2$	Yellow	λ_{max} = 400 nm, spherical; CTAB	69
Gold Nanoparticles			
$HSCH_2$	Pink	λ_{max} = 500 nm, spherical; Thiol	50
$HOOCCH_2$	Purple	λ_{max} = 500 nm, spherical; CTAB	68
$NH_2(CH_2)_4$	Pink	λ_{max} = 500 nm, rods; Thiol	50
$HOOC(CH_2)_2$	Pink	λ_{max} = 525 nm, spherical; CTAB	70
$HOPhCH_2$	Pink	λ_{max} = 500 nm, spherical; CTAB	71
Gold–Silver Nanocomposites			
H	Pink	λ_{max} = 500 nm, dumbbell; I, peanut-shaped	65
CH_3SCH_2	Pink	λ_{max} = 525 nm, dumbbell-shaped; CTAB	34
$NH_2(CH_2)_4$	Pink	λ_{max} = 500 nm, dumbbell-shaped; CTAB	34
imidazole	Pink	λ_{max} = 500 nm, peanut-shaped; CTAB	34
CH_3SCH_2	Pink	λ_{max} = 500 nm, corn-shaped; CTAB	34

a drop of silver sol in a carbon-coated standard copper grid (300 mesh) and allowing the solvent to evaporate. The reaction mixture containing the required concentrations of Ag^+ ions, CTAB and H_2O (for dilution) was thermally equilibrated at room temperature (30°C) and this was added in a glass-stoppered two-necked flask fitted with a spiral double-walled condenser to check evaporation. The reactions were started after the addition of measured amount of methionine and NaOH solutions, preequilibrated at the same temperatures. The reaction volume was 50 cm^3 throughout. The formation of yellow color (progress of reaction) was followed by measuring the absorbance at 550 nm (neither reactants nor products showed any absorbance at this wavelength) on the Spectronic 21D spectrophotometer. A control dynamic pH meter fitted with a combination electrode was used to measure the pH of the working solutions. The apparent first-order rate constants were calculated from the slopes of the plots of ln $(a/(1-a))$ versus time, where $a = A_t/A_\alpha$ and A_t and A_α are the absorbance at time t and α, respectively. Duplicate runs gave rate constants that were reproducible to within 5%.

The effect of $[OH^-]$ [range $(0.0–3.0) \times 10^{-4}$ mol dm^{-3}] was studied at constant $[Ag^+] = 10.0 \times 10^{-4}$ mol dm^{-3}, $[CTAB] = 8.0 \times 10^{-4}$ mol dm^{-3} and [methionine] = 10.0×10^{-4} mol dm^{-3}. The spectra of yellow color silver sol formation as a function of [NaOH] are depicted graphically in Fig. 64.1. The most characteristic part of the silver sol is the sharp surface plasmon resonance band observable at ~400 nm. The spectra of silver sol cover the whole visible region of the spectrum and is yellow-brown in color. The shape of the spectra gives information about the size, shape, the size distribution and the surface properties of the metal particles. The nature of the spectra was unsymmetric, indicating the presence of aggregated particles (polydispersity). The plots of log(absorbance) versus log(wavelength) are linear (Fig. 64.2). It is well known that the yellow color is due to the formation of colloidal silver particles in the spectrum, which be due mainly to the scattering of light (Rayleigh's law). Thus, we may safely conclude that the available data are consistent with the formation of colloidal silver nanosized particles under the present experimental conditions. The absorbance of the silver sol increases with

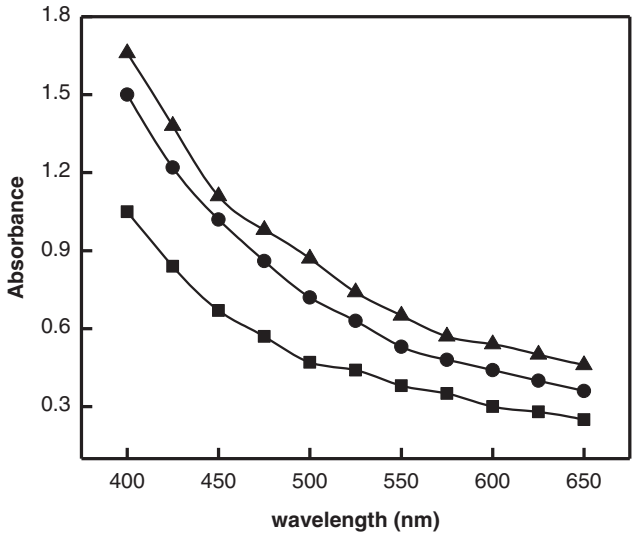


FIGURE 64.1 Spectra of silver nanoparticles. Reaction conditions: [methionine] = 10.0×10^{-4} mol dm^{-3}; $[Ag^+] = 10.0 \times 10^{-4}$ mol dm^{-3}; $[CTAB] = 8.0 \times 10^{-4}$ mol dm^{-3}; $[OH^-]$ = 2.0 (■), 8.0 (•) and 20.0×10^{-4} mol dm^{-3} (▲).

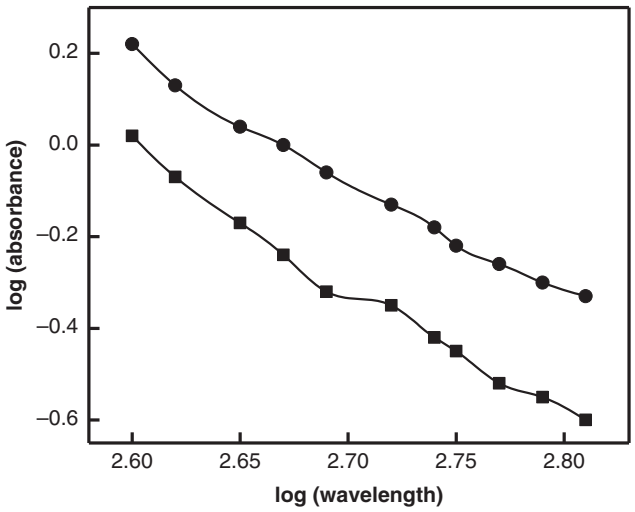


FIGURE 64.2 Plots of log(absorbance) versus log(wavelength) to the yellow color silver sol for the data in Fig. 64.1((■) and (•)).

increasing [OH^-] until it reaches a maximum, after which it decreases. These observations are summarized in Fig. 64.3 as an absorbance–[OH^-] profile. The increase/decrease behavior (hypochromic shift) of absorbance after a definite time interval (30 min) may be explained in terms of adsorption of OH^- onto the positive surface of metallic silver particles electrostatically, which, in turn, increases the Fermi level of particles. The nucleophiles and neutral stabilizing polymers have a strong effect on the plasmon absorption band of silver and/or metal nanometer particles and donate the electron density to the particles via lone pairs of electrons.

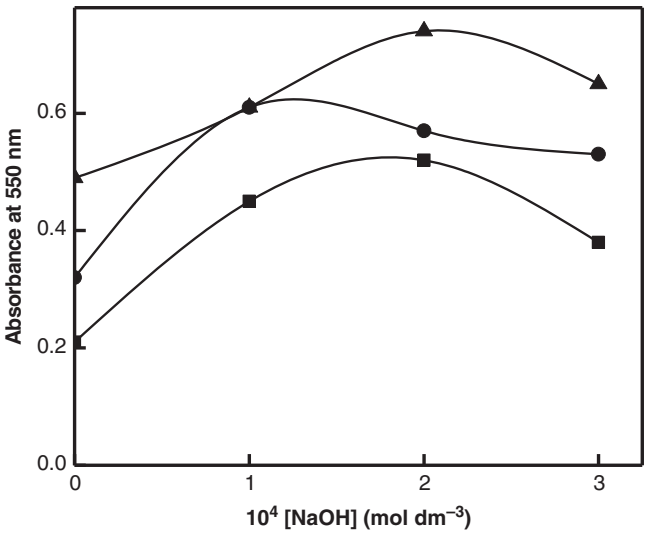


FIGURE 64.3 Plot showing the effect of [NAOH] on absorbance of silver nanoparticle formation after 30 min of mixing of silver(I) and methionine. Reaction conditions: [methionine] = 10.0×10^{-4} mol dm^{-3}; [Ag^+] = 10.0×10^{-4} mol dm^{-3}; [CTAB]= 8.0×10^{-4} mol dm^{-3}; [OH^-] = 2.0 (■), 8.0 (•) and 20.0×10^{-4} mol dm^{-3} (▲).

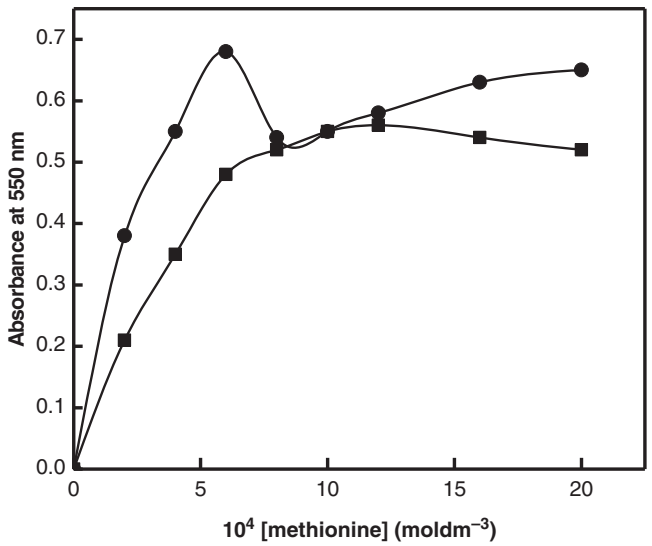


FIGURE 64.4 Plot showing the effect of [methionine] on the absorbance of silver nanoparticles formation after 30 min of mixing of silver(I) and methionine in absence (■) and presence (•) of [OH^-] (= 2.0×10^{-4} mol dm^{-3}). Reaction conditions: [Ag^+] = 10.0×10^{-4} mol dm^{-3}; [CTAB] = 8.0×10^{-4} mol dm^{-3}.

The effect of [methionine] on the silver sol formation was investigated at different methionine concentrations (2.0×10^{-4} to 20.0×10^{-4} mol dm^{-3}) at constant [CTAB] = 8.0×10^{-4} mol dm^{-3}, [Ag^+] = 10.0×10^{-4} mol dm^{-3} in absence and presence of [NaOH] (= 3.0×10^{-4} mol dm^{-3}) and temperature = 25°C. For a specific reaction time (viz., 30 min), the absorbance first increased until it reached a maximum, and then decreased with [methionine] (Fig. 64.4). Therefore, methionine also acts as a stabilizer. The presence of the $–NH_2$ group is responsible for the adsorption of

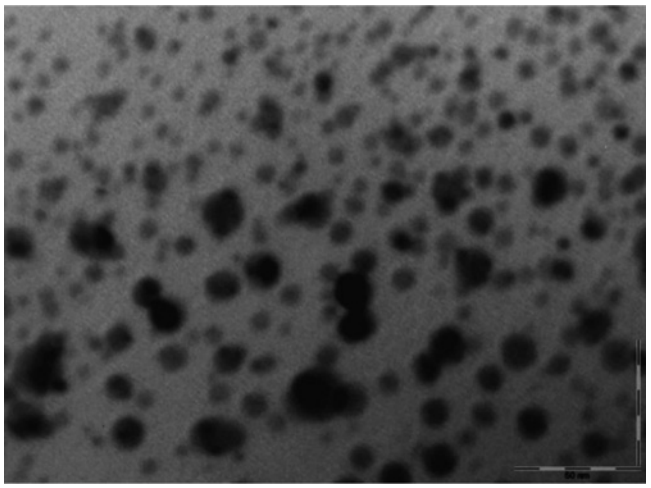
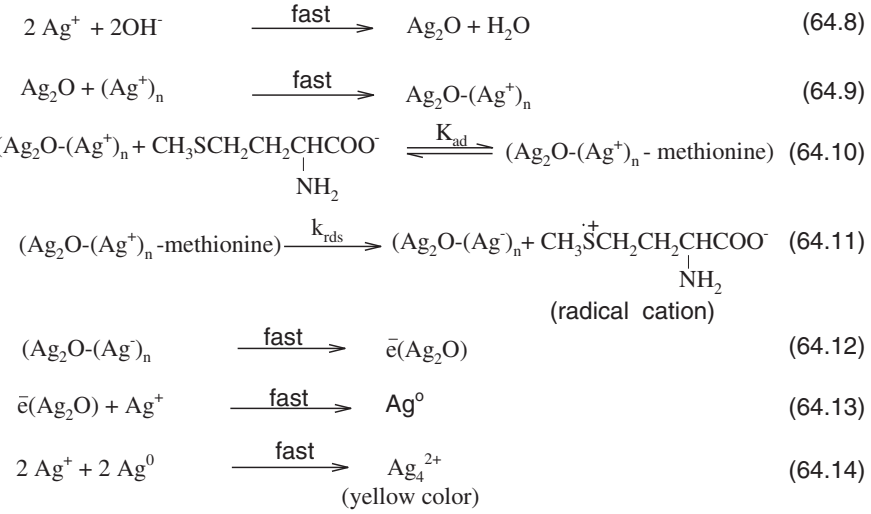


FIGURE 64.5 TEM images of silver nanoparticles. Reaction conditions: [methionine] = 10.0×10^{-4} mol dm^{-3}; [Ag^+] = 10.0×10^{-4} mol dm^{-3}; [CTAB] = 8.0×10^{-4} mol dm^{-3}; [OH^-] = 2.0×10^{-4} mol dm^{-3}.

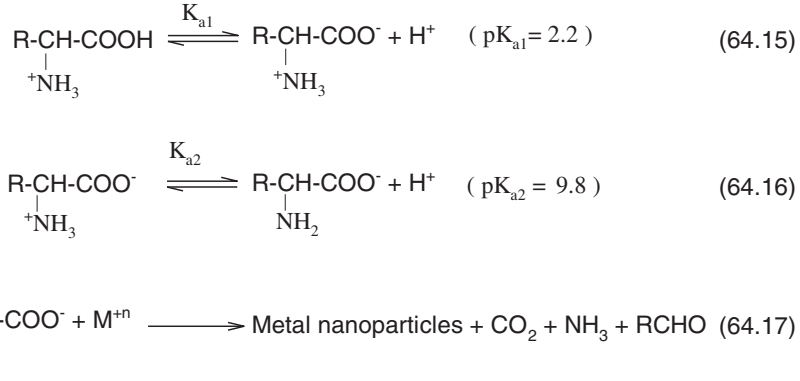


Scheme 64.1 Reduction of Ag^+ ions by mehtionine in basic medium.

methionine on the surface of silver particles, which easily donates the lone pairs of electrons, leading to the formation of stable water-soluble nanosized silver particles. The most interesting features of the present observations are the formation of yellow-color silver sol in presence of NaOH. The experimental finding is that the colorless reaction mixture became purple in absence of NaOH; instead of yellow, which is the characteristic of nanosized monodispersed silver particles. Hydroxide ions play a crucial role in the formation of silver nanoparticles (the hydroxide ions is known to have a catalytic effect on the formation of silver sols, providing a significant change in the reactivity of Ag^+ ions, thus allowing initiation of the electron transfer from reductant to Ag^+ ions, which in turn, prevents a fast corrosion of the very small silver particles at early stages of the reaction).

To evaluate the order with respect to [silver(I)], the measurements were made by recording the changes in the intensity of the plasmon absorption band at 550 nm. The reaction rate remains constant with an increase in [silver(I)] ($k_{obs} = 2.5 \pm 0.5 \times 10^{-4}$ s^{-1} at [silver(I)] = 1.0, 2.0, 4.0, 6.0, 8.0,10.0, and 12.0×10^{-4} mol dm^{-3}) at constant [methionine] (10.0×10^{-4} mol dm^{-3}), [CTAB] (8.0×10^{-4} mol dm^{-3}), indicating the first-order dependence on $[Ag^+]$.

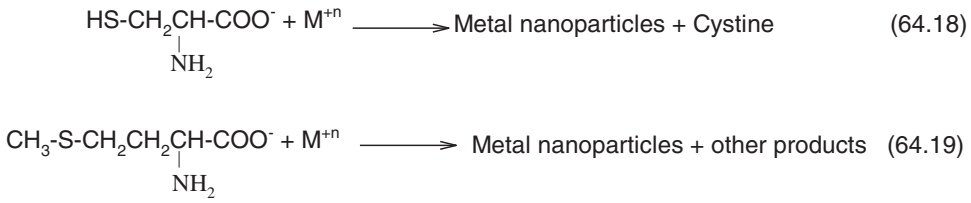
In order to determine the shape, size, and size distribution of silver nanoparticles, the TEM images were also determined by TEM. Figure 64.5 shows a TEM image of silver sol at a constant $[Ag^+]$ / [CTAB] ratio of 1.0. In agreement with the UV–Vis spectrophotometric observations, the TEM pictures reveal silvernanoparticles are aggregated and roughly spherical with a rather similar diameter of 20 nm. On



where R = H, CH_3, $HOOCCH_2$ and $HOOC(CH_2)_2$ for glycine, alanine, aspartic acid and glutamic acid

$M^{+n} = Ag^+$ and Au^{3+}

Scheme 64.2 Formation of silver and gold metal nanoparticles by amino acids.



Scheme 64.3 Formation of silver and gold metal nanoparticles by sulfur-containing amino acids.

the basis of the above results and discussion, the mechanism shown in Scheme 64.1 is proposed for the reduction of Ag^+ ions by methionine in presence of OH^- ions.

Scheme 64.1, Eqs. (64.8) and (64.9) represent the fast formation of colloidal Ag_2O and adsorption of Ag^+ from solution onto the surface of Ag_2O particles, respectively. The next step is the adsorption of methionine onto the surface of colloidal Ag_2O-$(Ag^+)_n$ particles [Eq. (64.10)] through the lone pair electrons of S and N atoms of methionine. In Eq. (64.11), one-step one-electron transfer occurs from the S atom to the Ag^+ ions. Silver ions adsorbed on the surface of Ag_2O are then reduced via reaction with the delocalized electrons [Eqs. (64.12) and (64.13)]. It is well known that various species such as Ag_2^+, Ag_3^{2+}, Ag_4^{2+}, $Ag_{8,}$ Ag^+, or Ag_9^+ and Ag_6^{4+} exist in aqueous solution and in zeolites. Out of these species, only Ag_4^{2+} can be stabilized for a long time in presence of a polyanion even under air and growth stops at the stage of this species. Under our experimental conditions of working solutions, the yellow color of the silver sol is due to the formation of Ag_4^{2+}. The participation of amino acid sidechain in the formation of metal nanoparticles is summarized in Schemes 64.2 and 64.3 for nonpolar or polar sidechains and sulfur-containing amino acids, respectively.

REFERENCES

[1] Faraday, M. (1857). The Bakerian lecture: Experimental relations of gold (and other metals) to light. *Phil. Transact.* **147**, 145–181.

[2] Henglein, A. (1989). Small-particle research: Physicochemical properties of extremely small colloidal metal and semiconductor particles. *Chem. Rev.* **89**, 1861–1873.

[3] Henglein, A., Mulvaney, P., Linnert, T. (1991). Chemistry of Ag_n aggregates in aqueous solution: Non-metallic oligomeric clusters and metallic particles. *Faraday Discuss.* **92**, 31–44.

[4] Schmid, G. (1992). Large clusters and colloids. Metals in the embryonic state. *Chem. Rev.* **92**, 1709–1727.

[5] Kamat, P.V. (1993). Photochemistry on nonreactive and reactive (semiconductor) surfaces. *Chem. Rev.* **93**, 267–300.

[6] Henglein, A. (1993). Physicochemical properties of small metal particles in solution: "Microelectrode" reactions, chemisorption, composite metal particles, and the atom-to-metal transition. *J. Phys. Chem.* **97**, 5457–5471.

[7] Pileni, M.P. (1993). Reverse micelles as microreactors. *J. Phys. Chem.* **97**, 6961–6973.

[8] Littau, K.A., Szajowski, P.J.Muller, A.J., Kortan, A.R., Brus, L.E. (1993). A luminescent silicon nanocrystal colloid via a high-temperature aerosol reaction. *J. Phys. Chem.* **97**, 1224–1230.

[9] Yonezawa, T., Toshima, N. (1995). Mechanistic consideration of formation of polymer-protected nanoscopic bimetallic clusters. *J. Chem. Soc. Faraday Transact.* **91**, 4111–4119.

[10] Lee, A.F., Baddeley, C.J., Hardacre, C., Ormerod, R.M., Lambert, R.M. (1995). Structural and catalytic properties of novel Au/Pd bimetallic colloid particles: EXAFS, XRD, and acetylene coupling. *J. Phys. Chem.* **99**, 6096–6102.

[11] Henglein, A. (1988). Mechanism of reactions on colloidal microelectrodes and size quantization effects. *Topics Curr. Chem.* **143**, 113–180.

[12] Watanabe, T., Gerischer, H. (1981). Photoelectrochemical studies on gold electrodes with surface oxide layers: Part II. Discrimination between the surface photoprocess and photohole emission. *J. Electroanal. Chem. Interfacial Electrochem.***122**, 73–91.

[13] Marignier, J.L., Belloni, J., Delcourt, M.O., Chevalier, J.P. (1985). Microaggregates of non-noble metals and bimetallic alloys prepared by radiation-induced reduction. *Nature* **317**, 344–345.

[14] Lin, S.-T., Franklin, M.T., Kalbunde, K.J. (1986). Nonaqueous colloidal gold. Clustering of metal atoms in organic media.12. *Langmuir* **2**, 259–260.

[15] Fischer, Ch.-H., Weller, H., Katsikas, L., Henglein, A. (1989). Photochemistry of colloidal semiconductors. 30. HPLC investigation of small CdS particles. *Langmuir* **5**, 429–432.

[16] Baxendale, J.H., Fielden, E.M., Keene, J.P. (1965). Formation of Cu^{III} in the radiolysis of Cu^{2+} solution. In Ebert, M., Keene, J.P., Swallow, A.J., Baxendale, A.J. (eds)., *Pulse Radiolysis*. Academic Press, London, p. 207.

[17] Ershov, B.G., Janata, E., Henglein, A. (1993). Growth of silver particles in aqueous solution: Long-lived "magic" clusters and ionic strength effects. *J. Phys. Chem.* **97**, 339–343.

[18] Ershov, B.G., Janata, E., Henglein, A., Fojtik, A. (1993). Silver atoms and clusters in aqueous solution: Absorption spectra and the particle growth in the absence of stabilizing Ag^+ ions. *J. Phys. Chem.* **97**, 4589–4594.

[19] Janata, E., Henglein, A., Ershov, B.G. (1994). First clusters of Ag^+ ion reduction in aqueous solution. *J. Phys. Chem.* **98**, 10888–10890.

[20] Mulvaney, P., Henglein, A. (1990). Long-lived nonmetallic silver clusters in aqueous solution: A pulse radiolysis study of their formation. *J. Phys. Chem.* **94**, 4182–4188.

[21] Wasowicz, T., Michalik, J. (1991). Reactions of silver atoms and clusters in Ag-NaA zeolites. *Radiation Phys. Chem.* **37**, 427–432.

[22] El-Sayed, M.A. (2001). Some interesting properties of metals confined in time and nanometer space of different shapes. *Acc. Chem. Res.* **34**, 257–264.

[23] Huynh, W.U., Dittmer, J.J., Alivisatos, A.P. (2002). Hybrid nanorod-polymer solar cells. *Science* **295**, 2425–2427.

[24] Wilson, O., Wilson, G.J., Mulvaney, P. (2002), Laser writing in polarized silver nanorod films. *Adv. Mater.* **14**, 1000–1004.

[25] Slot, J.W., Geuze, H.J. (1985). A new method of preparing gold probes for multiple-labeling cytochemistry. *Eur. J. Cell Biol.* **38**, 87–93.

[26] Khitrov, G.A., Strouse, G.F. (2003). ZnS nanomaterial characterization by MALDI-TOF mass spectrometry. *J. ACS* **125**, 10465–10469.

[27] Toshima, N., Harada, M., Yamazaki, Y., Asakura, K. (1992). Catalytic activity and structural analysis of polymer-protected gold-palladium bimetallic clusters prepared by the simultaneous reduction of hydrogen tetrachloroaurate and palladium dichloride. *J. Phys. Chem.* **96**, 9927–9933.

[28] Lee, A.F., Baddeley, C.J., Hardacre, C., Ormerod, R.M., Lambert, R.M., Schmid, G., West, H. (1995). Structural and catalytic properties of novel Au/Pd bimetallic colloid particles: EXAFS, XRD, and acetylene coupling. *J. Phys. Chem.* **99**, 6096–6102.

[29] Jana, N.R., Gearheart, L., Murphy, C.J. (2001). Seed-mediated growth approach for shape-controlled synthesis of spheroidal and rod-like gold nanoparticles using a surfactant template. *Adv. Mater.* **13**, 1389–1393.

[30] Yang, X.- H., Wu, Q.-S., Li, L., Ding, Y.-P., Zhang, G.-X. (2005). Controlled synthesis of the semiconductor CdS quasi-nanospheres, nanoshuttles, nanowires and nanotubes by the reverse micelle systems with different surfactants. *Colloids Surf. A* **264**, 172–178.

[31] Davis, R.J., Boudart, M. (1994). Structure of supported PdAu clusters determined by X-ray absorption spectroscopy. *J. Phys. Chem.* **98**, 5471–5477.

[32] Harada, M., Asakura, K., Toshima, N. (1993). Catalytic activity and structural analysis of polymer-protected gold/palladium bimetallic clusters prepared by the successive reduction of hydrogen tetrachloroaurate(III) and palladium dichloride. *J. Phys. Chem.* **97**, 5103–5114.

[33] Xie, J., Lee, J.Y., Wang, D.I.C., Ting, Y.P. (2007). Silver nanoplates: From biological to biomimetic synthesis. *ACS Nano* **1**, 429–439.

[34] Huang, Y.-F., Lin, Y.-W., Chang, H. (2006). Growth of various Au–Ag nanocomposites from gold seeds in amino acid solutions. *Nanotechnology* **17**, 4885–4894.

[35] Khan, Z., Talib, A. (2010). Growth of different morphologies (quantum dots to nanorod) of Ag-nanoparticles: Role of cysteine concentrations. *Colloids Surf. B: Biointerfaces* **76**, 164–169.

[36] Klabunde, K.J. (2001). *Nanoscale, Materials in Chemistry.* Wiley, New York. 292.

[37] Bahnemann, D.W. (1993). Ultrasmall metal oxide particles: Preparation, photophysical characterization, and photocatalytic properties. *Israel J. Chem.* **33**, 115–136.

[38] Satoh, N., Kimura, K. (1989). Metal colloids produced by means of gas evaporation technique. V. Colloidal dispersion of Au fine particles to hexane, poor dispersion medium for metal sol. *Bull. Chem. Soc. Japan* **62**, 1758–1763.

[39] Esumi, K., Tano, T., Torigoe, K., Meguro, K. (1990). Preparation and characterization of bimetallic palladium-copper colloids by thermal decomposition of their acetate compounds in organic solvents. *Chem. Mater.* **2**, 564–567.

[40] Pileni, M.P., Lisiecki, I., Motte, L., Petit, C., Cizeron, J., Moumen, N., Lixon P. (1993). Synthesis "in situ" of nanoparticles in reverse micelles. *Progress Colloid Polym. Sci.* **93**, 1–9.

[41] Toshima, N., Yonezawa, T., Kushihashi, K. (1993). Polymer-protected palladium–platinum bimetallic clusters: Preparation, catalytic properties and structural considerations. *J. Chem. Soc. Faraday Transact.* **89**, 2537–2543.

[42] Liz-Marzan, L.M., Philipse, A.P. (1995). Stable hydrosols of metallic and bimetallic nanoparticles immobilized on imogolite fibers. *J. Phys. Chem.* **99**, 15120–15128.

[43] De, S., Pal, A., Jana, N.R., Pal, T. (2000). Anion effect in linear silver nanoparticle aggregation as evidenced by efficient fluorescence quenching and SERS enhancementJ. *J. Photochem. Photobiol. A: Chem.* **131**, 111–123.

[44] Creighton, J.A., Blatchford, C.G., Albrecht, M.C. (1979). Plasma resonance enhancement of Raman scattering by pyridine adsorbed on silver or gold sol particles of size comparable to the excitation wavelength. *J. Chem. Soc. Faraday Transact.* **75**, 790–798.

[45] Creighton, J.A., Eadon, D.G. (1991). Ultraviolet–visible absorption spectra of the colloidal metallic elements. *J. Chem. Soc. Faraday Transact.* **87**, 3881–3891.

[46] Mostafavi, M., Marignier, J.L., Amblard, J., Belloni, J. (1989). Nucleation dynamics of silver aggregates simulation of photographic development processes. *Radiation Phys. Chem.* **34**, 605–617.

[47] Gersten, J.l., Nitzan, A. (1982). In Chang, R.K., Furtak, T.C. (eds.), *Surtace Enhanced Raman Scattering*. Plenum Press, New York, p. 89.

[48] Blatchford, C.G., Siiman, O., Kerker, M. (1983). Potential dependence of surface-enhanced Raman scattering from citrate on colloidal silver. *J. Phys. Chem.* **87**, 2503–2508.

[49] Huang, Y.F., Huang, K.M., Chang, H.T. (2006). Synthesis and characterization of Au core–Au–Ag shell nanoparticles from gold seeds: Impacts of glycine concentration and pH. *J. Colloid Interface Sci.* **301**, 145–154.

[50] Zhong, Z., Patskovskyy, S., Buovrette, P., Lung, J.H.T., Gedanken, A. (2004).The surface chemistry of Au colloids and their interactions with functional amino acids. *J. Phys. Chem. B* **108**, 4046–4052.

[51] Shoeib, T., Siu, K.W.M., Hopkinson, A.C. (2002). Silver ion binding energies of amino acids: Use of theory to assess the

validity of experimental silver ion basicities obtained from the kinetic method. *J. Phys. Chem. A* **106**, 6121–6128.

[52] Hodak, J.H., Henglein, A., Giersig, M., Hartland, G.V. (2000). Laser-induced inter-diffusion in AuAg core−shell nanoparticles. *J. Phys. Chem. B* **104**, 11708–11718.

[53] Yi-Heng, Z., Tian-Tang, Y., Shu-Quin, Y., Si-Yong, Z. (1999). Electroless copper deposition in the photographic gelatin layer. *J. Electrochem. Soc.* **146**, 1270–1272.

[54] Huang, Y., Lin, Y., Chang, H. (2006). Growth of various Au–Ag nanocomposites from gold seeds in amino acid solutions. *Nanotechnology* **17**, 4885–4894.

[55] Shao,Y., Jin, Y., Dong, S. (2004). Synthesis of gold nanoplates by aspartate reduction of gold chloride. *Chem. Commun.* **2004**, 1104–1105.

[56] Raso, A.G., Deya, P.M., Saa, J.M. (1986). Oxidation of a-amino acids and a-hydroxy acids by Fremy's salt. A model for oxidases. *J. Org. Chem.* **51**, 4285–4287.

[57] Khan, Z., Malik, M.A. (2009). Role of cetyltrimethylammonium bromide (cationic surfactant) on the tryptophan–MnO_4 reaction. *Colloids Surf. B: Biointerfaces* **72**, 253–258.

[58] Olatunji, M.A., Ayoko, G.A. (1988). Kinetics and mechanism of the oxidation of L-methionine by aqueous solution of chromium(VI). *Polyhedron* **7**, 11–15.

[59] Al- Thabaiti, S.A., Al- Nawaiser, F.M., Obaid, A.Y., Al-Youbi, A., Khan, Z. (2007). Formation, characterization and stabilization of water-soluble colloidal MnO_2 in the oxidation of methionine, thiourea and thioacetamide by permanganate. *Colloid Polym. Sci.* **285**, 1479–1485.

[60] Kapoor, S. (1998). Preparation, characterization, and surface modification of silver particles. *Langmuir* **14**, 1021–1025.

[61] Patakfalvi, R., Papp, S., Dekany, I. (2007). The kinetics of homogeneous nucleation of silver nanoparticles stabilized by polymers. *J. Nanopart. Res.* **9**, 353–364.

[62] Yu, D-G., Lin, W.-C., Lin, C.-H., Chang, L.-M., Yang, M.-C. (2007). An in situ reduction method for preparing silver/poly(vinyl alcohol) nanocomposite as surface-enhanced Raman scattering (SERS)-active substrates. *Mater. Chem. Phys.* **101**, 93–98.

[63] Wang, W., Wang, J., Sun, P., Yuan, Z., Ding, D., Chen, T. (2008). Polyvinylalcohol (PVA) induced wormhole-like mesoporous silica nano-fibers. *Mater. Lett.* **62**, 711–714.

[64] Crespilho, F.N., Lost, R.M., Travain, S.A., Oliveira Jr., O.N., Zucolotto, V. (2009). Enzyme immobilization on Ag nanoparticles/polyaniline nanocomposites. *Biosensors and Bioelectronis* **24**, 3073–3077.

[65] Huang, C-C., Yang, Z., Chang, H-T. (2004). Synthesis of Dumbbell-Shaped Au-Ag Core-Shell Nanorods by Seed-Mediated Growth under Alkaline Conditions. *Langmuir* **20**, 6089–6092.

[66] Zaheer, Z., Rafiuddin. (2012). Preparation, characterisation and kinetics of corn-shaped Ag nanoparticles. *J. Exp. Nano Sci.* **7**, 366–377.

[67] Zaheer, Z., Rafiuddin (2012). Nucleation and growth kinetics of silver nanoparticles prepared by glutamic acid in micellar media. *Int. J. Chem. Kinet*. **44**, 680–691.

[68] Rafey, A., Shrivastav, K.B.L., Iqbal, S.A., Khan, Z. (2011). Growth of Ag-nanoparticles using aspartic acid in aqueous solutions. *J. Colloid Interface Sci.* **534**, 190–195.

[69] Khan, Z., Al-Thabaiti, S.A., Obaid, A.Y., Khan, Z.A., Al-Youbi, A.O. (2012). Shape-directing role of cetyltrimethylammonium bromide in the preparation of silver nanoparticles. *J. Colloid Interface Sci.* **367**, 101–108.

[70] Wangoo, N., Bhasin, K.K., Mehta, S.K., Suri, C.R. (2008). Synthesis and capping of water-dispersed gold nanoparticles by an amino acid: Bioconjugation and binding studies. *J. Colloid Interface Sci.* **323**, 247–254.

[71] Bhargava, S.K., Booth, J.M., Agrawal, S., Coloe, P., Kar, G. (2005). Gold nanoparticle formation during bromoaurate reduction by amino acids. *Langmuir* **21**, 5949–5956.

65

NANOGEL, AN INTERNALLY NETWORKED POLY(AMINO ACID) NANOPARTICLE FOR pH-RESPONSIVE DELIVERY

Jong-Duk Kim and Chan Woo Park

Department of Chemical and Biomolecular Engineering, KAIST, 291 Daehak-ro, Yuseung-gu, Daejeon, Republic of Korea

65.1 INTRODUCTION

Nanogels are internally networked hydrophilic polymeric nanoparticles in nanoscale dimensions (i.e., <100 nm) [1], having hydrogel-like properties. Nanogels imbibe water when they are located in an aqueous environment, unlike dense nanospheres. Also, nanogels have high mechanical stability due to cross-linking, and their environment-sensitive swelling/deswelling can be observed likewise in hydrogel. In particular, the high surface area and small particle size enable nanogels to show faster swelling or deswelling in response to stimuli (pH, temperature, ions, light, etc.) compared to microgels [2].

Nanogels have several advantages in drug delivery system due to their affinity to water, high colloidal stability, inertness in blood and internal domains, as well as reduced drug degradation and toxicity [3]. The nanoscale size with narrow size distribution [4] also leads a delivery of oligonucleotides into the brain [5] and a rapid response to biological pH conditions. The surface functionalized nanogels are very useful for delivery of drugs to various diseases such as cancer or central nervous system via the blood–brain barrier [6].

In most physiological processes pH, is well controlled, and any deviation of pH can reflect systemic pathologies. For example, the extracellular pH of most tumors and inflamed and wound tissues is acidic (5.8–7.2), which is different from neutral normal tissue [7,8]. As the hydrostatic pressure builds up inside of tumors, the interior pH decreases as a result of the low oxygen concentration and high lactic acid concentration. Further, hydrolytic enzymes in lysosomes drop the interior pH to 4.5–5.0, and at Golgi complex to 6.4. Such pH differences between normal and pathological tissues, and endosomes as well as lysosome, would promote an excellent opportunity to explore a site-specific drug delivery from the pH-responsive nanogels.

65.1.1 pH Sensitivity of Nanogels

The pH sensitivity of nanogel is usually attributed to the functional groups of sidechains. For example, the polymer networks containing acidic groups (–COOH, $–SO_3H$), such as poly(acrylic acid) and poly(aspartic acid) (PAsp), are deprotonated and swell at neutral and basic pH. On the other hand, nanogels having basic groups ($–NH_2$), such as poly($_L$-lysine) (PLys), swell at acidic pH. In an environment where nanogel is ionized, the density of charged groups increases by a generation of mobile counterions inside of gels, and enhances swelling of gels due to electrostatic repulsion. In fact, the deionization of acidic or basic groups decreases both the charge density and the content of mobile counterions within nanogels, and the gel phase becomes compact, less hydrophilic, and enters a collapsed phase. Interestingly, this phase transition is highly nonlinear and occurs in narrow pH ranges near pK_a or pK_b of ionizable groups. Therefore, transition conditions could be modified by changing the chemical nature [9] or the structure of nanogels [10, 11]. Figure 65.1 shows the change in size, surface charge, or chemical nature induced by a pH change. As pH increases or decreases, the size of nanogels may be changed as a result of the collapsed networks, or the density of cross-links may be reduced by

Encyclopedia of Biocolloid and Biointerface Science, Volume 2, First Edition. Edited by Hiroyuki Ohshima.
© 2016 John Wiley & Sons, Inc. Published 2016 by John Wiley & Sons, Inc.

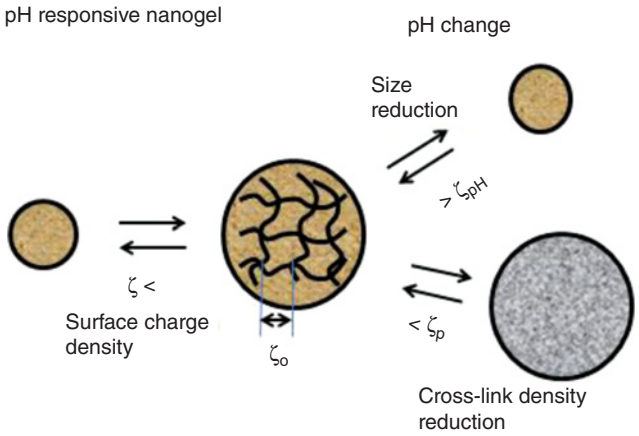


FIGURE 65.1 Dynamic change of nanogels in response to stimuli.

the chemical degradation or ζ-potential of surface decreases by reduction.

The preparation methods of nanogels can be divided into four groups:

1. The physical cross-linking or self-assembly of polymers [12]. The principles of the physically noncovalent cross-linking includes the ionic interaction, the polyelectrolyte complexation (coacervation), and the self-assembly of hydrophobically modified polymers.
2. The chemical cross-linking by the addition or radical polymerization of monomers in a homogeneous phase or in a micro- or nanoscale heterogeneous environment [13, 14].
3. The cross-linking of preformed polymers as well-defined building blocks.
4. The template-assisted nanofabrication of nanogel particle, including photolithography, micromolding, and microfluidics [15].

65.1.2 Modified Poly(amino acid)s

Poly(amino acid)s, polymerized from natural or synthetic amino acids, may be used in biomedical applications because of their biocompatibility, biodegradability, nontoxicity, and in vivo stability [16]. The diversity of amino acid monomers may influence the various properties of hydrophobicity, polarity, and stimuli responsive property. For these reasons, poly(amino acid)s are regarded as good materials for stimulus-responsive drug carriers. The pH-responsive core–shell poly(amino acid) nanogels were prepared from copolymers having reactive poly(succinimide) blocks that can be converted into poly(amino acid)s [17]. The preparation method of pH-responsive nanogels should be a high-throughput method that does not require the use of surfactants, emulsions, or expensive coupling agents. The chemically cross-linked nanogels can be synthesized from reactive amphiphilic diblock or graft copolymers as presented in Fig. 65.2.



FIGURE 65.2 Types of copolymers.

Amphiphilic copolymers form diverse nanostructures such as spherical and tubular micelles, vesicles, and lamellae through the spontaneous self-assembly in a selective solvent [18]. Additionally, the diverse morphology of self-aggregates that are prepared from reactive amphiphilic polymer can provide various nanogel architectures. Figure 65.3 illustrates nanogel architectures, including sphere, hairy shell, core–shell, and hollow shell. The favored morphologies of amphiphilic polymers depend on the hydrophilic/hydrophobic ratio, molecular geometry, concentration, temperature, solvent, and force balance such as the degree of stretching of core-forming blocks, intercorona chain interactions, and interfacial energy between the micelle core and the solvent. These polymeric nanostructures are thermodynamically and kinetically more stable than the surfactant systems. In particuar, the polymer vesicles of a layer have become a subject of special interest, because they can entrap hydrophilic molecules within their aqueous cavity [19, 20].

In this chapter, we address the various synthesis strategies of poly(amino acid) nanogels with respect to physicochemical cross-linking. Also, the structure and physical property analysis by small-angle neutron scattering (SANS),

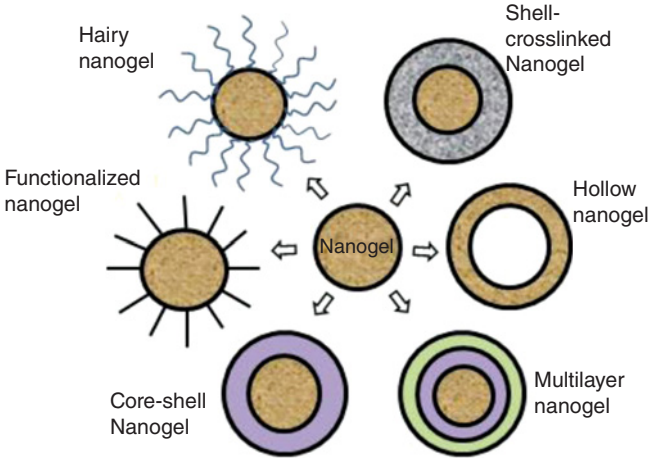


FIGURE 65.3 Diverse structure of nanogels.

pH-responsive behaviors, and their potentials as drug delivery carriers are comprehensively discussed.

65.2 PREPARATION OF POLY(AMINO ACID) NANOGELS

Poly(amino acid) nanogels can be prepared from physical or chemical cross-linking reactions of as-synthesized poly(amino acid)s or prepolymers for poly(amino acid)s.

The copolymers of poly(amino acid)s are typically synthesized from the ring-opening polymerization (ROP) of *N*-carboxyanhydride (NCA) of amino acids using nucleophiles and aprotic bases [i.e., aminopoly(ethylene glycol) (PEG-amine)] [21]. The polymerization of NCAs can provids high molecular weight and relatively narrow polydispersity of poly(amino acid)s [22].

On the other hand, a reactive poly(succinimide) (PSI) can be employed as reactive polymer blocks to be converted to poly(amino acid)s. The acid-catalyzed polycondensation of L-aspartic acid produces the PSI [23]. Amphiphilic graft poly(amino acid)s have been prepared from ring-opening reaction of the PSI backbone with hydrophobic nucleophiles such as alkyl amines [24]. Also, PSI can be converted into diverse poly(amino acid)s including poly(L-aspartic acid) (PAsp), and poly(L-asparagine) (PAsn), poly(aspartamide), by hydrolysis or an aminolysis reaction in NaOH, NH_4OH, and ethanolamine solution.

Because of the diversity of amino acids, the ionizable groups and reactive side groups of poly(amino acid)s can be modulated by the selection of monomers, thereby poly(amino acid)s can be designed to be appropriate for the physically or chemical cross-linking reaction.

65.2.1 Physical Association

The physically associated nanogels have been widely studied. In general, multivalent ions, charged protein, surfactants, DNA, and RNA have been employed as ionic cross-linkers to form an ionic linkage with oppositely charged polyelectrolyte polymers. Such a polyionic interaction generates a stable self-assembled nanostructure, and the charged biomolecules (proteins and nucleotides) are participated in the physical aggregation; in this way, biomolecules can be stabilized within nanogels for drug delivery applications.

Negatively charged nucleotides, DNA and RNA, can induce a polyionic complexation with cationic poly(amino acid)s and produce nanogels. One team of investigators prepared cationic *N*-(2-aminoethyl)-2-aminoethyl group–grafted PEG-*b*-poly(aspartic acid) backbone, denoted as PEG-*b*-P[Asp(DET)] [25]. The nanogels were synthesized from aminolysis reaction of PEG-*b*-poly(*β*-bezyl-L-asparate) (PEG-*b*-PBLA) with diethylenetriamine [25]. Here, the amine/phosphate (N/P) ratio and pH of the aqueous solution play a crucial role in the nanogel preparation process. Protonation states differ depending on the chemical structure of polycation and pH. In fact, the complexation of PEG-P[Asp(DET)] with DNA was more efficient at pH 5 than at pH 7.4, and also at the higher N/P ratio than at the lower N/P ratio. The prepared poly(amino acid)-based nanogels show higher biocompatibility than do poly(ethyleneimine)-based nanocomplexes with DNA.

Similarly, ribozyme-entrapped nanogels (∼100 nm) can be prepared from the complexation of cationic PEG-*b*-PLys with negatively charged ribozyme molecules, and PLys of having high positive charges contributes to form small nanogels [26].

Physically aggregated nanogels can also be utilized as templates for further chemical cross-linking to improve the stability of nanogels. Another team [27] prepared pyridyldithiopropionyl (PDP) group conjugated PEG-*b*-PLys by reaction of amine groups on PLys with the *N*-succinimidyl 3-(2-pyridyldithio)-propionate (SPDP). The removal of mercaptopyridine groups from PDP groups generated free thiol groups on PEG-*b*-PLys by oxidation reaction. After the physical complexation of the polymer with DNA, free thiol groups could form disulfide cross-links by the self-oxidation reaction during dialysis [27].

65.2.2 Chemical Cross-Linking of Poly(amino acid)s

Physical cross-linking by ionic association or complexation could successfully prepare nanogels, and chemical cross-linking is believed to be more stable than the physically associated nanogels. The chemical cross-linking uses the formation of a covalent bond in the process of chemically joining two or more molecules with specific functional groups (primary amines, sulfhydryls, etc.). In a direct polymerization, the size of macrogels can also be reduced by increase of the cross-linker concentration or initiator concentration [28]. For water-soluble polymers grafted with vinyl groups, the size of nanogels can be controlled using nano- or microemulsion in the presence of surfactants or PEGylated macromers, namely, the oil-in-water emulsion method for poly(ethylene glycol)-*cl*-polyethyleneimine nanogels [29] or the free-radical precipitation polymerization of poly(*N*-isopropylacrylamide) (pNIPAm) [30].

Since the nanogels of UV-induced cross-linked polymer were first developed [31], various cross-linking methods were introduced, including radiation-induced cross-linking [32], reaction with bifunctional cross-linker [33], and click cross-linking [34]. For example, the shell cross-link of polystyrene-*b*-poly(acrylic acid) was accomplished by cross-linking of carboxylic groups with diamine via the carbodiimide coupling method [33]. Since amine has strong reactivity with carboxylic acids, activated esters [35], and isocyanates [36], the amidation with carboxylic acid forms a stable and pH-responsive cross-linked network [37].

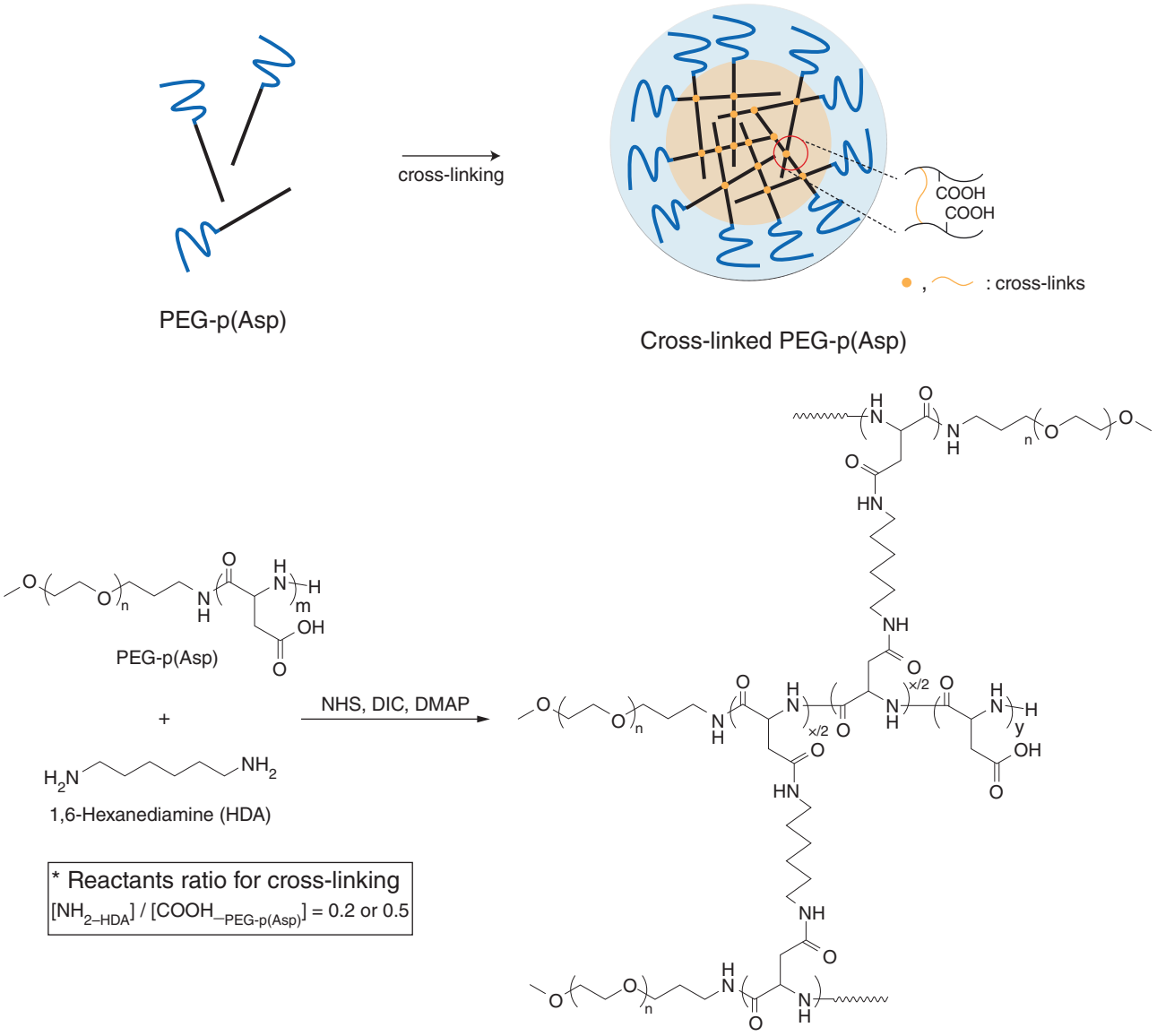


FIGURE 65.4 Preparation of PEG-PAsp nanogels by carbodiimide coupling reaction [38].

65.2.2.1 Coupling Reactions. The preparation of chemically cross-linked poly(amino acid)s have been attempted by cross-linking of reactive groups of poly(amino acid)s, carboxylates or amines, with the use of coupling agents.

Figure 65.4 illustrates the cross-linking method of the PEG-*b*-PAsp which is prepared from hydrolysis of PEG-*b*-PBLA [38]. The carboxylates of PAsp groups were cross-linked with hexamethylenediamines (HDA) by the coupling reaction of carbodiimide in DMSO. When the carboxyl groups of PAsp were reacted with 50% of HDA, PEG-PAsp nanogels can be successfully prepared with a high yield of 80%. The NMR and GPC analyses indicated that a total of 11 block copolymers were cross-linked in each nanogel, which has 253 of Asp units. Similarly, the PAsp inner shells of PEG-*b*-PAsp-*b*-poly(L-phenylalanine) (PEG-*b*-PAsp-*b*-PPhe) self-aggregates were also cross-linked with diamine cross-linkers by carbodiimide chemistry [39].

Despite this success, the cross-link of poly(amino acid)s with coupling agents is not desirable because of the high cost of coupling agents. In addition, the synthesis of PEG-*b*-poly(amino acid)s from NCA monomers requires the application of toxic phosgene-based chemistry.

65.2.2.2 Cross-Linkable Block Copolymer. Another approach for cross-linked nanogels employs a cross-linkable amphiphilic block copolymer of PEG-PSI. The hydrophobic succinimide in PSI backbone can react with nucleophiles such as primary and secondary amines; therefore, PSI is directly cross-linked by diamines. Also, the PSI can turn into

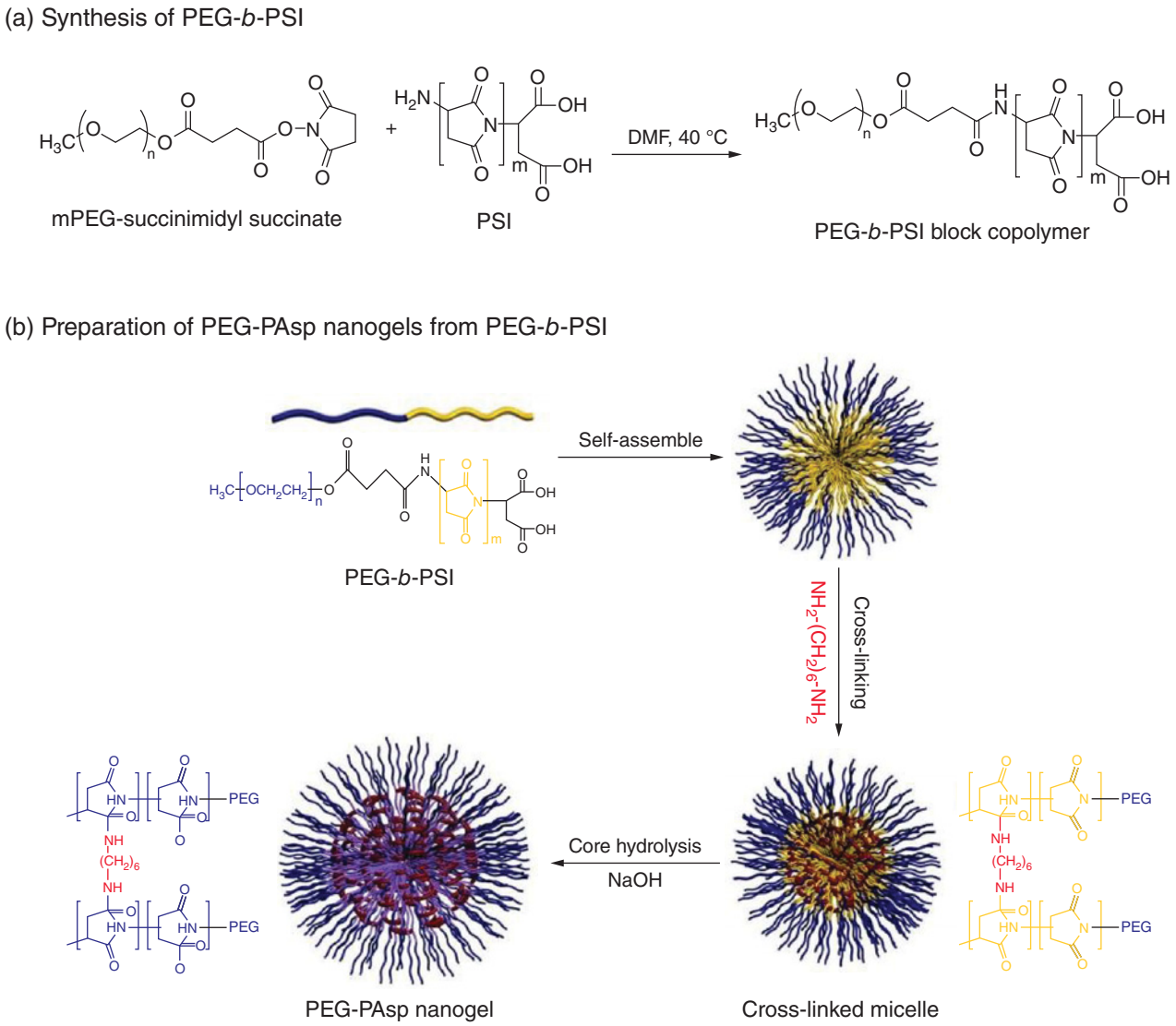


FIGURE 65.5 (a) Synthetic scheme of PEG-*b*-PSI block copolymer; (b) preparation method of PEG-PAsp nanogels from the PEG-*b*-PSI [17, 40].

diverse poly(amino acid)s, including poly(L-aspartic acid) (PAsp), and poly(L-asparagine) (PAsn), poly(aspartamide), by hydrolysis or an aminolysis reaction in NaOH, NH_4OH, and ethanolamine solution.

Figure 65.5 shows the amphiphilic cross-linkable PEG-*b*-PSI and core-hydrolyzed nanogel [17, 40]. In Fig. 65.5a, mPEG–succinimidyl succinate reacts with PSI in *N,N*-dimethyl formamide by the amidation reaction of the ester linkage in mPEG-succinimidyl succinate with a primary amine of PSI. Since PEG-*b*-PSI consists of hydrophilic PEG and hydrophobic PSI, the diblock copolymer has a surface-active property, and the PEG-*b*-PSI forms micelle structures stabilized by the PEG hairy shell with the hydrophobic PSI core in an aqueous solution. The diameter of the PEG-*b*-PSI self-aggregates is generally smaller than 100 nm.

The cross-linked nanostructure of PEG-PSI can be fabricated by adding diamine, hexamethylenediamine, to the micellar solution of PEG-*b*-PSI. As diamine diffuses into the PSI core, amine groups react with succinimide units, and induce cross-linked networks within the PSI core region of self-aggregates.

The degree of cross-link of nanogels, namely, the mole percentage of PSI groups that interconnected by diamine, can be controlled through adjustment of the feed mole of diamine. The degree of cross-links can be analyzed by monitoring the increment of nitrogen atoms after the cross-linking reaction by element analysis, because nitrogen atoms increase with cross-links. After the cross-linking with 5%, 50%, and 100% (1.1-fold excess of amine was added for 100% cross-linking) of diamines to succinimide units, the calculated degrees of

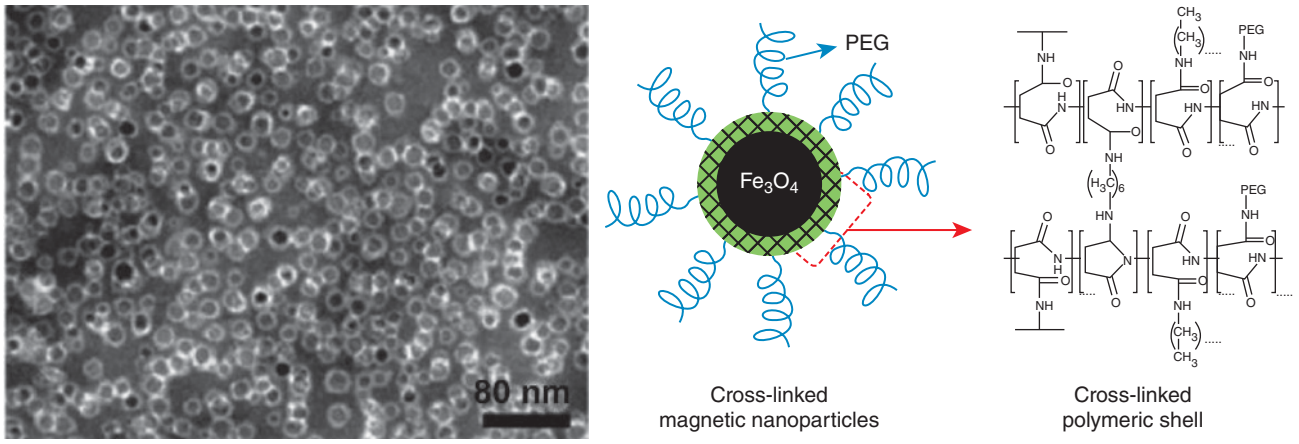


FIGURE 65.6 Nanogel-coated magnetic nanoparticles prepared from PSI-*g*-PEG [43].

cross-links were found to be 2.7%, 26%, and 66%, respectively. Hereafter, these will be denoted as Nanogels 5, 50, and 100, respectively, for the targeted degrees of cross-links.

The fully hydrophilic nanogel can be obtained when the hydrophobic PSI core is converted into hydrophilic poly(amino acid)s [17]. After cross-linking, the residual SI units are converted into the hydrophilic and negatively charged backbone of aspartic acid (Asp) by a hydrolysis reaction in NaOH solution [41]. Therefore, the cross-linked PAsp nanogels with hairy PEG were obtained by cross-linking the core of PEG-*b*-PSI aggregates. If the internal structures of diblock polymer aggregates are not chemically cross-linked, the copolymer cannot maintain the particle structure because of the high water solubility of both PEG and PAsp. In this microscopic analysis, however, the PEG-PAsp nanogels maintained their spherical structure after the hydrolysis of the partially cross-linked hydrophobic core.

65.2.2.3 Cross-Linkable Graft Copolymer. Along with block copolymer systems, graft copolymer systems have also been studied for nanogel preparations. Among various polymer systems, PSI has been widely studied for the graft polymers of poly(amino acid)s. As PSI can react with amine-containing molecules, the desired molecules with amine groups can be simply grafted by an aminolysis reaction. Therefore, any multifunctional polymer system can be readily prepared by multiple grafts in a single PSI backbone. As sidechains, any of long polymers, small molecules (alkyls, lipids, cholesterol), and nanoparticles has been used to prepare the graft copolymers [24]. Instead of covalent bonding, the noncovalent interactions such as ionic interactions, π–π interactions, and hydrogen bonding can also be introduced to PSI as graft groups [42].

The properties of graft copolymers can also be controlled by the chemical composition of backbone and grafts. Thus, the chemical nature can be defined with the graft density, such as the degree of substitution (DS) by the number of sidechains in a polymer backbone and the length of sidechain as the degree of polymerization (DP) of a branch.

To take advantage of the graft polymer system, one team of investigators developed cross-linkable PSI-*g*-PEG as shown in Fig. 65.6 [43, 44]. The amphiphilic copolymer of PSI-*g*-PEG-C_{12} was synthesized from subsequent aminolysis reaction of PSI with PEG-amine and dodecyl amine. The hydrophobic alkyl group was employed to coat hydrophobic iron oxide nanoparticles by the hydrophobic interaction in aqueous solution, and the nanoparticles coated with PSI inner shell with hairy PEG outer shell were obtained. The PSI inner shell was successfully cross-linked by adding hexamethylenediamine. To determine whether HMD reacts with two succinimide units without generation of dangling cross-linkers on PSI, X-ray photoelectron spectroscopy (XPS) analysis was carried out. The generation of amide peak at 399.4 eV was observed as a result of the successful cross-linking, while the free amine (NH_2) peak at 397.1 eV did not appear in the XPS spectrum. Thus, the reaction of only one side of diamine with PSI is negligible in the PSI-diamine cross-links.

65.2.3 Morphology of Nanogels Prepared from Amphiphilic Polymers

The advantage of PSI-based prepolymer of poly(amino acid)s is that the amphiphilic property of the copolymer is easily adjusted; therefore, the diverse morphology of nanogels can be generated in a derivative family. Amphiphilic polymers of the same building blocks could form not only spherical assemblies but also cylindrical and tubular aggregates, vesicles, disks, or lamellar structures by self-assembly in a selective solvent, and also the favored morphology can be obtained with the variation of hydrophilic/hydrophobic ratio, chemical nature, and external design factors such as concentration, temperature, and solvent [18].

The amphiphilc property, especially hydrophilic/hydrophobic ratio, of PEG-*b*-PSI can be modulated by

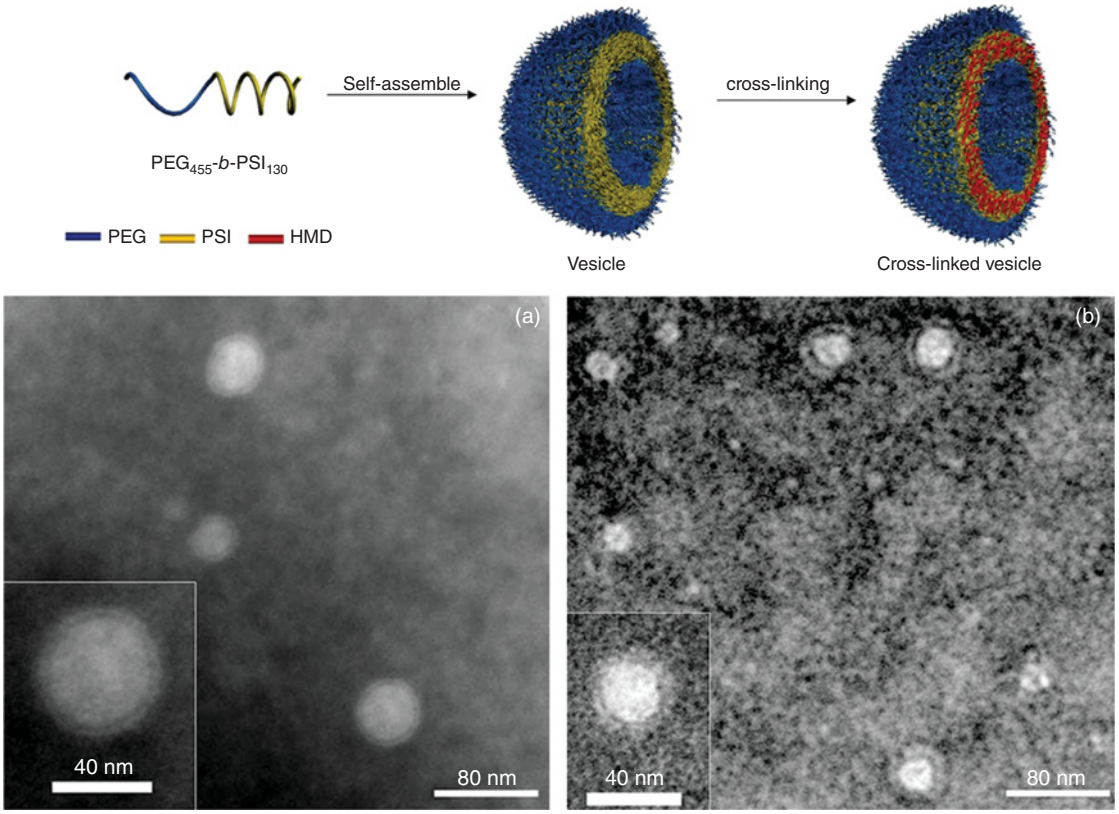


FIGURE 65.7 TEM images of the (a) PEG20k-PSI vesicle and (b) cross-linked vesicle [40].

adjusting the block length of PEG and PSI. When the molecular weight for PEG of PEG-*b*-PSI is reduced from 30 to 20 kDa, the morphology of self-aggregates changes from spherical micelles to vesicles whose diameter is 74.9 ± 18.3 nm in Fig. 65.7 [17]. Generally, the self-assembled morphology of diblock copolymers transforms from sphere, cylinder, to vesicle as increasing the weight fraction of hydrophobic moieties or decreasing the molecular weight of PEG blocks [18]. As were the spherical nanogels of PEG-*b*-PSI, the vesicle nanogels can also be fabricated by adding hexamethylenediamine to the PEG-PSI vesicle solution [17]. The 43.3% of cross-linking can be achieved at 1:2 molar ratio of amine groups and succinimide. After cross-linking, the hollow structure of vesicular nanogels remained undisturbed.

The hydrophilic/hydrophobic ratio of graft polymers can be controlled by changing the degree of substitution (DS) and degree of polymerization (DP) of sidechains. In the case of PSI-*g*-PEG, the polymers became hydrophobic with decrease in the molecular weight of PEG grafts (DP) and the number of PEG branches (DS) on PSI backbone. Further, the additional grafts of hydrophobic alkyl chains can modulate the hydrophilic/hydrophobic ratio [43, 44]. The PSI-*g*-PEG:C_{12} showed that structure changes from sphere to cylinder with increases in the grafted alkyl chains.

65.3 STRUCTURE AND CHARACTERISTICS OF NANOGEL

65.3.1 Shape and Size

Nanogels are swellable in a good solvent, and their shape architectures will vary with monomers and polymer solubility, reactivity of cross-linkers, and reaction temperature [45]. Nanogels are generally prepared in a specific size, having size distribution (polydispersity) [46, 47] and with the architectures of core–shell [48], hollow [49], or nonspherical, di- or trimeric structures as shown in Fig. 65.3 [50].

65.3.1.1 Hairy Shell. The "hairy nano-/microgels," as a cross-linked core surrounded by covalently grafted polymer chains (hairs), are synthesized by radical cross-linking polymerization [51, 52]. On the other hand, hydrophobic cores of partially cross-linked PEG-*b*-PSI micelles can be chemically converted into hydrophilic PAsp and to form PEG–PAsp nanogels (Fig. 65.5). So far, the direct chemical conversion methods have rarely been reported [53]. The nanogels consisting of a hydrophilic anionic PAsp core exhibit not only the high water uptake but also pH-responsive swelling and drug release behavior. In a macromonomer approach, PEGylated microgels in heterogeneous conditions in the presence of

stabilizing macromonomers also can provide the hairy structure [54, 55].

65.3.1.2 Sphere, Core–Shell, Hollow Gels. Hollow nanogels, which are also called *nanocapsules*, can encapsulate payloads, such as drugs, dyes, inks, and DNA [56]. Spherical nanogels are designed to avoid the formation of long-range networks in the prepolymer cross-linking as well as the formation of noncovalent microgel [46, 57, 58]. Cross-linking reactions can be carried out on preformed colloidal self-assemblies of synthetic or natural polymers, and "free radical cross-linking copolymerization" of monovinylic monomers with cross-linkers [59]. Most core–shell hydrogel particles are synthesized by two-step radical polymerization. First, the core is prepared by (co)polymerization in the presence of a bifunctional monomer as a cross-linker. Then, a second monomer is added for the shell synthesis (seed and growth process), but there is no chemical linking between the core and the shell, only a low interpenetration of chains at the interface exists as in hollow nanogels.

Alternatively, the diblock or graft copolymer with hydrophilic and hydrophobic groups can be dissolved in water to form a self-assembly of vesicle type, and cross-linkers can be placed into the vesicle layer for cross-linking. This structure is different from the shell cross-link hollow particle, because both sides of the shell have hydrophilic corona and the hydrophobic chains of shell may be bilayered or interdigitized as they become a thin layer.

65.3.2 Internal Structure

Figure 65.8 illustrates a model nanogel having the hairy shell or core–shell structure. The volume ratios between the core and the shell (giving access to the thickness of the shell) and the cross-linking density of the shell, were studied by dynamic light scattering (DLS) and small angle neutron scattering (SANS) [60].

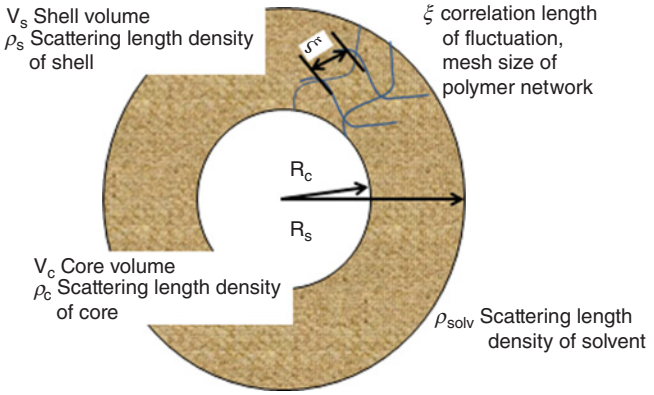


FIGURE 65.8 Core–shell nanogel model.

65.3.2.1 SANS Model for Nanogels. The small-angle neutron scattering (SANS) technique can probe macromolecular and microstructures of micelles, polymers, protein, and many other materials. The SANS technique is also utilized to analyze the structure and physical properties of nanogels. A model equation for core–shell nanogels, which have PEG shells and cross-linked PAsp cores, has been suggested [17]. The model function is designed to include the two independent major contributions of scattering intensity, with both intensities derived from the isolated core–shell particles and the fluctuation of the cross-linked network shown in Fig. 65.8. The total scattering intensity $I(q)$ measured for the nanogel particle solution can be modeled as

$$I(q) = I_{\text{particle}}(q) + I_{\text{fluct}}(q) + bkg \tag{65.1}$$

where $I_{\text{particle}}(q)$ is the scattered intensity that arises from a homogeneous core–shell structure, $I_{\text{fluct}}(q)$ are the dynamic fluctuations of networks in nanogels $[I_{\text{fluct}}(q)]$, and bkg denotes the residual incoherent scattering [61].

In a dilute particle system, the interparticle interference becomes negligible, and the scattering intensity of particles can be expressed as $I_{\text{particle}}(q) = n_{\text{p}}P(q)$, where n_{p} is the number density of particles and $P(q)$ is the particle form factor. Here, the particle form factor of the polydisperse core–shell model is employed, and the spherical core–shell model can be expressed as

$$\begin{aligned} P_{\text{core–shell}}(q) = {} & [3V_{\text{c}}(\rho_{\text{c}} - \rho_{\text{s}})j_1(qR_{\text{c}})/qR_{\text{c}} \\ & + 3V_{\text{s}}(\rho_{\text{s}} - \rho_{\text{solv}})j_1(qR_{\text{s}})/qR_{\text{s}}]^2 \\ & j_1(x) = (\sin x - x\cos x)/x^2 \end{aligned} \tag{65.2}$$

where V_{c} and V_{s} are the volume of the core and shell, respectively; R_{c} and R_{s} are the radius of the core and shell, respectively; and ρ_{c}, ρ_{s}, and ρ_{solv} are the scattering length density (SLD) values of the core, shell, and solvent, respectively. In modeling the distribution of the core size, the particle form factor is normalized with the width parameter of the Schulz distribution [62].

Unlike the solid core–shell structure, nanogel is swellable in water, and the swelling of core and shell of nanogel leads to change in the ρ_{c} and ρ_{s} values depending on the swelling degree. Consequently, the SLD values of nanogel core and shell can be expressed as

$$\rho_{\text{c}} = \varphi_{\text{CL-PAsp}} \times \rho_{\text{CL-PAsp}} + \varphi_{\text{D2O}} \times \rho_{\text{D2O}} \qquad (0 \le r \le R_{\text{c}}) \tag{65.3}$$

$$\rho_{\text{s}} = \varphi_{\text{PEG}} \times \rho_{\text{PEG}} + \varphi_{\text{D2O}} \times \rho_{\text{D2O}} \qquad (R_{\text{c}} \le r \le R_{\text{s}}) \tag{65.4}$$

$\varphi_{\text{CL-PAsp}}$, φ_{PEG} and φ_{D2O} are the volume fractions of cross-linked PAsp, PEG, and D_2O, respectively [17].

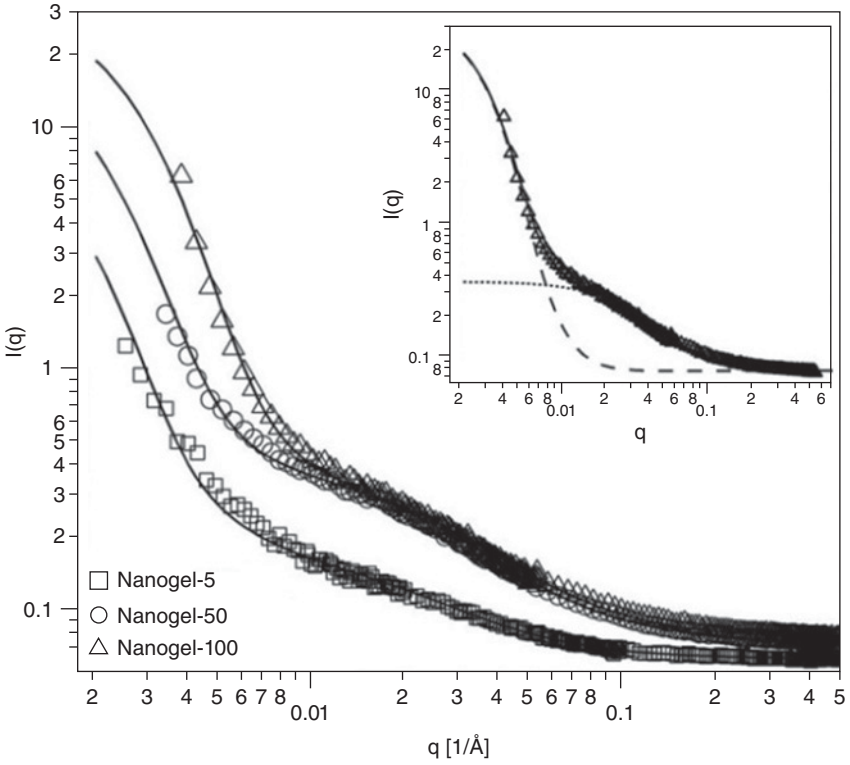


FIGURE 65.9 SANS scattering profile of PEG-PAsp nanogels. The solid lines represent the fitting results. The inset shows the contribution of $I_{\text{particle}}(q)$ (dashed line) and $I_{\text{fluct}}(q)$ (dotted line) [17].

Along with the change in SLD values in core and shell by swelling of the network, the scattering arises from the dynamical fluctuation of the polymer network in solvent is also important in the SANS analysis of nanogels. For this reason, the $I_{\text{fluct}}(q)$ in Eq. (65.1) is essential to describe the scattering from the polymer network [63]. The Lorentzian function that describes the ensemble average of correlations in the polymer network is used as the $I_{\text{fluct}}(q)$ term by [64]

$$I_{\text{fluct}}(q) = I_{\text{fluct}}(0)/(1 + \xi^2 q^2) \tag{65.5}$$

where $I_{\text{fluct}}(0)$ is the intensity at $q = 0$ and ξ is the correlation length of the fluctuation, which is related to the mesh size of networks [17, 65].

65.3.2.2 SANS Analyses of Nanogels. The SANS measurements and model-fitting analyses allow the better understanding of the structure and swelling behavior of nanogels. Figure 65.9 shows the SANS scattering profiles of PEG-PAsp nanogels in D_2O, and the inset shows the two distinct scattering intensities of $I_{\text{particle}}(q)$ and $I_{\text{fluct}}(q)$ [17]. The scattering from the isolated particles, $I_{\text{particle}}(q)$, is dominant in the low-q region (dashed line), whereas the scattering that arises from the fluctuation of the network, $I_{\text{fluct}}(q)$, is dominant in the high-q region (dotted line). Also, the SANS analysis showed that the scattering intensity of the PEG-PAsp nanogels decreases as approximately q^{-4} in the low-q region by following the classical Porod's law, and thus, this behavior is attributed to the scattering from a particle surface.

The model-fitting results for Nanogels 5, 50, and 100 provide various types of information on nanogel structures in aqueous solvent. Table 65.1 shows that the average particle size decreases as the degree of cross-link increases. The

TABLE 65.1 Parameters Obtained from Fitting Analysis of SANS Data

Parameter	Nanogel 5	Nanogel 50	Nanogel 100
R_{SANS} (nm) [a]	65.9	55.0	47.7
R_{DLS} (nm) [b]	67.6	57.4	44.5
R_c (nm)	57.1	45.7	37.1
δ_{shell} (nm) [c]	8.8	9.3	10.6
ρ_{core} ($\times 10^{10}$ cm^{-2})	6.22	5.94	5.38
ρ_{shell} ($\times 10^{10}$ cm^{-2})	5.79	5.58	5.25
ξ (Å)	43	40.6	37.2
$\varphi_{\text{CL-PAsp}}$	0.032	0.096	0.210
φ_{PEG}	0.098	0.135	0.193
Q_v^{core} [d]	31.25	10.42	4.76

[a,b] Radius of nanogel measured by SANS and DLS.
[c] Thickness of the PEG shell.
[d] Q_v^{core}=(swollen volume of core)/(polymer volume in core).
Source: Ref. 17.

higher degree of cross-linking provides the smaller mesh size of network, and the lower ability of nanogels to swell. Similarly, the core size of PEG-PAsp nanogels decreases with the degree of cross-link. When the degree of cross-link increases from 2.7% to 66%, the core size decreases from 57.1 to 37.1 nm. Therefore, this indicates that the cross-linking would particularly affect the swelling of the core.

On the other hand, the thickness of hairy PEG shell is independent of the cross-link density. In fact, the thickness of PEG shells is in the range of 8.8–10.6 nm depending on the molecular weight of PEG.

The mesh size of a polymer network in nanogel, which is related to the correlation length (ξ) of the Lorenzian function, also can be obtained from SANS analysis. One team of researchers proved that ξ of a poly(*N*-isopropylacrylamide) (pNIPAm) microgel decreases as the cross-link density of microgel increases [64]. Similarly, the ξ values of the PEG–PAsp nanogels decrease as the degrees of cross-link increase (Table 65.1) [17]. Thus, it is believed that the mesh size of the hydrogel network decreases as the degree of cross-link increases.

65.3.3 Swelling of Nanogel

The smart or responsive nanogel particles retain their volume and morphology change in response to a stimuli such as pH, temperature, and ionic strength. The dimensions of nanogels depend on the solubility of both monomers and polymers [66]. The solvent properties change the interfacial energies and the mechanism of a particle formation.

The volume fractions of polymer and water can be calculated using Eqs. (65.3) and (65.4) with SANS analysis data [17]. Swelling of the polymer network reduces the volume or weight fraction of polymer in nanogels to extremely low levels, and increases those of water molecules. In general, less-cross-linked hydrogels may exhibit significantly higher water uptake than do the more highly cross-linked hydrogels. For Nanogels 5, 50, and 100, the volume fractions in core (φ_c) of PEG-PAsp nanogels increases from 0.032 to 0.210 when the degree of cross-linking increases from 2.7% to 66%. If the swelling ratio of the core ($Q_v{}^{core}$) is defined by the ratio of the swelled volume to the polymer volume of the core, this indicates that the less-cross-linked nanogel can imbibe water approximately 30 times greater than the polymer volume of the core. The swelling ratio of the core ($Q_v{}^{core}$) could be calculated from $Q_v{}^{core} = 1/\varphi_{CL\text{-}PAsp}$, and was assumed to be 31.25 when the degree of cross-link was 2.7% [17]. Compared to the hydrogels, the cross-linked nanogels prepared here are less swellable. In general, maximum swelling ratio values of bulk PAsp hydrogels, when cross-linked by various diamines, can be in range of 90–280 g g^{-1} depending on the cross-linking agents (measured in deionized water, with 5 mol% cross-linkers used) [67]. During the cross-linking process, the polymer concentration as well as the amount of cross-linking agent is important for determining the mesh size of network, which is related to the swelling property of hydrogels. The nanogel system prepared from cross-linked polymer micelles have the highly confined geometry during the cross-linking reaction and less local water pocket; therefore, the nanogel system may show a relatively low swelling ratio.

65.4 pH-RESPONSIVE NANOGELS

65.4.1 pH-Sensitive Property of Nanogels

Nanogels can be designed to swell or deswell in response to stimuli such as temperature, pH, redox, or multiple stimuli [68]. In particular, a small variation in pH can change the ionization degree of the polyelectrolyte chain, and thus, suffice to induce the swelling of nanogels [69]. Therefore, a change in external pH can alter the ionic interaction, hydrogen bonding, and hydrophobic interaction, resulting in a reversible microphase separation or self-organization phenomenon. Thus, the active drug release from a delivery system can be triggered by physiological pH environments. Such pH-triggered delivery systems can be achieved by (1) incorporation of a pH-responsive moiety to the polymer structure, (2) cross-linking with pH-labile cross-linkers, and (3) chemical conjugation of pH-liable linkage between polymers and drugs.

Also the pH-responsive nanogel with a pH-dependent charge conversion can be used as a possible anticancer drug carrier. The transition from a negatively charged to a positively charged form in slightly acidic environments enhances the cellular uptake of nanogels and the efficiency of drug release in killing cancer cells. Positively charged nanoparticles show a higher affinity for negatively charged cell membranes to be readily internalized by the cells. In contrast, negatively charged carriers have a high potential for protein resistance, exhibiting prolonged circulation in vivo [70].

The PEG-PAsp nanogels have shown pH-responsive swelling/shrinking behavior based on the ionization/deionization of the polyanionic PAsp. The hydrodynamic diameters of PEG-PAsp nanogels, which are prepared from the cross-linking of PEG-*b*-PSI, ranged from 80 to 130 nm at pH 7, while the diameters were significantly reduced to 75–90 nm at pH 2 (Fig. 65.10) [17]. Furthermore, the pH-responsive swelling/shrinking of nanogels can be observed by AFM. Nanogel showed a smaller size at pH 2 compared to that at pH 7 even after drying ((Fig. 65.10). Similarly, PEG-PAsp nanogels, prepared by the cross-linking of PEG-PAsp with coupling agents, showed the swelling (>40 nm) and shrinking (< 20 nm) behavior depending on the surrounding pH [38].

The pH-responsive degradable nanogels can be prepared by employing pH-degradable polymers or pH-labile

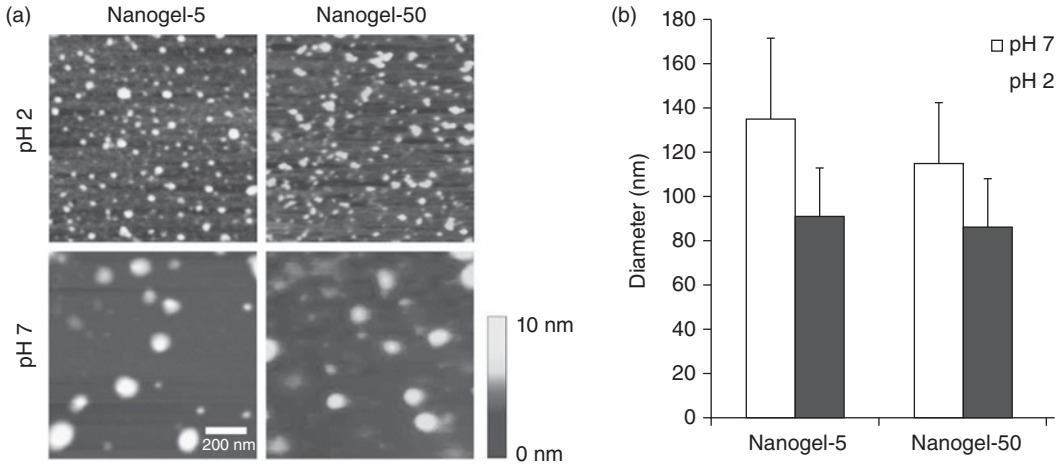


FIGURE 65.10 (a) AFM images of PEG-PAsp nanogels dried on mica at pH 2 and 7; (b) hydrodynamic diameters of the nanogel at pH 2 and 7 [17].

cross-linkers. One team developed ketal cross-linked nanogels of poly(amino acid)s by cross-linking PAsp groups of PEG-*b*-PAsp-*b*-PPhe aggeregates with ketal-containing diamines in the presence of carbodiimide coupling agents [39]. The ketal cross-link can be cleaved by hydrolysis, with the reaction rate increasing under acidic conditions. From hydrolysis kinetics, the hydrolysis half-life of ketal cross-links would be estimated as 0.7 h at pH 5.0 but 52 h at pH 7.4, which is 74-fold faster at the endosomal pH than at nomal plasma.

65.4.2 pH-Responsive Release of Payloads from Nanogels

The pH-responsive nanogels hold great promise as drug carriers for the delivery of hydrophilic drugs via pH-controlled drug release at target sites. The pH-sensitive hydrogel, whose volume can change by swelling and shrinking, can control the release of payload depending on the pH. Polycationic polymer-based nanogels show facilitated drug release at acidic pH, while polyanioic polymer nanogels, such as poly(methacrylic acid-*g*-poly(ethylene glycol)) P(MAA-*g*-EG), show slow release at acidic pH. The nanoparticles of P(MAA-*g*-EG) shrinks at an acidic condition due to the deionization below pK_a 4.5, and the nanoparticles can entrap drugs stably in the stomach when they are applied orally.

Insulin-drug-loaded PEG-PAsp nanogels can be produced by a simple postincubation of nanogels in an insulin solution, and a loading efficiency of ≤40% can be achieved. The pH-responsive release of insulin from nanogels was monitored in buffer solutions of pH 2 and 7.4; the release profiles are shown in Fig. 65.11. At pH 7.4, the insulin release was completed within 48 h, whereas 50% of the drugs were released at pH 2 within 48 h, due to the shrinkage of nanogels. The release behavior of drug carriers can be analyzed by employing a power-law equation, and the initial slope of log(released amount %)–log(t) plot, defined as the diffusional exponent (n), is closely related to the drug transport mechanism. The diffusional exponents for nanogels at pH 7.4 and 2 were found to be 0.78 and 0.66, respectively [17]. The results imply that the drug release from the PEG-PAsp nanogel is the anomalous transport system, which is a combination of Fickian diffusion and polymer relaxation by swelling. However, the n value is close to 1 at pH 7.4 because the drug release by swelling becomes dominant.

On the other hand, the utilization of ionic interactions between ionized drugs and nanogels is another approach for drug loading in nanogels [38]. An amino group of doxorubicin (DOX), an anticancer drug, forms an ionic bond with a carboxylic acid group of PEG-PAsp nanogel, and DOX can be entrapped in nanogels up to 27%. The DOX-loaded nanogels also displayed a pH-responsive shrinking at

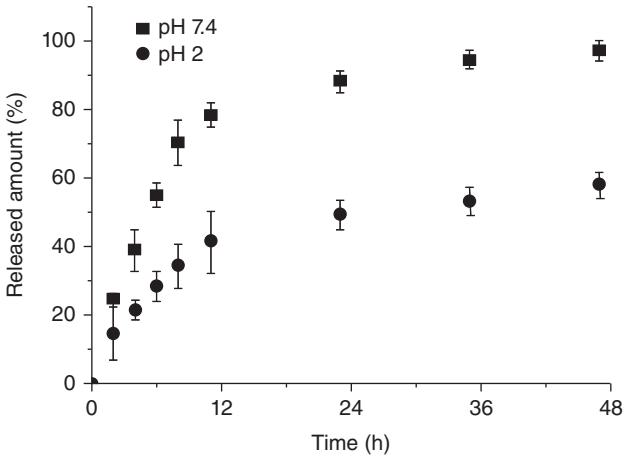


FIGURE 65.11 rh-insulin release profile from PEG-PAsp nanogel in pH 2 and pH 7.4 buffer solutions [17].

acidic pH due to free carboxylates. Furthermore, nanogels showed accelerated DOX release at pH 5 compared to that at pH 7.4. This is attributed to the ionic interaction between DOX and Asp, which becomes weaker as the carboxyl groups are deionized in acidic pH.

Also, the pH-labile bond of cross-links and drug conjugation provides pH-responsive drug release from nanogel networks. The DOX-loaded ketal cross-linked nanocarrier showed the minimized drug release at pH 7.4, whereas the release was accelerated at pH 5, due to the hydrolysis of cross-linkers and destabilization of the carrier [39]. On the other hand, the drug conjugation by an acid-labile hydrazone linker was also realized by the reaction of hydrazide group of PEG-*b*-poly(aspartate hydrazide) with the carbonyl group of DOX [71]. The hydrazone bond is typically stable at a neutral pH and degradable in acidic environments, and thus the conjugated drugs release at acidic pH. For this reason, the accelerated drug release was observed at pH 5.0 by 1.78–3.91-fold with respect to pH 7.4.

65.5 CONCLUSIONS

Nanogels have the distinctive properties of not only hydrogel-like behavior but also advantageous properties of nanoparticles. Nanogels can be prepared by ionic cross-linking or chemical cross-linking of functional groups on poly(amino acid)s. The physical and chemical properties of poly(amino acid)s can be readily modulated from the selection of amino acid monomers. Furthermore, the poly(amino acid) nanogels can have a stimulus-responsive property, especially pH sensitivity, which originates from ionizable polymer backbone, and stimulus-labile cross-link or drug conjugation. The stimulus-responsive destabilization or swelling/deswelling of nanogels induces the release of payloads from nanogels at a specific target site. Since poly(amino acid)s have great biocompatibility and biodegradability, the poly(amino acid)-based stimulus-responsive nanogels have great potential as smart drug delivery carriers. The development of new chemical technologies for multifunctional nanogel synthesis, such as diagnostics, sensing, imaging, and active targeting of tumors, is expected to open up new opportunities for their clinical applications.

REFERENCES

[1] Kabanov, A.V., Vinograv, S.V. (2009). *Agnew. Chem. Int. Ed.* **48**, 5418–5429.

[2] Reese, C.E., Mikhonin, A.V., Kamenjicki, M., Tikhonov, A., Asher, S.A. (2004). *J. ACS* **126**, 1493–1496.

[3] Allermann, E., Gury, R., Doelker, E. (1993). *Eur. J. Pharm. Biopharm.* **39**, 173–191.

[4] Soni, S., Babbar, A.K., Sharma, R.K., Maitra, A. (2006). *J. Drug Target.* **14**, 87–95.

[5] Vinogradov, S.V., Batrakova, E.V., Kabanov, A.V. (2004). *Bioconjug. Chem.* **15**, 50–60.

[6] Patel, M.M., Goyal, B.R., Bhadada, S.V., Bhatt, J.S., Amin, A.F. (2009). *CNS Drugs* **23**, 35–58.

[7] Vaupel, P., Kallinowski, F., Okunieff, P. (1989). *Cancer Res.* **49**, 6449–6465.

[8] Watson, P., Jones, A.T., Stephens, D.J. (2005). *Adv. Drug Deliv. Rev.* **57**, 43–61.

[9] Gil, E.S., Hudson, S.M. (2004). *Progress Polym. Sci.* **29**, 1173–1222.

[10] Dupin, D., Fujii, S., Armes, S.P., Reeve, P., Baxter, S.M. (2006). *Langmuir* **22**, 3381–3387.

[11] Weaver, J.V.M., Adams, D.J. (2010). *Soft Matt.* **6**, 2575–2582.

[12] Daud-Mahammed, S., Couvreur, P., Gref, R. (2007). *Int. J. Pharm.* **332**, 185–191.

[13] Sanson, N., Rieger, J. (2010). *J. Polym. Chem.* **1**, 965–977.

[14] Oh, J.K., Drumright, R., Siegwart, D.J., Matyjaszewski, K. (2008). *Progress Polym. Sci*. **33**, 448–477.

[15] Van Thienen, T.G., Lucas, B., Flesch, F.M., van Nostrum, C.F., Demeester, J., De Smedt, S.C. (2005). *Macromolecules* **38**, 8503–8511.

[16] Chilkoti, A., Dreher, M.R., Meyer, D.E. (2002). *Adv. Drug Deliv. Rev.* **54**, 1093–1111.

[17] Park, C.W., Yang, H.-M., Lee, H.J., Kim, J.-D. (2013). *Soft Matt.* **9**, 1781–1788.

[18] Zhang, L., Eisenberg, A. (1995). *Science* **268**, 1728–1731; Yu, K., Eisenberg, A. (1996). *Macromolecules* **9**, 6359–6361.

[19] Discher, D.E., Eisenberg, A. (2002). *Science* **297**, 967–973.

[20] Lee, H.J., Yang, S.L., An, E.J., Kim, J.D. (2006). *Macromolecules* **39**, 4938–4940.

[21] Lavasanifar, A., Samuel, J., Kwon, G.S. (2002). *Adv. Drug Deliv. Rev.* **54**, 169–190; Bae, Y., Kataoka, K. (2009). *Adv. Drug Deliv. Rev.* **61**, 768–784.

[22] Yui, N., Mrsny, R., Park, K. (eds.). (2004). *Reflexive Polymers and Hydrogels*. CRC Press, Boca Raton, FL, Chapter 18, pp. 373–400.

[23] Masayuki, T., Takeshi, N., Shigeyuki, M., Kakuchi, T. (1997). *Polymer* **38**(18), 4733–4736.

[24] Kang, H.S., Shin, M.S., Kim, J.-D., Yang, J.W. (2000). *Polym. Bull.* **45**, 39–43; Jeong, J.H.; Kang, H.S.; Yang, S.R.; Kim, J.-D. (2003). *Polymer* **44**, 583–591.

[25] Kanayama, N., Fukushima, S., Nishiyama, N., Itaka, K., Jang, W.-D., Miyata, K., Yamasaki, Y., Chung, U., Kataoka, K. (2006). *Chem. Med. Chem.* **1**, 439–444.

[26] Jeong, J.H., Cho1, Y.W., Jung, B., Park, K., Kim, J.-D. (2006). *Jpn. J. Appl. Phys.* **45**, 591–595.

[27] Oba, M., Aoyagi, K., Miyata, K., Matsumoto, Y., Itaka, K., Nishiyama, N., Yamasaki, Y., Koyama, H., Kataoka, K. (2008). *Mol. Pharm.* **5**(6), 1080–1092.

[28] Sato, T., Higashida, N., Hirano, T., Seno, M.J. (2004). *Polym. Sci. A: Polym. Chem.* **42**, 1609–1617.

[29] Vinogradov, S.V., Batrakova, E.V., Kabanov, A.V. (1999). *Colloids Surf., B* **16**, 291–304.

[30] Blackburn, W.H., Lyon, L.A. (2008). *Colloid Polym. Sci.* **286**, 563–569; Cuggino, J.C., Alvarez, C.I., Strumia, M.C., Welker, P., Licha, K., Steinhilber, D., Mutihac, R.-C.; Calderon, M. (2011). *Soft Matt.* **7**, 11259–11266.

[31] Prochazka, K., Baloch, M.K., Tazar, Z. (1979). *Makromol. Chem.* **180**, 2521–2523.

[32] Stewart, S., Liu, G.J. (1999). *Chem. Mater.* **11**, 1048–1054.

[33] Huang, H.Y., Kowalewski, T., Remsen, E.E., Gertzmann, R., Wooley, K.L. (1997). *J. ACS* **119**(48), 11653–11659; Li, Y.T., Lokitz, B.S., Armes, S.P., McCormick, C.L. (2006). *Macromolecules* **39**, 2726–2728.

[34] Joralemon, M.J., O'Reilly, R.K., Hawker, C.J., Wooley, K.L. (2005). *J. ACS* **127**, 16892–16899.

[35] Li, Y., Lokitz, B.S., Armes, S.P., McCormick, C.L. (2006). *Macromolecules* **39**, 2726–2728.

[36] Butu, V., Lowe, A.B., Billingham, N.C., Armes, S.P. (1999). *J. ACS* **121**, 4288–4289.

[37] Huang, H., Remsen, E.E., Wooley, K.L. (1998). *Chem. Commun.* 1415–1416; Li, Y., Du, W., Sun, G., Wooley, K.L. (2008). *Macromolecules* **41**, 6605–6607.

[38] Lee, H.J., Bae, Y. (2011). *Biomacromolecules* **12**, 2686–2696.

[39] Lee, S.J., Min, K.H., Lee, H.J., Koo, A.N., Rim, H.P., Jeon, B.J., Jeong, S.Y., Heo, J.S., Lee, S.C. (2011). *Biomacromolecules* **12**, 1224–1233.

[40] Park, C.W., Lee, H.J., Yang, H.-M., Woo, M.-A., Park, H.G., Kim, J.-D. (2011). *J. Polym. Sci. A: Polym. Chem.* **49**, 203–210.

[41] Kang, H.S., Yang, S.R., Kim, J.-D., Han, S.-H., Chang, I.-S. (2001). *Langmuir* **17**, 7501–7506.

[42] Jo, Y.M., Park, C.W., Jung, B.-K., Yang, H.-M., Kim, J.-D. (2010). *Macromol. Chem. Phys.* **211**, 2434–2442.

[43] Yang, H.-M., Park, C.W., Lim, S., Park, S.-I., Chung, B.H., Kim, J.-D. (2011). *Chem. Commun.* **47**, 12518–12520.

[44] Yang, H.-M., Park, C.W., Bae, P.K., Ahn, T., Seo, B.-K., Chung, B.H., Kim, J.-D. (2013). *J. Mater. Chem. B.* **1**, 3035–3043.

[45] Matyjaszewski, K., Gnanou, Y., Leibler, L. (2007). *Macromolecular Engineering: Precise Synthesis, Materials Properties, Applications*. Wiley, Weinheim.

[46] Auer, S., Frenkel, D. (2001). *Nature* **413**, 711–713.

[47] Iyer, A.S.J., Lyon, L.A. (2009). *Angew. Chem. Int. Ed.* **48**, 4562–4566.

[48] Jones, C.D., Lyon, L.A. (2003). *Macromolecules* **36**, 1988–1993.

[49] Nayak, S., Gan, D., Serpe, M.J., Lyon, L.A. (2005). *Small* **1**, 416–421.

[50] He, T., Adams, D.J., Butler, M.F., Yeoh, C.T., Cooper, A.I., Rannard, S.P. (2007). *Angew. Chem. Int. Ed.* **46**, 9243–9247.

[51] Oishi, M., Nagasaki, Y. (2007). *React. Funct. Polym.* **67**, 1311–1329.

[52] Raemdonck, K., Demeester, J., De Smedt, S. (2009). *Soft Matt.* **5**, 707–715.

[53] Ma, Q., Remsen, E.E., Kowalewski, T., Schaefer, J., Wooley, K.L. (2001). *Nano Lett.* **1**, 651–655.

[54] Amalvy, J.I., Wanless, E.J., Michailidou, Y., Li, V., Armes, S.P., Duccini, Y. (2004). *Langmuir* **20**, 8992–8999.

[55] Dupin, D., Fujii, S., Armes, S.P., Reeve, P., Baxter, S.M. (2006). *Langmuir* **22**, 3381–3387.

[56] Tamber, H., Johansen, P., Merkle, H.P., Gander, B. (2005). *Adv. Drug Deliv. Rev.* **57**, 357–376.

[57] Staudinger, H., Husemann, E. (1935). *Chem. Ber.* **68**, 1618–1634.

[58] Snowden, M.J., Chowdhry, B.Z., Vincent, B., Morris, G.E. (1996). *J. Chem. Soc. Faraday Trans.* **92**, 5013–5016.

[59] Funke, W., Okay, O., Joos-muller, B. (1998). *Adv. Polym. Sci.* **136**, 139–234.

[60] Berndt, I., Pedersen, J.S., Richtering, W. (2005). *J. ACS* **127**, 9372–9373.

[61] Stieger, M., Richtering, W., Pedersen, J.S., Linder, P. (2004). *J. Chem. Phys.* **120**, 6197–6206.

[62] Bartlett, P., Ottweill, R.H. (1992). *J. Chem. Phys.* **96**, 3306–3316.

[63] Fernandez-Barbero, A., Fernandez-Nieves, A., Grillo, I., Lopez-Cabarcos, E. (2002). *Phys. Rev. E* **66**, 051803.

[64] Kratz, K., Hellweg, T., Eimer, W. (2001). *Polymer* **42**, 6631–6639.

[65] Stieger, M., Pedersen, J.S., Linder, P., Richtering, W. (2004). *Langmuir* **20**, 7283–7292.

[66] Kawaguchi, H., Kawahara, M., Yaguchi, N., Hoshino, F., Ohtsuka, Y. (1988). *Polym. J.* (Tokyo) **20**, 903–909.

[67] Kim, J.-H., Lee, J.H., Yoon, S.-W. (2002). *J. Industr. Eng. Chem.* **8**, 138.

[68] Saunders, B.R., Vincent, B. (1990). *Adv. Colloid Interface Sci.* **80**, 1–25; Das, M., Sanson, N., Kumacheva, E. (2008). *Chem. Mater.* **20**, 7157–7163.

[69] Bontha, S., Kabanov, A.V., Bronich, T.K. (2006). *J. Control. Release* **114**, 163–174.

[70] Yoon, S.R., Yang, H.-M., Park, C.W., Lim, S., Chung, B.H., Kim, J.-D. (2012). *J. Biomed. Mater. Res. A* **100**, 2027–2033.

[71] Lee, H.J., Bae, Y. (2013). *Nano Bull.* **2**, 2, 130210.

66

STRATEGIES OF METAL NANOPARTICLES FOR NANOBIOLOGY

DAISUKE MATSUKUMA AND HIDENORI OTSUKA
Faculty of Science Division I, Department of Applied Chemistry, Tokyo University of Science

66.1 INTRODUCTION

With the development of science and technology, numerous scientific phenomena have been investigated in microscopic dimensions. The pertinent scientific issue has progressed from big to small. The quantum invention of analytical methods such as an electron microscope helped investigators examine phenomena in the regime of nanometer. Because of the electronic confinement of nanosized objects, their chemical and optical properties are significantly different from those of larger objects. As we look at lifeforms in smaller and smaller dimensions, we end up with biological objects, which are involved in fundamental life processes. The key molecules in biology such as DNA, enzymes, receptors, antigens, antibodies, and oxygen carriers can be included in the dimension of nanometers. Thus, all fundamental processes in biology are taking place in the dimension of 1–100 nm. Molecular self-organization around nanoparticles based on surface science can be used as probes for understanding fundamental life processes. The coupling of surface science and molecular biology has given birth to a new subject called *nanobiology*, which symbolizes a path-breaking evolution in the progress of biology. This new subject is able to reveal many fundamental secrets of lifeforms that are yet to be discovered.

The science of nanobiology has progressed significantly and can be grouped into several disciplines of life science such as cellular biology, genomics, proteomics, oncology, immunology, diagnosis, and targeted drug delivery. The idea of creating the hybrid systems of inorganic nanoparticles with biological moieties has helped solve several technical difficulties in medical and biosciences. Using nanomaterials, instead of conventional materials, in life science applications has increased efficiency while decreasing cost. Thus, the hybridization of nanotechnology and biotechnology has laid the ground for many novel methodologies, which are capable of solving several technical difficulties in bioanalysis. The ideas and innovations of nanoiology can be extended to the frontiers of biotechnology. In this chapter, we highlight the currently employed metal nanoparticles and their bioconjugation strategies for nanobiology.

66.2 METAL NANOPARTICLES

Unlike bulk materials, metal nanoparticles have characteristic physical, chemical, electronic, electrical, mechanical, magnetic, thermal, dielectric, optical, and biological properties [1–4]. Decreasing the dimension of nanoparticles has a pronounced effect on the physical properties that significantly differ from those of the bulk material. These physical properties are caused by their large surface atom, large surface energy, spatial confinement, and reduced imperfections. Obviously, metal nanoparticles are considered as building blocks of the next generation of optoelectronics, electronics, and various chemical and biochemical sensors [5–8]. In fact, a number of significant technologies such as catalysis, electronics, high-density information storage, photoluminescence devices, targeted drug delivery, and enzyme immobilization have been applied in various disciplines (Fig. 66.1);

Encyclopedia of Biocolloid and Biointerface Science, Volume 2, First Edition. Edited by Hiroyuki Ohshima.
© 2016 John Wiley & Sons, Inc. Published 2016 by John Wiley & Sons, Inc.

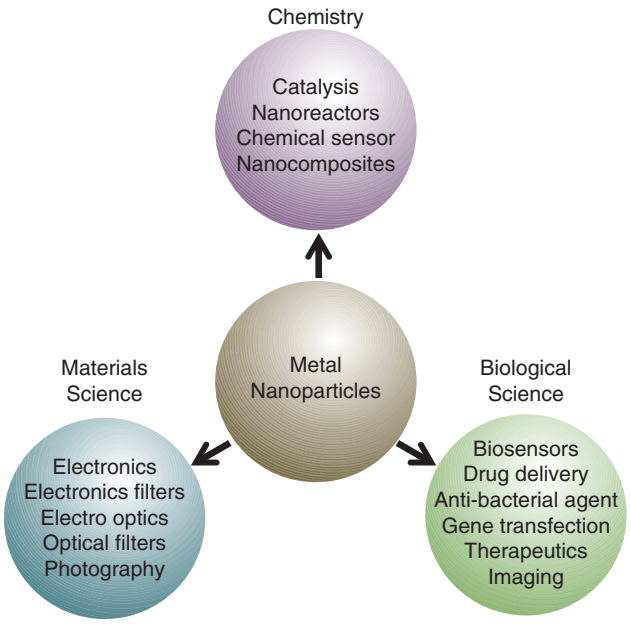


FIGURE 66.1 Significant applications of nanoparticles in various disciplines.

there have been many efforts to synthesize nanoparticles with different functionalities [9].

66.2.1 Basic Key Aspects of Metal Nanoparticles for Nanobiology

The key point for the fabrication of metal nanoparticles for biological applications is related to its mode of usage. It is applied orally or directly injected into the blood. For example, the drug delivery vehicle should be chemically stable at the locations to which it is transported. Thus, key aspects in biological applications are (1) lack of cytotoxicity, (2) absence of side effects, (3) chemical stability at transported locations, and (4) targeted drug delivery.

66.2.2 Noble Metal Nanoparticle

Generally, several types of noble nanomaterials such as nanoparticles, nanorods, metal nanoshells, and nanocages, made from gold and silver, are used for biological applications. For example, nanoshells constitute a novel class of optically tunable nanoparticles that consist of a dielectric core surrounded by a thin gold shell [10,11]. Antibodies can be immobilized to the gold surface of nanoshells. The gold surfaces of nanoshells are considered to be biocompatible, and polymers such as poly(ethylene glycol) (PEG) may be attached to nanoshell surfaces to further enhance biocompatibility and improve circulation in the bloodstream [12]. Silver [13] and gold [14] nanoparticles are used as intracellular surface-enhanced Raman scattering (SERS) probes. The advantages of noble metal nanoparticles are listed as (1) ideal immunolabels for transmission electron microscopy, (2) efficient contrast agents for optical microscopy, (3) powerful SERS probes, (4) inert to physiological conditions, (5) effective biocompatibility, and (6) ideal vehicles for immobilization of biomolecules.

Since 2005, biological delivery applications utilizing gold nanoparticles as inert, nontoxic, and biocompatible vehicles have been extensively studied and reviewed [15,16]. Modification with biomolecules such as oligonucleotide, peptide/protein, carbohydrate, and lipid has provided not only dispersive stabilization for nanoparticles under physiological conditions but also efficient transport of biomacromolecules with minimal cytotoxicity. In fact, gold nanoparticles with monolayers generated by biomolecules can address various delivery issues such as endosomal escape and specific targeting without conjugation of additional moieties. For example, endosomal trapping can be avoided by using a cell-penetrating peptide-based coating on the nanoparticle surface [17].

In addition, a critical requirement in molecular cell biology is the local mapping of specific biomolecules in cells and tissues. Immunofluorescent labeling is the standard approach, but fluorescence-based imaging is limited in spatial resolution by the wavelength of light. Hence, the application of transmission electron microscopy (TEM) in conjunction with immunolabeling has proved to be advantageous for high-resolution structural studies [18]. The prevalent strategy for immunolocalization via TEM is to employ antibodies conjugated with gold nanoparticles of various dimensions [19].

66.2.3 Quantum Dots

Quantum dots are small (<10-nm) inorganic nanocrystals that possess unique luminescent properties. Their fluorescence emission is stable and can be tuned by varying the particle size or composition. Quantum dots are generally composed of atoms from II–VI or III–V elements in the periodic table and are defined as particles with physical dimensions smaller than the exciton Bohr radius [20]. This size leads to a quantum confinement effect, which endows nanocrystals with unique optical and electronic properties. Semiconductor nanocrystals can be capped with inert oxides or sulfides and can be attached to a biomolecule with a specific function. The salient features of semiconductor nanocrystals are (1) size-tunable emission (from the UV to the IR) of quantum dots, (2) narrow spectral linewidths, (3) high luminescence, (4) continuous absorption profiles, (5) stability against photobleaching, and (6) ideal immunolabels for in vitro and in vivo fluorescent imaging.

One group of researchers reported that in vivo targeting by using semiconductor quantum dots has proved to be highly feasible [21]. It was found that ZnS-capped CdSe quantum

dots coated with a lung-targeting peptide accumulate in the lungs of mice after injection, whereas two other peptides specifically direct quantum dots to blood vessels or lymphatic vessels in tumors. It was also seen that on adding PEG to the quantum dot, coating prevents the nonselective accumulation of quantum dots in reticuloendothelial tissues. These results encourage the construction of more complex nanostructures with capabilities such as disease sensing and drug delivery. ZnS-capped CdSe quantum dots emitting in the green and the red (550 nm and 625 nm fluorescence maxima, respectively) were coated with peptides by using a thiol exchange reaction. These peptide-coated quantum dots were injected into the tail vein of a mouse and allowed to circulate for a given time. Then each dot was frozen, sectioned, and examined under an inverted fluorescent microscope or confocal microscope. The use of peptides to target drug-carrying nanostructures such as those composed of dendrimers or stabilized drug nanocrystals is also possible.

66.2.4 Magnetic Nanoparticles

The phenomenon of magnetism has received significant attention in life sciences and medical sciences. The magnetic particles in nanoscales can be synthesized by various methods, including soft chemical methods such as coprecipitation of hydroxides [22], hydrothermal synthesis [23], sol–gel transformation, and ball milling [24]. More recently, microbial synthesis of nanoparticles has been developed as a green chemistry approach that consists in interconnecting nanotechnology and microbial biotechnology. Intracellular ferrimagnetic nanocrystals of greigite (Fe_3S_4) magnetite (Fe_3O_4) have been found in magnetotactic bacteria [25]. These ferrimagnetic nanocrystals are aligned in a linear fashion in the intracellular part called *magnetosome*, which helps the bacteria in its alignment and motion parallel to the geomagnetic field. A variety of remarkable applications in biology such as biosensors, magnetic resonance imaging, drug delivery, and magnetic fluid hyperthermia can be attained by the synergy of magnetic nanocrystals and biomolecules. Magnetic nanocrystals are size-compatible, sufficiently competent to interrelate with biological entities, detectable in an applied magnetic field, and capable of conveying energy from an alternating magnetic field. Magnetic nanomaterials have various applications such as proteomics, molecular cell biology, medical science, analytical biochemistry, clinical diagnostics, microbiology, immunology, biotechnology, and targeted drug delivery.

66.3 BIOCONJUGATION OF METAL NANOPARTICLES FOR NANOBIOLOGY

Accurate and sensitive detection of water-soluble bioanalytes such as toxins, carbohydrates, ionic species, and various biomolecules including DNA, proteins, and peptides is one of scientific goals with implications in healthcare and industrial applications [26]. The interaction of a target molecule with a protein receptor in a biological recognition process is often associated with a change in the protein conformation as a response to the binding event. Many scientists focus on the design and development of recognition-based sensing assemblies that can account for such changes through signal transduction in a medium of interest.

These observations and methods lead us to the key issue concerning the fabrication of nanobiological hybrid systems. First, we have to consider about inorganic nanoparticles in aqueous medium. These nanoparticles have an either positive or negative charge on their surfaces depending on the synthetic methodology adopted for their preparation. A majority of biomolecules have electrostatic charge due to the presence of acidic and basic functional (amino) groups. Thus electrostatic self-assembly of biomolecules around the nanoparticle can be used to fabricate nanobiological hybrid systems.

Another protocol used for the fabrication of assemblies is the immobilization of biomolecules on the surface of inorganic nanoparticles by using covalent bonding with the aid of an anchor molecule. Both the methodologies can be used depending on the requirement of the desired application. The tactics used in the construction of nanoprobes for a specific purpose can be adopted from the logic of bioconjugation. This means that we are utilizing the principle of molecular interactions in the construction of nanoprobes. Immobilization of the molecular conjugate of the target molecule on the nanoparticle surface is the most efficient protocol. For example, antibody–nanoparticle hybrid systems can be used for the detection of antigens and vice versa. Such nanoprobes are now commercially available on the market. The kind of nanoprobes used for optical microscopy depends on the nature of the inorganic nanoparticles. For instance, semiconductor quantum dots are used for confocal fluorescence microscopy of biological samples, while noble metal nanoparticles are used for transmission electron microscopy of biological samples. Among the metal nanoparticles, gold nanoparticles are widely used because of their unique properties such as strong optical absorption, chemical inertness, and ease of surface functionalization.

Inorganic nanoparticles such as noble metal nanoparticles, magnetic metal oxide nanoparticles, and semiconductor nanocrystals are used for bioconjugation. They are further utilized in different analytical applications. In normal protocols, an antibody of biologically important molecule is immobilized on the surface of the nanoparticle, which, in turn, is used for applications such as molecular detection, targeted drug delivery, and biological imaging. Sensing studies utilizing fluorescence resonance energy transfer (FRET) between a fluorescent donor molecule bound to the target and an acceptor attached to a receptor protein have been widely used to study receptor–ligand interactions and

changes in protein conformation on binding to a target analyte [27]. FRET has also been used to study changes in the solution conditions (temperature, pH conditions, etc.). FRET is extremely sensitive to the separation distance between the donor and acceptor, and is ideal for probing such biological phenomena. For example, one team [28] used luminescent CdSe-ZnS core–shell quantum dots as energy donors in FRET assays. The interface of biological systems and inorganic nanomaterials has recently attracted widespread interest in biology and medicine. Nanoparticles are believed to have potential as novel intravascular probes for both diagnostic (e.g., imaging) and therapeutic purposes (e.g., drug delivery) [29].

66.4 SURFACE MODIFICATION OF METAL NANOPARTICLES BY FUNCTIONAL POLYMERS

As mentioned above, conjugation with biomolecules on nanoparticle surface is an effective tool because of the specific interaction between biomolecules and the target objective. On the other hand, this is a very important issue with respect to the disposition of nanoparticles under the existence of many substances in physiological conditions. Thus, surface modification of nanoparticles to yield nonfouling properties is also required to avoid the aggregation and/or uptake by the mononuclear phagocytes system [30]. The enhanced permeability and retention (EPR) effect is the best example of this aspect and observed to be universal in solid tumors. Nanosized objects (including liposomes, nanoparticles, and macromolecular drugs) with long circulation times leak preferentially into tumor tissue through a leaky tumor vasculature and then are retained in the tumor to reduced lymphatic drainage.

In this case, functional polymers have proved very useful, and have been extensively studied. Polymer-assisted or polymer template synthesis of metal nanoparticles have received substantial attention because of very low concentrations of homopolymer and block copolymers capable of stabilizing nanoparticles effectively by steric stabilization, and the possibility of controlling the size, morphology of nanoparticles by varying the polymer/metal salt ratio. Moreover, the use of polymers containing appropriate functional groups serves as both reducing and stabilizing (capping) agent, and offers to prepare novel metal–polymer nanocomposites.

66.4.1 Natural Polymer Coating of Nanoparticles

Because of their nontoxic and biocompatible nature, natural polymers have always been the first choice of material scientists for synthesis of their composites with metal nanoparticles. In fact, coating with natural polymers ultimately improves the colloidal stability, oxidation resistance, mechanical stability, and functionalization characteristics of the composite systems. For example, chitosan, derived from chitin by partial deacetylation is a natural polymer with polycationic properties in dilute acidic solutions, enabling electrostatic attraction toward the negatively charged gold nanoparticle surfaces. Addition of aliquots of chitosan solution to gold colloidal solution results in a chitosan-capped gold nanoparticle dispersion–composite system [31]. Nanoparticles of ferromagnetic character (e.g., magnetite, maghemite) have been embedded into natural polymers such as chitosan for the purpose of wastewater treatment and medicinal/biotechnological applications (e.g., separation of microorganisms, extracorporal blood detoxification and targeted drug delivery) [32]. The magnetite nanoparticles including in chitosan microspheres are prepared by a suspension crosslinking technique [33]. The magnetite nanoparticles are prepared by coprecipitation of ferrous and ferric salts in alkaline medium, and the resulting product is mixed into acidified solution of chitosan, followed by addition of the cross-linker, glutaraldehyde. This suspension is now added dropwise into dispersion medium, which is composed of mineral oil, petroleum ether, and emulsifier. The magnetic chitosan microspheres, so produced, are collected with the help of magnet.

A few formulations based on superparamagentic nanoparticles coated by dextran polymer are being approved by the Food and Drug Administration (FDA, USA) for clinical imaging applications, and some of them are under clinic investigations. Recent reviews provide outstanding information about the magnetic nanoparticle formulations to a number of clinical applications [34,35]. These reviews suggest that superparamagnetic iron oxide nanoparticles coated with or incorporated in the biodegradable polymers can serve as contrasting agents as well as targeted delivery applications. Gum arabic or gum acacia (GA) is widely known as natural polysaccharide. A few recent studies indicate that gum acacia is extensively useful as a stabilizer, as well as reducing agent for nanoparticles synthesis [36]. The acacia polymer can produce 5–10-nm silver nanoparticles with good dispersion property over a long period of time. The reduction capacity of the acacia polymer progresses with higher amounts of polymer.

66.4.2 Synthetic Polymer Coating of Nanoparticles

Coating of nanoparticles with biocompatible synthetic polymers is a promising approach to generating core–corona particles for biomedical applications [37]. A survey of the more recent literature shows that indeed many different polymers have been used, for example, to stabilize gold colloids in aqueous media. Among these are Nafion 117 [38], poly(ethylene glycol) (PEG) [37], poly(vinyl alcohol) (PVA) [39], polyphosphate [40], polyacrylate [41,42], poly(ethylene imine) (PEI) [43], poly(*N*-vinylpyrrolidone) (PVP) [44], and poly(methyl methacrylate) (PMMA) [45].

These polymers have to provide solubility in the desired medium (mainly aqueous media) and at the same time bond to the metal colloids.

PEG is one of the most efficient dispersants, and has proved to be effective in suppressing the opsonization process because of its ability to prevent protein adsorption [37,46–50]. This feature is particularly interesting for particles that are intended for intravenous injections, because their half-life in blood circulation will be extended. This is usually so-called PEGylation of surfaces. To consider several parameters, the concept of PEGylation is also applied to biomolecules such as protein and antibody. To obtain an optimum protein activity by the PEGylation, estimation of the appropriate molecular weight of PEG can be based on the size of the given protein and the desired in vivo half-life increase. The selection of the activated PEGylating agent and the coupling method are less straightforward. To ensure a high retention of biomolecules by polymer coupling tethered to those amino acids, it is necessary to retain the biological function. The conjugated polymer should avoid the shielding of amino acid sequences to recognize the specific biological interaction. Consequently, a case-by-case approach is necessary to achieve the desired outcomes [51].

One team reported that surface PEGylation of gold particles by CH_3O–PEG–SH significantly improved their dispersion stability in aqueous milieu due to steric repulsion effects of tethered PEG strands [52]. Yet, the CH_3O–PEGylated nanoparticles possess no reactive groups to further immobilize ligand molecules. Thus, a system possessing both sufficient colloidal stability and biofunctionality is strongly desired to construct quantitative bioassays using gold nanoparticles [53,54]. Another group of researchers reported a facile route to functionalize PEGylated gold nanoparticles, having a potential utility for colloidal sensor systems [37], by the use of newly designed heterobifunctional PEG derivatives. That strategy to synthesize various types of heterobifunctional PEGs is based on the ring-opening polymerization of ethylene oxide using a metal alkoxide initiator with a protected functional group. Other researchers have reported the synthesis of heterobifunctional PEG containing both mercapto and acetal terminal groups (α-acetal-ω-mercapto-PEG, acetal-PEG-SH) [55–60]. The acetal moiety can readily be transformed into a reactive aldehyde group by simple treatment with dilute acid. An aldehyde-functionalized PEGylation of gold nanoparticles using this acetal-PEG-SH was successfully achieved, and the obtained gold nanoparticles expressed high dispersion stability, particularly in physiological condition. Furthermore, appreciable aldehyde reactivity to immobilize ligand molecules on the PEG coronas additionally impart them sensitivity and selectivity because of their nonfouling properties. As a model ligand, lactose was successfully introduced in the distal end of PEG chain to induce lectin-mediated quantitative and reversible association of gold nanoparticles under physiologically relevant conditions, producing a concomitant color change (Fig. 66.2) [61].

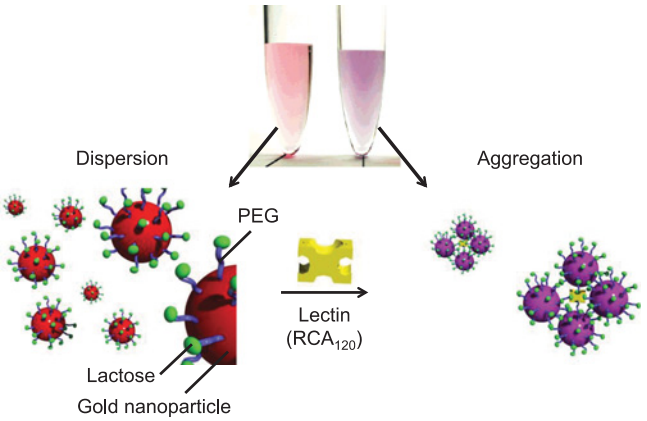


FIGURE 66.2 Schematic representation of the aggregation–dispersion behavior of lactose-modified gold nanoparticles by the addition of RCA_{120} lectin with change in color from red to purple [60].

66.4.3 Structural Regulated Copolymer for Coating Agent

The great advantage of synthetic polymers contrasted with natural polymers is the regulation of their primary structure. Amphiphilic block copolymers are versatile materials being explored for applications in medical, cosmetic, environmental, and industrial fields. The more recent developments of different synthetic techniques and the availability of numerous types of core and corona blocks with varying properties have provided a wide range of block copolymers [62]. In typical micellar applications, these copolymers are composed of a hydrophobic core block and a hydrophilic corona block. Under appropriate conditions, these amphiphilic copolymers can produce different aggregates of a wide range of shapes and sizes (especially spheres, rods, and vesicles) [63–71]. These aggregates can serve as versatile delivery vehicles for both hydrophobic and hydrophilic agents [72–82]. Block copolymers can provide nanoscale environments of varying and tunable shape, dimensions, mobility, local polarity, concentration, and reactivity. Reagents can be loaded into and react with functional polymers. The nanoscale domains formed by block copolymers can provide loci for the growth of metal and inorganic nanoparticles [83,84], while the block architecture can facilitate both the modification of the nanoparticle surface and the long-range positioning of nanoparticles [85–88].

Another group of coworkers successfully prepared the extremely high density PEG brush surface (~0.7 chains/nm^2) compared with other general methods (~0.3 chains/nm^2) [89–91]. The most peculiar aspect of the fabrication of the high-density PEG brush is the applyication of comb- and block-type copolymer (PEG-*co*-Py, PEG-*b*-Py), which is composed of a PEG segment as the hydrophilic part and a pyridine segment as the hydrophobic part [89,92–94] (Fig. 66.3). It is known that pyridine shows a high

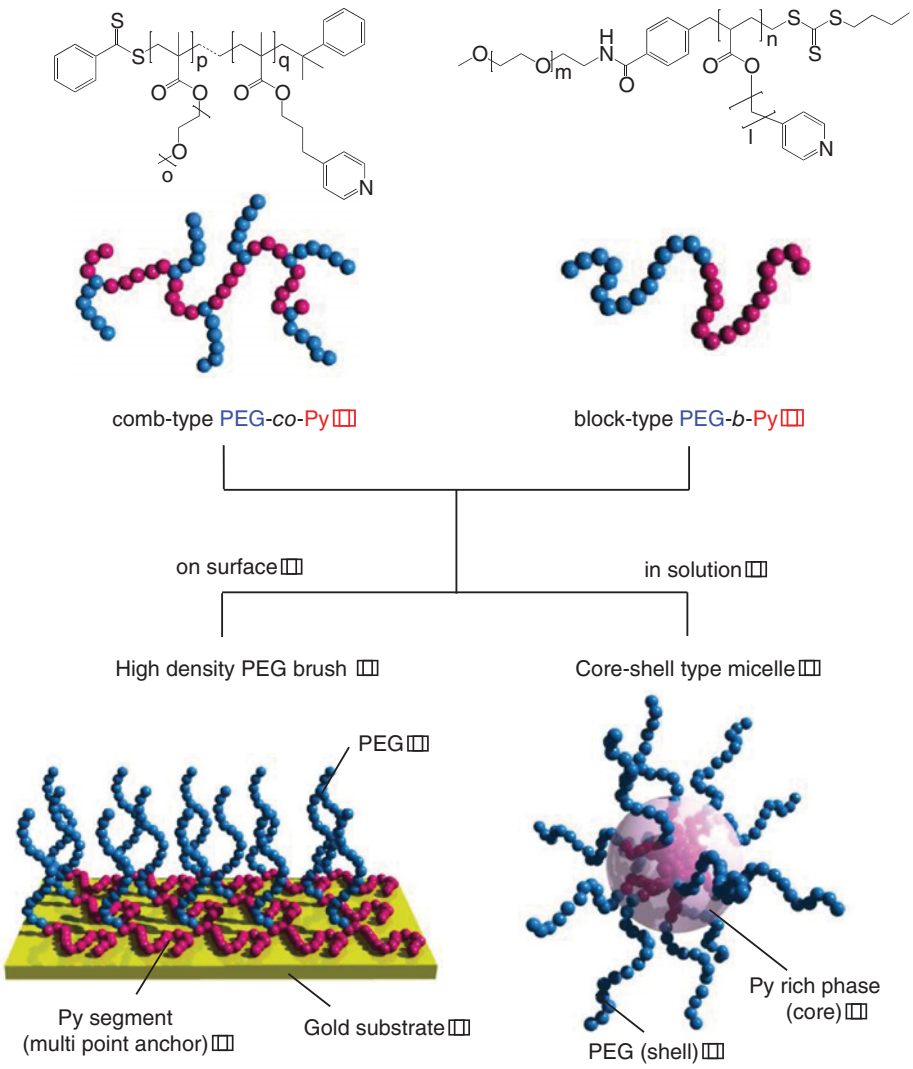


FIGURE 66.3 Chemical structure and schematic illustration of amphiphilic copolymers consisting PEG and polymerized pyridine on surface and in solution [91–93].

affinity to various metal surfaces. Thus, polymerized pyridine segment acts as the multipoint anchor to a metal surface. It is important that copolymer shows the phase-separated conformation in aqueous media, leading to the multipoint anchoring to provide exothermic enthalpy by adsorption compensating for entropy loss by crowding chain formation. This high-density PEG surface shows the specific features: excellent oil-repellent property based on their hydrophilicity, the molecule barrier property depending on the molecular weight of analytes such as biological protein, even at low molecule weight (myoglobin; MW = 17,600, R_g = ~2 nm) based on the exclusion volume effect of PEG, and the antioxidation activity in an oxidant environment likely in vivo. Moreover, when PEG-*co*-Py-modified gold nanoparticles are exposed to high salt concentration (1 M NaCl), they show long-term dispersion stability compered with PEG-SH modification [92].

66.5 REDUCING POLYMERS ACT AS DISPERSANTS FOR NANOPARTICLES

Nanotechnology research is emerging as cutting-edge technology interdisciplinary with physics, chemistry, biology, materials science, and medicine. Nanoparticles are usually 10–100 nm in each spatial dimension and are commonly synthesized using two strategies: top–down and bottom–up. In the top–down approach, the bulk materials are gradually broken down to nanosized materials, whereas in bottom–up approach, atoms or molecules are assembled in molecular structures in the nanometer range. The bottom–up approach is commonly used for chemical and biological synthesis of nanoparticles, and also for regulation of size and shape of nanoparticles. Obtaining monodispersed nanoparticles of different sizes and shapes has been a challenge in nanotechnology. The development of simple and versatile methods for the

preparation of nanoparticles in a size- and shape-controlled manner has attracted significant attention [95].

As mentioned above, nontoxicity of nanoparticles is of consequence for nanobiology. Although various physical and chemical methods are extensively used to produce monodispersed nanoparticles, the stability and the use of toxic chemicals is the subject of paramount concern. The use of toxic chemicals on the surface of nanoparticles and nonpolar solvents in the synthesis procedure limits their applications in clinical fields. Therefore, development of clean, biocompatible, nontoxic, and ecofriendly methods for nanoparticles synthesis deserves merit.

On the basis of these observations, a substitute method for one-step polymer-mediated synthesis has been developed [96]. If we use a polymer with reducing capacity as both the reducing agent and the stabilizer, covering the nanoparticles immediately after they are synthesized, then highly stabilized nanoparticles can be produced and the limitations mentioned above can be avoided as well [97]. This one-step method introduces no more reducing agents into the reaction system except for the polymer, so the product tends to be of high purity. Besides, by adjusting the polymer structure, reaction temperature, reactant ratio, and reacting time, it is possible to control the shape and size of metal nanoparticles. According to some previous experiments, metal nanoparticles synthesized this way are surprisingly stable and homogeneous. Although this one-phase process has only recently been proposed, much wider application can be forecast for future because of the low cost and relatively high efficiency of this method. As many more varieties of polymers are being used as the dual-functional reductant and stabilizer, metal nanoparticles with different dimensions, morphologies, structures, and optical properties are likely to be easily synthesized according to our needs. Therefore, potential applications of polymer-coated nanocomposites can be quite promising in future therapeutic applications and biomolecular manipulations, including detection, drug transfer, and genetic engineering. These newer production methods of metal nanoparticles based on polymer science and material science are also evolving to improve the nanobiology.

66.6 CONCLUSION

An overlap of nanotechnology, biotechnology, and bioinformatics has resulted in the advent of a new technology called *nanobiotechnology*, which is defined as a field that applies the principles of nanotechnology and bioinformatics to probe and modify biological systems or to apply the principles of life sciences and surface sciences to develop novel devices and systems for biocatalysis. Since 2005 or so, this technology has reached a level that has enabled it to develop probes for understanding the intracellular and intercellular biological process, novel targeted labels for biological systems, and efficient nanoparticle-based immunoassays for the detection of biomarkers at extremely low concentrations and preconcentration probes for selectively adsorbing the analyte from crude samples. Nanobiotechnology has a high potential for catering to societal needs, and can be used in common applications such as clinical assay and medical diagnosis, and can provide cheaper and more efficient solutions.

REFERENCES

[1] Goesmann, H., Feldmann, C. (2010). *Angew. Chem. Int. Ed.* **49**, 1362.

[2] Grzelczak, M., Pérez-Juste, J., Mulvaney, P., Liz-Marzán, L.M. (2008). *Chem. Soc. Rev.* **37**, 1783.

[3] Kamat, P.V. (2002). *J. Phys. Chem. B* **106**, 7729.

[4] Link, S., El-Sayed, M.A. (1999). *J. Phys. Chem. B* **103**, 8410.

[5] Zamborini, F.P., Bao, L., Dasari, R. (2012). *Anal. Chem.* **84**, 541.

[6] Agasti, S.S., Rana, S., Park, M.-H., Kim, C.K., You, C.-C., Rotello, V.M. (2010). *Adv. Drug Deliv. Rev.* **62**, 316.

[7] Anker, J.N., Hall, W.P., Lyandres, O., Shah, N.C., Zhao, J., van Duyne, R.P. (2008). *Nat. Mater.* **7**, 442.

[8] Murphy, C.J., Gole, A.M., Stone, J.W., Sisco, P.N., Alkilany A.M., Goldsmith, E.C., Baxter, S.C. (2008). *Acc. Chem. Res.* **41**, 1721.

[9] Thomas, V., Namdeo, M., Murali Mohan, Y., Bajpai, S.K., Bajpai, M. (2008). *J. Macromol. Sci. A.* **45**, 107.

[10] Hirsch, L.R., Jackson, J.B., Lee, A., Halas, N.J., West, J.L. (2003). *Anal. Chem.* **75**, 2377.

[11] Loo, C., Lowery, A., Halas, N., West, J., Drezek, R. (2005). *Nano Lett.* **5**, 709.

[12] Talley, C.E., Jusinski, L., Hollars, C.W., Lane, S.M., Huser, T. (2004). *Anal. Chem.* **76**, 7064.

[13] Kneipp, J., Kneipp, H., Rice, W.L., Kneipp, K. (2005). *Anal. Chem.* **77**, 2381.

[14] Rosi, N.L., Mirkin, C.A. (2005). *Chem. Rev.* **105**, 1547.

[15] Ghosh, I.P., Han, G., De, M., Kim, C.K., Rotello, V.M. (2008). *Adv. Drug Deliv. Rev.* **60**, 1307.

[16] Ranaa, S., Bajaja, A., Mouta, R., Rotelloa, V.M. (2012). *Adv. Drug Deliv. Rev.* **64**, 200.

[17] Nativo, P., Prior, I.A., Brust, M. (2008). *ACS Nano.* **2**, 1639.

[18] Cheng, L.-C., Jiang, X., Wang, J., Chen, C., Liu, R.-S. (2013). *Nanoscale* **5**, 3547.

[19] Chan, W.C.W., Nie, S. (1998). *Science* **281**, 2016.

[20] Bruchez, M. Jr., Moronne, M., Gin, P., Weiss, S., Alvisatos, A.P. (1998). *Science* **281**, 2013.

[21] Åkerman, M.E., Chan, W.C.W., Laakkonen, P., Bhatia, S.N., Ruoslahti, E. (2002). *Proc. Natl. Acad. Sci.* **99**, 12617.

[22] Grigorova, M., Blythe, H.J., Blaskvo, V., Rusanov, V., Petkov, V., Musheva, V., Nihtianova, D., Martinez, L.M., Munoz, J.S., Mikhov, M. (1998). *J. Magn. Magn. Mater.* **183**, 163.

[23] Yang, X., Jiang, W., Liu, L., Chen, B., Wu, S., Sun, D., Li, F. (2012). *J. Magn. Magn. Mater.* **324**, 2249.

[24] Zhang, L., Papaefthymiou, G.C., Ziolo, R.F., Ying, J.Y. (1997). *Nanostruct. Mater.* **9**, 185.

[25] Narayanan, K.B., Sakthivel, N. (2010). *Adv. Colloid Interface Sci.* **156**, 1.

[26] Looger, L.L., Dwyer, M.A., Smith, J.J., Hellinga, H.W. (2003). *Nature* **423**, 185.

[27] Medintz, I.L., Uyeda, H.T., Goldman, E.R., Mattoussi, H. (2005). *Nat. Mater.* **4**, 435.

[28] Clapp, A.R., Medintz, I.L., Mauro, J.M., Fisher, B.R., Bawendi, M.G., Mattoussi, H. (2004). *J. ACS* **126**, 301.

[29] Niemeyer, C.M. (2001). *Angew. Chem. Int. Ed.* **40**, 4128.

[30] Bazile, D., Prudhomme, C., Bassoullet, M.-T., Marlard, M., Spenlehauer, G., Veillard, M. (1995). *J. Pharm. Sci.* **84**, 493.

[31] Sugunan, A., Thanachayanont, C., Dutta, J., Hilborn, J.G. (2005). *Sci. Technol. Adv. Mater.* **6**, 335.

[32] Elaïssari, A., Bourrel, V. (2001). *J. Magn. Mater.* **225**, 151.

[33] Denkbas, E.B., Kiliçay, E., Birlikseven, C., Öztürk, E. (2002). *React. Funct. Polym.* **50**, 225.

[34] Zhang, Z., Zhang, L., Wang, S., Chen, W., Lei, Y. (2001). *Polymer* **42**, 8315.

[35] Corot, C., Robert, P., Idée, J.-M., Port, M. (2006). *Adv. Drug Deliv. Rev.* **58**, 1471.

[36] LaConte, L., Nitin, N., Bao, G. (2005). *Mater. Today* **8**, 32.

[37] Otsuka, H., Nagasaki, Y., Kataoka, K. (2012). *Adv. Drug Deliv. Rev.* **64**, 246.

[38] Quinn, M., Mills, G. (1994). *J. Phys. Chem.* **98**, 9840.

[39] Longenberger, L., Mills, G. (1995). *J. Phys. Chem.* **99**, 475.

[40] Henglein, A., Ershov, B.G., Malow, M. (1995). *J. Phys. Chem.* **99**, 14129.

[41] Keita, B., Nadjo, L., De Cointet, C., Amblard, J. (1996). *J. Chem. Phys. Lett.* **249**, 297.

[42] Strelow, F., Fojtik, A., Henglein, A, (1994). *J. Phys. Chem.* **98**, 3032.

[43] Ershov, B.G. (1994). *Russ. Chem. Bull.* **43**, 16.

[44] Bradley, J.S., Hill, E.W., Chaudret, B., Duteil, A. (1995). *Langmuir* **11**, 693.

[45] Nakao, Y. (1995). *Colloid Interface Sci.* **171**, 386.

[46] Prime, K.L., Whitesides, G.M. (1991). *Science* **252**, 1164.

[47] Lewis, L. (2000). *Colloids Surf. B* **18**, 261.

[48] Harder, P., Grunze, M., Dahint, R. (1998). *J. Phys. Chem. B* **102**, 426.

[49] Szleifer, I. (1997). *Curr. Opin. Solid State Mater. Sci.* **2**, 337.

[50] Katira, P., Agarwal, A., Hess, H. (2008). *Adv Mater.* **20**, 1.

[51] Veronese, F.M., Pasut, G. (2008). *Drug Discov. Today Technol.* **5**, e57.

[52] Wuelfing, W.P., Gross, S.M., Miles, D.T., Murray, R.W. (1998). *J. ACS* **120**, 12696.

[53] Quaroni, L., Chumanov, G. (1999). *J. ACS* **121**, 10642.

[54] Buining, P.A., Humbel, B.M., Philipse, A.P., Verkleij, A.J. (1997). *Langmuir* **13**, 3921.

[55] Nagasaki, Y., Iijima, M., Kato, M., Kataoka, K. (1995). *Bioconjug. Chem.* **6**, 702.

[56] Nagasaki, Y., Ogawa, R., Yamamoto, S., Kato, M., Kataoka, K. (1997). *Macromolecules* **30**, 6489.

[57] Nakamura, T., Nagasaki, Y., Kataoka, K. (1998). *Bioconjug. Chem.* **9**, 300.

[58] Akiyama, Y., Otsuka, H., Nagasaki, Y., Kataoka, K. (2000). *Bioconjug. Chem.* **11**, 947.

[59] Nagasaki, Y. (2008). *Chem. Lett.* **37**, 564.

[60] Nagasaki, Y. (2010). *Sci. Technol. Adv. Mater.* **11**, 1.

[61] Otsuka, H., Akiyama, Y., Nagasaki, Y., Kataoka, K. (2001). *J. ACS* **123**, 8226.

[62] Hadjichristidis, N., Pispas, S., Floudas, G.A. (2003). *Block Copolymers: Synthetic Strategies, Physical Properties, and Applications.* Wiley, Hoboken, NJ.

[63] Zhang, L., Eisenberg, A. (1995). *Science* **268**, 1728.

[64] Antonietti, M., Wenz, E., Bronstein, L., Seregina, M. (1995). *Adv. Mater.* **7**, 1000.

[65] Shen, H., Zhang, L., Eisenberg, A. (1999). *J. ACS* **121**, 2728.

[66] Zhang, Q., Remsen, E.E., Wooley, K.L. (2000). *J. ACS* **122**, 3642.

[67] Discher, D.E., Eisenberg, A. (2002). *Science* **297**, 967.

[68] Jain, S., Bates, F.S. (2003). *Science* **300**, 460.

[69] Wang, X.-S., Arsenault, A., Ozin, G.A., Winnik, M.A., Manners, I. (2003). *J. ACS* **125**, 12686.

[70] Liu, G., Yan, X., Li, Z., Zhou, J., Duncan, S. (2003). *J. ACS* **125**, 14039.

[71] Lim Soo, P., Eisenberg, A. (2004). *J. Polym. Sci. B: Polym. Phys.* **42**, 923–938.

[72] Gref, R., Minamitake, Y., Peracchia, M.T., Trubetskoy, V., Torchilin, V., Langer, R. (1994). *Science* **263**, 1600.

[73] Kwon, G.S., Naito, M., Kataoka, K., Yokoyama, M., Sakurai, Y., Okano, T. (1994). *Colloids Surf. B* **2**, 429.

[74] Allen, C., Maysinger, D., Eisenberg, A. (1999). *Colloids Surf. B* **16**, 3.

[75] Kataoka, K., Matsumoto, T., Yokoyama, M., Okano, T., Sakurai, Y., Fukushima, S., Okamoto, K., Kwon, G.S. (2000). *J. Control. Release* **64**, 143.

[76] Torchilin, V.P. (2001). *J. Control. Release* **73**, 137.

[77] Lavasanifar, A., Samuel, J., Kwon, G.S. (2002). *Adv. Drug Deliv. Rev.* **54**, 169.

[78] Rapoport, N., Pitt, W.G., Sun, H., Nelson, J.L. (2003). *J. Control. Release* **91**, 85.

[79] Jones, M.-C., Ranger, M., Leroux, J.-C. (2003). *Bioconjug. Chem.* **14**, 774.

[80] Riley, T., Heald, C.R., Stolnik, S., Garnett, M.C., Illum, L., Davis, S.S., King, S.M., Heenan, R.K., Purkiss, S.C., Barlow, R.J., Gellert, P.R., Washington, C. (2003). *Langmuir* **19**, 8428.

[81] Francis, M.F., Piredda, M., Winnik, F.M. *J. Control. Release* **93**, 59.

[82] Tang, Y., Liu, S.Y., Armes, S.P., Billingham, N.C. (2003). *Biomacromolecules* **4**, 1636.

[83] Liu, S.Y., Weaver, J.V.M., Save, M., Armes, S.P. (2002). *Langmuir* **18**, 8350.

[84] Simon, P.F.W., Ulrich, R., Spiess, H.W., Wiesner, U. (2001). *Chem. Mater.* **13**, 3464.

[85] Bockstaller, M.R., Mickiewicz, R.A., Thomas, E.L. (2005). *Adv. Mater.* **17**, 1331.

[86] Grubbs, R.B. (2005). *J. Polym. Sci. A: Polym. Chem.* **43**, 4323.

[87] Vaia, R.A., Maguire, J.F. (2007). *Chem. Mater.* **19**, 2736.

[88] Pozzo, D.C., Walker, L.M. (2008). *Eur. Phys. J. E* **26**, 183.

[89] Satomi, T., Ueno, K., Fujita, Y., Kobayashi, H., Tanaka, J., Mitamura, Y., Tateishi, T., Otsuka, H. (2006). *J. Nanosci. Nanotechnol.* **6**, 1792.

[90] Zdyrko, B., Klep, V., Luzinov, I. (2003). *Langmuir* **19**, 10179.

[91] Taylor, W., Jones, R.A.L. (2010). *Langmuir* **26**, 13954.

[92] Otsuka, H., Fukaishi, M., Ishizuka, T., Saito, Y. (2013). *J. Nanosci. Nanotechnol.* **13**, 537.

[93] Otsuka, H., Sanbai, T., Matsukuma, D., Ikenaga, Y. (2014). *Colloid Polym. Sci.* **292**, 291.

[94] Matsukuma, D., Maejima, Y., Ikenaga, Y.Sanbai, T., Ueno, K., Otsuka, H. (2014). *J. Nanosci. Nanotechnol.* **9**, 6774.

[95] Buck, M.R., Schaak, R.E. (2013). *Angew. Chem. Int. Ed.* **52**, 6154.

[96] Zhang, A.-Q., Cai, L.-J., Sui, L., Qian, D.-J., Chen, M. (2013). *Polym. Rev.* **53**, 240.

[97] Wang, L.Y., Cai, L.J., Shen, D., Feng, Y.G., Chen, M., Qian, D.J. (2010). *Progress Chem.* **22**, 580.

67

ON-CHIP ELECTROPHORESIS FOR EVALUATING ZETA-POTENTIAL OF NANOLIPOSOMES

Takanori Akagi and Takanori Ichiki
Department of Bioengineering, Graduate School of Engineering, University of Tokyo

67.1 INTRODUCTION

Liposomes are artificially prepared vesicles composed of a lipid bilayer and are widely used in various fields such as pharmacy, medicine, cosmetics, and the food industry. In recent years, extensive study has been carried out toward their application in drug delivery systems (DDSs), where liposomes are used as smart carriers of encapsulated drugs to disease sites. As a step toward realizing future applications such as DDSs, in which nanoliposomes will be utilized in a more sophisticated manner, the accurate characterization of nanoparticles is becoming increasingly important [1, 2].

The zeta-potential is one of the major physical properties of liposomes that determines the behavior in liquid. As for a liposomal DDS, it appreciably improves the physical stability and dispersibility of liposomes in the blood as well as the interaction of such vesicles with living bodies. Hence, the zeta-potential of liposomes has essential significance in correlation with nanoliposome application. Conventionally, laser Doppler electrophoresis has been the most widely used method for measuring the zeta-potential of nanoparticles [3]. However, it usually measures the intensity and wavelength shift of light scattered by a particle ensemble and cannot be used to evaluate the zeta-potential of individual nanoparticles in principle. Therefore, it is difficult to obtain an accurate zeta-potential distribution for nanoliposomes. Recently, we developed an Electrophoretic mobility (EPM) measurement system for individual nanoliposomes and applied it to comprehensively study the zeta-potential distribution of nanoliposomes [4].

67.2 NANOLIPOSOME PREPARATION

The materials used for the preparation of liposomes were 1,2-dilauroyl-*sn*-glycero-3 (DLPC) as the neutral lipid, L-α-phosphatidylserine (PS) as the anionic lipid, and cholesterol (chol) (Avanti Polar Lipids, Inc., AL, USA). The lipid mixture at an appropriate molar ratio dissolved in chloroform was deposited on a vial by evaporating the organic solvent, and the dried lipid film was then hydrated with phosphate-buffered saline (PBS) (pH=7.4), (GIBCO) containing 50 mM calcein (Kanto Chemical), a fluorescent dye encapsulated in liposomes for imaging. The mixture was incubated at 353 K for 2 h and then vortexed for 5 s. During the preparation, calcein (0.2 mM) was encapsulated in liposomes to enable fluorescent imaging. Subsequently, the liposomes were extruded through a polycarbonate membrane (pore size 50, 200, 400, and 1000 nm) to tailor their sizes [5]. The size distribution of liposomes extruded through different membrane pore sizes was measured using a Zetasizer nano ZS (Malvarn) by dynamic light scattering, and the average EPM of liposomes extruded through 50 nm pore size was measured by laser Doppler electrophoresis to investigate the effect of the composition ratio of the negatively charged PS lipid (Figs. 67.1 and 67.2).

Encyclopedia of Biocolloid and Biointerface Science, Volume 2, First Edition. Edited by Hiroyuki Ohshima.
© 2016 John Wiley & Sons, Inc. Published 2016 by John Wiley & Sons, Inc.

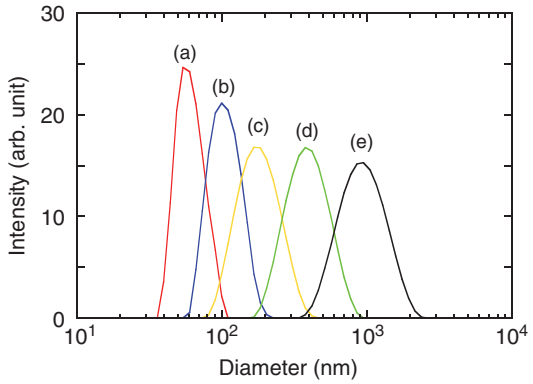


FIGURE 67.1 Size distribution of liposomes extruded through membranes with pore sizes of (a) 50 nm, (b) 200 nm, (c) 400 nm, and (d) 1000 nm.

67.3 ZETA-POTENTIAL MEASUREMENT SYSTEM

Figure 67.3 shows a schematic diagram of the on-chip zeta-potential measurement system. The system comprised a microcapillary electrophoresis (μCE) chip, a pair of platinum electrodes, a high-voltage dc power supply [HVL-1.1P(A), Matsusada Precision Inc., Japan], a 488-nm laser source (50 mW, 85-BCD-030-053, Melles Griot, USA), an inverted microscope (Ti-U, Nikon, Japan), and an EM-CCD camera (iXon3 897, Andor, UK). The details of μCE chip fabrication were described elsewhere [6]. Briefly, a chip made of poly(dimethylsiloxane) (PDMS) was fabricated by soft lithography. It was equipped with a microfluidic channel (length 1 cm; width 100 μm; height 50 μm) with reservoir tanks on both ends. To suppress nonspecific adsorption and electroosmotic flow, the inner surface of the microchannel was coated with 2-methacryloyloxyethylphosphorylcholine (MPC) polymer.

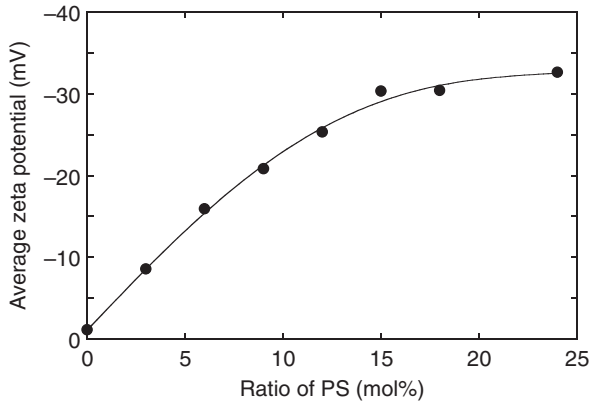


FIGURE 67.2 Average EPM of liposome measured by the PALS method as a function of lipid (PS) composition ratio.

The electrodes used to apply voltage were placed in the reservoir tanks of the μCE chip mounted on the inverted microscope. Fluorescence from individual liposomes excited by laser light was detected using an EM-CCD camera, which enabled the sensitive imaging of individual nanoliposomes.

67.4 CALCULATION OF ZETA-POTENTIAL OF LIPOSOMES

Liposomes suspended in PBS (pH=7.4, ionic strength 0.16) were introduced into the flow channel of the μCE chip, and the electrophoretic migration of liposomes was recorded while an electric field of 100 V/cm was being applied. Since the measured velocity of the migrating liposomes includes the electroosmosis velocity weakly observed in the microchannel, the true EPM of the liposomes was calculated using

$$\mu_{ep} = (U_{em} - U_{eo})/E \tag{67.1}$$

where μ_{ep} is the true EPM, U_{em} is the apparent electrophoretic velocity, U_{eo} is the electroosmotic flow velocity, and E is the electric field strength (V/cm). Electroosmosis velocity was measured by suspending charge-free beads of 500 nm diameter (Otsuka Electronics) in the electrophoresis buffer in the control experiment. According to the Henry equation, the EPM at low zeta-potentials (< 25 mV) can alternatively be given by

$$\mu_{ep} = \frac{\varepsilon_r \varepsilon_0 \zeta}{\eta} f(\kappa R) \tag{67.2}$$

where, ζ is the zeta-potential, η is the viscosity coefficient of the buffer solution, ε_r and ε_0 are the relative permeability of the solution and the permeability of vacuum, and $f(\kappa R)$ is Henry's function, in which κ, the Debye–Hückel parameter, is the reciprocal of the electric double-layer thickness, and R is the radius of the particle. Since the thickness of the electric double-layer in our experiments was approximately 0.8 nm, when R is a few hundreds of nanometers ($\kappa R \gg 1$), Henry's function is approximately 1.5; therefore, Smoluchowski approximation is applicable. However, for more accurate evaluation of Henry's function for a smaller R ($R < 100$ nm), we used the following formula derived by Ohshima to evaluate $f(\kappa R)$, which results in relative errors within 1% [7]:

$$f(\kappa R) = \frac{2}{3}\left[1 + \frac{1}{2[1 + 2.5/\{\kappa R(1 + 2\exp(-\kappa R))\}]^3}\right] \tag{67.3}$$

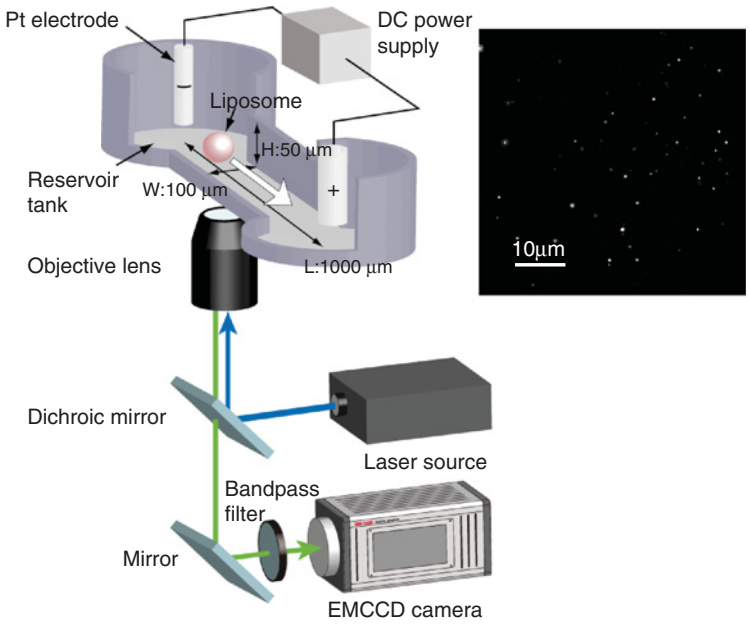


FIGURE 67.3 Schematic diagram of on-chip zeta-potential measurement system for nanoliposomes (left). Fluorescence microscopy image of nanoliposomes (extruded through filters with 50 nm pore size) in microchannel (right).

67.5 CAPILLARY ELECTROPHORESIS OF LIPOSOMES

Individual liposomes of different sizes were measured by on-chip electrophoresis. The sensitive fluorescence imaging system employed in this study enabled the direct observation of the electrophoretic migration of individual nanoliposomes. The histograms in Fig. 67.4 show the zeta-potential of liposomes prepared by extrusion through polycarbonate membranes with pore sizes of (a) 50 nm, (b) 100 nm, (c) 200 nm, (d) 400 nm, and (e) 1000 nm. Interestingly, although the averages are almost the same regardless of particle size, the apparent broadening of the zeta potential distribution was observed for the case of (a) 50 nm. In fact, the nanoliposomes extruded with a pore size of 50 nm showed a standard deviation approximately twofold that of the liposomes extruded with a pore size of 1000 nm.

From these data, we plotted the relationship between the average liposomal diameter and the standard deviation of EPM in Fig. 67.5 (solid circles) and found a size-dependent

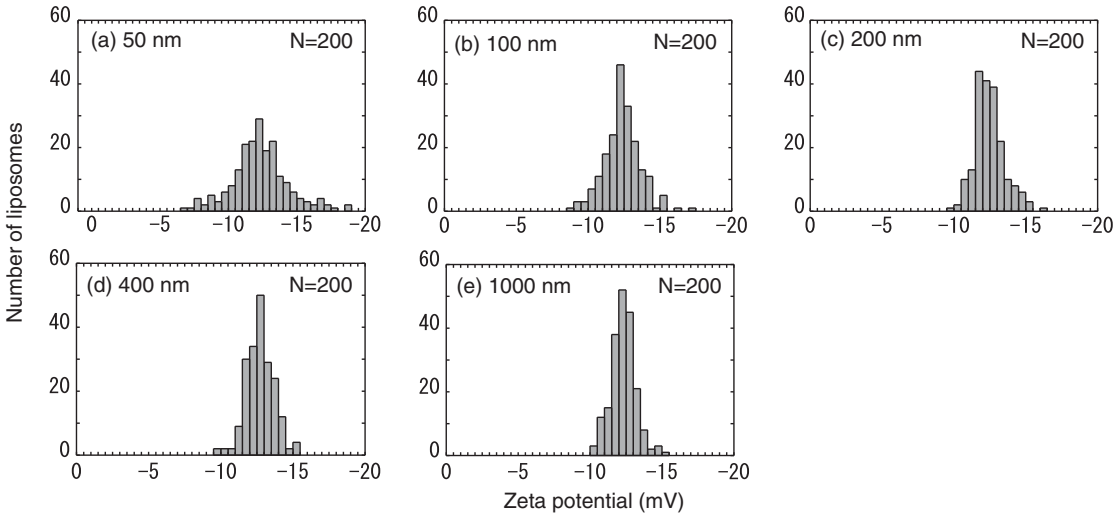


FIGURE 67.4 Zeta-potential distribution of liposomes of different sizes. The liposomes were extruded through membranes with pore sizes of (a) 50 nm, (b) 100 nm, (c) 200 nm, (d) 400 nm, and (e) 1000 nm. The liposomes were composed of DLPC:PS:Chol at molar ratio 5.55:0.45:4.00.

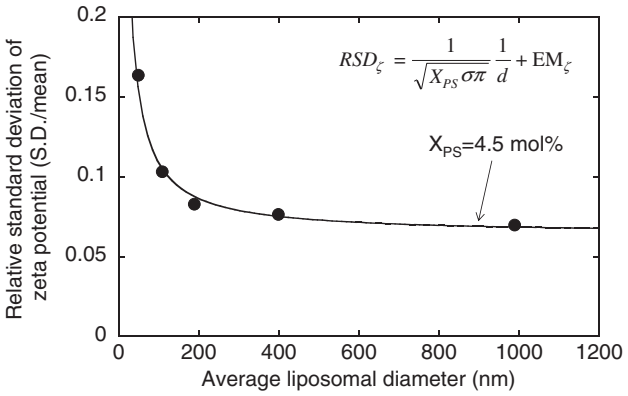


FIGURE 67.5 Relationship between average liposomal diameter and relative standard deviation of zeta-potential. Closed circles show experimental data. The solid line is a fitted curve obtained using the inverse curve given by Eq. (67.4). The curve was fitted by least-squares approximation using the experimental value of 4.5 mol% for the nominal composition of PS molecules, X_{PS}. The best-fit values of σ and EM_ζ are 0.41 nm^{-2} and 0.064, respectively.

broadening of the EPM distribution of nanoliposomes. We will now discuss the theoretical prediction of the zeta-potential distribution, considering this statistical fluctuation of anionic lipid PS molecules. Since the relative standard deviation of the zeta-potential RSD_ζ of nanoliposomes is expected to be the sum of the inherent deviation formulated above and other error margins EM_ζ that do not depend on liposomal diameter, it is expressed by the following equation and is inversely proportional to liposomal diameter:

$$RSD_\zeta = \frac{1}{\sqrt{X_{PS}\sigma\pi}}\frac{1}{d} + EM_\zeta \qquad (67.4)$$

Here, X_{PS} is the molar ratio of PS, d is the liposomal diameter, and σ is the surface density of lipid molecules. The solid line is the curve fitted using the inverse function given by Eq. (67.4). The curve was fitted by least-squares approximation using the experimental value of 4.5 mol% for the nominal composition of PS molecules, X_{PS}. From this curve fitting, σ and EM_ζ are obtained as 0.41 nm^{-2} and 0.064, respectively.

67.6 CONCLUSION

The zeta-potential measurement system that combines on-chip μCE with sensitive fluorescence imaging using an EM-CCD camera was developed to evaluate the electrokinetic behavior of individual nanoparticles, and was applied to a comprehensive study of the zeta-potential distribution of ternary-component nanoliposomes.

REFERENCES

[1] Jingkun, J., Oberdorster, G., Biswas, P. (2009). *J. Nanopart. Res.* **11**, 77–89.

[2] Powers, K.W., Brown, S.C., Krishna, V.B., Wasdo, S.C., Moudgil, B.M., Roberts, S.M. (2006). *Toxicol. Sci.* **90**, 296–303.

[3] Barchini, R., van Leeuwen, H.P., Lyklema, J. (2000). *Langmuir* **16**, 8238–8247.

[4] Kato, K., Koido, M., Kobayashi, M., Akagi, T., Ichiki, T. (2013). *Electrophoresis* **34**, 1212–1218.

[5] Zhu, T.F., Szostak, J.W. (2009). *PLoS ONE* **4**, e5009.

[6] Akagi, T., Ichiki, T. (2008). *Anal. Bioanal. Chem.* **391**, 2433–2441.

[7] Ohshima, H. (1994). *J. Colloid Interface Sci.* **168**, 269–271.

68

PHASE SEPARATION IN PHOSPHOLIPID BILAYERS INDUCED BY CHOLESTEROL

Nobutake Tamai, Masaki Goto, and Hitoshi Matsuki
Department of Life System, Institute of Technology and Science, The University of Tokushima, Tokushima, Japan

68.1 INTRODUCTION

Phospholipids are amphiphiles and self-assemble in the presence of excess water to form molecular aggregates of closed bilayer membranes, which are generally called *vesicles* or *liposomes*. Phospholipid vesicles provide the structural basis of biological membranes, or biomembranes, and therefore, various types of artificial phospholipid vesicles have long been used as models of the biomembranes to investigate their physicochemical properties and fundamental structure.

Dipalmitoylphosphatidylcholine (C16PC) is one of the phospholipid species that have most frequently been used in model membrane studies [1], and the structure and properties of the C16PC bilayer have been thoroughly investigated using various physical techniques, such as X-ray diffraction [2,3], differential scanning calorimetry (DSC) [4,5], nuclear magnetic resonance (NMR) [6], fluorescence spectroscopy [7, 8], and density measurements [9, 10]. It is well known that the C16PC bilayer exhibits several types of structural changes (i.e., phase transitions) with the variation in its surrounding conditions; for example, it undergoes the transition from the lamellar gel ($L_\beta{}'$) phase to the ripple gel ($P_\beta{}'$) phase (i.e., pretransition) and subsequently the transition from the $P_\beta{}'$ phase to the liquid–crystalline (L_α) phase (i.e., main transition) with the rise in temperature. Now we have ample information about the bilayer phase behavior of various kinds of phospholipids [11], which provides a deeper understanding of how the variation in the chemical structure of the constituent phospholipid molecules alters the bilayer phase behavior.

As a recent trend in model membrane studies, use of multicomponent phospholipid bilayer membranes containing cholesterol has increased [12, 13]. This recent trend is not due simply to the fact that cholesterol is a major component of animal cell membranes but is largely due to the proposal of a new concept that describes the structure and functions of the cell membrane [14]. According to this concept, there exist microdomains composed of specific kinds of phospholipids and cholesterol (i.e., *lipid rafts*) within the cell membrane, and signaling membrane molecules are localized in the microdomains. This means that the microdomains are essentially relevant to biological functions of the cell membrane, such as protein sorting [14] and signal transduction [15]. As a result, the significance of cholesterol within the cell membrane is highlighted as one of the key components directly related to the formation of the microdomains within the membrane. To state this boldly, a cholesterol-containing multicomponent phospholipid bilayer is preferable as a more "realistic" model of the biomembrane.

To date, a large number of basic studies have been performed to investigate the biophysical and biochemical properties of cholesterol-containing phospholipid bilayers, and many of the outcomes from those model membrane studies underpin the lipid raft concept. For example, the domain formation, which is a significant characteristic of the lipid raft concept, can be rationalized by the fact that cholesterol incorporated into a phospholipid bilayer has a propensity to induce phase separation within the bilayer. In fact, some relatively recent studies using various visualization techniques [16–18] have demonstrated the formation of domains due to

Encyclopedia of Biocolloid and Biointerface Science, Volume 2, First Edition. Edited by Hiroyuki Ohshima.
© 2016 John Wiley & Sons, Inc. Published 2016 by John Wiley & Sons, Inc.

the heterogeneous distribution of the constituent lipids within cholesterol-containing ternary model membranes. However, the physical and chemical origin of the heterogeneous distribution induced by cholesterol has not been completely elucidated yet. This means that further basic studies are still needed to obtain a full understanding of the cholesterol effect on the lateral organization of the phospholipid bilayer.

A compositional phase diagram of a cholesterol-containing binary bilayer (i.e., temperature (T)–cholesterol mole fraction (X_{ch}) phase diagram) provides a strong basis for studying the lateral organization of the binary bilayer. It also provides useful information about the cholesterol–phospholipid interaction within the bilayer in terms of thermodynamics, because in general the shape of the compositional phase diagram of a binary system is influenced by the affinity (or miscibility) between the two components. We have recently reported on the T–X_{ch} phase diagrams for the cholesterol-containing binary bilayers of a series of linear saturated diacylphosphatidylcholines (CnPCs) with different acyl chain length n (n = 14–18) [19–21] and also proposed a molecular picture of the distribution of cholesterol within the CnPC–cholesterol binary bilayers that can be deduced from the phase diagrams by taking several known effects of cholesterol into account. In this chapter, we describe the effect of cholesterol on the lateral organization of the CnPC bilayers on the basis of these recent studies and also discuss how the thermodynamic features of the phase diagrams are influenced by the variation in the acyl-chain length of the host PC molecule. In addition, we also give a brief overview of the historical background of the model membrane studies on the phase behavior of phospholipid–cholesterol binary bilayers to review previous studies on this subject and also a simple explanation of solid–liquid phase equilibria for binary mixtures.

68.2 HISTORICAL BACKGROUND

The physical and chemical properties and structure of cholesterol-containing phospholipid model membranes have been studied for almost 50 years. Especially in the first two decades, many such fundamental studies focused on the characterization of the molecular properties of cholesterol and phospholipids within the bilayer, and a wide variety of the experimental techniques were used in those studies, such as NMR [22–28], electron paramagnetic resonance (EPR) [29–32], X-ray or neutron scattering [33–36], DSC [32, 33,37–39], fluorescence techniques [40–42] and freeze fracture electron microscopy [42–45]. These earlier studies provided the physicochemical basis necessary for understanding the behavior of cholesterol within the bilayer at the molecular level, which revealed several key features of the cholesterol-containing phospholipid bilayer. For example, cholesterol decreases the membrane fluidity (i.e., lateral diffusion of lipid molecules within the bilayer) above the main transition temperature, whereas it increases the fluidity below that temperature. Another significant feature is that the orientational order of the phospholipid hydrocarbon chains is enhanced by the presence of cholesterol above the main transition temperature. Some review articles [46,47] are also helpful in reviewing earlier studies on this subject. From the viewpoint of phase behavior, these features can be interpreted as signifying that cholesterol has a propensity to induce an "intermediate" state between the gel and the L_α states and thereby to stabilize the bilayer structure on the whole.

On the other hand, earlier attempts to elucidate how cholesterol affects the lateral organization of the phospholipid bilayer do not seem to have been successful. For this purpose, considerable efforts were made to determine the phase diagram of the cholesterol-containing binary bilayer, but the phase diagrams reported in earlier studies [32,41,42,48] were not sufficiently consistent with one another to give a unified picture explaining the cholesterol effect on the lateral organization of the bilayer successfully. A major reason for this is the experimental difficulty in determining the transition temperatures accurately for a phospholipid–cholesterol binary bilayer with relatively higher cholesterol content, because the thermotropic bilayer phase transitions tend to be obscured with increasing content of cholesterol in the binary bilayer owing to the abovementioned propensity of cholesterol to induce an intermediate state.

A breakthrough was achieved by Ipsen et al. [49], who predicted the phase boundaries of the binary bilayer of C16PC and cholesterol by theoretical calculation based on a thermodynamic and a simple microscopic model. Although the phase diagram they presented was not experimental, it could explain several major cholesterol effects that had been already known, and it also indicated several significant features of the thermotropic phase behavior of the phospholipid–cholesterol binary bilayer, most of which are universally accepted today. For example, they identified the phase state of the binary bilayer with a higher cholesterol content ($X_{ch} > \sim 0.3$) as a third phase that was distinguishable from the solid ordered (S_o) phase, including the L_β' and the P_β' phase, and the liquid disordered (L_d) phase like the L_α phase. This third phase was termed *liquid ordered* (L_o) *phase* by taking into account the characteristics of this phase, namely, higher conformational order of the acyl chains and relatively faster lateral diffusion. In addition, they revealed that there is a two-phase region due to the miscibility gap between the L_d and L_o phases in an intermediate cholesterol composition region of the phase diagram, which means that the incorporation of the corresponding amount of cholesterol induces phase separation. Today, this cholesterol-induced phase separation is considered to be a physicochemical basis for rationalizing the formation of the microdomains within the biomembrane. A few years later, Vist and Davis [50] reported an experimental phase diagram of the perdeuterated

C16PC (d_{62}-C16PC)–cholesterol binary bilayer determined by means of ^{2}H NMR and DSC. Their experimental phase diagram was qualitatively very similar to their theoretical phase diagram. This qualitative agreement between the theoretical prediction and the experimental result strongly supported the validity of the theoretical consideration by Ipsen et al. [49], and at the same time, enhanced the reliability of the experimental phase diagram. For this reason, these theoretical and experimental phase diagrams were widely accepted as among the most reliable phase diagrams for the cholesterol-containing binary bilayer.

After that, numerous compositional phase diagrams of cholesterol-containing binary bilayers were reported for various kinds of phospholipid, such as dimyristoyl-PC (C14PC) [51] and unsaturated PCs [52]. It is interesting that most of them indicated some common features regarding the effect of cholesterol on the bilayer phase behavior; for example, the L_o phase is formed at higher cholesterol compositions and the two-phase state consisting of the L_o phases and the L_d (or S_o) phase is observed at intermediate cholesterol compositions above (or below) the main-transition temperature. A more recent review [53] is very helpful in considering these common features, where many of the phase diagrams that have so far been reported for various kinds of cholesterol-containing binary bilayers are collected together to compare and contrast those obtained by different experimental techniques. On the other hand, it has been also pointed out in this review that there is incomplete agreement between different determinations of the phase diagrams for the same binary bilayer. In fact, several dissimilar phase diagrams of the C16PC–cholesterol binary bilayer [54–56] have so far been reported even after that of the same system given by Vist and Davis [50] was widely accepted. This implies that the phase behavior of the cholesterol-containing binary bilayer has not been completely elucidated yet and that there are still some issues that need to be investigated for the complete elucidation.

One of those issues is how the thermotropic phase behavior of cholesterol-containing binary bilayers is affected by the variation in the chemical structure of the constituent phospholipid molecule. In order to clarify this, systematic investigations for binary bilayers of various phospholipids with cholesterol are indispensable. Another group has systematically studied the effect of cholesterol on the thermotropic bilayer phase transitions of various kinds of phospholipids [57–61] by means of high-sensitivity DSC and Fourier transform infrared spectroscopy (FT-IR) in detail. Their extensive studies have clearly revealed how the effects of cholesterol on thermodynamic properties of the bilayer phase transitions (e.g., transition temperatures and transition enthalpies) depend on the chemical structure of the host phospholipid and also found that those cholesterol effects can be classified into two types in terms of whether the effect is dependent on or independent of the acyl chain lengths of the host phospholipid molecules. Their studies, however, did not show how thermodynamic features of the phase diagram of the cholesterol-containing binary bilayers change with variations in the chemical structure of the constituent phospholipid, because the main aim of their studies was not to construct the phase diagrams. To our knowledge, the only study that has addressed this issue is that of Huang et al. [54] (see also Ref. 62), who investigated the phase behavior of cholesterol-containing binary bilayers of C16PC, distearoyl-PC (C18PC), and diarachidoyl-PC (C20PC) by means of solid-state NMR and high-sensitivity DSC to construct the phase diagrams of those binary bilayers excluding the C20PC–cholesterol binary bilayer. Although their phase diagram of the C16PC–cholesterol binary bilayer is essentially different from that of the same binary bilayer given by Vist and Davis [50], it can be directly compared to their own result for the C18PC–cholesterol binary bilayer to deduce what effect the difference in the acyl chain length has on the phase behavior of those binary bilayers. This means, as was emphasized in their paper, that examination of just one lipid species, such as C16PC, is insufficient and that a variety of phospholipids must be sampled to determine the overall trend.

It should be also mentioned that although some cholesterol effects directly related to the lateral organization of the binary bilayer and the distribution of cholesterol within the binary bilayer (e.g., condensation effect and the formation of cholesterol–phospholipid complexes [30,37,39,46,63–70]) have been well known, it has not been fully clarified how relevant this type of cholesterol effects are to the overall phase behavior of cholesterol-containing binary bilayers. This may be due to the fact that quantitative features of the phase diagram have been regarded as comparatively less significant while the qualitative similarities, as described above, were often emphasized, although those cholesterol effects are expected to be reflected in quantitative features of the phase diagram, especially with respect to the cholesterol composition. In order to clarify this relevance, therefore, it is important to determine quantitative characteristics of the phase behavior of the binary bilayers on the basis of the phase diagram.

68.3 SOLID–LIQUID PHASE DIAGRAMS OF BINARY MIXTURES

A solid–liquid phase diagram for a binary mixture is very useful for understanding the melting/freezing behavior of the mixture. It also helps us to predict the microscopic structure of the mixture in the solid state. We will briefly explain the significant features of typical solid–liquid phase diagrams of binary mixtures, along with the terminology, in terms of thermodynamics of the solid–liquid phase equilibria.

Figure 68.1a depicts the liquid–solid phase diagram of an ideal binary mixture of components A and B, which are

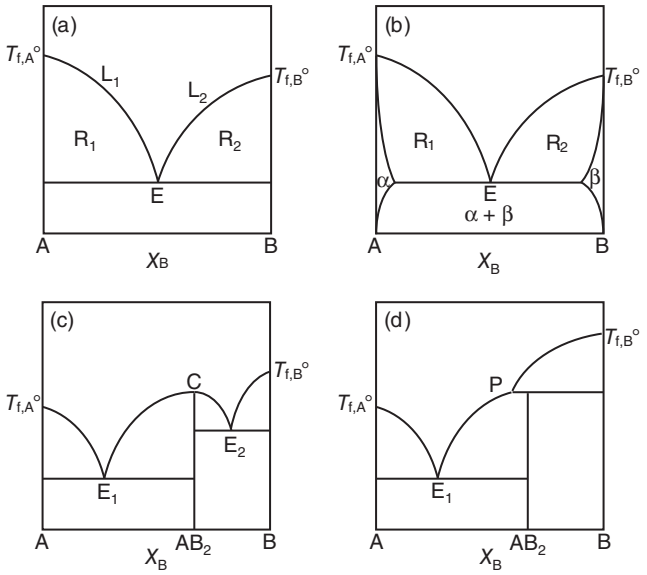


FIGURE 68.1 Typical solid–liquid phase diagrams for various types of binary mixtures: (a) a eutectic ideal binary mixture; (b) a eutectic binary mixture where the two components of A and B are partially miscible in a solid state; (c) a binary mixture that exhibits congruent melting behavior; (d) a binary mixture that exhibits incongruent melting behavior.

completely miscible in all proportions in the liquid phase (i.e., perfect solution) and completely immiscible in the solid state. The phase boundary labeled L_1 (or L_2) is the freezing-point–depression curve of A (or B) due to B (or A), given by the following relation between $T_{f,A}$ and X_B (for L_1):

$$\ln\left(1 - X_B\right) = \frac{\Delta H^\circ_{fus,A}}{R}\left(\frac{1}{T_{f,A}} - \frac{1}{T^\circ_{f,A}}\right) \qquad (68.1)$$

Here, X, ΔH_{fus}, T_f, and R are mole fraction, molar enthalpy of fusion, freezing-point temperature, and the gas constant, respectively. The superscript ° and the subscripts A and B denote quantities for pure substances and for components A and B, respectively. When a liquid solution of A and B with a given composition is cooled to $T_{f,A}$ (or $T_{f,B}$), pure solid A (or B) begins to freeze out, giving a two-phase region (i.e., region R_1 or R_2) in which pure solid A (or B) and a liquid solution coexist in equilibrium. Therefore, L_1 (or L_2) is a phase boundary that separates a liquid phase and a solid-containing phase and is called *liquidus*. The two liquidus lines L_1 and L_2 intersect at point *E*. This characteristic point is called a *eutectic point*. Below the eutectic temperature, both components exist as pure solids A and B independent of the composition, which means that the region below the horizontal line passing through the eutectic point corresponds to a two-phase region in which pure solids A and B coexist in equilibrium.

When components A and B are partially miscible in the solid state, the phase diagram of the binary mixture resembles Fig. 68.1b, in which there are three different solid-phase regions, each of which is labeled α, β, or α + β. The α and β phases correspond to solid solutions of B in A and of *A* in *B*, respectively. The α + β region corresponds to the two-phase region in which the saturated solid solutions of B in A and of A in B coexist in equilibrium. The boundaries that separate these three different solid phases are called *solvus*, and the boundary between α and the R_1 region, as well as that between β and the R_2 region, is called *solidus*. The presence of solidus and solvus lines in a binary phase diagram signifies that both components are partially miscible in the solid phase.

As is often the case with binary alloys and hydrated crystals, the two components A and B interact to produce a solid compound with a certain stoichiometry in the mixture. As typical examples, Figure 68.1c,d shows the compositional phase diagrams of the binary mixtures where the solid compound of AB_2 is formed. The common feature of these phase diagrams is that there is an isopleth (i.e., a vertical line) at $X_B = 0.67$, corresponding to the stoichiometric composition of AB_2, in each diagram. In the case of Figure 68.1c, when solid compound AB_2 is heated, it melts at the temperature of point C to give a liquid solution of A and B with the mixing composition equal to the stoichiometric composition of AB_2 (i.e., $X_B = 0.67$). This means that point C is the melting point of solid AB_2 and is called a *congruent melting point* in general. The overall melting/freezing behavior can be easily understood by regarding the phase diagram of Fig. 68.1c as consisting of two simple eutectic diagrams of A–AB_2 and AB_2–B mixtures adjacent to each other. When the melting point of pure solid B is much higher than that of solid compound AB_2, the freezing-point–depression curve of B (curve BE_2) no longer intersects the right-hand freezing-point–depression curve of AB_2 (curve CE_2), yielding a phase diagram of the type shown in Fig. 68.1d. In this diagram, the eutectic point between AB_2 and B and the congruent melting point disappear, and instead a new characteristic point (point P) occurs. This point is called a *peritectic point*. In this case, when solid AB_2 is heated, it begins to melt at the same temperature as that of point P to produce a liquid solution of A and B, and at the same time, pure solid B, which can coexist with the liquid solution in equilibrium, is also formed. The mixing composition of the resulting liquid solution is given by the composition of point P, which is obviously not equal to the stoichiometric composition of AB_2. For this reason, point P is also called an *incongruent melting point*. Qualitatively, the phase diagram of this type is not difficult to understand, because it is essentially the same as the congruent-melting type phase diagram (Fig. 68.1c) except that the increase in the melting temperature of pure solid B elevated the eutectic line between AB_2 and B along with the two-phase region between liquid solution and pure solid B in Fig. 68.1c, and as a result, eliminates

the right-hand two-phase region between AB_2 and liquid solution.

68.4 PHASE TRANSITIONS OF C*n*PC–CHOLESTEROL BINARY BILAYERS

In our studies, DSC and fluorescence spectroscopy using Prodan [6-propionyl-2-(dimethylamino)naphthalene] as a probe were utilized to determine the transition temperatures of a series of C*n*PC–cholesterol binary bilayers. DSC has often been used in many previous studies on the thermotropic phase behavior of phospholipid bilayers because of its high sensitivity to energetic thermotropic events such as conformational changes of the acyl chains of phospholipid molecules. On the other hand, Prodan is a polarity-sensitive fluorescent probe [71] and has a good potential as a membrane probe for investigating surface properties of phospholipid bilayers [72–84]. The emission spectrum of Prodan changes sensitively in response to the variation in the microenvironmental polarity around the probe molecule, and the bilayer phase transition can be detected from the spectral change. It has been also reported that the Prodan fluorescence technique is adequately applicable to cholesterol-containing phospholipid binary bilayers [78,81]. Thus, the combined use of these two complementary techniques enables us to investigate the phase transitions of the C*n*PC–cholesterol binary bilayers in detail from different aspects.

68.4.1 Prodan Fluorescence Spectra of Pure and Cholesterol-Containing C*n*PC Bilayers

Figure 68.2a shows the Prodan fluorescence spectra obtained for the pure C16PC bilayer at different temperatures ranging from 20°C to 55°C. It can be seen from these spectra that every spectrum has a unique local emission maximum, and that the wavelength at the maximum (λ_{max}) tends to shift toward higher wavelengths as the temperature is elevated. This spectral change is attributable to the thermotropic phase transitions (i.e., pretransition and main transition) of the C16PC bilayer, which can be clearly understood from the temperature dependence of λ_{max}, shown in Fig. 68.2b. The λ_{max} value changes from ~440 nm to a slightly higher wavelength around 34°C and sharply increases to nearly 490 nm at ~42°C. These temperatures are almost equal to those of the pretransition and main transition of the C16PC bilayer [4, 5]. Our previous study [27] has shown that there is a positive correlation between the λ_{max} value and the polarity of the solvent in which Prodan is dissolved. In addition, it is well known that the polarity inside the phospholipid bilayer membrane steeply decreases with the bilayer depth from the surface to the midplane along the longer axis of the constituent phospholipid molecule, as depicted by the zone model given by Okamura and Nakahara [85]. Taking these facts into account, the λ_{max} change with the bilayer phase transition is considered to be due to the relocation of the Prodan molecules in the bilayer depth direction caused by the change in the bilayer packing state at the transition. A similar λ_{max} change is observed for other C*n*PC bilayers, although the magnitude of the λ_{max} shift at the pretransition tends to be smaller as the acyl chain length becomes shorter. This can be roughly interpreted as follows: λ_{max} values of approximately 440 and 490 nm in the Prodan fluorescence spectra signify an ordered and a disordered membrane state, respectively.

There is another way to characterize the variation in the Prodan fluorescence spectra with the bilayer transitions. Since the wavelengths of 440 and 490 nm are characteristic wavelengths, the fluorescence intensities at those wavelengths, namely F_{440} and F_{490}, can be used as measures of the order of the bilayer packing state. Figure 68.2c

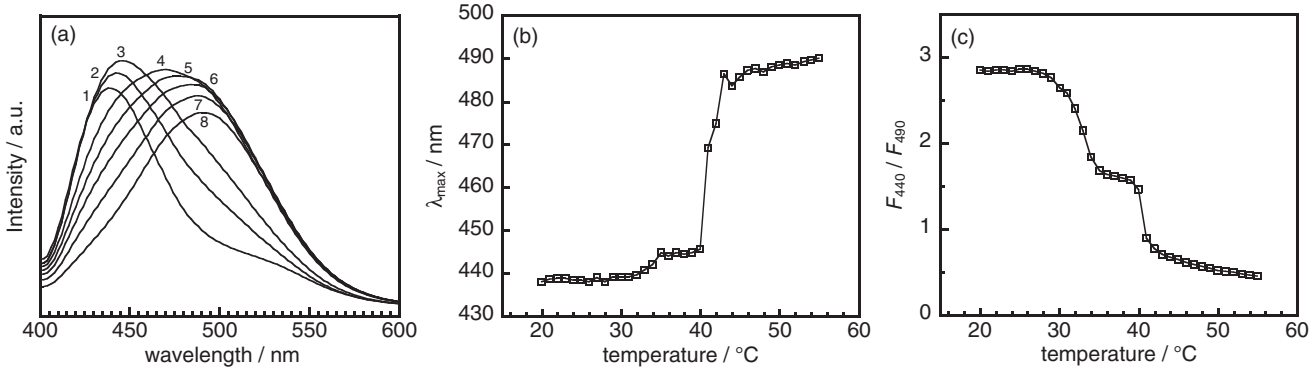


FIGURE 68.2 (a) Emission spectra of Prodan in C16PC bilayer at various temperatures: (1) 27.9°C, (2) 33.9°C, (3) 39.9°C, (4) 40.9°C, (5) 41.9°C, (6) 43.9°C, (7) 47.9°C, (8) 54.9°C. (b) Temperature dependence of wavelength at the maximum emission (λ_{max}) for C16PC bilayer. (c) Temperature dependence of ratio of the intensity at 440 nm (F_{440}) to that at 490 nm (F_{490}), namely, F_{440}/F_{490}, for C16PC bilayer.

shows the temperature dependence of the ratio, F_{440}/F_{490}, for the C16PC bilayer. This temperature dependence curve clearly shows two stepwise decreases in the intensity ratio of F_{440}/F_{490} with increasing temperature, which are consistent with the stepwise increases in λ_{max} with increasing temperature. As evident from the consistency, the decreases in F_{440}/F_{490} at a lower and a higher temperature are attributed to the pretransition and the main transition, respectively. Especially, the stepwise change corresponding to the pretransition can be more clearly seen in the temperature dependence curve of F_{440}/F_{490} than in that of λ_{max}. Therefore, the combined use of these two types of the temperature dependence curves allows us to determine the pre- and the main-transition temperatures of the C*n*PC bilayers with more reliability. Note that the intensity ratio F_{440}/F_{490} is too simple to use as a parameter to quantify membrane properties. Generalized polarization (GP) or three-wavelength GP (3wGP), which has been introduced by Parasassi et al. [77, 78], is more suitable as a quantitative parameter. As long as these intensity-based parameters are used only for the purpose of determining the transition temperatures, however, it should make no significant difference in the results what type of intensity-based parameter is used.

Figure 68.3 shows the temperature dependence curves of λ_{max} and F_{440}/F_{490} for the C16PC–cholesterol binary bilayers with different cholesterol compositions (X_{ch}). It can be seen that there is an overall tendency in the temperature dependence curves of λ_{max}: the temperature at which the λ_{max} reaches close to 490 nm moves to higher temperatures as X_{ch} increases, and at the same time, the λ_{max} shift to 490 nm itself becomes a gradual increase occurring in a finite temperature range. An obvious tendency can be seen also in the temperature dependence curves of F_{440}/F_{490}, which corresponds well to the above tendency in those of λ_{max}: the decrease in F_{440}/F_{490} with temperature also becomes gentle progressively with increasing X_{ch}. These tendencies suggest that in the C16PC–cholesterol binary bilayers, the conversion from an ordered state to a disordered state is not a discontinuous change like a first-order phase transition, but rather a continuous transformation process occurring over a finite temperature range. This means that two temperatures, namely, an onset and a completion temperature, can be defined to characterize this process of the conversion in the cholesterol-containing bilayers, whereas the conversion can be characterized by a single temperature (i.e., the main transition temperature) for the pure C16PC bilayer. Similar overall tendencies are also observed for the C*n*PC–cholesterol binary bilayers (n = 14,15,17), which suggests that, similarly, the conversion from the ordered state to the disordered state in these binary bilayers changes from a discontinuous transition to a continuous transformation process by the presence of cholesterol. The thermodynamic origin of the continuous process is explained later on the basis of the compositional phase diagram. On the other hand, the C18PC–cholesterol

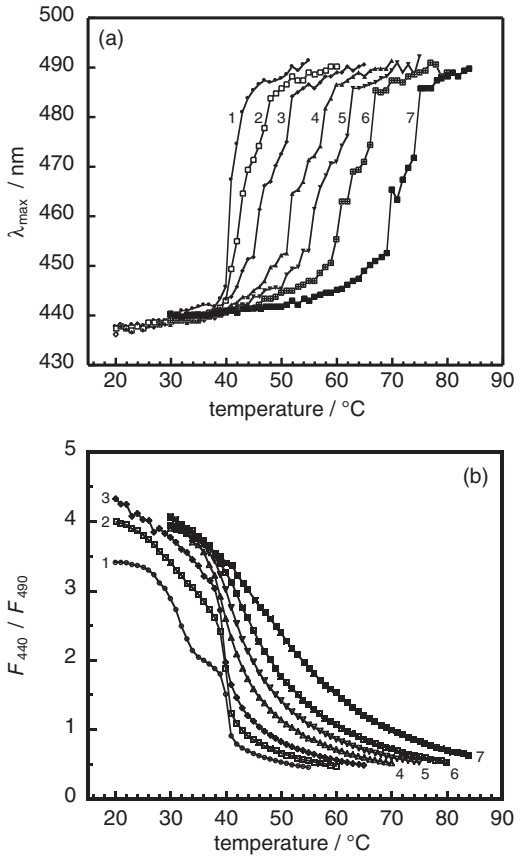


FIGURE 68.3 Temperature dependence of (a) wavelength at the maximum emission (λ_{max}) and (b) ratio of the intensity at 440 nm (F_{440}) to that at 490 nm (F_{490}), specifically, F_{440}/F_{490}, for C16PC–cholesterol binary bilayers at different cholesterol compositions (X_{ch}): (1) X_{ch} = 0.01, (2) 0.05, (3) 0.10, (4) 0.15, (5) 0.19, (6) 0.24, (7) 0.31.

binary bilayer exhibits very slightly different behavior: as X_{ch} increases, initially the temperature range of the process becomes wider, but it becomes narrow once around X_{ch} = 0.1 and then it becomes wider again with increasing X_{ch}. As seen from the phase diagram later, this shrinking of the temperature range around X_{ch} = 0.1 can be interpreted as attributable to the presence of a eutectic point around that cholesterol composition.

68.4.2 Characterization of Phase Transitions of C*n*PC–Cholesterol Binary Bilayers by DSC

Figure 68.4 shows the DSC thermograms of the pure C16PC and the C16PC–cholesterol binary bilayers with different cholesterol compositions. Two endothermic peaks are clearly seen in the thermogram of the pure C16PC bilayer (curve 1), and a small endothermic peak at 34.5°C and a large sharp one at 41.6 °C arise from the pretransition and the main transition, respectively. When cholesterol is incorporated into

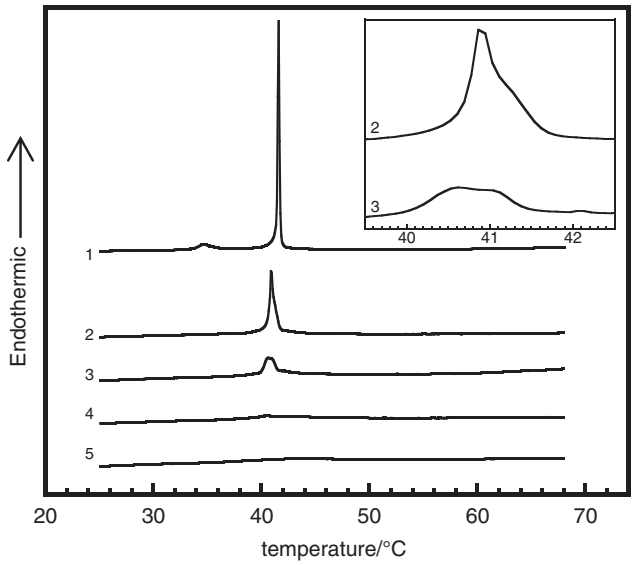


FIGURE 68.4 DSC thermograms of C16PC–cholesterol binary bilayers at different cholesterol compositions (X_{ch}): (1) $X_{ch} = 0$, (2) 0.07, (3) 0.14, (4) 0.20, (5) 0.30. The magnified view of the endothermic peaks of thermograms 2 and 3 are shown in the inset. Each thermogram is vertically shifted appropriately to avoid overlapping one another.

the C16PC bilayer, the endothermic peak of the pretransition becomes smaller with increasing X_{ch} and eventually undetectable above $X_{ch} = 0.08$. This indicates that the pretransition is abolished when the mole fraction of cholesterol within the binary bilayer exceeds at least 0.08. The X_{ch} value at which the pretransition is abolished is slightly different depending on the acyl-chain length n: $X_{ch} = 0.03$–0.035 for C18PC and $X_{ch} = 0.05$–0.06 for C14PC, C15PC and C17PC. The main transition is also affected by the presence of cholesterol within the binary bilayer, which is reflected in the variation in the shape and the size of the endothermic peak with increasing X_{ch}. As X_{ch} increases, the endothermic peak of the main transition gradually increases in width but steeply decreases in height, and as a whole, it becomes smaller. In the case of the C16PC–cholesterol binary bilayer, as seen from Fig. 68.4 (curve 2), the main transition peak is obviously asymmetric at $X_{ch} = 0.07$, signifying that the endothermic peak is composed of at least two component peaks with different heights and widths. At $X_{ch} = 0.14$ (curve 3), the heights of the two component peaks become apparently almost comparable, and only the broad peak remains above $X_{ch} = \sim 0.20$ (curve 4). This broad peak also becomes progressively smaller and markedly broader with further increases in X_{ch} (curve 5) and finally undetectable above $X_{ch} = 0.35$. Qualitatively, the other C*n*PC–cholesterol binary bilayers ($n = 14,15,17,18$) exhibit similar X_{ch}-dependent behavior with respect to the variation in the endothermic peak of the main transition, although there seems to be a tendency for the asymmetry of the main transition peak to become less noticeable in appearance as the acyl chain length becomes longer. Quantitatively, on the other hand, there is a definite difference in the X_{ch} value at which the main transition becomes undetectable as a peak: it can be detected even at $X_{ch} = 0.45$ for the C18PC–cholesterol binary bilayer whereas it becomes undetectable above $X_{ch} = 0.35$ for the remaining C*n*PC–cholesterol binary bilayers ($n = 14$–17).

The main transition temperature T_m and the enthalpy change with the main transition ΔH_m can be determined as the temperature at the peak maximum and as the peak area from the baseline, respectively. The half width of the endothermic peak $\Delta T_{1/2}$, defined as the so-called full width at half height, is also an important property relating to the cooperativity of the transition [86]. Figure 68.5 shows the X_{ch} dependence of ΔH_m, T_m and $\Delta T_{1/2}$ for all the C*n*PC–cholesterol binary bilayers ($n = 14$–18). As seen from Fig. 68.5a, the ΔH_m value decreases almost linearly with increasing X_{ch} and becomes zero at $X_{ch} = 0.45$–0.50 for the C18PC–cholesterol binary bilayer and at $X_{ch} = 0.30$–0.35 for the remaining C*n*PC–cholesterol binary bilayers ($n = 14$–17). As described in Section 68.2, earlier studies established that when cholesterol is incorporated into a phospholipid bilayer it suppresses the thermally induced *trans–gauche* conformational change in the hydrocarbon chains (i.e., chain melting) of the constituent phospholipid molecules with which it interacts. Therefore, the almost linear decrease in ΔH_m with X_{ch} indicates that the population of the C*n*PC molecules that still undergo the chain melting (i.e., main transition) decreases nearly in proportion to the amount of cholesterol incorporated into the bilayer. Furthermore, the fact that ΔH_m becomes zero at $X_{ch} = 0.45$–0.50 (C18PC) or at $X_{ch} = 0.30$–0.35 (C*n*PCs, $n = 14$–17) suggests that no constituent C*n*PC molecules undergo the chain melting in the binary bilayer above $X_{ch} = 0.50$ or 0.35. Conversely speaking, that amount of cholesterol is enough to suppress the *trans–gauche* conformational change in the acyl chains of all the constituent C*n*PC molecules. The difference in those X_{ch} values is discussed in the following section.

The X_{ch} dependence of T_m (Fig. 68.5b) shows that the main transition temperature decreases slightly with increasing X_{ch} in the relatively low X_{ch} region. This tendency is common to all the C*n*PC–cholesterol binary bilayers ($n = 14$–18). The solid lines in Fig. 68.5b represent the freezing-point–depression curves calculated by applying Eq. (68.1). Note that X_B, $\Delta H^\circ_{fus,A}$, $T^\circ_{f,A}$, and $T_{f,A}$ in Eq. (68.1) need to be replaced by X_{ch}, ΔH_m(at $X_{ch} = 0$), T_m(at $X_{ch} = 0$), and T_m, respectively. As described above, Eq. (68.1) is based on the simple thermodynamic concept of solid–liquid phase equilibrium of an ideal binary mixture, and thus assumes several thermodynamically ideal conditions for simplification: (1) the two components are perfectly immiscible in a solid state, (2) the binary mixture behaves as an ideal dilute solution in

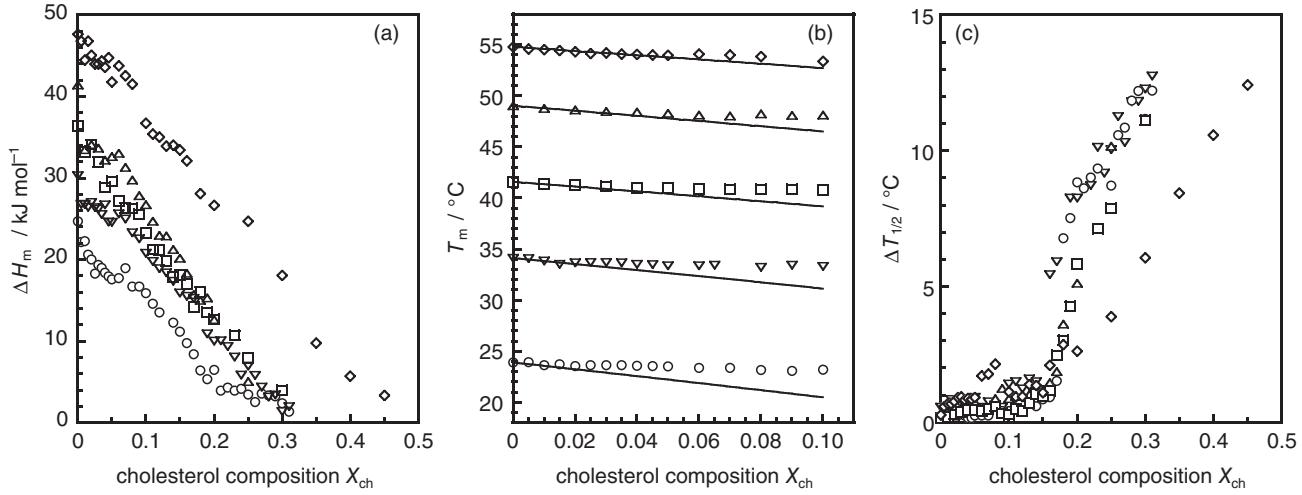


FIGURE 68.5 Cholesterol composition (X_{ch}) dependence of (a) enthalpy change with main transition (ΔH_m), (b) main transition temperature (T_m), and (c) peak width at half height ($\Delta T_{1/2}$) for C*n*PC–cholesterol binary bilayers (n = 14–18): (○) C14PC–cholesterol, (▽) C15PC–cholesterol, (□) C16PC–cholesterol, (△) C17PC–cholesterol, (◇) C18PC–cholesterol binary bilayer. In panel (b), solid lines represent the results of the calculation using the general thermodynamic relation of Eq. (68.1).

a liquid state, and (3) the molar enthalpy of fusion of the solvent in solution is invariant and equal to that of the pure solvent. As seen from Fig. 68.5b, the agreement between the experimental result and the calculated curve is recognized in a very dilute region for all the C*n*PC–cholesterol binary bilayers (n = 14–18). Therefore, these binary bilayers can be regarded as thermodynamically ideal binary mixtures in this dilute region; that is, the C*n*PC and the cholesterol molecules are almost completely immiscible in the P_β' phase while they are almost ideally miscible in the L_α phase. It is also interesting that there is a tendency concerning this dilute region; it extends to higher compositions with an increase in the acyl chain length [$X_{ch} \leq \sim 0.01$ (C14PC), $\leq \sim 0.02$ (C15PC and C16PC), $\leq \sim 0.03$ (C17PC), and $\leq \sim 0.04$ (C18PC)]. This may suggest that the miscibility of cholesterol and C*n*PC in the gel state becomes lower as the acyl chain of the host C*n*PC molecule becomes longer. On the other hand, when X_{ch} exceeds the upper limit of the dilute region, the experimental values begin to deviate from the calculated curve, which may be indicative that cholesterol becomes partially miscible with the C*n*PC bilayers even in the gel phase.

The X_{ch} dependence of $\Delta T_{1/2}$, as shown in Fig. 68.5c, suggests the possible existence of a threshold-like cholesterol composition around $X_{ch} = 0.15$ for all the C*n*PC–cholesterol binary bilayers (n = 14–18). The dependence changes drastically around this composition: the variation in $\Delta T_{1/2}$ with X_{ch} is relatively small in the X_{ch} region below ~0.15, whereas the $\Delta T_{1/2}$ value increases steeply with increasing X_{ch} in the X_{ch} region above ~0.15. The remarkable increase in $\Delta T_{1/2}$ in the higher X_{ch} region is consistent with the results of the Prodan fluorescence measurements; that is, the temperature range where the gradual increase in λ_{max} from 440 to 490 nm is observed becomes noticeably wider with increasing X_{ch} in the X_{ch} region above ~0.15. Therefore, it is reasonable to regard this X_{ch} of ~0.15 as a characteristic cholesterol composition related to some change in the phase behavior of these binary bilayers. Taking into account the fact that the reciprocal of $\Delta T_{1/2}$ is generally related to the cooperativity of the transition, the marked increase in $\Delta T_{1/2}$ in the X_{ch} region above ~0.15 indicates that the intermolecular cooperation when the chain melting occurs is considerably reduced in this X_{ch} region. It is discussed later on the basis of the compositional phase diagram what kind of change in the phase behavior causes the marked reduction in the intermolecular cooperation, but it is interesting that the change commonly occurs at almost the same composition in all the binary bilayers independent of the acyl chain length.

It may be useful to compare the above DSC results with several previous results. The DSC study by McMullen et al. [57] is one of the most systematic studies performed for a homologous series of C*n*PCs (n = 13–21). They have demonstrated that the endothermic peak is composed of a sharp and a broad component and also that the broad component remains until $X_{ch} = \sim 0.50$ while the sharp component fades out in the X_{ch} range between 0.20 and 0.25. In addition, their results showed that the $\Delta T_{1/2}$ value of the broad component increases steeply with increasing cholesterol composition above $X_{ch} = \sim 0.15$ for the C14PC– and the C16PC–cholesterol binary bilayer. Another team [54] also reported that the main transition of the C16PC–cholesterol

binary bilayer is eliminated at $X_{ch} = \sim 0.50$ while those of the C18PC– and the C20PC–cholesterol binary bilayer are not eliminated at the same X_{ch}. Our DSC results are qualitatively consistent with these previous results: the asymmetry of the endothermic peak becomes noticeable in the intermediate X_{ch} region and the $\Delta T_{1/2}$ value increases steeply with increasing X_{ch} in the X_{ch} region above ~0.15. On the other hand, quantitatively, they are not always in agreement with those previous calorimetric studies. With respect to the abolition of the main transition, the X_{ch} values estimated from Fig. 68.5a for these binary bilayers are overall lower than the values reported in those studies. This disagreement is presumably due to the uncertainty in accurately identifying the endothermic peak at higher X_{ch}. It is extremely difficult to determine the onset and the completion temperature accurately without any ambiguity for a broad endothermic peak with small height, especially when the peak height is small as compared to the variation or instability in the baseline. At least, the X_{ch} value estimated from our DSC results for the C16PC–cholesterol binary bilayer is supported by several recent studies using different techniques [87–89] that provide experimental evidence indicating that the homogeneous L_o phase is formed in the C16PC–cholesterol binary system above $X_{ch} = 0.33$.

68.5 PHASE DIAGRAMS OF C*n*PC–CHOLESTEROL BINARY BILAYERS

Figure 68.6 shows possible T–X_{ch} phase diagrams of all the C*n*PC–cholesterol binary bilayers (n = 14–18) constructed on the basis of the experimental results from the Prodan fluorescence and DSC measurements. In appearance, these phase diagrams resembles a typical solid–liquid phase diagram for a binary mixture that exhibits incongruent melting behavior, and this provides the information about important features of the phase behavior of these binary bilayers. First, it can be inferred from the shapes of the phase boundaries that cholesterol and these C*n*PCs are, on the whole, immiscible within the bilayer membranes below the eutectic temperature. Note that this never means the perfect immiscibility as assumed in Eq. (68.1). In fact, a noticeable increase in T_m with X_{ch} is observed in a higher X_{ch} region (X_{ch} > ca. 0.25) for the C*n*PC–cholesterol binary bilayers (n = 14–16). This increase in T_m is considered to correspond to the solidus line on each phase diagram. As described in a previous section, solidus and solvus lines appear in a solid–liquid phase diagram of a binary mixture that can form a homogeneous solid phase like a solid solution within a limited temperature range, whereas no solidus and no solvus lines exist on the solid–liquid phase

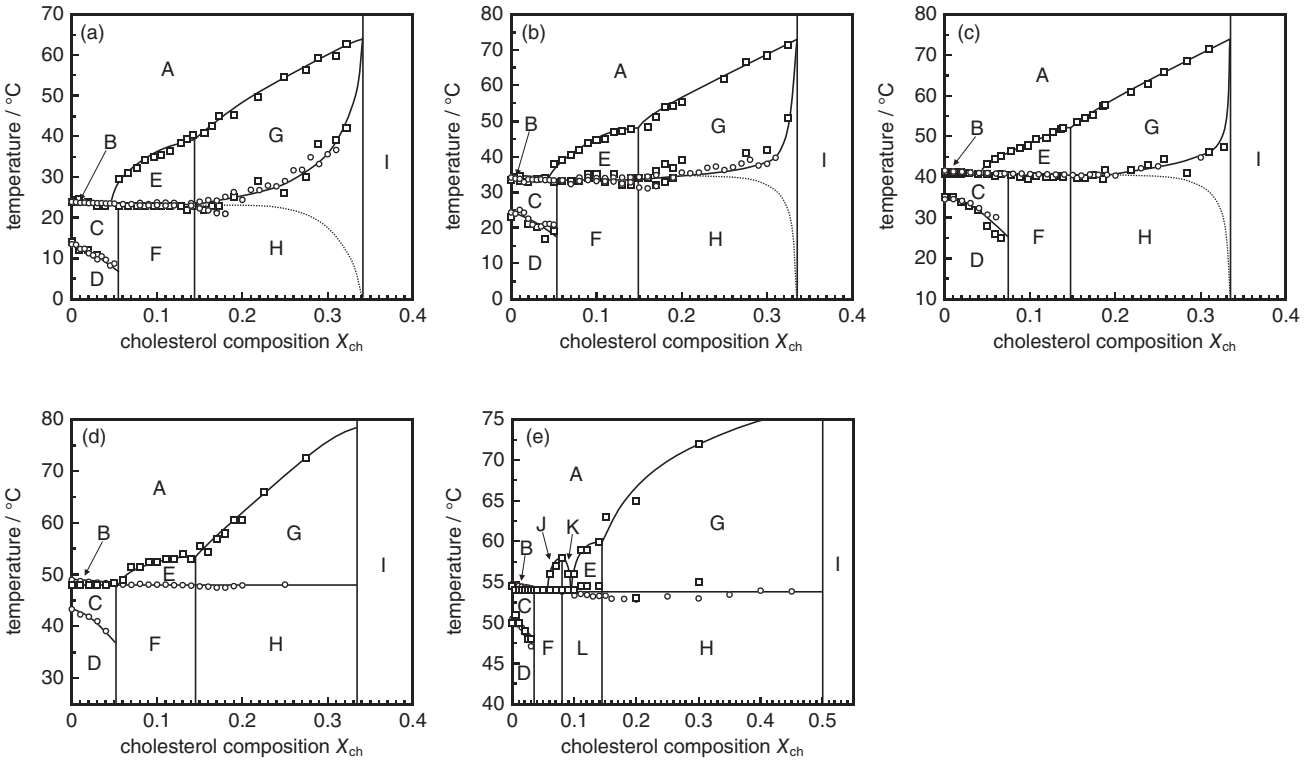


FIGURE 68.6 Temperature (T)–cholesterol composition (X_{ch}) phase diagrams of (a) C14PC–cholesterol, (b) C15PC–cholesterol, (c) C16PC–cholesterol, (d) C17PC–cholesterol, and (e) C18PC–cholesterol binary bilayer, all of which are constructed on the basis of the data from Prodan fluorescence (□) and DSC (○) measurements. See text for phase assignments.

diagram of the ideal binary mixture. Therefore, this increase in T_m can be interpreted as an indication of partial miscibility between the phase structures formed in the higher X_{ch} region in the C*n*PC–cholesterol binary bilayers ($n = 14$–16). On the other hand, such increase in T_m in the higher X_{ch} region is not clearly observed for the C17PC– and the C18PC–cholesterol binary bilayers, suggesting that in the case of these binary bilayers the phase structures formed in the higher X_{ch} region are almost immiscible with each other. Furthermore, it can be seen that there is a tendency among the variations in T_m of the respective binary bilayers: the increase in T_m in the higher X_{ch} region tends to be less noticeable as the acyl chain length of the host C*n*PC molecule increases, suggesting that the partial miscibility between the phase structures formed in the higher X_{ch} region tends to be lower as the acyl chain length increases. This is very interesting because this tendency is consistent with the tendency regarding the miscibility between C*n*PC and cholesterol deduced from the consideration on the decrease in T_m in the low-X_{ch} region.

Another feature of our phase diagram is that there is a characteristic point at $X_{ch} = \sim 0.15$ in each phase diagram. This point can be regarded as a point thermodynamically equivalent to the peritectic point on the basis of the fact that the phase diagrams of these C*n*PC–cholesterol binary bilayers are similar in shape to a typical solid–liquid phase diagram containing a peritectic point. In general, a peritectic point occurs as a result of incongruent melting, and as described in a previous section, this type of melting behavior is usually observed for such binary systems where the two components react to produce a solid compound with a specific stoichiometry that is stable in a solid state but unstable in a liquid state. The stoichiometry of the solid compound is also reflected in the compositional phase diagram; that is, an isopleth (i.e., a vertical line) always appears at the composition corresponding to the stoichiometry on the phase diagram. Taking this thermodynamic generalization into account, the presence of a peritectic point in our T–X_{ch} phase diagrams for all these C*n*PC–cholesterol binary bilayers ($n = 14$–18) suggests that a cholesterol molecule interacts with several C*n*PC molecules within the bilayer membrane to form a complex, or a molecular cluster, which is relatively stable below T_m but rather unstable above T_m. The stoichiometry of this complex can be presumed to be 1:6 (cholesterol:C*n*PC, $X_{ch} = 0.143$) independent of the acyl chain length, because the isopleth corresponding to the formation of this complex can be drawn at $X_{ch} = 0.15$ in our T–X_{ch} phase diagrams of all these binary bilayers on the basis of the X_{ch} dependence of $\Delta T_{1/2}$ (Fig. 68.5c). As described above, the dependence changes drastically around $X_{ch} = 0.15$, which suggests that this composition can be regarded as a threshold indicative of some drastic change in the phase behavior of the binary bilayer.

It is also a suggestive feature of our phase diagram that two or three other isopleths are drawn at characteristic X_{ch} in addition to that at $X_{ch} = 0.15$. The isopleths at the lowest and the highest X_{ch} on each phase diagram are relevant to the abolition of the pretransition and main transition, respectively. Although all these isopleths do not always signify the formation of complexes of cholesterol and C*n*PC, the concept of the complex formation is useful to estimate the average properties of the binary bilayers and to understand the X_{ch}-dependent phase behavior. Furthermore, the X_{ch}-dependent phase behavior can be linked with the distribution of cholesterol within the binary bilayer by applying the so-called *superlattice view* [90–92]. According to this view, cholesterol molecules tend to be distributed regularly within the binary bilayer and the distribution is well represented schematically by a typical hexagonal lattice. In fact, it has been reported as evidence for the regular distribution [93–102] that there are discontinuous changes in some measurable properties of the cholesterol-containing binary bilayers at specific cholesterol compositions. Figure 68.7 shows the schematic illustrations of several possible types of regular distributions of cholesterol within the binary bilayer using the hexagonal lattice, where an open circle and a closed circle on a lattice point represent a C*n*PC and a cholesterol molecule, respectively. Here, it should be noted that in the original superlattice model, either a cholesterol molecule or an acyl chain of a phospholipid molecule is assigned to a lattice point. However, we use simpler geometry (i.e., one molecule to one site) taking into account the fact that the cross-sectional areas of a fully extended hydrocarbon chain, a cholesterol molecule and a C*n*PC molecule have been roughly estimated at 0.20, 0.40, and 0.55–0.70 nm^2 (depending on X_{ch}) on insoluble monolayers or mixed monolayers, respectively [65, 66,103, 104]. The fundamental unit shown in Fig. 68.7a, for example, is composed of a cholesterol molecule and 30 C*n*PC molecules within the next-next-next-nearest-neighbor sites around the cholesterol molecule [i.e., Unit (1:30)], and when the binary bilayer is entirely occupied with only fundamental units of this type, the X_{ch} value is equal to 0.032. Similarly, the fundamental units shown in (b) and (c) of Fig. 68.7 are composed, respectively, of a cholesterol molecule and its surrounding 18 C*n*PC molecules [i.e., Unit (1:18)] and of a cholesterol and its 12 surrounding C*n*PC molecules [i.e., Unit (1:12)], and these units correspond to the X_{ch} values of 0.053 and 0.077, respectively. These X_{ch} values of 0.032, 0.053, and 0.077 are very close to the experimentally determined X_{ch} values of the abolition of the pretransition, respectively, for the C18PC–cholesterol binary bilayer (i.e., $X_{ch} = 0.03$–0.035), for the C14PC–, C15PC–, and C17PC–cholesterol binary bilayers (i.e., $X_{ch} = 0.05$–0.06) and for the C16PC–cholesterol binary bilayer (i.e., $X_{ch} = 0.07$–0.08). The abolition of the pretransition of the C*n*PC bilayer by the incorporation of cholesterol is generally attributed to the conversion of both L_β' and P_β' phases into an L_β-like phase induced by the presence of cholesterol, where the orientation of the acyl chains of the C*n*PC molecules is more perpendicular to the bilayer surface [57]. Therefore, this cholesterol effect of inducing such

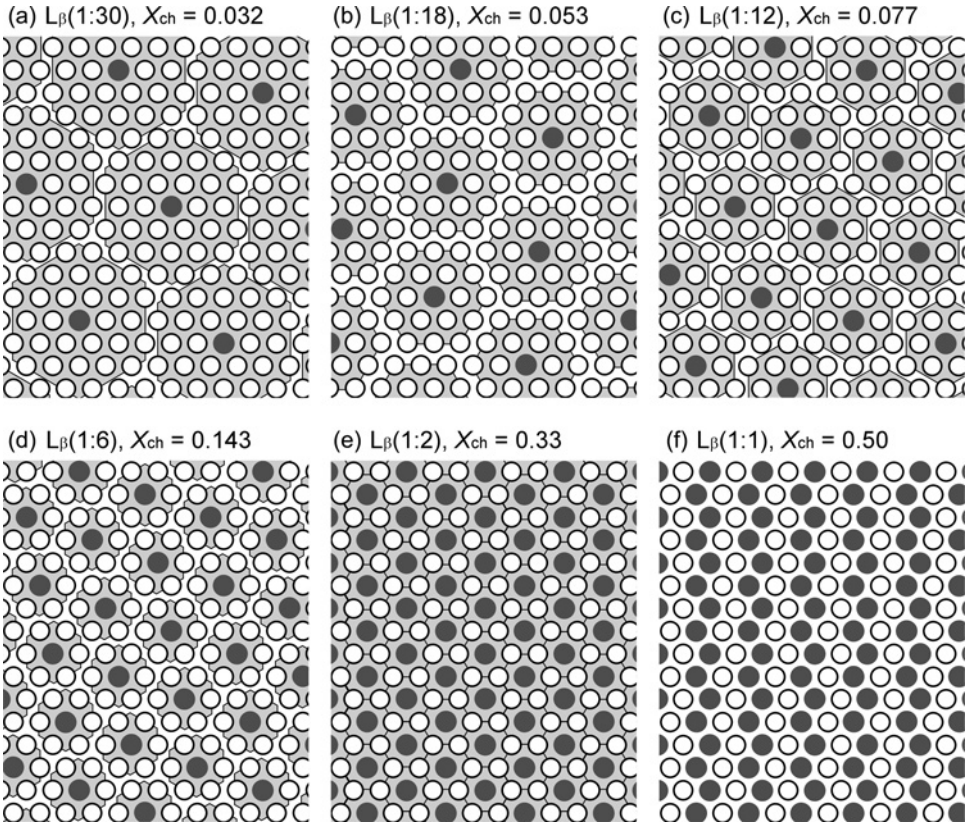


FIGURE 68.7 Schematic illustration of various types of regular distribution of cholesterol in binary bilayers based on hexagonal lattice model. A closed circle and an open circle represent a cholesterol and a C*n*PC molecule, respectively. A fundamental unit is indicated as a dark shaded area around a cholesterol molecule in each panel: (a) L_β (1:30) state ($X_{ch} = 0.032$) composed of only one unit [Unit (1:30)]; (b) L_β (1:18) state ($X_{ch} = 0.053$) composed of only unit [Unit (1:18)]; (c) L_β (1:12) state ($X_{ch} = 0.077$) composed of only one unit [Unit (1:12)]; (d) L_β (1:6) state ($X_{ch} = 0.143$) composed of only one unit [Unit (1:6)]; (e) L_o state ($X_{ch} = 0.333$) composed of only one unit [Unit (1:2)]; (f) L_o state in C18PC–cholesterol binary bilayer ($X_{ch} = 0.50$).

perpendicular orientation is presumed to propagate, on average, over the 30 C*n*PC molecules around a cholesterol molecule in the case of the C18PC–cholesterol binary bilayer, over the 18 C*n*PC molecules around a cholesterol molecule in the case of the C14PC–, C15PC–, and C17PC–cholesterol binary bilayers and over the 12 C*n*PC molecules around a cholesterol molecule in the case of the C16PC–cholesterol binary bilayer. Hereafter, we use the notation of L_β (1:*p*) to represent those gel states of the binary bilayers composed only of Units (1:*p*), as shown in Fig. 68.7. Note that all the L_β (1:*p*) phases with different *p* values given in Fig. 68.7 are regarded as thermodynamically different phases in respect of the interaction between the C*n*PC and cholesterol molecules, although the acyl chains of all the constituent C*n*PC molecules are oriented perpendicular to the bilayer surface in any L_β (1:*p*) phase.

Figure 68.7 also gives the schematic illustrations of three different types of distributions of cholesterol within the binary bilayer. Two of these three types correspond to other types of regular distributions, each of which is based on Unit (1:6) and Unit (1:2), as shown in (d) and (e) of Fig. 68.7, respectively. The other represents a distribution state of the binary bilayer composed of the 1:1 complexes of cholesterol and C*n*PC (Fig. 68.7f), and does not correspond, in a strict sense, to the superlattice. However, it can be regarded as virtually equivalent to a type of regular distribution, because an ample amount of cholesterol molecules are distributed almost homogeneously all over the binary bilayer. As apparent from the stoichiometry, Unit (1:6) is in accordance with the 1:6 complex of cholesterol and C*n*PCs deduced from the presence of a peritectic point on all the phase diagrams shown in Fig. 68.6, which means that the formation of the 1:6 complex does not conflict with the superlattice view. In this state, the orientation of the hydrocarbon chains of all the C*n*PC molecules within the binary bilayer is expected to be still perpendicular to the bilayer surface. Taking this into

account, we denote this phase state of the C*n*PC–cholesterol binary bilayer as L_β (1:6). As described above, this L_β (1:6) phase is a thermodynamically distinct phase from the other L_β (1:*p*) phases in terms of the molecular interaction between cholesterol and C*n*PC. As for Unit (1:2), it is obvious that the X_{ch} value becomes 0.33 when the binary bilayer is occupied entirely with this type of fundamental units. This X_{ch} value of 0.33 is very close to the experimental X_{ch} value for the abolition of the main transition of all the C*n*PC–cholesterol binary bilayers except the C18PC–cholesterol binary bilayer. The abolition of the main transition is generally considered to be due to the complete formation of the L_o phase within the binary bilayer membrane. Therefore, the L_o phase is presumed to be a homogeneous state composed by Units (1:2) as illustrated in Fig. 68.7e, where the thermally induced *trans–gauche* conformational changes in the acyl chains of all the C*n*PC molecules are completely suppressed by the cholesterol–C*n*PC interaction. In the C18PC–cholesterol binary bilayer, on the other hand, the main transition persists to $X_{ch} = 0.50$. Therefore, it can be said that the L_o phase formed in the C18PC–cholesterol binary bilayer corresponds to the homogeneous state where the 1:1-complexes of cholesterol and C18PC are distributed uniformly over the binary bilayer.

The above consideration of the X_{ch}-dependent phase behavior of a series of C*n*PC–cholesterol binary bilayers and the distribution of cholesterol within the binary bilayer may be somewhat speculative, but it is supported by several recent studies on the effects of cholesterol on the structure and properties of phospholipid bilayers. For example, other authors [105] have reported that the formation of the complexes containing large numbers of molecules in the binary bilayer is rationalized by the thermodynamic calculation based on the extended condensed complex model. Another team [106] also reported that the formation of complexes of cholesterol and constituent phospholipids is indicated by the disagreement between the calculated and the experimental values of the ratio of the translational diffusion coefficient to the rotational diffusion coefficient. Finally, the phase assignments based on the above consideration are given below. For the phase diagrams of the C14PC–, C15PC–, and C17PC–cholesterol binary bilayers, each of the areas labeled A to I in the phase diagram shown in Fig. 68.6 is assigned as follows: (A) L_d phase, (B) $L_d + P_\beta'$, (C) $P_\beta' + L_\beta$ (1:18), (D) $L_\beta' + L_\beta$ (1:18), (E) $L_d + L_\beta$ (1:6), (F) L_β (1:18) + L_β (1:6), (G) $L_d + L_o$, (H) L_β (1:6) + L_o, and (I) L_o. The same assignment is applicable to the phase diagram of the C16PC–cholesterol binary bilayer by replacing L_β (1:18) with L_β (1:12). In addition, it is also applicable to that of the C18PC–cholesterol binary bilayer except for the following: (C) $P_\beta' + L_\beta$ (1:30), (D) $L_\beta' + L_\beta$ (1:30), (F) L_β (1:30) + L_β (1:12), (J) $L_d + L_\beta$ (1:12), (K) $L_d + L_\beta$ (1:12), and (L) L_β (1:12) + L_β (1:6). Regarding the gel-phase structure, an X-ray diffraction study [107] has revealed that the periodically undulated structure (i.e., ripple structure) is observed for the C14PC– and the C16PC–cholesterol binary bilayers, and most part of the gel phase region in their phase diagram has been identified as P_β or P_β' phase on the basis of those structural data. However, such ripple structure can be also formed in the L_β'- L_β coexisting state.

68.6 ACYL CHAIN LENGTH DEPENDENCE OF CHARACTERISTIC CHOLESTEROL COMPOSITIONS

In the previous section, we described the X_{ch}-dependent phase behavior of a series of C*n*PC–cholesterol binary bilayers ($n = 14$–18) in connection with the distribution of cholesterol within the binary bilayer deduced from several characteristic X_{ch} values observed on the T–X_{ch} phase diagrams by applying the superlattice view. In this section, we discuss how the cholesterol effect on such X_{ch}-dependent phase behavior is affected by the variation in the acyl chain length *n* of the host C*n*PC molecules. First, we would like to briefly mention the miscibility of cholesterol and these C*n*PCs in the binary bilayer. As described above, our phase diagrams suggest that there is a qualitative tendency that the miscibility between them becomes slightly lower as the acyl chain length increases. This may be attributed to the fact that the van der Waals interaction between the acyl chains of the adjacent C*n*PC molecules in the bilayer becomes stronger with an increase in the acyl chain length, because in general two components in a binary mixture tend to separate out when the molecular interaction between the same species becomes stronger.

Figure 68.8 shows the acyl chain length dependence of the two characteristic X_{ch} values: one is the X_{ch} at which

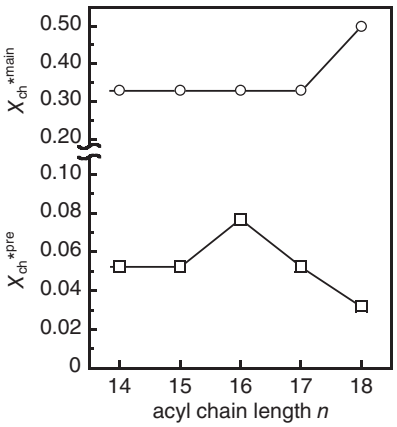


FIGURE 68.8 Acyl chain length (*n*) dependence of X_{ch}^{*main} (○), specifically, the cholesterol composition at which the main transition is abolished, and of X_{ch}^{*pre} (□), that is, the cholesterol composition at which the pretransition is abolished.

the main transition is abolished (X_{ch}^{*main}) and the other is the X_{ch} at which the pretransition is abolished (X_{ch}^{*pre}). As seen from the figure, the X_{ch}^{*main} value is constant at ca. 0.33 independent of n for $n = 14$–17, whereas it increases to ca. 0.50 at $n = 18$. As described above, this X_{ch}^{*main} value of ca. 0.33 for CnPC ($n = 14$–17) is surely low as compared to those from previous calorimetric studies [54,57], but the n-dependence of X_{ch}^{*main} shown in Fig. 68.8 is partly consistent with the tendency observed in each of those previous calorimetric studies; the constant X_{ch}^{*main} value for $n = 14$–17 is consistent with the results in Ref. 57, and the increase in X_{ch}^{*main} at $n = 18$ is consistent with the results in Ref. 54. Furthermore, this n-dependence of X_{ch}^{*main} can be successfully explained by the view proposed in Ref. 57. According to that view, there is no marked dependence on the acyl chain length of the host CnPC molecule in the effect of cholesterol on the thermotropic bilayer phase behavior of CnPCs with few exceptions, and the exceptions arise chiefly from the mismatch in the effective length of the hydrophobic region between cholesterol and CnPC in the bilayer. Taking into account the fact that this hydrophobic mismatch is minimized at $n = 17$ [57], the increase in X_{ch}^{*main} to ~0.50 at $n = 18$ can be interpreted as due to the reversal of the hydrophobic mismatch. Thus, in the case of CnPC with shorter acyl chains ($n \leq 17$), it is expected that the acyl chains of the CnPC molecules around a cholesterol molecules tend to be forcibly extended to minimize the hydrophobic mismatch, and consequently, the incorporation of the relatively small amount of cholesterol (i.e., at lower X_{ch}) can induce the homogeneous L_o phase within the entire binary bilayer. On the other hand, for $n \geq 18$, as has been discussed in Ref. 54, the hydrophobic mismatch can create a free volume in the middle of the bilayer, which is energetically unfavorable. This could contribute negatively to the complete suppression of the melting of the acyl chains, because the ends of the acyl chains would tend to have a kink to minimize the unfavorable effect of the voids. As a result, the relatively large amount of cholesterol is required to abolish the main transition of the bilayer of CnPC with longer acyl chains ($n \geq 18$).

As for X_{ch}^{*pre}, it is understandable that the acyl chain length dependence is biphasic: X_{ch}^{*pre} increases with an increase in the acyl chain length up to $n = 16$, whereas it decreases with an increase in the acyl chain length for $n \geq 16$. As described above, the abolition of the pretransition by the incorporation of cholesterol is thought to be due to the induction of an L_β-like orientation. Therefore, the biphasic n dependence of X_{ch}^{*pre} suggests that there are at least two antagonistic acyl-chain-length-dependent factors involved in the process of the induction of the L_β-like orientation: a factor that accelerates the induction of the L_β-like orientation when the acyl chains of the host CnPC molecule increase in length and the other one that promotes it when they decrease in length. Although the molecular mechanism of the induction of the L_β-like orientation by cholesterol has not yet been fully revealed, we currently speculate as follows. Van der Waals interaction is one of the most dominant interaction acting between the neighboring phospholipid molecules in the bilayer and tends to be stronger as the acyl chains becomes longer. The stronger van der Waals interaction is expected to facilitate wider propagation of the cholesterol effect of inducing the L_β-like orientation, and as a result, a smaller amount of cholesterol is required to induce the L_β-like orientation within the entire binary bilayer as the acyl chain length increases. This means that the pretransition is abolished completely at a lower X_{ch} as the acyl chain length increases. Second, we should also take the hydrophobic mismatch into account as an essential factor. In fact, the n value of 16, at which X_{ch}^{*pre} reaches maximum, is very close to that for the minimum hydrophobic mismatch (i.e., $n = 17$). The bilayer of CnPC with shorter acyl chains ($n < 17$) does not have a sufficient thickness of hydrophobic core to accommodate the cholesterol molecule, and thus, the cholesterol molecules are expected to be relatively forced out toward the bilayer surface as compared with those in the bilayer of CnPC with longer acyl chains ($n \geq 17$). This relative protrusion of the cholesterol molecule will inevitably become greater with a decrease in the acyl chain length for $n < 17$, which can interfere with repulsive interaction between the adjacent choline headgroups of the host CnPC molecules. The weakening of the repulsion will contribute to wider propagation of the cholesterol effect of inducing the L_β-like orientation. As a result, the hydrophobic mismatch for $n < 17$ can also cause the reduction in the amount of cholesterol needed to induce the L_β-like orientation within the entire binary bilayer. This can be the other factor that accelerates the induction of the L_β-like orientation as the acyl chain length decreases.

Finally, we mention a third characteristic X_{ch} value of 0.14. This X_{ch} value is relevant to the 1:6 complex of cholesterol and CnPCs, and the formation of this type of complex is common to all the CnPC–cholesterol binary bilayers ($n = 14$–18). This means that there is no definite n dependence in this characteristic X_{ch}. In addition, as seen from the T–X_{ch} phase diagrams shown in Fig.68.6, the L_o phase begins to be formed within the binary bilayers at this composition; that is, this characteristic X_{ch} corresponds to the minimum composition for the formation of the L_o phase. As far as we know, there have been no reports discussing the minimum composition for the formation of the L_o phase in connection with the molecular structure of constituent phospholipids. At present, we do not fully understand the physical and chemical origins of the formation of the 1:6 complexes within the binary bilayers regardless of the acyl chain length, as well as how relevant those origins are to the minimum composition for the formation of the L_o phase, but this result will support the applicability of the superlattice view based on the hexagonal lattice for all these binary bilayers.

68.7 SUMMARY

In this chapter, we described the phase behavior of the cholesterol-containing binary bilayers of a homologous series of C*n*PCs (n = 14–18) on the basis of the T–X_{ch} phase diagrams constructed by means of Prodan fluorescence and DSC. Our phase diagrams exhibited several significant features of the thermotropic phase behavior of these binary bilayers. First, the presence of a peculiar point like a peritectic point at $X_{ch} = \sim 0.15$ was indicated for all these binary bilayers. This finding indicates that these binary bilayers commonly exhibit peritecticlike melting behavior with the formation of 1:6 complexes of cholesterol and C*n*PCs, and not simple eutectic melting behavior, regardless of the acyl chain length. This characteristic X_{ch} was also found to correspond to the minimum composition for the formation of the L_o phase within the binary bilayer. Second, two more significant X_{ch}, in addition to this characteristic X_{ch} of 0.15, were seen in each phase diagram: the X_{ch} at which the main transition is abolished (i.e., ${X_{ch}}^{*main}$) and the X_{ch} at which the pretransition is abolished (i.e., ${X_{ch}}^{*pre}$). Although these characteristic X_{ch} values do not always suggest the formation of molecular complexes, they could be well explained by applying the concept of the complex formation based on the superlattice view (i.e., regular distribution of cholesterol within the binary bilayer). The distribution states of cholesterol and C*n*PC molecules at those characteristic X_{ch} were successfully represented by schematic illustrations using the hexagonal lattice, in each of which a single type of fundamental unit is contained depending on the X_{ch} value [e.g., Unit (1:30) for X_{ch} = 0.032, Unit (1:18) for 0.053, Unit (1:12) for 0.077]. These illustrations are also applicable to explain the two-phase coexisting state at an intermediate X_{ch}. Third, it was suggested from the change in the shape of the phase boundaries with the acyl chain length of the host C*n*PC molecule that there is a qualitative tendency for the miscibility cholesterol and C*n*PC to become slightly lower as the acyl chain length increases. This is presumably due to the fact that the van der Waals interaction between the acyl chains of adjacent C*n*PC molecules becomes stronger as the acyl chain length increases.

We also considered the acyl chain length dependence of ${X_{ch}}^{*main}$ and ${X_{ch}}^{*pre}$ in this chapter. The ${X_{ch}}^{*main}$ value was almost constant at 0.33 for n = 14–17, whereas it increased to ~0.50 at n = 18. This increase in ${X_{ch}}^{*main}$ at n = 18 can be explained in terms of the mismatch in the effective length of the hydrophobic region between the cholesterol and the C*n*PC molecule. As for ${X_{ch}}^{*pre}$, on the other hand, biphasic acyl chain length dependence was seen: it increased with an increase in the acyl chain length for $n \leq 16$, whereas it decreased with an increase in the acyl chain length for $n \geq 16$. Since the abolition of the pretransition is generally considered to be due to the induction of more perpendicular orientation of the acyl chains with respect to the bilayer surface (i.e., L_β-like orientation), this biphasic acyl chain length dependence suggests that there are at least two antagonistic acyl-chain-length-dependent factors involved in the process of the induction of the L_β-like orientation. A possible explanation for this is as follows. Increasing van der Waals interaction would contribute to wider propagation of the cholesterol effect of inducing the L_β-like orientation, which results in a decrease in ${X_{ch}}^{*pre}$ with an increase in acyl chain length. On the other hand, the location of the cholesterol molecule in the direction of bilayer depth is expected to move nearer to the bilayer surface as a result of the mismatch in the effective length of the hydrophobic region as the acyl chain length decreases for $n < 17$. This would weaken the repulsion between the neighboring choline headgroups, and this repulsion weakening would also contribute to wider prevalence of the cholesterol effect. As a result, ${X_{ch}}^{*pre}$ decreases with a decrease in the acyl chain length for $n < 17$.

REFERENCES

[1] Koynova, R., Caffray, M. (1998). *Biochim. Biophys. Acta* **1376**, 91–145.

[2] Ruocco, M.J., Shipley, G.G. (1982). *Biochim. Biophys. Acta* **684**, 59–66.

[3] Nagle, J.F., Zahng, R., Tristram-Nagle, S., Sun, W., Petrache, H.I., Suter, R.M. (1996). *Biophys. J.* **70**, 1419–1431.

[4] Lewis, R.N.A.H., Mak, N., McElhaney, R.N. (1987). *Biochemistry* **26**, 6118–6126.

[5] Ichimori, H., Hata, T., Matsuki, H., Kaneshina, S. (1998). *Biochim. Biophys. Acta* **1414**, 165–174.

[6] De Kruijff, B., Cullis, P.R., Radda, G.K. (1975). *Biochim. Biophys. Acta* **406**, 6–20.

[7] Kawato, S., Kinosita, K.Jr., Ikegami, A. (1977). *Biochemistry* **16**, 2319–2324.

[8] Kusube, M., Matsuki, H., Kaneshina, S. (2005). *Colloid Surf. B: Biointerfaces* **42**, 79–88.

[9] Nagle, J.F., Wilkinson, D.A. (1978). *Biophys. J.* **23**, 159–175.

[10] Tamai, N., Nambu, Y., Tanaka, S., Goto, M., Matsuki, H., Kaneshina, S. (2012). *Colloid Surf. B: Biointerfaces* **92**, 232–239.

[11] Caffrey, M. (1993). *Lipidat*. CRC Press, Boca Raton, FL.

[12] Kapoor, S., Werkmüller, A., Denter, C., Zhai, Y., Markgraf, J., Weise, K., Opitz, N., Winter, R. (2011). *Biochim. Biophys. Acta* **1808**, 1187–1195.

[13] Pinto, S.N., Fernandes, F., Fedorov, A., Futerman, A.H., Silva, L.C., Prieto, M. (2013). *Biochim. Biophys. Acta* **1828**, 2099–2110.

[14] Simons, K., Ikonen, E. (1997). *Nature* **387**, 569–572.

[15] Zajchowski, L.D., Robbins, S.M. (2002). *Eur. J. Biochem.* **269**, 737–752.

[16] Feigenson, G.W., Buboltz, J.T. (2001). *Biophys. J.* **80**, 2775–2788.

[17] Veatch, S.L., Keller, S.L. (2002). *Phys. Rev. Lett.* **89**, 268101.

[18] Veatch, S.L., Keller, S.L. (2003). *Biophys. J.* **85**, 3074–3083.

[19] Tamai, N., Uemura, M., Takeichi, T., Goto, M., Matsuki, H., Kaneshina, S. (2008). *Biophys. Chem.* **135**, 95–101.

[20] Tamai, N., Uemura, M., Goto, M., Matsuki, H., Kaneshina, S. (2008). *Colloids Surf. B: Biointerfaces* **65**, 213–219.

[21] Tamai, N., Izumikawa, T., Fukui, S., Uemura, M., Goto, M., Matsuki, H., Kaneshina, S. (2013). *Biochim. Biophys. Acta* **1828**, 2513–2523.

[22] Chapman, D., Penkett, S.A. (1966). *Nature* **211**, 1304–1305.

[23] Kroon, P.A., Kainosho, M., Chan, S.I. (1975). *Nature* **256**, 582–584.

[24] Opella, S.J., Yesinowski, J.P., Waugh, J.S. (1976). *Proc. Natl. Acad. Sci. USA* **73**, 3812–3815.

[25] Haberkorn, R.A., Griffin, R.G., Meadows, M.D., Oldfield, E. (1977). *J. ACS* **99**, 7353–7355.

[26] Brown, M.F., Seelig, J. (1978). *Biochemistry* **17**, 381–384.

[27] Dufourc, E.J., Parish, E.J., Chitrakorn, S., Smith, I.C.P. (1984). *Biochemistry* **23**, 6062–6071.

[28] Smith, R.L., Oldfield, E. (1984). *Science* **225**, 280–288.

[29] Hubbell, W.L., McConnell, H.M. (1971). *J. ACS.* **93**, 314–326.

[30] Shimshick, E.J., McConnell, H.M. (1973). *Biochem. Biophys. Res. Commun.* **53**, 446–451.

[31] Marsh, D., Smith, I.C.P. (1973). *Biochim. Biophys. Acta* **298**, 133–144.

[32] Recktenwald, D.J., McConnell, H.M. (1981). *Biochemistry* **20**, 4505–4510.

[33] Ladbrooke, B.D., Williams, R.M., Chapman, D. (1968). *Biochim. Biophys. Acta* **150**, 333–340.

[34] Franks, N.P. (1976). *J. Mol. Biol.* **100**, 345–358.

[35] Worcester, D.L., Franks, N.P. (1976). *J. Mol. Biol.* **100**, 359–378.

[36] McIntosh, T.J. (1978). *Biochim. Biophys. Acta* **513**, 43–58.

[37] Hinz, H.J., Sturtevant, J.M. (1972). *J. Biol. Chem.* **247**, 3697–3700.

[38] Mabrey, S., Mateo, P.L., Sturtevant, J.M. (1978). *Biochemistry* **17**, 2464–2468.

[39] Estep, T.N., Mountcastle, D.B., Biltonen, R.L., Thompson, T.E. (1978). *Biochemistry* **17**, 1984–1989.

[40] Kawato, S., Kinosita, K.Jr., Ikegami, A. (1978). *Biochemistry* **17**, 5026–5031.

[41] Rubenstein, J.L.R., Smith, B.A., McConnell, H.M. (1979). *Proc. Natl. Acad. Sci. USA* **76**, 15–18.

[42] Lentz, B.R., Barrow, D.A., Hoechli, M. (1980). *Biochemistry* **19**, 1943–1954.

[43] Verkleij, A.J., Ververgaert, P.H.J., van Deenen, L.L.M., Elbers, P.F. (1972). *Biochim. Biophys. Acta* **288**, 326–332.

[44] Verkleij, A.J., Ververgaert, P.H.J.Th., de Kruyff, B., van Deenen, L.L.M. (1974). *Biochim. Biophys. Acta* **373**, 495–501.

[45] Copeland, B.R., McConnell, H.M. (1980). *Biochim. Biophys. Acta* **599**, 95–109.

[46] Demel, R.A., de Kruyff, B. (1976). *Biochim. Biophys. Acta* **457**, 109–132.

[47] Yeagle, P.L. (1985). *Biochim. Biophys. Acta* **822**, 267–287.

[48] Koynova, R.D., Boyanov, A.I., Tenchov, B.G. (1985). *FEBS Lett*. **187**, 65–68.

[49] Ipsen, J.H., Karlström, G., Mouritsen, O.G., Wennerström, H., Zuckermann, M.J. (1987). *Biochim. Biophys. Acta* **905**, 162–172.

[50] Vist, M.R., Davis, J.H. (1990). *Biochemistry* **29**, 451–464.

[51] Almeida, P.F.F., Vaz, W.L.C., Thompson, T.E. (1992). *Biochemistry* **31**, 6739–6747.

[52] Thewalt, J.L., Bloom, M. (1992). *Biophys. J.* **63**, 1176–1181.

[53] Marsh, D. (2010). *Biochim. Biophys. Acta* **1978**, 688–699.

[54] Huang, T.-H.; Lee, C.W.B., Das Gupta, S.K., Blume, A., Griffin, R.G. (1993). *Biochemistry* **32**, 13277–13287.

[55] McMullen, T.P.W., McElhaney, R.N. (1995). *Biochim. Biophys. Acta* **1234**, 90–98.

[56] Karmakar, S., Raghunathan, V.A., Mayor, S. (2005). *J. Phys. Condens. Matt.* **17**, S1177–S1182.

[57] McMullen, T.P.W., Lewis, R.N.A.H., McElhaney, R.N. (1993). *Biochemistry* **32**, 516–522.

[58] McMullen, T.P.W., Lewis, R.N.A.H., McElhaney, R.N. (1999). *Biochim. Biophys. Acta* **1416**, 119–234.

[59] McMullen, T.P.W., Lewis, R.N.A.H., McElhaney, R.N. (2000). *Biophys. J.* **79**, 2056–2065.

[60] McMullen, T.P.W., Lewis, R.N.A.H., McElhaney, R.N. (2008). *Biochim. Biophys. Acta* **1778**, 2814–2822.

[61] Mannock, D.A., Lewis, R.N.A.H., McMullen, T.P.W., McElhaney, R.N. (2010). *Chem. Phys. Lipid*s **163**, 403–448.

[62] Blume, A., Griffin, R.G. (1982). *Biochemistry* **21**, 6230–6242.

[63] Engleman, D.M., Rothman, J.E. (1972). *J. Biol. Chem.* **247**, 3694–3697.

[64] Martin, R.B., Yeagle, P.L. (1978). *Lipids* **13**, 594–597.

[65] Müller-Landau, F., Cadenhead, D.A. (1979). *Chem. Phys. Lipids* **25**, 299–314.

[66] Müller-Landau, F., Cadenhead, D.A. (1979). *Chem. Phys. Lipids* **25**, 315–328.

[67] Radhakrishnan, A., McConnell, H.M. (1999). *Biophys. J.* **77**, 1507–1517.

[68] Radhakrishnan, A., Anderson, T.G., McConnell, H.M. (2000). *Proc. Natl. Acad. Sci. USA* **97**, 12422–12427.

[69] McConnell, H.M., Radhakrishnan, A. (2003). *Biochim. Biophys Acta* **1610**, 159–173.

[70] Radhakrishnan, A., McConnell, H.M. (2005). *Proc. Natl. Acad. Sci. USA* **102**, 12662–12666.

[71] Weber, G., Farris, F.J. (1979). *Biochemistry* **18**, 3075–3078.

[72] Chong, P.L. (1988). *Biochemistry* **27**, 399–404.

[73] Chong, P.L., Capes, S., Wong, P.T.T. (1989). *Biochemistry* **28**, 8358–8363.

[74] Zeng, J.W., Chong, P.L. (1991). *Biochemistry* **30**, 9485–9491.

[75] Zeng, J.W., Chong, P.L. (1995). *Biophys. J.* **68**, 567–573.

[76] Parasassi, T., Giusti, A.M., Gratton, E., Monaco, E., Raimondi, M., Ravagnan, G., Sapora, O. (1994). *Int. J. Radiation Biol.* **65**, 329–334.

[77] Krasnowska, E.K., Gratton, E., Parasassi, T. (1998). *Biophys. J.* **74**, 1984–1993.

[78] Krasnowska, E.K., Bagatolli, L.A., Gratton, E., Parasassi, T. (2001). *Biochim. Biophys. Acta* **1511**, 330–340.

[79] Kusube, M., Tamai, N., Matsuki, H., Kaneshina, S. (2005). *Biophys. Chem.* **117**, 199–206.

[80] Kusube, M., Matsuki, H., Kaneshina, S. (2005). *Colloids Surf. B: Biointerfaces* **42**, 79–88.

[81] Wilson-Ashworth, H.A., Bahm, Q., Erickson, J., Shinkle, A., Vu, M.P., Woodbury, D., Bell, J.D. (2006). *Biophys. J.* **91**, 4091–4101.

[82] Goto, M., Kusube, M., Tamai, N., Matsuki, H., Kaneshina, S. (2008). *Biochim. Biophys. Acta* **1778**, 1067–1078.

[83] Goto, M., Sawaguchi, H., Tamai, N., Matsuki, H., Kaneshina, S. (2010). *Langmuir* **26**, 13377–13384.

[84] Goto, M., Matsui, T., Tamai, N., Matsuki, H., Kaneshina, S. (2011). *Colloids Surf. B: Biointerfaces* **84**, 55–62.

[85] Okamura, E., Nakahara, M. (2000). In Volkov, A.G. (ed.), *Liquid Interfaces in Chemical, Biological and Pharmaceutical Applications*. Marcel Dekker, New York, pp. 775–805.

[86] Lewis, R.N.A.H., Mannock, D.A., McElhaney, R.N. (2007). In Dopico, A.M. (ed.), *Methods in Membrane Lipids*. Humana Press, Totowa, pp. 171–195.

[87] Yuan, C., Johnston, L.J. (2002). *J. Microsc.* **205**, 136–146.

[88] Zhang, J., Cao, H., Jing, B., Almeida, P.F.F., Regen, S.L. (2006). *Biophys. J.* **91**, 1402–1406.

[89] Su, Y., Li, Q., Chen, L., Yu, Z. (2007). *Colloids Surf. A: Physicochem. Eng. Aspects* **293**, 123–129.

[90] Somerharju, P., Virtanen, J.A., Cheng, K.H. (1999). *Biochim. Biophys. Acta* **1440**, 32–48.

[91] Chong, P.L.-G., Zhu, W., Venegas, B. (2009). *Biochim. Biophys. Acta* **1788**, 2–11.

[92] Somerharju, P., Virtanen, J.A., Cheng, K.H. (2009). Hermansson, M. *Biochim. Biophys. Acta* **1788**, 12–23.

[93] Hyslop, P.A., Morel, B., Sauerheber, R.D. (1990). *Biochemistry* **29**, 1025–1038.

[94] Chong, P.L. (1994). *Proc. Natl. Acad. Sci. USA* **91**, 10069–10073.

[95] Virtanen, J.A., Ruonala, M., Vauhkonen, M., Somerharju, P. (1995). *Biochemistry* **34**, 11568–11581.

[96] Parasassi, T., Giusti, A.M., Raimondi, M., Gratton, E. (1995). *Biophys. J.* **68**, 1895–1902.

[97] Tang, D., van der Meer, B.W., Chen, S.-Y.S. (1995). *Biophys. J.* **68**, 1944–1951.

[98] Virtanen, J.A., Somerharju, P. (1999). *J. Phys. Chem. B* **103**, 10289–10293.

[99] Huang, J. (2002). *Biophys. J.* **83**, 1014–1025.

[100] Cannon, B., Heath, G., Huang, J., Somerharju, P., Virtanen, J.A., Cheng, K.H. (2003). *Biophys. J.* **84**, 3777–3791.

[101] Parker, A., Miles, K., Cheng, K.H., Huang, J. (2004). *Biophys. J.* **86**, 1532–1544.

[102] Cuevas, F.J., Jameson, D.M., Sotomayor, C.P. (2006). *Biochemistry* **45**, 13855–13868.

[103] Brzozowska, I., Figaszewski, Z.A. (2002). *Biophys. Chem.* **95**, 173–179.

[104] Dynarowicz-Łątka, P., Hąc-Wydro, K. (2004). *Colloids Surf. B: Biointerfaces* **37**, 21–25.

[105] Anderson, T.G., McConnell, H.M. (2002). *Biophys. J.* **83**, 2039–2052.

[106] Ariola, F.S., Li, Z., Cornejo, C., Bittman, R., Heikal, A.A. (2009). *Biophys. J.* **96**, 2696–2708.

[107] Karmakar, S., Raghunathan, V.A. (2005). *Phys. Rev. E* **71**, 061924.

69

PHASE SEPARATION PHENOMENA IN DRUG SYSTEMS

Andleeb Z. Naqvi[1] and Kabir-ud-Din[2]

[1]*Department of Chemistry, Aligarh Muslim University, Aligarh 202 002, India*
[2]*Department of Applied Chemistry, Aligarh Muslim University, Aligarh 202 002, India*

69.1 INTRODUCTION

Various studies have been carried out to address structures and phase behavior of amphiphiles in aqueous solutions [1–3]. This interest is due to the vital role played by amphiphiles in industry as well as in biophysics, biotechnology, and pharmacology [4,5]. An amphiphilic molecule consists of two parts: solvent-loving (solvophilic/hydrophilic, in the context of water as solvent) and solvent-repelling (solvophobic/hydrophobic) parts. The sizes of both parts, as well as their shape and the hydrophilic–hydrophobic balance (HHB) [2,6], determine their self-assembly and ensuing fascinating physical properties. The presence of discrete hydrophilic and hydrophobic parts is, however, a prerequisite for self-assembly. The aggregates formed by the amphiphiles are commonly known as *micelles*, which are primarily the result of hydrophobic interactions [7]. The mean size of these aggregates (or micelles) is 1–100 nm. Micelles are dynamic as amphiphile monomers can exchange between the micelles and bulk phase. The threshold concentration at which the aggregates form [the so-called critical micelle concentration (cmc)], and the size, shape, and nature of the aggregates depend on the solution conditions as well as the nature of the amphiphile. The cmc values of nonionic amphiphiles are usually lower than those of ionic ones because of the absence of charge in the former ones. Similarly, block copolymers and triblock polymers also form aggregates, called *polymeric micelles*. Their size varies between 20 and 50 nm and they are relatively more stable than the surfactant micelles.

On the basis of their structure, the amphiphilic molecules may be classified into the following four categories: (1) flexible chain compounds (surfactants, etc.), (2) aromatic or heterocyclic ring or fused structures (dyes, drugs, etc.), (3) alicyclic compounds (bile salts, etc.), and (4) macromolecules (polymers, proteins, etc.) [8]. On the basis of studies of different features of molecular structure that influence the association pattern of amphiphiles, one researcher [8, 9] suggested that a high degree of flexibility and distinct polar and nonpolar parts are the necessary requirements of micellization. Rigid ring structures such as those found in cationic dyes and purines/pyrimidines result in face-to-face stacking in a continuous association pattern. In cationic dyes, the charge is delocalized in the ring system, and in purines/pyrimidines the structure is not flexible. Structures of amphiphilic drugs are intermediate to these two groups; although they have aromatic/heteroaromatic rings in their hydrophobic parts, they also have flexibility/rigidity in the molecules; and their charge is normally localized at a terminal group of a sidechain. These drugs belong to the families of phenothiazine and benzodiazepine tranquilizers, analgesics, peptide and nonpeptide antibiotics, tricyclic antidepressants, antihistamines, anticholinergics, β-blockers, local anesthetics, and nonsteroidal anti-inflammatory drugs [10–13]. Their aggregation is dependent on concentration, temperature, and pH. Some of these drugs form micelle-like aggregates; others associate by continuous stacking [14] with small aggregation numbers [10,15]. Their site of action is usually the plasma membrane. Even if their target is intracellular, they first interact with plasma membrane, resulting in various effects that have been studied in detail using a variety of spectroscopic [viz., electron paramagnetic resonance (EPR), nuclear magnetic resonance (NMR), fluorescence, Fourier transform infrared, circular dichroism (CD)] and biophysical [viz., X-ray and neutron diffraction, differential

Encyclopedia of Biocolloid and Biointerface Science, Volume 2, First Edition. Edited by Hiroyuki Ohshima.
© 2016 John Wiley & Sons, Inc. Published 2016 by John Wiley & Sons, Inc.

scanning calorimetry (DSC), titration calorimetry, monolayer] techniques.

Undoubtedly, there are numerous drugs in the market (and every day new therapeutic agents are identified and/or synthesized), but the successful development of the field of pharmaceutics has been hampered by the requirement of a drug delivery system (DDS) for their safe delivery to the site of action. In addition to the solubility enhancement of the newly developed therapeutic agents (as they are hydrophobic, almost 50% are never marketed mainly because of their solubility, and hence, bioavailability problems), the properties of the many currently existing drugs could be improved with the use of an effective DDS. Hence, to increase their bioavailability and to protect them from degradation (hydrolysis and enzymatic decomposition), these drugs must be administered with carriers in the form of micelles (surfactant/ polymeric), liposomes, niosomes, cyclodextrin inclusion complexes, liquid crystalline phase, microemulsions, and self-emulsifying drug delivery systems [16–22]. In this context micelles and mixed micelles show great promise as DDSs as these systems are easy to prepare, have a long shelf life, and have low toxicity [23], and, above all, the size of such DDSs as well as drug loading can be tuned according to the need.

Another type of drug carrier is the biosurfactants, the bile acid salts [24]. Bile salts, when mixed with AMT or ADP, decrease the cmc of the drug–bile salt mixtures [25,26]. Here also a very small amount of bile salts is needed, because of their comparatively greater contribution in mixed micelles.

It is well documented that the presence of surfactants in DDS could change the physicochemical properties of drugs, such as their aqueous solubility [27], stability [28], bioactivity [29], skin penetration [30], and bioavailability. In general, nonionic surfactants (due to their low cmc values, better stability, biocompatibility, minimum binding to proteins, and extremely low hemolytic activity [31]) are considered as better DDSs than ionic surfactants [32]. However, ionic surfactants with positive charge (cationics) are considered as more efficient membrane permeation enhancers than anionic or nonionic ones, although cytotoxicity of cationics is more than that of the other two types [33, 34]. Among cationics, alkylammonium bromide gemini surfactants are known to efficiently modulate the order of bioavailability [35].

Recently, there has been increased interest in the development of drug delivery systems with improved properties and effectiveness as well as reduced side effects of drugs. The aim of any DDS is to (1) increase the solubility and stability of drugs in vivo, (2) improve bioavailability, and (3) reduce side effects. Various DDSs have been developed depending on the route of administration, which is selected on the basis of biological properties of therapeutic agent as well as on the pathological condition being approached. Development of pharmaceutical formulations is a complex and time-consuming process involving the application of various aspects of physical chemistry, microbiology, and engineering [36, 37]. The process requires an in-depth understanding of the physicochemical properties of the drug (e.g., stability toward degradation), its detailed thermodynamic solubility data, and the solution properties of the final formulation. The capability of a drug solution to micellize or self-aggregate along with the effect of excipients on this phenomenon imparts product design [3,38] and is an important parameter to reckon with [3].

69.2 DRUG-DDS INTERACTIONS: EFFECT OF TEMPERATURE ON SOLUTION

A common observation for a solution of nonionic surfactants/polymers (and ionic surfactants under special conditions [39–43]) is that, on heating, the solution (at a well-defined temperature range) starts to scatter light strongly; it becomes cloudy. The isotropic solution region is bordered, at higher temperatures, by a lower consolute curve, above which there is a phase separation into one surfactant-rich solution and one surfactant-poor solution (Fig. 69.1). The onset of phase separation is manifested by a cloudiness of the solutions accompanied by strong scattering of light due to critical fluctuations. At cloud point (CP) a single isotropic micellar phase spontaneously turns cloudy and, on standing, separates into two phases—one very small in volume composed almost totally of surfactant with a small amount of water, referred to as the *surfactant-rich phase*, and another aqueous phase containing a concentration of surfactant close to cmc (referred to as *surfactant-poor*). The process of clouding is reversible, and when the temperature falls below the CP, the two phases merge to form a clear solution. The phase-to-volume ratio, that is, the ratio of the volume of the aqueous phase to that of the surfactant coacervate phase following the phase separation step, can be very high in such systems ($\leq$1:0.007) [44].

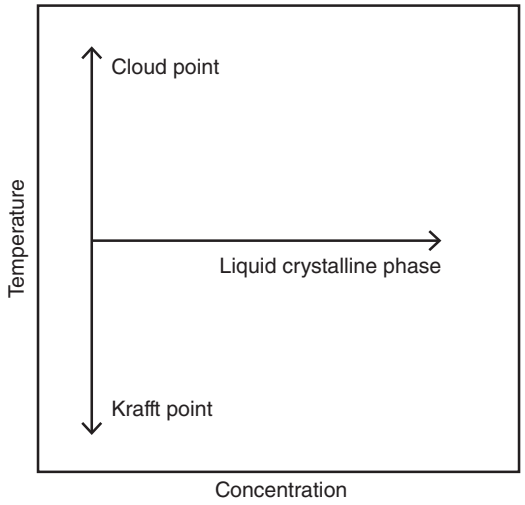


FIGURE 69.1 Schematic temperature–concentration phase diagram showing the types of aggregates encountered by moving away from the micellar region.

From simple thermodynamics, the primary reason for the CP behavior of nonionic surfactants is that the water around a polyoxyethylene chain (of amphiphiles) is more structured than bulk water; it has a lower enthalpy and entropy than bulk water. Existence of CP implies that the heat of mixing of the polyoxyethylene chain with water below the CP is exothermic. As the temperature increases, the hydration shells of two neighboring chains overlap, water is forced to leave these shells, and both the enthalpy and entropy of the system increase. At elevated temperature, the entropy gain in this destructuring of water is high enough to overcome the repulsive enthalpy contribution and the loss in entropy due to increased concentration—at this stage phase separation occurs.

It has been shown [45, 46] that few mixed nonionic and ionic surfactant solutions show preclouding; solutions first become faintly turbid and then fully clouded at a higher temperature. This phenomenon is generally called a *double cloud point* or an *apparent cloud point* [47]. Maclay [47] was the first to report it in 1956. A solution containing a nonionic surfactant and a small amount of an ionic surfactant will contain both charged and uncharged aggregates, with the former incorporating one or more ionic species. As the temperature is raised, these micelles coalesce to form large bodies of either two uncharged micelles or a charged micelle and an uncharged micelle. Two charged micelles could not be expected to coalesce because of mutual repulsion. This process results in aggregates that are all charged and therefore do not coalesce further, constituting a relatively stable suspension. The size of such aggregates is dictated by the relative proportions of the two types of surfactants and, hence, the resulting suspension will be colloidal only for certain compositions. These solutions correspond to the ones that undergo preclouding.

Reports in the literature reveal that phase separation can also occur in cyclodextrin- containing solutions, in reverse micellar systems, and in microemulsions [48–50].

Some nonionic surfactants, including dimethyldecylphosphine oxide, dimethyldodecylphosphine oxide, dimethyloleylamine oxide, tetraoxyethylene decyl ether, and pentaoxyethylene decyl ether, show a different type of clouding [51–53]. The phase-separated solutions again mix at higher temperatures of around 170–300°C, and the temperature – concentration phase diagram is a closed-loop type.

The CP depends strongly on both the polyoxyethylene chain length and hydrophobe size, although the effect of the hydrophobe size is marginal. It also depends on micellar size, which varies with the structure and nature of surfactant. A high micellar aggregation number is found to be equivalent to a high degree of polymerization of a polymer and thus gives a low cloud point.

The mechanism of phase separation is not fully understood yet. Some authors have discussed it in terms of an increase in the micellar aggregation number with the increase in temperature [54, 55]. One group of investigators [56–58] explained their SANS and viscosity results on nonionic surfactants through micellar growth. They found that with increase in temperature, spherical micelles change to rod-shaped ones that become so large that the solution becomes visibly turbid. However, the large scattering cross section in SANS results could be due to long-range concentration fluctuations, and some researchers have suggested change in micellar interactions, which changes from repulsive to attractive when temperature is increased [47,59,60]. Another team [61, 62] interpreted their SANS and light-scattering results by assuming attractive interactions among micelles with increasing temperature; the shape of micelles remained spherical throughout. The fact that addition of salts in nonionic surfactants increases the CP also supports the role of attractive interactions in producing CP.

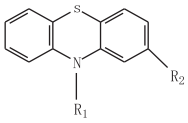
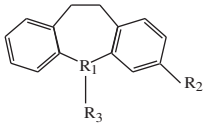
Some other authors attributed this phenomenon to the dehydration of polyoxyethylene chains as the temperature is increased [63–65]. This dehydration is thought to be induced by the conformational change of the surfactant chains with increase in temperature [66, 67]. Also, with increasing temperature, the dielectric constant of water decreases, making it a poor solvent for the hydrophilic parts of the surfactants. Another team [68] studied the solution behavior of thermoresponsive polymer using differential scanning calorimetry (DSC) and found that the bound water plays an important role in its phase separation process.

Attempts have also been made to apply Flory–Huggins theory for polymer solutions [69–72]. Rupert [72] also interpreted the phase separation as a result of change in balance between the hydrophilic and hydrophobic interactions among micelles as well as with surroundings. Hence, any factor that can change this balance can change the CP of the systems also.

Another point that is still unclear is the nature of micellar solutions. In the low- concentration region the solution contains micelles, but at very high concentrations micelles cannot persist [73]. In micellar solutions above CP, it is usually stated in the literature that in surfactant-rich areas no micelles are present as the surfactants are segregated from the aqueous phase. However, there are many reports that provide evidence for the existence of different structures such as micelles, lamellae, or hexagonal structures [74, 75]. At temperatures high above the CP, the dilute phase becomes increasingly dilute and the concentrated phase may become nonmicellar [73].

Amphiphilic drugs of the families of tricyclic antidepressants and phenothiazines, like surfactants, also undergo phase separation. Drugs of these families are chemically similar (see Table 69.1), containing a planar tricyclic ring system as a hydrophobic part and a short alkylamine part as hydrophilic portion. The pK_a values of these drugs range between 9.1 and 9.5 [76–80]. The nature and charge of these drugs are pH-dependent. At low pH values the N atom of amine acquires a positive charge, whereas at high pH values it becomes neutral.

TABLE 69.1 Amphiphilic Drugs Used and Their Basic Properties

Class	Name of drug	Abbreviation used in text	Structure	CP (°C)	Ref.
Phenothiazine					
	Promazine HCl	PMZ	$R_1 = -CH_2CH_2CH_2N(CH_3)_2$; $R_2 = H$	33 at 50 mM and pH = 6.7	122
	Chlorpromazine HCl	CPZ	$R_1 = -CH_2CH_2CH_2N(CH_3)_2$; $R_2 = Cl$	38 at 50 mM and pH = 6.7	90
	Promethazine HCl	PMT	$R = -CH_2CH(CH_3)N(CH_3)_2$; $R_2 = H$	26 at 50 mM and pH = 6.7	118
Tricyclic antidepressant					
	Imipramine HCl	IMP	$R_1 = N$; $R_2 = H$; $R_3 = CH_3–CH_2–CH_2–N(CH_3)_2$	49 at 100 mM and pH = 6.7	138
	Clomipramine HCl	CLP	$R_1 = N$; $R_2 = Cl$; $R_3 = CH_2–CH_2–CH_2–N(CH_3)_2$	32 at 50 mM and pH = 6.25	95
	Amitriptyline HCl	AMT	$R_1 = C$; $R_2 = H$; $R_3 = >CH–CH_2–CH_2–N(CH_3)_2$	25 at 50 mM and pH = 6.7	107
	Nortriptyline HCl	NOT	$R_1 = C$; $R_2 = H$; $R_3 = >CH–CH_2–CH_2–NH(CH_3)$	45 at 30 mM and pH= 7.07	119

The preceding discussion pertaining to mechanism of clouding in pure (or almost pure) systems is given as a prelude to the CPs observed in drug systems. Here, too, the phenomenon is related to hydration/dehydration of the entities, as well as their charge, concentration, size and shape, and other properties. In developing liquid formulations of these drugs, their CPs can be the key parameter as the normal body temperature is 12° above ambient. Phase separation of drug formulation under elevated temperatures such as in steam sterilization of parenteral product often leads to content heterogeneity. In the case of dispersed dosage forms, phase separation can result in physical instability. If the CP of pure drug is above room temperature, it may be close to physiological temperature. Also, it may change because of the presence of other components of the formulation (the pharmaceutical excipients). Human blood plasma has a pH close to 7.4. In some diseases pH may increase or decrease [81], which can also induce phase separation in the drug formulation administered during this time. All these points indicate that the effect of solution properties (effect of pH, buffer) of those additives that may be found in the body and of different pharmaceutical excipients on the clouding phenomenon in drug solutions is crucial in the rational design of more effective DDSs. Pharmaceutical excipients are the constituents of a drug formulation that are added in order to increase the stability, solubility, or bioavailability of the formulation. These are also used as preservatives and flavorings. Although they do not produce a medical effect, they cannot be considered as inert, as they can alter the physical properties of drugs, as can cmc and CP. Because clouding is concentration-dependent, it is essential to have a knowledge of clouding behavior of drugs under varying conditions of concentration, pH, and presence of additives. As the literature on the phase separation phenomenon in amphiphilic drugs is scarce, this chapter mainly summarizes the work done by our group on four antidepressants (AMT, NOT, IMP, CLP) and three phenothiazines (PMT, PMZ, CPZ) (for abbreviations, see Table 69.1). The experimental results shown in the figures are for PMT (50 mM). The CP values of pure drugs in SP buffer at the concentration used are listed in Table 69.1.

69.2.1 Effect of pH/Concentration

As per the requirement within a 24-h period, the body pH changes from a weak acid to a weak base. The question is then how pH may affect the phase behavior of a drug. One team [82, 83] observed a CP of ∼50°C for aqueous solution of 200 mM of AMT ($pK_a = 9.4$). They used sodium phosphate (SP) buffer and varied its concentration to see its effect on CP in terms of AMT. In yet another article, AMT concentration was varied at two SP concentrations of 10 mM and 500 mM [84]. They found an increase in CP with increase in drug and buffer concentrations. Also, the increase was less sensitive to drug concentration at higher SP concentration.

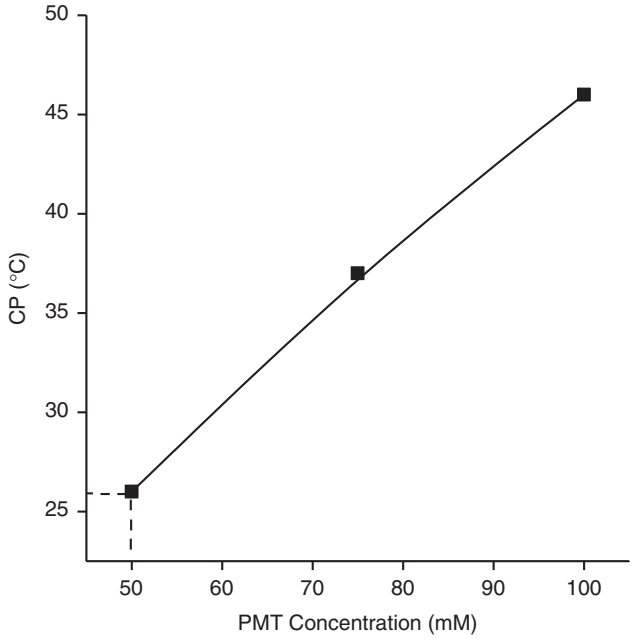


FIGURE 69.2 Effect of drug concentration on CP of PMT solution, prepared in 10 mM sodium phosphate buffer (pH = 6.7). Symbols depict the experimental points, and solid lines are drawn to guide the eye. (The same applies to all subsequent figures in which the various effects are shown.)

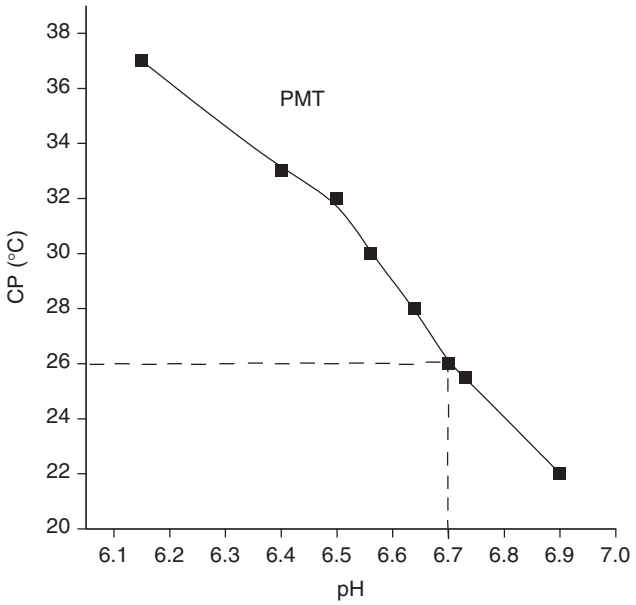


FIGURE 69.3 Effect of pH on CP of 50 mM PMT solution, prepared in 10 mM sodium phosphate buffer.

In these studies, pH was maintained at 6.7. At this pH most of the drug molecules would be in cationic form. They explained that excess of phosphate ions reduces the repulsion among drug headgroups and CP remains more or less constant. Kabir-ud-Din and coworkers fixed the concentration of buffer at 10 mM and varied the pH to observe the changes in the CP of the drug solutions. For all drugs the CP decreased with the increase in pH (Fig. 69.2). As stated above, charge of drug molecule is pH-dependent, and with increase in pH, an increasing number of molecules become neutral. This decreases the electrostatic repulsions experienced by the molecules at low pH values, and the molecules may come closer to each other. This also reduces the space among the headgroups [85], and CP decreases. An increase in the drug concentration increases the number of micelles. As drug monomers are positively charged, high drug concentration means more charged entities in the solutions (either micelles or monomers). This increases interparticle electrostatic repulsion (effect opposite to that of pH increase), and hence the CP increases (Fig. 69.3).

69.2.2 Effect of Electrolytes

Human muscles and neurons are activated by electrolyte activity between extracellular fluid or interstitial fluid, and intracellular fluid (fluid inside and outside or between cells). Sodium is concentrated in extracellular fluid and potassium, in intracellular fluid. Electrolytes may change the CP in any direction depending on their nature and concentration. Addition of electrolytes produces ions that can be classified into Hofmeister series [86] according to their size and other solution properties; ions on the right side of this series are known as *water structure breakers* or *chaotropes*, whereas ions on the left side are known as *water structure makers* or *kosmotropes* [87]. Alternatively, ions can also be classified on the basis of their adsorption/desorption ability [88]. Ions affect the CP by forming complexes with amphiphiles. Other authors [89] who studied the effect of sodium halides and alkali chlorides on the CP of 100 mM AMT (pH = 6.7), found that CP increases with the increase in salt concentration. The research group of Kabir-ud-Din also used inorganic salts to study their effect on CP of drugs [90–95]. The CP increased in the order: NaF < NaCl < NaBr and LiBr < NaBr < KBr (Fig. 69.4). F^-, Cl^-, and Br^- are counterions for the cationic drug micelles and directly interact with them. Although they decrease the charge of the drug micelles, at the same time, they increase the hydration of the micelles (as these ions are highly hydrated). The trend of CP increase is opposite to the hydrated size of the ion; hydrated radii of these ions increase in the order $Br^- < Cl^- < F^-$ [96]. Interaction of F^- with the drug micelles increases the micelle hydration more than with the addition of Cl^- or Br^-, and hence CP increase is sharper in presence of F^-. Results of UV–visible spectroscopy also support the above explanation: absorbance of Sudan III in drug–salt systems increased more with NaBr as compared to NaF. Because of its small hydrated size, Br^- could interact more strongly with the micelles and reduce the repulsions more than F^-. This results in micellar

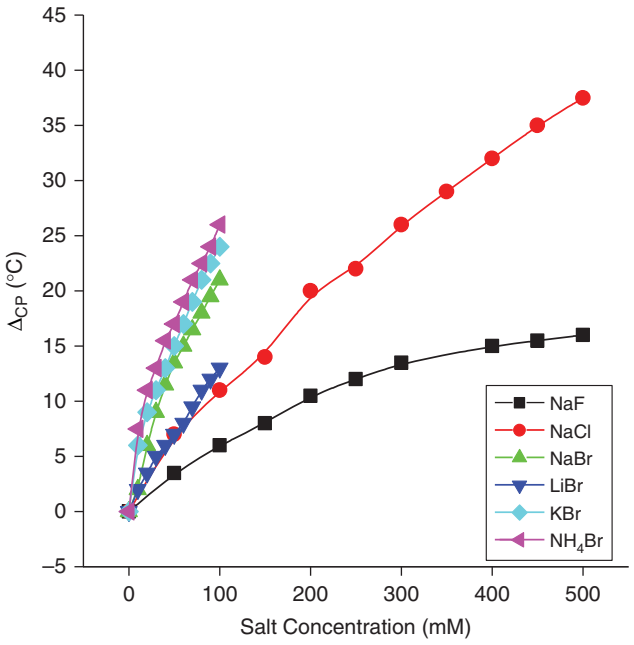


FIGURE 69.4 CP shift values (Δ_{CP}) of 50 mM PMT solutions, prepared in 10 mM sodium phosphate buffer (at pH = 6.7) as a function of electrolyte concentration.

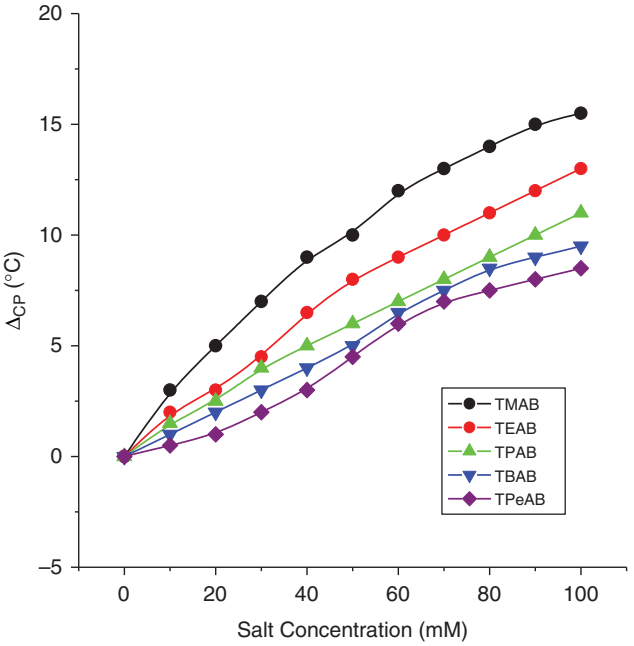


FIGURE 69.5 CP shift values (Δ_{CP}) of 50 mM PMT solutions, prepared in 10 mM sodium phosphate buffer (at pH = 6.7) as a function of quaternary ammonium salt concentration.

growth and more dye solubilized in these micelles, resulting in increase in the absorbance [94, 95].

Coions also affect the CP in the same way, although their line of action is different [90–95] (Fig. 69.4). These ions (Li^+, Na^+, K^+) affect the micelle hydration indirectly as they remain in the aqueous phase and decrease the availability of water to the micelles according to their hydrated radii. The larger the hydrated radius, the more water an ion pulls from the micelles. These cations affect the solvent structure, too; Li^+ and Na^+ ions exhibit stronger interactions with water molecules than with water itself and, hence, behave as water structure makers, while K^+ ion exhibits weaker interactions with water and acts as water structure breaker. Therefore, CP increase is slower with Li^+ than with K^+ (Na^+ is intermediate). The results also indicate that cations are less effective in changing the CP (as the difference in CP of solutions with K^+ and Na^+ is not significant). This is consistent with the Schulze–Hardy [97] rule, namely, that the main effect of the valence of the ion oppositely charged to the colloid is on the stability of the colloid.

Addition of quaternary ammonium bromides also increases the CP (Fig. 69.5); CP increase is greater with short alkyl chain salt [90–92,94,95]. The order of increase is as follows: tetramethylammonium bromide (TMAB) > tetraethylammonium bromide (TEAB) > tetrapropylammonium bromide (TPAB) > tetrabutylammonium bromide (TBAB) > tetrapentylammonium bromide (TPeAB). The salt cations contain alkyl chains and are water structure makers. As their chain length increases, their hydrophobicity also increases and TBA/TPeA are almost nonhydrated ions. Short-chain salts adsorb to the drug molecules, while long-chain ones form mixed micelles. Their adsorption/mixed micelle formation predominates over their water-structure-forming ability [98], and they increase the CP. Also, these salts increase the micelle hydration; the least hydrated salt is least effective in increasing the CP.

69.2.3 Effect of Urea/Thiourea



Urea ($H_2N—C—NH_2$) is a protein decomposition product that is being produced continuously in the human body in large quantities. This nitrogeneous waste is removed from the body to avoid toxicity. Urea is known to affect the micelles in two different ways depending on its concentration [99]. To explain the behavior of urea, two mechanisms have been proposed [100–102]. In one mechanism urea replaces water in the hydration shells of the solutes. As urea is thought to interact directly with the micelles, this mechanism is known as a *direct mechanism*. In the other one, urea affects the water structure and indirectly affects the micelles. This mechanism is, hence, known as an *indirect mechanism*. Urea is generally considered as a water structure breaker (following indirect mechanism) [103, 104]. However, molecular

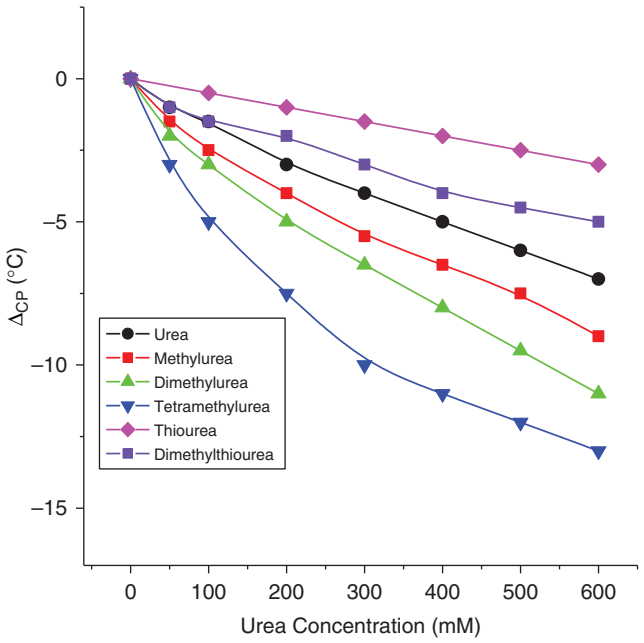


FIGURE 69.6 CP shift values (Δ_{CP}) of 50 mM PMT solutions, prepared in 10 mM sodium phosphate buffer (at pH = 6.7) as a function of urea/thiourea concentration.

dynamic studies indicate that there is only a small difference in the properties of water present in the solvation region of urea and those of bulk water [105, 106], which supports direct mechanism. In fact, urea follows both mechanisms depending on its concentration. In drug systems, urea decreases the CP [84,91,92,107–110] (Fig. 69.6). In these systems urea follows a direct mechanism. It replaces water molecules from the headgroup region and dehydrates micelles. One team [111] also explained their results of *n*-dodecylhexadecylethylene–urea systems by a direct mechanism. Alkylureas also decrease the CP; the rate of decrease is higher with a greater number of alkyl groups in the molecule. This again confirms the theory that urea in drug systems follows the direct mechanism as the addition of methyl groups increases the size of urea molecules and replaces more water from the hydrophilic region of the micelles.

Thiourea, on the other hand, increases the CP. Thiourea is considered as a better water structure breaker [112]. If we assume that urea follows an indirect mechanism and decreases the CP, then CP should decrease more with the addition of thiourea. However, opposite behavior is observed with thiourea. This is due to the difference in the nature of >C=O and >C=S bonds. As O atoms are more electronegative than S atoms, the electrons around S atoms will be delocalized and hence it would act as Lewis acid. An S atom in thiourea would behave as a positive center, and its addition would increase repulsions in the micellar system and CP would increase.

69.2.4 Effect of Alcohols

Alcohol is absorbed through the stomach or small intestine directly into the bloodstream, travels through the body, reaches every organ, and distributes throughout the water in the human body. The body immediately begins to try to get rid of the alcohol. Alcohol can change brain chemistry and become lethal in high doses. Alcohol molecules are slightly amphiphilic in nature as they possess a hydrophilic OH group and an alkyl chain. Their amphiphilicity depends on the length of their alkyl chain. Such molecules affect the structural and dynamic properties of micelles in two different ways: either by interacting with micelles or by changing the solvent properties [113]. Short-chain alcohols are hydrophilic molecules, while long-chain alcohols are hydrophobic in nature. Short- and medium-chain alcohols decrease the aggregation and size of surfactant micelles, whereas long-chain ones increase the aggregation number [114, 115]. Micelles even disappear when short-chain alcohols are added in large quantities [116]. They modify the properties of the solvent [117], and a mixed "water + alcohol" system would be a better solvent for amphiphilic monomers. The CP of drug solutions either remains unaffected or increases slightly [108,118–122] (Fig. 69.7). Pentanol and higher alcohols affect the CP strongly. Long-chain alcohols, because of the presence of long alkyl chains, solubilize in the micelles by forming mixed micelles and affect the micellar properties. The OH group of such alcohols intercalates between the charged headgroups [123], reducing the

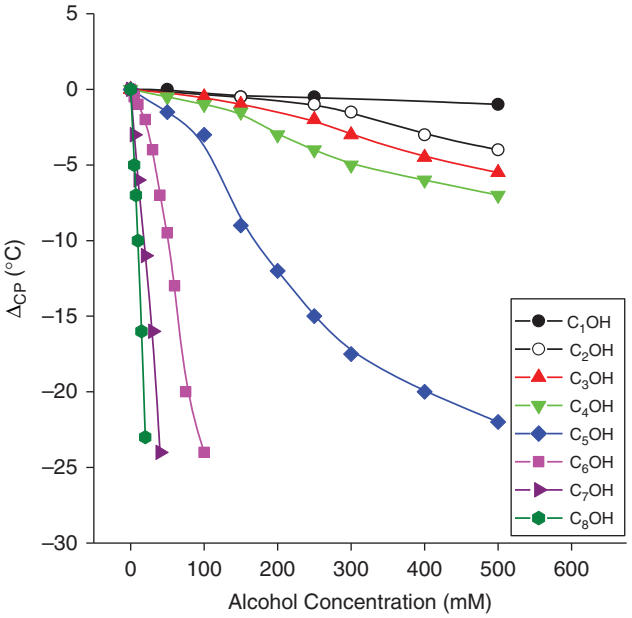


FIGURE 69.7 CP shift values (Δ_{CP}) of 50 mM PMT solutions, prepared in 10 mM sodium phosphate buffer (at pH = 6.7) as a function of alcohol (*n*-alkanols) concentration.

electrostatic repulsions, and results in compact micelles with a small headgroup area (a_0). Also, their hydrocarbon chains interact with the hydrophobic part and increase the hydrophobic interactions. This increases the volume of hydrophobic part (v_c) without affecting the length of hydrocarbon chain (l_c). Both these factors result in large and compact micelles (with high values of Mitchell–Ninham parameter [124], $R_p = v_c/a_0 l_c$). This compactness decreases the micelle hydration, and CP decreases. As the chain length of alcohol increases, hydrophobic volume or v_c also increases, which results in increase in the R_p value. A high R_p value ($^1/_3 \leq R_p \leq {}^1/_2$) indicates larger micelles with low hydration. Therefore, octanol and decanol decrease CP very sharply. The effect of change in position of OH of the alcohol molecules on the CP of 200 mM AMT has been studied [83] by taking three pentanol isomers. The authors [83] observed that CP increases in all the three systems; only the magnitude of increase was different for the three isomers. At a given alcohol concentration, 1-pentanol increased the CP most, while 3-pentanol was least effective. They explained this on the basis of the length of alcohol molecule. 2-Pentanol has chain length equal to that of butanol, and its effect is also equal to that of butanol. The CP with 3-pentanol was lower than the CP with either butanol or 2-pentanol.

Ethane-diol and propane-1,2-diol were found to be ineffective in changing the CP (Fig. 69.8) as these diols are highly hydrophilic and completely miscible with water. Allyl alcohol and cyclopentanol decreased the CP at high

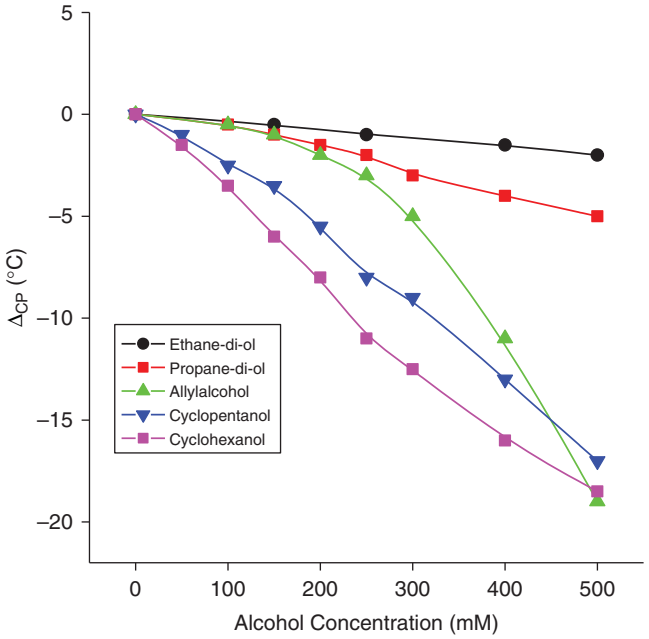


FIGURE 69.8 CP shift values (Δ_{CP}) of 50 mM PMT solutions, prepared in 10 mM sodium phosphate buffer (at pH = 6.7) as a function of alcohol (diols and cyclanols) concentration.

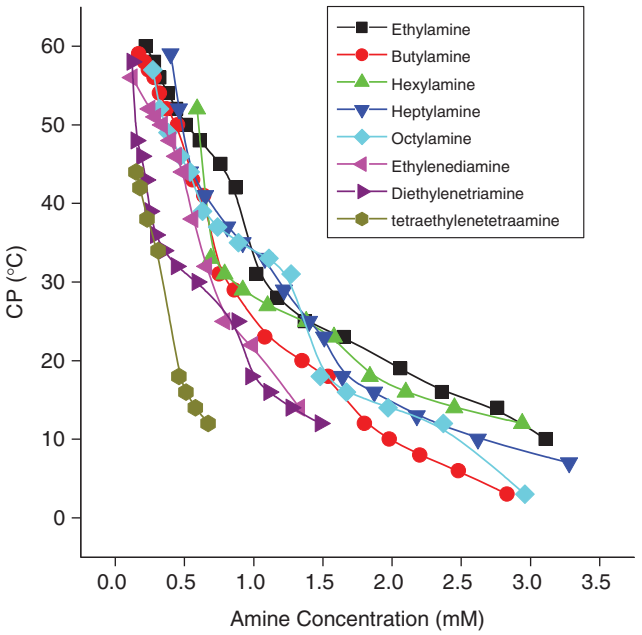


FIGURE 69.9 Variation of CP of 50 mM aqueous AMT solutions as a function of amine concentration.

concentrations, whereas cyclohexanol decreased it from the very beginning. Among these three, cyclohexanol is most hydrophobic and hence replaces more water from the micellar headgroup region [125].

69.2.5 Effect of Amines

Amines, like alcohols, are also slightly amphiphilic molecules. Blood and saliva contain amines and polyamines [126–129]. Stimulated mixed saliva contains lysine and arginine in ranges from 4 to 15 and 33 to 100 μg/mL, respectively [129], while stimulated parotid saliva contains even higher concentrations of these amines [129]. Other polyamines are also reported in saliva [126,127,130]. As shown in Fig. 69.9, 50 mM aqueous solutions of AMT exhibit CP with the addition of amines [131], which decreases with concentration. Amines, because of the presence of NH_2 group, hydrolyze on the surface of micelles [132]. Ethylenediamine, diethylenetriamine. and tetraethylenepentamine also decrease the CP of AMT solution. Nitrogen atom of amines forms hydrogen bond with the water molecules and decreases the CP. However, as solutions with amines are in water (without buffer), we cannot compare their results with those for alcohols.

69.2.6 Effect of Amino Acids

The role of amino acids is pivotal both as building blocks of proteins and as intermediates in metabolism. Outside proteins, they perform critical roles in processes such as neurotransmitter transport and biosynthesis. All amino acids

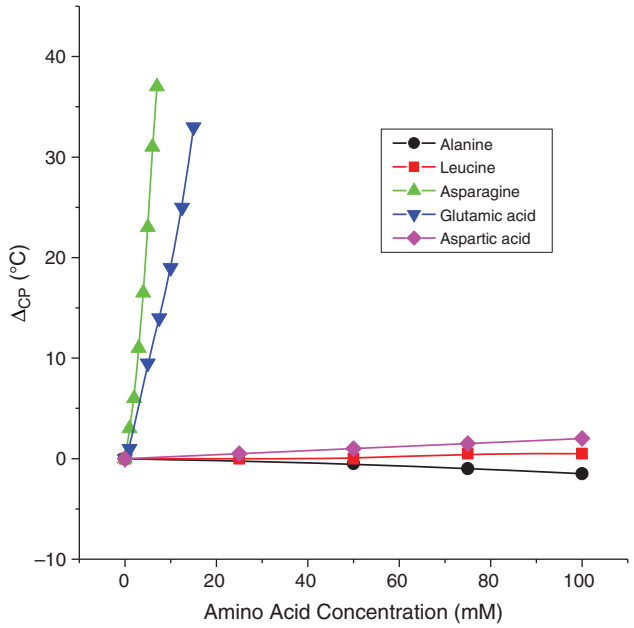


FIGURE 69.10 CP shift values (Δ_{CP}) of 50 mM PMT solutions, prepared in 10 mM sodium phosphate buffer (at pH = 6.7) as a function of amino acid concentration.

have similar functional groups but different sidechains, and their behavior in changing the CP of drug systems was found to be dependent on the nature of sidechains [107, 108,118,120–122] (Figs. 69.10 and 69.11). Acidic amino acids (aspartic acid, glutamic acid) carry negatively charged sidechains, and their interactions with micelles would increase the micelle hydration; hence CP increases sharply. Uncharged polar (glycine, serine, asparagine) and nonpolar amino acids (alanine, leucine, threonine, proline, methionine, phenylalanine) either remain in the bulk or partition in micellar interior and do not affect the CP. Basic amino acids (lysine, arginine, histidine) decreased the CP by replacing water from the headgroup region. Hydrochloride salts (histidine.HCl, histidine methylester.2HCl, lysine.HCl, arginine.HCl) have a positive charge, and on interacting with the micelles they increased the repulsions among headgroups, resulting in loose micelles. This increased the hydration of micelles as well as the CP.

69.2.7 Effect of Sugars

Sugars work as fuel for the body by providing the required energy for sustenance. Blood sugar is transported through the bloodstream to all the body cells. Sugars decrease the CP of drug solutions [107, 108,118–122] (Fig. 69.12), although the mechanism is different from that in long-chain alcohols. Sugars act as kosmotropes [133] and shift the equilibrium

$$nH_2O \rightleftharpoons (H_2O)_n$$

to the right. Thus they decrease the availability of water to the drug micelles, thereby decreasing the hydration of the

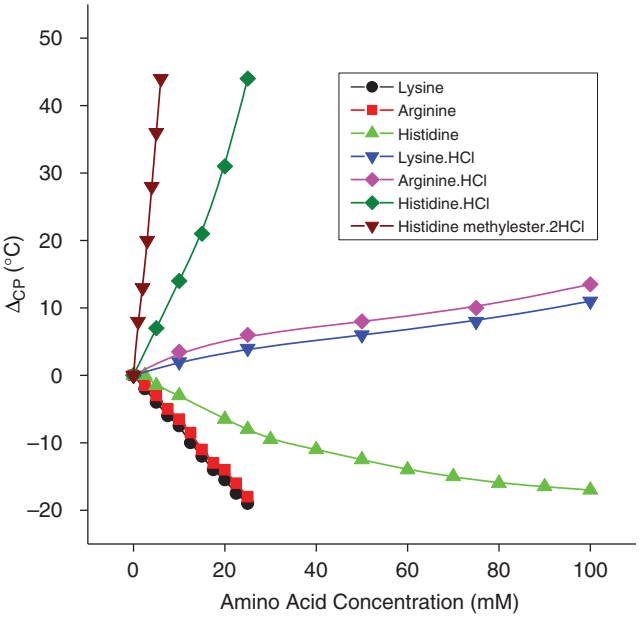


FIGURE 69.11 CP shift values (Δ_{CP}) of 50 mM PMT solutions, prepared in 10 mM sodium phosphate buffer (at pH = 6.7) as a function of amino acid concentration.

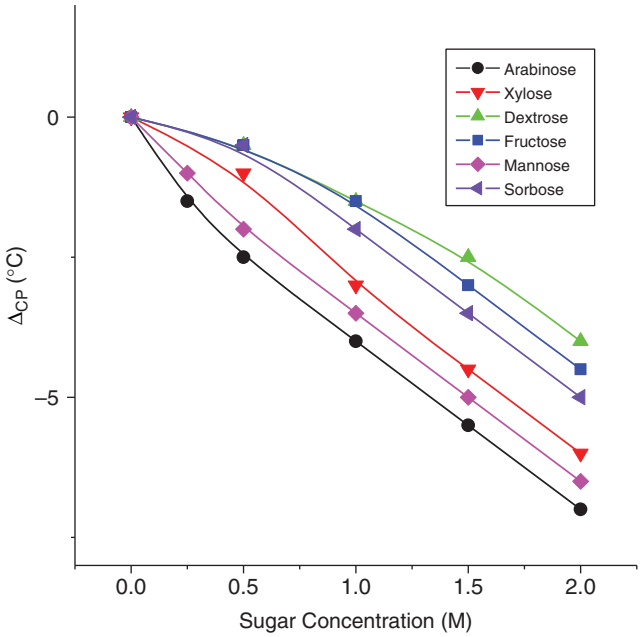


FIGURE 69.12 CP shift values (Δ_{CP}) of 50 mM PMT solutions, prepared in 10 mM sodium phosphate buffer (at pH = 6.7) as a function of sugar concentration.

micelles and, as a result, CP decreases. This decrease in hydration increases the repulsion among drug headgroups, and micellar size decreases. This is confirmed by the dye solubilization experiments performed on PMZ–sugar systems [122], where solubilization of Sudan III dye decreases in presence of sugars.

69.2.8 Effect of Polymers

Pluronics are the triblock copolymers of hydrophilic ethylene oxide (EO) and hydrophobic propylene oxide (PO). They are widely studied for applications in drug delivery [134, 135]. Polymers of the category of polyvinylpyrrolidone (PVP) of different molecular weights also affect the CP [107,136,137] (Fig. 69.13). With PVP 15, three regions––constancy, slight decrease and increase––were observed. As the molecular weight of the polymer increases, the constancy region disappears, the CP-decreasing region increases, and the CP-increasing region decreases. For the highest-molecular-weight polymer used (PVP 90), the CP at all concentrations remained below that of the CP of the pure drug. Polymers interact with drug micelles and affect the micelle hydration to a different extent. Pluronic PF127 increases the CP, while 10R8 decreases it [82]. In PF127, the PO part is in between two EO blocks, whereas in 10R8, EO is in between two PO blocks. As hydrophilic parts in PF127 are at the side, the copolymer increases the CP slightly while the opposite occurs in 10R8 –AMT systems.

69.2.9 Effect of Surfactants

There are many applications of pharmaceutical surfactants; the most important ones are solubilization, inclusion, and vectorization of hydrophobic drugs. Presence of surfactants in drug solutions affects the CP of drugs depending on their concentration, structure, and nature [107,109,110,119,136–140]. Very low concentrations of an ionic surfactant increase the solubility and the cloud point. This is due to either mixed micelle formation (in the case of a clouding surfactant) or an association between the surfactant and the polymer (in the case of clouding polymer). This results in the formation of charged aggregates which are much more difficult to concentrate in one of the phases due to the unfavorable electrostatic interaction. CPs of drug solutions in presence of anionic surfactants sodium dodecylsulfate (SDS) and sodium dodecylbenzenesulfonate (SDBS) show a peaked behavior (Fig. 69.14). The increase is found to be steeper with SDS than SDBS, while the decrease is more pronounced for SDBS. When added in low amounts, these anionic surfactants form ion pairs with the cationic drug molecules and hinder micellar association. Therefore, CP increases up to a certain concentration. Above it, these surfactants begin to form mixed micelles. Because of their long hydrophobic tails, the surfactant monomers intercalate between drug molecules in the micelles. As a result, they increase the hydrophobic interactions and v_c. At the same time, their charge, opposite to the charge of drug molecules, reduces the electrostatic repulsions among micellar heads and decreases the value of a_0.

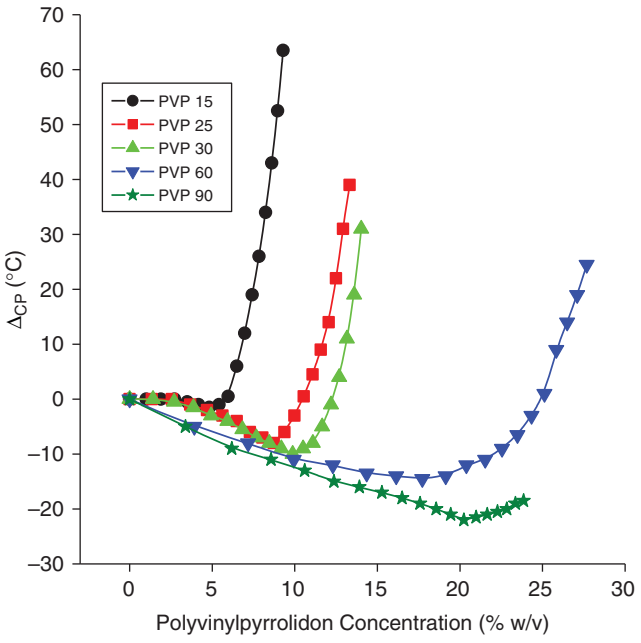


FIGURE 69.13 CP shift values (Δ_{CP}) of 50 mM PMT solutions, prepared in 10 mM sodium phosphate buffer (at pH = 6.7) as a function of polymer concentration.

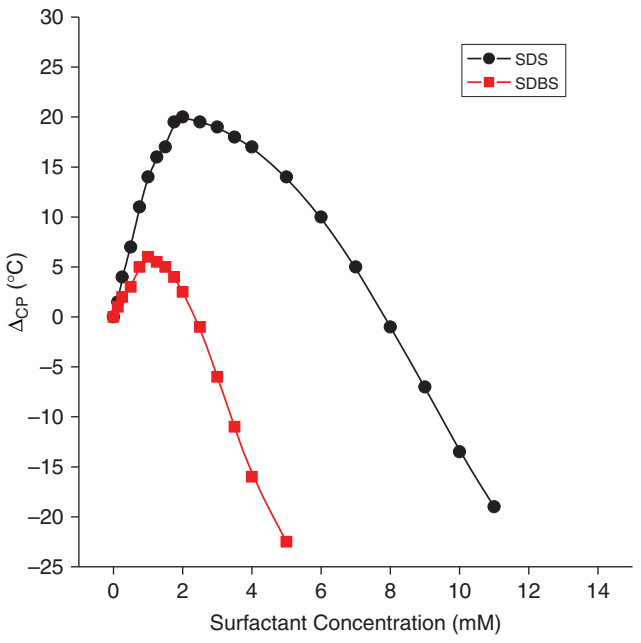


FIGURE 69.14 CP shift values (Δ_{CP}) of 50 mM PMT solutions, prepared in 10 mM sodium phosphate buffer (at pH = 6.7) as a function of anionic surfactant concentration.

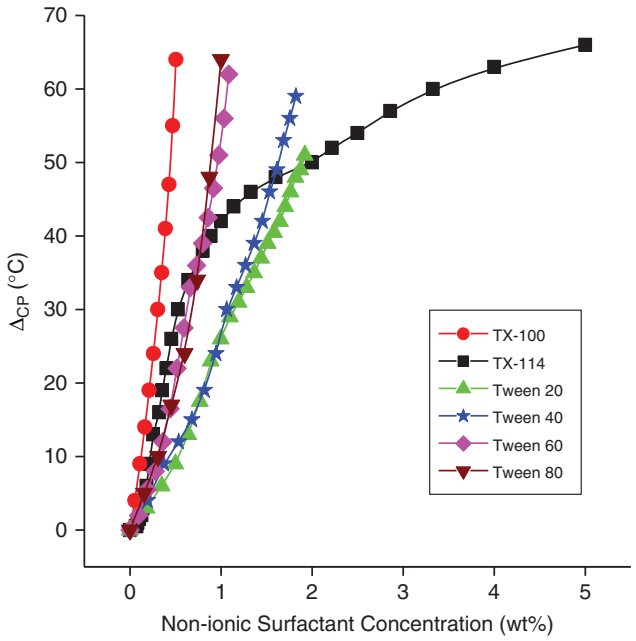


FIGURE 69.15 CP shift values (Δ_{CP}) of 50 mM PMT solutions, prepared in 10 mM sodium phosphate buffer (at pH = 6.7) as a function of nonionic surfactant (TX and Tweens) concentration.

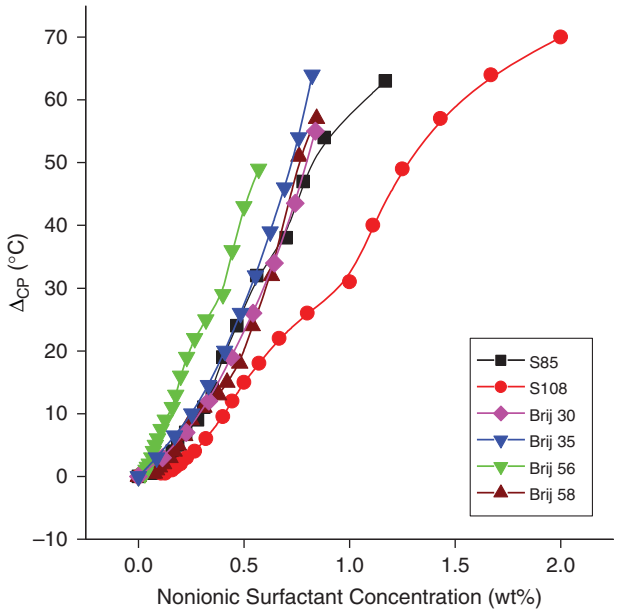


FIGURE 69.16 CP shift values (Δ_{CP}) of 50 mM PMT solutions, prepared in 10 mM sodium phosphate buffer (at pH = 6.7) as a function of nonionic surfactant concentration.

These two factors increase the R_p value, and CP decreases. SDBS contains a benzene ring in addition to the dodecyl chain. As a phenyl group is considered equivalent to three or four carbons in straight chain [141], the hydrophobic part of SDBS can be taken as longer than that of SDS. That is why CP increase is slower and decrease is sharper with SDBS than with SDS.

Nonionic surfactants of all types increase the CP (Figs. 69.15 and 69.16). As they contain highly hydrophilic oxyethylene chains, the resultant drug–nonionic surfactant mixed micelles would be highly hydrated and extra heating would be required to dehydrate these micelles. As a result, phase separation occurs at higher temperatures.

Cationic surfactants too increase the CP (Fig. 69.17), although the cause of increase is different from that in nonionic or anionic surfactants. Cationic surfactants, as already stated, form mixed micelles with these drugs. During this process they increase the hydration of the mixed micelles. As the chain length of the cationic surfactants increases, their tendency to form mixed micelles also increases. Therefore, surfactant with longer hydrophobic tail begins to increase the CP at lower concentrations.

The addition of cationic geminis of the class alkanediyl – α, ω – bis(dimethylalkylammonium bromides) (m-s-m type) also increases the CP (Fig. 69.18). Their cmc values are much lower [142] than those of conventional surfactants, and hence their CP-boosting effect is found to be higher than that of conventional surfactants. Within a series of geminis (either 16-*s*-16 or 14-*s*-14), the CP-boosting effect increases with increasing spacer length *s*. Increase in length of spacer increases the surface charge of the micelles [142], and the mixed micelles experience more electrostatic repulsions. This increases the headgroup area occupied by a single molecule, and hydration increases which, in turn, results in increase in the CP.

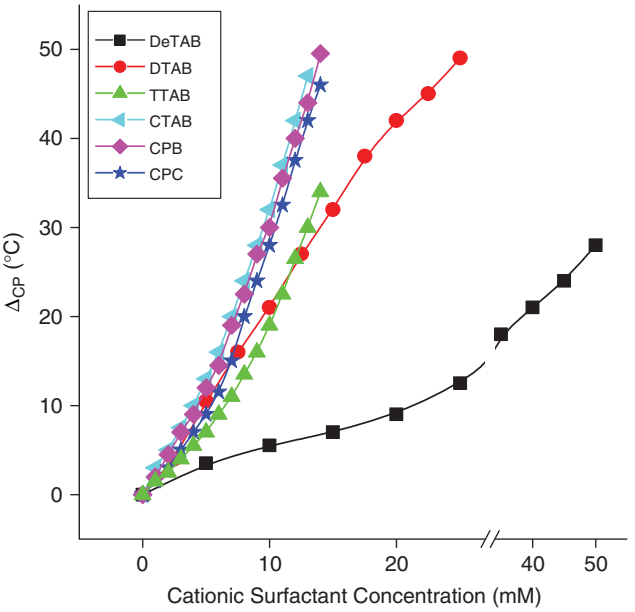


FIGURE 69.17 CP shift values (Δ_{CP}) of 50 mM PMT solutions, prepared in 10 mM sodium phosphate buffer (at pH = 6.7) as a function of cationic surfactant concentration.

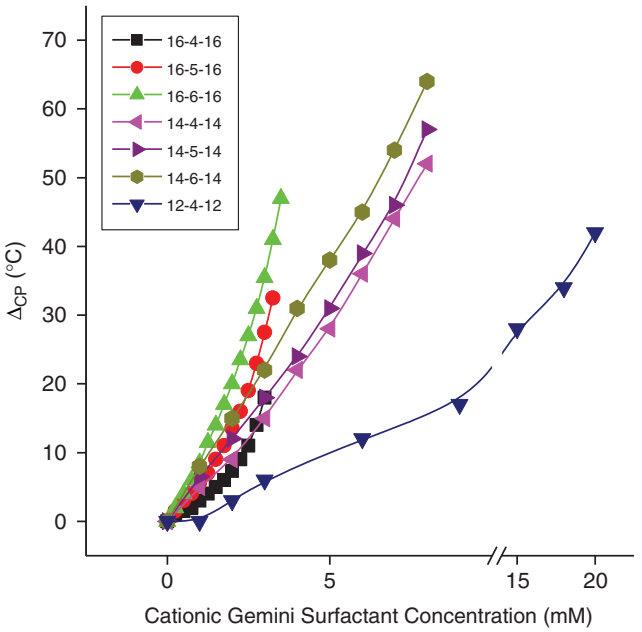


FIGURE 69.18 CP shift values (Δ_{CP}) of 50 mM PMT solutions, prepared in 10 mM sodium phosphate buffer (at pH = 6.7) as a function of cationic gemini surfactant concentration.

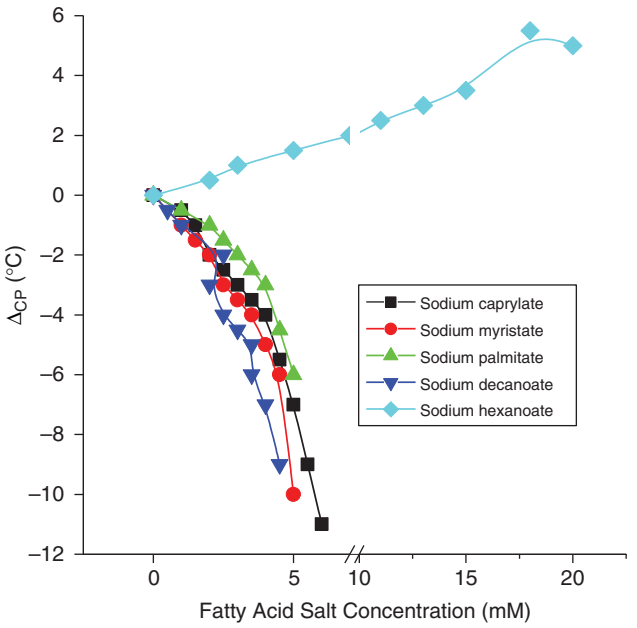


FIGURE 69.19 CP shift values (Δ_{CP}) of 50 mM PMT solutions, prepared in 10 mM sodium phosphate buffer (at pH = 6.7) as a function of fatty-acid concentration.

69.2.10 Effect of Fatty Acids (Sodium Salts)

The essential fuels of the heart are fatty acids, and thus their role is important in life and death of cardiac cells. Fatty-acid salts with 8-, 10-, 14-, and 16-carbon chains cause a peaked behavior in CP of drugs (except in PMT), while salt with 6-carbon chains continuously increases the CP [139, 140] (Fig. 69.19). As these are sodium salts, their moieties carry a negative charge and their behavior is similar to that of anionic surfactants. The carboxyl group is a highly hydrated group, and its presence in the headgroup region of the micelles increases the water content there. As a result, the fatty acids initially show a CP-boosting effect. However, these fatty-acid salts also possess long alkyl chains, and their penetration into the palisade layer increases the hydrophobic interactions. At low concentrations, the first factor dominates, whereas at high concentrations the second factor dominates and CP decreases. Sodium hexanoate has a relatively shorter chain and is slightly hydrophilic. Therefore, the CP-decreasing region is absent in this salt–drug system.

69.2.11 Effect of Bile Salts

Bile salts are synthesized in the liver, concentrate in the gallbladder, and are discharged into the duodenum through a biliary duct. Hence, the amphiphilic moiety of bile salts carries a negative charge. The effect of NaC and NaDC on the CP of drug solutions is similar to that of fatty acids (Fig. 69.20). NaC and NaDC both showed peak behavior in CP–[bile salt] curves (in all drugs except PMT) [139, 140]. At low concentrations these salts increase the hydration of the micelles, while at high, added concentrations, compact micelles form and hydration of the micelles decreases. Of the two, NaC contains an extra OH group and is more hydrophilic. Therefore,

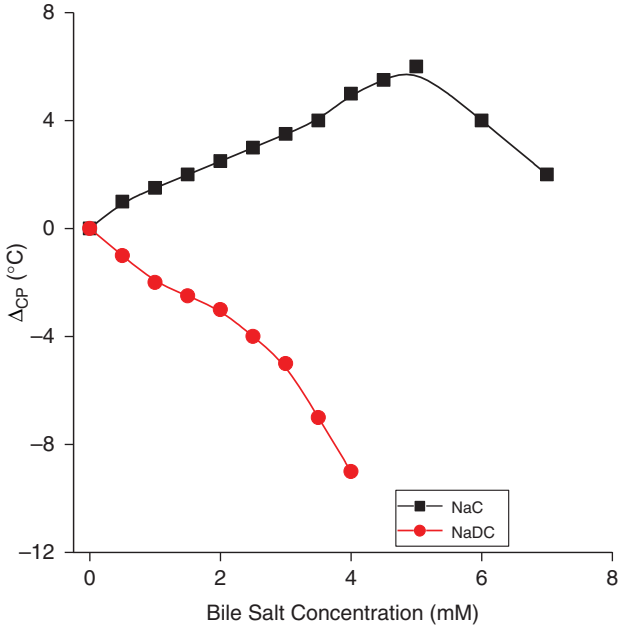


FIGURE 69.20 CP shift values (Δ_{CP}) of 50 mM PMT solutions, prepared in 10 mM sodium phosphate buffer (at pH = 6.7) as a function of bile acid salt concentration.

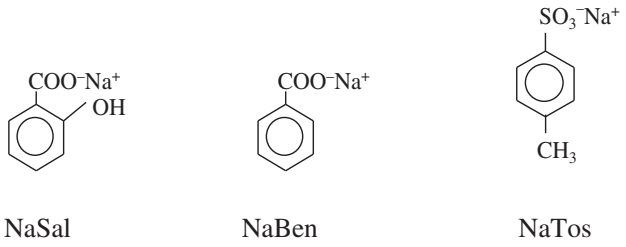


FIGURE 69.21 Structures of hydrotropes used.

CP increase is high and CP decrease is slow in the presence of NaC, as NaC increases the hydration to a greater extent and a higher concentration is required to decrease the CP.

69.2.12 Effect of Hydrotropes

Hydrotropes are surface-active and highly water-soluble compounds that can increase the solubility of sparingly soluble solutes in water. These organic salts are important in pharmaceutical processes such as microemulsion and drug formulations [143, 144]. We have used three hydrotropes having benzene (or substituted benzene) as the hydrophobic part and carboxylate/sulfonate as the hydrophilic part or the headgroup [e.g., sodium salicylate (NaSal), sodium benzoate (NaBen), and sodium tosylate (NaTos)] (Fig. 69.21). Hence, the amphiphilic moiety carries a negative charge. These salts also provide an anionic moiety when dissolved in water and neutralize the charge on drug molecules. At the same time they increase the hydration and also micellar growth by intercalating between the headgroups of drugs (as they contain the hydrophilic groups). The CP of drug solutions shows first an increase and then a decrease with increase in hydrotrope concentration [139, 140] (Fig. 69.22) wherein the magnitude of increase and decrease depends on the structure and nature of hydrotrope. NaBen possesses a carboxylate group, NaSal contains a carboxylate group and a hydroxyl group, and NaTos has a sulfonate group. Hence, the order of their hydrophilicity is as follows: NaSal > NaBen > NaTos. In NaSal, the OH group is at *ortho* position, and in cationic micelles it intercalates between the cationic headgroups [145]. This favors micellar growth, and CP decrease is the fastest with NaSal. Also, the π-electron cloud of the phenyl ring of the hydrotropes interacts with the cationic amine group of drugs.

69.2.13 Effect of Cyclodextrins

Cyclodextrins are toroidally shaped oligosaccharides composed of α-D-glucopyranoside units. α, β, γ-Cyclodextrins contain six, seven, and eight glucose units, respectively, in a ring creating a cone-shaped structure. Cyclodextrins have wide applications in food, pharmaceutical, and chemical industries [146]. β-Cyclodextrin is known for its ability to

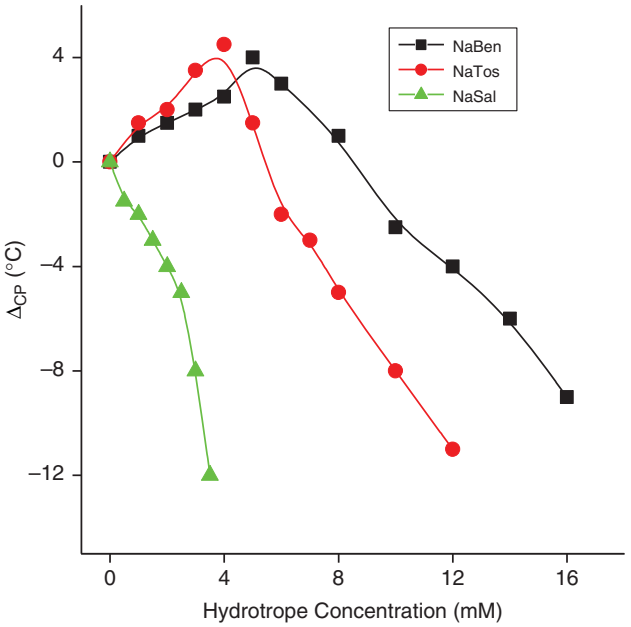


FIGURE 69.22 CP shift values (Δ_{CP}) of 50 mM PMT solutions, prepared in 10 mM sodium phosphate buffer (at pH = 6.7) as a function of hydrotrope concentration.

form inclusion complexes with surfactants [147] and is found to increase the CP of nonionic surfactants [148]. However, in drug systems, the CP decreases in its presence [139, 140] (Fig. 69.23). Perhaps, with the cationic drugs, cyclodextrin acts as water structure maker and does not form inclusion

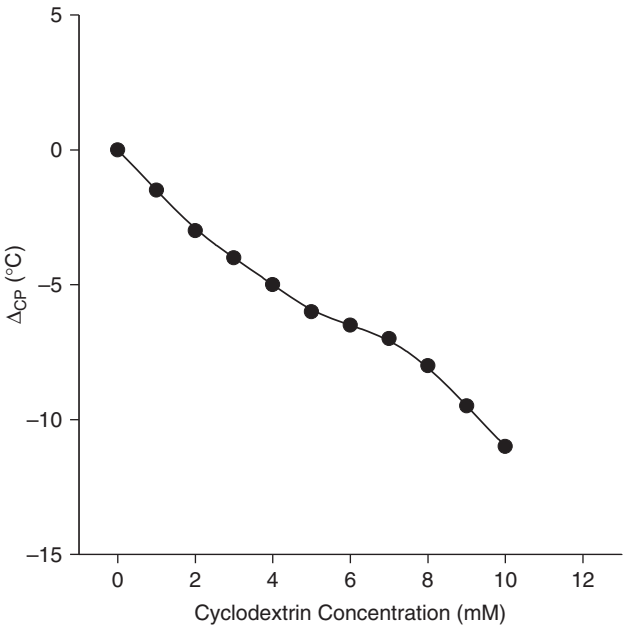


FIGURE 69.23 CP shift values (Δ_{CP}) of 50 mM PMT solutions, prepared in 10 mM sodium phosphate buffer (at pH = 6.7) as a function of cyclodextrin concentration.

complexes. It was mentioned earlier that water structure makers decrease the cmc by increasing the hydrophobic interaction. Increase in hydrophobic interactions decreases the CP also.

69.2.14 Effect of Phospholipids

Phospholipids, the essential constituents of biological membranes, are involved in numerous biological activities in living organisms [149]. Phospholipids and phospholipid derivatives, under special conditions, form mixed micelles with suitable amphiphiles [150, 151]; an important example is the mixed micelles formed between phospholipids (lecithin) and bile salts [152] in the human digestive tract to dissolve cholesterol. Cloud-point temperature measurements, performed with drugs as a function of added phospholipid type and concentration [153] (Fig. 69.24), show that in AMT, all the phospholipids decrease the CP, whereas in CLP systems, the phospholipids increase the CP only at low concentrations. Although PMZ and PMT are almost similar in structure, their behaviors are different. Adding phospholipids to PMZ solutions not only leads to transition temperatures shifted toward lower values but also results in a broader transition as in PMT solutions. For CLP and IMP the behavior is similar, only the values are higher and broader for IMP. Presence of Cl atom in CLP renders the molecule slightly more hydrophobic, and hence increase in CP is higher and decrease in CP is lower.

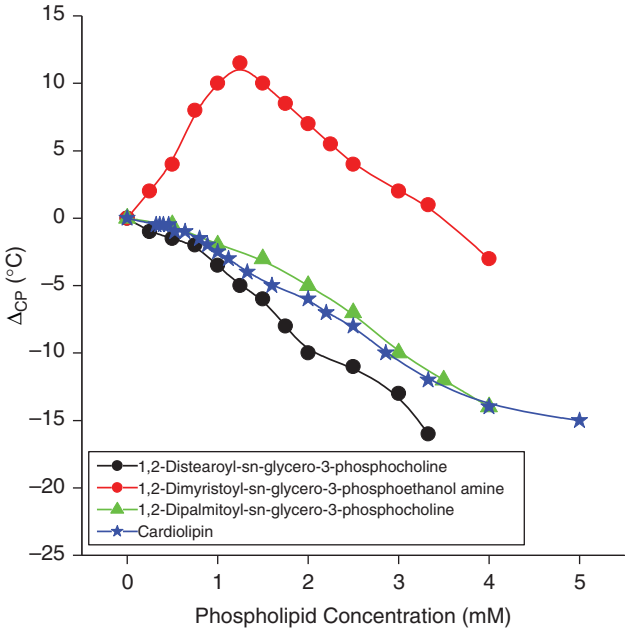


FIGURE 69.24 CP shift values (Δ_{CP}) of 50 mM PMT solutions, prepared in 10 mM sodium phosphate buffer (at pH = 6.7) as a function of phospholipid concentration.

REFERENCES

[1] Luzatti, V. (1968). The structure of the liquid crystalline phases of lipid-water systems. In Chapman, D. (ed.), *Biological Membranes.* Academic Press, New York.

[2] Israelachvili, J.N. (1986). *Intermolecular and Surface Forces*. Academic Press, London.

[3] Schreier, S., Malheiros, S.V.P., de Paula, E. (2000). Surface active drugs: Self-association and interaction with membranes and surfactants. Physicochemical and biological aspects. *Biochim. Biophys. Acta* **1508**, 210–234.

[4] Lasic, D.D. (1993). *Liposomes: From Physics to Applications*. Elsevier Science, Amsterdam.

[5] Barenholz, Y., Lasic, D.D. (eds.) (1996). *Handbook of Nonmedical Applications of Liposomes*. CRC Press, New York.

[6] Griffin, W.C. (1949). Classification of surface-active agents by "HLB." *J. Cosmetic Sci.* **1**, 311–326.

[7] Tanford, C. (1980). *The Hydrophobic Effect: Formation of Micelles and Biological Membranes.* Wiley, New York.

[8] Mukerjee, P. (1975). In van Olphen, H., Mysels, K.J. (eds.), *Physical Chemistry: Enriching Topics from Colloid and Surface Science*. Theorex, La Jolla, CA.

[9] Mukerjee, P. (1974). Micellar properties of drugs: Micellar and nonmicellar patterns of self-association of hydrophobic solutes of different molecular structures-monomer fraction, availability, and misuses of micellar hypothesis. *J. Pharm. Sci.* **63**, 972–981.

[10] Attwood, D., Florence, A.T. (1983). *Surfactant Systems, Their Chemistry, Pharmacy and Biology*. Chapman & Hall, New York.

[11] King, S.Y., Basista, A.M., Torosian, G. (1989) Self- association and solubility behaviors of a novel anticancer agent, Brequinar sodium. *J. Pharm. Sci.* **78**, 95–100.

[12] Rades, T., Muller-Goymann, C.C. (1997). Investigations on the micellisation behaviour of fenoprofen sodium. *Int. J. Pharm.* **159**, 215–222.

[13] Hwang, P.M., Vogel, H. (1998). Structure-function relationships of antimicrobial peptides. *Int. J. Biochem. Cell Biol.* **76**, 235–246.

[14] Attwood, D. (1995). The mode of association of amphiphilic drugs in aqueous solution. *Adv. Colloid Interface Sci.* **55**, 271–303.

[15] Taboada, P., Attwood, D., Ruso, J.M., Garcia, M., Mosquera, V. (2000). Static and dynamic light scattering study on the association of some antidepressants in aqueous electrolyte solutions. *Phys. Chem. Chem. Phys.* **2**, 5175–5179.

[16] Kommuru, T.R., Gurley, B., Khan, M.A., Reddy, I.K. (2001). Self-emulsifying drug delivery systems (SEDDS) of coenzyme Q10: Formulation development and bioavailability assessment, *International J. Pharm.* **212**, 233–246.

[17] Malmsten, M. (2006). Soft drug delivery systems. *Soft Matt.* **2**, 760–769.

[18] Rangel-Yagui, C.O., Junior, A.P., Tavares, L.C. (2005). Micellar solubilization of drugs. *J. Pharm. Pharm. Sci.* **8**, 147–163.

[19] Malmsten, M. (2002). *Surfactants and Polymers in Drug Delivery*, Marcel Dekker, New York.

[20] Chan, J., El Maghraby, G.M.M., Craig, J.P., Alany, R.G. (2007). Phase transition water-in-oil microemulsions as ocular drug delivery systems: In vitro and in vivo evaluation. *Int. J. Pharm*. **328**, 65–71.

[21] Omray, L.K., Kohli, S., Khopade, A.J., Patil, S., Gajbhiye, A., Agrawal, G.P. (2008). Development of mesophasic microreservoir-based transdermal drug delivery system of propranolol. *Indian J. Pharm. Sci*. **70**, 578–584.

[22] Aggarwal, G., Dhawan, S. (2009). Development, fabrication and evaluation of transdermal drug delivery system–a review. *Pharm. Rev*. **7**, paper # 5.

[23] Strickley, R.G. (2004). Solubilizing excipients in oral and injectable formulations. *Pharm. Res.* **21**, 201–230.

[24] Ross, B.P., Braddy, A.C., McGeary, R.P., Blanchfield, J.T., Prokai, L., Toth, I. (2004). Micellar aggregation and membrane partitioning of bile salts, fatty acids, sodium dodecyl sulfate, and sugar-conjugated fatty acids: Correlation with hemolytic potency and implications for drug delivery. *Mol. Pharm.* **1**, 233–245.

[25] Kabir-ud-Din, Rub, M.A., Naqvi, A.Z. (2011). Aqueous amphiphilic drug (amitriptyline hydrochloride)-bile salt mixtures at different temperatures. *Colloids Surf. B: Biointerfaces* **84**, 285–291.

[26] Kabir-ud-Din, Al-dahbali, G.A., Naqvi, A.Z., Akram, M. (2015). Adsorption and micellization behavior of mixtures of amphiphilic drugs with small amounts of bile salts. *Tenside, Surfac. Deterg.* **52**, 271–279.

[27] Sheu, M.T., Chen, S.Y., Chen, L.C., Ho, H.O. (2003). Influence of micelle solubilization by tocopheryl polyethylene glycol succinate (TPGS) on solubility enhancement and percutaneous penetration of estradiol. *J. Control. Release* **88**, 355–368.

[28] Hulsmann, S., Backensfeld, T., Bodmeier, R. (2001). Stability of extruded 17β- estradiol solid dispersions. *Pharm. Devel. Technol.* **6**, 223–229.

[29] Amsellem, E., Derrien, F., Lanquetin, M., Paris, J., Marty, J.P. (1998). In vitro studies on the influence of carbomers on the availability and acceptability of estradiol gels. *Arzneimittel Forschung Drug Res*. **48**, 492–496.

[30] Fang, J.Y., Yu, S.Y., Wu, P.C., Huang, Y.B., Tsai, Y.H. (2001). In vitro skin permeation of estradiol from various proniosome formulations. *Int. J. Pharm.* **215**, 91–99.

[31] Söderlind, E., Wollbratt, M., von Corswant, C. (2003). The usefulness of sugar surfactants as solubilizing agents in parenteral formulations. *Int. J. Pharm.* **252**, 61–71.

[32] Sparreboom, A., van Zuylen, L., Brouwer, E., Loos, W.J., de Bruijn, P., Gelderblom, H., Pillay, M., Nooter, K., Stoter, G., Verweij, J. (1999). Cremophor EL-mediated alteration of paclitaxel distribution in human blood: Clinical pharmacokinetic implications. *Cancer Res*. **59**, 1454–1457.

[33] Vieira, O.V., Hartmann, D.O., Cardoso, C.M.P., Oberdoerfer, D., Baptista, M., Santos, M.A.S., Almeida, L., Ramalho-Santos, J., Vaz, W.L.C. (2008). Surfactants as microbicides and contraceptive agents: A systematic in vitro study. *PLoS ONE* **3**(8), e2913.

[34] Incio, A.C., Mesquita, K.A., Baptista, M., Vaz, W.L.C., Vieira, O.V. (2011). In vitro surfactant structure-toxicity relationships: Implications for surfactant use in sexually transmitted infection prophylaxis and contraception. *PLoS ONE* **6**(5), e19850.

[35] Almeida, J.A.S., Marques, E.F., Jurado, A.S., Pais, A.A.C.C. (2010). The effect of cationic gemini surfactants upon lipid membranes. An experimental and molecular dynamics simulation study. *Phys. Chem. Chem. Phys.* **12**, 14462–14476.

[36] Wiedmann, T.S., Bhatia, R., Wattenberg, L.W. (2000). Drug solubilization in lung surfactant. *J. Control. Release* **65**, 43–47.

[37] Barber, T.A. (1999). *Control of Particulate Matter Contamination in Healthcare Manufacturing*. Interpharm Press, Englewood, CO.

[38] Akers, M.K., Larrimore, D., Guazzo, D. (2003). *Parenteral Quality Control: Sterility, Pyrogen, Particulate, and Package Integrity Testing*, 3rd ed. Informa HealthCare, New York.

[39] Appell, J., Porte G. (1983). Cloud points in ionic surfactant solutions. *J. Phys. Lett.* **44**, 689–695.

[40] Warr, G.G., Zemb, T.N., Drifford, M. (1990). Liquid-liquid phase separation in cationic micellar solutions. *J. Phys. Chem.* **94**, 3086–3092.

[41] Yu, Z.J., Xu, G. (1989). Physicochemical properties of aqueous mixtures of tetrabutylammonium bromide and anionic surfactants. 1. Temperature-induced micellar growth and cloud point phenomenon. *J. Phys. Chem.* **93**, 7441–7445.

[42] Smith, A.M., Holmes, M.C., Pitt, A., Harrison, W., Tiddy, G.J.T. (1995). Lamellar phases in contact with the lower consolute loop of ionic surfactant-water systems. *Langmuir* **11**, 4202–4204.

[43] Kumar, S., Sharma, D., Kabir-ud-Din (2000). Cloud point phenomenon in anionic surfactant + quaternary bromide systems and its variation with additives. *Langmuir* **16**, 6821–6824.

[44] Quina, F.H., Hinze, W.L. (1999). Surfactant-mediated cloud point extractions: An environmentally benign alternative separation approach. *Industr. Eng. Chem. Res.* **38**, 4150–4168.

[45] McCarroll, M.E., Toerne, K., von Wandruszka, R. (1998). Micellar fluidity and preclouding in mixed surfactant solutions. *Langmuir* **14**, 2965–2969.

[46] McCarroll, M.E., Toerne, K., von Wandruszka, R. (1998). Preclouding in mixed micellar solutions. *Langmuir* **14**, 6096–6100.

[47] Maclay, W.N. (1956). Factors affecting the solubility of nonionic emulsifiers. *J. Colloid Sci*. **11**, 272–285.

[48] Szejtli, J. (1983). Dimethyl-β-cyclodextrin as parenteral drug carrier. *J. Inclusion Phenom. Macrocycl. Chem.* **1**, 135–150.

[49] Chen, S.H., Ku, C.Y., Rouch, J., Tartaglia, P., Cametti, C., Samseth, J. (1993). Structure and dynamics of dense water-in-oil microemulsions below percolation threshold. *J. Phys. IV* **3**, C1-143

[50] Warner-Schmid, S., Hoshi, S., Armstrong, D.W. (1993). Removal of organic compounds from water via cloud-point

extraction with permethyl hydroxypropyl-β-cyclodextrin. *Separ. Sci. Technol.* **28**, 1009–1018.

[51] Herrmann, K.W., Brushmiller, J.G., Courchene, W.L. (1966). Micellar properties and critical opalescence of dimethyalkylphosphine oxide solutions. *J. Phys. Chem.* **70**, 2909–2918.

[52] Lang, L.C., Morgan, R.D. (1980). Nonionic surfactant mixtures. I. Phase equilibria in $C_{10}E_4$–H_2O and closed-loop coexistence. *J. Chem. Phys.* **73**, 5840–5861.

[53] Imae, T., Ikeda, S. (1986). The pH dependence of upper and lower consolute phase boundaries for aqueous NaCl solutions of dimethyloleylamine oxide. *J. Colloid Interface Sci.* **113**, 449–455.

[54] Corti, M., DeGiorgio, V., Hayter, J.B., Zulauf, M. (1984). Micelle structure in isotropic $C_{12}E_8$ amphiphile solutions. *Chem. Phys. Lett.* **109**, 579–583.

[55] Lindman, B., Wennerstrom, H. (1991). Nonionic micelles grow with increasing temperature. *J. Phys. Chem.* **95**, 6053–6054.

[56] Brunner-Popela, J., Glatter, O. (1997) Small-angle scattering of interacting particles. I. Basic principles of a global evaluation technique. *J. Appl. Crystallogr.* **30**, 431–442.

[57] Weyerich, B., Brunner-Popela, J., Glatter, O. (1999). Small-angle scattering of interacting particles. II. Generalized indirect Fourier transformation under consideration of the effective structure factor for polydisperse systems. *J. Appl. Crystallogr.* **32**, 197–209.

[58] Glatter, O., Fritz, G., Lindner, H., Brunner-Popela, J., Mittelbach, R., Strey, R., Egelhaaf, S.U. (2000). Nonionic micelles near the critical point: Micellar growth and attractive interaction. *Langmuir* **16**, 8692–8701.

[59] Corti, M., Degiorgio, V. (1981). Micellar properties and critical fluctuations in aqueous solutions of nonionic amphiphiles. *J. Phys. Chem.* **85**, 1442–1445.

[60] Degiorgio, V., Piazza, R., Corti, M., Minero, C. (1985). Critical properties of nonionic micellar solutions. *J. Chem. Phys.* **82**, 1025–1031.

[61] Hayter, J.B., Zulauf, M. (1982). Attractive interactions in critical scattering from non-ionic micelles. *Colloid Polym. Sci.* **260**, 1023–1028.

[62] Zulauf, M., Rosenbusch, J.P. (1983). Micelle clusters of octylhydroxyoligo(oxyethylenes). *J. Phys. Chem.* **87**, 856–862.

[63] Schick, M.J. (1962). Surface films of nonionic detergents—I. Surface tension study. *J. Colloid Sci.* **17**, 801–813.

[64] Nakagawa, T. (1966). In Schick, M.J. (ed.), *Nonionic Surfactants*. Marcel Dekker, New York.

[65] Nilsson, P.G., Wennerström, H., Lindman, B. (1983). Structure of micellar solutions of nonionic surfactants. Nuclear magnetic resonance self-diffusion and proton relaxation studies of poly(ethylene oxide) alkyl ethers. *J. Phys. Chem.* **87**, 1377–1385.

[66] Hey, M.J., Ilett, S.M., Davidson, G. (1995). Effect of temperature on poly(ethylene oxide) chains in aqueous solution. A viscometric, 1H NMR and Raman spectroscopic study. *J. Chem. Soc. Faraday Transact.* **91**, 3897–3900.

[67] Tasaki, K. (1996). Poly(oxyethylene)−water interactions: A molecular dynamics study. *J. ACS* **118**, 8459–8469.

[68] Maeda, T., Yamamoto, K., Aoyagi, T. (2006). Importance of bound water in hydration–dehydration behavior of hydroxylated poly(N-isopropylacrylamide). *J. Colloid Interface Sci.* **302**, 467–474.

[69] Goldfarb, J., Sepulveda, L. (1969). Application of a theory of polymer solutions to the cloud points of nonionic detergents. *J. Colloid Interface Sci.* **31**, 454–459.

[70] Kjellander, R. (1982). Phase separation of non-ionic surfactant solutions. A treatment of the micellar interaction and form. *J. Chem. Soc. Faraday Transact. 2* **78**, 2025–2042.

[71] Weckström, K., Zulauf, M. (1985). Lower consolute boundaries of a poly(oxyethylene) surfactant in aqueous solutions of monovalent salts. *J. Chem. Soc. Faraday Transact. 1* **81**, 2947–2958.

[72] Rupert, L.A.M. (1992). A thermodynamic model of clouding in water alcohol ethoxylate mixtures. *J. Colloid Interface Sci.* **153**, 92–105.

[73] Degiorgio, V., Degiorgio, V., Corti, M. (eds.) (1983). Nonionic micelles, in *Physics of Amphiphiles: Micelles, Vesicles and Microemulsions*. North-Holland Publishers, Amsterdam.

[74] Hoffmann, H., Kielman, H.S., Pavlovic, D., Platz, G., Ulbricht, W. (1981). Kinetic investigations at the cloud point of nonionic surfactants. *J. Colloid Interface Sci.* **80**, 237–254.

[75] Turro, N.J., Kuo, P.L. (1985). Fluorescence probes for aqueous solutions of nonionic micelles. *Langmuir* **1**, 170–172.

[76] Marshal, P.B. (1955). Some chemical and physical properties associated with histamine antagonism. *Br. J. Pharmacol. Chemother.* **10**, 270–278.

[77] Green, A.L. (1967). Ionization constants and water solubilities of some aminoalkylphenothiazine tranquillizers and related compounds. *J. Pharm. Pharmacol.* **19**, 10–16.

[78] Moffat, A.C. (1983). *Clark's Isolation and Identification of Drugs*, 2nd ed. The Pharmaceutical Press, London.

[79] Hansch, C. (1990). *Comprehensive Medicinal Chemistry: The Rational Design, Mechanistic Study and Therapeutic Application of Chemical Compounds*. Pergamon Press, Oxford, UK.

[80] Katzung, B.G. (2004). *Basic and Clinical Pharmacology*, 9th ed., McGraw-Hill, New York.

[81] Lehninger, A.L. (1987). *Principles of Biochemistry*. CSB, Delhi.

[82] Kim, E.J., Shah, D.O. (2003). Effect of surfactants on the cloud point of amphiphilic drug solutions. *Colloids Surf. A: Physicochem. Eng. Aspects* **227**, 105–111.

[83] Kim, E.J., Shah, D.O. (2003). A cloud point study on the micellar growth of an amphiphilic drug in the presence of alcohol and ionic surfactant. *J. Phys. Chem. B* **107**, 8689–8693.

[84] Kim, E.J., Kim, S., Yoo, I.-K., Chung, J.S., Kim, J.S., Shah, D.O. (2006). Cloud point and dye solubilization studies of

amphiphilic drug solutions: The effect of electrolytes and nonelectrolytes. *Chem. Eng. Commun.* **193**, 1065–1074.

[85] Wajnberg, E., Tabak, M., Nussenzveig, P.A., Lopes, C.M.B., Louro, S.R.W. (1988). pH-dependent phase transition of chlorpromazine micellar solutions in the physiological range. *Biochim. Biophys. Acta* **944**, 185–190.

[86] Hofmeister, F. (1888). On the understanding of the effects of salts. Second report. On irregularities in the precipitating effect of salts and their relationship to their physical behaviour. *Arch. Exp. Pathol. Pharmacol.* **24**, 247–260.

[87] Franks, F. (1972). *Water: A Comprehensive Treatise*. Plenum Press, New York.

[88] Hall, D.G. (1974). Thermodynamics of solutions of interacting aggregates by methods similar to surface thermodynamics. Part 2. Solutions of non-associating macromolecules. *J. Chem. Soc. Faraday Transact. 2* **70**, 1526–1541.

[89] Kim, E.J., Shah, D.O. (2002). Cloud point phenomenon in amphiphilic drug solutions. *Langmuir* **18**, 10105–10108.

[90] Alam, M.S., Naqvi, A.Z., Kabir-ud-Din (2006). Effect of electrolytes on the cloud point of chlorpromazine hydrochloride solutions. *Colloids Surf. B: Biointerfaces* **53**, 60–63.

[91] Alam, M.S., Naqvi, A.Z., Kabir-ud-Din (2007). Influence of electrolytes/non-electrolytes on the cloud point phenomenon of the aqueous promethazine hydrochloride drug solution. *J. Colloid Interface Sci.* **306**, 161–165.

[92] Kabir-ud-Din, Al-Ahmadi, M.D.A., Naqvi, A.Z., Akram, M. (2007). Study of the additive effect on the cloud point of nortriptyline hydrochloride solutions. *J. Surfact. Deterg.* **10**, 231–236.

[93] Alam, M.S., Naqvi, A.Z., Kabir-ud-Din (2008). Cloud point phenomenon in amphiphilic drug promethazine hydrochloride + electrolyte systems. *J. Dispersion Sci. Technol.* **29**, 783–786.

[94] Kabir-ud-Din, Al-Ahmadi, M.D.A., Naqvi, A.Z., Akram M. (2009). Effect of electrolytes on the cloud point and dye solubilization of promazine hydrochloride solutions. *J. Dispersion Sci. Technol.* **30**, 439–444.

[95] Naqvi, A.Z., Al-Ahmadi, M.D.A., Akram, M., Kabir-ud-Din (2012). Study of clouding and dye solubilization in clomipramine hydrochloride–electrolyte systems. *Chem. Eng. Commun.* **199**, 461–471.

[96] Nightingale, E.R.Jr. (1959). Phenomenological theory of ion solvation. Effective radii of hydrated ions. *J. Phys. Chem.* **63**, 1381–1387.

[97] Evans, D.F., Wennerström, H. (1999). *The Colloidal Domain: Where Physics, Chemistry, and Biology Meet*, 2nd ed. Wiley-VCH, New York.

[98] Schott, H., Royce, A.E., Han S.K. (1984). Effect of inorganic additives on solutions of nonionic surfactants VII. Cloud point shift values of individual ions. *J. Colloid Interface Sci.* **98**, 196–201.

[99] Kumar, S., Parveen, N., Kabir-ud-Din (2004). Effect of urea addition on micellization and the related phenomena. *J. Phys. Chem. B* **108**, 9588–9592.

[100] Nozaki, Y., Tanford, C. (1963). The solubility of amino acids and related compounds in aqueous urea solutions. *J. Biol. Chem.* **238**, 4074–4081.

[101] Watlaufer, D.B., Malik, S.K., Stoller, L., Coffin, R.L. (1964). Nonpolar group participation in the denaturation of proteins by urea and guanidinium salts. Model compound studies. *J. ACS* **86**, 508–514.

[102] Enea, O., Jolicoeur, C.J. (1982). Heat capacities and volumes of several oligopeptides in urea-water mixtures at 25°C. Some implications for protein unfolding. *J. Phys. Chem.* **86**, 3870–3881.

[103] Bonner, O.D., Bednarek, J.M., Arisman, R.K. (1977). Heat capacities of ureas and water in water and dimethylformamide. *J. ACS* **99**, 2898–2902.

[104] Manabe, M., Koda, M., Shirahama, K. (1980). The effect of 1-alkanols on ionization of sodium dodecyl sulfate micelles. *J. Colloid Interface Sci.* **77**, 189–194.

[105] Kuharski, R.A., Rossky, P.J. (1984). Molecular dynamics study of solvation in urea water solution. *J. ACS* **106**, 5786–5793.

[106] Tanaka, H., Nakanishi, K., Touhara, H. (1985). Computer experiments on aqueous solutions. VII. Potential energy function for urea dimer and molecular dynamics calculation of 8 mol % aqueous solution of urea. *J. Chem. Phys.* **82**, 5184–5191.

[107] Alam, M.S., Kumar, S., Naqvi, A.Z., Kabir-ud-Din (2006). Study of the cloud point of an amphiphilic antidepressant drug: Influence of surfactants, polymers, and nonelectrolytes. *Colloids Surf. A: Physicochem. Eng. Aspects* **287**, 197–202.

[108] Alam, M.S., Naqvi, A.Z., Kabir-ud-Din (2008). Influence of additives on the clouding phenomenon of chlorpromazine hydrochloride solutions. *Colloids Surf. B*: *Biointerfaces* **63**, 122–128.

[109] Kabir-ud-Din, Al-Ahmadi, M.D.A., Naqvi, A.Z., Akram, M. (2008). Phase separation study of a surface-active drug, promazine hydrochloride, in presence of surfactants and ureas. *Tenside Surfact. Deterg.* **45**, 131–136.

[110] Naqvi, A.Z., Al-Ahmadi, M.D.A., Akram, M., Kabir-ud-Din (2010). Surfactants and ureas affect the cloud point of amphiphilic drug, clomipramine hydrochloride. *Colloids Surf. B: Biointerfaces* **81**, 152–157.

[111] Briganti, G., Puvvada, S., Blankschtein, D. (1991). Effect of urea on micellar properties of aqueous solutions of nonionic surfactants. *J. Phys. Chem.* **95**, 8989–8995.

[112] Burke, S.E., Rodgers, M.P., Palepu, R. (2001). A thermodynamic and photophysical study of the effects of thiourea on the micellar properties of aqueous sodium dodecyl sulphate solution. *Mol. Phys*. **99**, 517–524.

[113] Myers, D. (1992). *Surfactant Science and Technology*. VCH, New York.

[114] Forland, G.M., Samseth, J., Hoiland, H., Mortensen, K. (1994). The effect of medium chain length alcohols on the micellar properties of sodium dodecyl sulfate in sodium chloride solutions. *J. Colloid Interface Sci.* **164**, 163–167.

[115] Caponetti, E., Chillura, M.D., Floriano, M.A., Triolo, R. (1997). Localization of n-alcohols and structural effects in aqueous solutions of sodium dodecyl sulfate. *Langmuir* **13**, 3277–3283.

[116] Suzuki, H. (1976). Studies of the effect of ethanol and sodium chloride on the micellization of sodium dodecyl sulfate by gel filtration. *Bull. Chem. Soc. Japan* **49**, 1470–1474.

[117] Almgren, M., Swarup, S., Loefroth, E. (1985). Effect of formamide and other organic polar solvents on the micelle formation of sodium dodecyl sulfate. *J. Phys. Chem.* **89**, 4621–4626.

[118] Alam, M.S., Naqvi, A.Z., Kabir-ud-Din (2007). Influence of organic additives on the clouding phenomena of promethazine hydrochloride solutions. *Colloid Polym. Sci.* **285**, 1573–1579.

[119] Kabir-ud-Din, Al-Ahmadi, M.D.A., Naqvi, A.Z., Akram, M. (2008). Study of the cloud point of nortriptyline hydrochloride: Effect of additives. *Chem. Eng. Commun.* **195**, 948–957.

[120] Alam, M.S., Naqvi, A.Z., Kabir-ud-Din (2010). Phase separation study of imipramine hydrochloride-additive systems. *J. Dispersion Sci. Technol.* **31**, 449 – 455.

[121] Naqvi, A.Z., Al-Ahmadi, M.D.A., Akram, M., Kabir-ud-Din (2010). Effect of non-electrolytes on the cloud point and dye solubilization of antidepressant drug, clomipramine hydrochloride. *Tenside Surfact. Deterg.* **47**, 396–401.

[122] Kabir-ud-Din, Al-Ahmadi, M.D.A., Naqvi, A.Z., Akram, M. (2012). Phase separation study of surface–active drug promazine hydrochloride in absence and presence of organic additives. In Paul, B.K., Moulik, S.P. (eds.), *Statistical Science and Interdisciplinary Research*, Vol. 12, Recent Trends in Surface & Colloid Science Series. World Scientific Publishers, Singapore.

[123] De Gennes, P.G., Taupin, C. (1982). Microemulsions and the flexibility of oil/water interfaces. *J. Phys. Chem.* **86**, 2294–2304.

[124] Mitchell, D.J., Ninham, B.W. (1981). Micelles, vesicles and microemulsions. *J. Chem. Soc. Faraday Transact.2* **77**, 601–629.

[125] *The Merck Index*, 13th ed. (2001). Merck, Kenilworth, NJ.

[126] Kirch, E.R., Kesel, R.G., O'Donnell, J.F., Wach, E.C. (1947). Amino acids in human saliva. *J. Dent. Res*. **26**, 297–301.

[127] Feller, R.P., Shannon, I.L., Wescott, W.B. (1974). Total amino acid levels of parotid saliva at different rates of gland function. *J. Dent. Res*. **53**, 772.

[128] McEvoy, F.A., Hartley, C.B. (1975). Polyamines in cystic fibrosis. *Pediatr. Res.* **9**, 721–724.

[129] Imahori, K., Suzuki, F., Suzuki O., Bachrach, U. (eds.) (1985). *Polyamines: Basic and Clinical Aspects*. VNU Science, Utrecht.

[130] Vratsanos, S.M., Mandel, I.D. (1985). Polyamines of dental plaque in caries-resistant vs. caries-susceptible adults. *J. Dent. Res*. **64**, 422–424.

[131] Ahmad, T., Khan, Z.A., Naqvi, A.Z., Kabir-ud-Din (2009). Study of the cloud point variation of amitriptyline hydrochloride solutions in presence of amines and amino acids. *Colloid J*. **71**, 725–728.

[132] Yamashita, T., Yano, H., Harada, S., Yasunaga, T. (1983). Kinetic studies of the hydrolysis of n-octylamine on the surface of a sodium dodecyl sulfate micelle by the ultrasonic absorption method. *J. Phys. Chem*. **87**, 5482–5485.

[133] Lakshmi, T.S., Nandi, P.K. (1976). Effects of sugar solutions on the activity coefficients of aromatic amino acids and their N-acetyl ethyl esters. *J. Phys. Chem*. **80**, 249–252.

[134] Kabanov, A.V., Batrakova, E.V., Melik-Nubarov, N.S., Fedoseev, N.A., Dorodnich, T.Y., Alakhov, V.Y., Chekhonin, V.P., Nazarova, I.R., Kabanov, V.A. (1992). A new class of drug carriers: Micelles of poly(oxyethylene)-poly(oxypropylene) block copolymers as microcontainers for drug targeting from blood in brain. *J. Control. Release* **22**, 141–157.

[135] Rapoport, N.Y., Herron, J.N., Pitt, W.G., Pitina, L. (1999). Micellar delivery of doxorubicin and its paramagnetic analog, ruboxyl, to HL-60 cells: Effect of micelle structure and ultrasound on the intracellular drug uptake. *J. Control. Release* **58**, 153–162.

[136] Alam, M.S., Naqvi, A.Z., Kabir-ud-Din (2007). Tuning of cloud point of promethazine hydrochloride with surfactants and polymers. *J. Surfact. Deterg.* **10**, 35–40.

[137] Alam, M.S., Naqvi, A.Z., Kabir-ud-Din (2008). Study of the cloud point of the phenothiazine drug chlorpromazine hydrochloride: Effect of surfactants and polymers. *J. Dispersion Sci. Technol.* **29**, 274–279.

[138] Alam, M.S., Naqvi, A.Z., Kabir-ud-Din (2007). Role of surfactants in clouding phenomenon of imipramine hydrochloride. *Colloids Surf. B: Biointerfaces* **57**, 204–208.

[139] Naqvi, A.Z., Rub, M.A., Kabir-ud-Din (2011). Effects of pharmaceutical excipients on cloud points of amphiphilic drugs. *J. Colloid Interface Sci.* **361**, 42–48.

[140] Naqvi, A.Z., Rub, M.A., Kabir-ud-Din (2012). Phase behavior study of amphiphilic drugs: Effect of pharmaceutical excipients. *Colloids Surf. B: Biointerfaces* **95**, 30–41.

[141] Lindman, B., Wennerstrom, H. (1980). Micelles. *Topics Curr. Chem*. **87**, 1–83.

[142] Zana, R., Benrraou, M., Rueff, R. (1991). Alkanediyl-α, ω-bis(dimethylalkylammonium bromide) surfactants. 1. Effect of the spacer chain length on the critical micelle concentration and micelle ionization degree. *Langmuir* **7**, 1072–1075.

[143] Horváth-Szabó, G., Yin, Q., Friberg, S.E. (2001). The hydrotrope action of sodium xylenesulfonate on the solubility of lecithin. *J. Colloid Interface Sci.* **236**, 52–59.

[144] Nathan, M.S., Jayakumar, C., Gandhi, N.N. (2009). Effect of hydrotropes on solubility and mass transfer coefficient of methyl benzoate. *Modern Appl. Sci.* **3**, 101–111.

[145] Rao, U.R.K., Manohar, C., Valaulikar, B.S., Iyer, R.M. (1987). Micellar chain model for the origin of the viscoelasticity in dilute surfactant solutions. *J. Phys. Chem.* **91**, 3286–3291.

[146] Uekama, K., Hirayama, F., Irie, T. (1998). Cyclodextrin drug carrier systems. *Chem. Rev*. **98**, 2045–2076.

[147] Muller, B.W., Albers, E. (1992). Complexation of dihydropyridine derivatives with cyclodextrins and 2-hydroxypropyl-β-cyclodextrin in solution. *Int. J. Pharm.* **79**, 273–288.

[148] Na, G.C., Yaun, B.O., Stevens, H.J.Jr., Weekley, B.S., Rajagopal, N. (1999). Cloud point of nonionic surfactants: Modulation with pharmaceutical excipients. *Pharm. Res*. **16**, 562–568.

[149] Hauser, H., Poupart, G. (1992). In Yeagle, P. (ed.), *Lipid Structure. The Structure of Biological Membrane*. CRC Press, London.

[150] Mu, L., Elbayoumi, T.A., Torchilin, V.P. (2005). Mixed micelles made of poly(ethylene glycol)-phosphatidylethanolamine conjugate and D-α-tocopheryl polyethylene glycol 1000 succinate as pharmaceutical nanocarriers for camptothecin. *Int. J. Pharm.* **306**, 142–149.

[151] Rupp, C., Steckel, H., Müller, B.W. (2010). Solubilization of poorly water-soluble drugs by mixed micelles based on hydrogenated phosphatidylcholine. *Int. J. Pharm.* **387**, 120–128.

[152] Danielsson, H. (1973). In Nair, P.P., Kritchevsky, D. (eds.), *The Bile Acids: Chemistry, Physiology and Metabolism*, Vol. 2. Plenum Press, New York.

[153] Naqvi, A.Z., Rub, M.A., Kabir-ud-Din (2015). Study of phospholipid-induced phase-separation in amphiphilic drugs. *Colloid Journal*, **77**, 525–531.

70

BILAYER IMAGING OF PHOSPHATIDYLCHOLINES BY HIGH-PRESSURE FLUOROMETRY

MASAKI GOTO, NOBUTAKE TAMAI, AND HITOSHI MATSUKI

Department of Life System, Institute of Technology and Science, The University of Tokushima, 2-1 Minamijosanjima-cho, Tokushima 770-8506, Japan

70.1 INTRODUCTION

Phospholipids form bilayer aggregates called *vesicles* or *liposomes* in aqueous solutions, and they undergo structural changes, namely, phase transitions depending on environmental variables such as temperature, pressure, pH, and added salts. Allthough most studies on the impact of environmental variables on lipid bilayers have focused on the effects of temperature and/or concentration, there have been a few studies on the effect of pressure. The adoption of pressure as an environmental variable enables us to (1) estimate the complete thermodynamic quantities of the bilayer phase transitions, including volume information in addition to thermal information; (2) construct a two-dimensional (2D) temperature (T)–pressure (p) phase diagram; and (3) observe low-temperature transitions that cannot be detected by conventional experimental methods. Pressure studies on phospholipid bilayers have concentrated on bilayers of phosphatidylcholines (PCs) with linear identical acyl chains such as dimyristoyl-PC (DMPC), dipalmitoyl-PC (DPPC), and distearoyl-PC (DSPC). In particular, the DPPC bilayer has been thoroughly examined by using various physicochemical techniques including differential scanning calorimetry (DSC), X-ray diffraction, neutron diffraction, NMR, ESR, Raman spectroscopy, dynamic light scattering, and light transmittance [1–10]. On the other hand, fluorescence measurements using fluorescent membrane probes have also been performed under high pressure, and there have been several reports on microscopic environments around the probe molecules in phospholipid bilayers [11–14].

This review summarizes the high-pressure fluorometry that we have established in our recent high-pressure studies on phospholipid bilayers. We have focused on one polarity-sensitive membrane probe among many probes, 6-propionyl-2-(dimethylamino)naphthalene (Prodan), which changes the maximum fluorescence wavelength (λ_{max}) sensitively in response to the microscopic polarity environment in the phospholipid bilayer [15], and we have shown that an analysis of second derivatives of the Prodan fluorescence spectra in the bilayer can be used for the accurate determination of phase transitions. Subsequently, we demonstrated that a correlation between the location of Prodan molecules in the bilayer and the phase state of the bilayer can be visualized by constructing a three-dimensional (3D) image plot in terms of the second derivatives of fluorescence spectra [16–22]. We call this visualization *bilayer imaging*. Here, using this technique, we explain the packing state of PC molecules in the bilayers of (1) DPPC homologs with different acyl chain lengths, (2) those with different vesicle sizes, and (3) asymmetric PCs with different linear acyl chains at the *sn*-1 and *sn*-2 positions. Furthermore, the formation of a lamellar crystal (L_c) phase of the asymmetric PC bilayer, which is clarified by the technique, is also described.

70.2 PRODAN FLUORESCENCE SPECTRA

70.2.1 Fluorescence Measurements

We employed a Bangham method of liposome preparation [23], or combined use of this method and sonication

Encyclopedia of Biocolloid and Biointerface Science, Volume 2, First Edition. Edited by Hiroyuki Ohshima.
© 2016 John Wiley & Sons, Inc. Published 2016 by John Wiley & Sons, Inc.

treatment to prepare the PC vesicle suspension containing the fluorescence probe Prodan [19, 20]. The total concentration of PC was 1.0 mmol kg^{-1}, and the molar ratio of Prodan to PC was 1:500. Fluorescence spectra of Prodan in the PC bilayers under high pressure were measured by a F2500 fluorescence spectrophotometer (Hitachi High Technology Corp., Tokyo, Japan) equipped with a high-pressure cell assembly PCI-400 (Syn Corp. Ltd., Kyoto, Japan). The spectra were observed by an isobaric thermotropic method with a heating rate of 0.50°C min^{-1}; details of the measurement procedure were described previously [16–22]. The excitation wavelength was 361 nm, and the emission spectra were recorded in the wavelength range from 400 to 600 nm. The second derivative of the emission spectrum was obtained by attached software FL solutions (Hitachi High Technology Corp., Tokyo, Japan) of the apparatus and Origin 7.0 (Lightstone Corp., Tokyo, Japan). Three dimensional image plots were constructed from the spectra by employing SigmaPlot 12 (HULINKS Inc., Tokyo, Japan).

70.2.2 Location of Prodan Distributed in PC Bilayer Membranes

The λ_{max} values of Prodan change depending on the kind of solvent, and there is good correlation between the λ_{max} value and the dielectric constant of a solvent around the probe molecules. A higher value of λ_{max} indicates that the probes exist in a polar or hydrophilic environment, while a lower λ_{max} value indicates that the probes exist in a less polar or hydrophobic environment (Fig. 70.1a) [24]. On the other hand, when the Prodan molecules distribute in the bilayer, the fluorescence spectra of Prodan are highly dependent on the phase states of the lipid bilayers; thus, the λ_{max} value drastically varies at the phase transitions. Alteration of the wavelength accompanying the phase transition is related to the local dielectric constant of the lipid molecule in the bilayer, which has been demonstrated as the *zone model* [25]. Since phospholipids are amphiphilic molecules, the dielectric gradient along the molecular axis of a lipid molecule in the hydrated lipid bilayer is produced, then, the gradient can be divided into three zones by the portions of the lipid molecule with different gradients. Figure 70.1b schematically illustrates the zone model of the lipid bilayer. *Zone I*, the hydrophilic part of the bilayer including the polar headgroups, consists of choline and phosphate groups and exhibits a high dielectric constant. *Zone III*, the hydrophobic part of the bilayer including the hydrocarbon core, exhibits a low dielectric constant. *Zone II*, the interfacial region in which the dielectric constant changes from that of zone I to that of zone III, includes the glycerol backbone and ester carbonyl group. When the PC bilayers form the gel, liquid crystalline (L_α), and interdigitated gel ($L_\beta I$) phases, the λ_{max} values exhibit wavelengths of approximately 430, 480, and 500 nm, respectively. Thus, the 430-nm peak indicates that the Prodan

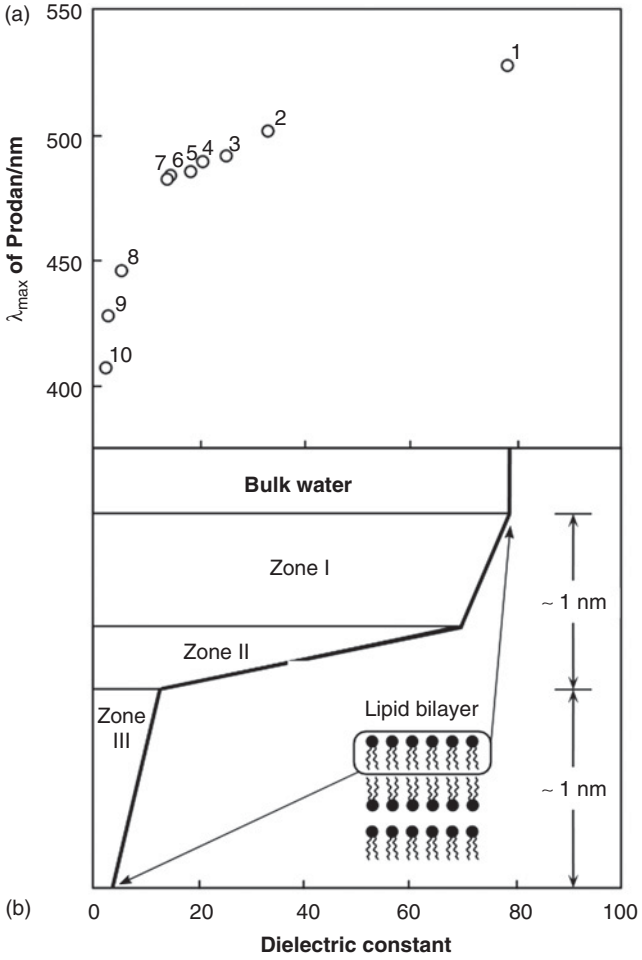


FIGURE 70.1 (a) Wavelength of fluorescence emission maximum for various solvents as a function of solvent dielectric constant at 25°C and 0.1MPa: (1) water, (2) methanol, (3) ethanol, (4) 1-propanol, (5) 1-butanol, (6) 1-pentanol, (7) 1-hexanol, (8) chloroform, (9) benzene, and (10) cyclohexane. (b) A schematic representation of the variation in the dielectric constant from the bilayer core to the bulk water. Three zones of lipid bilayer proposed by the zone model are drawn together with the size of the zones.

molecules exist in less polar regions around the glycerol backbone (zone II); the 480-nm peak, that they exist around the phosphate group (between zones I and II); and the 500-nm peak, that they exist in the hydrophilic region around the lipid headgroup (zone I). This fact signifies that the location of the Prodan molecules distributed in the PC bilayer is closely related to the molecular packing in the bilayer.

The location of the Prodan molecules distributed in the bilayer can be estimated to some extent from the zone model. However, the shape of the emission spectrum of Prodan is not always symmetric, and the spectrum often has a main peak containing shoulder peaks, suggesting that the Prodan molecules are not distributed into only one site in the bilayer. To investigate the location of the Prodan molecules

distributed in the bilayer more accurately, we have developed an analytical method by using the second derivatives of the fluorescence spectra. This method allows us to detect small spectra contained in the shoulder of the fluorescence spectrum [16–22]. The λ_{max} value of the original fluorescence spectrum generally corresponds to the wavelength (λ''_{min}) of minimum intensity in the second-derivative spectrum, whereas the λ''_{min} values of the Prodan spectrum are not always exactly identical to that of the λ_{max} values because the Prodan spectrum in the bilayer is composed of multiple components. In other words, a detailed analysis of the second derivatives of fluorescence spectra provides accurate estimation of the location of the Prodan molecules distributed in multiple sites in the bilayer.

When a series of the Prodan spectra are measured as a function of wavelength, temperature, and pressure, it is possible to construct a 3D image plot of the isobaric thermotropic and/or isothermal barotropic change of the Prodan spectra only if the temperature and/or pressure intervals for a spectrum measurement are narrow and interpolated between consecutive temperatures and/or pressures. The constructed plots provide the visual imaging of packing states of various phases in the PC bilayer by Prodan fluorescence [19–22]. In the next section, we show and discuss bilayer imaging of several PCs with different molecular structures.

70.3 FACTORS AFFECTING THE PACKING STATE IN THE PC BILAYER

70.3.1 Effect of Acyl Chain Length

Figure 70.2 shows *T–p* phase diagrams of the DPPC, diheptadecanoyl-PC (C17PC), and DSPC bilayers together with schematic drawings of each phase state. The DPPC bilayer undergoes the pretransition at 34.3°C from the lamellar gel (L'_β) phase to the ripple gel (P'_β) phase and the main transition at 42.0°C from the P'_β phase to the L_α phase under atmospheric pressure. Both transition temperatures increase by applying pressure, and the pressure-induced $L_\beta I$ phase, whose structure is a kind of nonbilayer that one side of monolayers constituting bilayers mutually interpenetrate the other side of monolayers, appears between the L'_β and P'_β phases at pressures higher than 100 MPa. The phase behavior of the C17PC and DSPC bilayers is similar to that of the DPPC bilayer. The transition temperatures of the PC bilayers increase with an increase in acyl chain length, while the minimum pressure value required for the interdigitation [minimum interdigitation pressure (MIP)] decreases [16,17].

Three 3D image plots of the DPPC, C17PC, and DSPC bilayers obtained under thermotropic conditions at high pressures are depicted in Fig. 70.3 [26]. The heating process of the plots for these PC bilayers under high pressure is given by arrows in Fig. 70.2, and they all undergo the $L'_\beta/L_\beta I$, pre-($L_\beta I/P'_\beta$) and main transitions in turn by this process. Here, the fluorescence intensity is drawn by a color scale as an indicator in the plots; the change from low to high intensity is indicated by the change in color from blue to red in the order of the rainbow colors. Therefore, the location of the Prodan molecules distributed in the PC bilayer can be evaluated from the depth of bluish valleys in the plot. In the case of the DPPC bilayer (Fig. 70.3a), four valleys are seen in the plot, and the respective valleys correspond to the four phase states. Two very deep bluish valleys at ~430 nm correspond to the L'_β (431 nm from 20°C to 45°C) and P'_β (434 nm from 58°C to 74°C) phases, one deep greenish valley at

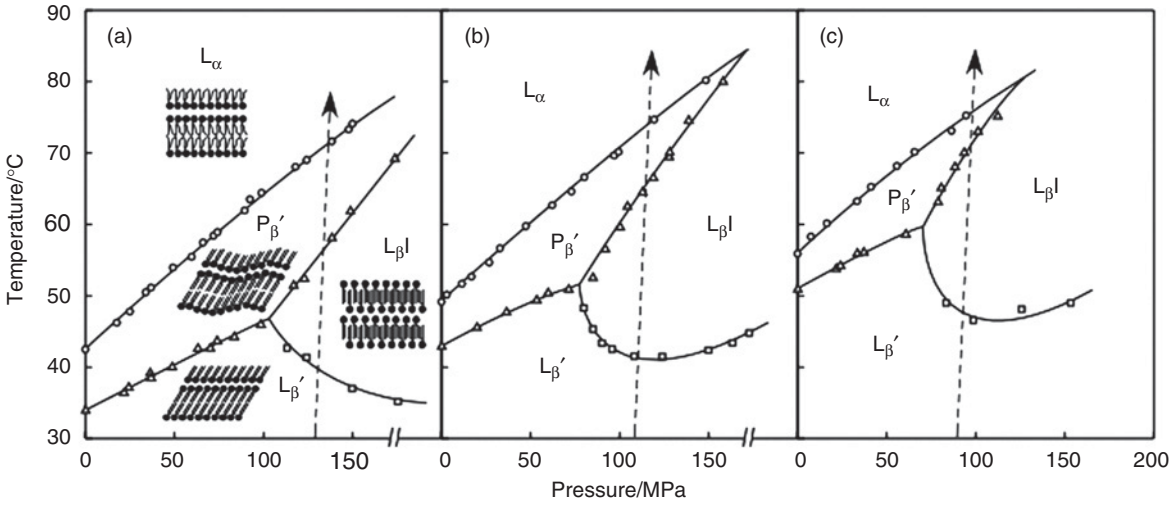


FIGURE 70.2 Temperature–pressure phase diagrams for (a) DPPC, (b) C17PC, and (c) DSPC bilayers. An arrow in each diagram indicates the heating process for Prodan fluorescence measurements in Fig. 70.3.

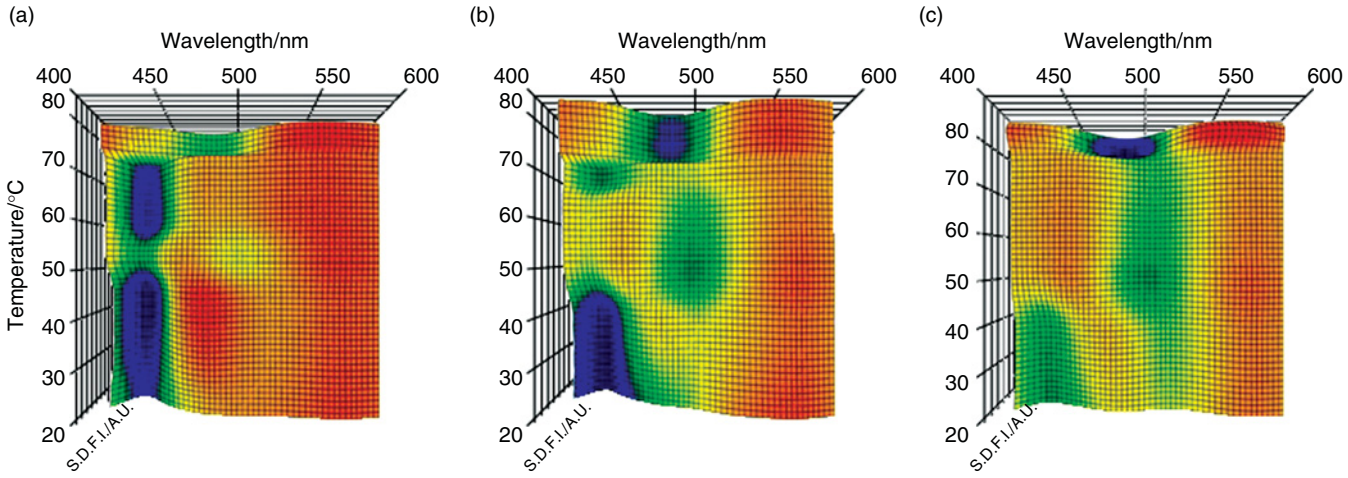


FIGURE 70.3 Image plots for the second derivatives of the fluorescence spectra of Prodan in the (a) DPPC, (b) C17PC, and (c) DSPC bilayers.

482 nm corresponds to the L_α phase (from 74°C to 80°C), and one shallow yellowish valley at 499 nm with a greenish valley at ~430 nm (from 45°C to 58°C) corresponds to the $L_\beta I$ phase. The valleys clearly change at three temperatures corresponding to the $L'_\beta/L_\beta I$ transition, pretransition and main transition temperatures of the DPPC bilayer, which are in good agreement with the transition temperatures in the T–p phase diagram (Fig. 70.2a), except for the $L'_\beta/L_\beta I$ transition. Concerning the $L'_\beta/L_\beta I$ transition, the transition temperature in the plot is ~8°C higher than that shown in the T–p phase diagram. This is attributable to the fact that the second-derivative spectra of the $L_\beta I$ phase in the DPPC bilayer have two $\lambda''_{\min}$ values of 431 and 499 nm and the former minima are greater than the values of the latter minima, suggesting that the packing in the $L_\beta I$ phase of the DPPC bilayer is looser and the Prodan molecules can localize near the glycerol backbone region even in the $L_\beta I$ phase. On the other hand, the valleys of ~500 nm corresponding to the $L_\beta I$ phase in the C17PC and DSPC bilayers become clearer than that in the DPPC bilayer, and their $L'_\beta/L_\beta I$ transition temperatures in the plots agree with those in the T–p phase diagram (Fig. 70.3b,c). This means that the Prodan molecules in both PC bilayers can significantly change the location at the bilayer interdigitation.

Comparing the image plots of the PC bilayers, the bluish valleys for the L'_β and P'_β phases at ~430 nm become shallower with an increase in acyl chain length, whereas the valley for the L_α phase at ~480 nm conversely deepens with an increase in acyl chain length. This contrastive change of the bilayer gel and L_α phases indicates that the quantity of the Prodan molecules distributed in the glycerol backbone region decreases while that in phosphate region increases with chain elongation. Therefore, we can say that the relative ease with which the Prodan molecules partition in the gel phase is inversely proportional to the hydrophobicity of the PC molecules, with an opposite or reverse situation observed in partitioning into the L_α phases. The valleys for the $L_\beta I$ phase observed in the C17PC and DSPC bilayers become deeper than that in the DPPC bilayer. The change in valley depth indicates that greater numbers of Prodan molecules partition into the hydrophilic region around lipid headgroup in the C17PC and DSPC bilayers in comparison with the DPPC bilayer; in other words, the enhanced packing of the $L_\beta I$ phase with the chain elongation excludes the Prodan molecules from the adjacent glycerol backbone to the hydrophilic region. Furthermore, another shallow light greenish valley at ~515 nm and <40°C appears together with the greenish valley at ~430 nm in the plot of the DSPC bilayer (Fig. 70.3c), and the two valleys incorporate into one greenish valley of the $L_\beta I$ phase at ~500 nm with an increase in temperature. The 515-nm valley reflects the fact that the Prodan molecules are distributed within the most hydrophilic region almost at bilayer surface. More specifically, a part of the Prodan molecules is squeezed out from the vicinity of glycerol backbone to the hydrophilic region because of the tight gel-phase packing of the DSPC bilayer.

70.3.2 Effect of Vesicle Size

It is also known that the size of bilayer aggregates affects the bilayer property. DSC, dynamic heat capacity, and solvent relaxation [27–30] measurements indicate that the pretransition of small unilamellar vesicles (SUVs) disappears after excessive sonication and drastically reduces the cooperativity of the main transition. Using high-pressure fluorometry, we investigated the difference in bilayer properties between large multilamellar vesicles (LMVs) with nanometer (nm) sizes described in Section 70.3.1 and giant multilamellar

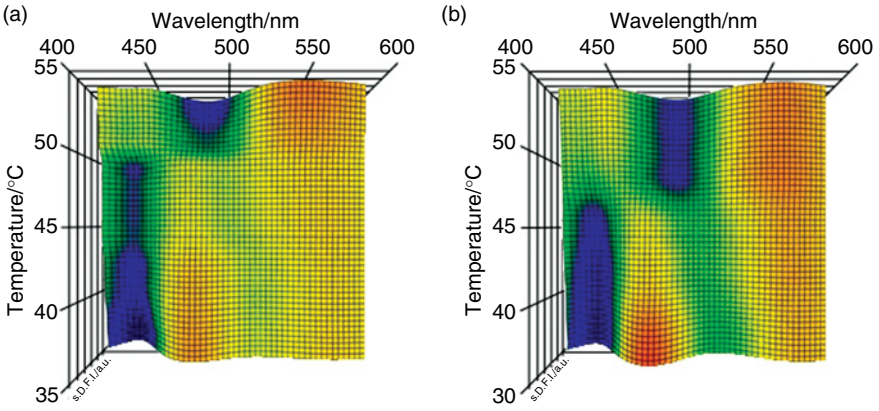


FIGURE 70.4 Image plots for the second derivatives of the fluorescence spectra of Prodan for (a) LMV and (b) GMV of C17PC bilayer.

vesicles (GMVs) with micrometer (μm) sizes. For this purpose, the GMV samples of the C17PC bilayer were prepared by a technique of static hydration using Bangham's method and the corresponding LMV ones were prepared by short-term sonication on the GMV sample immediately after the preparation. The mean diameters of LMVs and GMVs were 170 ± 15 nm and 5000 ± 800 nm, respectively; these sizes were determined by dynamic light-scattering measurements.

Figure 70.4 shows two 3D image plots for LMV and GMV of the C17PC bilayer obtained under thermotropic conditions at atmospheric pressure [20]. Valley depth changed from 431 to 484 nm at ∼50 °C for LMV and from 431 to 491 nm at ∼47 °C for GMV, indicating that the bilayers of LMV and GMV undergo the main transition at those temperatures. Although the pretransition of LMV can be observed as a variation in width of a blue band near 430 nm at ∼43°C, the variation for GMV is barely discernible in the plot. For GMV, a clear green valley band corresponding to another minimum in the second-derivative spectra appears in the wavelength range between approximately 500 and 525 nm in the plot as observed in the DSPC bilayers, indicating that a part of the Prodan molecules partitions into the hydrophilic region at the membrane surface even though the phase is L'_β . Packing stress exists between the outer and inner layers in LMV, which arises from the mismatch between the curvature of the membrane and its spontaneous curvature. The packing stress decreases with increasing vesicle size; as a result, the PC molecules in GMV can be packed more densely and tightly than those in LMV. Then a part of the Prodan molecules is squeezed out of the glycerol backbone region to the most hydrophilic region at the membrane surface near bulk water. It is noteworthy that the depths of the minima corresponding to the three phases are more enhanced in GMV than in LMV. The enhancement of the minima results from an increase in fluorescence intensity. As the partitioning of the Prodan molecules does not seem to change appreciably at the same molar ratio of Prodan and PC in GMV and LMV, enhancement of the minima in GMV is attributable to the increase in surface density of the Prodan molecules per unit area in GMV as compared with that in LMV. On the other hand, the blueish valley corresponding to the P'_β phase for GMV shrinks in the direction of the temperature axis while that to the L_α phase extends as compared with that of LMV. This means that the Prodan molecules in the P'_β phase of GMV can easily transfer from the glycerol backbone region to the adjacent phosphate group because of the tighter packing of the PC molecules in GMV than in LMV, which is in accord with a lower main transition temperature in GMV than in LMV. In addition to the abovementioned behavior, the difference between the $\lambda''_{\min}$ values of the L_α phase in GMV (491 nm) and LMV (484 nm) also support the view that the exclusion effect of Prodan molecules is higher in GMV and that the main transition occurs at a lower temperature in GMV. These results clearly show that the curvature of the vesicle markedly affects the distribution of Prodan molecules in various phases and that Prodan can be an good indicator of change in packing stress or the curvature of lipid bilayers [20].

A 3D image plot for GMV of the C17PC bilayer obtained under thermotropic conditions at a high pressure is depicted in Fig. 70.5, which corresponds to the plot for LMV under high pressure shown in Fig. 70.3b. The four wavelengths characteristic of the L'_β, P'_β, L_α, and $L_\beta I$ phases for LMV under high pressure are 430, 433, 480, and 497 nm, respectively, whereas those for GMV are respectively 430, 433, 482 and 501 nm. The difference in the shape of the spectra in the image plots between LMV and GMV under high pressure is essentially the same as the difference observed for these spectra under atmospheric pressure. The $\lambda''_{\min}$ values in the L_α phase for LMV and GMV under high pressure are lower than those under atmospheric pressure. This is probably because the high pressure almost cancels out the exclusion effect of the Prodan molecules as mentioned above [20].

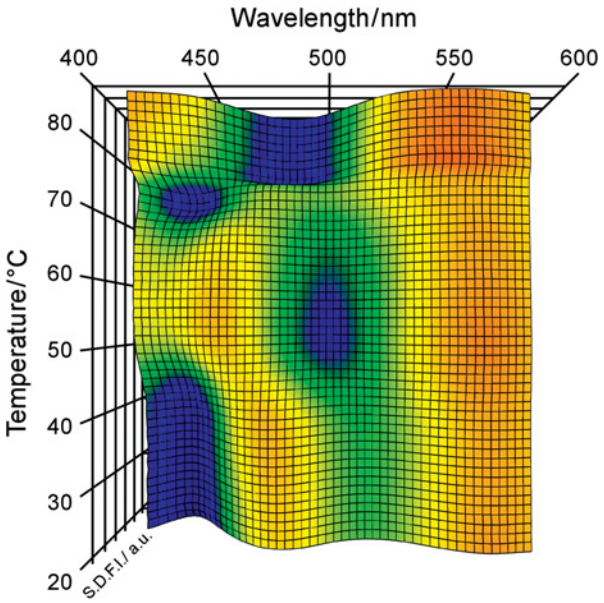


FIGURE 70.5 Image plot for the second derivatives of fluorescence spectra of Prodan for GMV of C17PC bilayer.

70.3.3 Effect of Acyl Chain Asymmetry

Symmetric phospholipids with two identical acyl chains such as DPPC and DSPC are rather minor components of lipids contained in biological membranes. Actually, asymmetric phospholipids with two different acyl chains (length and/or unsaturation) are found abundantly in the membranes. Thus, it is important to study bilayer properties of asymmetric phospholipids for an intrinsic understanding of the biological membranes. We have constructed *T–p* phase diagrams of various asymmetric PC bilayers and evaluated the thermodynamic quantities associated with the phase transitions. Consequently we showed that the bilayer properties of asymmetric PCs are significantly influenced by the effective chain length between the *sn*-1 and *sn*-2 acyl chains; that is, the acyl chain alignment at the terminal methyl ends in the PC molecule [22]. We will now discuss the results of the bilayer imaging for two kinds of asymmetric PCs, palmitoylstearoyl-PC (PSPC), and stearoylpalmitoyl-PC (SPPC). The total carbon number of acyl chains for each PC molecule is 34 and is equivalent to C17PC, and the degree of chain alignment at the terminal methyl ends increases in the order of SPPC < C17PC < PSPC [16]. Figure 70.6 shows *T–p* phase diagrams of the PSPC and SPPC bilayers. Here we focus on the behavior of the $L_\beta I$ phase; detailed discussion of the phase behavior is described elsewhere [16]. The MIP values of the PSPC, SPPC, and C17PC bilayers are different from one another, at 50.6, 93.0, and 79.1 MPa, respectively. In the $L_\beta I$ phase, since two acyl chains of the PC molecule orient perpendicularly to the membrane surface, the alignment of terminal methyl ends that can cause the enhanced cohesive interaction between acyl chains is advantageous for bilayer interdigitaion at a lower pressure. Furthermore, as shown in Fig. 70.6b, we observed in the SPPC bilayer that the $L'_\beta/L_\beta I$ phase transition proceeds stepwise and speculated that the peculiar transition may be ascribed to the appearance of the two-phase (i.e., L'_β and $L_\beta I$) coexistence state at the bilayer interdigitation due to the great chain asymmetry of the SPPC molecules [16].

Figure 70.7 shows 3D image plots for the PSPC and SPPC bilayers obtained at a thermotropic condition under high pressure [22]. The heating process of the plots for both PC bilayers under high pressure is given by arrows in Fig. 70.6, and they undergo the $L'_\beta/L_\beta I$, pre- ($L_\beta I/P'_\beta$), and main transitions in turn by this process. The distinct four bluish valleys are observed in the plot for the PSPC bilayer similar to that for the C17PC bilayer. One deepest valley at ~430 nm

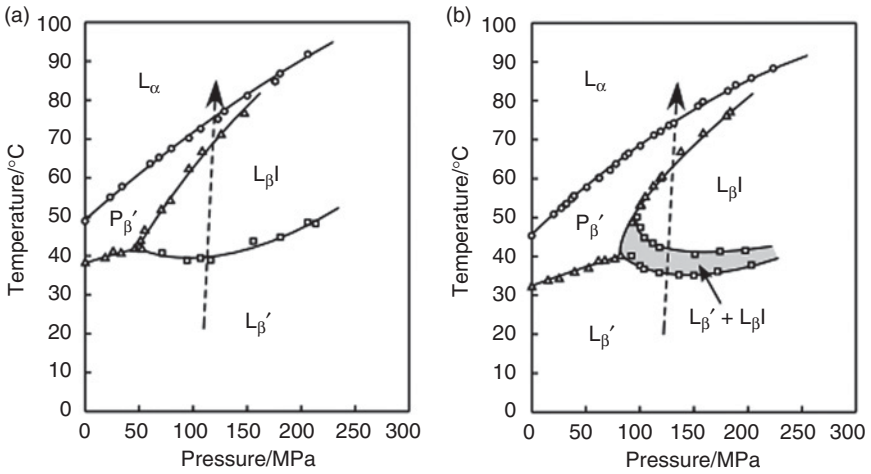


FIGURE 70.6 Temperature–pressure phase diagrams for (a) PSPC and (b) SPPC bilayers. An arrow in each diagram indicates the heating process for Prodan fluorescence measurements in Fig. 70.7.

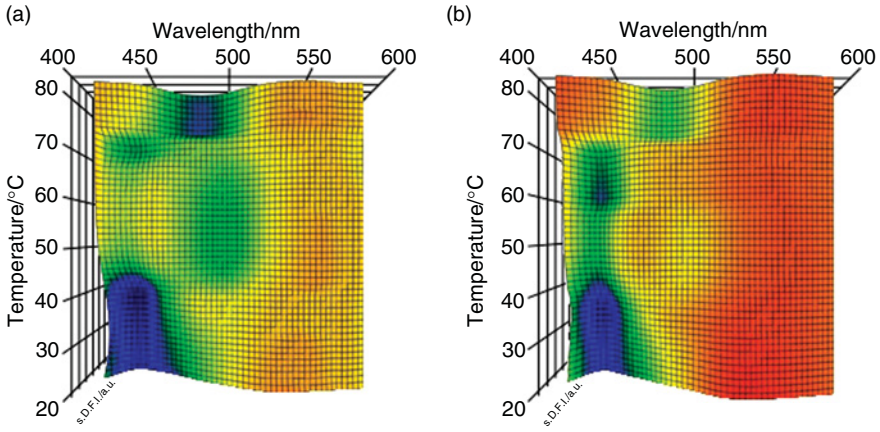


FIGURE 70.7 Image plots for the second derivatives of the fluorescence spectra of Prodan in the (a) PSPC, (b) SPPC bilayers.

(from 20°C to 42°C) corresponds to the L'_β phase, and another bluish valley at ~480 nm (from 78°C to 85°C) corresponds to the L_α phase. Two greenish valleys correspond to the P'_β (~430 nm from 70°C to 78°C) and $L_\beta I$ (~500 nm from 42°C to 70°C) phases. The transition temperatures obtained from the image plots are in good agreement with those from the *T–p* phase diagram in Fig. 70.6a. The image plot of the PSPC bilayer displays behavior similar to that observed in the C17PC bilayer, but the areas of the valleys for the PSPC bilayer extend further than those in the C17PC bilayer, indicating weaker immobilization of the Prodan molecules in the PSPC bilayer than in the C17PC bilayer.

On the other hand, the image plot of the SPPC bilayer is definitely different from those of the PSPC and C17PC bilayers. All valleys corresponding to four phases become shallow; in particular, the valley at 497 nm corresponding to the $L_\beta I$ phase becomes very shallow, to a faintly recognizable degree. In contrast with these behaviors, a distinct green band around 430 nm from 40°C to 60°C is observed, which implies that the Prodan molecules in the $L_\beta I$ phase of the SPPC bilayer partition not into the hydrophilic region, but into the adjacent glycerol backbone. This finding suggests that the great chain asymmetry of the SPPC molecules probably produces a less polar "pocket" in the interdigitated structure in which a Prodan molecule can remain and that they are hardly excluded to the hydrophilic region even if the $L_\beta I$ phase is induced. The fact that the Prodan molecules in the $L_\beta I$ phase of the SPPC bilayer can reside in two locations in the bilayer (i.e., that the Prodan fluorescence exhibits properties such as the L'_β phase even in the $L_\beta I$ phase); this is consistent with the appearance of the two-phase coexistence in the *T–p* phase diagram of the SPPC bilayer. In addition, we have also obtained some interesting data with respect to the effect of vesicle size on asymmetric PC bilayers, described elsewhere [22].

70.4 PACKING STATE IN THE L_c PHASE

Finally, we show the bilayer packing of the most stable phase at a low-temperature, L_c, phase of the PC bilayers examined by the imaging technique. Phospholipid bilayers can form the L_c phase at a low temperature in addition to the gel and L_α phase. Since the L_c phase is usually induced by dehydration of the polar headgroups of lipid molecules in the bilayer, the formation requires a pretreatment, termed *thermal annealing*, which facilitates dehydration prior to experimentation [31]. A period of the annealing treatment for complete L_c phase formation of symmetric PC bilayers increases with an increase in acyl chain length of the PC molecule; for example, about a week is needed for complete induction of the L_c phase in the DPPC bilayer. For the slow kinetics of the phase formation, it is difficult to study the properties and structures of the L_c phase by conventional measurement methods, and there have been few reports on the L_c phase of phospholipid bilayers. To make matters worse, because the annealing treatment enhances the bilayer packing, the probe molecules contained in the bilayer are squeezed out of the bilayer, which makes it difficult to observe the spectrum characteristic of the L_c phase.

We have found that one of the asymmetric PCs, a myristoylpalmitoyl-PC (MPPC) bilayer, can form the L_c phase in an extremely short period of time, unlike the case of symmetric PC bilayers, and that MPPC is suitable for investigation of L_c phase formation [17]. A *T–p* phase diagram of the MPPC bilayer is depicted in Fig. 70.8. In the MPPC bilayer, the subtransition in the low-pressure region is the L_c/P'_β transition, not the L_c/L'_β transition. Since the subtransition temperatures are higher than the pre- (L'_β/P'_β) transition temperatures in the whole range of pressure, the L'_β and P'_β phases and part of the $L_\beta I$ phase become the metastable phase. Therefore, the triple point at which the three gel

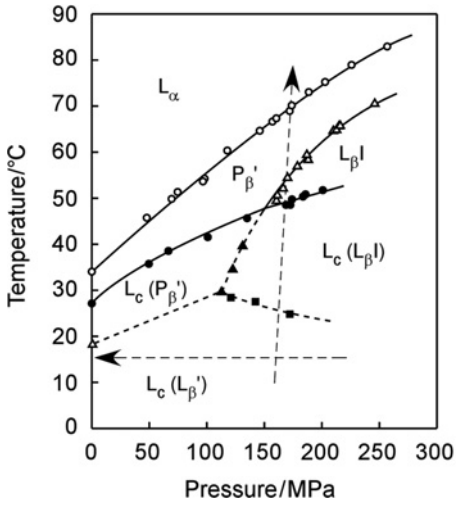


FIGURE 70.8 Temperature–pressure phase diagram for MPPC bilayers. Arrows in the diagram indicate the heating process for Prodan fluorescence measurements in Figs. 70.9 and 70.10.

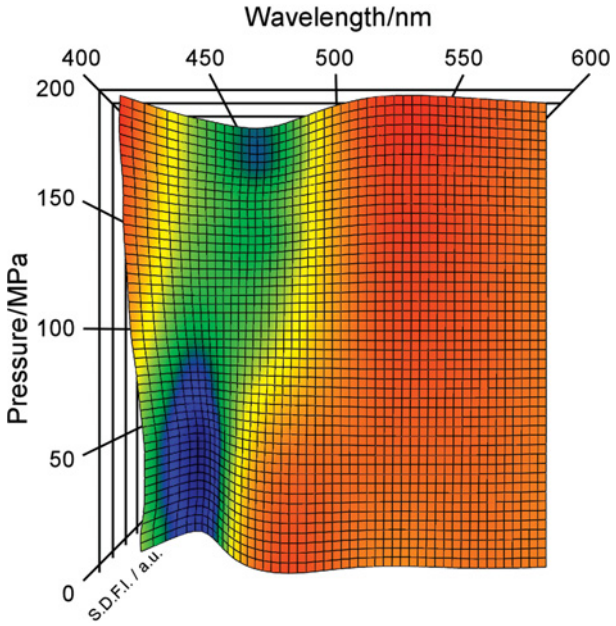


FIGURE 70.9 Decompression effect on image plot for second-derivative spectra of Prodan in MPPC bilayer.

phases coexist is located in the metastable region, and the MIP value is 113 MPa. Although pressure generally facilitates the formation of the L_c phase and hinders observation of the transitions between the gel phases, the Prodan fluorescence measurement can allow us to observe the transitions and simultaneously provide useful information regarding the structure of the L_c phase. The Prodan fluorescence in the L_c phase, which we observed for the first time using fluorometry, is explained here.

Figure 70.9 shows a 3D image plot of the MPPC bilayer obtained under isothermal (15.3°C) barotropic conditions [19]. The decompression process of the plot is indicated by an arrow in Fig. 70.8, and the bilayer undergoes no phase transitions in the process. During the pressurizing process at 15.3°C, the bluish valley at ~430 nm becomes shallower at ~100 MPa while that at ~460 nm becomes deeper, which results in the marked broadening of the valley. With further increasing pressure, the greenish valley at ~460 nm becomes broad but deep abruptly at pressures above ~200 MPa. Since the phase state was identified as the L_c phase by DSC and light transmittance measurements under atmospheric pressure, we judged the broad spectra to be characteristic of the L_c phase. Interestingly, the spectra at pressures below 50 MPa cannot be distinguished from those of the L'_β and P'_β phases. Because this spectral shift is completely reversible, sufficient pressure is essential to form the spectrum characteristic of the L_c phase, suggesting that the packing state of the structure of the L_c phase differs from those of the other phases.

Figure 70.10 shows an image plot of temperature dependence for the MPPC bilayer obtained under thermotropic conditions at a high pressure [19]. Here, the heating process of the plot under high pressure is indicated by an arrow in Fig. 70.8 and the MPPC bilayer undergoes the $L_c/L_\beta I$, pre-($L_\beta I/P'_\beta$), and main transitions in turn by this process. At 10°C, the bluish valley at ~460 nm, which is characteristic of the L_c phase, is broad. In the temperature range from ~10°C to ~20°C, the valley gradually shifts to the short-wavelength region, and the single valley at ~460 nm starts to separate into double local valleys at ~430 and 500 nm at ~26°C. Since

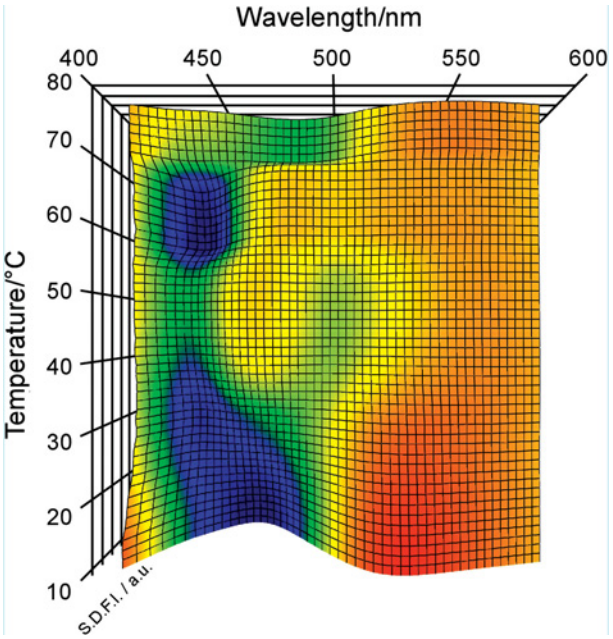


FIGURE 70.10 Image plot for the second derivatives of fluorescence spectra of Prodan in MPPC bilayer.

the temperature is consistent with the metastable $L'_\beta/L_\beta I$ phase transition temperature, we can conclude that the Prodan molecules in the L_c phase can sensitively recognize the metastable $L_\beta I$ phase region and quickly translocate the distribution sites at the transition. This fact suggests that the L_c phase of the MPPC bilayer transforms into two kinds of L_c phases, namely, L_c and interdigitated L_c (L_cI) phases. With an increase in temperature, the double local valleys become sharp while the valley at ~460 nm becomes shallow, and a typical image pattern of the $L_\beta I$ phase is observed at ~48°C. Further increases in temperature produce the valley at 430 nm and subsequently that at 480 nm in response to the pre- and main transitions, respectively, in the same pattern as that observed for the DPPC bilayer. From the bilayer imaging, we could propose a hypothesis that the MPPC molecules in the L_c phase form a staggered configuration, where adjacent polar headgroups of the molecules mutually shift the position up and down against the membrane surface. A detailed explanation is provided elsewhere [19].

70.5 CONCLUSIONS

We showed that a 3D image plot based on the second derivatives of the isobaric thermotropic and/or isothermal barotropic change in the Prodan fluorescence spectra can examine the correlation between the location of the Prodan molecules distributed in the bilayer and the bilayer phase behavior as a function of both temperature and pressure. This imaging method also enables us to visually evaluate the packing state of lipid molecules in the bilayer and the effects of several pertinent factors on the packing state of the PC molecules in the bilayer. Fluorometry is an easier technique than X-ray and neutron scattering for investigating the microscopic states of the phospholipid bilayer; however, several probes of hydrophobic and/or hydrophilic nature are required to observe multiple phase transitions such as gel/gel and gel/L_α transitions simultaneously. It is very significant that the fluorescence measurements using a amphiphilic probe Prodan enables us to observe such plural phase transitions by the only single probe at the same time and makes it possible to construct a map of the packing states in the bilayer. We expect that the bilayer and/or nonbilayer packing of other kinds of phospholipids such as phosphatidylethanolamines, phosphatidylglycerols, and phosphatidylserines will be clarified by this imaging method.

ACKNOWLEDGMENTS

We appreciate Shoji Kaneshina, professor emeritus of The University of Tokushima, for his kind help and advise in discussion of Prodan fluorescence under high pressure. We are also grateful to Mr. Yuji Yamashita, president of Yamashita Technology System Co. Ltd., for development of several experimental devices and continuous technical support.

REFERENCES

[1] Utoh, S., Takemura, T. (1985). Phase transition of lipid multilamellar aqueous suspension under high pressure I. Investigation of phase diagram of dipalmitoyl phosphatidylcholine bimembrane by high pressure-DTA and –dilatometry. *Jpn. J. Appl. Phys.* **24**, 356–360.

[2] Yager, P., Peticolas, W.L. (1980). Statistical mechanical analysis of Raman spectroscopic order parameter changes in pressure-induced lipid bilayer phase transitions. *Biophys. J.* **31**, 359–370.

[3] Wong, P.T.T., Mantsch, H.H. (1985). Effects of hydrostatic pressure on the molecular structure and endothermic phase transitions of phosphatidylcholine bilayers: A Raman scattering study. *Biochemistry* **24**, 4091–4096.

[4] Russell, N.D., Collings, P.J. (1982). High pressure measurements in phospholipid bilayers using adiabatic compression. *J. Chem. Phys.* **77**, 5766–5770.

[5] Chong, P.L.G., Weber, G. (1983). Pressure dependence of 1,6-diphenyl-1,3,5-hexatrien fluorescence in single-component phosphatidylcholine liposomes. *Biochemistry* **22**, 5544–5550.

[6] Lakowicz, J.R., Thompson, R.B. (1983). Differential polarized phase fluorometric studies of phospholipid bilayers under high hydrostatic pressure. *Biochim. Biophys. Acta* **732**, 359–371.

[7] Braganza, L.F., Worcester, D.L. (1986). Hydrostatic pressure induces hydrocarbon interdigitation in single-component phospholipid bilayers. *Biochemistry* **25**, 2591–2596.

[8] Winter, R., Pilgrim, W.C. (1989). A SANS study of high pressure phase transitions in model biomembranes. *Ber. Bunsenges. Phys. Chem.* **93**, 708–717.

[9] Maruyama, S., Matsuki, H., Ichimori, H., Kaneshina, S. (1996). Thermotropic and barotropic phase behavior of dihexadecylphosphatidylcholine bilayer membrane. *Chem. Phys. Lipids* **82**, 125–132.

[10] Driscoll, D.A., Jonas, J., Jonas, A. (1991). High pressure ^{2}H nuclear magnetic resonance study of the gel phases of dipalmitoylphosphatidylcholine. *Chem. Phys. Lipids* **58**, 97–104.

[11] Chong, P.L.-G., van der Meer, B.W., Thompson, T.E. (1985). The effects of pressure and cholesterol on rotational motions of perylene in lipid bilayers. *Biochim. Biophys. Acta* **813**, 253–265.

[12] Flamm, M., Okubo, T., Turro, N.J., Schachter, D. (1982). Pressure dependence of pyrene excimer fluorescence in human erythrocyte membranes. *Biochim. Biophys. Acta* **687**, 101–104.

[13] Turley, W.D., Offen, H.W. (1986). Lipid microviscosity of DMPC vesicles at high pressures. Dipyrenylpropane excimer fluorescence. *J. Phys. Chem.* **90**, 1967–1970.

[14] Chong, P.L.-G., Fortes, P.A.G., Jameson, D.M. (1985). Mechanisms of inhibition of (Na,K)-ATPase by hydrostatic pressure

studied with fluorescent probes. *J. Biol. Chem.* **260**, 14484–14490.

[15] Chong, P.L.-G. (1988). Effects of hydrostatic pressure on the location of PRODAN in lipid bilayers and cellular membranes. *Biochemistry* **27**, 399–404.

[16] Goto, M., Kusube, M., Tamai, N., Matsuki, H., Kaneshina, S. (2008). Effect of hydrostatic pressure on the bilayer phase behavior of symmetric and asymmetric phospholipids with the same total chain length. *Biochim. Biophys. Acta* **1778**, 1067–1078.

[17] Goto, M., Ishida, S., Tamai, N., Matsuki, H., Kaneshina, S. (2009). Chain asymmetry alters thermotropic and barotropic properties of phospholipid bilayer membranes. *Chem. Phys. Lipids* **161**, 65–76.

[18] Goto, M., Kusube, M., Nishimoto, M., Tamai, N, Matsuki, H., Kaneshina, S. (2010). Pressure study on symmetric and asymmetric phospholipid bilayers: Effect of vesicle size on Prodan fluorescence. *Ann. NY Acad. Sci.* **1189**, 68–76.

[19] Goto, M., Wilk, A., Kataoka, K., Chodankar, S., Tamai, N., Fukui, M., Kohlbrecher, J., Ito, H., Matsuki, H. (2012). Study on the subgel-phase formation using an asymmetric phospholipid bilayer membrane by high-pressure fluorometry. *Langmuir* **28**, 12191–12198.

[20] Goto, M., Sawaguchi, H., Tamai, N., Matsuki, H., Kaneshina, S. (2010). Effect of vesicle size on the Prodan fluorescence in diheptadecanoylphosphatidylcholine bilayer membrane under atmospheric and high pressures. *Langmuir* **26**, 13377–13384.

[21] Goto, M., Wilk, A, Kazama, A., Chodankar, S., Kohlbrecher, J., Matsuki, H. (2011). Chain elongation of diacylphosphatidylcholine induces fully bilayer interdigitation under atmospheric pressure, *Colloids Surf. B: Biointerfaces* **84**, 44–48.

[22] Goto, M., Matsui, T., Tamai, N., Matsuki, H., Kaneshina, S. (2011). Prodan fluorescence detects the bilayer packing of asymmetric phospholipids. *Colloids Surf. B: Biointerfaces* **84**, 55–62.

[23] Bangham, A.D., De Gier, J., Greville, G.D. (1967). Osmotic properties and water permeability of phospholipids liquid crystals. *Chem. Phys. Lipids* **1**, 225–246.

[24] Kusube, M., Matsuki, H., Kaneshina, S. (2005). Effect of pressure on the Prodan fluorescence in bilayer membranes of phospholipids with varying acyl chain lengths. *Colloids Surf. B: Biointerfaces* **42**, 79–88.

[25] Okamura, E., Nakahara, M. (2000). In Volkov, A.G. (ed.), *Liquid Interfaces in Chemical, Biological, and Pharmaceutical Applications.* Marcel Dekker, New York, p. 775.

[26] Matsuki, H., Goto, M., Kusube, M., Tamai, N. (2011). Imaging of phosphatidylcholines bilayers by a high-pressure fluorescence technique: Detection of the packing difference. *Bull. Chem. Soc. Japan* **84**, 1329–1335.

[27] de Kruijff, B., Cullis, P.R., Radda, G.K. (1975). Differential scanning calorimetry and ^{31}P NMR studies on sonicated and unsonicated phosphatidylcholine liposomes. *Biochim. Biophys. Acta* **406**, 6–20.

[28] van Dijck, P.W.M., de Kruijff, B., Aarts, P.A.M.M., Verkleij, A.J., de Gier, J. (1978). Phase transitions in phospholipid model membranes of different curvature. *Biochim. Biophys. Acta* **506**, 183–191.

[29] Nagano, H., Nakanishi, T., Yao, H., Ema, K. (1955). Effect of vesicle size on the heat capacity anomaly at the gel to liquid-crystalline phase transition in unilamellar vesicles of dimyristoylphosphatidylcholine. *Phys. Rev. E* **52**, 4244–4250.

[30] Sýkora, J., Jurkiewicz, P., Epand, R.M., Kraayenhof, R., Langner, M., Hof, M. (2005). Influence of the curvature on the water structure in the headgroup region of phospholipid bilayer studied by the solvent relaxation technique. *Chem. Phys. Lipids* **135**, 213–221.

[31] Lewis, R.N.A.H., Mak, N., McElhaney, R.N. (1987). A differential scanning calorimetric study of the thermotropic phase behavior of model membranes composed of phosphatidylcholines containing linear saturated fatty acyl chains. *Biochemistry* **26**, 6118–6126.

71

PHYSIOLOGICAL AND MOLECULAR ASPECTS OF MECHANISMS INVOLVED IN PLANT RESPONSE TO SALT STRESS

Xiaoli Tang[2] and Hongbo Shao[1]

[1]*Jiangsu Key Laboratory for Bioresources of Saline Soils; Provincial Key Laboratory of Agrobiology, Institute of Agro-Biotechnology, Jiangsu Academy of Agricultural Sciences, Nanjing 210014, China*

[2]*Sericultural Research Institute of Shandong, Shandong Academy of Agricultural Sciences, Yantai 264002, China*

71.1 INTRODUCTION

Globally, soil salinity is becoming an increasing threaten to plant growth [1, 2]. According to FAO, at least 800 million hectares (ha) of land are subjected to salinity [3], accounting for as much as 6% of the world's total land area. Although some of the salt-affected influence is the result of natural causes, most is derived from the degraded cultivated agricultural land [4, 5]. At present the world's cultivated land affected by salinity has achieved 20% [6]. Currently, food supply is basically sufficient, but approximately 800 million people are undernourished [7]. It has been reported that food production must increase to 150% to meet the constantly growing population by 2050 [3,8]. The amount of cultivated agricultural land is narrowed by the increasingly serious salinization, and there is an increasing demand for food with the increase in population. To meet these challenges, breeding crops which are able to survive abiotic stress, and to maximize performance under unfavorable conditions seem to be the major topics for research [9].

Generally, the so-called saline soil has a high concentration of soluble salts. Soils are regarded as saline if the soil solution electrical conductivity (EC) values reach ≥4 dS/m [10]. The solution concentration is equivalent to 40 mM NaCl, generating an osmotic pressure of approximately 0.2 MPa and significantly reducing the yields of most cereal crops [4]. However, the deleterious effects vary according to several related factors, including climatic conditions, plant species, and soil regime. For instance, rice is the most sensitive species among the grain crops, while barley displays a relatively pronounced resistance [11, 12]. High salinity can threaten plant health by imposing two general types of stress: hyperosmotic stress and hyperionic stress [13]. On the basis of their capacity to grow in high-salinity soil, plants are classified into two types: glycophytes and halophytes [14]. Some of the halophytes have the ability to exclude salts from their roots and shoots, some are able to endure high-concentration salt, and others adopt measures such as ion compartmentalization, synthesis of compatible solute, and osmotic adjustment [15]. Yet almost all the crops are glycophytes, thus two key measures (producing salt-tolerant lines/cultivars through conventional breeding or genetic engineering) to overcome this challlenge have been put forward for a long time [16]. Growing halophytes and salt-tolerant crops on saline soil is regarded as the *biotic approach*, which is similar to the concept of *biosaline agriculture* [17–19]. As is well known, other than animals, plants maintain a sessile lifestyle subjected to various types of environmental stress [20]. Modern-day plants are all the products of primal living, experienced eons of evolution with abiotic and biotic changes. Thus they have acquired various adaptive mechanisms to optimize growth and development under stress [21]. Sodium chloride is the most common and widespread salt in soil, so the evolved

Encyclopedia of Biocolloid and Biointerface Science, Volume 2, First Edition. Edited by Hiroyuki Ohshima.
© 2016 John Wiley & Sons, Inc. Published 2016 by John Wiley & Sons, Inc.

mechanisms of plants regulate its accumulation and distribution [22a]. For glycophytes, high-concentration salts can produce ionic stress, osmotic stress, and secondary stress [23]. In order to guarantee survival under such detrimental circumstances, plants have evolved a series of biochemical and molecular processes to acclimatize themselves to the environment [24–27]. The specific biochemical strategy consists in (1) ion regulation and compartmentalization, (2) induced biosynthesis of compatible solutes, (3) induction of antioxidant enzymes, (4) induction of plant hormones, and (5) changes in the photosynthetic pathway [28]. The molecular mechanism includes (1) the SOS (salt overly sensitive) pathway for ion homeostasis, (2) the protein kinase pathway for stress signaling, (3) the phytohormone signaling pathway under high salt stress [23], and (4) the associated genes encoding salt stress proteins (e.g., genes for photosynthetic enzymes, for synthesis of compatible solutes, for vacuolar sequestering enzymes, and for radical-scavenging enzymes) [29].

In recent years, tremendous advances have been achieved in salt stress studies. Plant breeders have fostered some salt-tolerant lines of crops by conventional breeding; moreover, a transgenic approach is employed to improve the crop salt tolerance, and a number of transgenic lines have been confirmed effective under control conditions [16]. *Metabolomics* is becoming a tool to help researchers understand the cellular mechanism of abiotic stress and is also a viable option for the biotechnological improvement of halophytes [30]. Small noncoding RNAs, mainly microRNAs and siRNAs (short interfering RNAs), can regulate gene expression by silencing of the genes [31]. MiR393 has been reported to be strongly upregulated by drought and high-salinity treatment [32, 33]. In the most recent study, ribosomal RNA methylation was discovered to response to abiotic stress [34]. In addition, the mitogen-activated protein kinase (MAPK) signaling pathways, which are involved in stress response, are highly conserved and important regulating systems in plants [35, 36].

Reviews on salinity responses began to appear three decades ago, and new reports have appeared continuously [1,4,13,14,28,37]. The molecular, cellular, and holistic mechanisms of plant salt tolerance have been discussed in detail [4]. One team of researchers chose to stand at the point of uptake and transport of ions to review the concrete mechanisms of salt tolerance [15]. Two investigators described how plants manage to control ion homeostasis by sensing, transduction, and responding to salt stress signaling [13]. Thanks to the rapid development of life science, our understanding of salinity tolerance in both physiological and molecular fields has experienced a qualitative leap. In this chapter we will focus on the molecular, cellular, and physiological mechanisms of salt tolerance in detail, especially the latest findings in this sphere.

71.2 GROWTH AND PHOTOSYNTHESIS

Environmental stress can trigger various plant responses ranging from gene expression to metabolism, and all the way to growth rate and productivity [38]. Salinity, which is the most common and comprehensive negative influence, can lead to apparent stunting of plant growth [39, 40]. From another perspective, slower growth is an available measure for ensuring plant survival under stress [1]. In other words, adverse environments affect the plant, and the plant takes the necessary measures to accommodate it. Actually, all physiological functions or activities are adaptive strategies for plants under salt stress. Research on *Arabidopsis* revealed a link between stress and cell division, illustrating the mechanism at the molecular level [41]. Cyclin-dependent protein kinase inhibitor (ICK1), which is induced by abscisic acid (ABA), can reduce the activities of cyclin-dependent protein kinase to restrain cell division, and ABA is a central plant hormone under abiotic stress, involved in cellular signaling, regulation of plant growth, and stomatal conductance [37,42]. Yet studies on barley displayed that ABA concentration increased transiently under salt stress and returned to normal after 24 h, with leaf growth rate reduced [43]. More recent research shows that it is a Asp-Glu-Leu-Leu-Ala (DELLA) protein, which is a common negative factor in plant growth and a key component in gibberellic acid (GA) signal transduction that integrates signals from hormones and abiotic stress to plant growth [44].

The accumulated Na^+ within plants also can produce ionic toxicity. With only a few exceptions, the glycophytes, especially a large proportion of crops, cannot tolerate Na^+ concentration at $\geq$50 mM [4]. The excess salt can inhibit enzyme activity and lead to death to leaves [22a]. Or salt may build up in the chloroplast exerting a toxic effect on photosynthetic processes and photosynthetic components directly [4]. Mitogen-activated protein kinase 6 (MPK6) has been demonstrated to play an important role in sodium detoxification through phosphorylation of the Na^+/H^+ antiporters and inducing the efflux of sodium [42].

Biomass is only a broad and morphological parameter, while photosynthesis is one of the most direct and conclusive factors in determining plant growth and crop yields. Photosynthetic rate would decrease if any part of its process was affected [27]. For instance, stress can reduce stomatal and mesophyll conductance and decrease CO_2 availability, ultimately lowering photosynthesis [42]. Carbon fixation can be destroyed by salt stress directly; for example, this can occur in ribulose-1,5-bisphosphate (RuBP) carboxylase/oxygenase (Rubisco) activity, which is the key enzyme in photosynthesis [40,45,46]. Gas exchange and chlorophyll a fluorescence are used to monitor photosynthesis to reflect the disadvantageous influence of salt stress [47]. In order to resist salt stress, some plants choose to change the

photosynthetic pathway to cope with this problem [28]. The plant *Mesembryanthemum crystallinum* opted to transform the C3 pathway to crassulacean acid metabolism (CAM) to reduce water loss [48]. The halophytic plant *Atriplex lentiformis* is able to shift from C3 to C4 to combat salt stress [49]. Some transgenic C3 plants displayed higher photosynthetic efficiency and better growth characteristics [50]. Moreover, salt stress can weaken photosynthesis indirectly by reducing chlorophyll and total carotenoid content. It was reported that the contents of total chlorophyll and carotene were depleted by NaCl stress in leaves of tomato and *B. parviflora* [51, 52]. Overall, salinity is accompanied by a significant reduction in photosynthesis.

71.3 OSMOTIC STRESS EFFECTS AND TOLERANCE

As is mentioned above, there are two aspects of salt tolerance: osmotic stress and ionic stress. Osmotic stress is not only confined to drought but is also a result of salinity. The abundance of ions in saline soil lowers the flow of water, inhibiting water uptake or even causing loss of intracellular water [27]. In such cases, to resist these effects, the plant accumulates many metabolites, which are usually called *compatible solutes*, to increase its osmotic tolerance [13]. These compatible solutes include sugars (fructose, sucrose, and glucose), complex sugars (trehalose, raffinose, and fructans), quaternary amino acid derivatives, tertiary amines, and sulfonium compounds [4]. They are able to not only counteract the ion load but also balance the osmotic potential of Na^+ and Cl^- that are sequestered into the vacuole [53]. Among the compatible solutes, proline (Pro) and glycine betaine (GB) are the most common and efficient. In 1977, a research team reported that Pro or GB is able to accumulate at high concentration, producing as much as 0.1 MPa osmotic pressure [14]. With the continuing in-depth research, their vital functions in salt stress are becoming increasingly clear.

Pro is able to act as molecular chaperone to stabilize the protein conformation, buffer cytosolic pH, and balance cell redox conditions [54]. Under stress, the accumulation of Pro is due to increased biosynthesis and decreased degradation. In leaves of two rice cultivars with different salinity tolerance, the accumulative rate of proline is quicker in the tolerant line [55]. Research on sorghum also illustrated that the proline concentration is at a higher level when subjected to salt stress [56]. It is now known that there are two pathways and three enzymes involved in the synthesis of Pro [57]. For the three synthetic enzymes [pyrroline-5-carboxylate synthase and reductase (P5CS, P5CR) and ord-δ-aminotransferase (OAT)], P5CS is the rate-limiting enzyme and is adjusted by feedback and transcriptional regulation [58, 59]. In *Arabidopsis* the signaling pathway for the induction of P5CS1 expression during salt stress depends on phospholipase C (PLC) and ABA-responsive (ABRE) element [60,61]. Identifciation of the molecular mechanism in Pro metabolism has been accompanied by progress in transgenic engineering. The first transgenic plant with accumulated Pro was acquired in 1995 [62]. In *Arabidopsis*, overexpression P5CS antisense or the insertional mutant of this gene can reduce the salt tolerance of transgenic plants [63,64]. Meanwhile, we may lessen the degradation of Pro to maintain its concentration, so the key enzyme in degradation, proline dehydrogenase (PDH), is also manipulated. However, in PDH antisense, lines with higher stress tolerance have emerged at times but not always [63,65].

Glycine betaine (GB) is synthesized and accumulated under a variety of abiotic stress and acts as an osmolyte to protect PSII under salinity [66]. It can also protect the integrity of membrane and the activity of enzymes against osmotic stress [67]. Generally, high-concentration salt is able to increase GB concentration in many crop plants, such as sugarbeet, spinach, barley, wheat, and sorghum [68–70]. In view of its powerful features, transgenic engineering was also employed to operate GB concentration. Transgenic *Arabidopsis* expressing *N*-methyltransferase gene, which is one of the three key enzymes in GB synthesis, showed improved seed yield compared to the control under salt stress [71]. Similarly, overexpression of galactinol peroxidase 2 (GOLS2), a GB synthase, enhanced tolerance to high salinity in *Arabidopsis* [72].

In fact, there are many other compatible solutes. For example, in *Arabidopsis*, overexpression of mannose-6-phosphate reductase was reported to increase growth and photosynthesis in saline treatment [73]. Some plants that are able to tolerate Na^+ at high levels, such as barley, tend to adapt and maintain turgor in the face of high soil salinities by Na^+ directly. In addition, some plants tend to accumulate carbohydrates such as sugars and starch to cope with salt stress [52]. In conclusion, to survive salt stress successfully, plants have to accumulate high concentrations of compatible solutes to maintain low water potential in cells.

71.4 ION TOXICITY AND ION HOMEOSTASIS

Because of their similarity in physicochemical properties, Na^+ competes with K^+ to bind to the active site of the enzymes, causing the inactivation or degeneration of the enzymes and the disorder of protein synthesis and ribosome function [4]. The toxic position of Na^+ is mainly in the leaf blade, since Na^+ in the transpiration stream is deposited here or in the roots [22b]. One study indicated that the functions of chloroplast were disturbed when K^+ was replaced by Na^+, resulting in uncontrolled water loss [74]. Although Cl^-

is a necessary micronutrient for cells in regulating enzyme activity, maintaining membrane protein and pH gradients, it is toxic to cells at high levels [75, 76]. Accumulated Na^+ in shoots is associated with a decrease in stomatal conductance, while Cl^- in high concentration can damage chloropyll and inhibit photosystem II (PS II) [77]. More seriously, the toxic effects of Na^+ and Cl^- have a cumulative effect. Hence, balancing intracellular ion concentrations by maintaining high K^+ and low Na^+ concentration in the cytosol are crucial for plants [27].

Fortunately, during the lengthy evolution, most plants have acquired capabilities to regulate ions accumulation and to uptake ions selectively. Plants can exclude the toxic excess Na^+ ions from cytosol [78], and almost all the plants are able to take up water and exclude Na^+ and Cl^- from soil effectively [22a]. Some plants, especially halophytes, possess succulent leaves and stems to dilute the concentration of the toxic ions; others evolve salt glands or bladders to secret excess ions [27]. Studies in wheat and wild soybean with better salt tolerance demonstrated that the Na^+ concentration in shoots is maintained at lower levels by withholding it in roots [79, 80]. In other words, the abilities to exclude Na^+ from the cytoplasm and to accumulate Na^+ in vacuoles efficiently are the most important means of maintaining ion homeostasis in cells [81]. By either exclusion by roots or compartmentalization into vacuoles, the transport of ions is mediated by H^+-ATPase, ion channels, and cotransporters in plants. The plasma membrane Na^+/H^+ antiporter SOS1 and the tonoplast membrane antiporters vacuolar Na^+ /H $^+$ antiporter (NHX) are the most important transporters in salt stress and have been investigated extensively [37].

Salinity exposure triggers complicated signaling events, so the means by which stresses are sensed and transported by salt stress signaling provides us with a clue to understand the regulation mechanism of plants. The SOS signaling pathway has been identified in earlier studies as consisting of three key components: SOS3, SOS2, and SOS1. SOS3 is a Ca^{2+} sensor [82]. SOS2 is a serine/threonine protein kinase [83]. SOS3 can sense the perturbation of Ca^{2+} levels in cytoplast caused by salt stress and then bind to the SOS2. Then the SOS3/SOS2 complex phosphorylates and activates SOS1; hence the activated SOS1 has the ability to export excess ions and contribute to Na^+ ion homeostasis [82–84]. SOS1 was also discovered to be the downstream target of MPK6 by GST pulldown assay [85]. Moreover, during salt stress the phosphorylation degree of SOS1 increases [42]. Many other studies have stated that the components of the signaling pathway may be regulated by salt stress directly or influence other signaling pathways of the stress to affect responses indirectly [86–88].

The NHXs are vacuolar Na^+/H^+ antiporters. In one review, NHXs were demonstrated to participate in cell expansion, cell volume regulation, ion homeostasis, osmotic adjustment, pH regulation, protein processing, and other processes [2]. In genetic engineering, the hypersensitive phenotype of *sos1* demonstrated powerfully the key position of SOS signaling pathway in salt stress. Compared to control leaves, the H^+-ATPase in tonoplast vesicles increased twofold in salt-treated leaves [89]. Overexpression of NHX may reduce cytosolic Na^+ concentration and improve salt tolerance by efficient sequestration [90]. Its overexpression confers salt tolerance to a wide range of plants [91]. In Table 71.1, transgenic plants for different ion transporters with enhanced ion homeostasis are listed for reference.

In addition, the HKT family also plays vital functions in maintaining ions homeostasis. The HKT proteins act as Na^+/K^+ symporters and Na^+-selective transporters, involved in balancing of Na^+ and K^+. More recently, AtHKT1 was demonstrated to take charge of the resorption of Na^+ from xylem to reduce the amount of Na^+ reaching the shoot in *Arabidopsis* [112]. In durum wheat, TmHKT1 is correlated with Na^+ exclusion and a high K^+/Na^+ rate in leaves [113]. In rice, OsHKT1 appears to have the same function as AtHKT1 [114], yet much more work is needed to clarify the multiple functions of the gene family.

Recently, maintaining intracellular high cytosolic K^+/Na^+ ratio has been accepted as the key determinant in salinity tolerance [4]. K^+ possesses a significant role in activating enzymes, regulating osmotic pressure, regulating stoma movement, and balancing turgor [115]. In wheat cells, the contents of K^+ and Na^+ are kept at 150 mM and 30 mM, respectively, so the K^+/Na^+ ratio is approximately 5 [116]. Indeed, increasingly reports show that it should be the cytosolic K^+/Na^+ ratio that determine the plant salt tolerance. Two other authors proposed that the low level of KNO_3 could alleviate NaCl-induced stress [117]. Another group further claimed that NaCl stress symptoms can be alleviated by simultaneously applied KNO_3 and that the optimal K^+/Na^+ ratio should be 100:16 for both salt-tolerant and salt-sensitive cultivar [118]. Similarly, overexpression of LeENH1 (a tomato enhancer of SOS3-1) in tobacco enhanced salinity tolerance by excluding Na^+ from cytosol and retained high K^+ levels in the cytosol [119]. Studies on NHXs also attest to this point. More recently, mineral analysis of the transgenic plants with overexpressed NHXs seems to indicate that salt resistance is provided by a high K^+/Na^+ ratio through K^+ retention rather than Na^+ exclusion [120]. In *Arabidopsis*, the phenotype of *sos* mutants may be alleviated by an exogenous supply of K^+ [37]. Compared to *Arabidopsis*, the *Thellungiella* species (see Table 71.1) possess stronger ability to adapt to saline soil. One reason is that the cytosolic K^+ concentration in *Thellungiella* is higher. One group claimed that the transgenic tomato with high resistance depended on cytosolic K^+ homeostasis rather than on vacuolar Na^+ accumulation [121].

TABLE 71.1 Improving Plant Salt Tolerance by Bioengineering Ion Homeostasis

	Donor	Acceptor	Gene function	Elevated character	Ref.
Vacuolar Na^+/H^+ Antiporter AtNHX1	*A. thaliana*	Wheat	Na^+/H^+ antiporters in tonoplast, exchange Na^+ or Li^+ for H^+	Biomass production, grain output, and leaf K^+ accumulation	92
Vacuolar Na^+/H^+ antiporter AtNHX1	*A. thaliana*	Tall fescue	Na^+/H^+ antiporters in tonoplast, exchange Na^+ or Li^+ for H^+	Activity of vacuolar Na^+/H^+ antiporter	93
Vacuolar Na^+/H^+ antiporter AtNHX1	*A. thaliana*	Tall fescue	Na^+/H^+ antiporters in tonoplast, exchange Na^+ or Li^+ for H^+	Better growth at 200 mM NaCl	94
Vacuolar Na^+/H^+ antiporter PgNHX1	Pennisetum glaucum	Rice	Na^+/H^+ antiporters in tonoplast, exchange Na^+ or Li^+ for H^+	Advanced root system	95
Vacuolar Na^+/H^+ antiporter OsNHX1	Rice	Perennial ryegrass	Na^+/H^+ antiporters in tonoplast, exchange Na^+ or Li^+ for H^+	Elevated concentration of Na^+, K^+, and proline	96
Vacuolar Na^+/H^+ antiporter MsNHX1	Alfalfa	*A. thaliana*	Na^+/H^+ antiporters in tonoplast, exchange Na^+ or Li^+ for H^+	Increased osmotic adjustment	97
Vacuolar Na^+/H^+ antiporter AlNHXI	*Aeluropus littoralis*	Tobacco	Na^+/H^+ antiporters in tonoplast, exchange Na^+ or Li^+ for H^+	A relatively high K^+/Na^+ ratio in leaves and roots	98
Vacuolar H^+ pyrophosphatase AVP1	*A. thaliana*	Alfalfa	Na^+/H^+ antiporters in tonoplast, exchange Na^+ or Li^+ for H^+	Increased content of Na^+, K^+, and Ca^{2+} in leaves and roots	99
Vacuolar Na^+/H^+ antiporter AtNHX1	*A. thaliana*	Kiwifruit	Na^+/H^+ antiporters in tonoplast, exchange Na^+ or Li^+ for H^+	Improved salt tolerance	94
Vacuolar Na^+/H^+ antiporter SsNHX1	Salsola soda	Alfalfa	Na^+/H^+ antiporters in tonoplast, exchange Na^+ or Li^+ for H^+	Growth in high concentrations of NaCl over 50 days	100a
Vacuolar Na^+/H^+ antiporter MdNHX1	Malus	Apple	Na^+/H^+ antiporters, exchange Na+ or Li+ for H+	A relatively high K^+/Na^+ ratio in leaves	100b
Vacuolar Na^+/H^+ antiporter AtNHX1	*A. thaliana*	Groundnut	Na^+/H^+ antiporters in tonoplast, exchange Na^+ or Li^+ for H^+	Resistant to high concentration of salt	101
Vacuolar Na^+/H^+ antiporter NHX1	*Aopiptanthus mongolicus*	*A. thaliana*	Na^+/H^+ antiporters in tonoplast, exchange Na^+ or Li^+ for H^+	Lower Na^+ content in leaves	102
Plasma membrane Na^+/H^+ antiporter sodium 2 (SOD2)	Yeast	Rice	Na^+/H^+ antiporters in plasma membrane, exchange Na^+ or Li^+ for H^+	Enhanced net photosynthetic rate, higher K^+, lower Na^+	103
H^+-pyrophosphatase (PPase) gene TsVP	*T. halophila*	Tobacco	Pumping H^+ from the cytoplasm into vacuoles to form the pH gradient	Greater dry weight at 300 mM NaCl	104
H^+-pyrophosphatase (PPase) gene TsVP	*T. halophila*	Cotton	Pumping H^+ from the cytoplasm into vacuoles to form the pH gradient	Accumulating more Na^+, K^+, Ca^{2+}, Cl^{2-} and soluble sugars in their root and leaf tissues	105
H^+-pyrophosphatase (PPase) gene AVP1	*A. thaliana*	Alfalfa	Pumping H^+ from the cytoplasm into vacuoles to form the pH gradient	Accumulating more Na^+, K^+, and Ca^{2+} in leaves and roots	106
H+-pyrophosphatase (PPase) gene AVP1	*A. thaliana*	Cotton	Pumping H^+ from the cytoplasm into vacuoles to form the pH gradient	More vigorous growth in the presence of 200 mM NaCl	107

TABLE 71.1 (*Continued*)

	Donor	Acceptor	Gene function	Elevated character	Ref.
Plasma membrane Na^+/H^+ antiporter SOS1	*A. thaliana*	*A. thaliana*	Na^+/H^+ antiporters in plasma membrane, exchange Na^+ or Li^+ for H^+	Accumulating less Na^+ in the xylem transpirational stream and in the shoot	108
Plasma membrane Na^+/H^+ antiporter sodium 2 (SOD2)	Yeast	*A. thaliana*	Na^+/H^+ antiporters in plasma membrane, exchange Na^+ or Li^+ for H^+	Accumulating less Na^+ and more K^+ in the symplast	109
Plasma membrane Na^+/H^+ antiporter SOS	*A. thaliana*	*A. thaliana*	Na^+/H^+ antiporters in plasma membrane, exchange Na^+ or Li^+ for H^+	Increased salt tolerance	91
Plasma membrane Na^+/H^+ antiporter SISOS	Tomato	Tomato	Na^+/H^+ antiporters in plasma membrane, exchange Na^+ or Li^+ for H^+	Active loading of Na^+ into the xylem, and Na^+ and K^+ compartmentalization	110
Plasma membrane Na^+/H^+ antiporter SOS1, SOS2, SOS3	*A. thaliana*	Tall fescue	Na^+/H^+ antiporters in plasma membrane, exchange Na^+ or Li^+ for H^+	Superior growth and accumulated less Na^+ and more K^+ in roots after 350 mM NaCl treatment	111

71.5 OXIDATIVE STRESS AND ANTIOXIDANT DEFENSE RESPONSES

Besides osmotic stress and ion toxicity, salinity can also induce the generation of reactive oxygen species (ROS) and lead to oxidative stress. ROS derive from the excitation of O_2 including singlet oxygen ($^1O_2$), superoxide anion (O_2^-), hydrogen peroxide (H_2O_2), and hydroxyl radical (OH·), respectively [27]. Unlike atmospheric oxygen, ROS are able to oxidize the various cellular components without unrestriction, leading to the oxidative destruction of plant cells [122]. Actually, ROS are the common byproducts of the metabolic pathways such as photosynthetic electron transport, respiration, and photorespiration processes [123]. For example, salt stress limits the supply of CO_2, causing overreduction of the photosynthetic electron transport chain and a vast production of ROS [13]. The overabundant ROS can oxidize cellular components, hinder metabolic activities, and affect organelle integrity [124]. The destructive effect of ROS is the lipid peroxidation estimated by the content of malonyldialdehyde (MDA) [125]. Generally, under normal conditions, the production and eliminate of ROS are in an equilibrium state [26]. However, under salt stress conditions, the generation rate of ROS overwhelms the scavenging of the antioxidant system, and then oxidative damage occurs, leading to oxidation to lipids, proteins, and nucleic acids. This occcurs precisely because these biomacromolecules are components of the plasma membrane; thus the membrane system is the main subject of the ROS [27].

In higher plants, the ROS removal system includes ROS-scavenging antioxidant enzymes and small nonenzymatic molecules such as ascorbate, glutathione, flavonoids, anthocyanines, and carotenoids [13]. The nonenzymatic molecules are able to donate electrons or hydrogen to scavenge free radicals [26]. The antioxidant enzyme system consists of superoxide dismutase (SOD), peroxidase (POD), ascorbate peroxidase (APX), glutathione peroxidases (GPX), glutathione reductase (GR), catalase (CAT), and the ascorbate–glutathione cycle [16]. The SOD, APX, and GR (glutathione reductase) are reported to scavenge H_2O_2 in chloroplasts and mitochondria, and the others are believed to be capable of removing H_2O_2, neutralizing or scavenging free radicals [126]. Among them, SOD and CAT are the most efficient enzymes. Under salt stress, the second metabolites increased more quickly than did the antioxidant enzyme activities in *Swertia chirata* [127]. The levels and contents of superoxide and hydrogen peroxide can be decreased by most of the antioxidant obviously, so in many species the antioxidant capacity is associated with salinity tolerance tightly. For example, the antioxidant enzyme activities of SOD, APX, and GR increased 10–18 times after salt stress in *P. popularis* [128]. The correlation between antioxidant capacity and salinity tolerance is being discovered in an increasing number of species, containing cotton, citrus, foxtail millet, purslane, sugarbeet, pea, and plantago [13].

During the last few decades, engineering the genes of some antioxidant enzymes has been employed to ameliorate plants exposed to stress. By observing the changes in the

expression level of related genes, researchers were able to produce transgenic plants to probe the effects. Finally, in the transgenic plants, overexpression antioxidant enzymes such as SOD, CAT, and APX displayed elevated tolerance to oxidative stress [13]. The transgenic *Arabidopsis* and *Lycopersicon esculentum* possess a significant increase in salt tolerance with the overexpression of a Mn-SOD [129, 130]. Details are shown in Table 71.2. More importantly, most of the transgenic plants with some overexpressed antioxidant enzymes acquire an elevated tolerance to almost all abiotic stresses instead of a specific stress. In our opinion, the possible reason for this is that the oxidative stress is the result of almost all the abiotic stresses, so the enhancement of the antioxidative capacity is able to boost resistance in general. Although the transgenic plants with overexpressed antioxidant enzymes acquire enhanced tolerance, there exist inevitable contradictions. The *Arabidopsis* mutants with loss of either or both cytosolic and chloroplastic APX show enhanced tolerance on the contrary [131]. Likewise, there is a decline in CAT activity in *Anabaena doliolum* under NaCl stress [132]. In *Glycyrrhiza uralensis* seedlings, CAT activity is also decreased by salt and drought stress [133]. In conclusion, the ROS pathway is plastic and redundant, more strategies and principles remain to be seen.

Reactive oxygen species play a dual role in plants. Superfluous ROS are detrimental to plant cells, yet moderate ROS components are necessary, playing important roles in signaling transduction and cell homeostasis [85]. In fact, upregulation of the expression levels of enzyme genes or the enhancement of their enzymatic activities results from cell signaling. Ahead of their detoxification, the genes will have initiated a series of signaling in cells. MAK3 and MAK6 can be activated by the elevated content of ROS [150], and the activated MAK3 and MAK6 were relocated in the nucleus to strengthen or weaken gene expression, triggering plant responses to ROS. Nevertheless, the MAPK phosphatase 2 (MKP2), which is induced by oxidative stress, is able to dephosphorylate MPK3 and MPK6 to promote oxidative stress tolerance [85]. Therefore, the signal regulatory pathways are intricate.

71.6 PHYTOHORMONE IN SALT STRESS

Plant hormones partipate in almost all plant contents and processes, including different positions, different tissues, and different developmental stages. ABA is the foremost one and is induced by various obvious types of stress. It is able to regulate the adaption of plants to stresses such as cold, drought, salinity, pathogen attacks, injury, and oxidative stress [85]. It has been proved responsible for the change in salt-stress-induced genes back in the 1990s [151]. Its powerful functions in salt stress are reflected in its involvement in the photosynthesis and growth, osmotic tolerance, ion homeostasis, and antioxidant defense responses that we mentioned above. Two decades ago, Popova and colleagues proposed that the inhibitory effect of salt stress on growth and photosynthesis can be alleviated by ABA [152]. Moreover, ABA participates in regulating stress-related gene expression. In ABA-deficient mutants, P5CS, which is the rate-limiting enzyme of the synthesis of Pro, is reduced or completely blocked [153]. For ion homeostasis, ABA has the ability to reduce anion channels to reduce Cl^- transfer in saline conditions [154]. The type 2C protein, phosphatase ABI2, which acts as a vital component in ABA signaling, is able to bind to SOS2 directly and dephosphorylate it [155]. The involvement of ABA in antioxidant defense responses is the induction of antioxidant defense. During the ABA-induced antioxidant defense, hydrogen peroxide (H_2O_2), nitric oxide (NO), and mitogen-activated protein kinase (MAPK) are the major components [156–160]. Zhang and coworkers reported that the zinc finger protein ZFP182 also mediated the ABA-induced antioxidant defense [161]. In rice, ABA can significantly induce the expression and activity of OsCAT to control the accumulation of H_2O_2 under stress [159]. More recently, ABA was discovered to induce the production of primary and secondary metabolites, the photosynthetic capacity, the antioxidant ability, and the antioxidant enzymes [162].

In recent years, phytohormone—salicylic acid (SA) was repeatedly reported to participate in salt stress responses as well [42]. The exogenous SA can ameliorate toxicity stress induced by salt stress, and its vital function under salt stress manifests in its enhancement on antioxidant system. In periwinkle, nonenzymatic and enzymatic antioxidants can be induced by exogenous SA [163]. In mungbean, SA alleviates decreases in photosynthesis by means of enhancing antioxidant metabolism [164]. Furthermore, SA can lessen salt stress by maintaining ion homeostasis. It is well known that ion homeostasis, especially the optimum K^+/Na^+ ratio, is crucial for plants under salt stress. Discoveries achieved by noninvasive microelectrode ion flux estimation (MIFE) technique [165] revealed that SA pretreatment can enhance K^+ retention, increase H^+-ATPase activity, and reduce K^+ loss under salt stress [166]. Generally speaking, the potential mechanism of SA to enhance salt tolerance lies in improving photosynthesis, enhancing antioxidant protection, and maintaining optimum K^+/Na^+ ratio [164,166,167].

71.7 CONCLUSIONS

Salt stress is one of the most common types of abiotic stress. Its negative influence on plants is comprehensive. High-concentration salt can interfere with normal growth and development tremendously and even lead to death to plant. Fortunately, plants have acquired the abilities to ameliorate these adverse effects by physiological, molecular, and genetic by means of regulation. Plants reduce their growth rate to

TABLE 71.2 Genetic Transformation of Antioxidant Enzymes for Enhancing Salt Tolerance

Gene symbol	Donor	Acceptor	Gene functions	Elevated character	Ref.
Ascorbate peroxidase (APX)	*A. thaliana*	Tobacco	Primary H_2O_2-scavenging enzyme	Enhanced tolerance to active oxygen-generating paraquat and sodium sulfite	134
Superoxide dismutase (SOD)	*A. thaliana*	*A. thaliana*	A critical enzyme for eliminating reactive oxygen species (ROS) in plant cells	Lower content of malondialdehyde (MDA) and better growth than control under salt stress	129
Ascorbate peroxidase (APX)	Pea	Tobacco	Primary H_2O_2-scavenging enzyme	Higher germination rate and minimized leaf damage under salt stress	135
Dehydroascorbate reductase (DHAR)	Rice	*A. thaliana*	A critical enzyme for ascorbate recycling	Enhanced resistance to salt stress	136
Ascorbate peroxidase (APX)	Rice	*A. thaliana*	Primary H_2O_2-scavenging enzyme	Longer root length and higher total chlorophyll content	137
Ascorbate peroxidase (APX) Superoxide dismutase (SOD) and DHAR	Tobacco	Tobacco	Primary H_2O_2-scavenging enzyme; A critical enzyme eliminating reactive oxygen species (ROS) in plant cells; a critical enzyme for ascorbate recycling	More resistant to paraquat-induced stress and enhanced tolerance to NaCI	138
Monodehydroascorbate reductase (MDAR)	*A. thaliana*	Tobacco	Crucial for ascorbate (AsA) regeneration and essential for maintaining a reduced pool of AsA	Higher net photosynthesis rates and greater PS II effective quantum yield under salt stress	139
Catalase (CAT)	*Escherichia coli*	Tobacco	Catalyzing the dismutation of H_2O_2 into water and oxygen	Increased the resistance of the chloroplast's translational machinery under salt stress	140
Superoxide dismutase (SOD)	*Avicennia marina*	Rice	The first enzyme in the enzymatic antioxidative pathway	More tolerant to methyl viologen–mediated oxidative stress	141
Superoxide dismutase (SOD)	Tobacco	Pepper	The first enzyme in the enzymatic antioxidative pathway	Increased resistance to oxidative damage	142
Ascorbate peroxidase (APX)	Tomato	Tobacco	Primary H_2O_2-scavenging enzyme	Higher seed germination rate and elevated stress tolerance during postgermination	143
Suaeda salsa glutathione S_transferase gene (GST)	*Suaeda salsa*	*A. thaliana*	Involved in the reduction of most active oxygen radicals generated by stress	Higher photosynthesis rate and fresh weight	144
Monodehydroascorbate reductase (MDAR)	*Avicennia marina*	Tobacco	Crucial for ascorbate (AsA) regeneration and essential for maintaining a reduced pool of AsA	Enhanced redox state of ascorbate and reduced levels of malondialdehyde	145
Ascorbate peroxidase (APX)	*P. populus*	Tobacco	Primary H_2O_2-scavenging enzyme	Resistance to methyl viologen and salt stress	146
Ascorbate peroxidase (APX), Superoxide dismutase (SOD)	Tobacco	Tobacco	Primary H_2O_2-scavenging enzyme; the first enzyme in the enzymatic antioxidative pathway	Improved seed longevity and germination under various types of environmental stress	147
Glutathione peroxidases (GPXs)	Wheat	*A. thaliana*	Reducing H_2O_2 and organic hydroperoxides to water and correspondingly alcohols	Strong tolerance to salt, H_2O_2, and ABA treatment	148
Ascorbate peroxidase (APX), superoxide dismutase (SOD)	Plums	Plums	Primary H_2O_2-scavenging enzyme; the first enzyme in the enzymatic antioxidative pathway	Higher contents of nonenzymatic antioxidants glutathione and ascorbate and lower accumulation of hydrogen peroxide	149

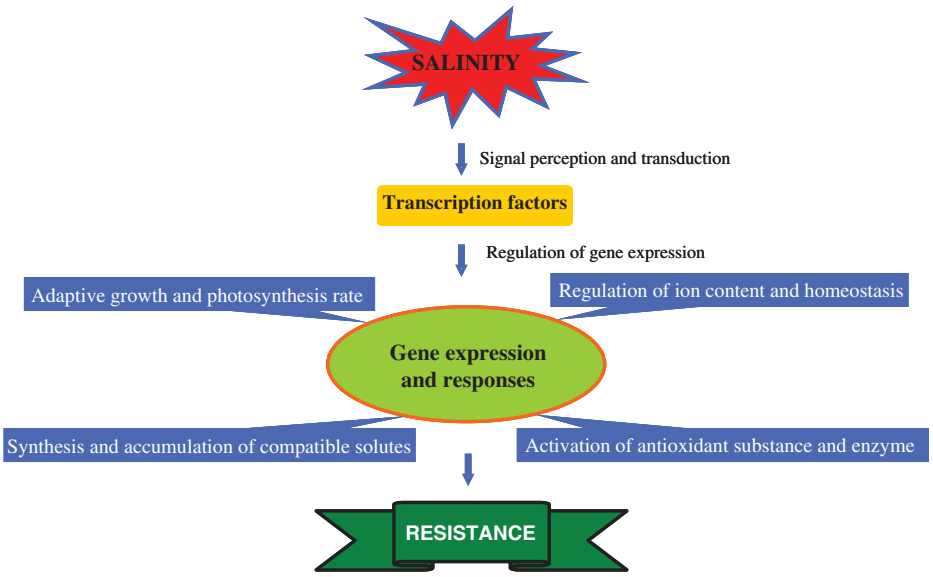


FIGURE 71.1 The general pathway under salt stress.

guarantee their survival and maintain regular photosynthesis by regulating enzymatic activities under salt stress [1]. Facing the osmotic stress produced by salt, plants accumulate compatible solutes actively to reduce cell water potential [4]. Different channels and transporters are activated or inhibited to regulate and maintain ion homeostasis. The clarified signaling pathways tell us the complicated regulatory mechanisms employed by plants under salt stress. The discovery of the SOS signaling pathway is a milestone of the signal pathway in salt stress [82]. The antioxidant system covering nonenzymatic and enzymatic antioxidant systems can help plants escape the damage due to salt stress [26]. Plant hormones are the growth regulators of plants and are involved in the processes in every regard, so salt stress is no exception. ABA plays a pivotal role in the metabolomic, physiological, and signaling procedures. Thus we can conclude that the relationships between salt stress and plants are processes of both influence and adaptation. Exploring and understanding the regulatory mechanisms underlying salt stress can provide us with more methods and ideas to improve plant resistance.

In view of the research and developments in molecular biology and transgenic engineering, plants with enhanced tolerance are generating continuously. For example, overexpression of the synthetic genes of Pro and GB can improve the content of Pro and GB obviously and endow the transgenic plants with enhanced tolerance [62,71]. Similarly, transgenic plants with more SOS1 or NHX1 transporters are able to regulate ion transport more quickly and effectively to improve their growth under salt stress [83, 84,91]. Increasing the antioxidants levels through genetic engineering is widely adopted in breeding to produce crops with enhanced salt stress. Yet the salt tolerance trait is a multigenic property, as salt tolerance is related to physiological, biochemical, and molecular processes, so the ability of genetic engineering to produce salt-tolerant crops is seriously limited by these natural plant processes [37]. More energy, materials, and financial resources are needed to invest in the research. Only in this way can the mechanisms and principles be discovered and corresponding ameliorative solutions be proposed. In addition, there are other factors such as LEA proteins and WRKY and MYB transcriptional factors affecting salt tolerance of plants, which should also arouse attention [168–170]. In the most recent reports, the microorganism in soil is found to be involved in phytohormonal signaling to improve plant nutrition, photosynthesis, and biomass production, thereby enhancing crop salt tolerance [171]. Finally, we summarize our points of view and blueprint for future research in Fig. 71.1.

ACKNOWLEDGMENTS

This work was jointly supported by the National Natural Science Foundation of China (Grant 41171216), Jiangsu Autonomous Innovation of Agricultural Science and Technology [CX(15)1005], National Basic Research Program of China (2013CB430403) and Shuangchuang Talent Plan of Jiangsu Province.

REFERENCES

[1] Zhu, J.K. (2001). Plant salt tolerance. *Trends Plant Sci.* **6**, 66–71.

[2] Rengasamy, P. (2010). Soil processes affecting crop production in salt-affected soils. *Funct. Plant Biol.* **37**, 613–620.

[3] FAO (2008). FAO Land and Plant Nutrition Management Service (http://wwwfaoorg/ ag/agl/agll/spush).

[4] Munns, R., Tester, M. (2008). Mechanisms of salinity tolerance. *Annu. Rev. Plant Biol.* **59**, 651–681.

[5] Lee, G., Boerma, H., Villagarcia, M., Zhou, X., Carter, T.Jr., Li, Z., Gibbs, M. (2004). A major QTL conditioning salt tolerance in S-100 soybean and descendent cultivars. *Theor. Appl. Genet.* **109**, 1610–1619.

[6] Rhoades, J., Loveday, J. (1990). Salinity in irrigated agriculture. *Agronomy* **30**, 1089–1142.

[7] Conway, G. (1998). The doubly green revolution. *Biologist* **45**, 85–86.

[8] Rengasamy., P (2006). World salinization with emphasis on Australia. *J. Exp. Bot.* **57**, 1017–1023.

[9] Abreu, I.A., Farinha, A.P., Negrão, S., Gonçalves, N., Fonseca, C., Rodrigues, M., Batista, R., Saibo, N.J.M., Oliveira, M.M. (2013). Coping with abiotic stress: Proteome changes for crop improvement. *J. Proteomics* **93**, 145–168.

[10] George, E., Brown, J. (2008). Mechanisms of salinity tolerance. *Annu. Rev. Plant Biol.* **59**, 651–681.

[11] Aslam, M., Qureshi, R., Ahmed, N. (1993). A rapid screening technique for salt tolerance in rice (Oryza sativa L.). *Plant Soil* **150**, 99–107.

[12] Colmer, T., Munns, R., Flowers, T. (2006). Improving salt tolerance of wheat and barley: Future prospects. *Animal Prod. Sci.* **45**, 1425–1443.

[13] Türkan, I., Demiral, T. (2009). Recent developments in understanding salinity tolerance. *Environ. Exp. Bot.* **67**, 2–9.

[14] Flowers, T., Troke, P., Yeo, A. (1977). The mechanism of salt tolerance in halophytes. *Ann. Rev. Plant Physiol.* **28**, 89–121.

[15] Flowers, T.J., Colmer, T.D. (2008). Salinity tolerance in halophytes. *New Phytol*. **179**, 945–963.

[16] Ashraf, M., Akram, N.A. (2009). Improving salinity tolerance of plants through conventional breeding and genetic engineering: An analytical comparison. *Biotechnol. Adv.* **27**, 744–752.

[17] Wright, M.J., Ferrari, S. (1976). *Plant Adaptation to Mineral Stress in Problem Soils.* PhD thesis, Cornell Univ.

[18] Kingsbury, R., Epstein, E. (1984). Selection for salt-resistant spring wheat. *Crop Sci*. **24**, 310–315.

[19] Ashraf, M., Wu, L. (1994). Breeding for salinity tolerance in plants. *Crit. Rev. Plant Sci.* **13**, 17–42.

[20] Sarwat, M., Ahmad, P., Nabi, G., Hu, X. (2013). Ca^{2+} signals: The versatile decoders of environmental cues. *Crit. Rev. Biotechnol.* **33**, 97–109.

[21] Xue, X.X., Shao, H.B., Ma, Y.Y., Xu, G., Sun, J.N., Guo, D.G., Ruan, C.J. (2010). Biotechnological implications from abscisic acid (ABA) roles in cold stress and leaf senescence as an important signal for improving plant sustainable survival under abiotic-stressed conditions. *Crit. Rev. Biotechnol.* **30**, 222–230.

[22] (a) Munns, R. (2005). Genes and salt tolerance: Bringing them together. *New Phytol*. **167**, 645–663; (b) Munns, R. (2002). Comparative physiology of salt and water stress. *Plant Cell Environ.* **25**, 239–250.

[23] Zhu, J.K. (2002). Salt and drought stress signal transduction in plants. *Annu. Rev. Plant Biol*. **5**, 247–269.

[24] Dufty, A.M. Jr., Clobert, J., Møller, A.P. (2002). Hormones, developmental plasticity and adaptation. *Trends Ecol. Evolut.* **17**(4), 190–196.

[25] Glombitza, S., Dubuis, P.-H., Thulke, O., Welzl, G., Bovet, L., Götz, M., Affenzeller, M., Geist, B, Hehn, A., Asnaghi, C. (2004). Crosstalk and differential response to abiotic and biotic stressors reflected at the transcriptional level of effector genes from secondary metabolism. *Plant Mol. Biol.* **54**, 817–835.

[26] Jaleel, C.A., Riadh, K., Gopi, R., Manivannan, P., Inès, J., Al-Juburi, H.J., Zhao, C.X., Shao, H.B., Panneerselvam, R. (2009). Antioxidant defense responses: Physiological plasticity in higher plants under abiotic constraints. *Acta Physiol. Plant* **31**, 427–436.

[27] Yan, K., Shao, H.B., Shao, C.Y., Chen, P., Zhao, S.J., Brestic, M., Chen, X.B. (2013). Physiological adaptive mechanisms of plants grown in saline soil and implications for sustainable saline agriculture in coastal zone. *Acta Physiol. Plant* **35**, 2867–2878.

[28] Parida, A.K., Das, A.B. (2005). Salt tolerance and salinity effects on plants: A review. *Ecotoxicol. Environ. Safety* **60**, 324–349.

[29] Winicov, I. (1998). New molecular approaches to improving salt tolerance in crop plants. *Ann. Bot.* **82**, 703–710.

[30] Ruan, C.J., Teixeira da Silva, J.A. (2011). Metabolomics: Creating new potentials for unraveling the mechanisms in response to salt and drought stress and for the biotechnological improvement of xero-halophytes. *Crit. Rev. Biotechnol.* **31**, 153–169.

[31] Carrington, J.C., Ambros, V. (2003). Role of microRNAs in plant and animal development. *Science* **301**, 336–338.

[32] Dharmasiri, N., Dharmasiri, S., Estelle, M. (2005). The F-box protein TIR1 is an auxin receptor. *Nature* **435**, 441–445.

[33] Kepinski, S., Leyser, O. (2005). The Arabidopsis F-box protein TIR1 is an auxin receptor. *Nature* **435**, 446–451.

[34] Baldridge, K.C., Contreras, L.M. (2013). Functional implications of ribosomal RNA methylation in response to environmental stress. *Crit. Rev. Biochem. Mol. Biol.* **30**, 1–21.

[35] Colcombet, J., Hirt, H. (2008). Arabidopsis MAPKs: A complex signalling network involved in multiple biological processes. *Biochem. J.* **413**, 217–226.

[36] Sinha, A.K., Jaggi, M., Raghuram, B., Tuteja, N. (2011). Mitogen-activated protein kinase signaling in plants under abiotic stress. *Plant Signal. Behav.* **6**, 196–203.

[37] Zhu, J.K. (2003). Regulation of ion homeostasis under salt stress. *Curr. Opin. Plant Biol.* **6**, 441–445.

[38] Shao, H.B., Chu, L.Y., Jaleel, C.A., Manivannan, P., Panneerselvam, R., Shao, M.A. (2009). Understanding water deficit stress-induced changes in the basic metabolism of higher plants - biotechnologically and sustainably improving agriculture and the ecoenvironment in arid regions of the globe. *Crit. Rev. Biotechnol.* **29**(2), 131–151.

[39] Gorai, M., Ennajeh, M., Khemira, H., Neffati, M. (2011). Influence of NaCl-salinity on growth, photosynthesis, water relations and solute accumulation in Phragmites australis. *Acta Physiol. Plant* **33**, 963–971.

[40] Tarchoune, I., Degl'Innocenti, E., Kaddour, R., Guidi, L., Lachaâl, M., Navari-Izzo, F., Ouerghi, Z. (2011). Effects of NaCl or Na_2SO_4 salinity on plant growth, ion content and photosynthetic activity in Ocimum basilicum L. *Acta Physiol. Plant* **34**, 607–615.

[41] Wang, H., Qi, Q., Schorr, P., Cutler, A.J., Crosby, W.L., Fowke, L.C. (1998). ICK1, a cyclin-dependent protein kinase inhibitor fromArabidopsis thalianainteracts with both Cdc2a and CycD3, and its expression is induced by abscisic acid. *Plant J.* **15**, 501–510.

[42] Davies, W.J., Kudoyarova, G., Hartung, W. (2005). Long-distance ABA signaling and its relation to other signaling pathways in the detection of soil drying and the mediation of the plant's response to drought. *J. Plant Growth Regul.* **24**, 285–295.

[43] Fricke, W., Akhiyarova, G., Veselov, D., Kudoyarova, G. (2004). Rapid and tissue-specific changes in ABA and in growth rate in response to salinity in barley leaves. *J. Exp. Bot.* **55**, 1115–1123.

[44] Achard, P., Cheng, H., De Grauwe, L., Decat, J., Schoutteten, H., Moritz, T., Van Der Straeten, D., Peng, J., Harberd, N.P. (2006). Integration of plant responses to environmentally activated phytohormonal signals. *Science* **311**, 91–94.

[45] Brugnoli, E., Björkman, O. (1992). Growth of cotton under continuous salinity stress: Influence on allocation pattern, stomatal and non-stomatal components of photosynthesis and dissipation of excess light energy. *Planta* **187**, 335–347.

[46] Yang, X., Liang, Z., Wen, X., Lu, C. (2008). Genetic engineering of the biosynthesis of glycinebetaine leads to increased tolerance of photosynthesis to salt stress in transgenic tobacco plants. *Plant Mol. Biol.* **66**, 73–86.

[47] Jedmowski, C., Ashoub, A., Brüggemann, W. (2013). Reactions of Egyptian landraces of Hordeum vulgare and Sorghum bicolor to drought stress, evaluated by the OJIP fluorescence transient analysis. *Acta Physiol. Plant* **35**, 345–354.

[48] Cushman, J.C., Meyer, G., Michalowski, C.B., Schmitt, J.M., Bohnert, H.J. (1989). Salt stress leads to differential expression of two isogenes of PEP case during CAM induction in the common ice plant. *Plant Cell* **1989**, 715–725.

[49] Meinzer, F.C., Zhu, J. (1999). Efficiency of C4 photosynthesis in Atriplex lentiformis under salinity stress. *Funct. Plant Biol.* **26**, 79–86.

[50] Ruan, C.J., Shao, H.B., Teixeira da Silva, J.A. (2012). A critical review on the improvement of photosynthetic carbon assimilation in C3 plants using genetic engineering. *Crit. Rev. Biotechnol.* **32**, 1–21.

[51] Khavari-Nejad, R., Mostofi, Y. (1998). Effects of NaCl on photosynthetic pigments, saccharides, and chloroplast ultrastructure in leaves of tomato cultivars. *Photosynthetica* **35**, 151–154.

[52] Parida, A., Das, A.B., Das, P. (2002). NaCl stress causes changes in photosynthetic pigments, proteins, and other metabolic components in the leaves of a true mangrove, Bruguiera parviflora, in hydroponic cultures. *J. Plant Biol.* **45**, 28–36.

[53] Wyn Jones, R., Storey, R., Leigh, R., Ahmad, N., Pollard, A. (1977). *A Hypothesis on Cytoplasmic Osmoregulation. Regulation of Cell Membrane Activities in Plants*. Wiley, New York, pp. 121–136.

[54] Maggio, A., Miyazaki, S., Veronese, P., Fujita, T., Ibeas, J.I., Damsz, B., Narasimhan, M.L., Hasegawa, P.M., Joly, R.J., Bressan, R.A. (2002). Does proline accumulation play an active role in stress-induced growth reduction? *Plant J.* **31**, 699–712.

[55] Demiral, T., Türkan, I. (2004). Does exogenous glycinebetaine affect antioxidative system of rice seedlings under NaCl treatment? *J. Plant Physiol.* **161**, 1089–1100.

[56] Yan, K., Chen, P., Shao, H.B., Zhao, S.J., Zhang, L.H., Zhang, L.W., Xu, G., Sun, J.N. (2012). Photosynthetic characterization of Jerusalem artichoke during leaf expansion. *Acta Physiol. Plant.* **34**(1), 353–360.

[57] Verbruggen, N., Hermans, C. (2008). Proline accumulation in plants: A review. *Amino Acids* **35**, 753–759.

[58] Savouré, A., Jaoua, S., Hua, X.J., Ardiles, W., Van Montagu, M., Verbruggen, N. (1995). Isolation, characterization, and chromosomal location of a gene encoding theΔ1-pyrroline-5-carboxylate synthetase in Arabidopsis thaliana. *FEBS Lett.* **372**, 13–19.

[59] Zhang, C.S., Li, Q., Verma, D.P.S. (1995). Removal of feedback inhibition of D1-pyrroline-5-carboxylate synthetase, a bifunctional enzyme catalyzing the first two steps of proline biosynthesis in plants. *J. Biol. Chem.* 20491–20496.

[60] Parre, E., Ghars, M.A., Leprince, A.-S., Thiery, L., Lefebvre, D., Bordenave, M., Richard, L., Mazars, C., Abdelly, C., Savouré, A. (2007). Calcium signaling via phospholipase C is essential for proline accumulation upon ionic but not nonionic hyperosmotic stresses in Arabidopsis. *Plant Physiol*. **144**, 503–512.

[61] Abrahám, E., Rigó, G., Székely, G., Nagy, R., Koncz, C., Szabados, L. (2003). Light-dependent induction of proline biosynthesis by abscisic acid and salt stress is inhibited by brassinosteroid in Arabidopsis. *Plant Mol. Biol.* **51**, 363–372.

[62] Kavi, K.P., Hong, Z., Miao, G., Hu, C., Verma, D. (1995). Overexpression of D1-pyrroline-5-carboxylate synthetase increases proline production and confers osmotolerance in transgenic plants. *Plant Physiol.* **108**, 1387–1394.

[63] Nanjo, T., Kobayashi, M., Yoshiba, Y., Kakubari, Y., Yamaguchi-Shinozaki, K., Shinozaki, K. (1999). Antisense suppression of proline degradation improves tolerance to freezing and salinity in Arabidopsis thaliana. *FEBS Lett.* **461**, 205–210.

[64] Székely, G., Abraham, E., Cséplő, Á., Rigo, G., Zsigmond, L., Csiszar, J., Ayaydin, F., Strizhov, N., Jasik, J., Schmelzer, E. (2008). Duplicated P5CS genes of

Arabidopsis play distinct roles in stress regulation and developmental control of proline biosynthesis. *Plant J*. **53**, 11–28.

[65] Mani, S., Van de Cotte, B., Van Montagu, M., Verbruggen, N. (2002). Altered levels of proline dehydrogenase cause hypersensitivity to proline and its analogs in Arabidopsis. *Plant Physiol.* **128**, 73–83.

[66] Jagendorf, A.T., Takabe, T. (2001). Inducers of glycinebetaine synthesis in barley. *Plant Physiol.* **127**, 1827–1835.

[67] Mäkelä, P., Kärkkäinen, J., Somersalo, S. (2000). Effect of glycinebetaine on chloroplast ultrastructure, chlorophyll and protein content, and Rubisco activities in tomato grown under drought or salinity. *Biol. Plant* **43**, 471–475.

[68] Weimberg, R., Lerner, H., Poljakoff-Mayber, A. (1984). Changes in growth and water-soluble solute concentrations in Sorghum bicolor stressed with sodium and potassium salts. *Physiol. Plant* **62**, 472–480.

[69] Fallon, K., Phillips, R. (1989). Responses to water stress in adapted and unadapted carrot cell suspension cultures. *J. Exp. Bot.* **40**, 681–687.

[70] Yang, W.J., Rich, P.J., Axtell, J.D., Wood, K.V., Bonham, C.C., Ejeta, G., Mickelbart, M.V., Rhodes, D. (2003). Genotypic variation for glycinebetaine in sorghum. *Crop Sci*. **43**, 162–169.

[71] Waditee, R., Bhuiyan, M.N.H., Rai, V., Aoki, K., Tanaka, Y., Hibino, T., Suzuki, S., Takano, J., Jagendorf, A.T., Takabe, T. (2005). Genes for direct methylation of glycine provide high levels of glycinebetaine and abiotic-stress tolerance in Synechococcus and Arabidopsis. *Proc. Natl. Acad. Sci. USA* **102**, 1318–1323.

[72] Sun, Z., Qi, X., Wang, Z., Li, P., Wu, C., Zhang, H., Zhao, Y (2013). Overexpression of TsGOLS2, a galactinol synthase, in Arabidopsis thaliana enhances tolerance to high salinity and osmotic stresses. *Plant Physiol. Biochem.* **69**, 82–89.

[73] Sickler, C.M., Edwards, G.E., Kiirats, O., Gao, Z., Loescher, W. (2007). Response of mannitol-producing Arabidopsis thaliana to abiotic stress. *Funct. Plant Biol.* **34**, 382–391.

[74] Slabu, C., Zörb, C., Steffens, D., Schubert, S. (2009). Is salt stress of faba bean (Vicia faba) caused by Na^+ or Cl^- toxicity? *J. Plant Nutr. Soil Sci.* **172**, 644–651.

[75] White, P.J., Broadley, M.R. (2001). Chloride in soils and its uptake and movement within the plant: A review. Ann. Bot. **88**, 967–988.

[76] Xu, G., Magen, H., Tarchitzky, J., Kafkafi, U. (1999). Advances in chloride nutrition of plants. *Adv. Agron.* **68**, 97–150.

[77] Tavakkoli, E., Fatehi, F., Coventry, S., Rengasamy, P., McDonald, G.K. (2011). Additive effects of Na+ and Cl– ions on barley growth under salinity stress. *J. Exp. Bot.* **62**, 2189–2203.

[78] Janicka-Russak, M., Kabała, K., Wdowikowska, A., Kłobus, G. (2013). Modification of plasma membrane proton pumps in cucumber roots as an adaptation mechanism to salt stress. *J. Plant Physiol.* **170**, 915–922.

[79] Islam, S., Malik, A., Islam, A., Colmer, T.D. (2007). Salt tolerance in a Hordeum marinum–Triticum aestivum amphiploid, and its parents. *J. Exp. Bot.* **58**, 1219–1229.

[80] Luo, Q., Yu, B., Liu, Y. (2005). Differential sensitivity to chloride and sodium ions in seedlings of glycine max and G. soja under NaCl stress. *J. Plant Physiol.* **162**, 1003–1012.

[81] Silva, P., Gerós, H. (2009). Regulation by salt of vacuolar H^+-ATPase and H^+-pyrophosphatase activities and Na^+/H^+ exchange. *Plant Signal. Behav.* **4**, 718–726.

[82] Liu, J., Zhu, J.K. (1998). A calcium sensor homolog required for plant salt tolerance. *Science* **280**, 1943–1945.

[83] Liu, J., Ishitani, M., Halfter, U., Kim, C.S., Zhu, J.K. (2000). The Arabidopsis thaliana SOS2 gene encodes a protein kinase that is required for salt tolerance. *Proc. Natl. Acad. Sci. USA* **97**, 3730–3734.

[84] Quintero, F.J., Ohta, M., Shi, H., Zhu, J.K., Pardo, J.M. (2002). Reconstitution in yeast of the Arabidopsis SOS signaling pathway for Na^+ homeostasis. *Proc. Natl. Acad. Sci.* **99**, 9061–9066.

[85] Smékalová, V., Doskočilová, A., Komis, G., Šamaj, J. (2013). Crosstalk between secondary messengers, hormones and MAPK modules during abiotic stress signalling in plants. *Biotechnol. Adv.* **S0734-9750**(13)00123-7 (doi:10.1016/j.biotechadv.2013.07.009).

[86] Shabala, L., Cuin, T.A., Newman, I.A., Shabala, S. (2005). Salinity-induced ion flux patterns from the excised roots of Arabidopsis sos mutants. *Planta* **222**, 1041–1050.

[87] Mahajan, S., Tuteja, N. (2005). Cold, salinity and drought stresses: An overview. *Arch. Biochem. Biophys.* **444**, 139–158.

[88] Qiu, Q.S., Guo, Y., Dietrich, M.A., Schumaker, K.S., Zhu, J.-K. (2002). Regulation of SOS1, a plasma membrane Na^+/H^+ exchanger in Arabidopsis thaliana, by SOS2 and SOS3. *Proc. Natl. Acad. Sci.* **99**, 8436–8441.

[89] Qiu, N., Chen, M., Guo, J., Bao, H., Ma, X., Wang, B. (2007). Coordinate up-regulation of V-H^+-ATPase and vacuolar Na^+/H^+ antiporter as a response to NaCl treatment in a C3 halophyte Suaeda salsa. *Plant Sci*. **172**, 1218–1225.

[90] Apse, M.P., Aharon, G.S., Snedden, W.A., Blumwald, E. (1999). Salt tolerance conferred by overexpression of a vacuolar Na^+/H^+ antiport in Arabidopsis. *Science* **285**(5431), 1256–1258.

[91] Yang, Q., Chen, Z.Z., Zhou, X.F., Yin, H.-B., Li, X., Xin, X.F., Hong, X.H., Zhu, J.K., Gong, Z. (2009). Overexpression of SOS (salt overly sensitive) genes increases salt tolerance in transgenic Arabidopsis. *Mol. Plant* **2**, 22–31.

[92] Xue, Z.-Y., Zhi, D.-Y., Xue, G.-P., Zhang, H., Zhao, Y.-X., et al. (2004). Enhanced salt tolerance of transgenic wheat (Tritivum aestivum L.) expressing a vacuolar Na+/H+ antiporter gene with improved grain yields in saline soils in the field and a reduced level of leaf Na+. *Plant Sci.* **167**, 849–859.

[93] Zhao, J., Zhi, D., Xue, Z., Liu, H., Xia, G. (2007). Enhanced salt tolerance of transgenic progeny of tall fescue (Festuca arundinacea) expressing a vacuolar Na^+/H^+ antiporter gene from Arabidopsis. *J. Plant Physiol.* **164**, 1377–1383.

[94] Tian, L.M.H.C., Yu, R., Liang, R.F, Li, Z.L., Zhang, L.S., Wang, Y.Q., Zhang, X.H., Wu, Z.Y. (2006). Overexpression AtNHX1 confers salt-tolerance of transgenic tall fescue. *Afr. J. Biotechnol.* **5**, 1041–1044.

[95] Verma, D., Singla-Pareek, S.L., Rajagopal, D., Reddy, M.K., Sopory, S.K. (2007). Functional validation of a novel isoform of Na+/H+ antiporter from Pennisetum glaucum for enhancing salinity tolerance in rice. *J. Biosci*. (Bangalore) **32**, 621–628.

[96] Wu, Y.-Y., Chen, Q.-J., Chen, M., Chen, J., Wang, X.-C. (2005). Salt-tolerant transgenic perennial ryegrass (Lolium perenne L.) obtained by Agrobacterium tumefaciens-mediated transformation of the vacuolar Na+/H+ antiporter gene. *Plant Sci*. **169**, 65–73.

[97] An, B.-Y. (2008). Expression of a vacuolar Na^+/H^+ antiporter gene of alfalfa enhances salinity tolerance in transgenic Arabidopsis. *Acta Agron. Sinica* **34**, 557–564.

[98] Zhang, G.-H., Su, Q., An, L.-J., Wu, S. (2008). Characterization and expression of a vacuolar Na+/H+ antiporter gene from the monocot halophyte Aeluropus littoralis. *Plant Physiol. Biochem.* **46**, 117–126.

[99] Bao, A.-K., Wang, S.-M., Wu, G.-Q., Xi, J.-J., Zhang, J.-L., et al. (2009). Overexpression of the Arabidopsis H^+-PPase enhanced resistance to salt and drought stress in transgenic alfalfa (Medicago sativa L.). *Plant Sci*. **176**, 232–240.

[100a] Tian, N., Wang, J., Xu, Z.Q. (2011). Overexpression of Na+/H+ antiporter gene AtNHX1 from Arabidopsis thaliana improves the salt tolerance of kiwifruit (Actinidia deliciosa). *S. Afr. J. Bot.* **77**, 160–169.

[100b] Li, W., Wang, D., Jin, T., Chang, Q., Yin, D., et al. (2010). The vacuolar Na^+/H^+ antiporter gene SsNHX1 from the halophyte Salsola soda confers salt tolerance in transgenic alfalfa (Medicago sativa L.). *Plant Mol. Biol. Rep.* **29**, 278–290.

[101] Li, Y., Zhang, Y., Feng, F., Liang, D., Cheng, L., et al. (2010). Overexpression of a Malus vacuolar Na+/H+ antiporter gene (MdNHX1) in apple rootstock M.26 and its influence on salt tolerance. *Plant Cell Tissue Organ Cult.* **102**, 337–345.

[102] Asif, M.A., Zafar, Y., Iqbal, J., Iqbal, M.M., Rashid, U., et al. (2011). Enhanced expression of AtNHX1, in transgenic groundnut (Arachis hypogaea L.) improves salt and drought tolerence. *Mol. Biotechnol*. **49**, 250–256.

[103] Wei, Q., Guo, Y.J., Cao, H.M., Kuai, B.K. (2011). Cloning and characterization of an AtNHX2 -like Na+/H+ antiporter gene from Ammopiptanthus mongolicus (Leguminosae) and its ectopic expression enhanced drought and salt tolerance in Arabidopsis thaliana. *Plant Cell Tissue Organ Cult*. **105**, 309–316.

[104] Zhao, F., Guo, S., Zhang, H., Zhao, Y. (2006). Expression of yeast SOD2 in transgenic rice results in increased salt tolerance. *Plant Sci*. **170**, 216–224.

[105] Gao, F., Gao, Q., Duan, X., Yue, G., Yang, A., et al. (2006). Cloning of an H+-PPase gene from Thellungiella halophila and its heterologous expression to improve tobacco salt tolerance. *J. Exp. Bot*. **57**, 3259–3270.

[106] Lv, S.-L., Lian, L.-J., Tao, P.-L., Li, Z.-X., Zhang, K.-W., et al. (2009). Overexpression of Thellungiella halophila H+-PPase (TsVP) in cotton enhances drought stress resistance of plants. *Planta* **229**, 899–910.

[107] Pasapula, V., Shen, G., Kuppu, S., Paez-Valencia, J., Mendoza, M., et al. (2011). Expression of an Arabidopsis vacuolar H+-pyrophosphatase gene (AVP1) in cotton improves drought- and salt tolerance and increases fibre yield in the field conditions: Using AVP1 to improve drought and salt tolerance in cotton. *Plant Biotechnol. J*. **9**, 88–99.

[108] Shi, H., Quintero, F.J., Pardo, J.M., Zhu, J.-K. (2002). The putative plasma membrane Na+/H+ antiporter SOS1 controls long-distance Na+ transport in plants. *Plant Cell*. **14**, 465–477.

[109] Gao, X., Ren, Z., Zhao, Y., Zhang, H. (2003). Overexpression of SOD2 increases salt tolerance of Arabidopsis. *Plant Physiol.* **133**, 1873–1881.

[110] Huertas, R., Olías, R., Eljakaoui, Z., Gálvez, F.J., Li, J., et al. (2012). Overexpression of SlSOS2 (SlCIPK24) confers salt tolerance to transgenic tomato. *Plant Cell Environ*. **35**, 1467–1482.

[111] Ma, D.-M., Xu, W.-R., Li, H.-W., Jin, F.-X., Guo, L.-N., et al. (2013). Co-expression of the Arabidopsis SOS genes enhances salt tolerance in transgenic tall fescue (Festuca arundinacea Schreb.). *Protoplasma* **251**, 219–231.

[112] Davenport, R.J., Munoz-Mayor, A., Jha, D., Essah, P.A., Rus, A., Tester, M. (2007). The Na^+ transporter AtHKT1 controls retrieval of Na^+ from the xylem in Arabidopsis. *Plant Cell Environ*. **30**, 497–507.

[113] Huang, S., Spielmeyer, W., Lagudah, E.S., James, R.A., Platten, J.D., Dennis, E.S., Munns, R. (2006). A sodium transporter (HKT7) is a candidate for Nax1, a gene for salt tolerance in durum wheat. *Plant Physiol*. **142**, 1718–1727.

[114] Horie, T., Costa, A., Kim, T.H., Han, M.J., Horie, R., Leung, H.-Y., Miyao, A., Hirochika, H., An, G., Schroeder, J.I. (2007). Rice OsHKT2 transporter mediates large Na^+ influx component into K^+ starved roots for growth. *EMBO J.* **26**, 3003–3014.

[115] Chérel, I. (2004). Regulation of K^+ channel activities in plants: from physiological to molecular aspects. *J. Exp. Bot.* **55**, 337–351.

[116] Carden, D.E., Walker, D.J., Flowers, T.J., Miller, A.J. (2003). Single-cell measurements of the contributions of cytosolic Na^+ and K^+ to salt tolerance. *Plant Physiol*. **131**, 676–683.

[117] Neid, S.L., Biesboer, D.D. (2005). Alleviation of salt-induced stress on seed emergence using soil additives in a greenhouse. *Plant Soil* **268**, 303–307.

[118] Zheng, Y., Jia, A., Ning, T., Xu, J., Li, Z., Jiang, G. (2008). Potassium nitrate application alleviates sodium chloride stress in winter wheat cultivars differing in salt tolerance. *J. Plant Physiol.* **165**, 1455–1465.

[119] Li, D., Ma, N.N., Wang, J.R., Yang, D.Y., Zhao, S.J., Meng, Q.W. (2013). Over-expression of tomato enhancer of SOS3-1 (LeENH1) in tobacco enhanced salinity tolerance by

excluding Na+ from the cytosol. *Plant Physiol. Biochem.* **70**, 150–158.

[120] Hueras, R., Rubio, L., Cagdac, O., Garcia-Sanchez, M.J., Alche, J.D.D., Venema, K., Fernandez, J., Rodriguez-Rosales, M.P. (2013). The K^+/H^+ antiporter LeNHX2 increases salt tolerance by improving K^+ homeostasis in transgenic tomato. *Plant Cell Environ*. **36**, 2135–2149.

[121] Leidi, E.O., Barragán, V., Rubio, L., El-Hamdaoui, A., Ruiz, M.T., Cubero, B., Fernández, J.A., Bressan, R.A., Hasegawa, P.M., Quintero, F.J. (2010). The AtNHX1 exchanger mediates potassium compartmentation in vacuoles of transgenic tomato. *Plant J*. **61**(3), 495–506.

[122] Mittler, R. (2002). Oxidative stress, antioxidants and stress tolerance. *Trends Plant Sci*. **7**, 405–410.

[123] Ahmad, P., Jaleel, CA., Salem, M.A., Nabi, G., Sharma, S. (2010). Roles of enzymatic and nonenzymatic antioxidants in plants during abiotic stress. *Crit. Rev. Biotechnol.* **30**, 161–175.

[124] Suzuki, N., Koussevitzky, S., Mittler, R., Miller, G. (2012). ROS and redox signalling in the response of plants to abiotic stress. *Plant Cell Environ*. **35**, 259–270.

[125] Hernández, J.A., Almansa, M.S. (2002). Short-term effects of salt stress on antioxidant systems and leaf water relations of pea leaves. *Physiol. Plant* **115**, 251–257.

[126] Karpinski, S., Muhlenbock, P. (2007). Genetic, molecular and physiological mechanisms controlling cell death, defenses, and antioxidant network in response to abiotic and biotic stresses in plants. *Compar. Biochem. Physiol. A: Mol. Integr. Physiol.* **146**, S60.

[127] Abrol, E., Vyas, D., Koul, S. (2012). Metabolic shift from secondary metabolite production to induction of antioxidative enzymes during NaCl stress in Swertia chirata Buch.-*Ham*. *Acta Physiol. Plant* **34**, 541–546.

[128] Chen, S., Polle, A. (2010). Salinity tolerance of populus. *Plant Biol*. **12**, 317–333.

[129] Wang, Y., Ying, Y., Chen, J., Wang, X. (2004). Transgenic Arabidopsis overexpressing Mn-SOD enhanced salt-tolerance. *Plant Soi1* **67**, 671–677.

[130] Wang, Y., Wisniewski, M., Meilan, R., Uratsu, S., Cui, M., Dandekar, A., Fuchigami, L. (2007). Ectopic expression of Mn-SOD in Lycopersicon esculentum leads to enhanced tolerance to salt and oxidative stress. *J. Appl. Hortic*. **9**, 3–8.

[131] Miller, G., Suzuki, N., Rizhsky, L., Hegie, A., Koussevitzky, S., Mittler, R. (2007). Double mutants deficient in cytosolic and thylakoid ascorbate peroxidase reveal a complex mode of interaction between reactive oxygen species, plant development, and response to abiotic 122] stresses. *Plant Physiol*. **144**, 1777–1785.

[132] Srivastava, A.K., Bhargava, P., Rai, L.C. (2005). Salinity and copper-induced oxidative damage and changes in the antioxidative defence systems of Anabaena doliolum. *World J. Microbiol. Biotechnol.* **21**, 1291–1298.

[133] Pan, Y., Wu, L.J., Yu, Z.L. (2006), Effect of salt and drought stress on antioxidant enzymes activities and SOD isoenzymes of liquorice (Glycyrrhiza uralensis Fisch). *Plant Growth Regul.* **49**, 157–165.

[134] Badawi Ghazi Hamid, K.N., Tamauchi, Y., Shimada, E., Sasaki, R., Kubo, A., Tanaka, K. (2004). Over-expression of ascorbate peroxidase in tobacco chloroplasts enhances the tolerance to salt stress and water deficit. *Physiol. Plant*. **121**, 231–238.

[135] Wang, Y.W., Meilan, R., Cui, M., Webb, R., Fuchigami, L. (2005). Overexpression of cytosolic ascorbate peroxidase in tomato confers tolerance to chilling and salt stress. *J. Am. Soc. Hort. Sci*. **130**, 167–173.

[136] Ushimaru, T., Nakagawa, T., Fujioka, Y., Daicho, K., Naito, M., et al. (2006). Transgenic Arabidopsis plants expressing the rice dehydroascorbate reductase gene are resistant to salt stress. *J. Plant Physiol.* **163**, 1179–1184.

[137] Lu, Z., Liu, D., Liu, S. (2007). Two rice cytosolic ascorbate peroxidases differentially improve salt tolerance in transgenic Arabidopsis. *Plant Cell Rep*. **26**, 1909–1917.

[138] Lee, Y.P., Kim, S.H., Bang, J.W., Lee, H.S., Kwak, S.S., et al. (2007). Enhanced tolerance to oxidative stress in transgenic tobacco plants expressing three antioxidant enzymes in chloroplasts. *Plant Cell Rep*. **26**, 591–598.

[139] Eltayeb, A.E., Kawano, N., Badawi, G.H., Kaminaka, H., Sanekata, T., et al. (2007). Overexpression of monodehydroascorbate reductase in transgenic tobacco confers enhanced tolerance to ozone, salt and polyethylene glycol stresses. *Planta* **225**, 1255–1264.

[140] Al-Taweel, K., Iwaki, T., Yabuta, Y., Shigeoka, S., Murata, N., et al. (2007). A bacterial transgene for catalase protects translation of d1 protein during exposure of salt-stressed tobacco leaves to strong light. *Plant Physiol*. **145**, 258–265.

[141] Prashanth, S.R., Sadhasivam, V., Parida, A. (2008). Over-expression of cytosolic copper/zinc superoxide dismutase from a mangrove plant Avicennia marina in indica rice var Pusa Basmati-1 confers abiotic stress tolerance. *Transgenic Res*. **17**, 281–291.

[142] Tsaftaris, A., Chatzidimitriadou, K., Nianiou-Obeidat, I., Madesis, P., Perl-Treves, R. (2009). Expression of SOD transgene in pepper confer stress tolerance and improve shoot regeneration. *Electron. J. Biotechnol.* **12**, 78—95.

[143] Sun, W.H., Duan, M., Shu, D.F., Yang, S., Meng, Q.W. (2010). Over-expression of StAPX in tobacco improves seed germination and increases early seedling tolerance to salinity and osmotic stresses. *Plant Cell Rep*. **29**, 917–926.

[144] Qi, Y.C., Liu, W.Q., Qiu, L.Y., Zhang, S.M., Ma, L., et al. (2010). Overexpression of glutathione S-transferase gene increases salt tolerance of arabidopsis. *Russ. J. Plant Physiol.* **57**, 233–240.

[145] Kavitha, K., George, S., Venkataraman, G., Parida, A. (2010). A salt-inducible chloroplastic monodehydroascorbate reductase from halophyte Avicennia marina confers salt stress tolerance on transgenic plants. *Biochimie* **92**, 1321–1329.

[146] Li, Y.J., Hai, R.L., Du, X.H., Jiang, X.N., Lu, H. (2009). Over-expression of a Populus peroxisomal ascorbate peroxidase (PpAPX) gene in tobacco plants enhances stress tolerance. *Plant Breed*. **128**, 404–410.

[147] Lee, Y.P., Baek, K.H., Lee, H.S., Kwak, S.S., Bang, J.W., et al. (2010). Tobacco seeds simultaneously over-expressing Cu/Zn-superoxide dismutase and ascorbate peroxidase display enhanced seed longevity and germination rates under stress conditions. *J. Exp. Bot.* **61**, 2499–2506.

[148] Zhai, C.-Z., Zhao, L., Yin, L.-J., Chen, M., Wang, Q.-Y., et al. (2013). Two wheat glutathione peroxidase genes whose products are located in chloroplasts improve salt and H_2O_2 tolerances in Arabidopsis. *PLoS ONE* **8**, e73989.

[149] Diaz-Vivancos, P., Faize, M., Barba-Espin, G., Faize, L., Petri, C., et al. (2013). Ectopic expression of cytosolic superoxide dismutase and ascorbate peroxidase leads to salt stress tolerance in transgenic plums. *Plant Biotechnol. J.* **11**, 976-985.

[150] Lumbreras, V., Vilela, B., Irar, S., Solé, M., Capellades, M., Valls, M., Coca, M. (2010). MAPK phosphatase MKP2 mediates disease responses in Arabidopsis and functionally interacts with MPK3 and MPK6. *Plant J.* **63**, 1017–1030.

[151] De Bruxelles, G., Peacock, W.J., Dennis, E.S., Dolferus, R. (1996). Abscisic acid induces the alcohol dehydrogenase gene in Arabidopsis. *Plant Physiol.* **111**, 381–391.

[152] Popova, L.P., Stoinova, Z.G., Maslenkova, L.T. (1995). Involvement of abscisic acid in photosynthetic process in *Hordeum vulgare* L. during salinity stress. *J. Plant Growth Regul.* **14**, 211–218.

[153] Xiong, L., Zhu, J.K. (2001). Abiotic stress signal transduction in plants: Molecular and genetic perspectives. *Physiol. Plant* **112**, 152–166.

[154] Gilliham, M., Tester, M. (2005). The regulation of anion loading to the maize root xylem. *Plant Physiol.* **137**, 819–828.

[155] Ohta, M., Guo, Y., Halfter, U., Zhu, J.K. (2003). A novel domain in the protein kinase SOS2 mediates interaction with the protein phosphatase 2C ABI2. *Proc. Natl. Acad. Sci.* **100**, 11771–11776.

[156] Hu, X., Jiang, M., Zhang, A., Lu, J. (2005). Abscisic acid-induced apoplastic H_2O_2 accumulation up-regulates the activities of chloroplastic and cytosolic antioxidant enzymes in maize leaves. *Planta* **223**, 57–68.

[157] Zhang, A., Jiang, M., Zhang, J., Tan, M., Hu, X. (2006). Mitogen-activated protein kinase is involved in abscisic acid-induced antioxidant defense and acts downstream of reactive oxygen species production in leaves of maize plants. *Plant Physiol.* **141**, 475–487.

[158] Zhang, A., Jiang, M., Zhang, J., Ding, H., Xu, S., Hu, X., Tan, M. (2007). Nitric oxide induced by hydrogen peroxide mediates abscisic acid-induced activation of the mitogen-activated protein kinase cascade involved in antioxidant defense in maize leaves. *New Phytol.* **175**, 36–50.

[159] Ye, N., Zhu, G., Liu, Y., Li, Y., Zhang, J. (2011). ABA controls H_2O_2 accumulation through the induction of OsCATB in rice leaves under water stress. *Plant Cell Physiol.* **52**, 689–698.

[160] Miller, G., Suzuki, N., Ciftci-Yilmaz, S., Mittler, R. (2010). Reactive oxygen species homeostasis and signalling during drought and salinity stresses. *Plant Cell Environ.* **33**, 453–467.

[161] Zhang, H., Ni, L., Liu, Y., Wang, Y., Zhang, A., Tan, M., Jiang, M. (2012). The C_2H_2 -type zinc finger protein ZFP182 is involved in abscisic acid–induced antioxidant defense in RiceF. *J. Integr. Plant Biol.* **54**, 500–510.

[162] Ibrahim, M.H., Jaafar, H.Z. (2013). Abscisic acid induced changes in production of primary and secondary metabolites, photosynthetic capacity, antioxidant capability, antioxidant enzymes and lipoxygenase inhibitory activity of *Orthosiphon stamineus* Benth. *Molecules* **18**, 7957–7976.

[163] Idrees, M., Naeem, M., Aftab, T., Khan, M.M.A. (2011). Salicylic acid mitigates salinity stress by improving antioxidant defence system and enhances vincristine and vinblastine alkaloids production in periwinkle [*Catharanthus roseus* (L.) G. Don]. *Acta Physiol. Plant* **33**, 987–999.

[164] Nazar, R., Iqbal, N., Syeed, S., Khan, N.A. (2011). Salicylic acid alleviates decreases in photosynthesis under salt stress by enhancing nitrogen and sulfur assimilation and antioxidant metabolism differentially in two mungbean cultivars. *J. Plant Physiol.* **168**, 807–815.

[165] Shabala, S.N., Newman, I.A., Morris, J. (1997). Oscillations in H^+ and Ca^{2+} ion fluxes around the elongation region of corn roots and effects of external pH. *Plant Physiol.* **113**(1), 111–118.

[166] Jayakannan, M., Bose, J., Babourina, O., Rengel, Z., Shabala, S. (2013). Salicylic acid improves salinity tolerance in Arabidopsis by restoring membrane potential and preventing salt-induced K^+ loss via a GORK channel. *J. Exp. Bot.* **64**, 2255–2268.

[167] Horváth, E., Szalai, G., Janda, T. (2007). Induction of abiotic stress tolerance by salicylic acid signaling. *J. Plant Growth Regul.* **2**, 290–300.

[168] Gao, W., Bai, S., Li, Q., Gao, C., Liu, G., Li, G., Tan, F. (2013). Overexpression of TaLEA gene from Tamarix androssowii improves salt and drought tolerance in transgenic poplar (Populus simonii P. nigra). *PloS ONE* **8**, e67462.

[169] Scarpeci, T.E., Zanor, M.I., Mueller-Roeber, B., Valle, E.M. (2013). Overexpression of AtWRKY30 enhances abiotic stress tolerance during early growth stages in *Arabidopsis thaliana*. *Plant Mol. Biol.* 1–13.

[170] Cheng, L., Li, X., Huang, X., Liang, Y., Ma, X., Peng, X., Jia, J., Chen, S., Chen, Y., Deng, B. (2013). Overexpression of sheepgrass R1-MYB transcription factor LcMYB1 confers salt tolerance in transgenic Arabidopsis. *Plant Physiol. Biochem.* **70**, 252–260.

[171] Dodd, I.C., Pérez-Alfocea, F. (2012). Microbial amelioration of crop salinity stress. *J. Exp. Bot.* **63**, 3415–3428.

72

INTERFACIAL PHENOMENA OF PULMONARY SURFACTANT PREPARATIONS

HIROMICHI NAKAHARA, SANNAMU LEE, AND OSAMU SHIBATA

Department of Biophysical Chemistry, Graduate School of Pharmaceutical Sciences, Nagasaki International University; 2825-7 Huis Ten Bosch, Sasebo, Nagasaki 859-3298, Japan

72.1 INTRODUCTION

Pulmonary surfactant (PS) is a surface-active material that lines the air−alveolar fluid interface. It plays an important role in vital physiological processes, such as respiratory movement and natural immunity (first-line defense). The main interfacial property of PS is to reduce the surface tension at the interface during respiratory movement, preventing alveolar collapses at the end-expired state and minimizing the work of breathing [1]. These functions are based on the formation of a surface-active film that consists of lipid monolayers, and bilayer or multilayer structures (surface-associated reservoirs) closely attached to the alveolar surface. These layered structures have been confirmed in vitro by fluorescence microscopy (FM) and atomic force microscopy (AFM) [2–5], and in vivo by electron microscopy[6].

Pulmonary surfactant is a lipid mixture composed of lipids (∼90 wt%) and proteins (∼10 wt%). The lipids consist mainly of phosphatidylcholines (especially dipalmitoylphosphatidylcholine or DPPC, ∼50 wt%) and smaller but significant amounts of phosphatidylglycerol (PG) and palmitic acid (PA) [7–9]. Among the proteins, the hydrophobic surfactant protein B (SP-B) has a crucial role in lung functions because of the experimental results with its gene knockout in mice [10] and its gene mutation in preterm infants [11, 12]. Moreover, the genetic absence of SP-B induces a deficiency in another hydrophobic surfactant protein, surfactant protein C (SP-C), due to dysfunction of the SP-C proprotein [10]. The human SP-B has a net charge of +7, which is quite important for electrostatic interactions with the headgroups of negatively charged lipids, such as PG [4, 13] and dissociated PA [14].

Fluid components in PS monolayers with less ability to take an ordered and close-packed orientation at the interface are preferentially eliminated from the surface on lateral compression so that the monolayers are enriched in rigid phospholipids (mainly DPPC) [15, 16]. This is known as the "squeeze-out" phenomenon. After the squeeze out of the surface, the organized multilayers are formed just below the interface as a repository for the excluded material. This surface reservoir enables the excluded molecules to respread onto the interface on subsequent expansion [4]. The release of squeezed-out molecules from the surface-associated reservoir is facilitated mainly by SP-B and SP-C. Thus, the composition and molecular structure of the reservoirs are issues of main importance. Synthetic and mimicking peptides based on the amino acid sequence of SP-B have been designed to clarify the mechanism of lipid–protein interactions around the interface and to develop PS preparations for the replacement therapy to patients with respiratory distress syndrome (RDS); examples are KL_4 (KLLLLKLLLLKLLLKLLLLK) [17–19] and Hel 13-5 (KLLKLLLKLWLKLLKLLL) [5, 20–22]. Hel 13-5 is a monomeric synthetic peptide based on the *N*-terminal segment of human SP-B. Its structure and surface activity have been investigated thoroughly both in vitro [5, 21–23] and in vivo [24, 25]. The secondary conformation of Hel 13-5 in the aqueous medium containing various phospholipids is mainly α-helix [26]. The

Encyclopedia of Biocolloid and Biointerface Science, Volume 2, First Edition. Edited by Hiroyuki Ohshima.
© 2016 John Wiley & Sons, Inc. Published 2016 by John Wiley & Sons, Inc.

in vivo experiments show that the PS preparations containing Hel 13-5 improve lung functions and activities in surfactant-deficient rats more than does Surfacten (Surfactant TA) [24], which is an analog to Survanta (Ross Laboratories, Columbus, OH). Surfacten is a bovine lung surfactant extract supplemented with DPPC, PA, and tripalmitin, and is commonly administered to RDS infants in Japan [27].

The polarization-modulation infrared reflection-absorption spectroscopy (PM-IRRAS) measurement provides information on molecular structure of the mimicking peptide of Hel 13–5 in the presence of lipids. SP-B and SP-C have been studied for several decades to understand the PS function at the molecular level. However, the change in protein structures such as α-helix and β-sheet across the interface and their interaction site with lipid monolayers and multilayers, have not been fully discussed. The proteins have several α-helical moieties with different amphiphilicity, hydrophobicity, and amino acid residues in a molecule. Therefore, intramolecular interactions of the proteins such as hydrogen bonding, S–S bonding as a linkage of the moieties, van der Waals force, and electrostatic force among the respective α-helical parts complicate the abovementioned issues. Thus, the lipid/Hel 13-5 systems provide a useful model for in vitro biophysical studies on the surface-associated reservoirs that are formed during respiration in the alveoli. Indeed, in the PS model systems including Hel 13-5, the formation of surface-associated reservoirs has been confirmed [5, 22, 23]. The preparations with the other peptide analogs have also revealed that the reservoirs form at the surface pressure (π) of around 40 mN m^{-1} [4, 13]. One research team have suggested from NMR investigations on interaction between PG and SP-C that positively charged parts of SP-C are located near the bilayer surface [28]. In more recent work, another group has quantitatively revealed the multilayer transition in the DPPC/dipalmitoylphosphatidylglycerol (DPPG)/SP-C system using the IR spectroscopy of films transferred at continuously varying π [29]. In the report, the π-induced formation of reservoirs is possibly based on the intermolecular interaction between the positively charged protein (or peptide) and the negatively charged phospholipid such as PG. As mentioned above, the hysteresis behavior in PS preparations is often observed for a thermodynamic parameter such as π against molecular area (A) during the compression– expansion cycle of monolayers. In addition, other studies have shown the hysteresis for secondary structure of peptides with respect to π employing the IRRAS technique [30–33]. However, it is not yet established at the molecular level how the hysteresis behavior is generated in respective physicochemical parameters, although it is closely related to the reservoir formation beneath the surface monolayer.

In this chapter, we review the hysteresis behavior of π–A isotherms, surface potential (ΔV)–A isotherms, and vibration mode in in situ PM-IRRAS spectra during the compression and successive expansion of PS monolayers. Herein, the following synthetic PS preparations are utilized: DPPC/Hel 13-5, DPPG/Hel 13-5, DPPC/PA(= 90/10, wt/wt)/Hel 13-5, DPPC/PG(= 68/22, wt/wt)/Hel 13-5, DPPC/DPPG(= 4/1, mol/mol), and DPPC/PG/PA(= 68/22/9, wt/wt/wt)/Hel 13-5. PM-IRRAS is almost insensitive to the strong IR absorption of water vapor and allows the extraction of faithful information on conformation and orientation of proteins in the monolayer. It is evident that secondary structure determination of surfactant proteins and their analog peptides in monolayers is essential for understanding their in vivo function during respiration and for designing model peptides toward the replacement therapy to the RDS patients. Unfortunately, however, the peak intensity of PM-IRRAS spectra for monolayers is relatively low because of the low surface density of the peptide. Therefore, attenuated total reflectance (ATR)-FTIR has been employed to confirm the peak frequency of PM-IRRAS spectra. PM-IRRAS spectra of the monolayers are separately analyzed for methylene vibration of the lipid hydrocarbons and for the amide mode of Hel 13-5.

72.2 ISOTHERM BEHAVIOR OF THE LIPIDS AND PEPTIDE

The Hel 13-5 peptide consists of 13 hydrophobic residues (12 Leu and 1 Trp) and 5 hydrophilic residues (5 Lys) [26,34]. The hydrophobic–hydrophilic balance (HHB) was estimated both theoretically from the calculated hydrophobicity value (or the magnitude of hydrophobic faces) and experimentally from the retention times in reverse phase high-performance liquid chromatography (RP-HPLC) [34]. For this modulation (hydrophobicity of Hel 13-5 is 0.07), it is assumed that Hel 13-5 mimics the amphipathic helical structure of SP-B at the alveolar air−liquid interface rather than the transmembrane helical structure of SP-C. In addition, when it forms an ideal α-helical structure, it has the amphiphilic structure with a 260° hydrophobic sector region [20, 26, 34–36]. This means that the hydrophobic part and the hydrophilic one are completely separated in the α-helical structure. Indeed, the α-helical form of Hel 13-5 has been confirmed in the aqueous solution [20, 26, 36]. However, the peptide assuming the α-helical conformation in the bulk is not always estimated to be in the same conformation at the air−water interface. Hel 13-5 forms an expanded monolayer at the interface (Fig. 72.1a). The surface pressure (π)−molecular area (A) isotherm shows no kink corresponding to a phase change such as lipid-expanded (LE)/lipid-condensed (LC) transition. The collapse pressure (π^c) of monolayers is $\sim$ 42.0 mN m^{-1} at $\sim$2.0 nm^2. Above π^c, Hel 13-5 is squeezed out of the surface into the bulk, which reflects slight variation of surface pressure in $A < 2.0$ nm^2. This behavior is also supported by the

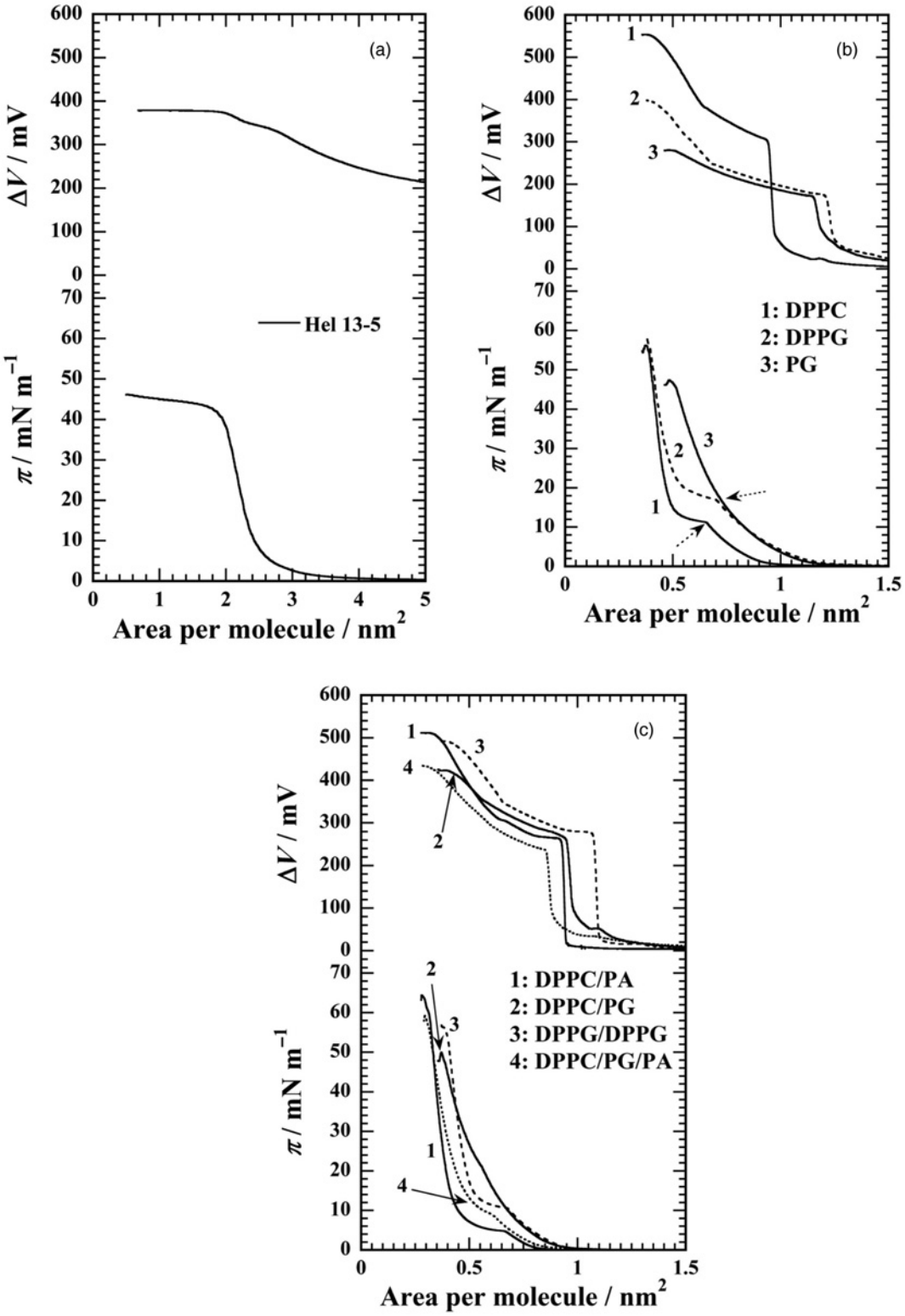


FIGURE 72.1 π–A and ΔV–A isotherms of monolayers on a 0.02 M Tris buffer solution (pH 7.4) with 0.13 M NaCl at 298.2 K: (a) Hel 13-5; (b) DPPC, DPPG, PG; (c) DPPC/PA (= 90/9, wt/wt), DPPC/PG (= 68:22, wt/wt), DPPC/DPPG (= 4/1, mol/mol), DPPC/PG/PA (= 68:22:9, wt/wt/wt).

corresponding surface potential (ΔV)–A isotherm. The ΔV value increases monotonously with decreasing A until 2.0 nm^2. This means that the improved ordering of Hel 13-5 on compression. However, below $A = 2.0$ nm^2, the ΔV value is kept almost constant in spite of monolayer compressing; that is, the extra Hel 13-5 molecules are considered to be excluded into the bulk [21]. The extrapolated area calculated from the π–A isotherm, which can provide information on molecular conformation at the close-packed state, is ~2.6 nm^2. The value is the mean surface area of Hel 13-5 under the assumption of the closest packing. This value can translate into ~0.15 nm^2/amino acid, which is consistent with the values of ~0.2 nm^2/amino acid for SP-B [37]. Thus, when we assume that the α-helical peptide assumes a conformation with its backbone parallel to the interface, the cross-sectional area becomes ~2.6 nm^2 [21]. The dimension of such an α-helix is found to agree well with the experimental value. However, it is noted that the extrapolated area derived from the π–A isotherm expresses the means of molecular ordering at the surface. The secondary structure of peptide at the surface on compression and expansion should be elucidated from the diversified aspects as will be mentioned in a later section.

The DPPC and DPPG monolayers respectively have the first-order LE/LC transitions at ~11 (A = 0.65 nm^2) and ~17 mN m^{-1} ($A = 0.70$ nm^2) on a 0.02 M Tris buffer solution with 0.13 M NaCl (pH 7.4) at 298.2 K, which are indicated by dashed arrows in Fig. 72.1b. The π^c values are ~55 (A = 0.38 nm^2) for DPPC and ~56 mN m^{-1} (A = 0.39 nm^2) for DPPG, respectively. On the other hand, PG forms a typical LE monolayer with π^c = ~46 mN m^{-1} ($A = 0.50$ nm^2), due to its unsaturated hydrocarbon chains. Under these conditions, PA cannot form a stable monolayer at the interface because of the lack of insolubility into the water. The ΔV value of monolayers in Fig. 72.1b always indicates a positive variation on compression. The variational mode is sharper compared than that for Hel 13-5 monolayers, which means that the orientation of the lipid monolayers changes more in degree. The detailed discussion on orientational variation with respect to each phase transition in ΔV–A isotherms has been described elsewhere [38–43]. The maximum ΔV value at the close-packed state is different among the three monolayers. The difference is attributed mainly to the headgroup species of the lipids according to the three-layer model proposed by Demchak and Fort, which postulates independent contributions of the subphase, polar headgroup, and hydrophobic chain to the surface dipole moment [44].

The binary DPPC/PA (= 90/9, wt/wt) monolayer (Fig. 72.1c, curve 1) shows lower LE/LC transition pressure (π^{eq}) and larger π^c than the DPPC monolayer (Fig. 72.1b, curve 1) [14]; that is, the addition of PA causes the condensation of DPPC monolayers. Furthermore, it is found that PA can be located stably at the interface in the system by means of the interactions such as van der Waals forces and miscibility with DPPC. On the other hand, the π^{eq} and π^c values for the DPPC/PG (= 68/22, wt/wt) monolayer become larger and lower, respectively (Fig. 72.1c, curve 2) [5]. This means that PG fluidizes DPPC monolayers as opposed to the DPPC/PA system. However, the similar system of DPPC/DPPG (= 4/1, mol/mol) forms more condensed monolayers to some extents (Fig. 72.1c, curve 3) [23]. The difference in additional effect on DPPC monolayers is significantly related with the ratio of saturation in aliphatic chains of PG molecules. In the case of the ternary DPPC/PG/PA (= 68/22/9, wt/wt/wt) system (Fig. 72.1c, curve 4), the solidifying effect of PA on DPPC monolayers is superior slightly to the fluidizing effect of PG [22].

72.3 INTERACTION BETWEEN THE LIPIDS AND PEPTIDE

The mutual interaction between lipids and Hel 13-5 can be elucidated by measuring the isotherm data as a function of mole fraction of Hel 13-5 ($X_{\text{Hel 13-5}}$). The representative data for the DPPG/Hel 13-5 and the DPPC/PG/PA (= 68/22/9, wt/wt/wt)/Hel 13-5 systems are shown in Fig. 72.2. For the DPPG/Hel 13-5 systems (Fig. 72.2a), the π^{eq} values of monolayers in the presence of Hel 13-5 ($0 < X_{\text{Hel 13-5}} \leq 0.1$) are almost the same as that of DPPG monolayers (~17 mN m^{-1}). The result indicates that the interaction between DPPG and Hel 13-5 is very weak at low surface pressures. At high surface pressures, the π–A isotherms at $X_{\text{Hel 13-5}} = 0.1$ have a plateau at ~50 mN m^{-1} (indicated by a dashed arrow), where Hel 13-5 begins to be gradually squeezed out of the monolayers. It is noted that the surface pressure of the squeeze out is different from the π^c value of Hel 13-5 monolayers (~42 mN m^{-1}). This difference will be discussed below. In the DPPC/PG/PA/Hel 13-5 system (Fig. 72.2b), all of the π–A isotherms indicate the phase transition. As opposed to the DPPG/Hel 13-5 system, the π^{eq} value slightly increases with increasing $X_{\text{Hel 13-5}}$, which means the fluidization of monolayers induced by the addition of Hel 13-5. At ~42 mN m^{-1}, the π–A isotherms in $0.025 \leq X_{\text{Hel 13-5}} \leq 0.1$ exhibit plateau regions, which typically indicated by dashed arrows (curves 3 and 4). These plateaus correspond to the squeeze out of Hel 13-5 from surface monolayers as mentioned above. On further compression, the surface pressures rapidly increase up to a monolayer collapse, resulting in the production of close-packed monolayers (DPPC/PA) at the interface. This surface refining is supported by the fact that the π^c values for the DPPC/PG/PA/Hel 13-5 systems are almost the same as those for the DPPC/PA/Hel 13-5 systems at $X_{\text{Hel 13-5}} = 0.05$ and 0.1[5, 22].

At surface pressures below the plateau, the ΔV–A isotherms for both systems shift to larger ΔV values with increasing $X_{\text{Hel 13-5}}$ (Fig. 72.2). This is attributed to a monotonous increase in ΔV value for Hel 13-5 monolayers

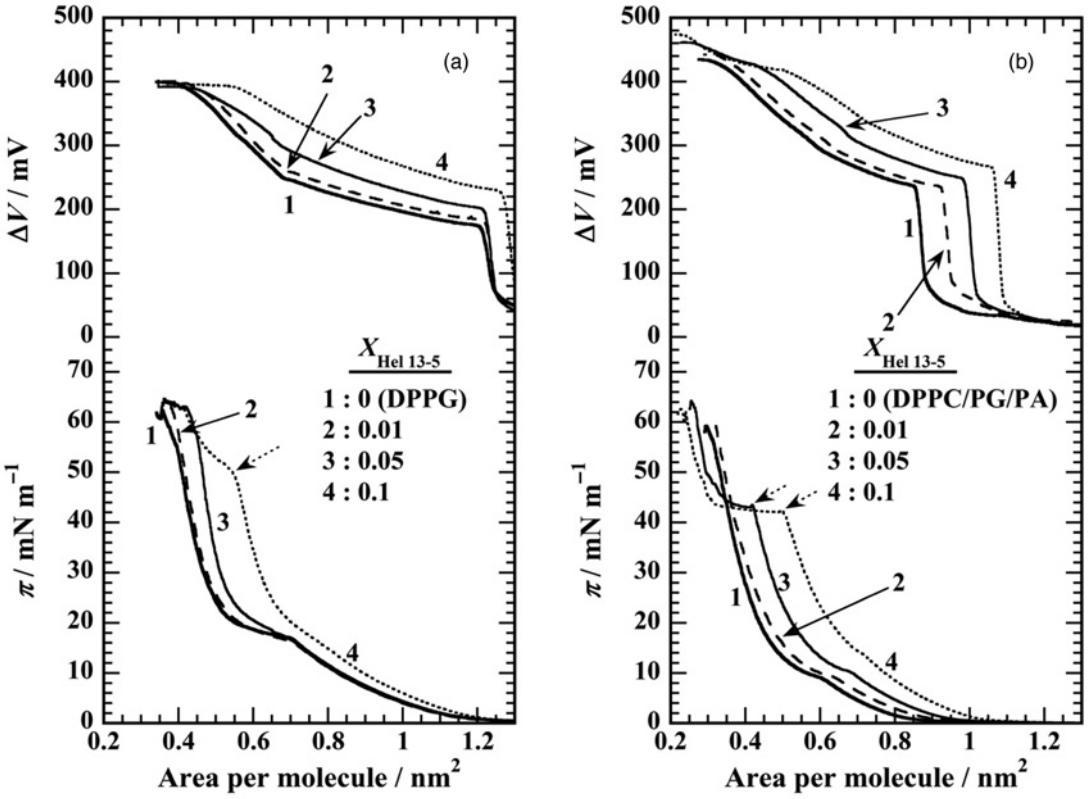


FIGURE 72.2 π–A and ΔV–A isotherms of (a) DPPG and (b) DPPC/PG/PA (= 68:22:9, wt/wt/wt) monolayers containing different amounts of Hel 13-5 on a 0.02 M Tris buffer solution (pH 7.4) with 0.13 M NaCl at 298.2 K.

on compression (Fig. 72.1a). On further compression beyond the plateau on π–A isotherms, however, ΔV–A isotherms for DPPG/Hel 13-5 (Fig. 72.2a) finally converge to the similar ΔV value of ~400 mV, which corresponds to the maximum values of DPPG monolayers (Fig. 72.1b, curve 2). In the DPPC/PG/PA/Hel 13-5 system (Fig. 72.2b), however, the maximum values slightly increase as opposed to the DPPC/PG/PA monolayers (curve 1). Considering the maximum value in Fig. 72.1c, it is found that the dominant exclusion of Hel 13-5 together with PG from surface monolayers in the plateau region at the expense of the improvement in the orientation of the binary DPPC/PA monolayer. On further compression, all of the ΔV–A isotherms converge to ~460 mV, suggesting that the close-packed DPPC/PA monolayers are formed near 60 mN m^{-1}.

The surface pressure where Hel 13-5 is squeezed out of the monolayers is an index for determining the interaction between Hel 13-5 and lipids at the surface. As seen in Fig. 72.3, preparations containing fewer PG components indicate the squeeze-out pressure of ~42 mN m^{-1}, which corresponds to the π^c value of Hel 13-5 monolayers (Fig. 72.1a). Furthermore, the squeeze-out pressure is kept almost constant regardless of $X_{\text{Hel 13-5}}$, which indicates immiscibility among the components. On the other hand, binary DPPG/Hel 13-5 systems show a variation in the squeeze-out pressure (range: 39–49 mN m^{-1}) against $X_{\text{Hel 13-5}}$. The variation demonstrates that cationic Hel 13-5 electrostatically interacts with

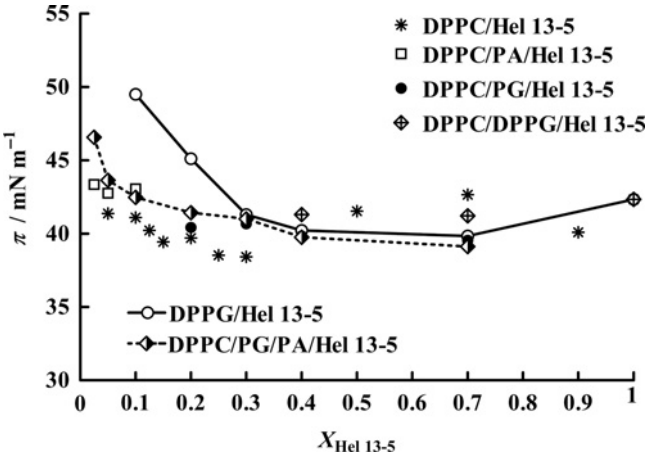


FIGURE 72.3 Changes in surface pressure at onset of the plateau against a molar amount of Hel 13-5 ($X_{\text{Hel 13-5}}$) for DPPC/, DPPG/, DPPC/PA (= 90/9, wt/wt)/, DPPC/PG (= 68:22, wt/wt)/, DPPC/DPPG (= 4/1, mol/mol)/, and DPPC/PG/PA (= 68:22:9, wt/wt/wt)/Hel 13-5.

anionic DPPG at high surface pressures, similarly to miscible behavior between normal lipid monolayers [45–50]. In other words, the positive change in pressure at $X_{\text{Hel 13-5}} = 0.1$ suggests that the mutual electrostatic attractive force prevents Hel 13-5 from being squeezed out of the binary monolayers. A similar variation is also caused in the DPPC/PG/PA/Hel 13-5 system at $X_{\text{Hel 13-5}}$ smaller than 0.05, not in the DPPC/PG/Hel 13-5 system. The carboxyl group in a PA molecule has a pK_a value of 5.1–5.7 [51–54]. Thus, at pH 7.4, the carboxyl group is partially dissociated (30−44%) to be negatively charged [14]. Thus, in addition to the PG components, the dissociated PA molecules are considered to promote the electrostatic interaction with Hel 13-5 in the DPPC/PG/PA/Hel 13-5 system.

72.4 HYSTERESIS IN π−A AND ΔV−A ISOTHERMS

Fluid components such as PG and Hel 13-5 are ejected from the air−water interface to be stored in surface-associated reservoirs on compression above the squeeze-out pressure, which prevents alveolar collapse. During the successive expansion, the squeezed-out molecules reenter with a delay and then spread back into the surface, which is commonly called respreading. The delay produces a large hysteresis loop in π−A isotherms. Both the large hysteresis area and reproducible hysteresis loops are very important for elucidating pulmonary function and activity [55]. In our study [32], the monolayer was compressed up to the respective π^c value and then expanded to the starting molecular areas. This process was successively repeated to examine the reproducibility of the respreading process within a monolayer. All of the preparations ($X_{\text{Hel 13-5}} = 0.1$) shown in Fig. 72.4 exhibit large hysteresis loops in π−A isotherms and good reproducible isotherms during the cycling. The π−A hysteresis curves have a plateau at high surface pressures (∼50 mN m^{-1} for DPPG/Hel 13-5 and ∼42 mN m^{-1} for the others) during lateral compression, where the squeeze-out action and the subsequent formation of 3D aggregates adjacent to the interface gradually occur. Under the expansion, the squeezed-out Hel 13-5 molecules reenter the interface from the aggregates at the slower speed relative to the expansion rate of movable barriers, resulting in a rapid reduction of surface pressures or surface concentrations of monolayers [56]. In this regard, large hysteresis is generated on the cyclic π−A isotherms. An enclosed area in hysteresis loops for the systems here is plotted against the number of cycles in Fig. 72.5. Apparently, the hysteresis areas are kept almost constant irrespective of the cycling number, which supports the reproducibility of repeated compression and expansion isotherms. Furthermore, the DPPG/Hel 13-5 system indicates the maximum hysteresis area among the preparations. This suggests that the PS preparation requires PG components which interact electrostatically with cationic Hel 13-5.

When the π−A hysteresis isotherms for DPPC/PG/Hel 13-5 (Fig. 72.4d) are compared to those for DPPC/DPPG/Hel 13-5 (Fig.72.4e), we would find differences in appearance of the isotherms. In particular, during expansion, the surface pressure indicates a rapid and monotonous decrease until 25 mN m^{-1} for DPPC/DPPG/Hel 13-5. On the other hand, the DPPC/PG/Hel 13-5 system shows a rapid decrease in surface pressure up to 40 mN m^{-1}, and then the decreasing mode becomes slow in magnitude. This difference demonstrates that the PG molecule with unsaturated hydrophobic chains has a closer relationship with stabilization of the surface-associated reservoir formed just below the monolayers.

Among the systems, the π−A hysteresis isotherms for the DPPC/PG/PA/Hel 13-5 system (Fig. 72.4f) have the longest plateaus at ∼44 mN m^{-1}. Commonly, the length of plateau is directly proportional to the amount of squeezed-out molecules. Considering that all the systems contain the same amount of Hel 13-5 ($X_{\text{Hel 13-5}} = 0.1$), it is found that parts of PA molecules are actually eliminated from the surface besides Hel 13-5 and PG. This confirms the abovementioned squeeze-out phenomenon of Hel 13-5 together with dissociated PA molecules. In addition, in terms of a liftoff area, shape, plateau length, and collapse pressure, this preparation possesses surface activity that is similar to that of Surfacten, which contains small amounts of native SP-B and SP-C [22].

It is also notable that the ΔV−A isotherms for the DPPG/Hel 13-5 preparation (Fig. 72.4b) show large and reproducible hysteresis loops. During compression, the ΔV−A isotherms have a plateau, similar to the corresponding π−A isotherms. In the plateau region under compression, Hel 13-5 is preferentially eliminated into the bulk, with the molecular orientation of surface monolayers kept almost constant. Then, the specific interaction stabilizes both the squeezed-out Hel 13-5 beneath the monolayers and the mixed monolayers with Hel 13-5 at the interface. During expansion, the packed monolayers laterally respread in the first stage, and then the molecular ordering and orientation are released again along the expansion of molecular area in the region of 0.40 nm^2 $< A \leq$ 0.70 nm^2. In the subsequent plateau (0.70 nm^2 $< A \leq$ 0.85 nm^2), the squeezed-out Hel 13-5 molecules stepwise reenter to the surface, due to the low surface concentration of the monolayers [23]. The other preparations show the hysteresis only on π−A isotherms, not on ΔV−A isotherms. Although the preparations have the same Hel 13-5 content, a depression in the proportion of PG (especially DPPG) is found to reduce hysteresis properties on ΔV−A isotherms, which means that the specific (or electrostatic) interaction between DPPG and Hel 13-5 specifically promotes the hysteresis behavior of lipid orientation at the surface. This interaction contributes strongly to pulmonary functions such as regulation of the squeeze-out event, 3D aggregates, and orientation of surface monolayers.

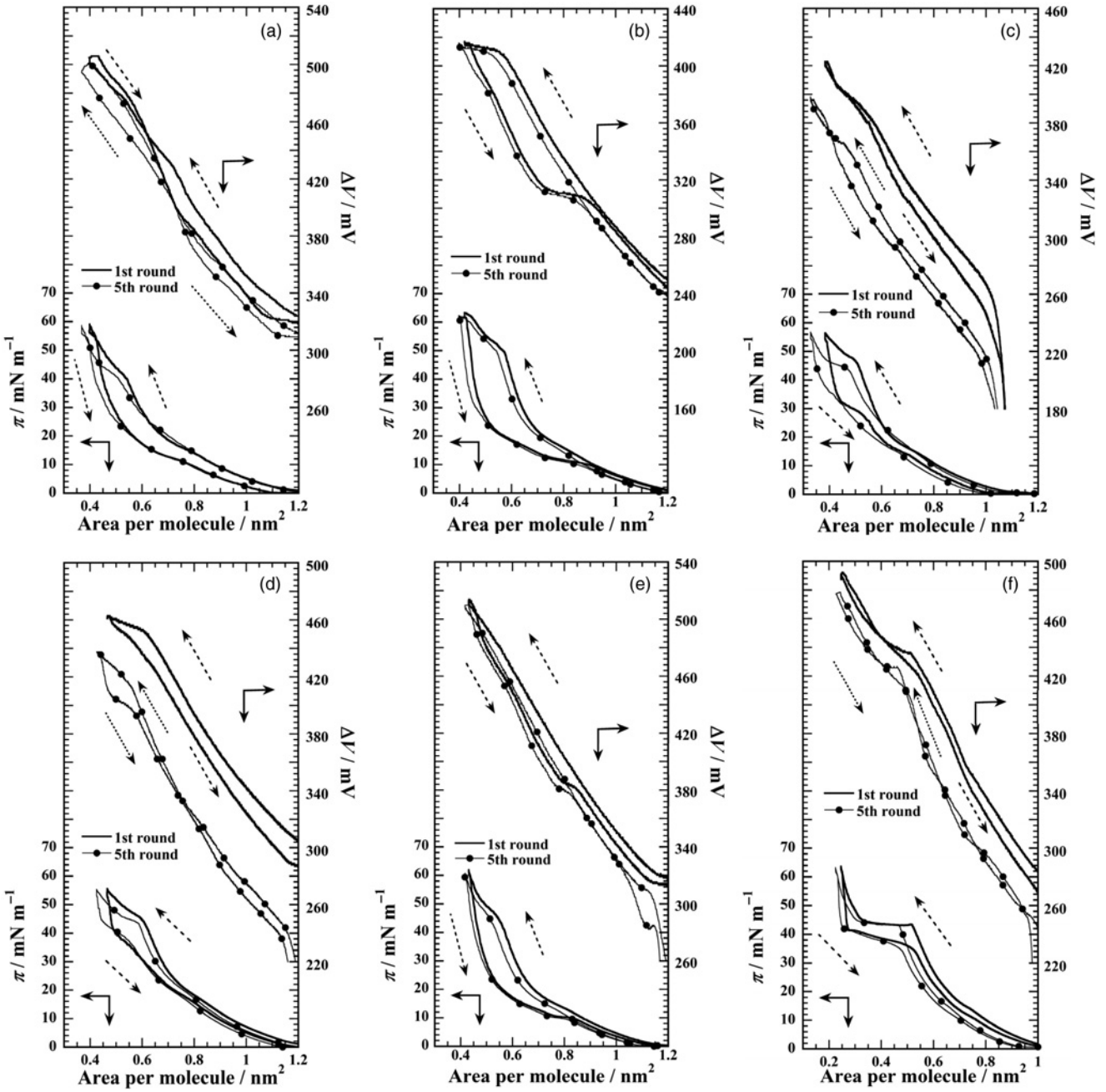


FIGURE 72.4 Cyclic compression and expansion isotherms of the (a) DPPC/, (b) DPPG/, (c) DPPC/PA (= 90/9, wt/wt)/, (d) DPPC/PG (= 68/22, wt/wt)/, (e) DPPC/DPPG (= 4/1, mol/mol)/, and (f) DPPC/PG/PA (= 68/22/9, wt/wt/wt)/Hel 13-5 preparations at $X_{\text{Hel 13-5}} = 0.1$ on a 0.02 M Tris buffer solution (pH 7.4) with 0.13 M NaCl at 298.2 K. The compression–expansion cycle was performed at a compression rate of ~ 90 cm^2 min^{-1}.

72.5 MORPHOLOGICAL PHASE BEHAVIOR

72.5.1 Fluorescence Microscopy (FM)

The in situ morphological behavior of phase transitions for monolayers can be visualized by Brewster angle microscopy (BAM) and fluorescence microscopy (FM). In particular, FM observations provide better performance of surface characteristics in resolution and magnification, although there remains the possibility that FM probes (or dyes) will affect the original phase behavior of monolayers. Thus, it is very important to rule out any influence of the probe on the original properties.

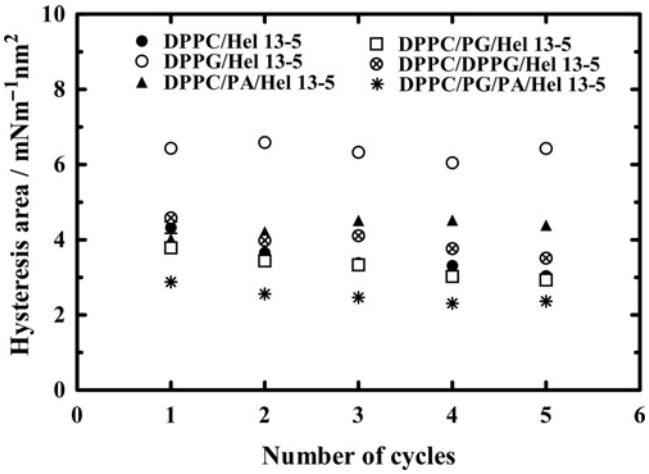


FIGURE 72.5 Changes in integrated hysteresis area surrounded by the compression isotherm and the accompanying expansion isotherm with cycling number of hysteresis measurements.

This is easily accomplished by the isotherm measurement or BAM observation. The LE/LC transition can be analyzed by screening the probe distribution in monolayers. The contrast in FM images depends on the difference in solubility of the probe between LE (disordered) and LC (ordered) phases. As a result, the probe molecules are selectively dissolved in LE phases due to the bulkiness of fluorescent moieties in a probe molecule. The shape of the LC domain is mainly controlled by the line tension of phase boundaries and long-range dipole interactions. The representative FM images for the DPPG/Hel 13-5 system are shown in Fig. 72.6. For DPPG monolayers, the phase behavior and domain shape are quite similar to those obtained from BAM [23]. The LC domains of DPPG monolayers are characterized as a roughly circular shape. FM images of Hel 13-5 alone are homogeneously bright over the entire range of surface pressures as expected obviously from the π–A isotherm (Fig. 72.1a). When Hel 13-5 is added to DPPG monolayers, a unique trend is observed. In the range of $0 < X_{\text{Hel 13-5}} \leq 0.01$, the LC domains of DPPG gradually and monotonously shrink in size with increasing $X_{\text{Hel 13-5}}$. This shows that at low and middle surface pressures, the electrostatic interaction between the two molecules is very weak for the change in phase behavior, nucleation process, and domain shape, due to low surface concentrations of Hel 13-5. In $0.01 < X_{\text{Hel 13-5}} \leq 0.05$, FM images show two kinds of nonfluorescent domains, which are indicated by solid-line and dashed-line circles typically at $X_{\text{Hel 13-5}} = 0.025$. With a decrease in $X_{\text{Hel 13-5}}$ from 0.025, the two populations are observed until $X_{\text{Hel 13-5}} = 0.013$. This indicates that the phase behavior for the DPPG/Hel 13-5 monolayer varies on the border of $X_{\text{Hel 13-5}} = 0.01$[23]. The smaller domains indicated by the dashed-line circles are not intermediate to the larger ones; rather, the two domains grow independently in size and number with an increase in surface pressure. As a result, the small and large domains are found to consist of free DPPG molecules and DPPG/Hel 13-5 complexes, respectively. This irregular behavior suggests the existence of a specific interaction between DPPG and Hel 13-5 such as a miscible monolayer [23].

The domain shape for the DPPC/DPPG (= 4/1, mol/mol) monolayer is different from that of pure DPPG [23, 57] and DPPC [43, 58–60], which indicates that DPPC and DPPG form a miscible monolayer at the surface (Fig. 72.7). When Hel 13-5 is added to the DPPC/DPPG mixture, anticlockwise LC domains shrink in size. As opposed to the DPPG/Hel 13-5 system, the FM images do not show specific behavior. This behavior results from the fact that the ratio of DPPG to Hel 13-5 is too small in the system and/or that the miscible interaction between DPPC and DPPG predominates over the electrostatic interaction between DPPG and Hel 13-5. With an increase in surface pressure to 20 mN m^{-1}, the LC domains become irregular in edge and confused. The variation is attributed to the fact that the electrostatic interaction becomes stronger and stronger as a result of the shortened intermolecular distance between DPPG and Hel 13-5, and thus DPPG can interact with DPPC as well as Hel 13-5.

72.5.2 Atomic Force Microscopy (AFM)

Langmuir–Blodgett (LB) films for the PS preparations deposited onto mica have been visualized by AFM in tapping mode to understand the mechanism of hysteresis behavior in the isotherms at the molecular level. Figure 72.8 shows are the representative AFM images for the DPPC/Hel 13-5, DPPG/Hel 13-5, and DPPC/DPPG/Hel 13-5 systems at $X_{\text{Hel 13-5}} = 0.1$ in the stages of compression and expansion. For the DPPC/Hel 13-5 preparation, the AFM topographic image at 35 mN m^{-1} under the compression shows two different phases in contrast. Considering the diameter of Hel 13-5 (∼1.0 nm) and the height of nontilted phospholipids with saturated dipalmitoyl chains (∼2.5 nm) [21], bright networks and dark domains represent DPPC and Hel 13-5 monolayers, respectively. On further compression of the monolayer, protrusion masses (or dotlike aggregates) are formed at 55 mN m^{-1}, where Hel 13-5 is squeezed out of the interface. The protrusions with a height difference of ∼3.0 nm consist of the ejected Hel 13-5 molecules. In the DPPG/Hel 13-5 system, the image at 35 mN m^{-1} during compression shows a phase behavior similar to that of the DPPC/Hel 13-5 system. However, the protrusions observed at 55 mN m^{-1} differ considerably in shape and number. The squeezed-out Hel 13-5 has a tendency to fuse into new protrusions (or disklike aggregates: tens of nanometers in diameter) with the height difference of ∼3.3 nm. As for the DPPC/DPPG/Hel 13-5 preparation, when the film is compressed to 55 mN m^{-1}, the protrusions are formed on the DPPC/DPPG monolayers but are fewer in number and lateral size compared to the DPPG/Hel 13-5 system. These results strongly suggest that the electrostatic

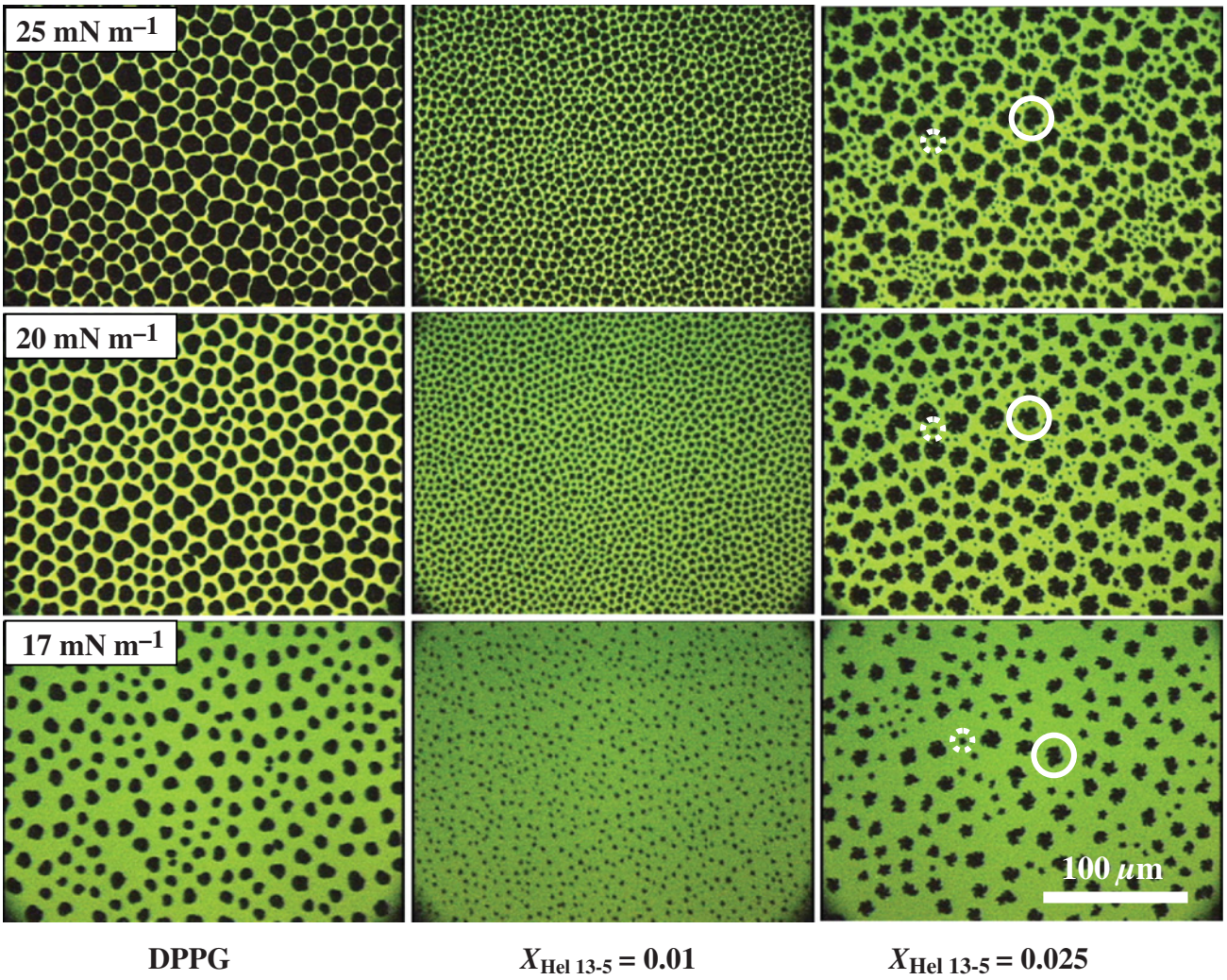


FIGURE 72.6 FM images of the binary DPPG/Hel 13-5 preparations at $X_{Hel\ 13\text{-}5} = 0$ (DPPG), 0.01, and 0.025 at selected surface pressures on a 0.02 M Tris buffer solution (pH 7.4) with 0.13 M NaCl at 298.2 K. The monolayers contain 1 mol% fluorescent probe (NBD-PC). The scale bar in the lower-right corner represents 100 μm.

interaction between DPPG and Hel 13-5 plays an important role in the lateral growth and organization of squeezed-out products at high surface pressures. The surface concentration of anionic charged monolayers are considered to control stabilization of the ejected Hel 13-5. During the first expansion cycle, for the DPPC/Hel 13-5 and DPPC/DPPG/Hel 13-5 systems, the protrusions become smaller in diameter and number, and correspondingly the dark regions of Hel 13-5 monolayers increase with decreasing surface pressures from 55 to 35 mN m^{-1}. On the other hand, the protrusions continue to retain their shape and size laterally and vertically in the DPPG/Hel 13-5 system. This means that the squeezed-out Hel 13-5 molecules do not reenter to the interface, but are rather maintained below the DPPG monolayer for a while after expanding monolayers. It is demonstrated that the squeezed-out Hel 13-5 is stabilized beneath the interface under expansion by the electrostatic interaction with the surface DPPG monolayers. Accordingly, the surface monolayers are restricted to some extents by the ejected Hel 13-5. This retention of the protrusions strongly supports the above-mentioned notion that the independent emergence of the eliminated Hel 13-5 to the surface takes place after the relaxation of surface monolayers under expansion.

Scheme 72.1 provides a possible explanation for the molecular action in the DPPG/Hel 13-5 system across the surface during the compression–expansion cycle. At low surface pressures, the electrostatic interaction is very weak because of the long intermolecular distance between DPPG and Hel 13-5. The lateral compression [route (a) in Scheme 72.1] of the monolayers reduces such distance and the mutual

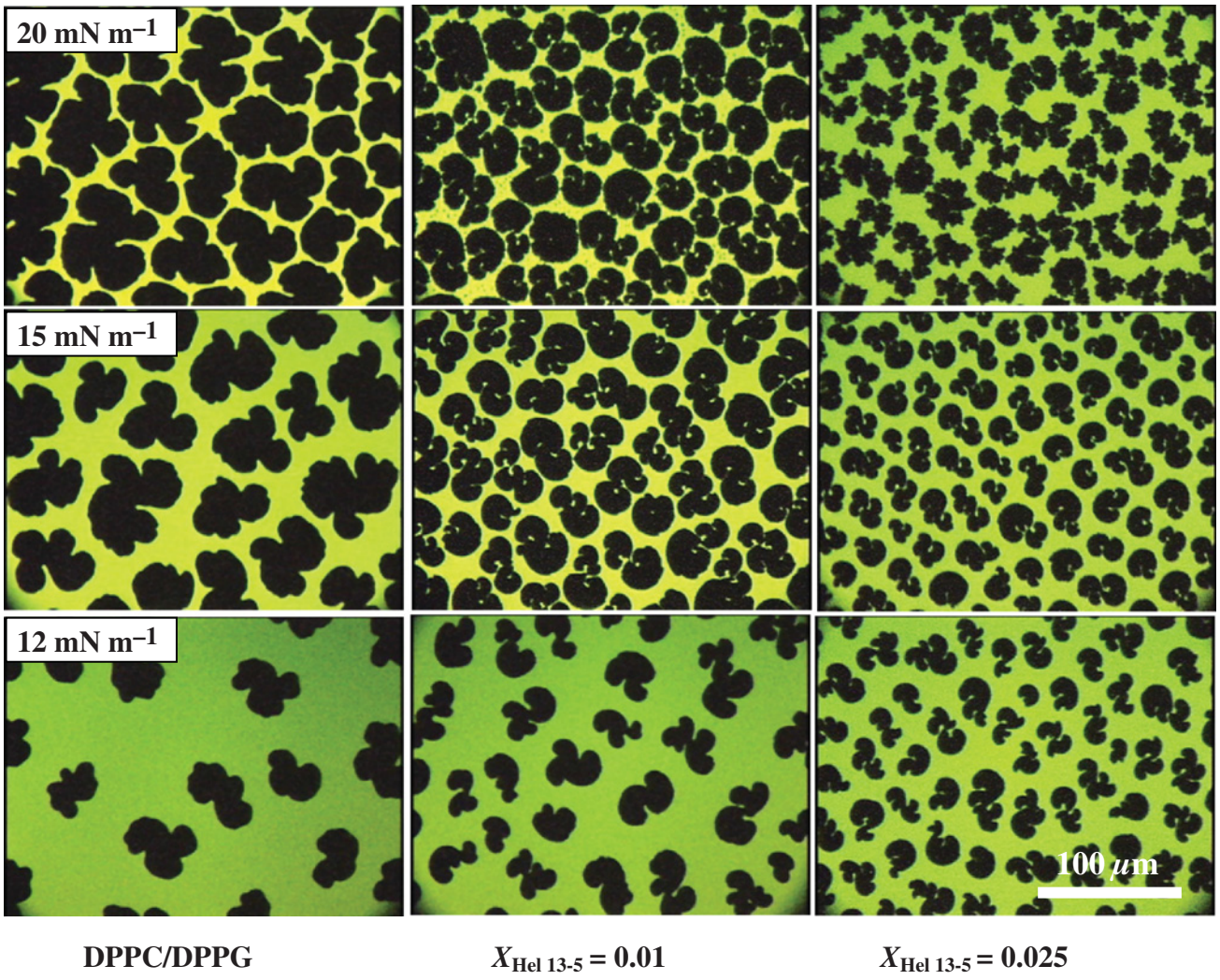


FIGURE 72.7 FM images of the ternary DPPC/DPPG (= 4/1, mol/mol)/Hel 13-5 preparations at $X_{\text{Hel 13-5}} = 0$ (DPPC/DPPG), 0.01, and 0.025 at selected surface pressures on a 0.02 M Tris buffer solution (pH 7.4) with 0.13 M NaCl at 298.2 K. The monolayers contain 1 mol% fluorescent probe (NBD-PC). The scale bar in the lower right corner represents 100 μm.

interaction accordingly strengthens, resulting in variation of the squeeze-out pressure (Figs. 72.1a and 72.3). On further compression beyond the squeeze-out pressure [route (b) in Scheme 72.1], Hel 13-5 is preferentially eliminated from the interface and forms mass aggregates like surface-associated reservoirs beneath the surface DPPG monolayer. Considering the saturated acyl chains of DPPG and the results of compression isotherms (Fig. 72.1b), almost all parts of DPPG would not be ejected together with Hel 13-5, but would remain at the interface during the squeeze-out process. The electrostatic interaction across the surface contributes to the formation and stabilization of the aggregates. During the expansion cycle [route (c) in Scheme 72.1], the surface monolayers respread to the interface, where the ejected Hel 13-5 is maintained beneath the monolayers. Then, when the surface concentration of monolayers decreases to a proper extent, the squeezed-out Hel 13-5 molecules reenter to the surface [route (d) in Scheme 72.1]. On further expansion to the initial molecular area [route (e) in Scheme 72.1], both components are completely released up to the gaseous phase of monolayers. Consequently, the specific interaction generates larger hysteresis loops on both the cyclic π–A and ΔV–A isotherms compared to the other preparations.

72.6 POLARIZED ATR-FTIR SPECTRA

It is well established that the frequency and peak of the amide band in the amide I (1600–1700 cm^{-1}) and II (1500–1600 cm^{-1}) regions depend critically on the secondary

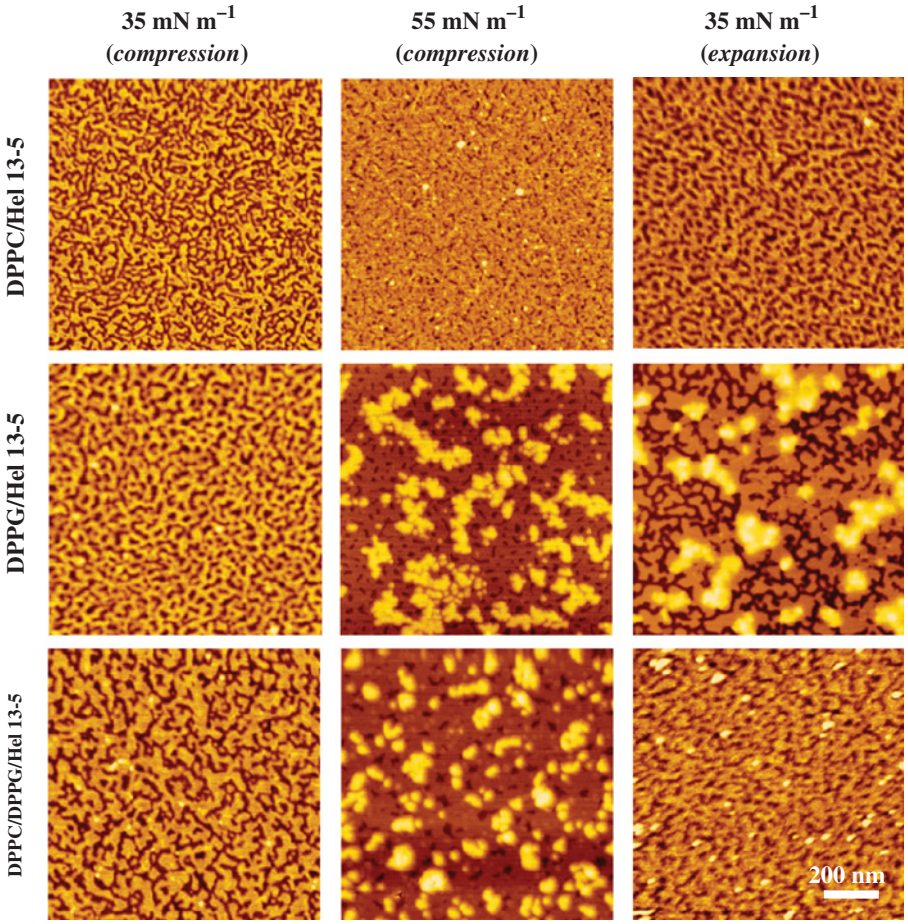


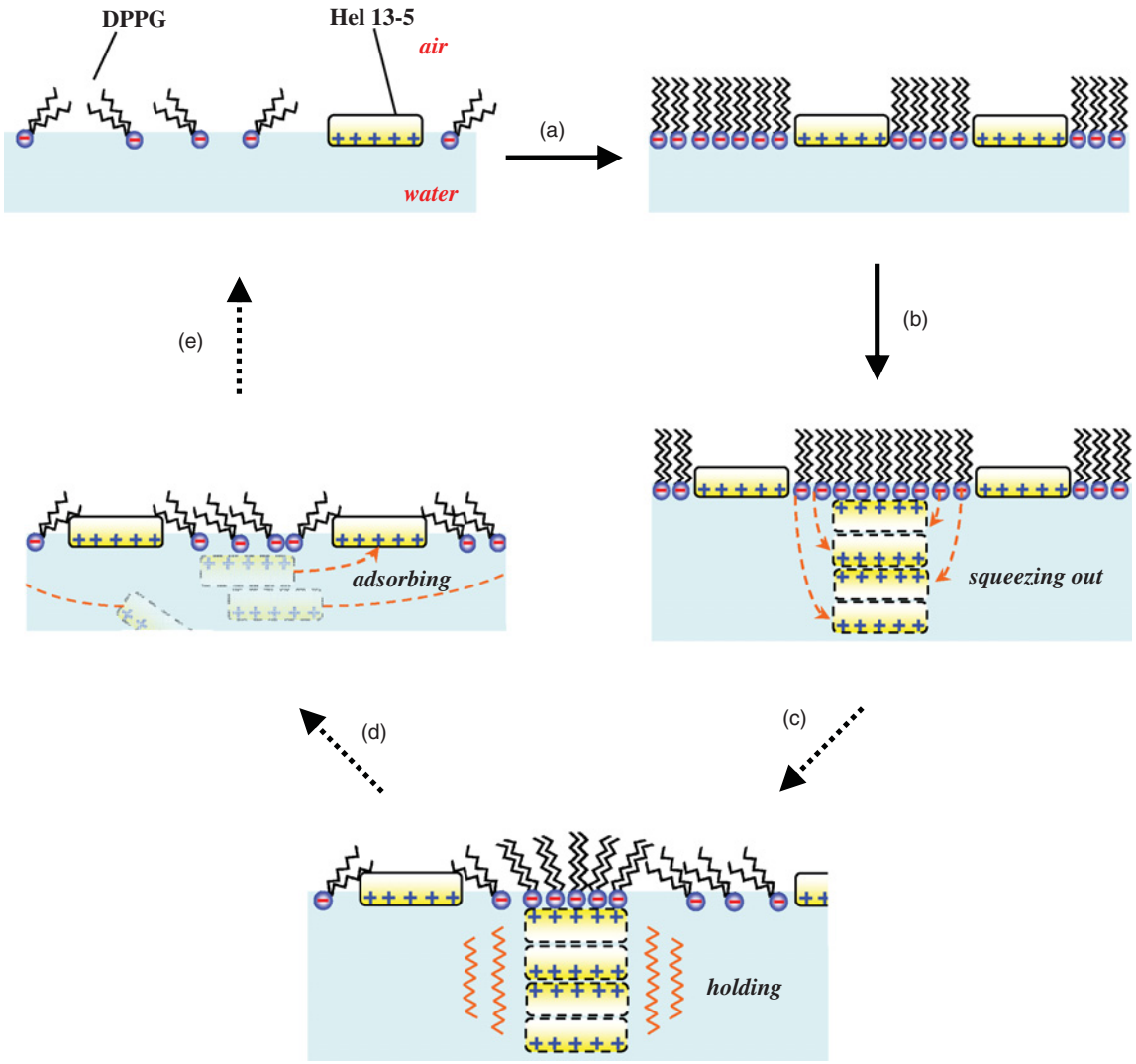
FIGURE 72.8 AFM topographic images of DPPC/, DPPG/, and DPPC/DPPG (4/1, mol/mol)/Hel 13-5 preparations at $X_{\text{Hel 13-5}} = 0.1$ on a 0.02 M Tris buffer solution (pH 7.4) with 0.13 M NaCl at 298.2 K. The monolayers were transferred onto mica at 35 (left column) and 55 (middle column) on the first compression, and 35 mN m^{-1} (right column) on the following first expansion. The scan area is 1 × 1 μm, and the scale bar in the lower right corner represents 200 nm.

structure of peptide and protein films [61–63]. Polarized attenuated total reflectance (ATR)-FTIR spectra of Hel 13-5 films in the amide region are shown in Fig. 72.9. There exist two positive bands at 1656 (amide I) and 1541 (amide II) cm^{-1}, which are indicative of the α-helical structure. In terms of peak intensity, the *p*-polarized spectrum is larger than the *s*-polarized one, which indicates that the molecular backbone of Hel 13-5 is tilted against the germanium (Ge) surface. The ATR-FTIR spectra for the DPPC/Hel 13-5, DPPG/Hel 13-5, and DPPC/PG/PA/Hel 13-5 films containing the fixed amount of Hel 13-5 ($X_{\text{Hel 13-5}} = 0.1$) are shown in Fig. 72.10. All the systems exhibit four major peaks at ∼1740, 1650, 1540, and 1465 cm^{-1}. The peaks at ∼1740 and 1465 cm^{-1} are assigned to the C=O stretching and CH_2 bending vibrations of lipid aliphatic chains, respectively. Both the amide bands at ∼1650 and 1540 cm^{-1} indicate the existence of α-helix in the films. Consequently, it can be concluded that the secondary structure of Hel 13-5 in the phospholipid films is predominantly the α-helix.

72.7 PM-IRRAS SPECTRA AT THE AIR–WATER INTERFACE

72.7.1 The in situ PM-IRRAS Spectra in the Amide Region

The in situ PM-IRRAS spectra of Hel 13-5 monolayers at the air–water interface are shown in Fig. 72.11. Below 35 mN m^{-1}, the amide I band is kept to be located at ∼1660 cm^{-1}, corresponding to the α-helix secondary structure. In addition, the indicative of the α-helix is also observed in the amide II region at ∼1539 cm^{-1}. The surface selection rules of the PM-IRRAS experiment at the interface specify that



Scheme 72.1 Possible explanation for specific interaction between anionic DPPG and cationic Hel 13-5 in the model pulmonary system of DPPG/Hel 13-5 during compression and successive expansion. Hel 13-5 with dashed-line squares means the squeezed-out one: (a) monolayer compression from $A =$ 1.20 to 0.60 nm^2 in Fig. 72.4b; (b) further compression from $A = 0.60$ to 0.40 nm^2; (c) monolayer expansion from $A = 0.40$ to 0.70 nm^2; (d) following expansion from $A = 0.70$ to 0.85 nm^2; (e) further expansion from $A = 0.85$ to 1.20 nm^2.

strong positive absorption bands in the spectrum indicate IR transition dipole moments, which are aligned parallel to the interface [64]. Therefore, the α-helical backbone of Hel 13-5 is found to be oriented parallel to the surface. Above the collapse pressure (~42 mN m^{-1}) of Hel 13-5 monolayers, the spectrum at 45 mN m^{-1} clearly indicates two different peaks at ~1645 and ~1612 cm^{-1} in the amide I region. The former peak frequency somewhat shifts to lower wavenumber, which means that the α-helical structure of Hel 13-5 is exposed by the surrounding water molecule [30, 65]. The latter band is assigned to an extended form, including the antiparallel β-sheet [31, 66]. In other words, the over-compression of Hel 13-5 monolayers induces the structural transformation from the α-helix to β-sheet at the air−water interface.

The PM-IRRAS spectra for the DPPC/Hel 13-5 monolayer at $X_{\text{Hel 13-5}} = 0.1$ during compression are shown in Fig. 72.12a. In comparison to Fig. 72.11, the peak intensities in the amide regions decrease as a result of the small surface concentration of Hel 13-5. To overcome this defect, peak separation to the Gaussian components is faithfully accomplished [32, 33]. At 5 mN m^{-1}, the intense constituents of the amide I (at ~1653 cm^{-1}) and II (at ~1534 cm^{-1}) modes are assigned to the α-helix. As surface pressure increases toward 60 mN m^{-1}, the α-helical marker band almost disappears. Instead, the component near ~1617 cm^{-1} corresponding to

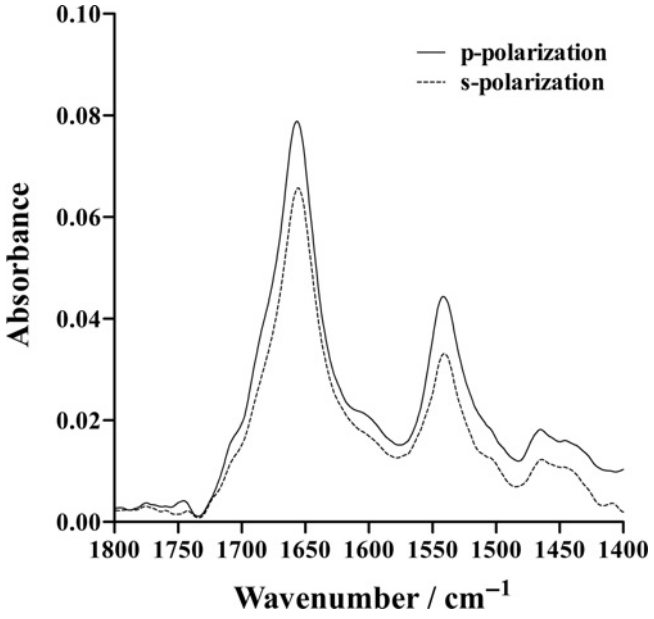


FIGURE 72.9 Polarized ATR-FTIR spectra of Hel 13-5 films in the region of 1400– 1800 cm^{-1} at room temperature. Solid line corresponds to p-polarization and dashed line, to s-polarization of the incident radiation.

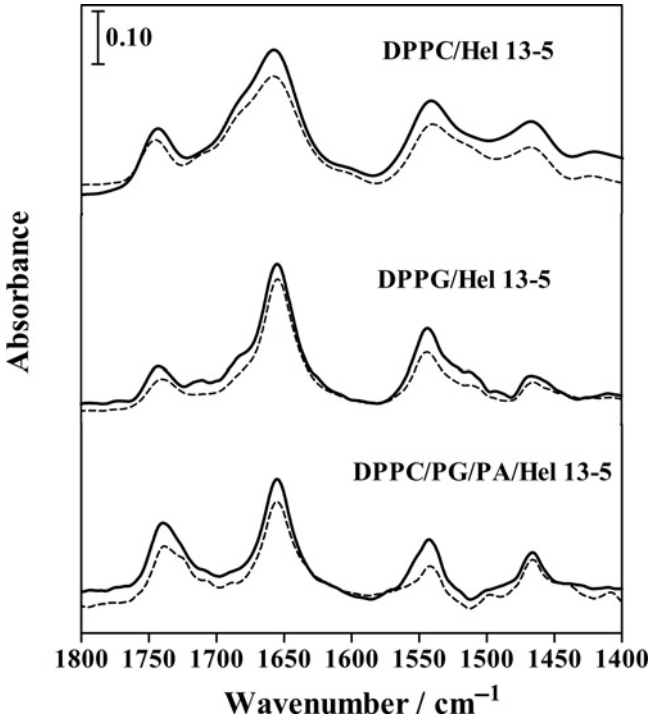


FIGURE 72.10 Polarized ATR-FTIR spectra of films of DPPC/Hel 13-5 (upper), DPPG/Hel 13-5 (middle), and DPPC/PG/PA (= 68/22/9, wt/wt/wt; lower)/Hel 13-5 systems at $X_{\text{Hel 13-5}} = 0.1$ in the region of 1400 – 1800 cm^{-1} at room temperature. Solid lines correspond to p-polarization and dashed lines, to s-polarization of the incident radiation.

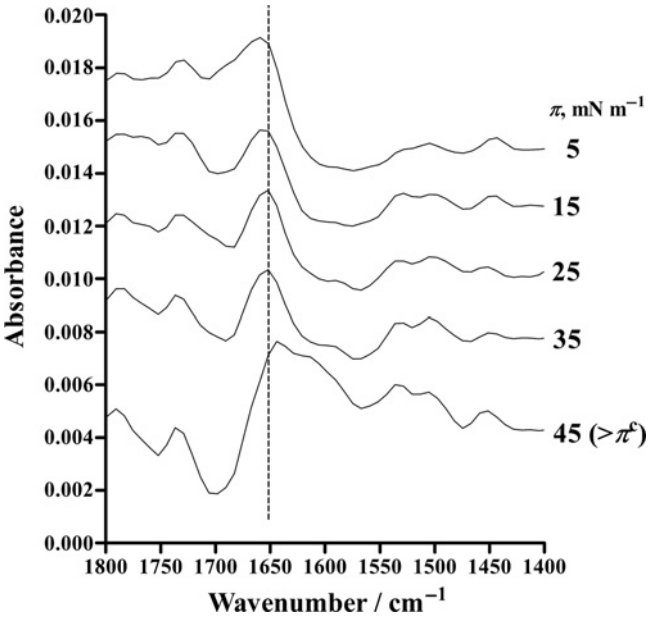


FIGURE 72.11 In situ PM-IRRAS spectra of Hel 13-5 monolayers as a function of surface pressure (π) in the region of 1400 – 1800 cm^{-1} on a 0.02 M Tris buffer solution (pH 7.4) with 0.13 M NaCl at 298.2 K.

the antiparallel β-sheet appears in the spectra, and the peak intensity of the β-sheet marker band increases relative to the α-helical marker band. The β-sheet marker bands near ∼1606 cm^{-1} also emerge in the spectrum for the DPPG/Hel 13-5 system at high surface pressures (Fig. 72.12b). The interconversion from the α-helix to the β-sheet is possibly attributed to the destruction particularly of intramolecular hydrogen bonding, based on the peptide secondary structure, which is facilitated by reduction in intermolecular distance between Hel 13-5 and the aliphatic chains of lipids. The transition of peptide secondary structures in lipid environments has been reported as well by other researchers [31, 67]. In this regard, the peptide structure is strongly deformed by the environmental lipid (especially phospholipids with saturated hydrocarbon chains, e.g., DPPC) density rather than applied surface pressures.

72.7.2 Secondary Structure Transformation of Hel 13–5

An α-helix ratio of Hel 13–5 relative to the (α-helix + β-sheet) component for Hel 13-5 monolayers and all the lipid/Hel 13-5 systems treated here at $X_{\text{Hel 13–5}} = 0.1$ during the compression (solid line with filled circles) and expansion (dashed line with open circles) cycle is plotted against surface pressure in Fig. 72.13. The ratio can be calculated from integrated peak areas of the α-helix (∼1650 cm^{-1}) and of the β-sheet (∼1620 cm^{-1}) marker bands (Gaussian bands) in the amide I region; the ratio α/(α+β) means the peak area

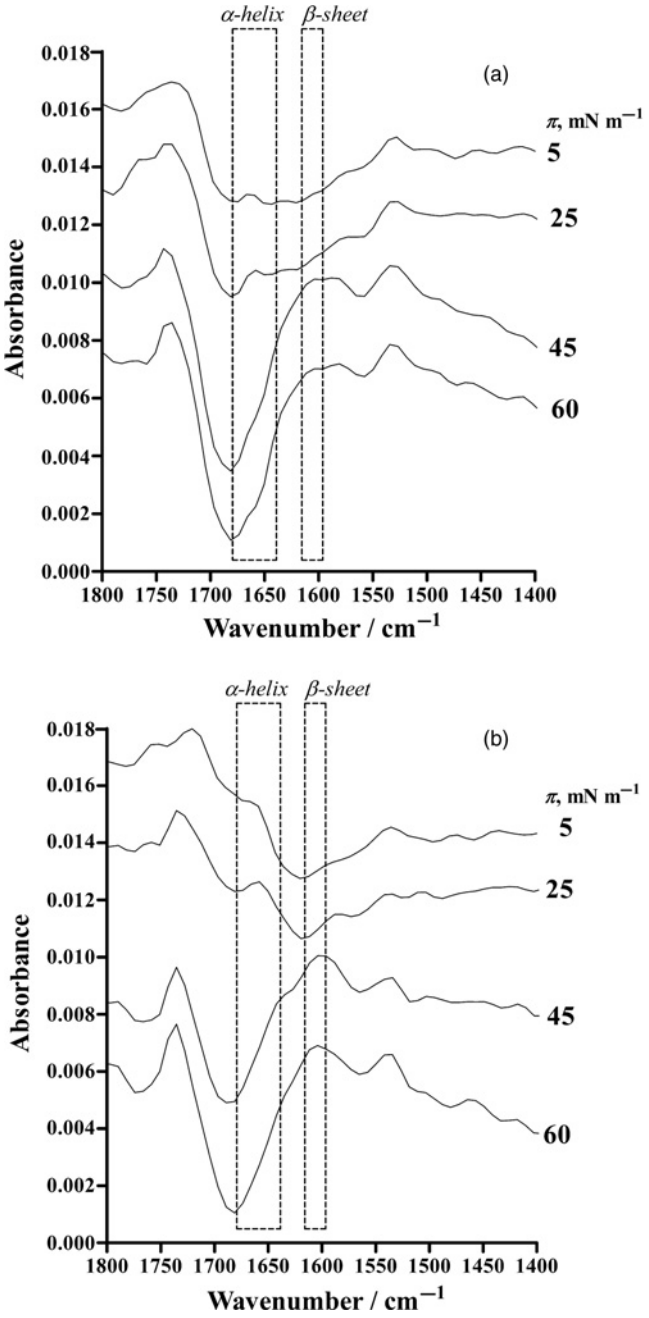


FIGURE 72.12 In situ PM-IRRAS spectra of monolayers of the (A) DPPC/Hel 13-5 and (b) DPPG/Hel 13-5 systems at $X_{\text{Hel 13-5}} = 0.1$ as a function of surface pressure (π) during compression in the region of 1400–1800 cm^{-1} on a 0.02 M Tris buffer solution (pH 7.4) with 0.13 M NaCl at 298.2 K. The marker band regions of the α-helix and the β-sheet in the amide I contour are emphasized in the dashed rectangles.

ratio of amide I band intensities for ~1650 cm^{-1}/(~1650 + ~1620) cm^{-1} [31–33]. Hel 13-5 monolayers in the absence of lipids at the air–water interface are in approximately >70% α-helical structure during compression. However, overcompression above the collapse pressure decreases the α-helix ratio by ~20%. During the successive expansion, the α-helix ratio is kept at >50%. In the DPPC/Hel 13-5 system, the percentage of the α-helical component decreases from 50% to 80% down to near zero with increasing surface pressures up to 60 mN m^{-1} on compression. During the subsequent expansion, the percentage immediately recovers up to ~30%, and the value is kept almost constant as surface pressure reduces further. This suggests the irreversible interconversion of Hel 13-5 secondary structures from the α-helix into the β-sheet, when Hel 13-5 is surrounded by DPPC monolayers. On the other hand, in the DPPG/Hel 13-5 monolayer, it is quite interesting that the percentage of the α-helix marker band reduces from ~60% down to ~30%, not to zero, on compression. As opposed to the DPPC/Hel 13-5 system, interconversion into the β-sheet is restrained by the surrounding DPPG monolayer, which may result from the electrostatic interaction between both components. During the subsequent expansion, the percentage does not return to the initial value but maintains the value of ~30% up to lower surface pressures. In the case of the DPPC/PA/Hel 13–5 system, the percentage of the α-helical component decreases from 30% to 40% down to 20% with increasing surface pressures on compression. This suggests that PA promotes the destruction of hydrogen bonding in Hel 13-5 secondary structures. In the subsequent expansion process, the ratio rapidly restores to the initial values of 30−40%, which indicates that PA components are effective in recovery of the secondary structure. From these results, it is found that the lipid species such as PG and PA are an important factor for deformation of the secondary structure: (1) the hydrogen bonding involved in construction of the secondary structure of Hel 13–5 is broken mainly by DPPC, (2) the surface-associated reservoir including charged PA and PG disturbs the transformation of the secondary structure into β-sheet, and (3) PA promotes the recovery of a secondary structure during expansion. Interestingly, PA exerts effects 2 and 3 during compression and expansion, respectively. The carboxyl group in PA molecules is partially dissociated by 30–40% under the present conditions [14]. Thus, a switching motion between COOH and COO^- is considered to be an effective driving force for the recovery of Hel 13–5 secondary structure from the β-sheet and for the release of surface-associated reservoirs onto the interface during expansion. Considering the predominant α-helical structure of Hel 13–5 in the aqueous solutions containing phospholipids [20, 26] and in the bilayer form [32, 33], it is demonstrated that the surface-associated reservoir prevents the protein structure transition (or surface denaturation) by incorporating the proteins into the reservoir.

72.7.3 Lipid Stretching Vibration Modes

The PM-IRRAS spectra in the region of 2800–3000 cm^{-1} commonly catch stretching vibrations of methylene and

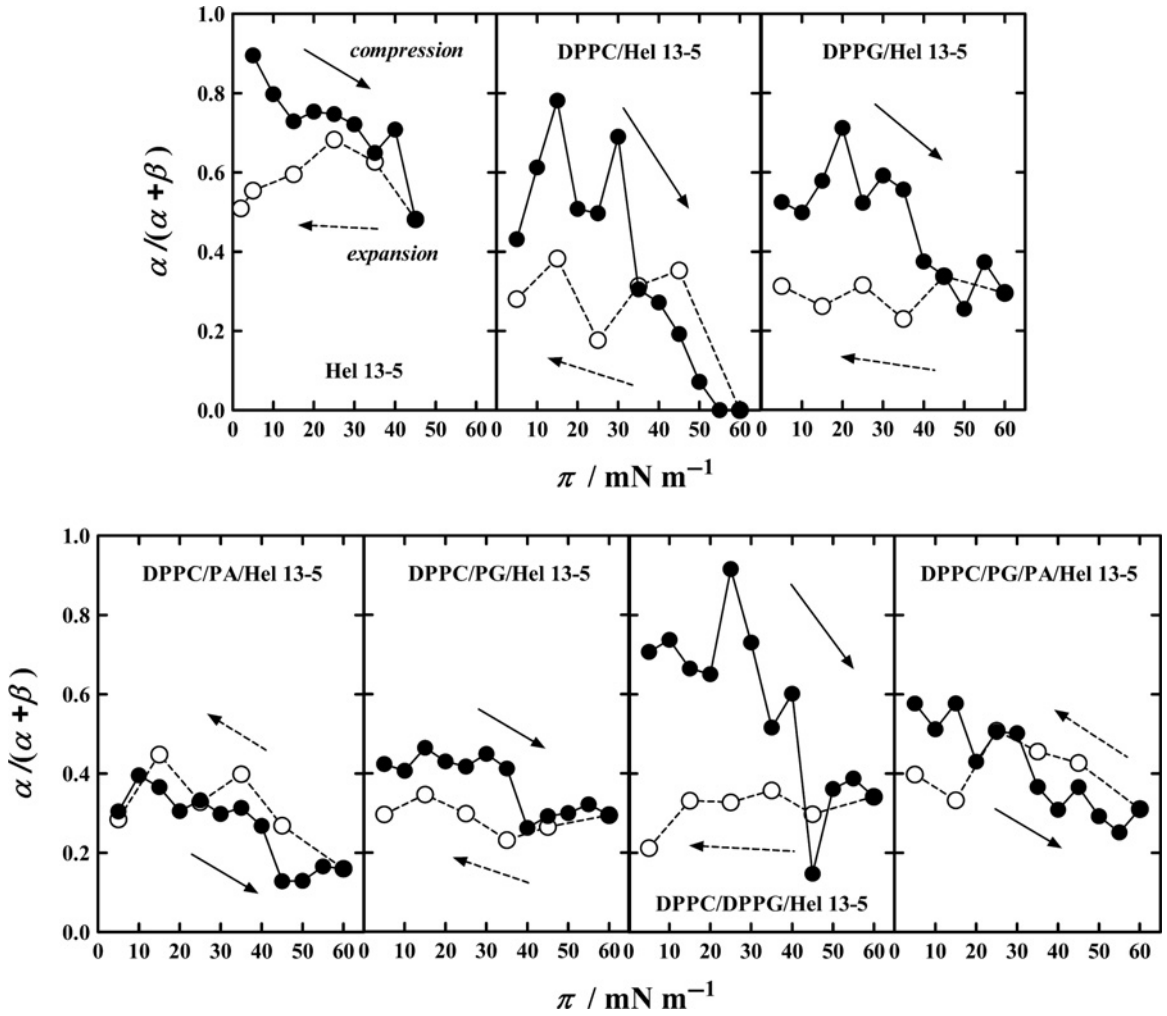


FIGURE 72.13 Peak area ratio $\alpha/(\alpha+\beta)$ of the amide I band intensity for ~1650 cm^{-1}/(~1650 + ~1620) cm^{-1} against surface pressure (π) during compression (filled circles and solid lines) and expansion (open cycles and dashed lines) for the DPPC/, DPPG/, DPPC/PA (= 90/9, wt/wt)/, DPPC/PG (= 68/22, wt/wt)/, DPPC/DPPG (= 4/1, mol/mol)/, and DPPC/PG/PA (= 68/22/9, wt/wt/wt)/Hel 13-5 preparations at $X_{\text{Hel 13-5}} = 0.1$. The peak at ~1650 cm^{-1} is assigned to the α-helical secondary structure and the peak at ~1620 cm^{-1} is assigned to the antiparallel β-sheet.

methyl groups for lipid components [33, 68–70]. The region includes three kinds of specific peaks of the lipids such as a symmetric methylene stretching vibration [or $\nu_s(CH_2)$] at ~2850 cm^{-1}, an asymmetric methylene stretching vibration {or $\nu_a(CH_2)$} at ~2920 cm^{-1}, and a methyl stretching vibration [or $\nu(CH_3)$] at ~2950 cm^{-1}. Among the three, the $\nu_a(CH_2)$ peak is, in general, the largest in intensity and is most sensitive to external stimuli such as lateral compression (or surface concentration) and temperature. Therefore, the $\nu_a(CH_2)$ mode allows us to probe changes in surface concentration and orientation of the lipid components. The intensity of $\nu_a(CH_2)$ modes increases with an increase in surface pressure and subsequently decreases during the expansion cycle. The $\nu_a(CH_2)$ RA intensity at ~2920 cm^{-1} for all the lipid/Hel 13–5 systems at $X_{\text{Hel 13–5}} = 0.1$ during compression (solid line with filled circles) and expansion (dashed line with open circles) is plotted against surface pressure in Fig. 72.14. On compression, the RA value increases with an increase in surface pressure and finally reaches 0.004−0.009 at 60 mN m^{-1}. Considering the maximum $\nu_a(CH_2)$ RA intensity (~0.004) for the binary DPPC/Hel 13–5 system [32], all the systems here indicate larger RA values, which indicates an increase in surface concentration (or density) of aliphatic chains induced by the addition of PA and PG (or DPPG) at the close-packed state. During the expansion stage, the RA intensity decreases with decreasing surface pressure. Notably, all the systems exhibit a hysteresis loop in intensity during the compression–expansion process. The hysteresis regarding the interfacial

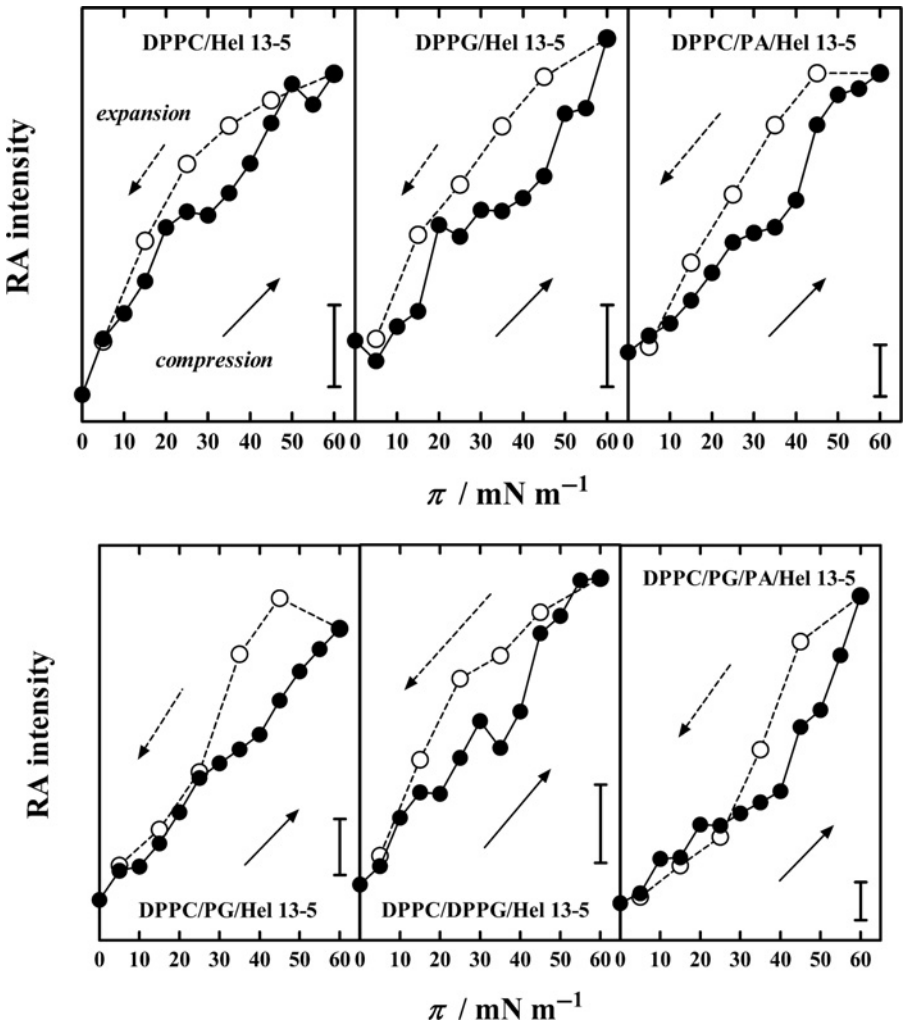


FIGURE 72.14 RA intensity of the asymmetric CH_2 stretching vibrations $\nu_a(CH_2)$ of lipids in the PM-IRRAS spectra at different surface pressures (π) during compression (filled circles and solid lines) and successive expansion (open circles and dashed lines) for the DPPC/, DPPG/, DPPC/PA (= 90/9, wt/wt)/, DPPC/PG (= 68/22, wt/wt)/, DPPC/DPPG (= 4/1, mol/mol)/, and DPPC/PG/PA (= 68/22/9, wt/wt/wt)/Hel 13-5 preparations at $X_{\text{Hel 13-5}} = 0.1$ on a 0.02 M Tris buffer solution (pH 7.4) with 0.13 M NaCl at 298.2 K. Each scale bar in the lower right corner represents 0.001 of RA intensity.

orientation of hydrophobic chains in lipid components is also supported by ΔV–A isotherms (Fig. 72.4). RA intensities for the DPPC/PA/Hel 13–5 system under the expansion stage from 60 down to 10 mN m^{-1} are maintained larger compared with those at the same surface pressures during compression. On the other hand, in the systems containing PG (DPPC/PG/Hel 13-5 and DPPC/PG/PA/Hel 13-5), RA intensities on expansion restore to the initial value down by 25 mN m^{-1}. These results suggest that the addition of PA and PG accelerates monolayer packing at high surface pressures under the compression and respreading of tightly packed monolayers under the expansion, respectively. However, the influence on the respreading in the systems containing DPPG seems to be different from those containing PG. This is considered to result from the saturated hydrocarbon chains in DPPG, which remains at the surface during cycling. Thus, it is demonstrated that the hysteresis behavior of orientation of hydrophobic chains in the lipids could be related to the formation of surface-associated reservoirs.

Besides the RA intensity, a wavenumber (or peak frequency) of $\nu_a(CH_2)$ modes for lipid monolayers is more strongly influenced by packing, orientation, and conformational change of their hydrophobic chains. In particular, the wavenumber near 2920 cm^{-1} is characteristic of all-*trans* conformations of these chains [71–73]. As seen in Fig. 72.15, the wavenumber of $\nu_a(CH_2)$ modes for the DPPC/PA/Hel

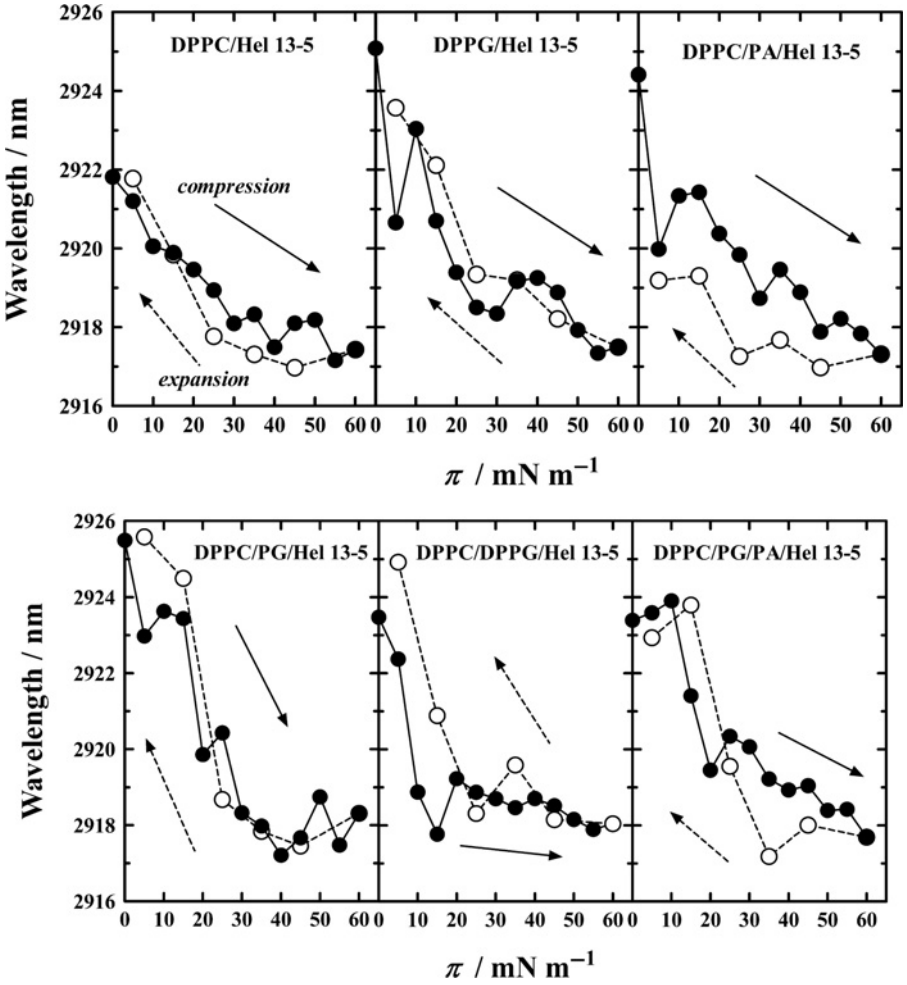


FIGURE 72.15 Wavenumber of the asymmetric CH_2 stretching vibrations $\nu_a(CH_2)$ of lipids in the PM-IRRAS spectra at different surface pressures (π) during compression (filled circles and solid lines) and successive expansion (open circles and dashed lines) for the DPPC/, DPPG/, DPPC/PA (= 90/9, wt/wt)/, DPPC/PG (= 68/22, wt/wt)/, DPPC/DPPG (= 4/1, mol/mol)/, and DPPC/PG/PA (= 68/22/9, wt/wt/wt)/Hel 13-5 preparations at $X_{\text{Hel 13-5}} = 0.1$ on a 0.02 M Tris buffer solution (pH 7.4) with 0.13 M NaCl at 298.2 K.

13–5 and DPPC/PG/PA/Hel 13-5 systems indicates a hysteresis loop during compression and expansion, not for the DPPG/Hel 13-5, DPPC/PG/Hel 13–5, DPPC/DPPG/Hel 13-5 systems. The hysteresis in the wavenumber plots also indicates the condensing effect of undissociated PA components on the monolayer, which prevents it from respreading during expansion. On the other hand, the PG components are found to improve the relaxation of the packed chains of lipid monolayers on expansion.

72.8 CONCLUSIONS

The large hysteresis in the π–A and ΔV–A isotherms for the DPPG/Hel 13-5 system demonstrates that the mutual specific (or electrostatic) interaction triggers completely independent processes for Hel 13-5 during repeated compression and expansion processes: (1) squeeze-out into subsolution and (2) close packing as a monolayer with DPPG at the interface. In addition, the AFM observations reveal that the electrostatic interaction contributes to the formation of the squeezed-out Hel 13-5 aggregates beneath the monolayers under the compression process and to their stabilization up to low surface pressures under the expansion process. In other words, the specific interactions between the PG headgroup and the polarized moiety of Hel 13-5 are closely related to the physiological and biophysical functions of PS. Moreover, the reservoir formation causes a hysteresis in π–A and ΔV–A isotherms as well as spectrum parameters regarding lipid orientations and peptide secondary structures during the compression–expansion cycle. The formation and function of reservoirs across the surface are controlled not only

by the electrostatic attraction between lipids and peptide but also by the structural transition of peptides. The structural transition is considered to be induced by destruction of the hydrogen and S–S bonding constructing higher-order structures of a peptide or protein. In the monolayer study, the destructive factors are typically an applied surface pressure and a surface density of lipids (in particular, their hydrocarbon chains). DPPC-rich surroundings cause the structural transition of Hel 13-5 to β-sheet almost completely. However, the existence of PA and/or PG preserves the α-helical structure. Furthermore, it is suggested that the release of squeezed-out lipids and peptides from the surface-associated reservoir is accelerated by partially charged PA molecules and that PG assumes a strong resistance to the secondary structure transition on compression.

REFERENCES

[1] Schürch, S., Goerke, J., Clements, J. A. (1976). Direct determination of surface tension in the lung. *Proc. Natl. Acad. Sci. USA* **73**, 4698–4702.

[2] Amrein, M., Von Nahmen, A., Sieber, M. (1997). A scanning force and fluorescence light microscopy study of the structure and function of a model pulmonary surfactant. *Eur. Biophys. J.* **26**, 349–357.

[3] Krol, S., Ross, M., Sieber, M., Kunneke, S., Galla, H.-J., Janshoff, A. (2000). Formation of three-dimensional protein-lipid aggregates in monolayer films induced by surfactant protein B. *Biophys. J.* **79**, 904–918.

[4] Takamoto, D.Y., Lipp, M.M., Von Nahmen, A., Lee, K.Y.C., Waring, A.J., Zasadzinski, J.A. (2001). Interaction of lung surfactant proteins with ANIONIC phospholipids. *Biophys. J.* **81**, 153–169.

[5] Nakahara, H., Lee, S., Sugihara, G., Shibata, O. (2006). Mode of Interaction of hydrophobic amphiphilic α-helical peptide/dipalmitoylphosphatidylcholine with phosphatidylglycerol or palmitic acid at the air-water interface. *Langmuir* **22**, 5792–5803.

[6] Schürch, S., Qanbar, R., Bachofen, H., Possmayer, F. (1995). The surface-associated surfactant reservoir in the alveolar lining. *Biol. Neonate* **67**(Suppl. 1), 61–76.

[7] Veldhuizen, R., Nag, K., Orgeig, S., Possmayer, F. (1998). The role of lipids in pulmonary surfactant. *Biochim. Biophys. Acta* **1408**, 90–108.

[8] Krüger, P., Baatz, J.E., Dluhy, R.A., Lösche, M. (2002). Effect of hydrophobic surfactant protein sp-c on binary phospholipid monolayers. Molecular machinery at the air/water interface. *Biophys. Chem.* **99**, 209–228.

[9] Yu, S.-H., Possmayer, F. (2003). Lipid compositional analysis of pulmonary surfactant monolayers and monolayer-associated reservoirs. *J. Lipid Res.* **44**, 621–629.

[10] Clark, J.C., Wert, S.E., Bachurski, C.J., Stahlman, M.T., Stripp, B.R., Weaver, T.E., Whitsett, J.A. (1995). Targeted disruption of the surfactant protein B gene disrupts surfactant homeostasis, causing respiratory failure in newborn mice. *Proc. Natl. Acad. Sci. USA* **92**, 7794–7798.

[11] Nogee, L.M., Garnier, G., Dietz, H.C., Singer, L., Murphy, A.M., Demello, D.E., Colten, H.R. (1994). A mutation in the surfactant protein B gene responsible for fatal neonatal respiratory disease in multiple kindreds. *J. Clin. Invest.* **93**, 1860–1863.

[12] Ballard, P.L., Nogee, L.M., Beers, M.F., Ballard, R.A., Planer, B.C., Polk, L., Demello, D.E., Moxley, M.A., Longmore, W.J. (1995). Partial deficiency of surfactant protein B in an infant with chronic lung disease. *Pediatrics* **96**, 1046–1052.

[13] Pérez-Gil, J., Casals, C., Marsh, D. (1995). Interactions of hydrophobic lung surfactant proteins SP-B and SP-C with dipalmitoylphosphatidylcholine and dipalmitoylphosphatidylglycerol bilayers studied by electron spin resonance spectroscopy. *Biochemistry* **34**, 3964–3971.

[14] Nakahara, H., Lee, S., Shoyama, Y., Shibata, O. (2012). The role of palmitic acid in pulmonary surfactant systems by Langmuir monolayer study: Lipid-peptide interactions. *Soft Matt.* **7**, 11351–11359.

[15] Nahmen, A.V., Schenk, M., Sieber, M., Amrein, M. (1997). The structure of a model pulmonary surfactant as revealed by scanning force microscopy. *Biophys. J.* **72**, 463–469.

[16] Lipp, M.M., Lee, K.Y.C., Takamoto, D.Y., Zasadzinski, J.A., Waring, A.J. (1998). Coexistence of buckled and flat monolayers. *Phys. Rev. Lett.* **81**, 1650–1653.

[17] Revak, S.D., Merritt, T.A., Cochrane, C.G., Heldt, G.P., Alberts, M.S., Anderson, D.W., Kheiter, A. (1996). Efficacy of synthetic peptide-containing surfactant in the treatment of respiratory distress syndrome in preterm infant rhesus monkeys. *Pediatr. Res.* **39**, 715–724.

[18] Ma, J., Koppenol, S., Yu, H., Zografi, G. (1998). Effects of a cationic and hydrophobic peptide, KL4, on model lung surfactant lipid monolayers. *Biophys. J.* **74**, 1899–1907.

[19] Wiswell, T.E., Smith, R.M., Katz, L.B., Mastroianni, L., Wong, D.Y., Willms, D., Heard, S., Wilson, M., Hite, R.D., Anzueto, A., Revak, S.D., Cochrane, C.G. (1999). Bronchopulmonary segmental lavage with surfaxin (KL(4)-surfactant) for acute respiratory distress syndrome. *Am. J. Respir. Crit. Care Med.* **160**, 1188–1195.

[20] Lee, S., Furuya, T., Kiyota, T., Takami, N., Murata, K., Niidome, Y., Bredesen, D.E., Ellerby, H.M., Sugihara, G. (2001). De novo-designed peptide transforms golgi-specific lipids into golgi-like nanotubules. *J. Biol. Chem.* **276**, 41224–41228.

[21] Nakahara, H., Nakamura, S., Hiranita, T., Kawasaki, H., Lee, S., Sugihara, G., Shibata, O. (2006). Mode of interaction of amphiphilic α-helical peptide with phosphatidylcholines at the air-water interface. *Langmuir* **22**, 1182–1192.

[22] Nakahara, H., Lee, S., Sugihara, G., Chang, C.-H., Shibata, O. (2008). Langmuir monolayer of artificial pulmonary surfactant mixtures with an amphiphilic peptide at the air/water interface: comparison of new preparations with surfacten (surfactant TA). *Langmuir* **24**, 3370–3379.

[23] Nakahara, H., Lee, S., Shibata, O. (2009). Pulmonary surfactant model systems catch the specific interaction of an

amphiphilic peptide with anionic phospholipid. *Biophys. J.* **96**, 1415–1429.

[24] Nakahara, H. (2008). *Investigation and Development of Artificial Lung Surfactant Preparations with a Novel Amphiphilic Peptide for Respiratory Distress Syndrome (RDS)*. PhD thesis, Kyushu Univ., Fukuoka. Japan.

[25] Yukitake, K., Nakamura, Y., Kawahara, M., Nakahara, H., Shibata, O., Lee, S. (2008). Development of low cost pulmonary surfactants composed of a mixture of lipids or lipids-peptides using higher aliphatic alcohol or soy lecithin. *Colloids Surf. B* **66**, 281–286.

[26] Kitamura, A., Kiyota, T., Tomohiro, M., Umeda, A., Lee, S., Inoue, T., Sugihara, G. (1999). Morphological behavior of acidic and neutral liposomes induced by basic amphiphilic α-helical peptides with systematically varied hydrophobic-hydrophilic balance. *Biophys. J.* **76**, 1457–1468.

[27] Tanaka, Y., Takei, T., Aiba, T., Masuda, K., Kiuchi, A., Fujiwara, T. (1986). Development of synthetic lung surfactants. *J. Lipid Res.* **27**, 475–485.

[28] Morrow, M R., Taneva, S., Simatos, G.A., Allwood, L.A., Keough, K.M.W. (1993). Deuterium NMR studies of the effect of pulmonary surfactant SP-C on the 1,2-dipalmitoyl-*sn*-glycero-3-phosphocholine headgroup: A model for transbilayer peptides in surfactant and biological membranes. *Biochemistry* **32**, 11338–11344.

[29] Mao, G., Desai, J., Flach, C.R., Mendelsohn, R. (2008). Structural characterization of the monolayer-multilayer transition in a pulmonary surfactant model: IR studies of films transferred at continuously varying surface pressures. *Langmuir* **24**, 2025–2034.

[30] Bi, X., Flach, C.R., Perez-Gil, J., Plasencia, I., Andreu, D., Oliveira, E., mendelsohn, r. (2002). Secondary structure and lipid interactions of the *N*-terminal segment of pulmonary surfactant SP-C in Langmuir films: IR reflection-absorption spectroscopy and surface pressure studies. *Biochemistry* **41**, 8385–8395.

[31] Cai, P., Flach, C.R., Mendelsohn, R. (2003). An infrared reflection-absorption spectroscopy study of the secondary structure in $(KL_4)_4K$, a therapeutic agent for respiratory distress syndrome, in aqueous monolayers with phospholipids. *Biochemistry* **42**, 9446–9452.

[32] Nakahara, H., Lee, S., Shibata, O. (2010). Specific interaction restrains structural transitions of an amphiphilic peptide in pulmonary surfactant model systems: An in situ PM-IRRAS investigation. *Biochim. Biophys. Acta* **1798**, 1263–1271.

[33] Nakahara, H., Lee, S., Shibata, O. (2013). Surface pressure induced structural transitions of an amphiphilic peptide in pulmonary surfactant systems by an in situ PM-IRRAS study. *Biochim. Biophys. Acta* **1828**, 1205–1213.

[34] Kiyota, T., Lee, S., Sugihara, G. (1996). Design and synthesis of amphiphilic α-helical model peptides with systematically varied hydrophobic-hydrophilic balance and their interaction with lipid- and bio-membranes. *Biochemistry* **35**, 13196–13204.

[35] Ohmori, N., Niidome, T., Kiyota, T., Lee, S., Sugihara, G., Wada, A., Hirayama, T., Aoyagi, H. (1998). Importance of hydrophobic region in amphiphilic structures of a-helical peptides for their gene transfer-ability into cells. *Biochem. Biophys. Res. Commun.* **245**, 259–265.

[36] Furuya, T., Kiyota, T., Lee, S., Inoue, T., Sugihara, G., Logvinova, A., Goldsmith, P., Ellerby, H.M. (2003). Nanotubules formed by highly hydrophobic amphiphilic a-helical peptides and natural phospholipids. *Biophys. J.* **84**, 1950–1959.

[37] Taneva, S., Keough, K.M. (1994). Pulmonary surfactant proteins SP-B and SP-C in spread monolayers at the air-water interface: I. Monolayers of pulmonary surfactant protein SP-B and phospholipids. *Biophys. J.* **66**, 1137–1148.

[38] Rusdi, M., Moroi, Y., Nakamura, S., Shibata, O., Abe, Y., Takahashi, T. (2001). Mixed Langmuir monolayer of *N*-(1,1-dihydroperfluorododecyl)-*N*,*N*,*N*-trimethylammonium chloride with perfluorocarboxylic acids. *J. Colloid Interface Sci.* **243**, 370–381.

[39] Hiranita, T., Nakamura, S., Kawachi, M., Courrier, H.M., Vandamme, T.F., Krafft, M.P., Shibata, O. (2003). Miscibility behavior of dipalmitoylphosphatidylcholine with a single-chain partially fluorinated amphiphile in Langmuir monolayers. *J. Colloid Interface Sci.* **265**, 83–92.

[40] Nakahara, H., Nakamura, S., Kawasaki, H., Shibata, O. (2005). Properties of two-component Langmuir monolayer of single chain perfluorinated carboxylic acids with dipalmitoylphosphatidylcholine (DPPC). *Colloids Surf. B* **41**, 285–298.

[41] Nakahara, H., Nakamura, S., Lee, S., Sugihara, G., Shibata, O. (2005). Influence of a new amphiphilic peptide with phospholipid monolayers at the air-water interface. *Colloids Surf. A* **270–271**, 52–60.

[42] Nakamura, S., Nakahara, H., Krafft, M.P., Shibata, O. (2007). Two-component Langmuir monolayers of single-chain partially fluorinated amphiphiles with dipalmitoylphosphatidylcholine (DPPC). *Langmuir* **23**, 12634–12644.

[43] Nakahara, H., Krafft, M.P., Shibata, A., Shibata, O. (2011). Interaction of a partially fluorinated alcohol (*F*8*H*11OH) with biomembrane constituents in two-component monolayers. *Soft Matt.* **7**, 7325–7333.

[44] Demchak, R.J., Fort, T.Jr. (1974). Surface dipole moments of close-packed nonionized monolayers at the air-water interface. *J. Colloid Interface Sci.* **46**, 191–202.

[45] Pagano, R.E., Gershfeld, N.L. (1972). Physical chemistry of lipid films at the air-water interface. II. Binary lipid mixtures. Principles governing miscibility of lipids in surfaces. *J. Phys. Chem.* **76**, 1238–1243.

[46] Chen, K.B., Chang, C.H., Yang, Y.M., Ma, J.R. (2000). On the interaction of dipalmitoyl phosphatidylcholine with normal long-chain alcohols in a mixed monolayer: A thermodynamic study. *Colloids Surf. A* **170**, 199–208.

[47] Keller, S. L., Anderson, T.G., McConnell, H.M. (2000). Miscibility critical pressures in monolayers of ternary lipid mixtures. *Biophys. J.* **79**, 2033–2042.

[48] Sseoane, R., Minones, J., Conde, O., Minones, J. Jr., Casas, M., Iribarnegaray, E. (2000). Thermodynamic and Brewster angle microscopy studies of fatty acid/cholesterol mixtures at the air/water interface. *J. Phys. Chem. B* **104**, 7735–7744.

[49] Oliveira, R.G., Maggio, B. (2002). Compositional domain immiscibility in whole myelin monolayers at the air-water interface and Langmuir-Blodgett films. *Biochim. Biophys. Acta* **1561**, 238–250.

[50] Okonogi, T.M., McConnell, H.M. (2004). Contrast inversion in the epifluorescence of cholesterol-phospholipid monolayers. *Biophys. J.* **86**, 880–890.

[51] Nyrén, V., Back, E. (1958). The ionization constant, solubility product and solubility of lauric and myristic acid. *Acta Chem. Scand.* **12**, 1305–1311.

[52] Caspers, J., Goormaghtigh, E., Ferreira, J., Brasseur, R., Vandenbranden, M., Ruysschaert, J.-M. (1983). Acido-basic properties of lipophilic SUBSTANCES: A surface potential approach. *J. Colloid Interface Sci.* **91**, 546–551.

[53] Taylor, D.M., Oliveira, O.N., Morgan, H. (1989). The surface potential of monolayers formed on weak acidic electrolytes: Implications for lateral condition. *Chem. Phys. Lett.* **161**, 147–150.

[54] Calvez, E.L., Blaudez, D., Buffeteau, T., Desbat, B. (2001). Effect of cations on the dissociation of arachidic acid monolayers on water studied by polarization-modulated infrared reflection-absorption spectroscopy. *Langmuir* **17**, 670–674.

[55] Banerjee, R., Bellare, J.R. (2001). Scoring of surface parameters of physiological relevance to surfactant therapy in respiratory distress syndrome. *J. Appl. Physiol.* **90**, 1447–1454.

[56] Notter, R.H. (2000). *Lung Surfactants: Basic Science amd Clinical Applications.* Marcel Dekker, New York/Basel, pp. 1–444.

[57] Yokoyama, H., Nakahara, H., Shibata, O. (2009). Miscibility and phase behavior of DPPG and perfluorocarboxylic acids at the air-water interface. *Chem. Phys. Lipids* **161**, 103–114.

[58] Nakahara, H., Hirano, C., Fujita, I., Shibata, O. (2013). Interfacial properties in Langmuir monolayers and LB films of DPPC with partially fluorinated alcohol (*F*8*H*7OH). *J. Oleo Sci.* **62**, 1017–1027.

[59] Nakahara, H., Hirano, C., Shibata, O. (2013). Two-component Langmuir monolayers and LB films of DPPC with partially fluorinated alcohol (*F*8*H*9OH). *J. Oleo Sci.* **62**, 1029–1039.

[60] Nakahara, H., Ohmine, A., Kai, S., Shibata, O. (2013). Monolayer compression induces fluidization in binary system of partially fluorinated alcohol (*F*4*H*11OH) with DPPC. *J. Oleo Sci.* **62**, 271–281.

[61] Menikh, A., Saleh, M.T., Gariépy, J., Boggs, J.M. (1997). Orientation in lipid bilayers of a synthetic peptide representing the *C*-terminus of the A1 domain of Shiga toxin. A polarized ATR-FTIR study. *Biochemistry* **36**, 15865–15872.

[62] Tatulian, S.A. (2003). Attenuated total reflection Fourier transform infrared spectroscopy: A method of choice for studying membrane proteins and lipids. *Biochemistry* **42**, 11898–11907.

[63] Vinchurkar, M.S., Chen, K.H., Yu, S.S., Kuo, S.J., Chiu, H.C., Chien, S.H., Chan, S.I. (2004). Polarized ATR-FTIR spectroscopy of the membrane-embedded domains of the particulate methane monooxygenase. *Biochemistry* **43**, 13283–13292.

[64] Blaudez, D., Buffeteau, T., Cornut, J.C., Desbat, B., Escafre, N., Pezolet, M., Turlet, J.M. (1993). Polarization-modulated FT-IR spectroscopy of a spread monolayer at the air/water interface. *Appl. Spectrosc.* **47**, 869–874.

[65] Kerth, A., Erbe, A., Dathe, M., Blume, A. (2004). Infrared reflection absorption spectroscopy of amphipathic model peptides at the air/water interface. *Biophys. J.* **86**, 3750–3758.

[66] Flach, C.R., Cai, P., Dieudonne, D., Brauner, J.W., Keough, K.M.W., Stewart, J., Mendelsohn, R. (2003). Location of structural transitions in an isotopically labeled lung surfactant SP-B peptide by IRRAS. *Biophys. J.* **85**, 340–349.

[67] Dieudonné, D., Mendelsohn, R., Farid, R.S., Flach, C.R. (2001). Secondary structure in lung surfactant SP-B peptides: IR and CD studies of bulk and monolayer phases. *Biochim. Biophys. Acta* **1511**, 99–112.

[68] Gericke, A., Flach, C.R., Mendelsohn, R. (1997). Structure and orientation of lung surfactant SP-C and L-A-dipalmitoylphosphatidylcholine in aqueous monolayers. *Biophys. J.* **73**, 492–499.

[69] Flach, C.R., Gericke, A., Mendelsohn, R. (1997). Quantitative determination of molecular chain tilt angles in monolayer films at the air/water interface: Infrared reflection/absorption spectroscopy of behenic acid methyl ester. *J. Phys. Chem. B* **101**, 58–65.

[70] Nakahara, H., Dudek, A., Nakamura, Y., Lee, S., Chang, C.H., Shibata, O. (2009). Hysteresis behavior of amphiphilic model peptide in lung lipid monolayers at the air–water interface by an IRRAS measurement. *Colloids Surf. B* **68**, 61–67.

[71] Gericke, A., Hühnerfuss, H. (1993). In situ investigation of saturated long-chain fatty acids at the air/water interface by external infrared reflection-absorption spectrometry. *J. Phys. Chem.* **97**, 12899–12908.

[72] Mendelsohn, R., Brauner, J.W., Gericke, A. (1995). External infrared reflection absorption spectrometry of monolayer films at the air-water interface. *Annu. Rev. Phys. Chem.* **46**, 305–334.

[73] Wen, X., Lauterbach, J., Franses, E.I. (2000). Surface densities of adsorbed layers of aqueous sodium myristate inferred from surface tension and infrared reflection absorption spectroscopy. *Langmuir* **16**, 6987–6994.

73

USING THIN LIQUID FILM FOR STUDY OF PULMONARY SURFACTANTS

Dotchi Exerowa,[1] Roumen Todorov,[1] and Dimo Platikanov[2]

[1]*Institute of Physical Chemistry, Bulgarian Academy of Sciences, 1113 Sofia, Bulgaria*
[2]*Department of Physical Chemistry, University of Sofia, 1164 Sofia, Bulgaria*

73.1 INTRODUCTION

Surface-active substances, or *surfactants*, are grouped under a large class of various substances with specific physicochemical properties [1]. A vast variety of chemical compounds (synthetic or natural) are surfactants; one distinguishes cationic, anionic, nonionic, zwitterionic, and polymeric surfactants. These include block copolymers, grafted polymers, and proteins, and also complicated natural mixtures such as saponins or pulmonary surfactants, and many others. Their molecules are *amphiphilic*; that is, one part of the molecule is characteristically polar and the other part is nonpolar. That is why the surfactant molecules, dissolved in a liquid solvent, adsorb on the interfaces of the liquid phase (liquid–gas, liquid–solid, or liquid–liquid interfaces), thus modifying the interfacial properties.

The surfactants play an important role in microheterogeneous systems, where the total area of the interfaces is very large. Such systems are all *disperse systems*, like foams, emulsions, sols, and suspensions as well as more complicated systems. The adsorption layers of surfactant molecules usually stabilize the disperse systems. The stability of these systems is bound by the stability and properties of the *thin liquid films*, which are formed when two particles of the disperse phase (solid particles, liquid drops, or gas bubbles) come close to each other [2–7]. The liquid film is symmetric when the two particles are identical; for instance, a symmetric *foam film* appears between two gas bubbles. In the more complicated case, when a gas phase approaches a solid surface, an asymmetric *wetting liquid film* is formed.

Obviously the properties and stability of the thin liquid films strongly depend on the surfactant *adsorption layers* at their interfaces. The experimental study of a single thin liquid film provides important information about the corresponding disperse system stabilized by the same surfactant. On the other hand, the experimental results obtained for single thin liquid film yield knowledge about the surfactant, from the solution of which the thin liquid film was formed. Hence the thin liquid film becomes a felicitous tool for studying surfactant properties. Thus the method involving the use of thin liquid film for studying surfactants was developed.

In this chapter we will briefly review two types of thin liquid films: foam film (symmetric, thin liquid film existing between two identical gas phases) and wetting film (asymmetric thin liquid film existing between a solid phase and a gas phase). The foam films and wetting films studied are circular, horizontal, and microscopic films, formed in special cells under strictly defined conditions. This method allows measurement of some parameters that can be used for physicochemical characterization of the surfactants involved. Further, this method using thin liquid film will be applied for studies of pulmonary surfactants, which will be illustrated by typical experimental results.

73.2 EXPERIMENTAL TECHNIQUE

Small, circular, horizontal foam films or wetting films, the radius of which is within the range of 10–500 μm, are considered as *microscopic films* [3,5,7]. The experimental technique

Encyclopedia of Biocolloid and Biointerface Science, Volume 2, First Edition. Edited by Hiroyuki Ohshima.
© 2016 John Wiley & Sons, Inc. Published 2016 by John Wiley & Sons, Inc.

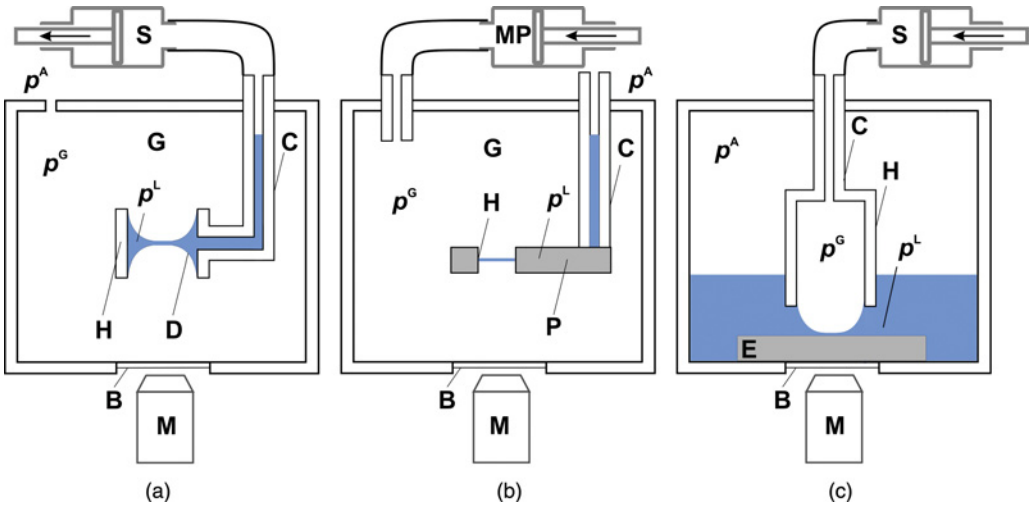


FIGURE 73.1 Measuring cells for microscopic thin liquid films: (a,b) for foam films; (c) for wetting films.

for their study allows the measurement of thermodynamic quantities, to follow the kinetic behavior, the formation of black films, the realization of metastable states, and so on. An advantage is the possibility of working at very low surfactant concentrations. Microscopic thin liquid films are formed and studied in special glass cells.

Figure 73.1a is a conceptual sketch (not to actual scale) of a cell reported [8, 9] for microscopic foam films, which can also be used for emulsion films. This is already a classical cell, used by many researchers for a long time in different countries. The foam film is formed in the middle of a biconcave drop D situated in a film holder H (glass cylinder of inner radius R) by withdrawing liquid (surfactant solution) from it. The suitable range of R is 0.2 - 0.6 cm, whereas the film radius r ranges from 100 to 500 μm. The holder H together with the foam film is situated in the closed space G of the cell, saturated with the solution vapor; the gas pressure p^G there is equal to the atmospheric pressure p^A. The film holder is welded to the sucking capillary C. The liquid is sucked out of the drop D by decreasing the pressure in the sucking capillary using a fine micrometric syringe S, connected to C. Thus the pressure p^L in the biconcave liquid phase is decreased and a pressure difference $\Delta p = p^G - p^L$ is created, which causes the thinning of the microscopic foam film.

As a result of the thinning process, either the film ruptures or an *equilibrium foam film* is formed. The periphery of the film is in contact with the double meniscus (bulk solution), the radius of curvature of which determines, together with the surface tension γ of the solution studied, the *capillary pressure* P_c. The equilibrium of the foam film is determined by the pressure balance $\Pi = P_c = \Delta p$, where Π is the *disjoining pressure*, which arises in all types of thin liquid films as a result of the action of the surface forces at sufficiently small film thickness [5–7]. The temperature is kept strictly constant. In this cell the microscopic foam films with fixed radius r are studied at constant capillary pressure P_c.

The foam films can be studied at a wide range of capillary pressures using the *porous plate cell* [10]. A conceptual sketch (not to actual scale) of this cell is given in Fig. 73.1b, which shows that the film holder H is a cylindrical hole drilled in a porous sintered glass plate P; the actual hole radius is considerably smaller (e.g., <250 μm). Plates of various pore radii can be used. If the meniscus penetrates into the pores, their radius determines the radius of curvature; that is, the small pore size allows for increase in the capillary pressure P_c until the gas phase can enter the pores. The capillary pressure can be increased to more than 10^5 Pa, depending on the pore size and the surface tension of the solution. A capillary tube C is welded to the porous plate, and its free end is open to the atmosphere. The film holder, together with the foam film, is also situated in the closed space G of the cell, saturated with the solution vapor. The increase in P_c is achieved by increasing the gas pressure p^G in the space of the cell using a membrane pump MP, with the pressure p^L in the liquid phase (in the pores) remaining constant. Thus a high pressure difference $\Delta p = p^G - p^L$ can be created, which at equilibrium is equal to $P_c = \Pi$. The pump MP allows the operator to set each desired p^G value, respectively, the desired P_c and Π values, in a wide range of pressures at constant temperature.

Figure 73.1c is a conceptual sketch (not to actual scale) of a cell described in the literature [11, 12] for formation and study of microscopic wetting films on a solid surface. The films are formed between the horizontal, flat surface of the solid substrate E and the hemispherical meniscus aqueous solution–air that is exiting from the orifice of a vertical tube–film holder H toward the solid plate E. The plate lies on the bottom B of the vessel, filled with the

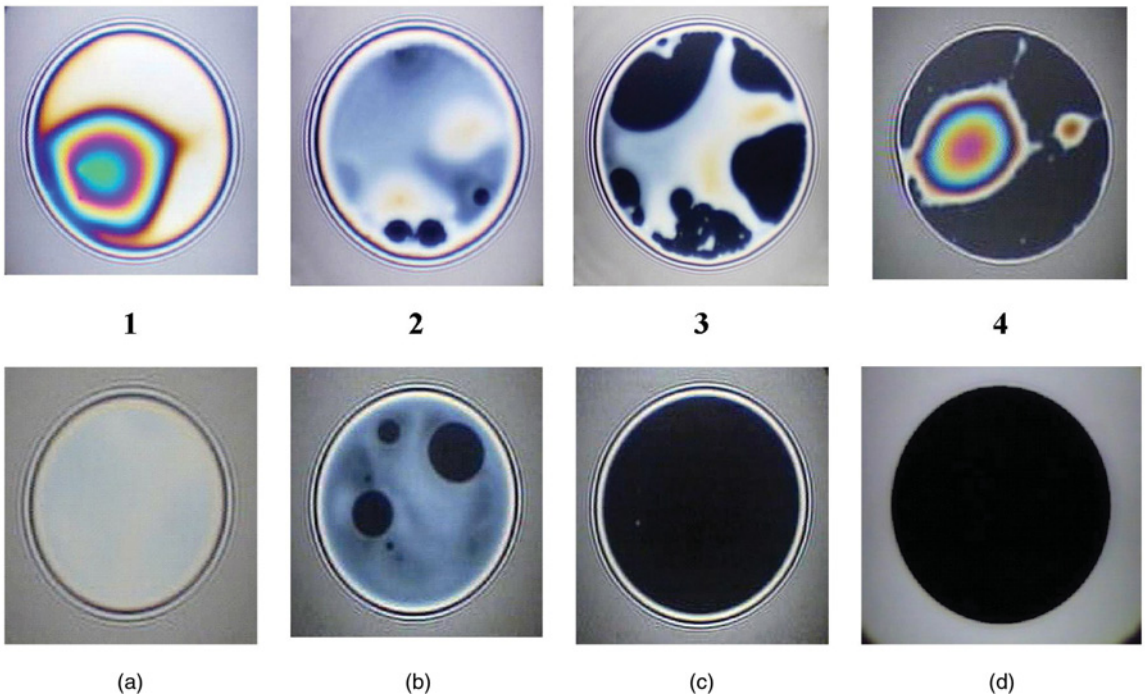


FIGURE 73.2 Photographs of microscopic foam films: (a–d) smooth thinning and formation of black spots and film; (1–4) irregular film drainage that impedes formation of black film.

solution studied; the gas pressure in the cell above the solution is equal to the atmospheric pressure. Hence the pressure p^{L} in the liquid phase at the level of the solid surface remains constant. The distance between the solid surface and the film holder orifice should be less than the inner radius R of the tube–film holder H, which is connected to the capillary C. The meniscus is placed very close to the solid plate, using a fine micrometric syringe S, which increases the gas pressure p^{G} in the tube H and thus creates the pressure difference $\Delta p = p^{G} - p^{L}$ between the gas phase in the glass film holder and the liquid phase in the vessel, around the tube. Here also $\Delta p = P_c = \Pi$ at equilibrium and constant temperature.

The cells illustrated in Fig. 73.1 are housed in a thermostat, fixed on the table of an inverted microscope M, and the thin liquid films are observed through the optically transparent bottom B of the cells in reflected monochromatic light [5].

73.3 PHYSICOCHEMICAL PROPERTIES STUDIED BY THE THIN LIQUID FILM METHOD

The process of formation, thinning, rupture, or establishment of equilibrium films, as well as formation of black spots and black films, can be followed through the microscope. Two typical series of microphotographs of different states of microscopic foam films, taken during the process of film thinning in the cell of Fig. 73.1a, are presented in Fig. 73.2. Photos (a)–(d) show a smooth, regular drainage of the thicker film, with formation of black spots and black film. On the contrary, photos (1)–(4) show irregular film drainage and impeded formation of black spots and black film, due to complicated rheological properties of the aqueous surfactant solution used.

The *film thickness* is measured using the microinterferometric method based on measurement of the intensity of monochromatic light reflected from the film. Foam film thickness is calculated from the ratio between the measured intensities of the reflected monochromatic light I, corresponding to a certain thickness, and I_{max}, corresponding to the interference maximum, according to the formula [13–15]

$$h_w = \frac{\lambda}{2\pi n}\left(k\pi \pm \arcsin\sqrt{\frac{I/I_{max}}{1+[(n^2-1)/2n]^2(1-I/I_{max})}}\right) \tag{73.1}$$

where k is order of interference, λ is the wavelength of light, n is the refractive index of the liquid in the film, and h_w is the *equivalent film thickness* (i.e. the thickness of a foam film with uniform refractive index n of the bulk solution from which the film is formed). For the asymmetric wetting films this formula is more complicated [14]. It is clear that h_w is not exactly equal to the real physical film thickness h. The difference between h_w and h could be neglected for any

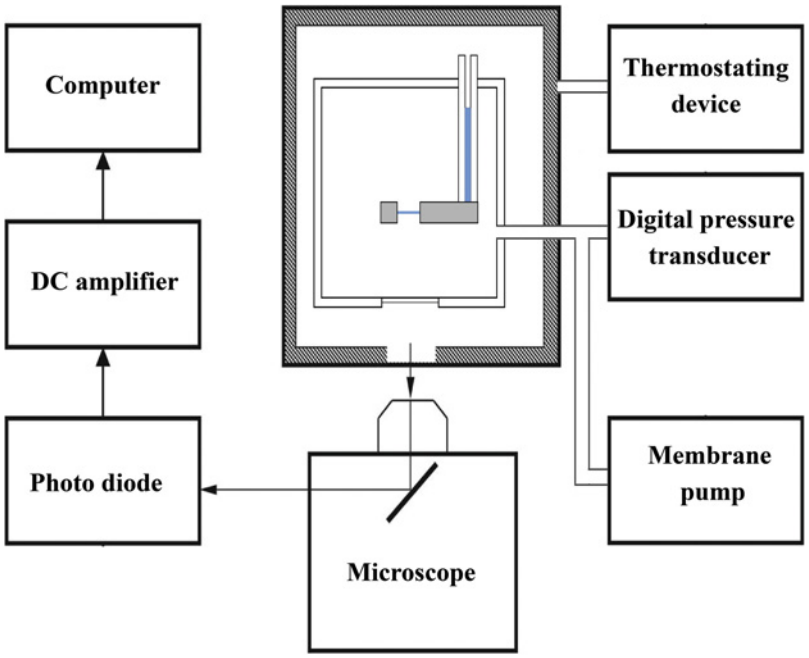


FIGURE 73.3 Block scheme of the microinterferometric method and pressure balance technique for study of black foam films.

thickness exceeding 30 nm. However, for thinner liquid films it is necessary to also account for the film structure [16].

For determination of *disjoining pressure* Π and its dependence on h [disjoining pressure isotherms $\Pi(h)$], an experimental method called the *thin liquid film–pressure balance technique* [5] is used. This is a combination of the microinterferometric technique and the porous plate cell method (Fig. 73.1b). The experimental block scheme of this method is shown in Fig. 73.3. Using the membrane pump, different capillary pressures P_c can be created and measured in a wide range up to 3×10^5 Pa. Since a thickness value can be measured interferometrically at equilibrium $\Pi = P_c$ for each disjoining pressure value, it is possible to obtain the isotherm $\Pi(h)$.

Foam films lose their stability during thinning when they reach a certain critical thickness h_{cr}. There are two plausible explanations for this; either (1) the film ruptures or (2) a local jumplike thinning in the film occurs. As a foam film appears to be black in reflected light at very narrow thicknesses, the jumplike local thinning appearance is called *formation of black spots* (Fig. 73.2). A black spot is a very small round area of a *black film* [2–5] that is much thinner than the surrounding area of the unstable foam film (Fig. 73.2). Black foam films can attain an extremely small thickness. Therefore, they could be called *nanofilms* as well. The IUPAC nomenclature [17] distinguishes two equilibrium phase states of black films: *common black film* (CBF) (Fig. 73.2c) and *Newton black film* (NBF) (Fig. 73.2d), which constitutes a bilayer of amphiphilic molecules.

The stability in respect to *rupture of the bilayer NBF* can be considered as a process of nucleation of a nucleus holes, which, by irreversible overgrowth, cause its rupture [18, 19]. This is possible only at surfactant concentrations C lower than the so-called bilayer equilibrium concentration C_e. When $C \geq C_e$, the bilayer is truly stable. An important quantity proved to be the probability W for black film formation, which depends on C. The nucleation theory [18, 19] yields W as a function of $C \leq C_e$

$$W(C) = \exp[-t_r/A \ \exp[B/\ln(C_e/C)]] \qquad (73.2)$$

where A, B, and t_r are constants. Equation (73.2) shows that W sharply increases with the bulk surfactant concentration C in a relatively narrow range. The dependence $W(C)$ in dimensionless coordinates is shown in Fig. 73.4. The curve runs steep, which justifies the introduction of two new characteristics of black foam film stability: (1) the minimum concentration C_c (critical concentration) required for black film formation and (2) the concentration C_t (threshold concentration) rendering 100% black films [5].The theoretical dependence $W(C)$ can be easily checked since W and C are measurable quantities, and experimental values of C_c and C_t can be obtained. Because of the fluctuation character of the film rupture, the probability W is a random parameter; hence it should be determined by averaging data from a large number of measurements.

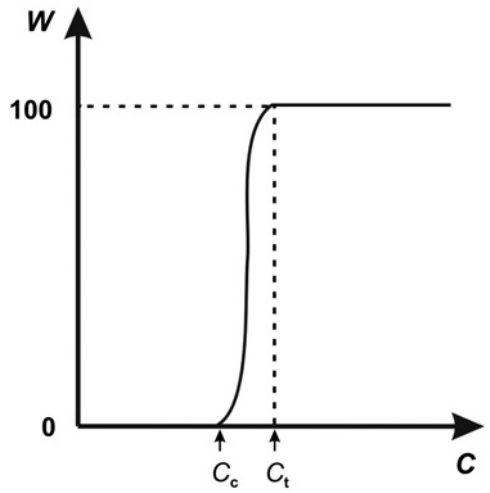


FIGURE 73.4 Probability W for black film formation versus surfactant concentration C [C_c, minimum (critical) concentration required for black film formation; C_t, threshhold concentration rendering 100% black films].

73.4 PULMONARY SURFACTANTS

The surface-active substance covering lung alveolar surface is called *pulmonary surfactant* (or *lung surfactant* or *alveolar surfactant*). It is well known that pulmonary surfactant is crucial for the normal breathing function [20]. Its deficiency, dysfunction, or inactivation can lead to development of the *respiratory distress syndrome* (RDS), an important cause of neonatal mortality of premature newborns [21, 22]. The treatment of such newborns with animal-derived pulmonary surfactant preparations has been shown to be very useful; in most cases it is a decisive factor for survival of premature infants. Clinical practice has proved the benefits of these *therapeutic surfactant preparations*, such as Curosurf, Infasurf, Survanta, and Exosurf, which have been widely applied [20, 23].

The pulmonary surfactant is a multicomponent composition of polar phospholipids [mainly dipalmitoylphosphatidylcholine (DPPC), phosphatidylglycerol (PG)], as well as specific hydrophilic proteins (SP-A and SP-D) and hydrophobic low-molecular-weight proteins (SP-B and SP-C). Table 73.1 illustrates this complicated natural mixture [24].

TABLE 73.1 Pulmonary Surfactant Composition

	DPPC	PC	PG	PE	PI	Sm	Chol	Prot	Specific Prot
Content (%)	45	23	8	3	4	2	5	8	2

Abbreviations: Chol = cholesterol; DPPC = dipalmitoylphosphatidylcholine; PC = phosphatidylcholines; PE = phosphatidylethanolamine; PG = phosphatidylglycerols; PI = phosphatidylinozitol; Prot = proteins; Sm = sphingomyelin.

The most common approach to physicochemical characterization of pulmonary surfactants has been to measure surface tension or surface pressure at the aqueous solution–air interface [25]. The widely spread hypothesis about alveolar surface structure perceives it as being covered by a phospholipid monolayer that is in contact with the hypophase. Our hypothesis differs from the abovementioned one, and we believe that it reflects the in vivo situation better. We have introduced a new method for the study of alveolar surface and stability [26, 27] and have also proposed a new diagnostic method for fetal lung maturity assessment [28]. The model employed in these methods is the black foam film one, including bilayer film. The black foam film model accounts for not only lateral interactions between first-neighbor molecules in the adsorption monolayer but also normal interactions in the bidimensional ordered system such as the bilayer black foam film [5].

73.5 METHOD FOR LUNG MATURITY ASSESSMENT

As mentioned earlier, pulmonary surfactant insufficiency in premature infants leads to RDS and quite frequently, to death. That is why fetal lung maturity requires an approach that enables proper assessment [27, 28]. The black foam film method proved to be very suitable as it possesses a number of advantages compared to the other methods employed; it is very precise (90%), fast (takes only ~20 min), and requires a small quantity of amniotic fluid [5, 28, 29]. For the purpose of this method, surfactant insufficiency (premature lung) versus absence of a black film has been studied. Amniotic fluid (AF) samples are diluted in order to map the dependence between threshold dilutions versus gestation weeks.

Figure 73.5 presents the dependence of threshold dilution [from the $W(C)$ curve] for each sample of amniotic fluid. The immature samples from the clinical result are plotted with filled circles and the mature samples, with open circles. Comparison with clinical results allows us to establish a threshold dilution: a horizontal line (Fig. 73.5) that distinguishes mature from immature samples [5, 28].

Test results obtained by this method correlate very well with the clinical status of newborns (proved by blind comparison of >1000 samples). Clinical application involves AF sample dilution and matching with the *threshold dilution*, that is, by establishing sample maturity or surfactant insufficiency/sufficiency. The approach described has provided a method for rapid and accurate assessment of fetal lung maturity, respectively, for RDS diagnostics [30]. The method is applicable also for blood- and meconium-contaminated AF, as well as for samples of nasopharyngeal aspirates of newborns. Early RDS diagnostics provides for adequate surfactant insufficiency treatment during the prenatal period and for reducing the risk of RDS infants.

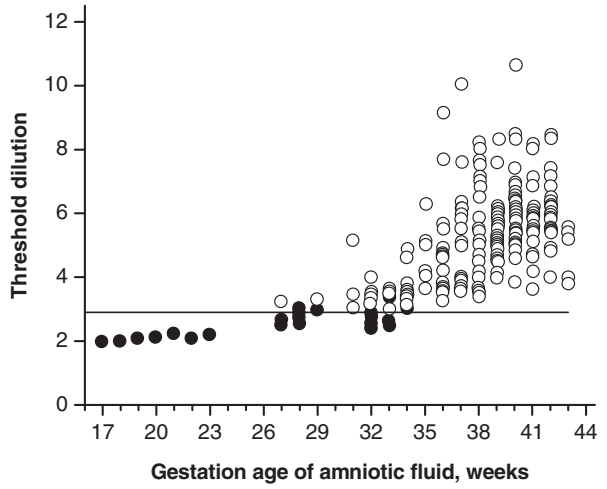


FIGURE 73.5 Dependence of the threshold dilution of amniotic fluid on its gestation age (• development of RDS in neonates; ∘ no RDS in neonates); the line indicates the dilution separating the mature from immature AF samples.

A schematic representation of the black foam film method for assessment of fetal lung maturity is presented in Fig. 73.6. The threshold concentration distinguishes between surfactant insufficiency/surfactant sufficiency, respectively, and lung immaturity/lung maturity. Photos of the corresponding microscopic foam films are also given in Fig. 73.6: (a) unstable film with black spots and (b) stable black foam film.

73.6 FOAM FILMS FROM PULMONARY SURFACTANT AND ITS COMPONENTS

Studies of foam films from pulmonary surfactant began with samples of amniotic fluid and lung lavages about 30 years ago [26,28,29].The conditions of formation of a microscopic foam film in order to "serve" the in vivo situation are close to the physiological: film radius r from 100 to 400 μm, with capillary pressure between 0.3 and 3 kPa and electrolyte (NaCl) concentration at 0.15 mol/dm^3, and ensuring formation of black films [5]. Under such conditions it is possible to study the dependences for foam films and to use parameters related to formation and stability of black foam films (BFFs). Introduction of the "black foam film" model creates new options in the study of pulmonary surfactant behaviors in vitro [5, 27], at the same interface as it is in the alveoli, providing opportunities to measure dependences such as probability for black foam film formation versus surfactant concentration, film thickness versus electrolyte concentration, and interaction forces (disjoining pressure) versus film thickness.

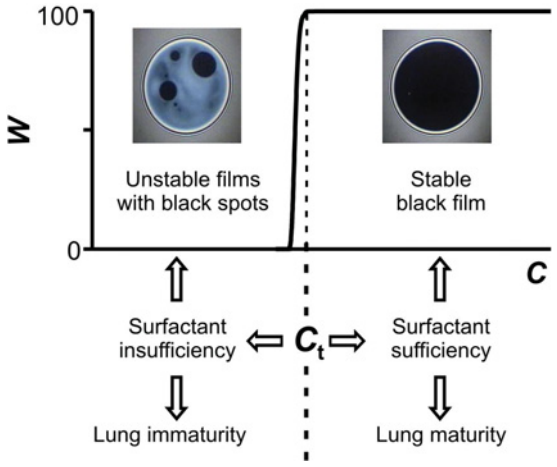


FIGURE 73.6 A schema of the black foam film method for assessment of fetal lung maturity.

The probability W for the formation of a stable black foam film depends strongly on the concentration C of the amphiphile molecules in the film forming bulk solution, according to the hole nucleation theory of Kashchiev and Exerowa [18, 19]; see Eq. (73.2). The $W(C)$ dependence was checked experimentally with a number of phospholipids, and the results revealed that for the phospholipids W changed sharply from 0% to 100 % in a very narrow concentration interval [5, 31]. W can be calculated using the equation $W = (\Delta N/N) \times 100$, where N is the total number of trials and ΔN is the number of trials in which stable BFFs are formed. As already pointed out above, studies of the probability W for black foam film formation versus concentration make it possible to determine two characteristics of black foam film stability: (1) the minimum (critical) concentration C_c required for black film formation and (2) the threshold concentration C_t rendering 100% black films [5,29]. Figure 73.7 depicts three $W(C)$ dependences for amniotic fluid, the main

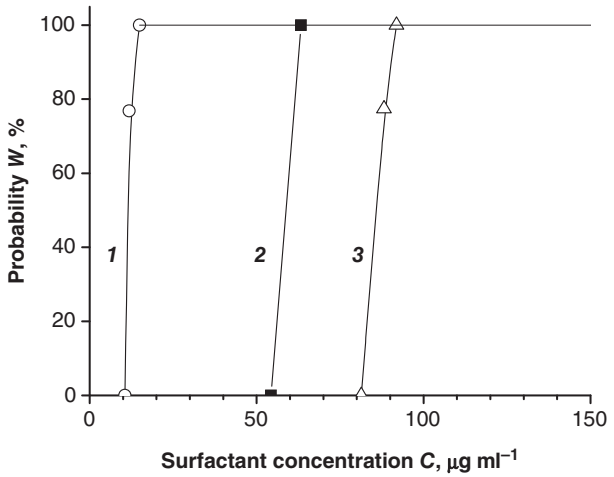


FIGURE 73.7 $W(C)$ dependence for black foam films from AF in 47% ethyl alcohol + 0.07 M NaC1 aqueous solution (curve 1); HF in 0.15 M NaCl aqueous solution (curve 2); DPPC in 47% ethyl alcohol + 0.07 M NaC1 aqueous solution (curve 3).

PS component (DPPC) and hydrophobic fraction (HF)–full set of PS lipids, and hydrophobic surfactant proteins.

The foam films were obtained from a solution of AF in the presence of 47% ethanol and 7×10^{-2} mol/dm^3 NaCl. The above percentage of ethanol ensures predominant adsorption of the phospholipid molecules at the air–solution interface with respect to the proteins present in the AF [5, 31]. The presence of alcohol in the solutions of both the AF and the individual phospholipids also resulted in an increase in the CMC, so that the concentration of monomer lipid could still respond to changes in the total lipid concentration. The electrolyte in the solution is sufficient to eliminate the effect of the electrostatic component of the disjoining pressure and to obtain black foam films. The composition of the hydrophobic fraction (HF) resembles those of the pulmonary surfactant and natural exogenous surfactant preparations.

As can be seen, the $W(C)$ curves run steeply, and the critical concentrations C_c, are quite different: 13 μg/cm^3 for AF, 54 μg/cm^3 for HF, and 80 μg/cm^3 for DPPC. Biochemical analysis of the AF reveals that the maximum weight content of individual phospholipids in the AF is orders of magnitude lower than that of the corresponding to C_c [29]. Thus, only the concentration of the DPPC remains to be considered as close to C_c in the AF. It could be concluded that DPPC is the phospholipid from which the foam bilayer of AF is almost completely formed. The lower C_c for HF in comparison to those for DPPC could be related to the effect of all the remaining phospholipid components and surfactant proteins. They play an essential role in the formation and stability of foam films.

The probability W of black film formation depends not only on concentration C but also on the phase state of the phospholipids. Black film has shown that the lamellar phases disintegrated at air/water interface with a greater tendency than the cubic phase [32]. Studies of the temperature dependence of C_c and film stabilization have revealed that an increase in temperature causes increases in both C_c and phase transitions of the phospholipids in the film. The sharp change in the binding energy of disaturated phospholipid molecule in the foam bilayer is obviously due to the occurrence of a chain melting phase transition in the bilayer. In cases of AF and HF there was no phase transition, in the range around the relevant physiological temperature, even though they contain 80% DPPC [33].

The lateral mobility of adsorbed molecules at the air–water interface is of great importance in the process of breathing. The foam film model has been employed to study molecular interactions at interfaces by estimating the molecular lateral mobility (surface diffusion coefficient D) by the FRAP method [34–36]. It is shown that the D value in the pure DPPC films remains at the immobile level up to 45°C and that higher temperatures only induce small increases in D. In contrast, the D value in films stabilized by the pulmonary phospholipid fraction is much higher. The higher D of the fraction compared with that of DPPC could be explained both by the presence of phospholipids other than DPPC in the fraction and by a shift in the phase transition temperature of the fraction to a lower temperature comparable to that of DPPC, with resultant fluidization of the film surfaces.

The probability of black foam film formation is very sensitive to the addition of surface-active agents to the bulk solution. The shift in the $W(C)$ dependence of pulmonary surfactant to higher C_c after addition of agent is interpreted as an effect of film destabilization. Such a destabilizing effect is observed in the presence of lysophosphatidylcholine and rhamnolipid, well-known inhibitors of pulmonary surfactant [37, 38]. These results indicate that the BFF method can be successfully applied to study the inhibitory effect that diminishes surface activity of endogenous surfactant as well as exogenous surfactant preparations [31, 39].

The black foam film used as a model system opens new horizons to obtain insights into molecular interaction forces, operating in foam films from pulmonary surfactant and to establish the range of long- and short-range molecular interaction forces and the transitions between them. Molecular interaction forces in foam films have been assessed by means of direct measurements of film thickness h versus electrolyte concentration C_{el} and disjoining pressure/film thickness isotherms $\Pi(h)$ [40, 41].

Figure 73.8 shows the dependence of equilibrium thickness h of foam films from AF, DPPC, and HF on NaCl concentration C_{el}. As can be seen, the results are consistent with the general tendency of decreasing h with increase in C_{el} until rather high C_{el}-values at which black films begin to form. For foam films stabilized with AF and DPPC, further increase of electrolyte concentration leads to the formation of only Newton black films (NBFs) with h of the order of 8 nm.

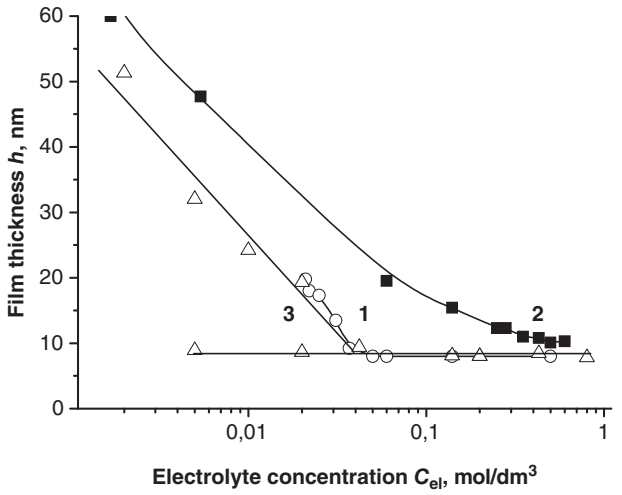


FIGURE 73.8 $h(C_{el})$ dependence for foam films from AF in 47% ethyl alcohol aqueous solution (curve 1); HF in aqueous solution (curve 2); DPPC in aqueous solution (curve 3).

Following the DLVO theoretical assumptions, the decrease in h with increase of C_{el} for AF and DPPC can be considered as evidence of the electrostatic stabilization of films. In the case of DPPC films, $C_{el} = 10^{-3}$ mol/dm^3 marks the onset of a metastable region where both thick and black films are formed in different experiments. The steady thickness of the black films in the metastable region indicates that these are NBF.

For foam films from HF, increased C_{el} leads to a decrease in h (Fig. 73.8). The thickness of BFF films decreases with the increase of C_{el}, showing that these films are *common black films* (CBFs). The range of CBF formation comprises the physiological electrolyte concentration, where $h = 11.7$ nm. Similar results have been obtained for films stabilized by exogenous surfactant preparations under the same conditions. The decrease in h of the CBF with the increase in C_{el} confirms the action of repulsive electrostatic forces in the film. Here it is possible to infer that the continuous film thinning is caused by the action of an additional positive component of the disjoining pressure. The experimental results also show that the HF-stabilized NBFs are ~2 nm thicker than the DPPC ones. Probably, this is again a result of the complex composition of HF leading to a different structure of the adsorbed layers compared to that of the DPPC films. These findings would help us clarify the influence of molecular interaction forces on the interfacial behavior of pulmonary surfactant layer as well as on the stability of DPPC-rich protrusions formed at alveolar surface during expiration.

Additional information about the inhibitor's activity on pulmonary surfactant interfacial properties may be obtained from the $h(C_{el})$. In the case of rhamnolipids, it was found that the rhamnolipid is adsorbed predominantly and participates more significantly in the formation of black film adsorption layers [37].

Disjoining pressure isotherms $\Pi(h)$ provide direct information about molecular interaction forces and have been studied extensively for phospholipids, amniotic fluid, pulmonary surfactant fractions, and a number of exogenous surfactant preparations [5, 26, 29, 40, 41]. Figure 73.9 shows $\Pi(h)$ isotherms measured for films from amniotic fluid and hydrophobic fraction of pulmonary surfactant.

In the case of AF, after a smooth initial decrease of h to ~14 nm, a transition from CBF to NBF is observed. On further increase in Π, the thickness of NBF remains constant and equal to film thickness from the $h(C_{el})$ curve in Fig. 73.8. At higher electrolyte concentration, h does not change with increasing Π and always retains the value of ~8 nm. Thus, by varying the thickness of the foam film through C_{el} or Π the same limiting thickness of ~8 nm is always reached, corresponding approximately to a bilayer of phospholipid molecules.

The steep curves in Fig. 73.9 (squares) show the $\Pi(h)$ isotherms for CBF and NBF from HF. The thickness of the CBF decreases from 19.5 to 10.9 nm with the increase in

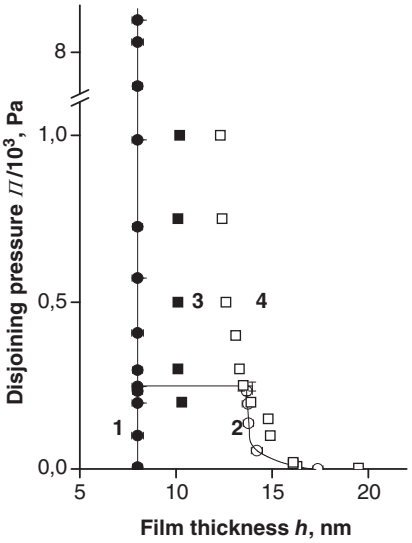


FIGURE 73.9 Disjoining pressure Π versus film thickness h for AF in 47% ethyl alcohol aqueous solution: curve 1 with 0.5 M NaCl and curve 2 with 0.03 M NaCl; HF aqueous solution: curve 3 with 1 M NaCl and curve 4 with 0.15M NaCl.

Π. It is noteworthy to mention that unlike films from AF the studied CBF film does not exhibit jumplike transition to NBF, although it does not rupture until the highest applied pressure. Besides, the smallest h of the films measured at the highest applied pressure does not reach that of the NBF, suggesting the action of additional repulsive forces in the film. In the case of the $\Pi(h)$ isotherm obtained for films formed from HF solutions with higher NaCl concentration, h remains practically constant with the increase in Π. This course of the isotherm demonstrates the lack of a free water core in the film and corroborates the assumption of NBF formation at high C_{el} (see Fig. 73.8).

The black foam film method provides options to assess the effects exerted by pulmonary surfactant components on surface properties of alveolar lining layer. The parameters (critical concentrations, thickness, disjoining pressure, etc.) obtained support the notion that black foam films are a realistic structural analog of surface films existing in vivo in the lung. These parameters may be used as a standard in the process of developing of therapeutic surfactant preparations for RDS therapy.

73.7 THIN LIQUID WETTING FILMS FROM PULMONARY SURFACTANT SOLUTIONS

Many observations show that the breathing function can be strongly affected by air pollution, as inhalation of crystalline silica particles is associated with numerous pathologies [42]. However, the interaction of the particles with the pulmonary surfactant layers in the alveoli has still not been sufficiently

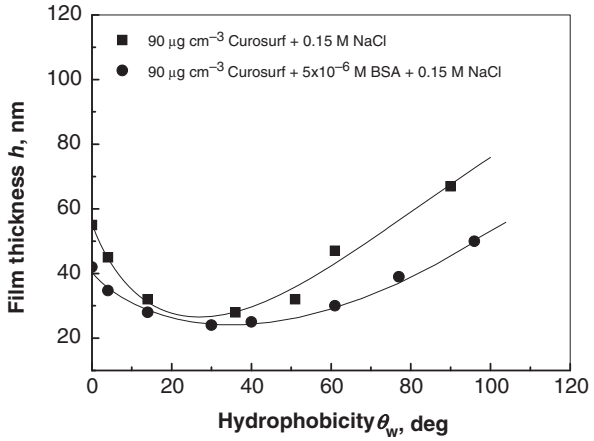


FIGURE 73.10 Dependence of equilibrium film thickness h on hydrophobicity θ_w of the SiO_2-glass surface for Curosurf aqueous solutions with and without bovine serum albumin (BSA) added.

studied. The method of the thin liquid film has been applied [43] to wetting films from pulmonary surfactant aqueous solutions on SiO_2-glass surfaces with different degrees of hydrophobicity.

The well-polished SiO_2-glass smooth, flat plates are carefully washed with acid mixtures and rinsed with doubly distilled water, thereby yielding a substrate with a completely hydrophilic surface. A special procedure for hydrophobization of this hydrophilic surface using trimethylchlorosilane allows the preparation of glass surfaces with different degrees of hydrophobicity [43]. As a measure of the degree of hydrophobicity, the contact angle θ_w of a drop of triple-distilled water on this surface is used.

Measurements of the equilibrium film thickness h have been carried out with thin liquid wetting films from 90 μg/cm^3 Curosurf + 0.15 M NaCl at different degrees of hydrophobicity θ_w of the solid surface. The influence of the addition of bovine serum albumine (BSA) to this solution on the equilibrium film thickness h has been studied as well. Figure 73.10 shows two h (θ_w) dependences for the two solutions, with and without BSA added. An interesting minimum at about $\theta_w = 30°$ in these curves has been obtained in both cases. The equilibrium thickness h, respectively the minimum in the h (θ_w) curves, is determined by the balance of all surface forces operative in the thin liquid wetting film. At 0.15 MNaCl the Van der Waals and the electrostatic disjoining pressures may be neglected. The attractive, hydrophobic (structural), and repulsive steric disjoining pressures actually determine the film thickness [44–46]. Their values depend on the hydrophobic and hydrophilic patches of the solid surface as well as the orientation and conformation of the adsorbed molecules of the phospholipids and the surfactant specific proteins. The minimum in the $h(\theta_w)$ curves could be due to changes in the structure and thickness of the adsorption layer at different areas of the hydrophobic and hydrophilic patches (different hydrophobicity) of the solid surface.

In a short range of θ_w around the minimum, the two curves are close to each other; however, the whole h (θ_w) curve for the aqueous solution, which contains 5×10^{-6} mol/dm^3 BSA, lies below the corresponding h (θ_w) curve for the 90 μg/cm^3 Curosurf + 0.15 mol/dm^3 NaCl solution without BSA added. These results show that BSA decreases the hydrophobization of the solid surface, due to the pulmonary surfactant. It is well known that BSA is an inhibitor of pulmonary surfactant activity [22]. It seems that albumin inhibits Curosurf by competitive adsorption on the alveolus surface (water–air interface). Similar competitive adsorption should occur also at the aqueous solution/solid interface. The BSA molecules prevent the adsorption of the molecules of pulmonary surfactant. Thus they decrease the hydrophobicity of the solid interface. Obviously there is a direct connection between the inhibition of Curosurf activity and the decreased (because of BSA) hydrophobization of solid surface due to the pulmonary surfactant.

73.8 CONCLUSION

Methods employing thin liquid film are useful tools for studying the pulmonary surfactants, including the therapeutic pulmonary surfactant preparations. In particular, the method using microscopic black foam film makes it possible to characterize pulmonary surfactants with the values of physicochemical parameters, such as disjoining pressure, critical surfactant concentration, threshold surfactant concentration, and probability of forming bilayer Newton black foam film. The black foam film method has been further developed into a diagnostic method for fetal lung maturity assessment. The method using microscopic thin wetting film allows for studies on the wetting behavior of pulmonary surfactant solutions on solid surfaces with different hydrophobicities.

REFERENCES

[1] Lyklema, J. (2000). *Fundamentals of Interface and Colloid Science*, Vol. 3, Chapter 4. Academic Press, London, pp. 4.68-4.93.

[2] Mysels, K.J., Shinoda, K., Frankel, S. (1959). *Soap Films.* Pergamon Press, New York.

[3] Scheludko, A. (1967). *Adv Colloid Interface Sci* **1**, 391.

[4] Clunie, I.S., Goodman, J.F., Ingram, B.T. (1971). Thin liquid films. In Matijevic, E. (ed.), *Surface and Colloid Science*, Vol. 3. Wiley, New York.

[5] Exerowa, D., Kruglyakov, P.M. (1998). *Foam and Foam Films.* Elsevier, Amsterdam.

[6] Ivanov, I. (ed.) (1988). *Thin Liquid Films*. Marcel Dekker, New York.

[7] Platikanov, D., Exerowa, D. (2005). Thin liquid films. In Lyklema, J. (ed.), *Fundamentals of Interface and Colloid Science*, Vol. 5, Chapter 6. Elsevier, Amsterdam.

[8] Scheludko, A., Exerowa, D. (1959). *Commun. Dept. Chem. Bulg. Acad. Sci.* **7**, 123.

[9] Scheludko, A., Exerowa, D. (1960). *Kolloid-Z.* **168**, 24.

[10] Exerowa, D., Scheludko, A. (1971). *Compt. Rend. Acad. Bulg. Sci.* **24**, 47.

[11] Platikanov. D. (1964). *J Phys. Chem.* **68**, 3619–3624.

[12] Zorin, Z., Platikanov, D., Kolarov, T. *Colloids Surfaces A* 1987, **22**, 147–159.

[13] Vašiček, C.J. (1960). *Optics of Thin Films*. North Holland Publishing, Amsterdam.

[14] Scheludko, A., Platikanov, D. (1961). *Kolloid-Z* **175**, 150.

[15] Scheludko, A. (1962). *Proc. Koninkl. Nederl. Akad. Wetenschap* **B65**, 76.

[16] Duyvis, E.M. (1962). PhD thesis. Univ. Utrecht.

[17] Ter Minassian-Saraga, L. (1994). Thin films including layers: Terminology in relation to their preparation and characterization. *Pure Appl. Chem.* **66**, 1667.

[18] Exerowa, D., Kashchiev, D. (1980). *J. Colloid Interface Sci.* **77**, 501.

[19] Exerowa, D., Kashchiev, D. (1986). *Contemp. Phys.* **27**, 429.

[20] Scarpelli, E., Mautone, A., Lalchev, Z., Exerowa, D. (1997). *Colloids Surfaces B: Biointerfaces* **8**, 133–145.

[21] Kramer, B.W. (2007). *Intensivmed* **44**, 403–408.

[22] Zuo, Y.Y., Veldhuizen, R.A., Neumann, A.W., Petersen, N.O., Possmayer, F. (2008). *Biochim. Biophys. Acta* **1778**, 1947–1997.

[23] Robertson, B., Curstedt, T., Johansson, J., Jornvall, H., Kobayashi, T. (1990). *Progress Respir. Res.* **25**, 237–246.

[24] Blanco, O., Pérez-Gil, J. (2007). *Eur. J. Pharmacol.* **568**, 1–15.

[25] Wustneck, R., Perez-Gil, J., Wustneck, N., Cruz, A., Fainerman, V.B., Pison, U. (2005). *Adv. Colloid Interface Sci.* **117**, 33–58.

[26] Exerowa, D., Lalchev, Z. (1986). *Langmuir* **2**, 668–671.

[27] Lalchev, Z., Todorov, R., Exerowa, D. (2008). *Curr. Opin. Colloid Interface Sci.* **13**, 183–193.

[28] Exerowa, D., Lalchev, Z., Marinov, B., Ognianov, K. (1986). *Langmuir* **2**, 664–667.

[29] Exerowa, D., Lalchev, Z., Kashchiev, D. (1984). *Colloids Surf.* **10**, 113–121.

[30] Lalchev, Z., Christova, E. (2010). *Alveolar Surfactant and Neonatal Resp-iratory Distress Syndrome: Physiological Aspects and Therapy*. Sofia Univ. Press, Sofia, pp. 1–267.

[31] Lalchev, Z. (2007). Phospholipid foam films: Types, properties and applications. In Tadros Th. (ed.), *Colloid Stability*, Vol. 1. Wiley-VCH, Weinheim.

[32] Jordanova, A., Lalchev, Z, Tenchov, B. (2003). *Eur. Biophys. J.* **31**, 626–632.

[33] Exerowa, D. (2002). *Adv Colloid Interface Sci.* **96**, 75–100.

[34] Lalchev, Z., Todorov, R., Ishida, H., Nakazawa, H. (1995). *Eur. Biophys. J.* **23**, 433–438.

[35] Lalchev, Z., Wilde, P., Mackie, A., Clark, D. (1995). *J. Colloid Interface Sci.* **174**, 283–288.

[36] Lalchev, Z, Todorov, R, Christova, V, Wilde, P, Mackie, A., Clark, D. (1996). *Biophys. J.* **71**, 2591–2601.

[37] Cohen, R., Vladimirov, G., Todorov, R., Exerowa, D. (2010). *Langmuir* **26**, 9423–9428.

[38] Alexandrov, S., Todorov, R., Jordanova, A., Lalchev, Z., Exerowa, D. (2009). *Biotechnol. Biotechnol. Enq.* **23**, 684–687.

[39] Georgiev, G., Vassilieff, C., Jordanova, A., Tsanova, A., Lalchev, Z. (2012). *Soft Matt.* **8**, 12072–12079.

[40] Cohen, R., Todorov, R., Alexandrov, S., Christova, Y., Lalchev, Z., Exerowa, D. (2006). *Colloid Polym. Sci.* **284**, 46–50.

[41] Todorov, R., Cohen, R., Exerowa, D. (2007). *Colloids Surf. A* **310**, 32–38.

[42] Davis, G.S. (1986). *Chest* **89**, 166S–169S.

[43] Alexandrova, L., Nedyalkov, M., Platikanov, D., Razzetti, R., Bianco, F. (2013). *Colloid Polym. Sci.* **291**, 2725–2731.

[44] Derjaguin, B.V., Landau, L.D. (1941). *Acta Physicochim. USSR* **14**, 633–642.

[45] Verwey, E.J.W., Overbeek, J.T.G. (1948). *Theory of the Stability of Lyphobic Colloids.* Elsevier, Amsterdam.

[46] Israelachvilli, J. (1991). *Intermolecular and Surface Forces.* Academic Press, New York.

74

PROBING RECEPTOR–LIGAND INTERACTIONS ON A *SINGLE* MOLECULE LEVEL USING OPTICAL TWEEZERS

Tim Stangner,[1] Carolin Wagner,[1] Christof Gutsche,[1] Konstanze Stangner,[2] David Singer,[3] Stefano Angioletti-Uberti,[4] and Friedrich Kremer[1]

[1]*Department of Experimental Physics I, Leipzig University, Leipzig, Germany*
[2]*Molecular Oncology, Leipzig University Medical School, Leipzig, Germany*
[3]*Center for Biotechnology and Biomedicine (BBZ), Institute for Bioanalytical Chemistry, Leipzig University, Leipzig, Germany*
[4]*Department of Physics, Humboldt University Berlin, Berlin, Germany*

74.1 INTRODUCTION

Structure and dynamics of living matter depend strongly on the principle of *receptor–ligand binding*, meaning specific interactions between biomolecules, such as peptides, DNA, antibodies, enzymes, and other biological matter. Furthermore, these interactions play a key role in almost every essential process in the human body (e.g., DNA replication [1], activation of signal cascades [2]). In particular, the immune system has to be emphasized, as being an impressive example for the precision achieved by the principle of specific binding; polyclonal antibodies are able to detect one "wrong" molecule out of 10^9 molecules [3]. In contrast to polyclonal antibodies that bind to multiple epitopes, monoclonal antbodies (mAbs) are targeted only to a single epitope. Therefore, mAbs provide a consensus between achievable specificity and flexibility in the framework of receptor–ligand interactions. On the basis of these special features, the development of monoclonal antibodies and the investigation of their interactions with different ligands are of highest interest for industrial applications (e.g., in the treatment of cancer [4–9] and rheumatoid arthritis [9]).

Recognizing their potential, receptor–ligand interactions also became a focus of research in modern biochemistry and biophysics. In addition, through the rapid development of single-molecule techniques, spectacular research into cellular, molecular, and even atomic structures and processes has been ongoing. Thus, in recent years the elastic properties of double-stranded DNA [10–12] as well as its interaction with binding partners such as transcription factors [13], architectural proteins [14–18], or intercalating dyes [19] have been studied. Other investigations have focused on individual steps of single motor proteins [20] or the translation of a ribosome at the level of single codons [21]. By means of the forced unfolding of proteins or RNA aptamers, new insights in the energetics of molecular folding processes could be gained [22–24].

This book chapter is concerned primarily with the biophysical investigation of receptor–ligand interactions, focusing on optical tweezers–assisted dynamic force spectroscopy. By using this technique it is possible to investigate these interactions on a single-molecule level, and to extract specific binding parameters. In Section 74.2, the methodology of optical tweezers is discussed in detail and other standard methods of investigating these receptor–ligand interactions are briefly introduced. Basic theoretical concepts of analyzing the experimental data are also presented (Section 74.3). In Section 74.4, three case studies, investigating the interactions between the antihuman tau monoclonal antibodies and synthetic τ-peptides with different phosphorylation patterns, are presented.

Encyclopedia of Biocolloid and Biointerface Science, Volume 2, First Edition. Edited by Hiroyuki Ohshima.
© 2016 John Wiley & Sons, Inc. Published 2016 by John Wiley & Sons, Inc.

74.2 METHODOLOGY

The idea of manipulating objects with light goes back to the beginning of the twentieth century, based on the theoretical description of light pressure by Peter Debye [25] and the discovery of wave–particle dualism. However, the realization of a *single-beam gradient force optical trap* took almost 70 years and was finally achieved in 1986 by Arthur Ashkin [26]. Eleven years later one of his former coworkers, Steven Chu, reeived the Nobel Prize for the "development of methods to cool and trap atoms with laser light" [27]. As a result of their extraordinary resolution in determining the relative position (±2 nm) of a microscopic object (radius ∼ 1 μm) and in measuring the forces acting on it (±50 fN), without any mechanical contact, optical tweezers became a standard tool in terms of biophysical and other related issues [28, 29]. In the following sections, we will briefly introduce our setup as well as some theoretical models to describe the forces acting on a trapped particle. The main focus will be on the detection of microparticles with nanometer resolution in all three dimensions, which is required for the experiments described below. In addition, we will briefly describe other biophysical and biochemical methods of characterizing the interactions between receptors and ligands.

74.2.1 The Setup

In order to ensure stable three-dimensional (3D) trapping of microparticles, certain requirements are necessary: (1) an intensive light source, (2) a microscope with high numerical aperture, and (3) that a trapped object must have a higher index of refraction than the surrounding medium. Therefore, every optical tweezers setup has in principle the same basic building blocks: a laser, a (inverted) microscope, and a detection unit, including a CCD camera and a photosensitive detector (PSD), respectively.

Figure 74.1 illustrates the setup we used for the pair interaction measurements described in Section 74.4; based on an inverted microscope (Axiovert S 100 TV, Carl Zeiss, Jena, Germany), the optical trap was realized with a diode pumped Nd:YAG laser (1064 nm, 1 W, LCS-DTL 322; Laser 2000, Wessling, Germany). Power stabilization is achieved with a

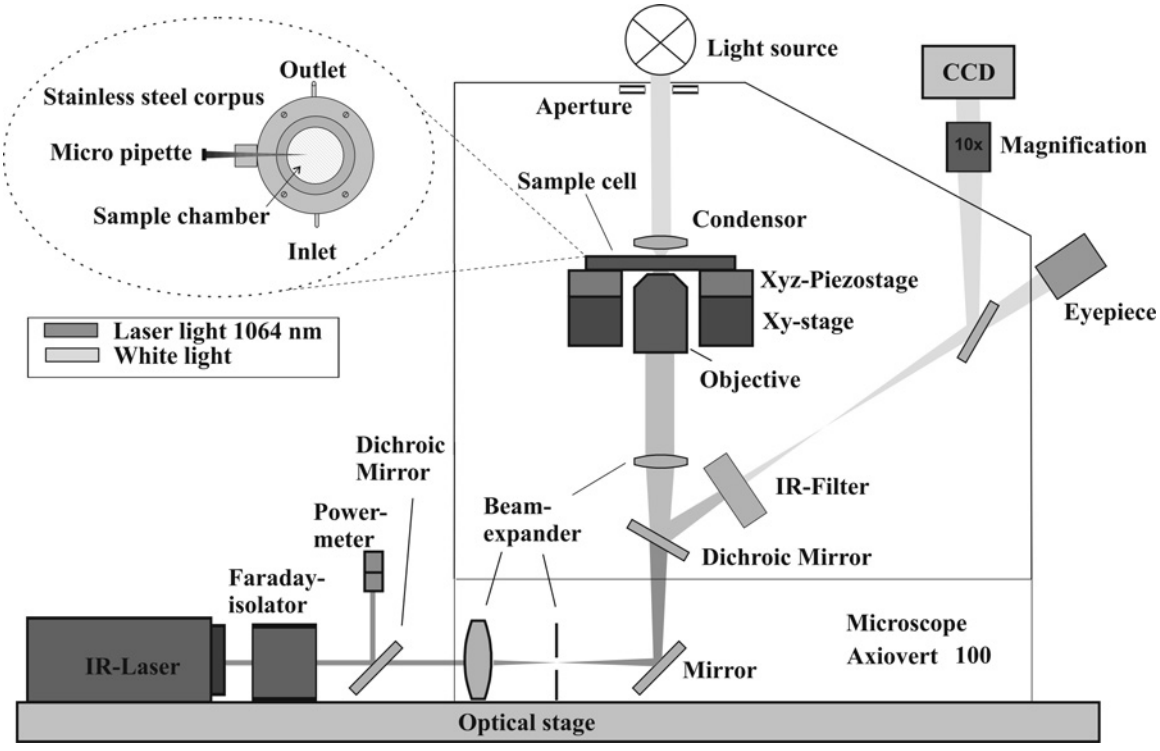


FIGURE 74.1 The optical tweezers setup is shown. The pathway of the laser beam is marked in dark gray. After passing a Faraday isolator, the beam is expanded and coupled into the back aperture of the microscope objective. Afterward it is focused in the sample plane. The path of the illumination light is indicated in light gray. The sample is illuminated from the top by a halogen lamp with an IR filter using Köhler illumination. The microscopic image can be detected from the eyepiece and is acquired, after a further 10-fold magnification, by a CCD camera. The sample cell is mounted on an *xyz* piezo stage for nanopositioning, which is built on a motor stage for rough positioning in a wide range (∼1 cm).

custom-made *LabView* program in order to guarantee long-term stability. Additionally, the profile of the laser beam is monitored to ensure optimal trapping conditions. After passing an optical isolator, a quarter-waveplate is used to produce circularly polarized light to exclude effects due to reflection differences of the mirrors between the *p*- and *s*-polarizations of the laser light. Subsequently, the beam is expanded and coupled into the back aperture of the microscope objective (Plan-Neofluor 100×, NA = 1.30 oil immersion, Carl Zeiss, Jena, Germany). Video imaging and optical particle tracking are accomplished by a digital camera (1M60, Dalsa, Munich, Germany). The optical stage is positioned in three dimensions with nanometer resolution by using piezo actuators (P-5173CD, Physik Instrumente, Karlsruhe, Germany). The sample cell (Fig. 74.1, inset) consists of a closed chamber that can be flushed by a syringe pump with varying solutions. A custom-made micropipette with an inner diameter at the tip of ≈0.5 μm is inserted into the chamber to hold one colloid by capillary action. The whole experimental setup is mounted in an air-conditioned room (T = 298±1 K) [30–32].

74.2.2 Trapping Basics and Force Calculation

Optical tweezers provide an experimental tool to manipulate microscopic objects only by photonic forces – without any mechanical contact. These forces can be divided into the scattering force and the gradient force. Scattering forces tend to push objects in the direction of propagation of the laser beam. In contrast, the gradient force attracts the particle toward the region of highest intensity, the laser focus (Fig. 74.2). Stable trapping is achieved when the gradient forces exceed the scattering forces.

Adequate models for calculating these forces theoretically depend on the ratio between the laser wavelength λ and the particle diameter D. Three cases can be distinguished: (1) $D/\lambda \ll 1$, (2) $D/\lambda \gg 1$, and (3) $D/\lambda \approx 1$. Case 1, where the particle is much smaller than the wavelength, is called the *Rayleigh regime* [33]. Forces are determined according to the formalism of wave optics [34]. The particles are considered as induced dipoles in an electromagnetic field. The forces are generated by changes in momentum of the electromagnetic wave due to the scattering by the dipole and the Lorentz force acting on the induced dipole, respectively [33].

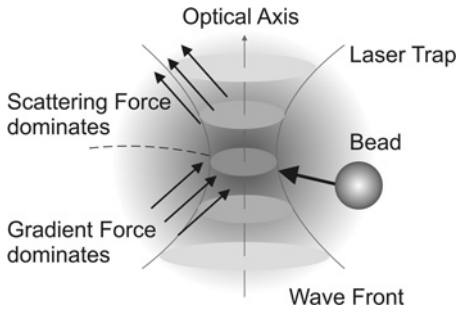


FIGURE 74.2 Schematic representation of photonic forces generated by a laser trap. Stable trapping is achieved when the gradient forces exceed the scattering forces. In this case, the microparticle is pulled into the laser focus and can be manipulated in three dimensions.

For particles having a much larger diameter than the wavelength of the laser light (the so-called Mie regime [34, 35]), the acting forces can be calculated using ray optics. Here, the beads are considered as collecting lenses. Light incident on a bead changes the propagation direction as well as the momentum of the light, generating a force [34].

The colloids used for the experiments in Section 74.4 have a diameter that corresponds approximately to twice the wavelength of the laser light. Therefore, an adequate description with the aforementioned models for Rayleigh and Mie particles is not possible. To determine the forces in this regime (generalized Lorentz–Mie regime [36, 37]), complex models are needed that allow only partly an analytical calculation.

To overcome these inconveniences in calculating the exact forces, different force calibration methods for optical tweezers measurements have been employed. All of them determine the trap stiffness. By knowing the exact bead position and using Hooke's law, one can calculate the acting forces [38,39]. Therefore, force calibration is reduced to calibrating the trap stiffness and separately measuring the relative displacement of the trapped particle. The most commonly used ways to compute the trap stiffness accurately are the drag force method, power spectrum analysis, and application of the equipartition theorem to fluctuation measurements [40]. For a melamine–resin particle having a diameter of ∼1 μm, typical values for optical trap stiffness can be varied in the range of (10^{-4}–1) pn/nm by adjusting the laser power from 10 to 1000 mW [28].

74.2.3 Position Detection in Three Dimensions

74.2.3.1 Position of Colloids in the xy Plane. As mentioned previously, to perform accurate position and force measurements with optical tweezers, it is imperative to localize spherical microparticles with nanometer resolution. Usually this is done either with a quadrant photodiode (QPD) or alternatively by image analysis [40]. In order to perform the measurements described in Section 74.4, we use image analysis for position detection, resulting in a lateral resolution of ±2 nm. This precision is clearly below the pixel size (13.25 nm/pixel) and has to be separated from the optical resolution of a microscope. The Abbe limit [41] describes the minimal separation of two objects that can be resolved by microscope and depends on the wavelength of the illumination, as well as the numerical aperture of the microscope lenses. Typically it is in the order of the half of the wavelength of illumination light. In contrast, the relative position of a single object with known geometry can be determined

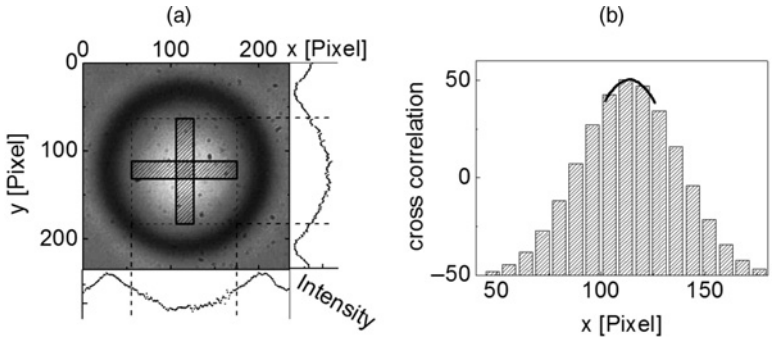


FIGURE 74.3 Position detection using cross-correlation. (a) Diffraction pattern of a melanin–resin microparticle (diameter 2.23 μm) and one-dimensional intensity at $[x, y] = 120$. The ROI is labeled by the dashed black square containing two strips (width 20 pixels) for detection of the position. The upper left corner of the ROI is defined as x_0 and y_0. (b) Shifted cross-correlation $K(d + \frac{L}{2} + x_0)$ (shaded bars) of the one-dimensional intensity profile in x convoluted with the direction inverted. The peak is fitted with a second-degree polynomial (solid line). Its maximum corresponds to the center position of the colloid.

with much higher precision [42]. All image analysis methods used to determine the lateral position are based on identification of the center of a spherical particle. However, they differ in computation time and resolution. An overview of different algorithms has been given [43].

Finding the suitable image analysis algorithm depends strongly on the aim of the measurement. In the case of pair interaction investigations, overlapping diffraction pattern may produce artifacts in the force separation dependence [44]. One method used to overcome these inconveniences is *edge detection* [43, 45, 46]. Here, a certain section, where the two diffraction patterns are overlapping, is omitted from the analysis, and the pathway of the remaining inner edge (given by maximum intensity contrast) is detected and fitted to a circle. The center of the circle defines the center position of the colloid. This algorithm is quite robust (e.g., against intensity fluctuations in the background and in the profile of the colloid), but it requires intensive computation resources, meaning that it is not applicable during the measurement [43, 45].

Another method, realizing pair interaction measurements in real time ("online"), is based on analyzing one-dimensional cross sections along an intensity profile by the use of cross-correlation. In this approach much fewer pixels have to be considered for the calculation; therefore it is more sensitive to image noise and thus, results in a higher uncertainty (usually twice that of edge detection [43]). The primary benefit of the cross-correlation method is the ability to perform a real-time analysis up to a frame rate of 10 kHz [47, 48] and the fact that no image storing is required.

To determine the position of a colloid by the cross-correlation method, a quadratic region of interest (ROI) containing the intensity maximum of a colloid with the edge length L and the coordinates of the upper left edge x_0 and y_0 is selected. The edge length is adjusted according to the reproduction scale and bead size. The pixels inside the ROI are defined as $\tilde{x} = x - x_0$ and $\tilde{y} = y - y_0$, with $\tilde{x}, \tilde{y} \in \mathbb{N}_0 \cap [0, L-1]$. In our particular case, two perpendicular stripes with a width of 20 pixels around position $\tilde{x} = (L-1)/2$ and $\tilde{y} = (L-1)/2$ are selected over the full length of the ROI to determine the center of the bead with the coordinates $\tilde{x}_K$ and $\tilde{y}_K$ (Fig. 74.3a). In the following only the stripe in x direction will be considered. In the y direction the algorithm will proceed in a similar manner.

To obtain a smooth one-dimensional intensity profile at each position $\tilde{x}_i$, the intensity is averaged over all 20 pixels in the y direction. This profile is defined as $A(\tilde{x})$. To determine the colloid center position, the cross-correlation K is calculated by averaging the product of $A(\tilde{x})$ and the direction inverted function $B(\tilde{x}) = A(L - \tilde{x})$:

$$K(d) = \frac{1}{L} \sum_{\tilde{x}=0}^{L-1} (A(\tilde{x}) - \bar{A})(B(\tilde{x} - d) - \bar{A}) = (A * B)(d) \tag{74.1}$$

where d is the offset and $\bar{A}$ is the mean value of the intensity profile. The fact that the cross-correlation is identical to the convolution of two functions enables one to calculate K taking the Fourier transformation of $A(\tilde{x})$ and $B(\tilde{x})$:

$$K(d) = \mathcal{F}^{-1}(\mathcal{F}((A * B)(d))) = \mathcal{F}^{-1}(\mathcal{F}(A)^* \mathcal{F}(B)) \tag{74.2}$$

where $\mathcal{F}(A)^*$ equals the complex conjugated. To calculate the maximum coordinate of $K(d)$, a polynom of the second order is fitted in the range of a few pixels around the (expected) maximum, which enables one to determine the

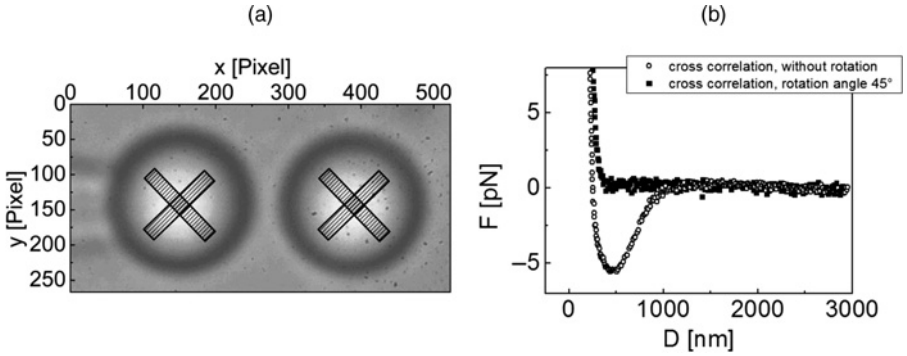


FIGURE 74.4 Position detection in pair interaction measurements using rotated cross-correlation (a) In order to avoid artifacts in the position detection of two colloids in the near contact region, the cross-correlation is rotated by an angle of 45°. Thus, the area where both diffraction patterns overlap is omitted from the analysis. (b) Resulting force–distance dependence without (open spheres) and with (solid squares) the rotated cross-correlation. In the image analysis without 45° rotation, artifacts occur at small surface distances (attractive behavior). These are caused by the overlapping diffraction patterns. To avoid this, the used strips for the cross-correlation algorithm are rotated by 45°.

extremum $\tilde{x}_{\max}$. The center of the colloid is then given by $x_K = \tilde{x}_{\max} + \frac{L-1}{2} + x_0$. Figure 74.3b shows the shifted cross-correlation $K(d + \frac{L}{2} + x_0)$ (shaded bars) and the quadratic fitting (solid line). The maximum corresponds directly to the center position of the colloid (in pixel units). Tracking of a particle is realized by moving the ROI by $\tilde{x}_{\max}$ and $\tilde{y}_{\max}$ to ensure that the center of the colloid is inside the ROI. This procedure provides an accuracy of about ± 2 nm.

For pair interaction measurements this method is only partially applicable, because artifacts based on the overlapping of the diffraction pattern may occur [44] (see Fig. 74.4). These artifacts depend on several parameters such as reproduction scale, colloid size, the colloid's index of refraction, the chosen edge length, and the overall illumination conditions. To avoid unphysical results, the abovementioned cross-correlation was expanded to the rotated cross-correlation [43]. Artifacts as described above occur mainly in the region where the diffraction pattern of the particles touch each other. To omit this area from position analysis, the image is rotated by 45° (see Fig. 74.4a) before the cross-correlation algorithm is used. Afterward the resulting center positions are projected back to the corresponding x and y axes. This enables one to determine the positions of colloids in close proximity (see Fig. 74.4b) without artifacts, as shown by direct comparison with other approaches [43].

74.2.3.2 Height Detection. Knowledge of the axial position (z postion) of a microparticle is usually of major importance, even if the experiment is performed in the xy plane. One example is the pair interaction measurement where the two colloid centers should be positioned in the same lateral plane. Additionally, exact knowledge of the z position enables one to compensate drift effects during long-term measurements (e.g., caused by the movement of a micropipette). However, a fast and stable z position detection based on image analyses is still challenging.

In the literature many methods are described to detect the height of a spherical particle. Most of them are based on a lookup table, where the diffraction patterns of colloids in different heights are stored [49, 50]. However, these methods require an illumination with parallel and monochromatic light to ensure that the diffraction pattern contains a sequence of several diffraction rings. Their number and distance are related to the axial position of the colloid to the focal plane. The height can then be obtained by averaging the diffraction profile over 360° and comparing the obtained value with the lookup table. Alternatively, the radius of the first diffraction ring can be fitted and compared with a lookup table [51].

For the experiments described in Section 74.4, another approach for fast and stable height detection was used. This method enables one to measure the axial position at ordinary white light conditions with a precision of ± 2 nm [46]. The principle for determining the relative height of a microparticle is based on a change in its diffraction pattern in the xy plane. The main maximum of the diffraction pattern depends on the z position with regard to the focal plane. For the used configuration it has been empirically determined that a square of 81*81 pixel (ROI) around the center position of the colloid shows a pronounced height dependence in the xy plane (Fig. 74.5). The matrix elements in the ROI are labeled with $I_{i,j}$, where $i, j \in \mathbb{Z} \cap [-40, 40]$, whereas the colloid center corresponds to $i = j = 0$. The relative height is calculated using a predefined reference polynomial. To calculate this reference polynomial, the diffraction pattern of the colloid at the micropipette is analyzed at different heights. Therefore, an arbitrarily chosen image close to the focal plane is defined as reference image, according to $z = 0$, and is saved.

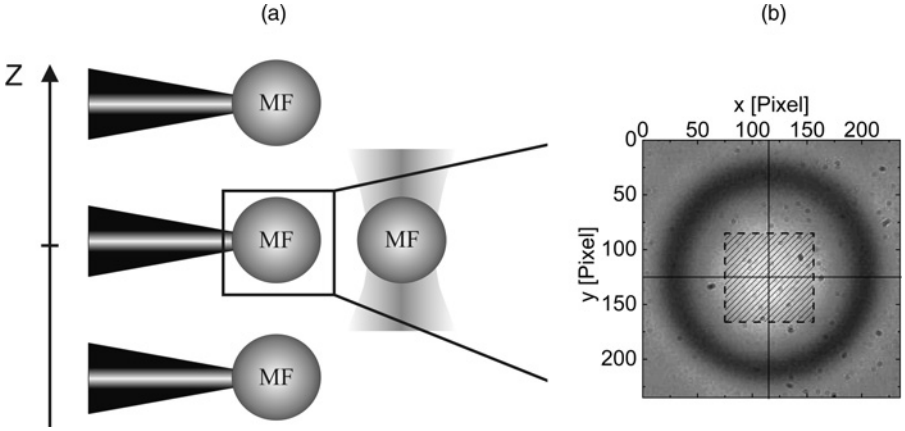


FIGURE 74.5 (a) Sketch of the height detection. The reference polynomial is calculated from the diffraction pattern of a colloid, fixed at the tip of the micropipette. Therefore, the height of the colloid is changed by moving the piezo stage in defined steps of 100 nm in the z direction, over a total distance of 1400 nm around the focal plane. At each height at least 20 images are analyzed. (b) A typical diffraction pattern of a colloid is shown. The center position is indicated by the black cross. The dashed square represents the ROI for the height detection having a width of 81*81 pixels and containing the elements $I_{i,j}$; $i, j \in \mathbb{Z} \cap [-40, 40]$. $i = j = 0$ equals to the center position of the colloid.

Afterward the micropipette is moved with a piezo stage in defined steps of 100 nm in the $\pm z$ direction. At each position the value of $I_{i,j}^{\text{current}}(z)$ is estimated and pointwise subtracted from the initial value $I_{i,j}^{\text{init}}$. Finally, the sum $S(z)$ of all matrix elements is determined, using

$$S(z) = \sum_{i,j} \left(I_{i,j}^{\text{current}}(z) - I_{i,j}^{\text{init}} \right). \tag{74.3}$$

In each height at least 20 images are acquired and the mean of $S(z)$, namely, $\langle S(z) \rangle$, is calculated. Therefore $\langle S(z) \rangle$ gives the relation between the current diffraction pattern and the relative height with regard to the reference image. As can been seen in Fig. 74.6 for the whole range of 1400 nm, a monotonically increasing dependence of $S(z)$ on the height is found and can be described by a polynomial of third order. From here on, we will refer to it as a *reference polynomial*. The height of a microparticle can then be determined by calculating $S(z)$ for the actual image and finding the root of interest of the master curve [46].

74.2.4 Other Methods for Characterizing Receptor–Ligand Interactions

Besides optical tweezers, several other prominent techniques have been established to investigate receptor–ligand interactions in biophysical and biochemical contexts. Their application depends strongly on the aim of the measurement. In order to study nucleic acid enzymes, particularly DNA topoisomerases [52, 53] and the molecular motors [28, 54] using superparamagnetic particles as force sensors, magnetic tweezers (MT) are ideally suited. In contrast to optical tweezers, the concept of MT consists in manipulating the force probe through magnetic field gradients created by a permanent magnet. Therefore, magnetic tweezers can be used to manipulate and rotate magnetic beads ranging from 0.5 to 5 μm in diameter. The trap stiffness can be varied between 10^{-6} and 10^{-3} pN nm^{-1}, resulting in a force range of 10^{-3}–100 pN [28].

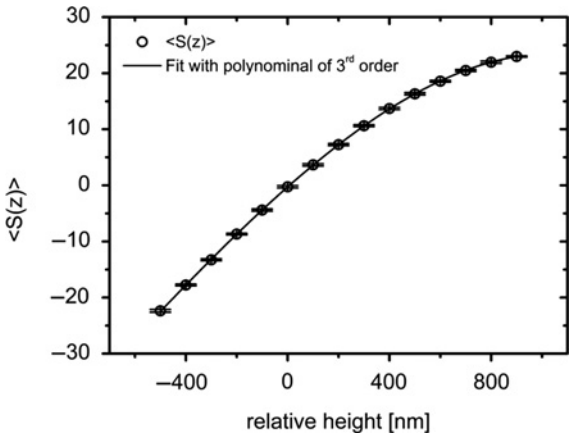


FIGURE 74.6 The reference polynomial. The figure shows the sum $S(z)$ in dependence of the relative height z. The height of the colloid was changed in steps of 100 nm using a piezo stage. The mean value $\langle S(z) \rangle$ (open circles) is calculated out of 20 acquired pictures at one height and is described by the reference third-degree polynomial. For the entire range of 1400 nm a monotonically increasing dependence is found. Finally, the height of the colloid is determined by calculating $S(z)$ for the current image and solving the reference polynomial for that value.

To apply high forces up to the nanonewton (10^{-9} N) range with subnanometer spatial resolution, atomic force microscopes (AFMs) can be used to study biological interactions under physiological conditions [28]. In general, the AFM is counted to the scanning probe techniques and consists of a cantilever with a sharp tip (force sensor) positioned above a piezoelectric scanner and an optical deflection system [55]. Force detection is accomplished using a laser detecting the vertical movement of the cantilever. By applying the TREC (topography and recognition imaging) mode, both surface properties measurements and localizing specific binding sites of a receptor can be performed simultaneously with nanometer resolution [56]. The cantilever stiffness ranges from 10 to 10^5 pN nm^{-1}. However, for biological applications softer cantilevers are used, which allow detection of piconewton forces [57]. Using this technique, phenomena such as the interaction between two complementary DNA strands [58] and the unzipping behavior of DNA [59] have been studied.

In order to perform high-throughput measurements to determine the specificity of biomolecules, other techniques (e.g., EILSA and Western blot) have been developed and became standard tools in biochemical/pharmaceutical research [60]. Enzyme-linked immunosorbent assay (ELISA [61,62]) is a biochemical method used to quantify the amount of an antigen (e.g., proteins, viruses, hormones, or toxins) in different liquid samples (e.g., blood, urine, water) using target-specific antibodies. In recent years, many different ELISA types (e.g., indirect ELISA, sandwich ELISA, competitive ELISA) have been developed. However, the basic principle remains the same; a specific antibody recognizing the antigen of interest is incubated with the sample (e.g., ligand on well plate). Either the first antibody itself or a second antibody specific for the first one is coupled with an enzyme that catalyzes most commonly a color-changing reaction. After addition of the enzyme-specific substrate, the measurable color change indicates the amount of antigen in the sample. From these data, binding constants (e.g., relative affinity) can be derived as well.

Western blotting [63] is another biochemical method employed to detect proteins in tissue homogenates or in other sample mixtures, using specific antibodies against the antigen of interest. Before these proteins/antigens were accessible and detectable by detection antibodies, the sample (e.g., protein mixture) has to be separated according to molecular weight, to isoelectric point, and/or to electric charge by gel electrophoresis. Subsequently, the proteins are transferred from the gel onto a membrane [nitrocellulose or polyvinylidenedifluoride (PVD)], most commonly by *electroblotting*. After blocking of nonspecific binding sites with various chemical agents [e.g., bovine serum albumin (BSA), dry milk, or fetal bovine serum (FBS)], the membrane is incubated with the antigen-specific primary antibody. Finally the protein of interest is visualized, by methods such as chemiluminescence. For this purpose, a secondary antibody against the Fc region of the detection antibody coupled with an enzyme [e.g., horseradish peroxidase (HRP)] is used, similar to EILSA. The HRP catalyzes either the conversion of chromogenic substrates into colored products, or a redox reaction of chemiluminescent substrates leading to a detectable light signal.

74.3 THEORETICAL DESCRIPTION OF RECEPTOR–LIGAND INTERACTIONS

Many biologically relevant interactions such as the binding of an enzyme to a particular substrate, or the detection of foreign substances by antibodies causing an immune response, are based on the principle of a noncovalent specific binding (receptor–ligand binding). The latter is a superposition of several attractive, short-range interactions. These are hydrogen bonds (~2–7 k_BT), van der Waals (<1 k_BT), electrostatic (0.2–10 k_BT), and hydrophobic (1–5 k_BT) interactions (values taken from Ref. 64). Since each of these interactions is in the order of k_BT, only the complex interplay between all of them results in a specific and stable bond. In contrast, the binding energy of a covalent bond exceeds 100 k_BT. Experimentally, the interactions between receptors and ligands are analyzed by *dynamic force spectroscopy* (DFS). By definition, DFS is the investigation of a force-induced dissociation of a single bond and provides information about kinetic parameters as well as parameters that characterize the energy landscape of the binding from the distribution of rupture forces (see Section 74.4). This section focuses on introducing the theoretical concepts to analyze the experimental data by means of characterizing the specific binding between receptor and ligand. In recent years, many reviews [65–67] on theoretical descriptions have been published. Here we restrict ourselves to an ideal bond description and application of the Dudko—Hummer–Szabo [68] approach.

74.3.1 An Ideal Bond

Figure 74.7 displays the simplified energy landscape for an idealized bond along the reaction coordinate x. The bound state (1) is represented as a deep local minimum, which is separated by a barrier from the unbound state (2). Overcoming the barrier is a stochastic process that can be characterized by the kinetic rates k_{on} (ON rate, association) and k_{off} (OFF rate, dissociation). For the dissociation process, the height of the barrier, with its maximum at position x_{ts}, corresponds to the activation energy ΔG. However, it has to be mentioned that representation of the potential along a one-dimensional reaction coordinate is a simplified picture. In more advanced approaches, x is the energetically preferred path in a multidimensional, structured energy landscape. Furthermore, if a force is applied to the bond, the reaction path is not randomly chosen, but often follows the direction of the force. It must

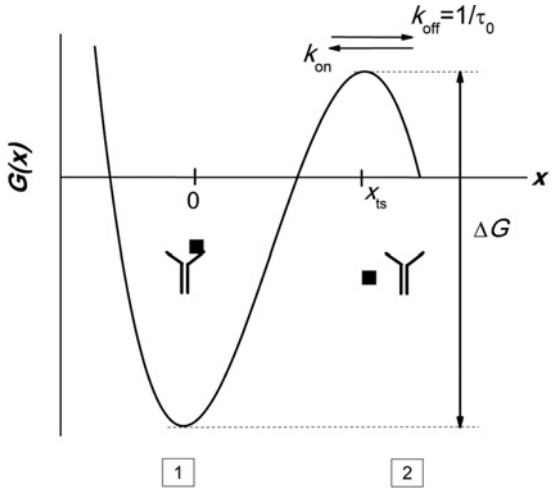


FIGURE 74.7 Depicted is the one-dimensional energy landscape of an idealized specific binding. The reaction coordinate x corresponds to the preferred path for binding and dissociation, respectively. The bound state (1) is separated from the unbound state (2) by an energy barrier with the height of ΔG. x_{ts} denotes binding length and is a measure of the distance between the state (1) and the transition state (local maximum). The kinetic transition rates are given by k_{on} and k_{off}, where the latter is the inverse of the bond lifetime without externally applied force τ_0.

also be noted that the potential form is an idealization, too. Since the bond is the sum of multiple interactions, the true energy landscape is structured and may vary in shape. However, despite these limitations, a majority of the investigated specific binding can be considered as an ideal, single bond as described above [66, 68, 69].

74.3.2 Force-Induced Bond Rupture: The Dudko—Hummer–Szabo Model

Appling a constant external force to a single bond lowers the enthalpic barrier of bond dissociation, making the rupture more probable. Additionally, the position and the shape of the barrier in Fig. 74.7 can be changed as well. The first phenomenological model to describe the dependence of the bond lifetime on the force was proposed in 1978 by Bell [70]:

$$\tau_{\text{Bell}}(F) = \tau_0 \exp\left(-\frac{Fx_{\text{ts}}}{k_B T}\right). \tag{74.4}$$

This equation contains two parameters, which are characteristic of each bond: τ_0, the lifetime of the bond without force, and x_{ts}, the characteristic length, which corresponds to the distance between the energetic minimum of the bound state and the maximum of the barrier. Furthermore, F denotes the applied force; k_B, the Boltzmann constant; and T, the absolute temperature. Obviously, reduction of the energy barrier causes an exponential increase in the OFF rate.

However, in the experiments described in Section 74,4, the applied force rises continuously with time. With increasing load the likelihood of a bond rupture grows. On the other hand, the limited force-dependent bond lifetime determines the moment when the bond breaks, too. Therefore, the rate with which the bond is loaded plays a central role in dynamic force spectroscopy measurements [57]. This correlation is called *loading rate dependence*. The *loading rate* is defined as the increase in force over a certain time interval in which the bond remains intact.

Almost 20 years after Bell, Evans and Ritchie [71] established the cornerstone for dynamic investigation of the forced rupture of single specific bindings by extending Kramers' theory for reaction kinetics in liquids [72] to bond dissociation under force. They obtained the probability density distribution of rupture forces [31]. It depends strongly on the loading rate $\dot{F}(F) = \Delta F/\Delta t$:

$$p(F) = \frac{\exp\left(-\int_0^F [\dot{F}(f)\tau(f)]^{-1} df\right)}{\dot{F}(F)\tau(F)} \tag{74.5}$$

For theoretical description of the following experiments, we use the theory published by Dudko et al. (DHS model) [68]. Here the bond is characterized by three parameters: x_{ts}, which denotes the binding length; τ_0, the bond lifetime in absence of an external force; and ΔG, the potential depth. Applying Kramers' theory to different energy profiles and adding ΔG as a further parameter results in a force dependent bond lifetime $\tau_{\text{DHS}}(F)$ [68]:

$$\tau_{\text{DHS}}(F) = \tau_0 \left(1 - \frac{\nu F x_{\text{ts}}}{\Delta G}\right)^{1-1/\nu} \exp\left(-\frac{\Delta G}{k_B T}\left[1 - \left(1 - \frac{\nu F x_{\text{ts}}}{\Delta G}\right)^{1/\nu}\right]\right). \tag{74.6}$$

This equation holds for forces below a critical force at which the barrier vanishes:

$$F_{\text{crit}} = \frac{\Delta G}{\nu x_{\text{ts}}} \tag{74.7}$$

The factor υ corresponds to the geometry of the underlying free energy profile, which is for $\upsilon = 0.5$ a harmonic well with a cusplike barrier and for $\upsilon = 0.66$ a potential containing linear and cubic terms. For $\upsilon = 1$, it passes into the model from Bell and Evans, which constitutes a special case within the formalism. The rupture-force distributions can be transformed into $\tau(F)$ by inverting Eq. (74.5). Therefore, rupture-force histograms, which are obtained experimentally, are converted into $\tau(F)$ as described in Dudko et al. [68].

By inserting $\tau_{\mathrm{DHS}}(F)$ in Eq. (74.5), we can derive the distribution of rupture forces. An analytical solution of the integral is possible for stiff molecules when the loading rate does not depend on the force:

$$p(F) = \frac{1}{\dot{F}\,\tau_0}\left\{\exp\left[\frac{\Delta G}{k_B T}\left(1-\left(1-\frac{\nu F x_{\mathrm{ts}}}{\Delta G}\right)^{1/\nu}\right)\right.\right. \\ \left.\left.-\left(\frac{\left(-1+\exp\left[\frac{\Delta G}{k_B T}\left(1-\left(1-\frac{\nu F x_{\mathrm{ts}}}{\Delta G}\right)^{1/\nu}\right)\right]\right)k_B T}{x_{\mathrm{ts}}\,\dot{F}\,\tau_0}\right)\right]\right. \\ \left.\left(1-\frac{\nu F x_{\mathrm{ts}}}{\Delta G}\right)^{-1+1/\nu}\right\}. \tag{74.8}$$

74.4 CASE STUDIES

In this section, we describe experimental details of the measurement procedure as well as of three experiments using DFS to characterize the interactions between receptors and ligands. The systems of interest are the interactions between τ-peptides having a varying phosphorylation pattern and their respective monoclonal antibodies. The microtubule-associated protein tau promotes the assembly and stabilization of neuronal microtubules [73]. In Alzheimer's disease tau becomes hyperphosphorylated and self-associates to form paired helical filaments (PHF). This PHF-tau aggregates in tangles in cortical brain areas, which are essential for cognitive function, and is found to be one of the pathological characteristics of Alzheimer's disease [74]. The number and density of tangles correlates well with the progress of the disease [75]. However, up to now the causal background of Alzheimer's disease has remained unclear. Monoclonal antibodies can be used for the histological detection of hyperphosphorylated τ-protein and even to discriminate between different phosphorylation patterns. For the following experiments τ-peptides containing two typical phosphorylation sites (Thr231 and Ser235) have been synthesized and the interactions with the respective mAb are analyzed under different points of view.

74.4.1 Measurement Procedure

The interactions between the receptors and ligands are measured by the following procedure. A particle with one kind of ligand (we will discuss different τ-peptides later) on its surface is trapped with optical tweezers and brought in the vicinity of the custom-made micropipette. This colloid is fixed on the tip of the pipette by capillary forces. Next, a colloid covered with one type of receptor (we discuss different monoclonal antibodies below) is captured and placed in close vicinity to the immobilized bead on the pipette (Fig. 74.8a). Using a custom-made *LabView* program, both particles are approached until a force of (8±2) pN is reached and retracted with a distinct velocity after one second of contact. If a bond has formed, the particle in the optical trap is displaced out if its equilibrium position until the rupture force is exceeded. At this force (*e.g.* rupture force) the bond breaks and the particle snaps back into its initial position (Fig. 74.8b). All experiments are carried out in PBS buffer solution at pH 7.4 and (298±1) K. The force calibration of the bead in the optical trap was accomplished by displacing the particle from

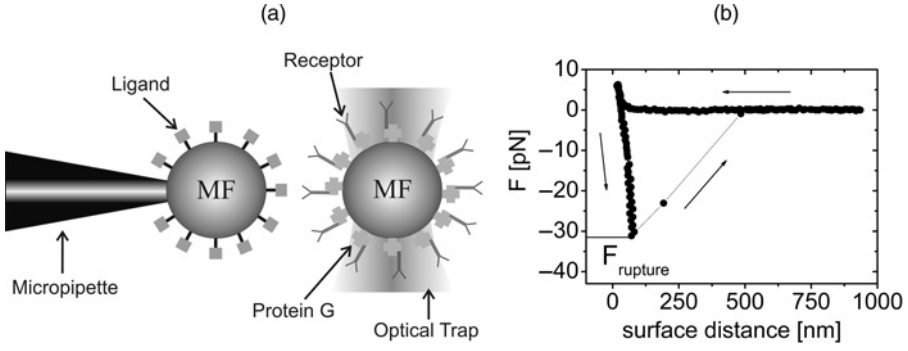


FIGURE 74.8 (a) Sketch of the measurement procedure. One colloid, grafted with the ligand (τ-peptide), is captured by a micropipette via capillary forces, while the other particle, coated with the receptor (monoclonal antibody), is held in the optical trap. The monoclonal antibodies (mAbs) are oriented via protein G in order to ensure optimized binding efficiency. (b) Force–distance curve of a typical measurement cycle. Both particles approached each other until a force of (8±2) pN is reached. After one second of contact, they are again separated with a certain loading rate. If a receptor–ligand bond has been established, the particle in the trap is pulled out of its equilibrium position until the bond breaks (rupture force).

its equilibrium position and applying Stokes' formula to the data. For the experiments this results in a force constant of 0.09 pN nm^{-1} at a laser power of 225 mW [32].

For the following measurements the colloids are prepared according to specific published protocols [31]. Therefore, two types of surface-modified microparticles (melamide group and carboxyl group, respectively) are used; the first is coated with the τ-peptide, and the second one bears the respective protein G oriented mAbs on its surface (Fig. 74.8a).

74.4.2 Ensuring Single Binding Events and Specificity

In order to ensure that the observed binding events originate from specific receptor–ligand interactions, control experiments have to be performed. For this purpose the specificity of the used antibodies against the epitopes of the respective τ-peptides was proved using ELISA [76]. Furthermore, background events (e.g., interactions among peptide/mAb and the functional surface groups of the colloids) are determined to be less frequent than 2% of the cases and are found to be negligible.

Additionally, to guarantee that only single binding events are investigated, the grafting density Σ (e.g., the number of immobilized peptides/mAb on the colloid surface) on the microparticles was varied. It can be assumed that the higher the added volume (of, e.g., peptide solution) during the preparation process, the higher the resulting Σ, meaning that the volume of the peptide solution is directly proportional to the coating density. For the purpose of determining the optimal Σ, relative binding frequencies and median rupture forces are recorded for each surface coverage, by measuring 200 approaches and retraction cycles (see Fig. 74.8b) for at least five pairs of colloids. Figure 74.9 shows the median of the relative binding frequency h_B (a) and the rupture force F (b) at different grafting densities for the interaction between the mAb HPT-110 and the monophosphorylated peptide tau[pSer235]. In order to obtain different coating densities, the added amount of τ-peptide solution was varied during the preparation process. At a fixed antibody volume (5 μL, $c = 1$ mg mL^{-1}), the peptide solution volume ($c = 1.3$ mg mL^{-1}) was reduced successively from 2 μL to 0.1 μL, giving a surface coverage range from 0.11 to 0.005 nm^{-2}, respectively. As shown in Fig. 74.9, this results in a decrease of the binding frequency (shaded bars), while F_{Median} does not undergo a systematic change (open circles). From this it follows that $V_{\text{peptide}} = 2$ μL and $V_{\text{mAb}} = 5$ μL are suitable to investigate the interactions between the mAb and the peptide on single and specific binding events.

This approach provides a simple way to find the best settings for the preparation and measurement procedure, but a reproducible control of the surface coverage and the reduction of the error bars in Fig. 74.9 is not possible using this method.

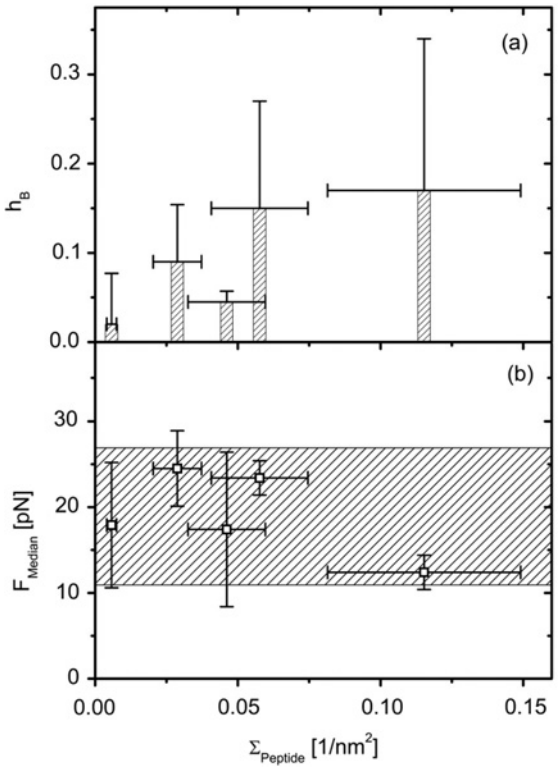


FIGURE 74.9 Adjustment of the surface coverage of peptide-coated colloids for the interaction between mAb HPT-110 and the monophosphorylated peptide tau[pSer235]. The coating density of the mAb-grafted colloids is kept constant. (a) Median of the relative binding frequency h_B and (b) median rupture force for five different coating densities Σ. The coating density is calculated from the respective volume of peptide solution that has been added during the preparation procedure. In order to determine h_B and F_{median}, at least 200 approach and retraction cycles (see Fig. 74.8b) for five colloid pairs and for each surface coverage have been analyzed. The error bars represent the median error. While the binding frequency is reduced with decreasing grafting density (shaded bars), the median rupture force (open symbols) remains unchanged, as indicated by the shadowed area.

74.4.3 Reducing the Data Variance in Dynamic Force Spectroscopy Measurements Using Presorted Particles [32]

Investigation of the bond formation and dissociation process with dynamic force spectroscopy can be reduced to the measurement of the ON rate (k_{on}) and the OFF rate (k_{off}), respectively. However, a major problem in studying these two quantities between surface-attached molecules is their dependence on many parameters [2]. One of these factors is the surface coverage or the grafting density Σ. By influencing both, k_{on} and k_{off}, the grafting density plays a crucial role in measuring relative binding frequencies h_B, which are a measure for the association rate between biomolecules [2].

Because the grafting density on particles out of one preparation procedure is Gaussian-distributed around a mean surface coverage, the varying Σ causes a large data variance (error bars) in relative binding frequency measurements, as can be seen in Fig. 74.9. Therefore, reducing differences in the grafting density results in a more sensitive measurement of h_B values [32]. One method for determining the number of immobilized biomolecules of coated particles is the *fluorescence-activated cell sorting* (FACS [77]) approach. With FACS it is possible to sort and accumulated particles according to their fluorescence intensity and their surface coverage, respectively. Another great advantage of FACS is that dynamic force spectroscopy experiments can be performed with the same colloids as previously sorted using the FACS spectrometer. By combining FACS analysis and DFS, a comparison between different measurements of relative binding frequencies is more sensitive, since smaller differences can be resolved.

For the experimental proof, the interactions between the monoclonal antibody HPT-104 and the carboxyfluorescein-labeled monophosphorylated peptide tau226-240[pThr231] are investigated. The peptides are synthesized according to the protocol published by Stangner et al. [32], and the colloid-coating procedure follows the instructions described in Section 74.4.1. Because of hydrophobic properties and the close vicinity of the fluorescein molecule to the binding site of the mAb, it is necessary to prove that the dye does not influence the specific interaction between peptide and antibody. By performing dynamic force spectroscopy and comparing the bond parameters obtained to data using unsorted beads covered with the nonfluorescence peptide analogue, no effect was found.

To obtain peptide-labeled colloids with similar grafting densities by taking the fluorescence intensity as a measure for a certain surface coverage, a FACS analysis is performed (Fig. 74.10). The plot shows the two fluorescence intensities to record the characteristic emission spectra of carboxyfluorescein. The 2D density plot before the selection process reveals two different populations (Fig. 74.10a). Area A1 contains blank, uncoated particles, whereas A2 comprises the target population with the peptide covered beads. To emphasize that A1 and A2 can be distinguished by the FACS spectrometer, additional blank beads are added. By choosing a narrow region of A2, including roughly the dark area, the selection process is started. After sorting a sufficient number of colloids the solution is reanalyzed to verify the accuracy of the method (Fig. 74.10b). Population A1 is almost removed. The remaining number in this area is less than 0.5% of the total bead number. To compare the population A2 before and after the selection process by grayscale as well as by data variance, it is important to mention that the basic population is kept constant within the experimental accuracy. The used gray code scales with the data point number in each bin and is equal for both plots. Comparing the color scheme of

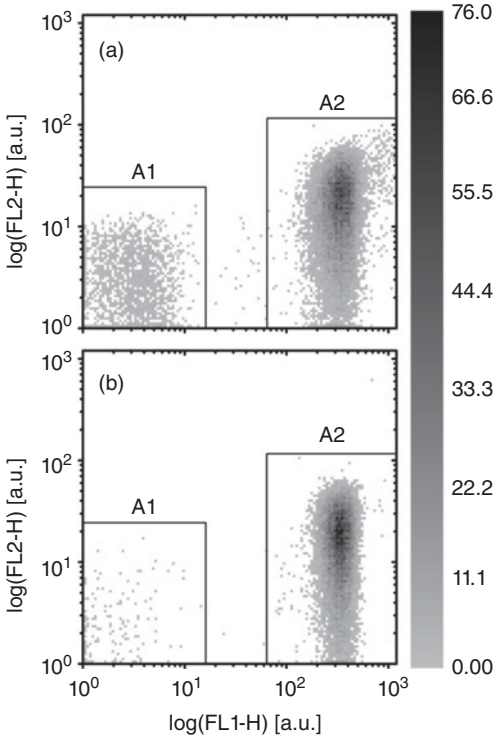


FIGURE 74.10 2D density plot of τ-peptide-labeled MF particles (diameter 2.31 μm) in dependence on intensity signal of channel FL2-H versus FL1-H before (top) and after (bottom) FACS sorting. The grayscale corresponds to the amount of colloids within each bin, whereas black is equivalent to high count numbers and light gray, to low ones. In order to maintain comparability, the color code was kept constant for both plots. (a) FACS data before the selection process. Two populations are visible: A1 contains uncoated colloids, and A2 contains the fluorescence tagged tau-particles. (b) Same batch of colloids as in (a), but after sorting. Population A1 is sorted out, only the target population A2 remains with a significant reduction in width and a pronounced increase in density (dark color).

Fig. 74.10a,b, it becomes obvious that (1) after the selection process the width of A2 is reduced and (2) the density in the middle of A2 is shifted to much higher values (black color). To quantify the difference in the width of both distributions, their standard deviations σ_{FL1-H} are calculated. They deviate by approximately 33% and significance was proven by applying the F test [78].

This implies that by presorting colloidal solutions using FACS, it is possible to accumulate particles with a similar grafting density compared to the unsorted solution. Furthermore, this procedure provides a reliable method for comparing different receptor–ligand systems under the same surface coverage conditions by using the same FACS protocol.

Next, the influence of a constant coating density on the data variance in relative binding frequency (h_B) measurements using presorted tau particles instead of unsorted ones is investigated. For this purpose, the approach and retraction

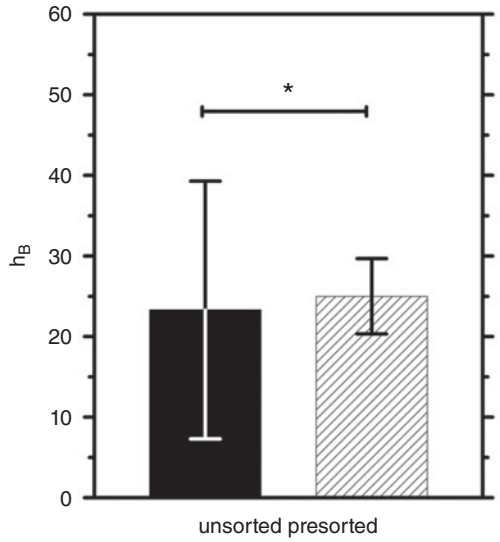


FIGURE 74.11 Median relative binding frequency h_B for unsorted (solid) and sorted (shaded) colloids. The median values are given by $h_B^{\text{solid}} = (23.3 \pm 16.0)\%$ and $h_B^{\text{shaded}} = (25.0 \pm 4.7)\%$. The median variance is decreased significantly, which accounts for an almost constant surface coverage of the presorted colloids.

cycles are recorded for each case (presorted dye-labeled τ-colloids and unsorted unlabeled τ-colloids, respectively) as described in Section 74.4.1. After counting the rupture events, the resulting relative binding frequencies between labeled, presorted, and unlabeled, unsorted colloids are compared (Fig. 74.11). For the unsorted solution large fluctuations in the h_B values are observed (solid bar). In contrast, the presorted colloids constituting a homogeneous surface coverage exhibit only a small spread (shaded bar). Interestingly, the median h_B value for the unsorted colloids differs only slightly from the median relative binding frequency of the presorted ones, but the data variance is reduced significantly. This effect is caused by an almost constant surface coverage achieved by presorting particles via FACS.

74.4.4 Dynamic Force Spectroscopy on the Binding of Monoclonal Antibodies and τ-Peptides [31]

The molecular accuracy of receptor–ligand systems is imperative for all living organisms. These systems play a key role in almost every biological relevant process, including the immune response of the human body. However, specific binding always carries a certain probability for an error, namely, that the receptor may bind to a ligand for which it is not specific. Such unspecific binding is explained by the fact that molecules always interact; there is always a competition between the kinetic energies to be independent and forces of intermolecular attraction. However, a perfect discrimination between "correct" ligands, which are detected by the receptor, and "wrong" ligands, which are discarded, is never possible [79]. The unspecific interaction of the mAbs to the peptides to which the respective mAbs are not specific implies that detected binding events originate from interactions besides the specific binding sites. Therefore it can be assumed that these unspecific attachments occur also between the mAb and its specific peptide. In other words, the distributions of rupture forces (see Section 74.3.2) for the specific interaction contain events that do not only originate from the interaction between specific binding site and epitope. These might be caused by hydrophobic or charged sites on the surface of the molecules. It is not possible to distinguish between specific and unspecific rupture events according to properties of their force–distance curves.

In one report [31] the unspecific interactions of the monoclonal antibodies HPT-110 and HPT-104 were characterized and separated from the specific ones. Except for the respective phosphorylation (at Thr231 and Ser235), both tau226-240 peptides used consist of the same sequence. It was shown by ELISA that HPT-110 binds specifically to the peptide carrying a phosphorylation at Ser235, whereas HPT-104 is specific for tau[pThr231].

To determine the contribution of unspecific binding, the rupture-force distribution of HPT-110 binding specifically to the τ-peptide that is phosphorylated only at Ser235 is analyzed as described in Section 74.4.1. The rupture-force histogram (Fig. 74.12a) is evaluated by means of the DHS model, and the bond parameters are displayed in Fig. 74.12d–f (black circles). The rupture-force distribution of the unspecific interaction between the same mAb HPT-110, and the peptide phosphorylated only at Thr231 is shown in Fig. 74.12b. The histogram is shifted toward lower forces compared to that obtained for the specific interaction. The distribution is broad and cannot be described using the DHS model. As the unspecific interaction is not caused by defined binding sites, the authors assume that the sites and mechanisms of the attachments differ, for example, independently of the direction of the interacting molecules. Such varying interactions cannot be described by the same energy well, which forms the basis for the theoretical description.

Furthermore, it is assumed that the contribution of specific and unspecific interactions to the rupture-force distributions of specific bindings is purely additive. This allows for them to be separated by subtracting the rupture-force histograms. The difference, meaning the corrected distribution of rupture forces, which corresponds to the specific binding between epitope and binding site, is shown in Fig. 74.12c. This distribution is narrower, and the maximum is shifted to higher forces. The corrected dataset is analyzed analogously to the raw data as described above. The resulting parameters are shown in Fig. 74.12d–f (open triangles). Especially the bond lifetime τ_0 determined for the corrected data shows the strongest deviation from the parameter set obtained from the raw data (black circles). But also, the characteristic length from the corrected data is roughly 4 times larger than

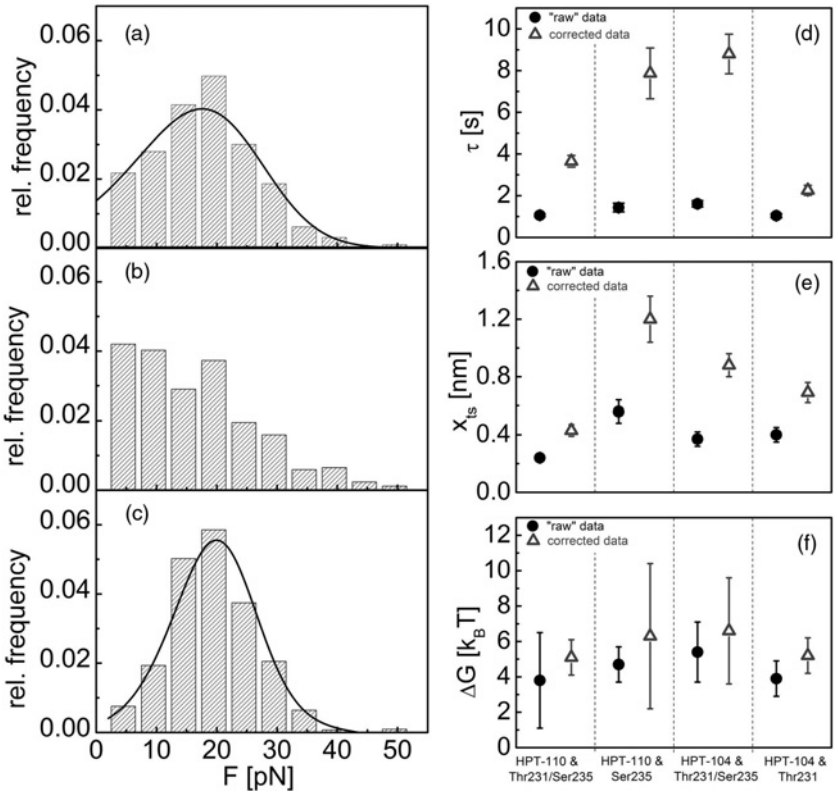


FIGURE 74.12 The rupture-force histogram for (a) the specific interaction between HPT-110 and the monophosphorylated peptide tau[pSer235], (b) the unspecific interaction between HPT-110 and the peptide only phosphorylated at Thr231, and (c) the difference between rupture-force distributions of specific and unspecific binding. The solid line depicts the theoretical description of the rupture-force distribution $p(F)$ [Eq. (74.8)] for the parameters obtained by fitting $\tau_{DHS}(F)$ [Eq. (74.6)] for $\upsilon = 0.5$. (d–f) The binding parameters lifetime τ_0, characteristic length x_{ts}, and free energy of activation ΔG for the specific interactions HPT-110 binding to the double-phosphorylated peptide and to the peptide monophosphorylated at Ser235, respectively, as well as HPT-104 binding to the double-phosphorylated peptide and to the peptide monophosphorylated at Thr231, respectively. For each interaction, the values obtained by fitting the raw data (circles) are opposed to the values from fitting the corrected data after separating the specific from the unspecific interactions (open triangles). The corrected data correspond to a longer lifetime and a higher value for x_{ts}. For the free activation energy, no significant difference is found between the values obtained from the raw data and those from the corrected histograms.

that from the raw data. For the free energy of activation ΔG no significant change is observed.

Following the same procedure, the corrected rupture-force distribution of HPT-110 binding to the double-phosphorylated peptide are obtained. Likewise, the specific binding of HPT-104 and the double-phosphorylated τ-peptide as well as to the one monophosphorylated at Thr231 is separated from the contribution of unspecific interactions. Analyzing the interaction of HPT-104 binding to the peptide monophosphorylated at Ser235 yields the rupture-force distribution of the unspecific interactions. The data are distributed similarly to the unspecific binding of HPT-110 to the peptide monophosphorylated at Thr231 as shown in Fig. 74.12b. In the next step, the resulting rupture-force histogram is subtracted from the one of the respective specific interaction. The parameters obtained by analyzing the raw and the corrected histograms by use of the DHS model are opposed in Fig. 74.12d–f. As the data are no longer overlaid by unspecific interactions, it is assumed that the parameters obtained from the corrected histograms give the better description of the specific binding between the mAbs and the respective peptides.

74.4.5 Determining the Specificity of a Monoclonal Antibody Using Dynamic Force Spectroscopy [80]

Because of the unique properties of mAbs, they are also being used in medical applications. Since their first in vitro

production by Köhler and Milstein [81] in 1975 and two decades of advances in genetic engineering, mAbs are now widely applied medical agents [e.g., in the treatment of cancer using antibody drug conjugates (ADCs) [4–9], rheumatoid arthritis [9], Crohn's disease, multiple sclerosis, and prophylaxis for transplant rejection [82]). In 2012 approximately 30 therapeutic mAbs are being marketed in the United States and/or Europe, and a record number of mAbs are in clinical development [82]. The key feature of mAbs-based therapies is the targeted administration of highly potent drugs in combination with the reduction of negative side effects to healthy tissue due to so called cross-reactions. To achieve this goal a high target selectivity (or specificity) of the used mAb is imperative [5], meaning that the antibody must bind only to the disease-specific marker whereas no cross-reactivity to other tissue should occur. Apart from their applications in drug delivery, mAbs are also being used and developed as diagnostic tools in immunohistochemistry [76, 83] and flow cytometry [84]. In the context of neurodegenerative diseases (e.g., Alzheimer's disease), when symptoms are heterogeneous or their initial manifestation is ambiguous and can be mistaken with that of other conditions [85], the specificity of mAbs can be of invaluable help for the early detection of the disease.

Standard procedures to determine the specificity of a mAb in biochemical and pharmaceutical research include ELISA and Western blot [60] (see Section 74.2.4). Despite their outstanding performance in screening applications, a fundamental understanding of the dynamic binding process is not accessible for both techniques, since they provide only a static, equilibrated picture. However, to comprehend the overall receptor–ligand interaction (e.g., specificity of the mAb), more details on the binding kinetics (e.g., ON and OFF rates) are required [80].

For this purpose, the interactions between mAb HPT-101 and three τ-peptides (tau[pThr231/pSer235], tau[pThr231], and tau[pSer235]), each with a different phosphorylation pattern, are investigated on a single molecule level using DFS. In advance of these measurements, the specificity of mAb HPT-101 to the abovementioned τ-peptides was determined using ELISA. Interestingly, these assays showed that mAb HPT-101 binds specifically only to the epitope of the double-phosphorylated peptide tau226-240[pThr231/pSer235]. Cross reactions to monophosphorylated peptides with the same amino acid sequence were not observed, although the epitope differs only by a single isolated phosphorylation site [76].

In order to determine the ON-rate k_{on} the relative binding frequency h_B for all three mAb/peptide combinations have been measured (Fig. 74.13a), as described in Section 74.4.1. Although the highest binding frequency has been observed for the interaction between mAb HPT-101 and tau[pThr231/pSer235], this single-molecule approach also shows an appreciable binding of mAb HPT-101 to the monophosphorylated peptides. Therefore, the supposed specificity of mAb HPT-101 to the biphosphorylated peptide cannot be confirmed [80]. However, the binding frequency constitutes a measure for the relative ON rate only [2], whereas the affinity of a bond is defined by the association

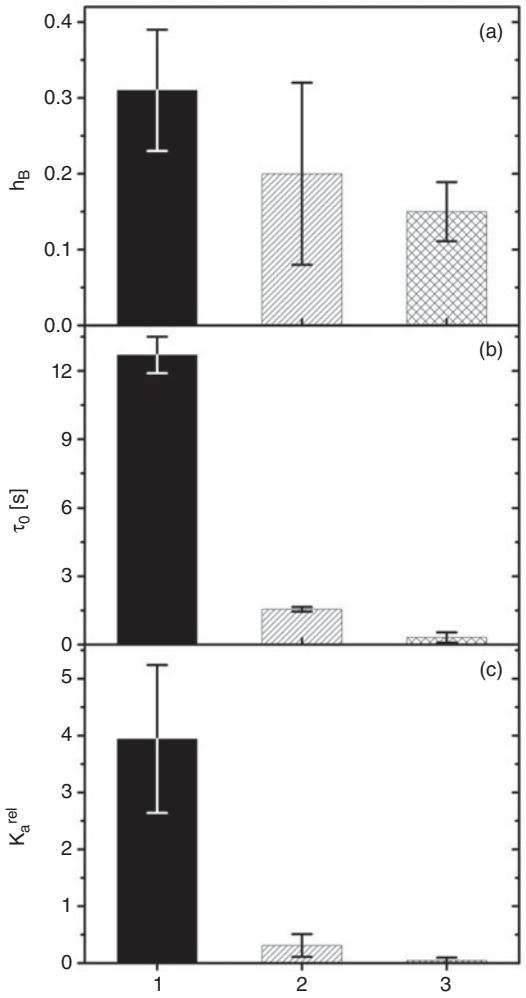


FIGURE 74.13 Median relative binding frequency h_B, bond lifetime τ_0, and relative affinity K_a^{rel} for the binding of mAb HPT-101 to the peptides (1) tau[pThr231/pSer235], (2) tau[pThr231], and (3) tau[pSer235]. (a) The interaction between the mAb and the double-phosphorylated peptide (1) shows the highest binding frequency. In contrast to ELISA measurements, mAb HPT-101 also binds to both monophosphorylated mutants. (b) Bond lifetime without external force, obtained by fitting $\tau_{DHS}(F)$ using Eq. (74.6) (for $\upsilon = 0.5$) to the rupture-force data. The highest τ_0-value is observed for the binding of mAb HPT-101 to tau[pThr231/pSer235] again, followed by the peptide carrying a phosphorylation at Thr231. The shortest lifetime is represented by the interaction between mAb HPT-101 and tau[pSer235]. (c) The relative affinity follows the trend observed for the binding frequency and bond lifetime. The highest relative affinity is obtained for the mAb HPT-101/tau[pThr231/pSer235] system and decreases by reducing the number of phosphorylation sites. The result is in accordance with ELISA measurements.

constant K_a, which is the ON/OFF-rate ratio. Thus, a full characterization requires the determination of the OFF rate as well.

Therefore, the OFF rate k_{off} is determined in a similar manner to that described in previous sections by analyzing the rupture-force distribution with the DHS model ($\nu = 0.5$). Figure 74.13b shows the bond lifetime for all three interactions. Again, the longest lifetime τ_0 is given for the binding of mAb HPT-101 to the double-phosphorylated peptide. MAb HPT-101 binds also to both monophosphorylated peptides, but with bond lifetimes reduced by one order of magnitude compared to the peptide tau[pThr231/pSer235]. In essence, the trend detected for the binding frequencies is reproduced, meaning that the strongest bond occurs for mAb HPT-101 and tau[pThr231/pSer235], followed by the two monophosphorylated peptides tau[pThr231] and tau[pSer235], respectively [80].

Subsequently, the affinity constant (i.e., the ON/OFF-rate ratio) from this single-molecule measurement can be calculated and compared to the data obtained by ELISA. The dissociation rate follows directly from the DFS measurements by the relation $k_{\text{off}} = \tau_0^{-1}$. The ON rate k_{on} is related to the binding frequency h_B in the following way. Neglecting the dissociation process, the mass action law reads as

$$\frac{d\,[RL]}{dt} = k_{\text{on}}\,[R]\,[L] \tag{74.9}$$

where $[RL]$ is the number of formed receptor–ligand complexes in a certain time dt, $[R]$ and $[L]$ are the receptor and ligand concentrations, respectively. For the following calculations $[RL]$ equals the binding frequency h_B. By assuming that the surface coverage of the different microparticles is identical, the product $[R]\,[L]$ becomes a constant. However, this assumption is not totally fulfilled, as can be seen from the error bars Fig. 74.13a. The incubation time dt is set as one second (see discussion of relative binding frequency measurements). Consequently it follows that the ON rate is directly proportional to the binding frequency. Finally the relative affinity is given by

$$K_a^{\text{rel}} = h_B \cdot \tau_0 \propto k_{\text{on}} \cdot \tau_0 = \frac{k_{\text{on}}}{k_{\text{off}}^0} = K_a. \tag{74.10}$$

The relative affinity of mAb HPT-101 to the different types of peptides is shown in Fig. 74.13c. It is evident that the interaction between the mAb and the biphosphorylated peptide shows the highest relative affinity. Compared to this, the affinity of tau[pThr231] is decreased by a factor of 10 and to tau[pSer235] by a factor of almost 100. This strong splitting is caused mainly by the large differences in τ_0 since binding frequencies differ only slightly. By multiplying both quantities to get the relative affinity, this effect is enhanced strongly, resulting in the highest specificity of mAb HPT-101 to the biphosphorylated peptide. This result is in accordance with ELISA. However, the abovementioned cross-reactivity indicates that not only a distinct phosphorylation pattern contributes to the receptor–ligand bond, but also the surrounding amino acids, as they may slightly influence the free energy landscape of the epitope. By assuming that the binding is dominated by the electrostatic interactions between antibody and the negatively charged phosphorylation sites of the peptide, it can be concluded that the cross-reactions between mAb HPT-101 and tau[pThr231] as well as tau[pSer235], respectively, are too weak to be detected by ELISA [80].

74.5 CONCLUSION

The application of physical concepts and measurement procedures to relevant biological and biochemical issues have been well established in recent years. Especially optical tweezers, with the ability to hold and manipulate microscopic objects in three dimensions and with subpiconewton forces, became a standard tool in biophysics. By using appropriate position detection algorithms (e.g., cross-correlation and edge detection) force measurements can be performed with nanometer resolution. Additionally, dynamic force spectroscopy has proved to be a powerful tool for investigating biologically relevant processes, such as receptor–ligand interactions, on a single molecule level. By extracting specific bond parameters such as bond lifetime, binding length, and free energy of activation, DFS measurements offer new insights into the nature of such noncovalent bonds. In this chapter, three experimental studies on small, hyperphosphorylated τ-peptides and their respective monoclonal antibody have been presented. Such well-defined and small systems make it possible to compare the binding of mAbs to peptides containing the sites responsible for specific binding with those not containing them. In this context, the appearance of the distribution of rupture forces of unspecific interactions can be characterized and separated from the specific interactions. From this, detailed insight into the specific binding of different mAbs binding to the respective sorts of τ-peptides can be gained. Furthermore, the abovementioned measurements might help to increase the target specificity of mAbs since cross-reactions to epitopes with similar amino acid sequence can be detected and characterized, even if they are not observed in commonly used ensemble techniques. This precise knowledge might be of fundamental interest in the development and optimization of future therapeutic/diagnostic antibodies that can be used in human medicine.

REFERENCES

[1] Berg, J.M., Tymoczko, J.L., Stryer, L. (2002). *Biochemistry*, 5th ed. Freeman, New York, Chapter 27, Section 2.

[2] Robert, P., Benoliel, A., Pierres, A., Bongrand, P. (2007). What is the biological relevance of the specific bond properties revealed by single-molecule studies? *J. Mol. Recognit.* **20**, 432–447.

[3] Sackmann, E., Merkel, R. (2010). *Lehrbuch der Biophysik*. Master. Wiley-VCH-Verlag, Weinheim.

[4] Casi, G., Neri, D. (2012). Antibody–drug conjugates: Basic concepts, examples and future perspectives. *J. Control. Release* **161**, 422–428.

[5] Gerber, H., Koehn, F.E., Abraham, R.T. (2013). The antibody-drug conjugate: An enabling modality for natural product-based cancer therapeutics. *Nat. Prod. Reports* **30**, 625.

[6] Lin, K., Tibbitts, J. (2012). Pharmacokinetic considerations for antibody drug conjugates. *Pharm. Res*. **29**, 2354–2366.

[7] Nelson, A.L., Dhimolea, E., Reichert, J.M. (2010). Development trends for human monoclonal antibody therapeutics. *Nat. Rev. Drug Discov.* **9**, 767–774.

[8] Reichert, J.M., Dhimolea, E. (2012). The future of antibodies as cancer drugs. *Drug Discov. Today* **17**, 954–963.

[9] Reichert, J.M. (2013). Antibodies to watch in 2013: Mid-year update. *mabs 5* (doi 10.4161/mabs.24990).

[10] Salomo, M., Kegler, K., Gutsche, C., Struhalla, M., Reinmuth, J., Skokow, W., Hahn, U., Kremer, F. (2006). The elastic properties of single double-stranded DNA chains of different lengths as measured with optical tweezers. *Colloid Polym. Sci.* **284**, 1325–1331.

[11] Marko, J.F., Siggia, E.D. (1995). Stretching DNA. *Macromolecules* **28**, 8759–8770.

[12] Smith, S.B., Cui, Y., Bustamante, C. (1996). Overstretching B-DNA: The elastic response of individual double-stranded and single-stranded DNA molecules. *Science* **271**, 795–799.

[13] Tolić-Nørrelykke, S.F., Rasmussen, M.B., Pavone, F.S., Berg-Sørensen, K., Oddershede, L.B. (2006). Stepwise bending of DNA by a single TATA-box binding protein. *Biophys. J.* **90**, 3694–3703.

[14] Bennink, M.L., Leuba, S.H., Leno, G.H., Zlatanova, J., Grooth, B.G. de, Greve, J. (2001). Unfolding individual nucleosomes by stretching single chromatin fibers with optical tweezers. *Nat. Struct. Biol.* **8**, 606–610.

[15] Dame, R.T., Noom, M.C., Wuite, G.J.L. (2006). Bacterial chromatin organization by H-NS protein unravelled using dual DNA manipulation. *Nature* **444**, 387–390.

[16] Wagner, C., Olbrich, C., Brutzer, H., Salomo, M., Kleinekathöfer, U., Keyser, U., Kremer, F. (2011). DNA condensation by TmHU studied by optical tweezers, AFM and molecular dynamics simulations. *J. Biol. Phys.* **37**, 117–131.

[17] Salomo, M., Kroy, K., Kegler, K., Gutsche, C., Struhalla, M., Reinmuth, J., Skokov, W., Immisch, C., Hahn, U., Kremer, F. (2006). Binding of TmHU to single dsDNA as observed by optical tweezers. *J. Mol. Biol.* **359**, 769–776.

[18] Salomo, M., Keyser, U.F., Kegler, K., Gutsche, C., Struhalla, M., Immisch, C., Hahn, U., Kremer, F. (2007). Kinetics of TmHU binding to DNA as observed by optical tweezers. *Microsc. Res. Tech.* **70**, 938–943.

[19] Sischka, A., Toensing, K., Eckel, R., Wilking, S.D., Sewald, N., Ros, R., Anselmetti, D. (2005). Molecular mechanisms and kinetics between DNA and DNA binding ligands. *Biophys. J.* **88**, 404–411.

[20] Block, S.M., Goldstein, L.S.B., Schnapp, B.J. (1990). Bead movement by single kinesin molecules studied with optical tweezers. *Nature* **348**, 348–352.

[21] Wen, J., Lancaster, L., Hodges, C., Zeri, A., Yoshimura, S.H., Noller, H.F., Bustamante, C., Tinoco, I. (2008). Following translation by single ribosomes one codon at a time. *Nature* **452**, 598–603.

[22] Bertz, M., Rief, M. (2009). Ligand binding mechanics of maltose binding protein. *J. Mol. Biol.* **393**, 1097–1105.

[23] Preiner, J., Janovjak, H., Rankl, C., Knaus, H., Cisneros, D.A., Kedrov, A., Kienberger, F., Muller, D.J., Hinterdorfer, P. (2007). Free energy of membrane protein unfolding derived from single-molecule force measurements. *Biophys. J.* **93**, 930–937.

[24] Onoa, B. (2003). Identifying kinetic barries to mechanical unfolding of the T. thermophila ribozyme. *Science* **299**, 1892–1895.

[25] Debye, P. (1909). Der Lichtdruck auf Kugeln von beliebigem Material. *Ann. Phys.* **11**, 57–136.

[26] Ashkin, A., Dziedzic, J.M., Bjorkholm, J.E., Chu, S. (1986). Observation of a single-beam gradient force optical trap for dielectric particles. *Opt. Lett.* **11**, 288

[27] Ekspong, G. (2002). *Nobel Lectures: Including Presentation Speeches and Laureates' Biographies*. World Scientific, Singapore.

[28] Neuman, K.C., Nagy, A. (2008). Single-molecule force spectroscopy: Optical tweezers, magnetic tweezers and atomic force microscopy. *Nat. Methods* **5**, 491–505.

[29] Merkel, R. (2001). Force spectroscopy on single passive biomolecules and single biomolecular bonds. *Phys. Reports* **346**, 343–385.

[30] Gutsche, C., Elmahdy, M.M., Kegler, K., Semenov, I., Stangner, T., Otto, O., Ueberschär, O., Keyser, U.F., Krueger, M., Rauscher, M., Weeber, R., Harting, J., Kim, Y.W., Lobaskin, V., Netz, R.R., Kremer, F. (2011). Micro-rh eology on (polymer-grafted) colloids using optical tweezers. *J. Phys. Condens. Matt.* **23**, 184114.

[31] Wagner, C., Singer, D., Ueberschär, O., Stangner, T., Gutsche, C., Hoffmann, R., Kremer, F. (2011). Dynamic force spectroscopy on the binding of monoclonal antibodies and tau peptides. *Soft Matt*. **7**, 4370.

[32] Stangner, T., Singer, D., Wagner, C., Gutsche, C., Ueberschär, O., Hoffmann, R., Kremer, F. (2013). FACS-sorted particles reduce the data variance in optical tweezers-assisted dynamic force spectroscopy measurements. *Phys. Biol.* **10**, 46004.

[33] Harada, Y., Asakura, T. (1996). Radiation forces on a dielectric sphere in the Rayleigh scattering regime. *Opt. Commun.* **124**, 529–541.

[34] Ashkin, A. (1970). Acceleration and trapping of particles by radiation pressure. *Phys. Rev. Lett*. **24**, 156–159.

[35] Gouesbet, G., Maheu, B., Grehan, G. (1985). The order of approximation in a theory of the scattering of a Gaussian beam by a Mie scatter center. *J. Opt.* **16**, 239–247.

[36] Ren, K.F., Gréha, G., Gouesbet, G. (1994). Radiation pressure forces exerted on a particle arbitrarily located in a Gaussian beam by using the generalized Lorenz-Mie theory, and associated resonance effects. *Opt. Commun.* **108**, 343–354.

[37] Neves, A.A.R., Fontes, A., Cesar, C.L., Camposeo, A., Cingolani, R., Pisignano, D. (2007). Axial optical trapping efficiency through a dielectric interface. *Phys. Rev. E* **76**, 61917.

[38] Svoboda, K., Block, S.M. (1994). Biological applications of optical forces. *Ann. Rev. Biophys. Biomol. Struct.* **23**, 247–285.

[39] Williams, M.C. (2002). Optical tweezers: Measuring piconewton forces. In Schwille, P. (ed.), *Single Molecule Techniques*. Biophysical Society, Bethesda, MD.

[40] Neuman, K.C., Block, S.M. (2004). Optical trapping. *Rev. Sci. Instrum.* **75**, 2787–2809.

[41] Cox, G. (2012). *Optical Imaging Techniques in Cell Biology*, 2nd ed. CRC Press, Boca Raton, FL.

[42] R., Ficz, G. (2006). Breaking the resolution limit in light microscopy. *Brief. Funct. Genom. Proteom.* **5**, 289–301.

[43] Ueberschär, O., Wagner, C., Stangner, T., Gutsche, C., Kremer, F. (2012). A novel video-based microsphere localization algorithm for low contrast silica particles under white light illumination. *Opt. Lasers Eng.* **50**, 423–439.

[44] Baumgartl, J., Bechinger, C. (2005). On the limits of digital video microscopy. *Europhys. Lett.* **71**, 487–493.

[45] Gutsche, C., Keyser, U.F., Kegler, K., Kremer, F., Linse, P. (2007). Forces between single pairs of charged colloids in aqueous salt solutions. *Phys. Rev. E: Stat. Nonlin. Soft Matt. Phys.* **76**, 31403.

[46] Wagner, C., Stangner, T., Gutsche, C., Ueberschär, O., Kremer, F. (2011). Optical tweezers setup with optical height detection and active height regulation under white light illumination. *J. Opt.* **13**, 115302.

[47] Otto, O., Czerwinski, F., Gornall, J.L., Stober, G., Oddershede, L.B., Seidel, R., Keyser, U.F. (2010). Real-time particle tracking at 10,000 fpsusing optical fiber illumination. *Opt. Express* **18**, 22722–22733

[48] Otto, O., Gornall, J.L., Stober, G., Czerwinski, F., Seidel, R., Keyser, U.F. (2011) High-speed video-based tracking of optically trapped colloids. *J. Opt.* **13**, 44011.

[49] Gosse, C., Croquette, V. (2002). Magnetic tweezers: Micromanipulation and force measurement at the molecular level. *Biophys. J.* **82**, 3314–3329.

[50] Kim, K., Saleh, O.A. (2009). A high-resolution magnetic tweezer for single-molecule measurements. *Nucleic Acids Res*. **37**, e136.

[51] Chen, Y., Blab, G.A., Meiners, J. (2009). Stretching submicron biomolecules with constant-force axial optical tweezers. *Biophys. J.* **96**, 4701–4708.

[52] Charvin, G., Strick, T.R., Bensimon, D., Croquette, V. (2005). Tracking topoisomerase activity at the single-molecule level. *Annu. Rev. Biophys. Biomol. Struct.* **34**, 201–219.

[53] Strick, T.R., Croquette, V., Bensimon, D. (2000). Single-molecule analysis of DNA uncoiling by a type II topoisomerase. *Nature* **404**, 901–904.

[54] Gore, J., Bryant, Z., Stone, M.D., Nollmann, M., Cozzarelli, N.R., Bustamante, C. (2006). Mechanochemical analysis of DNA gyrase using rotor bead tracking. *Nature* **439**, 100–104.

[55] Binnig, G., Quate, C.F., Gerber, C. (1986). Atomic force microscope. *Phys. Rev. Lett.* **56**, 930–933.

[56] Stroh, C.M., Ebner, A., Geretschläger, M., Freudenthaler, G., Kienberger, F., Kamruzzahan, A.S.M., Smith-Gill, S.J., Gruber, H.J., Hinterdorfer, P. (2004). Simultaneous topography and recognition imaging using force microscopy. *Biophys. J.* **87**, 1981–1990.

[57] Hinterdorfer, P., Dufrêne, Y.F. (2006). Detection and localization of single molecular recognition events using atomic force microscopy. *Nat. Methods* **3**, 347–355.

[58] Lee, G.U., Chrisey, L.A., Colton, R.J. (1994). Direct measurement of the forces between complementary strands of DNA. *Science* **266**, 771–773.

[59] Rief, M., Clausen-Schaumann, H., Gaub, H.E. (1999). Sequence-dependent mechanics of single DNA molecules. *Nat. Struct. Mol. Biol.* **6**, 346–349.

[60] Lequin, R.M. (2005). Enzyme immunoassay (EIA)/enzyme-linked immunosorbent assay (ELISA). *Clin. Chem.* **51**, 2415–2418.

[61] Engvall, E., Perlmann, P. (1971). Enzyme-linked immunosorbent assay (ELISA) quantitative assay of immunoglobulin G. *Immunochemistry* **8**, 871–874.

[62] van Weemen, B.K., Schuurs, A.H.M. (1971). Immunoassay using antigen—enzyme conjugates. *FEBS Lett.* **15**, 232–236.

[63] Renart, J., Reiser, J., Stark, G.R. (1979). Transfer of proteins from gels to diazobenzyloxymethyl-paper and detection with antisera: a method for studying antibody specificity and antigen structure. *Proc. Natl. Acad. Sci.* **76**, 3116–3120.

[64] Noy, A. (2008). *Handbook of Molecular Force Spectroscopy*. Springer, New York.

[65] Bongrand, P. (1999). Ligand-receptor interactions. *Reports Progress Phys*. **62**, 921–968.

[66] Evans, E., Williams, P. (2002). *Dynamic Force Spectroscopy.* Springer, pp. 145–204.

[67] Zhou, H., Gilson, M.K. (2009). Theory of free energy and entropy in noncovalent binding. *Chem. Rev.* **109**, 4092–4107.

[68] Dudko, O.K., Hummer, G., Szabo, A. (2008). Theory, analysis, and interpretation of single-molecule force spectroscopy experiments. *Proc. Natl. Acad. Sci.* **105**, 15755–15760.

[69] Evans, E. (2001). Probing the relation between force – lifetime – and chemistry in single molecular bonds. *Annu. Rev. Biophys. Biomol. Struct.* **30**, 105–128.

[70] Bell, G. (1978). Models for the specific adhesion of cells to cells. *Science* **200**, 618–627.

[71] Evans, E., Ritchie, K. (1997). Dynamic strength of molecular adhesion bonds. Biophys. *J.* **72**, 1541–1555.

[72] Kramers, H.A. (1940). Brownian motion in a field of force and the diffusion model of chemical reactions. *Physica* **7**, 284–304.

[73] Schaap, I.A.T., Hoffmann, B., Carrasco, C., Merkel, R., Schmidt, C.F. (2007). Tau protein binding forms a 1 nm thick layer along protofilaments without affecting the radial elasticity of microtubules. *J. Struct. Biol.* **158**, 282–292.

[74] Wiltfang, J., Lewczuk, P., Riederer, P., Grünblatt, E., Hock, C., Scheltens, P., Hampel, H., Vanderstichele, H., Iqbal, K., Galasko, D., Lannfelt, L., Otto, M., Esselmann, H., Henkel, A.W., Kornhuber, J., Blennow, K. (2005). Consensus paper of the WFSBP Task Force on Biological Markers of Dementia: The role of CSF and blood analysis in the early and differential diagnosis of dementia. *World J. Biol. Psychiatr.* **6**, 69–84.

[75] Dickson, D.W., Crystal, H.A., Mattiace, L.A., Masur, D.M., Blau, A.D., Davies, P., Yen, S., Aronson, M.K. (1992). Identification of normal and pathological aging in prospectively studied nondemented elderly humans. *Neurobiol. Aging* **13**, 179–189.

[76] Singer, D., Lehmann, J., Hanisch, K., Härtig, W., Hoffmann, R. (2006). Neighbored phosphorylation sites as PHF-tau specific markers in Alzheimer's disease. *Biochem. Biophys. Res. Commun.* **346**, 819–828.

[77] Fulwyler, M.J. (1965). Electronic separation of biological cells by volume. *Science* **150**, 910–911.

[78] Lomax, R.G., Hahs-Vaughn, D.L. (2012). *Statistical Concepts: A Second Course*, 4th ed. Routledge Academic, New York.

[79] Kirkwood, T.B.L., Rosenberger, R.F., Galas, D.J. (1986). *Accuracy in Molecular Processes: Its Control and Relevance to Living System*. Springer, Dordrecht, Chapter 3, p. 37.

[80] Stangner, T., Wagner, C., Singer, D., Angioletti-Uberti, S., Gutsche, C., Dzubiella, J., Hoffmann, R., Kremer, F. (2013). Determining the specificity of monoclonal antibody HPT-101 to tau-peptides with optical tweezers. *ACS Nano* (doi:10.1021/nn405303u).

[81] Köhler, G., Milstein, C. (1975). Continuous cultures of fused cells secreting antibody of predefined specificity. *Nature* **256**, 495–497.

[82] Buss, N.A., Henderson, S.J., McFarlane, M., Shenton, J.M., Haan, L. de (2012). Monoclonal antibody therapeutics: History and future. *Curr. Opin. Pharmacol.* **12**, 615–622.

[83] Ducry, L., Stump, B. (2009). Antibody−drug conjugates: Linking cytotoxic payloads to monoclonal antibodies. *Bioconjug. Chem.* **21**, 5–13.

[84] Borrebaeck, C.A.K. (2000). Antibodies in diagnostics – from immunoassays to protein chips. *Immunol. Today* **21**, 379–382.

[85] Cahill, D.J. (2001). Protein and antibody arrays and their medical applications. *J. Immunol. Methods* **250**, 81–91.

75

AC ELECTROKINETICS OF CONCENTRATED SUSPENSIONS OF SOFT AND HAIRY NANOPARTICLES: MODEL AND EXPERIMENTS

Silvia Ahualli,[1] Ángel V. Delgado,[1] Félix Carrique,[2] and María L. Jiménez[1]

[1]*Department of Applied Physics, School of Sciences Campus Fuentenueva, University of Granada, Granada, Spain*
[2]*Department of Applied Physics II, School of Sciences, Campus Teatinos, University of Málaga, Málaga, Spain*

75.1 INTRODUCTION

It is a well-known fact that dispersions of micro- or nanoparticles are often used in the form of concentrated slurries in very different applications. Volume fractions of solids can be indeed very high (as much as 30–50%) in ceramic or drug suspensions, for example [1–4]. However, many techniques used in the characterization of dilute suspensions are practically useless in the evaluation of such systems, although this chapater focuses on electrokinetic techniques. These methods are based on determination of the response of the solid–solution interface (or of its macroscopic manifestations) to the application of an external field, often (but not always) electric [5–9]. Among these methods, (micro)electrophoresis, electroosmosis, or streaming potential are best known and most frequently employed, and their origins date back to the nineteenth century [10]. More recently, "indirect" techniques based on the measurement of some collective property have be used. In such cases, a theoretical treatment is required even for obtaining single-particle properties as a prior step in surface charge or potential evaluation. To this group belong two of the available techniques for the electrokinetic evaluation of concentrated suspensions. They are based on the application of alternating electric or pressure fields to the disperse system, and conclusions about the particles properties are based on analysis of the electrical permittivity of the suspension, or of the ["dynamic" or alternating-current (AC)] electrophoretic mobility of a single particle. They are obtained, respectively, from the frequency dependences of the conductivity of the system, and of the amplitude and phase of the ultrasound generated when an electric field with frequency in the MHz range is applied.

In both cases we can gain access to rich information about the dynamic processes in very varied systems, considering that the underlying microscopic mechanisms (field-induced or permanent polarization) can have a number of different origins. The associated methodologies are termed *low-frequency dielectric spectroscopy* (LFDD) and *electroacoustics*, respectively. In the first case, the frequency region of interest ranges from approximately 1 kHz to 1 MHz, while the 1–20 MHz interval is preferred for electroacoustic determinations [6, 9, 11–13].

Indeed, while the dielectric spectrum of a pure electrolyte solution in this region is flat, a suspension presents clear relaxation (or frequency dispersion) phenomena, regardless of whether the particles are large or small, polymeric or inorganic, or natural or artificially produced; with the only requirement is that their surface distributed electric charge be nonzero. On the other hand, the dynamic mobility also exhibits frequency dispersion processes related to polarization of the charged particles. Additionally, the shapes of the spectra depend in a nontrivial manner on the surface structure, particle size, conductivity, and permittivity, as well as

Encyclopedia of Biocolloid and Biointerface Science, Volume 2, First Edition. Edited by Hiroyuki Ohshima.
© 2016 John Wiley & Sons, Inc. Published 2016 by John Wiley & Sons, Inc.

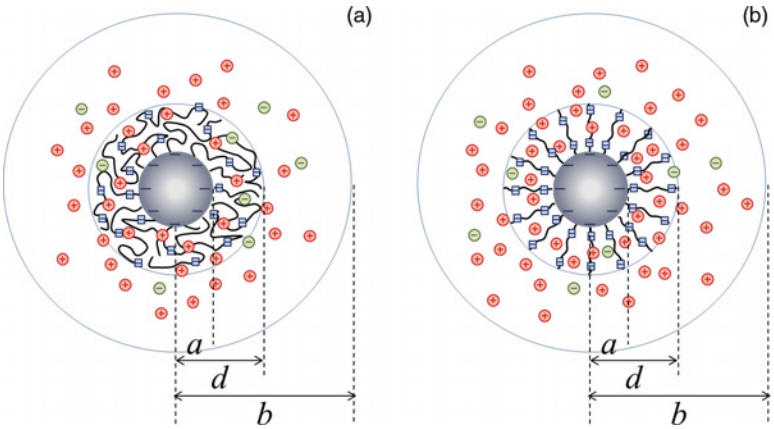


FIGURE 75.1 Schematic illustrations of the structure of a soft particle (a) and a spherical polyelectrolyte brush (b), where a is the core radius, d is the particle+layer thickness, and b is the radius of the electrolyte cell used for simulation of particle–particle interactions at moderate concentrations.

the ionic composition of the dispersion medium and the concentration of dispersed particles.

The number of studies dedicated to the AC electrokinetics of suspensions of rigid (or hard) particles is rather high (although experimental difficulties still limit the use of the technique) [14, 15]. Nevertheless, more recently it was found [16–18] that such properties are very sensitive to the presence of an external layer or shell of polymer or polyelectrolyte, grafted or adsorbed on the rigid core. Such a layer will be deformable, partially penetrable to the liquid, and (often) highly charged, and for this reason the resulting structures are known as *soft particles*, as schematically shown in Fig. 75.1a.

Interest in such particles is fundamental and related to the extremely varied phenomenology of such systems. Furthermore, in many situations modeling the particles as rigid is absolutely wrong, and in many instances the particles are used precisely because of their soft surface structure. In this respect, optimization of layer-by-layer deposition techniques has made it possible to construct model particles with soft interface properties [19]. Of particular importance is the occurrence of these types of structures in biological entities, including viruses and bacteria [20–25], for which the complexity of their external membranes (in the case of bacteria) or capsids (in viruses) rules out the description of their electrokinetic properties in terms of zeta-potential, no matter how sophisticated the theoretical model used.

Applications of soft-particle electrokinetics are very important in these biological systems, but they are not limited to them. Microgels and nanogels, which are of increasing interest, are extreme examples of soft entities in which even the rigid core can be considered absent. Again, these particles have found application in the field of drug transport and release [26–28].

The present contribution is devoted to showing some of the special features of the frequency dependence of the electric permittivity and dynamic mobility of suspensions of these types of materials. The chapter is organized as follows. In Section 75.2, the basic equations of the problem of determining the dielectric permittivity and dynamic mobility of concentrated suspensions of soft particles are presented. In Section 75.3, some representative predictions are discussed. Section 4 is devoted to our experimental results for both homogeneous and brushlike structure of the polymer layer. Finally, Section 75.5 summarizes the contents of the chapter.

75.2 BASIC EQUATIONS

75.2.1 General Overview and Notation Used

The first rigorous evaluations of the electrokinetics of concentrated systems date back to the 1970's, thanks to the contributions of Levine and Neale [29, 30], based on so-called cell models, previously introduced by Happel and Brenner [31] and Kuwabara [32] to account for hydrodynamic interactions between particles, and extended to the case of particles subjected to electrical or any other external fields. The model later received a more solid theoretical basis in work by another team [33–35]. In general terms, it is based on the assumption that an effective way to consider interactions between dispersed particles involves solving the problem for a single particle (a sphere of radius a) immersed in a concentric sphere of solution (the cell) with radius b (Fig. 75.1). The basics of the approach are as follows:

1. b can be defined by the volume fraction of solids in the suspension, ϕ:

$$\left(\frac{a}{b}\right)^3 = \phi \tag{75.1}$$

2. The interactions are mimicked by proper selection of boundary conditions for the velocity of the liquid, the

electric potential, and the concentration of ions on the cell limit, $r = b$.

3. The model can be extended to soft particles with adsorbed or grafted polymer layers, if the thickness of the layer is smaller than b.

Electrokinetic calculations based on the cell approach are very abundant [36] (although not free from criticism). One group of investigators [37,38] clarified some inconsistencies in earlier uses of the model, and several authors have more recently considered the so-called Shilov–Zharkikh method [39–42] as a well-founded alternative.

The basic equations of the problem are well established, in any case. A mean field approach is followed, so that the quantities of interest are functions of the position $\mathbf{r}$ (the position vector has its origin at the particle center). The quantities of interest are the electric potential $\Psi(\mathbf{r})$, the fluid velocity $\mathbf{v}(\mathbf{r})$, and the concentrations and velocities $n_i(\mathbf{r})$, $\mathbf{v}_i(\mathbf{r})$ of each ionic species. The fundamental equations are [11,17,43–45] (an alternating electric field, of frequency ω, $\mathbf{E}\exp(-i\omega t)$, is applied, hence a dependence $\exp(-i\omega t)$ is implicit in all quantities):

1. Poisson–Boltzmann equation

$$\nabla^2\Psi(\mathbf{r}) = \begin{cases} -\dfrac{\rho_{\mathrm{el}}(\mathbf{r})}{\varepsilon_0\varepsilon_{\mathrm{m}}}, & d < r < b \\ -\dfrac{\rho_{\mathrm{el}}(\mathbf{r})}{\varepsilon_0\varepsilon_{\mathrm{m}}} - \dfrac{3Q_{pol}(\mathbf{r})}{4\pi\varepsilon_0\varepsilon_{\mathrm{m}}(d^3 - a^3)}, & a < r < d \end{cases} \tag{75.2}$$

where $\rho_{\mathrm{el}}(\mathbf{r})$ is the local volume charge density $\rho_{\mathrm{el}}(\mathbf{r}) = \sum_{i=1}^{N} z_i e n_i(\mathbf{r})$, and Q_{pol} is the total charge carried by the polyelectrolyte cover.

2. Navier–Stokes equations for an incompressible fluid

$$\rho_m \frac{\partial}{\partial t}[\mathbf{v}(\mathbf{r}) + v_e] = \begin{cases} \eta_m\nabla^2\mathbf{v}(\mathbf{r}) - \nabla p(\mathbf{r}) - \rho_{\mathrm{el}}\nabla\Psi(\mathbf{r}), & d < r < b \\ \eta_m\nabla^2\mathbf{v}(\mathbf{r}) - \nabla p(\mathbf{r}) - \rho_{\mathrm{el}}\nabla\Psi(\mathbf{r}) - \gamma\mathbf{v}, & a < r < d \end{cases}$$
$$\nabla\cdot\mathbf{v}(\mathbf{r}) = 0 \tag{75.3}$$

where $\mathbf{v}$ is the fluid velocity with respect to the particle. The particle velocity with respect to the laboratory frame of reference is the electrophoretic velocity $\mathbf{v}_e exp(-i\omega t)$, and η_m, ρ_m are, respectively, the viscosity and density of the liquid medium. The extra friction in the polyelectrolyte layer is represented by the term $-\gamma\mathbf{v}$ in the Navier–Stokes equation, meaning that the Debye–Bueche model (where the charged layer is represented by a uniform distribution of friction centers) is assumed [16,17,46]. It is customary to use a different quantity to measure the layer resistance; this is the dimensionless product λa, where $\lambda = (\gamma/\eta_m)^{1/2}$. The reciprocal of λ is known as the *Brinkman screening length*, and it is a measure of the permeability of the porous layer or, equivalently, the thickness of the transition region between open flow of the liquid and the Darcy flow inside the pore thickness [46,47].

3. Ion conservation and Nernst–Planck equations

$$\begin{aligned} &\nabla\cdot[n_i(\mathbf{r})\mathbf{v}_{\mathbf{i}}(\mathbf{r})] = -\frac{\partial}{\partial t}[n_i(\mathbf{r})] \\ &\mathbf{v}_{\mathbf{i}} = \mathbf{v} - \frac{D_i}{k_B T}\nabla\mu_i \\ &\mu_i(\mathbf{r}) = \mu_i^{\infty} + z_i e\Psi(\mathbf{r}) + k_B T\ln n_i(\mathbf{r}) \end{aligned} \tag{75.4}$$

where $\mu_i(\mathbf{r})$ is the chemical potential of the ith ions, μ_i^{∞} is the corresponding standard value, and D_i is their diffusion coefficient.

It will be assumed that all quantities can be expressed as the sum of an equilibrium (superscript 0) and a field-dependent perturbation term. For low field strengths, as is the case in the problems considered, the perturbations are linearly dependent on the field, with its same frequency, and complex [44,48]:

$$\mu_i(\mathbf{r}) = \mu_i^0(r) + \delta\mu_i(\mathbf{r}) = \mu_i^0(r) - z_i e\phi_i(r)E\cos\theta \qquad (i = 1,\ldots,N) \tag{75.5}$$

$$\Psi(\mathbf{r}) = \Psi^0(r) + \delta\Psi(\mathbf{r}) = \Psi^0(r) - \Gamma(r)E\cos\theta \tag{75.6}$$

$$\mathbf{v}(\mathbf{r}) = \left\{ -\frac{2}{r}h(r)E\cos\theta, \quad \frac{1}{r}\frac{d}{dr}[rh(r)]\,E\sin\theta, \quad 0 \right\} \tag{75.7}$$

The obvious spherical symmetry in the absence of field renders the equilibrium quantities exclusively dependent on the radial spherical coordinate r. In addition, the perturbed quantities display axial symmetry with respect to the field direction, z. The unknown functions will hence be $h(r)$, $\phi_i(r)$, and $\Gamma(r)$, and θ is the angle between $\mathbf{r}$ and the field axis.

In terms of these new quantities, the partial differential equations of Poisson, Navier–Stokes, and ion conservation become ordinary differential equations, the form of which can be found in the literature [45, 49, 50]. The boundary conditions of the problem are as follows:

1. The surface charge of the particles Q or their surface density σ is defined as follows:

$$\varepsilon_m \varepsilon_0 \left.\frac{d\Psi^0}{dr}\right|_{r=a} = -\sigma = -\frac{Q}{4\pi a^2} \tag{75.8}$$

2. Electroneutrality of the cell is as follows:

$$\left.\frac{d\Psi^0}{dr}\right|_{r=b} = 0 \tag{75.9}$$

Equations (75.8) and (75.9) refer to the equilibrium situation. The conditions in presence of the field follow below.

3. Continuity of the potential and displacement vector perturbations on the particle surface, and on the polyelectrolyte layer, are as follows:

$$\left.\begin{array}{c} \delta\Psi(a^-) = \delta\Psi(a^+) \\ \varepsilon_p \left.\dfrac{\partial\delta\Psi}{\partial r}\right|_{a^-} = \varepsilon_m \left.\dfrac{\partial\delta\Psi}{\partial r}\right|_{a^+} \\ \delta\Psi(d^-) = \delta\Psi(d^-) \\ \left.\dfrac{\partial\delta\Psi}{\partial r}\right|_{d^-} = \left.\dfrac{\partial\delta\Psi}{\partial r}\right|_{d^+} \end{array}\right\} \rightarrow \begin{array}{c} \left.\dfrac{d\Gamma}{dr}\right|_a - \dfrac{\varepsilon_p}{\varepsilon_m a}\Gamma(a) = 0 \\ \Gamma(d^-) = \Gamma(d^+) \\ \left.\dfrac{d\Gamma}{dr}\right|_{d^-} = \left.\dfrac{d\Gamma}{dr}\right|_{d^+} \end{array} \tag{75.10}$$

Here, ε_p is the particle's relative permittivity.

4. The fluid velocity is stagnant on the core surface, and continuous at the polyelectrolyte layer. The vorticity is also taken as continuous on the same ideal surface $r = d$:

$$\left.\begin{array}{l} \mathbf{v}(\mathbf{r})|_{r=a} = 0 \\ \mathbf{v}(\mathbf{r})|_{r=d^-} = \mathbf{v}(\mathbf{r})|_{r=d^-} \\ \nabla\times\mathbf{v}(\mathbf{r})|_{r=d^-} = \nabla\times\mathbf{v}(\mathbf{r})|_{r=d^-} \end{array}\right\} \rightarrow \left\{\begin{array}{l} h(a) = 0 \\ \left.\dfrac{dh}{dr}\right|_{r=a} = 0 \\ h(d^-) = h(d^+) \\ \left.\dfrac{dh}{dr}\right|_{r=d^-} = \left.\dfrac{dh}{dr}\right|_{r=d^+} \\ Lh|_{r=d^-} = Lh|_{r=d+} \end{array}\right. \tag{75.11}$$

Here, L is the differential operator $L(\cdot) = d^2(\cdot)/dr^2 + 2/r\, d(\cdot)/dr - 2(\cdot)/r^2$.

5. Ions cannot penetrate the particle:

$$\left.\mathbf{v}_j \cdot \hat{\mathbf{n}}\right|_{r=a} = 0 \rightarrow \left.\frac{d\phi_j}{dr}\right|_{r=a} = 0, \quad j = 1, \ldots, N \tag{75.12}$$

6. The concentrations and velocities of ionic species are continuous at the interface between the polyelectrolyte layer and the solution:

$$\left.\begin{array}{l} \mathbf{v}_j(d^-) = \mathbf{v}_j(d^+) \\ n_j(d^-) = n_j(d^+) \end{array}\right\} \rightarrow \left\{\begin{array}{l} \phi_j(d^-) = \phi_j(d^-) \\ \left.\dfrac{d\phi_j}{dr}\right|_{d^-} = \left.\dfrac{d\phi_j}{dr}\right|_{d^+} \end{array}\right. , \quad j = 1, \ldots, N \tag{75.13}$$

A careful discussion is available [50] concerning the conditions on the cell external surface $r = b$. We will follow another approach [45], in which a set of general physical statements on the cell dynamics is all that is needed, as given next.

7. The macroscopic electric field $\mathbf{E}$ is given by

$$\mathbf{E} = \langle -\nabla\delta\Psi(\mathbf{r})\rangle \rightarrow \Gamma(b) = -b \tag{75.14}$$

where the average $\langle\bullet\rangle$ must be evaluated throughout the whole cell volume. This is equivalent to Dirichlet conditions as stated elsewhere [38].

8. Similarly, the average of the concentration perturbations is:

$$\langle\nabla\delta n_j(\mathbf{r})\rangle = 0 \rightarrow \delta n_j(b) = 0 \rightarrow \phi_j(b) = b \tag{75.15}$$

9. The average of the pressure perturbation (δp) gradient in the cell volume can be neglected, as no external pressure is imposed on the system:

$$\langle\nabla\delta p(\mathbf{r})\rangle = 0 \rightarrow \left.\frac{d}{dr}\left[r(L+\gamma^2)h\right]\right|_{r=b} - 2h(b)\gamma^2 - \frac{\sum_{i=1}^{N} z_i e n_i^0(b)}{\eta_m} \tag{75.16}$$

Here, $n_i^0(b)$ is the equilibrium concentration of the ith species on the cell boundary.

10. An additional condition is equivalent to Kuwabara's condition, which states that the radial velocity of the fluid on the cell coincides (except for a change of sign) with the component of the electrophoretic mobility in the same direction:

$$\left.\begin{array}{c} v_r(b) = -u_e E\cos\theta \\ \text{or} \\ \langle\mathbf{v}(\mathbf{r})\rangle = 0 \end{array}\right\} \rightarrow u_e = \frac{2h(b)}{b} \tag{75.17}$$

11. Finally the force balance on the cell is required [51]:

$$\oint_{S(r=b)} \overleftrightarrow{\boldsymbol{\tau}} \cdot \hat{\mathbf{n}} dS = -i\omega \left[\frac{4\pi}{3} a^3 \rho_P u_e \mathbf{E} + \rho_m \int_{V_m} [\mathbf{v}(\mathbf{r}) + \mathbf{v}_e] dV \right]$$
$$\rightarrow L[h(r)]|_{r=b} = \gamma^2 \phi \left(\frac{\rho_p - \rho_m}{\rho_m} \right) h(b) \tag{75.18}$$

Here, ρ_p is the particle density and $\overleftrightarrow{\boldsymbol{\tau}}$ is the total stress tensor on the $r = b$ surface. It can be demonstrated that it contains only hydrodynamic interactions.

75.2.2 The Case of Grafted Polymer: Spherical Polyelectrolyte Brushes (SPBs)

This problem has been treated both experimentally and theoretically [18,52]. Typical soft particles are distinguished by the additional assumption that the charged polymer chains are long and grafted on the particle from whose surface they appear to extend as rays; hence the denomination of brush particles [53–55], as schematically shown in Fig. 75.1b. If the ionic strength of the medium is low, the charged groups along the chains will keep them stretched. Shrinking of the chains will likely take place if the ionic concentration is raised or, as it is of interest to us here, if the concentration of SPBs is also large. This radial structure of the polyelectrolyte on the core requires modification of the soft-particle model described above. The homogenous distribution of charged groups is modified and an r^{-2} dependence of the volume charge density of the layer, the drag of the liquid, and the diffusion coefficient of the ions must be considered instead:

$$\rho_{pol} = \frac{Q_{pol}}{4\pi(d-a)} \frac{1}{r^2}$$
$$\lambda = \lambda_0 \frac{a}{r} \tag{75.19}$$
$$D = D_0 \frac{r^2}{d^2}$$

Here, the 0 subscript corresponds to the situation where all charge and frictions centers are homogeneously distributed.

75.2.3 Expressions for Electrophoretic Mobility and Permittivity of the Suspension

Details on the evaluation of the dynamic mobility or the electric permittivity are provided in Ref. 16. For the sake of brevity, only the final expressions will be shown here. These equations reflect the need to obtain the values of h, ϕ_j, and Γ as well as their derivatives on the cell limit. In the case of mobility, the result is rather straightforward:

$$u_e = \frac{2h(b)}{b} \frac{1}{1 + \phi \dfrac{\rho_c - \rho_m}{\rho_m}} \tag{75.20}$$

Here, ρ_c (ρ_m) is the mass density of the core (solution). The permittivity is obtained in a more indirect way, as one starts from the complex frequency-dependent conductivity of the suspension:

$$K^*(\omega) = \sum_{i=1}^{N} \left[\frac{z_i^2 e^2 n_i^\infty k_B T}{D_i} \left(1 - \frac{3\phi}{a^3} \Omega_i \right) - u_e z_i n_i^\infty \right]$$
$$\times \exp\left(-\frac{z_i e \Psi^0(b)}{k_B T} \right) - i\omega \varepsilon_m \varepsilon_0 \left(1 - \frac{3\phi}{a^3} \Omega \right) \tag{75.21}$$

Here

$$\Omega_i \equiv -\frac{b^2}{3} \left(r \frac{d\phi_i}{dr} - \phi_i \right)_{r=b}, \quad i = 1, \ldots, N$$
$$\Omega \equiv -\frac{b^2}{3} \left(\Gamma - r \frac{d\Gamma}{dr} \right)_{r=b} \tag{75.22}$$

From the conductivity, the permittivity follows by simply considering that a complex conductivity can equally be interpreted as a complex permittivity, except for the DC ($\omega = 0$) contribution:

$$K^*(\omega) = K^*(\omega = 0) - i\omega \varepsilon^*(\omega) \varepsilon_0$$
$$= K^*(\omega = 0) - i\omega \varepsilon'(\omega) \varepsilon_0 + \omega \varepsilon''(\omega) \varepsilon_0 \tag{75.23}$$

where we have introduced the real and imaginary components of the relative permittivity (frequently designated as dielectric constant). For practical reasons, the (also complex) dielectric increment is used:

$$\Delta\varepsilon^*(\omega) = \varepsilon^*(\omega) - \varepsilon_m = \Delta\varepsilon'(\omega) - i\Delta\varepsilon''(\omega) \tag{75.24}$$

Let us finally mention that, according to the Maxwell–Wagner derivation [6], a relationship can be established between the complex conductivity of the suspension and the induced dipole coefficient of each particle (in our case, the solid particle plus its electric double layer), C^* (ω):

$$K^*(\omega) = K_m^*(\omega) \frac{1 + 2\phi C^*(\omega)}{1 - \phi C^*(\omega)} \underset{\phi \to 0}{\approx} K_m^*(\omega)(1 + 3\phi C^*(\omega)) \tag{75.25}$$

In this equation, $K_m^*(\omega)$ is the complex conductivity of the liquid medium, which, keeping in mind that the liquid does not

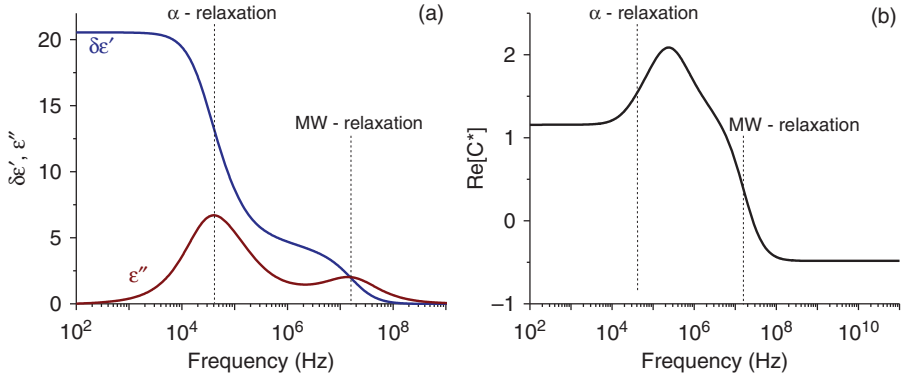


FIGURE 75.2 Schematic representation of the real and imaginary parts of the relative permittivity (a) of a dilute suspension, and real part of the induced dipole coefficient (b) of a 100 nm spherical particle in a 0.1 mM KCl solution with surface charge 10^{-14} C, as a function of the frequency of the field.

undergo any relaxation for frequencies below the microwave regime, can be simplified in terms of the (constant) DC conductivity and the dielectric constant of the medium: $K_m^*(\omega) = K_m + i\omega\varepsilon_m\varepsilon_0$. From this we obtain

$$\varepsilon'(\omega) = \varepsilon_m + 3\phi\varepsilon_m \left\{ \mathrm{Re}[C^*(\omega)] + \frac{K_m}{\omega\varepsilon_m\varepsilon_0} \mathrm{Im}\left[C^*(\omega)\right] \right\} \tag{75.26}$$

an expression allowing us to interpret the dielectric spectra in terms of a microscopic quantity as the polarizability of the particles.

Figure 75.2 shows the two relaxations typically encountered in the dielectric spectrum of a suspension: the α relaxation and the Maxwell–Wagner relaxation. The *α relaxation* is due to polarization of the concentration clouds induced by the field on both sides of the particle (so-called concentration polarization; the neutral electrolyte concentration increases on one side and is depleted on the other). If the frequency is high enough, the relaxation takes place because the clouds cannot be formed. The *Maxwell–Wagner* (*MW*) *relaxation* is higher in frequency and is associated with the heterogeneity of the dispersed system, that is, the fact that the particle and the medium may have different permittivities and/or conductivities. As mentioned, these processes have different timescales [13]: 10^{-7} s in the case of the MW relaxation (typically the time required for the ions to diffuse at a distance equal to the double- layer thickness), and 10^{-4} s (the time for the formation of the electrolyte cloud with characteristic dimension equal to the particle dimension). The correlation with the dipole coefficient is also illustrated in Fig. 75.2. Because the concentration polarization tends to decrease the magnitude of the dipole, the disappearance of the former leads to an increase in the real part of C^*; for high frequencies it is the MW relaxation that appears, and produces a decrease in Re[C^*] because the ions cannot follow the field oscillations. The limiting value of Re[C^*] is $-1/2$, but at low frequency the value will be larger (even positive and equal to 1) for a highly charged particle [7]. For little or no charge, the $-1/2$ value remains constant for the whole frequency range.

75.3 SOME PREDICTIONS

75.3.1 Soft Particles

Figure 75.3 enables comparison between the dielectric behavior of a suspension of hard particles and one with soft structures; the charges of the rigid particle in the former case and of the polyelectrolyte layer in the latter are identical. It is evident that the amplitude of the relaxation is significantly larger in coated particles, an effect hindered by the increase in friction (i.e., the increase in λa), as expected from the subsequent reduction in ion mobility in the layer. The fact that ions in the coating are on the average at larger distances from the rigid core can explain the enhanced response. On the other hand, note that the frequency of the relaxation is not affected by the presence of the layer.

In the same figure, the dynamic mobility is shown. Note that maxima and minima in (minus) the imaginary component of u_e correspond roughly to the decrease (inertial) and increase (Maxwell–Wagner), respectively, of the real part. It is clear that the mobility of the coated particles can be considerably larger than that of the bare ones, as long as the friction in the layer is not too high, becoming a dominant decreasing factor. The presence of the volume-distributed counterions in the layer produces an extended charged interface where the electroosmotic flow is largely favoured; hence the large mobility. We can also see evidence of the well-known fact that at high field frequencies, neither the liquid flow nor the particle motions can follow the fast field oscillations, and the mobility drops to zero in all cases. This so-called inertia relaxation takes place, in the case of rigid particles, at

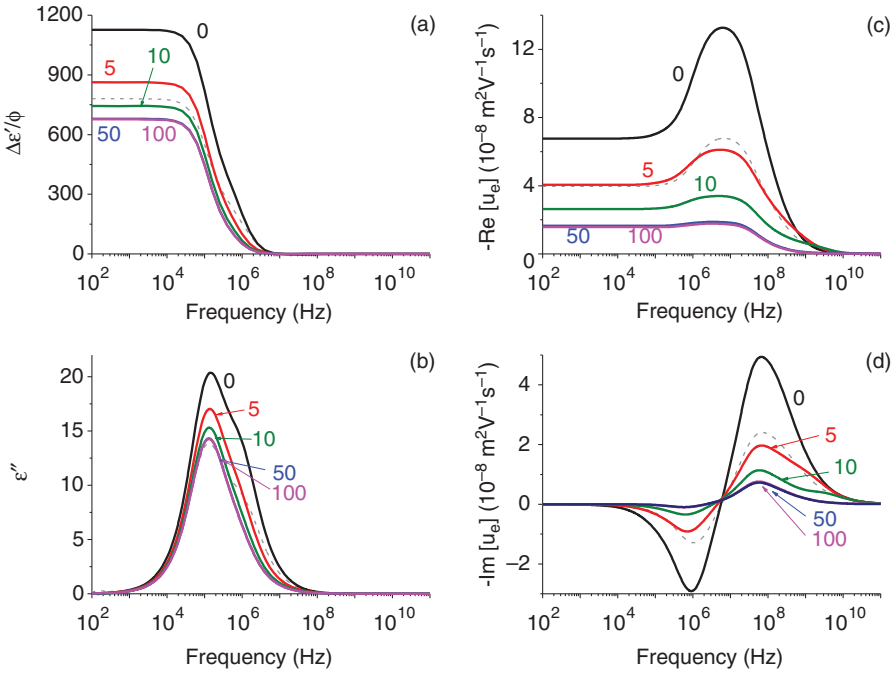


FIGURE 75.3 (a) Specific (per unit volume fraction) dielectric increment, (b) imaginary component of the relative permittivity, and real (c) and imaginary (d) components of the dynamic mobility in suspensions of soft spheres, as a function of frequency. The case of hard particles (dashed lines) is included for comparison. In all cases, the charge (on the bare particles or in the polymer layer) equals -1×10^{-15} C, the volume fraction of solids is 5%, the core radius is 100 nm. The thickness of the polyelectrolyte coating is 40 nm and the dispersion medium is 0.1 mM KCl solution. λa values as indicated.

a frequency $\omega_{in} = 2\pi\eta_m/a^2\rho_m$; the fact that the position of maxima in $-\mathrm{Im}(u_e)$ in Fig. 75.3d does not change in presence of the layer indicates that the inertia relaxation is controlled by the core size, except if the layer is too rigid, when the coated particle differs only slightly from a rigid one with radius d (data not shown).

The effect of the volume fraction on the dielectric and mobility dispersions is depicted in Fig. 75.4. Two features are immediately noticeable. *First*, both the dielectric amplitude and the low-frequency mobility decrease when the volume fraction is increased. In the former case, the reason is the partial compensation of the polarized clouds of neighbor particles when the average interparticle distance (roughly the b parameter of the cell, Fig. 75.1) decreases as a result of particle concentration. In the case of the mobility, the effect of hydrodynamic and electrical interactions can be assumed responsible for the reduction in the dielectric dispersion amplitude [56]. *Second*, Fig. 75.4 shows an increase in α relaxation toward higher frequencies the larger the volume fraction, again well explained in terms of the size of the polarization clouds, controlled by the particle radius at low volume fractions and by the distance b at moderate and high ϕ values. The effect on the inertia relaxation of u_e of the particle concentration is also clear; increasing ϕ raises the characteristic frequency as well. The same reasons can be given for such behavior. It is also apparent that the effect of the volume fraction is more relevant in the case of soft particles; because of the spatial extension of the polymer layers, increasing the volume fraction (i.e., reducing b in Fig. 75.1) more easily affects the volume available for concentration polarization clouds in that case, due to the closer proximity of the polymer layers to the cell limits, or, equivalently, to neighbor particles.

75.3.2 Brushlike Particles

The first point to consider is the difference between the model predictions corresponding to soft-particle and SPB models. Figure 75.5a,b clearly demonstrates the larger amplitude of the α relaxation and the different frequency dependences in the case of brush-like particles. This is because the characteristic dimensions and the magnitudes of the gradients of neutral electrolyte concentration established around the three kinds of particles are significantly different. For soft layers the equilibrium space charge distribution is homogeneous, and both the perturbed concentration of ions and the region where diffusion is maximum (limit of the space charge region) are smaller in comparison to SPBs. In such particles,

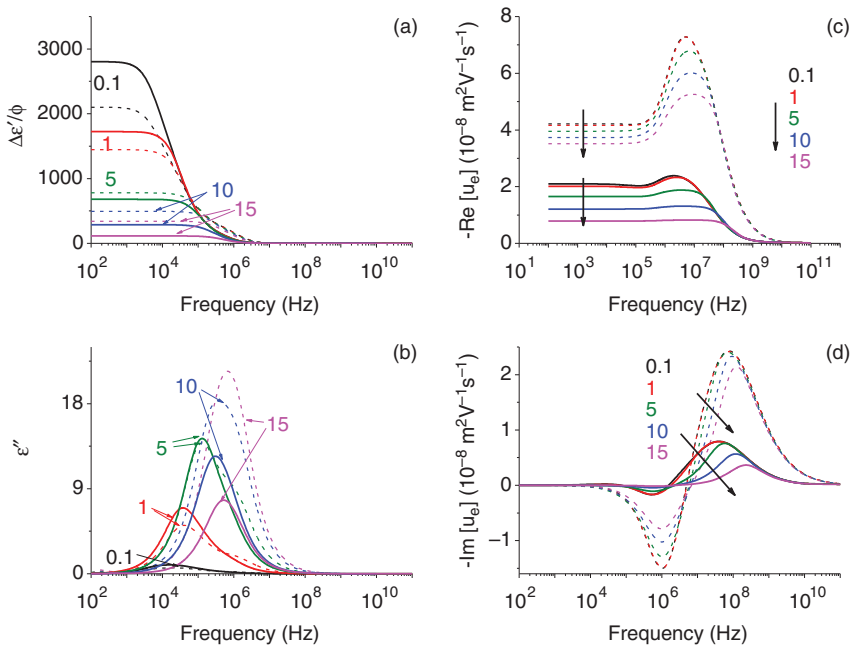


FIGURE 75.4 (a) Specific dielectric increment, (b) imaginary component of the relative permittivity, and real (c) and imaginary (d) components of the dynamic mobility of suspensions of soft (solid lines) and hard (dashed lines) spheres, as a function of frequency. In each case, the figures show the variations with the indicated volume fractions in percent, keeping constant the remaining parameters; the charge equals -1×10^{-15} C (in the polymer layer for soft particles, and on the particle surface for hard ones), the friction parameter $\lambda a = 50$, and the core radius is 100 nm. The thickness of the polyelectrolyte coating is 40 nm, and the dispersion medium is 0.1 mM KCl solution.

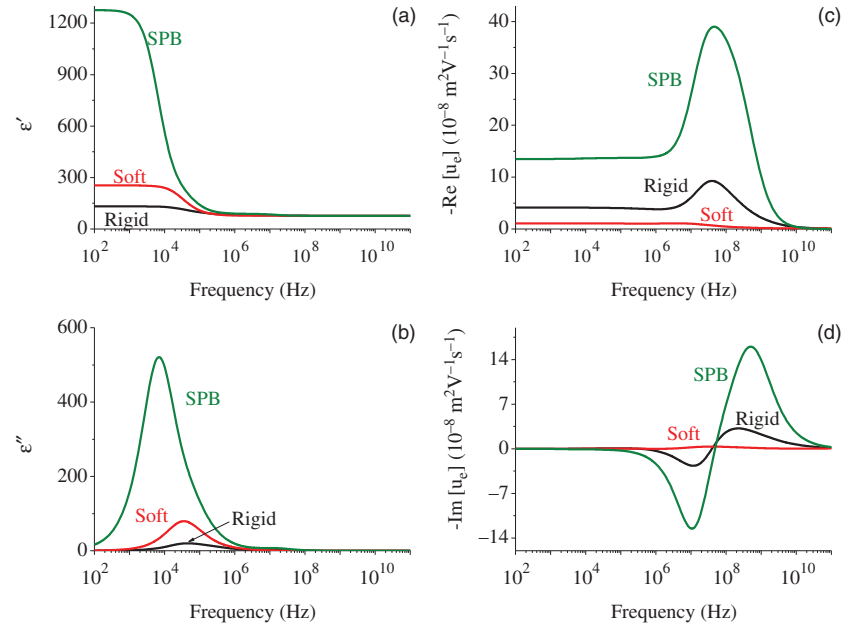


FIGURE 75.5 Real (a) and imaginary (b) parts of the relative permittivity, and real (c) and imaginary (d) components of the dynamic mobility for rigid, soft, and SPB particle suspensions under the same conditions. The total charge (-1×10^{-14} C) in the polymer layer for soft and SPB models is distributed on the core in the case of the rigid model. The friction parameter is $\lambda a = 50$, the core radius is 100 nm, and the volume fraction is 1%. The thickness of the polyelectrolyte coating is 100 nm, and the dispersion medium is 1 mM KCl solution.

the charge is not homogeneously distributed inside the brush, and the cloud of neutral electrolyte can be formed even inside the polyelectrolyte brush. This leads to a considerable concentration polarization and, from this, to a large increase in low-frequency permittivity, as has been found experimentally. Together with the r dependence of the diffusion coefficient, this results in a shift in the relaxation frequency to lower values. For the same reasons, the electrophoretic mobility is much larger in SPBs, as the region of volume charge extends to large distances from the interface, giving rise to a wide conducting layer, and, correspondingly, to a large region where electroosmotic flow can develop around the particle. Therefore, it can be assumed that a thick layer of charged liquid is accelerated by the field. As a result, from the laboratory frame of reference, the mobility will undergo a clear increase.

75.4 EXPERIMENTAL VERIFICATION

75.4.1 Soft Particles

A number of predictions of the models described can be confirmed experimentally [57–59]. For this work, we have used spherical hematite particles (manufactured by Lanxess, Germany) under the tradename of Bayferrox 130. A Malvern Mastersizer 2000 (Malvern Instruments, UK) was used for estimating an average diameter $d_{50} = 253$ nm. Two coatings were deposited on them, one cationic [poly(dialildimethyl ammonium chloride) (PDADMAC)] and the other anionic [sodium polystyrene sulfonate (PSS)]. Figure 75.6 presents data on the electrophoresis of the particles, showing that the coating has been produced as expected, with both polyelectrolytes behaving as strong ones, with full dissociation at any pH.

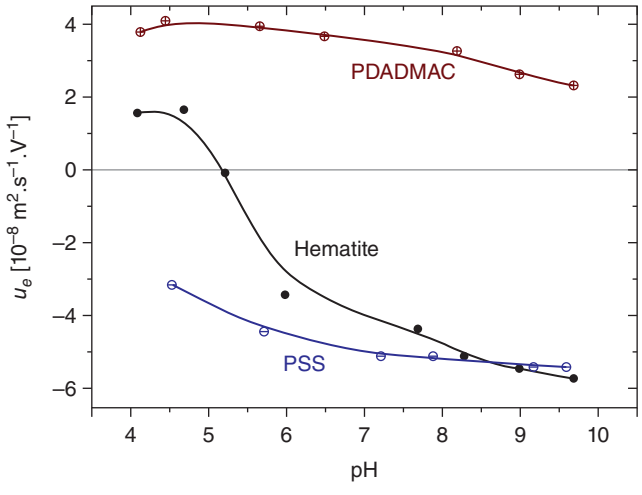


FIGURE 75.6 Effect of pH on electrophoretic mobility of hematite particles, both uncoated and coated with either PDADMAC or PSS. Ionic strength: 1 mM $NaClO_4$.

The permittivity of the hematite suspensions was in this case obtained from the measurements of the complex impedance of the systems in a cylindrical cell with platinized platinum electrodes, with variable separation, using the logarithmic derivative of the real component of the permittivity in order to minimize the effect of electrode polarization [14,15]. The results refer to the imaginary part of the relative permittivity, as shown in Figs. 75.7 and 75.8. The tremendous effect of the coating is clear, and, in addition, our model is capable of fitting the spectra very precisely. Furthermore, these data can be fitted using our model, with the following (reasonable) parameters: Q_{pol} (PDADMAC) $= 15 \times 10^{-15}$ C, Q_{pol}(PSS) $= -6 \times 10^{-15}$ C, λ (PDADMAC) $= 8 \times 10^7$ m^{-1}, and λ (PSS) $= 7 \times 10^7$ m^{-1}. The inner core charges used in the model are pH-dependent as expected in an oxide–solution interface. Some representative values for Q were (units: 10^{-15} C): +1 (pH 4), −1.8 (pH 5.6), −4 (pH 6.7), −6 (pH 7.6), −9 (pH 8.6).

Finally, we point out the following:

- The permittivity increment of coated particles is larger than that of rigid ones.
- The relaxation frequency decreases on coating, something not predicted by the model. This may be a manifestation of an increase in particle size because the coating encloses several particles instead of single ones.
- For negatively charged coating, the permittivity increases clearly with the polymer charge. This is found both experimentally and theoretically. The effect is not so clear for positive layers, because of the interplay between the signs of the core and the coating.

75.4.2 Polyelectrolyte Brushes

Although the most common technique of electrophoresis can be used for inferring structural changes in SPBs, the AC methods presented in this chapter are presumably much more informative. In a more recent contribution from the authors [18, 52] it was found that it is very unlikely that electrokinetic data in AC fields obtained with SPBs can be reasonably explained not only with a rigid particle model but even with a soft particle approach. Indeed, Fig. 75.9 demonstrates that the spectra of dynamic mobility reach values as high as 10^{-7} m^2 V^{-1} s^{-1}, between 2 and 5 times larger than expected for standard, rigid particles. Moreover, the absolute value of the mobility increases with the volume fraction of solids, again a strongly unexpected behavior. The fact that the mobility can be higher in the case of SPBs than in comparable rigid particles was predicted theoretically as described, and was already reported by other authors [46], in cases of highly coated layers. This is an indication of strong electroosmotic flows in the layer (recall that a high velocity of the particles in the laboratory reference frame is equivalent to a high electroosmotic

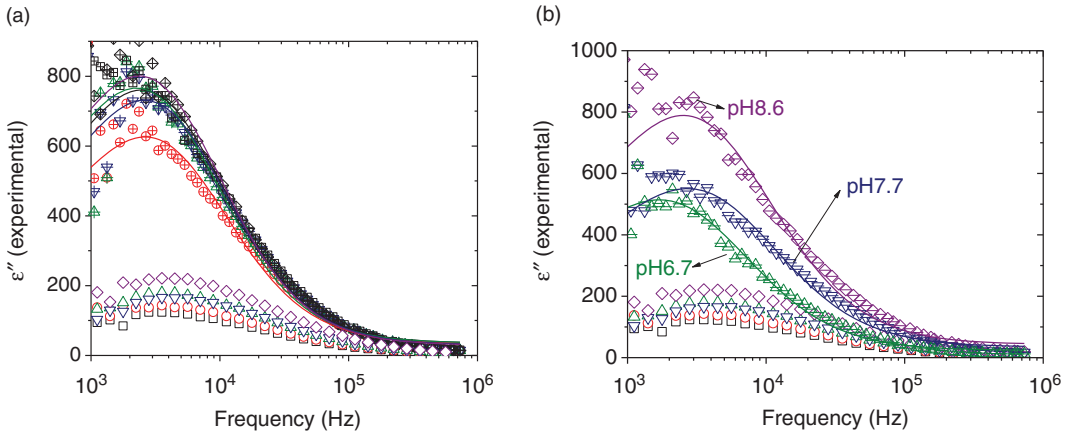


FIGURE 75.7 Experimental values (symbols with "+"/"−") of the imaginary part of the permittivity of suspensions of hematite coated with PDADMAC: (a) (pH 4, squares; pH 5.6, circles; pH 6.7, up triangles; pH 7.6, down triangles; pH 8.6, diamonds) and PSS (b), for different pH values as indicated. Lines: best fit to the model presented. Open symbols: bare hematite.

velocity of the liquid referred to the particle), associated with mobile counterions. Although some data have been reported indicating that the mobility of ions in the layer is reduced as compared to that of free ions, the abundance of ions for highly charged coatings must compensate for that and lead to fast flows.

As discussed, as in other electrokinetic studies dealing with complex systems, the use of more than one technique applied to the very same system is very clarifying, as long as the same set of fundamental parameters can be used to explain both sets of data. In our case, we focus on the electric permittivity spectra of SPBs. The results are depicted in Fig. 75.10, showing that the observed relaxation is significantly high, not comparable to that of rigid particles. In Fig. 75.11 we compare the permittivity of an SPB suspension to that of pure, rigid polystyrene particles with the size of either the core or the whole particle. Note that in neither case do the permittivity spectra of the polystyrene particles approach that of the brush-coated cores.

On the contrary, our model, described above, is capable of explaining the entire set of data using a single set of parameters, as illustrated in Figs. 75.9 and 75.10. It must be admitted that only at low frequency are some discrepancies found between the experimental data and our predictions. Nevertheless, it is also well known that in this range of frequencies, the effect of electrode polarization can be more noticeable, in spite of the methods used for eliminating (or, more realistically speaking, minimizing) such effects. Fortunately, the frequency interval used in dynamic mobility measurements, ranging from 1 to 18 MHz, is much less affected.

The values of the parameters used for fitting can be considered reasonable and comparable to values found

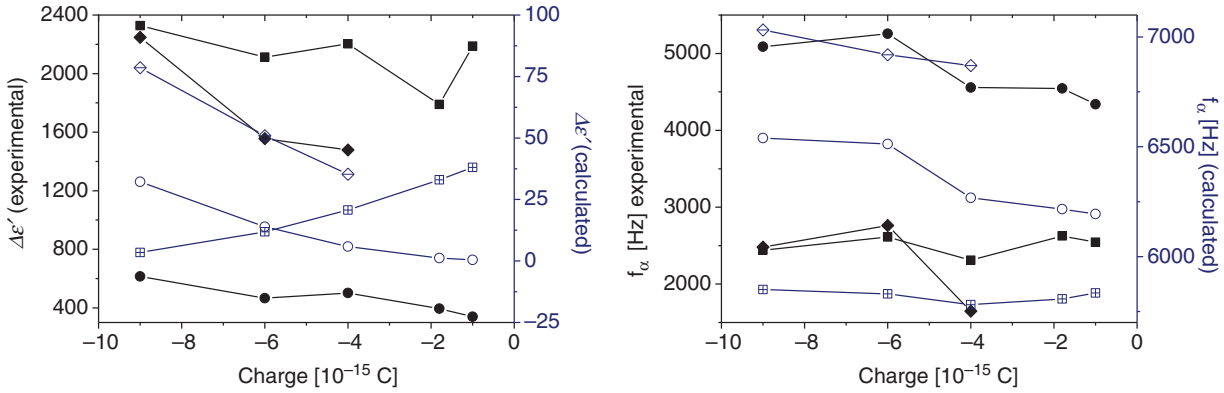


FIGURE 75.8 Comparison between the experimental (left axes, full symbols) and calculated (right axes, open symbols) permittivity increments (a) and relaxation frequencies (b) of hematite particles either bare (circles) or coated with PDADMAC (squares) and PSS (diamonds), as a function of the charge of the bare particle.

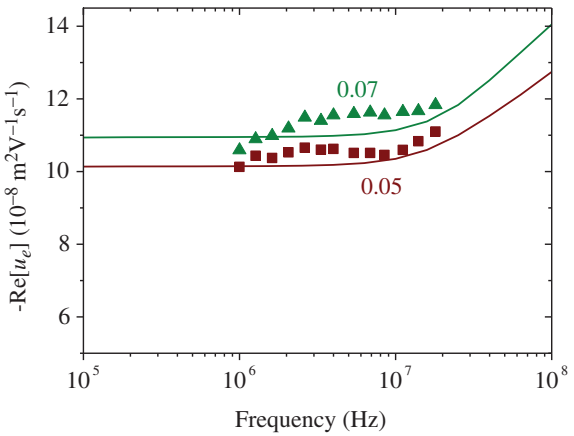


FIGURE 75.9 Symbols: real part of the experimental values of the dynamic mobility of SPBs (polystyrene sulfonate chains grafted on polystyrene core) as a function of frequency, for the volume fractions indicated, in 0.5 mM NaCl. The lines correspond to the best fit to our theoretical predictions, obtained using the following parameters: Particle charge: -5×10^{-16} C; charge of the polyelectrolyte layer plus condensed counterions: -8.5×10^{-14} C, dimensionless friction parameter: $\lambda_0 a = 110$; polymer layer thicknesses: 85 and 55 nm for volume fractions $\phi = 5$ and 7%, respectively. (From Ahualli et al. 2012 [52], p. 16372. © American Chemical Society; reproduced with permission.)

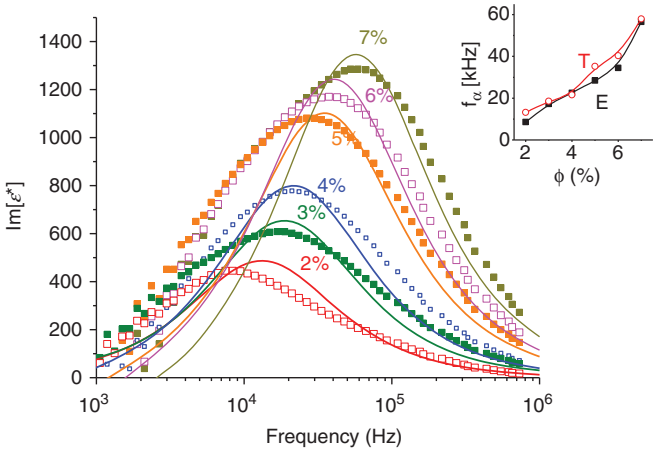


FIGURE 75.10 Symbols: imaginary part of the experimental values of the relative permittivity of SPB suspensions as a function of frequency, for the volume fractions indicated, in 0.5 mM NaCl. The lines correspond to the best fit to our theoretical predictions, obtained using the parameters detailed in the caption to Fig. 75.9; polymer layer thicknesses: 156, 136, 94, 85, 75, and 55 nm for volume fractions $\phi = 2\%$, 3%, 4%, 5%, 6%, and 7%, respectively. The inset allows the comparison between measured (full symbols, E) and fitted (open symbols, T) relaxation frequencies f_α as a function of ϕ. (From Ahualli et al. 2012 [52], p. 16372. @ American Chemical Society; reproduced with permission.)

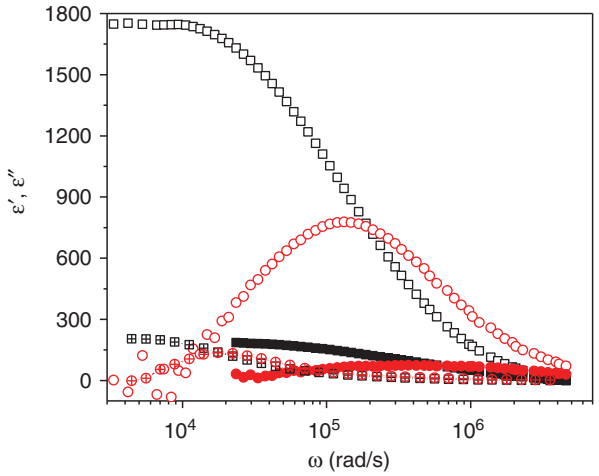


FIGURE 75.11 Real (squares) and imaginary (circles) parts of the relative permittivity of suspensions of SPBs (open symbols), polystyrene 50 nm in radius (filled sysmbols) and polystyrene 168 nm in radius (crossed symbols) as a function of the field frequency. Particle concentration: 4% by weight. Ionic strength 0.5 mM NaCl. (Details in Jiménez et al. 2011 [18]; http:pubs.rsc.org/en/content/articlelanding/2011/sm/c0sm01544j. Reproduced with permission of the Royal Society of Chemistry.)

using other methods. For instance, the core particle charge ($Q = -5 \times 10^{-16}$ C) corresponds to a surface charge density of 6 μ C/cm^2, a very typical value. The polymer charge (-8.5×10^{-14} C) is equivalent to 40 mM, again a moderate charge amount. Finally, the layer thickness changes from 156 nm for 2% volume fraction to 55 nm for 7%; these values should be compared with the thickness deduced from hydrodynamic radius determinations (i.e., very low volume fractions), namely, 150 nm [62]. Concerning the Brinkman screening length that best fits the data, $\lambda^{-1} = 0.5$ nm, it is quite close to the theoretical result of 1 nm [55].

75.5 CONCLUSION

We have given a brief account of the basic features of the dielectric relaxation in suspensions of spheres coated by a polyelectrolyte layer. The predictions are physically explained in terms of polarization mechanisms in the electric double layer. The modeling compares favorably with experimental data obtained with hematite spheres coated with PDADMAC (positive) and PSS (negative), as well as with spherical brushes of polystyrene with polystyrene sulfonate. It is especially worthwhile to mention that the results presented demonstrate that AC electrokinetic techniques provide, if a proper model is used in each case, an amount of information impossible to acquire with standard electrokinetic methods. In particular, the combination of dielectric dispersion and dynamic mobility data yields in situ values

of parameters completely characterizing the soft or SPB particle, including particle and polymer charge, polyelectrolyte thickness, and layer permeability, which are perfectly comparable to those accessible with specifically designed methods.

ACKNOWLEDGMENT

Financial support from Junta de Andalucía, Spain (Project PE2012-FQM694) MINECO, Spain (projects FIS2013-47666-C3-1-R and FIS2013-47666-C3-2-R) and EU FEDER Funds are gratefully acknowledged.

REFERENCES

[1] Barrientos, A.B. (2009). Model for yield stress of quartz pulps and copper tailings. *Int. J. Mineral Process.* **93**(3–4), 213–219.

[2] Beirowski, J., Inghelbrecht, S., Arien, A., Gieseler, H. (2012). Freeze-drying of nanosuspensions, Part 3: Investigation of factors compromising storage stability of highly concentrated drug nanosuspensions. *J. Pharm. Sci.* **101**(1), 54–362.

[3] Johnson, S.B., Franks, G.V., Scales, P.J., Boger, D.V., Healy, T.W. (2000). Surface chemistry-rheology relationships in concentrated mineral suspensions. *Int. J. Mineral Process.* **58**(1–4), 267–304.

[4] Vauthier, C., Cabane, B., Labarre, D. (2008). How to concentrate nanoparticles and avoid aggregation? *Eur. J. Pharm. Biopharm.* **69**(2), 466–475.

[5] Ohshima, H. (2012). *Electrical Phenomena at Interfaces and Biointerfaces.* Wiley, Hoboken, NJ.

[6] Delgado, A.V. (2002). *Interfacial Electrokinetics and Electrophoresis.* Marcel Dekker, New York, p. 106.

[7] Hunter, R.J. (1987). *Foundations of Colloid Science*, Vol. I. Clarendon Press, Oxford, UK.

[8] Lyklema, J. (2005). *Fundamentals of Interface and Colloid Science*, Vol. IV. Elsevier, Amsterdam.

[9] Stoilov, S.P., Stoimenova, M.V. (2007). *Molecular and Colloidal Electro-optics.* Taylor & Francis, Boca Raton, FL, p. 134.

[10] Wall, S. (2010). The history of electrokinetic phenomena. *Curr. Opin. Colloid Interface Sci.* **15**(3), 119–124.

[11] Delacey, E.H.B., White, L.R. (1981). Dielectric response and conductivity of dilute suspensions of colloidal particles. *J. Chem. Soc. Faraday Transact. Ii* **77**, 2007–2039.

[12] Dukhin, S.S., Shilov, V.N. (1974). *Dielectric Phenomena and the Double Layer in Disperse Systems and Polyelectrolytes*. Wiley, New York.

[13] Shilov, V.N., Delgado, A.V., González-Caballero, E., Horno, J., López-García, J.J., Grosse, C (2000). Polarization of the electrical double layer. Time evolution after application of an electric field. *J. Colloid Interface Sci.* **232**(1), 141–148.

[14] Tirado, M.C., Arroyo, F.J., Delgado, A.V., Grosse, C. (2000). Measurement of the low-frequency dielectric properties of colloidal suspensions: Comparison between different methods. *J. Colloid Interface Sci.* **227**(1), 141–146.

[15] Jiménez, M.L., Arroyo, F.J., van Turnhout, J., Delgado, A.V. (2002). Analysis of the dielectric permittivity of suspensions by means of the logarithmic derivative of its real part. *J. Colloid Interface Sci.* **249**(2), 327–335.

[16] Ahualli, S., Jiménez, M.L., Carrique, F., Delgado, A.V. (2009). AC electrokinetics of concentrated suspensions of soft particles. *Langmuir* **25**(4), 1986–1997.

[17] López-García, J.J., Grosse, C., Horno, J. (2003). Numerical study of colloidal suspensions of soft spherical particles using the network method - 1. DC electrophoretic mobility. *J. Colloid Interface Sci.* **265**(2), 327–340.

[18] Jiménez, M.L., Delgado, A.V., Ahualli, S., Hoffmann, M., Witteman, A., Ballauff, M. (2011). Giant permittivity and dynamic mobility observed for spherical polyelectrolyte brushes. *Soft Matter* **7**(8), 3758–3762.

[19] Decher, G., Hong, J.D., Schmitt, J. (1992). Buildup of ultrathin multilayer films by a self-assembly process .3. Consecutively alternating adsorption of anionic and cationic polyelectrolytes on charged surfaces. *Thin Solid Films* **210**(1–2), 831–835.

[20] Duval, J.F.L., Gaboriaud, F. (2010). Progress in electrohydrodynamics of soft microbial particle interphases. *Curr. Opin. Colloid Interface Sci.* **15**(3), 184–195.

[21] Duval, J.F.L., Ohshima, H, (20006). Electrophoresis of diffuse soft particles. *Langmuir* **22**(8), 3533–3546.

[22] de Kerchove, A.J., Elimelech, M. (2005). Relevance of electrokinetic theory for "soft" particles to bacterial cells: Implications for bacterial adhesion. *Langmuir* **21**(14), 6462–6472.

[23] Ohshima, H. (2013). Electrokinetic phenomena of soft particles. *Curr. Opinion Colloid Interface Sci.* **18**(2),73–82.

[24] Ohshima, H. (2012). Electrical phenomena in a suspension of soft particles. *Soft Matter* **8**(13), 3511–3514.

[25] Makino, K., Ohshima, H. (2011). Soft particle analysis of electrokinetics of biological cells and their model systems. *Sci. Technol. Adv. Mater.* **12**(2).

[26] Baipaywad, P., Udomluck, N., Pyo, S.-G., Park, H.H., Park, H. (2014). Fabrication of nanogels for delivery of molecules. *J. Nanosci. Nanotechnol.* **14**(10), 7363–7373.

[27] Coll Ferrer, M.C., Dastgheyb, S., Hickok, N.J., Eckmann, D.M., Composto, R.J. (2014). Designing nanogel carriers for antibacterial applications. *Acta Biomater.* **10**(5), 2105–2111.

[28] Wang, C., Mallela, J., Garapati, U.S., Ravi, S., Chinnasamy, V., Girard, Y., Howell, M., Mohapatra, S. (2013). A chitosan-modified graphene nanogel for noninvasive controlled drug release. *Nanomed. Nanotechnol. Biol. Med.* **9**(7), 903–911.

[29] Levine, S., Neale, G. (1974). Electrophoretic mobility of multiparticle systems. *J. Colloid Interface Sci.* **49**(2), 330–332.

[30] Levine, S., Neale, G. (1974). Prediction of electrokinetic phenomena within multiparticle systems.1. Electrophoresis and electroosmosis. *J. Colloid Interface Sci.* **47**(2), 520–529.

[31] Happel, J., Brenner, H. (1957). Viscous flow in multiparticle systems—motion of spheres and a fluid in a cylindrical tube. *AIChE J.* **3**(4), 506–513.

[32] Kuwabara, S. (1959). The forces experienced by randomly distributed parellel circular cylinders or spheres in a viscous flow at small reynolds numbers. *J. Phys. Soc. Japan* **14**(4), 527–532.

[33] Zholkovskij, E.K., Masliyah, J.H., Shilov, V.N., Bhattachalgee, S. (2007). Electrokinetic phenomena in concentrated disperse systems: General problem formulation and spherical cell approach. *Adv. Colloid Interface Sci.* **134–135**, 279–321.

[34] Shilov, V.N., Borkovskaja, Y.B., Dukhin, A.S. (2004). Electroacoustic theory for concentrated colloids with overlapped DLs at arbitrary kappa a - I. Application to nanocolloids and nonaqueous colloids. *J. Colloid Interface Sci.* **277**(2), 347–358.

[35] Dukhin, A.S., Shilov, V.N., Ohshima, H., Goetz, P.J. (1999). Electroacoustic phenomena in concentrated dispersions: New theory and CVI experiment. *Langmuir* **15**(20), 6692–6706.

[36] Delgado, A.V., Rica, R.A., Arroyo, F.J., Ahualli, S., Jiménez, M.L. (2014). AC electrokinetics in concentrated suspensions. In *Colloid and Interface Chemistry for Nanotechnology*. CRC Press, Boca Raton, FL, pp. 313–346.

[37] Dukhin, A.S., Shilov, V.N., Borkovskaya, Y. (1999). Dynamic electrophoretic mobility in concentrated dispersed systems. Cell model. *Langmuir* **15**(10), 3452–3457.

[38] Shilov, V.N., Zharkikh, N.I., Borkovskaya, Y.B. (1981). Theory of non-equilibrium electrosurface phenomena in concentrated disperse systems. 1. Application of non-equilibrium thermodynamics to cell model of concentrated dispersions. *Colloid J. USSR* **43**(3), 434–438.

[39] Carrique, F., Arroyo, F.J., Delgado, A.V. (2001). Electrokinetics of concentrated suspensions of spherical colloidal particles: Effect of a dynamic stern layer on electrophoresis and dc conductivity. *J. Colloid Interface Sci.* **243**(2), 351–361.

[40] Carrique, F., Arroyo, F.J., Delgado, A.V. (2001). Sedimentation velocity and potential in a concentrated colloidal suspension—effect of a dynamic Stern layer. *Colloids Surf. A: Physicochem. Eng. Aspects* **195**(1–3), 157–169.

[41] Carrique, F., Arroyo, F.J., Delgado, A.V. (2002). Electrokinetics of concentrated suspensions of spherical colloidal particles with surface conductance, arbitrary zeta potential, and double-layer thickness in static electric fields. *J. Colloid Interface Sci.* **252**(1), 126–137.

[42] Hsu, J.P., Lee, E., Yen, F.Y. (2002). Dynamic electrophoretic mobility in electroacoustic phenomenon: Concentrated dispersions at arbitrary potentials. *J. Phys. Chem. B* **106**(18), 4789–4798.

[43] O'Brien, R.W., White, L.R. (1978). Electrophoretic mobility of a spherical colloidal particle. *J. Chem. Soc. Faraday Transact. Ii* **74**, 1607–1626.

[44] Ohshima, H. (1997). Dynamic electrophoretic mobility of spherical colloidal particles in concentrated suspensions. *J. Colloid Interface Sci.* **195**(1), 137–148.

[45] Ahualli, S., Delgado, A.V., Miklavcic, S.J., White, L.R. (2006). Dynamic electrophoretic mobility of concentrated dispersions of spherical colloidal particles. On the consistent use of the cell model. *Langmuir* **22**(16), 7041–7051.

[46] Hill, R.J., Saville, D.A., Russel, W.B. (2003). Electrophoresis of spherical polymer-coated colloidal particles. *J. Colloid Interface Sci.* **258**(1), 56–74.

[47] Saville, D.A. (2000). Electrokinetic properties of fuzzy colloidal particles. *J. Colloid Interface Sci.* **222**(1), 137–145.

[48] Arroyo, F.J., Carrique, F., Ahualli, S., Delgado, A.V. (2004). Dynamic mobility of concentrated suspensions. Comparison between different calculations. *Phys. Chem. Chem. Phys.* **6**(7), 1446–1452.

[49] Ohshima, H. (1999). Electrical conductivity of a concentrated suspension of spherical colloidal particles. *J. Colloid Interface Sci.* **212**(2), 443–448.

[50] Carrique, F., Cuquejo, J., Arroyo, F.J., Jiménez, M.L., Delgado, A.V. (2005). Influence of cell-model boundary conditions on the conductivity and electrophoretic mobility of concentrated suspensions. *Adv. Colloid Interface Sci.* **118**(1–3), 43–50.

[51] Ohshima, H. (2000). Cell model calculation for electrokinetic phenomena in concentrated suspensions: An Onsager relation between sedimentation potential and electrophoretic mobility. *Adv. Colloid Interface Sci.* **88**(1–2), 1–18.

[52] Ahualli, S., Ballauff, M., Arroyo, F.J., Delgado, A.V., Jiménez, M.L. (2012). Electrophoresis and dielectric dispersion of spherical polyelectrolyte brushes. *Langmuir* **28**(47), 16372–16381.

[53] Pincus, P. (1991). Colloid stabilization with grafted polyelectrolytes. *Macromolecules* **24**(10), 2912–2919.

[54] Barbati, A.C., Kirby, B.J. (2012). Soft diffuse interfaces in electrokinetics—theory and experiment for transport in charged diffuse layers. *Soft Matter* **8**(41), 10598–10613.

[55] Ballauff, M. (2007). Spherical polyelectrolyte brushes. *Progress Polym. Sci.* **32**(10), 1135–1151.

[56] Ahualli, S., Delgado, A.V., Grosse, C. (2006). A simple model of the high-frequency dynamic mobility in concentrated suspensions. *J. Colloid Interface Sci.* **301**(2), 660–667.

[57] Delgado, A.V., Ahualli, S., Arroyo, F.J., Carrique, F. (2005). Dynamic electrophoretic mobility of concentrated suspensions—comparison between experimental data and theoretical predictions. *Colloids Surf. A: Physicochem. Eng. Aspects* **267**(1–3), 95–102.

[58] Zukoski, C.F., Saville, D.A. (1987). Electrokinetic properties of particles in concentrated suspensions. *J. Colloid Interface Sci.* **115**(2), 422–436.

[59] Zukoski, C.F., Saville, D.A. (1989). Electrokinetic properties of particles in concentrated suspensions—heterogeneous systems. *J. Colloid Interface Sci.* **132**(1), 220–229.

76

ELECTROPHORETIC BEHAVIOR OF pH-REGULATED SOFT BIOCOLLOIDS

LI-HSIEN YEH[1] AND JYH-PING HSU[2]

[1]*Department of Chemical and Materials Engineering, National Yunlin University of Science and Technology, Yunlin 64002, Taiwan*
[2]*Department of Chemical Engineering, National Taiwan University, Taipei, Taiwan 10617, Republic of China*

76.1 INTRODUCTION

Electrophoresis has been widely applied to characterize the physicochemical properties of colloidal particles. Among these, soft biocolloids, biocolloidal particles composed of a rigid core and an ion-penetrable soft layer, belong to a distinct category. Typical examples include biological entities, such as cells, viruses, and proteins, and synthetic particles, such as particles covered by an artificial or a biological membrane layers [1–5], to name only a few. Note that a special case of soft particles is that the rigid core vanishes, becoming a fully porous particle, typically termed a *polyelectrolyte* (PE). Considering the wide variety of applications using soft biocolloids, a systematic approach for the description of the abovementioned electrophoresis problem under general conditions is highly desirable.

Convectional electrophoresis analysis on soft particles is based on assumptions of the low surface potential [6–17] and a constant fixed charge density of the soft layer [7–34]. The former assumption implies that the effect of double-layer polarization (DLP) [23, 24], one of the most interesting phenomena in electrophoresis arising from the deformation of ionic cloud when the particle is in motion, is neglected. That effect, which usually restrains the particle mobility, is most important when the surface potential of a particle is high and its characteristic size is comparable to the thickness of an electrical double layer (EDL) [23]. It has been proved that most biocolloids such as cells and proteins are of charge-regulated nature [35–37]. Stemming from the presence of the dissociation/association reactions of functional groups in the soft layer of a particle, its charge properties and, accordingly, electrophoretic behavior are highly dependent on the solution properties, such as pH and salt concentration. This implies that the assumption of constant fixed charge density of the soft layer is inappropriate for the description of biocolloids.

In this chapter, a continuum-based mathematical model comprising a Poisson equation for the electrical potential, multiple-ion Nernst–Planck equations for the ionic concentrations, and modified Stokes–Brinkman equations for the hydrodynamic field, combined with a skillful superposition solution procedure through a perturbation approach [38], is introduced to evaluate the electrophoretic behavior of a pH-regulated soft biocolloid. The model proposed is verified by comparing its predictions to the existing experimental data obtained from the literature. Therefore, the model is suitable for estimating the charge properties and the electrophoretic mobility of biocolloids under various background solution properties, pH, and salt concentration, because the DLP effect arising from the convective motion of multiple ionic species is taken into account. This chapter is structured as follows. Section 76.2 details the general theoretical model and that based on the perturbation approach for the case of an isolated, pH-regulated, soft particle in an infinite electrolyte solution containing multiple ionic species. Section 76.3 describes the numerical procedures, code validation, and the typical results of the charge properties and the electrophoretic behavior of a pH-regulated soft biocolloid. Section 76.4 concludes the

Encyclopedia of Biocolloid and Biointerface Science, Volume 2, First Edition. Edited by Hiroyuki Ohshima.
© 2016 John Wiley & Sons, Inc. Published 2016 by John Wiley & Sons, Inc.

chapter; this is followed by a list of symbols used in this chapter (Section 76.5).

76.2 THEORETICAL MODEL

Referring to Fig. 76.1, we consider the electrophoresis of a pH-regulated, soft spherical particle of radius a constituting a rigid core of radius b and an ion-penetrable soft layer of thickness c subject to an applied uniform electric field $\mathbf{E_z}$ of strength E_z. The spherical coordinates, r, θ, and φ, are adopted with the origin located at the center of the particle, and E_z is applied in the z direction (parallel to $\theta = 0$), resulting in the electrophoretic velocity U_p in the same direction. Note that, if the rigid core of a soft particle shrinks to a point, it becomes a completely porous particle or a polyelectrolyte (PE) particle.

We assume that (1) the system under consideration is at a pseudo–steady state; (2) the liquid phase is an incompressible Newtonian fluid containing N kinds of ionic species; (3) the rigid core of the particle is nonslip, nonconducting, and impenetrable to ionic species; (4) the soft layer of the particle is penetrable to ions and fluid, and the permittivity and viscosity of the liquid phase inside the soft layer are the same as those outside the particle; (5) the flow field is in the creeping flow regime; (6) both the flow and the electric fields at the point far away from the particle are uninfluenced by its presence; and (7) the dispersion of particles is so dilute that the particle-particle interaction is neglected.

76.2.1 General Electrokinetic Equations

On the basis of the abovementioned assumptions, the electric and ionic concentration fields of the problem illustrated in Fig. 76.1 can be described by the Poisson–Nernst–Planck (PNP) equations [35, 37, 39]:

$$\nabla^2 \phi = -\frac{\rho + h\rho_s}{\varepsilon_f}, \; h = 0, \; 1 \tag{76.1}$$

$$\nabla \cdot \mathbf{J}_i = 0, \; i = 1, \; 2, \ldots, N \tag{76.2}$$

$$\mathbf{J}_i = n_i \mathbf{u}_i = n_i \mathbf{u} - D_i \left(\nabla n_i + \frac{e z_i n_i}{k_B T} \nabla \phi \right), \; i = 1, 2, \ldots, N \tag{76.3}$$

In the above, ∇ and ∇^2 are the gradient and Laplace operators, respectively; ϕ is the electrical potential in the liquid phase; $\mathbf{u}$ and $\mathbf{u}_i$ are the flow velocity of the fluid and that of the ith mobile ionic species, respectively; e, ε_f, k_B, and T are the elementary charge, permittivity of the liquid phase, Boltzmann constant, and absolute fluid temperature, respectively; $\rho = \sum_{i=1}^{N} e z_i n_i$ is the space charge density of mobile ions; ρ_s is the charge density of the soft layer; z_i, n_i, D_i, and $\mathbf{J}_i$ are the valence, number concentration, diffusivity, and flux of ionic species i, respectively; h is a unit step region function ($h = 0$ for the liquid phase outside the particle, $h = 1$ inside the soft layer). Equation (76.3) implies that the mobile ion species are driven by the liquid flow (convective process), the concentration gradient (diffusion process), and the electric field (electromigration process).

Since the Reynolds numbers of the electrokinetic flows in electrophoretic devices are extremely low, the flow field at steady state can be described by the following continuity equation and the modified Stokes–Brinkman equation [35, 37, 39]:

$$\nabla \cdot \mathbf{u} = 0 \tag{76.4}$$

$$-\nabla p + \eta \nabla^2 \mathbf{u} - h\eta \lambda_s^2 \mathbf{u} - \rho \nabla \phi = \mathbf{0}, \; , \; h = 0, \; 1 \tag{76.5}$$

Here, p and η are the pressure and dynamic viscosity of the liquid phase, respectively; $\lambda_s = (\gamma_s/\eta)^{1/2}$ is the reciprocal softness degree (or Brinkman screening length) of the soft layer, where γ_s is the hydrodynamic frictional coefficient of that layer. For biocolloids, λ_s^{-1} typically ranges from 0.1 to 10 nm [1]. The third ($-\eta \lambda_s^2 \mathbf{u}$) and fourth terms ($-\rho \nabla \phi$) of the left-hand side (LHS) of Eq. (76.5) represent the frictional force exerted on the fluid by the molecular chains of the soft layer [40, 41] and the electrical body force acting on the liquid. Note that in the free-draining limit, γ_s can be expressed as $6\pi\eta R_s N_s$, where R_s and N_s respectively are the Stokes radius and the number density of the hydrodynamic frictional polyelectrolyte segments of the entirely soft particle [3].

The charge properties of the soft layer of biocolloids such as cells, virus, and proteins are typically of a charge-regulated nature. This implies that the distribution of ρ_s in Eq. (76.1) is

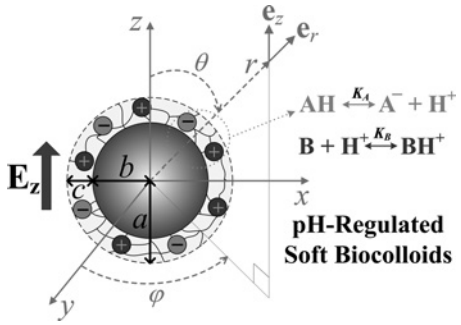


FIGURE 76.1 Electrophoresis of a pH-regulated, soft spherical particle of radius a constituting a rigid core of radius b and an ion-penetrable soft layer of thickness c in an applied uniform electric field $\mathbf{E_z}$. The soft layer carries both acidic and basic functional groups AH and B, respectively, capable of undergoing dissociation and association reactions with protons, and, therefore, its charges possess pH-regulated nature. $\mathbf{e_r}$ and $\mathbf{e_z}$ are the unit vectors in the r and z directions, respectively.

strongly dependent on the degree of dissociation/association reactions of the functional groups contained inside the soft layer of the particle, thus affecting the electrophoretic behavior of soft biocolloids. For illustration, we consider the case where the soft layer of the particle carries zwitterionic functional groups (e.g., lysine), AH (e.g., ∼COOH), and B (e.g., $\sim NH_2$), respectively, capable of undergoing the following dissociation/association reactions:

$$\mathrm{AH} \leftrightarrow \mathrm{A}^- + \mathrm{H}^+ \quad \text{and} \quad \mathrm{B} + \mathrm{H}^+ \leftrightarrow \mathrm{BH}^+ \tag{76.6}$$

Let K_A and K_B be the equilibrium constants of these reactions, as follows:

$$K_A = \frac{N_{\mathrm{A}^-}\left[\mathrm{H}^+\right]}{N_{\mathrm{AH}}} \tag{76.7}$$

$$K_B = \frac{N_{\mathrm{BH}^+}}{N_{\mathrm{B}}\left[\mathrm{H}^+\right]} \tag{76.8}$$

In the above, N_k represents the number density of species k and $[H^+]$ denotes the molar concentration of H^+. Let N_{As} and N_{Bs} be the total number densities of the acidic and the basic functional groups in the soft layer, respectively:

$$N_{As} = N_{\mathrm{A}^-} + N_{\mathrm{AH}} \tag{76.9}$$

$$N_{Bs} = N_{\mathrm{B}} + N_{\mathrm{BH}^+} \tag{76.10}$$

Applying Eqs. (76.7)–(76.10) yields the charge density of the soft layer

$$\begin{aligned}\rho_s &= F(-N_{\mathrm{AH}^-} + \Gamma_{\mathrm{BH}^+}) \\ &= F\left(-\frac{K_A N_{As}}{K_A + [\mathrm{H}^+]} + \frac{K_B N_{Bs}\left[\mathrm{H}^+\right]}{1 + K_B\left[\mathrm{H}^+\right]}\right)\end{aligned} \tag{76.11}$$

where F is Faraday constant. For biocolloids, N_{As} or N_{Bs} typically ranges from 10 to 2635 mol/m^3 [1, 42].

76.2.2 Boundary Conditions

The boundary conditions associated with Eqs. (76.1)–(76.5) include the following. For convenience, we first let the soft particle be fixed and the liquid far away from it moves with a relative velocity $\mathbf{u}_\infty = -U_p\mathbf{e}_z$, where $\mathbf{e}_z$ is the unit vector in the z direction. To simulate biocolloids [22, 39], we assume that the rigid core ($r = b$) of the soft biocolloids is uncharged [22, 39], impenetrable to ionic species, and nonslip. These yield the following boundary conditions:

$$\mathbf{n} \cdot \nabla\phi = 0 \tag{76.12}$$

$$\mathbf{n} \cdot \mathbf{J}_i = \mathbf{n} \cdot \mathbf{u}_i = 0 \tag{76.13}$$

$$\mathbf{u} = \mathbf{0} \tag{76.14}$$

Here, $\mathbf{n}$ is the unit outer normal vector on the surface of the rigid core. Note that Eq. (76.12) stems from the assumption that the permittivity of the rigid core is much smaller than that of the liquid phase. Equation (76.14) implies that the shear plane on which $\mathbf{u} = \mathbf{0}$ is located on the surface of the rigid core.

Because the values of ε_f and η for the liquid phase inside the soft layer are the same as those outside the particle, the electrical potential, the electric field, the ionic concentrations, the ionic fluxes, the flow velocity, and the flow field are continuous on the soft particle–liquid interface ($r = a$) [23]:

$$\phi|_{r=a^-} = \phi|_{r=a^+} \tag{76.15}$$

$$\mathbf{n} \cdot \nabla\phi|_{r=a^-} = \mathbf{n} \cdot \nabla\phi|_{r=a^+} \tag{76.16}$$

$$n_i|_{r=a^-} = n_i|_{r=a^+} \tag{76.17}$$

$$\mathbf{J}_i|_{r=a^-} = \mathbf{J}_i|_{r=a^+} \tag{76.18}$$

$$\mathbf{u}|_{r=a^-} = \mathbf{u}|_{r=a^+} \tag{76.19}$$

$$\mathbf{n} \cdot \mathbf{u}|_{r=a^-} = \mathbf{n} \cdot \mathbf{u}|_{r=a^+} \tag{76.20}$$

$$\mathbf{n} \times \mathbf{u}|_{r=a^-} = \mathbf{n} \times \mathbf{u}|_{r=a^+} \tag{76.21}$$

$$\mathbf{n} \cdot (\boldsymbol{\sigma}^{\mathbf{H}} \cdot \mathbf{n})\Big|_{r=a^-} = \mathbf{n} \cdot (\boldsymbol{\sigma}^{\mathbf{H}} \cdot \mathbf{n})\Big|_{r=a^+} \tag{76.22}$$

$$\mathbf{n} \times (\boldsymbol{\sigma}^{\mathbf{H}} \cdot \mathbf{n})\Big|_{r=a^-} = \mathbf{n} \times (\boldsymbol{\sigma}^{\mathbf{H}} \cdot \mathbf{n})\Big|_{r=a^+} \tag{76.23}$$

In the above, $\boldsymbol{\sigma}^{\mathbf{H}} = -p\mathbf{I} + 2\eta\Delta$ is the hydrodynamic stress tensor, and $\mathbf{I}$, $\Delta = [\nabla\mathbf{u} + (\nabla\mathbf{u})^{\mathrm{T}}]/2$, and the superscript $\mathbf{T}$ are the unit tensor, the rate of deformation tensor, and the matrix transpose, respectively.

Because the particle is in an infinite liquid medium and the particle–particle interaction is neglected, the electric field, the ionic concentrations, and the flow field far away from the particle ($r \to \infty$) are not influenced by its presence. This assumption yields the following boundary conditions:

$$\nabla\phi = -\mathbf{E}_z \tag{76.24}$$

$$n_i = n_{i0} \tag{76.25}$$

$$\mathbf{u} = -U_p\mathbf{e}_z \tag{76.26}$$

Note that for the case where the aqueous solution takes multiple ionic species into account [36, 37, 43, 44], the electroneutrality must be satisfied in the bulk phase:

$$\sum_{i=1}^{N} ez_i n_{i0} = 0 \tag{76.27}$$

76.2.3 Forces Acting on a Soft Particle

The spatial distributions of the electrical potential (ϕ), the fluid velocity ($\mathbf{u}$), and the number concentration of ith ionic

species (n_i) can be obtained by simultaneously solving the electrokinetic governing equations [Eqs. (76.1)–(76.5) and (76.11)] subject to the appropriate boundary conditions, such as those expressed in Eqs. (76.12)–(76.26). Then, the sum of forces, including the electrical force F_e and the hydrodynamic force F_h acting on the soft particle in the z direction, can be evaluated by integrating the Maxwell stress tensor ($\boldsymbol{\sigma}^{\mathbf{E}} = \varepsilon_f \mathbf{E}_z \mathbf{E}_z - (1/2)\varepsilon_f E_z^2 \mathbf{I}$) and the hydrodynamics stress tensor ($\boldsymbol{\sigma}^{\mathbf{H}}$) over the particle surface Ω_p. It can be shown that [32,38,39,42,45]

$$F_e = \int_{\Omega_p} (\boldsymbol{\sigma}^{\mathbf{E}} \cdot \mathbf{n}) \cdot \mathbf{e}_z d\Omega_p = \int_{\Omega_p} \varepsilon_f \left[\frac{\partial \phi}{\partial n}\frac{\partial \phi}{\partial z} - \frac{1}{2}\left(\frac{\partial \phi}{\partial n}\right)^2 n_z - \frac{1}{2}\left(\frac{\partial \phi}{\partial t}\right)^2 n_z \right] d\Omega_p \tag{76.28}$$

$$F_h = \int_{\Omega_p} \left(\boldsymbol{\sigma}^{\mathbf{H}} \cdot \mathbf{n}\right) \cdot \mathbf{e}_z d\Omega_p = \int_{\Omega_p} \left[-p n_z + 2\eta \frac{\partial u_n}{\partial n} n_z + \eta \left(\frac{\partial u_n}{\partial t} + \frac{\partial u_t}{\partial n} \right) t_z \right] d\Omega_p \tag{76.29}$$

In the above, $\mathbf{E}_z = -\nabla\phi = \mathbf{n}(\partial\phi/\partial n) + \mathbf{t}(\partial\phi/\partial t)$, $\mathbf{u} = \mathbf{n}u_n + \mathbf{t}u_t = \mathbf{n}(\mathbf{u}\cdot\mathbf{n}) + \mathbf{t}(\mathbf{u}\cdot\mathbf{t})$, and $E_z^2 = \mathbf{E}_z \cdot \mathbf{E}_z$; $\mathbf{t}$ is the unit tangential vector on Ω_p; n_z and t_z are the z components of the unit normal vector $\mathbf{n}$ and the unit tangent vector $\mathbf{t}$, respectively; $\partial/\partial n$ and $\partial/\partial t$ are the derivatives along the normal and tangential directions on the particle surface, respectively.

At steady state, the electrophoretic velocity U_p of the soft biocolloid can be determined based on the balance of the z-component forces acting on the particle:

$$F_e + F_h = 0 \tag{76.30}$$

However, solving this problem under general conditions is nontrivial, if possible, because of the coupled, highly nonlinear nature of the partial differential equations involved. In addition, a tedious trial-and-error procedure is typically needed to obtain U_p. To circumvent this difficulty, the perturbation approach described below [38, 46, 47] has been developed.

76.2.4 Perturbation Approach

Suppose that the strength of the applied electric field ($\mathbf{E}_z$) is much weaker than that established by the soft biocolloidal particle, which is usually satisfied in practice. For example, the surface potential of a biocolloid is typically lower than ~200 mV and its Debye length ranges from 0.1 nm to 1 μm, yielding the strength of the equilibrium electrical field established by a charged particle ranging from 2×10^5 to 2×10^9 V/m. Because the strength of $\mathbf{E}_z$ is much lower than this level, the assumption of weak applied electric field is realistic. Therefore, all the relevant dependent variables, ϕ, n_i, p, and $\mathbf{u}$, can be partitioned into an equilibrium term, denoted with a subscript e, and a perturbed term, denoted with a prefix δ, as follows:

$$\phi = \phi_e + \delta\phi \tag{76.31}$$

$$n_i = n_{ie} + \delta n_i \tag{76.32}$$

$$p = p_e + \delta p \tag{76.33}$$

$$\mathbf{u} = \mathbf{u}_e + \delta\mathbf{u} \tag{76.34}$$

In these expressions, the equilibrium terms arise from the presence of the particle in the absence of the applied electric field $\mathbf{E}_z$, and the perturbed terms arises from the application of $\mathbf{E}_z$. Suppose that $\mathbf{u}_e = \mathbf{0}$ if $\mathbf{E}_z$ is not applied and, therefore, Eq. (76.34) becomes $\mathbf{u} = \delta\mathbf{u}$. Substituting Eqs. (76.31)–(76.34) into the general electrokinetic equations, Eqs. (76.1)–(76.5), governing this problem yields two sets of linear expressions, one describing the equilibrium-dependent variables and the other describing the perturbed dependent variables [38].

76.2.4.1 Equilibrium Problem. Collecting terms involving the equilibrium variables yields the following set of equations for the equilibrium electric, concentration, and flow fields:

$$\nabla^2\phi_e = -\sum_{i=1}^{N} \frac{e z_i n_{ie}}{\varepsilon_f} - \frac{h\rho_s}{\varepsilon_f},\ h = 0,\ 1 \tag{76.35}$$

$$\nabla n_{ie} + \frac{e z_i n_{ie}}{k_B T}\nabla\phi_e = 0 \tag{76.36}$$

$$-\nabla p_e + \left[\varepsilon_f \nabla^2\phi_e + h\rho_s\right]\nabla\phi_e = \mathbf{0} \tag{76.37}$$

The Boltzmann distribution for the concentration of ith ionic species can be obtained by integrating Eq. (76.36) from a point far away from the particle, where $\phi_e = 0$ and $n_{ie} = n_{i0}$, to a point near the particle, where $\phi_e = \phi_e$ and $n_{ie} = n_{ie}$:

$$n_{ie} = n_{i0} \exp\left(-\frac{e z_i \phi_e}{k_B T}\right),\ i = 1,\ 2,\ \ldots,\ N \tag{76.38}$$

Substituting this expression into Eq. (76.35), we obtain the following governing equation for the equilibrium electric potential (ϕ_e):

$$\nabla^2\phi_e = -\sum_{i=1}^{N} \frac{e z_i n_{i0}}{\varepsilon_f} \exp\left(-\frac{e z_i \phi_e}{k_B T}\right) - \frac{h\rho_s}{\varepsilon_f},\ h = 0,\ 1 \tag{76.39}$$

76.2.4.2 Perturbation Problem. As is well known, the effect of double-layer polarization (DLP), arising from the convective flow of ionic species and thus yielding a deformation of a double layer surrounding a particle, has a significant effect on its electrophoretic behavior [22–24, 32, 37]. In general, the DLP of a particle induces an internal polarized electric field, the direction of which is opposite that of the applied electric field, making the electrophoretic velocity of the particle slower than that for the case where the double layer is not polarized. To take the DLP effect into account, the spatial number concentration of the ith ionic species, n_i, can be expressed by [37, 38, 46]

$$n_i = n_{i0} \exp\left[-\frac{ez_i(\phi_e + \delta\phi + g_i)}{k_B T}\right], \quad i = 1, 2, \ldots N \tag{76.40}$$

where g_i is a hypothetical perturbed potential function for a polarized double layer. Note that although this expression is of Boltzmann type, the actual distribution of n_i, depending on the value of g_i, can deviate appreciably from that distribution.

Based on Eqs. (76.1), (76.30), (76.35), and (76.40), one obtains the following governing equation for the perturbed potential $\delta\phi$:

$$\begin{aligned}\nabla^2\delta\phi &= \nabla^2\phi - \nabla^2\phi_e \\ &= -\sum_{i=1}^{N} \frac{ez_i n_{i0}}{\varepsilon_f}\left\{\exp\left[-\frac{ez_i(\phi_e + \delta\phi + g_i)}{k_B T}\right]\right. \\ &\quad \left. - \exp\left(-\frac{ez_i\phi_e}{k_B T}\right)\right\}\end{aligned} \tag{76.41}$$

Applying Eqs. (76.31), (76.38), and (76.40) yields

$$\begin{aligned}\delta n_i &= n_{i0}\exp\left[-\frac{ez_i(\phi_e + \delta\phi + g_i)}{k_B T}\right] \\ &\quad -n_{i0}\exp\left(-\frac{ez_i\phi_e}{k_B T}\right),\ i = 1, 2, \ldots, \quad N\end{aligned} \tag{76.42}$$

Substituting Eqs. (76.30), (76.33), and (76.42) into Eqs. (76.2) and (76.3) yields

$$\begin{aligned}&\nabla^2 g_i - \frac{ez_i}{k_B T}\nabla\phi_e \cdot \nabla g_i \\ &= \frac{1}{D_i}\mathbf{u}\cdot\nabla\phi + \frac{1}{D_i}\mathbf{u}\cdot\nabla g_i + \frac{ez_i}{k_B T}\nabla\delta\phi\cdot\nabla g_i \\ &\quad + \frac{ez_i}{k_B T}\nabla g_i\cdot\nabla g_i, \quad i = 1, 2, \ldots, N\end{aligned} \tag{76.43}$$

If the applied electric field is weak compared to that established by the particle, then $\phi_e \gg \delta\phi$ and $\phi_e \gg \delta\phi + g_i$. In this case, Eq. (76.40) can be approximated by [38]

$$\begin{aligned}n_i &\cong n_{i0}\exp\left(-\frac{ez_i\phi_e}{k_B T}\right)\left[1 - \frac{ez_i}{k_B T}(\delta\phi + g_i)\right], \\ &\quad i = 1, 2, \ldots, N\end{aligned} \tag{76.44}$$

This expression describes the concentration of ith ionic species after the external electric field is applied. Because the perturbed variables, $\delta\phi$, δn_i, δp, and $\delta\mathbf{u}$ are all on the order of E_z, substituting Eq. (76.44) into Eqs. (76.41) and (76.43) and neglecting terms involving the product of two or more those perturbed terms, one obtains the following approximated equations for the disturbed electrical field:

$$\nabla^2\delta\phi = -\sum_{i=1}^{N}\frac{ez_i n_{i0}}{\varepsilon_f}\left[-\exp\left(-\frac{ez_i\phi_e}{k_B T}\right)\right]\left[-\frac{ez_i}{k_B T}(\delta\phi + g_i)\right] \tag{76.45}$$

$$\nabla^2 g_i - \frac{ez_i}{k_B T}\nabla\phi_e\cdot\nabla g_i = \frac{1}{D_i}\mathbf{u}\cdot\nabla\phi_e, \quad i = 1, 2, \ldots, N \tag{76.46}$$

Substituting Eqs. (76.1), (76.31), (76.33), and (76.34) into Eqs. (76.4) and (76.5) and collecting terms of the order of E_z, one obtains the following perturbed expressions for the flow field:

$$\nabla\cdot\mathbf{u} = 0 \tag{76.47}$$

$$\begin{aligned}&-\nabla\delta p + \eta\nabla^2\mathbf{u} - h\eta\lambda_s^2\mathbf{u} + \left(\varepsilon_f\nabla^2\phi_e + h\rho_s\right)\nabla\delta\phi \\ &\quad + \varepsilon_f\nabla^2\delta\phi\nabla\phi_e = \mathbf{0},\ h = 0, 1\end{aligned} \tag{76.48}$$

Note that after applying the perturbation approach, the linearized expressions, Eqs. (76.39) and (76.45)–(76.48), are applicable to arbitrary charge density of soft layer, double-layer thickness, and geometry.

76.3 ELECTROPHORESIS OF A pH-REGULATED SOFT BIOCOLLOID

Let us first discuss the electrophoretic behavior of pH-regulated soft biocolloids. For illustration, we consider the general case where a soft particle of radius a consisting of a rigid core of radius b and an ion-penetrable soft layer of thickness c, $a = b + c$, in an infinite general electrolyte solution containing N kinds of ionic species, is electrophoretically driven by an uniform applied electric field $\mathbf{E_z}$ of strength E_z, as depicted in Fig. 76.2. For convenience, a cylindrical computational domain of radius d ($d \gg a$) is defined and the cylindrical coordinates, r, θ, and z, are chosen with the origin located at the center of the domain. $\mathbf{E_z}$ is in the z direction. Let Ω_p, Ω_r, Ω_w, and Ω_e be the soft layer–liquid interface and the rigid core of the particle, and the lateral and the end surfaces

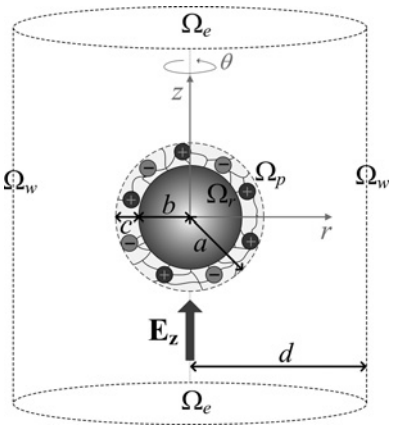


FIGURE 76.2 Electrophoresis of a soft spherical particle of radius a making up a rigid core of radius b and an ion-penetrable soft layer of thickness c along the axis of a cylindrical computational domain of radius d ($d \gg a$); r, θ, and z are the cylindrical coordinates with the origin at the center of the domain; $\mathbf{E_z}$ is in the z direction; Ω_p, Ω_r, Ω_w, and Ω_e represent the soft layer–liquid interface and the rigid core of the particle, and the lateral and the end surfaces of the computational domain, respectively.

of the computational domain, respectively. For convenience, the slipping plane, where the liquid velocity relative to the particle vanishes, is assumed to be on the surface of the rigid core of the particle, that is, the computational domain moves with a relative velocity of $-U_p\mathbf{e}_z$.

To simulate experimental conditions, we assume that the background salt is KCl (or NaCl), and the solution pH is adjusted by HCl and KOH (or NaOH). Therefore, four kinds of ionic species (i.e., $N = 4$) need be considered: K^+ (or Na^+), Cl^-, H^+, and OH^-. Let $C_{i0} = n_{io}/1000N_a$ (in the unit of M), i =1,2,3,4, be the bulk molar concentrations of these ions, respectively. Electroneutrality yields the following relations [37, 48]: $C_{10} = C_{\mathrm{KCl}}$, $C_{20} = C_{\mathrm{KCl}} + 10^{-\mathrm{pH}} - 10^{-(14-\mathrm{pH})}$, $C_{30} = 10^{-\mathrm{pH}}$, and $C_{40} = 10^{-(14-\mathrm{pH})}$ for pH ≤ 7; $C_{10} = C_{\mathrm{KCl}} - 10^{-\mathrm{pH}} + 10^{-(14-\mathrm{pH})}$, $C_{20} = C_{\mathrm{KCl}}$, $C_{30} = 10^{-\mathrm{pH}}$, and $C_{40} = 10^{-(14-\mathrm{pH})}$ for pH > 7. Here, N_a is the Avogadro constant, and C_{KCl} (C_{NaCl}) is the background salt concentration when KCl (NaCl) is used.

To simulate biocolloids, it is assumed that the soft layer carries pH-regulated, zwitterionic, functional groups, AH and B, capable of experiencing dissociation and association equilibrium reactions, expressed in Eq. (76.6), with protons. If we assume that the equilibrium concentration of H^+ follows the Boltzmann distribution, $[H^+] = C_{30}\exp(-e\phi_e/k_BT)$, the charge density of the soft layer expressed in Eq. (76.11) can be expressed as

$$\rho_s = F\left(-\frac{K_A N_{As}}{K_A + C_{30}\exp\left(-\dfrac{e\phi_e}{k_BT}\right)} + \frac{K_B N_{Bs} C_{30}\exp\left(-\dfrac{e\phi_e}{k_BT}\right)}{1 + K_B C_{30}\exp\left(-\dfrac{e\phi_e}{k_BT}\right)}\right) \tag{76.49}$$

where C_{30} is the bulk molar concentration of H^+. This expression implies that ρ_s is not uniformly distributed, and depends on the physicochemical properties (e.g., K_A, K_B, N_{As}, N_{Bs}) of the soft layer of biocolloids and the background solution properties such as pH and salt concentration.

76.3.1 Governing Equations

If the applied electric field is relatively weak compared to that established by the soft particle, the electrostatics, ionic mass transport, and momentum transport of the problem described in Fig. 76.2 can be governed by the electrokinetic equations, Eqs. (76.39) and (76.45)–(76.48), based on the perturbation approach described in Section 76.2. To provide a more concise presentation, we have rewritten Eqs. (76.39) and (76.45)–(76.48) in dimensionless forms, as follows [37]:

$$\nabla^{*2}\phi_e^* = -\frac{(\kappa a)^2}{\sum_{i=1}^{4}\alpha_{21}}\sum_{i=1}^{4}\alpha_{11}\exp\left(-\alpha_{10}\phi_e^*\right) - h\rho_s^*,\ h = 0,\ 1 \tag{76.50}$$

$$\nabla^{*2}\delta\phi^* = \frac{(\kappa a)^2}{\sum_{i=1}^{4}\alpha_{21}}\sum_{i=1}^{4}\alpha_{21}\left(\delta\phi^* + g_i^*\right)\exp\left(-\alpha_{10}\phi_e^*\right) \tag{76.51}$$

$$\nabla^{*2}g_i^* = \alpha_{10}\nabla^*\phi_e^*\cdot\nabla^* g_i^* + Pe_i\left(\mathbf{u}^*\cdot\nabla^*\phi_e^*\right),\ i = 1, 2, 3, 4 \tag{76.52}$$

$$\nabla^*\cdot\mathbf{u}^* = 0 \tag{76.53}$$

$$-\nabla^*\delta p^* + \nabla^{*2}\mathbf{u}^* - h\left(\lambda_s a\right)^2\mathbf{u}^* + \left[\left(\nabla^{*2}\phi_e^* + h\rho_s^*\right)\nabla^*\delta\phi^* + \nabla^{*2}\delta\phi^*\nabla\phi_e^*\right] = \mathbf{0},\ h = 0,\ 1 \tag{76.54}$$

In these expressions, $\nabla^* = a\nabla$, $\nabla^{*2} = a^2\nabla^2$, $\phi_e^* = \phi_e/\phi_{\mathrm{ref}}$, $\delta\phi^* = \delta\phi/\phi_{\mathrm{ref}}$, $g_i^* = g_i/\phi_{\mathrm{ref}}$, $\rho_s^* = \rho_s a^2/\varepsilon_f\phi_{\mathrm{ref}}$, $\delta p^* = \delta p/[\varepsilon_f(\phi_{\mathrm{ref}})^2/a^2]$, and $\mathbf{u}^* = \mathbf{u}/U_{\mathrm{ref}}$, where $\phi_{\mathrm{ref}} = k_BT/ez_1$ and $U_{\mathrm{ref}} = \varepsilon_f(\phi_{\mathrm{ref}})^2/\eta a$ are a reference potential and a reference velocity, respectively; $\alpha_{\beta\zeta} = z_i^\beta n_{i0}^\zeta/z_1^\beta n_{10}^\zeta$; $\kappa = \left(\sum_{i=1}^{4}\left[n_{i0}(ez_i)^2/\varepsilon_f k_BT\right]\right)^{1/2}$ is the reciprocal Debye length; $\mathrm{Pe}_i = \varepsilon_f(\phi_{\mathrm{ref}})^2/\eta D_i$ the electric Peclet number of ith ionic species. As an example for an aqueous general NaCl solution at $T =$ 298K, $D_1(Na^+) = 1.33\times10^{-9}\mathrm{m}^2/\mathrm{s}$, $D_2(C1^-) = 2.03\times10^{-9}\mathrm{m}^2/\mathrm{s}$, $D_3(H^+) = 9.31\times10^{-9}\mathrm{m}^2/\mathrm{s}$, $D_4(OH^-) = 5.30\times10^{-9}\mathrm{m}^2/\mathrm{s}$, $\varepsilon_f = 7.08\times10^{-10}$ F/m, $\eta = 1\times10^{-3}\mathrm{Pa}\cdot\mathrm{s}$, $e = 1.602\times10^{-19}\mathrm{C}$, and $k_B = 1.38\times10^{-23}\mathrm{J/K}$, yielding $\mathrm{Pe}_1(Na^+) = 0.351, \mathrm{Pe}_2(Cl^-) = 0.230, \mathrm{Pe}_3(H^+) = 0.050$, and $\mathrm{Pe}_4(OH^-) = 0.088$ [24].

76.3.2 Boundary Conditions

Let us introduce next the boundary conditions associated with the governing equations for the electric, the ionic concentration, and the flow fields for the problem illustrated in Fig. 76.2. We assume the following: (1) the rigid core surface (Ω_r) of the soft particle is uncharged, nonconductive, impermeable to ionic species, and nonslip; (2) both the electrical potential and the corresponding electric field are continuous on the soft layer–liquid interface (Ω_p); (3) both the concentration and the flux of *i*th ionic species are continuous on the soft layer–liquid interface (Ω_p); (4) the fluid velocity and both the normal and the tangential components of the hydrodynamic stress tensor are continuous on the soft layer–liquid interface (Ω_p); and (5) the electric field, the concentration, and the flow fields at a point far away from the soft particle (i.e., on the cylindrical computational domain, Ω_e and Ω_w) are uninfluenced by its presence. If the permittivity ε_f and the viscosity η of the liquid phase inside the soft layer are identical to those outside it, the above conditions yield the following boundary conditions associated with Eqs. (76.50)–(76.54) [22, 35, 37]:

$$\mathbf{n}\cdot\nabla^*\phi_e^* = 0 \text{ on } \Omega_r \tag{76.55}$$

$$\mathbf{n}\cdot\nabla^*\delta\phi^* = 0 \text{ on } \Omega_r \tag{76.56}$$

$$\mathbf{n}\cdot\nabla^* g_i^* = 0,\ i = 1,1,2,3,4 \text{ on } \Omega_r \tag{76.57}$$

$$\mathbf{u}^* = 0 \text{ on } \Omega_r \tag{76.58}$$

$$\phi_e^*\big|_{\Omega_p^-} = \phi_e^*\big|_{\Omega_p^+} \text{ and } \mathbf{n}\cdot\nabla^*\phi_e^*\big|_{\Omega_p^-} = \mathbf{n}\cdot\nabla^*\phi_e^*\big|_{\Omega_p^+} \tag{76.59}$$

$$\delta\phi^*\big|_{\Omega_p^-} = \delta\phi^*\big|_{\Omega_p^+} \text{ and } \mathbf{n}\cdot\nabla^*\delta\phi^*\big|_{\Omega_p^-} = \mathbf{n}\cdot\nabla^*\delta\phi^*\big|_{\Omega_p^+} \tag{76.60}$$

$$g_i^*\big|_{\Omega_p^-} = g_i^*\big|_{\Omega_p^+} \text{ and } \mathbf{n}\cdot\nabla^* g_i^*\big|_{\Omega_p^-} = \mathbf{n}\cdot\nabla^* g_i^*\big|_{\Omega_p^+},\ i = 1,2,3,4 \tag{76.61}$$

$$\mathbf{u}^*\big|_{\Omega_p^-} = \mathbf{u}^*\big|_{\Omega_p^+},\ \mathbf{n}\cdot\mathbf{u}^*\big|_{\Omega_p^-} = \mathbf{n}\cdot\mathbf{u}^*\big|_{\Omega_p^+}, \text{ and } \mathbf{n}\times\mathbf{u}^*\big|_{\Omega_p^-} = \mathbf{n}\times\mathbf{u}^*\big|_{\Omega_p^+} \tag{76.62}$$

$$\mathbf{n}\cdot(\boldsymbol{\sigma}^{\mathbf{H}^*}\cdot\mathbf{n})\Big|_{\Omega_p^-} = \mathbf{n}\cdot(\boldsymbol{\sigma}^{\mathbf{H}^*}\cdot\mathbf{n})\Big|_{\Omega_p^+} \text{ and } \mathbf{n}\times(\boldsymbol{\sigma}^{\mathbf{H}^*}\cdot\mathbf{n})\Big|_{\Omega_p^-} = \mathbf{n}\times(\boldsymbol{\sigma}^{\mathbf{H}^*}\cdot\mathbf{n})|_{\Omega_p^+} \tag{76.63}$$

$$\mathbf{n}\cdot\nabla^*\phi_e^* = 0 \text{ on } \Omega_e \tag{76.64}$$

$$\mathbf{n}\cdot\nabla^*\delta\phi^* = -E_z^* \text{ on } \Omega_e \tag{76.65}$$

$$g_i^* = -\delta\phi^* \text{ on } \Omega_e \tag{76.66}$$

$$\mathbf{u}^* = -U_p^*\mathbf{e}_z \text{ on } \Omega_e \tag{76.67}$$

$$\mathbf{n}\cdot\nabla^*\phi_e^* = 0 \text{ on } \Omega_w \tag{76.68}$$

$$\mathbf{n}\cdot\nabla^*\delta\phi^* = 0 \text{ on } \Omega_w \tag{76.69}$$

$$\mathbf{n}\cdot\nabla^* g_i^* = 0,\ i = 1,2,3,4 \text{ on } \Omega_w \tag{76.70}$$

$$\mathbf{u}^* = -U_p^*\mathbf{e}_z \text{ on } \Omega_w \tag{76.71}$$

In the above, $\boldsymbol{\sigma}^{\mathbf{H}^*} = \boldsymbol{\sigma}^{\mathbf{H}}/[\varepsilon_f(\phi_{\text{ref}})^2/a^2]$, $E_z^* = E_z/(\phi_{\text{ref}}/a)$ and $U_p^* = U_p/U_{\text{ref}}$, where U_p is the electrophoretic velocity of the soft particle in the z direction. Equation (76.65) depicts the fact that the local electric field on Ω_e arises from the applied electric field [49]. Equation (76.66) implies that the number concentration of *i*th ionic species on the outer computational domain, which is very large compared to the size of the particle, reaches the Boltzmann distribution at equilibrium state:

$$n_i = n_{ie} = n_{i0}\exp\left(-\frac{ez_i\phi_e}{k_BT}\right),\ i = 1,2,3,4 \tag{76.72}$$

Here, n_{ie} is the bulk number concentration of *i*th ionic species at equilibrium.

76.3.3 Solution Procedure

The forces acting on the particle include an electric force and a hydrodynamic force. In this case, only z components of these forces, F_e and F_h, respectively, need to be considered. Because the problem under consideration is θ-symmetric, F_e and F_h, expressed in Eqs. (76.28) and (76.29), can be rewritten, in the cylindrical coordinates, as [32, 42]

$$F_e = \int_{\Omega_p}\varepsilon_f\left[\frac{\partial\phi}{\partial z}\frac{\partial\phi}{\partial r}n_r - \frac{1}{2}\left(\frac{\partial\phi}{\partial z}\right)^2 n_z - \frac{1}{2}\left(\frac{\partial\phi}{\partial r}\right)^2 n_z\right]d\Omega_p \tag{76.73}$$

$$F_h = \int_{\Omega_p}\left[-pn_z + 2\eta\frac{\partial u_z}{\partial z}n_z + \eta\left(\frac{\partial u_z}{\partial r} + \frac{\partial u_r}{\partial z}\right)n_r\right]d\Omega_p \tag{76.74}$$

Here, n_r is the r component of $\mathbf{n}$ and u_r and u_z are the r and the z components of $\mathbf{u}$, respectively.

Suppose that the applied electric field is weak relative to that established by the charged particle and the equilibrium electric field induced by the particle has no contribution to its movement. Substituting $\phi = \phi_e + \delta\phi$ into Eq. (76.73), neglecting the terms involving $(\partial\phi_e/\partial z)(\partial\phi_e/\partial r)$, $(\partial\phi_e/\partial z)^2$, and $(\partial\phi_e/\partial r)^2$ because the particle is unable to be driven by its equilibrium electric field, and the terms associated with the product of two perturbed quantities, $(\partial\delta\phi/\partial z)(\partial\delta\phi/\partial r)$, $(\partial\delta\phi/\partial z)^2$, and $(\partial\delta\phi/\partial r)^2$ because they are relatively small, and collecting the rest terms that are on the order of E_z, one

obtains

$$F_e = \int_{\Omega_p} \left\{ \varepsilon_f \left[\frac{\partial \phi_e}{\partial z}\frac{\partial \delta\phi}{\partial r} + \frac{\partial \delta\phi}{\partial z}\frac{\partial \phi_e}{\partial r} \right] n_r - \varepsilon_f \left[\frac{\partial \phi_e}{\partial z}\frac{\partial \delta\phi}{\partial z} + \frac{\partial \phi_e}{\partial r}\frac{\partial \delta\phi}{\partial r} \right] n_z \right\} d\Omega_p \quad (76.75)$$

This expression is suitable for various kinds of biocolloids with arbitrary geometry and arbitrary level of the charge density of soft layer. If we let $\mathbf{u} = u_r \mathbf{e}_r + u_z \mathbf{e}_z$, then it can be shown that Eq. (76.74) can be rewritten as [32, 38]

$$F_h = \int_{\Omega_p} \left[\left(-\delta p + 2\eta \frac{\partial u_z}{\partial z} \right) n_z + \eta \left(\frac{\partial u_z}{\partial r} + \frac{\partial u_r}{\partial z} \right) n_r \right] d\Omega_p \quad (76.76)$$

In terms of the scaled symbols, $F_e^* = F_e/\varepsilon_f(\phi_{\text{ref}})^2$ and $F_h^* = F_h/\varepsilon_f(\phi_{\text{ref}})^2$, results in

$$F_e^* = \int_{\Omega_p^*} \left\{ \left[\frac{\partial \phi_e^*}{\partial z^*}\frac{\partial \delta\phi^*}{\partial r^*} + \frac{\partial \delta\phi^*}{\partial z^*}\frac{\partial \phi_e^*}{\partial r^*} \right] n_r - \left[\frac{\partial \phi_e^*}{\partial z^*}\frac{\partial \delta\phi^*}{\partial z^*} + \frac{\partial \phi_e^*}{\partial r^*}\frac{\partial \delta\phi^*}{\partial r^*} \right] n_z \right\} d\Omega_p^* \quad (76.77)$$

$$F_h^* = \int_{\Omega_p^*} \left(\boldsymbol{\sigma}^{\mathbf{H}^*} \cdot \mathbf{n} \right) \cdot \mathbf{e}_z d\Omega_p^* = \int_{\Omega_p^*} \left[\left(-\delta p^* + 2\frac{\partial u_z^*}{\partial z^*} \right) n_z + \left(\frac{\partial u_z^*}{\partial r^*} + \frac{\partial u_r^*}{\partial z^*} \right) n_r \right] d\Omega_p^* \quad (76.78)$$

Here, $z^* = z/a$, $r^* = r/a$, $u_r^* = u_r/U_{\text{ref}}$, $u_z^* = u_z/U_{\text{ref}}$, and $\Omega_p^* = \Omega_p/a^2$ is the scaled surface area of the soft particle. The electrophoretic mobility of the soft particle can be determined from the fact that the net force acting on it in the z-direction vanishes at steady state:

$$F_e^* + F_h^* = 0 \quad (76.79)$$

In general, the procedure for solving Eqs. (76.49)–(76.54) subject to the prespecified boundary conditions, such as Eqs. (76.55)–(76.71), involves a tedious trial-and-error numerical procedure. However, because the problem under consideration is of linear nature, that procedure can be avoided by adopting a supposition method [23, 37, 50]. Similar to the treatment of O'Brien and White [46], the present electrophoresis problem is decomposed into two subproblems: (1) the soft particle moves with a constant scaled velocity U_p^* in the absence of $\mathbf{E}_z$; and (2) $\mathbf{E}_z$ is applied, but the particle is held fixed. Let F_{ej}^* and F_{hj}^* be the scaled electric and hydrodynamic forces acting on the soft particle in the z direction in subproblem j, $j = 1,2$, respectively. Then, the total force acting on the soft particle in the z direction in subproblem j, that is, F_j^*, is

$$F_j^* = F_{ej}^* + F_{hj}^*, \; j = 1, 2 \quad (76.80)$$

Because the total force acting on the particle in the z direction must vanish at steady state, $F_1^* + F_2^* = 0$, yielding

$$\mu^* = \frac{U_p^*}{E_z^*} = -\frac{f_2}{f_1} \quad (76.81)$$

where μ^* is the scaled electrophoretic mobility of the soft particle, $F_1^* = f_1 U_p^*$ and $F_2^* = f_2 E_z^*$, where the proportional constants f_1 and f_2 are independent of U_p^* and E_z^*, respectively. The solution procedure for μ^* includes the following steps [23, 51]: (1) assume an arbitrary value for U_p^* in Eqs. (76.67) and (76.71), and solve the governing equations for the electric, the concentration, and the flow fields [Eqs. (76.49)–(76.54)] numerically, subject to the associated boundary conditions [Eqs. (76.55)–(76.71); (2) calculate F_{ej}^*, F_{hj}^*, and F_j^* $(= F_{ej}^* + F_{hj}^*)$, $j = 1$ and 2, using Eqs. (76.77) and (76.78); and (3) apply $F_1^* = f_1 U_p^*$ and $F_2^* = f_2 E_z^*$ to obtain f_1 and f_2, and then to evaluate μ^* using Eq. (76.81). Several finite-element method based commercial software, such as COMSOL, Fluent, FlexPDE, FIDAP, to name only a few, can be applied to directly solve the system under consideration.

76.3.4 Model Validation by Experimental Data

The applicability of the numerical model introduced above is verified by fitting it to experimental data given in two studies [52, 53]. In the former, the electrophoresis of creatine-covered gold nanoparticles of radius $a = 15$ nm, comprising a rigid gold core of radius $b = 10.5$ nm and an biological creatine soft layer of thickness $c = 4.5$ nm, in an aqueous NaCl solution at pH = 7.4 was conducted, and, in the latter, the electrophoresis of succinoglycan polyelectrolytes (PEs) of radius $a = 10.8$ nm, viewed as a fully porous spherical particle (i.e., $a = c$ and $b = 0$), was examined in an aqueous NaCl solution at pH = 10.3. Figure 3 shows the variation of the electrophoretic mobility of the creatine-covered gold nanoparticle, $\mu = U_p/E_z = \mu^* \times (aU_{\text{ref}}/\phi_{\text{ref}})$, as a function of the background NaCl concentration C_{NaCl}; both the experimental results of Lopez-Viota et al. [52] (symbols with error bars) and the result predicted by the abovementioned numerical model (solid line) are presented. In this case, pK_A and pK_B, with $pK_m = -\log K_m$ ($m = A$ or B), are fixed at 3.43 and -10.57 [54, 55], respectively, because the soft layer of the particle is creatine. As can be seen in Fig. 76.3, the

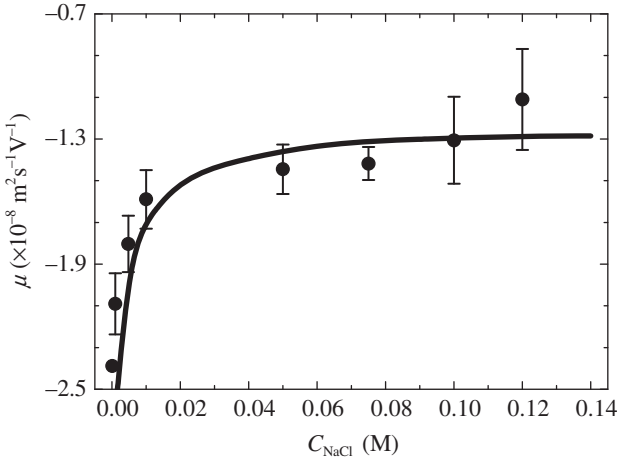


FIGURE 76.3 Dependence of the electrophoretic mobility μ on NaCl concentration C_{NaCl} for the case where the liquid phase contains creatine-covered gold nanoparticles of radius 15 nm, comprising a rigid gold core of radius 10.5 nm and an ion-penetrable creatine soft layer of thickness 4.5 nm, at pH = 7.4. Circles with error bars: experimental data of Lopez-Viota et al. [52]; solid line: results predicted by the present model at $pK_A = 3.43$, $pK_B = -10.57$, $N_{As} = 338$ mol/m^3, $N_{Bs} = 322$ mol/m^3, and $\lambda_s a = 3$.

prediction from the present model, with $N_{As} = 338$ mol/m^3, $N_{Bs} = 322\,x$mol/m^3, and $\lambda_s a = 3$, is in good agreement with the general trend of the experimental data.

To model succinoglycan in the second case, we let $pK_A = 4.58$ and $pK_B = -8.6$ [53], implying that it is negatively charged at the experimental condition of pH = 10.3. In addition, we further let $b = 0$ to simulate a PE, an entirely porous particle, and therefore, the corresponding boundary conditions on the rigid core of a soft particle, Eqs. (76.55)–(76.58), should be replaced by the fact that the electrical potential, the concentration of ionic species i, and the fluid velocity are all finite in the interior of PE. Figure 76.4 illustrates the variation of the scaled electrophoretic mobility of the succinoglycan μ^* with the ionic strength of NaCl. The solid line represents the abovementioned numerical result with considering the DLP effect, and circles with error bars represent the experimental data obtained by Duval et al. [53]. For comparison, the corresponding result for the case where the DLP effect is neglected (dashed line) is also presented. As shown in Fig. 76.4, the present model with $N_{As} = 213$ mol/m^3, $N_{Bs} = 26$ mol/m^3, and $\lambda_s^{-1} = 0.635$ nm successfully captures the dependence of the scaled electrophoretic mobility on the ionic strength of NaCl, and its predictions agree well with the experimental results. However, if the DLP effect is neglected, the predicted μ^* increases monotonically with decreasing ionic strength, and significantly deviates from the experimental data, especially at low ionic strength. This arises from the fact that the effect of DLP, which retards the particle motion [22, 23, 37], is significant when the Debye length is comparable to the particle radius (i.e., $\kappa a \cong 1$).

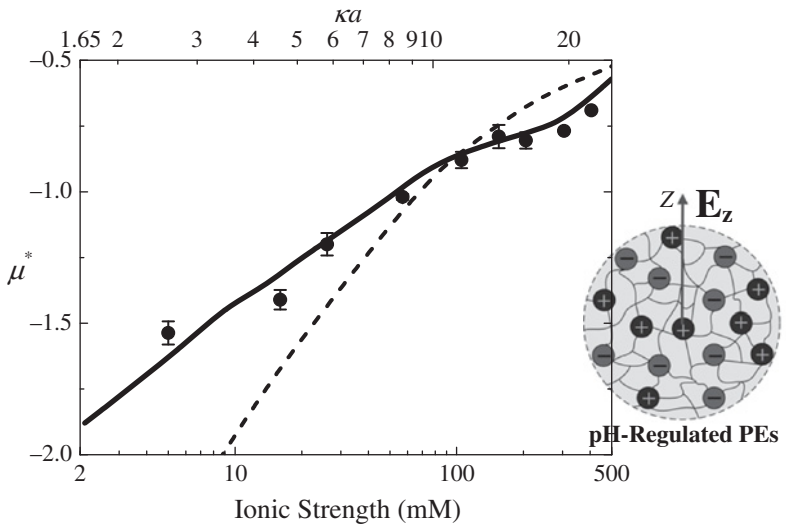


FIGURE 76.4 Dependence of the scaled electrophoretic mobility μ^* on NaCl ionic strength (and the corresponding κa) for the case where the liquid phase contains pH-regulated succinoglycan PEs, schematically represented in the inset, of radius 10.8 nm at pH = 10.3. Circles with error bars: experimental data of Duval et al. [53]; solid (dashed) line: results predicted by the present model with (without) taking into account the DLP effect at $pK_A = 4.58$, $pK_B = -8.6$, $N_{As} = 213$ mol/m^3, $N_{Bs} = 26$ mol/m^3, and $\lambda_s^{-1} = 0.635$ nm. (Adapted with permission from Yeh et al. 2012 [37], pp. 7575—7584.)

76.3.5 Electrokinetics of a pH-Regulated Soft Biocolloid

In the last section, it was verified that the numerical procedure described earlier is capable of capturing the underlying physics of the electrophoretic mobility of pH-regulated biocolloids, including soft particles and PEs. For example, the numerical model is applied to examine the electrophoretic behavior of a pH-regulated soft biocolloid under various general background solution properties such as pH and salt concentration. To simulate a pH-regulated soft biocolloid, we consider the typical case of a soft particle of radius $a = 10$ nm, constituting a rigid core of radius $b = 7$ nm and a soft layer composed of amino acid with thickness $c = 3$ nm, $pK_A = 2.5$ (α-carboxyl), $pK_B = -9.5$ (α-amino) [56], $N_{As} = 500$ mol/m^3, and $N_{Bs} = 500$ mol/m^3 [1]. The values of pK_A and pK_B considered imply that the isoelectric point (IEP) of the soft particle is 6. For illustration, we assume that the liquid phase is filled with KCl electrolyte and that its pH is adjusted by KOH and HCl, implying that four major kinds of ionic species, namely, K^+, Cl^-, H^+, and OH^-, are considered. Therefore, the following electric Peclet number of the ionic species i, $Pe_1(K^+) = 0.238$, $Pe_2(Cl^-) = 0.230$, $Pe_3(H^+) = 0.050$, and $Pe_4(OH^-) = 0.088$ [24], are used in the simulations.

As is well known, the electrophoretic behavior of soft biocolloids is highly dependent on the charge properties of the ion-penetrable soft layer in contact with an aqueous electrolyte solution, due to the dissociation/association chemistry reactions of molecular chains in the soft layer. The charge properties of soft biocolloids, therefore, depend apparently on the background medium environments such as pH and salt concentration [35–37, 39]. To clearly visualize these effects, the influences of the solution properties, pH and the background salt concentration C_{KCl}, on the scaled volume-averaged charge density of the soft layer, $\bar{\rho}_s^*$, of a pH-regulated soft particle are illustrated in Fig. 76.5, and those on its scaled Donnan potential, $\psi_d^* = \psi_d/\phi_{ref}$, where ψ_d is defined as the electric potential (i.e., Donnan potential) on the rigid core–liquid interface of the soft particle [3,4,7], in Fig. 76.6. Here, $\bar{\rho}_s^*$ is defined as [36, 37]

$$\bar{\rho}_s^* = \frac{\int_{V_s^*} \rho_s^* dV_s^*}{\int_{V_s^*} dV_s^*} \tag{76.82}$$

where $V_s^* = V_s/a^3$, where V_s is the volume of the soft layer. As expected, because the IFP of the soft layer of a soft particle is 6, the soft particle is positively charged (i.e., $\bar{\rho}_s^* > 0$) if pH < 6 and negatively charged (i.e., $\bar{\rho}_s^* < 0$) if pH > 6, as depicted in Fig. 76.5a, which also shows that $\left|\bar{\rho}_s^*\right|$ increases with a more significant deviation of the solution pH from 6. This arises from the fact that the larger the deviation, the more amounts of A^- (or BH^+) formed from AH (B), yielding more amount of fixed charges in the soft layer. It is worth noting in Fig. 76.5b that $\left|\bar{\rho}_s^*\right|$ increases monotonically with an increase in C_{KCl}. This interesting behavior is unexpected and can be explained by the spatial distribution of H^+ illustrated in Fig. 76.7, where the radial variations in the scaled equilibrium number concentration of H^+, n_{3e}/n_{30}, for various levels of C_{KCl} are presented. Because the soft particle is negatively charged at pH = 10, counterions, including K^+ and H^+, are electrostatically attracted into the soft layer (light gray region) of a soft particle. As C_{KCl} increases, most of H^+ are excluded by the other cations, K^+, from the interior of the soft layer of a soft particle to its exterior. In this case, a greater number of A^- are dissociated from HA molecules and, therefore, a higher negative $\left|\bar{\rho}_s^*\right|$.

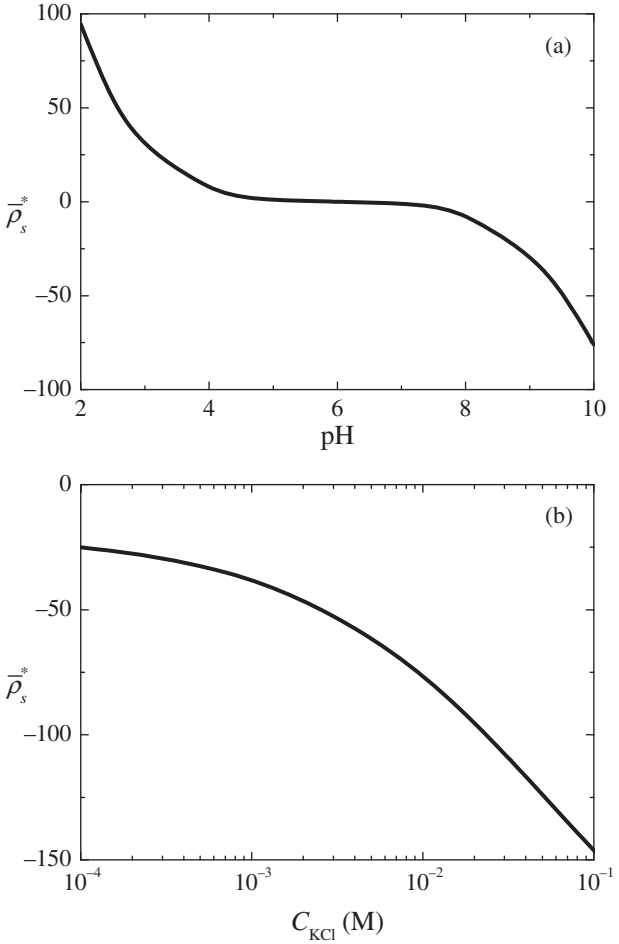


FIGURE 76.5 Scaled volume-averaged charge density of the soft layer $\bar{\rho}_s^*$ of a pH-regulated soft particle as a function of pH at the background salt concentration $C_{KCl} = 0.01$M (a) and as a function of C_{KCl} at pH = 10 (b).

Figure 76.6a indicates that the magnitude of ψ_d^*, namely, $\left|\psi_d^*\right|$, increases with an increase in the deviation of the solution pH from 6, which is expected because of an increase in

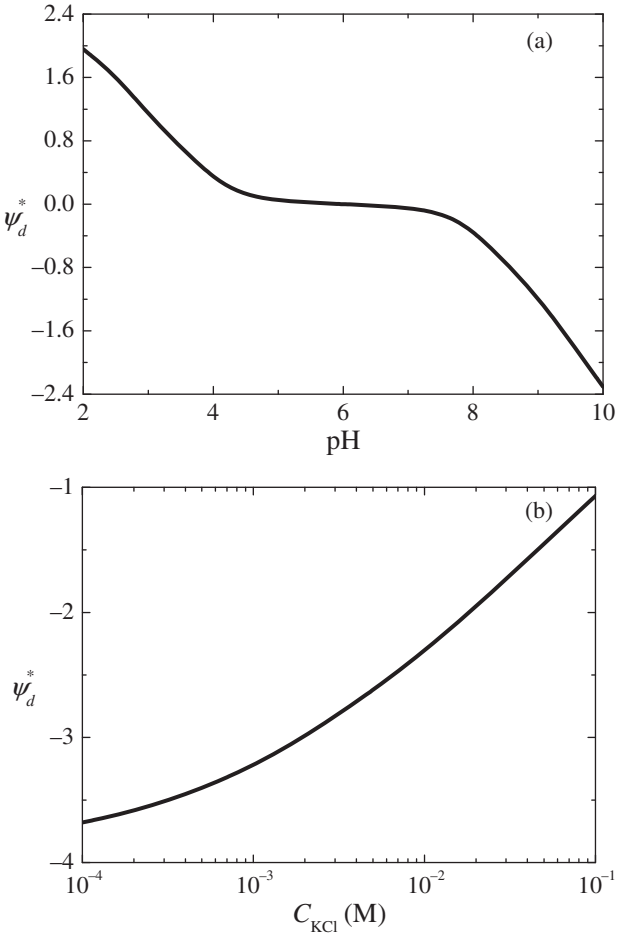


FIGURE 76.6 Scaled Donnan potential ψ_d^* of a pH-regulated soft particle as a function of pH at the background salt concentration $C_{KCl} = 0.01$M (a) and as a function of C_{KCl} at pH = 10 (b). Other parameters are the same as those in Fig. 76.5.

the corresponding $\bar{\rho}_s^*$ observed in Fig. 76.5a. It is interesting to note in Fig. 76.6b that $\left|\psi_d^*\right|$ decreases monotonically with increasing C_{KCl}, which is opposite to the trend of the corresponding $\left|\bar{\rho}_s^*\right|$ depicted in Fig. 76.5b. This is because although $\left|\bar{\rho}_s^*\right|$ increases with increasing C_{KCl}, the increases in $\left|\bar{\rho}_s^*\right|$ and C_{KCl} also lead to an increase in the net amount of counterions condensed inside the soft layer of a soft particle, yielding a lower $\left|\psi_d^*\right|$.

Figure 76.8 summarizes the influence of the background salt concentration C_{KCl} and pH on the scaled electrophoretic behavior μ^* of a pH-regulated soft particle for various values of the scaled softness parameter $\lambda_s a$. As expected, the larger the value of $\lambda_s a$, the more compact is the structure of the soft layer of a soft particle, yielding a larger hydrodynamic drag force originating from the soft layer and a smaller electrophoretic mobility. Figure 76.8a indicates that μ^* is positive if pH < 6 and becomes negative if pH > 6, and that the

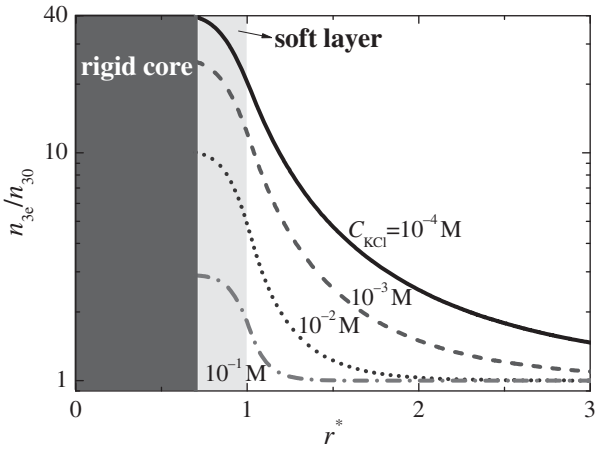


FIGURE 76.7 Variations of the scaled equilibrium number concentration of H^+, namely, n_{3e}/n_{30}, as a function of r^* $(= r/a)$ near a pH-regulated soft particle for various background salt concentrations C_{KCl} at pH = 10. The deep and light gray regions highlight, respectively, the interiors of the rigid core and the ion-penetrable soft layer of the soft particle. Other parameters are the same as those in Fig. 76.5b.

magnitude of μ^* increases with increasing deviation of pH from 6. These findings are consistent with the qualitative behaviors of $\bar{\rho}_s^*$ and ψ_d^* seen in Fig. 76.5a and 76.6a and can be explained by the same reasoning.

Figure 76.8b suggests that the qualitative behavior of μ^* as C_{KCl} varies depends highly on the level of $\lambda_s a$. If $\lambda_s a$ is small (a loose-structured soft layer), $|\mu^*|$ shows a local minimum as C_{KCl} varies; however, if $\lambda_s a$ is large (a compact-structured soft layer), then $|\mu^*|$ decreases monotonically with increasing C_{KCl}. The former can be attributed to the DLP effect, which becomes significant and remarkably reduces electric driving force acting on a particle when the thickness of the electric double layer is comparable to the particle radius (i.e., $\kappa a \cong 1$) and its surface potential is apparently larger than a thermal potential (25.68 mV) [24,37,44]. In the present case, because the Donnan potential of the soft particle is extremely high at low salt concentration, as shown in Fig. 76.6b, the effect of DLP becomes significant and apparently reduces the particle mobility when $C_{KCl} \approx 0.001$ M (i.e., $\kappa a \cong 1$). On the other hand, a monotonic decrease in $|\mu^*|$ with C_{KCl} at sufficiently high $\lambda_s a$ can be explained by the fact that the DLP effect is offset by the electroosmotic flow of counterions [24]. As pointed out by Yeh and Hsu [24], the more compact the structure of the soft layer of a soft particle the less significant is the convective flow of ionic species inside the soft layer.

76.4 SUMMARY

A multiple-ion model for analyzing both the charge properties and the electrophoretic behavior of a pH-regulated soft

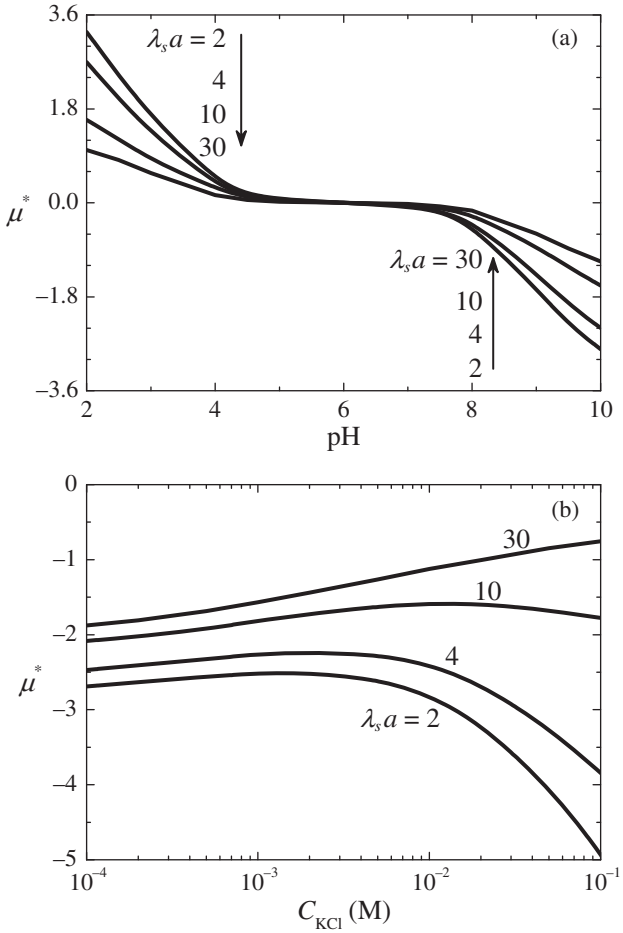


FIGURE 76.8 Scaled electrophoretic mobility μ^* of a pH-regulated soft particle as a function of pH for various scaled softness parameters $\lambda_s a$ at the background salt concentration $C_{\mathrm{KCl}} = 0.01$ M (a) and as a function of C_{KCl} at pH = 10 (b). Other parameters are the same as those in Fig. 76.5.

particle, making up a rigid core and a porous soft layer containing both dissociable acidic functional groups AH and associable basic functional groups B, has been developed and verified. This type of soft particle is capable of simulating biocolloids such as proteins, viruses, and cells. The model introduced takes into account the effect of double-layer polarization (DLP) arising from the convective flow of ionic species surrounding a charged particle, and its predictions agree well with the existing experimental data of creatine-covered gold nanoparticles and succinoglycan polyelectrolytes, fully porous charged particles. Therefore, the model successfully captures the underlying physics of the electrophoresis of pH-regulated soft biocolloids. Simulations exemplified show that in addition to its softness degree of the soft layer, the qualitative electrophoretic behavior of a pH-regulated soft particle depends highly on the solution properties such as pH and background salt concentration. If pH deviates apparently from the isoelectric point of a pH-regulated soft particle, yielding a higher charge density of the soft layer and Donnan potential, the DLP effect becomes significant, which limits the mobility of a soft particle. For a loose-structured soft particle, the behavior of its mobility is significantly influenced by the DLP effect and shows a local minimum as the salt concentration varies. On the contrary, for a compact-structured soft particle, the effect of DLP on its electrophoretic behavior is insignificant, and, therefore, the mobility decreases with increasing salt concentration. The model proposed can be applied directly to interpret the observed experimental data of pH-regulated biocolloids, to estimate the key adjustable parameters in the model, and to design a relevant electrophoresis apparatus.

76.5 NOTATIONS

a = radius of a soft particle (m)
b = radius of rigid core of a soft particle (m)
A^- = dissociated form of the functional group AH (–)
AH = acidic functional group (–)
B = basic functional group (–)
BH^+ = associated form of B (-)
c = thickness of soft layer (m)
C_{i0} = bulk molar concentration of ionic species i (M)
C_{10} = bulk molar concentration of K^+ (or Na^+) (M)
C_{20} = bulk molar concentration of Cl^- (M)
C_{30} = bulk molar concentration of H^+ (M)
C_{40} = bulk molar concentration of OH^- (M)
C_{KCl} = background KCl concentration (M)
C_{NaCl} = background NaCl concentration (M)
d = radius of cylindrical computational domain (m)
D_i = diffusivity of ionic species i (m^2/s)
e = elementary charge (C)
$\mathbf{e}_r$ = unit vector in radial direction (–)
$\mathbf{e}_z$ = unit vector in z direction (-)
E_z = strength of applied electric field (V/m)
E_z^* = $E_z/(\phi_{\mathrm{ref}}/a)$, scaled E_z (–)
$\mathbf{E}_z$ = applied uniform electric field (V/m)
f_1, f_2 = proportional constant (–)
F = Faraday constant (C/mol)
F_1^* = $F_{e1}^* + F_{h1}^*$, z component of scaled forces in subproblem 1 (see Section 76.3.3) (–)
F_2^* = $F_{e2}^* + F_{h2}^*$, z component of scaled forces in subproblem 2 (–)
F_e = electrical force acting on a particle in z direction (N)
F_e^* = $F_e/\varepsilon_f(\phi_{\mathrm{ref}})^2$, scaled form of F_e defined by Eq. (76.77) (–)
F_{ej}^* = z component of scaled electrical force in subproblem j (–)
F_h = hydrodynamic force acting on a particle in z direction (N)

F_h^* = $F_h/\varepsilon_f(\phi_{\text{ref}})^2$, scaled form of F_h defined by Eq. (76.78) (α)
F_{hj}^* = z component of scaled hydrodynamic force in subproblem j (–)
F_j^* = $F_{ej}^* + F_{hj}^*$, scaled total force acting on a particle in z direction in subproblem j (N)
g_i = perturbed potential associated with ionic species i (V)
g_i^* = g_i/ϕ_{ref}, scaled form of g_i (–)
h = unit step region function"n ($h = 0$ for the liquid phase outside of a soft particle $h = 1$ inside soft layer) (–)
H^+ = hydrogen ion (–)
$[H^+]$ = molar concentration distribution of H^+ (M)
i = index for ionic species (–)
$\mathbf{I}$ = unit tensor (–)
$\mathbf{J}_i$ = flux of ionic species i (1/s/m^2)
k_B = Boltzmann constant (J/K)
K_A = equilibrium dissociation constant defined by Eq. (76.7) (mol/m^3)
K_B = equilibrium association constant defined by Eq. (76.8) (mol/m^3)
n_i = number concentration of ionic species i (#/m^3)
n_{ie} = number concentration of ionic species i at equilibrium (#/m^3)
n_{3e} = number concentration of H^+ at equilibrium (#/m^3)
n_{i0} = bulk number concentration of ionic species i (#/m^3)
n_{30} = bulk number concentration of H^+ (#/m^3)
$\mathbf{n}$ = unit outer normal vector on particle or boundary surface (-)
n_r = r component of unit normal vector $\mathbf{n}$
n_z = z component of unit normal vector $\mathbf{n}$
N = total number of ionic species j (-)
N_{A^-} = number density of A^- in soft layer (mol/m^3)
N_{AH} = number density of AH in soft layer (mol/m^3)
N_{As} = ($= N_{A^-} + N_{AH}$) total number density of acidic functional groups in soft layer (mol/m^3)
N_B = number density of B in soft layer (mol/m^3)
N_{BH^+} = number density of BH^+ in soft layer (mol/m^3)
N_{Bs} = ($= N_B + N_{BH^+}$) total number density of basic functional groups in soft layer (mol/m^3)
N_k = number density of molecular species in soft layer (mol/m^3)
N_s = number density of hydrodynamic frictional polyelectrolyte segments in soft layer (#/m^3)
p = hydrodynamic pressure (Pa)
pK_A = $-\log K_A$, equilibrium dissociation constant of acidic function groups AH (–)
pK_B = $-\log K_B$, equilibrium association constant of basic function groups B (–)
Pe_i = $\varepsilon_f(\phi_{\text{ref}})^2/\eta D_i$, electric Peclet number of ionic species i (–)
r = radial coordinate (m)
R_s = Stokes radius of hydrodynamic frictional polymer segments in soft layer (m)
t_z = z component of unit tangent vector $\mathbf{t}$
$\mathbf{t}$ = unit tangential vector on particle surface (-)
T = absolute fluid temperature (K)
$\mathbf{T}$ = matrix transpose (–)
u_n = normal component of liquid velocity (m/s)
u_t = tangential component of liquid velocity (m/s)
u_r = r component of liquid velocity (m/s)
u_t = z component of liquid velocity (m/s)
$\mathbf{u}$ = velocity of liquid phase (m/s)
$\mathbf{u}_i$ = velocity of ionic species i (m/s)
$\mathbf{u}_\infty$ = liquid velocity at a point far from the particle (m/s)
$\mathbf{u}^*$ = $\mathbf{u}/U_{\text{ref}}$, scaled velocity of liquid phase (–)
U_p = z component of particle velocity (m/s)
U_p^* = U_p/U_{ref}, scaled electrophoretic velocity (–)
U_{ref} = $\varepsilon_f(\phi_{\text{ref}})^2/\eta a$ (–)
V_s = volume of soft layer (m^3)
V_s^* = V_s/a^3, scaled volume of soft layer (–)
z = axial coordinate (m)
z_i = valence of ionic species i (–)

Greek Letters

$\alpha_{\beta\zeta}$ = $z_i^\beta n_{i0}^\zeta / z_1^\beta n_{10}^\zeta$ (–)
$\delta\phi$ = perturbed potential in the presence of $\mathbf{E}_z$ (V)
$\delta\phi^*$ = $\delta\phi/\phi_{\text{ref}}$, scaled perturbed potential (–)
δp^* = $\delta p/[\varepsilon_f(\phi_{\text{ref}})^2/a^2]$, scaled perturbed hydrodynamic pressure (–)
∇ = gradient operator (1/m)
∇^* = $a\nabla$, scaled gradient operator (–)
∇^2 = Laplace operator (1/m^2)
∇^{*2} = $a^2\nabla^2$, scaled Laplace operator (–)
ε_f = permittivity of liquid phase (C^2 N^{-1} m^{-2})
ϕ = total electrical potential (V)
ϕ_e = equilibrium potential in absence of $\mathbf{E}_z$ (V)
ϕ_e^* = ϕ_e/ϕ_{ref}, scaled equilibrium potential (–)
ϕ_{ref} = k_BT/ez_1,reference potential (V)
ψ_d = Donnan potential of a soft particle (V)
ψ_d^* = ψ_d/ϕ_{ref}, scaled Donnan potential of a soft particle (–)
γ_s = $6\pi\eta R_s N_s$, hydrodynamic frictional coefficient inside soft layer per unit volume of the fluid (kg m^{-3} s^{-1})
η = dynamic viscosity of liquid phase (kg/m/s)
κ = $\left(\sum_{i=1}^4 \left[n_{i0}(ez_i)^2/\varepsilon_f k_B T\right]\right)^{1/2}$, reciprocal Debye length (m^{-1})
λ_s = $(\gamma_s/\eta)^{1/2}$, reciprocal softness degree (or Brinkman screening length) of soft layer (m^{-1})

$\lambda_s a$ = $(\gamma_s a^2/\eta)^{1/2}$, scaled softness parameter of soft layer (–)
μ = U_p/E_z, electrophoretic mobility of a soft particle ($m^2\ V^{-1}\ s^{-1}$)
μ^* = U_p^*/E_z^*, scaled electrophoretic mobility of a soft particle defined in Eq. (76.81) (–)
θ = angular coordinate (–)
ρ = space charge density of mobile ions (C/m^3)
ρ_s = fixed charge density in soft layer of a soft particle (C/m^3)
ρ_s^* = $\rho_s a^2/\varepsilon_f \phi_{\text{ref}}$, scaled charged density of soft layer (–)
$\bar{\rho}_s^*$ = scaled volume-averaged charge density of soft layer defined in Eq. (76.82) (–)
$\boldsymbol{\sigma}^{\mathbf{E}}$ = Maxwell stress tensor (N/m^2)
$\boldsymbol{\sigma}^{E*}$ = $\boldsymbol{\sigma}^{\mathrm{E}}/[\varepsilon(\phi_{\text{ref}})^2/a^2]$, scaled Maxwell stress tensor (–)
$\boldsymbol{\sigma}^{\mathbf{H}}$ = hydrodynamic stress tensor (N/m^2)
$\boldsymbol{\sigma}^{\mathbf{H}*}$ = $\boldsymbol{\sigma}^{\mathbf{H}}/[\varepsilon_f(\phi_{\text{ref}})^2/a^2]$, scaled hydrodynamic stress tensor (–)
Ω_e = surface (area) of ends of the computational domain (m^2)
Ω_p = surface (area) of a soft particle (m^2)
Ω_p^* = Ω_p/a^2, scaled surface area of a soft particle (–)
Ω_r = surface (area) of rigid core of a soft particle (m^2)
Ω_w = surface (area) of the lateral of computational domain (m^2)

Superscripts

$*$ = scaled property

Subscripts

e = equilibrium property
j = subproblem j

Prefix

δ = perturbed property

REFERENCES

[1] Duval, J.F.L., Gaboriaud, F. (2010). Progress in electrohydrodynamics of soft microbial particle interphases. *Curr. Opin. Colloid Interface Sci.* **15**, 184–195.

[2] Ramos, J., Imaz, A., Callejas-Fernandez, J., Barbosa-Barros, L., Estelrich, J., Quesada-Perez, M., Forcada, J. (2011), Soft nanoparticles (thermo-responsive nanogels and bicelles) with biotechnological applications: From synthesis to simulation through colloidal characterization. *Soft Matt.* **7**, 5067–5082.

[3] Ohshima, H. (1995). Electrophoresis of soft particles. *Adv. Colloid Interface Sci.* **62**, 189–235.

[4] Ohshima, H. (2012), Electrical phenomena in a suspension of soft particles. *Soft Matt.* , **8**, 3511–3514.

[5] Duval, J.F.L., Ohshima, H. (2006), Electrophoresis of diffuse soft particles. *Langmuir* **22**, 3533–3546.

[6] Zhang, X.G., Hsu, J.P., Chen, Z.S., Yeh, L.H., Ku, M.H., Tseng, S. (2010). Electrophoresis of a charge-regulated soft sphere in a charged cylindrical pore. *J. Phys. Chem. B* **114**, 1621–1631.

[7] Ohshima, H. (1994). Electrophoretic mobility of soft particles. *J. Colloid Interface Sci.* **163**, 474–483.

[8] Ohshima, H. (2000). On the general expression for the electrophoretic mobility of a soft particle. *J. Colloid Interface Sci.* **228**, 190–193.

[9] Ohshima, H. (2002). Modified Henry function for the electrophoretic mobility of a charged spherical colloidal particle covered with an ion-penetrable uncharged polymer layer. *J. Colloid Interface Sci.* **252**, 119–125.

[10] Ohshima, H. (2002). Electrophoretic mobility of a charged spherical colloidal particle covered with an uncharged polymer layer. *Electrophoresis* **23**, 1995–2000.

[11] Ohshima, H. (2005). Approximate expression for the electrophoretic mobility of a spherical colloidal particle covered with an ion-penetrable uncharged polymer layer. *Colloid Polym. Sci.* **283**, 819–825.

[12] Hsu, J.P., Chen, Z.S., Tseng, S. (2009). Effect of electroosmotic flow on the electrophoresis of a membrane-coated sphere along the axis of a cylindrical pore. *J. Phys. Chem. B* **113**, 7701–7708.

[13] Hsu, J.P., Chou, C.H., Kuo, C.C., Tseng, S., Wu, R.M. (2012). Electrophoresis of a soft toroid of nonuniform structure. *Colloid Surf. B: Biointerfaces* **98**, 36–42.

[14] Yeh, L.H., Hsu, J.P., Tseng, S. (2010). Electrophoresis of a membrane-coated cylindrical particle positioned eccentrically along the axis of a narrow cylindrical pore. *J. Phys. Chem. C* **114**, 16576–16587.

[15] Chou, C.H., Hsu, J.P., Kuo, C.C., Ohshima, H., Tseng, S., Wu, R.M. (2012). Importance of the porous structure of a soft particle on its electrophoretic behavior. *Colloid Surf. B: Biointerfaces* **93**, 154–160.

[16] Keh, H.J., Liu, C.P. (2010). Electric conductivity and electrophoretic mobility in suspensions of charged porous spheres. *J. Phys. Chem. C* **114**, 22044–22054.

[17] Chen, W.J., Keh, H.J. (2013). Electrophoresis of a charged soft particle in a charged cavity with arbitrary double-layer thickness. *J. Phys. Chem. B* **117**, 9757–9767.

[18] Huang, C.H., Cheng, W.L., He, Y.Y., Lee, E. (2010). Electrophoresis of a soft particle within a cylindrical pore: Polarization effect with the nonlinear Poisson-Boltzmann equation. *J. Phys. Chem. B* **114**, 10114–10125.

[19] Huang, C.H., Hsu, H.P., Lee, E. (2012). Electrophoretic motion of a charged porous sphere within micro- and nanochannels. *Phys. Chem. Chem. Phys.* **14**, 657–667.

[20] Liu, K.L., Hsu, J.P., Tseng, S. (2011). Influence of membrane layer properties on the electrophoretic behavior of a soft particle. *Electrophoresis* **32**, 3053–3061.

[21] Tseng, S., Lin, C.Y., Hsu, J.P., Yeh, L.H. (2013). Electrophoresis of deformable polyelectrolytes in a nanofluidic channel. *Langmuir* **29**, 2446–2454.

[22] Yeh, L.H., Fang, K.Y., Hsu, J.P., Tseng, S. (2011). Influence of boundary on the effect of double-layer polarization and the electrophoretic behavior of soft biocolloids. *Colloid Surf. B: Biointerfaces* **88**, 559–567.

[23] Yeh, L.H., Hsu, J.P. (2011). Effects of double-layer polarization and counterion condensation on the electrophoresis of polyelectrolytes. *Soft Matt.* **7**, 396–411.

[24] Yeh, L.H., Liu, K.L., Hsu, J.P. (2012). Importance of ionic polarization effect on the electrophoretic behavior of polyelectrolyte nanoparticles in aqueous electrolyte solutions. *J. Phys. Chem. C* **116**, 367–373.

[25] Hsu, J.P., Lo, H.M., Yeh, L.H., Tseng, S. (2012). Importance of boundary on the electrophoresis of a soft cylindrical particle. *J. Phys. Chem. B* **116**, 12626–12632.

[26] Hsu, J.P., Lin, C.Y., Yeh, L.H., Lin, S.H. (2012). Importance of the shape of a polyelectrolyte on its electrophoretic behavior. *Soft Matt.* **8**, 9469–9479.

[27] Min, W.L., Lee, E., Hsu, J.P. (2006). Dynamic electrophoresis of a spherical dispersion of soft particles subject to a stress-jump condition. *J. Colloid Interface Sci.* **299**, 464–471.

[28] Lee, E., Chou, K.T., Hsu, J.P. (2004). Electrophoresis of a concentrated dispersion of spherical particles covered by an ion-penetrable membrane layer. *J. Colloid Interface Sci.* **280**, 518–526.

[29] Hsu, H.P., Lee, E. (2013). Electrophoresis of a single charged porous sphere in an infinite medium of electrolyte solution. *J. Colloid Interface Sci.* **390**, 85–95.

[30] Hsu, H.P.; Lee, E. (2012). Electrophoresis of a charged porous sphere normal to an air-water interface. *Phys. Chem. Chem. Phys.* **14**, 15729–15738.

[31] Cheng, W.L., He, Y.Y., Lee, E. (2009). Electrophoresis of a soft particle normal to a plane. *J. Colloid Interface Sci.* **335**, 130–139.

[32] Zhang, M.K., Ai, Y., Kim, D.S., Jeong, J.H., Joo, S.W., Qian, S.Z. (2011). Electrophoretic motion of a soft spherical particle in a nanopore. *Colloid Surf. B: Biointerfaces* **88**, 165–174.

[33] Bhattacharyya, S., Gopmandal, P.P. (2013). Effects of electroosmosis and counterion penetration on electrophoresis of a positively charged spherical permeable particle. *Soft Matt.* **9**, 1871–1884.

[34] Gopmandal, P.P., Bhattacharyya, S. (2014). Nonlinear effects on electrokinetics of a highly charged porous sphere. *Colloid Polym. Sci.* **292**, 905–914.

[35] Tseng, S., Hsieh, T. H., Yeh, L.H., Wang, N., Hsu, J.P. (2013). Electrophoresis of a charge-regulated soft sphere: Importance of effective membrane charge. *Colloid Surf. B: Biointerfaces* **102**, 864–870.

[36] Yeh, L.H., Hsu, J.P., Qian, S., Tseng, S.J. (2012). Counterion condensation in pH-regulated polyelectrolytes. *Electrochem. Commun.* **19**, 97–100.

[37] Yeh, L.H., Tai, Y.H., Wang, N., Hsu, J.P., Qian, S. (2012). Electrokinetics of pH-regulated zwitterionic polyelectrolyte nanoparticles. *Nanoscale* **4**, 7575–7584.

[38] Hsu, J.P., Yeh, L.H., Ku, M.H. (2007). Evaluation of the electric force in electrophoresis. *J. Colloid Interface Sci.* **305**, 324–329.

[39] Yeh, L.H., Zhang, M.K., Joo, S.W., Qian, S., Hsu, J.P. (2012). Controlling pH-regulated bionanoparticles translocation through nanopores with polyelectrolyte brushes. *Anal. Chem.* **84**, 9615–9622.

[40] Brinkman, H.C. (1947). A calculation of the viscous force exerted by a flowing fluid on a dense swarm of particles. *Appl. Sci. Res. A* **1**, 27–34.

[41] Debye, P., Bueche, A.M. (1948). Intrinsic viscosity, diffusion, and sedimentation rate of polymers in solution. *J. Chem. Phys.* **16**, 573–579.

[42] Zhang, M.K., Yeh, L.H., Qian, S.Z., Hsu, J.P., Joo, S.W. (2012). DNA electrokinetic translocation through a nanopore: Local permittivity environment effect. *J. Phys. Chem. C* **116**, 4793–4801.

[43] Ma, Y., Yeh, L.H., Qian, S., Hsu, J.P., Tseng, S. (2014). Analytical model for surface charge property of pH-regulated nanorods. *Electrochem. Commun.* **45**, 75–78.

[44] Hsu, J.P., Tai, Y.H. (2010). Effect of multiple ionic species on the electrophoretic behavior of a charge-regulated particle. *Langmuir* **26**, 16857–16864.

[45] Yeh, L.H., Zhang, M., Qian, S., Hsu, J.P. (2012). Regulating DNA translocation through functionalized soft nanopores. *Nanoscale* **4**, 2685–2693.

[46] O'Brien, R.W., White, L.R. (1978). Electrophoretic mobility of a spherical colloidal particle. *J. Chem. Soc. Faraday Transact. 2* **74**, 1607–1626.

[47] Masliyah, J.H., Bhattacharjee, S. (2006). *Electrokinetic and Colloid Transport Phenomena*. Wiley, Hoboken, NJ.

[48] Yeh, L.H., Zhang, M., Qian, S. (2013). Ion transport in a pH-regulated nanopore. *Anal. Chem.* **85**, 7527–7534.

[49] Zydney, A.L. (1995). Boundary effects on the electrophoretic motion of a charged particle in a spherical cavity. *J. Colloid Interface Sci.* **169**, 476–485.

[50] Lee, E., Chu, J.W., Hsu, J.P. (1998). Electrophoretic mobility of a sphere in a spherical cavity. *J. Colloid Interface Sci.* **205**, 65–76.

[51] Hsu, J.P., Kao, C.Y. (2002). Electrophoresis of a finite cylinder along the axis of a cylindrical pore. *J. Phys. Chem. B* **106**, 10605–10609.

[52] Lopez-Viota, J., Mandal, S., Delgado, A.V., Toca-Herrera, J.L., Moller, M., Zanuttin, F., Balestrino, M., Krol, S. (2009). Electrophoretic characterization of gold nanoparticles functionalized with human serum albumin (HSA) and creatine. *J. Colloid Interface Sci.* **332**, 215–223.

[53] Duval, J.F.L., Slavykova, V.I., Hosse, M., Buffle, J., Wilkinson, K.J. (2006). Electrohydrodynamic properties of succinoglycan as probed by fluorescence correlation spectroscopy, potentiometric titration and capillary electrophoresis. *Biomacromolecules* **7**, 2818–2826.

[54] Eadie, G.S., Hunter, A. (1926). The apparent dissociation constants of creatine and creatinine. *J. Biol. Chem.* **67**, 237–44.

[55] Cannan, R.K., Shore, A. (1928). The creatine-creatinine equilibrium. The apparent dissociation constants of creatine and creatinine. *Biochem J.* **22**, 920–929.

[56] Switzer, R., Garrity, L. (1999). *Experimental Biochemistry*. Freeman, New York.

77

ELECTROPHORETIC MOBILITY OF SOFT PARTICLES

Kimiko Makino and Hiroyuki Ohshima

Faculty of Pharmaceutical Sciences, Tokyo University of Science, 2641 Yamazaki Noda, Chiba 278-8510, Japan

77.1 INTRODUCTION

Measurement of the electrophoretic mobility of charged colloidal particles in an electrolyte solution is a powerful tool for estimating their surface properties. Under an external electric field $\boldsymbol{E}$, charged colloidal particles move with a constant velocity $\boldsymbol{U}$ in a liquid, as a result of the balance between the electric force accelerating the particles and a viscous force exerted by the liquid on the particles tending to retard the particles. This phenomenon is called *electrophoresis*. Usually, we treat the case where the magnitude of the applied electric field $\boldsymbol{E}$ is not very large. In such cases the velocity $\boldsymbol{U}$ of the particles, which is called *electrophoretic velocity*, is proportional to $\boldsymbol{E}$ in magnitude. The magnitude ratio of $\boldsymbol{U}$ to $\boldsymbol{E}$ is called *electrophoretic mobility* μ, which is defined by $\mu = U/E$ (where $U = |\boldsymbol{U}|$ and $E = |\boldsymbol{E}|$). In this chapter we consider the electrophoretic mobility of a soft particle (i.e., a hard particle covered with an ion-penetrable surface layer of polyelectrolytes) in comparison with that of a hard particle without surface structures.

77.2 ELECTROPHORETIC MOBILITY OF HARD PARTICLES

The most widely employed formula for the electrophoretic mobility μ of a charged spherical particle of radius a in an electrolyte solution is Smoluchowski's formula [1], which relates the electrophoretic mobility μ of the particle to its zeta-potential ζ:

$$\mu = \frac{\varepsilon_r \varepsilon_0}{\eta} \zeta \tag{77.1}$$

Here, ε_r and η are, respectively, the relative permittivity and the viscosity of the electrolyte solution and ε_0 is the permittivity of a vacuum. The *zeta-potential* ζ is defined as the potential at the plane where the liquid velocity relative to the particle is zero. This plane, which is called the *slipping plane* or the *shear plane*, does not necessarily coincide with the particle surface. Only if the slipping plane is located at the particle surface does the zeta-potential ζ become equal to the surface potential ψ_0. Equation (77.1) is the correct limiting mobility equation for very large particles and is valid irrespective of the shape of the particle, provided that the dimension of the particle is much larger than the Debye length $1/\kappa$, where κ is the Debye–Hückel parameter, and thus the particle surface can be considered to be locally planar. For a symmetric electrolyte solution of valence z and bulk concentration (number density) n, the Debye–Hückel parameter κ is given by

$$\kappa = \left(\frac{2z^2 e^2 n}{\varepsilon_r \varepsilon_0 kT} \right)^{1/2} \tag{77.2}$$

where e is the elementary electric charge, k is Boltzmann's constant, and T is the absolute temperature.

For a planar surface, the surface potential ψ_0 is related to the surface charge density σ of the particle by

$$\sigma = (8n\varepsilon_r \varepsilon_0 kT)^{1/2} \sinh\left(\frac{ze\psi_0}{2kT} \right) \tag{77.3}$$

or

$$\psi_0 = \left(\frac{2kT}{ze} \right) \ln \left[\frac{\sigma}{(8n\varepsilon_r \varepsilon_0 kT)^{1/2}} + \left(\frac{\sigma^2}{8n\varepsilon_r \varepsilon_0 kT} + 1 \right)^{1/2} \right] \tag{77.4}$$

Encyclopedia of Biocolloid and Biointerface Science, Volume 2, First Edition. Edited by Hiroyuki Ohshima.
© 2016 John Wiley & Sons, Inc. Published 2016 by John Wiley & Sons, Inc.

77.3 ELECTROPHORETIC MOBILITY OF SOFT PARTICLES

This section deals with a general theory of electrophoresis of soft particles and approximate analytic expressions for the mobility of soft particles [2–15]. This theory unites the electrophoresis theories of hard particles and of polyelectrolytes, since a soft particle tends to become a hard particle in the absence of the polymer layer and to become a polyelectrolyte in the absence of the particle core.

Consider a spherical soft particle, that is, a charged spherical particle covered with an ion-penetrable layer of polyelectrolytes moving with a velocity $\boldsymbol{U}$ in a liquid containing a general electrolyte in an applied electric field $\boldsymbol{E}$. We assume that the uncharged particle core of radius a is coated with an ion-penetrable layer of polyelectrolytes of thickness d and that fixed charges are distributed at a density of $\rho_{\text{fix}}(\boldsymbol{r})$. If ionized groups of valence Z are distributed within the polyelectrolyte layer at a uniform density N, then the polyelectrolyte later is uniformly charged at a constant density $\rho_{\text{fix}} = ZeN$. The polymer-coated particle has thus an inner radius a and an outer radius $b \equiv a + d$ (Fig. 77.1).

We adopt the model of Debye–Bueche [16] that the polymer segments are regarded as resistance centers distributed in the polyelectrolyte layer, exerting frictional forces on the liquid flowing in the polyelectrolyte layer. In the following text, we consider the case where a is much larger than $1/\kappa$ so that the particle surface can be considered as planar (Fig. 77.2).

We take an x axis perpendicular to the particle surface with its origin at $x = 0$ so that the region $-d < x < 0$ corresponds to the surface layer and the region $x > 0$ corresponds to the external region of the surface layer. The fundamental electrokinetic equations for the liquid velocity $u(x)$ at position

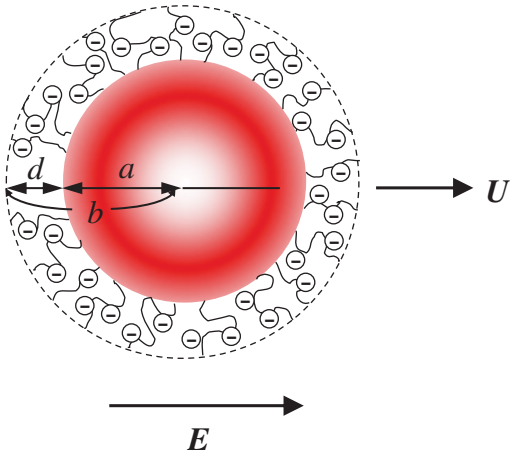


FIGURE 77.1 Spherical soft particle consisting of the particle core of radius a covered with an ion-penetrable surface layer of thickness d; $b = a + d$ is the outer radius. The particle moves with a velocity $\boldsymbol{U}$ in an applied electric field $\boldsymbol{E}$.

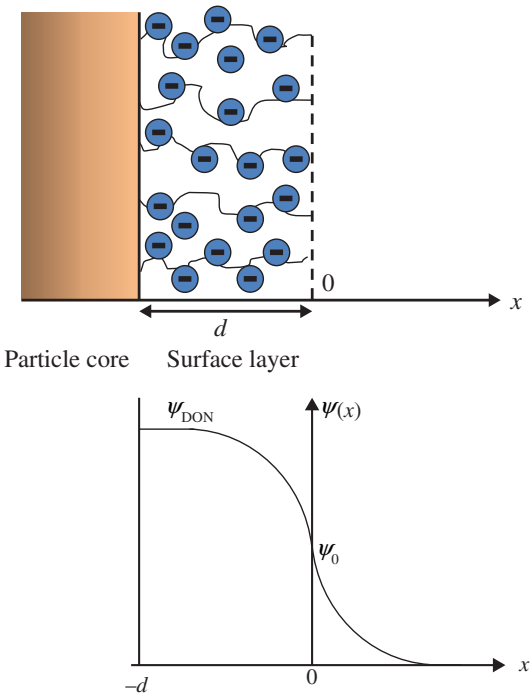


FIGURE 77.2 Schematic representation of the distribution of electrolyte ions and the potential distribution across a surface layer of thickness d.

x relative to the particle [$u(x) \to -U$ as $x \to \infty$] follow the one-dimensional Navier–Stokes equations for the regions outside and inside the surface layer:

$$\eta \frac{d^2u}{dx^2} + \rho_{\text{el}}(x)E = 0, \quad 0 < x < +\infty \tag{77.5}$$

$$\eta \frac{d^2u}{dx^2} - \gamma u + \rho_{\text{el}}(x)E = 0, \quad -d < x < 0 \tag{77.6}$$

Here, Eq. (77.5) is the usual Navier–Stokes equation. The term γu on the left-hand side (LHS) of Eq. (77.6) represents the frictional forces exerted on the liquid flow $u(x)$ by the polymer segments in the polyelectrolyte layer, and γ is the frictional coefficient. If it is assumed that each resistance center corresponds to a polymer segment, which, in turn, is regarded as a sphere of radius a_{p} and the polymer segments are distributed at a uniform volume density of N_{p} in the polyelectrolyte layer, then each polymer segment exerts the Stokes resistance $6\pi\eta a_{\text{p}}u$ on the liquid flow in the polyelectrolyte layer so that

$$\gamma = 6\pi\eta a_{\text{p}} N_{\text{p}} \tag{77.7}$$

Similarly, the Poisson equations relating the charge density $\rho_{\text{el}}(x)$ resulting from the mobile charged ionic species and

the electric potential $\psi(x)$ are also different for the different regions:

$$\frac{d^2\psi}{dx^2} = -\frac{\rho_{\rm el}(x)}{\varepsilon_{\rm r}\varepsilon_0}, \quad 0 < x < +\infty \tag{77.8}$$

$$\frac{d^2\psi}{dx^2} = -\frac{\rho_{\rm el}(x) + \rho_{\rm fix}(x)}{\varepsilon_{\rm r}\varepsilon_0}, \quad -d < x < 0 \tag{77.9}$$

Here, the relative permittivity $\varepsilon_{\rm r}$ is assumed to take the same value both inside and outside the polyelectrolyte layer. Note that the right-hand side (RHS) of Eq. (77.9) contains the contribution of the fixed-charges of density $\rho_{\rm fix}(x)$.

It can be shown that Eqs. (77.5) and (77.6) are solved to give

$$u(x) = \frac{\varepsilon_{\rm r}\varepsilon_0 E}{\eta}\psi(x) - U \text{ for } x \geq 0 \tag{77.10}$$

$$\begin{aligned} u(x) = \frac{\varepsilon_{\rm r}\varepsilon_0 E}{\eta}\Bigg[&\psi(x) - \psi(-d)\frac{\cosh(\lambda x)}{\cosh(\lambda d)} \\ &- \frac{\lambda\sinh(\lambda(x+d))}{\cosh(\lambda d)}\int_{-d}^{0}\psi(x)\cosh(\lambda x)\,dx \\ &+ \lambda\int_{-d}^{x}\psi(x')\sinh(\lambda(x-x'))\,dx'\Bigg] \\ &+ \frac{E}{\eta\lambda}\Bigg[\int_{-d}^{x}\rho_{\rm fix}(x')\sinh(\lambda(x-x'))\,dx' \\ &- \frac{\sinh(\lambda(x+d))}{\cosh(\lambda d)}\int_{-d}^{0}\rho_{\rm fix}(x)\cosh(\lambda x)dx\Bigg] \\ &\text{for } -d < x < 0 \end{aligned} \tag{77.11}$$

where λ is defined by $\lambda = (\gamma/\eta)^{1/2}$.

The electrophoretic mobility $\mu = U/E = -u(\infty)/E$ is thus

$$\begin{aligned} \mu = \frac{\varepsilon_{\rm r}\varepsilon_0}{\eta}\cdot\frac{1}{\cosh(\lambda d)}\left[\psi(-d) + \lambda\int_{-d}^{0}\psi(x)\sinh(\lambda(x+d))\,dx\right] \\ + \frac{1}{\eta\lambda}\cdot\frac{1}{\cosh(\lambda d)}\int_{-d}^{0}\rho_{\rm fix}(x)\sinh(\lambda(x+d)\,dx \end{aligned} \tag{77.12}$$

We treat the case where $\rho_{\rm fix}(x) = ZeN$ and κd, $\lambda d \gg 1$. In such cases the potential $\psi(x)$ inside the polyelectrolyte layer can be approximated by

$$\psi(x) = \psi_{\rm DON} + (\psi_0 - \psi_{\rm DON})e^{\kappa_{\rm m}x} \text{ for } -d < x < 0 \tag{77.13}$$

with

$$\psi_{\rm DON} = \left(\frac{kT}{ze}\right)\ln\left[\frac{ZN}{2zn} + \left\{\left(\frac{ZN}{2zn}\right)^2 + 1\right\}^{1/2}\right] \tag{77.14}$$

$$\begin{aligned} \psi_0 = \frac{kT}{ze}\Bigg(&\ln\left[\frac{ZN}{2zn} + \left\{\left(\frac{ZN}{2zn}\right)^2 + 1\right\}^{1/2}\right] \\ &+ \frac{2zn}{ZN}\left[1 - \left\{\left(\frac{ZN}{2zn}\right)^2 + 1\right\}^{1/2}\right]\Bigg) \end{aligned} \tag{77.15}$$

$$\kappa_{\rm m} = \kappa\left[1 + \left(\frac{ZN}{2zn}\right)^2\right]^{1/4} \tag{77.16}$$

where $\kappa_{\rm m}$ is the Debye–Hückel parameter in the surface layer and $\psi_{\rm DON}$ and $\psi_0 = \psi(0)$ are, respectively, the Donnan potential and the surface potential of the surface charge layer. Note that the surface potential ψ_0 is determined by the surface charge density σ (C/m^2) but for a soft particle it is determined by the volume charge density ZeN (C/m^3).

Similarly, from Eq. (77.11) we obtain

$$\begin{aligned} u(x) = \frac{\varepsilon_{\rm r}\varepsilon_0 E}{\eta}(\psi_0 - \psi_{\rm DON})\frac{\kappa_{\rm m}(\kappa_{\rm m}e^{\kappa_{\rm m}x} - \lambda e^{\lambda x})}{\kappa_{\rm m}^2 - \lambda^2} \\ + \frac{ZeNE}{\eta\lambda^2}\{e^{-\lambda(x+d)} - 1\} \text{ for } -d < x < 0 \end{aligned} \tag{77.17}$$

We thus obtain the following expression for the electrophoretic mobility of a soft particle [3]:

$$\mu = \frac{\varepsilon_{\rm r}\varepsilon_0}{\eta}\frac{\psi_0/\kappa_{\rm m} + \psi_{\rm DON}/\lambda}{1/\kappa_{\rm m} + 1/\lambda} + \frac{ZeN}{\eta\lambda^2} \tag{77.18}$$

Equation (77.18) consists of two terms; the first term is a weighted average of the Donnan potential $\psi_{\rm DON}$ and the surface potential ψ_0. It should be stressed that only the first term is subject to the shielding effects of electrolytes, tending to zero as the electrolyte concentration n increases, while the second term does not depend on the electrolyte concentration. In the limit of high electrolyte concentrations, all the potentials vanish and only the second term of the mobility expression remains:

$$\mu \to \mu^\infty = \frac{ZeN}{\eta\lambda^2} \tag{77.19}$$

This last equation shows that as $\kappa \to \infty$, μ tends to a nonzero limiting value μ^∞. This is a characteristic of the electrokinetic behavior of soft particles, in contrast to the case of the electrophoretic mobility of hard particles, which should reduce to zero as a result of the shielding effects, since the mobility expressions for rigid particles do not have μ^∞.

It is also to be noted that in the limit of $1/\lambda$ tending to zero, Eq. (77.18) becomes Smoluchowski's formula [Eq. (77.1)]. This means that in this limit a soft particle becomes a hard particle carrying zeta-potential $\zeta = \psi_0$. In other words, the parameter $1/\lambda$ can be regarded as a softness parameter.

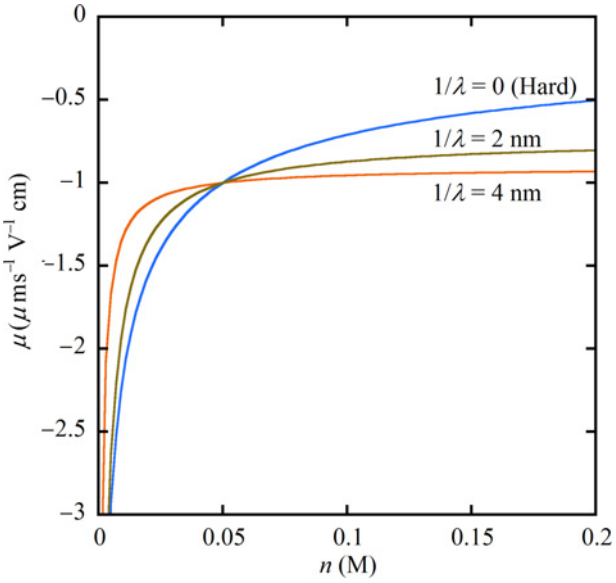


FIGURE 77.3 The electrophoretic mobility μ of soft particles as a function of the electrolyte concentration n for three values of the softness parameter $1/\lambda$. A particle with $1/\lambda = 0$ corresponds to a hard particle. Calculated via Eq. (77.18) with z = l, $\eta = 0.891$ mPa · s, $\varepsilon_r = 78.5$, and $T = 298$ K. The values of the fixed charge density ZeN for the soft particles and the surface charge density σ for the hard particle are chosen so that three curves give the same μ value at $n = 0.05$ M, that is, $ZN = 16.9$ mM for a curve with $1/\lambda = 2$ nm, $ZN = 5.2$ mM for a curve with $1/\lambda = 4$ nm, and $\sigma = 6.6$ mC/m^2 for a curve with $1/\lambda = 0$ nm (hard particle).

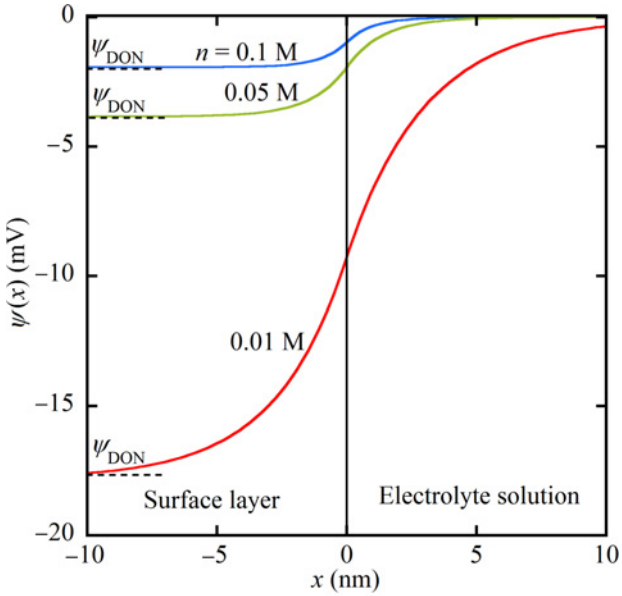


FIGURE 77.4 The potential distribution $\psi(x)$ across the uniformly charged surface layer for several values of n, calculated with z = l, $ZN = -0.015$ M, $d = 10$ nm, $\eta = 0.891$ mPa · s, $\varepsilon_r = 78.5$, and $T = 298$ K for $n = 0.1$ M, 0.05 M, and 0.01 M [2].

Figure 77.3 shows the electrophoretic mobility μ of soft particles (curves with $1/\lambda = 2$ nm and 4 nm) in comparison with the mobility of a hard particle (curve with $1/\lambda = 0$).

The values of the charge density N or σ are chosen so that the mobility values for all the cases show the same value of -1 μm s^{-1} V^{-1} cm^{-1} at $n = 0.05$ M. We see that for a hard particle μ approaches zero but for a soft particle it tends to a nonzero limiting value μ^∞.

In order to see this more clearly, in Figs. 77.4 and 77.5 we give examples of the liquid velocity $u(x)$ and the potential distributions $\psi(x)$ and the liquid velocity $u(x)$ across the surface layer of thickness 10 nm on a soft particle [2].

It is seen that the liquid velocity $u(x)$ in the middle region of the surface charge layer (the plateau region) (Fig. 77.5), where the potential is almost equal to the Donnan potential ψ_{DON} (Fig. 77.4), gives μ^∞. It is this term that yields the term independent of the electrolyte concentration. We also note that $1/\lambda$ is the distance between the slipping plane at the core surface at $x = 0$ and the bulk phase of the surface layer (the plateau region in Fig. 77.5), where $u(x)/E$ is given by $-\mu^\infty$. Figure 77.5 shows that a small shift of the slipping plane causes no effects on the mobility value. Therefore the mobility of soft particles is insensitive to the position of the slipping plane, and the zeta-potential loses its meaning.

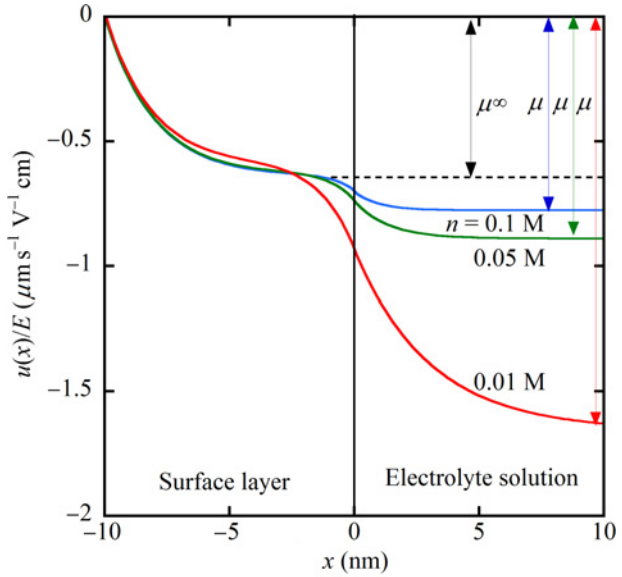


FIGURE 77.5 The velocity distribution of liquid flow $u(x)$ across the uniformly charged surface layer for several values of n. Calculated with $z = 1$, $ZN = -0.015$ M, $d = 10$ nm, $l/\lambda = 2$ nm, $\eta = 0.891$ mPa · s, $\varepsilon_r = 78.5$, and $T = 298$ K for $n = 0.1$ M, 0.05 M, and 0.01 M. The value of - $u(+\infty)/E$ gives the mobility μ. The dashed line indicates the contribution from the term independent of the electrolyte concentration μ_∞ [2].

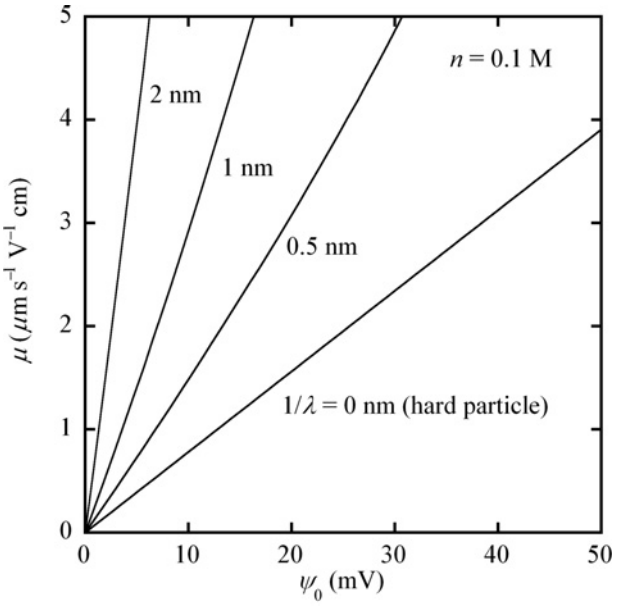


FIGURE 77.6 The electrophoretic mobility μ as a function of the surface potential ψ_0 for several values of $1/\lambda$. Calculated with Eq. (77.18) at $z = 1$, $\eta = 0.891$ mPa · s, $\varepsilon_r = 78.5$, and $T = 298$ K. The curve with $1/\lambda = 0$ (or $\lambda = \infty$) corresponds to the mobility of hard particles [Eq. (77.1)] [12].

It has been shown that the electrical behaviors of soft particles are quite different from those of hard paticles. As is seen from Eqs. (77.1) and (77.18), the magnitude and the electrolyte concentration dependence of the electrophoretic mobility μ of soft particles, in particular, differ considerably from those of hard particles. Figure 77.6 shows the electrophoretic mobility μ as a function of the surface potential ψ_0 at $n = 0.1$ M for various values of the softness parameter $1/\lambda$. The curve with $1/\lambda = 0$ corresponds to hard particles [Eq. (77.1)]. Figure 77.4 demonstrates a remarkable difference between soft and hard particles. For example, at $n = 0.1$ M, $ZN = 0.15$ M and $1/\lambda = 2$ nm, despite the fact that the surface potential ψ_0 is only 1 mV, the mobility μ amounts to 0.78 μm s^{-1} V^{-1} cm^{-1}. With Smoluchowski's formula [Eq. (77.1)], on the other hand, this mobility value is converted to the surface potential (or the zeta-potential) of approximately 10 mV. Thus, in order to analyze the mobility data of soft particles, the soft particle theory [Eq. (77.18)] should be applied, instead of Smoluchowski's formual [Eq. (77.1)]. Otherwise the surface potential would be considerably overestimated.

77.4 ANALYSIS OF ELECTROPHORETIC MOBILITY OF SOFT PARTICLES

Equation (77.18) contains two unknown parameters: the density of fixed charges ZN and the softness parameter $1/\lambda$. We calculate the electrophoretic mobility μ as a function of the electrolyte concentration n in the suspending medium for various ZN and $1/\lambda$ in order to determine the values of ZN and $1/\lambda$ by a curve-fitting procedure. A number of experimental studies have been carried out in order to analyze experimental mobility data by using Eq. (77.18) [17–36]. Note that N and n are given in units of m^{-3}. If one uses the units of M, then N and n must be replaced by $1000N_AN$ and N_An, where N_A is Avogadro's number. In the remainder of this section we present some examples of the analysis of the electrophoretic mobility of soft particles.

77.4.1 RAW117 Lymphosarcoma Cells and Their Variants

Makino et al. [18] measured the electrophoretic mobilities of the cells of malignant lymphosarcoma cell line RAW117-P and its variant H10 with a highly metastatic property to the liver at various ionic strengths. The cells of the parental cell line (RAW117-P) show mobility values that are higher in magnitude than those of its variant line (RAW117-H10) in the whole range of electrolyte concentration measured. The mobility data obtained have been analyzed via Eq. (77.18). By a curve-fitting procedure, we have found that the best-fit curves (shown as solid lines in Fig. 77.7) are obtained with $zN = -0.04$ M and $1/\lambda = 1.5$ nm for RAW117-P cells and $zN = -0.03$ M and $1/\lambda = 1.7$ nm for RAW117-H10 cells.

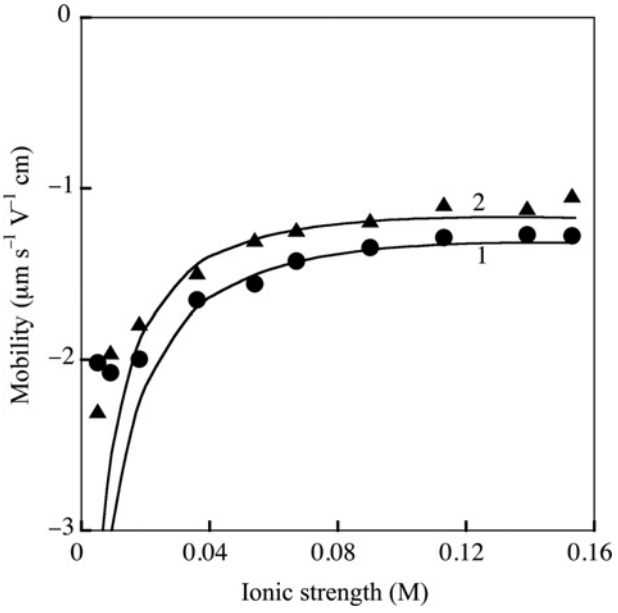


FIGURE 77.7 Electrophoretic mobilities of RAW117-P cells and RAW117-H10 cells. Symbols represent experimental data measured as a function of the ionic strength in the suspending medium at pH 7.4 and 37°C: ●, RAW117-P cells ▲, RAW117-H10 cells. Solid-line curves indicate theoretical results calculated via Eq. (77.18) with $ZN = -0.04$ M and $1/\lambda = 1.5$ nm (curve 1), and $ZN = -0.03$ M and $1/\lambda = 1.7$ nm (curve 2). (From Ref. 18.)

It is observed that the theoretical curves and the experimental data points are in good agreement with each other over a wide range of electrolyte concentration. The mobility difference between RAW117-P and RAW117-H10 cells is attributed to the differences in both $1/\lambda$ and charge density ZeN in their surface layers. Among these differences, the difference in N is corresponds to the difference in sialic acid contents in both cells, while the difference in $1/\lambda$ may possibly reflect a change of packing state of polymer chains in the cell surface layer. The result that $1/\lambda$ is greater for RAW117-H10 cells than for RAW117-P cells implies that the friction exerted by the surface layer on the liquid flow around the cells is less for RAW117-H10 than for RAW117-P. In other words, the surface layer of RAW117-H10 cells is "softer" than that of RAW117-P cells.

77.4.2 Poly(*N*-isopropylacrylamide) Hydrogel–Coated Latex

Poly(*N*-isopropylacrylamide) hydrogel is known to be temperature-sensitive, exhibiting a phase transition at about 32°C [17,18]; that is, it swells below 32°C and shrinks above 32°C. In Refs. 17 and 18, the measurements and the analysis are given for the electrophoretic mobility of latex particles composed of a poly(styrene-*co*-ethylhexyl methacrylate) core and a poly(*N*-isopropylacrylamide) hydrogel layer in an electrolyte solution as a function of the ionic strength and temperature of the suspending media. Although poly(*N*-isopropylacrylamide) is itself electrically neutral, the hydrogel layer on the particle carries fixed negative charges, arising from dissociation of sulfate groups in the hydrogel layer, since potassium persulfate is used as an initiator of soap-free emulsion copolymerization.

Figure 77.8 shows that the electrophoretic mobility of the latex particles was measured in a phosphate buffer solution at pH 7.4 at four different temperatures, namely, 25°C, 30°C, 35°C, and 40°C [above and below the phase transition temperature of the poly(*N*-isopropylacrylamide) hydrogel] [17].

Figure 77.8 shows results of the calculation of the mobility as a function of the electrolyte concentration on the basis of Eq. (77.18). Theoretical curves calculated via Eq. (7718) with a single value of each of N and $1/\lambda$ are found to be in good agreement with the experimental data over a wide range of the ionic strength except in cases where it is too low. The deviation at very low ionic strengths at 35°C and 40°C, where Eq. (77.18) yields overestimation in magnitude, may be due to the fact that the hydrogel layer suffers an additional minor expansion due to reduction of the ionic shielding effects, resulting in a decrease in N. The overall agreement between theory and experiment implies that hydrogel-layer-coated latex particles show the electrophoretic behavior of "soft particles" described by Eq. (77.18) and also enables us to estimate the values of the unknown parameters N and $1/\lambda$ via a curve-fitting procedure.

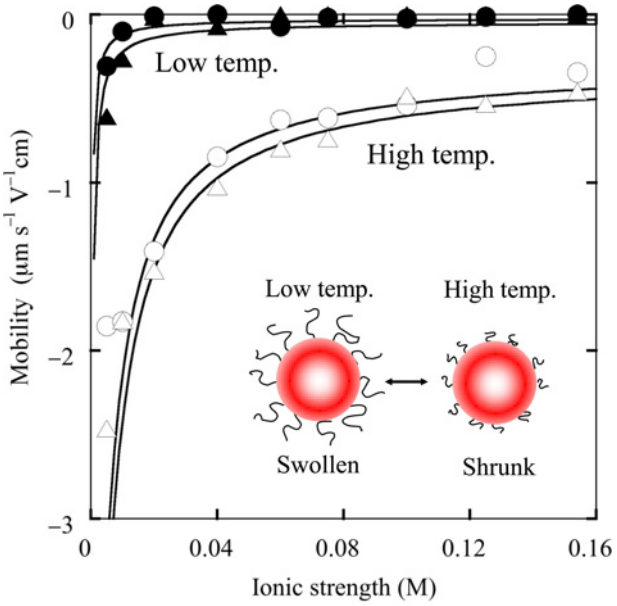


FIGURE 77.8 Electrophoretic mobility of latex particles with temperature-sensitive poly(*N*-isopropylacrylamide) hydrogel layers as a function of ionic strength at pH = 7.4 at several values of the temperature of the suspending medium. Symbols represent experimental data: ●, 25°C; ▲, 30°C (below the phase transition temperature); ○, 35°C; △, 40°C (above the phase transition temperature). Solid-line curves give theoretical results calculated from Eq. (77.18) with $ZN = -0.0015$ M and $1/\lambda = 1.2$ nm at 25°C; $ZN = -0.0025$ M and $1/\lambda = 1.2$ nm at 30°C, $ZN = -0.03$ M and $1/\lambda = 0.9$ nm, both at 35°C and 40°C. (From Ref. 17.)

The best-fit curves (shown as solid lines in Fig. 77.8) at different temperatures are obtained with $zN = -0.0015$ M and $1/\lambda = 1.2$ nm at 25°C, $zN = -0.0025$ M and $1/\lambda = 1.2$ nm at 30°C, and $zN = -0.03$ M and $1/\lambda = 0.9$ nm, at both 35°C and 40°C. The best-fit values of zN and $1/\lambda$ are thus the same for 35°C and 40°C. The observed small difference in the mobility values between 35°C and 40°C can be explained by the temperature dependence of the relative permittivity ε_r and viscosity η of the suspending media, that is, ($\varepsilon_r = 75.1$ and $\eta = 0.719 \times 10^{-3}$ mPa • s at 35°C and $\varepsilon_r = 73.4$ and $\eta = 0.653 \times 10^{-3}$ mPa • s at 40°C). This implies that the values of N and $1/\lambda$ do not change appreciably in the temperature range 35–40°C. On the other hand, the large mobility increase from 30°C to 35°C across the phase transition temperature (which correlates with the large change in size of the latex particles) is due mainly to an increase in the charge density ZeN. Thus, below the phase transition temperature, where the hydrogel layer swells, the charge density decreases, while above the phase transition temperature the hydrogel layer shrinks and the charge density increases, causing a large change in the mobility. Note that the mobility given by Eq. (77.18) is determined not by the total amount of fixed charges carried by a colloidal particle but by their volume density. Thus, below

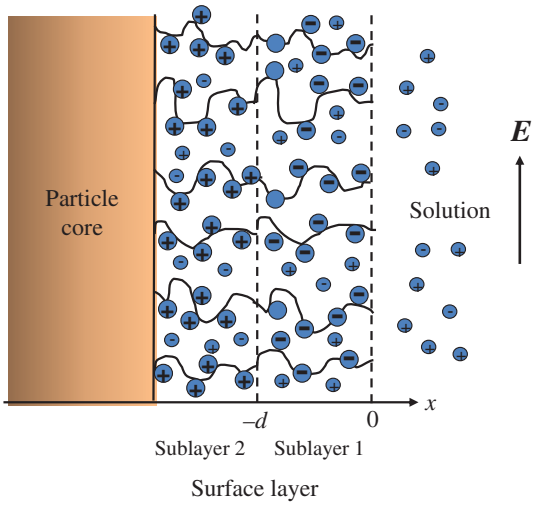


FIGURE 77.9 A surface charge layer consisting of two oppositely charged sublayers 1 and 2.

the phase transition temperature, when the hydrogel layer swells, the decreased charge density leads to a large reduction of the mobility, even if the total number of the fixed charges remains constant. The minor difference in the estimated values of N between 25°C and 30°C may also be due to a small change in the thickness of the hydrogel layer in this temperature range. The observed reduction of the "softness parameter" $1/\lambda$ implies that the hydrogel layer becomes "harder," which is inconsistent with the observed shrinkage of the hydrogel.

77.5 ELECTROPHORESIS OF NONUNIFORMLY CHARGED SOFT PARTICLES

We consider the case in which the surface charge layer consists of a positive-charge inner sublayer and a negative-charge outer sublayer (Fig. 77.9).

In such cases the surface potential is negative at high electrolyte concentrations but may become positive at low concentrations. The reason for the sign reversal of the surface potential can be explained as follows. It is the fixed charges located through the depth (from the boundary between the outer sublayer and the surrounding electrolyte solution) of the order of the Debye length $1/\kappa$ that mainly contribute to the membrane surface potential. At high electrolyte concentrations, $1/\kappa$ is small, so that the sign of the surface potential is determined mainly by the sign of the fixed charges present in the outer layer. On the other hand, at low electrolyte concentrations, $1/\kappa$ is large and the contribution from the fixed-charges in the inner layer becomes appreciable. Thus, if the inner layer is sufficiently highly charged, then at low electrolyte concentrations the sign of the surface potential may coincide with the sign of the fixed charges in the inner layer.

The sign reversal takes place also in the electrophoretic mobility of a nonuniformly charge soft particles, as shown below. We treat a large soft particle. The x axis is taken to be perpendicular to the soft surface with its origin at the front edge of the surface layer (Fig. 77.9). The soft surface consists of the outer layer ($-d < x < 0$) and the inner layer ($x < -d$), where the inner layer is sufficiently thick so that the inner layer can be considered practically to be infinitely thick. Consider the case where the outer sublayer (sublayer 1) carries ionized groups of valence Z_1 and number density N_1, while the inner sublayer (sublayer 2) carries ionized groups of valence Z_2 and number density N_2. Let the thickness of layer 1 be d. Then, we have

$$\rho_{\text{fix}}(x) = \begin{cases} Z_1 eN_1, & -d \le x \le 0 \\ Z_2 eN_2, & x \le -d \end{cases} \tag{77.20}$$

where $Z_1 eN_1$ and $Z_2 eN_2$ are, respectively, the charge densities of fixed charges in sublayers 1 and 2.

By solving the Navier–Stokes equations for sublayers 1 and 2, we finally obtain the following expression for the electrophoretic mobility:

$$\mu = \mu_1 + \mu_2 \tag{77.21}$$

with

$$\mu_1 = \frac{Z_1 eN_1}{\eta\lambda^2}\left[1 + \left(\frac{\lambda}{\kappa}\right)^2 \left\{\frac{1+\lambda/2\kappa}{1+\lambda/\kappa} + \frac{\lambda}{2(\kappa-\lambda)}e^{-\kappa d}\right\} - \frac{\kappa^2}{(\kappa^2-\lambda^2)}e^{-\lambda d}\right] \tag{77.22}$$

$$\mu_2 = -\frac{Z_2 eN_2}{\eta\lambda^2}\left[\left(\frac{\lambda}{\kappa}\right)^2 \frac{\lambda}{2(\kappa-\lambda)}e^{-\kappa d} - \frac{\kappa^2}{(\kappa^2-\lambda^2)}e^{-\lambda d}\right] \tag{77.23}$$

Variation of the mobility with electrolyte concentration n is caused not only by the shielding effects of electrolyte ions but also by the change in the relative contributions from the fixed-charges in layer 1 and from those in layer 2. The latter effects correspond to the fact that fixed charges located through the depth of around $1/\kappa$ mainly contributes to the mobility. Figure 77.10 gives μ_1 and μ_2 and their sum $\mu = \mu_1 + \mu_2$ plotted as functions of electrolyte concentration n, showing the sign reversal of the electrophoretic mobility μ.

Makino et al. [25] measured the electrophoretic mobility of four types M_1–M_4 of hydrophilic gel microcapsules containing water prepared by an interfacial polymerization method. Each type of microcapsules has membranes of different compositions. The results of the analysis of the measured mobilitiy values on the basis of Eq. (77.21) are given in Figs. 77.11 and 77.12, showing good agreement between theory and experiment.

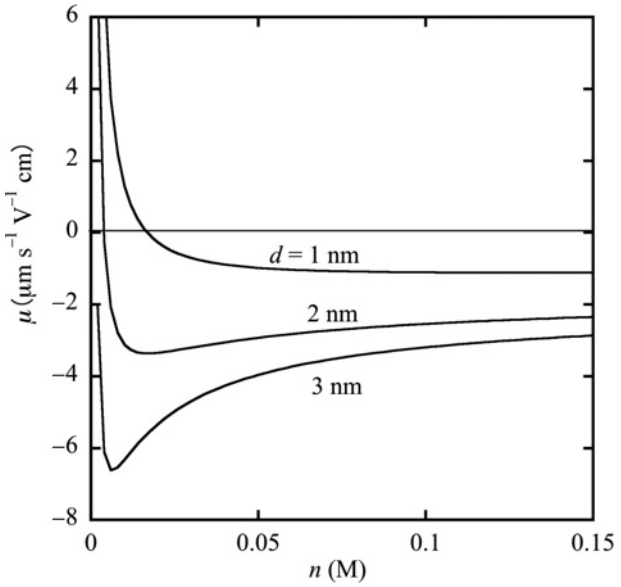


FIGURE 77.10 Electrophoretic mobility μ as a function of electrolyte concentration n for various values of d at $1/\lambda = 1$ mm, calculated using Eq. (77.21) with $z = 1$, $Z_1N_1 = -0.2$ M, $Z_2N_2 = 0.1$ M, $\eta = 0.89$ mPa • s, $\varepsilon_r = 78.5$, and $T = 298$ K. Curves: (1) $d = 0.2$ nm; (2) $d = 1$ nm; (3) $d = 2$ nm; (4) $d = 3$ nm.

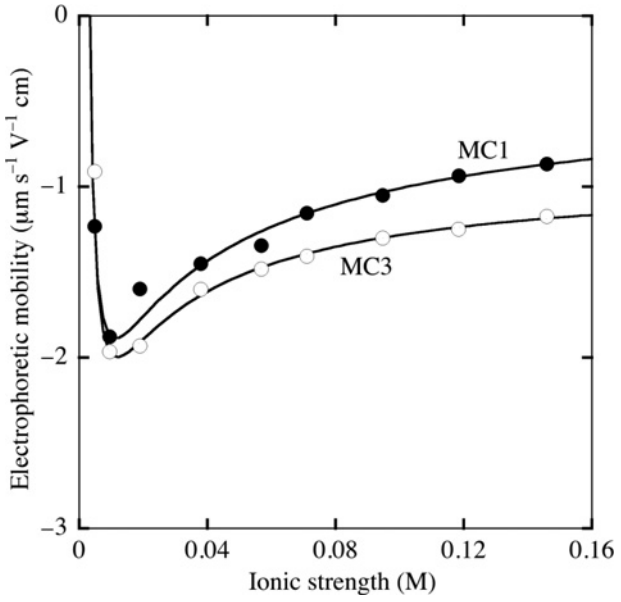


FIGURE 77.11 Electrophoretic mobility of MC 1 and 3. Symbols represent experimental data with MC 1 and 3 measured as a function of ionic strength in surrounding medium at pH 7.4 and 37°C. Solid-line curves represent theoretical vaues calculated with $Z_1N_1 = -0.111$ M, $Z_2N_2 = 0.041$ M, $1/\lambda = 0.505$ nm, $d = 1.706$ nm (MC 1), and with $z_1N_1 = -0.048$ M, $z_2M_2 = 0.048$ M, $1/\lambda = 1{,}230$ nm, Z_1N_1, $d = 3.758$ nm (MC 3). (From Ref. 24.)

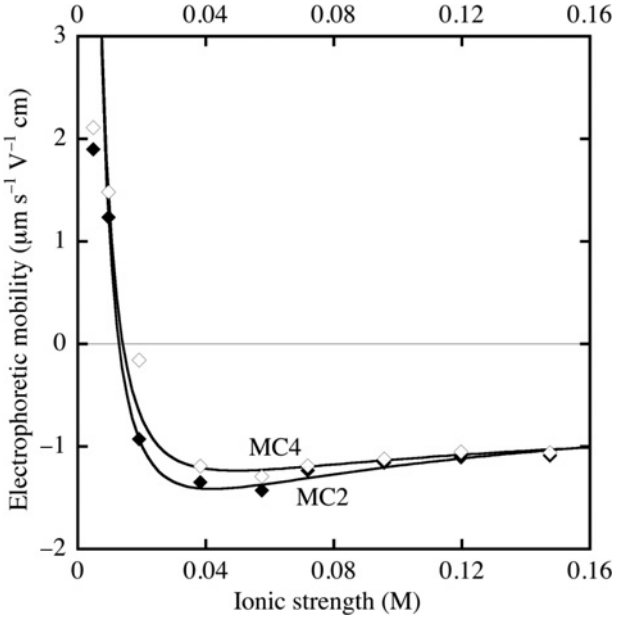


FIGURE 77.12 Electrophoretic mobility of MC 2 and 4. Symbols represent experimental data with MC 2 and 4 measured as a function of ionic strength in surrounding medium at pH 7.4 and 37°C. Solid-line curves represent theoretical values calculated with $Z_1N_1 = -0.140$ M, $Z_2N_2 = 0.166$ M, $1/\lambda = 0.471$ nm, $d = 2.090$ nm (MC 2), and with $Z_1N_1 = -0.084$ M, $Z_2N_2 = 0.159$ M, $1/\lambda = 0.778$ nm, $d = 2.751$ nm (MC 4). (From Ref. 25.)

REFERENCES

[1] von Smoluchowski, M. (1921). In Graetz, L. (ed.), *Handbuch der Elektrizität und des Magnetismus*. Barth, Leipzig, Vol 2, p. 366.

[2] Ohshima, H., Kondo, T. (1991). *Biophys. Chem.* **39**, 191.

[3] OhshiIma, H. (1994). *J. Colloid Interface Sci.* **163**, 474.

[4] Ohshima, H. (1998). In Ohshima, H., Furusawa, K. (eds.), *Electrical Phenomena at Interfaces. Fundamentals, Measurements, and Applications*, 2nd ed. (revised and expanded). Marcel Dekker, New York, Chapter 2.

[5] Ohshima, H. (2000). *J. Colloid Interface Sci.* **228**, 190.

[6] Ohshima, H. (2006). *Theory of Colloid and Interfacial Electric Phenomena.* Elsevier/Academic Press.

[7] Duval, J.F.L., Ohshima, H. (2006). *Langmuir* **22**, 3533.

[8] Ohshima, H. (2007). *Colloid Polym. Sci.* **285**, 1411.

[9] Ohshima, H. (2009). *Sci. Technol. Adv. Mater.* **10**, 063001.

[10] Ohshima, H. (2010). *Biophysical Chemistry of Biointerfaces.* Wiley, Hoboken, NJ.

[11] Ohshima, H. (2012). In Ohshima, H. (ed.), *Electrical Phenomena at Interfaces and Biointerfaces: Fundamentals and Applications in Nano-, Bio-, and Environmental Sciences*. Wiley, Hoboken, NJ, Chapter 4.

[12] Ohshima, H. (2012). *Soft Matt.* **8**, 3511.

[13] Ohshima, H. (2012). *J. Phys. Chem. A* **116**, 6473.

[14] Ohshima, H. (2013). *Curr. Opinion Colloid Interface Sci.* **18**, 73.

[15] Ohshima, H. (2014). *Colloids Surf. A: Physicochem. Eng. Aspects* **440**, 151.

[16] Debye, P., Bueche, A. (1948). *J. Chem. Phys.* **16**, 573.

[17] Ohshima, H., Makino, K., Kato, T., Fujimoto, K., Kondo, T., Kawaguchi, H. (1993). *J. Colloid Interface Sci.* **159**, 512.

[18] Makino, K., Taki, T., Ogura, M., Handa, S., Nakajima, M., Kondo, T., Ohshima, H. (1993). *Biophys. Chem.* **47**, 261.

[19] Makino, K., Suzuki, K., Sakurai, Y., Okano, T., Ohshima, H. (1995). *J. Colloid Interface Sci.* **174**, 400.

[20] Mazda, T., Makino, K., Ohshima, H. (1995). *Colloids Surf. B.* **5**, 75; erratum (1998), ibid. **10**, 303.

[21] Takashima, S., Morisaki, H. (1997). *Colloids Surf. B.* **9**, 205.

[22] Bos, R., van der Mei, H.C., Busscher, H.J. (1998). *Biophys. Chem.* **74**, 251.

[23] Larsson, A., Rasmusson, M., Ohshima, H. (1999). *Carbohydr, Res*. **317**, 223.

[24] Morisaki, H., Nagai, S., Ohshima, H., Ikemoto, E., Kogure, K. (1999). *Microbiology* **145**, 2797.

[25] Makino, K., Umetsu, M., Goto, Y., Kikuchi, A., Sakurai, Y., Okano, T., Ohshima, H. (1999). *J. Colloid Interface Sci*. **218**, 275.

[26] Rasmusson, M., Vincent, B., Marston, N. (2000). *Colloid Polym. Sci*. **278**, 253.

[27] Hayashi, H., Tsuneda, S., Hirata, A., Sasaki, H. (2001). *Colloids Surf. B* **22**, 149.

[28] Garcia-Salinas, M.J., Romero-Cano, M.S., de las Nieves, F.J. (2001). *Progress Colloid Polym. Sci.* **118**, 180.

[29] Kiers, P.J.M., Bos, R., van der Mei, H.C., Busscher, H.J. (2001). *Microbiology* **147**, 757.

[30] Molina-Bolivar, J.A., Galisteo-Gonzalez, F., Hidalgo-Alvalez, R. (2001). *Colloids Surf. B: Biointerfaces* **21**, 125.

[31] Lutterodt, G., Basnet, M., Foppen, J.W.A., Uhlenbrook, S. (2009). *Water Res*. **43**, 595.

[32] Hori, K., Matsumoto, S. (2010). *Biochem. Eng. J.* **48**, 424.

[33] Makino, K., Ohshima, H. (2011). *Sci. Technol. Adv. Mater*. **12**, 023001.

[34] Morille, M., Passirani, C., Dufort, S., Guillaume, B., Pitard, B., Coll, J.L., Benoit, J.P. (2011). *Biomaterials* **32**, 2327.

[35] Morisaki, H. (2012). In Ohshima, H. (ed.), *Electrical Phenomena at Interfaces and Biointerfaces: Fundamentals and Applications in Nano-, Bio-, and Environmental Sciences*. Wiley, Hoboken, NJ, Chapter 42.

[36] Loui, S.M., Phenrat, T., Small, M.J., Tilton, R.D., Lowry, G.V. (2012). *Langmuir* **28**, 10334.

78

POTENTIAL DISTRIBUTION AROUND A HARD PARTICLE AND A SOFT PARTICLE

Hiroyuki Ohshima

Faculty of Pharmaceutical Sciences, Tokyo University of Science, 2641 Yamazaki Noda, Chiba 278-8510, Japan

78.1 INTRODUCTION

Around a charged colloidal particle immersed in an electrolyte solution, mobile electrolyte ions form an ionic cloud around the particle. In the ionic cloud the concentration of counterions (electrolyte ions with charges of the sign opposite to that of the particle surface charges) becomes very high while that of coions (electrolyte ions with charges of the same sign as the particle surface charges) is very low, due to electrostatic interaction between electrolyte ions and particle surface charges. Figure 78.1 schematically shows the distribution of ions around a charged spherical particle of radius a. The ionic cloud together with the particle surface charge forms an electrical double layer.

Such an electrical double layer is often called an *electrical diffuse double layer*, since the distribution of electrolyte ions in the ionic cloud takes a diffusive structure because of the thermal motion of ions. Electrostatic and electrokinetic behaviors (interaction between colloidal particles and motion of colloidal particle in an external field, e.g., electric field and gravitational field) depend on the distribution of electrolyte ions and of the electric potential across the electrical double layer around the particle surface [1–6].

78.2 HARD PARTICLES

Consider a uniformly charged particle immersed in a liquid containing N ionic species with valence z_i and bulk concentration (number density) n_i^∞ ($i = 1,2,\ldots,N$) (in units of m^{-3}). From the electroneutrality condition, we have

$$\sum_{i=1}^{N} z_i n_i^\infty = 0 \tag{78.1}$$

The electric potential $\psi(\boldsymbol{r})$ at position $\boldsymbol{r}$ outside the particle, measured relative to the bulk solution phase, where ψ is set equal to zero, is related to the charge density $\rho_{\mathrm{el}}(\boldsymbol{r})$ at the same point by the Poisson equation as

$$\Delta\psi(\boldsymbol{r}) = -\frac{\rho_{\mathrm{el}}(\boldsymbol{r})}{\varepsilon_{\mathrm{r}}\varepsilon_{\mathrm{o}}} \tag{78.2}$$

where Δ is the Laplacian, ε_{r} is the relative permittivity of the electrolyte solution, and ε_{o} is the permittivity of a vacuum. We assume that the distribution of the electrolyte ions $n_i(\boldsymbol{r})$ obeys Boltzmann's low as

$$n_i(\boldsymbol{r}) = n_i^\infty \exp\left(-\frac{z_i e\psi(\boldsymbol{r})}{kT}\right) \tag{78.3}$$

where $n_i(\boldsymbol{r})$ is the concentration (number density) of the i th ionic species at position $\boldsymbol{r}$, e is the elementary electric charge, k is Boltzmann's constant, and T is the absolute temperature. The charge density $\rho_{\mathrm{el}}(\boldsymbol{r})$ at position $\boldsymbol{r}$ is thus given by

$$\rho_{\mathrm{el}}(\boldsymbol{r}) = \sum_{i=1}^{N} z_i e n_i(\boldsymbol{r}) = \sum_{i=1}^{N} z_i e n_i^\infty \exp\left(-\frac{z_i e\psi(\boldsymbol{r})}{kT}\right) \tag{78.4}$$

Encyclopedia of Biocolloid and Biointerface Science, Volume 2, First Edition. Edited by Hiroyuki Ohshima.
© 2016 John Wiley & Sons, Inc. Published 2016 by John Wiley & Sons, Inc.

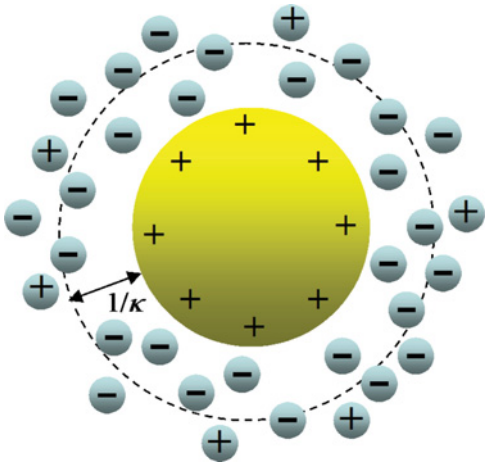


FIGURE 78.1 Electrical double layer around a charged colloidal particle. The thickness of the electrical double layer is given by the Debye length $1/\kappa$.

Combining Eqs. (78.2) and (78.4) gives

$$\Delta\psi(\boldsymbol{r}) = -\frac{1}{\varepsilon_r\varepsilon_o}\sum_{i=1}^{N} z_i e n_i^{\infty} \exp\left(-\frac{z_i e\psi(\boldsymbol{r})}{kT}\right) \tag{78.5}$$

This is the Poisson–Boltzmann equation for the potential distribution $\psi(\boldsymbol{r})$, which is subject to the following boundary conditions:

$$\psi(\boldsymbol{r}) = \psi_o \text{ at the particle surface} \tag{78.6}$$

$$\psi(\boldsymbol{r}) \to 0 \text{ as } r = |\boldsymbol{r}| \to \infty \tag{78.7}$$

If the internal electric fields inside the particle can be neglected, then the surface charge density σ of the particle is related to the potential derivative normal to the particle surface as

$$\frac{\partial\psi}{\partial n} = -\frac{\sigma}{\varepsilon_r\varepsilon_o} \tag{78.8}$$

where n is the outward normal at the particle surface.

If the potential ψ is low, that is

$$\left|\frac{z_i e\psi}{kT}\right| \ll 1 \tag{78.9}$$

then Eq. (78.5) reduces to the following linearized Poisson–Boltzmann equation (Debye–Hückel equation):

$$\Delta\psi = \kappa^2\psi \tag{78.10}$$

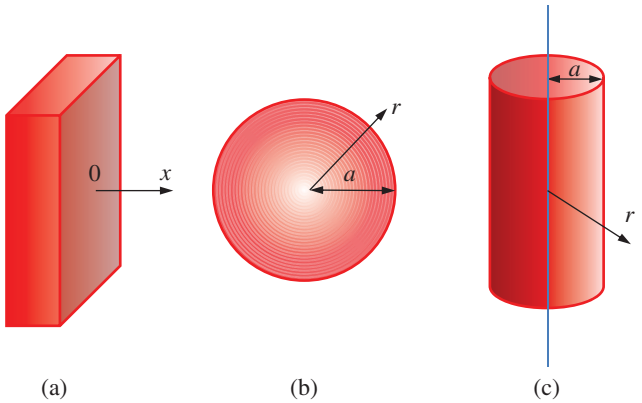


FIGURE 78.2 Colloidal particles of various geometry: (a) plate; (b) sphere; (c) cylinder.

with

$$\kappa = \left(\frac{1}{\varepsilon_r\varepsilon_o kT}\sum_{i=1}^{N} z_i^2 e^2 n_i^{\infty}\right)^{1/2} \tag{78.11}$$

where κ is called the *Debye–Hückel parameter*. The reciprocal of κ (i.e., $1/\kappa$), which is called the *Debye length*, corresponds to the thickness of the double layer. Note that n_i^{∞} in Eqs. (78.5) and (78.10) is given in units of m^{-3}. If one uses the units of M (mole/liter), then n_i^{∞} must be replaced by $1000N_A n_i^{\infty}$, where N_A is Avogadro's number.

The linearized equation [Eq. (78.10)] can be solved for particles of various shapes. We give below the potential distribution for a planar surface, a sphere of radius a, and a cylinder of radius a, which can be obtained by solving Eq. (78.10) (with $\Delta = d^2/dx^2$ for a planar surface, $\Delta = d^2/dr^2 + 2/r\cdot\, d/dr$ for a sphere, and $\Delta = d^2/dr^2 + 1/r\cdot\, d/dr$ for a cylinder) subject to Eqs. (78.6) and (78.7), where x is the distance from the planar surface located at $x = 0$ and r is the distance from the sphere center or the cylinder axis (Fig. 78.2):

1. Planar surface

$$\psi(x) = \psi_o e^{-\kappa x} \tag{78.12}$$

with

$$\psi_o = \frac{\sigma}{\varepsilon_r\varepsilon_o\kappa} \tag{78.13}$$

2. Sphere of radius a

$$\psi(r) = \psi_o\frac{a}{r}e^{-\kappa(r-a)} \tag{78.14}$$

with

$$\psi_o = \frac{\sigma}{\varepsilon_r \varepsilon_o \kappa (1 + 1/\kappa a)} \tag{78.15}$$

3. Cylinder of radius a

$$\psi(r) = \psi_o \frac{K_0(\kappa r)}{K_0(\kappa a)} \tag{78.16}$$

with

$$\psi_o = \frac{\sigma}{\varepsilon_r \varepsilon_o \kappa} \frac{K_0(\kappa a)}{K_1(\kappa a)} \tag{78.17}$$

where $K_n(z)$ is the modified Bessel function of the second kind of order n.

For the arbitrary potential case, one must solve the nonlinear Poisson–Boltzmann equation [Eq. (78.5)]. For a planar surface in contact with a z:z symmetric electrolyte solution, a 2:1 electrolyte solution, or a mixed solution of 1:1 electrolyte of bulk concentration n_1 and 2:1 electrolyte of bulk concentration n_2, the potential distribution $\psi(x)$ and the surface potential ψ_0/surface charge density σ relationship are as follows:

1. Symmetric electrolytes of valence z

$$\psi(x) = \frac{2kT}{ze} \ln\left(\frac{1 + \gamma e^{-\kappa x}}{1 - \gamma e^{-\kappa x}}\right) \tag{78.18}$$

with

$$\sigma = \frac{2\varepsilon_r \varepsilon_o \kappa kT}{ze} \sinh\left(\frac{ze\psi_o}{2kT}\right) \tag{78.19}$$

$$\gamma = \tanh\left(\frac{ze\psi_o}{4kT}\right) = \frac{\exp(ze\psi_o/2kT) - 1}{\exp(ze\psi_o/2kT) + 1} \tag{78.20}$$

2. 2:1 electrolyte solution

$$\psi(x) = \frac{kT}{e} \ln\left[\frac{3}{2}\left(\frac{1 + \frac{2}{3}\gamma' e^{-\kappa x}}{1 - \frac{2}{3}\gamma' e^{-\kappa x}}\right)^2 - \frac{1}{2}\right] \tag{78.21}$$

with

$$\sigma = \frac{2\varepsilon_r \varepsilon_o \kappa kT}{e} \left\{1 - \exp\left(-\frac{e\psi_o}{kT}\right)\right\} \times \left\{\frac{2}{3}\exp\left(\frac{e\psi_o}{kT}\right) + \frac{2}{3}\right\}^{1/2} \tag{78.22}$$

$$\gamma' = \frac{3}{2}\left\{\frac{\left(\frac{2}{3}e^{y_o} + \frac{1}{3}\right)^{1/2} - 1}{\left(\frac{2}{3}e^{y_o} + \frac{1}{3}\right)^{1/2} + 1}\right\} \tag{78.23}$$

where $y_o = e\psi_o/kT$ is the scaled surface potential.

3. Mixed solution of 1:1 electrolyte of concentration n_1 and 2:1 electrolyte of concentration n_2

$$\psi(x) = \frac{kT}{e} \ln\left[\left(\frac{1}{1 - \eta/3}\right)\left\{\frac{1 + \left(1 - \frac{\eta}{3}\right)\gamma'' e^{-\kappa x}}{1 - \left(1 - \frac{\eta}{3}\right)\gamma'' e^{-\kappa x}}\right\}^2 - \left(\frac{\eta/3}{1 - \eta/3}\right)\right] \tag{78.24}$$

with

$$\sigma = \frac{2\varepsilon_r \varepsilon_o \kappa kT}{e}(1 - e^{-y_o})\left[\left(1 - \frac{\eta}{3}\right)e^{y_o} + \frac{\eta}{3}\right]^{1/2} \tag{78.25}$$

$$\gamma'' = \left(\frac{1}{1 - \eta/3}\right)\left[\frac{\left\{\left(1 - \frac{\eta}{3}\right)e^{y_o} + \frac{\eta}{3}\right\}^{1/2} - 1}{\left\{\left(1 - \frac{\eta}{3}\right)e^{y_o} + \frac{\eta}{3}\right\}^{1/2} + 1}\right] \tag{78.26}$$

$$\eta = \frac{3n_2}{n_1 + 3n_2} \tag{78.27}$$

For a sphere, the nonlinear Poisson–Boltzmann equation has not been solved analytically. Loeb et al. [7] tabulated numerical computer solutions to the nonlinear spherical Poisson–Boltzmann equation, and approximate analytic solutions are given in Refs. 8 and 9.

$$\psi(r) = \frac{2kT}{ze} \ln\left[\frac{(1 + Bs)\left(1 + \frac{Bs}{2\kappa a + 1}\right)}{(1 - Bs)\left(1 - \frac{Bs}{2\kappa a + 1}\right)}\right] \tag{78.28}$$

with

$$s = \frac{a}{r}\exp(-\kappa(r - a)) \tag{78.29}$$

$$B = \frac{\left(\frac{2\kappa a + 1}{\kappa a + 1}\right)\tanh\left(\frac{y_o}{4}\right)}{1 + \left\{1 - \frac{2\kappa a + 1}{(\kappa a + 1)^2}\tanh^2\left(\frac{y_o}{4}\right)\right\}^{1/2}} \tag{78.30}$$

Approximate analytic expressions for the relationship between the surface charge density σ and the surface

potential ψ_o of a plate in various types of electrolyte solutions are given below [8, 9].

1. Symmetric electrolytes of valence z

$$\sigma = \frac{2\varepsilon_r\varepsilon_o\kappa kT}{ze}\sinh\left(\frac{ze\psi_o}{2kT}\right) \times \left[1 + \frac{1}{\kappa a}\frac{2}{\cosh^2(ze\psi_o/4kT)} + \frac{1}{(\kappa a)^2}\frac{8\ln[\cosh(ze\psi_o/4kT)]}{\sinh^2(ze\psi_o/2kT)}\right]^{1/2} \quad (78.31)$$

2. 2:1 electrolyte solution

$$\sigma = \frac{\varepsilon_r\varepsilon_o\kappa kT}{e}pq\left[1 + \frac{4}{\kappa a}\frac{(3-p)q-3}{(pq)^2} + \frac{4}{(\kappa a)^2(pq)^2}\left\{6\ln\left(\frac{q+1}{2}\right) + \ln(1-p)\right\}\right]^{1/2} \quad (78.32)$$

3. Mixed solution of 1:1 electrolyte of concentration n_1 and 2:1 electrolyte of concentration n_2

$$\sigma = \frac{\varepsilon_r\varepsilon_o\kappa kT}{e}\left[pt + \frac{2}{\kappa apt}\left\{(3-p)t - 3 - \frac{3^{1/2}(1-\eta)}{2\eta^{1/2}}\ln\left(\frac{\{1+(\eta/3)^{1/2}\}\{t-(\eta/3)^{1/2}\}}{\{1-(\eta/3)^{1/2}\}\{t+(\eta/3)^{1/2}\}}\right)\right\}\right] \quad (78.33)$$

Here

$$p = 1 - \exp(-e\psi_o/kT) \quad (78.34)$$

$$q = \left[\frac{2}{3}\exp\left(\frac{e\psi_o}{kT}\right) + \frac{1}{3}\right]^{1/2} \quad (78.35)$$

$$t = \left[\left(1 - \frac{\eta}{3}\right)\exp\left(\frac{e\psi_o}{kT}\right) + \frac{\eta}{3}\right]^{1/2} \quad (78.36)$$

where η is given in Eq. (78.27).

For the case of an infinitely long cylindrical particle of radius a, approximate solutions are derived in Refs. 8 and 10. The potential distribution around a cylinder of radius a and surface potential ψ_o are given by

$$\psi(r) = \frac{2kT}{ze}\ln\left[\frac{(1+Dc)\left\{1 + \left(\frac{1-\beta}{1+\beta}\right)Dc\right\}}{(1-Dc)\left\{1 - \left(\frac{1-\beta}{1+\beta}\right)Dc\right\}}\right] \quad (78.37)$$

with

$$c = \frac{K_0(\kappa r)}{K_0(\kappa a)} \quad (78.38)$$

$$\beta = \frac{K_0(\kappa a)}{K_1(\kappa a)} \quad (78.39)$$

$$D = \frac{(1+\beta)\tanh\left(\frac{y_o}{4}\right)}{1 + \left\{1 - (1-\beta^2)\tanh^2\left(\frac{y_o}{4}\right)\right\}^{1/2}} \quad (78.40)$$

Approximate analytic expressions for the relationship between the surface charge density σ and the surface potential of a cylinder of radius a in various types of electrolyte solutions are given below:

1. Symmetric electrolytes of valence z

$$\sigma = \frac{2\varepsilon_r\varepsilon_o\kappa kT}{ze}\sinh\left(\frac{y_o}{2}\right) \times \left[1 + \left(\frac{1}{\beta^2} - 1\right)\frac{1}{\cosh^2(y_o/4)}\right]^{1/2} \quad (78.41)$$

2. 2:1 electrolyte solution

$$\sigma = \frac{\varepsilon_r\varepsilon_o\kappa kT}{e}pq\left[1 + 2\left(\frac{1}{\beta^2} - 1\right)\frac{(3-p)q-3}{(pq)^2}\right]^{1/2} \quad (78.42)$$

where p and q are given by Eqs. (78.34) and (78.35), respectively.

3. Mixed solution of 1:1 electrolyte of concentration n_1 and 2:1 electrolyte of concentration n_2

$$\sigma = \frac{\varepsilon_r\varepsilon_o\kappa kT}{e}pt\left[1 + \frac{2(\beta^{-2}-1)}{(pt)^2}\left\{(3-p)t - 3 - \frac{\sqrt{3}(1-\eta)}{2\sqrt{\eta}}\ln\left(\frac{\left(t-\sqrt{\frac{\eta}{3}}\right)\left(1+\sqrt{\frac{\eta}{3}}\right)}{\left(t+\sqrt{\frac{\eta}{3}}\right)\left(1-\sqrt{\frac{\eta}{3}}\right)}\right)\right\}\right]^{1/2} \quad (78.43)$$

where t and η are given by Eqs. (78.36) and (78.27), respectively.

78.3 SOFT PARTICLES

We consider the case where the particle core is covered by an ion-penetrable surface layer of polyelectrolytes, which we term a *surface charge layer* (or, simply, a *surface layer*). Polyelectrolyte-coated particles are often called *soft particles* (Fig. 78.3) [3–6].

Soft particles serve as a model for biocolloids such as cells. Figure 78.3 is a schematic representation of ion and potential distributions around a soft surface, which shows that the potential deep inside the surface layer is practicably equal to the Donnan potential ψ_{DON}, if the surface layer is much thicker than the Debye length $1/\kappa$. Also we denote $\psi_0 \equiv \psi(0)$ (which is the potential at the boundary between the surface layer and the surrounding electrolyte solution) as the surface potential of the polyelectrolyte layer.

Consider a surface charge layer of thickness d coating a planar hard surface in a general electrolyte solution containing M ionic species with valence z_i and bulk concentration (number density) n_i^{∞} ($i = 1,2, \ldots, M$). We treat the case where fully ionized groups of valence Z are distributed at a uniform density of N in the surface charge layer and the particle core is uncharged. We take an x axis perpendicular to the surface charge layer with its origin $x = 0$ at the boundary between the surface charge layer and the surrounding electrolyte solution, so that the surface charge layer corresponds to the region $-d < x < 0$ and the electrolyte solution corresponds to $x > 0$ (Fig. 78.3). The Poisson–Boltzmann equations for the regions inside and outside the surface charge layer are given by

$$\frac{d^2\psi}{dx^2} = -\frac{1}{\varepsilon_r \varepsilon_\circ} \sum_{i=1}^{M} z_i e n_i^{\infty} \exp\left(-\frac{z_i e \psi(x)}{kT}\right), 0 < x < +\infty \tag{78.44}$$

$$\frac{d^2\psi}{dx^2} = -\frac{1}{\varepsilon_r \varepsilon_\circ} \sum_{i=1}^{M} z_i e n_i^{\infty} \exp\left(-\frac{z_i e \psi(x)}{kT}\right) - \frac{ZeN}{\varepsilon_r \varepsilon_\circ}, -d < x < 0 \tag{78.45}$$

We have assumed here that the relative permittivity ε_r takes the same value in the regions inside and outside the surface charge layer. Note that the right-hand side (RHS) of Eq. (78.45) contains the contribution of the fixed charges of density $\rho_{\mathrm{fix}} = ZeN$ in the polyelectrolyte layer. The boundary conditions are

$$\left.\frac{d\psi}{dx}\right|_{x=-d^+} = 0 \tag{78.46}$$

$$\psi(-0^-) = \psi(-0^+) \text{ and } \left.\frac{d\psi}{dx}\right|_{x=-0^+} = \left.\frac{d\psi}{dx}\right|_{x=-0^+} \tag{78.47}$$

$$\psi(x) \to 0 \text{ and } \frac{d\psi}{dx} \to 0 \text{ as } x \to \infty \tag{78.48}$$

Equation (78.46) corresponds to the situation in which the particle core is uncharged.

For the low-potential case, we give below analytic approximate expressions for the potential distribution $\psi(x)$ for a soft plate or $\psi(r)$ for a soft sphere or cylinder of radius a, where x is the distance from the planar soft surface located at $x = 0$ and r is the distance from the sphere center or the cylinder axis (Fig. 78.4) and the surface potential ψ_o/charge density N.

The following equations are relevant for soft particles:

1. Planar soft surface

$$\psi(x) = \frac{ZNkT}{4z^2ne}(1 - e^{-2\kappa d})e^{-\kappa x}, \mathrm{x} > 0 \tag{78.49}$$

$$\psi(x) = \frac{ZNkT}{2z^2ne}\left\{1 - \frac{e^{\kappa x} + e^{-\kappa(x+2d)}}{2}\right\}, -d < x < 0 \tag{78.50}$$

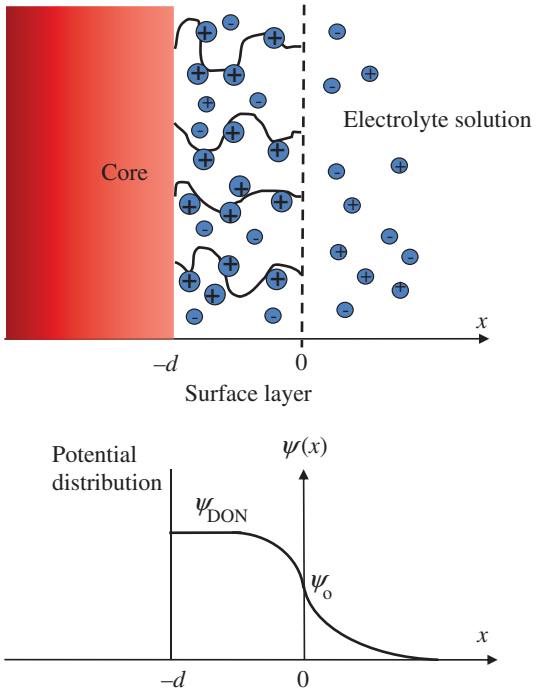


FIGURE 78.3 A soft surface, that is, a hard surface covered with an ion-penetrable surface layer of polyelectrolytes of thickness d and the potential distribution around the soft surface.

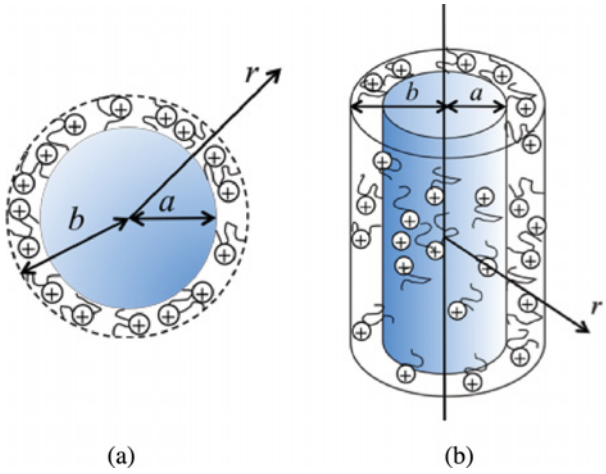


FIGURE 78.4 A soft sphere (a) and a soft cylinder (b).

with

$$\psi_o = \frac{ZeN}{2\varepsilon_r\varepsilon_o\kappa^2}(1 - e^{-2\kappa d}) \tag{78.51}$$

2. Soft sphere

$$\psi(r) = \frac{ZeN}{\varepsilon_r\varepsilon_o\kappa^2}\left[1 - \left(\frac{1+\kappa b}{1+\kappa a}\right)e^{-\kappa(b-a)} \times \left\{\frac{\sinh[\kappa(r-a)]}{\kappa r} + \frac{a\cosh[\kappa(r-a)]}{r}\right\}\right] a < r < b \tag{78.52}$$

$$\psi(\boldsymbol{r}) = \psi_o\frac{b}{r}\exp[-\kappa(r-b)], r > b \tag{78.53}$$

with

$$\psi_o = \frac{ZeN}{2\varepsilon_r\varepsilon_o\kappa^2}\left\{1 - \frac{1}{\kappa b} + \frac{(1-\kappa a)(1+\kappa b)}{(1+\kappa a)\kappa b}e^{-2\kappa(b-a)}\right\} \tag{78.54}$$

3. Soft cylinder

$$\psi(r) = \frac{ZeN}{\varepsilon_r\varepsilon_o\kappa^2}\left[1 - \kappa bK_1(\kappa b)\left\{I_0(\kappa r) + \frac{I_1(\kappa a)}{K_1(\kappa a)}K_0(\kappa r)\right\}\right], \quad a < r < b \tag{78.55}$$

$$\psi(r) = \psi_o\frac{K_0(\kappa r)}{K_0(\kappa b)}, r > b \tag{78.56}$$

with

$$\psi_o = \frac{ZeN}{\varepsilon_r\varepsilon_o\kappa^2}\kappa bK_0(\kappa b)\left\{I_1(\kappa b) - \frac{I_1(\kappa a)}{K_1(\kappa a)}K_1(\kappa b)\right\} \tag{78.57}$$

For the arbitrary potential case, we give below an approximate expression for the potential distribution $\psi(x)$ for the case where a planar soft surface is in contact with a z–z symmetric electrolyte solution and the thickness of the surface layer d is much greater than the Debye length $1/\kappa$.

$$\psi(x) = \psi_{DON} + (\psi_o - \psi_{DON})e^{-\kappa_m|x|}, x \le -d \tag{78.58}$$

with

$$\kappa_m = \kappa\cos\ h^{1/2}y_{DON} = \kappa\left[1 + \left(\frac{ZN}{2zn}\right)^2\right]^{1/4} \tag{78.59}$$

$$\psi_{DON} = \left(\frac{kT}{ze}\right)\ln\left[\frac{ZN}{2zn} + \left\{\left(\frac{ZN}{2zn}\right)^2 + 1\right\}^{1/2}\right] \tag{78.60}$$

$$\psi_o = \left(\frac{kT}{ze}\right)\left(\ln\left[\frac{ZN}{2zn} + \left\{\left(\frac{ZN}{2zn}\right)^2 + 1\right\}^{1/2}\right] + \frac{2zn}{ZN}\left[1 - \left\{\left(\frac{ZN}{2zn}\right)^2 + 1\right\}^{1/2}\right]\right) \tag{78.61}$$

where $\psi_0 = \psi(0)$ is the surface potential of the soft plate, that is, the potential at the front edge of the surface layer, and ψ_{DON} is the Donnan potential in the surface layer. Note that for the low-potential case, Eqs. (78.60) and (78.61) tend to

$$\psi_{DON} = \frac{ZeN}{\varepsilon_r\varepsilon_o\kappa^2} \tag{78.62}$$

$$\psi_o = \frac{\psi_{DON}}{2} = \frac{ZeN}{2\varepsilon_r\varepsilon_o\kappa^2} \tag{78.63}$$

78.4 DISCRETE-CHARGE EFFECT

The Donnan potential and surface potential of soft particles (i.e., polyelectrolyte-coated hard particles) in an electrolyte solution play an essential role in their electrical behaviors. As described before, these potential are usually derived via a continuum model in which fixed charges inside the surface layer are distributed with a continuous charge density. As shown below, for a platelike soft particle consisting of a cubic lattice of fixed point charges, on the basis of the

linearized Poisson–Boltzmann equation, we derive expressions for the electric potential distribution in the regions inside and outside the surface layer [11], by extending a method of Nelson and McQuarrie [38],who considered a charged surface carrying a squared lattice of point charges and solved the two-dimensional linearized Poisson–Boltzmann equation for the potential distribution.

Consider the case where fixed charges are distributed within the surface layer ($-\infty < z \leq 0$) at a discrete density of $\rho(\boldsymbol{r})$, which is not uniform but a function of position $\boldsymbol{r}(x, y, z)$. Here we consider the case where the thickness of the surface layer is much thicker than the Debye length $1/\kappa$ so that the surface layer can be considered to be infinitely thick. Let us obtain the electric potential $\psi(\boldsymbol{r})$ at position $\boldsymbol{r}$, which depends not only on z but also on x and y. In this case Eqs. (78.44) and (78.45) are replaced by the following three-dimensional linearized Poison–Boltzmann equations:

$$\left(\frac{\partial^2}{\partial x^2}+\frac{\partial^2}{\partial y^2}+\frac{\partial^2}{\partial z^2}\right)\psi(\boldsymbol{r})=\kappa^2\psi(\boldsymbol{r})-\frac{\rho(\boldsymbol{r})}{\varepsilon_r\varepsilon_o}, -\infty < z \leq 0 \tag{78.64}$$

$$\left(\frac{\partial^2}{\partial x^2}+\frac{\partial^2}{\partial y^2}+\frac{\partial^2}{\partial z^2}\right)\psi(\boldsymbol{r})=\kappa^2\psi(\boldsymbol{r}), 0 < z < +\infty \tag{78.65}$$

In order to solve Eqs. (78.64) and (78.65), we write $\psi(\boldsymbol{r})$ and $\rho(\boldsymbol{r})$ by their Fourier transforms as

$$\psi(\boldsymbol{r})=\psi(s,z)=\frac{1}{(2\pi)^2}\int\hat{\psi}(\boldsymbol{p},z)\exp(i(\boldsymbol{p}\cdot s))d\boldsymbol{p} \tag{78.66}$$

$$\rho(\boldsymbol{r})=\rho(s,z)=\frac{1}{(2\pi)^2}\int\hat{\rho}(\boldsymbol{p},z)\exp(i(\boldsymbol{p}\cdot s))d\boldsymbol{p} \tag{78.67}$$

where $\hat{\psi}(p,z)$and$\hat{\rho}(p,z)$are the Fourier coefficients, $\boldsymbol{s}=(x,y)$ and $\boldsymbol{p}=(p_x,p_y)$.

Substitution of Eqs. (78.22) and (78.23) into Eq. (78.12) yields

$$\begin{aligned}\psi(\boldsymbol{r})=\frac{1}{2(2\pi)^2\varepsilon_r\varepsilon_o}\Bigg[&\int\frac{1}{\sqrt{\kappa^2+p^2}}\\&\times\left\{\int_{-\infty}^{z}\hat{\rho}(\boldsymbol{p},z')\exp(+\sqrt{\kappa^2+p^2}\cdot z')dz'\right\}\\&\times\exp(-\sqrt{\kappa^2+p^2}\cdot z)\cdot\exp(i(\boldsymbol{p}\cdot s))d\boldsymbol{p}\\&+\left\{\int_{z}^{0}\hat{\rho}(\boldsymbol{p},z')\exp(-\sqrt{\kappa^2+p^2}\cdot z')dz'\right\}\\&\times\exp(+\sqrt{\kappa^2+p^2}\cdot z)\cdot\exp(i(\boldsymbol{p}\cdot s))d\boldsymbol{p}\Bigg], -\infty < z \leq 0\end{aligned} \tag{78.68}$$

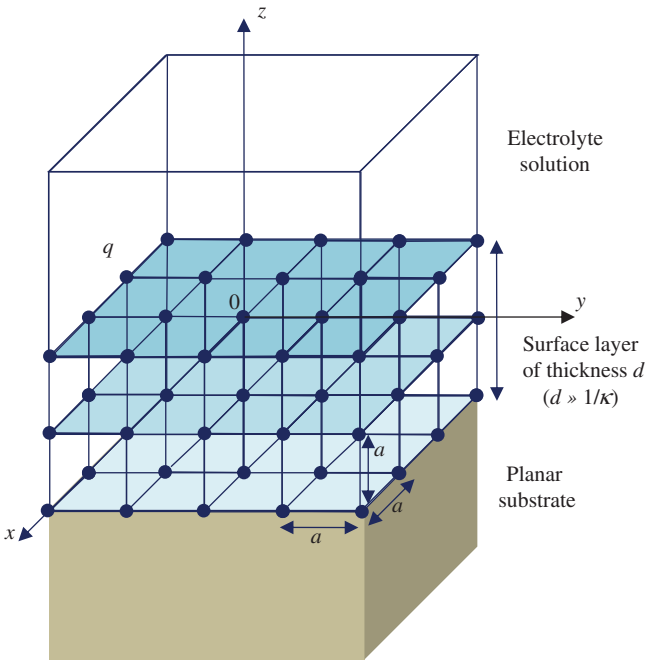


FIGURE 78.5 Soft plate consisting of a discrete cubic lattice of fixed point charges q with a spacing of a within a surface layer.

$$\begin{aligned}\psi(\boldsymbol{r})=&\frac{1}{2(2\pi)^2\varepsilon_r\varepsilon_o}\int\frac{1}{\sqrt{\kappa^2+p^2}}\\&\times\left\{\int_{-\infty}^{0}\hat{\rho}(\boldsymbol{p},z')\exp(+\sqrt{\kappa^2+p^2}\cdot z')dz'\right\}\\&\times\exp(-\sqrt{\kappa^2+p^2}\cdot z)\cdot\exp(i(\boldsymbol{p}\cdot s))d\boldsymbol{p}, 0 < z < \infty\end{aligned} \tag{78.69}$$

where

$$p=|\boldsymbol{p}|=\sqrt{p_x^2+p_y^2} \tag{78.70}$$

Now we deal with the case in which a surface layer consists of a cubic lattice of point charges q with spacing a (Fig. 78.5).

The point charges are thus located at lattice point (la, ma, na), where m and n take both positive and negative integers and n takes only negative integers, since the surface layer occupies the half-space $-\infty< z \leq 0$. The volume charge density $\rho(\boldsymbol{r})$ ($-\infty< z \leq 0$) is then expressed as

$$\begin{aligned}\rho(\boldsymbol{r})&=\rho(s,z)\\&=q\sum_{\substack{-\infty<l,m<\infty,\\-\infty<n\leq 0}}\delta(x-la)\delta(y-ma)\delta(z-na), -\infty < z \leq 0\end{aligned} \tag{78.71}$$

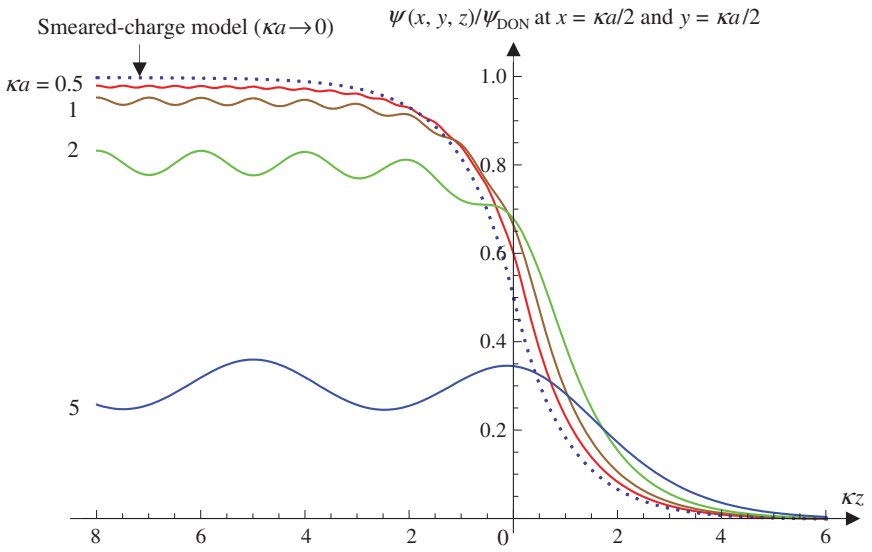


FIGURE 78.6 Change in $\psi(x, y, z)/\psi_{\mathrm{DON}}$ along the z direction at $x = \kappa a/2$ and $y = \kappa a/2$. (From Ref. 11.)

Thus Eqs. (78.66) and (78.71) give

$$\psi(\boldsymbol{r}) = \frac{q}{4\pi\varepsilon_{\mathrm{r}}\varepsilon_{\mathrm{o}}} \sum_{\substack{-\infty<l,m<\infty,\\ -\infty<n\le 0}} \times \frac{\exp[-\kappa\sqrt{(x-la)^2+(y-ma)^2+(z-na)^2}]}{\sqrt{(x-la)^2+(y-ma)^2+(z-na)^2}}, \quad -\infty < z < +\infty \tag{78.72}$$

Equation (78.72) is the required expression for the potential distribution $\psi(\boldsymbol{r})$ for the case of the cubic lattice of charges. The surface potential, which is a function of x and y, is given by the potential at $z = 0$, that is, $\psi(x, y, 0)$, which is a function of x and y, is given by

$$\psi(x, y, 0) = \frac{q}{4\pi\varepsilon_{\mathrm{r}}\varepsilon_{\mathrm{o}}} \sum_{\substack{-\infty<l,m<\infty,\\ -\infty<n\le 0}} \times \frac{\exp[-\kappa\sqrt{(x-la)^2+(y-ma)^2+(na)^2}]}{\sqrt{(x-la)^2+(y-ma)^2+(na)^2}} \tag{78.73}$$

It is seen that Eq. (78.72) is just a sum of screened Coulomb potentials produced by point charges located at the lattice points. The results of some calculations for the electric potential $\psi(\boldsymbol{r})$ are given in Fig. 78.6, which shows $\psi(x, y, z)/\psi_{\mathrm{DON}}$ as a function of scaled distance κz calculated at $x = \kappa a/2$ and $y = \kappa a/2$ for several values of κa in comparison with the continuous model (given by the dotted line).

We see that $\psi(x, y, z)$ oscillates with a period of κa and the amplitude of the oscillation decreases with decreasing κa. The potential $\psi(x, y, z)$ in the region outside the surface layer shows no oscillation, monotonically decreasing in magnitude with increasing z. It should also be noted that there is considerable deviation of the continuous-charge model. This deviation becomes smaller as the ratio κa of the lattice spacing a to the Debye length $1/\kappa$. Indeed, in the limit of $\kappa a \to 0$, the continuous-charge model approaches the discrete-charge model, as shown in Fig. 78.6.

It can be shown analytically on the basis of Eq. (78.72) that the discrete charge model approaches the continuous charge model in the limit of $\kappa a \to 0$. In this limit, the discrete sum with respect to l, m, and n in Eq. (78.72) can be replaced by a continuous integration. By introducing a smeared continuous charge density $\rho = q/a^3$, we consider the following potential in the deep inside the surface layer, which is shown to equal to the Donnan potential below:

$$\lim_{\substack{z\to-\infty\\ \kappa a\to 0}} \psi(\boldsymbol{r}) = \lim_{\substack{z\to-\infty\\ \kappa a\to 0}} \frac{q}{4\pi\varepsilon_{\mathrm{r}}\varepsilon_{\mathrm{o}}} \sum_{-\infty<l,m,n<\infty} \times \frac{\exp[-\kappa\sqrt{(x-la)^2+(y-ma)^2+(z-na)^2}]}{\sqrt{(x-la)^2+(y-ma)^2+(z-na)^2}} \tag{78.74}$$

Here the range of n (i.e., $-\infty < n \le 0$) has been extended to approximately $-\infty < z < +\infty$, since we are treating the limiting case of $z \to -\infty$. We introduce $r = \sqrt{(x-la)^2+(y-ma)^2+(z-na)^2}$ and replace the discrete sum with a continuous integration:

$$\sum_{-\infty<l,m,n<+\infty} \to \frac{1}{a^3}\int_0^\infty 4\pi r^2 dr \text{ as } \kappa a \to 0 \tag{78.75}$$

Then Eq. (78.74) becomes the Donnan potential, that is

$$\psi_{\mathrm{DON}} = \frac{\rho}{4\pi\varepsilon_{\mathrm{r}}\varepsilon_{\mathrm{o}}} \int_0^{\infty} \frac{e^{-\kappa r}}{r} 4\pi r^2 dr = \frac{\rho}{\varepsilon_{\mathrm{r}}\varepsilon_0\kappa^2} \tag{78.76}$$

which agrees with the result obtained by the continuous-charge model [Eq. (78.62)]. We thus see that integration of the screened Coulomb potential over the entire space $-\infty < z < +\infty$ yields the Donnan potential. If the integration is made over a half-space $-\infty < z \leq 0$, then the surface potential ψ_0 is obtained and its value is half the Donnan potential (i.e., $\psi_0 = \psi_{\mathrm{DON}}/2$), which agrees with the result of the continuum approximation [Eq. (78.63)]. The overall potential distribution in the limit of $\kappa a \to 0$ can also be derived in a similar manner. We introduce cylindrical coordinates: $s = \sqrt{(x - la)^2 + (y - ma)^2}$ and $z = na\text{-}z'$, and replace the discrete sum with a continuous integration:

$$\sum_{\substack{-\infty<l,m<+\infty \\ -\infty<n\leq 0}} \to \frac{1}{a^3} \int_{s=0}^{\infty} \int_{z'=-\infty}^{-z} 2\pi s ds dz' \text{ as } \kappa a \to 0 \tag{78.77}$$

Then Eq. (78.70) tends to

$$\begin{aligned} \psi(z) &= \frac{\rho}{4\pi\varepsilon_{\mathrm{r}}\varepsilon_{\mathrm{o}}} \int_{s=0}^{\infty} \int_{z'=-\infty}^{-z} \frac{\exp[-\kappa\sqrt{s^2 + z'^2}]}{\sqrt{s^2 + z'^2}} 2\pi s ds dz' \\ &= \begin{cases} \dfrac{\rho}{\varepsilon_{\mathrm{r}}\varepsilon_{\mathrm{o}}\kappa^2} \left(1 - \dfrac{1}{2} e^{\kappa z}\right), -\infty < z \leq 0 \\ \dfrac{\rho}{\varepsilon_{\mathrm{r}}\varepsilon_{\mathrm{o}}\kappa^2} e^{-\kappa z}, 0 < z < +\infty \end{cases} \end{aligned} \tag{78.78}$$

Equation (78.78), which depends only on z, agrees with Eqs. (78.49) and (78.50) for the case of $d \to \infty$.

REFERENCES

[1] Derjaguin, B.V., Landau, L. (1941). *Acta Physicochim.* **14**, 633.

[2] Verwey, E.J.W., Overbeek, J.Th.G. (1948). *Theory of the Stability of Lyophobic Colloids.* Elsevier, Amsterdam.

[3] Ohshima, H., Furusawa, K. (eds.) (1998). *Electrical Phenomena at Interfaces: Fundamentals, Measurements, and Applications*, 2nd ed. (revised and expanded). Marcel Dekker, New York.

[4] Ohshima, H. (2006). *Theory of Colloid and Interfacial Electric Phenomena*. Elsevier/Academic Press, Amsterdam.

[5] Ohshima, H. (2010). *Biophysical Chemistry of Biointerfaces.* Wiley, Hoboken, NJ.

[6] Ohshima, H. (2012). *Electrical Phenomena at Interfaces and Biointerfaces: Fundamentals and Applications in Nano-. Bio-, and Environmental Sciences*. Wiley, Hoboken, NJ.

[7] Loeb, A.L., Overbeek, J.Th.G., Wiersema, P.H. (1961). *The Electrical Double Layer around a Spherical Colloid Particle.* MIT Press, Cambridge, MA.

[8] Ohshima, H., Healy, T.W., White, L.R. (1982). *J. Colloid Interface Sci.* **90**, 17.

[9] Ohshima, H. (1995). *J. Colloid Interface Sci.* **171**, 525.

[10] Ohshima, H. (1998). *J. Colloid Interface Sci.* **200**, 291.

[11] Ohshima, H. (2014). *Colloid Polym. Sci.* **292**, 749.

[12] Nelson, A.P., McQuarrie, D.A. (1975). *J. Theor. Biol.* **55**, 13.

79

SOIL INTERFACIAL ELECTRICAL PHENOMENA

Munehide Ishiguro

Laboratory of Soil Conservation, Research Faculty of Agriculture, Hokkaido University, Sapporo, Japan

79.1 INTRODUCTION

Soils have electric charges. In particular, clayey soil contains a significant amount of negative charge, roughly equivalent to 1 mole of electron per kilogram of soil [i.e., equal to the Faraday constant, 9.64×10^4 C (coulmbs)]. As the typical soil density is about 1000 kg/m^3, the soil has 100 million C in 1 cubic meter. When we use an electric heater of 1 kW ($=3.6 \times 10^6$ J/h) at 100 V, it requires a charge current of 3.6×10^4 C/h. Thus, the soil can theoretically supply electric current to such a heater for about 120 days [1]. Practically, however, the soil cannot do this because its charge cannot be separated. Nonetheless, the electric charge stored in soils is significant. This charge affects various soil phenomena such as soil structure, permeability, soil erosion, nutrient transport, and contaminant transport. These phenomena also strongly affect agricultural technology and environmental problems. In this chapter, such phenomena induced by soil electric charge are introduced.

79.2 ION TRANSPORT IN SOILS

79.2.1 Influence of Electric Charge on Ion Transport

An ion transport experiment was conducted using a soil column 30 cm in height and 5 cm in diameter. Allophanic andisol, which is a typical volcanic ash soil, was uniformly packed and saturated with a $CaCl_2$ solution. Then, a $SrBr_2$ solution was continuously infiltrated vertically into the column, and the ion concentrations of the outflow solution were measured. Figure 79.1 shows the experimental result. The abscissa indicates the normalized cumulative volume of the outflow solution divided by the water volume in the soil column. The units of the normalized volume are called *pore volume*; 1 pore volume equals the water volume in the soil column. The Sr^{2+} breakthrough curve shifted to the right as the pH increased; that is, Sr^{2+} moved more slowly in the soil when the pH increased. On the other hand, the Br^- breakthrough curve shifted to the left as the pH increased; Br^- moved more quickly in the soil when the pH increased. Figure 79.2 shows the cation exchange capacity (CEC) and the anion exchange capacity (AEC) of the soil; the CEC and AEC correspond to the negative and positive charge densities of the soil, respectively. The CEC increased and AEC decreased as the pH increased. Therefore, Sr^{2+} moved more slowly and Br^- more quickly as the pH increased because the Sr^{2+} adsorption increased and the Br^- adsorption decreased in the soil [2, 3].

The delay of ion transport corresponds to the amount of electric charge in the soil. When we use the normalized cumulative volume (pore volume) as the abscissa, the average delay of the ion transport by the adsorption is equal to the distribution ratio D_g, which is defined by

$$D_g = \frac{\rho q_0}{\theta c_0} \tag{79.1}$$

where ρ is the bulk density (kg/m^3), q_0 is the ion exchange capacity (mol$_c$/kg), θ is the volumetric water content (m^3/m^3), and c_0 is the input ion concentration (mol$_c$/m^3) [4]. The relative concentration of the outflow solution becomes about 0.5 at $D_g + 1$ pore volumes in the breakthrough curve. That is because Dg is the ratio of ions in the adsorption phase to ions in the solution phase.

Encyclopedia of Biocolloid and Biointerface Science, Volume 2, First Edition. Edited by Hiroyuki Ohshima.
© 2016 John Wiley & Sons, Inc. Published 2016 by John Wiley & Sons, Inc.

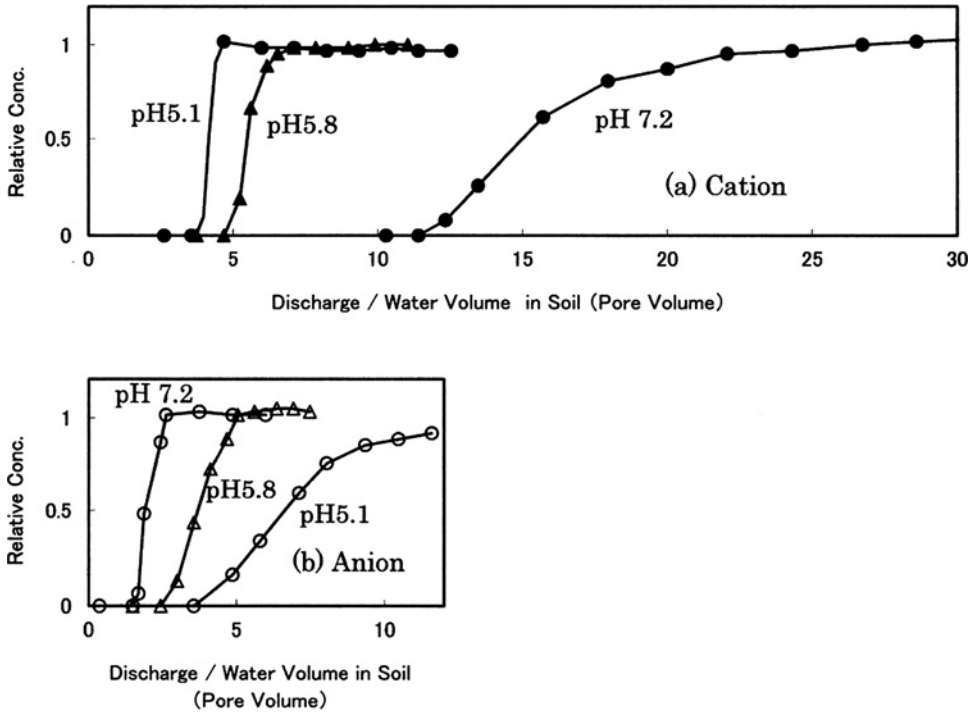


FIGURE 79.1 Breakthrough curves of the allophanic andisol for (a) cations and (b) anions. Inflow solution concentration was 0.01 $mmol_c/L$ [3].

Affinity of adsorbed ions to the soil affects the ion transport when two ions with the same sign of charge are present. Figure 79.3 shows the SO_4^{2-} and NO_3^- adsorption amounts in the soil at pH 3.3 and 1.0 $mmol_c/L$ with a mixture of H_2SO_4 and HNO_3. Because the SO_4^{2-} adsorption is stronger than that of NO_3^- in the allophanic andisol, the amount of SO_4^{2-} adsorption was much larger than that of NO_3^-. Figure 79.4 shows the state of SO_4^{2-} adsorption at pH 3.3 and 1.0 $mmol_c/L$ with a mixture of H_2SO_4 and HNO_3. Exchangeable SO_4^{2-} was obtained by exchanging the solution with 1 mol_c/L KCl solution after the soil was equilibrated at the prescribed solution condition. SO_4^{2-} in the diffuse layer was calculated by the Stern–Gouy–Chapman model, assuming that the adsorbed NO_3^- was all in the diffuse layer. The adsorbed SO_4^{2-} obtained by subtracting the exchangeable SO_4^{2-} from the total SO_4^{2-} is assumed to be an inner-sphere complex that is chemically adsorbed. More than 95 % of the adsorbed SO_4^{2-} remained on the soil surface from the calculation [5] because SO_4^{2-} is strongly adsorbed. Figure 79.5 shows the influence of coexisting SO_4^{2-} on NO_3^-

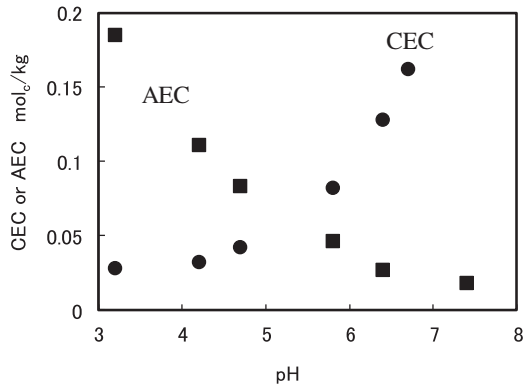


FIGURE 79.2 Amounts of electric charges of the allophanic andisol (AEC, anionic exchange capacity; CEC, cation exchange capacity) [2].

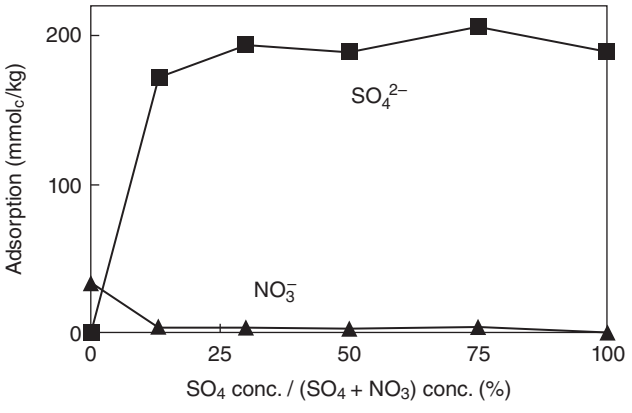


FIGURE 79.3 SO_4^{2-} and NO_3^- adsorption in the allophanic andisol at pH 3.3 and 1.0 $mmol_c/L$ with the mixture of H_2SO_4 and HNO_3 [5].

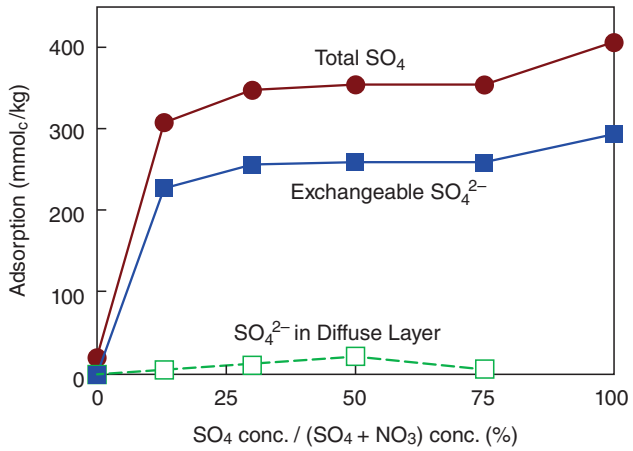


FIGURE 79.4 SO_4^{2-} adsorption in the allophanic andisol at pH 3.3 and 1.0 $mmol_c$/L with the mixture of H_2SO_4 and HNO_3. Exchangeable SO_4^{2-} was exchanged with a 1 mol_c/L KCl solution. SO_4^{2-} in diffuse layer was calculated by the Stern–Gouy–Chapman model [5].

breakthrough curves when a 10 $mmol_c$/L NO_3^- solution was percolated in the allophanic andisol. NO_3^- flowed out faster from the soil when SO_4^{2-} coexisted, because the affinity of SO_4^{2-} to the soil is much larger than that of NO_3^-. NO_3^- flowed out more slowly as a result of adsorption when SO_4^{2-} was not there. However, NO_3^- flowed out more quickly when the soil was initially equilibrated with a 10 $mmol_c$/L SO_4^{2-} solution (symbol □ in Fig. 79.5). The NO_3^- flow also became faster when SO_4^{2-} was included in the inflow NO_3^- solution at the same concentration of 10 $mmol_c$/L (symbol △ in Fig. 79.5). Because NO_3^- is a water contaminant and yet an important nutrient input for crops, it must be effectively used in the crop fields, and it must not be allowed to

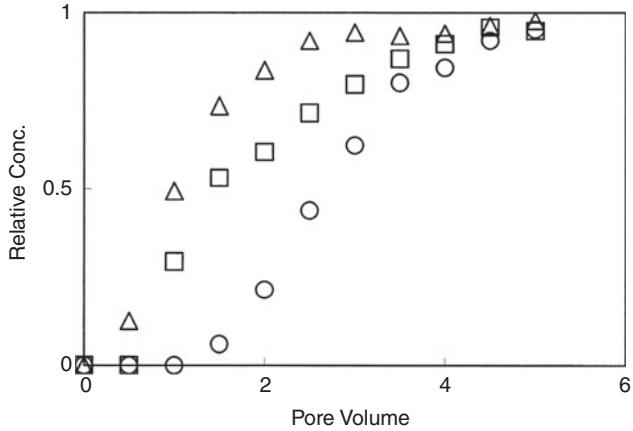


FIGURE 79.5 Effect of coexisting SO_4^{2-} on NO_3^- transport. NO_3^- breakthrough curves at10 $mmol_c$/L for the allophanic andisol; with no SO_4^{2-}(○), for the soil initially equilibrated with a 10 $mmol_c$/L SO_4^{2-} solution (□), and with a 10 $mmol_c$/L SO_4^{2-} solution(△) [6].

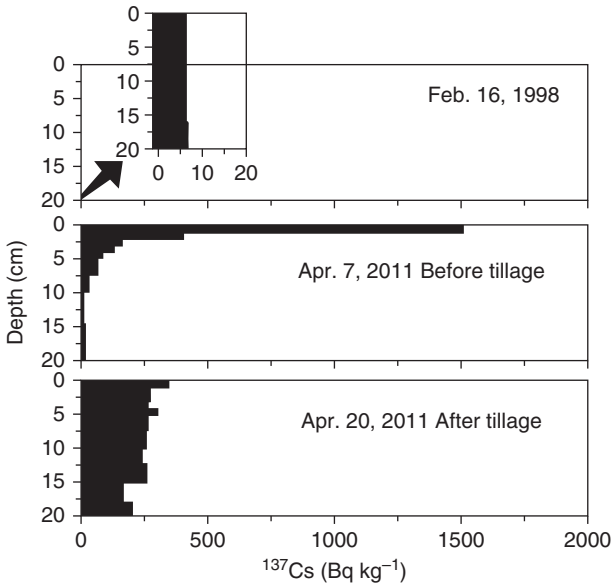


FIGURE 79.6 Radioactive Cs accumulation at the surface volcanic ash soil in Tsukuba, Japan after the accident at the Fukushima atomic power plant on March 11, 2011 [7].

leach. Therefore, sulfate application to the crop fields is not recommended in allophanic andisol, because it accelerates NO_3^- discharge [6].

Figure 79.6 shows radioactive cesium (Cs) accumulation in surface volcanic ash soil in Tsukuba, Japan after the accident at the Fukushima atomic power plant on March 11, 2011 [7]. Because the selectivity of Cs is about 1000 times larger than that of K at the frayed edge sites of some clay minerals, radioactive Cs was fixed strongly at the surface soil [8]. Such strong fixation occurs at the frayed edge of clays having a 2:1 layer structure and negative charges in Si tetrahedral layers such as vermiculite and illite [9]. Figure 79.7 shows the Cs fixation in the frayed edge of

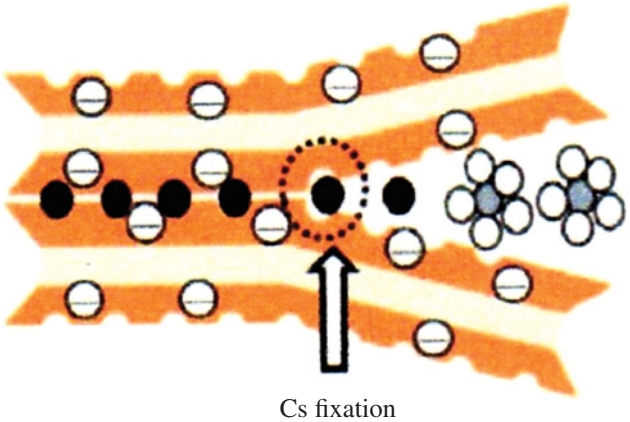


FIGURE 79.7 Cesium fixation in a frayed edge of vermiculite or illite [6].

vermiculite or illite [7]. Because the half-life of the radioactive Cs is 30.2 years, the soil contamination continues for a long time unless it is removed.

The electric charge density significantly influences ion transport in soils. Because ions are important nutrients for crops and sometimes harmful contaminants for living organisms, understanding the electric charge characteristics of soils is important when we consider effective nutrient use in agriculture and environmental conservation.

79.2.2 Influence of Selectivity Coefficient, Distribution Ratio, and Peclet Number on Ion Transport

The shape of the breakthrough curve is determined by the Peclet number for mass transfer, Pe, the selectivity coefficient, $k_{1/2}$, and the distribution ratio, D_g, as is shown in the following advective–dispersive equation with ion exchange [10]. The Peclet number is defined by

$$Pe = \frac{uL}{D} \tag{79.2}$$

where u is the mean pore water velocity (m/s), L is the soil length (m), D is the dispersion coefficient (m^2/s), and $k_{1/2}$ is a coefficient that indicates the distribution of Ions 1 and 2 between solution and adsorbed phases. Thus

$$\frac{q_1}{q_2} = k_{1/2}\frac{c_1}{c_2} \tag{79.3}$$

where q_1 and q_2 are the amounts of ions 1 and 2, respectively, in the exchange phase (mol_c/kg), and c_1 and c_2 are the concentrations of ions 1 and 2, respectively, in the soil solution (mol_c/m^3) [11, 12]. The input ion concentration, which is equal to the total ion concentration, c_0, is

$$c_0 = c_1 + c_2 \tag{79.4}$$

We assume that the total ion concentration is time-invariant in this binary system and that the two ions have the same valence in order to indicate basic transport phenomena. The ion exchange capacity, q_0 (mol_c/kg), is

$$q_0 = q_1 + q_2 \tag{79.5}$$

From Eqs. (79.3)–(79.5), we obtain

$$Q_1 = \frac{k_{1/2}C_1}{(k_{1/2}-1)C_1 + 1} \tag{79.6}$$

where Q_1 is the relative amount of ion 1 in the exchange phase and C_1 is the relative concentration of ion 1 in the soil solution [12]. They are represented as

$$Q_1 = q_1/q_0 \tag{79.7}$$

$$C_1 = c_1/c_0 \tag{79.8}$$

The one-dimensional advective–dispersive equation with ion exchange in a soil is

$$R_f\frac{\partial C_1}{\partial t} = D\frac{\partial^2 C_1}{\partial x^2} - u\frac{\partial C_1}{\partial x} \tag{79.9}$$

where t is time (s) and x is distance (m) [13]. R_f is defined by

$$R_f = 1 + D_g\frac{\partial Q_1}{\partial C_1} \tag{79.10}$$

Equation (79.9) can be expressed in dimensionless form by introducing the following dimensionless variables [10,14]:

$$X = x/L \tag{79.11}$$

$$T = \frac{ut}{(D_g+1)L} \tag{79.12}$$

The dimensionless time T equals the ratio of the real time to the mean time required for ion 1 to move through the distance $x = L$. We define the effluent volume at $T = 1$ as the apparent pore volume [15]. Given these data, we can rewite Eq. (79.9) in dimensionless form

$$\frac{\partial C_1}{\partial T} = \frac{1}{fPe}\frac{\partial^2 C_1}{\partial X^2} - \frac{1}{f}\frac{\partial C_1}{\partial X} \tag{79.13}$$

where f is

$$f = \frac{R_f}{D_g+1} = \frac{1}{D_g+1} + \frac{D_g}{D_g+1}\frac{\partial Q_1}{\partial C_1} \tag{79.14}$$

The derivative $\partial Q_1/\partial C_1$ in Eq. (79.14) is determined by the exchange isotherm. Differentiating Eq. (79.6) by C_1, we obtain

$$\frac{\partial Q_1}{\partial C_1} = \frac{k_{1/2}}{[(k_{1/2}-1)C_1 + 1]^2} \tag{79.15}$$

When the selectivity coefficient $k_{1/2}$ equals 1.0, that is, when the adsorption energy of ion 1 is the same as that of ion 2, f becomes 1 and the dimensionless advective–dispersive equation [Eq. (79.13)] becomes

$$\frac{\partial C_1}{\partial T} = \frac{1}{Pe}\frac{\partial^2 C_1}{\partial X^2} - \frac{\partial C_1}{\partial X} \tag{79.16}$$

which is similar to the equation for nonreactive solute. In this case, the normalized breakthrough curve can be determined by Pe as shown in Fig. 79.8 [16]. When Pe becomes larger, the breakthrough curve becomes steeper.

Figure 79.9 shows numerically calculated breakthrough curves of ion 1 using Eq. (79.13). When $k_{1/2}$ is smaller than 1.0, the ion 1 breakthrough curve is flatter than that for $k_{1/2} =$ 1.0 (Fig. 79.9a), because the displaced ion, ion 2, is preferred to the input ion, ion 1. When $k_{1/2}$ is larger than 1.0,

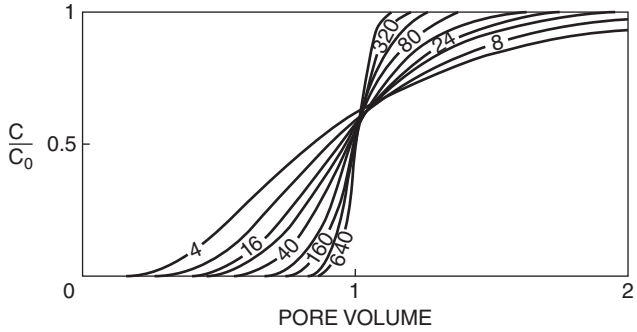


FIGURE 79.8 Breakthrough curves derived from one-dimensional advective–dispersive equation. The numbers on the curves denote Peclet numbers [16].

the ion 1 breakthrough curve is steeper than that for $k_{1/2} = 1.0$ (Fig. 79.9b), because ion 1 is preferred to ion 2.When D_g becomes larger, the breakthrough curve for $k_{1/2} < 1.0$ becomes flatter (Fig. 79.9a) and that for $k_{1/2} > 1.0$ becomes steeper (Fig. 79.9b). However, when D_g is much larger than 1.0, the breakthrough curves are almost the same; the breakthrough curves for $D_g = 10$ are almost same as those for $D_g = 50$, as shown in Fig. 79.9 [10].

Figure 79.10 shows the measured breakthrough curves and calculated breakthrough curves fitted using the measured exchange isotherm data shown in Fig. 79.11. The abscissa of the figure is the normalized cumulative volume, which is the same as T in Eq. (79.12), and is defined by

$$\frac{1}{D_g + 1}\frac{\text{outflow water volume}}{\text{water volume in the soil column}}$$

(unit; apparent pore volume)

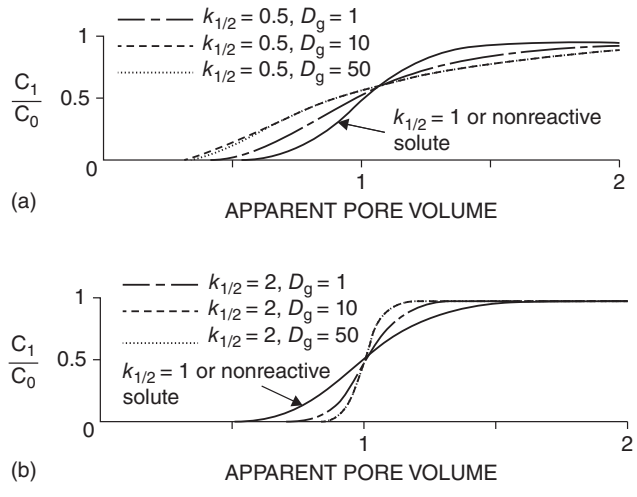


FIGURE 79.9 Effect of distribution ratio and selectivity coefficient on the breakthrough curve: (a) $k_{1/2} = 0.5$; (b) $k_{1/2} = 2$; Pe = 50 [10].

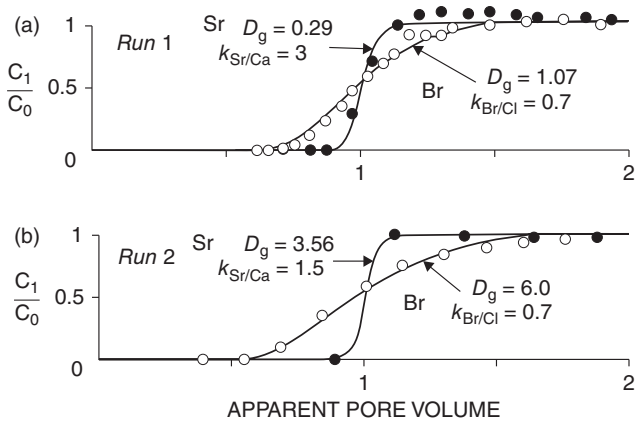


FIGURE 79.10 Comparison of measured breakthrough curves (symbols) and calculated breakthrough curves (solid lines): (a) run 1—pH 4.2, 100 mol_c/L; (b) run 2—pH 5.05, 10 mol_c/L [10].

We can confirm that when $k_{1/2}$ becomes larger, the breakthrough curve is steeper [10], as mentioned before.

79.3 SOIL DISPERSION AND FLOCCULATION

Figure 79.12 shows the result of a dispersion flocculation experiment for allophanic andisol in an Na-H-Cl-OH system at 1 $mmol_c$/L. The ordinate indicates the *dispersion ratio*, which is the ratio of the turbidity of the soil suspension after standing for 12 h to that just after shaking. When pH was lower (pH $\leq$ 4) or higher (pH $\geq$ 10), the soil suspension dispersed well. This is because the positive charge dominates at a lower pH and the negative charge dominates at a higher pH (Fig. 79.2). When the pH was in between, it flocculated well because considerable numbers of both negative and positive charges were present [17].

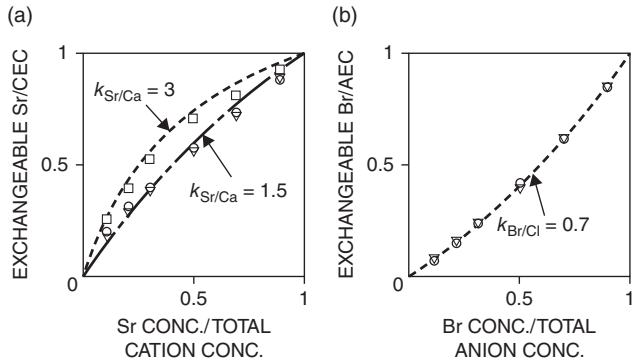


FIGURE 79.11 Measured exchange isotherms (symbols) and the isotherms calculated from Eq. (79.6) (dotted lines): (a) Sr-Ca exchange isotherms; (b) Br-Cl exchange isotherms (□ pH 4.55 and 100 mol_c/L; ○ pH 4.9 and 10 mol_c/L; ▽ pH 5.5 and 10 mol_c/L) [10].

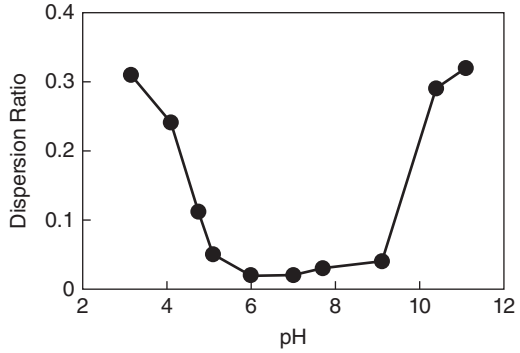


FIGURE 79.12 Influence of pH on dispersion and flocculation of allophanic andisol at 1 $mmol_c/L$ for Na-H-Cl-OH system [17]. Dispersion ratio = (turbidity of soil suspension for 12 h standing) / (turbidity of soil suspension just after shaking).

Figure 79.13 shows the result of the dispersion–flocculation experiments for SO_4^{2-} and NO_3^-solutions at 1 $mmol_c/L$ using allophanic andisol. The solutions were an Na-H-SO_4-OH system and an Na-H-NO_3-OH system. The soil dispersed well at lower pH for the NO_3^- solution. However, it flocculated at lower pH for SO_4^{2-} solution [18]. Zeta-potentials of the soil in the mixture of H_2SO_4 and HNO_3 at pH 3 and pH 4 are shown in Fig. 79.14. The ζ-potential was smaller when the SO_4^{2-} ratio was larger. It was larger when the NO_3^- ratio was larger. Figure 79.15 shows the repulsive potential energy when two soil particles come closer to each ζ-potential plane in the dilute acid. The following equations and ζ-potential obtained were used for the calculation:

$$V_\varsigma = -2\int_b^0 \Pi dD \tag{79.17}$$

$$\Pi = RT\sum(C_i - C_{0,i}) \tag{79.18}$$

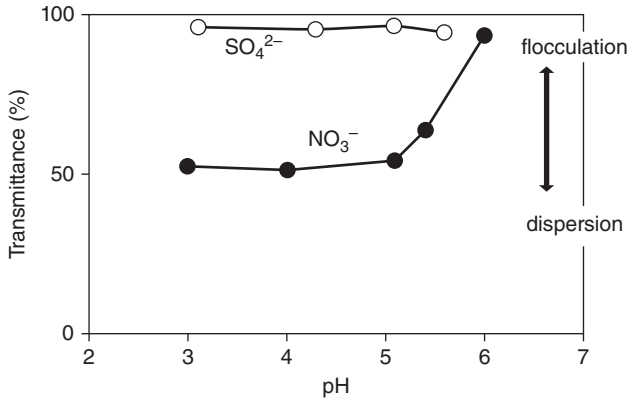


FIGURE 79.13 Effect of anion species on dispersion / flocculation of allophanic andisol at low pH [18].

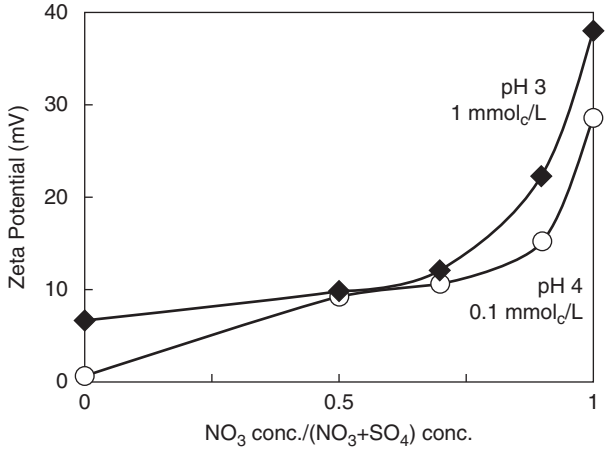


FIGURE 79.14 Zeta-potentials of allophanic andisol in dilute acids [17].

$$C_i(x) = C_{0,i}\exp\left(-\frac{z_i F\Psi_m}{RT}\right) \tag{79.19}$$

$$\Psi_m = 2\Psi \tag{79.20}$$

Here, V_ζ is the repulsive potential energy, D is the distance from the ζ-potential plane to the midpoint between the two soil particles, and b is the distance from the ζ-potential plane to the boundary of the bulk solution. The point at which the repulsive potential energy is equal to 0 is given in the bulk solution. Π is the osmotic pressure difference for each D, R is the gas constant, T the absolute temperature, C_i is the concentration of ion i at the midpoint between the soil particles, $C_{0,i}$ is the concentration of ion i in the bulk solution, z_i the valence of ion i, F is the Faraday constant, Ψ_m is the potential at the midpoint, and Ψ is the potential at the midpoint when the particle exists alone, as calculated by the Gouy–Chapman

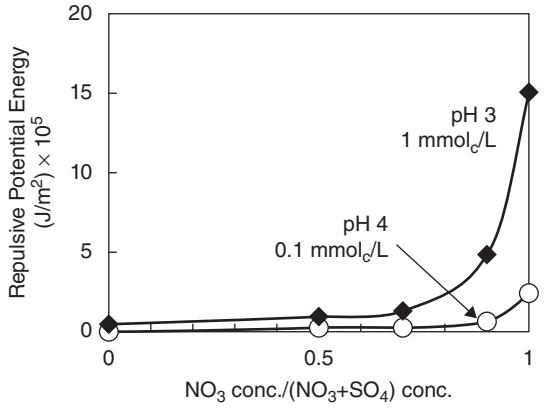


FIGURE 79.15 Calculated electrical repulsive potential energy between particles of allophanic andisol when they approach the ζ-potential plane [19].

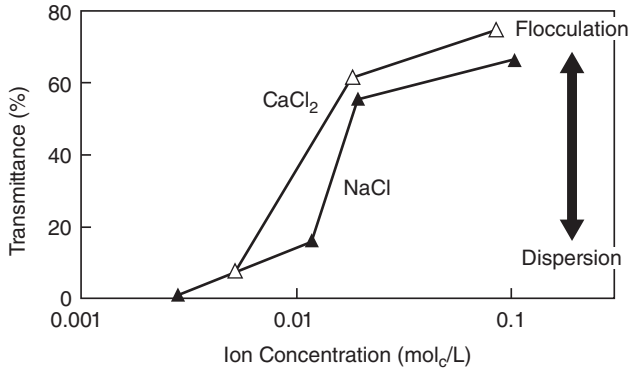


FIGURE 79.16 Effect of ion concentration and cation species on dispersion–flocculation of sediment soil in Lake Kojima; the solutions are at pH 7 [20].

theory. The repulsive potential energy is larger when the NO_3^- ratio in the acid mixture solution is larger (Fig. 79.15). This confirms the result that the soil dispersed well in NO_3^- solution at lower pH and flocculated well in SO_4^{2-} solution (Fig. 79.13) [19]. The behavior of dispersion or flocculation is caused by the difference of adsorption state between the anions because the positive charge is predominant at lower soil pH. Most SO_4^{2-} is strongly adsorbed on the soil surface (Fig. 79.4), while NO_3^- is adsorbed in a diffuse layer, as mentioned before. When most of the anions are adsorbed only on the positively charged soil surface, a diffuse layer does not develop. Then, the soil flocculates well because the electric repulsive potential between the soil particles is small (Fig. 79.15).

Figure 79.16 shows the result of the dispersion–flocculation experiment for the sediment soil of Lake Kojima at pH 7. A well-mixed soil suspension was settled for 8.3 h. Then, the soil suspension was sampled at 3 cm in depth from the water surface and the light transmittance through it at 500 nm wavelength was measured. The soil under an Na^+ system dispersed more than did soil under a Ca^{2+} system because Na^+ is a monovalent cation while Ca^{2+} is a divalent cation, which corresponds to the Shulze–Hardy rule. Cation species influence the dispersion flocculation because the negative charge is predominant in this soil. The soil flocculated well when the ion concentration increased, because the diffuse layer became thin and the repulsive force between soil particles became smaller at a higher ion concentration, due to the shielding of the electric field [20]. This phenomenon is observed at seashore estuaries. Dispersed soil suspensions that adsorb nutrients flow down from rivers. They flocculate and deposit at estuaries because of their high salt concentrations. These regions provide good fisheries as nutrients are accumulated. The fate of radioactive Cs is similarly affected by this phenomenon. Accumulation of radioactive Cs was observed at the mouth of the Arakawa River in Tokyo Bay after the nuclear accident at the Fukushima atomic power plant on March 11, 2011, as shown in Fig. 79.17. The distribution in the sediments above 5 cm in depth sampled from August 2011 to November 2012 was observed. Part of the radioactive Cs that was scattered into the air from the Fukushima atomic power plant flowed down to the Kanto region. The radioactive Cs was fixed to clays in the surface soil, as mentioned earlier. The dispersed clays on which Cs was strongly adsorbed were conveyed by water and gathered in the Arakawa estuary. They flocculated and deposited at that estuary [21]. The discharge of dispersed soil suspensions from paddy fields to the water environment can also cause environmental problems because soil suspensions contain nutrients. Discharge after fertilizer application before transplanting is especially problematic. Plans for appropriate water contaminant mitigation have been proposed [22–25]. Soil dispersion and flocculation are key processes in material cycles in nature; understanding these processes is crucial to addressing environmental contamination associated with agriculture and industry.

79.4 INFLUENCE OF DISPERSION ON SOIL PERMEABILITY

Figure 79.18 shows the change of saturated hydraulic conductivity of allophanic andisol during the percolation of solutions at different pH levels in a 1-$mmol_c$/L Na-H-Cl-OH system. The hydraulic conductivity decreased at lower ($pH \leq 4$) and higher ($pH \geq 10$) levels. The positive charge predominated at more acidic levels and the negative charge, at more alkaline levels, as mentioned before (see also Fig. 79.2). Therefore, the soil dispersed well at lower and higher pH (Fig. 79.12) because the electric repulsive potential energy increased. This led to a decrease in the hydraulic conductivity because macropores in the soil became narrower as a result of swelling of the soil and clogging in the macropores [17]. Figure 79.19 shows the surface of the soil sample before and after percolation of the HCl solution at pH 3. Before the dilute HCl percolation, many aggregates were observed; after the percolation, the aggregates were dispersed. Figure 79.20 shows a vertical cross section of the soil sample after dilute HCl percolation at pH 3. The soil structure of the surface layer changed by soil swelling and macropore clogging [3]. The influence of the electric repulsive force was clearly observed [3,17].

Figure 79.21 shows the change in saturated hydraulic conductivity of allophanic andisol during percolation of dilute HNO_3 and H_2SO_4. While the hydraulic conductivity decreased during HNO_3 percolation, that during H_2SO_4 percolation did not decrease but rather increased [18]. The result corresponds to the results of the dispersion flocculation experiment in Fig. 79.13 and the calculated repulsive potential energy in Fig. 79.15. The repulsive potential energy for HNO_3 was significant, and the soil dispersed well. Therefore,

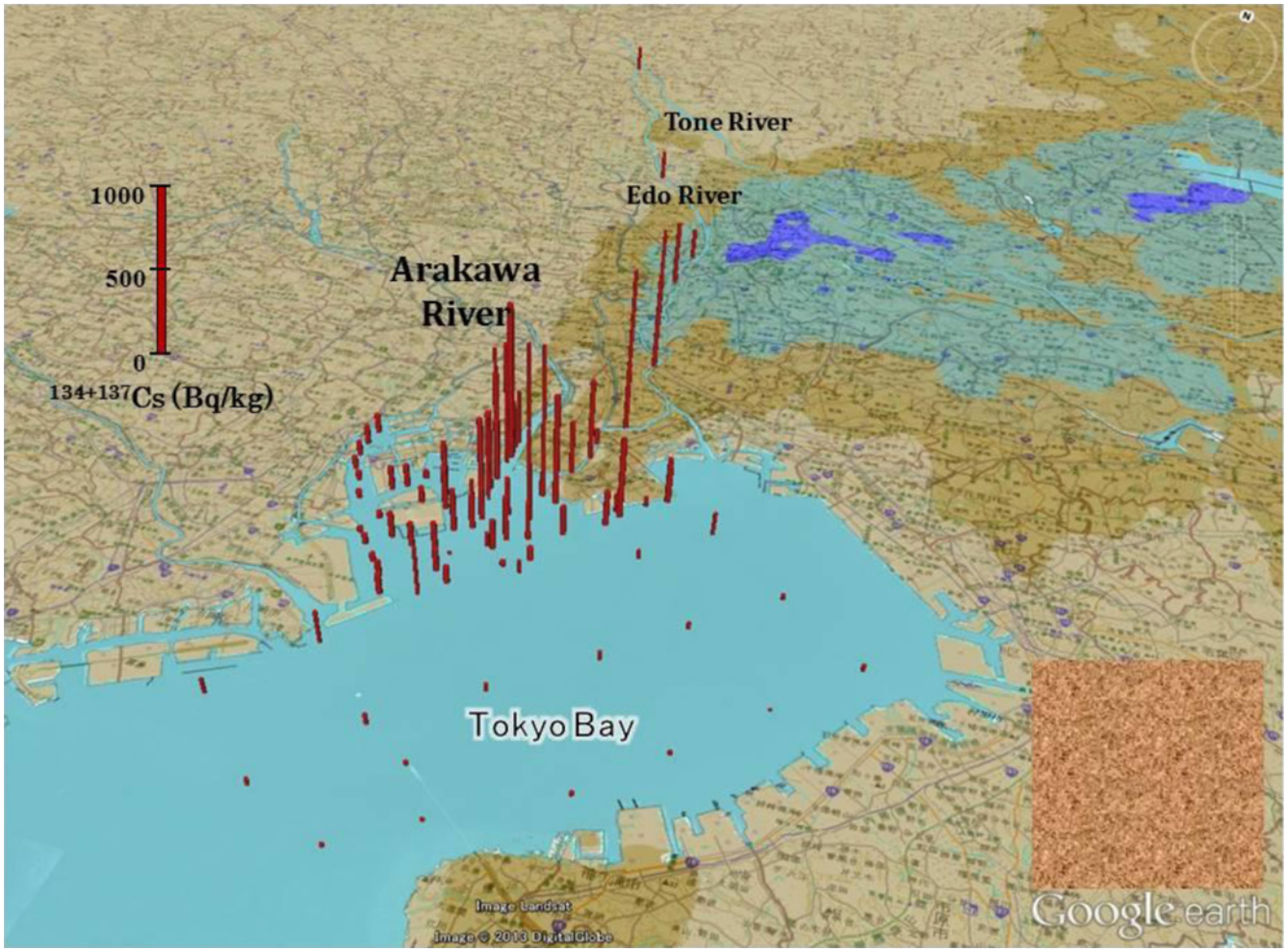


FIGURE 79.17 Radioactive cesium distribution in Tokyo Bay. Cs accumulated at the mouth of Arakawa river [21]. (Map data: Google, DigitalGlobe.)

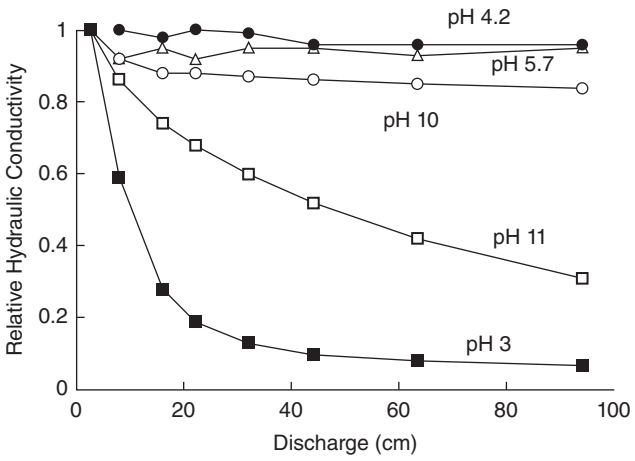


FIGURE 79.18 Effect of pH on saturated hydraulic conductivity of allophanic andisol. The electrolyte concentration was 1 mol_c/L for Na-H-Cl-OH system [3].

the hydraulic conductivity decreased as a result of swelling and dispersion. The hydraulic conductivity for HNO_3 at pH 3 decreased more than that at pH 4, because the repulsive potential energy at pH 3 was greater than that at pH 4. The hydraulic conductivity for H_2SO_4 did not decrease because the repulsive potential energy was smaller and the soil was well flocculated [19]. The difference is due to the variation in adsorption state; NO_3^- is adsorbed into the diffuse layer while SO_4^{2-} is strongly adsorbed just on the soil surface. The adsorption state also influences soil structure and permeability.

Figure 79.22a shows the changes in saturated hydraulic conductivity of the sediment soil in Lake Kojima at different pH levels in a Na system. The soil was initially equilibrated with a 0.1 mol_c/L NaCl solution at the prescribed pH. Then, the NaCl solution was percolated by decreasing the concentration ($0.1 \rightarrow 0.01 \rightarrow 0.001 \rightarrow 0$ mol_c/L) stepwise. The hydraulic conductivity decreased with increase in pH and

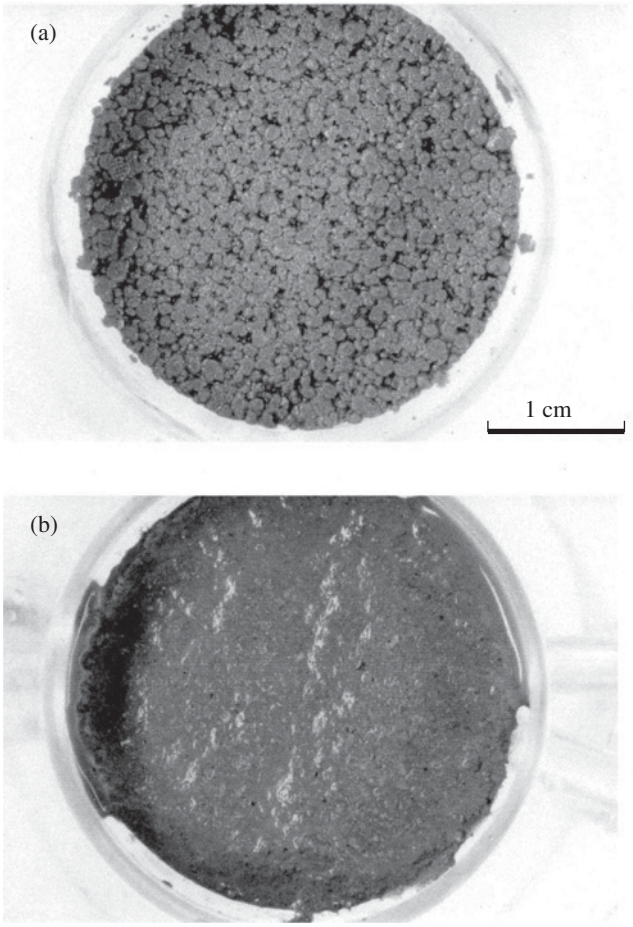


FIGURE 79.19 Surface soil structure of the allophanic andisol (a) before and (b) after HCl at pH 3 percolation (1.33 m) [3].

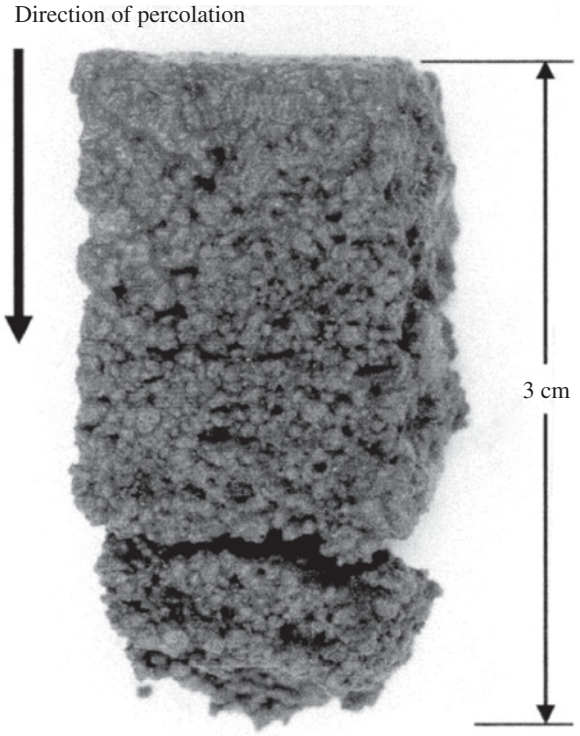


FIGURE 79.20 Vertical cross section of allophanic andisol sample after percolation of HCl solution at pH 3 (1.33 m) [3].

decrease in ion concentration. When the pH increases, the negative charge of the soil increases and the repulsive potential energy between soil particles increases. Then, the soil disperses well and the hydraulic conductivity decreases. When the ion concentration decreases, the diffuse layer becomes thicker and the repulsive potential energy between soil particles increases. Therefore, the soil disperses well, as mentioned before, and the hydraulic conductivity decreases. Figure 79.22b shows the same experiment conducted in a Ca system. The decrease in hydraulic conductivity in the Ca system with the decrease of ion concentration was smaller than that in Na system, because Ca^{2+} is divalent while Na^{+} is monovalent and the soil in a Ca system is more flocculative, as mentioned before. The hydraulic conductivity in a Ca system at pH 11 only slightly decreased with the decrease in ion concentration and was greater than that at pH 9. This was because the soil structure stabilized at pH 11 in a Ca system, due to the chemical reaction between Ca and the soil under alkaline conditions. Historically, reflecting this reaction, a method that consisted in using lime to improve ground stability was used in road construction during the ancient Roman era [20].

When the soil contains Na^{+}, the permeability tends to decrease and the discharge from the soil proceeds very slowly. This condition corresponds to the land reclaimed from below seawater level, such as the Na-salt-accumulated land damaged by tsunami seawater. Because the soil permeability required to wash out Na salt decreases when land is irrigated, a proper drainage plan must be considered. In

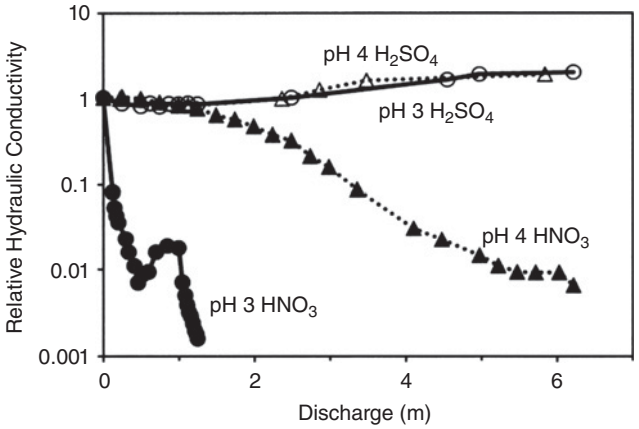


FIGURE 79.21 Effect of anion species of acid solution on saturated hydraulic conductivity of allophanic andisol [18].

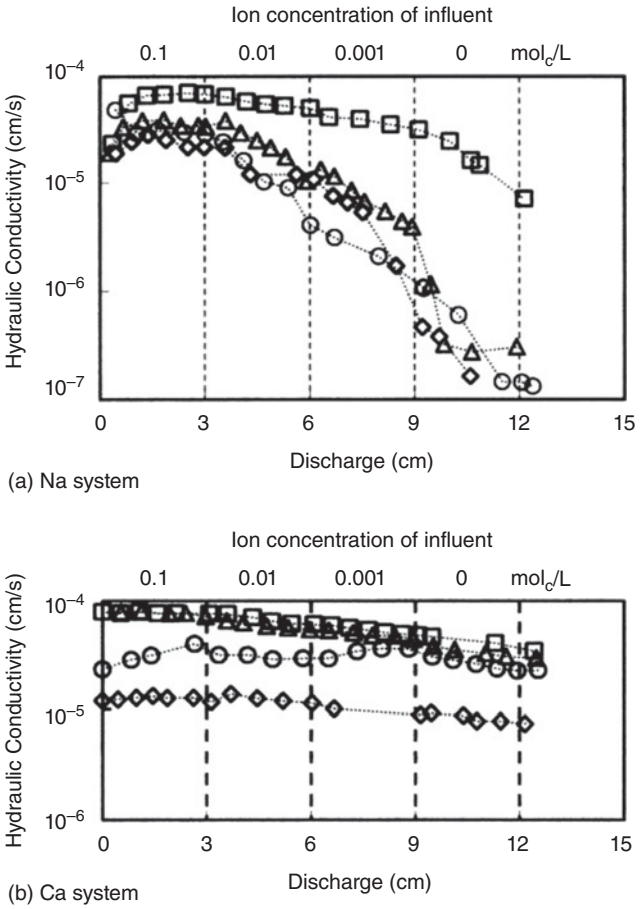


FIGURE 79.22 Effect of soil pH on saturated hydraulic conductivity of the sediment soil of Lake Kojima: (a) Na system; (b) Ca system (□ pH 5; △ pH 7; ◇ pH 9; ○ pH 11) [20].

particular, the permeability decreases at higher pH. Research of this type has been conducted since ancient times because damage due to salt accumulation in crop fields easily occurs in semiarid regions. One theory for the collapse of ancient civilizations is that crop fields were damaged by salt accumulation [26]. Although this theory is not new, current research is focusing on similar problems generated in many areas in the world.

79.5 SURFACTANT ADSORPTION

Surfactants are used for many purposes such as in domestic, industrial, and agricultural applications. When they are discharged into the environment, they can damage the ecosystem, because they can destroy the cells of living organisms. On the other hand, they are sometimes used for remediation of contaminated soils. Because surfactants can change the characteristics of solid surfaces, they affect the physicochemical nature of the soils into which they are introduced.

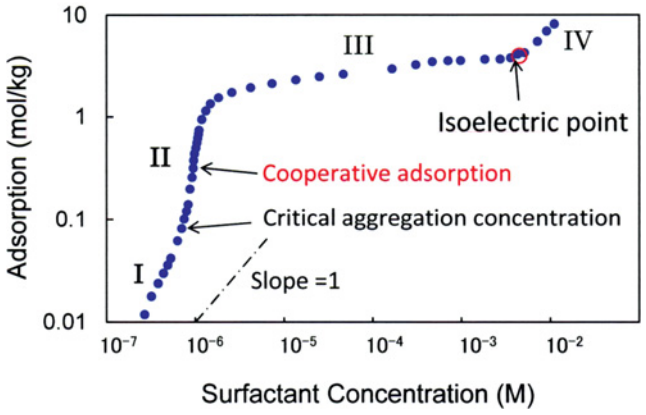


FIGURE 79.23 Cationic surfactant adsorption on anionic polymer in a 5-mmol/L NaCl solution [27].

Before showing the adsorption on soils, it is appropriate to discuss the adsorption on a simple polymer because the fundamental phenomena can be introduced using the polymer adsorption as an example; soils themselves consist of many kinds of materials, and the phenomena are more complicated. Figure 79.23 shows the adsorption of a cationic surfactant, dodecylpyridinium chloride, on an anionic polymer, sodium polystyrene sulfonate. The adsorption isotherm, which is plotted in double-logarithmic scale, is divided into four regions. In *region I*, representing very low adsorption, each monomer surfactant is adsorbed independently on the polymer chain as a result of electrostatic attraction. The slope is close to one unit, the *Henry slope*, which indicates adsorption on isolated *equal-energy sites*. In *region II*, the slope is much larger than one. This indicates cooperative adsorption by which surfactants gather and are adsorbed together because surfactant hydrophobic chains attract each other by hydrophobic interaction. The crosspoint of regions I and II is called the *critical aggregation concentration* (CAC), where surfactants begin to aggregate into polymer chains. In *region III*, the slope gradually becomes smaller because the negative-charge sites decrease. In *region IV*, the net charge becomes positive because the adsorption of surfactant exceeds the negative charge of the polymer as a result of hydrophobic attraction [27].

Humic substances are one of the important components of soils. They characterize soils and play important roles in the material cycle in Nature. Humic substances can be classified into three types: *fulvic acids*, which are soluble in water; *humic acids*, which are soluble in water at pH > 3; and *humins*, which are insoluble in water. Figure 79.24 shows the adsorption of the cationic surfactant, dodecylpyridinium chloride, on three kinds of humic acid and two kinds of fulvic acid. They adsorb the cationic surfactant by electrostatic attractive force as they have negative charges. Cooperative adsorption is not observed because their structures are complicated and surfactants do not aggregate easily. The

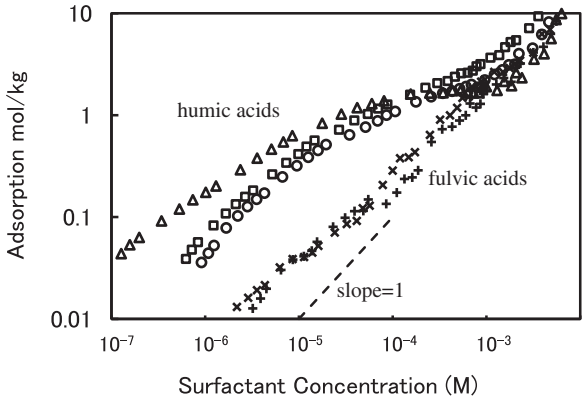


FIGURE 79.24 Cationic surfactant adsorption on fulvic acids and humic acids in a 5 mmol/L NaCl solution (△ Aldrich humic acid; □ Inogashira humic acid; ○ Dando humic acid; × Strichen fulvic acid; + Laurentian fulvic acid) [29].

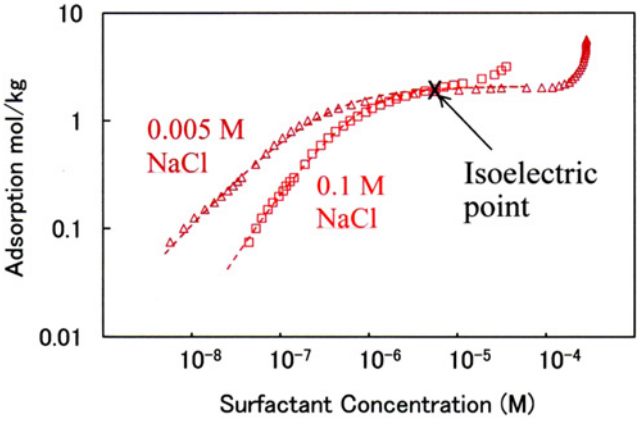


FIGURE 79.26 Effect of ion concentration on surfactant, cetylpyridinium chloride, adsorption in Aldrich humic acid [29].

surfactant begins to adsorb on the humic acids at lower surfactant concentration compared to the fulvic acids, which reflects the difference in hydrophobicity. Figure 79.25 shows the influence of carbon chain length on surfactant adsorption. The effect of hydrophobic chain length of the surfactant on adsorption on Aldrich humic acid is clear. The longer-linear-chain surfactant, cetylpyridinium chloride, has 16 carbons. The shorter-linear-chain surfactant, dodecylpyridinium chloride, has 12 carbons. Both surfactants are positively charged, but the surfactant with longer carbon chain is more hydrophobic. The longer-chain surfactant is adsorbed at lower surfactant concentration. This reflects the stronger adsorption that was caused by the lateral hydrophobic interaction among the carbon chains of the surfactant. One research team [28] indicated that the chain length dependence of the free energy of adsorption per CH_2 group amounts to approximately 3.1 kJ/mol in an alkylpyridinium fulvic acid system and 2.3 kJ/mol in an alkylpyridinium humic acid system. Figure 79.26 shows the effect of ion concentration on the adsorption of the surfactant, cetylpyridinium chloride, on Aldrich humic acid. The surfactant adsorption at 0.1 M NaCl is less than that at 0.005 M NaCl at lower surfactant concentration where the humic acid–surfactant complex is negatively charged. On the other hand, the surfactant adsorption at 0.1 M NaCl is greater than that at 0.005 M NaCl at higher surfactant concentration where the humic acid–surfactant complex is positively charged. This result was induced by the screening effect of the higher ion concentration. As a result of the screening effect at the higher ion concentration, the attractive electric force on the negatively charged surface becomes smaller at lower surfactant concentration, and the repulsive electric force on the positively charged surface becomes smaller at higher surfactant concentrations. Therefore, the adsorption decreased in the former case and increased in the latter case [29].

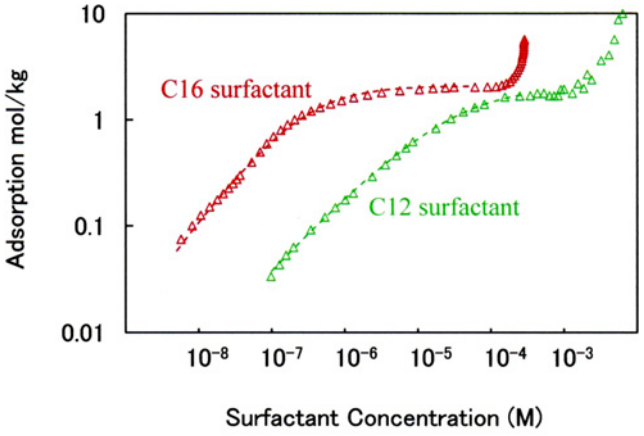


FIGURE 79.25 Effect of surfactant chain length on adsorption in Aldrich humic acid in a 5 mmol/L NaCl solution (C16 surfactant = cetylpyridinium chloride, C12 surfactant = dodecylpyridinium chloride) [29].

When a surfactant is adsorbed on a solid surface, the surface characteristics completely change, because a surfactant is a surface-active agent. Figure 79.27 shows the influence of adsorption of the cationic surfactant dodecylpyridinium chloride on silica stability and the contact angle of water on the silica surface. When the surfactant is adsorbed on the silica, the negative-charge sites of the silica are covered with the surfactant. The stability decreases and the silica gradually becomes flocculative. When the surfactant is adsorbed on more than only the negative-charge sites of the silica, the silica–surfactant complex becomes positively charged. The complex becomes dispersive when the surfactant adsorption is sufficient. When the surfactant covers all negative charge sites and the charge is canceled, the contact angle of water on the silica is largest because the silica surface is covered with the hydrophobic carbon chain of the surfactant [30].

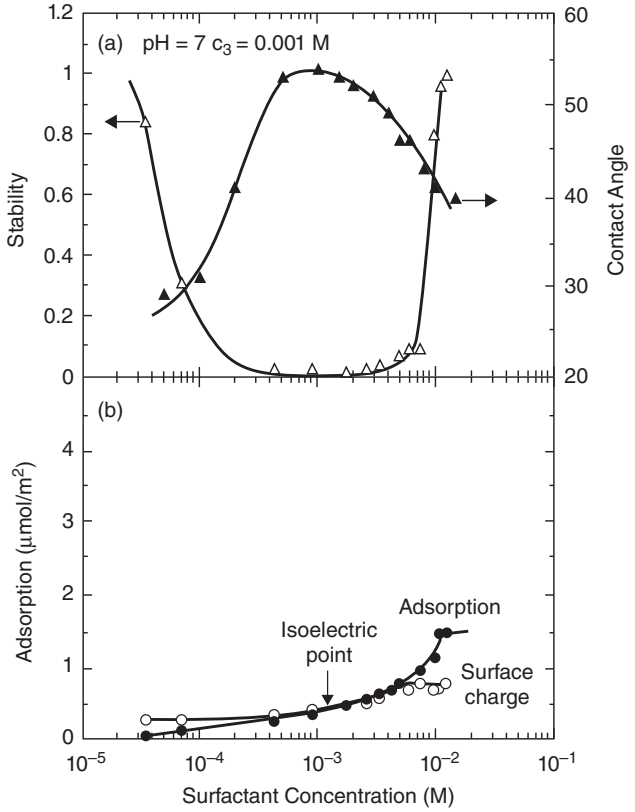


FIGURE 79.27 Stability, contact angle, cationic surfactant adsorption, and surface charge of silica [30].

Figure 79.28 shows the effect of pH on anionic surfactant adsorption in highly humic soil at 100 mM NaCl. The anionic surfactant is sodium dodecylbenzene sulfonate. The highly humic soil has only a negative charge. Therefore, an electric repulsive force is generated between the surfactant and the soil. However, the anionic surfactant is adsorbed by hydrophobic attraction. The adsorption decreases with

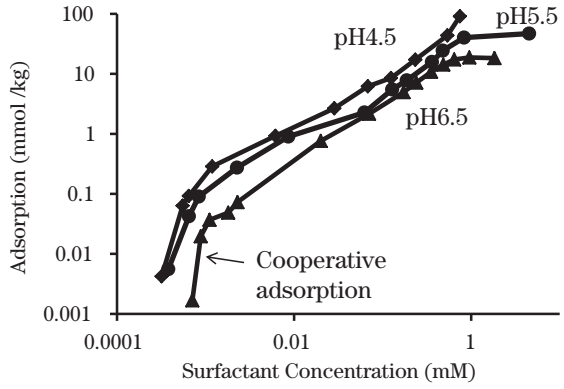


FIGURE 79.28 Effect of pH on anionic surfactant adsorption in highly humic soil [31].

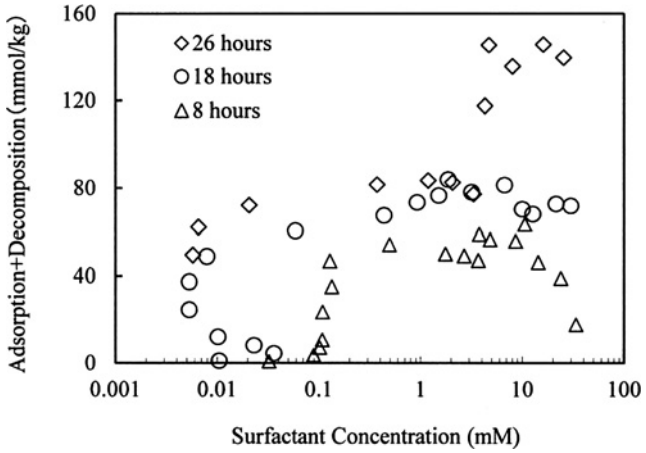


FIGURE 79.29 Sodium dodecyl sulfate (SDS) adsorption and decomposition in highly humic soil. The number denotes the elapsed time after mixing the surfactant and the soil [39].

increasing pH because the negative charge of the soil increases and the repulsive force increases with increasing pH. The increase in negative charge can be detected by the increase in magnitude of the ζ-potential of the soil particles. At lower surfactant concentrations, cooperative adsorption is observed where the slope is larger than one in a double-logarithmic plot [31]. Surfactant adsorption correlates positively with the organic matter content of the soils [32–37] and increases with increasing alkyl chain length [38].

Sodium dodecyl sulfate (SDS) is an anionic surfactant that has a simple linear carbon chain. It decomposes well in humic soil. Figure 79.29 shows the SDS adsorption decomposition in highly humic soil. The number in the figure denotes the elapsed time after mixing the surfactant and the soil. The adsorption–decomposition amount increases with time as a result of decomposition. Surfactants with such simple carbon chains decompose easily in humic soil. At lower surfactant concentrations, the slopes of the curves are steep or skewed, which indicates cooperative adsorption. Figure 79.30 shows the SDS breakthrough curve and the saturated hydraulic conductivity for highly humic soil. After the soil was saturated with a 1 mM NaCl solution, an SDS solution at 5 mM was continuously percolated into the 30-cm-height, 5-cm-diameter soil column. The effluent surfactant concentration initially increased, but after the initial small peak, it gradually decreased to zero—even though the surfactant was continuously percolated. This indicates the process of adsorption and decomposition of the surfactant in the soil. The saturated hydraulic conductivity of the soil decreased gradually with decrease of the breakthrough curve. Because the negative charge of the soil increased as the surfactant adsorption increased, the repulsive force among soil particles increased during the surfactant percolation. This caused a change in

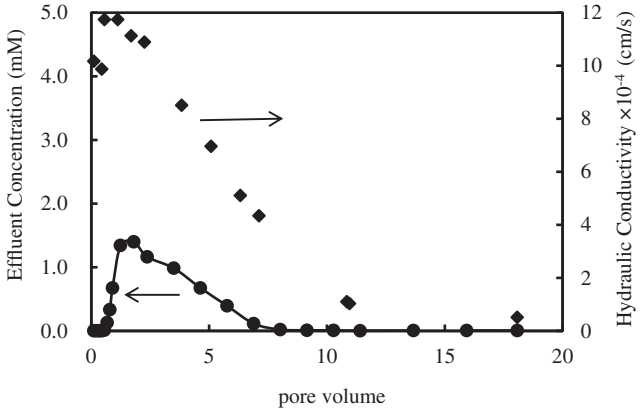


FIGURE 79.30 Sodium dodecyl sulfate (SDS) breakthrough curve and saturated hydraulic conductivity for the highly humic soil; SDS solution at 5 mM was continuously percolated [39].

the soil structure and a decrease in hydraulic conductivity. The surfactant adsorption clearly affects transport phenomena [39].

79.6 ION EXCLUSION AND SALT SIEVING

Ions having same-sign electric charges with the soil itself are excluded from the diffuse layer of the soil. The ions are not only excluded from the diffuse layer but also excluded from the larger pores surrounded by the narrow pores in which diffuse layers overlap. Such ion exclusion affects the ion transport in soils [40–45]. Figure 79.31 shows the NO_3^- breakthrough curve during percolation of 1-mol_c/L NO_3^- solution for the A horizon of allophanic andisol; the soil has negative charge and no positive charge. Because of the anion exclusion, NO_3^- flowed out slightly faster than a nonreactive solute. If there is no interaction with the soil surface, the solute breakthrough curve shows an increase at around 1 pore volume and the relative effluent concentration becomes 0.5

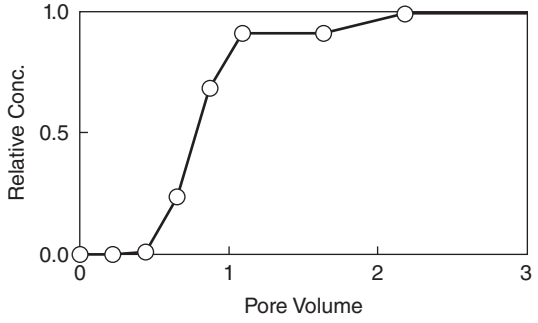


FIGURE 79.31 NO_3^- breakthrough curve during percolation of 1-mol_c/L NO_3^- solution for soil that has a negative charge and no positive charge [6].

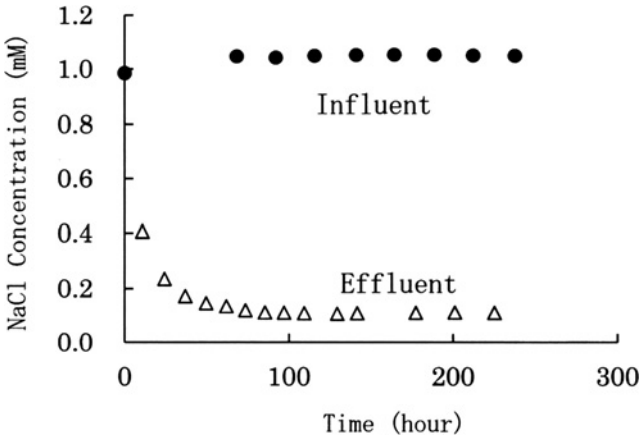


FIGURE 79.32 Salt sieving of montmorillonite membrane.

at 1 pore volume [6]. The NO_3^- breakthrough curve shifted slightly to the left compared to that for the nonreactive solute.

Figure 79.32 shows the salt-sieving effect of a montmorillonite membrane 0.5 mm in thickness. Because montmorillonite is a clay mineral that has a large cation exchange capacity (80–150 $cmol_c$/kg) and specific surface (600–800 m^2/g) [46], its diffuse layer can develop well and the clay is heaviy influenced by its electric charge; it disperses and swells effectively under low electrolyte concentration. When its diffuse double layer overlaps, salts are sieved by it, as shown in Fig. 79.32. The effluent NaCl concentration became 10% of the influent NaCl concentration of 1 $mmol_c$/L [47]. The clay membrane shows the characteristics of a reverse-osmosis membrane.

Transport phenomena in a clay layer are restricted by the water pressure difference ΔP, the osmotic pressure difference $\Delta\pi$, and the electric potential difference ΔV between both ends of the layer under isothermal conditions. Figure 79.33 shows those measured values of a thin montmorillonite clay subject to different NaCl concentrations of 1 $mmol_c$/L and 0.1 $mmol_c$/L under the condition of zero net flux of liquid [48]. The concentration difference between the clay layer induced a pressure difference and an electric potential difference . Groenevelt et al. [49] applied the following phenomenological equations derived from irreversible thermodynamics and evaluated the results:

$$j_V = L_V F_V + L_{VD} F_D + L_{VE} F_E \tag{79.21}$$

$$j_D = L_{VD} F_V + L_D F_D + L_{DE} F_E \tag{79.22}$$

$$I = L_{VE} F_V + L_{DE} F_D + L_E F_E, \tag{79.23}$$

In these equations, j_V is the water flux, j_D is the salt flux, I is the electric current, L represents the phenomenological coefficients, $F_V = -\Delta P/\Delta X$, $F_D = -\Delta\pi/\Delta X$, $F_E = -\Delta V/\Delta X$, and ΔX denotes the thickness of the thin clay layer. Such

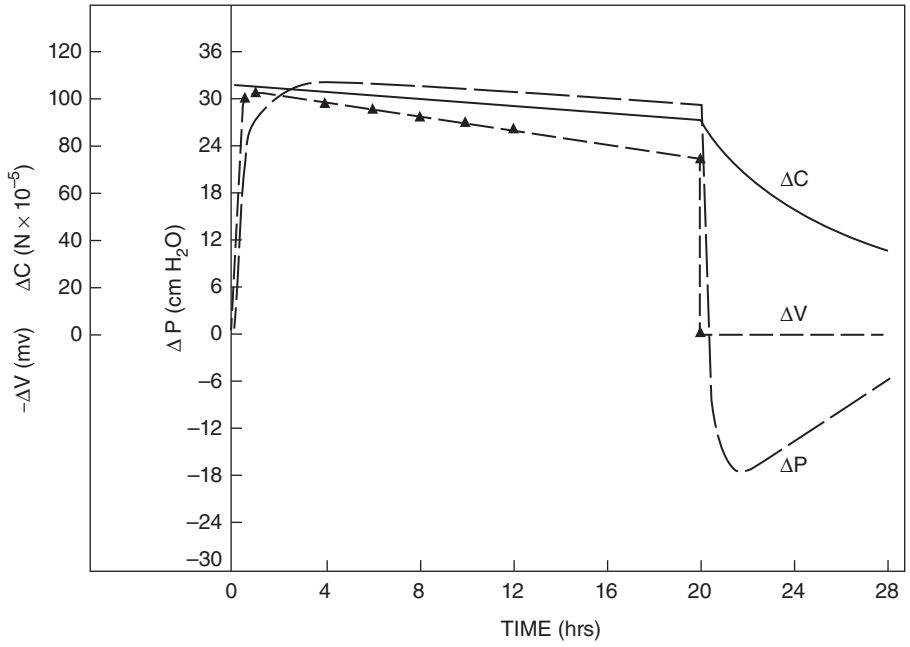


FIGURE 79.33 Changes in concentration difference ΔC, pressure difference ΔP, and voltage difference ΔV, with time for a thin clay layer [48].

coupling phenomena occur during salt sieving and transport in clayey soils [45]. Further research efforts are required to evaluate these interesting phenomena that will relate to environmental technology.

REFERENCES

[1] Iwata, S. (1985). *Soil Is the Origin of Life*. Ohtsuki Publishing Co., Tokyo (in Japanese).

[2] Ishiguro, M., Song, K.-C., Yuita, K. (1992). *Soil Sci. Soc. Am. J.* **56**, 1789–1793.

[3] Ishiguro, M. (2005). *Soil Sci. Plant Nutr.* **51**, 637–640.

[4] Bolt, G.H., Bruggenwert, M.G.M. (eds.) (1978). *Soil Chemistry: A: Basic Elements.* Elsevier, Amsterdam.

[5] Ishiguro, M., Makino, T. (2011). *Colloids Surf. A: Physicochem. Eng. Aspects* **384**, 121–125.

[6] Ishiguro, M., Manabe, Y., Seo, S., Akae, T. (2003). *Soil Sci. Plant Nutr.* **49**, 249–254.

[7] Yamaguchi, N., Takada, Y., Hayashi, K., Ishikawa, S., Kuramata, M., Eguchi, S., Yoshikawa, S., Sakaguchi, A., Asada, K., Wagai, R., Makino, T., Akahane, I., Hiradate, S. (2012). *Bull. Natl. Inst. Agro-Environ. Sci.* **31**, 75–129 (in Japanese with English abstract).

[8] Brouwer, E., Baeyens, B., Maes, A., Cremers, A. (1983). *J. Phys. Chem.* **87**, 1213–1219.

[9] Sawhney, B.L. (1972). *Clays Clay Minerals* **20**, 93–100.

[10] Ishiguro, M. (1992). *Soil Sci. Soc. Am. J.* **56**, 1738–1743.

[11] Rubin, J., James, R.V. (1973). *Water Resources Res.* **9**, 1332–1356.

[12] Valocchi, A.J., Street, R.L., Roberts, P.V. (1981). *Water Resources Res.* **17**, 1517–1527.

[13] Hashimoto, I., Deshpande, K.B., Thomas, H.C. (1964). *Industr. Eng. Chem. Fund.* **3**, 213–218.

[14] Selim, H.M., Mansell, R.S. (1976). *Water Resources Res.* **12**, 528–532.

[15] Schulin, R.H., Flühler, R.S., Mansell, R.S., Selim, H.M. (1986). *Geoderma* **38**, 311–322.

[16] Rose, D.A., Passioura, J.B. (1971). *Soil Sci.* **111**, 252–257.

[17] Nakagawa, T., Ishiguro, M. (1994). *J. Environ. Qual.* **23**, 208–210.

[18] Ishiguro, M., Nakajima, T. (2000). *Soil Sci. Soc. Am. J.* **64**, 813–818.

[19] Ishiguro, M., Nakaishi, K., Nakajima, T. (2003). *Colloids Surf. A: Physicochem. Eng. Aspects* **230**, 81–88.

[20] Ishiguro, M., Iwamoto, R., Ishida, T., Akae, T. (2001). *Transact. Jpn. Soc. Irrigat. Drain. Reclam. Eng.* **216**, 65–70 (in Japanese with English abstract).

[21] Nakagawa, R., Ishida, M., Baba, D., Tanimoto, S., Okamoto, Y., Yamazaki, H. (2012). *Proc. Int. Symp. Environmental Monitaring and Dose Estimation of Residents after Accident of TEPCO's Fukushima Daiichi Nuclear Power Stations*, pp. 133–136.

[22] Akae, T. (1992). *Soil Phys. Cond. Plant Growth* (Japan) **64**, 37–44 (in Japanese with English abstract).

[23] Akae, T. (1992). *Soil Phys. Cond. Plant Growth* (Japan) **64**, 45–52 (in Japanese with English abstract).

[24] Akae, T. (1994). *Soil Phys. Cond. Plant Growth* (Japan) **69**, 3–10 (in Japanese with English abstract).

[25] Tabuchi, T., Hasegawa, S. (eds.) (1995). *Paddy Fields in the World*. The Japanese Society of Irrigation, Drainage and Reclamation Engineering, Tokyo, pp. 332–338.

[26] Hillel, D. (1998). *Environmental Soil Physics.* Academic Press, San Diego, p. 262.

[27] Ishiguro, M., Koopal, L.K. (2009). *Colloids Surf. A: Physicochem. Eng. Aspects* **347**, 69–75.

[28] Yee, M., Miyajima, T., Takisawa, N. (2006). *Colloids Surf. A: Physicochem. Eng. Aspects* **272**, 182–188.

[29] Ishiguro, M., Tan, W., Koopal, L.K. (2007). *Colloids Surf. A: Physicochem. Eng. Aspects* **306**, 29–39.

[30] Koopal, L.K., Goloub, T., Keizer, A. (1999). *Colloids Surf. A: Physicochem. Eng. Aspects* **151**, 15–25.

[31] Ahmed, F., Ishiguro, M., Akae, T. (2012). *J. Jpn. Soc. Soil Phys.* **120**, 45–54.

[32] Krishna, M., Volk, G., Jackson, M. (1966). *Soil Sci. Soc. Am. Proc.* **30**, 685–688.

[33] Urano, K., Saito, M., Murata, C. (1984). *Chemosphere* **13**, 293–300.

[34] Hand, V.C., Williams, G.K. (1987). *Environ. Sci. Technol.* **21**, 370–373.

[35] Fytianos, K., Voudrias, E., Papamichali, A. (1998). *Chemosphere* **36**, 2741–2746.

[36] Westall, J.C., Chen, H., Zhang, W., Brownawell, B.J. (1999). *Environ. Sci. Technol.* **33**, 3110–3118.

[37] Rodriguez-Cruz, M.S., Sanchez-Martin, M.J., Sanchez-Camazano, M. (2005). *Chemosphere* **61**, 56–64.

[38] Hand, V.C., Williams, G.K. (1987). *Environ. Sci. Technol.* **21**, 370–373.

[39] Ishiguro, M., Torigoe, T., Kameoka, Y., Akae, T. (2008). *Transact. Jpn. Soc. Irrigat. Drain. Reclam. Eng.* **258**, 7–13 (in Japanese with English summary).

[40] Kemper, W.D. (1961). *Soil Sci. Am. Proc.* **25**, 255–260.

[41] Smith, S.J. (1972). *Soil Sci.* **114**, 259–263.

[42] Bresler, E. (1973). *Soil Sci. Am. Proc.* **37**, 663–669.

[43] Sakuma, T. (1982). *Jpn. J. Soil Sci. Plant Nutr.* **53**, 333–336 (in Japanese with English summary).

[44] Hatano, R., Sakuma, T., Okajima, H. (1985) *Soil Sci. Plant Nutr.* **31**, 199–213.

[45] Iwata, S., Tabuchi, T., Warkentin, B.P. (1995). *Soil-Water Interactions.* Marcel Dekker, New York, pp. 198–228.

[46] Sparks, D.L. (2003). *Environmental Soil Chemistry.* Academic Press, Amsterdam.

[47] Ishiguro, M., Matsuura, T., Detellier, C. (1995). *J. Membr. Sci.* **107**, 87–92.

[48] Elrick, D.E., Smiles, D.E., Baumgartner, N., Groenevelt, P.H. (1976). *Soil Sci. Am. J.* **40**, 490–491.

[49] Groenevelt, P.H., Elrick, D.E., Blom, T.J.M. (1978). *Soil Sci. Am. J.* **44**, 671–674.

80

PHARMACEUTICAL SOLID–WATER INTERFACE PHENOMENA MEASURED BY NEAR-INFRARED SPECTROSCOPY

YUSUKE HATTORI AND MAKOTO OTSUKA

Research Institute of Pharmaceutical Sciences, Musashino University, 1-1-20, Shin machi, Nishitokyo, Tokyo 202-8585, Japan

80.1 INTRODUCTION

Because of its portability, countability, and ease of administration, solid dosage is one of the most popular drug formulations. In the more recent decades, the large-scale manufacturing process has significantly improved. New drug additives have been developed for suitable in vivo dissolution of active ingredients. Dissolution and controlled release of active ingredients are critical to an efficient drug delivery, and both have been the object of active investigations [1–7].

On oral administration of a solid dosage, drug absorption rate depends on (1) the release rate of the drug substance from the product, (2) the dissolution rate of the active ingredient under physiological conditions, and (3) the permeability across the gastrointestinal tract. In vitro studies investigating the process of dissolution can bring significant insight into predicting the properties of solid formulations in vivo. Thus, in vitro dissolution tests for solid dosage forms, such as tablets and capsules, are conducted in order to ensure lot-to-lot reproducibility and product quality [2, 8]. When drug formulations, manufacturing processes, or manufacturing sites are changed, in vitro dissolution tests provide useful information to ensure continued quality.

The theory on the dissolution of solids was first introduced by Noyes and Whitney [9], while Nernst presented a diffusion-controlled dissolution model based on Fick's first law [10]. The in vitro dissolution of active ingredients from solid dosage forms is classically interpreted by the Noyes–Whitney–Nernst dissolution model. In this model, the dissolution rate $\mathrm{d}C/\mathrm{d}t$ of a substance from a solid state is calculated as

$$\frac{\mathrm{d}C}{\mathrm{d}t} = \frac{DS}{Vh}(C_s - C) \tag{80.1}$$

where C_s and C represent its solubility concentration and the concentration of the dissolved substance in the bulk solution at a time t, respectively; D, V, and S are the diffusion coefficients of the dissolved substance in the bulk solution, the volume of the solution, and the exposed surface of the solid, respectively. Additionally, Nernst described a zone of nonequilibrium concentration gradient commonly known as the *diffusion layer*, at the interface between the solid and the bulk solution. At the surface of a solid, the concentration of a substance reaches saturation and then decreases toward the bulk concentration. The thickness of the diffusion layer is represented by h in Eq. (80.1).

The diffusion of particles at nonequilibrium is described by Fick's second law:

$$\frac{\partial C}{\partial t} = D\frac{\partial^2 C}{\partial x^2} = \frac{\partial}{\partial x}\left(D\frac{\partial C}{\partial x}\right) \tag{80.2}$$

In the dissolution theory proposed by Nernst, it is assumed that the diffusion layer of thickness h exists at the solid surface undergoing dissolution; thus, the concentration gradient at the interface is calculated as follows:

$$\frac{\mathrm{d}C}{\mathrm{d}x} = \frac{C_s - C}{h} \tag{80.3}$$

Encyclopedia of Biocolloid and Biointerface Science, Volume 2, First Edition. Edited by Hiroyuki Ohshima.
© 2016 John Wiley & Sons, Inc. Published 2016 by John Wiley & Sons, Inc.

By substituting Eq. (80.3) into the diffusion equation Eq. (80.2), the equation thus becomes

$$\frac{\mathrm{dC}}{\mathrm{dt}} = \frac{D}{xh}(C_s - C) \tag{80.4}$$

When a partial, flat, and small area of a solid surface is being considered, the solid surface area S and the volume of the solution V may be substituted by x, which is the distance from a solid surface, with $x = V/S$ in Eq. (80.1). Finally, given h, the thickness of the diffusion layer, the dissolution equation [Eq. (80.1)] is derived from the diffusion equation as presented in Fick's second law.

On oral administration, drug release and dissolution rates from a solid dosage form coincide with its disintegration into particles or granules [11–13]. The total surface area of disintegrated granules may become 10^3 times larger than that of a tablet. At microscopic scale, the distance x from a solid surface is used, instead of S and V, as constant surface area. However, the surface area has a significant contribution in controlling the macroscopic dissolution of active ingredients from a solid dosage form.

The process of disintegration and dissolution of an active ingredient from solid dosages has been empirically characterized by several models such as first-order [14], Hixson–Crowell [15], Higuchi [1], Weibull [16–18], and Korsmeyer–Peppas [19] functions.

A first-order dissolution kinetics represents a dissolution model similar to the one described in the Noyes–Whitney equation, with a constant surface area. Expression of the drug dissolution rate of uniformly sized particles is based on the cube root of the particle weight in accordance with the Hixson–Crowell cube root law.

Higuchi developed theoretical models of drug release from semisolid and solid matrixes, such as ointments and polymer matrices. In the Higuchi model, the amount of released drug is proportional to the square root of time, and the matrix surface is assumed to be constant.

Another model to describe dissolution profiles is the empirical use of the Weibull function

$$C(t) = 1 - \exp(-at^b) \tag{80.5}$$

where a and b are constants. However, there is currently a lack of meaning in these parameters, and this is a pending issue [4, 16]. Recently, this empirical model nicely described the dissolution profiles in both Euclidian and fractal spaces, and the relation between the exponent b and the fractal geometry of its solid structure has been investigated [16, 20, 21]. One research team [20, 21] reported the results of Monte Carlo simulation illustrating the relationship between b and the drug release substrate structure as follows: (1) when $0.35 < b < 0.69$, the drug is released from fractal or disordered substrate; (2) when $0.69 < b < 1$, the drug is released from Euclidian substrate; (3) and when $b = 1$, there is a first-order drug release in accordance with Fick's first law of diffusion [20, 21].

Earlier, another team reported a method that predicts the specific surface area of solid dosages during diffusion and disintegration-controlled dissolution using a model-dependent function [22]. According to this method, the surface area at a given time t may be obtained using the function for area variations during dissolution. According to the authors, the calculated profiles are in good agreement with experimental profiles in describing drug dissolution using the Weibull function.

Another team proposed a model-free function based on the Noyes–Whitney–Nernst equation [23]

$$C(t) = C_s \int_0^{\tau} KS(t) \exp\{-KS(t)t\}\, dt \tag{80.6}$$

where $K = D/Vh$. The cumulative concentration at time τ is expressed using an integral equation, where the surface area of solid exposed to bulk solution is a function of time. Thus the concept of this function is that $S(t)$ can be calculated from the dissolution profile. While a thick diffusion layer slows down the dissolution process, a thinner layer provides a faster dissolution. However, what defines a thick or a thin diffusion layer? If the diffusion layer does exist, what are the dissolution mechanisms within this layer? In this review, we explore the phenomena associated with the initial dissolution of solids based on the Noyes–Whitney–Nernst dissolution model using near-infrared spectroscopic measurements.

80.2 EXPLORATION OF INTERFACE PHENOMENA USING NEAR-INFRARED SPECTROSCOPY

Macroscopic dissolution phenomena were empirically or semiempirically described using multiple models [4]. These models mat be classified into two groups: (1) the models based on Fick's law and (2) those based on a power law. As described above, the power-law models are applicable for solids such as polymeric matrices without a disintegration process. Classically, solid dosage is presented as a compressed solid incorporating monomer additives such as lactose, polymer additives such as cellulose, and a small amount of the active ingredient. In this chapter, we focus on the dissolution of solid dosages.

The Noyes–Whitney–Nernst dissolution model is based on the assumption that the formation of a diffusion layer between the solid and the bulk solution occurs. This layer may be formed prior to the dissolution process. A number of studies have been conducted to investigate the interfacial phenomena by means of contact angle between solid and water [24–29], water adsorption [30–34], microcalorimetry

[25], and inverse gas chromatography [24, 27] methods. These methods evaluate the surface energy of solids on the basis of macroscopic measurements. Microscopic interactions between solids and water molecules have not been investigated using these methods.

Spectroscopic measurements are widely used for measuring molecular interactions. In particular, in situ vibrational spectroscopic measurements, such as Raman [35–37], infrared (IR) [38, 39], and near-infrared (NIR) [40–44] spectroscopy, are noninvasive tools that may provide useful information without any prior sample treatments. IR and NIR spectroscopic measurements are more sensitive to water molecules than Raman spectroscopy; however, IR spectroscopy is too sensitive to measure water rich sample in situ. Although it remains difficult to use NIR spectroscopy to measure sample completely dissolved in water, it is a sufficiently sensitive method for in situ measurements of the initial stages of the dissolution process, when the amount of water is low.

80.2.1 Initial Dissolution of Compressed Solids

Figure 80.1 shows the in situ NIR spectra of compressed lactose with penetrating water. In the initial spectrum (before water penetration), a strong band at 4730 cm^{-1} and a sharp peak at 5170 cm^{-1} can be observed. These two peaks are assigned to the combination of O–H stretching and C–O–H bending modes of disaccharide molecules and the combination of H–O–H stretching and bending modes of water, respectively. Interdependently, the former peak is reduced and the latter peak is enhanced and broadens with water penetration. Several sharp and weak peaks in the 5900–5500 cm^{-1} region and broad peaks in the 6500–6000 cm^{-1} region are assigned to the first overtones of the C–H stretching O–H stretching modes, respectively.

The peaks in the 4800–5200 cm^{-1} and 6500–7200 cm^{-1} regions are due to a combination of O–H stretching and bending modes and first overtone of O–H stretching mode of water molecules, respectively. These bands involve several species of water molecules with different grades of hydrogen bonds [42, 45]. The multiple bands cause a complex overlap of spectra. The differential spectrum is one of the analytical methods used to extract spectral changes from peak-overlapped spectra.

Differential spectra of the in situ NIR spectra of lactose tablets are shown at various times of water penetration in Fig. 80.2a–c. There are bands due to different water species at 5245 and 5108 cm^{-1} and a shoulder at 4921 cm^{-1} involving both of water and a C–O–H combination band of lactose. In Fig. 80.2b,c, these spectra indicate secondary change at around 20 min and 45 min, respectively. The secondary change was not observed with the higher-porosity tablets

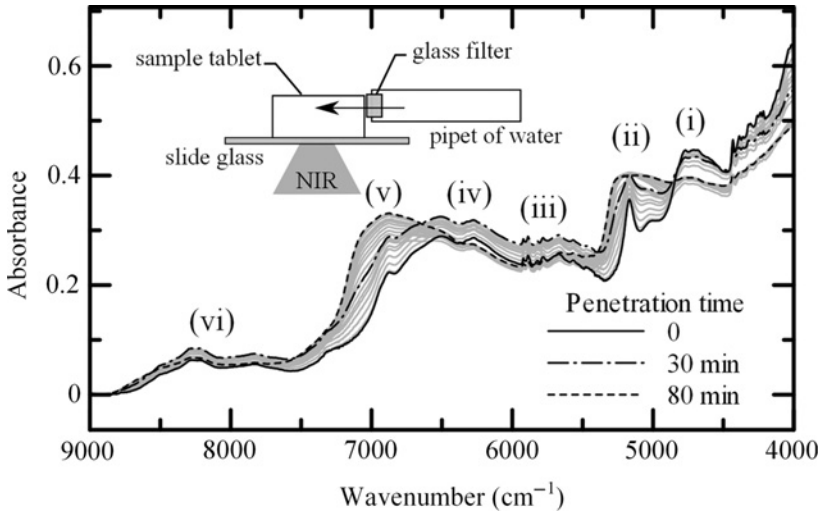


FIGURE 80.1 In situ diffuse reflectance NIR spectra of lactose tablet with penetrating water. The tablet was compressed under 189 MPa. Its dimensions were 8 mm in diameter and 3.1 mm in thickness. The spectra were collected using a FT-NIR spectrophotometer (MPA, Bruker Optics, Ettlingen, Germany). Each spectrum was accumulated 32 times between 4000 cm^{-1} and 9000 cm^{-1} with a 4 cm^{-1} spectral resolution. The spectral measurements were performed at 1-min intervals after the start of water penetration from the glass tube into the tablet via a glass filter (pore size 10–16 μm). The collected spectra were processed using multiplicative scatter to correct the baseline. The bands were assigned to (1) a combination of O–H stretching and C–O–H bending modes, (2) a combination of O–H stretching and H–O–H bending modes, (3) first overtone of C–H stretching, (4) first overtone of O–H stretching (lactose), (5) first overtone of O–H stretching (water), and (6) second overtone of C–H stretching.

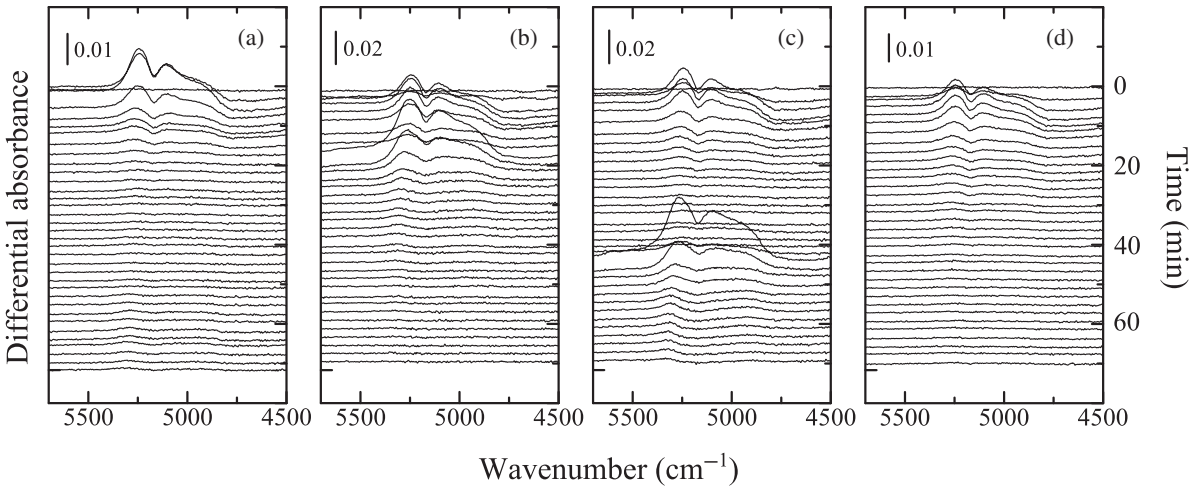


FIGURE 80.2 Differential NIR spectra in the range of bands due to a combination of O–H stretching and bending modes with a time series of penetrating water (a–c) and lactose-saturated solution (d). The tablets were compressed under 118 (a), 189 (b,c), and 243 (c) MPa. The void fractions were 0.149, 0.113, and 0.0898, respectively. The spectral difference was calculated at intervals of 2 min. The two-stage changes were observed in (b) and (c). The time of onset of the second change was delayed when the void fraction of tablets decreased. It is assumed that the second change occurred too rapidly to be detected in the tablet with the highest void fraction (a). The second change disappeared on penetration of lactose-saturated solution (d).

because the fast secondary change coincided with the prior change.

The first change is assigned to the increment of water due to penetration. The time of onset of the secondary change is delayed by the decreasing porosity of tablets. The secondary change may due to the formation of a diffusion layer between lactose solids and the bulk solution.

Figure 80.2d shows the differential spectra of a lactose tablet with penetrating lactose-saturated solution. The porosity of the tablet is shown in Fig. 80.2b; however, the secondary change failed to occur.

In the diffusion layer, the substance concentration decreases from a saturated concentration to a bulk concentration as a function of distance from the solid surface. Therefore, if the bulk concentration is already saturated, the diffusion layer should be absent. In Fig. 80.2d, the disappearance of the secondary change in the differential spectra indicates that it occurred independently of the diffusion layer, and the secondary change indicates the formation of a diffusion layer.

The peak decomposition of spectra provides quantitative information on water molecules, with their different grades of hydrogen bonding, as shown in Fig. 80.3. The decomposition was modelled using a Gaussian function:

$$\Delta A(\nu) = \sum_{i=1}^{n} \Delta A_i(\nu) \exp\left\{ -B \frac{(\nu - \nu_{i,max})^2}{\Gamma_i^2} \right\} \qquad (80.7)$$

Here, $A(\nu)$ is the absorbance at a wavenumber ν; n is the number of components; $\nu_{i,\max}$ and Γ_i are the peak

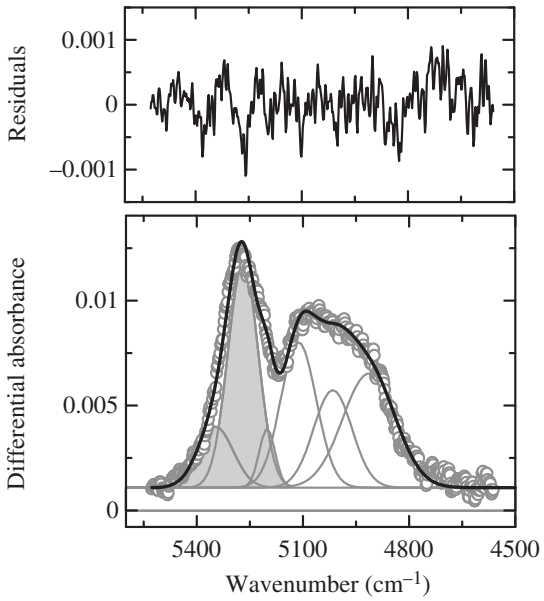


FIGURE 80.3 Spectral decomposition of differential NIR spectrum between 22 and 20 min by nonlinear least-squares method according to Eq. (80.7) and with fitting residuals. The open circles and the solid line represent the experimental and calculated spectra, respectively. The calculation was performed using six Gaussian components (solid gray lines), and the filled components at higher wavenumber indicate free or loosely binding species of water molecules. The other nonfilled components are due to strongly binding water molecules.

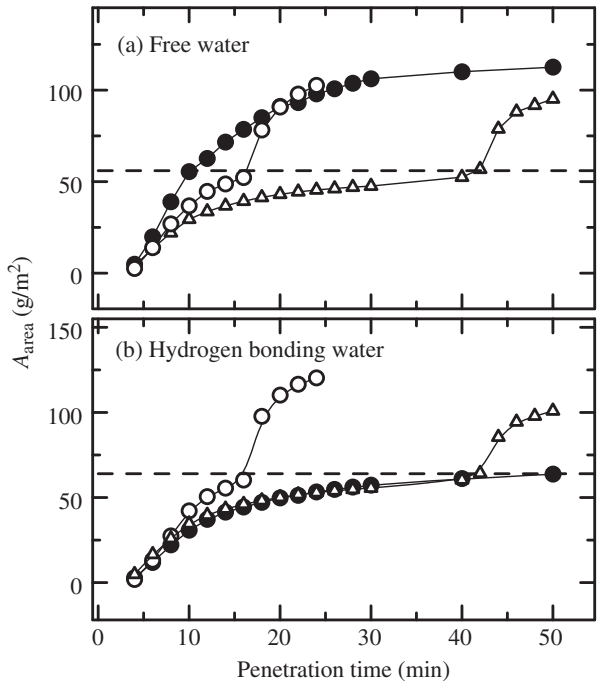


FIGURE 80.4 Surface-area-normalized absorbance (A_{area}) profiles of free/loosely binding water (a) and strongly binding water molecules (b) as a function of water penetration time. The open and closed circles represent the profiles of compressed solids under 189 MPa pressure with penetrating water and saturated lactose solution, respectively. The triangles indicate the profile of the solid compressed under 243 MPa with penetrating water. The values of A_{area} were obtained as the sum of the peak area for each component and normalized by the specific surface area of a compressed solid. The specific surface area was measured using a surface area analyzer (Monosorb, Quantachrom Instruments, FL) and a bulk solid cell (QS-620).

wavenumber and the half-width of a component, respectively; and B is a constant. In this study, six components were used to decompose the spectra because the calculated curve showed an excellent fit to the experimental spectrum. In fact, determination of the number of components should be considered carefully. Here, the meaning of decomposition is the quantitative separation between free (or loosely hydrogen bonding) water and hydrogen bonding water species.

Figure 80.4 shows the peak area profiles of hydrogen bonding and free species of water, which are normalized by the solid surface area of compressed lactose solid. The secondary changes in both hydrogen bonding and free species are simultaneously induced at 16 min and 42 min for highly and loosely compressed tablets, respectively. Noticeably, the threshold area intensity, which relates to the amount of hydration water, necessary to induce the formation of diffusion layer, is independent of tablet porosity.

When a lactose-saturated solution is used, a corresponding increase in free water species occurs with the profiles of secondary change in water penetration. On the other hand, hydrogen-bonded water exhibits the same profile as in the prior change. As a consequence of the spectral decomposition, an initial dissolution model was proposed and is shown in Fig. 80.5. In the early stage, free water molecules attach to the solid surface, and saturation of the attached water molecules induces the formation of a diffusion layer. This represents the initial dissolution of the solid.

80.2.2 Hydration and Swelling of Disintegrating Agents: Two-Dimensional Correlation Spectroscopy (2DCOS)

Disintegrating agents are used in order to accelerate tablet dissolution, as the dissolution rate of an active ingredient is controlled by the disintegration rate of the tablet [23, 31]. Thus the disintegrating properties of tablets depend on the loaded amount and the efficiency of the agent. Starch and microcrystalline cellulose (MCC) are traditionally used as disintegrating agents, while carboxymethyl cellulose sodium (CMC) [46–48] and polyvinilpyrrolidone (crospovidone) [31, 49, 50] are widely employed as "superdisintegrating agents," as they confer a very high efficiency of disintegration. Both traditional and superdisintegrating agents swell up on contact with water. The swelling rate drives the disintegration rate of the tablet, and the swelling rate of superagents is much higher than that of traditional agents [46, 48, 49]. A high swelling rate with a low amount of water creates pores in the tablet to allow water penetration, which, in turn, induces rapid tablet disintegration.

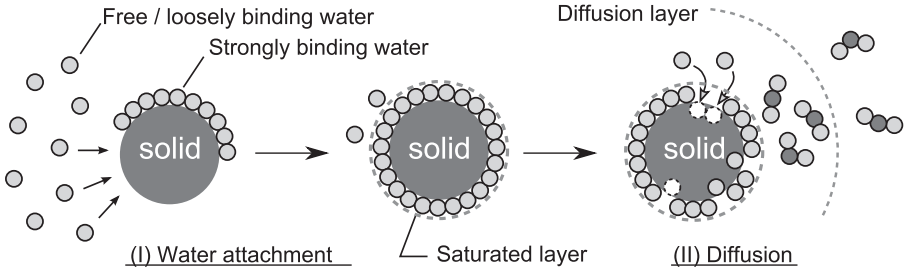


FIGURE 80.5 The dissolution model based on in situ NIR spectroscopy and decomposition. In the first stage, water molecules bind to the solid surface followed by a second stage of diffusion.

The characteristics of disintegrating agents have been macroscopically evaluated by water absorption rate [31, 32, 51] and disintegration force [12]. One team described the linear relationship between disintegration force and the amount of absorbed water [12]. CMC exhibited a high water absorption rate compared to other agents [48]. Microscopic interactions between disintegrating agents and water molecules have been investigated via sorption isotherms [52, 53]. One research group described a model of hydrogen bonding between cellulose and water using moisture sorption isotherms [52]. According to this model, water interacts with cellulose through three stages: (1) strong binding of water to cellulose with two binding sites per water molecule, (2) dissociation of some hydrogen bonds between water and cellulose, and (3) loose hydrogen bonding between water molecules. Both starch and MCC obey this three-stage swelling process upon contact with water.

Figure 80.6 shows the in situ reflectance NIR spectra of cellulose powder with vapor flowing and the differential spectra (i.e., difference between two consecutive spectra). The bands due to the combination between stretching and bending modes of water molecules increased. The differential spectra were decomposed into two species on the basis of strong versus loosely hydrogen-bonded water molecules, as shown in Fig. 80.7. The bands at lower and higher wavenumbers can be assigned to the strongly and loosely bonded water, respectively.

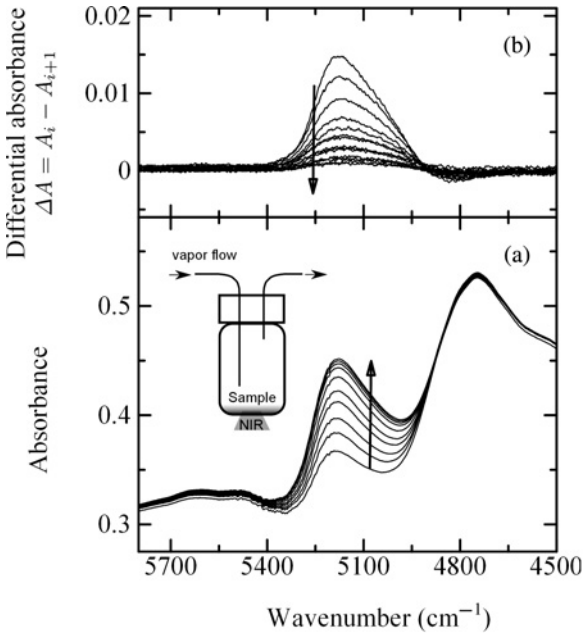


FIGURE 80.6 In situ diffuse reflectance NIR spectra (a) and differential spectra (b) of powder samples in the wavenumber range of O–H combination between stretching and bending modes. The spectra were collected by accumulation of 32 scans and collected at intervals of 60 s for 2 h with flowing vapor at 100 mL/min. Before measurement, the powders were dehydrated for 2 h under reduced pressure. The dehydrated sample (1.0 g) was placed into a glass sample cell, as shown in the figure.

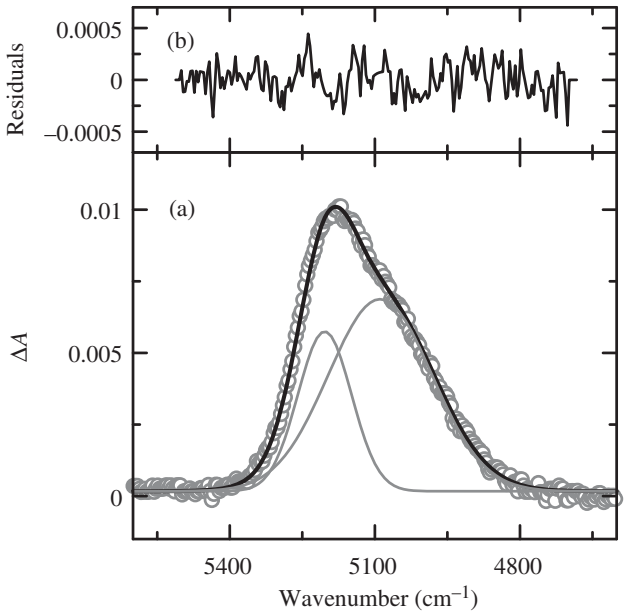


FIGURE 80.7 The decomposition of a differential NIR spectrum into two components of loosely (indicated in gray) and strongly binding water species by nonlinear least-squares method using Eq. (80.7) (a) and with residuals (b). The circles and solid lines indicate the experimental and calculated profiles, respectively. Gray lines indicate the decomposed spectra of each component. The decomposition was performed for all the collected spectra.

The peak area profiles of the two species calculated by the decomposition are shown in Fig. 80.8. The MCC and CMC powder samples denote a faster increment of strongly bonded water compared to that of loosely bonded water, while starch exhibited a reversed profile. In line with the water–cellulose interaction model [52], water molecules bind to cellulose with strong bonding first, followed by the dissociation of some hydrogen bonds. Thus, CMC and MCC feature similar water bonding kinetics.

Next, the wetting process of disintegrating agents was demonstrated by in situ measurements of NIR spectra using a transmittance attachment, as shown in Fig. 80.9. Approximately 20 mg of sample was loaded to the cell and water was added via a syringe pump at a rate of 2.3 μL/min.

Figure 80.10 shows synchronous 2DCOS maps of in situ NIR spectra of wetted powder of MCC, starch, and CMC. 2DCOS is an analytical method employed to visualize spectral changes as a correlation between spectral intensities at the spectral variables of ν_1 and ν_2 for N number of spectra [54, 55]. In the spectral data set of $y(\nu, p)$, ν and p are the wavenumber and the perturbation variable, respectively. The synchronous $\Phi(\nu_1, \nu_2)$ and asynchronous $\Psi(\nu_1, \nu_2)$ 2D correlation spectra between $y(\nu_1, p)$ and $y(\nu_2, p)$ are calculated

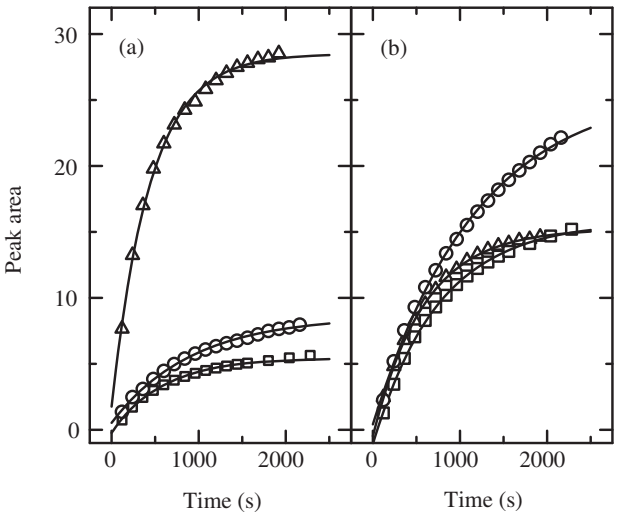


FIGURE 80.8 Profiles of decomposed peak area of loosely (a) and strongly (b) binding water species in starch (triangles), MCC (squares), and CMC (circles) as a function of flowing time. These profiles were fitted using $A = A_{max}(1 - e^{-kt}) + A_0$, where A is the peak area at time t and A_{max}, A_0, and k are the area of maximum, area at $t = 0$, and the rate constant, respectively. The rate constants obtained were 0.00226 s^{-1} (starch), 0.00170 s^{-1} (MCC), and 0.00109 s^{-1} (CMC) for loose component (a), and 0.00171 s^{-1} (starch), 0.00132 s^{-1} (MCC), and 0.000840 s^{-1} (CMC) for strong component (b).

from the mean-centered dynamic spectra $\tilde{y}(\nu, p)$ as detailed in the following equations:

$$\Phi(\nu_1, \nu_2) = \frac{1}{N-1} \sum_{j=1}^{N} \tilde{y}(\nu_1, p_j) \cdot \tilde{y}(y_2, p_j)$$
$$\Psi(\nu_1, \nu_2) = \frac{1}{N-1} \sum_{j=1}^{N} \tilde{y}(\nu_1, p_j) \cdot \sum_{k=1}^{N} M_{jk} \cdot \tilde{y}(\nu_2, p_k) \quad (80.8)$$

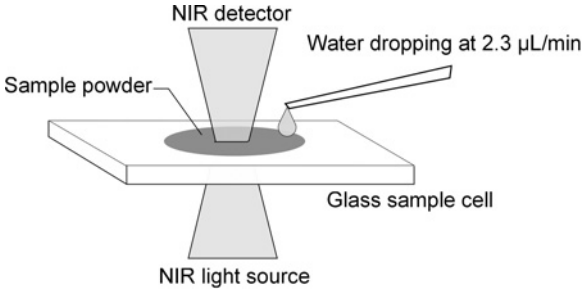


FIGURE 80.9 Transmittance attachment setup for in situ NIR measurements (MPA) of the powder wetting process. Approximately 20 mg of sample was loaded and water was dropped via a syringe pump at 2.3 μL/min. Spectra were repeatedly collected in the range from 10,000 to 5800 cm^{-1} with a spectral resolution of 8 cm^{-1}. The collection interval was 30 s, and spectra were accumulated with 16 scans.

where

$$\tilde{y}(\nu, p) = y(\nu, p) - \frac{1}{N} \sum_{j=1}^{N} y(\nu, p_j) \quad (80.9)$$

and M_{jk} is the element of the discrete Hilbert–Noda transformation matrix. The NIR spectrum of water indicates an overlap in the broad range with several water species of different hydrogen-bonding levels. 2DCOS allows a good visualization of spectral changes, without the effect of spectral overlap.

The autocorrelation spectra can be obtained, as the correlation intensity profiles are equal at ν_1 and ν_2. All synchronous maps indicated similar patterns, with a single autocorrelation peak at ~7200–6800 cm^{-1} due to the first overtone of O–H stretching mode of water. The autocorrelation peak indicates whether the corresponding band changes

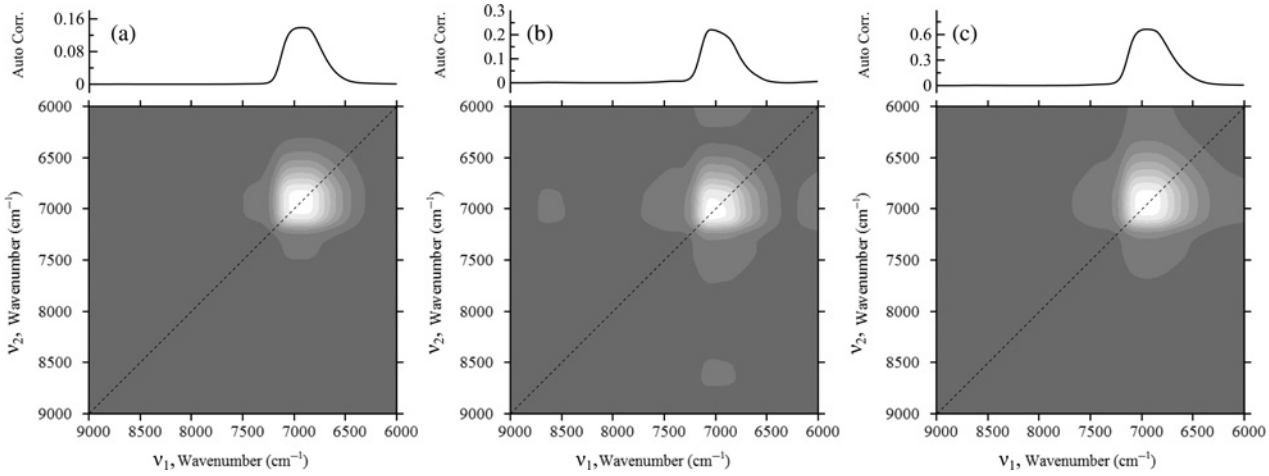


FIGURE 80.10 Synchronous 2DCOS maps of in situ transmittance NIR spectra of starch (a), MCC (b), and CMC (c) with wetting. Autocorrelation spectra correspond to the diagonal line on the 2D map.

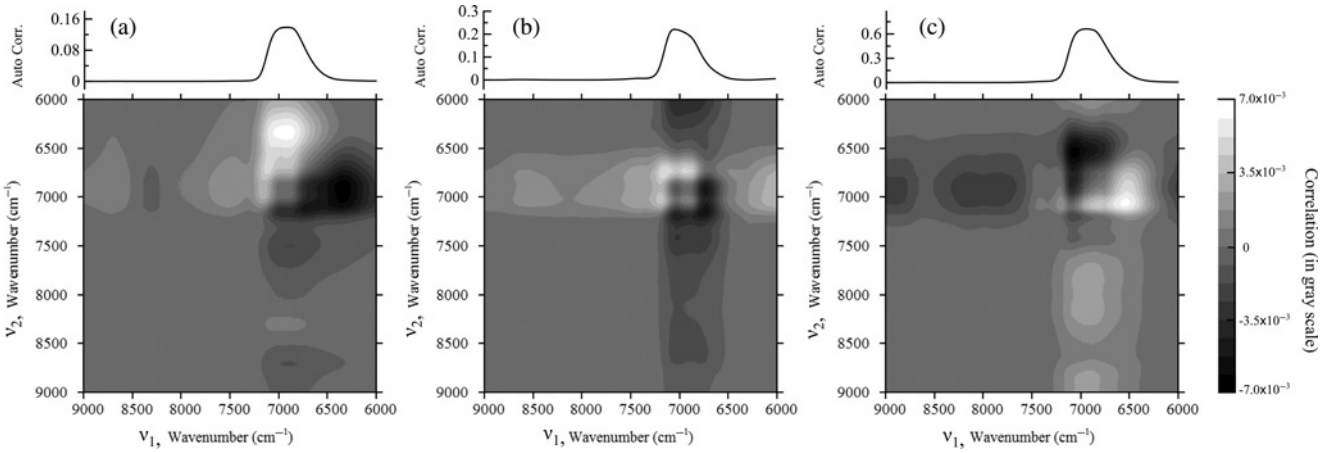


FIGURE 80.11 Asynchronous 2DCOS maps of in situ transmittance NIR spectra corresponding to the synchronous maps, shown in Fig. 80.10.

as a result of perturbation. When the band changes, there is a positive peak in the autocorrelation. In all samples, simply, the first overtone of O–H increased with the addition of water.

In the asynchronous 2DCOS maps shown in Fig. 80.11, several cross-correlation peaks were observed. In the MCC, triple peaks were found at (7021, 7193), (6743, 7153), (6721, 6924), which were due to the first overtone of O–H stretching mode of water in different hydrogen bonding forces. Starch denotes a broad peak at (6908, 6331), unlike MCC. Similarly, CMC denotes a band around (7066, 6541). The two peaks observed at 6331 and 6541 cm^{-1} are due to the first overtone of O–H stretching mode of the associating polymer with water or interpolymer. Thus, the addition of water induced changes in the interaction within the polymer; however, the interactions within MCC were affected by water to a lesser degree. The interpolymer association corresponds to gel formation.

The key information provided by asynchronous 2DCOS maps is the sequence of changes in band intensity. The positive and negative cross-correlation peaks indicate which peak at ν_1 or ν_2 changes prior to the other. The synchronous maps shown in Fig. 80.10a indicate positive cross-correlation in the range 7250–6500 cm^{-1} for both ν_1 and ν_2; thus, the positive cross-correlation in the asynchronous maps indicates that the peak at ν_2 changes prior to the peak at ν_1. Conversely, negative cross-correlation indicates that the peak at ν_1 changes prior to the peak at ν_2. In Fig. 80.11, cross-correlation peaks at around (7100–7000, 7000–6700) are positive for MCC and starch; however, those of CMC are negative. Thus, MCC and starch indicated that the band in the range of 7100–7000 cm^{-1} changes prior to the band in the 7000–6700 cm^{-1} range, and the map of CMC denotes an opposite sequence of events in the spectral changes. These spectral changes are due to water molecules of different hydrogen bonding components. The loosely bound water is assigned to the band at 7100–7000 cm^{-1} and the bands at lower wavenumber are due to strongly bound water. CMC displayed an increment in strongly bound water followed by an increment in loosely bound water. As shown in the asynchronous 2DCOS maps, starch and MCC both showed an increment in loosely bound water prior to that of strongly bound water.

The interaction process of starch and MCC with water molecules has been reported in a number of studies [40, 52, 53,56]. Given the results obtained in the in situ NIR measurements of MCC with vapor flowing and the 2DCOS analysis of MCC powder wetting process, it may be concluded that, initially, water strongly binds to the cellulose ensued by loose water penetration. In the case of CMC, water initially binds to the polymer in a manner similar to MCC; however, the number of bound water molecules is much larger than that of CMC. In the wetting process, an increase in strongly bound water to MCC occurs prior to an increase in loose water. The swelling process of CMC is reminiscent of the gel formation process. Starch exhibits a loose water increment in both the vapor flowing and the wetting processes. Hygroscopic starch contains a much larger amount of water molecules in the absence of strong hydrogen bonds. If starch binds strongly to water molecules, it may form a gel state similarly to CMC.

80.3 CONCLUSION

Current understanding of the interactions between water molecules and solids such as lactose, starch, cellulose, and carboxymethyl cellulose sodium, was reviewed in the context of NIR spectroscopic investigations. In pharmaceuticals, these materials are used not only to dilute a solid dosage but also to control the dissolution of an active ingredient, thus ensuring the mechanical strength of the tablet. The dissolution process has been well described using the Noyes–Whitney–Nernst dissolution model from a macroscopic perspective. One of the key aspects in this theory is the

assumption that a diffusion layer exists between the solid and the bulk solution. It is important to investigate the existence of a miscroscopic diffusion layer. In situ NIR measurements of the initial dissolution of lactose demonstrated a two-stage behavior. In a first stage, water molecules bind onto solid surface followed by diffusion of lactose in a subsequent stage. NIR spectroscopy and 2DCOS analyses revealed that starch, MCC, and CMC act as disintegrating agents according to different processes. The specific mode of interaction with water is strongly related to the swelling characteristics of the materials.

Finally, NIR spectroscopy provides quantitative and qualitative information at the molecular level. NIR spectroscopy is particularly useful for measuring water molecule interactions because of its high sensitivity to water. In this review, analytical techniques such as differential spectroscopy, decomposition, and 2DCOS were described to further elucidate the interaction between water with solids. NIR spectroscopy has been utilized in many fields such as agriculture, food science, medical science, and pharmaceuticals; however, its potential remains to be fully uncovered. We thus hope that a more advanced use of NIR spectroscopy occurs in both fundamental and applied research contexts.

REFERENCES

[1] Higuchi, T. (1963). Mechanism of sustained-action medication. Theoretical analysis of rate of release of solid drugs dispersed in solid matrices. *J. Pharm. Sci.* **52**, 1145–1149.

[2] Dokoumetzidis, A., Macheras, P. (2006). A century of dissolution research: From Noyes and Whitney to the biopharmaceutics classification system. *Int. J. Pharm.* **321**, 1–11.

[3] Amidon, G.L., Lennernas, H., Shah, V.P., Crison, J.R. (1995). A theoretical basis for a biopharmaceutic drug classification: The correlation of in vitro drug product dissolution and in vivo bioavailability. *Pharm. Res.* **12**, 413–420.

[4] Costa, P., Sousa, L.J.M. (2001). Modeling and comparison of dissolution profiles. *Eur. J. Pharm. Sci.* **13**, 123–133.

[5] Harland, R.S., Dubernet, C., Benoît, J.-P., Peppas, N.A. (1988). A model of dissolution-controlled, diffusional drug release from non-swellable polymeric microspheres. *J. Control. Release* **7**, 207–215.

[6] Higuchi, W.I. (1967). Diffusional models useful in biopharmaceutics. Drug release rate processes. *J. Pharm. Sci.* **56**, 315–324.

[7] Shefter, E., Higuchi, T. (1963). Dissolution behavior of crystalline solvated and nonsolvated forms of some pharmaceuticals. *J. Pharm. Sci.* **52**, 781–791.

[8] Dressman, J.B., Amidon, G.L., Reppas, C., Shah, V.P. (1998). Dissolution testing as a prognostic tool for oral drug absorption: Immediate release dosage forms. *Pharm. Res.* **15**, 11–22.

[9] Noyes, A.A., Whitney, W.R. (1897). The rate of solution of solid substances in their own solutions. *J. ACS* **19**, 930–934.

[10] Nernst, W. (1904), Theorie der Reaktionsgeschwindigkeit in heterogenen Systemen. *Z. Phys. Chem.* **47**, 52–55.

[11] Morrison, A.B., Campbell, J.A. (1965). Tablet disintegration and physiological availability of drugs. *J. Pharm. Sci.* **54**, 1–8.

[12] Catellani, P.L., Predella, P., Bellotti, A., Colombo, P. (1989). Tablet water uptake and disintegration force measurements. *Int. J. Pharm.* **51**, 63–66.

[13] Nelson, K.G., Wang, L.Y. (1978). Determination of time course of tablet disintegration II: Method using continuous functions. *J. Pharm. Sci.* **67**, 86–89.

[14] Schwartz, J.B., Simonelli, A.P., Higuchi, W.I. (1968). Drug release from wax matrices I. Analysis of data with first-order kinetics and with the diffusion-controlled model. *J. Pharm. Sci.* **57**, 274–277.

[15] Hixson, A.W., Crowell, J.H. (1931). Dependence of reaction velocity upon surface and agitation. *Industr. Eng. Chem.* **23**, 1160–1168.

[16] Papadopoulou, V., Kosmidis, K., Vlachou, M., Macheras, P. (2006). On the use of the Weibull function for the discernment of drug release mechanisms. *Int. J. Pharm.* **309**, 44–50.

[17] Itai, S., Kouchikawa, S., Nemoto, M., Murayama, H., Nagai, T. (1986). Effect of compression pressure and formulation on the available surface area of flufenamic acid in tablets. *Chem. Pharm. Bull.* **34**, 1264–1274.

[18] Dokoumetzidis, A., Papadopoulou, V., Macheras, P. (2006). Analysis of dissolution data using modified versions of Noyes–Whitney equation and the Weibull function. *Pharm. Res.* **23**, 256–261.

[19] Korsmeyer, R.W., Peppas, N.A. (1981). Effect of the morphology of hydrophilic polymeric matrices on the diffusion and release of water soluble drugs. *J. Membr. Sci.* **9**, 211–227.

[20] Kosmidis, K., Argyrakis, P., Macheras, P. (2003). A reappraisal of drug release laws using Monte Carlo simulations: The prevalence of the Weibull function. *Pharm. Res.* **20**, 988–995.

[21] Kosmidis, K., Argyrakis, P., Macheras, P. (2003). Fractal kinetics in drug release from finite fractal matrices. *J. Chem. Phys.* **119**, 6373–6377.

[22] Kouchikawa, S., Nemoto, M., Itai, S., Murayama, H., Nagai, T. (1985). Prediction of available surface area of powdered particles of flufenamic acid in tablets. *Chem. Pharm. Bull.* **33**, 1641–1651.

[23] Hattori, Y., Haruna, Y., Otsuka, M. (2013). Dissolution process analysis using model-free Noyes–Whitney integral equation. *Colloids Surf. B: Biointerfaces* **102**, 227–231.

[24] Dove, J.W., Buckton, G., Doherty, C. (1996). A comparison of two contact angle measurement methods and inverse gas chromatography to assess the surface energies of theophylline and caffeine. *Int. J. Pharm.* **138**, 199–206.

[25] Buckton, G., Choularton, A., Beezer, A.E., Chatham, S.M. (1988). The effect of the comminution technique on the surface energy of a powder. *Int. J. Pharm.* **47**, 121–128.

[26] Buckton, G., Bulpett, R., Verma, N. (1991). Surface analysis of pharmaceutical powders: X-ray photoelectron spectroscopy (XPS) related to powder wettability. *Int. J. Pharm.* **72**, 157–162.

[27] Pepin, X., Blanchon, S., Couarraze, G. (1997). A new approach for determination of powder wettability. *Int. J. Pharm.* **152**, 1–5.

[28] Lippold, B.C., Ohm, A. (1986). Correlation between wettability and dissolution rate of pharmaceutical powders. *Int. J. Pharm.* **28**, 67–74.

[29] Kiesvaara, J., Yliruusi, J. (1993). The use of the Washburn method in determining the contact angles of lactose powder. *Int. J. Pharm.* **92**, 81–88.

[30] Muller, E.A., Rull, L.F., Vega, L.F., Gubbins, K.E. (1996). Adsorption of water on activated carbons: A molecular simulation study. *J. Phys. Chem.* **100**, 1189–1196.

[31] Kornblum, S.S., Stoopak, S.B. (1973). A new tablet disintegrating agent: Cross-linked polyvinylpyrrolidone. *J. Pharm. Sci.* **62**, 43–49.

[32] Zografi, G., Kontny, M.J., Yang, A.Y.S., Brenner, G.S. (1984). Surface area and water vapor sorption of macrocrystalline cellulose. *Int. J. Pharm.* **18**, 99–116.

[33] Zografi, G., Kontny, M.J. (1986). The interactions of water with cellulose- and starch-derived pharmaceutical excipients. *Pharm. Res.* **3**, 187–194.

[34] Dabrowski, A. (2001). Adsorption–from theory to practice. *Adv. Colloid Interface Sci.* **93**, 135–224.

[35] Amado, A.M., Nolasco, M.M., Ribeiro-Claro, P.J.A. (2007). Probing pseudopolymorphic transitions in pharmaceutical solids using Raman spectroscopy: Hydration and dehydration of theophylline. *J. Pharm. Sci.* **96**, 1366–1379.

[36] Balbuena, P.B., Blocker, W., Dudek, R.M., Cabrales-Navarro, F.A., Hirunsit, P. (2008). Vibrational spectra of anhydrous and monohydrated caffeine and theophylline molecules and crystals. *J. Phys. Chem. A* **112**, 10210–10219.

[37] Starbuck, C., Spartalis, A., Wai, L., Wang, J., Fernandez, P., Lindemann, C.M., Zhou, G.X., Ge, Z. (2002). Process optimization of a complex pharmaceutical polymorphic system via in situ Raman spectroscopy. *Cryst. Growth Design* **2**, 515–522.

[38] Belton, P.S., Gil, A.M. (1994). IR and Raman spectroscopic studies of the interaction of trehalose with hen egg white lysozyme. *Biopolymers* **34**, 957–961.

[39] Lie, G.C., Clementi, E. (1986). Molecular-dynamics simulation of liquid water with an ab initio flexible water-water interaction potential. *Phys. Rev. A* **33**, 2679–2693.

[40] Delwiche, S.R., Pitt, R.E., Norris, K.H. (1991). Examination of starch-water and cellulose-water interactions with near infrared (NIR) diffuse reflectance spectroscopy. *Starch - Stärke* **43**, 415–422.

[41] Giangiacomo, R. (2006). Study of water–sugar interactions at increasing sugar concentration by NIR spectroscopy. *Food Chem.* **96**, 371–379.

[42] Fisher, H.F., McCabee, W.C., Subramanian, S. (1970). Near-infrared spectroscopic investigation of the effect of temperature on the structure of water. *J. Phys. Chem.* **74**, 4360–4369.

[43] Hattori, Y., Otsuka, M. (2011). NIR spectroscopic study of the dissolution process in pharmaceutical tablets. *Vibrat. Spectrosc.* **57**, 275–281.

[44] Hattori, Y., Otsuka, M. (2012). Time-resolved near-infrared spectroscopic study of the dissolution of crystalline lactose. *Eur. J. Pharm. Sci.* **47**, 884–889.

[45] Choppin, G.R. (1972) Near-infrared studies of the structure of water. III. Mixed solvent systems. *J. Chem. Phys.* **56**, 5890

[46] Shah, N.H., Lazarus, J.H., Sheth, P.R., Jarowski, C.I. (1981). Carboxymethylcellulose: Effect of degree of polymerization and substitution on tablet disintegration and dissolution. *J. Pharm. Sci.* **70**, 611–613.

[47] Bi, Y.X., Sunada, H., Yonezawa, Y., Danjo, K. (1999). Evaluation of rapidly disintegrating tablets prepared by a direct compression method. *Drug Devel. Industr. Pharm.* **25**, 571–581.

[48] Fukami, J., Yonemochi, E., Yoshihashi, Y., Terada, K. (2006). Evaluation of rapidly disintegrating tablets containing glycine and carboxymethylcellulose. *Int. J. Pharm.* **310**, 101–109.

[49] Carli, F., Colombo, I., Magarotto, L., Motta, A., Torricelli, C. (1986). Influence of polymer characteristics on drug loading into crospovidone. *Int. J. Pharm.* **33**, 115–124.

[50] Bolhuis, G., Zuurman, K., te Wierik, G.H. (1997). Improvement of dissolution of poorly soluble drugs by solid deposition on a super disintegrant. II. The choice of super disintegrants and effect of granulation. *Eur. J. Pharm. Sci.* **5**, 63–69.

[51] Assaf, A.G., Haas, R.H., Purves, C.B. (1944). A new interpretation of the cellulose-water adsorption isotherm and data concerning the effect of swelling and drying on the colloidal surface of cellulose. *J. ACS* **66**, 66–73.

[52] Khan, F., Pilpel, N. (1987). An investigation of moisture sorption in microcrystalline cellulose using sorption isotherms and dielectric response. *Powder Technol.* **50**, 237–241.

[53] Blair, T.C., Buckton, G., Beezer, A.E., Bloomfield, S.F. (1990). The interaction of various types of microcrystalline cellulose and starch with water. *Int. J. Pharm.* **63**, 251–257.

[54] Noda, I. (1993). Generalized two-dimensional correlation method applicable to infrared, Raman, and other types of spectroscopy. *Appl. Spectrosc.* **47**, 1329–1336.

[55] Ozaki, Y., Liu, Y., Noda, I. (1997). Two-dimensional infrared and near-infrared correlation spectroscopy: Applications to studies of temperature-dependent spectral variations of self-associated molecules. *Appl. Spectrosc.* **51**, 526–535.

[56] Zhou, S., Tashiro, K., Hongo, T., Shirataki, H., Yamane, C., Ii, T. (2001). Influence of water on structure and mechanical properties of regenerated cellulose studied by an organized combination of infrared spectra, X-ray diffraction, and dynamic viscoelastic data measured as functions of temperature and humidity. *Macromolecules* **34**, 1274–1280.

81

COLLOID STABILITY OF BIOCOLLOIDAL DISPERSIONS

Tharwat Tadros
89 Nash Grove Lane, Wokingham, Berkshire RG40 4HE, United Kingdom

81.1 INTRODUCTION

Colloid and interface science plays a major role in most biocolloidal dispersions [1]. For example, all biocolloidal dispersions such as nanoemulsions, nanosuspensions, and liposomes require application of colloid and interface science phenomena. Section 81.2 deals with the colloid stability of these dispersions by considering the balance between repulsive and attractive forces. Both electrostatic (produced by the presence of electrical double layers) and steric (produced by adsorbed surfactant and polymer layers) forces will be considered. Combination of repulsive and attractive forces results in a quantitative description of colloid stability/instability of biological dispersions. Application of these principles for nanoemulsions such as those used for drug delivery will be considered. This is followed by application to nanobiodegradable dispersions that are used for targeted delivery of drugs. A third example where the colloid and interface principles are applied is in the field of liposomes and vesicles that are used for solubilization of lipophilic and hydrophilic drugs. Stabilization of liposomes by using block and graft copolymers is also described.

81.2 KINETIC STABILITY OF BIOCOLLOIDAL DISPERSION SYSTEMS AND GENERAL STABILIZATION MECHANISMS

Disperse systems lack thermodynamic stability and tend to reduce their surface energy by aggregation and/or coalescence of the particles or droplets. The main driving force for the aggregation process is the universal van der Waals attraction, which will be discussed in subsequent sections. To overcome the aggregation and/or coalescence processes, one must overcome the van der Waals attraction by some repulsive mechanism, and this will give the system kinetic stability with an adequate shelf life. Normally one requires a shelf life of 2–3 years under various storage conditions (e.g., temperature variation). Several stabilization mechanisms are encountered with disperse systems, and these are summarized below.

81.2.1 Electrostatic Stabilization

In this case a repulsive energy is produced by formation of electrical double layers, for example, by adsorption of ionic surfactants. This repulsive energy increases with increase in the surface (or zeta-) potential and decrease of electrolyte concentration. The repulsive energy counteracts the van der Waals attraction at intermediate distance of separation, thus producing an energy barrier that prevents flocculation of the dispersion. A summary of the van der Waals attraction and electrostatic repulsion as well as their combination is given below.

81.2.1.1 Van der Waals Attraction. For two particles or droplets with equal radius R, and surface-to-surface separation h, the van der Waals attractive energy G_A (when $h \ll R$) is given by [2]

$$G_A = -\frac{AR}{12h} \tag{81.1}$$

Encyclopedia of Biocolloid and Biointerface Science, Volume 2, First Edition. Edited by Hiroyuki Ohshima.
© 2016 John Wiley & Sons, Inc. Published 2016 by John Wiley & Sons, Inc.

where A is the effective Hamaker constant, which is given by

$$A = \left(A_{11}^{1/2} - A_{22}^{1/2}\right)^2 \tag{81.2}$$

where A_{11} is the Hamaker constant of the particles or droplets and A_{22} is the Hamaker constant of the medium. The Hamaker constant of any material depends on the number of atoms per unit volume q and the London dispersion constant β:

$$A = \pi^2 q^2 \beta \tag{81.3}$$

It can be seen that G_A increases very sharply with decrease in h when the latter reaches small values. In the absence of any repulsion between the particles or droplets, the latter will aggregate (flocculate) by simple diffusion through the medium. This leads to rapid flocculation kinetics. The rate constant for the process k_0 has been calculated by Smolulokowski [3] as

$$k_0 = \frac{4kT}{3\eta} = 5.5 \times 10^{-18}\ \mathrm{m^3 s^{-1}} \tag{81.4}$$

where k is the Boltzmann constant, T is the absolute temperature, and η is the viscosity of the medium.

81.2.1.2 Double-Layer Repulsion. An electrical double layer can be created at the solid–liquid or liquid–liquid interface by charge separation due to the presence of ionogenic groups (e.g., –OH, –COOH) or by adsorption of ionic surfactants at the interface. The double layer is characterized by the following parameters [4]: (surface charge σ_0) – (charge in Stern layer σ_s) – (carge of diffusion layer σ_d). Note that $\sigma_0 = \sigma_s + \sigma_d$ – (surface potential ψ_0) – (Stern potential ψ_d) ($\sim$ zeta-potential). The double-layer extension is determined by the electrolyte concentration, and the valence of the counterions is given by the reciprocal of the Debye–Hückel parameter ($1/\kappa$), referred to as the *thickness of the double layer*

$$\left(\frac{1}{\kappa}\right) = \left(\frac{\varepsilon_r \varepsilon_0 kT}{2n_0 Z_i^2 e^2}\right) \tag{81.5}$$

where ε_r is the permittivity (dielectric constant) of the medium, ε_0 is the permittivity of free space, k is the Boltzmann constant, T is the absolute temperature, n_0 is the number of ions per unit volume of each type present in bulk solution, Z_i is the valence of the ions, and e is the electronic charge. The double-layer thickness increases with decrease in electrolyte concentration: 10^{-5} mol dm^{-3} NaCl ($1/\kappa$) = 100 nm, 10^{-3} mol dm^{-3} NaCl ($1/\kappa$) = 10 nm.

When two particles or droplets with double layers of the same sign approach at a distance of separation h that is smaller than twice the double-layer thickness, double-layer repulsion occurs, since the two double layers cannot be fully extended in the confined space. This leads to repulsion energy G_{el} that is given by the following expression [5]:

$$G_{el} = \frac{[4\pi\varepsilon_r\varepsilon_0 R^2 \psi_0^2 \exp(-\kappa h)]}{[2R + h]} \tag{81.6}$$

This expression shows that G_{el} decreases exponentially with increase in h, and the rate of this decrease depends on electrolyte concentration.

81.2.1.3 Total Energy of Interaction. Combination of G_A with G_{el} at various values of h results in the total energy G_T–distance curve illustrated in Fig. 81.1. This presentation forms the basis of the theory of colloid stability due to Deryaguin–Landau–Verwey–Overbeek (DLVO) theory [5, 6]. The G_T/h curve shows two minima and one maximum: a shallow minimum (of the order of few kT) units at large distances of separation. This may result in weak and reversible flocculation. A deep primary minimum (several 100 kT units) at short distances of separation. This results in strong flocculation (coagulation). An energy maximum G_{max} at intermediate distances prevents flocculation into the primary minimum.

To ensure adequate colloid stability, G_{max} has to be greater than 25 kT. The height of the maximum depends on the surface (or zeta-) potential, electrolyte concentration, particle radius, and Hamaker constant. When the zeta-potential is higher than 40 mV and the electrolyte concentration is $<10^{-2}$ mol dm^{-3} for 1:1 electrolyte, $G_{max} > 25\ kT$.

In the presence of an energy barrier one can define a slow rate of flocculation k [7], which is related to the fast flocculation rate k_0 by the stability ratio W as

$$W = \frac{k_0}{k} \tag{81.7}$$

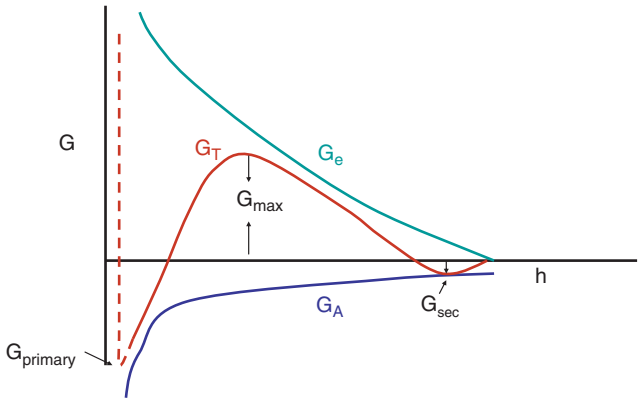


FIGURE 81.1 Energy–distance curves according to the DLVO theory [5, 6].

where W is related to the energy maximum G_{max} by [8]

$$W = \frac{1}{2}k \exp\left(\frac{G_{max}}{kT}\right) \tag{81.8}$$

For maintenance of colloid stability over a long period of time (i.e., 2–3 years), one needs to ensure the following conditions: (1) high ζ-potential by ensuring adequate coverage of the particles or droplets by ionic surfactant, (2) low electrolyte concentration, and (3) low valence of the electrolyte (multivalent ions should be avoided)

81.2.2 Steric Stabilization

Many polymers are used for the preparation of disperse systems (suspensions and emulsions) in pharmaceutical formulations. An example of such systems is the A-B-A block copolymer of poly(ethylene oxide)—poly(propylene oxide)—poly(ethylene oxide) (PEO-PPO-PEO), commercially available as poloxamers and pluronics (BASF). On hydrophobic drug particles or oil droplets, the polymer adsorbs with the B hydrophobic chain (PPO) close to the surface, leaving the two hydrophilic A chains dangling in solution. These nonionic polymers provide stabilization against flocculation and/or coalescence by a mechanism, usually referred to as *steric stabilization* [9]. In order to understand the principles of steric stabilization, one must first consider the adsorption and conformation of the polymer at the solid–liquid or liquid–liquid interface. The PPO chain adsorbs on the surface with many attachment points forming small "loops," whereas the A chains (sometimes referred to as "tails" extend to some distance (a few nanometers) from the surface [10].

The adsorption of polymers at interfaces differ significantly from that of simple surfactant molecules. The adsorption isotherm is of the high-affinity type; that is, the first added molecules are almost completely adsorbed and the plateau adsorption is reached at low equilibrium concentration. Adsorption is practically irreversible, because the molecule is attached by several segments to the surface.

The adsorption isotherm depends on the structure, molecular weight, and environment (temperature, electrolyte) for the chains. To fully characterize polymer adsorption, one needs to obtain information on the following parameters: (1) the amount of adsorption Γ; (2) the fraction of segments in "trains" and the adsorption energy per segment; and (3) extension of the A chains in bulk solution, usually described as *segment density distribution* $\rho(z)$, or *hydrodynamic thickness* δ_h. It is essential to know how these parameters vary with system parameters such as proportion of hydrophobic to hydrophilic chains, molecular weight, flexibility, temperature, and addition of electrolyte.

The most important parameters for steric stabilization are the strong "anchoring" of the B chain to the surface and the extension of the A chains (adsorbed layer thickness δ_h) and its solvation by the molecules of the medium.

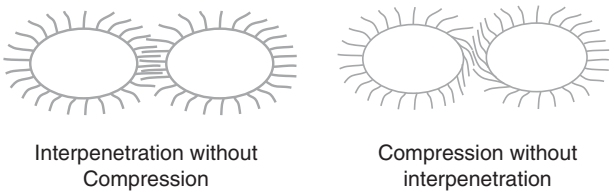


FIGURE 81.2 Schematic representation of interaction between adsorbed layers.

When two particles or droplets each with a radius R and containing an adsorbed surfactant or polymer layer with a hydrodynamic thickness δ_h, approach each other at a surface–surface separation distance of separation h that is smaller than $2\delta_h$, the surfactant or polymer layers interact with each other, resulting in one or both of two main scenarios: (1) the polymer chains may overlap with each other, or (2) the polymer layers may undergo compression. In either case, there will be an increase in the local segment density of the chains in the interaction region. This is schematically illustrated in Fig. 81.2.

The real situation is perhaps in between the two abovementioned cases; specifically, the polymer chains may undergo some interpenetration and some compression. Provided the dangling chains (A chains) are in good solvent (i.e., strongly solvated by the solvent molecules), this local increase in segment density will result in strong repulsion as a results of two main effects.

Two main repulsive energies can be defined: (1) osmotic repulsion arising from the (tnfavourable mixing of the stabilising A chains when these are in good solvent conditions (this is referred to as *mixing interaction* G_{mix}) and (2) entropic, volume restriction or elastic interaction resulting from the loss of configurational entropy of the chains on considerable overlap (this is referred to as *elastic interaction* G_{el}).

As a result of the unfavorable mixing of the chains, when these are in good solvent, an increase in the osmotic pressure in the interaction zone occurs, and G_{mix} is given by the following expression [9] as

$$\frac{G_{mix}}{kT} = \left(\frac{2V_2^2}{V_1}\right)\nu^2\left(\frac{1}{2} - \chi\right)\left(\delta - \frac{h}{2}\right)\left(3R + 2\delta + \frac{h}{2}\right) \tag{81.9}$$

where k is the Boltzmann constant, T is the absolute temperature, V_2 is the molar volume of polymer, V_1 is the molar volume of solvent, ν_2 is the number of polymer chains per unit area, and χ is the Flory–Huggins interaction parameter.

The sign of G_{mix} depends on the value of the Flory–Huggins interaction parameter. When the chains are under favorable solvent conditions (strongly solvated by the

molecules of the medium), $\chi < {}^1/_2$ and G_{mix} is positive; that is, the mixing interaction free energy is positive, and this leads to strong repulsion as soon as $h < 2\delta$. Clearly, to maintain stability of a suspension or emulsion, one must ensure that χ is less than ${}^1/_2$ under all conditions of storage (temperature variation, addition of electrolyte, etc.).

The coefficient G_{el} may be given by the following simple expression (assuming the chains to be represented by simple rods that rotate in a circle with a radius δ)

$$\frac{G_{el}}{kT} = 2kTv^2 \ln\left[\frac{\Omega(h)}{\Omega(\infty)}\right] \tag{81.10}$$

where $\Omega(h)$ is the number of chain configuration after overlap ($h < \delta$), and $\Omega(\infty)$ is the number of chain configurations before overlap ($h > 2\delta$).

The elastic interaction G_{el} is always positive and could play a major role in steric stabilization. The steric free energy of interaction G_s is given by the sum of G_{mix} and G_{el}, and when this is added to the van der Waals attraction, we obtain the total interaction energy G_T:

$$G_T = G_s + G_A = G_{mix} + G_{el} + G_A \tag{81.11}$$

A schematic representation of the variation of G_{mix}, G_{el}, G_A, and G_T with h is given in Fig. 81.3.

The mixing interaction G_{mix} increases very sharply with decrease of h when $h < 2\delta$. G_{el} increases very sharply with decrease of h when $h < \delta$. G_T versus h shows a minimum, G_{min}, at separation distances comparable to 2δ; G_T shows a rapid increase with further decrease in h [9]. Unlike the G_T/h curve predicted by the DLVO theory (which shows two minima and one energy maximum), the G_T/h curve for systems that are sterically stabilized dispersions shows only one minimum G_{min}, followed by a sharp increase in G_T when $h < 2\delta$. The depth of the minimum depends on the Hamaker constant A, particle radius R, and adsorbed layer thickness. At a given A and R, G_{min} increases with decrease of δ. When δ is small (say, <5 nm), G_{min} may reach sufficient depth (a few kT units) for weak flocculation to occur. However, this flocculation is reversible, and by gentle shaking of the container, the suspension or emulsion can be easily redispersed.

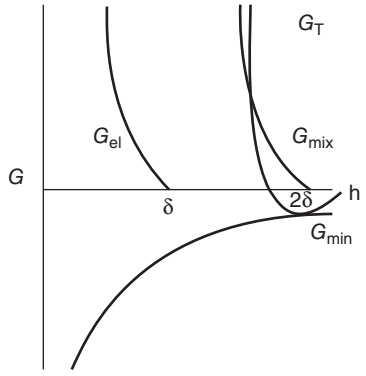


FIGURE 81.3 Variation of G_{mix}, G_{el}, G_A, and G_T with surface–surface distance between the particles.

When δ is sufficiently large (e.g., > 10 nm), G_{min} may become so small that no flocculation will occur. In this case the suspension or emulsion approach thermodynamic stability and no aggregation occurs over very long periods (>2 years). Clearly the particle radius also plays a major role. The larger the particles, the deeper G_{min} becomes (at a given δ value).

Several criteria for effective steric stabilization can be defined:

1. The particles or droplets should be completely covered by the surfactant or polymer (the amount should correspond to the plateau value). Any bare patches may cause flocculation either by van der Waals attraction (between the bare patches) or by bridging flocculation (where a polymer molecule will become simultaneously adsorbed on two or more particles or droplets).
2. The polymer should be strongly anchored to the particles or droplets surface, to prevent any displacement during particle approach. This is particularly important for concentrated suspensions or emulsions. With an A-B-A block copolymer, the B chain is chosen to be highly insoluble in the medium and has a strong affinity to the surface.
3. The stabilizing chain(s) A should be highly soluble in the medium and strongly solvated by its molecules. In other words, the Flory–Huggins interaction parameter for the A chains should always be less than ${}^1/_2$. The most commonly used A chains are those based on PEO (e.g., with poloxamers).
4. The adsorbed layer thickness δ should be sufficiently large (> 5–10 nm) to prevent weak flocculation. This is particularly the case with concentrated suspensions and emulsions, since such flocculation may cause increase in the viscosity of the system and makes it difficult to redisperse on shaking.

81.3 NANOEMULSIONS

Nanoemulsions are transparent or translucent systems mostly covering the size range 20–200 nm [11, 12]. Nanoemulsions are also referred to as *miniemulsions* [13–15]. Unlike microemulsions (which are also transparent or translucent and thermodynamically stable), nanoemulsions are only kinetically stable. However, the long-term physical stability of nanoemulsions (with no apparent flocculation or coalescence) make them unique, and they are sometimes referred to as *approaching thermodynamic stability*.

The inherently high colloid stability of nanoemulsions can be well understood from a consideration of their steric stabilisation (when using nonionic surfactants and/or polymers) and how this is affected by the ratio of the adsorbed layer thickness to droplet radius, as will be discussed below.

Unless adequately prepared (to control the droplet size distribution) and stabilized against Ostwald ripening (which occurs when the oil has some finite solubility in the continuous medium), nanoemulsions may lose their transparency with time as a result of increase in droplet size.

The attraction of nano-emulsions for application in drug delivery is due to the following advantages:

1. The very small droplet size causes a large reduction in the gravity force, and the Brownian motion may be sufficient for overcoming gravity. This means that no creaming or sedimentation occurs on storage.
2. The small droplet size also prevents any flocculation of the droplets. Weak flocculation is prevented, and this enables the system to remain dispersed with no separation.
3. The small droplets also prevent their coalescence, since these droplets are nondeformable and hence surface fluctuations are prevented. In addition, the significant surfactant film thickness (relative to droplet radius) prevents any thinning or disruption of the liquid film between the droplets.
4. The transparent nature of the system, their fluidity (at reasonable oil concentrations) as well as the absence of any thickeners, give them an advantage in application, in particular for intravenous injection.
5. Nanoemulsions can be applied for delivery of lipophilic drugs.
6. Nanoemulsions may be applied as a substitute for liposomes and vesicles (which are much less stable).

81.3.1 Preparation of Nanoemulsions

Two methods may be applied for the preparation of nanoemulsions (covering the droplet radius size range 20–200 nm): (1) use of high-pressure homogenizers (aided by appropriate choice of surfactants and cosurfactants) or (2) application of the phase inversion temperature (PIT) concept. The production of small droplets (<1 μm) requires application of high energy; the process of emulsification is generally inefficient. Simple calculations show that the mechanical energy required for emulsification exceeds the interfacial energy by several orders of magnitude. For example, to produce an emulsion at a volume fraction $\phi = 0.1$ with a Sauter diameter $d_{32} = 0.6$ μm, using a surfactant that gives an interfacial tension $\gamma = 10$ mN m^{-1}, the net increase in surface free energy is $A\gamma = 6\phi\gamma/d_{32} = 10^4$ J m^{-3}. The mechanical energy required in a homogenizer is 10^7 J m^{-3}, that is, an efficiency of 0.1%. The remainder of the energy (99.9%) is dissipated as heat.

The intensity of the process or the effectiveness in making small droplets is often governed by the net power density $[\varepsilon(t)]$ as

$$p = \varepsilon(t)dt \tag{81.12}$$

where t is the time during which emulsification occurs.

Breakup of droplets will only occur at high ε values, which means that the energy dissipated at low ε levels is wasted. Batch processes are generally less efficient than continuous processes. This shows why, with a stirrer in a large vessel, most of the energy applied at low intensity is dissipated as heat. In a homogenizer, p is simply equal to the homogenizer pressure.

Several procedures may be applied to enhance the efficiency of emulsification when producing nanoemulsions; for instance, one should optimize the efficiency of agitation by increasing ε and decreasing dissipation time. The emulsion is preferably prepared at high volume fraction of the disperse phase and diluted afterward. However, very high ϕ values may result in coalescence during emulsification. The addition of more surfactant may result in a smaller γ_{eff} and possibly diminishing recoalescence. It may be desirable to use a surfactant mixture that shows more reduction in the individual components. If possible, dissolve the surfactant in the disperse phase rather than the continuous phase; this often leads to smaller droplets. It may be useful to emulsify in steps of increasing intensity, particularly with emulsions having highly viscous disperse phase.

The phase inversion principle for preparation of nanoemulsions is based on the concepts introduced by Shinoda and coworkers [16–18], who showed that by increasing the temperature of an oil-in-water (o/w) emulsion prepared using a nonionic surfactant of poly(ethylene oxide) type, inversion to a w/o emulsion occurs at a critical temperature that is defined as the phase inversion temperature (PIT). At the PIT the interfacial tension reaches a minimum and very small droplets are produced. By rapid cooling the system near the PIT nanoemulsion droplets are produced.

81.3.2 Steric Stabilisation and Role of Adsorbed Layer Thickness

Since most nanoemulsions are prepared using nonionic and/or polymeric surfactants, it is necessary to consider the interaction forces between droplets containing adsorbed layers (steric stabilization). This was described earlier, and only a summary is given here. When two droplets, each containing an adsorbed layer of thickness δ, approach at a distance of separation h, whereby h becomes less than 2δ, repulsion occurs as a result of two main effects: (1) unfavorable mixing of the stabilizing chains A of the adsorbed layers,

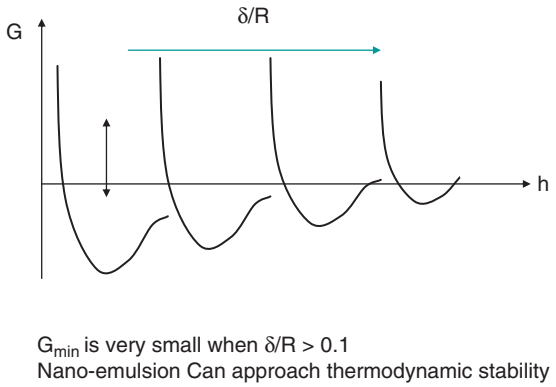


FIGURE 81.4 Importance of adsorbed layer thickness to particle size ratio (δ/R).

when these are in good solvent conditions—referred to as the *mixing* [osmotic interaction G_{mix}, given by Eq. (81.9)] and (2) reduction in configurational entropy of the chains on significant overlap—referred to as *elastic* (entropic) *interaction*, given by Eq. (81.10). Combination of G_{mix} and G_{el} with the van der Waals attraction G_A gives the total energy of interaction G_T, as given by Eq. (81.11)

Figure 81.3 gave a schematic representation of the variation of G_{mix}, G_{el}, G_A, and G_T with h. As can be seen form Fig. 81.3, G_{mix} increases very rapidly with decrease of h as soon as $h < 2\delta$, G_{el} increase very rapidly with decrease of h when $h < \delta$. G_T shows one minimum, G_{min}, and it increases very rapidly with decrease of h when $h < 2\delta$. The magnitude of G_{min} depends on the following parameters: (1) the particle radius R, (2) the Hamaker constant A, and (3) the adsorbed layer thickness δ. Figure 81.4 shows the variation of G_T with h at various ratios of δ/R. It can be seen from the figure that the depth of the minimum decreases with increasing δ/R. This is the basis of the high kinetic stability of nanoemulsions. With nanoemulsions having a radius in the region of 50 nm and an adsorbed layer thickness of, say, 10 nm, the value of δ/R is 0.2. This high value (when compared with situations in macroemulsions where δ/R is at least an order of magnitude lower) results in a very shallow minimum (which could be less than kT). This situation results in very high stability with no flocculation (weak or strong). In addition, the very small size of the droplets and the dense adsorbed layers ensures lack of deformation of the interface, lack of thinning, and disruption of the liquid film between the droplets, and hence coalescence is also prevented. The only instability problem with nanoemulsions is Ostwald ripening, which is discussed below.

81.3.3 Ostwald Ripening

One of the main problems with nanoemulsions is *Ostwald ripening*, which results from the difference in solubility between small and large droplets. The difference in chemical potential of dispersed phase droplets between different sized droplets as given by Lord Kelvin [19]

$$c(r) = c(\infty) \exp\left(\frac{2\gamma V_m}{rRT}\right) \tag{81.13}$$

where $c(r)$ is the solubility surrounding a particle of radius r, $c(\infty)$ is the bulk phase solubility and V_m is the molar volume of the dispersed phase.

The quantity ($2\gamma V_m$/RT) is termed the characteristic length. It has an order of ~1 nm or less, indicating that the difference in solubility of a 1-μm droplet is of the order of ≤0.1%. Theoretically, Ostwald ripening should lead to condensation of all droplets into a single drop (i.e. phase separation). This does not occur in practice since the rate of growth decreases with increase of droplet size.

For two droplets of radii r_1 and r_2 (where $r_1 < r_2$), we obtain

$$\left(\frac{RT}{V_m}\right) \ln\left[\frac{c(r_1)}{c(r_2)}\right] = 2\gamma\left(\frac{1}{r_1} - \frac{1}{r_2}\right) \tag{81.14}$$

This equation shows that the larger the difference between r_1 and r_2, the higher the rate of Ostwald ripening.

Ostwald ripening can be quantitatively assessed from plots of the cube of the radius versus time; this is known as the *Lifshitz–Slesov–Wagner* (LSW) *theory* [20, 21]

$$r^3 = \frac{8}{9}\left[\frac{c(\infty)\gamma V_m D}{\rho RT}\right] t \tag{81.15}$$

where D is the diffusion coefficient of the disperse phase in the continuous phase and ρ is the density of the disperse phase.

Several methods may be applied to reduce Ostwald ripening [22–25]:

1. Addition of a second disperse phase component that is insoluble in the continuous phase (e.g., squalane). In this case significant partitioning between different droplets occurs, with the component having low solubility in the continuous phase expected to be concentrated in the smaller droplets. During Ostwald ripening in two component disperse phase system, equilibrium is established when the difference in chemical potential between different size droplets (which results from curvature effects) is balanced by the difference in chemical potential resulting from partioning of the two components. If the secondary component has zero solubility in the continuous phase, the size distribution will not deviate from the initial one (the growth rate is equal to zero). In the case of limited solubility of the secondary component, the distribution is the same as governed by Eq. (81.15); that is, a mixture growth rate is obtained that is still lower than that of the more soluble

component. This method is of limited application since one requires a highly insoluble oil as the second phase which is miscible with the primary phase.

2. Modification of the Interfacial film at the o/w interface. According to Eq. (81.15), reduction in γ results in reduction of Ostwald ripening. However, this alone is not sufficient since one has to reduce γ by several orders of magnitude. One author [25] suggested that by using surfactants that are strongly adsorbed at the o/w interface (i.e. polymeric surfactants) and that do not desorb during ripening, the rate could be significantly reduced. An increase in the surface dilational modulus and decrease in γ would be observed for the shrinking drops. The difference in γ between the droplets would balance the difference in capillary pressure (i.e., curvature effects).

To achieve this effect it is useful to use A-B-A block copolymers that are soluble in the oil phase and insoluble in the continuous phase. The polymeric surfactant should enhance the lowering of γ by the emulsifier. In other words, the emulsifier and the polymeric surfactant should show synergy in lowering γ.

81.4 NANOBIODEGRADABLE DISPERSIONS

Nanobiodegradable dispersions offer a potentially attractive method for targeted delivery of drugs to its pharmacologically site of action in a controlled manner [26–32]: (1) protection of the drug against metabolism or recognition by the immune system; (2) reduction of toxic side effects, especially for potent chemotherapeutic drugs and poor tissue specificity; and (3) improved patient compliance by avoiding repetitive administration.

Polymeric nanoparticles have some advantages in terms of their long-term physical stability and also their stability in vivo. Both model nondegradable and biodegradable particulate drug carriers have been investigated. The main problem that needs to be overcome is their removal by phagocytic cells (macrophages) of the reticuloendothelial system (RES) and in particular the Kupffer cells of the liver. The main target of any research on nanoparticles is to modify the surface of the particles in such a way to avoid RES recognition.

The above approach has been investigated for both nonbiodegradable polymer particles (such as polystyrene or cyanoacrylate) and biodegradable particles (such as poly(lactic acid)/poly(lactic acid-*co*-glycolic acid) [25].

Several particle characteristics play a major role in controlled delivery:

1. *Particle Size*. Particles >7 μm are larger than blood capillaries (∼ 6 μm) and become entrapped in the capillary beds of the lungs (which may have fatal effects). The majority of particles that pass the lung capillary bed accumulate in the elements of the RES (spleen, liver, and bone marrow). The degree of splenic uptake increases with particle size. Removal of particles >200 nm is due to nonphagocytic process (physical filtration) in the spleen and phagocytosis (by Kupffer cells) by the liver. Particles < 200 nm decrease splenic uptake and are cleared by the liver and bone marrow. Colloidal particles not cleared by the RES can potentially exit the blood circulation via the sinusoidal fenestration of the liver and bone marrow.
2. *Surface Charge*. Surface charges only influence particle–protein or particle–macrophage interactions at very short distances. The surface charge may affect the surface hydrophobicity, which can affect protein adsorption.
3. *Surface Hydrophobicity*. Serum components adsorb on the surface of colloidal particles via their hydrophobic sites. Increase in surface hydrophobicity increases opsonization. To reduce opsonization, a predominantly hydrophilic surface is required. This has led to the conclusion that by adsorption of poly(ethylene glycol (PEG)-type block copolymers on the surface of the particles should reduce the opsonisation process. This will be discussed in the next section.

Polystyrene nanoparticles have been used as model systems for investigation of the effect of surface modification in the various processes of phagocytosis, opsonization, and dysopsonization. It was possible to modify the surface of polystyrene particles either by adsorption of block copolymers containing PEG or by grafting PEG chains on the surface of the particles. PEG has the advantage of being nontoxic and approved by the FDA. Earlier work using liposomes containing PEG-phospholipid derivatives showed prolonged circulation times and prevention of phagocytic clearance. The PEG chains act as a barrier towards adsorption of proteins thus preventing phagocytic clearance.

Two methods for surface modification could be applied:

1. Adsorption of block copolymers of PEO-PPO-PEO, namely, poloxamers, or poloxamines that are made of polyethylene diamine with four branches of PEG chains. The molecular weight of the PEG chain and hence the adsorbed layer thickness was crucial in preventing phagocytosis. For example, Poloxamer 338 (with PEG chains of $M_w = 5600$) was more efficient in preventing phagocytosis when compared with Poloxamer 108 (with PEG $M_w = 1800$). A long PPO chain was also important to ensure anchoring of the block copolymer to the surface. The particle size of the polystyrene particles was also important. For example, 60- and 150-nm particles coated with

Poloxamer 407 were not sequestered by the macrophages in the bone marrow (they avoided capture by the Kupffer cells). In contrast to the 250-nm particles (also coated with Poloxamer 207), which were absorbed by the spleen and liver, only a small portion of the smaller particles reached the bone marrow.

2. Chemically grafting the PEG chains. Particles with different surface densities of PEG were prepared by copolymerization of styrene with methoxy(PEG) acrylate macromonomer. Particle uptake by the Kupffer cells (in rat studies) showed a decrease with increase in graft density. Only particles with a very low PEG density resulted in considerable liver deposition. However, the higher PEG density achieved with grafting did not improve the blood circulation time when compared with particles containing adsorbed block copolymers.

Several biodegradable polymers have been investigated as drug carriers [26]: (1) poly(lactic acid)/poly(lactic acid-*co*-glycolic acid), (2) poly(anhydrides), (3) poly(*ortho*-esters), (4) poly(β-malic acid-*co*-benzyl malate), and (5) poly(alkylcyanoacrylates). The most widely used biodegradable polymer was poly(lactic) (PLA)/poly(lactic acid-*co*-glycolic acid) (PLGA), which have been used to produce a wide range of drug delivery formulations (microparticles, implants, and fibers). To avoid contamination, the nanoparticles were produced by precipitation by mixing acetone solution with water. PLGA nanoparticles < 150 nm in diameter were produced. The surface of the PLGA particles was modified by adsorption of water-soluble PLA-PEG block copolymer or Poloxamine 908 (forming an adsorbed layer thickness ~ 10 nm). Block copolymer micelles were also used as drug carriers; the A-B or A-B-A block copolymers can produce micelles with aggregation numbers of several tens or hundreds of molecules (10–30 nm diameter). The hydrophobic core can be used to solubilise insoluble drugs (lipophilic molecules), whereas the hydrophilic chains provide the steric barrier, preventing protein adsorption and phagocytosis.

The most systematically studied micelle forming block copolymers are those based on PLA-PEG assemblies. The structure of the PLA-PEG micelles depend on the copolymer composition, including the PLA to PEG ratio. With a fixed PEG block ($M = 5000$), the size of the PLA-PEG micelle increases with increase in the PLA molecular weight. The characteristics of the corona, in a good solvent, are determined by the aggregation number and surface curvature. PLA-PEG nanoparticles prepared from a copolymer with PLA molecular weight ≤ 15,000 are colloidally stable with a reasonable high surface coverage of stabilizing PEG chain. The grafting density of PEG chains appears to increase as the molecular weight of the PLA block increases from 2000 to 15,000, which results in increase in the thickness of the steric layer. As the PEG chains become radially more extended, they become less compressible. As the PLA molecular weight increases above 15,000, the colloid stability of the nanoparticles is impaired, suggesting a reduction in PEG surface coverage. For PLA-PEG copolymer with a PLA block $M >$ 45000, it is possible to increase the aggregation number and particle size. To produce long-circulating particulate carriers (i.e., to reduce opsonisation), one has to enhance the surface coverage of the brushlike PEG chains; copolymers with intermediate PLA to PEG ratio (e.g., PLA-PEG 15: 5) appear to give optimal protein-resistant surface properties. To study the effect of nanoparticle structure on blood circulation, a hydrophobic radiolabeled γ-emitter ^{111}In-oxine (8-hydroxy quinoline) was incorporated within PLA and PLA-PEG nanoparticles [27, 28]. The PLA nanoparticles (~125 nm) were rapidly cleared from blood circulation with only 13% of the injected dose still circulating after 5 min. After 3 h, 70% of the nanoparticles were removed by the liver. The rate and extent of release of the radiolabeled compound (using in vitro studies with rat serum) was higher for nanoparticles produced from the PLA-PEG copolymers with a lower M PLA. After 3 h, 77% and 88% radiolabeled compound remained associated with the PLA-PEG 6: 5 and 30: 5.

In vivo studies showed that free radiolabeled compound remained in the blood at moderate levels after 3 h, and there was low liver accumulation. Contrary to expectation, it was found that smaller micelles of PLA-PEG copolymers did accumulate in the liver. It was necessary to have micelles with size > 100 nm to evade phagocytosis. By optimizing the size of the micelles and controlling the surface characteristics, it is possible to produce nanoparticles that can be applied as drug carriers.

81.5 LIPOSOMES AND VESICLES IN PHARMACEUTICALS

Liposomes are multilamellar structures consisting of several bilayers of lipids (several micrometers). They are produced by simply shaking an aqueous solutions of phospholipids, such as egg lecithin. When sonicated, these multilayer structures produce unilamellar structures (with size range of 25–50 nm) that are referred to as *liposomes*. A schematic representation of liposomes and vesicles is given in Fig. 81.5.

Glycerol-containing phospholipids are used for the preparation of liposomes and vesicles: phosphatidylcholine→phosphatidylserine→phosphatidylethanolamine→phosphatidylanisitol→phosphatidylglycerol→phosphatidic acid→cholesterol. The chemical structures of some of these lipids were given earlier. In most preparations, a mixture of lipids is used to obtain the most optimum structure.

Liposomes and vesicles are ideal systems for drug delivery, due to their high degree of biocompatability, in particular for intravenous delivery [33]. For effective application, larger unilamellar vesicles are preferred (diameter

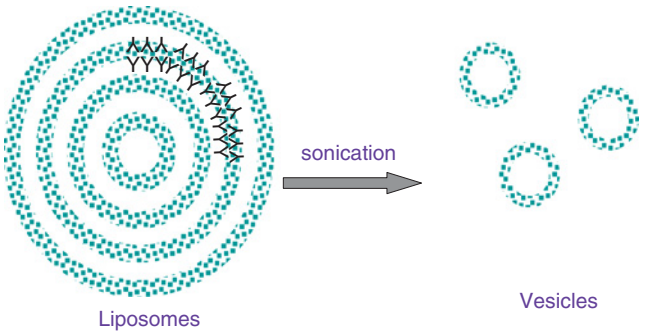


FIGURE 81.5 Schematic representation of liposomes and vesicles.

100–500 nm). In addition to drug delivery, liposomes have been used as model membranes, as carriers of drugs, DNA, ATP, enzymes, and diagnostic agents. Both water-soluble and water-insoluble drugs can be incorporated by encapsulation in the aqueous space or intercalation into the lipid bilayer.

Liposomes are capable of solubilizing both water-soluble and lipid-soluble drugs. The amount and location of a drug within a liposome are dependent on a number of factors: (1) the location of a drug within a liposome is based on the partition coefficient of the drug between aqueous compartments and lipid bilayers, (2) the maximum amount of drug that can be entrapped within a liposome is dependent on its total solubility in each phase, (3) drugs with limited solubility in polar and nonpolar solvents cannot be encapsulated in liposomes, and (4) efficient capture depends on the use of drugs at concentrations that do not exceed the saturation limit in the aqueous compartment (for polar drugs) or the lipid bilayers (for nonpolar drugs).

If liposomes are prepared by mixing the drug with the lipids, the drug will eventually partition to an extent depending on the partition coefficient of the drug and the phase volume ratio of water to bilayer. Release rates are highest when the drug has intermediate partition coefficient.

The bilayer/aqueous compartment partition coefficient is usually estimated by determining the partition coefficient between octanol and water (the log P number). Drug solubilization in liposomes has important biological effects: (1) the ultimate efficacy of a liposomal dosage depends on the control of the amount of free drug that can reach the exact *site of action*; (2) generally, the exact site of action is not known, and one must rely on attaining reproducible blood levels of the drug; (3) with nonparenteral dosage forms, only the free drug is absorbed and hence one can measure the amount of drug that enters the blood as a function of time.

With parenteral, especially intravenous, administration of drugs encapsulated in liposomes requires control of the pharmacokinetics of the drug and this requires control of the following factors: (1) concentration of the free drug in the blood, (2) concentration of liposomes and their entrapped drug in blood, (3) leakage rate of drug from liposome in the blood, and (4) disposition of the intact drug-carrying liposomes in the blood.

To control the pharmacokinetics of these complex systems, one must separate out the leakage rate of the drug from the liposome in the blood and the disposition of the intact carrying liposomes in the blood.

One of the major problems with application of liposomes for drug delivery is their interaction with high-molecular-weight substances such as albumin. The instability of liposomes in plasma appears to be the result of transfer of bilayer lipids to albumin and high-density lipoproteins (HDLs). Some protein is also transferred from the lipoprotein to the liposome. Both lecithin and cholesterol can exchange with membranes of red blood cells. The susceptibility of liposomal phospholipid and phspholipase is strongly dependent on liposome size and type. Generally MLVs are most stable and SUVs are least stable. Liposomes prepared with higher chain length phospholipids are more stable in buffer and in plasma. Cholesterol and sphingomyelin are very effective in reducing instability. As we will see later, incorporation of block copolymers such as poloxamers can enhance the stability of liposomes.

Despite the above limitations, the therapeutic promise of liposomes as a drug delivery system is becoming a reality in the following applications: (1) parenteral administration, (2) inhalation treatment, (3) percutaneous administration, (4) ophthalmics, (5) cancer treatment, and (6) controlled-release formulations.

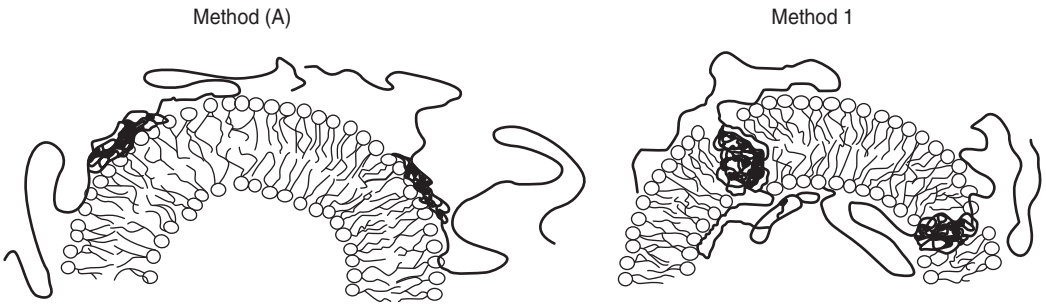


FIGURE 81.6 Schematic representation of vesicle structure in the presence of block copolymers.

The preparation of sterically stabilized vesicles with the addition of triblock copolymers of the polyethylene oxide (PEO)- polypropylene oxide (PPO) type, Namely, poloxamers or pluronics (PEO-PPO-PEO) have been shown to enhance stabilization [34]. The steric stabilization of phospholipid vesicles by the copolymer molecules was attempted by following two different techniques: (1) addition of the block copolymer to performed vesicles (denoted as method A) and (2) addition of the block copolymer to the lipid before formation of the vesicles (denoted as method I). In this case both the lipid and copolymer participate in the construction of the vesicle. A schematic representation of the resulting vesicle structure for both methods is given in Fig. 81.6. Vesicles prepared according to method I are more stable than those prepared according to method A for the following reasons: Association of the block copolymer as an integral part of the bilayer (method I) gives better "anchor" to the bilayer when compared to those prepared by simple adsorption (method A). Increased rigidity of the lipid-polymer bilayer structure (for method I). The increased rigidity decreases the interaction with HDL. The (I) vesicles do not exhibit osmotic swelling.

REFERENCES

[1] Tadros, Th.F. (ed.) (2013). *Encyclopedia of Colloid and Interface Science.* Springer, Heidelberg, Germany.

[2] Hamaker, H.C. (1937). *Physica* (Utrecht), **4**, 1058.

[3] Smulochowsi, M.V. (1927). *Z. Phys. Chem*. **92**, 129.

[4] Kruyt, H.R. (1952). *Colloid Science.* Elsevier, Amsterdam, Vol. I.

[5] Verwey, E.J.W., Overbeek, J.Th.G. (1948). *Theory of Stability of Lyophobic Colloid*. Elsevier, Amsterdam.

[6] Deryaguin, B.V., Landau, L. (1941). *Acta Physicochem. USSR* **14**, 633.

[7] Fuchs, N. (1936). *Z. Physik.* **89**, 736.

[8] Reerink, H., Overbeek, J.Th.G. (1954). *Discuss. Faraday Soc.* **18**, 74.

[9] Napper, D.H. (1983). *Polymeric Stabilisation of Colloidal Dispersions*. Academic Press, London.

[10] Tadros, Th.F. (1985). Polymer adsorption. In Buscall, R., Corner, T., Stageman, J. (eds.), *Polymer Colloids.* Applied Sciences, London.

[11] Nakajima, H., Tomomossa, S., Okabe, M. (1993). First Emulsion Conf., Paris.

[12] Nakajima, H. (1997). In Solons, C., Konieda, H. (eds.), *Industrial Applications of Microemulsions*. Marcel Dekker, New York.

[13] Ugelstadt, J., El-Aassar, M.S., Vanderhoff, J.W. (1973). *J. Polym. Sci.* **11**, 503.

[14] El-Aasser, M. (1997). In Asua, J.M. (ed.), *Polymeric Dispersions*. Kluwer Academic Publishers, Amsterdam.

[15] Forgiarini, A., Esquena, J., Gonzalez, J., Solans, C. (2000). *Progress Colloid Polym. Sci.* **115**, 36.

[16] Shinoda, K., Kunieda, H. (1983). In Becher, P. (ed.), *Encyclopedia of Emulsion Technology*. Marcel Dekker, New York.

[17] Shinoda, K., Saito, H. (1969). *J. Colloid Interface Sci.* **30**, 258.

[18] Shinoda, K., Saito, H. (1968). *J. Colloid Interface Sci.* **26**, 70.

[19] Thompson, W. (Lord Kelvin) (1871). *Phil. Mag.* **42**, 448.

[20] Lifshitz, I.M., Slesov, V.V. (1959). *Soviet Phys. JETP* **35**, 331.

[21] Wagner, C. (1961). *Z. Electrochem.* **35**, 581.

[22] Kabalnov, A.S., Shchukin, E.D. (1992). *Adv. Colloid Interface Sci.* **38**, 69.

[23] Kabalnov, A.S. (1994). *Langmuir* **10**, 680.

[24] Weers, J.G. (1998). In Binks, B.P. (ed.), *Modern Aspects of Emulsion Science*. Royal Society of Chemistry Publication, Cambridge, UK.

[25] Walstra, P. (1993). *Chem. Eng. Sci.* **48**, 333.

[26] Kreuter, J. (1994). *Colloidal Drug Delivery Systems*. Marcel Dekker, New York.

[27] Moghimi, S.M., Davis, S.S. (1994). Innovations in avoiding particle clearance from blood by Kupffer cells: Cause for reflection. *Crit. Rev. Ther. Drug Carriers Syst.* **11**, 31–36.

[28] Douglas, S.J., Davis S.S., Illum, L. (1987). Nanoparticles in drug delivery. *Crit. Rev. Ther. Drug Carriers Syst.* **3**, 233–261.

[29] Stonik, S., Dunn, S.E., Davies, M., Coombes, A.G.A., Taylor, D.C., Irving, M.P., Purkiss, S.C., Tadros, Th.F., Davis, S.S., Illum, L. (1994). Surface modification of poly(lactide-co-glycolide) nano-spheres by biodegradable poly(lactide)-poly(ethylene oxide) copolymers. *Pharm. Res.* **11**, 1800–1808.

[30] Hagen, S., Coombes, A.G.A., Garnett, M.C., Dunn, S.E., Davies, M.C., Illum, L., Davis, S.S. (1996). Poly(lactide)-poly(ethylene glycol) ciopolymers as drug delivery systems. 1. Characterisation of water dispersible micelle forming systems. *Langmuir* **12**, 2153–2161.

[31] Moghimi, S.M., Porter, C.J., Muir, L.S., Illum L., Davis, S.S. (1991). Non-phagocytic uptake of i.v. injected microspheres in the rat spleen: Influence of particle size and hydrophilic coating. *Biochem. Biophys. Res. Commun*. **177**, 861–866.

[32] Stolnik, S., Illum, L., Davis, S.S. (1995). Long circulating drug carriers. *Adv. Drug Deliv. Rev.* **16**, 195–214.

[33] Cartensen, J.Th. (1973). *Theory of Pharmaceutical Systems.* Academic Press, London/New York.

[34] Kostarelos, K., Tadros, Th.F., Luckham, P.F. (1999). Physical conjugation of (tri-) block copolymers to liposomes toward the construction of sterically stabilised vesicle systems. *Langmuir* **15**, 369–376.

82

STABILITY RATIO AND EARLY-STAGE AGGREGATION KINETICS OF COLLOIDAL DISPERSIONS

HIROYUKI OHSHIMA

Faculty of Pharmaceutical Sciences, Tokyo University of Science, 2641 Yamazaki Noda, Chiba 278-8510, Japan

82.1 INTRODUCTION

The stability of dispersions of colloidal particles can be analyzed by the DLVO (Derjaguin–Landau–Verwey–Overbeek) theory of colloid stability [1, 2]. This theory factors in the repulsive electrostatic interaction and the attractive van der Waals interaction between colloidal particles [3–12]. There are a number of theoretical studies on colloidal aggregation kinetics [13–33]. A quantitative measure of the stability of colloidal dispersions based on the DLVO theory is the stability ratio, which is expressed by the ratio of the rapid and slow aggregation rates of colloidal particles. The rapid aggregation process is caused only by the van der Waals attractive interaction in the absence of the electrostatic repulsion. In the presence of the electrostatic repulsion, under certain conditions, the potential curve for the interparticle interaction can exhibit a maximum, a primary deep minimum, and a secondary shallow minimum. The slow aggregation rate is related to the height of a maximum on the potential curve of the interaction energy between two approaching particles. The aggregation kinetics of colloidal particles is usually analyzed via the probability that association of two single-particle monomers occurs at the primary minimum to form an irreversibly aggregated dimer after overcoming the potential energy barrier at the potential maximum. Behrens and Borkovec [25], in particular, considered a set of coupled nonlinear differential rate equations for the early-stage aggregation kinetics of colloidal particles by taking into account the influence of the secondary minimum. In this chapter we derive a simple analytic solution to these rate equations.

82.2 DLVO THEORY OF COLLOID STABILITY AND THE STABILITY RATIO

Following the DLVO theory of colloid stability [1, 2], we consider the interaction between two identical spherical particles of radius a carrying unperturbed surface potential ψ_0 at separation H between their surfaces immersed in a symmetric electrolyte solution of valence z and bulk concentration (number density) n. The interaction energy $V(H)$ between the two spheres can be given by the sum of the repulsive electrostatic interaction energy $V_R(H)$ and the attractive van der Waals interaction energy $V_A(H)$, namely, $V(H) = V_R(H) + V_A(H)$.

The most widely employed expressions for $V_R(H)$ and $V_A(H)$ are given by

$$V_R(H) = \frac{64\pi ankT\gamma^2}{\kappa^2} e^{-\kappa H} = \frac{G\kappa akT}{12} e^{-\kappa H} \tag{82.1}$$

$$V_A(H) = -\frac{Aa}{12H} \tag{82.2}$$

with

$$\kappa = \sqrt{\frac{2z^2e^2n}{\varepsilon_r\varepsilon_0 kT}} \tag{82.3}$$

$$\gamma = \tanh\left(\frac{ze\psi_0}{kT}\right) \tag{82.4}$$

$$G = \frac{12 \times 64\pi\gamma^2 n}{\kappa^3} = \frac{384\pi\gamma^2\varepsilon_r\varepsilon_0 kT}{(ze)^2\kappa} \tag{82.5}$$

Encyclopedia of Biocolloid and Biointerface Science, Volume 2, First Edition. Edited by Hiroyuki Ohshima.
© 2016 John Wiley & Sons, Inc. Published 2016 by John Wiley & Sons, Inc.

where κ is the Debye–Hückel parameter, e is the elementary electric charge, ε_r is the relative permittivity of the electrolyte solution, ε_0 is the permittivity of a vacuum, k is Boltzmann's constant, T is the absolute temperature, and A is the Hamaker constant.

The total interaction energy $V(H) = V_R(H) + V_A(H)$ between the two spheres is thus given by

$$V(H) = \frac{64\pi ankT\gamma^2}{\kappa^2} e^{-\kappa H} - \frac{Aa}{12H} \tag{82.6}$$

which can be rewritten as

$$V(H) = \frac{A\kappa a}{12}\left(\frac{GkT}{A} e^{-\kappa H} - \frac{1}{\kappa H}\right) \tag{82.7}$$

The potential curves of $V_R(H)$, $V_A(H)$, and $V(H) = V_R(H) + V_A(H)$ are schematically given as function of the separation H between the two spheres in Fig. 82.1 for the case where there exists a potential maximum V_{max} at $H = H_m$. Figure 82.1 gives the scaled interaction energy $V^*(H) = V(H)/(\kappa aA/12)$ as a function of the scaled separation κH for various values of GkT/A [33].

The following three types of the stability ratio have been proposed for a dispersion of colloidal particles of radius a with the inter-particle interaction potential $V(H) = V_R(H) + V_A(H)$:

$$W = q \tag{82.8}$$

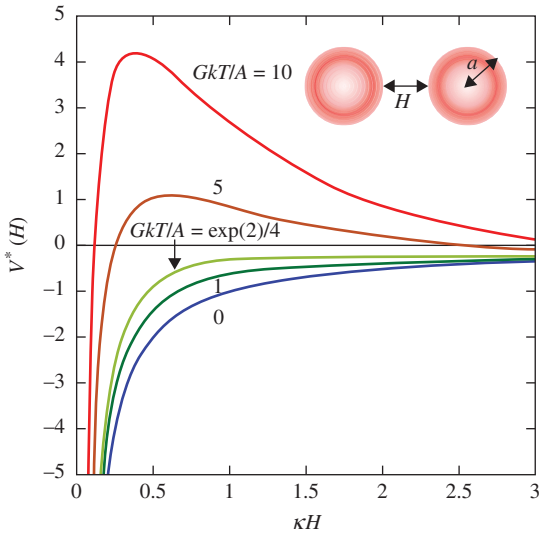


FIGURE 82.1 The scaled potential energy $V^*(H) = V(H)/(\kappa aA/12)$ as a function of the scaled separation κH for several values of GkT/A. The potential curve exhibits a maximum if $GkT/A >$ exp(2)/4, while there is no maximum if $0 \le GkT/A \le$ exp(2)/4 [33].

$$W = \frac{q}{q^o} \tag{82.9}$$

$$W_{visc} = \frac{q_{visc}}{q^o_{visc}} \tag{82.10}$$

In these three equations

$$q = 2a\int_0^\infty \frac{e^{V(H)}}{(2a+H)^2} dH = 2\int_0^\infty \frac{e^{V(u)}}{(2+u)^2} du \tag{82.11}$$

$$q^o = 2a\int_0^\infty \frac{e^{V_A(H)}}{(2a+H)^2} dH = 2\int_0^\infty \frac{e^{V_A(u)}}{(2+u)^2} du \tag{82.12}$$

$$q_{visc} = 2\int_0^\infty \beta(u)\frac{e^{V(u)}}{(2+u)^2} du \tag{82.13}$$

$$q^o_{visc} = 2\int_0^\infty \beta(u)\frac{e^{V_A(u)}}{(2+u)^2} du \tag{82.14}$$

with

$$\beta(u) = \frac{6u^2+13u+2}{6u^2+4u} = \frac{(6u+1)(u+2)}{2u(3u+2)} \tag{82.15}$$

where $u = H/a$. Equation (82.8) is Fuch's stability formula [13], in which the rapid coagulation is considered to be a pure diffusion-limited process. Equation (82.9), which is the stability ratio modified by McGown and Parfitt [15], accounts for the fact that the rapid coagulation is caused by the attractive van der Waals interaction (which is neglected in Fuch's formula). Further improvement was made by Spielman [16] and Honig et al. [17], who derived Eq. (82.10), in which a function $\beta(u)$ is introduced to account for viscous interactions between particles. Also Honig et al. [17] provide the following analytic expressions q^o and q^o_{visc}:

$$q^o = 1 - \frac{A}{24kT}\exp\left(\frac{A}{24kT}\right) E_1\left(\frac{A}{24kT}\right) \tag{82.16}$$

$$q^o_{visc} = \frac{11}{8}\exp\left(\frac{A}{24kT}\right) E_1\left(\frac{A}{24kT}\right) - \frac{9}{8}\exp\left(\frac{A}{8kT}\right) E_1\left(\frac{A}{8kT}\right) \tag{82.17}$$

where $E_1(z)$ is the first-order exponential integral, defined by

$$E_1(z) = \int_1^\infty \frac{e^{-zt}}{t} dt \tag{82.18}$$

82.3 APPROXIMATE ANALYTIC EXPRESSIONS FOR THE STABILITY RATIO *W*

We present a novel method in which $\exp[V_R(H)/kT]$ is expanded in a Tylor series:

$$\begin{aligned} q &= 2\int_0^\infty \frac{e^{V(u)/kT}}{(u+2)^2}du = 2\int_0^\infty \frac{1}{(u+2)^2}e^{V_R(u)/kT}e^{V_A(u)/kT}du \\ &= 2\int_0^\infty \frac{1}{(u+2)^2}e^{V_A(u)/kT}\left\{1+\sum_{m=1}^{\infty}\frac{1}{m!}\left(\frac{V_R(u)}{kT}\right)^m\right\}du \\ &= q^o + 2\int_0^\infty \frac{1}{(u+2)^2}e^{-A/12kTu} \\ &\quad\times\left\{\sum_{m=1}^{\infty}\frac{1}{m!}\left(\frac{G\kappa a e^{-\kappa a u}}{12}\right)^m\right\}du \\ &\approx q^o + \frac{1}{2}\int_0^\infty e^{-A/12kTu}\left\{\sum_{m=1}^{\infty}\frac{1}{m!}\left(\frac{G\kappa a e^{-\kappa a u}}{12}\right)^m\right\}du \end{aligned} \tag{82.19}$$

Here, $2/(u+2)^2$ in the integrand has approximately been replaced by $^1/_2$. Further, Eq. (82.19) becomes

$$q = q^o + \sqrt{\frac{A}{12kT\kappa a}}\sum_{m=1}^{\infty}\frac{1}{m!\sqrt{m}}\left(\frac{\kappa a G}{12}\right)^m K_1\left(\sqrt{\frac{A\kappa a m}{3kT}}\right) \tag{82.20}$$

where $K_1(z)$ is the first-order Bessel function of the second kind and the following relation has been employed:

$$\int_0^\infty e^{-C_1u-C_2/u}du = 2\sqrt{\frac{C_2}{C_1}}K_1(2\sqrt{C_1C_2}) \tag{82.21}$$

We thus obtain

$$W = \frac{q}{q^o} = 1 + \frac{1}{q^o}\sqrt{\frac{A}{12kT\kappa a}}\sum_{m=1}^{\infty}\frac{1}{m!\sqrt{m}}\left(\frac{G\kappa a}{12}\right)^m \times K_1\left(\sqrt{\frac{A\kappa a m}{3kT}}\right) \tag{82.22}$$

This is the required expression for the stability ratio W without viscous interactions between particles [33].

Similarly, we obtain the stability ratio W_{visc} with viscous interaction as follows:

$$\begin{aligned} q_{visc} &= 2\int_0^\infty \beta(u)\frac{e^{V(u)/kT}}{(u+2)^2}du \\ &= 2\int_0^\infty \frac{\beta(u)}{(u+2)^2}e^{V_R(u)/kT}e^{V_A(u)/kT}du \\ &= 2\int_0^\infty \frac{\beta(u)}{(u+2)^2}e^{V_A(u)/kT}\left\{1+\sum_{m=1}^{\infty}\frac{1}{m!}\left(\frac{V_R(u)}{kT}\right)^m\right\}du \\ &= q^o_{visc} + 2\int_0^\infty \frac{\beta(u)}{(u+2)^2}e^{-A/12kTu} \\ &\quad\times\left\{\sum_{m=1}^{\infty}\frac{1}{m!}\left(\frac{G\kappa a e^{-\kappa a u}}{12}\right)^m\right\}du \\ &\approx q^o_{visc} + \frac{1}{4}\int_0^\infty \frac{e^{-A/12kTu}}{u} \\ &\quad\times\left\{\sum_{m=1}^{\infty}\frac{1}{m!}\left(\frac{G\kappa a e^{-\kappa a u}}{12}\right)^m\right\}du \end{aligned} \tag{82.23}$$

Here, $2\beta(u)/(u+2)^2$ in the integrand has approximately been replaced by $^1/_4u$. We thus obtain

$$q_{visc} = q^o_{visc} + \frac{1}{2}\sum_{m=1}^{\infty}\frac{1}{m!}\left(\frac{G\kappa a}{12}\right)^m K_0\left(\sqrt{\frac{A\kappa a m}{3kT}}\right) \tag{82.24}$$

where $K_0(z)$ is the zeroth-order Bessel function of the second kind and the following relation has been employed:

$$\int_0^\infty \frac{1}{u}e^{-C_1u-C_2/u}du = 2K_0(2\sqrt{C_1C_2}) \tag{82.25}$$

We thus obtain

$$W_{visc} = \frac{q_{visc}}{q^o_{visc}} = 1 + \frac{1}{2q^o_{visc}}\sum_{m=1}^{\infty}\frac{1}{m!}\left(\frac{\kappa a G}{12}\right)^m \times K_0\left(\sqrt{\frac{A\kappa a m}{3kT}}\right) \tag{82.26}$$

This is the required expression for the stability ratio W_{visc} with viscous interactions between particles [33]. Note that in Eqs. (82.22) and (82.26), q^o and q^o_{visc} are given by Eqs. (82.16) and (82.17), respectively.

The expressions obtained [Eqs. (82.22) and (82.26) as combined with Eqs. (82.16) and (82.17)] involve modified Bessel functions K_0(z), K_1(z) and an exponential integral E_1(z), which can easily be calculated via programs such as Mathematica. It is found that the present results are in excellent agreement with the exact numerical results obtained directly from Eqs. (82.11)–(82.14). Examples are shown in Fig. 82.2, which compares the exact numerical results and the stability expressions obtained [Eq. (82.22) as combined with Eq. (82.16) for W and Eq. (82.26) as combined with Eq. (82.17) for W_{visc}] calculated at $A/kT = 1$ and $\kappa a = 50$.

We see that the approximate stability expressions obtained are in excellent agreement with the exact numerical results within the line width for all values of G/AkT.

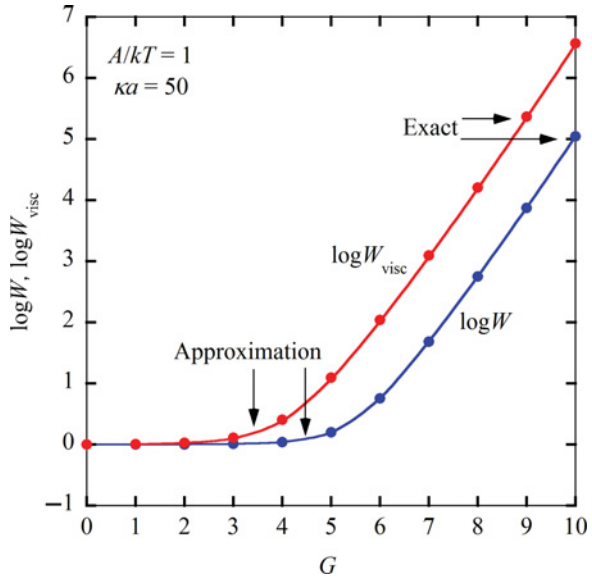


FIGURE 82.2 Logarithm of the stability ratio without viscous interaction between particles (log W) and that with viscous interactions (log W_{visc}) as function of G at $A/kT = 1$ and $\kappa a = 50$. The solid line represents the approximate results [Eqs. (82.22) and (82.26) as combined with Eq. (82.16) and (82.17)], which agree with exact numerical results represented by • within the line width [33].

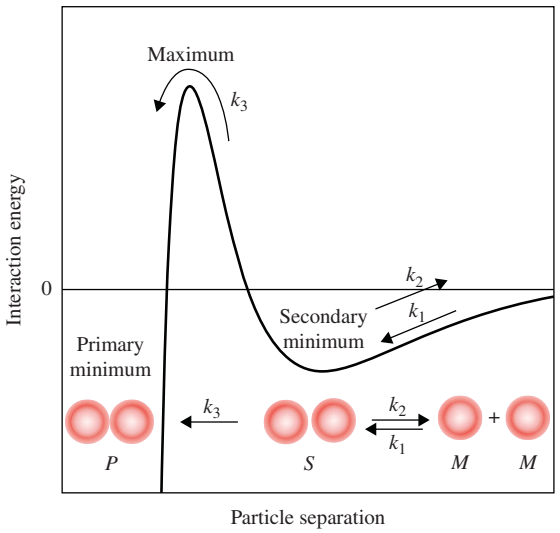


FIGURE 82.3 A typical interaction energy profile leading to the association of two single-particle monomers M to form both irreversibly aggregated dimes P (primary aggregated dimers) and reversibly aggregated dimers S (secondary aggregated dimers). (Adapted from Behrens and Borkovec 2000 [25], Fig. 1.)

82.4 RATE EQUATIONS FOR EARLY-STAGE AGGREGATION KINETICS OF COLLOIDAL PARTICLES

The potential energy of the interaction between two approaching colloidal particles obtained by the DLVO theory can exhibit a maximum, a primary minimum, and a secondary minimum on the potential curve of the interparticle interaction energy. Behrens and Borkovec [25] considered a set of coupled nonlinear differential rate equations for the early-stage aggregation kinetics of colloidal particles by factoring in the influence of the secondary minimum.

Following Behrens and Borcovec [25], we consider a dilute suspension of colloidal particles for the case in which the interaction energy between two approaching particles has a maximum, a primary minimum, and a secondary minimum (Fig. 82.3).

We assume two-step early-stage aggregation kinetics, in which association of two single-particle monomers M forms a reversibly aggregated dimer S in the secondary minimum (secondary aggregated dimer) before an irreversibly aggregated dimer P in the primary minimum (primary aggregated dimer) is formed:

$$2M \underset{k_2}{\overset{k_1}{\rightleftharpoons}} S \xrightarrow{k_3} P \tag{82.27}$$

Here, k_1 is the rate constant for association of two single-particle monomers M into a secondary aggregated dimer S, k_2 is the rate constant for dissociation of a secondary aggregated dimer S into two single-particle monomers M, and k_3 is the date constant of a secondary aggregated dimer S into a primary aggregated dimer P after overcoming the potential energy maximum. These rate constants are related to the potential energy of the interparticle interaction [25]. We assume that initially at time $t = 0$ there exist only single-particle monomers. Equation (82.27) holds good for the early stage of the aggregation kinetics, in which formation of higher-order aggregates can be neglected (early-stage approximation).

We denote the concentrations of single-particle monomers M, secondary aggregated dimers S, and primary aggregated dimers P at time t by $n_1(t)$, $n_{2S}(t)$, and $n_{2P}(t)$, respectively. The time evolution of the concentrations $n_1(t)$, $n_{2S}(t)$, and $n_{2P}(t)$ for the two-step reaction [Eq. (82.27)] is thus governed by [25]

$$\frac{dn_1(t)}{dt} = -k_1 n_1^2(t) + 2k_2 n_{2S}(t) \tag{82.28}$$

$$\frac{dn_{2S}(t)}{dt} = \frac{1}{2}k_1 n_1^2(t) - (k_2 + k_3) n_{2S}(t) \tag{82.29}$$

$$\frac{dn_{2P}(t)}{dt} = k_3 n_{2S}(t) \tag{82.30}$$

which are subject to the following boundary conditions

$$n_1(0) = n_0,\ n_{2S}(0) = 0,\ n_{2P}(0) = 0 \tag{82.31}$$

where n_0 is the initial concentration of the single-particle monomers. Note that the above set of rate equations satisfies the conservation law: $n_1(t) + 2\{n_2\mathrm{S}(t)+n_2\mathrm{P}(t)\} = n_0$. These rate equations [Eqs. (82.28)–(82.30)], which neglect higher-order aggregates, can be applicable only when the concentration of aggregated dimers is much smaller than the concentration of monomers. Since the above coupled rate equations [Eqs. (82.28)–(82.30)] are nonlinear with respect to $n_1(t)$, they can be solved only numerically.

82.5 APPROXIMATE SOLUTION TO THE RATE EQUATION

In order to obtain an approximate solution to Eqs. (82.28)–(82.30), we put

$$n_1(t) = n_0\{1 + \Delta(t)\} \tag{82.32}$$

where $\Delta(t)$ is a small quantity and linearize ${n_1}^2(t)$ in Eqs. (82.28) and (82.30) as

$$n_1^2(t) = n_0^2\{1 + \Delta(t)\}^2 \approx n_0^2\{1 + 2\Delta(t)\} \tag{82.33}$$

The rate equations [Eqs. (82.28)–(82.30)] thus become

$$\frac{d\Delta(t)}{dt} = -k_1 n_0^2\{1 + 2\Delta(t)\} + 2k_2 n_{2S}(t) \tag{82.34}$$

$$\frac{dn_{2S}(t)}{dt} = \frac{1}{2}k_1 n_0^2\{1 + 2\Delta(t)\} - (k_2 + k_3)n_{2S}(t) \tag{82.35}$$

$$\frac{dn_{2P}(t)}{dt} = k_3 n_{2S}(t) \tag{82.36}$$

which are subject to the following boundary conditions:

$$\Delta(0) = 0,\ n_{2S}(0) = 0,\ n_{2P}(0) = 0 \tag{82.37}$$

Note that the above set of rate equations satisfies the conservation law: $n_1(t) + 2\{n_2\mathrm{S}(t)+n_2\mathrm{P}(t)\} = n_0$. Equations (82.34)–(82.36), subject to Eq. (82.37), which are linear, can easily be solved to give

$$\begin{aligned} n_1(t) &= n_0\{1 + \Delta(t)\} \\ &= \frac{n_0}{2}\left\{1 + \left(\frac{K_\mathrm{a} + K_\mathrm{b} - 2k_1 n_0}{2K_\mathrm{b}}\right) e^{-(K_\mathrm{a}-K_\mathrm{b})t}\right. \\ &\quad \left. - \left(\frac{K_\mathrm{a} - K_\mathrm{b} - 2k_1 n_0}{2K_\mathrm{b}}\right) e^{-(K_\mathrm{a}+K_\mathrm{b})t}\right\} \end{aligned} \tag{82.38}$$

$$n_{2S}(t) = \frac{k_1 n_0^2}{4K_\mathrm{b}}\{e^{-(K_\mathrm{a}-K_\mathrm{b})t} - e^{-(K_\mathrm{a}+K_\mathrm{b})t}\} \tag{82.39}$$

$$\begin{aligned} n_{2P}(t) &= \frac{n_0}{4}\left\{1 - \left(\frac{K_\mathrm{a} + K_\mathrm{b}}{2K_\mathrm{b}}\right) e^{-(K_\mathrm{a}-K_\mathrm{b})t}\right. \\ &\quad \left. + \left(\frac{K_\mathrm{a} - K_\mathrm{b}}{2K_\mathrm{b}}\right) e^{-(K_\mathrm{a}+K_\mathrm{b})t}\right\} \end{aligned} \tag{82.40}$$

and

$$\begin{aligned} n_2(t) &= n_{2S}(t) + n_{2P}(t) \\ &= \frac{n_0}{4}\left\{1 - \left(\frac{K_\mathrm{a} + K_\mathrm{b} - 2k_1 n_0}{2K_\mathrm{b}}\right) e^{-(K_\mathrm{a}-K_\mathrm{b})t}\right. \\ &\quad \left. + \left(\frac{K_\mathrm{a} - K_\mathrm{b} - 2k_1 n_0}{2K_\mathrm{b}}\right) e^{-(K_\mathrm{a}+K_\mathrm{b})t}\right\} \end{aligned} \tag{82.41}$$

where

$$K_\mathrm{a} = \frac{k_2 + k_3}{2} + k_1 n_0 \tag{82.42}$$

$$K_\mathrm{b} = \left(K_\mathrm{a}^2 - 2k_1 k_3 n_0\right)^{1/2} \tag{82.43}$$

Note here that $K_\mathrm{a} > K_\mathrm{b}$. Equations (82.38)–(82.41) are the required results for the time evolution of the concentrations $n_1(t)$, $n_{2\mathrm{S}}(t)$, $n_{2\mathrm{P}}(t)$, and $n_2(t) = n_{2\mathrm{S}}(t) + n_{2\mathrm{P}}(t)$ [32].

In Fig. 82.4, we compare two results for the concentration $n2(t)$ of the total aggregated dimers $(S + P)$, that is, the analytic result [Eq. (82.41)] and exact numerical solutions.

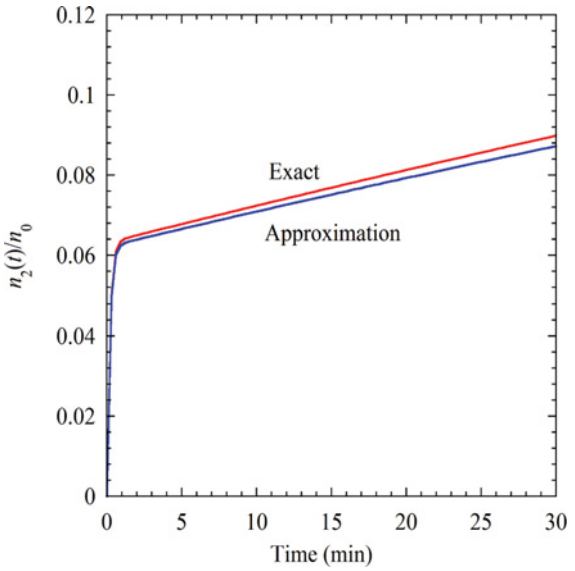


FIGURE 82.4 Comparison of results for the time evolution of concentration $n_2(t)$ of the total aggregated dimers $(S + P)$, that is, the analytic approximate result [Eq. (82.41)] [32] and exact numerical solutions to Eqs. (82.2)–(82.4). Calculated with $n_0 = 10^{15}$ m^{-3}, $k_1 = 1.1 \times 10^{-17}$ m^3 s^{-1}, $k_2 = 6.6 \times 10^{-2}$ s^{-1}, and $k_3 = 3.2 \times 10^{-4}$ s^{-1} from Behrens and Borkovec [25].

Following Behrens and Borkovec [25], we have used the following parameter values: $n_0 = 10^{15}$ m^{-3}, $k_1 = 1.1 \times 10^{-17}$ m^3 s^{-1}, $k_2 = 6.6 \times 10^{-2}$ s^{-1}, and $k_3 = 3.2 \times 10^{-4}$ s^{-1}, which are considered to be a suitable example for real colloidal dispersions showing an appreciable secondary minimum on the potential energy of the interparticle interaction.

We see that the analytic results are in excellent agreement with the numerical results. The relative error is found to be less than ∼3% for $t \leq 30$ min.

The most remarkable feature of the time evolution of $n_2(t)$ shown in Fig. 82.4 is that $n_2(t)$ increases almost linearly with time t after its initial sharp increase with a transient time $\tau_1 = 1/(K_a + K_b)$. Indeed, for the time region $t \ll \tau_2 = 1/(K_a - K_b)$, Eq. (82.41) tends to

$$n_2(t) \approx \frac{n_0}{4}\left[\left\{\frac{k_1 n_0 (k_3 - K_a + K_b)}{K_b}\right\} t - \left(\frac{K_a - K_b - 2k_1 n_0}{2K_b}\right)\{1 - e^{-(K_a + K_b)t}\}\right] \quad (82.44)$$

It follows from Eq. (82.44) that the slope of linear increase in $n_2(t)$ is given by

$$\frac{k_1 n_0^2 (k_3 - K_a + K_b)}{4K_b} \quad (82.45)$$

which agrees well with the exact numerical results.

REFERENCES

[1] Derjaguin, B.V., Landau, L.D. (1941). *Acta Physicochim.* **14**, 633.

[2] Verwey, E.J.W., Overbeek, J.Th.G. (1948). *Theory of the Stability of Lyophobic Colloids.* Elsevier/Academic Press, Amsterdam.

[3] Derjaguin, B.V. (1989). *Theory of Stability of Colloids and Thin Films.* Consultants Bureau, New York/London.

[4] Lyklema, J. (1995). *Fundamentals of Interface and Colloid Science, Solid-Liquid Interfaces.* Academic Press, New York, Vol. 2.

[5] Ohshima, H. (1998). In Ohshima H., Furusawa, K. (eds.), *Electrical Phenomena at Interfaces: Fundamentals, Measurements, and Applications*, 2nd ed. (revised and expanded). Marcel, New York, Chapter 3.

[6] Delgado, A.V. (ed.) (2000). *Electrokinetics and Electrophoresis.* Marcel Dekker, New York.

[7] Spasic, A., Hsu, J.-P. (eds.) (2005). *Finely Dispersed Particles. Micro-. Nano-, Atto-Engineering.* CRC Press, Boca Raton, FL.

[8] Ohshima, H. (2006). *Theory of Colloid and Interfacial Electric Phenomena.* Elsevier/Academic Press, Amsterdam.

[9] Tadros, Th.F. (ed.) (2007). *Colloid Stability, The Role of Surface Forces*—Part 1. Wiley-VCH, Weinheim.

[10] Ohshima, H. (2010). *Biophysical Chemistry of Biointerfaces.* Wiley, Hoboken, NJ.

[11] Israelachvili, J.N. (2011). *Intermolecular and Surface Forces*, 3rd ed. Academic Press, New York.

[12] Ohshima, H. (ed.) (2012). *Electrical Phenomena at Interfaces and Biointerfaces: Fundamentals and Applications in Nano-, Bio-, and Environmental Sciences.* Wiley, Hoboken, NJ, Chapters 1–4.

[13] Fuchs, N. (1934). *Z. Physik* **89**, 736.

[14] Reerink, H., Overbeek, J.Th.G. (1954). *Discuss. Faraday Soc.* **18**, 74.

[15] McGown, D.N.L., Parfit, G.D. (1967). *J. Phys. Chem.* **71**, 449.

[16] Spielman, L.A. (1970). *J. Colloid Interface Sci.* **33**, 562.

[17] Honig, E.P., Roebersen, G.J., Wiersema, P.H. (1971). *J. Colloid Interface Sci.* **36**, 97.

[18] Ruckenstein, E. (1978). *J. Colloid Interface Sci.* **66**, 531.

[19] Marmur, A. (1979). *J. Colloid Interface Sci.* **72**, 41.

[20] Prieve, D.C., Ruckenstein, E. (1980). *J. Colloid Interface Sci.* **73**, 539.

[21] Fornes, J.A. (1985). *Colloid Polym. Sci.* **263**, 1004.

[22] Kostoglou, M., Karabelas, A.J. (1991). *J. Colloid Interface Sci.* **142**, 297.

[23] Gisler, T., Borkovec, M. (1993). *Langmuir* **9**, 2247.

[24] Dukhin, S.S. (1995). *Adv. Colloid Interface Sci.* **61**, 17.

[25] Behrens, A.H., Borkovec, M. (2000). *J. Colloid Interface Sci.* **225**, 460.

[26] Wu, K.L., Lai, S.K. (2005). *Langmuir* **21**, 3238.

[27] Urbina-Villalba, G., García-Sucre, M. (2005). *Langmuir* **21**, 6675.

[28] Guaregua, J.A., Squitieri, M.E., Mujica, V. (2006). *J. Mol. Struct. THEOCHEM* **76**, 165.

[29] Guaregua J.A., Squitieri, M.E., Mujica , V. (2009). *J. Comput. Methods Sci.* Eng. **9**, 223.

[30] Chen, K.L., Smith, B.A., Ball, W.P., Fairbrother, D.H. (2010). *Environ. Chem.* **7**, 10.

[31] Rahn-Chique, K., Puertas, A.M., Romero-Cano, M.S., Rojas, C., G. Urbina-Villalba, G. (2012). *Adv. Colloid Interface Sci.* **178**, 1.

[32] Ohshima, H. (2013). *Colloid Polym. Sci.* **291**, 3013.

[33] Ohshima, H. (2014). *Colloid Polym. Sci.* **292**, 2269.

83

CATANIONIC SURFACTANTS: NOVEL SURROGATES OF PHOSPHOLIPIDS

Kausik Manna and Amiya Kumar Panda
Department of Chemistry, University of North Bengal, Darjeeling 734 013, West Bengal, India

83.1 INTRODUCTION

Because of the complications in isolation, purification, and characterization as well as their stability, it has been necessary to develop phospholipid mimetic synthetic amphiphiles in order to understand their various biophysical properties at the molecular level. Recently, a new class of bipolar amphiphiles has been developed that consists of two oppositely charged long-chain surfactants and thus are named as *catanionic surfactants*. The various aggregates formed by synthetic catanionic surfactants in aqueous media are considered to serve as feasible substitutes of phospholipids in comparison with the high cost, stability, and ease of preparation of liposomes [1–8]. Besides, they can serve as novel drug–DNA delivery agents [9–13] and templates for the synthesis of nanomaterials [14–17]. The ease of availability and low cost of single-chain surfactants, compared to the double-tailed phospholipids, provide significant motivation in using catanionic surfactants as neoteric materials for the synthesis of vesicles. Structure of the catanionic surfactants resembles that of the zwitterionic phospholipids (Fig. 83.1), although their polar head moieties are generally composed of two oppositely charged groups bound electrostatically. Despite their structural differences, the aggregates they form in the bulk solution exhibit the same rich diversity of morphologies that are also observed in phospholipids; these range from stable vesicles to liquid crystals, depending on the composition, temperature, and ionic strength of the medium [9, 18]. The designation *catanionic surfactant* was first coined in 1987 by Jokela et al. [19]. It may be noted that the studies on such systems started earlier; in 1943, Scott et al. [20] prepared the crystalline surfactants octyltrimethylammonium–octanesulfonate and decyltrimethylammonium–decylsulfonate for the first time and termed those as *double long-chain salts*. They investigated the colloidal electrolytic properties of those synthesized catanionic surfactants in aqueous media. In 1987, Jokela et al. [19] synthesized four different catanionic surfactants: dodecylammonium–dodecanoate, dodecylammonium–dodecyl sulfate, dodecyltrimethylammonium–dodecyl sulfate and dodecylethyldimethylammonium–dodecyl sulfate, and they studied the detailed phase equilibria of those systems. For the first time such a study revealed the existence of various phases, including isotropic micellar, lamellar (Fig. 83.2), and liquid crystalline phases. They noticed the structural and behavioral similarity between the prepared catanionic surfactants and naturally occurring zwitterionic phospholipids (Fig. 83.3) and proposed that the catanionic surfactant–water systems can be used as suitable theoretical models for studies to identify and clarify the properties of phospholipids.

In the last few decades catanionic surfactants have attracted the attention of scientists throughout the world and have been studied with focus on several aspects. Among them, the most striking outcome is the formation of vesicles by catanionic surfactants and its successful

Encyclopedia of Biocolloid and Biointerface Science, Volume 2, First Edition. Edited by Hiroyuki Ohshima.
© 2016 John Wiley & Sons, Inc. Published 2016 by John Wiley & Sons, Inc.

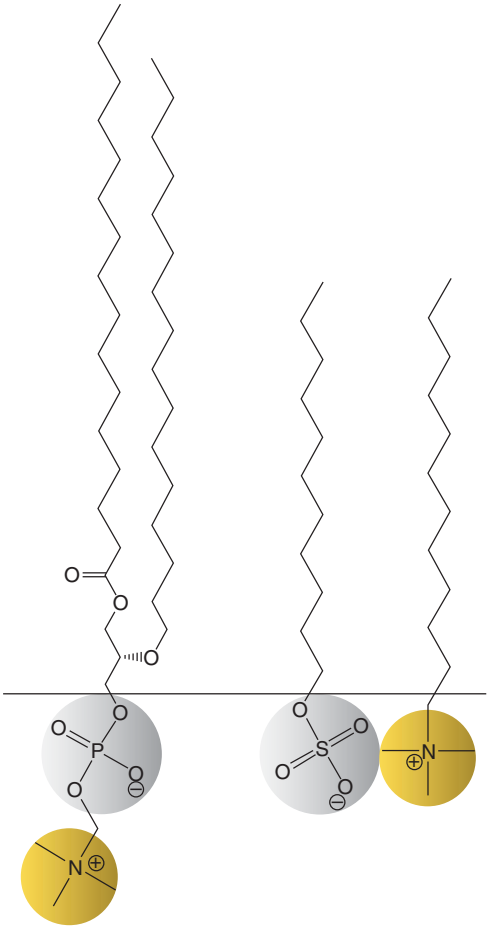


FIGURE 83.1 Structural comparison between a phospholipid (DPPC, shown on left) and a typical catanionic surfactant molecule (shown on right).

application in drug or DNA delivery [9–13, 21]. Besides, the other aggregates of catanionic surfactants such as liquid crystalline phase [22–27], monolayer at air–water interface [24,28–34], micelles [23,26,31,35–38], have also fascinated scientists for their resemblance to phospholipids. They can be considered as a new class of pseudo-double-chained surfactants, which have been developed with a potential as the

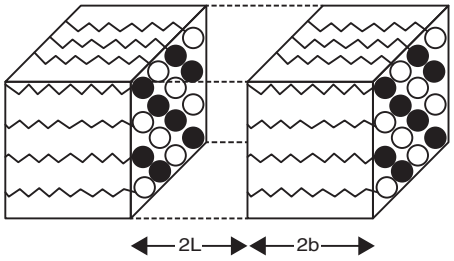


FIGURE 83.2 Schematic representation of the lamellar phase, where 2*L* is the thickness of the water layer and 2*b* is the thickness of the hydrocarbon layer. (Adapted from Jokela et al. 1987 [19], pp. 3291–3298.)

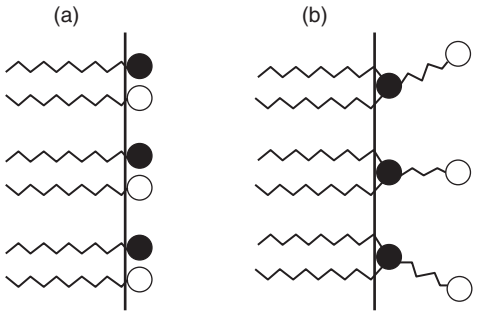


FIGURE 83.3 Orientation of the polar headgroups relative to the hydrocarbon surface: (a) catanionic and (b) zwitterionic phospholipid. (Adapted from Jokela et al. 1987 [19], pp. 3291–3298.)

substitute of phospholipids for the study of various biophysical phenomena [5, 39, 40].

It should be noted that the synthesis, properties, and applications of catanionic surfactants cover a vast area of colloid science, so in this chapter we briefly discuss the synthesis of catanionic surfactants and its characterization procedures, the properties of catanionic surfactants of various compositions and fixed compositions (isolated IPA) in aqueous media, and its applications based on the aqueous media and pure molecular state of IPA.

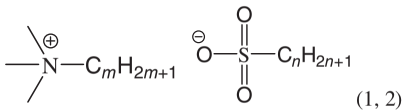
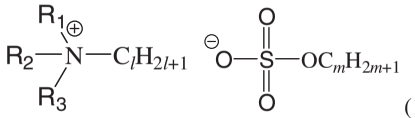
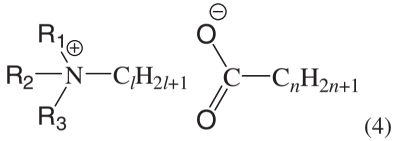
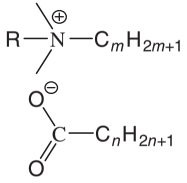
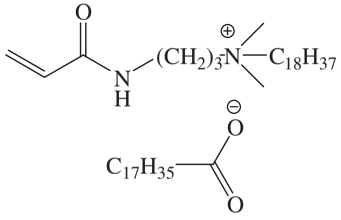
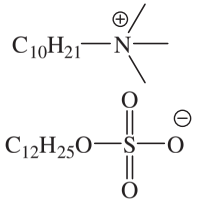
83.2 CLASSIFICATIONS

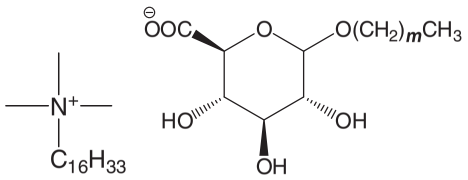
On the basis of their differences in precursors, structure, properties, and applicability, catanionic surfactants can be divided into four main categories:

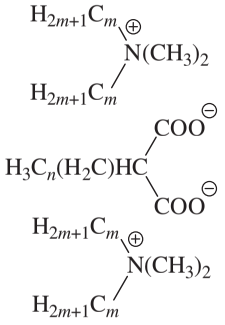
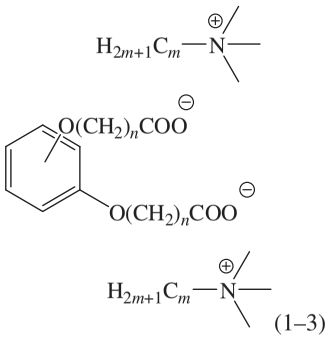
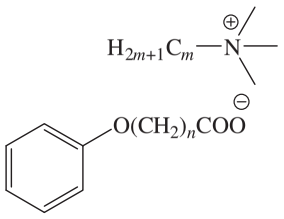
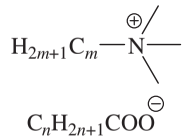
1. *Pseudo-double-chain catanionic surfactants*–the simplest class of catanionic surfactants, obtained by the combination of two oppositely charged single- chain surfactants
2. *Pseudo-triple- and quadruple-chained catanionic surfactants*–combination of two oppositely charged multiple-chain or multiple-head surfactants (gemini surfactants, bolaamphiphiles)
3. *Polymerizable catanionic surfactants*–combination of surfactants containing a polymerizable group
4. *Amino acid–and amino sugar–derived catanionic surfactants*–synthesized by either cationic or anionic surfactants, both derived from amino acid and sugar.

Details on the structure, synthetic methods, and investigated properties of these four types of surfactants are listed in Table 83.1. Each individual catanionic surfactant serves a unique purpose. Table 83.1 also lists the various IPA systems synthesized and studied by various research groups in chronological order.

TABLE 83.1 Chronological Order of Some IPA Systems Synthesized, Isolated, and Investigated and Available in the Literature

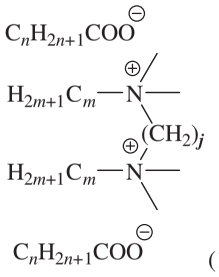
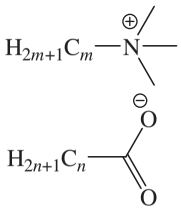
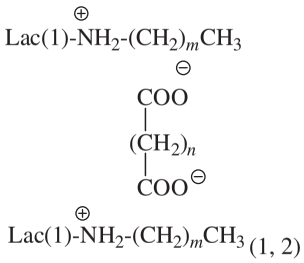
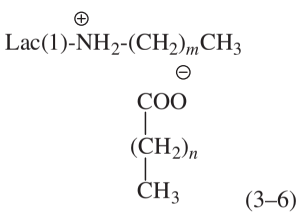
IPA system	Chain length	Synthetic method(s)	Investigation highlights	Ref. (year of report)
 (1, 2)	1. $m = 8$, $n = 8$ 2. $m = 10$, $n = 10$	Precipitation method (a)	3. Conductance in aqueous media 4. Micellar composition	20 (1943)
 (1–3)  (4)	1. $R_1 = R_2 = R_3 = CH_3$, $l = 12$, $m = 12$ 2. $R_1 = R_2 = R_3 = H$, $l = 12$, $m = 12$ 3. $R_1 = R_2 = CH_3$, $R_3 = C_2H_5$, $l = 12$, $m = 12$ 4. $R_1 = R_2 = R_3 = H$, $l = 12$, $n = 12$	Precipitation method (b), extraction method, and ion exchange method	1. ^{2}H-NMR spectroscopy (phase equilibria) 2. Phase behavior 3. Effect of polar headgroup	19 (1987)
 (1–4)	1. $m = n = 14$; R = H 2. $m = n = 16$; R = H 3. $m = n = 18$; R = H 4. $m = n = 18$; R = CH_2CH_2OH	Ion exchange followed by precipitation method (b)	1. Vesicle (TEM image) 2. Gel filtration 3. Surface pressure–area isotherm	45 (1990)
	–	Ion exchange method	1. Polymerized vesicle 2. Gel permeation chromatography 3. Vesicle stability	46 (1991)
 (1–3)	1. $m = n = 10$ 2. $m = n = 12$ 3. $m = n = 14$	Precipitation method (b)	1. Catanionic surfactants 2. Liquid crystals 3. Polymorphism 4. Thermal analysis 5. X-ray diffraction	47 (1997)

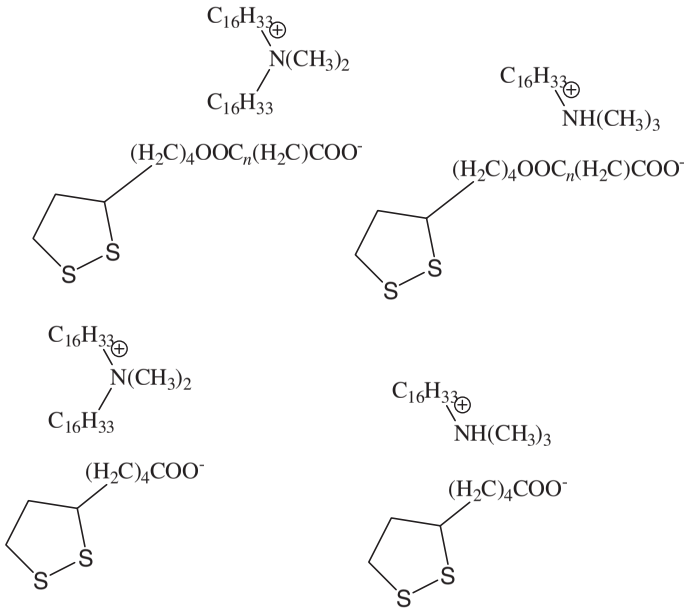
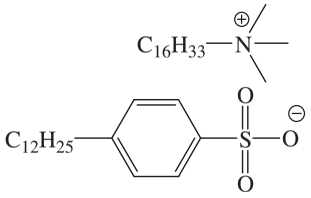
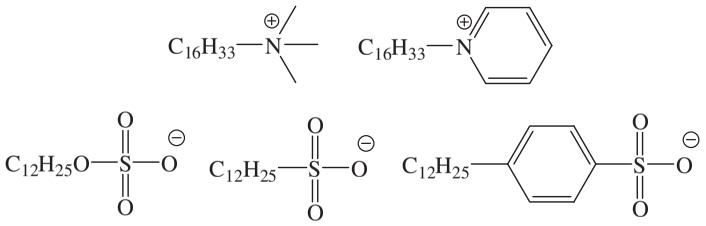


	m = 3, 7, 11	Extraction method	1. Interfacial properties 2. Aggregate size	48 (1997)
 (1–3)	1. m = 13, n = 13 2. m = 15, n = 15 3. m = 17, n = 17	Ion exchange method	1. Bilayer properties 2. Liposome 3. Carboxyfluoresceine release	49 (1998)
 (1–3)	m = 15, n = 10 *1.* Ester group in *ortho* *2.* Ester group in *meta* 3. Ester group in *para*	Ion exchange method	1. Bilayer structures 2. Membrane properties 3. Riboflavin encapsulation	2 (1998)
	m = 15, n = 10			
	m = 15, n = 15			

(continued)

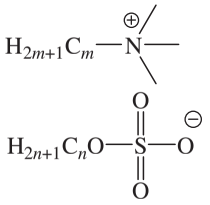
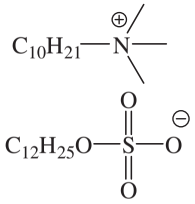
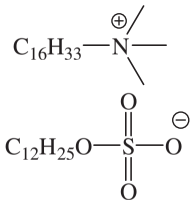
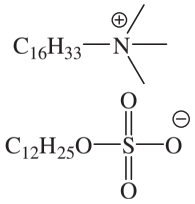
TABLE 83.1 ***(Continued)***

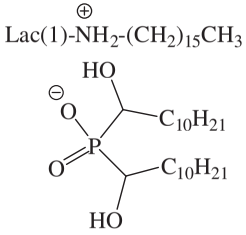
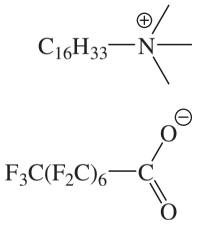
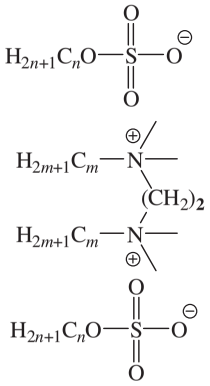
IPA system	Chain length	Synthetic method(s)	Investigation highlights	Ref. (year of report)
 (1–8)	$m = 15$, $n = 15$ $j = 2$–6,8,10,12	Ion exchange method	1.Polyethylene spacer 2.Riboflavin ncapsulation 3. Ion transport phenomena 4. Bilayer structures 5. Membrane properties	1 (1999)
	$m = 16$, $n = 15$	Ion exchange method	1. Bilayer structure 2. Ion-sensing properties	50 (1999)
 (1, 2)  (3–6)	1. $m = 7$, $n = 12$ 2. $m = 15$, $n = 12$ 3. $m = 7$, $n = 6$ 4. $m = 7$, $n = 10$ 5. $m = 15$, $n = 6$ 6. $m = 15$, $n = 10$	Proton exchange method	1. Aminoglucose-derived catanionic surfactant 2. Surface properties 3. Lamellar phase 4. Anti-HIV activity	41,42 (1999)

	–	Ion exchange method	1. Polymerization of IPA 2. Liposome 3. Encapsulation and release of fluorescence markers	3 (2002)
	–	Ion exchange method	1. Catanionic vesicles 2. Glucose encapsulation 3. Permeation kinetics	51 (2002)
	IPA systems were prepared by permutation and combination of cationic and anionic surfactants	Precipitation method (b)	1. Thermotropic liquid crystals 2. Effect of headgroups 3. Asymmetric chain length	52 (2005)

(continued)

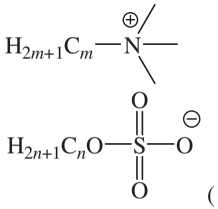
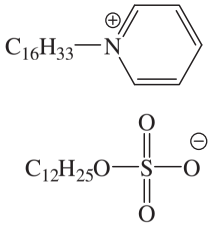
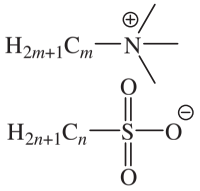
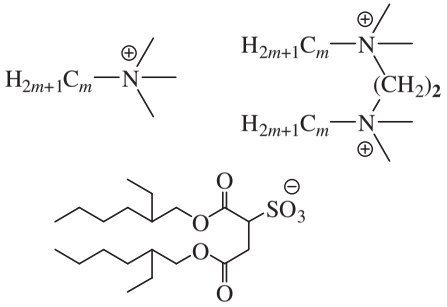
TABLE 83.1 ***(Continued)***

IPA system	Chain length	Synthetic method(s)	Investigation highlights	Ref. (year of report)
 (1–4)	1. $m = 12$, $n = 12$ 2. $m = 14$, $n = 12$ 3. $m = 16$, $n = 12$ 4. $m = 14$, $n = 14$	Precipitation method (b)	1. Cosolvent effect 2. Stability of catanionic vesicles 3. Lifetime of catanionic vesicles	40 (2005)
	–	Precipitation method (b)	1. Cosolvent effect 2. Phospholipid 3. Comparison between stabilities of liposomes and catansomes	8 (2008)
	–	Precipitation method (b)	1. Catanionic vesicles 2. Reactive oxygen species 3. Mitochondrial membrane potential 4. Cell cycle 5. Flow cytometry 6. Apoptosis	Kuo et al. (2008) [53]
	–	Precipitation method (b)	1. Monolayer at air–water interface 2. Monolayer stability	5 (2008)

	–	Proton exchange method	1. Stable vesicle 2. Drug vectorization 3. Encapsulation efficiency 4. Entrapment stability	54 (2008)
	–	Precipitation method (b)	5. Hydro-genated/fluorinated catanionic surfactant 6. Interfacial monolayer 7. Surface pressure–area isotherm 8. Atomic force microscopy	55 (2009)
	m = 14,16,18 n = 14,16	Evaporation method	1. Mesophase 2. Soft crystal 3. Smectic liquid crystal 4. Van der Waals interactions 5. Electrostatic interactions 6. Birefringence	44 (2010)

(continued)

TABLE 83.1 ***(Continued)***

IPA system	Chain length	Synthetic method(s)	Investigation highlights	Ref. (year of report)
 (1–5)	1. $m = 10$, $n = 12$ 2. $m = 12$, $n = 12$ 3. $m = 14$, $n = 12$ 4. $m = 16$, $n = 12$ 5. $m = 18$, $n = 12$	Extraction method	1. Conductance behavior 2. Phase behavior 3. Liquid crystalline behavior 4. Interfacial monolayer 5. Film morphology.	24 (2010)
	–	Extraction method	1. Catanionic micelle 2. Regular solution theory 3. Interaction parameter 4. Surface pressure–area isotherm 5. IPA morphology 6. Liquid crystal	25 (2010)
	$m = 12$–16 $n = 6$ - 10	Precipitation method (b)	1. Headgroups 2. Thermotropic liquid crystals 3. Chain length mismatch 4. Interdigitation	56 (2013)
	m = 12–18 IPA systems were prepared by permutation and combination of cationic and anionic surfactants	Extraction method	1. Mesophase structure 2. Ion pair amphiphile 3. Room-temperature liquid crystal 4. Amphiphilic liquid crystal	57 (2013)

83.3 PREPARATION AND ISOLATION

Catanionic surfactants are also known as *ion pair amphiphiles* (IPA) as they are synthesized by mixing two oppositely charged amphiphiles. It is worth mentioning that the catanionic surfactants are generated only when an equimolar amount of two oppositely charged surfactants are mixed. It should be kept in mind that as a catanionic surfactant is generally a neutral molecule, the term *ionic equivalence* is more appropriate than *equimolar* in some cases where either of the ionic surfactants holds two headgroups (e.g., gemini surfactants, bolaamphiphiles). Therefore, in such cases one mole equivalence of double-headed ionic surfactant should be mixed with two mole equivalence of single-headed oppositely charged surfactants to obtain neutral catanionic surfactant or IPA. Several methods have been used to synthesize catanionic surfactants or IPA by several research groups [41–44]. Among those, five distinguished methods can be described in general. T

83.3.1 Extraction Method

This method consists in mixing oppositely charged surfactants in water whereby the precipitate of the IPA is formed; the formed IPA is then extracted using suitable organic solvents and the salts remaining in the aqueous phase.

83.3.2 Precipitation Method

Surfactants prepared by this method can be processed in one of two ways:

(a) Precipitation of the potassium, sodium, or lithium salt of the anionic surfactant with silver ions in the aqueous phase. After purification of the precipitate, it is dissolved in a mixture of water and organic solvent, and an equivalent amount of the cationic surfactant with a chloride or bromide counterion is then added to the solution. The pure catanionic surfactant is finally b

(b) Preparation of IPA generated by mixing of supersaturated aqueous solution of two oppositely charged surfactants. The IPA precipitates are removed by filtration or centrifugation where the residual salts remain in solution.

83.3.3 Ion Exchange Method

In this method the cationic surfactant is converted into its hydroxide form and the anionic surfactant into its protonated form by passing through suitable ion exchange resin. The two surfactant solutions are then mixed to produce the pure catanionic surfactant through an acid–base reaction.

83.3.4 Evaporation Method

In this method constituent cationic and anionic surfactants are dissolved in low-boiling-point organic solvents and are mixed in ionic equivalent ratio. The solvents are then evaporated out, leaving solid IPA molecules.

83.3.5 Proton Exchange Method

This method consists in mixing an equimolar quantity of an amino sugar–derived surfactant with an amphiphile bearing an acidic function in water. By a simple acid–base reaction, equimolar catanionic amphiphiles are obtained without residual salts.

83.4 CHARACTERIZATION OF ISOLATED IPA

Since the catanionic surfactants are formed by means of electrostatic attraction between the oppositely charged headgroups of the cationic and the anionic species, characterization of the catanionic surfactants is based on the headgroups and their surrounding environments. Isolated catanionic surfactants are generally characterized by ^{1}H-NMR, FT-IR, or XRD analysis. It may be mentioned that each and every method has its own advantages and disadvantages. The methods are described below, with examples.

83.4.1 ^{1}H-NMR Spectroscopy

In ^{1}H-NMR spectra of catanionic surfactants significant changes in the chemical shift (δ) values of the protons near the headgroups (α and β protons) are observed and compared to those of the precursors [1, 2, 24, 25, 58, 59]. Symmetric and asymmetric chain catanionic surfactants show different δ values for the same headgroups [24]. Results on the NMR studies for a catanionic surfactant comprising hexadecyltrimethylammonium cation and the dodecylsulfate anion are mentioned here in as catanionic surfactants represent one of the simplest systems. The different protons for the IPA can be assigned as shown in Fig. 83.4.

It is obvious that for the IPA, the peaks for the α,α', β,β', and γ γ' protons will be shifted because of the proximity of the charged headgroups. On the other hand, the NMR peak for the terminal protons as well and the other protons will not be significantly changed. Such an observation was reported by Maiti et al. [24]. According to that team of researchers, the following peaks are representative for the IPA: $C_{16}TA^+$ DS^- : 0.87 (t, 6H, ω,$\acute{\omega}$), 1.25 [s, 40H, (CH2)12, 8], 1.33 (s, br, 4H γ, γ'), 1.62–1.72 (q, 2H, β'), 1.89 (s, br, 2H, β), 3.27 [s, 9H,N(CH_3)$_3$], 3.37-)3.42 (t, 2H, α), 3.99 (t, 2H, $\acute{\alpha}$) (where the abbreviations s, d, t ,q, br, etc. have their usual meanings). The same research group described the structural characterization of ion pair amphiphiles formed between hexadecyl pyridinium ion and dodecyl sulfate ion in another report [25].

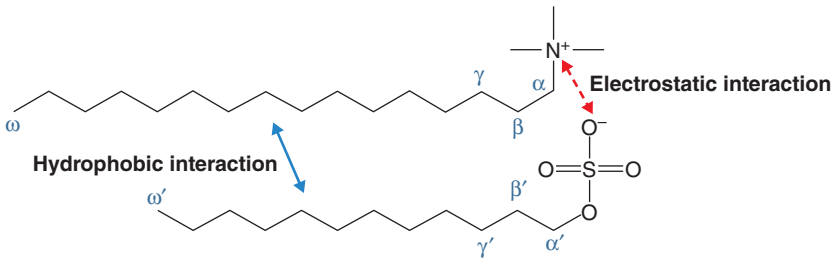


FIGURE 83.4 Cetyltrimethylammonium dodecylsulfate (CTA^+DS^-) molecule.

83.4.2 FT-IR Spectroscopy

The stretching and bending modes of vibration of the various bonds with and around the headgroups are affected by the electrostatic attraction in catanionic surfactants [24, 25, 31]. Vibrational spectroscopy is a very simple yet informative tool used to characterize catanionic surfactants by means of the changes in those vibrational frequencies with respect to the individual precursors. Table 83.2 summarizes the FTIR vibrational frequencies of the individual C–H bonds of an isolated catanionic surfactant, octadecyltrimethylammonium–dodecylsulfate ($C_{18}TA^+DS^-$), and its precursors. Data show that the vibrational frequencies of headgroups and the methylene groups near them change significantly during formation of the catanionic surfactant.

83.4.3 X-Ray Diffraction Study

X-ray diffraction studies on catanionic surfactants can provide useful information on the surfactants' crystal lattice structures [24, 25, 59]. Usually they remain in the form of interdigitated bilayers. The headgroups remain separated by two paraffinic layers with an equimolar mixing of the alkyl chains of the cationic and anionic surfactants and remain in *trans* configuration [59]. Figure 83.5 illustrates the powder XRD pattern of hexadecylylpyridinium–dodecylsulfate (CP^+DS^-).

Characteristic XRD diffraction lines confirm the bilayer lamellar structure of catanionic surfactants [24, 25]. Size and nature of the headgroup plays an important role in describing the structure of crystal lattice. Electrostatic interaction between two oppositely charged headgroups and the hydrophobic–hydrophobic interaction between their alkyl chains are key factors in the packing arrangements of the crystal lattice of the catanionic surfactants. Interlamellar electrostatic interactions between headgroups neutralize the surface charge density and thus help to form closely packed ion pairs, while the van der Waals interaction between their hydrophobic tails forces their alkyl chains into a compact packing arrangement.

TABLE 83.2 FT-IR Results of Precursors (SDS and $C_{18}TAB$) and Their IPAs ($C_{18}TA^+DS^-$) at 298 K

	Wavenumber (cm^{-1})						
Compound	$\gamma_{as}(CH_3\text{-}N^+)$	$\gamma(CH_3)$, $\gamma(CH_2)$	$\delta(CH_3)$, $\delta(CH_2)$	δ_{as}(S–O)	δ_s(S–O)	δ_{as}(C–N)	$\delta(CH_2)_p$ rocking
SDS	ab	2955 (s) 2920 (s) 2853 (s)	1472 (s) 1440 (w) 1399 (vw) 1380 (w)	1252 1222	1083		722 (s)
$C_{18}TABr$	3015 (m)	2955(sh) 2920 (s) 2853 (s)	1460 (s) 1440 (w) 1399 (w) 1380 (w)	ab	ab	970 (vw)	722 (w)
$C_{18}TA^+DS^-$	3036 (m)	2955(sh) 2920 (s) 2853 (s)	1473 (s) 1430 (wm) 1397 (vw) 1380 (w)	1252 1222	1059	990 (ms)	722 (ms)

Abbreviations: ab—absent; m—medium; ms—medium strong; mw—medium weak; s—strong; sh— shoulder; sm—small; vs—very strong; vw—very weak; w—weak.
Source: Table reconstructed from Panda et al. [24].

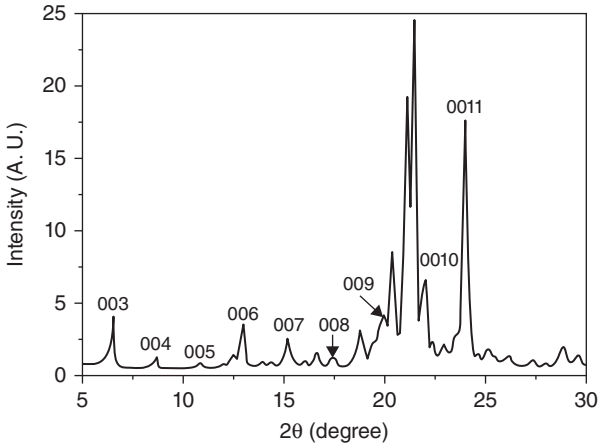


FIGURE 83.5 Powder XRD pattern of catanionic surfactant hexadecylpyridinium–dodecylsulfate, (Adapted from Maiti et al. 2010 [25], pp. 88–98.)

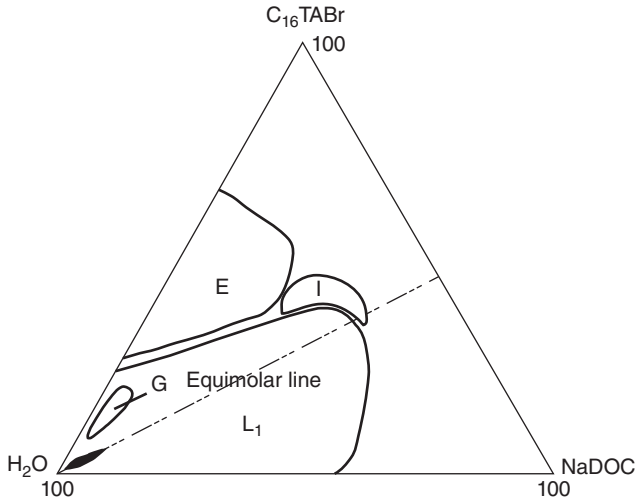


FIGURE 83.6 Pseudoternary phase diagram of NaDOC/C_{16}TABr/H_2O system at 25°C. The dashed line represents the equimolar region. (Different phases: E, normal hexagonal phase; I, normal cubic phase; G, gel phase; L_1, isotropic micellar phase.) (Adapted from La Mesa et al. 1985 [62], pp. 373–391.)

83.5 PROPERTIES

The properties of catanionic surfactant systems have been grouped into two main categories according to surfactant composition and synthesis and how they are studied:

1. Solutions of oppositely charged surfactant solutions are mixed as a function of variable composition in a wide range surfactant concentration. The compositional and total surfactant concentration effects on phase equilibria and aggregation behavior are studied mainly in this way. However, catanionic surfactant systems are accompanied by impurities of either of the constituent surfactants and counterions, which influence the properties of such systems.
2. The catanionic surfactant is synthesized at fixed compositions, isolated, purified, and studied. The selective and targeted study of catanionic surfactants or IPA thus can be performed in an impurity-free environment.

83.5.1 Properties of Catanionic Surfactants as Functions of Composition and Concentration

83.5.1.1 Phase Equilibria. A single-chain cationic or anionic surfactant exhibits only one (isotropic micellar) phase in water. The combination of two oppositely charged surfactants in aqueous media introduces more components of the surfactant–water systems. In addition to that, the synergism between opposite charges and dissimilarity in structure and some other physicochemical properties between two kinds of surfactants introduce both complexity and versatility in the phase behavior of catanionic surfactant systems. The packing parameter, defined as $p = v/al$ (where v is volume of the hydrocarbon chain, l is optimal length close to the fully extended chain length, and a is surfactant headgroup area), is expected to play a major role in the aggregation pattern of surfactants. The assembly of two surfactants with different structures can result in a variety of curvatures of amphiphilic films and, therefore, a wide variety of aggregates and hence various phases. Owing to the suppleness of their structure, catanionic surfactants reveal various phases in semidilute and concentrated aqueous solutions such as micelle, gel, vesicle, lamella, and liquid crystal [21,24,26,27,35,60,61]. The concurrence of two inverted hexagonal phases in different systems has also been observed. Precipitation or coacervation is one of the most significant features of the phase behavior for most catanionic surfactant systems at the equimolar region, which occurs irrespective of the overall surfactant concentration [24, 35].

In the high-concentration region the phase behavior of catanionic surfactants is more diverse than in the semidilute and dilute regions. Liquid crystalline phases, such as normal and cubic hexagonal, normal cubic, and lamellar, dominate over other phases in the higher-concentration region [27, 62]. Vesicles are seldom formed in the extremely high concentration range. Figure 83.6 represents the ternary phase diagram for the sodium deoxycholate (NaDOC)/hexadecyltrimethylammonium bromide (C_{16}TABr)/water system. The phase diagram shows occurrence of normal hexagonal, normal cubic phases at high concentration range, while the gel and isotropic micellar phases are formed in the semidilute region of the surfactants. Formation of the precipitates or coacervates at equimolar composition generally take place in the dilute or semidilute region.

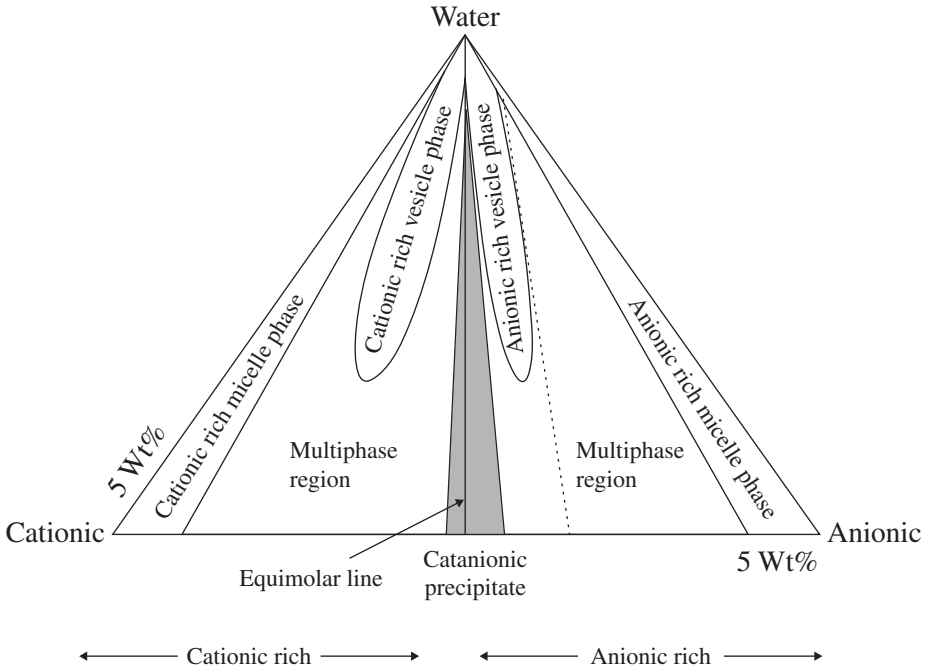


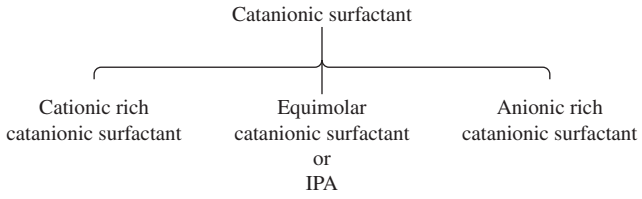
FIGURE 83.7 Schematic phase diagram of symmetric pseudo-double-tail catanionic surfactant mixture, single-chain cationic (12-carbon)–single-chain anionic (12-carbon)–water system, in the very dilute region of the pseudoternary system. Compositions are in wt%. (Adapted from Khan et al. 1996 [63], pp. 614–623.)

The phase behavior is equally diverse even in the semidilute and dilute regions [24, 35]. Figure 83.7 is a schematic phase diagram of a symmetric pseudo-double-chain catanionic surfactant. Catanionic precipitates are formed in the equimolar region, and in the cationic and anionic surfactant–rich regions, the precipitates are redissolved to form the stable vesicle phase. On further increase in the parent surfactant concentration, transition from vesicle to micellar phase occurs. Reports on the formation of rodlike and wormlike micelles in cationic- or anionic-rich regions are also available in the literature [26, 35]. The vesicle phase remains in equilibrium with multiphase regions and with catanionic precipitate. The phase behavior is predominantly dependent on the surfactant structure: number of alkyl chains, chain length, and alkyl chain symmetry; however, the surfactant polar headgroups were found to have minor effects on the phase behavior in the dilute region (e.g., the asymmetric pair hexadecyltrimethylammonium bromide and sodium octylsulfate [64]). One of the most interesting findings of the phase manifestation of catanionic surfactants is the concurrence of precipitate and vesicle phases near the equimolar region. Cationic- and anionic-rich mixed surfactants form vesicles very near to the equimolar region, which led scientists to believe that the formation of pseudo-double-chain surfactants in the equimolar region explains why the surfactants are insoluble in aqueous medium as a result of enhanced hydrophobicity.

All combinations of oppositely charged surfactants do not exhibit phase variation. Occurrence of the different phases depend mainly on the nature of the surfactants, apart from the other physicochemical conditions. According to the report of Panda et al. [35], sodium cholate (NaC) exhibits only one (isotropic micellar) phase in combination with alkyltrimethylammoniumbromhides (C_nTABr), whereas in the case of its derivative sodium deoxycholate (NaDC), various phases are observed in aqueous media. Interestingly, only slight variation in the structure of bile slats (NaC and NaDC) abruptly changes the macroscopic phase behavior. Formation of only small micelles by catanionic surfactants of NaC and C_nTABr implies that the spontaneous curvature of the aggregates is sufficiently higher. Although the NaDC-C_nTABr catanionic surfactants exhibit various phases and form various aggregates (normal micelles, wormlike micelles, and vesicle), the radii of the vesicles formed are shorter than those of vesicles formed by conventional long-chain catanionic surfactants.

Review of the above mentioned phase manifestations clearly implies that the different phases in catanionic surfactants lie in three main regions: cationic-rich, anionic-rich, and equimolar catanionic surfactants. In both the cationic- and anionic-rich regions, various phases are observed and in the equimolar region the complete precipitation of catanionic surfactant occurs; therefore, this can be considered as a signature composition where formation of catanionic surfactants are confirmed. The mixture thus formed at equimolar cationic

and anionic surfactant ratio is often known as *coacervate* or *ion pair amphiphile* (IPA):



The separation of IPA from the bulk phase through precipitation completely frees the IPA from counterions. The removal of counterions further strengthens the electrostatic interactions between the two surfactants, which changes the total area occupied by these polar headgroups and subsequently the packing parameter (p). As a result, IPA is significantly different from the catanionic surfactants at nonequimolar compositions in various physicochemical aspects.

83.5.1.2 Electrical Properties. Replacement of small counterions from the individual surfactants by long-chain oppositely charged ionic surfactants can abruptly change the electrical property of aqueous cationic surfactants owing to the strong synergism between oppositely charged surfactants. In the first report on catanionic surfactants [20], the electrical behaviors of two synthesized catanionic surfactants were studied by means of electrical conductance. The appearance of sharp breakpoints in the conductance–surfactant concentration profiles implied that the change in the strong long-chain noncolloidal electrolytes in the premicellar region might be due to the weak colloidal electrolytes (micelle) in the postmicellar region (Fig. 83.8). In this study the bulk as well as micellar compositions were quantified by means of electrical conductometry. The unexpected nonneutrality of micelles of catanionic surfactants, as indicated by the increase in conductance of catanionic surfactants (Fig. 83.8) after micellization, revealed the stoichiometric inequality of the oppositely charged surfactants in their mixed micelles. Either anionic or cationic excess exists in the micelles even at equimolar composition. Similar results were also found by Panda and his coworkers [35] in the zeta-potential (ZP) measurements of catanionic surfactants of alkyltrimethylammonium bromide and bile salts (Fig. 83.9). The ZP values were found to be nonzero at equimolar composition of cataionic surfactants. The results again prove that micellar composition differs from that of bulk depending on the nature of the surfactants.

Conductometric titrations can also conveniently sense the pulse of the formation of different phases in the aqueous catanionic surfactant solutions. Onset of the formation of different phases and various aggregates lead to the change in conductivity of catanionic surfactant systems ranging from

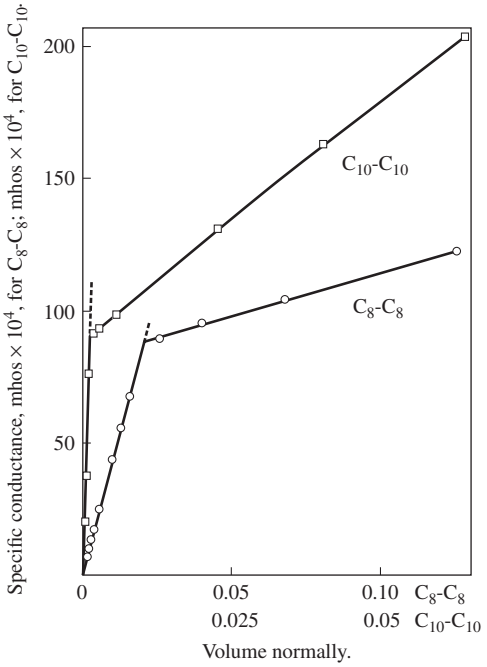


FIGURE 83.8 Specific conductance of aqueous solutions decyltrimethylammonium decanesulfonate (at 40°C) and octyltrimethylammonium octanesulfonate (at 25°C). (Adapted from Scott et al. 1943 [20], pp. 698–701.)

cationic rich to anionic rich region. Some catanionic surfactant systems have been studied conductometrically at a wide range of concentrations by Panda et al. [24,35]. In those studies the onset of various phases could be identified for both variable and fixed total surfactant concentrations (Fig. 83.10). Like phase behavior, the conductance behavior of catanionic surfactants also changes from dilute to concentrate region as a function of overall surfactant concentration (Fig. 83.10). The conductance behavior just reversed from dilute to concentrate region. The onset of micellization or formation of aggregates can clearly be predicted from the breakpoints.

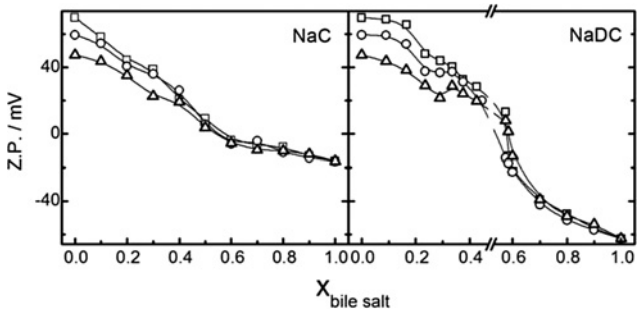


FIGURE 83.9 Variation in zeta-potential (ZP) with the mole fraction of bile salt ($x_{\text{bile salt}}$) at 25°C; bile salts are labeled in the figure (symbols: □ C_{16}TABr; ∘: C_{14}TABr; Δ C_{12}TABr; total surfactant concentration = 50 mM) [35].

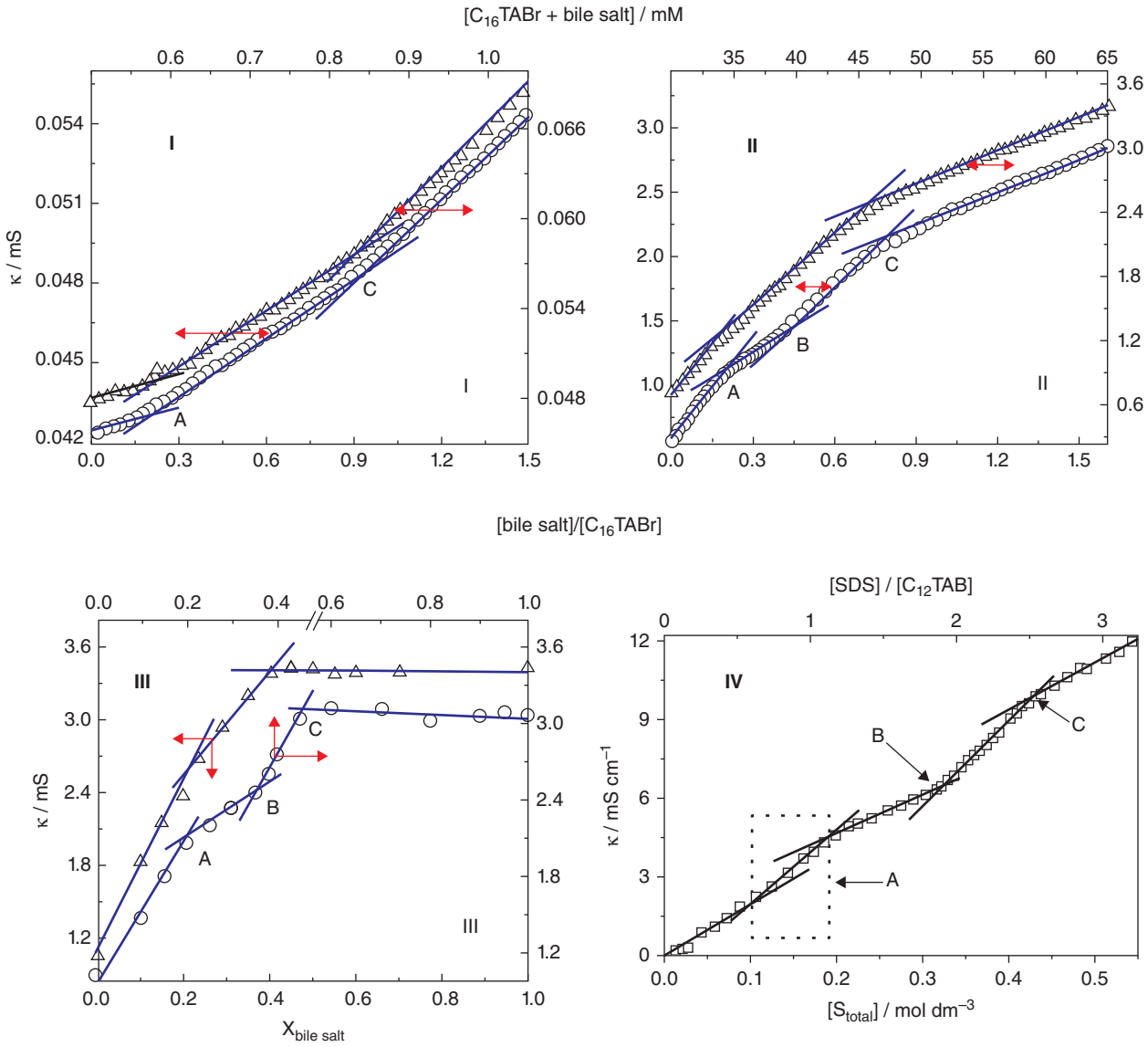


FIGURE 83.10 Variation in electrical conductance with surfactant composition/concentration of some catanionic surfactant systems. Bile salt–C_{16}TABr systems [35], at variable lower (I) and higher (II) total surfactant concentration and mole ratio; (III) bile salt–C_{16}TABr systems [35] at fixed total surfactant concentration (50 mM) and variable mole ratio (∘ NaDC/C_{16}TABr; Δ NaC/C_{16}TABr). (*A* indicates onset of IPA formation; *B*, onset of gel formation; and *C*, onset of coacervation .) (IV) SDS–C_{12}TABr system [24] (*A* indicates onset of coacervation; *B*, onset of gel formation; *C*, onset of clear solution formation). Temperature: 25°C.

83.5.1.3 Aggregation Behavior in Water. Spontaneous aggregation (like normal surfactants in solution) of IPA is hindered because of its poor solubility in water. Strategies to stabilize IPA suspensions have been suggested by introducing additives [8, 24, 40, 65]. The aqueous solubility of IPA decreases with the increase of hydrophobic chain length of the individual surfactants. Besides, the aqueous solubility or insolubility of IPA resembles that of the phospholipids. Although additives such as cholesterol or bile salts themselves are poorly soluble in water, their presence enhances the aqueous solubility of IPA. Only a small amount of cholesterol (3.5–7.0 mol%) acts most effectively as solubilizing agent; an excess amount of it can have an adverse effect on the solubilization, due to an antagonistic effect. Similar phenomena are also common in living cell membranes; the presence of a trace amount of cholesterol facilitates the solubilization of lipids and hence lipid bilayer formation [66]. In mammalian bile, bile salts help in the solubilization of cholesterol. Through the formation of mixed micelles with lecithin, it increases the water solubility of IPA as well. It is

found that bile salts are better solubilizers at their postmicellar concentrations [24].

Introduction of cosolvents such as alcohol additives enhance the solubility of IPAs in water [40, 65]. It has been found that the cosolvent effect on the enhancement of the solubility of IPA in water follows the order 1-butanol→1-propanol→ethanol→methanol for a given IPA. For a particular cosolvent, the solubility of IPA increases with the concentration of cosolvent, and at sufficiently higher concentration, IPAs prefer to remain in the molecular dispersion state instead of forming aggregates [40].

83.5.2 Properties of Isolated IPA

83.5.2.1 Special Features of IPA: Liquid Crystalline Behavior. The ability to pass through the liquid crystalline (LC) phase in case of catanionic surfactants at aqueous cationic or anionic rich regions were discussed in a previous section. In the aqueous cationic- and anionic-rich regions, the formed LCs are lyotropic, formed due to the amphiphilic aggregation in solvents. Several reports [67–72] are available on the liquid crystalline behavior exhibited by phospholipids. But those lamellae, hexagonal liquid crystalline phases are observed for hydrated phospholipids, which are also lyotropic in nature. However, the liquid crystalline behavior of pure isolated IPA has recently been explored with some unique observations that are typical for IPA. IPA shows thermotropic LC behavior [24, 25, 44, 47, 56, 73] at higher temperatures. It may be noted that catanionic surfactants coomprising quaternary ammonium/pyridinium as cationic headgroups and sulfate/sulfonate as anionic headgroups show thermotropic LC (shown in Table 83.1). Smectic phases are observed for such catanionic surfactants in the majority of cases except the hexagonal columner (discotic) [52, 57] and nematic phases [57]. Some of them show liquid crystalline behavior even at room temperature [57]. Variation in the phase transition temperature depends on the hydrocarbon of the catanionic surfactant systems. It has been observed that double-chain catanionic surfactants exhibit smectic phases and triple- and quadruple-chain catanionic surfactants exhibit hexagonal and nematic phases. The existence of smectic phases is an outcome of the formation of layered structure by the pseudo-double-chain catanionic surfactants and their orientation. Figure 83.11 shows various LC textures observed for some synthesized catanionic surfactants.

83.5.2.2 Insoluble Monolayer at Air–Water Interface. Catanionic surfactants form a two-dimensional (2D) insoluble monolayers at the air–water interface that are considered to be similar to those of the phospholipid monolayers. Decoration of the ensuing monolayer depends on the balance of a competition between hydrophilic and lipophilic groups among the surfactant molecules at the interface through intermolecular interactions; therefore, intermolecular hydrophilic–lipophilic balance (HLB) among the surfactant molecules plays an important role in such cases. Although this fact is similarly applicable to the bulk solution, the nature of this competition is not so prominent in bulk as in Langmuir monolayers. This is because the surfactant molecules are limited to orientation at the 2D interface. Configuration of the monolayer depends mainly on three parameters: (1) tilting of the surfactant chains, (2) minimum area per surfactant molecule, and (3) relative distance between them and their penetration into the bulk phase. All these parameters are governed by the nature of the hydrophilic head and hydrophobic chain of the surfactants [32]. On compression and expansion of the monolayer film, the surfactant molecules reorganize themselves into lower- and higher-energy states, respectively, by changing these structural parameters.

The selective preparation of insoluble IPA monolayer is generally performed by following the same procedure as in case of phospholipids [33, 34]. The IPA monolayer is formed at the air–water interface by spreading a solution of IPA (generally prepared in pure or mixed organic solvents) dropwise at the interface. The films are then characterized by following a procedure similar to that adapted for phospholipid monolayers. While the functionality of the monolayer is generally investigated by surface pressure measurements, structure of the monomolecular films of the IPA are characterized by different techniques, such as fluorescence microscopy, Brewster angle microscopy (BAM), IR spectral analysis, ellipsometry, and atomic force microscopy (AFM). The equilibrium surface tension of IPA dispersions is characteristically lower than those of the solutions of each ionic surfactant separately [29] even at higher concentrations of their CMCs. This demonstrates two factors: (1) that the 2D interface covered by the catanionic surfactant is higher than the area covered by a single-chain surfactant and (2) the existence of strong synergism. The interfacial behavior of IPA monolayer is best understood in surface pressure measurement using the Langmuir technique. Figure 83.12 plots the surface pressure (π)–area (A) behavior of various IPAs at the air–water interface for different catanionic surfactants prepared from alkyltrimethylammonium bromide and sodium dodecyl sulfate. The π–A isotherm for pure DPPC has also been shown in the figure for comparison of the surface activity of the IPA.

Individual components of the IPA are individually highly soluble in water and less likely to form Langmuir monolayer at the air–water interface; instead, they prefer to remain in the bulk through micellization. With the variation in hydrocarbon chain length, IPAs are inclined to exhibit variances in π– A isotherm behavior that are governed by the relative strength of intramonolayer hydrophobic interactions. An IPA with a longer hydrophobic chain prefers to stay at the air–water interface compared to the IPA of shorter hydrocarbon chain. On compression, a 2D monolayer is formed with various

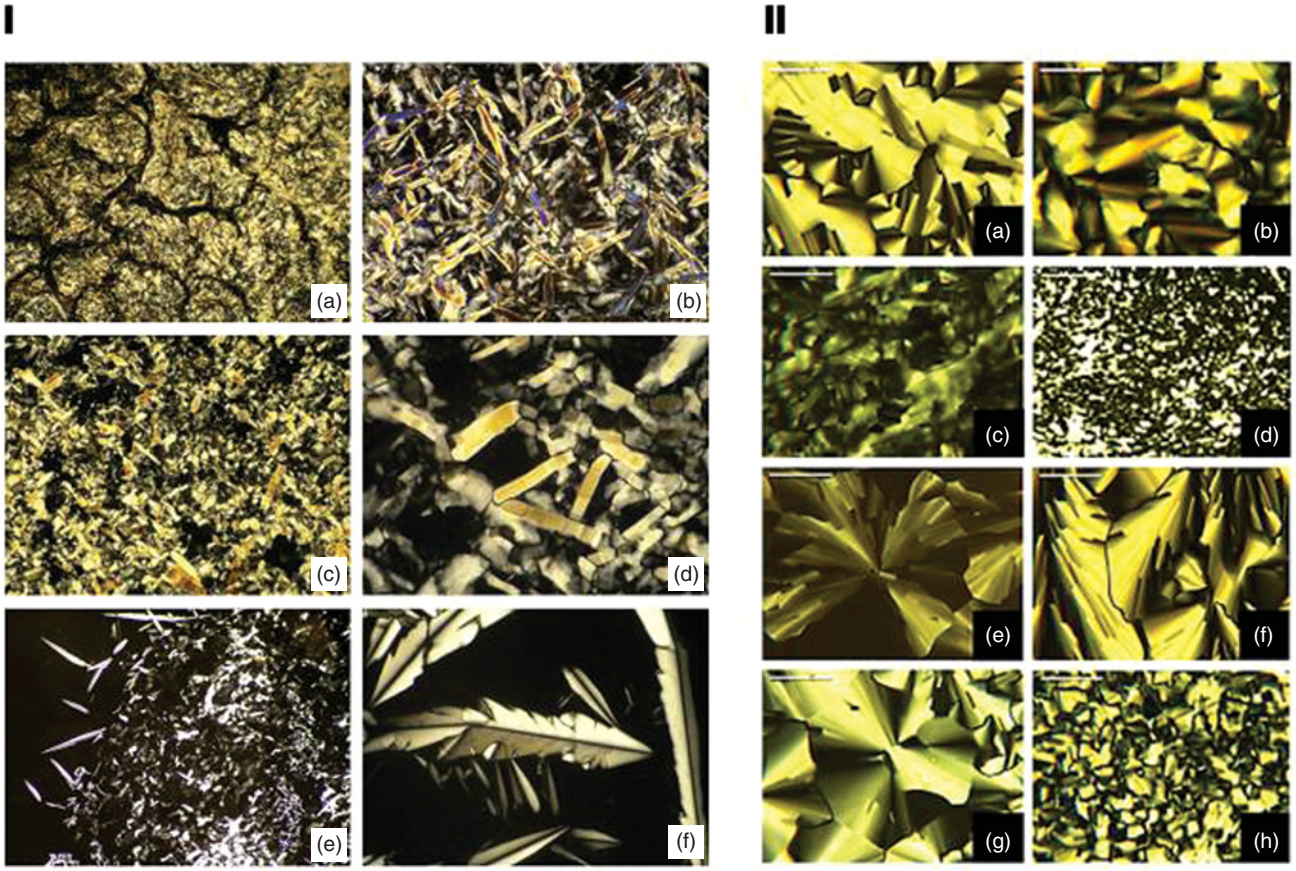


FIGURE 83.11 Optical microscopic texture of liquid crystal phases exhibited by catanionic surfactants: (I) smectic phases—mosaic and featherlike lancet textures (from Matos et al. 2013 [56], reproduced with permission of Elsevier); (II) hexagonal and nematic (D) phases—fan-shaped and nematic textures (from Jose et al. 2013 [57], reproduced with permission of Elsevier).

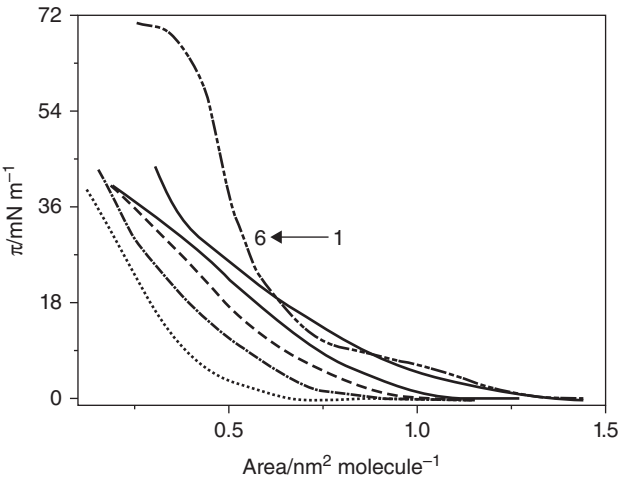


FIGURE 83.12 $\pi - A$ isotherms of IPA at the air–water interface at 298 K. Curves: (1) DPPC; (2) $C_{10}TA^+DS^-$; (3) $C_{12}TA^+$ DS^- ; (4) $C_{14}TA^+$ DS^- ; (5) $C_{16}TA^+$ DS^- ; (6) $C_{18}TA^+DS^-$. (Adapted from Maiti et al. 2010 [24], pp. 867–879.)

patterns depending on surface pressure. Thus the IPAs could be considered to have potentials to act as novel substitutes for the conventional phospholipids. However, the cytotoxicity of the IPA needs to be explored for a particular formulation.

83.6 CATANIONIC MICELLES

The CMC for a binary mixed surfactant system can be theoretically calculated according to the Clint formalism [74]:

$$\frac{1}{CMC} = \frac{x_1}{CMC_1} + \frac{1 - x_1}{CMC_2} \tag{83.1}$$

where, CMC, CMC_1, CMC_2, and x_1 are the CMCs of mixed micelle, surfactant 1, surfactant 2, and mole fraction of cationic surfactant, respectively. The rationale could simply be made applicable to the catanionic surfactants also. Interaction among the constituent surfactants are defined and evaluated by employing the Rubnigh's *regular solution*

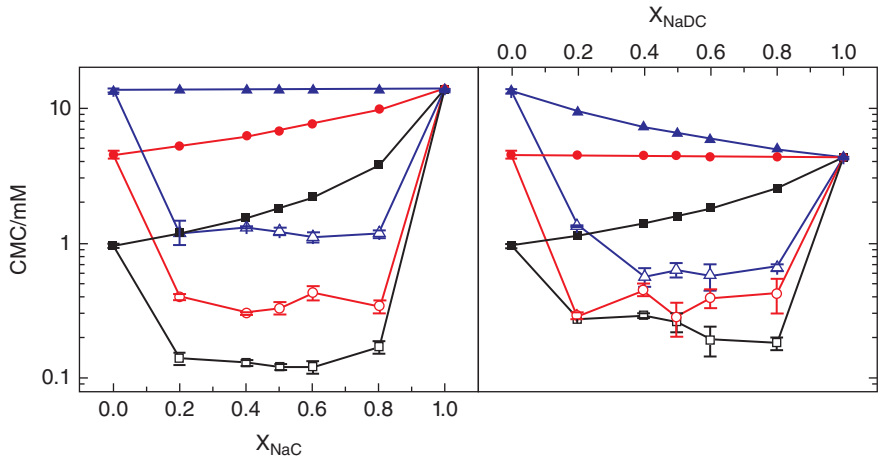


FIGURE 83.13 Variation of CMC for C_nTABr-NaC (left panel) and C_nTABr-NaDC (right panel) mixed surfactant systems with the mole fraction of bile salt ($X_{\text{bile salt}}$). Systems: -□- C_{16}TABr; -○- C_{14}TABr; -Δ- C_{12}TABr. Open symbols correspond to the experimental values, and solid symbols correspond to the theoretically calculated values obtained by Clint formalism. Temperature: 25°C. (From Manna et al. 2012 [35], pp. 10–21.)

theory (RST) [75]. The interaction parameter (β) can be evaluated according to the following equation

$$\beta = \frac{\ln(x_1 CMC / x_1^R CMC_1)}{(1 - x_1^R)^2} \tag{83.2}$$

where x_1^R is the micellar mole fraction of component 1 (herein the cationic surfactants, C_nTABr). x_1^Rcan be obtained from the following equation:

$$\frac{\left(x_2^R\right)^2 \ln\left(\dfrac{CMCx_1}{CMC_1 x_1^R}\right)}{\left(1 - x_1^R\right)^2 \ln\left[\dfrac{CMC\left(1 - x_1\right)}{CMC_2\left(1 - x_1^R\right)}\right]} = 1 \tag{83.3}$$

The equation is repeatedly solved for x_1^R using a computer program by iterative method. The activity coefficient (f^{R}) also reflects the nonideality of a multicomponent mixed micellar system. The f^{R} values of both the surfactants in their mixture can respectively be evaluated using the following equations:

$$\begin{aligned} f_1^R &= \exp[\beta_i (x_1^R)] \\ f_2^R &= \exp[\beta_i (1 - x_1^R)] \end{aligned} \tag{83.4}$$

where subscripts 1 and 2 denote surfactant 1 and surfactant 2, respectively. $f^{\mathrm{R}} = 1$ indicates an ideal mixed system. Several reports [26,31,35–38,76,77] are available on micellization of catanionic surfactants, where remarkable differences in micellization parameters of catanionic surfactants, with significant negative deviation from the ideal values, were noticed. These were attributed to change in both hydrophilic and hydrophobic environments. Abrupt lowering of experimental CMC is found to occur with respect to theoretical values. Figure 83.13 describes the variation in CMC of the mixed micellar systems of alkyltrimethylammonium bromide and bile salts [sodium cholate (NaC) and sodium deoxycholate (NaDC)] with the composition. Significant negative deviations from the ideal values (calculated by the Clint equation) were due to strong synergism between the oppositely charged surfactants.

83.7 CATANIONIC VESICLES: CATANOSOMES

Because of their structural similarities, catanionic surfactants can form liposomelike ensembles, which are known as *catanosomes*.

83.7.1 Preparation Methods

Catanionic vesicles are generally prepared by spontaneous, semispontaneous, or mechanical disruption approaches [45, 78, 79] (see Fig. 83.14).

83.7.1.1 Spontaneous Process. Vesicle dispersion of IPA is prepared by gentle mixing of the cationic and anionic surfactant solutions for several hours at room temperature. All solutions are then left to stand at room temperature to attain equilibrium for 24 h.

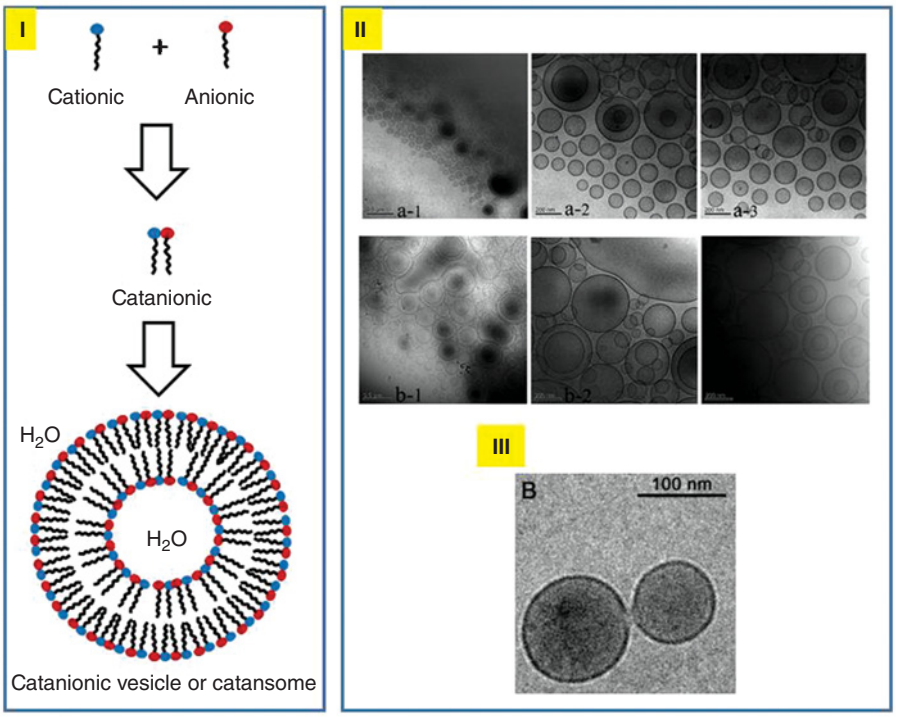


FIGURE 83.14 Schematic representation of catanosome preparation: (I) cryo-TEM images of C_nDMAO/C_7F_{15}CF=CHCOOH catanosomes; (II) [80], Cryo-TEM image of liposome (III) [81]. [Panel (II) is from Li et al. 2009 [80], from the journal *Soft Matter* (published by Royal Society of Chemistry); panel (III) is from Urbán et al. 2011 [81], from the journal *Nanoscale Research Letters* (published by Springer).]

83.7.1.2 Semispontaneous Method. In this method [8], the aid of cosolvent addition is applied. In a typical experiment of vesicle preparation, a suitable amount of IPA is dissolved in the alcohol. Water is then added and the solution sample is passed through a homogenizer for few minutes at room temperature in a sealed container specially designed for this vesicle preparation process.

83.7.1.3 Mechanical Disruption Process. In this method [8], an appropriate amount of IPA is dissolved in suitable organic (easily vaporizable) solvent and dried to form thin films on the surfaces of glass beads in a test vessel by blowing of nitrogen gas. The resulting films are then hydrated in absence or presence of additives and vortexed for a few minutes. A heterogeneous suspension is generated, which is then exposed to ultrasonic dispersion. The translucent solution is then extruded under nitrogen pressure through a membrane filter sequentially at higher temperature (above the phase transition temperature) whereby a stable vesicular diepersion is obtained.

83.7.1.4 Modified Reversed-Phase Evaporation. This method can also be applied for the preparation of vesicles from catanionic surfactants. IPA, dissolved in a small volume of suitable organic solvent, was added to large amount of water, and the two-phase mixture was briefly bath-sonicated (for 15–20 min) at ambient temperature to produce a stable emulsion. The organic solvent from this emulsion was gradually evaporated under reduced pressure. The resulting suspension was then subjected to freeze–thaw cycles several times. Then a brief bath sonication (5 min) above 70°C (well above the chain melting temperature) afforded a stable, translucent suspension of the catanosomes.

83.7.2 Stability of Catanosomes

Some recent investigations revealed that through the dispersion of IPA in aqueous medium, stable IPA vesicles can also be prepared by introducing double-chain ionic surfactants. In consideration of intravesicle interaction, addition of cholesterol or fatty alcohol can modify the molecular packing or intermolecular interaction within the bilayer. For the intervesicle aspect, additional ionic surfactant can increase the electrostatic repulsion to prevent the vesicle fusion or aggregation. Consequently, an appropriate amount of additives can effectively enhance the physical stability of the vesicles.

83.8 APPLICATIONS OF IPA/CATANIONIC SURFACTANTS

Their versatile phase behaviors and their tunability in enabling different desired formulations have opened doors to multifaceted applications of catanionic surfactants in various fields, especially in drug delivery, synthesis of nanomaterials, and liquid crystalline systems. In addition, researchers are investigating the applications of catanionic surfactant systems in ion sensing, molecular recognition, and catalysis. Such applications of catanionic surfactant systems are relatively recent phenomena in the progress of colloidal science. Some of the applications of catanionic surfactants are mentioned below.

83.8.1 Drug Delivery

Liposomes have attracted the attention of different research groups in various interdisciplinary fields because of their biomimetic cell membrane like structures. However, because of the high cost, difficulties in isolation and purification, and biological stability of the naturally occurring phosopholipids, catanionic surfactants have emerged as an important substitute because of their phospholipidlike structure and easy preparation, isolation, and purification and because of the low cost of their precursors. Because of their liposomelike structure, catanionic vesicles are now good biomimetic systems for researchers in biophysical chemistry and pharmaceutics. Encapsulation or entrapment efficiency of the drug carrier and vectorization, or the specific delivery of drugs, are the major challenges in pharmaceutical research. Several research groups have investigated the encapsulation ability of hydrophilic probes of catanionic vesicles. However, vectorization using catansomes is still limited. Major hurdles of such entities are their cytotoxicity, which are still in infancy stage.

In 1989, Kaler et al. [78] found that glucose could be efficiently encapsulated in CTAT/SDBS vesicles (T = tosylate), which remained stable for at least 1 year. Caillet et al. [82] studied the encapsulation of riboflavine and glucose in CTAB/SOS vesicles as well as in the corresponding IPA vesicles. The encapsulation was extremely low (<0.01%), which was attributed to the ionic character of the probe, which might destabilize the vesicles. The release of glucose was rapid, complete, and independent of the presence or absence of a membrane disrupting agent, indicating that the amphiphilic membrane has a very dynamic and permeable nature. Fischer et al. [51] investigated CTAT/SDBS systems, in which three vesicle compositions were used: a vesicle with an excess of CTAT, a vesicle with an excess of SDBS, and pure IPA vesicles without counterions. The CTAT-rich vesicles were the least efficient in entrapping glucose, whereas the SDBS-rich and the pure IPA vesicles were approximately equivalent in efficiency. The intrinsic encapsulated volume, even at very low surfactant concentrations, was greatest for the IPA vesicles, but in the long term the IPA vesicles seemed to be less stable than the SDBS-rich. Therefore, the entrapment capacity is better in the IPA vesicles where all counterions had been removed, provided, that the IPA system is allowed to age for 24 h. In 1990, Fukuda et al. [45] investigated the riboflavin encapsulation ability of the vesicles formed by the catanionic surfactant (Table 83.1) in water for the first time. They found that the catanionic vesicles were able to encapsulate 0.9 % riboflavin. A similar study by Bhattacharya et al. [2] in their synthesized catanionic vesicles of bolaamphiphile and long-chain quaternary ammonium hydroxide (Table 83.1) showed 2.28% encapsulation efficiency. Tondre et al. [9] were able to encapsulate 2.5% glucose in their catansomes. A glucose retention stability study revealed that after 24 h only 8% of the initially encapsulated glucose was retained in the hydrophilic core of the catanionic vesicles, which indicates the high permeability of this system.

Polymerization of the ion pair amphiphiles is another approach that can be adopted to increase the encapsulation efficiency and the tightness of the bilayer membrane of the vesicles. Chung et al. [3] tried to polymerize different combinations of ion pair amphiphiles using an amphiphile with ammonium headgroup and carboxylate chain amphiphile (Table 83.1) with a lipoyl group at the chain end, to study the encapsulation and release of fluorescent markers. Their study revealed that the uncharged polymerized catansomes prepared from an anionic surfactant with two carboxylic groups with the same cationic surfactant showed an almost complete encapsulation, while the negatively charged vesicles (made from one ammonium and one dicarboxylate surfactant) only partially encapsulated the fluorescence markers. The release also differed between the two vesicles, with the uncharged vesicle showing a much slower release than the negatively charged one.

Vectorization using catanionic vesicles has remarkably improved with studies involving the vesicles of nontoxic amino acid– [11, 83] or amino sugar– [41, 42] derived catanionic surfactants. Such entities are found to be highly efficient as drug and DNA delivery systems. Studies by Blanzat et al. [41, 42] revealed that the aminoglucose-derived gemini catanionic analog possesses both low toxicity and strong anti-HIV activity. The low toxicity of the gemini analog compared with the other catanionic analogs was attributed to its unique aggregation characteristics. Further studies by Brun et al. [84] suggested that the gemini analog would probably not penetrate into a biological membrane. In a more recent study, Blanzat et al. [54] showed an 8% encapsulation efficiency and very good drug entrapment stability (30 h) of the catanionic vesicles of amino sugar–derived catanionic surfactants, regardless of medium used (water or phosphate buffer), and this is the highest encapsulation efficiency by the catanionic vesicles reported to date.

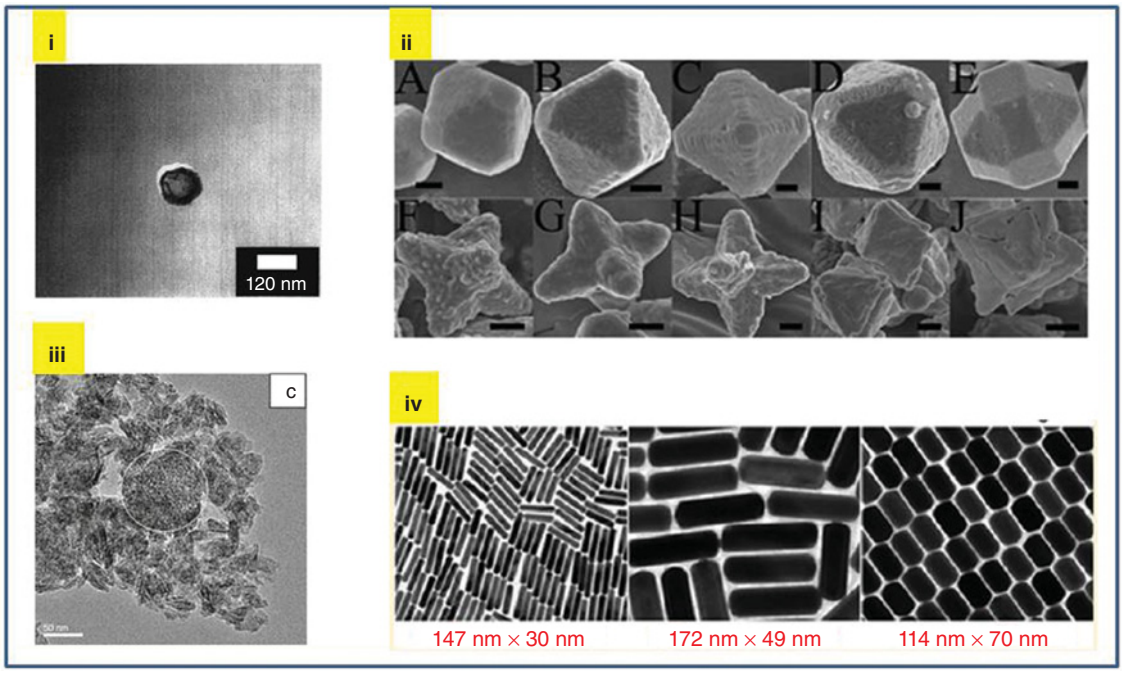


FIGURE 83.15 TEM images of various nanomaterials synthesized in catanionic surfactant media: (i) silica hollow sphere synthesized by Kaler et al. [14]; (ii) different-shaped copper oxide nanocrystals at different catanionic surfactant (SDS/CTAOH) compositions: 1:0 (A), 7:1 (B), 7:2 (C), 7:3, (D), 7:4 (E), 4:7 (F), 3:7 (G), 2:7 (H), 1:7 (I) and 0:1 (J) Shen et al. [15]; (iii) mesoporous alumina [16] and (iv) gold nanorods synthesized by CTAB/NaOL catanionic templates [17].

83.8.2 Templates for Nanomaterial Synthesis

Surfactant-mediated nanomaterial synthesis has given a new direction to nanochemistry. In the last two decades several approaches have been made by several research groups to synthesize nanomaterials using micelles and reverse micelles as templates. But those most of the synthesized materials are spherical in shape. Surfactant-templated controlled syntheses of nanoparticles are limited and are mainly performed using microemulsions, whereas the fabrication of synthesized nanoparticles is still absent. In the last few years, catanionic aggregates have been used for that purpose and found capable of fabricating the nanomaterials in various shapes and geometry in a controlled manner in aqueous media. Various stable aggregates formed by catanionic surfactants in aqueous media have added a further dimension and velocity in surfactant mediated nanomaterial synthesis.

In 2003 Kaler et al. [14] synthesized silica hollow spheres of size 60–120 nm, using catanionic vesicles as templates from tetramethoxysilane (TMOS). They used two different catanionic surfactant formulations, CTAB/SDBS and CTAT/SDBS, for the preparation of vesicle dispersions. The reaction was performed at room temperature and acidic condition (pH = 3) whereby fairly monodispersed nanocrystalline materials could be synthesized [Fig. 83.15(i)].

The catanionic surfactants CTAOH/SDS were introduced as shape and size modifiers by Shen et al. [15] for the syntheses of cuprous oxide (Cu_2O) nanocrystals. The presence of SDS-rich catanionic surfactants could induce the formation of polyhedral Cu_2O structures with eight triangular structures. The presence of SDS-rich catanionic surfactants could induce the formation of polyhedral Cu_2O structures, while the CTAOH-rich catanionic surfactants led to the generation of hexapod-shaped Cu_2O mesostructures with tiny nanoparticles on these symmetrical branches [Fig. 83.15(ii)].

Wang et al. [16] synthesized mesoporous γ-alumina nanoparticles using CTAB/SDS catanionic micelles as templates. The synthesized materials consisted mainly of nanoparticles with length about 50–100 nm, high specific surface area (261 $m^2\ g^{-1}$), large pore volume (0.79 $cm^3\ g^{-1}$), and large pore size (12.1 nm) [Fig. 83.15(iii)].

In a very recent study Murray et al. [17] showed a dramatically improved synthesis of colloidal gold nanorods using catanionic surfactants CTAB/NaOL. Both thin (diameter < 25 nm) and thicker (diameter > 30 nm) gold nanorods with exceptional monodispersity and broadly tunable longitudinal surface plasmon resonance could be synthesized using seeded growth at reduced CTAB concentrations (as low as 0.037 M). The CTAB/NaOL catanionic surfactants helped to overcome the difficulty of growth of the nanomaterials,

which is often associated with the single-component CTAB system.

83.9 CHALLENGES AND FUTURE PERSPECTIVES

In terms of drug delivery, *toxicity* is a major concern. Assurance of nontoxicity or negligible toxicity of the catansomes is one of the most important factors before developing such systems. The involvement of toxic cationic surfactants increases the cytotoxicity of catansomes since they increase the generation of reactive oxygen species (ROS). One team [53] investigated the cytotoxic effect of positively charged catansomes of HTMADS/DTDAB/cholesterol on a wide range of concentration on the U-937 human macrophages. At sufficiently low concentration (40– 80 nM), catansome dispersions were found to be nontoxic.

REFERENCES

[1] Bhattacharya, S., De, S. (1999). Vesicle formation from dimeric ion-paired amphiphiles. Control over vesicular thermotropic and ion-transport properties as a function of intra-amphiphilic headgroup separation. *Langmuir* **15**, 3400–3410.

[2] Bhattacharya, S., et al. (1998). Synthesis and vesicle formation from hybrid bolaphile/amphiphile ion-pairs. Evidence of membrane property modulation by molecular design. *J. Org. Chem.* **63**(22), 7640–7651.

[3] Chung, M.-H., Chung, Y.-C. (2002). Polymerized ion pair amphiphile that shows remarkable enhancement in encapsulation efficiency and very slow release of fluorescent markers. *Colloids Surf. B: Biointerfaces* **24**(2), 111–121.

[4] Chung, M.-H., et al. (2003). Encapsulation and permeation properties of the polymerized ion pair amphiphile vesicle that has an additional carboxyl group on anionic chain. *Colloids Surf. B: Biointerfaces* **28**(2–3), 83–93.

[5] Li, W.-T., Yang, Y.-M., Chang, C.-H. (2008). Stability enhancement effect of normal long-chain alcohols on ion pair amphiphile monolayers at the air/water interface. *J. Colloid Interface Sci.* **327**(2), 426–432.

[6] Meure, L., Foster, N., Dehghani, F. (2008). Conventional and dense gas techniques for the production of liposomes: A review. *AAPS Pharm. Sci. Technol.* **9**, 798–809.

[7] MozafarI, M.R. (2005). Liposomes: An overview of manufacturing techniques. *Cell. Mol. Biol. Lett.* **10**, 711–719.

[8] Yang, Y.-M.Y., et al. (2008). On the stability of liposomes and catansomes in aqueous alcohol solutions. *Langmuir* **24**, 1695–1700.

[9] Tondre, C., Caillet, C. (2001). Properties of the amphiphilic films in mixed cationic/anionic vesicles. *Adv. Colloid Interface Sci.* **93**(1–3), 115−134.

[10] Dias, R.S., Lindman, B., Miguel, M.G. (2002). DNA interaction with catanionic vesicles. *J. Phys. Chem. B* **106**, 12600–12607.

[11] Rosa, M., et al. (2007). The association of DNA and stable catanionic amino acid-based vesicles. *Colloids Surf. A: Physicochem. Eng. Aspects* **301**, 361–375.

[12] Bramer, T., Dew, N., Edsman, K. (2007). Pharmaceutical applications for catanionic mixtures. *J. Pharm. Pharmacol.* **59**, 1319–1334.

[13] Soussan, E., et al. (2009). Drug delivery by soft matter: Matrix and vesicular carriers. *Angew. Chem. Int. Ed.* **48**, 274–288.

[14] Hentze, H.-P., et al. (2003). Silica hollow spheres by templating of catanionic vesicles. *Langmuir* **19**(4), 1069–1074.

[15] Kang, W., et al. (2011). The catanionic surfactant-assisted syntheses of 26-faceted and hexapod-shaped Cu_2O and their electrochemical performances. *CrystEngCommun*.

[16] Jiao, W., et al. (2012). Catanionic-surfactant templated synthesis of organized mesoporous γ-alumina by double hydrolysis method. *J. Porous Mater.* **19**(1), 61–70.

[17] Ye, X., et al. (2013). Using binary surfactant mixtures to simultaneously improve the dimensional tunability and monodispersity in the seeded growth of gold nanorods. *Nano Lett.* **13**(2), 765–771.

[18] Khan, A., Marques, E. (1997). Catanionic surfactants. In Robb, J.D. (ed.), *Specialist Surfactants*. Blackie Academic and Professional Publishers, London.

[19] Jokela, P., Joensson, B., Khan, A. (1987). Phase equilibria of catanionic surfactant-water systems. *J. Phys. Chem.* **91**(12), 3291–3298.

[20] Scott, A.B., Tartar, H.V., Lingafelter, E.C. (1943). Electrolytic properties of aqueous solutions of octyltrimethylammonium octanesulfonate and decyltrimethylammonium decanesulfonate. *J. ACS* **65**(4), 698–701.

[21] Bramer, T., et al. (2003). Catanionic drug–surfactant mixtures: Phase behavior and sustained release from gels. *Pharm. Res.* **20**(10), 1661–1667.

[22] Edlund, H., Sadaghiani, A., Khan, A. (1997). Phase behavior and phase structure for catanionic surfactant mixtures: Dodecyltrimethylammonium chloride-sodium nonanoate-water system. *Langmuir* **13**(19), 4953–4962.

[23] Emo, M., et al. (2013). Metastable micelles and true liquid crystal behaviour of newly designed "cataniomeric" surfactants. *Soft Matt.* **9**(9), 2760–2768.

[24] Maiti, K., et al. (2010). Physicochemical studies on ion-pair amphiphiles: Solution and interfacial behaviour of systems derived from sodium dodecylsulfate and *n*-alkyltrimethylammonium bromide homologues. *J. Chem. Sci.* **122**(6), 867–879.

[25] Maiti, K., et al. (2010). Physicochemistry of the binary interacting mixtures of cetylpyridinium chloride (CPC) and sodium dodecylsulfate (SDS) with special reference to the catanionic ion-pair (coacervate) behavior. *Colloids Surf. A: Physicochem. Eng. Aspects* **355**, 88–98.

[26] Vethamuthu, M.S., et al. (1996). The hexagonal phase and cylindrical micelles in the system alkyltrimethylammonium bromide - sodium desoxycholate - water as studied by x-ray diffraction and fluorescence quenching. *J. Colloid Interface Sci.* **178**(2), 538–548.

[27] Vethamuthu, M.S., et al. (1995). Aggregate structure, gelling, and coacervation within the L phase of the quasi-ternary system alkyltrimethylammonium bromide-sodium desoxycholate-water1. *J. Colloid Interface Sci.* **174**, 461–479.

[28] Eastoe, J., et al. (1996). Interfacial properties of a catanionic surfactant. *Langmuir* **12**(11), 2706–2711.

[29] Kume, G., Gallotti, M., Nunes, G. (2008). Review on anionic/cationic surfactant mixtures. *J. Surfact. Deterg.* **11**, 1–11.

[30] Liu, L., et al. (2013). Effects of oriented surface dipole on photoconversion efficiency in an alkane/lipid-hybrid-bilayer-based photovoltaic model system. *ChemPhysChem* **14**(12), 2777–2785.

[31] Panda, A.K., et al. (2005). Physico-chemical studies on mixed oppositely charged surfactants: Their uses in the preparation of surfactant ion selective membrane and monolayer behavior at the air water interface. *Colloids Surf. A: Physicochem. Eng. Aspects* **264**(1–3), 106–113.

[32] Schwartz, D.K., Viswanathan, R., Zasadzinski, J.A. (1994). *J. Chem. Phys.* **101**, 7161–7168.

[33] Shigenobu, H., McNamee, C.E. (2012). The interaction of insulin, glucose, and insulin–glucose mixtures with a phospholipid monolayer. *J. Colloid Interface Sci.* **388**(1), p. 274.

[34] Soussan, E., et al. (2007). Physical study of the arrangement of pure catanionic glycolipids and interaction with phospholipids, in support of the optimisation of anti-HIV therapies. *Colloids Surf. A: Physicochem. Eng. Aspects* **303**, 55–72.

[35] Manna, K., Chang, C.-H., Panda, A.K. (2012). Physicochemical studies on the catanionics of alkyltrimethylammonium bromides and bile salts in aqueous media. *Colloids Surf. A: Physicochem. Eng. Aspects* **415**, 10–21.

[36] Marques, E.F., et al. (2000). Micelles, dispersions, and liquid crystals in the catanionic mixture bile salt-double-chained surfactant. The bile salt-rich area. *Langmuir* **16**(22), 8255–8262.

[37] Šegota, S., Heimer, S., Težak, D. (2006). New catanionic mixtures of dodecyldimethylammonium bromide/sodium dodecylbenzenesulphonate/water: I. Surface properties of dispersed particles. *Colloids Surf. A: Physicochem. Eng. Aspects* **274**(1–3), 91–99.

[38] Tah, B., et al. (2011). Aggregation behavior of SDS/CTAB catanionic surfactant mixtu*r*e in aqueous solution and at the air/water interface. *J. Phys. Chem. B* **115**(26), 8493–8499.

[39] Chang, D.P., et al. (2012). Adsorption of lipid liquid crystalline nanoparticles: Effects of particle composition, internal structure, and phase behavior. *Langmuir* **28**(29), 10688–10696.

[40] Yeh, S.-J., Yang, Y.-M., Chang, C.-H. (2005). Cosolvent effects on the stability of catanionic vesicles formed from ion-pair amphiphiles. *Langmuir* **21**, 6179–6184.

[41] Blanzat, M., et a1. (1999). Synthesis and anti-HIV activity of catanionic analogs of galactosylceramide. *New J. Chem.* **23**(11), 1063–1065.

[42] Blanzat, M., et al. (1999). New catanionic glycolipids. 1. Synthesis, characterization, and biological activity of double-chain and gemini catanionic analogues of galactosylceramide (galβ1cer). *Langmuir* **15**(19), 6163–6169.

[43] Khan, A., Marques, E. (1997). Catanionic surfactants. In Robb, J.D. (ed.), *Specialist Surfactants.* Springer, Amsterdam, pp. 37–80.

[44] Wang, Y., Marques, E.F. (2010). Mesophase formation and thermal behavior of catanionic mixtures of gemini surfactants with sodium alkylsulfates. *J. Thermal Anal. Calorim.* **100**(2), 501–508.

[45] Fukuda, H., et al. (1990). Bilayer-forming ion pair amphiphiles from single-chain surfactants. *J. ACS* **112**(4), 1635–1637.

[46] Hirano, K., Fukuda, H., Regen, S.L. (1991). Polymerizable ion-paired amphiphiles. *Langmuir* **7**(6), 1045–1047.

[47] Filipovic-Vincekovic, N., et al. (1997). Solid-phase transitions of catanionic surfactants. *J. Colloid Interface Sci.* **188**, 396–403.

[48] Menger, F.M., Binder, W.H., Keiper, J.S. (1997). Cationic surfactants with counterions *of* glucuronate glycosides. *Langmuir* **13**(12), 3247–3250.

[49] Chung, H.-C., Lee, H.-J., Park, J.-Y. (1998). Bilayer properties of the multiple-chain ion pair amphiphiles. *Bull. Korean Chem. Soc.* **19.**

[50] Chung, Y.-C., Lee, J.-J. (1999). Ion-sensing property of an ion pair amphiphile. *Bull. Korean Chem. Soc.* **20**, 16–18.

[51] Fischer, A., M.Hebrant, and C.Tondre, *Glucose Encapsulation in Catanionic Vesicles and Kinetic Study of the Entrapment/Release Processes in the Sodium Dodecyl Benzene Sulfonate/Cetyltrimethylammonium Tosylate/Water System*. Journal of Colloid and Interface Science, 2002. **248**(1): p. 163-168.

[52] Silva, B.F.B., Marques, E.F. (2005). Thermotropic behavior of asymmetric chain length catanionic surfactants: The influence of the polar head group. *J. Colloid Interface Sci.* **290**(1), 267–274.

[53] Kuo, J.-H.S., et al. (2008). Flow cytometric characterization of interactions between U-937 human macrophages and positively charged catanionic vesicles. *Colloids Surf. B: Biointerfaces* **64**(2), 307–313.

[54] Soussan, E., et al. (2008). Sugar-derived tricatenar catanionic surfactant: Synthesis, self-assembly properties, and hydrophilic probe encapsulation by vesicles. *Langmuir* **24**.

[55] Blanco, E., et al. (2009). Langmuir monolayers of a hydrogenated/fluorinated catanionic surfactant: From the macroscopic to the nanoscopic size scale. *Langmuir* **25**, 8075–8082.

[56] Matos, M.R.A., Silva, B.F.B., Marques, E.F. (2013). Chain length mismatch and packing effects on the thermotropic phase behavior of salt-free catanionic surfactants. *J. Colloid Interface Sci.* **405**, 134–144.

[57] Jose, R., et al. (2013). Room temperature thermotropic liquid crystalline phases of catanionic surfactants derived from quaternary ammonium surfactants and bis(2-ethylhexyl)sulfosuccinate. *J. Colloid Interface Sci.* **411**, 61–68.

[58] Maiti, K., et al. (2007). *J. Phys. Chem. B* 1111–4175.

[59] Tomasic, V. et al. (1997). *Ber. Bunsenges. Phys. Chem.* **101**, 1942.

[60] Youssrya, M., et al. (2008). Unravelling micellar structure and dynamics in an unusually extensive DDAB/bile salt catanionic solution by rheology and NMR-diffusometry. *J. Colloid Interface Sci*. **324**, 192–198.

[61] Caria, A., Khan, A. (1996). Phase behavior of catanionic surfactant mixtures: Sodium bis(2-ethylhexyl)sulfosuccinate-didodecyldimethylammonium bromide-water system. *Langmuir* **12**, 6282–6290.

[62] La Mesa, C., et al. (1985). Phase diagrams and NMR studies of some ternary sodium deoxycholate-surfactant-water systems. *J. Colloid Interface Sci.* **103**(2), 373–391.

[63] Khan, A. (1996). Phase science of surfactants. *Curr. Opinion Colloid Interface Sci.* **1**, 614–623.

[64] Yatcilla, M.T., et al. (1996). Phase behavior of aqueous mixtures of cetyltrimethylammonium bromide (CTAB) and sodium octyl sulfate (SOS). *J. Phys. Chem.* **100**(14), 5874–5879.

[65] Yu, W.-Y., Yang, Y.-M., Chang, C.-H. (2005). Cosolvent effects on the spontaneous formation of vesicles from 1:1 anionic and cationic surfactant mixtures. *Langmuir* **21**, 6185–6193.

[66] Panda, A.K., et al. (2003). *Indian J. Biochem. Biophys.* **40.**

[67] Bangham, A.D., De Gier, J., Greville, G.D. (1967). Osmotic properties and water permeability of phospholipid liquid crystals. *Chem. Phys. Lipids* **1**(3), 225–246.

[68] Chapman, D. (1967). Liquid crystalline nature of phospholipids. In *Ordered Fluids and Liquid Crystals*. American Chemical Society, pp. 157–166.

[69] Chapman, D. (1l71). Living systems. Liquid crystalline properties of phospholipids and biological membranes. *Symp. Faraday Soc.* **5**, 163–174.

[70] Gupta, A., et al. (2014). Nanoassemblies of Gd-DTPA-monooleyl and glycerol monooleate amphiphiles as potential MRI contrast agents. *J. Mater. Chem. B* **2**(9), 1225–1233.

[71] Papahadjopoulos, D., Watkins, J.C. (1967). Phospholipid model membranes. II. Permeability properties of hydrated liquid crystals. *Biochim. Biophys. Acta Biomembr.* **135**(4), 639–652.

[72] Steim, J.M., et al. (1969). Calorimetric evidence for the liquid-crystalline state of lipids *in* a biomembrane. *Proc. Natl. Acad. Sci. USA* **63**(1), 104–109.

[73] Sjöbom, M.B., Edlund, H. (2002). Dependence of alkyl chain asymmetry on the phase equilibria of three catanionic surfactant mixtures containing dodecyltrimethylammonium chloride−sodium alkylcarboxylate−water. *Langmuir* **18**(22), 8309–8317.

[74] Clint, J.H. (1975). Micellization of mixed non-ionic surface active agents. *J. Chem. Soc. Faraday Transact. l* **71**, pp. 1327–1334.

[75] Rubingh, D.N. (1979). In Mittal, K.L. (ed.), *Solution Chemistry of Surfactants*. Plenum Press, New York, Vol. **1**, pp. 337–354.

[76] Eastoe, J., et al. (1996). Micelles of asymmetric chain catanionic surfactants. *Colloids Surf. A: Physicochem. Eng. Aspects* **117**, 215–225.

[77] Rubingh, D.N. (1979). Mixed micelle solutions. *Solution Chem. Surfact.* **1**, 337–354.

[78] Kaler, E., et al. (1989). Spontaneous vesicle formation in aqueous mixtures of single-tailed surfactants. *Science* **245**, 1371–1374.

[79] Marques, E.F., et al. (2003). Self-organization of double-chained and pseudodouble-chained surfactants: Counterion and geometry effects. *Adv. Colloid Interface Sci.* **100–102**, 83–104.

[80] Li, X., Dong, S., Hao, J. (2009). Phase behavior, rheological properties, and vesicles of alkyldimethylamine oxide and fluorinated acidic surfactant mixtures. *Soft Matt.* **25**.

[81] Urbán, P., et al. (2000). Study of the efficacy of antimalarial drugs delivered inside targeted immunoliposomal nanovectors. *Nanoscale Res. Lett.* **6**.

[82] Caillet, C., Hebrant, M., Tondre, C. (2000). Sodium octyl sulfate/cetyltrimethylammonium bromide catanionic vesicles: Aggregate composition and probe encapsulation. *Langmuir* **16**(23), 9099–9102.

[83] Rosa, M., et al. (2006). Spontaneous formation of vesicles and dispersed cubic and hexagonal particles in amino acid-based catanionic surfactant systems. *Langmuir* **22**(13), 5588–5596.

[84] Brun, A., et al. (2003). Interaction between phospholipids and new gemini catanionic surfactants having anti-HIV activity. *Colloids Surf. A: Physicochem. Eng. Aspects* **228**(1–3), 3–16.

84

PHASE BEHAVIOR OF NATURAL-SOURCED SURFACTANT SYSTEMS

KENJI ARAMAKI

Graduate School of Environment and Information Sciences, Yokohama National University, Yokohama, Japan

84.1 INTRODUCTION

Surfactants is widely used in many industrial fields. In terms of performance and cost, synthetic surfactants obtained from petrochemical materials are commonly used in most industries. However, growing demands for low environmental impacts and low toxicity allow people to consider employing surfactants produced by/from natural-sourced materials. Phospholipids are one of the most important natural-sourced surfactants and are already used in pharmaceutical and cosmetic products. Recently biosurfactants produced by microorganisms have expanded application fields because of their characteristic properties and the development of low-cost production processes [1]. Contrary to those naturally produced surfactants, there are several synthetic surfactants from natural-sourced materials such as sugar, glycerol, amino acids, and fatty acids. In this chapter, such surfactants are called *natural-sourced surfactants*. Advantages for these surfactants can be obtained at relatively low cost and flexibility of molecular architecture to meet demands regarding physicochemical properties such as cmc, Krafft point, and HLB.

84.2 SUGAR-BASED SURFACTANTS

Sugars are natural and renewable materials and are used for the surfactant hydrophilic group because of their strong hydrogen-bonding ability. Alkyl glucosides are nonionic surfactants with a glucose headgroup. One team studied the phase behavior of aqueous dodecyl glucoside ($C_{12}G_1$) in a composition-temperature diagram (Fig. 84.1) [2, 3].

The aqueous $C_{12}G_1$ system gives a Krafft point at ~40°C, while poly(oxyethylene) lauryl ethers do not give any Krafft point. Above the Krafft point, a lamellar phase (L_α) and an isotropic phase (L_2) are formed, and the composition range for those phase regions are temperature-insensitive. The same group also reported the effect of chain branching for the hydrophobic chain with the same carbon number, showing that the Krafft point vanishes for $C_{12}G_1$ with a branched hydrophobic chain [2]. Another group studied the aqueous phase bahavior of octyl, nonyl, and decyl glucosides (C_8G_1, C_9G_1, and $C_{10}G_1$) as shown in Fig. 84.2. C_8G_1 and C_9G_1 give micelles at low concentration, and no Krafft and cloud points are apparent. $C_{10}G_1$ also give micelles, but phase separation occurs in the dilute region [4, 5].

Phase separation in the dilute region of the water/$C_{10}G_1$ system is due to the LCST-type phase separation or the clouding phenomena commonly observed in poly(oxyethylene)-type surfactant systems, which was suggested by earlier work for a mixed $C_9G_1/C_{10}G_1$ system [6]. The C_8G_1 and C_9G_1 systems give a hexagonal phase, a bicontinuous cubic phase, and a lamellar phase in the concentrated region.

Sucrose alkanoates or sucrose fatty-acid esters are also a type of sugar-based surfactant and are sysnthesized from sucrose and fatty acids. They are approved as a food-grade emulsifier or solubilizer in most countries. Because of the stronger hydrogen- bonding ability of sucrose compared to glucose, the monoester-type sucrose fatty-acid ester is a more hydrophilic surfactant than alkyl glucoside with the same hydrophobic chain length. One team of researchers reported aqueous phase diagrams of sucrose monooctanoate,

Encyclopedia of Biocolloid and Biointerface Science, Volume 2, First Edition. Edited by Hiroyuki Ohshima.
© 2016 John Wiley & Sons, Inc. Published 2016 by John Wiley & Sons, Inc.

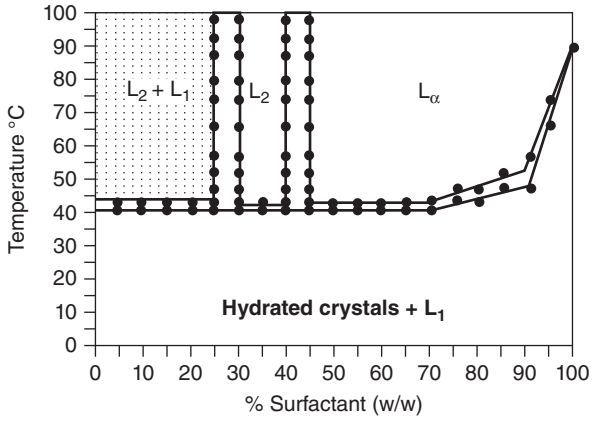


FIGURE 84.1 Phase diagram of the water/racemic (±)-2*R*-dodecyl β-D-glucopyranoside system.

monodecanoate, monododecanoate, and monohexadecanoate (C_8SE, C_{10}SE, C_{12}SE, and C_{16}SE) as shown in Fig. 84.3 [7].

As described previousely, both $C_{10}G_1$ and $C_{12}G_1$ behave as hydrophobic surfactants while C_{12}SE and even C_{16}SE give micelles in the dilute region. A Krafft point appears at around 20°C in the water/C_{16}SE systems, but no cloud points appear in any of the systems studied. A discontinuous cubic phase is formed in the C_8SE and C_{10}SE systems but in a limited composition and temperature range. A hexagonal phase is formed at a high-concentration region for all the systems, and the hexagonal region continues to >100°C, which is again similar to the temperature-insensitive behavior found in the alkyl glucoside systems. Although no full phase behavior has not been shown, one team [8] reported micellar formation in an aqueous sucrose monooleate ($C_{18:1}$SE) system at 25°C, indicating that the Krafft point is below this temperature for this sugar surfactant with an unsaturated hydrophobic chain. They also reported that 10 wt% of the aqueous solution of $C_{18:1}$SE gives relatively high viscosity, approximately 100 Pa • s, and shows a viscoelastic nature, suggesting the formation of wormlike micelles in a binary water/surfactant system. Sucrose fatty-acid esters are more suitable surfactants compared to poly(oxyethylene)-type surfactants in terms of the formation of wormlike micelles as the former combine monoglycerides [9], fatty alcohols [10], and fatty acids [11]. Strong hydrogen-bonding ability of the sucrose fatty-acid esters also allows for the formation of reverse wormlike micelles in alkanes [12].

As found in the mixture of nonyl- and decyl glucosides (C_9G_1 and $C_{10}G_1$) [6], cloud points are found in a mixed sucrose laurate system [13]. In this literature, authors studied the dependence of cloud points against the surfactant HLB number for the sucrose laurate systems and compared then with that for the poly(oxyethylene) dodecyl ether ($C_{12}EO_n$) systems as shown in Fig. 84.4.

Contrary to moderate increase in cloud points for the $C_{12}EO_n$ systems, cloud points of the sucrose laurate systems drastically increase, indicating that the clouding phenomenon is observed only in a limited HLB number range. The authors pointed that this is the reason for a common observation of "no clouding phenomenon for polyol-type nonionic surfactants," which is actually incorrect.

A sucrose molecule contains eight hydroxyl groups, and therefore hydrophile–lipophile balance (HLB) of the sucrose fatty-acid esters can be tuned by the relative degree of

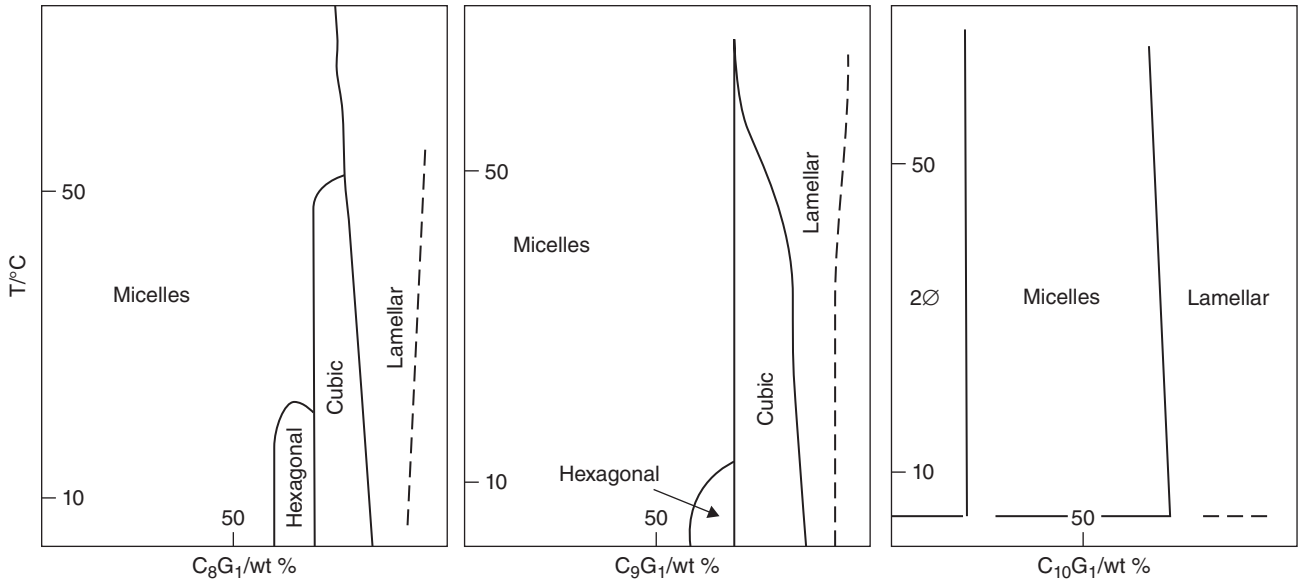


FIGURE 84.2 Phase diagram of binary aqueous systems of *n*-octyl β-D-glucopyranoside (C_8G_1), *n*-nonyl β-D-glucopyranoside (C_9G_1) and *n*-decyl β-D-glucopyranoside ($C_{10}G_1$).

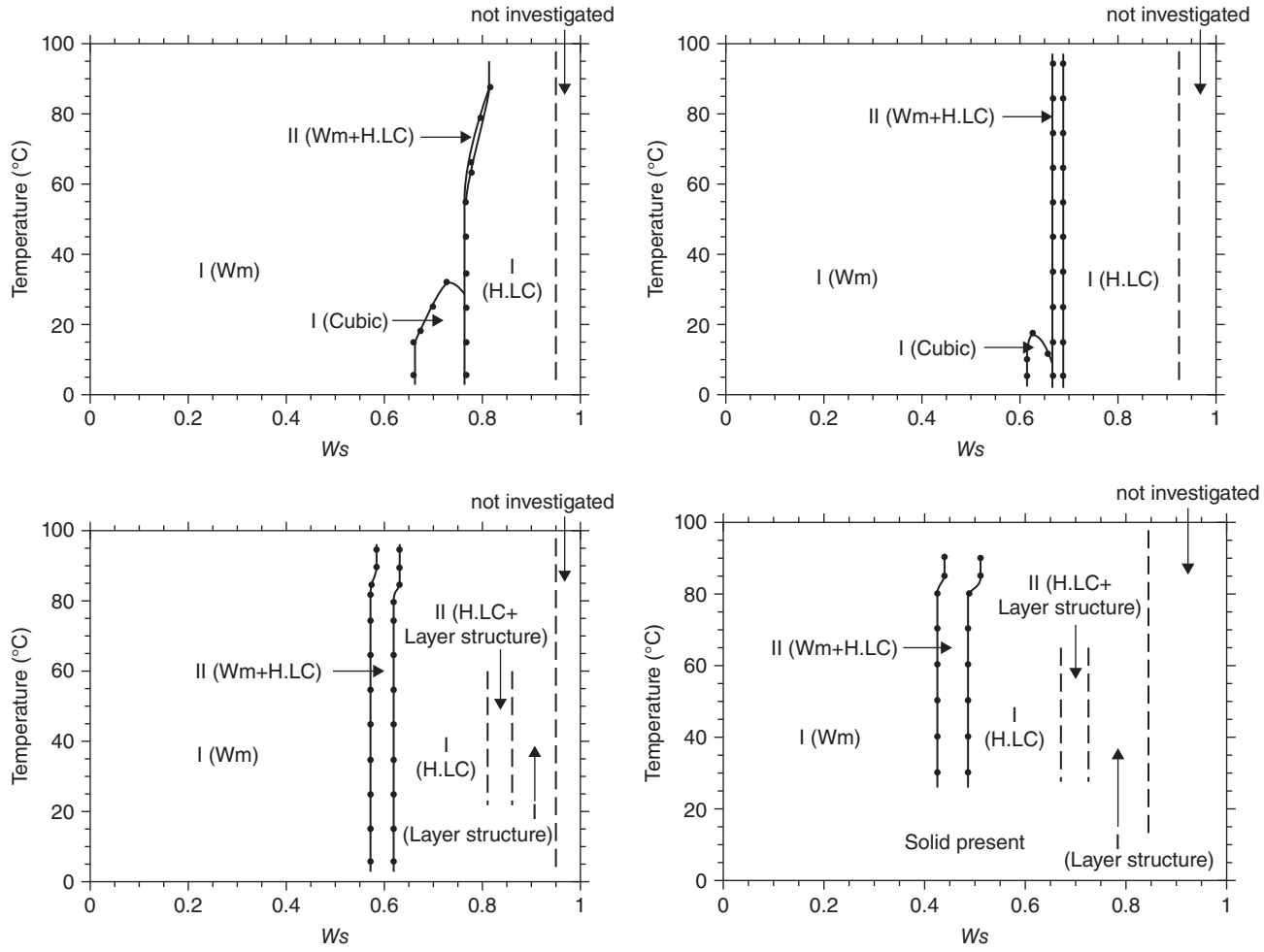


FIGURE 84.3 Phase diagram of binary aqueous systems of C_8SE (upper left), C_{10}SE (upper right), C_{12}SE (lower left), and C_{16}SE (lower right). W_S indicates weight fraction of surfactant.

esterification. As mentioned previously, the monoesters are hydrophilic but diesters are already hydrophobic and form lamellar liquid crystal [14], which is similar to the behavior of other double-tailed amphiphiles such as phospolipids and dialkyl dimethyl ammonium halides. As shown in Fig. 84.5, mixing sucrose mono- and dilaurates induces curvature change of a self-assembled structure from a highly positive one (micelle and hexagonal phase) to zero curvature (lamellar phase), but the phase behavior is rather simple compared to that of other mixed amphiphile systems.

However, as shown in Fig. 84.6, adding oils expands the variety of phases as found in the same study cited above [14], in which a phase transition occurs from lamellar to hexagonal and discontinuous cubic phases occur by solubilization of *n*-dexadecane. Also, the solubilized content of oil in the discontinuous cubic phase is reached with almost the same composition of water, and the authors referred to this cubic phase as *cubic-phase microemulsions*.

General microemulsion, especially the bicontinuous type, formation, and phase behavior have been reported in a sucrose fatty-acid mixture system [15] and also by combining cosurfactants such as fatty alcohols [16–18] and diethyleneglycol mono ethyl ether [19]. Formulation of food-grade microemulsions is also attempted [20, 21]. Similar to high thermal stability of liquid crystalline phases as described previously, thermal stability of bicontinuous microemulsions in sucrose fatty-acid ester systems is relatively high [15,16]. As shown in Fig. 84.7, a abicontinuous phase region (I) exists in a wide temperature range above $X = 0.1$.

84.3 GLYCEROL-BASED SURFACTANTS

Glycerol fatty-acid esters or monoglycerides are one of the most popular food additives for emulsifying or foaming. Since only two hydroxyl groups exist in a

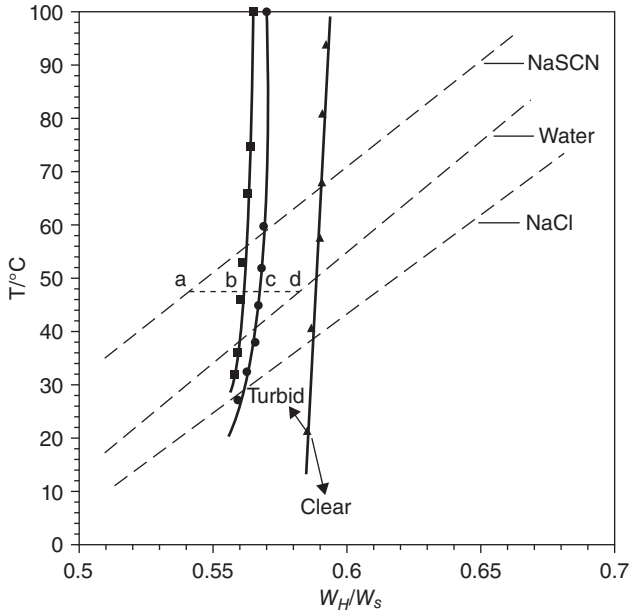


FIGURE 84.4 Cloud points of aqueous sucrose laurate system at 2 wt% without salt (circles) and with 5 wt% of NaCl (triangles) and NaSCN (squares). Dotted lines indicate loci of cloud points for aqueous poly(oxyethylene) lauryl ether ($C_{12}EO_n$) systems.

monoglyceride molecule, the nature of monoglycerides as a surfactant is hydrophobic. Therefore monoglycerides with a long acyl chain generally form lamellar (L_α), reverse hexagonal (H_2), and reverse bicontinuous cubic (V_2) phases

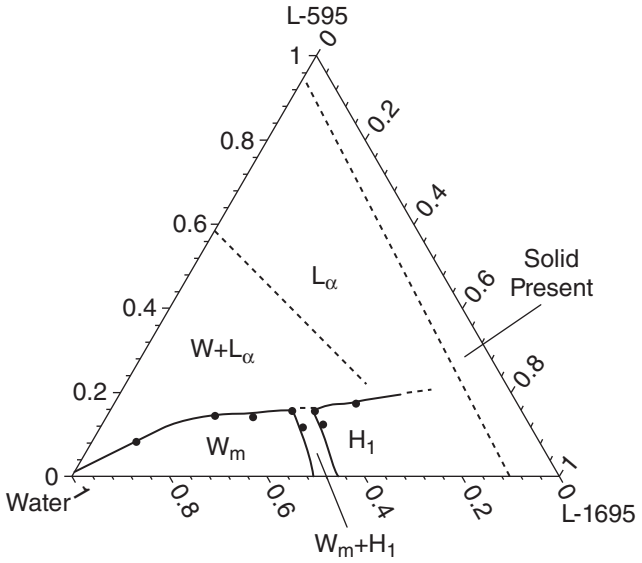


FIGURE 84.5 Phase diagram of the ternary water/L-1695/L-595 system at 30°C. L-1695 and L-595 are sucrose laurate mixture containing mono-, di-, and trilaurates. Averaged esterification degree is 1.16 for L-1695 and 1.79 for L-595. W_m indicates aqueous micellar phase.

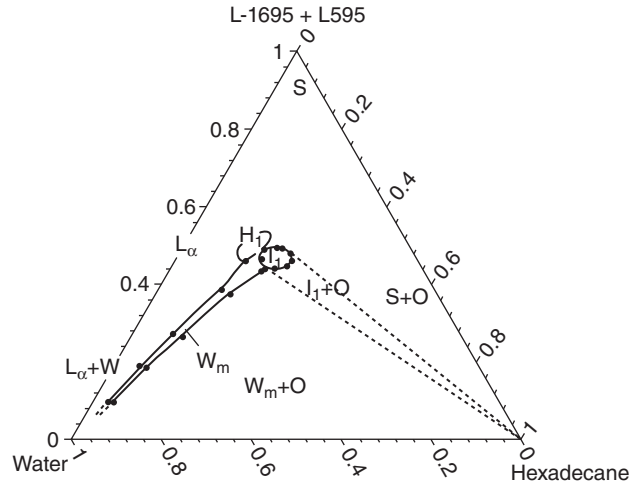


FIGURE 84.6 Phase map of quaternary water/L-1695/L-595/hexadecane system with equiweight mixture of L-1695 and L595 at 30°C.

with low contents of water. For this reason, temperature–composition phase diagrams in a binary water/surfactant system have normally been drawn as a function of water concentration in spite of surfactant concentration in conventional surfactant systems. Another team reported a series of temperature-composition phase diagrams of monoglycerides

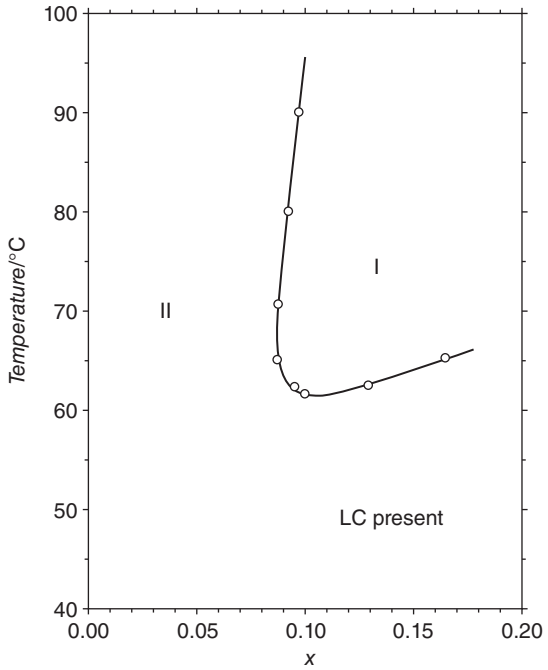


FIGURE 84.7 Phase map of quaternary water/L-1695/L-595/heptane system with a constant weight ratios water/oil = 1/1 and L-1695/L-595 = 2/8. *X* indicates the weight fraction of sucrose ester mixture in the whole system.

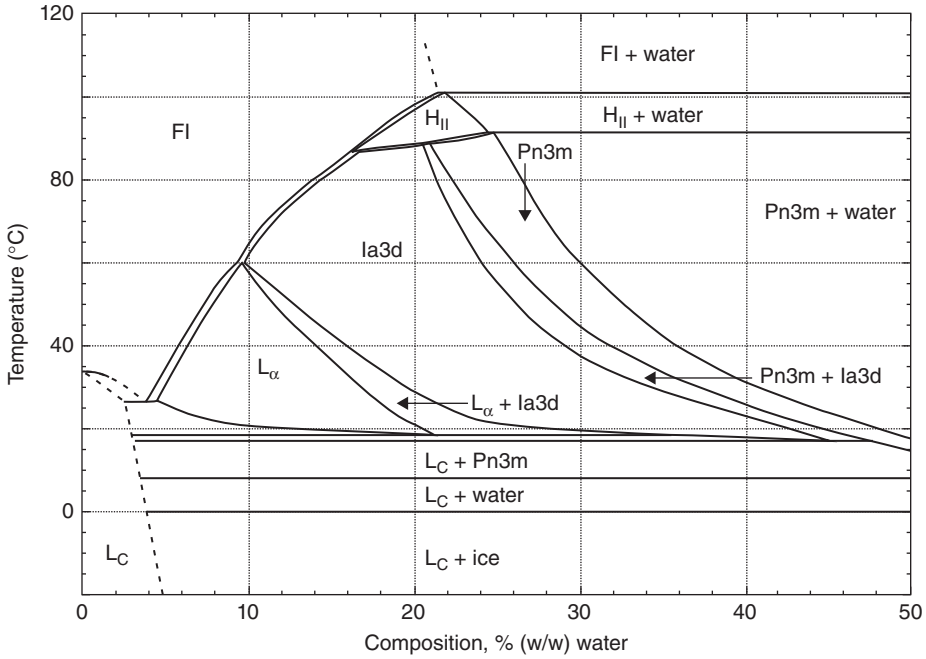


FIGURE 84.8 Phase diagram of binary water/monoolein system. L_C, *FI*, and H_{II} indicate hydrated crystalline, fluid isotropic, and reverse hexagonal phases, respectively. Two different space groups (*Ia3d* and *Pn3m*) for bicontinuous cubic phases are characterized.

with saturated (monolaurin, monomyristin, monopalmitin, monostearin, monoarachidin, monobehenin) and unsaturated (monoolein, monolinolein, monoelaidin, monoerucin) acyl chain [22]. Formation of the V_2 phase in some aqueous monoglycerides systems have been paid people's attention since dispersion of the V_2 phase in excess water with a dispersant was found to formulate fine particles called cubosome which is a potential nanocarrier of drugs and active molecules. Particle size of cubosomes is typically several tens to a few hundreds of nanometer and each particle has the V_2 phase structure in the interior. The most well-known system forming cubosomes are water/monoolein system in which Pn3m-type V_2 phase is equilibrated with water between 20 and 90°C as shown in Fig. 84.8 [23].

Monolinolein, which has one more unsaturated bond in the acyl chain than monoolein, also forms the *Pn3m*-type V_2 phase but in a narrow temperature range between 20°C and 40°C; instead, it forms the H_2 phase between

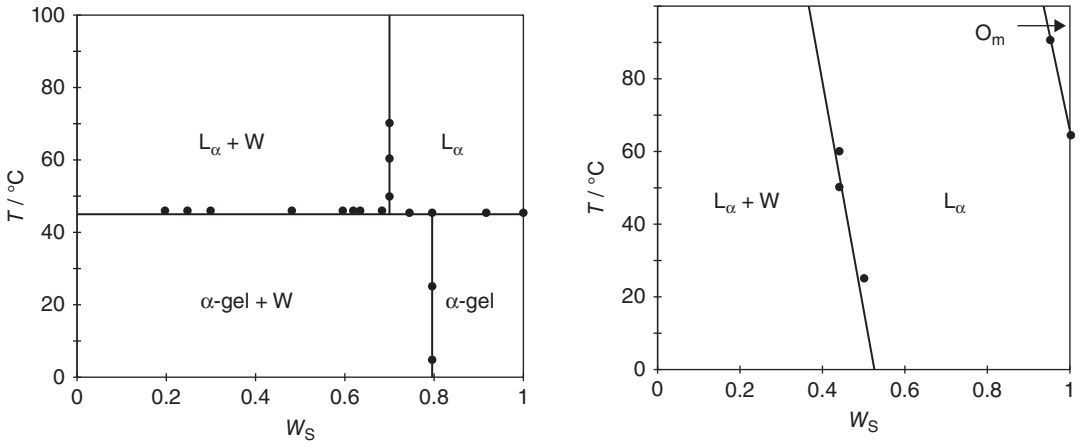


FIGURE 84.9 Phase diagrams of binary water/pentaglycerol monostearate ($C_{18}G_5$, left) and water/monooleate ($C_{18:1}G_5$, right) systems; α-gel indicates a hydrated α-type crystalline phase.

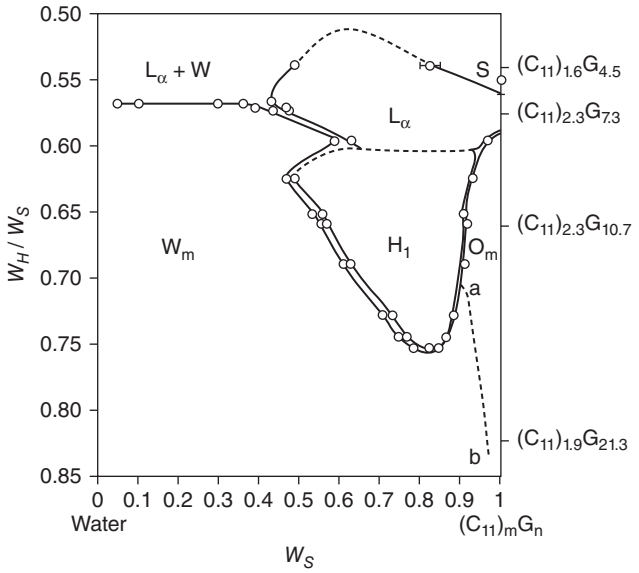


FIGURE 84.10 Phase diagrams of binary water/polyglycerol laurate, $(C_{11})_mG_n$, system as a function of weight ratio of polyglycerol group (W_H) to whole surfactant molecule (W_S) at 25°C.

40°C and 90°C, whose nanoparticles are called *hexosomes* [24].

Polyglycerol fatty acid esters are also used as food additives in some countries but basic phase study had not been done before Ishitobi and Kunieda in 2000 [25]. Similar to the sucrose fatty-acid esters, an advantage of this surfactant is availability of various HLBs by changing polymerization degree of the polyglycerol. Diglycerol monomyristate ($C_{14}G_2$) and monopalmitate ($C_{16}G_2$) are still hydrophobic, and their aqueous phase behavior is similar to that of monoglycerides such as monolaurin and monomyristin, in which an L_α phase is formed at high surfactant concentration and above Krafft points, 25°C for $C_{14}G_2$ and 45°C for $C_{16}G_2$ [26]. Pentaglycerol monostearate ($C_{18}G_5$) and monooleate ($C_{18:1}G_5$) are still hydrophobic, and an L_α phase is formed above 45°C for $C_{18}G_5$ and above 0°C for $C_{18:1}G_5$ as shown in Fig. 84.9 [27].

Another group studied aqueous phase bahavior of polyglycerol dilaurate as a function of weight ratio of polyglycerol in a surfactant molecule (W_H/W_S) [28]. As shown in Fig. 84.10, a phase transition from lamellar to micelle takes place at $W_H/W_S = 0.57$ with an increase in the polymerization degree of polyglycerol.

In another study the same group also observed cloud points for the same surfactant and showed very sensitive cloud-point change against the W_H/W_S value, which is similar to the behavior found in the sucrose fatty-acid esters described before (see Fig. 84.4) [29].

Another group reported several phase diagrams of mono- and diglycerol fatty-acid esters in nonpolar solvents. Monoglycerides such as monocaprylin (glycerol monooctanoate), monocaprin (glycerol monodecanoate), and monolaurin (glycerol monolaurate) do not form any liquid crystalline phases in liquid paraffin, squalene, and squalene as shown in Fig. 84.11 [30]. Instead of ordered phases, an isotropic phase with reverse micelles is formed in a wide composition range above a melting temperature of a solid phase. In the squalane system, the isotropic phase is separated into two liquid phases, while no phase separation is observed in the other systems. This clouding curve in the squalane system shows an UCST-type miscibility gap and is caused by increasing lipophilicity of the monoglyceride. Therefore the phase separation takes place in all oil systems with monocaprylin but not in those with monolaurin.

In diglycerol fatty-acid ester/oil systems, phase behavior becomes more complicated, as shown in Fig. 84.12 [31]. The single-phase region of the lamellar phase (L_α) appears at high surfactant concentration, and an oil phase is separated out in lower surfactant concentration. However, the variety of

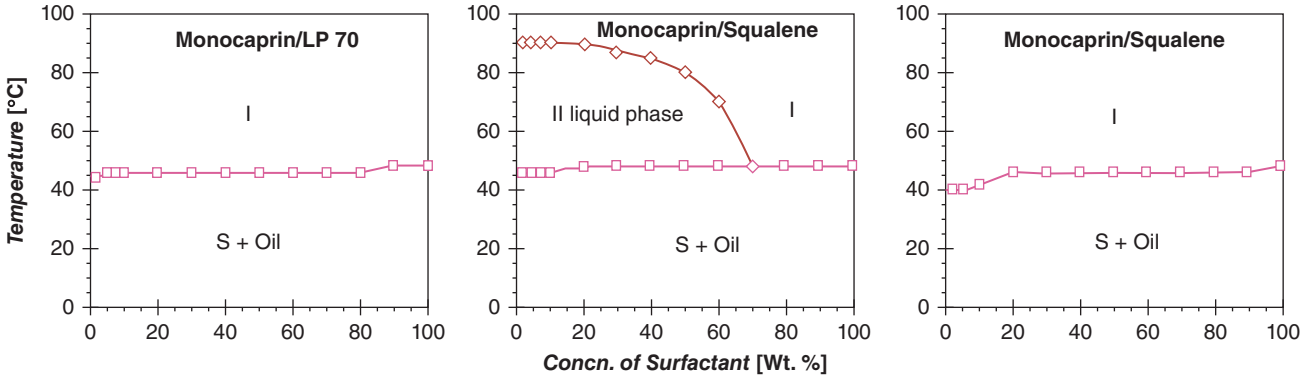


FIGURE 84.11 Composition–temperature phase diagrams of monocaprin/oil system. LP 70 indicates a liquid paraffin (hydrocarbon mixture). I indicates an isotropic phase in which reverse micelles are formed.

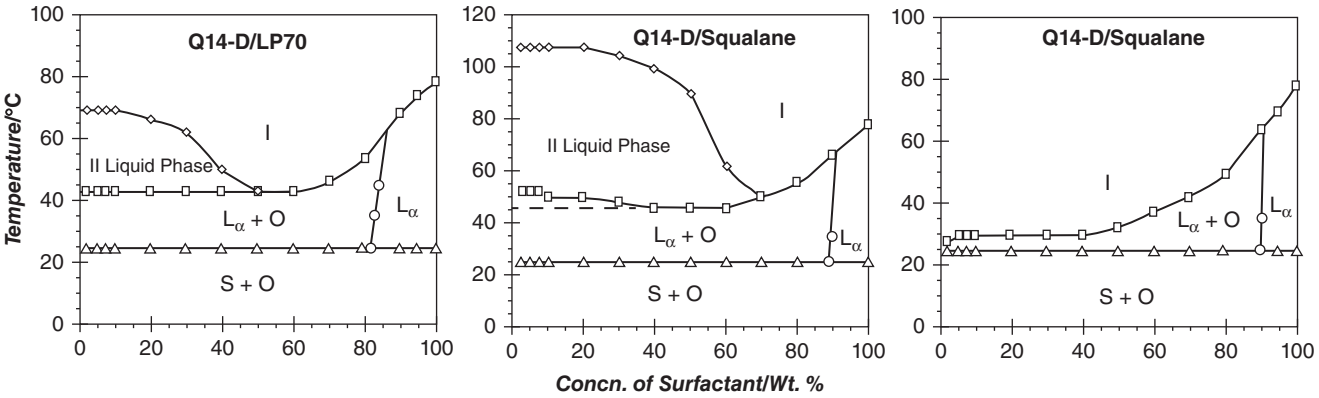


FIGURE 84.12 Composition–temperature phase diagrams of diglycerol monomylistate.

phases is narrower than that of aqueous surfactant systems. Again, a UCST-type miscibility gap appeared in the liquid paraffin and squalane systems.

REFERENCES

[1] Kitamoto, D., Morita, T., Fukuoka, T., Konishi, M., Imura, T. (2009). *Curr. Opin. Colloid Interface Sci.* **14**, 315–328.

[2] Boyd, B.J., Drummond, C.J., Krodkiewska, I., Weerawardena, A., Furlong, D.N., Grieser, F. (2001). *Langmuir* **17**, 6100–6107.

[3] Boyd, B.J., Krodkiewska, I., Drummond, C.J., Grieser, F. (2002). *Langmuir* **18**, 597–601.

[4] Whiddon, C., Söderman, O., Hansson, P. (2002). *Langmuir* **18**, 4601–4618.

[5] Kocherbitov, V., Söderman, O., Wadsö, L. (2002). *J. Phys. Chem. B* **106**, 2910–2917.

[6] Whiddon, C., Söderman, O. (2001). *Langmuir* **17**, 1803–1806.

[7] Kanei, N., Imae, T., Kihara, K., Tagawa, T., Kunieda, H. (1996). *J. Oleo Sci.* **45**, 849–855.

[8] Ishizuka, C., Ahmed, T., Arima, S., Aramaki, K. (2009). *J. Colloid Interface Sci.* **339**, 511–516.

[9] Sato, T., Acharya, D.P., Kaneko, M., Aramaki, K., Singh, Y., Ishitobi, M., Kunieda, H. (2006). *J. Dispers. Sci. Technol.* **27**, 1–6.

[10] Aramaki, K., Hoshida, S., Arima, S. (2010). *Colloids Surf. A* **366**, 58–62.

[11] Aramaki, K., Hoshida, S., Arima, S. (2012). *Colloids Surf. A* **396**, 278–282.

[12] Shrestha, L.K., Yamamoto, M., Arima, S., Aramaki, K. (2011). *Langmuir* **27**, 2340–2348.

[13] Kabir, Md.H., Aramaki, K., Ishitobi, M., Kunieda, H. (2003). *Colloids Surf. A* **216**, 65–746.

[14] Aramaki, K., Kabir, Md.H., Nakamura, N., Kunieda, H., Ishitobi, M. (2001). *Colloids Surf. A* **183–185**, 371–379.

[15] Kunieda, H., Ushio, N., Nakano, A., Miura, M. (1993). *J. Colloid Interface Sci.* **159**, 37–44.

[16] Pes, M.A., Aramaki, K., Nakamura, N., Kunieda, H. (1996). *J. Colloid Interface Sci.* **178**, 666–672.

[17] Aramaki, K., Kunieda, H., Ishitobi, M., Tagawa, T. (1997). *Langmuir* **13**, 2266–2270.

[18] Nakamura, N., Tagawa, T., Kihara, K., Tobita, I., Kunieda, H. (1997). *Langmuir* **13**, 2001–2006.).

[19] Bolzinger-Thevenin, M.A., Grossiord, J.L., Poelman, M.C. (1999). *Langmuir* **15**, 2307–2315.

[20] Garti, N., Clement, V., Leser, M.E. (2000). *J. Agric. Food Chem.* **48**, 3945–3956.

[21] Glatter, O., Orthaber, D., Strandner, A., Scherf, G., Fanun, M., Garti, N., Clement, V., Leser, M.E. (2001). *J. Colloid Interface Sci.* **241**, 215–225.

[22] Lutton, E.S. (1965). *J. Am. Oil Chem. Soc.* **42**, 1068–1070.

[23] Qui, H., Caffrey, M. (2000). *Biomaterials* **21**, 223–234.

[24] de Campo, L., Yaghmur, A., Sagalowicz, L., Leser, M.E., Watzke, H., Glatter, O. (2004). *Langmuir* **20**, 5254–5261.

[25] Ishitobi, M., Kunieda, H. (2000). *Colloid Polym. Sci.* **278**, 899–904.

[26] Shrestha, L.K., Shrestha, R.G., Iwanaga, T., Kunieda, H. (2007). *J. Dispers. Sci. Technol.* **28**, 883–891.

[27] Shrestha, L.K., Acharya, D.P., Sharma, S.C., Aramaki, K., Asaoka, H., Ihara, K., Tsunehiro, T., Kunieda, H. (2006). *J. Colloid Interface Sci.* **301**, 274–281.

[28] Kunieda, H., Akahane, A., Feng, J., Ishitobi, M. (2002). *J. Colloid Interface Sci.* **245**, 365–370.

[29] Kunieda, H., Kaneko, M., Fujiyama, R., Ishitobi, M. (2002). *J. Oleo Sci.* **51**, 379–386.

[30] Shrestha, L.K., Sato, T., Acharya, D.P., Iwanaga, T., Aramaki, K., Kunieda, H. (2006). *J. Phys. Chem. B* **110**, 12266–12273.

[31] Shrestha, L.K., Kaneko, M., Sato, T., Acharya, D.P., Iwanaga, T., Kunieda, H. (2006). *Langmuir* **22**, 1449–1454.

85

SURFACTANTS AND BIOSURFACTANTS

YOUICHI TAKATA

Department of Chemical and Biological Engineering, Ube National College of Technology, Ube, Yamaguchi, Japan

85.1 INTRODUCTION

The surfactant molecule is composed of hydrophilic and hydrophobic groups. Hydrophilic groups are attracted to ("like") water, whereas hydrophobic groups are repelled by ("dislike") water (or are attracted to oil). In this respect, a surfactant molecule possesses two totally different groups. This causes interesting phenomena characteristic of surfactant, such as surface adsorption and micelle formation in the solution.

The various kinds of groups are well known for both hydrophilic and hydrophobic characteristics. The wide global variety of surfactants is due to the fact that the surfactant molecule is structurally fixed by the combination of hydrophilic and hydrophobic groups. Such versatility in surfactant synthesis is useful for designing a novel surfactant applied for a specific purpose. The function of synthetic surfactants has also been improved to meet demands based on the needs of society. More recent developments in surfactant preparation also reflect the "greening effect" or the need to produce surfactants that are ergonomic or compatible with the natural environment (i.e., that are "environmentally friendly").

In this chapter, the basic structure and properties of general surfactants are first reviewed. Next, the novel surfactants that have been widely studied recently are discussed. The chapter concludes with an introduction to the surfactants associated with the field of biology, the so-called biosurfactant.

85.2 GENERAL SURFACTANTS

Surfactants are usually classified into four basic types, according to the charge on the hydrophilic groups: cationic, anionic, zwitterionic, and nonionic. The typical hydrophilic groups in each type are shown below, after some information on the hydrophobic groups is mentioned.

85.2.1 Hydrophobic Group

The term *hydrophobic* means to be repelled by or to "dislike" water. In other words, hydrophobic groups prefer oil to water. Therefore, the hydrophobic groups have structures similar to those of organic compounds. In general, the hydrophobic groups are actually alkyl groups composed of hydrogen and carbon atoms, which are often called *hydrocarbon chains* (Fig. 85.1).

In order to exert the function of surfactant, the length of the hydrocarbon chain is important. If its length is too short, the molecules indicate fairly strong water-soluble properties and their hydrophobic properties are hardly observed. This results in a loss of driving force for the adsorption to the interface, the micelle formation in solution, and so on. On the contrary, when the hydrocarbon chain is too long, the molecules become insoluble in water because of their strong hydrophobic properties. It is usually assumed that the 8–18 carbon atoms in the hydrocarbon chain are suitable for the surfactant.

In some cases, one surfactant molecule has two hydrocarbon chains (Fig. 85.2).

Encyclopedia of Biocolloid and Biointerface Science, Volume 2, First Edition. Edited by Hiroyuki Ohshima.
© 2016 John Wiley & Sons, Inc. Published 2016 by John Wiley & Sons, Inc.

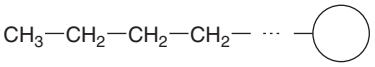


FIGURE 85.1 Example of hydrocarbon chain. Circle shows hydrophilic group.

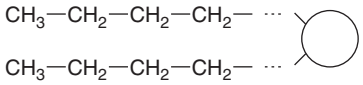


FIGURE 85.2 Example of surfactant with two hydrocarbon chains. Circle shows hydrophilic group.

Obviously, the hydrophobic property of a surfactant with two hydrocarbon chains increases in comparison to a surfactant with one hydrocarbon chain. Also, this modification affects the aggregate formation in the solution. The packing parameter, which is determined by the geometry of one surfactant molecule [1], of the typical surfactant is about $1/3$, and this suggests the formation of a spherical micelle. When the number of the hydrocarbon chain varies from one to two, the hydrophobic group becomes bulky and as a result its packing paramater approaches 1. Therefore the surfactant with two hydrocarbon chains tends to form a vesicle or lamellar structure rather than the spherical micelle.

Fluorocarbon chains composed of fluorine and carbon atoms are known as the other hydrophobic groups (Fig. 85.3).

It is well known that fluorine compounds show a high water repellency. This fact reveals that fluorocarbon chains have a strong hydrophobic property. Furthermore, the hydrocarbon and fluorocarbon compounds do not mix with each other and are separated into two phases [2]. This is because the interaction between hydrocarbon and fluorocarbon compounds is very week, and therefore the same species are condensable. This immiscible effect brings about an interesting behavior regarding the adsorbed film and micelles of the hydrocarbon and fluorocarbon surfactant mixture system. For example, the mixed micelle in the binary system of hydrocarbon surfactants is formed at any micelle composition by adjusting the bulk composition. On the other hand, the mixed micelle in the hydrocarbon–fluorocarbon surfactant mixture system is not formed at any micelle composition, and either hydrocarbon-rich micelles or fluorocarbon-rich ones appear in the aqueous solution [3]. This is due to the very weak interaction between hydrocarbon and fluorocarbon chains.

The unique properties of surfactants are produced by including two totally different groups, namely, hydrophilic and hydrophobic groups, in one molecule. At this point, the research on surfactants having both hydrocarbon and fluorocarbon chains as hydrophobic groups becomes

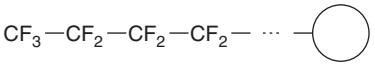


FIGURE 85.3 Example of fluorocarbon chain. Circle shows hydrophilic group.

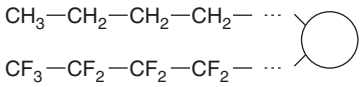


FIGURE 85.4 Example of hybrid surfactant. Circle shows hydrophilic group.

interesting. Such surfactants are called *hybrid surfactants* (Fig. 85.4).

As expected, hybrid surfactants exhibit unusual properties (critical micelle concentration, morphology of micelle, viscosity and so on) that are different from those of general surfactants [4]. It is anticipated that the hybrid surfactants will be applied in new fields in the future.

85.2.2 Hydrophilic Group

The term *hydrophilic* means to be attracted to or "like" water. The hydrophilic groups are divided into four types on the basis of their charges. As each hydrophilic group exhibits an inherent property, we can choose the surfactants depending on the purpose.

Ionic surfactants dissociate into cations and anions in water. The ion that has a charge opposite to that of the hydrophilic group is called a *counterion*. Even if both hydrophobic and hydrophilic groups of surfactants are the same, the different counterions greatly affect the properties of their surfactants [5]. Although the existence of counterions is not negligible, we omit further discussions here.

85.2.2.1 Cationic Surfactant. The hydrophilic group of cationic surfactant has a positive charge. The representative cationic group is the ammonium one. The substitution of hydrogen atom for methyl group leads to a series of ammonium groups, namely, (mono)methylammonium, dimethylammonium, and trimethylammonium groups (Fig. 85.5).

The properties of cationic surfactants are highly influenced by a slight change in hydrophilic group due to methylation [6].

In general, the main component of hair rinse is cationic surfactants. This is because the cationic hydrophilic group binds to the negatively charged surface of wet hair and its hydrophobic group provides the lubrication of hair.

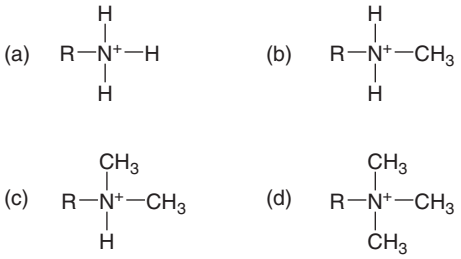


FIGURE 85.5 Example of cationic hydrophilic group: (a) ammonium; (b) monomethylammonium; (c) dimethylammonium; (d) trimethylammonium group (R denotes hydrophobic group).

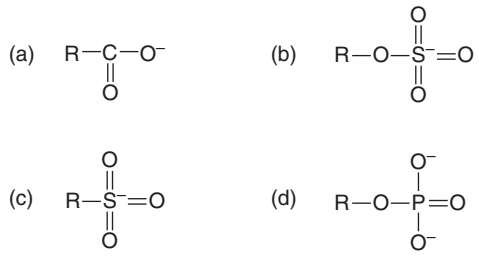


FIGURE 85.6 Example of anionic hydrophilic group: (a) carboxyl; (b) sulfate; (c) sulfonate; (d) phosphate group (R denotes hydrophobic group).

85.2.2.2 Anionic Surfactant. The hydrophilic group of anionic surfactant has a negative charge. There are various kinds of anionic surfactants compared with cationic ones. The most popular anionic surfactant is alkali salt of fatty acid (Fig. 85.6a), which is so-called soap. Sodium dodecyl sulfate (SDS), which contains an anionic sulfate group (Fig. 85.6b), is often utilized not only in ordinary household detergents but also in professional biological experiments such as electrophoresis. Besides, the sulfonate and phosphate groups are included in the typical hydrophilic groups of anionic surfactants (Fig. 85.6c,d).

85.2.2.3 Zwitterionic Surfactant. Amphoteric electrolyte such as amino acid and protein can possess both positive and negative charges in their molecules, depending on the pH. When the positive and negative charges are equal, the pH is defined as the *isoelectric point*. If the pH is less than the isoelectric point (i.e., if the solution is strongly acidic), the amphoteric electrolyte has a positive charge. On the other hand, if the pH is greater than the isoelectric point (i.e., if the solution is strongly basic), the amphoteric electrolyte has a negative charge. Thus the property of the amphoteric electrolyte depends on the pH.

In a similar manner, some surfactants can have both positive and negative charges in their hydrophilic groups. Such surfactants are called *zwitterionic* surfactants. The *critical micelle concentration* (cmc or CMC, depending on context) in the solution and ability of adsorption to the surface of zwitterionic surfactants are changeable by adjusting the pH in analogy with the amphoteric electrolyte because of the alteration in charge of hydrophilic group depending on the pH [7].

The most popular zwitterionic surfactant is alkyldimethyl betaine (Fig. 85.7a).

Phospholipid molecules such as diacylphosphatidyl choline (Fig. 85.7b) are also classified as zwitterionic surfactants. From a biological perspective, it is useful to clarify the pH dependence of the property of phospholipid molecules, which constitute the cell membrane.

85.2.2.4 Nonionic Surfactant. The hydrophilic group of nonionic surfactants has neither positive nor negative charge.

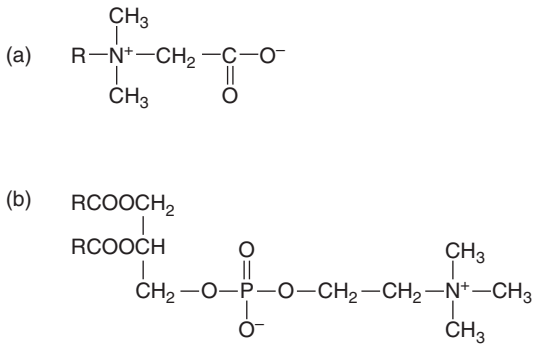


FIGURE 85.7 Example of zwitterionic hydrophilic group: (a) alkyldimethyl betaine; (b) diacylphosphatidyl choline (R denotes hydrophobic group).

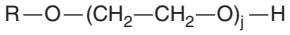


FIGURE 85.8 Example of nonionic hydrophilic group (polyoxyethylene group) (R denotes hydrophobic group).

Thus, the cmc is lower in nonionic surfactants than in ionic surfactants because there is no electrostatic repulsive force between the hydrophilic groups of the nonionic surfactant. Therefore, nonionic surfactants play an important role in products such as household detergents.

The most popular nonionic surfactant includes a polyoxyethylene chain (Fig. 85.8) in the hydrophilic group.

The nonionic surfactant polyoxyethylene alkylether is o ften presented as C_iE_j, where i and j denote the numbers of carbon atoms in the alkyl chain and in the oxyethylene group, respectively. The C_iE_j surfactants are available for various commercial purposes because it is possible to adjust their hydrophobicity or hydrophilicity simply by changing the number of i or j. Furthermore the solubility of C_iE_j surfactants into water or oil can change with temperature. For instance, an elevation in temperature causes the dehydration from the oxyethylene group and the C_iE_j surfactants to gradually acquire an oil-soluble property. The temperature at which the phase separation occurs is the *cloud point*.

85.2.3 Novel Surfactants

In addition to the abovementioned conventional surfactants, novel types of surfactants have been developed recently. These novel surfactants have two main advantages: (1) a smaller quantity is needed for use and (2) they are environmentally friendly.

If the surfactants exhibit outstanding performances, the required amount of surfactants decreases. For this reason much research has focused on gemini surfactants. *Gemini surfactants* are those surfactants to which the hydrophilic groups of two surfactant molecules are connected by a spacer composed of a shorter hydrocarbon chain (Fig. 85.9).

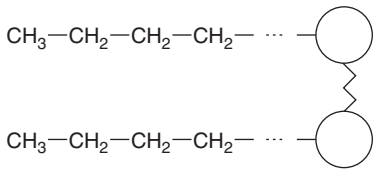


FIGURE 85.9 Example of gemini surfactant. Circle shows hydrophilic group. The shorter hydrocarbon chain between hydrophilic groups is a spacer.

As the gemini surfactants have two hydrophobic chains, the performance of adsorption is high. On the other hand, the solubility of gemini surfactants in water is maintained because of two hydrophilic groups. Therefore the critical micelle concentration of gemini surfactants becomes lower than that of ordinary surfactants [8].

The inherently low degradation power of synthetic surfactants is a major problem. In order to address this problem, sugar-based surfactants have been developed [9]. The hydrophilic group of a sugar-based surfactant is a monosaccharide such as glucose or galactose (Fig. 85.10). It is also suspected that sugar-based surfactants possess a higher degree of biodegradability compared to other synthetic surfactants.

There are several ongoing studies on the other novel surfactants focusing on the control of properties of a surfactant under an external field. As mentioned above, the properties of zwitterionic surfactants depend on the pH. Also the properties of C_iE_j surfactants depend on temperature, and it is possible that the same surfactant can possess both water-soluble and oil-soluble properties at certain temperatures. Research on light-sensitive (or photoresponsive) surfactants is increasing. The light-sensitive surfactant has a group characterized by a chemical structure that varies according to the relative absorption of light. Therefore, the irradiation of light switches the properties of light- sensitive surfactants. For example the irradiation of visible and ultraviolet light results in a change in chemical structure between *cis*- and *trans*-azobenzene (Fig. 85.11). If the hydrophobic group contains azobenzene, the properties of the surfactant depend on the light absorption [10, 11].

85.3 BIOSURFACTANTS

Surfactants are classified into synthetic and natural groups. The surfactants described above are mainly examples of

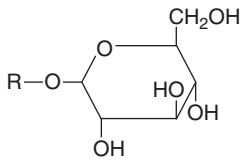


FIGURE 85.10 Example of sugar surfactant (R denotes hydrophobic group).

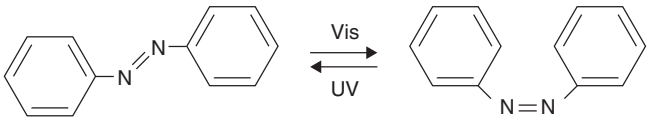


FIGURE 85.11 Change in chemical structure of azobenzene due to the absorption of light. If the hydrophobic group in surfactant molecule contains such a structure, the irradiation of light affects the properties of the surfactant.

synthetic surfactants and those synthesized from organic compounds. On the other hand, natural (i.e., nonsynthetic) surfactants originate from within the human body. The representative natural surfactant is a biosurfactant. More recent the research on biosurfactants has increased because of their environmentally friendly properties, although the ability of their surface activities is not as good as that of synthetic surfactants.

The most popular biosurfactant is a phospholipid, as shown in Fig. 85.7b. The packing parameter of phospholipid is close to 1, and therefore formation of the liposome and lamellar structure is easy. In fact, phospholipids are one of major components of the cell membrane.

Cholesterol constituting the cell membrane may also be regarded as a biosurfactant (Fig. 85.12).

The distinction between hydrophilic and hydrophobic groups in cholesterol molecules is not as clear as that for the usual (ordinary) surfactants, and in addition, the solubility of cholesterol in water is low. However, the interfacial tension acting on the water/oil solution of the cholesterol interface decreases with increasing cholesterol concentration [12]. Therefore, cholesterol has higher surface activity.

Bile acid and its salts are often investigated from the standpoint of surface chemistry [13]. Their chemical structures are similar to those of cholesterol (Fig. 85.13).

The micelle formation of bile acid is related to the function of digestion in the human body, and therefore, its research is important.

Surfactants that assist lung function are called *pulmonary surfactants*. The pulmonary surfactant exists at the surface of alveoli and reduces the surface tension acting at the air–water surface on the alveoli [14]. The pulmonary surfactant is

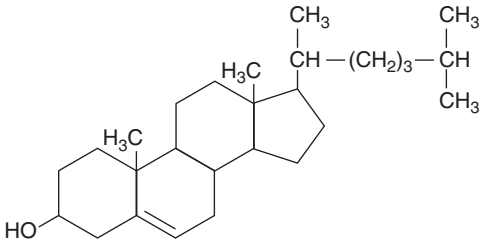


FIGURE 85.12 Chemical structure of cholesterol.

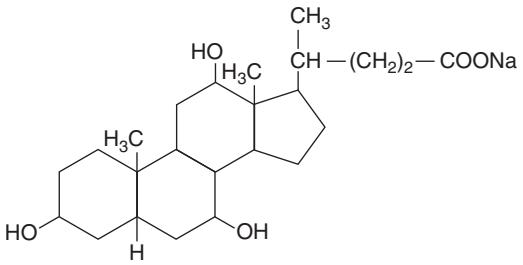


FIGURE 85.13 Chemical structure of sodium cholate.

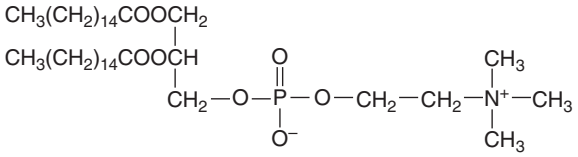


FIGURE 85.14 Chemical structure of dipalmitoylphosphatidylcholine.

composed mainly of phospholipids such as dipalmitoylphosphatidylcholine (Fig. 85.14).

As shown above, the origin of biosurfactants is the human body; therefore, its effect on the natural environment is low. From that perspective, research on biosurfactants, such as improvement of their functions and synthesis of surfactants having structures similar to those of biosurfactants, is widespread globally.

REFERENCES

[1] Israelachvili, J.N. (2011). *Intermolecular and Surface Forces*, 3rd ed. Academic Press, New York.

[2] Kashimoto, K., Yoon, J., Hou, B., Chen, C., Lin, B., Aratono, M., Takiue, T., Schlossman, M.L. (2008). *Phys. Rev. Lett.* **101**, 076102.

[3] Villeneuve, M., Nomura, T., Matsuki, H., Kaneshina, S., Aratono, M. (2001). *J. Colloid Interface Sci.* **234**, 127–136.

[4] Kondo, Y., Yoshino, N. (2005). *Curr. Opinion Colloid Interface Sci.* **10**, 88–93.

[5] Takata, Y., Miyayama, T., Nagahashi, T., Hyono, A., Ohshima, H. (2009). *J. Oleo Sci.* **58**, 557–563.

[6] Aratono, M., Okamoto, T., Ikeda, N., Motomura, K. (1988). *Bull. Chem. Soc. Japan* **61**, 2773–2778.

[7] Wang, X., Liu, J., Yu, L., Jiao, J., Wang, R., Sun, L. (2013). *J. Colloid Interface Sci.* **391**, 103–110.

[8] Yoshimura, T., Esumi, K. (2004). *J. Colloid Interface Sci.* **276**, 231–238.

[9] Hato, M. (2001). *Curr. Opinion Colloid Interface Sci.* **6**, 268–276.

[10] Cicciarelli, B.A., Elia, J.A., Hatton, T.A., Smith, K.A. (2007). *Langmuir* **23**, 8323–8330.

[11] Song, B., Zhao, J., Wang, B., Jiang, R. (2009). *Colloids Surf. A: Physicochem. Eng. Aspects* **352**, 24–30.

[12] Matsubayasi, N., Motomura, K. (1986). *Langmuir* **2**, 777–780.

[13] Posa, M., Kevresan, S., Mikov, M., Cirin-Novta, V., Kuhajda, K. (2008). *Colloids Surf. B: Biointerfaces* **64**, 151–161.

[14] Lunkenheimer, K., Winsel, K., Fruhner, H., Fang, J., Wantke, K.D., Siegler, K. (1996). *Colloids Surf. A: Physicochem. Eng. Aspects* **114**, 199–210.

86

EFFECT OF ADDITIVES ON SELF-ASSOCIATION AND CLOUDING PHENOMENA OF VARIOUS SURFACE-ACTIVE DRUGS

Md. Sayem Alam[1] and Asit Baran Mandal[1,2]

[1]*Industrial Chemistry Laboratory, Council of Scientific and Industrial Research (CSIR) — Central Leather Research Institute (CLRI), Adyar, Chennai 600 020, India*

[2]*Chemical Laboratory, Council of Scientific and Industrial Research (CSIR)—Central Leather Research Institute (CLRI), Adyar, Chennai 600 020, India.*

86.1 INTRODUCTION

The amphiphiles are molecules, which contain two parts: (1) oil-preferring or water-hating, referred to as *lipophilic* or *hydrophobic*, respectively, and (2) water-preferring, or *hydrophilic*. In aqueous environments, these molecules, including surfactants [1–24], drugs [25–38], and polymers [39–46], can form a kind of self-organized molecular assembly of thermodynamically stable colloidal dimension above their critical micelle concentrations (cmc's), which are termed *micelles* or *association colloids*. The self-organization and self-assembly are spontaneous and natural processes. They occur mainly through noncovalent interactions such as van der Waals, hydrogen bonding, hydrophobic/hydrophilic, electrostatic, donor and acceptor, and metal–ligand coordination networks [47]. The interests in micelle solutions stem from their potential as functional molecular assemblies for use in various fields of pure and applied sciences. They can be used as models for several biochemical and pharmacological systems. These solutions of amphipathic systems can solubilize water-insoluble substances (including certain medicines/drugs) in their hydrophobic cores [48].

Amphiphilic compounds bear an ionic (anionic, cationic, or zwitterionic) or nonionic polar headgroup and a hydrophobic portion. In aqueous medium, they are able to organize themselves as micelles, bilayers, monolayers, or as hexagonal or cubic phases. The spatial separation between the polar and nonpolar moieties, as well as the molecular shape [49] and the hydrophilic–lipophilic balance (HLB) [50], determine their tendency to form the different structures, which eventually can be interconverted as a function of pH, temperature, ionic strength, and concentration.

Surface-active drugs of quite different chemical structures are reported to self-associate and bind to membranes, causing disruption and solubilization, in a surfactantlike manner. Classes of surface-active drugs include phenothiazine [25–27,51–58] and benzodiazepine [25–27,59] tranquilizers, analgesics [25,60], peptide [61] and nonpeptide [25–27,62, 63] antibiotics, tricyclic antidepressants [25–27,64–66], antihistamines [67], anticholinergics [68], β-blockers [69], local anesthetics [25–27,70–73], nonsteroidal antiinflammatory drugs [74], and anticancer drugs [75]. Many of these drugs contain one or more (condensed or not) aromatic nuclei, while others are of peptide nature. A list of cmc and aggregation number N_{agg} (under specific conditions) of some commonly used nonpeptide surface-active drugs is given in Table 86.1.

The surface-active behavior among many diverse classes of drugs has been reported in order to correlate surface activity with biological activity [25–27]. The aggregation of the drugs listed in Table 86.1 follows same principles as those of

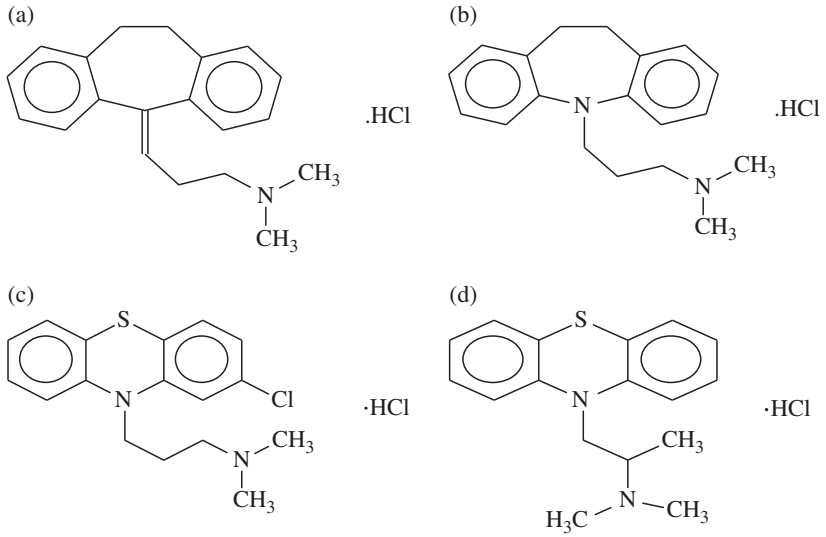
Encyclopedia of Biocolloid and Biointerface Science, Volume 2, First Edition. Edited by Hiroyuki Ohshima.
© 2016 John Wiley & Sons, Inc. Published 2016 by John Wiley & Sons, Inc.

TABLE 86.1 Some Surface-Active Drugs (Nonpeptide) and Their Micellar Properties in Aqueous Solution

Name of drug	Class	cmc (mM)[a]	N_{agg}
Dextropropoxyphene	Analgesics	100.0	7
Actinomycin D	Antibiotics	0.10	–
Penicillin G		250	–
Streptomycin		0.90	–
Adiphenine·HCl	Anticholinergics	82.0	10
Chlorphenoxamine·HCl		45.0	13
Orphenadrine·HCl		96.0	7
Penthianate methobromide		220.0	6
Piperidolate·HCl		82.0	12
Amphotericin B	Antifungal polyenes	6.0×10^{-4}	–
Nystatin		3.0×10^{-3}	–
Bromodiphenylhydramine·HCl	Antihistamines	54.0	11
Chlorcyclizine·HCl		127.0	3
Diphenhydramine·HCl		90.0	9
Diphenylpyraline·HCl		40.0	9
Thenyldiamine·HCl		100.0	3
Tripelennamine·HCl		120.0	3
Acetobutolol·HCl	Antihypertensives (with β-blocking action)	170.0	4
Oxprenolol·HCl		170.0	3
Propranolol·HCl		100.0	12
Thiopental	General anesthetics	7.0	–
Dibucaine·HCl	Local anesthetics	66.0	–
		11.0	9
Stadacaine·HCl		76.0	17
Tetracaine·HCl		130.0	7
		60.0	–
Chlorpromazine·HCl	Phenothiazines	19.0	11
		22.0	12
Promazine·HCl		36.0	11
		12.0	–
Promethazine·HCl		44.0	9
		58.0	12
Thioridazine·HCl		5.9	8
		1.5	–
Trifluoperazine		0.042	–
Trifluopromazine		4.5	–
Flupenthixol	Thioxanthene tranquilizers	8.5	19
Amitriptyline·HCl	Tricyclic antidepressants	36.0	7
Butriptyline·HCl		42.0	9
Clomipramine·HCl		22.0	6
Desipramine·HCl		49.0	7
Imipramine·HCl		47.0	8
Nortriptyline·HCl		23.0	4

Sources: Refs. 25–27 and 112.

conventional surfactants [25,27]. The "surfactantlike" behavior is due to the presence of an almost planar tricyclic ring system and a short hydrocarbon chain carrying a terminal nitrogen atom (see Scheme 86.1) [25–27]. It is well known that the cmc values of amphiphiles vary in presence of additives, as the interfacial and micellar properties of these compounds in solutions are governed by a subtle balance of hydrophobic and hydrophilic interactions. As additives are known to modify those interactions and drugs that are used in combination with additives (salts, surfactants, excipients, etc.), it is necessary to have some knowledge of the additive's effect on the cmc and the thermodynamics of amphiphilic



SCHEME 86.1 Molecular structure of surface-active drugs used in the present study: (a) 3-(10, 11-dihydro-*5H*-dibenzo[*a*,*d*]cycloheptane-5-ylidene)-*N*,*N*-dimethyl-1-1-propanamine hydrochloride [amitriptyline hydrochloride (AMT)]; (b) 5-[3-(dimethylamino)propyl]-10,11-dihydro-*5H*-dibenz[*b*,*f*]azepine hydrochloride [imipramine hydrochloride (IMP)]; (c) 2-chloro-10-(3-dimethylaminopropyl)phenothiazine hydrochloride [chlorpromazine hydrochloride (CPZ)]; and (d) 10-[2-(dimethylamino)propyl]phenothiazine hydrochloride [promethazine hydrochloride (PMT)].

drugs. Because surfactants have long shelf-lives and their preparation is usually simple, they have been widely used as drug delivery vehicles or drug carriers.

The excellent colloidal properties of amphiphilic drugs are determined largely by the nature of the aromatic ring system of their hydrophobic moieties. Such drugs are useful in probing relationships between the molecular architecture and physicochemical properties [25–27,76]. In pharmaceutical applications, the interaction between small molecules and drugs has been studied extensively. In this respect, it is worthwhile to mention here that many drugs, particularly those with local anesthetic, antidepressant, tranquillizer, and antibiotic actions, exert their activities by interaction with biological membranes, which can be considered as complex forms of amphiphilic bilayers. Thus, a full knowledge of the mechanism of the interactions of drugs with other foreign materials is essential prior to their actual application in the human body. This is so because drugs are always used in presence of a variety of additives (excipients).

Clouding is a well-known phenomenon, which is generally observed in nonionic surfactants. When the temperature is raised, the system becomes cloudy and phase separation occurs at a well-defined temperature, which called the *cloud point* (CP) [77–80]. To the best of our knowledge, the mechanism of clouding in nonionic surfactants is not yet clearly understood, and continues to be a source of controversy among various research groups. This clouding phenomenon rarely occurs in charged micelles, presumably because of the electrostatic repulsions between the micelles in addition to the van der Waals attraction force, which prevents phase separation in most cases [81–83]. The appearance of CPs in ionic surfactant solutions is rare except under certain special conditions [84–93], namely, high salt concentration [84–89], salt-free aqueous solutions of certain surfactants with large headgroups [90, 91] or large counterions [92, 93], and in some mixed cationic–anionic surfactant solutions [93]. The occurrence of CPs in these systems is explained in terms of increased hydrophobic interactions, dehydration of the hydrophilic group [89], and formation of large aggregates or clusters [88,92].

The clouding phenomena of amphiphilic drugs are rare, as are like ionic surfactants. However, under special conditions, they showed clouding phenomena and phase separation occurred [94–111]. The pK_a values of these drugs lie in the range 9.1– 9.4 [112], and, depending on the solution pH, the drug monomers may acquire cationic (i.e., protonated) or neutral (i.e., deprotonated) forms (see Scheme 86.1) [94]. Some surface-active drugs, such as ionic surfactants, undergo phase separation, depending on pH, concentration, and temperature [94=-111]. It was observed that their CP values can vary with additives [94–111]. The thermodynamic parameters of some surface-active drugs in presence of additives have recently been reported [113–119].

The work presented here is aimed at obtaining a better understanding of the role of the presence of additives in the surface properties, micellization or mixed micellization and the thermodynamic quantities of micellization of two basic types of amphiphilic

drugs: (1) tricyclic antidepressants [3-(10, 11-dihydro-*5H*-dibenzo[*a*,*d*]cycloheptane-5-ylidene)-*N*,*N*-dimethyl-1-1-propanamine hydrochloride, i.e., amitriptyline hydrochloride (AMT) and 5-[3-(dimethylamino)propyl]-10 ,11-dihydro-*5H*-dibenz[*b*,*f*]azepine hydrochloride, i.e., imipramine hydrochloride (IMP)] and (2) phenothiazines [2-chloro-10-(3-dimethylaminopropyl)phenothiazine hydrochloride, i.e., chlorpromazine hydrochloride (CPZ) and 10-[2-(dimethylamino)propyl]phenothiazine hydrochloride, i.e., promethazine hydrochloride (PMT)] (see Scheme 86.1). The Gibbs energies at the air–water interface ($G_{\min}^{(s)}$), standard Gibbs energy of micellization (ΔG_{mic}°), standard Gibbs free energy change of adsorption (ΔG_{ads}°), and excess Gibbs energy change of micellization (ΔG_{ex}) are calculated and discussed here.

Clouding phenomena in both absence and presence of additives have also been reported. It was found that the CP of these drugs can vary with additives. It is worthwhile to mention here that the thermodynamics of clouding (phase separation) of the above four amphiphilic drugs—AMT, IMP, CPZ, and PMT—in the presence of additives (electrolytes, surfactants, etc.), with a view to stimulate further studies in drug delivery andmodel drug delivery systems.

86.2 SURFACE PROPERTIES, SELF-ASSOCIATION, AND MIXED MICELLIZATION OF SURFACE-ACTIVE DRUGS WITH AND WITHOUT ADDITIVES

Representative plots of surface tension versus log [drug] for surface-active drugs with different additives are indicated in Fig. 86.1a. The cmc values of all the drugs have been found to decrease in the presence of additives (see representative plot in Fig. 86.1b). On the basis of the spectra of Sudan III in x mM drug (AMT, IMP, CPZ, and PMT) solutions with and without fixed concentrations of additives, the cmc values of the drugs were determined using the dye solubilization method also (Fig. 86.1c) and revealed a similar trend in the cmc values, which decreased in the presence of additives (e.g., NaCl; see Fig. 86.1d). The cmc values for pure drugs are in good agreement with the literature values [25–27,112].

The cmc values of all drugs are found to decrease in the presence of additives. Counterions are bound to micelles primarily not only by the strong electric field created by the headgroups but also by specific interactions that depend on the headgroup and the counterion type. Two mechanisms were proposed: (1) inorganic salts affecting the solvent property of water and (2) ions affecting the micelles directly by adsorbing/desorbing to the headgroup region of the micelles [120, 121]. Counterion binding plays a role in determining the effective charge on the micelles and hence its formation, shape, and mutual interactions [122]. Added Cl^- ions (in the form of NaCl) follow mechanism 2 and adsorb to the cationic headgroup region of the drug monomers. This adsorption decreases the electrostatic repulsion among headgroups, and less electrical work is required to form micelles. The cmc values of the drugs also decreased in the presence of CTAB and TX-100. The concentrations of these surfactants were lower than or equal to their cmc values (which are 1 mM – CTAB and 0.36 mM – TX-100 [124]). Furthermore, these surfactants are known to form mixed micelles with the drugs [31,124].

Rodriguez et al. [31,124] studied the effect of dodecyltrimethylammonium bromide concentration on the cmc of AMT in aqueous solution using conductivity and static fluorescence measurements. They explained their results on the basis of mixed micelle formation. Theoretical calculations of their results predict an apparent ideal but nonsynergistic behavior of the mixed micelles. Our results also suggest mixed micelle formation, although the slope of cmc decrease is lower in the case of CTAB.

The values of the surface pressure at the cmc (Π_{cmc}) were obtained using the following equation

$$\Pi_{cmc} = \gamma_0 - \gamma_{cmc} \tag{86.1}$$

where $\gamma_{0,}$ and γ_{cmc} are the surface tension of the solvent and the surface tension of the mixture at the cmc, respectively. The values of Π_{cmc} increase, with increase in concentration of the additives, indicating that the efficiency increases.

The surface excess concentration is an effective measure of the Gibbs adsorption at the liquid–air interface, which was calculated by employing Eq. (86.2) [125] as

$$\Gamma_{max} = -\frac{1}{2.303nRT}(d\gamma/\log c)_T \tag{86.2}$$

where γ, R, T, and c are surface tension, gas constant, absolute temperature, and concentration, respectively. The variable n is introduced to allow for the simultaneous adsorption of ions (anions and cations). The expression used in the calculation of n was that proposed by two investigators [126], $n = 1+ m/(m+m_s)$, where m_s is the concentration of the added electrolyte. Hence, n has a value of 2 in water and approaches 1 in the presence of excess inert electrolyte. The slope of the tangent at the given concentration of the γ *vs* log c plot was used to obtain Γ_{max}, and A_{min} and evaluated using the following relation [127]

$$A_{min} = 10^{16}/N_A\Gamma_{max} \tag{86.3}$$

where N_A is the Avogadro number.

A thermodynamic quantity for the evaluation of synergism in mixing, i.e., the free energy of the given air/water interface $G_{min}^{(s)}$, which was proposed by another team [128, 129], is defined as follows:

$$\Delta G_{min}^{(s)} = A_{min}\Pi_{cmc}N_A \tag{86.4}$$

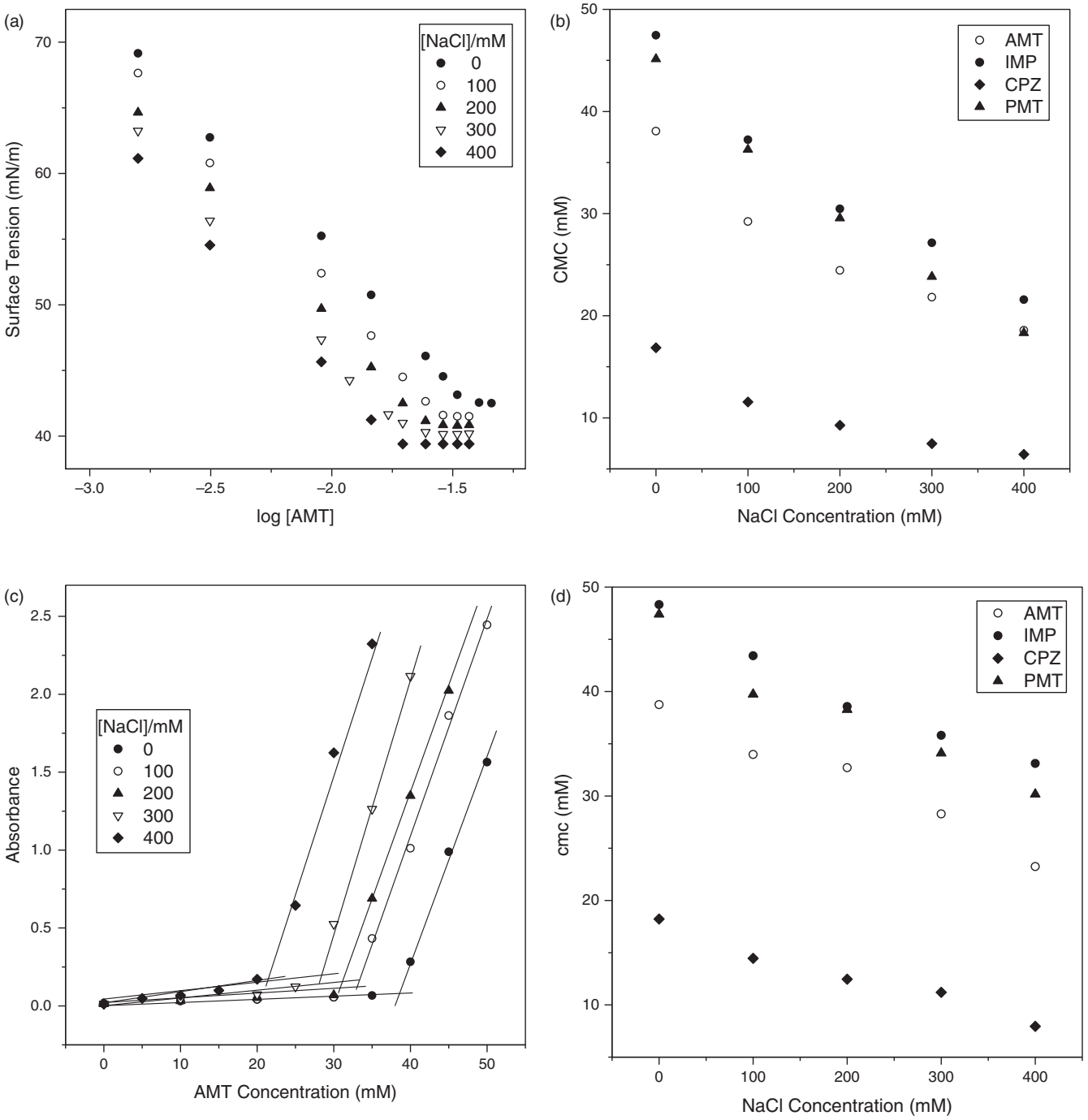


FIGURE 86.1 Plots of surface tension versus logarithm of AMT concentration at different fixed concentrations of NaCl: (a) effect of NaCl concentration on cmc values of drugs in aqueous solutions at ~27°C determined by surface tension measurements; (b) plots of absorbance versus concentration of AMT at different fixed concentrations of NaCl at 510 nm; (c) effect of NaCl concentration on cmc values of drugs in aqueous solutions at ~27°C determined by the dye solubilization method (d).

The Gibbs energy $G_{\min}^{(s)}$ is regarded as the work needed to construct an interface per mole or the free-energy change accompanied by the transition from the bulk phase to the surface phase of the solution components. In other words, the lower the values of $G_{min}^{(s)}$, the more thermodynamically stable surface is obtained. With increase in the additives' concentration/mole fractions, the $G_{\min}^{(s)}$ values are found to decrease (Fig. 86.2a).

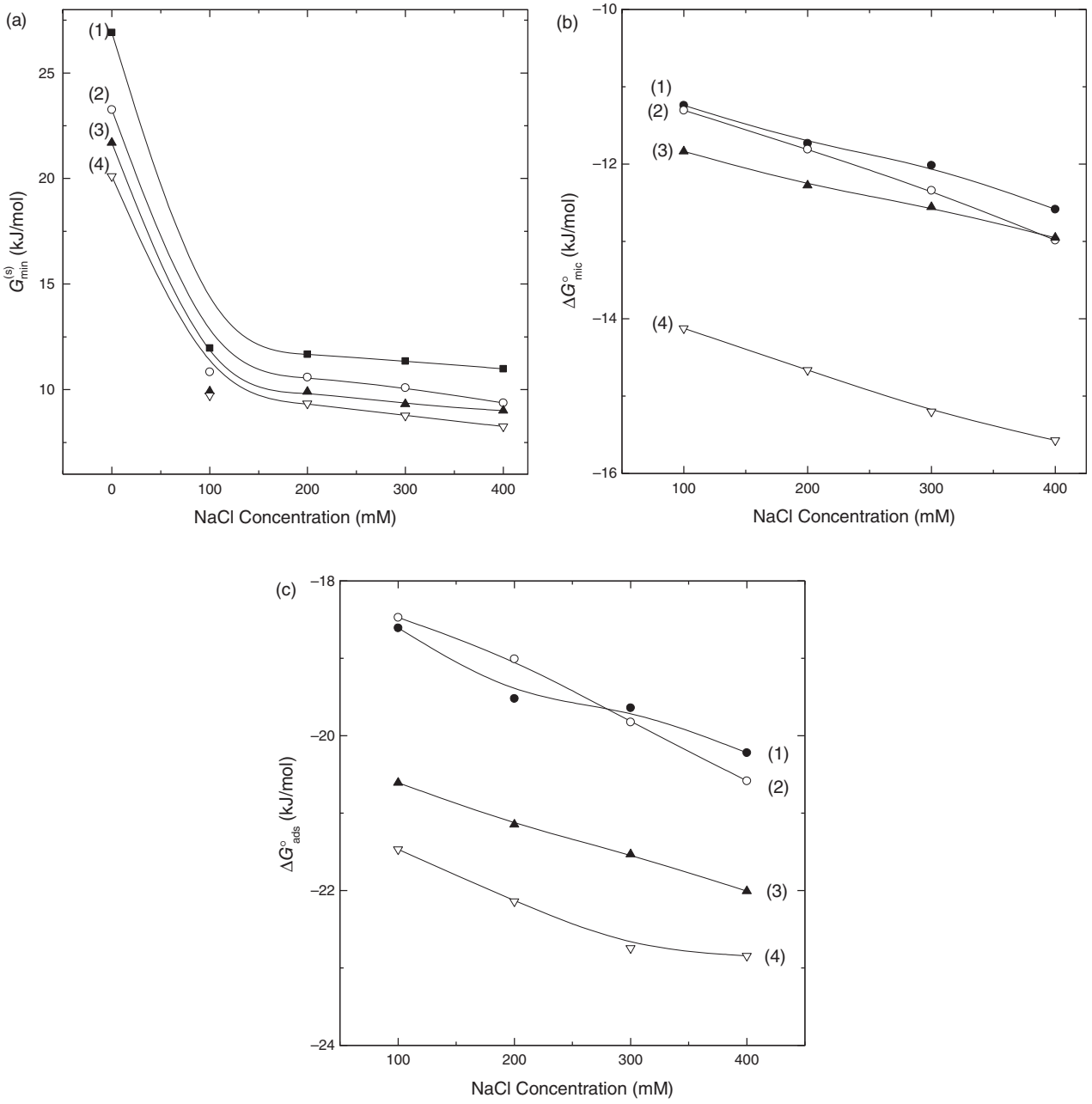


FIGURE 86.2 Variation in Gibbs free energy at the air–water interface: (a) the standard Gibbs energy change of micellization ΔG°_{mic}; (b) Gibbs energy change of micellization, ΔG°_{ads}; (c) surface-active drugs [(1) amitriptyline hydrochloride (AMT), (2) chlorpromazine hydrochloride (CPZ), (3) imipramine hydrochloride (IMP), (4) promathiazine hydrochloride (PMT) at different concentration of NaCl.

In order to quantify the effect of additives in the mixture on the micellization process, the standard Gibbs free-energy change of micellization ΔG°_{mic} and standard Gibbs energy of adsorption ΔG°_{ads} were calculated using Eqs. (86.5) and (86.6) as

$$\Delta G^{\circ}_{mic} = RT \ln \mathrm{cmc}_m \tag{86.5}$$

where cmc_m is the cmc of the mixture of the two components at a given mole fraction.

$$\Delta G^{\circ}_{ads} = \Delta G^{\circ}_{mic} - \Pi_{\mathrm{cmc}}/\Gamma_{\max} \tag{86.6}$$

A decrease in ΔG°_{mic} and ΔG°_{ads} values with increasing additive concentrations was observed (see Fig. 86.2b,c). The

standard state (at zero surface pressure) for the adsorbed surfactant is a hypothetical monolayer at its minimum surface area per molecule. The last term in Eq. (86.6) expresses work involved in transferring the surfactant molecule from a monolayer at zero surface pressure to the micelle. In all the cases (in absence/presence of additives), ΔG°_{mic} values are negative and decreased with increasing additive concentration/mole fraction (Fig. 86.2b). This indicates that the micellization is more spontaneous in presence of the additives (Fig. 86.2b). All the ΔG°_{ads} values were also found to be negative, implying that the adsorption of the surfactants at the air–mixture interface takes place spontaneously (see Fig. 86.2c).

The nature and strength of the interactions between the drugs and surfactants can be determined by finding the values of their β^m parameters [130]. The intermicellar interaction coefficient in the mixed micelles is calculated from the following equations:

$$\frac{\left\{\left(x_1^m\right)^2 \ln(\mathrm{cmc}\alpha_1/\mathrm{cmc}_1 x_1^m\right\}}{\left[\left(1-x_1^m\right)^2 \ln\left\{(\mathrm{cmc}(1-\alpha_1)/\mathrm{cmc}_2(1-x_1^m)\right\}\right]} = 1 \quad (86.7)$$

$$\beta^m = \ln\left(\mathrm{cmc}\alpha_1 x_1^m\right)/\left(1-x_1^m\right)^2 \quad (86.8)$$

Here, x_1^m is the mole fraction of component 1 in the micelles and cmc_1; cmc_2 and cmc are the cmc values for component 1, component 2, and their mixture at mole fraction of component 1, α_1, in the solution.

Equation (86.7) was solved iteratively for x_1^m, which was then substituted into equation (8) to obtain the β^m values.

The activity coefficients f_1 and f_2 are related to β and calculated by Eqs. (86.9) and (86.10):

$$f_1 = \exp\left\{\beta^m\left(1-x_1^m\right)^2\right\} \quad (86.9)$$

$$f_2 = \exp\left\{\beta^m x_1^m\right)^2\right\} \quad (86.10)$$

The excess free-energy change of micellization, ΔG_{ex}, is calculated by using the following equation:

$$\Delta G_{ex} = \left\{x_1^m \ln f_1 + \left(1-x_1^m\right)\ln f_2\right\}RT \quad (86.11)$$

In addition of surfactants (CTAB/TX-100), first they adsorbed and then formed mixed micelles. The negative ΔG_{ex} indicates a positive synergism [128]. The values of ΔG_{ex} are negative for all mole fraction/concentration values of additives, and the magnitude increases (ΔG_{ex}values become more negative) with increase in the additives' mole fractions/concentrations. This negative magnitude increase of ΔG_{ex} indicates stability of the micelles as well as more effective (positive) synergism.

86.3 EFFECT OF ADDITIVES ON CLOUDING BEHAVIOR OF AMPHIPHILIC DRUG SOLUTIONS

86.3.1 Effect of pH

As we have mentioned before, drugs (see Scheme 86.1) used in the present investigations can behave as cationic surfactants at pH < 7, and intermolecular and intermicellar interactions depend on the polar head charge and counterion concentration. Hence, the clouding behavior of surface-active drug solutions should be influenced by both pH and ionic strength. Indeed, maintaining the [drug] fixed [50 mM (or 100 mM for IMP)—all above the cmc of the drugs] and increasing the pH permitted us to observe the clouding phenomenon. We showed that the CP decreases as the pH value of the drug soltions increases (regardless of whether an additive is present); the results are plotted in Fig. 86.3a. In the pH range employed, this decrease in CP implies a significant change in the micellar surface charge. Depending on the solution pH, the hydrophilic *tert*-amine of the drug molecule (see Scheme 86.1) becomes protonated (i.e., cationic) or deprotonated (i.e., neutral). With the increase in solution pH, number of un-ionized (deprotonated) drug molecules in the micelles increases. Thus the observed behavior can be explained in terms of reduction of electrical repulsion due to increased fraction of the deprotonated drug with the concomitant enhancement in micellar aggregation number leading to decrease in the CPs. The behavior remains the same in the presence of additives, except that the CP values (increasing or decreasing as compared to the no-additive case) are dependent on the nature of the additive.

86.3.2 Effect of Electrolytes

86.3.2.1 Inorganic Salts. Figure 86.3b depicts the effect of inorganic counterions (F^-, Cl^- and Br^-) on the CP of drug solutions. Addition of electrolytes causes an increase in CP, and the order of increase is NaF < NaCl < NaBr. As halide ions carry charge opposite to that of the drug micelles (which is cationic), they should interact electrostatically with the micelles. The degree of counterion binding is known to affect the size and shape of the micelles [27,122]. The fluoride ion binding to the cationic headgroup is weak (as F^- is highly hydrated; crystal radius is 1.36 Å and hydrated radius is 3.52 Å) [131]. Therefore, with addition of NaF, micelle shape/size changes slowly and CP increase is slow. For NaBr, Br^- binds strongly to the micelles and increases the size of micelles. However, as Br^- is also hydrated, although less than F^- (crystal radius, 1.95 Å; hydrated radius, 3.30 Å) [131], and it increases micelle hydration as well as CP. The size of Cl^- (crystal radius, 1.81 Å; hydrated radius, 3.32 Å) [131] is in between F^- and Br^-, therefore, CP increase is intermediate to F^- and Br^-. The CP increase with micellar growth has been proposed [94, 95]. Those same authors observed a

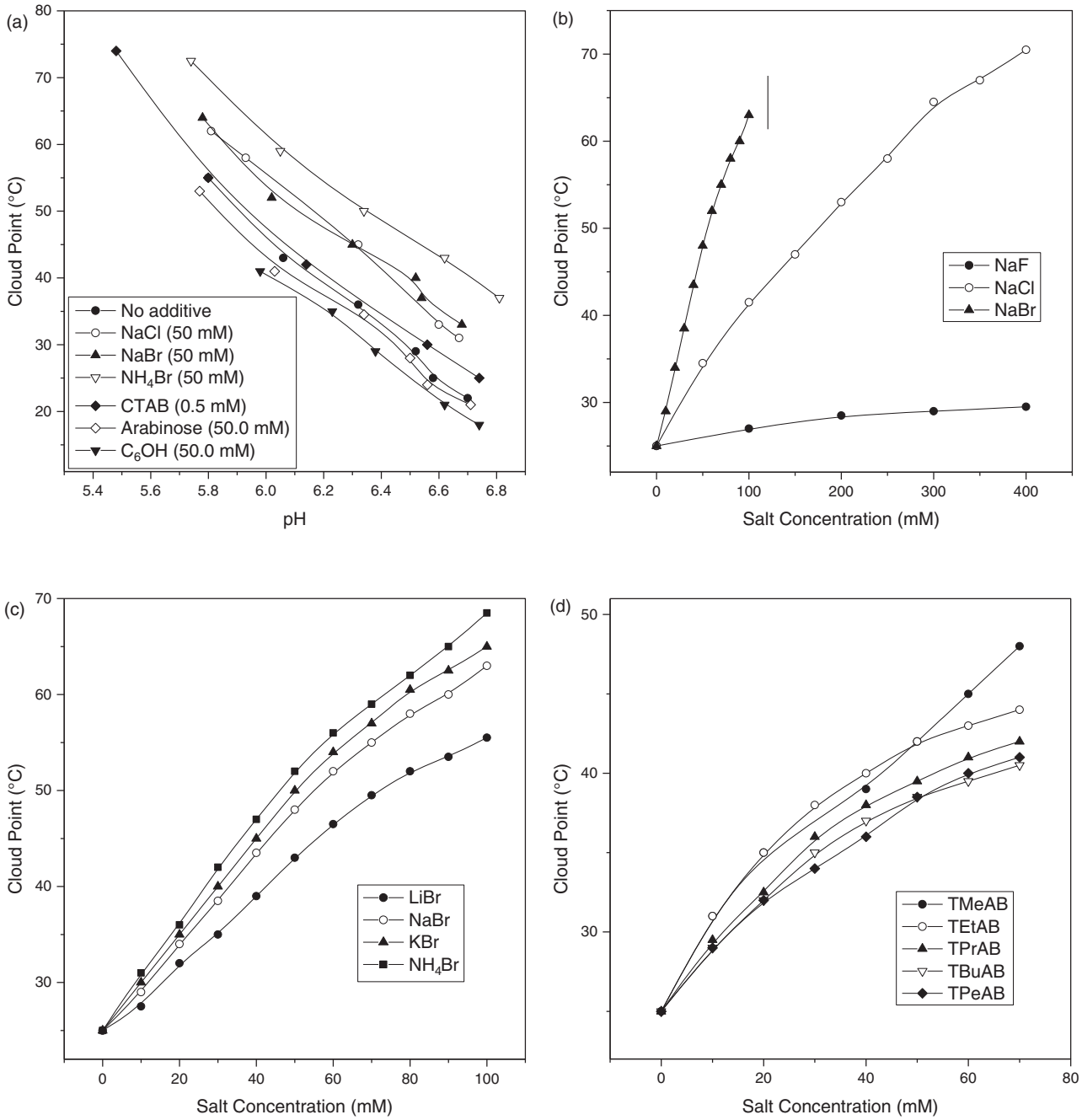


FIGURE 86.3 Effect of pH (containing no or a fixed additive concentration): (a) anionic counterions (| indicates precipitation occurring beyond [NaBr] > 100 mM at room temperature (which could be due to formation of nonmicellar phases); (b) cationic coions; (c) quaternary ammonium bromide salts; (d) concentration on the CP of 50 mM AMT solution, prepared in 10 mM sodium phosphate buffer (pH = 6.7).

larger increase in CP as well as in UV–visible intensity of AMT drug solutions with the addition of NaBr as compared to NaF addition [94, 95].

The variation in cloud points of drug solutions in presence of inorganic coions (Li^+, Na^+, K^+ and NH_4^+) is shown in Fig. 86.3c. The order of CP increase is LiBr < NaBr < KBr < NH_4Br. Ions can be classified into Hofmeister series according to their hydrated radius and salting-out strength [132]: (1) salts on the left-hand side of the series are water-structure makers and decrease the solute solubility; and (2) salts on the right-hand side are considered as water-structure breakers and increase the solute

solubility in water [120]. Another mechanism for Hofmeister series behavior relates salting-in and salting-out phenomena directly to adsorption or desorption of ions to the hydrophilic parts of the organic compounds [133]. In the series of MBr salts, Li^+ is highly hydrated (r_h = 3.82 Å) [131] and would act as a water-structure promoter, decreasing the availability of water to the micelles, which results in a slow increase in CP. Na^+, K^+, or $NH_4{}^+$ are comparatively less hydrated (for Na^+, r_h = 3.58 Å, for K^+ and $NH_4{}^+$, r_h = 3.31 Å) [131] and result in increase in micelle hydration. Hence, CP increases sharply.

86.3.2.2 Quaternary Ammonium Bromides. Figure 86.3d illustrates the variation in CP of drug solutions prepared in 10 mM SP buffer (pH = 6.7) as a function of the concentration of added quaternary ammonium bromides (QABs). All the salts cause an increase in CP. The increase is in the following order: TMeAB>TEtAB>TPrAB>TBuAB>TPeAB. The QABs are less hydrated than the inorganic salts. It was reported that the tetraalkylammonium ions are water-structure formers, and this effect increases with increase in the length of the alkyl group. The CP rising in the case of QA^+ cations is ascribed to adsorption–mixed micelle formation predominating over water-structure formation [134]. In such cases, micelles would experience greater intermicellar repulsions and consequently higher CPs. This, indeed, has been observed experimentally (Fig. 86.3d).

86.3.3 Effect of Surfactants

86.3.3.1 Anionic Surfactants. The effect of anionic surfactants on drug solutions is shown in Fig. 86.4a. In drug solutions, the added anionic surfactants (SDS/SDBS) would behave as counterions to the drug micelles. Also, penetration of dodecyl/dodecylbenzene chain into the micelles is probable. These factors should decrease the CP. However, we observe a different behavior with SDS/SDBS. The CP increases up to a certain surfactant concentration and then decreases (Fig. 86.4a). At low concentrations surfactant molecules adsorb at the micellar interface and inhibit micellization resulting in an increase in CP; whereas, at higher concentrations the added surfactant increases the compactness of the micelles and leads to micellar growth. Intercalation of DS^-/DBS^- anions into the drug micelles would reduce the headgroup repulsions and enhance the hydrophobic interactions. This, in turn, would reduce a_o and increase v. Hencee, R_p increases with anionic surfactants.

The addition of SDBS shows a slight increase and a sharp decrease in CP, which indicates that SDBS is more hydrophobic than SDS. A phenyl group is considered to be equivalent to three or four carbons in a straight chain [135]. This is reflected in a lower cmc value for SDBS [123]. As a result, greater hydrophobic interactions occur between the benzene ring of the SDBS monomer and the hydrophobic portion of the drug molecule. Also, the presence of a benzene ring causes greater electrostatic interaction with cationic drug molecules. All of these factors make SDBS more effective in dehydrating the drug micelles causing a sharper decrease in CP at higher relative concentrations.

86.3.3.2 Cationic Surfactants. The effects of cationic surfactants on the CPs are shown in Fig. 86.4b. The CP increases with addition of all the cationic surfactants. The magnitude of CP increase is found to be dependent on the chain length of the alkyl chain present in the surfactant. Increasing the chain length (longer chain lengths) results in increasing the CP to a higher degree. The presence of a counterion (Br^-) is responsible for the decrease in surface area occupied per drug headgroup, with a simultaneous increase in R_p [136]. An increase in R_p results in micellar growth. The added cationic surfactants exist in the surface-active drug solutions as monomers, micelles, and mixed micelles depending on their cmc values. The addition of CTAB, which forms larger micelles than TTAB, generates stronger electrostatic repulsion between micelles and produces a higher CP (Fig. 86.4b).

86.3.3.3 Nonionic Surfactants. Data on CP variation in surface-active drug solutions in presence of various nonionic surfactants are clearly illustrated in Fig. 86.4c. All the nonionic surfactants cause an increase in CP. All these surfactants contain oxyethylene chains. When the nonionic surfactant-drug mixed micelles are formed, they contain relatively more hydrated water in comparison to that with a micelle of a pure drug. This increase in water hydration provided by oxyethylene chains seems to be the primary cause of CP increase in drug solutions. It can also be seen from figure Fig. 86.4b that the CP increase is highest with TX-100 and lowest with Tween 20. This may be due to the presence of unidentical as well as different numbers of hydrophobic and hydrophilic groups, which would affect the CP behavior of drug solutions in a different manner.

86.3.4 Effect of Additives at Different Fixed pHs

The variation in CP of surface-active drug solutions at different fixed pHs (= 6.5, 6.7 and 6.9) prepared in 10 mM SP buffer (see representative plot, Fig. 86.5a). Additive concentration variations at different fixed pHs (all below pK_a values of the drugs) [112] show that increase/decrease in pH causes a decrease/increase in CP. With all the additives, the trend of CP variation remains exactly the same as observed at pH = 6.7 (for comparison, plots of pH = 6.5, 6.7 and 6.9 are shown in Fig. 86.5a).

86.3.5 Effect of Additives at Different Fixed Drug Concentrations

Figure 86.5b illustrates the effects of additive concentrations on the CPs of drug solutions at different fixed concentrations, prepared in 10 mM sodium phosphate buffer (pH = 6.7). The

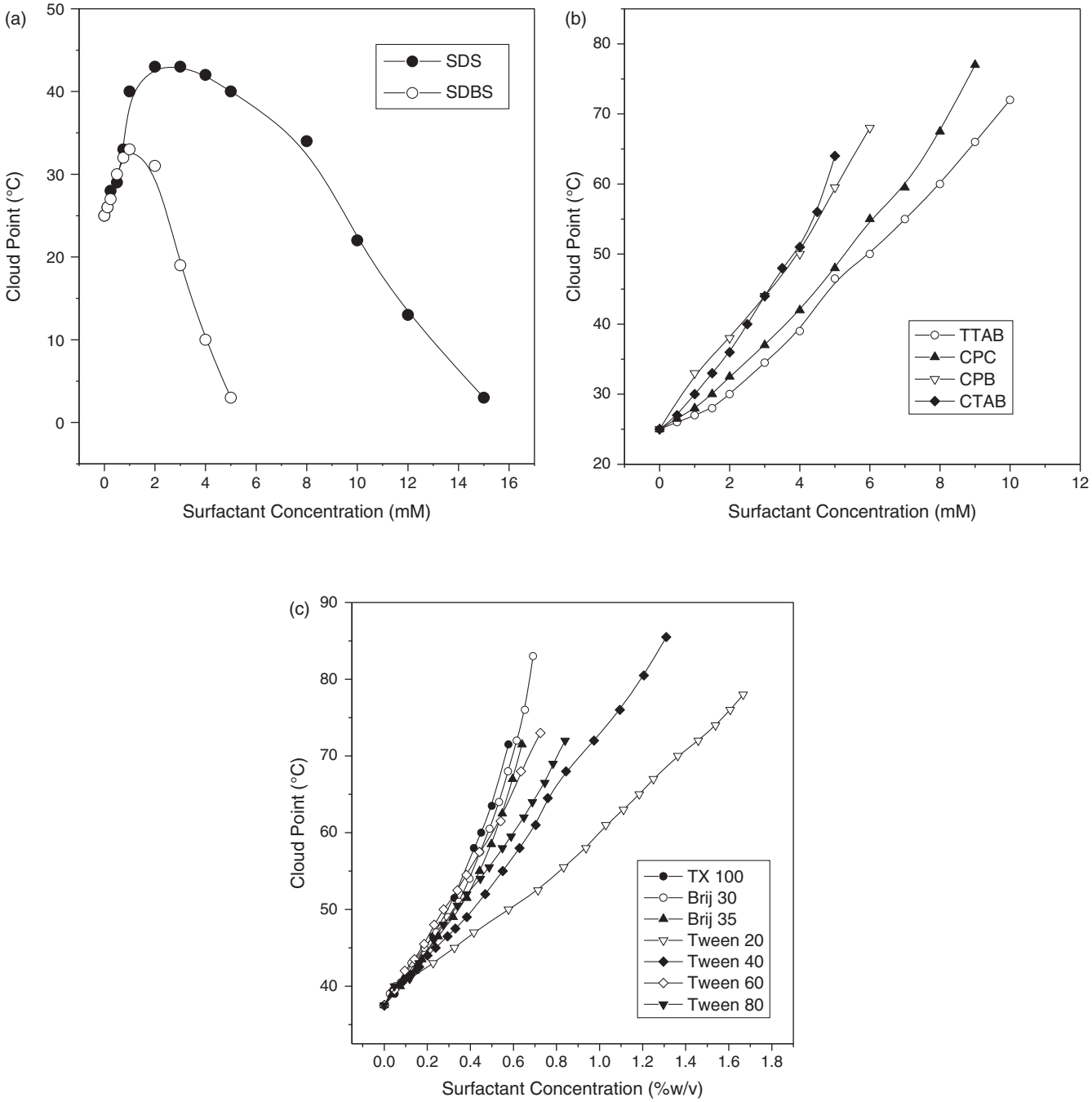


FIGURE 86.4 Effects of anionic (a), cationic (b), and nonionic (c) surfactant concentrations on the CP of 50 mM AMT solution, prepared in 10 mM sodium phosphate buffer (pH = 6.7).

trend in CP variations with different additives is the same as described earlier. With increase in drug concentrations, there is a corresponding increase in the number of micelles (which are charged). This increased number of micelles increases the degrees of intermicellar and intramicellar repulsion, and hence the CP also increases (Fig. 86.5b).

86.4 THERMODYNAMICS AT CP

As the amphiphile phase separates at temperatures above CP, the CP of a given amphiphile can be considered as the limit of its solubility. The clouding components release their solvated water and separate out from the solution. Hence, the standard

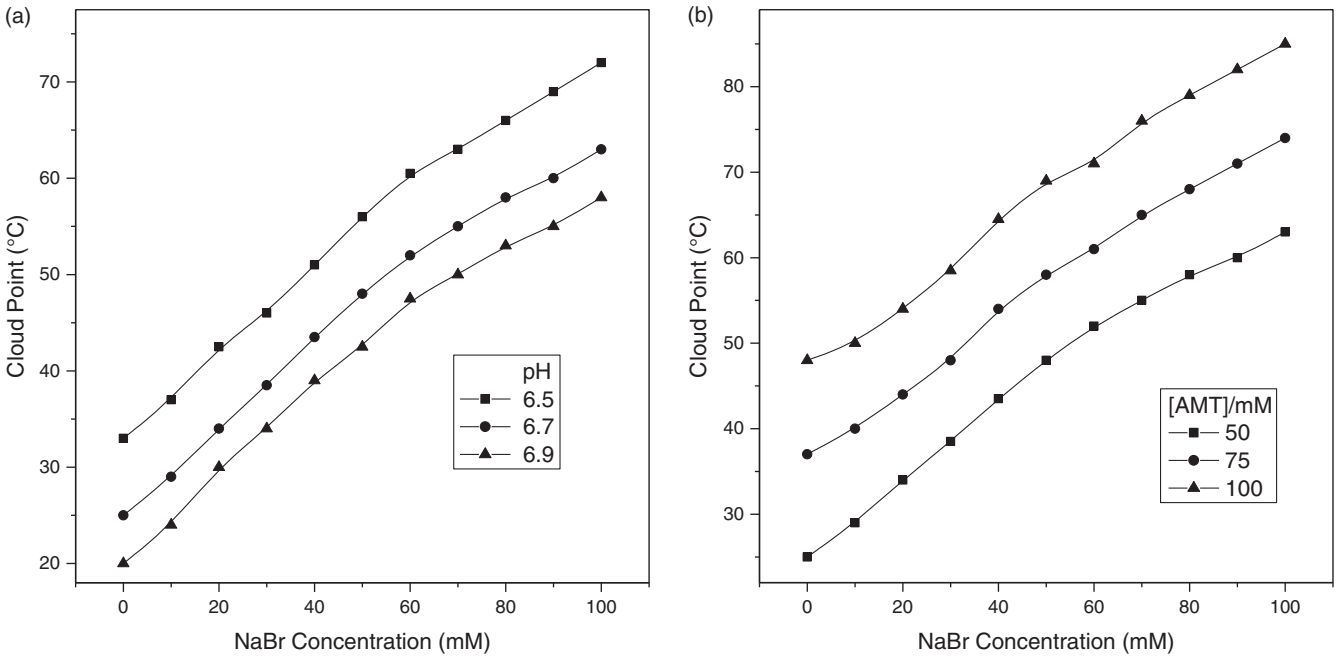


FIGURE 86.5 Effect of NaBr concentration on the CP of 50 mM AMT solution, prepared in 10 mM sodium phosphate buffer at different pH levels (a) and the effect of NaBr concentration on the CP of different fixed concentrations of AMT solutions, prepared in 10 mM sodium phosphate buffer (pH = 6.7) (b).

Gibbs energy of solubilization (ΔG_s°) of the amphiphile can be evaluated from the relation

$$\Delta G_s^\circ = -RT \ln X_s \tag{86.12}$$

where X_s is the mole fraction concentration of additive at CP, R is gas constant, and T is the clouding temperature in Kelvin scale.

The standard enthalpy and entropy of clouding, ΔH_s° and $T\Delta S_s^\circ$, respectively, can be calculated by the following equations:

$$\Delta H_s^\circ = \frac{\delta\left(\Delta G_s^\circ/T\right)}{\delta(1/T)} \tag{86.13}$$

$$T\Delta S_s^\circ = \Delta H_s^\circ - \Delta G_s^\circ \tag{86.14}$$

The thermodynamic parameters were calculated by employing Eqs. (86.12) – (86.14). The $\Delta G_s^\circ/T$ versus $1/T$ curves have two stages (a representative plot is shown in Fig. 86.6): (1) an enthalpy-controlled stage (i.e., $\Delta H_s^\circ > T\Delta S_s^\circ$) and (2) a stage that is controlled by both enthalpy and entropy (i.e., $\Delta H_s^\circ \approx T\Delta S_s^\circ$).

The thermodynamics of clouding data for surface-active drugs in the presence of additives are evaluated. The thermodynamic parameters ΔG_s° are found positive for all additives, whereas ΔH_s° and $T\Delta S_s^\circ$ values are negative or positive depending on the type and nature of the additives.

86.4.1 Effect of Surfactants

86.4.1.1 Anionic Surfactants. In presence of anionic surfactants (both SDS and SDBS), the values of thermodynamics parameters (ΔH_s° and $T\Delta S_s^\circ$) change sign from positive to

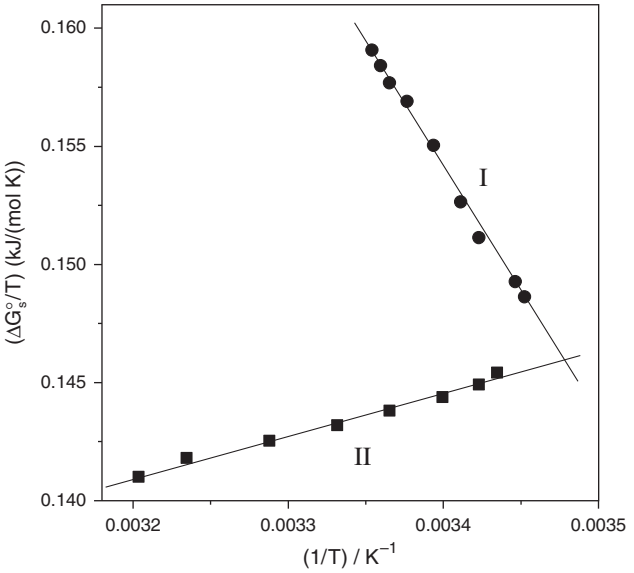


FIGURE 86.6 Plot of $\frac{\Delta G_s^\circ}{T}$ versus $\frac{1}{T}$ of surface-active drug–additive system for derivation of the enthalpy change of clouding (ΔH_s°). The stages are denoted by the labels I and II.

negative in all mole fractions. First they have positive values ΔH_s° and $T\Delta S_s^\circ$; and then after a certain concentration (cmc), the values of ΔH_s° and $T\Delta S_s^\circ$ become negative:

1. At low concentration of anionic surfactants, ΔH_s° and $T\Delta S_s^\circ$ become positive and $\Delta H_s^\circ > T\Delta S_s^\circ$. At low concentrations, these surfactants hinder micelle formation, and the overall system is in a disordered state.
2. As the concentration of surfactant increases, micellar growth increases and large aggregates form and ΔH_s° and $T\Delta S_s^\circ$ become positive with $\Delta H_s^\circ \approx T\Delta S_s^\circ$.

86.4.1.2 Cationic Surfactants. At all mole fractions of cationic surfactants, the thermodynamic parameters, both ΔH_s° and $T\Delta S_s^\circ$ are found to be positive. The added cationic surfactants exist in the solution as monomers, micelles, or mixed micelles [32], which increase the degree of interaggregate repulsion. The longer the alkyl chains of the cationic surfactant, the lower the values of ΔH_s° and $T\Delta S_s^\circ$.

86.4.1.3 Nonionic Surfactants. For all nonionic surfactants, the values of both ΔH_s° and $T\Delta S_s^\circ$are positive. These surfactants possess hydrophilic oxyethylene chains, and they form mixed micelles. Therefore, the drug–surfactant system [32] would be highly hydrated. Undoubtedly, the increase in CP with the addition of nonionic surfactants is due to this headgroup hydration, and the randomness of the systems also increases (i.e., $T\Delta S_s^\circ$ increases).

At standard conditions, the dissolution of one mole of drug in presence of additives releases heat with an overall ordering of the drug–additive system. These additives are only partially soluble in water. Hence, they solubilize more in micelles with their headgroups facing toward the surface and alkyl chain penetrating into the micelles. This results in the formation of larger aggregates that ultimately release heat with overall ordering in the system. It is clear that the exothermicity of the clouding phenomenon is due to the aggregation of weakly solvated amphiphile molecules and their phasing out into the condensed phase. This is a simplified explanation; otherwise, various environmental and structural factors and their combinations (desolvation, solvent modification, micellar growth, morphological transition, intermicellar interactions, etc.) have their due share on the energetics of clouding.

86.5 CONCLUSIONS

Like surfactants, a large number of drug molecules are amphiphilic; that is, they self-associate in aqueous environments to form small aggregates. The effect of additives on self-association, mixed micellization, and clouding phenomena of four surface-active drugs [viz., tricyclic antidepressants—amitriptyline hydrochloride (AMT) and imipramine hydrochloride (IMP) and phenothiazines—chlorpromazine hydrochloride (CPZ) and promethazine hydrochloride (PMT)]. The cmc values of all drugs have been found to decrease in the presence of additives. The thermodynamics of these four surface- active drugs in the absence and presence of additives and evaluated Gibbs energies [at the air–water interface ($\Delta G^s_{\min}$), standard Gibbs energy change of micellization (ΔG°_{mix}), standard Gibbs energy change of adsorption (ΔG°_{ads}), and excess free-energy change of micellization (ΔG_{ex})] were evaluated. In all cases (in absence/presence of additives), these values are negative and decrease with increasing additive concentration/mole fraction. This indicates that the micellization is more spontaneous in presence of the additives. Under special conditions, these surface-active drugs undergo phase separation or cloud point (CP). Like ionic surfactants, these drugs undergo phase separation, which depends on the pH, concentration, and temperature. It was observed that their cloud point (CP) can vary with additives. At cloud point the thermodynamics parameters are evaluated. In all cases standard Gibbs free-energy changes are found to be positive; but the values of ΔH_s° and $T\Delta S_s^\circ$ are found to be positive as well as negative, depending on the nature of the additive. Additives that increase the micelle size decrease the randomness of the system, and hence the $T\Delta S_s^\circ$ value becomes negative. On the other hand, additives that cause breakdown of micelles and are water structure breakers give positive ΔH_s° and $T\Delta S_s^\circ$. The above two points have clearly been demonstrated by studying the cloud points of these drugs in the presence of various additives.

ACKNOWLEDGMENT

The authors are grateful to the Department of Science and Technology (DST), New Delhi, India for financial support (Grant SR/FT/CS-48/2011) and also for financial support from Project CSC0201 of the Council of Scientific and Industrial Research (CSIR), New Delhi, India.

REFERENCES

[1] Tanford, C. (1980). *The Hydrophobic Effect: Formation of Micelles and Biological Membranes*. Wiley, New York.

[2] Mandal, A.B., Nair, B.U., Ramaswamy, D. (1988). *Langmuir* **4**, 736–740.

[3] Mandal, A.B., Nair, B.U. (1991). *J. Phys. Chem.* **95**, 9008–9013.

[4] Geetha, B., Mandal, A.B., Ramasami, T. (1993). *Macromolecules* **26**, 4083–4088.

[5] Mandal, A.B. (1993). *Langmuir* **9**, 1932–1933.

[6] Mandal, A.B., Wang, L., Brown, K., Verrall, R.E. (1993). *J. Colloid Interface Sci.* **161**, 292–298.

[7] Geetha, B., Mandal, A.B. (1995). *Langmuir* **11**, 1464–1467.

[8] Geetha, B., Mandal, A.B. (1996). *J. Chem. Phys.* **105**, 9649–9656.

[9] Geetha, B., Mandal, A.B. (1997). *Chem. Phys. Lett.* **266**, 443–450.

[10] Geetha, B., Mandal, A.B. (1997). *Langmuir* **13**, 2410–2414.

[11] Geetha, B., Mandal, A.B. (2000). *Langmuir* **16**, 3957–3963.

[12] Geetha, B.; Gaspar, M.; Mandal, A.B. *Langmuir* 2003, **19**, 9051-9057.

[13] Mandal, A.B., Ramesh, D.V., Dhar, S.C. (1987). *FEBS Eur. J. Biochem*. **169**, 617–628.

[14] Mandal, A.B., Jayakumar, R. (1993). *J. Chem. Soc. Chem. Commun.* **1993**, 237–238.

[15] Mandal, A.B., Jayakumar, R. (1994). *J. Chem. Soc. Faraday Transact.* **90**, 161–165.

[16] Jayakumar, R., Mandal, A.B., Manoharan, P.T. (1994). *J. Chem. Soc. Faraday Transact.* **90**, 2725–2730.

[17] Rose, C., Mandal, A.B. (1996). *Int. J. Biol. Macromol.* **18**, 41–53.

[18] Lawrence, M.J. (1994). *Chem. Soc. Rev.* **23**, 417–424.

[19] Ramya, S., Thennarasu, S., Mandal, A.B. (2003). *Chem. Phys.* **291**, 195–205.

[20] Ramya, S., Thennarasu, S., Mandal, A.B. (2004). *J. Phys. Chem. B* **108**, 8806–8816.

[21] Khan, I.A., Mohammad, R., Alam, Md.S., Kabir-ud-Din (2009). *J. Dispers. Sci. Technol.* **30**, 1486–1493.

[22] Khan, I.A., Mohammad, R., Alam, Md.S., Kabir-ud-Din (2010). *J. Chem. Eng. Data* **55**, 370–380.

[23] Khan, I.A., Mohammad, R., Alam, Md.S., Kabir-ud-Din (2010). *J. Dispers. Sci. Technol.* **31**, 129–137.

[24] Khan, I.A., Mohammad, R., Alam, Md.S., Kabir-ud-Din (2010). *J. Surf. Deterg.s* **13**, 179–188.

[25] Attwood, D., Florence, A.T. (1983). *Surfactant Systems: Their Chemistry, Pharmacy and Biology*. Chapman & Hall, New York.

[26] Attwood, D. (1995). *Adv. Colloid Interface Sci.* **55**, 271–303.

[27] Schreier, S., Malheiros, S.V.P., de Paula, E. (2000). *Biochim. Biophys. Acta* **1508**, 210–234.

[28] Tiwary, L.K., Mandal, A., Alam, Md.S., Thennarasu, S., Mandal, A.B. (2011). *Colloids Surf. B* **82**, 126–133.

[29] Mandal, A., Krishnan, R.S.G., Thennarasu, S., Panigrahi, S., Mandal, A.B. (2010). *Colloids Surf. B.* **79**, 136.

[30] Taboada, P., Attwood, D., Ruso, J.M., Garcia, M., Mosquera, V. (2000). *Phys. Chem. Chem. Phys.* **2**, 5175–5179.

[31] Rodriguez, A., Junquera, E., del Burgo, P., Aicart, E. (2004). *J. Colloid Interface Sci.* **269**, 476–483.

[32] Alam, Md.S., Naqvi, A.Z., Kabir-ud-Din (2007). *J. Chem. Eng. Data* **52**, 1326–1331.

[33] Alam, Md.S., Ghosh, G., Kabir-ud-Din (2008). *J. Phys. Chem. B* **112**, 12962–12967.

[34] Alam, Md.S., Mandal, A., Mandal, A.B. (2011). *J. Chem. Eng. Data* **56**, 1540–1546.

[35] Alam, Md.S., Ghosh, G., Mandal, A.B., Kabir-ud-Din (2011). *Colloids Surf. B* **88**, 779–784.

[36] Alam, S., Mandal, A., Mandal, A.B. (2011). In Moreno-Piraján, J.C. (ed.), *Thermodynamics—Systems in Equilibrium and Non-Equilibrium*. Intech International, Rijeka, Chapter 11, pp. 229–254.

[37] Alam, Md.S., Samanta, D., Mandal, A.B. (2012). *Colloids Surf. B* **92**, 203–208.

[38] Alam, Md.S., Mandal, A.B. (2012). *J. Mol. Liquids* **168**, 75–79.

[39] Jeong, B., Bae, Y.H., Kim, S.W. (1999). *Colloids Surf. B*, **16**, 185–193.

[40] Nakayama, M., Kawahara, Y., Akimoto, J., Kanazawa, H., Okano, T. (2012). *Colloids Surf. B* **99**, 12–19.

[41] Naskar, B., Dan, A., Ghosh, S., Moulik, S.P. (2010). *Carbohydr. Polym.* **81**, 700–706.

[42] Marangoni, B.P. (2011). *Colloids Surf. B* **83**, 69–77.

[43] Kadam, Y., Yerramilli, U., Bahadur, A., Bahadur, P. (2011). *Colloids Surf. B* **83**, 49–57.

[44] Samanta, D., Sankar, R.M., Jaisankar, S.N., Alam, Md.S., Mandal, A.B. (2011). *Chem. Commun.* **47**, 11975–11977.

[45] Samanta, D., Murali, A., Prakash, J.A., Nagaraju, P., Ramesh, R., Mitra, T., Gnanamani, A., Jaisankar, S.N., Mohan, R., Alam, Md.S., Mandal, A.B. *RSC (Royal Society of Chemistry) Adv.* **3**, 16626–16631.

[46] Khalil, H.P.S.A., Bhat, A.H., Yusra, A.F.I. (2012). *Carbohydr. Polym.* **87**, 963–979.

[47] Whitesides, G.M., Grzybowski, B. (2002). *Science* **295**, 2418–2421.

[48] Barzykin, A.V., Tachiya, M. (1996). *Heterogen. Chem. Rev.* **3**, 105–167.

[49] Israelachvili, J.N. (1986). *Intermolecular and Surface Forces*. Academic Press, London.

[50] Griffin, W.C. (1949). *J. Soc. Cosmetic Chem.* **1**, 311–320.

[51] Atherton, A.D., Barry, B.W. (1985). *J. Colloid Interface Sci.* **106**, 479–489.

[52] Wajnberg, E., Tabak, M., Nussenzveig, P.A., Lopes, C.M., Louro, S.R. (1988). *Biochim. Biophys. Acta* **944**, 185–190.

[53] Attwood, D., Mosquera, V., Pérez-Villar, V. (1989). *J. Chem. Soc. Faraday Transact. I* **85**, 3011–3017.

[54] Wanbahdi, W., Mwakibete, H., Bloor, D.M., Palepu, R., Wyn-Jones, E. (1992). *J. Phys. Chem.* **96**, 918–925.

[55] Perez-Villar, V., Vazquez-Iglesias, M.E., Degeyer, A. (1993). *J. Phys. Chem.* **97**, 5149–5154.

[56] Attwood, D., M1squera, V., Lopez-Fontan, J.L., Garcia, M., Sarmiento, F. (1996). *J. Colloid Interface Sci.* **184**, 658–662.

[57] Attwood, D., Boitard, E., Dubès, J.P., Tachoire, H. (1997). *J. Phys. Chem.* **101**, 9586–9592.

[58] Perez-Rodrigues, M., Prieto, G., Rega, C., Varela, L.M., Sarmiento, F., Mosquera, V. (1998). *Langmuir* **14**, 4422–4426.

[59] Attwood, D., Blundell, R., Mosquera, V., Garcia, M. (1993). *J. Colloid Interface Sci.* **161**, 19–23.

[60] Attwood, D., Tolley, J.A. (1980). *J. Pharm. Pharmacol.* **32**, 761–765.

[61] Hwang, P.M., Vogel, H.J. (1998). *Biochem. Cell Biol.* **76**, 235–246.

[62] Taboada, P., Attwood, D., Ruso, J.M., Garcia, M., Sarmiento, F., Mosquera, V. (1999). *Colloid Interface Sci.* **216**, 270–275.

[63] Varela, L.M., Rega, C., Suarez-Filloy, M.J., Ruso, J.M., Prieto, G., Attwood, D., Sarmiento, F., Mosquera, V. (1999). *Langmuir* **15**, 6285–6290.

[64] Atherton, A.D., Barry, B.W. (1985). *J. Pharm. Pharmacol.* **37**, 854–862.

[65] Attwood, D., Mosquera, V., Garcia, M., Suarez, M.J., Sarmiento, F. (1995). *J. Colloid Interface Sci.* **175**, 201–206.

[66] Sarmiento, F., López-Fontán, J.L., Prieto, G., Attwood, D., Mosquera, V. (1997). *Colloid Polym. Sci.* **275**, 1144–1147.

[67] Causon, D., Gettins, J., Gormally, J., Greenwood, R., Natarajan, N., Wyn-Jones, E. (1981). *J. C.hem. Soc. Faraday Transact. II* **77**, 143–151.

[68] Yokoyama, S., Fujino, Y., Kawamoto, Y., Kaneko, A. (1994). *Chem. Pharm. Bull.* **42**, 1351–1353.

[69] Ruso, J.M., Attwood, D., Rey, C., Taboada, P., Mosquera, V., Sarmiento, F. (1999). *J. Phys. Chem.* **103**, 7092–7096.

[70] Fernandez, M.F. (1980). *Biochim. Biophys. Acta* 5**97**, 83–91.

[71] Attwood, D., Fletcher, P. (1986). *J. Pharm. Pharmacol.* **38**, 494–498.

[72] Wakita, M., Kuroda, Y., Fujiwara, Y., Nakagawa, T. (1992). *Chem. Phys. Lipids* **62**, 45–54.

[73] Matsuki, H., Hashimoto, S., Kaneshina, S., Yamanaka, M. (1994). *Langmuir* **10**, 1882–1887.

[74] Rades, T., Muller-Goymann, C.C. (1997). *Int. J. Pharm.* **159**, 215–222.

[75] King, S.Y., Basista, A.M., Torosian, G. (1989). *J. Pharm. Sci.* **78**, 95–100.

[76] Cheema, M.A., Taboada, P., Barbosa, S., Castro, E., Siddiq, M., Mosquera, V. (2007). *Biomacromolecules* **8**, 2576–2585.

[77] Gu, T., Galera-Gomez, P.A. (1999). *Colloids Surf. A* **147**, 365-370.

[78] Wang, Z., Xu, J.-H., Zhang, W., Zhuang, B., Qi, H. (2008). *Colloids Surf. B* **61**, 118–122.

[79] Susan, Md.A.B.H., Ishibashi, A., Takeoka, Y., Watanabe, M. (2004). *Colloids Surf. B* **38**, 167–173.

[80] Tsubouchi, T., Nishida, K., Kanaya, T. (2007). *Colloids Surf. B* **56**, 265–269.

[81] Yu, Z.-J., Xu, G. (1989). *J. Phys. Chem.* **93**, 7441–7445.

[82] Yu, Z.-J., Zhang, X., Xu, G., Zhao, G.-X. (1990). *J. Phys. Chem.* **94**, 3675–3681.

[83] Raghavan, S.R., Edlund, H., Kaler, E.W. (2002). *Langmuir* **18**, 1056–1064.

[84] Gomati, R., Appell, J., Bassereau, P., Marignan, J., Porte, G. (1987). *J. Phys. Chem.* **91**, 6203–6210.

[85] Warr, G.G., Zemb, T.N. (1990). *J. Phys. Chem.* **94**, 3086–3092.

[86] Yu, Z.-J., Neuman, R.D. (1994). *Langmuir* **10**, 2553–2558.

[87] Kumar, S., Sharma, D., Kabir-ud-Din (2000). *Langmuir* **16**, 6821–6824.

[88] Kumar, S., Sharma, D., Khan, Z.A., Kabir-ud-Din (2002). *Langmuir* **18**, 4205–4209.

[89] Kumar, S., Sharma, D., Kabir-ud-Din (2003). *Langmuir* **19**, 3539–3541.

[90] Buckingham, S.A., Garvey, C.J., Warr, G.G. (1993). *J. Phys. Chem.* **97**, 10236–10244.

[91] Smith, A.M., Holmes, M.C., Pitt, A., Harrison, W., Tiddy, G.J.T. (1995). *Langmuir* **11**, 4202–4204.

[92] Bales, B.L., Zana, R. (2004). *Langmuir* **20**, 1579–1581.

[93] Panizza, P., Cristobal, G., Curely, J. (1998) *J. Phys. Condens. Matt.* **10**, 11659–11678.

[94] Kim, E.J., Shah, D.O. (2002). *Langmuir* **18**, 10105–10108.

[95] Kim, E.J., Shah, D.O. (2003). *Colloids Surf. A* **227**, 105–111.

[96] Kim, E.J., Shah, D.O. (2003). *J. Phys. Chem. B* **107**, 8689–8693.

[97] Kumar, S., Alam, Md.S., Parveen, N., Kabir-ud-Din *Colloid Polym. Sci.* (2006). **284**, 1459–1463.

[98] Alam, Md.S., Kumar, S., Naqvi, A.Z., Kabir-ud-Din (2006). *Colloids Surf. A* **287**, 197–202.

[99] Alam, Md.S., Kumar, S., Naqvi, A.Z., Kabir-ud-Din (2006). *Colloids Surf. B* **53**, 60–63.

[100] Alam, Md.S., Naqvi, A.Z., Kabir-ud-Din (2007). *J. Colloid Interface Sci.* **306**, 161–165.

[101] Alam, Md.S., Naqvi, A.Z., Kabir-ud-Din (2007). *J. Surfact. Deterg.* **10**, 35-40.

[102] Alam, Md.S., Naqvi, A.Z., Kabir-ud-Din (2007). *Colloids Surf. B* **57**, 204-208.

[103] Alam, Md.S.; Naqvi, A.Z., Kabir-ud-Din (2007). *Colloid Polym. Sci.* **285**, 1573–1579.

[104] Alam, Md.S., Naqvi, A.Z., Kabir-ud-Din (2008). *J. Dispers. Sci. Technol.* **29**, 274–279.

[105] Alam, Md.S., Naqvi, A.Z., Kabir-ud-Din (2008). *Colloids Surf. B* **63**, 122–128.

[106] Alam, Md.S., Naqvi, A.Z., Kabir-ud-Din (2008). *J. Dispers. Sci. Technol.* **29**, 783–786.

[107] Alam, Md.S., Kabir-ud-Din (2008). *Colloids Surf. B* **65**, 74–79.

[108] Alam, Md.S., Kabir-ud-Din (2008). *Acta Phys. Chim. Sinica* **24**, 411–415.

[109] Alam, Md.S., Naqvi, A.Z., Kabir-ud-Din (2010). *J. Dispers. Sci. Technol.* **31**, 449–455.

[110] Mandal, A.B., Alam, Md.S., Mandal, A., Baskar, G. (2010). *J. Surf. Sci. Technol.* **26**, 321–352.

[111] Kabir-ud-Din, Rub, M.A., Alam, Md.S. (2010). *J. Dispers. Sci. Technol.* **31**, 1182–1187.

[112] Katzung, B.G. (2004). *Basic and Clinical Pharmacology*, 9th ed. McGraw-Hill, New York.

[113] Alam, Md.S., Kabir-ud-Din (2008). *Proc. NCTCS-2008*, Vol. 3, pp. 93–99.

[114] Alam, Md.S., Kabir-ud-Din, Mandal, A.B. (2010). *Colloids Surf. B* **76**, 577–584.

[115] Alam, Md.S., Kabir-ud-Din, Mandal, A.B. (2010). *J. Chem. Eng. Data* **55**, 1693–1699.

[116] Alam, Md.S., Kabir-ud-Din, Mandal, A.B. (2010). *J. Chem. Eng. Data* **55**, 1893–1896.

[117] Alam, Md.S., Kabir-ud-Din, Mandal, A.B. (2010). *J. Chem. Eng. Data* **55**, 2630–2635.

[118] Alam, Md.S., Kabir-ud-Din, Mandal, A.B. (2010). *J. Dispers. Sci. Technol.* **31**, 1721–1726.

[119] Alam, Md.S., Kabir-ud-Din, Mandal, A.B. (2013). *Colloids Surf. B* **105**, 236–245.

[120] Franks, F. (1975). *Water: A Comprehensive Treatise*. Plenum Press, New York.

[121] Hall, D.G. (1974). *J. Chem. Soc. Faraday Trans.2* **70**, 1526–1541.

[122] Rosen, M.J. (2004). *Surfactants and Interfacial Phenomena*, 3rd ed. Wiley, New York.

[123] Mukerjee, P., Mysels, K.L. (1971). *Critical Micelle Concentration of Aqueous Surfactant Systems*, NSRDS-36 (National Standard Reference Data Series Vol. 36), Washington, DC.

[124] Kabir-ud-Din, Khan, A.B., Naqvi, A.Z. (2010). *Colloid Surf. B* **80**, 206–212.

[125] Chattoraj, D.K., Birdi, K.S. (1984). *Adsorption and the Gibbs Surface Excess*. Plenum Press, New York.

[126] Matijevic, E., Pethica, B.A. (1958). *Transact. Faraday Soc.* **54**, 1382–1389.

[127] Anand, K., Yadav, O.P., Singh, P.P. (1991). *Colloids Surf.* **55**, 345–358.

[128] Sugihara, G., Miyazono, A., Nagadome, S., Oida, T., Hayashi, Y., Ko, J.-S. (2003). *J. Oleo Sci.* **52**, 449–461.

[129] Ko, J.-S., Oh, S.-W., Kim, Y.-S., Nakashima, N., Nagadome, S., Sugihara, G. (2004). *J. Oleo Sci.* **53**, 109–126.

[130] Rubingh, D.N. (1979). In Mittal, K.L. (ed.), *Solution Chemistry Chemistry of Surfactants*, Vol. 1. Plenum Press, New York.

[131] Nightingale, E.R.Jr. (1959). *J. Phys. Chem.* **63**, 1381–1387.

[132] Hofmeister, F. (1888). *Arch. Exp. Pathol. Pharmacol.* **24**, 247–260.

[133] Hall, D.G. (1974). *J. Chem. Soc. Faraday Transact. 2* **70**, 1526–1541.

[134] Ruiz, C.C. (1999). *Colloid Polym Sci.* **277**, 701–707.

[135] Lindman, B., Wennerstrom, H. (1980). *Topics Curr. Chem.* **87**, 1–87.

[136] Kabir-ud-Din, Kumar, S., Kirt Goyal, P.S. (1996). *Langmuir* **12**, 1490–1494.

87

THERMODYNAMIC ANALYSIS OF PARTIAL MOLAR VOLUME IN BIOCOLLOIDAL SYSTEMS

MICHIO YAMANAKA,[1] HIDEYUKI MAEKAWA,[1] TAMAKI YASUI,[1] AND HITOSHI MATSUKI[2]

[1]*Department of Chemistry, Faculty of Sciences, Kyushu University, 6-10-1 Hakozaki, Higashi-ku, Fukuoka 812-8581, Japan*
[2]*Department of Life System, Institute of Technology and Science, The University of Tokushima, 2-1 Minamijosanjima-cho, Tokushima 770-8506, Japan*

87.1 INTRODUCTION

It is well known that the partial molar properties provide fundamental, useful information about solute–solute, solute–solvent, and solvent–solvent interactions in solutions [1, 2]. The partial molar quantities such as enthalpy, entropy, and volume are determined by experiments. However, because enthalpy and entropy of a solution are measured relative to some reference system, they are the difference between the values of the partial molar enthalpy and entropy in the solution and in the reference system. In contrast, volume of a solution can be measured, so that the partial molar volume (PMV) in the solution is directly obtained from experiments [3].

Biocolloids such as lipid membrane aggregates and proteins are involved in many biophysical and biochemical processes. The main events in the processes could be the protein–ligand binding and/or the incorporation of biomolecules into membranes. Since PMV of a solute contains information about the interaction of the solute molecule with molecules around it in solution, one can bring out useful information about the processes from PMV measured for the biocolloidal systems [4]. Since, for example, the phenomena of pressure reversal of general anaesthesia [5–8] indicate that general anaesthesia is a process with a volume increase, the analysis of PMVs provides useful information to elucidate the molecular mechanism of general anaesthesia.

In this chapter, we develop thermodynamic approaches to analyze PMVs to obtain the binding parameters of ligand molecules to protein such as the binding constant and the binding number and to obtain information about the miscibility in the mixed vesicle membrane and the partition of water-soluble molecules and ions into the membrane. In Section 87.2, we first review the definition of PMV in a multicomponent solution and elementary thermodynamic equations describing volume behavior of the solution. Section 87.3 concerns a thermodynamic treatment of the binding of protein and ligand in solution from the standpoint of PMVs. A Method for obtaining a binding isotherm from PMV is shown. The application of the treatment to aqueous solutions of globular proteins and short chain alcohols is also described. In Section 87.4, we develop a thermodynamic treatment of PMVs for aqueous solutions of vesicles of binary water-insoluble lipid mixtures and for aqueous solutions of binary vesicles of a water-insoluble lipid and a water-soluble compound. Using the treatment for the former system, we can obtain information about the miscibility of lipids in the bilayer membrane from the analysis of PMVs. On the other hand, for the latter system, the partition of the water-soluble compound into the membrane can be examined using PMVs. The application of the derived equations to the latter system is demonstrated.

Encyclopedia of Biocolloid and Biointerface Science, Volume 2, First Edition. Edited by Hiroyuki Ohshima.
© 2016 John Wiley & Sons, Inc. Published 2016 by John Wiley & Sons, Inc.

87.2 DEFINITION OF PARTIAL MOLAR VOLUME AND ELEMENTARY THERMODYNAMIC EQUATIONS OF THE VOLUME BEHAVIOR OF SOLUTIONS

Let us consider a solution of solute components 1,2, . . . , c dissolved in solvent w. The volume of the solution V' is given as a function of temperature T, pressure p, number of moles of solvent n_w, and number of moles n_i of solute component i (=1,2, . . . , c). The partial molar volume v_i of solute i in the solution is defined as the infinitesimal change of solution volume associated with the addition of an infinitesimal amount of the component i at constant T, p, n_w, and the numbers of moles of all solutes other than component i, $n_{j\neq i}$, and given by

$$v_i = \left(\frac{\partial V'}{\partial n_i}\right)_{T,p,n_w,n_{j\neq i}} = \lim_{\delta n_i \to 0} \frac{V'(T,p,n_w,n_{j\neq i};n_i+\delta n_i) - V'(T,p,n_w,n_{j\neq i};n_i)}{\delta n_i} = \lim_{\delta n_i \to 0} \frac{\delta V}{\delta n_i} \tag{87.1}$$

where the index $j \neq i$ indicates all components other than i and δV is defined by

$$\delta V = V'(T,p,n_w,n_{j\neq i};n_i+\delta n_i) - V'(T,p,n_w,n_{j\neq i};n_i) \tag{87.2}$$

Therefore, PMV of component i includes information about the intrinsic geometric volume of a molecule of component i, the contribution of the solute–solute interactions between molecules of component i and between a molecule of component i and that of other solute components, the solute–solvent interaction (solvation of molecules of solute component i), and change in the solvent structure by the addition of small amounts of component i (see Fig. 87.1). The total differential of the solution volume V' at constant T and p is written in the form

$$dV' = v_w dn_w + \sum_{i=1}^{c} v_i dn_i \tag{87.3}$$

and, according to the Euler's theorem, the solution volume is given by

$$V' = v_w n_w + \sum_{i=1}^{c} v_i n_i \tag{87.4}$$

From an experimental perspective, it is convenient to consider the solution volume per 1 kg of solvent and to adopt

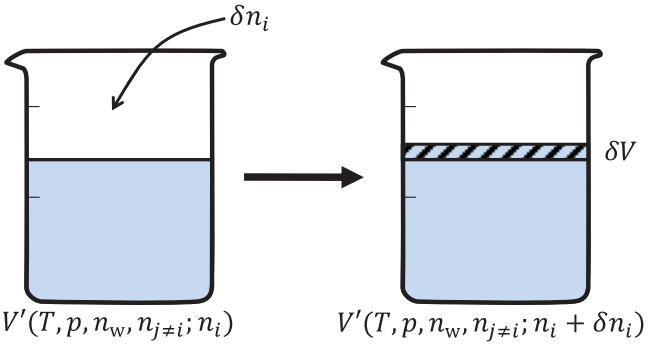


FIGURE 87.1 Schematic illustration of variation in solution volume with the addition of small amount of component i.

molality of solute components as the concentration variables. The solution volume V and the molality m_i of solute component i are defined by

$$V = \frac{V'}{n_w M_w} \tag{87.5}$$

and

$$m_i = \frac{n_i}{n_w M_w} \qquad (i = 1,2,\ldots,c) \tag{87.6}$$

where M_w is the molar mass of solvent in the unit of kg mol^{-1}. The total differential of the solution volume V at constant T and p is written in the following form:

$$dV = \sum_{i=1}^{c} v_i dm_i \tag{87.7}$$

Thus, PMV of component i is redefined by

$$v_i = \left(\frac{\partial V}{\partial m_i}\right)_{T,p,m_{j\neq i}} \tag{87.8}$$

and the solution volume is given by

$$V = \frac{v_w}{M_w} + \sum_{i=1}^{c} v_i m_i. \tag{87.9}$$

The values of PMVs are obtained experimentally from the dependence of V on molality of component i at constant T, p, and molalities of components other than i. V is related to solution density ρ by

$$V = \frac{1 + \sum_{i=1}^{c} m_i M_i}{\rho} \tag{87.10}$$

where M_i is the molar mass of component i (= 1,2, . . . , c) in unit of kg mol^{-1} and density ρ is in kg per unit volume.

Thus, one can obtain PMVs of solute components from density measurements for solutions. In the following sections, we will develop thermodynamic treatments for protein and membrane systems using the molalities.

87.3 PARTIAL MOLAR VOLUMES IN A PROTEIN–LIGAND SYSTEM

In this section, we will derive thermodynamic equations to estimate the binding parameters such as the binding constant between protein and ligand molecules and the maximum number of ligand molecules per protein molecule. Let us consider a solution that contains 1 kg of solvent w, $m_{\mathrm{M}}^{\mathrm{T}}$ moles of protein M, and $m_{\mathrm{X}}^{\mathrm{T}}$ moles of ligand X. The protein M is assumed to have $b_{\max}$ binding sites of ligand X, each site able to bind with only one ligand molecule. Thus, the dissolved species in the solution are free protein M, free ligand X, and protein–ligand complexes MX_i ($i = 1,2,\ldots,b_{\max}$). When the molalities of these dissolved species are represented by m_{M}, m_{X}, and m_i ($i = 1,2,\ldots,b_{\max}$), respectively, the preparation molality of protein $m_{\mathrm{M}}^{\mathrm{T}}$ is given by

$$m_{\mathrm{M}}^{\mathrm{T}} = m_{\mathrm{M}} + \sum_{i=1}^{b_{\max}} m_i \tag{87.11}$$

and the preparation molality of ligand $m_{\mathrm{X}}^{\mathrm{T}}$ by

$$m_{\mathrm{X}}^{\mathrm{T}} = m_{\mathrm{X}} + \sum_{i=1}^{b_{\max}} i m_i. \tag{87.12}$$

The total differential of the solution volume per 1 kg of solvent at constant T and p is given by

$$dV = \upsilon_{\mathrm{M}} dm_{\mathrm{M}} + \upsilon_{\mathrm{X}} dm_{\mathrm{X}} + \sum_{i=1}^{b_{\max}} \upsilon_i dm_i \tag{87.13}$$

where v_{M}, v_{X}, and v_{i} are PMVs of free protein, free ligand, and protein–ligand complexes MX_i ($i = 1,2,\ldots,b_{\max}$). These equations are fundamental to treat volume behavior of protein–ligand system.

According to our thermodynamic treatment of protein–ligand binding [9], Eq. (87.13) is rewritten as a function of the preparation molalities of protein and ligand at constant T and p in the form

$$\mathrm{d}V = (\upsilon_{\mathrm{M}} + b\Delta V)\mathrm{d}m_{\mathrm{M}}^{\mathrm{T}} + \upsilon_{\mathrm{X}}\mathrm{d}m_{\mathrm{X}}^{\mathrm{T}} + m_{\mathrm{M}}^{\mathrm{T}}\Delta V \mathrm{d}b, \tag{87.14}$$

where we have introduced the averaged number of ligand molecules bound to a protein molecule, b, defined by

$$b = \frac{\sum_{i=1}^{b_{\max}} i m_i}{m_{\mathrm{M}} + \sum_{i=1}^{b_{\max}} m_i} = \frac{m_{\mathrm{X}}^{\mathrm{T}} - m_{\mathrm{X}}}{m_{\mathrm{M}}^{\mathrm{T}}} \tag{87.15}$$

and the averaged partial molar volume change of the complex formation per ligand molecule (volume change of binding) ΔV, defined by

$$\begin{aligned}\Delta V &= \frac{\sum_{i=1}^{b_{\max}} i m_i \left(\dfrac{\upsilon_i - \upsilon_{\mathrm{M}} - i\upsilon_{\mathrm{X}}}{i}\right)}{\sum_{i=1}^{b_{\max}} i m_i} \\ &= \frac{\sum_{i=1}^{b_{\max}} i m_i \left(\dfrac{\upsilon_i - \upsilon_{\mathrm{M}}}{i}\right)}{\sum_{i=1}^{b_{\max}} i m_i} - \upsilon_{\mathrm{X}} \\ &= \upsilon_{\mathrm{X}}^{\mathrm{M}} - \upsilon_{\mathrm{X}}\end{aligned} \tag{87.16}$$

where $v_{\mathrm{X}}^{\mathrm{M}}$ is the averaged partial molar volume of ligand binding to protein molecules defined by

$$\upsilon_{\mathrm{X}}^{\mathrm{M}} = \frac{\sum_{i=1}^{b_{\max}} i m_i \left(\dfrac{\upsilon_i - \upsilon_{\mathrm{M}}}{i}\right)}{\sum_{i=1}^{b_{\max}} i m_i}. \tag{87.17}$$

It should be noted that $v_{\mathrm{X}}^{\mathrm{M}}$ includes the contribution of the changes of hydration state and conformation of protein molecule by the binding of ligand molecules. Thus, PMV of total protein $V_{\mathrm{M}}^{\mathrm{T}}$, which is determined experimentally, provides PMV of free protein unbound by ligand molecules, v_{M}, the volume change of ligand binding per mole of protein, $b\Delta V$, and a term relating to the dependence of the binding number on protein molality;

$$\begin{aligned}V_{\mathrm{M}}^{\mathrm{T}} &= \left(\frac{\partial V}{\partial m_{\mathrm{M}}^{\mathrm{T}}}\right)_{T,p,m_{\mathrm{X}}^{\mathrm{T}}} \\ &= \upsilon_{\mathrm{M}} + b\Delta V + m_{\mathrm{M}}^{\mathrm{T}}\Delta V\left(\frac{\partial b}{\partial m_{\mathrm{M}}^{\mathrm{T}}}\right)_{T,p,m_{\mathrm{X}}^{\mathrm{T}}}\end{aligned} \tag{87.18}$$

When the V vs. $m_{\mathrm{M}}^{\mathrm{T}}$ plot is almost linear, the third term of the right-hand side (RHS) of Eq. (87.18) is negligible and therefore $V_{\mathrm{M}}^{\mathrm{T}}$ is independent of $m_{\mathrm{M}}^{\mathrm{T}}$. Further, if the value of v_{M} at $m_{\mathrm{X}}^{\mathrm{T}}$ is the same as that of PMV of protein in the solution at $m_{\mathrm{X}}^{\mathrm{T}} = 0$ which is free from ligand, the value of $b\Delta V$ is obtained from the difference between the value of $V_{\mathrm{M}}^{\mathrm{T}}$ at $m_{\mathrm{X}}^{\mathrm{T}}$ and the value at $m_{\mathrm{X}}^{\mathrm{T}} = 0$ on the $V_{\mathrm{M}}^{\mathrm{T}}$ vs. $m_{\mathrm{X}}^{\mathrm{T}}$ curve. Since b approaches to $b_{\max}$ and the dependence of b on $m_{\mathrm{M}}^{\mathrm{T}}$ at constant $m_{\mathrm{X}}^{\mathrm{T}}$ becomes very small when $m_{\mathrm{X}}^{\mathrm{T}}/m_{\mathrm{M}}^{\mathrm{T}}$ becomes large, the experimental partial molar volume of total protein

at high ligand molality relative to protein molality is given by

$$V_{\mathrm{M}}^{\mathrm{T}} = v_{\mathrm{M}} + b_{\max}\Delta V \tag{87.19}$$

Thus, we can approximate the value of $b_{\max}\Delta V$ by the value of $(V_{\mathrm{M}}^{\mathrm{T}} - v_{\mathrm{M}})$ obtained from the $V_{\mathrm{M}}^{\mathrm{T}}$ vs. $m_{\mathrm{X}}^{\mathrm{T}}$ curve at high $m_{\mathrm{X}}^{\mathrm{T}}$.

On the other hand, PMV of total ligand obtained from the V vs. $m_{\mathrm{X}}^{\mathrm{T}}$ plot provides

$$V_{\mathrm{X}}^{\mathrm{T}} = \left(\frac{\partial V}{\partial m_{\mathrm{X}}^{\mathrm{T}}}\right)_{T,p,m_{\mathrm{M}}^{\mathrm{T}}} = v_{\mathrm{X}} + m_{\mathrm{M}}^{\mathrm{T}}\Delta V\left(\frac{\partial b}{\partial m_{\mathrm{X}}^{\mathrm{T}}}\right)_{T,p,m_{\mathrm{M}}^{\mathrm{T}}} \tag{87.20}$$

It may be assumed that v_{X} on the RHS of Eq. (87.20) has the same value as PMV of ligand has at $m_{\mathrm{M}}^{\mathrm{T}} = 0$. Introducing the site occupancy $\theta = b/b_{\max}$, we have

$$V_{\mathrm{X}}^{\mathrm{T}} = v_{\mathrm{X}} + m_{\mathrm{M}}^{\mathrm{T}} b_{\max}\Delta V\left(\frac{\partial \theta}{\partial m_{\mathrm{X}}^{\mathrm{T}}}\right)_{T,p,m_{\mathrm{M}}^{\mathrm{T}}} \tag{87.21}$$

which gives

$$\left(\frac{\partial \theta}{\partial m_{\mathrm{X}}^{\mathrm{T}}}\right)_{T,p,m_{\mathrm{M}}^{\mathrm{T}}} = \frac{V_{\mathrm{X}}^{\mathrm{T}} - v_{\mathrm{X}}}{m_{\mathrm{M}}^{\mathrm{T}} b_{\max}\Delta V} \tag{87.22}$$

The value of $(V_{\mathrm{X}}^{\mathrm{T}} - v_{\mathrm{X}})/m_{\mathrm{M}}^{\mathrm{T}}$ on the RHS of this equation is obtained ftom the $V_{\mathrm{X}}^{\mathrm{T}}$ vs. $m_{\mathrm{M}}^{\mathrm{T}}$ curve and the value of $b_{\max}\Delta V$ from the $V_{\mathrm{M}}^{\mathrm{T}}$ vs. $m_{\mathrm{X}}^{\mathrm{T}}$ curve using Eq. (87.19). Integration of Eq. (87.22) by $m_{\mathrm{X}}^{\mathrm{T}}$ yields

$$\theta = \int_0^{m_{\mathrm{X}}^{\mathrm{T}}} \frac{V_{\mathrm{X}}^{\mathrm{T}} - v_{\mathrm{X}}}{m_{\mathrm{M}}^{\mathrm{T}} b_{\max}\Delta V}\mathrm{d}m_{\mathrm{X}}^{\mathrm{T}} \tag{87.23}$$

Thus, we can obtain, in principle, the site occupancy as a function of $m_{\mathrm{X}}^{\mathrm{T}}$ at constant T and p from the concentration dependence of PMVs of protein and ligand.

In order to examine in detail the binding behavior, it is necessary to evaluate the maximum binding number $b_{\max}$ and the binding constant K by applying a binding isotherm to the site occupancy data. In this chapter, we adopt a binding isotherm of Langmuir type. The extension of the isotherm to more complex one is quite easy. The Langmuir binding isotherm is expressed by

$$\theta = \frac{b}{b_{\max}} = \frac{Km_{\mathrm{X}}}{1 + Km_{\mathrm{X}}} = \frac{K\left(m_{\mathrm{X}}^{\mathrm{T}} - bm_{\mathrm{M}}^{\mathrm{T}}\right)}{1 + K\left(m_{\mathrm{X}}^{\mathrm{T}} - bm_{\mathrm{M}}^{\mathrm{T}}\right)} \tag{87.24}$$

where we have used Eq. (87.15) on the RHS of this equation. Rearranging this equation, we obtain a quadratic equation of θ:

$$Kb_{\max}m_{\mathrm{M}}^{\mathrm{T}}\theta^2 - \left(1 + Km_{\mathrm{X}}^{\mathrm{T}} + b_{\max}Km_{\mathrm{M}}^{\mathrm{T}}\right)\theta + Km_{\mathrm{X}}^{\mathrm{T}} = 0 \tag{87.25}$$

Solving this equation analytically and accounting for the fact that θ has to be close to 0 in the limit of $m_{\mathrm{X}}^{\mathrm{T}} \to 0$, we obtain the solution as follows:

$$\theta = \frac{\left(1 + Km_{\mathrm{X}}^{\mathrm{T}} + b_{\max}Km_{\mathrm{M}}^{\mathrm{T}}\right) - \sqrt{\left(1 + Km_{\mathrm{X}}^{\mathrm{T}} + b_{\max}Km_{\mathrm{M}}^{\mathrm{T}}\right)^2 - 4b_{\max}K^2m_{\mathrm{M}}^{\mathrm{T}}m_{\mathrm{X}}^{\mathrm{T}}}}{2Kb_{\max}m_{\mathrm{M}}^{\mathrm{T}}} \tag{87.26}$$

By differentiating both sides of this equation by $m_{\mathrm{X}}^{\mathrm{T}}$ at constant T, p, and $m_{\mathrm{M}}^{\mathrm{T}}$, we have

$$\left(\frac{\partial \theta}{\partial m_{\mathrm{X}}^{\mathrm{T}}}\right)_{T,p,m_{\mathrm{M}}^{\mathrm{T}}} = \frac{\sqrt{\left(1 + Km_{\mathrm{X}}^{\mathrm{T}} + b_{\max}Km_{\mathrm{M}}^{\mathrm{T}}\right)^2 - 4b_{\max}K^2m_{\mathrm{M}}^{\mathrm{T}}m_{\mathrm{X}}^{\mathrm{T}}} - \left(1 + Km_{\mathrm{X}}^{\mathrm{T}} - b_{\max}Km_{\mathrm{M}}^{\mathrm{T}}\right)}{2b_{\max}m_{\mathrm{M}}^{\mathrm{T}}\sqrt{\left(1 + Km_{\mathrm{X}}^{\mathrm{T}} + b_{\max}Km_{\mathrm{M}}^{\mathrm{T}}\right)^2 - 4b_{\max}K^2m_{\mathrm{M}}^{\mathrm{T}}m_{\mathrm{X}}^{\mathrm{T}}}} \tag{87.27}$$

Although this is an exact equation which expresses the slope of the θ vs. $m_{\mathrm{X}}^{\mathrm{T}}$ curve as a function of $m_{\mathrm{X}}^{\mathrm{T}}$ and $m_{\mathrm{M}}^{\mathrm{T}}$, it is very difficult to fit this to the experimental values on the RHS of Eq. (87.22) to obtain the values of $b_{\max}$ and K.

Instead, let us consider the initial slope of the θ vs. $m_{\mathrm{X}}^{\mathrm{T}}$ curve. When $m_{\mathrm{X}}^{\mathrm{T}}$ approaches zero, Eq. (87.27) gives the initial slope of the θ vs. $m_{\mathrm{X}}^{\mathrm{T}}$ curve

$$\left(\frac{\partial \theta}{\partial m_{\mathrm{X}}^{\mathrm{T}}}\right)_{T,p,m_{\mathrm{M}}^{\mathrm{T}}}^{m_{\mathrm{X}}^{\mathrm{T}} \to 0} = \frac{K}{1 + b_{\max}Km_{\mathrm{M}}^{\mathrm{T}}} \tag{87.28}$$

and Eq. (87.22) is rewritten in the form

$$\left(\frac{\partial \theta}{\partial m_{\mathrm{X}}^{\mathrm{T}}}\right)_{T,p,m_{\mathrm{M}}^{\mathrm{T}}}^{m_{\mathrm{X}}^{\mathrm{T}} \to 0} = \frac{V_{\mathrm{X}}^{\mathrm{T},0} - v_{\mathrm{X}}}{m_{\mathrm{M}}^{\mathrm{T}} b_{\max}\Delta V} \tag{87.29}$$

where $V_{\mathrm{X}}^{\mathrm{T},0}$ is PMV of ligand at its infinite dilution. When the V vs. $m_{\mathrm{X}}^{\mathrm{T}}$ curve is linear, the value of $V_{\mathrm{X}}^{\mathrm{T},0}$ is identical to that of $V_{\mathrm{X}}^{\mathrm{T}}$. Thus, Eq. (87.28) says that the initial slope of the θ vs. $m_{\mathrm{X}}^{\mathrm{T}}$ curve, evaluated from the experimental data of PMVs of protein and ligand by using Eq. (87.29), is related to the biding parameters and depends on the preparation molality of protein. At low concentrations of protein where the second term $b_{\max}Km_{\mathrm{M}}^{\mathrm{T}}$ of the denominator on the RHS of

Eq. (87.28) is negligibly smaller than unity, the initial slope of the θ vs. m_X^T curve provides the binding constant K.

Now, let us apply the equations derived above to the experimental data for the systems of globular proteins and short chain alcohols. Proteins used were myoglobin (Mgb, from equine skeletal muscle, Sigma, St. Louis, MO) and lysozyme (Lys, from chicken egg white, Sigma, St. Louis, MO). Mgb is larger in the molar mass, smaller in the surface hydrophilicity, and softer in the rigidity than Lys [10]. Alcohols used were 1-hexanol (C_6OH, Tokyo Chemical Industry, Tokyo, Japan), 1-butanol (C_4OH, Tokyo Chemical Industry, Tokyo, Japan), ethanol (C_2OH, Wako Pure Chemical Industries, Osaka, Japan), and 2,2,2-trifluoroethanol (TFE, Tokyo Chemical Industry, Tokyo, Japan). We measured densities of solutions of the proteins dissolved in dilute aqueous solutions of the alcohols at 298.15 ± 0.02 K under atmospheric pressure using a vibrating tube density meter (DMA 60/602, Anton Paar, Austria). The experimental error in the density was within $\pm 0.002\,\mathrm{kg\,m^{-3}}$. The values of the solution volume per 1 kg of solvent water were calculated by

$$V = \frac{1 + M_M m_M^T + M_X m_X^T}{\rho} \tag{87.30}$$

which is derived from Eq. (87.10). M_M and M_X in Eq. (87.30) are the molar mass of protein and ligand.

In Figs. 87.2 and 87.3, the values of V are plotted against m_M^T at constant m_X^T for the Mgb and Lys systems, respectively. It is observed that, for all of the V vs. m_M^T curves, V increases with increasing m_M^T linearly. The linearity of the curves indicates that the value of PMV of protein V_M^T at m_M^T is identical to that at infinite dilution of protein. The values of V_M^T obtained from Figs. 87.2 and 87.3 are plotted against m_X^T in Fig. 87.4, and the values of PMVs of Mgb and Lys in their aqueous solutions which are free from ligand are listed in Table 87.1. For both proteins, subtracting the v_M values in Table 87.1 from the values of V_M^T at $m_X^T = 100\,\mathrm{mmol\,kg^{-1}}$ for C_4OH, C_2OH, and TFE and at $m_X^T = 50\,\mathrm{mmol\,kg^{-1}}$ for C_6OH from corresponding V_M^T vs. m_X^T curves, we obtained the values of $b_{max}\Delta V$ using Eq. (87.19) and listed them in Table 87.2. It is found that the values of $b_{max}\Delta V$ for Mgb and Lys are positive, i.e., the values of ΔV are positive for the present systems. According to Eq. (87.16), this fact indicates that the averaged partial molar volume of alcohol binding to protein molecules is larger than PMV of alcohol in the bulk solution. Moreover, the magnitude of $b_{max}\Delta V$ increases in the order of $C_6OH < TFE < C_2OH < C_4OH$ for both proteins. The value of ΔV includes the contributions of the changes in the hydration states of alcohol and protein molecules and the conformation change of protein molecule associated with the binding. Therefore, in order to explain in detail the reason of

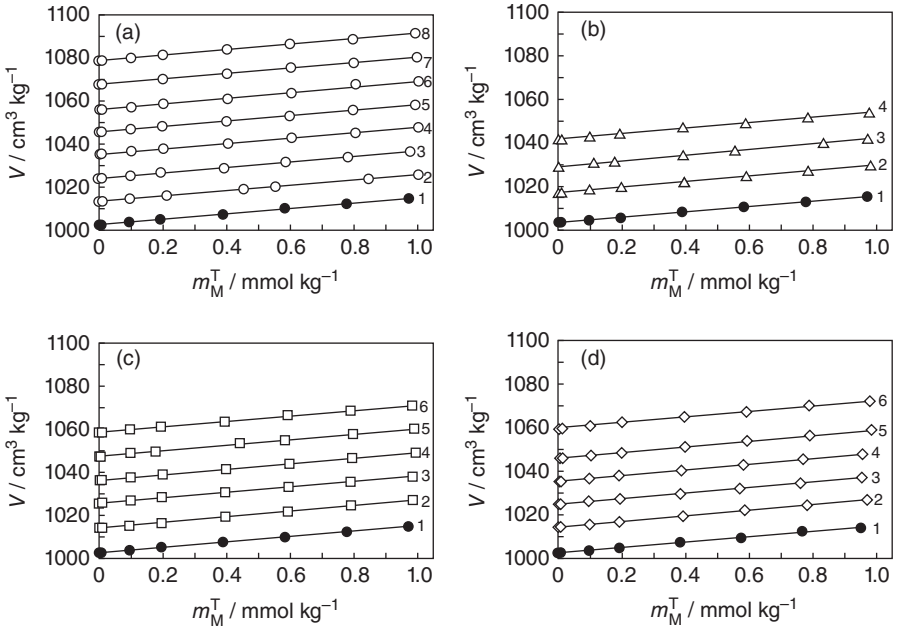


FIGURE 87.2 Solution volume per 1 kg of water versus total protein molality curves for Mgb systems: (a) C_6OH, $m_X^T/\mathrm{mmol\,kg^{-1}}$ = (1) 0, (2) 4.950, (3) 11.61, (4) 20.07, (5) 24.93, (6) 29.94, (7) 40.89, (8) 48.82; (b) C_4OH, (1) 0, (2) 50.54, (3) 75.08, (4) 101.7; (c) C_2OH, (1) 0, (2) 20.17, (3) 49.48, (4) 60.53, (5) 81.64, (6) 101.1; (d) TFE, (1) 0, (2) 20.42, (3) 30.25, (4) 39.77, (5) 50.42, (6) 100.6. In order to avoid overlap of the curves, all curves other than curve 1 in each graph are shifted upward by (2) +10, (3) +20, (4) +30, (5) +40, (6) +50, (7) +60, (8) +70 $\mathrm{mmol\,kg^{-1}}$.

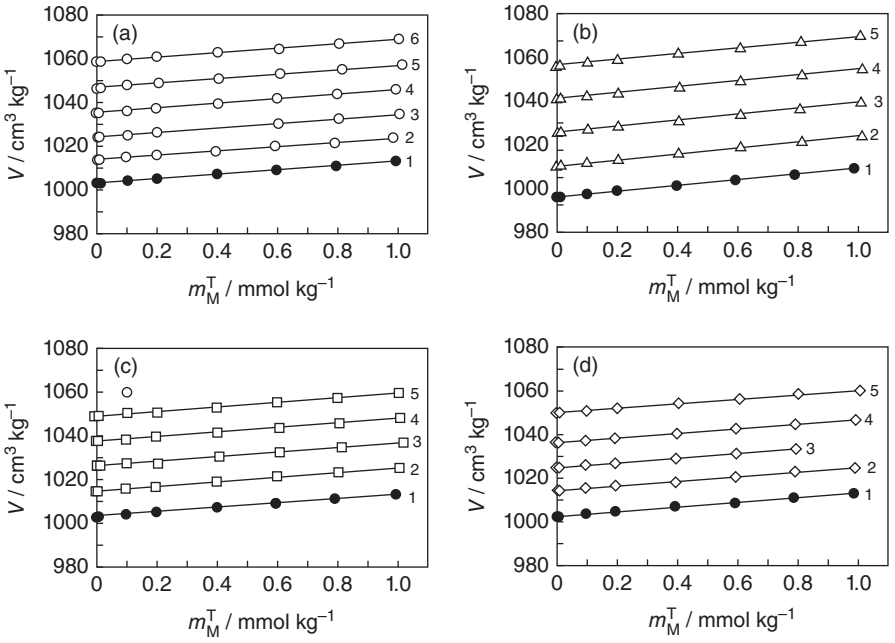


FIGURE 87.3 Solution volume per 1 kg of water versus total protein molality curves for Lys systems: (a) C_6OH, m_X^T/mmol kg^{-1} = (1) 0, (2) 5.011, (3) 10.26, (4) 20.05, (5) 29.87, (6) 49.08; (b) C_4OH, (1) 0, (2) 25.35, (3) 50.03, (4) 75.81, (5) 100.7; (c) C_2OH, (1) 0, (2) 25.47, (3) 50.57, (4) 75.90, (5) 101.5; (d) TFE, (1) 0, (2) 20.68, (3) 30.41, (4) 50.43, (5) 102.1. In order to avoid overlap of the curves, all curves other than curve 1 in each graph are shifted upward by (2) +10, (3) +20, (4) +30, (5) +40, (6) +50 mmol kg^{-1}.

the order of the magnitude of $b_{max}\Delta V$, it is necessary to know the value of b_{max}, the hydrophobicity of the binding sites of the short chain alcohol molecules, effect of the addition on the conformation of the proteins, and the hydration state of protein and alcohol molecules.

Since the influence of the polar group on the hydrophobic hydration around alkyl chains of the solutes becomes more significant for shorter-chain alcohols [11, 12], it may be difficult to compare the order of ethanol and TFE with the order of C_4OH and C_6OH simply. If the binding sites of C_6OH and C_4OH molecules are in the hydrophobic domain, the volume of the hydrophobic process [13] may contribute the smaller value of $b_{max}\Delta V$ for C_6OH than for C_4OH; in other words, the longer the hydrophobic alkyl chain, the larger the volume lost due to the release of hydrating water molecules within the transfer of an alcohol molecule from the bulk solution to the surface of the protein molecules. The volume of the hydrophobic process may also explain the negative value of $b_{max}\Delta V$ for octanol (C_8OH) binding to bovine serum albumin (BSA) (see Fig. 87.9, later) [9]. Further, the value of $b_{max}\Delta V$ is smaller for Lys than for Mgb. This fact may be attributable to the difference in the rigidity and the compactness of the structure between Lys and Mgb.

TABLE 87.1 Partial Molar Volumes of Proteins and Alcohols

	v_M (cm^3 mol^{-1})	v_X (cm^3 mol^{-1})
Mgb	12,440	—
Lys	10,454	—
C_6OH	—	118.1
C_4OH	—	86.4
C_2OH	—	55.1
TFE	—	66.4

The values of V at constant m_M^T taken from the V vs. m_M^T curves in Figs. 87.2 and 87.3 are plotted against m_X^T for the Mgb and Lys systems in Figs. 87.5 and 87.6, respectively. The curves show the linear dependence of V on m_X^T. Thus, the values of V_X^T at m_X^T are identical to those of PMV of alcohol at its infinite dilution, $V_X^{T,0}$. The values of V_X^T obtained from the curves in Figs. 87.5 and 87.6 are plotted against m_M^T in Fig. 87.7, and the PMVs of alcohols in their aqueous solutions free from proteins are listed in Table 87.1. For all alcohols used here, V_X^T increases linearly with increasing m_M^T. According to Eq. (87.21), this fact indicates that the left-hand side (LHS) of Eq. (87.22) is almost constant for the present systems. The slope of the curves in Fig. 87.7 is larger for Mgb than for Lys, corresponding to the difference in the magnitude of $b_{max}\Delta V$.

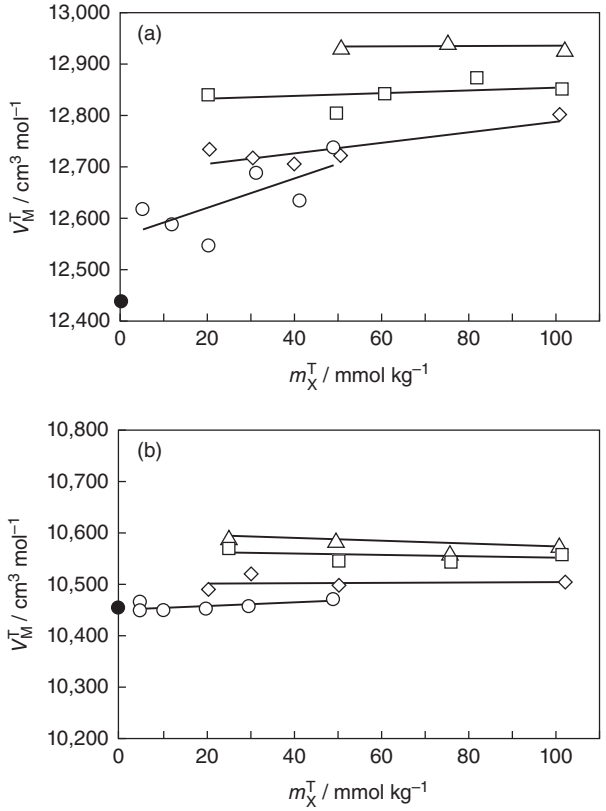


FIGURE 87.4 Partial molar volume of total protein in water (•) and partial molar volume of total protein versus total alcohol molality curves at 298.15 K (a) for Mgb in aqueous solutions of (○) C_6OH, (△) C_4OH, (□) C_2OH, and (◇) TFE and (b) for Lys in aqueous solutions of (○) C_6OH, (△) C_4OH, (□) C_2OH, and (◇) TFE.

Since the V_X^T vs. m_M^T curves of the present systems are linear, the slopes of the curves provide the values of $(V_X^{T,0} - v_X)/m_M^T$ in Eq. (87.29), which are listed in Table 87.2. Combining these values with the values of $b_{max}\Delta V$ and using Eq. (87,29), we obtained the values on the LHS of Eq. (87.28) listed in Table 87.2. Because of the small value of $b_{max}\Delta V$, we excluded the value for the Lys-C_6OH system from the list. Using these values, we calculated the values of K at infinite dilution of alcohols of the present systems for the values of $b_{max}m_M^T = 1$ and 5 mmol kg^{-1} and listed the results in Table 87.2. The values on the LHS of Eq. (87.28) correspond to the K values at $b_{max}m_M^T = 0$. The values of K at different $b_{max}m_M^T$ seem to be in agreement with each other. As compared with the value of the binding constant BSA and C_8OH [14], the magnitude of the K values for the present systems may be reasonable. Further, it is interesting that, contrary to that of C_4OH, the affinity of C_2OH and TFE to protein is stronger for Lys than for Mgb. This fact may be attributable to difference in the size and hardness of the structure between Lys and Mgb.

The procedure described above is a simple one to obtain the binding isotherm and the value of K from PMV data, but it is not able to determine the respective values of b_{max} and ΔV. In order to do this, it is necessary to arrange the procedure a little. From Eqs. (87.28) and (87.29), the following equation is obtained:

$$V_X^{T,0} = v_X + \frac{b_{max}\Delta V K m_M^T}{1 + b_{max}K m_M^T} \tag{87.31}$$

This equation expresses the dependence of the PMV of the ligand at its infinite dilution on the preparation molality of protein, if v_X has the same value with that of PMV of ligand in the solution free from protein. Rearranging Eq. (87.31) further, we obtain the following equation

$$\frac{1}{V_X^{T,0} - v_X} = \frac{1}{b_{max}\Delta V K} \cdot \frac{1}{m_M^T} + \frac{1}{\Delta V} \tag{87.32}$$

which implies that the slope and vertical intercept of the $1/(V_X^{T,0} - v_X)$ vs $1/m_M^T$ plot provide $1/(b_{max}\Delta V K)$ and $1/\Delta V$, respectively. Since the value of $b_{max}\Delta V$ is obtained

TABLE 87.2 Volume and Binding Parameters of Protein-Ligand Systems

Protein	Alcohol	$\frac{b_{max}\Delta V}{cm^3\ mol^{-1}}$	$\frac{(V_X^{T,0}-v_X)/m_M^T}{(cm^3\ mol^{-1})/(mol\ kg^{-1})}$	$\frac{(\partial\theta/\partial m_X^T)_{T,p,m_M^T}^{m_X^T\to 0}}{(mol\ kg^{-1})^{-1}}$	$\frac{K}{(mol\ kg^{-1})^{-1}}$	
Mgb	C_6OH	264[a]	4.08	15.5	15.7[c]	16.8[d]
	C_4OH	495[b]	5.01	10.1	10.2[c]	10.7[d]
	C_2OH	418[b]	3.19	7.6	7.7[c]	7.9[d]
	TFE	350[b]	2.74	7.8	7.9[c]	8.1[d]
Lys	C_6OH	13[a]	0.39	—	—	—
	C_4OH	113[b]	1.02	9.1	9.1[c]	9.5[d]
	C_2OH	93[b]	0.88	9.4	9.5[c]	9.9[d]
	TFE	50[b]	0.50	10.1	10.2[c]	10.6[d]

The values of $b_{max}\Delta V$ were obtained at [a]$m_X^T = 50$ mmol kg^{-1} and at [b]m_X^T=100 mmol kg^{-1}. The values of K were calculated by assuming [c]$b_{max}m_M^T = 1$ mmol kg^{-1} and [d]$b_{max}m_M^T = 5$ mmol kg^{-1}.

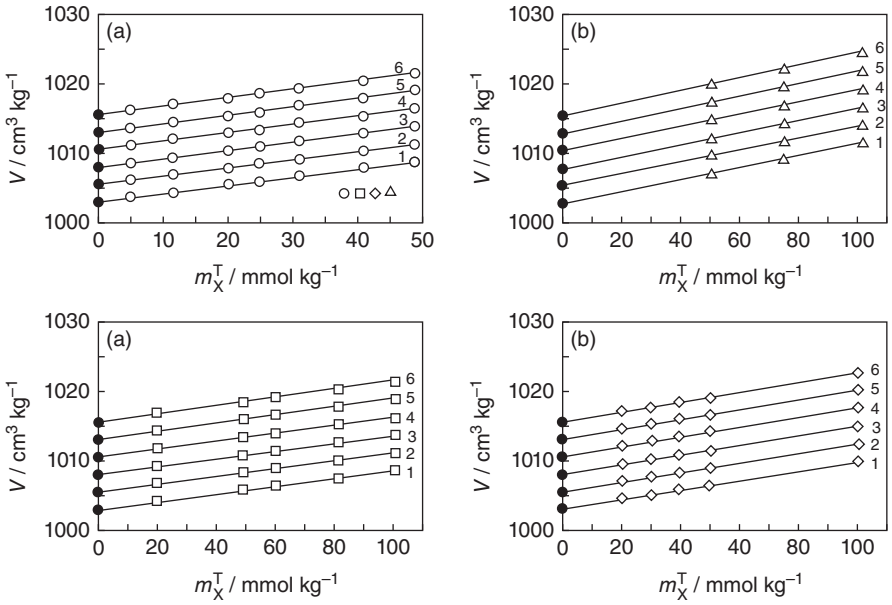


FIGURE 87.5 Solution volume per 1 kg of water versus total alcohol molality curves for Mgb systems: (a) C_6OH; (b) C_4OH; (c) C_2OH; (d) TFE; $m_M^T/\text{mmol kg}^{-1}$ = (1) 0, (2) 0.2, (3) 0.4, (4) 0.6, (5) 0.8, (6) 1.0.

from the V_M^T vs. m_X^T plot, the values of b_{max} and K can be estimated. In the following, we show the application of Eq. (87.32) to the binding between BSA and C_8OH [9].

Figure 87.8 shows the PMV of BSA at infinite dilution $V_M^{T,0}$ as a function of C_8OH molality m_X^T at 298.15 K. Evidently, the value of $b_{max}\Delta V$ is negative for the BSA-C_8OH system. In Fig. 87.9, the PMV of C_8OH $V_X^{T,0}$ is shown as a function of BSA molality m_M^T. The value of $V_X^{T,0}$ decreases with increasing BSA molality. This decrease corresponds to the negative value of $b_{max}\Delta V$. The

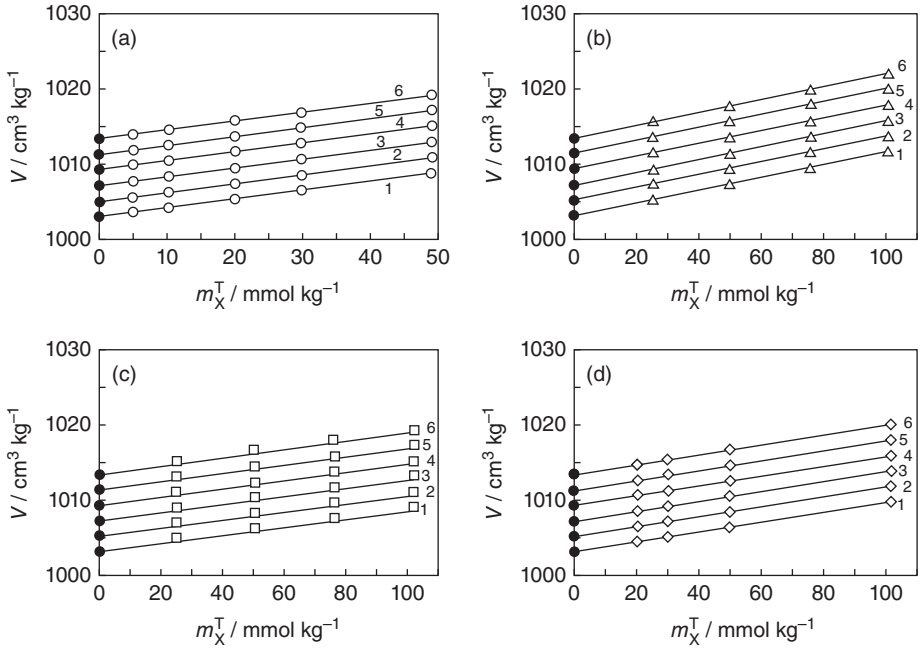


FIGURE 87.6 Solution volume per 1 kg of water versus total alcohol molality curves for Lys systems: (a) C_6OH; (b) C_4OH; (c) C_2OH; (d) TFE; $m_M^T/\text{mmol kg}^{-1}$ = (1) 0, (2) 0.2, (3) 0.4, (4) 0.6, (5) 0.8, (6) 1.0.

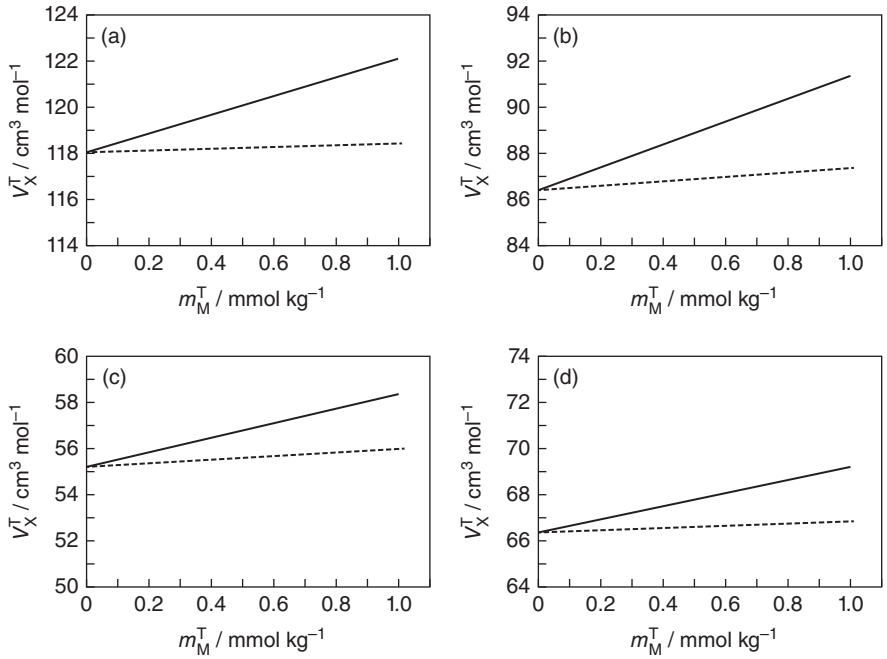


FIGURE 87.7 Partial molar volume of total alcohol versus total protein molality curves at 298.15 K: (a) C_6OH; (b) C_4OH; (c) C_2OH; (d) TFE; (—) Mgb and (- - -) Lys.

values of $V_X^{T,0} - v_X$ at m_M^T were obtained by assuming the value of v_X was equal to PMV of C_8OH in the solution free from BSA. In Fig. 87.10, the values of $1/(V_X^{T,0} - v_X)$ are plotted against $1/m_M^T$. It is found that $1/(V_X^{T,0} - v_X)$ decreases linearly with increasing $1/m_M^T$. This fact indicates that Eq. (87.32) is valid for the BSA-C_8OH system. Using the values of the slope and vertical intercept of the plot and the value of $b_{max}\Delta V$ obtained from Fig. 87.7, the values of $\Delta V = -109\,\text{cm}^3\,\text{mol}^{-1}$, $b_{max} = 1.9$, and $K = 392\,\text{kg mol}^{-1}$ were obtained.

87.4 PARTIAL MOLAR VOLUME IN MIXED MEMBRANE SYSTEMS

Let us consider an aqueous vesicle dispersion composed of n_w moles of solvent water and n_i moles of solute i (= 1,2, . . . , c). It is presumed that n_m moles of vesicles are monodispersed in the solution with volume V'. In a manner similar to that used for the micellar systems [15], the thermodynamic quantities of the bilayer membrane can be defined as the surface excess quantities in reference to two

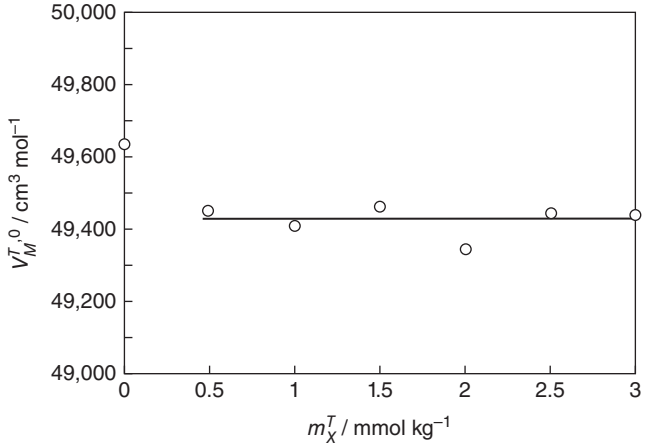


FIGURE 87.8 Partial molar volume of BSA at infinite dilution of BSA versus total molality of C_8OH curve. (Adapted from Yamanaka et al. 2001 [9].)

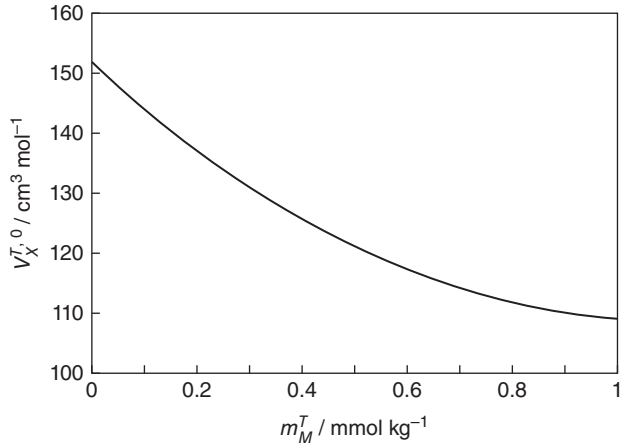


FIGURE 87.9 Partial molar volume of C_8OH at infinite dilution of C_8OH versus total molality of BSA curve. (Adapted from Yamanaka et al. 2001 [9].)

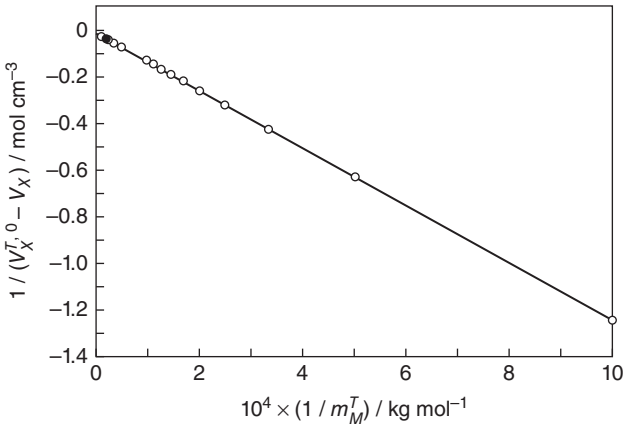


FIGURE 87.10 Reciprocal plot of partial molar volume of C_8OH. (Adapted from Yamanaka et al. 2001 [9].)

curved dividing surfaces at each side of the bilayer membrane. The locations of the dividing surfaces are determined so as to make the surface excess moles of water zero:

$$n_{\mathrm{w}} - c_{\mathrm{w}}^{\mathrm{W,I}} V'^{\mathrm{W,I}} - c_{\mathrm{w}}^{\mathrm{W,O}} V'^{\mathrm{W,O}} = 0 \tag{87.33}$$

Here, $c_{\mathrm{w}}^{\mathrm{W,I}}$ and $c_{\mathrm{w}}^{\mathrm{W,O}}$ are the number of moles of water per unit volume at positions far from the membrane surfaces in the interior and exterior bulk solutions of vesicle particles, respectively, whose volumes are denoted by $V'^{\mathrm{W,I}}$ and $V'^{\mathrm{W,O}}$. (See Fig. 87.11.)

The number of molecules of solute i per mole of vesicle is defined by

$$N_i^{\mathrm{M}} = \frac{n_i - c_i^{\mathrm{W,I}} V'^{\mathrm{W,I}} - c_i^{\mathrm{W,O}} V'^{\mathrm{W,O}}}{n_{\mathrm{m}}} \tag{87.34}$$

where $c_i^{\mathrm{W,I}}$ and $c_i^{\mathrm{W,O}}$ are the number of moles of solute i per unit volume in the interior and exterior bulk solutions, respectively, of the vesicle particles. Similarly, the molar thermodynamic quantity y^{M} of the membrane is defined by

$$y^{\mathrm{M}} = \frac{Y' - c_y^{\mathrm{W,I}} V'^{\mathrm{W,I}} - c_y^{\mathrm{W,O}} V'^{\mathrm{W,O}}}{n_{\mathrm{m}}} \tag{87.35}$$

where Y' is the thermodynamic quantity of the whole solution and $c_y^{\mathrm{W,I}}$ and $c_y^{\mathrm{W,O}}$ the thermodynamic quantity per unit volume in the interior and exterior bulk solutions, respectively. Since $c_v^{\mathrm{W,I}} = c_v^{\mathrm{W,O}} = 1$, the molar volume of the membrane is written in the following form:

$$v^{\mathrm{M}} = \frac{V' - V'^{\mathrm{W,I}} - V'^{\mathrm{W,O}}}{n_{\mathrm{m}}} \tag{87.36}$$

Since it is appropriate to use the molality as a concentration variable in the investigation of the volume properties in solution, let us now consider the solution per 1 kg of water. The molality of solute i in the whole solution and those in the bulk solutions are given by

$$m_i = \frac{n_i}{n_{\mathrm{w}} M_{\mathrm{w}}} \tag{87.37}$$

$$m_i^{\mathrm{W,I}} = \frac{c_i^{\mathrm{W,I}} V'^{\mathrm{W,I}}}{c_{\mathrm{w}}^{\mathrm{W,I}} V'^{\mathrm{W,I}} M_{\mathrm{w}}} \tag{87.38}$$

$$m_i^{\mathrm{W,O}} = \frac{c_i^{\mathrm{W,O}} V'^{\mathrm{W,O}}}{c_{\mathrm{w}}^{\mathrm{W,O}} V'^{\mathrm{W,O}} M_{\mathrm{w}}}, \tag{87.39}$$

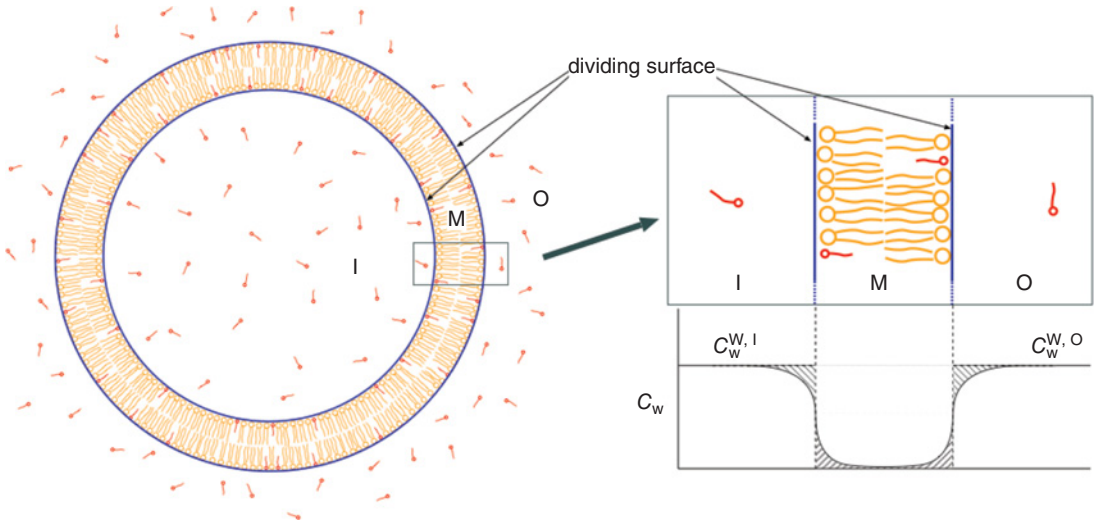


FIGURE 87.11 Schematic illustration of the relation between the variation in the concentration of water and the locations of the dividing surfaces.

respectively, where M_{w} is the molar mass of water. Using these equations, we can rewrite Eq. (87.34) as

$$N_i^{\mathrm{M}} = \frac{m_i - m_i^{\mathrm{W,I}}\alpha_{\mathrm{w}}^{\mathrm{W,I}} - m_i^{\mathrm{W,O}}\alpha_{\mathrm{w}}^{\mathrm{W,O}}}{m_{\mathrm{m}}} \tag{87.40}$$

where $\alpha_{\mathrm{w}}^{\mathrm{W,I}}$ and $\alpha_{\mathrm{w}}^{\mathrm{W,O}}$ are the fractions of the number of moles of water in the interior and exterior solutions, respectively, to the total moles of water of the whole solution defined by

$$\alpha_{\mathrm{w}}^{\mathrm{W,I}} = \frac{c_{\mathrm{w}}^{\mathrm{W,I}} V'^{\mathrm{W,I}}}{n_{\mathrm{w}}} = \frac{c_{\mathrm{w}}^{\mathrm{W,I}} V'^{\mathrm{W,I}}}{c_{\mathrm{w}}^{\mathrm{W,I}} V'^{\mathrm{W,I}} + c_{\mathrm{w}}^{\mathrm{W,O}} V'^{\mathrm{W,O}}} \tag{87.41}$$

$$\alpha_{\mathrm{w}}^{\mathrm{W,O}} = \frac{c_{\mathrm{w}}^{\mathrm{W,O}} V'^{\mathrm{W,O}}}{n_{\mathrm{w}}} = \frac{c_{\mathrm{w}}^{\mathrm{W,O}} V'^{\mathrm{W,O}}}{c_{\mathrm{w}}^{\mathrm{W,I}} V'^{\mathrm{W,I}} + c_{\mathrm{w}}^{\mathrm{W,O}} V'^{\mathrm{W,O}}} \tag{87.42}$$

Similarly to Eqs. (87.37)–(87.39), the volumes per 1 kg of water of the whole solution and of the interior and exterior solutions are given by

$$V = \frac{V'}{n_{\mathrm{w}} M_{\mathrm{w}}} \tag{87.43}$$

$$V^{\mathrm{W,I}} = \frac{V'^{\mathrm{W,I}}}{c_{\mathrm{w}}^{\mathrm{W,I}} V'^{\mathrm{W,I}} M_{\mathrm{w}}} \tag{87.44}$$

$$V^{\mathrm{W,O}} = \frac{V'^{\mathrm{W,O}}}{c_{\mathrm{w}}^{\mathrm{W,O}} V'^{\mathrm{W,O}} M_{\mathrm{w}}} \tag{87.45}$$

respectively. Using Eqs. (87.41)–(87.45), and rearranging Eq. (87.36), we can redefine the molar volume of membrane v^{M} by

$$v^{\mathrm{M}} = \frac{V - V^{\mathrm{W,I}}\alpha_{\mathrm{w}}^{\mathrm{W,I}} - V^{\mathrm{W,O}}\alpha_{\mathrm{w}}^{\mathrm{W,O}}}{m_{\mathrm{m}}} \tag{87.46}$$

Assuming that the vesicle membrane is a solution of film components, we can write

$$v^{\mathrm{M}} = \sum_{l=1}^{\mathrm{c}} v_l^{\mathrm{M}} N_l^{\mathrm{M}} \tag{87.47}$$

$$\mathrm{d}v^{\mathrm{M}} = \sum_{l=1}^{\mathrm{c}} v_l^{\mathrm{M}} \mathrm{d}N_l^{\mathrm{M}} \tag{87.48}$$

where v_l^{M} is PMV of solute l in the vesicle membrane. Using Eq. (87.40), we obtain

$$v^{\mathrm{M}} m_{\mathrm{m}} = \sum_{l=1}^{c} v_l^{\mathrm{M}} \left[m_l - \left(m_l^{\mathrm{W,I}}\alpha_{\mathrm{w}}^{\mathrm{W,I}} + m_l^{\mathrm{W,O}}\alpha_{\mathrm{w}}^{\mathrm{W,O}} \right) \right] \tag{87.49}$$

$$\mathrm{d}\left(v^{M} m_{\mathrm{m}}\right) = \sum_{l=1}^{c} v_l^{\mathrm{M}} \mathrm{d}\left[m_l - \left(m_l^{\mathrm{W,I}}\alpha_{\mathrm{w}}^{\mathrm{W,I}} + m_l^{\mathrm{W,O}}\alpha_{\mathrm{w}}^{\mathrm{W,O}} \right) \right] \tag{87.50}$$

Rearranging Eq. (87.46) and substituting Eq. (87.49), we obtain the equation for the volume of the whole solution per 1 kg of water in the following form:

$$V = V^{\mathrm{W,I}}\alpha_{\mathrm{w}}^{\mathrm{W,I}} + V^{\mathrm{W,O}}\alpha_{\mathrm{w}}^{\mathrm{W,O}} + \sum_{l=1}^{c} v_l^{\mathrm{M}} \left[m_l - \left(m_l^{\mathrm{W,I}}\alpha_{\mathrm{w}}^{\mathrm{W,I}} + m_l^{\mathrm{W,O}}\alpha_{\mathrm{w}}^{\mathrm{W,O}} \right) \right]. \tag{87.51}$$

Since, because the number of degree of freedom for the whole solution is $c + 2$, the volume V of the whole solution is a function of T, p, and the preparation molalities of solutes, m_1, m_2, …, and m_c, the total differential of V at constant temperature T and pressure p is given by

$$\begin{aligned} \mathrm{d}V &= \mathrm{d}\left(V^{\mathrm{W,I}}\alpha_{\mathrm{w}}^{\mathrm{W,I}} + V^{\mathrm{W,O}}\alpha_{\mathrm{w}}^{\mathrm{W,O}} \right) + \mathrm{d}\left(v^{\mathrm{M}} m_{\mathrm{m}} \right) \\ &= \sum_{i=1}^{c} \left\{ \left[\frac{\partial \left(V^{\mathrm{W,I}}\alpha_{\mathrm{w}}^{\mathrm{W,I}} + V^{\mathrm{W,O}}\alpha_{\mathrm{w}}^{\mathrm{W,O}} \right)}{\partial m_i} \right]_{T,p,m_{j\neq i}} + v_i^{\mathrm{M}} \right. \\ &\quad \left. - \sum_{l=1}^{c} v_l^{\mathrm{M}} \left[\frac{\partial \left(m_l^{\mathrm{W,I}}\alpha_{\mathrm{w}}^{\mathrm{W,I}} + m_l^{\mathrm{W,O}}\alpha_{\mathrm{w}}^{\mathrm{W,O}} \right)}{\partial m_i} \right]_{T,p,m_{j\neq i}} \right\} \mathrm{d}m_i \end{aligned} \tag{87.52}$$

Thus, the PMV of solute i measured experimentally using the preparation molality is given by

$$\begin{aligned} V_i &= \left(\frac{\partial V}{\partial m_i} \right)_{T,p,m_{j\neq i}} \\ &= \left[\frac{\partial \left(V^{\mathrm{W,I}}\alpha_{\mathrm{w}}^{\mathrm{W,I}} + V^{\mathrm{W,O}}\alpha_{\mathrm{w}}^{\mathrm{W,O}} \right)}{\partial m_i} \right]_{T,p,m_{j\neq i}} + v_i^{\mathrm{M}} \\ &\quad - \sum_{l=1}^{c} v_l^{\mathrm{M}} \left[\frac{\partial \left(m_l^{\mathrm{W,I}}\alpha_{\mathrm{w}}^{\mathrm{W,I}} + m_l^{\mathrm{W,O}}\alpha_{\mathrm{w}}^{\mathrm{W,O}} \right)}{\partial m_i} \right]_{T,p,m_{j\neq i}} \end{aligned} \tag{87.53}$$

When the interior bulk solution of vesicles has the same composition as the exterior bulk solution, Eqs. (87.51) and (87.52) are rewritten as follows:

$$V = V^{\mathrm{W}} + v^{\mathrm{M}} m_{\mathrm{m}} = \frac{v_{\mathrm{w}}^{\mathrm{W}}}{M_{\mathrm{w}}} + \sum_{i=1}^{c} v_i^{\mathrm{W}} m_i^{\mathrm{W}} + v^{\mathrm{M}} m_{\mathrm{m}} \quad (87.54)$$

The total differential of V at constantan T and p is written in the following form:

$$\begin{aligned} \mathrm{d}V &= \mathrm{d}V^{\mathrm{W}} + \mathrm{d}\left(v^{\mathrm{M}} m_{\mathrm{m}}\right) \\ &= \sum_{i=1}^{c} \left\{ \left(\frac{\partial V^{\mathrm{W}}}{\partial m_i} \right)_{T,p,m_{j\neq i}} + v_i^{\mathrm{M}} - \sum_{l=1}^{c} v_l^{\mathrm{M}} \left(\frac{\partial m_l^{\mathrm{W}}}{\partial m_i} \right)_{T,p,m_{j\neq i}} \right\} \mathrm{d}m_i \end{aligned} \quad (87.55)$$

Therefore, PMV of solute i with respect to the preparation molality, is given by

$$\begin{aligned} V_i = \left(\frac{\partial V}{\partial m_i} \right)_{T,p,m_{j\neq i}} &= \sum_{k=1}^{c} v_k^{\mathrm{W}} \left(\frac{\partial m_k^{\mathrm{W}}}{\partial m_i} \right)_{T,p,m_{j\neq i}} \\ &+ v_i^{\mathrm{M}} - \sum_{l=1}^{c} v_l^{\mathrm{M}} \left(\frac{\partial m_l^{\mathrm{W}}}{\partial m_i} \right)_{T,p,m_{j\neq i}} \end{aligned} \quad (87.56)$$

where the total differential of the volume of the bulk solutions at constant T and p, as

$$\mathrm{d}V^{\mathrm{W}} = \sum_{k=1}^{c} v_k^{\mathrm{W}} \mathrm{d}m_k^{\mathrm{W}} \quad (87.57)$$

has been used. In Sections 87.4.1 and 87.4.2, we will consider application of the above equations to some mixed solute systems whose interior and exterior bulk solution vesicle compositions are the same.

87.4.1 Binary Mixtures of Water-Insoluble Lipids

In this section, we consider binary mixtures of water-insoluble lipids. Since the number of degree of freedom of the system is 4, we can choose two concentration variables other than temperature and pressure as the experimental variables. From the practical point of view on preparing vesicle solutions, it is convenient to adopt the combination of the molality m_{t} of total solutes in the whole solution given by

$$m_{\mathrm{t}} = m_1 + m_2 \quad (87.58)$$

and the mole fraction of solute 2 in the total solutes defined by

$$X_2 = \frac{m_2}{m_{\mathrm{t}}} \quad (87.59)$$

Since both lipids are water-insoluble, the number of molecules of solute $i(= 1, 2)$ per mole of vesicle given by Eq. (87.40) is written in the following form:

$$N_i^{\mathrm{M}} = \frac{m_i}{m_{\mathrm{m}}} \quad (87.60)$$

Thus, the total number of lipids and the mole fraction of solute 2 in the vesicle membrane are given by

$$N_{\mathrm{t}}^{\mathrm{M}} = N_1^{\mathrm{M}} + N_2^{\mathrm{M}} = \frac{m_t}{m_{\mathrm{m}}} \quad (87.61)$$

$$X_2^{\mathrm{M}} = \frac{N_2^{\mathrm{M}}}{N_{\mathrm{t}}^{\mathrm{M}}} = X_2 \quad (87.62)$$

respectively.

From Eq. (87.55), the total differential of V at constant T and p is given by

$$\mathrm{d}V = v_1^{\mathrm{M}} \mathrm{d}m_1 + v_2^{\mathrm{M}} \mathrm{d}m_2 \quad (87.63)$$

Changing the concentration variables from m_1 and m_2 to m_{t} and X_2 using Eqs. (87.58) and (87.59), Eq. (87.63) becomes

$$\mathrm{d}V = \frac{v^{\mathrm{M}}}{N_{\mathrm{t}}^{\mathrm{M}}} \mathrm{d}m_{\mathrm{t}} + m_{\mathrm{t}} \left(v_2^{\mathrm{M}} - v_1^{\mathrm{M}} \right) \mathrm{d}X_2 \quad (87.64)$$

Then, we have

$$\left(\frac{\partial V}{\partial m_{\mathrm{t}}} \right)_{T,p,X_2} = \frac{v^{\mathrm{M}}}{N_{\mathrm{t}}^{\mathrm{M}}} = v_1^{\mathrm{M}} X_1^{\mathrm{M}} + v_2^{\mathrm{M}} X_2^{\mathrm{M}} = v_1^{\mathrm{M}} X_1 + v_2^{\mathrm{M}} X_2 \quad (87.65)$$

$$\left(\frac{\partial V}{\partial X_2} \right)_{T,p,m_{\mathrm{t}}} = m_{\mathrm{t}} \left(v_2^{\mathrm{M}} - v_1^{\mathrm{M}} \right) \quad (87.66)$$

The LHSs of Eqs. (87.65) and (87.66) are obtained experimentally from the V vs. m_{t} curve at constant X_2 and the V vs. X_2 curve at constant m_{t}, respectively. By setting up these equations simultaneously, we can estimate the values of v_1^{M} and v_2^{M}, which provide information about the volume behavior and packing of the vesicle membranes.

The volume of mixing in the vesicle membrane is defined by

$$\Delta_{\mathrm{mix}} v = \frac{v^{\mathrm{M}}}{N_{\mathrm{t}}^{\mathrm{M}}} - \left(v_1^{\mathrm{M},0} X_1 + v_2^{\mathrm{M},0} X_2 \right) \quad (87.67)$$

where $v_i^{M,0}$ $(i = 1, 2)$ is the molar volume of vesicle membrane composed of solute i alone. Applying Eq. (87.67) to the v^M/N_t^M vs. X_2 curve for the mixtures of film-forming lipids, the miscibility and interaction between the lipids in the vesicle membrane can be examined. On the other hand, for mixtures of lipids, one of which, say, solute 2 cannot form vesicles alone like cholesterol [16, 17], Eq. (87.67), which is symmetric for solutes 1 and 2, is not appropriate. It is necessary, for example, to assume that $v_2^{M,0}$ in Eq. (87.67) is approximated by the molar volume of solute 2 in its crystalline state.

87.4.2 Binary Mixtures of a Water-Insoluble Lipid and a Water-Soluble Substance

In this section, we consider the binary mixtures of a water-insoluble lipid (solute 1) and a water-soluble substance (solute 2). Taking $m_1^W \cong 0$ into account, and then applying Eq. (87.56) to the present mixtures, we obtain expressions for PMVs of solute 1 and 2 as

$$V_1 = \left(\frac{\partial V}{\partial m_1}\right)_{T,p,m_2} = v_2^W \left(\frac{\partial m_2^W}{\partial m_1}\right)_{T,p,m_2} + v_1^M - v_2^M \left(\frac{\partial m_2^W}{\partial m_1}\right)_{T,p,m_2} \tag{87.68}$$

$$V_2 = \left(\frac{\partial V}{\partial m_2}\right)_{T,p,m_1} = v_2^W \left(\frac{\partial m_2^W}{\partial m_2}\right)_{T,p,m_1} + v_2^M - v_2^M \left(\frac{\partial m_2^W}{\partial m_2}\right)_{T,p,m_1} \tag{87.69}$$

respectively. Since we can write

$$m_2^W = m_2 - \frac{N_2^M}{N_1^M} m_1 \tag{87.70}$$

using Eq. (87.40), the partial derivatives of m_2^W with respect to m_1 and m_2 are given by

$$\left(\frac{\partial m_2^W}{\partial m_1}\right)_{T,p,m_2} = -\frac{N_2^M}{N_1^M} - m_1 \left[\frac{\partial \left(N_2^M/N_1^M\right)}{\partial m_1}\right]_{T,p,m_2} \tag{87.71}$$

$$\left(\frac{\partial m_2^W}{\partial m_2}\right)_{T,p,m_1} = 1 - m_1 \left[\frac{\partial \left(N_2^M/N_1^M\right)}{\partial m_2}\right]_{T,p,m_1} \tag{87.72}$$

respectively. Substituting Eqs. (87.71) and (87.72) into Eqs. (87.68) and (87.69), respectively, we have

$$V_1 = v_1^M + \left(v_2^M - v_2^W\right) \frac{N_2^M}{N_1^M} + \left(v_2^M - v_2^W\right) m_1 \left[\frac{\partial \left(N_2^M/N_1^M\right)}{\partial m_1}\right]_{T,p,m_2} \tag{87.73}$$

$$V_2 = v_2^W + \left(v_2^M - v_2^W\right) m_1 \left[\frac{\partial \left(N_2^M/N_1^M\right)}{\partial m_2}\right]_{T,p,m_1} \tag{87.74}$$

The value of V_1 can be obtained experimentally from the V vs. m_1 curve at constant m_2 and that of V_2 from the V vs. m_2 curve at constant m_1.

In order to estimate the partial derivatives of N_2^M/N_1^M on the RHSs of Eqs. (87.73) and (87.74), it is necessary to consider the partition equilibrium of water-soluble solute 2 between the membrane phase and the bulk solution using the chemical potentials of solute 2 in the bulk solution and in the bilayer membrane. Assuming that the bulk solution is an ideal-dilute solution of solute 2 in water, we can write the chemical potential of solute 2 in the bulk solution as

$$\mu_2^W = \mu_2^{W,\ominus} + RT \ln m_2^W \tag{87.75}$$

where $\mu_2^{W,\ominus}$ is the standard chemical potential of solute 2 in the bulk solution. Similarly, assuming that the membrane is an ideal-dilute solution of solute 2 in solute 1, we have the chemical potential of solute 2 in the membrane in the form

$$\mu_2^M = \mu_2^{M,\ominus} + RT \ln X_2^M \tag{87.76}$$

where $\mu_2^{M,\ominus}$ is the standard chemical potential of solute 2 in the membrane, X_2^M the mole fraction of amphiphile in the membrane defined by

$$X_2^M = \frac{N_2^M}{N_1^M + N_2^M}. \tag{87.77}$$

The equilibrium constant for the partition of solute 2 between the membrane and the bulk solution is defined by

$$P_{M/W} \equiv \exp\left(-\frac{\mu_2^{M,\ominus} - \mu_2^{W,\ominus}}{RT}\right) = \frac{X_2^M}{m_2^W}. \tag{87.78}$$

and is referred to as the partition coefficient. Accounting for the fact that the number of film-forming lipid molecules in a vesicle is generally very large [18–20] and that solute 2 is very dilute in the membrane, we may replace m_2^W by m_2 and

X_2^{M} by $N_2^{\mathrm{M}}/N_1^{\mathrm{M}}$. Thus, we have the partition coefficient in the form

$$P_{\mathrm{M/W}} = \frac{N_2^{\mathrm{M}}}{m_2 N_1^{\mathrm{M}}} \tag{87.79}$$

which provides the partial derivatives of $N_2^{\mathrm{M}}/N_1^{\mathrm{M}}$ with respect to the preparation molalities of solutes 1 and 2

$$\left[\frac{\partial\left(N_2^{\mathrm{M}}/N_1^{\mathrm{M}}\right)}{\partial m_1}\right]_{T,p,m_2} = 0 \tag{87.80}$$

$$\left[\frac{\partial\left(N_2^{\mathrm{M}}/N_1^{\mathrm{M}}\right)}{\partial m_2}\right]_{T,p,m_1} = P_{\mathrm{M/W}} \tag{87.81}$$

respectively. Substituting Eqs. (87.79)–(87.81) into Eqs. (87.73) and (87.74), we obtain

$$V_1 = v_1^{\mathrm{M}} + \left(v_2^{\mathrm{M}} - v_2^{\mathrm{W}}\right) P_{\mathrm{M/W}} m_2 \tag{87.82}$$

$$V_2 = v_2^{\mathrm{W}} + \left(v_2^{\mathrm{M}} - v_2^{\mathrm{W}}\right) P_{\mathrm{M/W}} m_1 \tag{87.83}$$

respectively. These equations say that the experimental values of PMVs of solutes 1 and 2 with respect to their preparation molalities include the volume change of the transfer of solute 2 from the bulk solution to the membrane.

At low concentrations of solute 2, it may be reasonable to use the molar volume of vesicle membrane composed of solute 1 alone, $v_1^{\mathrm{M},0}$, instead of v_1^{M} , and to introduce the apparent molar volume of solute 2 in the membrane, ϕ_2^{M}, defined by

$$v^{\mathrm{M}} = v_1^{\mathrm{M}} N_1^{\mathrm{M}} + v_2^{\mathrm{M}} N_2^{\mathrm{M}} = v_1^{\mathrm{M},0} N_1^{\mathrm{M}} + \phi_2^{\mathrm{M}} N_2^{\mathrm{M}} \tag{87.84}$$

Further, assuming that v_2^{W} can be replaced by PMV of solute 2 in the solution free from solute 1, $v_2^{\mathrm{W},0}$, we obtain

$$V_1 = v_1^{\mathrm{M},0} + \left(\phi_2^{\mathrm{M}} - v_2^{\mathrm{W},0}\right) P_{\mathrm{M/W}} m_2 \tag{87.85}$$

$$V_2 = v_2^{\mathrm{W},0} + \left(\phi_2^{\mathrm{M}} - v_2^{\mathrm{W},0}\right) P_{\mathrm{M/W}} m_1 \tag{87.86}$$

which are useful for examining the effect of the addition of solute 2 on the molar volume of the vesicle membrane. It is notable that Eq. (87.85) resembles Eq. (87.19) for the protein–ligand binding. Moreover, assuming that ϕ_2^{M} is independent of m_2 in the dilute concentration region, we have

$$\left(\frac{\partial V_1}{\partial m_2}\right)_{T,p,m_1} = \left(\frac{\partial V_2}{\partial m_1}\right)_{T,p,m_2} = \left(\phi_2^{\mathrm{M}} - v_2^{\mathrm{W},0}\right) P_{\mathrm{M/W}} \tag{87.87}$$

which is similar to Maxwell's equations.

TABLE 87.3 Temperature and Volume of Phase Transitions for Bilayer Membranes [21]

Lipid	Transition	T (K)	ΔV ($\mathrm{cm^3\,mol^{-1}}$)
DPPC	$P'_\beta \rightarrow L_\alpha$	315.2	25.4
	$L'_\beta \rightarrow P'_\beta$	307.5	1.9
DMPC	$P'_\beta \rightarrow L_\alpha$	297.1	17.6
	$L'_\beta \rightarrow P'_\beta$	287.1	1.8

Now, let us demonstrate the application of the present treatment to practical systems. In order to do this, we adopted two systems of zwitterionic phospholipids (component 1), 1,2-dipalmitoyl-*sn*-gylycero-3-phosphocholine (DPPC), and 1,2-dimyristoyl-*sn*-glycero-3-phosphocholine (DMPC), with octanol (C_8OH, nonionic water-soluble component 2). DPPC and DMPC are purchased from Sigma (St. Louis, MO) and C_8OH, 99+ %, anhydrous, from Aldrich (Milwaukee, WI). They were used after further purification. Distilled water was used as solvent. The bilayer membranes of phospholipids exhibit different phases, such as the lamellar gel (L'_β), the liquid crystal (L_α), and the ripple gel (P'_β), depending on the environmental variables such as temperature, pressure, and concentrations of the solutes coexisting with the membranes. In Table 87.3, the temperatures and the volume changes of the phase transitions are listed for DPPC and DMPC [21]. Since the molecular packing of phospholipid is different among these phases, effects of the addition of water-soluble solutes on the volume behavior of the membrane in each phase state may be different.

Densities ρ of aqueous vesicle dispersions were measured as functions of the preparation molality of phospholipid m_1 at constant C_8OH molality m_2 at 303.15 ± 0.02 K under atmospheric pressure using a vibrating-tube density meter (DMA 60/608, Anton Paar, Austria). The experimental error in the density was within $\pm 0.002\,\mathrm{kg\,m^{-3}}$. At 303.15 K, the membrane of DPPC is in the lamellar gel (L'_β) state and that of DMPC in the liquid crystal (L_α) state. The values of solution volume V were calculated from the solution densities using

$$V = \frac{1 + M_1 m_1 + M_2 m_2}{\rho} \tag{87.88}$$

where M_1 and M_2 are molar masses of phospholipid and C_8OH, respectively. In Fig. 87.12a,b, the V vs. m_1 plots are shown for the DPPC and DMPC systems, respectively. All of the curves are linear, which indicates that PMVs of phospholipids are independent of their concentrations.

The values of PMVs V_1 of DPPC and DMPC, estimated by applying $V_1 = (\partial V/\partial m_1)_{T,p,m_2}$ to the V / m_1 curves in Fig. 87.12, are plotted against m_2 in Fig. 87.13. The values of $v_1^{\mathrm{M},0}$ for DPPC and DMPC, given by the V_1 values at $m_2 = 0\,\mathrm{mmol\,kg^{-1}}$, are listed in Table 87.4. It is found that

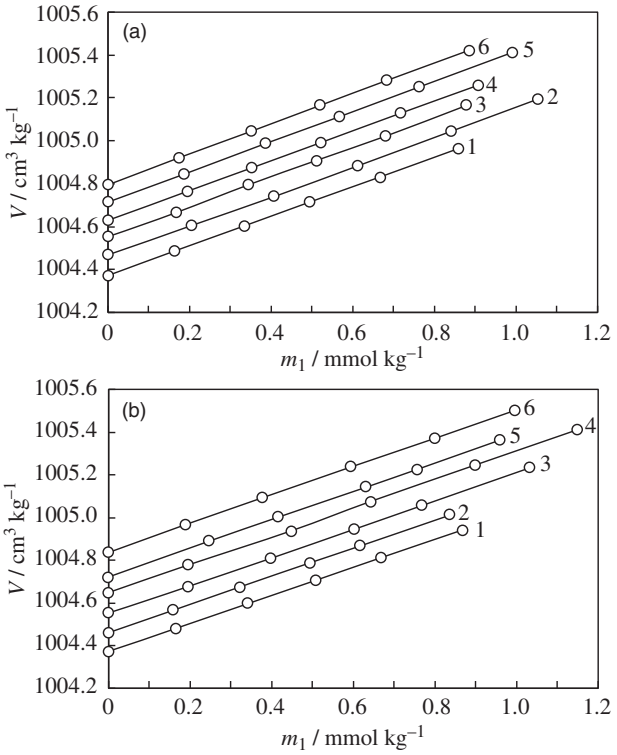


FIGURE 87.12 Solution volume versus phospholipid molality curves for phospholipid-C_8OH systems at 303.15 K: (a) DPPC, m_2/mmol kg^{-1} = (1) 0, (2) 0.548, (3) 1.115, (4) 1.604, (5) 2.184, (6) 2.731; (b) DMPC, m_2/mmol kg^{-1} = (1) 0, (2) 0.561, (3) 1.150, (4) 1.791, (5) 2.330, (6) 2.954.

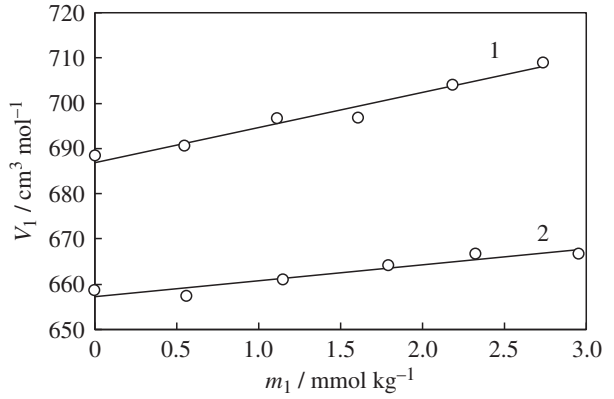


FIGURE 87.13 Partial molar volume of phospholiipid versus C_8OH molality curves at 303.15 K: (1) DPPC, (2) DMPC.

TABLE 87.4 Volume Parameters of Membrane Systems at 303.15 K

	$v_1^{M,0}$ (cm^3 mol^{-1})	$v_2^{W,0}$ (cm^3 mol^{-1})	$(\partial V_1/\partial m_2)_{T,p,m_1}$ (cm^3 kg mol^{-2})	$(\partial V_2/\partial m_1)_{T,p,m_2}$ (cm^3 kg mol^{-2})
DPPC	688		7509	7507
DMPC	659		3411	3429
C_8OH		155		

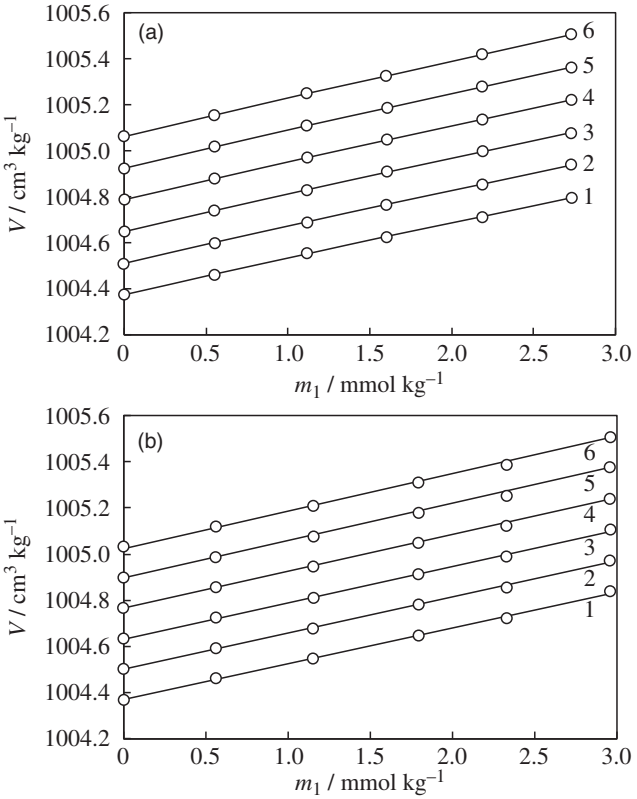


FIGURE 87.14 Solution volume versus phospholipid molality curves for phospholipid-C_8OH systems at 303.15 K: (a) DPPC, m_1/mmol kg^{-1} = (1) 0, (2) 0.2, (3) 0.4, (4) 0.6, (5) 0.8, (6) 1.0; (b) DMPC, m_1/mmol kg^{-1} = (1) 0, (2) 0.2, (3) 0.4, (4) 0.6, (5) 0.8, (6) 1.0.

the values of V_1 of DPPC and DMPC increase linearly with increasing C_8OH molality. The values of the slope of the curve, $(\partial V_1/\partial m_2)_{T,p,m_1}$, are listed in Table 87.4. The value for DPPC is found to be more than twice as large as that for DMPC.

In order to obtain the values of PMV of C_8OH V_2, the values of solution volume V taken from the V vs. m_1 curves in Fig. 87.13 at constant m_2, were plotted against m_2 in Fig. 87.14. The values of V are found to increase linearly with increasing m_2. Applying $V_2 = (\partial V/\partial m_2)_{T,p,m_1}$ to the curves, we determined the values of V_2, plotted against m_1 in Fig. 87.15. The value of $v_2^{W,0}$ of C_8OH in its solution free from phospholipid, given by the V_2 value at $m_1 = 0$ mmol kg^{-1}, is added in Table 87.4. It is observed that the value of V_2 increases linearly with increasing m_1 from the $v_2^{W,0}$ value. The slope of the curve, $(\partial V_2/\partial m_1)_{T,p,m_2}$, listed in Table 87.4, is larger for DPPC than for DMPC. For both DPPC and DMPC, the values of $(\partial V_2/\partial m_1)_{T,p,m_2}$ are in excellent agreement with those of $(\partial V_1/\partial m_2)_{T,p,m_1}$. This fact confirms the validity of Eq. (87.87). Quantitative examination of the value of $(\phi_2^M - v_2^{W,0})P_{M/W}$ requires the

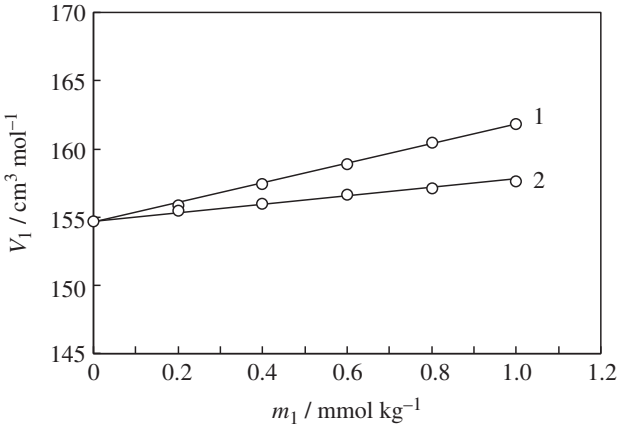


FIGURE 87.15 Partial molar volume of C_8OH versus phospholipid molality curves at 303.15 K: (1) DPPC, (2) DMPC.

numerical values of $P_{M/W}$, which is defined by Eq. (87.78), for the partition of C_8OH between its bulk solution and the bilayer membranes of DMPC and DPPC. The positive value of $(\phi_2^M - v_2^{W,0})P_{M/W}$ indicates that ϕ_2^M is larger than $v_2^{W,0}$ because $P_{M/W}$ assumes a positive value [22–24]. This fact suggests that the packing of the bilayer membranes is loosened by the incorporation of C_8OH molecules. A similar observation was found for the effect of hexanol on the molecular area of adsorbed film of 1,2-dihexanoyl-*sn*-gylycero-3-phosphocholine (DHPC) [25].

ACKNOWLEDGMENTS

This work was supported by JSPS KAKENHI Grant 21118515.

REFERENCES

[1] Atkins, P., Paula, J. (2006). *Physical Chemistry*, 8th ed. Oxford Univ. Press, New York.

[2] Rowlinson, J.S., Swinton, F.L. (1982). *Liquids and Liquid Mixtures*, 3rd ed. Butterworth Scientific, London.

[3] Levine, I.N. (1995). *Physical Chemistry*, 4th ed. McGraw-Hill, New York.

[4] Chalikian, T.V., Breslauer, K.J. (1998). *Curr. Opinion Struct. Biol.* **8**, 657–664.

[5] Johnson, F.H., Brown, D.E.S., Marsland, D.A. (1942). *J. Cell. Compar. Physiol.* **20**, 269–276.

[6] Johnson, F.H., Flagler, E.A. (1950). *Science* **112**, 91–92.

[7] Lever, M.J., Miller, K.W., Paton, W.D.M., Smith, E.B. (1971). *Nature* **231**, 368–371.

[8] Miller, K.W., Paton, W.D.M., Smith, R.A., Smith E.B. (1973). *Mol. Pharmacol.* **9**, 131–143.

[9] Yamanaka, M., Kaneshina, S., Kamaya, H., Ueda, I. (2001). *Colloids Surf. B: Biointerfaces* **22**, 23–29.

[10] Nishimoto, M., Komatsu, U., Tamai, N., Yamanaka, M., Kaneshina, S., Ogli, K., Matsuki, H. (2011). *Colloid Polym. Sci.* **289**, 1785–1797.

[11] Nakajima, T., Komatsu, T., Nakagawa, T. (1975). *Bull. Chem. Soc. Japan* **48**, 783–787.

[12] Sakurai, M., Nakamura, K., Nitta, K. (1994). *Bull. Chem. Soc. Japan* **67**, 1580–1587.

[13] Ben-Naim, A. (1980). *Hydrophobic Interactions.* Plenum Press, New York, Chapter 5.

[14] Ray, A., Reynolds, J.A., Polet, H., Steinhardt, J. (1966). *Biochemistry* **5**, 2606–2616.

[15] Motomura, K., Yamanaka, M., Aratono, M. (1984). *Colloid Polym. Sci.* **262**, 948–955.

[16] Tanford, C. (1980). *The Hydrophobic Effect: Formation of Micelles and Biological Membranes.* Wiley, New York.

[17] Greenwood, A.I., Tristram-Nagle, S., Nagle, J.F. (2006). *Chem. Phys. Lipids* **143**, 1–10.

[18] Mimms, L.T., Zampighi, G., Nozaki, Y., Tanford, C., Reynolds, J.A. (1981). *Biochemistry* **20**, 833–840.

[19] Huang, C. (1969). *Biochemistry* **8**, 344–352.

[20] Maulucci, G., De Spirito, M., Arcovito, G., Boffi, F., Castellano, A.C., Briganti, G. (2005). *Biophys. J.* **88**, 3435–3550.

[21] Ichimori, H., Hata, T., Matsuki, H., Kaneshina, S. (1998). *Biochim. Biophys. Acta* **1414**, 165–174.

[22] Lee, A.G. (1976). *Biochemistry* **15**, 2448–2454.

[23] Jain, M.K., Gleeson, J., Upreti, A., Upreti, G.C. (1978). *Biochim. Biophys. Acta* **509**, 1–8.

[24] Aagaard, T.H., Kristensen, M.N., Westh, P. (2006). *Biophys. Chem.* **119**, 61–68.

[25] Takajo, Y., Matsuki, H., Kaneshina, S., Aratono, M., Yamanaka, M. (2007). *Colloid Surf. B: Biointerfaces* **59**, 52–58.

88

VAN DER WAALS INTERACTION BETWEEN COLLOIDAL PARTICLES

HIROYUKI OHSHIMA

Faculty of Pharmaceutical Sciences, Tokyo University of Science, 2641 Yamazaki Noda, Chiba 278-8510, Japan

88.1 INTRODUCTION

The behaviors of colloidal dispersions are determined by the balance of the van der Waals attraction and the electrostatic repulsion acting between particles [1–9]. In this chapter we discuss the van der Waals interaction between colloidal particles. When two molecules are approaching each other, the van der Waals attractive intermolecular forces are acting as a result of interactions between the fluctuating dipoles. A most remarkable characteristic of the van der Waals interaction is that the additivity of interactions approximately holds. The interaction energy between two particles in a vacuum may thus be calculated approximately by a summation (or by an integration) of the interaction energies for all molecular pairs formed by two molecules belonging to different particles [10, 11]. As a result, although the van der Waals interaction energy between two single molecules is small, the interaction energy between two particles consisting of many molecules can be large. In this chapter we start with the van der Waals interaction between two molecules and then we derive analytic expressions for the van der Waals interaction energy between two approaching particles of various geometries.

88.2 VAN DER WAALS INTERACTION BETWEEN TWO MOLECULES

The potential energy $u(r)$ of the van der Waals forces between two similar molecules at separation r between their centers in a vacuum is given by

$$u(r) = -\frac{C}{r^6} \tag{88.1}$$

with

$$C = \frac{3\alpha^2 h\nu}{4(4\pi\varepsilon_0)^2} \tag{88.2}$$

where C is called the *London–van der Waals constant*; α and ν are, respectively, the electronic polarizability and the characteristic frequency of the molecule; and h is the Planck constant. Thus $h\nu$ corresponds to the ionization energy of the molecule. Equation (88.1) holds when the intermolecular distance is shorter than the characteristic wavelength $2\pi/\nu$. At large distances $u(r)$ becomes proportional to $1/r^7$ instead of $1/r^6$ (retardation effect).

For two interacting dissimilar molecules 1 and 2, $u(r)$ is given by

$$u(r) = -\frac{C_{12}}{r^6} \tag{88.3}$$

with

$$C_{12} = \frac{3\alpha_1\alpha_2 h}{2(4\pi\varepsilon_0)^2}\left(\frac{\nu_1\nu_2}{\nu_1+\nu_2}\right) \tag{88.4}$$

Encyclopedia of Biocolloid and Biointerface Science, Volume 2, First Edition. Edited by Hiroyuki Ohshima.
© 2016 John Wiley & Sons, Inc. Published 2016 by John Wiley & Sons, Inc.

where α_i and ν_i are, respectively, the electronic polarizability and the characteristic frequency of molecule i ($i = 1,2$). To a good approximation, Eq. (88.4) may be replaced by

$$C_{12} \approx \frac{3\alpha_1\alpha_2 h\sqrt{\nu_1}\sqrt{\nu_2}}{4(4\pi\varepsilon_0)^2} = \sqrt{C_1}\sqrt{C_2} \tag{88.5}$$

with

$$C_1 = \frac{3\alpha_1^2 h\nu_1}{4(4\pi\varepsilon_0)^2},\ C_2 = \frac{3\alpha_2^2 h\nu_2}{4(4\pi\varepsilon_)^2} \tag{88.6}$$

88.3 VAN DER WAALS INTERACTION BETWEEN TWO COLLOIDAL PARTICLES

Since the additivity of the van der Waals interactions holds well, the interaction energy between two particles in a vacuum may thus be calculated approximately by a summation (or by an integration) of the interaction energies for all molecular pairs formed by two molecules belonging to different particles (Fig. 88.1).

In other words, the interaction energy V between two particles 1 and 2, containing N_1 and N_2 molecules per unit volume, respectively, can be obtained by integration of the interaction energy u between two volume elements dV_1 and dV_2 at separation r, containing $N_1 dV_1$ and $N_2 dV_2$ molecules, respectively, over the volumes V_1 and V_2 of particles 1 and 2:

$$V = \int_{V_1}\int_{V_2} u(r)N_1N_2 dV_1 dV_2 \tag{88.7}$$

As a result, although the van der Waals interaction energy between two single molecules is small, the interaction energy between two particles consisting of many molecules can be large.

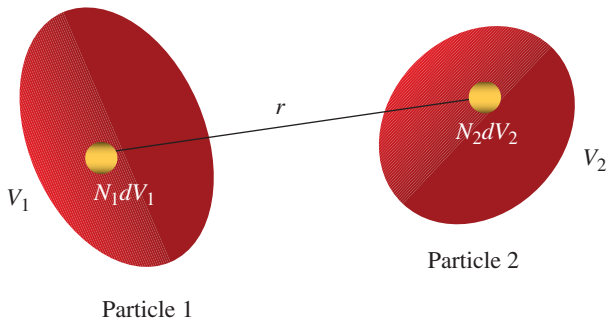


FIGURE 88.1 Integration of the interaction energy between two volume elements dV_1 and dV_2, containing N_1dV_1 and N_2dV_2 molecules, respectively, over the volumes V_1 and V_2 of particles 1 and 2.

88.4 VARIOUS GEOMETRIES

It is not always possible to calculate the van der Waals interaction energy on the basis of Eq. (88.7). In such cases, with the help of Derjaguin's approximation, one can calculate the interaction energy between two spheres or two cylinders of radii a_1 and a_2 at separation H between the closest distance between their surfaces by integrating the interaction energy between the corresponding two parallel plates [12–14]. This approximation holds good at small separations as compared with the particle size. It should also be mentioned that Derjaguin's approximation can be applied not only to the van der Waals interaction between colloidal particles but also to the electrostatic interaction between colloidal particles at small particle separations. Derjaguin's formulas are given here:

$$V_{sp}(H) = \frac{2\pi a_1 a_2}{a_1 + a_2}\int_H^\infty V_{p1}(h)dh \text{ for two spheres} \tag{88.8}$$

$$V_{cy//}(H) = \sqrt{\frac{2a_1a_2}{a_1+a_2}} \times \int_H^\infty V_{p1}(h)\frac{dh}{\sqrt{h-H}} \text{ for two parallel cylinders} \tag{88.9}$$

$$V_{cy\perp}(H) = 2\pi\sqrt{a_1a_2} \times \int_H^\infty V_{p1}(h)dh \text{ for two crossed cylinders} \tag{88.10}$$

We derive approximate analytic expressions for the van der Waals interaction energy between two particles directly on the basis of Eq. (88.7) or by using Derjaguin's approximation [Eqs. (88.8)–(88.10)] in the following sections.

88.4.1 A Molecule and a Plate

The interaction energy $V(h)$ between a pointlike molecule and an infinitely large plate of thickness d and molecular density N separated by a distance h in a vacuum can be calculated via Eq. (88.7) with the result that

$$V(h) = -\frac{\pi C_{12}N}{6}\left[\frac{1}{h^3} - \frac{1}{(h+d)^3}\right] \tag{88.11}$$

where C_{12} is the London–van der Waals constant for the interaction between the single molecule and a molecule within the sphere. In particular, as $d \to \infty$, Eq. (88.11) becomes

$$V(h) = -\frac{\pi C_{12}N}{6h^3} \tag{88.12}$$

which is the interaction energy between a molecule and an infinitely thick plate.

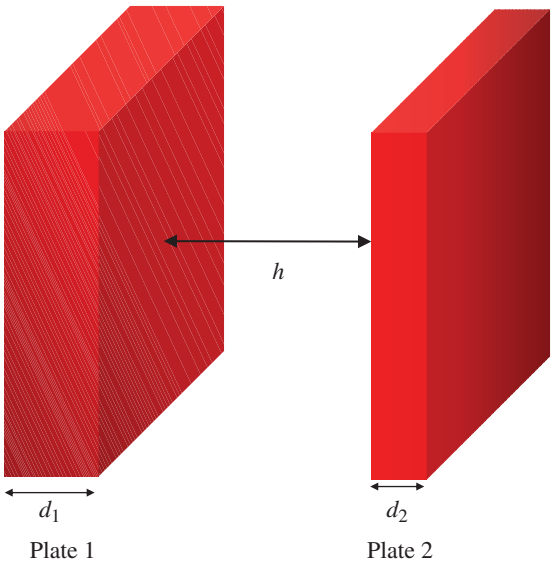


FIGURE 88.2 Two parallel plates of thicknesses d_1 and d_2 separated by a distance h.

88.4.2 Two Parallel Plates

For the interaction energy $V(h)$ per unit area between two parallel similar plates of thickness d separated by distance h between their surfaces in a vacuum (Fig. 88.2), from Eq. (88.7), we have

$$V(h) = -\frac{A}{12\pi}\left[\frac{1}{h^2} - \frac{2}{(h+d)^2} + \frac{1}{(h+2d)^2}\right] \tag{88.13}$$

where

$$A = \pi^2 C N^2 \tag{88.14}$$

is called the *Hamaker constant*.

Note that the Hamaker constant given by Eq. (88.11) can be applied to particles of arbitrary shape (plates, spheres, or cylinders).

Similarly, the interaction energy $V(h)$ between two parallel dissimilar plates 1 and 2 per unit area in a vacuum, which have molecular densities N_1 and N_2, London–van der Waals constants C_1 and C_2, and thicknesses d_1 and d_2, respectively is given by

$$V(h) = -\frac{A_{12}}{12\pi}\left[\frac{1}{h^2} - \frac{1}{(h+d_1)^2} - \frac{1}{(h+d_2)^2} + \frac{1}{(h+d_1+d_2)^2}\right] \tag{88.15}$$

with

$$A_{12} = \sqrt{A_1}\sqrt{A_2} = \pi\sqrt{C_1}\sqrt{C_2}N_1N_2,\ A_1 = \pi^2 C_1 N_1^2,\ A_2 = \pi^2 C_2 N_2^2 \tag{88.16}$$

where A_i is the Hamaker constant for the interaction between similar particles of substance i ($i = 1,2$) and A_{12} is that for dissimilar particles of substances 1 and 2. Equation (88.16) follows from approximate Eq. (88.5).

For small h ($h \ll d_1, d_2$), Eq. (88.15) tends to

$$V(h) = -\frac{A_{12}}{12\pi h^2} \tag{88.17}$$

which is the interaction energy between two infinitely thick plates 1 and 2.

88.4.3 A Molecule and a Sphere

The interaction energy $V(R)$ between a single molecule and a sphere of radius a and molecular density N separated by a distance R between their centers can be calculated via Eq. (88.7) to give

$$V(R) = -\frac{4\pi C_{12} N}{3}\frac{a^3}{(R^2 - a^2)^3} \tag{88.18}$$

where C_{12} is the London–van der Waals constant for the interaction between the single molecule and a molecule within the sphere.

88.4.4 Two Spheres

The interaction energy $V(R)$ between two dissimilar spheres 1 and 2, having radii a_1 and a_2, respectively, separated by a distance R between their centers (Fig. 88.3) can be calculated via Eq. (88.7) to give

$$V(R) = -\frac{A_{12}}{6}\left\{\frac{2a_1a_2}{R^2 - (a_1+a_2)^2} + \frac{2a_1a_2}{R^2 - (a_1-a_2)^2} + \ln\left[\frac{R^2 - (a_1+a_2)^2}{R^2 - (a_1-a_2)^2}\right]\right\} \tag{88.19}$$

where A_{12} is given by Eq. (88.16).

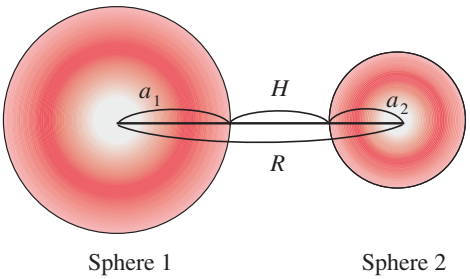


FIGURE 88.3 Two spheres of radii a_1 and a_2 separated by a distance R between their centers.

For the special case of two identical spheres ($a_1 = a_2 = a$, $C_1 = C_2 = C$, and $N_1 = N_2 = N$), Eq. (88.19) becomes

$$V(R) = -\frac{A}{6}\left\{\frac{2a^2}{R^2 - 4a^2} + \frac{2a^2}{R^2} + \ln\left(1 - \frac{4a^2}{R^2}\right)\right\} \quad (88.20)$$

where A is given by Eq. (88.14).

For small H ($H \ll a_1, a_2$), Eq. (88.20) tends to

$$V(H) = -\frac{A_{12}a_1a_2}{6(a_1 + a_2)H} \quad (88.21)$$

with

$$H = R - (a_1 + a_2) \quad (88.22)$$

where H is the closest distance between the surfaces of two spheres 1 and 2. For the special case of two identical spheres, Eq. (88.21) gives

$$V(H) = -\frac{Aa}{12H} \quad (88.23)$$

Equation (88.21) can also be obtained with the help of Derjaguin's approximation, that is, by substituting Eq. (88.17) into Eq. (88.8).

The interaction energy between two dissimilar shells separated by R, having outer radius a and thicknesses d (Fig. 88.4) can be calculated by

$$V(R) = V(a, a, R) - 2V(a, a - d, R) + V(a - d, a - d, R) \quad (88.24)$$

where $V(a_1, a_2, R)$ is given by Eq. (88.19).

88.4.5 A Molecule and a Rod

The interaction energy between a pointlike molecule and an infinitely long thin rod carrying the line density N of molecules along the rod separated by a distance R can be calculated via Eq. (88.7) to give

$$V(R) = -\frac{3\pi NC_{12}}{8R^5} \quad (88.25)$$

where C_{12} is the corresponding London–van der Waals constant for the interaction energy between the single molecule and a molecule within the rod.

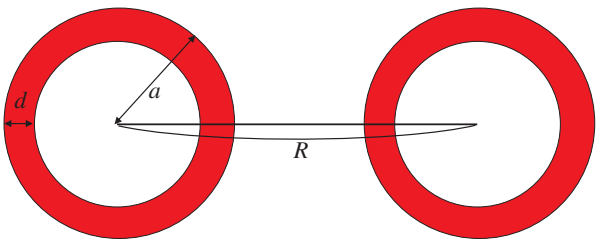


FIGURE 88.4 Interaction between two shells of outer radius a and thickness d separated by a distance R between their centers.

88.4.6 Two Parallel Rods

The interaction energy $V(R)$ per unit length between two dissimilar thin rods 1 and 2, having molecular densities N_1 and N_2, respectively, separated by a distance R between their axes can be calculated via Eq. (88.7) to give

$$V(R) = -\frac{3\pi N_1N_2C_{12}}{8R^5} \quad (88.26)$$

88.4.7 A Molecule and a Cylinder

The interaction energy $V(R)$ between a single molecule and an infinitely long cylinder of radius a and molecular density N separated by a distance R can be calculated via Eq. (88.7) to give [15]

$$V(R) = -\frac{3\pi^2C_{12}Na^2}{8R^5}F\left(\frac{5}{2}, \frac{5}{2}, 2; \left(\frac{a}{R}\right)^2\right) \quad (88.27)$$

with

$$F(\alpha, \beta, \gamma, z) = \frac{\Gamma(\gamma)}{\Gamma(\alpha)\Gamma(\beta)}\sum_{n=0}^{\infty}\frac{\Gamma(\alpha + n)\Gamma(\beta + n)z^n}{\Gamma(\gamma + n)n!} \quad (88.28)$$

where $F(\alpha, \beta, \gamma; x)$ is the *hypergeometric* function and C_{12} is the corresponding London–van der Waals constant.

88.4.8 Two Parallel Cylinders

The interaction energy $V(R)$ per unit length between two parallel dissimilar cylinders 1 and 2, having radii a_1 and a_2, molecular densities N_1 and N_2, respectively, separated by a distance R between their axes (Fig. 88.5), can be calculated via Eq. (88.7) to give [15]

$$V(R) = -\frac{2A_{12}}{3R}\sum_{m=0}^{\infty}\sum_{n=0}^{\infty}\frac{\Gamma^2(m + n + 1/2)}{m!n!(m - 1)!(n - 1)!} \times \left(\frac{a_1}{R}\right)^{2m}\left(\frac{a_2}{R}\right)^{2n} \quad (88.29)$$

where A_{12} is given by Eq. (88,16).

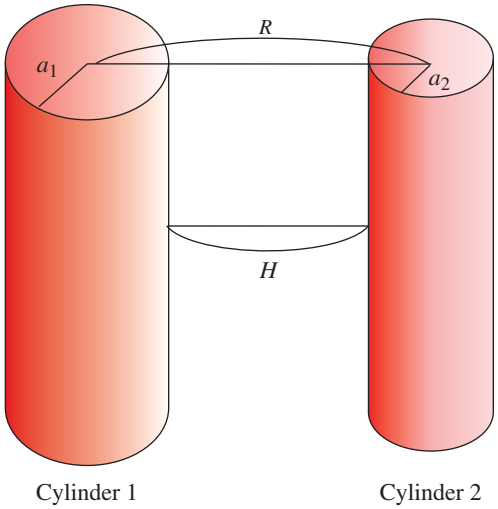


FIGURE 88.5 Two parallel cylinders of radii a_1 and a_2 separated by a distance H.

For the special case of two identical cylinders ($a_1 = a_2 = a$, $C_1 = C_2 = C$, $N_1 = N_2 = N$, and $A_{12} = A$), Eq. (88.29) becomes

$$V(R) = -\frac{2A}{3R}\sum_{m=0}^{\infty}\sum_{n=0}^{\infty}\frac{\Gamma^2(m+n+1/2)}{m!n!(m-1)!(n-1)!}\left(\frac{a}{R}\right)^{2(m+n)} \tag{88.30}$$

where A is given by Eq. (88.14).

For small $H = R - (a_1 + a_2)$ ($H \ll a_1$ and a_2), Eq. (88.29) tends to

$$V(H) = -\frac{A_{12}}{12\sqrt{2}H^{3/2}}\left(\frac{a_1 a_2}{a_1 + a_2}\right)^{1/2} \tag{88.31}$$

For the special case of two identical cylinders per unit length, Eq. (88.31) gives

$$V(H) = -\frac{A\sqrt{a}}{24H^{3/2}} \tag{88.32}$$

Equation (88.31) can also be obtained with the help of Derjaguin's approximation, that is, by substituting Eq. (88.17) into Eq. (88.9).

88.4.9 Two Crossed Cylinders

With the help of Derjaguin's approximation, one can derive the van der Waals interaction energy between two crossed cylinders of radii a_1 and a_2 at separation H between their surfaces (Fig. 88.6).

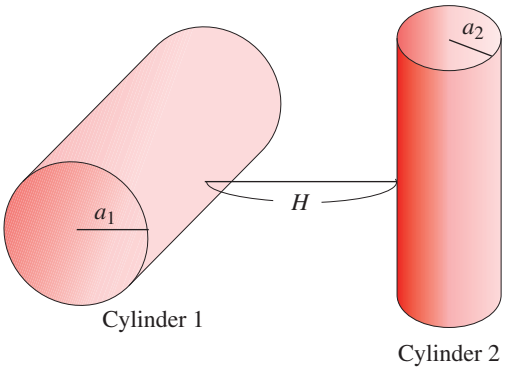


FIGURE 88.6 Two crossed cylinders of radii a_1 and a_2 separated by a distance H.

By substituting Eq. (88.17) into Eq. (88.10), we obtain

$$V(H) = -\frac{A\sqrt{a_1 a_2}}{6H} \tag{88.33}$$

which is applicable for small H ($H \ll a_1, a_2$).

88.4.10 Two Parallel Rings

Consider two parallel rings 1 and 2 of radii r_1 and r_2, respectively, separated by a distance h. The two rings are of the same substance. Let $\tilde{N}$ be the number of molecules on each ring; that is, let $\tilde{N}$ be the line density of molecules on each ring. For the interaction energy between rings 1 and 2, we thus obtain

$$V(r_1, r_2, h) = -\frac{4\pi^2 C\tilde{N}^2 r_1 r_2\left[\left\{h^2 + (r_1 + r_2)^2\right\}\left\{h^2 + (r_1 - r_2)^2\right\} + 6r_1^2 r_2^2\right]}{\left[h^2 + (r_1 + r_2)^2\right]^{5/2}\left[h^2 + (r_1 - r_2)^2\right]^{5/2}} \tag{88.34}$$

Note that for two identical parallel rings ($r_1 = r_2 = r$) in the limit of very small h, Eq. (88.34) becomes

$$V(r_1, r_2, h) = -\frac{3\pi C\tilde{N}^2}{8h^5}\cdot 2\pi r \tag{88.35}$$

It is interesting to note that Eq. (88.35) agrees with the energy between two parallel rods of length $2\pi r$ carrying molecules of line density $\tilde{N}$.

88.4.11 Two Parallel Torus-Shaped Particles

A torus-shaped particle can serve as a model for biocolloids such as biconcave human red blood cells. The interaction between two parallel biconcave-shaped red blood cells can be

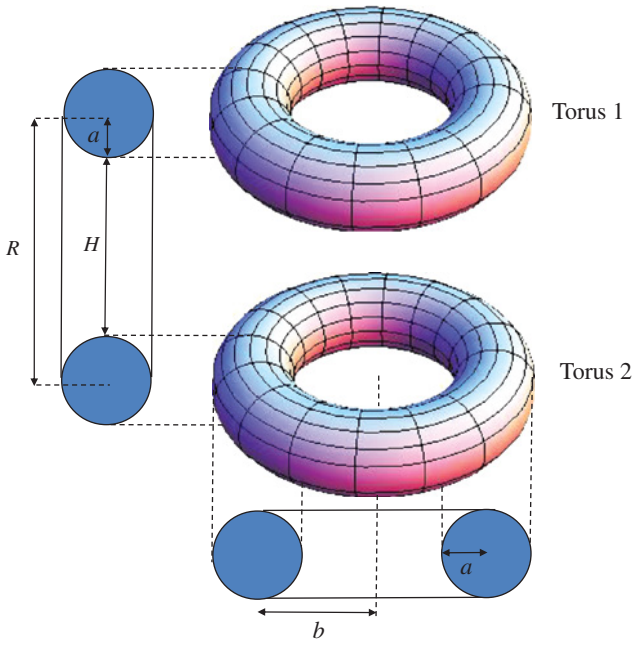


FIGURE 88.7 Two parallel torus-shaped particles at separation R between their centers, where a is the radius of the tube and b is the distance from the center of the tube to the center of the torus. (From Ref. 16.)

approximated by the interaction between two parallel torus-shaped particles.

Consider two parallel similar torus-shaped particles at separation R between their centers (Fig. 88.7) [16].

A torus can be constructed by joining the ends of a cylindrical tube. We denote the radius of the tube by a and the distance from the center of the tube to the center of the torus by b. The length of the cylindrical tube is thus $2\pi b$, and the closest distance H between the surfaces of these tori is $H = R - 2a$. Let N be the number of molecules contained within the particles. The interaction energy $V(R)$ between two parallel tori can be calculated with the help of Eq. (88.34), as

$$V(R) = -4A \int_{\rho_1=0}^{a} \int_{\rho_2=0}^{a} \int_{\phi_1=0}^{2\pi} \int_{\phi_2=0}^{2\pi} \left(\frac{r_1 r_2 \left[\{h^2 + (r_1 + r_2)^2\} \{h^2 + (r_1 - r_2)^2\} + 6r_1^2 r_2^2 \right]}{\left[h^2 + (r_1 + r_2)^2\right]^{5/2} \left[h^2 + (r_1 - r_2)^2\right]^{5/2}} \right) \times \rho_1 \rho_2 d\rho_1 d\rho_2 d\phi_1 d\phi_2 \tag{88.36}$$

with

$$r_1 = b - \rho_1 \cos\phi_1 \tag{88.37}$$

$$r_2 = b - \rho_2 \cos\phi_2 \tag{88.38}$$

$$h = R + \rho_1 \sin\phi_1 - \rho_2 \sin\phi_2 \tag{88.39}$$

As is well known, a torus and the corresponding cylindrical tube of radius a and length $2\pi b$ have the same surface area $(2\pi a \cdot 2\pi b)$ and interior volume $(\pi a^2 \cdot 2\pi b)$ (the Pappus–Guldinus theorem). Therefore, the interaction energy between two parallel tori is expected to be close to that between the corresponding two parallel cylinders. It follows from Eq. (88.36) that the interaction energy $V(R)$ between two parallel similar cylinders of radius a and length $2\pi b$ is given by

$$V(R) = -\frac{2A}{3R} \sum_{m=0}^{\infty} \sum_{n=0}^{\infty} \frac{\Gamma^2(n + m + 1/2)}{m!n!(m-1)!(n-1)!} \left(\frac{a}{R}\right)^{2(m+n)} \times 2\pi b \tag{88.40}$$

For small $H/a < 2$, Eqs. (88.36) and (88.40) give results very close to each other. Indeed, in the limit of small H/a, Eqs. (88.36) and (88.40) both tend to the same limiting value

$$V(R) = -\frac{A\sqrt{a}}{24H^{3/2}} \times 2\pi b \tag{88.41}$$

which also agrees with the results obtained by applying Derjaguin's approximation to the interaction between two parallel cylinders.

88.4.12 Two Particles Immersed in a Medium

The expressions for the interactions between particles derived in this chapter so far are based on the assumption that the interacting particles are interacting in a vacuum. If the medium between the particles is no longer a vacuum, but a second substance (e.g., water), we have to account for the fact that each particle replaces an equal volume of water. It follows from the assumption of the additivity of the van der Waals interaction energies that the Hamaker constant A_{132} for the interaction two different particles of substances 1 and 2 immersed in a medium of substance 3 is

$$A_{132} = \left(\sqrt{A_1} - \sqrt{A_3}\right)\left(\sqrt{A_2} - \sqrt{A_3}\right) \tag{88.42}$$

$$|A_{132}| = \sqrt{A_{131}}\sqrt{A_{232}} \tag{88.43}$$

where A_1 and A_2 are, respectively, the interactions between two similar particles of substances 1 and 2 immersed in a vacuum. In particular, the Hamaker constant for the interaction two similar particles of substance 1 immersed in a medium of substance 3 is

$$A_{131} = \left(\sqrt{A_1} - \sqrt{A_3}\right)^2 \tag{88.44}$$

Note that while A_{131} is always positive, A_{132} may be positive or negative depending the relative magnitudes of A_1, A_2, and

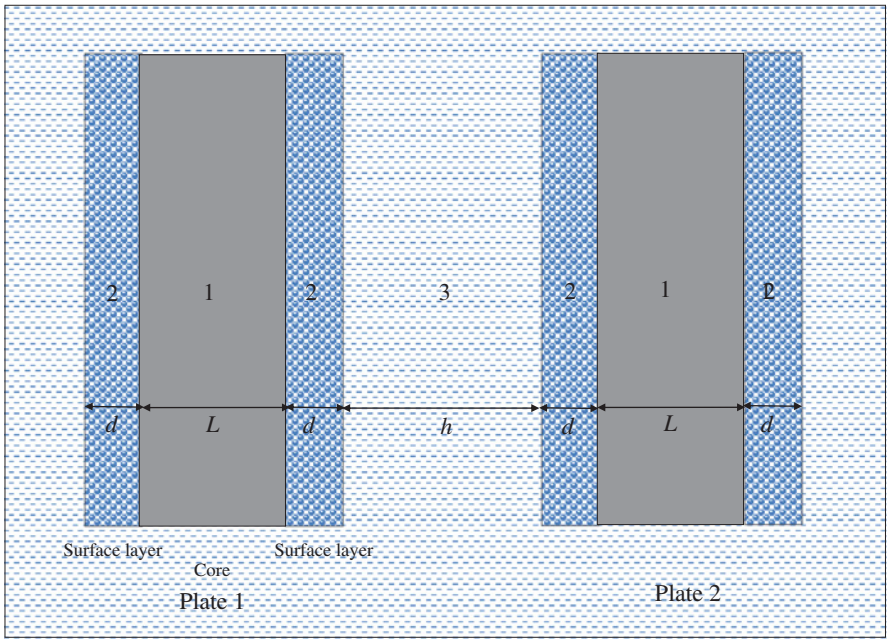


FIGURE 88.8 Two similar parallel plates of substance 1 and thickness L covered by a surface layer of substance 2 and thickness d separated at a separation h in a medium 3.

A_3. Thus, if two particles of substances 1 and 2 are interacting in medium 3, then A_{12} appearing in the expressions given in previous sections must be replaced by A_{132}.

88.4.13 Two Parallel Plates Covered with Surface Layers

It is possible to derive the interaction energy between particles with multilayer structures [8, 16, 17]. Consider the interaction between two parallel similar plates separated by a distance h (Fig. 88.8).

Let the thicknesses of the plate core and the surface layer be L and d, respectively. The interaction energy per unit area between the plates is thus given by

$$V(h) = -\frac{1}{12\pi}\left[\frac{A_{232}}{h^2} - \frac{2A_{123}}{(h+d)^2} + \frac{A_{121}}{(h+2d)^2} + \frac{2A_{123}}{(h+d+L)^2} - \frac{2(A_{232}+A_{121})}{(h+d+L)^2} + \frac{A_{121}}{(h+2d+2L)^2} + \frac{2A_{123}}{(h+3d+L)^2} - \frac{2A_{123}}{(h+3d+2L)^2} + \frac{A_{232}}{(h+4d+2L)^2}\right] \tag{88.45}$$

For very small h ($h \ll d$ and $h \ll L$), Eq. (88.45) becomes an expression of the interaction energy between the two surface layers of substance 2 in a medium 3:

$$V(h) = -\frac{A_{232}}{12\pi h^2} \tag{88.46}$$

For large h such that $L \gg h \gg d$, on the other hand, Eq. (88.45) approaches the interaction between the two plate cores of substance 1 in a medium 3:

$$V(h) = -\frac{(A_{232} - 2A_{123} + A_{121})}{12\pi h^2} = -\frac{A_{131}}{12\pi h^2} \tag{88.47}$$

REFERENCES

[1] Derjaguin, B.V., Landau L.D. (1941). *Acta Physicochim.* **14**, 633.

[2] Verwey, E.J.W., Overbeek, J.Th.G. (1948). *Theory of the Stability of Lyophobic Colloids.* Elsevier/Academic Press, Amsterdam.

[3] Derjaguin, B.V. (1989). *Theory of Stability of Colloids and Thin Films*. Consultants Bureau, New York/London.

[4] Israelachvili, J.N. (1992). *Intermolecular and Surface Forces*, 2nd ed. Academic Press, New York.

[5] Lyklema, J. (1955). *Fundamentals of Interface and Colloid Science, Solid-Liquid Interfaces.* Academic Press, New York, Vol. 2.

[6] Ohshima, H. (1998). In Ohshima, H., Furusawa, K. (eds.) (1998). *Electrical Phenomena at Interfaces: Fundamentals, Measurements, and Applications*, 2nd ed. (revised and expanded). Marcel Dekker, New York, Chapter 3.

[7] Tadros, Th.F. (ed.) (2007). *Colloid Stability, The Role of Surface Forces—Part 1*. Wiley-VCH, Weinheim.

[8] Ohshima, H. (2010). *Biophysical Chemistry of Biointerfaces*. Wiley, Hoboken, NJ.

[9] Ohshima, H. (ed.) (2012). *Electrical Phenomena at Interfaces and Biointerfaces: Fundamentals and Applications in Nano-, Bio- and Environmental Sciences*. Wiley, Hoboken, NJ.

[10] Hamaker, H.C. (1937). *Physica* **4**, 1058.

[11] Langbein, D. (1974). *Theory of van der Waals Attraction*. Springer, Berlin.

[12] Derjaguin, B.V. (1934). *Kolloid Z.* **69**, 155.

[13] Sparnaay, M.J. (1959). *Recueil* **78**, 680.

[14] Ohshima, H., Hyono, A. (2009). *J. Colloid Interface Sci.* **333**, 202.

[15] Kirsch, V.A. (2003). *Adv. Colloid Interface Sci.* **104**, 311.

[16] Ohshima, H., Hyono, A. (2009). *J. Colloid Interface Sci.* **332**, 251.

[17] Vold, M.J.J. (1961). *Colloid Sci.* **16**, 1.

[18] Vincent, B. (1973). *J. Colloid Interface Sci.* **42**, 270.

89

WORMLIKE MICELLES WITH NONIONIC SURFACTANTS

Rekha Goswami Shrestha,[1,3] Kenji Aramaki,[2] Hideki Sakai,[1] and Masahiko Abe[1]

[1]*Department of Pure and Applied Chemistry, Faculty of Science and Technology, Tokyo University of Science, 2641 Yamazaki, Noda, Chiba 278-8510, Japan*

[2]*Graduate School of Environment and Information Sciences, Yokohama National University, Tokiwadai 79-7, Hodogaya-ku, Yokohama 240-8501, Japan*

[3]*Nano-Functionality Integration Group, Nano Functionality Integration Group, National Institute of Material Science, Tsukuba, Sengen, 305-0047, Japan*

89.1 INTRODUCTION

In 1913, J.W. McBain [1] proposed the idea of self-assembled aggregates in aqueous solution. The amphiphilic molecules have the remarkable ability to form a variety of self-assembled structures in aqueous or nonaqueous media depending on composition and temperature such as micelles, liquid crystals, and vesicles. The thermodynamics of the micelle would reflect a balance of repulsive interaction between the surfactant headgroups and van der Waals's attractive forces between the hydrocarbon tails [2, 3]. At any local packing environment, the packing free energy per molecule f is the sum of the average interaction (steric and/or electrostatic) energy per molecule resulting from headgroup repulsion f_h, the surface energy associated with the hydrocarbon–water interface f_s and the chain (hydrocarbon tail) contribution to the free energy f_t as follows;

$$f = f_h + f_s + f_t \tag{89.1}$$

All three terms, f_h, f_s, and f_t, depend on the average cross-sectional area per molecule at the interface a_s, and on the local interfacial curvatures [4]. The geometry of the aggregates formed may be predicted by the critical packing parameter (CPP) of an amphiphilic molecule, CPP = $v/a_s l_c$, where v is the volume of the lipophilic chain having maximum effective length l_c and a_s. Generally, hydrophilic amphiphiles having large headgroups self-assemble into spherical micelles (CPP $\leq 1/3$) in a dilute aqueous region. A reduction in a_s, namely, an increase in CPP, tends to induce micellar growth. The spherical micelles often undergo 1D growth to form long, linear cylindrical micelles on change in the concentration or temperature, on the addition of salt, or in the presence of specific counterions. These cylindrical micelles, which are commonly modeled as rods, consist of a cylindrical body and two hemispherical endcaps [5.6]; both the body and the endcaps have the same diameter; however, some theoretical [7,8] and experimental [9,10] evidence suggests that the endcaps actually have a larger diameter than the cylindrical body. The molecules packed at the hemispherical ends have excess free energy, called the *endcap energy*, and a thermodynamic driving force for the linear growth [11]. They can reach a few nanometers to micrometers in length. When the number density of these long aggregates exceeds a certain threshold value, they entangle with each other to form a transient network called *wormlike micelles* or *giant micelles* [12], which exhibit viscoelastic properties.

When the equilibrium condition for a wormlike micellar system is disturbed, it tries to relax and restore the equilibrium condition within a definite time τ_R. A system that deforms faster than it relaxes exhibits an elastic property characteristic of a solid material with a Hookean constant G_0, called the *shear modulus*. For a slow deformation, the stress imposed on the system dissipates easily, and behaves as a viscous fluid with a zero-shear viscosity η_0. In many cases, there is only one characteristic relaxation time for wormlike

Encyclopedia of Biocolloid and Biointerface Science, Volume 2, First Edition. Edited by Hiroyuki Ohshima.
© 2016 John Wiley & Sons, Inc. Published 2016 by John Wiley & Sons, Inc.

micellar systems; in such cases the rheological properties can be interpreted in terms of the Maxwell model of a viscoelastic fluid [13, 14], consisting of an elastic spring with the Hookean constant G_0 and a dashpot with viscosity η_0. The variation of elastic (storage) modulus (G') and viscous (loss) modulus (G'') with shear frequency ω is given by the equations

$$G'(\omega) = \frac{\omega^2 \tau_R^2}{1 + \omega^2 \tau_R^2} G_0 \tag{89.2}$$

$$G''(\omega) = \frac{\omega \tau_R}{1 + \omega^2 \tau_R^2} G_0 \tag{89.3}$$

where τ_R is the Maxwelllian relaxation time. As may be evident from the equations, in the low-frequency region, $\omega \ll \omega_c$, G' and G'' scale with ω according to $G' \propto \omega^2$ and $G'' \propto \omega$. In the high-frequency region, or more specifically, in the region of $\omega \ll \omega_c$, however, G' attains a plateau value equal to G_0, whereas G'' shows a monotonic decrease. The shear frequency corresponding to $G' - G''$ crossover is $\omega_c = 1/\tau_R$. For wormlike micellar solutions, the τ_R and G_0 gives information about average micellar length and the number density of the entanglements in the transient network, respectively. A $G'(\omega)$ versus $G''(\omega)$ (Cole–Cole) plot would give a semicircle for Maxwellian behavior. The terms G_0, τ_R, and η_0 are related as follows:

$$\eta_0 = G_0 \tau_R \tag{89.4}$$

Alternately, the following relationship allows one to estimate η_0 by extrapolating the complex viscosity values ($|\eta^*|$) to zero-shear frequency:

$$|\eta^*| = \frac{(G'^2 + G''^2)^{1/2}}{\omega} = \frac{\eta_0}{\sqrt{1 + \omega^2 \tau_R^2}} \tag{89.5}$$

The wormlike micelles are often called *living polymers* as they break and re-form spontaneously, and their molecular weight fluctuates with time [15], unlike the conventional polymers, where the covalently bonded repeat units maintain constant molecular weight. The mean field model developed by M. Cates and coworkers [16–18], has shown that the viscoelastic behavior for wormlike micelles consists in two processes: reptation (reptilelike motion of the micelle along its own contour) and reversible scission of micelles, taking place at two timescales, namely, reptation time τ_{rep} and breaking time τ_b. It is assumed that when a chain breaks, the two resulting chains become uncorrelated and recombine with the micellar end in a random way. For fast scission kinetics ($\tau_b \ll \tau_{rep}$), a single-exponential stress decay is observed, and the viscoelastic behavior of such systems in the low-frequency region follows the Maxwell model with a single relaxation time τ_R, given by $(\tau_b . \tau_{rep})^{1/2}$. Although the Maxwell equations predict a monotonic decrease of G'' in the high-frequency region, wormlike micelles usually deviate from this behavior, showing an increase of G'' in the high-frequency region and a deviation from the semicircle predicted by the Maxwell model in the G'' versus G' (Cole–Cole) plot. This deviation is often associated with the stress relaxation by additional "faster" processes such as Rouse modes of cylindrical micelles, analogous to polymer chains. The minimum value of G'' in the high-frequency region is related to L according to the relation.

$$\frac{G_{min}}{G_0} \approx \frac{l_e}{L} \tag{89.6}$$

where l_e is the entanglement length, that is, the contour length of the section of wormlike micelles between two entanglement points. For flexible micelles, the correlation length ξ, which gives the mesh size of the micellar network, is related to l_e according to

$$l_e = \xi^{5/3} / l_p^{2/3} \tag{89.7}$$

The persistence length l_p provides an estimate of micellar flexibility. Even though the micelles are flexible, at a small length scale (comparable to l_p), they behave as rigid rods. The correlation length ξ is related to T and G_0 as follows:

$$\xi \approx \left(\frac{kT}{G_0} \right)^{1/3} \tag{89.8}$$

The combination of Eqs. (89.7) and (89.8) yields an equation that relates l_e to G_0 as follows:

$$G_0 \approx \frac{kT}{l_e^{9/5} l_p^{6/5}} \tag{89.9}$$

For $\tau_b \ll \tau_{rep}$, the living-polymer model predicts the following scaling laws for the viscoelastic parameters [19]: $G_0 \approx \phi^{2.25}$, $\tau_R \approx \phi^{1.25}$, $\eta_0 \approx \phi^{3.5}$, and $\frac{G_{min}}{G_0} \approx \phi^{-1.75}$. When $\tau_b \gg \tau_{rep}$, the micelles behave like ordinary polydisperse unbreakable polymers, and the stress–relaxation function is strongly nonexponential. For neutral or highly screened ionic micelles [20], the zero-shear viscosity scales as $\eta_0 \propto \phi^{5.25}$. For branched or interconnected micelles, the exponents of the scaling laws are significantly different [21, 22]. For a saturated interconnected network, $G''_{min}/G_0 \ \phi^{-0.75}$ has been proposed [23].

Analysis of small-angle scattering data using indirect Fourier transformation (IFT) followed by deconvolution [24–26] allows us to extract information about the shape and internal structure of the aggregate without having an a

priori assumption of the model. An brief description of the principle involved is presented here.

The overall scattering intensity $I(q)$ for the systems of monodisperse spherical particles is given by

$$I(q) = nP(q)S(q) \tag{89.10}$$

where $P(q)$ is the intraparticle contribution, known as the *form factor*, and $S(q)$ is the interparticle contribution or structure factor. When the system is sufficiently dilute, $S(q) \approx 1$, the spatially averaged $I(q)$, is given by

$$I(q) = 4\pi \int_0^\infty p(r) \frac{\sin(qr)}{qr} dr \tag{89.11}$$

where $p(r)$ is the pair distance distribution function (PDDF), which provides the overall information about the shape and of the scattering particles such as micellar aggregates. The Fourier transform of $p(r)$ gives $P(q)$. The PDDF for a particle of an arbitrary shape with a scattering density difference of $\Delta\rho(r)$ is given by

$$p(r) = r^2 \Delta\tilde{\rho}^2(r) \tag{89.12}$$

where $\Delta\tilde{\rho}^2(r)$ is the convolution square of $\Delta\rho(r)$ averaged for all directions in space. The form factor and the structure factor can be determined by the *generalized indirect Fourier transformation* (GIFT) technique [27–29] simultaneously from the scattering data without any assumption for the form factor, whereas we need appropriate assumptions for the interparticle interaction potential for the structure factor. A hard-sphere interaction model is the common choice. The detailed theoretical description on the method has been reported elsewhere. Note that when particle geometry deviates from an ideal spherical symmetry, the output parameters from $S(q)$ analysis are no longer exact. Nevertheless, the GIFT approach efficiently suppresses the influence of the interparticle interference scattering in the calculation of $p(r)$ and allows us to deduce a sufficiently reliable $p(r)$ value.Wormlike micelle systems are most commonly reported in ionic surfactants, especially with cationic surfactants with long hydrophobic chain (C16 or longer) induced by adding salts, strongly binding counterions or cosurfactants [30–39]. Ionic surfactants, however, are sometimes undesirable for commercial products, because of their toxicity and sensitivity to electrolytes. Growing environmental awareness has prompted the search for nontoxic and biodegradable nonionic surfactants from renewable sources for the formation of wormlike micelles. Therefore, it is important to understand the underlying basic principle of the formation and rheological properties of nonionic systems and have novel insight into the thermodynamics of micellar growth.

89.2 WORMLIKE MICELLES IN NONIONIC SURFACTANTS

Nonionic surfactant solutions can undergo temperature- or concentration-induced micellar growth through adequate modulation of the specific surface area and interfacial curvature [40–42]. Fluorocarbon surfactants show high hydrophobicity and CMC lower than the hydrocarbon surfactants of similar chain length, high electronegativity, relatively large van der Waals radius, and less conformational freedom that produce bulky and stiff chains with their skeletons covered by a dense electron-rich environment. The resulting high cohesive energy facilitates a more dense packing at the interface, that is, small interfacial areas per molecule, which favors micellar growth. The compound $C_8F_{17}SO_2(C_3H_7)N(CH_2CH_2)_{10}H$ (Fig. 89.1a) is one of the nonionic fluorocarbon surfactants that shows interesting phase behavior [43]. It forms a micellar solution over a wide range of compositions (up to 38 wt% at 5°C) at low temperature. Hexagonal (H_1), bicontinuous cubic (V_1), and lamellar (L_α) liquid crystalline phases are formed successively with an increase in surfactant concentration. Micellar solutions at low temperature transforms into highly viscous solutions with increasing surfactant concentration. Small-angle X-ray scattering (SAXS) patterns show a broad scattering band, ruling out the possibility of the presence of an isotropic micellar cubic phase. With increasing temperature, the viscosity of the solution gradually decreases, and ultimately, a less viscous easily flowing isotropic solution is formed. At higher temperatures, clouding behavior is observed.

Figure 89.1b shows the variation of η_0 of $C_8F_{17}EO_{10}$ with concentration. The low surface area of fluorinated surfactant favors micellar growth and an onset of the overlapping of wormlike micelle leading to η_0 increase even at low concentration; the η_0 of 2 wt% $C_8F_{17}EO_{10}/H_2O$ is $\sim$ 4 orders of magnitude that of water. With further increase in concentration, the viscosity shows a maximum and then decreases. The η_0 versus temperature curves (Fig. 89.1c) for concentrations between 1 and 7 wt% also show a maximum. The η_0 of 1 wt% $C_8F_{17}EO_{10}/H_2O$ increases by ~ 2 orders of magnitude on increasing temperature from 5°C to 35°C. The temperature for viscosity maximum ($T_{\eta\text{-max}}$) shifts to lower values with increasing surfactant concentration. The viscosity of the micellar solution is very sensitive to the concentration at low temperatures, but at and above 25°C, the viscosity is nearly the same over a wide range of concentrations (2–25 wt%). At high surfactant concentration, the degree of hydration of the EO chain decreases. This reduces the specific surface area and increases aggregation numbers, inducing decrease in the spontaneous curvature of the aggregate and favoring 1D micellar growth increasing the viscosity. With an increase in concentration, the formation of micellar joints with faster relaxation is expected to take place at lower temperatures,

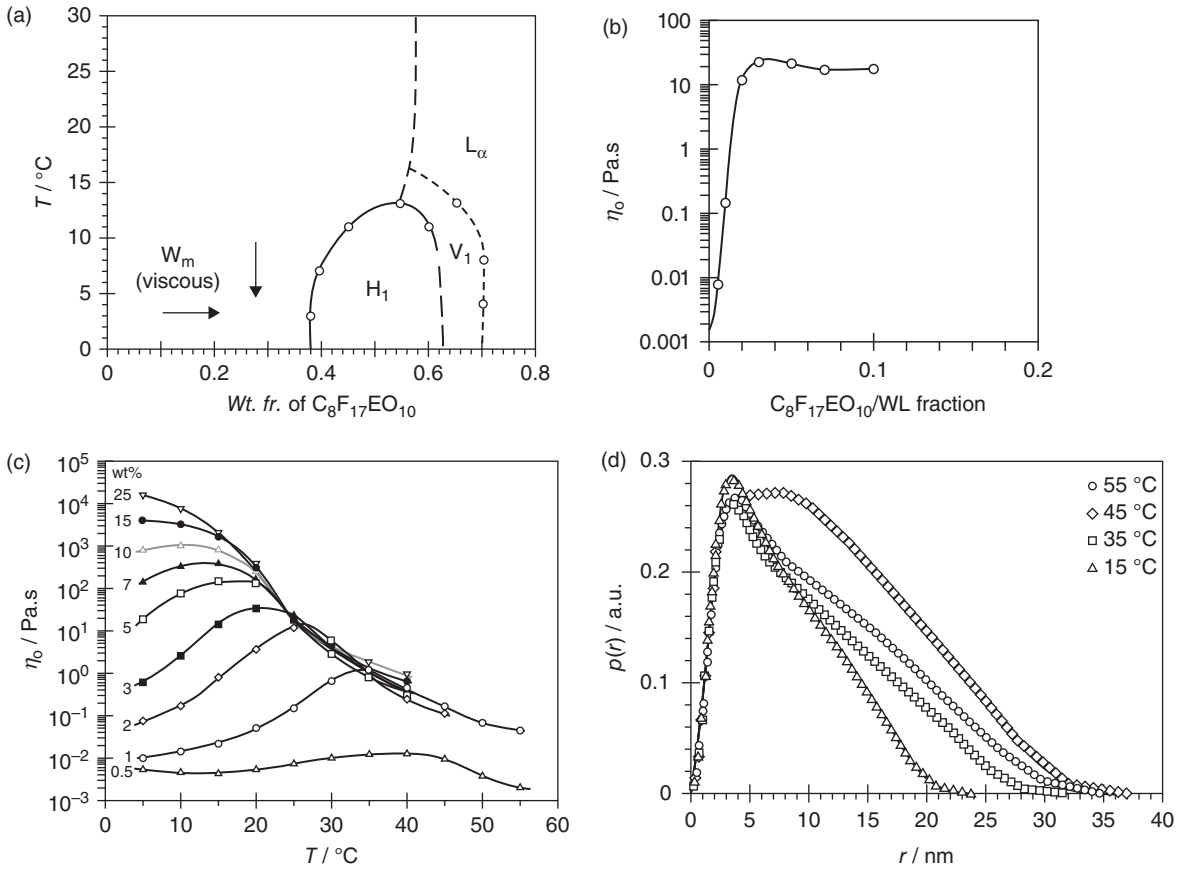


FIGURE 89.1 (a) Partial phase diagram of $C_8F_{17}EO_{10}/H_2O$ binary system; W_m, H_1, V_1, and L_α stand for micellar, hexagonal, bicontinuous cubic, and lamellar liquid crystalline phases, respectively. The arrows in the W_m domain show the direction of the viscosity increase for the systems at surfactant concentration of 15 wt% and above. At lower concentrations, viscosity increases and then decreases with increasing temperature. (b) Variation of η_0 with $C_8F_{17}EO_{10}$ concentration in water at 25°C. (c) Variation of zero-shear viscosity (η_0) as a function of temperature at different concentrations (in wt%) of $C_8F_{17}EO_{10}$ in water. (d) Pair distance distribution function, $p(r)$ of 1 wt% $C_8F_{17}EO_{10}$/ H_2O binary system at different temperatures. (Panels (a), (c), and (d) reprinted from Acharya et al. 2006 [43], pp. 20224–20234; reproduced with permission of the American Chemical Society. Panel (b) reprinted from Sharma et al. 2007 [47], p. 223; reproduced with permission of Elsevier.)

which can explain the gradual shift of $T_{\eta\text{-max}}$ toward lower temperatures.

Figure 89.1d shows the $p(r)$ curves of 1 wt% $C_8F_{17}EO_{10}/H_2O$ solutions with increasing temperature. The local maximum and minimum in the $p(r)$ function in the low r region arise from the productive contribution of the negative and positive electron densities from the hydrophobic core and hydrophilic shell, respectively. The value of r corresponding to the maximum inflexion after the second maxima of the $p(r)$ function gives the cross-sectional diameter of cylindrical aggregate, including the headgroup. The $p(r)$ plots at 15°C, 35°C, and 45°C are typical of rodlike particles. The D_{max} increases with increasing temperature, while the cylindrical cross-sectional diameter of the aggregates remains almost constant (≈ 5.8 nm). It should be noted that the D_{max} measured is not the actual length of the micelles as it is biased by the maximum resolution (or q_{min}) of the measurement. Nevertheless, the trend in the variation of D_{max} values as obtained here can be taken as the evidence of 1D micellar growth with increase in temperature. The 1D micellar growth seems to continue even above 35°C ($T_{\eta\text{-max}}$), until 55°C. Importantly, there is a significant change in the pattern of $p(r)$ observed in the middle-r region, which suggests a gradual evolution of the local structure toward a lamellar pattern, with nil curvature and a packing parameter close to 1.

A more hydrophilic nonionic fluorinated surfactant, $C_8F_{17}EO_{20}$, forms isotropic micellar solution over a wide concentration range (~ 80 wt%) in water at 25°C [44]. However, it can form viscoelastic wormlike micelles only with a less hydrophilic cosurfactant, $C_8F_{17}EO_1$ [45], $C_8F_{17}EO_3$

[46], or $C_8F_{17}EO_{10}$ [47]. With successive addition of the cosurfactant, viscosity of aqueous micellar solution of $C_8F_{17}EO_{20}$ increases rapidly, reaches a maximum, and then decreases, and ultimately phase separation occurs. The viscosity increases by ~ 5 orders of magnitude that of pure water. It has been suggested that after the saturation of micellar growth, further addition of cosurfactant to the system results in the formation of joints that can slip along its length, thereby allowing a faster and easier way of stress relaxation [48,49] and causing a decrease in viscosity. There are reports on micellar connections or branching points [50, 51]. On the other hand, addition of perfluoropolyether oil, $(C_3F_6O)_nCOOH$, and perfluorodecalin oil, $C_{10}F_{18}$, to the viscoelastic solution of $C_8F_{17}EO_{20}/H_2O/C_8F_{17}EO_3$, decreases the viscosity until phase separation. Small-angle X-ray scattering (SAXS) measurements confirm that $C_8F_{17}EO_1$, $C_8F_{17}EO_3$, and $C_8F_{17}EO_{10}$ induced spherical–cylindrical while fluorinated oils, $(C_3F_6O)_nCOOH$ and $C_{10}F_{18}$ induced wormlike–sphere micellar transition in $C_8F_{17}EO_{20}/H_2O/C_8F_{17}EO_3$ system responsible for different rheology.

Similarly, a mixture of nonionic dimeric poly(oxyethylene) gemini surfactants having the structure, $(C_{n\text{-}2}H_{2n\text{-}3}CHCH_2(OCH_2CH_2)_mOH)_2(CH_2)_6$ with alkyl and ethoxy chain lengths ranging from $n = 12-20$ and $m = 5-30$ can also form wormlike micelles in aqueous solution [52], especially for the $n = 20$ and $m = 15$ surfactant, a shape transition is accompanied by an increase in viscosity at low concentration and gelation at higher concentrations. The size and shape of micelles formed have been determined using small-angle neutron scattering (SANS).

The hydrophobic sterol group of poly(oxyethylene) cholesterol and poly(oxyethylene) phytosterol ether surfactants are of natural origin; they can also be a good candidates for wormlike micelle formation. The interfacial curvature of poly(oxyethylene) alkyl ethers [53], poly(oxyethylene) cholesteryl ethers ($ChEO_m$) [54–56], poly(oxyethylene) phytosterol ethers ($PhyEO_m$) [57–62] micelles can be tuned to induce sphere-to-wormlike micelles transition. Aqueous micellar solutions of $ChEO_m$ and $PhyEO_m$, where $m =$ 10,5,20,30, can solubilize a considerable amount of $C_{12}EO_n$, where $n = 3$–4 system at 25°C. Successive additions of $C_{12}EO_n$ to the aqueous micellar solutions of the $ChEO_m$ or $PhyEO_m$ results in optically isotropic highly viscous samples that show shear birefringence. At higher mixing fractions of $C_{12}EO_n$, phase separation takes place, and a vesicular dispersion is observed in the multiphase region due to the decrease in surfactant layer curvature with the incorporation of $C_{12}EO_n$. In $ChEO_{10}/H_2O/C_{12}EO_n$ systems [63], with decreasing headgroup size (smaller n), a sharp increase in η_0 begins at lower $C_{12}EO_n$ concentration and micellar growth occurs more "rapidly." On increasing the n of cosurfactant, a higher cosurfactant/surfactant ratio is required to form viscoelastic solution, which is attributed to the decreased ability of the cosurfactant to reduce the aggregate curvature. While an increase in m of the $ChEO_m$ shifts it toward higher concentrations (see Fig. 89.2a).

Structural information on the mixed systems can be extracted from X-ray [64, 65] and neutron-scattering measurements [66]. SANS measurement in dilute mixed nonionic system ($ChEO_m$+$C_{12}EO_n$) provides evidence for 1D micellar growth (see Fig. 89.2b). The $p(r)$ functions indicate

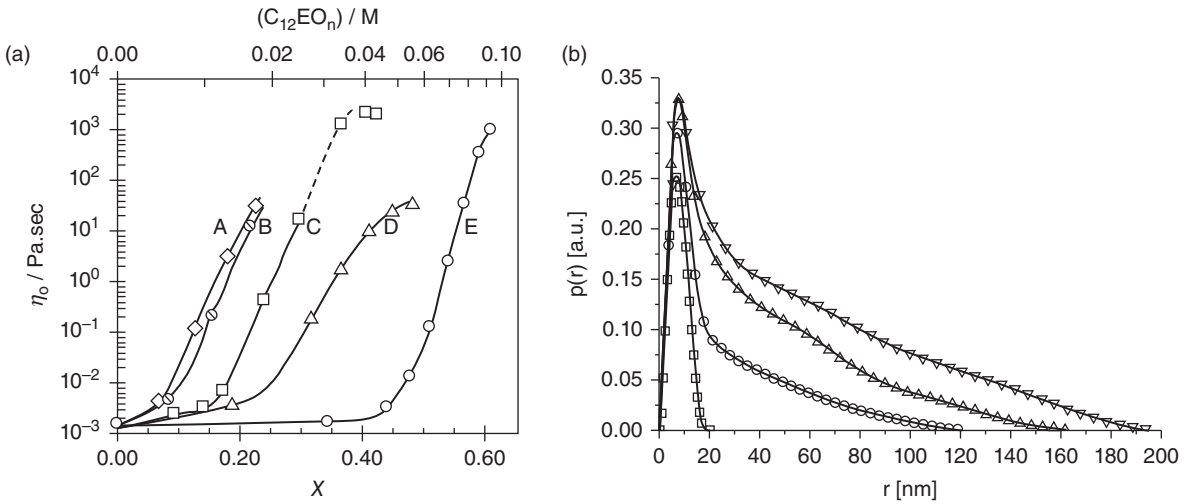


FIGURE 89.2 (a) Variation of η_0 with mixing fraction of $ChEO_n$ (X) in different 0.06 M $ChEO_{10}/ChEO_n/H_2O$ systems: (A) $C_{12}EO_1$, (B) $C_{12}EO_2$, (C) $C_{12}EO_3$, (D) $C_{12}EO_4$, and (E) 0.06 M $ChEO_{15}/C_{12}EO_3/H_2O$. (b) Pair distance distribution functions $p(r)$ for 1 wt% of $ChEO_{10}$ and 0 wRt% (squares), 0.05 wt% (circles), 0.10 wt% (upward-pointing triangles), and 0.15 wt% (downward-pointing triangles) $C_{12}EO_3$, respectively. (Both panels reprinted from Moitzi et al. 2005 [66], p. 16161. Reproduced with permission of American Chemical Society.)

that the geometry is close to a sphere for $ChEO_m$ (where $m = 10,20,30$) alone. Addition of $C_{12}EO_n$ induces spherical to cylindrical micelles transition. Figure 89.2b shows elongation for an increasing concentration of $C_{12}EO_3$, in agreement with the conclusions drawn from rheology. The decay to large r values is not linear, but is slightly convex, indicating polydispersity in length. It should be noted that a length of 200 nm (for 0.15 wt% $C_{12}EO_3$) is longer than the resolution of the instrument, so only qualitative analysis is possible in this case.

Alkanolamides like lauryldiethanolamide (L-DEA) and cocamid monoethanolamide (C-MEA) are also capable of transforming spherical micelles of $ChEO_{20}$ into wormlike micelles. The wormlike micelles could be obtained with lower concentration in the case of the L-DEA-added system, while a higher maximum η_0 could be obtained with a C-MEA-added system. Rheological, SAXS measurements and cryo-TEM (see Fig. 89.3) images confirm the formation of wormlike micelles on addition of alkanolamides in both cases [64, 65].

Lipophilic monoglycerides, like monolaurin ($C_{12}MG$), monocaprin ($C_{10}MG$), and monocaprylin (C_8MG), can induce wormlike micelles in aqueous micellar solutions of $ChEO_{10}$ [67]. Higher amounts of small hydrophobic tailed surfactant, C_8MG (0.60), compared to those of $C_{10}MG$ (0.34) and $C_{12}MG$ (0.30), are needed to induce the 1D growth. Aliphatic oils, ethyl butyrate (EB), and ethyl caprylate (EC) and cyclic oils such as peppermint (PP), and tea tree (TT) oils can also induce wormlike micelle formation in aqueous micellar solutions of $ChEO_{10}$. The wormlike micelles with maximum η_0 are obtained in the order $C_{12}MG > C_{10}MG > C_8MG$ for the monoglycerides, while for the oils, they are obtained in the order TT > PP > EC > EB. Both SANS and cryo-TEM confirm an increase in contour length on the addition of C_nMG and oils. The oils intercalate at the core–shell interface of the micelles. In the presence of an entangled network, however (at higher cosurfactant concentration), the addition of oil reduces the viscoelasticity, possibly because of competition with the monoglyceride surfactant and solubilization of the oil in the hydrophobic core, ultimately leading to phase separation. In yet another report, wormlike micelles have been observed in an aqueous mixture of poly(oxyethylene) phytosterol ether ($PhyEO_m$; $m = 10,20,30$) and glycerin fatty acid monoester (C_nGFA; $n = 8,10,12$) [60]. The η_0 value increases dramatically with changing ratio of C_nGFA in the system. The rheological measurements confirm the presence of entangled wormlike micelles in $PhyEO_{10}/C_8GFA/H_2O$ and $PhyEO_{20}/C_{10}GFA/H_2O$ systems.

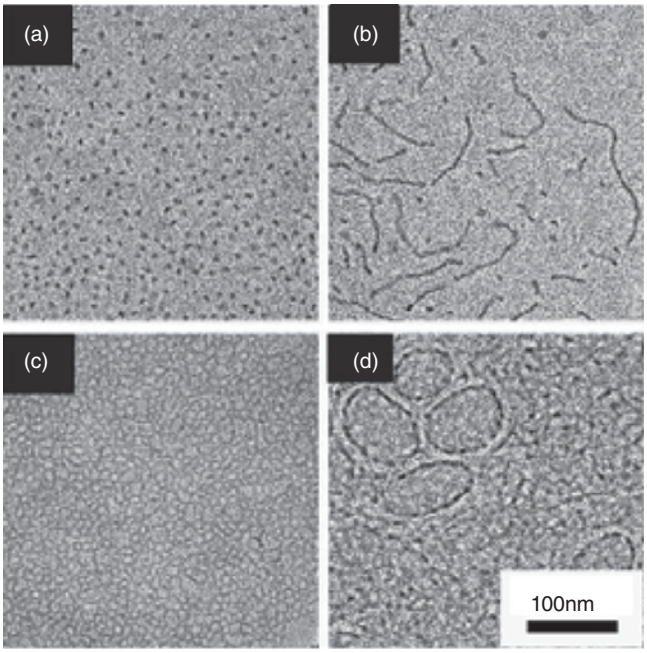


FIGURE 89.3 Cryo-TEM micrographs of micelles formed by 2 wt% $ChEO_{20}$ with (a) no L-DEA, (b) 1 wt%, (c) 2 wt%, and (d) 2.6 wt% of L-DEA. (All panels reprinted from Shrestha et al. 2011 [65], p. 12877. Reproduced with permission of American Chemical Society.)

Among those forming wormlike micelles, substantial work has focused on sugar-based surfactants [68, 69]. Aqueous binary solutions of sucrose alkanoate surfactants (C_xSE, where $x = 12,16,18$) can form viscous wormlike micellar solutions over a wide range of concentration and temperature [70–73]. Such micelles have also been reported in an aqueous mixtures of sucrose dodecanoate (C_xSE, where $x = 12,16$) and poly(oxyethylene) ethers ($C_{12}EO_n$) [74]. A successive addition of C_mEO_n or monolaurin (ML) to the aqueous micellar solutions of sucrose alkanoates promotes highly viscoelastic micelles in the system that disappears with further addition of cosurfactant followed by phase separation, observed for all the cases studied (see Fig. 89.4a). The value of η_0 increases by several orders of magnitude if a small amount of C_mEO_n is added to $C_{16}SE$ and then decreases at higher ratios C_mEO_n/C_xSE ratios (R) up to phase separation. The η_0-increasing capacity is in the following order: ML $\approx C_{12}EO_1 \approx C_{12}EO_2 > C_{12}EO_3 > C_{12}EO_4$. A comparatively higher concentration of the more hydrophilic ethoxylated amphiphile is needed for similar rise in the $C_mEO_n/C_xSE/H_2O$ system.

The $p(r)$ functions of 5% $(C_{16}SE+C_{12}EO_3)/H_2O$ at different mixing fractions of $C_{12}EO_3$ (W_1) (see Fig. 89.4b) are typical of cylindrical aggregates [75, 76], with nonlinear (slightly convex) decay at large r values indicating polydispersity in length. In the $C_{16}SE/H_2O$ binary system the maximum dimension of the aggregate is ~12.5 nm. On addition of $C_{12}EO_3$, the maximum length increases, and at a composition corresponding to the maximum viscosity, it is ~23 nm (the actual length is limited by the resolution limit). The data confirm the elongation of the micelles with addition of $C_{12}EO_3$. Further increase in $C_{12}EO_3$ concentration decreases

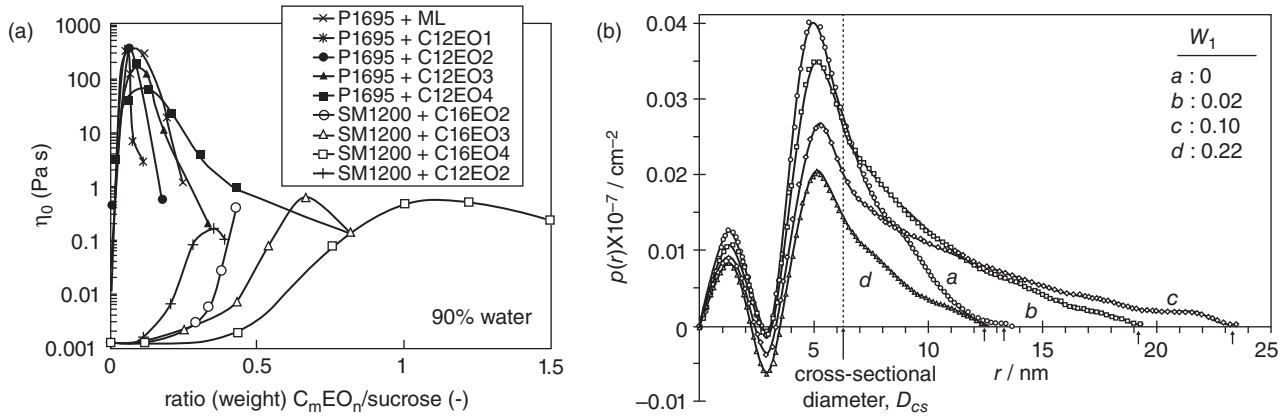


FIGURE 89.4 (a) Zero-shear viscosity η_0 for ($C_xSE + C_mEO_n$) + 90% H_2O at various C_mEO_n/C_xSE ratios (R) (ML = monolaurin). (b) Pair distance distribution function $p(r)$ for 5% ($C_{16}SE + C_{12}EO_3$) system at different mixing fractions of $C_{12}EO_3$ (W_1). (Panel (a) reprinted from Maestro et al. 2004 [74], p. 14009; reproduced with permission of American Chemical Society. Panel (b) reprinted from Acharya and Kuneida 2006 [76], p. 401; reproduced with permission of Elsevier.)

the aggregate size, in consistence with the rheological data.

The oil induced structural transition in the micellar aggregates is of particular relevance for their use in cosmetics or pharmaceutical applications. The effects of oils in the rheology of $C_{16}SE/C_{12}EO_3/H_2O$ and $C_{16}SE/C_{12}MG/H_2O$ systems have been reported [77]. When $C_{12}EO_3$ is added in the presence of decane, most of the $C_{12}EO_3$ is solubilized in decane(hydrophobic core), and the availability of $C_{12}EO_3$ at the interface is very low. Further addition of $C_{12}EO_3$ increases its interfacial concentration and the curvature of the C_mSE/H_2O aggregate is reduced, increasing the viscosity. On the other hand, as $C_{12}MG$ is not soluble in decane, it is readily adsorbed at the interface regardless of the presence of decane, and hence the tendency to increase the viscosity by $C_{12}MG$ is almost the same as in the system without oil. These oils, in the absence of $C_{12}EO_3$ or $C_{12}MG$, do not increase the viscosity of $C_{16}SE/H_2O$. On the other hand, relatively rigid and elongated amphiphilic oil, *p*-xylene, is preferentially solubilized in the surfactant palisade layer, and it increases the viscosity of $C_{16}SE/H_2O$ binary solution sharply even in the absence of $C_{12}EO_3$ or $C_{12}MG$ [78]. Moreover, less cosurfactant ($C_{12}EO_3$ or $C_{12}MG$) is needed to induce micellar growth, and also micellar branching, which causes the viscosity decrease after the maximum, at lower cosurfactant fraction. SAXS confirms that further elongation of long wormlike micelles is favored by *p*-xylene, while decane promotes the formation of globular, small micelles, responsible for the different rheological behavior.

Another research team further confirmed that monohydroxy alcohols (C_3–C_9) can also induce wormlike micelles formation in sucrose monohexadecanoate ($C_{16}SE$) [79]. The η_0 of the aqueous micellar solution of $C_{16}SE$ increases, shows a maximum, and then decreases for all the alcohols except for 1-propanol. Rheological study confirms the presence of wormlike micelles. Micelles show 1D growth with alcohol and lead to branched micelles at higher concentration, losing the viscoelastic properties. Long-chain alcohol induces higher maximum η_0 and slow relaxation time τ_R.

In aqueous binary solutions of poly(ethylene oxide)–poly(propylene oxide) (PEO-PPO), block copolymers can aggregate into temperature-sensitive wormlike micelles as confirmed by rheological study [80]. In aqueous mixtures of poly(butadiene-*co*-ethylene oxide) (PBD_{46}-PEO_{30}), copolymer and a commercial nonionic surfactant (Triton X-100), long micelles have been observed by cryo-TEM [81].

Nonaqueous wormlike micelles or reverse wormlike micelles are formed by lipophilic surfactants in nonaqueous solvents. The most popular system forming reverse wormlike micelles investigated so far is a ternary mixture of lecithin/H_2O/oil [82–84]. Lecithin, a zwitterionic phospholipid with two alkyl chains, forms globular or ellipsoidal micelles in a variety of organic solvents. A trace amount of water into lecithin reverse micellar solution can induce axial micellar growth and exhibit viscoelastic behavior due to the entanglement of long cylindrical micelles into a transient network [85, 86]. The η_0 increases by several orders of magnitude. This increase depends on the molar ratio of water to lecithin. Another team of investigators reported wormlike micelles in lecithin/decane system by substituting water with urea, sucrose fatty acid esters [87, 88], sugars of RNA and DNA, and polyglycerol [89, 90]. The substituting additives form hydrogen bonds with the phosphate group of lecithin, thereby reducing the interfacial curvature of the molecular assembly and inducing an axial growth of lecithin micelles, leading to the formation of reverse wormlike micelles. The η_0 increases by $\sim$ 6 orders of magnitude. Similarly, other researchers [91, 92] replaced water with a trace amount of a

bile salt, sodium deoxycholate, in lecithin/hydrocarbon oil–based reverse wormlike micelles. They proposed that facially amphiphilic bile salts promote the longitudinal aggregation of lecithin molecules into viscoelastic wormlike micelles. The η_0 increases by ~ 5 orders of magnitude, which is controlled by the molar ratio of bile salt to lecithin. They [91,92] have also illustrated the formation of light-responsive reverse wormlike micelles in a combination of lecithin/*p*-coumaric acid/oils [93]. Shrestha et al. have reported that addition of relatively less lipophilic nonionic surfactant sucrose dioleate, SDO to semidilute solutions of sucrose trioleate (STO) in hexadecane forms transient networks of viscoelastic reverse wormlike micelles even in the absence of water. The η_0 increases by ~ 4 orders of magnitude, determined by the mixing fraction of SDO and STO [94]. The growth of reverse wormlike micelles has been confirmed by small-angle scattering (SAXS or SANS) experiments.

89.3 CONCLUSION

Viscoelastic wormlike micellar solutions are formed in both binary and mixed nonionic surfactants and amphiphilic block copolymers. Experimental techniques such as rheology, small-angle X-ray scattering, and cryo-TEM provide evidence of the change in morphology and size when wormlike micelles are formed, and also provide valuable information on the dynamics of the systems, which show several relaxation and diffusion mechanisms, associated with micellar breaking, micellar reptation, and entanglement. Micellar growth in 1D is favored by an increase in the average surfactant molecular packing parameter, which can be induced by a reduction in the effective surface area when a cosurfactant is added to the system. The wormlike micellar solutions formed by ethoxylated nonionic surfactants are very sensitive to temperature, and dehydration of the surfactant headgroups promotes elongation. The rheological behavior of nonionic wormlike micelles is affected by the additives. Relatively hydrophobic cosurfactants that tend to reside in the surfactant palisade layer and reduce the specific surface area favor larger elongation, whereas long and bulky oils, which tend to be solubilized in the micellar core, induce a rod–sphere transition, thereby decreasing viscosity. In mixed systems, the effect of oil also depends on the solubility of the cosurfactant in the oil phase. Reverse wormlike micelles can be formed in nonpolar solvents, even in the absence of ionic components or water. The possibility of obtaining highly viscoelastic wormlike micellar solutions with nonionic surfactants expands the field of applications and provides new insight on the study of living polymers.

REFERENCES

[1] McBain, J.W. (1913). *Transact. Faraday Soc.* **9**, 99.

[2] Debye, P. (1949). *J. Phys. Colloid Chem.* **53**, 1–8.

[3] Tanford, C. (1973). *The Hydrophobic Effect.* Wiley, New York.

[4] May, S., Bohbot, Y., Ben-Shaul, A. (1997). *J. Phys. Chem. B* **101**, 8648–8657.

[5] McMullen, W.E., Ben-Shaul, A., Gelbart, W.M. (1984). *J. Colloid Interface Sci.* **98**, 523–536.

[6] Vila-Romeu, N., Taddei, G. (1999). *Colloid Polym. Sci.* **277**, 1093–1097.

[7] Karaborni, S., Esselink, K., Hilbers, P.A.J., Smit, B., Karthauser, J., van Os, N.M., Zana, R. (1994). *Science* **266**, 254–256.

[8] May, S., Ben-Shaul, A. (2001). *J. Phys. Chem. B* **105**, 630–640.

[9] Bernheim-Groswasser, A., Zana, R., Talmon, Y. (2000). *J. Phys. Chem. B* **104**, 4005–4009.

[10] Zheng, Y., Won, Y., Bates, F.S., Davis, H.T., Scriven, L.E., Talmon, Y. (1999). *J. Phys. Chem. B* **103**, 10331–10334.

[11] Debye, P., Anacker, E.W. (1951). *J. Phys. Colloid Chem.* **55**, 644–655.

[12] Porte, G. (1983). *J. Phys.Chem.* **87**, 3541.

[13] Larson, R.G. (1999). *The Structure and Rheology of Complex Fluids*. Oxford Univ. Press, New York.

[14] Marin, G. (1998). In Collyer, A.A., Clegg, D.W. (eds.), *Rheological Measurement*, 2nd ed. Chapman & Hall, London.

[15] Candau, S., Hirsch, E., Zana, R. (1985). *J. Colloid Interface Sci.* **105**, 521–528.

[16] Cates, M.E., Candau, S.J. (1990). *J. Phys. Condens. Matt.* **2**, 6869–6892.

[17] Granek, R., Cates, M.E. (1992). *J. Chem. Phys*. **96**, 4758–4767.

[18] Cates, M.E. (1988). *J. Phys. Fr.* **49**, 1593–1600.

[19] Berret, J.F., Appell, J., Porte, G. (1993). *Langmuir* **9**, 2851–2854.

[20] Magid, L.J. (1998). *J. Phys. Chem. B* **102**, 4064–4074.

[21] Drye, T.J., Cates, M.E. (1993). *J. Chem. Phys.* **98**, 9790–9797.

[22] Lequeux, F. (1992). *Europhys. Lett*. **19**, 675–681.

[23] Khatory, A., Lequeux, F., Kern, F., Candau, S.J. (1993). *Langmuir* **9**, 1456–1464.

[24] Glatter, O. (1977). *J. Appl. Crystallogr*. **10**, 415–421.

[25] Glatter, O. (1981). *J. Appl. Crystallogr*. **14**, 101–108.

[26] Strey, R., Glatter, O., Schubert, K.V., Kaler, E.W. (1996). *J. Chem. Phys.* **105**, 1175–1188.

[27] Brunner-Popela, J., Glatter, O. (1997). *J. Appl. Crystallogr*. **30**, 431–442.

[28] Weyerich, B., Brunner-Popela, J., Glatter, O. (1999). *J. Appl. Crystallogr.* **32**, 197–209.

[29] Bergmann, A., Fritz, G., Glatter, O. (2000). *J. Appl. Crystallogr.* **33**, 1212–1216.

[30] Shikata, T., Shiokawa, M., Imai, S. (2003). *J. Colloid Interface Sci.* **259**, 367–373.

[31] Rehage, H., Hoffmann, H. (1988). *J. Phys. Chem.* **92**, 4712–4719.

[32] Kern, F., Lemarechal, P., Candau, S.J., Cates, M.E. (1992). *Langmuir* **8**, 437–440.

[33] Clausen, T.M., Vinson, P.K., Minter, J.R., Davis, H.T., Talmon, Y., Miller, W.G. (1992). *J. Phys. Chem.* **96**, 474–484.

[34] Khatory, A., Kern, F., Lequeux, F., Appell, J., Porte, G., Morie, N., Ott, A., Urbach, W. (1993). *Langmuir* **9**, 933–939.

[35] Berret, J.-F., Appell, J., Porte, G. (1993). *Langmuir* **9**, 2851–2854.

[36] Lin, Z., Cai, J.J., Scriven, L.E., Davis, H.T. (1994). *J. Phys. Chem.* **98**, 5984–5993.

[37] Soltero, J.F.A., Puig, J.E.Manero, O., Schulz, P.C. (1995). *Langmuir* **11**, 3337–3346.

[38] Hassan, P.A., Candau, S J., Kern, F., Manohar, C. (1998). *Langmuir* **14**, 6025–6029.

[39] Hoffmann, H. (1994). In Herb, C.A., Prudhomme, R. (eds.), *Structures and Flow in Surfactant Solutions*. ACS Symposium Series Vol. 578, American Chemical Society, Washington, DC, p. 2031.

[40] Kato, T., Terao, T., Seimiya, T. (1994). *Langmuir* **10**, 4468–4474.

[41] Schurtenberger, P., Cavaco, C., Tiberg, F., Regev, O. (1996). *Langmuir* **12**, 2894–2849.

[42] Arrigo, G.D., Briganti, G. (1998). *Phys. Rev. E* **58**, 713–723.

[43] Acharya, D.P., Sharma, S.C., Rodriguez-Abreu, C., Aramaki, K. (2006). *J. Phys. Chem. B* **41**, 20224–20234.

[44] Shrestha, R.G., Shrestha, L.K., Sharma, S.C., Aramaki, K. (2008). *J. Phys. Chem. B* **112**, 10520–10527.

[45] Sharma, S.C., Acharya, D.P., Aramaki, K. (2007). *Langmuir* **23**, 5324–5330.

[46] Sharma, S.C., Shrestha, R.G., Shrestha, L.K., Aramaki, K. (2009). *J. Phys. Chem. B* **113**, 1615–1622.

[47] Sharma, S.C., Rodríguez-Abreu, C., Shrestha, L.K., Aramaki, K. (2007). *J. Colloid Interface Sci.* **314**, 223–229.

[48] Khatory, A., Kern, F., Lequeux, F., Appell, J., Porte, G., Morie, N., Ott, A., Urbach, W. (1993). *Langmuir* **9**, 933–939.

[49] Candau, S.J., Oda, R. (2001). *Colloid Surf. A: Physicochem. Eng. Aspects* **183–185**, 5–14.

[50] Danino, D., Talmon, Y., Levy, H., Beinert, G., Zana, R. (1995). *Science* **269**, 1420–1421.

[51] Lin, Z., Cai, J.J., Scriven, L.E., Davis, H.T. (1994). *J. Phys. Chem.* **98**, 5984–5993.

[52] Fitzgerald, P.A., Davey, T.W., Warr, G.G. (2005). *Langmuir* **21**, 7121–7128.

[53] Jerke, G., Pedersen, J.S., Egelhaaf, S.U., Schurtenberger, P. (1998). *Langmuir* **14**, 6013–6024.

[54] Acharya, D.P., Kunieda, H. (2003). *J. Phys. Chem. B* **107**, 10168–10175.

[55] Ahmed, T., Aramaki, K. (2008). *J. Colloid Interface Sci.* **327**, 180–185.

[56] Shrestha, R.G., Sharma, S.C., Sakai, K., Sakai, H., Abe, M. (2012). *Colloid Polym. Sci.* **290**, 339–348.

[57] Kunieda, H., Rodriguez, C., Tanaka, Y., Kabir, Md.H., Ishitobi, M. (2004). *Colloids Surf. B* **38**, 127–130.

[58] Acharya, D.P., Hossain, Md.K., Feng, J., Sakai, T., Kunieda, H. (2004). *Phys. Chem. Chem. Phys.* **6**, 1627–1631.

[59] Sato, T., Hossain, Md.K., Acharya, D.P., Glatter, O., Chiba, A., Kunieda, H. (2004). *J. Phys. Chem. B* **108**, 12927–12939.

[60] Hashizaki, K., Tamaki, N., Taguchi, H., Saito, Y., Tsuchiya, K., Sakai, H., Abe, M. (2008). *Chem. Pharm. Bull.* **56**, 1682–1686.

[61] Sharma, S.C., Shrestha, L.K., Tsuchiya, K., Sakai, K., Sakai, H., Abe, M. (2009). *J. Phys. Chem. B* **113**, 3043–3050.

[62] Naito, N., Acharya, D.P., Tanimura, J., Kunieda, H. (2004). *J. Oleo. Sci.* **53**, 599–606.

[63] Acharya, D.P., Kunieda, H. (2003). *J. Phys. Chem. B* **107**, 10168–10175.

[64] Shrestha, R.G., Sakai, K., Sakai, H., Abe, M. (2011). *J. Phys. Chem. B* **115**, 2937–2946.

[65] Shrestha, R.G., Abezgauz, L., Danino, D., Sakai, K., Sakai, H., Abe, M. (2011). *Langmuir* **27**, 12877–12883.

[66] Moitzi, C., Freiberger, N., Glatter, O. (2005). *J. Phys. Chem. B* **109**, 16161–16168.

[67] Afifi, H., Karlsson, G., Heenan, R.K., Dreiss, C.A. (2011). *Langmuir* **27**, 7480–7492.

[68] Stradner, A., Glatter, O., Schurtenberger, P. (2000). *Langmuir* **16**, 5354–5364.

[69] Sanz, M.A., Granizo, N., Gradzielski, M., Rodrigo, M.M., Valiente, M. (2005). *Colloid Polym. Sci.*, **283**, 646–652.

[70] Gallegos, C., Muñoz, J., Guerrero, A., Berjano, M. (1994). In Herb, C.A., Prudhomme, R.K. (eds.), *Structure and Flow in Surfactant Solutions*. ACS Symposium Series Vol. 578, American Chemical Society, Washington, DC, pp. 217–228.

[71] Ericsson, C.A., Soderman, O., Garamus, V.M., Bergstrom, M., Ulvenlund, S. (2005). *Langmuir* **21**, 1507–1515.

[72] Ericsson, C.A., Soderman, O., Garamus, V.M., Bergstrom, M., Ulvenlund, S. (2004). *Langmuir* **20**, 1401–1408.

[73] Whiddon, C., Soderman, O., Hansson, P. (2002). *Langmuir* **18**, 4610–4618.

[74] Maestro, A., Acharya, D.P., Furukawa, H., Gutierrez, J.M., López-Quintela, M.A., Ishitobi, M., Kunieda, H. (2004). *J. Phys. Chem. B* **108**, 14009 –14016.

[75] Glatter, O. (2002). *Neutrons, X-rays and Light-Scattering Methods Applied to Soft Condensed Matter*. Elsevier, pp. 73–102.

[76] Acharya, D., Kunieda, H. (2006). *Adv. Colloid Interface Sci.* **123–126**, 401–413.

[77] Rodríguez, C., Aramaki, K., Tanaka, Y., López-Quintela, M.A., Ishitobi, M., Kunieda, H. (2005). *J. Colloid Interface Sci.* **291**, 560–569.

[78] Sato, T., Acharya, D.P., Kaneko, M., Aramaki, K., Singh, Y., Ishitobi, M., Kunieda, H. (2006). *J. Dispers. Sci. Technol.* **27**, 611–616.

[79] Aramaki, K., Hoshida, S., Arima, S. (2010). *Colloids Surf. A: Physicochem. Eng. Aspects* **366**, 58–62.

[80] Waton, G., Michels, B., Steyer, A., Schosseler, F. (2004). *Macromolecules* **37**, 2313–2321.

[81] Dan, N., Shimoni, K., Pata, V., Danino, D. (2006). *Langmuir* **22**, 9860–9865.

[82] Shchipunov, Y.A. (2001). *Colloid Surf. A* **183–185**, 541–554.

[83] Willard, D.M., Riter, R.E., Levinger, N.E. (1998). *J. ACS.* **120**, 4151–4160.

[84] Scartazzini, R., Luisi, P.L. (1988). *J. Phys. Chem.* **92**, 829–833.

[85] Schurtenberger, P., Scartazzini, R., Magid, L.J., Leser, M.E., Luisi, P.L. (1990). *J. Phys. Chem.* **94**, 3695–3701.

[86] Schurtenberger, P., Magid, L.J., King, S.M., Lindner, P. (1991). *J. Phys. Chem.* **95**, 4173–4176.

[87] Hashizaki, K., Taguchi, H., Saito, Y. (2009). *Colloid Polym. Sci.* **287**, 1099–1105.

[88] Hashizaki, K., Chiba, T., Taguchi, H., Saito, Y. (2009). *Colloid Polym. Sci.* **287**, 927–932.

[89] Hashizaki, K., Taguchi, H., Saito, Y. (2009). *Chem. Lett.* **38**, 1036–1037.

[90] Hashizaki, K., Sakanishi, Y., Yako, S., Tsusaka, H., Imai, M., Taguchi, H., Saito, Y. (2012). *J. Oleo Sci.* **61**, 267–275.

[91] Tung, S.H., Huang, Y.E., Raghavan, S.R. (2006). *J. ACS* **128**, 5751–5756.

[92] Tung, S.H., Huang, Y.E., Raghavan, S.R. (2007). *Langmuir* **23**, 372–376.

[93] Kumar, R., Ketner, A.M., Raghavan, S.R. (2010). *Langmuir* **26**, 5405–5411.

[94] Shrestha, L.K., Yamamoto, Y., Arima, S., Aramaki, K. (2011). *Langmuir* **27**, 2340–2348.

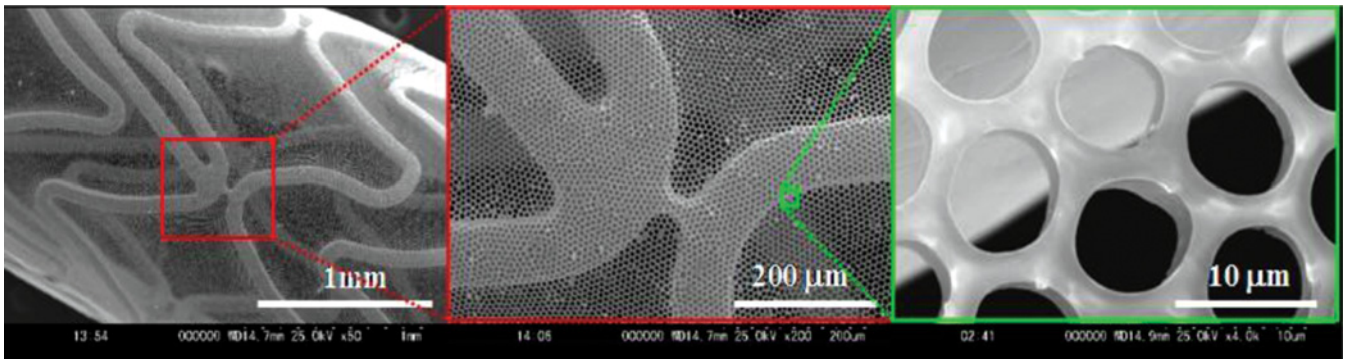


FIGURE 6.11 Novel stent covered with a vertically open-pored honeycomb film.

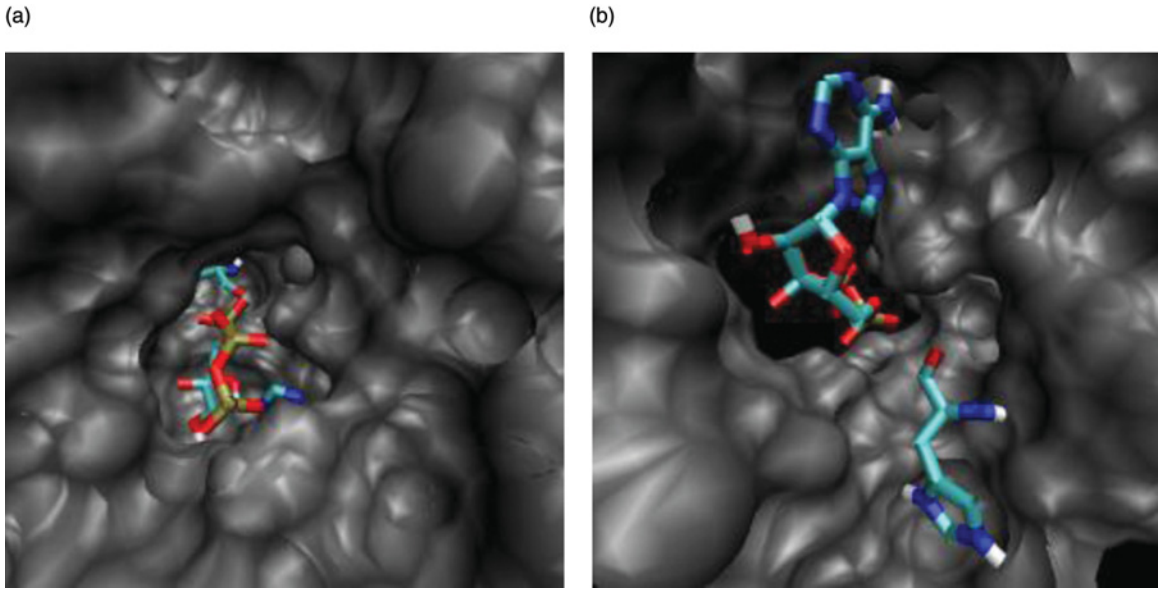


FIGURE 14.2 The active-site geometry of HisRS (1KMN.pdb) from *Escherichia coli* [26]. The ATP and histidinol are shown as bound substrate and substrate analog (analog of histidine), respectively. Two different views of the active site are shown: (a) from the perspective of the active site as viewed from the opening of the cavity; (b) as viewed from the amino acid binding site (few residues are omitted for clarity). The opening of the active site is ∼1.1 nm, and the tunnel length spanning the substrate and analogue is ∼1.7 nm. Images are prepared using VMD [108].

Encyclopedia of Biocolloid and Biointerface Science, Volume 1, First Edition. Edited by Hiroyuki Ohshima.
© 2016 John Wiley & Sons, Inc. Published 2016 by John Wiley & Sons, Inc.

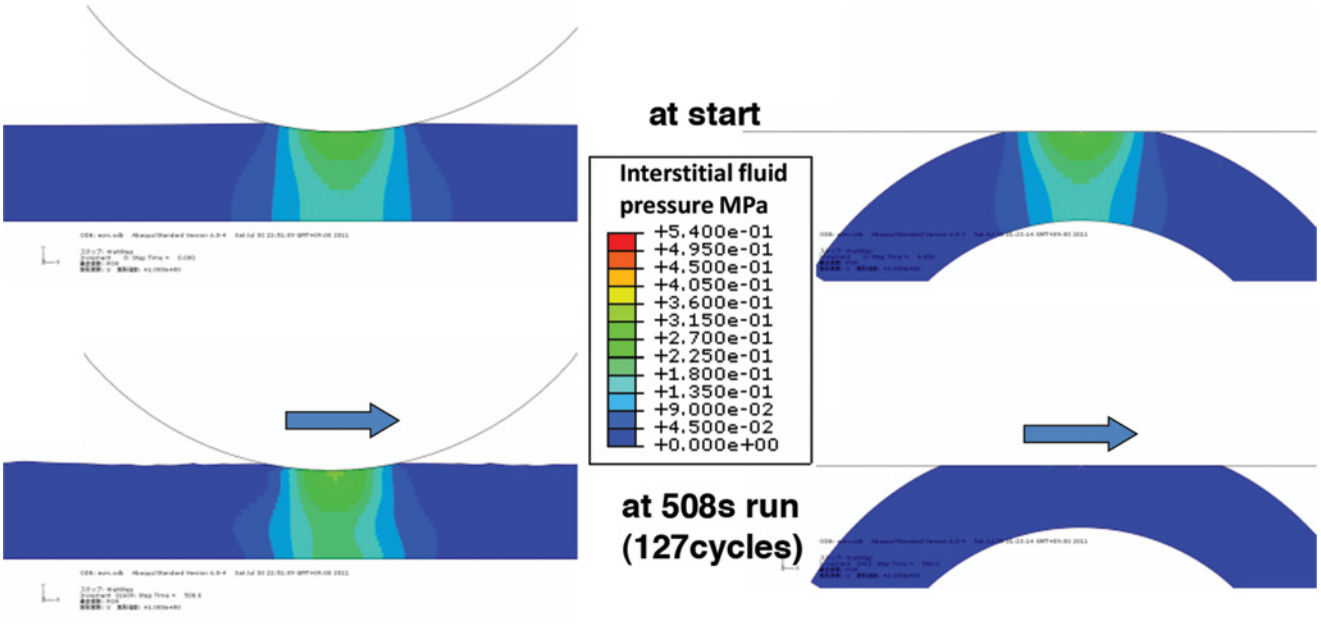


FIGURE 22.5 Changes in interstitial fluid pressure of articular cartilage: (a) on/off loading to cartilage; (b) continuous loading to cartilage (modified from Ref. 26).

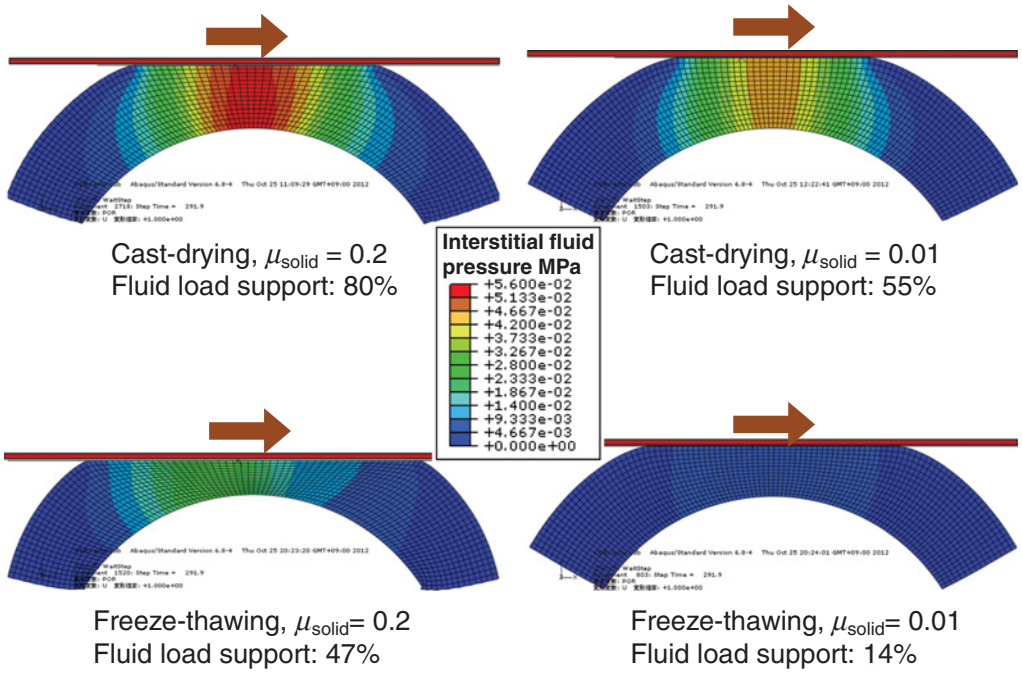


FIGURE 22.12 Changes in interstitial fluid pressure and fluid load support of PVA hydrogel [41].

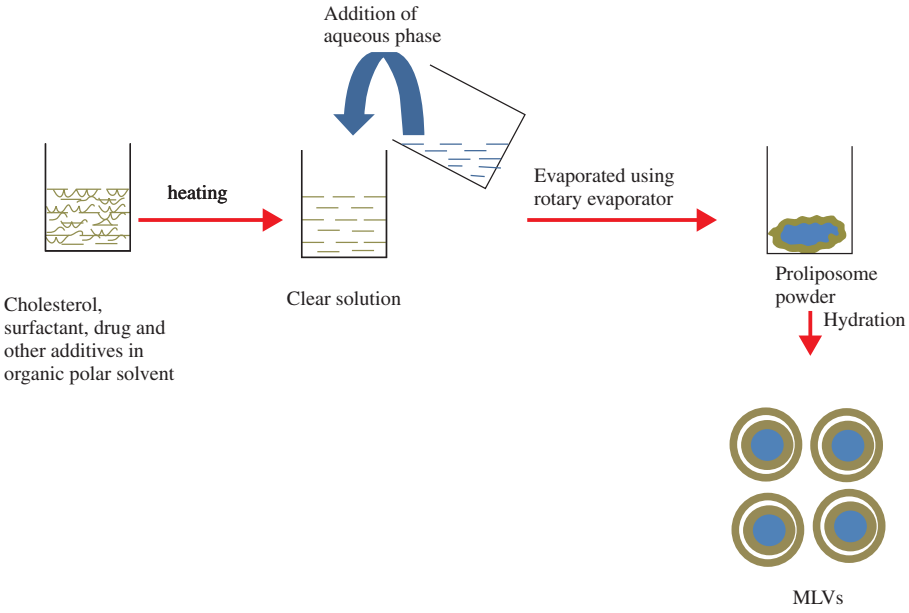


FIGURE 23.7 Formation of liposomes from proliposomes.

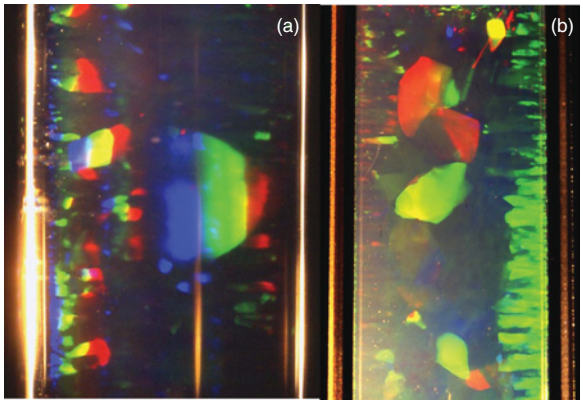


FIGURE 28.1 Close-up images of colloidal crystals in test tube (a) and in a plain cell (b) at 25°C. (a) CS91, ϕ; = 0.00083, 18 days after preparation and 1 h after mixing; (b) CS81, ϕ = 0.00095, 7 days after preparation and 40 min after mixing.

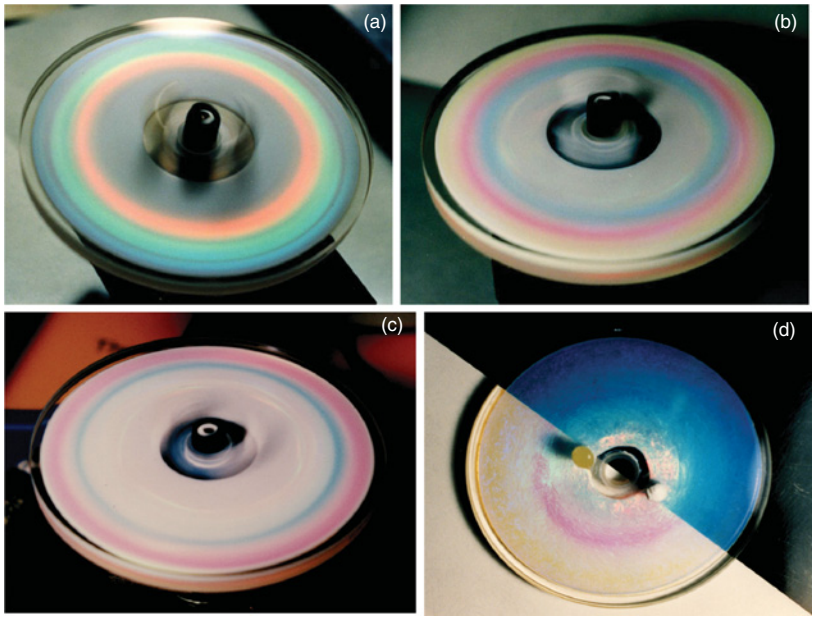


FIGURE 28.8 Close-up color images of colloidal single crystals of D1K88 (a,b) and D1B72 spheres (c,d) in a rotating cell. ϕ_{D1K88} = 0.0617, ϕ_{D1B72} = 0.0820. Images captured with (a) obtuse-angle illumination and (b,c) acute-angle illumination, and (d) photograph showing the observation cell on black and white papers.

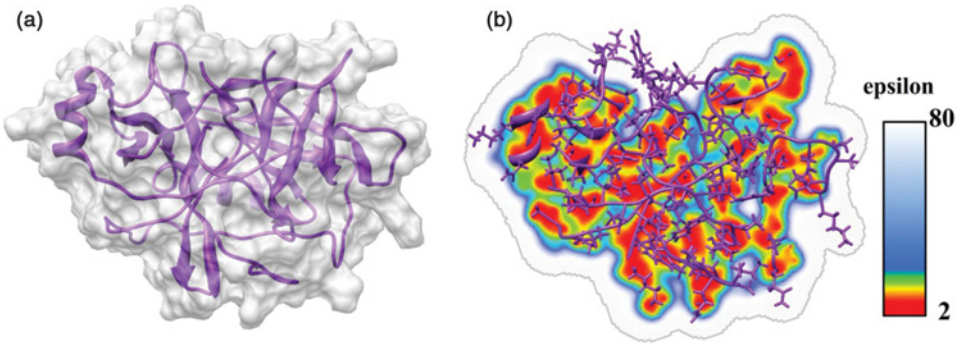


FIGURE 29.4 (a) Structure of the Bovine Eglin protein (PDB ID 1ACB); (b) dielectric distribution of the Gaussian smooth method for this protein. [Molecular graphics and analyses were performed with the UCSF Chimera package. Chimera is developed by the Resource for Biocomputing, Visualization, and Informatics at the University of California, San Francisco (supported by NIGMS P41-GM103311).]

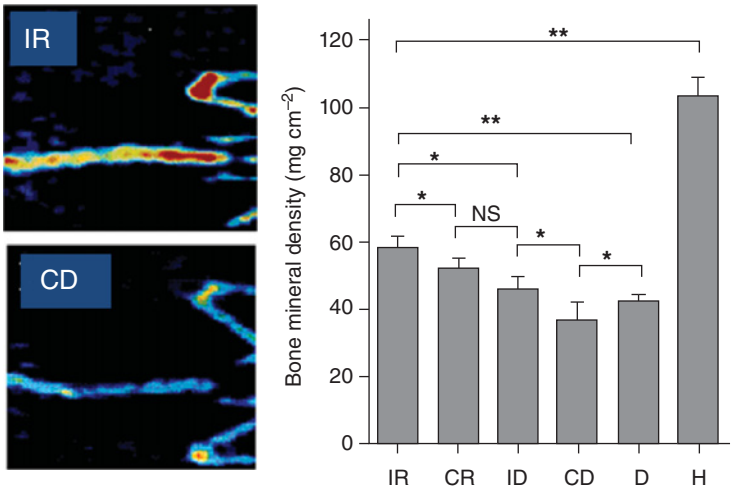


FIGURE 31.3 BMD of implanted apatite cement containing estradiol in osteoporotic rats.

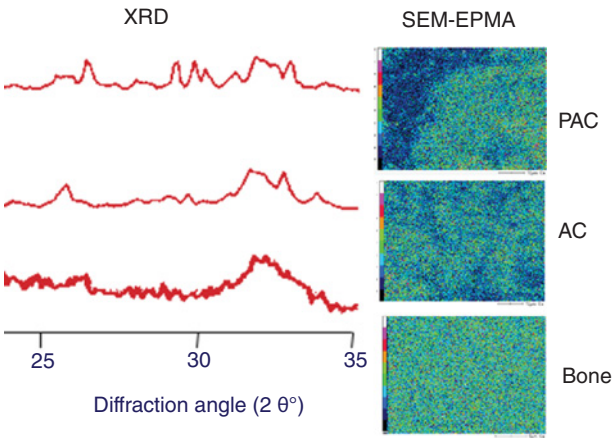


FIGURE 31.4 Effects of grinding of element dispersibility of AC and PAC by electron probe microanalyzer.

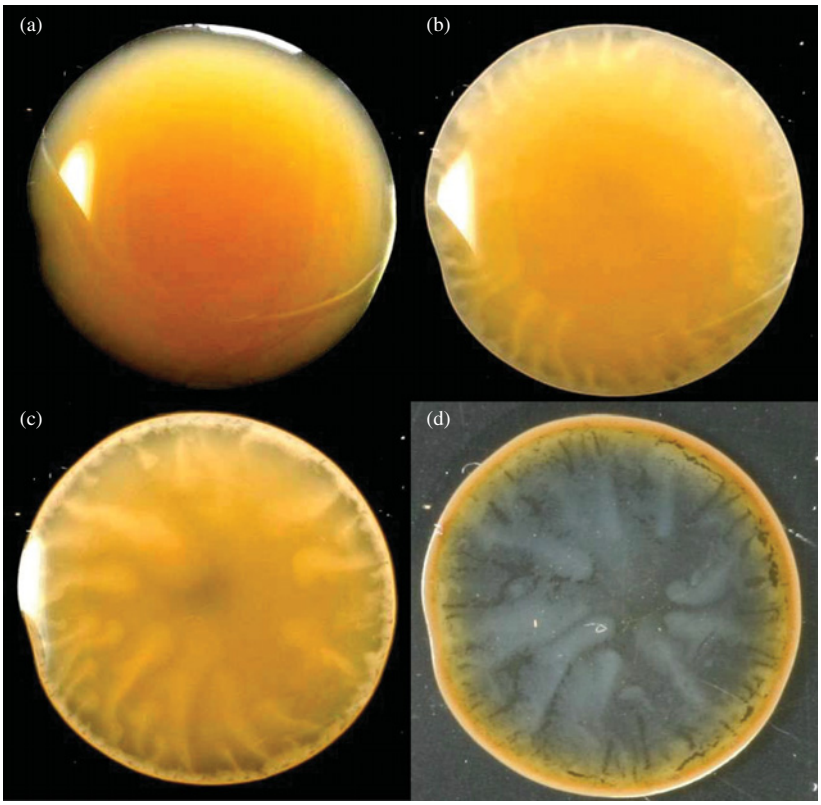


FIGURE 32.1 Convectional, sedimentary, and drying patterns of coffee (for iced coffee) with cream on a coverglass at 27°C, 1.26 wt%, 0.1 mL: (a) 10 min; (b) 50 min; (c) 1 h 40 min; (d) 3 h 25 min after setting.

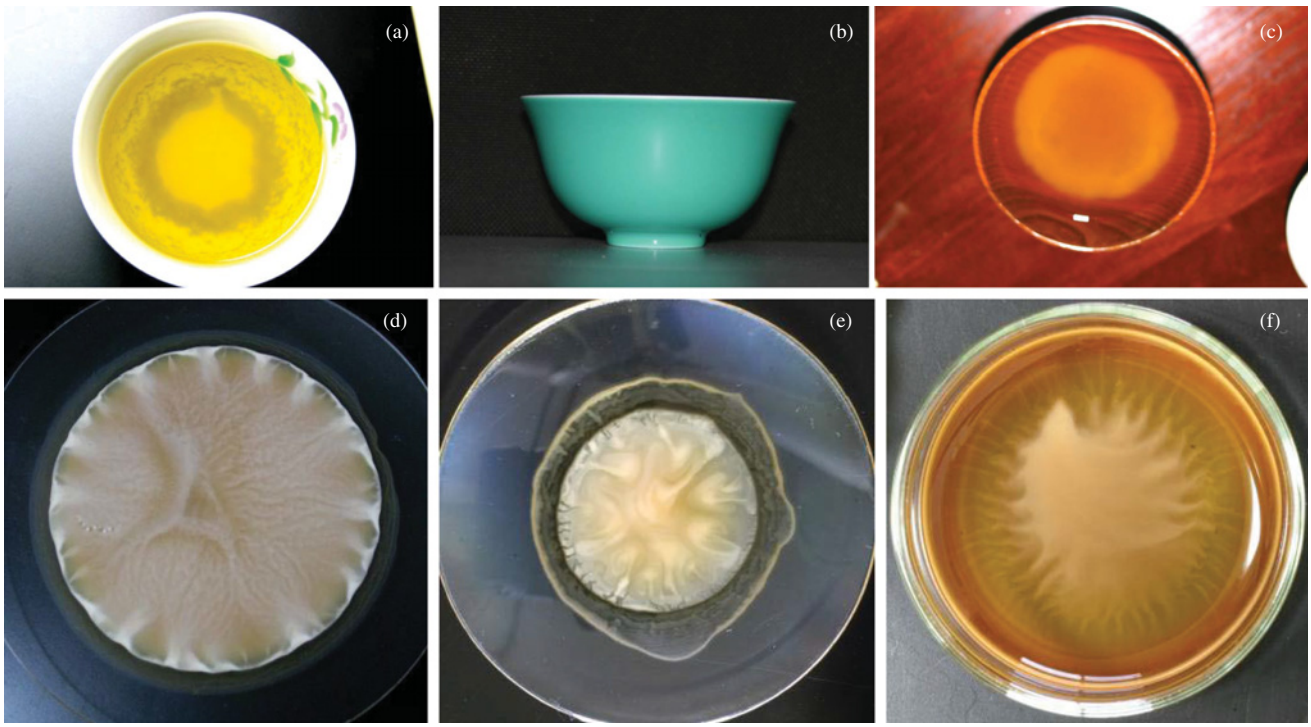


FIGURE 32.3 Typical examples of broad ringlike (a–c), cluster (d), bundle (e), and flamelike (f) sedimentation patterns of (a,b) green tea, (c) miso soup, and (d–f) coffee. (a) In a teacup at 24°C; (b) side view of a teacup; (c) in a bowl at 24°C; (d) in a watchglass (150 mm), 10 mL, 2.3 wt%, with cream, from 70°C to 20°C, after 12 h 25 min; (e) in a watchglass (50 mm), 1 mL, 0.7 wt%, with cream, after 9 h 20 min; (f) in a glass dish (42 mm), 3 mL, 2.3 wt%, with cream, after 20 h 5 min.

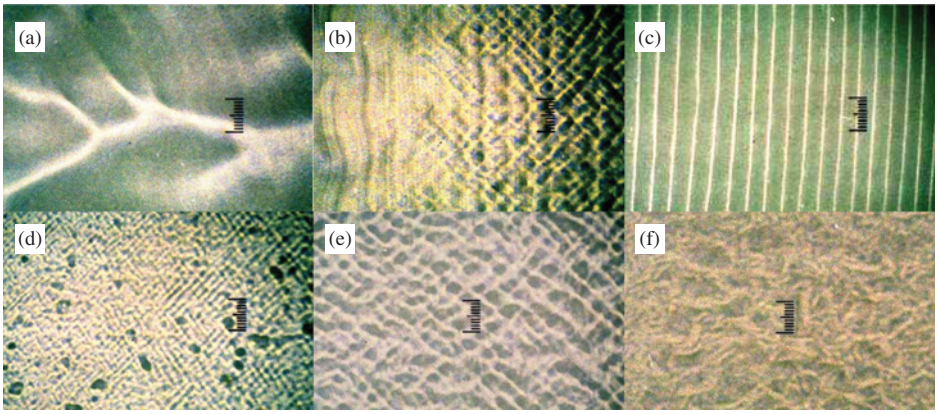


FIGURE 32.7 Typical examples of microscopic drying patterns of (a,b) pNIPAm(200-0.5): (c) pNIPAm(200-2); (d) pNIPAm(200-10); (e) pNIPAm(400-5); (f) pNIPAm(1500-5) at 45°C (humidity 35%, full scale at 100 μm): (a) 1.01 wt%, on a watchglass; (b)1.01, watchglass; (c) 0.039, glass dish; (d) 2.4, glass dish; (e) 0.97, glass dish; (f) 3.1, coverglass.

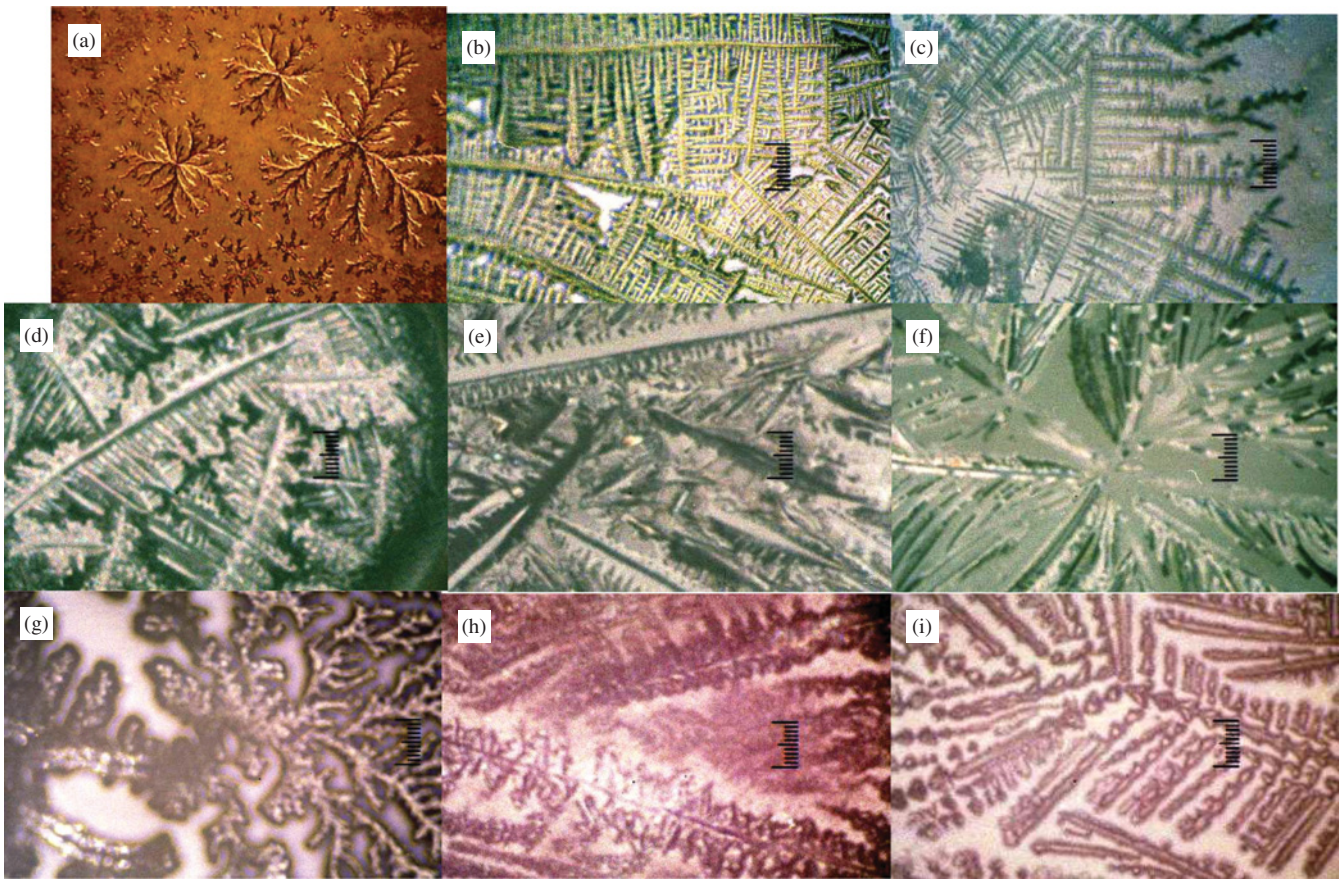


FIGURE 32.10 Typical examples of microscopic patterns of biopolymers: (a) NaPDGA + NaPLGA (1:1) [103], [NaPGA] = 0.01 monoM, on a coverglass, 0.1 mL, at 25°C; (b) NaPLGA + NaCl [103], [NaPLGA2] = 0.008 monoM, [NaCl] = 4 mM, on a watchglass, 0.7 mL, 25°C; (c) PDL-HBr + PLLHBr [40], [PDLHBr] = [PLLHBr] = 0.00005 monoM, on a watchglass, 0.7 mL, 24°C; (d) NaHLA [108], [NaHLA] = 0.004 monoM, [NaCl] = 0.06 mM, on a coverglass, 0.1 mL, at 25°C; (e) NaCMC2 [106], [NaCMC2] = 0.008 monoM, [NaCl] = 0.04 M, on a coverglass, 0.1 mL, 25°C; (f) βCD [107], [βCD] = 0.01 M, on a glass dish, 0.7 mL, at 20°C; (g) NaDNA [42], [NaDNA] = 0.01 monoM, on a watchglass, 0.7 mL, at 25°C; (h) KPolyA [109], [KPolyA] = 0.00414 monoM, [KCl] = 0.06 M, pH = 6.6, at 20°C; (i) PolyA + PolyU [110], [PolyA] = [PolyU] = 0.002 monoM, [KCl] = 0.01 M, on a coverglass, 0.1 mL, pH = 6.6, at 25°C. Full scale is at 100 μm (a–g) and 50 μm (h,i).

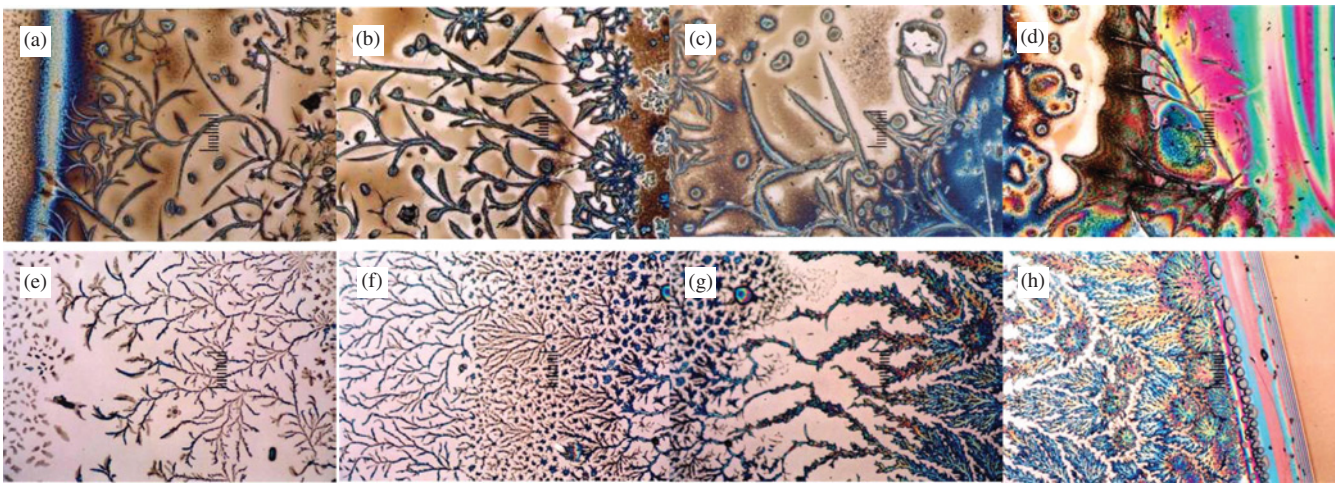


FIGURE 32.12 Microscopic drying patterns of Ge:GeO_2 film. (a–d) code 23b, on Si, 5×, full scale at 200 μm; (e–h) code 24b, on Si, 40×, full scale at 25 μm, from the central area to the right edge.

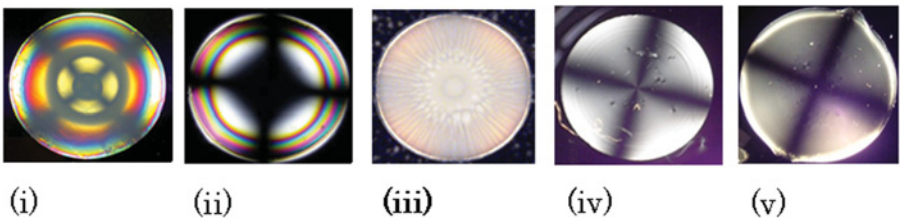


FIGURE 39.2 Gels observed under crossed nicols for polymer solution/medium systems using the boundary condition (a) or (c) in Fig. 39.1. The gels prepared under condition (a) were excised perpendicularly to the long axis of the dialysis tube, and the gels prepared under condition (c) were stripped off the plates. The photographs were taken from the top view: (i) Curdlan in NaOH solution/$CaCl_2$ solution (from Ref. 14, Fig. 2); (ii) DNA in buffer of pH 9.2/$CoCl_2$ solution (from Ref. 17, Fig. 1); (iii) CMC in pure water/$CaCl_2$ solution (from Ref. 18, Fig. 1); (iv) chitosan in acetic acid solution/NaOH solution (from Ref. 24, Fig. 1a); (v) myosin in pure water/glutaraldehyde solution.

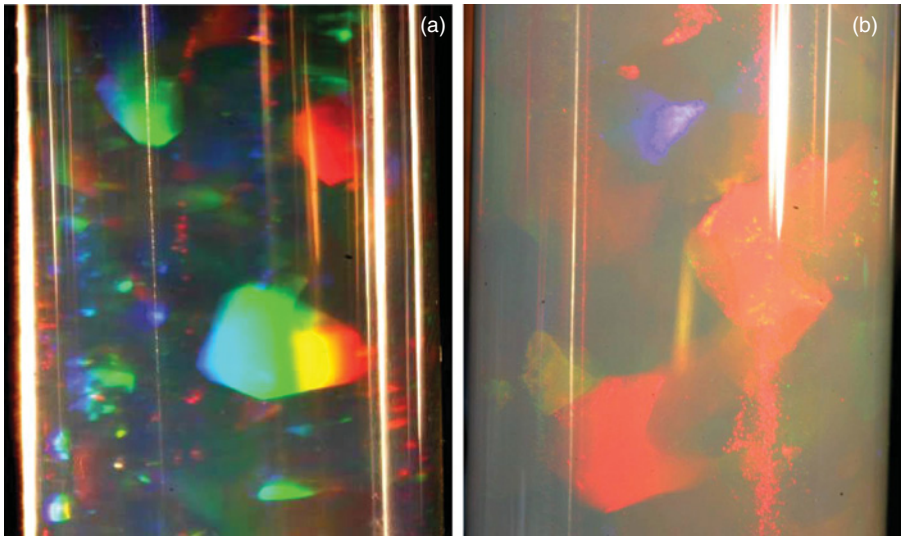


FIGURE 41.3 Close-up color images of PNIPAM(200-5) in a test tube: (a) [PNIPAM(200-5)] = 0.116 wt%, with resins, at 25°C; (b) 2.82 wt%, [NaCl] = 3.5×10^{-5} M, at 25°C.

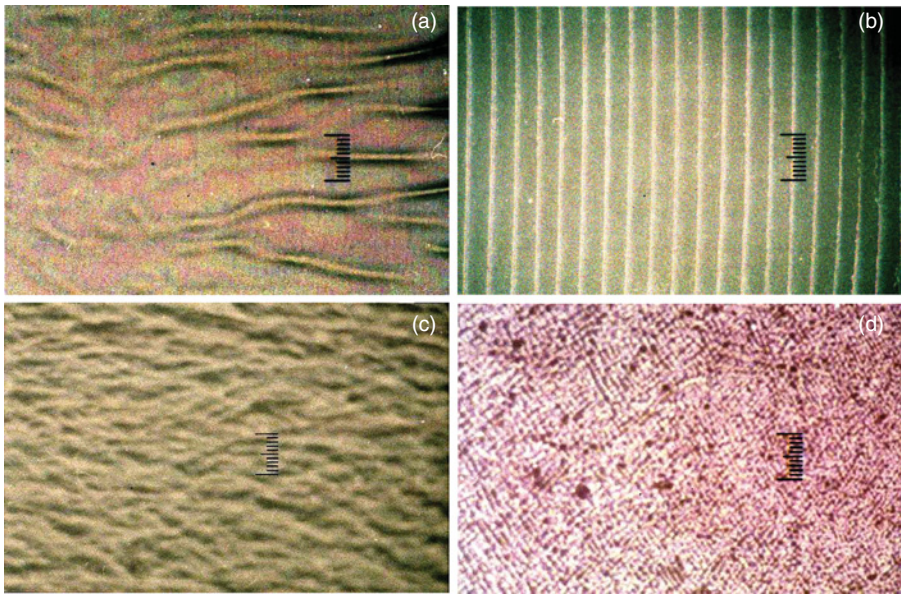


FIGURE 41.8 Typical microscopic drying structures of (a) *ordered spokelines*, (b) *ordered rings*, (c) *net* structure, and (d) *lattice*like ordered structures of the agglomerated particles of gel spheres. (a) pNIPAm(200-10), 0.119 wt%, on a coverglass, 20°C; full scale is 200 μm, (b) pNIPAm(200-0.5), 0.0336 wt%, on a glass dish, 45°C; full scale is 100 μm. (c) AIBA-P2VP(1), 3.45 wt%, on a watchglass, 22°C; full scale is 100 μm. (d) pNIPAm(200-5), 1.55 wt%, on a glass dish, 45°C; full scale is 200 μm.

INDEX

AAc, *see* acrylic acid
aaRS, *see* aminoacyl tRNA synthetase
ABA, *see* abscisic acid
ABC, *see* adenosine triphosphate (ATP)-binding cassette
ABS, *see* antigen binding site
abscisic acid (ABA), 871
absorption band, 270, 508, 646, 790, 896
AC electrokinetics, 933
acetic acid group, 272
acid phosphatase, 459
acid strength, 185
acidic amino acid, 792
ACM, *see* astrocyte-conditioning medium
acrylic acid (AAc), 223, 559, 775
activated sludge, 74
active layer, 465
active site, 29, 196, 313, 381, 467, 580, 791, 872
activity coefficient, 369, 461, 721, 1037, 1062
acute myelogenous leukemia (AML), 314
acyl-CoA synthetase, 19
adamantine, 325
adaptive multimode lubrication, 278
adenosine monophosphate (AMP), 18, 198, 223
adenosine triphosphate (ATP), 18, 223, 244
adenosine triphosphate (ATP)-binding cassette (ABC), 244
adenylate-forming superfamily, 22
adenylation, 202
adhesion force, 60, 84
adsorbed film, 280, 636, 1052, 1086
adsorbed layer, 45, 146, 284, 535, 668, 912, 1006
adsorption isotherm, 49, 249, 535, 988, 1006
adsorption layer, 905
advective-dispersive equation, 982
AEC, *see* anion exchange capacity
AEM, *see* anion exchange membrane
aerogel, 1, 498
affinity chromatography, 225, 609
affinity constant, 929
affinity latex, 609
AFM, *see* atomic force microscopy
AFS, *see* atomic force spectroscopy
agarose gel, 498, 549, 609
agglomerate, 6, 357, 420, 524, 558
agglutination, 610, 614
agglutination test, 614
aggregated structure, 642, 772
aggregation kinetics, 577, 1014
aggregation number, 189, 629, 645, 711, 774, 841, 1011, 1056, 1097
aggregation pattern, 1031
air–aqueous solution interface, 531, 637
air–water interface, 197, 262, 368, 535, 597, 604, 628, 674, 777, 886, 895, 911, 1021, 1035, 1059
alasan, 233
albumin, 84, 148, 225, 283, 615, 913, 1012
aligned collagen matrix, 340
alkanolamide, 1100
alkyl glucoside, 1044
alkylurea, 847
allosteric reaction, 382
alloy crystal, 361
alpha (α)-crystallin, 737
alpha (α)-helix, 31, 507, 580, 885, 895
alpha (α)-helix-rich protein, 31
alternative solvent, 135
alveolar collapse, 885
Alzheimer's disease, 256
amide I, 167, 577, 894
amide II, 167, 894
amide III, 167
amine, 848
amino acid surfactant, 573, 771
amino acid-derived surfactant, 573
aminoacyl tRNA synthetase (aaRS), 199
aminoacyl-AMP, 199
aminoacylation, 197
amitriptyline hydrochloride (AMT), 1058
AML, *see* acute myelogenous leukemia
amniotic fluid, 909
amorphous carbon, 325
amorphous region, 272
amorphous solid, 262, 355
AMP, *see* adenosine monophosphate
amphiphile, 123, 197, 242, 292, 307, 426, 530, 544, 597, 629, 750, 771, 841, 1020, 1046, 1056, 1083, 1095
amphiphile, bola, 773
amphiphilic block copolymer, 181, 580, 777, 802, 816, 1102
amphiphilic copolymer, 181, 800, 816
amphiphilic dendrimer, 189
amphiphilic drug, 841, 1058, 1062

Encyclopedia of Biocolloid and Biointerface Science, Volume 2, First Edition. Edited by Hiroyuki Ohshima.
© 2016 John Wiley & Sons, Inc. Published 2016 by John Wiley & Sons, Inc.

amphiphilic fluoropolymer, 151
amphiphilic molecule, 30, 36, 150, 198, 231, 292, 529, 774, 841, 861, 908, 1095
amphoteric polymer, 596
AMT, *see* amitriptyline hydrochloride
amyloid, 256, 575
anachelin, 152
analgesics, 841, 1057
ANC, *see Aspergillus niger* cellulose
anchoring group, 151
anesthesia phenomenon, 44
anesthetic action, 17, 56
anesthetic potency, 17, 45
ANG, *see* angiopoietin
angiopoietin (ANG), 245
anion exchange capacity (AEC), 979
anion exchange membrane (AEM), 721
anionic surfactant, 136, 296, 504, 531, 704, 773, 850, 990, 1020, 1039, 1053, 1058, 1064
anisotropic gel, 487
anisotropic interface, 134
anisotropic network structure, 277
ANN, *see* artificial neural network
anoikis, 313
anomalous transport, 809
antibacterial activity, 135, 256, 263
antibiofouling surface, 121
antibiotics, 95, 119, 131, 202, 456, 841, 1056
antibody, 211, 227, 249, 257, 316, 610, 814, 921
anticholinergics, 841, 1056
antifertility, 130
antifungal polyene, 1057
antigen, 1, 62, 161, 211, 244, 257, 304, 610, 614, 812, 921
antigen binding site (ABS), 616
antigen excess zone, 617
antigenicity, 161, 615
antimicrobial action, 451
antimicrobial activity, 71, 123, 134, 539
antimicrobial agent, 162, 242, 775
antimicrobial stress, 95
antioxidant, 131, 305, 785, 871
antioxidant defense, 875
antioxidation activity, 817
antirheumatoid antibody, 615
AO, *see* atomic orbital
apatite/collagen composite cement, 406
apoptosis, 132, 317, 1026
aptamer, 216, 915
AQP, *see* aquaporin
aquaporin (AQP), 245
aqueous organic solution, 721
Arabinosylcytosine (Ara-C), 316
Ara-C, *see* Arabinosylcytosine
articular cartilage, 269, 278
artificial hydrogel cartilage, 269, 278
artificial joint, 269, 278, 284
artificial neural network (ANN), 129
artificial vessel, 90
aryl-homoserine lactone, 71
Aspergillus niger cellulose (ANC), 712
astrocyte, 245
astrocyte-conditioning medium (ACM), 245
asymmetric field flow fractionation (AFFF), 303
asymmetric methylene stretching vibration, 899
asymmetric synthesis, 196
atom transfer radical polymerization (ATRP), 152, 222, 595, 774
atomic force microscopy (AFM), 5, 59, 173, 285, 303, 342, 536, 557, 597, 604, 636, 674, 885, 892, 1035
atomic orbital (AO), 336
atomistic model, 198
ATP, *see* adenosine triphosphate
ATR, *see* attenuated total reflection
ATR-FT-IR, *see* attenuated total reflection Fourier transform infrared
ATR-IR, *see* Attenuated total reflection infrared
ATRP, *see* atom transfer radical polymerization
attenuated total reflection Fourier transform infrared (ATR-FT-IR), 8
attenuated total reflection infrared (ATR-IR), 84
attenuated total reflection, polarized attenuated total reflection (ATR), 894
AuNP, *see* gold nanoparticle
autocorrelation function, 621, 747
axisymmetric particle, 692

bacteria adhesion, 118, 147
bacterial aggregate, 76
bacterial biofilm, 97
bacterial cell, 69, 95, 135, 202
bacterial cellulose, 356
bacterial interaction, 68, 74
bacterial membrane, 134
bacterial surface, 64
bactericidal potency, 545
ball-on-plate mode, 275
BAM, *see* Brewster angle microscopy
Bangham method, 860
basic amino acids, 849
BBB, *see* blood–brain barrier
bcc, *see* body-centered cubic
Belousov–Zhabotinsky (BZ) reaction, 560
Benard cell, 412
bending elasticity of bilayer, 293
bending energy, 294, 632
bentonite, 357, 417
beta (β)-lactoglobulin, 713
beta (β)-sheet, 507, 896
bicontinuous cubic phase, 534
bicontinuous phase, 1046
bilayer, 196, 292, 537, 772
bilayer fluidity, 305
bilayer permeability, 295
bile acid, 712, 842, 1054
bile salt, 123, 301, 705, 746, 841, 1033, 1102
bimetallic nanocolloid, 787
binary monolayer, 599, 890
binding constant, 32, 84, 711, 921, 1071
binding free energy, 399
binding isotherm, 705, 1071
binding number, 20, 1071
bioactive compound, 129, 220
biochirality, 196
biocolloid, 231, 260, 557, 946, 1004, 1071, 1091
biocompatibility, 1, 63, 82, 122, 145, 161, 263, 325, 406, 560, 593, 686, 800, 842
biocompatible polymer, 82, 136, 714
bioconjugation, 814
biodegradable polymer, 87, 815, 1010
biodegradation, 3, 407
biodispersan, 119, 233
biodistribution, 138
biofilm, 68, 94–107, 118–121, 147, 262
biofilm formation, 65, 74–76
bioflotation, 108
biofouling, 3, 100, 118–121
bioinspired material, 195
bioinspired microemulsion, 122
biointerface, 60, 231, 261, 303, 790
biological cell, 59, 261, 469, 631, 663, 684
biological macromolecule, 167, 280, 380
biological membrane, 17, 62, 126, 195, 383, 661, 674, 690, 825, 854, 865, 946, 1039, 1058
biomaterial, 14, 63, 82, 95, 145–150, 161–175, 343, 407
biomedical device, 82
biomimetic polymer aggregate, 181
biomimetic, 46, 122, 152, 181, 195, 198, 269, 687, 1039
biomolecule, 1, 59, 195, 211, 223, 257, 497, 554, 609, 668, 684, 785, 790, 801, 813, 915, 1071
biomolecule–water interface, 380, 384
bioscaffold, 686
biosensing, 211, 790
bioseparation, 133, 220, 609
biosurfactant, 76, 97, 128, 231–243, 704, 771, 842, 1044, 1051, 1054

biosynthetic pathway, 196
biosystem, 65, 195
biotechnology, 60, 133, 212, 227, 236, 260, 704, 790, 812, 841
biphasic finite element analysis, 278
biphasic lubrication, 280
birefringence, 356, 415, 488, 661, 663–671, 1027, 1099
BIS, *see* methylenebisacrylamide
bis(alkylphenyl)iodonium hexafluorophosphate, 188
bisimidazolium gemini, 551
bisphenol A, 391
black foam film, 908
black spot, 907
Bloch equation, 396
block copolymer, 151, 181, 214, 260, 302, 426, 580, 774, 800, 815, 841, 905, 1006, 1101
blocklike crystal, 359, 518
blood–brain barrier (BBB), 244
BNCT, *see* boron neutron capture therapy
BODIPY, *see* boron dipyrromethene
body-centered cubic (bcc) lattice, 360, 519
bola amphiphile, 773
Boltzmann distribution, 949
Born approach, 384
borocaptate sodium (BSH), 256
boron dipyrromethene (BODIPY), 258
boron neutron capture therapy (BNCT), 255
boron tracedrug, 255–259
boundary lubrication, 275, 278, 287
bovine serum albumin (BSA), 18, 63, 84, 212, 257, 709, 913, 921, 1076
Bragg diffraction, 356, 420, 515
Bragg distance, 520
breakthrough curve, 979
Brewster angle microscopy (BAM), 38, 597, 602, 629, 891, 1035
brick-wall-like aggregate, 698
bridging flocculation, 481, 1007
Brinkman screening length, 935
BrMA, *see* bromomalonic acid
broad ring, 412
bromomalonic acid (BrMA), 561
Brownian coagulation, 475
Brownian dynamics method, 692
Brownian motion, 295, 474, 620, 692, 1008
Brownian movement, 358
brush regime, 150, 213
BSA, *see* bovine serum albumin
BSH, *see* borocaptate sodium
budding of vesicles, 632
bundle, 174, 274, 340, 412, 753
burn wound, 451
C13 NMR, 325, 332, 647
C13 NMR spin-lattice relaxation time, 647
C6 glioma cell, 544
CAC, *see* critical aggregation concentration
CAC, *see* critical association concentration
cadmium nanoparticle (CdNP), 306
caffeine, 424
calcium phosphate, 404, 687
CAM-DR, *see* cell-adhesion-mediated drug resistance
cancer cell, 89, 133, 471, 581, 610, 690, 808
cancer resistance protein (CRP), 216
cancer therapy, 132, 778
capillary electrophoresis of liposomes, 823
capillary flow theory, 413
capillary pressure, 906, 1010
capping ligand, 260
carbodiimide, 616, 801
carbonization, 328
carboxybetaine (CB), 151
carboxybetaine methacrylate (CBMA), 152
carboxymethyl cellulose, 131, 714, 998
cardanol oil, 544
cardhouse structure, 453
cast-drying (CD), 270, 285
castor oil (CO), 2, 126
catanionic amphiphile, 307, 1029
catanionic micelle, 1028, 1036
catanionic microemulsion, 134
catanionic phospholipid, 1021
catanionic surfactant, 1020
catanionic system, 296
catanionic vesicle, 306, 1025, 1037
catanosome, 1037
cation exchange capacity (CEC), 979
cation exchange membrane (CEM), 466, 721
cationic gemini surfactant, 530, 539, 852
cationic surfactant, 125, 423, 531, 580, 631, 704, 776, 851, 988, 1029, 1052, 1064, 1067, 1097
caveola, 316, 674
CBF, *see* common black film
CBMA, *see* carboxybetaine methacrylate
CD, *see* cast-drying
CD, *see* circular dichroism
CdNP, *see* cadmium nanoparticle
CEBE, *see* core-electron binding energy
CEC, *see* cation exchange capacity
cell adhesion, 65, 82, 169, 228, 313
cell attachment, 65, 75, 95, 161, 340
cell behavior, 90, 340
cell function, 88, 352, 629
cell proliferation, 171, 244, 314
cell separation, 220, 227
cell viability, 7, 90, 171, 317, 581
cell-adhesion-mediated drug resistance (CAM-DR), 313
cell–cell communication, 68, 97
cellobiose, 241, 332
cell-sized giant vesicle (CSV), 393
cellular uptake, 64, 261, 401, 686, 791, 808
CEM, *see* cation exchange membrane
central nervous system (CNS), 56, 244, 799
centrifugal compression, 364
cetylpyridinium bromide (CPB), 708
cetylpyridinium chloride (CPC), 705, 989
cetyltrimethylammonium bromide (CTAB), 134, 293, 704, 792, 1039, 1059
CH_2 bending vibrations, 895
chain asymmetry, 865
chain density, 150, 213
chaotrope, 845
chaperone, 358, 738
charge distribution, 155, 195, 473, 505, 721, 939
charge effectiveness, 733
charge renormalization effect, 358, 514
CHEMFET, *see* chemically modified field effect transistor
chemical affinity, 460
chemical architecture, 772
chemical cross-linking, 800
chemical shift, 9, 336, 394, 652, 1029
chemically modified field effect transistor (CHEMFET), 709
Chinese black ink, 413
chiral discrimination, 196
chiral segregation, 197
chirality, 195
chitin, 263, 331, 775, 815
chitosan, 165, 249, 263, 325, 331, 488, 685, 712, 815
chlorpromazine hydrochloride (CPZ), 1058
cholesterol, 40, 54, 130, 196, 295, 392, 400, 629, 652, 674, 712, 804, 821, 825, 854, 1011, 1034, 1054, 1083
choline formate, 3
chromatogram, 221
circular dichroism (CD), 83, 136, 164, 507, 713, 841
circulating line, 414
cis–trans isomerization, 186
Clint formalism, 1036
close-packed state, 599, 888
cloud point (CP), 842, 1044, 1053, 1058

clouding temperature, 570, 1066
cluster size distribution, 696
CMC, *see* critical micelle concentration
CNS, *see* central nervous system
CO, *see* castor oil
coacervation, 710, 800, 1031
coaggregation, 76, 96
coagulation, 83, 109, 145, 356, 479, 554, 786, 1005, 1015
coagulation in shear flow, 479
coarse-grained, 198
coated-wire electrode (CWE), 708
coexistence state, 38, 865
coffee, 412
cohesive force, 605
coil-to-helix transition, 507
coimmobilization, 215
coion, 435, 515, 726, 846, 970, 1063
cold crystallization, 84
collagen (type I), 340, 347
collagen (type II), 280
collagen concentration, 342
collagen fibril, 340
collagen matrix, 164, 281, 348, 352
collagen reinforcement, 281
collagen scaffold, 161, 497
collagen self-assembly, 347
collapse pressure, 599, 674, 886
collision frequency function, 475
collision radius, 478
colloid probe, 59
colloid stability, 914, 1004
colloidal crystal, 355, 413, 514, 558
colloidal dispersion, 59, 300, 358, 417, 483, 514, 692, 771, 784, 1004, 1014, 1087
colloidal gas, 355
colloidal gold nanorods, 1140
colloidal liquid, 355
colloidal sensor, 816
colloidal silica sphere, 357, 414
colloidal stability, 483, 557, 615, 799, 815
comblike architecture, 775
common black film (CBF), 637, 908
community structure, 95
complementary studies, 125
complete wetting, 165, 423, 512, 625, 684, 706, 834, 1073
complex impedance, 941
complex ore beneficiation, 108
complex viscosity, 5
compressibility, 29, 261, 602, 697
compression method, 37
compression stress, 273
compression-expansion cycle, 901
concentration polarization, 886
condensation effect, 42, 827
conditioning film, 95, 118
conductivity dispersion, 369
conductivity method, 539
confinement, 6, 123, 195, 280, 686, 812
confocal reflection microscopy (CRM), 342
conformational change, 28, 84, 136, 147, 164, 380, 489, 570, 683, 737, 829, 900
congruent melting point, 828
constant-compliance region, 61
contact angle, 5, 88, 110, 227, 593, 634, 913, 989
CONTIN (Laplace inversion program), 622
continuity equation, 432, 460, 947
continuous charge model, 977
continuous transformation process, 830
continuum electrostatics, 380
contractile protein, 753
controlled delivery, 135, 1010
cooperative adsorption, 988
cooperative interaction among crossbridges, 759
cooperativity, 413, 586, 711, 762, 831
core-electron binding energy (CEBE), 332
core/shell, 559, 787
core–shell microgel, 555
core–shell nanogel, 806
correlation length, 557, 634, 806, 1096
correlation time, 392, 624, 647
corynomycolic acid, 233
Coulomb potential, 431, 723, 977
counterdiffusion, 687
counterion association, 358
coupling agent, 3, 800
coupling effect, 422, 525
coupling phenomena, 459, 992
coupling reaction, 220, 802
CP, *see* cloud point
CPB, *see* cetylpyridinium bromide
CPC, *see* cetylpyridinium chloride
C16PC, *see* dipalmitoylphosphatidylcholine
C17PC, *see* diheptadecanoyl-PC
CPP, *see* critical packing parameter
CPZ, *see* chlorpromazine hydrochloride
critical aggregation concentration (CAC), 507, 544, 710, 988
critical association concentration (CAC), 530
critical micelle concentration (CMC), 114, 240, 529, 539, 705, 774, 841, 1052
critical thickness, 908
CRM, *see* confocal reflection microscopy
cross correlation, 918, 929, 1001
cross reactivity, 928
crossbridge, 754
crossed polarization, 666
cross-link density, 523, 555, 562, 800
cross-linkable block copolymer, 802
cross-linkable graft copolymer, 804
cross-linked micelle, 803
cross-linked vesicle, 805
cross-linking point, 499
cross-linking-agent-induced gelation, 495
crossover time, 496
CRP, *see* cancer resistance protein
cryogenic transmission electron microscopy (cryo-TEM), 302, 530, 1038, 1100
cryo-TEM, *see* cryogenic transmission electron microscopy
crystal growth rate, 362, 521
crystallinity, 167, 270, 404, 688
crystallization kinetics, 355, 361
CSV, *see* cell-sized giant vesicle
CTAB, *see* cetyltrimethylammonium bromide
cubic phase, 534, 911, 1031, 1044, 1056, 1097
cubosome, 122, 1048
cumulant expansion, 622
cuprous oxide (Cu_2O) nanocrystal, 1040
Curosurf, 909
cutoff phenomenon, 17
CWE, *see* coated-wire electrode
cyclic chemical reaction, 566
cyclic dimeric guanosine monophosphate (c-di-GMP), 75
cyclodextrin, 423, 786, 842
cytotoxic effect, 547, 1041
cytotoxicity, 64, 133, 173, 544, 813, 842, 1036

D-amino acid, 100, 201
Davies equation, 571
D-band formation, 349
D-band periodic structure, 348
D-band periodicity, 340
DDS, *see* drug delivery system
deacetylation, 263, 815
deadspace minimization, 358
Debye length, 358, 430, 522, 946, 961, 971
Debye screening length, *see* Debye length
Debye–Bueche model, 935, 935, 962
Debye–Hückel equation, 971
Debye–Hückel parameter, 436, 446, 822, 971, 1005
Debye–Hückel theory, 502
decyltrimethylammonium-decylsulfonate, 1020
degradation, 3, 73, 86, 97, 122, 133, 156, 172, 313, 325, 350, 549, 872, 1054
degree of cross-linking, 419, 515, 803
degree of hydration, 727, 1097
degree of hydrolysis, 270

degree of hydrophobicity, 344, 913
degree of order, 671
degree of polymerization (DP), 270, 502, 610, 804, 843
degree of saponification, 285
deionization, 359, 525
delay time, 191, 621
DeMon, 333
denaturation enthalpy, 24
denaturation temperature, 19, 24, 163
dendritic cell-like domain, 679
density functional theory (DFT), 52, 207, 325, 656
deoxyribonucleic acid (DNA), 44, 59, 68, 94, 123, 181, 195, 215, 260, 305, 409, 488, 544, 609, 657, 685, 712, 777, 790, 812, 915, 1012, 1020, 1101
depth profile, 171, 325
Derjaguin–Landau–Verwey–Overbeek (DLVO) theory, 59, 118, 455, 912, 1005, 1014
Derjaguin's approximation, 440, 1088
dermal permeation, 130
detergent, 76, 100, 163, 297, 571, 642, 704, 772, 1053
dextran sulfate (DXS or DS), 685, 712
DFS, *see* dynamic force spectroscopy
DFT, *see* density functional theory
diacylphosphatidylcholine, 826
diagnosis, 64, 211, 597, 614, 812
diagnotherapeutics, 258
dialysis tubing, 304
dialysis-induced gelation, 487
diamagnetic shielding, 335
diaryliodonium salt, 190
dibutyltindilaurate, 4
dielectric constant, 358, 381, 502, 522, 624, 661, 706, 721, 843, 861, 937
dielectric dispersion, 369, 939
dielectric tensor, 661
differential scanning calorimetry (DSC), 24, 84, 149, 165, 270, 505, 563, 661, 733, 825, 843, 860
differentiation, 86, 109, 244, 320
diffusible signal factor (DSF), 69
diffusion, 48, 70, 98, 120, 225, 244, 295, 489, 508, 523, 621, 638, 684, 690, 725, 947, 1102
diffusion coefficient, 462, 521, 557, 621, 911, 935
diffusion controlled process, 129
diffusion layer, 994, 1002
diffusion potential, 722
diffusional flux, 459
diffusion-controlled dissolution model, 994
diffusion-controlled reaction, 399
diffusion-limited process, 489, 685, 1015
diheptadecanoyl-PC (C17PC), 862
dilute region, 270, 832, 1031
dimerization, 186
dimyristoyl phosphatidylcholine (DMPC), 39, 292, 395, 668, 860, 1084
dimyristoyl-PC, *see* dimyristoyl phosphatidylcholine
dimyristoylphosphatidylethanolamine (DMPE), 599
diol, 2, 610, 848
dioleoylphosphatidylcholine (DOPC), 632, 674
dipalmitoyl-PC, *see* dipalmitoylphosphatidylcholine
dipalmitoylphosphatidylcholine (DPPC), 32, 597, 674, 704, 825, 860, 885, 909, 1021, 1084
dipalmitoylphosphatidylglycerol (DPPG), 559, 886
diphenyliodonium hexaflurophosphate (DPI), 189
dipole–dipole interactions, 150, 367, 603, 647, 695, 892
direct force measurement, 60
direct mechanism, 846
discrete-charge effect, 975
disjoining pressure, 637, 906
disklike particle, 358, 696
disordered phase, 598
dispersed phase, 127, 455, 498, 625, 771, 1009
dispersion coefficient, 982
dispersion polymerization, 555
disproportionation, 182
dissipation function, 460
dissipative crystallization, 413
dissymmetry, 195
distearoyl-PC (DSPC), 827, 860
distribution function, 622
distribution ratio, 979
dividing surface, 1080
D-like carbon, 327
DLP, *see* double-layer polarization
DLS, *see* dynamic light scattering
DLVO, *see* Derjaguin–Landau–Verwey–Overbeek
DMPC, *see* dimyristoyl phosphatidylcholine
DMPE, *see* dimyristoylphosphatidylethanolamine
DNA, 74, 215, 422. *See also* deoxyribonucleic acid
DNA, complementary DNA, 611, 921
DNA-binding, 549
dodecanoic acid, 647
dodecylammonium-dodecanoate, 1020
dodecylammonium-dodecyl sulfate, 1020
dodecylethyldimethylammonium-dodecyl sulfate, 1020
dodecyltrimethylammonium bromide (DTAB), 134, 293, 712, 777, 851, 1059
dodecyltrimethylammonium-dodecyl sulfate, 1120
domain morphology, 603
donnan potential, 430, 444, 557, 722, 955–956, 963, 974
DOPC, *see* dioleoylphosphatidylcholine
Doppler frequency shift, 623
double cloud point, 843
double layer, *see* electrical double layer
double layer repulsion, 64, 1005
double-layer polarization (DLP), 433, 950
DOX, *see* doxorubicin
doxorubicin (DOX), 130, 249, 302, 319, 779, 809
DP, *see* degree of polymerization
DPI, *see* diphenyliodonium hexaflurophosphate or, *see* dual-polarization interferometry
DPPC, *see* dipalmitoylphosphatidylcholine
DPPG, *see* dipalmitoylphosphatidylglycerol
dropping method, 36
drug accumulation, 318
drug bioavailability, 136
drug delivery, 82, 122, 135, 162, 181, 244, 301, 391, 403, 539, 690, 772, 801, 812, 928, 994, 1004, 1039, 1058
drug delivery agent, 300
drug delivery carrier, 145, 801
drug delivery system (DDS), 1, 60, 82, 100, 135, 220, 331, 352, 403, 685, 690, 771, 799, 821, 842
drug release, 122, 246, 302, 325, 403, 685, 779, 805, 995
drug targeting, 122
drugs' tolerance, 129
dry ligand, 687
drying temperature, 272
DS, *see* dextran sulfate
DSC, *see* differential scanning calorimetry
DSF, *see* diffusible signal factor
DSPC, *see* distearoyl-PC
dual mechanism, 489
dual-functional, 818
dual-polarization interferometry (DPI), 667
Dudko–Hummer–Szabo model, 922
DXS, *see* dextran sulfate
dye solubilization method, 1059
dynamic binding probability, 394
dynamic elastic modulus, 364
dynamic (electrophoretic) mobility, 933

dynamic force spectroscopy (DFS), 915
dynamic light scattering (DLS), 125, 183, 302, 362, 484, 510, 517, 530, 557, 586, 619, 671, 712, 806, 821, 860

ECM, *see* extracellular matrix
edge detection, 918
edible microemulsion, 127
eDNA, *see* extracellular DNA
effective birefringence, 667
effective charge density, 723
effective charge number, 358
effective diffusion coefficient, 362
effective polydispersity, 359
effective soft-sphere model, 358, 522
effective surface potential, 442
egg phosphatidylcholine (EPC), 395
EHL, *see* elastohydrodynamic lubrication
Einstein's equation, viscosity, 26
Einstein's equation, diffusion, 649
Einstein–Stokes equation, 363, 621
elastic interaction, 1006
elastic modulus, 63, 278, 363, 417, 523
elastohydrodynamic lubrication (EHL), 280
electric field autocorrelation function, 621
electrical diffuse double layer, *see* electrical double layer
electrical double layer, 64, 356, 412, 433, 439, 474, 514, 522, 822, 937, 946, 970, 991, 1004
electrical equivalent circuit, 45
electroacoustics, 933
electrode polarization, 941
electroformation, 298
electrokinetic equations, 435, 947, 962
electrokinetics, 437, 955
electrolytic reduction ion water (ERI), 451
electro-mechano-acoustical analogy, 45
electron donors, 190
electron transfer-induced self-assembly, 182, 190
electrooptics, 366
electroosmosis, 470, 822, 933
electroosmotic flow, 470, 624, 822, 938, 956
electrophoresis, 163, 224, 258, 261, 430, 469, 549, 609, 624, 704, 785, 821, 921, 933, 946, 961, 1053
electrophoresis of nonuniformly charged soft particles, 967
electrophoresis of a pH-regulated soft biocolloid, 950
electrophoretic light scattering (ELS), 619
electrophoretic mobility (EPM), 98, 163, 303, 358, 420, 430, 469, 557, 619, 821, 933, 946, 961
electrophoretic mobility of colloidal particles, 430
electrophoretic mobility of soft and hairy particles, 933
electrophoretic mobility of soft particles, 435, 961
electrostatic interaction at constant surface charge density, 439
electrostatic interaction at constant surface potential, 439
electrostatic interaction between colloidal particles, 439
electrostatic interaction between hard particles, 439–442
electrostatic interaction between soft particles, 443–448
electrostatic interaction between two interpenetrating soft particles, 448
electrostatic interaction, 75, 99, 134, 148, 166, 198, 212, 222, 365, 384, 439, 469, 500, 554, 571, 594, 733, 850, 885, 929, 970, 1014, 1027, 1064, 1088
ELISA, *see* enzyme-linked immunosorbent assay
ELS, *see* electrophoretic light scattering
elution, 221, 273
emulsan, 98, 233
emulsification, 36, 124, 239, 452, 570, 704, 779, 1008
emulsion crystal, 368
emulsion polymerization, 429, 556, 610, 775
emulsion-phase structures, 771
enantiomeric excess, 197
enantiomeric pair, 197
enantiopurity, 197
encapsulation, 1, 72, 130, 712, 771, 1012, 1039
endothermic peak, 6, 24, 830
endothermic process, 505
endothermic shrinking, 502
energy flow, 762
energy liberation rate, 763
enflurane, 19, 44
engulfing, 448
enhanced permeability and retention (EPR) effect, 815
entrapment efficiency (EE), 301, 304, 1039, 1139
entropy controlled, 714
enzymatic degradation, 549
enzymatic reaction, 123, 197, 211, 306, 459, 684
enzyme membrane, 459
enzyme-catalyzed reaction, 133, 463
enzyme-linked immunosorbent assay (ELISA), 211, 617, 921
enzyme-linked immunosorbent assay, 221, 614, 921
enzyme-substrate complex, 461
EPC, *see* egg phosphatidylcholine
EPM, *see* electrophoretic mobility
EPR, *see* enhanced permeability and retention
EPS, *see* extracellular polymeric substance
ERI, *see* electrolytic reduction ion water
erythroid, 320
ethosome, 301
eutectic point, 828
evaporation, 2, 45, 273, 297, 368, 412, 421, 686, 793, 1027
excess Gibbs energy change of micellization, 1059
excess Gibbs free energy of mixing, 599
excess osmotic pressure, 439
exchange rate constant, 396
excitation wavelength, 746, 861
excluded volume, 413, 478, 522
excluded volume effect, 212, 355, 421, 522
exosome, 469–473
exothermic swelling, 502
expandability, 39, 53
extended critical micelle concentration, 710
extended DLVO model, 64
external field effect, 365
external stimuli, 63, 554, 684, 771, 889
extracellular DNA (eDNA), 76
extracellular matrix (ECM), 64, 85, 97, 146, 161, 248, 279, 317, 340, 350
extracellular polymeric substance (EPS), 68, 97, 260
extraction method, 98, 1022
extraordinary light, 662
eye lens, 737

fabrication, 86, 172, 276, 369, 558, 686, 800, 813, 822, 1040
face-centered cubic (fcc) lattice, 166, 358, 519
fatty acid ester, 125, 232, 571, 642, 656, 1044, 1101
fatty-acid homolog, 20
FBA, *see* force balance approach
fcc, *see* face-centered cubic
FCS, *see* fluorescence correlation spectroscopy
feedback effect, 561
FEL, *see* firefly luciferase
fengycin, 236
Fe_3O_4 nanoparticle, 161
FFL, *see* firefly luciferase

FF-TEM, *see* freeze–fracture transmission electron microscopy
fibrillogenesis, 340, 581
fibrinogen, 84, 145, 314, 576, 594
fibroblast, 93, 146, 164, 228, 320, 340
fibronectin, 152, 313
Fick's law, 491, 995
Fick's first law, 475, 994
Fick's second law, 994
Field, Korös and Noyes (FKN) mechanism, 565
firefly luciferase (FFL), 18
first-order autocorrelation function, 621
first-order kinetics, 714
fission, 296
fitting analysis, 807
five (5) FU, *see* fluorouracil
five-component monolayer, 683
fixed charge density, 448, 721, 946, 964
fixed charge group, 721
FKN, *see* Field, Korös and Noyes
flexibility, 2, 37, 86, 129, 153, 174, 341, 383, 416, 612, 841, 915, 1006, 1044, 1096
flipflop, 296, 392
floc, 74, 474
floc structure, 478, 480
flocculation, 116, 474, 556, 983
Flory's description, 500
flotation, 108
flow rate, 342, 668
fluid film lubrication, 279
fluid mosaic model, 44, 391
fluid phase load support, 281
fluidizing effect, 601, 888
fluorescence activated cell sorting, 925
fluorescence correlation spectroscopy (FCS), 306, 747
fluorescence dye, 424, 556
fluorescence intensity, 315, 578, 740, 862, 925
fluorescence microscopy (FM), 38, 59, 597, 629, 711, 814, 823, 891, 1035
fluorescence probing, 306
fluorescence resonance energy transfer (FRET), 65, 306, 745, 814
fluorescent probe, 306, 357, 603, 685, 737, 829, 893
fluorinated amphiphile, 597
fluorinated bisphenol A, 391
fluorinated gemini, 533
fluorinated pyridinium, 543
fluorinated surfactant, 533, 713, 1097
fluorocarbon chain, 1152
fluorouracil (5FU), 128, 395
FM, *see* fluorescence microscopy
FN, *see* fibronectin
FNIII14, 313
foam film, 637, 905
food-grade microemulsion, 128, 1046
force balance approach (FBA), 507
force curve, 62, 537
force–distance curve, 61, 537, 923
force–velocity relation, 764
foreign body reaction, 147
form factor, 520, 619, 663, 806, 1097
fouling release surface, 150
Fourier transform infrared (FT-IR) spectroscopy, 4, 111, 136, 149, 167, 270, 288, 577, 788, 827, 1030
fractal structure, 478
free water, 50, 84, 124, 149, 912, 998
free-draining behavior, 624
free-NCO, 8
freestanding membrane, 395, 686
freeze drying, 3, 300
freeze–fracture transmission electron microscopy (FF-TEM), 303
freeze–thawing (FT), 270, 285
freeze–thawing temperature, 272
freezing bound water, 84, 149
freezing-point–depression curve, 828
frequency beat, 623
FRET, *see* fluorescence resonance energy transfer
FT, *see* freeze–thawing
FT-IR, *see* Fourier transform infrared
full width at half height, 831
fulvic acid, 988
functional electrolyzed alkaline water, 451
functional electrolyzed water, 451
functional latex, 775
functionalization, 214, 264, 352, 814
fluorescent membrane probe, 860
Fuoss approach, 723
furanosyl borate diester (AI-2), 69
fusion, 37, 70, 87, 296, 350, 650, 828

gamma (γ)-ray irradiation, 505
ganglioside, 642, 674
gastrointestinal (GI) physiology, 124
gauche-type, 39
GAUSSIAN 09, 325, 333
Gaussian, 169, 198, 326, 385, 502, 925, 997
Gaussian component, 896, 997
Gaussian function, 997
GE100, 453
gel, 2, 33, 39, 123, 149, 163, 224, 270, 295, 325, 342, 350, 412, 419, 452, 487, 490, 497, 502, 515, 609, 636, 713, 721, 772, 799, 862, 921, 1001, 1031, 1048
gel crystal, 368, 420, 514
gel electrophoresis, 224, 258
gel permeation chromatography, 225, 1022
gel sphere, 357, 419, 523
gelatin, 85, 134, 164, 212, 249, 488, 657, 705, 785
gelation temperature, 5, 270
gel–sol transition temperature, 778
gemini pyridinium surfactant, 539
gemini surfactant, 529, 539, 773, 842, 1021, 1053, 1099
gene delivery, 137, 409, 539, 546, 554, 687
gene expression, 69, 94, 409, 871
gene transcription, 119, 260
gene transfer, 96, 257
generalized polarization (GP), 830
germanium, 895
giant multilamellar niosome, 307
giant multilamellar vesicle (GMV), 864
giant unilamellar vesicle (GUV), 61, 295, 631
Gibbs–Duhem equation, 723
gingerglycolipid, 233
glass dish, 413, 524
glass transition temperature, 368, 636
globular protein, 17, 163, 1071
glucosamine, 239, 332
glucose, 227, 260, 332, 466, 581, 685, 713, 775, 853, 872, 1039, 1044, 1054
glutalaldehyde, 616
glycerol backbone, 72, 236, 861
glycerol fatty acid ester, 571, 1046
glycerol-based surfactant, 1046
glycidyl methacrylate, 225, 556, 610
glycolipid, 130, 231, 674, 704, 773
glycophospholipid, 223, 236
glycosaminoglycan, 352
glycosidic bond, 233, 263
gold nanoparticle (AuNP), 189, 214, 264, 301, 550, 792–793, 813, 953
good solvent, 30, 805, 1009
GP, *see* generalized polarization
graft polymerization, 63, 555, 775
graft-from method, 152
graft-to method, 152
Gram-negative bacteria, 68, 97
Gram-positive bacteria, 68, 546
graphite, 325, 709
gravitational effect, 367, 427
green chemistry, 256, 261, 791, 814
green tea, 123, 416
greening effect, 1051
Griffin's equation, 571
GUV, *see* giant unilamellar vesicle

hairy nanogel, 800
Hamaker constant, 477, 1005, 1015, 1089
hard crystal, 355
hard particle, 439, 961
hard protein, 31

Hartree–Fock, 204, 332
Hasa–Ilavsky–Dusek theory, 502
heat exchange, 119
height detection, 919
hemagglutination, 614
hematite particle, 358, 693, 941
hemoglobin, 123, 321, 705
hemolysis test, 137
hemolytic activity, 242, 842
HeNe ion laser, 326
Henry slope, 988
Henry's equation, 430, 822
heparan sulfate, 313, 352
heparin, 263, 314, 352, 778
hepatoma operation using a microcatheter, 642
heterochiral, 197
heterocyclic cationic gemini surfactant, 539
heterodisperse, 622
heterodyne detection, 620
heterogeneous network, 288
heterogeneous nucleation, 359, 518, 636
heteropolysaccharide, 97, 238
hexadecanoic acid, 647
hexadecyltrimethyl ammonium bromide (HTAB), 264, 713
hexadecylylpyridinium–dodecylsulfate, 1030
hexagonal phase, 534, 1031, 1044
hexosome, 1049
HF/6-31G(*d*,*p*), 333
HHB, *see* hydrophobic–hydrophilic balance
hierarchical network structure, 277
high-dimensional structure, 181
high-field-gradient NMR, 393
high-performance liquid chromatography (HPLC), 303, 573, 580, 886
high-speed separation, 226
Hill number, 19
HisRS, *see* histidyl-tRNA synthetase
histidyl-tRNA synthetase (HisRS), 198, 202
HL60 cell, 319
HLB, *see* hydrophile–lipophile balance and, *see* hydrophilic–lipophilic balance
Hofmeister series, 845, 1063
hole nucleation theory, 910
hollow gel, 806
hollow sphere, 356, 665, 1040
homeostasis, 244, 871
homochirality, 196
homodyne-detected, 595
homogeneity, 150, 169, 270, 506, 535, 611
homogeneous nucleation, 359, 518
honeycomb, 86, 368, 419, 426, 453
honeycomb film, 87
Hooke's law, 60, 917
horizontally adhering type, 46
HPLC, *see* high-performance liquid chromatography
HSA, *see* human serum albumin
HTAB, *see* hexadecyltrimethyl ammonium bromide
Hückel's equation, 431
human serum albumin (HSA), 27, 63, 223, 249, 625, 713
humic acid, 97, 261, 988
humic substance, 97, 988
humidity, 2, 272, 413
humins, 988
hybrid gel, 288
hybrid microgel, 558
hybrid nanocapsule, 687
hybrid quantum-mechanical–semiempirical–molecular-mechanical theory (QM/MM), 198
hybrid surfactant, 1052
hybrid technique, 276
hybridization, 44, 215, 288, 612, 812
hydrate, 49–56
hydrated radius, 731, 846, 1062
hydrated state, 149
hydrated water, 32, 52, 84, 149, 593, 1064
hydration, 30, 49, 62, 85, 123, 148, 212, 261, 279, 296, 399, 504, 570, 595, 638, 727, 763, 776, 843, 864, 998, 1053, 1058, 1073, 1097
hydration force, 62
hydration lubrication, 279
hydraulic conductivity, 985
hydrazone bond, 810
hydrocarbon chain, 126, 231, 399, 530, 549, 599, 643, 774, 826, 848, 888, 1031, 1051, 1057
hydrodynamic diameter, 134, 182, 419, 519, 537, 557, 738, 808
hydrodynamic force, 261, 949
hydrodynamic interaction, 477, 692, 934
hydrodynamic radius, 512, 586, 621, 649, 784, 943
hydrodynamic stress tensor, 948
hydrogel, 122, 149, 169, 221, 269, 278, 456, 498, 524, 554, 799, 966
hydrogel, hybrid hydrogel, 277
hydrogel, poly(vinyl alcohol) (PVA) hydrogel, 278
hydrogel sphere, 421, 557
hydrogen bond, 29, 63, 123, 148, 168, 205, 270, 288, 380, 504, 776, 848, 921, 996, 1101
hydrogen bonding, 38, 62, 153, 181, 260, 289, 421, 489, 503, 577, 643, 710, 804, 886, 997, 1044, 1056
hydrolysis, 2, 95, 133, 247, 270, 459, 547, 610, 742, 755, 801, 842
hydropathy index, 30
hydrophile–lipophile balance (HLB), 124, 301, 1045
hydrophilic group, 37, 154, 240, 571, 606, 629, 704, 772, 853, 1044, 1051
hydrophilic interaction, 38, 583, 1057
hydrophilicity, 10, 17, 29, 36, 148, 161, 212, 227, 300, 341, 534, 558, 571, 593, 610, 817, 853, 1053, 1075
hydrophilic–lipophilic balance (HLB), 570, 774, 1035, 1056
hydrophobic alkyl chains, 36, 539, 778, 805, 1076
hydrophobic association, 504, 580, 774
hydrophobic attraction, 988
hydrophobic bond, 504
hydrophobic chain, 507, 529, 539, 599, 632, 657, 775, 806, 888, 988, 1006, 1034, 1044, 1054, 1097
hydrophobic core, 129, 148, 385, 580, 739, 804, 816, 837, 1011, 1056, 1098
hydrophobic effect, 292
hydrophobic energy, 30
hydrophobic environment, 17, 533, 861, 1037
hydrophobic group, 46, 151, 772, 806, 1051
hydrophobic interaction, 30, 62, 75, 121, 148, 212, 220, 347, 502, 535, 580, 636, 710, 737, 775, 804, 841, 988, 1030, 1058
hydrophobic process, 1076
hydrophobic–hydrophilic balance (HHB), 886
hydrophobic–hydrophobic interaction, 1030
hydrophobicity, 3, 21, 36, 64, 77, 88, 95, 113, 121, 135, 151, 220, 341, 400, 425, 577, 597, 610, 738, 778, 800, 846, 863, 886, 913, 989, 1010, 1032, 1053, 1076, 1097
hydrotrope, 853
hydroxylamine, 184
hydroxylamine hydrochloride, 183
hyperthermia, 814
hypochlorous acid, 119
hypochromic shift, 794
hysteresis, 886
hysteresis loop, 453, 890

ideal binary mixture, 827
identical interaction, 600
IER, *see* infrared external reflection
IFT, *see* indirect Fourier transformation
IL-based microemulsion, 135
image analysis, 108, 174, 342, 917

imidazolium amphiphile, 550
imidazolium gemini surfactant, 547
imipramine hydrochloride (IMP), 1058
immiscibility, 605, 833, 889
immobilized enzyme, 459
immunoassay, 83, 211, 614, 818
immunolatex, 610, 614
immunosensing, 211
immunosurface, 216
impedance analyzer, 46
in situ fluorescent observation, 283
in vitro release, 130, 303, 408
in vivo administration, 126
inclusion complex, 842
incongruent melting, 828
indirect Fourier transformation (IFT), 1096
indirect mechanism, 846
induced-fit, 21
induction period, 182, 361, 521, 561
induction time, 522
inert layer, 465
infrared external reflection (IER), 535
inhalation anesthetic, 18, 49
inhibitor, 19, 65, 130, 247, 256, 317, 539, 580, 585, 871, 911
inhibitor activity, 131
initial flash intensity, 21
inorganic nanoparticle, 554, 812
inorganic polymers, 771
insoluble monolayer, 535, 834, 1035
insulin, 127, 211, 222, 740, 809
insulin fibrillation, 575–588
integrated surfactant potency (ISP), 573
integrin, 146, 313–323
integrin-associated protein (IAP), 322
interaction parameter, 602, 1006, 1028
interdigitated gel ($L_{\beta}I$) phase, 861
interdigitated L_c (L_cI) phase, 868
interdigitation, 446, 862, 1028
interface displacement model, 634
interfacial energy, 125, 147, 293, 636, 800, 1008
interfacial layer, 51
interfacial polymerization, 127, 967
interfacial structured water, 50
interfacial tension, 124, 240, 628, 704, 1008, 1054
interfacial water, 82, 149, 592
interference light intensity, 665
intermediate water, 82
intermicellar interaction, 1062
interpenetration, 448, 806, 1006
interstitial fluid pressurization, 280
interstitial water, 95
intramembrane fluidity, 395
intramicellar repulsion, 1065
intramolecular movement, 647
intrapolymer complex, 625
intravenous route, 132
intrinsically disordered molecule, 383
inverted microscope, 470, 822, 907, 916
ion exchange capacity, 462, 726, 982
ion exchange chromatography, 222, 609
ion exchange membrane, 452, 466, 721, 726
ion exchange method, 1022
ion exclusion, 991
ion flux, 130, 491, 734, 876
ion homeostasis, 871
ion pair, 156, 475, 705, 721, 733, 850
ion pair amphiphile (IPA), 1029, 1033
ion toxicity, 872
ion transport, 721, 873, 979, 1024
ionic exchange, 540, 980
ionic liquid, 2–14, 135, 260, 368, 548
ionization energy, 325, 1087
ionomer membrane, 462
ion-selective field effect transistor (ISFET), 705
IPA, *see* ion pair amphiphile
IPDI, *see* isophorone diisocyanate
iron nanoparticle, 164
irreversible attachment, 75, 119
irreversible photoreaction, 186
ISFET, *see* ion-selective field effect transistor
isoelectric point, 504, 921, 955, 990, 1053
isoflurane, 19, 44, 52–55
isometric tension transient, 767
isophorone diisocyanate (IPDI), 4
isopleth, 828
isothermal titration calorimetry (ITC), 563, 710
isotonic velocity transient, 766
ISP, *see* integrated surfactant potency
ITC, *see* isothermal titration calorimetry
iturin, 236

J-aggregate, 426
Janus particle, 558
Joos equation, 602

K562 cell, 320
Katchalsky's model, 503
Kelvin equation, 1009
Kemp elimination, 207
ketal, 809
kinetic stability, 1004
Kirkwood–Alder transition, 358
kosmotrope, 154, 845
Kr^+ ion irradiation, 327
Krafft point, 539, 842, 1044

label-free, 211, 401, 667
lactose, 225, 816, 995
lag phase, 340, 577
lamellar phase, 50, 126, 296, 534, 911, 1021, 1044
lamination method, 276
Langmuir monolayer, 36, 597, 628, 639, 1035
Langmuir–Blodgett (LB) bilayer, 668
Langmuir–Blodgett (LB) film, 45, 675
Langmuir–Blodgett (LB) membrane, 357
Langmuir–Blodgett (LB) method, 369
Langmuir–Blodgett (LB) technique, 604
Laplace inversion program, 622
large multilamellar vesicle (LMV), 261, 863
large unilamellar vesicle (LUV), 295, 393, 1011
lateral diffusion, 392, 826
latex particle, 482, 511, 557, 610, 614, 966
lattice structure, 360, 421, 519
layer birefringence, 667
layered adsorbed film, 284
LC, *see* liquid crystal
LCST, *see* lower critical solution temperature
lectin, 65, 77, 98, 382, 816
lectin-mediated, 816
Lewy body dementia, 256
LFDD, *see* low-frequency dielectric spectroscopy
ligand-receptor, 62, 261
light intensity, 18, 99
light-sensitive surfactant, 1054
limiting molecular area, 38, 55
Lindemann's law, 364, 523
line tension, 603, 628, 892
line-active agent (linactant), 630
linear superposition approximation (LSA), 441
lipid bilayer, 44, 61, 181, 261, 297, 301, 391, 594, 661, 666, 684, 704, 861, 1012, 1034
lipid bilayer membrane, 661, 825, 860
lipid hypothesis, 18
lipid membrane, 32, 56, 62, 302, 391, 466, 663, 684, 1071
lipid monolayer, 36, 508, 599, 674, 885
lipid raft, 606, 629, 674, 825
lipiodol, 657
lipofectin, 546
lipoid hypothesis, 45
liponanocapsule, 684
lipopeptide, 231
lipophilic, 122, 181, 233, 546, 570, 657, 704, 772, 1004, 1011, 1035, 1049, 1056, 1095
lipopolysaccharide (LPS), 68, 98, 112, 246, 642

liposan, 233
liposomal drug formulations, 304
liposome, 261, 292, 300, 684, 821, 771, 825, 860, 1011
liquid crystal (LC), 2, 33, 295, 368, 391, 497, 535, 570, 631, 663, 684, 1020, 1046, 1084, 1095
liquid crystalline phase, 842, 1020, 1046, 1097
liquid disordered phase, 629
liquid membrane electrode (LME), 705
liquid ordered phase, 629
liquidus, 828
lithography, 86, 369
living polymer, 1096
LME, *see* liquid membrane electrode
LMV, *see* large multilamellar vesicle
loading rate, 922
London–van der Waals constant, 1087
lone pairs, 214, 337, 794
longitudinal relaxation time, 394
Lorentz–Mie regime, 917
loss modulus, 5, 1096
low water content, 721
lower critical solution temperature (LCST), 220, 507, 554
lower-shear layer, 284
low-frequency dielectric spectroscopy (LFDD), 933
LPS, *see* lipopolysaccharide
LSA, *see* linear superposition approximation
lubrication, 269
lubricin, 280
luciferin, 18
lung maturity assessment, 909
LUV, *see* large unilamellar vesicle
lycoposium, 419
Lys, *see* lysozyme
lysozyme (Lys), 18, 133, 224, 325, 361, 576, 705, 1075

MA, *see* malonic acid
macromolecule–water interface, 384
macromonomer, 511, 778, 805, 1011
macroscopic pattern, 419
magic bullet, 138, 304
magnesium aluminum silicate, 452
magnetic core particle, 690
magnetic drug delivery, 690
magnetic immunoparticle, 617
magnetic nanoparticle, 612, 693, 804, 814
magnetic particle-field interaction energy, 694
magnetic particle-particle interaction energy, 694
magnetic tweezer (MT), 920
main transition, 826, 862
main-transition temperature, 827
malonic acid (MA), 561
MAPK, *see* mitogen-activated protein kinase
mass transfer, 98, 120, 982
matrix metalloproteinase (MMP), 248, 313
maximum fluorescence wavelength, 860
Maxwell model, 1096
Maxwell stress tensor, 439, 949
Maxwell's equation, 662, 1084
Maxwell–Wagner derivation, 937
Maxwell–Wagner relaxation, 938
MBG, *see* microemulsion-based organogel
MCC, *see* microcrystalline cellulose
MCT, *see* medium chain triglyceride
mean field approach, 935
mean field approximation, 477
mean field model, 1096
mean-square radius, 512
medium chain triglyceride (MCT), 126, 453
melting peak, 6, 149
membrane binding, 396
membrane charge density, 723
membrane diffusion potential, 723
membrane dynamics, 391
membrane electrode, 704
membrane extrusion, 298
membrane filtration, 121
membrane fluidity, 46, 73, 395, 685, 826
membrane potential, 714, 721, 1026
membrane protein, 1, 18, 195, 244, 392, 668, 873
membrane reactor, 459
membrane surface, 33, 118, 391, 460, 632, 683, 722, 864, 967, 1080
membrane vesicle (MV), 68, 72, 469
mesh size, 564, 807, 1096
mesoporous γ-alumina nanoparticle, 1040
mesoscopic, 196, 692
messenger ribonucleic acid (mRNA), 197, 247, 469, 610
metagenome, 101
metal core-polymer shell nanoparticle, 182
metal nanoparticle, 263, 556, 791, 812
metallic nanocolloid, 784–789
metastable region, 867, 912
methionine, 100, 201, 776, 791, 849
methylation, 153, 871, 1052
methylenebisacrylamide (BIS), 498, 554
methylester, 650, 849
methyloctanoate, 648
Metrohm, 707, 727
Metropolis method, 692
Meyer–Overton rule, 17, 32
MFC, *see* microbial fuel cell
Mgb, *see* myoglobin
MIC, *see* microbially influenced corrosion
mica, 62, 174, 341, 347, 809, 892
micellar growth, 843, 1062, 1095
micellar protein, 737
micelle, 36, 50, 114, 122, 181, 240, 294, 392, 507, 529, 580, 631, 705, 771, 841, 1011, 1021, 1044, 1051, 1056, 1095
micelle hydration, 845, 1062
micellization, 181, 552, 776, 841, 1033, 1058, 1161
Michaelis constant, 459
Michaelis-Menten equation, 459
microbe, 72, 94, 119, 147, 545, 618
microbial fuel cell (MFC), 100
microbial surfactant, 231
microbially influenced corrosion (MIC), 95
microcapillary electrophoresis (μCE), 469, 822
microcapsule, 618, 967
microcapsule, hydrophilic gel microcapsule, 967
microcrystalline cellulose (MCC), 356, 998
microcrystallite, 270, 288
micro-culture method, 101
microdomain, 122, 316, 392, 674, 825
micro-EHL, 280
microelectrode, 466, 709, 790, 876
microemulsion-based organogel (MBG), 134
microenvironment, 100, 134, 148, 244, 257, 320, 609, 737, 773, 829
microfibril, 340
microfluidic, 298, 341, 497, 560, 800
microfluidization, 297
microgel, 403, 504, 511, 523, 554, 799, 934
microgravity, 367
microheterogeneous media, 136, 907
microorganism, 72, 94, 108, 118, 134, 231, 260, 704, 815, 878, 1044
microphase, 11, 510, 808
microscale of turbulence, 481
microscopic pattern, 417
microscopic solvent effect, 30
microvesicle, 469
microviscosity, 304
middle phase, 534
Mie regime, 917
Mie scattering, 625
migrating contact, 281
Miller's indices, 520
mineral analysis, 108, 873
mineralization, 97, 260, 684
miniemulsion, 614, 775, 1007

minimal residual disease (MRD), 315
minimum interdigitation pressure (MIP), 862
MIP, *see* minimum interdigitation pressure
miriplatin (MPT), 657
miscibility gap, 826, 1049
mismatched DNA, 612
Miso soup, 413
Mitchell–Ninham parameter, 848
mitogen-activated protein kinase (MAPK), 248, 871
mixed lubrication, 279
mixed micelle, 842, 1033, 1052
mixed micellization, 1059
mixing interaction, 1006
MLV, *see* multilamellar vesicle
MMP, *see* matrix metalloproteinase
MO, *see* molecular orbital
mobile phase, 220, 573
modified reversed-phase evaporation, 1038
modified Stokes–Brinkman equation, 946
modified Young equation, 636
modified Zimm plot, 626
moisture sorption, 5, 999
molecular alignment, 487
molecular lateral mobility, 911
molecular orbital (MO), 258, 331
molecular symmetry, 532
monoacylglycerol, 655
monochromatic light, 907
monoclonal antibody, 316, 927
monodispersity, 191, 264, 356, 554, 1040
monoglyceride, 1045, 1100
monolinolein, 1048
monolithic silica, 226
monometallic biocolloid, 785
mononuclear cell-like domain, 680
monoolein, 1048
monophasic region, 128
Monte Carlo, 690, 995
morphological transition, 1067
morphology of nanogel, 804
moving boundary picture, 491
MPPC, *see* myristoylpalmitoyl-PC
MPT, *see* miriplatin
MRD, *see* minimal residual disease
mRNA, *see* messenger ribonucleic acid
MRP, *see* multidrug resistance protein
MT, *see* magnetic tweezer
MTT assay, 8, 316
multidrug resistance, 247, 313
multidrug resistance protein (MRP), 247
multifunctional nanogel, 810
multifunctional polymer, 804
multilamellar bilayer, 671
multilamellar vesicle (MLV), 295, 303, 671
multilayer coating, 356, 685
multi-physisorption, 51
multiplex assay, 614
multipoint anchor, 215, 817
multivesicular body (MVB), 469
multivesicular vesicle (MVV), 295
multiwalled carbon nanotube (MWCNT), 549
muscle, 90, 100, 228, 487, 567, 753, 845, 1075
mushroom regime, 213
MV, *see* membrane vesicle
MVB, *see* multivesicular body
MVV, *see* multivesicular vesicle
MWCNT, *see* multiwalled carbon nanotube
myofibril, 753
myoglobin (Mgb), 18, 705, 817, 1075
myosin, 488
myosin head, 754
myosin molecule, 753
myristic acid, 19, 599
myristoylpalmitoyl-PC (MPPC), 866

nanobiodegradable dispersion, 1010
nanobiology, 206, 812
nanocapsule, 127, 306, 684–688, 779, 806
nanocarrier, 122, 248, 771–780, 810, 1048
nanocomposite, 166, 263, 408, 790, 813
nanodelivery, 135
nanodrop, 261, 300
nanoemulsion, 122, 302, 1004
nanogel, 511, 799–810, 934
nanolength, 195
nanoliposome, 821–824
nanomaterial, 1, 64, 257, 260, 297, 775, 791, 812, 1020
nanomedical application, 551
nanometer-scale homogeneity, 151
nanoparticle (NP), 64, 248, 260, 269, 325, 511, 550, 554, 575, 612, 686, 771, 784, 790, 799, 812, 821, 933, 953, 1010, 1040
nanoparticle–carbohydrate interaction, 261
nanoparticulate carrier, 551
nanoreactor, 191, 292, 305, 813
nanosensor, 260
nanotherapeutic material, 185
nasal delivery, 131
native state, 21, 195, 227, 742
natural immunity, 885
natural polymer, 212, 263, 331, 499, 560, 806, 815
natural synovial joint, 269, 278, 282
natural-sourced surfactant, 1044
Navier–Stokes equation, 412, 432, 935, 962
NBF, *see* Newton black film
N-carboxyanhydride, 778
near-infrared spectroscopy, 650, 994
necklace bead, 710
nematic order parameter, 699
Nernst–Planck equation, 721, 946
network homogeneity, 510
network inhomogeneity, 274, 510
neurovascular unit (NVU), 245
neutron dynamic therapy, 255
neutron scattering, 394, 661, 711, 826
neutron-induced prompt gamma (γ)-ray spectroscopy (NIPS), 256
Newton black film (NBF), 638, 908
NIH/3T3 cell, 320
niosome, 300–307, 842
NIPS, *see* neutron-induced prompt gamma (γ)-ray spectroscopy
NMR, *see* nuclear magnetic resonance
NOE, *see* nuclear Overhauser effect
NOESY, *see* nuclear Overhauser enhancement spectroscopy
nonequilibrium flocculation, 483
nonfouling material, 149
nonfreezing water, 84, 149
nonionic surfactant, 122, 300, 412, 452, 531, 573, 704, 773, 842, 1008, 1044, 1053, 1058, 1095
non-magnetic core particle, 690
nonpolar amino acid, 849
nonspecific adsorption, 147, 212, 610, 822
nonspecific binder, 22
normal healing response, 146
normalized intensity autocorrelation function, 621
Noyes–Whitney–Nernst dissolution model, 994
NP, *see* nanoparticle
NPOE, *see* ortho-nitrophenyl octyl ether
NPPE, *see* ortho-nitrophenylphenyl ether
nuclear Overhauser enhancement spectroscopy (NOESY), 394
nucleation rate, 360, 521
nucleophilic attack, 199
nutrient ion, 98

OAC, *see* oxoaminium chloride
occupied area, 531
octadecyltrimethylammonium–dodecylsulfate, 1030
octanoic acid, 20, 643
octan-1-ol, 643
octyltrimethylammonium-octanesulfonate, 1020
ocular delivery, 131

OEGMA, *see* oligo(ethylene glycol) methyl methacrylate
off-rate, 929
oil pollution remediation, 242
oleic acid, 125, 168, 236, 455, 529, 642
oleic acid-based surfactant, 529
oleic acid-cholesterol complex, 655
oleic acid–ethanol mixture, 654
oligo ethylene glycol (OEG), 149
oligo(ethylene glycol) methyl methacrylate (OEGMA), 152
oligolamellar (OLV), 295
oligolamellar vesicle, 295
OLV, *see* oligolamellar vesicle
omega (ω)-(perfluorooctyl)alkanol, 598
OMP, *see* outer membrane protein
on-chip electrophoresis, 821
one-electron oxidizing agent, 183
on-rate, 928
optical anisotropy, 664
optical axis, 662
optical constant, 619
optical microscopic texture, 1036
optical tweezer, 630, 915
optical waveguide lightmode spectroscopy (OWLS), 668
optically isotropic, 123, 1099
oral administration, 131, 778, 994
ordered ring, 420, 524
ordered spokeline, 524
ordinary light, 662
organic conceptual diagram, 571
organic solution, 297, 721
organogel, 134, 777
orientation angle, 343, 669
orientational distribution function, 694
orientational order, 661, 697, 826
orientation-dependent interaction, 197
Orion, 707
ortho-nitrophenyl octyl ether (NPOE), 706
ortho-nitrophenylphenyl ether (NPPE), 706
oscillating microgel, 560
oscillation circuit, 47
osmotic stress, 155, 870
Oster's mixing rule, 724
Ostwald ripening, 125, 362, 521, 1008
outer membrane protein (OMP), 72
OWLS, *see* optical waveguide lightmode spectroscopy
oxidative stress, 785, 875
oxidizing biocide, 119
oxoaminium chloride (OAC), 182
oxoaminium salt, 183

PA, *see* palmitic acid
packing density, 150, 358
packing parameter, 125, 202, 533, 772, 1031, 1052, 1095
packing stress, 864
pair distance distribution function (PDDF), 1097
pair potential, 198
palmitic acid (PA), 19, 606, 885
palmitoylstearoyl-PC (PSPC), 865
Pappus–Guldinus theorem, 1092
parallel polarization, 670
paramagnetic shielding, 335
parenteral administration, 126, 1012
Parkinson's disease, 247, 576
partial wetting, 633
particle analysis, 109
particle form factor, 520, 619, 806
particle-by-particle measurement, 469
particle-scattering function, 619
partition coefficient, 17, 49, 731, 1012, 1083
partition equilibrium, 124, 1083
PASt-*b*-PSt, *see* poly(4-allyloxystyrene)-*block*-polystyrene
patchlike packing, 600
PB, *see* phosphobetaine
p-boronophenylalanine (BPA), 256
p-BPA, *see p*-boronophenylalanine
PBSt-*b*-PSt, *see* poly(4-*tert*-butoxystyrene)-*block*-polystyrene
PC, *see* phosphorylcholine
PCS, *see* photon correlation spectroscopy
PDDF, *see* pair distance distribution function
PDGF, *see* platelet-derived growth factor
PDGFR, *see* platelet-derived growth factor receptor
PDMS, *see* poly(dimethylsiloxane)
Peclet number, 951, 982
PEG, *see* poly(ethylene glycol)
PEGylation, 214, 249, 816
PEI, *see* poly(ethylenimine)
PEMA, *see* poly(ethylene*alt*-maleic-acid)
PEO, *see* poly(ethylene oxide)
PEO-PPO-PEO, 151, 1006
peptide, 31, 59, 127, 154, 165, 197, 222, 307, 313, 382, 397, 575, 639, 668, 686, 741, 771, 790, 813, 841, 885, 915, 1056
peptidyl transferase center (PTC), 198
percutaneous penetration, 130
perfluorooctanoic acid (PFOA), 597
perfluorooctylation, 598
pericyte, 246
peritectic point, 828
permeability coefficient, 246, 725
permselectivity, 733
perturbation approach, 946
PET, *see* positron emission tomography
PFOA, *see* perfluorooctanoic acid
P-glycoprotein, 247, 248
pharmaceutical excipient, 844
pharmacokinetic parameter, 132
pharmacosome, 300
phase behavior, 123, 533, 602, 825, 841, 862, 891, 1031, 1044, 1097
phase diagram, 129, 296, 359, 518, 533, 601, 826, 843, 862, 1031, 1044, 1098
phase difference, 664
phase equilibria, 498, 826, 1020
phase inversion temperature, 129, 570, 1008
phase separation, 11, 86, 197, 276, 488, 501, 530, 604, 631, 715, 808, 825, 841, 1009, 1044, 1058, 1099
phase transition temperature, 222, 301, 868, 911, 966, 1035
phase transition, 39, 63, 85, 220, 295, 355, 498, 535, 550, 554, 598, 674, 696, 779, 825, 860, 888, 911, 966, 1035, 1046, 1084
PHEMA, *see* poly(2-hydroxyethyl methacrylate)
phenomenological equation, 459, 991
phenothiazine, 841, 1056
phenylhydrazine, 182
phopholipid, 860
phosphatidylcholine (PC), 182
phosphobetaine (PB), 83, 151, 592
phosphoglycolipid, 233
phospholipid, 73, 231, 295, 684, 773, 825, 854, 909
phospholipid bilayer membrane, 32, 825
photoacid generator, 188
photo-Claisen rearrangement, 189
photocleavage, 189, 613
photodecomposition, 190
photoelectron transfer, 190
photolithography, 709
photolysis, 186, 742
photon correlation spectroscopy (PCS), 303, 363, 617, 620
photon-counting heterodyne correlation function, 624
photonic bandgap, 369
photooxidation, 174, 186
photoreactive group, 187
photoresponsive surfactant, 1054
photosynthesis, 99, 186, 871
pH-responsive drug release, 810
pH-responsive nanogel, 799, 808
physical cross-link, 270
physical cross-linking, 800
physical entrapment, 505
physically cross-linked gel, 273
physisorption, 45, 115, 151
phytohormone, 871
pickering emulsion, 559, 636

pillarlike crystal, 359, 518
pincushion, 87
pinning efffect, 413
piperidinium gemini surfactant, 552
plant hormone, 871
plant surface, 96
plasma crystal, 369
plasma-induced polymerization, 227
plasmon excitation, 669
plasmon-waveguide resonance, 663
plasticizer, 212, 706
plateau border, 637
platelet-derived growth factor (PDGF), 320
platelet-derived growth factor receptor (PDGFR), 246, 320
ploughing component, 282
PMEA, *see* poly(2-methoxyethyl acrylate)
PM-IRRAS, *see* polarization-modulation infrared reflection absorption spectroscopy
PMMA, *see* poly(methyl methacrylate)
PMPC, *see* poly(2-methacryloyloxyethyl phosphorylcholine
PMT, *see* promethazine hydrochloride
PNIPAM, *see* poly(*N*-isopropyl acrylamide)
Poisson equation, 432, 946, 962, 970
Poisson–Boltzmann equation, 384, 439, 723, 935, 971
Poisson–Nernst–Planck equations, 947
polarity, 2, 157, 227, 425, 572, 705, 738, 771, 800, 816, 829, 860
polarity parameter, 30
polarizability tensor, 663
polarization, 132, 174, 244, 304, 326, 433, 593, 619, 662, 738, 759, 830, 886, 917, 933
polarization-modulation infrared reflection absorption spectroscopy (PM-IRRAS), 886, 895
polarized transmitted light, 669
pole vaulting motion, 341
poly(allylamine hydrochloride), 422
poly(4-allyloxystyrene)-*block*-polystyrene (PASt-*b*-PSt), 189
poly(α-DL-lysine) (α-PDLL), 507
poly(α-L-lysine) (α-PLL), 507
poly(amino acid), 778, 799
poly(amino acid) nanogel, 800
poly(amino acid) nanoparticle, 799
poly(aspartic acid), 778, 799, 801
poly(dimethylsiloxane) (PDMS), 11, 341, 470, 636, 822
poly(ethylene glycol) (PEG), 63, 126, 212, 302, 813
poly(ethylene oxide) (PEO), 64, 212, 774
poly(ethylene-*alt*-maleic-acid) (PEMA), 344
poly(ethyleneimine), 801
poly(ethylenimine) (PEI), 504
poly(2-hydroxyethyl methacrylate) (PHEMA), 84, 212
poly(lactide-*co*-glycolide) (PLGA) nanoparticle, 248
poly(L-lysine), 712
poly(2-methacryloyloxyethyl phosphorylcholine) (PMPC), 85, 212
poly(2-methoxyethyl acrylate) (PMEA), 83, 149, 212
poly(methyl methacrylate) (PMMA), 356, 413, 815
poly(*N*-isopropyl acrylamide) (PNIPAM), 63, 419, 515, 554, 775, 801
poly(*N*-isopropylacrylamide) hydrogel-coated latex, 966
poly(octadecene-*alt*-maleic acid) (POMA), 342
poly(oxyethylene) cholesterol ether, 1099
poly(4-pyridinemethoxymethylstyrene)-*block*-polystyrene (PPySt-*b*-PSt), 190
poly(succinimide), 801
poly(4-*tert*-butoxystyrene)-*block*-polystyrene (PBSt-*b*-PSt), 188
poly(vinyl alcohol) (PVA), 212, 269, 278, 815
poly(vinyl chloride) (PVC), 705
poly(2-vinyl pyridine) 517
poly(vinyl pyrrolidone), 367, 712
poly(4-vinylbenzyloxy-TEMPO)-*block*-polystyrene (PVTEMPO-*b*-PSt), 182
polyamine, 214, 547, 848
polyarginine, 685, 778
polydimethylsiloxane (PDMS), 341
polydispersity index, 365, 519, 622, 779
polyelectrolyte, 149, 243, 261, 356, 412, 430, 439, 484, 497, 503, 554, 592, 624, 684, 710, 775, 800, 934, 946, 961, 974
polyelectrolyte, zwitterionic polyelectrolyte, 154
polyelectrolyte brush, 445, 934
polyelectrolyte gel, 503
polyethylene glycol (PEG), 148, 249, 714
polyglycerol fatty acid ester, 571, 1049
polylactide nanoparticle, 132
polymer adsorption, 367, 988, 1006
polymer brush, 63, 150, 222, 280, 347, 444, 595
polymer complexation, 421
polymer flocculant, 474
polymer gel, 419, 498, 517
polymer saturation concentration, 710
polymeric amphiphile, 771
polymeric micelle, 771, 841
polymeric nanoparticle, 772, 779, 799, 1010
polymeric surfactant, 182, 231, 780, 905, 1008
polymerization, 63, 127, 152, 181, 221, 270, 285, 356, 498, 554, 595, 610, 614, 684, 721, 774, 800, 843, 966, 1011, 1025, 1039, 1049
polymerization degree, 285, 1049
polymerized pyridine, 817
polymer–liquid water interfaces, 592
polymer-mediated synthesis, 818
polymerosome, 302, 771
polynucleotide, 413, 619
polyoxyethylene alkyl ether, 126, 424
polyoxyethylene (POE) surfactant, 570
polypeptide, 62, 148, 163, 199, 340, 413, 507, 579, 611, 685, 711, 722
polypeptide gel, 507
polysaccharide, 18, 74, 85, 94, 115, 154, 238, 263, 413, 614, 619, 642, 684, 712, 815
polystyrene sphere, 356, 413, 524
polystyrene sulfonate (PSS), 707, 941, 988
polyurethane, 2, 285, 456
polyurethane-siloxane, 1
polyvinylpyrrolidone (PVP), 85, 850
POMA, *see* poly(octadecene-*alt*-maleic acid)
poor solvent, 30, 843
population balance, 474
porosity, 86, 172, 404, 524, 731, 996
positron emission tomography (PET), 256
potential maximum, 1014
potential well, 203, 758
potentiometric titration, 705, 727
power density, 1008
power stroke model, 753
PPySt-*b*-PSt, *see* poly(4-pyridinemethoxymethylstyrene)-*block*-polystyrene
PQS, *see* pseudomonas quinolone signal
precipitation method, 168, 1022
precipitation polymerization, 554, 610, 801
premicelle, 533
preparation molality, 1073
pressure antagonism, 17, 32
pressure balance technique, 908
pretransition, 825, 862
primary minimum, 1005, 1014
probability density function, 691
prodan, 860
prodan fluorescence spectrum, 829
prodan [6-propionyl-2-(dimethylamino) naphthalene], 829
proliferation, 7, 85, 146, 161, 244, 313

proliposome, 297
promethazine hydrochloride (PMT), 1058
proniosome, 301
propylene sulfoxide, 153
protein adsorption, 3, 63, 82, 148, 212, 224, 504, 779, 816, 1010
protein folding, 148, 181, 504
protein hypothesis, 18, 32
protein unfolding, 22
protein-ligand complex, 1073
proteoglycan, 245, 279
proton exchange method, 1029
proton (^{1}H)-NMR, 5, 50, 183, 394, 652, 1029
proton wire, 383
protrusion, 174, 394, 837, 892, 912
PS, *see* pulmonary surfactant
pseudo-double-chain catanionic surfactant, 1021
pseudo-double-chained surfactant, 1021
pseudomonas quinolone signal (PQS), 71
pseudo-partial wetting, 633
pseudo-triple- and quadruple-chained catanionic surfactants, 1021
PSS, *see* polystyrene sulfonate
PTC, *see* peptidyl transferase center
public consumption, 137
pulmonary surfactant (PS), 606, 704, 885, 905, 1054
pulsed-field-gradient (PFG) NMR, 392
PVA, *see* poly(vinyl alcohol)
PVC, *see* poly(vinyl chloride)
PVP, *see* polyvinylpyrrolidone
PVTEMPO-*b*-PSt, *see* poly(4-vinylbenzyloxy-TEMPO)-*block*-polystyrene
pyrene, 325, 530, 713, 738
pyridinemethoxymethyl group, 191
pyridinium amphiphile, 546
pyrrolidinium gemini surfactant, 552

QCI, *see* quartz crystal impedance
QCM, *see* quartz crystal microbalance
QCO, *see* quartz crystal oscillator
QD, *see* quantum dot
QELS, *see* quasielastic light scattering
QS, *see* quorum sensing
quadratic synchronous transient method 3 (QST3), 198
quantum dot (QD), 263, 306, 556, 618, 791, 813
quantum-mechanical, 198, 202, 207
quartz crystal impedance (QCI), 45
quartz crystal microbalance (QCM), 45, 83, 211
quartz crystal oscillator (QCO), 45
quasielastic light scattering (QELS), 620
quaternary ammonium bromide, 846
quaternary ammonium bromide salt, 1063
quaternary monolayer, 681
quinolone signal, 71
quorum sensing (QS), 69, 97

racemic pair, 198, 656
radial distribution function, 694
radioactive Cs, 981
radioimmunoassay (RIA), 211
radioimmunotherapy, 257
radius of gyration, 153, 512, 619
raftlike cluster, 696
Raman shift, 327
Raman spectra, 326
Ramos cell, 317
random coil, 164, 213, 502, 685
random displacement, 693
rapid aggregation, 1014
rapid coagulation, 477, 1015
rate of flocculation, 474, 1005
rate process model, 21
RAW117 lymphosarcoma cell, 965
Rayleigh ratio, 619
Rayleigh regime, 917
Rayleigh scattering, 261, 619
Rayleigh–Debye–Gans approximation (RDGA), 625
RDGA, *see* Rayleigh–Debye–Gans approximation
RDS, *see* respiratory distress syndrome
reaction layer, 466
reaction parameter, 263
reactive oxygen species (ROS), 784, 875, 1041
receptor-ligand bond, 923
reciprocating test, 274, 378
red cell, 615
redox catalyst, 182
redox polymerization, 505
redox potential, 304, 563
redox system, 182
reduced viscosity, 25, 365
reference polynomial, 919
reflection spectrum, 364, 521
refraction, 661, 916
region of interest (ROI), 918
regioselective cobromination, 544
rehydration, 262, 281
relative binding frequency, 924
relaxation effect, 433
relaxation length, 459
relaxation rate, 621
relaxation time, 398
relaxation time, structural relaxation time, 363
reorientation, 174, 362
repeated freeze-thawing method, 285
reptation, 1096
residence time, 248, 385
resistance function, 693
respiratory distress syndrome (RDS), 885, 909
respiratory movement, 885
restoration, 278, 289
retention time, 148, 221, 597, 886
reverse bicontinuous cubic phase, 1047
reverse micelle, 123, 791, 1040
reverse phase high-performance liquid chromatography (RP-HPLC), 886
reverse wormlike micelle, 1045, 1101
reversed passive hemagglutination (RPHA), 615
reversed-phase chromatography, 220, 572
reversible attachment, 75, 119
reversible photoreaction, 181
rhamnolipid, 128, 232, 911
RIA, *see* radioimmunoassay
ribosomal ribonucleic acid (rRNA), 101, 201, 679
rigidity, 40, 45, 364, 523
rigidity of bilayer, 294
ripple gel (P_β') phase, 825, 862, 1084
ripple structure, 836
rodlike particle, 695
ROI, *see* region of interest
root-mean-square distance, 626
ROS, *see* reactive oxygen species
rotational Brownian motion, 692
rotational correlation time, 394
rotational diffusion, 394
rotational diffusion coefficient, 370, 693
RPHA, *see* reversed passive hemagglutination
RP-HPLC, *see* reverse phase high-performance liquid chromatography
rRNA, *see* ribosomal ribonucleic acid
RST, *see* Rubnigh's regular solution theory
Rubnigh's regular solution theory (RST), 1036

S100, 456
saccharide-based material, 154
saline soil, 870
saline solution, 132, 172, 283
salt sieving, 991
salt stress, 870
salting-in and salting-out phenomena, 1064
SAM, *see* self-assembled monolayer
sandwich method, 489, 617
SANS, *see* small-angle neutron scattering
saponification, 240, 285, 571
sarcomere, 753
SAS, *see* solvent accessible surface

Sauerbrey equation, 45
SAW, *see* surface acoustic wave
SAXS, *see* small-angle X-ray scattering
SB, *see* sulfobetaine
SC, *see* stratum corneum
scaffold, 82, 161, 207, 256, 403, 497, 686
scanning electron microscopy (SEM), 6, 87, 109, 135, 171, 303, 406, 517, 556, 577, 636, 687
scanning tunneling microscopy (STM), 303
scattering intensity, 182, 362, 520, 620, 806, 1097
scattering length density, 806
scattering vector, 362, 519, 557, 620
SCFS, *see* single-cell force spectroscopy
screened Coulomb potential, 723, 977
screening effect, 522, 989
screen-printed electrode (SPE), 709
SDS-PAGE, *see* sodium dodecyl sulfate-polyacrylamide gel electrophoresis
SEC, *see* size exclusion chromatography
second virial coefficient, 619
secondary minimum, 638, 1014
second-derivative spectrum, 862
second-order autocorrelation function, 620
second-order harmonics, 366
secospiculisporic acid, 233
sedimentation, 119, 412, 421, 452, 474, 624, 690, 699
sedimentation equilibrium, 360, 523
sedimentation pattern, 416
segmental movements, 647
segregation, 197, 361, 417
selectivity, 45, 126, 200, 245, 706, 733, 816, 928, 981
selectivity coefficient, 45, 707, 982
self-aggregate, 774, 802, 842
self-aggregated structure, 774
self-assembled monolayer (SAM), 62, 153, 593, 1104
self-assembled system, 122, 292
self-assembly, 122, 155, 164, 181, 242, 261, 292, 340, 370, 512, 582, 639, 721, 772, 790, 814, 841, 1056
self-association, 577, 645, 1056
self-diffusion, 363, 392, 650
self-diffusion coefficient, 393, 642
self-microemulsifying drug delivery system (SMEDDS), 136
self-microemulsifying system, 137
self-organization, 82, 171, 350, 412, 487, 570, 650, 693, 808, 812
self-preserving antimicrobial, 123, 134
self-setting, 406, 409
self-similar solution, 477
SEM, *see* scanning electron microscope
semiconductor crystal, 370
semi-expanded state, 38
sensitization, 615
sevoflurane, 44, 391, 400
SFA, *see* surface force apparatus
shape factor, 664
shear flow, 341, 347, 362, 479, 630, 692
shear flow deposition, 341
Shear plane, 948, 961
Shear rate, 27, 341, 365, 479
Shearing deformation, 367
Shelf life, 124, 138
shielding tensor, 332
short-chain fatty acid, 20
shoulder peak, 337, 861
shrinkage temperature, 166
shrinking, 63, 500, 629, 808, 830, 937, 1010
Shultz–Hardy rule, 357
sialic acid, 248, 472, 966
sialidase, 472
SI-ATRP, *see* surface-initiated atom transfer radical polymerization
Siegert relation, 621
signal molecule, 97, 243
silane, 3, 168, 222, 333
silica aerogel, 1
silica bead, 220, 630
silica hollow sphere, 1040
silica nanoparticle, 2, 250, 262, 618, 779
silica particle, 6, 306, 357, 498, 536, 555, 630, 912
silica sphere, 357, 413, 520, 636, 779
siloxane, 1, 168, 249, 498, 713
silver and gold nanocomposite, 790
silver nanoparticle, 121, 162, 261, 792, 815
silver, 790
simple electrolyte, 424, 515
simulated synovial fluid, 275, 283
simulated valence X-ray photoelectron spectra (simulated VXPS), 329
simulator test, 285
single fiber, 753
single-cell force spectroscopy (SCFS), 65
single-molecule force spectroscopy (SMFS), 62
single-walled carbon nanotube, 708
SISE, *see* surfactant ion-selective electrode
site occupancy, 1074
site-specific delivery, 771
size distribution function, 477
size exclusion chromatography (SEC), 303, 609
Slater's transition state method, 332
SLB, *see* supported lipid bilayer
sliding-filament theory, 753
slipping plane, 430, 951, 961
slow aggregation, 1014
SLS, *see* static light scattering
small unilamellar vesicle (SUV), 295, 392, 671, 863
small-angle neutron-scattering (SANS), 128, 577, 711, 800, 807, 843, 1099
small-angle X-ray scattering (SAXS), 270, 303, 579, 1097
small-molecule surfactant, 186
smeared charge model, 977
smectite structure, 452
SMEDDS, *see* self-microemulsifying drug delivery system
SMFS, *see* single-molecule force spectroscopy
Smoluchowski approximation, 476, 824
Smoluchowski equation, 430, 470, 624, 961
smoothed surface, 12
SOD, *see* superoxide dismutase
sodium dodecyl sulfate-polyacrylamide gel electrophoresis (SDS-PAGE), 163, 224, 258
sodium phosphate buffer, 845, 1063
soft biocolloid, 946
soft colloidal particle, 95, 430
soft crystal, 355, 1027
soft EHL, 280
soft material, 269
soft particle, 69, 261, 430, 439, 934, 941, 946, 954, 961, 970
soft protein, 31
softness, 651, 947, 957
softness parameter, 558, 956, 963
soil dispersion, 983
soil flocculation, 983
soil permeability, 985
soil structure, 985
sol-gel, 1, 358, 814
solid lipid nanoparticle, 249
solid ordered phase, 826
solid solution, 111, 655, 828, 933
solid state NMR, 5, 738, 827
solidification, 276, 413, 421, 599
solid-phase catalyst, 134
solidus, 828
solubilization, 850, 1004, 1012
solubilization of lipids, 1034
solvation dynamics, 306, 747
solvent accessible surface (SAS), 384
solvus, 828
sophorolipid, 232
Soxhlet extraction, 3
spacer, 611, 1024
spacer length, 543, 851
SP-B, *see* surfactant protein B

SP-C, *see* surfactant protein C
SPE, *see* screen-printed electrode
specific base sequence, 611
specific binder, 18, 77
specific protein, 77, 211, 575, 610, 785, 909
specific viscosity, 365
spherulite, 422
sphingosome, 301
spiculisporic acid, 233
spin Brownian motion, 693
spokeline, 412
spontaneous curvature, 124, 294, 632, 864, 1031, 1097
SPPC, *see* stearoylpalmitoyl-PC
SPR, *see* surface plasmon resonance
squeeze out, 885
S–S bonding, 886
stability of catanosome, 1038
stability ratio, 1005, 1014
stabilization, 263, 265
stabilizer, 170, 263, 483, 554, 775, 784, 792, 815
staggered configuration, 868
standard Gibbs energy of micellization, 1059
standard Gibbs free energy change of adsorption, 1059
starch, 260, 872, 998
static light scattering (SLS), 362, 511, 519, 619
stationary contact, 281
steady-state coupling, 459
steady-state light intensity, 21
stealth liposome, 302
stealth surface, 147
stearic acid, 73, 606, 648
stearoylpalmitoyl-PC (SPPC), 865
Stejskal–Tanner equation, 393
stem cell, 88, 352
stent, 90, 686
step-temperature gradient, 223
stereoisomer, 18, 201
stereoselectivity, 200
steric interaction, 62, 537
steric repulsion effect, 816
steric stability effect, 355
steric stabilization, 212, 615, 684, 815, 1006
steroid, 40, 131, 221, 451, 642, 775
stiffness of muscle, 764
stimuli-responsive polymer, 63, 220
stimulus-responsive, 403, 558, 800
STM, *see* scanning tunneling microscopy
Stokes equation, 455, 649
Stokes–Brinkman equation, 946
Stokes–Einstein equation, 557
Stokes–Einstein radius, 649
Stokes–Einstein relation, 476, 621
storage modulus, 5, 365, 1096
storage stability, 136, 615
strain-dependent permeability, 281
stratum corneum (SC), 301, 529
stress-relaxation test, 286
Stribeck curve, 279
structural domain, 381
structural relaxation time, 363
structure factor, 363, 520, 697, 856, 1097
structured water, 50, 383
styrene, 555, 610, 779, 1011
subcellular compartment, 383
subcutaneous route, 132
succinoyl trehalose, 232
sucrose, 123, 260, 872, 1044, 1100
sucrose fatty acid ester, 1044, 1101
sugar ring, 201
sugar-based surfactant, 775, 1044
sulfide, 31, 108, 183, 306, 356, 546, 576, 776, 801
sulfobetaine (SB), 83, 151
sum frequency generation, 592
supercritical fluid, 86, 297
superlattice, 361, 687, 834
superoxide dismutase (SOD), 785, 875
supported lipid bilayer (SLB), 62, 594, 667
supposition method, 953
supraamphiphile, 774
supramolecular, 260
surface acoustic wave (SAW), 211
surface charge density, 134, 431, 439, 800, 943, 961, 971, 1030
surface charge density/surface potential relationship, 972
surface charge layer, 437, 557, 963, 974
surface conduction, 433
surface coverage, 685, 924, 1011
surface deformation, 61
surface energy, 2, 12, 639, 812, 996, 1004, 1095
surface excess, 1180
surface excess concentration, 531, 1059
surface force apparatus (SFA), 59
surface free energy, 10, 83, 605, 1008
surface gel hydration lubrication, 280
surface layer, 280, 415, 430, 439, 452, 511, 557, 624, 961, 974, 985, 1093
surface lubricity, 288
surface modification, 110, 151, 161, 212, 341, 615, 690, 699, 780, 792, 815, 1010
surface plasmon resonance (SPR), 83, 211, 265, 558, 793, 1040
surface potential, 64, 430, 439, 557, 597, 886, 946, 961, 972, 1005, 1014
surface pressure, 37, 367, 535, 597, 628, 674, 886, 909, 1022, 1035, 1059
surface roughness, 5, 12, 43, 75, 121, 163, 279, 697
surface tension, 10, 37, 98, 122, 231, 261, 425, 529, 539, 580, 597, 628, 711, 885, 906, 1035, 1059
surface tension measurement, 547, 713, 1060
surface-active drug, 1056
surface-active silica aerogel, 1
surface-associated reservoir, 885
surface-bound ion, 384
surface-initiated atom transfer radical polymerization (SI-ATRP), 152, 595
surfactant adsorption, 110, 536, 905, 988
surfactant ion-selective electrode (SISE), 705
surfactant monolayer, 125, 280
surfactant protein B (SP-B), 885
surfactant protein C (SP-C), 885
surfactant-bound gel, 508
surfactant-free emulsion, 451
surfactant-free stable emulsions, 451
surfacten (Surfactant TA), 886
surfactin, 98, 103, 233
suspension array, 618
SUV, *see* small unilamellar vesicle
swelling, 63, 183, 456, 498, 563, 675, 799, 808, 985, 998, 1013
swelling ratio, 270, 288, 500, 808
swelling-shrinking kinetics, 510
swollen membrane, 727
symmetric methylene stretching vibration, 899
synchronization, 426, 489
synchronous oscillation, 367
syndecan-4, 313
synergism, 32, 319, 368, 1031, 1059
synthon, 264

tau (τ) peptide, 915
tear energy, 274
tear resistance, 274
tecton, 292
TEER, *see* transendothelial electrical resistance
telomerase, 613
TEM, *see* transmission electron microscopy
TEMPO-containing micelle, 185
tenascin-C, 314, 323
tendon, 163, 340, 753
tensile modulus, 11
tensile strength, 11, 65, 174, 285, 577
Teorell, Meyer, and Sievers (TMS) theory, 721
TEOS, *see* tetraethylorthosilicate
Terada cell, 412
terminal methyl end, 865

ternary monolayer, 676
tert-butoxy group, 188
tert-butoxystyrene units, 188
tetradecyltrimethylammonium (TTA), 707
tetradecyltrimethylammonium bromide (TTAB), 712, 851
tetraethoxysilicate, 779
tetraethylorthosilicate (TEOS), 1
tetramethyl silane (TMS), 333
tetramethylorthosilicate (TMOS), 1
TGA, *see* thermogravimetric analysis
theranostic agent, 255
theranostics, 305
therapeutic surfactant preparation (TSP), 909
thermal annealing, 558, 866
thermal degradation, 549
thermal fluctuation, 364, 381, 399, 522, 759
thermal potential, 956
thermodynamic stability, 122, 399, 1004
thermodynamic-state-change-induced gelation, 495
thermogravimetric analysis (TGA), 549
thermoresponsive anionic copolymer, 223
thermoresponsive cationic copolymer, 223
thermoresponsive chromatography, 220
thermoresponsive hydrogel, 223
thermoreversible gel, 498
thermosensitive polymer, 501
thermotropic LC, 1035
thick filament, 754
thin filament, 753
thin layer chromatography, 573
thin liquid film, 628, 905–913
thin liquid wetting film, 912
thiourea, 846
thixotropy, 453
three-dimensional (3D) image plot, 860
three-wavelength GP (3wGP), 830
threshold concentration, 841, 908
threshold dilution, 909
thrombin (TB), 146, 216
thrombosis, 145
tight junction, 244–250
TIRFM, *see* total internal reflection fluorescence microscopy
tissue engineering, 85, 161, 228, 325, 352, 686
TMOS, *see* tetramethylorthosilicate
TMS, *see* tetramethyl silane
TMV, *see* tobacco mosaic virus
TNIIIA2, 313, 317
tobacco mosaic virus (TMV), 356
topographic image, 604, 892
topography, 5, 75, 83, 148, 161, 921
topology, 195, 384
tortuosity, 98, 404, 725
torus-shaped particle, 1091
total internal reflection fluorescence microscopy (TIRFM), 65, 284
total organic carbon (TOC) analyzer, 274
transdermal permeation, 130
transendothelial electrical resistance (TEER), 244
transfection, 411, 546, 813
transfer of information, 425
transfer ribonucleic acid (tRNA), 197–207
transferosome, 300, 301
trans–gauche conformational change, 831
transient phenomena, 766
transition pressure, 599, 888
transition state, 29, 37, 198, 332, 922
transition state theory, 21
transition temperature, 20, 39, 294, 501, 562, 826, 862
translational Brownian motion, 693
translational diffusion coefficient, 370, 693, 836
transmembrane 4 superfamily (TM4SF), 322
transmission electron microscopy (TEM), 134, 303, 556, 786, 813
transverse electric (TE) waveguide mode, 667
transverse magnetic (TM) waveguide mode, 667
transverse relaxation time, 398
trehalolipids, 232
trehalose 6,6′-bismycolate, 234
trehalose 6-mycolate, 234
trehalose tetraester, 232
triacylglycerol, 642
tricyclic antidepressant, 841, 1056
trifluoroethanol, 586, 1075
triphenylsulfonium triflate, 189
triple point, 866
triskelion, 602
Triton X 100, 136, 307, 631, 685, 704, 1101
tRNA, *see* transfer ribonucleic acid
TTA, *see* tetradecyltrimethylammonium
TTAB, *see* tetradecyltrimethylammonium bromide
tumbling, 341, 394, 511, 647
tungstic acid, 357
turbidity, 20, 59, 110, 525, 616, 670, 705, 983
two-dimensional colloidal crystal, 367
two-dimensional correlation spectroscopy (2DCOS), 998
two-dimensional (2D) micelle, 631
two-electron oxidation, 183
two-phase region, 826
U937 cell, 316
UCST, *see* upper critical solution temperature
UCST-type miscibility gap, 1049
undulation, 59, 392
uniaxial crystal, 661
unidirectional freezing, 276
unilamellar vesicle, 261, 295, 671, 1011
unspecific binding, 926
uPAR, *see* urokinase plasminogen activator receptor
upper critical solution temperature (UCST), 1049
urea, 712, 749, 846
urokinase plasminogen activator receptor (uPAR), 322
UTX boron tracedrug, 258
UTX-42, 258
UTX-44, 258
UTX-47, 258
UTX-50, 258
UTX-51, 258
UV-visible intensity, 1063
UV-visible spectra, 10
UV-visible spectrophotometer, 5
UV-visible spectroscopy, 111, 303, 845

vague wrinkled pattern, 417
valence X-ray photoelectron spectroscopy (valence XPS), 329
van der Waals (vdW) molecular surface, 384
van der Waals attraction, 1004, 1158
van der Waals force, 63, 474, 501, 605, 651, 772, 886
van der Waals interaction, 44, 148, 181, 571, 598, 605, 637, 737, 837, 1014, 1027, 1187
van der Waals interaction energy, 1014, 1087
vascular endothelium, 137
VBNC, *see* viable but nonculturable
vertebrate skeletal muscle, 753
vertical ionization potential (VIP), 325
vesicle, 292, 306, 684, 771, 805, 825, 860, 1011, 1137, 1179
vesicle phase, 1032
vesicle size, 294, 669, 863
viable but nonculturable (VBNC), 101
vinyl phenol units, 188
vinyl pyrrolidone (VP), 506
virosome, 304
viscoelasticity, 365, 1100
viscosity, 5, 26, 45, 122, 150, 211, 279, 347, 355, 365, 395, 430, 452, 470, 481, 544, 558, 566, 621, 642, 711, 731, 822, 935, 947, 961, 1005, 1045, 1095
viscous delivery sytems, 137

volume change of binding, 1073
volume of mixing, 1082
volume phase transition (VPT), 63, 498, 554
volume phase transition temperature (VPTT), 501, 562
VP, *see* vinyl pyrrolidone
VPT, *see* volume phase transition
VPTT, *see* volume phase transition temperature

waste water treatment, 77, 100, 120, 815
watch glass, 415
water content, 85, 98, 130, 149, 269, 368, 721, 979
water exchange, 272
water structure, 82, 292, 504, 845, 1063
water structure breaker, 845, 1063
water structure maker, 845, 1063
water treatment, 100, 262, 481
water-soluble complex, 625
waveform transformation, 366
waveguide mode, 667
waveguide spectroscopy, 667
WD, *see* work function and the other energies
wear, 269, 278
wear debris-induced osteolysis, 278
wear ratio, 274
wear resistance, 269, 284, 325
Weibull function, 995
weight-average molecular weight, 619
Weiner–Khinchine theorem, 624
Western blot, 221, 581, 921
Western blotting, 211, 614, 921
wetting transition, 155, 628
whole muscle, 753
Wilson model, 723
WLC, *see* wormlike chain
wobbling, 392
work function and the other energies (WD), 326, 337
wormlike chain (WLC) model, 62
wormlike micelle, 529, 1032, 1045, 1095
Wrap therapy, 451
Wurster's blue, 183

XAFS, *see* X-ray absorption fine structure
xerogel, 2
XPS, *see* X-ray photoelectron spectroscopy
X-ray absorption fine structure (XAFS), 734, 787
X-ray diffraction (XRD), 108, 166, 270, 288, 332, 577, 643, 661, 757, 786, 825, 860, 1022, 1030
X-ray photoelectron spectroscopy (XPS), 83, 168, 329, 331, 707, 786, 804
XRD, *see* X-ray diffraction

Young equation, 634
Young's modulus, 63, 174, 281

z-average radius of gyration, 619
zeolite, 791
zero shear viscosity, 1095
zeta-potential (ζ), 73, 109, 304, 413, 430, 455, 469, 517, 557, 619, 712, 779, 821, 934, 961, 984, 1004, 1033
Zimm plot, 620
zone model, 829, 861
zonula occluden (ZO), 244
zwitterionic phospholipid, 1020, 1084, 1101
zwitterionic polyelectrolyte, 154
zwitterionic polymer, 83, 152, 280, 592
zwitterionic surfactant, 707, 1053